

7th International Building Physics Conference

IBPC2018

Proceedings

SYRACUSE, NY, USA

September 23 - 26, 2018

Healthy, Intelligent and Resilient
Buildings and Urban Environments

ibpc2018.org | [#ibpc2018](https://twitter.com/ibpc2018)



Keynotes	1
Dynamic Environment, Adaptive Comfort, and Cognitive Performance (497).....	1
Green Infrastructure and Urban Sustainability Recent Advances and Future Challenges (499).....	7
Humans and Nature in the Loop (498).....	17
Multiphysics Modeling of Materials, Assemblies, Buildings and Cities (496).....	25
The Physics in Natural Ventilation of Cities and Buildings (501).....	35
BE-1 Diagnostics and Models for Building Performance	37
A state-space based method to predict thermal performance of pipe-embedded double skin façade case study in Guangzhou (115).....	37
Computer Tomography as a data acquisition tool for quantifying and modeling in-pore gypsum crystallization in building materials (84).....	43
Determination of the input data for computational simulation of active glazing with changeable optical properties (92).....	49
Predicting the thermal conductivity of porous building materials with nanopores or reduced gas pressures (80).....	55
Rational selection of experimental readouts for hygric material characterisation (197).....	61
Towards validation of a numerical model of a test cell laboratory (362).....	67
BE-2 Liquid Water in Buildings and Materials	73
Adsorption and film forming of train of water droplets impacting porous stones (373).....	73
Application of rain intensity dependent rain admittance factor (RAF) in hygrothermal performance assessment of wall systems (202).....	79
Do interface resistances matter in historic masonries - analysis based on X-ray tomography and heat, air and moisture modelling (33).....	85
Drainage and retention of water in small wall drainage cavities experimental assessment (253).....	91
Rain-tightness of door sill sealing (95).....	97
Water uptake in masonry effect of brickmortar interface (216).....	103
BE-3 Innovative Thermal Insulation Systems	109
Aerogel-enhanced blankets state-of-the-art, market readiness and future challenges (106).....	109
Hygrothermal analysis of a vapour-open assembly with vacuum insulation panels (440).....	115
Measurements of temperature dependency on thermal insulation thickness in ventilated attics (199).....	121
Prediction of the long-term performance of vacuum insulation panels installed in real building environments (342).....	127
Super insulation material in district heating pipes (187).....	133
Super insulation materials in the building sector field studies and future challenges (206).....	139

BE-4 Moisture in Buildings and Materials	145
Effect of air pressure on moisture transfer inside porous building materials three-dimensional behavior of moisture and air (116)	145
Evaluation of the impact of phase change humidity control material on energy performance of office buildings (167)	151
Experimental analysis of micro-cracks on the change of moisture transport properties of AAC (37).	157
Moisture monitoring of wood-frame walls with and without exterior insulation in a Midwestern U.S. cold climate (428).	163
Psychrometer method to measure the moisture retention curves of porous building materials in the full humidity range (59)	169
Semi-permeable membrane experiment for unsaturated liquid permeability of building materials potential and practice (58)	175
BE-5 Ventilation Systems for Buildings	181
Experimental analysis on a solar air heating façade system (235)	181
Experimental validation of a model for naturally ventilated double-skin facades (465)	187
Hygrothermal assessment of north facing, cold attic spaces under the eaves with varying single sided passive ventilation strategies and infiltration rates, in a cool, temperate climate (223)	193
Hygrothermal performance of sealed attics in climate zone 3A (446).	199
Moisture robustness of eaves solutions for ventilated roofs – experimental studies (331)	205
Thermal performance of novel natural ventilation apertures in a high-performance single-family house (240).	211
BE-6 Hygrothermal Performance and Mold Prevention	217
Application of radiant floor heating in large space buildings with significant cold air infiltration through door openings (131).	217
Evaluating the hygrothermal performance of wooden beam heads in 19th century town houses using in-situ measurements (419).	223
Experimental investigations of wooden beam ends in masonry with internal insulation results contrasting three years of the experiment (405)	229
On the hygrothermal behaviour of brick veneer clad timber frame walls the role of the vapour diffusion resistance of the wind barrier (123)	235
Performance evaluation of a highly insulated wall to withstand mould (208).	241
Renovation with internal insulation and heat recovery in real Life – energy savings and risk of mold growth (93).	247
BE-7 Energy Retrofits for Building Envelopes	253
A sustainable approach to the adaptive reuse of historic brick buildings analysis of energy efficiency	

strategies for historic facade retrofits (433)	253
Experimental investigation of latent heat thermal energy storage for highly glazed apartments in a continental climate (13)	259
Interior insulation retrofit of a brick wall using super insulation materials design of a field testing in an industrial brick building (99).....	265
Light transmissibility characterization of a new coating for window retrofit (444)	271
Monitoring and modelling of a prefabricated exterior envelope retrofit (474).....	277
Retrofit of the existing buildings using a novel developed aerogel-based coating results from an in-field monitoring (277).....	283
BE-8 High Performance Building Envelope Systems	289
Comparing exterior wall finishes using life-cycle assessment (372)	289
Experimental study of the performance of a double skin façade window under non-solar conditions (65)	295
Hygrothermal performance assessment of wall systems with various concrete and insulation configurations (194).....	301
Preparation and thermal performance of diatomite-based composite phase change materials wallboard (175).....	307
Study of the mechanical behavior of traditional Japanese mud wall on bamboo lath (272).....	313
Thermal stability of lightweight frame partitions exposed to pulsed wind load (41)	319
BE-9 Innovations in Wood	325
Determination of lead dust fall rates during deconstruction of wood frame buildings in an urban region in the Northeastern United States. (317)	325
Hygrothermal performance of a hygroscopic and permeable wall assembly impact of a vented wall cavity (468).....	331
Improving durability of wooden beam bearings in inside insulated walls by tempering the beam’s heads (407)	337
Sorption hysteresis in wood and its coupling to swelling a new modeling approach (369)	343
The effects of production technologies on the air permeability properties of cross laminated timber (410)	349
Understanding swelling of wood through multiscale modeling (395).....	355
BE-10 Solar Energy Harvesting and Management	361
A transparent insulation solar façade coupled with a selective absorber an experimentally validated building energy simulation model (300).....	361
Power generation and visual comfort performance of photovoltaic toplighting technologies in transient spaces (255)	367
Solar and lighting transmission in complex fenestration systems with perforated solar protection	

systems (436).....	373
Solar efficiency index of building envelopes and load matching in low energy buildings (215)	379
Study on the design method of integration of roof and photovoltaic based on aesthetics, technology and energy-saving characteristic (130)	385
Thermal performance of PCM-glazing unit under moderate climatic conditions (38).....	391
EC-1 Environmental Control Equipment and Systems	397
A deep reinforcement learning method for model-based optimal control of HVAC systems (66).....	397
Air cooling and dehumidification with a zeolite coated heat exchanger regenerated by solar thermal energy (352).....	403
Evaluating the energy consumption and heat loss in the hot water supply and heating systems of a nursing home (177)	409
Extracting radiant cooling from building exhaust air using the Maisotsenko-cycle principle (276)	415
Periodic alternation between intake and exhaust of air in dynamic insulation (328)	421
The energy saving performance of ventilation-heat-recovery system in residential buildings in the summer of hot-summer and cold-winter zone in China (145)	427
EP-1 Residential Energy Analysis and Management	433
Characterisation of the flexibility potential from space heating in French residential buildings (172).....	433
Evaluation of the impact of weather variability on a net zero energy building advantage of sensitivity analysis for performance guarantee (192).....	439
Numerical analysis of a ground-source heat pump system in traditional Japanese “Kyo-machiya” dwellings (166).....	445
Offsetting peak residential cooling loads using a medium temperature chiller and sensible cold thermal storage (181).....	451
Prosumer cluster of single-family houses under the Danish net metering policy (473).....	457
Visualizing the quantitative comparison between exergy & energy analysis results with ExFlow (198)...	463
EP-2 Urban Energy Generation, Analysis and Management	469
A review of microgrid energy systems (431).....	469
Impacts of climate change and its uncertainties on the renewable energy generation and energy demand in urban areas (146).....	475
Multi-stage optimal design of energy systems for urban districts (399).....	481
Novel gas-driven fuel cell HVAC and dehumidification prototype (244)	487
Optimization of electric vehicle charging in a fully (nearly) electric campus energy system (259).....	

.....	493
Studying the impact of local urban heat islands on the space cooling demand of buildings using coupled CFD and building energy simulations (386).....	499
GB-1 Environmental Design, Sensing and the Built Environment	505
An implementation for transforming a home energy management system to a multi-agent system (174).....	505
Bioclimatic tools for sustainable design – uncertainty perspective (422).....	511
Campus as a lab for computer vision-based heat mapping drones a case study for multiple building envelope inspection using unmanned aerial systems (UAS) (285).....	517
Optimal control strategies for passive heating and cooling elements reduce loads by two-thirds in the adaptive reuse of a San Francisco Bay Area office (153).....	523
Sensing and information technologies for the environment (SITE); hardware and software innovations in mobile sensing applications (430).....	529
GB-2 Green Roofs and Vegetation	535
Experimental study on the stomatal resistance of green roof vegetation of semiarid climates for building energy simulations (104).....	535
Greening rooftops to reduce heat islands how large is large enough (402).....	541
Integrated vegetation model for studying the cooling potential of trees in urban street canyons (338).....	547
.....	547
The use of a large, extensive green roof for multiple research objectives (447).....	553
Thermal performance of a green roof based on CHAMPS model and experimental data during cold climatic weather (423).....	559
Using rain and vegetation to improve thermal comfort in a hot street canyon with fully-integrated urban climate modeling (376).....	565
GB-3 Urban Microclimates and the Heat Island Effect	571
An investigate on the quantitative correlation between urban morphology parameters and outdoor ventilation efficiency indices (429).....	571
Effect of urban texture on building energy performance (287).....	577
New microclimate monitoring method and data process for investigating environmental conditions in complex urban contexts (231).....	583
Rapid cooling of urban surfaces during rainfall physical basis, dominant energy fluxes, and sensitivity to pavement and rainfall prop (400).....	589
Using advanced urban canopy models to investigate the potential of thermochromic materials as urban heat island mitigation strategies (283).....	595
HF-1 Office Buildings	601
A picture is worth a thousand words Smartphone photograph-based surveys for collecting data on	

office occupant adaptive opportunities (81).....	601
Benchmarking the energy efficiency of office buildings in Belo Horizonte, Brazil (52).....	607
Exploring occupants' impact at different spatial scales (147).....	613
Neural network models using thermal sensations and occupants' behavior for predicting thermal comfort (28).....	619
Quantification of building energy performance uncertainty associated with building occupants and operators (148).....	625
Towards a new way of capturing occupant well-being (484).....	631
HF-2 Occupant Comfort in Special Cases	637
Conserving energy, conserving buildings airtightness testing in historic New England homes (304).....	637
Field occupants' behavior monitoring integrated to prediction models impact on building energy performance (169).....	643
Modeling and spatial visualization of indoor micro-climates for personalized thermal comfort (316).....	649
Occupants' perception of historical buildings' indoor environment. Two case studies. (356).....	655
Towards human-centered intelligent envelopes A framework for capturing the holistic effect of smart façades on occupant comfort and satisfaction (466).....	661
HF-3 Residences	667
Energy flexibility of building cluster – part I occupancy modelling (186).....	667
HOUSE project Building understanding through an enabled boundary object (324).....	673
Inter-ActiveHouse users driven building performances for nearly zero energy buildings in Mediterranean climate.....	679
The influence of window opening habits on the residential energy use in nearly zero energy buildings (74).....	685
Utilization of heat recovery ventilation steady-state two-zone energy use analysis and field studies (72).....	691
HF-4 Lighting and Visual Quality	697
Application of C-SVM classification algorithm to the lighting visual comfort of university classrooms (46).....	697
Developing and testing visual privacy metrics (60).....	703
Environmental conditions and occupant satisfaction in the workplace a controlled study in a living lab (85).....	709
Generating design-sensitive occupant-related schedules for building performance simulations (87).....	715
Lighting systems and users interactions in classrooms and laboratory rooms (415).....	721

Visual comfort assessment of different shading strategies in a commercial office building in the southeastern US (411).....	727
IE-1 Assessment and Analysis	733
A method for an effective microclimate management in historical buildings combining monitoring and dynamic simulation the cas.....	733
Description method of outdoor climate characteristics considering comprehensive effect on indoor climate (469).....	739
IEQ measurement and assessment tools for plug-and-play deep renovation in buildings (102).....	745
Influence of illumination on paper and silk used in Chinese traditional painting and calligraphy based on Raman spectroscopy in museum (120).....	751
The impact of indoor temperature and CO2 levels on occupant thermal perception and cognitive performance of adult students and the implications on buildings (137).....	757
Thermal and mycological active protection of historic buildings on the example of the baroque residence of Polish kings in Wilanów (40).....	763
IE-2 Field Studies	769
Classification of the indoor environment in a high-school building by means of subjective responses (396).....	769
Comparison between qualitative and quantitative measurement in assessing thermal comfort in an elementary school (445).....	775
Empirical assessment of summertime overheating risk in new, retrofitted and existing UK dwellings (243).....	781
Indoor air quality and thermal comfort for elderly residents in Houston, TX – a case study (245).....	787
Method for detecting contaminant transport through leakages in a condemned school (195).....	793
The impact of physical environments on satisfaction in shopping centers (207).....	799
IE-3 Lighting and Windows	805
A novel methodology to spatially evaluate DGP classes by means of vertical illuminances. Preliminary results. (471).....	805
Comparative study of different design configurations based on the daylight and visual comfort performance of electrochromic glass in a side-lit office building (452).....	811
Daylight availability in a room equipped with PCM window (36).....	817
Development of an electric-driven smart window model for visual comfort assessment (269).....	823
Lighting quality study of shopping malls in China based on the evaluation experiment (88).....	829
Thermal performance of an electric-driven smart window experiments in a full-scale test room and simulation model (270).....	835
IE-4 Ventilation and Air Conditioning	841

A novel approach to near-real time monitoring of ventilation rate and indoor air quality in residential houses (249).....	841
Design and operational strategies for good indoor air quality in low-energy dwellings performance evaluation of two apartment blocks in East London, UK (162).....	847
Effects of semi-open space on micro-environmental control (173).....	853
Numerical investigation of a diffuse ventilation ceiling system for buildings with natural and hybrid ventilation (179).....	859
Research for the optimization of air conditioner sensor position based on the room spatial parameter (132).....	865
The impact of ventilation strategy on overheating resilience and energy performance of schools against climate change the evidence from two UK secondary schools (165).....	871
IE-5 Air Pollution and Control.....	877
Analysis of dynamic variation characteristics and influential factors of PM2.5 on subway platforms under air-conditioning condition and ventilation condition (364).....	877
Assessing the performance of photocatalytic oxidation of volatile organic compounds in three different scaled set-ups (363).....	883
Fate of particles released by a puff–dispersion with different air distributions (475).....	889
Radon levels in rented accommodation (5).....	895
IE-6 Thermal Environment and Control.....	901
Condensation-free radiant cooling using infrared-transparent enclosures of chilled panels (463).....	901
Experimental study on the impact of passive chilled beam in a room with displacement ventilation (42).....	907
Liquid desiccant-polymeric membrane dehumidification system for improved cooling efficiency in built environments (454).....	913
Simulation-based approach to optimize courtyard form concerning climatic comfort in hot and humid climate (105).....	918
The effect of the position and temperature difference of local radiant asymmetry on thermal comfort an experimental investigation (17).....	924
Thermal effect of metal fin inside elevated radiant floor based on the thermal utilization of a burning cave (479).....	930
IM-1 Intelligent Monitoring and Management Systems.....	935
Implementation of integrated wireless sensors technology in renovation of social housing buildings. A Danish case study. (7).....	935
LightLearn Occupant centered lighting controller using reinforcement learning to adapt systems to humans (34).....	941

Sequential Monte Carlo for on-line estimation of the heat loss coefficient (225)	947
The co-heating test as a means to evaluate the efficiency of thermal retrofit measures applied on residential buildings (464).	953
The thermal resistance of retrofitted building components based on in-situ measurements (377).	959
Wireless sensor system for intelligent facades (387).	965
MS-1 Whole Building, Resilience, and Life Cycle Analysis	971
A resilient refurbishment project for an Italian large sports hall (490)	971
Dynamic life cycle assessment integrating cultural value (11)	977
Investigation of energy modelling methods of multiple fidelities a case study (427).	983
Optimal passive design strategies for nearly zero-energy dwellings in different Chilean climates using multi-objective genetic algorithms (24).	989
Pareto optimality analysis for evaluating the tradeoff between visual comfort and energy efficiency (384)	995
Passive survivability in residential buildings during heat waves under dynamic exterior conditions (426)	1001
MS-2 Lighting, Daylighting, and Multi-Physics Models	1007
Comparison of daylighting simulation workflows and results using plugins for BIM and 3D Modelling programs application on early phases of design process (310).	1007
Existing energy performance and the potential of simulation in school buildings – a review (4).	1013
Lighting simulation for external Venetian blinds based on BTDF and HDR sky luminance monitoring (56).	1019
Modelling of a naturally ventilated BIPV system for building energy simulations (273).	1025
Numerical analysis of the influencing factors on the performance of a pipe-embedded window operated in summer (114)	1031
Validation of the EN 151932017 calculation method to estimate the daylight supply in a building comparison with dynamic climate-base (326).	1037
MS-3 Heat and Moisture Transfer in Materials and Assemblies	1043
Assessment of cumulative damage of selected building envelopes exposed to various environmental effects (32)	1043
Impact of the substrate thermal inertia on the thermal behaviour of an extensive vegetative roof in a semiarid climate (448).	1049
New algorithm for water leakages flow through rain screen deficiencies (205).	1055
PV-PCM system integrated into a double skin façade. A genetic optimization based study for the PCM type selection. (71)	1061

Stochastic modelling of hygrothermal performance of highly insulated wood framed wall (190).....	1067
Thermal insulation of radon stack systems to avoid freezing (73).....	1073
MS-4 Co-simulation and Platforms for Integrated Analysis	1079
A GIS based methodology to support multi-criteria decision making for the retrofitting process of residential buildings (398).....	1079
A new normative workflow for integrated life-cycle assessment (291).....	1085
Big-open-real-BIM data model - proof of concept (161).....	1091
BIM and game engine integration for operational data monitoring in buildings (383).....	1097
Cross-platform, public domain simulation tools for performing parametric IAQ and energy analysis (380).....	1103
Optimization of four-primary white LEDs based on protective effect and color quality-a solution for museum illumination (118).....	1109
MS-5 Computational Fluid Dynamics and Energy Performance	1115
Analytical and experimental investigation on depth and pipe configuration for coaxial borehole heat exchanger (281).....	1115
Comparison of lattice Boltzmann method and finite volume method of large eddy simulation in isothermal room flow (53).....	1121
Development of a supermarket prototype building model (232).....	1127
Improving the representation of convective heat transfer in an urban canopy model (424).....	1133
Streamlined CFD simulation framework to generate wind-pressure coefficients on building facades for airflow network simulations (358).....	1139
Unsteady-state exergy analysis on two types of building envelopes under time-varying boundary condition (33).....	1145
MS-6 Data Analytics, Model Reduction and Calibration	1151
Achieving faster building energy model optimization through selective zone elimination (86).....	1151
Comparison of data-driven building energy use models for retrofit impact evaluation (318).....	1157
Modeling and model calibration for model predictive occupants comfort control in buildings (361).....	1163
Neural networks to predict the hygrothermal response of building components in a probabilistic framework (91).....	1169
Optimization of night cooling of commercial premises using genetic algorithms and neural networks (49).....	1175
Use of calibrated building simulation to investigate comfort conditions in a healthcare facility (303).....	1181
MS-7 Material Characterization and Model Parameters	1187

An experimental and modelling study on the adsorption characteristics of activated carbon under different challenge concentration levels (229).....	1187
Development of a procedure for estimating the parameters of mechanistic emission source models from chamber testing data (308).....	1193
Evaluation of the physical interpretability of calibrated building model parameters (248).....	1199
Field experimental investigation of temperature, humidity and solar radiation impacts on formaldehyde emissions from interior furnish material (particle board): a preliminary study (261).....	1205
Study on improving the surface wet condition of subfloor by hygroscopic material in rural residences of China (260).....	1211
The application of computed tomography for characterising the pore structure of building materials (83).....	1217
MS-8 Building Enclosure Design.....	1223
A dynamic thermal network model applied to ventilated attics (27).....	1223
A holistic decision support tool for facade design (413).....	1229
Considerations on the thermal modeling of insulated metal panel systems (309).....	1235
Numerical thermal model of a double-glazed window filled with phase change materials (438).....	1241
On the compliance of thermal performance requirements for highly insulated building units (238).....	1247
The effect of ambient moisture conditions on heat flux time shift and decrement factor of multi-layered walls (392).....	1253
PE-1 Economic and Policy Aspects of Green Buildings.....	1259
Conceptual framework for improved management of risks and uncertainties associated with the performance of the building enclosure (57).....	1259
Effect of economic indicators on cost-optimal energy performance levels of residential building retrofits in the Mediterranean region of Turkey (347).....	1265
Evaluation of efficiency and renewable energy measures considering the future energy mix (274).....	1271
Optimization of government subsidization strategies for building stock energy refurbishment (357).....	1277
Techno economic analysis of individual building renovation roadmaps as an instrument to achieve national energy performance targets (233).....	1283
The impact of an energy efficiency regulation in northern Canada (107).....	1289
PS Poster Session.....	1295
A comparison of model order reduction methods for the simulation of wall heat transfer (70).....	1295

A framework for comfort assessment in buildings and districts retrofit process (101)	1301
A rain simulator to examine green roof and soil moisture sensor performance (417)	1307
A study on natural lighting design strategies for teaching buildings in hot-summer and cold-winter zone of china—a case of the Arts and Sciences building of Xinyang Normal University (133).	1313
Analysis of thermal bridges in insulated masonry walls a comparison between vacuum insulated panels and expanded polystyrene (307).	1319
Application of PCM-to-air heat exchanger for free cooling applications (289).	1325
Assessment of the BIPV potential at the city of Prague and their effect on the built environment (333).	1331
Bio-inspired outdoor systems for enhancing citizens thermal comfort in public spaces by learning from nature (219)	1337
Building information modeling (BIM) implementation for sustainability analysis a mega airport project case study (492)	1343
Chemical analysis of precipitation and stormwater runoff from a large green roof (453).	1349
Computational evaluation of the thermal performance of underground bunkers the case of Albania (150)	1353
Criteria for identifying failure optimization algorithms in building energy optimization and case studies (90)	1359
Effects of gaseous pollution and thermal conditions on the corrosion rates of copper and silver in data center environment a literature review (257)	1365
Elaboration of the decision space for an optimization of building retrofit (336)	1371
Energy flow through the Onondaga County Convention Center green roof (313).	1377
Estimating time constants for over 10,000 residential buildings in North America towards a statistical characterization of thermal dynamics (134)	1383
Experimental investigation of the impact of PCM containment on indoor temperature variations (470)	1389
Hygrothermal modelling of building enclosures reference year design for moisture accumulation and condensation risk assessment (211)	1395
Hygrothermal performance of historic massive wall when is 2D simulation necessary (239).	1401
Innovative composite materials with enhanced acoustic, thermal, and optical performance for urban pavements experimental characterization (230)	1407
Intrinsic evaporative cooling and weather-responsive natural ventilation for adaptive thermal comfort in tropical buildings (155).	1413
Long term measurements and HAM modelling of an interior insulation solution for an office building in cold climate (220).	1419
New technology creates new lightscape (39).	1425

Optical performance of polycarbonate multi-wall panels in the form of transparent insulation based on long-term outdoor measurements (406)	1431
Preliminary monitoring results of ventilated heavyweight building envelope from recycled aggregate (98)	1437
Review of the sky temperature and solar decomposition, and their impact on thermal modeling (458)	1443
Roof windows for passive houses – what can be improved (182)	1449
Sensitivity analysis using the SWMM LID control for an extensive green roof in Syracuse, NY (149)	1455
Simulation of building physics for beginning design students (442)	1461
Study on multivariate regression model of indoor and outdoor particulate pollution in severe cold area of China (26)	1467
The design, construction and commissioning of a small scale dynamic calibrated hot box (241)	1473
The effect of human walking on distribution characteristics of indoor particulate matter (67)	1479
Thermal performance analysis of traditional housing in Albania (94)	1485
Uncertainty in building energy performance characterization impact of gas consumption decomposition on estimated heat loss coefficient (371)	1491
Ventilation potential assessments for residential building arrangements based on exceedance probability analysis (157)	1497
Author Index	1503

Dynamic Environment, Adaptive Comfort, and Cognitive Performance

Richard de Dear^{1,*} and Fan Zhang^{1,2}

¹IEQ Laboratory, The University of Sydney, Sydney NSW 2006, Australia

²Griffith University, Southport QLD 4222, Australia

*Corresponding email: Richard.Dedear@sydney.edu.au

ABSTRACT

Since the invention of airconditioning over 100 years ago a central research challenge has been to define the indoor environmental temperatures best suited for occupants. The first scientific approach to this question was framed in terms of *optimising occupant thermal comfort*, commonly expressed as a U-function, symmetrical around a single optimum temperature for any given combination of the remaining comfort parameters (ISO, 2005). The inescapable conclusion drawn from such logic in the minds of risk-averse design engineers is that the only strategy able to reliably deliver occupant comfort is HVAC applied to sealed-façade architecture.

A rigorous scientific rebuttal of the “single temperature optimum” model of comfort came 30 years after PMV/PPD was first floated (e.g. de Dear and Brager, 1998; 2001). Known as the *adaptive comfort model*, a clear implication is that passive design solutions are capable of delivering comfortable internal environments across a broad swathe of climate zones, throughout most if not all of the year. But recently the “single temperature optimum” model has resurfaced, this time with its justification shifting away from the thermal comfort requirements of occupants towards their cognitive performance.

Beyond the building science domain, in disciplines such as psychology and ergonomics, the prevailing wisdom regarding temperature effects on cognitive performance is an *extended-U* rather than an inverted U function. The gist of the model is that cognitive performance is relatively stable throughout the moderate temperature range, but it rapidly deteriorates at the boundaries of thermal acceptability where stress drains the performers’ attentional resources. The *extended-U* model has garnered broad acceptance across a range of disciplines with the notable exception of HVAC engineering and indoor air sciences. But the weight of research evidence tends to support the extended- rather than inverted-U model. In this paper the arguments regarding thermal effects on cognitive performance are critically evaluated.

KEYWORDS

Cognitive performance, arousal theory, temperature optimum, adaptive model.

INTRODUCTION

The effect of the thermal environment on performance and productivity has been a focus of interest among indoor environmental researchers for nearly a century, but most of that work has been conducted in relative isolation from the cognate disciplines of human performance evaluation. In his wide-ranging survey of the indoor environmental research domain Corsi (2015) observed that “... *indoor air scientists all too often work in narrow trenches, interacting primarily with those they have interacted with for years, content to dig more deeply into that of which they already have significant knowledge, and unaware of the*

connections that their work may have to those who dig in other trenches.” This insularity is clearly evident in cognitive performance research theme.

The range of indoor temperatures deemed acceptable has a strong bearing on building energy requirements because it constrains the geographic scope as well as the seasonal duration when *passive* designs are able to achieve acceptable indoor environments. Secondly, the design temperature range indoors directly impacts energy required by active systems (HVAC) to achieve them. Up until about the end of the last century the range of indoor design temperatures was mostly couched in terms of thermal comfort. Simple comfort models suggested that a range of $\pm 1.5K$ around an invariant optimum temperature could ensure 90% occupant thermal acceptability (Fanger, 1970; ISO, 2005). However, more recent adaptive thermal comfort models have challenged these narrow temperature prescriptions with strong empirical evidence that indoor comfort temperatures are dependent on outdoor climatic conditions (e.g. de Dear and Brager, 1998, 2001). The adaptive comfort approach encourages warmer indoor temperatures in warmer climate zones and seasons, and *vice versa* in cooler climates and seasons. In response to this debunking of the comfort arguments HVAC peak bodies such as REHVA and ASHRAE have shifted their justifications for tight indoor temperature control away from occupant comfort towards occupant productivity (ASHRAE, 2013). Since these HVAC peak bodies exert a strong influence on air conditioning practices, HVAC-related energy and greenhouse gas emissions well beyond their European and North American jurisdictions, it behooves us to critically review the scientific evidence put forward in support of temperature effects on cognitive performance.

In this review we examine a broad collection of papers, all specifically examining the effects of thermal environment on cognitive performance, but from a variety of disciplinary perspectives *beyond* the indoor environmental sciences.

LITERATURE REVIEW

Moderate indoor thermal environments are far from hyper- and hypo-thermic scenarios because they pose no threat to health and safety. Nevertheless they are still capable of exerting adverse impacts on building occupants’ cognitive performance, although the literature remains conflicted on the significance of these impacts. Two distinct theoretical perspectives have emerged. The first posits a dose-response relationship between the indoor thermal environment and cognitive performance, with *any* deviation from thermal optimum leading to a decrement in performance and productivity. The second position asserts that, depending on the thermal intensity of exposure, type of cognitive activity, and other attenuating factors, externally imposed cognitive demands can be absorbed by the buffering capacity or “cognitive reserve” of the subject, with little or no deleterious effect appearing until those adaptive resources are depleted.

The inverted-U model

Arousal theory (e.g. Duffy, 1962) has been ubiquitous in the stress literature. Alternatively known as the *Yerkes-Dodson law*, it postulates an *inverted-U relationship*. Performance of a particular task improves as arousal increases until reaching an optimal level for the task in question. Beyond this optimum, performance starts to decline when the arousal level continues to rise, and likewise with reductions below the optimal level of arousal. In regards to the effects of thermal environment on cognitive performance, the same inverted-U relationship has been assumed, substituting arousal level with the intensity of the environmental thermal load (e.g. Griffith and Boyce, 1971).

In the indoor environmental science domain, arousal theory and the associated inverted-U relationship, has held sway for several decades, judging by the number of citations it has received. Arithmetic relationships have been proposed by different researchers to quantify the performance decrement in percentage terms as room temperature (or thermal sensation) deviates from the single optimum. These functions have then been widely applied to cost-benefit analyses that trade off the costs of lost performance from the building's workforce against the costs of variations in building and building services design, retrofits, and operational facilities management practices. Seppänen and Fisk (2006) along with Seppänen et al. (2006) have emerged as the most influential studies in the indoor environmental science literature. Their meta-analysis collated 24 previously published studies, then fitted an inverted-U relationship to the summary data. The resulting model shows performance increasing as temperatures increased towards 21.6 °C, then decreasing in temperatures beyond 22 °C. The same inverted-U relationship is mirrored in the *American Society of Heating, Refrigerating, and Air-Conditioning Engineers' Handbook of Fundamentals* (2013), but instead of room temperature, as in Seppänen et al. (2006), the *ASHRAE Handbook* shows the x-axis as room temperature relative to the optimal comfort temperature T_c for the group. Despite the large variance in data points in the meta-analysis, *ASHRAE's Handbook of Fundamentals* graph shows a smooth parabolic curve for performance, peaking at the optimum comfort temperature (corresponding to “neutral” thermal sensation), and then tapering off as soon as room temperature deviates from neutrality (Figure 1).

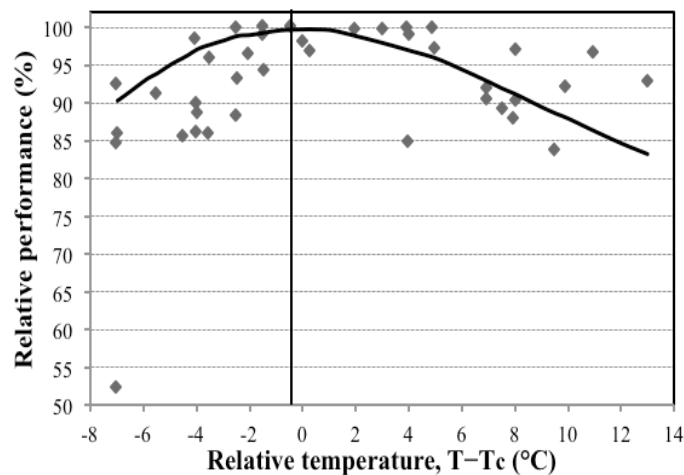


Figure 1 Relative performance of office work vs. deviation from optimal comfort temperature T_c (adapted from *ASHRAE Handbook of Fundamentals*, 2013).

The extended-U model

The extended-U model, initially proposed by Hancock and Warm (1989) and also known as the *Maximal Adaptability Model* contends that human performance remains relatively stable across a broad range, but rapidly deteriorates at the boundaries of thermal acceptability (Figure 2). Thermal stress exerts its adverse impacts on performance by consuming and ultimately depleting the performers' attentional resources (e.g. Kahneman, 1973). The normative zone falls in the middle of the continuum of input stress intensity, and it is here that zero compensatory effort is required of the participant in order for them to maintain optimal performance. The comfort zone encompasses broader conditions than the normative zone, but cognitive adjustments are easily accomplished within the comfort zone in order to maintain a

near-optimum level of performance. However, when the environmental stress exceeds the comfort zone, attentional resources begin to be depleted. At first, equivalent or even improved performance can still be achieved by psychological adaptive behaviours such as attentional focus. Because of the central role played by psychological adaptability this region is referred to as the psychological zone of maximal adaptability in Figure 2. When the stress level continues to increase, human performance deteriorates as attentional resources begin to be depleted, indicated by the dashed line at the boundary of the psychological zone of maximal adaptability.

The extended-U model has garnered broad acceptance and currency across a range of disciplines with the notable exception of HVAC engineering and the cognate indoor environmental sciences. It has been confirmed by several authoritative literature reviews on this topic, none of which were published in the HVAC engineering and building science outlets. For example, Ramsey (1995) performed a meta-analysis on 160 individual performance studies and concluded that mental or simple tasks would most likely undergo negligible performance loss in hot environments, and may even be enhanced, at least for exposures under two hours. For perceptual motor tasks other than mental tasks, performance decrements were discernible only beyond 30°C WBGT (approximately 32°C air temperature at 50% RH).

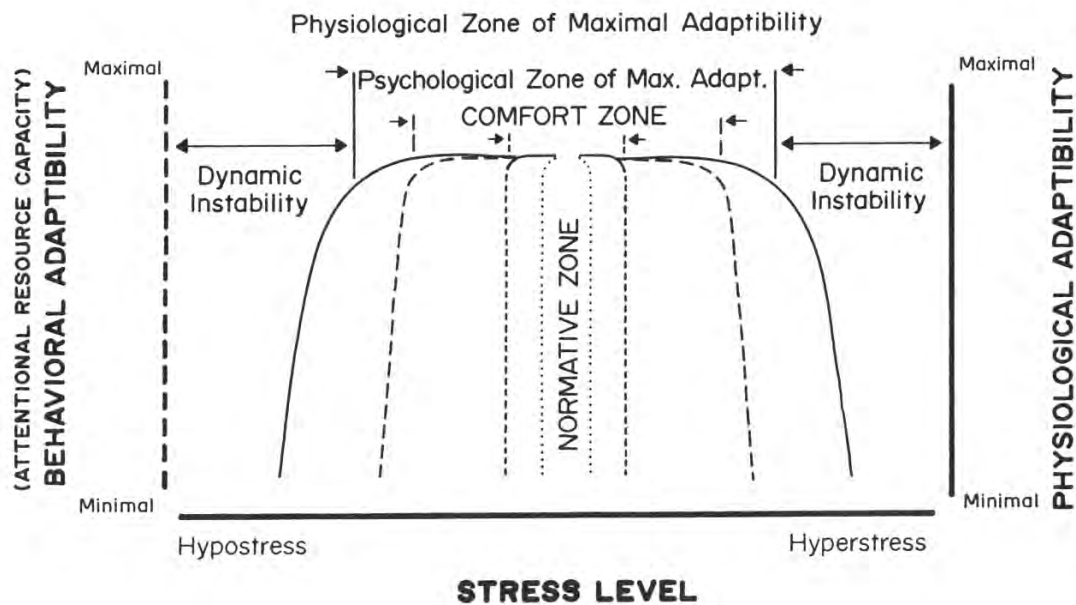


Figure 2 Extended-U model linking stress and performance (Hancock and Warm, 1989)

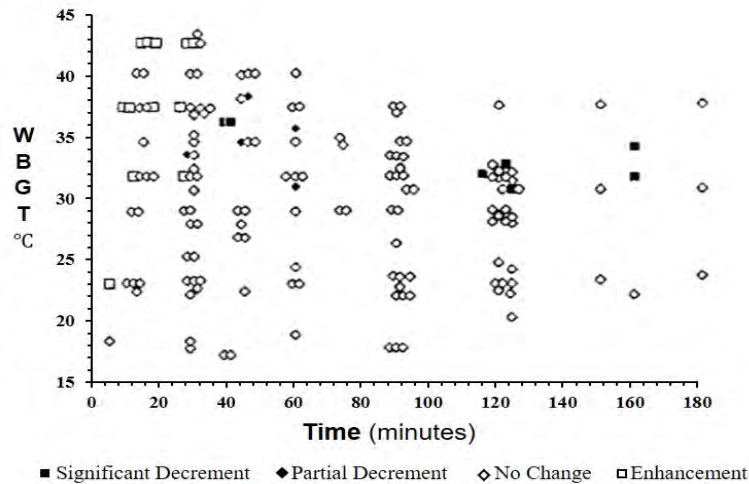


Figure 3 Mental or simple task performance under thermal stress (after Ramsay, 1995)

Another definitive meta-analysis by Pilcher et al. (2002) extracted 515 effects sizes from 22 original studies, and could find no effect of temperature on mental performance in the air temperatures ranging from 23-28.8°C at 50% RH. This meta-analysis provides some of the strongest confirmation of the extended-U model. In Hancock et al.'s (2007) meta-analysis of 49 separate studies providing 528 effect sizes, the original studies were classified into four effective temperature ranges: below 25.7°C, 25.7°C–29.4°C, 29.4°C–35.2°C, and above 35.2°C. It was found that, "... with the exception of the lowest temperature range, it is clear that the effect size variation sequentially increases across the three remaining categories. This gives rise to the proposition that performance is relatively stable over much of the temperature range but exhibits radical variation at the highest extreme " (p.862) and this observation represents a core feature of the extended-U theory of stress and performance.

CONCLUSIONS

Notwithstanding its overly simplistic concept and methodological flaws throughout its empirical bases, the inverted-U relationship has held sway in the indoor environment research literature on thermal environmental influences on cognitive performance and productivity. Moreover, it has permeated engineering practice, as reflected in design guidelines and handbooks published by HVAC peak bodies. The dose-response inverted-U model has been uncritically implemented across broad swathes of the world's commercial building sector. Enhancements in HVAC equipment and control technology over recent decades have facilitated ever-tighter tolerances on indoor temperatures around a speciously defined performance optimum. Scientifically illiterate tenants and their facility managers have begun specifying overly stringent temperature clauses in their commercial office space lease agreements under the mistaken belief that they will maximise productivity from their human resources. However, this multidisciplinary review conducted in this paper finds the evidence for the single-temperature optimum dose-response relationship between indoor environment and occupant performance less compelling, which calls into question the crude cost/benefit of productivity decrements prevalent in the indoor environmental and HVAC engineering

domains. Much stronger evidence in support of an extended-U relationship exists in literature published *outside* the usual for building science and indoor air fora.

REFERENCES

- ASHRAE. 2013 *ASHRAE handbook: Fundamentals*. Atlanta: American Society of Heating, Refrigerating and Air-Conditioning Engineers, Inc.
- ASHRAE. 2017. *ANSI/ASHRAE Standard 55-2017*, Thermal Environmental Conditions for Human Occupancy. Atlanta: American Society of Heating, Refrigerating, and Air-Conditioning Engineers, Inc.
- Corsi R.L. 2015. Connect or stagnate: The future of indoor air sciences. *Indoor Air*, 25, 231–4
- de Dear R.J. and Brager, G. 1998. Developing an adaptive model of thermal comfort and preference,” *ASHRAE Transactions*, 104(1a), 145-167.
- de Dear, R.J. and Brager, G.S. 2001. The adaptive model of thermal comfort and energy conservation in the built environment, *International Journal of Biometeorology*. 45(2), 100-108.
- Duffy E. 1963. *Activation and Behavior*. New York: Wiley.
- Fanger P.O. 1970. *Thermal Comfort*. Copenhagen: Danish Technical Press.
- Griffith I.D. Boyce P.R. 1971. Performance and Thermal Comfort. *Ergonomics*, 14, 457–68.
- Hancock P.A. and Warm J.S. 1989. A dynamic model of stress and sustained attention. *Journal of Human Factors*, 31, 519–37.
- Hancock PA, Ross JM, Szalma JL. 2007. A Meta-Analysis of Performance Response Under Thermal Stressors. *Human Factors*, 49, 851–77.
- ISO 2005 *International Standard 7730*. Moderate Thermal Environments - Determination of the PMV and PPD Indices and Specification of the Conditions of Thermal Comfort. Geneva: International Standards Organization.
- Kahneman D. 1973. *Attention and Effort*. Englewood Cliffs, NJ: Prentice Hall.
- Pilcher J.J, Nadler E. and Busch C. 2002. Effects of hot and cold temperature exposure on performance: A meta-analytic review. *Ergonomics*, 45, 682–98.
- Poulton E.C. Arousing Stresses Increase Vigilance. *Vigil. Theory, Oper. Performance, Physiol. Correl.* Mackie, R., Boston, MA: Springer US; 1977, p. 423–59.
- Poulton EC, Kerslake DM. Initial stimulating effect of warmth upon perceptual efficiency. *Aerosp Med* 1965;36:29–32.
- Ramsey J.D. 1995. Task performance in heat: A review. *Ergonomics*, 38, 154–65.
- Seppänen, O. and Fisk, W.J. 2006. Some quantitative relations between indoor environmental quality and work performance or health. *HVAC and R Research*, 12(4), 957-973.
- Seppänen O, Fisk WJ, Lei QH. 2006. Room temperature and productivity in office work. In: *Proceedings of Healthy Buildings*, Lisbon, V.1, 1-5.
- Wilkinson RT, Fox RH, Goldsmith R, Hampton IFG, Lewis HE. Psychological and physiological responses to raised body temperature. *J Appl Physiol* 1964;19:287–91.

Green Infrastructure and Urban Sustainability: Recent Advances and Future Challenges

Patricia J. Culligan*

Robert A.W. and Christine S. Carleton Professor of Civil Engineering
Columbia University, New York City, USA

* Corresponding author. Tel.: +1 212 854 3154; email: pjc2104@columbia.edu

ABSTRACT

Although the majority of urban green infrastructure (GI) programs in the United States, and elsewhere, are being driven by stormwater management challenges arising as a result of the impervious nature of modern cities, GI is also believed to provide other benefits that enhance urban sustainability. This paper discusses the role that GI systems might play in urban climate adaptation strategies for cities like New York City, where increases in both temperature and precipitation are projected over the coming decades. Examples of work conducted by the author and colleagues in New York City to quantify the performance of urban GI are first presented. This work includes monitoring efforts to understand how extensive green roofs retain rainfall, reduce surface temperatures and sequester carbon. Next, a discussion of the advantages that a distributed, or neighborhood level, GI system might bring to a climate adaptation strategy is provided. The paper then concludes with an outline of some of the future work that is needed to fully realize the potential of urban GI systems to address future climate change impacts.

Keywords: Green infrastructure, distributed infrastructure, urban sustainability, stormwater management, climate adaptation

1. INTRODUCTION

The term *green infrastructure* (GI) was coined in 1994 as part of a greenway planning report that advocated for land conservation through a system of greenways, or *green infrastructure*, that were as well-planned and financed as traditional built infrastructure [1]. Since then, the term has been used by planners, designers, scientists, and engineers alike to describe networks of green space, including *natural areas* such as waterways and woodlands, and *built areas* such as parks and community gardens - all of which are widely considered to provide an array of services to humans and the environment [2], [3]. More recently, green infrastructure has gained attention as a means of improving urban stormwater management. This focus has given rise to a class of *engineered green infrastructure*, whose primary design purpose is to reduce urban stormwater runoff and pollution. Examples of *engineered green infrastructure* (GI) include green roofs, porous pavement, rain-gardens and rain cisterns. It is these green infrastructure types that are those most closely associated with GI programs to promote sustainable buildings, neighborhoods and cities. Examples of US cities where large investments in engineered GI are currently underway include Philadelphia (\$2.4 billion), New York City (\$1.5 billion), Chicago (\$50 million), and Cleveland (\$42 million) [4]–[6].

Although the majority of urban GI programs in the US, and elsewhere, are being driven by stormwater management challenges arising as a result of the impervious nature of modern cities, GI is also believed to provide other benefits that advance urban sustainability. By increasing vegetation and perviousness within city boundaries, it is claimed that GI can help cool urban environments, thus reducing urban heat island impacts [7], trap harmful air-borne

particulates [8], sequester greenhouse gases [9], increase and/or restore urban biodiversity [10], improve public health and well-being [11], [12] and even create so-called “green collar jobs” [13], [14]. Thus, many GI programs are promoted not only on the basis of their stormwater management goals, but also on the basis of these claimed co-benefits.

The goal of this paper is to examine some of the advantages and hurdles associated with green infrastructure programs for urban sustainability. The paper will do so by using climate adaptation as an example urban sustainability challenge. In order to focus the paper, New York City (NYC) will be used as a case study. Nonetheless, many of the discussions and conclusions reached in the paper are also relevant to other urban settings, as well as other sustainability challenges.

2. CLIMATE CHANGE IMPACTS

Current climate change projections involve significant uncertainty, not least because scenarios for future green-house gas emissions are unknown. For high emissions scenarios (RCP8.5), mean global temperature rise is projected to be about 4°C (~ 8°F) over the course of the 21st Century, Figure 1, while mean global sea-level rise is projected to be about 2.5 meters (~ 8 feet), Figure 2. Local sea-level and temperature rises are projected to be above or below the mean global levels shown in Figures 1 and 2, depending upon the region under consideration.

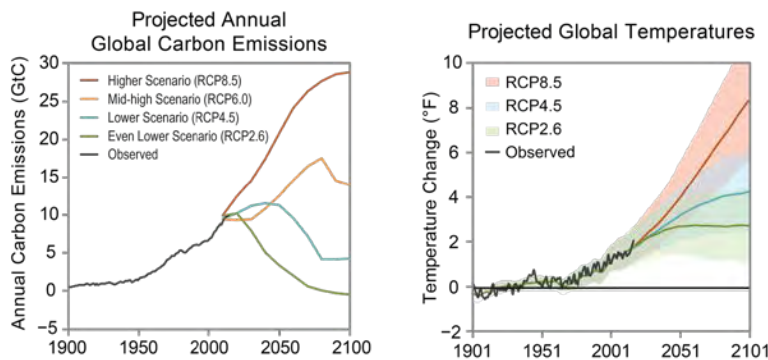


Figure 1. Past and projected changes in global mean temperature rise under different emissions scenarios, from [15].

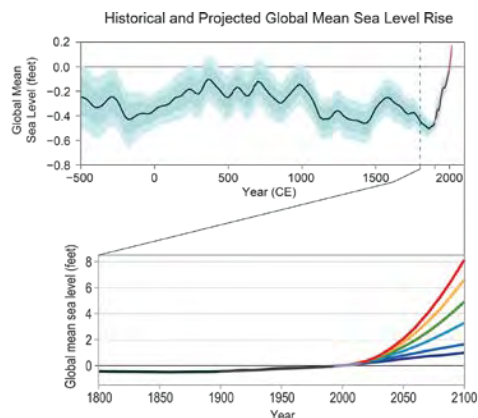


Figure 2. Past and projected changes in global mean sea level rise under different emissions scenarios, from [15].

Nonetheless, despite uncertainties in the projected magnitude of climate change effects, there are general trends that climate scientists and others agree upon. These include a raise in sea-levels; an increase in temperatures; changes in the patterns and amount of precipitation; a decline in snow-cover, permafrost and sea-ice; acidification of the oceans; an increase in the frequency, density and duration of extreme events, and a change in eco-system characteristics. These effects will negatively impact water resources, infrastructure, food supplies and eco-systems, as well as human health and well-being. Given the rapid pace of urbanization, adaptation to climate change impacts is especially important for the world's cities, which are expected to house 66% of the world's population by 2050 [16].

2.1 New York City Temperature and Precipitation Changes

In New York City, historic trends over the past 110 years indicate an increase in both the average temperature and annual precipitation, as recorded at the Central Park Meteorological Station [17]. From a baseline of the year 2000, projected climate change scenarios for a mid-range of emissions scenarios indicate temperature rises of up to 3°C and precipitation increases of up to 11% by the 2050s [18]. These increases will only intensify the present day challenges New York City faces with respect to its stormwater management issues [19] and mitigation of the urban heat island effect [20].

3. NEW YORK CITY GREEN INFRASTRUCTURE PLAN

In 2010, New York City (NYC) released the NYC Green Infrastructure Plan, which is a multi-decade, multi-billion-dollar plan to improve water quality in the City via the introduction of engineered interventions such as green roofs, right-of-way bioswales, green streets and urban street-trees into NYC's impervious landscape [19], Figure 3. By increasing the amount of vegetation in the City, the NYC Green Infrastructure plan aims to allow precipitation to be soaked up locally, thereby reducing contamination of local water bodies and also incidents of rain induced flooding.

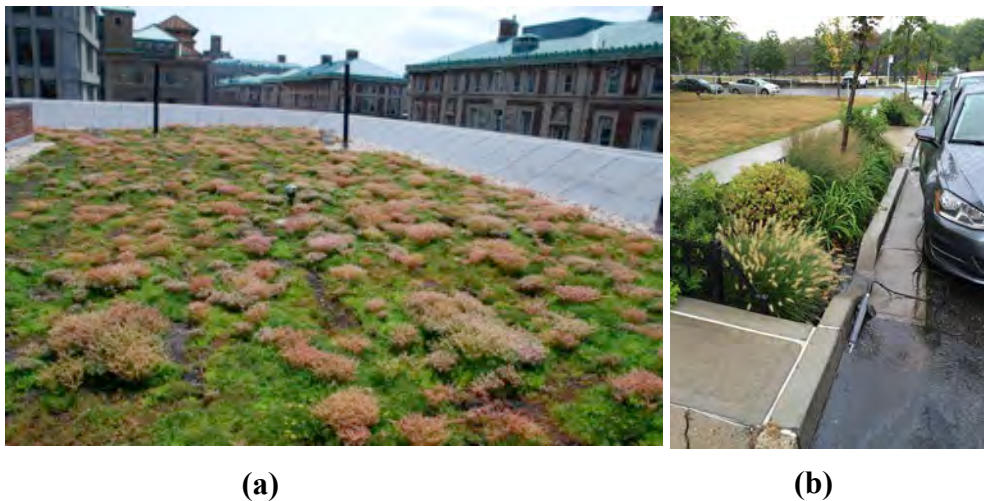


Figure 3. a) Green roof on a Columbia University building, and b) Right-of-way bioswale in the Bronx, New York City. Image (a) courtesy of Stuart Gaffin, Columbia University. Image (b) courtesy of Nandan Shetty, Columbia University.

3.1 Green Infrastructure Performance Monitoring in New York City

Over the past decade, the author and her colleagues have been researching the performance of green infrastructure in NYC from the vantage point of multiple sustainability metrics [21]–[32], including those relevant to climate adaptation. In the following paragraphs, some example findings are provided for the performance of a common building level GI intervention, namely green roofs.

The two major green roof categories include extensive green roofs, whose substrates are typically 15 cm thick or less and feature short rooting, drought resistant plants such as *sedum*, and intensive green roofs, whose substrates are greater than 15 cm thick and may be sowed with deeper rooting plants including shrubs and trees. Due to their lower cost, reduced maintenance requirements, and lighter weight per unit area, extensive green roofs are more frequently adopted than their intensive counterpart [27]. For this reason, the majority of green roof studies engaging the author and her colleagues involve extensive green roofs. Figure 4 provides the location of three of these extensive green roofs, each of which encompasses a popular construction type. W118 is a Xero Flor America XF301+2FL *vegetated mat system* with a substrate depth of 32 mm, ConEd is a GreenGrid-G2 *modular tray system* with a substrate depth of 100mm, while USPS is a Tecta Green *built-in-place system* with a substrate depth of 100mm. All three roofs are planted with *sedum* species. Monitoring of green roof performance began in 2009 and has been almost continuous since then. Further information on the characteristics of each green roof, monitoring equipment and set-up can be found in [21].

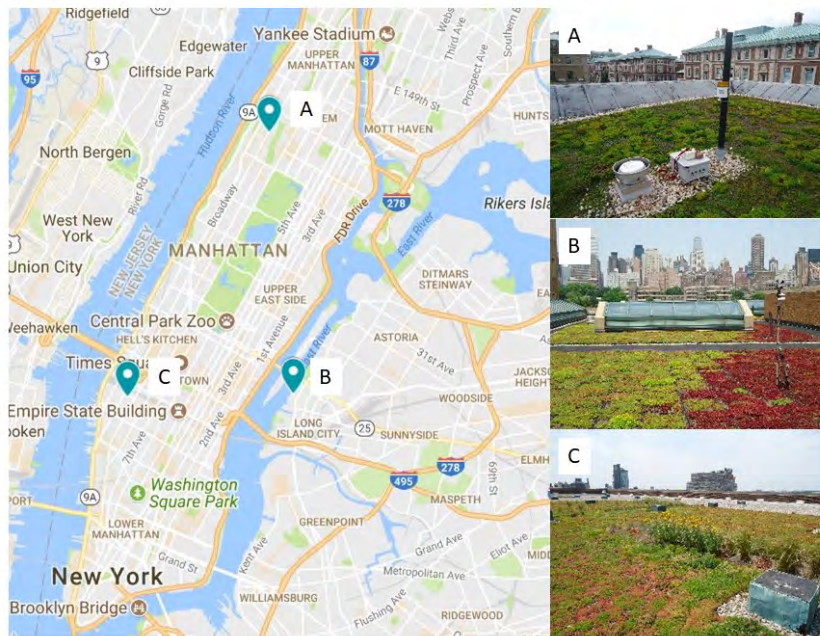


Figure 4. Locations and rooftop views of the W118 (A), ConEd (B) and USPS (C) green roofs, respectively. Map data retrieved from Google Maps (Google Chrome 2018).

Figure 5 summarizes stormwater retention values by storm size category for the three extensive green roof types. As would be expected, green roof rainfall retention reduces with increasing storm depth. Nonetheless, even for largest of storms (50mm +), rainfall retention is

30% or more of incident rainfall. In general, the thinner W118 green roof under-performs with respect to rainfall retention in comparison to the thicker ConEd and USPS systems. Since July 2011, the date when vegetation on all three roofs was considered fully established, the observed annual retention of the W118, ConEd and USPS green roofs has been 45.9%, 50.7% and 56.5%, respectively.

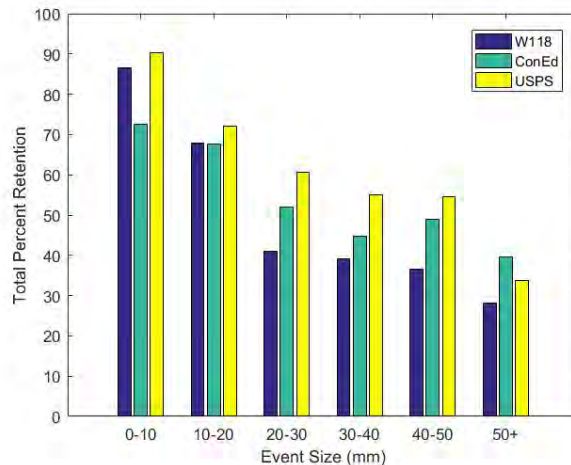


Figure 5. Green roof stormwater retention performance for the W118, ConEd and USPS *sedum* green roofs for different storm event categories.

Green roofs achieve air temperature reductions by transforming adsorbed sunlight into water vapor through evapotranspiration (ET), also termed latent heat loss. White or “cool” roofs, which achieve a high reflection of sunlight, are an alternative to green roofs for air temperature reduction. Temperature data collected over a period of a year from the ConEd green roof and nearby white and black roof treatments, show that white roof and green roof temperatures are actually fairly close, except during summer wet periods when the efficiency of latent heat loss lowers the green roof temperatures significantly below that of the white roof [33]. An illustration of the surface temperature differences that are possible between black, white and green roof areas are shown in Figure 6. It is the observation of large, surface temperatures differences like those shown in Figure 6 (e.g., a different of 46°C between the black and green roof surfaces) that has spurred interest in the use of vegetated GI to moderate extreme heat in urban spaces.

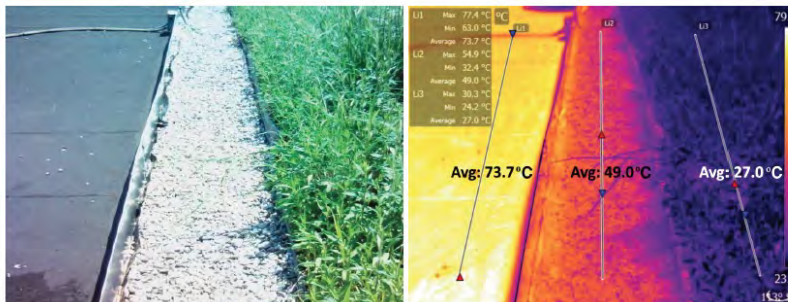


Figure 6. Standard (left) and Infra-red (right) photographs of an NYC based rooftop comprising black, white and green surfaces. Image courtesy of Stuart Gaffin, Columbia University.

Figure 7 provides measurements of diurnal surface-atmospheric CO₂ fluxes for the W118 green roof taken during the month of April. The data show the green roof to be a source of CO₂ during night-time hours (0 – 5am, and 9pm to midnight) and a sink during daylight hours. Overall, the calculated net ecosystem exchange (NEE) of CO₂ for the measurements shown in Figure 7 is -116.5 g CO₂ m⁻² month⁻¹, or -31.8 g C m⁻² month⁻¹. This value is very similar to values reported for an extensive sedum green roof located in Berlin, Germany during the Spring growing season [34]. The authors of [34] report an annual, cumulative NEE of -313 g CO₂ m⁻² year⁻¹, equivalent to -85 g C m⁻² year⁻¹, for the green roof that they studied. For comparison [35] estimate a NEE value of -7.33 kg C m⁻² year⁻¹ associated with carbon storage and sequestration of the NYC urban tree cover, where area refers to the canopy area, which was obtained from aerial photographs taken during a leaf-on state.

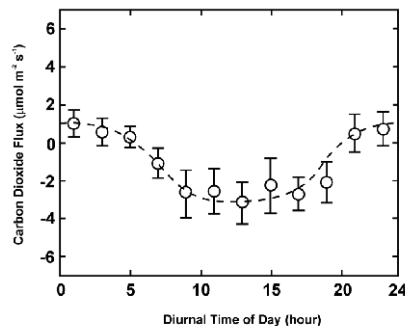


Figure 7. Measured values of CO₂ surface-atmospheric exchange during the Spring growing season for W118.

3.2 Green Infrastructure and Climate Adaptation

Like many other municipal green infrastructure plans, the NYC Green Infrastructure Plan is targeting the construction of thousands of GI interventions, located on both public and private property, to achieve the City's stormwater management goals. The plan is therefore relying on a distributed, or neighborhood scale, infrastructure approach to realize a city-wide objective.

Unlike centralized infrastructure approaches, which usually comprise a smaller number of large investments, distributed infrastructure approaches can be incorporated into urban fabrics at a range of densities and scales. These approaches can thus evolve as performative systems over space and time as needed. Given current uncertainty in climate change projections (see Figures 1 and 2), strategies for climate change adaptation need to be able to change as projections improve over time and/ or impacts are better quantified. Given the flexibility with which a distributed infrastructure system can evolve, the use of distributed infrastructure as part of an urban climate adaptation strategy has many advantages.

Although the NYC Green Infrastructure Plan was not developed as a climate adaptation strategy for NYC, the Plan's promotion of green infrastructure could help mitigate the projected effects of increased precipitation and temperatures in the City, as well as augment local carbon sequestration (refer to Figures 5, 6 and 7). Thus the Plan, inadvertently, encourages a climate adaptation strategy that relies on a distributed infrastructure approach in the face of ill-quantified climate impacts.

4. CHALLENGES AND FUTURE NEEDS

As discussed above, distributed GI appears to have promise as a strategy for climate change adaptation in urban environments. Nonetheless, as discussed below, there are still hurdles that need to be overcome in order to fully realize the actual potential of this promise.

Despite significant progress in documenting the performance of an individual GI intervention, an understanding of how thousands of GI interventions perform as a system of interventions remains lacking. Developing this understanding is essential to advancing system level optimization of multi-component GI schemes for climate adaptation, or other urban sustainability goals. Modeling approaches might be one way to make the necessary progress. However, even in the well-studied area of stormwater management, process-based predictive models have had limited success in forecasting the behavior of an individual GI installation [23], let alone a multi-component GI system. One reason for this, is poor parameterization of evapotranspiration processes for engineered GI. An alternative to systems level modeling is systems level monitoring. This approach has the advantage of providing direct, possibly real-time, information on neighborhood or city-wide GI performance. Furthermore, with enough data collection, it might be possible to create data driven models to inform future system design, optimization and operation strategies. Nonetheless, advancement of this approach will require the development of appropriate sensor networks as well as accompanying data-management and support systems: In other words, a “smart-cities’ type approach to urban GI programs.

Improved understanding of the role of engineered GI in mitigating urban heat island effects is also needed. While it is true that large patches of greenery, such as NYC’s Central Park, have measureable effects on air temperatures within the park boundary, the cooling effects exerted by smaller areas, such as the green roofs or right-of-way bio-swales shown in Figure 3, are less clear. Thus, more research is needed to define the scale and spatial patterns of urban vegetation required to significantly lower air temperatures in dense urban environments like NYC.

Different from larger-scale climate adaptation strategies, such as the installation of massive underground stormwater storage tanks, distributed GI systems are not only comprised of many more elements, they are also more likely to interface with urban social systems and communities. This can add complex facets of public acceptance and stewardship to the equation of GI performance, which are not always accounted for in GI design, siting and maintenance. Public acceptance and stewardship lessons learned to date from NYC’s Green Infrastructure program indicate the importance of greater public dialogue regarding infrastructure placement in the public right-of-way (e.g. Figure 3b). In general, public acceptance of right-of-way GI in NYC has been mixed, with many residents not embracing this vegetative intervention due to concerns about loss of parking, accumulation of trash in the GI, dislike of GI plant palettes – especially native grasses, and general dis-satisfaction about perceived lack of public consultation prior to implementation. In some instances, right-of-way GI has been vandalized in ways that actually compromise its physical performance. Survey work by the author and colleagues indicate that the public places more value on the cultural, social and aesthetic services provided by GI, than the environmental services. Thus, GI designs that account for public value systems, might have better long-term performance and stewardship outcomes than present-day designs.

Currently, efforts to design GI to maximize performance beyond stormwater management remain limited. For example, [34] note that carbon uptake by the sedum green roof they monitored in Berlin, Germany declined when substrate moisture content fell below $0.05 \text{ m}^3\text{m}^{-3}$, while [33] observed that high substrate moisture contents were linked to lower green roof temperatures. Yet, the active management of substrate moisture content to enable optimal rainfall capture, carbon uptake and the lowering of surface temperatures is neither a design nor

operational feature of most extensive green roofs. Going forward, more attention needs to be paid to the design and operation of GI interventions that maximize as many sustainability benefits as possible.

Finally, questions still remain as to how to define “acceptable” performance for a distributed GI system, whether for the purpose of climate adaptation or not. For example, with respect to performance redundancy, questions remain as to what is an acceptable factor of safety for a distributed system? And should a factor of safety be applied to each individual component of a GI system (i.e., each component has a built-in factor of safety) or the entire system itself (i.e., the system has redundant components)? In addition, there are questions regarding system resiliency. For example, are distributed systems more resilient because they are comprised of very, many components (so if several components fail the overall system performance is not compromised) or are they less resilient because it is hard to manage and secure a system of very many components? Furthermore, with respect to funding, what is the model for financing distributed GI systems that are installed on private land to perform public good? These, and other, questions will need answers if distributed GI systems are to become viable elements of urban climate adaptation strategies.

5. CONCLUSIONS

Distributed, or neighborhood level, systems of green infrastructure can contribute to urban sustainability goals in multiple ways. This paper discussed climate adaptation as one such example. Because GI can be incorporated into urban fabrics at a range of densities and scales, the performance of GI systems can evolve over space and time as needed. Given current uncertainty in climate change projections and impacts, the flexibility of an adaptation strategy whose performance can continually evolve has many advantages. Nevertheless, there are a number of challenges that need to be overcome to advance the use of GI for climate adaptation.

Despite the fact that significant progress has been made in documenting the performance capacity of individual GI interventions, an understanding of how thousands of GI interventions perform as a system remains lacking. Developing this understanding is essential to designing multi-component GI interventions for climate adaptation, or other urban sustainability goals. In addition, better understanding of the scale and patterns of urban vegetation required to mitigate urban heat island effects is needed, as are new designs for GI that optimize different performance attributes and improve public acceptability and stewardship outcomes for GI sited in the public-right-of-way. Finally, fundamental questions regarding what defines acceptable performance for a distributed GI system still need to be addressed.

ACKNOWLEDGEMENTS

This work was funded, in part, by the National Science Foundation awards CMMI-1325676 and CBET-1444745, as well as the Environmental Protection Agency contract EP-15-C-000016. Any opinions, findings, and conclusions expressed in this article are those of the author and do not necessarily reflect the views of any supporting institution.

REFERENCES

- [1] Florida Greenways Commission, “Creating a statewide Greenways system, for people... for wildlife... for Florida.” Tallahassee, 1994.
- [2] M. a Benedict and E. T. McMahon, “Green Infrastructure: Smart Conservation for the 21st Century,” *Renew. Resour. J.*, pp. 12–19, 2002.
- [3] J. P. Newell *et al.*, “Green Alley Programs: Planning for a sustainable urban

- infrastructure?,” *Cities*, vol. 31, pp. 144–155, 2013.
- [4] City of Chicago, “2014 Budget Overview,” Chicago, IL, 2014.
- [5] NEORS (Northwest Ohio Regional Sewer District), “Green Infrastructure Plan,” 2012.
- [6] Philadelphia Water Department, “Green City Clean Waters,” Philadelphia, 2011.
- [7] E. Oberndorfer *et al.*, “Green Roofs as Urban Ecosystems: Ecological Structures, Functions, and Services,” *Bioscience*, vol. 57, no. 10, pp. 823–833, 2007.
- [8] J. Yang, Q. Yu, and P. Gong, “Quantifying air pollution removal by green roofs in Chicago,” *Atmos. Environ.*, vol. 42, pp. 7266–7273, Oct. 2008.
- [9] K. L. Getter, D. B. Rowe, G. P. Robertson, B. M. Cregg, and J. A. Andresen, “Carbon sequestration potential of extensive green roofs,” *Environ. Sci. Technol.*, vol. 43, no. 19, pp. 7564–7570, Oct. 2009.
- [10] Toronto and Region Conservation Authority, “Evaluation of an Extensive Greenroof,” TORONTO, ONTARIO, 2006.
- [11] H. Niu, C. Clark, J. Zhou, and P. Adriaens, “Scaling of economic benefits from green roof implementation in Washington, DC,” *Environ. Sci. Technol.*, vol. 44, no. 11, pp. 4302–4308, Jun. 2010.
- [12] T. Van Renterghem and D. Botteldooren, “In-situ measurements of sound propagating over extensive green roofs,” *Build. Environ.*, vol. 46, pp. 729–738, Mar. 2011.
- [13] Center for American Progress, “New York City Green Collar Jobs Roadmap,” 2009.
- [14] The New York Times, “Millions of Jobs of a Different Collar,” *Online*. 2008.
- [15] D. J. Wuebbles, D. W. Fahey, K. A. Hibbard, D. J. Dokken, B. C. Stewart, and T. K. Maycock, “Climate science special report: fourth National Climate Assessment,” *U.S. Glob. Chang. Res. Progr.*, vol. 1, p. 470, 2017.
- [16] United Nations, “World Urbanization Prospects 2014,” 2014.
- [17] J. E. Rosenthal, K. M. Knowlton, C. Rosenzweig, R. Goldberg, and P. L. Kinney, “One Hundred Years of New York City’s ‘Urban Heat Island’: Temperature Trends and Public Health Impacts,” in *American Geophysical Union, Fall Meeting*, 2003.
- [18] “New York City panel on climate change 2015 report executive summary,” *Annals of the New York Academy of Sciences*, vol. 1336, no. 1, pp. 9–17, 2015.
- [19] NYC DEP, “NYC Green Infrastructure Plan: A sustainable strategy for clean waterways,” New York, NY, 2010.
- [20] S. R. Gaffin *et al.*, “Bright is the new black: multi-year performance of high-albedo roofs in an urban climate,” *Environ. Res. Lett.*, vol. 7, no. 1, 2012.
- [21] T. B. Carson, D. E. Marasco, P. J. Culligan, and W. R. McGillis, “Hydrological performance of extensive green roofs in New York City: Observations and multi-year modeling of three full-scale systems,” *Environ. Res. Lett.*, vol. 8, no. 2, 2013.
- [22] P. Culligan *et al.*, “Evaluation of Green Roof Water Quantity and Quality Performance in an Urban Climate,” 2014.
- [23] T. Carson, M. Keeley, D. E. Marasco, W. McGillis, and P. Culligan, “Assessing methods for predicting green roof rainfall capture: A comparison between full-scale observations and four hydrologic models,” *Urban Water J.*, vol. 14, no. 6, 2017.
- [24] D. E. Marasco, B. N. Hunter, P. J. Culligan, S. R. Gaffin, and W. R. McGillis, “Quantifying evapotranspiration from urban green roofs: A comparison of chamber measurements with commonly used predictive methods,” *Environ. Sci. Technol.*, vol. 48, no. 17, pp. 10273–10281, 2014.
- [25] D. E. Marasco, P. J. Culligan, and W. R. McGillis, “Evaluation of common evapotranspiration models based on measurements from two extensive green roofs in New

- York City,” *Ecol. Eng.*, vol. 84, 2015.
- [26] R. Hakimdavar, P. J. Culligan, M. Finazzi, S. Barontini, and R. Ranzi, “Scale dynamics of extensive green roofs: Quantifying the effect of drainage area and rainfall characteristics on observed and modeled green roof hydrologic performance,” *Ecol. Eng.*, vol. 73, 2014.
- [27] R. Hakimdavar, P. J. Culligan, A. Guido, and W. R. McGillis, “The Soil Water Apportioning Method (SWAM): An approach for long-term, low-cost monitoring of green roof hydrologic performance,” *Ecol. Eng.*, vol. 93, pp. 207–220, 2016.
- [28] R. M. Elliott, R. A. Gibson, T. B. Carson, D. E. Marasco, P. J. Culligan, and W. R. McGillis, “Green roof seasonal variation: Comparison of the hydrologic behavior of a thick and a thin extensive system in New York City,” *Environ. Res. Lett.*, vol. 11, no. 7, 2016.
- [29] R. M. Elliott, E. R. Adkins, P. J. Culligan, and M. I. Palmer, “Stormwater infiltration capacity of street tree pits: Quantifying the influence of different design and management strategies in New York City,” *Ecol. Eng.*, vol. 111, 2018.
- [30] N. Shetty, P. J. Culligan, B. Mailloux, W. R. McGillis, and H. Y. Do, “Bioretention Infrastructure to Manage the Nutrient Runoff from Coastal Cities,” in *Geotechnical Special Publication*, 2016, vol. 2016–Janua, no. 273 GSP.
- [31] D. Roman, A. Braga, N. Shetty, and P. Culligan, “Design and modeling of an adaptively controlled rainwater harvesting system,” *Water (Switzerland)*, vol. 9, no. 12, 2017.
- [32] L. J. Whittinghill, D. Hsueh, P. Culligan, and R. Plunz, “Stormwater performance of a full scale rooftop farm: Runoff water quality,” *Ecol. Eng.*, vol. 91, 2016.
- [33] S. R. Gaffin, C. Rosenzweig, J. Eichenbaum-Pikser, R. Khanbilvardi, and T. Susca, “A Temperature and Seasonal Energy Analysis of Green, White, and Black Roofs,” *Water Resour.*, p. 19, 2010.
- [34] J. Heusinger and S. Weber, “Extensive green roof CO₂ exchange and its seasonal variation quantified by eddy covariance measurements,” *Sci. Total Environ.*, vol. 607–608, pp. 623–632, 2017.
- [35] D. J. Nowak, E. J. Greenfield, R. E. Hoehn, and E. Lapoint, “Carbon storage and sequestration by trees in urban and community areas of the United States,” *Environ. Pollut.*, vol. 178, pp. 229–236, 2013.

Humans and Nature in the Loop: Integrating occupants & natural conditioning into advanced controls for high performance buildings

Vivian Loftness¹, Azizan Aziz¹, Volker Hartkopf¹, Khee Poh Lam¹, Bertrand Lasternas¹
¹Center for Building Performance & Diagnostics, Carnegie Mellon University

ABSTRACT

Post Occupancy Evaluation plus Measurements (POE+M) has revealed that thermal, visual, acoustic and even air quality standards derived through controlled experimentation alone does not ensure comfort or health in buildings. Introducing human input into environmental standards and into user centric controls is critically needed for a sustainable future. For over a decade, CMU's Center for Building Performance & Diagnostics has been gathering POE+M data from over 1500 workstations around the world and testing the benefits on innovative environmental control systems. The separation of ambient and task conditioning, the provision of task controls, the introduction of occupant voting and bio-signal inputs into ambient and task set-points, offers major gains in comfort, task performance, energy savings, as well as health and wellness.

KEYWORDS

Humans in the Loop, Internet of Things, Task and Ambient Conditioning, Bio-signals, POE

INTRODUCTION

Addressing the seriousness of climate change and resiliency necessitates breaking out of the control impoverished, reflective, sealed commercial buildings of today. These buildings are often driven by first least cost, treat humans as a liability by hiding sensors and controllers, and treat nature as a liability by blocking natural solar heating and sealing out natural ventilation and cooling. These buildings are not intelligent and not resilient. Next generation buildings will embrace the Internet of Things (IoT) to make every point of service – every air diffuser, light fixture, heating or cooling unit, window, shade and plug point - a point of sensing, control and intelligent feedback (figure 1). Sensor and control rich environments will engage humans and nature as assets for ensuring indoor environmental quality, organizational flexibility, individual health and productivity, as well as ecological sustainability.

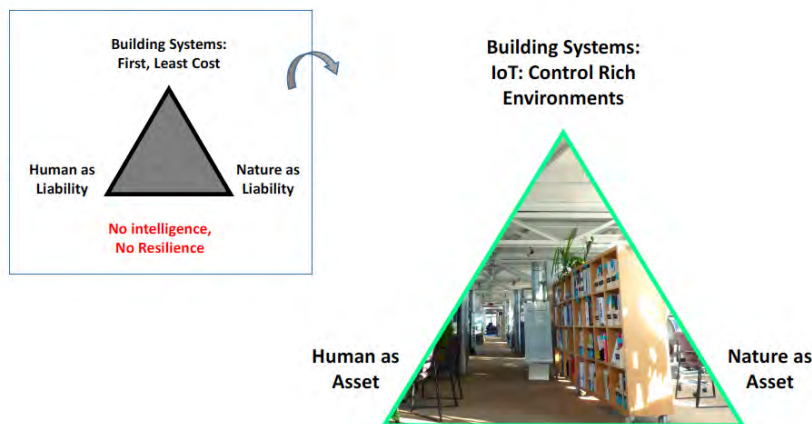


figure 1. Next generation buildings will be IoT control rich, treating humans and nature as assets

Post Occupancy Evaluation plus Measurement (POE+M) in 70 Federal Facilities

Over the past 20 years, The Center for Building Performance and Diagnostics (CBPD) at Carnegie Mellon University and the U.S. General Services Administration (GSA) launched a nation-wide effort to complete post occupancy evaluations in federal facilities before and after the investments to improve the quality of the federal workplace. A National Environmental Assessment Toolkit (NEAT) was developed that critically merged user satisfaction surveys (long term and right now surveys) with physical measurements of environmental conditions and expert walkthroughs and interviews to capture the technical attributes of the building systems that supplied the thermal, air quality, lighting, acoustic and spatial performance (Loftness 2009, Aziz 2012, Choi 2012). Armed with national and international IEQ standards & thresholds, teams of Carnegie Mellon faculty and graduate students surveyed, measured and recorded conditions in over 1600 Workstations in 70 GSA buildings to build the NEAT data base, completing studies with recommendations, and leading to numerous Masters and PhD dissertations. The term POE+M was coined to emphasize the importance of simultaneously recording user satisfaction at given environmental conditions and given physical configurations of the building systems.

$$\text{CMU POE+M} = \text{User Satisfaction (COPE)} + \text{Environmental Conditions (NEAT)} + \text{Technical Attributes of Building Systems (TABS)}$$

For example, comparing field measured air temperatures with “right now” satisfaction Reveals: that US buildings are unacceptably and unnecessarily cold in summer (figure 2); that highest user satisfaction with air quality is achieved at CO₂ thresholds of 600 ppm ($p < 0.05$) not the 1000 ppm presently used; that the highest satisfaction with lighting quality is achieved at less than 250 lux, given the computer intensive tasks in the office today. POE+M data bases offer a wealth of environmental learning and innovation (CBPD 2013), and should be the basis of both educational and professional commitments to field studies.

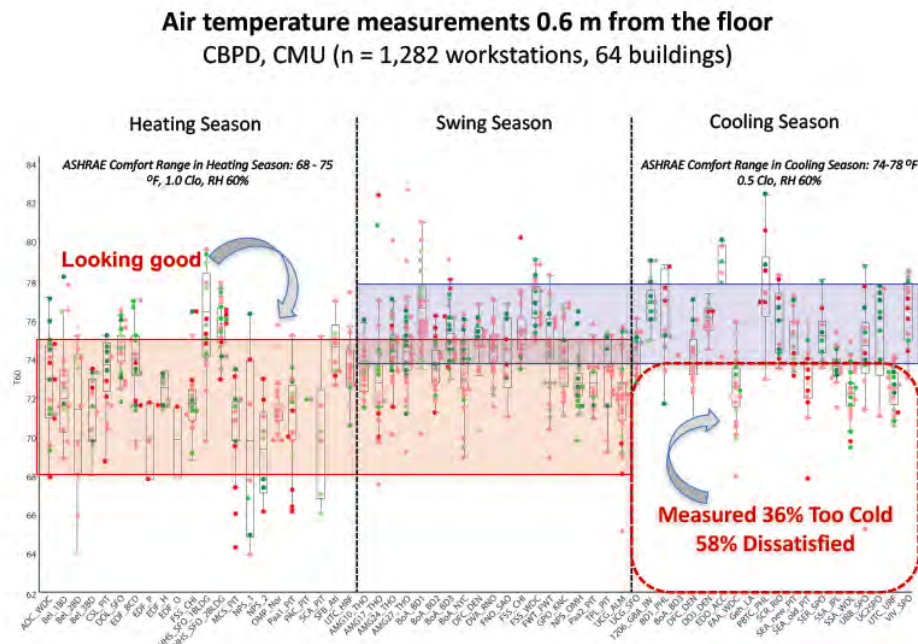


figure 2. Comparing field measured air temperatures with “right now” satisfaction reveals that US buildings are unacceptably and unnecessarily cold in summer.

“Are Humans Good IEQ Sensors? Using occupants as sensors for thresholds that matter.”

With measurements in 1600 workstations in 64 buildings in the POE+M database, the 2014 CMU Dissertation of Jihyun Park used a rich array of statistical methods to definitely answer the research question ‘Are Humans Good IEQ Sensors’. The thermal, air quality, lighting and acoustic findings are both critical to building operation and future design, and statistically significant (Park 2015). The dissertation identified five building environmental conditions (NEAT) or physical conditions (TABS) significantly impacted thermal satisfaction: Air temperature at 0.6 m from the floor; Radiant temperature asymmetry with façade; Size of Zone; Window Quality; and Level of Temperature Control. These findings challenge existing design and engineering practices as well as existing comfort standards. For example, in 391 perimeter workstations, satisfaction with thermal conditions (-1 to +1) cannot be achieved unless horizontal radiant asymmetry is contained below 3.4oF (p<.001), not the 18oF presently in the code (see figure 3). The highest user satisfaction with thermal conditions in summer is achieved at 76.5oF (p<0.05), not the 72oF so prevalent as a year round set-point in the field, and occupants in spaces with hidden or locked thermostats will be 20-40 % less satisfied with air temperature in their work area (p<0.01). Beyond thermal satisfaction, the research continued to identify the building environmental (NEAT) or physical (TABS) conditions that significantly impacted satisfaction with air quality, lighting quality and acoustic quality.

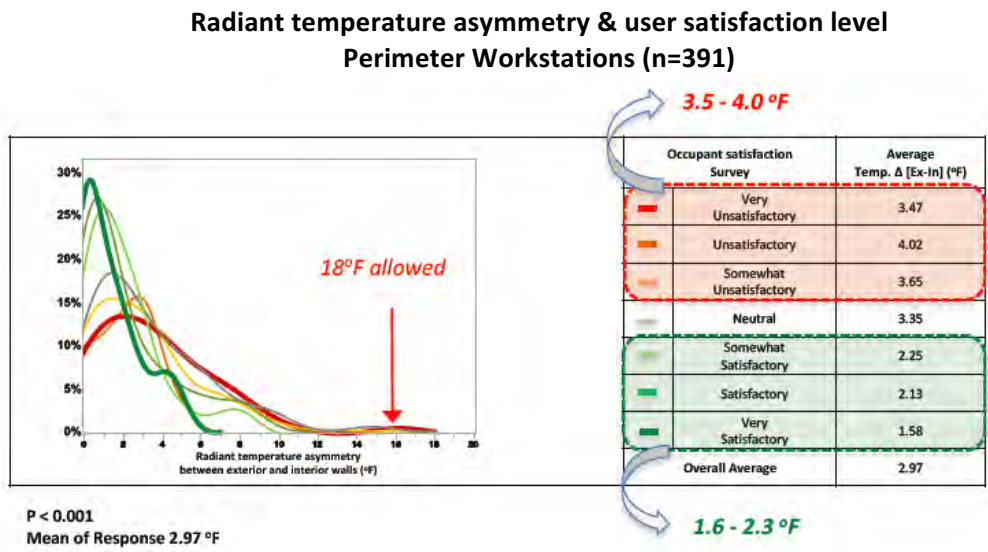


figure 3. Comparing measured horizontal temperature asymmetry with “right now” satisfaction suggest ASHRAE standards need to reduce acceptable delta’s from 18F to <5F (Park 2015).

The CMU Intelligent Workplace: A Living Laboratory of Systems Integration for Performance

The Intelligent Workplace is one of the most sensed and controllable workplaces worldwide, shifting from traditional settings with one control for every 20 occupants to 20 controls for every occupant. With the emergence of wireless sensors and controllers and the Internet of Things (IoT), the IW is a testbed for the engagement of occupants as both sensors and controllers for the improvement of environmental quality and energy conservation.

In addition to field POE+M studies, the faculty and graduates in the Center for Building Performance have been testing the performance of innovations in component and integrated systems in the Intelligent Workplace at CMU. In collaboration with Siemens Corporate Research, Siemens Building Technology and the U.S. Department of Energy (DOE), this living and lived in laboratory supported two years of research on “Advanced, Integrated Controls for 40% Energy Savings in Building Operations” (figure 4) (Siemens 2012). A combination of seasonal controlled experimentation and computer simulation revealed that up to 75% of the ventilation energy, 36% of the heating energy, 25% of the cooling energy, and 70% of the lighting energy could be saved in cool and temperate climates through learning, occupant and nature responsive controls.

For example, the 36% in heating energy savings from the 2010 Baseline of US commercial buildings with limited sensors, limited controllers and sloppy 7x24 operation could be cumulatively reduced:

- 7.7% through updated sensors, time of day operation, and no over/under start up times;
- 15.5% through night setback $\Delta 5^{\circ}\text{F}$ and weekend setback $\Delta 2\text{-}7^{\circ}\text{F}$; and
- 36.1% through lower ambient settings & occupant controlled low watt task heating.

The 70% in lighting energy savings from the same 2010 baseline could be cumulatively reduced:

- 40% savings by daylighting when it met space requirements alone;
- 64% savings by adding occupant scene control to daylighting; and
- 71% total savings by Daylighting + Occupant Scene Control + Daylight Harvesting (possible through dimming controls).

Intelligent Workplace Lighting/ Daylighting/Shading Systems

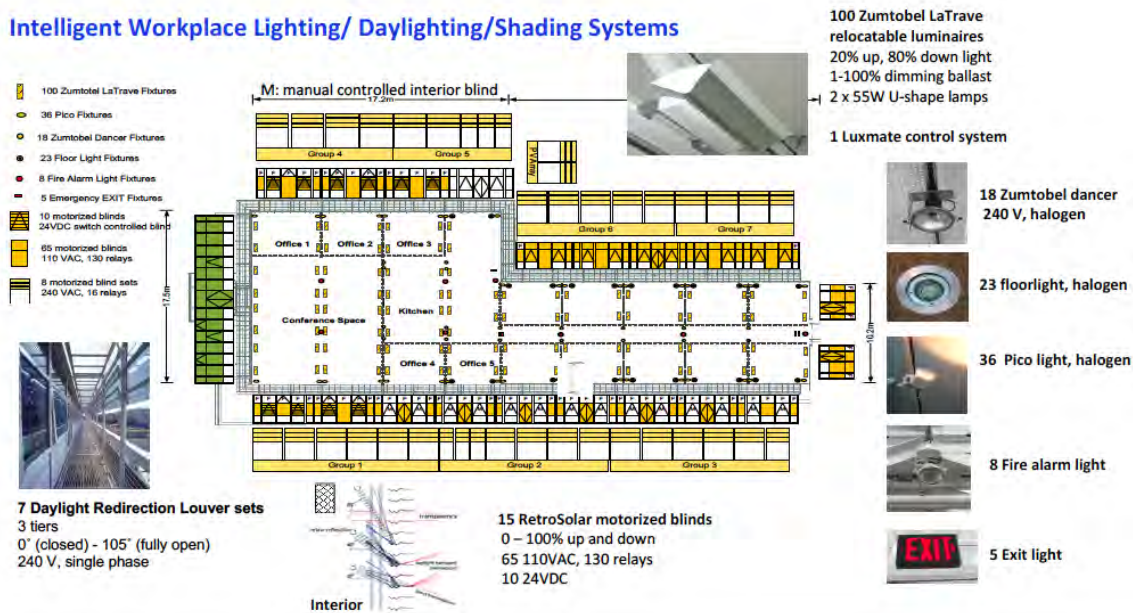


figure 4. The CMU Intelligent Workplace is a living and lived in laboratory for high performance building systems, the IoT, and human and nature responsive controls

The research also demonstrated that “control density is far more important than sensor density” and that the Internet of Things (IoT) offers a future where every node of service – every light fixture, air diffuser, heating or cooling coil, every plug – would support control optimization that

integrates across environmental conditioning systems, and includes occupant & natural conditioning strategies. These advances are key to net zero energy, resiliency, as well as human health and performance.

CoBi: Bio-Sensing Building Mechanical System Controls for Sustainably Enhancing Individual Thermal Comfort

The CMU Intelligent Workplace has also been the testbed for numerous Master and PhD thesis projects including the path-breaking work on human bio-signals completed by Joonho Choi (Choi 2010, 2012). With IRB certified human subject testing of a host of bio-signals to control thermal conditions - skin temperatures from ten body locations, heart rate, heart rate variability, and sweat rate – the research identified the wrist as one of the most responsive body location relative to thermal sensation and comfort, given variations in seasons, BMI, MET and CLO conditions. When each individual's variation in wrist temperature is correlated to their thermal sensation votes and enabled to control air temperature, over 93% neutral sensation votes can be achieved, with 5.9 % energy savings for office cooling. This thesis helps to illustrate the importance of distributed controls for environmental systems and engaging occupants as sensors and controllers for energy savings and maximum user comfort, health and task performance.

Smart Phone Controls for the Internet of Things (IoT)

The potential of micro-zoning, of separating thermal and ventilation, of layering ambient and task conditioning, and of controlling every plug - is unlocked by the Internet of Things (IoT). Every node of service – every light fixture, air diffuser, heating or cooling coil, window, window shade, and even every plug – will support control optimization that integrates across environmental conditioning systems, and includes occupant and natural conditioning strategies. In 2010, the IW faculty began a long term collaboration with the students of Dr. Bernd Bruegge in the Institut for Informatik at the Technical University of Munich. Through this collaboration, the IW has been the laboratory for Bachelor, Masters and PhD thesis projects exploring the capabilities of smart phones to provide communication, expert feedback and consulting, and intuitive control (Peters 2012, 2016). These efforts have introduced wifi triangulation for IoT locations, gesture and voice control, innovative smart phone based occupancy sensors, environmental sensing, geo-fencing, smart plug data analytics and more (figure 5).

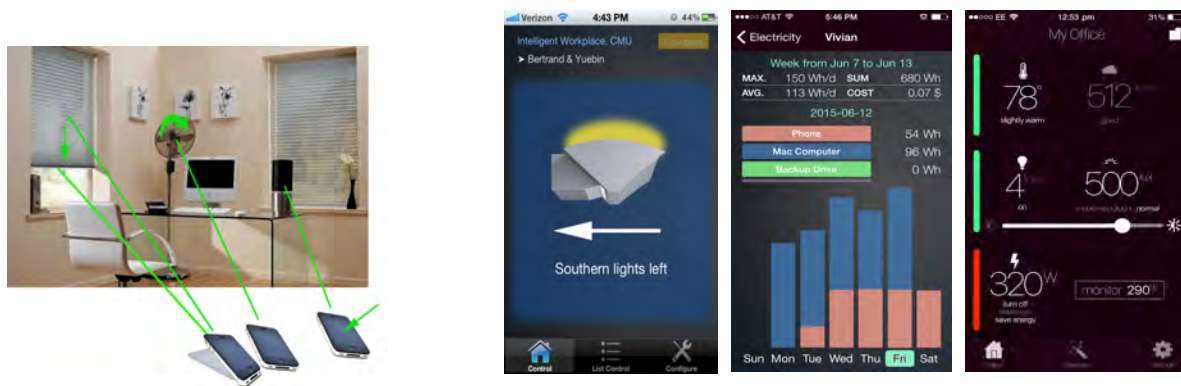


figure 5. Smart phones support intuitive gesture control of every fixture (left 2), provide energy use information (center) and readings of individual sensors and set points (right), (Peters, 2016)

Persistent Workplace Energy Savings and Awareness through Intelligent Dashboards

The importance of communication, feedback, expert consulting, and multiple levels of control are the basis of CMU's research into Intelligent Dashboards for Occupants (ID-O). The PhD thesis of *Ray Yun* explores the impact of nine critical interventions for behavioral change, structured in three sets: Instructional interventions – education, advice and self-monitoring; Motivational interventions – goal setting, comparison and engagement; and Supportive interventions – communication, control and reward (figure 6). With a focus on controlling plug loads, the fastest growing energy end use in commercial buildings, the nine-month controlled field experiment with 80 office workers at a leading green corporation in Pittsburgh revealed that occupant dashboards for controlling desktop technology, with ongoing energy communication and expert consulting generated by the occupants own data set, can generate up to 40% energy savings in plug loads (Yun, 2014).

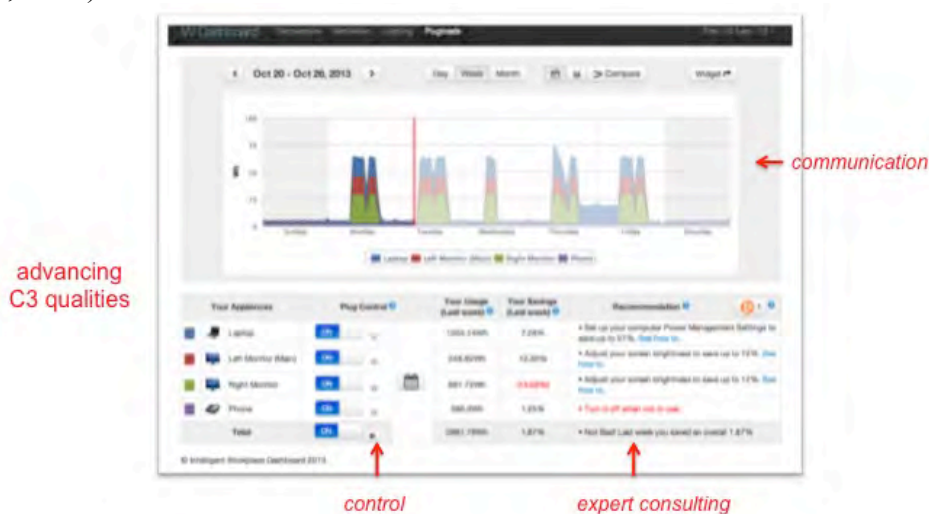


Figure 6 Desktop energy feedback and control dashboards for occupants yielded as much as 40% sustained savings from an already efficient workstation (Yun, 2014)

Occupant-oriented, mixed-mode, Energy+ predictive controls

In addition to engaging occupants directly, the power of occupancy and nature responsive building energy management (BEM) is also a critical development for the Internet of Things. The CBPD has been developing dynamic life-cycle building information models (DLC-BIM) into building energy models (BIM to BEM) focused on total building performance to ensure best practices in sustainable and green architecture. Jie Zhao completed a dissertation in 2015 demonstrating “Design-Build-Operate Energy Information Modeling for Occupant-Oriented Predictive Building Control”, moving from controlled experimentation in the IW to a partnership with a newly awarded Living Building in Pittsburgh. This dissertation developed and demonstrated the concept of design-build-operate Energy Information Modeling infrastructure (DBO-EIM), which can be used at different stages of the building life-cycle to improve energy and thermal comfort performance (figure 7). Given the Pittsburgh weather context and current operation, the Occupant-oriented Mixed-mode EnergyPlus predictive control (OME+PC) system provided a 29.37% reduction in annual HVAC energy consumption. In addition, OME+PC enables building occupants to control their thermal environment through an internet-based dashboard, updating a design stage EnergyPlus model for use through the entire DBO-EIM process.” (Zhao, 2015)

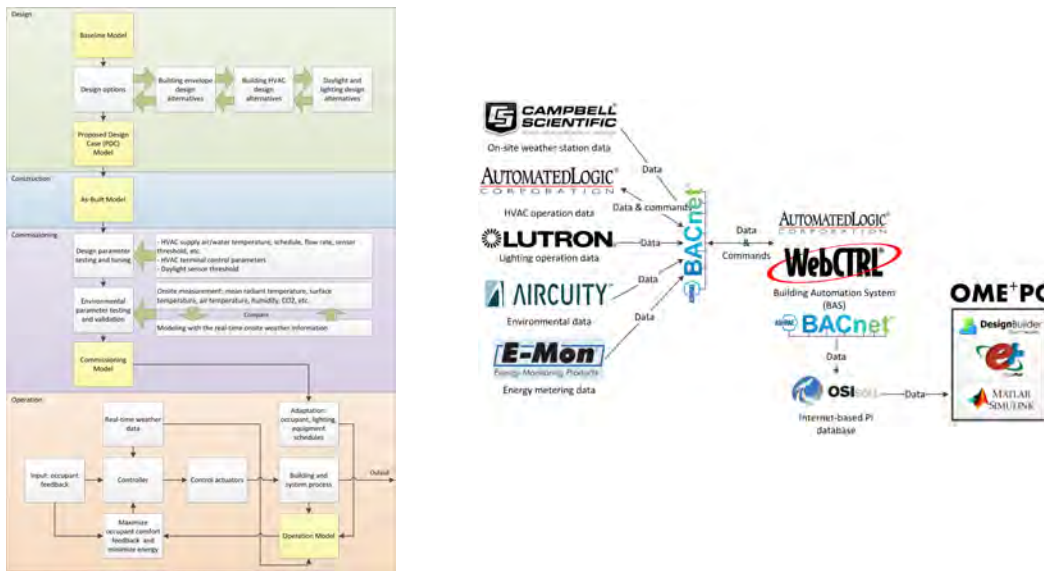


Figure 7 Design-build-operate Energy Information Modeling (DBO-EIM) infrastructure (left), and data collection and system integration architecture (Right) (Zhao, 2015)

Embracing Natural Conditioning

Erich Fromm used the term ‘biophilia’ to describe the psychological orientation of being attracted to all that is alive and vital. EO Wilson and Stephen Kellert, in their book ‘The Biophilia Hypothesis’ described biophilia as the links that human beings instinctively seek with other living systems (Kellert 1993). For those of us in the bricks and systems that define buildings, biophilia must include a passion for natural conditioning. Yet we know that advances in conditioning systems, sensors and controls are equally invaluable to our goals of intelligence, resiliency, health and productivity – especially in the warming and wildly fluctuating changes in our environment. Our future is in the marriage of the high tech and the low tech. First, we must pursue every possible hour of natural conditioning through environmental surfing for daylight, natural ventilation, night ventilation cooling, time lag cooling, passive solar heating, evaporative cooling and more. Then we must lightly introduce mechanical and electrical conditioning through mixed mode design. This demands no more heavy handed, pervasive overlighting or overcooling, and no more over-sealing, over-darkening our building facades. Instead, we must fully design for:

- Mixed Mode: Daylight & Electric Light
- Mixed Mode: Natural Cooling & Mechanical
- Mixed Mode: Natural Ventilation & Mechanical
- Mixed Mode: Outdoor & Indoor Work/Learn/Play/Heal

For each of these mixed design mode solutions, the disciplines must collaborate from the earliest stages of design – to integrate structure, enclosure, mechanical, lighting, interiors and control systems that fully engage nature and the building occupants in a sustainable future.

CONCLUSION

Several decades of field and lab experiments at the Center for Building Performance and Diagnostics at Carnegie Mellon University have demonstrated that humans are good environmental sensors and humans are good environmental controllers, especially when given information, recommendations, and rewards. Occupants contribution to both energy savings and the highest level of individual satisfaction and delight is even greater when natural conditioning opportunities are introduced – daylighting, natural ventilation, night ventilation cooling, passive solar heating and more. Nature offers abundant, albeit variable, free energy sources for environmental conditioning. The future of intelligent buildings for resiliency, health and productivity depends on building systems that engage humans and nature to save energy and increase environmental quality.

REFERENCES

- Loftness, V., Aziz, A., Choi, J., Kampschroer, K., Powell, K., Atkinson, M., & Heerwagen, J., (2009), The value of post-occupancy evaluation for building occupants and facility managers. *Intelligent Buildings International*, 1(4), 249-268.
- Choi, J., Loftness, V., & Aziz, A, 2012, Post-occupancy evaluation of 20 office buildings as basis for future IEQ standards and guidelines, *Energy and Buildings*, 46, 167-175.
- CBPD, 2013, National Environmental Assessment Toolkit (NEAT) manual, Carnegie Mellon University, Available at <http://neat-cbpd.arc.cmu.edu/neat/NEAT-manual.pdf>
- Park, J. (2015). “Are Humans Good Sensors? Using Occupants as Sensors for Indoor Environmental Quality Assessment and for Developing Thresholds that Matter”, CMU PhD.
- Siemens (2012) Lu, Yan, Loftness, V., Aziz, A., Lasternas, B. xxxx “Advanced, Integrated Controls for 40% Energy Savings in Building Operations” ARRA/DOE Final Report 2012.
- Choi, J., (2010)., “CoBi: Bio-Sensing Building Mechanical System Controls for Sustainably Enhancing Individual Thermal Comfort”, PhD Thesis Carnegie Mellon University
- Choi, J., and Loftness, V., (2012). “Investigation of human body skin temperatures as a bio-signal to indicate overall thermal sensations”, *Building and Environment*, 2012, 58, 258-269.
- Peters, S., (2011). “A framework for the intuitive control of smart home and office environments, Masters Thesis in Informatics”, TUM.
- Peters, S., (2016). “MIBO - A Framework for the Integration of Multimodal Intuitive Controls in Smart Buildings”, PhD Thesis in Informatics, TUM.
- Yun, R. (2014) “Persistent Workplace Energy Savings and Awareness through Intelligent Dashboards” PhD thesis, Carnegie Mellon University.
- Yun, R., Lasternas, B., Aziz, A., Loftness, V., Scupelli, P., Rowe, A., Kothari, R., Marion, F., Zhao, J., (2014b)., “Toward the Design of a Dashboard to Promote Environmentally Sustainable Behavior among Office Workers” *Persuasive Technology* (pp. 253-265). Springer Berlin 2014.
- Zhao, J., (2015). “Design-Build-Operate Energy Information Modeling for Occupant-oriented Predictive Building Control”, PhD Dissertation Carnegie Mellon University.
- Kellert (1993). edited by Stephen R. Kellert and Edward O. Wilson. *The Biophilia Hypothesis*. Washington, D.C.:Island Press 1993.

Multiphysics Modeling of Materials, Assemblies, Buildings and Cities

Jan Carmeliet^{1,*}, Jonas Allegrini², Aytac Kubilay² and Dominique Derome²

¹ETH Zurich, Chair of Building Physics, Switzerland

²Empa, Laboratory for Multiscale Studies in Building Physics, Switzerland

*Corresponding email: cajan@ETHZ.CH

ABSTRACT

There is growing evidence that heat waves are becoming more frequent under increased greenhouse forcing, associated with higher daytime temperatures and reduced night-time cooling, which might exceed the limits of thermoregulation of the human body and affect dramatically human health. Especially urban areas are affected, since these regions in addition experience an urban heat island (UHI) effect characterized by higher air temperatures compared to the surrounding rural environment. A necessary breakthrough is a shift away from a fragmented approach towards an integrated multiscale urban climate analysis. This type of research is a rather new domain of research and might be based on an all-physics understanding and modeling of the urban climate ranging from the scales of material and buildings, to the scales of a group of several buildings, street canyons, neighbourhoods, cities and urban regions, referred to as multiscale building physics. To adequately cover global and local urban heat island effect, regional and mesoscale climate analyses have to be downscaled to sub-kilometer resolution and linked with urban climate models at neighborhood and street canyon scales. Such a multiscale urban climate model allows to analyze the influence of urban and building parameters on thermal comfort and the building cooling demand. The importance of accounting for the local urban climate when quantifying the space cooling demands of buildings in an urban environment is demonstrated. The heat-moisture transport model for building materials allows the design of new building materials, which can help in the mitigation of local heat islands. With respect to evaporative cooling materials, we need to optimize their water retention and evaporative cooling by tailoring their pore structure. The understanding and information obtained from pore-scale investigations enables to understand macro-scale transport processes, and enabling us to explore the potential of new evaporative cooling materials at local urban scale.

KEYWORDS

IBPC 2018, building and urban physics, multiscale modelling, building energy demand, pore scale modelling

THE BROAD VIEW: URBAN CLIMATE AND CLIMATE CHANGE

There is growing evidence that heat waves are becoming more frequent under increased greenhouse forcing (e.g. Seneviratne et al. 2012, Hartmann et al. 2013, Schleussner et al. 2017). Climate simulations project an increase of the number and intensity of heatwaves and hot extremes in many regions in the world (Sillmann et al. 2013, Fischer et al. 2014) even for moderate scenarios of global warming of 1.5°C or 2°C (Seneviratne et al. 2016, Wartenburger et al. 2017, Dosio et al. 2018). In future, heat waves associated with higher daytime temperatures and reduced nighttime cooling might exceed the limits of thermoregulation of the human body and affect dramatically human health. Switzerland experienced important heat waves during the 2003 and 2015 summers, which were the two warmest summers over more than 150 years. For these summers, an excess mortality of 6.9% and 5.9% respectively

was estimated corresponding to 975 and 804 extra deaths for these years, see Figure 1a (Vicedo-Cabrera et al. 2016).

Urban areas are especially affected, since these regions, in addition, experience an urban heat island (UHI) effect characterized by higher air temperatures compared to the surrounding rural environment (Oke 1987, Moonen et al 2012b). Urban heat islands in cities have been reported for more than 400 cities around the world (Santamouris and Kolokotas 2016). The magnitude of UHI is found to vary from place to place with urban heat island intensities up to 6 - 7°C (Santamouris and Kolokotsa, 2016). For Zurich, we found an urban heat island intensity of around 4.5 degrees during the heat wave of 2015 (see Figure 1b-c, Mussetti et al. 2016). Li and Bou-Zeid (2013) showed that the combined effect of UHI and heat waves is larger than the sum of the two individual effects.

The UHI leads not only to a reduction of urban thermal comfort, but also to an increase in building energy demand, especially in space cooling demand during warm periods. Due to local and global climate change and growth of world's population and economic, the world global space cooling demand for buildings is expected to strongly increase in future. In 2010 the global cooling consumption of the residential sector represented 4.4 % of the total space conditioning of buildings. This number is expected to increase to 35 % in 2050 and 61% in 2100 (Santamouris 2016, Isaac and van Vuuren 2009). Not only the annual but also the peak cooling demands will strongly increase. This means that also the power capacity for cooling, and thus electricity, may have to be strongly increased to satisfy future peak energy needs (Santamouris 2016). Santamouris (2016) proposed three main actions to face the problem with the increase in cooling demands: (1) mitigation of the global and local climate change, (2) adaptation of the building sector and improvement of its energy performance and (3) improvement of mechanical air conditioning and alternative cooling technologies.

In addition to the global UHI effect, heat waves are accompanied with local hot spots in cities, called local heat islands (LHI), see Figure 1d (Allegrini and Carmeliet, 2016). Certain city quarters or zones between individual buildings may show much higher air temperatures compared to neighboring urban areas, due to lower wind speeds by wind sheltering leading to less removal of heat. On the other hand, at low wind speeds, higher urban surface temperatures due to solar radiation may lead to more buoyancy enhancing heat removal. As a result, the origin of LHIs is a complex phenomenon depending on a set of parameters such as lack of urban ventilation, lack of vegetation, densification and urban morphology.

The continuing spread of urban areas and the growing fraction of people living in cities direct nowadays a particular spotlight on urban climate and urban heat islands, and the corresponding effects on thermal comfort and heat stress during heat waves. As a result, many research teams worldwide aim at formulating adequate measures to adapt to and/or mitigate these threats, but most approaches remain fragmented focusing on specific scales or topics of the urban climate.

A necessary breakthrough is a shift away from a fragmented approach towards an integrated multiscale urban climate analysis. This type of urban climate research is a rather new domain of research and might be based on an all-physics understanding and modeling of the urban climate ranging from the scales of material and buildings, to the scales of a group of several buildings, street canyons, neighbourhoods, cities and urban regions. The final aim is to propose adequate urban adaptation measures for climate change (CC) at regional scale in view of different CC scenarios and to develop adequate UHI mitigation measures. Such an approach for urban heat island mitigation allows communities to identify spots of local heat islands, reduced urban comfort and increased health risks, to pinpoint the causes for the appearance of local urban heat islands, and to propose possible mitigation measures using high-resolution urban mapping techniques.

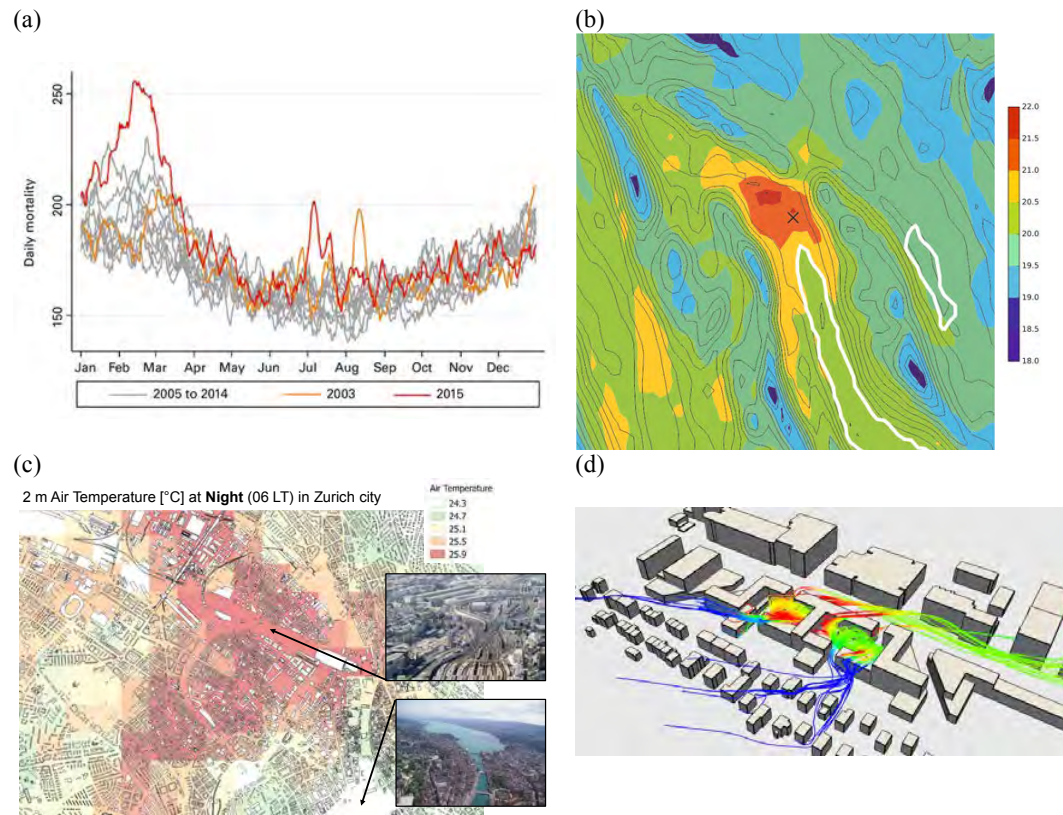


Figure 1. (a) All-cause daily mortality (number of deaths) in Switzerland in 2003, from 2005 to 2014 and in 2015. Two prominent mortality peaks in the summer months, July 2015 and August 2003. (b) Global heat island in Zurich during the heat wave of 2013: map of air temperatures at 2 m height at 12 pm averaged over 5 consecutive days. (c) Urban mapping of air temperatures at 2 m height at 6 am in city of Zürich showing higher air temperatures during the night. (d) Local climate at a neighborhood in Zurich determined with coupled Building Energy - CFD simulations. Selected streamlines where colours indicate local temperature increase due to new buildings (Allegrini and Carmeliet 2016).

WHY MULTISCALE BUILDING PHYSICS ? WHICH SCALES TO CONSIDER?

Traditional building physics focusses on the scales of materials towards building components and buildings systems, and finally whole buildings. The aim of building physics is assuring a correct indoor comfort with minimal building energy consumption, while guaranteeing a correct hygrothermal and acoustic performance, maintenance and durability. Urban physics focusses on physical processes from the scales of urban materials, to the scales of a group several buildings, street canyons, neighbourhoods and total cities. Urban physics can be seen as a complement to building physics, filling the missing link between studies at meteorological and climate scales and building physics. There is nowadays not only a high need of integrating urban and building physics, but also to develop a new discipline, called multiscale building physics. The challenge for multiscale building physics is not only to broaden its field over different scales from material to city scale, but also to link up with other fields. From one side urban climate scientists and planners generally consider only UHI mitigation measures to limit the negative impact of local heat islands. Climate model scientists on the other hand mainly focus on the effects of greenhouse gas mitigation to limit the climate change impact globally. A necessary breakthrough consists in the combination of regional climate modeling combining the effects of greenhouse gas forcing on larger scales with the assessment of UHI mitigation measures on smaller scales for local heat islands during heat waves, and the analysis of their interaction. Such a global approach allows the

formulation of more general UHI mitigation measures integrating the use of materials, energy and water on different scales, which can be considered in climate change projections and climate change adaptation.

Scales in urban climate analysis

To adequately cover global and local urban heat island effects, regional and mesoscale climate analyses have to be downscaled to sub-kilometer resolution and linked with urban climate models at neighborhood and street canyon scales. The scales to be considered are represented in Figure 2. We start from global climate models and scale them down to the European (~25 km resolution) and further to the regional scale (entire Switzerland and a portion of central Europe at 1-2 km resolution) using a regional/mesoscale climate model. The regional climate model is further downscaled for selected cities to resolve small-scale thermal circulations and intra-urban variability at sub-kilometer resolution (~200 m). At the urban level, we consider city, neighborhood and street canyon scales.

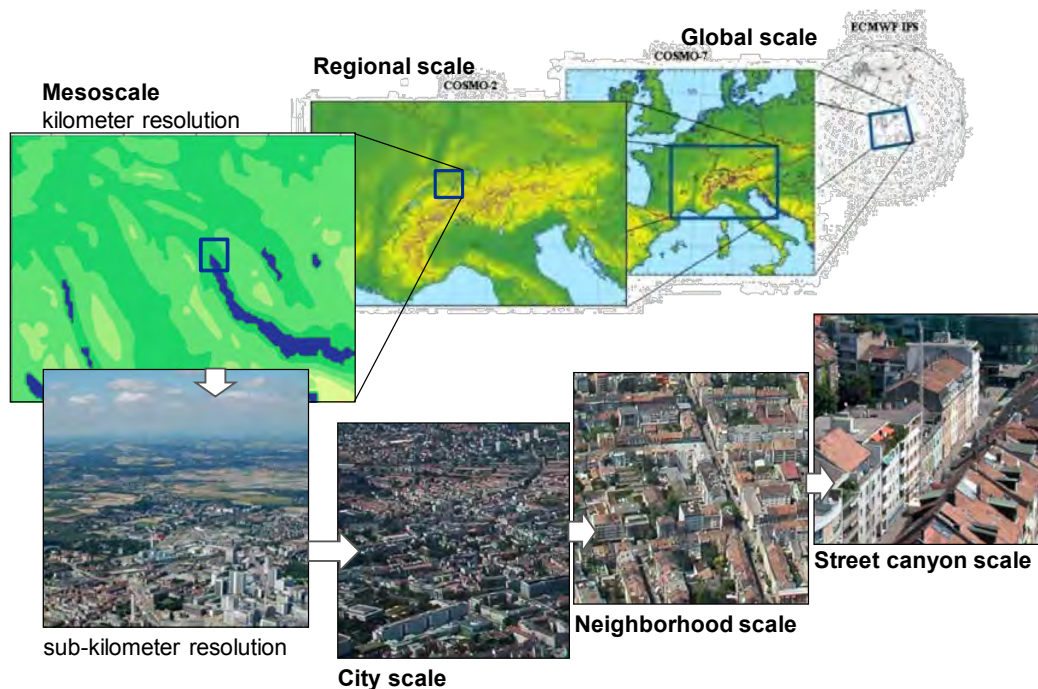


Figure 2. Different scales in urban climate modelling and multiscale building physics (photos from Christen 2005).

MULTISCALE MODELING?

Regional and urban climate interactions

Urban surfaces interact with mesoscale meteorology and climate in several different ways (Roth 2000; Masson 2006; Martilli 2007). Their roughness exerts enhanced drag on the flow and they alter the surface energy balance by trapping radiation, storing heat in urban materials, changing the ratio between sensible and latent heat fluxes, and releasing additional heat due to human activities. These interactions motivated the development of urban canopy parameterizations in atmospheric models enabling a better representation of the mesoscale forcing of urban weather and climate. These models describe the sub-grid scale effects of buildings and urban surfaces on the flow and on surface heat exchange in a parameterized fashion, for example by representing buildings within a grid cell as a statistical ensemble of

street canyons of different orientations and dimensions and calculating radiative transfer (including multiple reflections between surfaces) and energy and water vapor exchange between atmosphere and building and street surfaces in each canyon separately.

As an example, the urban heat island effect in Zurich was simulated with the climate version of COSMO in order to capture the local atmospheric circulation influenced by the orography and the presence of Lake Zurich, see Figures 1b-c (Mussetti et al. 2016). The model has currently been extended with the representation of street trees and a detailed representation of short- and long-wave radiation in the street canyons by ray tracing.

From urban to building scale: building-resolved analysis

At city scale, a CFD based urban climate model is used which, in contrast to mesoscale models, also resolves the physical phenomena at street canyon scale. These models take into account accurately the building and street geometry, where buildings are geometrically resolved in computational fluid dynamics (CFD) (figure 3a). They also take into account the used urban materials, particular weather conditions (wind, sunshine, rain, temperature, relative humidity), shadowing, as well as the local urban water cycle.

The influence of higher scales such as the global urban heat island are modeled via appropriate boundary conditions (wind velocity and orientation, surface temperatures) from simulations at sub-kilometer resolution using a nesting approach (Vonlanthen et al. 2017). In order to solve the mismatch between different scales and physics involved in the two models, we apply a blending layer. Transpirative cooling and shadowing effects from trees as well as the evaporative cooling effects of water bodies or absorbed water (by rain or spraying) can be considered. Figure 3b gives an example of the air temperatures at 3 m height in downtown Zurich during a heat wave day.

These models at city scale are further downscaled to neighborhood and street canyon scales for selected parts of a city. At this scale, an all-physics model is used considering solar and longwave radiation, three-dimensional turbulent wind flow and buoyancy, temperature and relative humidity in the air domain and heat and moisture transport in the porous domains of urban surfaces (see Figure 3c, Kubilay et al. 2016). The surface temperatures are determined by a thermal balance of solar and longwave radiation, convective heat transport at surfaces, heat conduction and storage of heat in the building materials and soil, and evaporative cooling effects. The urban climate model is extended with vegetation using a porous media approach with sink and source terms for moisture and heat to model the transpiration and the related transpirative cooling effect. The vegetation model includes moisture transport within the soil/roots, tree, stem, branches and leaves, allowing the consideration of the complete water cycle at street canyon scale between air, soil and tree. A multiphase Eulerian model for wind driven rain has been developed and validated in order to accurately determine the wetting of the building surfaces and soil, see Figure 3d (Kubilay et al. 2013). The wind driven rain model is able to predict the rain load and wetting of all urban surfaces including roofs, facades, pavements, streets, soils and other surfaces. The porous heat-moisture transport model allows the determination of the heat and moisture transport and storage in these materials. When evaporation occurs, evaporative cooling is considered.

The urban climate model is further integrated with an urban water cycle model including rain and drainage systems at city scale in order to explore the potential of using urban water resources locally for UHI mitigation, especially during heat waves. This enables the assessment of when stormwater can be used to reduce the local heat island effects via evaporative cooling. A thorough analysis on stormwater availability and storage potential in cities can then be performed. This provides answers to questions such as: Is the stormwater volume sufficient and available when required to mitigate urban heat island effects? How does

dedicated stormwater storage solutions compare with other existing urban water infrastructure in terms of city infrastructure retrofitting possibilities and costs?

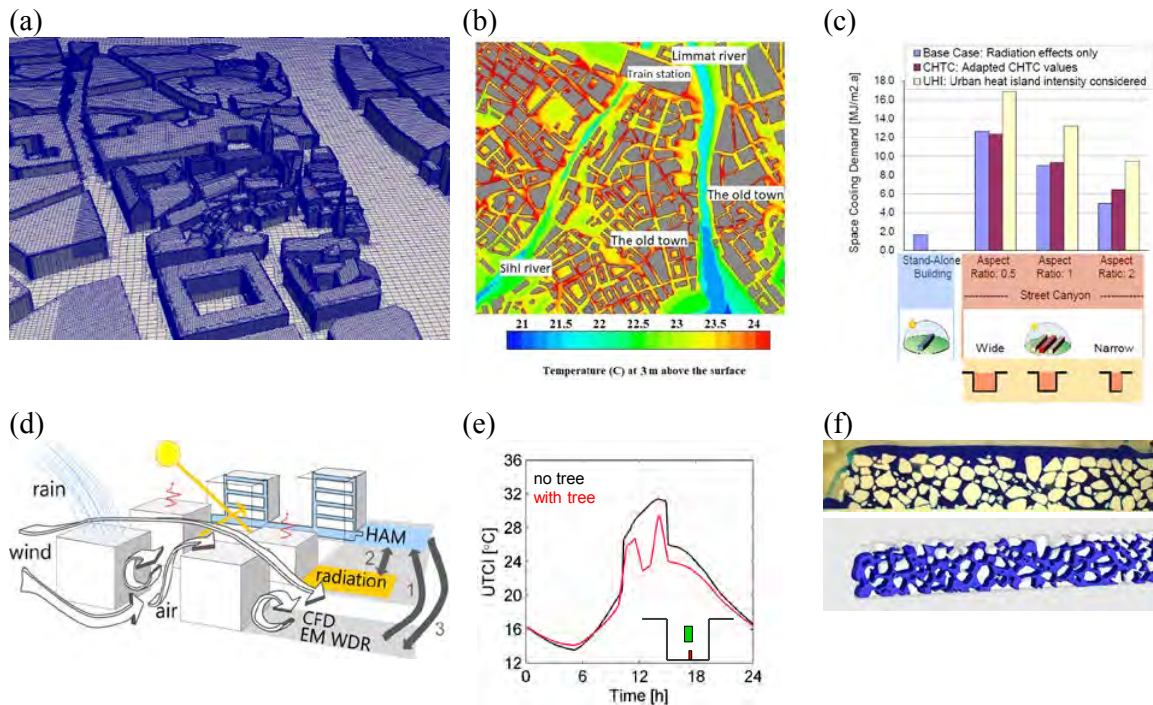


Figure 3. (a) CFD mesh for the old city of Zurich. The area of interest is represented with more geometric details (roofs), while the surrounding neighborhood is represented by simplified building blocks. (b) Air temperature at 3 m height in downtown Zurich during heat wave day June 23 2015 at 2 pm. (c) Annual space cooling demands for different building configurations and using different modelling approaches (Allegrini 2012). (d) All-physics approach of local urban climate model. The momentum, heat and moisture transport in the air domain is solved using computational fluid dynamics (CFD). Wind driven rain is modelled using an Eulerian Multiphase method. Results from the CFD simulation are exchanged with a model for heat and moisture transport (HAM) in urban materials like facades, roofs, pavements and soils. A radiation model solves for the solar radiation, shadowing and thermal radiation between the different surfaces and the environment. (e) Universal Thermal Climate Index (UTCI) for a person (red box) standing below a tree (green box) showing the positive effect of a tree mainly through shadowing on the thermal comfort. (f) top: Liquid distribution in micro-fluid device representing porous asphalt during drainage. bottom: PM-LBM simulation of drainage in porous asphalt (Son et al. 2016).

The urban climate model allows to analyze the influence of urban parameters on thermal comfort by determining the variables at a certain location in the street canyon, such as air temperature, air speed, radiant temperature and relative humidity. These variables are used to determine thermal comfort/heat stress using a common thermal comfort indicator, such as the UTCI (Universal Thermal Climate Index, Bröde et al., 2018). As an example we show the influence of a tree on the UTCI for a person (red box) standing below a tree (green box), showing the positive effect of a tree mainly through shadowing on the thermal comfort.

COUPLING URBAN CLIMATE AND BUILDING ENERGY

It is clear that space cooling demands of buildings in urban environments exposed to climate change and heat waves will increase in future due to hotter urban climates.

To propose new building designs and/or building energy systems and to adapt existing buildings to future urban climates, the impact of the local urban climate on the space cooling

demands of buildings has to be better understood. At the moment, no full scale studies where models for the different scales of the urban climate are coupled to accurately simulate the local urban climate for building energy simulations taking into account all interactions between the scales, exist. There is a strong need for a better understanding and quantification of the impact of local urban climate, its modification due to climate change as well as possible urban mitigation measures on the cooling demand of buildings in cities. Such knowledge will allow proposing new solutions to improve the energy performance of buildings taking into account their local urban climate.

Most of the building energy simulation models, which are used to predict energy demands of buildings, were originally developed for stand-alone buildings (Hensen 2011). For buildings in urban environments, the space cooling demand is strongly influenced by the local urban climate (Figure 3e) and can be quite different to buildings in rural areas (Allegrini et al. 2012a). The short and longwave radiation exchange between buildings in dense urban areas has a strong impact on the building performance (Allegrini et al. 2012a, Allegrini et al. 2016). The shortwave radiation entering the street canyons is entrapped between the buildings due to multiple reflections between the buildings. Additionally sunlit surfaces exchange hot and radiate longwave radiation with non-sunlit surfaces and heat them up. These increased surface temperatures have a direct impact on the energy performance of the buildings and on the local air temperatures. Another important impact is the increased local air temperatures due to the urban heat island effect. The lowest impact comes from the convective heat transfer coefficients. This study showed clearly the importance of accounting for the local urban climate when quantifying the space cooling demands of buildings in an urban environment.

DOWN TO MATERIAL SCALE

The multiscale urban climate model can be used to understand the impact of different urban parameters on the local heat island effect and to propose adequate mitigation measures. Especially one can study the impact of (1) radiation properties of building surfaces (albedo value), (2) the heat-moisture transport and capacity properties of building materials, (3) the presence of vegetation such as green roofs and facades, (4) the role of impervious versus porous substrates (different pavements and sublayers, different soils, cover ratio), (5) the presence of urban shadowing devices, (6) the role of active evaporative cooling by water spraying during heat waves of collected urban water.

The heat-moisture transport model allows the design of new building materials, which can help in the mitigation of local heat islands. With respect to evaporative cooling materials, we need to optimize their water retention tailoring their pore structure. This requires the use of pore-scale simulation of two-phase flow in porous media and an upscaling using pore-network models for the determination of the macroscopic fluid transport properties

As an example, we recently showed that hydrophobic macro-porous materials, such as porous asphalt with pore sizes ranging from micron to millimeter size, can retain water in their pore structure for long time after wetting by rain or artificial wetting (spraying), as such opening potentials for new evaporative cooling materials (Lal 2016). To study the two-phase flow in such complex materials, we developed a pseudopotential multiphase lattice Boltzmann model (PM-LBM). The use of LBM was motivated by the need for the explicit tracking of the liquid-vapor interface during gravity-driven drainage in macro-porous asphalt as well as the drying process. The PM-LBM was validated with micro-fluidic measurements, where liquid distributions were monitored by high speed camera on quasi-2D transparent micro-fluidic devices, where the porous structure was printed by additive manufacturing (Figure 3e-f) (Son 2016). To predict the unsaturated permeability of building materials, pore-network modeling

- Environment 61: 69-81.
- Kubilay A, Derome D, Carmeliet J. 2016. Urban microclimate model using a coupled approach for CFD, radiation, wind-driven rain and transport in building materials. 4th International Conference on Countermeasures to Urban Heat Island, 30-31 May and 1 June 2016, Singapore.
- Lal S. (2016) Multiscale investigation and numerical modelling of imbibition, drainage and drying of macroporous medium, PhD thesis ETH Zurich No. 23628.
- Li D, Bou-Zeid E. Synergistic interactions between urban heat islands and heat waves: the impact in cities is larger than the sum of its parts. *Journal Applied Meteorology and Climatology* 52 (9), 2051–2064, 2013.
- Martilli A (2007) Current research and future challenges in urban mesoscale modeling, *Int. J. of Climatology* 27: 1909-1918, doi:10.1002/joc.1620.
- Masson V (2006) Urban surface modeling and the meso-scale impact of cities, *Theor. Appl. Climatol.* 84: 35–45, doi:10.1007/s00704-005-0142-3.
- Moonen P, Defraeye T, Dorer V, Blocken B, Carmeliet J. 2012b. Urban Physics: Effect of the micro-climate on comfort, health and energy demand. *Frontiers of Architectural Research* 1 (3): 197-228.
- Mussetti G, Brunner D, Henne S, Allegrini J, Wouters H, Schubert S, Carmeliet J. 2016. Impact of model resolution and urban parameterization on urban climate simulation: a case study for Zürich. COSMO/CLM/ART User Seminar 2016. 7-9 March 2016, Offenbach.
- Oke T R, *Boundary Layer Climates*, 2nd ed., Methuen, London, 1987.
- Roth M (2000) Review of atmospheric turbulence over cities. *Quart J Roy Meteor Soc* 126: 941–990.
- Santamouris M; Kolokotsa D, 2016, 'Passive cooling of buildings: Present and future needs: Recent progress on passive cooling convective technologies', in *Advanced Environmental Wind Engineering*, pp. 75 - 88, 10.1007/978-4-431-55912-2_4.
- Santamouris M. Cooling the buildings – past, present and future. *Energy and Buildings* 128, 617-638, 2016.
- Schleussner, C.F., P. Pfleiderer, and E.M. Fischer, 2017: In the observational record half a degree matters. *Nature Climate Change*, 7, 460-462.
- Seneviratne, S.I., N. Nicholls, D. Easterling, C.M. Goodess, S. Kanae, J. Kossin, Y. Luo, J. Marengo, K. McInnes, M. Rahimi, M. Reichstein, A. Sorteberg, C. Vera, and X. Zhang, 2012: Changes in climate extremes and their impacts on the natural physical environment. In: *Managing the Risks of Extreme Events and Disasters to Advance Climate Change Adaptation* [Field, C.B., V. Barros, T.F. Stocker, D. Qin, D.J. Dokken, K.L. Ebi, M.D. Mastrandrea, K.J. Mach, G.-K. Plattner, S.K. Allen, M. Tignor, and P.M. Midgley (eds.)]. A Special Report of Working Groups I and II of the Intergovernmental Panel on Climate Change, pp. 109-230.
- Seneviratne, S.I., M. Donat, A.J. Pitman, R. Knutti, and R.L. Wilby, 2016: Allowable CO₂ emissions based on regional and impact-related climate targets. *Nature*, 529, 477-483, doi:10.1038/nature16542.
- Sillmann, J., V.V. Kharin, F. W. Zwiers, X. Zhang, and D. Bronaugh (2013), Climate extremes indices in the CMIP5 multimodel ensemble: Part 2. Future climate projections, *J. Geophys. Res. Atmos.*, 118, 2473–2493, doi:10.1002/jgrd.50188.
- Son S (2016) Lattice Boltzmann modeling of two-phase flow in macroporous media with application to porous asphalt, PhD thesis ETH Zurich No. 23627.
- Vandersteen K, Carmeliet J, Feyen J. (2003) A network approach to derive unsaturated hydraulic properties of a rough-walled fracture. *Transport in Porous Media* 50(3): 197-221.
- Vicedo-Cabrera AM, Ragettli MS, Schindler C, Rössli M (2016), Excess mortality during the warm summer of 2015 in Switzerland, *Swiss Med Wkly.* 2016;146:w14379.

- Vonlanthen M., Allegrini J., Carmeliet J. (2017) Multiscale interaction between a cluster of buildings and the ABL de-veloping over a real terrain, *Urban Climate*, 20:1-19.
- Wartenburger, R., Hirschi, M., Donat, M.G., Greve, P., Pitman, A.J. and Seneviratne, S.I., 2017: Changes in regional climate extremes as a function of global mean temperature: an interactive plotting framework. *Geosci. Model Dev.*, 10, 3609–3634, <https://doi.org/10.5194/gmd-10-3609-2017>.

The Physics in Natural Ventilation of Cities and Buildings

Yuguo Li

Department of Mechanical Engineering, The University of Hong Kong, Hong Kong SAR, China

Corresponding email: liyg@hku.hk

EXTENDED SUMMARY

Asian cities are mostly taller, denser, deeper and larger than those in the West, and the magnitudes of building drag or urban heat island circulation and their effects on city ventilation are also stronger. The physics of urban climate in these large cities is complex, as a combined result of local circulation and synoptic winds modified by the mountainous topography and land/sea breeze, if any. Natural ventilation of a city refers to the penetration and distribution of rural air into an urban canopy layer. The weakened city ventilation has become one major reason for worsening urban warming and air pollution in cities. Two distinct situations need to be considered, i.e. when the synoptic wind is strong; and when the synoptic wind is weak respectively. For the former, designers are interested to manage city ventilation for removal of the urban heat, moisture and pollutant, or retain of urban heat and moisture. The latter become mostly the conditions for the worst urban extreme heat or haze scenarios to occur. Natural ventilation of a building refers to the introduction of outdoor air into a building by natural forces such as wind and buoyancy. High-rise buildings present an interesting challenge as the top of the building may be in the urban roughness layer or even beyond the atmosphere boundary layer.

Many excellent review papers exist on relevant urban airflows (e.g. Roth, 2000, Britter and Hanna 2003, Arnfield, 2003, Belcher 2005), but not specifically on city ventilation. City ventilation is mainly driven by winds and buoyancy forces such as slope flows, sea-land breezes, etc. The importance of city ventilation may be seen by long recognition that the restricted air flows were the causes of the all major pollution disasters (Brimblecombe and Sturges, 2009). Rigby et al (2006) presented a rose analysis showing the influence of boundary layer ventilation. The wind speed in London is often found to be lower than in a rural area, whilst occasionally accelerated due to urban heat island effects (Lee, 1979).

The purpose here is to review the status of our understanding of the physics in city ventilation under both strong and weak wind conditions. It is known that understanding the urban air flows in calm wind conditions is crucial, as most urban heat wave and severe air pollution episodes occur when wind calmness and inversion coexist, leading to formation of a heat dome or urban heat island circulation. Heat dome comprises a convergent inflow at the lower atmospheric level, divergent outflow at the upper, and a dome-shaped flow field resulting from entrainment and overshoot at the top. Numerous field studies worldwide have confirmed the existence of UHIC during the day and night in many cities. It is interesting that though a strong wind would destroy the heat dome and breakup the inversion, a weak wind may only elongate the dome to become a plume or dome shadow, transport the pollutant downstream to other cities. How such a weak wind impact on the dome formation has not been well studied.

Examples given here including wind weakening phenomenon in a dense high-rise city (Peng et al. 2018), the roles of heat dome formation on urban extreme high temperature events,

spread of SARS CoV virus when there is inversion, and the urban heat domes (Fan et al 2017) and their merging (Fan et al 2018). Different methods are available for investigation, i.e. simple theoretical estimates (Fan et al 2017), water tank models (Fan et al 2016), city scale CFD (Wang and Li, 2016), and meso-scale WRF (Wang et al 2017).

It is concluded that there is a need to establish the need and an approach for designing city climate and environment as for buildings, for example, designing building density and height in a city for better urban climate, and between-city distance needed to avoid regional haze formation.

KEYWORDS

Natural ventilation, city ventilation, fluid mechanics, heatwave, heat dome, urban climate

ACKNOWLEDGEMENT

I thank Hong Kong RGC (HKU9/CRF/12G, E-HKU702/17, and 17201817) and NSFC of China (51778555) for financial support of our studies, and to all students (see co-authors) and collaborators for their contribution (Adrian Bejan, PW Chan, Julian Hunt, Jiaping Liu, Borong Lin, Sylvana di Sabatino, Yi Wang and Charles Wong).

REFERENCES

- Arnfield A.J. 2003. Two decades of urban climate research: a review of turbulence, exchanges of energy and water, and the urban heat island. *International Journal of Climatology*, 23(1), 1-26.
- Belcher S.E. 2005. Mixing and transport in urban areas. *Philosophical Transactions of the Royal Society A*, 363, 2947-2968.
- Brimblecombe P., Sturges K. 2009. History of atmospheric environment. *Atmospheric Environment*, 43, 2-8.
- Britter R.E., Hanna S.R. 2003. Flow and dispersion in urban areas. *Annual Review of Fluid Mechanics*, 35, 469-496.
- Fan Y., Li Y., & Yin S. 2018. Interaction of multiple urban heat island circulations under idealised settings. *Building and Environment*, 134, 10-20.
- Fan Y., Li Y., Bejan A., Wang Y. and Yang X. 2017. Horizontal extent of the urban heat dome flow. *Scientific Reports* 7, Article number: 11681
- Fan Y., Li Y., Wang X. and Catalano F. 2016. A new convective velocity scale for studying diurnal urban heat island circulation. *Journal of Applied Meteorology and Climatology*, 55, 2151-2164.
- Lee D.O. 1979. Influence of atmospheric stability and the urban heat island on urban-rural wind speed differences, *Atmospheric Environment*, 13(8), 1175-1180.
- Peng L., Liu J.-P., Wang Y., Chan P.-W. et al 2018. Wind weakening in a dense high-rise city due to over nearly five decades of urbanization. *Building and Environment*, 138, 207-220.
- Rigby M., Timmis R., Toumi R. 2006. Similarities of boundary layer ventilation and particulate matter roses. *Atmospheric Environment*, 40 (27), 5112-5124.
- Roth M. 2000. Review of atmospheric turbulence over cities. *Quarterly Journal of the Royal Meteorological Society*, 126, 941-990.
- Wang X. and Li Y. 2016. Predicting urban heat island circulation using CFD. *Building and Environment*, 99, 82-97.
- Wang Y., Di Sabatino S., Martilli A., Li Y., Wong M.S., Gutierrez E. and Chan P.W. 2017. Impact of land surface heterogeneity on urban heat island circulation and sea-land breeze circulation in Hong Kong. *Journal of Geophysical Research Atmosphere*, 122(8), 4332-4352.

A state-space based method to predict thermal performance of pipe-embedded double skin façade: case study in Guangzhou

Shuai Yan, Weihua Lv, Chong Shen and Xianting Li*

Department of Building Science, Tsinghua University, Beijing, China 100084

*Corresponding email: xtingli@tsinghua.edu.cn

ABSTRACT

Pipe-embedded double skin facade, which arranges pipes in shading device, is an alternative to reduce indoor demand and save energy. To simulate annual performance of this system, a simplified approach based on optical and thermal property is proposed at first, in which dynamic performance is acquired through state-space method. Then the model is validated with former investigation and shows good accuracy. Indoor room temperature with the pipe-embedded double skin façade is analyzed under different types of room in Guangzhou at last. Results show that the pipe-embedded double skin façade could guarantee a barely satisfactory indoor environment where indoor heat gain is small in most time. Besides, superiority would be obvious when solar radiation is strong, indicating the applicability in some typical region with abundant sunshine.

KEYWORDS

natural energy, pipe-embedded window, double skin facade, heat gain, free-running temperature

NOMENCLATURE

DSF	double skin façade
PDSF	pipe-embedded double skin façade
CFD	computational fluid dynamics
LMTD	logarithmic mean temperature difference

INTRODUCTION

Glass curtain has been widely applied in recent years. Nevertheless, heat transfer through transparent envelope is significant, which would lead to the increase heating and cooling load in building. To be specific, large amount of solar radiation transmitted directly into the room in summer while the heat dissipated through glass is remarkable in winter owing to its poor thermal insulation. Many researches concentrated on the thermal performance improvement of glass envelope consists: 1) substitution of high thermal performance glazing such as triple glazing (Manz et al., 2006), 2) development of high-efficiency shading devices (Cheng et al., 2013), 3) double skin façade (DSF) with ventilation. Better glazing aims to reduce heat dissipation in winter however better shading aims to decrease solar transmittance in summer, in other words, both the first and second approach is not designed for annual performance. By contrast, double skin façade could be of benefit for both heating and cooling.

Traditional DSF combined with ventilation is made up of the external glass, shading device and internal glass. Researches shows that the outlet air temperature could reach up to 50°C when solar radiation is strong, that is, conventional double skin façade combined with ventilation can't remove heat absorbed by venetian blinds efficiently in some cases. Thus, Shen and Li (2016) proposed the idea to arrange pipes in the shading device and simulated the performance by CFD method. Results shows that inner surface temperature can be reduced dramatically compared with traditional DSF, benefitting not only energy consumption but also thermal comfort.

Hourly indoor temperature prediction plays an important role in thermal comfort and

energy saving. It is difficult to get the hourly indoor temperature in the whole year by CFD method due to its complication and time-consuming character. Therefore, a state-space method based on optical and thermal property is proposed to calculate the hourly indoor temperature at first. Then thermal performance of pipe-embedded double skin façade(PDSF) in Guangzhou under two different types of room is analyzed.

METHODOLOGY

Description of PDSF

The detailed structure together with schematic diagram of the PDSF are shown in Figure 1. Compared with traditional DSF, cooling pipes are embedded into the shading device for the case of PDSF. Water flows inside pipes to take away the heat absorbed. On one hand, heat transfer coefficient of water to blinds is much larger than air to blinds, so PDSF would remove the radiation more efficiently. On the other hand, natural cooling source such as direct evaporative cooling, ground source heat exchanger is feasible and of low-cost according to the climate feature.

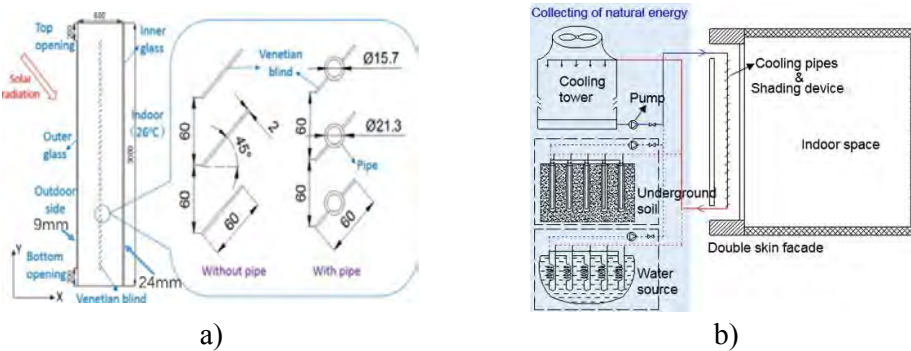


Figure1. description of PDSF system. a)structure, b) schematic diagram.

Solar radiation distribution

The dynamic optical properties of glazing should be calculated at first, then the overall optical character of DSF could be obtained including reflection, transmission and absorption. Solar radiation consists of two parts, namely direct fraction and diffuse fraction, whose optical character should be calculated separately (Wang et al.,2016)

$$\alpha_{eg}^{dir} + \alpha_{bl}^{dir} + \alpha_{ig}^{dir} + \rho^{dir} + \tau^{dir} = 1 \quad (1)$$

$$\alpha_{eg}^{dif} + \alpha_{bl}^{dif} + \alpha_{ig}^{dif} + \rho^{dif} + \tau^{dif} = 1 \quad (2)$$

where α , ρ and τ represents absorptivity, reflectivity and transmittance respectively; subscript eg , bl , ig represents external glass, blind and internal glass; super-script dir , dif represents direct radiation and diffuse radiation.

Optical property of diffuse fraction equals to that of direct radiation whose incidence angle is 60 degrees. Thus solar distribution in each layer is acquired, which is the fundamental to thermal performance calculation.

Energy balance equation

Thermal stratification in the cavity is neglected according to the CFD results (Shen and Li, 2016). Since heat transfer coefficient of water side is much larger than air side, we make the assumption that blind temperature is 0.5°C higher than water temperature, which corresponds to our previous study (Shen and Li, 2016). Thus, surface temperature can be calculated based on thermal network, as shown in Figure.2.

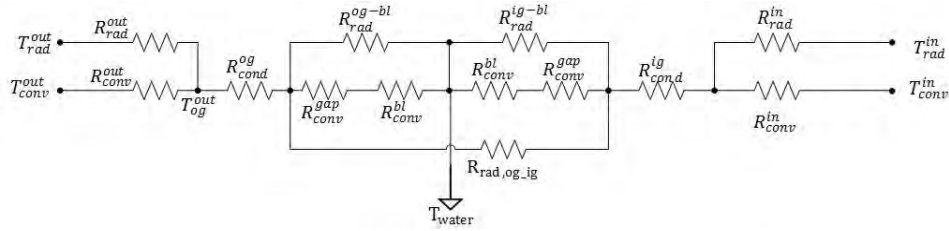


Figure 2. Thermal network of PDSF

where R represents thermal resistance ($m^2 \cdot K/W$); subscript conv, cond and rad indicates convective, conductive and radiative heat transfer respectively.

LMTD model (Utamura et al., 2008) is utilized to simulate the inlet and outlet water temperature difference.

Dynamic simulation based on state-space method

State space method, where space is discretized while time is continuous, was widely used (Parker and Bowman, 2012) and adopted in this study. Compared with conventional window, thermal performance of PDSF is related with not only meteorological parameter but also water temperature. That is, temperature of PDSF and other node temperature of room should be solved through two matrices below respectively.

$$M \overrightarrow{T_{glass}} = \vec{b} \tag{3}$$

where T_{glass} is node temperature of glass, M is the matrix based on thermal network, b is a vector related to climate data.

$$C \dot{\vec{T}} = A \vec{T} + B \vec{u} \tag{4}$$

where T is node temperature, C represents heat capacity, A is a matrix related to heat transfer between different node, u is a vector of thermal disturbance and B is its' distribution on each node.

By the thermal network in figure 2, there are only four nodes in state-space method, thus it is easier to describe the thermal character than conventional CFD approach.

Verification with CFD results

Total indoor cooling load simulated by this state-space based method in five typical cities were verified with that by CFD method (Shen and Li, 2016). Standard κ - ϵ turbulence model and DO radiation model were adopted in the CFD simulation. Results show that the simplified method can achieve the accuracy within 15 percent in all cases. The detailed information can be seen from Figure. 3. Nevertheless, computing time can be reduced from 2 days to 1 hour for each simulation.

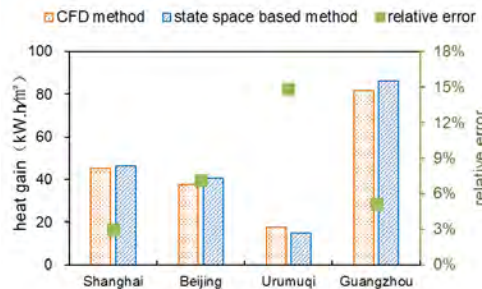


Figure 3. Validation with CFD results

CASE STUDY IN GUANGZHOU

Description of case setup

A typical room in Guangzhou which belongs to hot summer and warm winter zone was selected to investigate thermal improvement by PDSF. Hourly outdoor climate parameter including solar radiation, dry bulb temperature etc. can be obtained from China climate database and it is shown in Figure. 4. The dimension of the room is 5.0 m (length) \times 5.0 m (width) \times 3 m (height). All of the building envelope was designed according to the design standard GB 50189-2015. A PDSF, whose size is 5.0 m (length) \times 3.0 m (height), is installed at south orientation. This room locates in middle floor and the east wall is the external wall. Heat transfer through other internal structure is neglected. Thermal and optical properties of the pipe-embedded double skin façade is described as Table 1.

Table 1. Thermal properties of the PDSF

	External glass	Venetian blinds	Internal glass
Material	stalinite	aluminum	Double glazing
Thickness(mm)	9	2	6+12(air)+6
Heat conductivity Coefficient(W/(m·k))	0.28	180	0.09
Density (kg/m ³)	2200	2700	1000
Specific heat (J/kg·K)	840	100	880
Refractive index	1.4	/	1.4
Absorptivity(1/m)	5	/	20
Transmissivity	/	0.1	/

Two types of room, namely office room and residential room, in which indoor heat gain are different, are adopted in this study for the applicability discussion. Detailed information of these two rooms is listed in Table 2.

Table 2. Indoor heat gain and occupancy of office and residential room

	Office room		Residential room	
	Power(W/m ²)	Occupancy(hour)	Power(W/m ²)	Occu-
Occupant	8		3	All-time
Equip-	18	7:00-19:00	5	7:00-22:00
Lighting	8		3	18:00-22:00

Cooling water produced by cooling tower is analysed in this study. The temperature of cooling water is assumed to be considered 3°C higher than wet bulb temperature(Klimanek et al., 2015).

In this study, a triple glazing DSF whose external and internal glass are the same as pipe-embedded DSF was simulated as baseline.

Outdoor climate is described as figure 4. The average outdoor temperature hit the peak at July while solar radiation hit the peak at November.

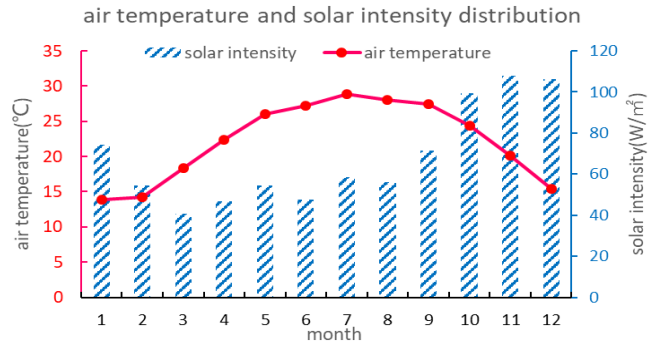


Figure 4. Monthly average outdoor temperature and solar radiation of Guangzhou

Performance of decreasing average indoor temperature

Cooling water provided by water pipes can decrease external glass temperature as well as block solar radiation, therefore room temperature can be reduced. Since heating is not required in Guangzhou, the PDSF is operated all-year around.

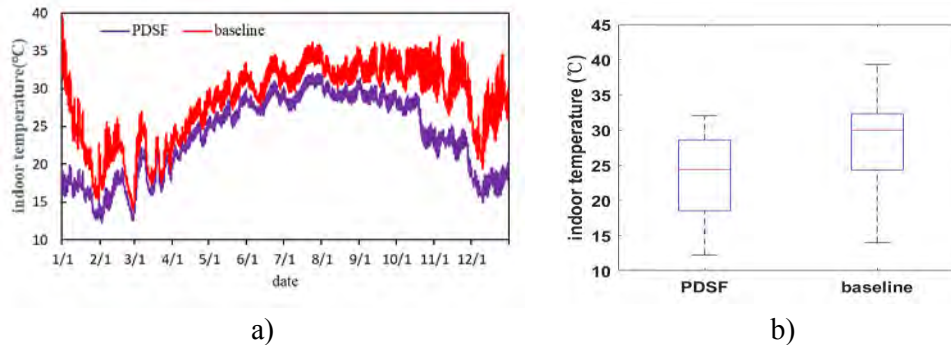


Figure 5. results of residential room. a) hourly indoor temperature, b) distribution

With built-in pipes in venetian blinds, room temperature can be decreased about 5°C for both office and residential room. Although with pipe-embedded, room temperature would still exceed 30°C in office for some time due to large indoor heat gain.

Superiority of PDSF is significant in spring and autumn when solar radiation is the strong while outdoor air temperature is not so high. What's more, average indoor temperature difference between office and residential rooms is only 3°C, approving that transmitted solar radiation has a tremendous impact on indoor temperature.

Effect of extending non-air-conditioning period

Accumulated satisfactory hours when indoor room temperature is below 25°C and 28°C, which can guarantee a barely satisfactory environment (Okuma et al., 2007) as to save energy, are utilized for the determination of non-air-conditioning period. From Figure. 6, we can conclude that hours when indoor temperature is within 25°C can be increased from 1000 to 3000 hours by applying PDSF in office room. If a broad range of indoor room temperature is acceptable, the accumulated time can reach more than 4000 hours.

Compared with office room, performance in residential room is more promising. There are 5900 hours when room temperature is under 28°C. It means that the pipe-embedded double skin façade is considerably efficient under this circumstance.

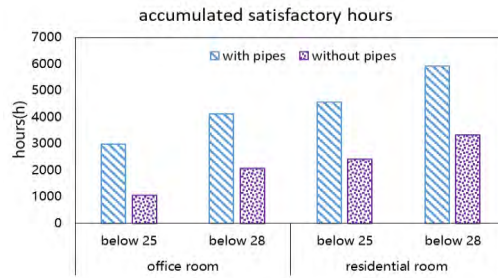


Figure 6 Satisfactory hours in different criteria

CONCLUSION

PDSF integrated with natural energy is a new approach to reduce heat gain. A state-space based method to evaluate dynamic thermal performance of PDSF is proposed in this paper. Performance of two typical rooms with different indoor heat gain in Guangzhou is analysed as a typical case. The main conclusions are as follows.

- 1) PDSF combined with cooling tower can reduce indoor room temperature significantly in Guangzhou. The average room temperature can be decreased about 5°C.
- 2) Accumulated hour when indoor temperature is within 28°C accounts for 5900 hours for residential room, indicating room temperature can meet the basic requirement in most time with the assistance of PDSF if indoor heat gain is small.
- 3) Performance in October is the most efficient when solar radiation is strong because shading blind embedded with water-pipes can block solar radiation and take it away directly, which indicates that PDSF could be promising in regions with strong solar radiation such as western china.

ACKNOWLEDGEMENT

This study was supported by the National Natural Science Foundation of China (Grant No. 51638010 and 51578306).

REFERENCE

- Cheng C L, Liao L M, Chou C P. A study of summarized correlation with shading performance for horizontal shading devices in Taiwan[J]. *Solar Energy*, 2013, 90(4):1-16.
- Klimanek A, Cedzich M, Bialecki R. 3D CFD modeling of natural draft wet-cooling tower with flue gas injection[J]. *Applied Thermal Engineering*, 2015, 91:824-833.
- Manz, H., Brunner, S., Wullschleger, L., 2006. Triple vacuum glazing: heat transfer and basic mechanical design constraints. *Sol. Energy* 80 (12), 1632–1642.
- Okuma R, Ishino H, Nakayama S. Thermal comfort for office occupants in air temperature of 28°C in summer [J]. *Journal of Environmental Engineering*, 2007, 72(618):31-36.
- Parker S T, Bowman V. State-space methods for calculating concentration dynamics in multizone buildings[J]. *Building & Environment*, 2011, 46(8):1567-1577.
- Shen C, Li X. Solar heat gain reduction of double glazing window with cooling pipes embedded in venetian blinds by utilizing natural cooling[J]. *Energy & Buildings*, 2016, 112:173-183.
- Shen C, Li X. Thermal performance of double skin façade with built-in pipes utilizing evaporative cooling water in cooling season[J]. *Solar Energy*, 2016, 137:55-65.
- Utamura M, Nikitin K, Kato Y. Generalization of Logarithmic Mean Temperature Difference Method for Heat Exchanger Performance Analysis[J]. *Thermal Science & Engineering*, 2008, 15(3):163-173.
- Wang Y, Chen Y, Zhou J. Dynamic modeling of the ventilated double skin façade in hot summer and cold winter zone in China[J]. *Building & Environment*, 2016, 106:365-377.

Computer Tomography as a data acquisition tool for quantifying and modeling in-pore gypsum crystallization in building materials

Steven Claes^{1,*}, Jelena Todorovic¹ and Hans Janssen¹

¹ KU Leuven, Department of Civil Engineering, Building Physics Section, Kasteelpark Arenberg 40, 3001 Heverlee, Belgium

**Corresponding email: Steven.claes@kuleuven.be*

ABSTRACT

In the last few decades a new type of persistent efflorescence has started appearing on ceramic brick facades in the UK, the Netherlands and in Belgium. Since the problem undermines the aesthetic appearance of masonry buildings, it results in a growing number of complaints from building owners.

In the laboratory, gypsum efflorescence is typically studied via wicking tests. However, these often yield gypsum subflorescence instead, leading to significant pore clogging just below the evaporation surface. To gain further insight in that subflorescence and pore clogging, a correct quantification of the amount and the distribution of the gypsum crystallised in the pore space is necessary. Micro-CT achieves this by allowing visual inspection as well as quantitative data gathering. Because of the non-destructiveness of micro-CT, samples can be scanned before and after subflorescence/pore clogging has occurred. The suggested methodology includes visualization and characterization of the pore space. Observing the changes in pore structure, with the assumption that these are induced only by the presence of the salt crystals, it is possible to accurately quantify the volume of gypsum present, as well as the location of the affected pores in 3D. Due to the partial volume effect, the CT dataset can be used to detect objects smaller than the voxel size because the density difference between gypsum and air is large enough.

The obtained results confirm the presence of a thin gypsum layer just below the evaporation surface of the sample. Other techniques such as the wicking test and MIP also confirm the observations regarding pore size change and gypsum content.

KEYWORDS

Salt crystallization, Pore clogging, Brick sample, Micro-CT, Pore network properties

INTRODUCTION

The development of gypsum efflorescence on newly erected ceramic brick facades is a rising problem in the UK, the Netherlands and Belgium (Chwast et al, 2015). Unlike the common efflorescence, composed of soluble salts which are easily washed away by natural weathering, the new efflorescence consists of slightly soluble gypsum, which makes it persistent and hard to remove. Once formed on the masonry surface, they stay and permanently spoil the facade's appearance.

Even though salt crystallization in porous materials has already been the subject of study for many decades, there is still a lack of knowledge and understanding in relation to the involved pore clogging and its impact on the moisture transfer properties of porous materials. In order to study this phenomenon in laboratory conditions, wicking experiments are often performed.

Such experiments usually reveal gypsum's tendency to crystallize under the surface, inducing significant pore clogging and resultantly a strong drop in the wicking rate.

In this paper, the resultant changes in the brick's pore structure, with the assumption that these are induced only by the presence of the salt crystals, will be quantified based on CT datasets. It will be shown that such CT analysis makes it possible to accurately quantify the volume of salts present as well as the location of the affected pores in 3D.

METHODS

Wicking test

The effect of gypsum pore clogging is generated with a wicking test. It is composed of a brick sample fed with a gypsum solution from the bottom side, while evaporation is permitted only from the top side. The gypsum solution for the wicking test is prepared by dissolving 2.2 g of calcium sulphate dihydrate (Fisher Chemicals, 99% pure) in 1l of distilled water (conductivity of pure water $1.2\mu\text{S}/\text{cm}$). The prepared solution is 85% saturated, and its concentration can be calculated as $2200\text{ g}/\text{m}^3$. The experimental set-up is composed of a glass container with at the bottom a layer of gypsum solution. The container is closed with a plastic lid, to which a brick sample is mounted. In this way, a constant contact between the solution and the brick sample is maintained throughout the experiment. The experiment is conducted in a climate chamber, under constant environmental conditions, at 21°C temperature and 40% relative humidity, for a duration of 14 days.

CT characterization

Computed tomography (CT) is a non-destructive visualization technique, generating images of slices of a sample based on the attenuation of X-rays. Hence, it enables the 3D visualization of the internal structures of the object. As CT is a fast and non-destructive technique, it has become a reliable method to analyze the heterogeneity of interior components as well as the porosity network of the studied sample. A more detailed explanation of the principles of CT can be found in Claes et al. (2018). Also Aikens (1991), Kak and Slaney (1988) and Herman (2009) provide more general information about the technique.

In order to determine the effect of the salt precipitation, the same sample is scanned by micro-CT before and after the above described wicking experiment. Both scans are performed using the same scan parameters (80 kV and $160\mu\text{A}$) and both have a resolution of $3.5\mu\text{m}$. The quantitative data are generated through the attenuation of X-rays, which are sensitive to sample density and atomic number, and are stored in voxels as relative gray scale values. Since in theory the only difference between both scans is the presence of salt, which will cause a higher attenuation of the x-rays compared to the air present in the pores of the original sample, resulting in higher greyscale values of the voxels. Thus, a subtraction of both datasets should result in the quantification of the precipitated salt. Hence, it becomes very important to subtract the correct corresponding voxels of both datasets, in order not to introduce artificial artefacts in the results. This is achieved by a registration process involving the determination of a geometrical transformation that aligns points in one view of an object with corresponding points in another view of that same object. The inputs of the registration algorithm are the two views to be aligned; the output is a geometrical transformation, which is a mere mathematical mapping from points in one view to points in the second. In order to retain cubic voxels, the values of the voxels of the transformed view will be linearly interpolated.

RESULTS & DISCUSSION

Effect on the pore network

A visual inspection of the micro-CT slices taken at the same depths from the top evaporation surface show that, in the top of the sample, gypsum is present at the edges of large pores and clogs smaller pore throats (Figure 1 A-B). Comparison of slices taken towards the bottom of the sample indicate that no visual gypsum is present (Figure 1 C-D).

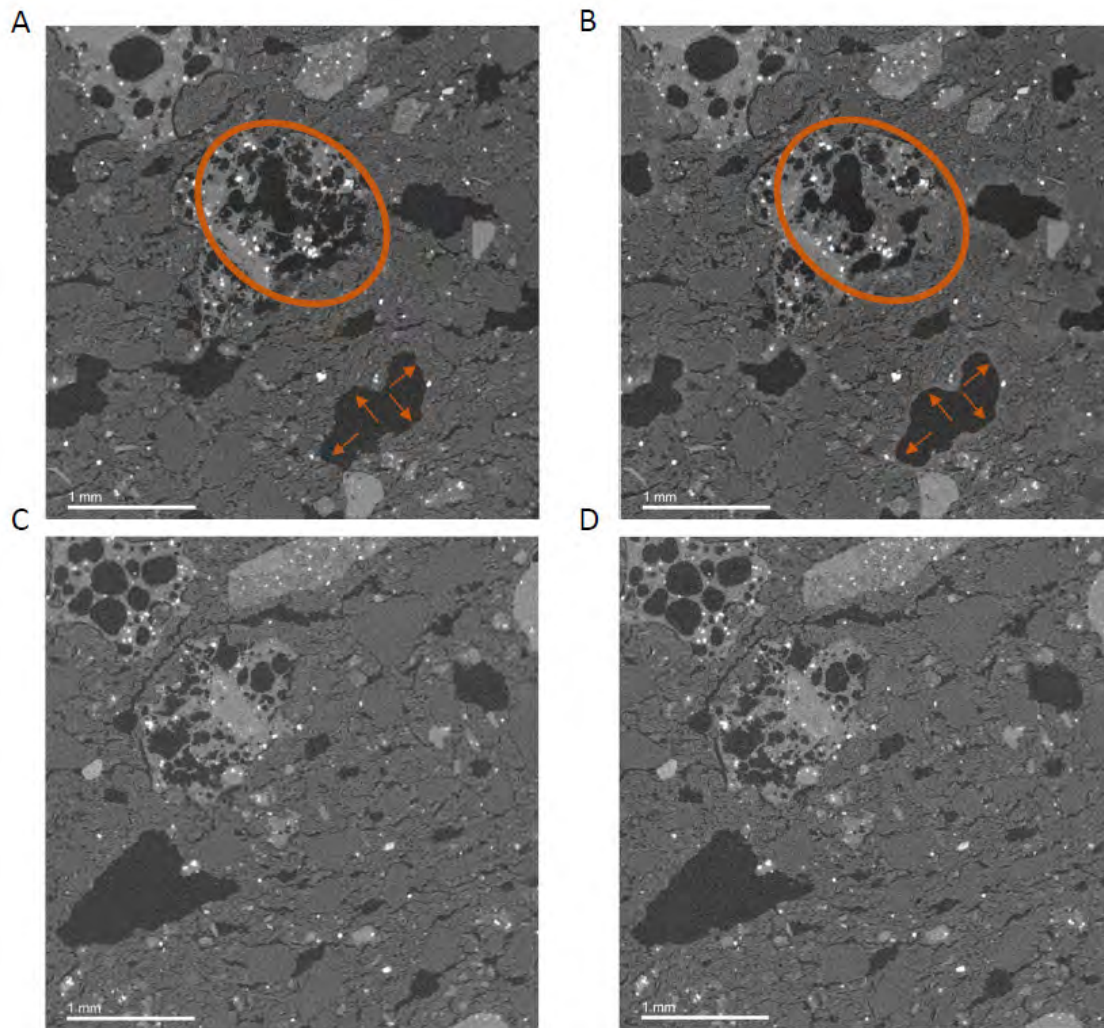


Figure 1. Micro-CT slices of the brick sample parallel to the evaporation surface. a) Original state at 130 μm below the evaporation surface, b) State with salt present at 130 μm below the evaporation surface; orange markers illustrate the differences, c) Original state at 1.5 mm from the evaporation surface, d) State with salt at 1.5 mm from the surface, no differences are visible between c and d.

These images are used to deduce the pore network in these volumes by applying a hysteresis segmentation (Claes et al., 2018). Subsequently these pore networks are split into pore bodies and pore throats using the workflow of Blunt et al. (2013).

Based on a visual inspection of the slices, the salt precipitation occurs in the top layer of the studied sample. Hence, two corresponding volumes of $500 \times 500 \times 120$ voxels ($1.75 \times 1.75 \times 0.42 \text{ mm}^3$) are selected in this layer.

In general the CT-detectable open porosity is decreased by 1.2 %, from 15.6 % porosity in the original sample to 14.4 % in the affected sample. Moreover, the salt subflorescence has a clear effect on the pore size as well as on the overall distribution of pore bodies and throats in the studied volumes. As expected from the visual observations in Figure 1, the number of pore bodies and throats increases in the volume affected by salt precipitation. The average pore radii become 5 % smaller when affected by the salt. This can be explained by the rims of salt formed at the edges of the pores. Figure 2 represents the calculated pore size distributions of the reference and affected volume. The number of pores in the bin with the smallest pore radii also increases from 2460 pores to 3283. Additionally a clear shift towards smaller coordination numbers can be noticed in the sample where salt is present, even though it has a larger number of throats in the same sample volume (8324 compared to 6777). This results in a halving of the simulated permeability but these simulations only take into account the visible porosity in the CT scan.

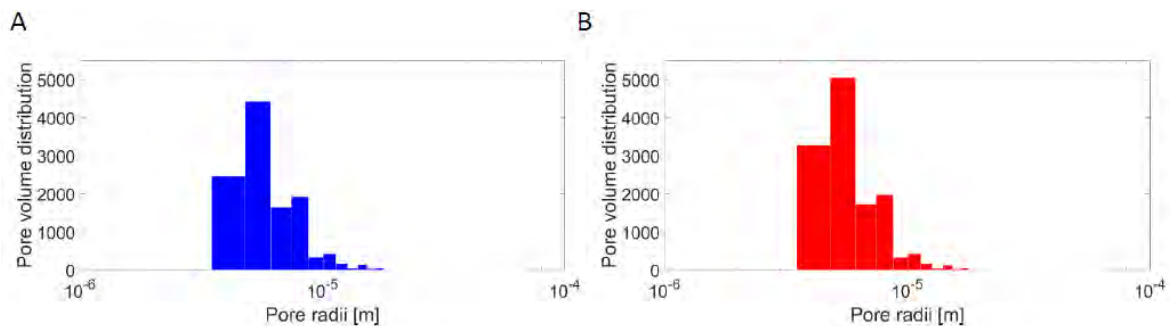


Figure 2. Pore volume distribution. a) Reference sample, b) Affected sample.

Validation

The results of the visual comparison of the slices agree with observations made in lab results and confirm the creation of a salt subflorescence layer just below the top evaporation surface. Admittedly, the influence of the scan resolution remains apparent, as only half of the open porosity can be CT-detected (15.6 % vs 31.8 % which is the actual open porosity of the brick samples). The obtained pore size distributions are further matched to distributions acquired by mercury intrusion porosimetry (MIP). Todorovic and Janssen (2018) noted that the curves of samples containing gypsum shifted in two general directions: firstly a downward shift corresponding to a decrease in open porosity, and secondly a shift to the left, towards smaller pore radii. The same observations can be partially made based on Figure 2. It is important to notice that due to the scanning resolution of 3.5 μm the spectrum of CT-detectable pore radii is limited. Hence, most of the clogged open porosity was not visible in the reference scan, since these pores fall below the resolution. The beginning of the shift to the left is visible but the main shift occurs for pores with radii of 10^{-6} m which are not captured in the micro-CT scan.

Quantification and spatial distribution of the salt

The validation of the results obtained in the prior section indicate that they are greatly affected by the limited scan resolution, as only half of the expected open pores are visible in the scan. Another approach is therefore necessary to accurately quantify the distribution of precipitated gypsum. Micro-CT datasets have the added advantage that objects smaller than the voxel size can still be detected if the density difference between the competing components is large

enough. For the studied problem this is the case because $\rho_{\text{gypsum}} (2300 \text{ kg/m}^3) > \rho_{\text{air}} (1.25 \text{ kg/m}^3)$. This is due to what is generally called the partial volume effect (Figure 3 A). Because the borders of the scanned sample or a component in the sample may not coincide with the borders of the pixels of the detector, the partial volume effect occurs: features smaller than the resolution will also contribute to the attenuation coefficient of the voxel in a linear way.

Hence, in order to quantify all gypsum present in one slice, slices corresponding to the same depth are subtracted from each other. In Figure 3 B-C the histograms of these subtractions are depicted. The histogram of a slice where no salt is visible corresponds to a symmetrical bell curve centered approximately around zero. Hence this curve is interpreted as a representation of the noise present in the subtracted images. For the slices nearer to the top of the sample, the histograms become asymmetrical, and show an increase in positive difference values around 1200. These curves will therefore be modeled as a sum of two normal distributions. Parameter p represents the contribution of the noise component to the overall model, while a factor $(1-p)$ is assumed to define the gypsum. The distributions are fitted using a maximum likelihood method. Table 1 summarizes the modeled parameters.

Table 1. Overview of typical values of the fitted parameters.

slice depth	p	μ_1	σ_1	μ_2	σ_2
0,2 mm	0.85	-112	568	903	1137
1,2 mm	0.98	5.6	620	25.5	1087

Based on these models the parameter $(1-p)$ represents the relative amount of voxels for which the composition has changed between the two scans. Hence, they can be used to characterize the volume percentage of salt in each slice. The profile is shown in Figure 3 D and clearly indicates the presence of a gypsum crust at the top of the sample. The top 49 μm are not processed as these are too much affected by the surface roughness of the brick sample. The sudden drops in the profile can be explained by spurious additional noise in some slices.

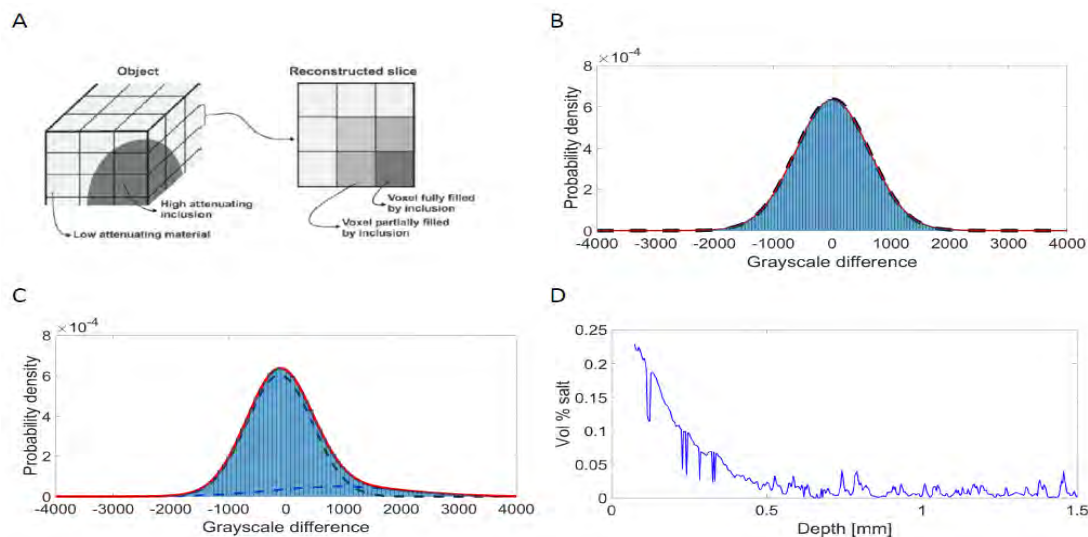


Figure 3. Localisation and quantification of the salt layer. a) Schematic overview of the linear partial volume effect (modified from Pullan et al., 1981), b) Histogram of the difference between two slices near the bottom of the sample (black dotted line represents the noise component, red line represents the overall model), c) Histogram of the difference between two slices near the top of the sample (black dotted line represents the noise component, blue

dotted line represents the salt component, red line represents the overall model), d) Volume percentage salt in function of sample depth.

Validation

In order to validate the results of the calculated presence of gypsum in the section above, these results are compared to the lab measurements. On average 0.046 g of gypsum precipitated in the 28.7 mm diameter ceramic brick plugs. This corresponds to a total amount of gypsum of 71 g/m². By calculating the surface below the curve in Figure 3 D up to 450 μm below the top surface, a total amount of 91 g/m² is obtained from our CT measurements. Both measurement methods are thus in agreement with each other.

CONCLUSIONS

In this paper the location and concentration of the gypsum subflorescence layer in bricks is successfully determined based on 3.5 μm resolution micro-CT scans. The evaporated gypsum is concentrated in the top 450 μm layer of the sample. Based on the pore network analysis general observations about the change in pore geometry can be made. However, comparison with MIP measurements indicate the strong importance of the contribution of pores below the scanning resolution. The partial volume effect can overcome some of these limitations, but additional visualization techniques with smaller resolutions will need to be used in the future in order to perform accurate fluid flow simulations.

ACKNOWLEDGEMENT

This project has received partial funding from the FWO Odysseus grant ‘Moisture transfer in building materials: analysis at the pore-scale level’. Their support is kindly acknowledged.

REFERENCES

- AIKENS, R. S. 1991. *Charge-Coupled Devices for Quantitative Electronic Imaging. International Amateur-Professional Photoelectric Photometry Communications*, 44, 1.
- Blunt, M. J., Bijeljic, B., Dong, H., Gharbi, O., Iglauer, S., Mostaghimi, P., Pentland, C. 2013. *Pore-scale imaging and modelling. Advances in Water Resources*, 51, 197-216.
- Claes, S., Van De Walle, W., Islahuddin, I. Janssen, H. 2018. *The application of Computed Tomography for characterising the pore structure of building materials*, IBPC 2018 (submitted).
- Chwast, J., Todorović, J., Janssen, H., Elsen, J. 2015. *Gypsum efflorescence on clay brick masonry: field survey and literature study*, Constr. Build. Mater. 85: 57 – 64.
- Herman, G. T. 2009. *Fundamentals of computerized tomography: image reconstruction from projections*, Springer Science & Business Media.
- Kak, A. C. & Slaney, M. 1988. *Principles of computerized tomographic imaging*. IEEE Press.
- Pullan, B., Ritchings, R. & Isherwood, I. 1981. *Accuracy and meaning of computed tomography attenuation values*. Technical Aspects of Computed Tomography. Mosby, St. Louis, 3904-3917.
- Todorović, J., & Janssen, H. 2018. *The impact of salt pore clogging on the hygric properties of bricks*. Construction and Building Materials, 164, 850-863.

Determination of the input data for computational simulation of active glazing with changeable optical properties

Dariusz Heim^{1*}, Dominika Knera¹ and Anna Wieprzkowicz¹

¹Department of Environmental Engineering, Lodz University of Technology, Poland

*Corresponding email: dariusz.heim@p.lodz.pl

ABSTRACT

Nowadays, many construction components applied in the energy efficient buildings are characterized by dynamically changeable physical properties. Some of them are actuated by the user or building management system, while the others are self-regulated. The second group of mentioned elements is often named intelligent or smart components. Change of their properties is triggered by physical processes e.g. thermal or chemical.

Energy performance of the building can be precisely determined based on the results of computational simulation obtained using one of the widely well-known computational tools e.g. Energy Plus or ESP-r. In the numerical analysis the effect of changeable properties can be also included towards better modelling of physical processes in the buildings. However, the exact material data and its characteristics are necessary for a proper definition of such component properties - thermal or optical characteristics. The main goal of this study is to refine the ESP-r material database, in order to include in the calculation the effect of changeable optical properties of glazing unit filled with material characterized by variable solar transmittance.

The basic general equation of transmittance, reflectance and absorptance as a function of incidence radiation were provided. The material optical database developed in this study consists of experimentally determined reflectance, absorption and transmittance of solar radiation for five angles of incident (as required for ESP-r optical databases). All these data were provided for double glazed unit where the inner cavity was filled with material characterized by changeable optical properties. All optical data were obtained based on the spectral characteristic of the material layer (in different thicknesses) in a wave length range of solar radiation (300-1200 nm). It was concluded, that overall transmittance is determined by the material filling the cavity, but the reflectivity mainly depends on the external surface of glazing and interrelations between glazing and subsequent layer.

KEYWORDS

Solar energy, heat transfer, transmittance, reflectance, phase change materials.

INTRODUCTION

The application of paraffin as a filling of transparent building components is well known since the end of the nineties. (Ismail and Henríquez 2002) proved that additional layer of PCM can improve the thermal efficiency of the whole window, while (Weinläder, Beck, and Fricke 2005) dedicated their research to comfort analysis. PCM was not only used as a layer of a glazing pane but also as a filing of the shading elements (Bianco et al. 2018) and in other technologies as well (Silva, Vicente, and Rodrigues 2016). Additionally, PCM was used in hybrid TPV systems where PV cells were thermally stabilized by PCM layer located at the back side of the panel (Machniewicz, Knera, and Heim 2015). Additionally, the application of PCM glazing components can also lead to achieve future energy standard according to the requirements of new energy performance directive (Firlag 2015). Determination of optical and

thermal properties of PCM-glazing component is very important for proper estimation of its efficiency using modelling techniques. Moreover, it is necessary to determine the optical data, especially of any complex glazing structure for the purpose of building energy performance simulation (Clarke 2001), (Hensen and Lamberts 2011). Many authors provided those data obtained experimentally using spectrophotometric techniques or direct measurements (Goia et al. 2012). Nevertheless, both techniques ignore the effect of local optical phenomena (Duffie and Beckman 2013) on interfaces between glass, air and PCM layer.

The main idea of using PCM in glazing was raised by the necessity of the improvement of their thermal inertia (Grynning, Goia, and Time 2015). Although PCM application in glazing is relatively brand new idea, some previous research study was devoted to analyse other liquids e.g. water as a glazing extender. (Chow, Li, and Lin 2011) revealed that water-flow window can work as a hot-water preheating device. (Sierra and Hernández 2017) showed the active behaviour of water flow glazing by a variable g factor. Additionally they concluded that the best glazing to manage the incoming solar energy is the one that allows to enter only visible spectra when the system is flowing and the absorption occurs only in the water chamber. The PCM glazing will play the similar role but the heat will not be extracted from the system to external storage tank but isothermally stored in the PCM layer.

The main purpose of this study was to develop the methodology for determining total solar transmittance, reflectance and absorptance in a glass pane with phase change material, in solid a liquid state. The basic equations were provided for double glazed window with PCM and optical data for standard angle of incidents was determined. Results were presented in the standard of ESP-r (Environmental System Performance) database format.

METHODOLOGY

The proposed methodology is based on the physical fundamentals of solar radiation’s transmission through transparent media like glazing (Chwieduk 2014). Physical fundamentals of the phenomena occurring within glazing are mostly related to the optics. The phenomena of radiation’s passage through two transparent covers should be analysed taking into account the multi inter reflections on all interfaces. These multi-reflections in double glazed window with air, argon or any other gases between glass panes are schematically presented in figure 1.

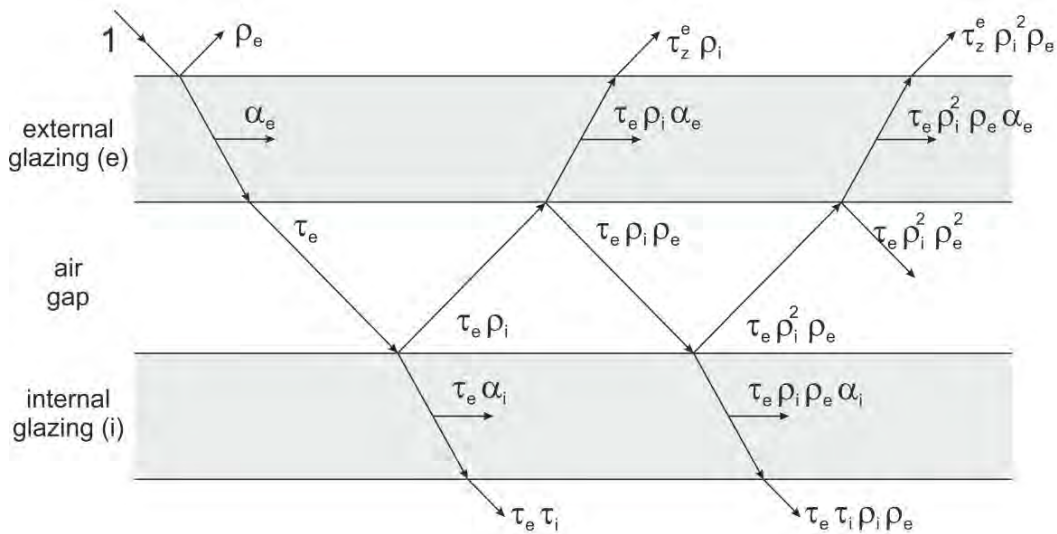


Figure 1. Transmittance, reflectance and absorptance components including inter reflections on glass surface and absorption in a glass pane.

Taking into account inter reflections on glass surface and absorption in a glass pane, the total reflectance (ρ), absorptance (α) and transmittance (τ) of the component can be calculated from the following formulas (eq. 1-3):

$$\rho = \rho_e + \frac{\tau_e^2 \rho_i}{1 - \rho_e \rho_i} \quad (1)$$

$$\alpha = \alpha_e + \frac{\tau_e (\alpha_i + \alpha_e \rho_i)}{1 - \rho_e \rho_i} \quad (2)$$

$$\tau = \frac{\tau_e \tau_i}{1 - \rho_e \rho_i} \quad (3)$$

where indexes i and e refer to the internal and external glass covers respectively.

When glazing cavity is filled with PCM the repeated reflection on all interfaces become more complex due to additional effect of reflection on PCM layer. This process is schematically presented in figure 2, where m means material between two glasses.

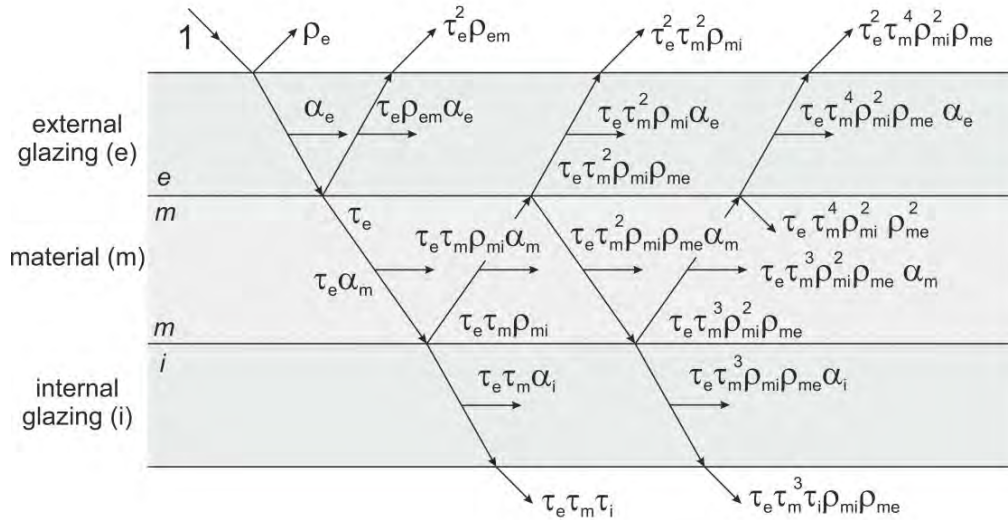


Figure 2. Transmittance, reflectance and absorptance components including inter reflections on glass surface and absorption in a glass pane filled with PCM (material).

The general formula for total solar reflectance (ρ), absorptance (α) and transmittance (τ) becomes as follows:

$$\rho = \rho_e + \tau_e^2 \rho_e + \frac{\tau_e^2 \tau_m^2 \rho_{mi}}{1 - \tau_m^2 \rho_{me} \rho_{mi}} \quad (4)$$

$$\alpha = \alpha_e \left(1 + \tau_e \rho_{em} + \frac{\tau_e \tau_m^2 \rho_{mi}}{1 - \tau_m^2 \rho_{me} \rho_{mi}} \right) + \alpha_m \left(\tau_z \frac{1 + \tau_m \rho_{mi}}{1 - \tau_m \rho_{me} \rho_{mi}} \right) + \alpha_i \left(\frac{\tau_e \tau_m}{1 - \tau_m^2} \right) \quad (5)$$

$$\tau = \frac{\tau_e \tau_m \tau_i}{1 - \tau_m \rho_{me} \rho_{mi}} \quad (6)$$

The indexes concerns the surface where optical processes appears, where i and e refer to the internal and external glass covers respective and m corresponds to PCM layer.

The equations presented above require very precise sets of data which are usually unavailable or impossible to be obtained during tests. Therefore, the following assumptions and simplifications were done:

- 1) The absorptivity of the single PCM layer in both phases is the same for all angles of incident. It means that reflectivity of the whole component is determined primarily by reflectivity of external glass surface.
- 2) The reflectivity of single PCM layer in liquid state changes versus angle of incident cognately as the glass – only direct reflectance is considered.
- 3) The transmissivity of single PCM layer in both phases is a function of the incident angle according to the optical length of the beam during transmission through the material.

OPTICAL PROPERTIES OF PCM DOUBLE GLAZED WINDOW

The results of presented analysis were obtained for glass pane that consists of two glasses 4 mm each with 16 mm air cavity or PCM layer between them. The cross section through the unit is presented in figure 3a - standard double glass pane and 3b - glass pane with PCM.

The main difference between both cases is the heightened potential to absorb solar radiation in a material layer located between glasses. Especially, when PCM is in solid state the absorption appears on the surface exposed to solar radiation. The total transmittance of single PCM (16 mm thick) layer in solid state is less than 10%, while in liquid state it is above 80%. It means that for the case considered here the solid PCM is similar to opaque material. The colour of solid paraffin or fatty acids is white or light grey. It means that reflectivity can be assumed as 0.5 - 0.7 and decreases when material melts. The liquid PCM is fully translucent and has neutral colour.

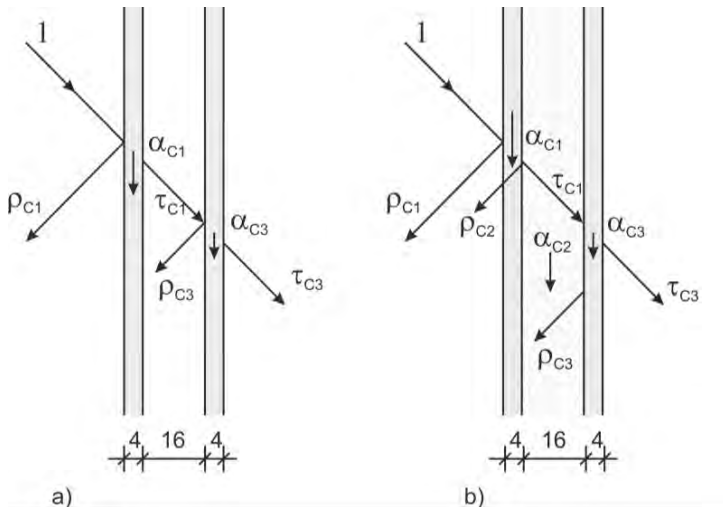


Figure 3. Cross section through glass pane a) standard, b) with PCM.

For the purpose of computational simulation the datasets including angular optical properties are necessary to analyse any physical processes in a glazing unit. The main goal of the work presented in the paper was to develop the characteristic data based on the physics of radiation transmission through glazing. Taking into account the formulas 1-6, the optical characteristics of double glazed unit without, with liquid and with solid PCM were determined. The results are presented in figure 4 a-c as a function of incident angle. It can be noted that when material is solid, PCM glazing characteristic is similar to standard glazing but transmittance is slightly lower as an effect of higher reflectance. In solid state the reflectance is much higher and strongly depends on reflectance of PCM.

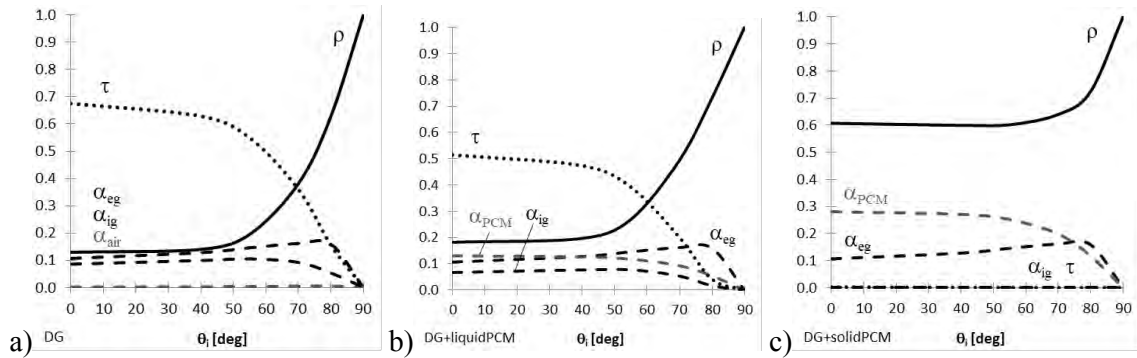


Figure 4. Transmittance, reflectance and absorptance versus angle of incident for a) clear glass double pane window unit, b) glass unit with liquid PCM, c) glass unit with solid PCM.

DISCUSSIONS

In a case of liquid PCM the obtained results show that total transmittance is more than 20% lower than for standard glazing unit and its function versus angle of incident has similar character. The absorptance of liquid PCM is similar to external glazing for the angles up to 50 deg. For higher angles the absorptance of external glazing increases due to the additional reflections between glass and PCM layer.

In solid state the glazing unit is almost blind and most of solar energy is absorbed on the PCM external surface due to the highest absorptivity, almost 0.3. This absorptivity decreases as a function of angle of incident while absorptivity of external glazing increases. This is caused by the longer optical path of the radiation beam, and as it was stated for the liquid state, the interreflections between glass and PCM occur.

In both cases the absorptance on the internal glass surface is very low and has no effect on thermal performance of the whole system. It means that PCM layer should protect building interior against overheating caused by solar radiation. The excessive solar heat gains will be stored as an latent heat in PCM layer and any heat transfer to external environment will be possible only by conduction (inside the component) and convection between glass surface and internal air. Heat exchange by radiation, when melting temperature will be close to indoor air temperature, seems to be negligible.

CONCLUSIONS

The paper presents the methodology of optical properties determination for complex glazing structure. The formulas were developed based on the physical fundamentals of solar radiation's transmission through transparent media. The problem was graphically illustrated and related formulas were also derived.

The final results of transmittance, reflectance and absorptance versus angle of incident were presented in a form of ESP-r optical database and compared with case of standard, double glazed clear glass window. In both phases, solid and liquid, PCM-glazing is characterized by the lower transmittance than standard glass unit. In solid phase the component is almost blind, but the absorptance of PCM layer is relatively high. This feature will determine the ability to absorb solar energy and convert it to heat.

ACKNOWLEDGEMENT

This work was funded in a framework of ERANet-LAC 2nd Joint Call on Research and Innovation by NCBiR as part of the project entitled: Solar hybrid translucent component for thermal energy storage in buildings (acronym: SOLTREN).

REFERENCES

- Bianco, Lorenza, Anna Komerska, Ylenia Cascone, Valentina Serra, Michele Zinzi, Emiliano Carnielo, and Dariusz Ksionek. 2018. "Thermal and Optical Characterisation of Dynamic Shading Systems with PCMs through Laboratory Experimental Measurements." *Energy and Buildings* 163 (March). Elsevier: 92–110. doi:10.1016/j.enbuild.2017.12.015.
- Chow, Tin Tai, Chunying Li, and Zhang Lin. 2011. "The Function of Solar Absorbing Window as Water-Heating Device." *Building and Environment* 46 (4). Pergamon: 955–60. doi:10.1016/j.buildenv.2010.10.027.
- Chwieduk, Dorota. 2014. *Solar Energy in Buildings - Chapter 4. Solar Energy in Buildings*. doi:10.1016/B978-0-12-410514-0.00004-9.
- Clarke, JA. 2001. "Energy Simulation in Building Design." *Energy Simulation in Building Design*, no. Second edition: 384. doi:10.1016/B978-075065082-3/50016-4.
- Duffie, John A., and William A. Beckman. 2013. *Solar Engineering of Thermal Processes. Solar Engineering of Thermal Processes*. Wiley Online Books. doi:doi:10.1002/9781118671603.fmatter.
- Firlag, Szymon. 2015. "How to Meet the Minimum Energy Performance Requirements of Technical Conditions in Year 2021?" In *Procedia Engineering*, 111:202–8. Elsevier. doi:10.1016/j.proeng.2015.07.077.
- Goia, Francesco, Michele Zinzi, Emiliano Carnielo, and Valentina Serra. 2012. "Characterization of the Optical Properties of a PCM Glazing System." In *Energy Procedia*, 30:428–37. Elsevier. doi:10.1016/j.egypro.2012.11.051.
- Grynning, Steinar, Francesco Goia, and Berit Time. 2015. "Dynamic Thermal Performance of a PCM Window System: Characterization Using Large Scale Measurements." In *Energy Procedia*, 78:85–90. Elsevier. doi:10.1016/j.egypro.2015.11.119.
- Hensen, Jan L M, and Roberto Lamberts. 2011. *Building Performance Simulation for Design and Operation*. Routledge. doi:doi:10.4324/9780203891612.
- Ismail, K. A R, and J. R. Henríquez. 2002. "Parametric Study on Composite and PCM Glass Systems." *Energy Conversion and Management* 43 (7). Pergamon: 973–93. doi:10.1016/S0196-8904(01)00083-8.
- Machniewicz, Anna, Dominika Knera, and Dariusz Heim. 2015. "Effect of Transition Temperature on Efficiency of PV/PCM Panels." In *Energy Procedia*, 78:1684–89. doi:10.1016/j.egypro.2015.11.257.
- Sierra, Pablo, and Juan A. Hernández. 2017. "Solar Heat Gain Coefficient of Water Flow Glazings." *Energy and Buildings* 139 (March). Elsevier: 133–45. doi:10.1016/j.enbuild.2017.01.032.
- Silva, Tiago, Romeu Vicente, and Fernanda Rodrigues. 2016. "Literature Review on the Use of Phase Change Materials in Glazing and Shading Solutions." *Renewable and Sustainable Energy Reviews*. Pergamon. doi:10.1016/j.rser.2015.07.201.
- Weinläder, Helmut, Andreas Beck, and Jochen Fricke. 2005. "PCM-Facade-Panel for Daylighting and Room Heating." In *Solar Energy*, 78:177–86. Pergamon. doi:10.1016/j.solener.2004.04.013.

Predicting the thermal conductivity of porous building materials with nanopores or reduced gas pressures

Wouter Van De Walle^{1,*}, Hans Janssen¹

¹KU Leuven, Department of Civil Engineering, Building Physics Section, Kasteelpark Arenberg 40, 3001 Heverlee, Belgium

**Corresponding email: wouter.vandewalle@kuleuven.be*

ABSTRACT

Porous materials with nanopores or reduced gas pressures like aerogels, nanocellular foams or vacuum insulation panels show a great potential as insulation materials, due to their extremely low thermal conductivity. Understanding the relation between their pore structure parameters and effective thermal conductivity is crucial for further optimization. This paper discusses the extension of a numerical framework simulating the heat transfer directly at the material's pore scale. A novel methodology to model the reduced gaseous conductivity in nanopores or at low pressures is presented, accounting for the three-dimensional pore geometry while remaining computationally efficient. Validation with experimental and numerical results from literature indicates the accuracy of the methodology over the full range of pore sizes and gas pressures. A simple case study is analysed, which shows the expected improvements of the thermal conductivity when reducing the pore size for materials with different porosities. The numerical framework thus offers the possibility for a more thorough understanding and optimization of the thermal conductivity of superinsulators.

KEYWORDS

Thermal conductivity; porous materials; superinsulators; nanopores; low-pressure

INTRODUCTION

Heat losses through opaque building components like walls and roofs account for a large part of the total heating demand in buildings. Hence, porous insulation materials are often applied, offering a relatively low thermal conductivity due to their porous nature (Smith et al., 2013). To comply with progressively stringent energy requirements though, increasingly large insulation thicknesses are needed, hindering the design and the refurbishment of new and existing buildings. In the search for better performing insulators, a promising solution is offered by materials having pores with diameters in the nanoscale range and/or with reduced gas pressures inside. Examples are aerogels or aerogel-based materials (Baetens et al., 2011), nanocellular foams (Liu et al., 2015) and vacuum insulation panels (Jelle et al., 2010). Research has shown that in these materials the gaseous conduction shifts from the Fourier to the Knudsen regime, resulting in a reduced gaseous and hence overall effective thermal conductivity (ETC) (Jelle et al., 2010). Furthermore, the effect becomes even more crucial at increasing material porosities where conduction through the gaseous phase becomes progressively more dominant in the total heat transfer (Solórzano et al., 2009). Modelling efforts so far though have mainly focussed on obtaining analytical expressions, predicting the ETC as a function of several pore scale parameters like porosity and pore size (He & Xie, 2015; Wang et al. 2017). A more detailed understanding of the pore structure influence on the total ETC is hence needed to improve their performance significantly. To this aim, a numerical framework was recently implemented predicting the ETC of porous building materials based on their pore structure. A 3D voxel image representation of the microstructure, obtained via either micro-CT scanning

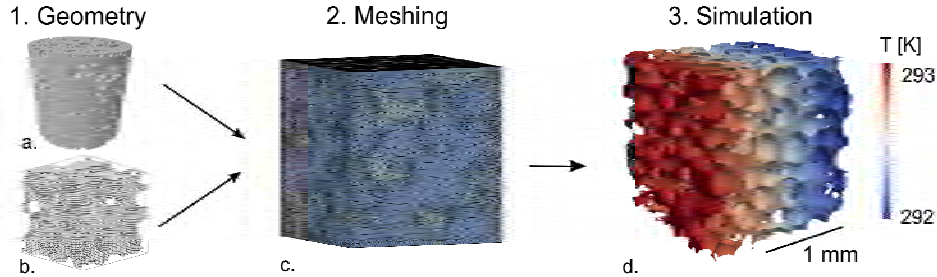


Figure 1: The numerical framework simulates the pore scale heat transfer to deduce the ETC. (a) micro-CT image of cellular concrete; (b) virtual material; (c) finite element mesh; (d) temperature profile.

or virtual generation, is used as input for the pore scale heat transfer simulation (Figure 1); more details can be found in the paper by Van De Walle & Janssen (2016). Currently, the model framework is limited though to porous materials with pore dimensions above several micrometres and containing gas at atmospheric pressure. Extension to a physical description of the Knudsen effect on the gaseous conductivity could enlarge its scope and facilitate the characterization of possible optimization strategies for superinsulating materials.

This paper discusses the implementation of the dimension- and pressure-dependent gaseous conduction in the aforementioned numerical framework. A novel simulation methodology based on the kinetic theory is introduced to obtain the local gaseous conductivities, offering an efficient calculation procedure while taking into account the pores' specific geometry. The proposed methodology is validated with experimental and numerical results from literature. Finally, the model is applied in an exploratory case study to investigate the effect of the pore size at different material porosities. Currently, only materials in dry conditions are targeted.

GASEOUS CONDUCTIVITY

The kinetic theory framework is used to model the microscopic gaseous heat transfer in pores. Firstly, the general theory is revisited for clarity, then the extension to reduced dimensions and/or gas pressures is explained. Finally, the implementation of the methodology in the numerical framework is discussed.

General kinetic theory

The kinetic theory framework allows to describe the heat conduction through gas as a function of the gas properties. Apart from the density ρ_{gas} [kg/m³], the specific heat capacity at constant volume $c_{V, gas}$ [J/kgK] and the mean molecule speed v_{mean} [m/s], the gaseous thermal conductivity depends on the mean free path L_{MFP} [m], which is the average distance a gas molecule travels before colliding with another gas molecule (eq. 1), (Zhang, 2007; Jiji, 2009).

$$q_{cond} = -\frac{1}{3} \cdot \rho_{gas} \cdot c_{V, gas} \cdot v_{mean} \cdot L_{MFP} \cdot \frac{dT}{dx} = -\lambda_{gas, bulk} \cdot \frac{dT}{dx} \quad (1)$$

Here, q_{cond} [W/m²] is the total heat flow caused by the temperature gradient dT/dx [K/m], and $\lambda_{gas, bulk}$ [W/mK] is the bulk gaseous thermal conductivity. The mean free path between successive collisions depends on the temperature and pressure of the gas, as well as on the gas molecule properties. However, as argued by Jiji (2009), the mean free path between collisions is not completely suited to describe the energy transport, since it doesn't consider the efficiency of energy exchange between two colliding particles. Therefore the 'energy' mean free path was introduced, which should be used in eq. 1 to obtain correct results. This energy mean free path can easily be deduced for bulk gases by reverse calculating equation 1, leading for example to an energy mean free path of 180 nm for air at 20 °C and atmospheric pressure.

Apart from gaseous heat conduction, the kinetic framework can equally be applied to describe heat conduction in solids by electrons, phonons (acoustic waves), and radiative heat transfer by photons (electromagnetic waves), considering the waves as particles (Chen, 2005). Although less accurate than more detailed simulation strategies like molecular dynamics or lattice Boltzmann simulations, the kinetic theory is capable of predicting reasonably well the thermal transport and thermal conductivity. This paper focusses solely on the implementation for gaseous conduction.

Extension to pore cavities with reduced dimensions and gas pressures

When the pore dimensions or gas pressure start to reduce, gas particles start colliding relatively more often with the pore boundaries instead of with each other, which is called the Knudsen effect. This translates to a reduction in the effective mean free path of the molecules and - according to eq. 1 - to a reduction of the gaseous conduction. The effective mean free path can be calculated according to Matthiessen's rule, combining the bulk mean free path and the mean free path induced by the boundaries, as shown in eq. 2 (Jiji, 2009).

$$\frac{1}{L_{MFP,eff}} = \frac{1}{L_{MFP,bulk}} + \frac{1}{L_{MFP,bdy}} \quad (2)$$

Again, the effectiveness of energy exchange between molecules and boundaries will influence the thermal transport. This is usually described with the thermal accommodation coefficient a , varying between 0 and 1, and very similar to the better-known absorptivity coefficient α used in thermal radiation simulations (Zhang, 2007; Jiji, 2009). Hence, an 'energy' boundary mean free path should be defined including this factor, thus directly incorporating the boundary resistance effect. Apart for simple structures like parallel plates, accurate calculation of this energy boundary mean free path is far from trivial. A novel method is therefore implemented in the model framework to account for the real 3D geometry of pores.

Including nanoscale gaseous conduction in the model framework

To calculate the gaseous conductivity in each pore, the energy boundary mean free path needs to be determined. A calculation methodology based on the analogy with radiative heat transfer is proposed, simplifying the simulation procedure. Introduced by Loeb (1954) and later extended by Van De Walle & Janssen (2016), the radiative heat transfer in a pore cavity can be described as a conductive process with a radiative conductivity depending – amongst others – on the pore dimensions and the wall's absorptivity. The formulas proposed by Van De Walle & Janssen (2016) to calculate this conductivity are shown in eq. 3 and 4. Eq. 3 is equalized to the more general form of the radiative conductivity originating from the kinetic theory.

$$\lambda_{rad,pore} = 4 \cdot \sigma \cdot T^3 \cdot d_{mean} \cdot C(\alpha, S_f) = \frac{1}{3} \cdot 16 \cdot \sigma \cdot T^3 \cdot L_{MFP,rad,eff} \quad (3)$$

$$S_{f,2D} = h_{mean} / d_{mean} ; S_{f,3D} = h_{mean} \cdot w_{mean} / d_{mean}^2 \quad (4)$$

Here, T [K] is the average temperature inside the pore, σ [W/m²K⁴] the Stefan-Boltzmann constant and d_{mean} , h_{mean} and w_{mean} [m] the mean distance between opposing pore walls parallel (d_{mean}) or perpendicular (h_{mean} , w_{mean}) to the heat transfer direction. $C(\alpha, S_f)$ [-] is a factor taking into account the effect of the absorptivity and the geometry of the pore walls using the directional slenderness factor S_f [-], and was defined based on a series of radiative simulations in several pores with varying geometries (Van De Walle & Janssen, 2016).

Since the bulk mean free path of photons $L_{MFP,rad,bulk}$ travelling in a non-absorbing medium like air is considered very large (\sim kilometres), the effective mean free path reduces to the boundary mean free path. Indeed, radiation is often modelled as only depending on the system boundaries. Using the analogy between gas particles and photons as well as between the thermal accommodation coefficient and the absorptivity, we can rewrite the last two parts from eq. 3 to finally formulate an expression calculating the energy boundary mean free path for gas particles in a certain pore (eq. 5).

$$L_{MFP,bdy,en} = \frac{3}{4} \cdot d_{mean} \cdot C(a, Sf) \quad (5)$$

Here, a is now the thermal accommodation coefficient instead of the radiative absorptivity. Hence, combining eq. 5, 4, 2 and 1, the reduced gaseous conduction can be calculated for every pore, knowing the gas state (pressure and temperature), the bulk gas properties (R_s [J/kgK], $c_{V,gas}$ and $\lambda_{bulk,gas}$) and the material properties (pore dimensions and thermal accommodation coefficient).

VALIDATION OF GASEOUS CONDUCTION CALCULATION

The implemented gaseous conductivity calculation procedure is validated against experimental and numerical results found in literature for different geometries, gasses and thermal accommodation coefficients.

Gas confined between parallel plates

The accuracy of the implemented calculation procedure to predict the gaseous conductivity variation is examined firstly for the simple case of parallel plates. Results are compared with experimental measurements of Braun & Frohn (1976) on Ar gas at pressures from 8.5 Pa to 66735 Pa, and with numerical DSMC simulations by Denpoh (1998) on N₂ gas at plate separation distances from 1.6 nm till 22 μ m. Details of both studies are summarized in Table 1, results are brought in Figure 2a. For both cases, the calculation procedure proves to accurately predict the gaseous thermal conductivity over the whole range of pressures and plate separation distances, even at varying thermal accommodation coefficients. Furthermore, they agree also very well with the often applied analytical prediction formula of Zhang (2007), derived for heat transfer between parallel plates.

Cuboid nanopore

The gaseous conductivity in real, more complex shaped pores depends (apart from the pore size and gas pressure) also on the pore's specific geometry. The performance of the novel calculation procedure – able to take the three-dimensional shape of the pore into account – is validated on a cuboid nanopore. Predicted results are compared with numerical DSMC simulations performed by Zhu et al. (2017) on Ar gas in a cuboid pore, varying the side length from 24 nm till 1.4 μ m; details are mentioned in Table 1. The gaseous conductivity predicted by our model agrees very well with the simulation results of Zhu et al. over the whole range of pore sizes, see Figure 2b. Furthermore, the model clearly outperforms the parallel plates formula of Zhang, underlining the importance of taking the true pore geometry into account.

Table 1. Properties used in the model to predict the gaseous thermal conductivity (NIST).

Study	Geometry	Gas	$\lambda_{gas,bulk}$ [W/mK]	a [-]
Braun & Frohn, 1976	// plates	Ar @ 323 K	0.0188	0.7385
Denpoh, 1998	// plates	N ₂ @ 343 K	0.0286	0.1 – 0.5 – 1
Zhu et al., 2017	Cuboid	Ar @ 300 K	0.0177	1

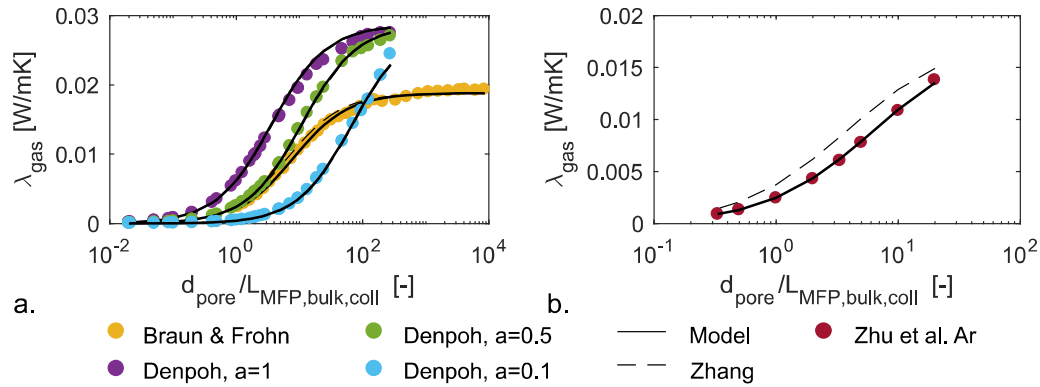


Figure 2: Gaseous conductivity results predicted by our model agree very well with experimental and numerical literature for gas confined between parallel plates (a) and gas in a cuboid nanopore (b).

CASE STUDY

Lastly, a case study is performed to investigate the potential impact of reducing the pore size and thus the gaseous conductivity on the total ETC of a porous sample. A body-centred cubic (BCC) unit cell is used as sample pore structure, considering the spheres as air-filled cavities inside a solid matrix. Three different material porosities are considered (50 %, 70 % & 90 %). The thermal conductivity of the matrix is set to 1 W/mK, simulations are performed at 20 °C mean temperature and 101325 Pa air pressure inside the pores. The specific heat capacity at constant volume is assumed to be 717 J/kgK (NIST), while a common value of 0.9 is taken for the thermal accommodation coefficient (Zhang, 2007). First, the ETC of each sample is calculated setting the pores' diameter to 1 mm, hence having the bulk air thermal conductivity inside them. Subsequently, the dimensions of each sample are rescaled five times, obtaining five different pore diameters between 1 nm and 10 μm. The total ETC of each sample is calculated using the numerical framework described in the introduction, taking into account the reduced gaseous thermal conductivity in every pore. The effect of the pore dimensions on the effective matrix conduction and radiative heat transfer is not taken into account here. A resolution of 400^3 for the voxel grid image is applied together with a mesh size of 3 times the respective voxel size, showing no further improvement with increasing grid and mesh refinement. As expected, the ETC generally decreases with increasing porosity and decreasing pore diameter (Figure 3). Furthermore, the effect of the pore size becomes more pronounced at increasing porosities, since gaseous conduction becomes progressively more dominant in the total heat transfer. The steepest drops are observed when decreasing the pore size from 10 μm to 100 nm, resulting in an ETC decrease of over 30 % for the sample with 90 % porosity. However, at the relatively high matrix conductivity involved here, the sample's porosity seems to remain the most important parameter. Future research will focus on studying

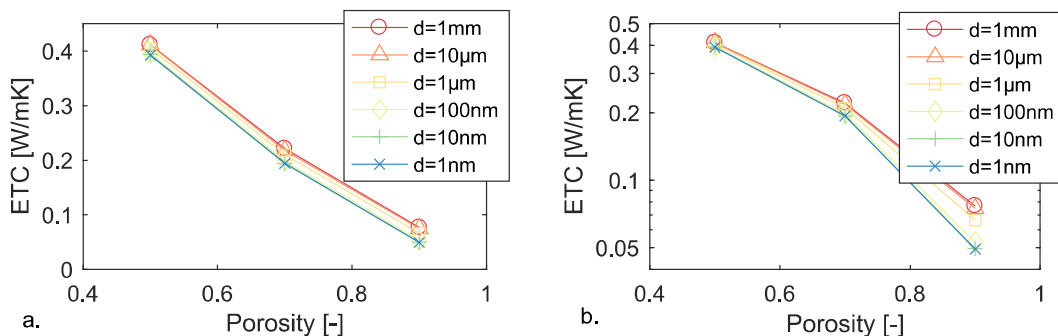


Figure 3: The ETC decreases with increasing porosity and decreasing pore size (a); at higher porosities the effect of a smaller pore size becomes more pronounced (b).

more complex materials and including the nanoscale effect on the matrix conduction and the radiative heat transfer in nanoporous materials.

CONCLUSIONS & FUTURE WORK

The paper presents the extension of a numerical framework to study the heat transfer in porous insulation materials showing low thermal conductivities due to the Knudsen effect. A novel computationally efficient method for calculating the gaseous conductivity in nanopores and at reduced gas pressures is discussed and validated against experimental and numerical results found in literature. An exploratory case study showed the effect of reduced pore dimensions on the ETC of a porous material, at three different porosities. Future work will focus on validating the model with experimental measurements on real materials having nanopores or reduced gas pressures.

ACKNOWLEDGEMENT

This research is being funded by a Ph.D. grant of the Agency for Innovation by Science and Technology (IWT - Vlaio), their support is gratefully acknowledged.

REFERENCES

- Baetens R., Jelle B.P., and Gustavsen A. 2011. Aerogel insulation for building applications: A state-of-the-art review. *Energ. Buildings*, 43(4), 761-769.
- Braun D. and Frohn A. 1976. Heat transfer in simple monatomic gases and in binary mixtures of monatomic gases. *Int. J. Heat Mass Transfer*, 19, 1329-1335.
- Chen G. 2005. *Nanoscale Energy Transport and Conversion*. Oxford University Press.
- Denpoh K. 1998. Modeling of rarefied gas heat conduction between wafer and susceptor. *IEEE. T. Semiconduct. M.*, 11(1), 25-29.
- He Y.-L. and Xie T. 2015. Advances of thermal conductivity models of nanoscale silica aerogel insulation material. *Appl. Therm. Eng.*, 81, 28-50.
- Jelle B.P., Gustavsen A., and Baetens R. 2010. The path to the high performance thermal building insulation materials and solutions of tomorrow. *J. Build. Phys.*, 34(2), 99-123.
- Jiji L.M. 2009. *Heat Conduction*, 3rd ed. Springer-Verlag Berlin Heidelberg.
- Liu S., Duvigneau J., and Vancso G.J. 2015. Nanocellular polymer foams as promising high performance thermal insulation materials. *Eur. Polym. J.*, 65, 33-45.
- Loeb A. 1954. Thermal conductivity: VIII, a theory of thermal conductivity of porous materials. *J. Am. Ceram. Soc.*, 37(2), 96-99.
- NIST. NIST Chemistry WebBook SRD 69 – Thermophysical properties of fluid systems. <https://webbook.nist.gov/chemistry/fluid/> (accessed 15/06/2018).
- Smith D.S., Alzina A., Bourret J., Nait-Ali B., Pennec F., Tessier-Doyen N., Otsu K., Matsubara H., Elser P., and Gonzenbach U.T. 2013. Thermal conductivity of porous materials. *J. Mater. Res.*, 28(17), 2260-2272.
- Solórzano E., Rodriguez-Perez M.A., Lázaro J., and de Saja, J.A. 2009. Influence of solid phase conductivity and cellular structure on the heat transfer mechanisms of cellular materials: diverse case studie. *Adv. Eng. Mater.*, 11(10), 818-824.
- Van De Walle W. and Janssen H. 2016. A thermal conductivity prediction model for porous building blocks. *Bauphysik*, 38(6), 340-347.
- Wang G., Wang C., Zhao J., Wang G., Park C.B., and Zhao G. 2017. Modelling of thermal transport through a nanocellular polymer foam: toward the generation of a new superinsulating material. *Nanoscale*, 9(18), 5996-6009.
- Zhang Z. 2007. *Nano/microscale heat transfer*. McGraw-Hill Education.
- Zhu C.-Y., Li Z.-Y., and Tao W.-Q. 2017. Theoretical and DSMC studies on heat conduction of gas confined in a cuboid nanopore. *J. Heat Transf.*, 139(5), 052405

Rational selection of experimental readouts for hygric material characterisation

Evy Vereecken^{1,*}, Hans Janssen¹ and Staf Roels¹

¹KU Leuven, Department of Civil Engineering, Building Physics Section, Belgium

*Corresponding email: Evy.Vereecken@kuleuven.be

ABSTRACT

To reduce the experimental effort and time required for the hygric characterisation of building materials, dynamic measurements in combination with parameter estimation are promising. However, noisy input data as well as limited and noisy output data complicate a reliable estimation of the material properties. A well-considered design of the dynamic experiments is advisable to reduce parameter uncertainty and to resolve non-identifiability issues.

Based on a virtual hygric test case, this paper shows the profile likelihood analysis to be an interesting starting point for the optimal design of hygric experiments. Trajectories of internal observables, such as relative humidity, plotted for the parameter sets along the profile likelihood curve are used to map highly uncertain ranges in the prediction space. This way, a first indication of information-rich (but originally non-measured) readouts that can reduce the parameter uncertainty is achieved. A *profile likelihood sensitivity (PLS) index* is used to quantify the individual uncertainty impact of the model parameters on a dynamic model prediction. Additionally, the *PLS entropy* quantifies the parameters' individual contribution to the *overall* prediction uncertainty. Both quantitative measures are applied to select the optimal readouts for reducing parameter uncertainty. The major advantage of the methodology is that it is a sample-based approach, and hence no gradient or curvature information of the objective function is required. This renders the methodology preferable over classical approaches based on Fisher information especially when dealing with non-linear problems.

KEYWORDS

Hygric properties, dynamic experiments, optimal experimental design, profile likelihood analysis, PLS index and entropy

INTRODUCTION

The reliable evaluation of moisture transfer in building materials is of great importance for the assessment of hygric damage patterns, building energy consumption, etc. In this respect, an accurate description of the moisture storage and transport properties of building materials is essential. Traditionally, these hygric properties are mainly determined based on steady-state measurements, which are tedious and time-consuming though. To reduce the experimental efforts required for such hygric material characterisations, dynamic measurements in combination with inverse parameter estimation show a lot of promise (Vereecken et al., 2018). However, noisy input data together with a limited and noisy output can complicate a reliable estimation of the properties. A well-considered design of the dynamic experiment helps reducing parameter uncertainty and could even resolve non-identifiability issues (i.e. parameters that cannot be uniquely derived from the available experimental output). Optimal Experimental Design (OED) methods can be applied to define such a purposeful information-rich design. Often, these OED methods aim at maximizing an optimality criterion that makes use of the Fisher information matrix (a.o. Dantas et al., 2002; Balsa-Canto et al., 2007), which is a matrix that quantifies the amount of information about an unknown model parameter

comprised in an observable. Unfortunately, the calculation of the Fisher information matrix requires information on the curvature or gradient of the log-likelihood objective function, which can be hard or even impossible to obtain for non-linear problems.

To resolve these issues, this paper explores, for a virtual hygric test case, the applicability of a sample-based OED approach evolved in systems biology research (Raue et al., 2009; Flassig et al., 2015). The method uses the information obtained in a profile likelihood analysis to map highly uncertain ranges in the prediction space. In this way, information-rich (but originally perhaps non-measured) readouts that reduce the parameter uncertainty can be selected. Quantitative measures for the uncertainty impact of the model parameters and their individual contribution to the overall prediction uncertainty are applied to make a rational selection between different potential readouts.

METHODS

The next paragraphs describe the virtual benchmark case, the parameter estimation method, the profile likelihood analysis and how to use this information to make a rational selection of suitable additional readouts in further experimental planning.

Initial benchmark description

In the benchmark case, the vapour resistance factor and the sorption isotherm of a calcium silicate sample are to be determined based on a dynamic experiment. The material's actual hygric properties (= target values) are shown in Figure 1a-b. A cylindrical sample with a diameter of 8 cm, a height of 4 cm and at an initial relative humidity of 12% is exposed to a dynamic step function in relative humidity (see Figure 1c). The sample's side and bottom are covered with a vapour-tight foil, which yields one-dimensional moisture transport. The mass transfer coefficient at the top of the sample is $3 \cdot 10^{-8} \text{ s/m} + N(\mu, \sigma^2)$ with $\mu = 0$ and $\sigma = 2 \cdot 10^{-9}$. The moisture transfer in the sample is simulated by use of a control volume model in order to create the virtual experimental output. Initially, the sample's mass change measured with a 1-hour time interval is assumed to be the experimental output. This output is subjected to white measurements noise $\varepsilon \sim N(\mu, \sigma^2)$ with $\mu = 0$ and $\sigma = 0.011$.

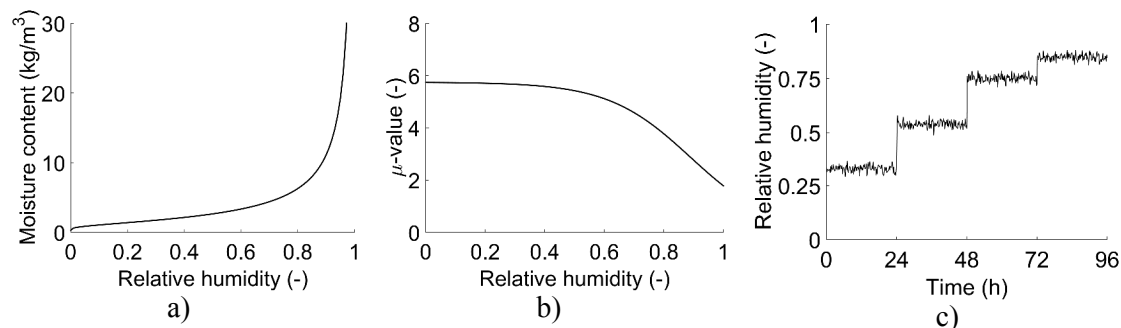


Figure 1. a) Actual sorption isotherm and b) actual vapour diffusion resistance of the calcium silicate sample; c) relative humidity in the environment above the top of the sample.

Parameter estimation

The parameters searched for are given in Table 1, together with the target values (= actual values in the benchmark case) and the lower and upper values of the search space. To estimate the unknown parameters, Bayesian inference is applied. Thereto, the Differential Evolution Adaptive Metropolis algorithm developed by Vrugt (2016) is used. In the estimation process, the moisture transfer in the calcium silicate sample is simulated with the same control volume model as used to simulate the benchmark experiment. A maximum log-likelihood (LL) is pursued, with the log-likelihood expressed as:

$$LL = \frac{-n_m}{2} \log(2\pi) - \sum_{t=1}^{n_m} \log(\hat{\sigma}_t) - \frac{1}{2} \sum_{t=1}^{n_m} \left(\frac{\bar{y}_t - y_t}{\hat{\sigma}_t} \right)^2 \quad (1)$$

where n_m the number of measurement points for the sample's mass increase, $\hat{\sigma}_t$ the standard deviation of the observations' measurement noise and \bar{y}_t and y_t the mass increase in the virtual experimental data set and simulated in the estimation process, respectively. For the priors in the Bayesian inference, a uniform distribution is assumed.

Table 1. Unknown parameters together with the target values and the upper and lower boundaries in the search space. The parameter w_{sat} in the sorption balance is assumed to be known (811.14 kg/m³). Additionally, $w(0.54)$ is assumed to be measured beforehand (= 2.9 kg/m³) and is used to infer the parameter k in the sorption balance.

	Vapour resistance $\mu(\text{RH}) =$ $1/(a+b \cdot \exp(c \cdot \text{RH}))$			Sorption isotherm $w(\text{RH}) =$ $w_{sat} \cdot [1 + (k \cdot \ln(\text{RH}))^{1/(1-m)}]^{-m}$	Noise balance σ_M	Mass transfer coefficient β
Parameters	a	b	c	m		
Target value	0.174	$2.806 \cdot 10^{-4}$	7.229	0.4321	0.011	$3 \cdot 10^{-8}$
Lower boundary	0.05	10^{-10}	4	0.1	10^{-5}	10^{-9}
Upper boundary	0.8	10^{-1}	30	0.8	1	10^{-6}

Profile likelihood analysis

To assess the identifiability and the confidence of the estimated model parameters, the profile likelihood analysis developed by Raue et al. (2009) is applied. In this approach, the profile likelihood PL curve for a model parameters θ_i is calculated by:

$$PL(\theta_i) = \max_{\theta_{j \neq i}} L(\theta_j) \quad (2)$$

with L the likelihood and θ_j the other parameters searched for in the estimation process. Hence, the PL curve for a parameter θ_i can be constructed by a re-optimisation of the parameters $\theta_{j \neq i}$ for fixed values of θ_i within an interval in the search space. In the current study, the knowledge on the likelihood of the candidate solutions analysed in the Bayesian inference procedure is used to draw the PL curves. A frequentist optimisation method as applied in (Vereecken et al., 2018) is furthermore used to create additional points to check and to complete the PL curves. The profile likelihood-based confidence region (CR) is defined by:

$$\left\{ \theta_i \mid -2 \log(PL(\theta_i)) \leq -2 \log(\hat{L}) + \chi_{\alpha}^2 \right\} \quad (3)$$

with χ_{α}^2 the α^{th} quantile of the χ_{df}^2 -distribution, with $df = 1$ degree of freedom and \hat{L} the maximum likelihood estimate. The borders of this confidence region define the confidence interval (CI). A finite CI indicates a practically identifiable parameter, which means that - based on the available data - for θ_i a limited range of values with a likelihood not significantly different from \hat{L} can be determined. A (semi-)infinite CI with a variable likelihood level is associated with practical non-identifiability, whereas an infinite CI with a constant likelihood

level below the desired threshold indicates that the parameter is both practically and structurally non-identifiable and, thus, that a unique parameterisation is theoretically not possible for the model.

Optimal experimental design

To define an OED, insight on the impact of the parameter's uncertainty on model predictions is required. To analyse this impact, in the current approach, the set of parameters along the PL curves in the confidence region are used (in case of a semi- or infinite confidence region the set of parameters along the PL curve in a region of a few orders of magnitude around the maximum likelihood estimate (MLE) can be used). The spread of the model prediction trajectories drawn for this set of parameters contains information on the parameter's uncertainty impact; a large spread indicates a large impact of the uncertainty of the specific parameter on the specific model prediction. To quantify the individual uncertainty impact of a model parameter θ_i on a model prediction $p_i(t_k)$, the profile likelihood sensitivity (PLS) as defined by Flassig et al. (2015) can be used:

$$s_i(t_k) = \left(\frac{\max(\{p_i(t_k)\}) - \min(\{p_i(t_k)\})}{\langle \hat{p}(t) \rangle_t} \right)^2 \quad (4)$$

where $\max(\{p_i(t_k)\})$ define the maximum/minimum for a model prediction p_i at time t_k and where the denominator corresponds to the time average of the model prediction for the MLE of the parameters. The overall uncertainty of the set of model parameters (n_θ) for a specific model prediction over a period defined by n_t time-points can be obtained as:

$$s_{tot} = \sum_{i=1}^{n_\theta} \sum_{k=1}^{n_t} s_i(t_k) \quad (5)$$

To reduce the uncertainty on a model prediction, and thus to reduce the uncertainty of the parameters that produce this prediction uncertainty, an additional readout that maximizes the PLS index (s_i or s_{tot} depending on the interest in a single parameter θ_i or in the total set of parameters, respectively) should be selected. When a reduction of the uncertainty of a set of model parameters it pursued, it is furthermore of importance to look for a design with a more or less equal contribution of these parameter uncertainties to the PLS index. Shannon's entropy gives information on this contribution and can be calculated as (Flassig et al., 2015):

$$J_{tot} = \sum_{k=1}^{n_t} J_k = \sum_{k=1}^{n_t} \sum_{i=1}^{n_\theta} - \frac{s_i(t_k)}{\sum_{i=1}^{n_\theta} s_i(t_k)} \log \left(\frac{s_i(t_k)}{\sum_{i=1}^{n_\theta} s_i(t_k)} \right) \quad (6)$$

The larger Shannon's entropy the more homogenous the PLS index of the individual parameters (s_i) contributes to the total PLS index (s_{tot}).

RESULTS

The OED methodology is applied to define the best position to measure the relative humidity in the sample. Four possible designs are compared: a RH-sensor at 1, 2, 3 or 4 cm from the top of the sample. Figure 2 shows the PL curves for the model parameters that define the

hygric properties, and this for the case when the experimental output is limited to the sample's mass increase (and thus without a RH-sensor). The four parameters are practically identifiable, as is the case with the other model parameters (not shown) as well. Based on the parameter sets along the PL curves below the 95% threshold, the trajectories of different model predictions are drawn. As an example, Figure 3a shows the trajectories for RH₄ (= RH at the bottom of the sample), and this for the model parameter m . The individual PLS indices as a function of time are given in Figure 3b, and this for the model prediction RH₄. Finally, Figure 3c shows for the four designs the criterion space with the total PLS index and entropy. The maximum PLS index and entropy is obtained for RH₄. Hence, of the four designs this is the best option to choose as an additional readout. Overall, the largest reductions of the confidence intervals are obtained when including data on RH₄, as indicated in Table 2. Note also that some CI's become slightly wider after including a RH-sensor, which might be the result of the extra noise term σ_{RH} included in the parameter estimation process.

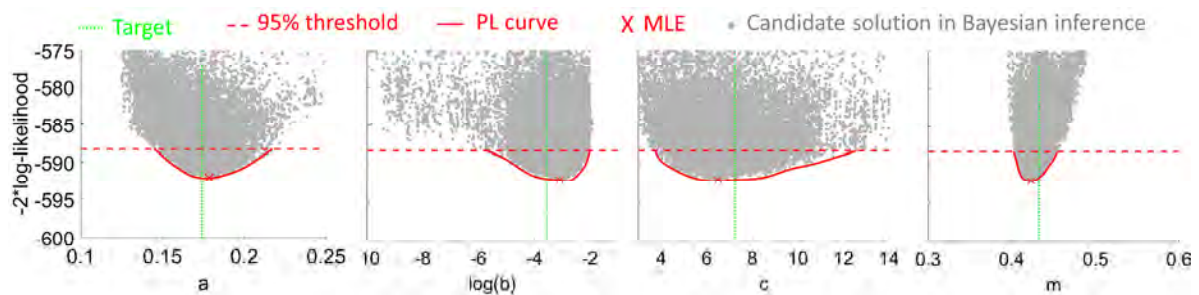


Figure 2. Profile likelihood curves for the model parameters a , $\log(b)$, c and m .

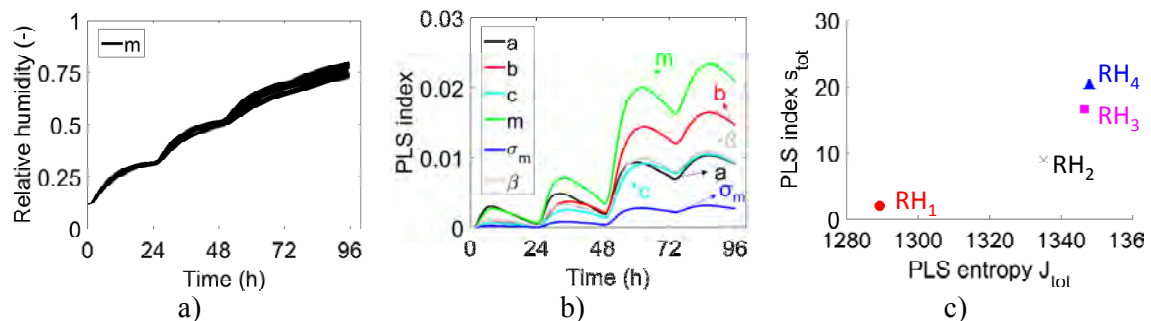


Figure 3. a) Trajectories of RH₄ along the PLS curve for the parameter m , b) PLS indices of the different model parameters for prediction RH₄ and c) criterion space.

Table 2. Upper and lower bounds of the CI's for the initial experiment and the experimental designs. The narrowest CI's are indicated in bold.

	Mass only	Mass + RH ₁	Mass + RH ₂	Mass + RH ₃	Mass + RH ₄
a	[0.145; 0.22]	[0.15; 0.2]	[0.154; 0.2]	[0.16; 0.19]	[0.142; 0.178]
$\log(b)$	[-6; -2]	[-6; -2]	[-6.8; -2.18]	[-5.8; -3]	[-4.0; -2]
c	[3.7; 14]	[4; 13.5]	[5; 15]	[5.6; 13]	[3.4; 8.7]
m	[0.405; 0.455]	[0.426; 0.442]	[0.428; 0.438]	[0.428; 0.438]	[0.426; 0.436]
σ_M	[-2; -1.88]	[-2; -1.94]	[-1.99; -1.87]	[-1.99; -1.87]	[-1.99; -1.88]
σ_{RH}	/	[-1.84; -1.72]	[-1.875; -1.77]	[-1.875; -1.77]	[-1.83; -1.72]
β	[-7.825; -6.85]	[-7.8; -6.5]	[-7.75; -6.9]	[-7.75; -6.9]	[-7.74; -6.93]

DISCUSSION

A sample-based approach that starts from the information in a profile likelihood analysis is used to make a decision on the optimal position of a RH-sensor in a hygric experiment. A RH-

sensor at the bottom of the sample is found to be most efficient in reducing the confidence region. However, it should be kept in mind that such a reduction is not necessarily always accompanied by a closer agreement with the target values.

One of the advantages of the presented sample-based approach is that it is based on information that is already at hand when analysing the practical identifiability based on the PL curves. Additionally, the method yields information on the uncertainty induced by the individual parameters and their contribution to the overall prediction uncertainty. This way, one can also focus on specific model parameters. A disadvantage of the sample-based approach might be its limitation to the readouts in experimental planning. In its current form no direct information on the best input conditions is achieved. Ultimately, as with all OED methods, the OED process is an iterative process that requires a priori knowledge. In the presented approach, a first experiment should be performed before a rational selection of further readouts can be made, whereas in the classical OED approaches initial parameter assumptions have to be made.

CONCLUSIONS

The profile likelihood analysis is shown to be a highly valuable starting point for the optimal design of hygric experiments. Based on the trajectories of internal observables plotted for the parameter sets along the profile likelihood curve uncertain ranges in the prediction space are mapped. A quantitative measure of the parameters' uncertainty (PLS index) and their contribution to the overall uncertainty (PLS entropy) enable a rational selection of highly informative readouts. The major advantage of the methodology is that it is a sample-based approach, which makes that no gradient or curvature information of the objective function is required. This way, especially when dealing with non-linear problems, the methodology is preferable over classical approaches based on Fisher information.

ACKNOWLEDGEMENT

Evy Vereecken is a postdoctoral fellow of the Research Foundation (FWO) – Flanders, Belgium (FWO project 12J5216N). This financial support is gratefully acknowledged.

REFERENCES

- Balsa-Canto E., Rodriguez-Fernandez M., Banga J.R., 2007. Optimal design of dynamic experiments for improved estimation of kinetic parameters of thermal degradation. *Journal of Food Engineering* 82, 178-188.
- Dantas L.B., Orlande H.R.B., Cotta R.M. 2002. Estimation of dimensionless parameters of Luikov's system for heat and mass transfer in capillary porous media. *International Journal of Thermal Sciences* 41, 217-227.
- Flassig R., Migal I., van der Zalm E., Rihko-Struckmann L., and Sundmacher K. 2015. Rational selection of experimental readout and intervention sites for reducing uncertainties in computational model predictions. *BMC Bioinformatics*, 16, 13p.
- Raue A., Kreutz C., Maiwald T., Bachmann J., Schilling M., Klingmüller U., Timmer J. 2009. Structural and practical identifiability analysis of partially observed dynamical models and exploiting the profile likelihood. *Bioinformatics*, 25(15), 1923-1929.
- Vereecken E., Roels S., and Janssen H. 2018. Inverse hygric property determination based on dynamic measurements and swarm-intelligence optimisers. *Building and Environment*, 131, 184-196.
- Vrugt J. 2016. Markov Chain Monte Carlo simulation using the DREAM software package: Theory, concepts, and MATLAB implementation. *Environmental Modelling & Software*, 75, 273-316.

Towards validation of a numerical model of a test cell laboratory

Johannes Brozovsky^{1,2}, Matthias Haase^{1,*}, Alessandro Nocente³ and Nicola Lolli¹

¹SINTEF, Norway

²Technical University Munich, Germany

³Norwegian University of Science and Technology, Norway

*Corresponding email: matthias.haase@sintef.no

ABSTRACT

This work represents the determination of the discharge coefficient c_d of a window in the Research Centre on Zero Emission Buildings' (ZEB) Test Cell Laboratory (TCL), located at the campus of the Norwegian University of Science and Technology (NTNU) in Trondheim, Norway, for the later use in building energy performance simulation (BEPS) software. For example, the BEPS program IDA Indoor Climate and Energy (IDA ICE) considers window openings to always be of rectangular shape and the user can only enter the percentage of window area to be opened together with a discharge coefficient c_d . By adjusting the c_d which depends on the actual shape of the window and whether the opening is used for single-sided natural ventilation or cross ventilation among others, it is possible to approximate other window opening forms such as tilted, pivoted etc.

While several studies found the discharge coefficient for large, sharp-edged openings such as windows or doors to be between 0.60 and 0.65 (Cruz & Viegas, 2016; Flourentzou, van der Maas, & Roulet, 1998; Heiselberg, Svidt, & Nielsen, 2001), it is still questionable which value to use for tilted windows.

For a subsequent calibration process of a simulation model of the TCL it was necessary to perform measurements for the discharge coefficient which describes flow losses in natural ventilation, based on the research of Heiselberg et al. (2001) in order to quantify airflows through the opened window. Measurements were carried out using Blowerdoor test equipment to determine c_d for the TCL's window. This was done for a tilted window with different opening angles and different pressure differences across the window. By experiment, the mean c_d was found to be 0.75. It can be seen that Heiselberg et al. results are slightly higher than the ones obtained in the present work. This is most likely a result of different window shapes (vertical vs. horizontal shape, but both bottom hung) and measurement inaccuracies. The results of these measurements can be used as input to BEPS programs.

KEYWORDS

Building energy performance simulation model, calibration, discharge coefficient, measurements

INTRODUCTION

Natural ventilation is often used to supply indoor environments with fresh air from the outside and it is considered to be able to reduce cooling energy demands of office buildings significantly, since people are found to be satisfied with a wider temperature range and their office indoor environment in general when given control over it (Brager, Paliaga, & de Dear, 2004; de Dear & Brager, 1998; Leaman & Bordass, 1999). The use of natural ventilation instead of mechanical cooling systems therefore can enhance working conditions while saving energy costs.

The quantification of air flowing through a window thus plays a critical role in determining the cooling potential and the indoor thermal comfort. While several studies confirmed the discharge coefficient c_d , which is often used in BEPS programs to account for turbulence and friction losses, for sharp-edged openings to be between 0.60 and 0.65 (e.g. Cruz & Viegas, 2016; Flourentzou et al., 1998; Heiselberg et al., 2001), it is still questionable which c_d to use in case of tilted windows since it is very much dependent on the specific case of application, as the following literature review will show.

Wang et al. (2017) investigated a row of windows typically used in buildings, both analytical and with Computational Fluid Dynamics (CFD) simulations. The model used for the analytical approach originally goes back to Awbi (1996) and describes the volume flow rate through a single opening due to temperature difference. Wang et al. found good coherence between their detailed CFD calculations and the analytical approach for the tilted window with a maximum deviation under 20 %. But they also suggested dismissing a constant c_d of 0.6 for all kinds of window openings when using the analytical model. The coefficient increases with increasing buoyancy and decreases with an increasing flow area.

The module for air flow networks in the simulation program TRNSYS (Transient System Simulation Tool) integrates a COMIS (Conjunction of Multizone Infiltration Specialists) type network into the program suite, that offers the possibility to calculate bidirectional air flows through opened (including tilted) windows and their c_d factor (TRNSYS, 2009). At standard opening angles from $\alpha = 3^\circ$ to 7° the equation gives discharge coefficients lower than 0.65 (mostly between 0.3 and 0.5).

Maas (1995) conducted CFD calculations and measurements for different opening angles ($\alpha = 1.02^\circ$ to 7.17°) of a tilted window (width w x height $h = 0.82$ m x 1.12 m) with and without a window reveal of 20 cm under realistic boundary conditions (measurements in an actual building). Similar to Hall (2004) Maas found that a radiator right below a window leads to a lower air exchange through the window. Furthermore, he quantified the impact of a window reveal with a decrease of air flows through the window with 50 % (Maas, 1995).

Grabe (2013) found that the assumption of equal in and outflow cross sections might not be right. Smoke visualizations showed the outflow area (in case of warmer indoor temperatures located at the window top) being constantly larger than the inflow area by the factor 2.5 (Grabe, 2013). In a precedent study Grabe, Svoboda, and Bäumler (2014) found that the incoming mass flow through a tilted window can be expressed through a logarithmic relation (Grabe et al., 2014).

Heiselberg et al. (2001) investigated the characteristics of air flow in rooms for a bottom hung (w x $h = 1.6$ m x 0.4 m) and a side hung window (w x $h = 0.81$ m x 1.38 m) in a series of laboratory measurements. The windows were mounted in a wall separating two rooms, one of which simulating outdoor conditions. A ventilation system was used to generate pressure differences and to measure the air flow rates through the openings. For the case of the bottom hung window with single sided ventilation three opening areas have been investigated: 0.019 m², 0.026 m² and 0.045 m². For this window, the measured discharge coefficients showed a significant dependency on the opening area, the window type and the pressure difference between the two rooms used for the experiment, but only a small dependency on the temperature difference. For the largest opening area the c_d was roughly between 0.78 and 0.85, for the intermediate between 0.87 and 0.92 and for the smallest between 0.96 and 1.02 (Heiselberg et al., 2001).

A comparison of the named studies is not trivial, as all the named authors pointed out that their findings would be valid for similar boundary conditions and window shapes only. The big difference from Heiselberg's findings to those from TRNFLOW for example, is mainly a result of different area calculations and different governing equations.

ZEB Test Cell Laboratory

The measurements for this study were conducted at the ZEB Test Cell Laboratory (Goia et al. 2017), a facility used for testing building envelope systems in calorimetric and comparative tests. It is located on the campus of the NTNU in Trondheim, Norway. The building consists of two 10.9 m² test cells, each surrounded by a guard volume. Both cells have one façade to the outside, facing exactly South, which can be replaced according to the research needs. This way it is possible to investigate different window types, window opening strategies, façade types, insulations, heating, ventilation and lighting strategies etc. with real weather conditions and, if required, with real occupants. Each cell and each guard volume can be conditioned independently from each other. This part also has an own, independent HVAC system. Fig. 1 shows a 3D perspective from inside the Test Cell Laboratory with highlighted investigated window (red).

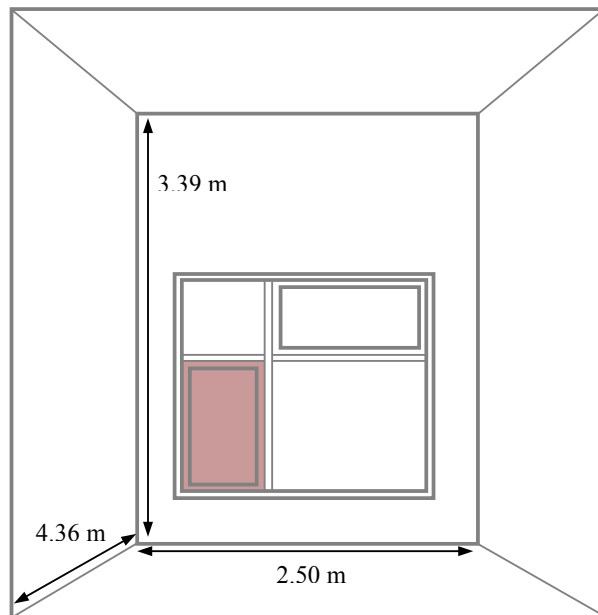


Fig. 1. 3D perspective from inside the Test Cell Laboratory. Highlighted, the investigated window.

The cell envelopes to the guard volume are made of prefabricated sandwich panels with two 0.6 mm stainless steel sheets and 10 cm injected polyurethane foam in between, resulting in a U-value of 0.23 W/m²K. Between the slab of the building and the test cell floor is a gap of ca. 0.5 m, which is also conditioned by the guard volume HVAC system. Its air exhausts are located along the test cell's surfaces to guarantee an even distributed air flow and temperature around it. A weather station on the roof is continuously collecting wind speed and direction, temperature, relative humidity, solar radiation and other weather data. These, along with the measurement values from the cells are stored on a server in the control room.

The facility is used for testing different building parts and conditioning strategies under real weather conditions, primarily for the purpose of indoor comfort analysis. A calibrated virtual model in a thermal simulation program therefore can help to reduce duration and costs of measurements by preselecting only the most promising set-ups for real life tests.

Research question

Many of the common BEPS tools, such as IDA ICE, require the input of a suitable discharge coefficient to consider special window opening forms (e.g. tilted window) for the

determination of natural ventilation air flows. As the literature review has shown, the discharge coefficient is not constant and it very much depends on the case of application. Due to simplifications IDA ICE cannot determine the air flow through a tilted window correctly, as only rectangular windows are supported (Bring et al., 1999). A possible solution for the problem can be to change the window geometry in the simulation model. The program's distributor EQUA therefore gives modelling guidelines which can be seen in Fig. 2. With this approach, the window is split into several smaller ones, which correspond to the same area as the original one, so that solar gains and losses through heat transmission etc. stay the same. Only the grey parts are (fully) openable (Moosberger, 2017). However, it is still questionable which discharge coefficient should be inserted when this method is used. Therefore it was decided to perform measurements for the discharge coefficient based on the research of Heiselberg et al. (2001).

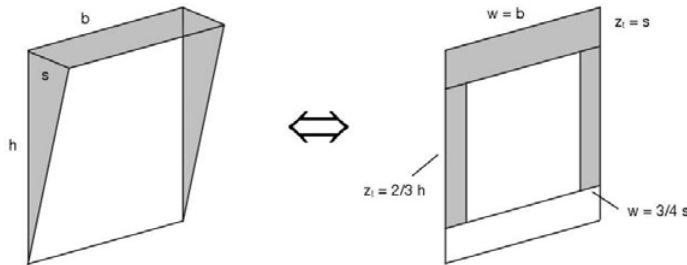


Fig. 2. EQUA's modelling guidelines for tilted windows (Brozovsky, 2018)

METHODS

Since the investigated window form significantly differs from the ones used in the previously listed studies, own measurements were taken. They were conducted at different pressure differences and opening degrees with Blowerdoor test equipment (Brozovsky, 2018). The pressure difference is measured by the Blowerdoor test equipment and the window's opening area was determined by measurements. Thereby the narrowest passage of the flow had to be found for the complex frame geometries. Following equations 1 - 3 were used for the calculations.

$$c_d = \frac{\dot{V}_{BD}}{\dot{V}_{theo}} \quad \text{eq. 1}$$

$$\dot{V}_{theo} = A_{op} \cdot u_{theo} = A_{op} \cdot \sqrt{2 \frac{\Delta p}{\rho_0}} \quad \text{eq. 2}$$

$$A_{op} = s \cdot (h + w) - A_c \quad \text{eq. 3}$$

with

\dot{V}_{BD}	Air volume flow measured by blower door [m ³ /h]
\dot{V}_{theo}	Theoretically achievable volume flow without friction [m ³ /h]
A_{op}	Opening area of window [m ²]
u_{theo}	Theoretically achievable mean air speed through opening without friction [m/s]
Δp	Pressure difference across opening [Pa]
ρ	Density of incoming air [kg/m ³]

The measures of the investigated window are $w \times h = 0.70 \text{ m} \times 1.21 \text{ m}$. The theoretically possible volume flow without friction then was obtained from the pressure difference and the density. The Blowerdoor equipment estimates the actually occurring air flow through the

rotational speed of the fan. Under realistic conditions, the actual air flow must always be lower than the theoretically possible flow. A high potential for error must be considered especially for small openings, when the clearance between the window frames is minimum. All measurements were taken under isothermal conditions. A_{op} was determined with equation 3 with tilt width s and window height h (according to Figure 2), window width w and constriction area A_c due to the window fitting etc.

RESULTS

Fig. 3 and Table 1 show the results of the analysed measurement data. As a comparison, also Heiselberg et al.'s findings (2001) with the largest window opening area are plotted on the figure. By experiment, the mean discharge coefficient was found to be $c_d = 0.75$ for the tilted window being used in the laboratory which is good accordance with the research by Heiselberg et al. (2001).

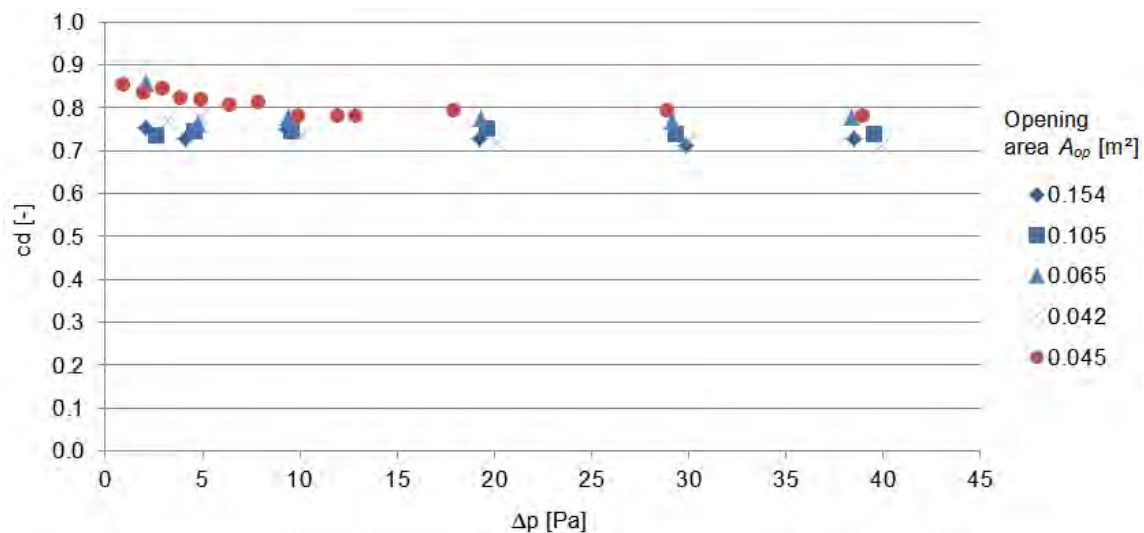


Fig. 3. Measured discharge coefficients for different opening areas and pressure differences (blue) and measurement results by Heiselberg et al. (2001) (red)

Table 1. Measured c_d values for different opening areas

Opening area A_{op} [m ²]	Tilt width s [m]	Tilt angle α [°]	Mean c_d [-]
0.042	0.024	4.1	0.74
0.065	0.037	5.4	0.79
0.105	0.060	7.1	0.74
0.154	0.088	8.5	0.73

DISCUSSIONS

It can be seen that Heiselberg et al. results are slightly higher than the ones obtained in the present work. This is caused by different window shapes (vertical vs. horizontal shape, but both bottom hung) and measurement inaccuracies. Still, the findings are in accordance with Heiselberg et al. as they assume that “[...] for large opening areas the discharge coefficient approaches the commonly used value of 0.6, while it will have a larger value for small opening areas” (Heiselberg et al., 2001) which was also found by Wang et al. (2017). The overall mean discharge coefficient for all opening sizes and pressure differences of the investigated and tilted window is $c_d = 0.75$.

CONCLUSIONS

The results of these measurements can be used as input to BEPS programs. It gives confidence in the use of discharge coefficients determined by Heiselberg et al. (2001). The obtained discharge coefficients were consequently used in a calibration process of an IDA ICE simulation model of the TCL (Brozovsky, 2018).

ACKNOWLEDGEMENT

This work is financed by the Norwegian Research Council and the industry partners StGobain, NorDan and Schüco.

REFERENCES

- Awbi, H. B. (1996). *Air Movement in Naturally Ventilated Buildings*. Reading, UK.
- Brager, G., Paliaga, G., & de Dear, R. (2004). *Operable windows, personal control and occupant comfort*. Retrieved from <http://escholarship.org/uc/item/4x57v1pf>
- Bring, A., Sahlin, P. and Vuolle, M. Models for Building Indoor Climate and Energy Simulations, a report of IEA Task 22: Building Energy Analysis Tools, Subtask B: Model Documentation, KTH Royal Institute of Technology, Stockholm, 1999.
- Brozovsky, J. (2018). Study of a Digital Twin for a Test Laboratory, Master thesis TU Munich, 2018
- Cruz, H., & Viegas, J. C. (2016). On-site assessment of the discharge coefficient of open windows. *Energy and Buildings*, 126, 463–476. <https://doi.org/10.1016/j.enbuild.2016.05.051>
- Flourentzou, F., van der Maas, J., & Roulet, C.-A. (1998). Natural ventilation for passive cooling: measurement of discharge coefficients. *Energy and Buildings*, 27(3), 283–292.
- Goia, F, Schlemminger C. and Gustavsen A. (2017). The ZEB Test Cell Laboratory. A facility for characterization of building envelope systems under real outdoor conditions. *Energy Procedia*, 132, 531-536.
- Grabe, J. von. (2013). Flow resistance for different types of windows in the case of buoyancy ventilation. *Energy and Buildings*, 65, 516–522. <https://doi.org/10.1016/j.enbuild.2013.06.035>
- Grabe, J. von, Svoboda, P., & Bäuml, A. (2014). Window ventilation efficiency in the case of buoyancy ventilation. *Energy and Buildings*, 72, 203–211. <https://doi.org/10.1016/j.enbuild.2013.10.006>
- Hall, M. (2004). Untersuchungen zum thermisch induzierten Luftwechsellpotential von Kippfenstern (Dissertation). Universität Kassel, Kassel.
- Heiselberg, P., Svidt, K., & Nielsen, P. V. (2001). Characteristics of airflow from open windows. *Building and Environment*, 36(7), 859–869. [https://doi.org/10.1016/S0360-1323\(01\)00012-9](https://doi.org/10.1016/S0360-1323(01)00012-9)
- Leaman, A., & Bordass, B. (1999). Productivity in buildings: the ‘killer’ variables. *Building Research & Information*, 27(1), 4–19. <https://doi.org/10.1080/096132199369615>
- Maas, A. (1995). Experimentelle Quantifizierung des Luftwechsels bei Fensterlüftung (Dissertation). Universität Kassel, Kassel.
- Moosberger, S. (2017) Gekipptes Fenster, personal communication (E-mail) October 27, 2017.
- TRNSYS. (2009). *TRNFLOW: A module of an airflow network for coupled simulation with TYPE 56 (multi-zone building of TRNSYS). User manual*.
- Wang, J., Wang, S., Zhang, T., & Battaglia, F. (2017). Assessment of single-sided natural ventilation driven by buoyancy forces through variable window configurations. *Energy and Buildings*, 139, 762–779. <https://doi.org/10.1016/j.enbuild.2017.01.070>

Adsorption and film forming of train of water droplets impacting porous stones

Dominique Derome^{1*}, Stephan Carl¹, Peter Vontobel², Jan Carmeliet³

¹Laboratory for Multiscale Studies in Building Physics, Swiss Federal Laboratories for Materials Science and Technology, Empa, Switzerland

²Laboratory for Neutron Scattering and Imaging, Paul Scherrer Institute, Switzerland

³Chair of Building Physics, ETH Zürich, Switzerland

*Corresponding email: dominique.derome@empa.ch

ABSTRACT

The phenomenon of droplets impacting porous media is ubiquitous in rain events. Rain is a major source of moisture in buildings. When a water droplet impacts a permeable surface, it spreads on the surface and is absorbed into the porous material due to capillary action. This paper presents an experimental investigation of the absorption and film forming during train of liquid droplets impacting porous stones, towards establishing the fate of rain droplets during rain events.

KEYWORDS

Rain water droplet, porous materials, impact, absorption, film forming.

INTRODUCTION

The phenomenon of drop impacting porous media is ubiquitous in nature and is associated with mechanisms found in various industrial applications. Rain is a major source of moisture in buildings and a main agent of degradation.

When a liquid droplet impacts a permeable surface, it spreads on the surface and is absorbed into the porous material due to capillary action. The spreading behavior of the impinging droplet on the surface is known to depend on the properties of the liquid, i.e. density, viscosity and surface tension, impact conditions such as drop size and impact velocity, and the surface wettability and roughness (Lee et al. 2016a). In porous media, absorption is governed by both the properties of the liquid and of the porous medium, i.e. porosity, pore size, wettability (Lee et al. 2016b). Once the deposited droplet is completely depleted from the surface, the liquid further redistributes within the porous medium due to capillary forces, while evaporation occurs at the surface (Reis et al. 2003). In case of saturation of the porous medium, the remaining water lies at the surface in a pool, and, in the event of further impacts, a water film can build up.

For a better understanding of the absorption process inside porous media, observing directly the liquid content redistribution in the porous medium is required. Absorption in porous media has been studied with several non-destructive techniques, namely X-ray, neutron and gamma-ray radiography, magnetic resonance imaging (MRI) and nuclear magnetic resonance, and destructive techniques.

In this study, we aim to capture the full deposited droplet contact area, absorption and film forming process of trains of impinging droplets on natural porous stones by using neutrons as the means of investigation. Neutron radiography allows visualizing the moisture content

distribution in porous stones. During the experiments, we measure the mass of deposited water to validate the neutron measurements. The deposition and absorption process of trains of impinging droplets is continuously characterized during deposition, absorption, evaporation and redistribution. We provide the total mass in/above the stone and moisture distribution, in a time-resolved manner.

METHODS

Samples

Three stones with varying porosity and uptake characteristics are selected: two sandstones (Meule and Bentheimer) and one limestone (Savonnières), Figure 1. The porous stones are cut in cubes of 20 x 20 x 10 mm³ for characterization and drop impact tests.



Figure 1. Photos of Bentheimer (left), Meule (center) and Savonnières samples.

Water droplet generation

Water droplets are generated at the flat tip of a needle by pushing a syringe pump. The droplets have an initial diameter of 2 mm. When the droplet is released, it accelerates by gravity reaching an impact velocity of 0.5 m/s, 1.0 m/s and 3.0 m/s, and the rates are varied to 4, 8 or 16 drops per minute.

Neutron radiography

The absorption process into the porous stone is captured by neutron radiography. In a nutshell, neutrons are attenuated by the hydrogen of water, but penetrate the porous stone, and then activate a scintillator which is photographed by a camera.

The experiment for the absorption of drop impact is performed at the NEUTron Transmission RADIography (NEUTRA) beamline of the Paul Scherrer Institut, Villigen, Switzerland. The NEUTRA beamline is operated with neutrons within a thermal spectrum (Lehmann 2008). The necessary exposure time for each image is 3 seconds and the nominal spatial resolution of the neutron radiography is 47.2 $\mu\text{m}/\text{pixel}$. Figure 2 shows a schematic overview of the neutron beamline and the experimental setup for drop impact.

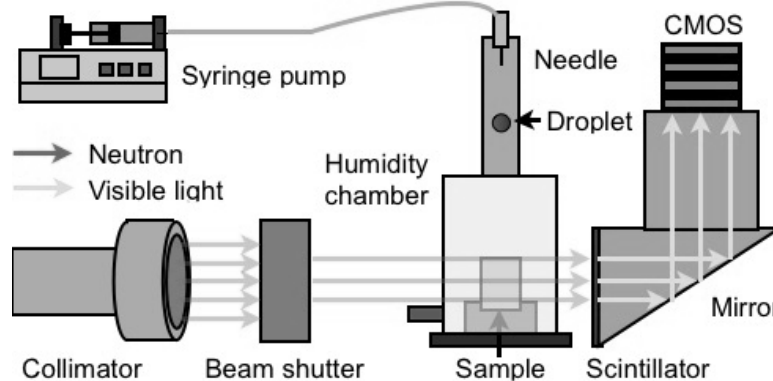


Figure 2. Schematic of experimental setup at NEUTRA beamline configuration.

Using Beer-Lambert law, the variation of attenuation of the neutron beam yields the moisture content, further details on image analysis and post-processing can be found in (Sedighi Gilani et al. 2012). Figure 3 shows the comparison between mass obtained from neutron images and deposition.

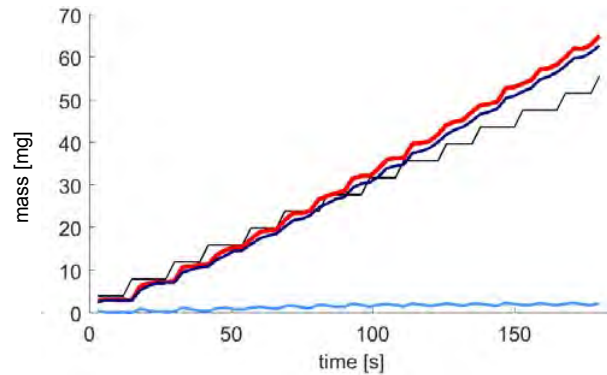


Figure 3. Validation by comparing total mass (mg) versus time comparing the total mass from neutron imaging (thick red) with actual water mass deposited (thin black). Total mass of water resting on the stone in blue, in the stone in dark blue.

RESULTS

We present here only the results for Savonnières but results of all 3 stones are presented at the conference. In general, the uptake is faster for Savonnières with more water in the stone and less on the surface. The other two stones undergo less moisture uptake in the same time and hence the surface water pool appears earlier and develops more.

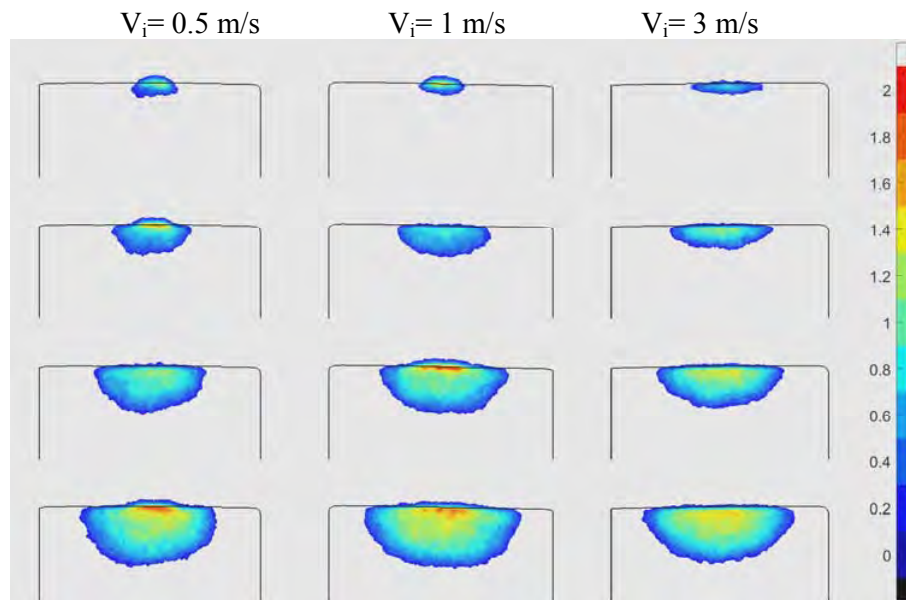


Figure 4. Moisture content (in thickness (mm) per pixel) for train of water droplets on Savonnières at the rate of 4 drops per minute for three impact velocities from top to bottom after 3, 33, 93 and 180 seconds.

In Figure 4, moisture content distribution is given after deposition of 1, 3, 7 and 13 droplets for three impact velocities. Absorption occurs from the deposited droplet into the stones via

the contact area, With time, water is transported in the stone further and further from the point of impact. In time water distribution has an elliptical shape that is quite independent from the impact velocities, as, by that time, the contact area is similar in all these cases.

Figures 5 and 6 provide moisture content profiles versus time above and below the stone surface, taken at the center of the droplet and right below/above the surface respectively. Faster droplet rate leads to the development of water accumulation and thus water pool and film on the surface.

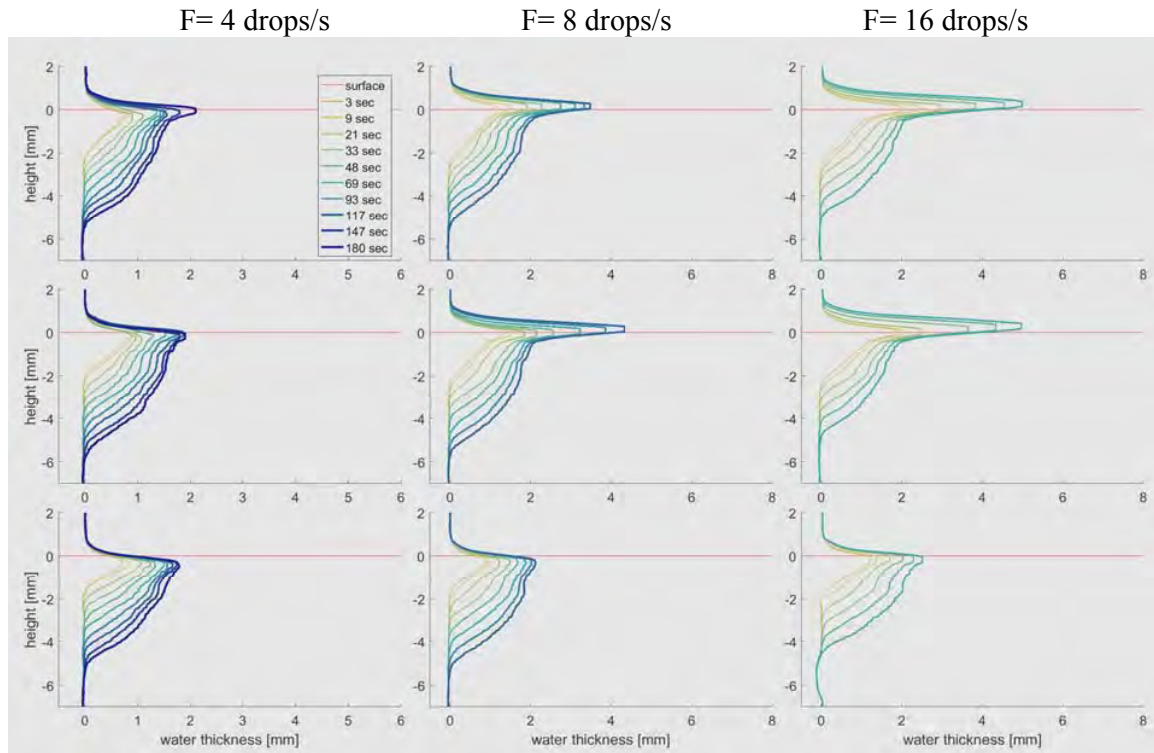


Figure 5. Vertical moisture content profiles for train of water droplets on Savonnières at the rate of 4, 8 and 16 drops per minute for three impact velocities from top to bottom of 0.5, 1 and 3 m/s. Pink line represents the stone surface.

Droplets spreading on the surface depends on impact velocities. Then, water is transported in the stone further and further from the point of impact. In time water distribution has an elliptical shape that is quite independent from the impact velocities. Faster droplet rate leads to the development of water accumulation and thus water pool and film on the surface. Film forming is found to be dependent on both transport properties and saturation degree of the stones. Moisture distribution within the porous stones, which are here all rather isotropic, is found to be dependent on impact velocity and thus of maximum spreading, for the first droplets of the train. Afterwards, the pooling of water yields similar moisture distribution.

CONCLUSIONS

This paper presents an experimental investigation of absorption and film forming during trains of liquid droplets impacting porous stones. Neutron radiography is used to quantify moisture absorption in three natural stones of varying porosity and moisture uptake characteristics. Film forming is found to be dependent on both transport properties and saturation degree of the stones. Moisture distribution within the porous stones, which are here all rather isotropic,

is found to be dependent on impact velocity, and thus maximum spreading, for the first droplets of the train. Afterwards, the pooling of water yields similar moisture distribution. This experiment provides very detailed information of rain droplet absorption and redistribution in porous materials and can be used in conjunction with rain deposition modeling to understand the fate of water with the built environment.

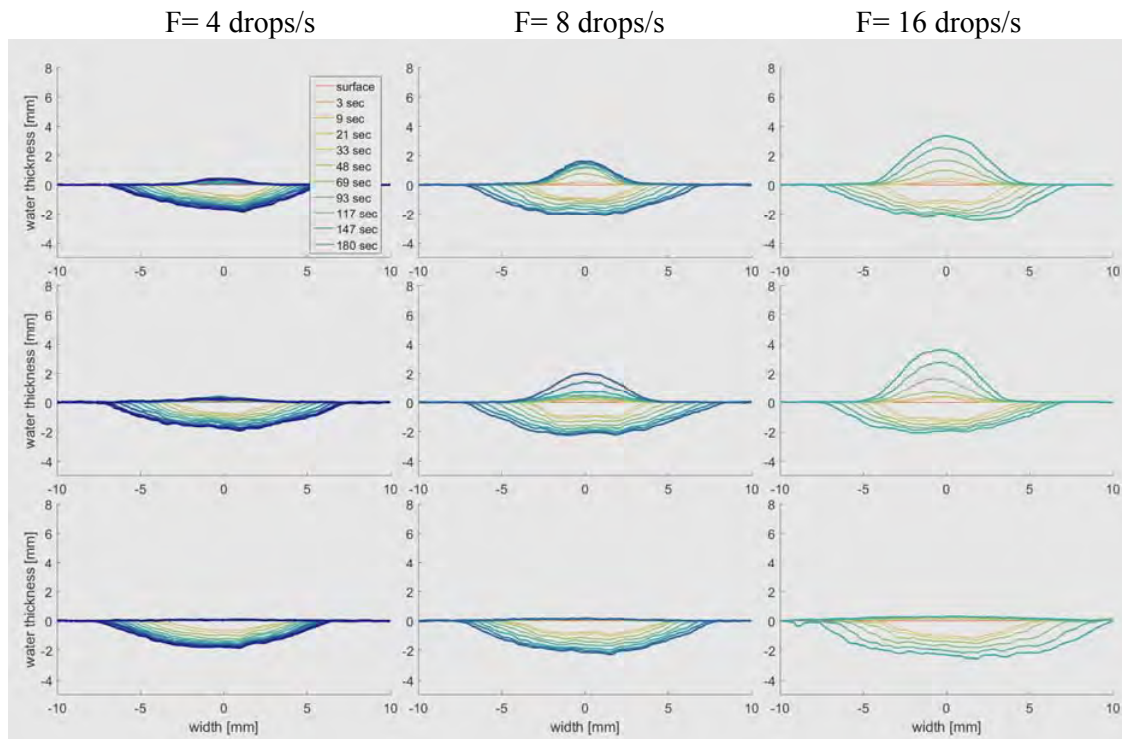


Figure 6. Horizontal moisture content profiles above and below the contact line for train of water droplets on Savonnières at the rate of 4, 8 and 16 drops per minute for three impact velocities from top to bottom of 0.5, 1 and 3 m/s.

ACKNOWLEDGEMENT

We acknowledge the important contribution of the PhD work of Dr. Jaebong Lee to this paper and for running the experiment. His PhD was made possible through Swiss National Science Foundation project no. 200021-135510. Guylaine Desmarais is acknowledged for the support in the preparation and running of the PSI Neutra experiment.

REFERENCES

- Lee J.B., D. Derome, J. Carmeliet. 2016a. Drop impact on natural porous stones. *J. Colloid and Interface Science*, 469:147-156.
- Lee J.B., D. Derome, J. Carmeliet. 2016b. Absorption of impinging water droplet in porous stones. *J. Colloid and Interface Science*, 471:59-70.
- Reis N.C., R.F. Griffiths, M.D. Mantle, L.F. Gladden. 2003. Investigation of the evaporation of embedded liquid droplets from porous surfaces using magnetic resonance imaging, *Intern. J. of Heat and Mass Transfer*, 46:1279–1292.

- Lehmann E.H. 2008. Recent improvements in the methodology of neutron imaging, *Pramana*, 71 () 653–661.
- Sedighi Gilani M., M. Griffa, D. Mannes, E, Lehmann, J. Carmeliet, D. Derome. 2012. Visualization and quantification of liquid water transport in softwood by means of neutron radiography, *Intern. J. of Heat and Mass Transfer*, 55:6211-6221.

Application of Rain Intensity Dependent Rain Admittance Factor (RAF) in Hygrothermal Performance Assessment of Wall Systems

Emishaw Iffa*, Fitsum Tariku

BCIT Building Science Centre of Excellence, BC, Canada

**Corresponding email: eiffa@bcit.ca*

ABSTRACT

Wind-driven rain (WDR) is one of the main moisture loading sources on the exterior enclosures. The direct impact of wind-driven rain on the hygrothermal performance of building envelope has been well documented. Rain admittance factor (RAF) and rain penetration values characterize the amount of water reaching the exterior surface and the exterior surface of the water-resistive barrier respectively based on measured horizontal rain intensity. In common RAF factor calculation from horizontal rainfall data procedures, such as ASHRAE 160, RAF values are not affected by the intensity of the rainfall. However, a previous study shows RAF coefficients are sensitive to the rainfall intensity. Thus it is important to investigate how the sensitivity of using horizontal rainfall intensity dependent RAF factors and the subsequent rain penetration relates to hygrothermal performance assessment of building envelope components. This study is based on five years of WDR and horizontal rainfall data collected at different orientations of façades at a two-story test building in a mild coastal climate. The data is categorized into two sets based on rain intensity. The correlation between the measured moisture content on the sheathing board of a building envelope at different points utilizing RAF values based on the proposed approach and the overall measured RAF values is studied using WUFI simulation. Results show that an average percentage difference between the moisture content values of a sheathing board using RAF values of the rain intensity dependent approach and the overall RAF measured value can be as large as 9 %.

KEYWORDS

hygrothermal performance, rain admittance factor, rain intensity, water penetration, wind-driven rain.

INTRODUCTION

Moisture ingress on building envelopes due to rain load along with vapour diffusion and built-in moisture is the main cause for moisture related problems such as corrosion, mould, rotteness and their consequential effects such as compromised structural integrity and health-related problems. Accumulated moisture in components of wall systems due to wind-driven rain (WDR) can be prominent in wet climates such as the coastal climate of British Columbia. Designers are expected to take the rain load effect into account on the overall hygrothermal performance of a building enclosure. Incorporating the wind-driven rain effect requires measuring or accurately estimating the number of raindrops that are impinging on the vertical building surfaces due to wind forces blowing towards the building.

Many factors affect the amount of wind-driven rain, including rain intensity, wind speed and direction, topography, building geometry, the orientation of the building assembly, and the location of the area of interest on the building elevation. However, the primary components to

wind-driven rain intensity are rain intensity, wind speed and wind direction. Most wind-driven rain computational models are based on semi-empirical and numerical analysis methods. The most commonly used numerical analysis method is mainly developed by Choi in the 1990s (Choi, 1994a, 1994b, 1999). According to Hens (2015), the semi-empirical analysis method was developed in the 1950s by Lacy (Lacy, 1965) using experimental-based relations of raindrop size, raindrop speed, and horizontal rain intensity. The calculation of raindrop size and terminal velocity was based on Best's work (Best, 1950a, Best, 1950b). Recently, based on Lacy's findings, a semi-empirical estimation formula is developed by Straube and Burnett (2000).

To estimate the amount of wind-driven rain without direct field measurement at the location of interest, historical weather data can be used. To account for other factors, such as the building geometry, orientation of the building assembly, and the area of interest on the wall façade, semi-empirical studies have provided coefficients to be used in calculations. The two commonly used factors are *the wall factor*, W (BSI EN 13013-3, 1997), and *Rain Admittance Factor*, RAF (Straube and Burnett, 2000), which considers the building aspect ratio, the presence of a roof overhang and the area of interest within the wall facade. The wind-driven intensity on a vertical surface according to Straube and Burnett's method (Straube and Burnett, 2000) can be calculated as:

$$R_{wdr} = RAF \times DRF(V_t) \times \cos(\theta) \times U(h) \times R_h \quad (1)$$

Where R_{wdr} is wind-driven rain intensity (mm), RAF is Rain Admittance Factor, $DRF(V_t)$ is Driving Rain Factor ($1/V_t$), θ is the angle of the wind to the wall's normal, $U(h)$ is the wind speed at the height of interest (m/s), R_h is horizontal rainfall intensity (mm/hr.m²).

The driving rain factor (DRF) is a multiplicative inverse of terminal velocity. A droplet size, the main parameter in terminal velocity calculation (Dingle and Lee, 1972), can be estimated based on horizontal rain intensity (by Best 1950a). The last 3-terms on the right side of equation 1, $\cos(\theta) \times U(h) \times R_h$, represent free-field wind-driven rain under the rain intensity through a 1 m² area of the unobstructed vertical field.

Commonly, a median droplet size is used while employing the Straube and Burnett model. A work by Cornick and Lacasse (2009) used the predominant raindrop diameter instead of the median drop size. Using the predominant raindrop diameter provides a lower terminal velocity and a higher WDR load (Van Den Bossche et al, 2013). A work by Van Den Bossche et al. (2013) stresses the drawbacks of using single rain droplet diameter and their simulation work shows using a median droplet in WDR calculation can introduce an error up to 20% as the horizontal rain intensity increases.

In this study, the dependency of the Rain admittance factor (RAF) on rainfall intensity for different orientations and elevations is examined. Based on the newly obtained RAF coefficients, the effect of RAF values variation between the existing RAF calculation and the proposed approach on hygrothermal performance of building enclosure is investigated.

WEATHER DATA ANALYSIS

In this study, fifty-seven months of weather data between January 2009 to September 2013 was collected at the BCIT's Building Envelope Test Facility in Burnaby (BETF), British Columbia, Canada. The horizontal rain intensity, vertical rain intensity, wind speed and

directions are measured using a horizontal rain gauge, 15 wall rain gauges, and an anemometer. The data is used to calculate the free-field wind-driven rain, the Driving Rain Factor (DRF) and the Rain Admittance Factor (RAF) at different elevations and orientations.

An hourly data of horizontal rain, wind speed and direction is used to calculate the free-field wind-driven rain using Equation 1. The weather data is categorized into classifications based on rain intensity as class I (high horizontal rain intensity) and Class II (low horizontal rainfall). The effect of small wind speed is found to be less significant in the computation of RAF values, thus classifying the data based on wind speed is excluded in this paper. The horizontal rain intensity of above 2mm/hr is classified as high rain intensity class. Correspondingly, horizontal rain intensity below and equal to 2mm/hr is considered as low rain intensity scenario. In order to accommodate the sensitivity of data sensors, rain intensity and wind speed values below 0.1mm/hr and 0.5 m/s are unused. The vertical rain intensity measured at different locations and orientations, as shown in Figure 1b, is used to find a semi-empirical RAF value. Once the free-field wind-driven rain is calculated, the RAF values are obtained as gradients of vertical rain intensity (the wind-driven rain) and the free-field wind-driven rain.

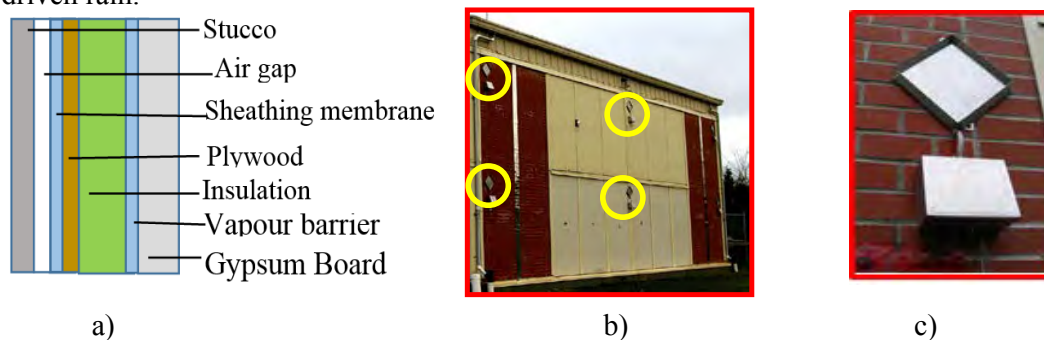


Figure 1 a) a rain-screen wall system b) rain gauge locations and c) vertical rain gauge

SIMULATION DESIGN

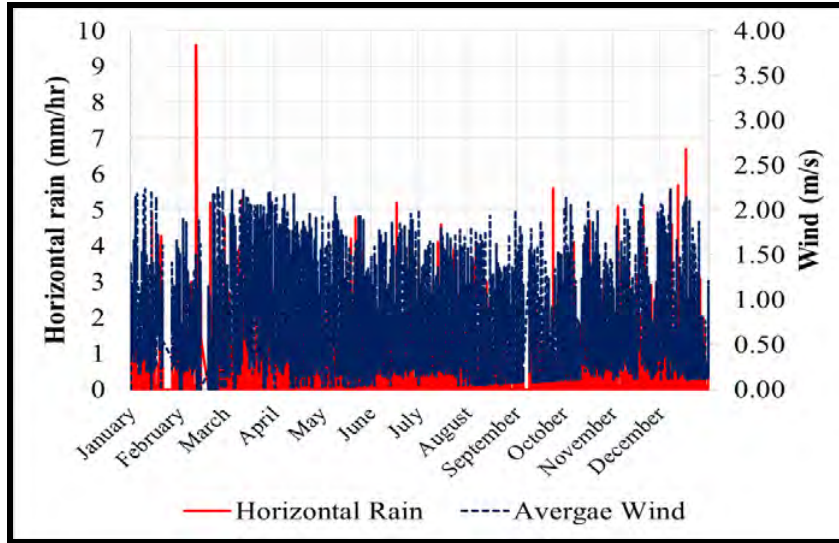
In order to study how the rain intensity dependant RAF values affect the hygrothermal performance of a building envelope, a WUFI simulation for rain screen wall system is conducted. The indoor conditions of relative humidity and temperature are set using ASHRAE 160P intermediate model.

As shown in Figure 1a, the components of the wall system are regular Portland Stucco which is used as an exterior cladding, 10mm rain- screen air-gap, spun bonded olefin as a sheathing membrane (as a second plane of protection from precipitation and water intrusion), plywood sheathing board, 6 mil polyethylene sheet as a vapour and air barrier material, and gypsum board as an interior finishing layer. The initial conditions of 20°C and 80% RH are used for all wall component members and the simulation is run for two consecutive years.

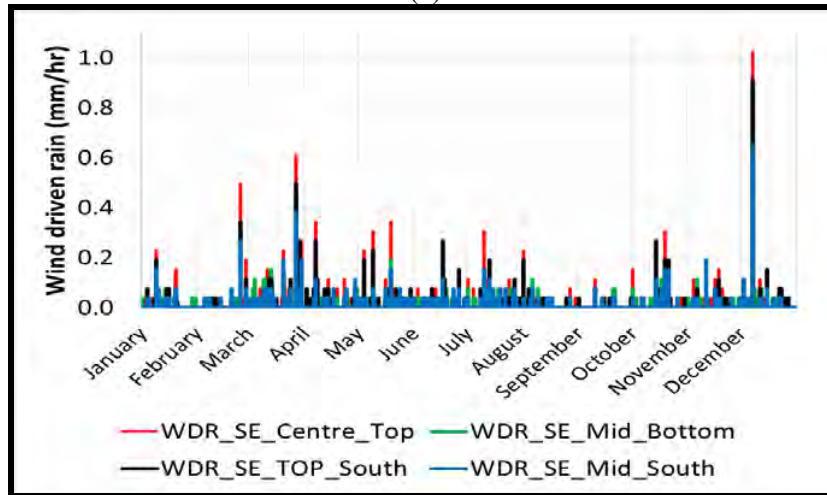
RESULTS AND DISCUSSIONS

The rain dependant RAF values were computed using the collected data of horizontal rain intensity, wind speed and direction and the wind-driven rain which is collected by vertical rain gauges at different elevations and directions of the BCIT Building Envelope Test Facility (BETF) walls. The horizontal and the vertical rain intensity values data used in this study are measured from January 1st, 2009 to September 30th, 2013. Figure 2 (a) shows the measured horizontal rain and wind speed of the year 2009. The wind-driven rain collected by vertical rain gauges on the South-East facing wall is shown in Figure2 (b). The selected elevations and the directions for the rain gauges are top-center, mid- centre, top-corner and mid-corner points

of the four walls of the BETF. This data is used to simulate the hygrothermal performance of a rain screen wall located in Metro Vancouver.



(a)



(b)

Figure 2. One year measured data. a) Horizontal rain and wind speed, b) WDR at different wall locations.

The horizontal rain intensity, the wind speed and direction data were used to calculate the free-field wind-driven rain and the DRF. The RAF values at each wall rain gauge location were determined by the slope of the plot of wind-driven rain intensity against the calculated free-field wind-driven rain (Tariku et al. 2016). The RAF values at the different locations on the walls are compared to the RAF values in literature and shown in Table 1.

Table 1. Calculated rain-dependent RAF and literature-based RAF values

Vertical Rain-gauge locations	Low rain Intensity	High rain intensity	BSI EN 13013-3, 1997
Top Centre	0.23	0.32	0.5
Middle Centre	0.23	0.31	0.4
Top Corner	0.26	0.38	0.5
Mid Corner	0.33	0.37	0.4

In order to study how this variation in RAF values affects the hygrothermal performance of building envelope, two types of simulations are conducted. The first simulation is using the measured variable RAF values based on the horizontal rainfall at the specific hour of interest. Thus in this simulation when the horizontal rain intensity class changes so does the RAF value used. In the second simulation category, the calculated constant RAF values are used.

Figure 3 shows the moisture content of the plywood sheathing board for a rain-screen wall system on three locations. As can be seen in the figure, the moisture content values for the Metro Vancouver weather data, the simulation based on constant RAF provides a lower moisture content value throughout the simulation periods of all three locations. The percentage difference of the water content of the plywood values between the two simulations for the gauges locations of top-centre, mid centre and top-corner has reached up to 5.8%, 9.0% and 6.2% respectively. The schematic diagram shown in Figure 3d shows the rain gauge locations used in the study.

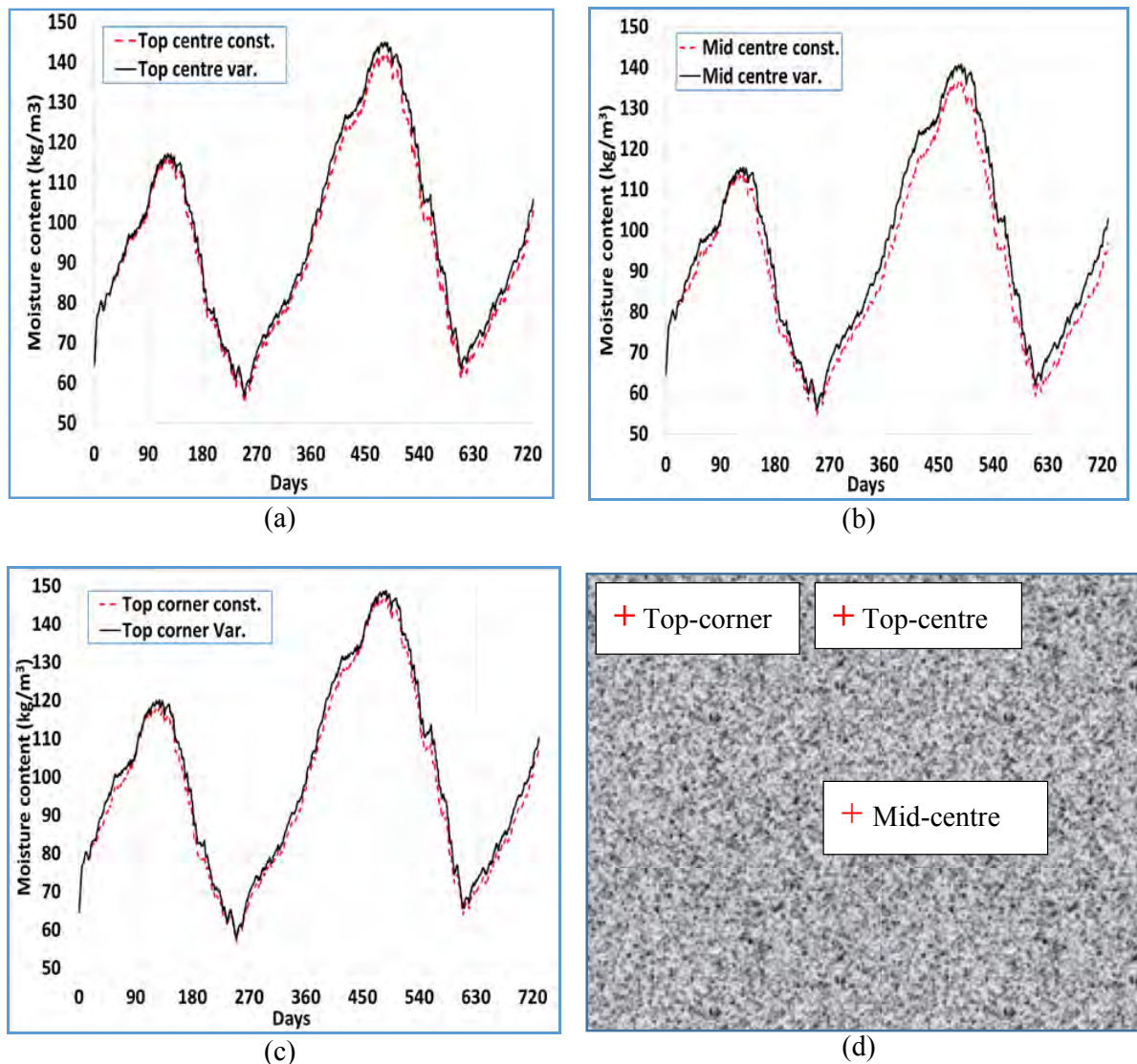


Figure 3. Water content of the plywood for constant and rain intensity dependant RAF values at (a) top-centre (b) mid-centre and (c) top-corner

Considering the above figure is moisture content values of a sheathing in a rain-screen wall design with a moisture barrier, it can be deduced that the variation between the two models can be pronounced in the absence of rain gap and prolonged time period.

CONCLUSIONS

In this study, the variation of the proposed approach's RAF values from the existing literature calculation method is studied and the variation's effect on the hygrothermal performance of rain screen wall system is examined. Results show that there is a direct relationship between rain intensity and calculated RAF values. The total water content of the plywood sheathing for wall systems with rain screen is simulated for both constant and rain intensity dependent RAF values developed under this study. A percentage variation up to 9% is observed between the new approach and constant RAF model for studied wall systems at different elevations. These findings support the initial hypothesis of this study that applying a constant RAF value for any rain load can affect the overall hygrothermal performance study of building enclosures.

REFERENCES

- Best, A. 1950a. The size distribution of raindrops. *Quarterly Journal of the Royal Meteorological Society*, 76(327), 16-36.
- Best, A. C. 1950b. Empirical formulae for the terminal velocity of water drops falling through the atmosphere. *Quarterly Journal of the Royal Meteorological Society*, 76(329), 302-311.
- BSI EN 13013-3. 1997. Hygrothermal performance of buildings - Climatic data - Part 3: Calculation of a driving rain index for vertical surfaces from hourly wind and rain data. British Standards Institution, Committee B/540/1.
- Choi, E. 1994a. Determination of wind-driven-rain intensity on building faces. *Journal of Wind Engineering and Industrial Aerodynamics*, 51(1): 55-69.
- Choi, E. C. 1994b. Parameters affecting the intensity of wind-driven rain on the front face of a building. *Journal of Wind Engineering and Industrial Aerodynamics*, 53(1): 1-17.
- Choi, E. C. 1999. Wind-driven rain on building faces and the driving-rain index. *Journal of Wind Engineering and Industrial Aerodynamics*, 79(1): 105-122.
- Cornick S.M., and Lacasse M.A. 2009. An investigation of climate loads on building facades for selected locations in the US. *J ASTM Int.* 6 (2):1-17
- Dingle, N., & Lee, Y. 1972. Terminal fall speeds of raindrops. *Journal of Applied Meteorology*, 11(5): 877-879.
- Hens, L.S.C.H. 2015. Combined heat, air, moisture modelling: A look back, how, of help? *Building and Environment* 91: 138-151.
- Lacy, R. E. 1965. Driving-rain maps and the onslaught of rain on buildings: Building Research Station.
- Straube, J. F., & Burnett, E. F. P. 2000. Simplified Prediction of Driving Rain on Buildings. *Proceedings of International Building Physics Conference, Eindhoven, The Netherlands*: 375-382.
- Tariku F., Simpson W., Ngudjiharto E. 2016. Analysis of wind-driven rain exposure based on long-term monitoring. In: *Proceedings of the Thermal Performance of the Exterior Envelopes of Whole Buildings XIII International*, Clearwater, FL USA.
- Van Den Bossche, N., Lacasse, M. and Janssens, A. 2013. A uniform methodology to establish test parameters for water tightness testing. *Building & Environment*, 63:145-156.

Do interface resistances matter in historic masonries? -Analysis based on X-ray tomography and heat, air and moisture modelling -

Klaas Calle^{1,*} and Nathan Van Den Bossche¹

¹Faculty of Engineering and Architecture, Ghent University, Ghent, Belgium

*Corresponding email: Klaas.Calle@ugent.be

ABSTRACT

For hygrothermal simulations it is often advised to homogenize masonry wall constructions into a 1D solid brick construction. This saves computational time, but it may lead to an underestimation of moisture related risks. Some literature states that the impact of mortar is negligible, but no specific attention was paid to historic masonries, which often have high absorptive mortars (e.g. lime) and/or bricks. Hence, this study investigates the impact of the interface resistance between brick and mortar, in relation to the properties of the adjacent materials during absorption as well as under real climate conditions. As expected the impact of interface resistances is more pronounced during an absorption test compared to under real climate conditions. Nevertheless, due to the interface resistance, increased frost risks do arise in a number of cases subjected to real climate conditions. The results are found to be highly dependent of the climate, the sequence of rain and frost events, and the properties of the adjacent materials. In conclusion, one can state that there can be an increased risk of frost damage due to the effect of interface resistances in historic masonries. However, deriving generic guidelines on the impact of these effects remains a challenge due to a high dependency on climate and material parameters.

KEYWORDS

Interface resistance, HAM simulations, Masonries, Frost damage

INTRODUCTION

The hygrothermal response of porous materials has been studied and documented intensively. (Pel, 1995; Kunzel,1995; Grunewald,1997) These studies have led to an increased reliability of risk assessment on building facades due to Heat, Air and Moisture (HAM) modelling software. In these models it is often advised to homogenize masonry constructions from a combination of mortar and bricks to solid brickwork to simplify the model and thereby save computational time (Dephin User Manual, 2006; Vereecken et al, 2013). This approach raises several questions. For instance, what happens in the mortar, which represents in reality +/- 20% of the masonry?

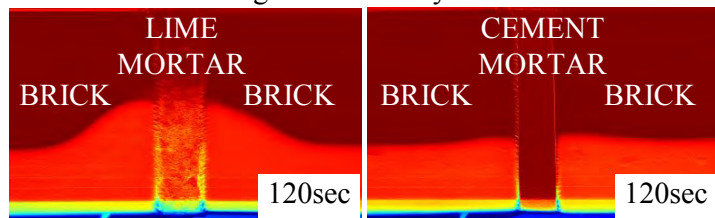


Figure 1. X-ray visualization of absorption in a brick/mortar sample. Left: Hydraulic lime mortar, Right: cement mortar. Red/blue= Low/high moisture content. In collaboration with UGCT.

To answer this question, Vereecken investigated the impact of the simplification in the article ‘Hygic performance of a massive masonry: How mortar joints influence the moisture flux?’ (Vereecken et al., 2013). This publication reported that for the investigated material properties massive masonry constructions can be homogenised to a solid brick construction in

perspective of HAM modelling. The statement is based on several simulations and measurements on ceramic brick and cement mortar. However, it can be assumed that the impact of mortars in historic constructions may be bigger, as mortars generally have higher absorption coefficients in comparison to cement mortars. This is visualized by means of tests with X-ray attenuation (Figure 1). It can be seen that the hydraulic lime mortar (often used in historic constructions) serves as a capillary highway and humidifies the brick sideways, which is not the case for the cement mortar. Due to these capillary highway, the moisture penetrates deeper into the structure, which may perhaps increase the frost risk. In (Figure 1, left) it is clear that the brick and the mortar influence each other's moisture content over the interface between them. Here the so called interface resistance (IR) will be decisive for the moisture flux. From this visualisation it can be concluded that the potential impact of mortars and their adjacent IR may be bigger for high absorptive mortars.

What is an IR between porous materials? Qui et al, 2003; Derluyn et al, 2011 and Guimarães et al, 2018 have listed several causes: a mismatch between the physical-chemical properties, the pore network and the surface energy of both systems, the modification of the hygric properties of the mortar and the transport of fine particles to the interface due to curing, the creation of compaction pores near the interface, and cracking of the interface due to hygric tensions.

The amount of research that addresses the impact of interface resistance (IR) between porous media is limited (Qui et al, 2003; Derluyn et al., 2011). The order of magnitude of an IR found by Derluyn et al, 2011 is between 0 and $5E10$ m/s. It must be noted that the highest IR was found for the combination of a ceramic brick and cement mortar, for a sample where the mortar was cured in contact with oven dried bricks. It can be discussed whether these values derived by Qui and Derluyn are representative for the combination of ceramic brick and hydraulic lime mortar. Next to that, to date the dependency of the IR on the moisture content and flow direction is unknown. On the other hand, it can be argued that these results provide at least an order of magnitude of the potential impact, which should suffice to indicate the impact on the hygrothermal performance of masonry constructions. This study will therefore proceed with adopting an IR of $5E10$ m/s. In preliminary simulations the IR was modified to see the impact, and it showed that the presence of the IR is more important than its magnitude in perspective of the amount of absorbed moisture.

Where does this interface resistance occur?

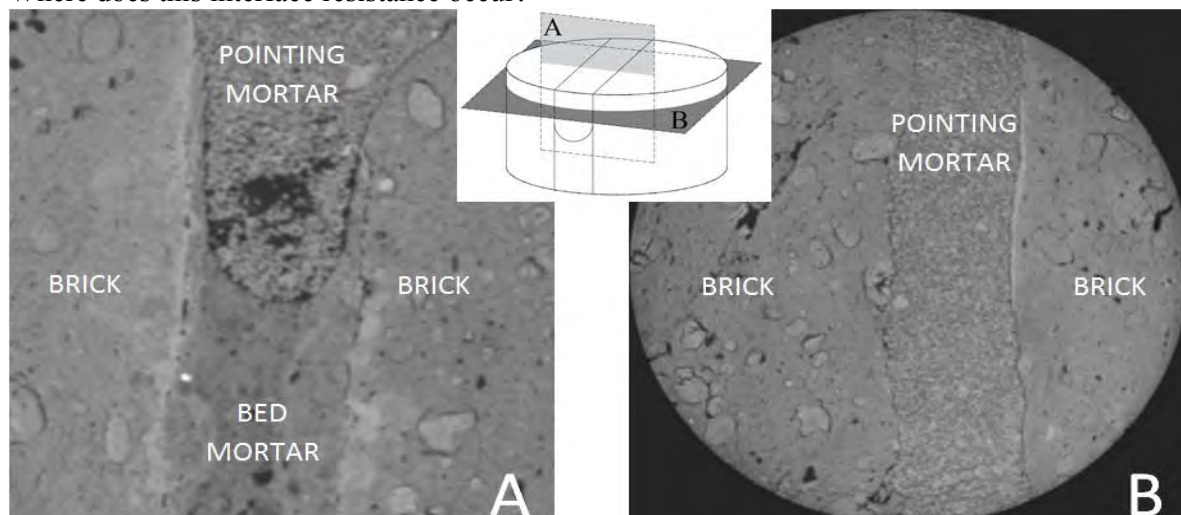


Figure 2. X-ray tomography, voxel size $90 \mu\text{m}$ A) perpendicular section to the building facade with the facade at the top side. B) parallel section to the building facade through the bed mortar. In collaboration with UGCT and the Belgian Royal Institute for Cultural Heritage.

With X-ray tomography a historic masonry core of a Flemish church was investigated to visualise the interfaces between the pointing mortar, the bed mortar and the bricks. From the images, shown in Figure 2, the following aspects can be deduced:

- pointing mortar – brick(A/B): very clear separation of materials, interface appears fractured ($\pm 0.3\text{mm}$).
- bed mortar – brick(A): very diverse interface; some places seem in perfect contact whereas in other places cracks are visible. Around the interface the attenuation changes. This may be the effect of a changed density/porosity at the interface (0-0.5mm).
- pointing mortar – bed mortar: poor compaction of the pointing mortar results in a poor contact.

To summarize, traditionally masonry constructions are homogenised in HAM simulations. This seems to be a valid approach based on the state-of-the-art literature, but no specific attention has been given yet to high absorptive mortars and interface resistances, which are as shown in figure 2 on different ways present in historic constructions. This study aspires to contribute to this understanding, in order to develop in depth guidelines for HAM simulations for historic masonry constructions.

METHODOLOGY

First, six types of historic bricks commonly found in historic buildings in Belgium are characterized by their density, capillary moisture content, absorption coefficient and vapor diffusion resistance. The same is done for three historic mortars, based on replicas made from contemporary raw materials.

Subsequently, some combinations of bricks and mortars were simulated in Delphin 5.9, mimicking a simple absorption test. The section of the materials was based on the absorption coefficients, extreme values are preferred to indicate clear but at the same time realistic differences. The material functions (moisture retention curve, liquid water conductivity and vapor permeability curve) were scaled based on the materials available in the software database. As a reference, the materials used by Vereecken (ceramic brick/cement mortar) were approximated as good as possible based on the available data and added to the simulations.

In a third phase, simulations under realistic climate conditions (Essen, Bremerhaven and Munich) were executed for four brick/mortar combinations and three types of interface resistances. To investigate the impact of the interface resistances in the construction, a combination of moisture saturation degree, freeze thaw cycles (FTC) and ice mass density outputs were analyzed.

Based on the literature reported above and the X-ray tomography (Figure 2), three variations on the interface resistances in the setups are simulated: 1) perfect hydraulic contact is assumed (IR0), 2) an interface resistance of $5\text{E}10 \text{ m/s}$ is added at all interfaces between brick – mortar (IR5), 3) on top of the IR's in IR5 an additional IR of $5\text{E}10 \text{ m/s}$ is added in the mortar at a depth of 20mm from the surface, to represent poor contact between the pointing mortar and the bed mortar (IR5PM).

RESULTS

Table 1 (the abbreviations represent brick type B_V: Veldovensteen (Dutch, literal translation: Field oven stone), M_H: Hydraulic lime mortar, B_REF/M_REF: Reference material from Vereecken Roels et al, 2013) shows the results of the material characterization

for the materials which are used in the simulations. Generally, the absorption coefficients of the historic bricks and mortars are higher than for the reference materials.

Table 1. Material properties bricks and mortars: Mean (Standard deviation)

	Density [kg/m ³]	A _w [kg/m ² .s ^{0.5}]	Θ _{cap} * [m ³ /m ³]	μ _{dry} ** [-]	Mat. func.*** /
B_V	1786 (87)	0.486 (0.237)	0.165 (0.058)	10.394 (3.652)	ID 97
B_REF	2087	0.116	0.130	24.79	ID 97
M_H	1459 (31)	0.518 (0.033)	0.180 (0.016)	28.302	ID 718
M_REF	1823	0.091	0.252	20.97	ID 717

*Capillary moisture content, **Vapor diffusion resistance, *** The material functions are scaled based on the software database, the material ID is shown.

Absorption

From the normalized (based on capillary moisture content) absorption curves it is clear that the absorption occurs in several linear phases (Figure 3). The number and transitions of these phases depends on the obstructions the moisture front has to overcome. These obstruction can be a low absorptive mortar (M_REF), an IR (IR5, IR5PM) or the top of the specimen. For example Figure 3A shows the moisture content of B_REF-M_H after 3.5 hours. At that point in time the moisture front reaches location 1, where the IR and the mortar result in a decline of the water absorption (point A). A similar observation can be made when the water front reaches location 2 after 16h for the same configuration (3B). The large difference in the absorption curves for high absorptive mortars (M_H) without (IR5) and with (IR5PM) pointing mortar IR are due to reduced moisture buffering in the mortar. In cases with the low absorptive reference mortar (M_REF) these difference are negligible.

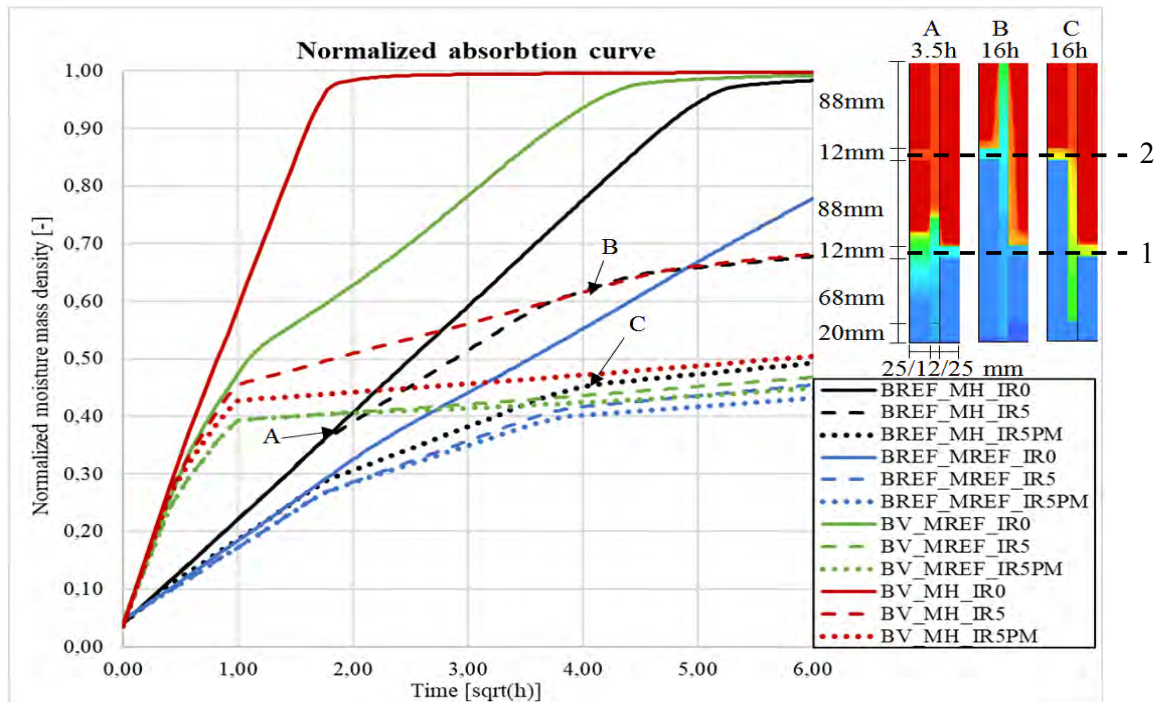


Figure 3. Normalized absorption curves, ABC moisture saturation degree after 3.5h/16h/16h of respectively BREF_MH_IR0/ BREF_MH_IR5/ BREF_MH_IR5PM

It is clear that in all cases the absorption is slowed down by the interface resistances, especially in combination with high absorptive mortars, which could insinuate a decreased frost damage risk. But is this also the case under real climate conditions?

Real climate conditions

For these simulations with realistic exterior climate conditions (Essen, Munich, Bremerhaven) the same configuration as shown in Figure 3 (A) was used, except for the lime plaster of 10 mm, which was added to the interior side. The normalized average moisture mass density reveals that the interface resistances affect the moisture distribution in the brickwork, especially during rain events, as well as during the convective drying phase (Figure 4). The interface resistances decreases the amount of absorbed water during a rain event due to a reduced redistribution of the moisture in the masonry, and the drying potential shortly after the rain event is increased as well. But in the second drying phase, indicated in figure 4 as zone a, the drying potential is decreased due to the hampering of moisture redistribution which makes the brickwork more vulnerable to critical frost cycles for a longer period of time after a rain event. To conclude the sequence of wetting and drying, and the trade-off between reducing absorption and hampering drying yields a complex balance that is very sensitive to material properties and boundary conditions.

In the analysis several effects of the interface resistances were found that induce increased frost risks:

- moist trapped in the bed mortar behind the IR between a pointing mortar and a bed mortar (Figure 4 A/B and zone a)
- generally a slight increase in of freeze thaw cycles due to a decreased redistribution and drying, biggest impact for case B_V, M_H due to higher moisture contents deeper in the construction
- reduced drying of the brick to the mortar due to the IR, especially in case of high absorptive mortars (Figure 4 DEF, case B_REF,M_H).
- reduced drying of the mortar to the brick, especially in case of high absorptive bricks combined with a low absorptive mortar (Figure 4 G/H/I, case B_V, M_REF).

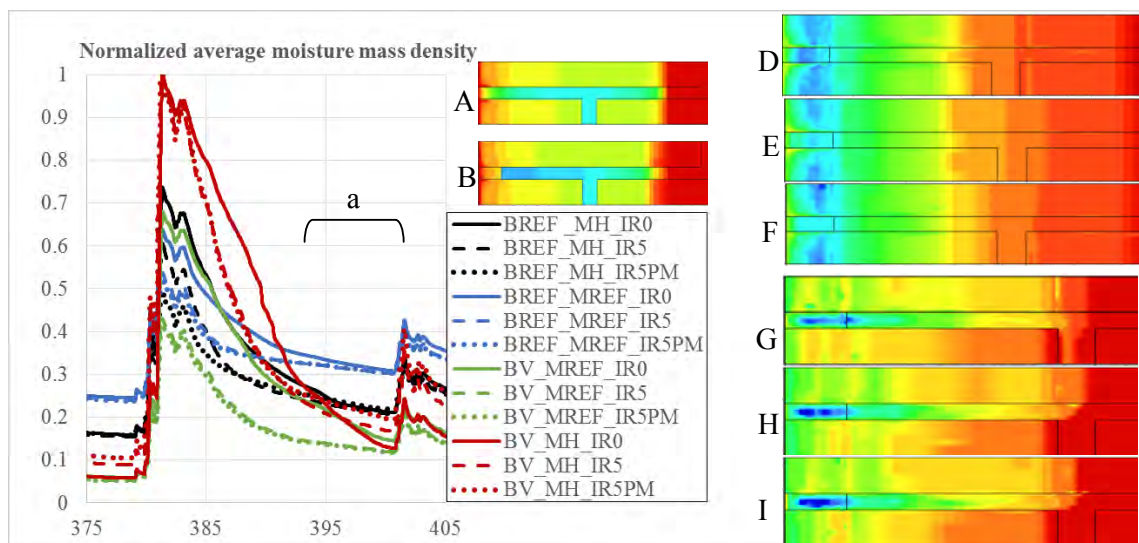


Figure 4 Normalized average moisture mass density during and after a rain event (Munich) based on the capillary moisture content, A/B: Ice mass density for respectively BREF_MH IR0/IR5PM at day 393.5 (Munich), D/E/F: cumulative critical FTC for respectively BREF_MH IR0/IR5/IR5PM (Munich) and G/H/I cumulative FTC for respectively BV_MREF IR0/IR5/IR5PM (Bremerhaven)

Despite the effects described above, it must be noted that the overall differences between IR0, IR5 and IR5PM are limited for the combinations that were studied here.

The risk for mould growth at the interior surface was investigated as well, the IR seems to have reduce the risk on mould growth in all cases. As expected, masonries with hydraulic lime mortar are far more vulnerable to mold growth at the interior surface due to the capillary highway effect described in (Figure 1).

CONCLUSIONS

Homogenisation of historic masonries whit lime mortars in HAM simulations can lead to an underestimation of several risks. Therefore it is advised to avoid homogenisation if possible in perspective of historic constructions.

Next to that, the described effects are found to be strongly dependent on several parameters such as the sequencing of wetting/freezing and the properties of the adjacent materials which hampers straight forward conclusions.

The impact on the moisture content of interface resistances in brickwork in real climate conditions seems rather limited compared to absorption tests. Therefore it is plausible that IR can be neglected but further validation of the reliability of this approach should be made. Follow up research is planned to validate the IR between historic materials more in depth based on CT(computerized tomography).

Due to the large number of uncertainties and highly sensitive trade-off between wetting and drying effects, additional research should also further investigate what the impact is of the variation in the material properties (pointing mortars, bed mortars and bricks), the interface resistances, and the climate conditions.

ACKNOWLEDGEMENTS

This research is funded by the Research Foundation - Flanders (FWO). The center for X-ray tomography (UGCT) at Ghent University is acknowledged for its help with the visualizations. The Royal Institute of Cultural Heritage (KIK) is acknowledged for providing the drilling core of historic masonry.

REFERENCES

- Pel L., PhD thesis, Moisture transport in porous building materials, Eindhoven University of Technology the Netherlands, (1995)
- Künzel M. H., PhD thesis, Simultaneous Heat and Moisture Transport in Building Components, (1995)
- Grunewald J., PhD thesis, Diffusiver und konvektiver Stoff- und Energietransport in kapillarporösen Baustoffen, (1997)
- Delphin 5 Version 5.2, User manual and Program reference, (2006)
- Vereecken E., Roels S., Hygric performance of a massive masonry wall: How do the mortar joints influence the moisture flux? *Construction and Building Materials* 41 (2013) 697-707
- Derluyn H., Janssen H., Carmeliet J., Influence of the nature of interfaces on the capillary transport in layered materials, *Constr. Build. Mater.* 25 (2011) 3685- 3693.A.S.
- Qiu, X., Haghighat, F., Kumaran, M.K., Moisture transport across interfaces between autoclaved aerated concrete and mortar, *Journal of Thermal Envelope & Building Science*, v. 26, no. 3, (Jan. 2003), pp. 213-236
- A.S. Guimarães, J.M.P.Q. Delgado, A.C. Azevedo, V.P. de Freitas, Interface influence on moisture transport in buildings, *Construction and Building Materials* 162 (2018) 480–488

Drainage and retention of water in small drainage cavities: Experimental assessment

Stéphanie Van Linden^{1,*}, Michael Lacasse² and Nathan Van Den Bossche¹

¹Faculty of Engineering and Architecture of Ghent University, Ghent, Belgium

²NRC Construction, National Research Council Canada, Ottawa, Canada

*Corresponding email: stephanie.vanlinden@ugent.be

ABSTRACT

Water that enters the drainage cavity of a rain screen wall assembly through deficiencies in the cladding will either be drained or retained by absorption or adhesion on the drainage surfaces. The objective of this study is to gain insight into the different factors that affect the quantity of water drained or retained in a drainage cavity. Drainage tests have been conducted for water flowing between two vertical polycarbonate plates with different gap widths to determine the effect on the drainage rate. Tests showed that even small cavities with a width of 1 mm can already drain more water than the amount that would enter the cavity during a rain event. Experiments were performed to determine the contact angle of water on a range of different sheathing materials such as asphalt saturated building paper, spun-bonded polyethylene wrap and cross-woven polyolefin wrap by the use of an optical goniometer. Drainage tests have been conducted for different combinations of these materials to quantify the effect of surface energy on the drainage rate. A larger contact angle results in a smaller quantity of water retained during the drainage test. These tests result in a retained portion of water and a drainage rate for different combinations of materials. The retained portion of water may be considered as a moisture load applied to the outer-most layer of the wall assembly's back-up wall in hygrothermal simulations.

KEYWORDS

Water drainage, small drainage cavities, contact angle, retention

INTRODUCTION

Rain screen wall systems or drained wall assemblies are commonly used to reduce the risk for moisture damage due to rain penetration behind the cladding. If openings or deficiencies are present in the cladding, raindrops may penetrate and enter the drainage cavity during a rain event. Most of the water that enters the drainage cavity will flow down along one of the drainage surfaces or between both as singular droplets, rivulets or multiple streams resulting in a film flow. Also some droplets may be retained in the cavity depending on the surface energy of the materials that define the drainage cavity, the gap width and the initial velocity and volume of the droplets entering the drainage cavity. Accurate knowledge of the retained portion of water is important given that in undertaking hygrothermal and durability analyses, it is considered to be the moisture load applied to the outer-most layer of the wall assembly's back-up wall. According to the Swedish SP Certification Rules no. 021, the quantity of retained water in drained facades should be determined by tests and be applied as input for hygrothermal simulations according to EN 15026 (SP Certification, 2009; Künzle et al., 2008).

Several detailed studies have been completed on film flow dynamics both in the laboratory or by numerical and analytical modelling (Ambrosini et al., 2002). Experimental studies have

been undertaken to investigate the transition from falling film flow to rivulet flow (Martin et al., 2015), rivulet geometry (McCreery et al., 2007) and the transition from laminar to meandering flow on both a single surface (Le Grand-Piteira, 2006) and between two planes (Drenckhan, 2004). As well, the retention of droplets has been studied (ElSherbini and Jacobi, 2006). Research on film flow dynamics has been conducted within the field of chemistry to improve applications such as heat exchangers, the field of geophysics to gain insight into the transport of contaminants in the Earth's substructure (McCreery et al. 2007) or within the field of building engineering mainly focusing on water runoff on a building facade due to wind driven rain (Blocken and Carmeliet, 2012; Van Den Bossche et al., 2015). Research concerning water flow and retention of water in wall drainage cavities however is very limited. Straube and Smegal (2007) performed drainage tests to obtain a better understanding of the drainage capacity in wall cavities given that, as it was stated by Onysko et al. (2007), even when hydrophobic materials are applied not all injected water drains out from the cavity. Drainage tests of smooth non-absorptive materials showed that a drainage gap of 1 mm between two stiff acrylic sheets (23-25 g/m²) stored less water than a single acrylic sheet (65 g/m²). Additionally, spray tests on a polyethylene sheet (35 g/m²) showed a smaller quantity of retained water compared to an acrylic sheet (65 g/m²) which is likely due to the increased hydrophobicity of the polyethylene as compared to the acrylic sheet. It was concluded that several wall assemblies even those having small gaps (< 1 mm) could drain more water than would ever enter the drainage cavity during a rain event as drainage rates exceeded 1 l/min.m. Given that wind driven rain loads on buildings seldom exceed 2 l/m².h, and infiltration rates are typically between 1% up to 10%, it can easily be assumed that the accumulated drainage rate, even for tall buildings, will never exceed 1 l/min/m. Blocken and Carmeliet (2006) performed an experimental study on different vertical surfaces (PVC, PMMA, PTFE, glass, glass with hydrophilic coating and glass with hydrophobic coating) to evaluate the impact of contact angle on the quantity of adhered water. Although it is often assumed that hydrophobic vertical surfaces promote drop run-off and therefore show less adhered water, no clear relation between the contact angle measurements and the quantity of adhesion water could be found.

To gain a better understanding of the parameters that affect drainage and retention in wall assemblies, an experimental research program was carried out. The objective of this research program was to evaluate the impact of the drainage cavity width and the surface characteristics of the drainage surfaces on the amount of water that is retained within the cavity. This program and the results derived from the work are described in detail in this paper.

METHODS

Drainage tests were conducted for water flowing down between two parallel vertical polycarbonate (PC) plates (609.6 x 609.6 mm). Gap widths of 0.99 mm, 1.96 mm, 3.12 mm and 4.84 mm (± 0.01 mm) were defined by use of spacers inserted between the PC plates at both vertical edges. A copper tube was installed on top of the test setup and aligned with the position of the rear PC plate. The tube contained 16 evenly spaced openings of 0.5 mm diameter located every 12.7 mm along its length; this arrangement provided an evenly distributed water deposition rate across the drainage cavity. A gutter located beneath the PC plates collected the drained water. To introduce a water flow, a peristaltic pump (Stenner Pumps 85 pump series) was connected to the copper water deposition tube by means of a flexible plastic tube. An average flow rate of 0.769 ± 0.002 l/min.m was applied during 3 cycles of 10 minutes and water deposition was evenly distributed over 16 openings in the copper tube. Both the mass of water that flowed through the pump and the mass of drained water were weighed with an accuracy of 0.1 g. By subtracting the mass drained from that

deposited, the mass of retained water in the cavity could be calculated for each setup. Before each experiment, the pump was turned on for a few minutes in order to reach a steady state for the water content of all tubes both before and after the experiment.

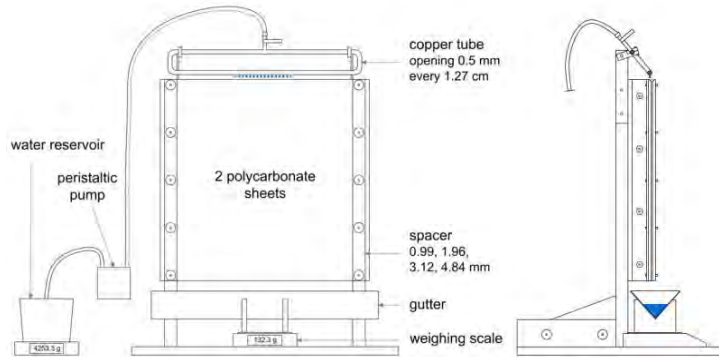


Figure 1: Test setup

Additionally, the drainage capacity of different commonly used sheathing membranes was evaluated. The sheathing membranes were taped onto the PC plate at the back of the test setup with a cavity width of 1.96 mm by means of two vertical strips of double-sided tape (350 mm o.c.). The same procedure as described above was applied to obtain the drainage characteristics of the sheathing membranes. To evaluate the impact of the surface characteristics of the plates or the sheathing membrane on the retention of water in the cavity, the contact angle of a distilled water drop on the different sheathing membranes was measured by means of a goniometer (Ramé Hart model 100-00-115). The optical sessile-drop method was applied to determine the static, advancing and receding contact angle. The reported values are the average of 8 contact angle measurements of different locations on the sample; these are in Table 1.

RESULTS

As water drops flow down, they leave behind smaller droplets, i.e. trace droplets. The impact of gap width on the volume of these trace droplets is evaluated by introducing water flow in between two PC sheets with different gap widths. During the test, the amount of water added to the drainage gap and the drained amount was measured and the retained portion is calculated. Results for the different gap widths and a single sheet are shown in Figure 2a).

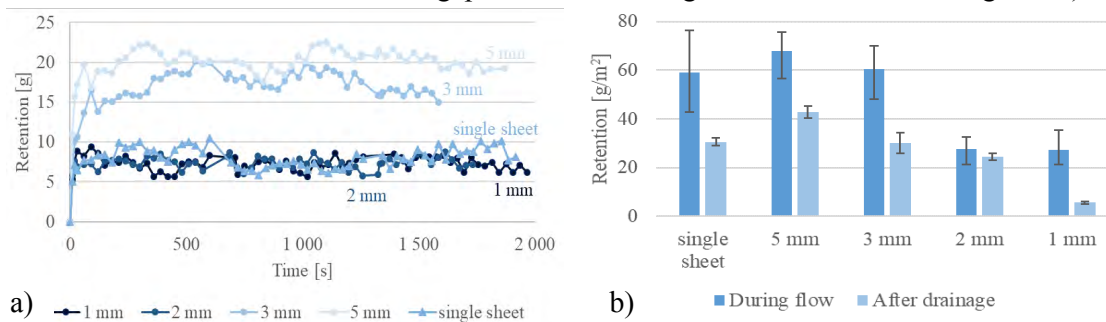


Figure 2: Drainage tests on PC a) Retention during test, b) Retention during test and after drainage has finished per m²

These measurements show that a steady-state is achieved after less than 100 seconds for all gap widths. Small peaks are visible which represent the droplets injected to the cavity from discharge of the copper tube. For gaps of 3 and 5 mm a larger variation is visible due to a smaller relative impact of forces due to surface tension compared to gaps of 1 and 2 mm

which causes larger deviation of the flow of drops after collision with other drops along their downward path. As a result, a larger wetted area is achieved for larger gap widths, i.e. the wetted area of the test setup with a 5 mm gap is 11.51% larger compared to the 1 mm gap. Figure 2b) shows the average amount of water retained per m^2 during the test including droplets adhered to the plate and drops flowing downwards. The error bars represent the minimum and maximum values. Additionally shown in Figure 2b) is the amount of water retained per m^2 after drainage has finished, i.e. the number of water droplets adhered to the PC plates. The latter was based on pictures captured after the test, assuming that the volume of the trace droplet is half a sphere (Blocken and Carmeliet, 2006). The amount of trace droplets and the average base area was measured at different locations of the test setup as it was observed that values at the top of the setup differed from values at the bottom. The error bars show the standard deviation of the retained amount of water based on three different experiments for each gap width. The graph illustrates that for an increasing gap width, an increasing amount of water was retained in the gap both during flow and after drainage. The retained volume during the test for a gap width of 2 mm was similar to the retained volume in a gap of 1 mm. However, it should be noted that this value also includes the capillary retained portion at the bottom of the test setup which was significantly larger for the 1 mm gap (3.3 g) compared to the 2 mm gap (< 1 g). The increasing amount of retained water for an increasing gap width was mainly due to an increasing amount of drops per m^2 . The average drop base area ranged from $1.155 \pm 0.045 \text{ mm}^2$ for a 2 mm gap to $1.300 \pm 0.108 \text{ mm}^2$ for a 5 mm gap. Only the average base area of the trace droplets of the 1 mm gap was significantly smaller, i.e. $0.563 \pm 0.044 \text{ mm}^2$. The vertical spacing between the drops ranged from 3 – 5 mm. It was visually observed that most of the drops adhered only to one of the plates. Only some drops were retained between both plates for the 1 mm gap.

The same measurements were conducted for test setups with a 2 mm gap and a sheathing membrane adhered to the back plate of the setup thus permitting evaluating the importance of membrane contact angle and surface roughness on retained water.

Table 1. Contact angles distilled water on sheathing membranes

No. Sample	Description	$\theta_{C, \text{static}}$	$\theta_{C, \text{advancing}}$	$\theta_{C, \text{receding}}$
0	Polycarbonate	79.1 ± 1.5	83.3 ± 1.5	48.7 ± 1.5
1	Cross-woven polyolefin wrap	77.7 ± 5.8	85.1 ± 4.0	50.8 ± 4.7
2	Spun-bonded polyethylene, grooved	84.2 ± 4.0	88.4 ± 1.8	57.3 ± 3.6
3	Spun-bonded polyethylene, continuous	90.4 ± 2.1	96.5 ± 3.3	73.1 ± 2.7
4	Asphalt saturated Kraft building paper	105.4 ± 6.4	111.3 ± 2.1	74.9 ± 2.1

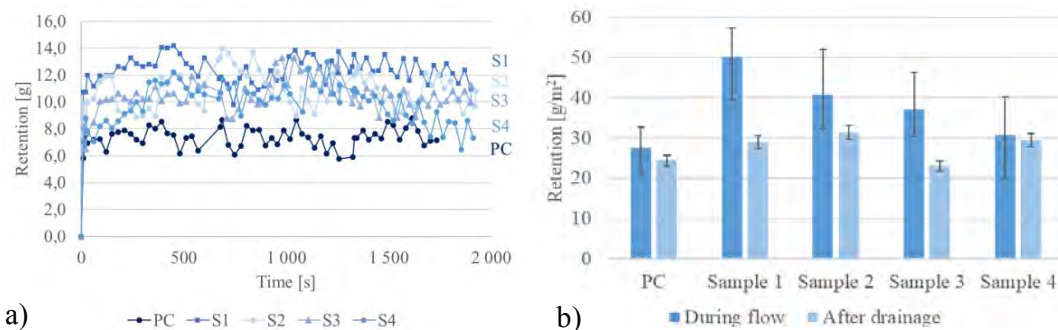


Figure 3: Drainage tests on sheathing membranes a) Water retained during test, b) Water retained during test and after drainage had finished per m^2

Figure 3a) shows the retained amount of water in the cavity as a function of time for the different sheathing membranes tested. For all sheathing membranes a steady-state is reached as for the PC plates with small peaks. However, a larger variation about the average value is apparent due to the surface roughness which causes deviation of the flow of drops and a difference in wetted area (woven pattern of sample 1, grooves of sample 2, ink on sample 3, bulging of sample 4). Sample 4 shows the largest wetted area (0.323 m^2) with an increase of 12.5% compared to the setup with two PC plates. The building paper, due to water absorption, bulges that in turn causes locally reduced thickness of the gap width. As a result, drops will not flow in a straight downward path but will follow the path of smallest resistance in between the bulged areas. Sample 1 on the other hand shows the smallest wetted area (0.248 m^2) which is 7.8% smaller than the wetted area of the PC. Due to the vertical threads of the sheathing membrane, the deviation of drops from their downward path is significantly less compared to drops flowing down, e.g. over sample 4 that were affected by the bulged areas on their way down. By comparing the average retention during the test for the different sheathing membranes (Figure 3b), it can be stated that the quantity of retained water decreased for increasing contact angle. The error bars of the measurements during flow represent the minimum and maximum values. After drainage had finished this trend was less apparent. The largest amount of retained water was measured for sample 2 and 4. The surface of sample 2 contained grooves resulting in locally reduced thickness of the gap width ($< 1 \text{ mm}$) which caused capillary retention at the top portion of the grooves. Locally reduced gap width is also observed for sample 4 due to bulging of the building paper resulting in a larger amount of retention. The larger contact angle of sample 3 ($\theta_{C, \text{static}} 90.4 \pm 2.1$) compared to polycarbonate ($\theta_{C, \text{static}} 79.1 \pm 1.5$), results in a smaller drop base area as well as fewer drops per mm^2 . In contrast, sample 1 had a contact angle similar to polycarbonate but the number of drops per mm^2 was larger. This is also apparent when the vertical spacing between the drops is compared (PC: $4.27 \pm 0.29 \text{ mm}$; S1: $3.41 \pm 0.32 \text{ mm}$). This is caused by the woven pattern of the sheathing membrane resulting in trace droplets every other thread.

DISCUSSIONS AND CONCLUSIONS

Drainage tests performed on two polycarbonate plates with different gap widths, showed that smaller quantities of water are retained in the cavity for gap widths of 2 mm and 1 mm compared to the retained quantity on a single sheet or in a gap of 3 and 5 mm. This confirms the results found by Straube and Smegal (2007) who stated that a drainage gap of 1 mm between two acrylic sheets stored less water than a single acrylic sheet. Further analysis should reveal whether this can also be stated for gaps smaller than 1 mm as more water drops will presumably be retained between both plates as a result of larger quantities of capillary retained water. The average base area and consequently the trace drop diameter differed over the area of the setup. This is in contrast with the observations of Blocken and Carmeliet (2006) who stated that the base diameter was fixed. This is probably due to a different method of adding water to the test setup, i.e. spraying of water onto the vertical sheet or water drops flowing downwards only from the top of the setup. De Vogelaere and Pacco (2012) developed a numerical model at Ghent University to simulate runoff patterns on building facades. By use of a micro model, a simulation was conducted of the cumulated runoff volume on a PMMA surface over time. The shape of the resulting graph is very similar to the graphs obtained from the experiments in this paper including a steady-state with small peaks achieved after less than 100 seconds. Further analysis should be carried out to confirm the results of the simulation model.

Drainage test were also performed for different sheathing membranes. These tests showed that the quantity of water in the gap between the polycarbonate plate and the sheathing membrane

during water flow depends on the contact angle of the sheathing membrane. After drainage has finished, this is however less apparent. As stated by Blocken and Carmeliet (2006) not all retained water is present in the gap as single drops, but also some portion is retained in between the PC plate and the membrane due to locally reduced thickness of the gap. Future research should include a broader range of contact angles and smooth surfaces as it was observed that the presence of grooves and threads affects the quantity of retained water and the size of the wetted area.

Overall, measurements showed that less than 0.5 % of water added over the course of the test (+/- 4.8 l) was retained in between the plates or on a single sheet both during water flow and after drainage has finished. Future research will focus on the development of a drainage model to predict the drainage capacity required for a drainage gap in function of the applied materials and gap width necessary to prevent the build-up of hydrostatic pressure which may cause water to penetrate further into the wall assembly.

REFERENCES

- Ambrosini W., Forgione N., Oriolo, F. 2002. Statistical characteristics of a water film falling down a flat plate at different inclinations and temperatures. *International Journal of Multiphase Flow*. Vol. 28, pp. 1521-1540.
- Blocken B. and Carmeliet J. 2006. On the accuracy of wind-driven rain measurements on buildings. *Building and Environment*. Vol. 41, pp. 1798-1810.
- Blocken B., Carmeliet J. 2012. A simplified numerical model for rainwater runoff on building facades: Possibilities and limitations. *Building and Environment*. Vol. 53, pp. 59-73.
- De Vogelaere T., Pacco M. 2012. Development of a numerical model for rainwater runoff on vertical planes extended with experimental verification. Ghent University, Belgium SP Certification. 2009. Certification Rules 021. Construction Systems for Exterior Walls and Facades. 28 pages.
- Drenckhan W., Gatz S., Weaire D. 2004. Wave patterns of a rivulet of surfactant solution in a Hele-Shaw cell. *Physics of Fluids*. Vol. 16, 3115.
- Elsherbini A., Jacobi A. 2006. Retention forces and contact angles for critical liquid drops on non-horizontal surfaces. *Journal of Colloid and Interface Science*. Vol. 299, pp. 841-849.
- Künzel H.M., Zirkelbach, D., Karagiozis, A., Holm A., Sedbauer, K. 2008. Simulating water leaks in external walls to check the moisture tolerance of building assemblies in different climates. In: *Proceedings of 11th DBMC International Conference on Durability of Building Materials and Components*, Istanbul.
- Le Grand-Piteira N., Daerr A., Limat L. 2006. Meandering rivulets on a plane: a simple balance between inertia and capillarity. *Physical review letters*. Vol. 96, 254503.
- Martin M., Defraeye T., Derome D., Carmeliet J. 2015. *International Journal of Multiphase Flow*. Vol. 73, pp. 207-216.
- McCreery, G.E., Meakin P., McEligot D.M. 2007. Measurements of rivulet flow between parallel vertical plates. *International Journal of Multiphase Flow*. Vol. 33, pp. 432-447.
- Onysko D.M. 2007. Drainage and retention of water by cladding systems. Part 8 – summary report. Canada Mortgage and Housing Corporation. 63 pages.
- Straube J., Smegal J. 2007. The role of small gaps behind wall claddings on drainage and drying. In: *Proceedings of 11th Canadian Conference on Building Science and Technology*. Alberta.
- Van Den Bossche N., Ge H., De Vogelaere T., Pacco M., Janssens A. 2015. Development of a 2D numerical model for rainwater runoff on vertical planes. In: *Proceedings of XIII International Conference on Durability of Building Materials and Components*.

Rain-tightness of door sill sealing

Lars Gullbrekken^{1,*}, Steinar Grynning¹

¹ Department of Materials and Structures, SINTEF Building and Infrastructure, Trondheim, Norway

**Corresponding email: Lars.gullbrekken@sintef.no*

ABSTRACT

The harsh Norwegian climate requires buildings designed according to high standards. The airtightness of the building envelope is crucial to attain an energy efficient building and to avoid moisture problems. A considerable part of building defects registered in the SINTEF Building defects archive are related to leakages through door sills especially in combination with balconies.

The aim of the study has been to examine the rain tightness of the joint below door sills. A laboratory investigation using a driving rain cabined according to EN 1027 has been conducted to provide answers to the matter. In total 14 different test were conducted. Two different sills were included, both a traditional "high" sill and a "lower" handicap-sill. Two different underlays for the sill were included in the investigation. In addition, 3 different heights of the joint-sealing below the sill were chosen (0, 5 and 10 mm). All the tests except two were performed with silicon as joint sealant material.

It was found that the workmanship of the joint-sealing was challenging due to the geometry of the detail. Even if the silicon sealant was carefully applied, voids between the sealant and door sill were found when inspecting closely. When improving the faults, the test showed that the joints was tight. 11 of the 14 tests showed no water leakages at 600 Pa pressure difference. However, leakages were observed at lower pressure differences for the sills with no silicon sealing and for the configurations where there were faults in the silicon sealing.

The laboratory study revealed that the joint below the door sill is vulnerable to small mistakes in the workmanship. Given a carefully application and control of the silicon sealing it is possible to achieve a high water tightness performance. However, improvements to the sealing detail is needed to further increase the robustness of the detail.

KEYWORDS

Laboratory investigation, Driving rain, Door sill

INTRODUCTION

Norway is characterized by an extremely varied climate, the rugged topography and long coastline being one of the main reasons for large local differences over short distances and extreme seasonal variations (O'Brien et al., 2004). The climate puts a great demand on the building envelope of Norwegian buildings. The building envelope may be exposed to severe winds, snow loads, precipitation, freeze/thaw cycles, and rather large temperature fluctuations. The Norwegian report "Climate in Norway 2100" is an updated scientific base for climate adaptation in Norway (Bauer et al., 2015). By assuming a further increase in the greenhouse gas emissions, the climate scenarios show an increase in the yearly precipitation by 10-20 %

depending on the climatic model used. Heavy showers will occur more frequently and rainfall flood become more powerful and occur more often.

Increased precipitation is also affecting the strain from wind-driven rain. Wind-driven rain is one of the most important moisture sources affecting the hygrothermal performance and the durability of building facades (Blocken and Carmeliet, 2012; 2004). Measures to adapt the built environment to the anticipated climate changes were studied by Lisø (2006). Lisø stresses the immediate need for information and research with respect to vulnerability in the built environment and technical solutions. This to prevent or minimize negative climatic impacts on buildings.

The SINTEF Building Research design guidelines recommends a rain tightness performance of the wind barrier of minimum 300 Pa (SINTEF, 2007). Skogstad et al. (2011) performed laboratory testing of the rain tightness of wind barriers and sealing around windows. The tests were performed with a pressure difference ranging from 0-600 Pa. Sealing compound of acrylic was found to be rain tight at 100 Pa pressure difference.

Both the Norwegian planning and building legislation (TEK) and the Equality and Anti-Discrimination Act (Lovdata, 2018) dictates that housings should be available for all people. This entails the need for level door sills which can easily be crossed by wheelchairs. As a result, the height of door sills must not exceed 25 mm. This applies to the height difference between the interior floor and the top of the door sills, as well as the difference in height between outdoor surfaces and the top of the door threshold. Hence, these solutions require level interior and exterior surfaces. This increases the risk for static pressure of water as well as presence of snow and freeze/thaw cycles in front of the sill. A robust solution is proposed in the SINTEF Building Research Design Guidelines which includes a gutter in front of the door to direct the water away from the detail (as seen in Figure 1). However, this solution is costly due to material and time use.

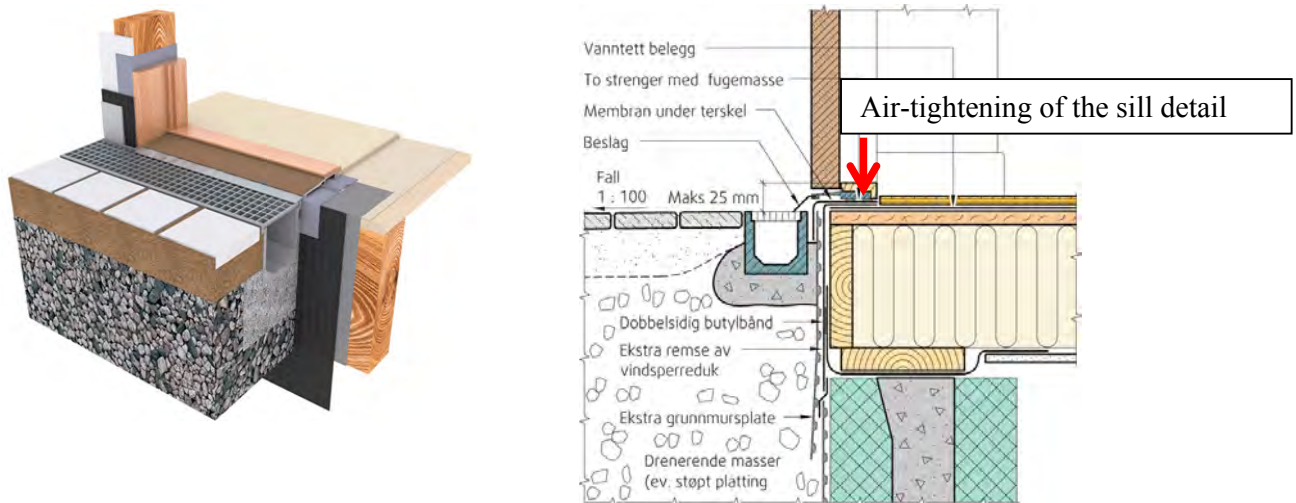


Figure 1. Level door details from the SINTEF Building Research design guidelines 523.731 (SINTEF, 2010).

The purpose of the study has been to examine the rain tightness of the joint below the door sill. A laboratory investigation using a driving rain cabin has been conducted to provide answers to the matter. Tests have been carried out according to EN 1027 (Standard Norge 2016). In total 14 different test sections were tested. Two different sills were included; a traditional "high" sill and a "lower" handicap-sill. Two different underlays (wood and radon-

membrane) for the sill were included in the investigation. In addition, 3 different heights of the joint below the sill were tested (0, 5 and 10 mm). All the tests except two were performed with silicon as the joint sealant material. The remaining were sealed with no use of sealant.

METHOD

Test method

The water tightness was tested in accordance with EN 1027 *Windows and doors Water tightness Test method, method 1A – static pressure* (Standard Norge, 2016). The method is designed to determine the water tightness of completely assembled windows and doors. It is also suitable to determine the water tightness of wall sections. Inside the test chamber a controlled static pressure can be applied across the specimen and a nozzle system can apply a continuous regularly dispersed film of water all over the surface of the test section. The water is sprayed by nozzles at an angle of 84° onto the test section at a rate of approximately 2 l/min per nozzle. The test begins with 15 minutes of water application before a static pressure is established over the test section. The water tightness are tested with 5 minute intervals at pressure differences of 50, 100, 150, 200, 250, 300, 450 and 600 Pa. The penetration of water is observed visually during the testing. Location, point in time and pressure is continuously registered during the tests.



Figure 3. Test equipment for testing according to EN 1027. (left) nozzle system. (right) an example of a door mounted in the apparatus.

Design of the specimens

Testing of a worst-case scenario with no exterior flashings and gutters gives conservative results. Hence, test specimens were designed by fixing the door sill to a wood sill or a radon membrane with three different joint heights, see Figure 4, 5 and 6. Six of the specimens were designed with a radon membrane between the door sill and the wood sill. A foam gasket was positioned into the joint as a backing material for the compound sealant. The joint was then sealed with silicon compound exterior to the gasket. The sealing of the test samples were carried out as close to a real-life situation for application as possible. The test specimens were positioned on the floor when applying the silicon compound.

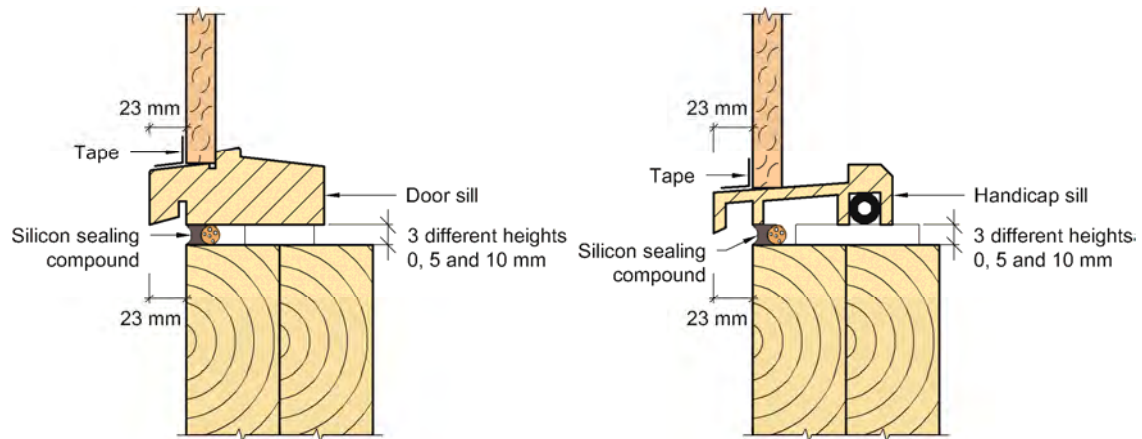


Figure 4. Design of the test specimen.



Figure 5. Standard door sill.



Figure 6. Handicap door sill.

RESULTS

Challenges related to the workmanship of the application of the silicon compound was encountered even in a controlled laboratory environment and when carried out by qualified craftsmen. When applying the sealing compound as carefully as possible (see Figure 7), small faults were found by close inspection, as seen in Figure 8.



Figure 7. Application of silicon compound.



Figure 8. Small defects in the silicon compound was found by closer inspection.

Visual inspections of the specimens were carried out during the tests. The location of leakages occurring at given air pressure differences were registered during tests. It was not practically feasible to register the amounts of the water leakages. Test results are shown in Table 1.

Table 1. Results from the driving rain measurements.

	Without sealing	0 mm	5 mm	10 mm
HC without radon	Leakages at 50 Pa	No leakages	No leakages	No leakages
HC with radon		No leakages	No leakages	No leakages
Regular without radon	Leakages at 250 Pa	No leakages	No leakages	Leakages at 0 Pa
Regular with radon		No leakages	No leakages	No leakages

DISCUSSIONS

Based on the performed tests it is possible to evaluate the resistance of water penetration through the door sill structure. Laboratory testing is carried out under controlled conditions and does not represent the variation in building materials and workmanship as it would be on a building site.

The workmanship of the sealing of the joint was challenging due to the geometry of the detail. Even if the silicon sealant was carefully applied, voids between the silicon sealant and the door sill were found when inspecting closely. When improving the faults, the test showed that the joints were surprisingly tight. Most of the tests showed no water leakages at 600 Pa pressure difference. According to the SINTEF Building Research design guidelines this is *high performance*. However, leakages were observed at lower pressure difference for the sills with no silicon sealing and at faults in the silicon sealing. This indicates that the detail is vulnerable and that great care should be taken when applying the silicon sealant. The performance of the sealed joint is depending on the workmanship of the craftsmen. In order to further improve the robustness of the detail there is a need to introduce sealing methods which ensure high performance more independently of workmanship.

The handicap sill with sealing compound was found to be watertight at 600 Pa. Without sealing compound water leakages were registered at 50 Pa pressure difference. High performance was also found for the regular door sill except for the 10 mm joint height without radon membrane where water leakages was observed at 0 Pa pressure difference. By closer inspection it was observed that the water leakage was caused by small imperfections in the sealing compound. Based on the measurement campaign we were not able to reveal any difference between underlay of wood and underlay of radon membrane indicating that the silicon sealant had sufficient adhesion between the door sill and radon membrane.

CONCLUSIONS

A laboratory study was conducted in order to examine the rain tightness of the joint below a door sill. Most of the tests showed no water leakages at 600 Pa pressure difference. Given a careful application and control of the silicon sealing it is possible to achieve high water tightness performance. However, the laboratory study revealed that the joint below the door sill is vulnerable to small mistakes in the workmanship. To further improve the robustness of the detail an improved sealing method is needed.

ACKNOWLEDGEMENT

The experiments were carried out as part of the *Tall Timber Facades* project (part of the WoodWisdom 2014-2017 program). The authors also acknowledge the Centre for Research-based Innovation "Klima 2050" for providing necessary funding.

REFERENCES

- Bauer, I.H., et al. 2015. Klima i Norge 2100 (Climate in Norway 2100) (In Norwegian), Norwegian environment Agency.
- Blocken, B. and Carmeliet, J. 2012. A simplified numerical model for rainwater runoff on building facades: Possibilities and limitations, *Building and Environment*, 53 (0), 59-73.
- Blocken, B. and Carmeliet, J. 2004. A review of wind-driven rain research in building science, *Journal of Wind Engineering and Industrial Aerodynamics*, 92 (13), 1079-130.
- Lisø K. R. 2006 Building envelope performance assessments in harsh climates: Methods for geographically dependent design. *PhD. Thesis 185:2006*, Norwegian University of Science and Technology (NTNU). Norway.
- Lovdata (2018) Equality and Anti-Discrimination Act. Lovdata. Norway
- Lovdata (2017) Forskrift om tekniske krav til byggverk. (Regulations on technical requirements for construction work) (In Norwegian). Lovdata. Norway.
- O'Brien, K, Sygna L. and Haugen J.E., Vulnerable or Resilient? A Multi-Scale Assessment of Climate Impacts and Vulnerability in Norway, *Climatic Change*, 64 (1-2), 193-225.
- Skogstad HB. Uvsløkk S. Asphaug O. 2011. Experimental testing of wind barrier and sealing around of window joints. In: *Proceedings of the 9 th Nordic Symposium on Building Physics NSB 2011* Tampere, Finland, vol 1, pp. 121-128
- SINTEF (2007). 523.255 Bindingsverk av tre. Varmeisolering og tetting (Timber frame. Heat insulation and airtightness) (In Norwegian), SINTEF; Byggforskserien
- SINTEF (2010). 523.731 Trinnfritt inngangsparti for småhus av tre. Tekniske løsninger. (Level door suitable for wooden houses) (In Norwegian) SINTEF; Byggforskserien
- Standard Norge (2016) NS-EN 1027 Windows and doors - Water tightness - Test method. Standard Norge. Norway

Water uptake in masonry: effect of brick/mortar interface

Xiaohai Zhou^{1,2*}, Guylaine Desmarais², Peter Vontobel³, Jan Carmeliet^{1,2} and Dominique Derome¹

¹Laboratory of Multiscale Studies in Building Physics, Empa, Dübendorf, Switzerland

²Chair of Building Physics, ETH Zürich, Zürich, Switzerland

³SINQ, Paul Scherrer Institute, Villigen, Switzerland

*Corresponding email: xiaohai.zhou@empa.ch

ABSTRACT

Water transport in masonry walls composed of bricks and mortar joints can be strongly affected by the interface between brick and mortar. In this study, water uptake experiments and numerical simulations are performed to study the effect of interface resistance on moisture transport in masonry samples with horizontal and vertical interfaces. Neutron radiography is used to measure moisture content distribution in different masonry samples. An interface resistance is introduced to consider the imperfect contact between brick and mortar in the numerical model. A good agreement between measured and simulated moisture contents is found for different masonry samples. The orientation, horizontal or vertical, of the interface between brick and mortar has no influence on the value of the interface resistance. However we found that the interface resistance is affected by capillary pressure at the interface. A lower capillary pressure at the interface leads to a larger interface resistance.

KEYWORDS

Masonry, interface resistance, neutron imaging, capillary moisture transport

INTRODUCTION

Liquid water transport in single materials such as masonry, brick or mortar, is well understood and explained with capillary transport theory. However, moisture transport in masonry walls composed of bricks and mortar joints deviates from what is expected from the capillary transport theory. Many researchers attribute the deviation to the imperfect contact and hence the interface resistance at the brick/mortar interface (Qiu et al. 2003, Derluyn et al. 2011, Janssen et al. 2012, Delgado et al. 2016), while some attribute the deviation to a change of the moisture properties of the mortar joint, compared to bulk mortar (Brocken 1998). Nevertheless, most numerical hygrothermal models still use the assumption of perfect hydraulic contact at the brick and mortar interface (Zhou et al. 2016). It is unclear how the interface resistance affects the hygrothermal performance of masonry walls. Moisture flow across the brick/mortar interface needs to be accurately quantified in order to better understand moisture transport in masonry.

The masonry samples used in previous studies on interface effects are quite simplified (Qiu et al. 2003, Derluyn et al. 2011, Delgado et al. 2016). The samples normally consist of a layer of brick, a layer of mortar, and a second layer of brick, where only horizontal interface exists between brick and mortar joint. By comparison, masonry is much more complex than this in reality. There are both horizontal and vertical interfaces between brick and mortar in masonry. The effect of interface resistance on moisture transport in such complex geometry is not yet studied.

The objective of this study is to understand capillary water transport in masonry with horizontal and vertical joints. Neutron radiography is used to measure moisture content distribution. Numerical model is used to study capillary moisture transport and to obtain the interface resistance at different brick/mortar interfaces. The effect of horizontal and vertical interfaces on moisture transport is described.

METHODS

Four masonry samples with horizontal and vertical interfaces between brick and mortar are used for capillary water uptake experiment. Two of them are shown in Figure 1. The type of brick is kiln-fired clay brick. Portland cement mortar is used for making mortar joints. The sand grain size in the mortar ranges between 0.1 and 3 mm. The water-cement ratio is 0.16. The masonry samples are made by joining wet bricks with fresh mortar. Then the masonry samples are covered with vapor tight sheeting for 72 h for initial curing. Afterwards, the plastic sheeting is removed and the masonry samples are let to be cured for 28 days at room condition. Given the power of the neutron beam, the thickness of all the masonry samples is 1 cm. Neutron radiography, a non-destructive imaging technique that uses thermal neutrons to probe the sample, is used to measure the time- and space-resolved moisture content distribution in different masonry samples. The experiments were performed at the NEUTRA (Neutron Transmission Radiography) beamline at PSI (Paul Scherrer Institute) in Villigen, Switzerland. The neutron beam passing through the experimental sample is recorded by a detector system. The detector system consists of a scintillator screen with a CCD camera. The CCD camera has a field of view of 254 x 214 mm². The pixel size is 0.196 x 0.196 mm². The exposure time in the experiments was 20 s per radiography.

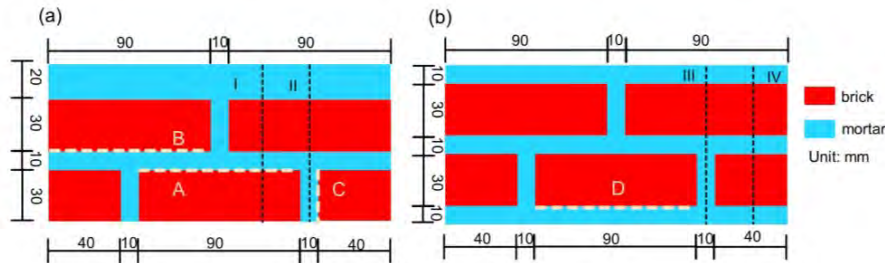


Figure 1. Two masonry samples for water uptake experiments showing the four types of interface (A, B, C and D) considered in this study.

The masonry samples are initially dried in an oven at 60 °C before capillary water uptake experiments. The experimental setup consists of a balance, a support for the samples that rests on the balance and a water reservoir. The sample is first installed on the support. Next, the water surface in the reservoir is brought up to the bottom of the masonry sample and then capillary water uptake starts. The mass of the experimental sample is measured at the start and end of each on a separated balance, as well as during the experiment with the balance in the experimental setup at an interval of 12 s.

The governing equation for 2-dimensional isothermal moisture transport in masonry is described by Richards equation:

$$\frac{\partial w}{\partial p_c} \frac{\partial p_c}{\partial t} + \frac{\partial}{\partial x} \left(K(p_c) \frac{\partial p_c}{\partial x} \right) + \frac{\partial}{\partial y} \left(K(p_c) \frac{\partial p_c}{\partial y} \right) = 0 \quad (1)$$

where w is the moisture content (kg/m³), p_c is the capillary pressure (Pa), $K(p_c)$ is the liquid permeability (s), which is a function of capillary pressure. At the interface between mortar and

brick, an interface resistance R (s/m) is introduced. Moisture flow across the interface is described by: $g_f = \frac{\Delta p_c}{R}$, where Δp_c is the capillary pressure difference between the interface

(Pa). At the bottom side of the masonry samples, a constant capillary pressure of -10 Pa is applied to represent capillary saturated condition. The capillary pressure curves of brick and mortar are described using a bimodal function of the van Genuchten model. The liquid permeability of the brick is determined based on the method proposed by Carmeliet et al. (2004). The moisture transport equation is solved using the finite element simulation program COMSOL. Rectangular meshes are used to discretize the geometric domain. More meshes are mapped around brick/mortar interface and the lower part of the domain. The COMSOL solver used is the direct solver MUMPS with its default solver options. Numerical time steps are automatically selected by the COMSOL solver.

The interface resistance is obtained by comparing simulated moisture profile results with measured moisture profile results. Only interfaces below the wetting front are considered for numerical simulation in this study. There are four types of interface between brick and mortar that affects moisture distribution in this study (Figure 1). Interface A is the horizontal interface between the first layer of brick and the second layer which is mortar. Interface B is the horizontal interface between this second layer, i.e. of mortar, and the third layer, i.e. of brick. Interface C is the vertical interface between two first layers, of brick and of mortar. Interface D is the horizontal interface between a first layer of mortar and a second layer of brick. Moisture transport in the two samples shows symmetric behavior. For sample (a), two profiles in the right part (profile I and II in Figure 1a) are selected for comparison. For sample (b), two profiles in the right part of this sample (profile III and IV in Figure 1b) are selected.

RESULTS

The moisture content distribution in the uptake experiment in sample (a) is given in Figure 2. The advance of wetting front is symmetric with respect to the middle of the sample. At the time of 409 s, the wetting front in the first layer of brick reaches the top of the brick element. By comparison, the wetting front in the two vertical mortar joints in the first layer shows an inverted bell curve. The wetting front reaches a higher height at the two edges of the mortar joints, while the middle part of the mortar joint shows the lowest height of wetting front. The higher wetting front at the two edges of the mortar is due to moisture transport from the surrounding bricks. At the time of 1525 s, the wetting front is already in the horizontal mortar joint above the first layer of brick, whereas the wetting front shows a shape of inverted triangle in the two vertical mortar joints. At the time of 10027 s, the wetting front is highest in the vertical mortar joint, in the third layer of the sample.

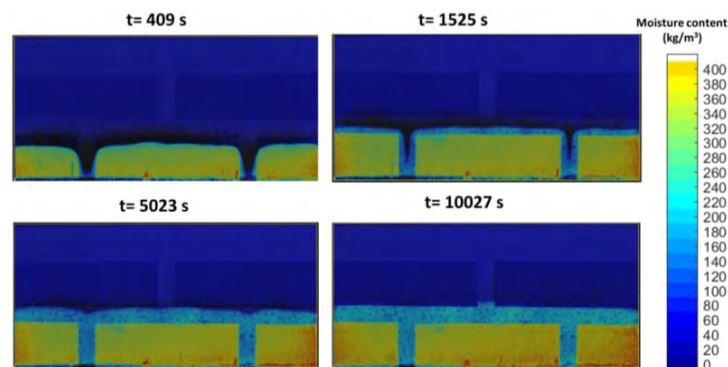


Figure 2. Moisture content distributions in sample (a) at different times.

The moisture content distribution in the uptake experiment in sample (b) is given in Figure 3. As the first layer of the sample is made of mortar, the advance of wetting front is very slow in this sample. For example, at the time of 5012 s, the wetting front only reaches the height of 1 cm. The wetting front shows an almost uniform distribution in the first layer of mortar joint. By comparison, at the time of 10026 s, the wetting front is higher at the location of the two vertical mortar joints than in the brick.

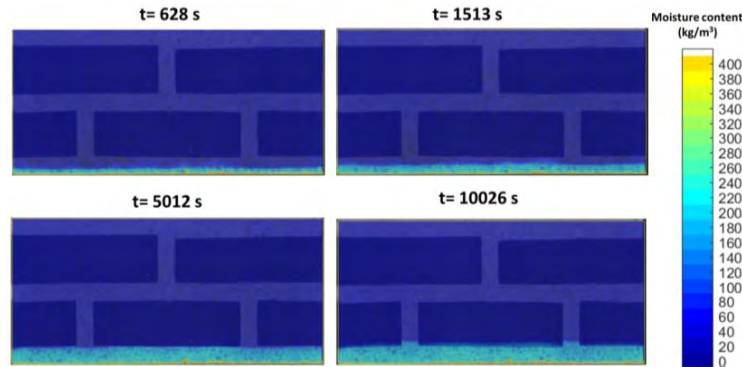


Figure 3. Moisture content distributions in sample (b) at different times

Figures 4 and 5 shows the comparison between simulated and measured moisture profiles in samples (a) and (b). In general, the simulated moisture content profiles agree mostly well with the simulated moisture content profiles. Not only the simulated locations of wetting front agree well with measurements, but also the simulated moisture contents at different locations agree well with the measured moisture contents. However, there are some disagreements between measurement and simulation at some profiles. This might be due to material heterogeneity. In the numerical model, the same brick and mortar material properties are used for each sample. In reality, the material properties of brick and mortar might be slightly different.

The obtained interface resistances for the four types of interface A, B, C and D are: 8.0×10^9 , 5.0×10^{12} , 4.0×10^9 and 20.0×10^9 m/s. A larger value of interface resistance means a larger capillary pressure drop across the interface and a smaller moisture flux across the interface.

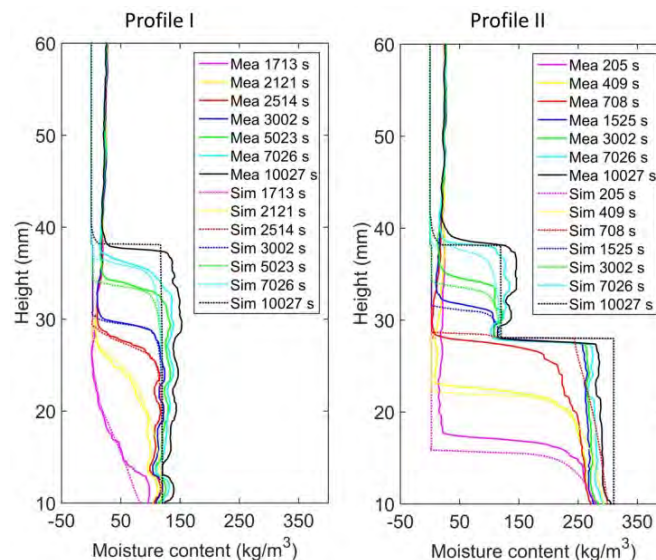


Figure 4 Measured and simulated moisture contents at profiles I and II for sample (a).

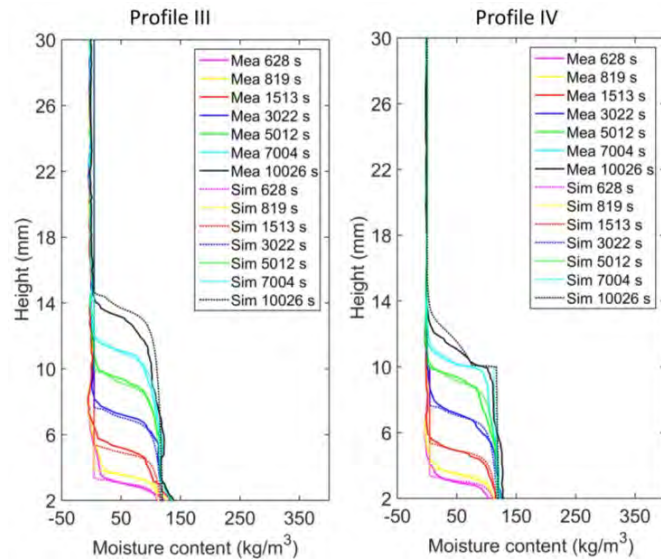


Figure 5 Measured and simulated moisture contents at profiles III and IV for sample (b).

DISCUSSIONS

Based on the results presented above, we propose that the interface resistance may be dependent on capillary pressure at the interface between two materials. A lower capillary pressure at the interface will lead to a larger interface resistance. Interface B has the largest interface resistance. The capillary pressure at Interface B is much lower than at the other types of interface. On the one hand, Interface B is at a higher location above two layers, i.e. of brick and mortar. There is already a large capillary drop when moisture reaches Interface B by capillary transport. On the other hand, the interface resistance at Interface A leads to an additional capillary pressure drop.

The interface resistance at Interface C (4.0×10^9 s/m) is slightly smaller than that at Interface A (8.0×10^9 s/m). Interface A is a horizontal interface between the first layer of brick and the second layer of mortar, whereas Interface C is a vertical interface between brick and mortar in the first layer. When wetting front reaches Interface A, there is already some capillary pressure drop. By comparison, Interface C is along the direction of moisture transport. Capillary pressure at lower location is larger than at higher location. The top location of Interface C is the same as that of Interface A. Therefore, the capillary pressure at Interface A is definitely larger than that at Interface C. The obtained interface resistance at Interface C is the averaged value along this interface. Due to higher capillary pressure at the interface, the interface resistance Interface C is smaller than that at Interface A. There are both horizontal and vertical interfaces between brick and mortar in masonry. Compared to the flow, the magnitude of interface resistance does not seem to be affected by the direction of interface. Instead, the interface resistance is apparently related to capillary pressure during wetting at the interface. The larger the capillary pressure, the smaller the interface resistance at the interface. The datasets offer more result, which will be studied in the next phase.

CONCLUSIONS

Different masonry samples with horizontal and vertical interfaces are used to study the resistance to moisture transport across the brick/mortar interface. Neutron radiography is used to measure the time- and space-resolved moisture content distribution in different masonry samples. A 2-dimensional moisture transport model is built to study moisture transport in

masonry samples. An interface resistance is introduced to consider the imperfect contact between brick and mortar. There is very good agreement between measured and simulated moisture contents for different masonry samples. Compared to the flow, the magnitude of interface resistance is not affected by the direction of interface. Horizontal interface or vertical interface between brick and mortar has no influence on the value of interface resistance. It is found that interface resistance seems to be affected by the capillary pressure at the interface, and not by the orientation of the interface. A lower capillary pressure at the interface will lead to a larger interface resistance.

ACKNOWLEDGEMENT

We acknowledge the support of the Swiss Competence Center for Energy Research project “Future Energy Efficient Buildings and Districts”.

REFERENCES

- Brocken, H.J.P. (1998) Moisture transport in brick masonry: the grey area between bricks, Technische Universiteit Eindhoven.
- Carmeliet, J., Hens, H., Roels, S., Adan, O., Brocken, H., Cerny, R., Pavlik, Z., Hall, C., Kumaran, K. and Pel, L. 2004. Determination of the liquid water diffusivity from transient moisture transfer experiments. *Journal of thermal envelope and building science* 27(4), 277-305.
- Delgado, J.M.P.Q., de Freitas, V.P. and Guimares, A.S. (2016) Water movement in building walls: interfaces influence on the moisture flux. *Heat and Mass Transfer* 52(11), 2415-2422.
- Derluyn, H., Janssen, H. and Carmeliet, J. (2011) Influence of the nature of interfaces on the capillary transport in layered materials. *Construction and Building Materials* 25(9), 3685-3693.
- Janssen, H., Derluyn, H. and Carmeliet, J. (2012) Moisture transfer through mortar joints: A sharp-front analysis. *Cement and Concrete Research* 42(8), 1105-1112.
- Qiu, X., Haghighat, F. and Kumaran, M.K. (2003) Moisture transport across interfaces between autoclaved aerated concrete and mortar. *Journal of thermal envelope and building science* 26(3), 213-236.
- Zhou, X.H., Derome, D. and Carmeliet, J. (2016) Robust moisture reference year methodology for hygrothermal simulations. *Building and Environment* 110, 23-35.

Aerogel-enhanced blankets: state-of-the-art, market readiness, and future challenges

Umberto Berardi^{1,*}, Syed (Mark) Zaidi¹, Bryan Kovisto¹

¹ Ryerson University, Ontario, Canada.

**Corresponding email: uberardi@ryerson.ca*

ABSTRACT

Aerogel-enhanced products are often indicated as promising materials for increasing the thermal resistance of the building envelope. In particular, aerogel-enhanced blankets have already showed their effectiveness in several retrofitting projects. This paper aims to review the current state of the art regarding aerogel-enhanced blankets. In these materials, a fiber matrix bonds together the aerogel structure, compensating the low mechanical properties of the aerogels without reducing their exceptionally low thermal conductivity. This paper describes current aerogel-enhanced blankets existing worldwide and produced by different companies. Then, a new aerogel-enhanced blanket developed by the authors is presented. Thermal characterization tests confirm the superior performance of aerogel-enhanced blankets, which show a thermal conductivity as low as 0.013 W/(mK). Finally, future research challenges for aerogel-enhanced blankets are presented.

KEYWORDS

High-performance envelope, aerogel, aerogel-enhanced blanket, super-insulating materials.

INTRODUCTION

The development of innovative materials aiming to achieve energy savings is a main focus in the building technology sector. In this context, silica aerogel-enhanced products are often indicated as promising materials for increasing the thermal resistance of the building envelope. While aerogels seem to be promising but still uncommon materials, the global market for silica-based aerogels continues to grow annually at over 10%, passing from US\$ 427 Million in 2016 to a forecast of US\$ 1.92 billion in 2022 (GVR, 2016). Nowadays, the primary market sector for aerogel-enhanced products is represented by the oil and gas fields which mainly use aerogel-enhanced blankets. However, the building and construction aerogel-market sector is supposed to increase more than the other sectors (Berardi and Nosrati, 2018).

Silica aerogels have extraordinary small pores, which result in remarkable thermal properties, and mechanical strength. Table 1 reports the main physical properties of silica aerogels. In Table 1, it emerges that while the compression strength of the aerogel has a value around 300 kPa, their tensile strength is only 16 kPa, making aerogel extremely fragile. In order to strengthen the tensile properties of the silica aerogels to be used as an insulating material, it has been recently proposed to reinforce the aerogels with mechanically stronger materials and non-woven fiber matrixes such as glass, mineral or carbon fibers. When the fibers or fibrous matrix are added to the pre-gel mixture which contains the gel precursors, the resulting dried composite is an aerogel-enhanced blanket (Aegerter et al., 2011, Baetens et al., 2011).

Nowadays, the main reasoning for the use of aerogel-enhanced insulation is related to the possible space saved resulting from the exceptional thermal properties and fire resistance. In

particular, aerogel-enhanced products during building retrofits guarantee the advantage of significant space saving and provide a high thermal resistance in thin layers (Ibrahim et al., 2014, Ghazi Wakili et al. 2014, Galliano et al., 2016). In fact, already a few years ago, the retrofit of a wall with 1 cm thick aerogel blankets on the interior side demonstrated to be economically feasible by Shukla et al. (2014), although the high material cost at that time.

Table 1. Main physical properties of silica (SiO₂) aerogels.

Property	Value
Density	3 to 350 kg/m ³ (typical 70 to 150 kg/m ³)
Pore diameter span	1 to 100 nm (~20 nm on average)
Pore particle diameter	2 to 5 nm
Average pore diameter	20 to 40 nm
Porosity	85 to 99.9 % (typical ~95%)
Thermal conductivity	0.01 to 0.02 W/mK
Primary particle diameter	2 to 4 nm
Surface area	600 to 1000 m ² /g
Tensile strength	16 kPa
Compression strength	300 kPa
Coefficient of linear expansion	2 to 4×10 ⁻⁶

Aerogel-enhanced blankets composed of synthetic amorphous silica are a valid possibility whenever space and weight constraints exist. Several studies have investigated the use of aerogel blankets in buildings and reported about the in-situ behaviour of such products. For example, at the University of Nottingham, the energy efficient retrofit project of a 1930's house was investigated. The research aimed to understand the impact of thermal bridging on the heat loss using aerogel blankets of 20 mm thickness implemented internally with 12 mm of gypsum plaster-board. Results showed that after retrofit, the heat loss through the retrofitted wall was highly reduced, while for the separating wall, there was an increase of the heat losses due to the growing thermal bridges (Cuce et al., 2014, Cuce and Cuce, 2016). Although these preliminary experiences seem promising, a systematic evaluation of the available aerogel-enhanced blankets is still missing. This paper aims to review thermal properties of products currently on the market, to present an innovative aerogel-enhanced blanket, and to review current challenges for these highly promising insulating products.

LITERATURE REVIEW

Aerogel-enhanced blankets are flexible, highly porous, and have a remarkably high thermal resistance. In fact, they have started to be produced and commercialized by several manufactures worldwide, such as Aspen Aerogel Inc., Cabot Corporation, Svenska Aerogel AB, Acoustiblok UK Ltd., Active Space Technologies, Joda, and Airglass AB. For example, Spaceloft developed by Aspen Aerogels Inc. (MA, US) is a flexible fiber-reinforced blanket with a declared thermal conductivity of 0.013 W/(mK) at 0°C. Other common aerogel blankets are Cryogel[®]Z by Aspen, available in 5 mm and 10 mm thickness and suitable for industrial application, and Thermal-Wrap[™], available in 5 mm and 8 mm thickness by Cabot Corporation. The thermal conductivity of these last two products is 0.014 W/(mK) and 0.023 W/(mK) respectively. Similarly, among the aerogel-based commercial blankets, Proloft by Advanced Technologies has attracted some attention as a thermal barrier strip to provide thermal bridging protection around window frames.

The advantages of aerogel-enhanced blankets are that the final panel does not show any granularity of the aerogel, since the aerogel particles are chemically attached to the fiberglass matrix. Commercially available aerogel-enhanced blankets are made with amorphous silica,

and they usually suffer for dust production. However, several health organizations, including the International Occupational Safety and Health Organization, have declared aerogel blankets not hazardous for the human health. The non-toxicity combined with the excellent fire protection are promising characteristics of these blankets, which are recyclable, have minimal to no Ozone Depleting Potential and a Global Warming Potential below than 5. Table 2 reports the main properties of different aerogel-enhanced blankets available on the market.

Table 2. Main properties of the most common aerogel-enhanced blankets available on the market.

Commercial name	Manufacture	Fiber composition	Density (kg/m ³)	λ (W/mK)
Thermal Wrap	Cabot	Polyestere and PET	~70	0.023
Cryogel x201	Aspen aerogel	Polyester/fiber glass	~130	0.014
Cryogel Z	Aspen aerogel	PET / fiber glass	~160	0.014
Dow Corning HPI 1000	Dow Corning	Fiber glass	-	0.015
Pyrogel HPS	Aspen aerogel	Fiber glass	~200	0.014
Pyrogel XTE	Aspen aerogel	Fiber glass	~200	0.014
Pyrogel XTF	Aspen aerogel	Fiber glass	~200	0.014
Spaceloft	Aspen aerogel	Polyester/fiber glass	~151	0.015
Silica aerogel fiberglass blanket	Joda	Fiber glass	<300	0.016
Silica aerogel ceramic fiber blanket	Joda	Ceramic fiber	<301	0.016

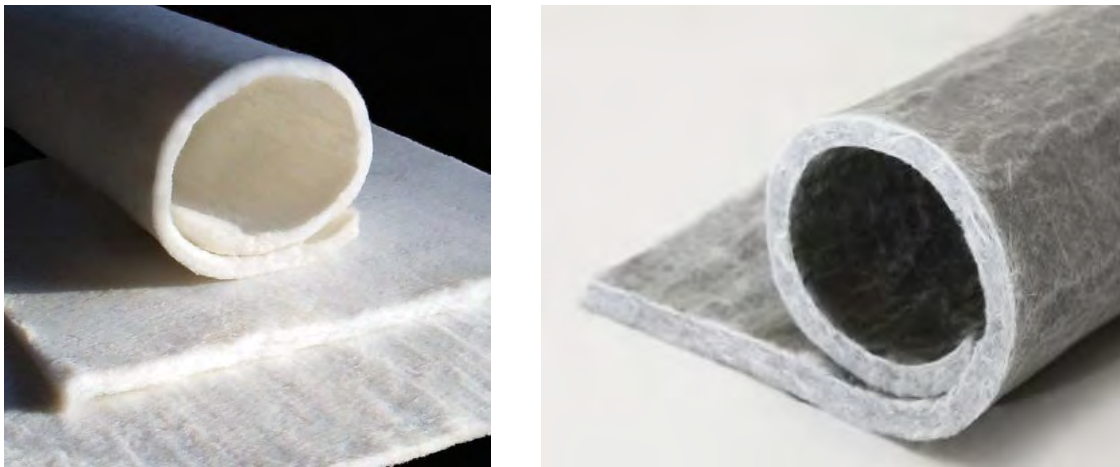


Figure 1. Aerogel blankets Cryogelx201 (left) and Dow Corning HPI 1000 (right).

Lakatos (2017) and Nosrati and Berardi (2018) assessed how the thermal conductivity of aerogel-blankets increases as a function of the moisture content. In particular, Lakatos (2017) studied the application of the aerogel-blanket to a brick-based wall. Firstly, sorption isotherms were investigated to understand the temperature sensitivity of moisture uptake. Each aerogel slab was tested after wetting the dried samples for 0, 4, 8, 12, 16, 20 hours at 293 K and 93% relative humidity, showing significant higher thermal conductivity in the wetting stage.

A comprehensive investigation of the thermal conductivity of the aerogel-enhanced Cryogel by Aspen Aerogel and Thermal Wrap by Cabot blankets in humid conditions at transient and steady-state regimes was made by Hoseini et al. (2017). The moisture build-up in the two aerogel blanket samples was measured as a function of the relative humidity and temperature. Transient plane source tests revealed that the thermal conductivity increased by up to approximately 15% as the ambient relative humidity increased from 0% to 90%. However, when the aerogel blankets were placed in a humid environment, it took hours for the moisture to diffuse towards the material core.

EXPERIMENTAL STUDIES

Comparison of existing products

Figure 2 shows the thermal conductivity values declared by the manufacturer for different aerogel blankets currently on the market. The results are particularly promising, especially at the temperature typically incurred in the building sector.

To help comparing several products, the authors performed hygrothermal tests in the Building Science Lab at Ryerson University. In particular, after exposing the different blankets to the same hygrothermal conditions, the thermal conductivity values for different aerogel blankets were measured using the heat flow meter apparatus HFM 436 Lambda. The temperature difference between the hot and cold plates was set to 20 °C, while the temperatures ranged from -20 °C to +50 °C. Figure 3 reports the results for four aerogel-enhanced blankets.

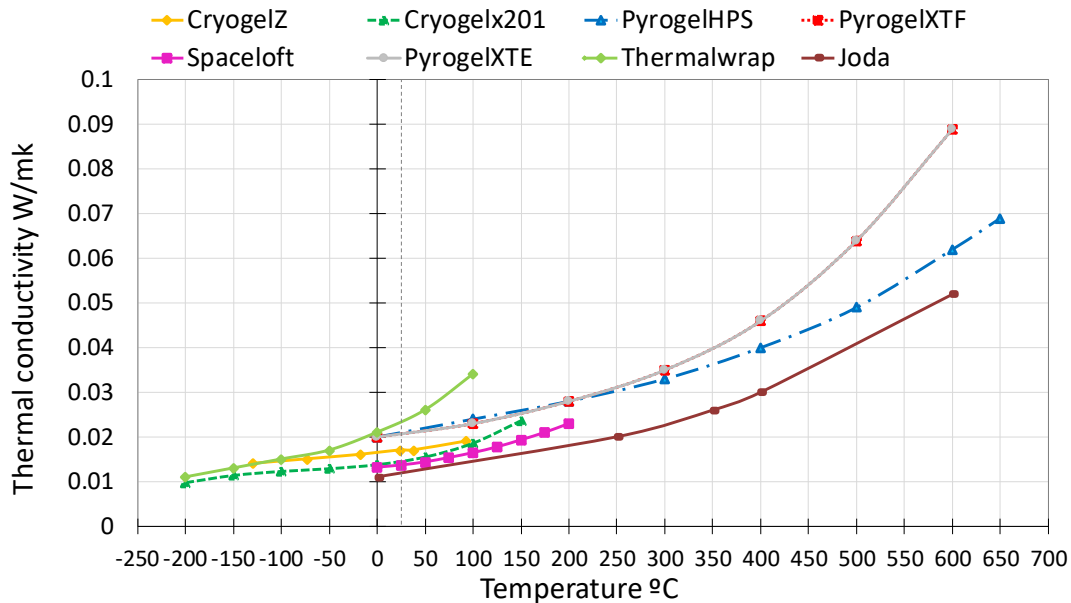


Figure 2. Thermal conductivity values across the temperature for different aerogel blankets (this figure was drawn using the values declared by the manufactures).

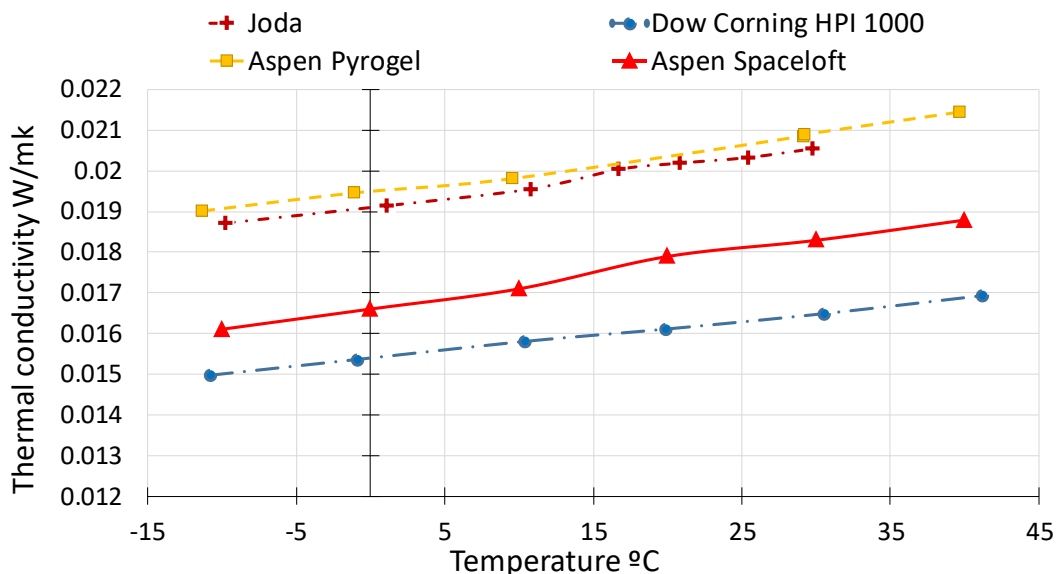


Figure 3. Thermal conductivity values across temperature for different aerogel blankets (these values were measured by the authors after having normalized the hygrothermal conditions).

Development of a new aerogel-enhanced blanket

The synthesis of silica aerogels is typically carried out in three phases: gel preparation, aging, and drying. In particular, three methods for drying the aerogels can be used: supercritical drying (SCD), ambient pressure drying (APD) and the freezing drying. SCD reduces capillary tension but comports higher costs. On the other hand, APD is more cost-effective but involves increased capillary tension which can lead to shrinking and possible fractures, therefore SCD is generally used for silica aerogels. The cost of the SCD process represents a limiting factor to obtain a competitive price for the aerogel. To lower the price of the blankets by avoiding to perform a SCD, the authors have obtained aerogels and aerogel-enhanced blankets drying the materials in a vacuum oven for 24 hours (Fig. 4).



Figure 4. Authors' produced aerogel granules (left) and aerogel-enhanced blankets obtained embedding a fiberglass panel with precursor aerogel before the drying process (right).

The silica aerogels were prepared using the 2-step Stöber process, as adapted from Shlyakhtina et al. (2007), using reagents purchased from Sigma Aldrich. Firstly, 120 ml of isopropanol was added to 123.2 ml of tetraethylorthosilicate in a graduated cylinder. The contents were then transferred to a beaker with a stir bar, set to stir for 30 minutes, and sealed with paraffin to prevent evaporation. Next, 29 ml of 0.1 M HCl was added dropwise, and set to stir for an additional hour until the mixture was completely hydrolyzed into silicic acid. A timer was started, and 28 ml of 0.15 M NH₄OH was added dropwise to initiate the polymerization. The solution was transferred into a cellophane-lined rectangular mould. Pre-cut and pre-weighed fiberglass samples 2 cm thick were dipped into the solution, and then the excess solution was squeezed out. Afterwards, the samples were set to cure, and were transferred to a heated vacuum furnace for 24 hours, similarly to the work of Padmanabhan et al. (2016). The samples were taken out and weighed to determine their final mass and that of aerogel, by subtracting from their initial mass. The thermal conductivity of the aerogel-enhanced blanket shown in Fig.4, tested using the same apparatus and conditions described previously, resulted to **be 0.029 W/(mK) at 0 °C and 0.031 W/(mK) at 20 °C**, generally above that of commercial aerogel-enhanced blankets, although the price of this bat would be extremely competitive and its manufacturing process would not require expensive equipment. In fact, the costs of the aerogel and of the aerogel-enhanced blankets were below \$4/gram and \$30/m² respectively.

CONCLUSIONS

This paper has presented ongoing research activities leading to the manufacture of aerogel-enhanced blankets. An overview of products available on the market has been reported. Meanwhile, a new aerogel-enhanced blanket has been presented. The hope is that soon APD processes could be improved to realize cheap aerogel-blankets with a thermal conductivity of 0.010 W/(mK), a target that would make these products preferable over traditional insulating ones.

ACKNOWLEDGEMENTS

The first author expresses his gratitude for the support of the NSERC DG #2016-4904 and for the ERA award sponsored by the Ontario Ministry of Research Innovation and Science, MRIS

REFERENCES

- Aegerter MA, Leventis N, Koebel MM. 2011. *Aerogels Handbook*. New York: Springer.
- Baetens R, Jelle BP, Gustavsen A. 2011. Aerogel insulation for building applications: A state-of-the-art review, *Energy Buildings* 43, 761–769.
- Berardi U, Nosrati R. 2018. Long-term performances of aerogel-enhanced insulating materials, *Energy* 147, 1188-1202.
- Berardi U. 2015. The development of a monolithic aerogel glazed window for an energy-retrofitting project, *Applied Energy* 154, 603–615.
- Cuce E, Cuce PM, Wood CJ, Riffat S. 2014. Toward aerogel based thermal superinsulation in buildings: A comprehensive review, *Renewable and Sustainable Energy Reviews* 34, 273–299.
- Dorcheh SA, Abbasi MH. 2008. Silica aerogel: synthesis, properties characterization, *Journal of Materials Processing Technology* 199, 10–26.
- Galliano R, Ghazi Wakili K, Stahl T, Binder B, Daniotti B. 2016. Performance evaluation of aerogel-based perlite-based prototyped insulations for internal thermal retrofitting: HMT model validation by monitoring at demo scale, *Energy and Buildings* 126, 275-286.
- Ghazi Wakili K, Binder B, Zimmermann M, Tanner C. 2014. Efficiency verification of a combination of high performance conventional insulation layers in retrofitting a 130-year old building, *Energy and Buildings* 82, 237-242
- Hoseini A, Malekian A, Bahrami M. 2016. Deformation and thermal resistance study of aerogel blanket insulation material under uniaxial compression, *Energy and Buildings* 130, 228-237.
- Ibrahim M, Biwole PH, Wurts E, Achard P. 2014. A study on the thermal performance of exterior walls covered with a recently patented silica-aerogel-based insulating coating, *Building and Environment* 81, 112–122.
- Lakatos Á. 2017. Investigation of the moisture induced degradation of the thermal properties of aerogel blankets: Measurements, calculations, simulations, *Energy and Buildings* 139, 506-516.
- Nosrati R, Berardi U. 2018. Hygrothermal characterization of aerogel-enhanced insulating materials under different humidity and temperature conditions. *Energy and Buildings* 158, 698-711.
- Padmanabhan, Kunjalukkal S, Ul Haq E, Licciulli A. 2016. Synthesis of silica cryogel-glass fiber blanket by vacuum drying. *Ceramics International* 42(6), 7216-222.
- Shlyakhtina AV, Young-Jei O. 2007. Transparent SiO₂ aerogels prepared by ambient pressure drying with ternary azeotropes as components of pore fluid. *Journal of Non-Crystalline Solids* 354(15-16), 1633-642.
- Shukla N, Fallahi A, Kosny J. 2014. Aerogel Thermal Insulation — Technology Review Cost Study, *ASHRAE Transactions* 120, 294-307.

Hygrothermal Analysis of a Vapour-Open Assembly with Vacuum Insulation Panels

Brock Conley¹, Cynthia Ann Cruickshank¹, Mark Carver²

¹Carleton University, Ottawa, Canada

²CanmetENERGY-Natural Resources Canada, Ottawa, Canada

ABSTRACT

The following paper studies the year-long moisture conditions associated with vacuum insulation as the exterior insulation. The exterior insulation of one assembly was renovated by using 50.8 mm (2 inch) of expanded polystyrene (EPS) and represents the baseline performance of current common practice. Another assembly was built with 20 mm (0.7 inch) vacuum insulation panels encased in the equivalent thickness of EPS to represent a high RSI-value retrofit. The thermal performance was evaluated using a guarded hot box facility at Carleton University and the in-situ Building Envelope Test Hut at CanmetENERGY-Ottawa. The temperature, humidity and moisture content in the sheathing measurements from February 2017 to March 2018 are presented. Experimental results were compared to failure criteria outlined by ASHRAE Standard 160 to determine if the proposed building envelope system would be suitable in a cold, humid climate.

KEYWORDS

Vacuum Insulation Panel, Retrofit, Building Envelope, Hygrothermal, Experimental

INTRODUCTION

In Canada, it is estimated that a single dwelling built before 1980 consumes 25% more space conditioning energy than a dwelling built after 2010 according to the National Energy Use Database (NRCan-OEE, 2016). Considering the disparity in energy consumption between vintages, and that there are 4.5 million dwellings in Canada (Statistics Canada, 2016) built before 1984, there is a significant amount of energy that can be saved by further insulating or improving the energy performance of these existing dwellings. Since space conditioning accounts for the majority of the energy consumption in a residential building, addressing the energy flow through the envelope of the building (e.g., conduction, air leakage) may provide significant benefits. A properly sealed and well insulated envelope, which older homes often lack, can reduce the energy transfer between the conditioned space and ambient environment.

Approximately 60% of existing residential buildings in Canada were constructed before 1984 (Statistics Canada, 2016). Since some of these buildings may be poorly insulated, and/or lacking airtightness and consequently represent a large portion of the energy usage of the residential building stock, that stock is a perfect candidate for retrofit. While these buildings may need upgrades to their envelopes, simply increasing the amount of insulation on the exterior face of the envelope may not be the best practice. Instead, it may be beneficial to use high performance (e.g., high resistance) materials, such as vacuum insulation panels (VIPs), to maintain or limit the increase of wall assembly thickness. While thermal improvements are a main driver of retrofitting the building envelope, the hygrothermal aspects of the wall assembly impact its lifespan and durability.

The paper outlines the investigation of using high performance exterior insulation on two wall assemblies to address the moisture requirements and thermal performance of a building envelope while maintaining the thickness compared to standard constructions.

WALL ASSEMBLIES

Since the desired wall assembly construction is thin profiled as well as thermally and hygrothermally sufficient for a cold and humid climate, a composite insulation panel using VIPs and Type 2 expanded polystyrene (EPS) as rigid exterior insulation board was proposed. The VIPs were surrounded by the EPS such that the RSI-value of the assembly was higher than an equivalent thickness of EPS. This configuration also mitigates the risk of punctured VIPs during installation, which was a concept previously investigated (Conley, et al., 2016; Carver, et al., 2017).

Construction

Two wall assemblies used for this study were developed to represent types of construction that could impact Canadian construction. As previously stated, retrofitting the existing building stock that is currently built below the current minimum insulation levels is an area that could provide a large change in national energy consumption. The first wall assembly under investigation was a 2x4 wood stud assembly with 600 mm spacing, filled with RSI-3.3 insulation without any interior vapour barriers and has undergone an exterior retrofit. The exterior retrofit involved removing all materials to the exterior of the sheathing, applying an air barrier, adding the VIP-EPS insulation panel, adding 1x3 strapping and finishing with siding (see Figure 1). The second wall assembly represented a typical new construction in Ottawa, Canada. The wall was construction with 2x6 wood studs with 600 mm spacing filled with insulation, internal vapour barrier, 40 mm of rigid insulation, an exterior air barrier and vinyl siding (similar to Figure 1). For the high performance assembly, the VIP-EPS insulation panel was used as 40 mm of rigid insulation. Both of the wall assemblies described are attempts at creating a durable, robust and high performing assembly that can be utilized in Canadian climates and must be evaluated for their applicability to the climate.

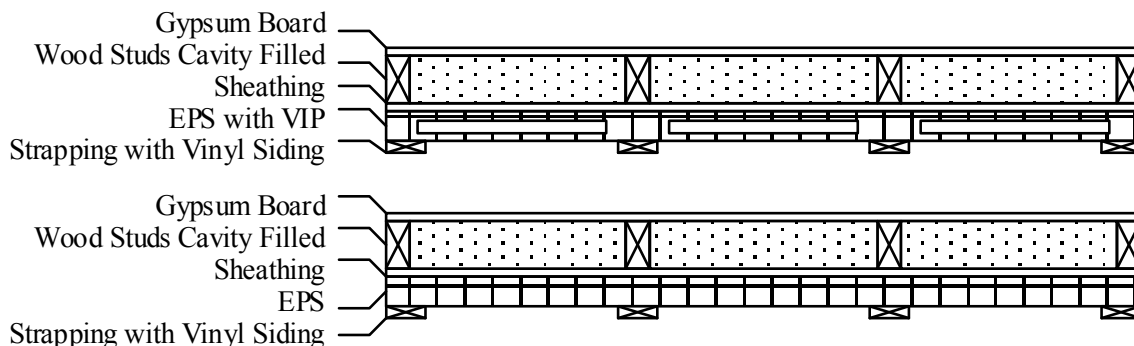


Figure 1: Cross section illustrating materials used for the wall assemblies in the study

Failure Criteria

For the wall assembly design to be considered a success, the thermal and hygrothermal goals must be met, in totality and in comparison to the baseline assemblies. These criteria were developed from standards such as ASHRAE 160 or voluntary building performance standards. The hygrothermal performance of the wall assembly is an indicator of its resilience to the wetting, and its drying potential. The following criteria is applicable for materials at temperatures between 5°C and 40°C:

1. Maintain the 30-day running average relative humidity at the sheathing below 80%;
2. Maintain the 5-day running average relative humidity at the sheathing below 98%;
3. Maintain the daily average relative humidity at the sheathing below 100%; and
4. Maintain a moisture content below 28% to eliminate the risk of mould and rot.

When the material is at a temperature below 5°C, most deterioration at high humidity levels is non-existent, while condensation and bulk wetting could still be an issue. The relative humidity set-points were developed by ASHRAE (ANSI/ASHRAE, 2016) as guidelines to minimize the risk associated with organic growth within the building envelope assembly. The moisture content of wood limits are based on studies that assessed the robustness or durability of wall assemblies and is related to the surface relative humidity.

THERMAL PERFORMANCE

The steady-state testing was performed using a guarded hot-box situated at Carleton University with the purpose of determining an accurate RSI-value of the proposed wall assemblies. The guarded hot-box, depicted schematically in Figure 2, is composed of three independently controlled chambers to force one-dimensional heat flow through the wall assembly specimen. The climate chamber is set to simulate the exterior temperature conditions (approximately -20°C) while the metering and guarded chambers have the same set-point, slightly above room temperature around 25°C, thus creating a substantial temperature difference across the specimen.

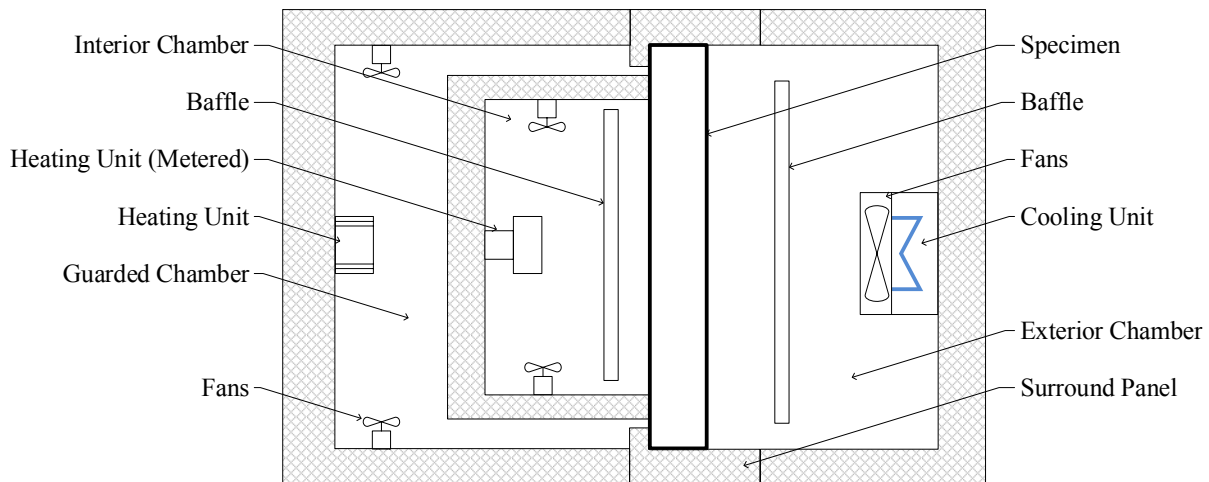


Figure 2: Schematic of the guarded hot-box at Carleton University

The electric heaters installed within the metering chamber are the only source of energy input to the area, and are therefore accurately monitored for the duration of the test period. Additionally, the interior and exterior surface temperatures are measured during the test period to find the effective RSI-value of the wall assembly through Equation (1), where ΔT is the temperature difference between surfaces in °C, A is the known area of the metering chamber in m^2 , t is the test period in seconds, and E is the energy input to the metering chamber in J.

$$RSI = \frac{\Delta T \cdot A \cdot t}{E} \quad (1)$$

The effective RSI-value of the wall assembly can be calculated from the measured data after steady-state is reached. Defined by ASTM C-1363, these test conditions are met when five consecutive test periods:

- The average specimen surface temperature in either chamber did not vary by more than $\pm 0.25^{\circ}\text{C}$.
- The average energy input to the metering chamber did not vary by more than $\pm 1\%$.

For this study, the wall assemblies were evaluated in the guarded hot-box and results were compiled into Table 1. The assemblies that were tested performed below the failure criteria previously described, however, the baseline values were improved by increasing the RSI-value by 31% and 21% for new construction and retrofit construction, respectively. It should be noted that the nominal values provided for the baseline assemblies do not incorporate thermal bridges from the vertical framing members, and constitute a highest permissible value, while the values calculated from the guarded hot-box experiments are the effective RSI-values, which would be a lowest possible RSI-value.

Table 1: Summary of steady-state effective RSI-value from guarded hot-box testing

Assembly	New Construction ($\text{m}^2\text{K}/\text{W}$)	Retrofit ($\text{m}^2\text{K}/\text{W}$)
Baseline	4.8 (nominal)	4.2 (nominal)
High Performance	6.3 (effective)	5.1 (effective)

HYGROTHERMAL PERFORMANCE

The hygrothermal assessment of the wall assemblies were conducted at the CanmetENERGY Building Envelope Test Hut (CE-BETH) in Ottawa, Canada. The test facility monitors the moisture and thermal conditions of wall assemblies by controlling the interior conditions and exposing the exterior to ambient conditions for a prolonged period of time. Instrumentation is placed within each specimen to monitor the moisture content, relative humidity, temperature and heat flux at various interfaces and materials within the assembly. The measured values were compared to failure criteria and the durability of the assembly was assess for the climate. Measurements were taken at 5 minute intervals and averaged over the hour to reduce the number of data points and have a better comparison for weather data. The instrumentation points are shown in Figure 3, which are identical for the new construction and retrofit wall assemblies.

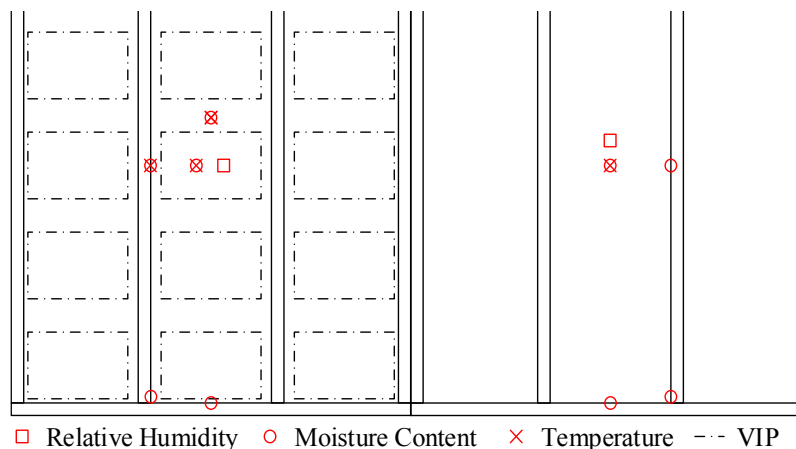


Figure 3: Plan view of instrumentation placed at the sheathing of bottom half of the assemblies

The durability of the wall assemblies were monitored from February 2017 to February 2018, however they were installed at the test facility beginning in December 2016. Therefore, the assemblies were exposed to a heating seasons worth of moisture loads prior to when the data acquisition began. During installation, various sensors were place on the sheathing surface and vertical framing members to assess the moisture content, temperature and relative humidity of the materials.

The interior conditions of the facility have different set-points for the heating and cooling seasons. During the heating season, the facility maintains an indoor air temperature of 24°C and a relative humidity between 35% and 40%. During the cooling season, the indoor air temperature is maintained at 20°C but the relative humidity may reach up to 70%. The lack of dehumidification in the space aligns with ASHRAE 160 interior design humidity for daily average outdoor temperatures 20°C or greater, which is experienced in Ottawa. For the one year test period, the interior temperature and relative humidity of CE-BETH is presented in Figure 4. Note that there were control and power issues during the monitoring program that caused dips in temperature and relative humidity.

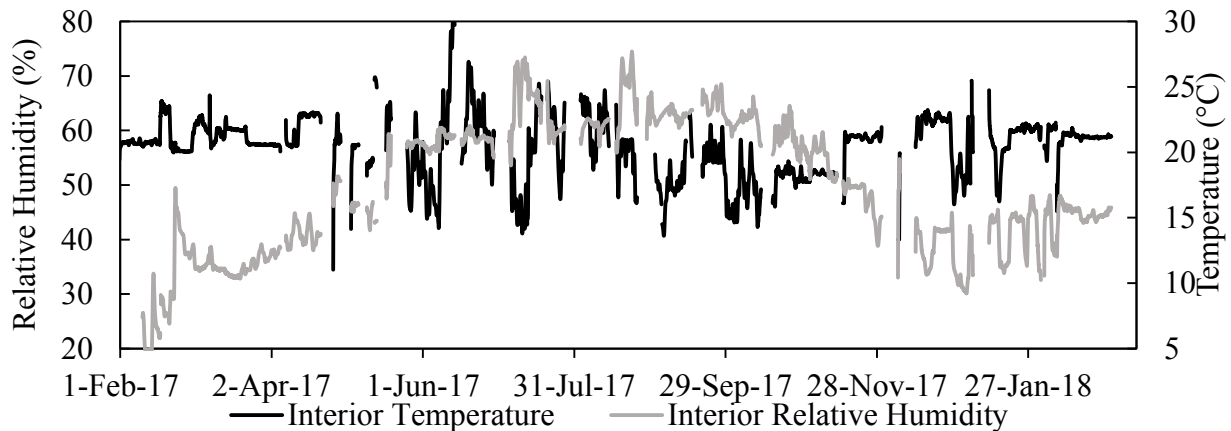


Figure 4: CE-BETH interior conditions for the February 2017 through February 2018

During the test period, the moisture content in the sheathing and vertical framing members were measured through resistance based instruments. In Figure 5, the moisture content of four locations in the high performance assembly designed for new constructions were plotted for the duration of the test period. The VIP and EPS labels are moisture content pins in the sheathing aligned to the labelled material outboard. The temperature of the sheathing aligned with a VIP is plotted to show the temperature dependence of the moisture content. The moisture contents in the assembly did not exceed 20%, except for a brief period in November and December, where the temperature decreased rapidly.

The findings suggests that the building envelope would pass the hygrothermal failure criteria outline, however, the assemblies would need to undergo further observation to ensure that the increasing trend of moisture content does not continue over time. An acceptable level of drying potential is shown for the 2017 annum, but with 2018 data, conclusive determinations can be made about the assembly and its feasibility in the environment.

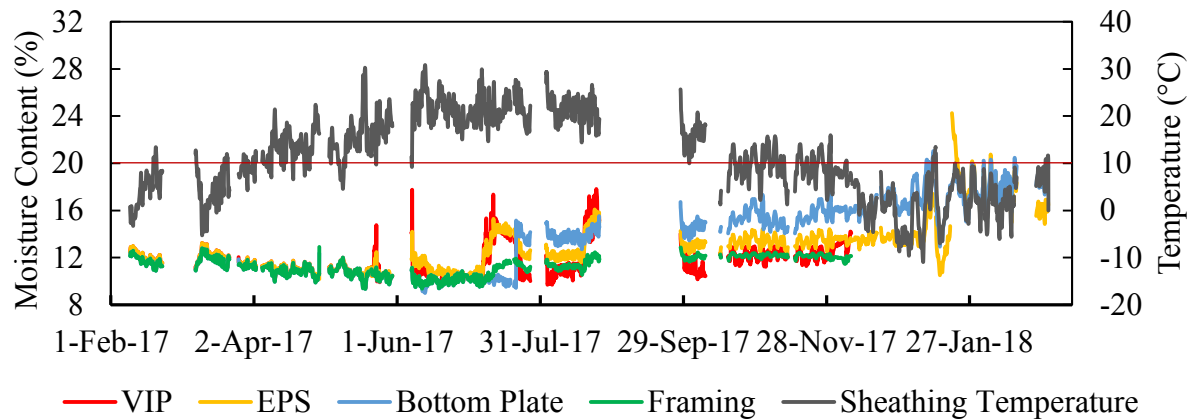


Figure 5: Monitored moisture content within the new construction wall assembly

CONCLUSION

In conclusion, two wall assemblies with VIPs were evaluated under steady-state and in-situ conditions in Ottawa, Canada. The thermal performance of the proposed assembly increased the thermal resistance by up to 32% compared to the baseline assembly. The hygrothermal parameters of the assemblies were and continue to be monitored and measured. After the first year of data collected, the wall assemblies passed the failure criteria outlined, however, it remains too early to make conclusive determinations about the durability and robustness of the wall assemblies in this climate.

The hygrothermal measurements continue to be logged, while the computer simulations will be used to verify the results from CE-BETH. After the in-situ study in Ottawa is completed and simulations are compared to the experimental data, the wall assemblies will be compared to other climates across Canada to ensure they are sufficiently robust and durable. Afterwards, hygrothermal simulations will be used to determine the sensitivity of the proposed assembly to parameters such as, interior relative humidity, sun exposure and varying weather files.

ACKNOWLEDGEMENTS

The authors would like to acknowledge the support of the Natural Sciences and Engineering Research Council of Canada (NSERC) for this work.

REFERENCES

- ANSI/ASHRAE. 2016. Criteria for Moisture Control Design Analysis in Buildings. ASHRAE.
- Carver, Mark, Anil Parekh, Christopher Baldwin, and Brock Conley. 2017. "Field Evaluation of Hygrothermal Performance and Constructability of a Vacuum-Insulated, Thin Wood-Framed Wall Assembly." Proceedings of the 15th Canadian Conference of Building Science and Technology. Vancouver.
- Conley, Brock, Cynthia Ann Cruickshank, Christopher Baldwin, and Mark Carver. 2016. "Comparison and Validation of Modelling Methods for Non-Homogenous Wall Incorporating Vacuum Insulation Panels." Proceedings of the 4th International High Performance Buildings Conference. West Lafayette.
- NRCan-OEE. 2016. National Energy Use Database. 01 04. Accessed 01 01, 2018. http://oee.nrcan.gc.ca/corporate/statistics/neud/dpa/data_e/databases.cfm?attr=0.
- Statistics Canada. 2016. "NHS Profile, 2011." Statistics Canada. 23 11. Accessed 01 01, 2018. statscan.gc.ca/nhs-enm/2011.

Measurements of Temperature Dependency on Thermal Insulation Thickness in Ventilated Attics

Thor Hansen^{1,*} and Eva B. Moeller¹

¹Aalborg University Copenhagen - SBI, A. C. Meyers Vaenge 15, Copenhagen SV 2450, Denmark

*Corresponding email: thh@sbi.aau.dk

ABSTRACT

The main objective of this paper is by measurements to investigate whether increased thermal insulation thickness reduces the temperature in ventilated attics. With lower heat flux through the ceiling in the winter, the theory is that the temperature in the attic decreases and consequently the relative humidity increases which may cause mold growth. While some simulations support this theory, others do not. To test the theory in practice, measurements were performed in 29 dwellings, mainly older single family houses with ventilated attics and insulation thicknesses varying between 150 and 600 mm (6" and 23"). The temperature was measured for more than one year in the attic, the living space below and outdoors.

All measured attics were ventilated as recommended in guidelines; i.e. with openings at the top and the bottom. The measurements in the attics showed high dependency on the outdoor temperature, while indoor temperature and the thickness of insulation were not significant.

Consequently, the thermal insulation thickness alone cannot explain possible increasing mold problems. However, extra insulation in attics may obstruct the ventilation openings and therefore, reduce the ventilation rate. Measurements of ventilation rates in non-problematic and moldy attics should therefore be the next step.

KEYWORDS

Ventilated attics, temperature, thermal insulation thickness, heat flux, energy efficiency

INTRODUCTION

Our recent, paper (Hansen & Møller, 2017) showed some indication that the measured temperature in the attics of the case buildings was independent of the thermal insulation in the ceiling. Another paper (Nielsen & Morelli, 2017) presented simulation results for temperature variation in cold ventilated attics, with insulation thicknesses varying from 50 to 450 mm, where the average temperature in the attic in January was 1.54 °C (50 mm), 0.29 °C (150 mm) and -0.39 °C (450 mm). In April the average temperatures in the attic were 9.7 °C (50 mm), 9.0 °C (150 mm) and 8.7 °C (450 mm). This indicates that an increased insulation thickness from 150 mm and up, has a minor influence on the temperature in a cold ventilated attic during winter time. Hagentoft & Sasic-Kalagasidis (2010) state that additional attic insulation leads to a colder attic space, but does not indicate the magnitude. Geving & Holme (2010) have made simulations with average monthly values of temperature and relative humidity for Oslo; they also conclude that the temperature in the attic decreases with increased insulation, but they do not state how much. However, from the increase in relative humidity the temperature difference can be calculated to be approximately 0.5 °C when the insulation thickness is changed from 100 mm to 500 mm. The outdoor temperature in Oslo in January is approximately 3 °C lower than in Denmark.

The general perception that energy-saving will decrease the temperature in a ventilated attic substantially and consequently increase the risk of mould growth is challenged in this paper. Instead of simulations, measurements of temperature were performed in 29 case buildings with different amounts of insulation on the ceiling against a ventilated attic.

METHODS

To assess the effect of the insulation thickness on the temperature in a cold ventilated attic, a series of field measurements was carried out in 29 Danish case buildings grouped in three groups depending on the insulation thickness:

- Group A: 7 case buildings with an insulation thickness ranging between 150-250 mm
- Group B: 9 case buildings with an insulation thickness ranging between 300-400 mm
- Group C: 13 case buildings with an insulation thickness ranging between 450-600 mm

The thermal insulation was applied either at construction or later as a part of improving the energy efficiency. When looking at temperature difference, the thermal resistance for the insulation material is the relevant parameter. As the insulation materials used in the case buildings had approximately the same thermal conductivity, the thickness was proportional to the thermal resistance. Most of the case buildings had a vapor barrier installed; some of them were old and probably not tight. However, this article only considers temperatures; the effectiveness of the vapor barriers is therefore not considered.

In each attic, a series of sensors (EL-USB-2+ from Lascar Electronics (Lascar electronics)) were installed in order to register the temperature and relative humidity for at least one year. Measurements were performed from July 2015 to June 2017. Not all houses were measured at the same time, and therefore two winters were covered. Sensor positions are shown in Figure 1. The sensors were controlled for uncertainty of measurements, which was registered to be within the 0.45 °C stated by the manufacturer. The sensors registered the climate every hour. Beside the sensors in the attic, one sensor registered the indoor climate and another sensor measured the outdoor climate.

The data analysis showed that the temperatures at the ridge and at the roof underlay were very much alike; the same applied for the two sensors located on top of the insulation material. The hypothesis that the temperatures in the attic space and above the insulation were the same in the groups was tested statistically by t-tests and test of correlation.

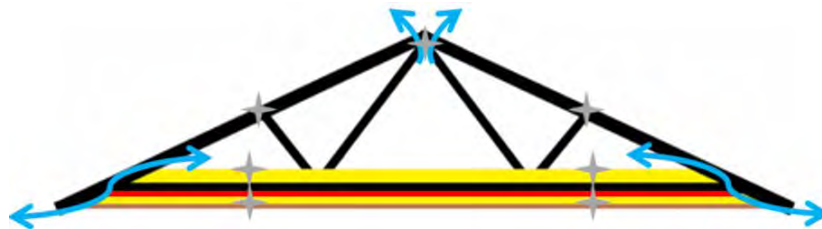


Figure 1. Principle sketch of a cold ventilated attic with sensor location (grey stars). Blue arrows indicate ventilation; red line indicates position of possible vapor barrier.

Ventilation rates in the attic were measured in seven of the case buildings by two passive tracer gasses (Heiselberg and Bergsøe, 1992) placed in attics and living spaces, respectively.

RESULTS

Data collected from the mounted loggers in the case buildings are presented in Figure 2 and Figure 3. In each group the case building has its own color so the legend in Figure 2 represents both figures. To avoid fluctuating data, moving average for a period of one week, is used for evaluating data.

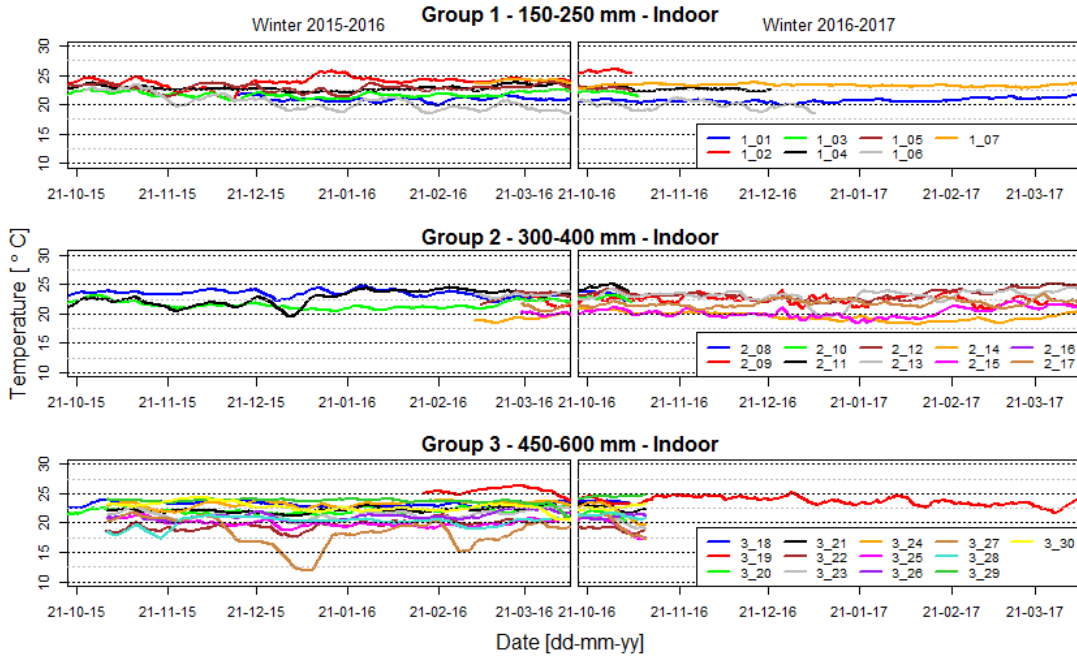


Figure 2. Measured indoor climate in every case building for the two winter periods 2015/16 and 2016/17 (November to March, both included) for the three different groups

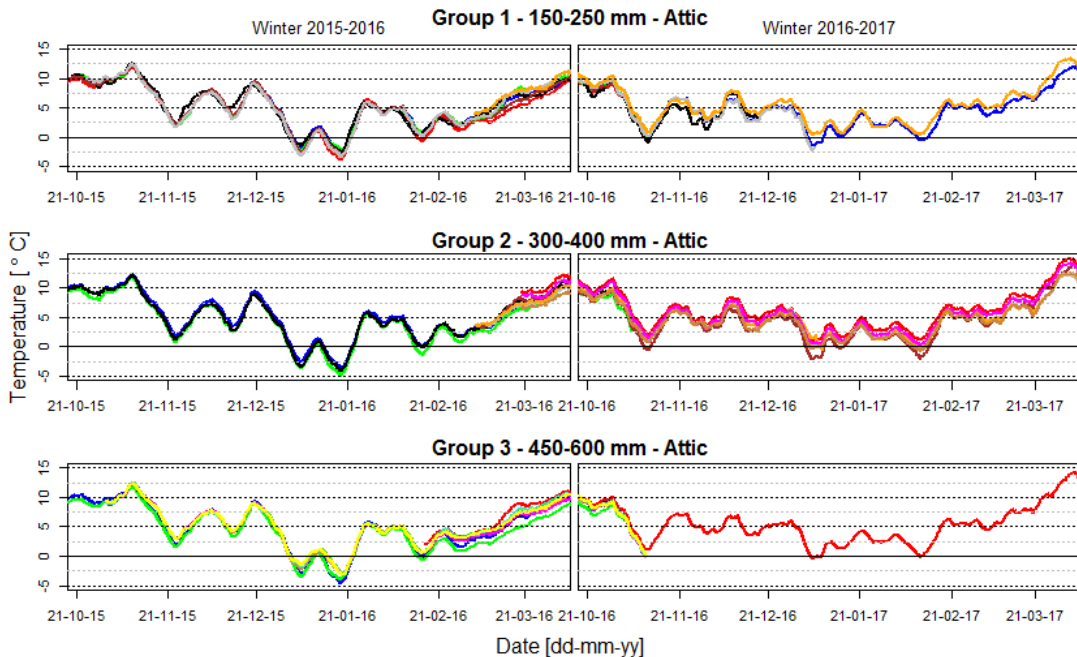


Figure 3. Measured attic temperature in every case building for the two winters 2015/16 and 2016/17 for the three different groups, see Figure 2 for legend

Figure 2 and Figure 3 illustrate the measured indoor temperature central in the house, and the average temperatures for the sensors located in the attic space, respectively. In the figures, the measured summer conditions are omitted, as the temperature difference between the indoor climate and the attic space are most significant during the winter period.

Table 1 shows the mean and standard deviation for the measured temperature in the three different groups for both winter periods (from 1 November to 31 March) in the attic and above the insulation. For comparison, the indoor and outdoor temperatures are shown as well.

Table 1. Mean and standard deviation for the measured temperature in the three different groups for both winter periods (from 1 November to 31 March). The numbers in brackets denotes the number of case buildings.

		Group 1 150-250 mm	Group 2 300-400 mm	Group 3 450-600 mm
Winter 2015/2016	Outdoor [°C]	4.9 ± 1.2 (14)		
	Indoor [°C]	22.1 ± 1.4 (6)	22.3 ± 1.5 (3)	21.5 ± 1.9 (12)
	Above insulation [°C]	4.9 ± 0.5 (6)	5.3 ± 0.7 (3)	5.3 ± 0.4 (12)
	Attic space [°C]	4.6 ± 0.4 (6)	4.2 ± 0.5 (3)	4.7 ± 0.4 (12)
Winter 2016/2017	Outdoor [°C]	4.5 ± 1.2 (10)		
	Indoor [°C]	21.8 ± 1.7 (2)	21.4 ± 1.7 (7)	23.6 (1)
	Above insulation [°C]	4.7 ± 1.2 (2)	5.1 ± 0.6 (7)	5.3 (1)
	Attic space [°C]	4.2 ± 0.6 (2)	4.5 ± 0.7 (7)	4.8 (1)

The ventilation openings were visually inspected; most of the case buildings had the recommended size of ventilation openings of 1/500 of the floor area (Brandt, et al., 2013). Only in one case the ventilation was insufficient. In that case, there was visible mold growth in the attic. Measurements of the ventilation rate in seven houses showed ventilation rates between 1.9 h⁻¹ and 24 h⁻¹. The ventilation rate was not measured in the attic with visible mold growth.

DISCUSSIONS

The measurements did not support the hypothesis that the attic temperature decreases with higher thickness of insulation. The tendency seems to be the opposite; in the winter 2016/2017 the attic temperature generally increased with higher amounts of insulation material. However, the measurements in Group 3 are only from one case and the indoor temperature was 1.8 °C higher in this building compared with the two Group 1 cases, so this might explain a 0.5 °C higher temperature. Nevertheless, the temperature rise in Group 2 of 0.3 °C compared with Group 1 cannot be explained by a higher indoor temperature as the average indoor temperature in Group 2 was 0.4 °C lower. In the winter 2015/2016, the temperature in the attic space in Group 3 was 0.1 °C higher than in Group 1 although the indoor temperature was 0.6 °C lower.

A series of t-tests shows no significant differences for the mean temperature between the different groups and as shown in Table 2, the temperature in the attics and above insulation were highly correlated within the group and each other. Furthermore, temperature differences of this magnitude in the attic are within the measurement uncertainties. Consequently, the temperatures in the attic space do not differ in the three groups and there is therefore no dependency on the insulation thickness. This corresponds to measured data from a laboratory test building with a controlled indoor climate (Hansen & Moeller, 2016).

Table 2. Correlation coefficients between temperature curves for different sensor positions. Green area indicates significant correlation.

	Out-door	Indoor climate			Above insulation			Attic		
		<i>G1</i>	<i>G2</i>	<i>G3</i>	<i>G1</i>	<i>G2</i>	<i>G3</i>	<i>G1</i>	<i>G2</i>	<i>G3</i>
Indoor	G1	0.59	1.00							
	G2	0.30	0.44	1.00						
	G3	0.06	-0.33	-0.52	1.00					
Above insulation	G1	0.98	0.64	0.30	0.06	1.00				
	G2	0.98	0.61	0.34	0.04	0.99	1.00			
	G3	0.97	0.62	0.28	0.10	0.99	0.99	1.00		
Attic	G1	0.98	0.65	0.34	0.03	1.00	1.00	0.99	1.00	
	G2	0.97	0.59	0.27	0.12	0.99	0.99	0.99	0.99	1.00
	G3	0.97	0.61	0.29	0.10	0.99	0.99	1.00	0.99	0.99

As expected, the temperature above the insulation is generally higher than the temperature in the attic space; the tendency was consistent throughout the two winters and the three groups. That the temperature in the attic space is the same as the outdoor temperature might be due to effective ventilation, but the surface temperature of the insulation should be lower in the case of reduced heat flux i.e. high insulation thickness. This was not the case; all temperatures above the insulation increased with increasing insulation thickness. In the winter 2015/2016 the temperature difference above the insulation was 0.4 °C higher in Group 3 than Group 1 despite a 0.6 °C lower indoor temperature in Group 3. There might be a simple technical explanation as to why the temperatures in Groups 2 and 3 are higher than in Group 1; while the insulation material in Group 1 is in general relatively firm plates, the insulation material in Groups 2 and 3 is more often a granulate. Consequently, the data loggers are more likely to sink a little into the insulation material in Groups 2 and 3 and therefore measure in an area where the temperature is higher. However, this cannot explain why the temperature above the insulation is higher in Group 3 than in Group 2.

Although some of the temperature differences cannot be explained, they are all small compared with the measurement uncertainties and the tendencies are not significant, therefore, the temperature above the insulation should be regarded as independent of the insulation thickness. This does not support simulations made by others. The reason for this discrepancy might be computational difficulties in the simulation of convection or because the ventilation rate in attics fluctuates, depending on wind speed and direction.

Some practitioners claim to have observed an increased number of attics with mold growth. This study shows that the assumption that a temperature decrease because of higher amounts of insulation in the ceiling is responsible for this is not correct. There must be other explanations. One could be that additional insulation in existing attics obstructs some of the ventilation openings and consequently less moisture is removed by ventilation. In some cases, ventilation openings have consciously been closed because of the wrong assumption that ventilation can be omitted in attics if the roof underlay is open for diffusion.

Knowing the appropriate ventilation rate would therefore be helpful. However, the rate varied considerably and no visual mold growth was detected in any of the attics where the ventilation rate was measured. The needed ventilation rate may also change with the season. Therefore, more studies of sufficient ventilation rates are needed. To test the influence of ventilation rates, WUFI (WUFI, 2018) was used for a series of preliminary simulations with insulation thickness of 150, 350, and 600 mm, simulated with two different ventilation rates:

2 and 15 h⁻¹. These showed that the temperature in the attic was influenced by neither the ventilation rate nor the insulation thickness. This supports that higher relative humidity in some attics are not caused by lower temperature. Contrary to the measurements, the simulations of temperature in the top of the insulation layer was influenced by the insulation thickness, winter average was 1 °C higher with 150 mm of insulation compared to 600 mm insulation, regardless of the ventilation rate. This illustrates how difficult it is to measure at intersections between materials when sensors have a size of approx. 2 cm.

CONCLUSIONS

Contrary to our expectations, the measurements showed that the temperature in ventilated attic spaces or just above the insulation material did not depend on the thickness of the insulation material. The assumption that additional insulation in ceilings reduced the temperature, therefore raises the relative humidity, and consequently is responsible for increased mold growth in attics, cannot be corroborated. However, additional insulation may have an influence on the relative humidity anyway e.g. because ventilation openings may be blocked by the additional insulation resulting in insufficient ventilation rates. The consequence of these findings is that if there is no mold problem in an attic, it is possible to increase the insulation limitless if the ventilation is not altered. Measurements of ventilation rates in attics with and without mold growth might bring further insight to why mold growth in attics seems to be an increasing problem.

ACKNOWLEDGEMENT

The authors would like to thank the Landowners' Investment Foundation, National Building Fund, Association of Danish Insulation Manufactures and the Danish Construction Association.

REFERENCES

- Brandt E. 2013. Moisture in buildings (In Danish) Fugt i bygninger, SBI-anvisning 224 (second edition), Danish Building Research Institute, Aalborg University, Copenhagen
- Geving S & Holme J. 2010. Highly insulated constructions and moisture (In Norwegian). Høyisolerte konstruksjoner og fukt. Analyse av fukttekniske konsekvenser av økt isolasjonstykkelse i yttervegger, tak, kryperom og kalde loft. Sintef project report 53, Trondheim Norway, 66 pages.
- Hagentoft C-E & Kalagasidis A.S. 2010. Mold Growth Control in Cold Attics through Adaptive Ventilation: Validation by Field Measurements. In: *Proceedings of the 11th International Conference on Thermal Performance of the Exterior Envelopes of Whole Buildings, Buildings XI*; Clearwater, USA
- Hansen T. & Moeller E.B. 2016. Full Scale Laboratory Test Building for Examining Moisture Penetration through Different Ceilings. *Proceedings pro112: International RILEM Conference Materials Systems and Structures in Civil Engineering 2016*. Rilem publications. Page 59-68.
- Hansen T. & Moeller E.B. 2017. Field measurements of moisture variation in cold ventilated attics with different ceiling constructions. *Energy Procedia* Vol. 132, pp. 801-806
- Heiselberg P. & Bergsøe N.C. 1992. Measurements of Contaminant Dispersion in ventilated Rooms by a Passive Tracer Gas Technique. *Indoor Environmental Technology*, R9255, Department of Building Technology and Structural Engineering, Aalborg, Denmark, Lascar electronics://www.lascarelectronics.com/easylog-data-logger-el-usb-2plus/.
- Nielsen, A. & Morelli, M. 2017. Measured temperature and moisture conditions in the roof attic of a one-and-a-half story house. *Energy Procedia*, Vol. 132, pp. 789-794
- WUFI. 2018. WUFI Pro 6.2 Fraunhofer – IBP, Holzkirchen, Germany

Prediction of the long-term performance of vacuum insulation panel installed in real building environments

Hideya Yamamoto^{1*,2}, Daisuke Ogura²

¹Asahi Fiber Glass Co., Ltd. Kanagawa, Japan

²Department of Architecture and Architectural Engineering, Kyoto University, Kyoto, Japan

*Corresponding email: h-yamamoto@afgc.co.jp

ABSTRACT

Vacuum insulation panels (VIPs) are high-performance insulating materials constructed by covering a core and adsorbent with an envelope and evacuating the air from the inside. VIPs have used to enhance the energy efficiency of devices including refrigerators, vending machines, and cooler boxes. In order to apply VIPs as heat-insulation materials in buildings and houses, it is necessary to predict the long-term performance of the VIPs and verify the accuracy of the prediction using actual measurements. VIPs using glass fiber as a core material are spreading in Japan, and VIPs using glass fiber core material as the core is also likely to be the mainstream in building applications. Therefore, in this paper, we report the comparison of the measurement results of the long-term performance in the building environment of VIPs using glass fiber and the calculation result. We also describe the calculation method of long-term performance prediction.

KEYWORDS

Vacuum insulation, Thermal conductivity, Long-term performance,

1. Introduction

Vacuum insulation panels (VIPs) are high-performance insulating materials constructed by covering a core and adsorbent with an envelope and evacuating the air from the inside. The VIP core is composed of glass fiber core or fumed silica core and covered by a laminated film. Upon evacuating the air from the VIPs, the gas thermal conductivity can be reduced to near zero, resulting in good thermal performance. Because it has high insulation performance, it is expected to be able to reduce wall thickness and enhance energy-saving when used for building applications. However, in many studies, long-term performance of VIPs under a constant environment had been discussed, but the long-term performance of VIPs itself in the building environment was not measured. Since there is no actual measurement data, accuracy of long-term performance prediction in the building environment cannot be confirmed. In addition, most of these studies are fumed silica core, and there are few studies on glass fiber core [1-6]. In order to solve this problem, we have been started to measure the thermal conductivity of VIPs that installed under the raised floor of a building. Glass fiber was used as the core material. VIPs was taken out from under the raised floor once every three months and measured the thermal conductivity by heat flow meter method. Furthermore, we measured the temperature and humidity of the front and back of VIPs, and examined the influence of environmental condition on long-term performance of VIPs.

2. Aging model^[7-10]

The parallel model is widely used to predict thermal conductivity. Heat transfer in the core material can be expressed as the conduction through solid and through gas in case of its presence and radiation:

$$\lambda_{cop} = \lambda_s + \lambda_g + \lambda_r, \quad (1)$$

Where λ_{cop} is the thermal conductivity of the center of panel, λ_s is the thermal conductivity of the solid skeleton, λ_r is the radiative thermal conductivity, and λ_g is the thermal conductivity of the gas within the pores. The units for all variables are provided in the Symbols section at the end of the paper. The thermal conductivities of the solid and gaseous components of the VIP are affected by the internal pressure and adsorption of water vapor on the core material.

2.1. Thermal conductivity of the VIP with desiccant

The thermal conductivity of the VIP containing desiccant can be expressed as,

$$\lambda_{cop} = \lambda_{sr,ini} + \lambda_{g(P_a,T)} = \lambda_{sr,ini} + \lambda_{ga}. \quad (2)$$

2.2. Permeability of dry air

Based on the mass-balance equation for air permeation into the VIPs and the state equation of an ideal gas ($P_i V_{eff} = m_i / M_i RT$), the change in internal pressure resulting from the permeation of dry air can be expressed b

$$\frac{dm_a}{dt} = \frac{M_a \cdot V_{eff}}{R \cdot T} \cdot \frac{dP_a}{dt} = K_{a,total} \cdot (P_{a,atm} - P_a) \quad (3)$$

$$P_a = P_{a,atm} - (P_{a,atm} - P_{a(0)}) \exp\left(-\frac{K_{a,total} RT}{M_a V_{eff}} t\right) \quad (4)$$

2.3. Relation of dry air pressure and thermal conductivity

Since the thermal conductivity of the VIPs relate to the internal pressure of VIPs, it can be expressed as follows using the Eq.(2)and (4).

$$\lambda_{cop} = \lambda_{sr,ini} + \lambda_g = \lambda_{sr,ini} + \frac{\lambda_{ga,0}}{1 + \frac{P_{1/2}}{P_a}} \quad (5)$$

$$\lambda_{cop} = \lambda_{sr,ini} + \frac{\lambda_{ga,0}}{1 + \frac{P_{1/2}}{P_{a0} + P'_{a,t} \cdot t}} \quad (6)$$

2.4. Thermal conductivity owing to difference in dimensions (metallized film)

Unlike the aluminum foil VIPs, considering the transmittance from the surface, the transmittance of the metallized VIPs is expressed as

$$K_{a,total} = K_{a,A} \cdot A + K_{a,L} \cdot L \quad (7)$$

From the time rate of the internal pressure, the relation of time rate of thermal conductivity can be obtained. Based on the measured value at a certain dimension, for a surface area A_{ref} and perimeter length L_{ref} , the change in internal pressure is expressed as

$$\frac{dP_{Aref,Lref}}{dt} \cong (P_{a,atm} - P_{a(0)}) \frac{K_{a,total(ref)} RT}{M_a V_{eff(ref)}} \quad (8)$$

$$\begin{aligned} \frac{dP_{A,L}}{dt} &\cong (P_{a,atm} - P_{a(0)}) \frac{K_{a,total} \cdot L_{ref} RT}{M_a V_{eff(ref)}} \\ &\cdot \frac{V_{eff(ref)}}{V_{eff}} \cdot \frac{K_{a,total}}{K_{a,total(A_{ref},L_{ref})}} \end{aligned}$$

$$= \frac{dP_{A_{ref},L_{ref}}}{dt} \cdot \frac{V_{eff}(ref)}{V_{eff}} \cdot \frac{K_{a,total}}{K_{a,total}(A_{ref},L_{ref})} \quad (9)$$

$$= \frac{dP_{A_{ref},L_{ref}}}{dt} \cdot \frac{V_{eff}(ref)}{V_{eff}} \cdot \frac{K_{a,total}}{K_{a,total}(A_{ref},L_{ref})} \quad (10)$$

2.5. Estimation of transmittance under different conditions (Arrhenius plot)

Supposing that the temperature and pressure of the environmental conditions to be found are $T_{ex}, P(T_{ex})$, from Eq. (8), the gas permeability $K_{a,total}$ of dry air is as follows:

$$K_{a,total} = \frac{1}{(P_{a,atm} - p(0))} \cdot \frac{M_a V_{eff}}{RT_{ex}} \cdot \frac{dP(T_{ex})}{dt} \quad (11)$$

When calculating the time rate of internal pressure from the measurement result of the thermal conductivity, it is necessary to convert by the average temperature at the time of measuring the thermal conductivity and the pressure ($\lambda_c, P(T_c)$).

$$P(T_{ex}) = \frac{P(T_c)}{T_c} T_{ex} \quad (12)$$

Substitute this equation into Eq.(11),

$$K_{a,total} = \frac{1}{(P_{a,atm} - p(0))} \cdot \frac{M_a V_{eff}}{RT_c} \cdot \frac{dP_a(T_c)}{dt} \quad (13)$$

3. Long term performance

In order to confirm the gas permeability (K_{air_total}) of the dependence of temperature and humidity, we carried out the aging test with thermostatic chamber. The Arrhenius plot was obtained based on Eq. (13). The details of the experimental VIPs are shown in Table 1. The Arrhenius plot does not consider the gas absorbed by the getter material.

3.1. Long-term performance in a thermostatic chamber

The VIPs was removed from the thermostatic chamber and cured at room temperature. The thermal conductivity was then measured using a heat flow meter (HC074 600, EKO instruments), and the results are shown in Fig. 3. The results of Arrhenius plot obtained from Eq.13 and experimental results are shown in Fig.4. The Arrhenius plot confirmed the temperature dependence of the VIPs air permeability under the tested aging conditions (23°C 50% RH and 50°C). The comparison of the aging conditions of 50°C and 50°C with 70% RH confirmed that the gas permeability increased by approximately 6% shown in table2. The transmittance of dry air increased with relative humidity, which may be influenced by the material of the film. The metallized film is provided with a vapor deposited layer based on Ethylene vinyl alcohol (EVOH), probably because the barrier property of the EVOH layer decreased under high temperature and high humidity. When estimating the transmittance using Arrhenius plot, it is also necessary to consider film properties of EVOH.

Table 1. Details of the VIPs and aging condition

VIP Size	① t10 x 495 x 495 *1	
Core	Glass fiber	
Film	Hybrid Type*2	
Desiccant	Calcium Oxide 20g	
Getter	Zeolite type 5g	
Protection	Covered by polyvinyl chloride(PVC) 75μm film	
Aging condition	1) 23°C, 50% RH 2) 35°C, 80% RH 3) 50°C4) 50°C, 70% RH	

*1: The four corners of the VIP contain 90-mm cutouts

*2: One side is an aluminium foil film and the other side is a metallized film with EVOH

Table2. Overall air permeability (K_{air_total}) of the VIP aged under different conditions

Temperature (T ; °C)	Relative Humidity (RH; %)	$1/T$	K_{air_total} [$\times 10^{-12}$ g/day·Pa]
23	50	0.00337	14.3
35	80	0.00325	21.0
50	-	0.00309	35.8
50	70	0.00309	37.7

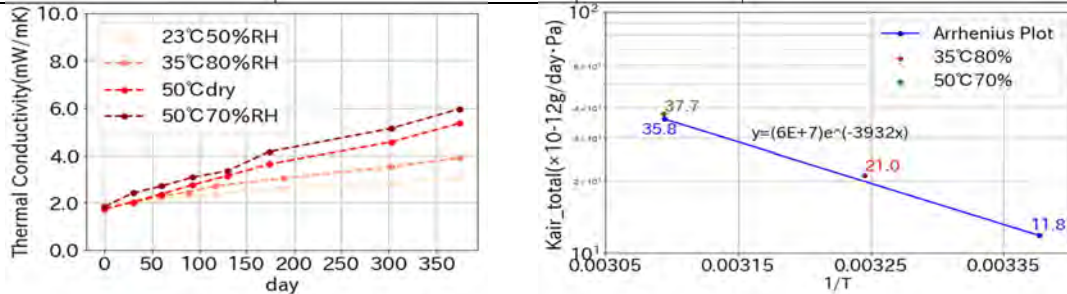


Fig.3: Long-term performance of the VIP under different static conditions

Fig.4: Arrhenius plot of the VIP

3.2. Long-term performance in a building condition

The VIPs were constructed on the concrete slab under the raised floor of a new building, the details of VIPs are shown in Table3. The VIPs were removed from under the floor every three months, and thermal conductivities were measured before reinstallation (Fig.5). The construction period and measurement period are shown in Table4. Thermo-hygrometers were installed on the front and back of each VIP to measure the temperature and humidity (Fig.7 and 8). Half of the VIPs installed in Room 2 (VIP01) was placed in the reverse of the front and back, and the effect of the orientation of the MF surface on the long-term VIPs performance was evaluated. First of all, we obtained the total gas permeability (K_{air_total}) based on the values of internal pressure which is calculated from measurement value of thermal conductivity. Secondly, Table5 shows a comparison of the internal pressure obtained from the time rate of thermal conductivity " ΔP_m " and the time rate of temperature data " ΔP_{cal} ". ΔP_{cal} was obtained total gas transmittance on site conditions which is calculated from Arrhenius plot and average temperature every 2 hours. As the result of calculating the among ΔP_{cal} obtained using the temperatures on the upper and lower surfaces of the VIPs in the room2, the error from the measured value was smaller in the result calculated by referring to the temperature on the metallized film's side than the aluminum foil's side. This is attributed to the higher temperature dependence of the transmittance of dry air on the metallized film compared to that on the aluminum foil. However, the error of this result should also consider that the exposure environment during the measurement period is ambiguous. In order to prevent errors, for example, it can be solved if pressure of inside the VIPs can be directly measured at the real building environment.

Table3. Characteristics of VIPs used in the test of building condition

VIP Size	① $t10 \times 495 \times 495$ *1 in table1 ② $t10 \times 372 \times 385$ ③ $t10 \times 372 \times 385$	
Core	① Glass fiber 1 ② Glass fiber 2 ③ Glass fiber 1	
Film	Hybrid Type	
Desiccant	Calcium Oxide	
Getter	Zeolite type	
Protection	Covered by PVC 75- μ m film	

Table4. Installation periods of the different VIPs used in the test of building condition

	Day installed	Day removed	Days after product was manufactured	
VIP①	333	48	381	
VIP②	331	58	389	
VIP③	333	48	381	

Table5. Comparison of measured and calculated values of internal pressure for each room

Place	Metallized film side	Reference temperature	Internal pressure (measured, ΔP_m)		Internal pressure (calculated, ΔP_{cal})		Error (%)	
			day	244	381	244	381	244
Room1	Upside (interior side)	Upside	10.3	13.8	9.98	17.42	9.80	26.2
		Lower			9.94	17.16	9.70	24.4
Room2	Lower (slab side)	Upside	8.18	12.9	10.3	17.73	40.0	37.4
		Lower			8.73	15.98	11.5	23.9
Room2	Upside (interior side)	Upside	10.74	14.5	10.3	17.73	7.3	22.3
		Lower			8.73	15.98	-14.9	10.0

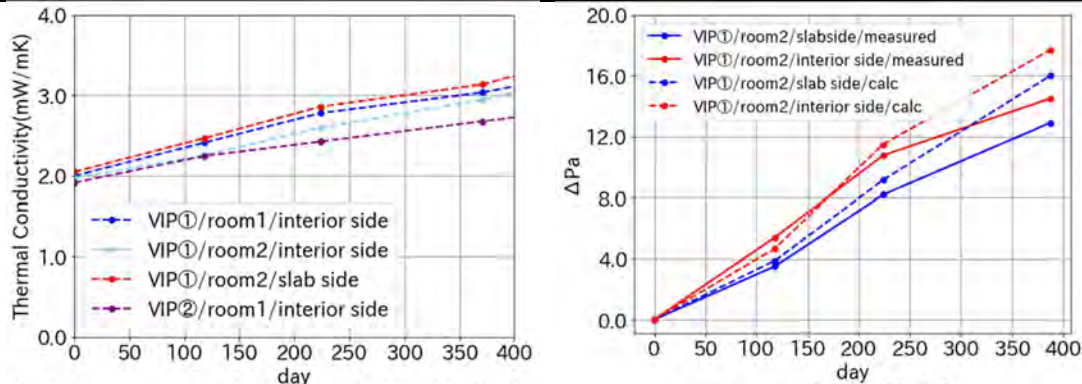


Fig.5. Long-term performance of the VIPs in different rooms and comparison of inside out

*VIP No/room No/Metallized film side

Fig.6. Comparison of measured value and calculated values of internal pressure (room2)

*VIP No/room No/Metallized film side/measured value or calculated value

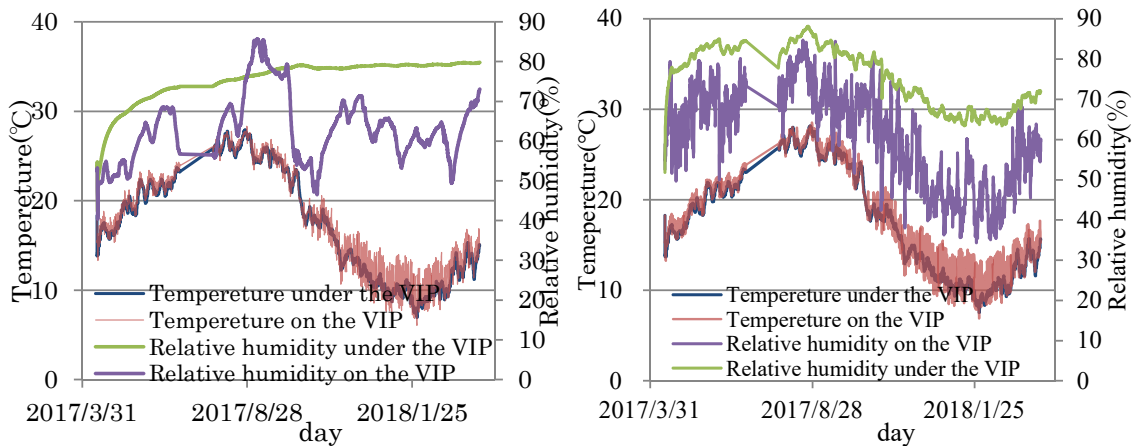


Fig.7. Temperature and relative humidity measured in room 1 on and under the VIPs

Fig.8. Temperature and relative humidity measured in room 2 on and under the VIPs

4. Summary

We constructed a VIPs under the raised floor of the building and periodically measured the thermal conductivity and the weight increase and the environmental conditions. We compared

the time change of internal pressure which was calculated by the relationship of thermal conductivity and internal pressure (Eq.6) using measurement result of thermal conductivity with calculated data which was obtained by temperature of environmental condition and Arrhenius plot (Eq.13). The results were roughly in agreement with the calculation results, but the prediction result of about 10% error as a whole at 227days increased further by 10% or more at 381 days (Fig.6). We consider the following three reasons why errors occurred.

- (1) It is necessary to separate the gas permeation of surface and edge.
- (2) Since the actual measurement range of Arrhenius plot is 23°C to 50°C, it is necessary to confirm the accuracy at 23 ° C. or less.
- (3) The influence of humidity in the actual measurement environment is expected to be low from the Arrhenius plot, but in order to make more accurate prediction it is necessary to consider the influence of humidity.

5. Future work

We will continue to measure and continue to verify whether long-term performance can be predicted from the measurement of environmental conditions. Meanwhile, we plan to develop a method that can be measured while it is being constructed on site. Specifically, we will consider improving the accuracy of prediction of durability by comparing it with the result of thermal conductivity measurement using VIPs equipped with micro pressure sensor. We will discuss the relation between external environment and internal pressure. And we will also study the influence of getter material, folded edges on gas permeability calculation, time rate of transmittance due to material deterioration, and another size of VIPs.

Acknowledgements

This study was performed in cooperation with everyone at the TODA CORPORATION RESEARCH and DEVELOPMENT CENTER. The authors express their sincere thanks.

References

- [1] S. Brunner, H. Simmler, In situ performance assessment of vacuum insulation panels in a flat roof construction (2007)
- [2] P. Mukhopadhyaya, D. Maclean, J. Korn, D. van Reenen, S. Molleti, Building application and thermal performance of vacuum insulation panels (VIPs) in Canadian subarctic climate (2014)
- [3] Par Johansson, Bijian Adl-Zarrabi, Angela Sasic Kalagasidis, Evaluation of 5 years' performance of VIPs in a retrofitted building facade (2015)
- [4] D. Maclean, P. Mukhopadhyaya, J. Korn, S. Mooney, Design details and long-term performance of VIPs in Canada's North (2016)
- [5] H. Simmler, S. Brunner, Vacuum insulation panels for building application Basic properties, aging mechanism and service life (2005)
- [6] E. Wegger, B. Petter-Jelle, E. Seipe, S. Grynning, A. Gustavsen, R. Baetens, J. V. Thue, Aging effects on thermal properties and service life of vacuum insulation panels (2011)
- [7] H. Simmler, S. Brunner, Vacuum insulation panels for building application Basic properties, aging mechanisms and service life (2005)
- [8] HiPTI-High Performance Thermal Insulation IEA/ECBCS Annex 39, Vacuum Insulation Panels Study on VIP-components and Panels for Service Life Prediction of VIP in Building Applications (Subtask A), (2005)
- [9] Daniel QUENARD, Hébert SALLEE: Micro-nano porous materials for high performance thermal insulation, 2nd International Symposium on NANOTECHNOLOGY in CONSTRUCTION BILBAO-13-16 (2005)
- [10] D. Ogura, A. Iwamae, T. Tasaka, K. Mabuchi, Y. Senda, K. Kugimiya, Prediction on long-term performance of vacuum insulation panels (VIP) using glass fiber core considering differences in hygrothermal environment and size of VIP and influence desiccant (2017)

Symbols λ_{cop} : thermal conductivity at the center of the panel [W/mK]; λ_{ini} : initial thermal conductivity [W/mK]; λ_s : solid thermal conductivity [W/mK]; λ_g : gaseous thermal conductivity [W/mK]; λ_r : radiative thermal conductivity [W/mK]; M_i : Avogadro's constant [kg/mol]; V_{eff} : volume of VIP [m³]; R : gas constant [J/Kmol]; K_i : mass transfer coefficient [g/h · Pa]; $P_{i,atm}$: partial pressure of gas under atmospheric pressure [Pa]; P_i : pressure inside the VIP [Pa]; P_{wv} : water vapor pressure inside the VIP [Pa]; $K_{i,total}$: overall transmittance ($i = a, v$) [g/day · Pa]; $K_{i,A}$: transmittance per unit area [g/m² · day · Pa]; $K_{i,L}$: transmittance per unit length [g/L · day · Pa]; A : surface area of VIP [m²], L : circumference of VIP [m].

Super insulation material in district heating pipes

Bijan Adl-Zarrabi^{1,*}

¹Chalmers University of technology, Sweden

*Corresponding email: zarrabi@chalmers.se

ABSTRACT

In Swedish district heating systems, 10% of the produced energy is lost at the distribution network. It is of interest to lower the energy losses both for economic and environmental reasons. Since 2011 the feasibility of using superinsulation material for insulation of the district heating pipes were studied. Apparent thermal conductivity and long term performance of vacuum panels has been identified as the crucial challenge for using vacuum insulation panels. The estimated life time of a vacuum panel in building applications at 90 °C is about 50 years. The life time estimation is based on the climate condition valid for building application. However, peak temperature in a district heating system can be about 140°C.

Hybrid insulated pipes with a Vacuum Insulated Panel (VIP) have been tested and evaluated by laboratory and field measurements. The results of numerical analyses of the measured data indicate a possible small degradation of the VIP at a similar rate as building application, even though the operative temperature is between 80-100 °C. In the laboratory a hybrid insulated pipe has withstood exposure to one sided heating at 115°C for over 5 years. The results indicate that hybrid insulated district heating pipes reduce heat losses by 20-30% for a twin pipe and with more than 50% in a single pipe. It can be concluded that VIP shows promising performance in district heating pipe applications.

KEYWORDS

Vacuum insulation panels, district heating pipe, heat losses, long-term performance

INTRODUCTION

More than 5000 district heating system are in operation within the European Union. Transferring heat and cold efficiently in urban areas is the main goal of district heating. Sweden is one of countries where more than 50% of heat demand of the building stock is covered by district heating systems. At present there are approximately 24,000 km of district heating network (DHN) in Sweden. The heat losses in DHN is 5-6 TWh (Swedish Energy Agency, 2017). There are a number of measures for reduction of heat losses e.g. a) using twin pipes instead of two single pipes, where the supply/carrier pipe and the return pipe are placed within the same insulation pipe, b) reduction of temperature level in DHN i.e. low temperature system, c) enhancing thermal properties of insulation material of the pipes.

In Nordic countries, the twin pipe concept has been used since the 1990's and utilization of low temperature district heating systems are under investigation in Sweden. However, the low temperature system was used in Denmark. Enhancing the insulation material in a DHN has been studied since the introduction of district heating systems and different types of insulations material, e.g. glass wool, mineral wool, stone wool and polyurethane (PUR), were used.

PUR is most common insulation material in new district heating pipe generation. The thermal conductivity of PUR is about 26 mW/mK at 50 °C. Research and development concerning

improving PUR insulation is ongoing. However, it is very difficult to achieve major improvements. An alternative is to replace a part of PUR insulation with Super Insulation Materials (SIM) which have 2-4 time lower thermal conductivity than PUR. Combining PUR and SIM, hybrid insulation, is the most technically feasible solution for development of high thermal performance district heating pipes.

Research related to hybrid insulation of the pipes, initiated in 2011 at Chalmers University of technology, department of Architecture and Civil engineering where a layer of SIM was added close to supply pipe. Two type of superinsulation material, aerogel blanket and vacuum insulated panels (VIP) were investigated as alternatives for hybrid insulation, see Figure 1.

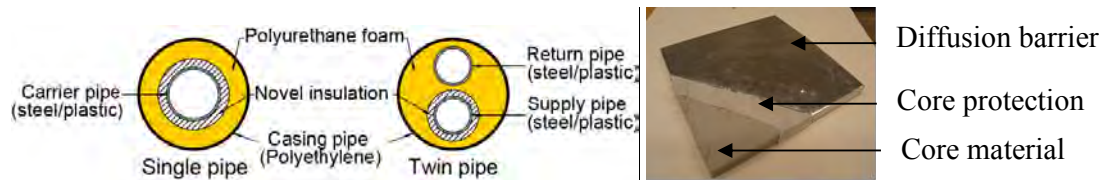


Figure 1. Hybrid insulation district heating (single/twin) pipe with VIP (left). In a VIP, the core material is enveloped by a diffusion barrier (right)

Samples and prototypes of hybrid insulation pipe were produced for investigating compatibility of SIM with polyurethane and investigating mechanical and thermal performance of the final product. Both types of selected SIM fulfilled the essential function described in (EN253, 2009). However, thermal performance of VIP was higher than aerogel blanket thus VIP was selected for further investigation.

Apparent thermal conductivity of VIP in a cylindrical geometry and expected lifetime of a VIP at a high temperature district heating network are of special interest for using VIP in district heating pipes. According to VIP manufacturer the maximum operative temperature of an ordinary VIP is about 80-90 °C which is lower than the peak temperature in a high temperature district heating system.

The aim of this paper is to present how the apparent thermal conductivity of a VIP can be determined and also present the results of analyses related to lifetime estimation of VIPs by measurement at laboratory and in operational environments.

APPARENT THERMAL CONDUCTIVITY

District heating pipes, single and twin pipe, vary in diameter thus the estimation of thermal performance of a hybrid insulated pipe with VIP needs determination of the apparent thermal conductivity of VIP for each pipe size. The thermal conductivity in the center of a VIP is declared to be between 3-5 mW/mK. To obtain the vacuum in a VIP, the core material is enveloped by an air and moisture diffusion barrier, see Figure 1, which is commonly a metalized polymer laminate or an aluminum laminate with a thermal conductivity 50-250 times higher than the center of VIP. The different thermal conductivities of the materials lead to thermal bridging effects at the edges of the panels. The linear thermal transmittance values for the edges of a plane panel can be calculated by procedures described in (ISO-102011, 2007). The influence of thermal bridges varies with the geometry of the panel, the core material and the type of diffusion barrier. The liner thermal transmittance of a number of different geometries for a plane VIP were calculated in (Sprenghard & Holm, 2014). However, the VIP in district heating pipes are cylindrical with a special formation on one surface, see Figure 3a. The non-

regular boundary between VIP and the pipe makes numerical calculation related to influence of thermal bridges on the overall thermal conductivity very difficult and uncertain. Thus, apparent thermal conductivity of VIP has been calculated in combination with measurements using the guarded hot pipe method (EN253, 2009).

The results of thermal and mechanical (fulfilling shear stress capacity caused by thermal expansions of different layers of the pipe) measurement indicates that a 10 mm thick VIP is the most reasonable thickness for a district heating pipe. Thus, the apparent thermal conductivity was determined for 10 mm thick VIP. Furthermore, manufacturing parameters related to production of a district heating pipes restrains the length of the VIP to 1 meter. The width of the panel is equal to the circumference of the supply pipe. The mounting of VIP around a supply pipe can be done in two ways 'edge to edge' or with overlapping, see Figure 3b.

Five measurements were performed for determination of steady state heat flow by the guarded hot pipe method. The first measurement, reference measurement, was performed in order to determine thermal properties of the pipe insulated by pure PUR. Two measurements were performed on hybrid insulated pipe for each mounting procedure. The pipes in the measurements were single pipe DN80/180 (supply pipe diameter/casing pipe diameter). The VIP insulation surrounding the supply pipe, see figure 1. The temperature of the supply pipe was about 80 °C and the temperature of casing pipe was about 22 °C.



Figure 2. a) Surface of a cylindrical VIP b) overlap mounting of VIP

The apparent thermal conductivity of the VIP can be calculated by using the measured heat flow and equation 1.

$$q = \frac{\Delta T}{\sum_{i=1}^N \frac{\ln(\frac{r_{i+1}}{r_i})}{2\pi \cdot \lambda_i}} \quad (1)$$

Where q (W/m) is heat flow, ΔT (°C) is the temperature difference cross insulation material, r (m) is the radius of each layer and λ (W/mK) is thermal conductivity of each layer.

The calculated apparent thermal conductivity of a 10 mm thick VIP with a length of 1 m and a width of 0.28 m (edge-to-edge) is presented in Table 1.

Table 1: Measured heat flow and calculated thermal conductivity for the pipes and apparent thermal conductivity of VIP for two different mounting procedures.

Sample	q [W/m]	λ_{50}^{Pipe} [mW/m.K]	$\lambda_{90}^{VIP/Apparant}$ [W/m.K]
Reference	14.7	28	-
Edge-to-Edge	10.8	19	12
Overlap	9,2	17	9

The results presented in Table 1 indicate that the thermal performance of the hybrid insulated pipe is 30-60% better than the reference pipe. However, it should be mentioned that the thermal conductivity of PUR insulation in this test is higher than ordinary PUR insulation. One reason is that the PUR in these measurements are handmade. In further investigations overlapping the edges of the VIP will be used. Furthermore, apparent thermal property of VIP was about 9 mW/mK which will be used for calculation of thermal performance of single and twin pipes.

LIFETIME ESTIMATION OF VIP

The hybrid insulation of the pipes was based on replacing 10-20 mm of PUR by VIP. As long as the VIP is not penetrated the thermal performance of the hybrid pipe will be better than a pipe insulated by pure PUR: If the VIP is penetrated for any reason, aging or damaged during production, then thermal conductivity of VIP will be around 21 mW/mK which is still better than thermal conductivity of PUR. Thus, the pipe will still fulfil its thermal performance.

According to manufacturer of VIP the maximum operating temperature of a VIP is around 80-90 °C. However, the declared values are based on laboratory measurements when all sides of a VIP is exposed to uniform temperature level. In a pipe the temperature will not be evenly distributed throughout the cross section of the insulation, but will rather form a gradient. Thus, laboratory and field tests concerning lifetime estimation of a hybrid insulated pipe and related temperature levels were initiated in 2012.

Laboratory test

The laboratory test was initiated at the end of 2012 and it is still ongoing. The tests were designed for mean temperature of 90°C over cross section of VIP in a hybrid insulated pipes (80/180) i.e. a supply pipe temperature of 115 °C and backside temperature of VIP 65°C. A hypothesis is that the sealing of the VIP envelope is the weak point of the diffusion barrier. Thus, the joints (sealing in a VIP) were folded around the edge making the distance to the service pipe as long as possible. Temperature gauges were installed inside the pipe, on backside of the VIP (center part) and on the service pipe, and on the casing pipe.

Using measured data and equation 2 make it possible to find a relation between thermal conductivity of PUR and thermal conductivity of VIP. Assuming that the ageing of PUR is negligible, it is possible to indicate the changes in thermal conductivity of the VIP.

$$\frac{\lambda_{PUR}}{\lambda_{VIP}} = \frac{\Delta T_{VIP}}{\Delta T_{PUR}} \cdot \frac{\ln(\Delta r_{PUR}/r_{0,PUR} + 1)}{\ln(\Delta r_{VIP}/r_{0,VIP} + 1)} \quad (2)$$

Where ΔT_{VIP} and ΔT_{PUR} are temperature gradients over the cross section of VIP and PUR, Δr_{VIP} and Δr_{PUR} are thickness of VIP and PUR respectively. $r_{0,VIP}$ and $r_{0,PUR}$ are internal radius of VIP and PUR in a cylindrical coordinate system.

The supply pipe temperature was controlled to be 115 ± 3 °C. The ambient temperature in laboratory varied between 21 and 27 °C. The measured results of five last years (2013-2015) were analyzed in order to determine a time dependent degradation coefficient for thermal conductivity of VIP. The results of the analyses are presented in figure 3. A decrease of the ratio indicates that the thermal conductivity of VIP increases.

The ratio is decreased during the first 13 weeks and between weeks 13-78 the ratio is stable around a mean value of 3.95. This means that the VIP has a thermal conductivity which is about 4 times better than PUR. The mean temperature of PUR is about 40°C, thermal conductivity of

PUR at 40 °C is about 27 mW/mK thus the center of VIP has a thermal conductivity of about 7 mW/mK in this setup.

A failure in the devices which maintain the supply pipe temperature lead to losing data for a number of weeks, see figure 3. The failure has no influence on the pipes and thermocouples. The measurements started again at week 86. The mean value of the ratio between week 86 to 260 is 4.25 i.e. 7% higher than the ratio before failure. There is no reasonable explanation for the increasing ratio before and after failure.

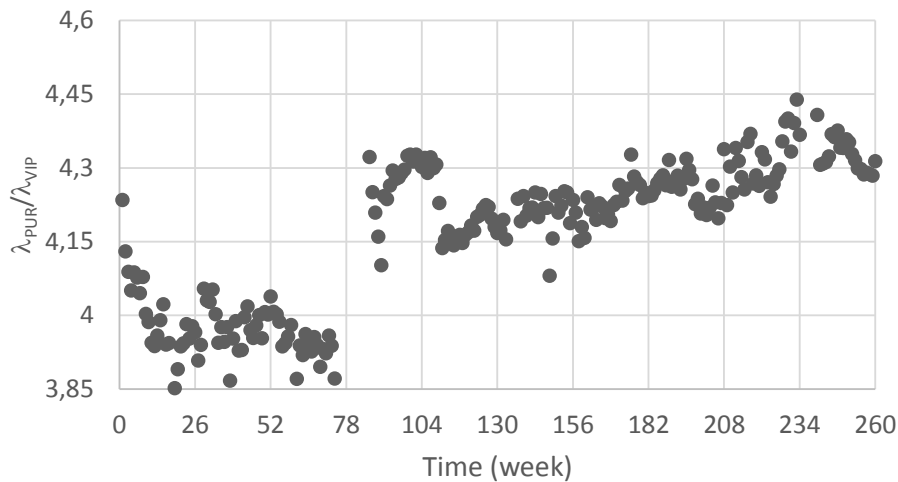


Figure 3. Variation of the ratio of thermal conductivity PUR and VIP in time.

There is a slight increase of the ratio observed between weeks 112 to 260, see figure 3. It is expected that both VIP and PUR will be degrade. It is difficult to determine the level of the degradation in each material. However, the results indicate a faster degradation of PUR than VIP.

Field measurement

Performance of the hybrid insulated pipes should be investigated in an operational environment. In field measurements the boundary condition of the pipes are quite different compared to laboratory tests i.e. the pipes lay about 1 meter below ground surface and they can be exposed to ground water flow. Furthermore, the pipes in the field station are generally twin pipes. The boundary conditions and the type of the pipes increases the complexity of analysing thermal performance of the hybrid insulated pipes.

Since 2013 five field stations were initiated in Sweden. The total length of pipe in each station is 6 meter. The pipe was divided in two parts, hybrid insulated pipe (3m) and reference pipe insulated by pure PUR (3m). The thickness and length of VIP were 10 mm and 1 meter. The VIP insulation enclosed the supply pipe. The size of the twin pipe was matched to size of the pipe in DHN. A number of thermocouples were imbedded in both parts of the pipe and on the casing pipe. The thermocouples in the reference pipe were placed in positions that they can be compared to the hybrid insulated pipe i.e. thermocouples S-VIP and S-PUR, see figure 4.

The temperature of the supply pipe follows the temperature level of DHN in the area. The results obtained from field measurement were used for validation of a numerical model. The numerical model and the results based on measurements during 2013-2016 were presented in (Berge,

Hagentoft, & Adl-Zarrabi, 2016) and (Berge A. & Adl-Zarrabi, 2014). The results of the numerical analyses showed that a total reduction in the energy loss between 20% and 30% compared to pipes of the same size with pure PUR insulation. Furthermore, the losses from the supply pipe decreased by up to 56%

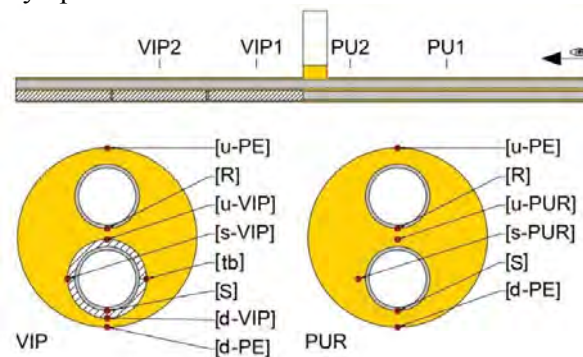


Figure 4 Position of VIP (dashed lines) and thermocouples in the twin pipe. PU1, PU2, VIP1 and VIP 2 sections where thermocouple positions were mounted.

The simulations also show that a slower deterioration process could be hidden in the responses to other variations in the system (Berge et al., 2016). The measured results during 2017-2018 were analysed and the results supported the same conclusions as presented in 2016.

CONCLUSIONS

The apparent thermal conductivity of a VIP in district heating pipes varies with dimension and type of the pipe. The apparent thermal conductivity of a 10 mm thick VIP at 50 °C used for insulation of a 40 mm supply pipe is about 9 mW/mK which can be used as a benchmark. Hybrid insulated district heating pipes reduce the heat losses by 20-30% for a twin pipe and by more than 50% in a single pipe. The results of field measurements show that hybrid insulated pipes using VIP fulfil their function after five years in an operational environment. Thus, hybrid insulated pipes by VIP have potential to improve long-term thermal performance of the district heating network.

REFERENCES

- Berge, A., Hagentoft, C.-E., & Adl-Zarrabi, B. (2016). Field measurements on a district heating pipe with vacuum insulation panels. *Renewable Energy*, 87, 1130-1138. doi:10.1016/j.renene.2015.08.056
- Berge A., & Adl-Zarrabi, B. (2014). *Evaluation of vacuum insulation panels used in hybrid insulation district heating pipes*. Paper presented at the 14th International Symposium on District Heating and Cooling, Stockholm, Sweden.
- EN253. (2009). District heating pipes-Pre insulated bonded pipe system for directly buried heat water networks-Pipe assembly of steel service pipe, polyurethane thermal insulation an outer casing of polyethylene. .
- ISO-102011. (2007). "Thermal bridges in building construction – Heat flows and surface temperatures: Detailed Calculations".
- Sprengard, C., & Holm, A. H. (2014). Numerical examination of thermal bridging effects at the edges of vacuum-insulation-panels (VIP) in various constructions. *Energy and Buildings*, 85, 638-643. doi:<https://doi.org/10.1016/j.enbuild.2014.03.027>
- Swedish Energy Agency. (2017). *Energiläget 2017*. Retrieved from <http://www.energimyndigheten.se/statistik/energilagget/>

Super insulation materials in the building sector: Field studies and future challenges

Pär Johansson^{1,*} and Bijan Adl-Zarrabi¹

¹Chalmers University of Technology, Gothenburg, Sweden

**Corresponding e-mail: par.johansson@chalmers.se*

ABSTRACT

The global rate of improvement in energy efficiency have to be increased to reach the UN sustainable development goals by 2030. Super insulation materials (SIM) can maintain the same thermal transmittance with a thinner insulation layer compared to conventional insulation materials. Recommendations and experiences from practical applications are needed to raise the knowledge and awareness of using SIM in buildings. Evidences related to real-condition performance need to be presented and independently assessed. The aim of this paper is to describe the state-of-the-art in the area of SIM in building applications based on monitoring data related to long-term performance of vacuum insulation panels (VIP). Both VIP and advanced porous materials (APM) have been successfully installed over the past 15 years in buildings. This paper presents a case study where the temperature and relative humidity of a wall were monitored for seven years. The results of the monitoring indicate that the VIP fulfil its function with no sign of degradation. By continuous product development, the performance of the SIM are improved for every generation which gives a promising outlook for the wider implementation of SIM in the building envelope.

KEYWORDS

Super insulation material, aerogel, VIP, renovation, energy efficiency, building

INTRODUCTION

There is presently a focus in the European Union to decrease the carbon dioxide emissions from the built environment. On the global arena, the UN sustainable development goals put focus on integrating climate change measures. By 2030 the global rate of improvement in energy efficiency should be doubled. This requires new and more energy efficient materials to be developed and evaluated. Conventional insulation materials require a certain thickness to reach a sufficient thermal transmittance. Super insulation materials (SIM) can maintain the same thermal transmittance with a thinner insulation layer. Products are available on the market which offer down to one tenth of the thickness required for conventional insulation materials. This is especially interesting in retrofit applications and in areas with limited land accessibility.

In many of the field studies reported in the literature only the thermal performance of the assembly was investigated (Johansson, 2012). However, also other parameters, such as the moisture performance, is important to consider. Recommendations and experiences from practical applications are needed to raise the knowledge and awareness of using SIM in buildings. Evidence related to real-condition performance needs to be presented and independently assessed. Full scale experiments provide knowledge of practical and technical difficulties as well as data for service life estimation. For certain conclusions to be drawn from case studies, long-term monitoring is needed. Unfortunately, monitoring is only performed in few case studies reported in the literature.

One of the International Energy Agency's (IEA) Energy in Buildings and Communities (EBC) Programme's objective is to enable research and development programmes (Annex) on the building envelope among its 24 member countries. During 2014 the Annex 65 'Long Term Performance of Super-Insulating Materials in Building Components and Systems' was initiated. The work was divided in 4 tasks where task 3 concerned field scale performance of SIMs. The focus of the work was to define the application areas of SIMs and to describe the conditions of the intended use of the products having building retrofit in mind (Adl-Zarrabi & Johansson, 2018).

The aim of this paper is to build on the conclusions of the Annex based on monitoring data related to real-life performance of VIP in buildings. By presenting the state-of-the-art in SIM applications in buildings and a case study with 7 years of monitoring data of a VIP wall installation, future research directions and recommendations for further actions are presented in the area of SIM in building applications.

SUPER INSULATION MATERIALS

Conventional insulation materials use entrapped air as insulator inside a porous matter. Examples of these are mineral wool, expanded polystyrene and polyurethane. By using different additives, the thermal conductivity can be reduced by targeting the three main heat transfer mechanisms presented in Figure 1 (Berge & Johansson, 2012).

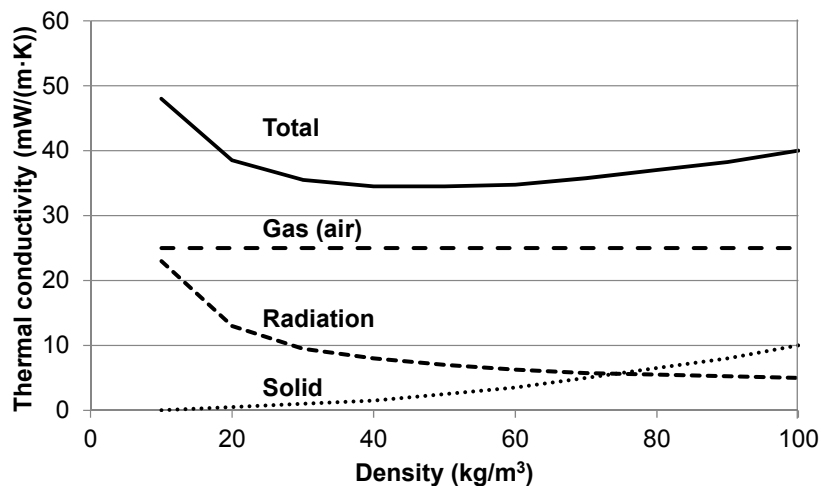


Figure 1. Thermal conductivity in porous materials divided into the three main heat transfer mechanisms (adapted from (Simmler et al., 2005)).

The total thermal conduction can be reduced down to a minimum around 30 mW/(m·K), which can be compared to stagnant air which has 25 mW/(m·K). Therefore, in this paper SIMs are defined as materials having a thermal conductivity lower than stagnant air ($\lambda = 25 \text{ mW/(m·K)}$). To reduce the thermal conductivity further, the heat transfer through the gas has to be reduced. This can be achieved by a) hindering the gas movements in the pores by reducing the pore size, b) removing the gas, or c) a combination of both a) and b) (Berge & Johansson, 2012).

In the context of Annex 65, SIM were divided in advanced porous materials (APM) and vacuum insulation panels (VIP). APM are materials where the heat transfer through the gas is hindered significantly by the fine pore structure. These can further be divided in two groups, porous silica, e.g. based on fumed silica, and aerogels. APM have been installed since the early 2000s in buildings (case studies) and assemblies. The products available on the market are more

similar to conventional insulation materials in most aspects. However, knowledge related to behavior of AMP are needed for performance prediction at the material, component and building scale. The aerogel based products, such as blankets, are in general vapor permeable and hydrophobic.

The second group of products is VIP. Here the contribution of heat transfer through the gas is suppressed by evacuation. These can be further divided in different core materials (fumed silica, glass fiber, polyurethane, expanded polystyrene and others), different envelopes (metalized film, aluminums laminate, stainless steel, glass, or combinations), and with or without a getter and/or a desiccant. Since VIP have less similarities to conventional insulation materials these products will be the focus of this paper.

Generally there are a number of challenges remaining when using VIP in buildings. The first challenge is the cost versus performance ratio. The thermal performance of VIP is practically 5 times better than conventional materials while the price is generally around 10 times higher. There are applications where the high performance and cost can be reasonable. The second challenge is the long-term performance of VIP. The service life of a building is 25-100 years while the VIP for building applications have been developed in the recent decades. The third challenge is that the construction market is a conservative market, regulated by numerous codes and standards, and thus, introducing new products takes a long time. The fourth challenge is knowledge and awareness among designers concerning using VIP. To provide answers to these challenges, field studies can provide insight on how the materials perform during normal use conditions (Adl-Zarrabi & Johansson, 2018).

During the years several research projects have focused on evaluating VIP in the field. The possibilities to use VIP in buildings was investigated during 2002-2005 by Binz et al. (2005). They studied in total 20 constructions with focus on the energy use, thermal bridges and moisture performance. In a study Heinemann and Kastner (2010) used infrared thermography to investigate the performance of the VIP after some years of use in the buildings. They concluded that as long as the VIP is not damaged at installation, about 95% of the VIP will maintain the vacuum several years. One of the most predominant building elements where VIP have been used is in flat roofs. At Empa in Switzerland researchers have monitored a roof construction containing VIP since 2004. Brunner and Ghazi Wakili (2014) measured the thermal conductivity of the VIP which had increased to 6.6-7.0 mW/(m·K) after 9 years. This is an increase of 65-75% from the initial thermal conductivity of 4 mW/(m·K). However, it is still well below the thermal conductivity of conventional insulation materials and the thermal conductivity of the core material at atmospheric conditions, 20 mW/(m·K).

CASE STUDIES USING VIP

Full scale experiments provide knowledge of practical and technical difficulties as well as data for service life estimations. For certain conclusions to be drawn from existing case studies, long-term monitoring is essential. Unfortunately, monitoring is only performed in few case studies. In total 22 case studies using VIPs, spread over 10 countries on 3 continents, were collected within Annex 65. The design process, practical aspects and results were described for each of these case studies. Of the 22 case studies only 4 were monitored and of these 2 were laboratory setups and 2 were field test of an external wall. The installation of the VIPs is the critical process which calls for inspection of the VIPs at the construction site before installing them. Considering the large amount of installed VIPs in case studies reported in Annex 65 in different countries (Figure 2) it is a pity that not more cases have been followed up.

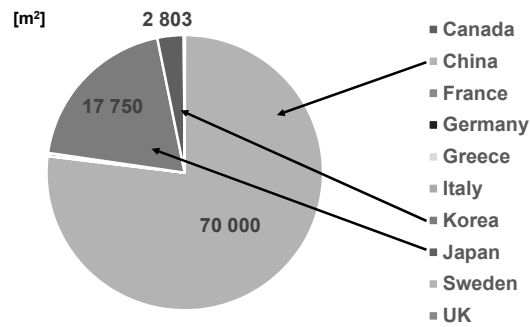


Figure 2. Installed VIP (m²) in case studies in Annex 65 (Adl-Zarrabi & Johansson, 2018).

In an ongoing study in Gothenburg, Sweden, a renovated building was monitored for 7 years with data presented for each year. The case study building was a listed building from 1930 which was insulated on the exterior with 20 mm VIPs. The calculated energy use for heating decreased by 24% (Johansson et al., 2014). Temperature and relative humidity sensors were installed in the test wall and in a neighboring (non-retrofitted) wall as reference, see Figure 3.

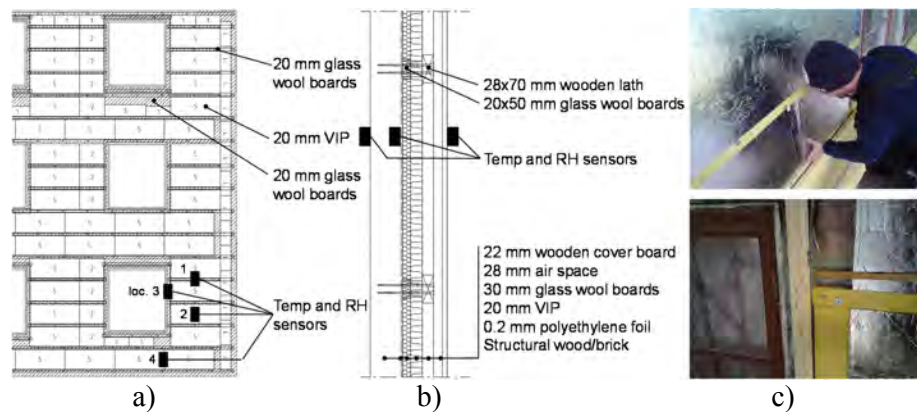


Figure 3. a) wall layout after retrofitting with 20 mm VIP and 30 mm glass wool boards, b) section of the wall layout with the location of the temperature and RH sensors in the wall marked by the black boxes (not in scale), c) installation of the VIP layer with the glass wool boards creating a thermal bridge between the VIP themselves and between the VIP and windows.

The hygrothermal performance was monitored by sensors integrated in the construction. The monitoring results for first 5 years were presented in (Johansson et al., 2016). The temperature and RH in the wall was recorded during 5 years, from January, 2011, to December, 2015. The measurements showed no sign of deterioration of the VIP and there was a low risk for condensation in the construction. It was concluded that the hygrothermal performance of the test wall was substantially better than that of the reference wall (Johansson et al., 2016).

The external air space made it impossible to identify the different panels by thermography. Only indirect methods, like evaluation of the measured temperatures in the wall, could be used to follow the long-term performance of the panels. For this analysis the average temperature for January each year 2011 to 2017 was used to calculate the temperature factor, see Figure 4. Unfortunately several sensors have been damaged why only one position can be evaluated for all 7 years.

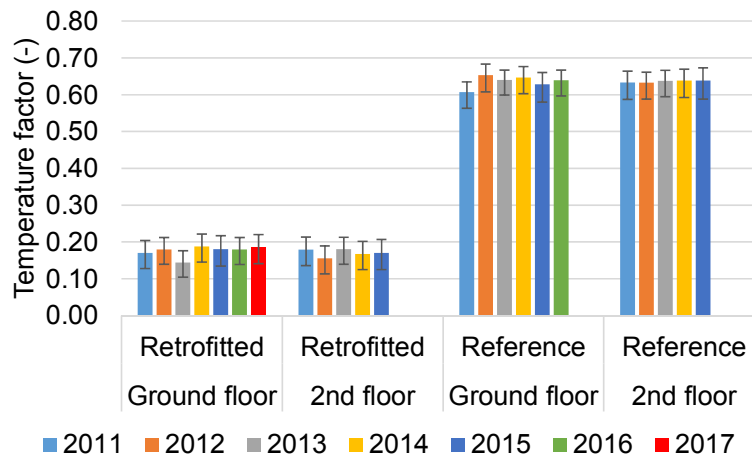


Figure 4. The temperature factor of January 2011 to 2017 for the retrofitted and reference walls. The temperature factor is the percentage temperature decrease over the original wall compared to the total temperature drop over the wall. The error bars show an accuracy of the sensor of $\pm 0.5^\circ\text{C}$ (adapted from (Johansson et al., 2016)).

In the reference wall about 64% of the temperature drop was over the uninsulated parts. After the retrofitting only about 17-18% of the temperature drop was over that part of the wall. The results indicate that after 7 years there was no sign of decreased insulation performance of the VIP. The results of this case study after 7 years are in good agreement with also the conclusion from several case studies that were collected in Annex 65 (Adl-Zarrabi & Johansson, 2018).

CONCLUSIONS

During the work of the Annex 65 several questions regarding the long-term performance of VIP and their application on the building scale were identified and discussed. Based on the experiences in the case studies, it was possible to identify application areas and the conditions of the intended use of VIP. It is clear that special care is necessary during installation compared to conventional insulation materials, since the VIP are sensitive to mechanical puncturing of the envelope. Therefore, there may be a need for certification of craftsmen and need of special training.

The building industry is generally conservative to new solutions and materials. The industry is regulated by numerous codes and standards, and thus, introducing new material takes a long time. Results obtained by activities in Annex 65 can be used for convincing the building industry about the performance of SIMs.

The ongoing standardization on the material and product levels may trigger building components with VIP to be introduced on the market. There are valuable savings of space when less area is needed for the building elements which leads to an increased rental income. There can also be technical reasons to select a VIP, i.e. when conventional insulation materials are not a practical alternative or for architectural reasons.

The theoretical investigations and first practical tests showed that VIP, especially those with fumed silica core, are expected to fulfil the requirements on durability in building applications for more than 50 years. Both VIP and APM have been successfully installed over the past 15 years in buildings. However, real experience from practical applications exceeding 15 years for VIPs is still lacking.

The long-term performance (25-100 years) cannot be entirely determined due to lack of data for longer time period exceeding 15 years. However, as seen above and more thoroughly discussed in the report of Annex 65, there were few claims concerning the malfunction of SIM in construction. The products are in continuous development and the VIP that were installed several years ago are no longer available on the market. By continuous product development the performance of the products are improved for every generation which gives a promising outlook for the wider implementation of SIM in the building envelope.

ACKNOWLEDGEMENTS

The work was financed by the Swedish Energy Agency project 40798-1 and 42856-1. The case studies and conclusions are results of the discussions throughout IEA EBC Annex 65. All the contributors and participants are acknowledged for their contributions.

REFERENCES

- Adl-Zarrabi, B., & Johansson, P. 2018. Annex 65 Long-Term Performance of Super-Insulating Materials in Building Components and Systems. Report of Subtask 3: Practical Applications – Retrofitting at the Building Scale – Field scale (Report to be published).
- Berge, A., & Johansson, P. 2012. Literature Review of Novel Thermal Insulation Materials. Gothenburg, Sweden: Chalmers University of Technology, Building Technology.
- Binz, A., Moosmann, A., Steinke, G., Schonhardt, U., Fregnan, F., Simmler, H., Brunner, S., Ghazi, K., Bundi, R., Heinemann, U., Schwab, H., Cauberg, J. J. M., Tenpierik, M. J., Jóhannesson, G. A., Thorsell, T. I., Erb, M., & Nussbaumer, B. 2005. Vacuum Insulation in the Building Sector. Systems and Applications (Subtask B): IEA/ECBCS Annex 39 High Performance Thermal Insulation (HiPTI).
- Brunner, S., & Ghazi Wakili, K. 2014. Hints for an additional aging factor regarding the thermal performance of vacuum insulation panels with pyrogenic silica core. *Vacuum*, 100(0), 4-6.
- Heinemann, U., & Kastner, R. 2010. VIP-PROVE: Vakuumisolationspaneele - Bewährung in der Baupraxis. Wissenschaftliche Begleitforschung. Schlussbericht Energieoptimiertes Bauen, ViBau Report ZAE 2-1210-11 (2010) (VIP-PROVE: Vacuum insulation panels - Testing in construction practice. Scientific evaluation. Final report energy optimized construction). [In German]. Würzburg, Germany: Bayerisches Zentrum für Angewandte Energieforschung e.V. ZAE Bayern.
- Johansson, P. 2012. Vacuum Insulation Panels in Buildings: Literature Review (No. 2012:1). Gothenburg, Sweden: Chalmers University of Technology, Department of Civil and Environmental Engineering.
- Johansson, P., Adl-Zarrabi, B., & Sasic Kalagasidis, A. 2016. Evaluation of 5 years' performance of VIPs in a retrofitted building façade. *Energy and Buildings*, 130, 488-494.
- Johansson, P., Hagentoft, C.-E., & Kalagasidis, A. S. 2014. Retrofitting of a listed brick and wood building using vacuum insulation panels on the exterior of the facade: Measurements and simulations. *Energy and Buildings*, 73, 92-104.
- Simmler, H., Brunner, S., Heinemann, U., Schwab, H., Kumaran, K., Mukhopadhyaya, P., Quénard, D., Sallée, H., Noller, K., Küçükpinar-Niarchos, E., Stramm, C., Tenpierik, M. J., Cauberg, J. J. M., & Erb, M. 2005. Vacuum Insulation Panels. Study on VIP-components and Panels for Service Life Prediction of VIP in Building Applications (Subtask A): IEA/ECBCS Annex 39 High Performance Thermal Insulation (HiPTI).

Effect of Air Pressure on Moisture Transfer inside Porous Building Materials: Three-dimensional Behavior of Moisture and Air

Kazuma Fukui^{1,*}, Chiemi Iba¹, Shuichi Hokoi² and Daisuke Ogura¹

¹Kyoto University, Kyoto

²Southeast University, China

*Corresponding email: be.fukui-k1820@archi.kyoto-u.ac.jp

ABSTRACT

The effect of air pressure on moisture transfer inside porous building materials cannot be ignored in cases in which air cannot escape through the surfaces of the materials; in such cases, the air is compressed by the movement of the moisture. Therefore, in a situation in which most surfaces of a specimen are sealed or treated with surface-protecting materials (a situation that is often encountered in typical water-absorption tests), the experimental results may differ from those without sealed or treated surfaces. In the present study, the influence of air pressure on moisture transfer was investigated quantitatively.

First, the following water-absorption test was conducted. Water infiltrated into a brick through its top surface, whereas the side surfaces were sealed to prevent the transfer of moisture and air. The bottom surface was exposed to the ambient air. The water content was measured two-dimensionally during the experiment using gamma-ray attenuation. Next, to investigate how air pressure affects water infiltration, another experiment was conducted after sealing the bottom surface. The air inside the brick was expected to be compressed by the infiltrating water when the bottom surface was sealed. A water-absorption test was then performed after a small hole was made in a side surface of the bottom-sealed brick to reduce the interior air pressure. Finally, we analyzed the experiments numerically using a three-dimensional calculation model for simultaneous air and moisture transfer, assessing the validity of the model by comparing the calculated and measured water contents.

The experimental and numerical results show that water infiltration is slowed by higher air pressure inside the specimen when it is difficult for air to escape. It is also shown that the hole in the side surface helped limit the rise in air pressure to some extent.

KEYWORDS

Air pressure, Water absorption, Numerical analysis, Gamma-ray attenuation

INTRODUCTION

In water-absorption tests and measurements of water permeability, it is common to seal the side surfaces (and sometimes also the bottom surface) of the specimen to make the moisture transfer unidirectional. In addition, water-absorption tests are widely used to understand how the water-absorption rate and moisture properties are changed by surface treatments such as waterproofing and water-repellent coatings. However, because the sealed or treated surfaces may prevent the movement of not only moisture but also air, moisture infiltration may increase the air pressure in the material, thereby affecting the moisture movement.

Descamps (1997) used water-absorption tests and numerical analysis to study how air entrapment affects moisture infiltration, finding agreement between the measured and calculated sorption coefficient and inflow-surface water content. However, the moisture distribution inside the material and its temporal evolution are yet to be examined in detail. By

comparing the results of water-absorption tests on (i) a brick whose side surfaces were sealed and (ii) one whose bottom surface was also sealed, we found previously that the water absorption was clearly delayed in the latter case in which air could not escape from the brick other than through the top surface where water was absorbed (Fukui et al. 2018). In addition, we analyzed those experiments numerically using a one-dimensional model of simultaneous air and moisture transfer. However, the validity of that numerical model was not demonstrated satisfactorily because we did not consider multidirectional air flow and non-uniform distribution of air pressure in the specimen. Such effects arise from non-uniform material properties and from air bubbles appearing locally and escaping from the water-absorption surface into the water. We expect that drilling a small hole in one of the sealed surfaces would help prevent the increased air pressure from hindering moisture transfer. However, how such a hole affects the moisture transfer inside the material is also yet to be revealed quantitatively.

Therefore, in the present study, we conducted water-absorption tests on a brick to investigate how air pressure affects moisture transfer and how drilling a small hole reduces that effect. We also analyzed the experiments numerically using a three-dimensional calculation model for simultaneous air and moisture transfer, examining the accuracy of the numerical results by comparing them with the experimental ones.

WATER-ABSORPTION TESTS

Specimens and method

We conducted three experiments (see Fig. 1) on a rectangular brick of size 210 mm × 100 mm × 60 mm. In the first experiment, the side surfaces were sealed (case 1). The brick was then dried and the experiment was repeated but with the 210 mm × 100 mm bottom surface now also sealed (case 2). Finally, the brick was dried again and a 10-mm-deep hole was made in one of the 100 mm × 60 mm side surfaces of the brick with a 3-mm-diameter drill (case 3). During each experiment, water was absorbed through the top surface.

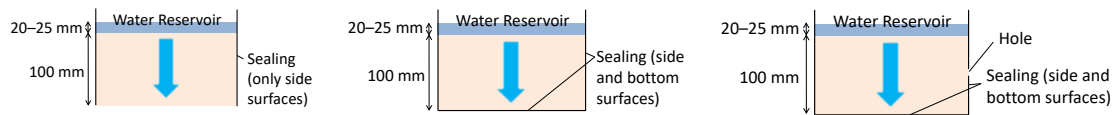


Figure 1. Schematic specimen cross sections for cases 1 (left), 2 (center), and 3 (right).

In the water-absorption tests, we used gamma-ray attenuation to measure the distribution of water content. Following Nielsen (1972), we determine the volumetric water content from the fraction of gamma rays absorbed as they pass through the brick:

$$\psi_w = -\frac{1}{\mu_{mw}\rho_w d} \ln\left(\frac{I_w}{I}\right), \quad (1)$$

where ψ_w is the volumetric water content [m^3/m^3], d is the specimen thickness [m], I_w is the gamma-ray intensity after passing through the wet specimen [cps], and μ_{mw} and ρ_w are the mass attenuation coefficient [m^2/kg] and the density [kg/m^3] of liquid water, respectively. I is the gamma-ray intensity after passing through the absolutely dry specimen [cps]. However, because the value of ψ_w is very low for an air-dried brick, instead of I we use the gamma-ray intensity after passing through the specimen in equilibrium with the ambient laboratory air. To determine I_w and I in Eq. (1), we used a measuring device whose gamma-ray source and detector could be moved vertically and horizontally on a plane normal to the direction of gamma-ray propagation (Fig. 2a). The 210 mm × 100 mm surface of the brick was irradiated

with gamma rays. At each measurement cycle, we measured the water content at 20 points (see Fig. 2b). We set the x and z axes as shown in Fig. 2b and the y axis as the direction of the gamma rays. To reduce noise, we measured for 40 s to obtain each data point. We stopped measuring from time to time to refill the water reservoir above the specimen, maintaining a water depth of 20–25 mm. We weighed the specimen before and after each experiment. We used an air conditioner to maintain the laboratory temperature at around 21°C, but we did not control the relative humidity (which fluctuated between 45% and 70%).

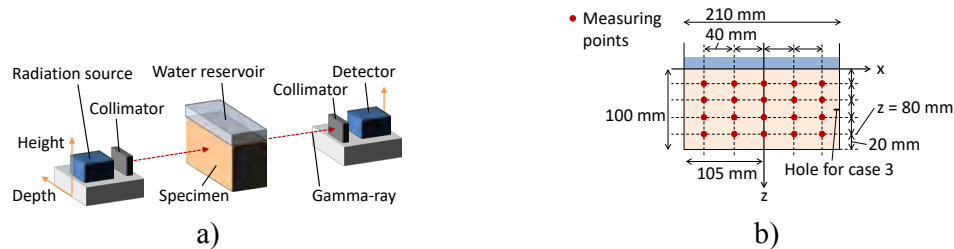


Figure 2. a) Schematic of apparatus used for gamma-ray attenuation. b) Points used to measure water content by gamma-ray attenuation.

Results and discussion

From observations made when the measurement was suspended, air bubbles appeared on the top surface of the brick and escaped into the water in case 2, whereas no such bubbles were observed in cases 1 and 3. Because air in the brick could escape through the bottom surface in case 1 and from the hole drilled in the side surface in case 3, air compressed by moisture infiltration near the top surface might have moved downward because of the air pressure gradient rather than escaping as bubbles through the top surface.

In Fig. 5, the water content measured in each experiment is shown as the data points, with the calculation results (described later) shown as the lines. Here, the results at $z = 80$ mm are shown as typical examples. Figure 5 shows only those data obtained during the 8 h after the start of each experiment; the water content changed little after that time. The water content clearly increases later in case 2 compared with case 1. In case 3, the water content increases at almost the same rate as in case 2, indicating that the hole did not completely prevent the rise in air pressure from hindering moisture infiltration. The results were nearly the same in cases 2 and 3 because the air bubbles (case 2) and the hole (case 3) might have suppressed the rise in air pressure inside the brick.

In each experiment, the increase in water content was slowest at $x = 0$ mm (i.e., the center of the brick), becoming faster nearer the side surfaces (i.e., larger absolute values of x). The sealed side surfaces and/or the horizontally non-uniform material property such as moisture diffusivity may have affected the moisture transfer. In case 3, the water content at $x = 80$ mm increased faster than did that at $x = -80$ mm. During that experiment, the air in the brick escaped from the hole, thereby lowering the air pressure at the right-hand side of the specimen. Therefore, the movement of moisture in the right half was hampered less than it was in the left half.

ANALYSIS OF SIMULTANEOUS AIR AND MOISTURE TRANSFER

In this section, we analyze case 1 numerically to estimate the moisture diffusivity of the brick. We then use that moisture diffusivity to analyze cases 2 and 3 to assess the validity of the calculation model for simultaneous air and moisture transfer.

Basic equations, calculation models, and calculation conditions

In the field of soil science, Green et al. (1970) proposed a model for air and moisture transfer and verified it using a water-absorption experiment. Referring to that model, we use the following two equations based on Darcy's law and mass conservation:

$$\frac{\partial \rho_a \psi_a}{\partial t} = \nabla \cdot \left\{ \frac{k_a}{g} (\nabla P_a - \rho_a g \mathbf{n}) \right\}, \quad (2)$$

$$\frac{\partial \rho_w \psi_w}{\partial t} = \nabla \cdot \left\{ \lambda'_p (\nabla P_w - \rho_w g \mathbf{n}) \right\}, \quad (3)$$

where ρ is the density [kg/m³], ψ is the volume fraction [m³/m³], t is time [s], k_a is the coefficient of air permeability [m/s], g is the acceleration due to gravity [m/s²], λ'_p is the water permeability due to the water pressure gradient [kg/(m·s·Pa)], P is the pressure [Pa], \mathbf{n} is the unit vector in the direction of gravity, and the suffixes a and w refer to air and water, respectively. Here, we consider the compressibility of air but neglect that of liquid water, it being very small in comparison. We use the finite-difference method in the analysis, and the basic equations are discretized by the central difference for space and the forward difference for time. The spatial differential interval is 1.67, 2, and 1 mm in the x , y , and z directions, respectively. The temporal differential interval depends on P_w : for case 1, it is 10⁻⁶ s for $P_w < -10^8$, 10⁻⁴ s for $-10^8 \leq P_w < -10^6$, and 0.02 s for $P_w \geq -10^6$; for cases 2 and 3, it is 10⁻⁶ s for $P_w < -10^8$, 5 × 10⁻⁵ s for $-10^8 \leq P_w < -10^6$, and 2.5 × 10⁻⁴ s for $P_w \geq -10^6$. Here, P_w is the water pressure relative to atmospheric pressure.

Figure 3 shows the calculation models. We used the average temperature and humidity over the previous 24 h in the laboratory as the initial conditions of the brick for each experiment (case 1: 20.9°C and 55.8%; case 2: 20.8°C and 49.1%; case 3: 20.8°C and 64.1%). In cases 2 and 3, we took the initial air pressure in the brick to be atmospheric pressure. In case 1, the bottom surface was exposed to the ambient laboratory air (the vapour pressure was in equilibrium with an average temperature of 21.0°C and humidity of 63.5% during the experiment); we set the coefficient of moisture transfer between the bottom surface and the ambient air to 1.25 × 10⁻⁸ kg/(m²·s·Pa).

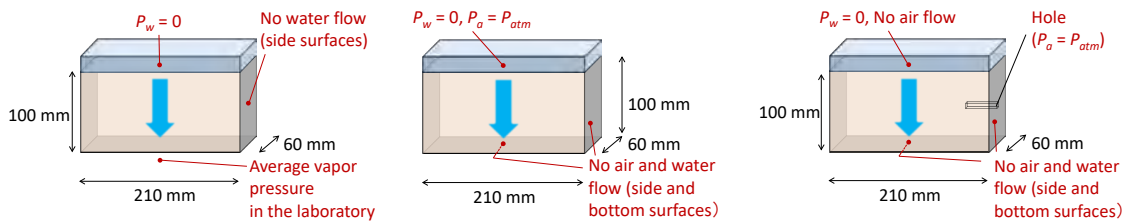


Figure 3. Calculation models for cases 1 (left), 2 (center) and 3 (right).

Because air bubbles were seen escaping from the top surface of the brick in case 2, the top surface was clearly not fully saturated with water. Therefore, in the calculation model we assumed water flow from the water reservoir to the top surface. We assumed there to be a moisture-transfer layer on the top surface of the brick, for which we used the Robin boundary condition. We set the coefficient of moisture transfer to 8.39 × 10⁻⁷ kg/(m²·s·Pa) to ensure that the experimental and numerical results agreed in case 1. In case 2, to simplify the model, we distributed the local air loss due to the air bubbles uniformly across the top surface. Therefore,

the boundary condition for the air at the top surface was again the Robin boundary condition; the external condition was atmospheric pressure and we set the coefficient of air transfer to $4.0 \times 10^{-10} \text{ kg}/(\text{m}^2 \cdot \text{s} \cdot \text{Pa})$. In case 3, we modelled the hole as a rectangular parallelepiped that was 9.17 mm long, 3 mm high, and 2 mm wide, thereby having nearly the same surface area as the actual hole. We took the air pressure at the hole surface to be atmospheric pressure, and we neglected any flow of moisture through the hole.

Material properties used in calculation

Figure 4a shows the adsorption isotherm of the brick, which we estimated from Kumaran (1996). However, we determined ψ_w at saturation by the mass of absorbed water in case 1. According to Descamps (1997), the air permeability decreases rapidly with water content in areas of high humidity. Therefore, we took k_a to be a function of ψ_w as in Fig. 4b. Here, we took k_a in the dry state to be $2.95 \times 10^{-9} \text{ m/s}$ so that the experimental and numerical results agreed in case 3. Figure 4c shows the moisture diffusivity D_ψ by volumetric water-content gradient at saturation as a function of x , and Fig. 4d shows D_ψ as a function of ψ_w at $x = 0$, ± 40 , and ± 80 mm. We introduced non-uniformity of D_ψ in the x direction because the calculated rate of increase of water content did not agree with the experimental results when the calculation model neglected the non-uniformity of this material property. In addition, the moisture diffusivity of a brick increases rapidly in regions of high water content (Kumaran 1996). We calculated λ'_p in Eq. (3) from D_ψ by $\lambda'_p = (D_\psi / \rho_w) \times (\partial \psi_w / \partial \mu)$, where μ is the water chemical potential for free water [J/kg]. In the analysis, we considered no other material properties to be non-uniform other than D_ψ . We did this (i) because the water content in the steady state is largely the same at all measuring points, as shown in Fig. 5, and (ii) to simplify the model.

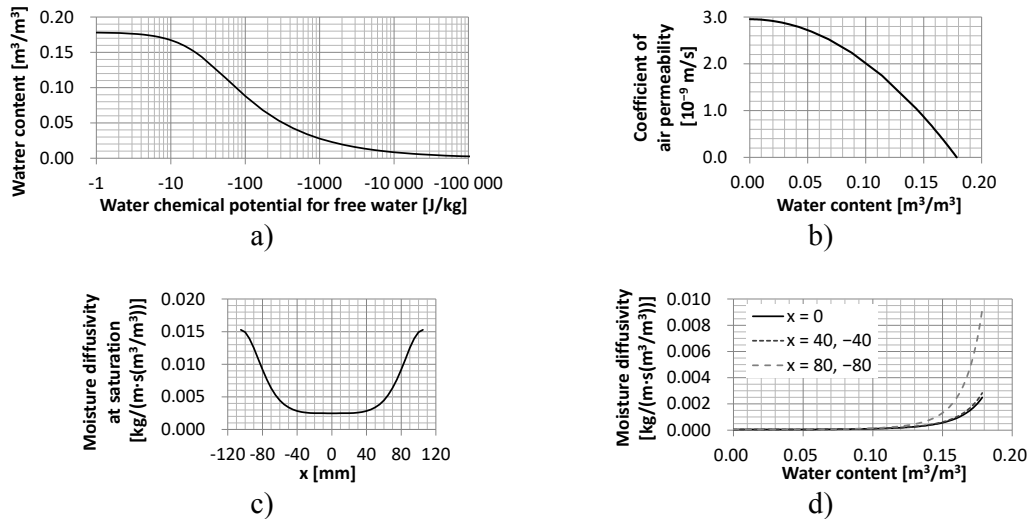


Figure 4. Material properties of the brick: a) adsorption isotherm; b) coefficient of air permeability as a function of water content; c) moisture diffusivity at saturation as a function of x ; d) moisture diffusivity as a function of water content.

Calculation results and discussion

The time profiles of the calculated water content for the first 4 h are shown in Fig. 5 along with the experimental results. Because the measured water content is the average along the line of the gamma rays, we show numerical results averaged in the y direction. Because the numerical results for case 1 agree well with the experimental ones (Fig. 5a), we applied the

moisture diffusivity identified in case 1 to cases 2 and 3. In cases 2 and 3, the numerical results (Fig. 5b and c, respectively) also agree reasonably with the experimental ones except for the point at $x = 0$ mm, where the calculated water content rises slower than in the experiment for case 3. Calculation models that consider non-uniformity in the y and z directions may improve such agreement.

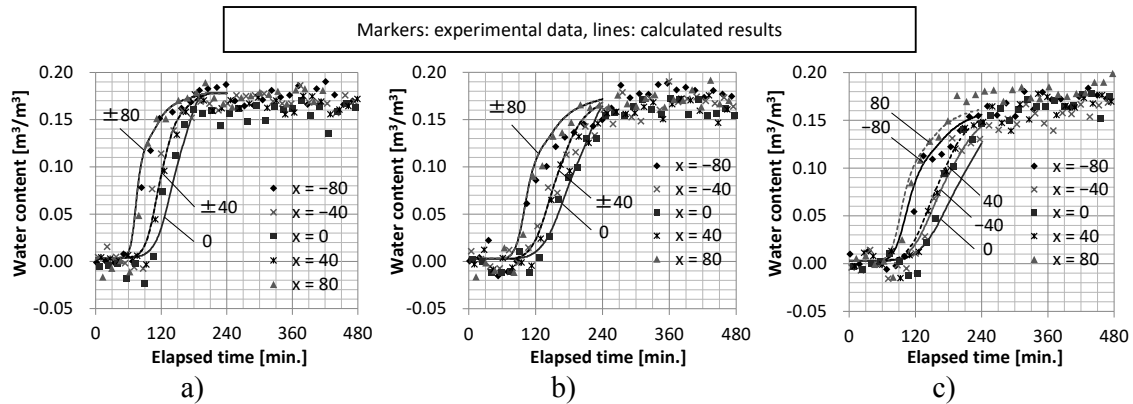


Figure 5. Calculated and measured water content for a) case 1, b) case 2, and c) case 3.

CONCLUSIONS

This study has shown that moisture infiltration in a water-absorption test is slowed considerably when air cannot escape from the specimen. It was also shown that making a small hole in the side of the specimen suppresses the rise in air pressure inside the specimen to the same extent as does air loss due to air bubbles; however, such a hole hardly changes the rate of increase of water content. Furthermore, a three-dimensional model of the simultaneous transfer of air and moisture can predict reasonably well the water content measured in the water-absorption test. Further studies of how the depth, area, and location of the small hole affect the ability of the rise in air pressure in a specimen to hinder moisture infiltration should be conducted.

ACKNOWLEDGEMENT

This research was supported by the JSPS Grant-in-Aid for Young Scientists (B) (grant no: 15K 21092; principal investigator: Chiemi Iba).

REFERENCES

- Descamps F. 1997. Continuum and discrete modelling of isothermal water and air flow in porous media. *Ph.D. Thesis*, K.U. Leuven (Belgium).
- Fukui K., Iba C., Hokoi S., and Ogura D. 2018. Effect of air pressure on moisture transfer inside porous building materials. *Japan Architectural Review*, <https://doi.org/10.1002/2475-8876.12047>.
- Green D.W., Dabiri H., Weinaug C.F., and Prill R. 1970. Numerical modeling of unsaturated groundwater flow and comparison of the model to a field experiment. *Water Resources Research*, 6(3), 862-874.
- Kumaran M.K. 1996. Heat, air and moisture transfer in insulated envelope parts. Final Report Volume 3 Task 3: Material Properties, International Energy Agency ANNEX24, Laboratorium Bouwfysica, K.U. Leuven (Belgium), pp. 30-36.
- Nielsen A.F. 1972. Gamma-ray-attenuation used for measuring the moisture content and homogeneity of porous concrete. *Building Science*, 7(4), 257-263.

Evaluation of the impact of phase change humidity control material on energy performance of office buildings

Zhimin Wu¹, Menghao Qin^{2,*}, Mingjie Zhang¹

¹ School of Architecture and Urban Planning, Nanjing University, Nanjing, China

² Department of Civil Engineering, Technical University of Denmark, Lyngby, Denmark

*Corresponding email: menqin@byg.dtu.dk

ABSTRACT

Phase change humidity control material (PCHCM) is a new kind of composite made of high performance PCM microcapsules and diatomite. The PCHCM composite can moderate the hygrothermal variations by absorbing or releasing both heat and moisture and significantly reduce the peak/valley values of indoor temperature and relative humidity. In this paper, a novel model is developed to evaluate the energy performance of office buildings with PCHCM. The model is validated by a series of experiments, and then applied to investigate the effect of PCHCM on energy consumption in different typical climates worldwide (i.e. Beijing, Paris, Atlanta, and Guangzhou). Results show that high values of energy efficiencies can be obtained in the climates which characterized by a wide amplitude of temperature and humidity difference all day along (Paris and Atlanta). Noteworthy, the highest potential energy saving rate could be up to 19.57% for the office building in Paris.

KEYWORDS

Phase change humidity control material, HAMT, Enthalpy method, Energy consumption

INTRODUCTION

Nowadays, increased energy demand has resulted in environmental issues worldwide (International Energy Agency, 2012). Building sector represents about 40% of global energy consumption and produces 30% of global greenhouse gas emissions annually (United Nations Environment Programme, 2009). The energy consumption of heating, ventilation and air-conditioning (HVAC) system accounts for 50% of building energy consumption in developed countries (Dincer, 1998). For this reason, it's essential to reduce the energy consumption of HVAC systems. The application of innovative building materials which can control the indoor hygrothermal condition at a relatively comfortable level is a promising way of energy saving.

The phase change materials (PCM) and porous hygroscopic materials are commonly used to moderate the indoor hygrothermal fluctuations (Barreneche et al. 2013; Evola et al. 2013; Andersen and Korsgaard, 1986; Toftum et al. 1998). However, those two kinds of material cannot simultaneously regulate the indoor temperature and humidity. Therefore, the phase change humidity control materials (PCHCM) that have the capability of both thermal and moisture buffering were prepared by our research group (Chen et al. 2015; Chen and Qin, 2016). The synthesis of novel phase change humidity control material (PCHCM) was achieved by using composite microencapsulated phase change material (MPCM) and diatomite. The PCHCM can moderate indoor air fluctuations of temperature and relative humidity by absorbing or releasing both heat and moisture.

Currently, the coupled heat and moisture transfer (HAMT) model proposed by Künel (1995) is the most used and validated model to calculate the coupled heat and moisture transfer

through porous building materials. On the other hand, the enthalpy method that can evaluate the general convection and diffusion phase change process was proposed by Voller et al (1987). However, very few models can be used to calculate the coupled heat, air and moisture transfer with phase change process.

The objectives of this study are: (1) to propose a novel mathematical model for calculating the coupled heat, air and moisture transfer with phase change process; (2) to analyse the energy saving effect of PCHCM in different climates.

METHODS

Methodology

The following equations are taken from HAMT model (Künzel, 1995). The heat balance of building envelopes can be described in equation (1):

$$\frac{\partial H}{\partial T} \frac{\partial T}{\partial t} = \frac{\partial}{\partial x} \left(k_{\omega} \frac{\partial T}{\partial x} \right) + h_v \frac{\partial}{\partial x} \left(\frac{\delta}{\mu} \frac{\partial(\varphi P_{\text{sat}})}{\partial x} \right) \quad (1)$$

where H is the total enthalpy of material (kJ/kg), T is the temperature ($^{\circ}\text{C}$), t is the time (s), x is the thickness (m), k_{ω} is the heat conductivity coefficient (W/m·K), h_v is the vaporization enthalpy of water (kJ/kg), δ is the vapor diffusion coefficient in air (kg/(m·s·Pa)), μ is the resistance coefficient of moisture, φ is the relative humidity, P_{sat} is the partial pressure of saturated water vapor (Pa).

The capacity of heat storage can be expressed as:

$$\frac{\partial H}{\partial T} = c_{\text{dry}} \rho_{\text{dry}} + c_{\text{p,vapor}} \omega \quad (2)$$

where c_{dry} is the specific heat capacity of dry materials (J/kg·K), ρ is the density of water (kg/m^3), $c_{\text{p,vapor}}$ is the specific heat capacity of water vapor (J/kg·K), ω is the water content (kg/m^3).

Equation (3) describes the mass conservation of building envelopes:

$$\frac{\partial \omega}{\partial \varphi} \frac{\partial \varphi}{\partial t} = \frac{\partial}{\partial x} \left(D_{\omega} \frac{\partial \omega}{\partial \varphi} \frac{\partial \varphi}{\partial x} \right) + \frac{\delta}{\mu} \frac{\partial}{\partial x} (\varphi P_{\text{sat}}) \quad (3)$$

According to the enthalpy method, the enthalpy H_{dry} can be expressed as:

$$H_{\text{dry}} = c_{\text{dry}} T + L_{\text{heat}} f_{\text{liq}} \quad (4)$$

where H_{dry} is the enthalpy of dry material (kJ/kg), L_{heat} is the latent enthalpy (J/kg), f_{liq} is the Liquid fraction.

The relationship between the specific heat capacity of dry material and temperature can be described by enthalpy method (Voller et al. 1987):

$$\rho_{\text{dry}} c_{\text{dry}} \frac{\partial T}{\partial t} = \rho_{\text{dry}} \frac{\partial H_{\text{dry}}}{\partial t} \quad (5)$$

The combined equation can be written by plugging the Eq. (2) and (4) into equation (1):

$$\rho_{\text{dry}} \frac{\partial H_{\text{dry}}}{\partial t} + \omega c_{\text{p,vapor}} \frac{\partial T}{\partial t} = \frac{\partial}{\partial x} \left(k_{\omega} \frac{\partial T}{\partial x} \right) + h_v \frac{\partial}{\partial x} \left(\frac{\delta}{\mu} \frac{\partial(\varphi P_{\text{sat}})}{\partial x} \right) \quad (6)$$

Combining with the moisture transfer Eq. (3), Eq. (6) and Eq. (3) are the whole heat and moisture governing equations of HAMT-Enthalpy (HAMT-E) model.

Validation

In order to verify the coupled HAMT-E model, a test facility with the PCHCM layer was built in Nanjing University.



Figure 1. Experimental cabin

As show in Fig. 2, the internal dimensions of the experimental cabin are 3m (depth) \times 2m (width) \times 2m (height). The cabin are made of 30 mm-thick wood boards and covered with an insulating material (thermal/humidity) on its four external sides. The 1m (width) \times 1.2m (height) double-glazed window are equipped in the south wall. The interior floor is covered with a 2 mm-thick PCHCM layer. The phase change temperature range of PCM is 25~27 °C. The tests are performed with a constant air change rate (ACH) of 0.5 h⁻¹. The experiment were conducted from July 1th to July 10th, 2017.

The temperature and relative humidity were measured both in the inside and outside space of the experimental cabin. The comparison between the experimental and simulated results is shown in Fig. 2 and Fig. 3. It can be seen that the high coincide results can be obtained with the HAMT-E model both in thermal and humidity aspect.

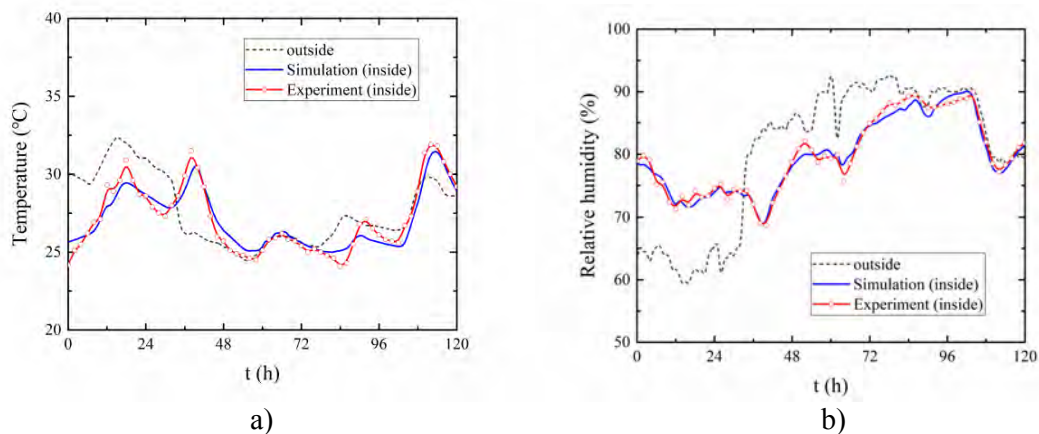


Figure 2. The comparison of simulated indoor temperature and relative humidity with the measured data

CASE STUDY

The validated HAMT-E model was applied to investigate the impact of PCHCM on building energy consumption under different climates. Four worldwide cities including Beijing, Paris, Atlanta and Guangzhou which characterized by typical urban climates were selected as boundary weather conditions for analysis. The BESTEST base case building (Fig. 3) from the IEA ECBCS Annex 21 was selected as the test office building (Zhang et al. 2017). The physical parameters of building envelopes are listed in Table 1. The simulation settings and boundary conditions can be seen in Table 2 as a office house.

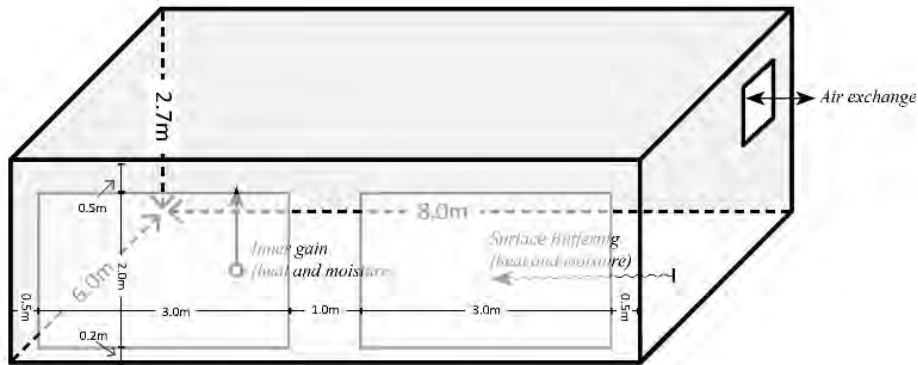


Figure 3. The BESTEST base case building adopted in application examples

Table 1. Physical parameters of different layers in building envelopes.

Construction	Material	d (m)	ρ (kg/m ³)	c_p (J/kg·K)	K (W/m·K)	U (W/m ² ·K)
Wall (from outer layer to inner layer)	Wooden board	0.010	530	900	0.14	0.474
	Rock wool board	0.066	60	850	0.04	
	Concrete	0.1	1400	1000	0.51	
	PCHCM layer	0.02	650	975	0.85	
Roof (from outer layer to inner layer)	Cement panel	0.012	1130	840	0.255	0.307
	Rock wool board	0.122	60	850	0.04	
	PCHCM layer	0.02	650	975	0.85	
Floor (from outer layer to inner layer)	Thermal insulating layer	1	60	850	0.04	0.04
	PCHCM layer	0.02	650	975	0.85	
Window	Double glazing unit	-	-	-	-	1.99

Table 2. Simulation settings and boundary conditions.

Conditions	Office case		
	Reference	CaseA.1	CaseA.2
Case ID	0	63.6	159.6
PCHCM area (m ²)		15 (occupied period)	6 (occupied period)
Heat power (W/m ²)		18-26 (occupied period)	≤65% (occupied period)
Moisture releasing rate (g/m ³ h)		0.5 (2ACH in unoccupied time)	No
Permissible room temperature range (°C)		09:00-17:00	The rest of the day
Permissible max relative humidity (RH)			
Air change rate (ACH)			
Air infiltration			
Occupied period (h)			
Unoccupied period			

RESULTS

In a typical year, the energy consumption and efficiency of PCHCM applied in office building are compared (Table 3). The energy saving quantity and efficiency tend to rise with the

increase of PCHCM's area. It illustrates that PCHCM could effectively moderate indoor hygrothermal environment; and a notable energy saving effect could be obtained.

Noteworthy, higher energy saving efficiency can be achieved in Paris and Atlanta, which have a temperate climate characterized by the wide amplitude of outdoor hygrothermal difference. Guangzhou has a hot and humid climate. It usually has a high temperature and relative humidity condition in the whole day. The high outdoor air temperature restrains the exothermic process of melting of the PCM. Similarly, the high outdoor relative humidity prevents the desorption process of diatomite. Therefore, the residual heat and moisture in PCHCM could not be efficiently discharged by the outside hygrothermal environment. As a result, the cooling loads of air conditioning system cannot be reduced by the efficiency of daily cyclic procedure of PCHCM.

The values of energy saving efficiency strictly follow the conclusions mentioned above. For instance, it can be seen that the utilization of PCHCM achieves the high values of energy saving efficiency in summer typical week. In Beijing, Paris, Atlanta and Guangzhou, the energy saving efficiencies are 10.22%, 19.57%, 17.82% and 8.76% in Case A.2, respectively. Additionally, the highest values of energy saving efficiency can be obtained in Paris with wide hygrothermal difference and the lowest can be obtained in Guangzhou with narrow hygrothermal difference.

Table 3. Energy consumption and energy saving of different cities in office buildings (Beijing, Paris, Atlanta and Guangzhou).

City	Load and efficiency	Area of PCHCM		
		0m ² (Reference)	63.6m ² (Case A.1)	159.6m ² (Case A.2)
Beijing	Total load (kWh m ⁻² a ⁻¹)	78.52	75.41	70.49
	Sensible heat saving(%)	-	0.77	7.40
	Latent heat saving(%)	-	18.98	23.48
	Total energy saving (%)	-	3.96%	10.22%
Paris	Total load (kWh m ⁻² a ⁻¹)	71.12	64.77	57.21
	Sensible heat saving(%)	-	0.87	8.82
	Latent heat saving(%)	-	38.13	58.51
	Total energy saving (%)	-	8.93%	19.57%
Atlanta	Total load (kWh m ⁻² a ⁻¹)	71.13	67.52	58.45
	Sensible heat saving(%)	-	0.72	14.83
	Latent heat saving(%)	-	17.41	26.31
	Total energy saving (%)	-	5.07%	17.82%
Guangzhou	Total load (kWh m ⁻² a ⁻¹)	104.57	102.09	95.41
	Sensible heat saving(%)	-	1.3	10.44
	Latent heat saving(%)	-	3.83	6.84
	Total energy saving (%)	-	2.37%	8.76%

CONCLUSIONS

This study intends to investigate the application of PCHCM in office buildings as a passive method to reduce energy consumption under different climate conditions. In this paper, a model for analyzing the energy consumption of the PCHCM is developed. The model is implemented in MATLAB-Simulink, and is validated by performing a series of experiments and validation tools. By using the model, the energy saving effect of PCHCM in office building is analyzed.

The research indicates that the application of PCHCM has the potential to reduce the energy consumption of office buildings. Overall, the PCHCM presents a melting point of 25~27 °C, which achieves the energy reduction of sensible heat in a summer typical week. Additionally, the porous structure of PCHCM enables the energy reduction of latent heat in moisture buffering process. From the analysis of energy saving, the overall energy saving potential of Paris with temperate maritime climate is found to be the best while the potential of energy reduction is limited in Guangzhou (located in subtropical humid climate) with high temperature and humidity all day long. Above all, the numerical results indicate that PCHCM is suitable for the areas that simultaneously manifest a wide amplitude of hygrothermal (temperature and humidity) difference.

ACKNOWLEDGEMENT

The present study was financially supported by the national key project of the Ministry of Science and Technology of China on "Green Buildings and Building Industrialization" (Grant No. 2016YFC0700500) and the National Natural Science Foundation of China (Grant No. 51578278).

REFERENCES

- Andersen I, Korsgaard J. Asthma and the indoor environment: assessment of the health implications of high indoor air humidity[J]. *Environment International*, 1986, 12(1-4): 121-127.
- Barreneche C, Navarro M E, Fernández A I, et al. Improvement of the thermal inertia of building materials incorporating PCM. Evaluation in the macroscale[J]. *Applied energy*, 2013, 109: 428-432.
- Buildings and Climate Change, Summary for Decision-Makers, United Nations Environment Programme, 2009.
- Chen Z, Qin M, Yang J. Synthesis and characteristics of hygroscopic phase change material: Composite microencapsulated phase change material (MPCM) and diatomite[J]. *Energy and Buildings*, 2015, 106: 175-182.
- Chen Z, Qin M. Preparation and hygrothermal properties of composite phase change humidity control materials[J]. *Applied Thermal Engineering*, 2016, 98: 1150-1157.
- Dincer I. Energy and environmental impacts: present and future perspectives[J]. *Energy sources*, 1998, 20(4-5): 427-453.
- Evola G, Marletta L, Sicurella F. A methodology for investigating the effectiveness of PCM wallboards for summer thermal comfort in buildings[J]. *Building and Environment*, 2013, 59: 517-527.
- International Energy Agency. CO₂ Emissions from fuel combustion: highlights (2012 ed.). Paris, France, 2012.
- Künzel H M. Simultaneous heat and moisture transport in building components[J]. One-and two-dimensional calculation using simple parameters. IRB-Verlag Stuttgart, 1995.
- Toftum J, Jørgensen A S, Fanger P O. Upper limits of air humidity for preventing warm respiratory discomfort[J]. *Energy and Buildings*, 1998, 28(1): 15-23.
- Voller V R, Cross M, Markatos N C. An enthalpy method for convection/diffusion phase change[J]. *International journal for numerical methods in engineering*, 1987, 24(1): 271-284.
- Zhang H, Yoshino H, Hasegawa K, et al. Practical moisture buffering effect of three hygroscopic materials in real-world conditions[J]. *Energy and Buildings*, 2017, 139: 214-223.

Experimental analysis of micro-cracks on the change of moisture transport properties of AAC

Jiří Maděra^{1,*}, Jan Kočí¹, Václav Kočí¹, Miloš Jerman¹, Magdaléna Doleželová¹

¹Czech Technical University in Prague, Czech Republic

*Corresponding email: madera@fsv.cvut.cz

ABSTRACT

In this paper, series of experiment measurements is carried out in order to study effect of freeze/thaw loading on the change of moisture transport properties of autoclaved aerated concrete. The samples were subjected to 15, 30 and 45 freeze/thaw cycles and subsequently basic physical properties, pore size distribution and water vapor and liquid water transport properties were investigated. The results showed significant changes in material properties of the material. The results of this research can be further implemented into computational models in order to bring the simulation results closer to the reality.

KEYWORDS

Autoclaved aerated concrete, freeze/thaw cycles, moisture transport properties, damage

INTRODUCTION

The effects of natural environment, such as air temperature, relative humidity, and solar and wind factors always vary in time, acting on the surface of building materials. Such effects may cause biological, chemical, or physical degradation of the material (Bertron, 2014; Kordatos et al., 2013; Sandrolini et al., 2007). When the materials are exposed to low temperatures, the ice damage needs to be considered in the first place. It is initiated through the nucleation, growth and interaction of micro-cracks, which usually occur internally. Such processes are manifested by volume expansion during cooling and by macroscopic cracks that develop after repeated cycles of freezing and thawing. (Beaudoin and MacInnis, 1972; Powers and Helmuth, 1953)

The ice damage is usually observed and investigated from a structural or esthetic point of view as usually strength loss of the material, surface cracks or detachment of renders are of interest. However, there exist some additional effects of ice damage, which are not apparent at a first glance. For example, building materials subjected to freeze-thaw loading become more permeable for the liquid water and water vapor due to the presence of micro- and macro-cracks in their structure. For that reason those materials become more vulnerable for the rest of their service life. Therefore, the freeze-thaw effects should be investigated also in this manner in order to analyze the effect of cracks on the change of moisture transport properties of building materials and to increase the credibility of service life analyses.

In this paper a series of experiments is conducted in order to investigate moisture transport properties of autoclaved aerated concrete after repeated freeze-thaw loading. The samples are fully saturated and subjected to different number of freeze-thaw cycles. Then, after drying process, for each sample the moisture transport properties, namely water vapor diffusion resistance factor and apparent moisture diffusivity, are determined and their dependence on the number of freeze-thaw cycles is investigated and discussed.

MATERIALS AND METHODS

Studied material

For the investigation of the effect of micro-cracks on the change of moisture transport properties, an autoclaved aerated concrete (AAC) P1.8-300 produced by company Xella was selected. Its basic physical, thermal and hygric properties (Jerman et al., 2013; Maděra et al., 2017) are shown in Table 1.

Table 1. Basic physical, thermal and hygric properties of studied AAC.

Parameter	Unit
Bulk density ρ (kg/m ³)	289
Open porosity ψ (%)	86.9
Specific heat capacity c (J/kg/K)	1090
Water vapor diffusion resistance factor μ_{dry} (-)	15.61
Water vapor diffusion resistance factor μ_{sat} (-)	6.17
Thermal conductivity λ_{dry} (W/m/K)	0.071
Thermal conductivity λ_{sat} (W/m/K)	0.548
Apparent moisture diffusivity κ (m ² /s)	$7.02 \cdot 10^{-8}$

For the further laboratory testing, the material was cut and different sets of samples having specific dimensions were prepared. For the measurement of apparent moisture diffusivity, rectangular prismatic specimens with the dimensions of 20 mm x 40 mm x 300 mm were prepared. The water vapor diffusion resistance factor was measured on block samples with the dimensions 100 mm x 100 mm and height of 20 mm (see Fig. 1), which were cut from the original AAC block.



Figure 1. AAC samples for measurement of water vapor resistance diffusion factor.

Experimental methods

The prepared samples were subjected to the freeze/thaw loading similarly to freeze resistance tests defined by ČSN EN 15304 (2010). First, the samples were dried, then submerged in water for 48 hours and left for another 24 hours in the laboratory in polyethylene bags to reach moisture content equilibration. After that, each sample was loaded by 15, 30 or 45 freeze/thaw cycles in order to create various amount of micro-cracks inside the material. Freezing period

was realized for 8 hours at -15 °C, thawing period 8 hours at 20 °C. The samples loaded by defined number of freeze/thaw cycles were then subjected to particular measurement of water vapor and liquid moisture transport properties. Simultaneously, the pore size distribution function of loaded samples was determined in order to provide preliminary information on changes in material's pore structure.

The apparent moisture diffusivity was obtained through the measurement of water absorption coefficient. The water absorption coefficient was determined by free water intake experiment. The cumulative mass of water in terms of the square-root-of-time rule commonly employed in the diffusion theory (Crank, 1975) can be expressed as

$$i = A \cdot t^{1/2}, \quad (1)$$

where i ($\text{kg} \cdot \text{m}^{-2}$) is the cumulative mass of water and A ($\text{kg} \cdot \text{m}^{-2} \cdot \text{s}^{-1/2}$) is the water absorption coefficient. Once A is known, the apparent moisture diffusivity can be calculated according to basic formula given by Kumaran (1999)

$$\kappa_{app} \approx \left(\frac{A}{w_{sat} - w_0} \right)^2, \quad (2)$$

where κ_{app} ($\text{m}^2 \cdot \text{s}^{-1}$) is the apparent moisture diffusivity, w_{sat} ($\text{kg} \cdot \text{m}^{-3}$) is the saturated moisture content and w_0 ($\text{kg} \cdot \text{m}^{-3}$) is the initial moisture content.

The water vapor transport properties were determined by means of water vapor diffusion resistance factor. For that reason the cup method was employed (Roels et al., 2004), which is the most frequently used in the practice. The method, defined by ISO (EN ISO 12572, 2001), is based on one-dimensional water vapor diffusion where the diffusion water vapor flux through the specimen and partial water vapor pressure in the air under and above specific specimen surface are measured. Water vapor transition properties of the investigated material are found by placing a specimen on the top of a cup and sealing it. The water vapor diffusion permeability δ (s) is calculated from the measured data according following equation

$$\delta = \frac{\Delta m \cdot d}{S \cdot \tau \cdot \Delta p_p}, \quad (3)$$

where Δm (kg) is the amount of water vapor diffused through the sample, d (m) is the sample thickness, S (m^2) is the specimen surface, τ (s) is the period of time corresponding to the transport of mass of water Δm , and Δp_p (Pa) is the difference between partial water vapor pressure in the air under and above specific specimen surface. Once the water vapor diffusion permeability is known, the water vapor diffusion resistance factor μ (-) can be calculated through water vapor diffusion coefficient D ($\text{m}^2 \cdot \text{s}^{-1}$) as

$$D = \frac{\delta \cdot R \cdot T}{M}, \quad (4)$$

$$\mu = \frac{D_a}{D}, \quad (5)$$

where R ($\text{kg} \cdot \text{m}^2 \cdot \text{s}^{-2} \cdot \text{K}^{-1} \cdot \text{mol}^{-1}$) is the universal gas constant, M ($\text{kg} \cdot \text{mol}^{-1}$) is the molar mass of water, T (K) is the absolute temperature, and D_a ($\text{m}^2 \cdot \text{s}^{-1}$) is the diffusion coefficient of water vapor in the air.

The pore size distribution function was determined using two different approaches. The distribution of pores up to 10 μm was determined using mercury intrusion porosimetry, while the amount of larger pores was calculated from total open porosity obtained by helium pycnometry.

RESULTS

Following data were obtained using experimental methods described in previous section. The basic physical properties such as bulk density, matrix density and open porosity are shown in Table 2. The distribution of pores is shown in Fig. 2.

Table 2. Basic physical properties of AAC

Sample	Matrix density ρ_{mat} ($\text{kg}\cdot\text{m}^{-3}$)	Bulk density ρ ($\text{kg}\cdot\text{m}^{-3}$)	Open porosity ψ (%)
unloaded (reference)	2034.0 ± 40.7	289.0 ± 4.3	85.1 ± 2.8
15 F/T cycles	2060.4 ± 41.2	281.7 ± 4.2	86.4 ± 2.9
30 F/T cycles	2016.1 ± 40.3	292.5 ± 4.4	85.5 ± 2.8
45 F/T cycles	2005.8 ± 40.1	285.0 ± 4.3	85.8 ± 2.8

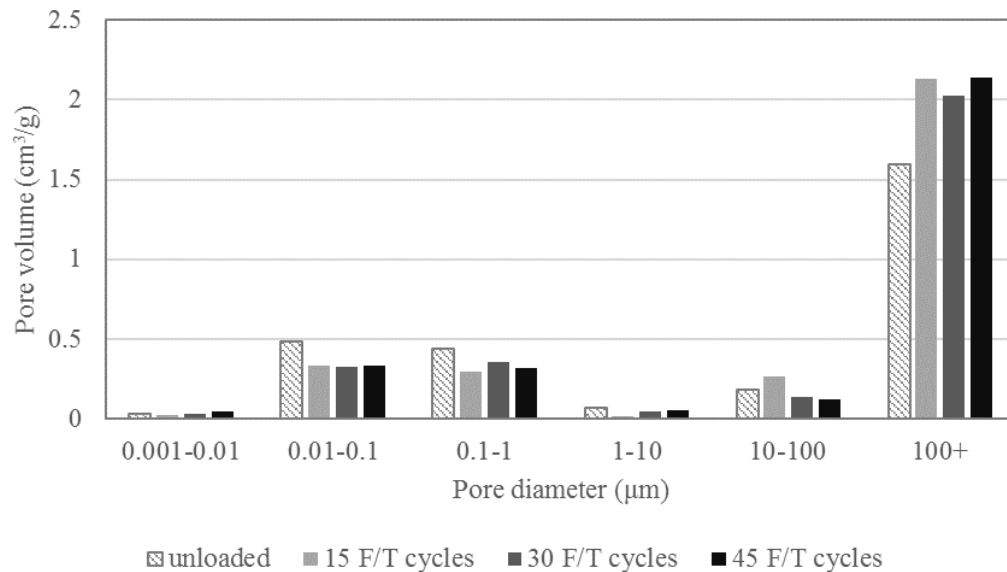


Figure 2. Pore size distribution of studied AAC

The measured water vapor and liquid water transport parameters are shown in Table 3.

Table 3. Water vapor and liquid water transport properties

Sample	Water vapor diffusion resistance factor μ (-)	Water absorption coefficient A ($\text{kg}\cdot\text{m}^{-2}\cdot\text{s}^{-1/2}$)	Apparent moisture diffusivity κ_{app} ($\text{m}^2\cdot\text{s}^{-1}$)
unloaded (reference)	15.6 ± 2.3	0.106 ± 0.005	$(7.020 \pm 0.351) \cdot 10^{-8}$
15 F/T cycles	5.7 ± 0.9	0.021 ± 0.001	$(2.652 \pm 0.133) \cdot 10^{-9}$
30 F/T cycles	6.4 ± 1.0	0.020 ± 0.001	$(2.450 \pm 0.123) \cdot 10^{-9}$
45 F/T cycles	6.5 ± 1.0	0.019 ± 0.001	$(2.139 \pm 0.107) \cdot 10^{-9}$

DISCUSSION

The presented results clearly show the change in material parameters of the sample before and after loading by certain numbers of freeze/thaw cycles. When basic physical properties are taken into account, it is obvious that freeze/thaw cycles generated some micro-cracks inside the material manifested by slight decrease of bulk density. However, the change is within the frame of measurement error. The increase of bulk density for the sample loaded by 30 freeze/thaw cycles can be explained by inhomogeneity of the original block from which the samples were cut. In the same way, the total porosity slightly increased. The changes of materials pore structure are evident from Fig. 2, where the amount of largest pores increased with the freeze/thaw loading.

The change of material structure affected the water vapor and liquid water transport properties. When water vapor diffusion resistance factor is discussed, it is evident that the material became more permeable for the water vapor. The values significantly decreased, however it seems that the number of freeze/thaw cycles does not have significant influence on the value change. Therefore, it can be concluded that major changes in material's pore structure appear after 1 to 15 freeze/thaw cycles and the additional loading does not affect the structure in significant way. In order to evaluate the critical number of freeze/thaw cycle that causes substantial change of material's structure, some additional testing should be performed with finer scale such as 1 or 2 freeze/thaw cycles.

The determination of water adsorption coefficient and apparent moisture diffusivity of AAC was very difficult. Basically, the reason for this is a coarse pore structure of the material making the gravity forces an important factor. With increasing pores in the material the absorption coefficient and apparent moisture diffusivity decreases. However, in order to provide more representative view on liquid moisture transport properties of studied material, another series of experiment needs to be conducted. The objective is to eliminate the effect of gravity forces and therefore the experiment should be designed to simulate moisture transport in horizontal position instead of vertical one.

Also, the cooling of material was done for -15 °C according to national standard, however, this temperature might not be sufficient enough. Using the Gibbs-Thompson equation for calculation of freezing point depression in the pores, the size of largest pore where the freezing occur may be calculated as

$$R = \frac{2T_0\gamma_{sl}v_l}{\Delta h_b\Delta T_f}, \quad (6)$$

where γ_{sl} ($\text{mJ}\cdot\text{m}^{-2}$) is the surface free energy (interfacial tension) of the solid/liquid interface ($\gamma_{sl} = 31.7 \pm 2.7 \text{ mJ}\cdot\text{m}^{-2}$), v_l ($\text{cm}^3\cdot\text{mol}^{-1}$) the molar volume of the liquid ($v_l = 18.02 \text{ cm}^3\cdot\text{mol}^{-1}$), and Δh_b ($\text{kJ}\cdot\text{mol}^{-1}$) the melting enthalpy in the unconfined (bulk) state ($\Delta h_b = 6.01 \text{ kJ}\cdot\text{mol}^{-1}$), all quantities taken at the bulk coexistence temperature T_0 ($T_0 = 273.15 \text{ K}$). ΔT_f (K) is the freezing temperature, i.e. $\Delta T_f = T_0 - T_{cooling}$. Based on Eq. (6), the largest pore with affected by freezing has a diameter of approximately $0.02 \mu\text{m}$. For that reason, it will be suggested in further experiments to decrease the freezing temperature to at least $-30 \text{ }^\circ\text{C}$ in order to affect the smallest pores (up to $0.008 \mu\text{m}$) by ice damage.

CONCLUSIONS

The water vapor and liquid water transport properties of the autoclaved aerated concrete were investigated in this paper. The samples were first loaded by various number of freeze/thaw cycles in order to induce ice damage to the material. Then, basic physical properties, pore size distribution and moisture transport properties were analyzed. The results proved significant

change in water vapor transport properties as the material become more permeable for the water vapor. The liquid water transport properties described by apparent moisture diffusivity decreased after loading by freeze/thaw cycles. However, the methodology for vertical water uptake was found not suitable for this kind of material due to significant effect of gravity forces. The analysis of pore size distribution revealed significant changes in pore structure of the material supporting the conclusions made in this paper.

ACKNOWLEDGEMENTS

This research has been financially supported by the Czech Science Foundation, under project No 17-01365S.

REFERENCES

- Beaudoin J.J. and MacInnis, C. 1972. The mechanism of frost damage in hardened cement paste. *Cement and Concrete Research*, 4, 139-147.
- Bertron A. 2014. Understanding interactions between cementitious materials and microorganisms: a key to sustainable and safe concrete structures in various contexts. *Materials and Structures*, 47(11), 1787-1806.
- Crank J. 1975. *The Mathematics of Diffusion*. Oxford: Clarendon Press.
- ČSN EN 15304. 2010. Determination of the freeze-thaw resistance of autoclaved aerated concrete. Czech Office for Standards, Metrology and Testing, Prague.
- EN ISO 12572. 2001. Hygrothermal performance of building materials and products. Determination of water vapor transmission properties. The European Committee for standardization, Brussels.
- Jerman M., Keppert M., Výborný J., and Černý R. 2013. Hygric, thermal and durability properties of autoclaved aerated concrete. *Construction and Building Materials*, 41(1), 352-359.
- Kordatos E.Z., Exarchos D.A., Stavrakos C., Moropoulou A., and Matikas T.E. 2013. Infrared thermographic inspection of murals and characterization of degradation in historic monuments. *Construction and Building Materials*, 48, 1261-1265.
- Kumaran M.K. 1999. Moisture diffusivity of building materials from water absorption measurements. *Journal of Thermal Envelope and Building Science*, 22, 349-355.
- Maděra J., Kočí V., Doleželová M., Čáchová M., Jerman M., and Černý R. 2017. Influence of weather-affected material characteristics on appearance of freeze/thaw cycles in building envelopes. *AIP Conference Proceedings*, 1866, 040023.
- Sandrolini F., Franzoni E., Cuppini G., and Caggiati L. 2007. Materials decay and environmental attack in the Pio Palace at Carpi: A holistic approach for historical architectural surfaces conservation. *Building and Environment*, 42(5), 1966-1974.
- Powers T.C. and Helmuth R.A. 1953. Theory of volume changes in hardened Portland-cement paste during freezing. In: *Proceedings, Highway Research Broad Annual Meeting, National Academy of Science*, 285-297.
- Roels S., Carmeliet J., Hens H., Adan O., Brocken H., Černý R., et al. 2004. Interlaboratory comparison of hygric properties of porous building materials. *Journal of Thermal Envelope and Building Science*, 27, 307-325.

Moisture monitoring of wood-frame walls with and without exterior insulation in a Midwestern U.S. cold climate

Samuel V. Glass^{1,*}, C.R. Boardman¹, Borjen Yeh², and Kingston Chow²

¹U.S. Forest Products Laboratory, Madison, Wisconsin, USA

²APA – The Engineered Wood Association, Tacoma, Washington, USA

*Corresponding email: svglass@fs.fed.us

ABSTRACT

Continuous exterior insulation is becoming more common in North American above-grade walls in both retrofit applications and new construction, as a means to improve the thermal performance of wall assemblies. Although moisture performance of wood-frame wall assemblies has been studied extensively, the drying capability of wall assemblies with exterior insulation and an interior vapor retarder in cold climates is not well characterized. This study monitored the hygrothermal performance of wall assemblies with and without exterior insulation under high and low interior humidity conditions and with intentional wetting of the wood structural panel sheathing. Moisture content and temperature of standard 38 mm × 140 mm wood framing and 11 mm thick oriented strand board (OSB) sheathing were measured over a two-year period in eight different wall assemblies, each with north or south orientation, in a conditioned test structure in Madison, Wisconsin. Wall configurations differed primarily in the interior vapor retarder (kraft paper or polyethylene film) and the exterior insulation (none, expanded polystyrene, extruded polystyrene, or mineral wool). OSB sheathing was wetted in a controlled manner at three different times of year to investigate drying response. Wintertime moisture accumulation in OSB in the tested climate zone was not a concern except in the wall with no exterior insulation and interior kraft vapor retarder, though rapid drying occurred in springtime. Drying of OSB after controlled wetting events was generally faster during warm weather than cold weather; faster with exterior insulation than without during cold weather; faster with vapor-open exterior insulation than low-permeance exterior insulation during cold weather; and faster with interior kraft vapor retarder than polyethylene.

KEYWORDS

moisture performance, hygrothermal performance, continuous insulation, building envelope, durability

INTRODUCTION

The building envelope is a key component affecting overall building energy use. Continuous exterior insulation is an increasingly common strategy to improve overall thermal performance in North American above-grade wall assemblies in both retrofit applications and new construction. This approach is particularly relevant for wood-frame construction in cold climates. While Performance Compliance Paths in the International Energy Conservation Code (IECC) (ICC, 2015) offer flexibility in the design of exterior walls, the Prescriptive Compliance Path requires wood-frame walls located in cold climates (IECC Climate Zone 6 or higher) to incorporate continuous insulation at a minimum thermal resistance of 0.88 m²·K/W (5 h·ft²·°F/Btu or “R-5”). This is often implemented with a combination of cavity insulation and continuous exterior insulation.

Long-term moisture performance of exterior wall assemblies is critical because moisture accumulation can lead to degradation of materials and poor indoor air quality. Moisture control strategies for exterior wall assemblies need to address sources of moisture from the interior and exterior of the building and the ways in which moisture migrates, including bulk water intrusion, uncontrolled air leakage, and vapor diffusion (TenWolde and Rose, 1996). In addition, the capacity to dry out when wetting occurs (either during construction or over the service life of the building) can improve the moisture tolerance and reduce the risk of problems, but the drying potential may be a concern for some wall assemblies that are insulated and air sealed to levels required by current model energy codes.

A recent literature review (Trainor and Smegal, 2017) concluded that adding exterior insulation to wood-frame walls in North American cold climates in nearly every case did not increase the risk of moisture-related durability problems. Continuous exterior insulation raised the temperature of wood structural members in exterior walls during cold weather (relative to walls without exterior insulation), thereby reducing the potential for wintertime moisture accumulation (Tsongas, 1991; Straube, 2011). With regard to drying potential, several studies found that walls with vapor-open exterior insulation allowed drying to the outside at a faster rate than walls with exterior foam insulation (Maref *et al.*, 2011; Fox *et al.*, 2014; Trainor *et al.*, 2016). In addition, faster drying rates were observed during spring and summer in exterior insulated walls without an interior polyethylene vapor barrier than in those with polyethylene (Craven and Garber-Slaght, 2014).

The studies mentioned above investigated a variety of wall configurations but did not include 38 by 140 mm framing (nominal 2×6) with 0.88 m²·K/W (R-5) exterior insulation, which meets the “R-20+5” IECC Prescriptive Compliance Path in cold climate zones (IECC Climate Zone 6 or higher). For this configuration, the ratio of exterior insulation to cavity insulation is not sufficient to permit the use of only a Class III interior vapor retarder (such as latex paint on gypsum board). The present study was initiated to characterize the moisture performance of 140 mm wood-frame wall assemblies with and without exterior insulation in a cold climate location. Specific objectives were to monitor wall assembly moisture and temperature conditions under ambient environmental conditions with high and low interior humidity conditions, and to characterize wall assembly drying rates after intentional wetting of the wood structural panel sheathing.

METHODS

Monitoring was carried out in a conditioned test structure located in Madison, Wisconsin (IECC Climate Zone 6). This cold climate has 4,074 heating degree days (18°C basis; 1981–2010 mean); 2015 and 2016 were warmer than normal, both with about 90% of the historic mean heating degree days. The 17.2 m x 4.9 m test structure was oriented with the long dimension running east to west. It had a preservative-treated wood post and beam foundation with an insulated floor. The 38 x 140 mm wood stud walls were refurbished for this study to create eight different north and south facing test bays (Figure 1). Each test bay was 1.2 m wide and 2.2 m high and consisted of three cavities with studs 406 mm on center. Test bays were isolated with a composite trim board on the exterior and by adding a 38 x 140 mm stud separated from the existing stud of the adjacent test bay using an impermeable self-adhering membrane. An entry door was located on the north side of a central area that houses the data acquisition system and heating and cooling equipment. Winter mean interior temperature was 20 °C; mean interior relative humidity (RH) was 42% during the first winter and 34% during the second winter. Summer mean interior conditions were 25 °C with RH between 45% and 55%.

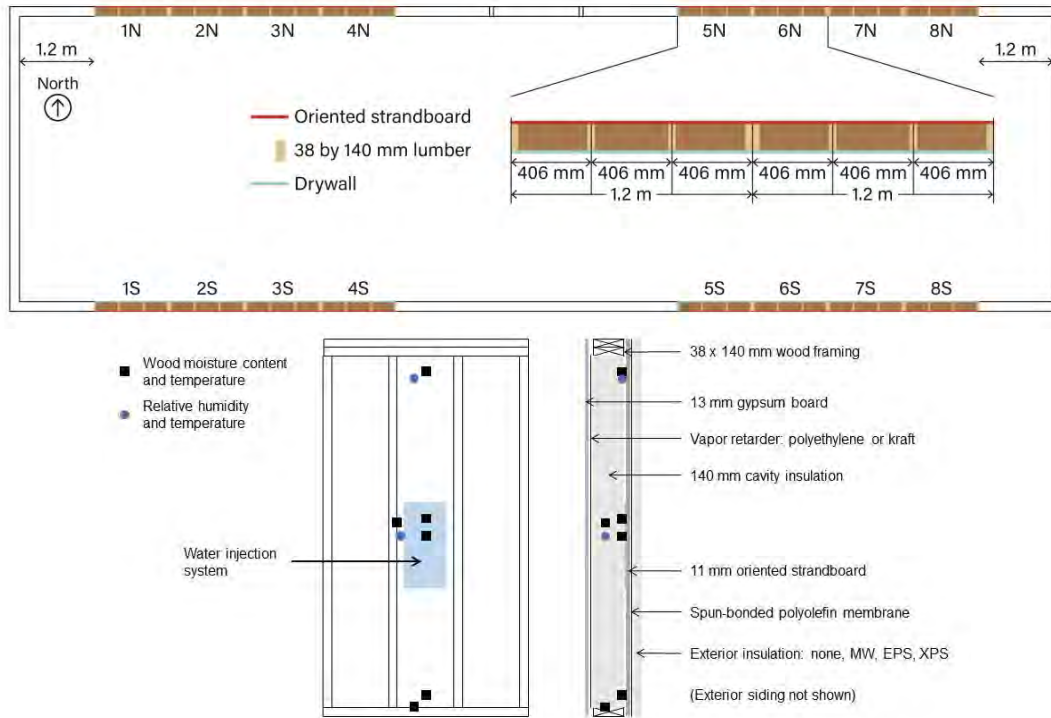


Figure 1. (top) Plan view of test structure with labelled test bays. (bottom) Wall elevation and section showing sensor layout.

All wall assemblies included vinyl siding, spun-bonded polyolefin house wrap, oriented strand board (OSB) sheathing, fiberglass batt cavity insulation ($3.7 \text{ m}^2 \cdot \text{K/W}$ or R-21), and interior gypsum drywall. Gasketing was installed between the framing and drywall for airtightness, and the drywall was finished with latex primer and latex paint. Test walls differed in the type of interior vapor retarder, water-resistive barrier, and exterior insulation (Table 1). Walls 1 and 2 provided base cases with no exterior continuous insulation (CI); Wall 1 had asphalt-coated kraft paper facing on the fiberglass batt insulation, whereas Wall 2 had 0.15 mm polyethylene sheet (with unfaced batt insulation). The remaining walls included one of the following exterior insulation materials: 38 mm mineral wool (MW) insulation ($1.1 \text{ m}^2 \cdot \text{K/W}$ or R-6); 38 mm expanded polystyrene (EPS) insulation ($1.1 \text{ m}^2 \cdot \text{K/W}$ or R-6); or 25 mm extruded polystyrene (XPS) insulation ($0.88 \text{ m}^2 \cdot \text{K/W}$ or R-5). Walls 1-7 had ordinary spun-bonded polyolefin membrane installed just exterior of the OSB sheathing, whereas Wall 8 used a “crinkled” version of the same material, structured to create vertical channels and a small air gap between the OSB sheathing and XPS insulation.

Table 1. Wall configurations.

Wall	Label	Interior Vapor Retarder	House Wrap	Exterior Insulation
1	No CI, kraft	Kraft paper	Flat polyolefin	None
2	No CI, poly	Polyethylene	Flat polyolefin	None
3	MW, kraft	Kraft paper	Flat polyolefin	38 mm MW
4	MW, poly	Polyethylene	Flat polyolefin	38 mm MW
5	EPS, kraft	Kraft paper	Flat polyolefin	38 mm EPS
6	XPS, kraft	Kraft paper	Flat polyolefin	25 mm XPS
7	XPS, poly	Polyethylene	Flat polyolefin	25 mm XPS
8	XPS, kraft, crinkled	Kraft paper	Crinkled polyolefin	25 mm XPS

Each test bay had an identical set of sensors installed in the central cavity (of the three that make up a bay; Figure 1). Wood moisture content (MC, percentage based on dry mass) and temperature were measured hourly at six locations in each test bay: four sensor pairs were located in OSB sheathing at various heights, one in the bottom plate, and one in a stud at mid-height. MC values in OSB were based on resistance measurements using the calibration of Boardman *et al.* (2017). Two additional sensors measured RH and temperature in the center of the cavity and at the interior surface of the OSB. Indoor RH and temperature and weather conditions were also recorded on site. Further details are given in Boardman *et al.* (2018).

Each wall assembly was subjected to an identical water injection schedule at three different times during the study. A shop towel was fastened to the interior side of the OSB in the center cavity to serve as a reservoir for the injected water (Figure 1), which was introduced through a vinyl tube from the interior near the drywall surface (Van Straaten, 2003). Each injection had a volume of 40 mL, which wetted the shop towel without water running down the OSB sheathing. The first series of injections occurred in late summer, starting August 13, 2015, with one injection per day for three days (total of 120 mL). The second series of injections occurred in late fall, starting November 6, 2015, and lasted five days (total of 200 mL). The last series of injections occurred the following spring, starting May 20, 2016, and lasted 4 days (total of 160 mL).

RESULTS AND DISCUSSION

OSB moisture content was higher in winter than summer, as illustrated in Figure 2 for north-facing walls (away from the wetting device). Two further trends are noted: first, walls with kraft vapor retarder had higher OSB MC in winter than corresponding walls with polyethylene; second, walls with exterior insulation had lower OSB MC than the base walls. Wintertime moisture contents were highest in the base wall with kraft vapor retarder; the peak was above 30% MC in the first winter and about 23% MC in the second winter, whereas the base wall with polyethylene vapor retarder remained below 16% MC. The difference is a result of water vapor migration from interior humidification through the more permeable kraft vapor retarder. Similar trends were observed in the south-facing walls, though the peak moisture contents were typically not as high as in the north-facing walls. The lower moisture levels in the south walls are due to the slightly higher temperature (as a result of solar radiation), but this effect was small and not consistent in all results. More consistent was the result that walls with exterior insulation had lower moisture levels than the base walls.

The response of OSB moisture content to water injections is depicted in Figure 3 for sensors placed within the field of the wetting device in north-facing walls. All wall configurations had a rapid increase in OSB MC after the water injections. Several observations about drying rates are noted. First, the drying rates in general were faster for the first injection (Aug 2015) and third injection (May 2016) than the second injection (Nov 2015). This was expected because drying is slower at colder temperatures. Second, for all three injections the walls with a kraft vapor retarder dried more rapidly than corresponding walls with polyethylene, consistent with the higher vapor permeance of kraft allowing drying to the interior. Third, for the second injection (in colder weather), walls with exterior insulation generally dried faster than the corresponding base walls, due to the exterior insulation keeping the OSB warmer. Fourth, the walls with exterior MW insulation dried faster than corresponding walls with exterior XPS insulation after the second injection; this is a result of the higher vapor permeance of MW and is consistent with prior research. Further analysis supporting these observations is presented by Boardman *et al.* (2018).

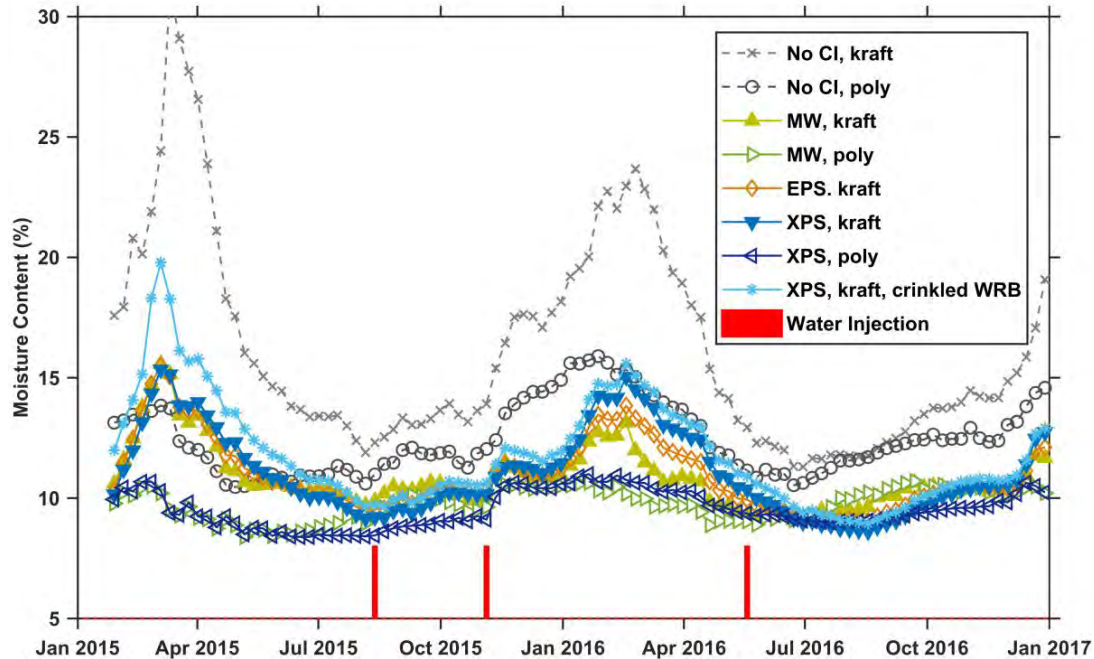


Figure 2. Weekly average moisture content of OSB in north-facing walls (average of sensors in OSB near top plate and bottom plate).

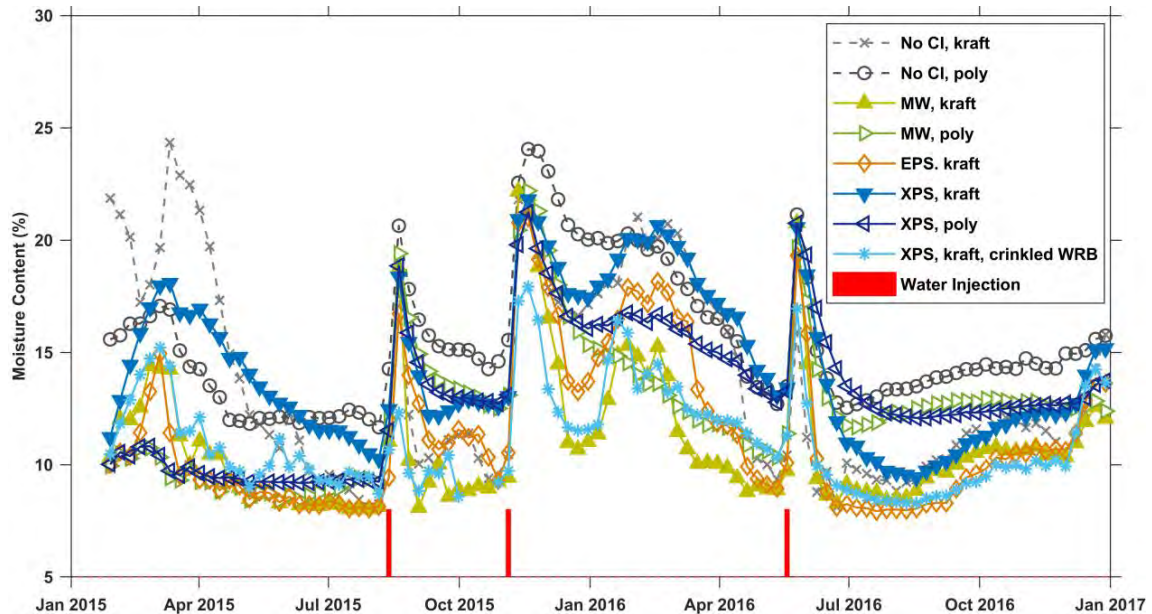


Figure 3. Weekly average moisture content of OSB at mid-height in north-facing walls (average of sensors in the field of the water injection system).

CONCLUSIONS

This cold-climate monitoring study provides further support to the conclusion that adding continuous exterior insulation lowers the wintertime moisture content in wood structural panel sheathing. The drying rate of a wall with low-permeance exterior insulation and interior polyethylene after modest wetting was similar to a corresponding base wall without exterior

insulation. Drying rates were faster for walls with an interior kraft vapor retarder than polyethylene. In cold weather walls with vapor-open exterior insulation dried faster than base walls and walls with low-permeance exterior insulation. Under cold weather conditions and high interior humidity levels, a kraft vapor retarder did not prevent moisture accumulation in the OSB sheathing in the base wall without exterior insulation, though it dried out quickly in warmer weather. This study did not quantify risk of moisture damage. Further work is ongoing to combine this field study with laboratory and modeling research to develop strategies to minimize moisture risks in energy efficient wood-frame walls.

ACKNOWLEDGEMENT

The authors gratefully acknowledge the help of many colleagues during the course of this investigation, especially Robert Munson of the Forest Products Laboratory. This work was funded by the U.S. Forest Service and APA – The Engineered Wood Association through Joint Venture Agreement 14-JV-1111136-054.

REFERENCES

- Boardman C.R., Glass S.V., and Lebow P.K. 2017. Simple and accurate temperature correction for moisture pin calibrations in oriented strand board. *Building and Environment*, 112, 250-260.
- Boardman C.R., Glass S.V., Yeh B., and Chow K. 2018. Field moisture performance of wood-frame walls with exterior insulation in a cold climate. Final Report for Joint Venture Agreement 14-JV-1111136-054, Forest Products Laboratory, Madison, WI (USA).
- Craven C.M., and Garber-Slaght R.L. 2014. Exterior insulation envelope retrofits in cold climates: implications for moisture control. *HVAC&R Research*, 20, 384-394.
- Fox M., Straube J., Ge H., and Trainor T. 2014. Field test of hygrothermal performance of highly insulated wall assemblies. In: *Proceedings of the 14th Canadian Conference on Building Science and Technology*, Toronto, pp. 101-110.
- ICC. 2015. International Energy Conservation Code. Country Club Hills, IL (USA): International Code Council.
- Maref W., Rousseau M.Z., Armstrong M.M., Lee W., Leroux M., and Nicholls M. 2011. Evaluating the effects of two energy retrofit strategies for housing on the wetting and drying potential of wall assemblies: summary report for year 2007-08 phase of the study. RR-315, National Research Council Canada, Ottawa.
- Straube J. 2011. Controlling cold-weather condensation using insulation. Building Science Digest 163, Building Science Press, Somerville, MA (USA).
- TenWolde A. and Rose W.B. 1996. Moisture control strategies for the building envelope. *Journal of Thermal Insulation and Building Envelopes*, 19, 206-214.
- Trainor T., and Smegal J. 2017. Analysis of exterior insulated high-R wall systems. Draft final report for Natural Resources Canada, Ottawa.
- Trainor T.M., Smegal J., Straube J., and Parekh A. 2016. Measured and predicted moisture performance of high-R wall assemblies in cold climates. In: *Proceedings of Thermal Performance of the Exterior Envelopes of Whole Buildings XIII International Conference*, Clearwater, FL (USA).
- Tsongas G.A. 1991. The effect of exterior insulating sheathing on wall moisture. In: Graves R.S. and Wysocki D.C., eds., *Insulation Materials: Testing and Applications*, Vol. 2, pp. 401-414. Philadelphia: American Society for Testing and Materials.
- Van Straaten R. 2003. Measurement of ventilation drying of vinyl siding and brick clad wall assemblies. Master's thesis, Department of Civil Engineering, University of Waterloo (Canada).

Psychrometer method to measure the moisture retention curves of porous building materials in the full humidity range

Chi Feng^{1,*}, Maria Fredriksson², Hans Janssen¹

¹KU Leuven, Department of Civil Engineering, Building Physics Section, 3001 Leuven, Belgium

²Division of Building Materials, Lund University, 22100 Lund, Sweden

*Corresponding email: fengchi860602@gmail.com

ABSTRACT

Moisture retention curves describe the moisture storage property of porous building materials. Currently available experimental methods for measuring moisture retention curves are often demanding in equipment and moreover not always suited for the adsorption process in most of the capillary moisture content range. This paper proposes a novel and simple technique – the psychrometer method – and validates it by the tests on calcium silicate and ceramic brick. In this experiment the moisture content of the samples experiencing adsorption and desorption processes is determined gravimetrically, while the corresponding capillary pressures in the samples are measured with a chilled-mirror dew-point psychrometer. Comparisons are made with results from mercury intrusion porosimetry, pressure plate/membrane and desiccator tests. It is shown that this psychrometer method is simple and reliable for both adsorption and desorption processes for capillary pressures below $-1 \cdot 10^5$ Pa. When the capillary pressure is around or above $-1 \cdot 10^5$ Pa, the psychrometer method is no longer very accurate, and other experimental techniques should be employed.

KEYWORDS

psychrometer, capillary pressure, moisture content, retention curve, porous building material

INTRODUCTION

Hygic properties of porous building materials are indispensable input parameters for analyzing the hygrothermal performance of building envelopes and the built environment (Defraeye et al. 2013; Zhao and Plagge, 2015). In general, hygic properties can be classified as moisture storage and transport properties, characterizing how much moisture can be stored in and how fast moisture can be transported through a material, respectively. Moisture storage properties are not constant; instead, they depend on the ambient humidity. Moisture storage properties are normally depicted either by moisture sorption isotherms, i.e. moisture content (w , kg/m³) as a function of relative humidity (RH, -), or by moisture retention curves, i.e. moisture content in function of capillary pressure (p_c , Pa). As RH and p_c are interchangeable through the Kelvin-Laplace equation, sorption isotherms and retention curves are equivalent. In this paper we use moisture retention curves to describe the moisture storage properties.

Because of hysteresis, moisture retention curves are usually not a single-valued function but process-dependent. As shown in Figure 1, for a complete characterization in the full humidity range, there are at least three important curves: the adsorption curve starting from the dry state, and two desorption curves, starting from the saturated moisture content (w_{sat} , kg/m³) and the capillary moisture content (w_{cap} , kg/m³) respectively.

In the hygroscopic range – where water vapor dominates – the static gravimetric method (e.g. the manual desiccator test (Feng et al. 2013) or the automatic sorption balance (Garbalińska et al. 2017)) is simple and reliable. In the over-hygroscopic range – where liquid water is more important – the currently available experimental techniques are unfortunately less satisfactory. Table 1 summarizes the characteristics of several of these methods. Clearly, none of them can measure the moisture retention curves completely. Even when combined, much information for the adsorption process in the capillary range is still not measurable.

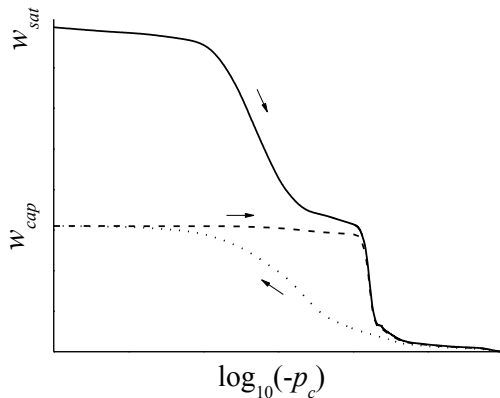


Figure 1. Moisture retention curves.

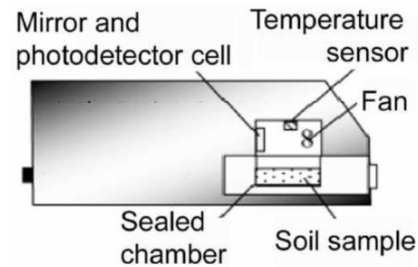


Figure 2. A schematic chilled-mirror dew-point psychrometer (Leong et al. 2003).

Table 1. Characteristics of several methods for measuring moisture retention curves

Method	Mercury intrusion porosimetry (Roels et al. 2001)	Traditional pressure plate/membrane (Hansen, 1998)	Modified pressure plate (Fredriksson and Johansson, 2016)
Equipment price	Very expensive	Expensive	Expensive
Availability	Common	Common	Rare
Toxicity	High (mercury)	Low	Low
Procedure	Simple	Complicated	Complicated
Data processing	Complicated	Simple	Simple
Applicable p_c range	$0 \sim -2 \cdot 10^8$ Pa	$0 \sim -1 \cdot 10^7$ Pa	$0 \sim -5 \cdot 10^5$ Pa
Applicable process	Desorption from w_{sat}	Desorption from w_{sat} and w_{cap}	Adsorption
Duration	Hours ~ days	Weeks ~ months	Weeks ~ months
Others	May not suit cement-based materials	Measurements easily fail	Measurements easily fail

To solve these problems, this paper proposes a novel experimental method – the psychrometer method. It features in simplicity, reliability and most importantly, the capability to do both adsorption and desorption measurements in the full humidity range. In the following sections, we will first introduce the principle of the psychrometer method. Then the validation measurements on calcium silicate and ceramic brick are explained. Finally, our experimental results are presented and compared with extra data from other methods.

METHODS

The key to obtaining moisture retention curves is to determine the corresponding w and p_c in the sample. Moisture content w can be easily obtained through the gravimetric method, while capillary pressure p_c can be obtained by holding the sample in a sealed chamber and measure the humidity of the air inside caused by the water evaporation from the sample. In the over-hygroscopic range the air humidity is close to saturation, thus the widely used RH sensors are no longer reliable and psychrometers instead become a much better choice. Cardoso et al

(2007) studied different types of psychrometers profoundly, and found that many factors – such as temperature, hysteresis, calibration and equilibrium time – all have an impact on the results. After comprehensive comparisons, the chilled-mirror dew-point psychrometer was recommended.

In this study, we adopted the chilled-mirror dew-point psychrometer for the humidity measurement. The instrument model is WP4C, produced by Decagon Devices, Inc (a schematic is illustrated in Figure 2). It is reported by the manufacturer that this psychrometer has an accuracy of $\pm 5 \cdot 10^4$ Pa in the range of $0 \sim -5 \cdot 10^6$ Pa and $\pm 1\%$ for $-5 \cdot 10^6 \sim -3 \cdot 10^8$ Pa. More details about the psychrometer can be found in (Leong et al. 2003).

During the test, calcium silicate (density: 271 kg/m^3) and ceramic brick (density: 1818 kg/m^3) were cut into samples with a diameter of 3 cm and a thickness of 0.5 cm. The dry mass of each sample was determined with a balance with a resolution of 1 mg after oven drying at 70°C for at least one week. For desorption measurements, the samples were first vacuum saturated and then exposed to 97% or 94% ambient RH (controlled by saturated salt solutions) at $23 \pm 0.5^\circ\text{C}$. At certain points in time, the desorption process was interrupted by sealing samples into the small sample cups. Trial tests showed that after several hours, the capillary pressure and moisture content distributions within the samples reached equilibrium, indicated by stable psychrometer readings. For this reason, we always carried out the measurements on samples having been isolated overnight. The capillary pressure was measured with the WP4C psychrometer and the wet mass was measured with the balance. Resultantly, the desorption curve starting from w_{sat} in the capillary range was determined. Reversibly, we measured adsorption curve in the capillary range by putting samples pre-conditioned by adsorption at 97% ambient RH above pure water in a closed container, with a similar process for the determination of capillary pressure and moisture content.

It should be mentioned that for calcium silicate the adsorption progressed very slowly when the humidity is extremely high, while for ceramic brick the adsorption directly from air can hardly result in an observable change in moisture content. For those cases, we applied some tiny water drops directly on the samples for acceleration of the conditioning. To check the applicability of the psychrometer method in the hygroscopic range, we also exposed samples to lower RHs for measurements, as in the desiccator test.

It should also be noted that according to the working principle of the chilled-mirror dew-point psychrometer, an underestimation of w is inevitable due to the evaporation. However, we estimate the total volume of the sealed chamber at 50 mL. A simple calculation reveals that under our experimental conditions 1.1 mg water vapor could yield 100% ambient RH in such volume. Our sample size is roughly $3.5 \cdot 10^{-6} \text{ m}^3$ in size, hence the underestimation of w is just around 0.3 kg/m^3 , which is completely negligible.

RESULTS

Figure 3 illustrates the experimental results obtained from the psychrometer method described in the previous section. For calcium silicate it is clearly reflected that both the adsorption and desorption curves have been obtained throughout the full humidity range. The results obtained by applying tiny water drops on the samples for accelerating the adsorption process also seem reasonable. It should be noted that even with the tiny water drops on the samples, the adsorption still progressed very slowly, as the whole adsorption process took more than 6 months. Consequently, for capillary pressures above $-1 \cdot 10^5$ Pa ($\log_{10}(-p_c) < 5$), we failed to obtain the adsorption curve.

For ceramic brick the general shape of the water retention curves can be observed. However, the data points display large scatters for the desorption process, and the hysteresis phenomenon also seems illogical (the desorption curve should stay above the adsorption curve). This should be explained by the fact that the ceramic brick used in this study has relatively large pores, with a median radius around $4 \cdot 10^{-6}$ m. Thus, a large drop/rise of the retention curves around $-3.2 \cdot 10^4$ Pa ($\log_{10}(-p_c) \approx 4.5$) is expected. The psychrometer used in this study has an accuracy of $\pm 5 \cdot 10^4$ Pa in that range. Consequently, the measured p_c here are not very reliable.

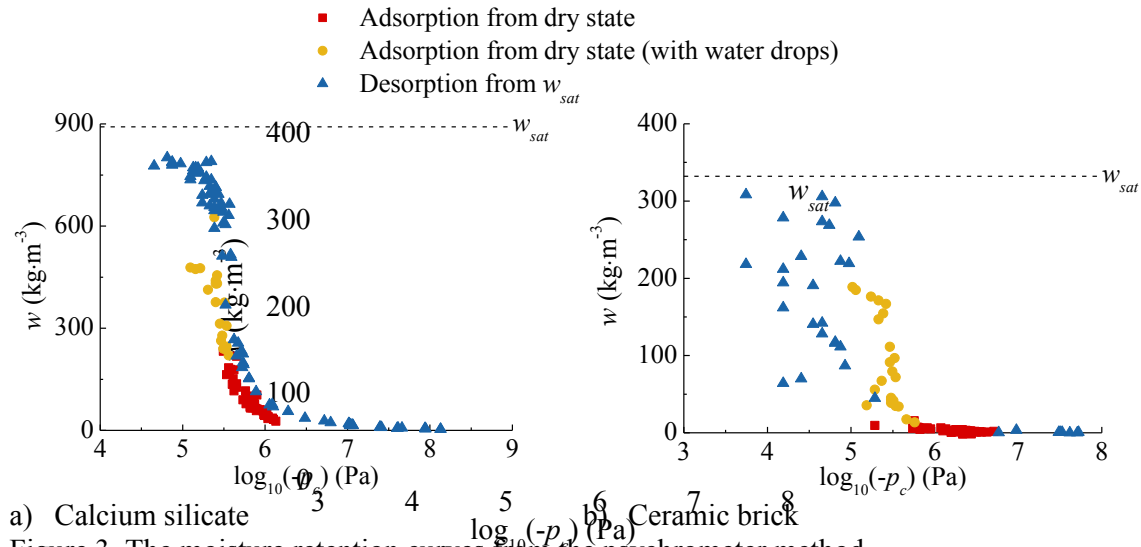


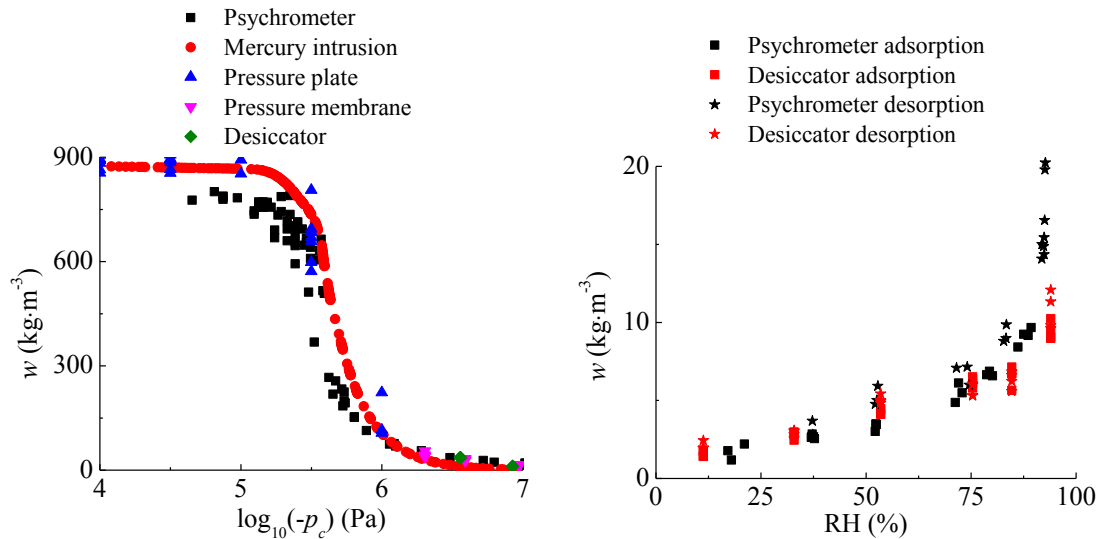
Figure 3. The moisture retention curves from the psychrometer method.

DISCUSSION

To validate the accuracy of the psychrometer measurements, we performed mercury intrusion porosimetry (Roels et al. 2001), pressure membrane (Hansen, 1998) and desiccator (Feng et al. 2013) experiments on the same batch of calcium silicate for comparison. Pressure plate results were also cited from the HAMSTAD project (Roels et al. 2003). As is clearly reflected in Figure 4.a, in the over-hygroscopic range the desorption results from the psychrometer method are generally close to the results from the other methods, albeit that the deviations around $-1 \cdot 10^5$ Pa ($\log_{10}(-p_c)=5$) appear to be more significant. Similarly shown in Figure 4.b, in the hygroscopic range for both adsorption and desorption processes the psychrometer method provides slightly different but reasonable results when compared to other methods.

For ceramic brick the situation is less promising. As illustrated in Figure 5, when compared to results from mercury intrusion and pressure plate tests, the psychrometer method results in a cloud of results – scattering irregularly in the range $\log_{10}(-p_c)=4-5$, reflecting the limitation of the psychrometer method, due to its limited accuracy in this p_c range. However, it should be noticed that the results from mercury intrusion and pressure plate tests are neither very close, and it is difficult to judge which method is more reliable here. Further experimental methods – such as the hanging water column method (Plagge et al. 2007) – are hence necessary to be developed and validated for the p_c range around and above $-1 \cdot 10^5$ Pa.

Last but not least, in this study we just performed the measurements starting from dry state and w_{sat} . The principle of the proposed psychrometer method is obviously also valid for the adsorption and desorption processes starting from other initial conditions.



a) In the over-hygroscopic range (desorption from w_{sat}). b) In the hygroscopic range (adsorption from dry state and desorption from w_{sat}).

Figure 4. Comparison of the experimental results from different methods on calcium silicate.

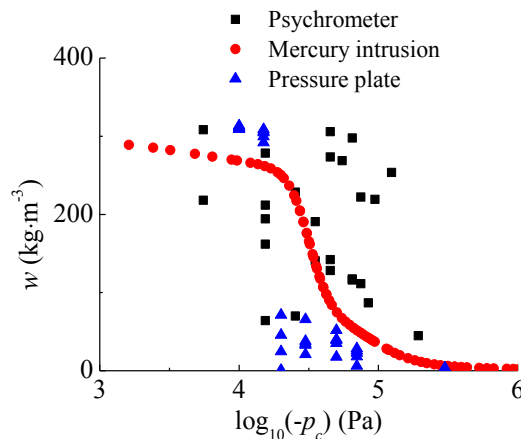


Figure 5. Comparison of the experimental results from different methods on ceramic brick (desorption from w_{sat} in the over-hygroscopic range).

CONCLUSIONS

This paper proposes a novel experimental approach – the psychrometer method – for determining the moisture retention curves of porous building materials. Measurements on calcium silicate and ceramic brick were conducted and the results were validated by comparing with experimental results obtained from the mercury intrusion porosimetry, pressure plate/membrane and desiccator tests. The psychrometer method demonstrates its simplicity, reliability and wide applicable range for capillary pressures below $-1 \cdot 10^5$ Pa, covering almost the full humidity range. When the capillary pressure is around or above $-1 \cdot 10^5$ Pa, other more reliable experimental techniques should be developed and validated.

ACKNOWLEDGEMENT

This project is supported by the FWO Odysseus grant "Moisture transfer in building materials: analysis at the pore-scale level" (No. G.0C55.13N).

REFERENCES

- Cardoso R., Romero E., Lima A., and Ferrari A. 2007. A comparative study of soil suction measurement using two different high-range psychrometers, *Experimental unsaturated soil mechanics*. Springer, 79-93.
- Defraeye T., Blocken B., and Carmeliet J. 2013. Influence of uncertainty in heat–moisture transport properties on convective drying of porous materials by numerical modelling. *Chemical Engineering Research and Design*, 91(1), 36-42.
- Feng C., Janssen H., Wu C., Feng Y., and Meng Q. 2013. Validating various measures to accelerate the static gravimetric sorption isotherm determination. *Building and Environment*, 69, 64-71.
- Fredriksson M. and Johansson P. 2016. A Method for Determination of Absorption Isotherms at High Relative Humidity Levels: Measurements on Lime-Silica Brick and Norway Spruce (*Picea abies*(L.) Karst.). *Drying Technology*, 34(1), 132-141.
- Garbalińska H., Bochenek M., Malorny W., and von Werder J. 2017. Comparative analysis of the dynamic vapor sorption (DVS) technique and the traditional method for sorption isotherms determination — Exemplified at autoclaved aerated concrete samples of four density classes. *Cement and Concrete Research*, 91, 97-105.
- Hansen M.H. 1998. Retention curves measured using pressure plate and pressure membrane apparatus: Description of method and interlaboratory comparison. *Nordtest Technical Report 367*.
- Leong E.C., Tripathy S., and Rahardjo H. 2003. Total suction measurement of unsaturated soils with a device using the chilled-mirror dew-point technique. *Géotechnique*, 53(2), 173-182.
- Plagge R., Scheffler G., and Nicolai A. 2007. Experimental methods to derive hygrothermal material functions for numerical simulation tools. *Building X Conference*. Clearwater, Florida.
- Roels S., Carmeliet J., Hens H., Adan O., Brocken H., Czerny R., Hall C., Hamilton A., Kumaran K., Pavlik Z., Pel L., Plagge R., and Tariku, F. 2003. *HAMSTAD Work Package 1: Final Report - Moisture Transfer Properties and Materials Characterisation*.
- Roels S., Elsen J., Carmeliet J., and Hens H. 2001. Characterisation of pore structure by combining mercury porosimetry and micrography. *Materials and structures*, 34(2), 76-82.
- Zhao J. and Plagge R. 2015. Characterization of hygrothermal properties of sandstones— Impact of anisotropy on their thermal and moisture behaviors. *Energy and Buildings*, 107, 479-494.

Semi-permeable membrane experiment for unsaturated liquid permeability of building materials: potential and practice

Chi Feng^{1,*}, Hans Janssen¹

¹KU Leuven, Department of Civil Engineering, Building Physics Section, 3001 Leuven, Belgium

*Corresponding email: fengchi860602@gmail.com

ABSTRACT

The unsaturated liquid permeability is a crucial hygric property of porous building materials. Its direct measurement is very challenging however, because currently available experimental protocols are either demanding in test facilities, complicated in data processing, or limited in moisture content range. Inspired by the osmosis phenomenon, we study the possibility to apply semi-permeable membranes for directly measuring the liquid permeability of porous building materials. The key principle is studied profoundly and a simple experimental set-up is constructed. Trial tests on calcium silicate insulation and autoclaved aerated concrete are performed. Results show that the experimental set-up can be used to measure the liquid permeability, but strongly underestimates its value in its current form. Based on an in-depth analysis, we believe that the underestimation should be attributed to the pore clogging to the semi-permeable membrane due to the extremely high concentration of salt in the solution. Hence, in a future iteration, we will turn to unsaturated solutions with lower salt concentrations to alleviate the problem.

KEYWORDS

liquid permeability, building material, semi-permeable membrane, hanging water column

INTRODUCTION

Hygric properties are key characteristics of porous building materials. They are indispensable for analyzing the hygrothermal performance of building envelopes and the built environment (Defraeye et al. 2013; Zhao and Plagge, 2015). Of all hygric properties, the liquid permeability (K_l , $\text{kg}\cdot\text{m}^{-1}\text{s}^{-1}\text{Pa}^{-1}$) is one of the most important.

Liquid permeability depends on moisture content. For (nearly) saturated samples, the liquid permeability can be easily measured by the water column test (Pedescoll et al. 2011) and the tension infiltrometer test (Zhao and Plagge, 2015). However, if the moisture content is lower, the direct measurement of the liquid permeability becomes rather difficult. One solution is to perform the Boltzmann transformation of the moisture content profiles visualized during a capillary absorption test for obtaining liquid diffusivity and subsequently liquid permeability. However, this protocol requires expensive experimental facilities – such as the X-ray set-up (Roels and Carmeliet, 2006) – and the data processing is complicated with large scatters. The drying test is another option for obtaining the liquid permeability below the capillary moisture content (Zhao and Plagge, 2015). However, this is basically an inverse method, requiring a lot of parameter tuning on the permeability model to approximate the measurement. It is therefore not straightforward and large uncertainties also exist.

From the review above, it's clear that current experimental protocols are either demanding in facilities, complicated in data processing, or limited in the moisture content range. Thus the

simple, reliable and full-range measurement of liquid permeability remains a challenging task. Inspired by the osmosis phenomenon, we investigate the possibility to employ the semi-permeable membrane for directly measuring the liquid permeability of porous building materials in a wide moisture content range. In this method, saturated salt solutions are used to exert a capillary pressure gradient across the sample, and semi-permeable membranes are used to protect against salts' interference. The permeability of the sample can hence be obtained from the measured liquid flux and the capillary pressure difference. Specifically, in the following section we will introduce the osmosis phenomenon. Next, our new experimental set-up with a semi-permeable membrane is described, and trial tests on calcium silicate insulation and autoclaved aerated concrete are explained. After that the experimental results are presented and analyzed. Finally, the future improvement of this method is discussed.

METHODS

In this section, we will first introduce the osmosis phenomenon. Then our new experimental set-up with a semi-permeable membrane is described, and trial tests on calcium silicate insulation and autoclaved aerated concrete are presented.

Osmosis phenomenon and the semi-permeable membrane

Osmosis is a common phenomenon in nature and has been widely adopted in many disciplines. As illustrated in Figure 1, when a solution and a pure solvent are separated by a proper semi-permeable membrane, the solvent particles can diffuse through the membrane in both directions while the solute particles are blocked. Due to the concentration difference of the solvent particles, a net flow of solvent from the pure solvent side towards the solution can be observed. This is the so-called osmosis phenomenon (Feher, 2017).

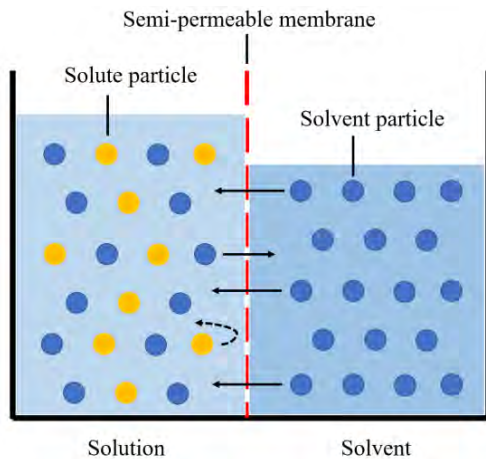


Figure 1. The osmosis phenomenon.



Figure 2. Photo of our semi-permeable membrane set-up

The osmosis phenomenon shows that a semi-permeable membrane exclusively allows the flow of solvent. It is therefore possible to use saturated salt solutions to exert a constant driving force for liquid water flowing through a sample, with semi-permeable membranes to protect the sample against salts' interference. The liquid permeability can thus be derived from the water flux and the capillary pressure difference. By altering the saturated salt solutions, the capillary pressure difference over and the moisture content in the sample can be controlled. This method is therefore in principle applicable to a wide moisture content range.

Experimental set-up

Based on the principle explained in the previous section, a simple experimental set-up is designed and constructed (Figure 2 and 3). In this set-up, a sample of known cross-sectional area (A , m^2) and thickness (T , m) is laterally sealed with epoxy to obtain a 1-D liquid flow. The top of the sample is in direct contact with pure water, for which the capillary pressure (p_c , Pa) is assumed 0 Pa. The sample bottom sits on a semi-permeable membrane in contact with a saturated K_2SO_4 solution with an RH of 97% at $22 \pm 1^\circ\text{C}$ corresponding to a p_c of $-3.6 \cdot 10^6$ Pa. The additional water head difference on both sides of the sample, originating from different water levels in the container and burette, is negligibly small relative to the used p_c difference ($\Delta p_c = 3.6 \cdot 10^6$ Pa). Consequently, the capillary pressure difference is assumed the only driving force for the water flow through the sample.

When the flow is ongoing, the pure water in the water tank passes through the sample and the semi-permeable membrane, entering the solution tank, where undissolved salt exists and a magnetic stirring system is installed to keep the solution saturated all the time. In this way a constant Δp_c can be maintained and a steady flow can be reached after an initial period. The volumetric flow rate (G , $\text{m}^3 \cdot \text{s}^{-1}$) can be easily measured by reading the burette regularly. Given that the burette is part of the container with the saturated solution, the volumetric flow rate thus relates to the inflowing pure water and the additionally dissolved salt.

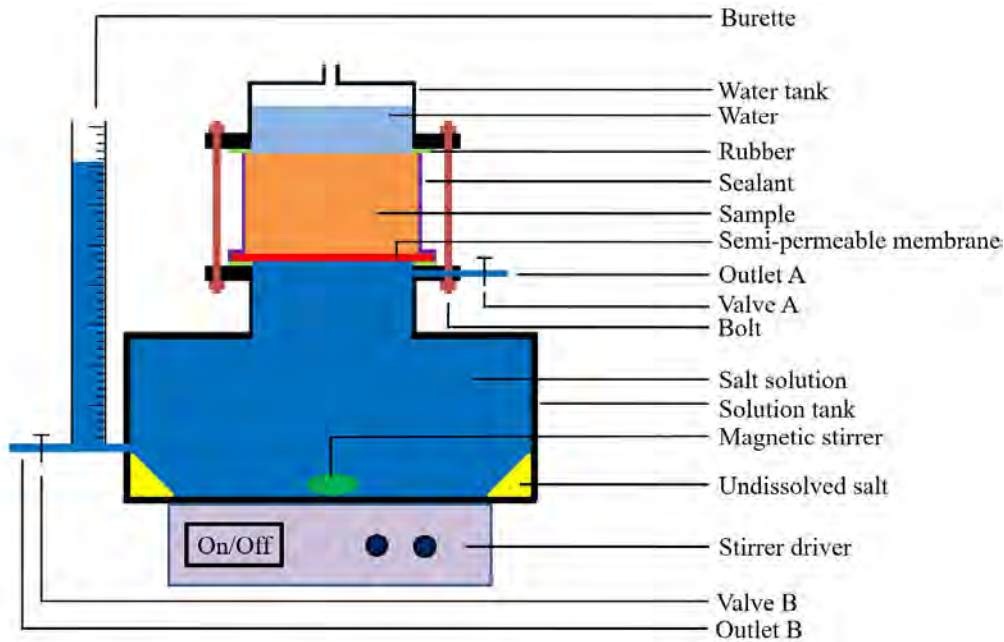


Figure 3. Schematic of our semi-permeable membrane set-up.

Assuming a certain amount of pure water (Δm_{water} , kg) passes through the sample and the membrane into the solution tank. The K_2SO_4 dissolved by it ($\Delta m_{\text{K}_2\text{SO}_4}$, kg) amounts to $s \cdot \Delta m_{\text{water}}$, where s is the solubility of K_2SO_4 , $\text{kg}(\text{K}_2\text{SO}_4) \cdot \text{kg}(\text{water})^{-1}$. Consequently, in the solution tank the increased saturated K_2SO_4 solution ($\Delta m_{\text{solution}}$, kg) occupies a volume of $\Delta V_{\text{solution}}$ (m^3):

$$\Delta V_{\text{solution}} = \frac{\Delta m_{\text{solution}}}{\rho_{\text{solution}}} = \frac{\Delta m_{\text{water}} + \Delta m_{\text{K}_2\text{SO}_4}}{\rho_{\text{solution}}} = \frac{\Delta m_{\text{water}} + s \cdot \Delta m_{\text{water}}}{\rho_{\text{solution}}} \quad (1)$$

where $\rho_{solution}$ is the density of saturated K_2SO_4 solution, $kg \cdot m^{-3}$. Since previously undissolved K_2SO_4 is now dissolved, its volume ($\Delta V_{K_2SO_4}$, m^3) should therefore be accounted for when calculating the net volume change (ΔV_{net} , m^3) in the solution tank:

$$\Delta V_{net} = \Delta V_{solution} - \Delta V_{K_2SO_4} = \frac{\Delta m_{water} + s \cdot \Delta m_{water}}{\rho_{solution}} - \frac{s \cdot \Delta m_{water}}{\rho_{K_2SO_4}} \quad (2)$$

where $\rho_{K_2SO_4}$ is the density of K_2SO_4 , $kg \cdot m^{-3}$. Now we define a coefficient c ($kg \cdot m^{-3}$) by:

$$c = \frac{\Delta m_{water}}{\Delta V_{net}} = \frac{1}{\frac{1+s}{\rho_{solution}} - \frac{s}{\rho_{K_2SO_4}}} \quad (3)$$

At 22°C we obtain $c=1009 \text{ kg} \cdot \text{m}^{-3}$, meaning that 1 m^3 increase in the net volume of the solution tank (indicated by the burette) reflects 1009 kg of inflowing pure water. With the help of the known c , we can describe the mass balance of the transport process by:

$$G \cdot c = \frac{\Delta p_c}{R_{total}} \cdot A \quad (4)$$

where R_{total} is the total liquid transport resistance, $m^2sPa \cdot kg^{-1}$. R_{total} is the sum of the membrane's resistance $R_{membrane}$ ($m^2sPa \cdot kg^{-1}$) and the sample's resistance R_{sample} ($m^2sPa \cdot kg^{-1}$):

$$R_{total} = R_{membrane} + R_{sample} = R_{membrane} + \frac{T}{K_l} \quad (5)$$

Combining Eq.(4) and (5), the liquid permeability of the sample can be finally derived:

$$K_l = \frac{T}{\frac{\Delta p_c \cdot A}{G \cdot c} - R_{membrane}} \quad (6)$$

After the test, the moisture content of the sample (w , $kg \cdot m^{-3}$) can be obtained gravimetrically, while $R_{membrane}$ can be obtained from similar measurements without the sample in the set-up.

To completely fulfill the measurements in a wide moisture content range, a double-membrane set-up with two semi-permeable membranes separating two different saturated salt solutions on both sides of the sample is needed. At this trial stage, we simplify the set-up to the single-membrane system described above. This set-up restricts the applicable moisture content range to near saturation, but is adequate for preliminary validation. Its success will call for a slightly more complicated double-membrane set-up.

Trial measurements

As two representative porous building materials, calcium silicate insulation and autoclaved aerated concrete are cut into duplicate cylindrical samples, with a diameter of 10 cm and a thickness of 2 to 4 cm. As a reference, falling-head water column tests are also performed for comparison. Due to the page limit of this paper, we will not explain the water column method specifically, and details can be found in (Pedescoll et al. 2011).

RESULTS

Figure 4 illustrates the experimental results obtained from the semi-permeable membrane approach described in the previous section. Results from water column tests are also included for reference. As is clearly shown, for both calcium silicate insulation and autoclaved aerated concrete, the measured K_l reflects an expected moisture content dependence – the higher the w is, the larger the K_l is. However, it is very noticeable that the measured K_l values from two methods differ about 4 orders of magnitude. This is far beyond what common experimental errors can explain, and more profound reasons must exist.

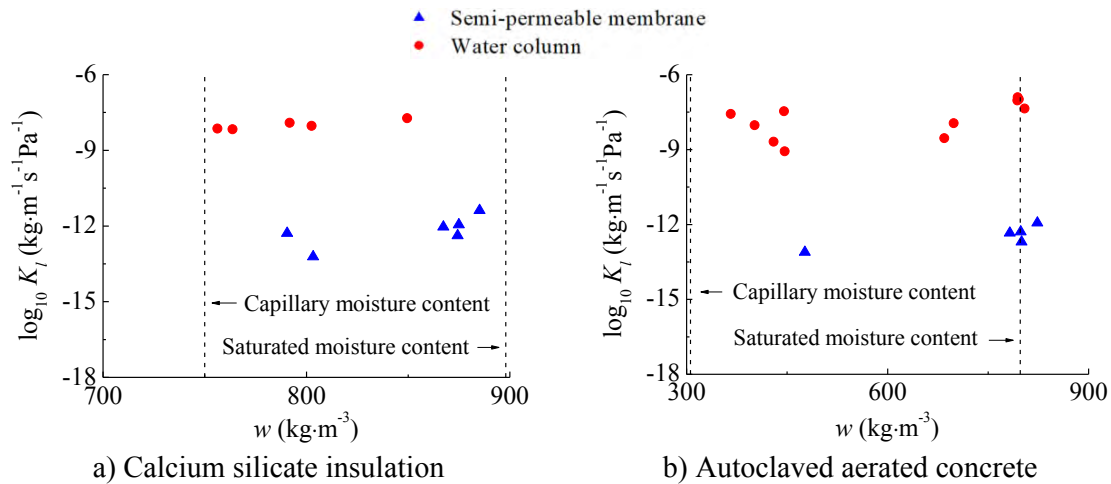


Figure 4. Experimental results of the semi-permeable membrane and water column tests.

DISCUSSIONS

The water column test is a well-established method. Our water column measurements on other materials agree nicely with other data sources. Thus we believe the water column results in Figure 4 are trustworthy and the semi-permeable membrane approach underestimates K_l .

The first explanation for the underestimation could be that the transport area of the sample should be corrected for the masked sample edge in the set-up. However, the total diameter of the sample is 10 cm while the unmasked diameter is roughly 9 cm. Simple estimation reveals that the underestimation of K_l caused by the masked edge should be less than $1-(9/10)^2 \approx 20\%$, while from Figure 4 we should focus on the difference amounting to 4 orders of magnitude. Consequently, the masked edge is not a primary reason for the underestimation.

The second possibility is the change of driving force. Ideally no salt can pass the semi-permeable membrane, while in practice a small amount of salt may still penetrate through the membrane and the sample into the tank for pure water, reducing the real driving force and causing the underestimation of the final K_l . However, reducing the Δp_c to $1/10^4$ of the assumed original value ($3.6 \cdot 10^6$ Pa) means that the pure water tank above the sample should almost get saturated. The membrane used in this study has a NaCl rejection capability as high as 99.5%, while the salt used in our test is K_2SO_4 , relatively more difficult to pass through the membrane. Consequently, it is unimaginable to assume an almost saturated solution in the upper tank due to the negligible salt transfer through the membrane. Direct measurements of the capillary pressure and electrical conductivity in both tanks also provide support.

Another explanation could be that the overall transport resistance is underestimated due to the existence of air layers on both sides of the membrane, which destroys the hydraulic continuity

of the system. An evidence is that the membrane resistance $R_{membrane}$, when measured separately by the semi-permeable membrane method and the water column method, comes to values of $1.4 \cdot 10^{10} \text{ m}^2\text{sPa}\cdot\text{kg}^{-1}$ and $1.1 \cdot 10^8 \text{ m}^2\text{sPa}\cdot\text{kg}^{-1}$ respectively. When there is only the membrane without the sample in the semi-permeable membrane set-up, the potential air layer between the membrane and the sample no longer exists, and this clearly reduces the difference between the measured $R_{membrane}$ values from both methods. To furthermore validate this hypothesis, we turned the presently vertical system into a horizontal one for complete elimination of the air layers. Unfortunately, the newly measured $R_{membrane}$ remained almost unchanged, indicating that the air layer should not be the most crucial reason.

The last and most plausible reason is that the pore clogging due to the extremely high salt concentration could happen to the semi-permeable membrane and hence increases the overall transport resistance. In our recent trials, we switched to unsaturated K_2SO_4 solution, obtaining $R_{membrane}$ around $2 \cdot 10^9 \text{ m}^2\text{sPa}\cdot\text{kg}^{-1}$, 10 times smaller than the saturated case. Encouraged by this supporting evidence, we plan to use unsaturated solutions of different salts and concentrations for further study and hopefully can succeed in the near future.

Albeit the semi-permeable membrane method is still under development, its principle is completely plausible. Theoretically, the liquid permeability below the capillary moisture content could be measured directly with two semi-permeable membranes on both sides of the sample, hence filling the gap of currently available experimental protocols.

CONCLUSIONS

This paper proposes a novel experimental approach – the semi-permeable membrane method – for determining the liquid permeability of porous building materials. A simple set-up has been constructed and trial tests on calcium silicate insulation and autoclaved aerated concrete are performed. Traditional water column tests are also conducted as a reference. Results show that our current semi-permeable membrane set-up strongly underestimates the liquid permeability, most plausibly due to the pore clogging to the semi-permeable membrane. In the future we are going to use unsaturated salt solutions to solve this problem.

ACKNOWLEDGEMENT

This project is supported by the FWO Odysseus grant "Moisture transfer in building materials: analysis at the pore-scale level" (No. G.0C55.13N). We express sincere gratitude to Prof. Bart Van der Bruggen in KU Leuven for sharing his expertise about semi-permeable membranes.

REFERENCES

- Defraeye T., Blocken B., and Carmeliet J. 2013. Influence of uncertainty in heat–moisture transport properties on convective drying of porous materials by numerical modelling. *Chemical Engineering Research and Design*, 91(1), 36-42.
- Feher J. 2017. *Quantitative Human Physiology (Second Edition)*. Boston: Academic Press.
- Pedescoll A., Samsó R., Romero E., Puigagut J. and García J. 2011. Reliability, repeatability and accuracy of the falling head method for hydraulic conductivity measurements under laboratory conditions. *Ecological Engineering*, 37(5), 754-757.
- Roels S. and Carmeliet J. 2006. Analysis of moisture flow in porous materials using microfocus X-ray radiography. *International Journal of Heat and Mass Transfer*, 49(25-26), 4762-4772.
- Zhao J. and Plagge R. 2015. Characterization of hygrothermal properties of sandstones— Impact of anisotropy on their thermal and moisture behaviors. *Energy and Buildings*, 107, 479-494.

Experimental analysis on a solar air heating façade system

Valeria Longo¹, Francesco Isaia^{1,*}, Stefano Fantucci¹, Lorenza Bianco¹ and Valentina Serra¹

¹TEBE Research Group, Department of Energy, Politecnico di Torino, Italy

*Corresponding email: francesco.isaia@polito.it

ABSTRACT

In this study, investigations on the thermal performance of a solar air heating façade system were carried out. The system consists of a double skin building envelope composed by an opaque internal face, with a novel solar absorbent layer and a glazed external face. This kind of system, particularly suitable to refurbish existing building envelopes, is designed to work as a fan-assisted air supply, which mitigates the heating and ventilation demand during the winter period.

An experimental campaign was set up using a full scale façade module in order to thoroughly characterize its thermal behavior and the air flow rate. This module was also compared with a similar one, having a conventional dark flat surface instead of the above mentioned solar absorbent layer. The system has proven great potential in both reducing the energy demand and maintaining proper the ventilation rates in the winter period. In fact, results show that the cavity air temperature reaches values close to 90°C (unventilated buffer mode) and that, in fan-assisted mode, the air temperature introduced in the indoor environment was up to 25°C higher than the external one. Moreover, the supplied air flow rate was of about 26 m³/h, providing about 0.5 air changes per hour (ACH) in a typical residential room (16 - 22 m² of floor area).

KEYWORDS Solar air heating; Opaque Double Skin Façade; Fan-assisted; Solar collector; Supply air façade

INTRODUCTION

Providing feasible solutions to take action against building energy consumption while promoting on-site energy generation through renewable resources is of paramount importance nowadays. Particular effort needs to be put into the energy refurbishment of the existing building stock, since it is largely composed by old, energy-demanding constructions, characterized by high total energy demands, not evenly distributed over time.

According to the Building Performance Institute Europe (BPIE), a deep renovation of the existing buildings could cut the 36% of their energy consumption by 2030 (Building Performance Institute Europe, 2018). Solar air heating façade systems can provide an effective solution: not only they guarantee an improvement in terms of thermal insulation, but they also mitigate buildings heating and ventilation demand by exploiting solar energy. The analysed façade system presents similar technological features of a classic Trombe Wall (Trombe and Michel, 1974), which consists of an external transparent layer and an internal opaque one, separated by an air gap. Usually, the classic Trombe Wall presents two vents installed at the bottom and at the top of the opaque layer. In this way, indoor air flows through the bottom air gap, it heats up due to the greenhouse effect and enters back into the internal environment through the top vent (Özbalta and Kartal, 2010).

Several studies have investigated different ventilation modes of the Trombe Wall. Considering a total of four vents, placed at the top and at the bottom of both the transparent (external) layer and the opaque (internal) layer, there are four main ventilation modes

(Tiantian, et al. 2014): not ventilated wall (Buffer mode); thermal insulation mode; natural ventilation mode (summer cross ventilation); space heating mode.

When the façade component is needed to function mainly as an insulation layer, the buffer or the thermal insulation mode are usually employed. The first mode is applied during the heating season, with all the vents closed, while the second one is used during the cooling season, with both the outer vents opened. It was demonstrated that by using these strategies the façade element was able to significantly reduce the thermal transmittance of the wall (in winter) and to improve solar heat removal (in summer) (Callegari, et al. 2015).

In the natural ventilation mode, the vents at the bottom of the opaque layer and at the top of the transparent part are opened. This ventilation mode results the most efficient during the cooling season (Krüger, et al. 2013; Gan, 1998).

The space heating mode is employed during the heating season in order to supply pre-heated air into the internal environment. In this ventilation mode the vent at the bottom of the transparent layer and at the top of the opaque layer are opened, and it was defined as the best mode during the heating season (Bajc, et al. 2015; Briga-Sá, et al. 2017).

This last ventilation mode is more efficient when the external layer of the opaque component is able to maximise the solar radiation-to-heat conversion, as a solar receiver (López-Herraiz, et al. 2017), and it was proved that the application of a high absorption coating on the exterior surface of the massive wall can improve the absorption and storage capacity of the Trombe Wall (Nwachukwu and Wilfred, 2008; Özbalta and Kartal, 2010). Usually, high absorption coefficient values correspond to dark colours. This might lead to have a limited choice of materials and coloured coatings to be used, slowing down the spread of this technology mainly for aesthetic reasons.

In the present study, the fan-assisted solar air heating façade operates in space heating mode. The analysed façade is provided of an outdoor vent, placed at the bottom of the external layer, which enables external air to flow through the entire height of the air cavity. This flow is generated by an axial fan placed at the top part of the opaque layer, connecting the air cavity with the indoor environment. In this way, a controlled rate of air can be introduced in the indoor environment. Moreover, while dark coloured surfaces are used in Trombe walls to enhance the greenhouse effect happening in the air cavity, a novel lightweight and light coloured layer was here used.

METHODS

During a previous experimental campaign carried out on a façade system called Naturwall[®] (Callegari, et al. 2015), two types of façade component were installed on the south side of the test apparatus, an outdoor test cell called TWINS (Testing Window INnovative System), in order to evaluate the behaviour of a solar air heating component.

Both components are characterized by a first external transparent layer (6 mm), an air gap and an inner opaque component. The opaque component consists of (from the inside to the outside) an OSB (Oriented Strand Board) layer (1.8 cm), a honeycomb cardboard insulation layer (8 cm) and another OSB panel (1.25 cm).

Module D (Figure 2) is 0.82 m high and 0.82 m wide and it is characterized by having the external OSB layer painted in black, a non-ventilated air gap and a clear glass as the external transparent layer. The original Module A (Figure 3), 3.07 m high and 0.82 m wide was modified by the Authors adding an additional 1.5 cm cellular polycarbonate layer with a particular geometry against the OSB panel face toward the air gap and installing an axial fan at the top of the opaque component in order to guarantee about 26 m³/h of air flow rate. Moreover, as external transparent layer a compact polycarbonate panel was chosen.

The main measured entities were the incident solar radiation, the temperatures (both air and surface ones) and the heat fluxes (between the cavity and the internal environment).

Measurements were performed through pyranometers, type T thermocouples and heat flux meter sensors (Figure 2, Figure 3) recorded every 15 minutes through a Datalogger. A first set of measurement was aimed at evaluating the effects of the cellular polycarbonate so to assess in the other analyses its influence on the global performance. A comparison between Module A and Module D was thus carried out, making the two modules operating in the same conditions: Module A fan was turned off and the vent was air-tight closed.



Figure 1 – Module A and module D installed on the outdoor test cell (TWINS)

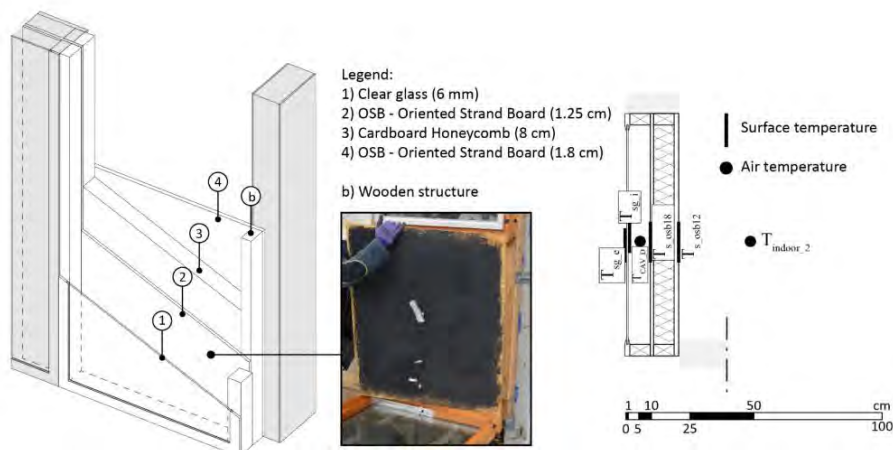


Figure 2- Scheme of the functional layers and the sensors used in Module D

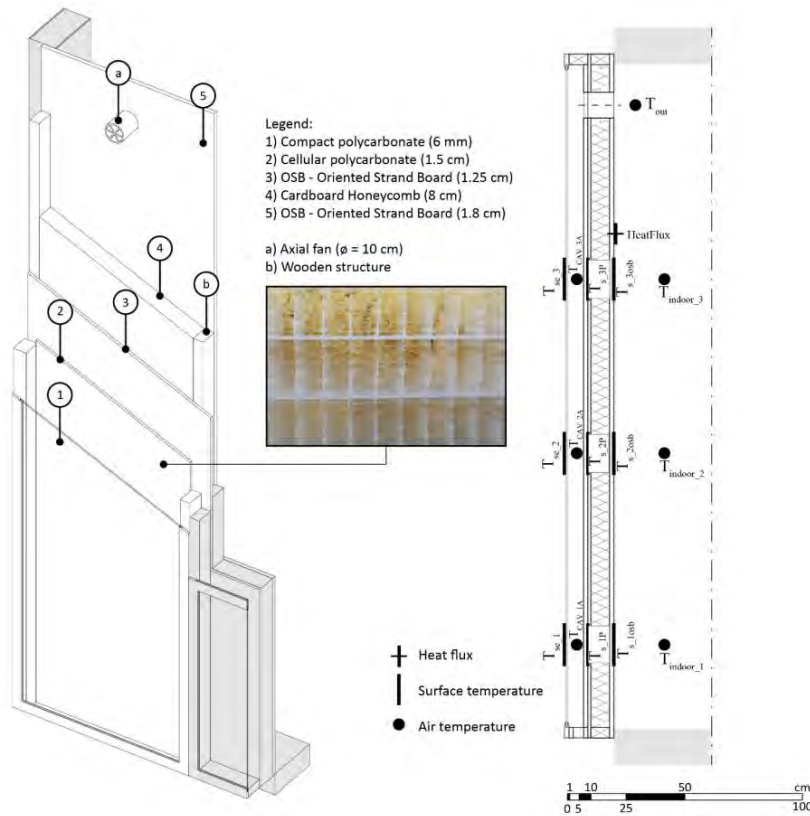


Figure 3 - Scheme of the functional layers and the sensors used in Module A.

In order to provide a quantitative indicator to assess the capability of the ventilated module to mitigate the heating and ventilation loads, solar efficiency (η_{sol}) was defined considering the heat supplied into internal environment (Q_{supply}) and the incident solar radiation measured on the vertical plane (Q_{sol}) according to Equation 1:

$$n_{sol} = \frac{\sum_n^m Q_{supply}}{\sum_n^m Q_{sol}} \cdot 100 = \frac{\sum_n^m \dot{V} \cdot C_p \cdot \rho \cdot (T_{out} - T_{ext})}{\sum_n^m I_{sol} \cdot A} \quad (1)$$

where n and m are respectively the beginning and the ending time of the examined day; \dot{V} is the air flow rate (m^3/s); C_p is the air specific heat (J/kgK); ρ is the air density (kg/m^3); T_{out} and T_{ext} are respectively the supply and the external air temperatures (K); I_{sol} is the incident solar radiation (W/m^2) and A is the surface area (m^2).

RESULTS AND DISCUSSIONS

Figure 4a shows a sunny winter day characterized by high solar radiation, which reaches values of $800 W/m^2$. It is possible to notice that, during the hours of maximum solar radiation, external air temperature ranges between $10^\circ C$ and $14^\circ C$, while the air temperatures in the two cavities are of $83^\circ C$ and of $89^\circ C$ respectively for Module A (T_{cav_2A}) and Module D (T_{cav_D}).

Figure 4b shows experimental data from Module A when ventilated by the above described axial fan. Solar radiation was stable throughout the day, with peak values of $800 W/m^2$ and external air temperature of about $20-23^\circ C$ between 12:00 and 18:00. At around 14:00 it is

possible to notice that the air cavity temperature at middle height ($T_{\text{cav_2A}}$) is of about 51°C , at the highest measurement point ($T_{\text{cav_3A}}$) is 53°C and enters the indoor environment (T_{out}) at 49°C ¹. In these conditions, the solar efficiency for the analysed day (April 8th) is of about 20%.

Results shown in Figure 4 show that the cellular polycarbonate layer, although being characterized by a much lower absorption coefficient (α), is able to heat up the cavity air roughly as much as the black-painted surface. This is due to its particular geometry, which provides more exposed surface to the solar radiation.

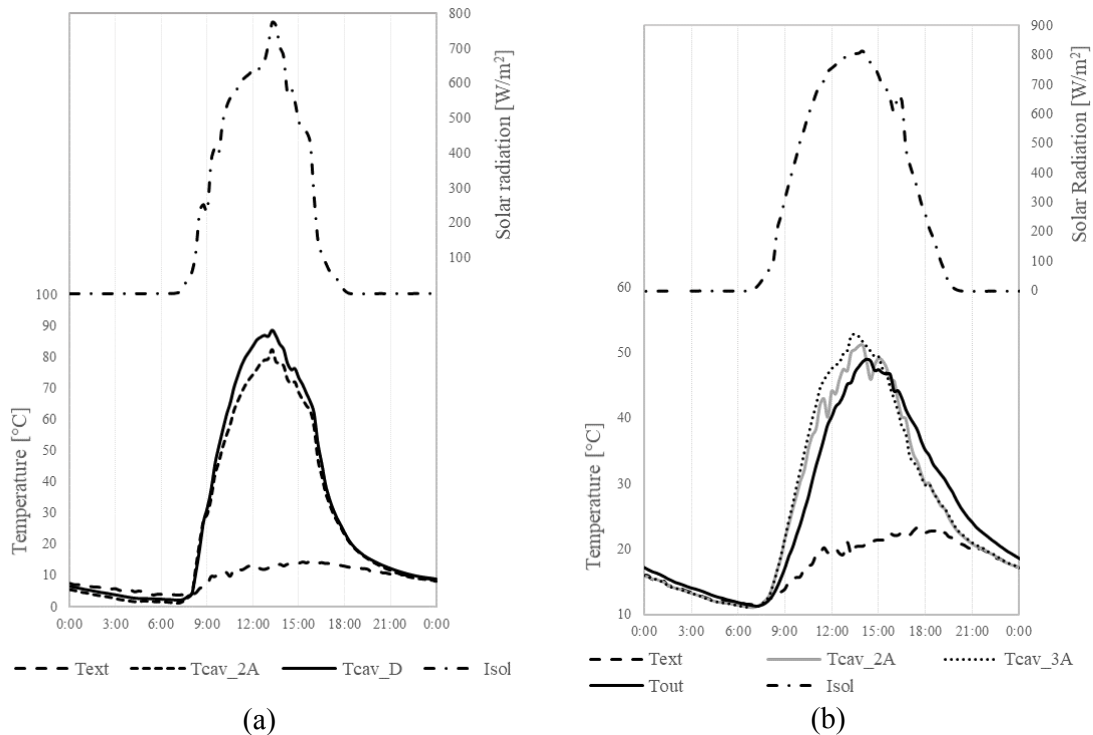


Figure 4 – (a) Experimental data measured of the cavities air temperatures. (b) Module A: experimental data measured of the cavity air temperatures at the different heights and of the outlet temperatures.

When working as a solar air heating façade module (ventilation turned on), it was observed that a significant increase in temperature between the intake and the supply air occurred. Figure 4b shows an increase of about 25°C between external air temperature and the outlet one, meaning that the system was providing $26 \text{ m}^3/\text{h}$ of air useful for both ventilation and heating purposes. Moreover, the solar efficiency (of about 20%) is in line with that of existing air heating collectors (VijayaVenkataRamana, et al. 2012).

CONCLUSIONS

In this study the behaviour of an adaptive façade system was investigated through an experimental campaign. As a first step, a comparison between a novel solar absorption layer (the cellular polycarbonate) and a traditional dark surface (typical of Trombe walls) was carried out, demonstrating how both have almost identical effects on the air cavity

¹ It is worthy to mention that the thermocouple used to measure the outlet temperature is placed on the internal side of the opaque component, therefore a little drop in temperature occurs between the air cavity and the outlet temperature.

temperature. Then, assessment in terms of performance and efficiency of the façade system were performed through additional experimental measurements of Module A working in space heating mode (ventilation turned on).

From the obtained results it is possible to state that more aesthetically pleasant solutions for solar air heating façades are possible. Indeed, the use of a lighter material colour with an adequate geometry has demonstrated to be comparable to a flat, black surface in terms of capability of heating the cavity. This outcome could enable similar solutions to arise, resulting in an easier integration of solar air heating façade systems in buildings.

When operating in space heating mode, the façade showed interesting capabilities in rising the air temperature, since a 25°C difference in temperature was observed between external and outlet air. Moreover, the system solar efficiency of about 20% is absolutely comparable with that of existing solar air heating technologies.

Given the great potential of the system to lower building energy need for heating and ventilation, further studies need to be carried out to assess the façade behaviour over a longer period (the entire heating season), also evaluating different technological solutions for both the transparent and the opaque components. Moreover, different control strategies can be explored to best modulate ventilation over time, with potentially great impact on the overall façade efficiency.

ACKNOWLEDGEMENT

This research was supported by be-eco s.r.l., who provided and installed the façade modules, and dott.gallina s.r.l., who supplied the polycarbonate components.

REFERENCES

- Bajc T, Todorovic M N, and Svorcan J. 2015. CFD analyses for passive house with Trombe wall and impact to energy demand. *Energy and Buildings*, Vol. 98, pp. 39-44.
- Briga-Sá A, Boaventura-Cunha J, Lanzinha J.C, and Paiva A. 2017. Experimental and analytical approach on the Trombe wall thermal performance parameters characterization. *Energy and Buildings*, Vol. 150, pp. 262-280.
- Building Performance Institute Europe. *BPIE*. 2018. <http://bpie.eu/> (accessed March 2018).
- Callegari G, Spinelli A, Bianco L, Serra V, and Fantucci S. 2015. NATURWALL© - A solar timber façade system for building refurbishment: optimization process through in field measurements. *Energy Procedia*, Vol. 78, pp. 291-296.
- Gan G. "A parametric study of Trombe walls for passive cooling of buildings. 1998. *Energy and Buildings*, Vol. 27, pp. 37-43.
- Krüger E, Suzuki E, and Matoski A. 2013. Evaluation of a Trombe wall system in a subtropical location. *Energy and Buildings*, Vol. 66, pp. 364-372.
- López-Herraiz M, Fernández A.B, Martinez N, and Gallas M. 2017. Effect of the optical properties of the coating of a concentrated solar power central receiver on its thermal efficiency. *Solar Energy Materials & Solar Cells*, Vol. 159, pp. 66-72.
- Nwachukwu N.P, and Wilfred I.O. 2008. Effect of an Absorptive Coating on Solar Energy Storage in a Trombe wall system. *Energy and Buildings*, Vol. 40, pp. 371-374.
- Zhang T, Yufei T, Hongxing Y, and Zhang X. 2014. The application of air layers in building envelopes: A review. *Applied Energy*, Vol. 165, pp. 651-659.
- Trombe F, and Michel J. Naturally Air-Conditioned Dwellings. United States Patent 3.832.992. 3 Settembre 1974.
- Özbalta T.G, and Kartal, S. 2010. Heat gain through Trombe wall using solar energy in a cold region of Turkey. *Scientific Research and Essays*, Vol. 5, pp. 2768-2778.
- VijayaVenkataRamana S, Iniyamb S, and Goicc R. 2012. A review of solar drying technologies. *Renewable and Sustainable Energy Reviews*, Vol. 16, pp. 2652- 2670.

Experimental Validation of a Model for Naturally Ventilated Double-Skin Facades

Alessandro Dama^{1,*}, Matteo Dopudi¹ and Olena Kalyanova Larsen²

¹Politecnico di Milano, Italy

²Aalborg University, Denmark

*Corresponding email: alessandro.dama@polimi.it

ABSTRACT

The steady state thermal model discussed in this paper is devoted to predict the temperatures and heat fluxes through a naturally ventilated DSF, having solar radiation and environmental temperatures as inputs. It is coupled with a fluid-dynamic model, based on a pressure loop, which takes into account both buoyancy and wind pressure at the openings.

The model has been validated against experimental data, basing on the prediction of the internal surface temperature of the DSF. Results show acceptable accuracy in the prediction of the heat flux towards the inside, even though they reveal a slight heat flux overestimation associated with dynamic effects. These observations lead to further investigate the role of DSF component capacities in order to increase the model accuracy and its applicability.

KEYWORDS

Building simulation, Airflow measurement, Natural ventilation, Temperature measurements.

INTRODUCTION

The Double Skin Facade (DSF) is a well-known technology, which might offer interesting adaptive features and improvements in terms of comfort and energy efficiency in buildings with large transparent facades. The evaluation of these benefits is still an open issue, due to reappearing difficulties in prediction of DSF thermal and energy performance as an integrated part of building envelope by means of well-established building simulation tools or recently developed models (Kalyanova et al. 2009; Manz & Frank, 2005).

Highly dynamic performance, initiated by fluctuating boundary conditions explain great complexity of experimental work for double-skin façade performance evaluation and thereby limited number of experimental studies to support validation of new and existing models for double-skin facades. Furthermore, existing experimental investigations (Kalyanova et al. 2007; Marques da Silva et al. 2015) underline multiple challenges related to investigation of DSF performance. Airflow measurement in a naturally ventilated cavity, measurement of the temperature under the strong solar exposure, as well as lack of standard, well-studied experimental methods for the measurement of the surface temperatures (with and without solar exposure) are found among the challenges. Experimental work carried in the of IEA ECBCS ANNEX 43/SHC Task 34 (IEA, 2007) had addressed some of these challenges in order to assemble a data set for empirical validation of building simulation software tools when double-skin façade performance evaluation is in question. This data set is applied for the validation of the model in this publication.

The thermal model discussed in this paper is an extension of a model already presented (Angeli et al. 2015, Dama et al. 2016 and 2017) in which the thermal and fluid dynamic ‘core’ of the ventilated cavity was validated having the channel surface temperatures as boundary conditions. In this work a suitable thermal network has been implemented to simulate the DSF having wind, solar radiation and environmental temperatures as inputs.

EXPERIMENTAL SETUP

The Cube is an outdoor full-scale test facility located near the main campus of Aalborg University, Denmark. A photo of Southern and Northern façade of the facility is shown in Figure 1.



Figure 1. The Cube. Photo of Southern façade (left) and photo of Northern façade (right).

The double-skin façade is facing South and consists of an internal double-glazed layer (4-Ar16-4) and a single-glazed exterior layer. Specifics of the material properties of all constructions in the Cube can be found in (Larsen et al. 2014). The experiments are performed in the external air curtain functioning mode, i.e. with naturally ventilated air cavity.

Particularly relevant to the task of this paper is to mention the procedures for the measurement of air and surface temperatures when the sensors are exposed to direct solar radiation, as well as the measurement of incident solar radiation. In (Kalyanova et al. 2007) it is explained that the presence of direct solar radiation is an essential element for the façade operation, but it can heavily affect measurements of air temperature and may lead to errors of high magnitude using bare thermocouples and even adopting shielding devices. Taking this into consideration, the thermocouples in DSF cavity were protected from the influence of direct solar radiation. The air temperature was measured using the silver coated and ventilated tube to reduce the impact of incident solar radiation. Meanwhile, surface temperature was measured by attachment of the thermocouples (type K) to a surface, using highly conductive paste and then fixed to the surface using the transparent tape. Surface temperature sensors were also protected from the impact of incident solar radiation, using two following strategies, depending on position of the sensor (Figure 2):

- Highly reflective film of apx. size 20x20 mm shields the thermocouple 1.
- Highly reflective shield made out of thin aluminum foil has the dimensions to ensure shielding both thermocouples 2 and 3.

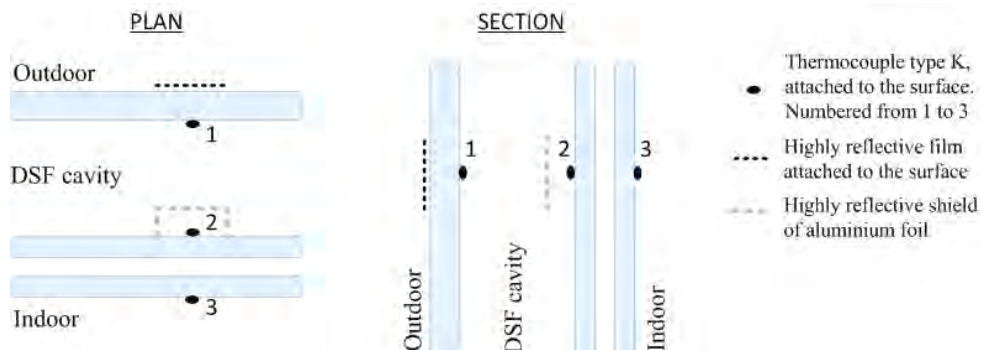


Figure 2. Shielding strategy from incident direct solar radiation. Left: Plan of DSF cavity. Right: Section of DSF cavity.

$$\varphi_i = \alpha_i(\theta)G_{beam}(\theta) + \alpha_i^{diff}G_{diff} \quad i = 1,2,3 \quad (3)$$

Table 1. Surface heat transfer

	External side	Channel	Internal side
Convective part	Sharples (1984)	McAdams (1954)	Churchill and Chu (1975)
Radiative part	T _{sky} based on Swinbank (1963)	Grey surfaces Linearized exchange	Grey surfaces Linearized exchange

RESULTS AND DISCUSSION

An experimental validation of the thermal and fluid dynamic model of the ventilated channel using as boundary condition the glass surface temperatures was already presented (Dama et al. 2017). This work focuses on the thermal network implementation, which employs as input the environmental temperatures and the solar irradiance and allows to calculate the convective and radiative (long wave) heat transfer through the DSF towards the interior. This flux strictly depends on the surface temperature of the internal glass of the inner skin (double glazed unit). Figure 3 shows the measured and modelled internal surface temperature (position 3 in the drawing of Figure 2) during the 15 days of the experimentation. Table 3 reports the daily integrated values of the surface heat fluxes from the DSF toward the inside of the Cube, separating the positive contributes to negative ones.

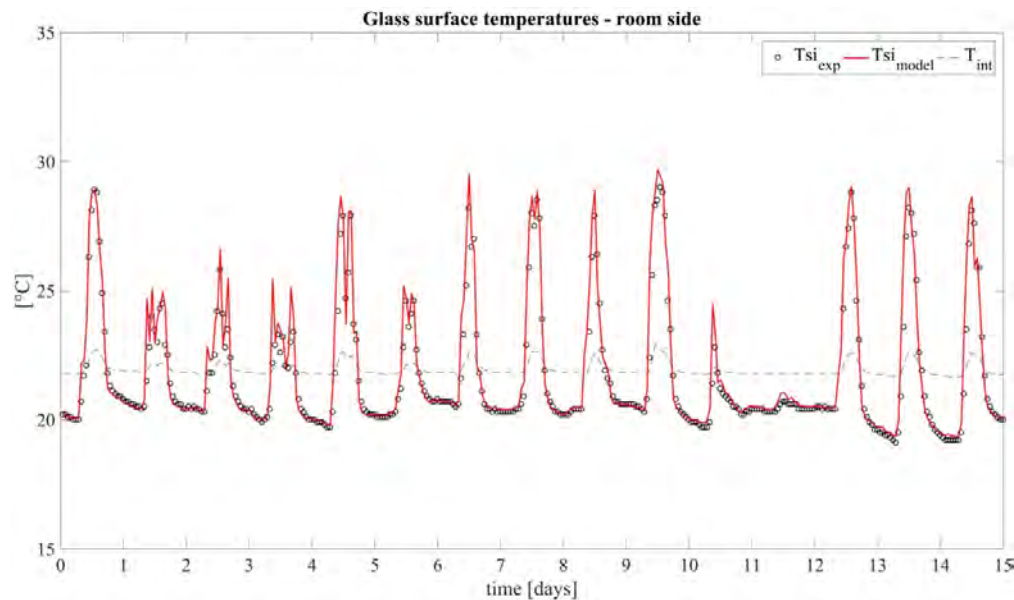


Figure 4. Internal surface temperature of the inner skin, model versus measurements (T_{si_model}/T_{si_exp}). T_{int} – internal air temperature.

The results show that the internal surface temperature is predicted with acceptable accuracy, even though a general overestimation is observed when solar irradiance heats up the DSF. For outward heat fluxes, the daily relative errors are below 6% during night time and around 12% in cloudy days. For inward fluxes the average overestimation is about 25%, and reduces to 15% in the last three days of the experimentation, with more stable solar and wind conditions. In order to have better picture of model predictions versus measurements, Figure 5 shows also inlet and outlet air temperatures and surface temperature of the glasses facing the channel. It can be noticed that, while the internal surface temperature is slightly overestimated, the outer surface temperatures, facing the ventilated channel, are underestimated.

It can also be observed that, while the modelled temperatures have the same dynamic profile, which instantaneously responds to the solar irradiance, the measured values show a bit more complex dynamics. The internal surface temperature increases slower than modelled and the surfaces temperature 1 and 2 (respectively of outer glass and external surface of the inner skin) decrease slower than modelled. Component capacities are often omitted when modelling DSF performances, in this case it might have led to an overestimation of the heat transmitted to the inside. Further investigation is therefore advisable first of all to identify the exact origin of heat gain overestimation and then to evaluate significance of the heat capacity of the glazing for better prediction of complex dynamic processes in the DSF and thereby increasing the accuracy and the applicability of the model.

Table 2. Heat exchange towards interior. Model versus experimental results. Daily integrated values calculated separately for hours with flux inwards (+) and hours with flux outwards (-)

Day	$Q_{\text{int}} (+)$ Model [Wh/m]	$Q_{\text{int}} (+)$ Exp. [Wh/m]	Rel error (+)	$Q_{\text{int}} (-)$ Model [Wh/m]	$Q_{\text{int}} (-)$ Exp. [Wh/m]	Rel. error (-)
1	1380	1238	11%	670	684	-2%
2	620	392	58%	723	684	6%
3	590	386	53%	708	703	1%
4	526	227	132%	850	827	3%
5	1415	1035	37%	891	900	-1%
6	481	367	31%	727	765	-5%
7	1016	790	29%	715	761	-6%
8	1309	1130	16%	784	819	-4%
9	808	697	16%	644	658	-2%
10	1857	1515	23%	753	717	5%
11	142	27	429%	1038	1176	-12%
12	0	0	-	1004	1144	-12%
13	1216	1073	13%	835	832	0%
14	1228	1040	18%	1157	1208	-4%
15	1133	988	15%	1079	1142	-6%

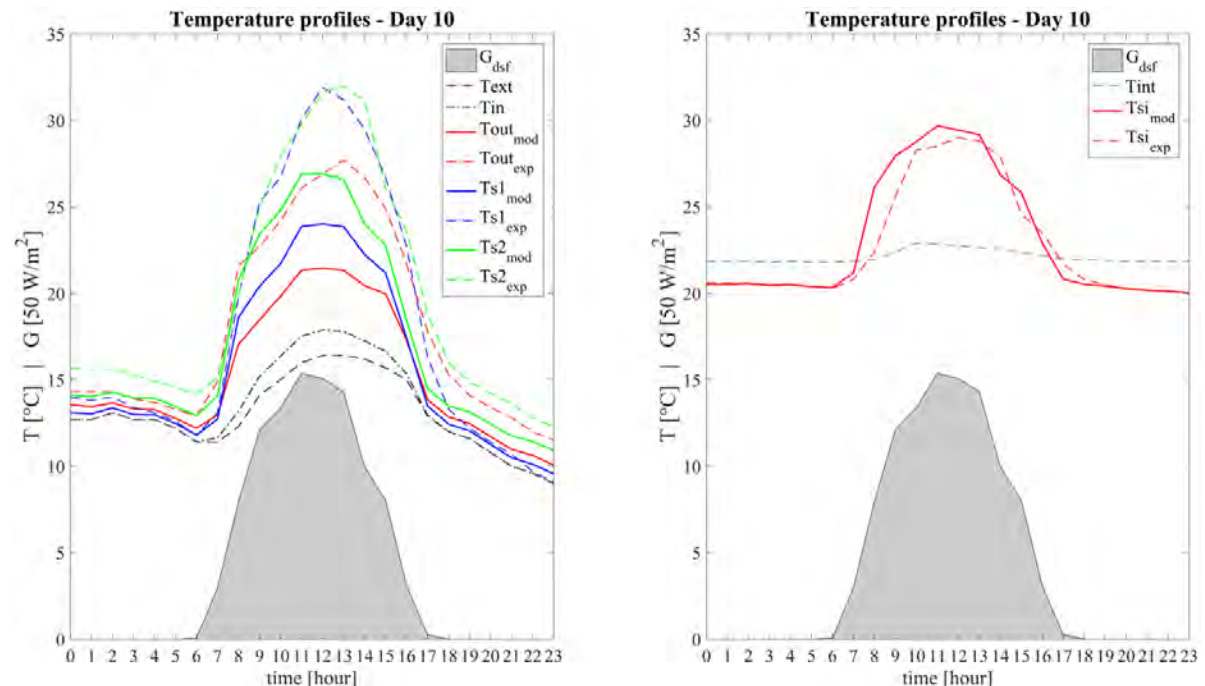


Figure 5. Glazing surface temperature and air temperature. Model versus measurements for a single day (October the 10th). On the left the air and the surface temperature of the glazing facing the ventilated cavity, on the right the internal surface temperature of the inner skin.

CONCLUSIONS

A thermal model for simulating naturally ventilated Double Skin Facades under variable boundary conditions – wind, solar radiation and environmental temperatures - has been implemented and results have been compared with measured data from a full scale test facility.

The validation, based on the prediction of internal surface temperature of the DSF, has showed acceptable accuracy even though an overestimation is observed when solar irradiance heats up the DSF. This leads to an overestimation of the heat transmitted inwards of about 15%, limiting to the three days with more stable wind and irradiance, and around 25% averaging over the 15 days of the experimental campaign.

The presence of dynamic effects, which might be associated to the DSF component capacities, has been observed and will be furtherly investigated in the future model implementation in order to increase its accuracy and applicability in the frame of building performance simulation.

REFERENCES

- Angeli D., Dama A., 2015. Modelling natural ventilation in double skin facade. *Energy Procedia*, Vol. 78, pp. 1537-1542.
- Churchill S.W., Chu H.H.S., 1975. Correlating equations for laminar and turbulent free convection from a vertical plate. *International Journal of Heat and Mass Transfer*, Vol. 18 No. 11, pp. 1323-1329.
- Dama A., Angeli D., Larsen O.K. 2017. Naturally ventilated double-skin facade in modelling and experiments. *Energy and Buildings*, Vol. 144, pp. 17-29.
- Dama A., Angeli D. 2016. Wind and buoyancy driven natural ventilation in double skin façades. *International Journal of Ventilation*, Vol.15(3-4), pp.288-301.
- IEA – SHC Task 34/ECBCS Annex 43: Testing and Validation of Building Energy Simulation Tools, 2007.
- Kalyanova, O. et al. 2009. An Empirical Validation of Building Simulation Software for Modelling of Double-Skin Facade (DSF). *Building Simulation : Proceedings of the 11th International Building Performance Simulation Association Conference*. Glasgow: University of Strathclyde.
- Kalyanova, O. et al., 2007. Measuring Air Temperature in Glazed Ventilated Facades in the Presence of Direct Solar Radiation. *The International Conference on Air Distribution in Rooms, Roomvent*.
- Larsen, O.K., Jensen, R.L. & Heiselberg, P.K., 2014. Experimental Data and Boundary Conditions for a Double-Skin Facade Building in External Air Curtain Mode, Aalborg, Aalborg University.
- LBNL, LBNL Window & Daylighting Software, <https://windows.lbl.gov/software/window>. Lawrence Berkeley National Laboratory, Berkeley, California, USA.
- Manz, H. & Frank, T., 2005. Thermal simulation of buildings with double-skin façades. *Energy and Buildings*, Vol.37, pp.1114–1121.
- Marques da Silva, F., Gomes, M.G. & Rodrigues, A.M., 2015. Measuring and estimating airflow in naturally ventilated double skin facades. *Building and Environment*, 87, pp.292–301.
- McAdams W.H. 1954. *Heat Transmission*. McGraw-Hill, New York, NY.
- Sharples S. 1984. Full-scale Measurements of Convective Energy Losses from Exterior Building Surfaces. *Building and Environment*, Vol. 19, No. I, pp. 31-39.
- Swinbank W.C., 1963. Long-wave radiation from clear skies. *Quart. J. R. Meteorol. Soc.*, Vol. 89, pp. 339-348.

Hygrothermal assessment of north facing, cold attic spaces under the eaves with varying single sided passive ventilation strategies and infiltration scenarios, in a cool, temperate climate

Nickolaj Feldt Jensen^{1,*}, Søren Peter Bjarløv¹, Christopher Just Johnston^{1,2}, Casper F. H. Pold³, Morten Hjorslev Hansen⁴, and Ruut Hannele Peuhkuri⁵

¹ Department of Civil Engineering, Technical University of Denmark, Brovej 118, 2800 Kgs. Lyngby, Denmark

² NIRAS Gruppen A/S, Building and Design, Sortemosevej 19, 3450 Allerød, Denmark

³ Goritas A/S, Lautrupvang 8, 2750 Ballerup, Denmark

⁴ Fonden BYG-ERFA, Ny Kongensgade 13, 1472 Copenhagen K, Denmark

⁵ Danish Building Research Institute, Aalborg University, Copenhagen, Denmark

**Corresponding email: nicf@byg.dtu.dk*

ABSTRACT

Relative humidity and temperature were measured in cold attic spaces under the eaves with diffusion-open roofing underlay to investigate different ventilation strategies, the influence of infiltration, and exterior insulated roofing underlay. The project was carried out as a full-scale experimental setup in the cool, temperate climate in Lyngby, Denmark. The objective was to test if the best practice recommendations concerning design of the cold attic space will prevent damaging moisture levels in the attics. Measurements do however indicate that complying with recommendations will not ensure satisfactory moisture levels in the attic spaces. A comparison of the passive ventilation strategies in combination with varying infiltration rates, for attic spaces fitted with diffusion-open roofing underlay, indicate that attic ventilation increases moisture levels. The exterior insulation of the attic space improved the hygrothermal performance.

KEYWORDS

Cold attics, ventilation, diffusion-open roofing underlay, insulated roofing underlay, moisture

INTRODUCTION

Recommendations regarding design of cold attics in cold, temperate climates are to ventilate moisture away using outdoor air, and to ensure air- and vapour tightness towards the conditioned spaces. Previous studies by the Technical University of Denmark (DTU) (Bjarløv et al., 2016) and other studies (Fugler, 1999; Harderup & Arfvidsson, 2013; Roppel & Lawton, 2014) do however indicate that moisture induced damages can be found in attics even when constructed in compliance with local best practice recommendations. Some studies (Essah et al., 2009; Harderup & Arfvidsson, 2013; Ojanen, 2001; Uvsløkk, 2005) have investigated the use of diffusion-open roofing underlay as an alternative to passive ventilation, indicating a lowering of the diffusion resistance may reduce moisture levels in the attic space. Single-sided passive ventilation with one or two ventilation valves have previously been investigated by DTU (Bjarløv et al., 2016; Pold, 2015) for attics with diffusion-open roofing underlay in a cool, temperate climate. Here reported results indicated that single-sided passive ventilation had a detrimental effect and led to an increase in humidity of air by volume. The authors hypothesized that the observed detrimental effect was a result of a lower air tightness allowing for more air to infiltrate from the conditioned interior. Simulations by Essah et al. (2009) for attics with diffusion-open roofing underlay suggests an increase in moisture levels

due to eave-to-eave ventilation. Meanwhile experimental studies by Hagentoft & Sasic Kalagasidis (2010) have investigated attics fitted with adaptive ventilation, indicating superior performance compared to eave-to-eave ventilation. Simulations by Nik et al. (2012) support these indications for adaptive ventilation, as well as suggest superior performance compared to attics with eave- and gable ventilation, and insulated roofing underlay. Furthermore, experimental studies including (Harderup & Arfvidsson, 2013) have investigated the influence of long-wave radiation, and observed lower temperatures in the attic construction than in the outdoor air, increasing the risk of condensation on the roofing underlay.

The objective of the research project was to test the best practice recommendations concerning design of the cold attic space. Especially whether compliance with the Danish building regulations (TBST, 2018) regarding the airtightness of the building envelope (less than 1 l/s per m² heated floor area at 50 Pa pressure difference) will prevent damaging moisture levels. According to official Danish guidelines, appropriate ventilation of the attic is recommended and this may be achieved with attic using “pressure equalization” (based on stack effect ventilation) (Brand et al., 2009). However, (Brand et al., 2013) state “It cannot be expected that a diffusion-open roofing underlay (Z-value < 3 GPa m² s/kg) will to a sufficient extent remove moisture from the attic rooms and attic rooms under the eaves (when the floor width > 1 m). Unless the vapour retarder toward the indoor climate is perfectly installed, these attics will need some degree of ventilation.” Therefore, the guidelines suggests to ventilate the attic using two ventilation valves. Measurements of relative humidity and temperature will be presented for different attic designs, as well as temperatures in the roofing underlay. Results are expected to contribute to enhancing the current best practice recommendations for design of cold attic space under the eaves, to reduce the risk of moisture induced damages.

METHODS AND MATERIALS

The experimental setup consisted of a 45° single sided pitched roof, constructed on top of a 40-foot reefer container, conditioned to 20 °C and 60% relative humidity (corresponding to an indoor climate class 3 (Brand et al., 2013)). The roof was subdivided into nine attics with the interior dimensions (LxWxH) 1.25 m x 1 m x 1 m, each with different design variations, of which seven are presented in this paper. Special care was taken to reduce potential sources of error like unintentional transport of heat, air, moisture and mould spores. Thus, hygric- and thermal decoupling were established between the attic spaces and to the conditioned spaces, using vapour retarders and thick layers of mineral wool. The attic spaces were fitted with a diffusion-open roofing underlay, with a vapour diffusion resistance, Z, of 0.1 GPa·s·m²/kg.

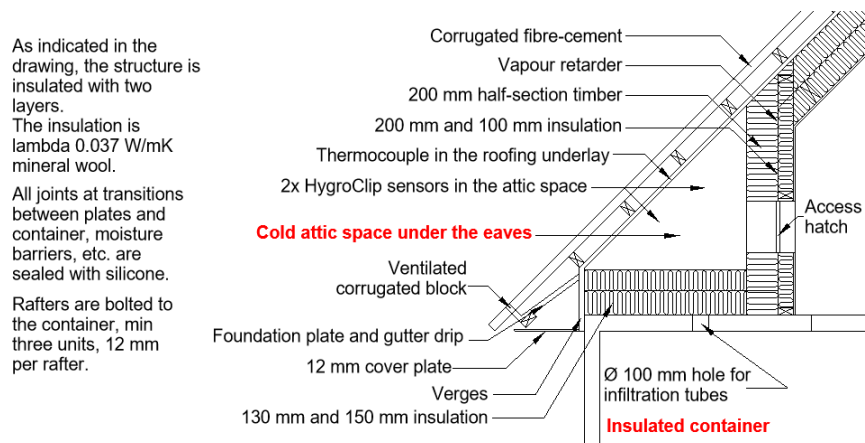


Figure 1 Vertical section of the cold attic space under the eaves

The attics were constructed as north facing, cold attic spaces under the eaves, as this represents the worst-case scenario, since the roof surface receive only a limited amount of solar radiation. A conditioned loft corridor was constructed on the southern side. The experiment was conducted at the test site of the Department of Civil Engineering at DTU in Lyngby, Denmark (55.79°N, 12.53°E). The experiment consisted of three series of variations, representing different structural roof scenarios. The series were infiltration rate, single-sided passive ventilation strategies, and exterior insulation. Two different infiltration scenarios were investigated: 1) 3.4 l/s at 50 Pa pressure difference; 2) No infiltration from the conditioned spaces. It is easier to construct tight walls, ceilings and floors than it is to construct tight joints. Leaks are therefore often found where the ceiling meets the walls. This means that attic spaces under the eaves are in risk of being subjected to (local) infiltration rates well above 1 l/s per square meter attic space at 50 Pa pressure difference over the building envelope that is allowed by BR18. The 3.4 l/s at 50 Pa pressure difference used in this experiment is used to approximate the effects of infiltration in an assumed worst-case scenario. Infiltration was established by fitting several attics with PVC tubes connecting the attics and the conditioned spaces. Three different ventilation strategies: 1) Un-ventilated (UV), in which attic spaces were not fitted with ventilation valves; 2) Pressure equalization (PE), in which attic spaces were fitted with a valve in the top corner. 3) Single-sided ventilation (SSV), in which attic spaces were fitted with two valves, diagonally in the top and bottom corners. The third series compared an unventilated attic space with infiltration, to an identical attic, fitted with a 50mm polystyrene insulation on the exterior side of the ventilated cavity. This series investigated the influence of long-wave radiation. An overview of the attic variations is presented in **Table 1**.

Table 1 Overview of attic variations

Attic space	B1	B2	B3	B4	B5	B6	B7
Infiltration rate at 50 Pa	-	-	-	3.4 l/s	3.4 l/s	3.4 l/s	3.4 l/s
Ventilation strategy	UV	PE	SSV	UV	PE	SSV	UV
Exterior insulation	-	-	-	-	-	-	+

Temperature and relative humidity sensors were installed in the attic spaces (two in each), outside, and inside the conditioned container, while temperature sensors were installed in the roofing underlay (see Figure 1). The presented results are based on measurements logged every 10 minutes from November 2014 to May 2017. Note that measurements from the two sensors in the attic spaces were averaged. The accuracy of the sensors is shown in **Table 2**.

Table 2 Accuracy of sensors

Instrument	Measurement	Accuracy	Range
Rotronic HygroClip	Temp.	± 0.1 K at 23 °C and 10, 35 and 80% RH	-50 to 100°C
2 S	RH	± 0.8 % at 23 °C and 10, 35 and 80% RH	1 to 100 %
Thermocouple type T	Temp.	± 0.5 K at 0 °C	-200 to 350 °C

RESULTS

In the following, the measured temperature and relative humidity in the attic spaces are presented as 15-days moving average of the derived daily average values, using 7 days before and after the current date (Figures 2-3). Figure 2 shows the relative humidity for attics without infiltration (B1-3) and with infiltration (B4-6), where higher relative humidity is seen for the cases with ventilation and/or infiltration. The highest relative humidity is seen for the PE attic (B5). Figure 3 shows the temperatures in the attic spaces. Since the measured temperatures were almost identical for attics B1-4, the measurements are shown in combination, against the PE attic (B5) and the SSV attic (B6). Slightly higher temperatures were seen for B5 and B6 during the cold periods (highest for B5,) and slightly lower during the warm periods.

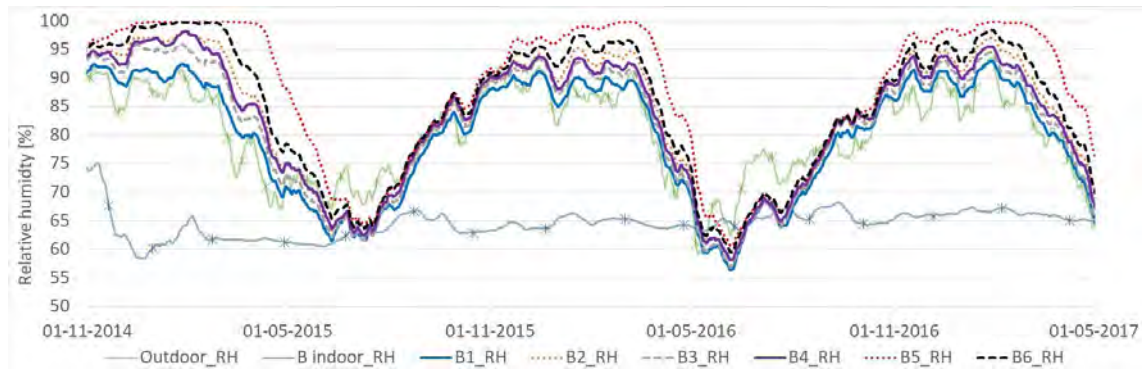


Figure 2 Relative humidity in the attics spaces, indoor, and outdoor.

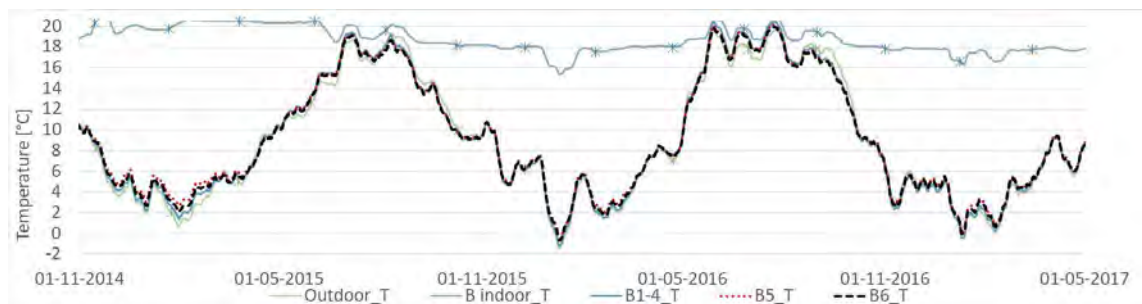


Figure 3 Temperatures in selected attic spaces, indoor, and outdoor.

Figure 4 shows the difference in temperatures measured in the roofing underlay and outdoor air, when the temperature in the roofing underlay is lower than the outdoor air. Temperatures are presented as hourly averages of the logged data. The difference in temperatures is the effect of the exterior insulation mounted on attic room B7 preventing heat loss by long-wave radiation. Heat losses from radiation will be greatest during cold nights with clear skies. Focus in the presented data is therefore on cold periods. November 1st, 2016 to May 1st, 2017 was chosen, as the lowest temperatures were observed during this winter period. Tendencies were similar for the other winter periods. In Figure 4 the roofing underlays are seen to experience temperatures several degrees below that of the outdoor air. The uninsulated underlay (B4) is seen to frequently experience the largest temperature difference to the outdoor air (when $B4 > B7$). Furthermore, the humidity of air by volume was calculated for the attics, and the insulated attic was seen to experience an increase of up to 0.35 g/m^3 during the winter periods.

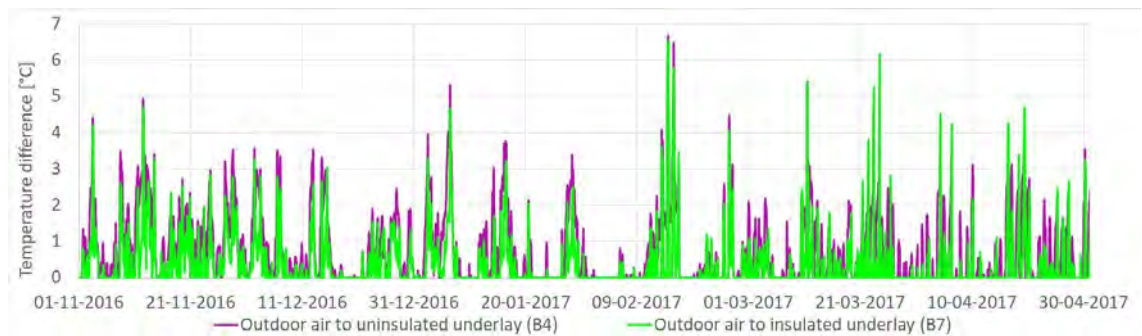


Figure 4 Temperature in the roofing underlay relative to the outdoor air.

DISCUSSIONS

Considering the humidities of B1 and B4 in comparison to B2-3 and B5-6 in Figure 2, measurements seem to indicate that ventilation of diffusion-open attic spaces under the eaves

in a cool temperate climate using PE or SSV will increase the relative humidity. While a comparison of B1 to B4, B2 to B5, and B3 to B6, indicate that the relative humidity also will increase in case of infiltration from the conditioned spaces. Lastly, a comparison of B1 to B4 and then to B5-6 show the compounding effect of infiltration and the tested ventilation strategies for the attic spaces with diffusion-open roofing underlay, where the relative humidity was observed to increase even further. The PE attic experienced the largest increase in temperature and relative humidity (B4 to B5). A smaller increase in relative humidity was observed for the SSV attic (B4 to B6). We believe that the observed increase in moisture levels is due to untight ceiling and roof constructions allowing a stack effect to cause an updraft of infiltration air. These indications correlate with findings of previous experimental studies by DTU (Bjarløv et al., 2016; Pold, 2015). However, in contrast to Bjarløv et al. (2016) but in agreement with Pold (2015), the ventilation strategy PE (B2 and B5) was shown to result in the largest increase in the moisture levels, compared to SSV (B3 and B6). Simulations by Pold suggested that PE will exacerbate infiltration from the indoor spaces due to negative pressure under the roof cladding, resulting in increased moisture levels. Pold's simulations also suggested that SSV increase moisture levels in attic spaces just to a smaller extent. Findings concerning lowered moisture levels due to reduced attic ventilation for attics with diffusion-open roofing underlay in cool temperature climate, correlate with the experimental studies by Harderup & Arfvidsson (2013) and Ojanen (2001), as well as the simulation results by Essah et al. (2009). Furthermore, as it was the case for these attic spaces, Harderup & Arfvidsson also observed relative humidity favorable for mould growth during the cold periods. In this study, relative humidity favorable for mould growth, was observed between mid-August to mid-April, when considering 75% relative humidity as critical limit as suggested in the best practice recommendations (Brand et al., 2013).

Considering the temperature difference between the outdoor air and the roofing underlays in Figure 4, measurements indicate that externally insulating the roofing underlay reduces the heat loss due to long-wave radiation for these attics. The roofing underlay temperatures in the externally insulated attic (B7) were seen to increase by up to 2.5 °C compared to the uninsulated attic (B4), and 0.5 °C on average. This difference between the two roofing underlays occurred around midnight on May 18th, 2017. The roofing underlays were observed to experience temperatures below that of the outdoor air (Figure 4); and despite the focus on clear, cold nights, the largest temperature difference between the roofing underlays and the outdoor air occurred around 14:00 on February 14th, 2017: a difference of 6.7 °C for the uninsulated attic and a difference of 6.6 °C for the insulated attic. Roofing underlay temperatures below that of the outdoor air and attic space air is a potential risk, as movement of warmer, moister air to the roofing underlay could lead to condensation on the interior surface. In the summer periods the attic spaces were almost identical. These findings correlate with Harderup & Arfvidsson (2013), who during the cold periods observed the highest temperatures in the externally insulating attics, compared to the uninsulated; also, a small increase in the moisture levels was observed. Finally, our measurements thus seem to indicate that the exterior insulation has both positive and negative effects on the moisture balance in this attic space with the temperature increase in the roofing underlay being good while the increase in the humidity of air by volume in the attic space is not.

CONCLUSIONS

Measurements from different cold attic spaces under the eaves fitted with diffusion-open roofing underlay, indicate that following the current best practice recommendations regarding passive ventilation does not guarantee safe moisture levels in attic spaces. Ventilation of these attic spaces seems to lead to an increase in moisture levels, and so does infiltration from the

conditioned spaces. Allowing for infiltration in combination with ventilation allows for even higher levels of moisture. From this, the results indicate that the assessed ventilation strategies under similar physical conditions does not mitigate moisture problems but may instead exacerbate moisture problems. Furthermore, exterior insulation of the attic spaces reduces the risk of condensation on the interior surface of the roofing underlay slightly. However, more data and analysis about other construction scenarios are needed for more general conclusions.

ACKNOWLEDGEMENT

This research was financially supported by Grundejernes Investeringsfond (The Landowners' Investment Foundation).

REFERENCES

- Bjarløv, S. P., Johnston, C. J., & Hansen, M. H. (2016). Hygrothermal conditions in cold, north facing attic spaces under the eaves with vapour-open roofing underlay in a cool, temperate climate. *Building and Environment*, 95, 272–282. <https://doi.org/10.1016/j.buildenv.2015.09.009>
- Brand, E., Bunch-Nielsen, T., Christensen, G., Gudum, C., Hansen, M. H., & Møller, E. B. (2009). *SBi-Anvisning 224 - Fugt i Bygninger (Danish)* (1st ed.). Hørsholm, Denmark: Statens Byggeforskningensinstitut, Aalborg University.
- Brand, E., Bunch-Nielsen, T., Christensen, G., Gudum, C., Hansen, M. H., & Møller, E. B. (2013). *SBi-Anvisning 224 - Fugt i Bygninger (Danish)* (2nd ed.). Hørsholm, Denmark: Statens Byggeforskningensinstitut, Aalborg University.
- Essah, E. A., Sanders, C. H., Baker, P., & Kalagasidis, A. S. (2009). Condensation and moisture transport in cold roofs: Effects of roof underlay. *Building Research and Information*, 37(2), 117–128. <https://doi.org/10.1080/09613210802645973>
- Fugler, D. W. (1999). Conclusions from ten years of Canadian attic research. *ASHRAE Transactions*.
- Hagentoft, C., & Sasic Kalagasidis, A. (2010). Mold Growth Control in Cold Attics through Adaptive Ventilation: Validation by Field Measurements. In *11th International Conference on Thermal Performance of the Exterior Envelopes of Whole Buildings, Buildings XI*. Clearwater Beach, Florida, US.
- Harderup, L.-E., & Arfvidsson, J. (2013). Moisture safety in cold attics with thick thermal insulation. *Journal of Architectural Engineering*, 19, 265–278.
- Nik, V. M., Sasic Kalagasidis, A., & Kjellström, E. (2012). Assessment of hygrothermal performance and mould growth risk in ventilated attics in respect to possible climate changes in Sweden. *Building and Environment*, 55, 96–109. <https://doi.org/10.1016/j.buildenv.2012.01.024>
- Ojanen, T. T. (2001). Thermal and Moisture Performance of a Sealed Cold-Roof System with a Vapor-Permeable Underlay. *Thermal Performance of the Exterior Envelopes of Buildings VIII Conference*.
- Pold, C. F. H. (2015). *Ventilation Design of Cold Attics for Avoiding Moisture-Related Problems*. Technical University of Denmark.
- Roppel, P., & Lawton, M. (2014). *Attic Ventilation and Moisture Research Study - Final Report*. <https://doi.org/10.1002/2014GB005021>
- TBST. Danish Buildign Regulations 2018 (2018). Denmark. Retrieved from <http://byggningsreglementet.dk/>
- Uvsløkk, S. (2005). Moisture and temperature conditions in cold lofts and risk of mould growth. *Proceedings of the 7th Symposium on Building Physics in the Nordic Countries*, 8.

Hygrothermal performance of sealed attics in climate zone 3A

Mikael Salonvaara^{1*}, Achilles Karagiozis¹, and William Miller, PhD²

¹Owens Corning, Granville, OH

²Oak Ridge National Laboratory, Oak Ridge, TN

*Corresponding email: mikael.salonvaara@owenscorning.com

ABSTRACT

Sealed attics with fiberglass have been in the US building codes for several codes cycles. Prior to the IRC 2018, air permeable insulation (such as fiberglass) was previously allowed to be deployed without continuous air impermeable insulation only in dry climate zones 2B and 3B in tile roofs systems. New research has revealed that asphalt shingles can also be allowed as implemented in the new IRC 2018 with a new addition to the section for sealed attics using air permeable insulations. The new building code also permits the use of air permeable insulation without air impermeable insulation in climate zones 1 to 3 (including moist climates “A”) when certain conditions are met in the design. To expand the use of the sealed attic system in moist climates (1A to 3A) field testing was needed to further understand the impacts of roof claddings and diffusion vent.

The authors identified the need for collection of field test data to validate the new sealed attic design that was being implemented in the IRC (2018 International Residential Code). Testing of sealed attics exposed to a southern climate (Charleston, SC) was launched in 2015. The goals were to determine a) if spray foam and fiberglass insulation perform differently in terms of moisture performance in sealed attics and if so, how and b) if the diffusion vent improves the moisture performance at the ridge by reducing the high humidity and moisture contents and c) if asphalt shingles could be used for unvented attics with air permeable insulations in IRC climate zones 1-3.

This paper summarizes the field testing and simulation results confirming that air permeable insulation as well as shingles can be used in humid southern climate zones. The new building code requirements regarding air permeable insulation should be required with all highly vapor-permeable insulations.

KEYWORDS

Sealed attics, moisture performance, diffusion vent, moist climate zone

INTRODUCTION

Sealed attics with air permeable (and vapor permeable) insulation had experienced moisture problems in the past (GBA 2010, JLC 2010, Colon 2011, Miller 2016). Some of the past problems had resulted in changes to the building codes that ultimately prevented using air permeable insulation in sealed attics. Even with these changes the problems continued occurring. In recent years further research has created better understanding of the reasons for failures and has enabled development of systems that fix the issues (Boudreaux et al. 2013, Salonvaara et al. 2013). However, field testing to prove the concepts was needed to allow for the sealed attic systems to be used in different climates and with air permeable insulation.

Conventional attic construction involves providing insulation on the floor of the attic and ventilation of the attic space (vented attic) from the outside. When an air distribution system is installed in the vented attic, any duct or air handler leakage creates an energy penalty in addition

to conduction and radiation losses. An alternative to conventional vented attics is an unvented attic which is also known as a sealed attic. Insulating the attic roof deck and blocking ventilation of the attic space to the outside moves the thermal boundary to the sheathing roof line. The air distribution system is now located within a semi-conditioned space, which increases its overall efficiency, durability, and maintainability. The sealed attic can be built as an unvented attic with insulation in direct contact with the roof deck or with a ventilated roof deck with an air tight interior layer in the attic side of the ventilation gap. The ventilated roof deck is not common in unvented attics, but is an option for a cathedral ceiling. The cathedral ceiling is over conditioned living space whereas the roof deck in the sealed attic is exposed to an attic space that is typically only indirectly conditioned.

Moisture problems in sealed attics and proposed solutions

The moisture problems experienced in some sealed attics are mainly of two types (Salonvaara et al, 2013): 1) High moisture in the roof sheathing mostly at the ridge and 2) high humidity or condensation in the attic space.

The latest changes to the International Residential Building code (IRC 2018) include a requirement for conditioning the sealed attic by supplying air from the ductwork at a rate of 50 cfm per 1000 sqft of ceiling (0.25 L/s,m^2) and the addition of a diffusion port when air-permeable insulation is used in sealed attics. The purpose of the diffusion port and conditioning are to provide control for moisture at the ridge and the attic humidity, respectively. A diffusion port is a gap at the ridge (greater than or equal to 1:600 of the ceiling area) covered by a vapor permeable membrane (vapor permeance 20 perms or more) to create water and air tightness but allowing for vapor transport between the ridge and outdoors. Previous studies have been carried out by Kohta and Lstiburek (2013) regarding the diffusion port. Attic conditioning is a new approach that has previously not been well investigated.

METHODS

Field tests were conducted at the Natural Exposure Test (NET) facility (Figure 1) located in Hollywood, SC, a suburb of Charleston. Charleston is in climate zone 3A which is described as warm-humid with cooling degree days CDD 10°C ranging from 2500 to 3500 and heating degree days HDD $18^\circ\text{C} \leq 3000$ and with precipitation more than 50cm annually. Personnel from Oak Ridge National Laboratory (ORNL) instrumented attic assemblies on the NET facility and collected data for two years. The instrumentation included temperature, relative humidity and moisture content sensors. The site has its own weather station recording hourly values.

Simulations with a hygrothermal simulation model (Fraunhofer IBP) were carried out to compare simulated predictions of performance to the field performance.

Studies in a Large Scale Climate Simulator at ORNL were performed in addition to the field tests to carry out side by side tests with different configurations. Data from these tests are shown in discussion of the performance of the diffusion port only.

The test period covered two years at the NET facility. Attics installed in the NET facility include three different insulation types: open cell spray foam (ocSPF, density 0.5 kg/m^3), closed cell spray foam (ccSPF, density 2 kg/m^3) and netted and blown fiberglass (FG, 21 kg/m^3). The solar reflectance of the shingles is 4% and 25% for conventional and cool roof shingles, respectively. The attics are listed in Table 1 in the order they appear in the test hut.

RESULTS

Installation of the roof sections occurred early 2016. Data has been collected from March 2016 till March 2018. Data are missing for October to mid-November 2016 due to storms causing unrecoverable power shortage. In the end of May 2017, computer fans were installed in the attics insulated with fiberglass to provide the venting rate 50 cfm/1000 sqft of ceiling area (0.25 L/s,m^2) as specified in IRC 2018 for sealed attics with air permeable insulation in southern

climate zones 1A-3A. The setup did not allow for conditioning the attics with air from the ductwork and instead the ventilation air is coming from the conditioned test hut.

Table 1. Types of attics, insulation and shingles details.

Attic #	Type	Insulation/R-value	Shingles type
2	Sealed	ocSPF, R-22/RSI-3.9	Conventional
3	Sealed	ccSPF, R-22/RSI-3.9	Conventional
4	Sealed	FG, R-38/RSI-6.7	Cool Roof
5	Vented	FG, R-38/RSI-6.7	Conventional
1	Sealed	FG, R-38/RSI-6.7	Conventional
7	Sealed, FG + Diffusion port	FG, R-38/RSI-6.7	Conventional

The roof planes (3:12 pitch) are facing South and North. Figure 1 shows the different attics as arranged in the test hut.

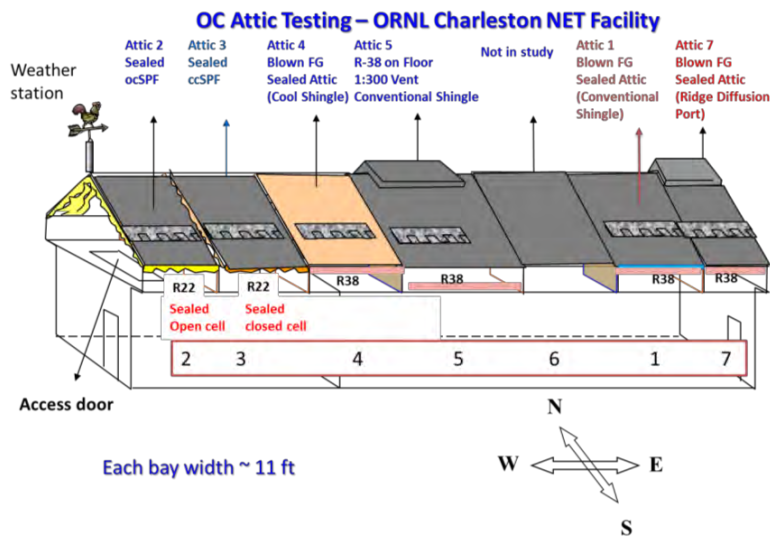


Figure 1. Schematics of the attics in NET facility. The arrangement includes 5 sealed attics and one vented attic.

Climate conditions and attic humidity

During summer in the first year the attic humidity in the attics with vapor permeable insulation rises quite high reaching 80% relative humidity and even higher above 90%-RH in the attic with open cell spray foam (Figure 2). In the end of May in 2017 fans were installed in attics 1, 4 and 7 to ventilate the attic spaces with indoor air at the rate 50 cfm/1000 sqft of ceiling area (0.25 L/s,m²). The humidity level in the attics dropped right after the fans were installed which is clearly seen in attics 1 and 7. Attic 4 has cool roof shingles with solar reflectance 0.25. This attic does not reach as high humidity in the attic space and the overall level is lower than in the other attics with fiberglass insulation. This is due to the cooler roof deck which creates less vapor flux from the roof deck into the attic space. Similarly, the low humidity in attic 3 with closed cell spray foam is a result of low vapor flux from the roof deck which is due to the low water vapor permeance of the insulation layer.

Roof deck moisture content

The moisture content of the roof deck (OSB=oriented strand board) never reached unacceptable levels and mostly stayed below 14% by weight (Figure 3).

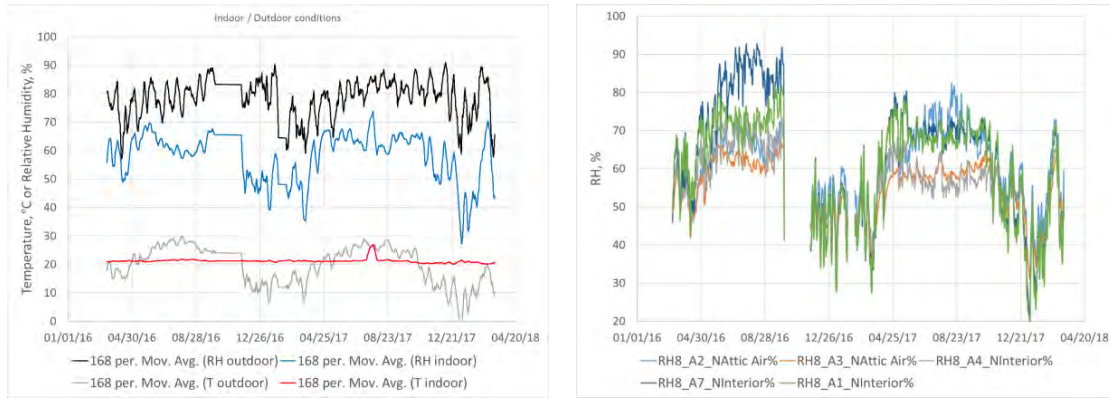


Figure 2. Indoor and outdoor temperature and relative humidity (7 day moving average, left) and attic air relative humidity during the two-year test period (right).

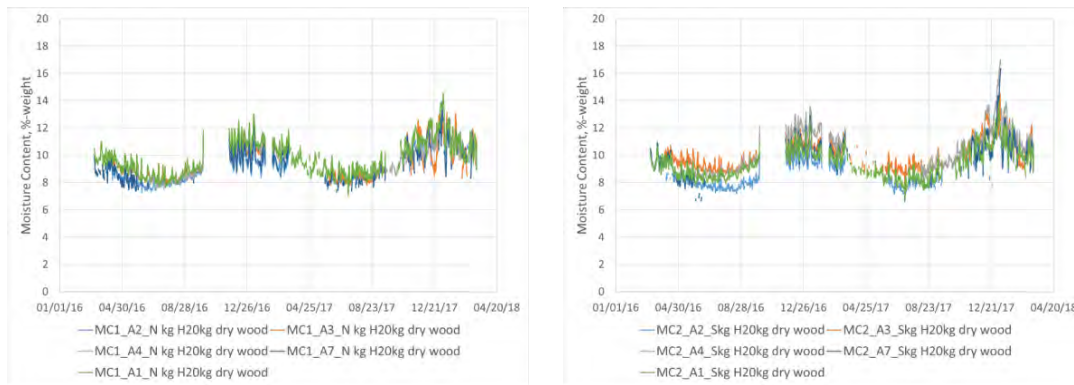


Figure 3. Moisture content of the roof deck in the north (left) and the south (right) roof slope.

Humidity at the ridge and the effect of diffusion port

Laboratory tests in a climate simulator for attic sections with and without a diffusion port allowed for close investigation of the effect of the diffusion port on moisture conditions at the ridge. Figure 4 shows the sensor mapping and the water vapor pressure contours in the attic in an afternoon with simulated weather data.

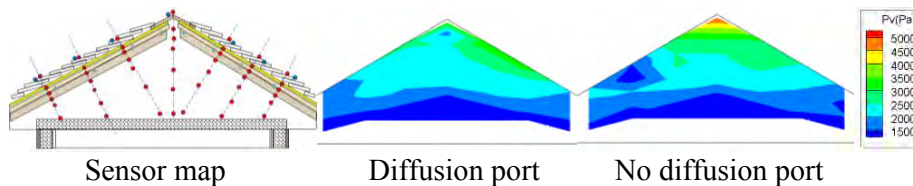


Figure 4. Water vapor pressure contours in a summer afternoon in the attics with shingles and fiberglass insulation with and without a diffusion port at the ridge. Results are from the Large Scale Climate Simulator tests.

The moisture removal was more isolated near the ridge area, Figure 4. Moist air is more buoyant than drier air because of the difference in molecular weight of air and water vapor. The hot roof deck during sunny hours also creates temperature differences that create buoyancy-driven flows towards the ridge. The higher the moisture content of the air the more water vapor displaces the

air, and the air-water density drops compared to air holding less water vapor. Therefore, the moist air moves toward the diffusion port which acts as a relief valve at the ridge during the hours of high humidity in the attic. Further down from the ridge the sheathing is not affected by the moist air even during periods of high humidity.

Simulated versus measured performance

Simulation models are extensively used today to design for building envelope systems to improve thermal and moisture performance. A whole building hygrothermal simulation model was used with the weather data measured on site to evaluate whether the model simulations agree with the measured performance. Simulated and measured data were found to agree well throughout the seasons. Figure 5 shows results for the roof deck temperature and humidity during one week in the summer. The results give confidence that hygrothermal modeling is a valid approach to use for designing attic systems.

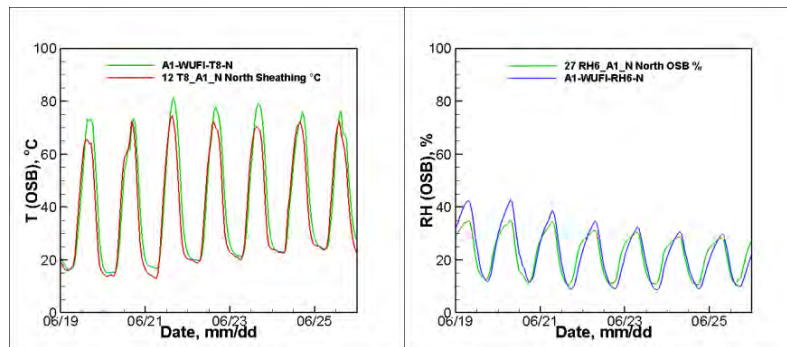


Figure 5. Measured temperature and relative humidity at the interface between the roof sheathing (OSB) and the fiberglass insulation in the north facing roof slope in attic 1.

DISCUSSIONS

Cool roof shingles reduce the temperature swings on the roof deck, which creates less vapor drive from the roof deck into the attic during sunny days. This has both positive and negative impacts. In the summer the attic humidity stays lower and high peaks in relative humidity are less likely with cool roof shingles than with standard shingles. In the winter the lower solar absorption coefficient keeps the shingles colder thus allowing more time for the roof deck to accumulate moisture and less vapor drive to dry the roof deck inwards, which results in higher moisture contents in the roof deck with cool roof shingles than with standard shingles.

Sealed attics (unvented attics) with fiberglass have shown acceptable performance in the test hut study: moisture contents of the roof sheathing panels have stayed in acceptable levels (per moisture pin evaluations) and the analyses have not revealed any mold growth risk. Visual inspection after two years showed no signs of mold at the roof deck.

The open cell spray foam attic performed similarly to the fiberglass insulated attics in terms of moisture performance. Open cell spray foam has slightly lower water vapor permeability than the blown in fiberglass, which creates slower movement of water vapor; thus the highest daily humidity in the roof deck was typically lower than in the fiberglass attics. Closed cell spray foam has much lower water vapor permeability and the attic with closed cell spray foam showed a slower response to climatic changes even seasonally by maintaining humidity with less variations over time than the attics with vapor permeable insulation.

Diffusion port size and design is currently not optimized. Additional work is recommended on the diffusion port design and to test the performance of these sealed attics in real full-size homes in a hot and humid climate. The presented results are for a test hut. Occupant behavior in real homes may change the indoor conditions that can affect the results.

CONCLUSIONS

The new building code requirements – diffusion port and conditioning of attic space – have proven effective in providing control of moisture in sealed attics. The diffusion port has been shown in this as well as in another study (Kohta and Lstiburek 2013) to reduce high moisture at the ridge. Conditioning of attics by introducing a small flow of conditioned air for the HVAC supply was shown to be critical for avoiding high humidity in the attic space. The attics in this study and in this climate zone (3A) had no moisture problems when the attics were conditioned. Without the conditioned air the attic space can reach high enough humidity levels that are conducive for mold growth.

ACKNOWLEDGEMENT

Owens Corning Roofing and Insulation provided cost sharing to enable this study. The support is greatly appreciated.

REFERENCES

- Boudreaux, P., Pallin, S., Jackson, R. 2013. Moisture Performance of Sealed Attics in the Mixed-Humid climate. Report ORNL/TM-2013/525. Building Technologies Research and Integration Center Energy and Transportation Science Division, Oak Ridge National Laboratory, TN, USA.
- Colon C. 2011. New Construction Builders Challenge: Sealed Attic and High Efficiency HVAC in Central Florida: A Year in Review. Report FSEC-PF-454-11, Florida Solar Energy Commission, USA.
- Fraunhofer IBP, Germany. WUFI ® Plus. <https://wufi.de/en/software/wufi-plus/>.
- Karagiozis, A. and Kunzel, H. M., and Holm, A, (2001), "WUFI-ORNL/IBP - A North American Hygrothermal Model", Proceedings for Performance of Exterior Envelopes of Whole Buildings VIII: Integration of Building Envelopes, December 2-7, Clearwater Beach, Florida.
- Miller, W., Railkar, S., Shiao, M. and Desjarlais, A. 2016. "Sealed Attics Exposed to Two Years of Weathering in a Hot and Humid Climate," Proceedings for Performance of Exterior Envelopes of Whole Buildings VIII: Integration of Building Envelopes, December 2-7, Clearwater Beach, Florida.
- GBA. 2010. High humidity issues in a spray foam attic. <http://www.greenbuildingadvisor.com/community/forum/general-questions/17488/high-humidity-issues-spray-foam-attic>.
- IRC 2018. International Residential Code. International Code Council. www.iccsafe.org.
- JLC. 2010. Moisture issue in an unvented attic..... <http://forums.jlconline.com/forums/showthread.php?52456-Moisture-issue-in-an-unvented-attic.....>
- Kohta U., Lstiburek, J. 2013. Monitoring of Two Unvented Roofs with Air-Permeable Insulation in Climate Zone 2A. Thermal Performance of the Exterior Envelopes of Whole Buildings XI International Conference, Clearwater Beach, FL, December 2013.
- Salonvaara, M., Karagiozis, A., Desjarlais, A. 2013. Moisture Performance of Sealed Attics in Climate Zones 1 to 4. Thermal Performance of the Exterior Envelopes of Whole Buildings XI International Conference, Clearwater Beach, FL, December 2013.

Moisture robustness of eaves solutions for ventilated roofs – experimental studies

Steinar Grynning^{1,*}, Silje Kathrin Asphaug^{2,1}, Lars Gullbrekken¹ and Berit Time¹

¹ Department of Materials and Structures, SINTEF Building and Infrastructure, Trondheim, Norway

² Department of Civil and Transport Engineering, Norwegian University of Science and Technology (NTNU), Trondheim, Norway

*Corresponding email: Steinar.grynning@sintef.no

ABSTRACT

Ventilated pitched wooden roofs with eaves (roof overhangs) is a common building practice in the Scandinavian countries. The eaves are protecting the façade from rain, wind driven rain (WDR) and snow, and it covers the roof ventilation aperture. The eaves should be designed so that the least possible amounts of rainwater and snow enters the ventilation aperture between the roof cladding- and underlayer roofing. At the same time, adequate ventilation of the roof must be ensured to promote proper drying-out capabilities of the roof and to avoid problems of snow melt and ice formation at eaves and gutters during winter season. Small or almost non-existing eaves is a trend in modern architecture. It is a common perception that such solutions are more vulnerable to moisture damages due to possible increase of water penetration into the roof aperture.

The aim of the study is to experimentally investigate the moisture robustness of the described risk area and to find answers to how the design of eaves influence the amount of rain that is driven on to the underlayer roofing under the aperture in ventilated roofs.

It was found that the amount of collected water in the different test series to a large extent are given by the water droplet size as well as the wind velocity inside the air cavity. The results from this study simulates an example of a rain event with heavy rain intensity and strong winds (storm). The test represents an example of a storm event with a given droplet size distribution. The results indicate that an increased pressure drop decreases the water ingress. Comparative tests showed that installation of a wire mesh largely decreases the measured water collection and the dynamic pressures inside the air cavity.

KEYWORDS

Roof design; eaves; robustness; precipitation, water ingress

INTRODUCTION

Moisture related damages pose significant challenges to the Norwegian built environment. Indoor moisture, damp building structures and precipitation stresses the building envelope and can provoke significant damages. 75 % of all damages and defects in the Norwegian building stock are caused by moisture related problems and 2/3 of defects are related to the building envelope (Lisø 2006). In pitched wooden roofs 67 % of the defects are caused by precipitation or indoor moisture (Gullbrekken, Kvande, et al. 2016). Climate change has been proven to increase the amount and intensity of precipitation. On average, an increase of more than 20 % has been registered over the last 100 years, and an increase of an additional 20% is expected

before the year 2100 (Pachauri and Meyer 2014). Changes in temperature leads to an increase in conditions where wood materials are susceptible to degradation (Lisø and Kvande 2007). These changes lead to higher demands on the entire building and the building envelope parts, where mould and other biological growth is critical. A state-of-the-art in modelling of mould failure is thoroughly investigated by Gradeci et al. (Gradeci, Labonnote et al. 2016).

Ventilated pitched wooden roofs with eaves (roof overhangs) is a common building practice in the Scandinavian countries. The traditional construction technique for ventilated wooden roofs uses relatively large roof overhangs. These overhangs have two main functions related to moisture robustness; Firstly, to reduce the amount of wind-driven rain (WDR) hitting the facade and secondly to reduce the amount of wind-driven precipitation entering the ventilated air cavity between the roof underlayer and the roof cladding. WDR is one of the largest moisture sources with potential negative effects on the hygrothermal performance and durability of building envelopes. A detailed (and comprehensive) review of WDR research is given in (Blocken and Carmeliet 2004, Blocken, Abuku et al. 2011, Kubilay, Derome et al. 2014). Large deposition chambers where the air-flow velocity is reduced, have traditionally been recommended for ventilated wooden roofs (Thiis, Barfoed et al. 2007). However, new trends in architecture calls for solutions with minimal roof overhangs and slender design of the eaves. It is a common perception that such solutions are more vulnerable to moisture damages. Quantifying the amount of precipitation is important to provide a basis for future design-recommendations of moisture robust eave solutions. The design of roofs and eaves (roof overhangs) and how they influence the quantity of WDR impinging on building facades are studied in several publications (Hersels 1996, Ge and Krpan 2009, Chiu, Ge et al. 2015). However, there is a need to obtain further and more fundamental knowledge on the performance and durability of commonly used solutions, especially through experimental studies (Fasana and Nelva 2011, Boardman and Glass 2013). Some experimental studies have been carried out (Inculet and Surry 1995, Inculet 2001, Blocken and Carmeliet 2005, Kvande and Lisø 2009). To the authors' knowledge, few studies have quantified the amount of precipitation accumulation in the apertures and eaves of sloped ventilated wooden roofs caused by WDR.

The aim of the study is to experimentally investigate the moisture robustness of eaves solutions and how the design of eaves influence the amount of rain which is driven inside the ventilated air cavity of the roof aperture. Influencing factors that will be studied are; the length of the roof overhang and the ventilation aperture opening size and position.

METHODS

Test series are described in Table 1 and 2 and Figure 1. The measurements were carried out in a *Rain and Wind apparatus* in accordance with principles in NS-EN 12865:2001 (ISO 2001) method B. Smaller quantities of rain than advised in the standard were used due to limitations in the equipment. The facility is described in (Kvande and Lisø 2009). The sample exposed to WDR had an area of 2.45 m x 2.45 m. The width of the roof surface was 1.8 m. Transparent acrylic boards were used as wind-barrier in the wall and as underlying roof and roof cladding to make visual inspection easier. The front of the roof cladding was covered with a 200 x 19 mm weatherboard, with a steel gutter in front to promote realistic air-flow vectors. An expansion chamber was used to adjust wind-speeds in the roof aperture. Ten eaves-solutions with three different overhang lengths and various closure-solutions of the eaves were tested. Table 1 and 2 shows illustrations and description of the different sample configurations. Test series B4 is identical to B3 apart from a wire mesh covering the ventilation opening in the eave. A mesh like this is used to prevent insects and birds from entering the eave in real buildings. It was chosen to add this for the series with the largest amount of water collected in the aperture (B3).

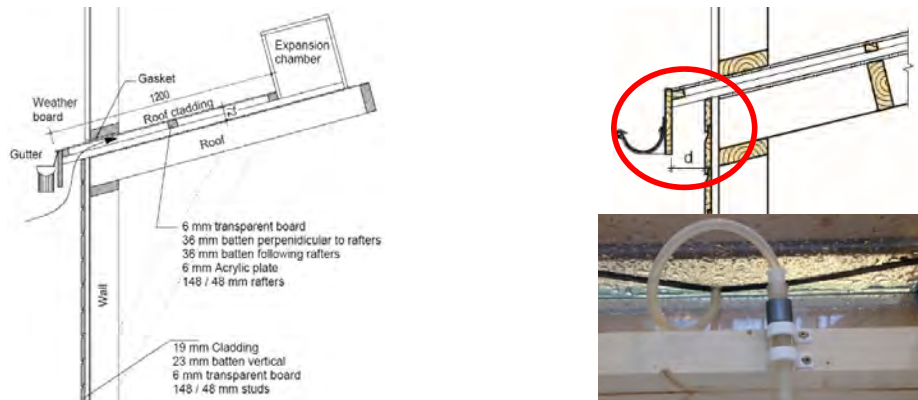


Figure 1. (left) Cross-section of the test sample. (top right) Different eaves overhang lengths (denoted d and circled in red). (bottom right) Water collection system used in the experiment.

Table 1. Test configurations. Test ID's A has 36 mm roof overhang, B has 100 mm and C has 200 mm. d = overhang length, Opening = opening size. I1 is the same as A1, but with driving rain application only. I2 is identical to I1, but w/ 300 Pa pressure difference. The Test ID numbers (1-5) aligns with weatherboard configurations presented in Table 2.

Test ID	I1	I2	A1	A2	B1	B2	B3	B4	C1	C2	C3	C4	C5
d (mm)	36	36	36	36	100	100	100	100	200	200	200	200	200
Opening (mm)	36	36	36	36	100	18	36	36	200	18*	36*	18**	36**
dP (Pa)	0 - 200	0 - 300	0 - 200	0 - 400	0 - 400	0 - 400	0 - 400	0 - 400	0 - 400	0 - 400	0 - 400	0 - 400	0 - 400
Duration (min)	20	20	40	40	40	40	40	40	40	40	40	40	40

* Opening in deposition chamber facing the weatherboard ** Opening in chamber facing cladding

Table 2. Test series A1 to C5 overview. Weatherboard placement and configurations marked in red. Series nr (1-5) relates to the number in the Test ID series presented in Table 1.

Test series	1	2	3	4	5
Configurations A-C					

Water was applied as driving-rain only, in I1 and I2. For the remaining series, both driving rain (large droplets) and a water mist (very small droplets) spray was used. This was done to cover a larger span of droplet-sizes and, thus, to represent a wider span of likely, realistic downpour conditions. No measurement of the actual droplet-size distributions was feasible to carry out. The total volume flow of water for the driving rain nozzles was measured to 660 l/h and 550 l/h after turning on the water-mist nozzles. The nozzles were positioned to create the maximum moisture load possible. Calculations were carried out to ensure the use of realistic air velocities in the aperture. A worst-case scenario of a *storm* (level 10 on the Beaufort scale) was chosen for the experiments. This corresponds to the pressure of 400 Pa used in the experiments. This gives a resulting air velocity of 26 m/s. The dynamic pressure in the aperture was measured using a pitot-tube. The pressure readings were highly irregular, indicating turbulent flow.

RESULTS

Calibration tests were carried out to achieve the desired water-load on the sample. Several pressure differences across the sample was tested, ranging from 200 to 400 Pa. It was found that the mean droplet-size of the applied water was too large for the droplets to be transported into the aperture. This was independent of the pressure difference. Hence, water application using water-mist nozzles were used in A1-C5. Figure 2 show the amounts of water collected during the test cycles. A qualitative description of the visual observations is given in Table 3

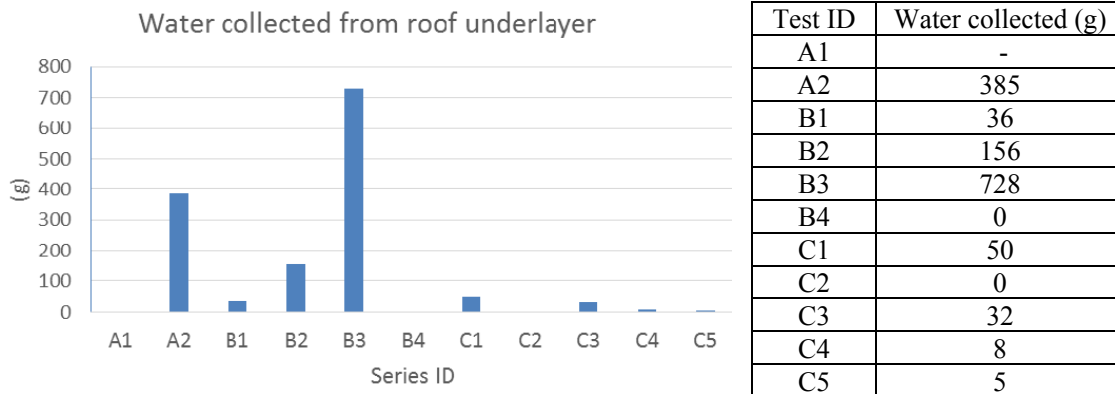


Figure 2. Test configurations and measured retained amounts of water from roof underlay after 40 min of water application for series A1-C5

Table 3. Visual observations during the test series A1 to C5. Location of water deposition are based on visual inspections and should be treated as qualitative observations.

ID	Observations
A1	No water accumulated on the roof underlayer (RU). No water deposited on the wind barrier (WB) of the wall (e.g. on the vertical board).
A2	Rapid wetting of RU. Small droplets deposited on RU up to the first furring strip (30-40 cm). Water deposited on RU in large droplets 15-20 cm from eave. Water running down WB
B1	Rapid accumulation of water on RU (more than for A2). A lot of water running down the WB. Fewer small droplets deposited on RU, deposition length same as for A2.
B2	More and bigger droplets are transported in the airstream than for A2 and B1. Deposition on cladding, but less than for A2 and B1.
B3	Similar behaviour as B2, but with more rapid wetting of RU. Water retained in vials after 5 minutes. Water driven further along the back-side of the roof cladding than previous series.
B4	Some droplets are deposited on the roof cladding and RU but no water is collected in the vials. Water droplets are deposited in/on the wire mesh.
C1	Some deposition on roof cladding but little on RU. Some small droplets in mid-and very little in left section. Some water running down WB.
C2	Some large droplets are deposited on the RU (8-10 cm from wall/roof joint). Some small droplets are deposited up to the first furring strip.
C3	Similar behaviour as B3, but fewer droplets on RU. Some water hitting WB
C4	Very little water (small droplets) deposited on RU. Some deposition of large droplets on RU up to approximately 5-10 cm from the wall/roof connection.
C5	Similar observations as for C4.

DISCUSSIONS

The amounts of collected water in the different test series are given by both the water droplet size as well as the air velocity inside the air cavity. The pressure difference of 400 Pa was necessary to transport water from the water-mist nozzles in through the eaves opening. Based on the strains from the applied pressure and the corresponding pressure loss through the system, the driving forces from wind can be categorized as "worst case". It is not expected that temperatures (above freezing) will affect the deposition of water on roof underlayer or wind-barrier of walls.

Water amounts collected in A2 and B3 was considerably higher than for the remaining. Close to 400 ml of water was collected in A2, which had a 36 mm long overhang and no weather-board covering the underside of the eave. The largest amount of water collected was 728 ml.

Visual observations made during the test, suggest that a possible reason was that the position and size of the opening gave a particularly disfavoured air-flow direction (vector) for this configuration. Large amounts of water were transported in the airflow and was deposited on the side of the roof cladding facing the ventilation aperture. The deposited water was then "dragged" along the surface until the water droplets became large enough for gravitational forces to force them off the cladding with a resulting deposition on the roof underlayer (RU). Furthermore, it was found that the solutions with a 100 mm roof overhang had the highest amounts of water deposition on the RU regardless of the opening size under the eave. The Norwegian building design guidelines suggests using a ventilation gap in the roof aperture with a height of 40-50 mm (SINTEF 2005).

C3 and C5 indicate that the placement of the ventilation opening in the eave toward the weather board reduce the amount of collected water. For the 18 mm cavity (C2 and C4) the comparable position gave little increase of the collected amount of water. The measured amount of water during C4 was rather low. This, Barfoed et al. (2007) also found that position of the ventilation opening towards the weather board was effective to reduce snow penetration to the roof compared to a position close to the cladding. This, Barfoed et al. (2007) also indicated that the snow concentration of the air entering the air channel decreased by increasing air pressure drop over the eaves construction. Hence, the measurements must be seen in connection to snow-draft which might be a bigger practical issue to solve.

Tests B1 by B2 and C2 by C3 indicate that an increased pressure drop decreases the water ingress. This is clearly demonstrated by the introduction of the wire mesh which is representing a large pressure drop. Comparing Test B4 and B3 shows that installation of the wire mesh decreases the measured water collection and the dynamic pressures inside the air cavity.

CONCLUSIONS

Measurements of how the design of eaves influence the amount of rain that is driven in to the ventilation aperture roofs have been carried out. The amount of water collected are given by the water droplet size and the wind velocity inside the air cavity. In practice the amount of WDR hitting the facade is dependent of wind speed, wind direction, rainfall intensity, raindrop size and the rain event duration. The results from this study simulates an example of an event with heavy rain intensity and strong winds (storm) with a given droplet size distribution. Hence, the actual amount of water collected in each of the test series are of less interest than the comparison of the amounts of water in the different series.

It can be assumed that a mesh like the one used in B4 will be effective in stopping rain with a large variation of droplet sizes and droplet size-distributions from entering the roof aperture.

There are limitations in the measurements that have been carried out. There was no feasible way of controlling the droplet size distribution other than that the use of water-mist nozzles created smaller droplets than the driving rain nozzles. Substantial amounts of water were deposited on the RU without being collected. Future measurements should take this into account. The air velocity inside the ventilation cavity was high. This was, however, necessary to induce rain penetration in the ventilation cavity. The effect of varying wind direction was not accounted for and should be included in future studies. Only rain accumulation in the ventilation aperture was studied in this paper. Future measurements should also be coupled to experiments studying challenges related to snow, which might be a bigger issue. Future studies should also include the combined effects and implications of eaves-design on WDR effects on cladding. Measurements studying real-climate performance should also be carried out.

ACKNOWLEDGEMENT

The experiments were carried out as part of the *Tall Timber Facades* project (part of the WoodWisdom 2014-2017 program). The authors also acknowledge the Centre for Research-based Innovation "Klima 2050" for providing necessary funding.

REFERENCES

- Blocken B., Abuku M., et.al. 2011. Intercomparison of wind-driven rain deposition models based on two case studies with full-scale measurements, *Journal of Wind Engineering and Industrial Aerodynamics* Vol. 99, pp. 448-459.
- Blocken B. and Carmeliet J. 2004. A review of wind-driven rain research in building science, *Journal of Wind Engineering and Industrial Aerodynamics*, Vol 92, pp. 1079-1130.
- Blocken, B. and Carmeliet J. 2005. High-resolution wind-driven rain measurements on a low-rise building—experimental data for model development and model validation, *Journal of Wind Engineering and Industrial Aerodynamics*, Vol 93, pp. 905-928.
- Boardman C. R. and Glass S. V. 2013, Investigating Wind-Driven Rain Intrusion in Walls with the CARWASH, *Thermal Performance of the Exterior Envelopes of Whole Buildings XII International Conference*, ASHRAE.
- Chiu V., Ge H., and Stathopoulos T. 2015, Overhang effect on reducing wind-driven rain for a mid-rise building, *6th International Building Physics Conference*, Vol. 78, pp.2506-2511.
- Fasana S. and Nelva R. 2011. Improvement of the performance of traditional stone roofs by wind driven rain experimental tests, *Constr. and Building Matr.*, Vol 25, pp. 1491-1502.
- Ge H. and Krpan R. 2009. Wind-driven Rain Study in the Coastal Climate of British Columbia. Final report, British Columbia Institute of Technology.
- Gradeci K., Labonnote N., et.al. 2016. A proposed probabilistic-based-design methodology against mould failure in timber façades, *World Conference on Timber Engineering*, Vienna.
- Gullbrekken L., Kvande T., et.al. 2016. Norwegian Pitched Roof Defects, *Buildings*, Vol 6.
- Hershfiels, M. 1996, Survey of Building Envelope Failures in the Coastal Climate of British Columbia" *AIVC* 11608.
- Inculet, D. 2001. The Design of Cladding Against Wind-driven Rain, *PhD thesis*.
- Inculet, D. and Surry D. 1995, Simulation of Wind-Driven Rain and Wetting Patterns on Buildings, *R. R. f. C. M. a. H. Corporation*. Ottawa.
- Kubilay A. Derome D., et.al. 2014, Numerical simulations of wind-driven rain on an array of low-rise cubic buildings and validation by field measurements, *Building and Environment* Vol 81, pp. 283-295.
- Kvande T. and Lisø K.R. 2009, Driving-rain protective design of parapet flashing, the Fourth International Building Physics Conference.
- Lisø K. R. (2006). Building envelope performance assessments in harsh climates: Methods for geographically dependent design. Doctoral thesis, Doctoral thesis submitted at NTNU.
- Lisø K. R. and Kvande T. 2007, Klimatilpasning av bygninger "Climate adaption of buildings" (In Norwegian).
- Lisø K.R., Kvande T. and Thue J.V. 2006, Learning from experience - an analysis of process induced building defects in Norway". Proceedings of the *3rd International Building Physics Conference*, London.
- Pachauri R.K. and Meyer L.A. 2014, IPCC Climate Change 2014: Synthesis Report. Contribution of Working Groups I, II and III to the Fifth Assessment Report of the Intergovernmental Panel on Climate Change - Annex II", *IPCC*, pp. 117-130.
- SINTEF 2005, 525.106 Skrå tretak med kaldt loft. *SINTEF Design Guidelines*, Trondheim.
- Thiis T.K., Barfoed P., et.al., 2007, Penetration of snow into roof constructions-Wind tunnel testing of different eave cover designs, *Journal of Wind Engineering and Industrial Aerodynamics*, Vol 95, pp. 1476-1485.

Thermal Performance of Novel Natural Ventilation Apertures in a High-Performance Single-Family House

Martha Bohm^{1,*}

¹ Department of Architecture, University at Buffalo, 319 Hayes Hall, South Campus, Buffalo, NY 14214 USA

* marthabo@buffalo.edu

ABSTRACT

Natural ventilation provides opportunities to reduce residential cooling load in summer, but increasing the operability of a façade potentially increases infiltration, which is already a source of significant winter heat load. Solving both of these simultaneously is challenging. The test building for this study was a prototype house containing a novel ventilator detail which allows for porosity for summer ventilation and a tight, insulated seal in winter. We aimed to determine whether the prototype had low enough infiltration and thermal bridging to be worthy of further laboratory testing and subsequent deployment in more buildings. The test home was blower door tested, following the Resnet standard to determine ACH50. While the house was depressurized, diagnostic photographs were taken with a smoke wand at each ventilator to qualitatively document air exchange. The ventilator plan and section details were modeled in THERM v7.6 to look for potential thermal bridging. These tests were conducted in February 2018 on the GRoW Home, a prototype house built for the 2015 Solar Decathlon at the University at Buffalo. The home contains thirteen instances of the ventilation detail in question. ACH50 was found to be 1.16, photographs showed observable infiltration at only five of the thirteen apertures, and only when the operable interior door was open. The thermal flux magnitude analysis did not evidence major thermal bridging. Thus this ventilation approach shows promise for naturally ventilated small buildings in cold climates. Further laboratory study is warranted to characterize and further improve the construction.

KEYWORDS

Natural ventilation, passive, thermal performance, residential, cold climate

INTRODUCTION

Natural ventilation provides opportunities to reduce residential cooling load in summer. Residential air conditioning loads represent 6% percent of total US residential energy consumption, and are responsible for 1.5% percent of residential energy consumption in cold/very cold US climates (EIA 2009). Natural ventilation is a viable option in residential projects to reduce reliance on energy-intensive cooling strategies. Ventilation typically requires increasing the operability of the façade to allow air into occupied spaces, but doing so introduces more opportunity for infiltration in winter as well, thereby increasing heating loads in winter. Typically 6 to 22% (mean 15%) of infiltration occurs at windows and doors in residential buildings (ASHRAE 2001). Winter space conditioning is responsible for 42% percent of total US residential energy consumption, and 54% percent of energy consumption in cold climates (EIA 2009). Infiltration rates can vary by a factor of ten in north America, so the impact on energy consumption is highly variable based on construction typology (ASHRAE 2001). Single family detached homes in the US have ACH50 values from 3 to 40, with a median of about 12 ACH50 (Chan, Joh, and Sherman 2013). Buildings in cold climates with energy recovery ventilation particularly need to control infiltration so as to make best use

of the mechanical heat exchange (ASHRAE 2001). However, infiltration is responsible for a third to a half of the space conditioning load of a home (Sherman 2009). Increasing the number of operable apertures would likely further increase winter infiltration. Wall apertures present opportunities for thermal bridging in addition to infiltration because frames are typically more conductive materials spanning the insulation layer. The detail studied in this project is similar to a window or door frame in this regard.

The ventilation apertures in the test home were designed to increase summer ventilation while minimizing winter infiltration and thermal bridging. However, the thermal and air movement performance of these in either field or laboratory conditions is currently unknown. This study seeks to assess whether winter performance in the field suggests viability of this envelope detail approach, and hence whether further lab testing is warranted.

Specific requirements or standards for whole-building ventilation provide an indication of whether a building has infiltration levels within a desired range for energy efficient operations. Significant relevant examples are shown in Table 1.

Requirement	Notes	ACH 50
Energy Star (EPA and DOE 2015)	Under the prescriptive path in climate zone 5.	<4
International Energy Conservation Code (IECC) and NY State Energy Conservation Construction Code (NYSECCC) (International Code Council 2015)	NYSECCC is based on IECC	<3
LEED v4 for Homes: 1 point (US Green Building Council 2013)		<2.75
LEED v4 for Homes: 2 points		<2.0
Passive House Standard (International Passive House Association)		<0.6

Thermal bridging may be studied using finite element analysis software that maps how heat will flow through all elements of an assembly under ideal specified conditions. Analyzing the magnitude of thermal flux should identify aspects of the test apertures that allow significant heat transfer from inside to outside during winter.

We predicted that infiltration levels would be lower than the published guidelines without major thermal bridging occurring, and we tested this hypothesis with a blower door test and analysis in THERM.

METHODS

Ventilator / House prototype

The ventilation apertures studied were a set of thirteen 0.121 m² operable through-wall openings, shown in Figures 1, 2. These openings cut through a 260mm SIP wall finished with 16mm gypsum board on the interior and 19mm larch rainscreen on the exterior. On the interior face, the units had an operable plywood door so the user could regulate ventilation in the summer, as shown in Figure 3. These had wing up hold open fittings to maintain ventilation when open, and magnetic touch latches to keep them closed. The exterior rainscreen was perforated with 50% openings where the ventilators occurred, as shown in Figure 4. Behind the perforated openings was an insect screen. Each ventilator had a wood-wrapped insulation plug that is inserted in winter. These plugs had an EPDM gasket and were fixed in place with a casement fastener.

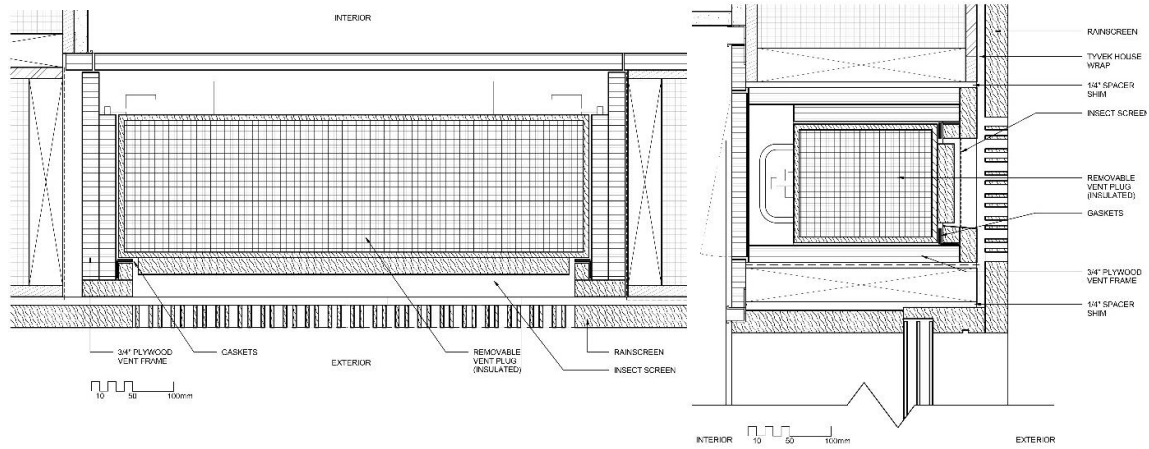


Figure 1: Ventilator construction, plan (left).

Figure 2: Ventilator construction, section (right).

The ventilators were located in a 71.5 m² prototype high-performance house located in Buffalo. Windows in the house, with the exception of an egress window in the bedroom, were fixed, triple-paned, and argon-filled. The ventilators are typically located above the windows from 2197mm to 2374mm. The house is equipped with a Greenheck Minicore-5-VG energy recovery ventilator equipped with a CO₂ sensor to cycle air when the house is occupied.



Figure 3: Ventilator as seen from inside test house (left).

Figure 4: Ventilator as seen from outside test house (right).

Blower Door Test + Smoke Analysis

The ACH50 was measured by following chapter 8 of the RESNET standards, which specifies procedures for conducting a one-point building enclosure airtightness test¹ (RESNET 2013). We used a Minneapolis Blower door with a single fan. Tests were performed in February and March of 2018, when temperature conditions were between -1 and 4 °C and conditions were not windy. While the house was depressurized to -50 Pascals relative to outside conditions, we performed a qualitative assessment of air infiltration at the ventilators. Using a smoke wand, we examined each of the thirteen ventilators with doors open and doors closed to look for evidence of infiltration, and documented each condition photographically. Ventilation plugs remained inserted for this test.

Therm analysis

The plan and the section detail for the ventilators were examined in THERM 7.6 using a temperature difference of 20.7 °C from inside to outside (with external temperature equal to

¹ Chapter 8 standards were replaced with ANSI/RESNET/ICC 380-2016 and addendum A-2017 as of January 1, 2018.

0.4 °C). Table 2 shows the material properties assigned to each of the component materials of the assembly. Emissivity was set to 0.90 for each material.

		Thickness (mm)	Thermal conductivity (W/m-K)
Wall assembly	External larch cladding	19	0.11
	Oriented strand board	13	0.13
	Expanded polystyrene (EPS)	235	0.03
	Oriented strand board	13	0.13
	Gypsum wall board	16	0.25
Insulation plug	Plywood	6	0.12
	Extruded polystyrene (XPS)	190	0.034
	Plywood	6	0.12
	EPDM Gasket (D-shaped)	16	0.2

Table 2: Material properties for THERM model

RESULTS

We have earlier postulated that the inclusion of the ventilators do not prevent the test home from meeting published air infiltration guidelines and at the same time introduce more natural ventilation possibilities. Our blower door test result (ACH50) of 1.16, indicate that the air infiltration levels of the whole house are well within the guidelines for Energy Star certification, IECC, NYECCC, LEED v4 for Homes, but do not meet the more stringent requirements for the Passive House standard, as shown in Table 1.

The smoke wand photographs taken while the house was depressurized help to identify qualitatively where infiltration is occurring in the house. Figures 6 is typical of the ventilators in the closed position, showing that there is no discernable air leakage. Figure 7 indicates some air leakage with the ventilator door is open. This occurred in five of the thirteen ventilators when the doors were open.



Figure 6: Photograph of smoke test with ventilator in closed position. No air leakage is evident in this condition at any ventilator (left).

Figure 7: Photograph of smoke test with ventilator in open position. Five of thirteen ventilators showed some discernable air leakage in this position, as shown here (right).

Smoke tests at other envelope locations in the home while it was depressurized show evidence of air infiltration at the base of the folding glass doors, the stove hood, the bathroom fan, and several of the HVAC diffusers suggesting that these are contributing measurably to the whole house air leakage.

Further, we have suggested that these apertures do not introduce substantial new thermal bridges into the building envelope. Our THERM analysis, shown in Figures 11 and 12, suggest that thermal bridging at this detail is not a primary concern but that a less conductive frame material may yield thermal improvements.

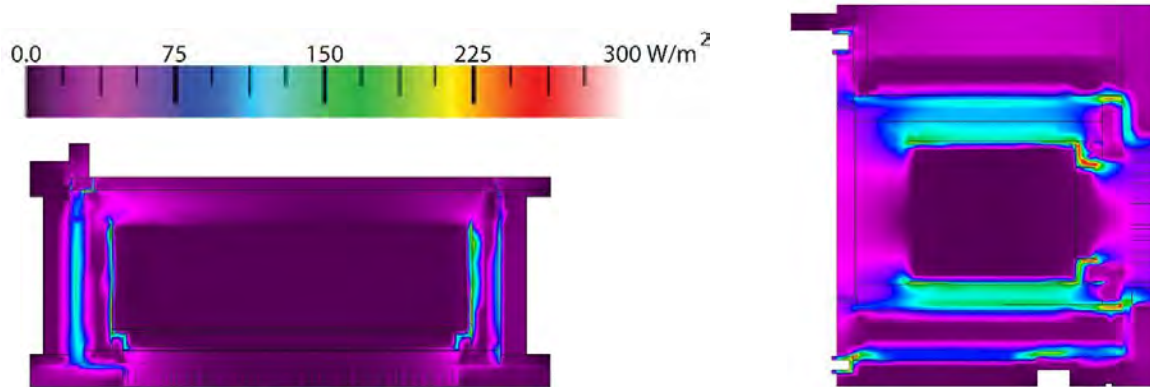


Figure 11: Results of THERM heat flux analysis, plan view (left).

Figure 12: Results of THERM heat flux analysis, section view (right).

We conclude from the results of the blower door testing and the THERM analysis that this ventilation approach is a viable one in cold climates, and may be applicable to other buildings beyond the test home. Thus further laboratory testing is warranted.

DISCUSSION

This study performed initial analysis and in-situ research into a novel natural ventilation aperture which indicates that it is a promising detail for cold climate residential construction. That is, whole house infiltration, including that from the thirteen ventilators, is within several energy efficiency guidelines for infiltration. Further, 2D heat flow analysis suggests that thermal bridging is not problematic. Further laboratory study is warranted to quantitatively characterize heat flow and infiltration. Laboratory studies should focus on heat flux measurements through the assembly, including a hot box test.

While the house meets most of the infiltration guidelines examined, it notably does not meet the PassiveHouse standard. Given that much attention was paid to air infiltration during design and construction, this is a surprise. For example, walls, ceilings, and floors are of SIP construction, where panels are tightly connected with a spline and adhesive. All windows are fixed, with spray foam insulation around the frame; all wall and roof penetrations are caulked. However, the photographic evidence points to air leakage under the folding glass panel doors, as well as at several mechanical system connections. It is recommended that these leaky areas be addressed in order to reduce air infiltration to meet the Passive House standard.

CONCLUSIONS

Design for high-performance residential buildings often includes novel applications of sophisticated active technologies, but may also benefit from novel applications of passive technologies. This paper reports on an investigation into the wintertime performance of novel natural ventilation apertures in a prototype high-performance single-family home in Buffalo, NY. This study assess whether the design approach of decoupling natural ventilation apertures from daylight/view windows can improve wintertime thermal performance of the home. In the test home, natural ventilation occurs through a set of thirteen 0.121 m^2 wood framed, screened openings located in the upper part of the SIP-constructed walls, typically above fixed view windows. Ventilation in summer is controlled with a manual wooden door.

In winter, a gasketed plug of insulation weatherizes the opening and minimizes conductive heat transfer and infiltration.

This design approach is new for cold climates. The operable, dedicated ventilation panels found in temperate locales is modified here to include seasonal insulation. The investigation methods included analysis of whole-building infiltration using blower door testing, diagnostic photography, and modeling in THERM. Results indicate that this approach is viable in cold climates, and should be further studied for implementation to maximum effect in future projects.

ACKNOWLEDGEMENTS

The author appreciates the data collection efforts of the following students: Leticia Avilla, Trezz Bailey, Tierra Bush, Laura Carless, Aubrey Fan, Zach Fields, Tom Foederer, Frank Kraemer, Jelani Lowe and Fatima Mohammed.

The information, data, or work presented herein was funded in part by the Office of Energy Efficiency and Renewable Energy (EERE), U.S. Department of Energy, under Award Number DE-EE0006549. The information, data, or work presented herein was funded in part by an *agency* of the United States Government. Neither the United States Government nor any agency thereof, nor any of their employees, makes any warranty, express or implied, or assumes any legal liability or responsibility for the accuracy, completeness, or usefulness of any information, apparatus, product, or process disclosed, or represents that its use would not infringe privately owned rights. Reference herein to any specific commercial product, process, or service by trade name, trademark, manufacturer, or otherwise does not necessarily constitute or imply its endorsement, recommendation, or favoring by the United States Government or any agency thereof. The views and opinions of authors expressed herein do not necessarily state or reflect those of the United States Government or any agency thereof.

REFERENCES

- ASHRAE. 2001. *2001 ASHRAE Handbook: Fundamentals*. Edited by Mark S. Owen. Atlanta, GA.
- Chan, Wanyu R., Jeffrey Joh, and Max H. Sherman. 2013. "Analysis of air leakage measurements of US houses." *Energy and Buildings* 66:616-625. doi: <https://doi.org/10.1016/j.enbuild.2013.07.047>.
- EIA, US. 2009. Residential Energy Consumption Survey.
- EPA, and DOE. 2015. "National Program Requirements ENERGY STAR Certified Homes, Version 3 (Rev. 08) Modified Prescriptive Path Allowance." https://www.energystar.gov/ia/partners/bldrs_lenders_raters/downloads/ES%20NPR%20v83%202015-07-07_clean_508.pdf.
- International Code Council. 2015. "2015 International Energy Conservation Code (2nd Printing as adopted by New York State)." <https://codes.iccsafe.org/public/document/IECC2015NY/chapter-4-re-residential-energy-efficiency>.
- International Passive House Association. "Passive House Guidelines." accessed February 14, 2018. https://www.passivehouse-international.org/index.php?page_id=80.
- RESNET. 2013. Mortgage Industry National Home Energy Rating Systems Standards. In *Chapter 8*. Oceanside, CA: Residential Energy Services Network, Inc.
- Sherman, Max. 2009. "Infiltration in ASHRAE's Residential Ventilation Standards." *ASHRAE Transactions* 115 (2):887-896.
- US Green Building Council. 2013. LEED v4 for Homes Design and Construction.

Application of Radiant Floor Heating in Large Space Buildings with Significant Cold Air Infiltration through Door Openings

Gang Liu¹, Siyu Cheng¹, Yi Xu¹ and Kuixing Liu¹

¹Tianjin University, Tianjin

**Corresponding email: 2016206004@tju.edu.cn*

ABSTRACT

Radiant Floor Heating System (RFHS) has been commonly used in railway stations in cold regions of China for its advantages in thermal comfort and energy efficiency. However, the uneven distribution and extremely cold area of the heating floor, caused by cold air infiltration through door openings, are commonly found in our field measurements. This impact is not considered in the standardized design methods, resulting in an underestimation of the design heat flux. In this paper, CFD simulations are used to quantify the impacts of natural infiltration on surface heat transfer process. Model validation was made against field measurements. 13 simulations were performed for different speeds. As a result, the mean radiant heat flux at floor surface decreased by 36.8% as the infiltration air speed increased from 0.05 m/s to 1.2 m/s, and the noneffective area increased more than 16 times. This result highlights a significant influence of natural infiltration. Regression models were finally developed as a simple method for rough estimation of this impact on radiation, which can make up the limitations of current methods and inform designers to improve their initial design of RFHS when natural infiltration is present.

KEYWORDS

Radiant floor heating system (RFHS), Large space buildings, Natural infiltration, Radiation heat transfer, CFD simulations.

INTRODUCTION

The proportion of radiant heat exchange in surface total heat flux counts much for the design and operation of Radiant floor heating system (hereinafter RFHS). For this system, the air temperature is allowed to be 1-2 K lower than the conventional all-air systems, due to its heat exchange mainly by radiation (Rhee K N et al, 2017). With the benefit of high energy efficiency, good thermal comfort and space saving potential, RFHS has been widely applied in most railway stations in cold regions of China and is considered as especially effective for heating this space. However, the uneven distributions and a wide low temperature region at the floor surface were commonly found in field measurements of six railway stations. This gap between the design and the reality indicates that the current design methods of RFHS are not applicable for buildings with high door opening frequency and increased ventilation heat loss. Therefore, the goals of this paper are to: 1) verify the impacts of natural infiltration on RFHS, 2) develop a simple method for rough estimation of radiation heat transfer, and 3) give reasonable advice for improving the initial design of RFHS when natural infiltration is present.

METHODS

Field measurement

There are mainly 3 types of waiting hall (Fig.1), categorized by the relative position of entrance and exits. A corner type was chosen for field measurements. The test was performed from 8am to 8pm on January 8th, which was an overcast day. The measuring details are listed in Table 2. Table 1. Three types of waiting hall

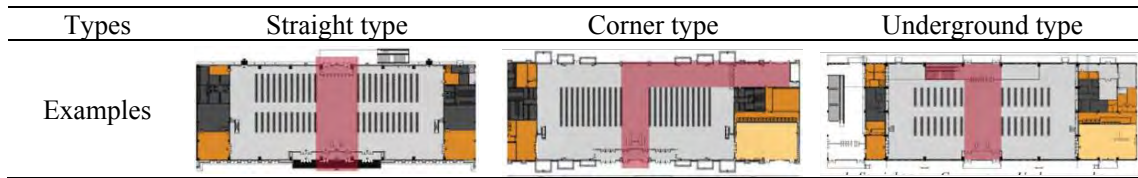
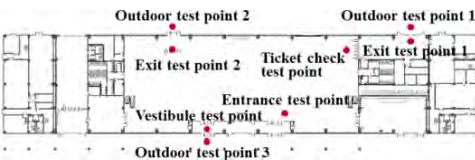


Table 2. Measuring summarization

Item	Instrument name	Range	Accuracy	Measuring points	Interval	Method
Ground temp and internal surface temp	 Sentry ST677 infrared thermometer	-32~1650°C	±2°C		2h	The average value of 5 measurements
Air temp	 HOBO UX100-003	-20~70°C	±0.21°C		5min	Air Temp and Humidity Measure Method of Public Place GB/T18204.13-2000
Airflow rate	 Tesco 425 Hot wire anemometer	0~50 m/s	±0.015 m/s		15min/h	Wind Speed Measure Method of Public Place GB/T18204.15-2000

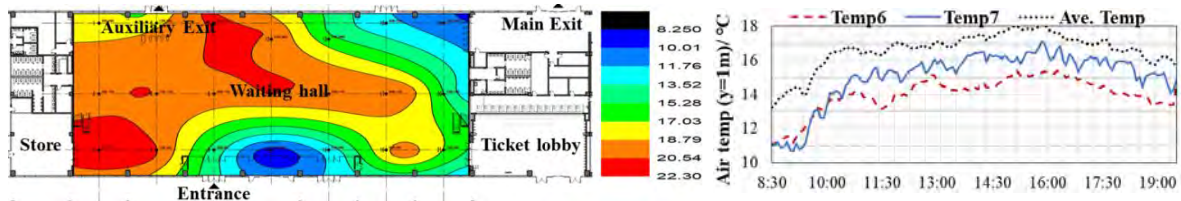


Figure 1. Measured results of waiting hall. a) Ground temp distribution, b) Air temp

The measurement interval of ground temperature was two hours. During the test period, six runs were tested, and the mean value of each point was used for interpolation. The matrix data of ground temperature was transferred into a color-filled contour image by Origin (Fig.1a). An uneven temperature distribution and a wide low-temperature region between the entrance and the main exit are observed from this image, leading to a decline of surface radiation in the combined heat transfer process. Besides, the air temperatures of point 6 and 7 are found always below average (Fig.1b), demonstrating a poor performance of convection heat transfer due to the increased ventilation heat loss.

CFD simulation

The ANSYS’s workbench platform was employed for CFD simulation. The size of the waiting hall is about 84 m (length)×33.6 m (width)×20.4 m (height). The geometry (Fig.2a) of the flow domain was modelled using ANSYS’s DESIGN MODELER. The developed physical model was then meshed using 3D hybrid meshing comprised of 4, 582,417 unstructured elements and 1,611,915 nodes. The maximum mesh size was 0.2 m. Meshes near wall surface are subdivided as $y^+ < 1$ using 10 layers inflation (Fig.2b). Separate grid independency was not tested due to the fine sizes. solar radiation, internal heat gains and heat loss of enclosures were not included, since they are often counterbalanced with one another. The associated air system was shut off

during the test periods. The flow was assumed to be 3D, steady-state, incompressible and turbulent. Buoyancy was modelled with Boussinesq approximation. Near-wall treatment was considered. The heat flux generated from the heating panel was assumed as a constant value of 80 W/m^2 . Based on the assumptions above, the airflow and temperature distribution were solved by the conservation laws of mass, momentum and energy. The detailed boundary conditions are given in Table 3. The airflow rates and temperatures were set equal to their actual values. Besides, RNG $k - \epsilon$ and Discrete Ordinate (DO) model were chosen to simulate the turbulence and radiation phenomena inside the room, respectively. The coupled-analysis model was solved as steady state using SIMPLE algorithm. Enough good convergence was obtained finally.

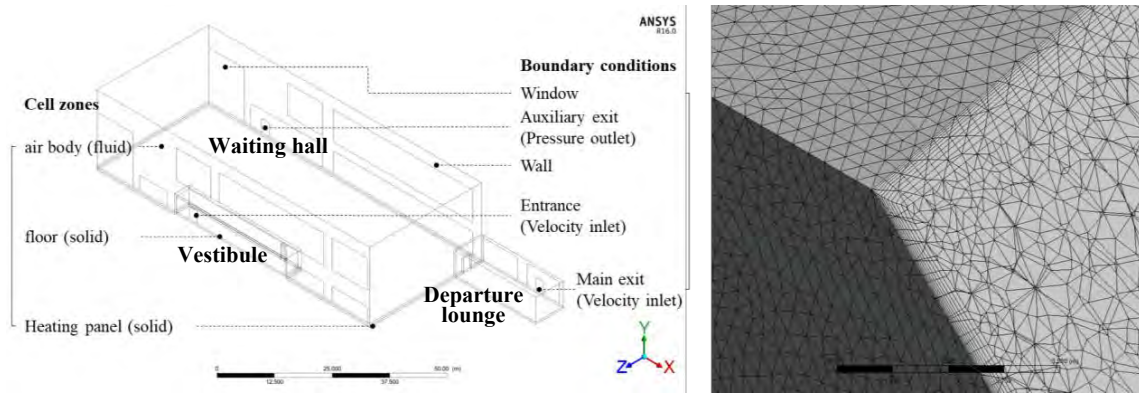


Figure 2. a) CFD drawing of the computing domain.

b) Near-wall mesh refinement

Table 3. Boundary conditions

Wall	Window	Internal wall	Floor	Heating panel
Wall temperature boundary condition (17°C)	Wall temperature boundary condition (10.5°C)	Adiabatic (heat flux = 0)	coupled boundary condition	Heat flux boundary condition (80W/m^2)

Validation of the model

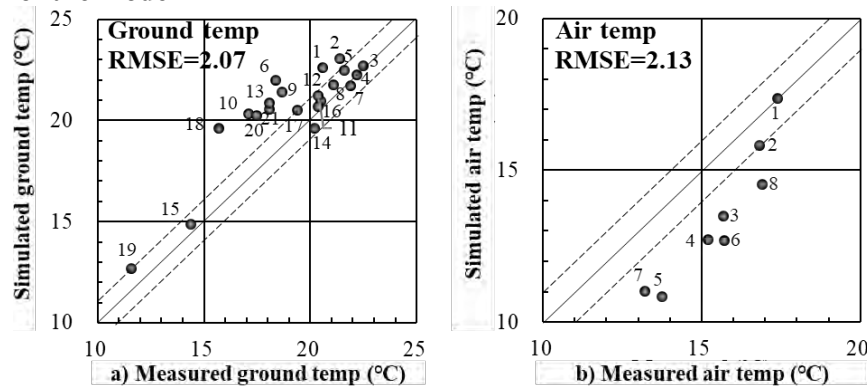


Figure 3. Correlations of actual measurements and simulated temperatures. a) Ground temperature of 21 measuring points ($y=0$), b) Air temperature of 8 measuring points ($y=1\text{m}$).

The measured floor surface temperatures at 21 points and air temperatures at eight points at 19:00 in the measured day were used for model validation. The occupancy rate was lowest. Fig.3 shows the correlation of actual measurement and simulation results. Dotted lines in the graphs represent the error range of $\pm 1^\circ\text{C}$, and RMSE denotes the root mean square error. Ground temperature shows general agreement with measurement (Fig 3a), considering the uncertainty

of 2°C with measurement accuracy of the infrared thermometer. In general, the overestimation of ground temperature may result from the assumption of constant heat flux and the limitations of steady state simulation, which neglect the temperature drop within the pipe and the delay effect of this system. This overestimation seems to be more prominent in the peripheral area, especially for points near entrance and exists (1, 6, 10, 13, 21 in Table 2). In contrast, the air temperature is much underestimated by CFD simulation (Fig 3b), especially for points in occupied area (3, 4, 5, 6 in Table 2). This discrepancy is due to the ignorance of internal load. Since the central area usually has more passengers than peripheral area, the bias error of point 1,2,7,8 was larger. Generally, these values verify the satisfactory performance of the CFD model, and the simplification allows a substantial decrease of the computational cost without affecting the performance of radiant heat exchange, which is the main interest to this study.

Assessment parameters

The RFHS is defined as a system that radiant heat transfer covers more than 50% of heat exchange within a conditioned space. As the case mentioned in Chapter 6 of ASHRAE Handbook, HVAC Systems and Equipment (1992), the surface heat flux can be calculated separately for convection and radiation. Poor performance for providing stable thermal environment of convective heat transfer has been found in field measurements, which is caused by the increased ventilation heat loss at doors. Therefore, radiation is preferred. In this study, the overall level of radiant heat flux is viewed as an indicator of the system's thermal performance. To numerically demonstrate this, an index named mean radiant heat flux ratio (hereinafter **MRR**) is defined, which is a direct comparison of mean radiant heat flux and the total heat flux (80 W/m²) at the floor surface. Here, the mean radiant heat flux is calculated by the sum of radiant heat flux at the heating surface divided by the total heating area. Suffering from the decrease of ground temperature, the MRR may drop to 50%, which is a minimum value given in ASHRAE, or even lower. In such area the performance of the system is identified as noneffective. The ratio of the noneffective area to the total heating floor area is defined as the noneffective heating area ratio (hereinafter **NAR**). The two indices above were employed to quantify the impact of natural infiltration.

RESULTS

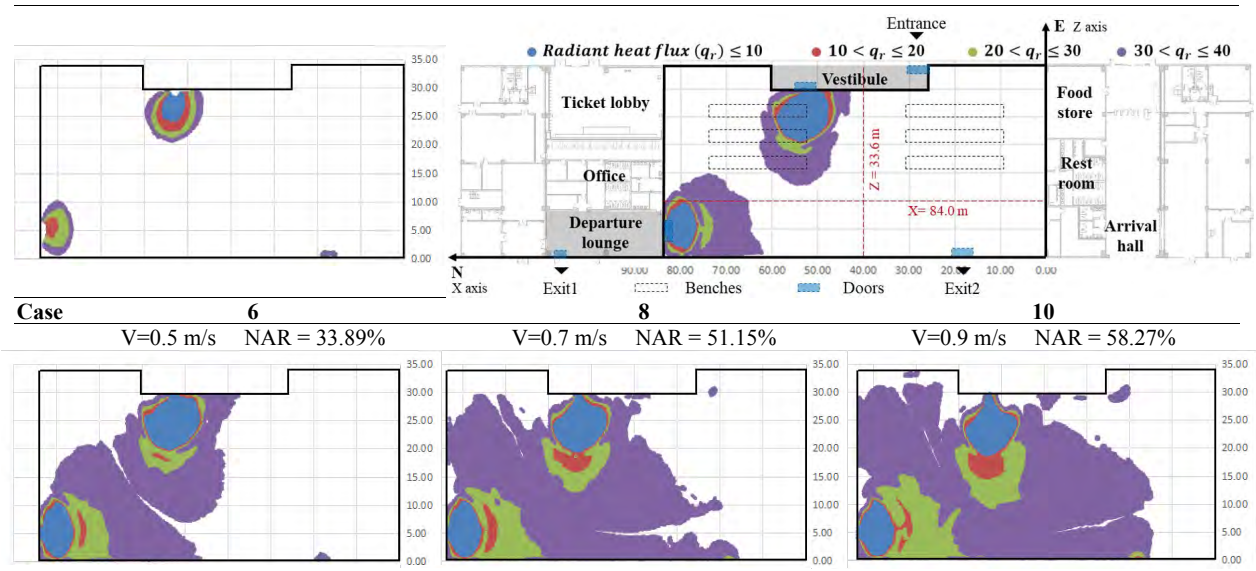
Table 4. CFD simulation results summarization

Case	1	2	3	4	5	6	7	8	9	10	11	12	13
Infiltration air speed (m/s)	0.05	0.1	0.2	0.3	0.4	0.5	0.6	0.7	0.8	0.9	1	1.1	1.2
Average radiant heat flux (W/m ²)	53.0	51.4	48.2	44.3	41.33	39.0	37.2	36.0	34.9	34.1	33.3	33.6	33.5
Average convective heat flux (W/m ²)	27	28.6	31.8	35.7	38.67	41	42.8	44	45.1	45.9	46.7	46.4	46.5
Mean radiant heat flux ratio (MRR)	70.0%	67.4%	61.7%	56.8%	52.9%	49.9%	47.7%	46.0%	44.6%	43.5%	42.5%	42.9%	42.8%
Noneffective heating floor area (m ²)	121	150	296	494	742	95679	1185	1445	1645	1775	1902	1973	2072
Noneffective area ratio (NAR)	4.3%	5.3%	10.5%	17.5%	26.3%	33.9	42.0%	51.2%	58.3%	62.9%	67.4%	69.9%	73.4%

According to the measured data, the wind speed at entrance and exits was initially set as 0.05m/s and then to increase from 0.1 to 1.2m/s at an increment of 0.1m/s. 13 scenarios in total were simulated. The main simulation results were tabulated in Table 4. Table 5 gives an intuitionistic exhibition of the noneffective heating area distributions under different wind speeds. In each figure, the noneffective area was categorized into four levels according to its radiant heat flux and filled with corresponding colors as the legend shows. The same coordinate system and room plan were only attached to case 4 as a reference. Part of cases are not shown due to limited space, but the gradually enlarging distribution pattern of the noneffective area is still obvious.

Table 5. Noneffective heating area distribution

Case	2	4
	V=0.1m/s NAR=5.34%	V=0.3 m/s NAR=17.54%



DISCUSSIONS

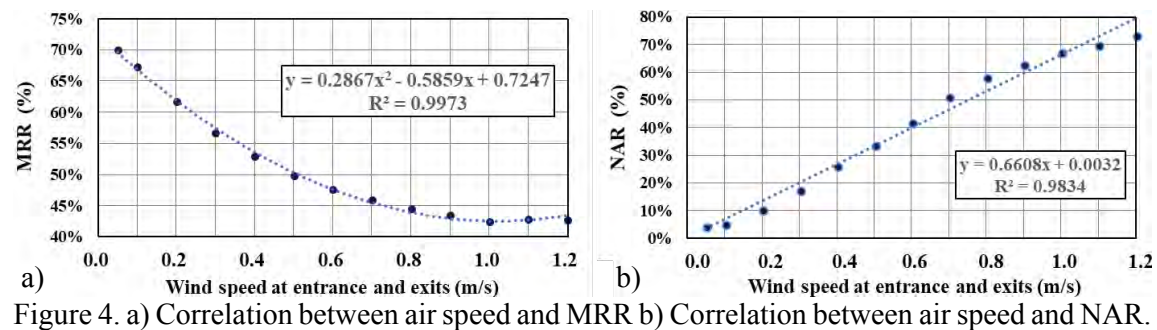


Figure 4. a) Correlation between air speed and MRR b) Correlation between air speed and NAR.

Scatterplots were used to evaluate the correlation of air velocity with MRR and NAR, and the acquired regression models were described in Fig.4. R^2 values over 0.9 show significant correlations between the input and output, indicating a deep impact of wind speed on radiation heat transfer. For MRR (Fig 4a), the decreasing rate is apparently higher when the air speed is increasing from 0.05 to 0.7 m/s, implying even a slight increase of wind speed could cause a significant drop. After that, the descending rate levels off, and the lowest ratio is about 43%. For NAR (Fig 4b), it is positively related to the infiltration air speed, which is considerably low at first but grows rapidly as the wind speed increases. Taking the distribution into account, the noneffective area only appears near the entrance and exits, and the MRR of occupied area is acceptable when air velocity is low, as shown in Table 5. However, the noneffective area becomes larger and gradually spreads to the occupied area with the increase of wind speed. The occupied area thus would be at great risk of discomfort. In this way, the impact of natural infiltration could be quantified at the initial design stage once the prevailing wind speeds at the entrance and exits are given. A microscopic correlation analysis was performed between near-surface-wind-speed ($y=1\text{mm}$) and the corresponding surface radiant heat flux ($y=0$) to further validate the findings above by using a large sample size and taking the position factor into account. To this end, 80857 sample points were investigated and 10% of them were selected with systematic sampling method for correlation analysis. These nodes were evenly distributed at the floor surface. The result is shown in Fig 5a, taking case 6 ($V=0.5\text{ m/s}$) as an example. The vertical axis represents the radiant heat flux, and the horizontal axis represents the node number which is defined sequentially according to its near-surface-wind-speed. An obvious piecewise

linear change was found at the two sides of the dividing line, which corresponds to a near-surface-wind-speed of 0.3 m/s. The left part of the dividing line shows a general decreasing trend. The discrete distribution shows a common influence of the speed and position factor. The near-surface-speed limit of 0.3 m/s and a decreasing amplitude of 33% are obtained as a design reference. While for the right part, which is replotted in Fig 5b, the highly linear correlation ($R^2=0.85$) highlights the dominate influence of speed factor. The decreasing rate is apparently higher than the left, and the surface radiation is extremely low. However, this part only accounts for a small portion of the entire sample size. In all cases, the near-surface-wind-speed shows 0~1.4 m/s at the occupied area regardless of the wind speed at the entrance and exits, and the results of piecewise correlations are found to be quite similar. Therefore, case 6 is representative for all other cases.

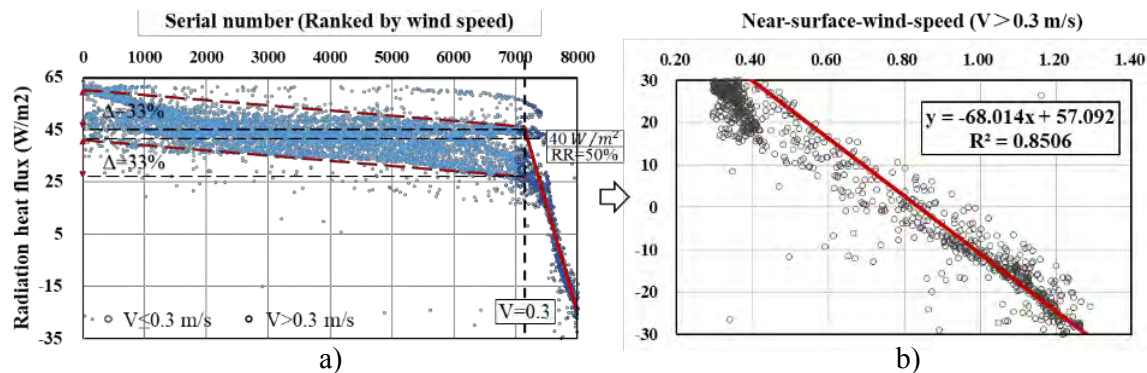


Fig.5 a) Surface radiant heat flux ($y=0\text{mm}$) according to the near-surface-wind-speed ($y=1\text{mm}$). b) the regression curve for $V>0.3\text{m/s}$

CONCLUSIONS

The results of field measurements provide evidences that the existing RFHS design methods are theoretically insufficient when this system operates with significant natural infiltration. Regression models for wind speed at doors and near-surface-wind-speed were developed in this paper. For a better performance of RFHS, the near-surface-wind-speed should be controlled under 0.3 m/s. Within this limit, comprehensive estimations are recommended for surface radiation, noneffective heating area and its distributions to guide reasonable design decisions. These assessments are easily to perform with the acquired regression models. When necessary, designers should take extra measures to increase the design heat flux at affected floor area, such as adding extra heat source, reducing pipe spacing or imposing the regional control methods.

ACKNOWLEDGEMENT

The research presented in this paper was financially supported by The National Natural Science Foundation of China (the Key Program) through grant No. 51338006;

REFERENCES

- Zhao K, Liu X H, Jiang Y. 2013. Application of radiant floor cooling in a large open space building with high-intensity solar radiation[J]. *Energy & Buildings*, 66(6):246-257.
- Rhee K N, Olesen B W, Kim K W t. 2017. Ten questions about radiant heating and cooling systems[J]. *Building & Environment*, 112:367-381.
- ASHRAE. *ASHRAE handbook-HVAC systems and equipment*. 2012. Atlanta, GA: American Society of Heating, Refrigerating, and Air Conditioning Engineers.
- Yi Xu, Rui Dang, Lixiong Wang, Gang Liu. 2016. The influence study of entrance air infiltration rate on energy consumption and optimal design of the high-speed railway station in cold climate regions[J]. *PLEA 2016 32nd Conference.*, 3: 238-245

Evaluating the hygrothermal performance of wooden beam heads in 19th century town houses using in-situ measurements

Paul Wegerer^{1,2*}, Thomas Bednar¹

¹TU Wien, Vienna, Austria

²Gassner & Partner Baumanagement GmbH, Vienna, Austria

*Corresponding email: paul.wegerer@tuwien.ac.at

ABSTRACT

Improving the energy efficiency of typical 19th century townhouses in middle Europe the focus on the wooden beam bearing's hygrothermal performance has become more and more important during the last years. There are several issues for the risk of rotting of the wooden parts of the ceiling, because the retrofitting process of the masonry totally changes the hygrothermal conditions inside the wall. Applying an interior insulation or changing the airtightness of the building envelope as well as the introduced moisture from the retrofitting process lead to a moisture increase inside the masonry and might cause rotting of the ceilings' wooden beam ends.

This paper introduces two demonstration objects which were retrofitted during the last years. Temperature and humidity sensors have been integrated at the wooden beams' ends to show the hygrothermal conditions during and after the retrofitting process. In the first building measurements started at the beginning of the renovation in September 2013 and are still being carried out. To compare different situations the monitored beam bearings are situated in two different retrofitted wall constructions, an inside insulated and a not insulated wall. Additionally, different indoor climates in the flats above and below the measured ceiling are monitored. In the second building 16 wooden beam heads situated in two different storeys with differing masonry thicknesses were measured. In this demonstration object the influence of building construction moisture from the renovation process as well as the drying out process were evaluated.

In conclusion, the wooden beam heads' durability will be assessed based on the measurement results and possible risk of damage influenced by the retrofitting process.

KEYWORDS

Wooden beam ceiling, interior insulation, in-situ measurements, hygrothermal performance

INTRODUCTION

During the course of the project „Improving Durability of Wooden Beam Bearings in Inside Insulated Walls by Tempering the Beam's Heads“ in-situ-trials on existing constructions with wooden beam ceilings were carried out in two late 19th century townhouses in Vienna. For a targeted analysis of the hygrothermal performance of wooden beam heads, sensors to measure temperature and relative humidity were installed in the floor-bearing-areas during a typical retrofitting process. Thus, the conditions in temperature and moisture could be examined during the state of construction and over the ensuing years of use.

Currently, no interior insulation is installed when a late 19th century townhouse is renovated conventionally, as there is no requirement for the thermal transmittance (U-value) with renovations according to the Austrian building code. However, due to noise abatement, a suspended ceiling is always mounted, which – because of the placement of mineral wool

results in cooling of the floor bearing area during wintertime. Future, energy-efficient renovations will stipulate the installation of an interior insulation, necessitating a detailed planning of accompanying measures on the ceiling-to-wall bearing. On the one hand, the measurement results document a long-term study on the functional efficiency of current methods of renovation. On the other hand, they form the basis for further research and the set-up of a bench test in a double climate chamber. The aim is to show that with constructions using interior insulation the floor bearing area cools of severely during winter and, because of the high relative humidity, the risk of wood rotting increases.

METHODS

Temperature and relative humidity sensors were installed in the construction of two demonstration buildings in selected apartments during the renovation works. Depending on the wooden beam's installation situation, the sensors were mounted in different positions. Figure 1 exemplarily shows, using the installation situation of building "Eckertgasse 10" that measurement points were chosen at the top, the bottom as well as in the middle of the beam head. Additionally, every wooden beam was spot-drilled, to be able to position a sensor in half of the beam's height in the air space between the wood and masonry. To measure the climatic boundary conditions, the indoor climate of the flat resp. the particular room and the outdoor climate on the façade were recorded.

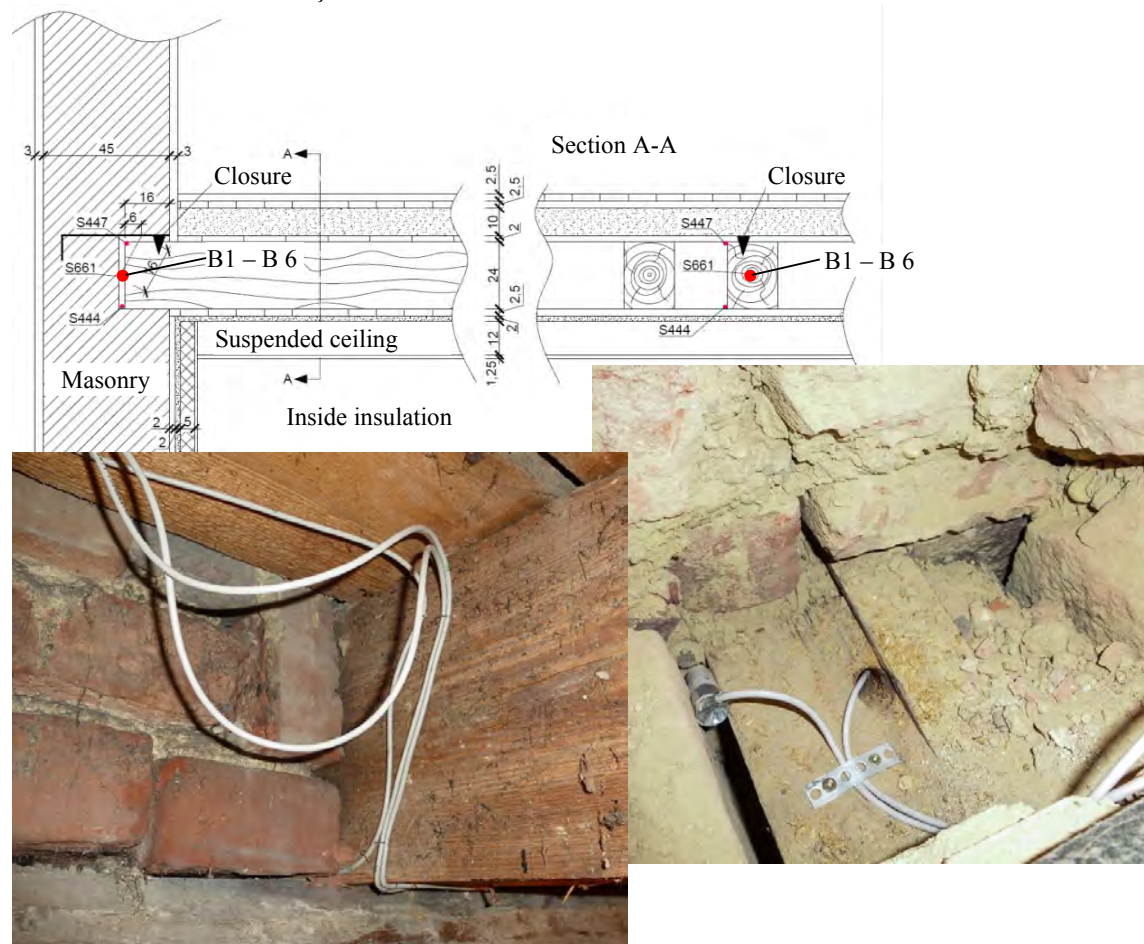


Figure 1. Example of sensor positions at the beams' end for long time monitoring; façade section of "Eckertgasse 10" (above), picture in the ceiling cavity (bottom left), picture of the sensor on top of the beam (bottom right);

There are different installation situations of beam head abutments (Wegerer et al., 2017) and thus also different hygrothermal behavioural patterns which are influenced by constructional parameters. While numerous publications (e.g. Kehl et al., 2013; Guizzardi et al., 2015; Strangfeld et al., 2012) often report on the calculation resp. the simulation of beam heads, there are little findings on the actual behaviour of wooden beam bearings in practice, especially after a retrofitting process.

The fundamental aims of this research paper consist in examining a sufficiently large enough sample of wooden beam heads as well as to achieve a multi-year measurement time. Figure 2 shows the façade of demonstration object “Trubelgasse 8”. In this building, 16 beam heads were equipped with sensors. The measurements on the two demonstration buildings started at construction level and, in the beginning, show the building moisture’s drying-up-process. The continuous, multi-year gathering of data that started in July 2016 gives information about the hygrothermal behaviour during the utilisation phase.



Figure 2. Façade (left) and section (right) of demooobject “Trubelgasse 8” with 16 schematically marked monitored beam heads.

RESULTS

Demonstration building “Eckertgasse 10”

So far, more than 4 years of measurement data are available from this monitoring. Beam heads B1 to B3 are located in the area of an outside wall with interior insulation analogous to the construction in fig. 1. Beam heads B4 to B6 are located in the area of the original outside wall without interior insulation and serve as a reference.

The results clearly show the fluctuations between winter and summer. Furthermore, a steady drying-up-process since the beginning of the measurements is noticeable with all beam heads on the basis of the relative humidity at at least one measurement position. An increase in relative humidity is noticeable with nearly all beam heads during the cold season, which dries up again during the summer months.

To obtain a direct comparison between a construction with and a construction without interior insulation, the measurement data of the sensor positions in the middle of the respective beam head are shown in the diagrams in fig. 3. These positions were made almost identically in all 6 beam heads using drill holes. This comparison shows that in the interior insulation’s area (B1 to B3) critical moisture conditions are reached at the wooden beam heads. Sensor positions on the beam heads bearing in the original, non-insulated construction yield only marginally to barely critical measurement values after the building moisture’s drying-up (B5 and B6). Only B4 shows a higher relative humidity during the winter months.

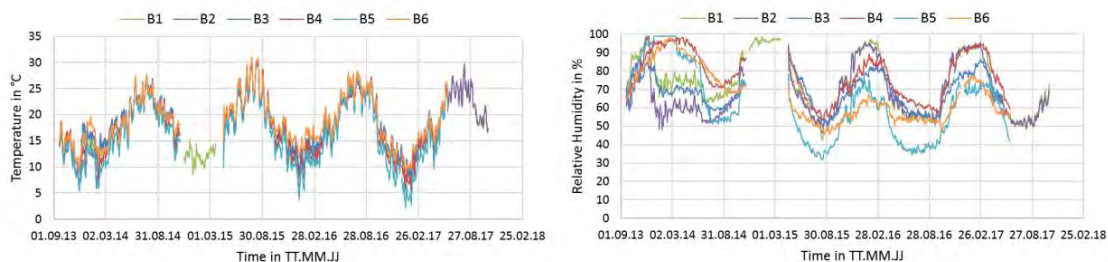


Figure 3. Temp. graphs (left) and rel. hum. graphs (right) over 4 years after the retrofitting process. The object “Eckertgasse 10” has an inside insulation below the measured floor.

The indoor climate (figure 4, left) shows a moisture load typical for residential use and can be classified into moisture class 3 according to EN ISO 13788.

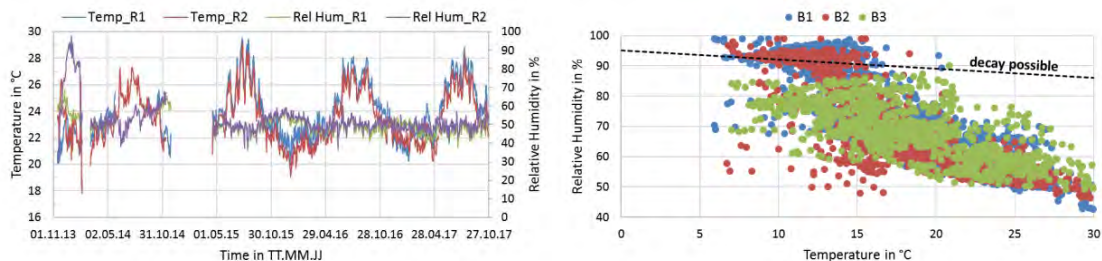


Figure 4. Left: Indoor climate; right: relation between temperature and relative humidity on the beam ends 1 to 3 (daily average values) and limiting curve according to WTA MB 6-8

The comparison of temperature and relative humidity (figure 4, right) in accordance with WTA MB 6-8 shows that only a few days during wintertime yield critical values. Most of the time there is a low risk of wood rotting because of the drying-up during summer.

Demonstration building “Trubelgasse 8”

In this demonstration building, 16 beam heads are examined after a conventional renovation of the façade without fitting an interior insulation. Three sensors were mounted on each beam head, one in the air cavity facing to the outside and two sensors on the abutment at the contact of wood and masonry. The outside wall has three different thicknesses (see figure 2). As a result, the hygrothermal conditions on the beam head vary highly depending on the storey. Beam heads 1 to 8 are situated in a 60cm thick wall and are covered by 45cm with masonry on the outside. Beam heads 9 to 16 are located in a 45cm thick wall and are covered by 30cm with masonry on the outside. This leads to lower temperature and higher relative humidity at the thinner outside covering. The influence of suspended ceilings is also discernible with this construction. Due to the thermal insulation in the ceiling level, increased cooling of the beam abutments occurs during the winter months. The following evaluation shows results from the 2017/18 winter period. Figures 5a and 5b display data with different wall thicknesses.

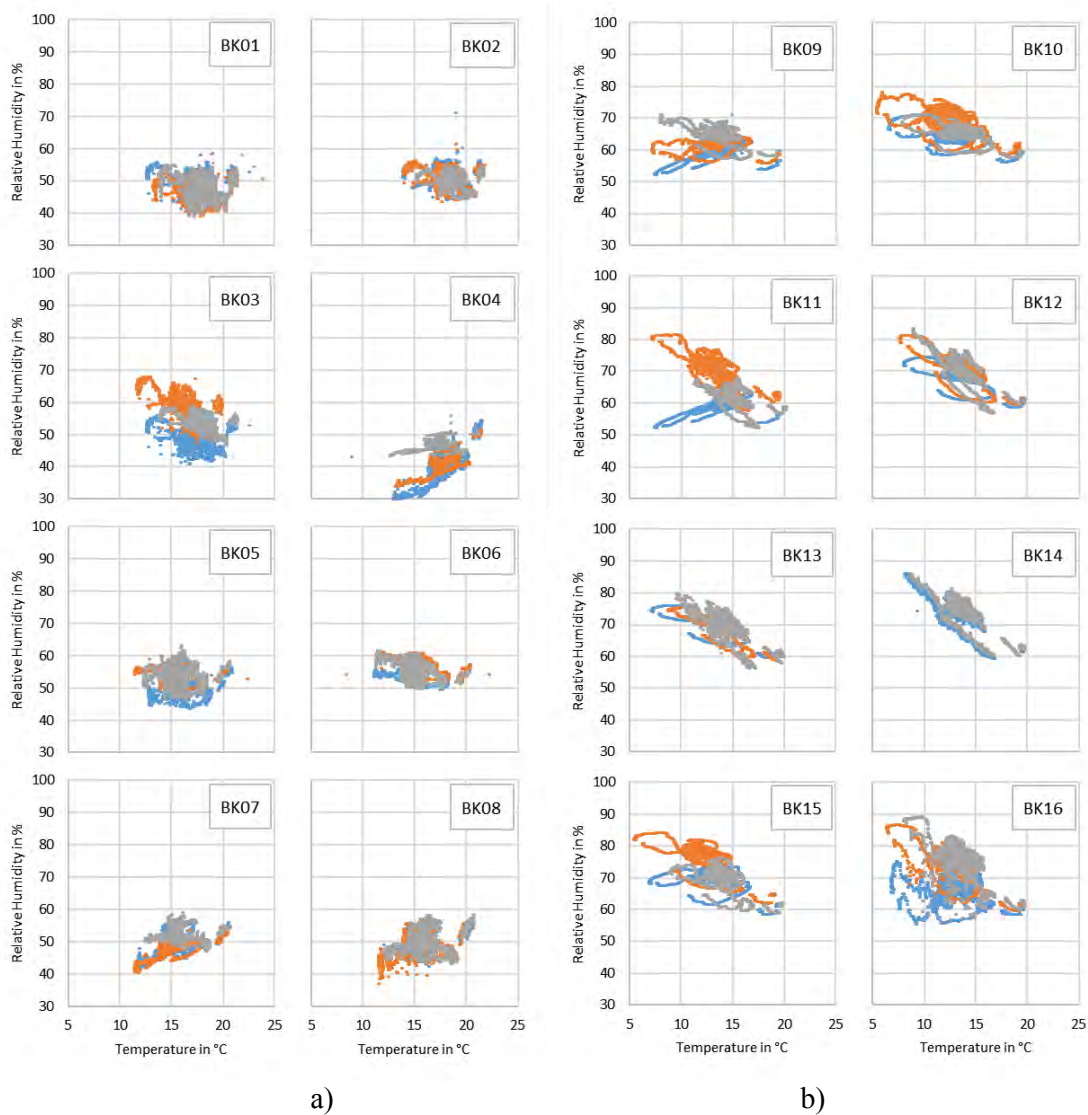


Figure 5. Measurement results at the three positions of the beam heads. a) Wall with 60cm thickness, b) wall with 45cm thickness. The object “Trubelgasse 8” has no inside insulation

on the outer wall below the measured floor. Only a suspended ceiling decreases the temperature of the beam end.

DISCUSSIONS

The combination of long-term measurement and a greater sample size of examined beam head details provides new findings on the functional efficiency and durability of current renovation methods. Most Wilhelminian style houses are over 100 years old and virtually no cases of damage on wooden beam ceiling abutments are known. However, renovations and thermal improvements of the building envelope, especially the fitting of more airtight windows, the mounting of an interior insulation system, or the installation of a suspended ceiling filled with mineral wool change the indoor climate and the hygrothermal performance of the outside wall. The measurement results show that certain renovation measures require detailed planning to minimise the risk of damage of the improved construction. Earlier research has shown the behaviour of wooden beam heads with a retrofitted interior insulation based on concrete examples of damage or case-specific hygrothermal simulations. This research paper's results are to emphasise the importance of monitoring and sample size, especially when particular renovation methods, e.g. an interior insulations, are planned. Additionally the findings show that the renovation measures used in the demonstration objects do not put the durability of the existing construction at risk when the building moisture may dry up and the room climate corresponds to average usage.

CONCLUSIONS

The results provide important feedback for the planner and the developer of the demonstration buildings presented. The long-term studies prove the well-tried constructions' functional efficiency and allow an apportionment on the developer's other renovation projects.

The monitoring results are important validation data for current laboratory tests, which are carried out on a true-to-life sample wall with ceiling-to-beam connection in a double climate chamber. The aim of further laboratory tests is to closer examine the beam head detail on the sample wall and to develop accompanying measures, e.g. a targeted tempering of components for constructions with interior insulation.

ACKNOWLEDGEMENT

The "Austrian Research Promotion Agency (FFG)" and "Gassner & Partner Baumanagement GmbH" supported this research. We are thankful to our colleagues Manfred Grüner and Harald Hofbauer who helped running the measurements that greatly assisted the research.

REFERENCES

- Guizzardi M., Derome D., Vonbank R., Carmeliet J. 2015. Hygrothermal behavior of a massive wall with interior insulation during wetting. In: *Building and Environment* 89 (2015) p. 59-71
- Kehl D., Ruisinger U., Plagge R., Grunewald J. 2013. Wooden Beam Ends in Masonry with Interior Insulation – A Literature Review and Simulation on Causes and Assessment of Decay. In: *2nd central European symposium of building physics, Vienna, September 9-11.*
- Strangfeld P., Staar A., Toepel T. 2012. Das hygrothermische Verhalten von Holzbalkenköpfen im innengedämmten Mauerwerk. In: *Bausubstanz Heft 2, 2012* p. 45-51.
- Wegerer P., Bednar T. 2017. Hygrothermal performance of wooden beam heads in inside insulated walls considering air flows. In: *Energy Procedia* 132:652-657. June 2017.
- EN ISO 13788:2013. Hygrothermal performance of building components and building elements - Internal surface temperature to avoid critical surface humidity and interstitial condensation - Calculation methods

Experimental investigations of wooden beam ends in masonry with internal insulation: results contrasting three years of the experiment

Pavel Kopecký¹, Kamil Staněk¹, Michal Bureš¹, Jan Richter¹, Jan Tywoniak¹

¹University Centre for Energy Efficient Buildings, Třinecká 1024, Buštěhrad, Czech Republic

**Corresponding email: pavel.kopecky@fsv.cvut.cz*

ABSTRACT

This paper deals with hygro-thermal performance of wooden beam ends embedded in masonry walls with lime-cement plaster applied on the external side. Three different insulation systems are attached on the internal side of masonry. The real scale experiment has been monitored for three consecutive years. Microclimatic conditions in joist pockets were assessed by VTT mold growth index. The paper shows the influence of two changes of boundary conditions on the microclimate in joist pockets. First, moisture load on the internal side of building enclosure was increased (24 °C, 60 % in winter 2016/2017 instead 20 °C, 50 % in winter 2015/2016). Then, the artificial short-time rain event brought liquid water onto the external surface of building enclosure in July 2017. The rain intensity was chosen so as to mimic the intensive summer thunderstorm. The increase of water vapor concentration in the air on the internal side led to suitable conditions for mold growth in unsealed joist pockets of a vapor open insulation system. On contrary, microclimate in sealed joist pockets in both vapor open and vapor closed insulation systems stayed in acceptable levels with no mold growth. The artificial rain event significantly changed the hygro-thermal performance of joist pockets. Drying season was shortened and the relative humidity in joist pockets overtook the time profile of external relative humidity.

KEYWORDS

internal insulation, wooden beam end, monitoring, moisture safety, mould growth

INTRODUCTION

Uninsulated brick buildings suffer from high energy consumption, poor thermal comfort and mould growth on the coldest spots of the internal side of the building enclosure. Such buildings were erected before the Second World War in many European cities and often form entire neighborhoods. Floors are often supported by wooden beams placed in pockets embedded in brick walls. The external insulation is usually excluded from refurbishment measures, either because of the fixed building line or because of the decorative façade with cultural value. The internal insulation is therefore the only possible technical solution in these cases. However, the internal insulation significantly changes hygro-thermal performance of the masonry wall.

As the wooden beam protrudes out thermal insulation it is also located in the cold part of the building enclosure. The lower temperature in this position inevitably leads to higher relative humidity of the air in the joist pocket. Moisture content of wood in contact with the air in the pocket is therefore higher (as follows from the sorption isotherm) than it would be if wood was placed on the warm side of the building enclosure. If moisture content of wooden beam end is high enough for sufficient period of time, mold growth or even biodegradation can occur.

This paper deals with hygro-thermal conditions in the air cavity behind wooden beam ends placed in masonry pockets. To study this phenomena long-time full-scale experiments were built in University Center for Energy Efficient Buildings (UCEEB) of Czech Technical University in Prague. Boundary conditions, temperatures, relative humidity, moisture content in wood, and heat fluxes, have been continually recorded for three years. It is assessed whether microclimate of the joist pockets was suitable for mold growth on the wooden beam ends.

EXPERIMENTAL SETUP

Two “test windows” on the south west façade, with the dimension 3.0 m x 3.2 m each, are occupied by brick masonry walls (30 cm) with lime cement plaster (2 cm) on the external side. A climatic room with controlled internal environment is located on the internal side of test walls. Three different internal insulation systems are attached on the internal side of masonry: S1 - wood fiber insulation (8 cm, 14 cm) with thin plaster applied on the internal side (5 mm), S2 - soft mineral wool (9 cm) placed between aluminum studs with smart water vapor retarder and gypsum boards, S3 - vacuum insulation plates (2 cm) covered by EPS (2 × 1 cm) with thin internal plaster (5 mm). Joist pockets were treated by different means, see Fig. 1. For more details on the experimental setup see (Kopecký et al., 2016).

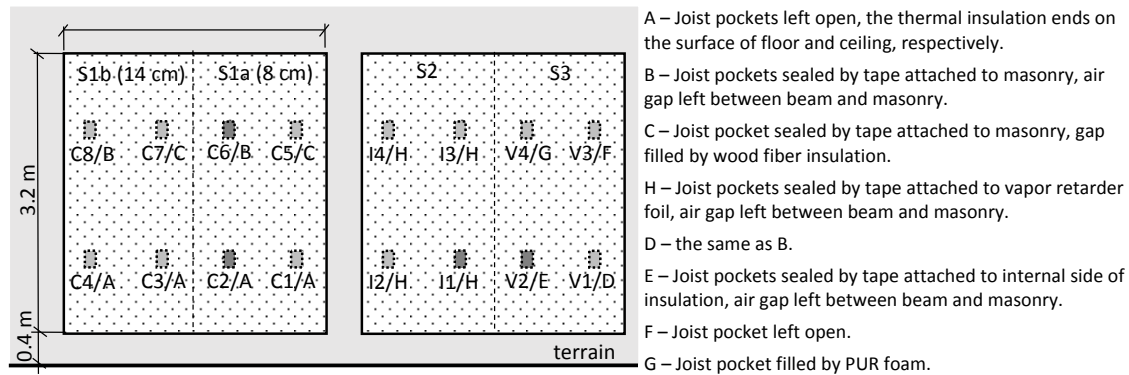


Figure 1. The view on the test fields (from exterior) with position of wooden beam ends.

The following sensors were used to monitor hygro-thermal conditions at the wooden beam end: 1) temperature sensors, 2) temperature + relative humidity sensors, 3) moisture content pins. Positions of the sensors are shown in Fig. 2. Thermostat and hygostat set points during the whole experiment are introduced in Fig. 3. The air handling unit is not equipped by dehumidifier. Therefore, the unit do not keep steady humidity during warm season.

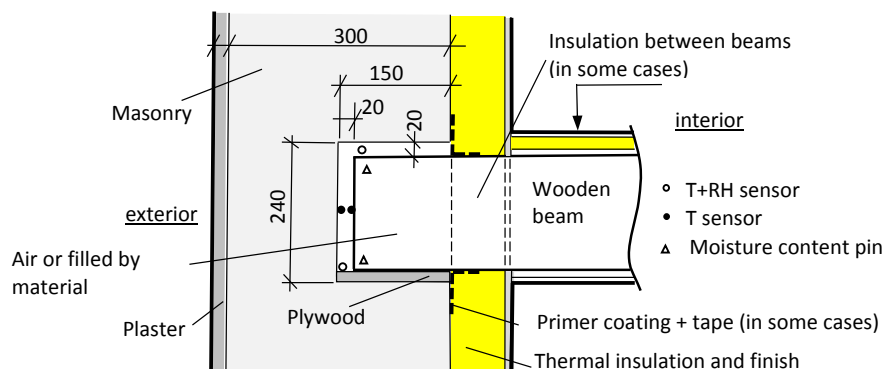


Figure 2. Position of measurement sensors in masonry pocket with wooden beam end.

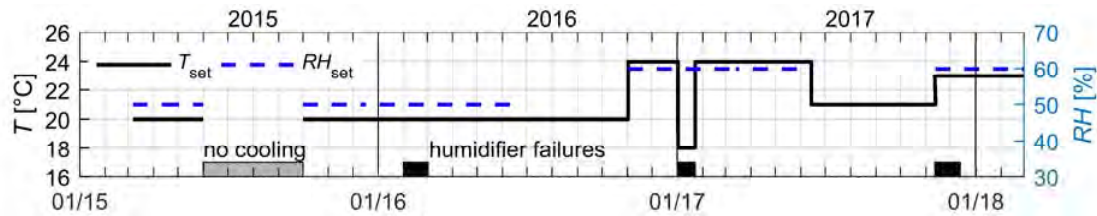


Figure 3. Thermostat and hygrostat setpoints during experiment.

The artificial rain experiment was realized on 19.7.2017 by means of nine nozzles mounted on a supporting frame (see Fig. 4). Time duration of showering was 40 minutes. The artificial rain imitated a summer thunderstorm with exceptional but still realistic rain intensity in the climatic locality. The experiment was intentionally performed during morning time (i.e. without direct solar irradiation on the south west facade) so evaporation was relatively low. Since sprinklers were positioned more in the central part of the test fields, the narrow stripe near the perimeter of test fields stayed dry (see. Fig. 4). The total inflow of water into the sprinkler device was 1,7 litres/m²/min (68 litres/m²/40min). The value is much higher than the strongest wind driven rain observed on site during monitoring campaign. The total volume of water sucked by the test field was 13,4 litres/m²/40 min (related to wet area, outflowing and bypassed water was taken into account). Due to the limited size of the sprinkler device joist pockets located on both vertical sides of test walls were not loaded as much as joist pockets located in the central part of test walls. Based on the porosity of the plaster and bricks and the total amount of water absorbed, it can be estimated that the saturated zone was approximately located up to a depth of 5 cm when the artificial rain was finished.

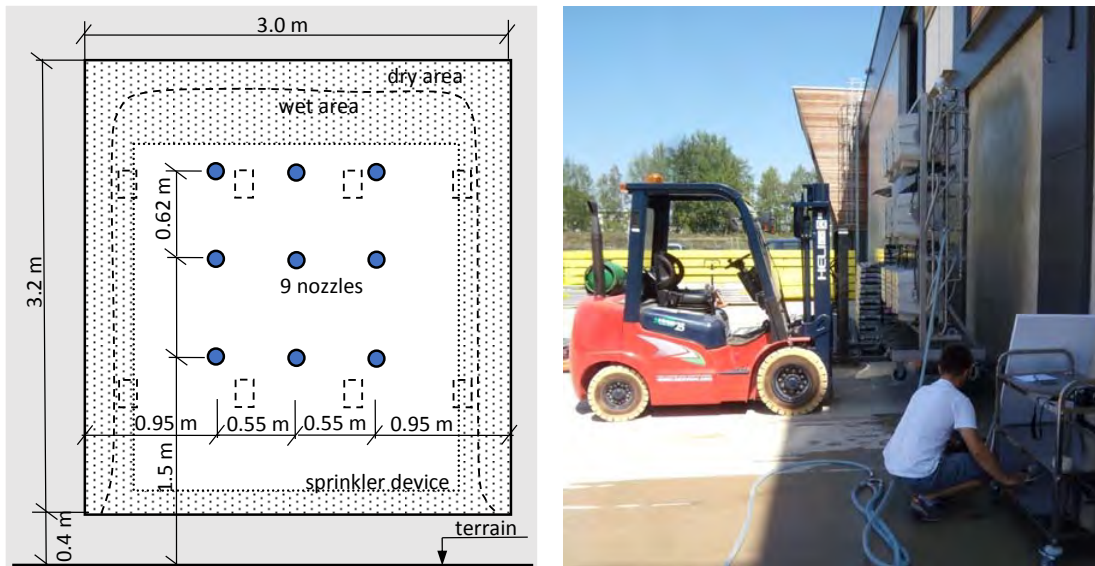


Figure 4. Left – the front view on the test field with position of sprinklers and wooden beam ends. Right – the sprinkler device positioned in the front of the test field.

RESULTS

Long-term measured data are summarized in Fig. 5.

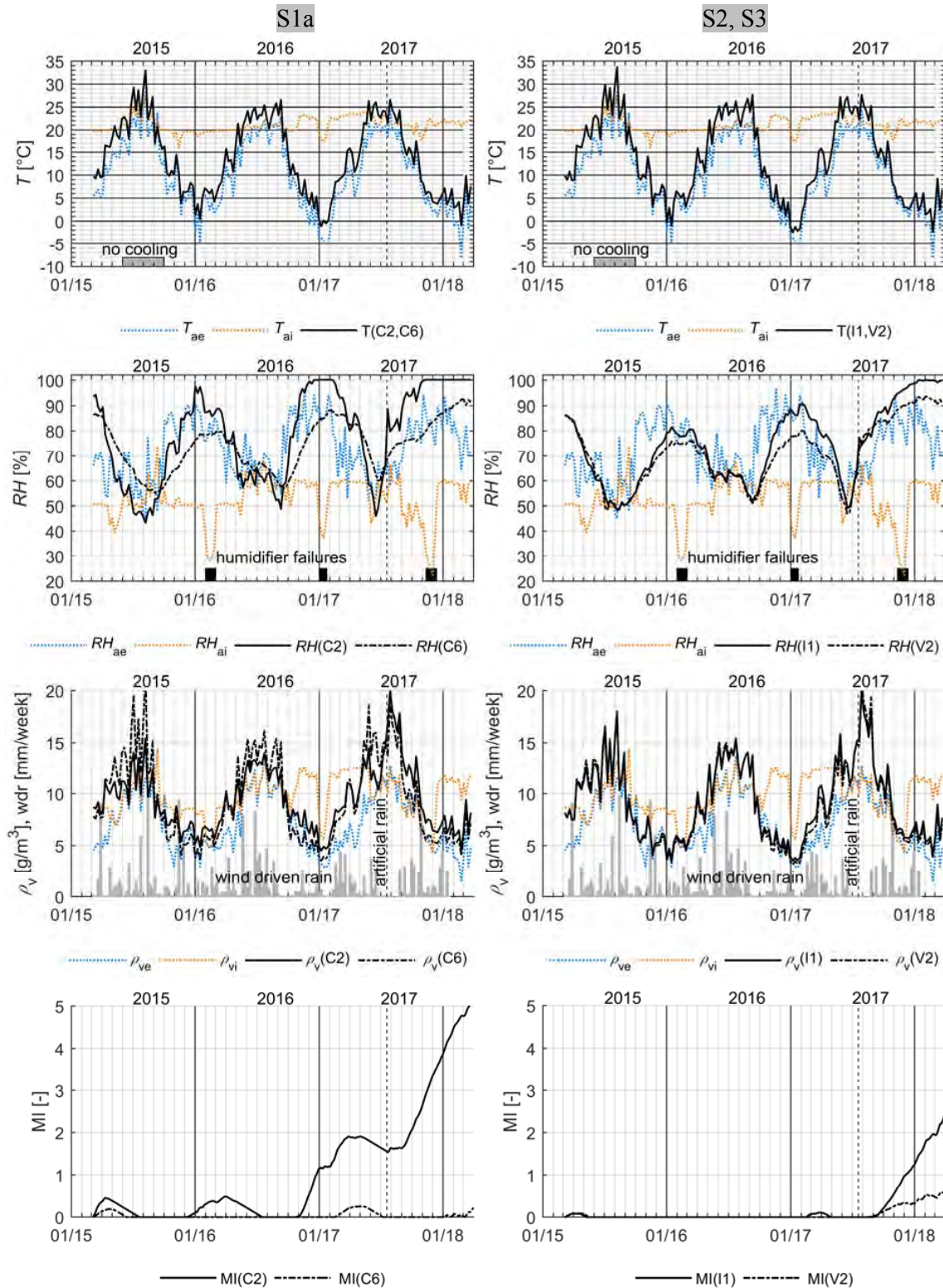


Figure 5. Measured data - temperature, relative humidity, water vapor concentration (weekly averages) and calculated mould growth index (hourly values) for selected joist pockets. Left column – system S1. Right column – systems S2 and S3. Temperature and relative humidity were measured in the bottom part of joist pockets (see Fig. 2).

Data depicted in Fig. 5 comprises weekly average values of temperature, relative humidity and water vapor concentration. Wind driven rain load was calculated by a simplified method of (Straube, 1998) for the spot near the ground in front of the test walls. Mould growth index was calculated by the improved version of VTT mold growth model (Viitanen and Ojanen 2007). The input parameters are material (spruce wood), wood surface quality (resawn) and hourly values of temperature and relative humidity measured in joist pocket.

Relative humidity in joist pockets exceeded 80 % during the experiment. Relative humidity in unsealed joist pocket (C2) of water vapor open system S1 reached 100 % in December 2016 resp. in November 2017. Relative humidity in sealed joist pocket (C6) of vapor open system S1 overshoot 90 % in February 2018. Relative humidity in the sealed pocket (I1) of vapor closed system S2 reached 100 % in January 2018. Relative humidity in the sealed pocket (V2) of vapor closed system S3 exceeded 90 %.

DISCUSSION

Similar patterns in time profiles of relative humidity in joist pockets were observed in the first two cold seasons of the experiment. There is obvious negative correlation of relative humidity in joist pocket with external air temperature. Moreover, relative humidity signals were delayed and dampened (with exception of amplitude amplification in the unsealed pocket C2) if compared with relative humidity of external air. Time lag and amplitude are related with the treatment of pockets and the type of insulation system. Relative humidity profiles during the last year of experiment differed from the patterns observed in the first two cold seasons. Relative humidity and water vapor concentration in joist pockets was increased after the rain experiment. Increase of relative humidity occurred even though mean external air temperature stayed near 20 °C for one and half month after the rain experiment. Relative humidity in joist pockets overtook relative humidity of the external air in time. Consequently, drying season was shortened. Surprisingly, only the sealed joist pocket C2 in vapor open system S1 did not show overtaking trend after the artificial rain experiment.

Water vapor concentration in joist pockets was systematically higher than water vapor concentration in the internal and external air during summer months. Both internal and external water vapor concentration were in equilibrium in summer months (no dehumidification incorporated in the air handling unit). Therefore, some other moisture sources than both ambient environments has to be responsible for that offset. Since the external surface temperature is on average higher than external air temperature during summer time and wind driven rain load tends to be higher in summer, it can be deduced that increased water vapor concentration in joist pockets is due to moisture flow from external side towards joist pockets. In addition, desorption of adsorbed moisture from wooden beam end also takes place.

Relative humidity in joist pockets was kept safe only during the first cold season of the experiment. Initial built-in moisture dried (as a consequence of very warm summer 2015). Even sealed joist pockets tended to overshoot the critical relative humidity 80 % in cold season under higher internal moisture load. Mould growth index indicated problems in unsealed joist pocket C2 in vapor open system S1 whereas mould growth was not predicted in joist pockets of vapor closed insulation systems S2 and S3 under higher internal moisture load. Even joist pockets in vapor closed systems suffered from possible mould growth after the artificial rain event (at the end of cold season 2018). It should be noted that probability of a rain event with similar intensity is low in the locality. Moreover, mould growth index is no

proof. Therefore, material samples will be taken from wooden beam ends at the end of the experiment (spring 2018). Samples will be tested in a laboratory for presence of molds. In addition, mutual comparisons of measured data in joist pockets with measured data from 1D section of insulation systems could introduce useful information.

Some unexpected results were registered after the artificial rain experiment:

- Sealed joist pocket C6 experienced slower increase of relative humidity than unsealed joist pocket C2. Due to the effect of tape on the outflow of vapor from joist pocket towards interior one would expect faster increase of vapor concentration than in unsealed joist pocket C2. Such performance might be caused by non-uniform rain load introduced by sprinkler device (i.e. joist pocket C6 did not receive the same amount of water as pocket C2).
- Sealed joist pocket V2 experienced slower increase of relative humidity than sealed joist pocket I1. This is suspect since diffusion resistance of internal layers should theoretically be much higher in case of insulation system S3. Such performance cannot be attributed with non-uniform rain load since both joist pockets are located next to each other at the same height. In this case, the slower increase of relative humidity might be related with joints between insulation plates of vacuum insulation panels (effective diffusion resistance of insulation system S3 is reduced).

The experiment will be modified in spring 2018. Some missing variants will be built (e.g. an unsealed joist pocket in uninsulated masonry either with or without metal anchor, joist pocket with non-hygroscopic beam, etc.). Moreover, sensor instrumentation so far is not sufficient to deduce directions of moisture flows. With this respect, combined temperature and relative humidity sensor should be placed at the external and internal side of test walls (close to the surfaces). Moreover, combined temperature and relative humidity sensor should be mounted at the interface of cold side of insulation layer and wooden beam.

CONCLUSIONS

The presented three-year long experimental results documented microclimatic conditions of wooden beam ends placed in joist pockets in three internal insulation systems attached to masonry walls located in semi-continental climate. The scope and nature of the data collected does not allow to state generally applicable recommendations. However, fundamental tendencies in performance and their relative significance can be evaluated. The more careful analysis of measured data and further real scale experiments are needed in future.

ACKNOWLEDGEMENT

This work has been supported by the Ministry of Education, Youth and Sports within National Sustainability Programme I (NPU), project No. LO1605 – University Centre for Energy Efficient Buildings.

REFERENCES

- Kopecký, P., Staněk, K., Bureš, M., Richter, J., Tywoniak, J., Experimental Investigations of Wooden Beam Ends in Masonry with Internal Insulation, *Energy Procedia* 132, 2017.
- Straube, J.F. Moisture Control and Enclosure Wall Systems. Ph.D. Thesis, Civil Engineering Department, University of Waterloo, Waterloo, Canada, 1998.
- Viitanen, J., Ojanen, T. Improved model to predict mold growth in building materials. In: *Proceeding of thermal performance of the exterior envelopes of whole buildings X*. American Society of Heating, Refrigerating and Air-Conditioning Engineers, 2007.

On the hygrothermal behaviour of brick veneer clad timber frame walls: the role of the vapour diffusion resistance of the wind barrier

Michiel Vanpachtenbeke^{1,2,*}, Jelle Langmans³, Jan Van den Bulcke², Joris Van Acker² and Staf Roels¹

¹KU Leuven, Department of Civil Engineering, Building Physics Section, Kasteelpark Arenberg 40 – box 2447, BE-3001 Heverlee, Belgium

²UGent, Department of Environment, Laboratory of Wood Technology (Woodlab), Coupure Links 653, BE-9000 Ghent, Belgium

³Baaphi bvba, Stropkaai 55, BE-9000 Ghent, Belgium

*Corresponding email: Michiel.Vanpachtenbeke@kuleuven.be

ABSTRACT

The present study looks into the hygrothermal behaviour of timber frame walls with brick veneer cladding in a moderate sea climate. It specifically focuses on the contradictory criterion for the wind barrier when it comes to the risk of interstitial condensation for summer and winter conditions: a vapour open wind barrier is advantageous during an outward vapour flow (i.e. in typical winter conditions for European climates), while during an inward vapour flow (i.e. in summer conditions) a more vapour tight wind barrier is appropriate. Therefore, a field study is conducted on two typical timber frame walls with brick veneer cladding and wind barriers with different vapour diffusion resistance: the s_d -value of the vapour open wind barrier and the more vapour tight wind barrier is 0.15 m and 1 m respectively at 70% relative humidity. The experimental results show little influence of the vapour tightness of the wind barrier: in general, relative humidity levels are similar in both walls. Outcomes of numerical HAM simulations indicate that this may be caused by the moisture buffer capacity of the different materials, which seems to play an important role to regulate the moisture levels inside the timber frame walls. Further research is needed, however, to draw general conclusions about the appropriate design of timber frame walls with brick veneer cladding.

KEYWORDS

Timber frame walls, brick veneer cladding, vapour diffusion resistance, moisture storage capacity, summer condensation

INTRODUCTION

The increasing environmental awareness has a substantial impact on the building sector. Past research made clear that timber as building material can help to reduce the carbon emission and the total energy requirement of buildings (Australian Government FWPRDC, 2004; Milne and Reardon, 2013). Therefore, the market share of timber frame constructions is increasing, even in countries with a tradition of masonry buildings. However, since wood is a moisture sensitive material, susceptible to mould growth and wood decay, it is essential to keep the moisture levels in the walls to an acceptable level, necessitating specific care when designing such walls. Today, it is common practice in Europe to provide a vapour barrier/retarder at the inside of the wall, while the layers to the outside have an increasing level of vapour permeability. In this way, the risk of interstitial condensation in the outer layers of the wall due to an outward vapour flow is limited. A rule of thumb suggests the layers at the warm side of the insulation to be at least 6 and preferable 15 times more vapour tight than the layers at the cold side of the insulation (WTCB, 2013). However, as already stated by different

researchers (Derome and Saneinejad, 2010; TenWolde and Mei, 1965), this design principle is based on cold climates where the ‘warm side of the insulation’ corresponds to the indoor environment. It does not consider possible inward vapour flow. In a country like Belgium with a masonry tradition, timber frame walls are often finished with a brick veneer cladding, which has a high buffer capacity for wind driven rain but low cavity ventilation rates (Langmans et al. 2016). Consequently, high moisture levels in the cavity behind the brick veneer cladding, resulting in an inward vapour flow, might occur. Different solutions influencing inward vapour flow do exist: hydrophobation of the brick veneer cladding, increasing the cavity ventilation rate or using a wind barrier with a higher vapour diffusion resistance (Sandin, 1993). The last solution is maybe the most simple solution, however increasing the risk of interstitial condensation in case of an outward vapour flow. Using the Glaser method (EN ISO 13788), one can get an idea of the potential problem. The relative humidity at the interface between the insulation (in casu mineral wool) and both the interior and exterior sheathing for a common timber frame inner wall has been calculated in function of the ratio of the vapour diffusion resistance of the interior and exterior sheathing (in terms of equivalent air layer thickness s_d : s_{din}/s_{dout}). The indoor conditions are 20°C and 50%. The cavity conditions are 3°C and 90% RH to simulate normal winter conditions and 35°C and 60% RH to simulate normal summer conditions. This simple calculation shows that only in a small range of s_{din}/s_{dout} the relative humidity at the interface between insulation and both sheathings will not reach 100% RH for the assumed winter as well as summer boundary conditions (Figure 1). In case the interior sheathing is 6 to 15 times more vapour tight than the exterior sheathing, the design will certainly lead to interstitial condensation in the assumed summer conditions according to this simple calculation.

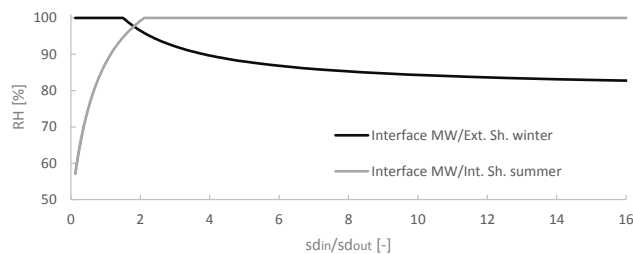


Figure 1: According to an elementary calculation, relative humidity conditions will be high at least at one side of the insulation layer, no matter the ratio s_{din}/s_{dout} .

The previous example suggests that summer condensation cannot be avoided with the common type of timber frame walls. Note, though, that the Glaser method does not take into account hygric buffering, nor liquid moisture transport. Therefore, the present paper studies, in detail, the overall hygrothermal performance of brick veneer cladded timber frame walls in a moderate sea climate and its risk of interstitial condensation, with focus on the role of the vapour permeability of the exterior sheathing. Field measurements have been conducted at KU Leuven, Belgium, on timber frame walls with different types of wind barrier. The experimental results are compared with the outcomes of numerical simulations, which allow for extrapolation of the different parameters.

EXPERIMENTAL SET-UP AND SIMULATION MODEL

Experimental set-up

In the VLIET test building of KU Leuven (Belgium), a long-term in-situ measuring campaign is conducted on two typical timber frame walls with brick veneer cladding. The measurements started in October 2015. The walls are 2.7m by 0.8-0.9m and consist of a brick veneer

cladding (9cm), a ventilated cavity (4cm), a wind barrier (1.8cm), mineral wool insulation between wooden studs (18cm) and an OSB board as interior finishing layer (2.2cm), as shown in Figure 2. The brick has an absorption coefficient of $0.2584 \text{ kg/m}^2\text{s}^{0.5}$ and its capillary moisture content is 256.13 kg/m^3 . The wooden studs are made of Scots pine sapwood. Furthermore, the cavity is ventilated by one open head joint ($3.5 \times 1.5 \text{ cm}^2$) at the bottom and top of the wall. The walls are South-West oriented, which is in Belgium the direction of prevailing winds and solar radiation. The temperature, relative humidity and moisture content of the materials is measured at different positions inside the wall. A weather station at the top of the building registers the outdoor climatic conditions.

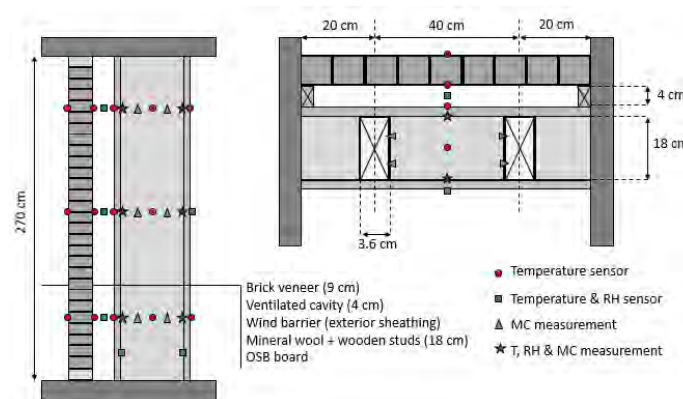


Figure 2: During field tests, the hygrothermal conditions inside real-scale timber frame walls with a brick veneer cladding are measured.

In one set-up (referred to as ‘open’) a vapour open bituminous impregnated wood fibre board (Celit¹) is used as wind barrier, whereas in the other set-up (referred to as ‘tight’) a more vapour tight wood fibre cement board (Duripanel²) is used. The vapour tightness of the interior finishing layer in both walls, in-casu OSB board, is in general still the highest however. Apart from a higher vapour diffusion resistance, the wood fibre cement board also has a higher moisture buffer capacity in the hygroscopic region compared to the wood fibre board (Figure 3).

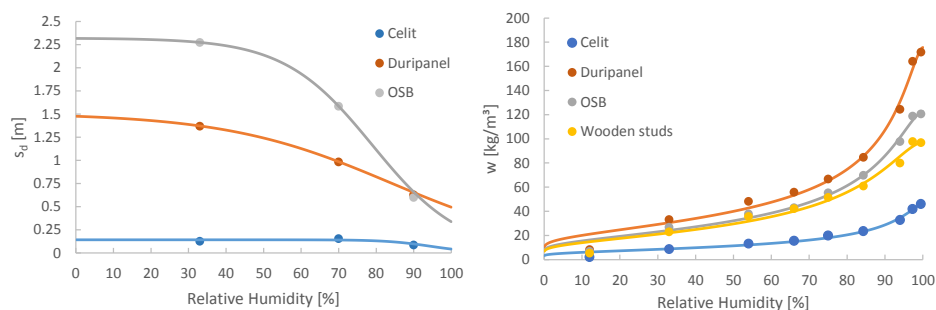


Figure 3: Vapour diffusion resistance (left) and moisture buffer capacity (right) of the building materials

Numerical simulation model

The same timber frame wall configuration is modelled in the numerical HAM-simulation program DELPHIN 5.9 (Grunewald, 1997; Nicolai, 2007). Only a simplified 1D model without wooden studs is considered. Since air change rates behind brick veneer cladding ranges from 1-10 air changes per hour (ACH) (Langmans, 2016), a constant cavity ventilation

¹ Isoproc Solutions. Celit 3D. <https://www.isoproc.be/nl/solutions/producten/detail/celit-3d/355>

² Siniat. Duripanel S3(B1). <https://www.siniat.be/nl-be/producten-en-systemen/producten/platen/vezelcementplaat-duripanel>

rate of 5 ACH is assumed. The real indoor and outdoor conditions as in-situ measured are imposed as boundary conditions.

RESULTS

In-situ measurements

By comparing the indoor vapour pressure (red line) with the cavity vapour pressure for the open and tight set-up (dark and light blue line respectively) on daily averaged basis, it is clear that in 2016 inward as well as outward vapour flow occurs (Figure 4). Outward vapour flow mainly occurs in winter periods, whereas inward vapour flow mainly occurs in spring and summer periods. In 2016, based on 10-minute in-situ measured data, 40% of the time the vapour pressure inside the cavity was higher than the indoor vapour pressure (Table 1). The vapour pressure difference in case of inward vapour flow is on average twice as high compared to outward vapour flow, the standard deviation approximately three times higher. These figures show that inward vapour flow in case of brick veneer cladded timber frame walls cannot be neglected.

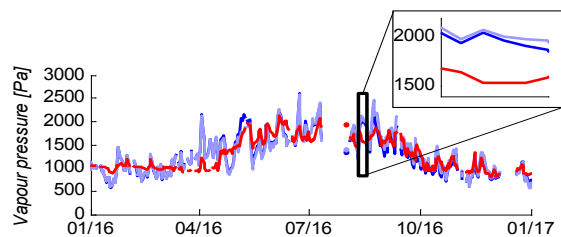


Figure 4: Daily averaged indoor (red line) and cavity (dark and light blue for open resp. tight set-up) vapour pressures indicate in- as well as outward vapour flow throughout the year.

Table 1: The occurrence of inward vapour flow and the vapour pressure difference between indoor climate and cavity (average and standard deviation) clearly show that inward vapour flows must be taken into account in case of brick veneer cladded timber frame walls.

	open		tight	
	In	Out	In	Out
Occurrence (%)	40	60	40	60
$\Delta P_{v,average}$ (Pa)	430	240	410	250
$\Delta P_{v,std}$ (Pa)	460	150	450	175

Next, the hygrothermal conditions at the potential condensation layers, the interface between mineral wool and interior and exterior sheathing, are analysed (Figure 5). At the interface between mineral wool and OSB board, a higher relative humidity is observed in summer conditions compared to winter conditions. However, the relative humidity rarely reaches values higher than 80% RH during the entire measurement period. Furthermore, little difference is observed between both set-ups. Only during springtime, when the cavity vapour pressure reaches high values while the indoor vapour pressure is still relatively low, the benefit of a more vapour tight wind barrier can be observed. At the interface between mineral wool and wind barrier, on the other hand, the relative humidity is higher in winter conditions than in summer conditions. Again, little difference is observed between both set-ups: the set-up with the more vapour tight wind barrier does not result in a higher condensation risk than the other set-up. A possible explanation for the fact that only small differences are noted between both set-ups is the moisture buffer capacity of the different materials inside the timber frame wall. To get more insight in the role of the moisture buffer capacity and vapour diffusion resistance, numerical simulations have been performed.

Numerical HAM-simulations

The trends in relative humidity at the interface between mineral wool and interior and exterior sheathing are quite well predicted by the numerical model (Figure 5). Only the relative humidity at the wind barrier in the tight set-up is underestimated in winter conditions. Although the wooden studs are not included in the numerical model, the simulations do not predict a higher condensation risk. This might indicate that the buffer capacity of the other materials inside the walls is already sufficient to lower the relative humidity peaks.

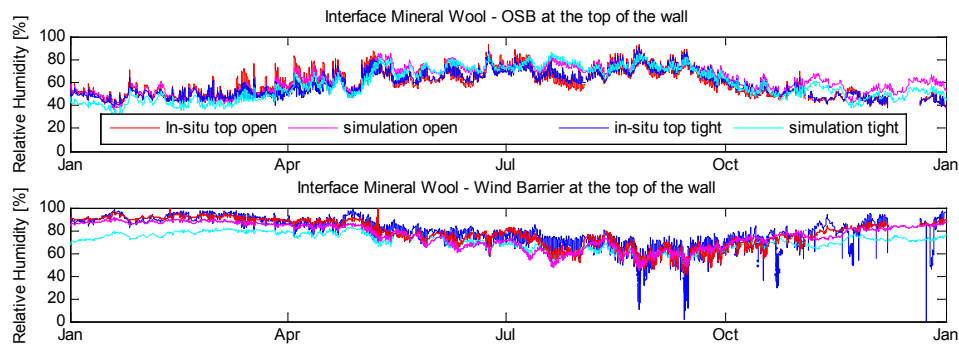


Figure 5: The in-situ measured relative humidity at both sides of the insulation layer shows only little differences between both set-ups. The numerical simulations are in line with the in-situ measured data.

To study the impact of the buffer capacity of the exterior sheathing on the potential condensation risk in winter conditions, the hygrothermal behaviour of the wall is simulated with a wind barrier as vapour tight as the wood fibre cement board, but with the same low moisture storage capacity of the wood fibre board. The results are compared with the original numerical outcomes (Figure 6). A lower moisture buffer capacity indeed leads to a higher relative humidity. In contrast, increasing the vapour diffusion resistance does not generally result in higher relative humidity. It must be stated, however, that the difference in vapour tightness of both wind barriers is less in the range of 80-90% RH compared to lower RH regions.

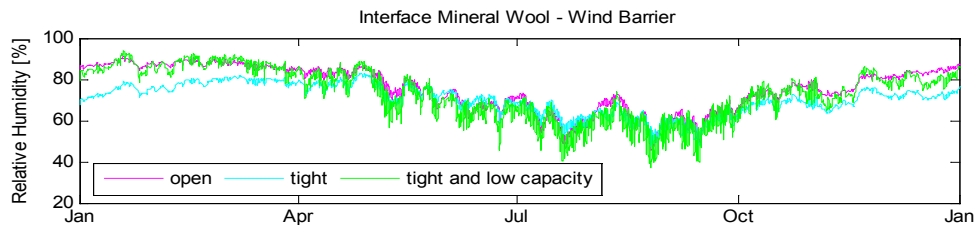


Figure 6: According to the simulations, the moisture buffer capacity of the wind barrier is more important than the vapour diffusion resistance.

A second simulation focuses on the buffer capacity of the OSB board. Figure 7 shows the change in relative humidity at the mineral wool – OSB interface with a theoretical OSB board without moisture buffer capacity. It is clear that in this case solar driven moisture transport leads to a condensation risk. Even the use of a more vapour tight wood fibre cement board as wind barrier does not eliminate this risk: the tight set-up is below 97% RH for only 6% of the time during which the open set-up is above this level. The different simulation assumptions, amongst them the exclusion of the wooden studs, may affect the hygrothermal conditions inside the wall. Nevertheless, the simulation outcomes emphasize the importance of the moisture buffer capacity of the different materials in the wall.

CONCLUSIONS

The present study investigated the contradictory criterion for the wind barrier in timber frame walls with brick veneer cladding when it comes to interstitial condensation for summer and winter conditions. Therefore, a field study on two typical timber frame walls with brick veneer cladding was conducted. One set-up had a vapour open wood fibre board as wind barrier, advantageous for outward vapour flows, the other set-up had a more vapour tight wood fibre cement board, which has potentially a higher resistance against solar driven

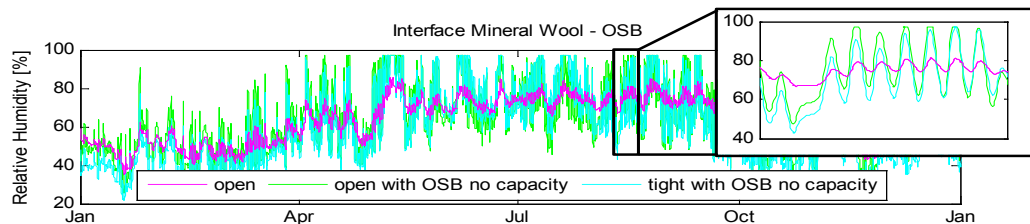


Figure 7: According to the simulations, the moisture buffer capacity of the OSB board is more important in avoiding summer condensation than the vapour diffusion resistance of the wind barrier.

moisture ingress. In contrast to an elementary calculation using the Glaser method, the experimental results showed only little differences in the hygrothermal behaviour of both walls. Numerical simulations indicate that this is probably caused by the moisture buffer capacity of the different materials in the wall, which is at least as important as the vapour diffusion resistance to lower the moisture levels inside the wall. However, to draw general conclusions about the design of timber frame walls, more numerical simulations should be performed. A 2D numerical model can point out the influence of the wooden studs on the hygrothermal behaviour. Also the climatic conditions should be treated as a varying parameter apart from the vapour diffusion resistance and moisture buffer capacity.

ACKNOWLEDGEMENT

The research presented in this paper is part of research project 3E140592 funded by the Fonds voor Wetenschappelijk Onderzoek – Vlaanderen (FWO): ‘A stochastic and dynamic risk assessment methodology for mould growth and wood rot on timber frame constructions.’

REFERENCES

- Australian Government FWPRDC. 2004. Environmental Properties of Timber – Summary Report.
- Derome D. and Saneinejad S. 2010. Inward vapor diffusion due to high temperature gradients in experimentally tested large-scale wall assemblies. *Building and Environment*, 45(12), 2790-2797.
- EN ISO 13788. 2001. Hygrothermal performance of building components and building elements – Internal surface temperature to avoid critical surface humidity and interstitial condensation – Calculation methods.
- Grunewald J. 1997. Diffusive and Convective Mass and Energy Transport in Capillary Porous Building Materials (in German). Ph.D. thesis.
- Langmans J., Desta T.Z., Alderweireldt L. and Roels S. 2016. Field study on the air change rate behind residential rainscreen cladding systems: A parameter analysis. *Building and Environment*, 95, 1-12.
- Milne G. and Reardon C. 2013. Embodied energy. *Your Home: Australia's guide to environmentally sustainable homes*.
- Nicolai A. 2007. Modelling and Numerical Simulation of Salt Transport and Phase Transitions in Unsaturated Porous Building Materials. Ph.D. thesis.
- Sandin K. 1993. Moisture conditions in cavity walls with wooden framework. *Build Res Inf*. 21.
- TenWolde A. and Mei H.T. 1986. In: *Proceedings of thermal performance of the exterior envelopes of buildings III*. Atlanta. American Society of Heating, Refrigerating and Air-Conditioning Engineers, Inc. pp. 570-582.
- WTCB. 2013. Vochtbeheersing bij houtbouw.
<https://www.wtcb.be/homepage/index.cfm?cat=publications&sub=bbri-contact&pag=Contact37&art=571>

Performance evaluation of a highly insulated wall to withstand mould

Klodian Gradeci^{1*} and Umberto Berardi²

¹SINTEF Building and Infrastructure, Norway

²Ryerson University, Canada

*Corresponding email: klodian.gradeci@sintef.no

ABSTRACT

In this paper, the performance to withstand mould growth of a highly insulated wall is evaluated by applying a probabilistic-based methodology that accounts for the involved uncertainties and investigates their significance. A sensitivity analysis according to the Morris method is conducted to understand the influence of each parameter and simplify the system representation. Deficiencies in terms of moisture and air leakages are accounted for. The mould growth outcome is evaluated by integrating different mould models and assessment criteria. The study demonstrates that a probabilistic-based methodology enables a more systematic approach to evaluate wall constructions since it accounts for the involved uncertainties, provides a clear association of the microbial growth to its likelihood, and enables the identification and significance of the dominant parameters; hence, it delivers a more comprehensive assessment of a building envelope.

KEYWORDS

Uncertainty; Sensitivity analysis; Probability; Mould; Building envelope.

INTRODUCTION

Highly insulated walls, which are walls with a considerable insulation thickness, have found increasing acceptance over the last few years to reduce the heat flow across the construction by increasing its thermal resistance. However, by increasing the thickness of the insulation the likelihood of moisture-related damages may increase significantly on the layers on the colder side of the insulation (Gullbrekken et al., 2015; Lepage et al., 2013). Especially when wood-based materials are used, biodeterioration presents a serious concern due to the lower requirements for microbial growth (Gradeci et al., 2017).

The design of wall constructions is replete with uncertainties. These are related to the outdoor and indoor climate, physical parameters of the materials properties and geometries, and the transfer of physical phenomena into numerical equations and models. Probabilistic-based methodologies can account for these uncertainties, and thus have found increasing acceptance over the last few years in the field of building performance simulation. Similarly, sensitivity analysis techniques have found increasing application since they can facilitate a better understanding of the system representation and the relationship between inputs and outputs (Gradeci et al., 2018b). The objective of this study is to evaluate the performance to withstand mould growth of a highly insulated wall by applying a probabilistic-based methodology. A sensitivity analysis is performed to simplify the system representation and to identify the most influential parameters. Finally, potential deficiencies from moisture or air leakages are accounted for.

METHODS

Building envelope

The building envelope investigated in this study is a stacked wood outside wall (Waltjen et al., 2008) using an MDF-board as the wind barrier and a membrane as the vapour barrier (see Figure 1 and Table 1). A construction with a wood-based material is selected due to the higher susceptibility to biodeterioration. A ventilated construction is chosen since the simulated rain data in current software may need further improvement, and these constructions are the least affected by rain.

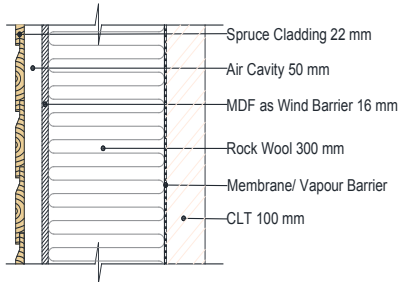


Figure 1. Configuration of the building envelope analysed in this paper.

Table 1. Mean values of material properties of the wall construction analysed in this paper.

Material	Thermal conductivity [W/mK]	Water vapour diffusion factor [-]	Density [kg/m ³]	Heat capacity [J/kgK]	Porosity [m ³ /m ³]
Spruce Cladding	0.09	130	455	1500	0.73
MDF-board	0.12	15	508	1700	0.667
Insulation	0.033	1.3	91	840	0.95
Membrane				$s_d=20$ m	
CLT	0.13	156	462	1400	0.627

Probabilistic-based methodology

The probabilistic-based methodology (Figure 2) as presented in (Gradeci et al., 2018a) has been further advanced by considering potential deficiencies, as described in the subsequent sections. The Monte Carlo Latin Hypercube Sampling is used to propagate, in a stratified way, the input variables by the simulation model to output variables. A total of 80 simulations are performed with this technique and a Beta distribution is fitted to the results.

The Morris method (Saltelli et al., 2008) varies one parameter at a time and screens important parameters by calculating two sensitivity measures: a) the mean μ , indicating the overall effect of the parameter; and b) the standard deviation σ , indicating either interaction or non-linear behaviour. A total of 24 parameters are considered for this study (see following sections); thus, $(24+1) \times 4 = 100$ simulations are performed. Three case scenarios are considered: the standard case without any deficiency, the second case when an amount of wind-driven rain (WDR) is assumed to penetrate, and the last case when an air leakage is accounted for.

Hygrothermal simulations and deficiencies

The hygrothermal simulations are performed by WUFI[®] 6.1. WUFI does not entirely model the air layer; therefore, a simplification that the temperature and relative humidity in the air are similar to exterior conditions can be assumed (Tietze et al., 2017). The effect of the wind-driven rain ($WDR = 0.2 \times \text{rain} \times \text{wind speed}$) is considered by applying moisture sources, while short-wave radiation absorptivity is set to 0.4 for untreated wood cladding (Tietze et al., 2017).

The initial conditions are set at RH = 80 % and T = 20 °C. The interface (wind barrier and insulation layer) is investigated due to the most favourable conditions for mould growth.

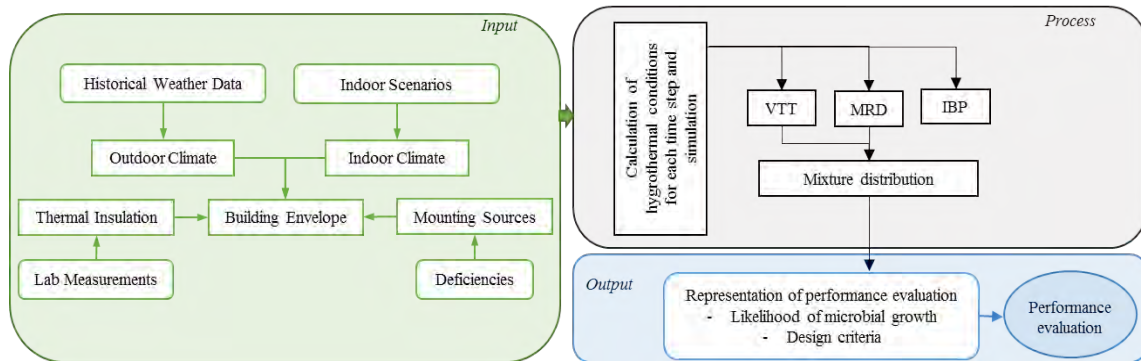


Figure 2. Schematic workflow of the probabilistic evaluation procedure.

In real life conditions, wall constructions are subject to moisture loads from a number of sources including wind-driven rain, bulk water (introduced by leakage), built-in moisture, water vapour (introduced by vapour diffusion or air leakage), and capillary transport through materials in contact with water or in contact with the ground (Lepage et al., 2013). Many of the latter may originate from human errors. They are difficult to identify and to represent quantitatively their distribution. Due to length requirements, this study considers only two scenarios, except for the base case, in a parametric way; 1 % moisture source representing moisture leaks from wind-driven rain according to ASHRAE recommendations and an interior air leak according to (Lepage et al., 2013). The moisture source is mounted between the MDF and insulation, while the air leak with airtightness class B is modelled according to recommendation in WUFI® (2017).

Representation of climate exposure and material parameters

The performance of the building envelope is evaluated when exposed to Oslo climate, which is a humid continental climate (ranked Dfb) with hot summers and very cold winters. The hourly-based historical data, from 01.01.1997 to 31.12.2016, are used to represent the outdoor climate. Each year among the 20-year long measurements is randomly distributed for each simulation as applied in (Hagentoft et al., 2015). In the current study, the initiation date of the simulation is also randomly sampled since it is another stochastic variable. Especially when the simulation period is one year long, the results of mould growth are very sensitive to the initiation (Gradeci et al., 2018a). The indoor climate is represented by a stochastic model based on a random distribution of the moisture categories and model uncertainties, as developed in previous study (Gradeci et al., 2018a).

A stochastic representation of the thermal conductivity of insulation material by conducting experiments is presented in (Gradeci et al., 2018b) and used in this study. Ideally, all parameters involved in the performance evaluation should be represented by their probabilistic models. However, due to limitations of the necessary data that are retrieved from experimental analyses, simplified assumptions are considered. A normal distribution (Salonvaara et al., 2001) is assumed for the parameters presented in Table 1, while the rest of the parameters were assumed as deterministic. The coefficient of variation is assumed 15 % for the vapour diffusion resistance, 8 % for the thermal conductivity of material other than insulation, 5 % for the density, 10 % for the heat capacity and 10 % for the porosity. The initial conditions for the relative humidity and temperature are also randomly distributed with mean values as presented in previous section and a coefficient of variation equal to 10%.

Representation of the failure event and performance evaluation

Different models have been developed to represent the mould growth and are characterised by specific strengths and limitations (Gradeci et al., 2017). Consequently, in the current study, the mould growth is calculated according to the integration of three most established mould models: VTT model (Viitanen et al., 2007), MRD model (Thelandersson et al., 2013) and IBP-biohygrothermal model (Sedlbauer, 2002), as previously presented in (Gradeci et al., 2018a). The *substrate class 1* is used for the biohygrothermal model, the standard case (*spruce, planed*) for the MRD, and the *very sensitive class* for the VTT model. Due to the lack of established design criteria related to building envelopes and biodeterioration, results are expressed as a density function associating potential levels of microbial growth to their respective likelihood.

RESULTS AND DISCUSSION

The sensitivity analysis results are presented in Figure 3 and Figure 4. The screening between influential and non-influential parameters, among the variables set up previously, is performed according to Morris method criteria (Saltelli et al., 2008). Only the influential parameters are depicted in the figures. They differ based on which mould model is applied. Similarly, the parameters' importance in the sensitivity analysis, as presented by the mean value, and its non-linearity or interaction, as presented by the standard deviation, differ based on which mould model is selected. The Mixture model and MRD model conclude that more parameters are important. The outdoor weather is screened as the most important parameter with non-linearity or interaction with other parameters. The indoor temperature is screened as important only from MRD model and the Mixture model. This parameter is judged as important considering engineering experience. The initial relative humidity is screened as an important parameter, which makes sense considering the short time of simulations. For the standard case and when an air leakage is accounted for, only the outdoor temperature and initial relative humidity are screened as important parameters. The reason might be the fact that this construction provides satisfactory performance, with low mould growth and/or due to one-dimensional simulations. The important screened parameters are increased when the wind-driven rain penetration is accounted for. The calculated mould growth is highly increased for this case.

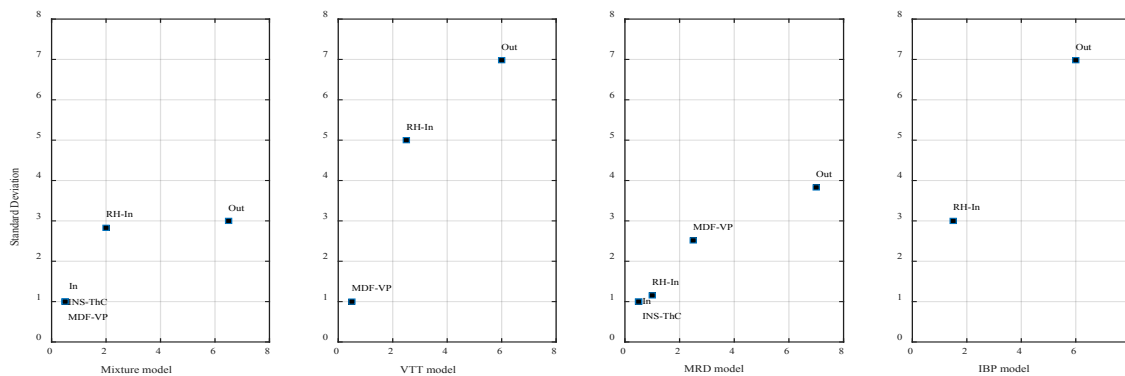


Figure 3. Sensitivity analysis results for the case when the wind-driven rain is accounted for. Difference between mould models. (In: indoor climate, Out: outdoor climate, RH-In: initial relative humidity, MDF-VP: water vapour diffusion factors of MDF, INS-ThC: thermal conductivity of insulation material.)

The results from sensitivity analysis enables a simplification of the system representation by reducing the number of variables, and thus the number of simulations. For the following calculation, only the influential parameters are accounted for as uncertain. The mould growth

results are shown in Figure 5 as the cumulative density function assessed against different available criteria. In addition, the results from applying the deterministic approach are shown as vertical lines when applying the MDRY (Moisture Design Reference Year), which is a conventional engineering approach, and the maximum mould growth during one year for the past 20 historical years in Oslo. The likelihood of obtaining the mould growth based on the historical data is high, while for MDRY is relatively lower implying that the probabilistic approach prevails the conventional one when representing the past twenty years.

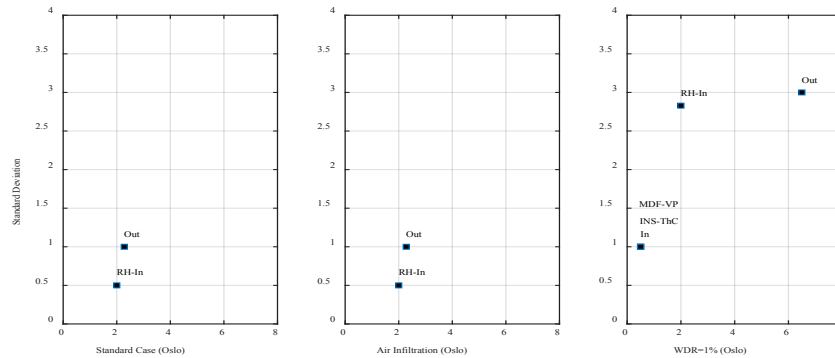


Figure 4. Sensitivity analysis results. The effect of deficiencies.

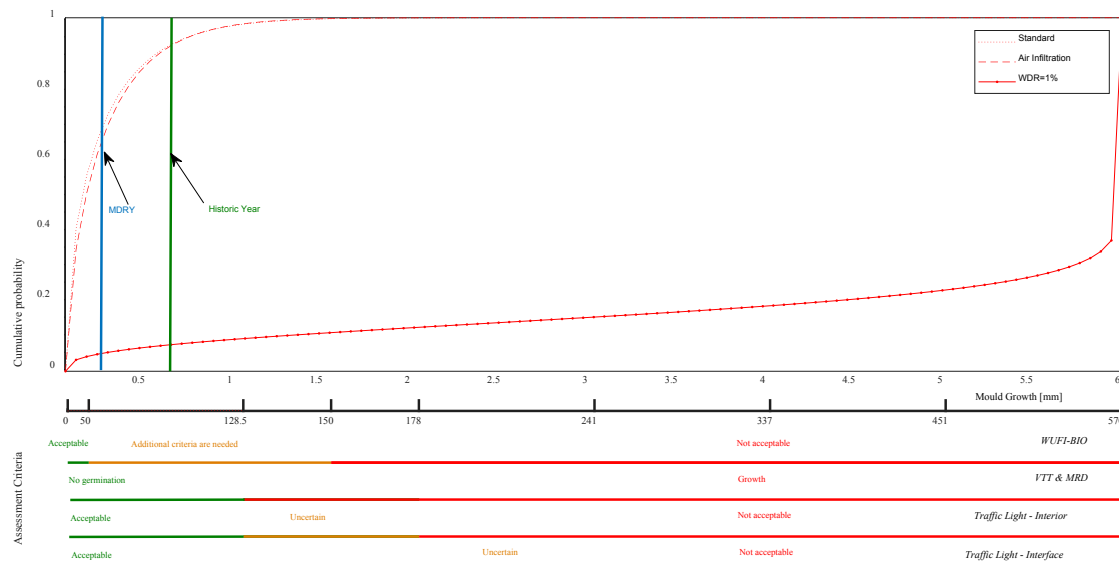


Figure 5 Cumulative density function of the mould growth according to three case scenarios assessed against different available criteria.

Moreover, a clear association can be retrieved between the different mould growth levels and their likelihoods. The performance of the investigated wall is satisfactory unless wind-driven rain penetration is simulated. However, it should be noted that there are no available criteria in codes/standards following simulations results with a duration of one year. Therefore, different assessment criteria can be considered, as shown in Figure 5, providing the flexibility to adapt the requirements and criterion based on the case study at hand. Otherwise, it is advised a longer time for the simulations to resemble the expected service life of the construction.

CONCLUSIONS

The probabilistic-based methodology enables a more systematic approach to performance evaluation of highly insulated walls since it accounts for uncertainties and delivers a clearer association of the mould growth to its likelihood. Furthermore, the application of sensitivity analysis is very beneficial in the design of wall constructions since it identifies and ranks the most dominant parameters influencing the outcome. The application of this methodology could be extended to different wall constructions, failure modes, climate exposures, and other deficiencies.

REFERENCES

- Gradeci, K., Berardi, U., Time, B., & Köhler, J. (2018b). Evaluating highly insulated walls to withstand biodeterioration: A probabilistic-based methodology (*under review*).
- Gradeci, K., Labonnote, N., Time, B., & Köhler, J. (2017). Mould growth criteria and design avoidance approaches in wood-based materials – A systematic review. *Construction and Building Materials*, 150, 77-88.
- Gradeci, K., Labonnote, N., Time, B., & Köhler, J. (2018a). A probabilistic-based methodology for predicting mould growth in façade constructions. *Building and Environment*, 128, 33-45.
- Gullbrekken, L., Geving, S., Time, B., Andresen, I., & Holme, J. (2015). Moisture conditions in well-insulated wood-frame walls. Simulations, laboratory measurements and field measurements. *Wood Material Science & Engineering*, 10(3), 232-244.
- Hagentoft, C. E., Kalagasidis, A. S., & Rode, C. (2015). 55, *Reliability of Energy Efficient Building Retrofitting-Probability Assessment of Performance & Cost (RAP-RETRO)*.
- Lepage, R., Schumacher, C., & Lukachko, A. (2013). *Moisture management for high R-value walls*.
- Salonvaara, M., Karagiozis, A., & Holm, A. (2001). Stochastic building envelope modeling—the influence of material properties. *Thermal Performance of Exterior Envelopes of Whole Buildings VIII*, 2-8.
- Saltelli, A., Ratto, M., Andres, T., Campolongo, F., Cariboni, J., Gatelli, D., . . . Tarantola, S. (2008). *Global sensitivity analysis: the primer*: John Wiley & Sons.
- Sedlbauer, K. (2002). Prediction of Mould Growth by Hygrothermal Calculation. *Journal of Building Physics*, 25(4), 321-336.
- Thelandersson, S., & Isaksson, T. (2013). Mould resistance design (MRD) model for evaluation of risk for microbial growth under varying climate conditions. *Building and Environment*, 65, 18-25.
- Tietze, A., Ott, S., Boulet, S., Gradeci, K., Labonnote, N., Grynning, S., . . . Pousette, A. (2017). *Tall Timber Facades – Identification of Cost-effective and Resilient Envelopes for Wood Constructions*.
- Viitanen, H., & Ojanen, T. (2007). *Improved model to predict mold growth in building materials*. Proceedings of the X International Conference on the Performance of the Exterior Envelopes of Whole Buildings, Clearwater, FL.
- Waltjen, T., Pokorny, W., Zelger, T., Torghelle, K., Mötzl, H., Bauer, B., . . . Unzeitig, U. (2008). *Details for passive houses. A catalogue of ecologically rated constructions*: Springer, Wien.
- WUFI®. (2017). *Guideline for Using the Air Infiltration Source in WUFI®*.

Renovation with Internal Insulation and Heat Recovery in Real Life – Energy Savings and Risk of Mold Growth

Martin Morelli^{1,*} and Eva B. Møller¹

¹Aalborg University, Danish Building Research Institute, Denmark

**Corresponding email: mmo@sbi.aau.dk*

ABSTRACT

This paper presents a pilot project for renovation of a large residential area; focus is on energy consumption and risk of mold growth. The renovation included internal insulation of walls with capillary active insulation material, balanced mechanical ventilation with heat recovery and insulation of floor towards basement. These types of measures are not completely new and have been used in other buildings as well, however the measures may be either risky regarding mold growth or the effect is uncertain with the specific external wall composition. A pilot project including six apartments was performed to test the measures in these specific buildings. Furthermore, six reference apartments were monitored simultaneously.

For two years, energy use for heating was measured as well as temperature and relative humidity in the internal insulation, indoors and outside. The insulation was dismantled in two apartments after two years, to test for mold growth at the original wall surface.

In extreme cases, the relative humidity in the walls behind the insulation system was up to 90 % RH shortly after installation, and mold growth models predicted growth of mold. However, the relative humidity decreased, typically to 70 % RH in the second winter. The inspection and measurements after the removal of the insulation material did not show signs of mold growth. Apparently, the used insulation material can be used in this specific case without risk of mold growth. Energy savings for heating was measured and calculated to around 25 %. However, the electricity use for ventilation was almost equal to savings from heat recovery.

KEYWORDS

Internal insulation; capillary active material; measurements; moisture; heat

INTRODUCTION

To save energy a large residential area from the 1950s is considered for renovation. The intent of the project is to demonstrate that energy savings are possible and moisture-safe using internal insulation with capillary active insulation materials combined with insulation towards a basement and mechanical ventilation with heat recovery. The case is Folehaven; a large urban area in Copenhagen, Denmark consisting of three-story apartment houses with approx. 74,200 m² heated floor area, rented out by a housing association. The brick masonry expression of the area is deemed worthy of preservation because of its architectural value. Internal insulation is therefore the only option for energy improving the walls. The Danish National Building Fund subsidizes energy-saving measures in social housing projects; however, the fund only subsidizes known and low risk measures. Traditional internal insulation with mineral wool and vapor barrier is not considered among these, due to high risk of mold growth, which has been experienced in other dwellings. Capillary active insulation materials have a specific pore size and pore distribution, allowing moisture to be transported by capillary suction from an area with capillary condensation to a more dry area, i.e. from the intersection wall/insulation material to the inside. Capillary active materials have been investigated by several researchers (e.g. Häupl et al, 2003; Pavlík and Černý, 2009; Vereecken

and Roels, 2015). However, well-documented projects with more than two years' experience are rare. Therefore, the objective of this pilot study is to provide documentation of the hygrothermal effects – including energy savings – of internal insulation with capillary active materials in these specific buildings. This would comply with The Danish National Building Fund requesting measurements conducted over a longer period e.g. five years in Denmark.

METHODS

The test site

The settlement Folehaven consists of 55 three-story apartment houses with 932 apartments. The buildings were built 1952-1962, and the materials may vary from building to building; generally, the walls are 360 mm thick made of bricks outside (110 mm) and lightweight concrete (240 mm) and plaster on the inside. The horizontal divisions are made of concrete. Attic and basement are unheated. Six apartments in the same staircase were chosen for the pilot project, see Figure 1. All apartments had a size of approx. 75m². Energy saving measures were installed in the summer of 2015. As a reference, six apartments were chosen, these were not renovated, however; layout, location and orientation were similar to the test apartments.

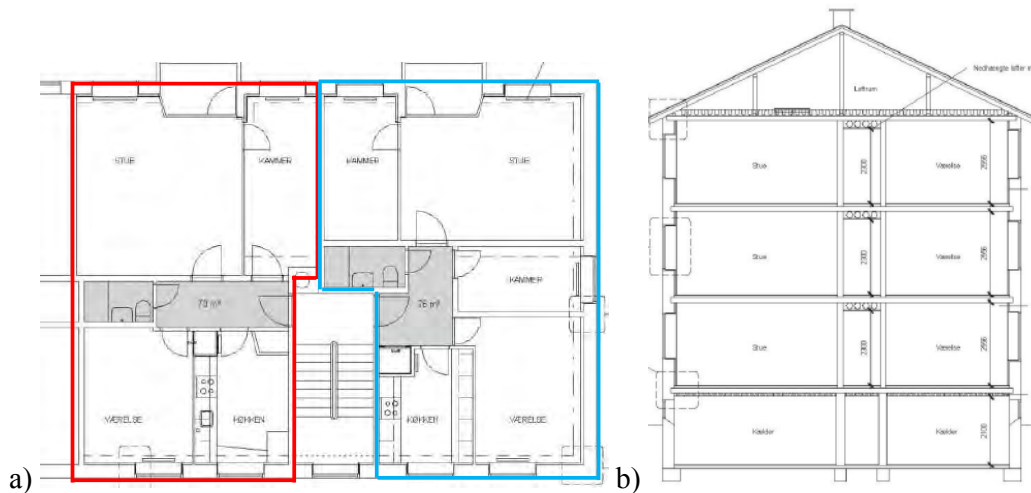


Figure 1. a) Layout of two apartments. Red designation is an internal apartment and blue designation is an apartment with a gable. In the grey area, a suspended ceiling is used to hide ventilation ducts. b) Cross section of the three apartments, basement and attic.

Several possibilities to reduce the energy consumption of the settlement Folehaven were considered but abandoned: External insulation was excluded for architectural reasons; internal mineral wool insulation with vapor barrier was deselected due to moisture risk from leaky vapor barriers; vacuum panels were rejected due to the high price and not being adjustable on site. New more energy efficient windows were considered, however, windows were renewed within the last 15 year and the building owner wanted to take advantage of the remaining service life. The attic floor was recently insulated. Conclusively, few options were left:

- Mechanical ventilation with heat recovery to replace the old system with natural ventilation through opening of windows and the stack effect of a ventilation shaft leading from the bathroom to the rooftop.
- Internal insulation with materials that need no vapor barrier (capillary active materials), and insulation of the floor division towards the basement.

The insulation material was chosen based on several criteria; i.e. thermal conductivity, price, robustness and flexibility. It was decided to test PUR foam with thin calcium silicate channels every 40 x 40 mm (λ -value of 0,031 W/m·K). The gable was insulated with 80 mm and the facades with 50 mm due to large windows and limited space behind installations.

Energy-saving potential

The energy savings were theoretically calculated and measured on site. The theoretical energy consumption for heating and ventilation was calculated using the software program Be10 (DBRI, 2015). U-values and Ψ -values were calculated through detailed 2D thermal calculations of assemblies before and after renovation and used in the Be10 model.

Energy consumption for room heating was measured with energy meter on the main heating pipes in the basement. Energy meters were installed on the mixing pipes before the after-heating surface of the ventilation system. Furthermore, the ventilation unit's electricity consumption was measured. The measurements covered the period April 2016 to March 2017 as a comparison between the test apartments and the reference apartments. The set point for the ventilation unit was 21 °C; however, at outdoor temperature above 18 °C, the after-heating surface was bypassed.

Onsite measurements of temperature and moisture

Temperature and relative humidity were measured and logged:

- Hourly in three rooms inside the six test apartments and six reference apartments with data logger Lascar EL-USB 2+ (Lascar Electronics) before and after the renovation. Data collection time: September 2014 to August 2015 and again March 2016 to June 2017.
- Hourly outside with similar data loggers and collection time as used inside. Alternatively, equivalent measurements were obtained from the Danish Meteorological Institute, as some loggers were stolen during the test period.
- Hourly inside the wall, at the intersection between original wall and the new interior insulation material. In each apartment, eight to ten sensors (Tramex Hygro-i connected to Transmitter IP65) were installed. The signals from the transmitters were collected by Profort mini data collector and were accessible via Internet. All instruments from BMT instruments (BMT Instruments). Data collection time: From December 2015 and ongoing.

Dismantling of insulation

Two years after installation, the interior insulation material was dismantled in two test apartments to inspect the area behind the insulation for mold growth; a check whether reality corresponds with mold growth models using actual hygrothermal measurements. One apartment was chosen because the installation of the insulation material was not in accordance with the guidelines of the manufacturer. The other apartment was chosen because the moisture load was high in this apartment before the renovation and measurements inside the wall showed high relative humidity the first winter after the installation of the insulation material. After dismantling the insulation material, the walls were visually inspected and Mycometer tests (Reeslev and Miller, 2000) were performed in critical areas. In the apartment with high moisture level behind the insulation material, additional mold tests were made with pressure plates and tape strips that were investigated in a microscope.

RESULTS

Energy consumption

The energy consumption for heating in the six renovated apartments during the heating season 2016/2017 was measured to 31.2 MWh at an average indoor temperature of 22.2 °C. The reference apartments with similar indoor temperature had a consumption of 41.1 MWh. This corresponds to a 24 % reduction in the energy consumption for heating or 9.9 MWh/year. Table 1 shows the theoretical calculation of the savings for the six apartments. The total energy savings for heating are 10.4 MWh/year. The specific fan power for the ventilation was 800 J/m³, which for an air change of 516 m³/h in constant run corresponds to 1.0 MWh/year.

Table 1. Theoretical calculation of U-value, air changes and energy saving for heating.

Measure	U-value ^A [W/m ² K]		Air change [m ³ /h]		Heating energy saving	
	Before	After	Before	After	MWh/year	%
Internal insulation of walls	1.05	0.65			7.3	70
Insulation of floor	0.70	0.40			2.2	22
Balanced ventilation ^B			344 ^C	516 ^C	0.9	8

^A U-values includes the linear thermal transmittance. ^B Heat recovery of 80%. ^C Air change before is 2/3 of the air change after which correspond to 0.5 h⁻¹.

Measurements of temperature and relative humidity

From October until March the average indoor temperature was 22.3 °C and 22.2 °C in the winter 2014/15 in the test apartments and the reference apartments, respectively. In the winter 2016/17 the average indoor temperature was 21.9 °C and 22.5 °C, respectively. The average outdoor temperature was 6.1 °C in the winter 2014/15 and 4.9 °C in the winter 2016/17.

Indoor relative humidity depends on moisture content in outdoor air, moisture supply depending on ventilation rate and use of the apartment, and the indoor temperature. To eliminate the influence of temperature of the indoor air, the results of the measurements in one room in a test apartment is presented in Figure 2 as moisture supply.

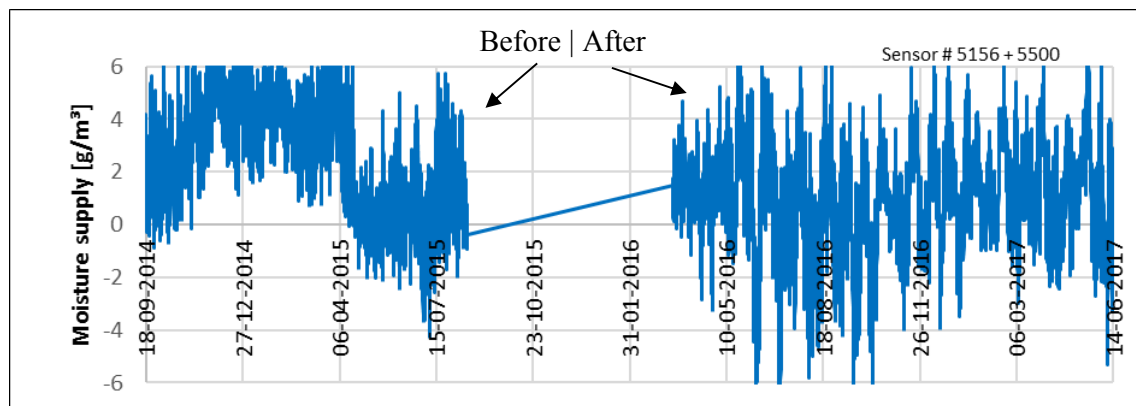


Figure 2. Moisture supply in a bedroom in one of the test apartments before and after the renovation. Compared to other apartments, the moisture supply was high before the apartment was renovated. The straight line in the middle covers the period without measurements.

Figure 3 shows a typical example of the temperature and relative humidity measured at the intersection of the interior insulation material and the existing wall. The most extreme case, and therefore, the one with the highest risk of mold growth, had a relative humidity of approx. 95 % RH in the winter 2015/16 at a temperature of 5-10 °C. The following winter the relative humidity had decreased to approx. 85 % RH at a temperature of 5-10 °C. The interior insulation was dismantled in that apartment.

The visual inspection of the walls after dismantling the interior insulation material did not show any signs of mold growth. This corroborates with the Mycometer tests, where only one test was higher than level A (background level). The highest Mycometer number was 34 i.e. very low number at level B (typical for e.g. dust), that goes from 25-450 (Reeslev and Miller, 2000). In the same point, the pressure plate test showed more than 50 colony forming units. All tape tests showed few spores but no mycelium on the wall.

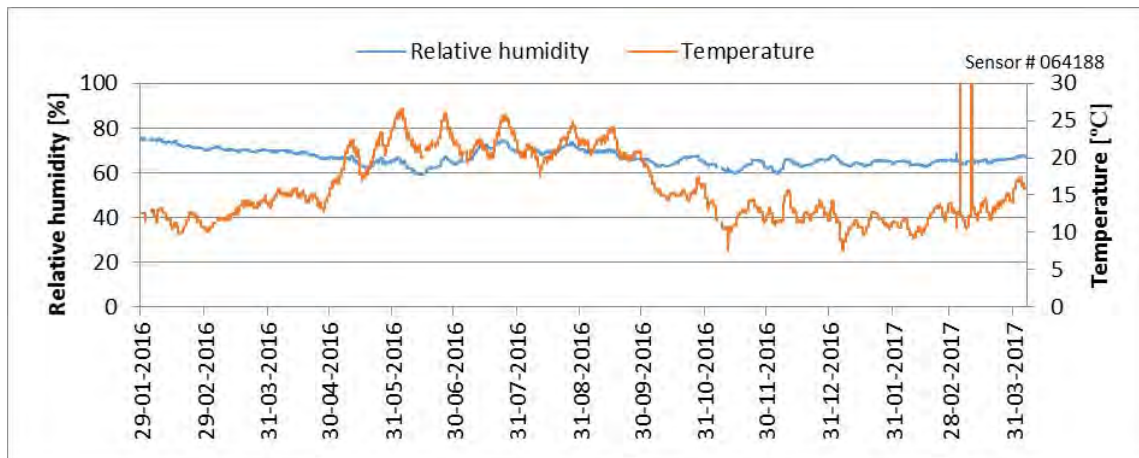


Figure 3. An example of typical conditions measured in the intersection between interior insulation material and existing wall.

DISCUSSIONS

Energy

The settlement Folehaven had from 2013-2016 an energy consumption for heating of 143-147 kWh/m², compared to key figures for the council housing sector, this is about 30 kWh/m² or 20 % higher than average. The findings from this study showed that the heating energy consumption could be reduced by 24 % when insulating the floor above the basement, installing internal insulation and balanced mechanical ventilation with heat recovery. If the savings found in the six apartments can be applied to the entire settlement, the heating energy consumption could be reduced to 109 kWh/m². These savings are obtained in six apartments where three have gables and three are internally located. As 1/3 of the staircases only have internally located apartments, the total savings might be lower. The indoor temperature was at a similar level before and after renovation, thus the rebound effect was minimal. In this pilot project, the energy use for running the ventilation corresponded to the heat savings obtained from the heat recovery. Furthermore, the ventilation rate was increased after renovation.

Temperature and relative humidity

The indoor climate varied in the different apartments but were within what was to be expected in apartments according to ISO 13788 (ISO, 2012). However, the moisture supply in Figure 2 was high before the renovation. After the renovation, the moisture supply decreased to normal level, probably due to the installation of a mechanical ventilation system. In apartments where the moisture supply was low before the renovation, no change could be detected.

When the measurements from behind the insulation material were used in mold growth models like Viitanen et al. (2011), mold index > 1 was to be expected in a few points, however, the inspection did not show mold in these areas. That may be because the walls were completely cleaned before the insulation material was installed, therefore, there was no organic material in the area, and theoretically dirt could not enter, i.e. no nutrients for the mold. In one point, the Mycometer level was B and there was mold growth on the pressure plate. However, the tape test combined with the Mycometer test indicated, that there was no active growth in the area. In areas where the relative humidity was high in the beginning, it decreased in the next winter; probably some build in moisture from the application with wet glue mortar had to dry out. Consequently, it is still necessary to follow the relative humidity and temperature in the wall to see how the system will perform over time. Especially because the two winters were mild compared to winter in the Danish reference year.

CONCLUSIONS

Renovation of buildings with special architectural appearance often ends in discussions of the possibility of applying external or internal insulation to save energy or improve the indoor environment. Therefore, it is important to decide what is most essential; obtaining energy savings, improving indoor environment, architectural value, etc. It is the author's opinion that moisture safety is crucial. When this is ensured, the heating energy savings in renovation projects can be calculated relatively easy. In this case, 24 % savings were documented.

When buildings are internally insulated, the indoor moisture supply becomes critical. Some users may not be aware of this; therefore, combining internal insulation with mechanical ventilation is a good idea, as the study confirms that mechanical ventilation reduces the moisture supply in apartments where the moisture supply was high.

Although the investigation of mold growth did not reveal any danger, it is still too soon to conclude that the investigated type of internal insulation is moisture safe in these apartments. Partly because mold models indicate, that mold growth may occur, partly because the two winters have been mild. Furthermore, it is important to notice, that the investigation only apply to these specific buildings. There is still a need to investigate how the internal insulation materials perform in other buildings; this applies to energy savings as well as moisture risk.

ACKNOWLEDGEMENT

The authors would like to thank Copenhagen municipality for financing the project, the building owner 3B housing association, Rambøll consulting engineers for performing the energy calculations and BMT Instruments for assisting with the measurement equipment.

REFERENCES

- BMT Instruments: <http://www.bmtinstruments.dk/shop/traadloest-maalesystem-23c1.html>
- DBRI, 2014. Energi-benchmark fra SBI. Available: <https://sbi.dk/it-vaerktoejer/Documents/Groent-regnskab/Energi-benchmark-fra-SBI.pdf>
- DBRI. 2015. Be10: Calculation Program for Documentation of the Energy Use in New Buildings. Available: <https://sbi.dk/beregningsprogrammet/Pages/Start.aspx>
- Häupl P., Jurk K. and Petzold H. 2003. Inside thermal insulation for historical facades. In: *Research in building physics: proceedings of the 2nd international conference on building physics, Leuven, Belgium, 14–18 September*, p. 463–469.
- ISO. 2012. *ISO standard 13788:2012*. Hygrothermal performance of building components and building elements - Internal surface temperature to avoid critical surface humidity and interstitial condensation - Calculation methods
- Lascar electronics: <https://www.lascarelectronics.com/easylog-data-logger-el-usb-2plus/>.
- Pavlik Z and Černý R., 2009. Hygrothermal performance study of an innovative interior thermal insulation system. *Applied Thermal Engineering*, Volume 29, Issue 10, July 2009, Pages 1941-1946
- Reeslev M. and Miller M. 2000. The MycoMeter-test: a new rapid method for detection and quantification of mould in buildings, p. 589–590. In: *Proceedings of Healthy Buildings 2000*, vol. 1. SIY Indoor Air Information OY, Helsinki, Finland.
- Viitanen H., Ojanen T., Peuhkuri R., Vinha J., and Lähdesmäki K. 2011. Mould Growth Modelling to Evaluate Durability of Materials, p. 409-416. In: *Proceedings of 12. International Conference on Durability of Building Materials and Components*. Porto.
- Evy Vereecken E. and Roels S. 2015. Capillary active interior insulation: do the advantages really offset potential disadvantages? *Materials and Structures*, September 2015, Volume 48, Issue 9, pp 3009–3021

A Sustainable Approach to the Adaptive Reuse of Historic Brick Buildings: Analysis of Energy Efficiency Strategies for Historic Facade Retrofits

Donghwan Kim¹ and Juliana Felkner^{2*}

¹School of Architecture, The University of Texas at Austin, Texas, USA

²Sustainable Built Environment Group, School of Architecture, The University of Texas at Austin, Texas, USA

**Corresponding email: juliana.felkner@austin.utexas.edu*

ABSTRACT

There are many historic brick buildings in downtown areas of the U.S. that are awaiting appropriate strategies for their adaptive reuse and preservation. The adaptive reuse method enables the adaptation of existing, obsolete historic buildings into new, mixed-use developments that will play an essential role in enhancing urban environments. However, many of these buildings have poor energy performance. This paper explores sustainable methods to balance between historic preservation and reduction of peak energy loads, through analyzing design strategies and conducting energy simulations for a building in downtown, Austin, TX. Energy retrofits related to windows, high performance of the facades with added insulation, and passive (spatial) interventions are covered in depth. Four retrofit scenarios were applied and simulated using the energy analysis tool in Revit, a popular BIM program. Analyzing the energy consumption data, we compare an existing building's facade condition to the retrofit scenarios' energy performances and record the energy performance data. This research proposes energy efficient preservation options for historic buildings and ultimately emphasizes potential values such as balancing the integrity of the original design with energy goals. We explore novel solutions for making historic buildings more sustainable through combining the adaptive reuse method with energy retrofit strategies that play up the historic buildings' unique passive potentials. The various solutions are found to be highly dependent on the climate.

KEYWORDS

Energy retrofit, adaptive reuse, historic preservation, facade, peak energy demand reduction

INTRODUCTION

Our research questions start from the growing trend of repurposing historic buildings. Because their original functions have been abandoned or new uses are emerging for them, architects and planners need to consider dealing with historic buildings economically, environmentally, and socially (Orbasli 2008). The act of extending the life of a building through adaptive reuse helps to lower material, transport and energy consumption; significantly contributing to sustainability goals and providing multiple benefits (Bullen and Love 2009).

Restored masonry buildings create vast opportunities for revitalizing communities and promoting cultural value. Instead of destroying the old brick materials and wooden structures, facade retrofits can create spaces that offer new experiences. Such reuse of buildings gives specific opportunities for the public to perceive the value of historic buildings and to make them attractive to neighborhoods and visitors. However, commonly, historic brick buildings are recognized for their poor energy performance with installed single pane glass windows. Therefore, they require a new approach to be adapted with appropriate uses and energy retrofits.

The method of dealing with existing facades comprises a large proportion of the adaptive reuse of old buildings. Because people tend to recognize buildings by the materials and patterns of their facade, facade retrofits can help preserve the historical significance of facades and meet modern energy standards. There are many articles dealing with the advantages of adaptive reuse or retrofits of old buildings, and the improvement of the building envelope, such as insulated roof and window replacements, could significantly reduce heating energy demand, for example, by 52% (Gourlis and Kovacic 2016).

This research addresses four retrofit scenarios for historic brick buildings in downtown Austin, TX. The study presents qualitative and quantitative comparisons of those scenarios, to help architects and planners to understand and apply the appropriate strategies for facade retrofits of old brick buildings in similar areas. The findings demonstrate which strategies are suitable for facade energy retrofits, while balancing energy goals and preserving the cultural value of old brick buildings.

METHODS

Facade retrofit scenarios are analyzed through Revit 2017, using the Energy Analysis for Autodesk Revit Engine. The 3D models represent a building that is 45 feet by 125 feet in plan and 35 feet high, typical for a historic building in downtown Austin. They comprise a ground floor and second floor with a stair opening. Southern and northern facades have four glass doors (7 feet wide by 12 feet high) on the first floor with wood framing and four windows (6 feet wide by 10 feet tall) on the second floor. We set up the input data as retail (building type), Austin (location), and occupancy rate (default of retail facility occupancy: 107.64 SF per person). The 3D models include brick facades and wooden structural systems. We obtain the energy data based on the information and change the specifications of windows and the glass front entry. This paper proposes four types of energy retrofit strategies for historical brick buildings and evaluates them by using the energy consumption data that we obtain from simulation in Revit (see Table 1).

Table 1. Retrofit typologies.

	Retrofit Option	Description	U-value (Btu/(h·ft ² ·°F))	R-value ((h·ft ² ·°F) Btu)
Existing	Single pane glass	8-inch masonry	1.18	0.85
		1/4-inch single pane glass with 3/8-inch cavity	0.50	1.98
Alt-1	Double glazed low-e	8-inch masonry	1.18	0.85
		1/4-inch double glazed glass (clear, low-e (e=0.05))	0.35	2.86
Alt-2	Wall insulation	3-inch thermal/Air layer + metal stud + gypsum wall board on interior of exterior wall	0.02	50
		1/4-inch double glazed glass (clear, low-e (e=0.05))	0.35	2.86
Alt-3	Secondary glazed windows	Alt-2 Secondary windows system	0.35	2.86
Alt-4	Double skin (glass)	Alt-2 Glass covered facade	0.35	2.86
		(system panel; 1/4-inch double glazed glass (blue-green, low-e (e=0.05))		

Through conducting the energy analysis in Revit, we obtained the data including annual energy consumption, monthly peak demands, and monthly cooling/heating load. This paper selects 'peak demands' representing peak cooling/heating load for comparing an existing building to

four facade retrofit scenarios. A growing number of retrofit interventions have started to take place around the world. All of them represent unique characteristics and respond to specific budgets, contexts, and functions. We re-classify those interventions into four categories of facade retrofit based on Martinez's table (Martinez 2013) (e.g. single pane glass, double glazed low-e, wall insulation applied to the interior of the exterior facade wall, secondary glazed windows, and double skin). Based on the proposed typologies, we create 3D models in Revit and run energy analyses in order to better understand how those strategies deal with energy improvements.

It should be noted that the simulated data would be different with measured results in an actual building because of orientation, climate condition, surroundings, and accuracy of simulation models. However, through modeling, this paper addresses facade retrofit typologies based quantitative and qualitative analysis of the simulation data, ultimately including the cultural value of the brick material, the design, and aesthetics. Thomas describes that successful sustainability should be evaluated by qualitative and quantifiable criteria simultaneously (Thomas 2004), which is why we chose to also value the aesthetic impact of retrofit measures - keeping our interventions as visually subtle as possible.

RESULTS

Five 3D models were designed in Revit for energy analysis based on the narrow rectangular type commercial building in downtown Austin. We gathered energy data to compare sustainable solutions for the adaptive reuse of historic brick buildings. Nagy explains that window replacement alone is able to reduce heating energy consumption by 12%, according to measured and simulated data for a building in Zurich, Switzerland (Nagy et al. 2014). Considering the total peak energy demands of an existing brick building in Austin, TX, which has a different climate and occupancy, the replacement of single pane glass with double low-e glass (low emissivity) enables the reduction of the peak energy demand by 0.70% (see Table 2).

Table 2. Comparison of energy simulation data. (1Btu=0.293Wh)

Retrofit Option	Floor Area (ft ²)	Peak Cooling total load (Btu/h)	Peak Heating total load (Btu/h)	Total Load (Btu/h)	WRT Single Pane Glass
Single pane glass	11,035	531,657.30	326,727.40	858,384.70	100.00%
Double glazed low-e	11,035	526,012.30	326,283.70	852,296.00	99.29%
Wall insulation	10,454	154,253.40	24,268.00	178,521.40	20.80%
Secondary glazed windows	10,194	130,663.10	14,465.70	145,128.80	16.91%
Double skin (glass)	11,084	188,675.40	32,413.10	221,088.50	25.76%

Table 2 illustrates peak energy demands of five typologies. 'Improvement of the wall insulation' resulted in approximately 80% total peak energy demands reduction as compared to the existing brick model, 'Single pane glass'. The 'secondary glazed windows' option allows for a reduction of 19% peak energy demand compared to 'improvement of insulation'.

According to Figure 1, the 'double skin scenario' reduces the peak energy demand less than the improvement of wall insulation. Rather, total peak energy demands are increased as compared to insulation improvement.

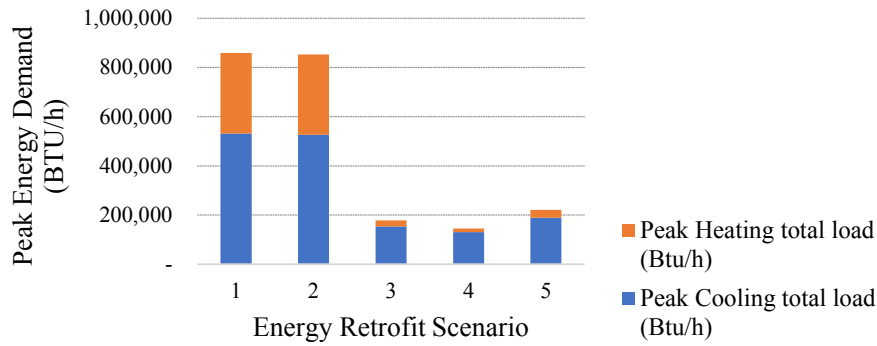


Figure 1. Peak energy demand comparison. (1-Single pane glass, 2-Double glazed low-e, 3-Wall insulation, 4-Secondary glazed windows, 5-Double skin (glass))

Table 3 shows the energy analysis models, plans, and section drawings. The double skin type has an additional seven feet wide corridor at the southern facade. Comparing facade visualization of five scenarios, the double skin option is only changed by layering the old brick material with glass (see Table 4). However, all the typologies enable the preservation of the brick material and its facade elements.

Table 3. Energy simulation models, plans, and southern facade section drawings in Revit.

	Single Pane glass	Double Glazed low-e	Wall insulation	Secondary glazed windows	Double skin (glass)
Energy model					
Section					

Table 4. Comparison of external facade visualization.

	Single pane glass ~ alt-4	Double skin (glass)
Southern facade render		

DISCUSSIONS

The building type analyzed is typical as part of downtown Austin's grid, planned by Edwin Waller in 1839. In general, most of the narrow rectangular type buildings face north and south, and are surrounded on the sides with adjacent buildings. Window to wall ratios are already low in such historic buildings, so replacement of the glass will not have as much of an impact as it would in buildings with larger windows. As seen in the second scenario, replacement of windows by low-e, the peak demand reduction is smaller than we expected, when looking at similar retrofit studies elsewhere. Moreover, as the occupancy is retail/commercial, and a narrow rectangular building facing south, it will not benefit as much from window replacement because there are more internal heat loads from the greater number of occupants, while the west and east facades are insulated by attached buildings.

The energy consumption significantly depends on building types or internal thermal loads, such as human activities. Replacing old single pane glass in this case helps to reduce peak cooling total loads more than peak heating loads. Improving specifications of facade wall type have positive effects on peak energy demand reduction. Upgrading old windows and doors to meet modern standards should be adopted into old buildings in Austin, with improving energy performance of the wall. These interventions are also visually unobtrusive to the original design.

Keeping old facades and preserving historic districts can produce social benefits to visitors and neighborhoods. The adaptive reuse and retrofit strategies for old buildings are produced by various decision makers. However, social aspects and the aesthetic value of historic brick buildings should also be considered as a positive solution for urban sustainability, and are not found to be in conflict with energy saving measures, according to our study. Moreover, a double skin type might be possible solution for harmony with modern goals while also preserving the historic brick material, but would most visually alter the facade and would also perform better in a climate less prone to overheating.

CONCLUSIONS

Austin, Texas has a humid subtropical climate, which requires a consideration to reduce cooling load from May to September. This study focuses on peak energy demand reduction for historic brick buildings, with retrofit alternatives evaluated and predicted with energy consumption data in balance with aesthetic impacts important for historic preservation. The best solution that balances the energy performance and aesthetic of the historic building is the option of adding an additional layer of glass on the interior side of the historic single pane windows (secondary glazed windows) in addition to better insulation. This totally preserves the character of the building from the outside, including the original window appearance, while greatly improving the energy performance with only a slight reduction of interior space.

This paper deals with balancing energy retrofit strategies and social-cultural value. Symbiotic strategies need to be considered in the early design phase of energy retrofit projects (Eliopoulou and Mantziou 2017). Unless the simulated data might be different with measured data in actual buildings, this paper proposes potential methods for the development of energy retrofits for historic buildings. Historic buildings are often limited in their energy retrofit options because of preservation requirements (Zagorskas et al. 2013). Therefore, this study does not cover shading options that would greatly alter the external appearance of the facade. However, it has been argued that the interaction between building regeneration, economic development and social renewal enables planners to make cities creative places (Sepe 2013). For this reason, balancing between historic preservation and energy retrofit strategies proves a significant step for architects and planners to make cities more sustainable.

REFERENCES

- Bullen, Peter A, and Peter E D Love. 2009. "Residential Regeneration and Adaptive Reuse: Learning from the Experiences of Los Angeles." *Structural Survey* 27 (5). Bradford: Emerald Group Publishing Limited: 351–60. doi:10.1108/02630800911002611.
- Eliopoulou, Eftychia, and Eleni Mantziou. 2017. "Architectural Energy Retrofit (AER): An Alternative Building's Deep Energy Retrofit Strategy." *Energy and Buildings* 150. Elsevier B.V.: 239–52. doi:10.1016/j.enbuild.2017.05.001.
- Gourlis, Georgios, and Iva Kovacic. 2016. "A Study on Building Performance Analysis for Energy Retrofit of Existing Industrial Facilities." *Applied Energy* 184. Elsevier Ltd: 1389–99. doi:10.1016/j.apenergy.2016.03.104.
- Martinez, Andrea. 2013. "Enhancing Energy Performance in Existing Buildings." University of Southern California.
- Nagy, Zoltán, Dino Rossi, Christian Hersberger, Silvia Domingo Irigoyen, Clayton Miller, and Arno Schlueter. 2014. "Balancing Envelope and Heating System Parameters for Zero Emissions Retrofit Using Building Sensor Data." *Applied Energy*. Elsevier B.V. doi:10.1016/j.apenergy.2014.06.024.
- Orbasli, Aylin. 2008. *Architectural Conservation: Principles and Practice*. Malden, MA: Blackwell Science.
- Sepe, Marichela. 2013. "Urban History and Cultural Resources in Urban Regeneration: A Case of Creative Waterfront Renewal." *Planning Perspectives* 28 (4): 595–613. doi:10.1080/02665433.2013.774539.
- Thomas, Randall. 2004. "OECD/IEA Joint Workshop on Sustainable Buildings : Towards Sustainable Use of Building Stock." *OECD/IEA Joint Workshop on Sustainable Buildings : Towards Sustainable Use of Building Stock*, 237.
- Zagorskis, Jurgis, Gražvydas Mykolas Paliulis, Marija Burinskiene, Jurate Venckauskaite, and Torben Valdbjørn Rasmussen. 2013. "Energetic Refurbishment of Historic Brick Buildings: Problems and Opportunities." *Environmental and Climate Technologies* 12 (1): 20–27. doi:10.2478/rtuct-2013-0012.

Experimental investigation of latent heat thermal energy storage for highly glazed apartments in a continental climate.

Shahrzad Soudian¹, Umberto Berardi^{1,*}

¹Ryerson University, Toronto, Ontario, Canada

*Corresponding email: uberardi@ryerson.ca

ABSTRACT

The high solar heat gains in highly glazed buildings are a major thermal discomfort factor leading to higher energy consumption for space cooling. Higher window to wall ratios (WWR) also entail large temperature fluctuations due to heat loss and temperature extremes in buildings. Passive latent heat thermal energy storage (LHTES) is a potential solution to regulate the indoor thermal environment in buildings through mitigating the indoor surface temperatures. In this study, the effectiveness of phase change materials (PCMs) in the context of a highly glazed apartment unit with 80% WWR is investigated for internal wall and ceiling applications. To provide thermal energy storage across the year, a composite PCM system with two melting temperatures is proposed, comprised of two PCM products, one with a melting temperature of 21.7 °C and the other with a melting temperature of 25 °C. To test the performance of this PCM, experimental tests were performed using test cells placed under climate conditions of Toronto to monitor changes in the phase change cycles of the PCMs and their impact on indoor air and surface temperatures. The results indicate improved thermal performance of the test cell containing the PCM system compared to a baseline cell in lowering peak indoor air and surface temperatures up to 6 °C. A relation was observed between the peak solar gain periods and the PCM behavior during the melting and solidification processes. This paper shows the potential of using PCMs as retrofit applications in highly glazed buildings by targeting specifically annual LHTES with two melting temperatures in one zone in a continental climate.

KEYWORDS

Thermal energy storage, phase change materials, thermal comfort, test cell, building retrofit.

INTRODUCTION

The thermal discomfort in buildings implies higher reliance on mechanical systems to provide a comfortable thermal environment. This is a critical issue considering the highest share of energy use in buildings is for space conditioning (Berardi, 2017). This effect is specifically important in buildings with high window to wall ratios (WWR) as they experience overheating in the cooling season and extreme heat loss in the heating one. Meanwhile, newer high-rise apartments in Canada often adopt transparent facades that are faced with high energy consumption and thermal discomfort levels (Touchie et al., 2014; Bennet and O'Brien, 2017).

To improve the thermal environment of highly glazed apartments, passive latent heat thermal energy storage (LHTES) has been considered through the incorporation of phase change materials (PCMs) as a retrofit measure for interior surfaces of apartment units. PCMs stabilize surface and indoor temperatures by undergoing a phase change at specific melting temperatures. It is argued by Heim (2010) and Navarro et al. (2016) that the isothermal behavior of PCMs allows for better surface temperature stabilization compared to traditionally high mass building structures with sensible storage. The high thermal storage capacity of PCMs in small volumes represents a main advantage of LHTES systems (Saffari et al., 2017).

Thermophysical properties of PCMs such as melting temperature, latent heat, and specific heat direct how PCMs affect the surface and indoor air temperatures. In particular, the melting temperature of PCMs is the most influential parameter of a PCM, and must be compatible with the environment and the climatic conditions the PCM is applied to (Cabeza et al., 2011, Kosny et al., 2012). The integration of PCMs in the Canadian climate has been investigated by Chen et al. (2014), Delcroix et al. (2017), Guarino et al. (2017) and Berardi and Soudian (2018) showing good potential in both heating and cooling seasons. Nevertheless, optimizing PCMs to operate for an entire year is difficult as PCMs with a melting point close to summer boundary conditions do not operate in other seasons. Consequently, recent studies have suggested optimizing PCMs for annual performance by using two or more melting temperatures in a hybrid PCM system (Hoes and Hensen, 2015, Kheradmand et al., 2016).

The aim of this paper is to evaluate the benefits of integrating thin layers of PCMs as unobtrusive retrofit measures to regulate indoor temperature swings. Considering the case specific design and performance of PCMs in relation to climate, this research focuses on the Canadian climate and looks at the annual thermal energy storage using a PCM system with two melting points to address both heating and cooling seasons with different boundary conditions.

METHODS

The composite PCM system investigated in this study is comprised of two commercially available PCM products with different melting temperatures as shown in Figure 1. The first layer in the composite PCM system has a melting temperature of 25 °C and the second layer in the system has a melting temperature of 21.7 °C, closer to winter boundary conditions. As shown in Fig. 1, the high latent heat storage capacity of this composite PCM system in a small thickness suggests a good potential for temperature stabilization in buildings. Both PCM products used in the composite PCM system are individual boards attached to each other.

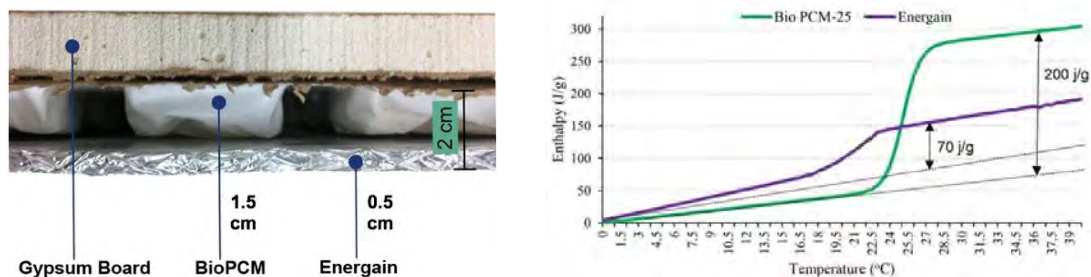


Figure 1. The composite PCM system (left) and temperature-enthalpy curves for the PCM boards (right).

Quantifying the performance of PCMs is more accurate using experimental test methods considering the simplifications of simulation modeling in calculating PCM behavior on a material scale (Cabeza et al., 2015). Therefore, in this study, two small scale test cells were constructed, one reference cell as a baseline and one cell with PCM-enhanced walls and ceiling. Test cells were constructed to represent typical highly glazed apartment units on a scale of 1:10 with one glazed wall covering 80% of one wall with an overhang shading (Fig. 2). The construction characteristics of the test cells are shown in Fig. 3.

The performance of the composite PCM system was assessed on a surface and room level through a comparative analysis between the reference test cell and the PCM integrated test cell. The main parameters of analysis were the rate of change in surfaces and room temperatures of

the composite PCM test cell compared to the reference cell in relation to ambient weather and solar gain variations. The experimental tests were conducted in Toronto under free floating conditions from July to October (2016) to assess the effects of different weather variations on the composite PCM's performance.



Figure 2. Experimental test cells: the test cell on the right contains the investigated PCM system.

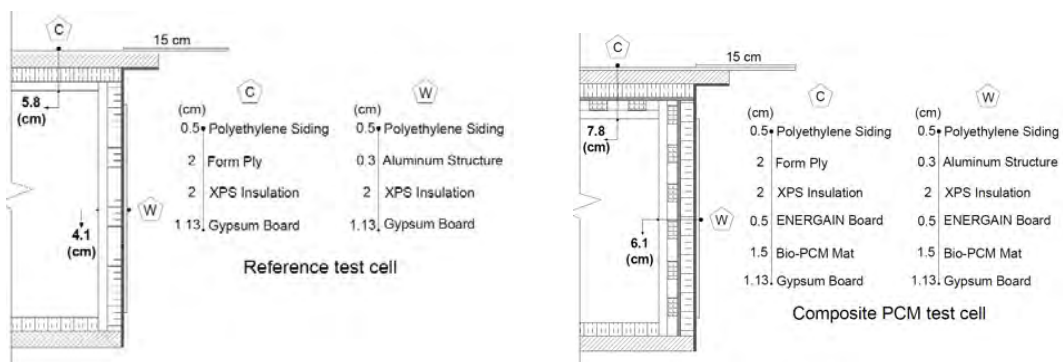


Figure 3. Construction characteristics of the experimental test cells.

RESULTS

Influence of solar gain on PCM performance

Figure 4a shows the indoor cell temperature variations in three days in July when the cells were facing south. The temperature changes are attenuated in the composite PCM test cell and overall, the air temperature swings are reduced by 6.8 °C. In particular, the effectiveness of the composite system at night is significant in maintaining indoor temperatures. An apparent peak temperature shifting of one hour happens in the composite PCM test cell. The maximum air temperature is shifted to later afternoon due to thermal lag in the composite PCM test cell. By rotating the test cells towards west, significant changes are observed as demonstrated in Fig. 4b. Unlike the south facing orientation, the highest temperatures in the test cells occur close to the sunset period from 5 to 7 pm when the benefits of PCM system also become more evident.

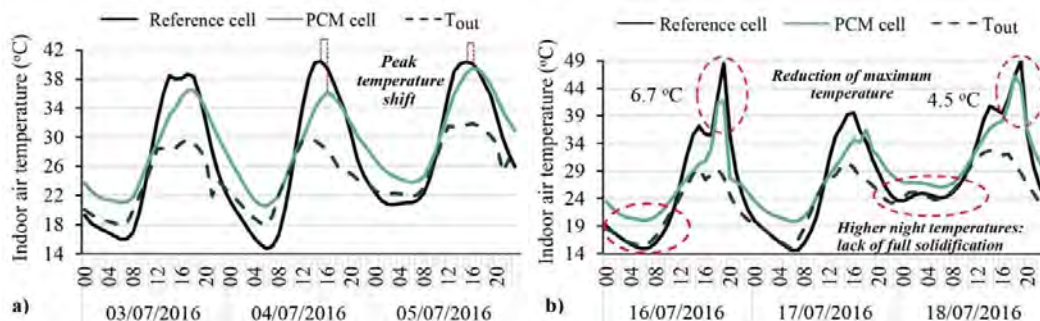


Figure 4. Hourly indoor room temperatures; a) South orientation – b) West orientation.

To further assess the influence of solar gain on the PCM performance, the shading part of the cells were removed to allow more solar radiation to get into the cells for one week in October. The reference test cell showed high dependence on outdoor weather conditions ultimately leading to average colder indoor air temperatures. Whereas, in the composite PCM test cell, indoor air temperatures were constantly above the outdoor temperatures. Removing the shading negatively affected PCMs performance in reducing excessive heat gain in the spaces. Figure 5 shows that by removing the shading, indoor air temperatures in the composite PCM test cell increased by 11 °C in the peak solar period in the south facing orientation. This sharp increase in the indoor air of the test cell is due to the sensible heat gain after the PCMs are melted.

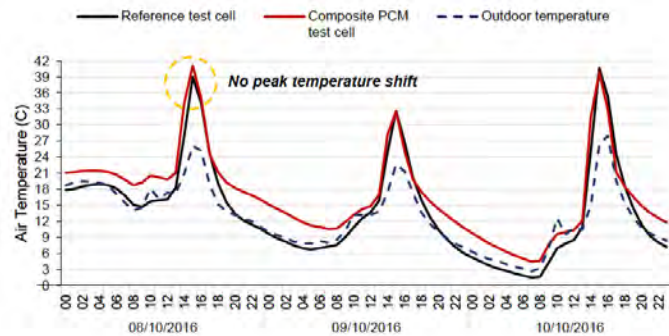


Figure 5. Hourly indoor room temperature variations from October 8th -10th.

Performance of PCM integrated surfaces

One side wall and the ceiling in the two test cells were simultaneously monitored. The primary parameter of analysis was the difference between the wall and ceiling surface temperature changes in relation to the room temperature. The hourly surface temperatures in the composite PCM wall show a faster response to ambient and indoor room temperature variations compared to the ceiling surface temperature changes. During the day, the wall heats up more rapidly, and at night, it loses heat faster as temperatures decrease compared to the composite PCM ceiling.

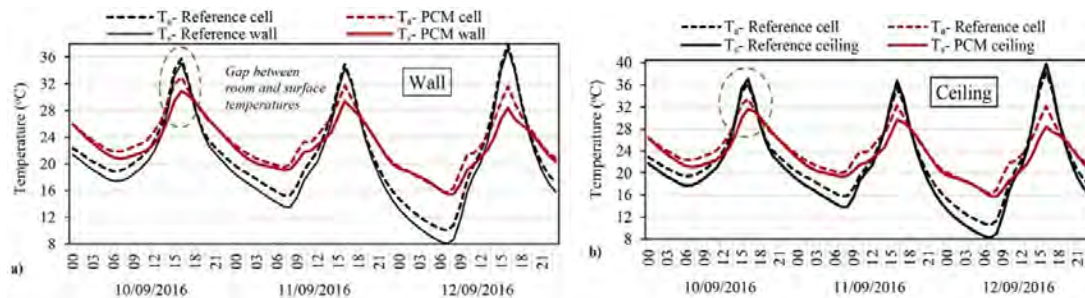


Figure 6. Hourly indoor air and surface temperature variations on wall (a) and ceiling (b)

Figure 6 shows hourly room (T_a) and surface temperature (T_s) variations in three consecutive days in September. Without PCMs, the indoor room temperatures of the reference cell show a close proximity to the reference wall and the ceiling's surface temperatures particularly in maximum peak periods in the day. Conversely, a gap is observed between the indoor air in the composite PCM cell and the composite PCM surface temperatures.

DISCUSSION

The focus in this study was to assess the impact of solar gain and ambient weather variations on PCM performance. The experimental results demonstrated that the impact of ambient weather is more significant as temperature variations control the entire transition of the composite PCM system during the day. Nevertheless, the exposure to solar radiation enhance the melting process periodically, specifically at times of highest solar intensity.

To better explain the impact of ambient weather on PCM performance, average data in the testing period are compared in Table 4. The trend of outdoor temperature variations and PCM activation points to the highest percentage of PCM being activated in July. Correspondingly in July, the composite PCM system reduced the indoor temperature swings and high peak temperatures significantly compared to other months. The benefit of a hybrid PCM system is evident as during the summer the Energain PCM is mostly in liquid form where in contrast, the BioPCM is often in the solid state during the fall.

Table 1. Summary of the impact of the composite PCM on indoor air temperatures.

	Average ambient conditions (°C)	Decrease of T _{max} (%)	Increase of T _{min} (%)	Decrease in temperature swings (%)	Frequency of PCM activation			
					PCM Layer	Solid	Phase change	Liquid
July	19.2 - 31.1	6%	18%	46%	BioPCM	29%	28%	43%
					Energain	6%	30%	64%
August	19.9 - 35.7	4%	16%	37%	BioPCM	7%	18%	74%
					Energain	0%	9%	91%
September	15.2 - 31.1	6%	19%	35%	BioPCM	57%	18%	25%
					Energain	41%	21%	38%
October	11.2 - 25.6	1%	24%	18%	BioPCM	86%	7%	6%

The relation of solar gain to PCM performance on surfaces and their influence on indoor air temperatures showed that in addition to peak temperature reductions, peak temperature shifting is another benefit of applying PCMs to highly glazed rooms. Similar observations were made by Kosny et al. (2012), showing that low peak temperatures were shifted to early morning and high peak temperatures in some instances were shifted to later evenings. However, in this study, it was discussed that the latter observations are relative to the orientation. Further testing on the factor of shading showed that due to lower temperatures, the availability of solar radiation was more important in the fall to ensure the activation of the PCMs, whereas in summer, the shading would be beneficial.

CONCLUSIONS

The performance of a composite PCM system proposed for annual thermal energy storage for retrofit applications in high-rise residential buildings in the climate of Toronto was investigated using experimental test cells for four months. The capability of the composite PCM system was clearly displayed as each PCM targeted the fall and summer months as expected. In conclusion, PCM systems constituted by two or more PCM products with different melting points offered potential in becoming a more prominent approach for PCM application in buildings, particularly in continental climates such as Toronto which undergo different weather patterns during the year. This research has shown that with an addition of layer only 2 cm thick of PCMs to interior surfaces, the temperature extremes could be significantly reduced.

ACKNOWLEDGEMENTS

The first author expresses his gratitude for the support of the NSERC DG #2016-4904 and for the ERA award sponsored by the Ontario Ministry of Research Innovation and Science, MRIS

REFERENCES

- Bennet, I. E., O'Brien, W. (2017). Field study of thermal comfort and occupant satisfaction in Canadian condominiums. *Architectural Science Review*, 60(1), 27–39.
- Berardi, U. (2017). A cross-country comparison of the building energy consumptions and their trends. *Resources, Conservation and Recycling*, 123, 230–241.
- Berardi, U., Soudian, S. (2018). Benefits of latent thermal energy storage in the retrofit of Canadian high-rise residential buildings, *Building Simulation*, 11, 709–723.
- Cabeza, L. F., Castell, A., Barreneche, C., De Gracia, A., Fernández, A. I. (2011). Materials used as PCM in thermal energy storage in buildings: A review. *Renewable and Sustainable Energy Reviews*, 15(3), 1675–1695.
- Chen, Y., Athienitis, A., Galal, K. (2014). A charging control strategy for active building-integrated thermal energy storage systems using frequency domain modeling, *Energy and Buildings*, 84, 651–661
- Delcroix, B., Kummert, M., Daoud, A. (2017). Building-scale experimental validation of a new model for walls with phase change materials. *Science and Technology for the Built Environment*, 23(6), 1049–1062.
- Guarino, F., Athienitis, A., Cellura, M., Bastien, D. (2017). PCM thermal storage design in buildings: Experimental studies and applications to solarium in cold climates. *Applied Energy*, 185, 95–106.
- Heim, D. (2010). Isothermal storage of solar energy in building construction. *Renewable Energy*, 35(4), 788–796.
- Hoes, P., Hensen, J. L. M. (2016). The potential of lightweight low-energy houses with hybrid adaptable thermal storage: Comparing the performance of promising concepts. *Energy and Buildings*, 110, 79–93.
- Kheradmand, M., Azenha, M., de Aguiar, J. L. B., Castro-Gomes, J. (2016). Experimental and numerical studies of hybrid PCM embedded in plastering mortar for enhanced thermal behavior of buildings. *Energy*, 94, 250–261.
- Kosny, J., Kossecka, E., Brzezinski, A., Tleoubaev, A., Yarbrough, D. (2012). Dynamic thermal performance analysis of fiber insulations containing bio-based phase change materials (PCMs). *Energy and Buildings*, 52, 122–131.
- Navarro, L., de Gracia, A., Niall, D., Castell, A., Browne, M., McCormack, S.J., Cabeza, L.F. (2016). Thermal energy storage in building integrated thermal systems: A review. Part 2. Integration as passive system. *Renewable Energy*, 85, 1334–1356.
- Saffari, M., de Gracia, A., Ushak, S., Cabeza, L.F. (2017). Passive cooling of buildings with phase change materials using whole-building energy simulation tools: A review. *Renewable and Sustainable Energy Reviews*, 80, 1239–1255.
- Touchie, M. F., Pressnail, K. D., Tzekova, E. S. (2014). Energy Savings by Retrofitting Multi-Unit Residential Buildings: Case Studies. Proceedings of the 3rd Building Enclosure Science and Technology (BEST3) Conference. Atlanta, Georgia, USA.

Interior insulation retrofit of a brick wall using super insulation materials: design of a field testing in an industrial brick building

Pär Johansson^{1,*} and Paula Wahlgren¹

¹Chalmers University of Technology, Gothenburg, Sweden

*Corresponding e-mail: par.johansson@chalmers.se

ABSTRACT

The societal demands on a more energy efficient building stock in Sweden creates challenges to find suitable retrofitting measures. One of the measures currently discussed is to use interior insulation. This measure leads to a reduced temperature in the wall, which increases the risk for elevated moisture levels in the wall. When the thickness of the insulation layer is limited, super insulation materials (SIM) may be used. SIM can be divided into advanced porous materials, such as aerogel blankets (AB), and vacuum insulation panels (VIP). Often moisture from the outside is the major moisture source why a solution may be to apply a water repellent substance on the surface. A previous study showed that it is difficult to predict all the uncertainties in the laboratory using hygrothermal numerical simulations. This paper presents the design of a field investigation of a homogenous brick wall where AB and VIP are installed as interior insulation.

KEYWORDS

Listed building, brick wall, interior insulation, super insulation material, moisture

INTRODUCTION

The demands on a more energy efficient building stock in Sweden creates challenges to find suitable retrofitting measures. Around 25% of the energy use in buildings in Sweden is used in buildings from before 1941. Out of these buildings many are built in brick masonry and have not been renovated before, which means they are practically non-insulated. The energy use in these buildings can be reduced by adding insulation to the walls. The conventional thermal insulation materials, such as fiber glass and EPS, often demand a thick layer of insulation to reach the energy targets. Super insulation materials (SIM) are thermal insulation components with a 2-10 times higher thermal resistance than the conventional insulation materials. The thermal transmittance (U-value) of the building envelope can thereby be substantially reduced using a limited additional insulation thickness.

Additional insulation can be added either to the interior or exterior side of a wall. Exterior insulation is preferred since the hygrothermal performance of the wall is in many cases improved compared to interior insulation. Interior insulation leads to a reduced temperature in the wall which increases the risk for elevated moisture levels in the wall (Künzel, 1998). Also, internal connections, such as intermediate floor beams, make it difficult to reach a continuous layer of insulation, thus resulting in large thermal bridges. Earlier research has shown that interior insulation decreases the drying-out capacity of the wall and thereby increases the risk for freeze-thaw damages in brick walls. In older brick constructions there is risk for frost damage when they are exposed to driving rain and fluctuating temperatures. Internal insulation can increase the risk of structural damages even more (Mensinga et al., 2010).

Often moisture from the outside is the major moisture source. Consequently, one solution may be to apply a water repellent substance on the surface. This measure leads to less moisture into

the construction (Sandin, 2003). There are several different impregnations available which can be applied to the surface of the façade. However, for brick masonry it is important to make sure that the surface is free from cracks and other defects. Otherwise, the impregnation can have adverse effect on the performance of the façade, since the drying out capacity is decreased while water can still enter the cracks. Slapø et al. (2017) tested four different impregnations on a brick wall with fresh mortar. They recommend great care when using the substances on brick walls in areas with much driving rain and frequent freeze-thaw cycles.

This paper presents results from a laboratory study of a brick wall and the first results from a field investigation of a homogenous brick wall insulated on the interior. Hygrothermal simulations in WUFI 2D were used to predict the hygrothermal performance for different designs. Previous studies have shown that it is difficult to predict the real performance of full-scale wall assemblies in the laboratory. For instance it is not possible to replicate old brick masonry walls in the laboratory and the climate is difficult to simulate (Johansson et al., 2014a). This calls for investigations in the field. Here, an old industrial brick building located in a cold and moist climate was selected where aerogel blankets (AB) and vacuum insulation panels (VIP) were installed as interior insulation. There were challenges to implement the internal insulation in the building. One of these was the ground water rising in the brick masonry which had to be taken into account.

INTERNAL INSULATION WITH SUPER INSULATION MATERIALS

When the thickness of the insulation layer is limited, SIM may be used. Two examples of SIM are AB and VIP, see Figure 1. VIP are rigid panels which cannot be cut on site and are sensitive to puncturing. Therefore, attention has to be paid in the design of details and envelope components. AB are more similar to conventional fiber-based insulation materials. They can be cut at the construction site and adapted to the specific measurements. VIP were first tested in buildings in the early 1990s which were later followed by several case studies both in laboratory and in the field. AB have been installed in various building assemblies since the early 2000s (Adl-Zarrabi & Johansson, 2018).

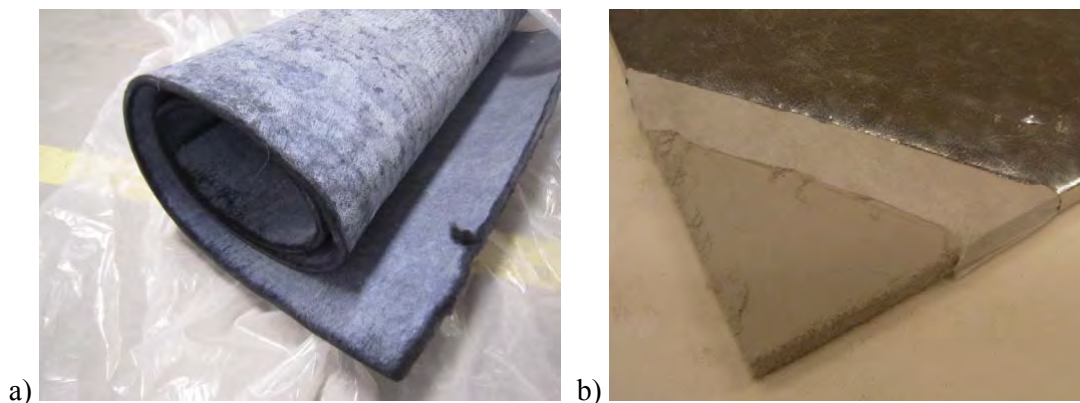


Figure 1. Super insulation materials; a) aerogel blanket (AB), b) vacuum insulation panel (VIP).

Among the important material properties for building materials are thermal conductivity, heat capacity and vapor diffusion resistance. The hygrothermal properties for AB and VIP differ substantially. The thermal conductivity of AB is 0.015-0.020 W/(m·K) and 0.002-0.008 W/(m·K) for VIP (Heinemann, 2018). The vapor diffusion resistance of AB is around $\mu=5$ which is a factor five higher than mineral wool. The blankets are coated with a water repellent substance which reduce the liquid water transfer. The VIP on the other hand, are

wrapped in an air and moisture tight metallized multi-layered polymer laminate which gives a vapor and liquid water transfer only at the edges between the VIP (Johansson et al., 2014b).

NUMERICAL SIMULATION AND LABORATORY STUDY RESULTS

Up until the early 1900s, hydraulic lime mortars were used in brick masonry buildings in Sweden. These have large tolerances to movements caused by temperature and moisture fluctuations, while one of the disadvantages is the longer curing time compared to mixtures of lime and cement mortar. In a previous numerical study to design a laboratory study (Johansson et al., 2014a), a mortar with a short curing and adhesion time, but with similar hygrothermal properties as the hydraulic lime mortar, was desired. To resemble the properties of an old brick wall it was also important to use a brick and mortar similar to what was used in Sweden during this time period. It was shown that the moisture content in the wall was highly influenced by the properties of the brick and mortar. The time before the walls were saturated differed with a factor of 6 between the least and most permeable bricks while the type of mortar influenced the drying of the wall. The mortar giving the lowest drying rate was the pure cement mortar while the mixture of lime and cement gave a lower drying rate than pure lime mortar.

In the numerical study, a historical brick was investigated with a thickness of 250 mm and a 10 mm thick layer of fine lime cement mortar between the bricks (Johansson et al., 2014a). On the interior of the bricks, 4 cases were simulated:

- 1) reference wall without insulation ($h = 8 \text{ W}/(\text{m}^2 \cdot \text{K})$, $s_d = 0.2 \text{ m}$),
- 2) vapor barrier (high performing) on the interior ($h = 8 \text{ W}/(\text{m}^2 \cdot \text{K})$, $s_d = 1.500 \text{ m}$),
- 3) 60 mm AB ($h = 0.242 \text{ W}/(\text{m}^2 \cdot \text{K})$, $s_d = 0.2 \text{ m}$),
- 4) 20 mm VIP (moisture resistance as vapor barrier) ($h = 0.242 \text{ W}/(\text{m}^2 \cdot \text{K})$, $s_d = 1.500 \text{ m}$).

The initial conditions of the materials were 20°C and 50% RH and the interior climate was 20°C and 40% RH. The exterior climate was based on the HAMSTAD benchmark with an exterior surface heat transfer coefficient of 25 W/(m²·K) and a wind dependent vapor surface transfer coefficient. The walls were well protected with a rain water absorption factor of 0.1, i.e. a small amount of rain was available for capillary absorption assuming that the remaining water runs down the façade or splashes off at impact. The results from the one-dimensional numerical simulations of the four cases are shown in Figure 2.

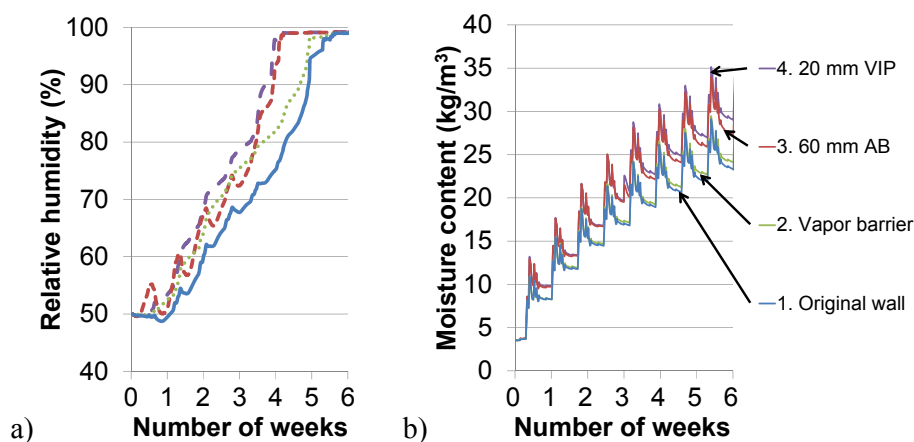


Figure 2. a) Numerically simulated RH 60 mm from the interior of the brick. b) Numerically simulated moisture content in a 250 mm thick wall (adapted from (Johansson et al., 2014a)).

Adding a vapor barrier to the interior of the brick wall does not change the total moisture content in the wall compared to the case without the vapor barrier. However, at the location 60 mm from the interior surface of the brick, the RH is higher than without the vapor barrier. This is caused by the restricted drying from the interior surface of the wall. In the two walls with a layer of interior insulation, both the RH and the moisture content increases compared to the case without interior insulation. The wall with the vapor open insulation has a slightly lower RH and moisture content than the wall with VIP. The main part of the vapor and water flow in the wall is caused by the rain on the exterior surface. Thus, the indoor moisture load is of minor importance for the conditions studied here.

Based on the results above, a brick wall was built in the laboratory of NTNU and SINTEF Building and Infrastructure in Trondheim, Norway. The wall was tested in a large-scale building envelope climate simulator where it was exposed to a temperature gradient and cycling climate with driving rain. The wall was first tested with 20 mm VIP on the interior and then without any layer on the interior side. The wall was divided in two parts (upper and lower) by a horizontal ledge made by a rubber strip to stop liquid water from being transported along the wall. Even though the temperature in the wall was lower in the case with interior VIP, the RH in the upper part of the wall increased more in the wall without VIP. For the lower part of the wall, the RH increased slower on the interior surface of the brick during the first few days, but was then equal to in the middle of the wall. The time before all sensors reached 100% was 180 h for the wall with interior VIP and 170 h for the wall without VIP.

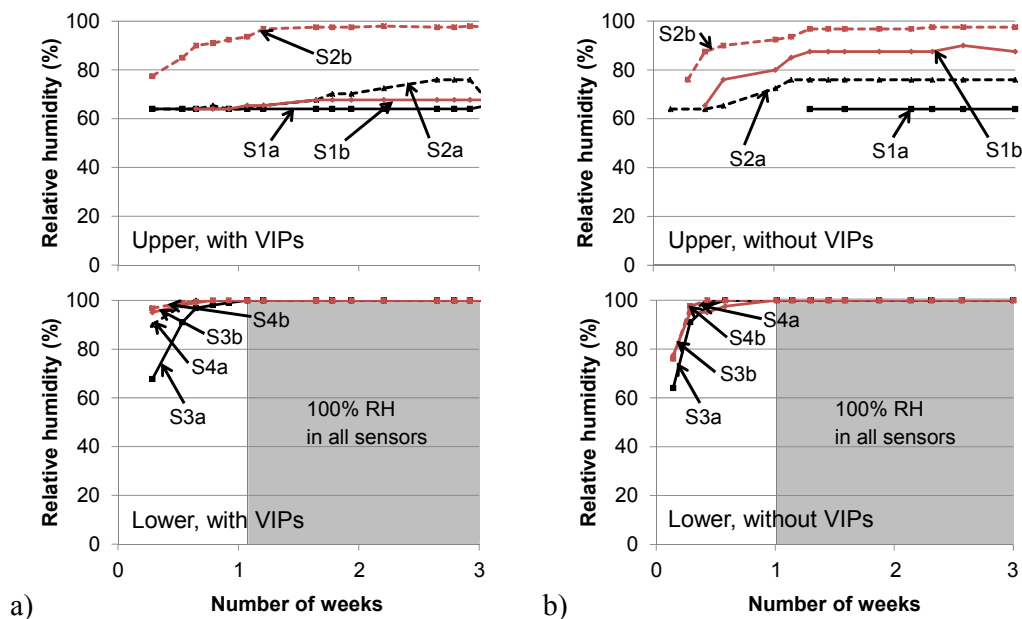


Figure 3. Measured moisture content: a) with VIP in the upper and lower parts of the wall. b) without VIP in the upper and lower parts of the wall. The sensors were located in the mortar in the middle of the wall (S1b-S4b) and in the mortar on the interior surface of the brick (S1a-S4a) (adapted from (Johansson et al., 2014a)).

CASE STUDY BUILDING

An old industrial brick building south of Gothenburg on the Swedish west-coast is under initial testing for evaluation of AB and VIP on the interior of the wall. The building was constructed in 1896 and has been reconstructed several times since then. The case study building was used for paper production which was in operation until the paper mill was closed in 2005. Left

deserted, the building was vandalized and degraded rapidly due to the cold and humid climate. The remaining heritage values and character defining elements of the building have been evaluated and one of the features that are considered important is the brick façade. Therefore, interior insulation is thought to be an interesting solution to reach sufficient energy performance. A small room was constructed inside the building with insulated (170 mm mineral wool) floor, walls and roof and the exposed brick wall, see Figure 4.

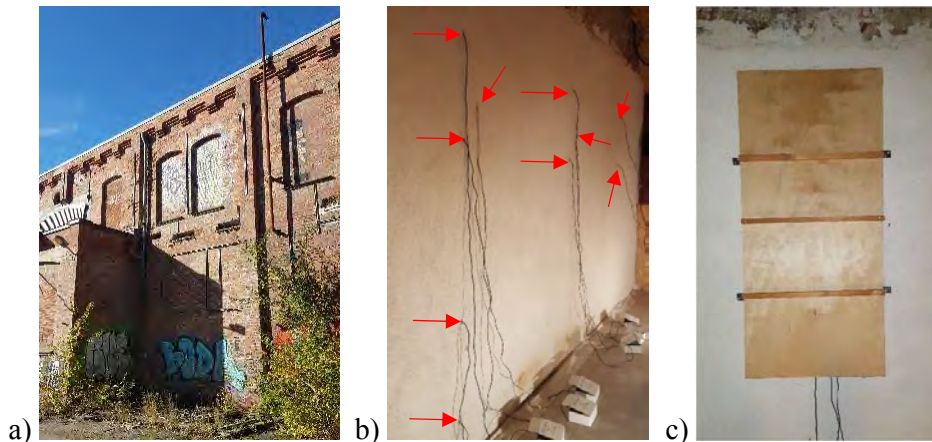


Figure 4. a) Industrial building from 1896 in south of Gothenburg, b) Sensors (marked with arrows) in the brick in the plastered brick wall, c) The test room with installed VIP and AB (removable for inspection of the wall).

Prior to the installation of the internal insulation, the existing plaster was removed from the interior brick surface. There was substantial capillary suction from the ground. The initial measurements showed that the rate of water flow in the bricks is approximately three times higher than that in modern bricks. The room on the inside of the brick wall was heated to around 22°C and ventilated by natural ventilation through two openings. The air in the room was circulated by a fan to create homogenous temperature and moisture conditions in the entire room. The temperature and relative humidity of the air is measured by three sensors. The measurement accuracy is $\pm 2.5\%$ for relative humidity in the range of 10 to 90% and $\pm 0.5^\circ\text{C}$ for temperature at 25°C. The temperature can be measured between -40 to 85°C (GE Sensing, 2007). A weather station monitors the outdoor temperature, relative humidity, wind speed and rain intensity on a free field, nearby the façade.

The brick wall is divided into three parts (500 x 1,200 mm) where AB and VIP is tested and compared to a non-insulated reference. The wall is equipped with 10 hygrothermal sensors that every hour register the temperature and relative humidity. The sensors are wireless Sahlén sensors (wood moisture sensors) which measure the weight percentage moisture in a piece of birch around the sensor. The measurement range corresponds to 60% to 100% RH. The size of the sensors is 40 mm x 13 mm (height x diameter), inserted in a 15 mm wide hole in the wall.

In the field study building, the temperature and relative humidity were measured during 20 December, 2017, to 29 January, 2018. The temperature was on average 4.1°C and varied between 0.9°C and 9.5°C. The relative humidity was on average 92.8% and varied between 66.7% and 100%. This can be compared to the outdoor temperature and relative humidity in a nearby weather station which was on average 3.0°C and 87% relative humidity. The outdoor temperature varied between -7.9°C and 10.0°C and the relative humidity varied between 48.0% and 100%. This gives a moisture excess of 0.8 g/m³ in the building. The moist and cold climate

give several challenges for the application of internal insulation in the field study building. Consequently, the installation of the AB and the VIP was delayed until mid-June, 2018.

CONCLUSIONS

A brick wall was insulated on the interior with AB and VIP to evaluate the hygrothermal performance before and after this measure. In a previous study, hygrothermal numerical simulations and laboratory measurements showed that it is important to investigate the amount of moisture from driving rain. The properties of the interior insulation material showed to have a lesser influence on the moisture accumulation rate. The rain load was the dominating factor determining the vapor and water transport in the wall. Having the possibility of inward drying lowered the moisture accumulation rate slightly. However, during dry periods with less rain, the VIP reduce the drying capacity of the moisture in the brick. In the end it was difficult to predict all the uncertainties in the laboratory measurements using the hygrothermal numerical simulations. This calls for field investigations.

ACKNOWLEDGEMENTS

This study is supported by the Swedish Energy Agency through the project 42856-1. We would also like to thank MölnDala Fastighets AB and our colleagues at the laboratory of NTNU and SINTEF Building and Infrastructure in Trondheim, Norway.

REFERENCES

- Adl-Zarrabi, B., & Johansson, P. 2018. Annex 65 Long-Term Performance of Super-Insulating Materials in Building Components and Systems. Report of Subtask 3: Practical Applications – Retrofitting at the Building Scale – Field scale (Report to be published).
- GE Sensing. 2007. Protimeter HygroTrac Remote Wireless Monitoring System: Instruction Manual. Billerica, MA, USA: GE Industrial, Sensing.
- Heinemann, U. 2018. Annex 65 Long-Term Performance of Super-Insulating Materials in Building Components and Systems. Report of Subtask 1: State of the Art on Materials & Components - Case Studies (Report to be published).
- Johansson, P., Geving, S., Hagentoft, C.-E., Jelle, B. P., Rognvik, E., Kalagasidis, A. S., & Time, B. 2014a. Interior insulation retrofit of a historical brick wall using vacuum insulation panels: Hygrothermal numerical simulations and laboratory investigations. *Building and Environment*, 79, 31-45.
- Johansson, P., Hagentoft, C.-E., & Kalagasidis, A. S. 2014b. Retrofitting of a listed brick and wood building using vacuum insulation panels on the exterior of the facade: Measurements and simulations. *Energy and Buildings*, 73, 92-104.
- Künzel, H. 1998. Effect of interior and exterior insulation on the hygrothermal behaviour of exposed walls. *Materials and Structures*, 31(2), 99-103.
- Mensinga, P., Straube, J., & Schumacher, C. 2010. Assessing the Freeze-Thaw Resistance of Clay Brick for Interior Insulation Retrofit Projects. In: *Proceedings of the 11th International Conference on Thermal Performance of the Exterior Envelopes of Whole Buildings*, Clearwater Beach, FL, USA, December 5-9, 2010.
- Sandin, K. 2003. Vattenavvisande impregnering - Fullskaleförsök 1992-2002. Slutrapport TVBM-3109 (Water repellent surface treatment - Full scale testing 1992-2002. Final report TVBM-3109). [In Swedish]. Lund, Sweden: Lund University, Division of Building Materials.
- Slapø, F., Kvande, T., Bakken, N., Haugen, M., & Lohne, J. 2017. Masonry's Resistance to Driving Rain: Mortar Water Content and Impregnation. *Buildings*, 7(3), 70.

Lighting characterization of a new coating for window retrofit

Umberto Berardi^{1,*}

¹ Ryerson University, Toronto, Ontario, Canada

*Corresponding email: uberardi@ryerson.ca

ABSTRACT

The present paper describes a new high-performance coating used for the retrofit of existing glazing systems. The easy application of this new coating on the internal side of the glazing makes possible to reduce quickly the solar heat gain coefficient of an existing window. A full laboratory characterization both from the thermal and light transmissibility point of views is presented. Moreover, the paper reports the results of long-term studies aiming at assessing the risks of aging and related performance reductions for the investigate coating.

KEYWORDS

Glazing coating; light transmissibility; window retrofit; high-performance window.

INTRODUCTION

The heat flow across a window assembly results by a combination of different heat transfer modes. In particular, two distinct types of radiation heat transfer take place: long-wave radiation heat transfer in the range from 3 to 50 microns (3000-50.000 nm), and short-wave radiation heat transfer in the range from 0.3 to 2.5 micron (300-2500 nm). The short-wave range includes the ultraviolet, visible (from 380 nm to 780 nm), and solar-infrared radiation. Common glass is transparent to solar-infrared radiation and it is opaque to long-wave infrared radiation. Strategic utilization of this behavior may allow to realize high-performance glazing. In fact, even though the physical process of heat radiation transfer is the same, there is no overlap in the heat transfer at long-wave radiation and short-wave radiation, and so the glass properties may be modified, adding coatings or through glass treatments.

The properties of glazing that affect the radiant energy transfer are the transmittance, reflectance, and emittance. These properties are generally expressed using three coefficients:

- Light Transmittance, which refers to the percentage of radiation that can pass through a glazing. In particular, the Visible Transmittance (VT) indicates the amount of visible light transmitted through the glass, i.e. the transmittance in the range from 380 nm to 780 nm;
- Solar Heat Gain Coefficient (SHGC), ruling the ability to control the heat gain by direct or indirect solar radiation, and hence a significant factor in determining the cooling and heating load of a building;
- U-factor (U-value), assessing the heat lost or gained by the combined effects of conduction, convection, and radiation.

Figure 1 helps to understand how ideally a glazing system should behave in different climates or for different building loads. Building envelope specialists typically target high transmittance in the visible range and aim to control the rest of the spectrum in different ways:

- If low solar heat gains are preferred, the glazing should have a treatment (typically a low-E coating) designed to transmit the visible light and reflect the solar-infrared radiation;
- If high solar heat gains are preferred, the idealized transmittance of a glazing should be such that the visible light and solar-infrared radiation are both transmitted.

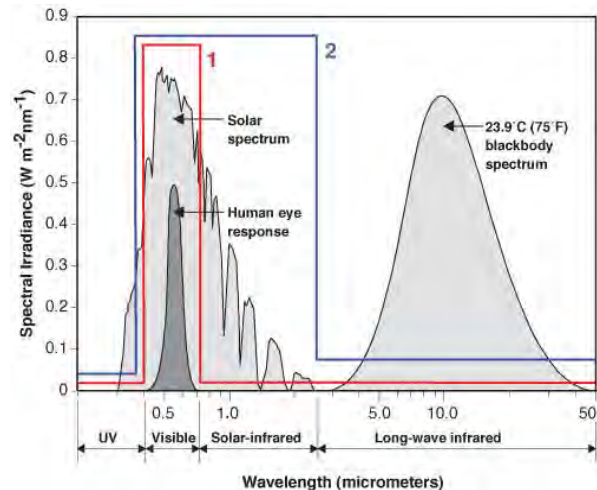


Figure 1. Ideal spectral transmittance: 1 for low-solar heat gains and 2 for high-solar heat gains.

With the recent advances in glazing technology, manufacturers can control how a glazing behaves in the different portions of the spectrum. For example, a window optimized for daylighting and for reducing overall solar heat gains should transmit light in the visible portion of the spectrum, while excluding heat gains from the near-infrared part of it.

Coatings may control the passage of long-wave solar radiation, through transmission and/or reflection. In the past, windows that reduced the solar gain (with tints or coatings) also reduced the visible transmittance. However, new high-performance tinted glass and low-solar-gain low-E coatings have made possible to reduce the solar heat gain with little reduction in the visible transmittance. This paper aims to present several tests done on single glazing and IGUs which were coated with a new product designed to be used for retrofit applications.

GLAZING COATING TRENDS

With conventional clear glazing, a significant amount of solar radiation passes through the windows; then, the heat radiated from internal surfaces within a space is radiated back towards the glass and from this to the outside. A glazing design for maximizing energy efficiency during the heating period should allow the solar spectrum to pass through, and should block the re-radiation of heat from the inside of the space (Rezaei et al., 2017).

Spectrally selective coatings, which act in specific portions of the spectrum, transmit the desirable wavelengths and reflect the rest. A coated glazing material can hence be designed to control (and optimize) the solar heating gain, daylighting, and cooling demand. Originally, the first low-E coatings, intended mainly for residential applications, were designed to have a high solar heat gain coefficient and a high visible transmittance to allow the maximum amount of sunlight into the interior. A glazing designed to minimize the (summer) heat gains, but to maximize the Visible Transmittance for daylighting purposes, would allow most visible light through, but would block all other portions of the solar spectrum, including the ultraviolet and near-infrared radiation, as well as the long-wave heat radiated from outside objects. These new low-E coatings which still allow to obtain a low U-factor, are designed to reflect the solar near-infrared radiation, thus reduce the total SHGC, while provide high Visible Transmittance (Fig.2).

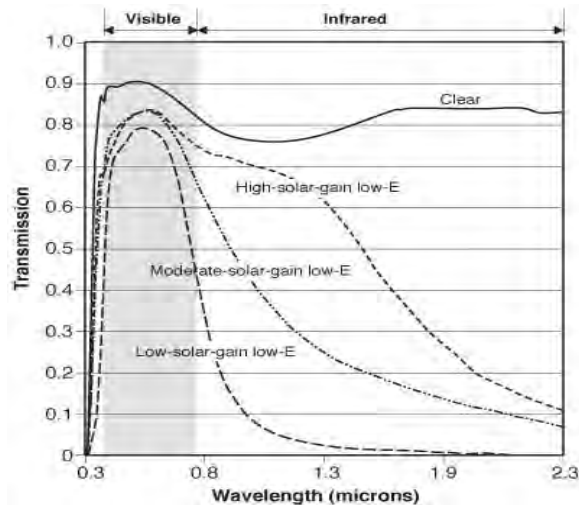


Figure 2. Sunlight transmitted by a clear glass with different coatings.

METHODOLOGY

A new coating (SNG) intended for window retrofit was investigated in this paper. This coating is composed of n-Butyl-acetate, Ethylene glycol monobutyl acetate, and 1-Methoxy-2-propanol acetate. For this study, the following samples were prepared: single glasses with a thickness of 3, 6, and 8 mm both clear and treated with the new SNG coating; insulating glass units (IGUs) clear, treated with a low-e coating, treated with the new coating, and treated with both a low-E coating and the new coating. The IGUs which had both a low-E coating and the SNG coating were realized with the coatings on the same glass (in positions #3 and #4 respectively) and on different glasses (in positions #2 and #4 respectively). The coating was applied with a special custom 6" high density foam rollers. The applied product was in the range of 25 grams of products per square meter. The thickness of the cured product was 8-10 microns. The product hardened in 2-4 hours (depending on the curing environment).

The intent of the study was to investigate the following properties: solar transmittance; visible transmittance (VT); UV transmittance; solar heat gains coefficient (SHGC); U-factor; and aging effects for exposure to extreme temperature and UV.

In order to determine the light transmittance, a spectrophotometer VARIAN CARY 5000 was used. This equipment makes possible to record the light passing through a glass between 190 nm and 3300 nm. The measurements were done at 5 nm intervals. Below the results will be shown only from 300 nm to 2500 nm, where the accuracy of the equipment is higher.

In order to predict the long-term performance, a series of accelerated aging tests was performed. Like any building material, which needs constant performance while being subject to weathering events, the thermal conductivity and light transmissibility of the glazing were tested after exposing the samples to various environmental loads designed to make sure the coating still performed as expected. Accelerated tests were performed at elevated temperature, extreme temperature fluctuations (freeze-thaw cycles), and combining UV exposure with high temperatures and relative humidity levels, following the methodology presented in previous studies (Berardi and Nosrati, 2018).

The samples were placed in several types of accelerated aging equipment and their long-term behaviour was assessed after an age acceleration equivalent to 10 years in natural outdoor conditions. The aging conditions included both thermal cycling aging (freeze-thaw cycles) and UV exposure aging. To investigate the durability of the different glazing against weathering caused by temperature, moisture, and UV light exposure, the effects of these factors were studied in the QUV accelerated weathering tester by Q-LAB Corp using the

cycle based on ASTM G154 standard (2016). Each cycle consisted of 8 hours of UV radiation at 60 °C black panel temperature, and 4 hours of condensation at 50 °C (Fig.3).



Figure 3. QUV accelerated weathering tester for studying the effects of temperature, moisture, and UV light exposure.

RESULTS

Figure 4 shows the light transmittance through a 6 mm clear glass and through the same 6 mm glass treated with the SNG coating. As it can be seen, the clear glass has a light transmittance in the range between 75% and 90% from 350 nm to 2500 nm. The 6 mm glass treated with SNG resulted in a lower light transmittance in the visible range, especially below 400 nm and above 600 nm (only reaching values above 70% from 400 nm to 600 nm), and had a transmittance below 20% in the range from 900 nm to 1750 nm. Similar results were obtained for the tests done for clear and treated 3 mm and 8 mm glass panes, which showed a shift of the results towards higher and lower absolute values of the light transmittance respectively.

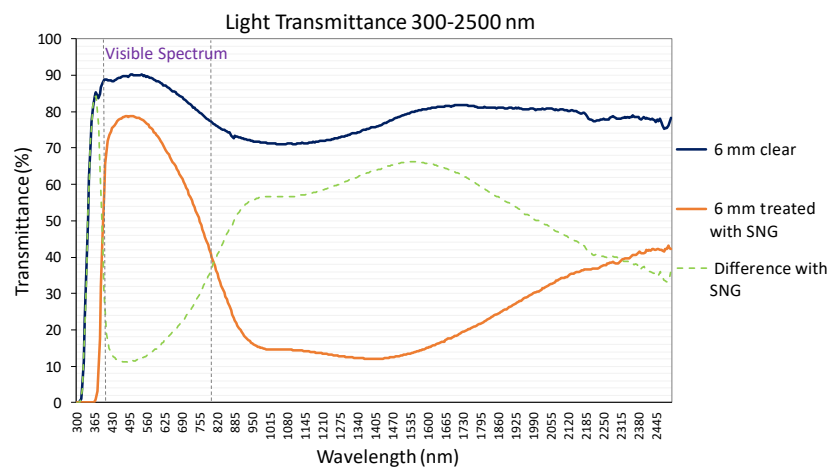


Figure 4 - Light Transmittance of 6 mm in the range from 300 nm to 2500 nm.

Figure 5 shows the light transmittance results for IGUs with clear non-treated (3mm /15mm space air filled/ 3mm), low-E non-treated, clear treated on one side on #4 and low-E treated glasses. The following resulted emerged:

- the clear non-treated IGU has a light transmittance consistently between 70% and 80% across the range from 300 nm to 2500 nm, with higher values in the visible range;
- the low-E non-treated IGU results in some lower transmittance in the wavelength range up to 400 nm, no significant difference in the rest of the visible range, and a significant lower

transmittance above 800 nm, with values linearly reducing down to a 10% transmittance above 2000 nm. However, the results in the range from 400 nm to 800 nm show minimal reduction compared to the clear non-treated IGU;

- the clear treated with SNG IGU results in lower transmittance in the wavelength range up to 430 nm compared to the low-E non-treated IGU. Light transmittance values between 10% and 20% were recorded in the range from 850 nm and 1800 nm, while the transmittance values increased above this wavelength. The light transmittance values increased linearly from 1400 nm to 2500 nm from 10% up to 40% respectively;
- the low-E treated IGU (basically the IGU with two coatings) results in lower transmittance in the wavelength range up to 430 nm, significant reduction above this wavelength, with values always below 10% above 900 nm.

Treating one glass in the IGU with a low-E coating resulted in a reduction of the transmittance mainly below 460 nm and again an appreciable reduction above 600 nm. The IGU with both a low-E and a SNG coating showed a transmittance substantially overlapping the IGU with the SNG coating, as the low-E showed a generally limited effect in the higher wavelengths in the visible range.

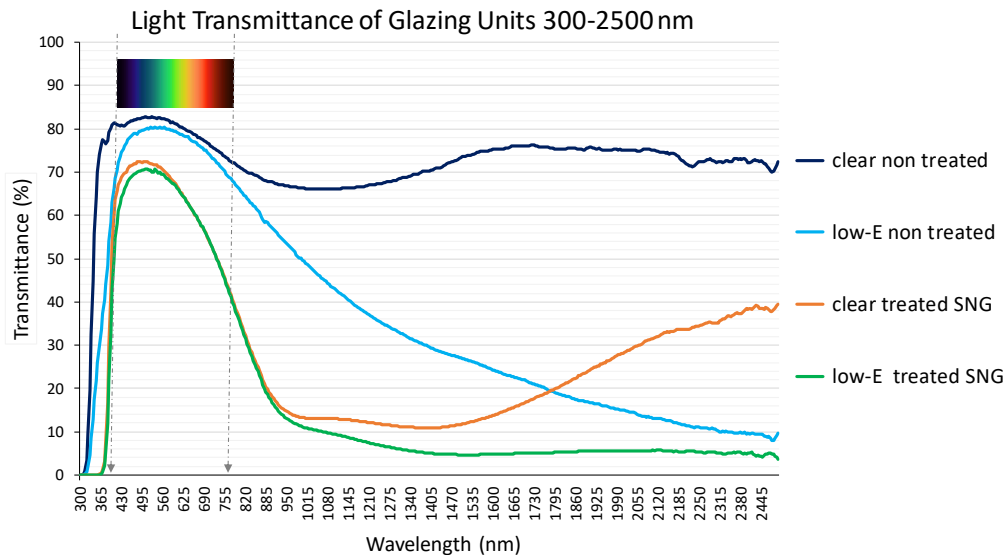


Figure 5 - Light Transmittance of the IGUs in the range from 300 nm to 2500 nm.

Table 1 reports a summary of the light transmissibility tests. The table reports the UV transmission factor, the VT Light transmission factor, the direct transmission of solar energy, and the color rendering index. The VT index for a clear glass decreases from 89% to 76% for a treated SNG glass, a reduction of 13%. Assessing the IGUs, it emerges that the VT was 82% for the clear non-treated glass, 80% for the low-E non-treated glass, which means that the low-E resulted in a particularly small reduction of the VT, and 70% and 69% for the clear treated with SNG and low-E treated with SNG IGUs respectively. This means that treating the IGU with a coating of SNG resulted in a reduction of 12% on average of the VT factor. The UV transmission factor which was 60% for a clear glass and 54% for a clear non-treated IGU, reduced significantly with a low-E coating and became zero once a SNG coating is applied.

The color rendering index (CRI) showed that the clear glass, the IGU clear non-treated and the IGU with a low-E only had a CRI close to a perfect perception of the color, whereas treating the glass with the new coating (SNG) resulted in a difference of the CRI of 4 to 5, and

in a final CRI value for clear treated SNG of 94 to 95. This may be considered a good result, since the coating does not alter the perception of the color in a substantial way.

Finally, the direct transmission of solar energy (%) shows a significant reduction from values as high as 81% for a clear glass and 75% for a clear non-treated IGU, to the value of 60% for a IGU with a low-E coating and 43% for a IGU with a face covered with a SNG coating. Applying the SNG coating to an IGU with a low-E coating resulted in a direct transmission of solar energy of 39%.

Table 1 – Indices resulting from the light transmissibility tests.

	UV transmission factor (%)	VT light transmission factor (%)	Direct transmission of solar energy (%)	Color rendering index
Clear 6 mm glass	60.16	89.30	80.98	99
Treated (SNG) 6 mm glass	0.91	75.98	46.59	94
IGU 3/15/3 clear non treated	54.39	81.89	74.61	99
IGU 3/15/3 low-E non treated	22.50	79.79	60.51	99
IGU 3/15/3 clear treated SNG	0.92	69.87	42.70	94
IGU 3/15/3 low-E treated SNG	0.61	68.70	39.46	95

The results of the aging tests performed on the different glazing systems proved no risks of the coatings over an equivalent life of 10 years. In particular, the light transmissibility tests showed results perfectly overlapping to the related sample in pristine, non-aged, conditions. This shows that the coating is strong and does not suffer thermal cycling or UV radiation at a rate equivalent to a life-span exposure.

Interesting tests regarded the UV exposure of the samples TOO. Based on the experiences of over four weeks of testing in the QUV machine which were calculated as a period equivalent to 10 years in typical application in a moderate climate following the methodology presented in Berardi and Nosrati (2018), no visible effect was perceived on the single panes and IGU systems, confirming the robust behavior of the SNG coating, and it was impossible to distinguish the sample that underwent the UV exposure to the one that did not.

CONCLUSIONS

Based on the measured results, it can be concluded that the application of the new coating on a glazing unit (IGU) allows to block 99% of the ultraviolet (UV), allows to block over 80% of the infrared (IR), with indices as high as 85% if assessed in the IR range where most of the sun radiation falls, allows to have a SHGC in the range between 0.30 and 0.33, and allows to obtain a visible transmittance in the range of 70%. This means that the performance of the coating overcomes that of a low-E coating with the only exception being the capability to limit transmittance above 2000 nm, which showed to be better for the low-E coating, and the reduced color rendering index which resulted in a slightly blue color of the glass.

REFERENCES

- ASTM G154 standard. 2016.. Operating Fluorescent Ultraviolet (UV) Lamp Apparatus for Exposure of Nonmetallic Materials.
- Berardi U, Nosrati R. 2018. Long-term thermal conductivity of aerogel-enhanced insulating materials under different laboratory aging conditions, *Energy* 147, 1188-1202.
- Rezaei SD, Shannigrahi S, Ramakrishna S. 2017. A review of conventional, advanced, and smart glazing technologies and materials for improving indoor environment, *Solar Energy Materials and Solar Cells*, 159, 26-51.

Monitoring and modelling of a prefabricated exterior envelope retrofit

Sébastien Brideau*, Mark Carver, Anil Parekh and Brock Conley

Natural Resources Canada, CanmetENERGY, Canada

*Corresponding email: sebastien.brideau@canada.ca

ABSTRACT

As part of a larger project to develop prefabricated technologies for retrofitting building envelopes of Canadian homes, a small building was retrofitted and instrumented. This prefabricated retrofit method is intended to be applied directly over existing cladding. Two prototype retrofit wall systems were installed on the building; a nailbase panel, and a wood frame panel. The existing wall had an RSI value of $1.80 \text{ m}^2\text{K/W}$ (including film coefficients) and the resulting retrofitted walls reached values of $6.40 \text{ m}^2\text{K/W}$ and $5.72 \text{ m}^2\text{K/W}$. With the addition of a new air barrier, blower door tests have shown a large reduction in infiltration from 7.62 ACH to 0.82 ACH at 50 Pa. This paper discusses the approach taken, the construction of the prefabricated panels, preliminary in-situ RSI measurements, and modelling of thermal bridging and energy savings for the pilot project.

KEYWORDS

Exterior wall retrofit, building energy simulation, prefabricated retrofit.

INTRODUCTION

Canada's housing stock consists of more than 11 million low-rise detached, semi and row-attached dwellings (Natural Resources Canada, 2018). More than two-thirds of these dwellings were built before the existence of residential energy efficiency standards. Although close to one million homes took advantage of retrofit program incentives to date, exterior wall insulation improvements have been uncommon, despite exterior walls often accounting for 25 to 35 percent of heat loss in residential buildings. Anecdotal barriers to exterior wall retrofits include: unpredictable costs; occupant and neighbour disruption; long completion times; and, perceived and real risk related to moisture issues.

This paper discusses Natural Resources Canada's Prefabricated Exterior Energy Retrofit (PEER) project (Natural Resources Canada, 2017a). This project seeks to develop technologies and processes for applying prefabricated components to retrofit existing homes and buildings from the exterior. Guided by a working group to provide technical guidance and market intelligence, the project team is collaborating with industry partners to develop technology specifications and build and test prefabricated panels. There are three main components: field dimensioning using 3D imaging and scanning; development of panel prototypes; and evaluation of their performance through field trial installations.

The PEER project team recently completed a proof-of-concept, pilot-scale field installation in Ottawa, Canada. The project involved surveying the existing building (using hand measurements, 3D laser scanning, and tacheometry), and fabricating and installing two prototype wall assemblies.

Many European projects have been addressing deep energy retrofits of the housing stock. (Ochs et al., 2016; Garay Martinez et al., 2017; Sandberg et al., 2016). The Energiesprong initiative

that started in the Netherlands has retrofit thousands of social housing units to achieve net-zero performance and is now being adopted in other countries. These projects often focus on prefabricated approaches to envelope retrofit to minimize on-site work. Prefabrication has a longer history and higher prevalence in Europe than in North America.

In Canada, off-site fabrication for low-rise residential construction is uncommon, and virtually non-existent for retrofit. However, prefabrication promises a host of benefits, including: minimized demolition and time on site; reduced waste and landfilling; improved quality control; and cost-savings if achieved at scale. The PEER project seeks to explore whether prefabrication may help realize these benefits and overcome technical barriers to traditional, piecemeal approaches - ultimately to enable a leap to industrialized deep retrofit.

Other North American organizations are actively working to overcome barriers to deep and net-zero energy retrofits and to adopt or adapt Energiesprong-type programs in their regions (PEMBINA Institute, 2018; Clean Foundation, 2018; Sustainable Buildings Canada, 2018; Rocky Mountain Institute, 2018; NYSERDA, 2018).

EXISTING WALL ASSEMBLY AND RETROFIT PANELS

The pilot field installation was performed on a construction trailer used for storage of material on the CanmetENERGY campus in Ottawa, Canada. The exterior wall assembly of this building is representative of typical Canadian home construction from 1961-1983. A pitched truss roof was assembled on top of the existing roof with a raised heel to achieve the target ceiling R-value. The existing wall assembly consists of the following layers from interior to exterior:

- 3 mm fibreboard interior finish surface
- 0.2 mm polyethylene
- 38 x 89 mm studs @ 405 mm O.C. (on-center) c/w RSI 2.29 (estimated) fibreglass batts
- 8 mm OSB (Oriented Strand Board) sheathing
- Building paper, lapped not taped
- Prefinished profiled galvanized sheet steel cladding

Based on the isothermal planes method, this provides a total RSI value of 1.80 m²K/W if a 23% framing fraction is assumed (Natural Resources Canada, 2016).

A narrow strip of the existing cladding was removed at the top and bottom of the existing walls, in order to tie-in the new air-barrier to the existing top plate and floor sheathing. Two different retrofit wall panels were installed directly over the remaining cladding. New windows and doors were preinstalled in the panels.

PEER Prototype 1: Nailbase

The nailbase panel consists of a high-density Expanded Polystyrene (EPS) core bonded to structural sheathing on the exterior and low-density batt adhered to the interior (“squishy layer”). The squishy layer is compliant and helps to plumb the panel and absorb surface irregularities. It also provides dimensional tolerance at panel corners and is vapour-open. This may aid upward drying by diffusion. The EPS core is factory cut to receive continuous structural members at the top and bottom of the panel. These members serve to connect several sub-panels together and provide strength and stiffness for transportation and hoisting. New windows and doors are installed in the EPS layer and supported by a wood perimeter buck. Vertical strapping is installed over a self-adhered, vapour permeable air and weather resistive barrier membrane to support cladding that is installed in the shop. A thicker EPS core layer could be specified to

achieve higher R-values. The nailbase panel is described from interior layer to exterior layer in Table 1.

Table 1. Retrofit panel descriptions

	Nailbase	Woodframe
Layer 1	50 mm low-density (24 kg/m ³) fiberglass or mineral wool batt	90mm continuous cellulose insulation (56 kg/m ³)
Layer 2	150 mm Type-II expanded polystyrene (EPS) core with continuous let-in structure	38 mm x 89 mm studs @ 405mm O.C. c/w cellulose insulation (56 kg/m ³)
Layer 3	11 mm OSB sheathing	11 mm (OSB) sheathing
Layer 4	Self-adhered vapour permeable air and weather resistive barrier	Self-adhered vapour permeable air and weather resistive barrier
Layer 5	19x89 mm strapping @ 405 mm O.C.	19 x 89 mm strapping @ 405 mm O.C.
Layer 6	Prefinished engineered wood siding	Prefinished engineered wood siding

PEER Prototype 2: Woodframe

The woodframe panel consists of a 38 x 89 mm stud wall, sheathed with OSB with a self-adhered vapour permeable air and water resistive barrier membrane, strapping and cladding installed prior to arrival to site. The prefabricated stud wall is stood-off from the existing cladding and supported on brackets anchored into the foundation. The stand-off gap is specified to achieve the target thermal resistance. Dense pack fibrous insulation is blown-in on-site through designated access zones at the top and bottom of the panel. In the case of the pilot, a 90 mm stand-off gap was selected. The woodframe panel is described from interior layer to exterior layer in Table 1.

Support

Steel brackets were anchored to the existing rim joist. Both panel systems sit on a continuous bearing plate placed atop the brackets. The wall panels were attached at the top with steel straps fastened to the existing and new top plates.

Air barrier details

Both prototypes utilize an exterior air barrier consisting of self-adhering vapour permeable air/weather resistive barrier applied outboard of the sheathing. This membrane wraps the top and bottom of both panels and connects to the existing building with transition membranes.

Fig. 1 shows the construction trailer before, during, and after the retrofit. The installation of all the wall panels was done in less than a day.

MONITORING RESULTS

In order to verify the thermal performance of the retrofitted walls, measurements of clear wall RSI values were taken in-situ. This was accomplished with Hukseflux HFP01 heat flux sensors on the existing sheathing, and 100 k Ω NTC thermistors on the indoor wall surface and in the ventilated cavity, in line with the heat flux sensors. A total of 7 days was used for the initial measurement, but the RSI value converged in approximately one day. The results for both panels, and a comparison with a calculated value can be seen in the first two rows of Table 2. In addition to increased wall RSI, blower door tests have shown a large increase in airtightness from approximately 7.62 to 0.82 air changes per hour at 50 Pa pressure difference.



a) b) c)
Figure 1. Construction trailer before (a), during (b), and after (c) retrofit.

EFFECTIVE RSI-VALUE AND SIMULATION

The effective RSI-value, considering the effect of thermal bridging through framing at the top and bottom of the panel was assessed using THERM (Lawrence Berkeley National Laboratory, 2018). THERM is a 2D steady-state finite element heat transfer software. A vertical section of each panel was modelled with the existing wall construction, roof and floor. To account for additional bridging in the layers with insulation in the stud cavities, an effective conductivity was imposed on those layers. A framing fraction of 23% was assumed for stud cavities, but the top and bottom plate were removed from this fraction as they are explicitly modelled in the 2D vertical section. The overall effective thermal resistance was then determined for two scenarios:

- The as-built case of the construction trailer without a foundation; and
- A more typical scenario with an insulated foundation. The two panels are depicted on a foundation in Fig. 2.

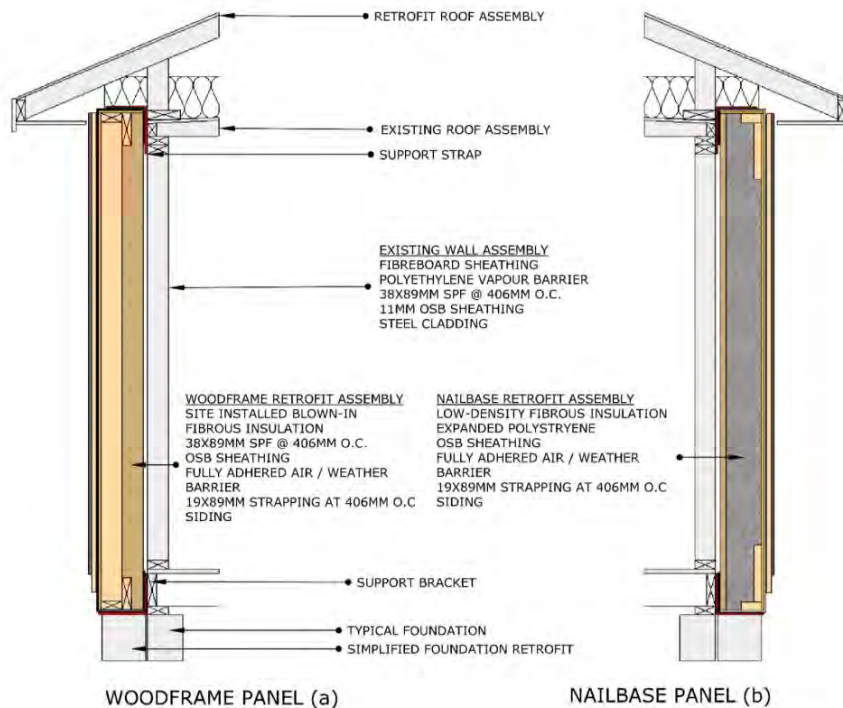


Figure 2. Section of Woodframe (a) and Nailbase (b) panels on existing hypothetical building.

The last three rows of Table 2 show the simulation results. The last row shows the results at the mid-point of the wall, where thermal bridging effects from the top and bottom of the wall are insignificant. There is a significant difference between the RSI values and the mid-point RSI

values for both panels. This is due to thermal bridging through the wood portions at the top and bottom of the assembly, as seen in Fig. 3 for the nailbase panel on insulated foundation. Additionally, the woodframe panel performs worse than the nailbase panel because of additional thermal bridging caused by studs.

Table 2. RSI values for retrofit assembly, including existing wall

	RSI (m ² K/W)		Notes
	Nailbase	Woodframe	
Measured Clear Wall	7.80	7.80	^a
Calculated Clear Wall	7.69	7.64	
Simulated Effective (insulated foundation)	6.77	6.03	
Simulated Effective (as-built)	6.40	5.72	
Simulated Mid-Point	7.07	6.24	

^a Uncertainty: ±0.47 m²K/W, method by Moffat (1988)

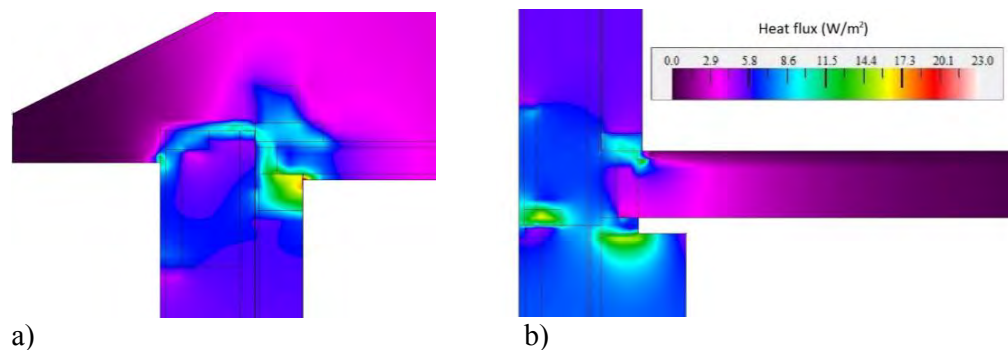


Figure 3. Plot of heat flux at top (a) and bottom (b) of Nailbase assembly.

WHOLE BUILDING ENERGY IMPACTS

The effective thermal resistance values of the retrofit building envelope components and the measured air leakage rates were used to estimate the annual energy use of the existing building and the improvements. In addition to the two prototype wall panels, other retrofit measures included blown-in insulation in the attic, floor batts replaced with spray applied polyurethane, windows replaced with triple glazed units and doors replaced with urethane insulated units. Simulation was performed using HOT2000 v 11.3 (Natural Resources Canada, 2017b). The results in Table 2 show significant improvements in many performance metrics, including a 71.9% improvement in the Thermal Energy Demand Intensity.

Table 2. Whole Building Energy Impacts

Performance Metric	Unit	Pre Retrofit	Post Retrofit	% improvement
Air leakage at 50Pa	ACH	7.6	0.82	89.2%
Annual Gross Heat Loss	MJ	39627.0	14290.0	63.9%
Annual Heat Loss via Walls	MJ	15242.8	4695.8	69.2%
Annual Heat Loss via Air Leakage	MJ	3677.2	393.7	89.3%
Design Heat Loss	W	5760.0	2540.0	55.9%
Design Cooling Load	W	2902.0	2324.0	19.9%
Thermal Energy Demand Intensity	kWh/m ²	230.3	64.7	71.9%

CONCLUSIONS

This paper presented preliminary results of a pilot project for prefabricated deep energy retrofit of building envelope for low-rise residential buildings. It was shown that thermal bridging can be an important source of heat loss, and that the bottom and top of the panels must be carefully designed while considering the existing building to minimize bridging. Additionally, annual simulations have shown significant improvements in thermal energy performance metrics. Field monitoring is continuing, and future work will include assessment of the hygrothermal performance of the envelope over an extended period.

ACKNOWLEDGEMENT

The authors would like to acknowledge funding from Natural Resources Canada's Energy Innovation Program. In addition, we would like to thank Jessica Webster for her help.

REFERENCES

- Clean Foundation, 2018. *Clean Net Zero*. Available at: <http://clean.ns.ca/clean-net-zero/> [Accessed 6 April 2018].
- Garay Martinez, R., Benito Ayucar, J. & Arregi Goikolea, B., 2017. Full scale experimental performance assessment of a prefabricated timber panel for the energy retrofitting of multi-rise buildings. Lausanne, 2017. Energy Procedia - CISBAT 2017.
- Lawrence Berkeley National Laboratory, 2018. *THERM*. Available at: <https://windows.lbl.gov/software/therm> [Accessed 4 April 2018].
- Moffat, R.J., 1988. Describing the Uncertainties in Experimental Results. *Experimental Thermal and Fluid Science*, 1, pp.3-17.
- Natural Resources Canada, 2016. *Tables for Calculating Effective Thermal Resistance of Opaque Assemblies*. Available at: <http://www.nrcan.gc.ca/node/14176#WA-1> [Accessed 29 March 2018].
- Natural Resources Canada, 2017a. *PEER – Prefabricated Exterior Energy Retrofit*. Available at: <http://www.nrcan.gc.ca/energy/efficiency/housing/research/19406> [Accessed 6 April 2018].
- Natural Resources Canada, 2017b. *HOT2000 – Residential Energy Analysis Program*. Available at: <http://www.nrcan.gc.ca/energy/efficiency/housing/home-improvements/17725> [Accessed 5 April 2018].
- Natural Resources Canada, 2018. *Comprehensive Energy Use Database*. Available at: http://oee.nrcan.gc.ca/corporate/statistics/neud/dpa/menus/trends/comprehensive_tables/list.cfm [Accessed 6 April 2018].
- NYSERDA, 2018. *Retrofit New York*. Available at: <https://www.nyserda.ny.gov/All-Programs/Programs/RetrofitNY> [Accessed 7 April 2018].
- Ochs, F., Hernandez-Maetschl, S. & Feist, W., 2016. Prefabricated Timber Envelopes for Retrofit with Integrated Heating System and Building Services. Bern, 2016. Advanced Building Skins Conference.
- PEMBINA institute, 2018. *Affordable Housing Renewal: Retrofits at Scale*. Available at: <http://www.pembina.org/pub/affordable-retrofits-workshop> [Accessed 6 April 2018].
- Rocky Mountain Institute, 2018. *REALIZE*. Available at: <https://rmi.org/our-work/buildings/residential-energy-performance/realize/> [Accessed 8 April 2018].
- Sandberg, K., Orskaug, T. & Andersson, A., 2016. Prefabricated wood elements for sustainable renovation of residential building façades. Tallin and Hellsinki, 2016. Energy Procedia - SBE16.
- Sustainable Buildings Canada, 2018. *Energiesprong*. Available at: <http://sbcanada.org/energiesprong/> [Accessed 6 April 2018].

Retrofit of the existing buildings using a novel developed aerogel-based coating: results from an in-field monitoring

Stefano Fantucci^{1,*}, Elisa Fenoglio¹, Giulia Grosso¹, Valentina Serra¹, Marco Perino¹, Marco Dutto² and Valentina Marino²

¹Politecnico di Torino - Department of Energy, C.so Duca degli Abruzzi 24 Torino

²Vimark Srl – Strada Spartafino 2, Peveragno CN

*Corresponding email: stefano.fantucci@polito.it

ABSTRACT

The energy retrofit of existing buildings and more in general building rehabilitation represents an important challenge in EU countries since a large part of their building stock is old, poorly insulated and affected by pathologies, i.e. mould growth, with relevant implications on users health other than aesthetical drawbacks. Unfortunately, the energy retrofit of existing buildings and particularly when dealing with historic buildings presents several issues, i.e. the compatibility between the identified solutions and the heritage value or the reduction of the internal space if internal solutions have to be adopted.

An emerging solution to address the target of the energy efficiency, according to the abovementioned issues, is the application of advanced materials characterized by high thermal performance and thus allowing to keep low layer thickness.

In the framework of an on-going Wall-ACE Horizon 2020 project, a set of aerogel-based novel super insulating plasters, particularly suitable for internal and external application on existing walls is under development. As far as the interior layer is concerned, so far two different aerogel-based products have been developed: an interior plaster and a thermal coating were developed respectively aimed at reducing the heating energy needs and mitigating thermal bridges mould issues.

The paper reports the first results of the laboratory tests carried out on the thermal coating. Moreover, a monitoring activity in a 1920s building in Torino (Italy, Lat.45°N, Long 7.65°E) was carried out to characterize the actual thermal performance of the insulating layer and to assess the technical and the hygrothermal compatibility of the intervention.

The monitoring results highlight that the application of a thin thermal coating finishing layer can lead to a significant increment of the indoor surface temperature of ~1.5°C with a decrease of the wall heat losses of ~30%. Moreover, a mitigation of the effect of the thermal bridge was also observed with an increment of the node surface temperature (wall-window frame) of up to 2°C.

KEYWORDS

Aerogel, coating, finish rendering, plaster, thermal performance

INTRODUCTION

The building sector is responsible for nearly 40% of the total energy consumption in Europe (Directive 2010/31/EU). About 50% of the European stock was built before the first thermal regulations in 1970s (EU Buildings Factsheets). Italy is a clear example, in fact, more than 60% of residential buildings were built before 1976, the year the first law on energy savings, and the 30% of buildings (12.5 million buildings) is dated before 1945 (ISTAT 2011), therefore, characterized by traditional construction systems. About 1.8% of this Italian

building stock can be classified as cultural heritage, according to the definition of the Legislative Decree no. 42 of 22/01/2004 pertaining to the Cultural Heritage and Landscape Code, that means subject to protection by the competent Ministerial Authorities.

In the last decade, the importance of energy efficiency and thermal comfort in historical buildings has increased immensely and, the most recent research shows a shift in viewpoints. While energy retrofits were previously seen as a potential threat to the character and fabric of historic and traditional buildings, they are now seen largely as an opportunity to protect these buildings and respond to global environmental concerns (Webb A.L - 2017))

There is a growing body of research facing the challenge of merging energy efficiency measures and internal thermal comfort with the requisite of maintaining the cultural and historic significance of buildings (De Bouw M. et al. - 2016). Among the technical solutions to reduce thermal losses, technologies for the indoor insulation are the most suitable for this purpose (Walker R. and Pavia S. - 2018). Innovative materials and products like aerogel-based plasters and renders shall be explored because of their reduced thickness of installation and their high insulation potential.

In the framework of an on-going Wall-ACE Horizon 2020 project a novel aerogel-based thermal coating has been developed, with the main aim of mitigating thermal bridges and mould growth issues.

In this paper first results coming from laboratory tests and in-field monitoring are presented.

METHODS

A novel aerogel-based thermal coating, here called R4, was developed adopting both mineral and organic binders, with Kward® granular aerogel (produced by Enersens), perlite, glass and ceramic spheres used, in various percentage, as lightweight aggregates (LWA).

A first series of preliminary tests, aimed at determining its thermal and mechanical properties were carried out in the laboratory to check its conformity to the market and its potentials in mitigating thermal bridges and avoiding mould growth. A monitoring campaign was then set-up and carried out on a case study building, in order to test its behaviour under actual operating conditions.

Laboratory test

The laboratory tests were aimed at determining the dry bulk density, the mechanical resistance and the thermal conductivity of the material.

The density was measured by weighing a specimen with a known volume of 0.4 x 0.4 x 0.05 m, previously dried in a climatic chamber (ACS DM 340, figure 1c) until any weight variation of more than 0.2%, occurs. Flexural and compression strength tests were carried out adopting prismatic samples according to UNI EN 1015-11:2007 (figure 1b). The dried specimen was also adopted for the thermal conductivity measurements carried out according to UNI EN 12667:2002, through a heat flux meter apparatus (Lasercomp FOX 600, figure 2d).

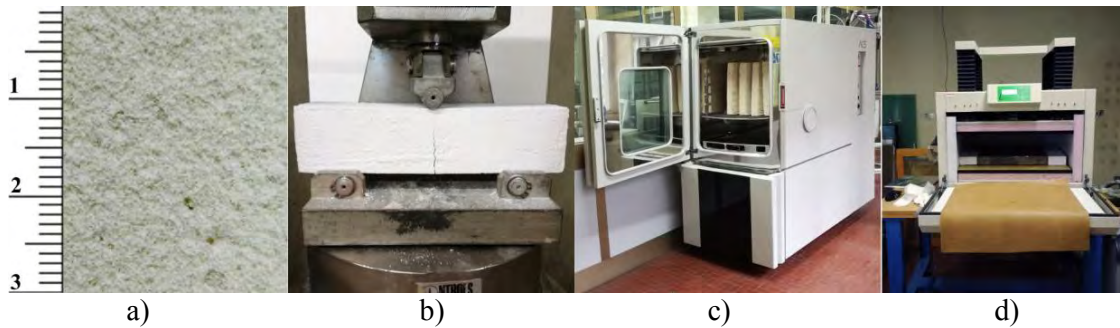


Figure 1: a) Coating sample surface aspect; b) Flexural strength measurement; c) Climatic chamber (ACS DM 340); d) Heat flux meter (Lasercomp FOX 600).

Application phase and in-field monitoring

In addition to laboratory measurements, an assessment of the behaviour under actual operating condition was performed aimed at investigating aspects related to the technical feasibility as well as energy effectiveness. A monitoring campaign on a 1920s building located in Turin (Italy, Lat. 45°N, Long. 7.65°E) was thus set-up and carried out. From the energy point of view, the aim of the in-situ measurements was to evaluate the capacity of the R4 coating, on one hand, to reduce heat losses through the solid masonry wall and on the other hand to mitigate thermal bridging effect due to the increasing of the wall indoor surface temperatures. An east-oriented room was chosen and two identical walls, named TW and RW, respectively the wall with the thermal coating (figure 3a) and the reference one (figure 3b) were continuously monitored.

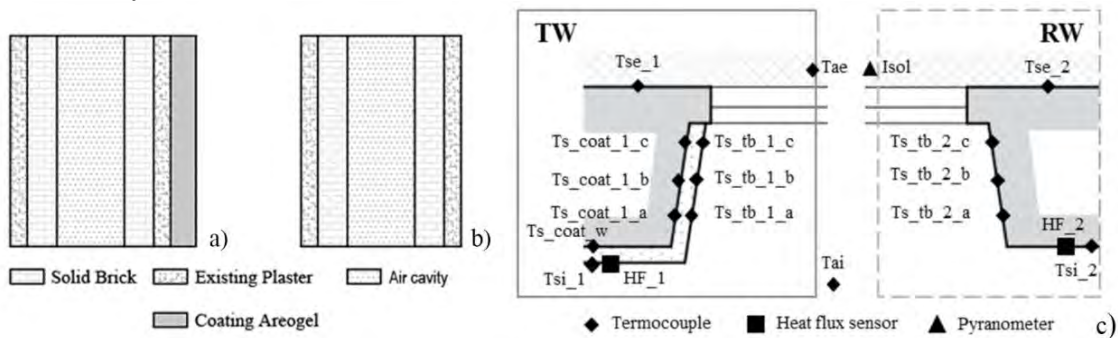


Figure 3: a) Coated wall (TW); b) Reference wall (RW); c) Schematic sensors position

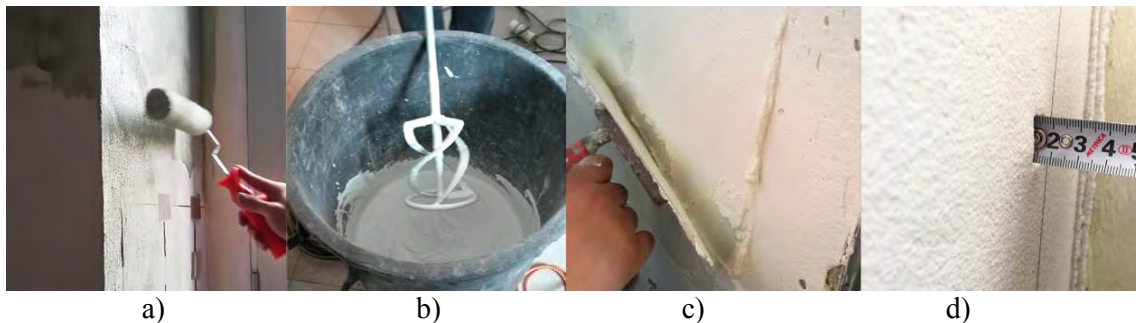


Figure 4: a) Primer application; b) Mixing; c) Coating application; d) Final thickness;

The coating was prepared and applied on TW and the related thermal bridge. To improve the adhesion of the thermal coating on the existent wall, a mono-component primer in thin layer

was firstly applied (figure 4a). The thermal coating, mechanically mixed with ~1:1 water ratio, was manually applied to reach a thickness of 12-15 mm (figure 4b, c, d).

For the monitoring campaign, carried out according to UNI ISO 9869-1:2015, temperature and heat flux sensors were placed both on TW and RW and on the relative thermal bridges. As reported in figure 3c, two heat flux sensors were applied in the centre of walls. T-type thermocouples were placed for measuring air and surface temperatures both on the walls and in the thermal bridges zones¹, in addition, thermocouples were also placed at the interface between the thermal coating and the wall (TW) (figure 3c).

In order to measure the incident solar radiation, a pyranometer sensor was adopted. To force the temperature difference between indoor and outdoor, reaching at least 10 °C, the indoor setpoint temperature maintained at $23 \pm 1^\circ\text{C}$.

RESULTS AND DISCUSSION

Physical properties

Laboratory test showed generally good properties (table 1). The density of dried specimen is ~50% lower than the value obtained from thermal insulating coat without aerogel grains (R0 table 1). As far as mechanical properties are concerned, flexural strength assumed the value of 0.8 MPa. Thermal conductivity was 0.051 W/mK for the dried specimen, that is ~65% lower than the λ -value assumed by mineral-based thermal insulation coating (R0 table 1).

Table 1: Results of laboratory measurements carried out on R4 sample

Sample	Density [kg/m ³]	Flexural strength [MPa]	λ [W/mK]		
			T _{avg} 10°C	T _{avg} 25°C	T _{avg} 40°C
R4	326	0.8	0.051	0.052	0.053
R0	617	1.1	0.138	0.143	0.151

Monitoring results

The temperature and heat flux analyses were focused on the last week of the entire monitored period; these days (from 26th February to 05th March) were considered the most representative due to the low solar radiation value and low external air temperature (figure 5).

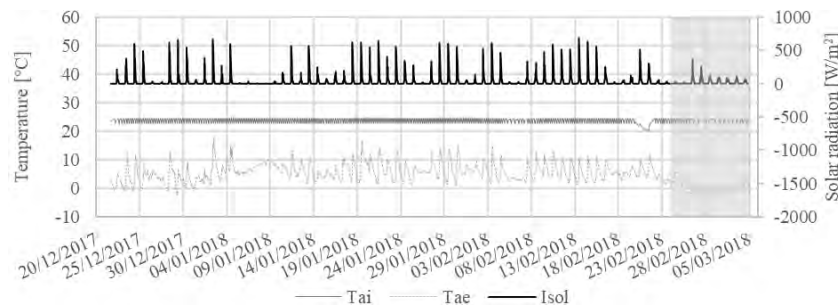


Figure 5: Boundary conditions

In figure 6a the boxplot analysis of the surface temperatures of the TW and RW in the centre of the walls and along the thermal bridge is reported. The graph shows an increase on W1 temperature surface due to the presence of the thermal coating. Particularly, near to the

¹ It is worth to be mentioned that the measurement set-up does not allow to quantify the linear thermal transmittance. For this sake, the measured wall-edge temperatures can be used to validate heat transfer models able to quantitatively assess the incidence of the thermal bridges.

window frame (●), the surface temperature increases of $\sim 2^{\circ}\text{C}$ compared to the uncoated surface. The thermographic analyses highlight the temperature increase on the TW thermal bridge due to the presence of the thermal coating (figure 7b, 7c). Looking at the TW external surface the temperature is, as expected, lower than that of RW, reaching a value below zero, which can determine freezing problems in rain-exposed façade (figure 6b, 7c). As well as the increasing of the internal surface temperature, a noticeable reduction of about 30% of the heat flux on the thermal coated wall, when compared to the RW wall (figure 7c), can be observed.

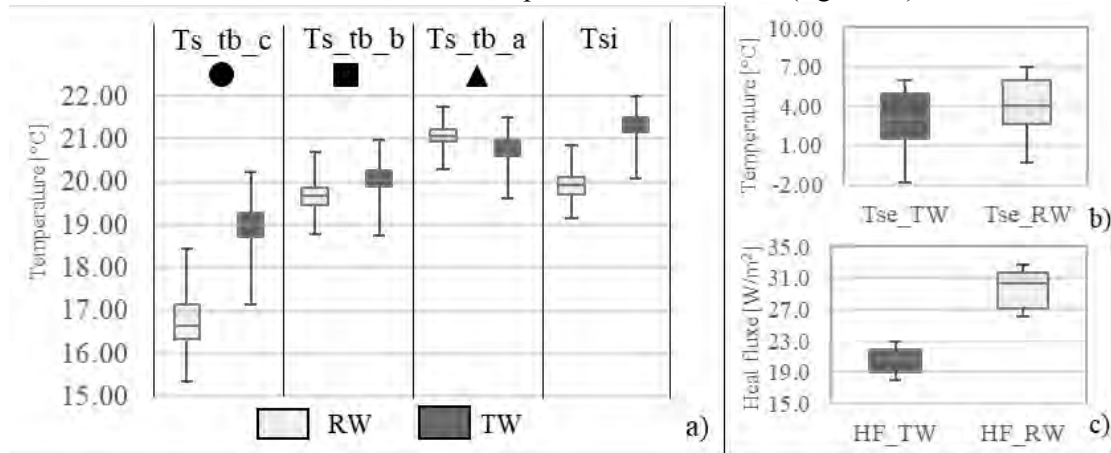


Figure 6: a) Thermal bridges and walls surface temperature monitored; b) external surface temperature monitored; c) Heat flux measured on TW and RW.

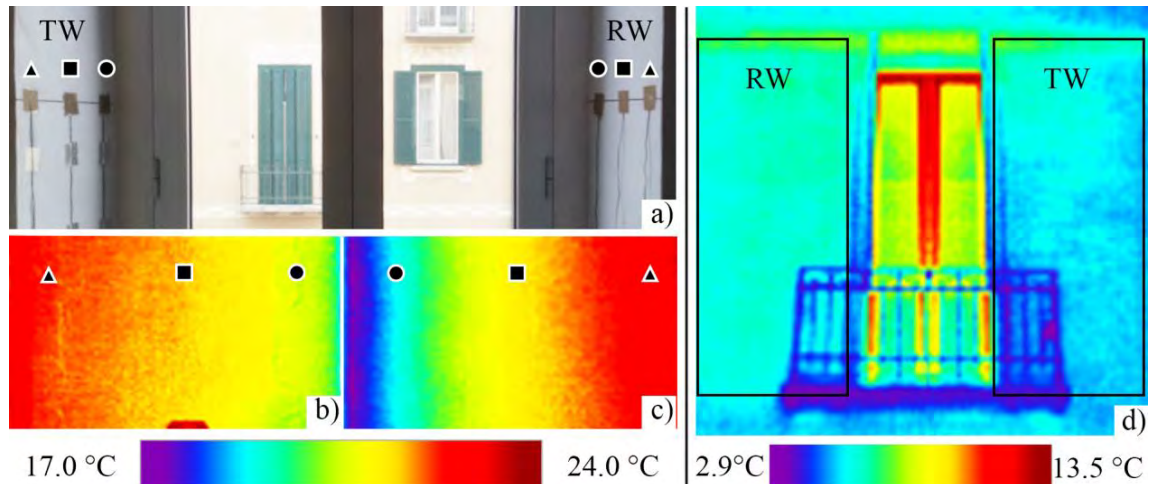


Figure 7: a) Thermocouples on thermal bridges; b) Infrared image of TW thermal bridge; c) Infrared image of RW thermal bridge; d) External infrared image.

CONCLUSIONS

In the framework of a Horizon-2020 project ‘Wall ACE’ a novel aerogel-based thermal coating finishing for interior insulation was developed.

As a first research step, the main physical properties of the developed material were assessed through laboratory analyses. The thermal results of the selected product show a low thermal conductivity value of ~ 0.05 W/mK. Furthermore, the material was applied to a 1920’ demonstration building in Turin. The thermal behaviour of the retrofitted wall was monitored for an entire winter season after the application and was compared with an uncoated reference wall. The monitoring results highlight that the application of a thin thermal coating finishing

layer can lead to a significant increment of the indoor surface temperature of $\sim 1.5^{\circ}\text{C}$ with a decrease of the wall heat losses of $\sim 30\%$. Moreover, a mitigation of the effect of the thermal bridge was also observed with an increment of the node surface temperature (wall-window frame) of up to 2°C . The obtained results reveal that the developed thermal coating finishing present a non-negligible reduction of the heat losses as well as significant mitigation of the condensation risks in thermal bridges demonstrating the suitability of the developed product for the application in all the buildings in which usual thick internal insulating solutions cannot be addressed for space, historical and technical constraints.

ACKNOWLEDGEMENT

The research project Wall-ACE has received funding from the EU Horizon 2020 research and innovation programme under the Grant Agreement No. 723574. The authors wish to thanks the project partner ATC (Agenzia Territoriale per la Casa del Piemonte Centrale) and CASE which make available the demonstration building and ENERSENS that provided the Kwark® aerogel for the development of the insulating coating finish.

REFERENCES

- Directive 2010/31/EU on the Energy Performance of buildings. <http://eur-lex.europa.eu/legalcontent/EN/TXT/PDF/?uri=CELEX:32010L0031&from=EN> (Accessed 2014-11- 17).
- EU Buildings Factsheets, Building stock characteristics, <https://ec.europa.eu/energy/en/eu-buildings-factsheets> (Accessed 2018 - 04- 03).
- ISTAT 2011, National Census - <http://dati-censimentopopolazione.istat.it/Index.aspx> (Accessed 2018 - 04- 03).
- Webb A.L., Energy retrofits in historic and traditional buildings: A review of problems and methods, *renewable and Sustainable Energy Reviews*, 77 (2017), pp. 748-759
- De Bouw M., Dubois S., Dekeyser L., Vanhellefont Y., *Proceedings of Energy Efficiency and Comfort of Historic Buildings (EECHB 2016)*, Brussels, Belgian Building Research Institute, Belgium, 19th-21st October, 2016
- Walker R., Pavía S., Thermal and moisture monitoring of an internally insulated historic brick wall, *Building and the environment* 133 (2018), pp. 178-186
- Enersens, Aerogel particles Kwark, <<http://enersens.fr/en/home/silica-aerogel-particles/>> (Accessed 2018 - 06 - 25)
- UNI ISO 9869-1:2015. Thermal insulation - Building elements – in-situ measurement of thermal resistance and thermal transmittance. Part 1: Heat flow meter method
- UNI EN 1015-11:2007. Methods of test for mortar for masonry - Determination of flexural and compressive strength of hardened mortar.
- UNI EN 12667:2002 Thermal performance of building materials and products. Determination of thermal resistance by means of guarded hot plate and heat flow meter methods. Products of high and medium thermal resistance

Comparing Exterior Wall Finishes Using Life-Cycle Assessment

Brandi Dodge¹, Rui Liu^{1,*}

¹College of Architecture and Environmental Design, Kent State University, Kent, Ohio

*Corresponding email: rliu5@kent.edu

ABSTRACT

Selecting products that are environmentally friendly can help reduce the negative environmental impacts associated with the built environment. However, the process can be difficult. Life-cycle assessment (LCA) is an approach used to measure the environmental performance of a product or service by considering all stages of a product's life-cycle from extraction of raw materials to its end of life. Many products that claim to be environmentally friendly are based on a single life-cycle stage or environmental impact. These claims are often misleading as they do not consider other life-cycle stages or other environmental impacts associated with the products. This study examines alternative exterior wall finishes for a traditional single-family home in the State of Ohio from an LCA approach to determine which finishes are friendlier on the natural and built environment. Advantages and disadvantages of exterior wall finishes including aluminum siding, brick, wood siding, fiber cement siding, stucco, and vinyl siding have been investigated, as well as the impact each finish has on each of the life-cycle stages. Their life-cycle environmental impacts during various life-cycle stages are compared using the BEES (Building for Environmental and Economic Sustainability) software developed by the National Institute of Standards and Technology. Each of the exterior wall finishes were compared in the following categories: overall life-cycle environmental impacts, global warming potential, recyclability, service life, and the cost of material and labor. Not one of the materials scores the best in every category. While vinyl siding does not have much potential for recycling or a long service life, it performs well in other categories and appears to be a better option from an environmental and cost perspective overall.

KEYWORDS

Exterior Wall Finishes; Life-cycle Assessment

INTRODUCTION

The construction industry consumes about 50% of the natural resources extracted from the earth. The process of extracting raw materials leads to resource depletion, creates pollution and landfill waste, and contributes to biological diversity losses. Also, transporting raw materials to manufacturing plants, and turning those materials into products, generates additional pollution and requires energy consumption resulting in higher greenhouse gas emissions. Products typically generate wastes during installation or have short service lives that result in disposal and the manufacture of replacement products. Energy consumption by the built environment is responsible for 40% of greenhouse gas emissions worldwide, so selecting building products that are environmentally friendly is one way to help reduce the negative environmental impacts associated with the built environment (Lippiatt, 2007). When considering products, people will typically look at the cost, lifespan, and product maintenance. However, people tend to only consider the end product and are not aware of the negative impacts that these products have on the environment from a life-cycle perspective (Robertson, 2008). By implementing life-cycle assessment (LCA), it is possible to optimize aspects of a product from the extraction of raw materials to the end of life. LCA helps to look

at the ways in which to improve environmental processes, ways in which to prevent adverse environmental impacts, how to enhance the quality of life, and ways to allow people to live in a healthy environment. In comparison between the findings of this study and existing studies, a lack of comparable research was discovered. Existing residential LCA studies on exterior walls tend to study entire wall assemblies rather than just the exterior wall finishes. The purpose of this study is to consider only the exterior wall finishes for a traditional single-family home in the northeast Ohio, United States. These finishes are compared to help aid in the selection of finishes that are environmentally friendlier from an LCA approach. The cost of the materials and installation are compared as well.

METHODS

The project is a 2-story residential house, located in a subdivision in the northeast Ohio. The house contains 4 bedrooms, 2.5 baths, and a 2-car attached garage. The house is constructed of 2x4 wood framing with batt insulation. The current materials on the envelope of the house include vinyl siding and asphalt shingles, shown in Figure 1. The finishes in this study include aluminium siding, brick, wood siding, fiber cement siding, stucco, and vinyl siding.



Figure 1. House used for the study (SketchUp Warehouse model by Paulwall)

The Building for Environmental and Economic Sustainability (BEES) software, developed by the U.S. National Institute of Standards and Technology, was used to compare the overall environmental performance of the exterior wall finishes according to their life-cycle stages.

BEES generates environmental performance scores for building products sold in the United States. The scores generated help with selecting products that are environmentally preferred. Manufacturing of a product involves several unit processes with inventory flows. The basis for the unit of comparison is the functional unit, which for this study will be 1 ft² of product lifetime for a 50-year period. Inventory analysis involves quantifying the inventory flows for a product. Data categories are used to group the inventory flows. For generic products, as used primarily in this study, assumptions concerning the associated unit processes were verified through industry experts.

The impact assessment quantifies the potential contribution of a product's inventory flows to a variety of environmental impacts. Twelve impacts include global warming, acidification, eutrophication, fossil fuel depletion, habitat alteration, criteria air pollutants, indoor air quality, human health, smog, ozone depletion, ecological toxicity, and water intake are addressed. Inventory flows contributing to each impact have been quantified and characterized in terms of U.S. flows per year per capita. Adding all characterized flows for each impact results in impact category performance measures. These measures represent a baseline against which to compare the environmental impacts of a product.

During interpretation, the normalized impact assessment results are analyzed. To compare the overall environmental performance of the alternative products, the performance scores for all the impact categories are synthesized. This is achieved by weighting each of the impact categories by its relative importance to the overall environmental performance, and then computing the weighted average impact score. The weighting used for this study is based on the EPA Science Advisory Board study (USEPA, 2000). Highest-risk problems include global warming and habitat alteration. High-risk problems include indoor air quality, ecological toxicity, and human health. Medium-risk problems include ozone depletion, smog, acidification, eutrophication, and criteria air pollutants. Fossil fuel depletion and water intake were not explicitly considered as impacts (Levin, 1996). These classifications are then converted into numerical importance weights using a method known as the analytic hierarchy process (ASTM International, 2002). Finally, the materials and installation costs are compared for these alternative exterior wall finishes using 2016 construction cost data (RS Means, 2016).

RESULTS AND DISCUSSIONS

The first step in the BEES assessment is to specify the analysis parameters. For this part of the study, other environment performance of the exterior wall finishes is being considered, so the environmental performance is set at 100% while the economic performance is set at 0%. In the building element for comparison section, shell is the major group element, exterior enclosure is the group element, and exterior wall finishes is the individual element. The product alternatives represent the six exterior wall finishes to be compared. The transportation distance represents the number of miles from the manufacturer to the site. Manufacturer locations and site locations vary for each analysis, so a default mileage, which represents an average, was used.

After selecting all the products for LCA comparison, the analysis was completed. The analysis looked at the overall environmental performance, the overall global warming potential, and the effect that each finish has on environmental impacts. Refer to Figures 2-4 for the results of the comparisons. The results are based on a performance score and do not represent absolute performance. Instead, these scores represent proportional differences in performance among the alternatives. The lower the number of the performance score, the more environmentally friendly the product is (Lippiatt, 2007).

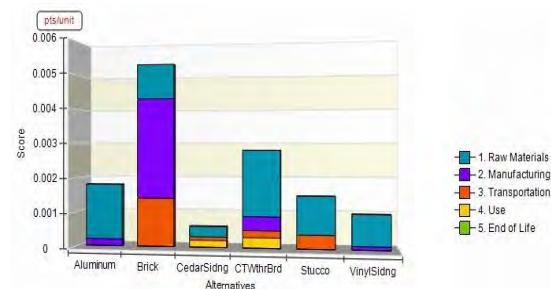


Figure 2. Environmental performance

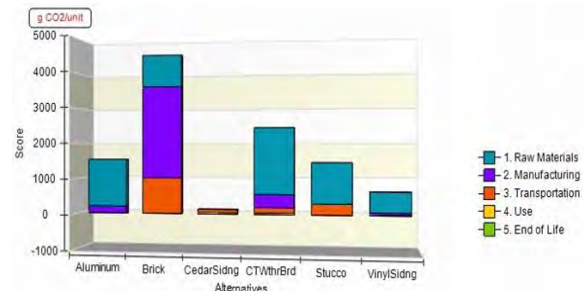


Figure 3. BEES global warming results

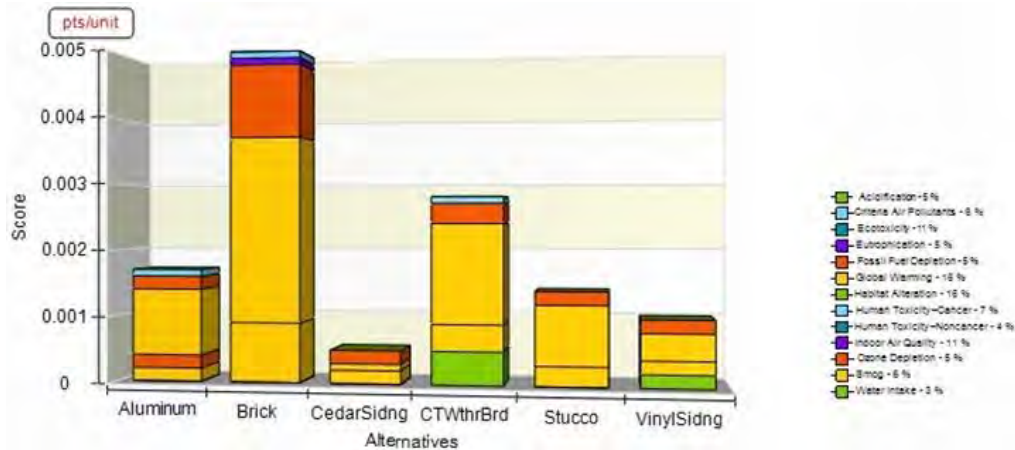


Figure 4. BEES results of each finishes' effect on environmental impacts

The results of the exterior wall finishes analyzed for comparison shows that of the five life-cycle stages, the extraction of raw materials has the greatest negative impact on the environment of each material except for brick. Wood siding has the least harmful impact on the environment, with a total performance score of 0.0006. Brick has the most harmful impact on the environment with a total impact performance of 0.0053. Viewing the global warming potential from these life-cycle stages, the results show that the extraction of raw materials is the greatest contributor to the negative impact on global warming of each material except for brick and wood siding. Wood siding has the least harmful impact on global warming with a total performance score of 126. Brick has the most harmful impact on global warming with a total performance score of 4513. The life-cycle stages of the finishes show that global warming has the greatest negative impact on the environment. Wood siding contributes the least to global warming with a total performance score of 0.0005. Brick contributes the most to global warming with a total performance score of 0.0050.

Based on the results from the BEES comparison studies, the exterior wall finish that is overall the most environmentally friendly, and contributes the least to global warming is wood siding. The exterior wall finish that is overall the least environmentally friendly, and contributes the most to global warming is brick. The other finishes, in order from most environmentally friendly to least environmentally friendly from all life-cycle stages combined are vinyl siding, stucco, aluminum siding, and fiber cement siding. Raw material extraction and manufacturing of these finishes are the life-cycle stages which contribute the most to a negative environmental impact. These two life-cycle stages also greatly impact the global warming potential and are the largest contributors of carbon dioxide emissions.

Some information to consider when performing LCA is that values associated with each model are representative of the year of the model. Data originating from surveys and/or forms submitted by industries to governments for national statistical purposes can be incomplete, thus underestimating actual data values. Economic input-output coefficients for stable industries may be similar to past coefficients, but may vary over time for rapidly changing industries. Also, environmental data can vary due to changes in efficiency, pollution regulations, or production levels (Carnegie Mellon University, 2016). In addition, products tend to be grouped into a single industry sector if their production requires a similar process, thus resulting in data and dissimilar products taking on contributions and impacts of another product. While uncertainties in data do not imply that LCA studies are unreliable, these uncertainties should be understood and the LCA results recognized (Williams, 2009).

The house in this study has a surface area of 3,292 ft² excluding all doors and windows. Accounting for a 5% material waste and rounding up to the nearest 100 ft², the total surface area increases to 3,500 ft². The cost of materials falls within a price range, so the lowest cost of each material and the highest cost of each material is calculated (Anderson, 2013; RS Means, 2016). The total costs exclude overhead and profit.

Table 1. Costs of Materials and Installations

	Material (\$/ft ²)		Labor (\$/ft ²)		Total (\$/ft ²)		Material Total (\$)		Material + Installation Total (\$)	
	Low	High	Low	High	Low	High	Low	High	Low	High
Aluminum	\$1.63	\$4.73	\$1.96	\$1.96	\$3.59	\$6.69	\$5,705	\$16,555	\$12,565	\$23,415
Brick	\$4.00	\$7.00	\$7.00	\$10.00	\$11.00	\$17.00	\$14,000	\$24,500	\$38,500	\$59,500
Wood (Cedar)	\$3.79	\$6.75	\$1.03	\$1.03	\$4.82	\$7.78	\$13,265	\$23,625	\$16,870	\$27,230
Fiber Cement	\$1.19	\$4.12	\$1.82	\$1.11	\$3.01	\$5.23	\$4,165	\$14,420	\$10,535	\$18,305
Stucco	\$1.00	\$1.00	\$1.30	\$1.50	\$2.30	\$2.50	\$3,500	\$3,500	\$8,050	\$8,750
Vinyl Siding	\$0.72	\$1.62	\$1.48	\$1.41	\$2.20	\$3.03	\$2,520	\$5,670	\$7,700	\$10,605

The costs of the exterior wall finishes in order from the cheapest to the most expensive are vinyl siding and stucco, fiber cement siding, aluminum siding, wood siding, and brick. Each of the exterior wall finishes were compared in various categories. Green represents the best in each category, yellow represents second to best, and red represents the worst in each category. Refer to Table 2 for the category comparisons.

Table 2. Overall Comparison

	Life-Cycle Impacts	Global Warming Potential	Recyclability	Service Life (Years)	Material + Install (\$ Low)	Material + Install (\$ High)
Aluminum	0.0018	1,538	100%	80	\$12,565	\$23,415
Brick	0.0053	45,134	75%	100+	\$38,500	\$59,500
Wood (Cedar)	0.0006	126	0%	40	\$16,870	\$27,230
Fiber Cement	0.0028	2,436	0%	50+	\$10,535	\$18,305
Stucco	0.0015	1,458	0%	100+	\$8,050	\$8,750
Vinyl Siding	0.001	655	0%	40	\$7,700	\$10,605

Not one of the materials scores the best in every category. Therefore, the best material cannot be selected without weighing the pros and cons. Brick has the worst score for life-cycle impacts and global warming potential, as well as the most expensive in cost compared to all the other materials. Brick has an advantage since 75% of it can be recycled at its end of life. Also, brick has a service life that can last over 100 years. However, a house's typical lifetime is about 60 years, so the service life far exceeds the house's lifetime. Aluminum siding does not have the worst scores in any of the categories, but requires continuous painting and can dent very easily. Stucco's life-cycle impacts and global warming potential fall near the middle, so environmentally, it is not the worst material, nor is it the best material. However, stucco is rarely used in the northeast Ohio. Fiber cement siding also falls near the middle range of the environmental impacts, but like aluminum siding and stucco, fiber cement is not a very common material in the northeast Ohio when compared to vinyl siding. Wood siding has the lowest life-cycle impacts and contributes the least to the global warming potential. It is more expensive than vinyl siding and is not typically recycled. Its service life is shorter than that of a house's typical lifetime, so the siding would need to be replaced at least once. Also, wood siding requires continuous painting or staining. While the material does not have much potential for recycling or a long service life, it does well in the other categories. Vinyl siding is a close second to wood as the best material according to life-cycle impacts and global warming potential, plus it is an affordable material. The service life of vinyl siding is

the shortest compared to those of the other materials but it can be replaced at the end of its service life, replacement material can be produced, and it will still have an overall life-cycle impact and global warming potential lower than that of aluminum, brick, wood, and fiber cement. Also, vinyl siding does not require painting or extensive maintenance.

While research shows that wood, fiber cement, stucco, and vinyl siding do not have much potential for recycling at end of life (Lippiatt, 2007), measures are being taken to prevent various building materials from ending up in landfills. Local regulatory measures, disposal fee increases, education, and green building are driving the market toward building material recovery. By recovering used building materials from waste streams, materials can be re-manufactured and refurbished (Liming, 2018).

CONCLUSIONS

Overall, vinyl siding appears to be the best option from an environmental and cost perspective. Based on the results carried out in this study, the most affordable material is not necessarily the most environmentally friendly. It is difficult to select a material that has both an appealing price tag as well as less of a negative impact on the environment. However, it is possible to weigh the options to responsibly select a material.

REFERENCES

- Anderson J. 2013. *Exterior Siding Materials: How Long Should they Last?* Improvement Center. Accessed on 3/22/2016 from <http://www.improvementcenter.com/siding/exterior-siding-materials-how-long-they-last.html>>
- ASTM International. 2002. *ASTM E1765-02*: Standard Practice for Applying the Analytic Hierarchy Process to Multiattribute Decision Analysis of Investments Related to Buildings and Building Systems. West Conshohocken, PA.
- ASTM International. 2005. *ASTM E1557-05*: Standard Classification for Building Elements and Related Sitework-UNIFORMAT II. West Conshohocken, PA.
- Carnegie Mellon University. 2016. Economic Input-Output Life-Cycle Assessment. *Assumptions, Uncertainty, and other Considerations with the EIO-LCA Method*. Accessed on 06/22/2018 from <http://www.eiolca.net/Method/assumptions-and-uncertainty.html>
- International Organization for Standardization (ISO). 2006. *International Standard 14040*: Environmental Management - Life-Cycle Assessment – Principles and Framework.
- Levin H. 1996. Best Sustainable Indoor Air Quality Practices in Commercial Buildings. Third International Green Building Conference and Exposition. *NIST Special Publication 908*, Gaithersburg, MD, November.
- Liming D. 2018. Careers in Green Construction, Bureau of Labor Statistics, United States Department of Labor. Accessed 06/22/2018 from <http://www.bls.gov/green/construction/>
- Lippiatt B. C. 2007. BEES 4.0: Building for environmental and economic sustainability technical manual and user guide. Gaithersburg, MD, National Institute of Standards and Technology. Accessed on 03/15/2016 from <http://nepis.epa.gov/Exe/ZyPDF.cgi/60000EQ6.PDF?Dockey=60000EQ6.PDF>
- Robertson T. 2008. Environmentally Friendly Siding. Los Angeles, CA. Accessed on 3/15/2016 from <http://www.scgh.com/go-green/siding/eco-friendly-siding/>
- RS Means. 2016. *Construction Cost Data*. Wellington, FL, USA.
- United States Environmental Protection Agency, Science Advisory Board. 2000. Toward Integrated Environmental Decision-Making. *EPA-SAB-EC-00-011*, Washington, D.C., August (2000).
- Williams E., Weber C., and Hawkins T. 2009. *Hybrid Framework for Managing Uncertainty in Life Cycle Inventories*, *Journal of Industrial Ecology*, 13 (6), 928-944.

Experimental Study of the Performance of a Double Skin Façade Window under Non-Solar Conditions

Jiayi Zhu, Guoqing He^{*}, Qihuan Luo and Yu Liu

College of civil engineering and architecture Zhejiang University Hangzhou China

**Corresponding email: guoqinghe@zju.edu.cn*

ABSTRACT

This paper reports measured heat transfer coefficient of a double skin façade (DSF) window measured 1.1 m by 0.7 m at varied depth in the absence of solar radiation using a calorimeter box. The results showed that the DSF had better insulation than the double glazing especially with cavity closed. All the studied factors (ventilation, cavity width, and outdoor temperature) had influence on the heat transfer coefficient and such influence could be season specific. Measurements confirmed the existence of an optimal width in winter for best insulation.

KEYWORDS

Double skin façade, U value, experiments, non-solar radiation

INTRODUCTION

Double skin façades (DSFs) have received increasing attention in research and in practice since their first appearance in northern Europe (Poirazis 2006). In addition to its freedom in aesthetic expression, the cavity between the two layers offers potential energy savings (Ghaffarianhoseini et al., 2016) and even carbon reduction in a life cycle (Pomponi and D'Amico, 2017). Recent studies explored the performance of varied forms of DSFs, such as phase change material attached blinds (Li et al., 2017), photovoltaic (PV) panel attached blinds (Kapsis and Athienitis, 2015; Luo et al., 2017), fan-coil combined DSF design (Bueno et al., 2017), and pipe-embedded DSF design (Shen and Li, 2016). These studies attempted to make the best of the double layers, which protect solar shading devices and other materials from the outdoor environment while keeping the heat absorbed in the cavity outdoors.

What makes the DSF unique is thought to be the double layers and various ventilation schemes to meet different needs in different seasons, i.e., one design that can work in both cooling and heating seasons, suitable for regions such as the hot summer and cold winter zone in China. Such capability requires the DSF to have good insulation, good shading performance in summer, and good solar heat gain in winter. The installation of blinds and its combination with other new materials aim to meet the later two needs. The double layer structure typically consisting of a double glazing and a single pane presumably provide better insulation than a normal double glazing, whose U values are typically around 2.80 W/m²/K. There are limited studies on the U values of DSFs. Recent studies have defined the U value of a DSF window based on total heat transferred through inner surface excluding the direct solar transmittance (here referred as heat transfer based U value, or U_{HT}). Luo et al. (2017) reported experimental data of U_{HT} as 2.2 to 2.8 W/m²/K for naturally ventilated DSFs, lower than 3.8 W/m²/K reported by Peng (Peng and Lu et al., 2015) for a naturally ventilated DSF with a semi-transparent PV film attached to the outer pane. Note that U_{HT} is not comparable to the conventional U value defined based on steady state heat transfer without solar radiation because the former includes part of the absorbed solar irradiation on the inner pane of the window which then enters into the room as heat gain by convection or irradiative heat transfer.

Chow et al. (2010) and He et al. (2016) used a different approach where total room heat gain of a window is expressed as a linear function of solar irradiation and the temperature difference between the room and the outside, which is confirmed by experiment in the case of DSF (He et al., 2016). The coefficient of the temperature term is defined as the U value (room heat gain based U value, or U_{HG}), which is difficult to measure directly. For common double glazing, Chow et al. (2010) showed that the calculated values of U_{HG} are close to the typical U values. For DSF, He et al. (2016) determined the U_{HG} value of a DSF window together with the solar shading coefficient by fitting the experimental data. However, the contribution of heat transfer through the DSF was shadowed by the solar radiation, making it difficult to obtain a U value with meaningful certainty. Nevertheless, their simulations indicated that the U value of DSF windows could be significantly lower than that of the corresponding double glazing indicating improved insulation by the addition of an extra layer.

Previously discussed U values of DSFs reflects the overall heating transfer coefficient in the present of solar radiation. To our best knowledge, there have not been any studies on the U value of DSF in the absence of solar radiation (conventional U values). Given the amount of non-solar time in a day, the conventional U value of the DSF is critical to the performance of DSF. This paper attempts to fill this gap by studying the conventional U value of a DSF window experimentally.

METHODS

Experiment setup

Experiments were carried out indoors with the same DSF model and calorimeter described in He et al. (2016). The model box was $1.3 \text{ m} \times 1.1 \text{ m} \times 0.88 \text{ m}$ (Figure 1) and consisted of a small version of DSF window on one wall. All other three walls, floor and ceiling were 0.1 m thick extruded polystyrene (XPS) panels, each covered by a thin (0.005 m) aluminum sheet outside. The outer layer of the DSF window was a single-pane glazing and the inner layer was a double glazing. All glazing panes were clear float glasses. There were two openings of equal height (0.02 m) at the top and the bottom of the single pane glazing. The double glazing separates the box into two spaces: the cavity of the DSF and the test chamber. By moving the double glazing, the distance between the single pane and the double glazing can be changed. An aluminum micro-channel heat exchanger was used as the heating source with the water flowed in from the bottom and out from the top. Inflow temperature was maintained constant at a desired value by a water bath. The pipe for connection is PPR (Polypropylene-Random, $\phi 20\text{mm}$) tube insulated using rubber foam. A rotameter ($\pm 2.5\%$) was used to measure the flow rate and its accuracy was checked by measuring the volume of the water at a given time.

In total, T-type thermocouples were used to measure temperatures of the aluminum plate (5 sets), double glazing (3 sets), single pane (1 set), room air (1 set), cavity air (3 sets), and test chamber air (6 sets), inflow water (1 set), and outflow water (1 set). For room air temperature measurement, a cup-shaped aluminum foil surrounded the thermocouple to reduce the radiative heat transfer from indoor environment. All thermocouples were calibrated against a platinum resistance thermometer (previously calibrated to 0.1 °C accuracy by the Center of Cryogenic Metrology in Chinese Academy of Sciences) in the range of -20 to 100 °C. The calibration results were used to correct the measured temperature to an accuracy of 0.2 K. Temperatures were recorded every 10 seconds using two data acquisition modules (NI 9213 and NI 9219).

Air velocity was measured at three positions (A, B, C) using thermal anemometers (Swema 03, 0.05~ 10 m/s, $\pm 0.04 \text{ m/s}$ or $\pm 4\%$). Position A is 30cm above the top surface of the test

chamber. Position B was 10 cm away from the center of the front glazing pane. Point C was used to measure the air speed inside the cavity at the bottom but 10cm from the opening.

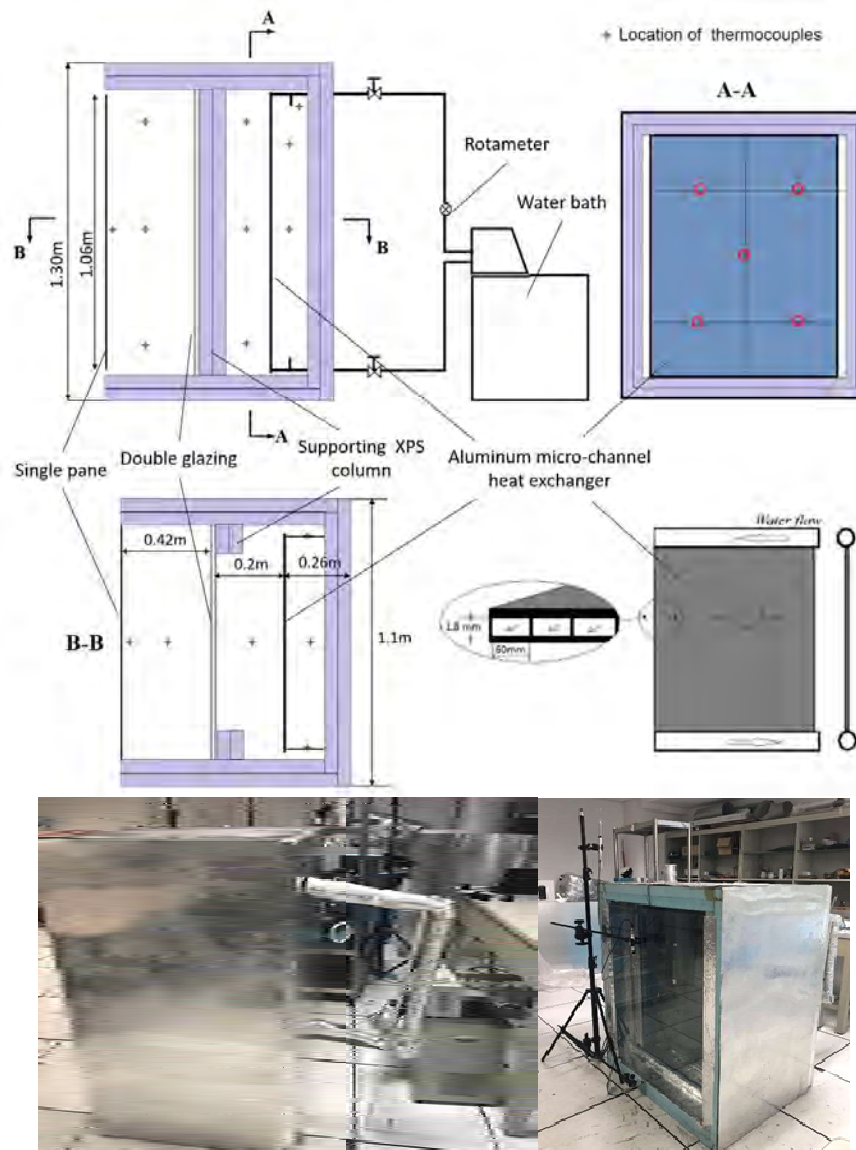


Figure 1. Sketches and photos of the DSF system and the location of measuring point

Determination of heat transfer coefficients

The energy change in the water flow from the inlet to the outlet is balanced by the heat transfers through the DSF and the envelope.

$$c_p(T_{in} - T_{out})q = u_{DSF}A_{DSF}(T_r - T_a) + u_0A_0(T_r - T_a) \quad (1)$$

where c_p is the specific heat of the water. T_{in} and T_{out} are the inlet and outlet temperatures, respectively. q is the mass flow rate. u_{DSF} is the overall heat transfer coefficient of DSF window and u_0 is the heat transfer coefficient of the XPS walls and needs to be determined separately. A_{DSF} is the area of the DSF and A_0 is the inner surface area of the envelope. T_r and T_a is the temperature of the chamber air and the room air, respectively.

The last term in Equation 1 is the heat loss through the XPS walls of the envelope. To determine u_0 , the single glaze pane was removed and the double glazing was covered by two 50 mm thick XPS plates on both sides. With this modification, the heat input by the water is assumed to be balanced by the heat loss through the XPS walls only. u_0 is determined by Eq. (1) with u_{DSF} being replaced by u_0 .

RESULTS AND DISCUSSION

Heat transfer coefficient of the XPS walls

The heat transfer coefficient of the XPS walls (u_0) was measured at three different temperature differences ($T_r - T_a$), each repeated at least 12 times (Figure 2). The standard deviations were less than 10% of the heat transfer coefficients indicating good repeatability. u_0 increased with the temperature difference. This is reasonable as larger temperature difference means stronger buoyancy force and convection on both sides of the walls. For the range of temperature considered, the heat transfer coefficient u_0 could be correlated to the temperature difference using the following formula:

$$u_0 = 0.0193 \ln(T_r - T_a) + 0.3391 \quad (2)$$

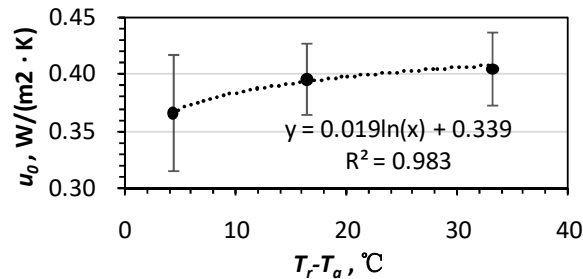


Figure 2. Plot of means and standard deviations of measured heat transfer coefficient of the XPS walls (u_0) at three temperature difference.

Although u_0 was determined in the heating mode, i.e., chamber air is hotter than the outside, it is assumed that it applies to the cooling mode as well, where chamber air is colder than the outside. u_0 can be converted to the conventional U value of the XPS walls if the convection coefficients on both sides of the wall can be determined. However this is irrelevant to the objective of this study.

Impact of cavity ventilation

In the non-ventilation mode, the upper and bottom openings of the outer pane were sealed using duct tape. Experiments were carried out under positive temperature difference and negative temperature difference, corresponding to the winter mode and summer mode, respectively. The range of the temperature difference covers the typical weather conditions in the hot summer and cold winter region of China. At least five repeat tests were conducted at each temperature difference and the results are shown in Figure 3. The repeat points are more clustered at higher temperature difference. In order to reach small temperature difference, the water flow rate had to be increased which resulted a small temperature drop from the inlet to the outlet. At 4 °C difference, the water temperature drop reduced to within 0.5 °C approaching to the uncertainty range of the temperature measurements, resulting greater uncertainties.

In either heating or cooling mode, the non-vented DSF had smaller u_{DSF} than the naturally ventilated DSF indicating better insulation. The measured u_{DSF} for the ventilated DSF window

ranged from 2 to 2.4 W/m²/K in summer condition and 1.5 to 2.1 W/m²/K in winter condition. When the opening was closed, the u_{DSF} value decreased by an average of 27% and 24% in summer and winter conditions, respectively.

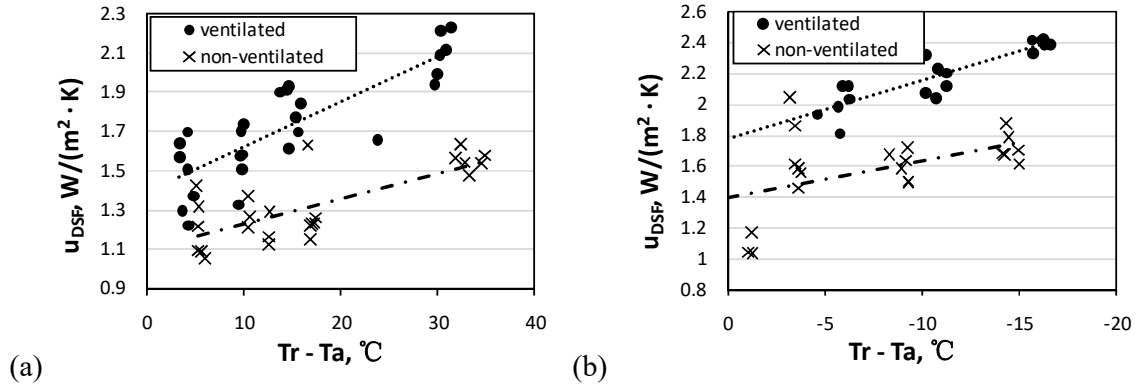


Figure 3. Heat transfer coefficient of the DSF window (u_{DSF}) at varied temperature difference with cavity ventilated or not (cavity width = 40 cm). a) winter mode; b) summer mode

Note that the averaged u_{DSF} under positive temperature difference (winter case, Figure 3a) was 16% smaller than the averaged u_{DSF} under negative temperature difference (summer case, Figure 3b) regardless the ventilation status. Similar phenomena could also be observed in other experiments. This indicates that downward draft along the double glazing in the cavity in summer is stronger than the upward buoyancy flow along the double glazing in summer. It might be explained by the direction of airflow and gravity. The upward draft in summer was against gravity and thus could be weakened while the downward draft could be strengthened by the gravity.

Impact of cavity width

Four cavity sizes were studied being 0cm, 10cm, 20 cm, and 40 cm with DSF operation in a ventilated mode and the u_{DSF} at cavity size of 0cm (pure double glazing) was measured as reference. Each case was repeated at least 3 times (Figure 4).

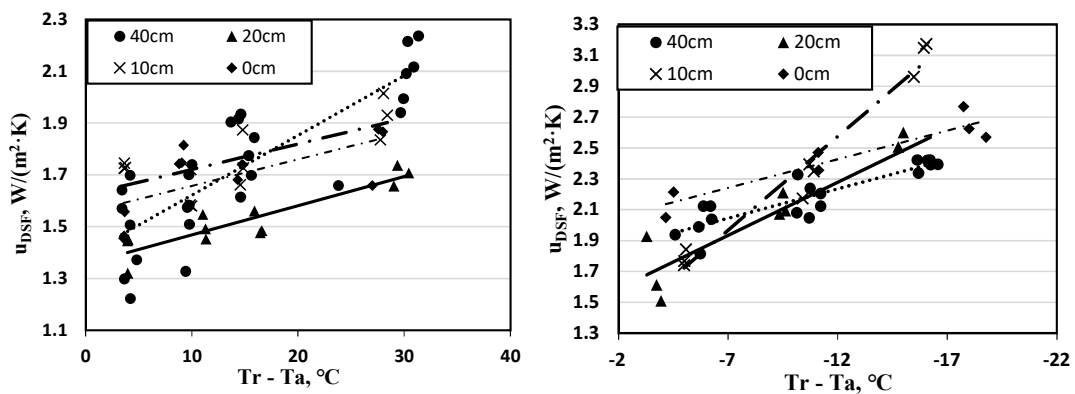


Figure 4. Heat transfer coefficient of the DSF window (u_{DSF}) at four cavity width and varied temperature difference. (left: winter mode; right: summer mode)

In the winter mode, u_{DSF} was lowest at cavity width = 20 cm indicating the existence of an optimal cavity width between 10 cm and 40 cm for the lowest heat transfer coefficient given

the range of the temperature difference. A similar phenomenon, however, was not observed in the summer case. The DSF had better insulation when the cavity was wider at high outdoor temperature while it had better insulation when the cavity was narrower at low outdoor temperature. Although u_{DSF} decreased in general with the decrease of the temperature, the decreasing rates varied for different cavity width and different season. In the summer mode, the impact of temperature difference tended to disappear as the width decreased while in the winter mode the impact of temperature difference was stronger for the narrower cavity. The results indicate that the cavity width is an important factor to the insulation performance but its influence is dependent on the operation season and the outdoor temperature.

CONCLUSION

The heat transfer coefficient of a DSF window was measured at different cavity width and at varied temperature in the absence of solar radiation. The results showed that DSF has better insulation than the double glazing especially with closed cavity. All the studied factors (ventilation mode, cavity width, and outdoor temperature) had influence on the heat transfer coefficient of the DSF window and such influence could be season related. Measurements confirmed the existence of optimal width in winter for the best insulation.

ACKNOWLEDGEMENT

This work was supported by the National Natural Science Foundation of China (Grant No.51678518).

REFERENCES

- Bueno, B. and M. Street, et al. (2017). A co-simulation modelling approach for the assessment of a ventilated double-skin complex fenestration system coupled with a compact fan-coil unit. *Energy and Buildings* 151: 18-27.
- Chow, T. and C. Li, et al. (2010). Innovative solar windows for cooling-demand climate." *Solar Energy Materials and Solar Cells* 94 (2): 212-220.
- Ghaffarianhoseini, A. and A. Ghaffarianhoseini, et al. (2016). Exploring the advantages and challenges of double-skin façades (DSFs). *Renewable and Sustainable Energy Reviews* 60: 1052-1065.
- He, G. and J. Xu, et al. (2016). Prediction of solar heat gain of double skin facade windows. *Building Simulation* 9 (4): 399-409.
- Kapsis, K. and A. K. Athienitis (2015). A study of the potential benefits of semi-transparent photovoltaics in commercial buildings. *Solar Energy* 115: 120-132.
- Li, Y. and J. Darkwa, et al. (2017). Heat transfer analysis of an integrated double skin façade and phase change material blind system. *Building and Environment* 125: 111-121.
- Luo, Y. and L. Zhang, et al. (2017). A comparative study on thermal performance evaluation of a new double skin façade system integrated with photovoltaic blinds. *Applied Energy* 199: 281-293.
- Peng, J. and L. Lu, et al. (2015). Comparative study of the thermal and power performances of a semi-transparent photovoltaic façade under different ventilation modes. *Applied Energy* 138: 572-583.
- Poirazis H (2006). Double skin facades: A literature review. A Report of IEA SHC Task 34, ECBCS Annex 43. Lund University, Sweden.
- Pomponi, F. and B. D'Amico (2017). Holistic study of a timber double skin façade: Whole life carbon emissions and structural optimisation. *Building and Environment* 124: 42-56.
- Shen, C. and X. Li (2016). Thermal performance of double skin façade with built-in pipes utilizing evaporative cooling water in cooling season. *Solar Energy* 137: 55-65.

HYGROTHERMAL PERFORMANCE ASSESMENT OF WALL SYSTEMS WITH VARIOUS CONCRETE AND INSULATION CONFIGURATIONS

Ali Vaseghi^{1*} and Fitsum Tariku¹

¹ Building Science Centre of Excellence· British Columbia Institute of Technology,

*Corresponding email: ali.vaseghi@yahoo.ca

ABSTRACT

The moisture performance of building envelope assemblies has always been a major concern of designers. Building envelope is constantly exposed to moisture loads such as exterior and interior humidity, rain, groundwater, snow and construction moisture. Therefore, it is critical to control the moisture migration mechanism within building envelope walls. Moisture accumulation occurs when the wetting potential of building envelope exceeds its drying potential due to applying inappropriate construction materials or configuration designs.

Moisture accumulation in mid-rise and high-rise concrete buildings has negative impacts on microbial growth, occupants' comfort, energy consumption, freeze thaw and compressive and tensile strength of concrete which lead to spent of millions of dollars on the repair in North America every year. Therefore, evaluation and prediction of moisture performance of building envelope components are important design factors that should be considered to minimize the risk of moisture accumulation in concrete buildings.

In this paper, the hygrothermal performance of a number of concrete wall systems with various configuration of concrete and insulation are studied. The performance of these systems in wet and cold climates of Vancouver and Winnipeg are evaluated using a hygrothermal model. The water content of concrete layers and moisture fluxes at the interior and exterior surface layers are analysed and the overall performance of the systems as related to moisture storage and drying behaviour are determined.

The results indicate that assemblies with thermal insulation placed on the exterior side of concrete have the highest hygrothermal performance while assemblies with concrete layer sandwiched between two wythes of thermal insulations have the poorest hygrothermal performance.

KEYWORDS

Hygrothermal performance, Building envelope, Concrete multilayer walls, Thermal insulation, Moisture content (MC)

INTRODUCTION

By rapid growth of construction trends and materials walls have started to turn into more complex assemblies. Thermal insulation from one side and vapour and air barrier materials from other side assemble together to form a whole building envelope system that could perform well in response to different interior and exterior climatic loads. However, there are still confusions and deficiencies exist regarding correct arrangements of materials and barriers in building envelope components (Hemmati et al. 2017).

Precipitation (rain and snow), groundwater, and in-borne humidity form exterior moisture sources while Interior moisture sources come from people, activities, abnormal loads and construction stage moisture. The holistic approach of any moisture management strategy

includes three main stages of deflection, drainage, storage or exclusion and drying (Tariku et al. 2015). Deflection consists of applying approaches or materials to control moisture entry or deposition into and on the wall. Drainage, storage and exclusion focus on limiting moisture accumulations inside the wall. Drying mechanism itself should consider as evaporation of water at surfaces, water vapour transport by diffusion or air movement, drainage and ventilation drying by air exchange. Failure in drying mechanism which results in excessive moisture accumulation that has undesirable influences on building envelope in variety of ways such as discoloration, mould, fungi, deterioration, corrosion and etc. (Lstiburek, 2002). Therefore, it is essential to design walls by applying appropriate materials and layers arrangement such that while limiting vapour intrusion from either interior or exterior, also letting the existing moisture within walls evacuated from timely (Kunzel, 1995).

Principle mechanisms of moisture transport through building envelope materials are vapour diffusion, capillary suction and surface diffusion. The water vapour is transported by vapour diffusion. Driving force of vapour diffusion is water vapour pressure difference. Vapour diffusion control layers (retarders or barriers) with low or none vapour permeability should be placed on the side of highest vapour pressure where this is on the interior side of the insulation in cold climates and this may be on the exterior side of the insulation in warmer climates. Capillary suction pressure acts as driving force of liquid water transport by capillary conduction. Materials with larger capillaries and pores show lower resistance behaviour to liquid water transport through which (capillary active materials). Lastly, the adsorbed water on material surfaces is conveyed by surface diffusion. The driving force of the surface diffusion is relative humidity (RH) difference.

The explanations given above indicate that material properties and their configurations within building envelope systems play significant roles on hygrothermal performance of assemblies. In designing of building envelope details not only energy efficiency of components has to come into account, but also their moisture performance should be considered. In other words, designing high thermal and moisture performance of building envelope systems has to be entirely based on building science principles to prevent improper hygrothermal performance designs that lead to damages to sensitive construction materials, increases of building thermal energy consumption and negative impacts on indoor air quality as well as occupants' comfort.

Comprehensive thermal analysis on a number of common concrete multilayer walls with similar material properties and thicknesses demonstrated that walls with two layers of insulation thermally perform more efficient compare to walls with single layer of insulation (Vaseghi, 2018). Also, it has been shown that among concrete multilayer walls with single layer of insulation, placing insulation material more toward exterior surface increases the thermal performance of wall.

In this research hygrothermal analysis has been performed on a number of common concrete multilayer walls. The goal is to compare moisture contents (MC) of concrete layers in various multilayer walls to indicate the impacts of configurations and properties of materials on moisture performance of walls.

SIMULATION SETUP

In this study, hygrothermal analysis is conducted using WUFI® Pro a simulation program for evaluating moisture conditions in building envelopes in dynamic conditions. WUFI® Pro takes into account hygrothermal properties including built-in moisture, driving rain, solar radiation, long-wave radiation, capillary transport, and summer condensation. The simulations

are performed for 10 years of hourly climate data. The outputs include moisture content of concrete layers.

Multilayer Walls Design

Seven multilayer walls are presented in this section (Figure 1). The walls are chosen in such a way to be relevant to ASHRAE standard 90.1 and local building code. The multilayer walls include:

- A. Concrete wall with interior XPS insulation wall,
- B. Concrete wall exterior XPS insulation wall,
- C. Insulated concrete form (ICF) with XPS insulation board on the interior and exterior side of the wall,
- D. Split insulation wall with XPS insulation board on the interior and mineral wool insulation on exterior face of the wall,
- E. Split insulation wall with XPS insulation board on the interior and fiberglass on exterior face of the wall,
- F. ICF with EPS insulation board on the interior and exterior of the wall,
- X. Also, a bare concrete wall is considered as a reference case as well

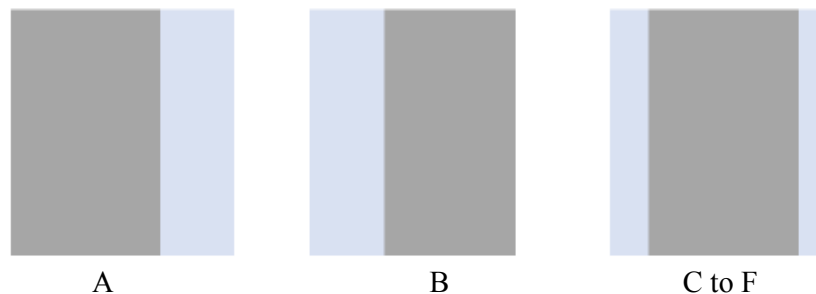


Figure 1. Schematics of multilayer walls, grey represents concrete and blue represents XPS

The hygrothermal properties of material are given as per WUFI material database. Some of the typical hygrothermal properties of the materials that are used in seven multilayer walls are described on Table 1. The total thickness of concrete layer is 0.20 meter while the total thickness of insulation layer for each individual multilayer wall is 0.10 meter.

Table 1. Hygrothermal properties of materials.

Material property	Concrete	XPS	EPS	Mineral wool	Fiberglass
Density (Kg/m ³)	2300	40	15	30	73
Porosity (m ³ /m ³)	18	0.95	0.95	0.99	0.95
Heat capacity (J/kg.K)	850	1500	1500	840	850
Thermal conductivity (kg/m.K)	1.6	0.03	0.04	0.035	0.032
Water vapour resistance diffusion factor (WVRDF)	180	100	30	1.3	1.1
Initial MC (kg/m ³)	150	0	0	0	0

Boundary Conditions

For the purpose of this study climate data of two locations of Vancouver and Winnipeg are considered. Vancouver represents a moderate oceanic climate (Köppen climate classification Cfb) while Winnipeg falls into the humid continental climate zone (Köppen Dfb). Simulation are done for south east elevation. For exterior vertical surface, heat transfer resistance of 0.0588 (K.m²/W) and for interior wall surfaces, the value of 0.125 (K.m²/W) are chosen. Short wave radiation absorptivity is equal to 0.4 while long wave radiation emissivity is 0.9.

WUFI built-in climate data contains global radiation, diffuse solar radiation, normal rain and interior and exterior temperature and RH.

RESULTS

Results are presented in Figures 2 to 4. Figure 2 represents annual wetting and drying performance of concrete layer over a 10-year period. Figure 3 illustrates total MC comparison of concrete layer for 10 years. Finally, Figure 4 demonstrates ratio of existent MC to initial MC of concrete (after 10 years of exposure).

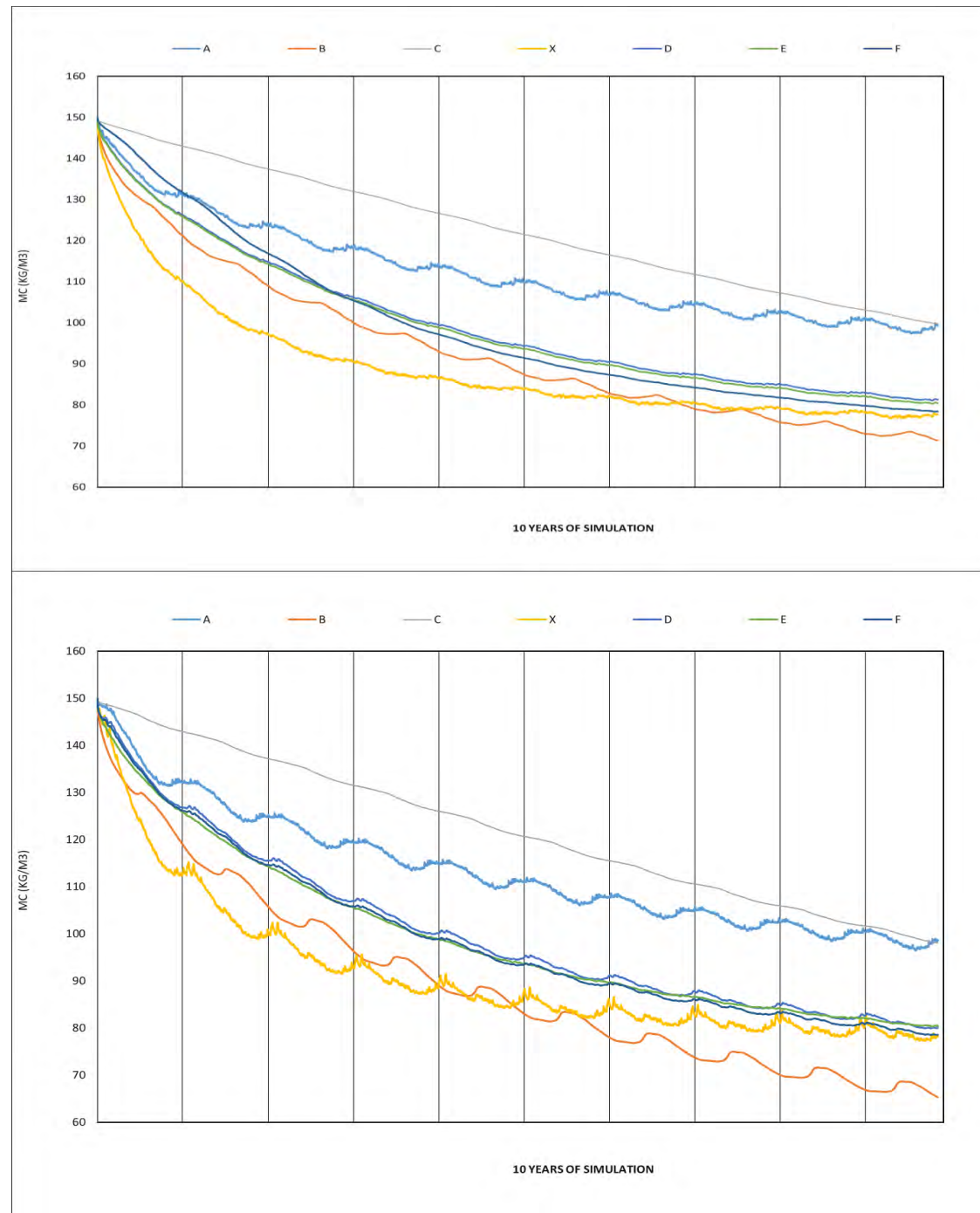


Figure 2. 10 years MC trends of multilayer walls (top: Vancouver, bottom: Winnipeg)

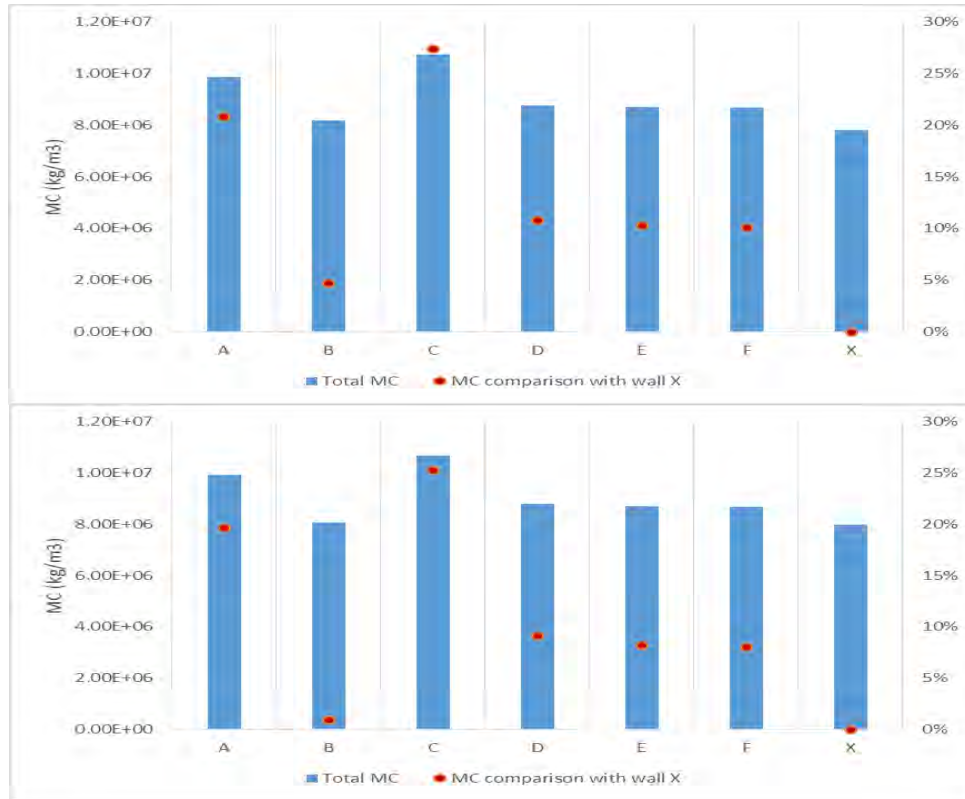


Figure 3. 10 years MC comparison of multilayer walls (top: Vancouver, bottom: Winnipeg)

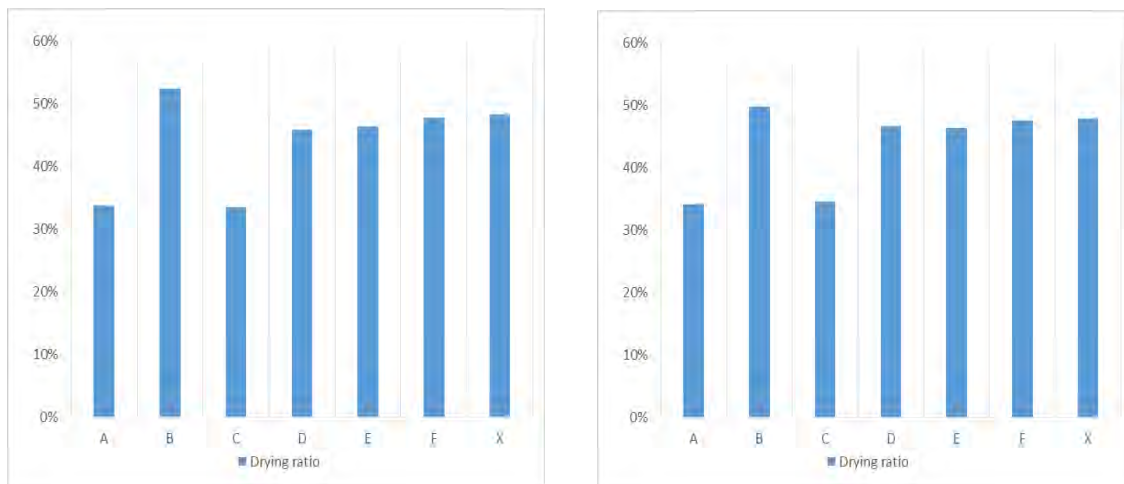


Figure 4. Drying performance ratio of multilayer walls (Left: Vancouver, Right: Winnipeg)

DISCUSSIONS

Studying the results for both climates indicates that wall “C” has the highest MC and the least drying ratio efficiency among the other walls. This is mostly due to the fact that concrete layer is sandwiched between the two low vapor permeable (high WVRDF) layers of XPS that limits the moisture flux and eventually drying potential toward exterior and interior sides of the wall. Following to wall “C”, wall “A” demonstrates fairly low drying performance too. Bare concrete layer in interior insulated wall is in direct exposure to frequent solar and rain which restricts the exterior drying potential. That likewise, explains the high fluctuation of its MC graph. Also, concrete is in direct contact with XPS on the interior side that reduces moisture flux toward inside. Walls “D” and “E” demonstrate a comparable hygrothermal behaviors.

Although both walls have a similar layers arrangement to ICF wall, however, the vapor open insulation materials on the exterior side of the walls increase the exterior moisture flux while protect the concrete layer from direct exposure to rain and wetness. Regarding total MC and drying behavior, wall “F” significantly performs better than wall “C” as EPS is more permeable compare to XPS which allows for more lateral drying potential. Wall “B” with exterior insulation has the best hygrothermal performance. Concrete layer in wall “B” is protected by XPS from rain deposition while it is exposed to interior condition that allows drying by vapor and surface diffusion. For the same reasons, drying performance ratio of wall “B” is slightly higher than reference wall. Although identical multilayer walls in both climates indicate similar wetting and drying trends, however multilayer walls located in Vancouver contain higher amount of MC. Solar heat gain of walls in much sunny weather of Winnipeg effectively increase their drying performance which result in lower existent moisture content compare to walls located in Vancouver.

CONCLUSIONS

Hygrothermal performance of six indivial concrete multilayer walls have been analysed. In contradiction with high thermal performance, multilayer concrete wall with two layers of XPS insulation has demonstrated the poorest moisture behaviour. This is an important factor for designers to take into consider that designing high thermal performance building envelope assemblies doesn’t necessarily lead to high efficient moisture performance or vice versa. The attention should be drawn to design building envelope details with “optimum performance” that consider all aspects of building science principles. Also, to increase the drying potential of ICF walls toward inside and outside space conditions, using material insulation with higher WVRDF are recommended. Overall, considering hygrothermal properties of building materials such as vapour permeability (WVRDF) along with their arrangement within the building envelope assemblies are key factors in a proper envelope design. Allowing for drying potential is only achievable by applying appropriate building materials and configurations.

ACKNOWLEDGEMENT

The authors are grateful for the financial support provided by the Natural Sciences and Engineering Research Council of Canada (NSERC), Canada Research Chair (CRC) and the School of Construction and the Environment at the British Columbia Institute of Technology (BCIT).

REFERENCES

- Hemmati F., Vaseghi A., and Tariku F. 2017. Risk of Condensation Analysis of Common Concrete Balcony Configurations. In: *Proceedings of ASHRAE 2017 Winter Conference - January 2017*, LasVegas, (LV-17-C063).
- Kunzel. (1995). *Simultaneous Heat and Moisture Trasport in Building Components*. Stuttgart, Germany: Fraunhofer IRB.
- Lstiburek, J. (2002). Moisture Control for Buildings. In: *Proceedings of ASHRAE 2002*, 36-41.
- Straube, & Burnett. (2005). *Building Science for Building Enclosures*. Massachusetts: Building Science Press Inc.
- Tariku, F., Simpson, Y., & Iffa, E. (2015). Experimental investigation of the wetting and drying potentials of wood frame walls subjected to vapor diffusion and wind-driven Rain Loads. *Building and Environment*, 368-379.
- Vaseghi A. 2018. Innovative building envelope designs to improve thermal performance of concrete buildings. Master’s Thesis, British Columbia Institute of Technology (Canada), 295 pages.

Preparation and Thermal Performance of Diatomite-Based Composite Phase Change Materials Wallboard

Chaoen LI, Hang YU*, Yuan Song

School of Mechanical Engineering, Tongji University, Shanghai 201804, China

*

Corresponding email: tjyuhang@163.com

ABSTRACT

Two kinds of diatomite-based composite phase change materials (the phase change temperature was 35°C and 42°C, respectively) were prepared by incorporating organic alcohol phase change materials into diatomite to form shape-stabilized composite PCMs. Then, diatomite-based phase change wallboards were fabricated, and the wallboards were attached to the exterior surface of the wall from a test small room to study the thermal performance. In this study, we investigated the effects on the wallboards location, the type of materials and the phase transition temperature on the thermal performance of the wallboards. It was found that comparing with the traditional polystyrene plastic insulation wallboard, the external surface temperature of the PCMs wallboards can be obviously lower than that of the traditional insulation wallboards due to thermal storage ability. But the thermal resistance of the PCMs wallboards was too small to reduce the indoor cooling load in summer comparing with the conventional polystyrene insulation wallboard. The suitable phase transition temperature for the PCMs wallboard was dependent on the orientation of the wall. At the same time, the optimal phase transition temperature is not just dependent on the outdoor meteorological conditions, but also relevant to the applied scenarios.

KEYWORDS

Phase change materials; PCMs wallboard; Diatomite; Insulation wallboard

INTRODUCTION

In China, the building energy consumption has up to 40% of the annual energy production during the last several years, which more attention has been taken to use the renewable-energy resources^[1]. One of the effective ways to minimizing the building consumption and keep the thermal comfort of the living room is to use the latent heat storage system such as PCMs, which has attracted more and more attention by abounding researchers. Phase change materials (PCMs) can be used storage and release large amount of energy during melting and solidification at a constant temperature.

It is well known that the thermal insulation performance of the envelope is one of the important factors that affect the energy consumption of the building^[1]. Thus, applying the PCMs to building envelope is a potential way for improving the indoor thermal comfort and energy saving. At the early stage, the combination of PCMs with building envelope, includes two principal types^[2]: directly incorporating PCMs with concrete or gypsum, and macro-encapsulation. However, the leakage and poor thermal conductivity of PCMs restrict their further application. Recently, there were two main technical routes developed to address above problems^[3]: 1) Encapsulating PCMs into porous materials to form shape-stabilized PCMs; 2) Another potential way is the encapsulation of PCMs into polymeric or inorganic materials. Comparing the second route, encapsulating PCMs into porous materials is more efficiency and low-cost. Diatomite, also called diatomaceous earth, it was lightweight, high porosity, high absorptivity, high purity, multi-shape, rigidity, and inertness. Both the chemical composition and the physical structure of diatomite make it suitable for many scientific and industrial purposes. Besides, diatomite has excellent compatibility with concrete as the inorganic supporting materials^[4].

In this study, diatomite was used as the supporting material. Commercial organic PCMs named MG35(tetradecanol) and MG42 (hexadecanol) was utilized as the working substance to prepare diatomite-based composite PCMs by physical adsorption method. Then the composite PCMs was directly mixed with concrete to fabricate phase change wallboards for test. In the earlier study, phase change wallboards were mainly placed on the interior surface of the wall to regulate the indoor temperature. However, there was few research was reported the application of PCMs wallboards placed on the exterior surface. Comparing with placing the PCMs wallboard on the interior surface, the fluctuates of exterior surface temperature was more obviously, which was helpful for the PCMs to undergo the whole phase transition process [5]. There was a large temperature difference during day and night, which was in favor of the PCMs store and release energy. In our study, the wallboards were attached to the exterior surface of the west wall from a real size room. Polystyrene insulation board and expanded perlite board were tested as a comparison group. The performances of heat insulation and temperature change of the wallboards were investigated.

MATERIALS & METHODS

Materials

90% particle size of expanded perlite used in this study was between 0.28-1.25mm. Two commercial PCMs named MG35(tetradecanol) and MG42(hexadecanol) were used in our study. The nominally latent heat of MG35 and MG42 is 178 J/g according to product information. The two materials were tested by the Q100-DSC instrument from TA company. Figure.1(a) displayed the DSC curves, which indicated that the phase transition temperature range of MG35 and MG42 is 33-36°C and 42-45°C, respectively. The main physical parameters of the four functional materials were shown in Table 1.

Table 1 Properties of raw materials

Type	Density (kg/m ³)	Thermal conductivity (W/m-k)	Phase change Temperature (°C)
Polystyrene	30	0.042	-
Expanded perlite	55	0.0235	-
MG35 (Tetradecanol)	835	0.147	35
MG42 (Hexadecanol)	840	0.148	42

Preparation of diatomite-based composite PCMs

(1) A simple physical blending method was adopted to adsorb these two kinds of PCMs into diatomite to form composite PCMs, respectively. Briefly, the diatomite was dried at 95°C for 24h. Then the PCMs particles were heated and blended with the diatomite to form composite PCMs. The mass content of PCMs in composite PCMs was 50%, due to the over high content of the PCMs is prone to serious agglomeration and leakage [6].

Preparation for wallboards

The cement and sand were mixed in a ratio of 5:3 with the addition of composite PCMs. Then, water was added (water/cement ratio is 1:2). Subsequently, wallboard samples were made by filling the mixture into homemade molds. The dimensions of boards and the percentages of composite PCMs were shown in Table 2. After 24h, the pre-prepared wallboards were cured in a standard curing room for 28 days. The prepared wallboards are shown in Figure 1 (d).

Table 2. Parameters of four types of wallboard

Type	Expanded perlite wallboard	MG35 diatomite-based wallboard	MG42 diatomite-based wallboard	Polystyrene wallboard (EPS)	
Size	300mm×300mm×30mm				
Composite PCM and mass percentage	Perlite 40%	MG35 diatomite composite 60%	MG42 diatomite composite 60%	Polystyrene	100%
Density (kg/m ³)	741	1344	1257	30	
Thermal conductivity	0.26	-	-	0.042	



Fig.1 (a) DSC curves of PCMs; picture of (b) Pure PCMs; (c) Composite PCMs; (d) prepared wallboards

Test methods

The as-prepared wallboards were respectively attached to the exterior surface of the east and west wall (the wall was built by regular vitrified bricks) of two adjacent test room located at Tongji University. A big frame (1200 × 1200mm) was divided into four small frames (600×600mm), and each small frame was attached with four same wallboards. The distribution of the four small frames with different wallboards was shown in Fig. 2(a). Finally, all the wallboards were coated with a layer of 5mm thick cement mortar. Thermocouples were arranged on the interior and exterior surfaces of each wallboard, and the data was recorded by a data acquisition instrument. The test was last six days from August 30 to September 5, 2016.

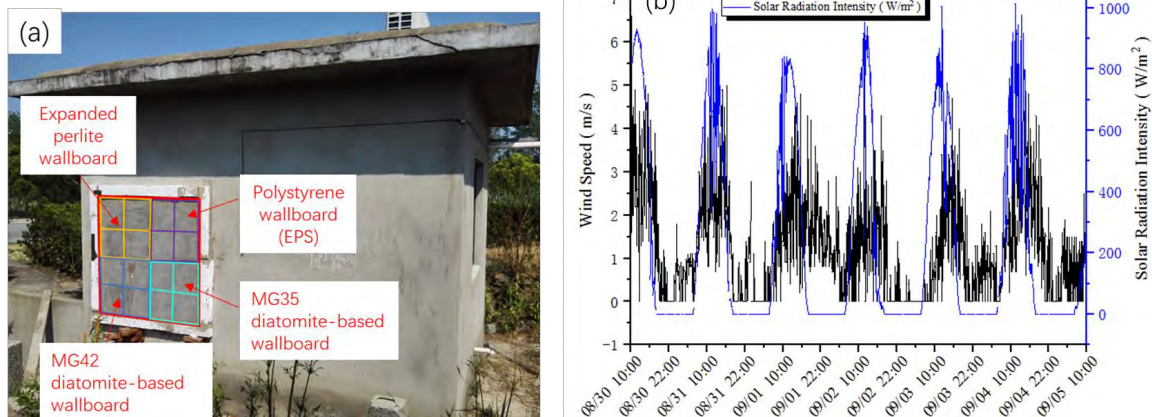


Fig.2 (a) Test room; (b) Outdoor weather data

RESULTS & DISCUSSIONS

Outdoor thermal environment

The as-prepared boards were all exposed to direct solar radiation at 14:30 until the sunlight was completely blocked by the tall buildings at 18:00. The outdoor weather data were plotted in Fig.2(b). As Fig.2(b) shown, all the test days were sunny and the total solar radiation intensity up to 1000W/m² at midday. The outdoor wind speed was between 1.5-2.5m/s.

Results of the west wallboard

The temperature history curves of the exterior surface of the four different kinds of wallboards on the west wall were displayed in Fig.3(a). During the daytime, the maximum temperatures of the exterior surface of the four wallboards were in order of the insulation board > perlite board > MG35>MG42. However, during the night, the minimum temperatures of the exterior surface of the four wallboards were in the order of MG35 > MG42 > perlite board > insulation board. The maximum and minimum temperatures of four kinds of wallboard occurred at around 4:00 pm and 5:30 am, respectively. Comparing with the common wallboard, there was no significant time delay was found from the exterior surface temperature of the PCMs wallboard.

Take the data of September 3 as an example for analysis, the results were displayed in Table 3. It is obviously found that the exterior surface temperature of the conventional polystyrene board could reach 54°C, which was nearly 16°C higher than the outdoor temperature. This phenomenon possible due to the polystyrene board has high thermal resistance and small heat

storage ability. The high temperature of exterior wall face will make people thermal discomfort when people move around the exterior wall because of the high radiation from the exterior wall. For the other three kinds of wallboards, the maximum temperatures of the exterior surface were lower 4-9°C then that of polystyrene board. The reason is that the other three kinds of wallboards have excellent thermal storage ability and high conductivity, which can store the heat from the outdoor radiation to reduce the temperature of the surface during the daytime. During the night, the exterior surface temperature of the insulation board was basically consistent with the outdoor air temperature. However, the exterior surface temperatures of other three kinds of wallboard were slightly higher than that of the polystyrene board. The reason is that the heat storage in the wallboard begins to release to the outdoor environment slowly.

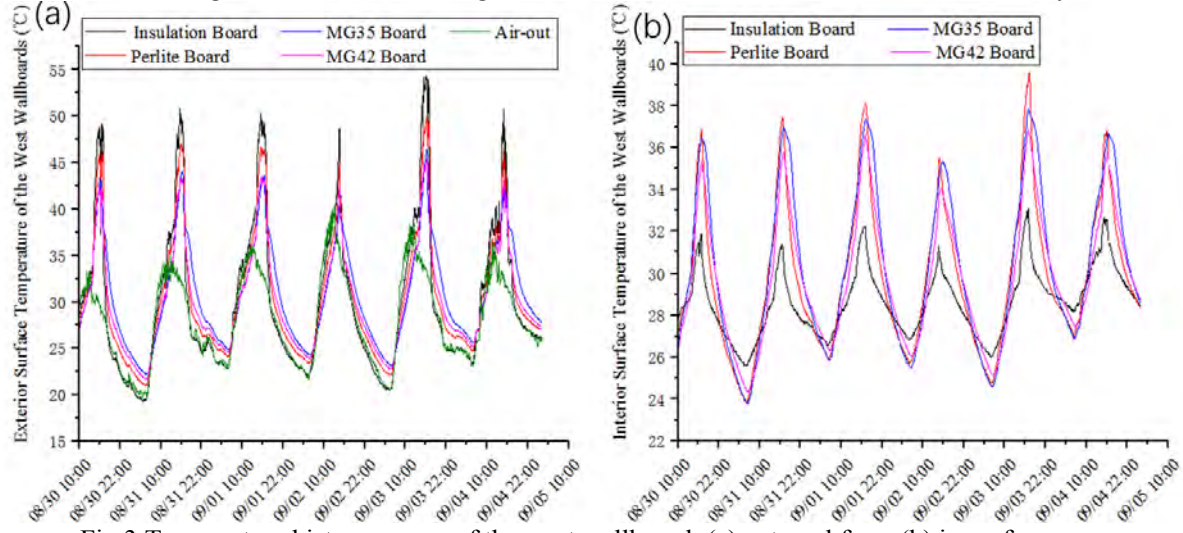


Fig.3 Temperature history curves of the west wallboard: (a) external face; (b) inner face
Table 3. Comparison of the surface temperature of the west wallboards (°C) (Data of September 3).

Type		Polystyrene wallboard (EPS)	Expanded perlite wallboard	MG35 board	MG42 board
Exterior surface	Maximum temperature (°C)/Time	54/16:00	49.5/16:00	46.5/16:20	45/16:20
	Maximum temperature difference (°C)	0	-4.5	-7.5	-9
	Minimum temperature (°C)/Time	20.5/05:22	20.2/05:30	23.2/05:35	22.9/05:30
	Minimum temperature difference (°C)	0	-0.3	+2.7	+2.4
	Temperature fluctuation range in a day (°C)	33.5	29.3	23.3	22.1
Interior surface	Maximum temperature (°C)/Time	33/17:00	39.5/17:11	37.8/16:37	36.8/17:23
	Maximum temperature difference (°C)	0	+6.5	+4.8	+3.8
	Minimum temperature (°C)/Time	26/06:09	24.7/06:21	24.6/06:21	25/06:30
	Minimum temperature difference (°C)	0	-1.3	-1.4	-1
	Temperature fluctuation range in a day (°C)	7	14.8	13.2	11.8
Temperature difference T_{in-ex} (°C)	Day (Maximum)	21	10	8.5	8.2
	Night (Minimum)	5.5	4.5	1.4	2.1

The maximum temperatures of the inner surface of the four wallboards were in order of the perlite board > MG35 > MG42 > insulation board. This order was different from that of the exterior surface temperatures, and the results were shown in Fig.3(b). The temperature fluctuation of the inner surface of the insulation board was significantly lower than that of other three kinds of wallboards, which means that the insulation board could effectively resist outside heat disturbance. During the daytime, the insulation board has the lowest inner surface

temperature among the four wallboards due to its highest thermal insulation, which was in favor of reducing the indoor cooling load in summer. Nevertheless, during the night, the interior surface temperature of the other three wallboards was about 1-2°C lower than that of the insulation board, which indicates that the other three wallboards were easy to release heat to the outdoor environment at night due to their high conductivities. This advantage also benefits for the wallboards storing part of the cold load at night.

Here, we define the temperature difference between the interior and exterior surfaces of the wallboard as T_{in-ex} . During the summer daytime, the larger T_{in-ex} is beneficial for reducing the indoor cooling load, which means the wallboard has good thermal resistance; However, during the summer night, to dissipate indoor heat and wall stored heat to outdoor is necessitous. Therefore, the smaller T_{in-ex} is favor of reducing the indoor cooling load at night. From the Table 3, it can be seen that during the day and night, the T_{in-ex} of the insulation board always bigger than that of other three wallboards. After midnight, the average temperature of both phase change wallboards was lower than the phase change temperature, which indicated that PCMs had completely solidified and the latent heat storage behavior of the material had been completed. Therefore, it can be concluded that the conventional insulation board is more helpful to reduce the indoor cooling load in the daytime, and the PCMs wallboards were more helpful to reduce the indoor cooling load at night.

Results of the east wallboard

When the four kinds of wallboards were installed on the east wall, the temperature history curves of the exterior surface were shown in Fig.4(a). The maximum temperatures of the exterior surface of the four wallboards were in order of the insulation board > MG42 > perlite board > MG35. Comparing with the west wall, the exterior surface temperatures of the MG42 board and the insulation board on the east wall were significantly increased. However, the temperature change trend of the perlite board and the MG35 wallboard on the east wall did not change much. Due to the influence of solar radiation and outdoor air environment, the exterior surface temperatures of the east wall exceeded the phase transition temperature of MG42, so the exterior surface temperature of the MG42 board rise rapidly. Nonetheless, the exterior surface temperature of the west wall was just within the phase transition temperature range of MG42. The process of phase change slowed down the rising rate of temperature. Comparing with the west wall, the exterior surface of the east wallboard was exposed to direct sunlight in the morning, so that the temperature rose rapidly, and the interior surface temperature quickly increased accordingly. As seen in Fig.4(b), the maximum interior surface temperature appeared at about 12 am.

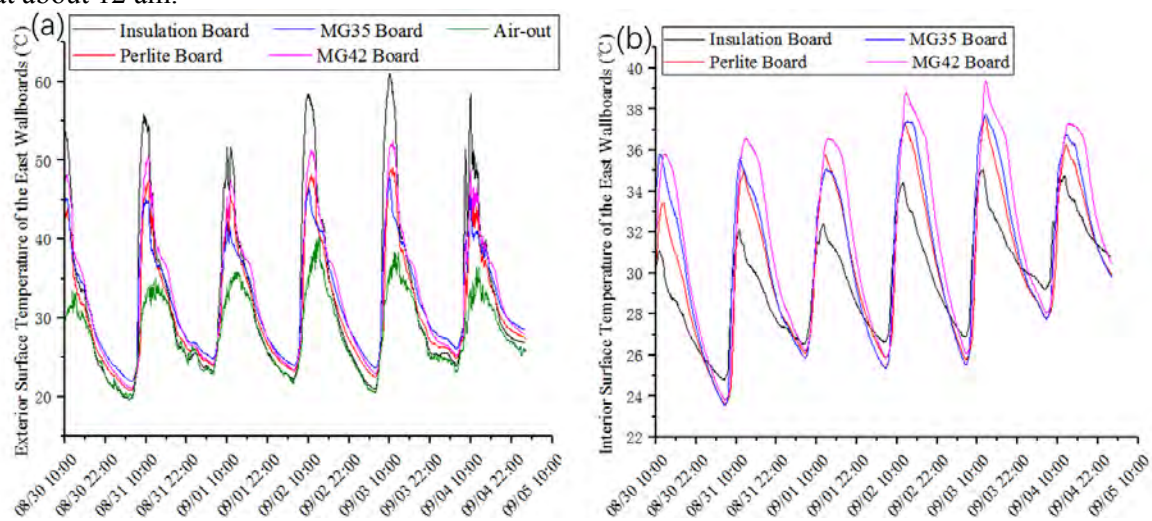


Fig.4. Temperature history curves of the east wallboard: (a) external face; (b) inner face

The influence of the phase transition temperature

When the PCMs wallboard undergoing the phase change process, the temperature rise rate of the wallboard was lower than that of the wallboard was stated in the solid state or liquid. When the PCMs wallboards were applied on the west wall, the largest interior surface temperature of the MG42 board was lower than other wallboards. The probable reason is that the exterior surface temperature of the wallboard on the west wall exceeded the phase transition temperature of MG35 during the daytime, which results in the external part of MG35 board completed the latent heat storage process, and then the temperature rapidly rose. However, when the phase change wallboards were applied on the east wall, the largest interior surface temperature of the MG35 board was lower than other wallboards. The reason is that the interior of MG42 board didn't undergoing the phase change process due to the low internal temperature of the east wall. It can be concluded that when the PCMs wallboards were applied on different direction of the wall should choose different phase-change temperature. Low phase change temperature PCMs is suitable for east wall and high phase change temperature PCMs is suitable for west wall.

CONCLUSIONS

(1) The interior surface temperature of the heat insulation board was the lowest during the daytime, which was good for heat insulation. However, the interior surface temperature of that was the highest during the night, which was unfavorable to the heat dissipation from the room. For the phase change wallboards, although the interior surface temperature of the wallboard was high than that of the heat insulation board, they could store a part of heat during the daytime and store some cold at night. In this study, the minimum interior surface temperature of the phase change wallboard was only 2°C lower than that of the insulation board, and the cold stored was not noticeable. Although, the phase change wallboards have the advantages for thermal storage performance. The thermal resistance of the phase change wallboards was too small to reduce the indoor cooling load in summer when used on the exterior surface of the wall compared with the conventional polystyrene insulation board.

(2) The suitable phase transition temperature for the wallboard on the east wall and west wall was different from each other. In this study, the exterior surface temperature of the east wall was generally higher than that of the west wall, but the interior surface temperature of the MG35 board was lower than that of the MG42 board. Therefore, the optimal phase transition temperature is not just positively correlated with the outdoor meteorological conditions, but it is also relevant to the scenarios applied.

ACKNOWLEDGEMENT

The study has been supported by the China National Key R&D Program "Solutions to heating and cooling of building in the Yangtze river region" (Grant No.2016YFC0700305-02)

REFERENCES

- [1] X. Mi, R. Liu, H. Cui, S.A. Memon, F. Xing, Y. Lo, Energy and economic analysis of building integrated with PCM in different cities of China, *Applied Energy*, 175 (2016) 324-336.
- [2] Kasaeian A, Bahrami L, Pourfayaz F, et al. Experimental Studies on the Applications of PCMs and Nano-PCMs in Buildings: A Critical Review[J]. *Energy & Buildings*, 2017, 154.
- [3] Milián Y E, Gutiérrez A, Grágeda M, et al. A review on encapsulation techniques for inorganic phase change materials and the influence on their thermophysical properties[J]. *Renewable & Sustainable Energy Reviews*, 2017, 73:983-999.
- [4] Li X, Sanjayan J G, Wilson J L. Fabrication and stability of form-stable diatomite/paraffin phase change material composites. *Energy & Buildings*, 2014, 76(2):284-294.
- [5] Li L, Yu H, Liu R. Research on composite-phase change materials (PCMs)-bricks in the west wall of room-scale cubicle: Mid-season and summer day cases. *Building & Environment*, 2017, 123.
- [6] Lv P, Liu C, Rao Z. Review on clay mineral-based form-stable phase change materials: Preparation, characterization and applications. *Renewable & Sustainable Energy Reviews*, 2017, 68:707-726.

Study of the Mechanical Behavior of Traditional Japanese Mud Wall on Bamboo Lath

Midori Yamada^{1,*} and Naoyuki Koshiishi²

¹ Dept. of Architecture, Kindai University, Japan

² Dept. of Architecture, Waseda University, Japan

*Corresponding email: yamada@arch.kindai.ac.jp

ABSTRACT

Mud wall on bamboo lath is a traditional Japanese method for constructing walls. Although the use of mud walls is environmentally friendly, it is necessary to evaluate the performances of the walls, especially their structural resistance, for broader and safe application. However, the performances of mud walls vary widely with various factors, including the locality, the natural materials used, the construction method adopted, and the quality of workmanship. In this study, the combinations of factors expected to improve the initial stiffness and toughness of mud walls were first determined based on previous studies. Subsequently, to reveal the influences of the bamboo lath configuration and properties of the wall mud on the structural resistance, structural experiments were conducted using full-section-sized specimens, the mechanical behavior observed, and characteristic values calculated. The results indicate that a mud wall of high initial stiffness can be practically achieved by avoiding gaps between the load-bearing elements and using wall mud with large elastic modulus and compressive strength. However, such walls tend to have reduced toughness because of marked delamination at the interface of the layers.

KEYWORDS

Mud wall, bamboo lath, mechanical behavior

INTRODUCTION

Mud wall on bamboo lathing, also referred to as “mud–bamboo wall construction,” is a traditional Japanese method of constructing walls using a timber framework, bamboo lathing, and plaster produced by mixing mud and straw. Although the use of mud wall on bamboo lathing is environmentally friendly, it is necessary to evaluate the performance of the walls, especially their structural resistance, so that they can be used widely and safely. However, the structural resistance of mud walls varies widely depending on factors such as their location, the natural materials used, the construction method adopted, and the quality of the workmanship. Furthermore, the influence of wall mud properties and plastering methods on their structural resistance mechanisms is unclear. This study investigated the fracture behavior and resistance mechanisms of mud–bamboo walls subjected to horizontal forces and clarified the factors that influence their mechanical properties.

METHODS

Mud wall specimen types employed

The specimens employed had the same cross-sectional dimensions of framework members as those used in real buildings, but were proportionally smaller. The timber framework was assembled using columns, a sill, a beam, and a batten. To create the bamboo lathing, which forms the bed required for the plastering of mud, split bamboo was woven into a grid-like pattern. This bed was created using two types of bamboo. The first type, called “bamboo

furring,” was inserted into holes in the sides of neighboring framework members every 30 cm. The other type, called “flying bamboo strip,” was secured with rope ties at the points where the ties intersect the bamboo furring. The mud–bamboo wall comprised mud layers, including two base-coat and two middle-coat layers in general (Fig. 1). All layers were completely dried before the loading tests were performed.

The specimens are listed in Table 1. Based on the findings of previous studies (Midori and Naoyuki, 2013a, 2013b), the combinations of factors expected to improve the initial stiffness, Specimen No. 1, and toughness, Specimen No. 6, of the mud walls were determined. The factors are described below.

(1) Difference in degree of looseness around the end of bamboo furring

Two types of specimens were prepared, as shown in Fig. 1: (i) with some looseness, Specimen Nos. 1–3; and (ii) without looseness, Specimen Nos. 4–6.

(2) Difference in properties of the wall mud

Previously, we investigated the compression properties of wall mud (Midori and Naoyuki, 2013a) and found that in the case of the base coat, the elastic modulus and compressive strength decreased with increasing straw content, whereas the absorbed energy increased. For the middle coat, in which the mud possessed a higher viscosity and water retentivity, the elastic modulus and compressive strength decreased, whereas the absorbed energy increased because the wall mud required a higher straw content to avoid cracking.

Based on these results, two combinations of wall mud, sand, and straw were adopted for the base and middle coat: (i) both base and middle coat had a large amount of absorbed energy, Specimen Nos. 1-2, (ii) both possessed a large elastic modulus and high compressive strength, Specimen Nos. 3-6. The compositions are detailed below.

(a) Base coat wall mud: we used mud from Kyoto and rice straw cut to a length of approximately 6 cm. Two types of straw content were used: 2.0, labelled "Much straw," and 1.0 %, labelled "Little straw," in terms of mass of dry mud.

(b) Middle coat wall mud: the same mud as the base coat was used. The mud was sieved and lumps of fine mud removed, with the resulting mud coarser than the base coat. The straw used was shorter and finer. Two compositions of sand and straw were used: 2.0 % straw without sand, labelled "Much straw," and 1.0 % straw with sand, labelled "Little straw."

(3) Specimens with differing ratios of layer thickness

Three combinations of thickness, constituting a total thickness of 70 mm, were adopted. As shown in Fig. 1, the thicknesses of the base-coat layer and both middle-coat layers were, respectively, (i) 50 mm and 10 mm for Specimen No. 1, (ii) 40 mm and 15 mm for Specimen Nos. 2–5, and (iii) 30 mm and 20 mm for Specimen No. 6.

(4) Difference in the plastering method “Plastering around framework”

The plastering method called “Plastering around framework” was investigated to determine whether the wall mud filled the gap between the base coat layer and the framework after shrinkage of the base coat layer. Two types of specimens were prepared (with and without “Plastering around framework”), Specimen Nos. 1–4 and Nos. 5–6.

Loading methods

Fig. 2 gives an overview of the apparatus used for the loading tests. The beam of the specimen was a joint actuator; the sill was a fixed reaction base. Axial force of 9 kN was applied to the two columns. Horizontal force was loaded to the positive and negative sides, alternating every three cycles until the deformation angle, 1/600, 1/450, 1/300, 1/200, 1/150, 1/100, 1/75, 1/50, 1/30, 1/20, 1/15 and 1/10 radian, was reached.

Calculating the characteristic values

The characteristic values were calculated in conformity with the methods for evaluating the structural resistance required by building regulations in Japan (CBL, 2013). The skeleton curve of the load-deformation relationship replaced perfect elastic plastic straight lines, and the initial stiffness and the absorbed energy until yield point and ultimate deformation were calculated.

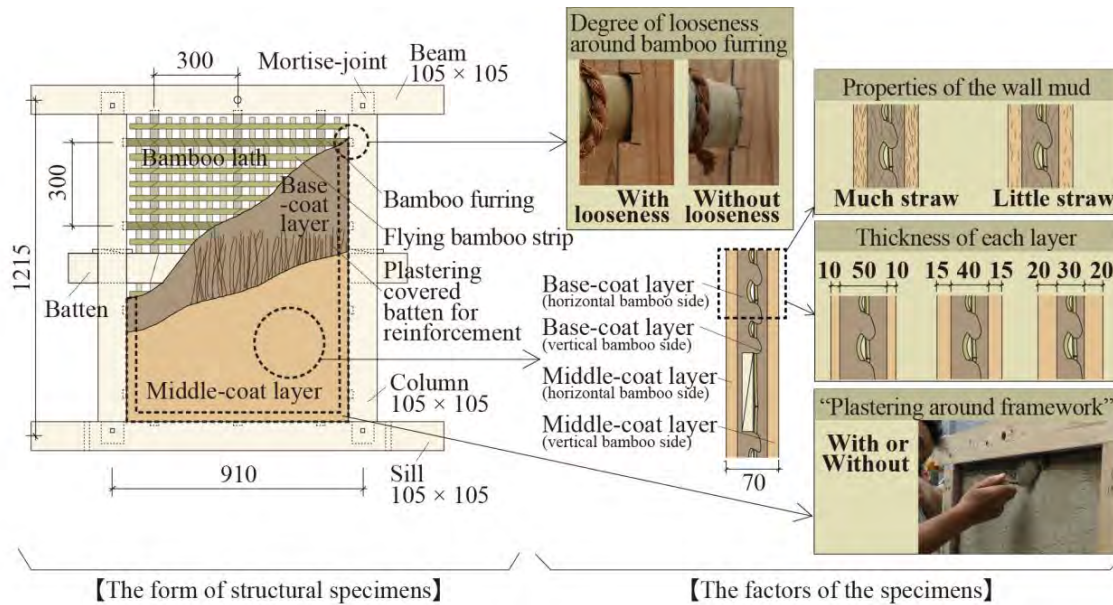


Figure 1. Mud-bamboo wall construction for a real building and for structural specimens.

Table 1. Types of specimens.

Specimen No.	Thickness of batten	Looseness around the end of bamboo furring	Properties of the wall mud		Thickness of each layer (mm)		With or without "Plastering around framework"
			Base-coat layer	Middle-coat layer	Base-coat layer	Middle-coat layer (with both side)	
1	15	with some looseness	Much straw (2.0%)	Much straw (2.0%) without sand	50	10	without
2					40	15	
3		20	30				
4							
5	10	without looseness	Little straw (1.0%)	Little straw (1.0%) with sand	30	20	with
6							

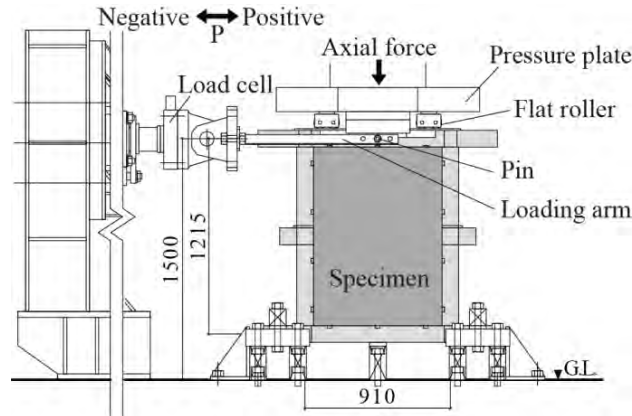


Figure 2. Overview of the loading test apparatus.

RESULTS

Load-deformation curve, fracture behavior, and mechanical characteristics

Fig. 3 shows the skeleton curves of the positive side, and Fig. 4 shows the state of fracture after loading. The skeleton curves and state of fracture differed with the types of specimens. The state of fracture had two types: with and without shearing crack.

Fig. 5 shows the mechanical characteristics values. It was established that the specimen that increased the initial stiffness had a high “K value,” which is the index of initial stiffness, and that the specimen that would improve the toughness would have high absorbed energy until yield point deformation. The absorbed energies until ultimate deformation did not differ significantly among the specimens.

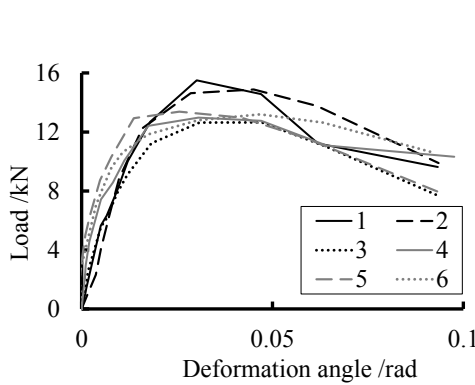


Figure 3. The skeleton curves.

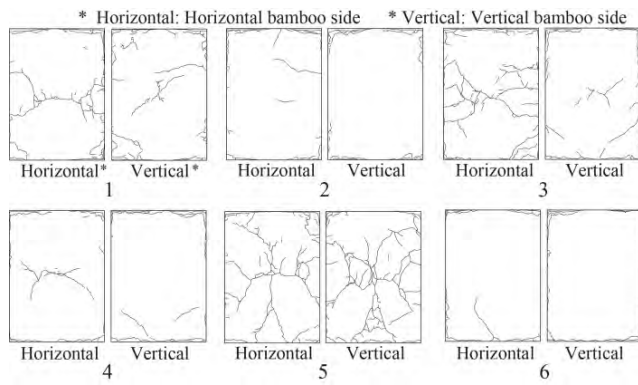


Figure 4. State of fracture after loading test.

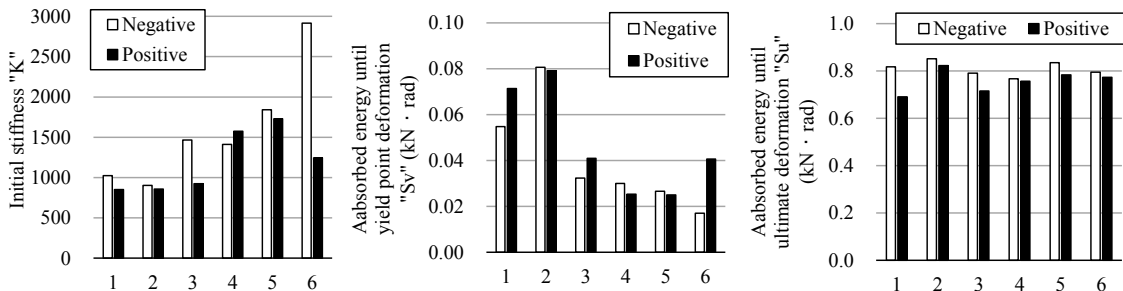


Figure 5. Mechanical characteristics values.

Resistance mechanisms

From the distresses observed during and after testing, we confirmed that four elements contributed to the resistance to the horizontal force observed in previous studies (Masahide et al., 2004). Fig. 6 shows the four elements. First, in the initial stage, even when the framework tilted because of the horizontal force, the plastered mud-wall layer rotated inside the framework without shear deformation. Consequently, the four corners of the mud-wall layers were found to have consolidated (I). Similarly, the mud-wall layer around the upper and lower sides of the batten was consolidated (II). After the rotation increased, the bamboo furring touched the edge of the hole made in the timber, which prevented further rotation. At that point, the bamboo furring began to separate the base-coat layer into the face and back layers (III). As the frame deformation angle increased, the flying bamboo strips began to prod against framework members, at which point the flying bamboo strips similarly caused the front and back sides of the base-coat layer to separate (IV).

A notable point is that there was a degree of looseness around the four resistance elements. For example, gaps related to load-bearing elements I and II were found because of drying shrinkage of the mud. In the case of III, looseness existed between the end of the bamboo furring and the hole. In the case of IV, clearance existed between the end of the flying bamboo strip and the framework member. Furthermore, as shown in Fig. 1, the mud wall comprised four layers. Therefore, the resistance elements that exist in each layer should differ. Table 2 shows the types of resistance elements in each layer.



Figure 6. Types of resistance elements.

Table 2. Types of resistance elements in each layer.

	Types of resistance element			
	I : Corners	II : Batten	III : Bamboo furring	IV : Flying bamboo strips
Base-coat layer (horizontal bamboo side)	○	○	○	○
Base-coat layer (vertical bamboo side)	○	-	○	○
Middle-coat layer (both side)	○	-	-	-

DISCUSSION

The influence of the factors were considered with reference to Figs. 3, 4, and 5.

(1) Influence of the properties of the wall mud (Comparison between Nos. 2 and 3)

The initial stiffness (Fig. 5) of Specimen No. 3 was higher than that of No. 2 for the mud layer labelled “Little straw,” which had a large elastic modulus and compressive strength. The other side, the absorbed energy until yield point deformation (Fig. 5) of “Little straw,” significantly decreased because of the low absorbed energy of the wall mud.

(2) Influence of looseness of the bamboo furring (Comparison between Nos. 3 and 4)

The initial stiffness (Fig. 5) of No. 4 was higher than that of No. 3 owing to resistance at the start by bamboo furring (the load-bearing element III). Although shearing deformation of No. 4 happened earlier to resist bamboo furring (III), shearing crack did not appear after the loading test (Fig. 4). This may be because larger delamination between the face and back of the base-coat layer is created without looseness, than that with looseness.

(3) Influence of “Plastering around framework” (Comparison between Nos. 4 and 5)

The initial stiffness (Fig. 5) of No. 5 was higher than that of No. 4 for initial resistance corners (the load-bearing element I) earlier with “Plastering around framework.” Shearing crack appeared with No. 5 in contrast to non-appearance with No. 4 (Fig. 4). This may be because larger delamination between the face and back of the base-coat layer of No. 4 is created by bearing bamboo furring (III) before start to bear corners (I).

(4) Influence of thickness of each layer (Comparison between Nos. 1 and 2, and 5 and 6)

Mechanical characteristics (Fig. 5) showed little difference between Nos. 1 and 2, and 5 and 6. On the other hand, the state of fracture of Nos. 1 and 5 appeared with shearing crack, in contrast to 2 and 6 (Fig. 4). This may be because delamination between the layers occurred before shearing crack was created when the middle-coat layer was thicker.

In summary, a mud wall possessing a high initial stiffness can be achieved by avoiding looseness around the resistance elements and using materials with large elastic modulus and compressive strength. However, such walls tend to develop delamination between the face and back of the base-coat layer, that are difficult to repair, because the behaviors of adjacent layers differ significantly in terms of the different load-bearing elements of each layer. In contrast, the advantage of toughness of mud walls can be maximally exploited by increasing looseness around the resistance elements and using materials that absorb large amounts of energy. Such walls tend to resist serious damage, namely delamination.

CONCLUSIONS

In this study, we conducted structural experiments to investigate the influence of various factors on the mechanical properties of traditional Japanese mud walls on bamboo lathing. The results obtained show that the mud walls developing initial stiffness tend to become seriously damaged because of delamination between the face and back of the base-coat layer. Originally, the Japanese mud walls can keep soundness for a long time period by repairing the slight damages such as around framework and finishing layer, which can easily repair. Accordingly, we should avoid the delamination between the face and back of the base-coat layer, for creating looseness around the bamboo lath.

ACKNOWLEDGMENT

This work was supported by JSPS KAKENHI Grant Number 26420565 and by the Gypsum Board Industry Association. We would like to thank Editage (www.editage.jp) for English language editing.

REFERENCES

- CBL. 2013. Center for Better Living. <http://www.cbl.or.jp/standard/kseino/11/file/01.pdf>
- Masahide M., Makoto K., Tamotsu S., and Masahiro I. 2004. Experimental clarification of load carrying mechanism of Japanese traditional mud walls subjected to static lateral force: Physical behavior of mud walls without initial failure in shear, *J. Struct. Constr. Eng., AIJ*, No. 582, 103–108.
- Midori Y. and Naoyuki K. 2013a. Properties of wall clays with straws: Wall clays for clay wall on bamboo lathing: Part 2, *J. Struct. Constr. Eng., AIJ*, No. 689, 1209-1218.
- Midori Y. and Naoyuki K. 2013b. The influence of the behaviors of layers upon their one united body: Wall clays for clay wall on bamboo lathing Part 3, *J. Struct. Constr. Eng., AIJ*, No. 693, 1831-1839.

Thermal stability of lightweight frame partitions exposed to pulsed wind load

Piotr Kosiński^{1,*}, Robert Wójcik¹, Beata Semen¹

¹University of Warmia and Mazury in Olsztyn, Olsztyn, Poland

*Corresponding email: piotr.kosinski@uwm.edu.pl

ABSTRACT

Much has been said about air infiltration, especially of ventilation losses and air quality. There is less information on heat losses through increased convection. This problem particularly concerns on one sided wind washing of the building envelope characterised with seeming airtightness of construction partitions. On the base of measurements undertaken in existing buildings constructed as lightweight timber structures filled with fiber materials it can be seen that air filtration also contributes to increased heat transfer through the building envelope. This paper presents the results of the research on the thermal stability of building partitions insulated with fiber materials and exposed to pulsed air filtration due to the wind load.

KEYWORDS

wind washing, air tightness, frame lightweight constructions, loose thermal insulations

INTRODUCTION

Fibrous thermal insulation materials, such as mineral wool, glass wool or natural materials, are characterized by high porosity. The tendency to reduce thermal conductivity of such materials causes increase of porosity and thus increased air permeability. Finally, thermal properties can be different than planned, because high air permeability increases natural convection in pores, which results in increased heat transmission through thermal insulation (Økland, 1998, Deseyve and Bednar 2006, Gullbrekken et al 2015). In addition, heat losses can also be caused by forced convection, e.g. wind washing. A qualitative and quantitative recognition of thermal losses caused by convection in fibrous insulation materials is particularly important, especially in lightweight frame constructions.

In many buildings the value of the heat transfer coefficient of the building envelope is significantly higher than the results of thermal calculations based on the thickness and thermal conductivity of embedded materials. As observed by the authors, the main reason for this phenomenon is the wind washing the porous thermal insulation. Nowadays, frame constructions are usually covered with barriers protecting against air filtration and wind washing. However, not all countries have the technical requirements for air and wind protection of the partitions. Hence many buildings are still constructed with thermal insulation layer exposed to wind washing. Although in the case of new buildings weather barrier requirements are well understood, the use of an exterior air barrier in existing buildings may not be feasible. What is important is that air sealing of the building envelope from the inside of the building partitions does not guarantee that the heat transfer coefficient of the envelope will meet the energy conservation criteria. If the inner layers (like vapour barrier) are set up continuously, the air tightness test can give a satisfactory result, despite the fact that the entire layer of thermal insulation is unprotected or only partly protected against wind washing (lack of weather barrier). Wójcik and Kosiński (2015) described this phenomena as the seeming air tightness of the building envelope, which is relevant for both existing and new buildings.

A PROBLEM OF WIND WASHING IN EXISTING BUILDINGS

Figure 1 presents thermograms registered within the attic (4th floor) of a public building. The building was renovated few years before this research and the attic was adopted for utility purposes. The knee and interior walls, as well as ceiling were constructed in the lightweight steel skeleton technology. The sheathing was made of single layer gypsum boards, while the thermal insulation consisted of loose mineral wool 12-20 cm thick. On the internal side, between the boards and thermal insulation, a polyethylene film was installed as a vapour retarder. The knee wall construction did not include wind prevention layers while in the roof construction the wind barrier membrane was used but its junctions were not glued (Figure 1a). The air tightness of the attic was measured using the Blower Door test, corresponding to standard EN 13829. The achieved n_{50} was lower than 3.0 h^{-1} for method B, which is claimed in Polish regulations. No leakages between sheathing boards were found, which shows a continuous sheath of polyethylene film. Leakages occurred at the electrical outlets area (Figure 1f) and in few roof window frames. A Flir B335 infrared camera with 50 mK thermal sensitivity was used to assess the thermal quality of the whole attic envelope. The boundary conditions of measurements: average internal temperature $+17 \text{ }^\circ\text{C}$, external temperature $-15.3 \text{ }^\circ\text{C}$ and average wind speed 3 m/s .

Figure 1b presents the junction of the interior and knee walls with roof and roof window, while Figure 1c presents the thermogram of this area. Figure 1d presents the junction of knee and interior walls with roof, while Figure 1e presents the thermogram of this area. Figure 1f presents the thermogram of the electrical socket installed in the knee wall during the air tightness measurements at 50 Pa underpressure. The hypothermia of the analyzed areas was caused by the wind washing of the mineral wool filling the frame partitions. Infrared (IR) analysis, based on surface and surrounding air temperature comparison revealed a 75% reduction of thermal resistance of the investigated partition.

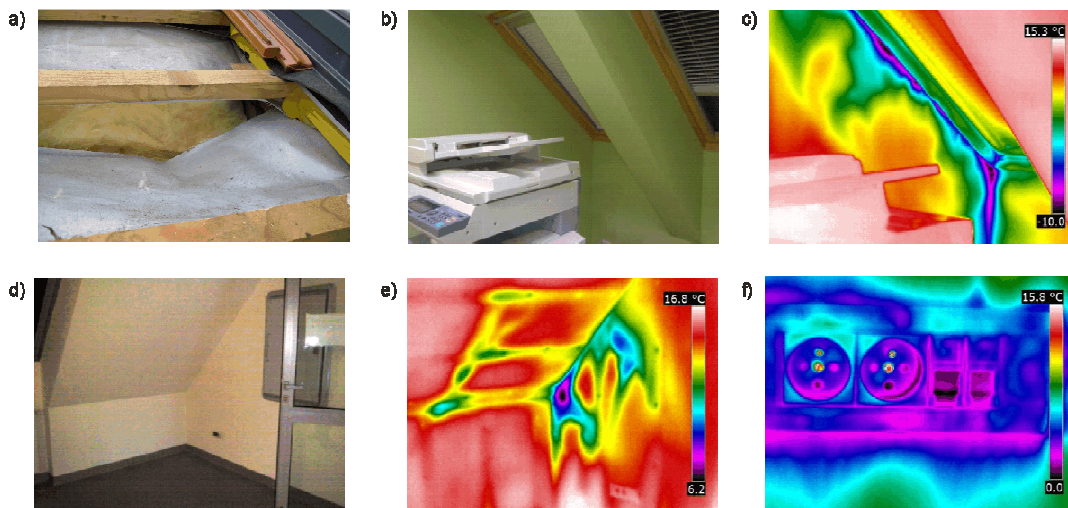


Figure 1. The described roof and attic. a) View of the roof construction, b-c) Problematic area of the walls and roof junction and its thermogram, d-e) Problematic area of the walls and roof junction and its thermogram, f) Thermogram of the electrical socket.

LABORATORY SET UP

A laboratory investigation was based on the results of air filtration measurements in existing Polish buildings. The purpose of the study was to investigate the thermal stability of

lightweight frame partitions filled with loose mineral wool exposed to wind washing. Figure 2 presents the scheme of the laboratory investigation – the climatic chamber and models.

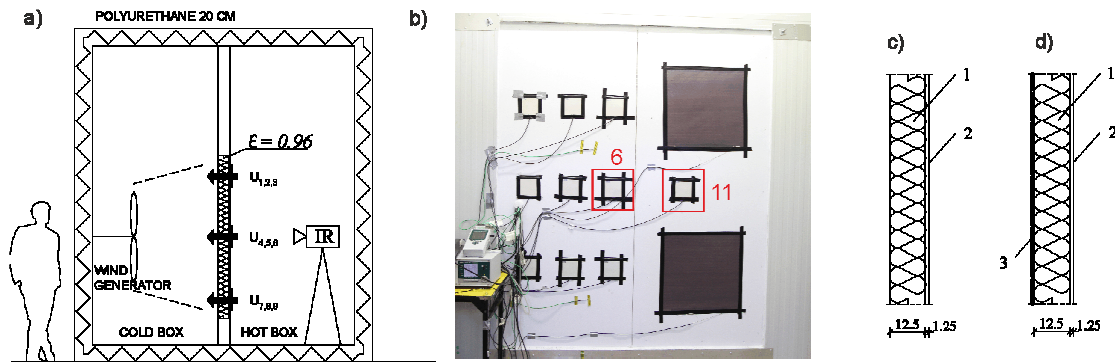


Figure 2. Schematic representation of the laboratory set-up. a) Cross section of the climatic chamber with a mounted specimen, b) View of the inner surface of the wall specimen, c, d) Cross sections of the specimen: c) 1st model, d) 2nd model, 1 – loose mineral wool, 2 – gypsum board, 3 – partial wind barrier.

For the purpose of this work, two wooden frame model partitions (Figure 2c, d) were investigated in a special non-isothermal climatic chamber at the building physics laboratory at the University of Warmia and Mazury in Olsztyn. The chamber (Figure 2a) allows the measurement of air filtration impact on heat transfer through building elements. Samples of natural dimensions are mounted in an inspection frame between hot and cold sections of the chamber. In the cold part an air supply system of adjustable power is used to generate wind. The chamber is mainly used for carried out tests with the wooden frame partitions filled with loose fiber materials.

The constructed models correspond to existing buildings, where authors found the seeming air tight partitions. The 1st model (Figure 2c) consists of frame partition, gypsum cardboards (1.25 cm) on the internal side, insulation (12.5 cm) made of loose mineral wool with a mean density of 120 kg/m^3 . The areas of different density were deliberately made in order to carry out a detailed analysis of the impact of fiber compaction on the thermal stability of partition (in future). The 2nd model (Figure 2d) – the same layers as the 1st, but with an additional wind retarder made of polypropylene membrane on the exterior side. The membrane junction was intentionally not connected or glued to imitate the leaks for wind washing and is placed at the level of sensors $U_{1,2,3}$ (Fig. 2a). Heat flux sensors (Figure 2b), thermocouples and thermal anemometers were placed on the wall surfaces. The Ahlborn system was used to measure and record the thermal parameters. During the research, the heat flux density (according to ISO 9869) and the temperature changes were registered in a function of wind speed. Simultaneously, infrared radiation emitted by the test specimen was being detected by the FLIR scientific camera SC7200 with a thermal sensitivity of 17 mK.

Two considered measurements areas (250 x 250 mm) are presented on Figure 2b. Both of them are in a distance from the windproof membrane junction. The 6th area is placed almost in the middle of the specimen height, 480 mm from the left and 770 mm from the upper edge of the specimen), while the 11th is placed 900 mm from the left and 770 mm from the upper edge. Four wind speeds corresponding to average local windy conditions were generated (0.46 m/s, 1.43 m/s, 2.36 m/s, 3.24 m/s). The wind load was generated in intervals: 4.5-5.0 hours of wind, 18.5-19.5 hours calm. The intervals were determined based on previous measurements

and experience, but a manual control was the reason for the differences in intervals length. The cycle for each wind speed was repeated 4 times. Thermal changes were converted to thermal resistance changes. During the measurements, the door to the hot part of the chamber was intentionally left open to imitate the daily thermal changes in the buildings.

RESULTS

Figures 3 and 4 present the changes of thermal resistance surface to surface for both models caused by the constant speed of wind washing the insulation. The results are presented for two analyzed areas: 6th and 11th differing with the position in examined models. The graphs present the results for 44.5 hours, what is almost two full cycles. Figures 3a and 4a present the results of the 1st model (without wind protection), while Figures 3b and 4b the results of the 2nd model (partial wind protection). The initial thermal resistance for both analyzed areas is approx. $5 \text{ m}^2\text{K/W}$, while theoretical value around $4 \text{ m}^2\text{K/W}$. It can be clearly seen that in the 1st model the reduction of thermal resistance starts simultaneously with the wind operating. The higher the wind speed, the faster the reduction.

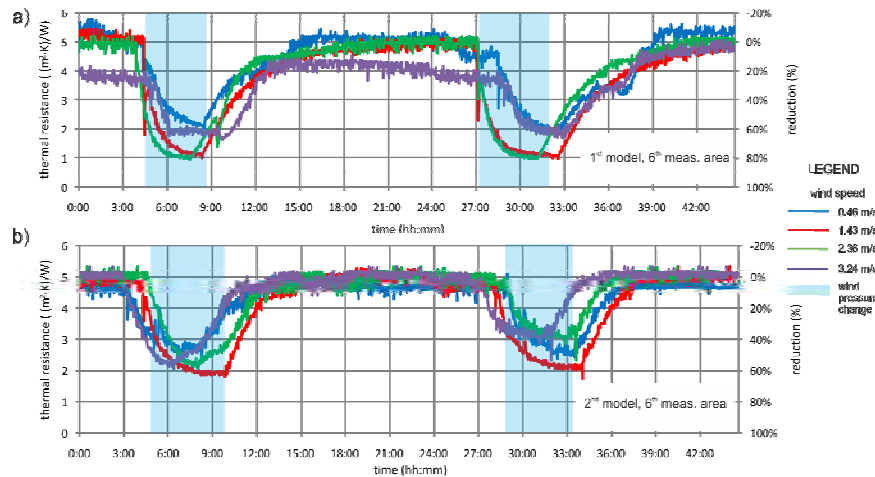


Figure 3. Changes of thermal resistance at constant wind speeds registered for the 6th measurement area for both models.

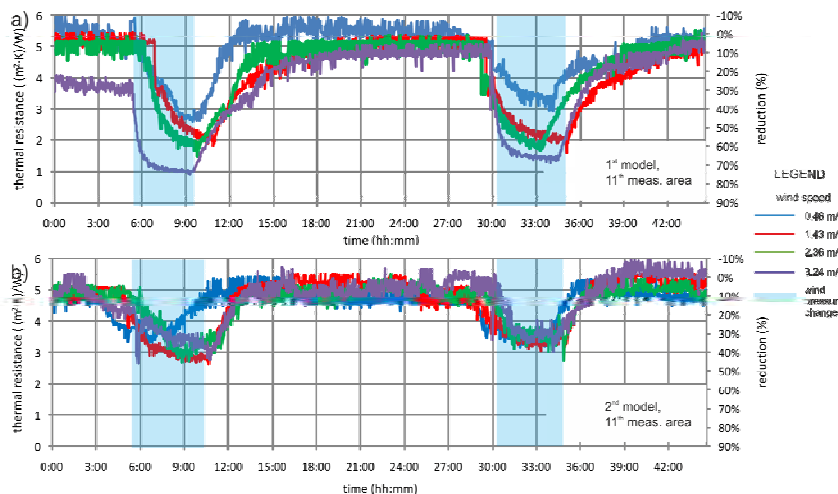


Figure 4. Changes of thermal resistance at constant wind speeds registered for the 11th measurement area for both models.

For the 1st model at a wind speed of 0.54 m/s, the reduction of the thermal resistance to the minimum value takes average 3 hours 18 min, for speed 3.24 m/s it is 1 hour 50 min. In the case of the 2nd model, the at a wind speed of 0.54 m/s, the reduction of the thermal resistance to the minimum value takes average 3 hours 20 min, while for speed 3.24 m/s it takes 2 hours 28 min. A detailed summary of the time needed to achieve the maximum reduction of the thermal resistance due to the wind speed is shown in a Figure 5a.

Table 1. The maximal reduction of thermal resistance surface to surface during wind washing

Symptom or Condition	0.54 m/s	1.43 m/s	2.46 m/s	3.24 m/s
1 st model	52-64%	69-82%	70-80%	60-75%
2 nd model	35-49%	48-65%	46-60%	46-58%

The reduction of thermal resistance surface to surface is presented in the Table 1. The time required for the partition to return to the thermal equilibrium after wind washing depends rather on the protection against wind than on the wind speed. For the 1st model the needed return time varies in the range 4 hours 50 min - 6 hours 04 min, while for the 2nd model varies in the range 2 hours 46 min - 4 hours 11 min. Detailed data are presented in the Figure 5b.

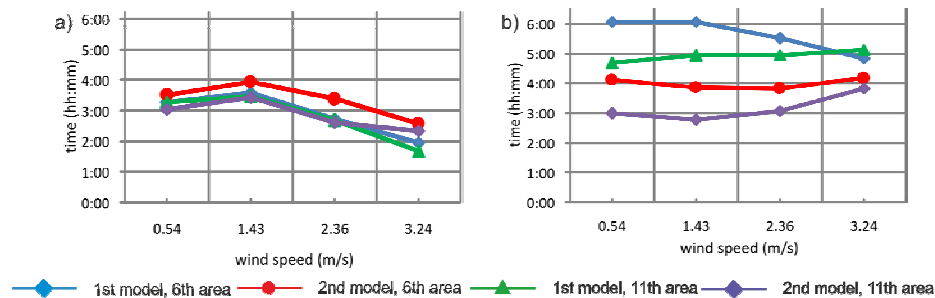


Figure 5. Time needed to achieve: a) Maximal thermal resistance reduction, b) Thermal equilibrium after wind washing.

DISCUSSIONS

The results of the study are similar to those presented in the work of Wójcik and Kosiński (2015). Slightly lower reduction of thermal resistance in this work results from higher density of loose mineral wool and thus its lower air permeability. The averaging during the data recording was used to eliminate accidental peaks resulting from the use of the building. However, even this procedure did not protect against irregular and various course of the thermal resistance changes curves. This is possible due to both the interaction of the environment as well as the natural convection which occurs in the fibrous thermal insulation even under windless conditions. The character of changes of the thermal resistance allows analysis of changes of its value due to the wind speed. In both models the maximum reduction of the thermal resistance was obtained for the average wind speed of 1.43 m/s, not for 3.24 m/s. This may be due to the loose fibers's susceptibility to deformation under the influence of wind pressure. In the case of the fastest wind the material was compressed and thus it obtains lower air permeability in this area.

The temperature of the cold side of chamber was maintained at the level of 0.5-1.3°C, while of the hot side, depending on the building heating, temperature range was 14.2-18.7°C. Exceptionally, during the test with a wind speed 3.24 m/s on the 1st model, the temperature range of the cold side was 3.9-7.9°C, which could have been caused by a cooling system failure. Fortunately, even in this case, the temperature range of the hot side was 17.4-18.7°C

and the temperature difference between hot and cold sides during the windless intervals did not drop below 13.0°C.

The time that models need to return to equilibrium does not depend on the wind speed, but on the reduction of thermal reduction caused by forced convection. The higher the changes the longer the return time. The time required to stabilize the partition is longer than the period of maximal reducing of the thermal resistance. It is also important to analyze the values registered for the maximum wind speed (3.24 m/s). As it is visible in the Figures 3a and 4a, the initial thermal resistance of both analyzed areas for this wind speed was smaller than in the other cases. Just after the second cycle, the resistance value was similar to the other cases. This may have resulted from measurement error or problems with the cooler, or the lack of full thermodynamic stabilization of the model. It should be also noticed that the measurements were conducted on the loose fiber thermal insulation which may deform under the wind load. This can be a source of potential differences between measurement cases.

CONCLUSIONS

Based on the research it can be stated that the thermal losses induced by wind washing in frame lightweight partitions filled with loose fiber insulation depend on many factors, including wind speed and construction of the partition. The greater the air permeability of the insulation, the more rapid thermal changes due to wind washing. The partial wind barrier causes a minimal reduction of heat losses due to air filtration in the partition, though only fully sheltered areas of partition are characterized by lower heat losses. Several hours of wind washing results in a longer period of transition of the partition into a state of thermal equilibrium, even 3 times longer than time needed to achieve a maximum reduction.

Current research is directed towards determining moisture distribution in the models. This may give an answer on the depth of the wind penetration in the frame lightweight partitions.

ACKNOWLEDGEMENT

This paper is supported by University of Josip Juraj Strossmayer Osijek, Croatia, under research project titled “Innovative simulation model for determination of heat losses in buildings due to infiltration”, 2017 - 2018, IZIP 2016 and by the by the Polish Ministry of Science and Higher Education with the statutory research.

REFERENCES

- Gullbreken L., Geving S., Time B., Andresen I., Holme J. 2015. Moisture conditions in well-insulated wood-frame walls. Simulations, laboratory measurements and field measurements, *Wood Material Science and Engineering* 10(3).
- Deseyve C, Bednar T. Wind induced airflow through lightweight pitched roof construction: Test roof element – measurements and model validation. *Proceedings of the 8th Symposium on Building Physics in the Nordic Countries*, Kopenhaga, 2008.
- Økland Ø. 1998. Convection in Highly – Insulated Building Structures. *Doctoral theses at NTNU*. Norwegian University of Science and Technology, Trondheim, 202 pages.
- ISO 9869, Thermal insulation–Building elements– In-situ Measurements of thermal resistance and thermal transmittance. Geneva: International Organization for Standardization.
- EN 13829:2000 - Thermal Performance of Buildings – Determination of Air Permeability of Domestic Buildings Fan Pressurization Method. Brussel: European Committee for Standardization.
- Wójcik R. and Kosiński P. 2015. Seeming air tightness of construction partitions, *Energy Procedia*, 78, 1519–1524.

Determination of lead dust fall rates during deconstruction of wood frame buildings in an urban region in the Northeastern United States.

Paul Crovella^{1*}, Marc Delaney², and Melisa Kohan³

¹ State University of New York College of Environmental Science and Forestry

²Widewaters Construction Inc.

³Comfort Systems Inc.

**Corresponding email: plcrovella@esf.edu*

ABSTRACT

Title: Lead dust fall deposition rates during deconstruction of wood frame buildings in an urban region in the Northeastern United States.

Objectives: Determine the lead dust fall deposition rate due to hybrid deconstruction (separation and removal of building components) of wood-frame structures, and compare that to the lead dust fall deposition rate from demolition (compression and collapse of building components).

Scope: A city block with a total of 11 wood-frame structures was selected as the location for the deconstruction leadfall testing. Testing was done during the deconstruction of 7 of the 11 pre-1950 homes (mean construction year 1928, mean floor area 283 square meter).

Method: During deconstruction, the lead deposition rate was measured by using the modified APHA 502 method (Mucha et al. 2009).

Findings: The geometric mean deposition rate for the lead dust fall at the property perimeter from the houses using deconstruction was 61.3 ug/sg m/hr. Published values for deposition rates from demolition in Chicago (Jacobs, et al. 2013) are 59.0 and 152 ug/sq m/hr for homes with and without the use of dust suppression. The deposition rate during hybrid deconstruction is similar to the deposition rate during demolition when dust suppression is employed.

Implications: Many older urban areas have abandoned buildings containing lead-based paint. Governments in these regions invest in removing these buildings, using a variety of methods. To avoid further lead contamination in the soil surrounding these buildings, methods which minimize the total lead dust fall must be employed. The proper quantification and evaluation of these methods will help policy makers with their decisions.

KEYWORDS

Environmental lead, soil contamination, lead deposition rate, deconstruction, demolition

INTRODUCTION

During the late 20th century major urban areas in US manufacturing regions experienced population loss, and an increase in abandoned homes. For cities in the Northeast and Midwest of the United States, this has become an acute problem. These homes create problems on many fronts, including the impact on investment in the community, use for illicit activities, danger due to arson, and loss of tax base. In many of these urban areas, these abandoned

buildings were built before the 1978 ban on lead paint, and as a result lead can be found on both exterior and interior surfaces.

The removal by demolition and landfilling of these homes can also create significant problems. First, the volume of landfill waste created is significant. Based on a 2014 EPA study, the waste from construction and demolition activities constitutes more than two-thirds of all landfill waste (by weight). Of this construction and demolition waste, more than 90% is from demolition (EPA, 2014). Another problem is that during the demolition of these homes the possibility exists for significant soil lead contamination from lead dust dispersion (Farfel, 2003).

However, many communities are looking for alternatives that will decrease the amount of material going to a landfill, return salvageable materials for new construction, help to provide employment for community members, and reduce the transportation impacts and greenhouse gas releases from materials transported and then left to decay in landfills. One way to do this is through deconstruction instead of demolition (Bell, 2012).

The disassembly and separation of building elements with the intent for reuse or recycling is known as “Deconstruction”. Traditional deconstruction involves an increased amount of labor and expense compared to demolition. However, depending on the costs of disposal, the value of the reclaimed materials, and the relative amount of labor in the process, under certain conditions deconstruction can be a lower cost solution (Pun, 2006). In an attempt to optimize these conditions, an adaptation of deconstruction known as “hybrid” deconstruction has been developed. In this process, the building’s planar surfaces are mechanically separated and then lowered to the ground where workers harvest the most easily separated materials, and avoid expending additional time for small amounts of reclaimed material. The goal of this method is to maximize the amount of materials salvaged per unit of labor invested.

Regardless of the method chosen, the presence of hazardous materials in the structure to be removed must be managed. During traditional demolition, the impact and crushing of the building materials creates a plume of dust that settles around the site. Some demolition contractors use a water stream sprayed at the materials to try to reduce this plume. Nevertheless, researchers have found that lead dust deposition measured around demolition sites represent a significant source of soil contamination. (Farfel, 2003)

The deleterious effects of exposure to environmental lead during childhood are well documented. In their 2015 report on Educational Interventions for Children Affected by Lead, the expert panel compiling the report cites 83 separate studies on the negative neurodevelopmental consequences of lead exposure (Educational Services for Children Affected by Lead Expert Panel, 2015). Results of such elevated childhood lead blood levels can range from anti-social and behavioural problems (Dietrich, 2001) to violent crime (Reyes, 2007). While guidelines from 1960 set safe lead blood levels at 60 $\mu\text{g}/\text{dL}$, recent studies show levels as low as 5 $\mu\text{g}/\text{dL}$, can have impacts on brain development in children (CDC, 2012).

Since the phase out of lead from gasoline beginning in the 1970s, to the elimination of lead from gasoline in 1996, lead blood levels in children have been shown to be correlated to soil lead levels (Johnson and Bretsch, 2002)(Mielke et al, 1997). The deposition of lead on soils from demolition activities has been identified as an important soil contamination pathway. Farfel (2003) found that lead dust fall rates during demolition increased by more than 40 fold from the background levels. In a study from St. Louis, MO., Rabito et al found a significant

correlation between multiple demolitions in a census block, and elevated blood lead levels in children (2007). Gulson and Taylor (2017) found that children's blood lead levels were found to be correlated both to leadfall on interior surfaces (100 $\mu\text{g}/\text{m}^2/30\text{d}$ rate corresponds to an increase in children's blood lead levels of about 1.5 $\mu\text{g}/\text{dL}$) and soil increases (0 to 1000 mg Pb/kg soil increase results in an increase of 1.7 $\mu\text{g}/\text{dL}$ of blood lead levels). Results from this study were suggested to be used for "action levels" to monitor activities such as housing demolition.

A study by Ayodle (2014) tracked aerosol lead concentrations and soil deposited lead from five homes in Detroit: One home was demolished, one home was fully deconstructed (ten days), and the remaining three homes were partially deconstructed (over one to five days), and then demolished. This study analysed the dust that was collected using a high volume air sampler. These particles were then analyzed using elemental ratios, and classified. Ayodle found that airborne dust concentration during demolition frequently exceeded National Ambient Air Quality Standards, and recommended dust suppression. The study recommended that the impacts of Deconstruction be measured by measuring lead depositional flux (dustfall rates) using buckets with liquid, rather than by determining the lead dustfall concentration in the soil. Due to the method of the study, the authors were unable to say if the total lead dustfall due to deconstruction was more or less than that during demolition.

Work to reduce pathways for blood lead contamination have shown that significant societal and economic benefits can be accrued from the investment to reduce lead hazards from indoor and outdoor paint using partial to full abatement. Protecting children from lead in buildings by remediating the building has shown to have significant economic benefits, with each dollar invested in lead paint hazard control resulting in a return of \$17–\$221 (Gould, 2009).

The present study proposed to measure the lead dustfall rate during the hybrid deconstruction of seven multi-family homes in an urban area in the Northeastern United States, and compare this to other methods of removal.

METHODS

A city block (85 m x 85 m) in the city of Syracuse, NY was chosen for the study. Eleven multi-family houses were located on this block and sequentially removed using hybrid deconstruction. During this process, lead dustfall rates were recorded for seven of the homes. The average size of the sampled homes was 283 sq. m., the average year of construction of the homes was 1928, and each of the homes had an interior lead survey performed before the deconstruction was done. The lead survey was performed on interior surfaces using an X-ray fluorescence (XRF) analyser by an accredited testing agency. HUD guidelines (1.0 milligram per square centimeter or greater) were used for the definition of lead paint, and all but one of the homes was found to contain interior lead paint. No testing was done for the presence of lead paint on the exterior. Detailed house information is shown in Table 1

Table 1. Housing characteristics for sampled multi-family homes

Home location	Year Built	Living Area (sq. m.)	Presence of interior lead paint
700 Raynor St.	1950	396	Yes
704 Raynor St.	1920	272	Yes
708 Raynor St.	1924	284	Yes
117 Standart St.	1940	164	No
119-21 Standart St	1922	283	Yes

125 Standart St.	1920	385	Yes
131-33 Standart St.	1922	283	Yes
Average	1928		

The houses were deconstructed over the course of two months, November and December of 2012. The approach selected for this work was a hybrid of demolition and deconstruction. Hybrid deconstruction entailed the planar building surfaces being separated into 2.5 m by 5m panel sections, and these sections being lowered to the ground for disassembly by hand or disposal. In this case, the larger wood members from the floor and roof assemblies were salvaged, while the smaller wood members (studs, plates, lath) located in the wall assemblies were not separated. The result of this approach was that the building could be broken down into these assemblies in one-two days, as opposed to the two-three weeks required for traditional on-site deconstruction.

The study data collection began by sampling the lead deposition rate during the deconstruction process. Previous studies (Mucha, 2009) placed their containers at an average distance of 5 m from the deconstruction activity. Containers for this study were placed just inside the perimeter at distances of 2-5 m from the deconstruction activity. Sampling was done just inside the property perimeter using the method described by Mucha et al. (2009) based on APHA 502. Four polyethylene sampling containers of 0.073 square meters surface area with 1 liter of water were located on portable stands that positioned them at approximately 2 m elevation above grade at the corners of the property. In some cases one or more of the corners of the site was inaccessible, or obstructed by machinery moving on the site. The containers were left open for dust fall for a period of 8 hours each day. At the end of the sampling period, the liquid in each container was transferred to a sterile bottle and transported to the laboratory. In the laboratory the liquid was filtered, and then the filter was dried and digested following EPA SW3050B. The remaining material was analyzed using inductively coupled mass spectrometry following EPA method SW6020. 30 total samples were taken from 7 different properties. Testing of samples included one control and processing included duplicate processing. The IC mass spectrometry measured weight of the lead was divided by the water surface area, and the hours left exposed, and the resulting value is reported as the deposition rate in ug/sq m/hr.

RESULTS

The geometric mean deposition rates were compared to two other studies, both from Chicago (Mucha, 2009)(Jacobs, 2013). One of these studies sampled lead dust fall at the perimeter of the work site, and the other study sampled the dustfall at an average distance of 5 m from the perimeter.

Table 2. Comparison of results from studies of lead deposition rate during demolition and deconstruction

Location	Condition	Dust suppression	N _{samples}	N _{address}	Geometric mean ($\mu\text{g Pb/m}^2/\text{h}$)	Sampler location	Year
Chicago	Background		18	6	12.9		2009
Chicago	Demolition	Hose	25	5	48	5 m outside perimeter	2009
Chicago	Demolition	None	22	6	74.6	5 m outside perimeter	2009
Syracuse	Deconstruction	None	29	7	61.3	Perimeter	2012

Chicago	Demolition	Hose	84	NR	59	Perimeter	2013
Chicago	Demolition	None	13	NR	152.6	Perimeter	2013

NR = Not Reported

Based on an assumed demolition (without dust suppression) time of 8 hours for a single structure, and an assumed hybrid deconstruction time for primary separation and lowering of materials of 8 hours, the cumulative geometric mean leadfall deposition at the site perimeter would be 1220 $\mu\text{g Pb/m}^2$ for demolition and 490 $\mu\text{g Pb/m}^2$ for deconstruction. Based on the work of Gilson (2017), if these lead levels were left exposed on a surface (e.g. inside an adjacent home) for 30 days, this difference in lead levels would correspond to an additional increase in blood lead level of 10.95 $\mu\text{g/dL}$ for the occupants next to the demolition site. The value of 10.95 $\mu\text{g/dL}$ is well above the 5 $\mu\text{g/dL}$ level of action recommended by the CDC (2012). The corresponding lead deposition due to deconstruction under a similar scenario, would cause a 4.40 $\mu\text{g/dL}$ increase, below the 5 $\mu\text{g/dL}$ level of action recommended by the CDC.

DISCUSSIONS

The lead deposition rate found in this study falls between the results for demolition with and without dust suppression found by Mucha (2009). The lead deposition rate found in this study is within 4% of the demolition with dust suppression found by Jacobs (2013).

Based on the comparison to both of the previous studies, the use of hybrid deconstruction reduces the lead fall deposition rate compared to demolition without dust suppression. Even in the case of demolition with dust suppression, deconstruction eliminates the water contamination and runoff resulting from dust suppression with a hose.

One difficulty with this study was that it was performed on buildings that were all deconstructed by the same firm. Measurements from hybrid deconstruction done by a variety of companies would provide a more representative sample.

A further difficulty is that location of the collection containers at the site perimeter does not accurately predict the impact on structures at a greater distance from the site.

CONCLUSIONS

While the result of the work clearly showed a reduction in leadfall deposition during the hybrid deconstruction process, there a number of considerations to note.

First, the deposition rate measured occurred over the eight-hour period of large panel separation and lowering to the ground. However, once on the ground, hand disassembly occurred over a number of days, and the possibility of continued elevated lead deposition exists. Ayodle (2014) found that during the full deconstruction process, aerosol lead increased during the third day when wall plaster and window frames were removed during the separation of wall elements, and the other days of deconstruction showed markedly less airborne dust. Comparison of total lead dustfall during the duration of the work could improve the direct comparison to demolition.

Second, the work that was done in this study set the measurement containers within the project perimeter. Because of this the comparison to other studies where the containers were located outside the worksite fencing is confounded. Jacobs (2013) study included sampling at distances up to 400 ft from the perimeter, and they found elevated levels at that distance.

ACKNOWLEDGEMENT

Partial support for this project was provided by the Syracuse University Environmental Finance Center.

REFERENCES

- Ayodele A. 2014. Changes In The Lead Concentration In Air And Soil During House Deconstruction And Demolition: Case Study Springwells, Detroit, Michigan. M.S Thesis, Wayne State University (USA), 115 pages.
- CDC. 2012. Response to Advisory Committee on Childhood Lead Poisoning Prevention Recommendations in “Low Level Lead Exposure Harms Children: A Renewed Call of Primary Prevention”. *Morbidity Mortality Weekly*. 2012, Vol. 61, Issue 20. pp. 1-16.
- Educational Services for Children Affected by Lead Expert Panel. 2015. Educational interventions for children affected by lead. Atlanta: U.S. Department of Health and Human Services.
- EPA, 2014 <https://www.epa.gov/smm/sustainable-management-construction-and-demolition-materials> Retrieved on April 8, 2018.
- Farfel, MR, Orlova, AO, Lees, PSJ, Rohde, C, Ashley, PJ, Chisolm, JJ. A study of urban housing demolitions as sources of lead in ambient dust: demolition practices and exterior dust fall. *Environ Health Perspect* 2003; 111:1228–34.
- Gould, E. Childhood Lead Poisoning: Conservative Estimates of the Social and Economic Benefits of Lead Hazard Control volume 117 | number 7 | July 2009 • *Environmental Health Perspectives* 1162-1167.
- Gulson, B and Taylor A. A simple lead dust fall method predicts children's blood lead level: New evidence from Australia. *Environ Res* 2017; 159: 76-81.
- Jacobs D. E et al. 2013. Lead and other Heavy Metals in Dust Fall from Single-Family Housing Demolition.
- Johnson D and Bretsch J. 2002. Soil lead and children’s blood lead levels in Syracuse, NY USA. *Environmental Geochemistry and Health*, Volume 24, Issue 4, pp 375–385.
- Kory T. Bell, One Nail at a Time: Building Deconstruction Law as a Tool to Demolish Abandoned Housing Problems, 45 *Ind. L. Rev.* 547 (2012)
- Mielke, H. et al, 1997. Associations between Soil Lead and Childhood Blood Lead in Urban New Orleans and Rural Lafourche Parish of Louisiana. *Environmental Health Perspectives*, Vol. 105, No. 9, pp. 950-954.
- Mucha, AP, Stites, N, Evens, A, MacRoy, PM, Persky, VW, and Jacobs, DE. Lead dustfall from demolition of scattered site family housing: developing a sampling methodology. *Environ Res* 2009; 109:143–8.
- Pun, Sung Kin, Liu, Chunlu and Langston, Craig 2006, Case study of demolition costs of residential buildings, *Construction management and economics*, vol. 24, no. 9, pp. 967-976.
- Rabito, F.A., Iqbal, S., Shorter, C.F., Osman, P., Philips, P.E., Langlois, E. and White, L.E., 2007. The association between demolition activity and children's blood lead levels. *Environmental research*, 103(3), pp.345-351.
- Reyes, J W. Environmental Policy as Social Policy? The Impact of Childhood Lead Exposure on Crime. 2007. *The B.E. Journal of Economic Analysis & Policy*, Volume 7, Issue 1, ISSN (Online) 1935-1682.

Hygrothermal Performance of a Hygroscopic and Permeable Wall Assembly: Impact of a Vented Wall Cavity

Diane Bastien^{1,*}, Martin Winther-Gaasvig¹

¹University of Southern Denmark, Denmark

*Corresponding email: dib@iti.sdu.dk

ABSTRACT

Building envelopes that are hygroscopic and permeable to water vapour can contribute to improve the Indoor Environmental Quality (IEQ) in buildings by reducing indoor humidity fluctuations and the concentration of some contaminants like CO₂. However, risks of interstitial condensation and mold growth need to be assessed to ensure the durability of such building envelopes. The objective of this paper is to perform hygrothermal simulations of a case study house designed with a Hygroscopic and Permeable Building Envelope (HPBE) and to assess the impact of having a vented cavity compared to a face-sealed wall.

This contribution presents hygrothermal simulations of a wall assembly performed with WUFI Plus and WUFI Pro. The mold index is calculated from the simulation results and the hygrothermal performance of the vented and unvented wall is compared. The resilience of the construction is assessed by introducing leaks within the envelope. Simulation results indicate a satisfactory performance of this wall assembly regardless of the presence of a vented wall cavity. The wall design with a vented cavity seems more resilient when subjected to large leakages, although the wood fibreboard surface seems more vulnerable to mold growth when unprotected by a plaster. Additional simulations and field data are needed for assessing the benefits of having a vented cavity for HPBE.

KEYWORDS

Moisture management, hygrothermal performance, durability, permeable building envelopes

INTRODUCTION

Scientific background

Sustainable building design goes beyond the achievement of a low energy consumption but also encompasses the creation of a healthy indoor environment while reducing the overall environmental impacts over the entire building life cycle. With around 75% of building failures that are caused by water (May 2005), establishing good water management practices is a key element for ensuring the durability of a building.

Overhangs and gutters, perimeter drains and a vapour retarder on the warm side of an assembly are common recommendations in many jurisdictions for controlling water and water vapour. Vapour retarders slow down the diffusion of water vapour, which mostly occurs from inside to outside in cold weather, hereby reducing risks of condensation on the cold side of an assembly. However, they also hinder their drying potential, which may cause significant moisture damage during accidental leakages (Kunzel 2005). As such, two-way drying is now recommended as a necessary climate change adaption measure, where it is now suggested to avoid interior vapour barriers in all but the most extreme climatic zones (Kesik 2017).

Hygroscopic and Permeable Building Envelopes (HPBE) can contribute to improve the IEQ in buildings by reducing indoor humidity fluctuations (Yang et al. 2014). Besides, the vapour permeability of building materials was found to correlate closely to their carbon dioxide permeability and simulations showed that bedrooms made of building materials with higher water vapour permeabilities experience reduced concentrations of CO₂ (Niemelä et al. 2017).

Surface condensation, visible mould and perceived mould odour are indicators of dampness and microbial growth. Since the relationship between microbial exposure and health effects cannot be quantified precisely, there are no recommended quantitative threshold; only preventing dampness and mould-related problems is recommended (WHO 2009). Recent evidence is showing that visible mould and mould odour are associated with new-onset wheezing in children in a dose-dependent manner, although the underlying mechanisms remain unidentified (Shorter et al. 2018).

A study of 1140 samples of visibly damaged building materials revealed highest median concentrations of fungi in wood and paper materials and lowest in mineral insulation, ceramic products, paints and glues. The percentage of building materials in which no growth was detected ranged from 9-14% for wood to 12-17% for mineral insulation materials. Microbial damage occurred in all material categories included in this study, confirming that microbial growth can occur in a wide variety of building products (Hyvärinen et al. 2002).

Vented and ventilated wall assemblies

Many studies have investigated the impact of ventilated or vented wall cavities on the moisture content and drying rates of building materials. A review about this topic is presented by Straube (2009), from which the main conclusions are presented below.

A vented wall assembly has an air cavity behind the exterior cladding with openings only at the bottom, usually provided for drainage, which also allow for some ventilation to take place. A ventilated wall has openings at both the top and bottom of an air cavity, which promotes higher ventilation airflow rates and drying.

Besides numerical airflow rate calculations, the three main modelling techniques used by researchers to approximate vented/ventilated wall assemblies using hygrothermal models are

1. Ignoring ventilation effects (insertion of a still air cavity)
2. Effective cladding permeance (user selects an increased exterior cladding permeance)
3. Removal of cladding (user removes external cladding, rain and solar radiation loads)

Experimental measurements from Straube showed that techniques # 2 and #3 are in relatively good agreement with experimental results, although the choice of the effective cladding permeance has a significant impact on the results. Thus, the modelling technique #3 was chosen to model the vented wall assembly in this contribution.

While some research reported conflicting results about the benefits of ventilation cladding, this review paper concluded that there was a general consensus in the last years that ventilation cladding can increase the drying potential of a wall, reduce wetting from absorptive cladding and sun-driven moisture.

Most of these studies have been carried with building constructions that included a low permeance layer on the interior. There are insufficient studies to confirm whether having a

ventilated wall cavity can significantly improve the hygrothermal performance of wall assemblies that are made of hygroscopic and permeable materials.

This paper aims to investigate the effect of cladding ventilation for a HPBE in a cold a wet climate such as northern Europe. As a first step, hygrothermal simulations of a house are carried out with WUFI Plus, a validated whole building simulation software (Künzel 1995). The mold index (ASHRAE 2016) is calculated over 2 and 5 years for different wall orientations for a vented and unvented wall assembly. Secondly, the resilience of a vented and unvented wall assembly is investigated by simulating water leakages with WUFI Pro.

METHODS

A model of a house was created in WUFI Plus V3.0.3.0 in order to investigate the effect of ventilation cladding in a HPBE. This house is located in Holbæk, Denmark, from which field data is currently being monitored. The weather file selected in WUFI is Lund, which is situated 120 km east of Holbæk at the same latitude.

The envelope of the house is made of a wood structure filled with blown-in woodfiber insulation, interior and exterior wood fibreboards, interior clay plaster and exterior mineral plaster. The house has a ventilated roof and crawl space. A floor plan and a south view of the house are presented in Figure 1. The walls do not have a vented cavity except for the south-east living room wall.

The characteristics of the wall assembly are presented in Figure 2. It can be seen that the mineral plaster is the material with the highest water vapour resistance factor with a μ of 21. In this given configuration, all layers are considered permeable with a s_d value smaller than 2 m where the woodfiber insulation provides the greatest water vapour resistance with $s_d = 0,68$ m.

The building model is divided in 6 zones: the living room (named *stue* on the floor plan) and the rest of the house are modelled as two conditioned zones, accompanied by their respective attic and crawl space, which are simulated as unconditioned zones each with continuous ventilation at 3 ACH. The carport and skylights are excluded from the simulation model.

The wind-driven rain coefficient is set to 0.07 for the walls. This value has been obtained by carrying a linear regression analysis of experimental driving rain data obtained for a 4 m high test wall at the center of the façade (Künzel 1995), which is deemed representative of the current situation. The wall with a vented cavity was modeled by removing the exterior cladding (mineral plaster) and rain and solar radiation loads.

The windows have a glass g-value of 0.55 and an overall U-value of 0.77 W/(m²K). There is mechanical ventilation at 0.5 ACH with 60% heat recovery and an infiltration rate of 0.1 ACH. Natural ventilation at 0.5 ACH takes place from May 15th until September 15th and a fictitious cooling set point of 28°C act as additional natural ventilation to control overheating. The building is occupied by a family of four following a typical occupancy schedule. In the main zone, the moisture generation is equal to 4610 g/day during the week and 8384 g/day during the weekend. In the living room, the moisture load is set at 432 g/ day.

The ASHRAE standard 160 (2016) provides a complete description on how to calculate the mold index at a location of interest in a building assembly. The value of the mold index was computed after two and five years of simulation. The exterior mineral plaster was treated as a medium sensitivity class and the wood fiberboard as a sensitive class.

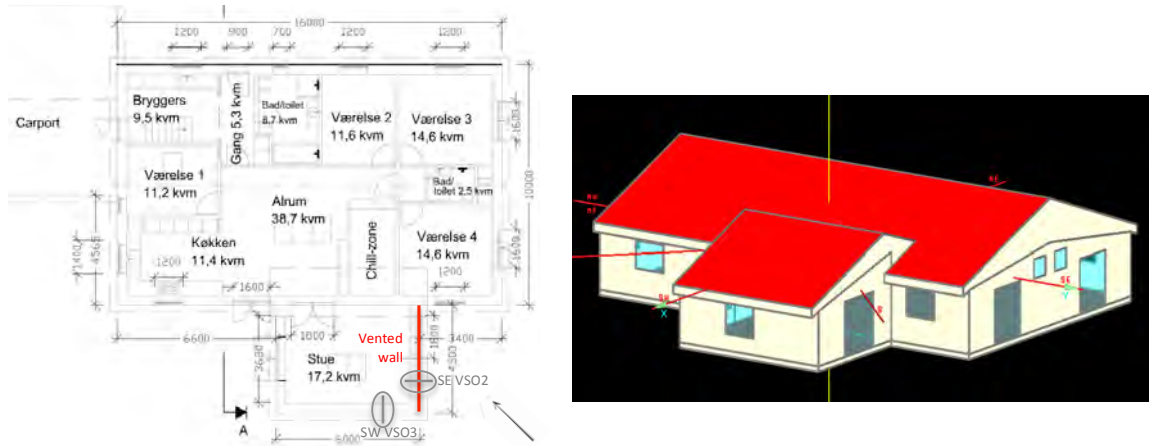


Figure 1. Floor plan and south view of the building model

Material/Layer (from outside to inside)	ρ [kg/m ³]	c [J/kgK]	λ [W/mK]	Thick. [m]	μ [-]	s_d [m]
Mineral cement Plaster	1434	850	0,9	0,006	21	0,126
Ext wood fibreboard	140	2100	0,04	0,06	3	0,18
Wood fiber insulation	50	2100	0,037	0,34	2,5	0,68
Clay board	615	2000	0,128	0,016	7,4	0,12
Basecoat clay plaster	1844	850	0,1	0,003	14,7	0,04
Topcoat clay plaster	1844	850	0,1	0,002	14,7	0,03

Figure 2. Wall assembly materials characteristics for the unvented wall. The mineral cement plaster is omitted in the vented wall section.

The hygrothermal performance of the vented and unvented wall assemblies subjected to internal moisture sources was also investigated. The assemblies were modeled in WUFI Pro, which can allow the introduction of heat, moisture and air change sources within the wall assembly. The vented and unvented wall assemblies were modeled, subjected to the climate of Lund on the exterior side and to EN 15026 conditions on the interior side with medium moisture loads. For modeling the vented wall, the mineral plaster and rain loads were removed, but the solar load remained, since it cannot be switched off in WUFI Pro. In these conditions, the moisture content is likely to be underestimated but the comparison of a vented and unvented wall can still reveal valuable information on the behavior of these assemblies.

Two different kinds of moisture intrusion were investigated: one based on a fraction of driving rain and one based on the IBP air infiltration model (WUFI 2017). The introduction of 0.01% and 1% of driving rain at the inner face of the wood fiberboard was simulated, as well as Class A and Class C air infiltrations (corresponding to $q_{@50 Pa}$ of 1 and 5 m³/m²h for the whole building and q of 0.07 and 0.33 m³/m²h through the component, respectively).

RESULTS AND DISCUSSION

Whole building simulations with WUFI Plus

Table 1 presents the maximum mold index (ASHRAE 2016) computed after two and five simulation years of the SE and SW walls of the building model, which have the highest

moisture content. M was calculated at the outer surface, 0.15 cm behind the exterior wood fibreboard and from the average temperature and relative humidity of the fibreboard.

Results show that the unvented wall exhibits a satisfactory hygrothermal performance, with a maximum mold index of 0.01 and 0.02 at the exterior plaster layer for a SE and SW wall respectively. The maximum mold index at 0.15 cm behind the external face of the wood fibreboard is 0.12 or less, well below the critical value of 3.

The unvented wall cavity has a mineral plaster as external rendering, which has a medium sensitivity class, while the external surface of the vented wall has a wood fibreboard as outermost layer, which is classified as a sensitive material. As such, the maximal mold index at the external surface of the vented assembly is higher, and reaches a maximum value of 1.37 over a two year period and of 2.13 over a five year period. A mold index of 3 is likely to be reached by performing simulations over a longer period of time. Therefore, the unvented wall assembly seems less likely to develop mold growth at the external surface. However, the maximum mean mold index is lower for a vented cavity for both wall orientations. Ongoing research will take place to evaluate long-term field performance.

Table 1. Maximum mold index for unvented and vented wall after 2 year (5 years)

Assembly type	Orientation	M , surface	M , 0.15 cm wood f.	M , mean
Vented	SE VSO2 (135°)	1.37 (2.13)	-	0.02 (0.02)
Unvented	SE VSO2 (135°)	0.01 (0.01)	0.09 (0.09)	0.05 (0.05)
Vented	SW VSO3 (225°)	1.37 (2.13)	-	0.02 (0.02)
Unvented	SW VSO3 (225°)	0.02 (0.02)	0.12 (0.12)	0.08 (0.08)

Hygrothermal simulation under water leakages with WUFI Pro

Performing hygrothermal simulations while introducing internal moisture sources within a wall assembly is a method that allows evaluating its resilience and drying potential under challenging situations. Simulations were performed with the presence of a fraction of driving rain or an air infiltration moisture source. The moisture source was introduced in the last element of the wood fibreboard, on the internal face. The maximum mold index for a SW vented and unvented walls under different moisture sources is presented in the Table 2 below.

Table 2. Mold index for unvented/vented walls after two years with various moisture sources

Assembly type	Moisture source	M , surface	M , 0.15 cm wood f.
Vented	None	1.24	0.89
Vented	0.01% driving rain	1.24	0.89
Vented	1% driving rain	1.24	0.89
Vented	IBP Air inf. Class A	1.24	0.89
Vented	IBP Air inf. Class C	1.24	0.89
Unvented	None	0.02	0.40
Unvented	0.01% driving rain	0.02	0.40
Unvented	1% driving rain	0.03	1.10
Unvented	IBP Air inf. Class A	0.02	0.40
Unvented	IBP Air inf. Class C	0.02	0.41

It can be seen that the maximum mold index at the external surface is not significantly affected by the introduction of the tested moisture sources. Observation of water content profiles and moisture fluxes reveal no significant difference (results not shown). The only significant change of the mold index at 0.15 cm behind the fibreboard is under the introduction of 1% of driving rain, when the index is increased from 0.40 to 1.10 for an

unvented wall. In light of these results, having a vented cavity for this type of assembly seems to increase its resiliency when subjected to significant, recurrent moisture sources.

In reality, leaks are usually localised and not uniformly distributed as assumed in these simulations. The location of the leak is also important in determining how it will be absorbed and redistributed within the building envelope; leaks at only one location have been investigated here. These simulations may be representative of well distributed leaks, but are not representative of substantial and localized leaks.

CONCLUSIONS

This paper investigated the hygrothermal performance of a vented and unvented permeable and hygroscopic wall assembly. Whole building hygrothermal simulations carried out with WUFI Plus and WUFI Pro indicate that the venting this assembly might increase its resilience and drying potential when subjected to significant moisture sources. However, the external face of the wood fibreboard seems more vulnerable to mold growth when unprotected by the mineral plaster.

From these limited results, it is unclear if providing a ventilated cavity yields significant improvement in terms of hygrothermal performance and resilience of the building envelope. Field data is currently being monitored and will shed additional light on this topic. The results presented in this contribution are applicable only for the specific wall assembly investigated here; additional simulations and field data for different types of hygroscopic and permeable wall assemblies are needed for making general conclusions for such assemblies.

ACKNOWLEDGEMENT

The first author is grateful to the Natural Science and Engineering Research Council of Canada for a Postdoctoral Fellowship.

REFERENCES

- ASHRAE, 2016. *Standard 160-2016 Criteria for Design Analysis in Buildings*, Atlanta: American Society of Heating, Refrigerating, and Air-Conditioning Engineers.
- Hyvärinen, A. et al., 2002. Fungi and actinobacteria in moisture-damaged building materials - Concentrations and diversity. *International Biodeterioration and Biodegradation*, 49(1), pp.27–37.
- Kesik, T., 2017. *Resilience Planning Guide*, University of Toronto.
- Kunzel, H.M., 2005. Adapted vapour control for durable building enclosures. In *10th DBMC International Conference on Durability of Building Materials and Components*. p. 8.
- Künzel, H.M., 1995. *Simultaneous heat and moisture transport in building components*, Fraunhofer Institute of Building Physics.
- May, N., 2005. *Breathability: The Key to Building Performance*, Available at: <http://www.ecotimberframe.ie/pdf/BreathabilityinbuildingsNBT.pdf>.
- Niemelä, T. et al., 2017. Carbon dioxide permeability of building materials and their impact on bedroom ventilation need. *Journal of Building Engineering*, 12(May), pp.99–108.
- Shorter, C. et al., 2018. Indoor visible mold and mold odor are associated with new-onset childhood wheeze in a dose-dependent manner. *Indoor Air*, 28(1), pp.6–15.
- WHO, 2009. *WHO guidelines for indoor air quality: dampness and mould*, WHO Regional Office Europe.
- WUFI, 2017. *WUFI Pro 6.1 help*, topic 65: Fraunhofer Institute.
- Yang, X. et al., 2014. Evaluation of Parameters Influencing the Moisture Buffering Potential of Hygroscopic Materials with BSim Simulations. *Buildings*, 4(3), pp.375–393.

Improving Durability of Wooden Beam Bearings in Inside Insulated Walls by Tempering the Beam's Heads

Paul Wegerer^{1,2*}, Thomas Bednar¹

¹TU Wien, Vienna, Austria

²Gassner & Partner Baumanagement GmbH, Vienna, Austria

*Corresponding email: paul.wegerer@tuwien.ac.at

ABSTRACT

Improving durability of wooden beam bearings after a thermal renovation via interior insulation is highly demanding for planners. Because of an isolated thermal bridge in the area of the wooden beam head the risk of condensation water forming in this area increases after installing interior insulation. The problem with wooden beam ends has been analysed increasingly in the last few years by many research institutions as wooden ceiling constructions are common in existing buildings. Furthermore, thermal renovation makes a vital contribution regarding improving the energy-efficiency of existing buildings.

In this paper a method to temper wooden beam ends is introduced. It is a patent pending which is currently developed further using laboratory-prototypes in a double climate chamber. This technology is based on thermo conductive types of sheet metal, which are driven into the construction at the joint between the wooden beam and the surrounding masonry. The thermal energy is provided by a heating pipe and fed into the metal. Because of the metal's high thermal conductivity, heat can be fed specifically into the beam's end in order to avoid wood rotting at this crucial point.

Calculating the beam's end temperature control was done using three-dimensional HAM simulations with air flows in the ceiling cavity being taken into account. The results of different measurements in the double climate chamber as well as the HAM simulations clearly show that the durability of an interior insulation can be increased via a temporary and local tempering of wooden beam bearings. At the same time the risk of wood rotting at the ceiling's bearing structure is minimised.

Comparative analyses show that this method of tempering the beam ends is especially energy-saving as the energy input is low due to the special feeding of heat via thermo conductive types of sheet metal.

KEYWORDS

Wooden beam ceiling, interior insulation, 3D HAM model, local temperature control, double climate chamber

INTRODUCTION

In-situ-measurements on existing buildings with wooden beam ceilings show that the thermal retrofitting via interior insulation can result in damage by moisture (IBO, 2017). Hygrothermal simulations (Wegerer and Bednar, 2017) prove this to be true and show that accompanying measures are to be made when planning an interior insulation with wooden beam ceilings. The interior insulation leads to the cooling-off of the entire outside wall in winter. The ceiling beams protrude into the cold area and are open to a greater risk of rotting. This can be prevented by a local, temporary heat input. The Research Center for Building Physics and Sound Protection at TU Vienna has developed a technology how the beam head area can be tempered. Thereby, harmful condensate formation can be prevented and thus the construction's durability secured.

At the same time, high energy efficiency and practical feasibility were taken into account. A prototype for a local beam head temperature control was developed and a patent filed (Wegerer and Bednar, 2012).

METHODS

Extensive tests were made in a double climate chamber on a true-to-life, 45cm-thick brick wall which is equipped with a ceiling connection over the entire length of its warm side (see fig. 1). Temperature and humidity sensors to examine the hygrothermal conditions were mounted on the – altogether five – wooden beam heads (see fig. 2a). In the bearing areas, sensors to measure the surface temperature were adhered directly to the surrounding bricks (see fig. 2b). Additionally, sensors were built into the wall's cross section to also examine the masonry's hygrothermal behaviour. These sensors serve as a reference for the one-dimensional temperature and moisture field. Finally, temperature and thermal flow measuring foils were applied to the wall's surface to gather a reference of the thermal resistance in comparison to in-situ-measurements.

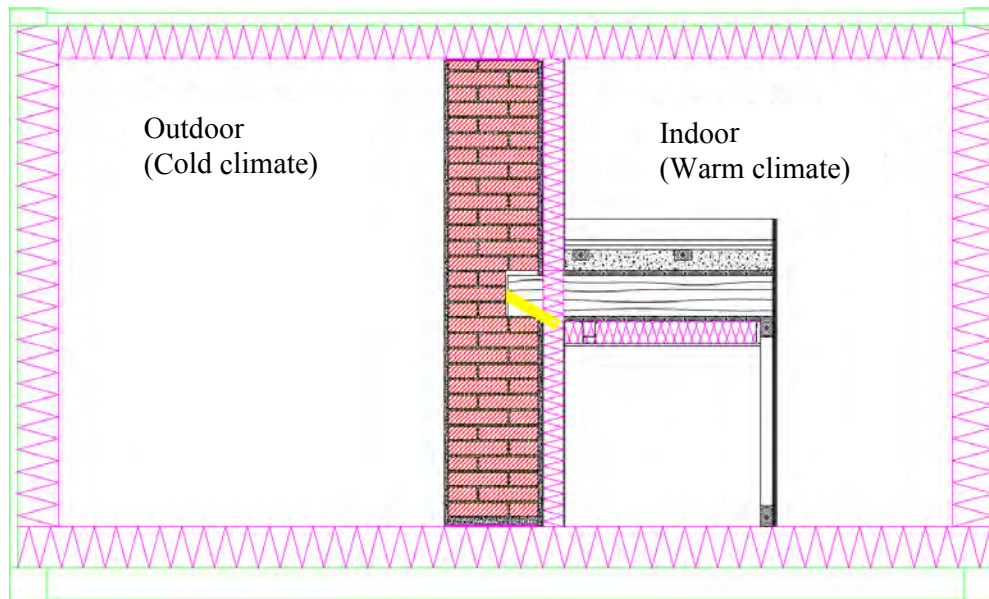


Figure 1. Cross section of the double climate chamber with test wall in middle. Ceiling structure is built into the right/warm climate side.

The tests in the double climate chamber were carried out in three phases. In the first testing phase, measurements were carried out on the test wall without interior insulation and without suspended ceiling. This construction corresponded with a typical existing wall of a Wilhelminian style house as it is found during renovation projects. The results were compared to in-situ-measurements to obtain true-to-life results during later tests with the test wall.

In the second testing phase, the wall was fitted with a 5cm-thick interior insulation made of Xella Multipor sheets. Furthermore, a suspended ceiling was constructed, as is currently usually the case with conventional renovations to improve noise protection. The results of the second testing phase provide information about the thermal enhancement of the existing wall and show the risk of moisture damage owing to the interior insulation. For a detailed analysis of the hygrothermal conditions, various climate scenarios were examined. In doing so, the outside climate was varied and the indoor climate was set with different moisture loads.

In the third testing phase, the beam head's temperature control was installed. Metal sheets made out of copper were driven into the airspace between wood and masonry with every wooden beam. A temperature sensor was stuck onto the outer end of every sheet (see fig. 3a). On the inner side, the heat conducting sheets were connected to a heating pipe (see fig. 4), which was laid in the interior insulation's area.

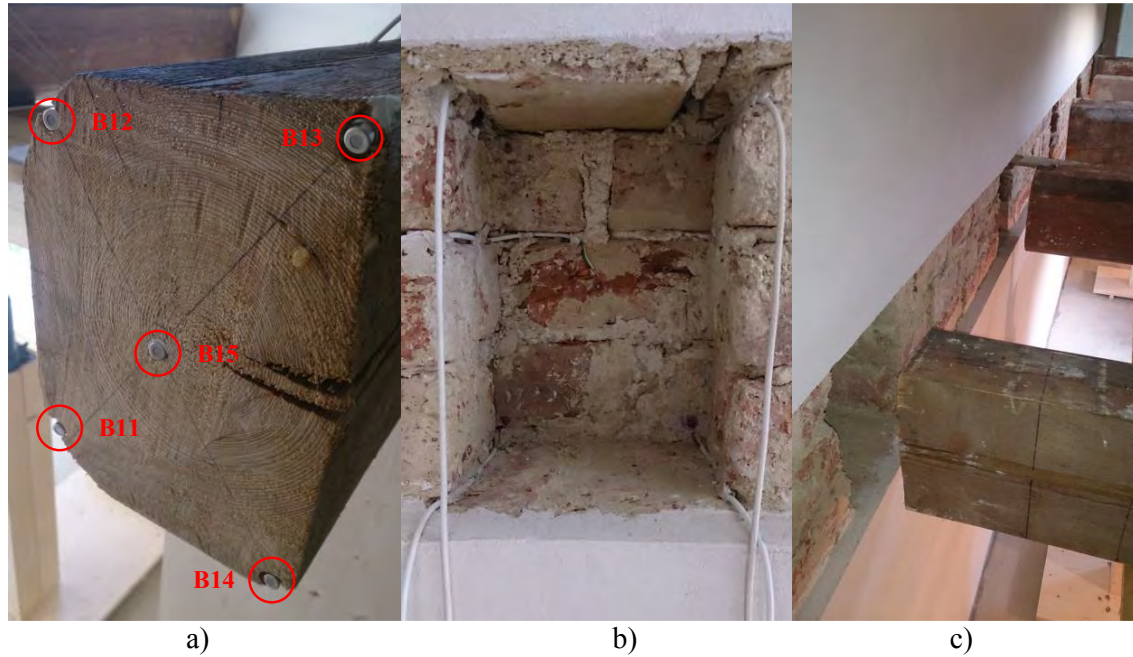


Figure 2. Sensor arrangement a) on beam head ends, b) in the bearing area, c) beam heads before mounting in brick wall



Figure 3. a) Prototype of heat conducting sheet, b) overhead beams without floor assembly

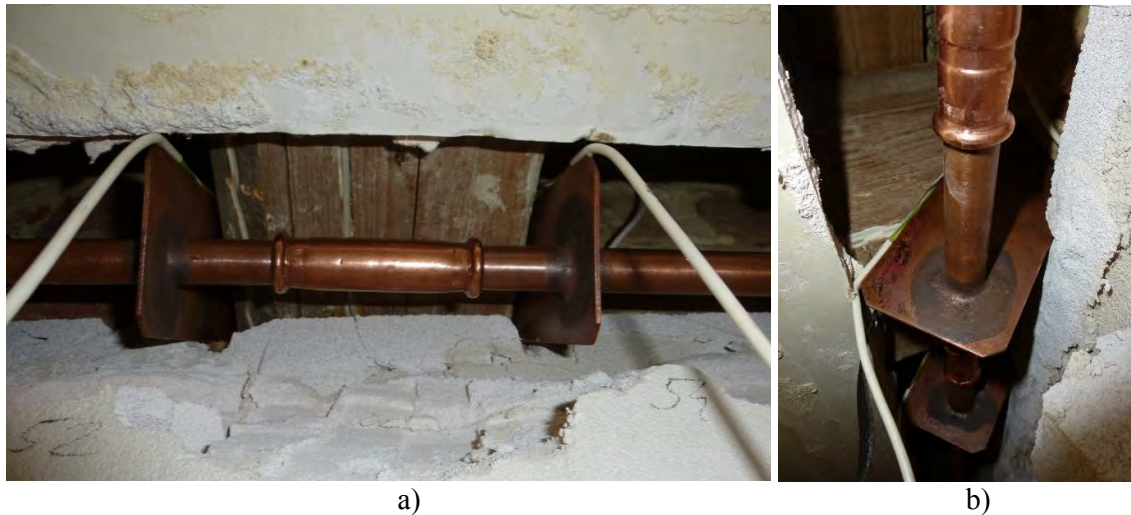


Figure 4. Installation of heat conducting sheets: a) view from below, b) view from side.

In addition to the measurements in the double climate chamber, hygrothermal simulations were made using Comsol Multiphysics and HAM4D_VIE. A model with dimensions geometrically identical to the test piece was generated in order to be able to validate the results and variations of every parameter. Besides, the energy demand was simulated and compared to real measurement data from the tests.

RESULTS

Temperature conditions at the beam's end

The results of the three testing phases show how the three-dimensional temperature field shapes itself within the different construction variants. The interior insulation's and temperature control's influences can be identified in the evaluations of the temperature field on the beam head's end. In figure 5, the measurement data of beam head 1 during the three testing phases are depicted exemplarily. It is evident that the installation of an interior insulation combined with a suspended ceiling leads to critical temperature conditions in the beam head area. This can be countered by temperature control of the beam head.

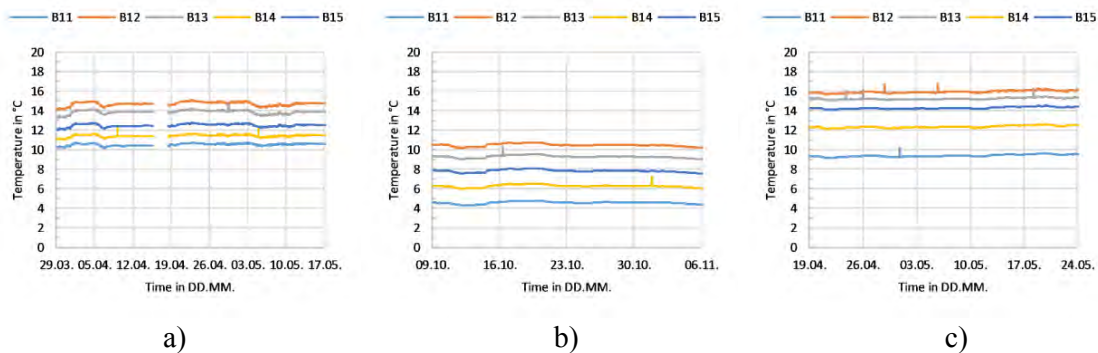


Figure 5. Temperature dispersion on beam head's end at stationary boundary conditions (-10°C outside temperature, 22°C inside temperature). Sensor positions as marked in fig. 2a: a) original construction, b) construction with interior insulation and suspended ceiling, c) construction with interior insulation, suspended ceiling and temperature control

The complex of problems regarding low surface temperatures near the beam head was elaborated by Wegerer and Bednar (2017). As a consequence of the perfusion near the airspace surrounding the wooden beam, warm and humid ambient air may condensate behind the wooden beam head resp. lead to mould growth or wood rotting.

Heating demand

During the experiments with the tempering of the beam head in the double climate chamber the energy consumption was also measured. The application of energy via all five beam heads' heat conducting sheets could be calculated by taking into account the difference in temperature between the heating line's flow and return as well as the flow rate. Additionally, the surface temperature was measured at every heat-conducting sheet directly at the junction from the heating pipe and at the outer end. The heat consumption and the flow rate as well as the surface temperatures are depicted in fig. 6a. Different scenarios were measured in which the same stationary climatic boundary conditions (-10°C outside and 22°C inside temperature) were always assured. The flow temperature was being held at a constant 45°C and only the flow rate was being varied. In spite of the sudden changes in temperature due to the flow rate's increase, the heat input into the construction remains almost the same.

To calculate the reference heating demand a simplified simulation model, which provides temperature control of the entire ceiling connection area was generated. It was assumed that a minimum temperature of 15°C at the beam head's end must not be gone below to prevent rotting of wood. The simulation model's geometry is shown in figure 7 and corresponds to the test wall in the double climate chamber. Figure 6b shows the cumulative heat consumption over a year.

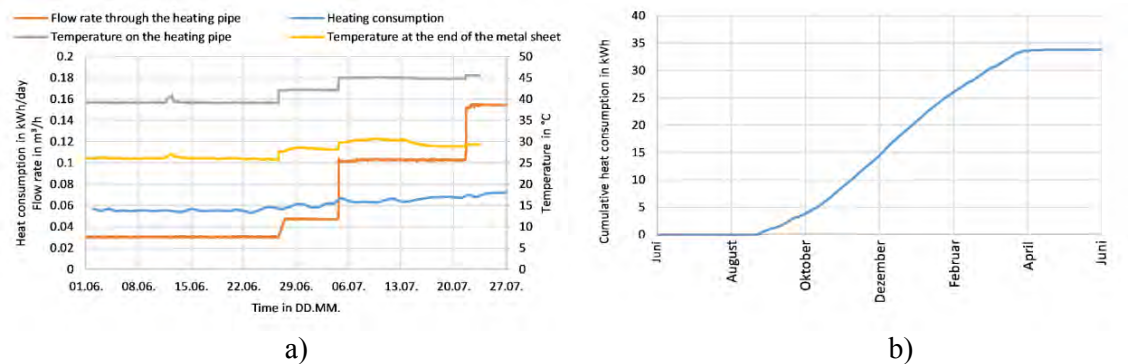


Figure 6. Heat consumption at respectively the same boundary conditions and component dimensions: a) energy consumption measured at prototype in the double climate chamber, b) Reference heating demand: simulated energy consumption corresponding to model in fig. 7 with temperature control of the entire ceiling connection area

From the data measured of the heat input per beam head (0.07kWh/day) and assuming a cold spell of two weeks (14 days), a yearly energy consumption of 1kWh per beam head can be gauged. If this is extrapolated onto a typical Wilhelminian style house, the theoretic energy demand of the beam head's temperature control via heat conducting sheets averages at 200kWh per year, not considering distribution losses. The comparison of the two temperature control models shows that the local heat input via the heat conducting sheets is distinctly more efficient.

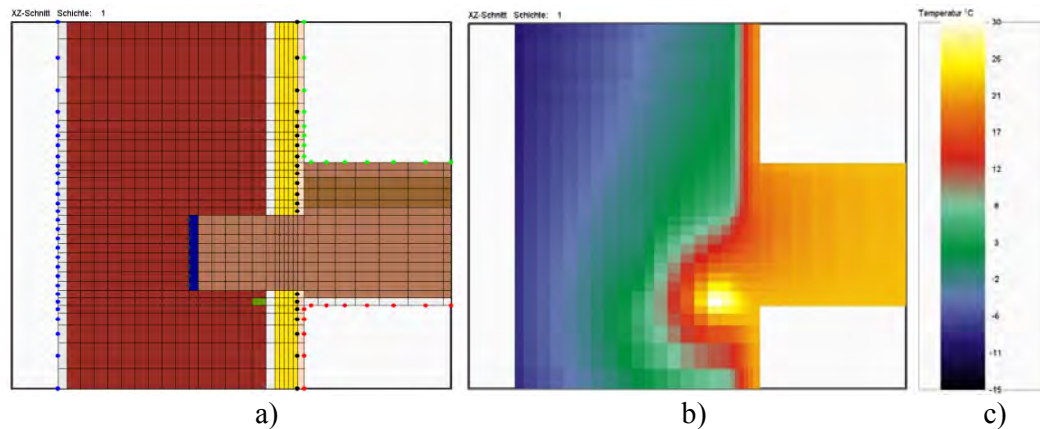


Figure 7. Simulation model of a wooden beam abutment in HAM4D_VIE: a) geometry of model with green cell as source of heat (heating pipe), b) temperature field with flow temperature of 30°C, c) legend with temperature scale.

DISCUSSIONS

The development of the prototype of a beam head's temperature control using a true-to-life brick wall has provided a wealth of data, which are of great relevance for construction practice. Currently, an interior insulation is installed in very little cases of existing constructions' renovations, however, the risk of damage of such construction is relatively high. With the selective temperature control of the beam abutments, greater insulation thicknesses and thus highly efficient renovations with interior insulation can be realised. The planning of such projects was in part dealt with in IEA Annex 55 (Bednar and Hagetoft, 2015), where a probabilistic calculation was developed.

CONCLUSIONS

In practice, the planning of a beam head's temperature control is of little relevance at the moment. The technology introduced is, however, of great significance when thermally renovating buildings using interior insulation. For its practical implementation, the cost-benefit ratio has to be examined above all. The hydraulic dimensioning and the controlling means of the beam head's temperature control require further research. The calculation by hygrothermal simulation associated with this is currently being processed. Further measurements in the double climate chamber are to provide data for the CFD simulation model's validation.

ACKNOWLEDGEMENT

The "Austrian Research Promotion Agency (FFG)" and "Gassner & Partner Baumanagement GmbH" supported this research. We are thankful to our colleagues Manfred Grüner and Harald Hofbauer who helped running the measurements that greatly assisted the research.

REFERENCES

- Bednar T., Hagetoft C.E. 2015. EBC Annex 55. Reliability of Energy Efficient Building Retrofitting - Probability Assessment of Performance & Cost. Risk management by probabilistic assessment. Development of guidelines for practice. Gothenburg 2015
- IBO (Ed.) 2017. Passivhaus Bauteilkatalog: Sanierung. Ökologisch bewertete Konstruktionen.
- Wegerer P., Bednar T. 2012. Wooden Beam Head Temperature Control in Interior Insulated Walls. Patent EP 2 511 439 A2; Temperierung von Holztramköpfen. Patent AT 510 965
- Wegerer P., Bednar T. 2017. Hygrothermal performance of wooden beam heads in inside insulated walls considering air flows. In: *Energy Procedia* 132:652-657. June 2017.

Sorption hysteresis in wood and its coupling to swelling: a new modelling approach

Jan Carmeliet^{1,2*}, Mingyang Chen^{1,2}, Dominique Derome²

¹Chair of Building Physics, Dep. of Mech. and Process Engineering, ETH Zurich, Switzerland

²Laboratory for Multiscale Studies in Building Physics, Empa, Switzerland

*Corresponding email: cajan@ethz.ch

ABSTRACT

Sorption hysteresis of amorphous cellulose is studied. Cellulose, as a renewable organic biopolymer, is an essential component of various natural composites such as wood. A coupling process between sorption and deformation leads to the hysteresis as observed in sorption and swelling, both experimental and simulated for cellulose and wood in general.

KEYWORDS

Sorption, hysteresis, swelling, cellulose, modelling.

INTRODUCTION

An appealing, but not fully understood characteristic of many porous building materials is the appearance of sorption hysteresis: i.e. the moisture content differs at same relative humidity (RH) depending on the loading history, ad -or desorption. Hysteresis has been commonly attributed to capillary condensation hysteresis and pore ink-bottle effects, where for the latter the pore body can only empty when the smaller neck pore is emptied. Such behavior can appropriately be described using models based on the independent domain theory, where hysteresis originates from hysteretic bottle elements, which do not interact necessarily with each other (see e.g. Coasne et al. 2005, Derluyn et al. 2012, Patera et al. 2016). The assumption of non-interaction and pore independence is for most materials however most likely not valid, and invasion percolation, where a pore can only empty when at least one neighboring pore is empty, has been adopted to model hysteresis. For an assembly of connected pores, invasion percolation effects appear where pores can only be emptied when a percolating path is present (see e.g. Carmeliet et al. 1999).

In the above mentioned approaches, the materials are assumed not to deform, remaining at constant volume and do not incorporate the influence of sorption induced swelling. However, many materials such as soft nano-porous materials as wood show an important sorption induced swelling. Soft nanoporous matter encompasses anthropic materials such as compliant porous solids, foams, intrinsically porous polymers, organic membranes, as well as natural materials such as wood, bamboo, plants, linen, kerogen in gas shale. Owing to their large internal surface area and compliant solid matrix, strong fluid-solid interactions lead to sorption-induced deformation or swelling. For example, cellulose, wood most redundant component, on adsorption of water may swell as much as 30% volumetrically (Mihrianyan et al. 2004). An important feature of nanoporous polymers is the hysteresis in sorption isotherms extending to very low RH, a different type of hysteresis to the one associated with capillary condensation, where the hysteresis disappears below a certain RH.

The coupling between sorption and swelling in porous materials has been investigated experimentally and with atomistic simulations (Derome et al. 2011). In parallel, much theoretical effort has been devoted to unify mechanical constitutive equations and surface thermodynamics relationships into the same framework known as poromechanics (Kulasinski et al. 2015). In spite of being successful at describing the coupling between sorption and

swelling, the physical microscopic mechanism behind this coupling is often ignored in studying the hygroscopic behavior of materials like wood. The question arises whether the swelling of the material and the accompanying pore structure changes play an important role in the sorption behavior and are at the origin of the observed sorption hysteresis. In this paper, we will show that this coupling effect is essential in explaining the observed sorption hysteresis effect.

SORPTION AND SWELLING HYSTERESIS OF SOFT MICRO-POROUS MATERIAL

In this paper, we study sorption hysteresis of amorphous cellulose considering its wide presence in nature. Cellulose, as a renewable organic biopolymer, is an essential component of various natural composites such as wood. Because of its abundance, cellulose is also a popular raw material to design innovative products for science, medicine and technology. Cellulose shows an important hygroscopic behavior because of the exposed hydroxyl sites in the nanoporous polymer. Understanding the hygroscopic hysteretic behavior of cellulose may lead to a better understanding of the origin of sorption hysteresis in wood. We use atomistic simulations to study the hysteresis behavior. Part of the atomistic model of cellulose used in this work is shown in Figure 1. The figure shows the material structure at RH=1 while the blue dashed line shows the non-swollen state of the system before adsorption.

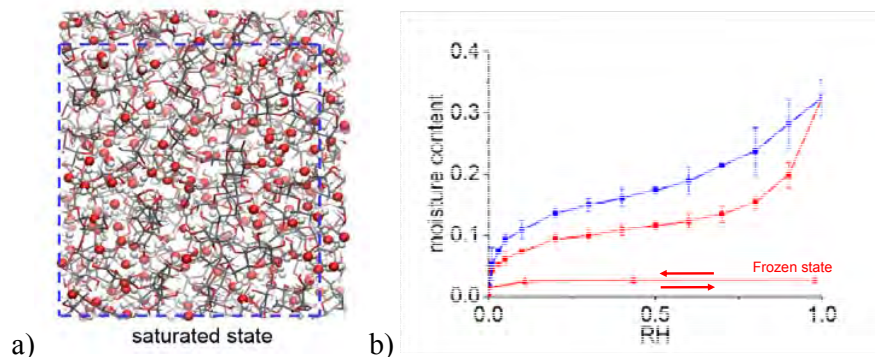


Figure 1 a). Atomistic model of cellulose in saturated state. The sticks are the bonds between the C, O and H atoms in cellulose, red and white spheres the O and H atoms of water. Box size $3.1 \times 3.3 \text{ nm}^2$. Blue dashed line shows the system size of dry material before adsorption. b) MD simulation of sorption hysteresis with swelling and adsorption in frozen state.

Water sorption and deformation are simulated with a hybrid Grand Canonical ensemble (GCMC)/ Molecular Dynamics (MD) method. Monte Carlo simulations in GCMC allow studying the sorption process by inserting or deleting a number of water molecules in order to reach the target RH (chemical potential). However, since the system is at constant volume, this method does not allow to study swelling and its effect on sorption. Therefore, MD simulations are consecutively used to obtain the deformation state. As the deformation changes the RH, we iterate between GCMC and MD until the target RH at equilibrium is reached. By using this hybrid strategy combining GCMC and MD, the atom-scale simulations probe adsorption phenomena while allowing for swelling of the host porous polymer.

Figure 2a shows the ad- and desorption isotherms, i.e. the moisture content (kg/kg) versus RH. Figure 2b shows the swelling isotherms, i.e. the swelling strain (m/m) versus RH. Figure 2a shows that the moisture content increases rapidly with RH in the low RH region and then increases less rapidly as initial pores in cellulose get filled. Upon further increasing RH, an inflection point in the adsorption isotherm is observed as pores open up upon swelling and significant subsequent adsorption occurs. The pore sizes in this nanoporous material, even upon swelling (0.2 – 0.4 nm), are too small to allow for capillary condensation (Coasne et al 2005). The sorption curves also exhibit significant hysteresis. The simulation results agree qualitatively well with experimental data (Mihiranyan et al. 2004). We note a systematic offset

of the experimental data (around 0.5 moisture content) with our simulations. This offset is attributed to the presence of residual water not being removed in the experimentally dried sample (presence of non-desorbable water).

Figure 2b shows the swelling isotherms. The volumetric strain shows significant swelling strains reaching as high as 36% close to $RH = 1$. Large hysteresis in sorption-induced swelling is observed reflecting the hysteretic sorption isotherm. Significant hysteresis in sorption and sorption induced deformation is observed. When we plot the swelling strain versus moisture content (Figure 2c), hysteresis disappears and the data collapse in a single almost linear curve. This is in agreement with experimental observations in wood (Patera et al. 2013). This shows that swelling is a direct consequence of filling of the deforming material with a number water molecules and therefore a linear relation between swelling and moisture content is observed.

The impact of swelling on the sorption isotherms was probed by simulating water adsorption keeping the material non-deformable (frozen material). We found that in this case, much less adsorption occurs (almost 10 times lower) and the hysteresis effect disappears. This indirectly shows that swelling of the material essentially contributes to the total sorption amount, and that hysteretic sorption depends on the swelling

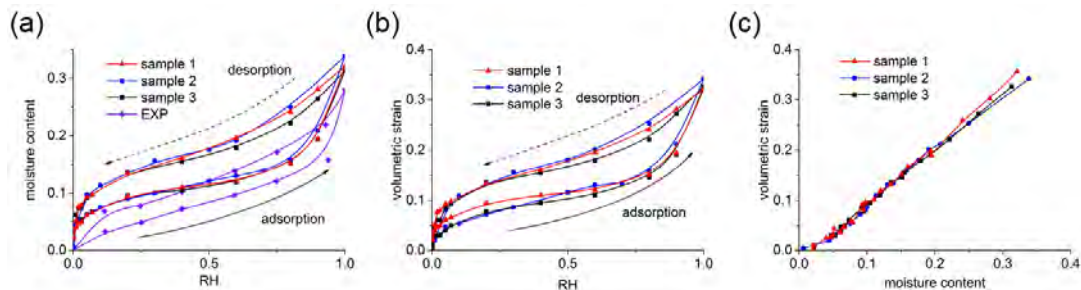


Figure 2. (a) Significant hysteresis in simulated and experimental sorption isotherms. (b) Hysteresis in simulated volumetric swelling strain isotherms. (c) Hysteresis disappears when plotting volumetric swelling strain in function of moisture content.

To better understand the coupling between sorption and swelling and more especially the origin of hysteresis, we further interrogate the systems looking at hydrogen bonding. Amorphous cellulose is a non-cross-linked polymer, where hydrogen bonds are a metric to monitor the interactions inside the polymer system, revealing different configurations of material and water molecules during adsorption and desorption. We study the number and nature of the hydrogen bonds in the material. Three types of hydrogen bonds (HB) are distinguished. In the dry material, polymer chains are interconnected with cellulose-cellulose hydrogen bonds (HB^{CC}). Upon adsorption of water molecules, swelling occurs and CC hydrogen bonds between the polymer chains are broken. Upon breaking the CC hydrogen bonds, new hydroxyl adsorption sites become available. Increasing RH , these new sites become occupied with new water molecules forming cellulose-water hydrogen bonds (HB^{CW}). Figure 4a-b show the normalized decrease of HB^{CC} and increase of HB^{CW} with moisture content. Increasing further the moisture content, water molecules start to form more and more water-water hydrogen bonds (HB^{WW}), since only a limited number of free hydroxyl sites is still available. In desorption, first water molecules in water-water hydrogen bonds will leave the system, while the remaining water molecules are attached to cellulose chains. As cellulose-water HBs are stronger than cellulose-cellulose HBs, hydroxyl sites will preferentially remain occupied by the water molecules at lower relative humidity. Cellulose-cellulose HBs between the polymer chains will only reform at lower RH . This process explains the lower number of cellulose-cellulose HBs during desorption.

In conclusion, at a given moisture content, the polymer system accommodates to receive the

same number of water molecules but distributes them differently as observed by different hydrogen bonding configurations during ab- and desorption. During adsorption process, new sites are created by breaking cellulose-to-cellulose hydrogen bonds between polymer chains due to material swelling. These sites become receptors for new water molecules changing cellulose-to-cellulose into cellulose-to-water hydrogen bonds. However, the recovery of these new adsorption sites back to cellulose-to-cellulose hydrogen bonds during desorption is less likely since the sites more likely remain occupied by water molecules. This coupling process between sorption and deformation leads to the hysteresis as observed in sorption and swelling, both experimental and simulated for cellulose and wood in general. The mechanism documented by observing configurations of hydrogen bonds gives a clear understanding of the coupling between sorption and swelling in soft porous matter that goes well beyond cellulose, wood and other soft polymer materials. While such mechanism was merely hypothesized in the literature, no experimental or theoretical evidence has been reported so far. With our atomistic approach, a clear understanding of hysteresis due to coupling between sorption and swelling in soft polymer materials is shown.

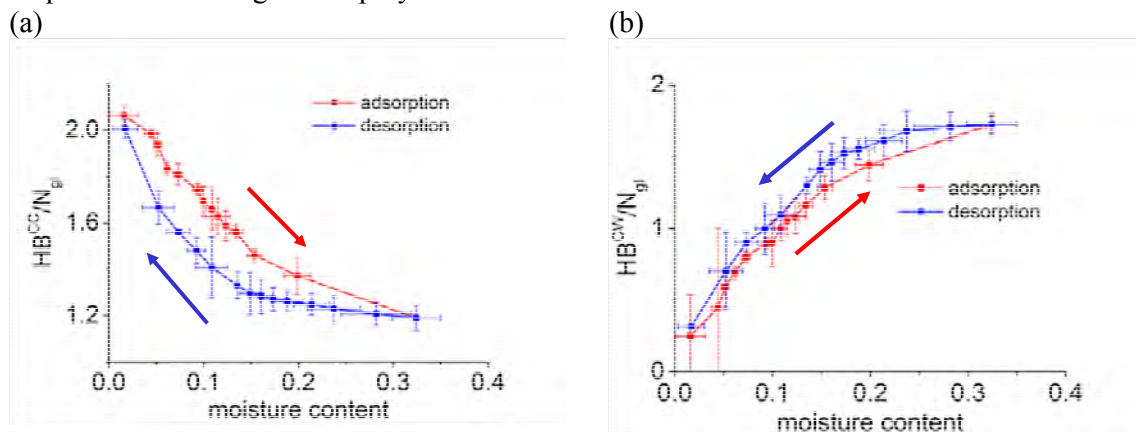


Figure 3. (a) Evolution of number of cellulose-to-cellulose hydrogen bonds with moisture content. (b) number of cellulose-to-water hydrogen bonds with moisture content.

DISCUSSION ON MODELLING HYSTERESIS USING INDEPENDENT/DEPENDENT DOMAIN THEORY

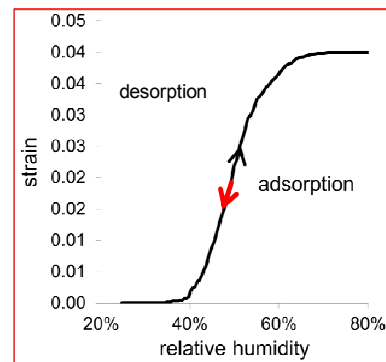
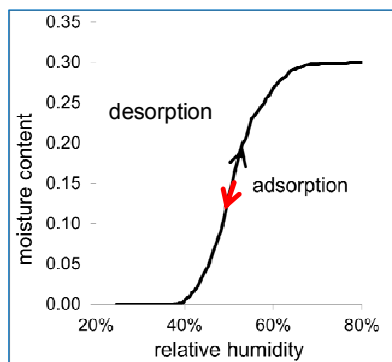
A common approach to describe sorption hysteresis in a phenomenological way is the independent domain theory, where hysteresis originates from local hysteretic elements, that do not interact with each other. In this approach, sorption hysteresis is explained by hysteretic pore scale phenomena like capillary condensation, contact angle or ink-bottle effects caused by smaller size entry pores. Based on these physical explanations, sorption hysteresis is considered to be merely a local pore phenomenon, i.e. sorption at the pore level itself is hysteretic. Thus, in the independent domain theory, pores are assumed not to interact with each other, and changes in moisture content are the outcome of the behavior of an assemblage of independent sorption sites. Different independent domain models have been proposed for different types of materials, where the main difference results from the way the distribution of hysteretic elements is derived from experimental data. These phenomenological models have appeared in different forms and fitted to experimental data. Although these phenomenological models seem to adequately simulate the observed behavior following the experimental data, no direct proof for their physical correctness has been yet given. Our recent atomistic modelling results show that independent theories, which do not include sorption induced swelling in nanoporous soft polymeric materials do not capture the correct physics.

Our atomistic analysis reveals that water molecules first adsorb at free sorption sites leading to a swelling of the material. The swelling is followed by an unravelling of the polymer

chains favoring the creation of new sorption sites. In desorption however, these extra-created sorption sites remain favorably occupied by water molecules and the material remains longer in a swollen state at higher moisture content. The question now remains how to model such a behavior in an elegant engineering way.

Based on the evidence that swelling plays a determining role in sorption hysteresis, a correct hysteresis model should incorporate swelling, which can only be modelled by an elastic dependent domain theory. In such model, the filling of a site depends not only on the relative humidity at the site but also on the strain state of the sorption site. In view of a dependent domain approach taking into account deformation, we assume the material to consist of a set of elastic interacting elements. A distribution of non-hysteretic pores is embedded in the elastic material. In the dry state, most of these pores are not accessible to water molecules since their size is too small to receive a water molecule. However, some smaller accessible pores become filled with water molecules, swell and will exert a swelling strain field on neighboring pores. Pores, which were not accessible before, will now become accessible due to the tensile strain exerted on the pore system. The filling and unfilling of an element is thus not only dependent on RH, but also on the strain exerted on the element. A positive strain originating from an internal strain field will lead to making pores accessible to sorption. Further, the tensile strain on an element is considered to produce extra volume for additional sorption of water molecules, which has also been observed in the atomistic simulations. The behavior of a distribution of such interacting elastic elements is studied by finite elements.

a)



b)

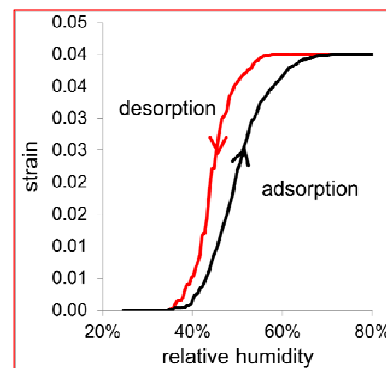
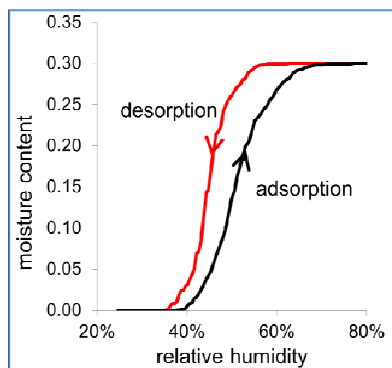


Figure 4. (a) Sorption and swelling isotherm of moisture content and strain versus RH for non-coupled dependent domain approach. No hysteresis is observed. (b) Sorption and swelling isotherm of moisture content and strain versus RH for coupled dependent domain approach, with interaction between filling and swelling process. Hysteresis both in sorption and swelling is observed (Guyer et. al 2011).

Our group in collaboration with R. Guyer from LANL (Guyer et. al 2011) developed such a dependent domain approach for an academic material. General results showing the model

performance are reported here. Figure 4a gives an example of predictions of sorption and swelling isotherms using the elastic dependent domain model of non-hysteretic elements where the coupling between sorption and swelling has been switched off. The curves show a non-hysteretic behavior. When switching on the coupling (figure 4b) meaning the filling of an element depends not only on the RH but also on the strain exerted in the element, we observe a hysteretic behavior both in sorption and in swelling. When plotting the swelling strain versus moisture content (Figure 5), we observe a quasi-linear relation between swelling strain and RH, showing no hysteresis. These results are in close qualitative agreement with our observations in experiments and atomistic simulations for wood components. This means that the elastic dependent domain approach seems to be the correct physical approach to model and predict sorption hysteresis.

In the next future, we will further develop and fine-tune this elastic dependent domain model showing its adequacy for modelling hysteresis of sorption induced swelling of nanoporous polymer materials as wood. Furthermore, we will implement this sorption model in a multiscale approach allowing modelling not only single woods components, but also layers in a wood cell wall like the S2 layer, and even wood. From there on, global macroscopic models can be improved for modelling materials behavior at macro- or structural scale. Final aim is to be able to adequately model sorption induced swelling and hysteresis. The models should be physically sound from one side, but also sufficiently simple to be used in engineering practice.

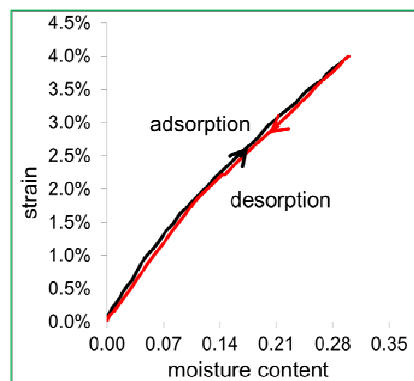


Figure 5. Swelling strain versus moisture content as determined by dependent domain. No hysteresis is observed (Guyer et. al 2011).

ACKNOWLEDGEMENT SNF Project 143601 is acknowledged.

REFERENCES

- Carmeliet J., Descamps F., Houvenaghel G. 1999. Multiscale network model for simulating water liquid and vapour transfer properties of porous materials. *Tr.Por. Media*, 35: 67-88.
- Coasne B, Gubbins KE, Pellenq RJM. 2005. Domain theory for capillary condensation hysteresis, *Phys. Rev. B*, 72: 024304.
- Derluyn H., Derome D., Carmeliet J., Stora E., Barbarulo R. 2012 Hysteretic moisture behavior of concrete: Modeling and analysis. *Cement and Concrete Res.*, 42:1379–1388.
- Derome D., Griffa M., Koebel M., Carmeliet J. 2011. Hysteretic swelling of wood at cellular scale probed by phase-contrast X-ray tomography, *J. Struct. Biol.*, 173:180-190.
- Guyer R.A., Kim H.A., Derome D., Carmeliet J., Ten Cate J. 2011. Hysteresis in modeling of poroelastic systems: Quasistatic equilibrium. *Physical Review E*, 83(6): 061408.
- Kulasinski K., Guyer R., Derome D, Carmeliet J. 2015. Poroelastic model for adsorption-induced deformation of biopolymers obtained from molecular simulations, *Phys. Rev. E*, 92:22605.
- Mihiranyan A., Llagostera A.P., Karmhag R., Strømme M., R. Ek R. 2004. Moisture sorption by cellulose powders of varying crystallinity, *Int. J. Pharm.*, 269:433-442.
- Patera A., Derome D., Griffa M., Carmeliet J. 2013. Hysteresis in swelling and in sorption of wood tissue, *J. Struct. Biol.*, 182, 226-234.
- Patera A., Derluyn H., Derome D., Carmeliet J. 2016. Influence of sorption hysteresis on moisture transport in wood, *Wood Sc. and Techn.*, 50:259-283.

The effects of production technologies on the air permeability properties of cross laminated timber

Villu Kukk^{1,*}, Targo Kalamees¹ and Jaan Kers²

¹Tallinn University of Technology, Tallinn. Department of Civil Engineering and Architecture

²Tallinn University of Technology, Tallinn. Department of Materials and Environmental Technology

*Corresponding email: villu.kukk@ttu.ee

ABSTRACT

In building envelope, the cross laminated timber (CLT) is often used as air barrier layer. The objective of this study was to evaluate the impact of production technologies such as edge bonding, different initial moisture content (MC) of lamination, and number of lamination layers (3 and 5) on the air-permeability properties of cross laminated timber. Air leakage and crack growth in CLT panels were measured after the panels were conditioned in environments with different relative humidity (RH) in progressive steps from humid to dry environments (RH 70%→ RH 50%→ RH 30%→ RH 10%). The test results showed that the most effective technologies for avoiding large crack growth and air leakages through panels were to use 5 layers of laminations with bonded edges. Overall, it can be recommended that for the production of CLT panels it is advisable to use primarily a larger number of layers, at least 5, for smaller growth of cracks on panel surfaces and thereby avoid air leakages during the time of use. The use of bonded edge technology helps to ensure the avoidance of possible air leakage threats, but in the long-term, this beneficial effect might decrease as bond layers may rupture or cracks may form in the middle of laminations.

KEYWORDS

Cross laminated timber, production technology, crack growth, air permeability

INTRODUCTION

Airtightness of building envelope has become an important property of building envelope. The more airtight envelope and more efficient heat recovery with reduced thickness of thermal insulation has a lower construction cost and lower energy consumption, making it financially viable (Saari, et al., 2012). The building envelope is locally sensitive to exfiltration airflow, as moisture convection could cause a remarkable increase in the moisture accumulation rate on the inner surface of the sheathing (Kalamees & Kurnitski, 2010). Kayello et al. (2017) showed that frost accumulation and condensation can happen very easily due to air leakage and pose a significant risk to the integrity of the envelope. In building envelope, the CLT is often used as air barrier layer. Crack formation in CLT influences its water vapour resistance and air permeability (Kukk et al. 2017) as well fire resistance, acoustic properties, and lower the quality (Brander, 2013).

Moisture movement in wood has a major role in crack formation. The important benchmark for the wood properties affected by moisture is the fibre saturation point (FSP). FSP is defined as the point where wood cell lumen does not contain free water but the cell wall is still saturated. Properties of wood, such as volume and mass, change if the MC changes below FSP point. A decrease or increase of MC results, respectively, in shrinkage or swelling of wood.

The unequal decrease of MC in different wood directions (tangential, radial and longitudinal) results in unequal shrinking of wood which causes internal stresses inside the wood. This, in turn, results in the formation of checks and cracks in the wood surface. Changes of MC in the laminations of a CLT panel result in shrinking and swelling of the wooden board's volume, which may cause cracks in board surfaces and also gaps between the edges of the boards.

This study is focused on analysing the effects of productions technologies on the air permeability properties of CLT panel. The objective is to study the effects of the number of layers in the panel, bonded edges and initial MC in lumber to crack growth in CLT panels' lamination surfaces and air permeability.

METHODS

Test specimens

Specimens were produced using three different technologies whose parameters are given in Table 1. Three specimens were made for each technology combination. According to this, 24 specimens of rectangle-shaped cross-laminated timber panels with dimensions of 1300x460mm, a thickness of 30mm and constructed from spruce wood (*Picea abies*) were designed and produced for the air permeability and crack evaluation test.

Table 1. Parameters of specimens produced with different technologies

Edge bonding	Number of layers	
	3 layer panel, thickness of one layer 10 mm	5 layer panel, thickness of one layer 6 mm
Edge bonded panels	Initial MC of laminations ≈ 13.1% (conditioned with RH of 70%)	Initial MC of laminations ≈ 13.1% (conditioned with RH of 70%)
	Initial MC of laminations ≈ 6.2% (conditioned with RH of 30%)	Initial MC of laminations ≈ 6.2% (conditioned with RH of 30%)
Panels without edge bonding	Initial MC of laminations ≈ 13.1% (conditioned with RH of 70%)	Initial MC of laminations ≈ 13.1% (conditioned with RH of 70%)
	Initial MC of laminations ≈ 6.2% (conditioned with RH of 30%)	Initial MC of laminations ≈ 6.2% (conditioned with RH of 30%)

Specimens were marked as follows: P30/70 W/BE 3/5L, where P30/70 defines panels initially conditioned in an environment with RH of 30% or 70%; W/BE- without or with bonded edges panels; 3/5L- panels with 3 or 5 layers.

Measurements

Three following parameters were measured during laboratory test: MC of panels, crack area on panels top surfaces and air permeability. Cracks area results were gained by measuring crack width and length using a crack width gauge and methodology developed by Brischke and Humar (Brischke *et al.* 2014). Air permeability was measured using a hermetic test rig and equipment for regulating and measuring air pressure differences and air flow (EN 12114, 2000), accuracy <5%, see Figure 1(b), (c). Airflow was measured by applying three overpressure impulses at a pressure difference of 550 Pa. To avoid any air leakages from the connection of the test rig and panels, all panels edges were sealed with vapour and air tight tape. Therefore the measurement area of each specimen for air permeability test was considered as 0.56 m² (1.25x0.45). The laboratory test process consisted of panel conditioning steps in environments with different RH supplied by a climate chamber, see Figure 1(a).

Conditioning steps for panels initially conditioned in an environment with RH 70% were as follows:

- I step: RH 50% → II step: RH 30% → III step: RH 10%;

And for panels initially conditioned in an environment with RH 30%:

- I step: RH 10%

Before and after each conditioning step all parameters were measured and recorded and corrected with an estimated error.

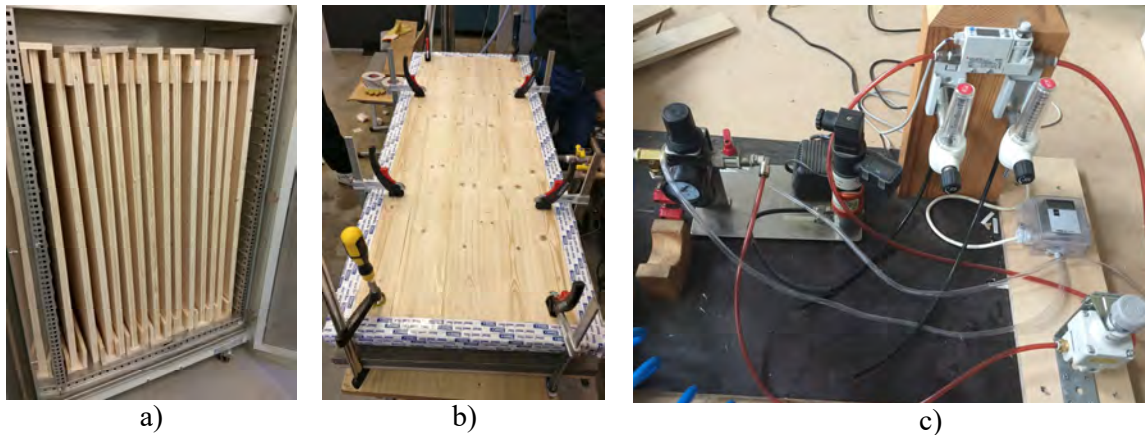


Figure 1.(a) Climate chamber Climacell 707 for panel conditioning, (b) hermetic test rig for air permeability tests, (c) equipment for measuring air pressure differences and air flow.

RESULTS

EMC of specimens

All specimens were conditioned equally and the equilibrium moisture content (EMC) after each conditioning step was almost the same in all panels, see Figure 2. Specimens conditioned initially in an environment with RH of 70% had an overall moisture loss after each conditioning step of RH of 10% of about 8%. Specimens P70WBE5L had a moisture loss of 12.2% due to a higher initial EMC. Specimens conditioned initially in a RH of 30% had an overall moisture loss after each conditioning step of RH of 10% of about 2.5%.

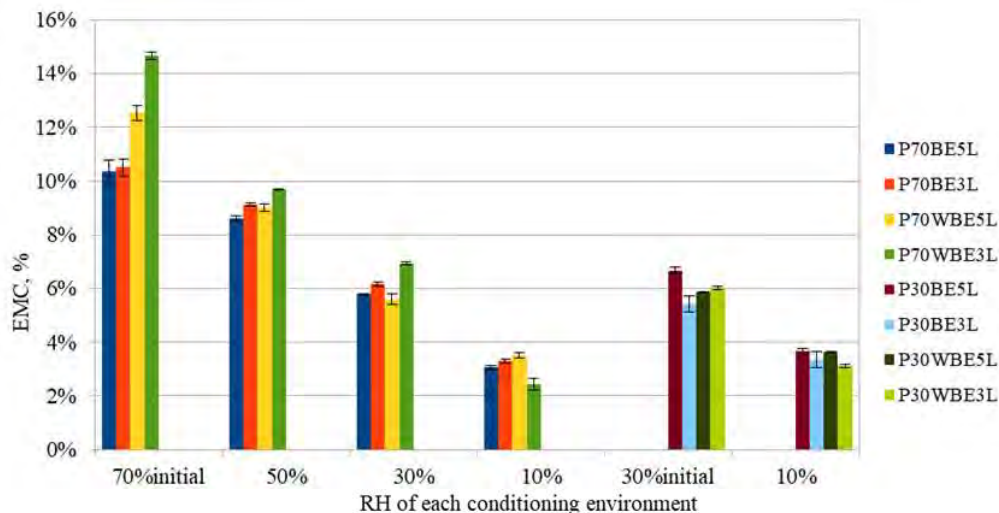


Figure 2. EMC of specimens after each conditioning step

Growth of crack area

A big difference in crack area growth between specimens P70 and P30 was expected due to the different number of conditioning steps, see Table 2. While a total crack growth in specimens P30 was from 16% to 55%, in specimens P70 it was from 516% to 22160%. The total crack growth of 22160% appeared in specimens P70WBE3L, which was about 10 times higher than rest of the specimens. Specimens P70WBE3L also had the biggest average crack area of 15456 mm² after conditioning steps of RH of 10%.

The smallest average crack area of 193 mm² after conditioning steps of RH of 10% was in specimen P30BE5L, and specimen P30BE3L had the smallest total crack growth of 16%. Overall, the greatest effect on smaller crack growth was in specimens with bonded edges and initially conditioned in an environment with RH of 30%.

Table 2. Average crack area and growth of specimens after each conditioning step

Specimen	70% _{initial}	50%	30%	10%	Total growth (RH 70-10 %), %			
	Av. existing crack area, mm ²	Av. crack area, mm ²	Growth, %	Av. crack area, mm ²		Growth, %		
P70BE5L	436	655	50%	1162	77%	2686	131%	516%
P70BE3L	194	246	27%	871	254%	2969	241%	1434%
P70WBE5L	202	1982	881%	3151	59%	5382	71%	2564%
P70WBE3L	69	1430	1959%	9064	534%	15456	71%	22160%
	30% _{initial}	10%	Total growth (RH 30-10 %), %					
P30BE5L	100	193	48%					
P30BE3L	1300	1551	16%					
P30WBE5L	1306	2918	55%					
P30WBE3L	1457	2677	46%					

Air permeability of specimens

The largest air leakages were in all specimens with three layers, when taking into account initial EMC in production and bonded and without bonded edge technology, see Figure 3. The greatest average air leakage of 0.53 m³/(h×m²) after conditioning steps of RH of 10% were in specimens P70WBE3L. The second greatest leakage of 0.52 m³/(h×m²) showed in specimens P30WBE3L after conditioning steps of RH of 10%.

Specimens with 5 layers and bonded edges and initially conditioned in an environment with RH of 30% were the most airtight which matched with pre-testing assumptions. Specimen P30BE5L showed an air leakage of 0.11 m³/(h×m²) and P70BE5L showed 0.25 m³/(h×m²) after conditioning steps of RH of 10%. Overall, 5 layer specimens had the most considerable effect on air permeability properties as a result of having less air leakages.

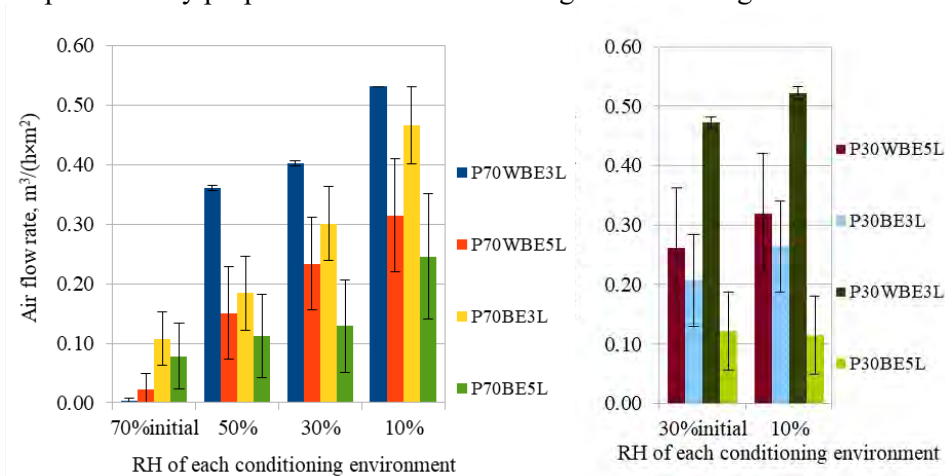


Figure 3. Air flow rate after each conditioning step of specimens a) initially conditioned in an environment with RH of 70%, b) with RH of 30%

The large estimated error of air flow rate results was probably a result of the small number of specimens for each type, quality variation of lumber and manufacturing defects on panels (such as existing gaps between laminations and some degree of uneven distribution of adhesive). Air flow rate of specimens P70WBE3L were measured maximum what used equipment could read and therefore no estimated error is shown in Figure 3.

DISCUSSIONS

The most effective technologies for avoiding large crack growth were using laminations with bonded edges and lumber initially conditioned in an environment with RH of 30%. Specimens initially conditioned in an environment with RH of 70% had a considerable resistance to crack growth when panels had 5 layers.

Using initially drier lumber together with edge bonded laminations seems to keep wood shrinkage lower and therefore keeps crack growth on the panels surface at a low percentage during the first stages of drying (conditioning steps from RH 30% to 10%). In the longer drying process (conditioning steps from RH 70% to 10%), 5 layer panels considerable resistance to crack growth was probably due to a larger number of bond layers and thinner lamination layer thickness. Bond layers and thin laminations seemed to keep the wood steadier and controlled the formation of internal stresses during the drying process better. Specimens with bonded edges that underwent the longer drying process showed, in the first conditioning steps, a lower crack growth compared to specimens without bonded edges, but during the last step, the growth percentage was higher. This shows that bonded edges can hold the formation of internal stresses due to shrinkage for a short period and later, when bonding connections might have been ruptured or cracks might have developed in the middle of laminations, crack growth can increase over time.

5 layer specimens combined with edge bonding had the most considerable effect on avoiding air leakages through the panel. The greater number of layers helps to avoid any overlapping of gaps between laminations which are possible sources of air leakages (Kukk, et al., 2017). The same argument was confirmed in this study as 3 layer specimens had considerably bigger air leakages, especially the specimens with laminations initially conditioned in an environment with RH of 70%. The reason for better airtightness in panels with a larger number of layers can be the same as it was for low crack growth which was a larger number of bond layers and thinner laminations. The use of bonded edge technology has been also previously recommended for avoiding overlapping of gaps and cracks and it was again confirmed with the results of this study, except specimen P70BE3L, which showed a quite high air flow rate (Brander, 2013) (Skogstad, Gullbrekken, & Nore, 2011).

Current research only covered the first cycle of the drying process and specimens with laminations initially conditioned in an environment with RH of 70% and 30% had different cycle durations. In other words, the results obtained in this experiment have given information about the behavior of the panels at the beginning of their service life. For a better understanding of the air-permeability properties of the panel in long-term of use the repeated test with several cycles is necessary to carry out.

In overall, it can be recommended that for the production of CLT panels one should primarily use a larger number of layers, at least 5, for the smaller growth of cracks on panel surfaces, thereby avoiding air leakages during the time of use. The use of bonded edge technology helps to ensure the avoidance of possible air leakage threats, but in the long-term, the effect might decrease as bond layers may rupture or cracks may form in the middle of laminations. Specimens with initially drier laminations did not show a significant resistance to air leakages but had considerable effect for avoiding large crack growth.

CONCLUSIONS

In this study, three production technologies of CLT panels were analysed to determine the influence of number of layers in the panel, bonded edges and initial MC in lumber. The main findings of this study were that the most effective technologies for avoiding large crack growth were using edge bonded and initially drier laminations and 5 layer specimens combined with edge bonding had the most considerable effect on avoiding air leakages through the panel. Based on the results it is recommended to primarily use a larger number of layers, at least 5, which helps to minimise the growth of cracks on panel surfaces, therefore, avoiding air leakages during the time of use. The use of bonded edge technology helps to ensure the avoidance of possible air leakage threats, but in the long-term, the effect might decrease as bond layers may rupture or cracks may form in the middle of laminations. Using initially drier lumber helps to avoid crack growth on panel surfaces, but does not have a significant effect on avoiding air leakages.

ACKNOWLEDGEMENT

This research was supported by the Estonian Centre of Excellence in Zero Energy and Resource Efficient Smart Buildings and Districts, ZEBE, grant TK146 funded by the European Regional Development Fund, and by the Estonian Research Council with Institutional research funding grant IUT1-15.

Participation in the conference was supported by the Estonian Ministry of Education and Research. EU Structural Fund (Cohesion Policy Funds) period 2014-2020, TUT Development Program for the period 2016-2022, Doctoral School of Civil and Environmental Engineering project code 2014-2020.4.01.16-0032 has made publishing of this article possible.

The author wishes to thank Estonian glulam producer Peetri Puit OÜ for helping to produce CLT specimens.

REFERENCES

- Brander, R. (2013). *Production and Technology of Cross Laminated Timber (CLT): A state-of-the-art report*. Graz, Austria.
- Brischke, C., Humar, M., Meyer, L., Bardage, S., & Bulcke, J. V. (2014). *COST Action FP 1303-Cooperative Performance Test*. COST Action FP 1303.
- EN 12114 (2000) Thermal performance of buildings - Air permeability of building components and building elements - Laboratory test method. Brussels: European Committee for Standardization.
- Kalamees, T., & Kurnitski, J. (2010). Moisture convection performance of external walls and roofs. *Journal of Building Physics*, 225-247.
- Kayello, A., Ge, H., Athienitis, A., Rao, J. (2017). Experimental study of thermal and airtightness performance of structural insulated panel joints in cold climates. *Building and Environment*, 115, 345-357.
- Kukk, V., Horta, R., Püssa, M., Luciani, G., Kallakas, H., Kalamees, T., & Kers, J. (2017). Impact of cracks to the hygrothermal properties of CLT water vapour resistance and air permeability. *Energy Procedia*, 132, 741-746.
- Saari, A., Kalamees, T., Jokisalu, J., Michelsson, R., Alanne, K., & Kurnitski, J. (2012). Financial viability of energy-efficiency measures in a new detached house design in Finland. *Applied Energy*, 76-83.
- Skogstad, H. B., Gullbrekken, L., & Nore, K. (2011). Air leakages through cross laminated timber (CLT) constructions. *9th Nordic Symposium on Building Physics*, (p. 8). Tampere.

Understanding swelling of wood through multiscale modeling

Dominique Derome^{1*}, Chi Zhang^{1,2}, Mingyang Chen^{1,2}, Jan Carmeliet²

¹Laboratory for Multiscale Studies in Building Physics, Swiss Federal Laboratories for Materials Science and Technology, Empa, Switzerland

²Chair of Building Physics, Dep. Mechanical Engin. and Processes, ETH Zürich, Switzerland

*Corresponding email: dominique.derome@empa.ch

ABSTRACT

Wood is a well-used building material where the capacity of wood to absorb water leads to swelling and reduced mechanical properties, and also to questions of durability. The origin of the hygroscopic behavior of wood lies at the nanoscale material that composes its cell walls. Using atomistic modeling, we study the hygromechanical behavior of the different polymeric components of wood, separately and in aggregate configurations. We report the coupled effects of water sorption on the hygric and mechanical properties of the S2 cell wall layer and we upscale the findings using a poromechanical framework.

KEYWORDS

Wood, hygroscopic behavior, swelling, multiscale modeling, atomistic modeling.

INTRODUCTION

Natural materials, from plant origin, are ubiquitous in our daily environment, where they are exposed to environmental loading like temperature and relative humidity variations. In particular, cellulose-based materials such as wood have been used traditionally and ubiquitously, and are particularly attractive nowadays as they offer sustainable solutions and as they can be a source of inspiration for biomimetic design of new materials. Wood, an orthotropic cellular biomaterial, has the capacity of adsorbing water molecules from the surrounding environment into its hierarchical material structure. This material displays remarkable properties combining low weight, high strength and high toughness, originating from the hierarchical organization of crystalline and amorphous polymers.

Wood is a well-used building material, for structure, façade, windows, indoor finishing and furnishing, etc., where the capacity of wood to absorb water is not only an issue of dimensional stability and modified material properties, but also of durability. In effect, as water molecules are adsorbed into the hydrophilic matrix in the cell walls, the induced fluid-solid interaction forces result in a swelling of the cell walls. The moisture-induced phenomena at cell wall scale are reflected in the hygromechanical behavior of wood at macroscale. Adsorption of moisture in wood, in the hygroscopic range i.e. until around 30% moisture content mass per mass, results in swelling up to 10% volumetrically and reduces considerable its mechanical properties.

We propose a multiscale approach to investigate and understand the hygromechanical behavior of wood. At cell wall material scale, using atomistic modeling, we study the different polymeric components of wood, separately and in aggregate configurations, in terms of the coupled effects of water sorption on hygric and mechanical properties. Then, we upscale the findings using a poromechanical approach. Such properties can then be employed in finite-element modeling to investigate the effects of cellular geometry and ring growth

pattern of wood. The work aims at elucidating the origin of the hygro-mechanical behavior of wood and such complex polymeric materials. In effect, wood is retained as a model hygroscopic material for further understanding of such hygromechanical behavior.

METHODS

Molecular Dynamics (MD) simulations

Materials

Wood cell wall is made of a network of stiff cellulose microfibrils which are embedded within complex matrixing polymers) and the S2 chemical content has been in large part identified. Figure 1 displays the cell wall layers and their components. We aim to reproduce all the main polymers present in the wood S2 layer, namely crystalline cellulose, galactoglucomannan (named GGM below), glucuronoarabinoxylan (referred as xylan below) and the different configurations of guaiacyl lignin.

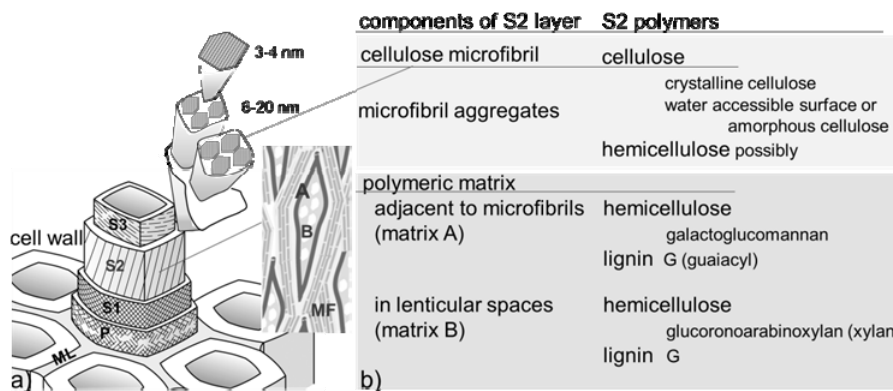


Figure 1. a) Schematic representation of the structure of wood cell wall, with P primary layer, S secondary layer, ML middle lamella (based on Derome et al. 2012), MF microfibril, A matrix close to fibrils, B lenticular matrix; b) components of S2 cell wall layer for a softwood like spruce.

Simulation

Molecular Dynamics simulations are carried out using Gromacs software (Hess et al 2008) with leap-frog algorithm for integration of Newton's equations of motion and the Gromos 53a6 united-atom force field (Oostenbrink et al 2004, Lins and Hünenberger 2005). The initial configuration of the polymer is constructed based on the position of atoms in the monomers and the proportion of different monomers in the chains as documented by previous studies. Using the main chemical components of wood, here softwood, the polymeric systems are reproduced, their hygromechanical behavior determined and analyzed. Nanoscale structures or composite systems are built and analyzed. MD results are validated with available experimental data. We note the capacity with this method to control exactly, as input, the polymeric constituents, their polymeric configuration and the configuration of layered or composite systems. Molecular dynamic provides a wealth of data, on which statistical physics is applied and then compared with theoretical and continuum approaches, like thermodynamics, providing a unique window on the fundamental hygromechanical behavior.

Tests

In order to study the different responses of the polymers to water, water molecules are introduced one by one to the system and the system let to equilibrate, as shown in Figure 2. We obtain water adsorption curves using One-Step Perturbation method for the determination of chemical potential. Calculated sorption curves, i.e. moisture content versus chemical

Swelling

The introduction of water molecules results in a displacement of the polymeric systems leading to material swelling. For the single components and the matrix system, made of amorphous components, swelling is found to be isotropic. Figure 4 shows that volumetric swelling strains vary linearly with moisture content, after an initial nonlinear behavior, the slope of this relationship yielding the swelling coefficient. Swelling coefficients are ranging from 1.07 for S2 to 2.0 for GGM. The different swelling coefficients stem from the combined effects of initial density and porosity, number of hydroxyl sites and bulk modulus, resulting from the different monomers content and arrangement of each system. As noted, the slope at low moisture content is always smaller and nonlinear.

The volumetric swelling of S2 layer is found to be smaller than those of hemicellulose and lignin alone. The crystalline cellulose acts as a stiff skeleton preventing the system from deformation. This effect is particularly pronounced in the longitudinal direction where, due to cellulose covalent bonds, the swelling coefficient is two orders of magnitude smaller ($\epsilon_z = 2 \times 10^{-3}$ at maximum moisture content) than in the other directions. This indicates that, for the microfibril systems, anisotropy directly results from the presence of crystalline cellulose that restrains most of the deformation in the direction along the crystal.

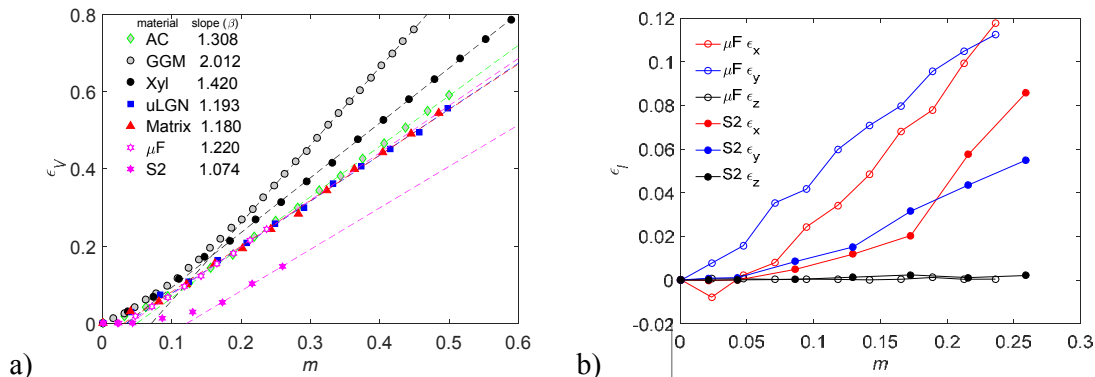


Figure 4. a) Volumetric swelling strain (ϵ_v) of four polymers and one amorphous composite system and of μF and S2, over the full range of moisture content (m). b) Orthotropic swelling strains (ϵ_i) of μF and S2, in function of moisture content (m) (from Derome et al. 2018).

Mechanical properties

As moisture content increases, all investigated polymeric systems show a decrease in elastic moduli. In single systems, the decrease of the bulk moduli, determined by imposing tensile or compressive stress, is seen to be in the range of factor 3 or 4. Remarkably the decrease in shear moduli is much more substantial, over one magnitude (Figure 5a, b). These lower shear moduli at higher moisture content are in part due to the presence of water layers offering almost no resistance in shear.

For anisotropic composite systems, Young's moduli are determined in the three principal directions. Results in the two directions x and y , perpendicular to the crystal orientation, are very similar. The weaker behavior with increasing moisture content is similar in all directions, but the magnitudes are very different for the behavior parallel to the crystal orientation (Figure 5c, d). The difference between microfibril and S2 is in large part due to the lignin which makes about one quarter of the S2 layer and which was here implemented with a low level of cross-polymerization, and as such is observed to weaken significantly.

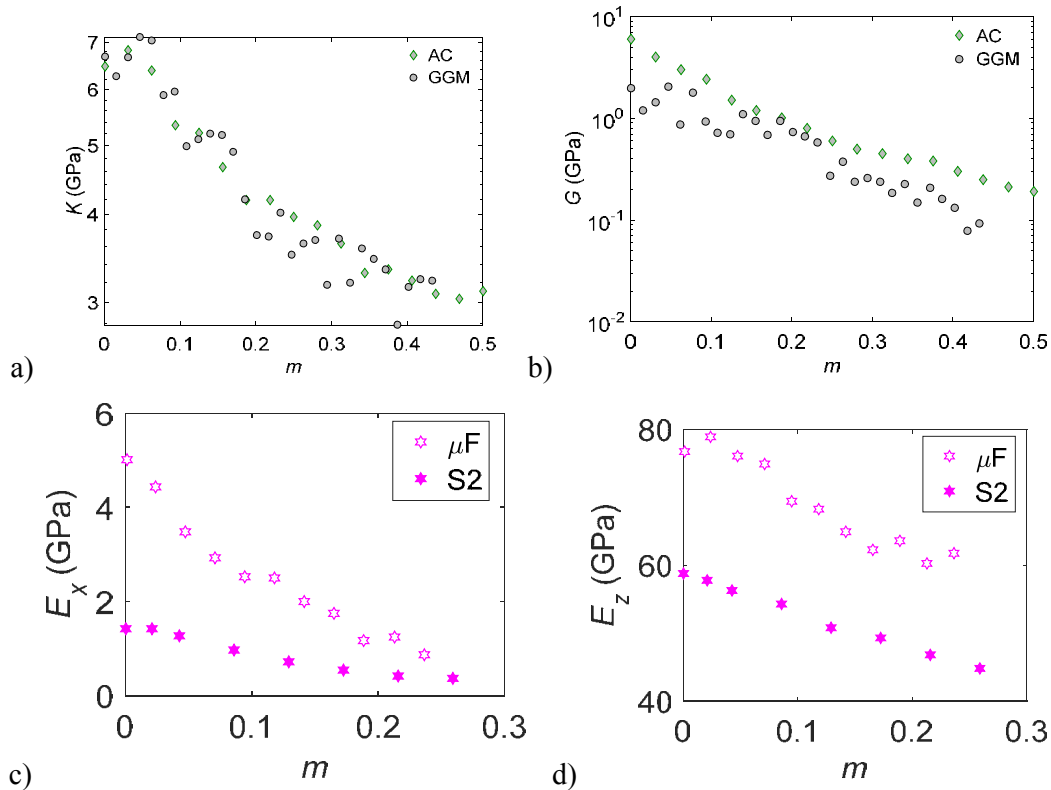


Figure 5. Mechanical properties, a) bulk (K) and b) shear modulus (G) of AC and GGGM, and Young's modulus of μF and S2 (E) c) perpendicular and d) parallel to crystalline cellulose, in function of moisture content (m) (from Derome et al. 2018).

CONCLUSIONS

Using Molecular Dynamics (MD) simulations, we construct and investigate atomistic models of wood polymers and of cellulose microfibril aggregates that consists of crystalline cellulose, amorphous hemicellulose and lignin. The atomistic results are upscaled and used in continuum models, using a poromechanical framework thus with full coupling of fluid transport and mechanical behavior. Upscaling to cellular scale is delineated, where the cellular scale is informed through accurate geometrical description using X-ray CT at different relative humidity.

The ensemble of results documents the full co-occurrence of sorption and swelling. This modeling methodology provides the capability to determine material properties and behavior which cannot be directly determined from experiments and to explore new pathways for material development and technology innovation, especially for capacity in terms of moisture-induced deformation.

ACKNOWLEDGEMENT

We acknowledge the support from Swiss National Science Foundation projects no. 200021-162957 and CRSI22-125184.

REFERENCES

Carmeliet J, Derome D, Dressler M, Guyer R. (2013). Nonlinear poro-elastic model for unsaturated porous solids, *Journal of Applied Mechanics*, 80(2), 020909.

- Derome D, Rafsanjani A, Patera A, Guyer R, Carmeliet J. (2012). Hygromorphic behaviour of cellular material: hysteretic swelling and shrinkage of wood probed by phase contrast X-ray tomography, *Philosophical Magazine*, 92: 3680-3698.
- Derome D, Rafsanjani A, Hering S, Dressler M, Patera A, Lanvermann C, Sedighi-Gilani M, Wittel FK, Niemz P, Carmeliet J. (2013). The role of water in the behavior of wood. *J. Build. Phys.* 36: 398–421.
- Derome D, Kulasinski K, Zhang C, Chen M, Carmeliet J. (2018). “Using modeling to understand the hygromechanical and hysteretic behavior of the S2 cell wall layer of wood”. In *Plant Biomechanics*, in press, edited by A. Geitmann and J. Gril. Springer.
- Hess B, Kutzner C, Van Der Spoel D, Lindahl E, 2008. GROMACS 4: algorithms for highly efficient, load-balanced, and scalable molecular simulation. *J. Chem. Theory Comput.* 4, 435–447.
- Kulasinski K, Guyer R, Derome D, Carmeliet J. (2015a). Water adsorption in wood microfibril-hemicellulose system: role of the crystalline-amorphous interface, *Journal Biomacromolecules*, 16, 2972-2978.
- Kulasinski K, Ketten S, Guyer R, Derome D, Carmeliet J. (2015b). Impact of moisture adsorption on structure and physical properties of amorphous biopolymers. *Macromolecules*, 48, 2793-2800.
- Kulasinski K, Guyer R, Derome D, Carmeliet J. (2015c). Poroelastic model for adsorption-induced deformation of biopolymers obtained from molecular simulations, *Phys. Rev. E*, 92, 022605.
- Kulasinski K, Guyer R, Derome D, Carmeliet J. (2015d) Water diffusion in amorphous hydrophilic systems: a stop and go process, *Langmuir*, 31:10843–10849.
- Kulasinski K, Derome D, Carmeliet J. (2017). Impact of hydration on the micromechanical properties of the polymer composite structure of wood investigated with atomistic simulations, *J. Mechanics and Physics of Solids*, 103: 221-235.
- The initial configuration of the polymer is constructed based on the position of atoms in the monomers and the proportion of different monomers in the chains as documented by previous studies
- Lins RD, Hünenberger PH, 2005. A new GROMOS force field for hexopyranose-based carbohydrates. *J. Comput. Chem*, 26:1400–1412.
- Oostenbrink C, Villa A, Mark AE, Van Gunsteren WF. 2004. A biomolecular force field based on the free enthalpy of hydration and solvation: The GROMOS force-field parameter sets 53A5 and 53A6. *J. Comput. Chem.* 25, 1656–1676
- Patera A, Derome D, Griffa M, Carmeliet J (2013). Hysteresis in swelling and in sorption of wood tissue. *Journal of Structural Biology*, 182:226-234.
- Patera A, Van den Bulcke J, Boone MN, Derome D, Carmeliet J. (2018). Swelling interactions of earlywood and latewood across a growth ring: global and local deformations, *Wood Sci technol.* 52:91-114.
- Rafsanjani A, Stiefel M, Jefimovs K, Mokso R, Derome D, Carmeliet J. (2014) Hygroscopic swelling and shrinkage of latewood cell wall micropillars reveal untrastructural anisotropy, *J. Royal Society Interface*, 11:20140126
- Rafsanjani A, Derome D, Carmeliet J. (2015). Poromechanical modeling of moisture induced swelling anisotropy in cellular tissues of softwoods. *RSC Advances* 5 (5): 3560-3566.

A Transparent Insulation Solar Façade Coupled with a Selective Absorber: An Experimentally Validated Building Energy Simulation Model

Miroslav Čekon ^{1,*} and Jakub Čurpek²

¹Brno University of Technology, Faculty of Civil Engineering, Centre AdMaS

²Slovak University of Technology, Faculty of Civil Engineering, Dept. of Building Constr.

*Corresponding email: cekon.m@fce.vutbr.cz

ABSTRACT

The development of various advanced materials and their subsequent integration into innovative building envelope concepts has the potential to achieve energy savings. Additionally, their usability in practical applications can be enhanced via the use of building energy simulation (BES) methods. Experimental procedures in conjunction with numerical computations could enable the prediction of the future performance of solar thermal façade concepts. The presented study is focused on the thermal response of a transparent insulation material (TIM) incorporated in a façade structure. An experimental prototype of a solar façade element with both a selective and a nonselective absorber was developed for use as part of an opaque building envelope. Experimental measurements were conducted using dynamic outdoor methods with the aim of verifying a BES model. Combined with the measured thermal and optical properties of key materials implemented, an integrated model was developed to simulate the effect on the thermal performance of the TIM-based façade prototype in the EnergyPlus computational engine. This was primarily focused on the capability of the thermo-optical properties of the proposed prototype to respond in an adequate way under transient boundary conditions. In the first part of this study, a specific characterization for the appropriate modelling and simulation of the given solar based prototype is presented. In the second part, the capability of one widely used BES tool is analysed in terms of its ability to model the energy and thermal performance of the presented façade model. The good consistency between the simulation results and the experimental data indicates that the simulation model was reliable when predicting the thermal performance of TIM based façade prototypes, though with some specific limitations. The methodology developed in this study is expected to provide a reference for simulating the thermal and energy performance of TIM-based building elements with two different solar absorbers.

KEYWORDS

Solar façade, Transparent insulation, Selective absorber, Building simulation, Outdoor tests

INTRODUCTION

The integration of transparent insulation material (TIM) as an interstitial structure between glazing panes reduces heat transfer and allows the penetration of solar radiation. It basically provides a combination of different solar and heat transfer processes. In addition, when these systems are also integrated into an opaque building envelope, e.g. as a specific type of transparent insulation façade (TIF) with solar absorber functionality, it can allow a completely different approach to a rather complicated issue. Current building energy simulation programs are not accurate enough to model these complex transparent insulation systems, often because of the simplified thermal and optical models used to solve heat transfer as well as light transmittance. Basically, one dimensional methods are used for both thermal transfer and solar transmittance through these systems (Sun et al. 2018). In practice, with the integration of a

more complex structure within the air cavity of a double glazing unit, there will be a significant effect on the free convection, longwave radiative heat transfer and solar energy transmitted through the system that has not been typically considered. This was recently analyzed by Sun et al. (2017), who comprehensively studied all these aspects in a glazing system with a TIM for building energy saving and daylight comfort. They aimed to develop a comprehensive method of analysing these specific glazing systems (Sun et al. 2017). Specifically, in most of the previously conducted studies, longwave radiation heat transfer, which accounts for two thirds of the total heat transfer across the air cavity (Gan 2001), is neglected within TIM-based structure during numerical modelling. In addition, when integrated in an opaque building envelope with a multilayer construction that employs several low-e barriers, this can result in a completely different situation and give rise to a more complex task that needs to be investigated. Although improved simulation methods have been implemented by Avedissian and Naylor (2008), who used a surface-to-surface model in order to include radiation, they only employed the model to calculate the U -value of the whole system instead of evaluating the effects of the internal structure on longwave radiative heat transfer. In order to create a proper computational model of a façade construction that contains TIM, it is necessary to determine the thermo-optical physical properties of the material. Through this approach, the required values were obtained from laboratory testing based on spectrophotometer measurements and outdoor in-situ measurements for solar transmittance quantification (Čekon and Slávik 2017). Additionally, the thermal and optical properties were obtained via experimental measurements. All of these are input into the building energy simulation (BES) program DesignBuilder that works under the EnergyPlus computational engine. The main goal of the simulation is to analyse the influence of two TIF prototypes with different solar absorbers on heat transfer through their components using outdoor climatic conditions and subsequently compare the results with real measured data. It is necessary to use this process to properly define the simulation model according to the results of experimental measurements.

EXPPERIMENTAL TRANSPARENT INSULATION FAÇADE MODELS

Two transparent insulation façade (TIF) samples were designed for the analysis of optical properties behind a transparent insulation system coupled with an additional air cavity layer. Two 1.19 m × 1.19 m test prototypes (Figure 1) were built using a system based on the Kapilux (2017) TIM fitted with honeycomb transparent (also may be considered as light translucent) PMMA-based insulation. Each was equipped with a different type of integrated solar absorber (a selective low-e SA and a nonselective nSA solar absorber). Thus, the absorber used was the main difference between both prototypes. Both had almost the same solar absorbance level (around 0.94 and 0.96, respectively), whilst their emissivity was diametrically opposite: 0.06 and 0.94, respectively. As a result the difference of the thermal performance between the TIFs is up to 18% due to different solar absorbers. Both prototypes were subsequently tested outdoors throughout the heating season. The TIM system comprises double low-e glazing incorporating honeycomb PMMA transparent insulation with a krypton-filled cavity. The declared thermal and optical properties are as follows: thermal transmittance U_g is 0.7 W/(m²·K), total solar energy transmittance or solar heat gain coefficient is 61%, and light transmission is 70%. As demonstrated in Figure 1, this prototype may allow the implementation of a ventilation function, though in this study related to the heating period this has not been applied. The second illustration presents a functional scheme of two identical boxes surrounded by a compensation room, in which both samples (reference (nSA) and experimental (SA)) were installed facing south-east at the Central Lab at the Faculty of Civil Engineering at the Slovak University of Technology (48°10'36" north and 17° 10'32" east). The twin-box measurement apparatus is used to identify and compare the non-steady state

heat transfer through the tested building elements (for more details see Čekon 2013). The monitoring of outdoor ambient temperature T_{ae} , indoor box air temperature T_{ai} and the total solar vertical radiation intensity I_{gv} represents an important part of the tests in relation to this stage of the presented analysis. The compensating room is a zone where both metering boxes are installed; it is controlled in order to eliminate heat flows through the internal box envelopes at a constant interior temperature T_{cr} .

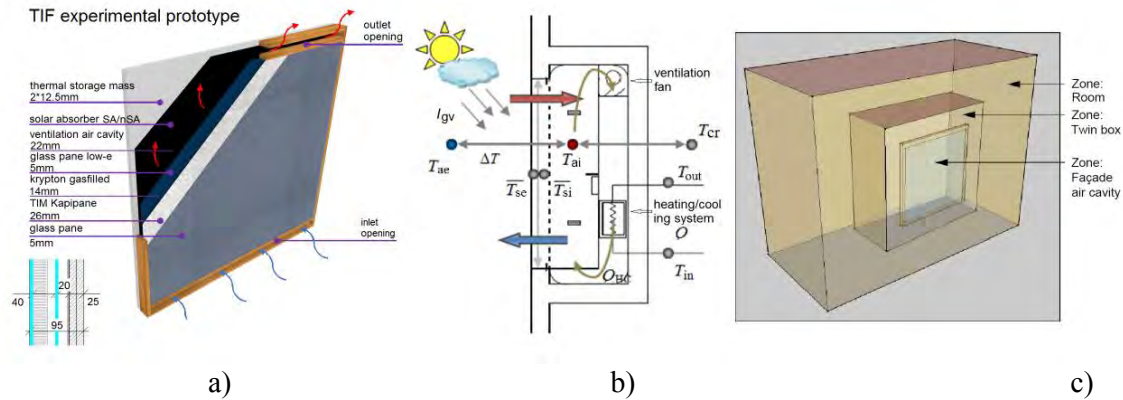


Figure 1. Test transparent insulation façade (TIF). a) TIF experimental model, b) Test experimental twin-box apparatus scheme, c) BES simulation model

BUILDING ENERGY SIMULATION MODEL

The simulation model was modelled based on experimental measurements in the building energy simulation (BES) tool DesignBuilder that works under the EnergyPlus dynamic simulation engine. The testing period covered the winter heating season. Real weather data was measured by every two minutes and then implemented in the simulation using the open-source program Elements for creating and editing custom weather files for building energy modelling. An overall experimental setup is assumed for the measured façade elements. It is divided into three zones covering the whole geometry of the simulation model. Each zone is specified and preadjusted with different interior thermal energy management regimes in correlation with real measured values. The façade's TIM component was modelled as a window because it allows solar radiation to penetrate the structure. Accordingly, it was necessary to create another two zones for the appropriate completion of the simulation model. The second zone represents a metering box space with 120 mm thermal insulation all around the envelope, except for the front south-east oriented wall with the measured sample. Depending on outside conditions, the real thermal regime of the zone varied with heat flux values (Q) ranging roughly from +50 W (nighttime) to -140 W (daytime) based on response of heating/cooling supply system. This phenomenon was included in the simulation by properly adjusting the schedule of process gains that set the design level of energy consumption due to process activity per unit of floor area. The third zone represents the air cavity between the TIM insulating glazing unit (IGU) and the absorber layer on the wall structure. The TIM IGU was modelled as a triple-glazed window, where the middle glass pane represents the honeycomb TIM with thermo-optical properties. The really small krypton-filled gas cavity (0.01 mm thick) between the outermost glass pane and the middle pane should be created by modelling the obstruction of the interstitial structure so that it is different from the gas cavity. The second larger gas cavity is modelled as a krypton gas cavity according to the dimensions of the façade structure. The innermost glass pane is modelled as low emissivity glass. The dimensions of the modelled glazed structure were completed by a wooden frame.

The above-mentioned methodology for modelling a façade prototype in computer software was implemented in the BES part of this research study. The airtightness of zone structures plays an important role in the modelling of zone air temperature. It is described by the infiltration rate ac/h, which is assumed to be constant throughout the simulation. The most suitable infiltration value in the Twin-boxes zone was set at 1.0 ac/h; the lowest values caused the air temperature to increase in the façade cavity. Additionally, it is more complex to adjust the appropriate thermal conductivity value of the TIM mainly due to its dynamic value – the function of the mean temperature of the TIM and the temperature difference between the two isothermal surfaces (glass panes). The parameters from laboratory measurements taken during a previous study (Čekon and Slávik, 2017) were used for the purpose of configuring thermal and optical properties, as those are considered highly sensitive variables in this study, and characteristics specifically related to transparently insulated components. Table 1 depicts the thermo-optical properties of each layer in both simulated TIF elements.

Table 1. Key thermo-optical properties of TIF elements

Material	Width [mm]	Thermal conductivity [W/(m.K)]	Solar transmittance / absorptance [-]	Outside emissivity [-]
Outermost glass pane	5	1.0	0.73	0.84
TIM Kapipane	26	0.069*	0.74*	0.9
Krypton	14	0.009	-	-
Innermost glass pane (coated)	5	1.0	0.73	0.1
Non-ventilated air cavity	22	-	-	-
<i>SA</i> solar absorber (TiNOx Al)	0.3	65	0.96*	0.06*
<i>nSA</i> black painted absorber			0.94*	0.96*
Gypsum board	25	0.2	-	0.9

* measured according to Čekon and Slávik (2017)

EXPERIMENTAL AND SIMULATION RESULTS

The experimental results were achieved under outdoor conditions where the maximum sun height above the horizon (about 31°) was at midday. It corresponds to a 31° incline from the normal angle of incidence representing the maximum solar incidence (I_{gv}) at the tested location. At the same time, the lowest outdoor ambient temperatures were reached that would allow the results to be used in BES modelling. The testing period was thus specified for the thermodynamic performance analysis of the time-transient winter heating aspect and solar heat gain. The outdoor ambient temperature (T_{ae}) varied from a nocturnal -15.0°C up to a diurnal +2.5°C. The incident solar radiation rate (I_{gv}) reached a maximum of 900 W/m² in the area where samples were measured during totally clear sky conditions. The data presented in the graph below (Figure 2) shows the results of both the real measured (exp) and simulated (sim) values. The difference in the internal air temperature (T_{ai}) response and thermal performance of the *SA* compared to the reference *nSA* sample is demonstrated. Although the solar absorptance values of both samples are very similar, the longwave spectrum and thermal emissivity, have a major influence on both obtained results. Low emissivity properties lead to a nearly 2K higher temperature under nocturnal conditions, thus the heat loss due to longwave radiation is recognizably reduced there by the low-e solar absorber. The simulated model *SA* reaches temperatures up to 1.5K higher compared to the real measured data. During the daytime, all simulated values are significantly higher. Here, the calibration of optical parameters seems to be needed in order to match the real measured values. With cloudy conditions and a low level of solar radiation exposure, i.e. the first two days of the study, the peak difference between the measured and simulated internal temperatures is up to 5 K, while between *SA* and *nSA* it corresponds to the measurements. The next two days are characterized

by the maximum level of solar radiation exposure obtained. At the beginning, good agreement was achieved with *SA*; however, *nSA* does not correspond well and additionally both models have their maximum peak at the same level. The second simulated clear sky day does not agree with the measured progressions. Instead, it responds in the following manner: the lower the outdoor temperature was, the higher the indoor air temperatures simulated.

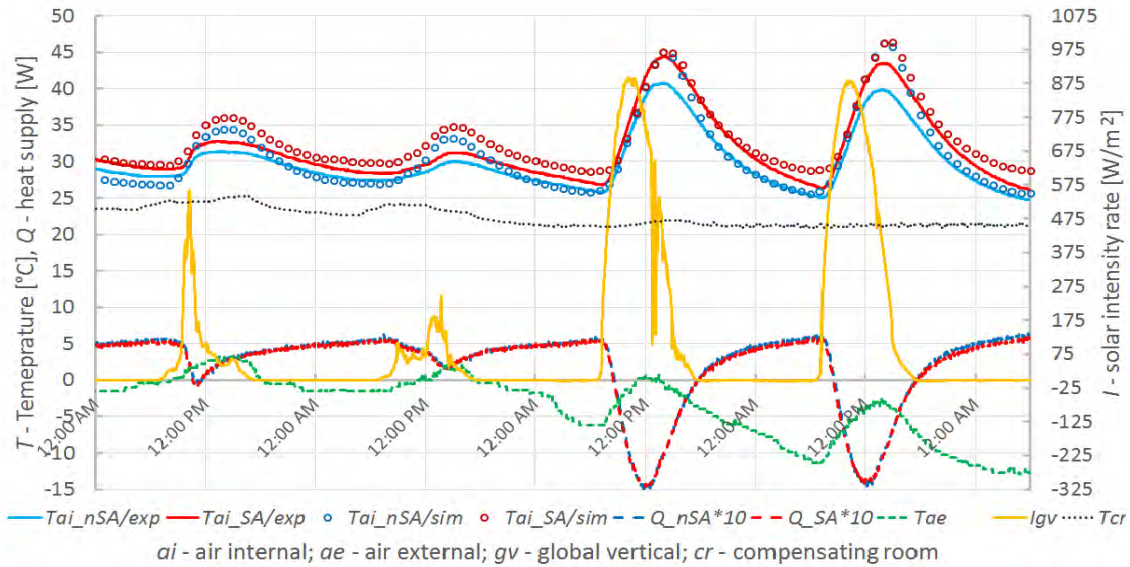


Figure 2. Experimental and simulation results for the presented period

DISCUSSIONS

The integration of solar based absorbers (selective/non-selective) behind a complex fenestration system enhanced with TIM is a challenge for building simulation modelling throughout the climatic year, mainly due to the difficulty of making reasonable performance predictions. The experimental part of the research demonstrates that the presence of low-emissivity surfaces within a façade air cavity based on Trombe wall principles has a significant effect on the internal space temperatures recorded during the presented experimental measurements. A comparison between experimental and simulation results indicated agreement occurred only during nighttime periods with the *nSA* model. At time periods with high solar radiation the temperature gap between the *nSA* and *SA* models is nearly zero. This leads to the fundamental obstructions of the BES calculation concerning the radiation exchange between surfaces with low-emissivity (view factors). The simulation also showed that the operating temperature of the façade cavity zone has nearly equal values to the air and radiant temperature, which indicates that low emissivity surfaces have a higher effect. In the case where a zone is defined as a cavity, it is also important to adjust the zone's inside convection algorithm in order to properly describe surface heat transfer phenomena. The utilised BES tool provides a "Cavity algorithm" that correctly calculates the convection coefficients for a narrow sealed vertical cavity based on the ISO 15099 standard as well as the "Full interior and exterior solar distribution algorithm" for the transmission of solar radiation through glazing. As the thermo-optical properties of the TIM layer inside the fenestration system were assumed to be static values, they might be used for the proper performance prediction of this façade system. Nevertheless, the above-mentioned complexity of the simulation of the dynamic value of thermal conductivity of a TIM glazing unit with regard to the temperature difference of each surface might be improved in a better manner through programming in the Energy Management System under EnergyPlus.

CONCLUSIONS

Based on experimental data concerning a transparent insulation façade (TIF) concept with a TIM glazing unit and two different solar absorber types (selective and non-selective), a performance prediction model was created in BES tool. The process of simulation modelling according to experimental measurements is quite a tricky affair but could provide the first insight into the thermal/optical process of a specific solar based building façade. It was demonstrated by this study that thermo-optical properties of the TIM layer inside the fenestration system as static values might be used for the performance prediction of this façade system. Though, the validation of the simulation model determined the causes of deviations between real and simulated outputs of the amount of overall heat transfer through the investigated TIF components. As result of that, current BES programs appear to have problems specifically with surface radiant heat exchange mainly during high levels of impinging solar radiation. BES coupling with computational fluid dynamics modelling could be further step of clarifying of this complex issue.

ACKNOWLEDGEMENT

This research is under the project GJ 16-02430Y "Contemporary concepts of climatically active solar façades integrating advanced material solutions" of Czech Science Found. and by the Slovak Research and Development Agency under the contract No. APVV-16-0126.

REFERENCES

- Avedissian T. and Naylor D. 2008. Free convective heat transfer in an enclosure with an internal louvered blind International, *J. Heat Mass Transf.* 51, 283–293.
- Brandl D., Mach T., Kaltenecker P., Sterrer R., Neururer C., Treberspurg M., Hochenauer C. 2015. CFD assessment of a solar honeycomb (SHC) façade element with integrated PV cells. *Sol. Energy* 118, 155–174.
- Brandl D., Mach T. and Hochenauer C. 2016. Analysis of the transient thermal behaviour of a solar honeycomb element with and without integrated PV cells. *Sol. Energy* 123, 1–16.
- Čekon M. 2013. Thermodynamic properties of reflective coatings. *Advanced Materials Research*, 649, 179-182.
- Čekon M., Slávik R. 2017. A Non-Ventilated Solar Façade Concept Based on Selective and Transparent Insulation Material Integration: An Experimental Study. *Energies*, 10, 815.
- DesignBuilder. 2016. *DesignBuilder EnergyPlus Simulation Documentation for DesignBuilder v5*. DesignBuilder Software Ltd.
- EnergyPlus. 2017. *EnergyPlus™ Version 8.8.0 Documentation*, Engineering Reference, U.S. Department of Energy.
- Gan G. 2001. Thermal transmittance of multiple glazing: computational fluid dynamics prediction, *Appl. Therm. Eng.* 21, 1583–1592.
- Kapilux. 2017. *Capillary system*, Okalux, <http://www.okaluxna.com/kapilux/#kapilux-twd>
- Sun Y., Wu Y., Wilson R., Lu S. 2016. Experimental measurement and numerical simulation of the thermal performance of a double glazing system with an interstitial Venetian blind, *Build. Environment* 103, 111–122.
- Sun Y. 2017. Glazing system with transparent insulation material for building energy saving and daylight comfort. *PhD thesis*, Fac. of Engineering, University of Nottingham, p. 201.
- Sun Y., Liang R., Wu Y., Wilson R., Rutheford P. 2017. Development of a comprehensive method to analyse glazing systems with Parallel Slit Transparent Insulation material (PS-TIM), *Appl. Energy* 205, 951–963.
- Sun Y., Liang R., Wu Y., Wilson R., Rutheford P. 2018. Glazing systems with Parallel Slits Transparent Insulation Material (PS-TIM): Evaluation of building energy and daylight performance, *Energy Build.*, 159, 213–227.

Power Generation and Visual Comfort Performance of Photovoltaic Toplighting Technologies in Transient Spaces

Nick Novelli^{1,*}, Brandon Andow², Scott Overall³, Mohamed Aly⁴, Christopher Morse³, and Berardo Matalucci³

¹ HeliOptix LLC, New York, NY

² Cornell University AAP, New York, NY

³ SHoP Architects, New York, NY

⁴ Center for Architecture Science and Ecology, Rensselaer Polytechnic Institute, Troy, NY

*Corresponding email: nen@heliOptix.com

ABSTRACT

Advances in long-span glazed structures and interest in high-performance building design has proliferated semi-conditioned spaces with large areas of overhead glazing. These spaces are often programmed with intermittent occupation where variability of the indoor climate is an intentional factor of the experience. Technological options for glazed canopy structures have likewise evolved, gaining functions such as power generation which diversifies the benefits of overhead glazing beyond weather protection and daylighting. Here we model the multiple benefits of current and emerging toplighting technologies deployed in the overhead glazing of a train station and compare power generation and visual comfort. A common building integrated photovoltaic system comprised of monocrystalline cells embedded in the interlayer of laminated glazing is compared with a dynamic, tracking solar collector technology that concentrates and largely intercepts direct solar energy but is transmissive to diffuse sky radiation. The concentrating system generates 6% more power annually with a 70% higher peak power production compared to a typical fixed PV system while at times significantly reducing glare.

KEYWORDS

Concentrating Photovoltaics, Building Integrated Photovoltaics, Daylighting, Active Envelopes, Glare

INTRODUCTION

Transparent and semi-transparent canopies are deployed in architecture to hybridize indoor and outdoor environments, providing the benefits of light and open space with some control of the indoor climate. These structures date to the first moments of technical possibility, with the cast iron and ribbon glass pavilions of the Victorian era, such as London's Crystal Palace in 1851. Contemporary designers incorporate emerging technologies into canopies to improve their performance against criteria of aesthetics, comfort, climate control, and the project's net energy use profile. The large surfaces of transportation structures offer unique opportunities to introduce photovoltaic (PV) generation. If employed correctly, PV not only generates power, but tempers the risk of over lighting and over heating the space under a canopy. Glazing-laminated building-integrated PV (LBIPV) has gained traction in this capacity.

The power output of LBIPV relative to fully opaque fixed panel photovoltaics has limited their desirability in larger projects. Alternatives to LBIPV are under development to increase power generation and lighting benefits. An Enclosure-Integrated, Daylighting, Tracking Solar Collector (EIDTSC) is designed to reduce glare and over-lighting by separating direct and diffuse insolation with Fresnel optics (Figure 1). By treating the direct and diffuse forms of

energy differently, sky-sourced luminance is transmitted through the optics to remain useful as light, but direct-beam energy is intercepted, and focused on multi-junction concentrator PV cells. Efficient generation, shading, and diffuse daylighting are simultaneously provided.

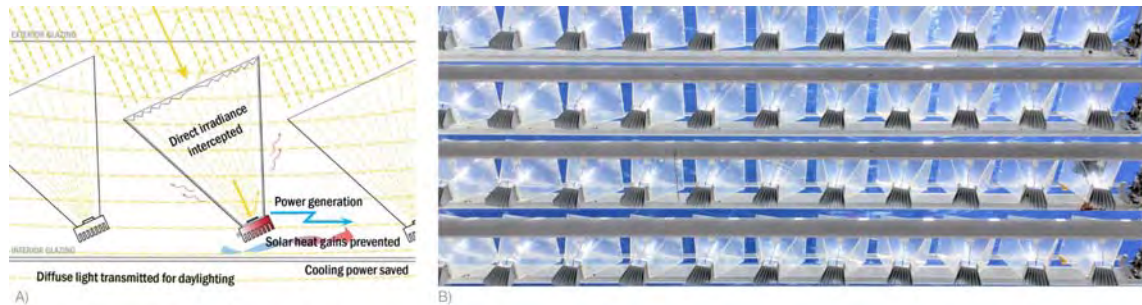


Figure 1. Envelope integrated daylighting tracking solar concentrator, A operational diagram and, B pre-production hardware. Image: HeliOptix LLC.

With physical mock-ups and testing, the EIDTSC is shown to moderate the solar luminance through a fenestration system, by reducing the intensity from direct sun, predominantly allowing diffuse daylight to transmit, and buffering fluctuations due to passing clouds or external shadows (Novelli et al., 2018). Additionally, simulations indicate the system produces power at levels similar to silicon flat-panel photovoltaics but incorporates less than 1% the semiconductor material (Novelli et al., 2015).

METHODS

A typical LBIPV system and an emerging EIDTSC system are simulated in the canopy over a transit platform in southern California and compared for power generation and visual comfort. Simulations assume TMY3 weather data from station #722970 with a 85m wide by 318m long canopy, for a total area of $\sim 27,000\text{m}^2$, oriented -2.6° from North. To manage simulation times, glare renderings use a subset of the canopy 85m wide by 132m long.

The total number of cells or tracking modules for both systems was non-trivial when deployed across the large area of the train station roof and required material functions and parametric scripting to manage the geometry. Additionally, the EIDTSC system tracks the direct beam of the sun to maintain high optical concentration ratios which requires a dynamic repositioning of the modules and racking in the model for each timestep requiring further parametric scripting. Simulating power generation for the two systems also required distinct methods due to the dynamic nature of the EIDTSC system. Where PV Watts (Dobos, 2014) is used for simulating the power output of the static LBIPV scheme, a custom model is used to calculate the EIDTSC output on an hourly timestep basis (Novelli, 2015). While the EIDTSC concept is capable of simultaneously producing both electricity and useful thermal energy, this study describes a version which is passively cooled and does not actively collect heat. Visual comfort and discomfort glare from train platform views are modeled using Radiance tools (Ward, 1994) and Evalglare (Wienold and Christofferson, 2006). The material representation of the LBIPV system employs a *mixfunc* material with a *perforate.cal* function (Mischler, 1993; Roudsari and Waelkens, 2015) which is suitable to describe the orthogonal array of PV cells in planar glazing. The EIDTSC system uses a custom material to model the concentrating optics also based on a *mixfunc* material with a *icsf4.cal* function (Aly et al., 2015). The *icsf4.cal* function reduces the transmittance to zero within a 2° angle of acceptance to model the concentration and absorption of light by the optical train and receiver assembly. Rays incident at an angle greater than 2° are transmitted according to the base *glass* material.

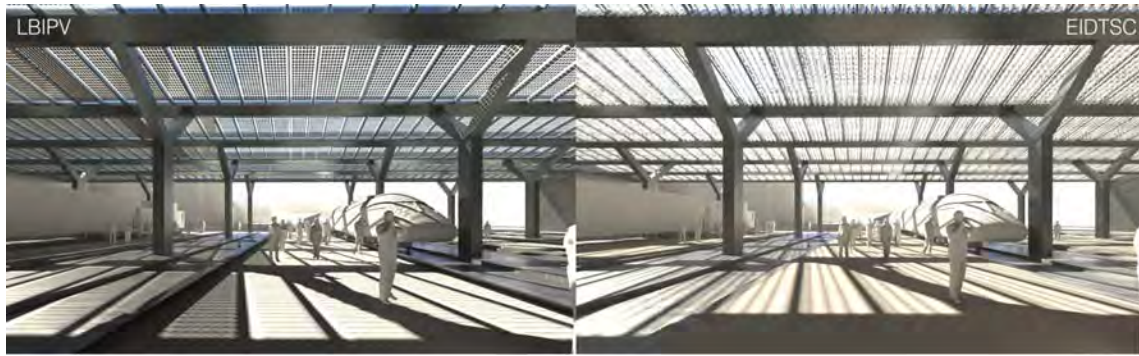


Figure 2. Visualizations of the train station canopy using laminated building integrated photovoltaics, LBIPV (left), and the envelope integrated daylighting tracking solar concentrator, EIDTSC (right).

The 3-d geometry of the train station is modelled in Rhinoceros using the Grasshopper plugin to parametrically generate and position the EIDTSC system geometry. For a glazing unit the custom grasshopper scripts will generate an array of concentrating Fresnel lenses, rear receiver assemblies, and aluminium racking rails based on dimension and clearance tolerance inputs. The EIDTSC array is aligned to track the sun using the Michalsky (1988) solar position algorithm with custom Grasshopper scripts. Additional Grasshopper plug-ins for various supplementary purposes include Elefront, and Ladybug/Honeybee.

Methods for simulating BIPV power generation are well-developed. Here we employ the PV Watts calculations (Dobos, 2014) to simulate the LBIPV, assuming monocrystalline silicon (CSPV) cells laminated into canopy glazing. Simulation of the EIDTSC is based on previous work by Novelli (2015), although the thermal generation described in that work is not modelled, only electricity. Multijunction CPV, Fresnel concentrating lenses, and active tracking is employed in this system. Table 1 lists relevant simulation parameter values.

Table 1. System simulation parameters for EIDTSC and LBIPV.

System Simulation Parameter	LBIPV	EIDTSC
PV type	CSPV, full wafer	MJ-CPV, 64mm ² format
PV or CPV efficiency	20.30%	38.50%
Temperature coefficient	-0.38/°C	-0.05%/°C
Active aperture – glazing area ratio	71%	79%
Cell-glazing area ratio	71%	0.06%
Initial degradation (sun exposure)	1.50%	0%
Wiring losses	2%	2%
Soiling losses	2%	2%
Module mismatch losses	2%	2%
Connector losses	0.50%	0.50%
Deviation from reference conditions	1%	1%
Optical Efficiency		85%
Range of motion limit		72°
Glazing transmittance (external)		87%
Parasitic losses (motor control)		5%

Visual comfort and glare under the glazing canopy of the train station are simulated from South and West facing viewpoints using Radiance validated software tools and Evalglare to calculate the Daylight Glare Probability (DGP) and Daylight Glare Index (DGI) from rendered views (Wienold and Christofferson, 2006; Hopkinson, 1973). Both daylighting systems modelled here require custom material definitions. The individual 0.152 m diameter cells of the LBIPV system are spaced at a distance of 0.16 m for an opaque coverage of 71%.

To reduce the LBIPV model geometry the glazing unit (1.52m width x 4.57m height) is modified with a *mixfunc* radiance material primitive that mixes a *glass* background material with a *plastic* foreground/cell material using the *perforate.cal* function developed by Georg Mischler (1993) to create an orthogonal array of dots to represent the LBIPV cell array with equal percent coverage. The glass material uses a 0.87 transmittance for a 6mm clear/1.52mm PVB/6mm clear laminate built in LBNL Optics. The plastic material uses a 0.02 reflectance material for the silicon cells. This mixfunc material definition allows for an accurate and fast representation of the BIPV array.

While the EIDTSC system cannot be accurately reduced to a bulk material property as is used for the LBIPV, components of the system can. Within a 2° cone of acceptance from the surface normal, the Fresnel concentrating optics focus direct normal solar radiation onto secondary optics and a high efficiency solar cell, while off axis radiation refracts through the lens. In order to model the light loss from the concentrating optics a custom material is defined for the planar lens geometry where transmittance drops sharply to 0 within the 2° angle of acceptance. Details of this material definition can be found in Aly (2015). This material definition allows for a reasonably accurate and fast representation of the complex optics useful glare renderings.

RESULTS AND DISCUSSION

The EIDTSC system generates 6% more power annually with a 70% higher peak power production compared to the LBIPV system while at times significantly reducing glare. The available surface incident insolation for the two systems is 1304 and 1970 kWh-I.m²a respectively. While the concentrating EIDTSC system has a higher effective annual power conversion efficiency of 19.3% it concentrates and converts only direct-beam insolation compared to the LBIPV system which can convert both direct and diffuse insolation. This higher available incident insolation for LBIPV in part accounts for the similar net annual power generation. However, the EIDTSC system generates a significantly higher peak power output of 202 W/m² compared to the LBIPV peak power of 119 W/m². Simulated power generation results are described in Table 2 and Figure 3.

Table 2. Simulated power generation of LBIPV and EIDTSC.

	LBIPV	EIDTSC	unit
Surface-incident insolation available	1970 (global)	1304 (direct)	kWh-I/m ² a
Net annual power generation	237	251	kWh-E/m ² a
Effective (annual) efficiency	12.0%	19.3%	
Peak power	119	202	W/m ²

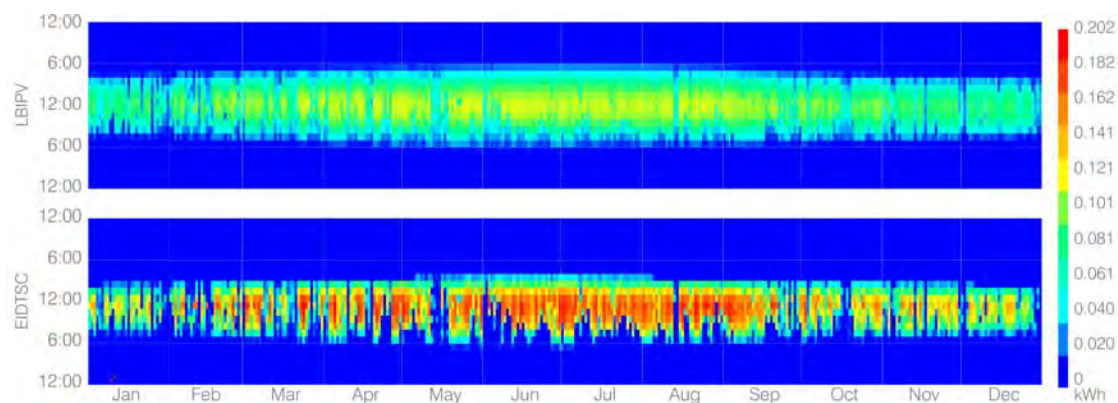


Figure 3. Annual power generation of LBIPV (top) and EIDTSC (bottom).

At times glare in the space is significantly reduced with the EIDTSC system due to the concentration and absorption of the direct beam component of the sun. This feature of the EIDTS system provides more even illumination under the canopy with less disturbing contrast between directly transmitted sun and diffusely illuminated shadows. However, the reduction in glare is not uniform at all times simulated particularly when the EIDTSC modules do not provide overlapping coverage around noon. At these times the EIDTSC canopy maintains or even slightly increases glare. In both canopies, when the sun is aligned through a gap in the PV cells or concentrating modules with the observer's viewpoint, glare is inevitable.



Figure 4. Daylight Glare Probability and Daylight Glare Index from a South facing viewpoint for the LBIPV and EIDTSC canopies at the solstices and spring equinox.

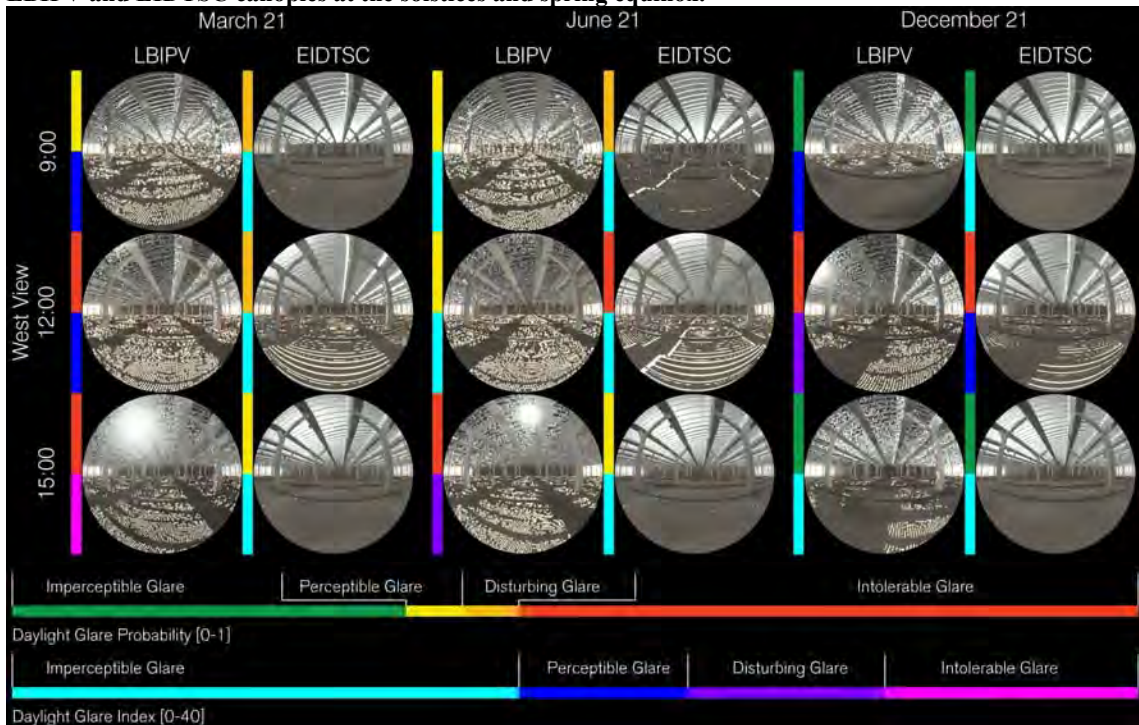


Figure 5. Daylight Glare Probability and Daylight Glare Index from a West facing viewpoint for the LBIPV and EIDTSC canopies at the solstices and spring equinox.

The DGP and DGI metrics do not always agree in magnitude across the times simulated, however the general trends of reducing or increasing the likelihood of glare are somewhat consistent. While DGP is generally considered to be the metric with better correlation in sidelit office settings, both of these commonly accepted daylight glare metrics may be inadequate for bright toplit spaces (McNeill, 2016). Modelling of the concentrating optics of the EIDTSC canopy may be further improved employing a high-resolution tensor tree BSDF with photon mapping for combined forward and backward ray tracing (McNeil, 2013; Schregle, 2015).

CONCLUSIONS

The large surfaces of transportation structures offer unique opportunities to introduce photovoltaic glazing canopies. If employed correctly a photovoltaic toplit roof canopy not only generates power but tempers glare in the space. The typical laminated BIPV system and emerging envelope integrated daylighting tracking solar concentrating system simulated here have comparable annualized power generation. However, the concentrating canopy enables a 70% higher peak power output and can at times significantly reduce glare. The EIDTSC canopy may be better suited in climates where direct solar loads dominate thermal and visual comfort. While the glare results are non-uniform for all timesteps simulated, annual simulations, improved optical representation of the concentrating optics, and the further development of metrics for brightly daylit spaces can reduce uncertainty.

REFERENCES

- Aly M. & Novelli N. & Shultz J. & Phillips K. & Andow B. & Dyson A. 2015. *Daylighting Effect of Separating Direct and Diffuse Insolation with Facade- Integrated, Transparent Solar Collector*. PLEA 2015 Architecture in (R)evolution. Bologna, Italy.
- Dobos A. 2014. PV Watts Version 5 Manual. NREL Technical Report NREL/TP-6A20-62641.
- Hopkinson R. 1972. Glare from Daylighting in Buildings. *Applied Ergonomics*. Vol 3, Issue 4, pp 206-215.
- McNeil A, Burrell G. 2016. *Applicability of DGP and DGI for Evaluating Glare in a Brightly Daylit Space*. ASHRAE and IBPSA-USA SimBuild 2016, Building Performance Modeling Conference. Salt Lake City, UT. Aug 8-12, 2016.
- McNeil A, Jonsson CJ, Appelfeld D, Ward G, Lee ES. 2013. A validation of a ray-tracing tool used to generate bi-directional scattering distribution functions for complex fenestration systems. *Solar Energy*, Vol. 98, pp 404-414.
- Michalsky J. 1988. The Astronomical Almanac's Algorithm for Approximate Solar Position (1950-2050). *Solar Energy*, Vol. 40, Issue 3, pp. 227-235.
- Mischler G. 1993. <https://radiance-online.org/pipermail/radiance-general/2005-April/002610.html>
- Novelli, N., Gordon, R., & Varfolomeev, I. 2018. *Separating Direct from Diffuse*. In Facade Tectonics Institute 2018 World Congress Proceedings Volume 2. Los Angeles.
- Novelli N., Shultz J., and Dyson, A. 2015. *Development of a Modelling Strategy for Adaptive Multifunctional Solar Energy Building Envelope Systems*. SimAUD '15 Proceedings of the Symposium on Simulation for Architecture & Urban Design. April 12-15. Alexandria, VA. Pages 35-42.
- Roudsari M., Waelkens A. 2015. *A New Approach to Modeling Frit Patterns for Daylight Simulation*. SimAUD '15 Proceedings of the Symposium on Simulation for Architecture & Urban Design. April 12-15. Alexandria, VA. Pages 22-27.
- Schregle R, Grobe L, Wittkopf S. 2015. Progressive photon mapping for daylight redirecting components. *Solar Energy*, Vol. 114, pp 327-336.
- Ward G. 1994. The RADIANCE Lighting Simulation and Rendering System. *Siggraph '94 Computer Graphics Proceedings*, Annual Conference Series. July 24-29. Orlando, FL.
- Wienold J., Cristoffersen J. 2006. Evaluation methods and development of a new glare prediction model for daylight environments with the use of CCD Cameras. *Energy and Buildings* 38(7), 743-757.

Solar and lighting transmission in complex fenestration systems with perforated solar protection systems

Waldo Bustamante^{1,3,*}, Daniel Uribe² and Sergio Vera^{2,3}

¹School of Architecture, Pontificia Universidad Católica de Chile

²Department of Construction Engineering and Management, School of Engineering, Pontificia Universidad Católica de Chile

³Center for Sustainable Urban Development, Pontificia Universidad Católica de Chile

**Corresponding email: wbustamante@uc.cl.*

ABSTRACT

Santiago de Chile is a city with a semi-arid climate, with prolonged periods of high temperature and solar radiation. In recent years, in this city, office buildings have been built with high window to wall ratio (WWR) facades. 65% of the office buildings built in the period 2005-2014 have a WWR higher than 60%. Only 5% of these buildings showed an efficient glazed façade solar protection device. One of these systems corresponds to an exterior textile solar protection. This type of systems, together with the perforated screens, could be effective solutions for the solar protection of glazed facades, reducing the cooling energy consumption of buildings, without risking the visual comfort of the occupants. The objective of this research is to evaluate the solar transmission and lighting of seven perforated solar protection systems. Three of these systems correspond to external textile solar protections, and the remaining four are perforated metallic screens. The evaluation was carried out by applying an experimental protocol in two different calorimeters that simulate an office space. In one of the calorimeters, the solar protection systems are installed while the other is used as a reference without any solar protection system. Measurements were made with illuminance sensors and pyranometers. The horizontal illuminance sensors from Konica Minolta (T10) were installed outdoor and at different points inside the calorimeters. Near the facade, vertical indoor and outdoor pyrometers were installed (Kipp Zonnen, CMP11 and Sp Lite 2). The measurements on the north facade are made in summer on clear days. The measurements showed a reduction in solar transmission of 82.1% (metallic screen, 40% drilling) to 94.7% (cloth, 3% drilling) and from 70.8% to 95.4% in the transmission of lighting respectively.

KEYWORDS

Complex fenestrations systems, perforated screens, solar protection fabrics.

INTRODUCTION

In recent decades the use of highly glazed facades in office buildings has become widespread. This has caused high cooling energy consumption and severe problems of thermal and visual comfort in users of these buildings. The problem described has also been observed in Santiago de Chile, a city with a semi-arid climate, with prolonged periods of high temperature and solar radiation. Office buildings of this city show a much higher cooling than heating energy consumption. To improve the thermal and lighting performance of these buildings, different external solar protection systems applied on glazed facades have been developed. The geometry and materiality of these systems are varied, and they can be fixed or mobile. The latter may be adapted automatically to the weather conditions of the exterior and the thermal and light standard required in the interior. The solar protection systems can be formed by a non-specular layer (i.e., louver or blinds), or perforated screens, which together with the glass of the envelope form a "complex fenestration system" (CFS).

CFSs may significantly reduce the solar heat gains through glazed facades and allow control of the natural light transmission so that these systems, as they are well designed, can significantly influence in decreasing buildings energy consumption, without affecting visual comfort (Bustamante et al., 2014). Given the possibilities offered by solar protection, in its natural lighting transmission properties, glare control, and outward vision, perforated or semi-transparent systems offer a good option for use on glazed facades. The use of perforated screens as solar and light protection is a current trend in the design of buildings (Blanco et al., 2014), and in Chile, it was with good results. On a completely sunny summer day, in a building in Santiago with an exterior textile screen on a south-west facade (see figure 1), the radiation and horizontal illuminance measured in the vicinity of the façades were reduced by approximately 95% and 75% respectively, about values measured abroad. (Bustamante et al., 2014)

Appelfeld et al. (2012) studied the solar transmission of a micro-perforated protection system and compared it with rollers and venetian blinds. They conclude that the effect of the micro-perforated system similar to venetian blinds. Mainini et al. (2014) studied different perforated and grilled metal screens with 40% perforations. They obtained the values of light transmission and solar experimentally. Blanco et al. (2014) developed a theoretical model to predict the thermal behaviour of double facades that was validated by experiments. The panels evaluated allow to filter the direct radiation and significantly reduce the temperature of the interior glass.

Stazi et al. (2014) studied the impact of perforated aluminum panels as solar protection system (SPS), on energy consumption and thermal comfort in a Mediterranean climate in Italy. Vera et al. (2016) and Bustamante et al. (2017) developed a tool for integrating the energy and light analysis of different solar protection systems with highly complex geometries. In particular, solar protection systems with curved and perforated aluminium horizontal slats are studied to implement the analysis during the early design stages of office buildings. They conclude that the use of this type of SPS allows achieving energy efficiency standards in buildings without risking visual comfort. On the other hand, Vera et al. (2017), in perforated SPS, studies variables such as the percentage of perforations, distance between the slats and the angle of inclination of these to minimize energy consumption ensuring visual comfort.

The impact of SPS on solar and light transmission in CFS has not been extensively studied through experimental techniques. The objective of this paper is to show and analyze the effects on the reduction of solar and light transmission in CFS that have an exterior SPS. To this end, an experimental protocol has been implemented in a laboratory that represents an office space.

METHODOLOGY

Experimental setup

The laboratory of solar protection systems corresponds to two calorimeters that simulate a real-scale office. Wall insulation of calorimeters correspond to 15 cm of polyurethane, and there exists a 100% glazed facade with double glazing, facing north. Dimensions of the calorimeter are 3,7 x 2.6 m, while it is 2,65 m high.

One of the calorimeters always remains without solar protection system, while in the other the protection system to be evaluated is installed, to determine the percentage of indoor reduction of lighting and solar radiation (see Figure 1).



Figure 1: Laboratory for solar and lighting transmission

To perform the measurements, the laboratory has two data acquisition units of Agilent Technologies. 9 lux meters T10 of Konica Minolta, three pyranometers CMP11 and 9 Spile 2 of Kipp & Zonen.

Illuminance measurements

Each calorimeter has 4 lux meters at the working plane level. Also, an exterior lux meter is available. See Figure 2.

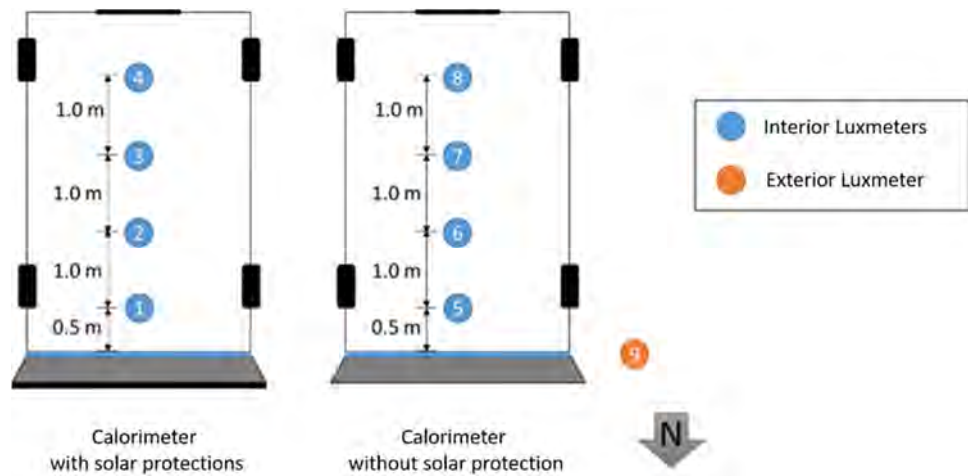


Figure 2. Position of lux meters in test cells

Solar radiation

The different types of pyrometers are located according as shown in figure 3.

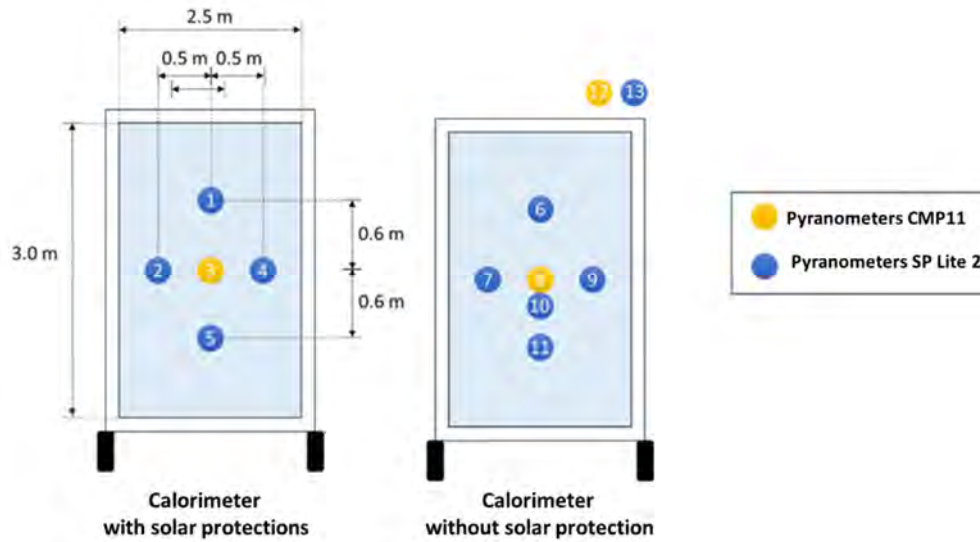


Figure 3. Position of different types of pyrometers in test cells.

Solar protection systems

The following table shows the sun protection systems that have been evaluated. The characteristics of its transparency or percentage of drilling are presented, together with the day considered for its evaluation. Each system was measured for six continuous days, of which a completely clear day was chosen. This is the day that has been denoted “day of measurement, and that is reported in Table 1. Measurements were made in summer 2016.

Table 1: Evaluated solar protection systems

ID	Description	Commercial name of Hunter Douglas	% of perforation	Day of measurement
1	Fabric 3mm	Texscreen	3%	17-Jan-16
2	Fzbric 5mm	Texscreen	5%	21-Jan-16
3	Fabric 10mm	Texscreen	10%	30-Jan-16
4	Metal	Screen Panel XL	10%	21-Feb-16
5	Metal	Screen Panel XL	20%	09-Feb-16
6	Metal	Screen Panel XL	30%	27-Feb-16
7	Metal	Screen Panel XL	40%	02-Mar-16

RESULTS

Table 2 shows the variation of the illuminance on the measurement day for system 7 (metal screen with 40% of perforation). On the left, test room results with solar protection are shown and on the right the results for test room without solar protection. Also, Table 3 shows the variation of solar radiation in system 7 for measurement day on the test room with and without solar protection respectively. Numbers on the graphs represent the position of the lux meter or pyrometers respectively.

Table 2: Illuminance (lux) for some of the solar protection systems

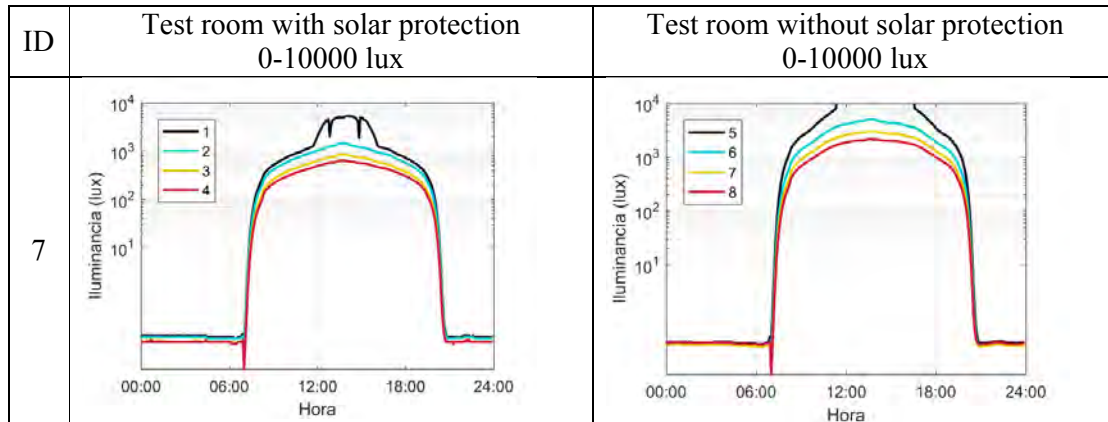


Table 3: Solar radiation transmission (W/m^2) for some of the solar protection systems

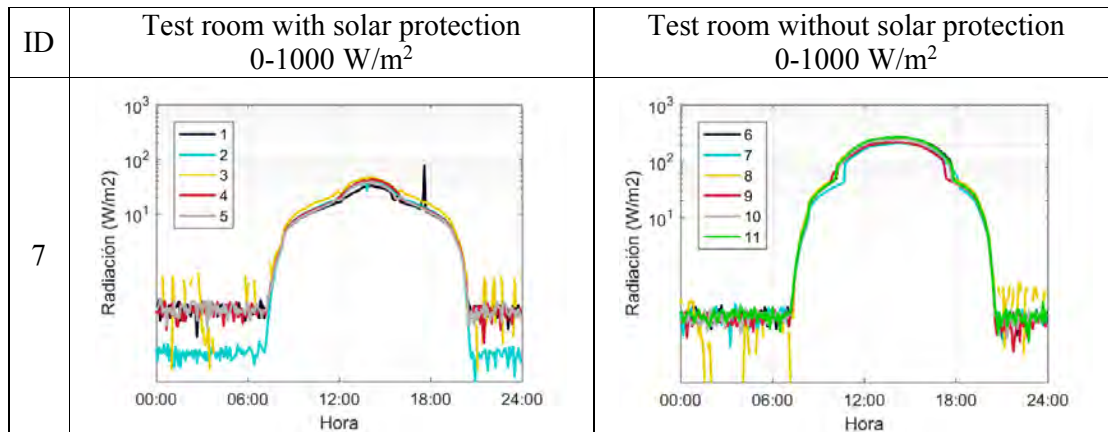


Table 4 shows the percentages of reduction of solar radiation for each protection system in Wh/m^2 , corresponding to the sum of the total radiation during the day of measurements. The calculations were made based on the results of pyrometers 2 and 7. Table 4 also shows the percentage of reduction of illuminance considering lux meters 2 and 6.

Table 4: Reduction on solar radiation and illuminance due to solar protection systems

ID	% of perforation	Solar radiation in test room with solar protection (Wh/m^2)	Solar radiation in test room without solar protection (Wh/m^2)	% of solar radiación reduction	% de illuminance reduction
1	3%	33.28	520.92	93.6%	95.4%
2	5%	27.39	744.95	96.3%	96.3%
3	10%	56.48	744.26	92.4%	90.7%
4	10%	42.28	1073.30	96.1%	93.3%
5	20%	82.51	931.60	91.1%	88.2%
6	30%	230.68	1201.90	80.8%	75.1%
7	40%	212.58	1302.20	83.7%	70.8%

CONCLUSIONS

The results show a very significant reduction in the light transmission (illuminance) and in the solar transmission through glazed façades that have perforated solar protection, compared with the case in which the glazed façade does not contain a solar protection system. Measurements showed a reduction of solar radiation transmission through facades with metallic screens between 96.1 % -when their perforation is 10 % - to 80.8% when they have a 30 % of perforation. Reductions in light transmission over 70% and up to more than 90% are observed in these metal protection systems. On façades with fabric solar protection systems, reductions of over 90% can be observed both in the transmission of solar radiation and lighting. The reductions shown in this report are valid for the period of measurements (summer 2016) and Santiago de Chile (33 ° 27 'S). Also, it is important to indicate that the measurements are made on different days, which present different meteorological conditions and in which the solar angle of incidence on the façade varies from day to day. This avoids a strict comparison of results between systems. However, for the analyzed scenarios, significant solar and light reductions is observed in the different types of perforated facades. This is an interesting property in these systems because together with it, these systems allow the vision to the outside, which is important for the comfort of the people.

Also, the measurements performed consider a north oriented glazed façade. It is recommended to carry out these measurements in different orientations in which the incident solar radiation is more critical, such as east or west orientations.

ACKNOWLEDGEMENT

This work was funded by the National Commission for Scientific and Technological Research (CONICYT) under project FONDECYT 1141240 and FONDECYT 1181686. The authors gratefully acknowledge the support provided by CEDEUS, CONICYT/FONDAP 15110020.

REFERENCES

- Appelfeld, D., McNeil, A., & Svendsen, S. (2012). An hourly based performance comparison of an integrated micro-structural perforated shading screen with standard shading systems. *Energy and Buildings*, 50, 166-176.
- Blanco, J., Arriaga, P., Roji, E., & Cuadrado, J. (2014). Investigating the thermal behavior of double-skin perforated sheet façades: Part A: Model characterization and validation procedure. *Building and Environment*, 81, 50-62.
- Bustamante, W., Vera, S., Prieto, A., & Vásquez, C. (2014). Solar and Lighting Transmission through Complex Fenestration Systems of Office Buildings in a Warm and Dry Climate of Chile. *Sustainability*, 6(5). 2786-2801.
- Bustamante, W., Uribe, D., Vera, S., Molina, G. (2017). “An integrated thermal and lighting simulation tool to support the design process of complex fenestration systems for office buildings”. *Applied Energy*. 198, 36–48.
- Mainini, A. G., Poli, T., Zinzi, M., & Speroni, A. (2015). Metal mesh as shading devices and thermal response of an office building: parametric analysis. *Energy Procedia* 48, 1292-1301.
- Vera, S., Uribe, D., Bustamante, W., Molina, G. (2017). Optimization of a fixed exterior complex fenestration system considering visual comfort and energy performance criteria. *Building and Environment*. 113. 163–174.
- Vera, S., Bustamante, W., Molina, G., D. Uribe. . (2016). A flexible and time-efficient schedule-based communication tool for integrated lighting and thermal simulations of spaces with controlled artificial lighting and complex fenestration systems. *Journal of Building Performance Simulation*. 9 (4):382-96.

Solar efficiency index of building envelopes and load matching in low energy buildings

Ellika Taveres-Cachat^{1,2*}, Francesco Goia¹ and Steinar Grynning²

¹NTNU, Department of Architecture and Technology, Trondheim, Norway

²SINTEF Building and Infrastructure, Trondheim, Norway

*Corresponding email: ellika.cachat@ntnu.no

ABSTRACT

Net-zero energy buildings oftentimes rely on solar-based building integrated technologies to offset energy use and achieve their goals. However, the value of a particular system is difficult to assess given that these technologies often bring about complex interactions with the indoor environment, and building energy management systems. The approach chosen in this study was to propose and test a simple index called the *Solar Efficiency index (SE index)*, which makes it possible to characterize the performance of building envelopes with integrated solar systems. The index was used to investigate the effect of different configurations of a PV integrated shading device on an office building in Norway. The results provided by the index allowed estimating how much solar energy was converted and how useful that energy was to the building in terms of load matching. This provided a picture of the building's energy autonomy.

KEYWORDS

Low Energy Buildings; Parametric Analysis; Load Matching; Solar Efficiency Index; Building Envelope.

INTRODUCTION

Sustainable building concepts such as net-Zero Energy Buildings (net-ZEB) or Zero Emission Buildings (ZEB) have increasingly become part of European building policies (D'Agostino et al., 2016). By definition, in order to reach a net zero balance, ZEBs and net-ZEBs must feed as much excess energy back into the grid as they purchase from the utility (Sartori et al., 2012). This design strategy is based on combining highly energy efficient building envelopes (Justo Alonso et al., 2015) with systems allowing to harvest and store renewable energy sources (RES). But reduced energy use and on-site production of heat and electricity, may lead to a seasonal load mismatch in the balance of energy use vs energy converted (Lindberg et al., 2016). This issue is especially critical in Nordic climates where solar radiation is relatively abundant during the summer while energy use is low, and the reciprocal during the winter.

As net-ZEBs and ZEBs become more popular, there is an increasing need to develop strategies in early design phase to improve load management and grid interactions. Increased energy autonomy can be achieved through energy storage, but isn't currently an economically viable option at single building scale given the techno-economic context (McKenna et al, 2017). Other approaches have been to optimize building systems such as heat pumps, or RES technology size and placement to best cover the energy loads (Dar et al., 2014). From a broader energy management point of view, load matching is an important topic of discussion, and fosters concern regarding the capacity of electric grids to adapt to future needs. In response to this need the International Energy Agency (IEA) in the Annex 67 created an energy flexibility indicator (Grønberg Junker et al., 2018). Previously, the IEA in the task 40 had reviewed Load Matching and Grid Interaction (LMGI) indicators and distributed them into four categories (Salom et al.,

2011). The findings showed that LMGIs are highly dependent on the timescale considered and more often than not, a shorter time step will improve their accuracy (Voss et al., 2011).

Designing low-energy buildings with RESs is not a straightforward task and requires careful balancing of parameters; this is because different uses of solar energy may have antagonistic purposes (e.g. visual comfort vs thermal comfort). The study presented in this paper deals with the development and testing of a new metric called the Solar Efficiency index (SE). The utility of the SE index is to characterize the extent to which different RES building envelope designs are able to utilize available solar radiation to reduce the building's energy use, while still maintaining high-quality indoor environments in terms of thermal and visual comfort. The goals of this study are: (i) define a new indicator called the solar efficiency index of the building skin; and (ii), to test the indicator on different envelope configurations in a Nordic climate by assessing its suitability to communicate the performance of the building in terms of solar energy use and load matching.

METHODS

This work was based on numerical simulations carried out in the dynamic building performance simulation tool IDA ice. The SE index was used to evaluate the simulation results of a case study based on a parametric analysis of the possible configurations for a PV integrated shading device (PVSD). The index was used to evaluate the amount of energy converted and how useful that energy was to the reference building in terms of hourly load matching.

Description of the reference building model

The reference model used for this study is a conceptual ZEB office building developed by (Dokka et al., 2013). The simulations were run using an EPW file for Trondheim, Norway. The inputs for the HVAC system, internal loads and domestic hot water demand were taken from the Norwegian Standard NS3031:2016 and Norwegian Passive House standard NS3701. A proportional control strategy for artificial lighting based on measured daylighting levels was used in peripheral zones during operation hours to ensure a minimum average of 500 lx at 0.8m from the floor level. Specifics about the building and energy systems are given in Table 1.

Table 1. Characteristics of the base case building model used in the study

Element	Area	Value
Heated floor area/volume	1 980 m ² / 7 128 m ³	
Building envelope	2 306 m ²	
External walls	860 m ²	U= 0.12 W/m ² K
External roof	495 m ²	U= 0.09 W/m ² K
Floor against cellar	495 m ²	U= 0.11 W/m ² K
Windows and doors	WWR 14%	U= 0.75 W/m ² K
Normalized thermal bridge value		Ψ''=0.03 W/m ² K
Air tightness		N ₅₀ <0.3 ach@50 Pa
Heat exchanger efficiency		86 %
Specific fan power		1.00 kWh/m ³ /s
Heat pump coefficient of performance for heating/ cooling		3 /4.5

Description of the different building envelope configurations investigated

Using a common basic building geometry, 7 scenarios were defined as case studies where the changing parameters were the presence or not of a photovoltaic shading device (PVSD), its design configuration in terms of spacing between the louvre-blades and angles, the orientation of the building site and the window to wall ratio (Table 2). The PVSD was modelled according to Taveres-Cachat et al. (2017). The conversion efficiency was assumed 15% after accounting for all the system losses, including self-shading and DC to AC conversion.

Table 2. Description of the scenarios investigated in the study

Case	Description
0	Base model with no shading system installed
1	Base model where all the south facing windows are equipped with an external shading system without PV coating. Inter-blade distance 132 mm, tilt angle 15°.
2	Base model where all the south facing windows are equipped with an external PVSD. Inter-blade distance 132 mm, tilt angle 15°.
3	Base model where all the south facing windows are equipped with an external PVSD. Inter-blade distance 111 mm, tilt angle 15°.
4	Base model where all the south facing windows are equipped with an external PVSD. Inter-blade distance 95 mm, tilt angle 0°.
5	Base model where all the south- and north facing windows are equipped with an external PVSD shading system. Inter-blade distance 132 mm, tilt angle 15°, WWR = 22%.
6	Case 1 with the building orientation changed by 90° and PVSD on east and west facing windows

Description of Solar Efficiency (SE) index

The models were first simulated in a theoretical context without solar radiation (neither direct nor diffuse), giving the hourly energy use $E_{0\ net}$ (kWh/m²). The simulations were run a second time with solar radiation which yielded the energy use defined as $E_{sun\ net}$ (kWh/m²).

These quantities were defined as follows:

$$E_{0\ net} = \int_{t_1}^{t_2} e_0(t) dt \quad (1)$$

$$E_{sun\ net} = \int_{t_1}^{t_2} (e_{sun}(t) - i(t)) dt \quad (2)$$

Where $e_{sun}(t)$ [W] and $e_0(t)$ [W] were respectively the electrical power demand required for heating, cooling and lighting for the building with and without the contribution of solar radiation at the instant t . $i(t)$ [W] was the amount of electric power being converted at the instant t .

The solar efficiency index was defined as:

$$SE_{index} = \frac{E_{0\ net} - E_{sun\ net}}{E_{0\ net}} \quad [-] \quad (3)$$

The solar efficiency index was calculated with hourly steps over the period of one year. Index values in the]0; 1] interval indicated that the building efficiently used solar radiation to lower its energy use compared to a situation with no solar radiation. An SE index value of one meant the building was completely self-sustaining (perfect load match) and any value above one meant excess energy was being sold back to the grid. An SE index value equal to zero implied that either no solar radiation was available, or the building was not able to use solar radiation to reduce its energy demand. Index values below zero indicated that the building had to use more energy to operate when there was solar radiation available than if there was not any.

RESULTS AND DISCUSSION

The SE index was calculated for all seven cases. The resulting SE index values are plotted as cumulated hourly frequency distributions to help visually assess the performance and identify both situations of under- and over energy production in Figure 1. Horizontal bars delimiting $SE = 0$ and $SE = 1$ highlight the different SE index value intervals. For all cases the SE index line crossed the lower threshold $SE = 0$ before the 0.15 marker, meaning that all configurations partially used solar energy to reduce energy use at least 85 % of the time. As anticipated, cases

0 and 1 performed the worst; crossing the lower threshold last and never yielding an SE index value above 0.7 because of the absence of energy conversion. Case 3 and 5 were seemingly the most efficient at using solar radiation with higher average SEs, but led to an energy surplus 15-20 % of the time. Cases 2 and 4 performed almost identically and provided the least conversion surplus. However, despite this, the values yielded were on average below those of other PVSD cases. Lastly, case 6 had satisfying SE index values with less energy surplus.

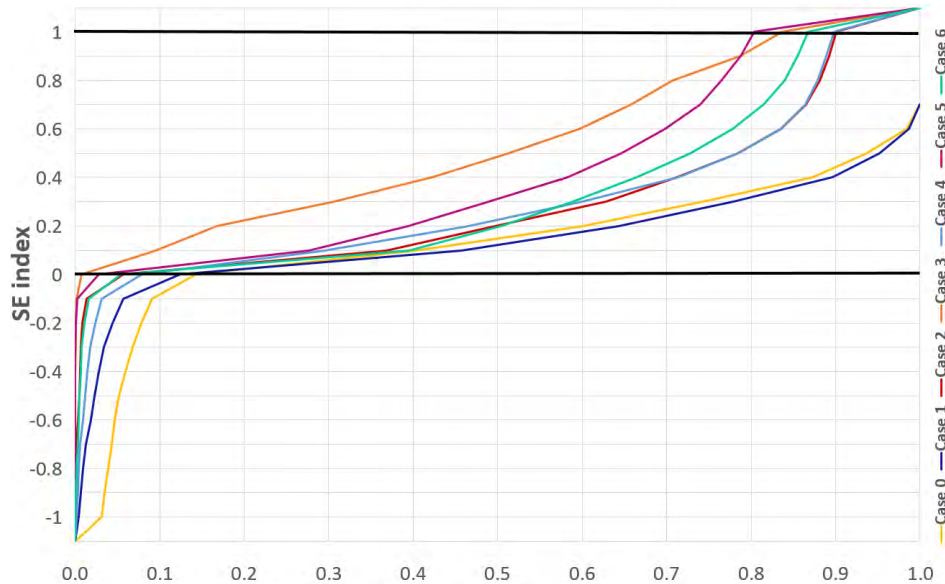


Figure 1 SE index for all cases as a cumulated frequency

The SE index results are analyzed further using the individual frequency distributions shown in Figure 2. The comparison of cases 0 and 1 shows that the increase in energy use due to lower solar gains did not outweigh the benefits of a reduced cooling demand, despite the study being in a heating dominated climate. Moreover, the results for cases 2-6 highlight that adding PV conversion was immediately sufficient to reduce the number of hours with negative values. However in case 2, the introduction of PV conversion seemed to have mainly shifted hours from the $SE < 0$ to the $SE > 1$ bracket. This occurred without significantly improving the rest of the hourly distribution when compared to case 1; suggesting that the energy converted was most often insufficient to cover the building load. Similarly, only small improvements were achieved in case 4, as the increase in energy use due to reduced solar gains counteracted the benefits of the additional PV material. Case 5 benefited from increased PV capacity and daylight availability thanks to a higher WWR. It yielded a relatively better SE index than the base cases but had the largest amount of hours with energy conversion surplus. Case 6 provided good SE index values, but showed that east and west facing PVSDS configurations are unlikely to be competitive with south facing systems at equal number of equipped windows. Finally, as previously suggested, case 3 which was an intermediate configuration in terms of louver-blade count, achieved the best performance with the highest mean SE index value for a WWR = 14%, and the most hours in the $0.6 \leq SE \leq 1$ range.

These findings supported the conclusion that the relationship between higher SEs and increased amounts of PV installed is not a linear. Thus, adding more PV material in the shading system using a larger count of blades was beneficial up to a certain point, beyond which the benefits of additional PV conversion no longer outweighed the additional energy use due to low solar gains.

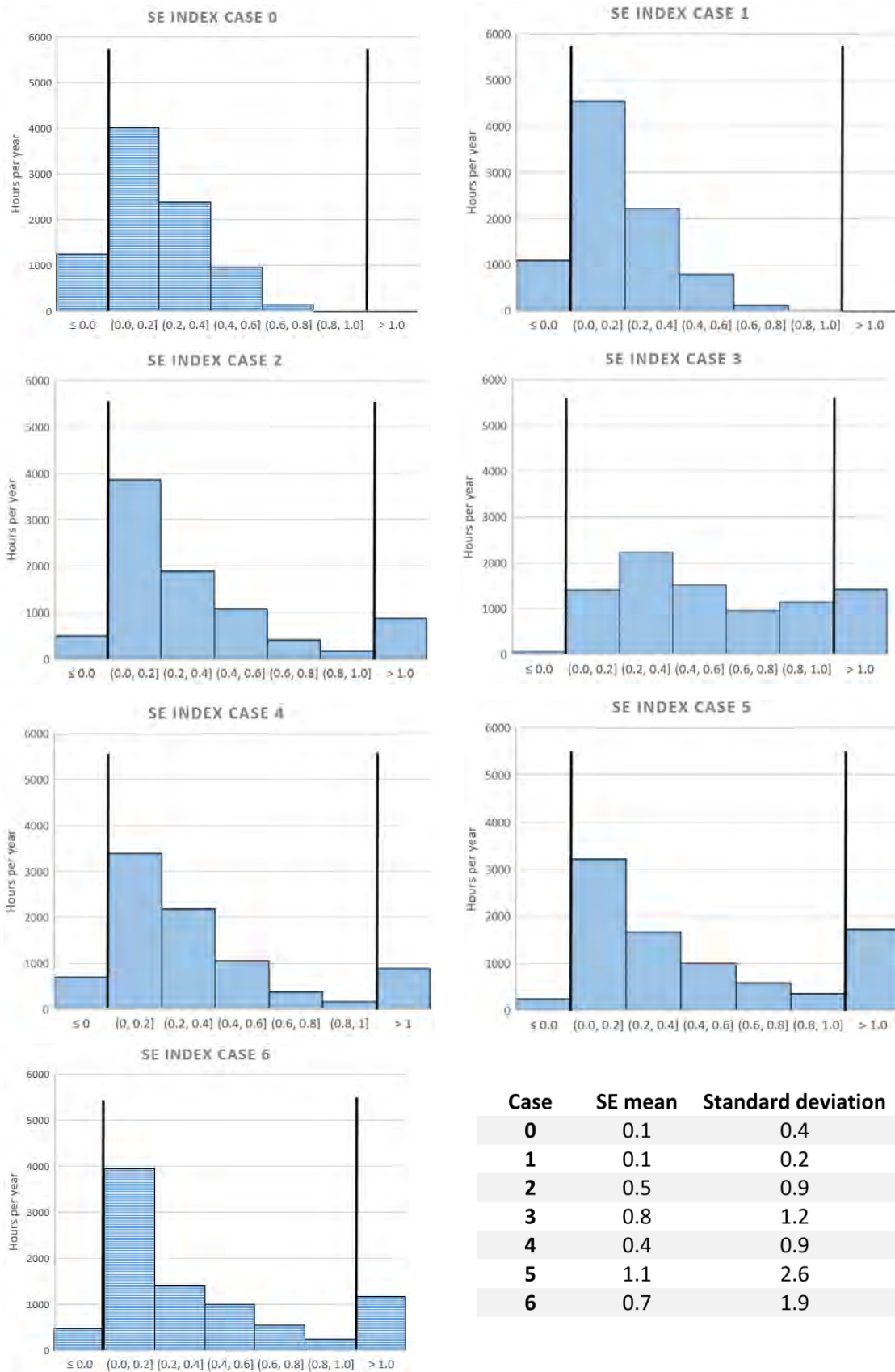


Figure 2 SE index values plotted as frequency distributions for each case.

CONCLUSION

The SE index was used to evaluate seven different design configurations of a building with PVSD through a parametric analysis. The SE index was successfully able to capture the differences between the cases investigated, and highlighted the most promising configuration. This scenario corresponds to the best balance between increased PV conversion and solar gains reduction, without raising significantly energy use for heating and lighting. Other parameters that could influence SE index results are the load profile of the building (energy use timing), and the total energy use for the building. Refining the index with smaller value intervals might also be useful in some cases, because two scenarios may perform very similarly in reality but may not appear to do so in the result visualization depending on how the thresholds are set. Plotting the cumulated frequency is therefore an important first step. Overall, the SE index is proposed as a simple approach to help communicate and compare the benefits of implementing different solar RESs aiming to increase energy autonomy. SE index results can be improved with control strategies in the building envelope or if integrated energy storage solutions are implemented. The SE index can also be combined with other existing load matching indicators as well as life cycle cost analysis to obtain a holistic view of the building's performance.

ACKNOWLEDGEMENTS

This paper is part of the SkinTech project supported by the Research Council of Norway under grant No. 255252/E20 and the industrial partners in the project.

REFERENCES

- D'Agostino, D., Zangheri, P., Cuniberti, B., Paci, D., Bertoldi, P., 2016. Synthesis Report on the National Plans for NZEBs. JRC Science Hub.
- Dar, U.I., Sartori, I., Georges, L., Novakovic, V., 2014. Advanced control of heat pumps for improved flexibility of Net-ZEB towards the grid. *Energy Build.* 69, 74–84.
- Dokka, T.H., Kristjansdottir, T., Time, B., Mellegård, S., 2013. A zero emission concept analysis of an office building.
- Grønborg Junker, R., Relan, R., Amaral Lopes, R., Renders, G., Byskov Lindberg, K., Madsen, H., 2018. Characterizing the Energy Flexibility of Buildings and Districts. *Appl. Energy* 225, 175–182.
- Justo Alonso, M., Liu, P., Mathisen, H.M., Ge, G., Simonson, C., 2015. Review of heat/energy recovery exchangers for use in ZEBs in cold climate countries. *Build. Environ.* 84, 228–237.
- Lindberg, K.B., Fischer, D., Doorman, G., Korpås, M., Sartori, I., 2016. Cost-optimal energy system design in Zero Energy Buildings with resulting grid impact: A case study of a German multi-family house. *Energy Build.* 127, 830–845.
- McKenna, R., Merkel, E., Fichtner, W., 2017. Energy autonomy in residential buildings: A techno-economic model-based analysis of the scale effects. *Appl. Energy* 189, 800–815.
- Salom, J., Widén, J., Candanedo, J., Sartori, I., Voss, K., Marszal, A.J., 2011. Understanding Net Zero Energy Buildings: Evaluation of load matching and grid interaction indicators. *Proc. Build. Simul.* 2011 6, 14–16.
- Sartori, I., Napolitano, A., Voss, K., 2012. Net zero energy buildings: A consistent definition framework. *Energy Build.* 48, 220–232.
- Taveres-Cachat, E., Bøe, K., Lobaccaro, G., Goia, F., Grynning, S., 2017. Balancing competing parameters in search of optimal configurations for a fix louvre blade system with integrated PV. *Energy Procedia* 122, 607–612.
- Voss, K., Sartori, I., Napolitano, A., Geier, S., Gonzalves, H., Hall, M., Widén, J., Candanedo, J. a, Marszal, A.J., 2011. Load Matching and Grid Interaction of Net Zero Energy Building. *Proc. Build. Simul.* 2011 6, 14–16.

Study on the design method of integration of roof and photovoltaic based on aesthetics, technology and energy-saving characteristic

Hongxin Feng¹, Juanli Guo^{1,*}, Gang Liu¹ and Jiehui Wang¹

¹School of Architecture, Tianjin University, China

**Corresponding email: fenghx@tju.edu.cn*

ABSTRACT

The development and utilization of new energy has been concerned due to the traditional energy is increasingly scarce. In recent years, solar building has developed rapidly in the construction industry which is a major energy consuming component. As an organic part of the building, the combination of roof and solar energy has become the focus of attention because of its large size, less shielding and other characteristics. Based on the works of recent years' Solar Decathlon, this paper analysed the design and implementation of the integration of solar building's roof and photovoltaic. Meanwhile, taking an office building in Xinjiang, China as an example, the paper analysed the design points and energy-saving situation of the roof photovoltaic building and prospected the application prospect of integrated design method of building's solar roof.

KEYWORDS

Roof, Photovoltaic, Integrated design, Energy-saving

INTRODUCTION

As an organic part of the building, roof is usually used to obstruct the unfavorable weather of outside (Li Baofeng and Li Gang, 2010), protect the bearing and maintain the basic function such as indoor micro climate environment. With the development of building energy-saving concept and the photovoltaic technology, it brings more green connotations into the design of roof (Tao Chengqian, 2004). In the whole life cycle of photovoltaic, it is hard to reduce energy consumption of the upper-middle without big manufacturing technology break through which has reached the limit. But on the other hand, the design quality of photovoltaic power generation system which can be optimized greatly affects the length of the payback period, and it can be achieved to improve efficiency and reduce building energy consumption through the optimal design of the building and photovoltaic. There are still some problems in the design of the integration of roof and photovoltaic, especially many traditional buildings do not reserve enough operation space for developing photovoltaic which makes a high cost of installation of photovoltaic power generation system but the effect is not ideal, such as roof space is not enough, the bearing capacity is insufficient, PV systems cannot select reasonable angle and direction because of the shape of building, components of pollution, severe hot spot effect and so on. At the same time, when designing the photovoltaic array, due to the limit of design method, it is unable to simulate accurately the shadow effect on the components and the component can't be designed toward the matching of peak power generation and peak power consumption, which make the power generation efficiency and profit are reduced greatly.

Up to now, developed countries have accumulated rich experience in the area of integrated design of photovoltaic and photothermal. In 1996, Friedrich Sick showed how to combine photovoltaic and building maximization and summed up the design guideline at the earliest. (Friedrich Sick and Thomas Erge, 1996). Peter Gevorkian put forward a series of main points of solar building design from basic theory to project planning, cost estimation and implemen-

tation methods (Peter Gevorkian, 2007). Bernhard Weller discussed the relation between integration of solar building and architectural design, and introduced the detailed design of several typical cases in detail (Bernhard Weller, 2010). Peder Vejsig Pedersen described the application of photovoltaic technology in the renovation of the new buildings in Copenhagen and the old buildings with low energy consumption (Peder Vejsig Pedersen et al, 2015). Hai Tao introduced the combination method of integration of roof and photovoltaic, and analysed design and energy saving effect of solar energy building (Hai Tao and He Jiang, 2015).

In summary, the scholars in various countries have a lot of theoretical research achievements in the field of integrated design of photovoltaic system and building. However, there are few researches on the application of photovoltaic technology in roof. Particularly, there are less researches discuss that how to combine photovoltaic systems better with roof from the perspective of architectural design.

Based on the current situation, it is important to summary and refine the current technical strategy and problems of integration of roof and photovoltaic, which aims to form the design idea of aesthetic, technology and energy-saving, through analysing the existing integrated design methods of different forms of roof, the paper put forward an integrated design method of roof and photovoltaic based on energy saving and increasing power generation efficiency.

METHODS

Through investigation and survey, the paper summarized the integrated design of roof and photovoltaic, classified design methods and analysed their characteristic based on the Solar Decathlon competition in recent years. In this paper, the integrated design method of photovoltaic and roof is divided into traditional design method and special design method, and the paper illustrated each design method by analysing concrete cases.

Through the summary and analysis of the current research results, the paper analysed the design points and energy-saving situation of the roof photovoltaic building and put forward a design method by using SKETCHUP and PVSYSYSTEM. Based on the characteristics of office buildings, such as large energy consumption, huge electricity supplement, most building load on day time, and higher photovoltaic matching rate, and also, South Xinjiang is endowed with abundant solar energy resources by nature, so we select Turpan, a city in cold area of Xinjiang Province in China, as the research area of office building, which is aimed for a qualitative comparison through the quantitative analysis concluding of the determination of the office building's materials selection and PV component's parameters, and simulating the photovoltaic power generation of the office building.

RESULTS

The implementation of integrated design methods

With the continuous development of roof design ideas, it no longer stay in the passive energy-saving design, but more positive active capacity design appears. In Solar Decathlon competition in recent years, the function of the system which on top of the roof is not overlooked with the limitations of human perspective. Meanwhile, in the architectural design, different roof forms can be used, the integration of solar energy system on the roof is divided into the integrated design of the flat roof, slope roof and curved roof.

Integrated design of flat roof

The solar radiation to the surface of the earth will be at a certain angle to the ground with the change of the longitude, latitude and time. Therefore, the integration of solar energy system and flat roof should generally make the solar angle equipment to adapt to the sun's angle of change, and the system should be set with a certain angle on the flat roof (Zheng Cunyao, 2007). Such as TUC separated the monocrystalline silicon battery array from the roof with the inclination is 2° by using the stent on the flat roof, which ensuring the safety of the system as

well as ensuring power generation efficiency by reducing the backside temperature of the battery (As shown in Figure.1). Many new forms of design arised based on the method of installing solar energy system on the flat roof directly which uses no inclination, such as the University of Florida team put the photovoltaic system directly on the top of the building structure system, which can save costs and cover the living room and the bedroom which have different elevations, so as to make the building to form a whole and to acquire a good physical environment and a unified architectural style (As shown in Figure.2).

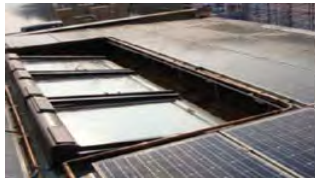


Figure1. Overhead PV panel of TUC



Figure.2. Photovoltaic roof of Florida

With the improvement of the solar energy system integration technology, the design of electro-optical system coupling has developed rapidly. For example, HFT has adopted the electro-optical heat collectors (PVT) on the flat roof. It covered PVT collectors as a building exterior finish on the flat roof surface, which replaced the building materials and reflected the high integration design. At the same time, the radiation boards are set under the dark black monocrystalline silicon cell array, it can not only generated electricity, but also recycled the heat generated by photovoltaic power generation to provide hot water. And the vacuum tube collectors installed on the glass ceiling of the "air gap" between the modules also provide heat, diffuse light and shading for the interior, as well as obtain special beauty as the application of the new material in the building (As shown in Figure.3).



Figure3. PVT collector and vacuum collector of HFT

Integrated design of slope roof

For the slope roof, with the development of integration, the system of solar energy utilization can be directly used as building material for the roof, instead of the additional installation design (Guo Juanli et al. 2012). For example, BER laid the monocrystalline silicon battery assembly directly on the roof of the building, supported by the southward corrugated aluminum and aluminum frames, which is integral with the exterior finish of the building and completed simultaneously with the construction of building, so that reducing the cost and difficulty of repeated construction. At the same time, the building material type's system of solar energy utilization also has the abilities of rain-proof, corrosion resistance, building decorative appearance and strength requirements (As shown in Figure.4).

Integrated design of curved roof

Considering the characteristics of photoelectric system, it is not suitable for integration on curved roof, but with the continuous development of technology and the improvement of efficiency, some new attempts have been started. For example, in 2013, the works "halo" integrated solar photovoltaic systems on the roof of the building (As shown in Figure.5), it uses a whole new solar technology that make the solar battery as the roof itself rather than fixed on the roof, so as to avoid the limitation of application of the traditional solar battery module

brings. The works can get maximum annual energy efficiency gains without summer housing overheating through the angle of roof for precision design. The roof consists of an area of 82m^2 polycarbonate film, and converting 18% of solar radiation to building usable energy through the integrated single crystal silicon solar cells. Meanwhile, there is a transition area under the eaves of the north and south, which provides a comfortable space for outdoor living.



Figure.4. Slope roof of BER



Figure.5. Curved roof of Halo

Special design

Obscure component boundary

In 2015, SURE HOUSE adopted a photovoltaic roof and a movable shading panel integrated with photovoltaic, not only provided the power, but also provided the building shading and natural lighting control. PV panels are not just a power generating device, but are designed to be a part of the roof. In daily weather conditions, the double folding anti-storm baffle is used to provide the function of shading for building, while in stormy weather, it serves as a major barrier to protect the building. Storm baffle is made of a lightweight composite glass fiber and a structural foam core, which can withstand the load required by the design, and can adjust the indoor light environment through manual operation. The panels are equipped with PV panels which can absorb solar energy and provide energy for the building.

Design of double-skin roof

Armadillo Box is designed by GRE. The interior roof of the building is built on an internal load-bearing frame, composite oriented strand board, and filled with thermal insulation material. The exterior roof is made of steel frames, supporting monocrystalline silicon solar cells, photovoltaic modules and low radiation sun curtains, so that a good ventilation corridor is formed between the inside and outside building roofs. (As shown in Figure.6) The low temperature radiation protection layer and the evaporation cooling system for spraying water by using water and rain water on the outside of the inner roof can be used to solve the ventilation problem between the double roofs. The interior of the building is also protected from adverse weather conditions due to the protective effects of the exterior roof. The photovoltaic square itself is controlled by the separation of the double roofs to achieve its own back temperature, while the power generation efficiency is guaranteed. (As shown in Figure.7).



Figure.6. SURE HOUSE

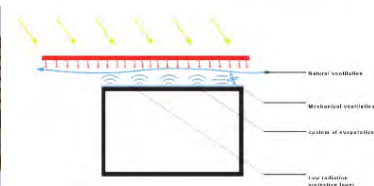


Figure.7. Analysis of double-skin roof of GRE

Analysis of design method of roof and photovoltaic for an office building in Xinjiang

Determination of orientation and dip angle parameters of photovoltaic module

Due to the hot summer in Turpan, the design is mainly aimed on diminishing the heat gain of enclosure, so the glass wall and lighting roof structure should not be considered. The paper built a building model with 1:1 scale that has flat roof and slope roof which laying solar pan-

els (As shown in Figure.8). Due to the angle and slope roof system has fixed, we mainly focus on the best angle and orientation of the flat roof. With the optimizing of PVSYST software, we can conclude that the 39 degrees is the best angle (As shown in Figure.9).

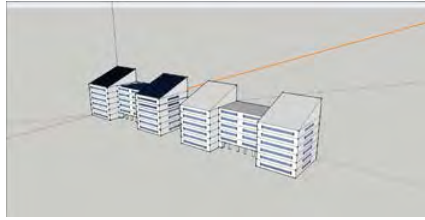


Figure.8. Model for analysis

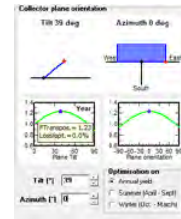


Figure.9. Inclination angle

At the same time, using the solar plugin SKELION to simulate the arrangement and shadow analyze, then choosing 9 to 15 o'clock to simulate without shading, providing the spacing of 3 meters (As shown in Figure.10). There are two kinds of measures to reduce shadow and hot spots loss. The first one is the shadow elimination, which is able to realize the unblocking during the specific time, but it will reduce the use of roof, another is to choose horizontal or vertical arrangement according to the shape of the shadow.

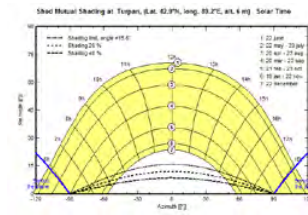
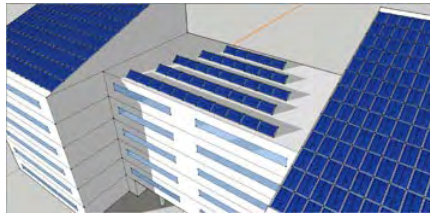


Figure.10. Model component layout in SKETCHUP and the sun time path diagram in Turpan

Calculation of photovoltaic power generation

Using PVSYST software for simulation and calculation, and arranging the number of PV modules by using SKETCHUP. The type of PV modules we choose is monocrystalline silicon component with the size of 1680*990*50, and its power is 240W. There are 468 pieces on the slope roof whose rated power is 120kw and there has an installing area of 750 m². And there are 41 pieces on the flat roof whose rated power is 11.3kw and there has an installing area of 375 m². The total rated power is 131.3kw, and we calculating respectively the power generation of flat roof and slope roof (As shown in Fig.11).

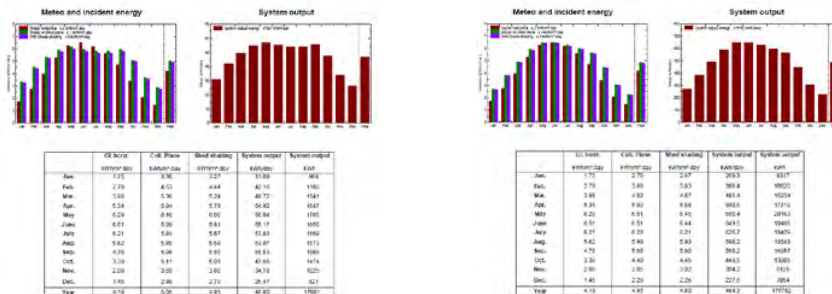


Figure.11. Calculation results of power generation from flat roof and curved roof

The calculation results show that the PV annual power generation of flat roof of the office building is 17081 kWh, and the figure for slope roof is 176782 kWh. Due to the characteris-

tics of office building that most of its power consumption is concentrated during the daytime which matches the high efficiency period of PV power generation. Therefore, the integration of solar building's roof and photovoltaic with optimized design will effectively reduce office building and other buildings' energy consumption (Yang Shanqin. 1997).

DISCUSSIONS

Through the above analysis, we can conclude that the integration of roof and photovoltaic has many forms based on the roof's type and the design concept, but these designs rarely synthetically consider aesthetics, technology and energy saving, which caused many problems such as roof space, hot spot, unreasonable PV panels' angle and direction. The paper put forward a new design method which synthetically used SKETCHUP and PVSYSYSTEM that can solutes problems which are common in the design of integration of roof and photovoltaic aims to aesthetics, technology and energy saving.

CONCLUSIONS

The integration of roof and photovoltaic not only makes architecture an energy consumer, but also an energy provider. A scientific and appropriate design of integration design will make a great contribution to energy-saving. Meanwhile, besides paying attention to form and style, meeting the elemental functions such as protection and isolation, the design should also be an integrated design based on the building which focusing on the use of environmental advantages, unifying with the whole structure of the building and paying more attention to the roof system's energy-saving design. With the development of the utilization of solar energy and integration of architecture, new design methods of roof integration are derived from many cases that the roof design is not only a traditional addition or a design with covert attitude anymore. This integrated design still should be an exploring direction which should not only ensure efficiency, meet demand and overall consideration of cost, but also truly integrate design with the building to achieve the perfect combination of technology and art.

REFERENCES

- Bernhard Weller. 2010. *Detail Practice: Photovoltaics, Technology, Architecture, Installation*. Birkhauser Press.
- Friedrich Sick and Thomas Erge. 1996. *Photovoltaics in Buildings: A Handbook for Architects and Engineers*. Birkhauser Press.
- Guo Juanli, Gao Hui, Wang Jiehui, Feng Ke. 2012. BIPV Design and Case Students of Solar Architecture Skin: Take the Solar Decathlon Europe 2010 for Example. *New Architecture*. (04):89-92.
- Hai Tao, He Jiang. 2015. *Application of integrated technology of solar energy building (Photovoltaic part)*. Science Press.
- Li Baofeng and Li Gang. 2010. Building skin——Study on building skin design in hot summer and cold winter zone. *China Architecture & Building Press*, 6-16.
- Peter Gevorkian. 2007. *Solar Power in Building Design: The Engineer's Complete Project Resource*. McGraw-Hill Professional Press.
- Peder Vejsig Pedersen, Jakob, Klint, Karin, Kappel. 2015. *Green Solar Cities*. Routledge Press.
- Tao Chengqian. 2004. The technical and artistic analysis of the roof—architectural entity factor. *Master Thesis*, Hefei University of technology (China), 104 pages.
- Yang Shanqin. 1997. *Civil building energy saving manual*. China Architecture & Building Press. 6.
- Zheng Cunyao. 2007. Research on design & application of integration of solar energy technology with roof. *Hebei University of Technology (China)*, 72 pages.

Thermal performance of PCM-glazing unit under moderate climatic conditions

Anna Wieprzkowicz^{1,*}, Dariusz Heim¹

¹Lodz University of Technology, Department of Environmental Engineering, Poland

*Corresponding email: anna.wieprzkowicz@p.lodz.pl

ABSTRACT

Considering physical properties, transparent or translucent building components like windows or glazing facades are the weakest elements of building envelope. The heat transfer coefficient of such elements is approximately four times higher than for opaque partitions, which causes considerable increase of heat loss during winter. In summer relatively high solar transmittance is a source of heat gains which results in undesirable overheating. Application of phase change materials in glazing components affects its thermal performance by the increase of its heat capacity and decrease of solar heat gains, with regard to the current physical state of the PCM.

The aim of this paper is investigation and determination of the thermal performance of PCM-glazing unit, under real, moderate climatic conditions in summer season. Analysis conducted by the authors aims to find the proper arrangement of PCM-glazing unit and proper material properties design, allowing effective overheating control.

To meet the stated goals, dynamic simulations of thermal performance of triple-glazing unit were carried out, using ESP-r software. It was assumed that one chamber, filled with PCM will adjust the solar heat gains flux while the second one will assure required thermal resistance of the partition. Original model of heat transfer through transparent partition, taking into account latent heat storage by effective heat capacity method was applied. Different phase change materials, characterized by various phase transition temperatures were considered in the analysis.

Based on the obtained results it can be concluded that application of a PCM in the external cavity of the triple glazing window effectively affects the thermal performance of the component, stabilizing the diurnal temperature fluctuations. Simulation results revealed that transition temperature should be close to the assumed cooling set point.

KEYWORDS

latent heat, façade, simulation, overheating, solar energy

INTRODUCTION

Transparent elements of the facades, in terms of physical parameters, are one of the weakest link of the building envelope. Because of approximately four times higher value of heat transfer coefficient for windows than for opaque partitions, glazing elements are the cause of the most heat losses during the winter. In addition, in the summer, their relatively high solar transmittance is a source of unwanted heat gains that cause overheating of single rooms and entire buildings. Moreover, during the whole year, the asymmetry of radiation in the areas next to the windows causes deterioration of thermal comfort conditions. Transparent elements cause both higher heat losses in winter and are the source of undesirable heat gains from solar radiation during the summer. An additional disadvantageous physical feature of these elements is their very low heat capacity due to which dynamic processes occurring in the glazing are reflected in the dynamic changes of parameters of the internal environment. On

the other hand, the transparent components are indispensable elements of the external partitions, ensuring the required amount of daylight in the rooms and the visual contact with the external environment, which is necessary for the users.

Modification of the optical and thermal properties of glass components using PCM is a relatively new issue. Nevertheless, some simulation analyses and laboratory-scale studies on this subject can be found in the literature. The first theoretical and experimental analyses concerning the determination of solar transmittance by double-glazed component filled with air and PCM were published fifteen years ago (Ismail and Henriquez, 2002). Similar studies, investigating the possibility of limitation of both heat losses and heat gains through transparent partitions by their modification with PCMs, were presented by Weinlader et al. (2005). In recent years, theoretical considerations to determine the thermal effect of PCM application with different transition temperatures under specific climatic conditions (Zhong et al. 2015) and their experimental validation (Li et al. 2014) have been also conducted. However, despite many attempts to develop the numerical model of the multi-pane system (Goia et al. 2012), the majority of experimental work was carried out for double glass unit (Goia et al. 2014) or commercially available glazing component with PCM (Grynning et al. 2015). Another important issue is analysis of the optical properties of transparent elements modified with PCM (Heim, 2011). The considerations presented in the paper start research project aiming to develop a translucent multi-layer component, adjusted for selected locations. In the framework of the project it is planned to develop and test a solution that, thanks to the use of PCM, will improve the energy efficiency of the transparent partition while maintaining (at least periodically) the physical characteristics of the translucent barrier. Theoretical analysis, presented in the paper, was carried out for moderate climate conditions, for the location of Lodz, Poland. The location have been selected due to the further experimental part of a research in a real scale, which will also be used to validate the numerical model of the developed PCM-glazing component.

MATERIALS AND METHODS

PCM-glazing arrangement

The scope of the analysis presented in the paper covers the design of the PCM-glazing parameters that will contribute to the reduction of overheating of the building under moderate climatic conditions. Similar concept was proposed by (Komerska et al. 2015), when PCM layer was used as a part of external dynamic solar shading system. In order to meet the stated goal of the research, preliminary analysis of the PCM-glazing arrangement was conducted. Furthermore, for the stated component composition analysis of the PCM melting temperature was done.

In accordance to the current requirements regarding thermal insulation of windows, it was assumed that for moderate climatic conditions, triple-glazed windows should be considered. Such window construction gives also the possibility of filling one of the window cavities with a phase-changing material, while the second one provides required thermal insulation. Two possible PCM-glazing arrangements allowing to meet the stated assumptions were presented in Figure 1.

Besides the possibility to regulate the daylight access, the main purpose of the PCM application was to decrease the energy demand for cooling by the reduction of the excessive solar heat gains. Based on the preliminary analysis it was stated that for summer conditions PCM should be placed in a cavity located from outside (Fig. 1a). In the cooling season the PCM will play a role of dynamic insulation by storing solar energy during a period of substantial solar heat gains. In that case the active layer (PCM) is located in a distance from indoor environment. The inner cavity limits the heat transfer from PCM layer to the room. During the night when external temperature drops down below solidification point the heat

will be released into external environment by conduction and radiation. Additionally, in a solid state the material is characterised by lower solar transmittance what will additionally contribute to the reduction of solar heat gains. Due to the further plan of experimental research, it was assumed that the case designed for the cooling period will be analysed for the east oriented façade, characterized by a significant heat gains in the morning hours.

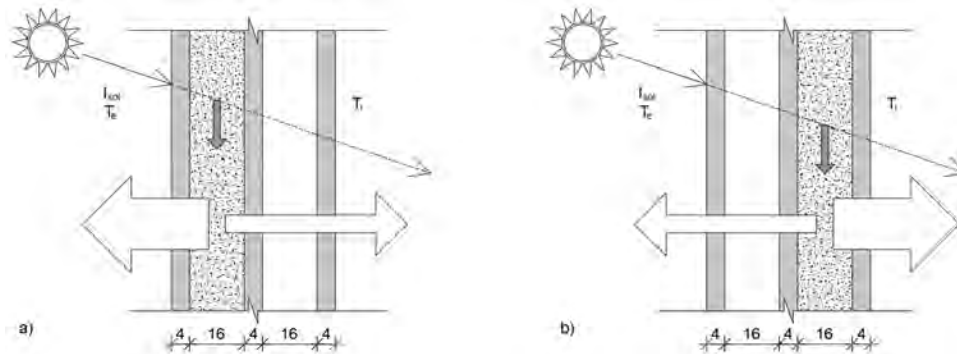


Fig. 1. Two possible arrangements of PCM glazing: a) PCM located from outside, b) PCM located from inside.

To confirm the above considerations, a simulation analysis was carried out, which allowed to compare distributions of the mean temperature in the three cases: reference one – without PCM, with PCM filling external cavity and with the PCM filling internal cavity (Fig. 2). It can be concluded that replacement of highly insulating but low capacity gaseous medium with PCM contributes to the lowering the temperature in the window. Moreover, PCM placed in the external cavity reveals greater ability to reduce the temperature rise due to solar radiation incidence on the facade, which confirms assumptions of preliminary analysis.

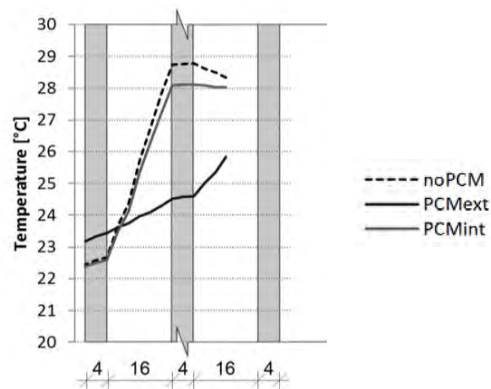


Fig. 2. Distribution of mean temperature in traditional window, PCM-glazing filled with external and internal cavity filled with PCM during cooling season.

Case study

Analysis of the transition temperature of the PCM was conducted for the single zone, office room with only one external wall equipped with centrally positioned, square window (1 m wide and high). Regarding considerations presented above, triple glazing unit with external cavity filled with PCM was further analysed. Numerical analysis was conducted in ESP-r computational environment (Clarke, 2001). Latent heat accumulation due to PCM application was calculated using effective heat capacity method, which was previously validated by the authors for opaque elements (Heim and Wieprzkowicz, 2016). Additionally, change of optical

properties of PCM-glazing was included in the analysis. Values of visible transmittance, absorbance and reflectance of solar radiation for the window component filled with liquid and solid PCM were determined based on the previously conducted measurements.

The materials considered in this research were selected based on the climate conditions analysis. It was assumed that, since the phase transition is triggered by the temperature rise, melting temperature of PCM placed in external cavity of the window should be suited for external temperature fluctuations (according to Typical Meteorological Year) characteristic for the analysed location (Lodz, Poland) and period of time (June-August). Thermal performance of the PCM-glazing window with four different paraffins (Table 1) was compared with the reference case of the triple glazed window with both cavities filled with argon. It was assumed that change of optical properties occurs at peak melting temperature, but material undergo phase transition in the whole given temperature range.

Table 1. Thermal properties of analysed paraffins.

PCM	Peak melting temperature [°C]	Phase transition temperature range [°C]	Latent heat capacity [kJ/kg]	Specific heat [kJ/kg·K]	Density [kg/m ³]
RT18HC	18	17-19	260	2000	880
RT22HC	22	19-24	190	2000	880
RT25HC	25	18-26	230	2000	880
RT28HC	28	26-29	250	2000	880

RESULTS

The analysis of the potential of PCM-glazing to limit the excessive solar heat gains was made based on the numerically calculated temperatures inside of the glazing unit and adjacent zone (Figure 3).

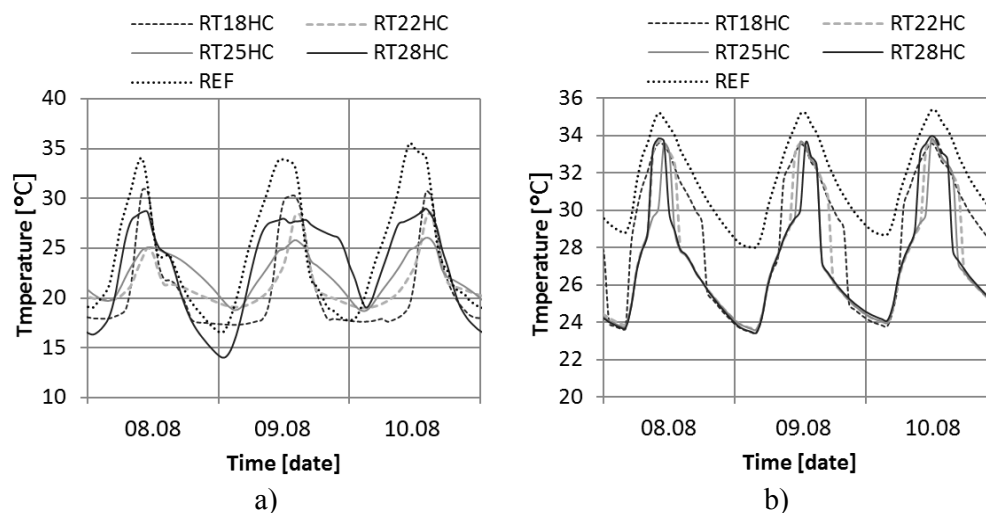


Figure 3. Temperature changes during 3 selected days: a) in the external glazing cavity, b) inside the room adjacent to the façade equipped with PCM-glazing.

Based in the results presented in Figure 3a it can be observed that in each case of PCM application the temperature is stabilized at the melting temperature level, during specific periods of time, during analysed days. It means that in all analysed cases the phase transition and latent heat accumulation occurred, but with different thermal effect. Analysing the

temperatures in the external cavity of the window, it can be observed that the highest daily peak temperatures were obtained for the paraffin with the lowest melting temperature, which stores the thermal energy mostly in the night hours. The lowest daily peak temperatures in that location were obtained for the paraffin RT25HC, which allowed to keep the temperature in the thermal comfort range for almost whole analysed 3-days period of time.

As the main purpose of the PCM application in the glazing unit was reduction of the temperature inside the adjacent room the results presented in Figure 3b reflects the thermal performance of four analysed paraffins compared to the reference case. Due to diversified melting temperatures, the increased rate of temperature rise can be observed in a different moments of the day. The material that allows to keep the possibly lowest zone temperature is paraffin with the melting temperature around 25°C.

Further, quantitative evaluation of the thermal effect of PCM-glazing application on the overheating control inside adjacent zone was done using the value of Degree-Hours of Overheating (*DHO*), which reflects the time and level of exceedance of maximum temperature of thermal comfort, calculated as:

$$DHO = \sum_{i=1}^n (T_i - 25) \cdot t \quad [\text{degC} \cdot \text{h}] \quad (1)$$

where T_i is instantaneous value of the room temperature [°C], t is length of the time step of calculation [h], i is subsequent number of the time step [-] and n is number of the time steps of analysis [-].

Additionally, number of hours of overheating was calculated (Fig. 4b), which showed that none of the analysed materials filling the cavity of glazing unit is able to totally prevent from overheating. For all analysed paraffins very similar number of hours of overheating was obtained, which confirmed the phenomena that could be observed for 3 selected days presented in Figure 3, that temperature below 25°C was register during the same periods of time. Together with the analysis of the calculated values of *DHO* parameter (Fig. 4a), it also proves (for the whole analysed period of time) that application of PCM contributes to the reduction of overheating but efficiency of such solution depends on the transition temperature of the material. The lowest value of *DHO* was obtained for the paraffin with melting temperature around upper limit of thermal comfort. Application of such kind of PCM in the glazing component allowed to obtain twice lower value of *DHO* parameter and reduces number of hours when overheating occurred by 26%.

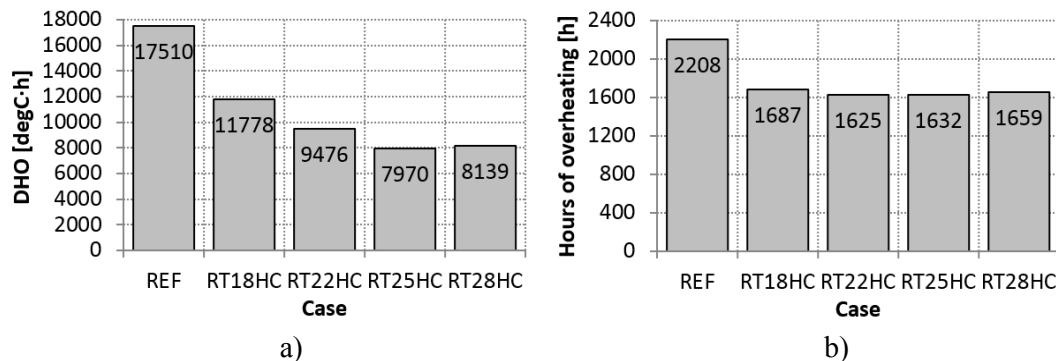


Figure 4. Calculated values of: a) Degree-Days of Overheating, b) Hours of overheating, for 5 analysed cases.

CONCLUSIONS

The paper presents the results of the theoretical analysis aiming to determine the basic technical parameters of the translucent construction component and thermal properties of the PCM filling the external window cavity. It was assumed that the component is to be designed for storing thermal energy of solar radiation and reducing overheating. The PCM-glazing arrangement dedicated to the selected location and the characteristic climatic conditions have been analysed. The main purpose of the presented research was selection of the phase change materials that could effectively reduce heat gains through a transparent partition.

On the basis of the analysis of the material transition temperature, the material recommended for further experimental investigation was selected. It was stated that the most effective performance was observed for paraffin with melting temperature of 25°C, which will be further experimentally tested in the real scale PCM-glazing component under moderate climatic conditions.

ACKNOWLEDGEMENT

This work was funded in a framework of ERANet-LAC 2nd Joint Call on Research and Innovation by NCBiR as part of the project entitled: Solar hybrid translucent component for thermal energy storage in buildings (acronym: SOLTREN).

REFERENCES

- Clarke J.A., 2001. *Energy Simulation in Building Design*, 2nd edition, Butterworth-Heinemann, Oxford 2001.
- Goia F, Perino M, Haase M. 2012. A numerical model to evaluate the thermal behaviour of PCM glazing system configurations. *Energy and Buildings*, 54, 141–153.
- Goia F, Perino M, Serra V. 2014. Experimental analysis of the energy performance of a full-scale PCM glazing prototype. *Solar Energy*, 100, 217–233.
- Grynning S, Goia F, Time B. 2015. Dynamic thermal performance of a PCM window system: characterization using large scale measurements. *Energy Procedia*, 78, 85–90.
- Heim D, Wieprzkowicz A. 2016. Positioning of an isothermal heat storage layer in a building wall exposed to the external environment. *Journal of Building Performance Simulation*, 9, 542-554
- Heim D. 2011. *Modyfikacja termo-optycznych właściwości transparentnych elementów obudowy budynków*. PAN, Warszawa.
- Ismail K.A.R, Henriquez J.R. 2002. Parametric study on composite and PCM glass systems. *Energy Conversion and Management*, 43, 973-993.
- Komerska A, Bianco L, Serra V, Fantucci S, Rosiński M. 2015. Experimental Analysis of an External Dynamic Solar Shading Integrating PCMs: First Results. *Energy Procedia*, 78, 3452-3457.
- Li S, Zhong K, Zhou Y, Zhang X. 2014. Comparative study on the dynamic heat transfer characteristics of PCM-filled glass window and hollow glass window. *Energy and Buildings*, 85, 483–492.
- Weinlader H., Beck A., Fricke J. 2005. PCM-facade-panel for daylighting and room heating. *Solar Energy*, 78, 177–186.
- Zhong K, Li S, Sun G, Li S, Zhang X. 2015. Simulation study on dynamic heat transfer performance of PCM-filled glass window with different thermophysical parameters of phase change material. *Energy and Buildings*, 106, 87–95.

A Deep Reinforcement Learning Method for Model-based Optimal Control of HVAC Systems

Zhiang Zhang^{1,*}, Chenlu Zhang¹ and Khee Poh Lam^{1,2}

¹Carnegie Mellon University, Pittsburgh, PA, USA

²National University of Singapore, SG

*Corresponding email: zhiangz@andrew.cmu.edu

ABSTRACT

Model-based optimal control (MOC) methods have strong potential to improve the energy efficiency of heating, ventilation and air conditioning (HVAC) system. However, most existing MOC methods require a low-order building model, which significantly limits the practicability of such methods. This study develops a novel model-based optimal control method for HVAC supervisory-level control based on the recently-proposed deep reinforcement learning (DRL) framework. The control method can directly use whole building energy model, a widely used flexible building modelling method, as the model and train an optimal control policy using DRL. By integrating deep learning models, the proposed control method can directly take the easily-measurable parameters, such as weather conditions and indoor environment conditions, as the input and controls the easily-controllable supervisory-level control points of HVAC systems. The proposed method is tested in an office building to control its radiant heating system. It is found that a dynamic optimal control policy can be successfully developed, and better heating energy efficiency can be achieved while maintaining the acceptable indoor thermal comfort. However, the “delayed reward problem” is found, which indicates the future work should firstly focus on the effective optimization of the deep reinforcement learning.

KEYWORDS

Deep Reinforcement Learning, HVAC Optimal Control, Energy Efficiency

INTRODUCTION

Heating, ventilation and air conditioning (HVAC) system is the major energy consumer in US office buildings. As a result, model-based optimal control (MOC) strategies become popular in the building industry in recent years due to its potential to save HVAC operation energy consumption. The most popular type of MOC is model predictive control (MPC) which, in real-time, uses a model to predict the future evolution of a process and calculates the optimal control decision for the current time step. However, MPC requires the model to be low-order, which is difficult for multi-zone buildings. This significantly limits its practicability. Therefore, some studies focus on using whole building energy model (BEM), a widely-used flexible physical-based building modelling method, in the predictive control of HVAC. However, the slow computational speed of BEM is the major limitation (Zhang and Lam, 2017).

Reinforcement learning (RL) is another alternative for the optimal control of HVAC systems. A standard RL control problem involves a learning agent (hereafter called “RL agent”) interacts with the environment in a number of discrete steps to learn how to maximize the returned reward from the environment, as shown in Figure 1 (Sutton and Barto, 2017). RL is a “model-free” method because the model is used as a simulator offline to let the RL agent learn

the optimal control policy. The slow computational speed of BEM is no longer a problem because of the “model-free” feature. However, conventional RL methods need the expert knowledge to design the algorithm and cannot be easily scaled for complicated control problems.

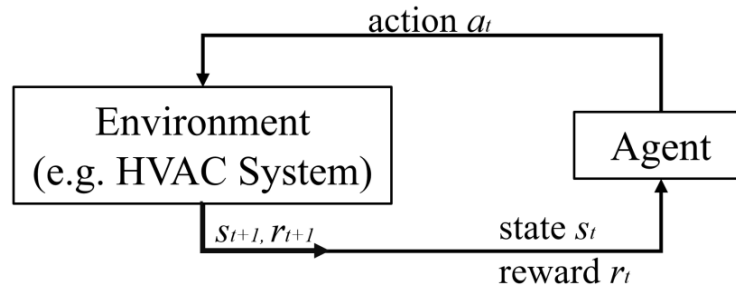


Figure 1. A Standard Reinforcement Learning Setting (Sutton and Barto, 2017)

Deep reinforcement learning (DRL), which uses deep learning models as the core of RL, becomes popular in recent years. DRL makes the "end-to-end" control possible, i.e. the DRL agent can take raw observations as the input and provide raw control actions as the output. Comparing with the conventional RL, DRL no longer requires the expert knowledge to design the algorithm and can be easily scaled for different control problems. However, HVAC optimal control using DRL is studied at an infant stage of research with very limited existing studies using only simple hypothetical building models as the case studies (Li et al., 2017; Wang et al., 2017; Wei et al., 2017).

This study proposes a framework (named “BEM-DRL”) that uses DRL to develop the optimal control policies of HVAC systems based on BEM. The processes, including building modelling, model calibration, DRL training, and control deployment, are explained by using a real-life office building as the case study. The energy efficiency and thermal comfort performance of the proposed control method are analysed using the building model. In addition, the optimization problems of the DRL training are discussed.

METHODS

The BEM-DRL framework is shown in Figure 2, which includes four steps:

1. BEM modelling: The building and its HVAC system are firstly modelled using BEM tools. In this study, EnergyPlus (Lawrence Berkeley National Laboratory, 2016) is used as the BEM tool.
2. HVAC model calibration: The BEM needs to be calibrated against real HVAC operation data. In this study, Bayesian calibration using the method proposed by Chong *et al.* (2017) is used.
3. DRL agent training: The DRL agent will be trained off-line using the calibrated BEM to learn the optimal control policy. The DRL state, reward and action design will be determined based on the building sensor data availability, control optimization objectives and HVAC system control capability. Asynchronous advantage actor critic (A3C) (Mnih et al., 2016) is the DRL training algorithm using this study. A3C surpasses other methods in its smaller computational memory usage and faster computational speed using only CPUs.
4. Control deployment: The trained DRL agent will be deployed to the actual HVAC system using the existing building automation system (BAS) infrastructure.

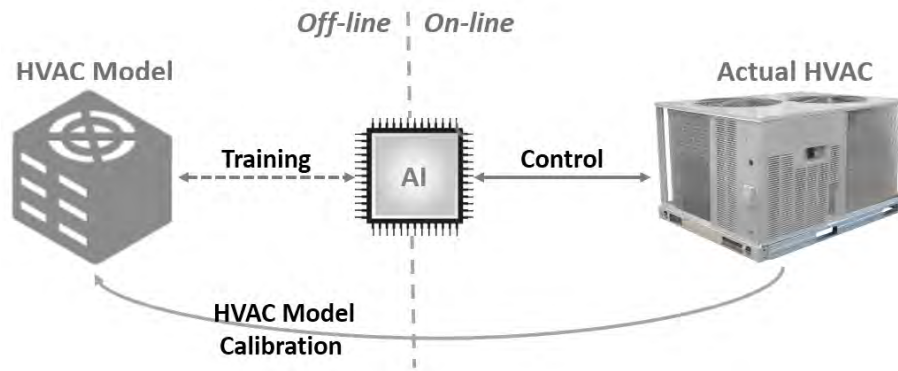


Figure 2. BEM-DRL Framework

RESULTS

The BEM-DRL framework is demonstrated using the Intelligent Workplace (IW) building located in Pittsburgh, PA, USA to control its heating system.

BEM Modelling and Calibration

The case study building, IW, is a one-level office building built on top of an existing building in 1997 with a complete building automation system installed. It has an area of approximately 600m², with about 20 regular occupants and a 30-person classroom.

IW uses a water-based radiant heating system that is integrated with the mullion of the window frames. The hot water for the radiant system is supplied by a steam-to-water heat exchanger in the campus. The hot water flow rate is constant while the hot water temperature is variable to respond to different heating demands. The hot water temperature setpoint is currently calculated by a PID controller based on the difference between the zones' average indoor air temperature and its setpoint.

Table 1. Modeling Errors after Calibration

Item	MBE	CVRMSE
Average Indoor Air Temperature	5-min: 0.52%	5-min: 4.82%
Heating Energy Consumption	Hourly: 0.43%	Hourly: 35.96%, Daily: 10.46%

MBE: Mean Bias Error, CVRMSE: Coefficient of Variation of the Mean Squared Error

The BEM of IW is calibrated for the heating energy consumption and indoor average air temperature. Three months measured data in the heating season of Pittsburgh, Jan 1st 2017 to Mar 31st 2017 with 5 minutes interval, is used for the calibration. The heating energy consumption is a calculated value based on the measured radiant system inlet/outlet water temperature and water mass flow rate. The modeling errors after the calibration is shown in Table 1. It is shown that the average indoor air temperature and aggregated heating energy consumption have been calibrated with the acceptable errors.

DRL Agent Training Setup

A DRL problem is defined by the design of the state, action and reward.

The state is a vector representing the environment observations, which includes the following items in this study:

[time, outdoor air temperature, outdoor air relative humidity, wind speed, wind direction, diffuse solar radiation, direct solar radiation, IW steam heat exchanger on/off status (HXOp),

IW average PPD (PPD)¹, IW Mullion system supply water temperature setpoint (MULLSSP), IW average indoor air temperature (IAT), IAT setpoint (IATSSP), IW occupancy mode flag (OCCU)², IW heating demand (E_{hvac})

All items can be easily accessed through the BAS of IW.

The action space includes the discretized Mullion system supply water temperature setpoints from 20 °C to 65 °C with 5 °C interval, and an action to turn the IW steam heat exchanger off.

The reward function determines the control optimization objective. The objective of the study is to minimize the heating energy consumption and maximize the thermal comfort. The design of the reward functions may significantly affect the convergence of the deep reinforcement learning and the final control performance. An empirical reward function combining the heating energy consumption and the indoor thermal comfort is shown in Equation (1):

$$reward = - \begin{cases} [\tau * ([PPD - 0.1]^+ * \rho)^2 + \beta * E_{hvac}]_0^1 |_{Occu=1} \\ [\tau * [Stpt_{low} - IAT]^+ * \lambda + \beta * E_{hvac}]_0^1 |_{Occu=0} \end{cases} \quad (1)$$

where τ , β , ρ , λ , $Stpt_{low}$ are the tunable hyperparameters. τ and β control the relative weight between the HVAC energy efficiency and the indoor thermal comfort for the optimization; ρ is a scale factor to penalize large PPD value; λ is the penalty level for the indoor air temperature violation during the unoccupied hours, $Stpt_{low}$ is the indoor air temperature penalty threshold. Note all parameters are normalized.

The calibrated BEM of IW is used for DRL training and testing in this study. The DRL agent is trained in heating season (Jan to Mar) using the TMY3 weather data. The trained DRL agent is tested also for heating season but using the actual Jan-Mar weather data of 2017. The BEM simulation time step and the control time step are both 5 minutes. The $Stpt_{low}$ in Equation (1) is the indoor air temperature setpoint calculated by the IW BAS control logic.

Table 2. DRL Simulated Control Performance in Heating Season (selected experiments)

#	Hyperparameters		Training Model			Testing Model		
	Action Repeat ³	τ, β, c^4	Heating Energy (kWh)	PPD _{mean} (%)	PPD _{std} (%)	Heating Energy (kWh)	PPD _{mean} (%)	PPD _{std} (%)
Basecase	N/A	N/A	45302	10.48	4.48	43709	9.46	5.59
1	1	1.0, 1.5, 20	52806	8.72	4.31	47522	8.23	2.46
2	1	1.2, 2.5, 20	44549	11.58	5.35	39484	11.11	4.53
3	1	1.0, 2.5, 10	40101	16.09	9.46	37238	14.20	8.65
4	3	1.0, 1.5, 20	42255	11.46	4.26	38550	10.63	3.34
5	3	1.0, 1.5, 20	43532	10.63	4.23	39109	10.44	3.75
6	3	1.0, 2.5, 10	42104	11.49	4.24	37131	11.71	3.76

¹ PPD is short for Predicted Percentage of Dissatisfied, which is calculated by the BEM engine with the assumptions $C_{lo} = 1.0$, $Met = 1.2$ and $V_{air} = 0.137\text{m/s}$.

² The occupancy mode flag is determined based on a fixed schedule (the occupancy mode flag is 1 between 7:00 AM and 7:00 PM of weekdays, and between 8:00 AM and 6:00 PM of weekends)

³ Action repeat means the DRL agent repeats the same control action for multiple time steps.

⁴ ρ is determined by a function $\rho = 1/(PPD_{thres}/100 - 0.1)$. $\rho = 20$ and $\rho = 10$ correspond to $PPD_{thres} = 15$ and $PPD_{thres} = 20$ respectively, meaning the reward function (Equation (1)) returns the minimum value if the PPD exceeds the PPD_{thres} .

Simulated Control Performance

The energy consumption and indoor thermal comfort (evaluated by the mean of PPD and standard deviation of PPD) of different DRL agents trained with different hyperparameters are shown in Table 2. The basecase in the table uses the current control logic in IW. Four key hyperparameters are tuned including action repeat, and τ , β , ρ in the reward function. Action repeat benefits the DRL training stability but lowers the flexibility of the trained optimal control policy. τ , β controls the relative weight on the energy efficiency and thermal comfort in the DRL training, and ρ determines the constraint for the maximum PPD during the DRL training. As shown in the table, the relationship between the hyperparameters and the control performance may not be intuitive. This is caused by the delayed reward problem of the DRL training, i.e. the control actions may not take effect soon because of the slow thermal response of the radiant heating system. Further study is needed for the delayed reward problem. Out of the six experiments in Table 6, case 6 performs comparably the best, which saves 15% of the heating energy with only slightly worse indoor thermal comfort quality in the testing model.

Control Deployment

The deployment is based on the existing building automation system (BAS) of IW using BACnet as the communication protocol. Figure 8 shows the deployment architecture. The DRL agent overwrites the Mullion supply water temperature setpoint every 15 minutes through BACnet, and the internal control logic of the BAS controls the three-way water valve to reach the defined water temperature setpoint. A phone app (OpenHAB) is used to collect the occupants' thermal sensation feedbacks. Occupants can select one of the 7 choices from "warmest" to "coolest" reflecting how they want the indoor thermal environment to be. The collected feedbacks are passed to the DRL agent for the control calculation.

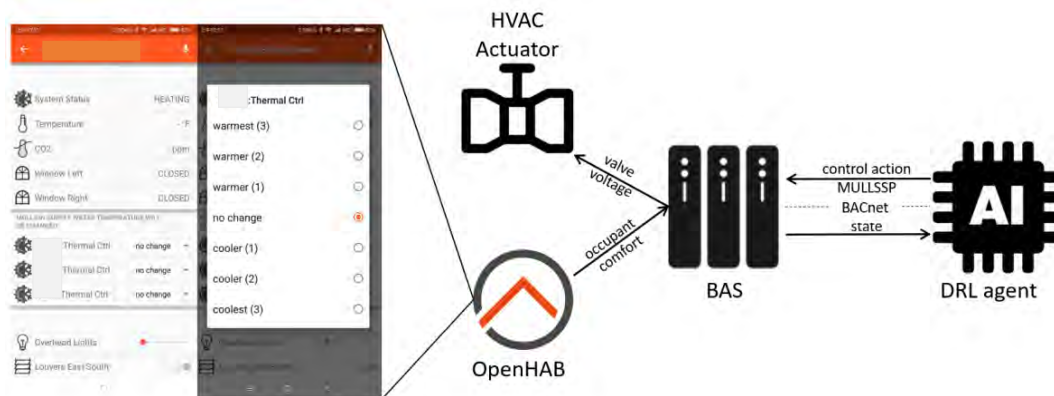


Figure 3. Deployment Architecture of the IW Case Study

DISCUSSIONS

The IW BEM has been calibrated with small error on most metrics, except the hourly CVRMSE for the heating energy consumption, as shown in Table 1. This may be because the hourly heating energy consumption of IW has large variance, which cannot be effectively captured by the BEM. However, aggregated energy consumption (e.g. daily) is more important than spot energy consumption (e.g. hourly) for energy efficiency research.

The slow thermal response of the IW radiant heating system causes the delayed reward problem in the DRL training. Therefore, the hyperparameters of the DRL must be tuned. It is found in Table 2 that some combinations of the hyperparameters can lead to better energy efficiency while maintaining the acceptable thermal comfort. However, no obvious trend has been found in the hyperparameter tuning. Structured method or guideline should be

developed, such as better reward function that can re-reward previous actions based on the future evolution of the controlled process.

The DRL agent has been deployed to IW using the architecture proposed in Figure 3. However, by the time this paper is written, the actual control performance test is not yet finished. Future work will study the actual control performance of the DRL agent.

CONCLUSIONS

This study develops a method to use deep reinforcement learning for the BEM-based HVAC optimal control. The method is demonstrated in a case study building with a radiant heating system. An EnergyPlus model is created for the building and calibrated using the Bayesian method. A3C is used to train a DRL agent to develop the optimal control policy for the system supply water temperature setpoint. By simulation, it is found that the optimal control policy can save about 15% heating energy while maintaining the acceptable indoor thermal comfort. This agent is deployed in IW through BACnet protocol and a phone app is used to collect the thermal sensation feedbacks from the occupants. Future work includes analyzing the actual control performance of the IW case study and developing a structured method to solve the delayed reward problem of the DRL training.

ACKNOWLEDGEMENT

The first author would like to thank the China Scholarship Council (CSC) for the financial support for the author's PhD study.

REFERENCES

- Chong, A., Lam, K. P., Pozzi, M., & Yang, J. (2017). Bayesian calibration of building energy models with large datasets. *Energy & Buildings*, 154, 343–355. <https://doi.org/10.1016/j.enbuild.2017.08.069>
- Lawrence Berkeley National Laboratory. (2016). EnergyPlus. Retrieved from <https://energyplus.net/>
- Li, Y., Wen, Y., Guan, K., & Tao, D. (2017). Transforming Cooling Optimization for Green Data Center via Deep Reinforcement Learning. Retrieved from <https://arxiv.org/abs/1709.05077>
- Mnih, V., Badia, A. P., Mirza, M., Graves, A., Lillicrap, T. P., Harley, T., ... Kavukcuoglu, K. (2016). Asynchronous Methods for Deep Reinforcement Learning. In *33rd International Conference on Machine Learning* (Vol. 48). New York, NY, USA. Retrieved from <http://arxiv.org/abs/1602.01783>
- Sutton, R. S., & Barto, A. G. (2017). *Reinforcement Learning: An Introduction* (Second Edi). Cambridge, MA, USA: MIT Press.
- Wang, Y., Velswamy, K., & Huang, B. (2017). A Long-Short Term Memory Recurrent Neural Network Based Reinforcement Learning Controller for Office Heating Ventilation and Air Conditioning Systems. *Processes*, 5(46). <https://doi.org/10.3390/pr5030046>
- Wei, T., Wang, Y., & Zhu, Q. (2017). Deep Reinforcement Learning for Building HVAC Control. In *Proceedings of the 54th Annual Design Automation Conference 2017*. Austin, TX, USA.
- Zhang, Z., & Lam, K. P. (2017). An Implementation Framework of Model Predictive Control for HVAC Systems: A Case Study of Energyplus Model-Based Predictive Control. In *ASHRAE 2017 Annual Conference*. Long Island, CA, USA.

AIR COOLING AND DEHUMIDIFICATION WITH A ZEOLITE COATED HEAT EXCHANGER REGENERATED BY SOLAR THERMAL ENERGY

Vincenzo Gentile¹, Marco Simonetti, Fabio Restagno

¹Politechnic of Turin, Department of Energy Galileo Ferraris, Turin, Italy

*Corresponding email: vincenzo.gentile@polito.it

ABSTRACT

This paper presents some experimental results of a new device for low energy/low exergy air conditioning system. The device can realize both dehumidification and sensible cooling of external air, and it is designed for very low pressure drops, drastically reducing the electricity consumption for the driving fans. It is composed by a finned coil heat exchanger, coated with a SAPO-34 zeolite layer, that handles both heat and mass transfer in a single component. During the adsorption a cold water flow at 20 °C circulates through the coil, cooling the air and realizing in a single step a complete air-treatment. Hot water produced with evacuated solar collector is then used to regenerate the zeolite.

Keywords: adsorption dehumidification, solar cooling, adsorption heat exchanger, experimental

1 INTRODUCTION

Cooling demand for air conditioning (AC) has continuously increased in the last decades. This because more and more buildings are provided with space cooling system to satisfy indoor comfort demand during warm and hot season (Werner, 2016) (Jakubcionis and Carlsson, 2017). Solar cooling is an alternative solution to traditional system that may attenuate the increase of electric consumptions associated to the cooling demand, and one of the simplest technology are the Desiccant Evaporative Cooling system (DEC). They are thermally-driven open cooling cycle, based on evaporative cooling and adsorption processes. In this technology, the dehumidification process is commonly carried out using desiccant rotors impregnated or covered by adsorption material (i.e. silica gel or lithium chloride) (Daou et al., 2006). Warm and dry air obtained from this step, is typically cooled using an indirect evaporative cooling module. Solar energy is used to regenerate the desiccant material, that dehumidifies moist air adsorbing vapor. Alternative configurations of the dehumidification component, the adsorption heat exchangers (ADS-HX) were explored (Finocchiaro et al., 2016), (Simonetti et al., 2016, 2017), (Zhao et al., 2016). These are static components in which there is the contemporaneous exchange of heat and mass between the air and the sorption material, and the heat between the adsorption material and a secondary fluid vector. The disposition of the adsorption material in a finned coil heat exchanger, typically used in air conditioning, can be different: surface coating on the fin or granular dispersion in the void volume. The goal of this research is to explore the use of renewable thermal energy, at temperature level between 55-80°C, to satisfy the latent load of the air conditioning using this type of technology in alternative of vapor compressor chillers. Savings in electricity consumption are attended.

2 METHODS

2.1 Adsorption heat exchanger

The component here presented is a fin and tube heat exchanger, typically used in HVAC system, in which all the exchanging surface, by tubes and fins, is coated with a zeolite. The advantage of this component, with respect to fixed packed bed (Finocchiaro et al., 2016), is the possibility to have contemporaneous heat and mass transfer between the air, the adsorptive mass, and a secondary thermal

vector fluid. The two working mode are represented in the scheme of Figure 1. During the **regeneration**, the heat is provided by hot water flow inside pipes of the heat exchanger. Then water vapor, previously captured by the zeolite, is released and transported by the air flow. The operation continues until the adsorption mean reach a sufficient level of drying to start the successive phase of dehumidification. After this operation the hot water flow is stopped and substituted by a cold water flow, circulating through the pipes of the same heat exchanger. This phase is the **cooled adsorption**: water vapor capture by zeolite reduces the moisture content of the air and produces heat, that is comparable with the latent heat of water evaporation. Previously tests of this component showed that the residual heat coming from the regeneration phase of the component influences significantly the dehumidification performance during the adsorption (Simonetti et al., 2016). This aspect combined with the heat generated by the adsorption phenomena result in low performance of the system. By cooling the coil during the adsorption, the increase of air and zeolite bed temperature is avoided and the material operates at its higher water adsorption capacity (Figure 2). Temperature level of water and flow rate regulates the equilibrium condition and the final temperature of the air at the outlet of the heat exchanger. Controlling these parameters, different air outlet condition can be achieved.

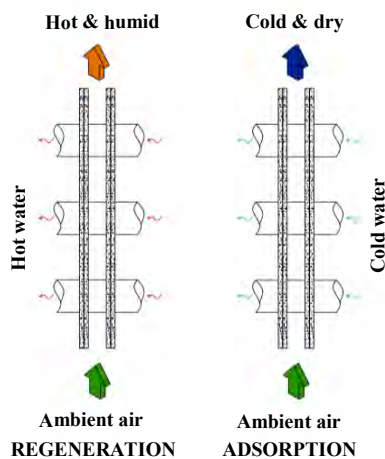


Figure 1. Scheme of the regeneration and adsorption phase of the zeolite SAPO-34 heat exchanger.

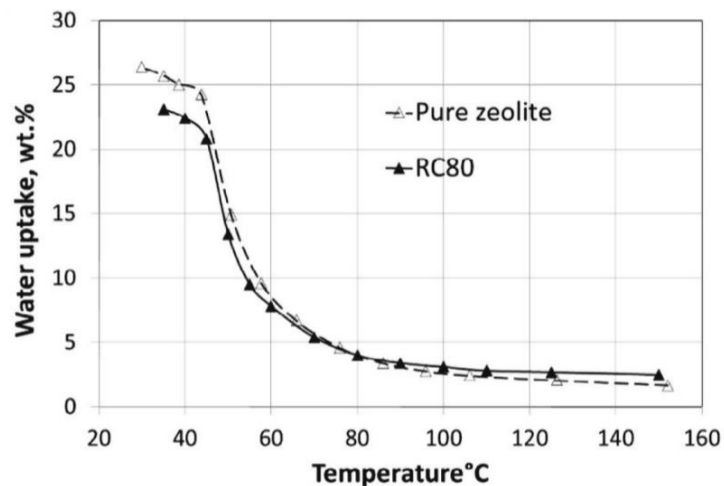


Figure 2. Comparison of the adsorption isotherm between pure zeolite SAPO-34, and the mixture coated on the surface of the heat exchanger (Simonetti et al.,2016) .

The type of zeolite used for this case study is the SAPO-34. Such material, belonging to the (silico) aluminophosphate family, shows a regular pores system, a three-dimensional network similar to zeolites and unusual adsorption properties regarding polar molecules, typically exhibiting a type V water vapor adsorption isotherm (Ng et al., 2008). These properties result in moderately low regeneration temperature (60- 100 °C) and a reduced desorption heat, while maintaining high performance within the adsorption cycle (Henninger et al. 2010). The coating procedure of the ADS-HX involves different steps (Simonetti et al.,2016), that influences the properties of the adsorption material. In particular the adsorption properties are slightly reduced respect to the pure SAPO-34, as showed in Figure 2. The final result of this manufacturing process is showed in Figure 4 and Figure 5.

2.2 Experimental set up

The experimental facility consists of two AHUs (Air Handling Units) that can process air flow rate (Q) in the range 100 ÷ 1500 m³/h (measured with calibrated flanges) controlling outlet temperature and humidity. Air temperature (T_a), humidity (X_a) and water temperature (T_w) sensors are distributed along the adsorption unit, as showed in Figure 3. In Table 1 the list of sensors and their accuracy employed in

the experimental activity is shown. The heat for regeneration is provided with 10 m² of evacuated solar thermal collectors and into a 500 lt thermal storage, equipped with an auxiliary electrical resistance of 3 kW. In Table 2 are reported the geometric characteristics of the finned coil heat exchanger, and the zeolite coating thickness is lower than 1 mm.

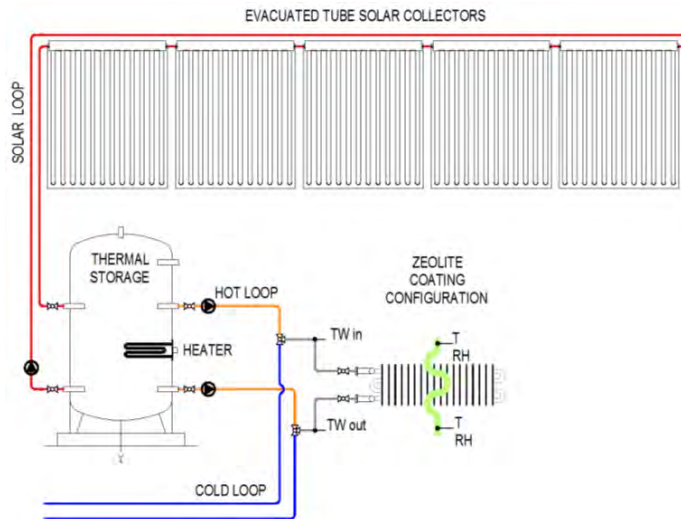


Figure 3. Scheme of the experimental set up for the test of the ADS-HX in laboratories of the Energy Department of Polytechnic of Turin.

Table 1. Sensor types and related accuracies.

Sensors	Accuracy	Unit
Air Pressure	± 0.2%	Pa
Air Temperature	± 0.4°C	°C
Water Temperature	± 0.3°C	°C
Relative Humidity	± 2%	%
Water flow rate	± 3%	kg/s
Air flow rate	± 7%	m ³ /h

Table 2. Dimensions of the finned coil

	d	n	p	L	D	H
	mm	-	mm	m	m	m
Fins	-	56	8	-	0.15	0.54
Tubes	15	24	-	0.45	-	-
Battery	-	-	-	0.45	0.10	0.54



Figure 4. Picture of the SAPO-34 ADS-HX

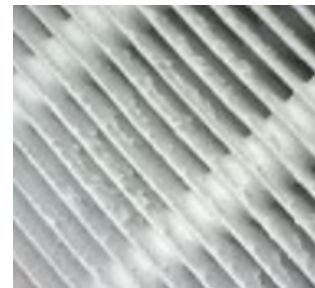


Figure 5. Zeolite coating on the HX

2.3 Test procedure

The tests aim to explore the transient dynamics of adsorption/regeneration cycle measuring air and water operational parameters at growing air flow rate. At the begin of each adsorption test the zeolite starts in a dry initial condition. The AHU prepares the air at the desired temperature and moisture content. Then adsorption tests start cooling down the zeolite with the cold-water loop; during this phase the air flow is mechanically driven by the fan of the AHU. When the air dehumidification goes below 1 g/kg the adsorption test ends. Then the fan of the AHU is stopped, and the water flow switched from cold to the hot circuit connected to the storage, fed by solar collectors. The same criteria of adsorption phase is used to stop the desorption one. During the regeneration natural ventilation of the heat exchanger occurs, thanks to the positive buoyancy, thermally generated. Air temperature and humidity as hot and cold water temperature and air pressure drops are continuously monitored and logged.

3 RESULTS

First, the adsorber air pressure drops were measured at different temperature (15 to 35 °C) ranging air velocity (v) from 0.2 to 1.6 m/s: the higher value is lower than 12 Pa (Figure 6). Further, three different operational tests have been carried out: air flow rate ranges from 220 to 430 m³/h; average regeneration temperature is 60°C; average cooling water is 20 °C; the water flow was around 2.7 liter/min throughout regeneration, and 22.4 during adsorption. Other information, such as operation time and moisture content are reported briefly in Table 3. The test 2 is depicted in Figure 7, to illustrate the behavior of all the physic parameters monitored during adsorption and regeneration.

Table 3. Average and deviation of the input test condition

	phase	time	Q	T _{a-in}	RH _{a-in}	T _w
		min	m ³ /h	°C	%	°C
Test 1	Ads	27	196.2 \pm 13.4	31.9 \pm 1.0	68.4 \pm 6.1	18.1 \pm 0.4
	Reg	29	67.4 \pm 21.0	28.7 \pm 1.0	48 \pm 6.9	61.5 \pm 3.7
Test 2	Ads	23	331.1 \pm 7.1	30.3 \pm 2.5	62 \pm 11.5	18.6 \pm 0.3
	Reg	25	67 \pm 21.0	29.7 \pm 0.6	30.5 \pm 3.5	63.1 \pm 3.2
Test 3	Ads	15	412.7 \pm 4.0	30 \pm 1.9	58.3 \pm 8.8	20.5 \pm 2.0
	Reg	22	83 \pm 20.0	29.8 \pm 0.4	27.4 \pm 4.3	62.7 \pm 2.9

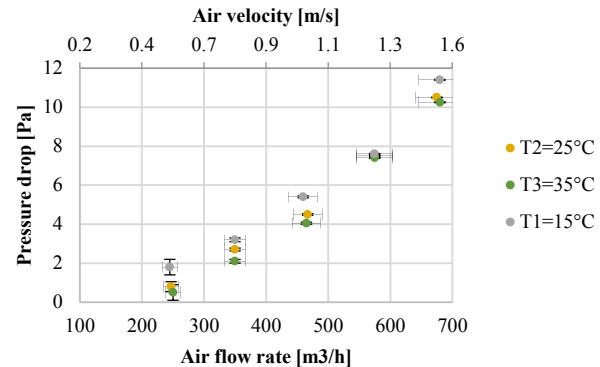


Figure 6. Zeolite SAPO-34 heat exchanger pressure drops

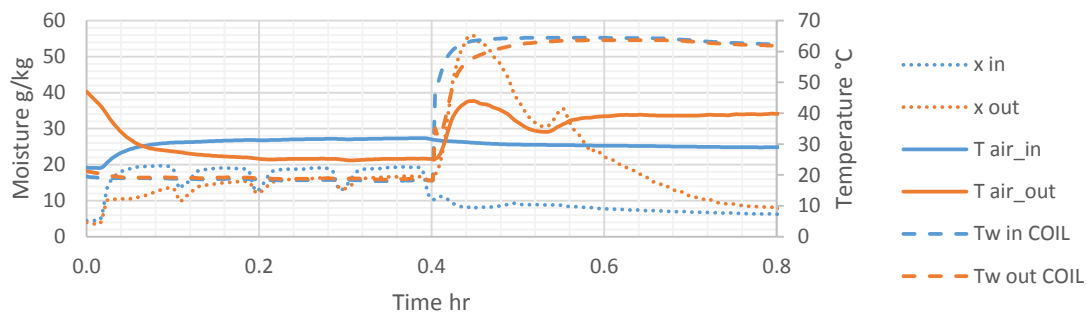


Figure 7. Behavior of the air and water physical parameters, temperature and moisture content, during an adsorption (time < 0,4) and regeneration (time > 0,4) test carried out on the adsorptive heat exchanger.

Adsorption had a duration of around 20 min, with an average dehumidification of 4 g/kg, and a maximum value of more than 8. Except for the initial transient, outlet temperature was always lower than the inlet. Regeneration had a similar duration, but with less than 1/5 of the adsorption air flow rate. Figure 8 and Figure 9 report the difference between a not cooled (with similar air inlet condition and flow rate of test n°2) and a cooled adsorption are showed. It can be observed how in the initial transient ($t < 1$ min) the cooling operation results in a higher exploitation of the zeolite, showing higher moisture removal, and a fast heat removal shifting air temperature below the inlet condition in less than 5 minutes. Increasing air flow rate, from the first to the last test, with similar air inlet condition during adsorption, has two significant results: a reduction of the maximum value of air dehumidification (from more than 8 to 6.5 g/kg), and an increase of the slope of the curve, as can be seen in Figure 10. This leads to a progressive reduction of the duration of the adsorption phase, from 30 to around 20 minutes. All these

characteristics are clearly depicted and summarized in Figure 11, in which the total thermal power (latent and sensible) exchanged between air and the ADS-HX is shown.

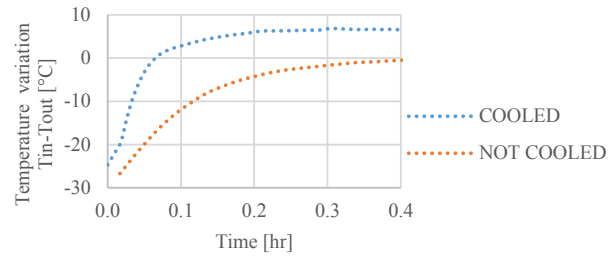
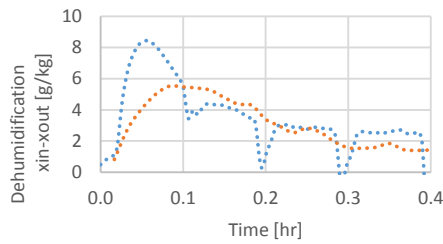


Figure 8. Differences on dehumidification curves in an adsorption test with and without cooling, at same air flow rate.

Figure 9. Differences on air temperature variation in an adsorption test with and without cooling, at same air flow rate.

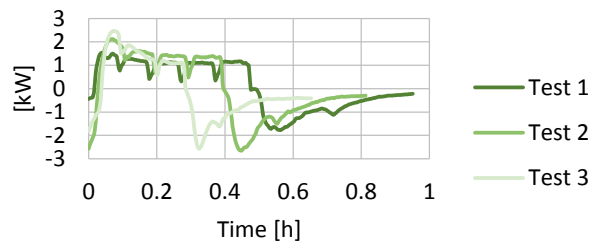
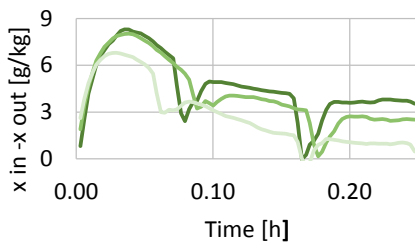


Figure 10. Effects of the air flow rate increase on air dehumidification during cooled adsorption, for the three different tests.

Figure 11. Thermal power exchanged between air and the ADS-HX during both adsorption (left part) and regeneration (right part), for the three different tests.

4 DISCUSSION

The integration of this component in traditional HVAC system (in particular for small size applications), to cool down and dehumidify humid air gives the possibility to directly exploit renewable energy. The low temperature of the hot source, 60°C, is compatible with the use of solar thermal systems to regenerate the component. In Figure 12 is compared the air transformation between the cooled adsorption and a typical condensing and re-heating process. Dehumidification by cooled adsorption ($\Delta h_{4-1} = -37$ kJ/kg) needs lower cooling energy at higher temperature ($T_{\text{cold water}}=18-20$ °C) than traditional system ($\Delta h_{4-1} = -45,3$ kJ/kg and $T_{\text{cold water}}=7-12$ °C). The temperature increase of the cold source enable the use of natural heat sink like groundwater. In order to guarantee a continuous supply service of cooling and dehumidification like in the graph, more components in parallel (at least two) have to be managed in a batch process. The frequency of switching between adsorption and regeneration is influenced by operational (temperature and vapor pressure) and geometric parameters such as the total exchange surface; the total amount of adsorbing mass; length of the exchange path. The optimization of these parameter need to be evaluated including the cost of the adsorbing material and installation costs related to the control system. A smarter geometric shape than the coated fin should lead to higher exchange surface per volume unit against a reduction of the manufacturing costs. Low switching frequency generally reduce the complexity of the control system resulting in a lean managing equipment.

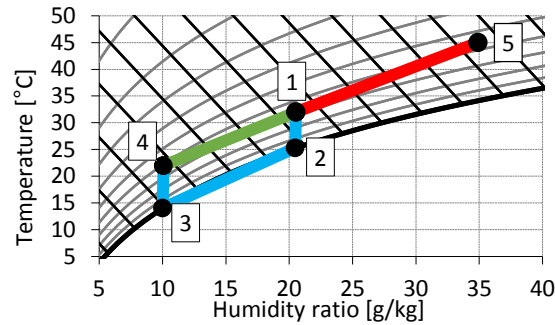


Figure 12. Comparison between cooled adsorption with traditional systems.

5 CONCLUSIONS

The coated-coil configuration presented is able to exchange heat and mass with the same device. The tested prototype can sustain for around 20 minutes an average dehumidification effect in the range 7-5 g/kg. Cooling the adsorption phase increased the dehumidification effect by around 30%, with evident benefits for the outlet air temperature. Similar devices can be considered for future applications in air-handling units substituting electrical consumptions of traditional cooling technologies with a sustainable heat demand, provided by solar energy and natural sink. The development of the prototype leads to increase performances and cost in order to obtain a more feasible solution for commercial applications.

REFERENCES

- Daou, K., Wang, R.Z., Xia, Z.Z. (2006). Desiccant cooling air conditioning: a review. *Renewable and Sustainable Energy Reviews*. Vol 10, pp. 55-77.
- Henninger, S., Schmidt, F., Henning, H.-M. (2010). Water adsorption characteristics of novel materials for heat transformation applications, *Applied Thermal Engineering*. Vol. 30, pp. 1692-1702.
- Jakubcionis, M, Carlsson, J. (2017). Estimation of European Union residential sector space cooling potential. *Energy Policy*. Vol 101, pp. 225-235.
- Simonetti, M, Gentile, V, Fracastoro, G V, Belmonte, R. (2017). Optimized low pressure solar DEC with zeolite based adsorption. *Energy Procedia*. Vol 122, pp. 1033-1038.
- Ng, Engh-Poh, Mintova, S. (2008). Nanoporous materials with enhanced hydrophilicity and high water sorption capacity. *Microporous Mesoporous Materials*. Vol. 114, pp.1-26.
- Simonetti, M, Gentile, V, Liggieri, L, Fracastoro, G V, Carrabba, M G. (2017). Experimental analysis of “NAC-wall” for hybrid ventilation mode. *Energy and Buildings*. Vol 152, pp. 399-408.
- Simonetti, M, Gentile, V, Freni, A, Calabrese, L, Chiesa, G. (2016). Experimental testing of the buoyant functioning of a coil coated with SAPO34 zeolite, designed for solar DEC (Desiccant Evaporative Cooling) systems of buildings with natural ventilation. *Applied Thermal Engineering*. Vol 103, pp. 781-789.
- Werner, S. (2016). European space cooling demands. *Energy*. Vol 110, pp. 148-156.
- Zhao, Y., Dai, Y., Ge, T., Wang, H., Wang, R. (2016). A high performance desiccant dehumidification unit using solid desiccant coated heat exchanger with heat recovery. *Energy and Buildings*. Vol 116, pp. 583-592.

Evaluating the Energy Consumption and Heat Loss in the Hot Water Supply and Heating Systems of a Nursing Home

Kana Inamoto¹, Chiemi Iba¹, Shuichi Hokoi², Daisuke Ogura¹ and Satoru Takada³

¹Kyoto University, Japan ²Southeast University, China ³Kobe University, Japan

*Corresponding email: be.inamotokana@archi.kyoto-u.ac.jp

ABSTRACT

The demand for nursing homes has increased recently due to an increase in the aging population in Japan. Nursing homes are generally equipped with hot water supply and heating systems for bathing, preparing meals, and heating rooms. This equipment utilizes a considerable amount of energy. Few studies have measured heat loss from the hot water supply and heating systems in such facilities. This study evaluated the hot water supply and heating systems of a nursing home located in a cold climate area in Japan.

The temperature and flow rate of the hot water were continuously measured, and the energy consumption and heat loss for each subsystem were calculated. These results clarified that the energy consumption in the hot water supply subsystem was slightly larger than that in heating subsystem. Inefficiencies of the system were also continuously evaluated throughout the study. Heat losses in piping attributed to 38% of the total energy consumed by the hot water supply subsystem. Subsequently, a thermal analysis of the hot water subsystem was performed. The calculated return temperature agreed with the measured return temperatures when the resistance of thermal insulation was decreased by an average of 45%; this result was possibly due to the deterioration of thermal insulation materials or the presence of thermal bridges.

KEYWORDS

Hot water supply, Energy consumption, Heat loss, Nursing home

INTRODUCTION

The aging population in Japan reached 26.7% of total population in 2017 and is expected to continue rising, thereby demanding more nursing homes for accommodation (Ministry of Health, Labor and Welfare 2016). These nursing homes consume a significant amount of hot water for bathing and preparing meals, thereby increasing the energy consumption. In addition, heating subsystems that use hot water are popular in cold regions, such as the location of the surveyed facility. While energy conservation in newly constructed buildings is being widely promoted, the importance of commissioning, which is a process to verify that the adopted building system is performing as planned, and energy management for existing buildings has attracted attention. The energy consumed by hot water supply systems accounts for 24%~38% in homes wherein energy consumption is <30 GJ/year (Murakami 2006). However, only a few studies have evaluated the hot water supply systems for nonresidential buildings. Nursing homes, in particular, have not been extensively studied; therefore, energy-saving strategies in such facilities are unavailable. Therefore, a quantitative evaluation of energy usage and heat loss from hot water systems in existing nursing homes will contribute to future energy conservation efforts in nursing homes.

In this study, we measured the temperature and flow rate for each part of the hot water supply and heating systems for a nursing home in Hokkaido, a cold region in Japan, and calculated

energy consumption based on the measurements. Furthermore, we identified the cause of heat loss in the hot water subsystems via numerical analysis.

CALCULATION OF ENERGY USED IN SYSTEMS

Methods

The surveyed building is a special nursing home for the elderly with a day service center situated in a cold region wherein the average temperature in the winter falls below 0°C. The building comprises a central part, which includes an office room, a meeting room, a day service room, a machine room and bathrooms, along with western and eastern wards with a total of 29 rooms for residents. Fig. 1 outlines the building.

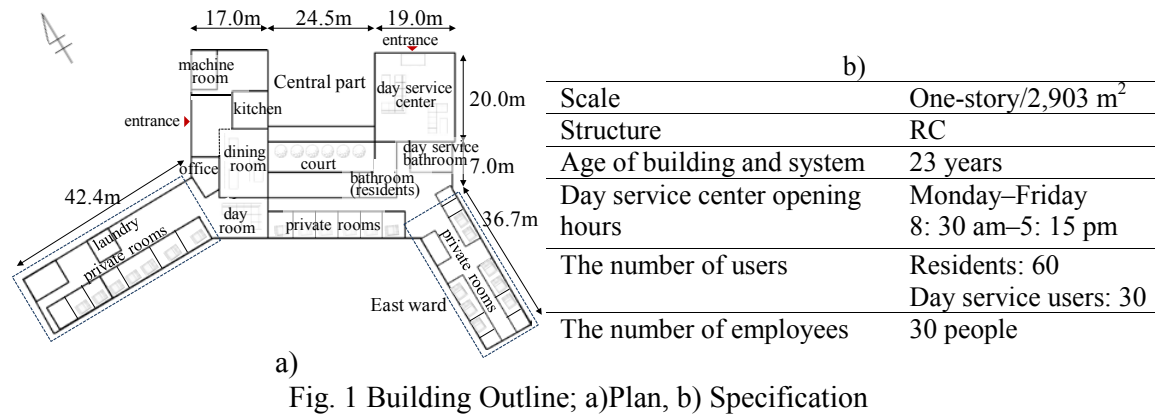


Fig. 1 Building Outline; a)Plan, b) Specification

Fig. 2 shows the schematic of the hot water supply and heating systems. The hot water is heated by two heavy-oil-fired boilers in the machine room and then used by the three subsystems. The first subsystem named “hot water supply subsystem (HWSS)” supplies hot water to each room. The second subsystem, named “heating subsystem,” circulates hot water to all hot water radiators and floor heating equipment throughout the facility. The third subsystem, “bathtub heating subsystem,” supplies heat to bathwater via a heat exchanger.

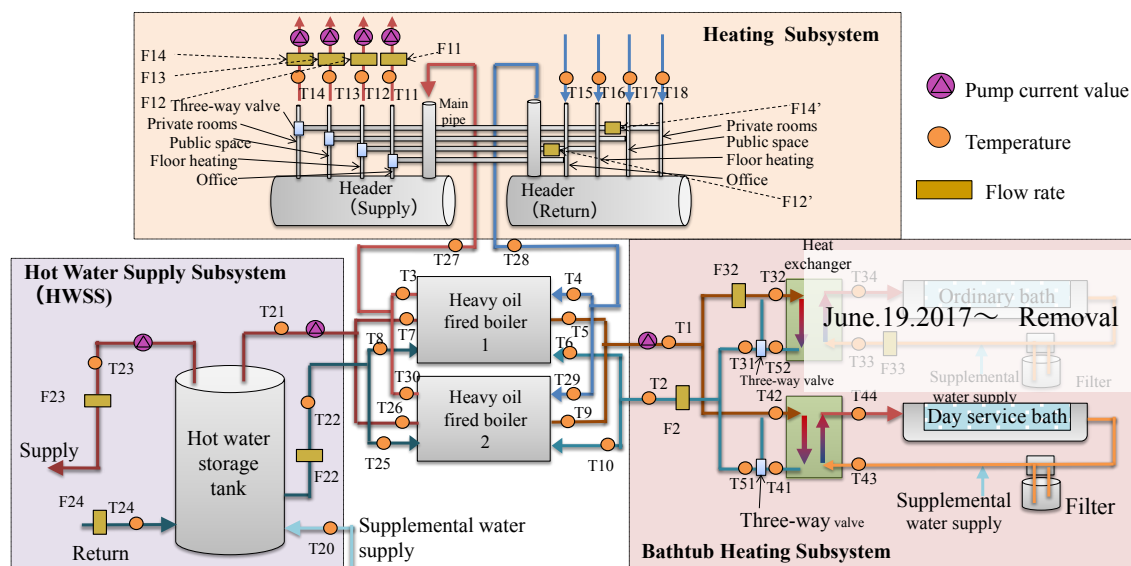


Fig. 2 Schematic of hot water supply and heating systems

Measured items

In this study, the hot water temperature, the flow rate in each subsystem, and the electric current for the pump were measured. The measurement points are shown in Fig. 2. T-type thermocouples were attached to the outer surface of the steel pipe, which was covered by thermal insulation material. The temperatures were mainly measured near the inlet and outlet of each component of the system, such as boilers, the hot water tank, hot water headers, and heat exchangers. The flow rate of the supplied hot water was measured continuously because it was not kept constant. On the other hand, the flow rates in the heating subsystem and bathtub heating subsystem were set to be constant, so measurements taken over a relatively short duration were used to estimate energy consumption. Since the pump was ON/OFF controlled, even in a subsystem with a constant flow rate, we determine the time when the hot water is flowing by the electric current for the pump. The measurements began on September 22, 2016, and the measurement interval was 1 min. The accuracy of T-type thermocouple is $\pm 0.5^\circ\text{C}$ and that of ultrasonic flowmeter is $\pm 1.0\%$ of flow rate. Taking these errors into consideration, the maximum error of heat amount is estimated to be $\pm 13.5\%$.

Use of heavy oil in each subsystem

Fig. 3 classifies the energy usage in the hot water supply and heating systems. Energy consumption indicated by the thick-lined frame was calculated by equations (1~5) using the measured data. We did not calculate the heat loss caused by the exhaust gas from the boilers or the heat release dissipation from the boiler surface.

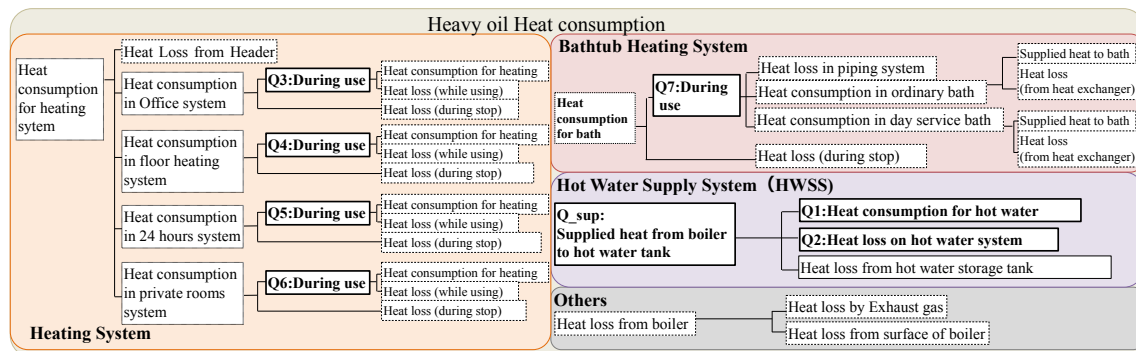


Fig. 3 Classification of energy use in hot water supply and heating systems

$$Q_{\text{sup}} = \sum_1^{1440} (T_{21}(t) - T_{22}(t)) \cdot F_{22} \rho c \Delta t, \quad (1)$$

$$Q_1 = \sum_1^{1440} (T_{23}(t) - T_{20}(t)) \cdot (F_{23}(t) - F_{24}(t)) \rho c \Delta t \quad (2)$$

$$Q_2 = \sum_1^{1440} (T_{23}(t) - T_{24}(t)) \cdot F_{24} \rho c \Delta t, \quad (3)$$

$$Q_3 = \sum_1^{1440} (T_{11}(t) - T_{16}(t)) \cdot F_{11} \rho c \Delta t, \text{ and} \quad (4)$$

$$Q_7 = \sum_1^{1440} (T_1(t) - T_2(t)) \cdot F_2 \rho c \Delta t. \quad (5)$$

In the HWSS, hot water is temporarily stored in the hot water storage tank (Q_{sup}). Q_{sup} is mainly transferred to the water as heat (Q_1), but some of the supplied heat is lost in the hot water pipes over the whole circulation pathway (Q_2) or from the hot water tank. The heating subsystem is comprised of four branches for office space, public space, private space and floor heating. Heat loss from the pipes occurs during both *on* and *off* operation. From the measured data, the total amount of heat consumed (including losses) during operation for the office space (Q_3) can be calculated. The heat consumption for the other spaces (Q_4 , Q_5 , and Q_6) are calculated in the same manner as Equation (4). In the bathtub heating subsystem, as with the heating subsystem, the total amount of heat during use (Q_7) can be calculated.

However, since the pumps are frequently *off* in this subsystem, it is necessary to take the heat loss during *off* operation into consideration. “T” and “F” in the equations correspond to those in Fig. 2, Q is the daily heat consumption [MJ/day], ρ is the water density [kg/m^3], c is the specific heat of water [$\text{MJ}/(\text{kg}\cdot\text{K})$], and F is the flow rate [m^3/min]. Δt is time interval [min].

Results and discussion

Fig. 4 shows the annual heavy oil use every week from Dec 1, 2016 to Dec 31, 2017. The bar graph shows each energy usage. While the energy consumption for the heating subsystem accounts for 17%, the HWSS accounts for 21%. Moreover, Heat losses in piping account for 38% of the energy consumption for the HWSS. The line graph shows the total energy consumption calculated based on heavy oil consumption. The difference between the sum of each energy usage and the total energy consumption can be 61% and is likely related to heat loss from the boilers. In this facility, the ON/OFF of the boiler was found to be very frequent. Every time the boiler is turned ON/OFF, it caused air purging to remove impurities, placing a large load on the boilers. In addition, a high air-fuel ratio of 1.3 or more is set. Heat loss from the boilers must be examined in detail in the future.

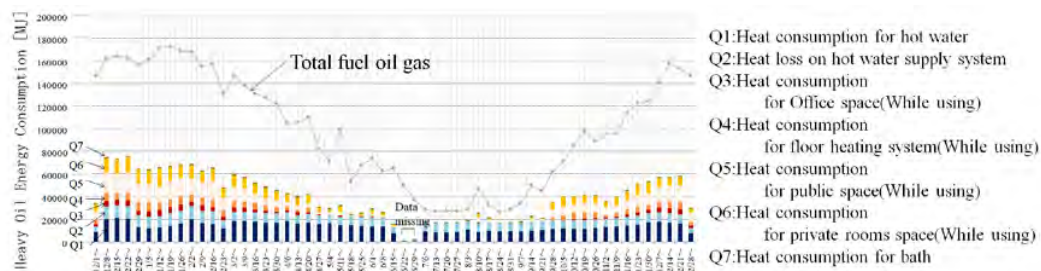


Fig. 4 Use of annual energy consumption of heavy oil in facilities

From Fig. 4, it can be seen that the energy consumption for the HWSS is quite large throughout the year, thus it would be efficient to lower the hot water set temperature. However, since the heat loss is also large, the hot water temperature may drop below a certain level ($45\sim 50^{\circ}\text{C}$) during the hot water circulation, which may no longer inhibit Legionella bacteria (JAHMEC Guideline 2017).

NUMERICAL ANALYSIS ON PIPING HEAT LOSS

In order to investigate measures to reduce the heat loss from the HWSS, a thermal analysis of the subsystem was conducted, focusing on the performance of the thermal insulation material, the construction situation in situ, and the heat bridge of equipment.

With reference to the equipment drawing of the facility, the HWSS was modeled as shown in Fig. 5. The specifications of the carbon steel piping and the thermal insulating material (fiberglass insulation) are listed in Table 1 and Table 2, referring to JIS G 3452 and JIS A 9504, respectively. The measured temperatures and flow rates used for calculation are listed in Table 3. The temperature just after the hot water tank exit (T23) was used as an input in this calculation. Then the calculated and the measured return temperatures just before entering the hot water storage tank (T24) were compared. The deterioration of the insulation materials and the portion without thermal insulation were considered to be the primary causes of piping heat loss. In this facility, there was no insulation at the holes of the building base and the floor slab through which the pipes run. These uninsulated segments, about 10 cm long each, were found every 5 to 8 m, and the total length was estimated to be 5 m of the 350 m total piping network. These uninsulated segments were taken into consideration in the simulation model. The calculation cases are given in Table 4. The calculation was carried out for 6 hours starting at

midnight on December 1st, during which the hot water is circulating at the constant flow rate (98 L / min). The heat balance equation of the hot water in the pipe and the boundary condition between the hot water and the underfloor air are given as follows:

$$C_w \rho_w \frac{\partial T_w}{\partial t} = \frac{\partial}{\partial x} \left(\lambda_w \frac{\partial T_w}{\partial x} \right) - C_w J \frac{\partial T_w}{\partial x}, \tag{6}$$

$$-\lambda_w \frac{\partial T_w}{\partial n} = K_w (T_a - T_w), \tag{7a}$$

$$K_w = \frac{\frac{1}{r_p}}{\left(\frac{\ln \frac{r_i}{r_p}}{\lambda_i} + \frac{1}{r_i h_a} \right)}, \tag{7b}$$

where x is the direction of water flow [m], J is the flow rate [kg/(m²·s)], C is the specific heat [J/(kg·K)], ρ is the density of water [kg/m³], T is temperature [K], λ is the thermal conductivity [W/(m·K)], h is the heat transfer coefficient [W/(m²·K)], K_w is the overall heat transfer coefficient [W/(m²·K)], r=D/2 (D is outer diameter [m]) $\frac{\partial}{\partial n}$ is the normal direction differential on the boundary between the pipe and insulation material, and the subscript w, a, i and p are water, air, insulation and piping, respectively. Equation (7b) refers to Transport Phenomena 2002.

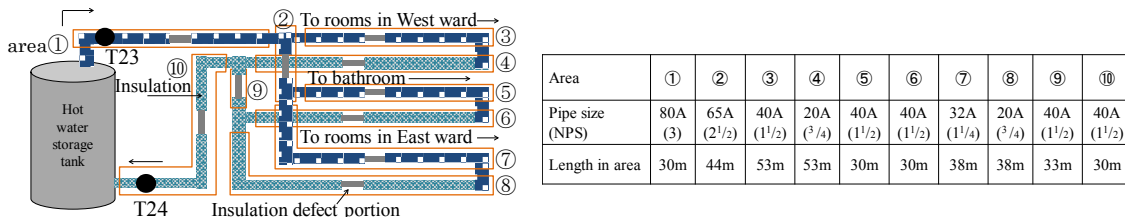


Fig. 5 Thermal model of the HWSS

Table 1 Specification of piping used for analysis

	80A(3)	65A(2½)	40A(1½)	32A(1¼)	20A(¾)
Pipe inner diameter [mm]	80.7	67.9	41.6	35.7	21.6
Lining thickness [mm]	4	3.5	3	3	2.5
Piping thickness [mm]	4.2	4.2	3.5	3.5	2.8
Insulation thickness [mm]	20	20	20	20	20

Table 2 Material properties used for analysis

	Hot water	Piping	Fiberglass	Air
Specific heat [J/(kg·K)]	4186	—	—	—
Density [kg/m ³]	1000	—	—	—
Thermal conductivity [W/(m·K)]	0.59	(pipe)53 (lining)0.17	0.043	—
Heat transfer coefficient [W/(m·K)]	—	—	—	9.3

Table 3 Measured temperature and flow rate used in calculation

Hot water supply temperature	T23 (near the hot water tank)
Underfloor temperature	20°C (constant)
Hot water supply flow rate	98L/min(constant)

Table 4 Computational condition

Case 1	no deterioration of thermal insulation and no insulation defect
Case 2	no deterioration of thermal insulation and 5 m insulation defect
Case 3	45% deterioration of thermal insulation and 5 m insulation defect

Calculation result

Fig. 6 shows the calculated results for the three cases compared with the measured results. In

Case 1, the return temperature of the hot water is 1.0°C lower than the supply temperature, while the measured return temperature decreased by 1.5 to 2.0°C. There is almost no difference in the return temperature between Case 1 and Case 2, although the heat loss at the uninsulated segment is about 2.2 times larger than the normal (insulated) pipe. This is probably because the total length of the uninsulated segments is very short compared to the total length of the hot water pipe. Since the actual length of the uninsulated segments has not been confirmed over the whole crawl space, a detailed check is necessary in the future. In Case 3, the calculated temperature agrees very well with the measured temperature. One possible reason that the thermal resistance of the insulation may have decreased by 45% on average is that the insulation material was wound up on the pipe too tightly (Masuda 2014). Another possible reason is that heat loss at thermal bridges such as piping flanges and hanging metal hooks may have a significant influence.

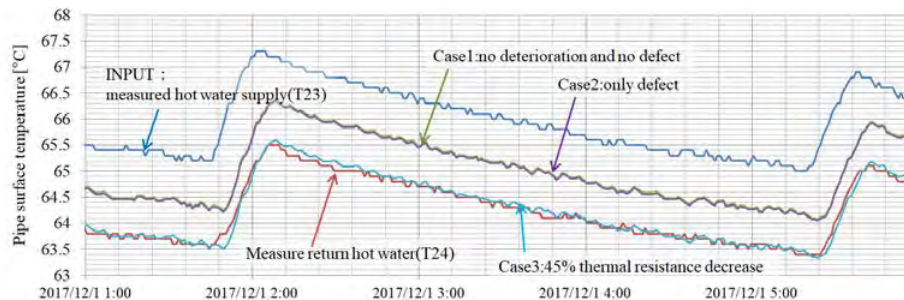


Fig. 6 Comparison of calculated and measured return temperatures of the hot water

CONCLUSION

We surveyed the annual heavy oil consumption in one nursing home, which served as reference data for energy conservation measures and performance verification of other facilities for elderly people. In the case of this considered building, we observed that piping heat loss in the HWSS was significant throughout the year. We investigated reasons for the large heat loss by conducting a thermal analysis and concluded that the heat insulation performance might have decreased by 45% on average. To identify the causes and locations of the heat loss, future work should consider temperature distribution in the underground space through which the hot water pipes run.

ACNOWLEDGEMENT

The authors would like to thank the related parties of elderly nursing home, and Public Interest Incorporated Foundation LIXIL JS Foundation for the generous cooperation.

REFERENCE PAPER

- JAHMEC, Guideline for Prevention of Legionnaires' Disease, The fourth version, July, 2017 Japanese Standard Association, JIS A 9504:2004 Man made mineral fibre thermal insulation materials, JIS G 3452:2014 Carbon Steel Pipes for Ordinary Piping
- Masuda Yoshinori et al.: Evaluation of Heat Loss from Hot Water Supply System and Insulation Retrofit in a Budget Hotel- Summaries of technical papers of annual meeting 2014 (Environmental Engineering), pp. 627 - 628, 2014 [in Japanese]
- Ministry of Health, Labour and Welfare: Outline of Nursing Care Facility Service • Office Survey, 2016, pp3, <http://www.mhlw.go.jp/toukei/saikin/hw/kaigo/service16/dl/gaikyo.pdf>
- Murakami Shuzo et al.: DETAIL SURVEY OF LONG-TERM ENERGY CONSUMPTION FOR 80 HOUSE IN PRINCIPAL CITIES JAPAN, Journal of Environmental Engineering (Transactions of AIJ), 603, pp.93-pp100, 2006
- Transport Phenomena 2nd Edition, John Wiley & Sons, Inc., p. 306, 2002

Extracting Radiant Cooling From Building Exhaust Air Using the Maisotsenko Cycle Principle

Théo Keeley-LeClaire¹, Eric Teitelbaum², Suin Shim³, Michael Bozlar^{2,4}, Howard A. Stone³, Forrest Meggers^{2,4}

¹Princeton University, Department of Chemical and Biological Engineering, USA

²Princeton University, School of Architecture, USA

³Princeton University, Department of Mechanical and Aerospace Engineering, USA

⁴Princeton University, Andlinger Center for Energy and the Environment, USA

* *Corresponding email: eteitelb@princeton.edu*

ABSTRACT

Indirect evaporative cooling has exciting implications for air based thermal comfort. With recent advances in the research and commercialization of Maisotsenko Cycle (M-Cycle), or dew-point, evaporative cooling, thermodynamics can be fully leveraged to provide effectively free air cooling. However, few studies seek to generate cool surfaces by evaporation for radiant cooling. As a method to reduce building energy consumption, such an evapo-radiative system would maintain occupant thermal comfort at higher ventilation air temperatures and provide cooling at low cost. This study explores an analytical model for an M-Cycle evapo-radiative cooling system that derives a 1-D temperature profile throughout an experimental module and compares the outputs to experimental data to begin the model validation process.

KEYWORDS

Radiant Cooling, Thermal Comfort, M-Cycle, Evaporative Cooling

INTRODUCTION

Maintaining comfortable conditions in buildings accounts for a significant portion of energy use and carbon dioxide emissions, both in the United States and around the world. According to the US Energy Information Administration, nearly 40% of total energy consumption in the US is accounted for by commercial and residential buildings (EIA, 2018); of total building energy use, 19% is used for ventilating and cooling building spaces (EIA, 2012). At a global scale, the International Energy Agency reports that the residential sector consumes approximately 20% of world energy demand (IEA, 2015).

Current air conditioning technologies rely on cooling air by exchanging heat with a refrigerant vapor compression cycle. Air conditioning refrigeration cycles typically have coefficients of performance, COP, between 2 and 4, and the compressor in the refrigeration cycle and the fan which circulates the building air account for the majority of the system energy demand (Duan et al. 2012). Using water for evaporative cooling is a common strategy for heat rejection and cooling.

Conventionally, the wet-bulb temperature is the maximum temperature depression achievable by conventional evaporative coolers, which are viable options only in very dry climates. But advancements in heat and mass exchanger integration and geometry have led to dew point evaporative cooling, known as the M-Cycle. The M-cycle was initially conceptualized by Valeriy Maisotsenko as a performance-enhancing modification of traditional IEC heat

exchangers (Duan et al. 2012). Both processes cool product air via heat exchange with a wetted working air channel, usually through a metallic plate separating the two channels. Whereas in the traditional process the working air is completely separate from the product air and is at the same temperature at the inlet, the M-cycle diverts some of the product air to the working air channel. This pre-cools the working air and the higher temperature difference between the two streams drives more effective heat exchange. This modification allows the M-cycle to approach much lower temperatures than the traditional process, which is desirable for a radiant panel because the temperature of the radiant surface determines its ability to cool effectively.

Hydronic radiant cooling systems have been gaining traction in the United States and abroad for providing comfort during cooling conditions. Traditionally, chilled water is circulated to cool ceiling panels, which condition spaces through both radiative and convective heat transfer, and are often effective at reducing energy consumption compared to forced air systems. However, radiant cooling still faces significant challenges, namely the need for precise temperature control and humidity sensing to prevent water from condensing on the panel and falling on building inhabitants below. The hydronics for a radiant system are rarely integrated with an evaporative system.

This project seeks to simultaneously address challenges to both hydronic radiant cooling and indirect evaporative cooling systems by developing a dew-point evaporatively cooled radiant panel. Using evaporation to cool the radiant surface promises to be more efficient than circulating chilled water and inherently avoids the possibility of condensation, as the lowest temperature that can be attained by evaporative cooling is above the dew point of the inlet air. Such a technology links surface temperatures in the room to air temperature and relative humidity, further simplifying controls and leveraging other low exergy technologies, such as desiccant dehumidification, to control for comfort using air dehumidification and subsequently lowered radiant temperatures for occupant control rather than air conditioning.

METHODS

Few studies exist on indirect evaporative cooling conducted in an integrated manner for radiative cooling. Younis et al. (2015) model such a similar system for small office environments, however the primary mode for occupant comfort is through chiller-based air conditioning. In this study, we propose a design methodology maintaining occupant thermal comfort in the absence of a chiller using a truly integrated approach to radiative and evaporative cooling requiring only control of the relative humidity of the inlet air.

In our integrated evaporative-radiant cooling system, it is crucial to have a highly conductive, but also easily tunable, material for thin film formation of water in the wet section. We suggest a boehmite nanostructure on an aluminum surface as a key material for the cooling system. Aluminum, when exposed to high temperature water, forms a nano-scale porous layer of aluminum oxide. A stable boehmite phase is achieved for a sufficiently high and also wide range of temperature of water (Bernard and Randall, 1960; Vedder and Vermilyea, 1968; Abdollahifar et al. 2015; Rani and Sahare, 2015); we choose the hydrothermal synthesis at ~ 80 °C for 24 hours as a standard treatment (Shim et al. 2018). The presence of the boehmite layer provides changes not only to the chemical composition of the substrate, but also to its physical structure, in terms of crystallography and surface roughness, which naturally turn the aluminum surface from hydrophilic to superhydrophilic (Shim et al. 2018). Such a superhydrophilic surface improves evaporative cooling performance by keeping the thermal mass of coolant (water) low compared to the regular hydrophilic aluminum surface.

Generating a thin film of water allows a large ratio of evaporating area to volume, which can be one of the most effective ways to enhance evaporative heat transfer.

Analytical Model

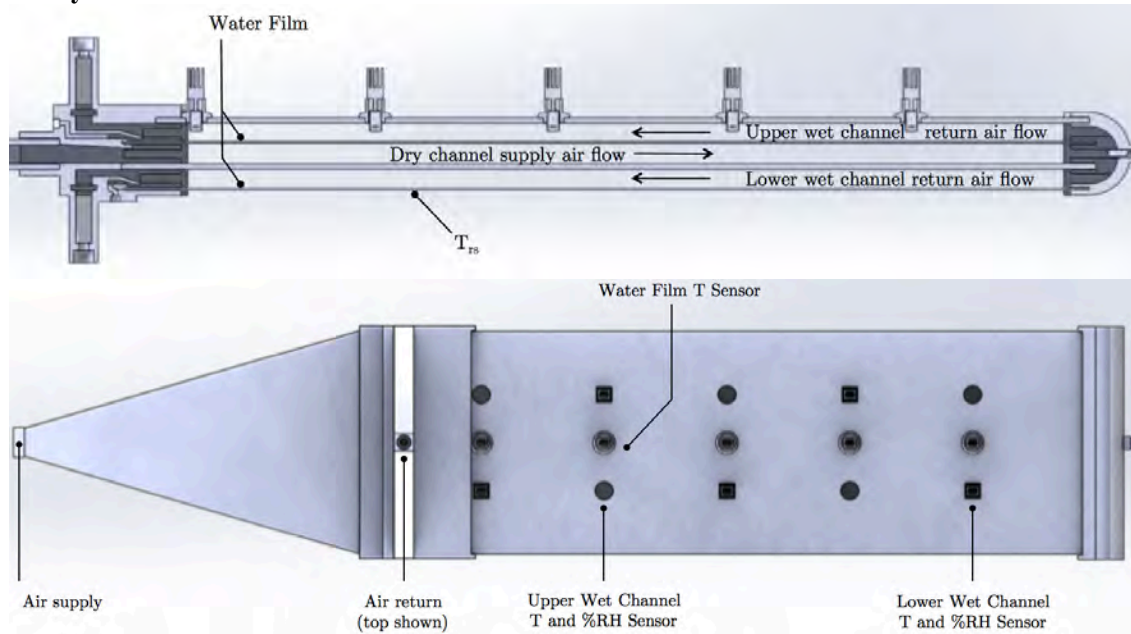


Figure 1: Section (top) and plan (bottom) drawings of the M-Cycle test apparatus, showing sensor locations and air flow directions. Starting from the top, the first and third horizontal plates are acrylic, chosen as an insulator; the second and fourth horizontal plates are wetted boehmitized aluminum. Air flow splits in the rounded baffle to the right, and flow can be modulated between 0 and 100% of supply air to either top or bottom stream.

A one-dimensional model tracking bulk average values was chosen to assess the performance of the prototype evapo-radiant device shown in figure 1. Because of its simplicity and relative accuracy (less than 10% error in the temperature of the product air), a previous simulation used by Hasan (2010) to model regenerative (M-cycle) evaporative coolers was used as a conceptual basis for the model developed here.

The conceptual basis is straightforward: air enters the panel (via the dry channel inlet) at ambient temperature and humidity and is cooled by heat exchange with the wet channel through the aluminum plate. At the end of the dry channel, the air flow is split into two streams that recirculate along the wet and radiant channels, respectively, at the end of which the air is collected and exhausted from the building. Thus, the bulk heat transfer equations account for (1) heat exchange between air in the dry channel and air in the wet channel, and (2) exchange between the room (via radiation and natural convection) and air in the radiant channel. The equations model the variation of the temperature, enthalpy, and humidity of the air streams with position in the panel (which is expressed synonymously by area $dA = Wdx$). Beginning with exchange between the dry and wet channels, the overall energy balance is given by:

$$M_w \frac{dh_w}{dA} = M_d C_p \frac{dT_d}{dA} \quad (1)$$

The heat (enthalpy) lost by air in the dry channel is given by Fourier's law as:

$$M_d C_p \frac{dT_d}{dA} = U(T_d - T_f) \quad (2)$$

where U , the overall heat transfer resistance from the dry air to the water film-wet air interface, is given by adding the heat transfer resistances of the air, aluminum, and water film, respectively:

$$U = (1/\alpha_d + \delta_{Al}/k_{Al} + \delta_f/k_f)^{-1} \quad (3)$$

The enthalpy gained by the air in the wet channel is given by both latent (water vapor mass transfer) and sensible (heat transfer) components:

$$M_w \frac{dh_w}{dA} = \alpha_w(T_f - T_w) + \beta(W_s - W_w) \quad (4)$$

However, assuming that the Lewis relation (5), which compares energy and mass propagation rates, can be taken as unity under these conditions, this equation can be simplified as an enthalpy driving force (6) between the water film and the bulk air as shown in Hasan (2010):

$$Le = \frac{\alpha_w}{\beta C_H} \approx 1 \quad (5)$$

$$\dot{M}_w \frac{dh_w}{dA} = \beta(h_s - h_w) \quad (6)$$

Solving equations (1), (2), and (6), and (7) will require relating the enthalpy and humidity of the saturated boundary layer at the air/water interface with the temperature of the water film. These relationships are tabulated in Chapter 6 of the 2001 ASHRAE Fundamentals Handbook and can be approximated as linear over the temperature range of interest with little loss of accuracy, the novel contribution to the field in this model. Thus, we can write the following linear relationships:

$$h_s = a_{s,h} T_f + b_{s,h} \quad (7)$$

Because the dry channel is insulated from the radiant channel by an acrylic plate, these equations fully define the temperature, humidity, and enthalpy profiles in the wet and dry channels. Before they can be solved, the heat and mass transfer coefficients need to be defined; for laminar flow between parallel plates, Burmeister (1983) gives the Nusselt number:

$$Nu = \frac{\alpha D_h}{k} = 4.861 \quad (8)$$

Thus, the heat transfer coefficient can be calculated, from which the mass transfer coefficient is known by the Lewis relation. Equation (1) can be integrated, which allows us to solve equations (2), (6), and (7) for the dry channel temperature, water film temperature, and wet channel enthalpy. The only difficulty here is in initial conditions; though the ambient conditions are known, none of the outlet conditions are given. Thus, we cannot set $x = 0$ to be the inlet of the panel because initial conditions would not be known for both the wet and dry air streams. Instead, we must guess the temperature at the recirculation point (the outlet of the dry channel where the air flow splits and recirculates to the wet and radiant channels). We can then calculate the outlet temperature and compare with known ambient conditions in order to adjust the guess and iterate to a solution. Heat transfer between the room and the radiant channel were then addressed to calculate the steady state temperature profile of the evapo-radiative M-Cycle apparatus for a given plate area and convective and radiative exchange with a fixed room condition. First, we assume that the heat transferred from the room to the water film is equivalent to the enthalpy lost by the water film to the air flow in the radiant channel:

$$\frac{dq_{room}}{dA} = \dot{M}_r \frac{dh_r}{dA} \quad (9)$$

The enthalpy gained by the air flow is analogous to that in the wet air channel, so we can write:

$$\dot{M}_r \frac{dh_r}{dA} = \beta(h_s - h_r) \quad (10)$$

Finally, the heat gained from the room is given by summing radiant and convective contributions. As shown by Lienhard and Lienhard,[3] radiant heat transfer can be expressed with a heat transfer coefficient analogous to that of natural convections for small temperature differences, so we can write an overall heat transfer coefficient:

$$U_{room} = (1/(\alpha_{radiant} + \alpha_{convective}) + \delta_{Al}/k_{Al} + \delta_f/k_f)^{-1} \quad (11)$$

$$\frac{dq_{room}}{dA} = U_{room}(T_{ambient} - T_f) \quad (12)$$

Equations (9), (10), and (12) can be solved analogously to the wet channel/dry channel case by first solving for T_f and then integrating.

RESULTS AND DISCUSSION

Initial experiments of the M-Cycle model produce intuitive results with reasonable outputs. Certain initial criteria were chosen to facilitate model validation in future experimentation. Figure 2a shows 9 data points where the ratio between air flowing to top and bottom wet channels is varied between 0 and 1. For example, a ratio of 0.25 indicates that 25% of the air supplied in the dry channel is diverted to the top wet channel, and the remaining 75% is diverted to the lower wet channel with the radiant panel facing the room. The y-axis is the average temperature across the lower radiant plate exposed to the room. Points are placed at the lowest average temperature value, with the entire dataset extending to the right y-axis to show the initial inlet air temperature. For all runs, the initial inlet air absolute humidity was 9 g/kg. Additionally, three runs of the model were conducted with plate spacings of 3.5, 6, and 10 mm.

Figure 2b shows experimental data compared to model outputs for the wet and dry channel temperatures as well as surface temperature data for the exposed panel. This data was taken at an air flow ratio of 0.23 and an inlet temperature of 20.7 °C and absolute humidity of 6 g/kg. Airflow was at a Reynolds number of $Re = 90$ inside the apparatus.

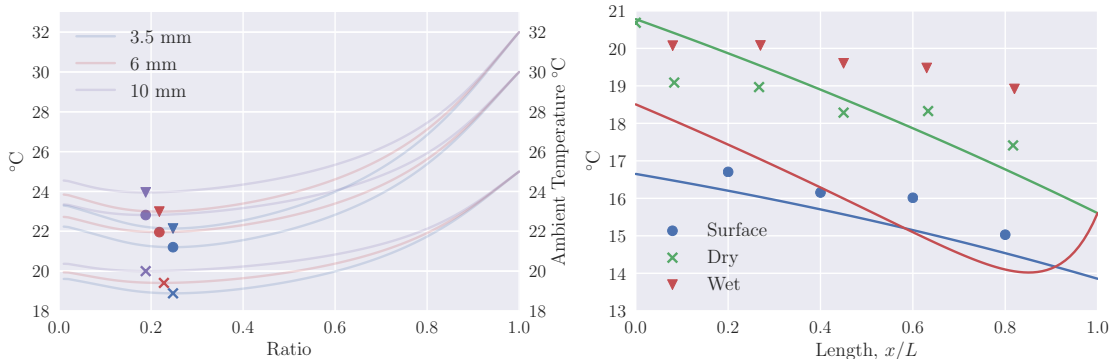


Figure 2: (a-left) The optimal ratio for air flow between top and bottom wet channels for producing a cold lower plate for three inlet air conditions and plate spacings. (b-right) Experimental data points compared to model outputs.

The wet bulb temperature for the experiment’s inlet air was 13 °C and the dew point was 7 °C. The average measured radiant surface temperatures from figure 2b was 16.0 °C for a wet bulb efficiency of 61% and a dew point efficiency of 34%. These low efficiencies of the test apparatus could be explained by the apparent ineffectiveness of the wet channel at remaining

wetted, which was visibly confirmed and shown in the data with the higher than expected temperatures for the wet channel compared to the model. This indicates that not enough precooling of the air occurs for the air entering the wet channels, and the lower channel is effectively a wet bulb radiant cooler rather than a dew point radiant cooler. Optimizing the setup was outside the scope of the experiment, as the ultimate goal is to begin validation on the analytical M-Cycle evapo-radiative cooling model. However, we will re-examine the surface wetting to make sure the physical data represents the modeled evaporative phenomena.

CONCLUSION

A major goal of the study was to develop an analytically solvable model for M-Cycle enhanced evapo-radiative cooling apparatus. The model is an exciting advance for describing this type of system. Linking air temperature, humidity, and surface temperatures is an innovative concept for control purposes, as fewer degrees of freedom simplify control and system response. Future work will be conducted to fully validate the model, drawing conclusions for the system design parameters, such as optimal airflow ratios between the channels, controls for comfort conditions based on climate data, and eventually an energy budget for the entire system.

REFERENCES

- Energy Information Administration. “*Energy Use in Commercial Buildings*”.
https://www.eia.gov/energyexplained/index.cfm?page=us_energy_commercial (accessed Feb 3, 2018).
- Energy Information Administration. “*2012 Commercial Buildings Energy Consumption Survey: Energy Consumption Summary*”.
<https://www.eia.gov/consumption/commercial/reports/2012/energyusage/>.
- International Energy Agency. “*World Final Consumption (2015)*”.
[https://www.iea.org/Sankey/#?c=World&s=Final consumption](https://www.iea.org/Sankey/#?c=World&s=Final%20consumption).
- Duan, Z.; Zhan, C.; Zhang, X.; Mustafa, M.; Zhao, X.; Alimohammadisagvand, B.; Hasan, A. Indirect Evaporative Cooling: Past, Present and Future Potentials. *Renew. Sustain. Energy Rev.* 2012, 16 (9), 6823–6850.
- Manar Younis, Kamel Ghali, and Nesreen Ghad- dar. Performance evaluation of the displacement ventilation combined with evaporative cooled ceiling for a typical office in beirut. *En- ergy Conversion and Management*, 105:655– 664, 2015.
- Hasan, A. Indirect Evaporative Cooling of Air to a Sub-Wet Bulb Temperature. *Appl. Therm. Eng.* 2010, 30 (16), 2460–2468.
- Burmeister, L. C. *Convective Heat Transfer*; John Wiley & Sons, Inc, 1983.
- Lienhard IV, J. H.; Lienhard V, J. H. *A HEAT TRANSFER TEXTBOOK*, 2.11.; Phlogiston Press, 2017.
- Bernard, W. J. and Randall, John J. Jr. An investigation of the reaction between aluminum and water. *J. Electrochem. Soc.* 1960, 107 (6), 483–487.
- Vedder, W. and Vermilyea, D. A. Aluminum + water reaction. *Transactions of the Faraday Society* 1968, 64, 561-584
- Abdollahifar, M., Karami, A. R., Haghazari, N. and Karami, C. Synthesis of porous boehmite nanostructures: effects of time and temperature in the hydrothermal method, 2015, *Ceramics – Silikáty* 59 (4), 305-310
- Rani, G. and Sahare, P. D. Effect of temperature on structural and optical properties of boehmite nanostructure, 2015, *Int. J. Appl. Ceram. Technol.* 12 (1), 124–132
- Shim, S., Bozlar, M., Teitelbaum, E. Meggers, F., Bou-Zeid, E. and Stone, H. A. Controlled evaporative cooling using boehmite nanostructure on aluminum surface, *In preparation*

Periodic alternation between intake and exhaust of air in dynamic insulation

Masaru Abuku^{1,*}, Akira Fukushima², Tsukasa Tsukidate³, Sayaka Murata³, Akinori Hosoi⁴, Hideo Ichiboji⁵, Daisuke Kitagawa⁵ and Kanako Makita⁵

¹Kindai University, Japan

²Hokkaido University of Science, Japan

³Northern Regional Building Research Institute, Hokkaido Research Organization, Japan

⁴Japan Woman's University, Japan

⁵Asahi Kasei Construction Materials Corporation, Japan

*Corresponding email: abuku@arch.kindai.ac.jp

ABSTRACT

Dynamic insulation (DI) can recover heat lost in conduction by drawing cold outdoor air into indoor through an insulation wall in winter. A “breathing DI” system we proposed in the past has functions both as an insulated envelope and as a highly efficient heat exchanger for ventilation. It is alternated periodically that the outdoor air is drawn through half of walls made of breathable inorganic concrete (BIC) and the indoor air is exhausted through the other half of the BIC walls. In order to put the breathing DI system into practice in housing construction, this paper presents some studies from various points of view in addition to the past studies on heat and moisture transport based on laboratory experiments and numerical simulations. We first experimentally studied the filtering efficiency and clogging of a BIC panel. This showed that approximately 30 % of the atmospheric dust can be captured by a BIC panel and no clogging would occur for at least 10 years. We also measured the sorption and desorption of formaldehyde by a BIC panel to confirm the effectiveness of a BIC wall to sorb gaseous state formaldehyde. We furthermore constructed a new test house at Ibaraki, Japan, to confirm the thermal performance of the breathing DI system based on full scale experiments.

KEYWORDS

Insulation, ventilation, heat recovery, indoor air quality,

1. INTRODUCTION

Dynamic insulation (DI) can recover heat lost in conduction by drawing cold outdoor air into indoor through an insulation wall in winter (Jensen, 1993; Taylor and Imbabi, 1997; Taylor et al. 1997; Dimoudi et al. 2004). A “breathing dynamic insulation” system (Abuku et al. 2012; Murata et al. 2015) we proposed in the past has functions both as an insulated envelope and as a highly efficient heat exchanger for ventilation. It is alternated periodically with a certain time interval that the outdoor air is drawn through half of walls made of breathable inorganic concrete (BIC) and the indoor air is exhausted through the other half of the BIC walls. After the heat in the exhaust air is stored inside the BIC walls, the stored heat in addition to the heat lost in conduction through the BIC walls is recovered by the supply air.

Our past numerical study (Abuku et al. 2012) showed that the inside surface temperature of the BIC walls can be kept the same as that of conventional “static” insulation walls and the recovery efficiency of the heat in the exhaust air can be improved to up to more than 90%. It was also experimentally shown that the BIC wall under study has recovery efficiencies of

almost 90% of the heat in the exhaust air, 18 to 35 % of the heat lost in conduction, and approximately 80% of the moisture lost through the BIC wall (Murata et al. 2015).

In order to put the breathing DI system into practice in housing construction, this paper addresses some other aspects of the system. We first experimentally studied the filtering efficiency and clogging of a BIC panel. We also measured the sorption and desorption of formaldehyde by a BIC panel to confirm the effectiveness of a BIC wall to sorb gaseous state formaldehyde. We furthermore constructed a new test house at Ibaraki, Japan, to perform full scale measurements of the hygrothermal performance, ventilation, energy consumption, and indoor air quality.

2. BREATHING DYNAMIC INSULATION SYSTEM

The breathing DI system consists of two distinct spaces that are enclosed by BIC walls and fans between the two spaces as illustrated in Fig.1. BIC has a high air permeability, a high insulation performance and a relatively large thermal storage. In this system, the outdoor air is drawn through half of the BIC wall, while the indoor air is exhausted through the other half. Intake and exhaust of air through the two halves of the wall are periodically alternated. An airflow from one space to the other is controlled by fans. After the heat in the exhaust air is stored inside the BIC walls, the stored heat in addition to the heat lost in conduction through the BIC walls is recovered by the supply air. Consequently, the “Breathing DI” system has functions both as an insulated envelope and as a highly efficient heat exchanger for ventilation.

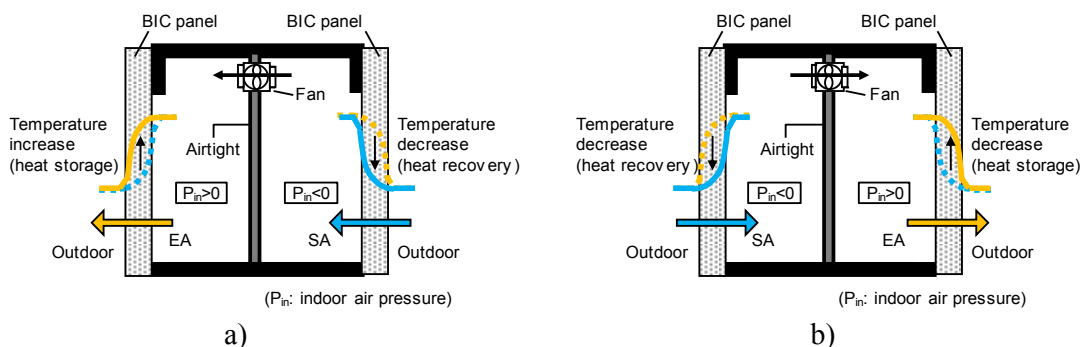


Figure 1. Schematic of the breathing DI system (slightly modified based on Murata et al. 2015). a) One operation mode with airflow in one direction, b) the other operation mode with airflow in the opposite direction.

3. FILTERING EFFICIENCY AND CLOGGING

The filtering efficiency of BIC panels for dust was measured outdoor. The measurement was conducted on the flat roof of building #34, Higashi-Osaka campus, Kindai University, Japan during October 24, 2016 – January 31, 2017. The building is located near busy roads and highways. The schematic of the experimental set-up is given in Fig. 2. The set-up is composed of wooden panels and frames, an electronic fan, a BIC panel (30 cm x 30 cm x 8 cm) with an air filter as well as a hygro-thermometer and a digital dust monitor both in and outside the box. The air filter was attached to the inner surface of the BIC panel to diminish the influence of powder remaining in the BIC panel on the dust concentration in the box. Note that it was confirmed that this air filter does not influence the dust concentration measured by the dust monitors. The difference between the outside dust concentration C_o (mg/m^3) and the inside dust concentration C_i (mg/m^3) is considered to be due to the BIC panel. In the current paper, the filtering efficiency E_f (%) is defined by

$$E_f = \frac{C_o - C_i}{C_o} \times 100. \quad (1)$$

In the breathing DI system, the direction of airflow through BIC panels changes with a certain interval of time (e.g. 10 minutes). However, in this experiment, the direction of airflow through a BIC panel was not changed to accelerate the decrease of the filtering efficiency of the BIC panel.

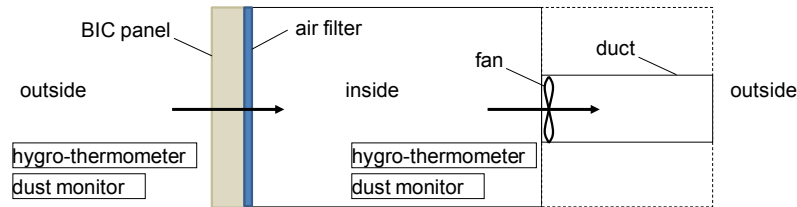


Figure 2. Schematic of the experimental set-up to measure the filtering efficiency of a BIC panel.

The inside and outside dust concentrations as well as the temperature and relative humidity (RH) values were measured and averaged over every 10 minutes. For each parameter, 211 data were successively obtained. The average outside dust concentration for all the data was 0.0135 mg/m^3 with a standard deviation of 0.0084 mg/m^3 and the maximum is 0.0350 mg/m^3 . E_f was 29.7 % on average with a standard deviation of 11.8 % and 61.5 % at the maximum. The relation between E_f and the number of measurement is given in Fig. 3a; the dependency of E_f on C_o is shown in Fig. 3b. Note that although in Fig. 3b there seems to be less number of data points, this means that some data show the same relation between E_f and C_o . The results show that the filtering efficiency did not decrease with time at least under the current study, although this is also supported by discussion on clogging in the last part of this section. It was also shown that the filtering efficiency is stably high when the outside dust concentration is high. This is probably because when the dust concentration is high, particles in the dust are large and thus easily captured by the BIC panel.

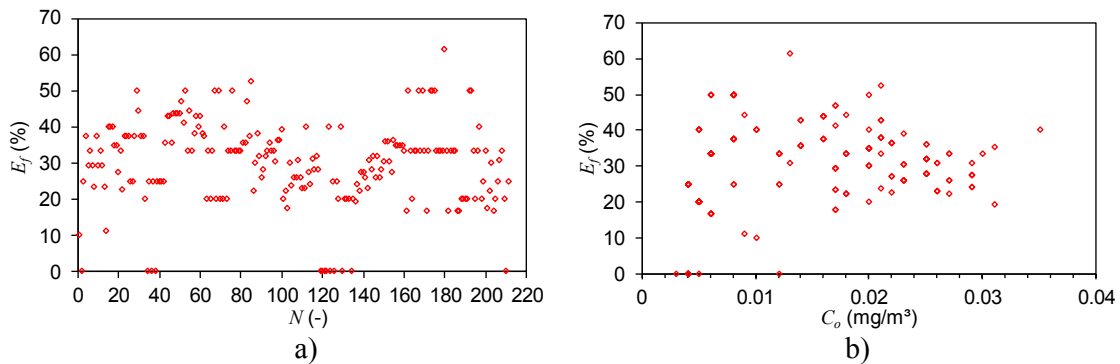


Figure 3. The dependency of the filtering efficiency E_f of the BIC panel on a) the number of measurement N and b) the outside dust concentration C_o .

In general, various factors affects the dust concentration (e.g. Csavina et al. 2014) that would eventually influence the filtering efficiency. In the current study, the relationships of E_f with the outside RH and humidity ratio are discussed as they would be considered to be one of the most important factors. Fig. 4. There is no correlation between E_f and the RH. However, only when the humidity ratio is high, E_f became stably high and there seems to be a positive

correlation between E_f and the humidity ratio. This is because particles in dust can swell when they absorb moisture and can be then captured by the pore structure of the panel more easily and because a wet surface of the pore structure can capture more dust.

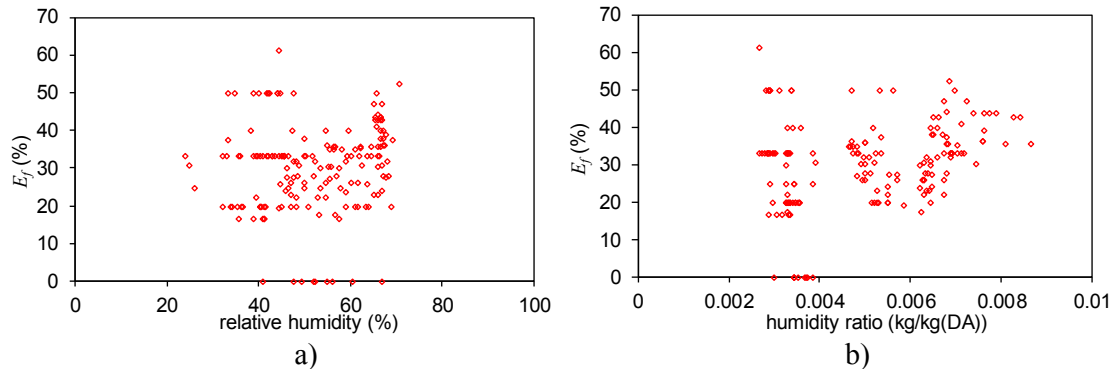


Figure 4. The dependency of the filtering efficiency E_f of the BIC panel on a) the outside relative humidity and b) the outside humidity ratio.

Apart from air filtering, when a large amount of atmospheric dust accumulates in the BIC panel, the air permeability might be reduced which affects the performance of the DI system. The possibility of clogging of a BIC panel due to atmospheric dust was also estimated here tentatively assuming some input values and summarised in Table 1. The air permeability value of the BIC panel was taken from our own measurements. The result show that as the dust mass captured by the panel is very small, almost no clogging of the BIC panel would occur at least for 10 years. It should be noted that in the breathing DI system, the intake and exhaust of air through the panel are alternated periodically and thus the dust mass captured by the panel should be the half of the one given in Table 1 if the indoor air is clean.

Table 1. Estimate of the possibility of clogging of the BIC panel due to atmospheric dust

Input/Output	Parameter	Value	Unit
	Atmospheric dust concentration	0.02	mg/m ³
	Air permeability	1.07	m/(h·Pa)
Input	Pressure difference between indoor and outdoor	20	Pa
	Service life	10	year
	Filtering efficiency	30	%
	Airflow rate	1.92	m ³ /h
Output	Airflow speed	5.93	m/s
	Dust mass captured by the panel	11.2	g/m ²

4. SORPTION AND DESORPTION OF FORMALDEHYDE

As one of drawbacks of the breathing DI system, a BIC panel can also sorb volatile organic compounds when the indoor air is exhausted through the BIC panel and then desorption of them to the inside might occur. According to Curling et al. (2012), the sorption and desorption of water and those of water plus formaldehyde were measured using the dynamic vapour sorption technique with a RH interval of 5 %. The results are given in Fig. 5a. The measured mass content of water plus formaldehyde was then subtracted by the measured water content to obtain the content of formaldehyde (Fig. 5b). Furthermore, the absorption/desorption rate was obtained by dividing the mass content increment/decrement for each RH step by the time used to obtain the equilibrium (Fig. 5c). The result means that after one cycle of absorption and desorption, most formaldehyde captured in the material is not desorbed. It was also shown that the desorption rate is lower than the absorption rate.

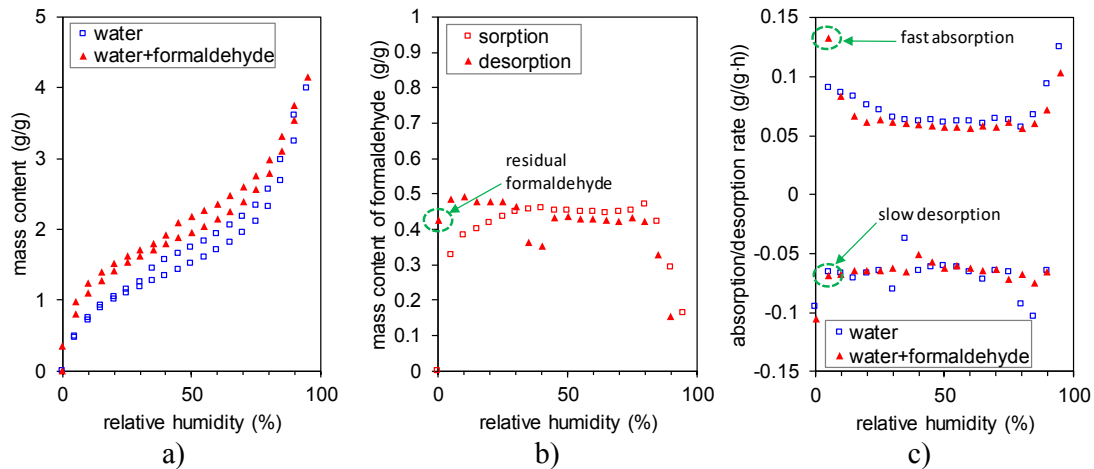


Figure 5. Measured sorption and desorption of water and formaldehyde by the BIC panel. a) sorption and desorption isotherm of water and water plus formaldehyde, b) the mass content of formaldehyde in the material, c) sorption and desorption rate of water and water plus formaldehyde.

5. FULL SCALE MEASUREMENTS AT A TEST HOUSE

Full scale measurements to confirm the thermal effectiveness of the breathing DI system were carried out at a two-storey test house (Fig. 6) located at Ibaraki prefecture, Japan. The test house has a gross floor area of 103 m² (1F: 52 m²; 2F: 51 m²), a total volume of approximately 300 m³ and a high insulation performance with the area-weighted average U-value of 0.25 W/(m²K). At this test house, we measured the vertical temperature distribution (Fig. 6b) in an atrium space of the house with or without the breathing DI system. For three days (January 13-15, 2017) when the breathing DI system was operated with a time interval of 15 minutes for alternation of intake and exhaust of air, the ventilation rate was kept at 150 m³/h. For other three days (February 3-5, 2017) without the breathing DI system, three mechanical ventilation fans were always operated in two rest rooms and an undressing room to obtain a total ventilation rate of ~ 200 m³/h. Fig. 7 plots the indoor temperatures measured at different heights as well as the outdoor temperature measured near the test house. The results confirm the effectiveness of the breathing DI system, showing that with the breathing DI system, the indoor temperatures can be kept both higher and more uniform. Note that there



Figure 6. A two-storey test house equipped with the breathing DI system at Ibaraki prefecture, Japan. a) A photograph, b) Plan (1st floor).

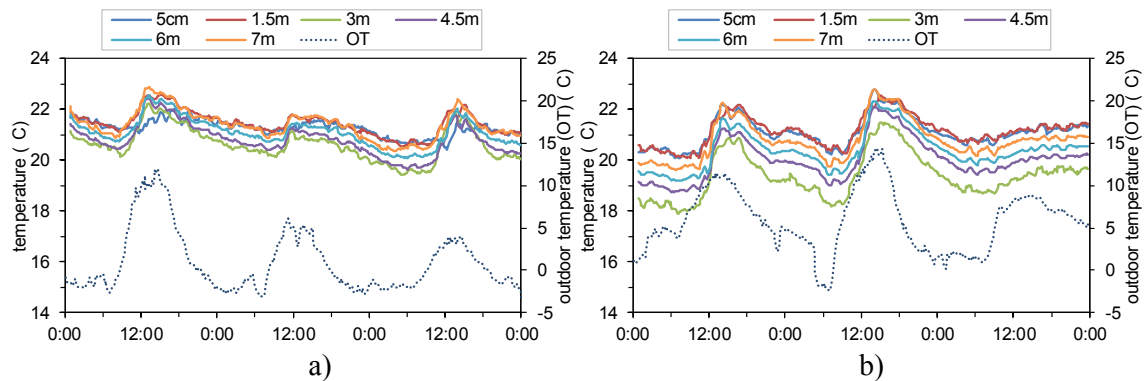


Figure 6. Indoor temperatures measured at different heights in an atrium of the test house compared to the outdoor temperature. a) Breathing DI system, b) Normal mechanical ventilation.

was a heat source under the floor of the 1st floor, so the temperatures measured at 5 cm and 1.5 m were higher than those at ≥ 3 m.

6. CONCLUSIONS

In order to put the breathing DI system into practice in housing construction, we first experimentally studied the filtering efficiency and clogging of a BIC panel. This showed that approximately 30 % of the atmospheric dust can be captured by a BIC panel and no clogging would occur for at least 10 years. By measuring the sorption and desorption of formaldehyde by a BIC panel, we also showed that a BIC wall is effective to reduce gaseous state formaldehyde. Lastly, full scale experiments at the test house demonstrated that the breathing DI system can keep the indoor temperature higher and more uniform in winter.

REFERENCES

- Abuku M, Fukushima A, Tsukidate T, Murata S, Iba C, Watanabe H, Ogawa A. 2012. Periodic alternation between intake and exhaust of air in dynamic insulation: A preliminary study. In: *Proceedings of the 5th International Building Physics Conference (IBPC)*, Kyoto, Japan, May 28-31, 2012, pp.303-307
- Csavina J, Field J, Félix m, Corral-Avitia AY, Eduardo Sáez A, Betterton EA. 2014. Effect of wind speed and relative humidity on atmospheric dust concentrations in semi-arid climates, *Sci Total Environ*, 487, 82–90.
- Curling SF, Loxton C, Ormondroyd GA. 2012. A rapid method for investigating the absorption of formaldehyde from air by wool. *Journal of Materials Science*, 47(7), 3248-3251
- Dimoudi A, Androutsopoulos A, Lykoudis S. 2004. Experimental work on a linked, dynamic and ventilated wall component, *Energy and Buildings*, 36, 443-453
- Jensen L. 1993. Energy impact of ventilation and dynamic insulation. In: *Proceeding of the 14th AIVC conference*, pp.251-260
- Murata S, Tsukidate T, Fukushima A, Abuku M, Watanabe H, Ogawa A. 2015. Periodic Alternation between Intake and Exhaust of Air in Dynamic Insulation: Measurements of Heat and Moisture Recovery Efficiency. *Energy Procedia*, 78, 531-536
- Taylor BJ, Imbabi MS. 1997. The effect of air film thermal resistance on the behaviour of dynamic insulation. *Building and Environment*, 32(5), 397-404
- Taylor BJ, Webster R, Imbabi MS. 1997. The use of dynamic and diffusive insulation for combined heat recovery and ventilation in buildings. In: *Proceedings of BEPAC/EPSC Sustainable Building Conference 1997*, pp.168-174

The energy saving performance of heat recovery ventilation system in residential buildings in the summer of hot-summer and cold-winter zone in China

Siyuan Cheng¹, Yao Ma¹, Menghao Qin^{2,*}

¹ School of Architecture and Urban Planning, Nanjing University, Nanjing, China

² Department of Civil Engineering, Technical University of Denmark, Copenhagen, Denmark

*Corresponding email: menqin@byg.dtu.dk

ABSTRACT

The rapid increase in space cooling and heating demand in recent years in the hot-summer and cold-winter (HSCW) zone in China (the most developed area in China) requires technology to be as efficient as possible, consuming the lowest amount of energy necessary. Heat recovery ventilation (HRV) system can meet this demand by lowering the building energy demand by pre-heating or pre-cooling. However, the climate in HSCW zone is humid and rainy all the year round, which may affect the energy performance of HRV system. The current research focuses on field measurements of the performance of HRV system in a test building located in east China to study the actual energy saving performance of the HRV system in the HSCW zone. The actual performance of the HRV system is measured. The experiment reveals that the system can save 14.5% of air-conditioning energy consumption in summer and 4.96% of air-conditioning energy consumption during rainy season. There is no significant energy saving effect in transition seasons. EnergyPlus is used to calculate the energy performance of the HRV system under different operating conditions. The simulation is compared with the test data. Both the measurements and simulation indicate that the use of HRV system can significantly reduce the energy consumption of the air-conditioned buildings in summer in HSCW zone.

KEYWORDS

Heat recovery ventilation; Energy-saving; Field measurement

INTRODUCTION

Improving indoor air quality and reducing building energy consumption have become an important area of research in architecture and related disciplines. Good indoor air quality is a guarantee for the health, comfort and productivity of occupants. The introduction of fresh air into room is one of the necessary conditions to improve indoor air quality ^[1]. However, the introduction of fresh air may result in a large fresh air cooling/heating load. There is a contradiction between the improvement of indoor air quality and the reduction of building energy consumption. Setting up a heat recovery system to exchange heat between fresh air and indoor exhaust air, and preheating or precooling the fresh air to reduce the heating or cooling load is an effective energy saving measure.

Many studies have been carried out to study the energy-saving effect of the heat recovery ventilation (HRV) system. For example, Roulet et al. ^[2] developed the evaluation method of heat recovery effect for different countries and regions based on energy gain method. However, the research on the energy-saving effect of HRV system for hot summer and cold winter zone in China mainly based on theoretical calculation or numerical simulation. Few experimental verifications have been carried out. Taking a library in Shanghai as an example,

Feng^[3] calculated hourly energy recovery of HRV system and obtained energy-saving heat recovery modes and air conditioning modes for different conditions during the whole year.

The HSCW zone is one of the most developed areas in China, which has a hot and humid summer and a mild winter. Cooling is required through the summer season, but there is no central heating in winter. It is of great importance to verify the applicability of HRV system in summer in this area. Field measurements of the energy performance of HRV system in a test building located in east China has been carried out in this research. Results from experiments and numerical simulation have been compared and discussed in the paper.

METHODS

Evaluation method of heat recovery ventilation system

This paper selects HRV system with plate-type enthalpy exchanger as the research object. This exchanger is more suitable for the residential buildings and the HSCW zone.

•Heat transfer efficiency

The evaluation index system of heat recovery unit includes several important performance indexes, and the heat transfer efficiency ^[4] is one of them. The heat transfer efficiency includes three different types. The formula is shown in Table 1 as follows.

Table 1 Calculation formula of different heat transfer efficiency

Heat transfer efficiency	
Sensible heat recovery	$\eta_{ts} = \frac{m_s(t_2 - t_1)}{m_{\min}(t_3 - t_1)}$
Latent heat recovery	$\eta_{ds} = \frac{m_s(d_2 - d_1)}{m_{\min}(d_3 - d_1)}$
Enthalpy recovery	$\eta_{is} = \frac{m_s(h_2 - h_1)}{m_{\min}(h_3 - h_1)}$

Where t is dry-bulb temperature ($^{\circ}\text{C}$), d is moisture content (g/kg) and h is enthalpy (kJ/kg). Subscript s means fresh air; 1 means supply-in air; 2 means supply-out air; 3 means exhaust-in air; 4 means exhaust-out air.

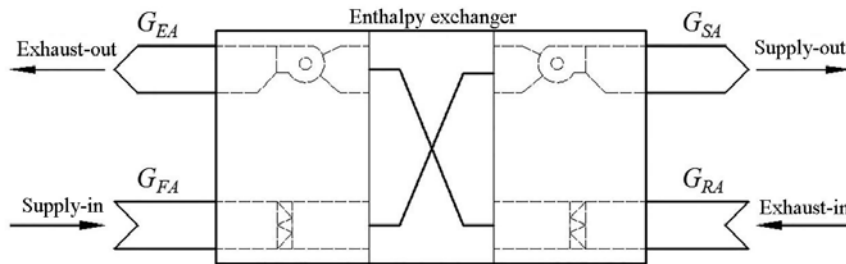


Figure 1 Energy test principle diagram of ventilation system

•Energy-saving evaluation method

According to the above enthalpy transfer efficiency, the heat energy recovered from HRV system is related to the fresh air volume, the enthalpy efficiency of the device, the enthalpy difference of air and the density of fresh air^[5] Calculation formula for heat recovery is as follows:

$$E = G\eta\rho(h_3 - h_1) \quad (1)$$

Where, E is the energy recovered by HRV system (kW), G is the fresh air volume (m^3/s), η is the enthalpy efficiency of heat recovery unit, ρ is air density (kg/m^3).

When HRV system is running, the resistance of the recovery system is increased and the energy consumption is increased. The energy consumption of HRV system is mainly produced by the fan, so the energy consumption energy of the fan is used as the energy consumption energy of HRV system. The formula is as follows:

$$W = \frac{(G_1 + G_2)\Delta p}{\eta_f} \quad (2)$$

Where, G_1 is the supply-in air volume through HRV system (m^3/s), G_2 is the exhaust-out air volume through HRV system (m^3/s), Δp the resistance of the air through HRV system (kPa), η_f is the fan efficiency. The energy consumption is converted to cooling / heating production

$$E' = W \cdot COP \quad (3)$$

$$W = \frac{(G_1 + G_2)\Delta p}{\eta_f} \quad (4)$$

When and only $E' < E$ HRV system is energy-saving, and the amount of cold (heat) recovery is $Q = E - E'$.

Experimental study

•The general information of the experiment site and the fresh air HRV system

The building used in the test is located in the Wujin District of Changzhou, Jiangsu province (HSCW). The test apartment consists of three main functional areas of the living room, the bedroom and the kitchen to simulate the ordinary residential space. The HRV system used in this test is plate-type HRV. The rated air volume is $250\text{m}^3/\text{h}$, and the power of the fan is 80 W/h. Heating and cooling of the experimental residential are applied by the VRF system. The rated cooling capacity is 33500W. The rated heating capacity is 37500W. The COP coefficient is 6.0.



Figure 2 The test building

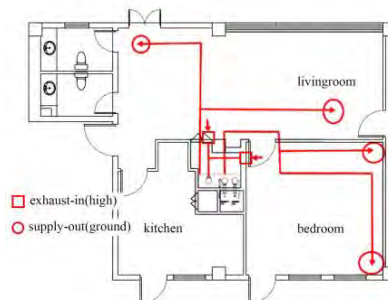


Figure 3 The plan of test apartment

•Experiment instrument and process

Main experimental instruments:

- (1) temperature and humidity recorder(testo-174H)
Accuracy Temperature: $\pm 0.5^\circ\text{C}$ ($-20 \sim +70^\circ\text{C}$);
Accuracy Humidity: $\pm 3\%$ RH ($2\% \text{ RH} \sim 98\% \text{ RH}$);
- (2) hot ball anemometer(TSI 9565-p): Accuracy: $\pm 0.015\text{m/s}$ ($0\text{m/s} \sim 30\text{m/s}$).

The experiment mainly includes two aspects: (1) to test the performance of the fresh air HRV system, which mainly includes air change rate, heat transfer efficiency, energy of the actual recovery etc.; (2) to measure the actual energy consumption of the test apartment, which includes energy consumption of all systems in the apartment. The heat gain or loss through the building envelope is also measured. Test process ^{[6]-[8]} is as follow:

- (1) start the HRV system / air conditioning preheating operation for 30min; keep the system running under the steady air volume.
- (2) fix the temperature and humidity recorder at a distance of 15cm from the air outlet and inlet; record the data every 5min;
- (3) use the hot ball anemometer to measure the air volume of the fresh air fan and record the wind speed of the cross section; calculate the air volume of the duct, and use the air volume hood to measure the air volume of the air conditioner;
- (4) Use power meter to test HRV system and air conditioning energy consumption separately;
- (5) keep the length of each working condition at the length of 2 hours.

RESULTS

•Experimental results

Air conditioning + mechanical ventilation with fresh air bi-directional flow in summer

HSCW zone is hot and humid in the summer, the daily average temperature is between 25-30°C, and the highest daily average temperature is over 30°C. The test condition is set as air conditioning temperature 26°C for cooling mode. The ventilation system keeps stable operation and the HRV system is on. The air enthalpy method is used to test the efficiency and energy consumption of summer air conditioning, and at the same time test the cooling load of the heat transfer, air infiltration and indoor heat source under the condition of air conditioning. The results are shown in Table 2 and 3.

Table 2 Test results of the ventilation system

Ventilation system	Temperature (°C)	Relative humidity (%)	Airflow (m ³ /h)	Enthalpy (kJ/kg)	Heat transfer efficiency
Exhaust-in	28.7	58.0	177.7	65.6	0.65(sensible heat)
Supply-in	35.4	63.0	166.3	95.2	0.52(latent heat)
Exhaust-out	33.3	57.5	175.1	86.1	0.55(enthalpy)
Supply-out	31.0	65.2	154.4	78.7	
Bedroom	26.6	48.7	/	/	
Living room	27.8	63.5	/	/	
Outdoor	35.0	58.0	/	/	

Table 3 Test results of the air conditioning

Air-conditioning	Temperature (°C)	Relative humidity (%)	Airflow (m ³ /h)	Enthalpy (kJ/kg)	COP
Bedroom (supply)	11.3	92.6	479.2	30.9	
Bedroom (exhaust)	27.1	44.9	/	52.9	
Living room (supply)	22.6	87.2	/	60.9	2.3
Living room (exhaust)	26.2	69.6	1545.0	64.4	
Energy consumption	5.8kwh=20880kJ				

Dehumidification by cooling + mechanical ventilation with fresh air bi-directional flow in plum rain season.

The plum rain season is a continuous phenomenon of rainy days in the middle and lower reaches of China's Yangtze River in June and July. In this period, the relative humidity is always over 90% during the whole month. Therefore, the dehumidification load of the air conditioner is huge. In the test, the condition of air conditioning is set as dehumidification mode, and the ventilation system is on. The results are shown in Table 4 and 5.

Table 4 Test results of the ventilation system

Ventilation system	Temperature (°C)	Relative humidity (%)	Airflow (m ³ /h)	Enthalpy (kJ/kg)	Heat transfer efficiency
Exhaust-in	23.4	64.9	175.0	53.3	0.62(sensible heat)
Supply-in	25.6	73.8	165.3	64.7	
Exhaust-out	25.4	67.2	177.1	60.5	0.33(latent heat)
Supply-out	24.2	67.2	152.4	56.7	
Bedroom	22.3	51.4	/	/	0.70(enthalpy)
Living room	22.4	72.	/	/	
Outdoor	23.3	97.0	/	/	

Table 5 Test results of the air conditioning

Air-conditioning	Temperature (°C)	Relative humidity (%)	Airflow (m ³ /h)	Enthalpy (kJ/kg)	COP
Bedroom (supply)	10.9	90.7	552.2	29.5	5.8
Bedroom (exhaust)	20.3	65.8	/	45.2	
Living room (supply)	16.9	96.0	/	46.3	
Living room (exhaust)	21.1	78.2	1604.6	55.0	
Energy consumption	3.1kwh=11268kJ				

Simulation of energy consumption by EnergyPlus

Numerical simulation is also carried out in the study. The EnergyPlus model adopted in this paper is built strictly according to the actual size of the test apartment. The indoor air conditioning system is simulated by using the VRF system in EnergyPlus. The modelling of HRV is based on the sensible and latent heat exchange efficiency of the enthalpy exchanger. Air change rate in modelling condition is 0.5. The outdoor conditions for simulation is obtained from the weather station on site.

Simulation results

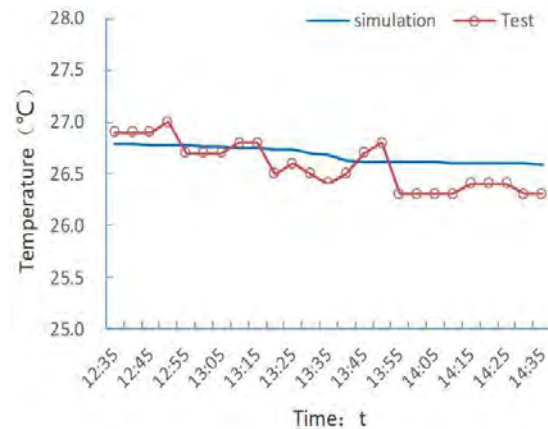


Figure 5 Temperature change curve of bedroom in summer

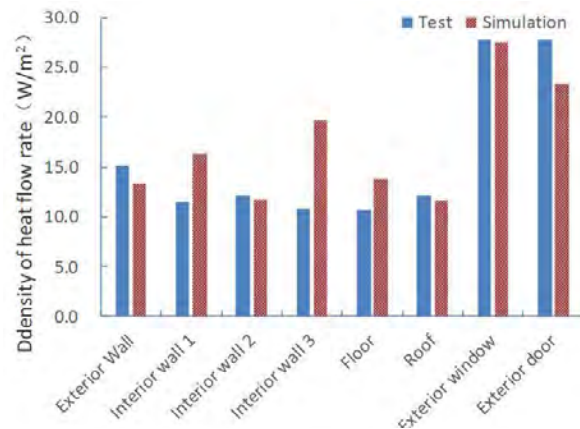


Figure 6 Comparison of average heat flux density of enclosure structure in summer

According to the measured and simulated results, the calculated value and the measured value are in good agreement with the accurate setting of the heat transfer and outdoor weather conditions. The relative error between the measured temperature and the simulated value of bedroom is 0.4%, the relative error of envelope heat transfer is 7%, and the heat transfer error of envelope is related to the actual construction quality and accuracy of the structure. In order

to verify the accuracy of the model, a longer verification experiment was conducted during the transition period.

CONCLUSION

The energy consumption of a residential building with HRV system in HSCW zone in China is measured experimentally. The energy saving effect of HRV system in the transitional season, summer season and plum rainy season is analysed (The accuracy of the instrument has a certain influence on the energy saving value.). The numerical model of a typical residential building with HRV system in HSCW zone is also established. The accuracy of the model is verified through the comparison of simulated and experimental results. This research draws the following conclusions:

- 1) In the summer of the HSCW zone, both indoor temperature and humidity are high, the room requires cooling and dehumidification by air conditioning system. Due to the big difference between the indoor and outdoor enthalpy, fresh air HRV system has a significant effect on the enthalpy recovery. The field measurements show that the HRV system can save energy 7059.68kJ within 2 hours and reduce 14.5% of the cooling load.
- 2) In the plum rain season, indoor air humidity is very high, which will cause large energy consumption for dehumidification. The fresh air HRV system has a great latent heat recovery effect. The experimental results show that the fresh air HRV system can save energy 3459.92kJ and reduce 4.96% of the dehumidification load within 2 hours.
- 3) Through the simulation results, it can be seen that the use of HRV system can significantly reduce the energy consumption of the air-conditioned buildings in summer. Compared with the natural ventilation, the energy consumption of the cooling system was reduced by 13.9% in summer after the introduction of the HRV system.
- 4) In hot summer and cold winter areas, air conditioning needs to be turned on in summer and winter, and the use of HRV system can save more energy.

ACKNOWLEDGEMENT

The present study was financially supported by the national key project of the Ministry of Science and Technology of China on “Green Buildings and Building Industrialization” (Grant No. 2016YFC0700500), and the National Natural Science Foundation of China (Grant No. 51578278).

REFERENCES

- [1] How much energy can be saved by heat recovery equipments from extract air ? [J]. Heating Ventilating & Air Conditioning, 2007.
- [2] Roulet C A, Heidt F D, Foradini F, et al. Real heat recovery with air handling units [J]. Energy & Buildings, 2001, 33(5):495-502.
- [3] Feng Xiaomei Shanghai Xian Dai Architectural Design (Group) Co, Shanghai. Energy consumption characteristics of exhaust air heat recovery units based on outdoor meteorological parameters [J]. Heating Ventilating & Air Conditioning, 2012.
- [4] Zhang L Z, Jiang Y. Heat and mass transfer in a membrane-based energy recovery ventilator [J]. Journal of Membrane Science, 1999, 163(1):29-38.
- [5] Zhao.R.Y, Fan C.Y, Xue.D.H, Air conditioning (Third Edition)[M]. China Construction Industry Press, 1994.
- [6] Room air conditioner [S] GB/T7725 – 2004
- [7] Air-to air energy recovery equipment [S] GBT 21087-2007
- [8] In-situ inspection on energy conversation for civil building [S] DGJ32/J 23-2006

Characterisation of the flexibility potential from space heating in French residential buildings

Jérôme Le Dréau^{1,*}, Johann Meulemans²

¹ LaSIE UMR CNRS 7356 / University of La Rochelle, France

² Saint-Gobain Recherche, France

*Corresponding email: jledreau@univ-lr.fr

ABSTRACT

Demand response (DR) at the building level (also named energy flexibility) will play an important role in facilitating energy systems based mostly or entirely on renewable energy sources. Flexibility is thus deemed necessary to control the energy consumption to match the actual energy generation from various renewable energy sources such as solar and wind power. However, there is lack of comprehensive knowledge about how much energy flexibility different building types and their usage may be able to offer to the present or future energy systems. In this study, the flexibility potential of space heating is characterised among the building stock in France. Five different typologies of buildings were chosen (post-1945, BR 1982, BR 2005, BR 2012 and BR 2020) with different levels of insulation, air-tightness and thermal mass. Building energy simulations were performed, with modulations (i.e. increase or decrease) of the space heating set-point during the heating season. From this study, the large influence of the envelope properties on the flexibility potential was highlighted: the storage efficiency for upward modulations and the rebound rates for downward modulations range from 40% up to 90% in poorly insulated and well-insulated buildings, respectively. This study describes a generic method and provides quantitative data to estimate the flexibility potential for demand response at the building level and to help designing future energy grids.

KEYWORDS

Energy flexibility; Demand response; Space heating; Building stock; Building envelope

INTRODUCTION

In order to decrease the environmental footprint of buildings, the European Union is encouraging the development of demand side management (DSM). These strategies consist in energy conservation measures to decrease the energy use of buildings on the long term and demand response (DR) to improve the operation of buildings taking into consideration the energy grids constraints. Demand response at the building level will play an important role in facilitating energy systems based mostly or entirely on renewable energy sources. Space heating, which accounts for 61% of the energy use in residential buildings in France (ADEME, 2013), can play an important role in providing flexibility to the energy grid. Recent studies in Denmark (Le Dréau and Heiselberg, 2016) and Belgium (Reynders et al., 2017) showed that the flexibility potential ranges from 50 up to 140 Wh/m²_{floor} for 4-hour modulations. Similarly, some field tests carried out in France (e.g., Modelec and Smart Electric Lyon projects) estimated this potential from 1 up to 3 kW per household (ADEME, 2016). However, these studies focussed on the type of control system and selected one or two building typologies to draw their conclusions. There is thus a lack of comprehensive knowledge about how much energy flexibility different building types and their usage may be able to offer to the present or future energy systems. The objective of this study is to evaluate the energy flexibility potential of single-family houses with respect to their thermal

characteristics, accounting for different types (i.e., upward or downward modulations) and durations of DR events. The objective of upward modulations is to fill the valleys, whereas the objective of downward modulations is to shed the peaks. The flexibility potential will be characterised by a virtual storage capacity as defined in previous studies (Le Dréau and Heiselberg, 2016; Reynders et al., 2018, 2017).

METHODOLOGY & DESCRIPTION OF BUILDINGS

Five buildings were selected to perform modulations of the space heating and can be classified according to the year of construction and the building regulation: 50's (no building regulation), BR 1982 (first building regulation in France), BR 2005, BR 2012 and BR 2020 (extrapolated from the actual building regulation in France). These five classes of buildings represent a large share of the building stock of single-family houses in France (around 30% of the single-family houses have been built within these periods). The main thermal characteristics of these buildings can be found in Table 1. The level of insulation of the buildings increases with the building regulations and the airtightness decreases. All buildings are insulated from the inside since this is a common feature in France. The building built in the 50's relies only on natural ventilation to ensure a good indoor air quality, whereas other buildings are equipped with a mechanical extraction (with either an automatic or a hygrometric regulation). It should be noted that the building layout varies with the cases (3 different geometries with a floor area from 110 up to 140 m²). Realistic occupation and internal loads scenarios were defined, resulting in a total sensible heat load of around 5000 kWh/year (which corresponds to an average load of 4.8 W/m²_{floor}). Due to these different characteristics, the space heating needs of the simulated buildings range from 21 kWh/m²_{floor}.year up to 290 kWh/m²_{floor}.year in Nancy (continental climate).

Table 1. Thermal properties of the simulated buildings.

	50's	BR 1982	BR 2005	BR 2012	BR 2020
Insulation walls	1 cm IWI ($U=2.75 \text{ W/m}^2\cdot\text{K}$)	4 cm IWI ($U=0.64 \text{ W/m}^2\cdot\text{K}$)	10 cm IWI ($U=0.32 \text{ W/m}^2\cdot\text{K}$)	15 cm IWI ($U=0.25 \text{ W/m}^2\cdot\text{K}$)	22 cm IWI ($U=0.14 \text{ W/m}^2\cdot\text{K}$)
Insulation roof	2 cm ($U=1.3 \text{ W/m}^2\cdot\text{K}$)	8 cm ($U=0.54 \text{ W/m}^2\cdot\text{K}$)	16 cm ($U=0.23 \text{ W/m}^2\cdot\text{K}$)	22 cm ($U=0.17 \text{ W/m}^2\cdot\text{K}$)	30 cm ($U=0.10 \text{ W/m}^2\cdot\text{K}$)
Insulation floor	2 cm ($U=1.93 \text{ W/m}^2\cdot\text{K}$)	8 cm ($U=0.45 \text{ W/m}^2\cdot\text{K}$)	20 cm ($U=0.19 \text{ W/m}^2\cdot\text{K}$)	16 cm ($U=0.23 \text{ W/m}^2\cdot\text{K}$)	15 cm ($U=0.20 \text{ W/m}^2\cdot\text{K}$)
Windows	Double glazing ($U_w=3.1 \text{ W/m}^2\cdot\text{K}$ & $g=0.75$)	Double glazing ($U_w=3.1 \text{ W/m}^2\cdot\text{K}$ & $g=0.75$)	Double glazing ($U_w=1.6 \text{ W/m}^2\cdot\text{K}$ & $g=0.60$)	Double glazing ($U_w=1.5 \text{ W/m}^2\cdot\text{K}$ & $g=0.63$)	Triple glazing ($U_w=0.8 \text{ W/m}^2\cdot\text{K}$ & $g=0.54$)
C_m [Wh/K.m²_{floor}]	75 (heavy)	50 (medium)	61 (heavy)	69 (heavy)	62 (heavy)
Ventilation	-	Mechanical ventilation by extraction (airflow 195 m ³ /h)		Mechanical ventilation by extraction (humidity controlled, mean 125 m ³ /h)	
Infiltration [ACH]	0.4	0.35	0.18	0.12	0.05
HLC [W/K]	601	330	165	120	90
G [W/m³_{heated}·K]	1.91	0.95	0.52	0.42	0.31
τ_{ISO 13790} [h]	16	21	47	65	81
Q_{heating needs} [kWh/m²_{floor}·y]	290	140	66	41	21

This study focusses on the flexibility that can be gained by controlling the space heating energy use. The heating system consists of radiators located in each room and emitting heat both by radiation (30%) and convection (70%). Upward and downward modulations (i.e. by increasing/decreasing the operative temperature set-point from 21°C to 23°C/19°C) were investigated for durations between 1 and 12 hours. These modulations do not jeopardise the thermal comfort of the occupants (as defined in the standard EN 15251). The starting time of the modulations (noon) was chosen to match with the peak of production in an energy production system dominated by solar panels. The controller of the radiators is a “perfect” rule-based controller, which pre-calculates at each time-step the amount of heat to be injected

in the thermal zone to reach the set-point (taking into consideration the limitations of the heating system). Each building was modelled by 11 thermal zones using a Building Energy Simulation (BES) software (EnergyPlus 8.8). The simulation time-step was set to 2 minutes. Two different climatic zones in France were considered: Nancy (continental climate) and Nice (Mediterranean climate). The results obtained for both climates were quite similar, so only the results from Nancy will be presented here for the sake of brevity.

From the simulations, the heating power and operative temperature with and without modulation are compared. An example is given in Figure 1 (left), where an upward modulation for 2 hours (grey area) is performed in the building built according to the BR 2012. Three indicators are then derived from these simulations to characterise the virtual storage capacity of each building: the energy charged in or discharged from the thermal mass during the modulation ($\Delta q_{heating\ DR}$), the energy change after the modulation ($\Delta q_{heating\ post-DR}$) and the efficiency (η) of the modulation. In case of an upward modulation, the efficiency is referred to as the storage efficiency. In case of a downward modulation, the efficiency is referred to as the rebound rate. The dimensionless power profiles were also plotted for the different days of the heating season (Figure 1, right) and a large variability can be observed.

$$\Delta q_{heating\ DR} = \int_{start\ DR}^{end\ DR} \Delta P_{heating} \cdot dt \quad [Wh/m^2_{floor}] \quad (1)$$

$$\Delta q_{heating\ post-DR} = \int_{end\ DR}^{\infty} \Delta P_{heating} \cdot dt \quad [Wh/m^2_{floor}] \quad (2)$$

$$\eta = \frac{-\Delta q_{heating\ post-DR}}{\Delta q_{heating\ DR}} \quad [-] \quad (3)$$

$$\overline{\Delta P_{heating\ DR}} = \frac{\int_{start\ DR}^{end\ DR} \Delta P_{heating} \cdot dt}{\int_{start\ DR}^{end\ DR} dt} \quad [W/m^2_{floor}] \quad (4)$$

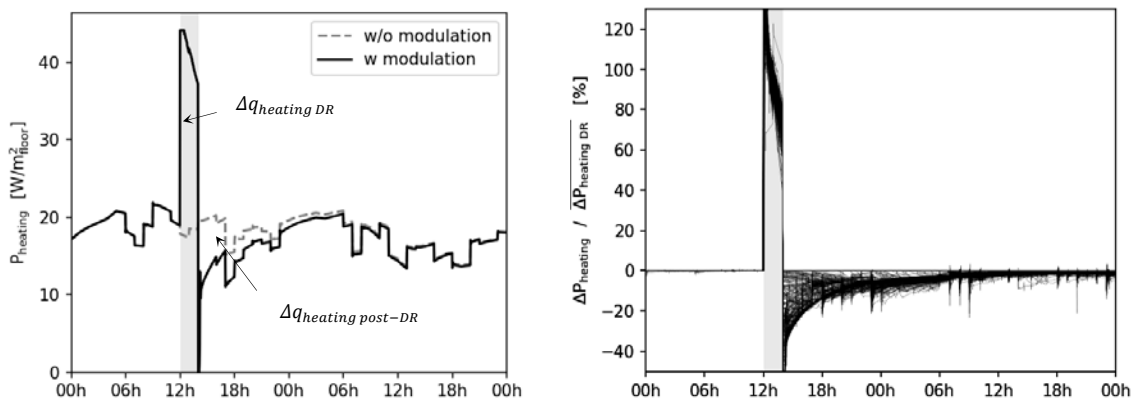


Figure 1. Heating power (26th of January) and dimensionless power profile (200 days of the heating season) for the building BR 2012.

RESULTS WITH SINGLE MODULATIONS

In a first part, single modulations were performed for each day of the heating season (resulting in more than 200 simulations for each building, each type and duration of modulation). By performing single modulations, the thermal mass has enough time to fully recover its initial state (which can last for several days) and interactions between different modulations can be dismissed.

Upward modulations

Figure 2 shows the discharged energy (post-DR) and the storage efficiency for the different buildings and the different upward modulation durations. In order to show the variability of

the potential over the heating season, boxplots were used. The box shows the 25th, 50th and 75th percentiles, the whiskers extend up to 0.5 times the interquartile range and the dots represent outliers. A large number of outliers can be observed especially during the transition season, which can be explained by the large diversity in power profiles as shown in Figure 1 (right). In terms of energy, the longer the modulation, the larger the energy shifted, and the lower the storage efficiency. The influence of the building envelope can also be clearly observed: the higher the level of insulation, the higher the storage efficiency. In other words, the additional energy use when activating the building thermal mass varies much, from 50% losses in a 50s' building down to 10% losses for a BR2020 building (for a 6-hour modulation). It can also be observed that the BR 2020 building is able to store more heat during long modulation times due to the intermittent heating.

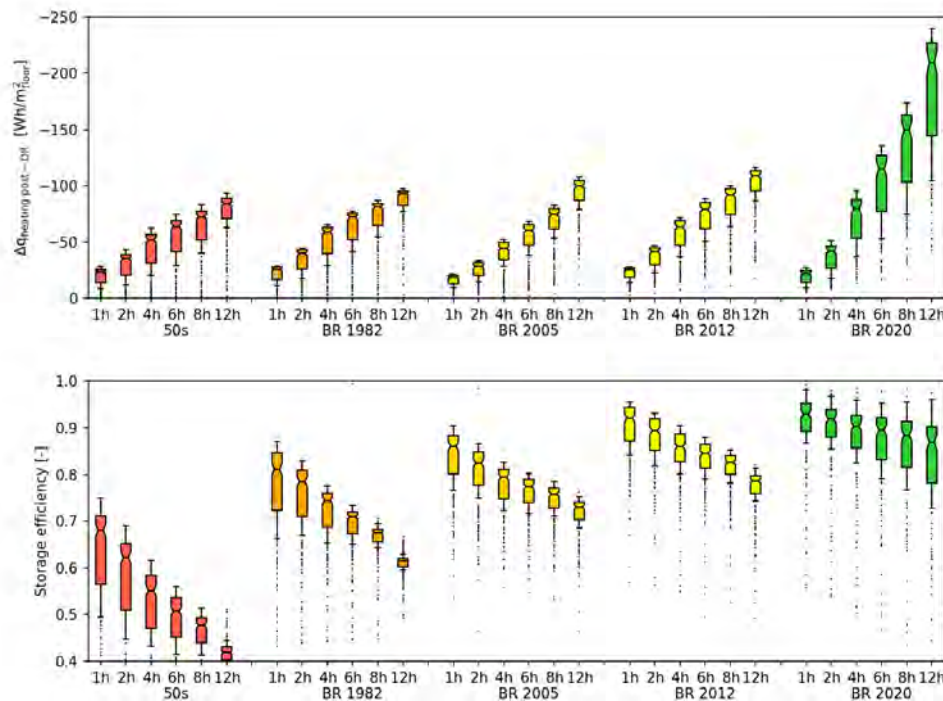


Figure 2. Heating energy post-DR (top) and storage efficiency for upward modulations (bottom).

Downward modulations

In order to harvest flexibility from buildings, downward modulations can also be performed to shave the peaks or shift part of the load. Figure 3 represents the discharged energy (during the DR) and the rebound rate for the different buildings and the different modulation durations. The lower the insulation level, the higher the energy savings. However, these higher savings come at the cost of a lower operative temperature in the building: the temperature decreases quickly in poorly insulated houses due to their lower time constant (cf. Table 1). It can also be observed that the energy shifted with downward modulations is lower than the one shifted with upward modulations, especially in relatively well insulated buildings: intermittent heating is more pronounced for well-insulated buildings. The rebound rate was also evaluated (Figure 4, bottom). A rebound rate of 100% means that the savings achieved during the downward modulation have to be fully “paid back” (resulting in no energy savings). The rebound rate exhibits a large variability within the building stock, ranging from 43% up to 87%.

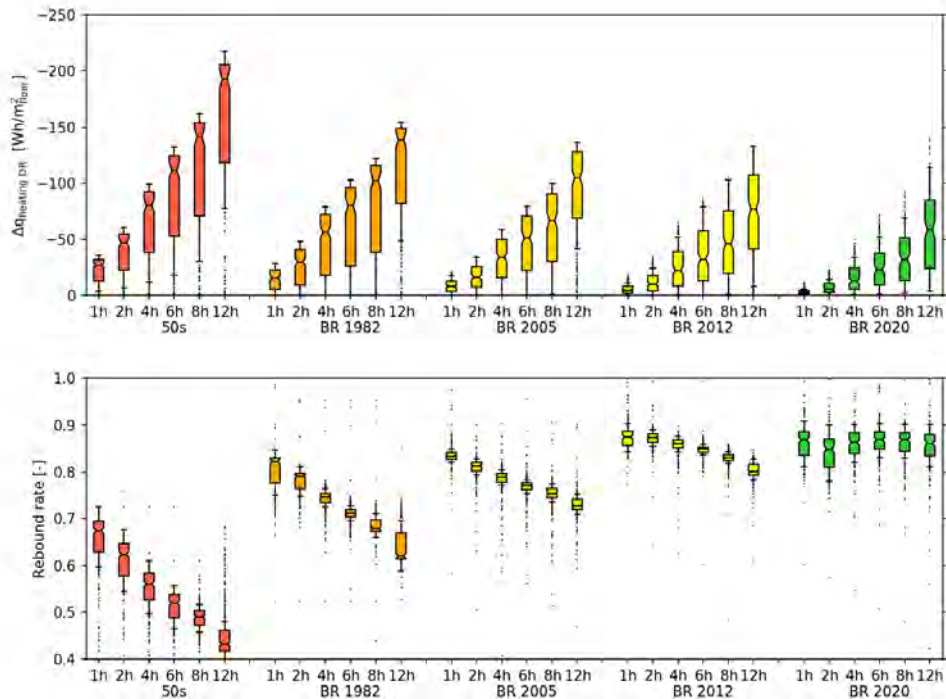


Figure 3. Heating energy DR (top) and storage efficiency for downward modulations (bottom).

RESULTS WITH DAILY MODULATIONS

In order to test a possible control strategy, the flexibility of buildings is activated once a day, starting at noon. The objectives of these simulations are both to validate the flexibility potential observed in the previous section and investigate the influence of flexibility on the yearly heating needs (energy flexibility vs. energy savings).

Figure 4 represents the annual space heating needs with upward modulations. The decreased energy use after the modulation (i.e. discharged energy) is almost constant in the building stock (around $12 \text{ kWh/m}^2_{\text{floor}\cdot\text{year}}$). However, the additional energy use by performing upward modulations differs and ranges from 4 up to 10% (2 up to $13 \text{ kWh/m}^2_{\text{floor}\cdot\text{year}}$). Figure 5 shows the resulting total energy needs with daily downward modulations. The energy savings are relatively small, around 3-4%. It can be explained by the high rebound rates (Figure 3, bottom).

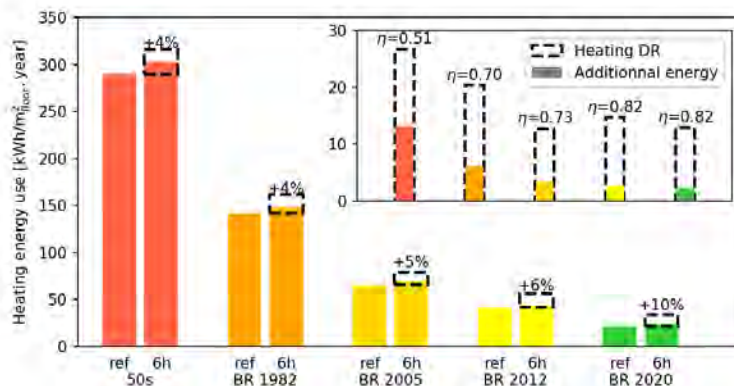


Figure 4. Annual heating need with a DR scenario (one upward modulation a day during 6 hours).

A good agreement can also be observed between the results of single and daily modulations in terms of efficiency and shifted energy. The results of single activations can thus be used by building designers to predict the flexibility potential. An example of the estimated charged energy is given below, for the BR2005 building and 6-hour upward modulations:

- from the single activations, $59 \text{ Wh/m}^2 / 0.77 \times 180 \text{ DR event} \approx 13.8 \text{ kWh/m}^2 \cdot \text{year}$
- from the daily modulations, $12.7 \text{ kWh/m}^2 \cdot \text{year}$

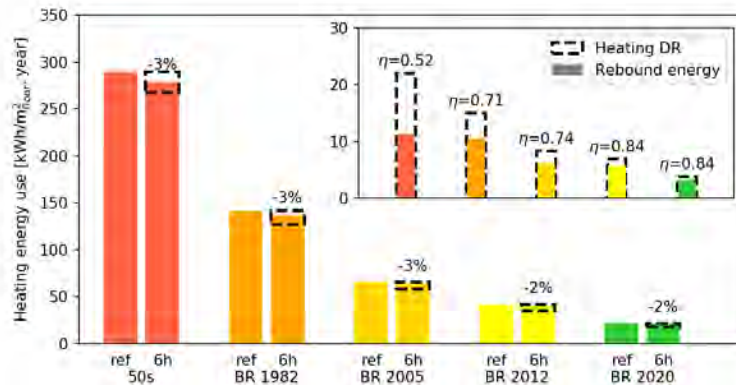


Figure 5. Annual heating need with a DR scenario (one downward modulation a day during 6 hours).

CONCLUSIONS

The energy flexibility potential of the space heating system was evaluated based on building energy simulations. Both upward and downward modulations were performed in buildings with different levels of insulation. A better characterization of the link between energy flexibility and envelope properties was achieved. Upward modulations in poorly insulated buildings should be avoided, as it leads to large storage losses (around 50% in average). Downward modulations can be performed, but they will induce rapid changes in indoor climate, which can exceed the acceptable limit set by ASHRAE ($1.1^\circ\text{C}/15 \text{ min}$). For relatively well-insulated buildings (built after the BR 2005), the efficiency and the stored energy did not change much and a good trade-off for flexibility was observed. If modulations are performed once a day for 6 hours, the decreased energy use as a consequence of the DR events amounts from 4 up to $22 \text{ kWh/m}^2_{\text{floor}} \cdot \text{year}$. This work also provides quantitative data to building designers to estimate the flexibility potential under a specific DR scenario and to help designing future energy grids.

ACKNOWLEDGMENT

The authors would like to gratefully acknowledge IEA EBC Annex 67 - Energy Flexible Buildings for providing excellent research networking.

REFERENCES

- ADEME, 2016. Systèmes Electriques Intelligents : Premiers résultats des démonstrateurs.
- ADEME, 2013. Chiffres-clés du bâtiment.
- Le Dréau, J., Heiselberg, P., 2016. Energy flexibility of residential buildings using short term heat storage in the thermal mass. *Energy* 111, 991–1002.
- Reynders, G., Amaral Lopes, R., Marszal-Pomianowska, A., Aelenei, D., Martins, J., Saelens, D., 2018. Energy flexible buildings: An evaluation of definitions and quantification methodologies applied to thermal storage. *Energy Build.* 166, 372–390.
- Reynders, G., Diriken, J., Saelens, D., 2017. Generic characterization method for energy flexibility: Applied to structural thermal storage in residential buildings. *Appl. Energy* 198, 192–202.

Evaluation of the impact of weather variability on a Net Zero Energy Building: advantage of sensitivity analysis for performance guarantee

Jeanne Goffart^{1,*}, Monika Woloszyn¹

¹Univ. Grenoble Alpes, Univ. Savoie Mont Blanc, CNRS, LOCIE, 73000 Chambéry, France

*Corresponding email: Jeanne.goffart@univ-smb.fr

ABSTRACT

Global sensitivity analysis associated with uncertainty analysis evaluates the robustness of a physical system and prioritises measurement and/or modelling efforts. The uncertainty analysis evaluates a confidence interval, whereas the sensitivity analysis quantifies the accountability of each uncertain input on the dispersion of the output.

These statistical methods are usually used to account for the variability of the static inputs, which are constant regarding the evolution of the system, for example the physical properties of the materials modelled. Dynamic inputs however, i.e. parameters that are variable over time, are rarely taken into account in the statistical analyses because of the difficulty managing correlations between the inputs in stochastic methods. Yet, the system's boundary conditions, such as meteorological input, are decisive for the evaluation of the behaviour of the building system.

This paper aims at quantifying the influence of six meteorological variables as well as 39 static inputs on the dynamic thermal behaviour of a net zero energy building. To do so, a method that stochastically generates consistent meteorological data is used and is adapted to the purpose of global sensitivity analysis. The results show a high dispersion of the cooling requirements, for which the direct solar radiation, the albedo and the window solar factor can be held accountable. Thus the variability of solar resources and their interaction with the building have the greatest impact on the performance of the building.

The variability of meteorological data needs to be considered to evaluate confidence intervals on energy performance. Furthermore, the impact of static parameters should not be overlooked, because their influence may remain significant. The considerable influence of the albedo and solar factor on the results of the present case study also shed light on the importance of assessing its value on site.

KEYWORDS

Global sensitivity analysis, Uncertainty analysis, Weather data, NZEB, solar gain

INTRODUCTION

Performance guarantee is a major issue in the context of the Net Zero Energy Building design. It consists of assigning a confidence bound to the building performance in order to guarantee a consumption level during the building's operation stage. The main concern is the strong variability of energy consumption due to the variation of weather and occupancy (Wang et al. 2012). Studies emphasise that an adjustment variable must be developed from the building's actual operating condition (weather, occupants, system settings) (Ligier et al. 2017). This makes dynamic thermal simulation combined with statistical methods essential tools. Uncertainty analysis and sensitivity analysis (USA) occur at different stages of the energy

performance guarantee process. By disturbing uncertain inputs, uncertainty analysis evaluates the confidence interval on the building performance so as to control the margin of error on the guarantee. In addition, sensitivity analysis identifies the most influential parameters on the variability in performance of the building modelled (Saltelli et al. 2008). This quest for the most influential parameter guides and/or warrants setting up a protocol for specific priority measures on the building delivered and/or the definition of the measurement and verification plan during the operation phase. This also allows one to identify the key elements in the pursuit of performance optimisation, while still in the design phase.

These statistical methods usually take into account the variability of the static inputs, which are constant regarding the evolution of the system, for example the physical properties of the materials modelled. Dynamic inputs, i.e. parameters that are variable over time, are rarely taken into account in the statistical analyses however, because of the difficulty managing correlations between the inputs in stochastic methods (Tian, 2013). Yet, the system's boundary conditions such as meteorological input, are decisive in evaluating the behaviour of the building system and therefore are one of the most important operating conditions for adjustment processes in the performance guarantee.

The purpose of the present study was to perform a UASA with dynamic and static inputs to illustrate the capabilities of this approach for the performance guarantee. The aim is to assign confidence bounds to model predictions by accounting for the natural variability of the weather inputs from year to year. This results in the characterisation of the robustness of the building performance, i.e. the stability of the performance predicted in an uncertain environment. Then we estimate the most influent input lead to measure and/or strategy to gain, respectively, confidence and/or performance. The study illustrates this on the cooling needs for July of a net zero energy single-family house with 39 static inputs and six weather variables.

METHODS

The building model

The detached house studied was built as part of the COMEPOS project, a French national program for the design, building, monitoring and feedback on 20 net zero energy single-family houses. The houses are occupied and located throughout France. The case study, in Figure 1, is situated in Strasbourg, which has a continental climate with hot summers and cold winters. The house is 137 m² on two levels. The airtightness is 0.4 m³/(h.m²) and the thermal resistance of the insulated exterior walls is 6 m². K/W. Annual energy needs are 43.6 kWh/m² for heating and 11.5 kWh/m² for cooling with, respectively, set points at 19 °C and 25 °C. Details and validation of the EnergyPlus model are available in (Josse, 2017).



Figure 1: 3D representation of the case study house, west-south façade, east-south façade.

The input variation for the UASA

To perform sensitivity and uncertainty analyses, a set of samples is generated based on the input variation defined. The variability definition of the input conditioned the results of the analysis. In this study the static and dynamic input uncertainty corresponds to the partial knowledge at the design stage.

A sampling-based method generates stochastic meteorological time series according to the typical meteorological EnergyPlus file. In this case study the Strasbourg IWEC (International Weather for Energy Calculations) is used and the generations are made for the month of July. The weather data set for UASA is built to be representative of the natural year-to-year variability of a summer month of July for Strasbourg. The sampling-based method is based on the procedure of Iman and Conover and maintains the statistical features of the meteorological time series (auto- and cross-correlations) (Goffart et al. 2017). The weather data sample generated allows the estimation of Sobol's indices (Sobol, 2001) of the first-order effect on the energy needs. The influence of each weather variable on the output variability can be quantified. The weather data set for the UASA is composed of six inputs: the dry bulb temperature, the relative humidity, the direct normal solar radiation, the diffuse horizontal solar radiation and the wind velocity and direction.

In the case of static inputs, the variability on the thermophysical properties of materials and windows are taken into account in the study as specific heat, conductivity, density in the case of materials and conductance and the solar factor for triple-glazing windows. Also considered in the study are airtightness, orientation, internal load of occupants for activity (90 W) and sleep (63 W), ventilation and ground reflectance. The variation of ground reflectance (albedo) is between 0.2 and 0.4, default values for asphalt and concrete, respectively. Both are potential exterior ground coating at the design phase. All variations are defined by uniform law and the range for each input is reported in Table 1.

Table 1: Variability of the static inputs

Input	Number of parameters	Range of the uniform law
Material properties (density, specific heat, conductivity)	31	$\pm 10\%$
Window properties (conductance, solar factor)	2	$\pm 10\%$
Orientation	1	$\pm 5^\circ$
Air-tightness	1	$\pm 20\%$
Ventilation	1	$\pm 10\%$
Internal load (occupants: activity and sleep)	2	$\pm 20\text{ W}$
Albedo (ground reflectance)	1	± 0.1 (33%)

Study protocol

According to the variability defined in Table 1 and the sampling-based method for weather data, coherent with natural weather variability for the month of July in Strasbourg, a set of 2000 values of the 39 static inputs and 2000 sequences of the six weather data variables was built and propagated into the EnergyPlus model of the single-family house. The 2000 simulations result in 2000 cooling need values, which are studied according to the 45-input variability in the next section.

RESULTS

Uncertainty analysis

First, we studied the output dispersion due to the propagation of the 45 uncertain inputs through the 2000 simulations. The cooling needs predicted for the month of July ranged from

1.30 to 5.31 kWh/m² with a mean of 3.07 kWh/m². The 95 % confidence interval of the energy need in July was 3.07 ± 1.31 kWh/m², *i.e.* 43%. To extract the elements responsible for this variability from the 45 inputs, the sensitivity indices were computed.

Sensitivity analysis

The Sobolj sensitivity indices of the most influential inputs are gathered in Table 2. They represent the variance part of each influential uncertain input on the output variance. The sum of the indices is close to 1, indicating that interactions between inputs do not influence the overall output dispersion. Its variability is bound to the effect of each input separately.

This result underscores the importance of the solar aspects on the cooling needs and especially the impact of the natural variability of direct solar radiation (34%). Then the second and third most influential inputs are the albedo (24%) and the solar factor (22%), respectively, with the same order of magnitude. Finally, the outside temperature and the conductivity of the exterior wall insulation explain the rest of the output dispersion.

Table 2. Sensitivity indices of the most influential inputs.

Input	Nature	Sensitivity index
Direct solar radiation	Dynamic	34%
Albedo	Static	24%
Solar factor	Static	22%
Dry bulb temperature	Dynamic	10%
Ext. wall insulation conductivity	Static	8%

Tendencies

It is possible to extract more information from the uncertainty and sensitivity analysis with the evolution of the output dispersion according to the variability of the most influential inputs. Figure 2 represents these tendencies for the albedo (a), the solar factor (b) and the monthly sum of the direct solar radiation (c). The shift of the average performance and the output uncertainty according to the value of an influential input can be visualised directly. For example, in Figure 2a), raising the albedo value to 0.2 from 0.4 results in a mean 45% increase in cooling needs. The same increase is observed in Figure 2b) with an increase in the solar factor to 0.44 from 0.54. The output dispersion in Figure 2a) and b) seems stable through the different albedo values and the solar factor.

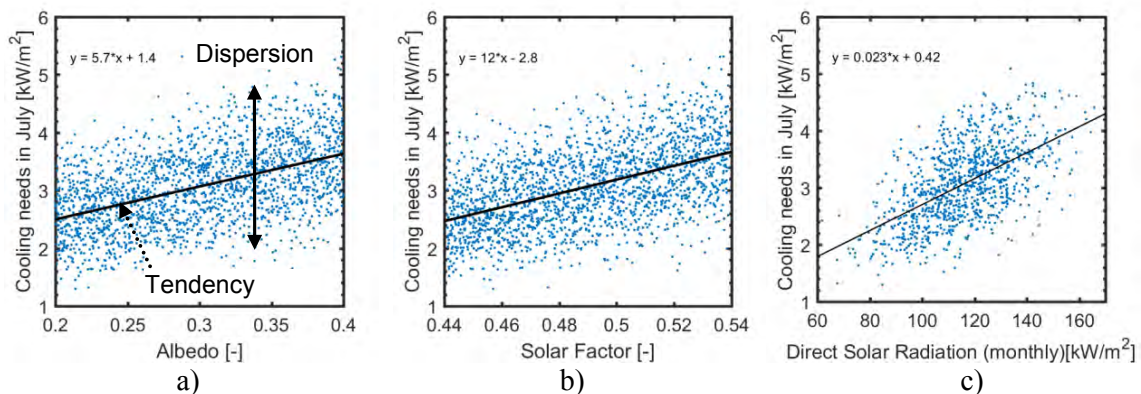


Figure 2. Evolution of the 2000 output values according to a) the albedo, b) the solar factor, c) the sum of direct solar radiation for each sequence generated for UASA. The tendency is represented by a black line.

The direct solar radiation is a time series and because of this dynamic characteristic, the dependence between output variability and weather data variability is more difficult to characterise. Figure 2c) represents the behaviour of the building performance according to the sum of direct solar radiation of each sequence. The sum variability is about 45%. This may help to better understand the variability in the solar impact on the cooling behaviour of the house.

DISCUSSION

The building performance uncertainty due to the natural variability in weather data and partial knowledge of the physical parameters of the building simulation is significant, with a variation of 43% at a 95% confidence bound. The sensitivity analysis quantifies the proportion of the influence of each input variability on the output variability: almost half of the output uncertainty is due to the variability of static parameters that determine solar radiation in the building: the ground reflectance and the window solar factor. The other part of output variability is explained by the natural weather variability of direct solar radiation (35%) and dry bulb air temperature (10%).

The interpretation takes into account the fact that the analysis results are conditioned by input variability: the solar radiation sum variability over stochastic sequences is about 45%, which explains 35% of the output dispersion; the albedo has 33% variability, which explains 24% of the output dispersion; and the solar factor has 10% variability, explaining 22% of the output dispersion. Thus, with variability at one-third of the variability of the albedo, the solar factor impacts the output variability equally, which must be the priority in characterising both the range of uncertainty and its nominal value.

The natural variability of direct solar radiation over the year cannot be reduced and is part of the operating uncertainty. More accurate in situ quantification of this entity might produce less bias in evaluating performance dependency in the guarantee process. Some of the input uncertainties may be reduced by expert knowledge by measuring the actual materials used and by the manufacturers' specifications. However, reducing uncertainties does not imply leaving them out. Indeed, the present study shows that ignoring uncertainty might result in underestimating the building performance variability and so may compromise the performance guaranteed.

CONCLUSIONS

This case study illustrates the capability of the sensitivity and uncertainty analysis for building performance. It focuses on the necessity of taking into account the natural variability of weather data and especially direct solar radiation when evaluating the interval bounds of cooling needs. Identification of the most influential static parameter prioritises in situ measurements of the solar aspects and thus increases confidence in the building's predicted energy performance. Uncertainty must be characterised so that it can be taken into account in the performance guarantee procedure and the accurate confidence bound assessed.

The building performance simulation coupled with uncertainty and sensitivity analyses makes it possible to test a large number of configurations on the model to evaluate the response of the building and thus extract the dependencies of the most influential variables on consumption. The UASA with natural variability assigns more realistic confidence bounds to the building performance and characterises the building's behaviour according to the weather data input from year to year. This might contribute to the adjustment process.

Because of the importance of a building's solar characteristics, one should focus on the sun management components such as opening and closing the shutters. Optimal management can be carried out by the occupant or using an automatic strategy and may decrease the cooling needs significantly. However, the occupants' behaviour is complex and highly uncertain. With in-situ sociological studies and measurements, it should be possible to characterise and include the building's specific occupancy in the UASA statistical approach.

REFERENCES

- Goffart J., Mara T. and Wurtz E. 2017. Generation of stochastic weather data for uncertainty and sensitivity analysis of a low-energy building. *Journal of Building Physics* 41(1): 41-57.
- Josse R. 2017. Méthode et outils pour l'identification de défauts des bâtiments connectés performants. Thesis. School of Genie Electrique of University of Grenoble Alpes. 227 pages. In French.
- Ligier S., Robillart M., Schalbart P. and Peuportier B. 2017. Energy Performance Contracting Methodology Based upon Simulation and Measurement. Proceedings of the International Building Performance Simulation Association – BS2017, San Francisco
- Saltelli A., Ratto M., Andres T., Campolongo F., Cariboni J., Gatelli D., Saisana M., and Tarantola S. 2008. Introduction to Sensitivity Analysis. In *Global Sensitivity Analysis. The Primer*, 1–51. John Wiley & Sons, Ltd. <https://doi.org/10.1002/9780470725184.ch1>.
- Sobol', I. M. 2001. Global Sensitivity Indices for Nonlinear Mathematical Models and Their Monte Carlo Estimates. *Mathematics and Computers in Simulation* 55 (1–3): 271–80. [https://doi.org/10.1016/S0378-4754\(00\)00270-6](https://doi.org/10.1016/S0378-4754(00)00270-6).
- Tian W. 2013. A review of sensitivity analysis methods in building energy analysis. *Renewable & Sustainable Energy Reviews* 20: 411–419.
- Wang L., Paul M. and Xiufeng P. 2012. Uncertainties in Energy Consumption Introduced by Building Operations and Weather for a Medium-Size Office Building. *Energy and Buildings*, 53, 152-58. doi:10.1016/j.enbuild.2012.06.017

Numerical analysis of a ground-source heat-pump system in traditional Japanese “Kyo-machiya” dwellings

Shun Takano^{1*}, Chiemi Iba¹ and Shuichi Hokoi²

¹Kyoto University, Japan

²Southeast University, China

*Corresponding email: be.takanoshun@archi.kyoto-u.ac.jp

ABSTRACT

Kyo-machiya, which is a traditional wooden dwelling in Kyoto, is generally equipped with a shallow well. The well water can be potentially utilized as a heat source with a geothermal heat-pump system without incurring a high drilling cost. Hereby, more energy saving in the traditional dwelling can be realized with the heat-pump system. However, an appropriate technique to utilize geothermal heat from a shallow well has not been established yet in Japan. To promote the geothermal use, we have continued an experiment to evaluate the practicability of a simple geothermal heat-pump system installed in a shallow well since the winter of 2013. In this study, the condition of the water flow in the well was examined using the computational fluid dynamics (CFD) technique, and the velocity of flow of the groundwater into the well was also estimated. We show that constant buoyancy was generated because of the temperature difference due to the heat-pump operation. Based on the results, a three-dimensional heat-transfer numerical analysis model, proposed in the previous study, was developed so that moisture transfer in the ground could be considered. Using the estimated buoyancy of the well water and the groundwater velocity, the calculated results seemed to reproduce the characteristic of the measured value. Furthermore, we show that the groundwater velocity has a large influence on the well water temperature.

KEYWORDS

Geothermal Heat Pump, Kyo-machiya, Well, Groundwater, CFD

INTRODUCTION

Geothermal heat is attractive as a stable energy source that is hardly affected by weather conditions and seasons. However, since the initial costs to utilize the geothermal heat such as those of drilling are very high, it is currently not widely used in Japanese dwellings (Nagano et al. 2006). Using geothermal heat, air conditioners can be operated without discharging cold air during winter. Additionally, the cooled ground can be used as a potentially cold heat source during summer. Since there are many unused shallow wells which were once used in a Kyo-machiya, a traditional wooden dwelling in Kyoto, energy saving may be realized by installing a ground-source heat pump (GSHP) system using the well water as the heat source, which will not involve a high initial cost. Therefore, the objective of this research is to spread the usage of GSHPs, which use the existing shallow wells in Japan, by providing basic information about the system and the efficient operational methods.

To promote the use of this system widely, it is necessary to evaluate the impact that this system has in real life and establish an optimum method whereby this system can be used. Hagihara et al. (2016) proposed a three-dimensional thermal model that can be used to predict the temperature change of the well water and showed the usefulness of the well water as a heat source. They also indicated that it is necessary for the well water to be restored to its original temperature for continuous heating. In their calculation, the water flow rate inside the well and

the inflow velocity of the groundwater into the well were estimated so that the calculation results agreed well with the measured results.

In this paper, we conducted a computational fluid dynamics (CFD) calculation to estimate the inflow velocity of the groundwater and the convective flow of the well water. Using the results, the heat and moisture transfer in and around the well during the heating operation was calculated by using the three-dimensional heat and moisture transfer model.

Nomenclatures			
c	Specific heat [J/kg·K]	ρ	Density [kg/m ³]
T	Temperature [K]	μ	Water chemical potential for free water [J/kg]
KS	Heat transfer coefficient [W/K]	λ	Thermal conductivity [W/(m·K)]
J	Flow rate [kg/m ² ·s]	V	Volume [m ³]
A	Area [m ²]	n	Gravity coefficient [-]
r	Latent heat [J/kg]	$\partial/\partial n$	Normal direction differential on boundary between Well water and antifreeze solution pipe
g	Gravity acceleration [m/s ²]		
Subscripts			
w	Well water	s	Soil
a	Air	b	Antifreeze solution
g	Gas	c	Convection

Surveyed system and CFD Calculation

The surveyed heating system using well water is shown in Fig.1 (a). The measured well is about 9 m deep from the ground surface and about 80 cm in diameter (Fig.1 (b)). It is in the living room of a Kyo-machiya, Kyoto city. The GSHP system installed in this well has been operational since the winter of 2013. In this system, the heat-collecting pipe is in contact with the well water and antifreeze solution circulates in the pipe to exchange heat with well water. The well water temperature was measured at three different heights: 4500 mm (upper), 2500 mm (middle), and 500 mm (lower) from the bottom. Also, the depth of the well water, the heat-pump inlet/outlet temperatures of the antifreeze solution, and electricity consumption were measured.

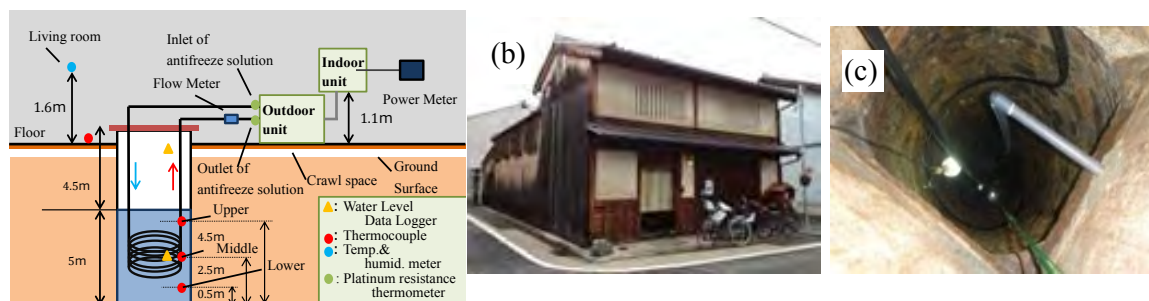


Fig.1 Surveyed system. (a) Schematics of measurement; (b) appearance of the Kyo-machiya; (c) well

Outline of the calculation

To simulate the characteristics of the temperature distribution of the well water when the heat pump was operated, and to clarify the water flow inside the well, a CFD analysis was performed. The simulation model is shown in Fig. 1(c) and (d), and the CFD calculation conditions are listed in Table 1. The model simulates the positional relation between the well and the antifreeze solution, and although the shapes of the well and the heat-collecting pipe are cylindrical, the shapes of these elements are approximated for simplicity as a square pipe of a volume and surface area equal to that of the actual well and the heat-collecting pipe, respectively. Based on the visual inspection of the well, the arrangement of the heat-collecting pipe was modelled to be concentrated at an approximate height of 3 m from the bottom. The CFD analysis software "Flow Designer 2017" was used for calculation.

According to a well drilling expert, the peripheral wall of this type of well is generally clogged

with mortar to the deep part and water does not easily permeate through it. Therefore, in this calculation, the groundwater was assumed to flow in only through the region which is 0.5 m from the bottom, which is different from that assumed in the previous study, (Hagihara et al. 2016) where the groundwater flows in through all parts of the well wall.

According to the literature (Fukukawa, 1969), several velocities of the groundwater were used to analyze the influence on the well water temperature by them. Only the results in case of a velocity of 2m/day, which agreed well with the measured results, were examined here. The remaining boundary surfaces were insulated.

The measured result during 07:30–13:00 h on December 22, 2015, which was the first day of the usage of heat pump during the winter, was used to verify the calculation.

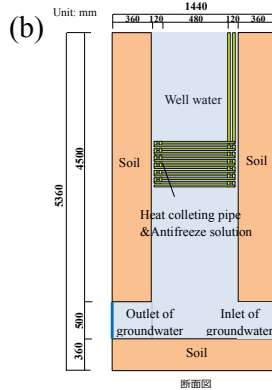
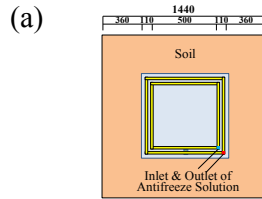


Table 1 Calculation condition

Space mesh number	$X \times Y \times Z = 38 \times 32 \times 119 = 144,704$
Size of calculated area	$X \times Y \times Z = 1.44 \times 1.44 \times 5.36 \text{ m}$
Minimum mesh increment	15 mm
Time interval	0.1 s
Flow type	laminar flow
Temperature of groundwater	18.5 °C
Velocity of groundwater	2.0 m/day
Inlet temperature of antifreeze solution	Given by the experimental result
Flowrate of antifreeze solution	result

Fig.2(a) Computational domain of CFD (plan); (b) computational domain of CFD (vertical section) ; Table 1: Calculation condition

Results and discussion

Fig. 3 (a) shows the comparison between the calculated and the measured temperatures, and Figs. 3 (b) and (c) show the water flow during and after the heating operation, respectively.

The points of the antifreeze solution that were obtained from the measurement and calculation were different. The point obtained from the measurement was located in the living room, whereas the point obtained from the calculation was located in the well water because of the limited calculation domain. Therefore, both the temperatures may not be in agreement after the termination of the operation.

The calculated temperatures agree well with the measured results; thus, it can be said that the

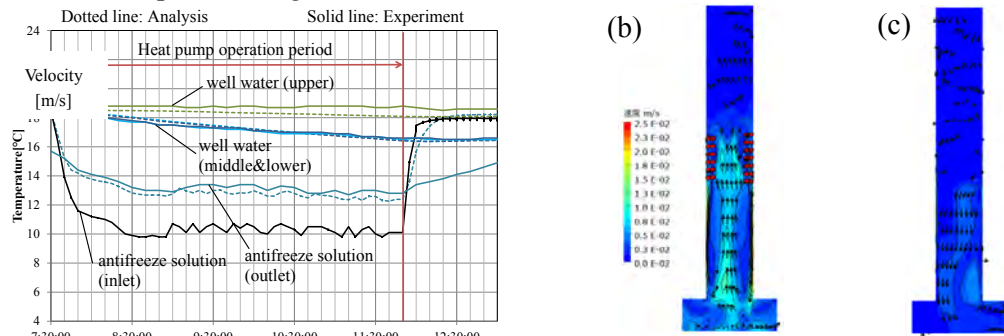


Fig. 3 Results of the CFD calculation. (a) Comparison of the calculated and measured temperatures. (b)(c) Water flow in the well: (b) 1 hour after the operation started and (c) 1 hour after the operation terminated.

inflow velocity of the groundwater and the location of the inflow inlet are accurately assumed. Fig. 3 (b) shows that water moves upward at about 0.01 m/s after commencing the heating operation. Since this upward flow did not occur after the heating was stopped, as shown in Fig. 3 (c), this water circulation was caused by the temperature difference between the inside and outside of the well. Judging from this result, the buoyant flow was taken into consideration in the three-dimensional heat and moisture analysis in the next section.

CALCULATION OF HEAT AND MOISTURE TRANSFER

Outline of calculation

A simulation model, as shown in Fig. 3, was proposed. The calculation area comprised soil, air, and water. The period considered for the calculation was from January 1, 2013 to January 16, 2014 (380 days), and the heating operation period was from December 27, 2013 to January 16, 2014 (20 days).

Therefore, on all sides of the calculation domain, the boundary temperature at a depth of more than 5 m was assumed to be 17.5°C, which was the annual average outdoor air temperature of Kyoto city (JMA 2014). The boundary temperature from the ground surface to a depth of 5 m was also approximated using the linear distribution by considering the results of one-dimensional thermal calculation. On the upper side of the calculation domain, three different values were used as the thermal boundary conditions: the temperature of the living room of the house (T_{room}); temperature of the crawl space (T_{U}); and temperature of the outside air (T_{o}). The inlet temperature (T_{in}) and the rate of flow of the antifreeze solution were also used as the boundary conditions.

The thermal conductance between the antifreeze solution and the well water as well as between the antifreeze solution and the well air are depicted in Fig. 3 as KS. Considering that the heat-collecting pipe was arranged in a bundle mainly in the middle height of the well, the thermal conductance was assumed to differ depending on the height.

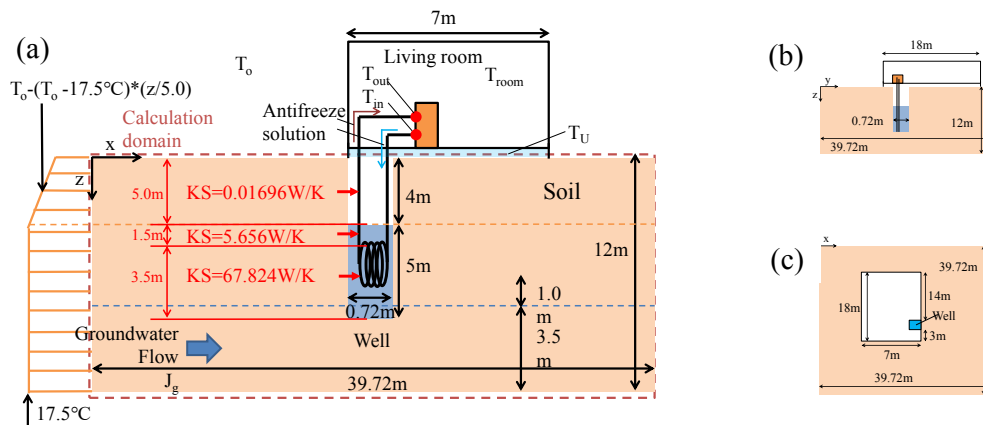


Fig. 4 Schematic of the simulation model: (a) x-z section; (b) y-z section; and (c) x-y plan

The equations (1)–(4) are the heat balance equations of the soil, well water, air in the well, and antifreeze solution proposed by Matsumoto et al. (1995); the basic equation of the groundwater flow is given by equation (5). The air in the well was dealt with as one mass. In the heat balance equation of the well water, both conductive and convective heat transfer were considered. From the results of the CFD analysis, it was assumed that the groundwater flow occurs by ground gradient, and the convective term by the groundwater flow is added to the heat balance equation. Table 2 shows the ground gradient coefficient and the liquid water conductivity related to the water chemical potential gradient. Also, from the results of the CFD analysis, it was assumed that a buoyant water flow of about 0.01 m/s occurs when the water temperature of the upper mesh is higher than that of the lower cell. In the calculation, two velocities of groundwater flow

were considered; as assumed in the CFD analysis, one is 2 m/day, and the other is two times larger. The boundary conditions between the well water and well air, and the well water and the antifreeze solution are given by equations (6) and (7).

$$c_s \rho_s \frac{\partial T_s}{\partial t} = \nabla \left[\left(\lambda_s + r \lambda'_s \right) \nabla T + r \lambda'_s \mu_g \nabla \mu \right] - c_w J_g \nabla T_s \quad (1)$$

$$c_w \rho_w \frac{\partial T_w}{\partial t} = \nabla (\lambda_w \nabla T_w) - c_w J_{buo} \frac{\partial T_w}{\partial z} - c_w J_c \frac{\partial T_w}{\partial x} - c_w J_c \frac{\partial T_w}{\partial y} \quad (2)$$

$$c_a \rho_a \frac{\partial T_a}{\partial t} = - \sum \frac{K_a S_a}{V_a} (T_a - T_b) - \sum \alpha_i A_i (T_a - T_i) \quad (3)$$

$$c_b \rho_b \frac{\partial T_b}{\partial t} = \nabla (\lambda_b \nabla T_b) - c_b J_{bx} \frac{\partial T_b}{\partial x} - c_b J_{by} \frac{\partial T_b}{\partial y} - c_b J_{bz} \frac{\partial T_b}{\partial z} \quad (4)$$

$$J_{gi} = -\lambda'_{i\mu} \left(\frac{\partial \mu}{\partial i} - n_i g \right) \quad (i = x, y, z) \quad (5)$$

$$-\lambda_w \frac{\partial T_w}{\partial z} = \alpha_a (T_a - T_w) \quad (6) \quad -\lambda_w \frac{\partial T_w}{\partial n} = K_w (T_b - T_w), -\lambda_b \frac{\partial T_b}{\partial n} = K_w (T_w - T_b) \quad (7)$$

Table 2 Moisture conductivity and ground gradient coefficient use in equation (5) ($Z \geq 8.5$ m)

direction	n	λ'_{μ} [kg/ms(J/kg)]
x	0.017	$1.5 \times 10^{-4} - 3.0 \times 10^{-4}$
y	0	0.0
z	0.999711	0.0

The material properties used are listed in Table 3. The density, specific heat, thermal conductivity, and moisture conductivity of the soil are assumed to change depending on its temperature and water content.

Table 3 Material properties used in the calculation

Material	c [J/kg·K]	λ [W/m·K]	ρ [kg/m ³]
Water	4,200	0.6	998
Air	1,005	(Heat transfer coefficient: 0.023[W/m ² K])	1.248
Antifreeze solution	4,100	0.5	1,020

Using these equations and conditions, the temperatures of the antifreeze solution and the well water were calculated. In the simulation, the space was discretized by using the central difference method and the time using forward difference. However, the heat balance equation of the antifreeze solution was discretized using the upwind difference method. The time increments were set as 0.15 s during the heating operation and 15 s in other cases.

Results and discussion

Figs. 5 (a) and 6 (b) compare the calculated temperatures of the well water with the measured results when the groundwater velocity was assumed to be 2 and 4 m/day, respectively. Figure 5 (c) compares the heat gain. In both cases (Figs. 5 (a) and 5 (b)), the measured tendency, i.e., that the water temperature in the upper region was higher than that in the middle and lower regions, was reproduced under the condition that the groundwater flows in only through the lower region of the well, which is different from that assumed in the previous study. Furthermore, it is likely that the groundwater velocity may be larger than that assumed in the CFD analysis since the result in (b) agrees with the measured result better than that from (a). Fig. 5 (c) shows that the heat gain is by 30% larger in the case of a groundwater velocity of 4 m/day. Thus, it can be said that the influence of the groundwater inflow on the well temperature

is very large.

However, shortly after beginning the calculation, the calculated well water temperature rapidly decreased as compared to the measured temperature, and the calculated upper temperature remained lower than the measured temperature. This may have occurred because the factors related to temperature recovery, such as infiltration of the ground water from the upper well wall, may not have been properly taken into consideration. To accurately evaluate the ground temperature and the water level of the well, it may be necessary to incorporate the aforementioned factors into the calculation model.

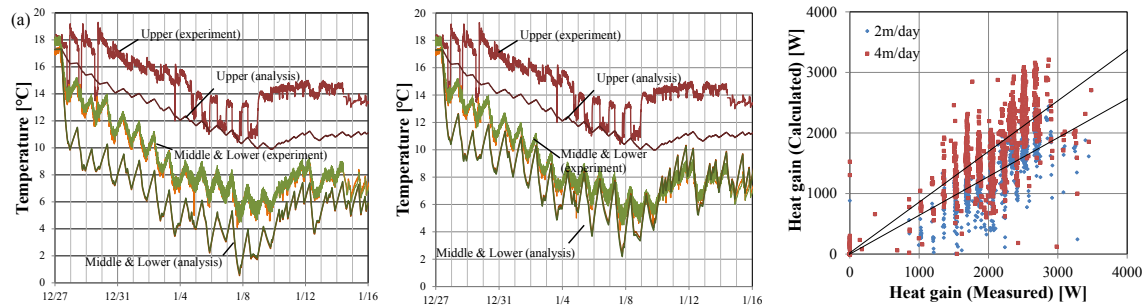


Fig. 5 Comparison of the calculated and measured results.

(a) Temperature (groundwater velocity of 2 m/day); (b) temperature (groundwater velocity of 4 m/day); (c) heat gain

(in Fig. 5(c), the measured heat gains are discretely distributed because they are calculated based on the measured temperatures in the units of 0.1°C)

CONCLUSION

In this study, the heat flow associated with water flow in and around the well with a heat-pump heating system was investigated by CFD analysis. It was shown that the water velocity due to the buoyancy amounted to about 0.01 m/s when the heating system was operated. Furthermore, previously proposed thermal model was extended to a heat and moisture transfer model based on the results of the CFD analysis, which show that the buoyancy and groundwater flow exist partially. The calculated results by the extended model agree well with the measured results that the water temperature in the upper region is higher than those in the middle and lower regions. It is also shown that the velocity of the groundwater has considerable impact on the well water temperature.

ACKNOWLEDGEMENT

The authors would like to thank the Kyo-machiya residents for their generous cooperation while setting up and using the heat pump.

REFERENCES

- Advanced Knowledge Laboratory Inc.: Flow Designer 2017
- Fukukawa Y, 1969, Functional deep well engineering, pp.4-13, Japan Road Technology Research Institute (in Japanese)
- Hagihara K, Iba, C and Hokoi S, 2016, Effective use of a ground-source heat-pump system in traditional Japanese “Kyo-machiya” residences during winter, *Energy and building*, 128, pp.262-269
- Japan Meteorological Agency 2014. URL: <http://www.jma.go.jp/jma/index.html> (Access date: 4 April 2018)
- Matsumoto M, Nagai H, and Ushio T. Numerical analysis of thermal behavior in and around the thermal well: Experimental studies on application of the ground for annual heat storage part 2 [in Japanese], *J. of architecture, planning and environmental eng.* 1995, 470, pp.37-44
- Nagano K, Katsura T, and Takeda S. , 2006, Development of a design and performance prediction tool for the ground source heat pump system, *Applied Thermal Eng.*, 26, pp.1578-1592

Offsetting Peak Residential Cooling Loads Using a Medium Temperature Chiller and Sensible Cold Thermal Storage

Christopher Baldwin^{1*} and Cynthia A. Cruickshank¹

¹Carleton University, Ottawa, Ontario, Canada

*Corresponding email: christopher.baldwin@carleton.ca

ABSTRACT

Space cooling places a significant peak load on the electrical grid during hot, sunny afternoons. With the introduction of time-of-use billing, space cooling during these periods has become very expensive. To reduce utility costs and shift peak loads, the use of a medium temperature chiller coupled with a sensible cold thermal storage system was investigated. Optimal configurations were found for seven cities located within each of the seven ASHRAE climate zones and an analysis on the energy consumption and annual utility costs are presented. It was found that in all locations, peak loads from air-conditioning could be reduced or eliminated, and that when the cooling load was great enough, or the peak utility rate was sufficiently greater than the off-peak period, annual utility costs savings, approaching 30% in some areas, could be realized.

KEYWORDS

Cold Thermal Storage, Demand Side Management, Residential Air-Conditioning, Peak Loading, Time-of-Use Billing

INTRODUCTION

As global temperatures increase with global warming, the demand for space cooling has seen a significant increase. This coupled with the increase in residential floor space, has caused a spike in air conditioning use, and consequently the amount of energy consumed for space cooling. Both the United States and Canada have seen an increase in energy consumed for space cooling in excess of 50% in the last 25 years, while total residential consumption has only increased 2% and 5% in the United States and Canada respectively (NRCan-OEE, 2013; U.S. EIA, 2018).

This demand for space cooling is greatest during afternoon and early evening, when daily temperatures and solar radiation are at their peak. Since electrical grids are sized to the anticipated peak load, an increase in generation and transmission capacity is required to meet these increasing loads. In order to address the required increase in grid capacity (which is also extremely expensive), utility providers are implementing measures to control when electricity is being used and to shift consumption from peak to off-peak periods. Of these, the most common strategy is implementing time-of-use billing. Electricity rates during hours of the day, when electricity demand is at its greatest, is more expensive than electricity during low demand or off-peak periods.

One approach for a utility customer to reduce the higher cost associated with time-of-use billing is lowering the air conditioning set-point, or turning off the unit entirely. This can impact the desired comfort of the occupant and is not always possible, particularly for elderly occupants. An alternative solution is to couple an air conditioning unit with cold thermal storage, allowing the air conditioner to run during off peak periods, and storing the cooling potential for use during peak periods.

In a previous study, Baldwin and Cruickshank (2016) explored this possibility using a standard liquid-to-liquid heat pump coupled to a cold thermal storage system. This was studied for Ottawa, Canada and in this study, it was found that peak loads from air conditioning can be eliminated if adequate storage is installed in the system. That being said, a significant increase in off-peak power was observed. This was caused by the substantial drop in performance of the heat pump when storing cooling potential at low temperatures, as well as the relatively low total cooling load of a residential building located in Ottawa. As a result, an increase in the annual electricity cost was observed.

This paper builds on the previous study, and looks at using a medium temperature chiller coupled with a sensible, cold thermal storage system using a 50/50 (by volume) water/glycol solution as the sensible storage medium. Medium temperature chillers are designed to operate with evaporator temperatures between 0°C and -25°C. By utilizing a chiller designed for lower temperatures, it was hypothesized that chiller performance would not degrade as storage temperatures near or below freezing are utilized. Additionally, multiple locations throughout all of ASHRAE's major climate zones are utilized to determine the impact of load on the potential for offsetting peak electrical loads as a result of air conditioning.

METHODS

To determine the potential of shifting electrical consumption to off-peak periods, a city in each ASHRAE climate zone was selected. Cities were selected where the major electrical provider either used only time-of-use billing or provided it as an option for customers who wished to opt-in to the program. The selected cities and the utility rates are provided in Table 1. All utility rates are as of March 2017 and are shown in local currency.

Table 1: Selected cities and the associated utility rate

Location	ASHRAE Climate Zone	Peak Rate* (\$/kWh)	Mid-Peak Rate* (\$/kWh)	Off-Peak Rate* (\$/kWh)
Miami, Florida	1	0.19165	N/A	0.0331
Phoenix, Arizona	2	0.1020-0.2226	N/A	0.0711-0.0741
Los Angeles, California	3	0.1456-0.2433	0.1456-.01641	0.1396-0.1492
Portland, Oregon	4	0.1998	0.1428	0.0421
Boston, Massachusetts	5	0.1973	N/A	0.0920
Toronto, Ontario	6	0.1564	0.1194	0.0894
Sudbury, Ontario	7	0.1504	0.1134	0.0834

* (FPL, 2018; SRP, 2018; LADWP, 2018; PGE, 2018; NG - ME, 2018; THC, 2018; GSU, 2018)

A model was developed in TRNSYS, and consisted of a two-storey house with a fully conditioned basement. The house had a total above grade floor area of 220 m² and a volume of 835 m³. The house was also modelled to the current Ontario building code, with an above grade wall RSI value of 4.5 m²K/W, and with windows on all 4 sides of the building, with an overall window to wall ration of 30%. A detailed description of the model is described in Baldwin and Cruickshank (2016).

For this study, baseline simulations to determine annual energy consumption using traditional heating and cooling methods were first run. In these models, space heating and cooling loads were met using a standard heat pump with a performance map developed by Baldwin and Cruickshank (2016). The domestic hot water demand was met using an instantaneous electric

water heater. Baseline results and annual utility costs for space heating, cooling and domestic hot water were then determined for each location.

Once the baseline energy consumption was determined, the medium temperature chiller and cold thermal storage were integrated into the house model. A performance map for the medium temperature chiller was experimentally determined at steady-state. A total of 315 tests were performed. A number of simulations were then performed to determine the optimal storage volume and tank set-point for each location. Using these results, an analysis was conducted to determine the feasibility in each of the chosen locations. The results of these simulations are shown and discussed in the next sections.

BASELINE ENERGY RESULTS

Baseline energy consumption and the resulting annual energy costs were calculated for each of the seven locations. Annual energy consumption was calculated first by end use (i.e., hot water, space heating, space cooling), neglecting any appliance, plug or lighting loads. A second baseline analysis was conducted on the time of day the energy is used, breaking down the peak, mid-peak and off-peak periods as defined by the local utility, as well as the utility costs for each period of the day. The results of two analysis are shown in Figure 1.

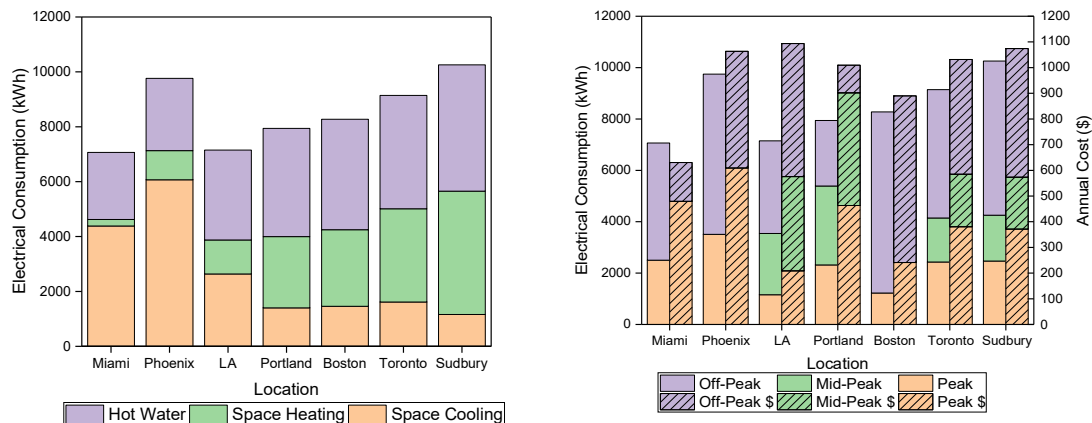


Figure 1: Energy consumption by: end use (left), time of day and annual utility costs (right)

From these results, it can be seen that as the ASHRAE climate zone number increases (going left to right on each graph), the proportion of heating to cooling of the building increases. It can also be noted that in all locations, the peak and mid-peak costs were disproportionately higher than the amount of energy used during the same period. Additionally, in general, the higher the percentage of the building load that is attributed to space cooling, the greater the percentage of utility costs as a result of energy used during peak periods.

OPTIMAL SET-POINT AND TANK VOLUME

Once the energy baseline was determined for each locale, a parametric study was undertaken to determine the optimal tank size and tank set-point for each location. The tank was controlled using the average tank temperature as the control variable and two set-points were implemented. The first was the tank set-point during peak and mid-peak periods, which was kept constant through all simulations at 15°C, and the second was the tank set-point during off-peak periods, which was varied through the simulations to determine the optimal value. During the study, the tank volume was varied from 0.25 m³ to 3 m³, in 0.25 m³ increments, while the off-peak tank set-point was varied from -10°C to 5°C, in 5°C increments. As such, a total of 48 simulations were completed for each locale. The annual utility costs were then calculated for each

simulation, and the results were plotted as a 3-dimensional surface plot, interpolating between the individual points, was developed for each city. The annual utility cost was the variable of interest, with the goal of minimizing the annual utility costs for the dwelling. Two examples for these plots for Phoenix and Portland are shown in Figure 2.

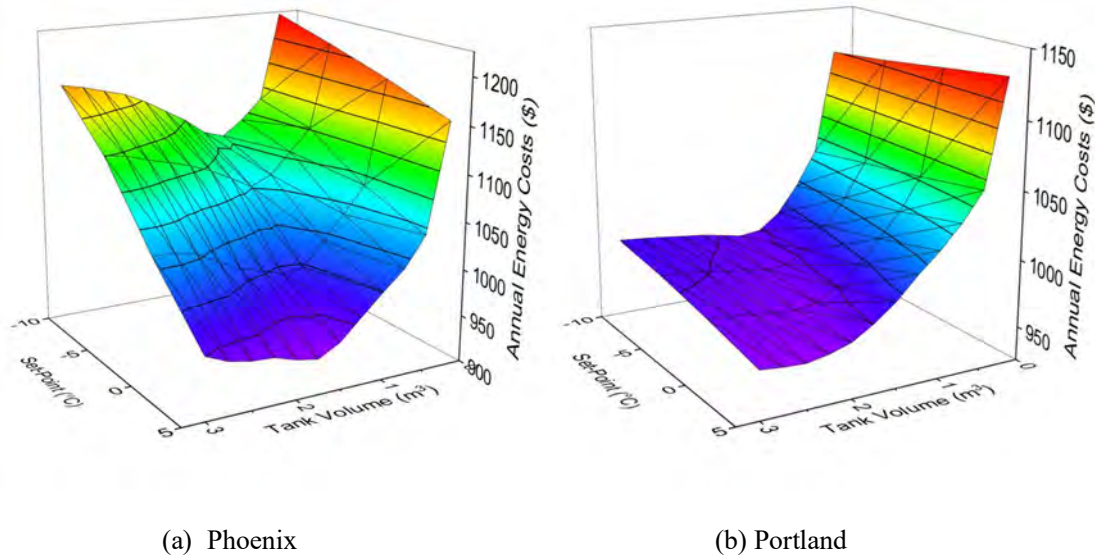


Figure 2: Example simulation results for Phoenix and Portland varying the off-peak set-point and tank volume

From this series of graphs, it can be seen that the optimal configuration for any given locations is dependent on both the cooling loads of the building, the ratio between peak and off-peak utility costs, and the total energy consumption. In all cases, it was concluded that it is paramount to find the correct storage capacity, as if not enough storage is integrated into the system, the amount of peak energy that is off-set is minimal, increasing the annual energy costs. On the other hand, it is seen that a second spike in energy costs occur in most locations if too much storage is integrated into the system, as the chiller must constantly operate at lower temperatures, near the set-point of the storage tank, without realizing the stored cooling potential. This decrease in operating temperature resulted in a significant drop in chiller performance, and consequently an increase in electrical energy required. Additionally, a trend towards higher set-point temperatures seeing lower annual costs was observed, as again, the performance of the chiller decreases with the lower operating temperatures. In contrast however, the higher the set-point temperature, the larger the tank volume typically required, and as such, more space and a higher initial capital cost is required.

Taking the results from each location, the optimal tank size and tank set-point was determined for each of the seven locations. When results from multiple configurations provided the same, or very similar results, the configuration in which the tank size was smallest was selected to reduce the required volume within the system. The optimal configuration in which annual energy costs are minimized for each location, and a comparison of cost compared to baseline for each of the locations is shown in Table 2. Further, a comparison of when energy is used between baseline and optimized configurations is shown in Figure 3.

Table 2: Optimal configuration and electrical costs per location

Location	Optimal Tank Volume (m ³)	Optimal Set-Point (°C)	Annual Energy Cost (\$)	Baseline Energy Cost (\$)	Difference (%)
Miami	1.50	0	446.39	630.44	-29.19%
Phoenix	1.75	5	937.65	1063.40	-11.83%
Los Angeles	0.50	5	1083.40	1093.78	-0.95%
Portland	2.00	0	963.93	1009.48	-4.51%
Boston	1.50	5	954.81	890.11	7.27%
Toronto	1.25	0	1046.52	1031.52	1.45%
Sudbury	1.00	5	1175.67	1074.24	9.44%

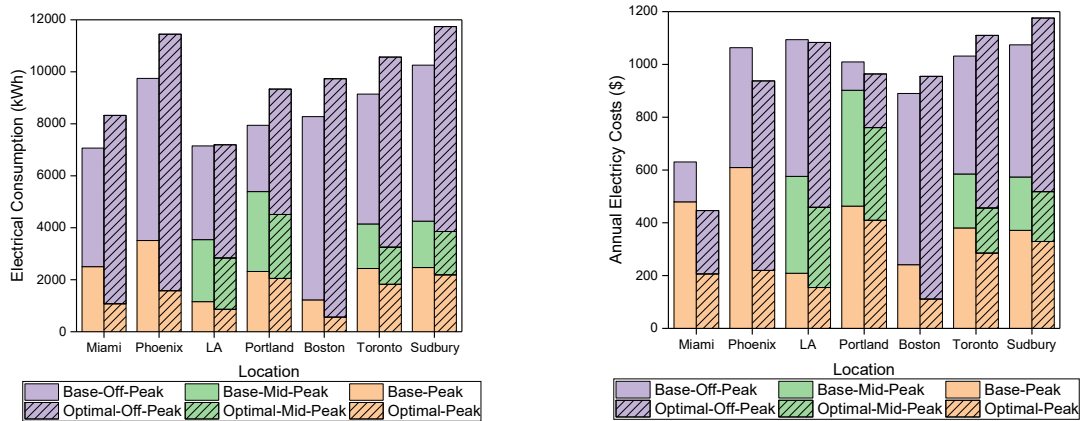


Figure 3: Comparison between baseline and optimal energy consumption and utility costs

DISCUSSION

Based on these results, a number of trends were observed. The first is the potential is greatest for offsetting significant peak loads in regions where building loads are dominated by cooling loads. In Northern climates a substantial reduction in peak loads can be obtained, however the economic benefits are not there when compared to southern climates. Even though climate appeared to be the most significant factor in determining the feasibility, the ratio between utility rates between peak and off-peak periods influenced the optimal configuration of the system. This can be seen in particular in the results for Los Angeles, where the small difference in peak to off-peak rates creates little economical benefits even though a high cooling load exists. When the ratio is high (peak to off-peak), it was beneficial to increase the storage capacity to offset as much of the peak load as possible, even if the increase in off-peak consumption is disproportionately large.

Although benefits were observed in most locations, additional benefits could be realized if heat recovery on the condenser side of the chiller was utilized, for one of, or both domestic hot water production or space heating. This could be in the form of a small hot water tank which is preheated using the waste heat from the chiller, or a direct heat exchanger between the condenser loop to the hot water inlet, warming up the water before it enters the on-demand heater.

In all locations, although the peak load is reduced, an increase in the overall annual energy consumption is also observed as a result of the decreased performance of the chiller in charging the thermal storage. Although the assumption is being made in the paper that it is always beneficial to switch consumption to off-peak periods, a more detailed analysis of each locations energy grid and specifically the generation methods used to produce power is required. If the

location has a clean generation base using sources such as hydro or nuclear that can't be turned off, that there is benefit to switching, however, if a location's electricity is met using fossil fuels (e.g., coal, natural gas), the increased power consumption would significantly increase the greenhouse gases released to generate the required electricity.

Finally, although many locations have seen an annual economic benefit, the benefits in terms of actual costs are quite small, in some cases only a few dollars. If a detailed life cycle economic analysis was completed, the system under today's economic conditions would not be profitable over the life of the system. A significant increase in both the absolute cost of electricity, as well as the ratio between peak to off-peak periods would need to occur to improve the economics of the system.

CONCLUSIONS

This paper has shown that using a medium temperature chiller coupled with cold thermal storage has the potential to reduce, and in some cases, eliminate the electrical consumption required for air-conditioning during peak utility periods. It was found that in southern climates, and those with a large ratio between peak and off-peak utility rates, significant savings can be realized on an annual basis. This paper shows there is significant potential, however before these systems see widespread implementation, significant research is still required to improve performance and further optimize the control strategy and configuration.

ACKNOWLEDGEMENT

The authors would like to acknowledge the support of the Natural Sciences and Engineering Research Council of Canada (NSERC) for this work.

REFERENCES

- Baldwin, C., & Cruickshank, C. A. (2016). Assessing the Potential for Reduction in Peak Residential Electrical Loads Using a Heat Pump and Thermal Storage System. *4th International High Performance Building Conference*. West Lafayette, Indiana
- Baldwin, C., & Cruickshank, C. A. (2016). Using TRNSYS Types 4, 60 and 534 to model residential cold thermal storage units using water and water/glycol solutions. *eSim 2016*, Hamilton, Ontario.
- Florida Power and Light. (2018, March). *Residential rates, clauses and storm factors*. Retrieved from <https://www.fpl.com/rates/pdf/Mar2018-Residential.pdf>
- Greater Sudbury Utilities. (2018, March). *Rates Schedule*. Retrieved from <http://gsuinc.ca>
- Los Angeles Department of Water and Power. (2018, March). *Electric Rates*. Retrieved from <https://www.ladwp.com>
- National Grid - Massachusetts Electric. (2018, March). *Service Rates*. Retrieved from <https://www.nationalgridus.com>
- Natural Resources Canada - Office of Energy Efficiency. (2013). *Energy Use Data Handbook*. Ottawa, Canada.
- Portland General Electric. (2018, March). *Time of Use Pricing*. Retrieved from <https://www.portlandgeneral.com>
- Salt River Project. (2018, March). *SRP Time-of-Use Price Plan*. Retrieved from <https://www.srpnet.com>
- Toronto Hydro Corporation. (2018, March). *Residential Electricity Rates*. Retrieved from <http://www.torontohydro.com>
- U.S. Energy Information Administration. (2018, March). *Residential Energy Consumption Survey*. Retrieved from <https://www.eia.gov/consumption/residential/data/2015/>

Prosumer Cluster of Single-Family Houses under the Danish Net Metering Policy

Marijana Larma^{*}, Rongling Li and Carsten Rode

Department of Civil Engineering, Technical University of Denmark, Denmark

**Corresponding email: marila@byg.dtu.dk*

ABSTRACT

In the energy sector, prosumers are typically houses with rooftop PV. With the drastically falling prices of PV panels, the number of installations is rising. Prosumers can have negative impacts, on power grids especially in the distribution grid. In order to mitigate this effect, and for the own benefit of the prosumers, they can function as groups sharing their resources. A literature overview is given focusing on studies that deal with this issue from the prosumer perspective, showing that many optimization studies focus on maximizing economical benefits and others on self-consumption or related indicators by means of energy management strategies and market models, most often hourly based. A case study is presented in the context of the current Danish net-metering scheme. The results show that savings for prosumers and increase of total self-consumption can be achieved by redistributing energy within the building cluster with rule-based control.

KEYWORDS

Energy prosumer, PV, net-metering, single-family house, building cluster

INTRODUCTION

Prosuming buildings are buildings that both “produce” and “consume” energy (Schleicher-Tappeser, 2012). Typically the term prosumer in the energy sector refers to a house with rooftop photovoltaic (PV) panels (www.energy.gov). An estimate of 25-35% of the global cumulative installed PV capacity is at the residential level (Couture et al., 2014). Because of the high electricity tariff, PV has reached grid-parity in Denmark, like in most other European countries (Schleicher-Tappeser, 2012). In order to support renewable energy, some countries have implemented net-metering schemes for residential prosumers. This means that the surplus energy can be stored in the grid within a set period. In Denmark the net metering is on an hourly basis (www.iea.org). Electricity production at the residential level can have a negative impact on the grid, especially at the local scale, amongst others by causing overvoltage in some cases (Vallée et al., 2013). In order to mitigate this, it has been suggested to increase the self-consumption (Luthander et al., 2015). The hypothesis of this study is that the impact on the grid can be decreased and the economical benefit of the users can be increased by forming groups of single-family house prosumers. A case study is carried out in the context of Danish hourly based net metering, based on a literature review.

LITERATURE REVIEW OF PROSUMER CLUSTERS

For the present literature search, a systematic search for documents containing the terms “prosumer” and “energy” on Web of Science and Scopus was done. Papers were selected based on the following two rules:

Table 1. – Studies of prosumer clusters						Technologies		
Objective function	KPI	reference	Time Step	Simulation Time	Method	PV	ES	other
case study	self-consumption	Bellekom et al., 2017	5 minutes	24 hours	5 scenarios combining residential storage and peer-to-peer exchange	x	x	
maximize self-consumption	profit	Broering and Madlener, 2017	15 minutes	1 month	3 scenarios in the German context varying grid-use and feed-in tariffs	x		battery cloud
reduce reverse flow	savings	Brusco et al., 2014	1 hour	24 hours	clustering in an energy district, energy management with trading			
maximize profit	net revenue	Giuntoli and Poli, 2014	15 minutes 1 hour	24 hours	MILP for a VPP including prosumers	x	x	CHP, thermal storage
self-consumption maximization	demand and supply ratio	Liu et al., 2016	1 hour	12 hours	dynamic pricing in non-cooperative game	x		Demand response
maximize profit	net loads and profits	Ma et.al., 2016	½ hour	24 hours	heuristic method to reach Stackelberg equilibrium	x	x	CHP, Demand response
minimize cost	cost and spillage savings	Martín-Martinez et. al., 2016	1 hour	12 representative days	MCP for prosumers in microgrid; game theory in imperfect competition case	x	x	Demand response, thermal storage
limit power flows	PV hosting capacity	Palacios-Garcia et al., 2017	1 minute	4 days 1 year	increasing self-consumption, soft and hard curtailment	x	x	
optimize dispatch with constraints	cost savings, self-consumption	Rigo-Marian et.al., 2014	1 hour	24 hours	heuristic methods; sequential forecast; microgrid	x		
investment resiliency	cost savings	Sanduleac et al., 2017	15 minutes	24 hours	Uni-directional Resilient Consumer (UniRCon) architecture	x	x	
minimize loss of delivery and cost	delivery loss, self-consumption, cost	Sha, Aiello, 2016	1 hour	24 hours	flow optimization with "Arc Dynamic Direction Matrix"	x		Wind turbines
minimize cost	simple payback period	Tedesco et. al., 2015	1 hour	1 year	Economic MPC for prosumer microgrid; battery lifetime considered		x	Wind turbines
maximize local consumption	local consumption	Velik, Nicolay, 2014 & 2015	1 hour	30 days	modified simulated annealing triple-optimizer/cognitive decision agent	x	x	
maximize social welfare	power imbalance	Verschae et al., 2016	10 minutes 1 hour	1 day	coordinated management approach based on ADMM	x	x	Demand response
three objectives translated to total annualised cost	cost, CO2 and unavailability	Wouters et al., 2017	1 hour	1 day	MILP for system design of small neighborhood	x	x	CHP

ES = Electric Storage, MILP = Mixed Integer Linear Programming, VPP = Virtual Power Plant, MCP=Mixed Complementarity Problem, ADMM = Alternating Direction Method of Multipliers, CHP = Combined Heat and Power KPI = Key Performance Indicator

1) included Q1 and Q2 journal papers focusing on groups of residential grid-connected prosumers of electricity from renewable energy sources and 2) -excluded the papers that focus on design of trading models, clustering method, demand response models, social science, politics or business, or has a more general viewpoint. An overview is given in Table 1. As can be seen, in the recent years, the number of optimization studies about energy prosumers has been growing rapidly. The objective function in most of these studies is either an economical indicator related to the interest of each prosumer or the prosumer cluster, or a grid-related indicator like maximizing the self-consumption or local consumption. These two objectives are correlated and studies that choose one often pick the other as a key performance indicator. In most studies, the focus is on the operational costs, as opposed to investments. It is difficult to compare the efficiency of the employed methods directly, as different system setups are used. The time step of the simulation is commonly one hour and the simulation time 24 hours. Also, the consumption profiles used are often generic ones, scaled down from national domestic consumption. Based on the above literature study, both economic benefits and self-consumption were chosen as indicators for this study. A one minute based time step is used with the simulation run for one year, in order to gain a helicopter view of the prosumer cluster.

METHODS

Consumption profiles and PV electricity generation

The energy consumption in one minute resolution for 2015 was generated with the open source generator “CREST Demand Model” provided by McKenna & Thomson (2016). Three single family houses of the same building type and each with four residents but with different orientations were considered. The house type was defined by “building index 1” in the CREST Demand Model, which is a detached house of 136 m².

The PV production was simulated with TRNSYS. For the weather file, a Meteonorm generated typical meteorological year for Copenhagen Taastrup was used. The Parameters for the PV panel were taken from the datasheet for REC (www.recgroup.com), for a panel with a nominal power of 300W. The model for PV production was validated by comparing the efficiency of the Panel in the simulation against the efficiency stated by the manufacturer.

Setup for simulation scenarios

The three single family houses were oriented towards east, south and west, respectively (see figure 1). The slope of the roofs with the PV panels installed was set to 55°, which is close to the latitude of Copenhagen, as recommended for all-year round PV systems with a fixed slope (Agrawal & Tiwari, 2009; Phadke, 2010). Each house was simulated with 10 PV-modules of 1.67 m², and a total PV installation of 16.7 m² aperture area. Two scenarios were considered: 1) base case scenario, in which each house is operated separately, and 2) cluster scenario, in which a common controller is used to redistribute energy flows from houses with excess production to houses with energy deficiency. This flow redistribution was performed in each simulation step.

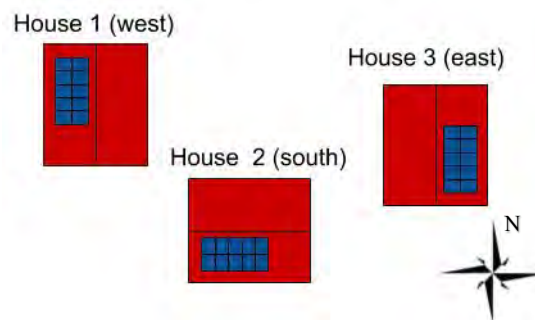


Figure 1. – Houses with orientations

Control algorithm for energy flow redistribution

Rule-based control was used for the flow redistribution. If any house has production at a given time, covering one's own demand is prioritized. After subtracting the energy use from the respective productions in a time step, the net energy flows are assessed and if there is simultaneous surplus and deficit, the surplus is then sent to the house with energy deficit. The prioritization is based on the absolute value of surplus or deficit, meaning electricity is first sent to/from the one with the larger deficit/surplus.

The indicators for the evaluation are self-consumption and electricity cost savings. Self-consumption is defined as the ratio of the momentary consumption of the power produced on-site (Luthander et al., 2015). It was calculated according to the following equations:

$$E_{SC}^{time\ step} = \min(E_{prod}^{time\ step}; E_{cons}^{time\ step}) \quad (1)$$

$$SC = \frac{E_{SC}^y}{E_{prod}^y} \quad (2)$$

Where $E_{SC}^{time\ step}$ is the self-consumed energy in each time step, $E_{prod}^{time\ step}$ is the energy produced and $E_{cons}^{time\ step}$ is the energy consumed in each time step. SC is the self-consumption ratio, E_{SC}^y is the yearly total self-consumed energy and E_{prod}^y the yearly total energy produced on-site. In the second scenario, the effective self-consumption SC_{eff} (or local consumption), for each house was based on the effective consumption (or local consumption of the energy produced by that house) ($E_{ec,i}^{time\ step}$), calculated as in equation (3), and the on-site production of each house, as in the base case scenario.

$$E_{ec,i}^{time\ step} = E_{cons,i}^{time\ step} + flow_{i_}^{time\ step} \quad (3)$$

$$SC_{eff} = \frac{E_{ec,i}^y}{E_{prod,i}^y} \quad (4)$$

Where $flow_{i_}^{time\ step}$ represents the total redirected flow from the given house i to other houses. The Danish Net-metering scheme is hour-based (iea.org), making it one of the most restrictive carryover provisions. This was taken into account when modelling the cash flow. When the net hourly energy was positive, it was multiplied with the feed-in tariff of 0.07 €. When it was negative it was multiplied with the retail electricity price of 0.31 €. Due to this difference, there is incentive to self-consume as much of the produced electricity as possible, in order to make the PV installation more profitable.

RESULTS

Self-consumption in the building cluster

Table 2. shows the self-consumption and its relative increase after clustering the three buildings and redirecting the surplus flows. The total self-consumption (or local consumption) is based on the total instantaneous production and the total instantaneous consumption.

	Separate scenario	Clustered scenario	Increased, %
House 1	40.56	54.41	34.2
House 2	36.91	51.07	38.4
House 3	44.14	57.61	30.5
Total	40.15	52.93	31.8

Electricity cost and savings

The calculated yearly electricity cost for each house, and in total, are presented in Table 3. For reference, the electricity cost without installed PV panels is shown in the third column. Based on this reference the savings were calculated for both the base case scenario and the clustered scenario. These can be seen in Table 4. The increase in savings of the clustered scenario is calculated in comparison with the separate scenario. The yearly electricity cost is reduced after clustering, with the increase in self-consumption. This is because the retail price of electricity from the grid is higher than the feed-in tariff for surplus electricity sent to the grid.

Table 3. Yearly electricity cost (€)			Table 4. Savings compared to baseline case (€)		
Baseline case (no PV)	Separate scenario	Clustered scenario	Separate scenario	Clustered scenario	Increased, %
House 1	1597	1190	407	476	17%
House 2	1551	1138	413	535	30%
House 3	1661	1236	425	523	23%
total	4809	3564	1245	1534	23%

DISCUSSIONS

In order to represent the grid-impact and the instantaneous self-consumption more accurately, in this study a time step of 1 minute was used, simulated over a year. The case setup was a simple example to give an indication of the effect on the correlation of the savings with the grid-impact reduction for the given tariff scheme. In this case study, it was assumed that the three houses freely share their surplus energy with rule-based control. The increase in self-consumption was slightly higher than the increase in electricity cost savings. The difference in savings is expected to be more pronounced with no net-metering. In this study the houses had a similar production and shared their surplus production freely and it was not necessary to consider the local trading dynamics. For a more general case, a remuneration has to be agreed upon, with a price between the feed-in tariff and the retail price. Additional wiring and controller costs for the local redistribution should be considered for making a more comprehensive economical analysis that also includes investment costs, for example by calculating the Net Present Value (NPV). This calculation was out of scope for this study. Some technologies for smart grids that enable local energy management are still in early stages and are expected to become more affordable in the future.

CONCLUSIONS

A literature overview was presented, focusing on studies about groups of prosuming buildings with PVs. It was found that most previous studies were on an hourly basis with a 24 hour time-frame. In those studies, both impact on grids and economic gains for users were often investigated. A case study of three prosumer houses was conducted under Danish hourly net metering conditions. Simulations were run for one year to investigate the effect of energy distribution within this building cluster. In the clustered scenario, self-consumption ratio increased 32% in total, indicating a decrease of the impact on the grid. Electricity cost savings with respect to the baseline case with no local production were calculated for both scenarios. In the clustered scenario, the savings increased 23% compared to the separated scenario. It is in line with the expectations that the savings increased when the self-consumption increased, as

the electricity retail price is higher than the feed-in tariff. The control in the current study is rule-based. In further research MPC for buildings will be considered with flexible electric load.

ACKNOWLEDGEMENT

This work is part of the strategic research centre “CITIES Centre for IT-Intelligent Energy Systems in Cities” (“CITIES Centre for IT-Intelligent Energy Systems in cities,” n.d.).

REFERENCES

- Agrawal, B., & Tiwari, G. N. (2009). Optimizing the energy and exergy of building integrated photovoltaic thermal (BIPVT) systems under cold climatic conditions. *Applied Energy*, *87*, 417–426. <http://doi.org/10.1016/j.apenergy.2009.06.011>
- Bellekom, S., Arentsen, M., & Van Gorkum, K. (n.d.). Prosumption and the distribution and supply of electricity. <http://doi.org/10.1186/s13705-016-0087-7>
- Broering, H., & Madlener, R. (2017). Simulation and Evaluation of the Economic Merit of Cloud Energy Storage for Prosumers: The Case of Germany. *Energy Procedia*, *105*, 3507–3514. <http://doi.org/10.1016/J.EGYPRO.2017.03.804>
- Brusco, G., Burgio, A., Menniti, D., Pinnarelli, A., & Sorrentino, N. (2014). Energy management system for an energy district with demand response availability. *IEEE Transactions on Smart Grid*, *5*(5), 2385–2393. <http://doi.org/10.1109/TSG.2014.2318894>
- CITIES Centre for IT-Intelligent Energy Systems in cities. (n.d.). Retrieved June 7, 2017, from <http://smart-cities-centre.org/>
- Consumer vs Prosumer: What's the Difference? | Department of Energy. (n.d.). Retrieved April 3, 2018, from <https://www.energy.gov/eere/articles/consumer-vs-prosumer-whats-difference>
- Couture, T., Barbose, G., Jacobs, D., Parkinson, G., Chessin, E., Belden, A., ... Rickerson, W. (2014). *Residential Prosumers: Drivers and Policy Options (Re-Prosumers)*. Berkeley, CA (United States). Retrieved from <http://www.osti.gov/servlets/purl/1163237/>
- Giuntoli, M., & Poli, D. (2013). Optimized thermal and electrical scheduling of a large scale virtual power plant in the presence of energy storages. *IEEE Transactions on Smart Grid*, *4*(2), 942–955. <http://doi.org/10.1109/TSG.2012.2227513>
- IEA - Denmark - Net-metering. (2012). Retrieved January 25, 2018, from <http://www.iea.org/policiesandmeasures/pams/denmark/name-42926-en.php>
- Liu, N., Wang, C., Lin, X., & Lei, J. (2016). Multi-Party Energy Management for Clusters of Roof Leased PV Prosumers: A Game Theoretical Approach. *Energies*, *9*(7), 536. <http://doi.org/10.3390/en9070536>
- Luthander, R., Widén, J., Nilsson, D., & Palm, J. (2015). Photovoltaic self-consumption in buildings: A review. *Applied Energy*, *142*, 80–94. <http://doi.org/10.1016/j.apenergy.2014.12.028>
- Ma, L., Liu, N., Zhang, J., Tushar, W., & Yuen, C. (2016). Energy Management for Joint Operation of CHP and PV Prosumers inside a Grid-connected Microgrid: A Game Theoretic Approach. *IEEE Transactions on Industrial Informatics*, *3203*(c), 1–1. <http://doi.org/10.1109/TII.2016.2578184>
- Martin-Martínez, F., Sánchez-Miralles, A., & Rivier, M. (2016). Prosumers' optimal DER investments and DR usage for thermal and electrical loads in isolated microgrids. *Electric Power Systems Research*, *140*, 473–484. <http://doi.org/10.1016/j.epsr.2016.05.028>
- McKenna, E., & Thomson, M. (2016). High-resolution stochastic integrated thermal-electrical domestic demand model. *Applied Energy*, *165*, 445–461. <http://doi.org/10.1016/j.apenergy.2015.12.089>
- Palacios-García, E., Moreno-Muñoz, A., Santiago, I., Moreno-García, I., & Milanés-Montero, M. (2017). PV Hosting Capacity Analysis and Enhancement Using High Resolution Stochastic Modeling. *Energies*, *10*(10), 1488. <http://doi.org/10.3390/en10101488>
- Phadke, V. (2010). Photovoltaic Power Systems. *US Patent App.* *12/976,495*, 1–33. Retrieved from <http://www.google.com/patents/US20120080943>
- REC. (n.d.). rec TwinPeak 2 SERIES datasheet. Retrieved from https://www.recgroup.com/sites/default/files/documents/ds_rec_twinpeak_2_series_ul_rev_f_eng.pdf
- Rigo-Mariani, R., Sareni, B., Roboam, X., & Turpin, C. (2014). Optimal power dispatching strategies in smart-microgrids with storage. *Renewable and Sustainable Energy Reviews*, *40*, 649–658. <http://doi.org/10.1016/j.rser.2014.07.138>
- Sanduleac, M., Ciomei, I., Albu, M., Toma, L., & Sturzeanu, M. (2017). Resilient Prosumer Scenario in a Changing Regulatory Environment — The UniRCon Solution. <http://doi.org/10.3390/en10121941>
- Schleicher-Tappeser, R. (2012). How renewables will change electricity markets in the next five years. *Energy Policy*, *48*, 64–75. <http://doi.org/10.1016/j.enpol.2012.04.042>
- Sha, A., & Aiello, M. (2016). A Novel Strategy for Optimising Decentralised Energy Exchange for Prosumers. *Energies*, *9*(7), 554. <http://doi.org/10.3390/en9070554>
- Tedesco, F., Mariam, L., Basu, M., Casavola, A., & Conlon, M. F. (2015). Economic Model Predictive Control-Based Strategies for Cost-Effective Supervision of Community Microgrids Considering Battery Lifetime. *IEEE Journal of Emerging and Selected Topics in Power Electronics*, *3*(4), 1067–1077. <http://doi.org/10.1109/JESTPE.2015.2446894>
- Vallée, F., Klonari, V., Lisiecki, T., Durieux, O., Moïny, F., & Lobry, J. (2013). Development of a probabilistic tool using Monte Carlo simulation and smart meters measurements for the long term analysis of low voltage distribution grids with photovoltaic generation. *International Journal of Electrical Power and Energy Systems*, *53*, 468–477. <http://doi.org/10.1016/j.ijepes.2013.05.029>
- Velik, R., & Nicolay, P. (2014). A cognitive decision agent architecture for optimal energy management of microgrids. *Energy Conversion and Management*, *86*, 831–847. <http://doi.org/10.1016/j.enconman.2014.06.047>
- Verschae, R., Kato, T., & Matsuyama, T. (2016). Energy Management in Prosumer Communities: A Coordinated Approach. *Energies*, *9*(7), 562. <http://doi.org/10.3390/en9070562>
- Wouters, C., Fraga, E. S., & James, A. M. (2017). A multi-objective framework for cost-unavailability optimisation of residential distributed energy system design. *Sustainable Energy, Grids and Networks*, *9*, 104–117. <http://doi.org/10.1016/j.segan.2017.01.002>

Visualizing the exergy destructed in exergy delivery chain in relation to human thermal comfort with ExFlow

Hongshan Guo^{1,*}, Forrest Meggers^{1,2}

¹School of Architecture, Princeton University, Princeton, NJ, USA

²Andlinger Center for Energy and the Environment, Princeton University, Princeton, NJ, USA

**Corresponding email: hongshan@princeton.edu*

ABSTRACT

Exergy analysis is an important tool to fully appreciate the usability of energy at different levels and has been widely applied in the building system analysis domain. It has become more useful as low temperature heating and high temperature cooling began to attract more attention both in Europe and the United States. Using low-grade energy to supply for these systems have, in return, led to an increase in awareness of low exergy (LowEx) system designs. The possibility of modeling the last missing link in the system that is to delivery thermal comfort, the human body, have therefore become a topic that increasingly draws the attention of many more researchers. Due to the complexity of these human body exergy models, it is very rare for these models to be linked back to building systems and produce an exergy efficiency for occupants' thermal comfort. Attempting to fill in the blanks of overall system exergy efficiency on delivery occupant thermal comfort, we have developed a visualization algorithm that could visually assess the exergy efficiency in comfort delivery. Using the ExFlow tool, it is much clearer and easier to determine the relationship of how much primary energy input is eventually converted to the energy that is used to condition for the occupants' comfort.

KEYWORDS

exergy analysis; thermal comfort; energy delivery; visualization

INTRODUCTION

The efficiency of systems to maintain a certain built environment is very often categorized by their energy efficiencies. How much primary energy input or levelized costs is necessary to deliver to the end of the chain where the users' demands are met. A common tool used to visualize this process is the Sankey diagrams (or occasionally referred to as the flow charts), where the total input and outputs can be visualized. Exergy analysis has gained popularity among many researchers as an addition to the existing analysis method during the last 20 years due to its capability of gauging not only the amount of energy, but also the usability of the energy.

With the growing popularity of systems that utilizes the low grade heat, or otherwise known as the low exergy (LowEx), exergy analysis has begun to receive a growing amount of attention from researchers. While the heat demand from the occupants stays the same, the same amount of exergy can be delivered with water warmed up by waste heat of a nearby factory than that heated with a gas boiler. Similar concepts of heat harvesting at stages of processing to be reused have been extensively used in chemical plants. This is particularly true for the domestic systems where the required water temperature rarely exceeds 75°C, but

are often supplied by primary energy sources that has high exergy and experience large amount of heat loss during distribution.

Acknowledging the magnitude of the question at hand, a tool named ExFlow was developed dedicated to visualize the exergy flow through a building systems' energy supply chain towards the occupants' thermal comfort. Basing off existing methods of calculating steady-state exergy consumption during the energy delivery for occupants, this tool specializes on visualizing both the exergies that are 'consumed' and the exergies that are used provide thermal comfort. Applying the ExFlow tool to three different types of building systems, a parametric study of an office study focusing mainly on its exergetic performance of components and thermal comfort is presented in this paper.

METHODS

Performing steady-state exergy analysis on a office building, we simulated the energy and exergy delivery chains for an office building, as was presented in Annex 37 for the heating case. Using simplified building geometry and thermal properties as inputs, the heat losses, heat demand and the amount of primary energy necessary to produce the heat necessary to maintain the room air condition can be calculated. Simplified system components assumptions were made including their inlet/outlet and operation temperatures as well as their individual efficiencies and required auxiliary energy consumptions. These parameters were then combined with the calculated energy consumption and heat losses along the energy delivery chain so that the exergy delivery chain can be determined.

Volume, net floor area and indoor air temperatures as well as the area and thermal transmit tan ce information of the envelope were used to generate basic estimation of the transmission heat losses. The ventilation heat losses is then determined through the designated air exchange rate and heat exchanger efficiencies. The solar heat gain is then calculated by assigning a window-wall ratio and pre-determined solar radiation rate per area. Internal heat gains were then obtained by using the number of occupants while the specific internal heat gains from equipments were obtained using equipment density per floor area. Same applied to lighting energy consumption and total ventilation power necessary. Subtracting the total heat gain from the heat loss, we then obtain the total building heating demand.

Splitting the energy delivery process into six distinctive stages, namely primary energy input, generation from primary energy input, distribution system from the generation system, emission system and room air towards envelope. The fundamental calculation behind the visualization algorithm of ExFLOW calculates the energy and exergy available at every stage of the delivery.

Previous investigations towards increasing the acknowledgement of the exergy consumption during the energy delivery process includes the I Schmidt, 2007), "Low Exergy Systems for Heating and Cooling of Buildings", Annex 49 , "Low Exergy Systems for High-Performance Buildings and Communities" (Angelotti & Caputo, 2007) and Annex 64, "LowEx Communities" (Schmidt, 2014). Annex 37, in particular, devised an excel tool that calculates steady-state flow of the energy as well as exergy when energy is being delivered to specific building cases. As a general rule of thumb, the exergy was calculated by multiplying the energy necessary with quality factors. These factors vary from 1.0 for electrical energy and mechanical energy, to 0.9 for fossil fuels and 0.06 for thermal energy at 40 degree Celsius. To determine the thermal exergies that are associated with different sources, their quality

factors can be written as the following Equation 1, where T_j and T_i are respectively the temperatures of the temperatures of the temperature generated and the temperature necessary at input.

$$F_p = 1 - \frac{T_j}{T_i} \quad (1)$$

As we are able to determine quantitatively both the energy and the exergies during the energy and exergy delivery to households, it is important to associate the resulting parameters with the human body exergy consumption models. Since the air temperature and the envelope temperatures were considered homogeneous per the original assumptions for the model, it is possible to be introduced into the human body exergy consumption models constructed by previous researchers. Among the three existing major human body exergy consumption hubs (Shukuya, Prek and Mady), the results were comparable as most resulted in a 4~5 W/m² for an adult man weighing 80 kg and 1.8 m² surface area of the body where the air temperature sits at about 21°C. This points to a total of 7~9 W for a single occupant, and with an assumed number of occupants at 13 for the entire building, this points to a 91~117 W for the entire building. Since the analysis is steady-state, it is reasonable to assume that the human body exergy consumption will remain constant as the other parameters of the building that is being simulated (Shukuya et al., 2010).

Specifically relating to the case study that we are examining within the scope of this paper, we are simulating an office building with the an overall volume of 6882.35 m³ and 2202.35 net floor area. For the indoor environment, we will be assuming indoor temperature was to maintain at 21°C while the outdoor temperature (or reference temperature for the calculation of exergy) remains at 0°C, we can simulate the energy and exergy required at every single level of the energy delivery (Sakulpipatsin & Schmidt, 2003).

To better understand the performance of ExFLOW as a tool to visualize both the energy and the exergy flow, three different variations of said building is considered and qualitatively compared between. We will be focusing mostly on how the generation level and the distribution level performance differences could have led to different scenarios of energy and exergy deliveries towards the end-goal, the human thermal comfort. More specifically, we would like to examine the possible implications in deploying larger surfaces for heat exchange (floor heating/radiators) vs. air-based heating and cooling as well as harvesting the primary energy generation/conversion systems through either standard boiler or taking in heat directly from district heating networks. These systems and their different parameters can be found in the following Table 1.

Table 1. Cases investigated with different building system combinations

Combination	Emission System	Generation System	Sup/Ret T (°C).	Generation Effi.
1	Floor Heating	District Heating w/ Waste Heat Recov.	35/30	0.89
2	Floor Heating	Standard Boiler	35/30	0.8
3	Air Heating/Cooling	Standard Boiler	35/25	0.8
4	Radiator	District Heating	70/60	0.89

It is important to point out that there are many other sources of primary energy input that would allow a significant decrease in primary energy input as the renewable energy sources essentially makes up the necessary primary energy input - such as various heat pump with

different sources, i.e. ground-sourced, air-sourced, etc. We will not be including any of these studies within the scope of this paper due to its length limitation.

RESULTS

Using the ExFLOW tool, it is possible to generate both the energy flow diagrams and exergy flow diagrams qualitatively with quantitative hover information as is shown in Figure 1. Qualitatively speaking, generating an energy flow diagram that includes the waste heat that is generated at different stages is the same with exergy consumption modeled in exergy analysis.

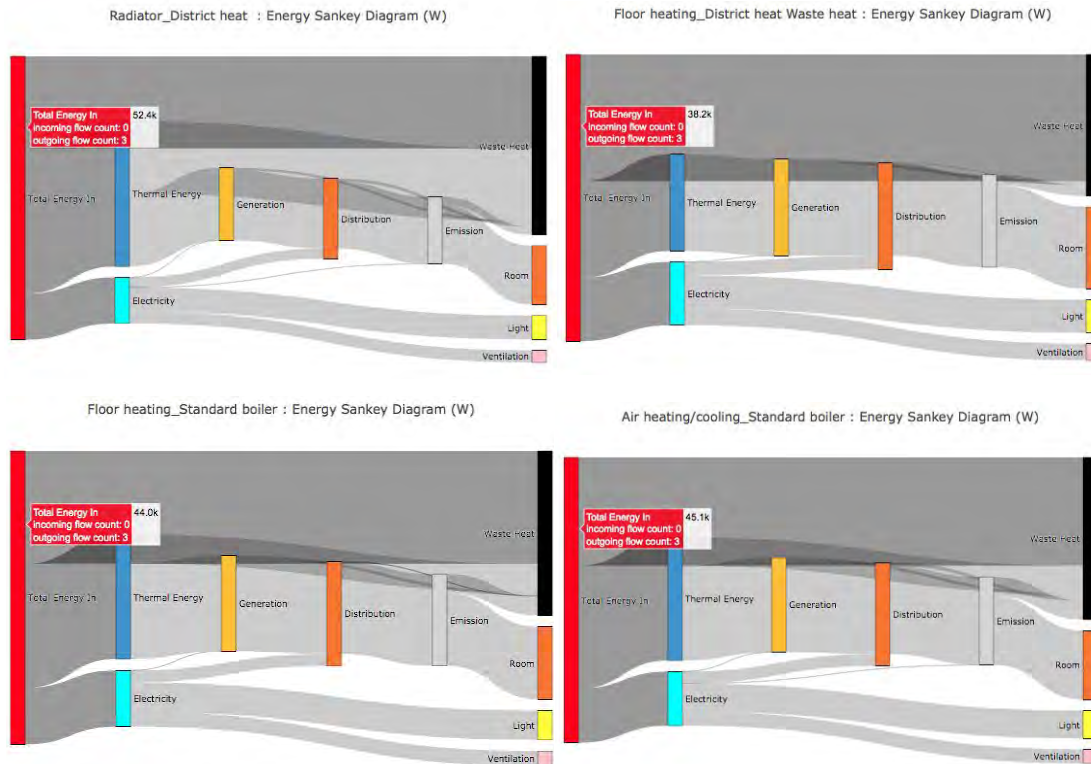


Figure 1. Energy Flow Sankey Diagrams generated by ExFLOW with four different combinations of energy generation and emission systems.

It is not very difficult to observe the discrepancy between the amount of waste heat is not quantitatively equivalent of that of exergy consumed. This is mostly because the amount of waste heat were in fact harvested at different levels of usability - or in other words, different amount of exergy. The total amount of waste heat as is shown in Figure 1 is, therefore, not representative of how much of which could have been harvested for secondary or further utilization.

Another interesting observation from the results generated by ExFLOW is its capabilities of showing how little amount of exergy is actually necessary at the end of the delivery. While the entire exergy/energy delivery chain is dedicated to provide for comfortable indoor conditions for the occupants, much of that is not dedicated to the comfort of the occupants, but rather conditioning the air indoor as is mandated by the design guidelines with respect to the supply and return temperature of the generation/distribution/emission systems.

DISCUSSIONS

The results from the ExFLOW tool brings ample of room for discussing its current and future room of applications. Looking at the similarities and discrepancies between the results of energy and exergy flow diagrams as shown in Figure 1 and Figure 2, the energy and exergy consumption concepts led to a very different understanding of the viability of various systems.

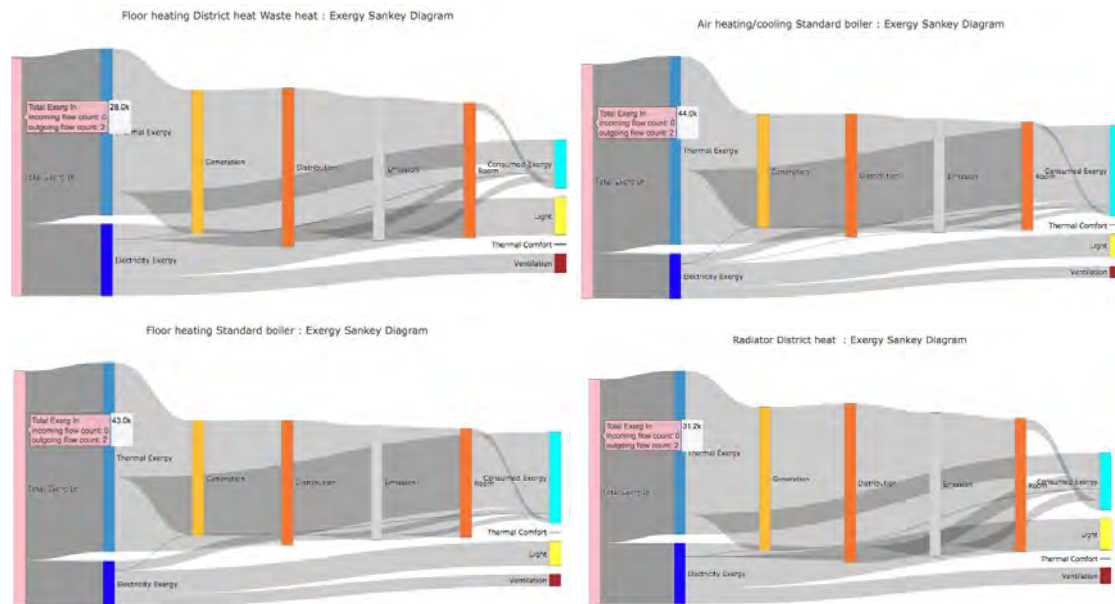


Figure 2. Exergy Flow Sankey Diagrams generated by ExFLOW with four different combinations of exergy generation and emission systems.

Combination of the floor heating system as emission system and district heating with waste heat harvesting was found to be the most energy and exergy efficient system of all four combinations. This is to be expected since their necessary supply temperatures are much lower and can benefit from generation system with a much smaller exergy input. The energy input then increases for the floor heating and standard boiler combination, further for air heating/cooling and standard boiler, and the largest for the combination of radiator and district heating combination. For the exergy side, this changes as the radiator plus district heating was found to require exergy input that was slightly larger than that of floor heating with district heating. This demand increases dramatically for floor heating and standard boiler combination, while the air heating and cooling was the least exergy-efficient combination of all four combinations.

Comparing the final exergy consumption at the human body reveals some even more interesting findings, where we can observe the final stage of exergy consumption being split into four categories, exergy consumed by system components, exergy consumed by the human body to maintain thermal comfort, and exergy required to maintain proper lighting and healthy ventilation. The energy that is necessary to maintain thermal comfort appears to be much smaller than that of the other three, while the light and ventilation exergy consumption remains the same since they are not subject to any change by any input parameters. This brings up a very interesting research question, as to whether we have positioned our energy assets in appropriate locations to achieve the maximized system efficiency. More importantly,

can we design systems that can deliver the same amount of comfort to the occupants without resulting with the same amount of exergy that is consumed by the transformation and distribution.

CONCLUSIONS

We developed a visualization tool for the energy and exergy flow to deliver satisfying indoor environment to occupants. Understanding the challenges of avoiding the stove-piped disciplines in understanding the overall system design, we compared four different combination of systems that could be used for a specific building with ExFLOW and quantitatively and qualitatively compared the results obtained from ExFLOW. Since exergy flows are by definition describes the quality of the energy flows, we were able to quantitatively understand the amount of exergy that are being consumed by the processes and compared against the necessary exergy consumption of a hypothetical human to understand the overall scope of comfort delivery.

REFERENCES

- Angelotti, A, and P Caputo. "The Exergy Approach for the Evaluation of Heating and Cooling Technologies; First Results Comparing Steady State and Dynamic Simulations," 2007, 8.
- Angelotti, Adriana, Paola Caputo, and Giulio Solaini. "Steady versus Dynamic Exergy Analysis: The Case of an Air Source Heat Pump." *International Journal of Exergy* 11, no. 4 (January 1, 2012): 460–72.
- Dietrich Schmidt. "EBC Annex64 LowEx Communities: Optimised Performance of Community Energy Supply Systems with Exergy Principles." Work Report, October 10, 2014.
- Poppong Sakulpipatsin, and Dietrich Schmidt. *Exergy Analysis Applied to Building Design*, 2004.
- Mosè Prandin. "Exergy Analysis at the Community Level: Matching Supply and Demand of Heat and Electricity in Residential Buildings." KTH Royal Institute of Technology, 2010.
- Schmidt, D, and M Shukuya. "New Ways towards Increased Efficiency in the Utilization of Energy Flows in Buildings", 2003.
- Schmidt, Dietrich. "Low Exergy Systems for High-Performance Buildings and Communities." In *Clima 2007 WellBeing Indoors*, 2007.
- Yan, Bing, Marialaura Di Somma, Nicola Bianco, Peter B. Luh, Giorgio Graditi, Luigi Mongibello, and Vincenzo Naso. "Exergy-Based Operation Optimization of a Distributed Energy System through the Energy-Supply Chain." *Applied Thermal Engineering* 101 (May 2016): 741–51.
- Shukuya, Masanori, Masaya Saito, Koichi Isawa, Toshiya Iwamatsu, and Hideo Asada. "Human-Body Exergy Balance and Thermal Comfort." *Low Exergy Systems for High - Performance Buildings and Communities*, 2010.

A Review of Microgrid Energy Systems

Lei Gao, Yunho Hwang*, Reinhard Radermacher

Center for Environmental Energy Engineering, Department of Mechanical Engineering
University of Maryland, College Park, MD, 20742, United States

**Corresponding email: yhhwang@umd.edu*

ABSTRACT

Microgrid combined cooling, heating and power energy systems are under intensive investigation owing to expansion of renewable energy generation and development of advanced technologies in distributed energy generation. Multi-generation systems serve as one of the core parts in any microgrid energy systems. This review paper presents the summary of state-of-the-art technologies in these multi-generation systems. The first part introduces the energy structure based on energy sources and the latest renewable energy harvesting technologies for solar, biomass and geothermal energy. In the second part, prime movers, including small-scale ones used in a microgrid energy system, are summarized. The third part shows the expanded microgrid system configurations mainly for desalination. The fourth part describes the control and operation strategies for complex multi-generation systems. In the first three parts, insufficient investigation or research gaps are also pointed out. Overall, this paper systematically summaries recent progress in microgrid multi-generation system, and suggest future researches for designing and optimizing a microgrid energy system.

KEYWORDS

Microgrid, CCHP, Renewable Energy, Multi-generation, Prime Mover

INTRODUCTION

Combined cooling, heating and power (CCHP) microgrid system can increase energy efficiency by recovering waste heat and eliminating transmission and distribution losses as compared with separate individual systems. And it will naturally decrease the operation cost and greenhouse gas (GHG) emission because of the energy input saving. In addition, microgrid systems are more reliable than centralized power plants from natural and man-made disasters since renewable energy serves as a localized energy source in most of the systems (Ebrahimi, 2014). A conventional CCHP microgrid system can be divided into four sub-components as shown in Figure 1: energy source (top), energy conversion technologies (middle left), energy demands (middle right) and storage systems (bottom). Different from traditional energy sources, more renewable energy including wind, solar, geothermal and biomass have been utilized in microgrid systems. The upstream of microgrid system will highly influence the system configuration and technologies applied.

RENEWABLE ENERGY SOURCES

Available renewable energy applied in CCHP systems has expanded from solar to biomass, geothermal and wind energy. Solar PVs and thermal collectors are two methods used for solar energy powered CCHP, in which solar thermal part can be integrated into the system as heat source of various energy conversion components due to its flexible temperature range. Solar thermal energy is always serving as a heat source for ORC, ABC or direct heating in CCHP. Wang et al. (2016) show that the solar thermal integrated CCHP system is more energy efficient but less exergy efficiency than the solar PV integrated system. However, due to the

intermittent and daytime-occur-only characteristics, CCHP systems powered by solar energy are sensitive to weather variation in its performance and cost change in its payback. Thus, accurate demand predictions and reliable control strategies are needed for efficient and effective solar integrated CCHP systems. While most of the research works considered parameters of solar PV as constant, Arsalis et al. (2018) provided detailed solar PV model experimentally validated in a CCHP system. Biomass as an alternative to natural gas has garnered researcher's attractions as it can produce more stable power than solar. In terms of structure, the biomass integrated CCHP system is similar to conventional one except that the fossil fuel is replaced by gasification subsystem. The increment of components and coupling within subsystems increases system complexity. Exergoeconomic analysis is the mainstream of biomass based system. Wang and Mao (2015) show that the biomass price greatly influence the product unit cost and the exergy cost of cooling water is the most sensitive among all the demand. However, the comparison of environmental and energy benefits between biomass powered CCHP system and conventional one has not been investigated sufficiently. Maraver et al. (2013) adopted ORC or Stirling engine to biomass-based CCHP system and found it is more favorable than stand-alone generation system in terms of the environmental aspect under small cooling-to-heating ratio. Nonetheless, the comparison is only limited to heat powered subsystems and other engines like gas turbines or internal combustion engines have been ignored. Similar to solar thermal energy, geothermal energy can be used to generate electricity. Figure 2 shows how geothermal energy is used in CCHP system. Kalina cycle is more utilized than ORC in system when geothermal is the only thermal source since the thermal efficiency is relatively low (Sun et al., 2017). ORC was used more often when solar thermal energy exists. The ground source heat pump is the most intensive investigation. Other researches were about supercritical CO₂ cycle power cycle, two-stage ORC cycle, combined with LNG gasification process. The utilization characteristics of geothermal in CCHP system is due to the lower temperature range. However, the pressure recovery of ground water has not been explored.

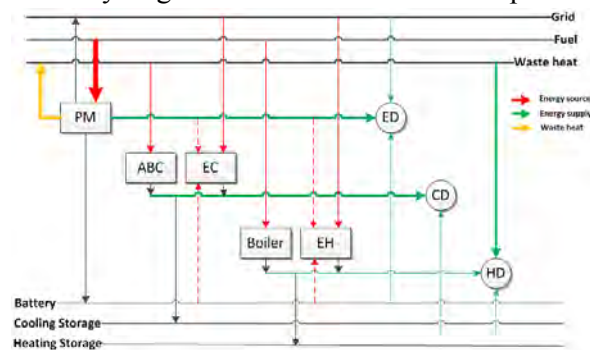


Figure 1. CCHP microgrid structure.

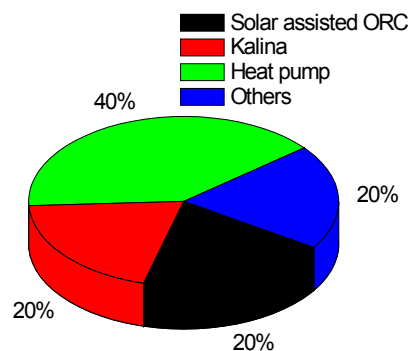


Figure 2. Research paper distribution of geothermal CCHP

PRIME MOVERS

Wu and Wang (2006) showed the characteristics, performance as well as economic information of main prime movers (PM), including steam turbine (ST), gas turbine (GT), microturbine (MT), internal combustion engine (ICE), Stirling engine (SE) and fuel cell (FC), utilized in CCHP microgrid system. The selection of prime mover in CCHP microgrid system varies based on the energy source, energy, environment and economic (3E) criteria. Wang et al. (2008) use multi-criteria (3E+society) to evaluate different PMs based trigeneration system and found gas turbine plus LiBr ABC is the best and SOFC based one is the worst. Ebrahimi and Keshavarz (2012) expanded this method to different climate regions. The results showed that the best to worst PMs are ICE, SE, separated system and MT, and climate difference has

little influence for selection. However, there are only limited hierarchy criteria in the second layer, which would limit the application of this method. Khorasaninejad et al. (2016) combined several other fuzzy approaches to the second layers criteria for selection of PMs in ORC based CCHP system. This work found PV panel is the best PM and GT is the worst when every primary criterion (3E+society) are segmented into 16 to 5 sub-criteria. Roman and Alvey (2016) provided following hybrid load operation-based selection method among ICE, MT and phosphoric acid FC. However, the selection is only one layer, so it can only provide the selection in each sub-criteria. Moreover, selection of PMs in these papers is based on some fixed configurations and no consideration of operation strategies for different PMs. The truth is that different PMs have their own optimal subsystem configuration and operation strategies, there is no work based on this premise. In addition, PMs can be driven by renewable energy, there is little concern about the influence of renewable energy on selection. For small size microgrid, FC, MT and SE are the main PMs in microgrid system based on the capacity range. Solid oxide fuel cell (SOFC) and proton exchange membrane (PEMFC) are the most common FC that are used in CCHP system, which can be seen from the distribution of published paper in Figure 3. Overall, FC based CCHP system has earned more attention recently. In system design and analysis, most of the research focused on energy saving potential and economic feasibility through parametric study. As for optimization, most of the work tried to solve multi-objective optimization through 3E criteria. Due to the research intensity and complex experiment setup, there is not much review work and test verification in this subtopic. The electricity to heat ratio for FC is relatively larger than conventional large-capacity PM, so it is sometimes insufficient to provide thermal cooling energy for ABC, however, the electric cooling can be designed in CCHP system, so there is need of comparison for FC based CCHP in which cooling is provided by ABC and EC.

Researchers have integrated MT integrated CCHP system based on cogeneration system since 2000. Figure 4 shows the research paper distribution from 2001 to 2018, in which 'others' includes dedicated investigation of MT and dynamic system modeling. Early stage research concerned about the system thermodynamic analysis, simple operation strategies and it always comes along with new system designs. Sugiarta et al. (2009) started to adopt 3E analysis in MT based CCHP system but no optimization analysis was provided until recent. Since MT is impaired under the variable ambient condition, so efficient and accurate system control is important for 3E benefits. However, there is not much work specified on control of MT based CCHP system. At last, limited research about combined cooling and power system is a special design in which heating demand is negligible compared with other two.

SE based system has not been explored much in recent research work. Limited investigators designed SE as supplementary PM in CCHP system to further improve energy efficiency of whole system (Ansarinassab and Mehrpooya, 2018). Other research chooses SE as main PM are all about system design and sizing. Kaldehi et al. (2017) designed a solar driven SE trigeneration system and mainly focused on the SE modeling and verification in different climate regions. However, when the authors tried to analysis the system performance, the thermal load was calculated based on ASHRAE standard, which is a fixed value and not reflects the actual demand. Thus it would not well suit for following electricity/thermal (FTL/FEL) load control strategies. Moghadam et al. (2013) use 3E criteria to optimize SE size under FTL/FEL. Nonetheless, auxiliary device or power is needed under these following strategies, so there is still some space for improvement of energy efficiency. Karami and Sayyaadi (2015) applied fuzzy-AHP decision-making method to choose the best optimization objective for different cities. However, the fuzzy-AHP method is subjective and depends on researchers' experience, so objective method should be considered. Harrod James et al. (2010) provided a sizing method for SE in CCHP through parametric study, however, the optimization is single objective which is not sufficient for SE design and selection. Moreover,

in the PM selection research mentioned above, SE is sometimes considered less competitive compared with other PMs when considering the capital cost. Overall, SE shows its developing potential in CCHP system and there is a need for more investigation of SE based CCHP, especially in related to the economic analysis.

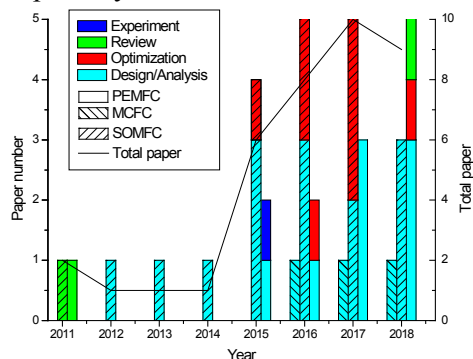


Figure 3. Research trend of fuel cell.

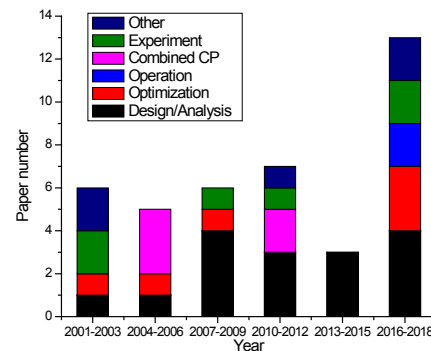


Figure 4. Research trend of microturbine.

SYSTEM CONFIGURATIONS

Desalination is an additional function that has been enriched in CCHP microgrid systems, especially for shipboard application. The system efficiency can be further improved. Shu et al. (2013) developed a fresh water producing CCHP system based on shipboard ICE. Mohammadi and Mehrpooya (2017) designed a desalination integrated CCHP system, which can provide 46.8 kW power, 451 kW heating, 52 kW cooling and 0.79 kg/s potable water, and optimal operational parameters were decided based on the sensitive analysis. Sadeghi et al. (2017) designed a novel multi-generation system for producing power, cooling and fresh water by adopting ejector and humidification /dehumidification desalination technology. The optimal exergy efficiency can reach 17%. Najafi et al. (2014) presented 3E modeling of a solid oxide fuel cell–gas turbine (SOFC–GT) hybrid system integrated with a multi-stage flash (MSF) desalination unit. The optimal design leads to an exergetic efficiency of 46.7% and 9 years payback period. However, the practical water demands have not been reflected in these researches. Besides, the most of these systems are not CCHP based and seldom provide optimal control strategies.

CONTROL AND OPTIMIZATION

The CCHP system optimization problems are always attributed to the multi-objective problem since almost all the investigations consider not only energy savings but also payback time and greenhouse gas emission reduction. The most common optimization algorithms used in CCHP system are genetic algorithm (GA) (Zhang et al., 2018), particle swarm optimization algorithm (PSO) (Luo and Fong, 2017a) and differential evolution algorithm (DEA) (Yao et al., 2017). The optimization of system control strategy has a great impact on system operation performance. The control strategies have gone from fixed pattern like following thermal load and following electricity load (Fumo et al., 2011) to model predictive control (Rossi et al., 2016) and discrepancy consideration (Luo and Fong, 2017b).

CONCLUSIONS

This review paper summarizes recent progress of CCHP microgrid systems from energy source, prime mover, system configuration, system control and optimization points of view. First, other renewable energy such as biomass and geothermal have been considered in microgrid systems in addition to conventional available distributed energy sources such as solar thermal and PV. Exergoeconomic analysis is the mainstream in biomass powered systems, and energy and environmental effects should be investigated more as

compared with other conventional energy sources. There exists research gap for pressure recovery in geothermal powered microgrid system. Second, research works related to MT, SE and FC are summarized in this paper. Current selection of prime movers is based on fixed system configuration which is not designed for various PMs. In addition, renewable energy should be considered when selecting PMs. FC, MT, and SE based small-scale CCHP microgrid systems focus on thermodynamic analysis and optimization through 3E criteria. There is a lack of experimental validation. Third, a microgrid system has expanded its function to desalination for further improving energy efficiency. However, the system becomes more complex and is not clear whether water demand is met when integrated with CCHP system. Last, the control and optimization work on the microgrid CCHP system has contributed to improving the performance. The control has upgraded from simple strategies to comprehensive and real-time ones.

REFERENCES

- Ansarinasab, H., and Mehrpooya, M., 2018, Investigation of a combined molten carbonate fuel cell, gas turbine and Stirling engine combined cooling heating and power (CCHP) process by exergy cost sensitivity analysis: *Energy Conversion and Management*, v. 165, pp. 291–303.
- Arsalis, A., Alexandrou, A.N., and Georghiou, G.E., 2018, Thermoeconomic modeling of a small-scale gas turbine-photovoltaic-electrolyzer combined-cooling-heating-and-power system for distributed energy applications: *Journal of Cleaner Production*, v. 188, pp. 443–455.
- Ebrahimi, M., 2014, Combined cooling, heating and power: decision-making, design and optimization: Elsevier, Waltham, MS.
- Ebrahimi, M., and Keshavarz, A., 2012, Prime mover selection for a residential micro-CCHP by using two multi-criteria decision-making methods: *Energy and Buildings*, v. 55, pp. 322–331.
- Fumo, N., Mago, P.J., and Smith, A.D., 2011, Analysis of combined cooling, heating, and power systems operating following the electric load and following the thermal load strategies with no electricity export: *Proceedings of the Institution of Mechanical Engineers, Part A: Journal of Power and Energy*, v. 225, no. 8, pp. 1016–1025.
- Harrod James, Mago Pedro J., and Luck Rogelio, 2010, Sizing analysis of a combined cooling, heating, and power system for a small office building using a wood waste biomass-fired Stirling engine: *International Journal of Energy Research*, v. 36, no. 1, pp. 64–74.
- Kaldehi, B.J., Keshavarz, A., Safaei Pirooz, A.A., Batooei, A., and Ebrahimi, M., 2017, Designing a micro Stirling engine for cleaner production of combined cooling heating and power in residential sector of different climates: *Journal of Cleaner Production*, v. 154, pp. 502–516.
- Karami, R., and Sayyaadi, H., 2015, Optimal sizing of Stirling-CCHP systems for residential buildings at diverse climatic conditions: *Applied Thermal Engineering*, v. 89, pp. 377–393.
- Khorasaninejad, E., Fetanat, A., and Hajabdollahi, H., 2016, Prime mover selection in thermal power plant integrated with organic Rankine cycle for waste heat recovery using a novel multi criteria decision making approach: *Applied Thermal Engineering*, v. 102, pp. 1262–1279.
- Luo, X.J., and Fong, K.F., 2017a, Control Optimization of Combined Cooling and Power System with Prime Mover of Solid Oxide Fuel Cell-gas Turbine for Building Application: *Energy Procedia*, v. 105, pp. 1883–1888.
- Luo, X.J., and Fong, K.F., 2017b, Development of multi-supply-multi-demand control strategy for combined cooling, heating and power system primed with solid oxide fuel cell-gas turbine: *Energy Conversion and Management*, v. 154, pp. 538–561.

- Maraver, D., Sin, A., Sebastián, F., and Royo, J., 2013, Environmental assessment of CCHP (combined cooling heating and power) systems based on biomass combustion in comparison to conventional generation: *Energy*, v. 57, pp. 17–23.
- Moghadam, R.S., Sayyaadi, H., and Hosseinzade, H., 2013, Sizing a solar dish Stirling micro-CHP system for residential application in diverse climatic conditions based on 3E analysis: *Energy Conversion and Management*, v. 75, pp. 348–365.
- Mohammadi, A., and Mehrpooya, M., 2017, Energy and exergy analyses of a combined desalination and CCHP system driven by geothermal energy: *Applied Thermal Engineering*, v. 116, pp. 685–694.
- Najafi, B., Shirazi, A., Aminyavari, M., Rinaldi, F., and Taylor, R.A., 2014, Exergetic, economic and environmental analyses and multi-objective optimization of an SOFC-gas turbine hybrid cycle coupled with an MSF desalination system: *Desalination*, v. 334, no. 1, pp. 46–59.
- Roman, K.K., and Alvey, J.B., 2016, Selection of prime mover for combined cooling, heating, and power systems based on energy savings, life cycle analysis and environmental consideration: *Energy and Buildings*, v. 110, pp. 170–181.
- Rossi, I., Banta, L., Cuneo, A., Ferrari, M.L., Traverso, A.N., and Traverso, A., 2016, Real-time management solutions for a smart polygeneration microgrid: *Energy Conversion and Management*, v. 112, pp. 11–20.
- Sadeghi, M., Yari, M., Mahmoudi, S.M.S., and Jafari, M., 2017, Thermodynamic analysis and optimization of a novel combined power and ejector refrigeration cycle – Desalination system: *Applied Energy*, v. 208, pp. 239–251.
- Shu, G., Liang, Y., Wei, H., Tian, H., Zhao, J., and Liu, L., 2013, A review of waste heat recovery on two-stroke IC engine aboard ships: *Renewable and Sustainable Energy Reviews*, v. 19, pp. 385–401.
- Sugiarta, N., Tassou, S.A., Chaer, I., and Marriott, D., 2009, Trigeneration in food retail: An energetic, economic and environmental evaluation for a supermarket application: *Applied Thermal Engineering*, v. 29, no. 13, pp. 2624–2632.
- Sun, Y., Lu, J., Wang, J., Li, T., Li, Y., Hou, Y., and Zhu, J., 2017, Performance improvement of two-stage serial organic Rankine cycle (TSORC) integrated with absorption refrigeration (AR) for geothermal power generation: *Geothermics*, v. 69, pp. 110–118.
- Wang, J.-J., Jing, Y.-Y., Zhang, C.-F., Shi, G.-H., and Zhang, X.-T., 2008, A fuzzy multi-criteria decision-making model for trigeneration system: *Energy Policy*, v. 36, no. 10, pp. 3823–3832.
- Wang, J., Lu, Y., Yang, Y., and Mao, T., 2016, Thermodynamic performance analysis and optimization of a solar-assisted combined cooling, heating and power system: *Energy*, v. 115, pp. 49–59.
- Wang, J., and Mao, T., 2015, Cost allocation and sensitivity analysis of multi-products from biomass gasification combined cooling heating and power system based on the exergoeconomic methodology: *Energy Conversion and Management*, v. 105, pp. 230–239.
- Wu, D.W., and Wang, R.Z., 2006, Combined cooling, heating and power: A review: *Progress in Energy and Combustion Science*, v. 32, no. 5–6, pp. 459–495.
- Yao, E., Wang, H., Wang, L., Xi, G., and Maréchal, F., 2017, Multi-objective optimization and exergoeconomic analysis of a combined cooling, heating and power based compressed air energy storage system: *Energy Conversion and Management*, v. 138, pp. 199–209.
- Zhang, J., Cao, S., Yu, L., and Zhou, Y., 2018, Comparison of combined cooling, heating and power (CCHP) systems with different cooling modes based on energetic, environmental and economic criteria: *Energy Conversion and Management*, v. 160, pp. 60–73.

Impacts of climate change and its uncertainties on the renewable energy generation and energy demand in urban areas

Vahid M. Nik^{1,2,3,*}, Yuchen Yang¹, Bijan Adl-Zarrabi²

¹Division of Building Physics, Department of Building and Environmental Technology, Lund University, Lund, Sweden

²Division of Building Technology, Department of Civil and Environmental Engineering, Chalmers University of Technology, Gothenburg, Sweden

³Institute for Future Environments, Queensland University of Technology, Brisbane, Australia

* *vahid.nik@byggtek.lth.se*

ABSTRACT

This work investigates the effects of future climate uncertainties in calculating the heating and cooling demand of buildings and estimating potentials for renewable energy generation (solar PV and wind). The building stock of Lund in Sweden is considered for energy simulations and for future climate, the most recent outputs of RCA4, which is the 4th generation of the Rossby Centre regional climate model (RCM), is used considering several two representative concentration pathways (RCPs) and four global climate models (GCMs). Simulations and assessment are performed for three 30-year time periods, from 2010 until 2099. Through comparing distributions of data sets, it is found that the uncertainty induced by climate models affects the estimation of renewable energy generation more than those induced by time periods. Changes in the heating demand due to climate change and uncertainties are surprisingly low while it is very large for cooling demand. This can be because of having a good quality for buildings on the average, however this should be more investigated for other cities in Sweden.

KEYWORDS

Climate change; regional climate model; Future climate uncertainties; energy demand in urban areas; renewable energy generation;

INTRODUCTION

By the advances in climate simulation and numerical modelling, it is possible to make better estimating the probable future conditions, which helps a lot in energy and infrastructure planning. A large amount of work exists on assessing the impacts of climate change on buildings as the main energy users, considering different types of buildings, their characteristics and their thermal comfort, retrofitting and energy saving potentials (e.g. (de Wilde and Coley 2012) (Nik 2012)). More than the energy demand, climate change may also alter generation out of renewable sources such as wind, hydropower and solar energy (Nik 2016).

The common approach in the impact assessment for engineering applications is introducing future weather files into building simulations. One of the big difference is the source and type of the future weather file. The origin of most of the available future weather files (in any temporal and spatial resolutions) which are used for energy simulations, are global climate models (GCMs) – also known as the general circulation models –which simulate climatic conditions under different initial and boundary conditions. GCMs simulate future climatic conditions for the spatial scale of 100-300km² which is coarse for the purpose of impact

assessment. Therefore, GCM data are downscaled by the means of statistical (such as morphing) or dynamic downscaling techniques. The latter is performed through using regional climate models (RCMs), which provide weather data with suitable temporal (down to 15 minutes) and spatial resolutions (down to 2.5km²) for direct use in building and energy simulations. It is not possible to rely on short time spans in the impact assessment of climate change the considered span should be 20 to 30 years. Moreover, there are different uncertainties which affect simulated climate data, such as the selected GCM, RCM, emissions scenario (which is not used anymore by IPCC) or representative concentration pathways (RCPs) and the spatial resolution (Nik, Sasic Kalagasidis, and Kjellström 2012). This means that a valid assessment should consider several future climate scenarios. Therefore, one important challenge is dealing with large data sets and uncertainties ((Nik, Sasic Kalagasidis, and Kjellström 2012) (Nik 2010)). Uncertainties due to climate change have been considered in several works (e.g. (Nik 2010)).

This work investigates the impacts of climate change on the energy demand of buildings and the renewable energy generation out of solar PVs and wind turbines. In this respect, the building stock in Lund is modelled for six different climate scenarios. The same scenarios are used for estimating the potentials of renewable generation. More information about the climate models and energy calculations are provided under the methodology section and results discussed afterwards.

METHODOLOGY

This section briefly describes the energy and climate models and some of the equations which are used for renewable generation calculations. Since most of the theory part have been discussed in previously published works, the reader is referred to the major references. For all the calculations, hourly weather data sets from six climate scenarios have been used for three 30-year periods of 2010-2039, 2040-2069 and 2070-2099.

Climate models and future weather data sets

The weather data sets are synthesized version of RCA4 (Samuelsson et al. 2015), the 4th generation of the RCM by the Rossby Centre at Swedish Meteorological Hydrological Institute, with the spatial resolution of 12.5km resolution and the temporal resolution down to 15 minutes. RCA4 downscaled four GCMs: CNRM-CM5, ICHEC-EC-EARTH, IPSL-CM5A-MR and MPI-ESM-LR. The first two GCMs are forced by two Representative Concentration Pathways (RCPs), RCP4.5 and RCP8.5, and the other GCMs are forced only by RCP8.5. This gives six different climate scenarios for Lund. RCPs are four greenhouse gas concentration trajectories adopted by the IPCC for its fifth Assessment Report (AR5) in 2014. All the RCM weather data were synthesized in Matlab before being used in energy simulations. For more details the reader is referred to (Nik 2016) and (Nik 2010).

Energy demand simulation

The residential building stock in Lund, Sweden is modelled in Simulink/Matlab. Lund is one the major cities in southern Sweden with the area of 25.75 km² and the population of around 88790. The building stock of Lund is statistically represented by 52 buildings using the data sets by the the Swedish National Board of Housing, Building and Planning (Boverket), which is the major information source for the energy performance of buildings in Sweden and has been used previously in several works (e.g. (Nik 2012) (Nik and Sasic Kalagasidis 2013) (Nik et al. 2016)). Figure 1 shows distributions of the U-values, heated floor areas and window areas of the buildings. For more details about modelling and assessing the future energy

performance of the building stock the reader is referred to (Nik 2012) and (Nik and Sasic Kalagasidis 2013).

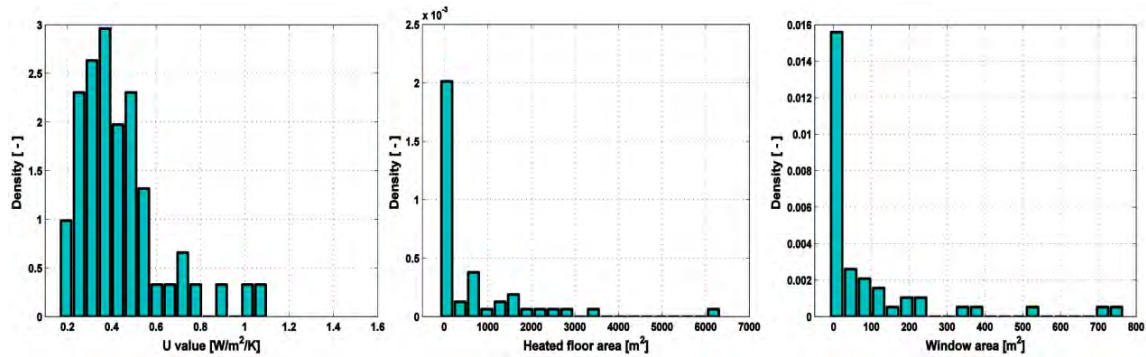


Figure 1. Distribution of the U values, heated floor areas and window areas of the building stock in Lund (figure is from (Nik 2012)).

Calculating the potentials for renewable generation

For comparing the effects of climate data uncertainties is estimating the solar energy potentials, the generated power from unit surface area (1 m²) is calculated according to relation (1) (Zervas et al. 2008):

$$P = A(0.128G_T - 0.239 \times 10^{-3}T_a) \quad (1)$$

where, P is the generated electrical power [W], A is the aperture surface area of PV module [m²], G_T is solar radiation flux (irradiance) on module plane [W/m²] and T_a is the ambient temperature [K].

Wind power generation is calculated according to relation (2) (Perera et al. 2012):

$$\bar{P}_w(t) = \begin{cases} P_w = 0 & V < V_{ci} \\ P_w = aV^3 - bP_r & V_{ci} < V < V_r \\ P_w = P_r & V_r < V < V_{co} \\ P_w = 0 & V_{co} < V \end{cases} \quad (2)$$

where \bar{P}_w is the power output from wind turbine [kW/m²], V is the wind speed at hub level [m/s] which is assumed 60 m, V_r , V_{ci} and V_{co} are respectively rated wind speed, cut in wind speed, cut off speed [m/s], P_r is rated power of the wind turbine [kW] which is assumed as 20. a and b are calculated as $a = P_r/(V_r^3 - V_{ci}^3)$ and $b = V_{ci}^3/(V_r^3 - V_{ci}^3)$.

RESULTS

Distributions for the heating and cooling demand of the building stock in Lund are shown in Figure 2 during 2070-2099. Differences due to climate change and its uncertainties are calculated in Table 1 and Table 2. Differences are visible and considerable in cooling demand; it can be even above 200% during 2070-2099 (depends on the climate scenario, e.g. 215% for ICHEC-rcp45 during 2070-2099) and depending on the selected climate scenario, differences (for one time period) can be also more than 200% (e.g. 234% for CNRM-rcp45 during 2010-2039 in Table 2). For Lund, which the cooling demand is much smaller than heating demand, differences between scenarios and time periods are quite negligible. This is in the contrary of the previous results using RCA3 (the older version of the RCM) which GCMs were forced by emissions scenarios defined by SRES IPCC (for more details, the reader is referred to (Nik 2012)(Nik and Sasic Kalagasidis 2013).

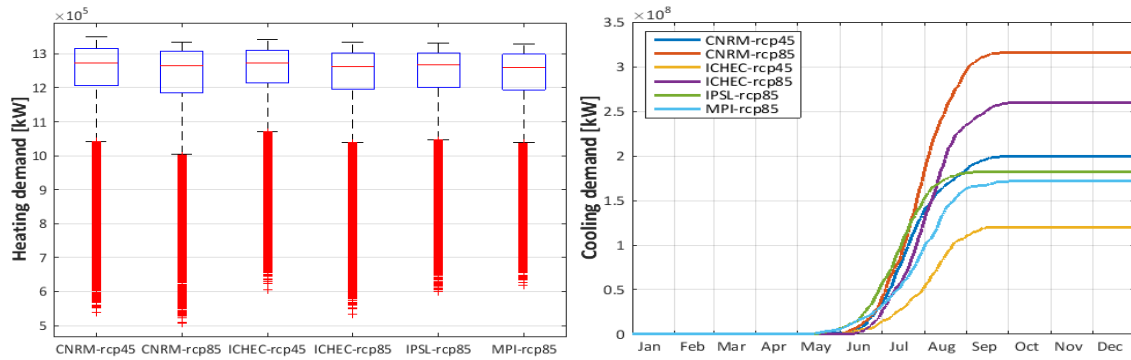


Figure 2. Distribution of the hourly heating demand (left) and cumulative cooling demand of the building stock in Lund for different climate scenarios during 2070-2099.

Table 1. Heating demand for different future climate scenarios.

Climate Scenarios	CNRM-rcp45	CNRM-rcp85	ICHEC-rcp45	ICHEC-rcp85	IPSL-rcp85	MPI-rcp85
Heating for 2010-2039 [kW]	10810408	10834448	10892567	10878912	10942434	10831818
Relative difference (RD) from 2010-2039 for each climate scenario [%]						
RD for 2040-2069	-0.5	-0.9	-0.6	-0.9	-0.7	-0.4
RD for 2070-2099	-0.8	-2.4	-1.0	-2.4	-2.1	-1.7
Relative difference (RD) of scenarios from IPSL-rcp85 for each time period [%]						
RD for 2010-2039	-1.2	-1.0	-0.5	-0.6	0.0	-1.0
RD for 2040-2069	-1.0	-1.2	-0.3	-0.7	0.0	-0.8
RD for 2070-2099	0.0	-1.3	0.6	-1.0	0.0	-0.6

Table 2. Cooling demand for different future climate scenarios.

Climate Scenarios	CNRM-rcp45	CNRM-rcp85	ICHEC-rcp45	ICHEC-rcp85	IPSL-rcp85	MPI-rcp85
Cooling demand for 2010-2039 [kW]	200277	182159	81052	82116	59964	87072
Relative difference (RD) from 2010-2039 for each climate scenario [%]						
RD for 2040-2069	17.1	15.2	39.0	49.0	53.7	15.8
RD for 2070-2099	-0.4	73.6	48.5	215.9	204.0	97.6
Relative difference (RD) of scenarios from IPSL-rcp85 for each time period [%]						
RD for 2010-2039	234.0	203.8	35.2	36.9	0.0	45.2
RD for 2040-2069	154.5	127.8	22.3	32.8	0.0	9.4
RD for 2070-2099	9.4	73.5	-33.9	42.3	0.0	-5.6

Impacts of climate change and its uncertainties on estimating the renewable energy potentials are presented in the following; Figure 3 and Table 3 show results for solar PV power generation and Figure 4 and Table 4 for wind turbine. Differences due to selection of the climate scenario are visible for both the renewable sources, affecting solar PV generation up to 20% (e.g. for ICHEC-rcp45 during 2070-2099 in Table 3) and wind power up to 22% (e.g. CNRM-rcp45 during 2070-2099 in Table 4). According to all the scenarios, potentials for PV power generation will be less in future while for wind power, some scenarios predict higher potentials and some less. In general, differences due to time period (climate change) are

smaller – which is around 8% at the maximum – than those induced by the selection climate scenario (climate uncertainty) – which is around 20% at the maximum. It is important to consider that these results can be highly dependent on the location and the considered time scale. In this work, all the calculations were done in the hourly time scale, however the relative differences have been calculated based on the annual production. These differences can vary if the time scale changes for example to seasonal.

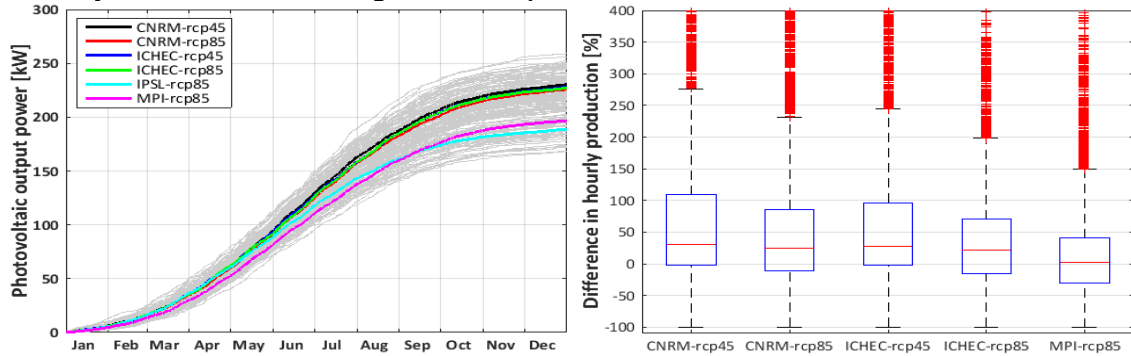


Figure 3. Cumulative solar PV power generation (left) and the relative differences on the hourly temporal resolution compared to IPSL-rcp85 (right).

Table 3. Solar PV power generation for different future climate scenarios.

Climate Scenarios	CNRM-rcp45	CNRM-rcp85	ICHEC-rcp45	ICHEC-rcp85	IPSL-rcp85	MPI-rcp85
PV power for 2010-2039 [kW]	238	240	235	229	204	213
Relative difference (RD) from 2010-2039 for each climate scenario [%]						
RD for 2040-2069	-2.4	-4.0	-0.7	-0.1	-2.6	-3.4
RD for 2070-2099	-3.3	-5.9	-3.0	-1.0	-7.6	-7.9
Relative difference (RD) of scenarios from IPSL-rcp85 for each time period [%]						
RD for 2010-2039	16.4	17.4	14.8	12.2	0.0	4.4
RD for 2040-2069	16.6	15.7	17.0	15.0	0.0	3.5
RD for 2070-2099	21.9	19.6	20.6	20.2	0.0	4.1

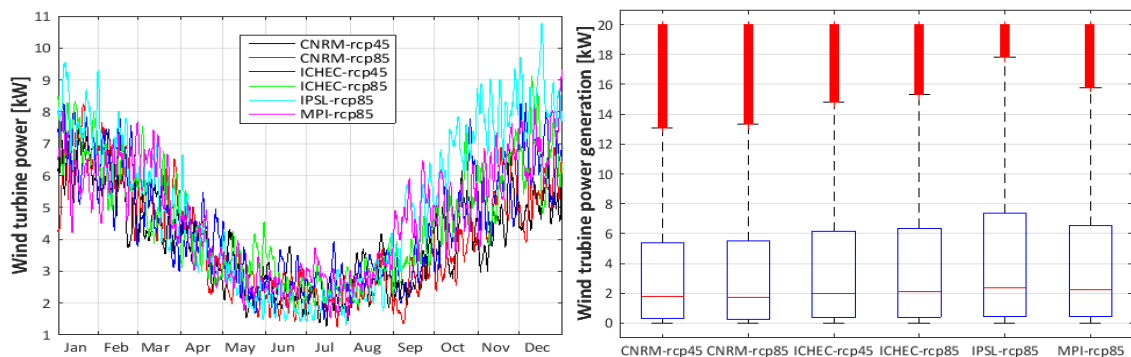


Figure 4. Wind power generation in hourly temporal scale for different climate scenarios.

Table 4. Wind power generation for different future climate scenarios.

Climate Scenarios	CNRM-rcp45	CNRM-rcp85	ICHEC-rcp45	ICHEC-rcp85	IPSL-rcp85	MPI-rcp85
Wind power for 2010-2039 [kW]	35166	36260	41232	40617	41077	38811
Relative difference (RD) from 2010-2039 for each climate scenario [%]						

RD for 2040-2069	-2.0	1.5	0.5	-0.8	4.7	-1.4
RD for 2070-2099	-2.0	-3.2	-6.3	-1.9	7.7	5.2
Relative difference (RD) of scenarios from IPSL-rcp85 for each time period [%]						
RD for 2010-2039	-14.4	-11.7	0.4	-1.1	0.0	-5.5
RD for 2040-2069	-19.9	-14.4	-3.6	-6.3	0.0	-11.1
RD for 2070-2099	-22.1	-20.7	-12.6	-9.9	0.0	-7.7

CONCLUSION AND DISCUSSION

According to the results, differences induced by climate change and its uncertainties in the cooling demand of buildings are very large, while there are negligible for heating demand of the building stock. The latter is contrary to the calculations using the older version of the climate model and should be investigated in more detail. Effects of climate change and uncertainties are visible in the renewable energy calculations, inducing differences up to 20% due to climate uncertainties and up to 8% due to climate change. In general, scenario point to less potential for renewable generation from solar PVs while for the wind turbine, numbers do not change considerably.

REFERENCES

- Nik, Vahid M. 2010. 'Climate Simulation of an Attic Using Future Weather Data Sets - Statistical Methods for Data Processing and Analysis'. Licentiate thesis, Sweden: Chalmers University of Technology.
- Nik, Vahid M. 2012. 'Hygrothermal Simulations of Buildings Concerning Uncertainties of the Future Climate'. PhD thesis, Gothenburg, Sweden: Chalmers University of Technology.
- Nik, Vahid M. 2016. 'Making Energy Simulation Easier for Future Climate – Synthesizing Typical and Extreme Weather Data Sets out of Regional Climate Models (RCMs)'. *Applied Energy* 177 (September): 204–26.
- Nik, Vahid M., Erika Mata, Angela Sasic Kalagasidis, and Jean-Louis Scartezzini. 2016. 'Effective and Robust Energy Retrofitting Measures for Future Climatic conditions—Reduced Heating Demand of Swedish Households'. *Energy and Buildings* 121 (June): 176–87.
- Nik, Vahid M., and Angela Sasic Kalagasidis. 2013. 'Impact Study of the Climate Change on the Energy Performance of the Building Stock in Stockholm Considering Four Climate Uncertainties'. *Building and Environment* 60 (February): 291–304.
- Nik, Vahid M., Angela Sasic Kalagasidis, and Erik Kjellström. 2012. 'Statistical Methods for Assessing and Analysing the Building Performance in Respect to the Future Climate'. *Building and Environment* 53 (July): 107–18.
- Perera, A. T. D., D. M. I. J. Wickremasinghe, D. V. S. Mahindaratna, R. A. Attalage, K. K. C. K. Perera, and E. M. Bartholameuz. 2012. 'Sensitivity of Internal Combustion Generator Capacity in Standalone Hybrid Energy Systems'. *Energy, Sustainable Energy and Environmental Protection* 2010, 39 (1): 403–11.
- Samuelsson, Patrick, Stefan Gollvik, Christer Jansson, Marco Kupiainen, Ekaterina Kourzeneva, and Willem Jan van de Berg. 2015. 'The Surface Processes of the Rossby Centre Regional Atmospheric Climate Model (RCA4)'. *Meteorologi* 157. Swedish Meteorological and Hydrological Institute (SMHI).
- Wilde, Pieter de, and David Coley. 2012. 'The Implications of a Changing Climate for Buildings'. *Building and Environment* 55 (September): 1–7.
- Zervas, P. L., H. Sarimveis, J. A. Palyvos, and N. C. G. Markatos. 2008. 'Model-Based Optimal Control of a Hybrid Power Generation System Consisting of Photovoltaic Arrays and Fuel Cells'. *Journal of Power Sources*, 181 (2): 327–38.

Multi-stage optimal design of energy systems for urban districts

Georgios Mavromatidis^{1,2*}, Kristina Orehounig² and Jan Carmeliet^{1,3}

¹Chair of Building Physics, ETH Zurich, Switzerland

²Laboratory for Urban Energy Systems, Empa Duebendorf, Switzerland

³Laboratory for Multiscale Studies in Building Physics, Empa Duebendorf, Switzerland

*Corresponding email: gmavroma@ethz.ch

ABSTRACT

Urban districts develop in a dynamic manner over multi-year horizons with new buildings being added and changes being made to existing buildings (*e.g.* retrofits). Nevertheless, optimization models used to design urban district energy systems (DES) commonly consider a single, “typical” year for the design. This practice, however, does not allow for energy design decisions to be made in multiple phases in order to reflect a district’s development phases. This paper addresses this issue and presents a novel optimization model that allows the multi-stage optimal design of urban DES. The model identifies the cost-optimal technology investment decisions across a horizon that spans multiple years, while also calculating the energy system’s optimal operating patterns in order to meet the district’s energy demands. The evolution of the district’s energy demands and aspects like the evolution of technology costs and energy carrier prices are considered in the model. The model is applied to a new urban district in Zurich, Switzerland, for which 5 development stages are considered with new buildings of various types constructed in each phase. A multi-stage DES design plan is developed for the period 2021-2050, which includes large energy technology investments for each new development phase, but also smaller ones in the intermediate years between 2021 and 2050. The model specifies the amount of energy generated by each technology installed in each year, as well as the contribution of renewable energy in covering the district’s energy demands.

KEYWORDS

Urban energy systems, District Energy Systems, Multi-stage energy planning, Optimization

INTRODUCTION

District energy systems (DES), incorporating multiple efficient energy technologies and locally available renewable sources, have the potential to sustainably transform the energy supply of existing and new urban districts. Designing DES is commonly performed using mathematical optimization models. These models aim to identify the optimal set of technologies that need to be installed in a DES, their capacities, and their operating patterns in order to cover the building energy demands and optimize a specific criterion (*e.g.* total system costs, CO₂ emissions etc.).

In these models, the DES design investment is typically assumed to occur in one stage, at the beginning of the project, without the possibility of further investments in later stages. Moreover, the design is usually performed for a “snapshot” in time, which corresponds either to the district’s current state or to the final state of a district. Multiple studies have presented such DES design models (see *e.g.* (Orehounig et al., 2015; Weber and Shah, 2011)).

This DES design paradigm, however, fails to consider the dynamic character of existing and new urban districts, which dynamically develop as buildings are getting retrofitted and/or new buildings are being added. Energy planning for urban districts should instead be able to account

for the developments in an urban district and involve multiple investment phases. This would allow the energy system plan to not only reflect the changes in the district, but also to take advantage of future investment opportunities *e.g.* due to reducing technology costs.

Therefore, this paper presents an optimization model, which enables the multi-stage design of urban DES. More specifically, the model outputs a multi-year investment plan for the DES design and calculates the system's optimal operation for each year. Additionally, the model is able to perform these tasks taking into account the evolution of a district's characteristics, as well as, the evolution of other external factors like energy prices and technology costs.

FORMULATION OF A MULTI-STAGE OPTIMAL DES DESIGN MODEL

In this section, the formulation of the multi-stage DES design model is presented. In order to be able to make DES design decisions in multiple stages, the model's horizon needs to include multiple years $y = \{1 \dots \mathcal{Y}\}$. Each year y is then represented with a set of days $d = \{1 \dots \mathcal{D}\}$, which are in turn represented with 24 hourly time steps $t = \{1 \dots 24\}$.

The developments considered in the model's multi-year horizon are: (i) the district's heating and electricity demands, (ii) the solar radiation availability, (iii) the energy carrier prices, (iv) the electrical grid's carbon factor (due to grid mix changes), and (v) the future technology costs.

The set of candidate energy generation and storage technologies for the DES are given in Fig. 1 and include a gas and a biomass boiler, a CHP engine, a ground-source heat pump (GSHP), PV panels, a thermal storage and batteries for the storage of electricity. Note that the connection to the electrical grid is maintained and accounted as a "generation technology" in the model.

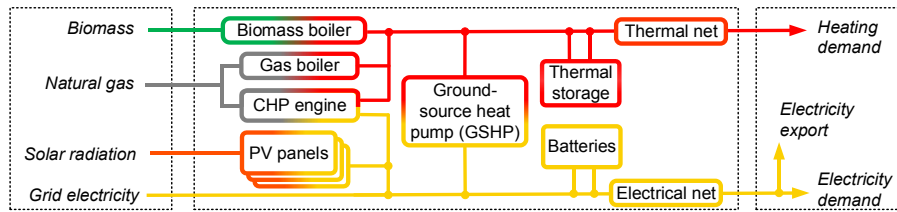


Figure 1. Candidate energy generation and storage technologies for the synthesis of a DES

The model aims to minimize the total DES cost, TC , over the modeled horizon. TC is expressed as the sum of the discounted annual costs (AC_y), which include an investment (Inv_y) and an operating expenditure (Op_y). All the relevant cost metrics are given in Eq. (1)-(3) (bold symbols indicate model variables).

$$TC = \sum_y (AC_y) \cdot (1 + DR)^{y-1} = \sum_y (Inv_y + Op_y) \cdot (1 + DR)^{y-1} \quad (1)$$

$$Inv_y = FC_{i,y} \cdot d_{i,y} + LC_{i,y} \cdot ncap_{i,y} + (L_y^{net} - L_{y-1}^{net}) \cdot LC_{net,y}, \quad \forall y \quad (2)$$

$$Op_y = \sum_{j,d,t} (P_{j,y,d,t} \cdot OC_{j,y}) - \sum_{d,t} (L_{y,d,t}^{exp} \cdot FiT_y), \quad \forall y \quad (3)$$

In all terms of Eq. (1)-(3), the indices y , d , and t signify that a term is indexed per year, day, and/or time, respectively. In Eq. (1), DR is the discount rate used for future expenditures. In Eq. (2), $FC_{i,y}$ and $LC_{i,y}$ are the fixed and the capacity-dependent costs of technology i , $d_{i,y}$ is a binary variable denoting the installation of technology i , while $ncap_{i,y}$ is the newly installed capacity of technology i . L_y^{net} is the length of the thermal network and $LC_{net,y}$ is the investment cost per m of network. These two variables form the *design decisions* of the model. In Eq. (3), $P_{i,y,d,t}$ is

the input energy flow to energy generation technology j , $OC_{j,y}$ is the price per kWh of the energy carrier used by generation technology j , $L_{y,d,t}^{exp}$ represents exported electricity to the grid, and FiT_y is the feed-in tariff for exported electricity. The variables $P_{j,y,d,t}$ and $L_{y,d,t}^{exp}$ are indexed per y , d , and t to calculate the system's operation for each year, day, and time step considered.

The carbon emissions, $Carb_y$, resulting from the system's operation in year y are defined in Eq. (4), in which $C_{j,y}$ is the emission factor [gCO₂/kWh] of the carrier used in technology i .

$$Carb_y = \sum_{j,d,t} (P_{j,y,d,t} \cdot C_{j,y}), \quad \forall y \quad (4)$$

An additional variable is needed in the model to track the total capacity of technology i in each year considering not only the introduction of new capacity, which is represented by $ncap_{i,y}$, but also the retirement of capacity that has reached the end of its lifetime. This variable is noted as $tcap_{i,y}$ and is defined in Eq. (5), in which $life_i$ represents the lifetime of technology i in years.

$$tcap_{i,y} = \sum_{\max(0,y-life_i+1)}^y ncap_{i,y}, \quad \forall y \quad (5)$$

An additional important set of model constraints are needed to ensure that the DES covers the district's energy demands in each time step. Eq. (6) expresses the energy balances for the heating and electricity demands of the district.

$$P_{j,y,d,t} \times \Theta_j + Q_{l,y,d,t}^{dis} - Q_{l,y,d,t}^{ch} = \eta_{net}^{dem} \cdot L_{y,d,t}^{dem} (+L_{y,d,t}^{exp}), \quad \forall y, d, t, dem \in \{Heat, Elec\} \quad (6)$$

In Eq. (6), Θ_j is a matrix of conversion efficiencies for each generation technology, $Q_{l,y,d,t}^{dis}$ and $Q_{l,y,d,t}^{ch}$ represent the charging/discharging flows from storage of type l , $L_{y,d,t}^{dem}$ are the district's heating/electricity demands, η_{net}^{dem} is the efficiency of the thermal/electrical network connecting the DES to the buildings, while $L_{y,d,t}^{exp}$ is only included in the electricity demand balance.

Additional constraints are included in the model to express the energy balance for the storage technologies, non-violation of capacities and charging/discharging rates, and other technical and operational constraints. These constraints have similar formulation to the constraints included in previous models that performed one-stage DES design. The difference, though, is that these constraints must also be indexed per year y instead of just per day d and time step t .

CASE STUDY

The developed model can be applied for both existing districts and new developments. In this paper, a hypothetical new urban district in Zurich, Switzerland is taken. New buildings of various types are added to the district every five years from 2021 to 2040. The analysis horizon is taken as 2021-2050 in order to analyze the DES operation for ten years after the district's construction is complete. The evolution of the district's building stock is shown in Fig. 2.

A centralized DES is envisioned for the district that will generate and distribute energy to the buildings using local thermal and electrical networks. The DES's location and thermal network are also shown in Fig. 2. Each new building of the district is assumed to be built with the newest standards defining U-values for the building envelope parts. The hourly heating and electricity demands and solar radiation patterns for each building and year are calculated using the software EnergyPlus. Future climate projections are sourced from the CORDEX project (Giorgi et al. 2009). The resulting annual district energy demands are shown in Fig. 3.

The evolution of energy carrier prices and the grid's emission factor are taken according to the New Energy Policy (NEP) scenario in the Swiss Energy Strategy 2050 (Prognos, 2012) and are shown in Fig. 3. The FiT is taken as 9 Rp./kWh for 2021 and is assumed to be linearly phased out until 2050. The evolution of technology prices is described using the approach of Gahrooei et al. (2006). The cost of technology i in year y , $C_{i,y}$, is described as: $C_{i,y} = C_{i,0}e^{-\gamma_i y}$, where $C_{i,0}$ is the price in 2021 and γ_i determines how fast future costs are reduced (this equation is applied to both $FC_{i,y}$ and $LC_{i,y}$). Base costs for year 2021 are taken from (Mavromatidis, 2017). A γ_i value equal to 0.01 is then used for the thermal storage and district heating network pipes, 0.02 for the GSHP and gas and biomass boilers, and 0.03 for PV panels and batteries.

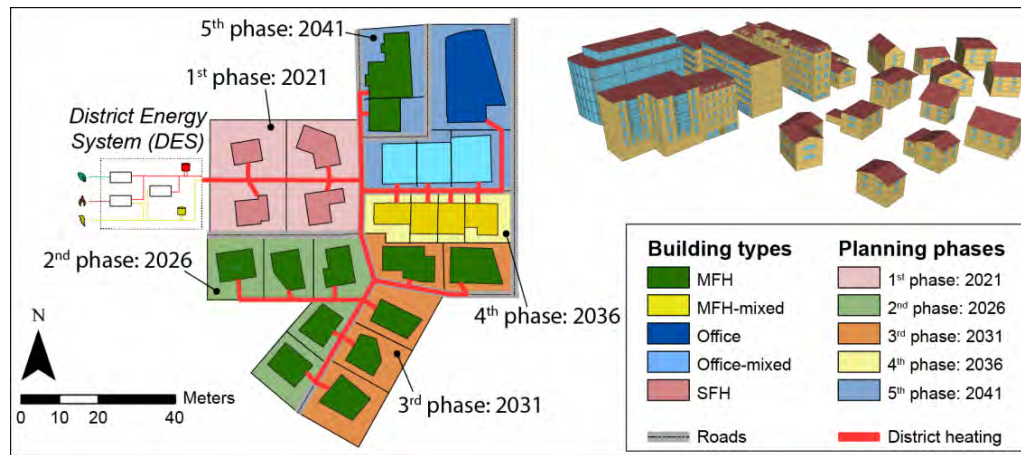


Figure 2. Evolution of urban district from 2021-2040

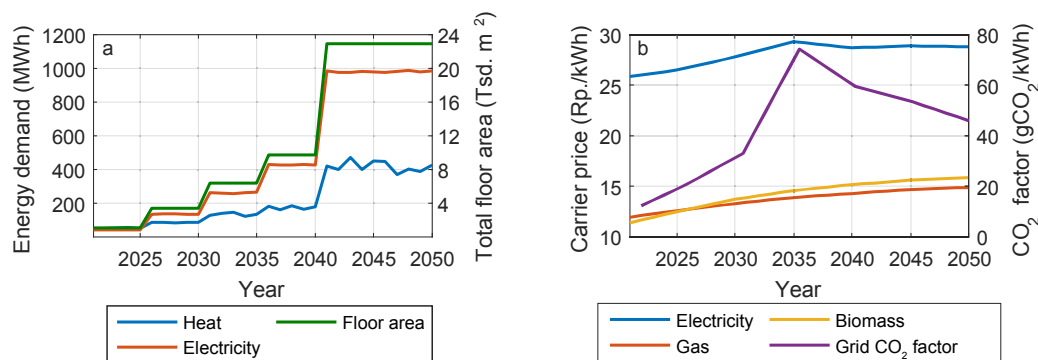


Figure 3. a. Evolution of district energy demands and total floor area, b. Evolution of energy carrier prices and the grid's emission factor

RESULTS

The first set of model results shown in Fig. 4a pertain to each year's operating and investment expenditures for the optimal DES design. The energy plan involves investments in primarily 5 stages, matching each development phase of the district. However, smaller investments are also necessary during the horizon (*e.g.* in year 2029). On the other hand, expenditure for the system's operation is necessary in each year and its evolution reflects the evolution of the district's energy demands and of the energy prices, leading to gradually increased costs in the future.

Fig. 4b presents the evolution of the system's CO₂ emissions along the modeled horizon. Initially, the emissions exceed the 10 tCO₂ per year during each year of the district's first phase. Then, during the second phase, the emissions reduce significantly only to increase again during

2031-2040. Finally, during the district's final phase after 2041, the emissions show a sharp increase. Despite the grid's CO₂ factor getting lower from 2041 on (see Fig. 3b), the district's increased floor area (see Fig. 3a) and the resulting increase in the total energy demands (see Fig. 2) offset this benefit and lead to higher CO₂ levels. Nevertheless, the CO₂ emissions per total floor area for the district remain at the same levels as the previous years.

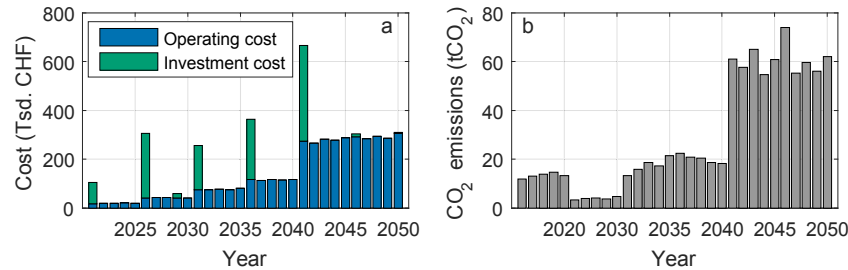


Figure 4. a. Investment and operating cost expenditures per year, b. CO₂ emissions per year

The evolution of the system's composition in terms of the energy generation and storage technologies and their capacities is shown in Fig. 5. On the generation side, the DES in the first phase consists of only a gas boiler of small capacity. A GSHP is first introduced in year 2026 and then in year 2036, while additional gas boilers are introduced in 2031, and, finally, a much larger boiler is added in year 2041. The evolution of the PV capacity is also shown in the figure with the first panels installed in 2026 and the maximum capacity being reached 2041. The figure also shows the generation capacity reduction when a device reaches the end of its lifetime (see e.g. year 2046 when the GSHP from year 2026 is retired). On the storage side, thermal storage capacity is added in two phases – in year 2026 and then in year 2036, reaching eventually a total capacity of approx. 560 kWh. Finally, in 2046 some storage capacity is retired and replaced in the final year of the modeled horizon.

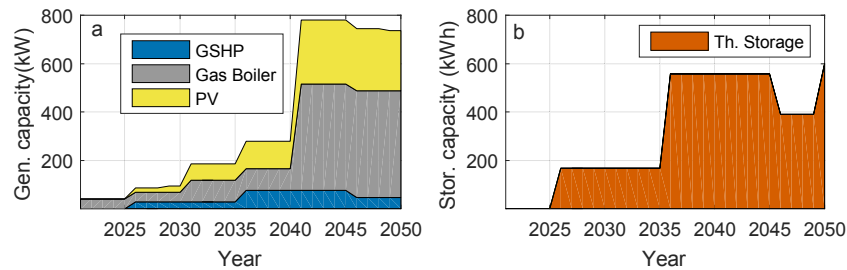


Figure 5. Total installed capacity for energy generation (a) and storage (b) technologies

The installed capacities, however, do not necessarily reflect the utilization of each technology. Thus, Fig. 6 shows the total annual heat and electricity supplied by the different technologies. During the first phase of the district, the heat demands are only covered by the gas boiler. After year 2026, though, the GSHP emerges as the main heat supply technology, and the utilization of the gas boiler remains low until 2040 and is only increased after 2041. These patterns can also explain the system's emissions in Fig. 4. Initially, when the system relies mostly on gas, the emissions are high. During the period 2026-2040 the emissions remain low as the GSHP is mainly used. Finally, from 2041 onwards the emissions increase due to both higher gas consumption, but also due to higher district energy demands.

On the electricity side, grid electricity is the primary source for covering the district's electricity demands, as well as the electricity needed by the GSHP. In the first 5 years, it is the only source

of electricity; however, as more PV capacity is installed after 2026, the contribution of PV electricity increases and reaches 28% of the total electricity supply in 2050.

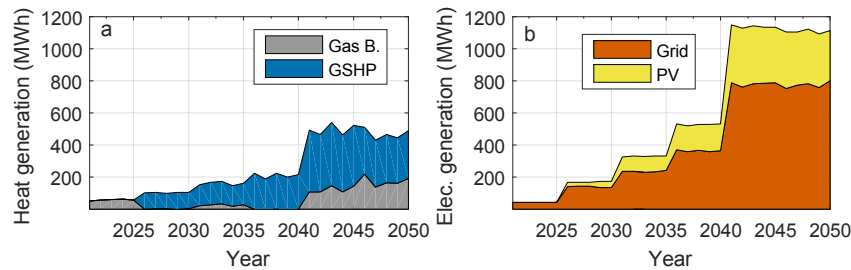


Figure 6. Heat (a) and electricity supply (b) by technology

CONCLUSIONS

In this paper, a model for the optimal multi-stage design of urban DES is presented and applied to a hypothetical urban district in Switzerland. The model is able to identify optimal energy technology investments and their timing along a multi-year horizon. Moreover, it calculates the system's optimal operation in each year and quantifies the contribution of each technology in meeting a district's energy demands.

The model's formulation is very flexible, as it can accommodate any number and type of energy technologies and be applied in urban districts of different scales. Moreover, the model can also be valuable for urban planning. Currently, urban DES are typically designed only after the district's development is finalized. By integrating the model in the urban planning process, the concurrent design of a district and its energy system can be performed, leading to potentially better solutions.

As future work, additional aspects like the efficiency improvements of energy technologies will be introduced. Additionally, the issue of uncertainty is very important, as predicting accurately the long-term evolution of energy demands, prices etc. can be very difficult. By introducing uncertainty considerations in the model, more robust DES strategies can be obtained.

ACKNOWLEDGEMENT

This research project is part of the Swiss Competence Center for Energy Research SCCER FEEB&D, which is funded by the Swiss Innovation Agency Innosuisse.

REFERENCES

- Gahrooei M.R, Zhang Y, Ashuri B, Augenbroe G. 2016. Timing residential photovoltaic investments in the presence of demand uncertainties. *Sustain Cities Soc* 20, 109–123.
- Giorgi F, Jones C, Asrar G.R. 2009. Addressing climate information needs at the regional level: the CORDEX framework. *World Meteorological Organization (WMO) Bulletin* 58, 175.
- Mavromatidis, G., 2017. Model-based design of distributed urban energy systems under uncertainty (Doctoral Thesis). ETH Zurich.
- Orehounig K, Evins R, and Dorer V. 2015. Integration of decentralized energy systems in neighbourhoods using the energy hub approach. *Appl Energy* 154, 277–289.
- Prognos AG, 2012. Die Energieperspektiven für die Schweiz bis 2050. Swiss Federal Office of Energy SFOE (Bundesamt für Energie BFE).
- Weber C, Shah N. 2011. Optimisation based design of a district energy system for an eco-town in the United Kingdom. *Energy* 36, 1292–1308.

Novel Gas-Driven Fuel Cell HVAC and Dehumidification Prototype

Daniel Betts¹, Moonis R. Ally^{*2}, Vishaldeep Sharma², Matthew Tilghman¹, Matthew Graham¹, Shyam Mudiraj³

¹Blue Frontier, LLC

²Oak Ridge National Laboratory

³Corning Inc.

**Corresponding email: allymr@ornl.gov*

ABSTRACT

Performance of a novel gas-driven, electricity-producing heating, ventilation, and air conditioning (HVAC) system with no vapor compression and no hydrofluorocarbon (HFC) refrigerant shall be discussed in the paper. The prototype was evaluated at ORNL under a Small Business Voucher (SBV) Cooperative Research and Development (CRADA) program. The target market is commercial buildings in the United States. The goal is to mitigate or eliminate grid-power for building air conditioning, coincident peak demand and associated spinning reserves, aiding in flattening of the “duck curve”. The technical goal is to transform the common packaged rooftop unit into a cost-effective distributed energy resource, opening a new range of small applications and broad markets for micro-combined cycle cooling, heating, and power with integral thermal energy storage. The test results indicate the prototype would be competitive with natural gas distributed power plants with average electrical production ranging from 45% to 60% natural gas to electricity conversion efficiency. The technology has a Primary Energy Savings Potential of 4.4 Quads, higher than any other air conditioning and heating technology.

KEYWORDS: Fuel Cell, Distributed Generation, Heating, Cooling, Dehumidification

INTRODUCTION

The first integrated electricity-producing heating, ventilation, dehumidification, and air conditioning (HVAC) system using a non-vapor compression cycle (VCC), packaged rooftop unit that also produces base-load electricity was evaluated¹. For convenience throughout this document we will call this integrated system Electricity-Production HVAC or EP-HVAC. The EP-HVAC unit represents a distributed energy resource with energy storage that eliminates the tremendous peak electricity demand associated with commonly used electricity-powered vapor compression air conditioning systems.

The objective is to enable the proliferation of renewable resources into the electric grid, reduce greenhouse gas emissions, eliminate the use of refrigerants used for air conditioning, and provide significant cost savings for utilities and ratepayers. This technology eliminates grid-powered electricity for building air conditioning, coincident peak demand and associated spinning reserves, aiding in the flattening of the “duck curve.” The technology is scalable from 2 to 20 tons and is applicable to 98% of US commercial buildings.

The results of the evaluation indicated that the technology, as tested would be competitive with natural gas distributed powerplants with average electrical power efficiency ranging from 45% to 60%. Test results indicate that the technology has a Primary Energy Savings Potential of 1.3×10^{12} kWh (4.4 Quads); higher than any other air conditioning and heating technology.

¹ Natural Gas Powered HVAC System for Commercial and Residential Buildings, ORNL/TM-2017/211, CRADA/NFE-16-016126, <https://resolution.ornl.gov/pub/preview/74419>

The project goal was to test and evaluate the performance metrics of a unit that provided 5 kW cooling capacity and generates electricity from burning natural gas using a commercially available solid oxide fuel cell (SOFC).

TECHNOLOGY DESCRIPTION

Principle of operation of the prototype:

A simplified description of the prototype is shown in Figure 1 and consists of three main sections: natural gas driven fuel cell for producing electricity; liquid desiccant regeneration; and dehumidification and air conditioning.

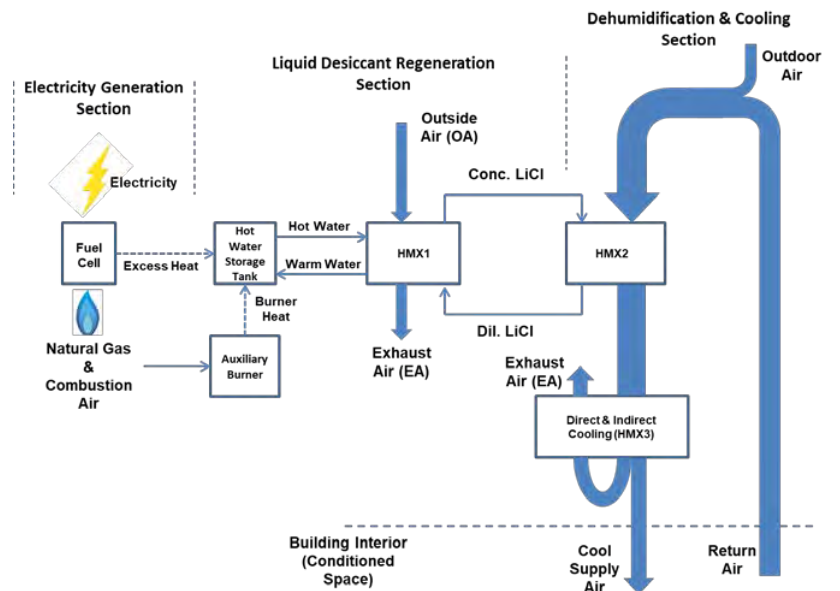


Figure 1 Schematic of the prototype EP-HVAC with three discrete sections: electricity Generation; LD regeneration; and Cooling and Dehumidification.

The prototype operates using a fuel cell and a burner to transform natural gas into electricity and heat. The heat generated is used to increase the concentration of a LiCl solution to 42% (mass fraction). This process occurs within a heat and mass exchanger (HMX) for liquid desiccant regeneration (HMX1). The concentrated LiCl is stored in a tank. When air conditioning is required, the concentrated LiCl is used to dehumidify process air (PA) within a dehumidifier (HMX2). PA for this prototype system is generally composed of a mixture of 30%–40% outdoor air (OA) with the remainder being return air (RA). The HMX2 is composed of a series of plates designed so that PA and high concentration LiCl flow on one surface. The LiCl is separated from the PA by a selectively permeable membrane that enables the interaction of water (in vapor form) with the air but prevents the flow of LiCl into the air. Because the liquid desiccant is at a high concentration, it will remove water from the air to reach water vapor pressure equilibrium with the air. This process, if adiabatic, would be isenthalpic dehumidification, resulting in a significant temperature increase of the process air. To mitigate this temperature rise, OA flows on the opposite side of the HMX2 plates, in cross-flow to the PA. The plate prevents both streams from mixing but enables heat transfer between the two flows. Water is also flown on the surface of the OA side of the plate. The OA in HMX2 absorbs the water, and this evaporation process (as well as sensible heat exchange with the air) cools the liquid desiccant dehumidification process on the other side of the plate. Consequently, the PA leaving HMX2 has a humidity that corresponds to a design dew point temperature, and a dry bulb temperature that is sometimes higher than the inlet air temperature but far lower than it would be if the dehumidification was isenthalpic (the exit temperature can be slightly lower

than inlet temperature if the outdoor conditions are very dry, which yields high-powered evaporative cooling).

To reduce the temperature of the PA down to supply air (SA) conditions, the stream is subjected to dew point-style indirect evaporative cooling (IEC) in a heat and mass exchanger (HMX3). HMX3 is composed of a series of plates. The entire PA flows over the plate's surface. However, at the exit of the plate approximately 30%–40% of the PA is redirected to flow counter to the bulk PA flow through HMX3, on the opposite side of the plates as the bulk PA flow. On this side of the plate water is flown, causing the redirected flow to cool to its wet bulb temperature. The redirected air flow leaves at close to 100% relative humidity (RH) and is exhausted. This reverse flow both cools the bulk flow, and is derived from the bulk flow, which means the lowest temperature achievable is the incoming air's dew point temperature, instead of its wet bulb temperature. At the outlet end of HMX3 plates, where a portion of the flow reverses its path, the exhaust air will indirectly cool the bulk air toward the exhaust air's wet bulb temperature. The cooler bulk air now has a lower wet bulb temperature, and it subsequently becomes the next batch of exhaust air, lowering the achievable temperature further. This continues until it cannot continue further, which (in theory) is when the dry bulb temperature of the bulk air equals the wet bulb temperature of the exhaust air, which, since they are the same stream, occurs when the bulk process air is exiting at its dew point. The bulk PA exiting HMX3 is the supply air (SA) to the building.

A more effective cooling process:

The air conditioning/dehumidification process is referred to as enhanced liquid desiccant air conditioning (ELD-AC). ELD-AC typically removes the latent heat duty of the air prior to cooling it down to as near the theoretical limit of the dew point temperature as possible. Compared to conventional VCC, the ELD-AC process is more energy efficient.

The ELD-AC process removes the more energy intensive latent first, followed by sensible indirect evaporative cooling using water extracted from the air. The change in enthalpy is typically roughly 30% lower than vapor compression (Figure 2). Most VCC systems introduce air into the space at near 100% RH and at a temperature much lower than for human comfort. VCC systems rely on heat from occupants and from building equipment (and sometimes supply their own reheat) to heat the air up to a comfortable temperature. Consequently, the prevailing method of air conditioning, VCC, is energy intensive.

In contrast, the ELD-AC dehumidification process is achieved through diffusion of water vapor from humid air across a semipermeable membrane into a flowing concentrated liquid desiccant. Liquids cannot penetrate the membrane, keeping the desiccant isolated from the conditioned air stream. This process of dehumidification is actively cooled using outside air so that it does not increase the DA temperature (however, even if it did, this would not increase the overall maximum enthalpy change, as long as the dehumidification process remains close to being isothermal). Air dehumidification, due to latent loads, is energy intensive and its removal by the above technique is more efficient than a VCC process. After removal of sufficient latent loads, further cooling in the ELD-AC process is achieved with indirect evaporative cooling.

RESULTS

The evaluation consisted of 29 data sets with varying conditions in the outdoor air chamber (Figure 3 and **Error! Reference source not found.**). The test showed a 1st law efficiency that ranged from 0.6 to 1.2. The average 1st law efficiency for all runs was 0.9, with a standard deviation of ± 0.15 . Supply air temperature varied from 15.4°C to 19.4°C, with an average SA temperature of 17.3°C and a standard deviation of ± 0.9 °C. SA average RH was 55%, and it ranged from 48% to 62%. Note that the 1st law efficiency in this case can be greater than 1 because the heat of water vaporization is not included in this calculation.

The first law efficiency is defined in Eq.(1) as,

$$\eta_{1st\ Law} = \frac{C+E}{F} \quad (1)$$

C is the air cooling is instantaneous steady state rate of enthalpy removed from air, corrected to eliminate liquid desiccant energy storage effects; E is the electrical power produced by the system; and F is the rate of chemical energy of the fuel provided to the system during a day. In this report, F is calculated using the lower heating value of the fuel.

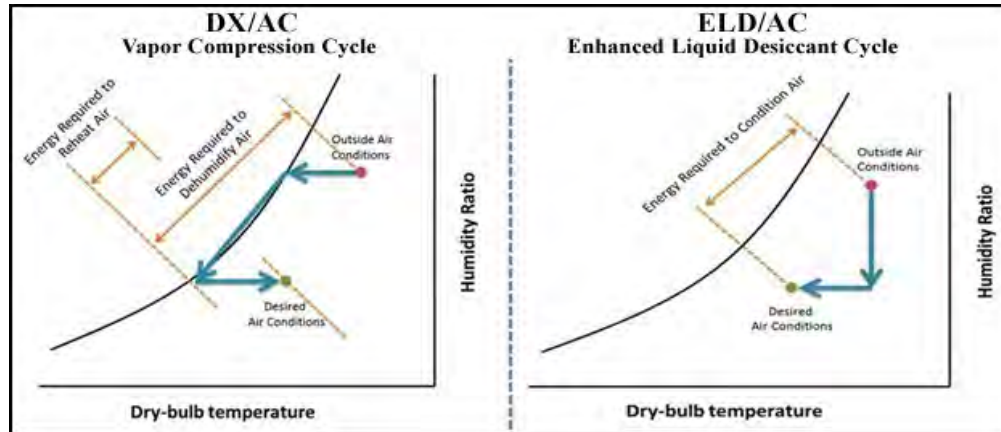


Figure 2 Difference in air conditioning and dehumidification processes between conventional vapor compression cycle (VCC) and the enhanced liquid desiccant evaporative cooling air conditioner (ELD/AC) cycle.

The testing was conducted at constant simulated outdoor and indoor air conditions. In other words, it did not take into account the daily varying requirements for air conditioning, which might have resulted in the air conditioning not being operated while the fuel cell continued to provide electrical power and regenerating liquid desiccant for later use. Under these test conditions, the heat supplied by the fuel cell was not sufficient to provide the heat required to sustain the air conditioning process, since these isolated tests could not rely on storage from daily continuous regeneration. For this reason, the supplemental natural gas burner was used to supply the extra heat required. Fuel cell performance was very predictable and repeatable. On average the fuel cell electrochemical efficiency was 47% (lower heating value based) with a combined heat and power efficiency of 90%, when producing 2.5 kW_e. Certain tests were performed without the fuel cell (burner only), in which case, for consistency, the expected power output and total natural gas input were calculated via the stable observed fuel cell electrical and combined heat and power efficiencies and included in the 1st law efficiency.

To provide a more insightful and comparative evaluation of the performance of the EP-HVAC, we define a distributed power efficiency (η_{DG}), as shown in Equation (2), where \dot{E} is the electrical power produced by the fuel cell system as a function of time, \dot{C} is the rate of cooling provided by the system as a function of time, COP_{VCC} is the coefficient of performance of an equivalent vapor compression system, \dot{F}_{FC} is the rate of fuel energy consumed by the fuel cell system as a function of time on a lower heating value basis, and \dot{F}_B is the rate of fuel energy consumed by the auxiliary burner as a function of time on a lower heating value basis. Note that \dot{F}_B is only required when the fuel cell is unable to produce enough excess heat to drive the air conditioning process. The heat required to run the air conditioning process can be calculated using the quantified $\eta_{1st\ Law}$ in Equation 1. τ is the operating time period under which the efficiency is calculated, and t is time. Equation 2 converts the air cooling produced into an

electrical equivalent output of the system. This efficiency definition enables the comparison of the EP-HVAC with a power plant that is providing both electrical power to the building and to run an air conditioning unit with equivalent output performance as the EP-HVAC.

$$\eta_{DG} = \frac{\int_0^{\tau} E dt + \int_0^{\tau} \frac{\dot{c}}{COP_{VCC}} dt}{\int_0^{\tau} \dot{F}_{FC} dt + \int_0^{\tau} \dot{F}_B dt} \quad (2)$$

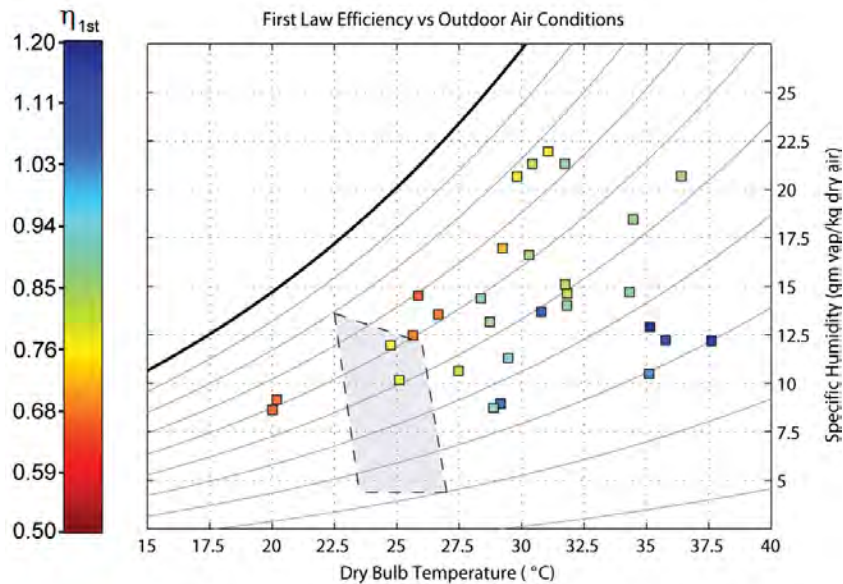


Figure 3. Psychrometric chart showing summary of outdoor air test points and $\eta_{1st\,Low}$ achieved (represented by point color and referenced to color bar on left) with the prototype unit. Comfort zone region is shown in dashed line polygon.

For illustration and simplicity, we have evaluated η_{DG} assuming the outdoor and indoor air conditions do not change during a day and that the air conditioning portion of the system operates in on/off operation (as most air conditioners do). Given this, a duty cycle can be defined as a ratio of the time the system spent cooling (air conditioner on) and the time the system produced electrical power. Also, for simplicity, we maintained the fuel cell power output constant during the day.

The tested conditions had two extremes: hot and humid (H&H), and hot and dry (H&D) conditions. These conditions are summarized in Table 1. Using the collected data and the simplifying assumptions previously described, where the power to cooling capacity ratio of the EP-HVAC is 1kW/RT, and a COP_{VCC} of 4.1 (EER = 14), which would correspond to a very high efficiency vapor compression cycle system, η_{DG} as a function of duty cycle was evaluated and the result is shown in Figure .

The results indicate that initially, η_{DG} increases as duty cycle increases, as the excess heat generated by the fuel cell is more than the heat required to drive the increasing air conditioning loads. In this regime, the excess heat from the fuel cell is better utilized and efficiency increases. As the duty cycle increases further, the fuel cell excess heat becomes insufficient to drive the cooling load, leading to increasing use of the auxiliary burner. This increases fuel consumption and decreases η_{DG} . For both H&H and H&D cases η_{DG} is higher than most distributed generation systems, ranging between 65% and 52% for the H&D case, and between 59% and 37% for the H&H case.

Table 1. Hot and Humid (H&H), and Hot and Dry (H&D) conditions tested

Hot and Humid Conditions			
First Law Efficiency:	90%	DG Efficiency Range:	37% to 57%
	Dry Bulb Temp. (°C)	Relative Humidity (%)	
Outdoor Air	31.8	72%	
Return Air	25.2	56%	
Hot and Dry Conditions			
First Law Efficiency	126%	DG Efficiency Range:	52% to 65%
	Dry Bulb Temp. (°C)	Relative Humidity (%)	
Outdoor Air	37.4	30%	
Return Air	25.5	55%	

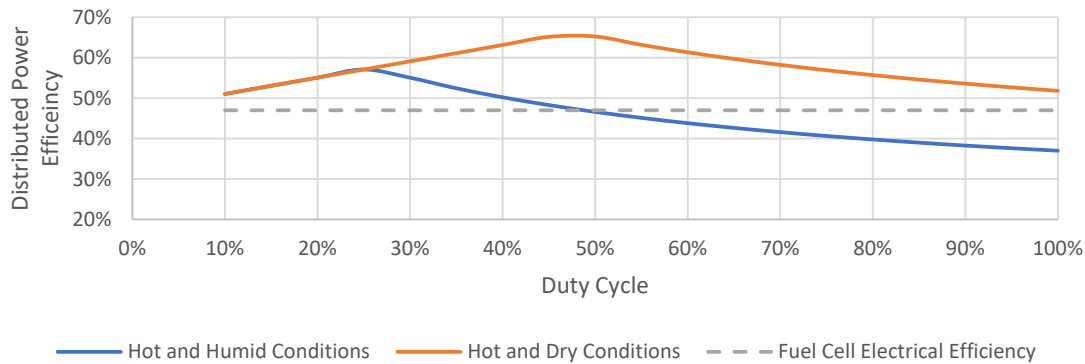


Figure 4. Distributed power efficiency of tested EP-HVAC as a function of duty cycle for constant return air and outdoor air conditions H&H and H&D. The COP_{VCC} is 4.1 and fuel cell power to air conditioner cooling capacity is 1kW/RT.

DISCUSSIONS

The EP-HVAC tested was the first prototype of its kind tested under varying outdoor air conditions. While the performance of the system measured in terms of $\eta_{1sr Law}$ is generally high, with improvements to the design it could be significantly higher.

EP-HVAC is an enhanced power generator and the most relevant comparative performance indicator is η_{DG} . The analysis of η_{DG} presented is sensitive to the assumptions made. In particular, COP_{VCC} and the power to cooling ratio. COP_{VCC} depends on outdoor air conditions and humidity, an effect that is not captured in the results presented. A COP_{VCC} of 4.1, the value used in our analysis, corresponds to the peak value found in the literature for high efficiency roof-top units.

Fuel cell electrical efficiency and CHP efficiency also play an important role and affect the optimization of the power to cooling design point in different weather conditions.

Further work is needed to complete a full evaluation of the EP-HVAC. This includes improving design of the system to reduce size and increase $\eta_{1sr Law}$ in all weather conditions. Additionally, there is a lot of room for system optimization for a particular building and weather conditions. To explore this, further dynamic, yearlong, location specific models should be developed.

CONCLUSIONS

The building and testing of this 1st EP-HVAC demonstrates that this is a technology with enormous potential to reduce energy consumption associated with electricity generation and powering air conditioners in buildings.

Optimization of Electric Vehicle Charging in a Fully (Nearly) Electric Campus Energy System

Jacques A. de Chalendar^{1,*}, Jason H. Frost¹ and Sally M. Benson¹

¹Stanford University, USA

*Corresponding email: jdechalendar@stanford.edu

ABSTRACT

The goal of this work is to build a set of computational tools to aid decision making for the modelling and operations of integrated urban energy systems that actively interact with the power grid of the future. District heating and cooling networks incorporating heat recovery and large-scale thermal storage, such as the Stanford campus system, dramatically reduce energy waste and greenhouse gas emissions. They have historically played a small, but important role at a local level. Here we explore the potential for other co-benefits, including the provision of load following services to the electrical grid, carbon emissions reductions or demand charge management. We formulate and solve the problem of optimally scheduling daily operations for different energy assets under a demand-charge-based tariff, given available historical data. We also explore the interaction and interdependence of an electrified thermal energy network with actively managed power sources and sinks that concurrently draw from the same electrical distribution feeder. At Stanford University, large-scale electric vehicle charging, on-site photovoltaic generation and controllable building loads could each separately represent up to 5 MW, or 15% of the aggregate annual peak power consumption in the very near future. We co-optimize financial savings from peak power reductions and shifting consumption to lower price periods and assess the flexibility of both the different components and the integrated energy system as a whole. We find that thermal storage, especially complemented with electric vehicle charging, can play the role that is often proposed for electrochemical storage for demand charge management applications and quantitatively evaluate potential revenue generators for an integrated urban energy system. Although there is little value to smart charging strategies for low penetrations of electric vehicles, they are needed to avoid significant increases in costs once penetration reaches a certain threshold – in the Stanford case, 750-1,000 vehicles, or 25% of the vehicle commuter population.

KEYWORDS

District energy system, electric vehicle charging, thermal energy storage, integrated urban energy.

INTRODUCTION

More than half of the world's population currently lives in urban areas (54% in 2014), and this fraction is expected to increase to 66% by 2050 (UN DESA, 2014). Increasingly, buildings and the urban environment are becoming a nexus for different energy networks across sectors such as electricity, heat and transportation (Keirstead et al., 2012). These networks will be denser, more complex and interdependent. Heat, electricity and transportation also account for two thirds of global carbon dioxide emissions from fuel combustion, which makes the urban environment a battleground for climate change mitigation efforts. A viable pathway to addressing climate change goals is to electrify the heat and transportation sectors while decarbonizing electricity generation. Along this pathway come serious challenges however: the demand for electricity is likely to rise significantly beyond the capacity of current infrastructure,

and current options for decarbonized electricity sources largely depend on the wind and sun, so they are more variable and less controllable than the traditional thermal power generation sources that constitute the backbone of current power grids (Apt, 2015). Unmanaged, the electrification of heat and transport represent a threat to the power system. On the other hand, exploiting the inherent flexibility in these sectors could also ease the integration of larger shares of renewable generation through demand side management (Callaway & Hiskens, 2010). Enhanced sensors and actuator controls are available to manage the interactions and energy flows between the heat, electrical and transportation networks (O'Malley et al., 2016).

District energy systems have historically played a small, but important role at a local level (Rezaie & Rosen, 2012). It is expected and desirable that they will play a larger one in future sustainable energy systems (Lund et al., 2014). In particular, the optimization of district electric heating and cooling systems offers a way of incorporating large thermal storage in power systems at the transmission and distribution levels as a major flexibility asset, while increasing the value of investments by broadening the services they can provide to an ever-expanding area (de Chalendar et al., 2017). Plug-in Electric Vehicles (PEVs) are expected to represent an increasing share of electric load in power systems in the near future, which is why a significant amount of recent work has focused on studying their impact on the grid (Richardson, 2013). Given the capital cost of chargers, it is likely that workplace charging will play a large role in future transportation networks. Whereas uncontrolled charging will present a risk if not managed adequately, when connected to the grid, the batteries of PEVs represent a potential storage asset for the system operator.

The Stanford Energy Systems Innovations project is a prime case study for this work. A schematic for the campus energy system is shown in Figure 1. The main energy requirements are those of the buildings, that consume cooling, heating and power. The heating and cooling needs are met through hot and chilled water distribution networks that are supplied by the onsite Central Energy Facility (CEF). The bulk of the thermal needs are met through electric heat pumps that leverage heat recovery and are backed by thermal storage tanks. These replaced the gas-fired co-generation plant that was decommissioned in 2015. Stanford University is a perfect example of a continually evolving urban environment: large-scale electric vehicle charging, on-site photovoltaic generation and controllable building loads could each separately represent up to 5 MW, or 15% of the aggregate annual peak power consumption in the very near future.

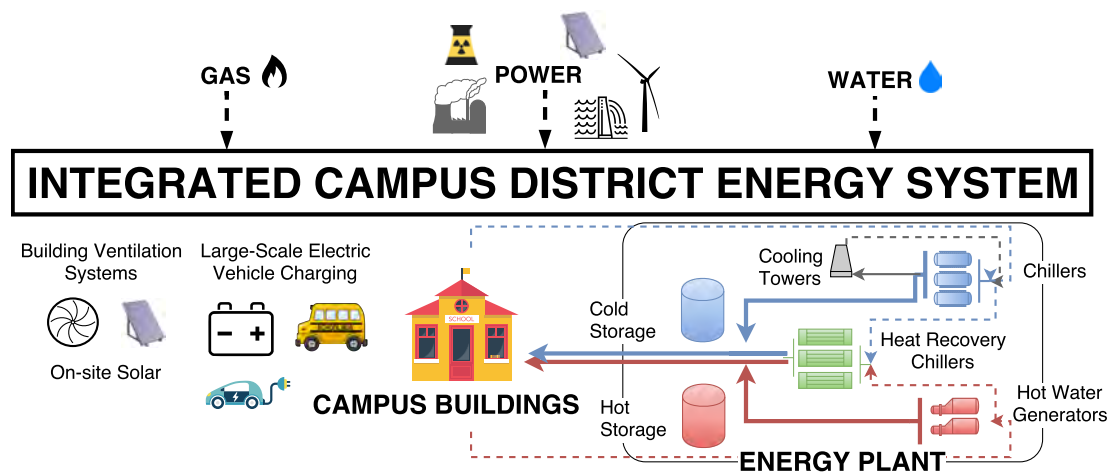


Figure 1. Schematic for an integrated campus district energy system.

The problem we are considering here is that of the optimal management of an integrated energy system in an urban environment. Since infrastructure investments in systems such as these are typically capital intensive and intended to last for many decades, ensuring that they are designed

in a way that they are not only flexible to short-term operating conditions but also longer-term evolution trends is critical to recovering invested value. In this paper we build on a previous model of the Stanford energy system to further explore the interdependence of the heat, electricity and transportation sectors at the urban energy system level. We assess the impact of different penetrations of electric vehicle charging on the campus distribution system and quantitatively determine the value of different PEV charging strategies.

METHODS

We consider an integrated urban energy system that meets its thermal needs through electric heat pumps backed by thermal storage. We call the operations scheduling problem that of determining the hourly operations at the CEF such that energy demands and technological constraints are met at minimum cost. This problem is formulated for the 8,760 hours in a year as a Linear Program (LP) with $\sim 130,000$ variables and $\sim 170,000$ linear constraints in de Chalendar et al. (2017). The objective function of this program is the campus aggregate energy bill, *i.e.* we consider financial savings in the context of a demand-charge-based system, where a time-varying, hourly price is paid for energy (measured in kWh), and a monthly price is paid for the peak power consumption (measured in kW). The decision variables of the program are the hourly power injections to the different machines at the CEF. At every time step, the campus heating and cooling loads must be met, as well as various operating constraints, *e.g.* available capacities and ramp rates. The machines available to contribute to the hot and chilled water streams are electric heat recovery chillers, electric chillers, and gas-fired boilers.

To model future interactions of the Stanford ecosystem with large-scale PEV charging, we now build a module to represent the population of PEVs on campus. This model also has an hourly resolution and tracks the energy and power flows associated with the different vehicles connected to campus chargers. The vehicles are characterized by the parameters in Table 1: they are present only for a portion of the day (arrival and departure times); their batteries have different technical characteristics (capacity and charge rate); the energy in their battery packs, or State of Charge (SoC), is different when they arrive in the morning; and finally they have different requirements for SoC levels when they leave the campus at the end of the day. We assume that when the drivers plug in to the campus chargers, they specify a minimum SoC for the end of the day and the time at which they leave, and then hand over control to the campus operator as to when the charging actually occurs. The dynamics of the SoC of the batteries in the vehicles is governed by the following equation during the hours when it is controlled by the system operator:

$$S_{t+1} = S_t + P_t^c \delta t \eta^c - \frac{P_t^d \delta t}{\eta^d} \quad (1)$$

where S_t is the SoC at time t , and P_t^c and P_t^d are the power charged and discharged during the time step of length δt at efficiencies of η^c and η^d , respectively. The power that is charged and discharged at every hour from the vehicle batteries are decision variables for the optimization program and represent bidirectional charging. During the hours where the vehicles are not connected to the campus chargers, we impose the constraint $S_t = 0$. The PEV module that was just described is tied to the main optimization program described in de Chalendar et al. (2017) through the total hourly electrical energy consumed by the PEV population, which is added to the aggregate campus consumption. A small penalty is also added to the objective to account for battery degradation (and prevent excessive charge/discharge cycles).

The storage dynamics represented by equation (1) hold for each of the vehicles that connects to the campus, and for small numbers of vehicles, each individual vehicle is tracked by the program. For large populations of PEVs however, the problem quickly becomes numerically intractable, and it is no longer reasonable to track every vehicle separately. Instead, we assume that the vehicles can be clustered into a set of commuter archetypes. Each archetype corresponds

to one set of parameters as defined by Table 1 (16 archetypes can be modelled here). For each archetype, a weight and the number of connected vehicles is used to scale the technical characteristics of the battery, such that all vehicles of a given archetype are grouped together as one large equivalent vehicle, and the 16 equivalent vehicles present the same technical characteristics to the distribution system as the full PEV fleet.

Table 1. Parameters for commuter archetypes in PEV model. We use $\eta^c = \eta^d = 90\%$, which corresponds to a round-trip efficiency of 81%. Arrival and departure times for each archetype are uniformly drawn from [6,7,8,9] AM and [5,6,7,8,9] PM.

Parameter	Value 1	Value 2
Storage capacity (kWh)	20	60
Charge/Discharge rate (kW)	4	20
Arrival state of charge (%)	20	70
Departure state of charge (%)	80	100

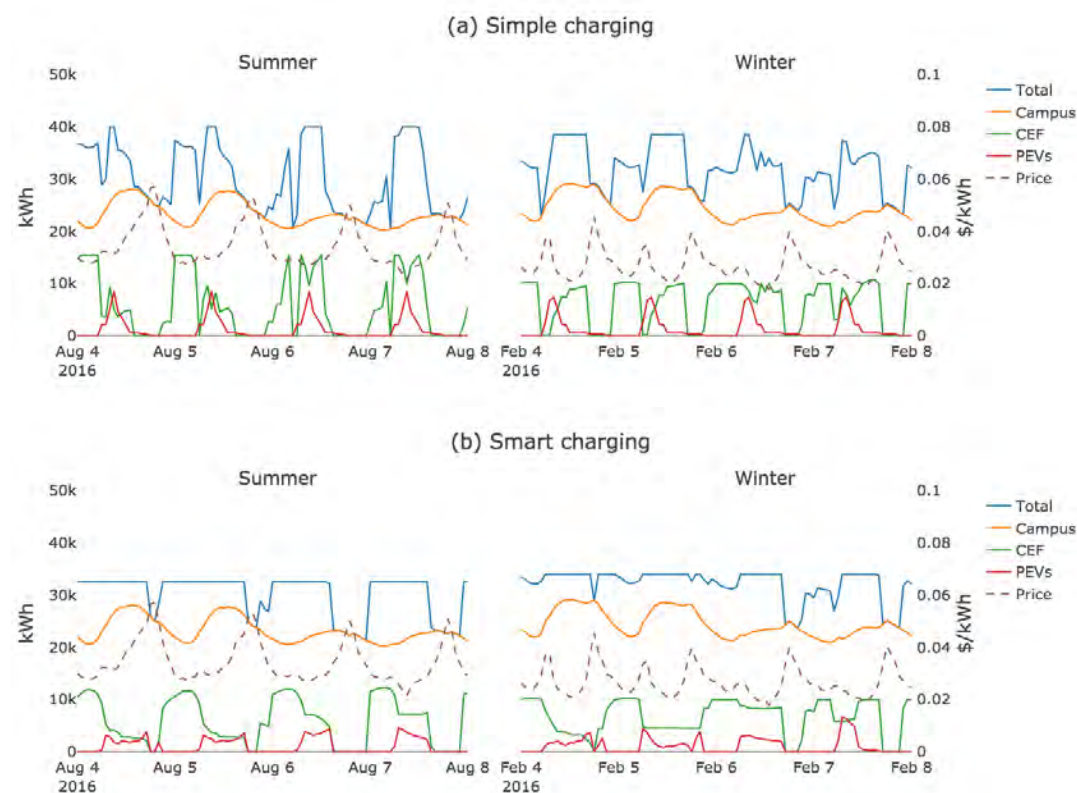


Figure 2. Typical summer and winter operations schedules for two charging strategies for 2,000 vehicles (~60% of campus commuter vehicles): (a) simple charging, where vehicles charge as soon as possible, and (b) smart charging, where the optimization program chooses when to charge the vehicles. The schedules report the energy (kWh) consumed by each component of the energy system during each hour.

RESULTS

To assess the impact of large-scale PEV charging on the Stanford energy system, we compute optimal operating schedules for the CEF with two operating modes for PEV charging: (i) “simple” charging where the PEVs charge as fast as possible when they arrive, until they reach their departure SoC level; and (ii) “smart” charging where the charging is handled by the optimization program. Real 2016 data is used for campus thermal and electrical loads. Figure 2 shows typical summer and winter operations schedules for the two charging strategies, for 2,000

vehicles. The (controllable) CEF, respectively PEV load, is represented in green, respectively red, while the (uncontrollable) background campus load is represented in orange, and the aggregate university load is represented in blue. In the top graphs where simple charging is adopted, the system operator does not control charging, so that the uncontrollable load consists of both building and PEV loads and presents a peak in the morning. By contrast, the smart charging strategy spreads charging throughout the day to avoid raising peak power demand and to target low price periods. The program is able to distribute charging throughout the day whether it is a summer, winter, weekend or week day and chooses never to use the Vehicle-to-Grid (V2G) capability: the discharge variable P_t^d is zero for every timestep. We also compare the financial and grid benefits at different PEV penetration levels from the considered charging strategies in Figure 3. We compute the average cost of charging the vehicles as the campus electric bill increase divided by the number of vehicles for Figure 3a, and the peak monthly power demand for Figure 3b. Data for Figures 3a and 3b are normalized to one for 100 vehicles. The results in Figure 3 show that although there is little benefit in smart charging strategies for low penetrations of PEVs, not applying them becomes extremely detrimental when penetrations rise above a critical threshold (here 750-1,000 PEVs for all months except March).

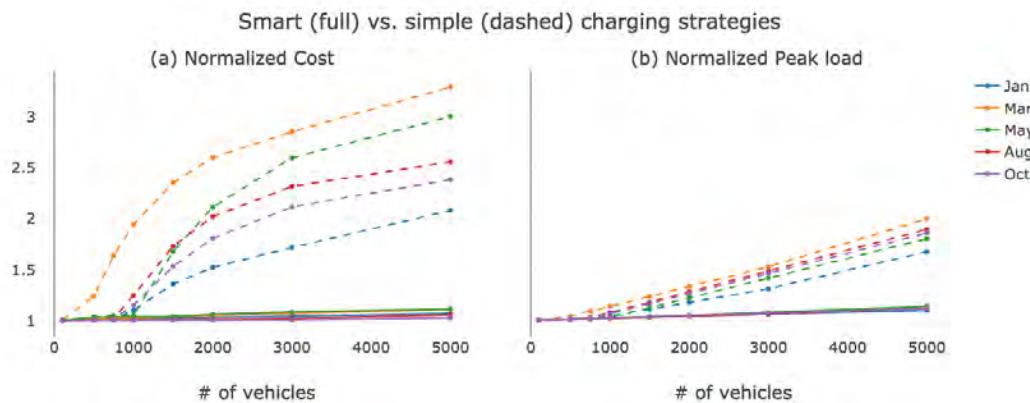


Figure 3. Comparing the benefits of charging strategies at different PEV penetration levels (from 0 to 160% of the current commuter population): (a) normalized average charging costs and (b) normalized monthly peak load. Average charging costs are computed as the increase in total campus costs from introducing PEVs, divided by the number of PEVs. In figure (a) charging costs are normalized to one for 100 vehicles, and similarly in figure (b), peak load is normalized to one for 100 vehicles. Solid lines represent smart charging, dashed lines represent simple charging.

DISCUSSION AND CONCLUSIONS

In the application presented here, multiple controllable electric loads interact, which means that different energy assets may be competing to generate the same value stream for the campus. Peak-shaving in particular is usually found to present substantial economic benefits for facilities such as the Stanford energy system. In a different setting where PEVs are the only controllable load, it could be expected that energy costs would decrease as PEV penetration increases, if the car batteries were used to provide electricity to the campus during peak demand (*e.g.* V2G). Since the CEF already possesses a very cheap way of shifting loads (by exploiting thermal energy storage) however, there is little added value left from peak shaving when PEV penetration increases. Here, the real value from smart charging lies in avoiding increased peak power charges when PEV penetration rises. As highlighted by Figure 3a, if smart charging is not adopted, the cost of charging will increase dramatically with penetration levels and peak demand will increase almost linearly, whereas charging costs can be kept almost constant through smart charging. We emphasize that only one value stream from PEV smart charging is considered here. Other more complex revenue streams may hold additional value, for instance to mitigate short-term power variations in local solar generation or to participate in frequency

response. The penetration threshold at which smart charging strategies start showing real value corresponds to a fleet of PEVs that can draw 15-20% of peak power demand, and 25% of the commuters are driving EVs¹, which demonstrates that significant interactions between the transportation and electricity sectors is not very far away. Injecting real data on PEV commuter patterns would bring even more value to this analysis to confirm these conclusions by more precisely segmenting vehicles in realistic customer archetypes. Additionally, coarser reduced-order-modeling of the PEV population may become necessary in order to increase the number of energy assets that can be managed by our optimization program. With 16 commuter archetypes, the size of the monthly optimization program jumps from 12,000 to 48,000 decision variables when adding the PEV module, which makes runtimes slower.

The results presented here have strong implications for policymakers and decision makers. They highlight how urban energy systems will become increasingly integrated across the transportation, heat and power sectors. This integration can bring real value but also presents corresponding risks if not properly managed. Given the high infrastructure costs associated with investments in urban environments, especial care should be taken in planning, in particular to consider the new energy networks that they will interact with.

ACKNOWLEDGEMENTS

Funding for this research was supported by the Global Climate and Energy Project and a Precourt State Grid Corporation of China Graduate Student Fellowship. The authors thank Joe Stagner, Executive Director of Sustainability and Energy Management Department at Stanford University, for providing energy load data for this study.

REFERENCES

- Apt, J. (2015). Recent results on the integration of variable renewable electric power into the US grid. *MRS Energy & Sustainability*, 2, 1–11. <https://doi.org/10.1557/mre.2015.7>
- Callaway, D. S., & Hiskens, I. A. (2010). Achieving Controllability of Electric Loads. *Proceedings of the IEEE*, 99(1). <https://doi.org/10.1109/JPROC.2010.2081652>
- Chalendar, J. A. De, Glynn, P. W., Stagner, J., & Benson, S. M. (2017). Decarbonization of Campus Energy Systems and Optimization of Grid-Friendly Electrified District Heating and Cooling with Thermal Storage. In *CIGRE US National Committee 2017 Grid of the Future Symposium*.
- Keirstead, J., Jennings, M., & Sivakumar, A. (2012). A review of urban energy system models: Approaches, challenges and opportunities. *Renewable and Sustainable Energy Reviews*, 16(6), 3847–3866. <https://doi.org/10.1016/j.rser.2012.02.047>
- Lund, H., Werner, S., Wiltshire, R., Svendsen, S., Thorsen, J. E., Hvelplund, F., & Mathiesen, B. V. (2014). 4th Generation District Heating (4GDH). Integrating smart thermal grids into future sustainable energy systems. *Energy*, 68, 1–11. <https://doi.org/10.1016/j.energy.2014.02.089>
- O'Malley, M., Kroposki, B., Hannegan, B., Madsen, H., Andersson, M., William, D., ... Dent, C. (2016). Energy Systems Integration : Defining and Describing the Value Proposition, (June).
- Rezaie, B., & Rosen, M. A. (2012). District heating and cooling: Review of technology and potential enhancements. *Applied Energy*, 93(May), 2–10. <https://doi.org/10.1016/j.apenergy.2011.04.020>
- Richardson, D. B. (2013). Electric vehicles and the electric grid: A review of modeling approaches, Impacts, and renewable energy integration. *Renewable and Sustainable Energy Reviews*, 19, 247–254. <https://doi.org/10.1016/j.rser.2012.11.042>
- UN DESA. (2014). *World Urbanization Prospects*. <https://doi.org/10.4054/DemRes.2005.12.9>

¹ ~3,500 drivers commute daily, according to: <https://gup.stanford.edu/transportation-no-net-new-commute-trips>.

Studying the impact of local urban heat islands on the space cooling demand of buildings using coupled CFD and building energy simulations

Jonas Allegrini^{1,2,*} and Jan Carmeliet^{1,2}

¹ Laboratory of Multiscale Studies in Building Physics, Empa, 8600 Dübendorf, Switzerland

² Chair of Building Physics, ETH Zurich, 8092 Zürich, Switzerland

*Corresponding email: jonas.allegrini@empa.ch

ABSTRACT

Surface as well as air temperatures are due to the urban heat island effect higher in urban compared to their surrounding rural areas. These increased temperatures have a strong impact on the building energy performance in urban environments and thermal comfort as well as health of inhabitants of these environments. At smaller scales, local heat islands are formed within urban environments, which have the same negative impacts. In this study, we investigate the influence of local heat islands on the space cooling demand of buildings. Commonly, climate information from one weather station is used for building performance simulations within a whole city. This climate information cannot take local hot spots into account, what can lead to inaccurate space cooling demand predictions. Here, we model the local urban climate with CFD (Computational Fluid Dynamics) simulations. With CFD also the local convective heat transfer coefficients (CHTC) for the building surfaces can be predicted. These local CHTC can strongly vary locally due to differences in local wind speeds. The commonly used coefficients are mostly based on measurements at facades of stand-alone buildings, where the local wind speeds are higher compared to urban areas. This study shows a dependency of the space cooling demands on the local urban climate. Space cooling demands are higher in areas with high local temperatures, where the wind-driven ventilation is decreased. Additionally to the higher local temperatures also the local CHTC are lower leading to lower heat losses from the buildings. It can be concluded that it is important to account for the local microclimate to accurately predict the space cooling demand of buildings in urban environments.

KEYWORDS

Urban climate, CFD, Building Energy Simulations, Space Cooling Demand, Local Urban Heat Island

INTRODUCTION

In the past decades, cities have been continuously growing and today about 54% of the world population lives in urban areas, a ratio that will increase to about 66% by 2050 (United Nations, 2015). Urban areas experience the urban heat island (UHI) effect, characterized by higher air temperatures compared to the surrounding rural environment (Oke, 1987). The UHI is expected to further increase due to the continuous growth of our cities, leading to even harsher urban climates in future. In addition to the UHI effect at city scale, local hot spots can be found in cities. Certain city quarters, neighbourhoods or zones between individual buildings may show much higher air temperatures compared to neighbouring urban areas, referred to as local heat islands (Allegrini and Carmeliet, 2017). These local hot spots are mainly due to lower wind speeds caused by wind sheltering. The intensity of these local heat islands depends on factors like building density, lack of shadowing by buildings and trees, type of building materials, lack of water bodies, vegetation or parks and deficiency of wind

flows to ventilate and remove heat. The local urban climate may highly influence the energy demand for buildings, especially the space cooling demand during hot periods. Most of the building energy simulation models, which are used to predict energy demands of buildings, were originally developed for stand-alone buildings (Hensen, 2011). For buildings in urban environments the building energy demand can be quite different to buildings in rural areas. The important impact of the local urban climate on the energy demand of buildings has been shown in a number of studies (e.g. Bouyer et al. 2011) with different approaches and levels of detail.

There exist a large number of numerical urban climate models, which predict the urban climate with different spatial resolutions and levels of accuracy. In this study a detailed urban microclimate model developed by Kubilay et al. (2017) is used to simulate the local urban heat islands in a small urban neighbourhood. This is a fully-integrated urban climate model, which solves for wind flow and for the transport of heat and moisture in the air and building materials. The predicted local air temperatures and local convective heat transfer coefficients for a period of 24 hours during a generic heat-wave event are used as inputs to building energy simulations (BES), which predict the space cooling demands. This study is conducted for the climate of Zürich (Switzerland).

NUMERICAL MODEL AND SIMULATION

An offline coupling between a CFD and a BES model is used to predict the impact of the local urban climate on the space cooling demands of a building in an urban neighbourhood. First the urban climate model based on CFD is conducted to predict the local urban climate for a time period of 24 hours. In a second step the local air temperatures around the studied building is used as an input parameter for the BES. The local air temperature is determined as the mean temperature in the air volume surrounding the building with a maximum distance of 0.3 m. For the convective heat transfer coefficients (CHTC) the correlations by McAdams (1954) are used (default correlations for the used BES model). For this study, for each building surface the local wind speed (mean over the façade or roof area) is used in the CHTC correlation instead of the wind speed from the climate file. With this offline coupling approach, we can account for the local microclimate, when simulating the space cooling demand of a building.

For the microclimate simulation the urban microclimate model by Kubilay et al. (2017) is used. This model solves the steady Reynolds-averaged Navier-Stokes (RANS) equations iteratively with the unsteady heat and moisture transfer in the building materials. The model includes long and shortwave radiation exchange between the urban (building and street) surfaces. The urban climate model is implemented in OpenFOAM 2.4 and a standard k- ϵ turbulence model is used. The building materials are modelled as porous domains and the heat and moisture transport equations are solved. The long and shortwave radiation is modelled based on a radiosity approach. For more details on the urban climate model, we refer to Kubilay et al. (2017).

For the Building Energy Simulation (BES), the program CitySim (Kämpf, 2009) is used. CitySim is a simulation tool which models the energy fluxes in a city, with a size ranging from a small neighbourhood to an entire city. In CitySim detailed radiation models for solar and longwave radiation are implemented that can account for the radiation exchange between neighbouring buildings, the ground and environment. The heat flow through the walls is determined with a model based on the analogy with an electrical circuit (resistor-capacitor network). CitySim uses an hourly timestep, which cannot be changed. CitySim also includes HVAC and energy conversion system models. CitySim determines the heat balances for all building materials and for the ground (e.g. street) materials.

In this study, urban microclimates for six different urban morphologies are studied and their impacts on the space cooling demands of the middle building (Fig. 1). All buildings are 10 m high and the lengths of the buildings are between 10 m and 50 m.

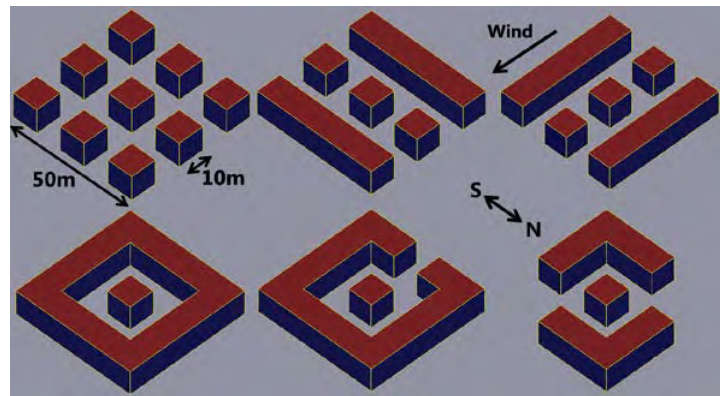


Figure 1. The layout and orientation of the urban morphologies under investigation.

All buildings are modelled as office buildings with corresponding occupancies and internal gains (SIA 2006). Ventilation and infiltration are considered. The glazing (G-value: 0.7, U-value: $1.1 \text{ W/m}^2\text{K}$) fraction of the buildings is 40 % and all façades have a solar reflectance of 0.4. The walls have a U-value of $0.5 \text{ W/m}^2\text{K}$ (with inner insulation); the roofs have a U-value of $0.23 \text{ W/m}^2\text{K}$ and the floors a U-value of $0.44 \text{ W/m}^2\text{K}$. The walls are made out of brick and the same material properties are used for the BES and urban climate simulations. External shading devices are used to protect the buildings from solar gains.

The simulations are conducted for the city of Zürich on June 21st. A generic heat-wave situation with ambient temperatures between $20 \text{ }^\circ\text{C}$ and $33 \text{ }^\circ\text{C}$ is assumed. Fig. 2 shows the variations of the ambient temperature during the day.

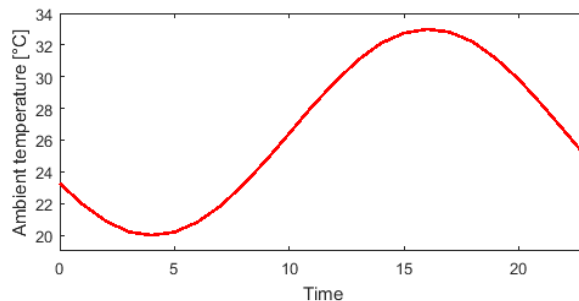


Figure 2. Daily variation of the ambient temperature.

The wind direction is assumed to be 270° for the whole 24 hours. At the inlet of the computational domain vertical profiles of the mean horizontal wind speed, the turbulent kinetic energy and the turbulence dissipation are imposed for a reference wind speed of 5 m/s at 10 m height. These profiles represent a neutral atmospheric boundary layer, where the turbulence originates only from friction and shear (Richards and Hoxey, 1993). The mesh, the computational domain size and the solution algorithm are in agreement with best practice guidelines (e.g. Franke et al. 2011).

Both the CFD as well as the BES are simulated for a number of 24 hour cycles until the results for the same hour of the day are the same for at least two consecutive cycles.

For each urban morphology four different BES are conducted. The first simulation is conducted with the default CHTCs used in CitySim and the ambient temperatures from the

weather file (shown in Fig. 2). A second simulation is conducted using the local air temperatures from CFD (with the default CHTCs). In the third simulation the local CHTC are used (with the ambient temperatures from the weather file) and finally the local CHTCs and local air temperatures are used for the simulations. Therefore it is possible to evaluate the impact of the different input parameters on the predicted space cooling demands.

RESULTS

Microclimate

First the predicted local microclimate is analysed, before the impact on the space cooling demands is studied. In Fig. 3, the local heat island intensities (temperature difference between the local temperature and the ambient temperature) for the warmest hour of the day are presented. The temperatures are locally 2 °C and more above the ambient temperature. This local temperature increase has an impact on the space cooling demands. Strong differences can be found for the different urban morphologies. Lower local heat island intensities (LHI) can be found for less dense morphologies and morphologies with open flow paths in wind direction. Fig. 4 shows the LHI shows during the coldest hour of the day. Here the LHI are lower, but the hot spots can be found in similar locations.

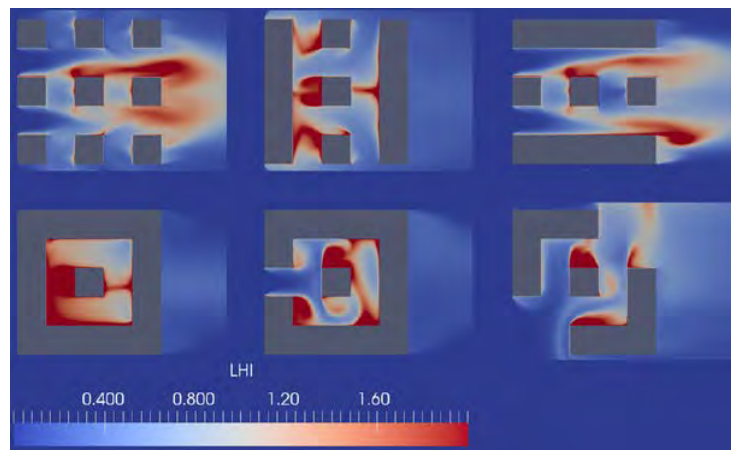


Figure 3. Local heat island intensities (LHI) at 2 m above the ground for an hour with an ambient temperature of 33 °C.

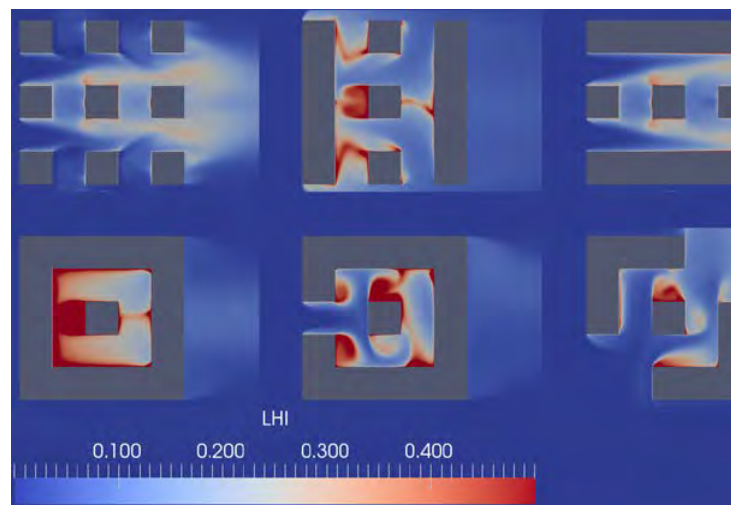


Figure 4. Local heat island intensities (LHI) at 2 m above the ground for an hour with an ambient temperature of 20 °C.

Space cooling demands

The differences in the local microclimate (discussed above) have an important impact on the energy performance of buildings in urban areas. The microclimate simulations show that the daily mean local heat island intensities in the air volume close to the studied building (used for the BES as input) are between 0.4 °C and 1.4 °C. The maximum local heat island intensities in this air volume are up to 2.7 °C. In Figure 5, the daily space cooling demands for the different urban morphologies are compared. For each morphology the space cooling demands are determined with the default settings of CitySim (“Base Case”), using the local air temperatures (“Local temperatures”), using the local CHTC (“Local CHTC”) or using local values for temperatures and CHTC (“Local temperatures and CHTC”). The results show that predicted space cooling demands of the same building can vary up to 20 % depending on the local microclimate and on the degree of detail that the microclimate is modelled in the BES. The urban morphology has first of all an impact on the radiation exchange between the buildings, what causes the differences between the different base cases. Urban morphologies also lead to different wind patterns and local air temperatures, what increases the space cooling demands in urban areas. The contribution of these two effects have a similar magnitude for the here studied cases. The combined effect of the local heat islands and the decreased wind speeds is approximately the sum of the individual effects.

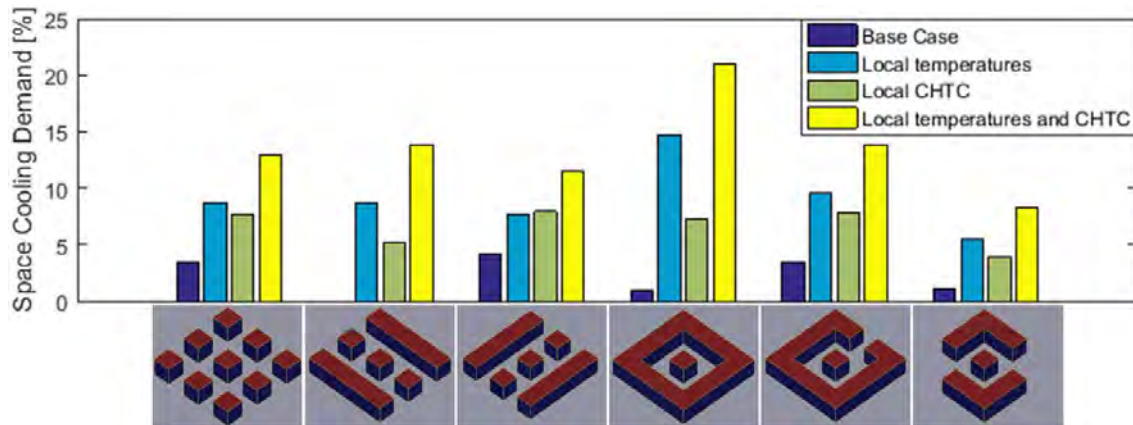


Figure 5. Normalized space cooling demands for different morphologies and microclimate boundary conditions (in percentage). Results are normalized by the case with the lowest daily space cooling demands (45.5 kJ/m^2).

DISCUSSIONS

The results of this study show a clear impact of the local microclimate on the space cooling demand of buildings in urban environments. Additional studies are needed to get more general conclusions, since the results here are limited to a (realistic) case study. Here the study is only conducted for one climate with the focus on a generic heat-wave. Also only one type of building was studied, but not all building types have the same sensitivity to the local climate. Additionally a number of simplifications were made here. The wind speed and wind direction are constant during the studied 24 hours and generic building configurations are used. Finally, the coupling between the CFD and BES can still be improved. With the models used in this study, the spatial resolution of energy fluxes and the temperatures of the building facades are significantly higher for the CFD compared to the BES.

CONCLUSIONS

In this study the impact of the local urban microclimate on the space cooling demand of a building during a heat-wave is investigated. A very detailed local urban climate model based

on CFD is used to predict the local microclimate for six different urban morphologies. The urban climate simulations show local hot spots between buildings with temperatures, which are more than 2 °C higher compared to the ambient air temperatures. The local heat island intensities are found to be larger during the day compared to the night. The BES show that the local hot spots lead to increased space cooling demands of an office building of 5-13 %. The lower wind speeds in the urban areas cause a further space cooling demand increase of 3-6 %. Finally, the radiation exchange with the neighboring buildings also has an impact on the space cooling demands of the studied building.

This study shows that it is important to not only account for the urban heat island effect in BES, but also considering the local heat islands that exist within the urban heat islands.

REFERENCES

- Allegrini J., Carmeliet J. 2017. Simulations of local heat islands in Zürich with coupled CFD and building energy models. *Urban Climate* <http://dx.doi.org/10.1016/j.uclim.2017.02.003>
- Bouyer J., Inard C., Musy M. 2011. Microclimatic coupling as a solution to improve building energy simulation in an urban context. *Energy and Buildings*, 43, 1549-1559.
- Franke J., Hellsten A., Schlünzen H., Carissimo B. 2011. The COST 732 best practice guideline for CFD simulation on flows in the urban environment: a summary. *International Journal of Environment and Pollution*, 44 (1-4), 419-427.
- Hensen J.L.M., Lamberts R. 2011. *Building Performance Simulation for Design and Operation*. Oxon: Spon Press.
- Kämpf J. 2009. *On the Modelling and Optimisation of Urban Energy Fluxes*. PhD thesis nr 4548, EPF Lausanne (Switzerland).
- Kubilay A., Derome D., Carmeliet J. 2017. Coupling of physical phenomena in urban microclimate: A model integrating air flow, wind-driven rain, radiation and transport in building materials. *Urban Climate* <https://doi.org/10.1016/j.uclim.2017.04.012>
- McAdams W.H. 1954. *Heat Transmission*. Tokyo: McGraw-Hill Kogakusha.
- Oke T. R. 1987. *Boundary Layer Climates*, 2nd ed., London: Methuen.
- Richards P.J., Hoxey R.P. 1993. Appropriate boundary conditions for computational wind engineering models using the k-ε turbulence model. *Journal of Wind Engineering and Industrial Aerodynamics*, 46-47, 145-153.
- United Nations. *World Urbanization Prospects: The 2014 Revision*, (ST/ESA/SER.A/366), 2015.

An Implementation for Transforming a Home Energy Management System to a Multi-agent System

Helia Zandi¹, Michael Starke¹, Teja Kuruganti¹

¹Oak Ridge National Laboratory (ORNL)

zandih@ornl.gov, starkemr@ornl.gov, kurugantipv@ornl.gov

ABSTRACT

In the United States, 41% of produced energy is consumed by the building sector, i.e. residential and commercial buildings (Building Energy Data Book, Buildings Sector, US Department of Energy, Office of Energy Efficiency and Renewable Energy, Building Technologies Office, 2012. n.d.). The anticipation is that Home Energy Management Systems (HEMS) will support energy efficiency gains through control of the devices in an optimal fashion. New opportunities are offering the ability to integrate grid type controls and the most suitable way to perform these controls is through a multi-agent system (MAS). In this paper, approaches on supporting a HEMS and MAS integration are discussed.

KEYWORDS

Home energy management system; home automation; multi- agent systems; demand response; smart grid; smart home; smart systems; internet of things; energy saving; interoperability; reusable mechanisms; system engineering; middleware

INTRODUCTION

Home Energy Management Systems (HEMS) today are consumer electronic devices that provide a home owner the option to monitor and control different end-use devices such as heating, ventilation, and air-conditioning (HVAC) systems, water heaters, and lighting to name a few, to support energy efficiency. For the most part, these systems have primarily focused on simple scheduling, control, and linkages (methods) such as IFFT (if this then that) that allow one device or application's output to trigger another. However, these systems are seeing rapid evolvement into a vision of smart homes that can support the smart grid with load and resource flexibility (Karlin et al. 2015). This evolvement is spawning potential grid supporting use cases that support the adoption of home owner HVAC, water heaters, energy storage, and photovoltaic (PV).

Significant research regarding HEMS has been actively pursued with several open-source and proprietary HEMS available (Lobaccaro, Carlucci, and Lofstrom 2016)(Aman, Simmhan, and Prasanna 2013)(Asare-Bediako, Kling, and Ribeiro 2012)(Helia Zandi, Teja Kuruganti, Edward Vineyard 2017). These HEMS typically support a specific suite of devices and methods from partnered vendors with communication protocols such as Wi-Fi, ZigBee (ZigBee. Retrieved from <http://www.zigbee.org/> n.d.), and Z-Wave (Z-Wave. Retrieved from <http://www.z-wave.com/> n.d.). As a result, interoperability across these devices is a key challenge as each of these devices has unique protocols, interfaces, and control functionality.

Hence, control flexibility from grid to devices through a HEMS has been a difficult proposition.

Multi-agent system (MAS) architectures have been proven as means to provide the necessary infrastructure for HEMS to achieve control goals (Asare-Bediako, Kling, and Ribeiro 2013). A MAS consists of agents that can communicate, and coordinate behaviour based on the overall system goals and status of other agents. By this transformation, the hardware and software components represented by agents can be grouped to collaborate to satisfy a main objective such as minimizing energy cost within the bounds of comfort. By utilizing a MAS architecture, the control strategies are distributed between agents that facilitates increased flexibility, less complexity, and better performance. In this paper, a general framework for integrating HEMS into a MAS using two general interfacing approaches is presented. This allows for a rapid development of new use options for load management and control to support the electric grid, which is also discussed.

METHODS

In this paper, the focus is not specifically on the development of an agent-based system, but on the integration of this type of system with a HEMS. Hence, an open-source distributed agent based platform, VOLTTRONTM, was used and will be referenced here forth in tandem with MAS (Haack et al. 2013). Also in this paper, a Home Assistants (HASS), which is an open-source home automation platform is chosen to represent the HEMS (Home Assistant n.d.). However, the architecture developed supports any general MAS and HEMS integration.

The first approach to adopting a MAS into HEMS is the potential utilization of a RESTful API (application programming interface) developed by the HEMS manufacturer as shown in Figure 1. This type of interface often exists in the cloud with direct access control and cyber security measures such as bearer tokens leading to a more seamless integration (Fielding 2000). For adopting the MAS, an agent (represented as HASS driver) is needed to communicate with the HEMS API and receive information about the devices for publishing on a local message bus for sharing with other agents. The agent also can send actuation commands to the devices using the HEMS API. An example is shown in Figure 1, and explanations is provided in Table I and Table II. While vendors may support the utilization of these APIs, these can be proprietary often reducing the ability to integrate with a MAS.

In the case where an API is not supported, the adoption can be performed by using a MQTT machine-to-machine communication protocol. In this case, a MQTT broker is needed as a communication median, represented by mosquito (an open-source broker (Mosquitto Broker n.d.)) in Figure 1. The broker provides the interface between a HEMS and MAS. An agent performing MQTT communications is required to bridge the data from the MQTT stream to a message bus. Also, a MQTT client is needed to publish the information about the devices supported by the HEMS to the broker. This client can also receive actuation commands from the HEMS MQTT Agent. An example along with description is provided in Table I and Table II.

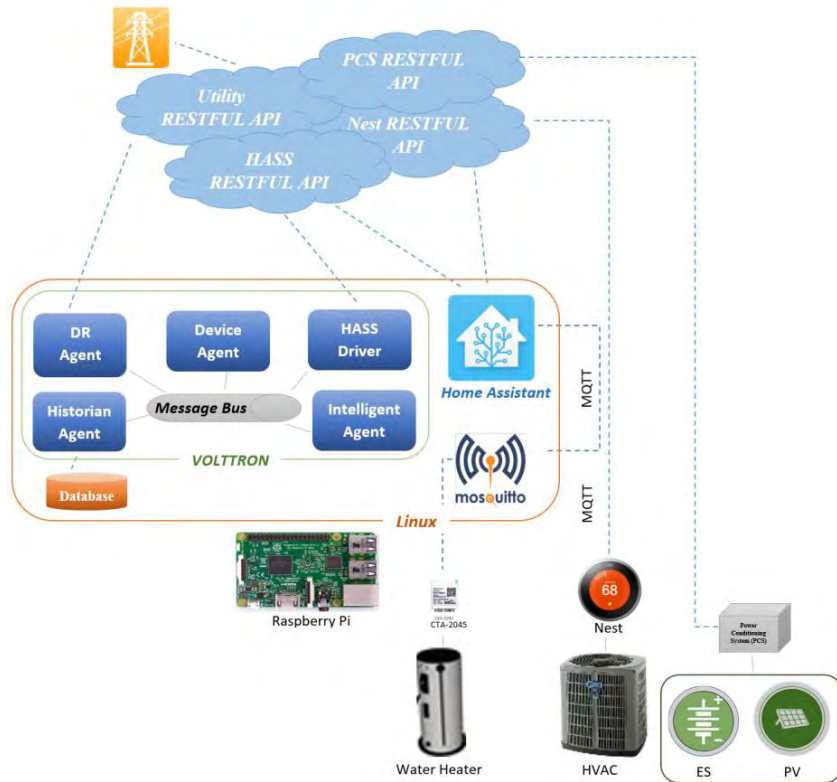


Figure 1- Integrating Home- Assistant with VOLTTRON USING RESTful API

Table I. Communication between HEMS and Devices

	MQTT	API
Communication to Device	<ol style="list-style-type: none"> 1. Water Heater interfaces with a device that communicates via CTA-2045 2. Home Assistant reads CTA-045 data 	<ol style="list-style-type: none"> 1. HVAC utilizing a NEST thermostat with available vendor API (NEST RESTful) 2. Home Assistant reads HVAC data from API (NEST RESTful)

Table II. Communication between HEMS and MAS

	MQTT	API
Communication to MAS	<ol style="list-style-type: none"> 1. Mosquito is the MQTT broker 2. Home Assistant MQTT client sends messages to broker and receives control messages 3. VOLTTRON MQTT agent subscribes to HASS messages on the broker and publishes them on message bus for decision making 4. MQTT Agent sends control messages to the broker 	<ol style="list-style-type: none"> 1. Home Assistant provides RESTful API. 2. MAS HASS Agent extracts device and provides control requests 3. HASS Agent publishes messages on VOLTTRON message bus for decision making

require utilities to enable device communications under a common framework. A HEMS supporting MAS has the opportunity to perform the appropriate decision making and control.

Table III. Grid Use Cases

Use Case	Description
1. Reduce Critical Peak Load	<p><u>Goal:</u> Reduce load during critical price period.</p> <p><u>Method:</u> Data is collected from each device by separate Device Agents and archived by the Historian Agent. A separate DR Agent assesses the current status of the loads and reports this information to utility distribution management system (DMS). The DMS performs an assessment of the data and estimates the needed overall load reduction. These reductions are issued to the DR Agent which sends control commands to the respective Device Agents and ultimately to the loads.</p>
2. High Penetration of Renewable Energy in Distribution Systems	<p><u>Goal:</u> Reduce voltage impact by renewable generation.</p> <p><u>Method:</u> Data is collected from each device by separate Device Agents and archived by the Historian Agent. A separate DR Agent assesses the current status of the loads and reports this information to utility distribution management system (DMS). The DMS performs an assessment of the data and estimates the needed overall change in load to support PV. The DMS issues the load change to the DR Agent which sends control commands to the respective Device Agents and ultimately the loads.</p>
3. Residential Resiliency through Islanding.	<p><u>Goal:</u> Improve residential resiliency with local energy storage and islanding features.</p> <p><u>Method:</u> Data is collected from each device by separate Device Agents and archived by the Historian Agent. A separate DR Agent assesses the current status of the loads and reports this information to utility distribution management system (DMS). The DMS performs an assessment of the current grid reliability and provides the DR Agent information regarding outage potential. Upon expected outage, the DR Agent issues islanding request to the energy storage Device Agent which is forwarded to the local energy storage system.</p>

CONCLUSIONS

In this paper, a general framework for integrating a multi-agent-system (MAS) into a home energy management system (HEMS) is proposed. MAS offer additional functionalities and decision making that go beyond the IFFT (if this then that) functionalities present with HEMS today. Two different communication methods between the MAS and HEMS are explained. One communication approach utilizes the RESTful API while the other demonstrates a MQTT broker approach. The MQTT local communication approach is demonstrated in the results. These communication schemes can be applied to any existing system regardless of the programming language implemented.

Besides addressing the interoperability challenge by supporting multiple pathways for communications, this work demonstrates a broadening of intelligence into the HEMS. The addition of an agent-based infrastructure provides new pathways and use case functionalities. In this paper, three utility-based use cases utilizing residential assets such as HVAC, water

heater, energy storage, and PV are discussed. These use cases include: reduction in critical peak load, high penetration of renewable energy in distribution systems, and residential resiliency through islanding.

ACKNOWLEDGEMENT

This work was funded by the Department of Energy, Energy Efficiency and Renewable Energy Office under the Buildings Technologies Program.

REFERENCES

- Aman, Saima, Yogesh Simmhan, and Viktor K Prasanna. 2013. "Energy Management Systems: State of the Art and Emerging Trends." *IEEE Communications Magazine* (January): 114–19.
- Asare-Bediako, B., W.L. Kling, and P.F. Ribeiro. 2013. "Multi-Agent System Architecture for Smart Home Energy Management and Optimization." *IEEE PES ISGT Europe 2013*: 1–5.
- Asare-Bediako, B, W L Kling, and P F Ribeiro. 2012. "Home Energy Management Systems: Evolution, Trends and Frameworks." *International Universities Power Engineering Conference (UPEC), 47th London*: 1–5. <http://ieeexplore.ieee.org/lpdocs/epic03/wrapper.htm?arnumber=6398441>.
- "Building Energy Data Book, Buildings Sector, US Department of Energy, Office of Energy Efficiency and Renewable Energy, Building Technologies Office, 2012."
- "CTA- 2045." https://standards.cta.tech/kwspub/published_docs/.
- Fielding, Roy Thomas. 2000. "Architectural Styles and the Design of Network-Based Software Architectures." *Building* 54: 162. <http://www.ics.uci.edu/~fielding/pubs/dissertation/top.htm>.
- Haack, Jereme et al. 2013. "Voltron: An Agent Platform for the Smart Grid." *Proceedings of the 2013 International Conference on Autonomous Agents and Multi-agent Systems (Aamas)*: 1367–68. <http://dl.acm.org/citation.cfm?id=2484920.2485228>.
- Helia Zandi, Teja Kuruganti, Edward Vineyard, David Fugate. 2017. "Home Energy Management Systems: An Overview." In *9th International Conference on Energy Efficiency in Domestic Appliances and Lighting (EEDAL2017)*, Irvine, 605–14.
- "Home Assistant." <https://home-assistant.io/>.
- Karlin, Beth et al. 2015. "Characterization and Potential of Home Energy Management (HEM) Technology." (February).
- Lobaccaro, Gabriele, Salvatore Carlucci, and Erica Lofstrom. 2016. "A Review of Systems and Technologies for Smart Homes and Smart Grids." *Energies* 9(5): 1–33.
- "Mosquitto Broker." <https://mosquitto.org/>.
- "Raspberry Pi." <https://www.raspberrypi.org/>.
- "Z-Wave. Retrieved from <Http://www.z-Wave.com/>."
- Zandi, Helia. "HomeAssistant-VOLTTRON Integration." <https://github.com/VOLTTRON/volttron-applications/tree/master/ornl/HomeAssistant-VOLTTRON-Integration-Agents>.
- "ZigBee. Retrieved from <Http://www.zigbee.org/>."

Bioclimatic tools for sustainable design – uncertainty perspective

Krystyna Pietrzyk*

Chalmers University of Technology, Gothenburg, Sweden

*Corresponding email: krystyna.pietrzyk@chalmers.se

ABSTRACT

Overall, holistic approach in which the building is integrated into its environment with respect to building physics principles allows for discussion of a variety of passive strategies regarding the building placement (local climatic conditions, microclimate etc.), building types, building materials and technical systems. Bioclimatic design is referred to as a proper approach to highlight the connection of a building with the natural environment, which can be treated as the prerequisite for energy efficient design.

The research results within the reliability studies of building performance become an inspiration for architects and engineers to further discuss tools supporting decisions at the early stage of design process from the reliability perspective. The bioclimatic tools allowing for interpretation of the sense of comfort as a variable dependent on the variability of climatic conditions, and human factors are suggested for the analysis at the early stage of building design. A framework for the probabilistic analysis of comfort performance to be included in bioclimatic design tools is proposed.

The uncertainty of the variables and unknown parameters are critically (qualitatively) examined. Further research is needed to quantify the uncertainty of the boundaries of the comfort caused by the variability of climatic conditions and the uncertainty of human perception of comfort.

KEYWORDS

Bioclimatic design, uncertainty, passive strategies, thermal comfort, reliability.

INTRODUCTION

Low-energy building design, ensuring comfort and safety in built environment, addresses mainly the following three sustainability goals as propagated by United Nations: number 3 – good health and well-being, number 7 – affordable and clean energy, and number 13 – climate action. ‘Energy is the dominant contributor to climate change, accounting for around 60% of total global greenhouse gas emissions’. Reducing the carbon intensity of energy is a key objective in long-term climate goals (goal 13). Hence, choosing a strategy based on integrating the building form and structure with its external environment to take advantage of natural forces (for wind induced ventilation, solar heating, etc.) is an example of design decisions leading towards mitigation of climate change (Pietrzyk & Czmocho 2018). It also promotes using affordable and clean energy (goal 7). Considering uncertainties coupled to climate and comfort conditions will give the chance to make the design process more reliable in achieving good health and well-being in built environment (goal 3).

To encourage architects to consider the passive design strategies to contribute to comfort and health in buildings, tools are needed. Such a tool could be a bioclimatic chart (Givoni 1998) which shows the relationships between climatic parameters (temperature, humidity) and a comfort zone. Introducing certain design solutions (lightweight construction or thermal mass,

natural or mechanical ventilation etc.) does influence the location of the boundaries of the climatic conditions within which the building design can provide interior comfort (Szokolay 2004). Some pedagogically described examples can be found in (Manzano - Agugliaro 2015) and the comfort boundary (in blue) of enhanced ventilation is shown in Figure 3. Significant research has been carried out within the field of thermal comfort in building resulting in the formulation of adaptive criteria that have been included in the International Standards such as ANSI/ASHRAE standard 55 (2013). However, the boundaries of the comfort zones do not include explicitly their uncertainty associated with human behavior (especially its psychological and cultural aspects) and the higher frequency of variability of climatic conditions. The discussion about the variability of comfort performance can be found in (Tuohy et al 2009; Humphreys et al 2013). For an architect it is important to design for the client representing a group of potential users. The uncertainty in human perception should be treated separately from the variability of climatic conditions. Within human perception physiological, behavioral and psychological requirements should be accounted for.

It is proposed to take into consideration the above uncertainties to elaborate on the uncertain boundaries of the adaptive comfort zone using uncertainty/risk analysis tools.

Architectural approach – climate as a generative principle for built form

Bioclimatic approach is not very common in the architectural practice. It seems to be still more related to the traditional architecture and certain climatic zones. One can also find the contemporary designs driven by the philosophy of ‘form follows climate’ where climate is given a generative roll for built form for ex. the houses designed by Philippe Rahm Architects (Rahm 2007).

Rahm creates spaces with stratified level of humidity to be occupied freely according to the weather and the season (Mollier’s house). Activities in the rooms are related to the climate existing in the different parts of the house. It means that functionality is secondary to the climate generated form. In that way the problem of building physics is transformed into an architectural question. Another example is Archimedes’s house designed as a vertical structure reflecting a relation between the house and the air, its temperature and its movement. The various temperature of interior spaces driven by the seasonal changes allow for the seasonal movement of the occupants within the house (migrations from downstairs to upstairs according to the vertical stratification of the temperature). In that way the functionality and the interior conditions are specified as different for various rooms. Those examples show how architect can be inspired by the opportunities created by nature. However, his philosophy can result in infinitely extended comfort zone.

Anyway, this kind of examples could suggest that bioclimatic chart is a good inspiration and communication tool for architects at the early stage of a design process promoting sustainable solutions. During the last 5 years new software became available to support climatic/environmental design based on bioclimatic tools (Climate Consultant, Grasshopper etc.). Starting design brief from the analysis of space in terms of bioclimatic parameters has been also appreciated by the students of architecture studying Building Climatology for Sustainable Design course at Chalmers University of Technology.

METHODS AND RESULTS

Communication of building climatology principles to support architect decisions at the early stage of design.

A design process promoting passive strategies should be supported by knowledge and analysis tools from different fields of building climatology (climatology, building physics, physiology/psychology and architecture). Climate is treated as a resource supporting natural ventilation, free cooling, and free heating. Results of the analysis of the climatic/environmental conditions could be synthesized and adapted to architectural expression. In that way, ‘architecture can mediate the design with the goals of sustainability’ (Brennan 2011).

Designed object offers passive and active controls over the interior climate according to the comfort requirements. A passive control creates an extra climate-comfort loop (see Figure 1).

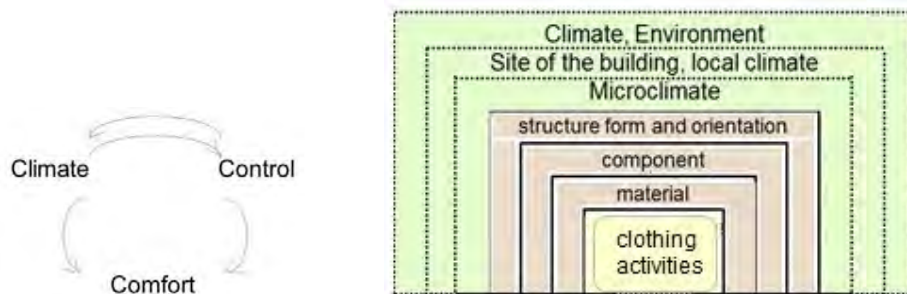


Figure 1 Bioclimatic thinking at the early stage of the design process – systemic approach; modified from (Pietrzyk 2015).

Climate: climate, local climate, microclimate (temperature, moisture content, wind speed, wind direction) in view of uncertainty (Pietrzyk & Czmocho 2018)

Control: materials (strengths and vulnerabilities), components, structures form and orientation, technical systems, topography, urban design, wind/surface interaction etc.

Comfort: uncertain adaptive comfort zones within enclosure extended by using passive or hybrid strategies of heating, cooling, and ventilating

Architectural criteria include the site of the building (also in urban context), the local environment being the result of feedback loop between natural and man-made elements, and the building orientation, form, layout/volume, material (see Figure 1). The criteria account also for integration of technical systems within building/environment system considering potential of the system to use locally produced renewable energy. The concept could be extended to include the user perception as a variable dependent on the climatic conditions and the design solution. A systems approach provides proper theoretical tool for the analysis of the interrelations between structure, its environment, and its performance. Use of bioclimatic chart (psychrometric chart with comfort zones) in the early stage of design process is considered. It can be considered as a means of raising awareness of the integration of a range of environmental and design parameters. The concept of bioclimatic design has been proposed in (Olgay 1953) and further developed (see Givoni 1998, Szokolay 2004, etc). The comfort zones refer to both seasonal climatic conditions and the traditional living style (clothing and the level of activity), see Figure 2. It is proposed to consider the relevant variables evaluated for local conditions and to elaborate on the uncertain comfort zone due to cultural/psychological and climatic aspect. In that way comfort zone could be treated as a dynamic concept addressing users’ perception related to the local climatic conditions, habits, behaviors, and the level of possible control.

The bioclimatic chart showing the properties of moist air is built on the analysis referred to the perfect gas relations. It could be the valuable visual aid for architects in analyzing different solutions at the early stages of the design process. First the local climate conditions

are collected in the form of averaged values over the period of hour, day or month. Then, the analysis of the neighborhood results in the microclimatic characteristics that are superimposed on the chart. The relation between the outdoor climatic conditions and the required interior conditions gives the indication about the passive/active strategies that could be designed for.

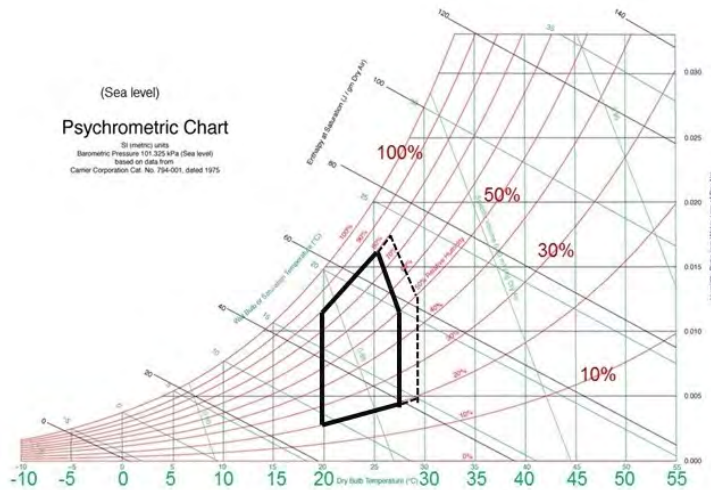


Figure 2 Bioclimatic chart with superimposed boundaries of climatic zones: temperate climate, summer - solid line; hot climate – dashed line from (Givoni 1998) modified from the psychrometric chart from Wikipedia

Building physics tools based on the rough modeling or/and qualitative evaluation are proposed to give the preliminary answers about the potentials of the building/environment system performance. The structure/environment interaction based on the source free enclosure (for example estimation of free running temperature – the temperature inside a naturally ventilated building without any heating source) accounting for wide boundary conditions could give the first evaluation (Ghiaus & Allard 2003). These results will constitute the reference for the qualitative tools developed based on psychrometric chart.

The boundaries of the comfort zones should be modified to visualize different design strategies directed to different groups of end-users. It is meant to be used as a communication tool at early stages of design

Boundaries of a comfort zone – a probabilistic approach

While evaluating a building performance the very important issue is to find criteria to differentiate between good and bad performance. A critical state dividing the space of the possible results into two subspaces the reliable one and the failure one is related to the performance criterion relevant for the chosen performance aspect. The critical state can be defined by a deterministic value, or by probability distribution function assigned to that parameter. The way of presenting performance criterion depends on the investigated problem and availability of data. Stochastic threshold criterion is built up because of the uncertainties regarding the climatic conditions or humans response (Pietrzyk 2008, Pietrzyk 2015).

Generally, variability in time, space, and among individuals can be included in the performance criterion R (see Figure 3). The chosen kind of variability depends on the performance aspect considered. In current case the performance aspect is the interior thermal comfort that can be presented in terms of temperature (sensible or operative). When considering the response of people to a certain state described by a physical parameter

(temperature), inter-individual variability in the form of the number of people being affected can be included in stochastic threshold. Variability among individuals in the response to specified interior conditions are caused by their different physical and behavioural conditions. Hence, a criterion for human's wellbeing can be stated for the population, specified group of people or for the individuals depending on the client group in focus, in the form of estimated for the group probability density function (uncertainty is represented by probability). Then, the general standards-based design or client controlled (adapted) design responding to the needs of target group can be considered.

Figure 3 shows the framework for the probabilistic analysis of thermal comfort performance. The results are proposed to be included in the description/communication of the comfort zones in terms of reliability. Reliability is understood as a complement to the probability of failure (P) as given in Figure 3.

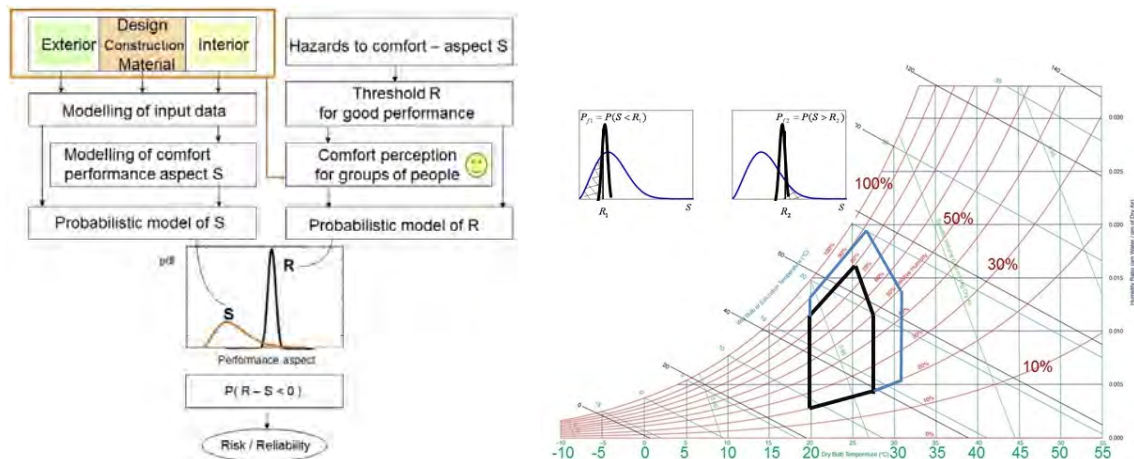


Figure 3 Framework (modified from (Pietrzyk 2015)) for the probabilistic analysis of comfort performance proposed to be included in the description/communication of the comfort zones: for temperate climate – black line: extended comfort zone because of ventilation – blue line. (Psychrometric chart modified from Wikipedia using data from (Manzano - Agugliaro et al 2015)).

Outdoor temperature is an important variable for the boundaries of the adaptive thermal comfort. They are given for each month by the regression equations characterizing lower and upper limits of the comfort zone. Those uncertain limits could be revised with the help of analysis of uncertainties coupled to the probability distribution of outdoor temperature (variability of S) as well as by analyzing the possible contribution of differences in perception/adaptation of various groups of people (variability of R). Eventually, the reliability of the stated boundaries would be estimated to be used in the design process.

Other thermal performance indicators like PPD (percentage of dissatisfied people) or allowable excess of operative temperature in offices could be used to estimate the uncertainties of thermal comfort performance R (Pietrzyk 2008).

CONCLUSIONS

The purpose of this paper is to elaborate on a reliable visualization tool based on bioclimatic approach that architects could use to effectively follow the strategies of passive environmental design of low energy, comfortable and healthy buildings. Climate is treated as a resource supporting natural ventilation, free cooling, and free heating. The theory and methods of the interdisciplinary field of building climatology (climatology, building physics,

physiology/psychology and architecture) are addressed. The performance aspects (air exchange, heating or cooling load, comfort indicators, etc.) are treated as random, as they are dependent on the random climatic characteristics and uncertain human perception. It is proposed to introduce to the bioclimatic chart the reliability of the boundaries of the adaptive comfort standard dependent on target group's perception. The paper presents only an idea that must be further developed. Research is needed to quantify the uncertainty of the boundaries of the comfort zones in relation to various passive strategies. Different thermal comfort standards and thermal comfort indicators could be considered.

ACKNOWLEDGMENTS

The financial support from KVVVS (Adlerbertska foundation) is gratefully acknowledged.

REFERENCES

- ANSI/ASHRAE Standard 55 (2013). Thermal environmental conditions for human occupancy ISSN 1041-2336.
- Brennan. J. (2011). Qualitative and quantitative traditions in sustainable design in *Aesthetics of Sustainable Architecture*. ed. by Lee S., 010 Publishers, Rotterdam 2011.
- Ghiaus C., Allard F. (2005). *Natural ventilation in the urban environment*. Earthscan, London.
- Givoni B. (1998). *Climate considerations in Building and Urban Design*. John Wiley & Sons.
- Humphrey M.A., Rijal H. B., Nicol J.F. (2013). Updating the adaptive relation between climate and comfort indoors; new insights and an extended database. *Building and Environment* 63 pp. 40-55.
- Manzano - Agugliaro F., Montoya F.G. Sabio-Ortega A., García-Cruz A. (2015). Review of bioclimatic architecture strategies for achieving thermal comfort. *Renewable and Sustainable Energy Reviews*. Vol. 49, pp 736-755, Elsevier.
- Olgyay V. (1953). Bioclimatic approach to architecture. Bldg. Res. Adv. Board, conf. Report No.5. National Research Council, Washington DC.
- Pietrzyk (2008). Stochastic versus deterministic approach to threshold criteria for Building/Environment system performance. The 8th *Nordic Symposium on Building Physics*, Copenhagen, Denmark, vol. 1 pp. 401-409.
- Pietrzyk K. (2015). A systemic approach to moisture problems in buildings for mould safety modelling. *Building and Environment*. Vol. 86, pp 50-60, Elsevier.
DOI: 10.1016/j.buildenv.2014.12.013
- Pietrzyk K. & Czmocho I. (2018) *On Risk and Reliability Studies of Climate Related Building Performance*. Invited book chapter of *Risk Assessment* ISBN 978-953-51-5702-1, InTech open science publishing, open access.
- Rahm P. (2004). Immediate Architecture. Rendell J., Hill J., Fraser M., Dorrian M. (eds). *Critical Architecture*. by Routledge Taylor and Francis Group.
- Tuohy P.G., Humphreys M.A., Nicol J.F., Rijal H. B., Clarke J.A. (2009). Occupant behavior in naturally ventilated and hybrid buildings. *ASHRAE Transactions*, CH-09-003.
- Szokolay, S. V. (2004). *Introduction to architectural science: the basis of sustainable design*. Architectural Press, Elsevier.
- United Nations. Sustainable Development Goals. Available from: <http://www.un.org/sustainabledevelopment/energy/>

Campus as a Lab for Computer Vision-based Heat Mapping Drones: A Case Study for Multiple Building Envelope Inspection using Unmanned Aerial Systems (UAS)

Tarek Rakha^{1*}, Amanda Liberty¹, Alice Gorodetsky¹, Burak Kakillioglu² and Senem Velipasalar²

¹School of Architecture, Syracuse University

²College of Engineering and Computer Science, Syracuse University

**Corresponding email: trakha@syr.edu*

ABSTRACT

Unmanned Aerial Systems (UAS – a.k.a. drones) have evolved over the past decade as both advanced military technology and off-the-shelf consumer devices. There is a gradual shift towards public use of drones, which presents opportunities for effective remote procedures that can disrupt a variety of design disciplines. In architecture praxis, UAS equipment with remote sensing gear presents an opportunity for analysis and inspection of existing building stocks, where architects, engineers, building energy auditors as well as owners can document building performance, visualize heat transfer using infrared imaging and create digital models using 3D photogrammetry. Comprehensive energy audits are essential to maximize energy savings in buildings realized from the design and implementation of deep retrofits for building envelopes, together with energy system repairs or changes. This paper presents a methodology for employing a UAS platform to conduct rapid building envelope performance diagnostics and perform aerial assessment mapping of building energy. The investigation reviews various literature that addresses this topic, followed by the identification of a standard procedures for operating a UAS for energy audit missions. The presented framework is then tested on a university campus site to showcase: 1) visually identifying areas of thermal anomalies using a UAS equipped with IR cameras; 2) detailed inspection applied to areas of high interest to quantify envelope heat-flow using computer vision techniques. The overall precision and recall rates of 76% and 74% were achieved in the experimental results, respectively. A discussion of the findings suggests refining procedure accuracy, as a step towards automated envelope inspection.

KEYWORDS

Unmanned Aerial System (UAS); building Inspection; retrofitting, energy audit; thermography

INTRODUCTION

The buildings sector accounts for about 76% of electricity use and 40% of all U.S. primary energy use and associated greenhouse gas (GHG) emissions. More than half of all U.S. commercial buildings in operation today were built before 1970 and this large existing building stock performs with general lower efficiency. HVAC and lighting loads in existing buildings consume 35% and 11% of total building energy, respectively, which totals more than 17 quads of residential and commercial building primary energy use (U.S. DOE, 2015). In order to achieve substantial energy savings in existing and deteriorating built environments, retrofitting strategies that respond to accurate and reliable energy audits should to be implemented. Unfortunately, predicted savings and delivered savings typically do not match. This can be attributed to imprecise energy audits, which may lead to lower than expected

energy savings, no energy savings or in some cases occasional increase in energy use. A myriad of negative effects follow, including environmental impacts that were not accounted for, discrediting energy efficiency retrofits as well as loss of investment monies. This is typically a result of many challenges that energy auditors face, including insufficient building information that leads to misrepresentation in energy models, overestimated savings, ineffective selection of improvement strategies and incomprehensive improvement scope that result in missed improvement opportunities (Shapiro, 2011). In this paper, we present a methodology to address these critical challenges by employing a UAS platform. More specifically, we employ a drone equipped with a thermal camera, to conduct rapid building envelope performance diagnostics and perform aerial assessment mapping of building energy. The paper aims to identify standard procedures for operating a UAS for energy audit missions, and to automate the envelope assessment method using computer vision algorithms.

Previous research work addressed the use of UAS and thermography in building inspection, diagnostics and energy audits. An earlier attempt by Martinez-De Dios and Ollero presented infrared-based automated detection techniques for thermal heat losses in building windows using UAS (Martinez-De Dios and Ollero, 2006). The use of impulse infrared thermography was introduced by Mavromatidis et al (2014) as a method to examine old civil infrastructure and residential buildings' energy consumption, ageing process and life cycle. A more comprehensive method to reduce manual workflows was introduced by Mauriello and Froehlich (2014). It utilized an unmodified Parrot AR. Drone 2.0 and a FLIR thermal camera to collect RGB and thermal images of a building and generate 3D reconstructions. Automation challenges were further presented, which included data quality, data overload, technical feasibility, privacy and problems of overreliance on automated scans (Mauriello et al, 2015). While UAS platforms were used in various building inspection activities, a comprehensive building envelope inspection procedure was not engaged. We aim to address this gap in the literature by presenting a twofold approach to the inspection of building envelopes: 1) using a geometric data-gathering process, tested in the field, and 2) a computer vision analysis approach for the automation of envelope anomaly detections.

METHODS

The research framework is divided into two methods. First, the design of flight paths and implementation of data collection using photogrammetry and thermal imaging. Second, the use of computer-vision workflows to analyse and segment thermal images, and autonomously detect thermal anomalies.

Energy Audit Flight Procedure

Preflight considerations: Energy leakage detection relies upon certain environmental conditions. Local climatic factors, such as rain, snow, and heavy wind are not typically appropriate weather conditions for drone flight. Certain environmental factors that can affect external surface temperatures of buildings such as indoor and outdoor temperature, humidity, wind speed, cloud coverage, solar radiation, and precipitation are considered. A temperature difference of about 10° Celsius, as well as a notable pressure difference should be observed between the interior and exterior of the building. (FLIR, 2012).

Flight path design: There are two common flight paths that can be adopted for the majority of typical buildings. For flat facades which are mostly vertical, the flight path should begin on a predetermined corner and follow vertical bays upward, move across to the next bay and downward. For flat facades that are mostly horizontal, the path should begin at a predetermined corner and continue to the right before moving up a bay and continuing in a

linear manner to the left. After capturing façades, the drone should move on to capture thermal images of the roof in a similar grid manner, starting from one corner and moving in either a horizontal or vertical pattern along a superimposed grid, until the entire roof has been captured (Eschmann et al, 2012). Based on empirical experimentation and a brief review of the literature, we propose a general distance of 20' away from a building, at changing bay heights of 7-10', with imaging gathered approximately every 5' along the flight path.

Post-flight analysis: Gathered data should include pre-flight environmental conditions, pre-flight interior conditions, IR images or videos, and corresponding non-thermal images or videos. The primary goal of drone-based energy audits is to visually identify thermal leaks and support these claims with temporal data extracted from the images (Lee and Ham, 2016). We hypothesize that the following building envelope issues can be identified in post-flight analysis using the designed procedure: 1) Exfiltration / infiltration, 2) Missing / deteriorating insulation, 3) Thermal bridges and 4) Regions of failure (cracks, etc.)

Computer Vision Algorithms

Our computer vision framework for heat leakage detection is composed of two stages: 1) A global lookup of a thermal image and 2) edge filtering and segmentation, where the actual leakage regions are identified. The detection framework assumes that a thermal anomaly is defined as regions where sudden or abnormal temperature changes happen in the thermal image. When an expert inspects a color-mapped thermal image which is taken outdoor during a cold winter season, she/he observes the leakage as a light (cold) region surrounded by darker (hotter) regions. Therefore, the main concept behind the detection algorithm is to find a sharp temperature change on the thermal image.

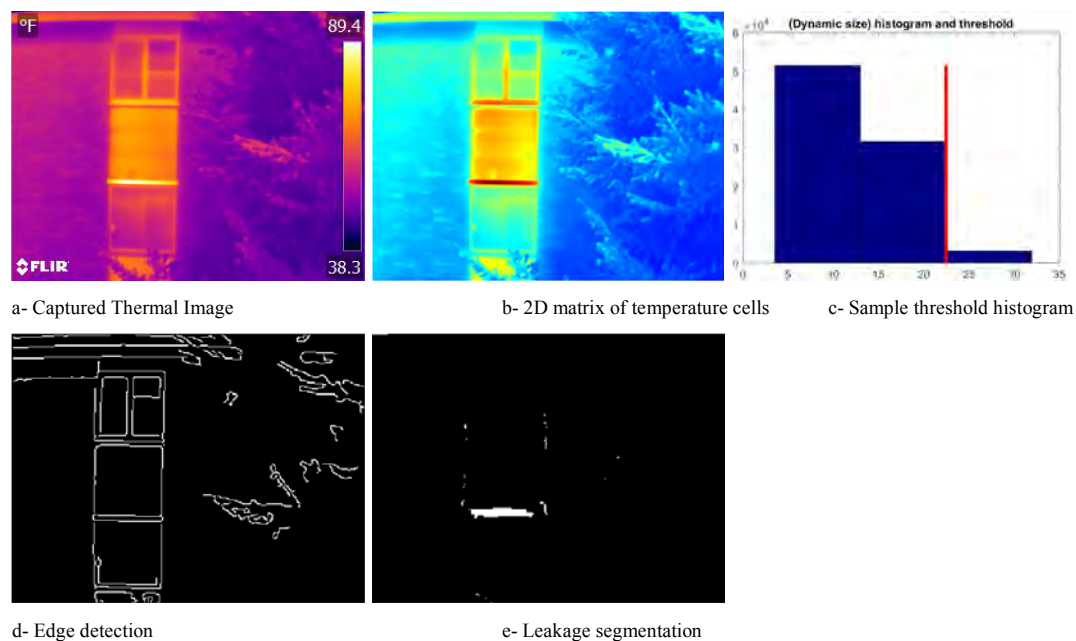


Figure 1. Edge processing and analysis of a sample thermal image.

In this framework, a thermal image is considered as a 2D matrix, whose cells, i.e. pixels, are temperature values. A naïve solution to segment out the heat leakage regions would be seeking “hot-enough” pixels (in winter, for outdoor images) and label them as leakage pixels. However, this approach is expected to introduce multiple false positive results, since this kind of strong, pixel-wise separation simply detects hot regions without taking any distinctive

characteristic of heat leakages into account. We observe that sharp temperature changes on a single-layer thermal image could be explained as nothing but thermal edges, which can possibly be the contours of leakage regions, and thermal anomalies are regions which have thermal edges. Consequently, by detecting those edges, anomaly regions would be segmented out. However, this argument is also not always true, since not all the edges found on thermal images are edges of leakage regions. For instance, red regions in Figure 1-b represent window leakage, and an edge detector would separate those regions. Yet, there are other visible edges, which will be detected on the same image such as trees as seen in Figure 1-c. Therefore, in our framework we eliminate those false detections, and eventually segment out the leakage regions by detecting edges, following them, and applying region growing.

Experiment Design

For this study, a proof-of-concept experiment was designed by the research team to inspect a cluster of dormitory buildings at a university campus in the United States. The team used a DJI Inspire 1 drone paired with a FLIR Zenmuse XT thermal camera. The accompanying DJI app was used during flight to monitor the thermal data. The flight path was predetermined and automated using the Pix4D app, and the images were processed and analysed using the FLIR Tools program. Figure 2 illustrates the flight path and data gathering processing for computer-vision analysis.

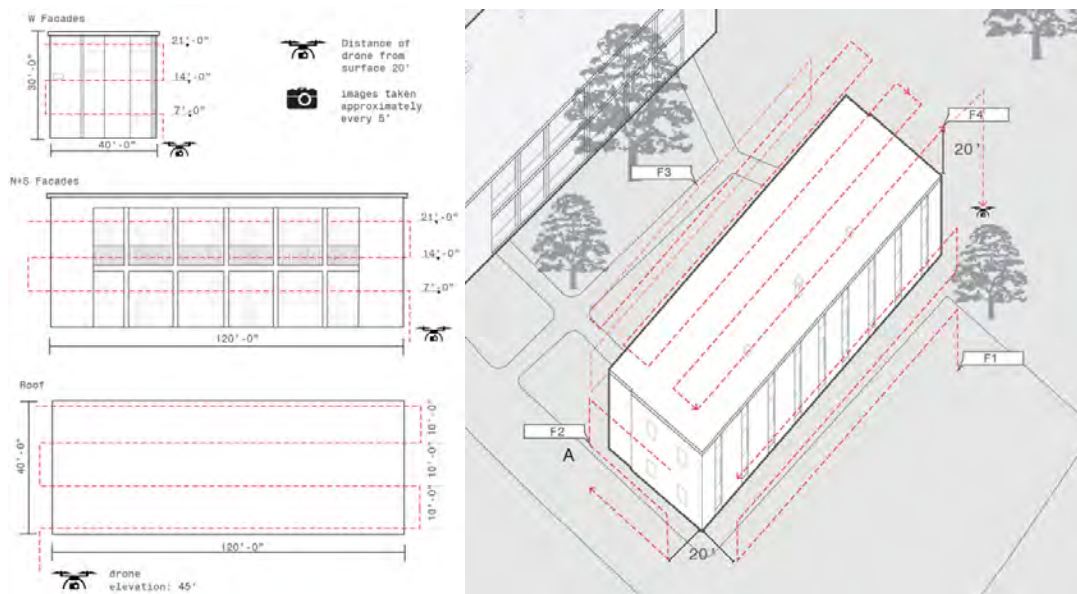


Figure 2. The experiment flight path and imaging procedure.

RESULTS

Building Envelope Audit

The audit flight took place on two separate days, the first day inspected 3 buildings using 3 batteries taking infrared video, and the second flight inspected two buildings taking still pictures. Building D was not fully inspected due to the proximity of trees on the southern façade as well. Each flight date was undertaken in 90 minutes. Figure 3 showcases 5 major categories of audit results that include: Rust – showcased through deterioration in the building façade. Water damage – infiltration and puddling of water on the roof at seams. Thermal bridges – due to faulty construction practice while installing roofs. Penetration – malfunction of envelope integrity (in façades and roofs). Brickwork deterioration – at openings and penetrations in the façade.

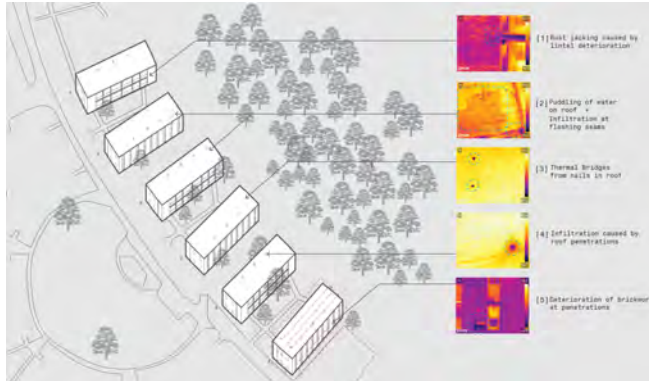


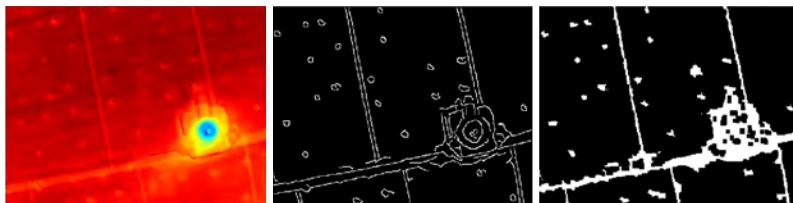
Figure 3. Sample results from building envelope audit.

Thermal Anomaly Segmentation

We tested the developed algorithm on 149 thermal images that contain a total of 1018 heat leakage regions. From these leakage regions, the algorithm successfully detects 751 of them, and missed 267 actual thermal anomaly regions. The workflow also reported 237 regions that are considered false positives. This resulted in precision and recall rates of 76% and 74%, respectively. These rates will increase as the algorithm is further developed to match expert identification of anomalies. Figure 4 highlights a series of sample heat leakage images and their corresponding detection results.



a) Successful infiltration detection.



b) Successful thermal bridge detection.

Figure 4. Experimental results from various sides of the inspected buildings. In each triplet, the left are IR scenes, middle are edge detection, and right are the segmented leakage regions.

DISCUSSION

The framework is presented as a workflow for building envelope diagnostic missions that would be administered by auditors to fly the UAS, which allows the use of thermal imaging for structural inspection, heat losses, infiltration, insulation conditions, glazing performance, as well as giving access to challenging to reach situations such as the roof. The proposed solution is being tested as a proof of concept that will significantly reduce the number of hours spent to produce high-quality, large-scale audits. Currently, an auditor may choose a repetitive pattern in a building envelope and assume that the performance is the same for all similar parts of the skin. The developed approach allows for comprehensive and accurate assessment with no such assumptions.

CONCLUSION

In regard to architectural practice, UAS equipped with thermal cameras present a unique opportunity for building inspection and more specifically, building energy auditing. The use of UAS in conjunction with building inspection and energy audits is ideal for a market saturated with degrading and energy inefficient infrastructure. In this paper, we presented an inspection framework that employs a developed computer vision algorithm to autonomously detect thermal anomalies. The ultimate goal is to enable assessments of entire campuses, neighborhoods and cities and map their energy performance accurately for identification of potential energy savings through retrofitting strategies.

ACKNOWLEDGEMENT

This publication is based on work funded in part by Gryphon Sensors, Syracuse University's Office of Research (Grant #SP- 29403-2), the Campus as a Lab for Sustainability program at Syracuse University, the National Science Foundation (NSF) under CAREER grant CNS-1206291, NSF Grant CNS-1302559 and NSF Grant 173978. The authors would like to thank Mr. Ian Joyce, the Center for Advanced Systems Engineering (CASE) and the Center of Excellence at Syracuse University for data gathering and faculty development support.

REFERENCES

- Eschmann, C., C. M. Kuo, C. H. Kuo, and C. Boller. 2012. "Unmanned Aircraft Systems for Remote Building Inspection and Monitoring." Proceedings of the 6th European Workshop on Structural Health Monitoring. Dresden, Germany.
- FLIR. 2012. Thermal Imaging Guidebook for Building and Renewable Energy Applications: An Informative Guide for the Use of Thermal Imaging Cameras for Inspecting Buildings, Solar Panels and Windmills. Breda: The Netherlands.
- Lee, J., and Y. Ham. 2016. "Impact Analysis on the Variations of the Thermo-Physical Property of Building Envelopes and Occupancy in Building Energy Performance Assessment." *Procedia Engineering* 145: 556–64.
- Martinez-De Dios, J. R., and Anibal Ollero. 2006. "Automatic Detection of Windows Thermal Heat Losses in Buildings Using UAVs." In *World Automation Congress 2006 (WAC '06)*, 1–6. Budapest, Hungary.
- Mauriello, M. L., and J. E. Froehlich. 2014. "Towards Automated Thermal Profiling of Buildings at Scale Using Unmanned Aerial Vehicles and 3D Reconstruction." In *Proceedings of the 2014 ACM International Joint Conference on Pervasive and Ubiquitous Computing: Adjunct Publication*, 119–22. Seattle, WA.
- Mauriello, M. L., L. Norooz, and J. E. Froehlich. 2015. "Understanding the Role of Thermography in Energy Auditing: Current Practices and the Potential for Automated Solutions." In *Proceedings of the 33rd Annual ACM Conference on Human Factors in Computing Systems, 1993–2002*. Seoul, South Korea.
- Mavromatidis, L. E., J. L. Dauvergne, R. Saleri, and J. C. Batsale. 2014. "First Experiments for the Diagnosis and Thermophysical Sampling Using Impulse IR Thermography from Unmanned Aerial Vehicle (UAV)." In *Proceedings of Quantitative InfraRed Thermography QIRT'14*. Bordeaux, France.
- Shapiro, Ian. 2011. "Ten common problems in energy audits." *ASHRAE Journal*, 53 (2): 26–32.
- U.S. Department of Energy. Sep 2015. "Chapter 5: increasing efficiency of building systems and technologies" In *Quadrennial technology review: an assessment of energy technologies and research opportunities*.

Optimal Control Strategies for Passive Heating and Cooling Elements Reduce Loads by Two-Thirds in the Adaptive Reuse of a San Francisco Bay Area Office

Rempel, Alexandra R.^{1*} and Lim, Serena²

¹Environmental Studies Program, University of Oregon, Eugene OR 97403

²Department of Architecture, University of Oregon, Eugene OR 97403

*Corresponding email: arempel@uoregon.edu

ABSTRACT

Housing crises in urban centers and growing climate concerns are encouraging city planners and building owners to explore the conversion of commercial buildings into energy-efficient dwellings. Passive solar heating, shading, and natural ventilation are attractive in such adaptive reuse projects since they minimize operational energy, but they suffer from the perception of limited effectiveness, and passive heating is often disregarded entirely in cloudy climates. At the same time, passive heating has recently shown promise in the cloudy winters of western Oregon and upstate New York, allowing the San Francisco Bay area to provide an excellent opportunity for further exploration. Passive cooling measures, in turn, are essential to prevent overheating. This work investigates the conversion of a brick office space in Berkeley, CA into a residential loft, using movable insulation, operable windows, thermal mass, and shading to diminish the need for mechanical conditioning to the extent possible. To determine this extent, preliminary explorations in EnergyPlus were followed by Hooke-Jeeves and particle-swarm optimizations of control thresholds, following field-validated techniques for passive heating and cooling simulation. Optimized parameters included skylight tilt; schedules for movable insulation, shading, and natural ventilation; and thermal mass quantity, each required to minimize annual sensible heating and cooling energy while maintaining adaptive thermal comfort. With optimal control, over half of the heating need could be met by passive solar collection and storage; likewise, most cooling (~80%) could be accomplished passively if shading and natural ventilation were well-controlled. Without these controls, most of the benefit was lost. We therefore propose replacing the term “passive” with “well-controlled passive” to reflect the importance of controls in sensing conditions and adjusting movable elements to maximize the performance of these systems.

KEYWORDS

passive solar heating; passive cooling; controls; optimization; adaptive reuse

INTRODUCTION

The U.S. population devotes one-tenth of all energy consumed to the active heating and cooling of living spaces in buildings. This considerable quantity—nearly 10 quadrillion Btu per year—is derived largely from fossil fuels, emitting an estimated 500 million metric tons of CO₂ each year (EIA 2018). As climate concerns increase the pressure to design buildings with smaller carbon footprints (e.g. Nejat 2015), passive heating and cooling systems are regaining interest (Chan 2010), building on historic technical and conceptual explorations (e.g. Olgyay 1963; Givoni 1969) as well as centuries of vernacular development. Operable elements are often essential to passive systems, and recent efforts have compared operational strategies in natural ventilation (Schulze 2013), night ventilation of mass (Santamouris 2010), and shading (e.g. van Moeseke 2007), showing that controls can greatly improve their effectiveness. Numerical optimizations have also been applied to passive heating and cooling systems to inform choices of glazing orientation and type, wall composition, overhang depth, ventilation rate, etc., reviewed by Stevanović (2013). While these efforts have considered the presence vs. absence of operable elements

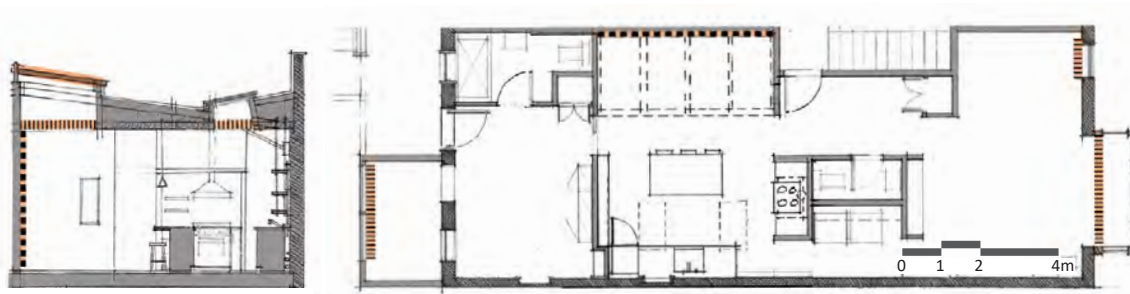


Figure 1. **Existing building** in (a) section and (b) plan, showing areas of investigation in orange, thermal mass in heavy dashes, and movable insulation in fine dashes.

as optimizable parameters, control thresholds have been pre-established in each case. To our knowledge, only Rempel (2015) has previously optimized threshold values themselves, and then only for cooling, without lower temperature limits. This work expands upon those findings by optimizing thresholds for passive heating and cooling simultaneously, incorporating upper and lower comfort limits throughout the year to predict the heating and cooling energy savings possible by these means. The renovation is planned for late 2018, and energy use will be monitored closely afterward, with the ultimate goal of providing compelling evidence that well-controlled passive systems have excellent performance potential in the Bay Area and similar climates.

METHODS

Simulations were conducted in EnergyPlus v8.7; windows and skylights were modeled in WINDOW 7.6 and referenced by EnergyPlus. Sensible heating and cooling loads were met by an Ideal Loads Air System, controlled by an adaptive comfort thermostat (Fig. 2a), to eliminate effects of mechanical system efficiency. Optimizations were conducted in GenOpt 3.1.1 using Hooke-Jeeves and particle-swarm optimizations for continuous and discontinuous variables, respectively, minimizing the annual sum of sensible heating + cooling energy.

Table 1. Baseline conditions and changes investigated

Parameter	Baseline Condition	Changes
Floor area	98.25m ²	-
Orientation	17° W of true south (i.e. 197°)	-
Roof assembly	Bitumen membrane o/ 75mm insul. board o/ 13mm pwd sheathing o/ 154mm batt insul. o/ 16mm gypsum board	-
Wall assemblies	N, S: adiabatic (party walls); E, W: 330mm solid brick (exterior); Porch: wood siding o/13mm pwd sheathing o/ 154mm batt insul. o/13mm pwd o/16mm gypsum board	-
Floor assembly	25mm Douglas fir o/19mm wood subfloor o/154mm batt insul. o/19mm gypsum board o/conditioned space	-
Thermal storage mass	None except for exterior brick walls	Mass wall
Window assemblies	E, W: Double clear, wood frame (7.8m ² , 1.0m ²); W porch: Double, alum. (3.9m ²); Sm skylights: Single, alum. (0.74m ²)	-
Skylight assembly	Acrylic dome, 7.2m ² : T _{vis} =0.53, SHGC=0.5, U=3.2 W/m ² K	Glazing, tilt
Movable insulation	None	Material, schedule
Infiltration	0.75 ACH	-
Natural ventilation	Operable E, W windows (2m ²); operable skylights (2m ²)	Temp. thresholds
Shading	None	Schedule
Internal gains	People = 2 adults; lighting power density = 1 W/m ² ; equipment power density = 1 W/m ²	-

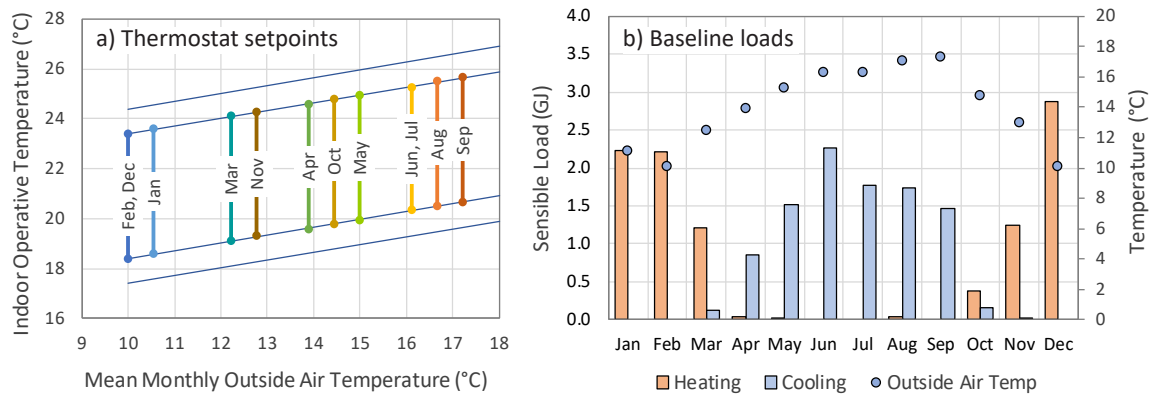


Figure 2. **Thermostat setpoints and resulting heating and cooling loads.** (a) Monthly heating and cooling setpoints, corresponding to the bounds of 90% acceptability in the adaptive thermal comfort zone (ASHRAE 2017); (b) Monthly sensible heating and cooling energy needed to raise or lower baseline-configuration air temperatures to thermostat setpoints.

RESULTS

The baseline building configuration (Fig. 1, Table 1) required 20.1 GJ of sensible heating and cooling energy annually to maintain conditions within the 90% acceptability limits of the adaptive thermal comfort zone (ASHRAE 2017), distributed between a heating season of October-March and a cooling season of April-September (Fig. 2b). Due to the large unshaded skylight, window heat gains were the greatest contributor to monthly cooling loads (Fig. 3), while infiltration and window heat losses contributed most to monthly heating loads. Because heat-recovery ventilation is generally not cost-effective in this climate, the infiltration target of approximately 0.75 ACH, consistent with provision of fresh air for four people, was not changed.

The first revision replaced the skylight's light-diffusing dome with double-clear uncoated glass (SHGC=0.67; $U=3.5\text{W/m}^2\text{K}$; $T_{\text{vis}}=0.72$), tilted 40° above horizontal to receive the greatest possible solar radiation during the six-month heating season as estimated by the model of Perez (1990) (Fig. 4). This change did not in itself appreciably diminish the heating load, since thermal mass and movable insulation were not yet present to retain collected heat, but its effects were apparent in subsequent steps (Fig. 7a), and optimally-tilted glazing is generally necessary for excellent passive solar performance when cloud cover is a factor (Rempel 2013).

The second revision added movable insulation ($k=0.03\text{ W/mK}$) and shading ($T_{\text{vis}}=0.3$) to all glazing, reflecting the choice of inexpensive, physically manageable, commercially-available materials.

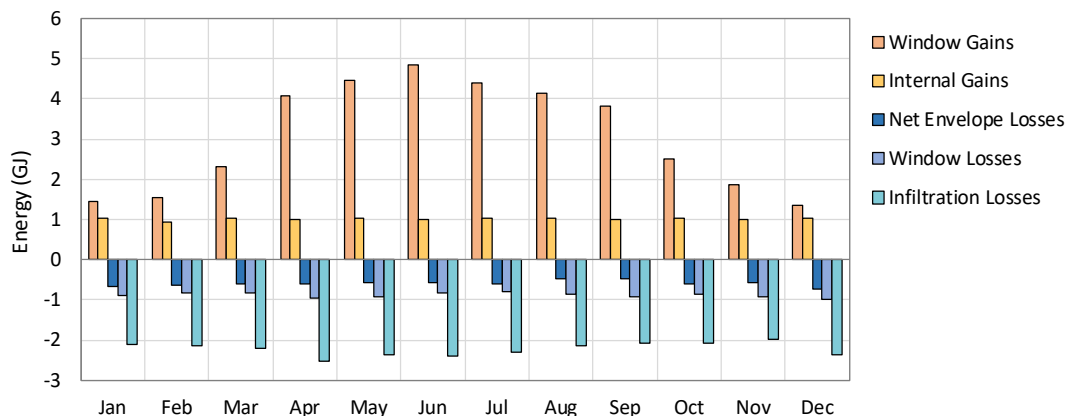


Figure 3. **Heat gain and loss pathways in the baseline configuration,** with prominent heat gains through the existing skylight and heat losses through windows and infiltration.

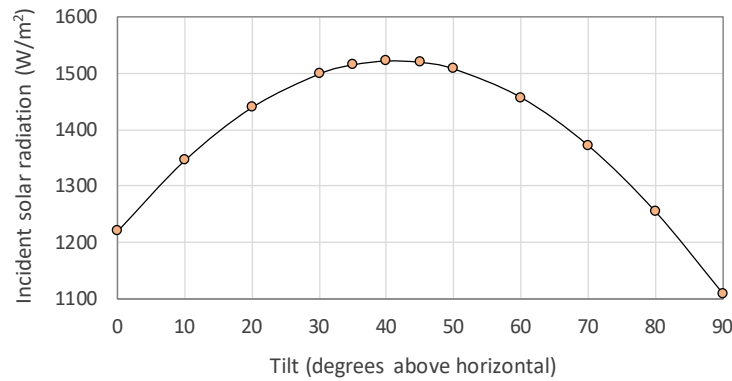


Figure 4. **Optimal tilt for solar-collecting glass**, shown by incident solar radiation during the heating season on surfaces of varying tilt to be approximately 40° above horizontal.

GenOpt was then used to find optimal hourly schedules for activation and retraction. Results showed, consistent with intuition from decades ago but contrary to recent assumptions (Stevanović 2013, van Moeseke 2007), that movable insulation was optimally activated hours before sunset in many months and often remained in place hours after sunrise; specific uninsulated hours depended on solar radiation utility (i.e. greater in Jan. than in Oct.) and heat loss vulnerability (i.e. greatest on Dec. mornings) (Fig. 5). Shading, similarly, was optimally activated well before the day's hottest hours and optimally retracted well before sunset, remaining retracted all night to promote cooling from glazed surfaces (Fig. 5). Together, these reduced the original heating load by about half and compensated for the cooling load introduced by the new skylight (Fig. 7a).

The third revision added thermal mass in the form of a brick wall north of the skylight (Fig. 1); its thickness was optimized alongside movable insulation and shading schedules due to strong interactions among these elements (Rempel 2015), yielding a final value of 25cm. The mass reduced annual loads only modestly (Fig. 7a), suggesting that seasonally-adjustable thermal mass (i.e. water or potted plants) should be explored. The fourth revision, in turn, sought optimal temperature thresholds, shown to be more effective than hourly schedules (Rempel 2015), for natural ventilation. These values, which reduced cooling loads by ~75% (Fig. 7a), fell within a surprisingly narrow range: above outside temperatures of ~25°C, and below indoor temperatures of ~23.5-24.5°C, natural ventilation had such a dramatic impact in this space, with amply-sized windows well-aligned to the prevailing wind, that overcooling easily resulted. This is evident, as well, in the appearance of small heating loads in April, May, and August (Fig. 6).

Table 2. Optimization parameters

Parameter	Range	Initial Step Size	Initiation Value	Result
Glazing tilt	0° - 90°	10°	n/a	Fig. 4
Movable insulation (Oct-Mar):				
time retracted (morning)	6:00 - 12:00	1:00	6:00	Fig. 5
time activated (evening)	15:00 - 20:00		15:00	
Shading (Apr-Sep):				
time activated (morning)	6:00 - 12:00	1:00	12:00	Fig. 5
time retracted (evening)	15:00 - 20:00		20:00	
Thermal mass thickness	0.01m - 0.3m	0.05m	0.01m	0.25m
Natural ventilation (Apr-Sep):				
indoor minimum temperature	16°C - 30°C	10°C	26°C	Fig. 6
outdoor maximum temperature	20°C - 38°C	10°C	26°C	

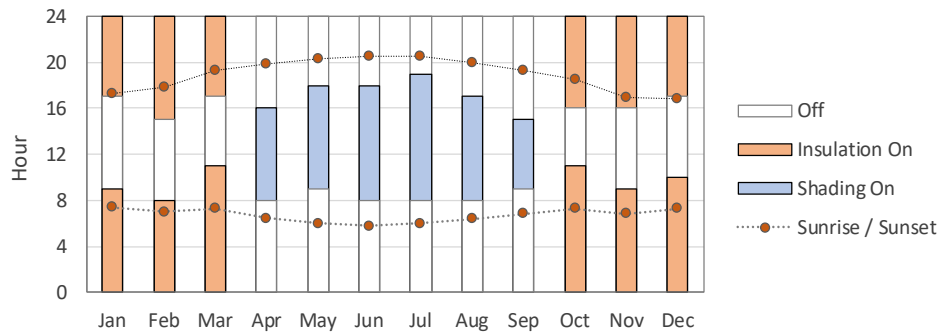


Figure 5. **Optimal hours for use of movable insulation** (orange bars) **and shading** (blue bars), as well as hours of full sunrise and full sunset (circles). Note nighttime retraction of shading.

DISCUSSION

Several useful observations emerge from these results. First, ideal thresholds for operation of movable elements are not necessarily intuitive, and despite accepted research practice (e.g. Ochoa 2008), they cannot be assumed. Here, movable insulation required activation of greater duration than the “nighttime” (sunset to sunrise) default found in EnergyPlus and other simulation engines; similarly, shading required activation hours before overheating occurred and also required removal at night. Where default activation settings exist, they must be overridden; likewise, effective manual operation by occupants cannot be assumed if thermal sensation and/or intuition are the only signals. Second, the penalties imposed by winter overheating and summer overcooling led to optimal thresholds that created small summer heating and winter cooling loads. If modest winter overheating and summer overcooling were permitted, which is not unrealistic given that mechanical heating is often made unavailable in the summer and vice-versa, these new loads would be reduced or eliminated. Third, it appears that even finer-grained optimizations would have been productive, particularly with respect to natural ventilation. The combination of summer overcooling penalties and ample operable window area, in this case, led to a high minimum indoor temperature threshold in May because so little time was necessary for natural ventilation to have sufficient cooling effect; optimizations that explore window area as well as sub-hourly timesteps might reveal better thresholds. The load reductions predicted here are therefore conservative, in the sense that they could be lowered even further, but optimistic in the sense that consistent, near-ideal operation is required to achieve them.

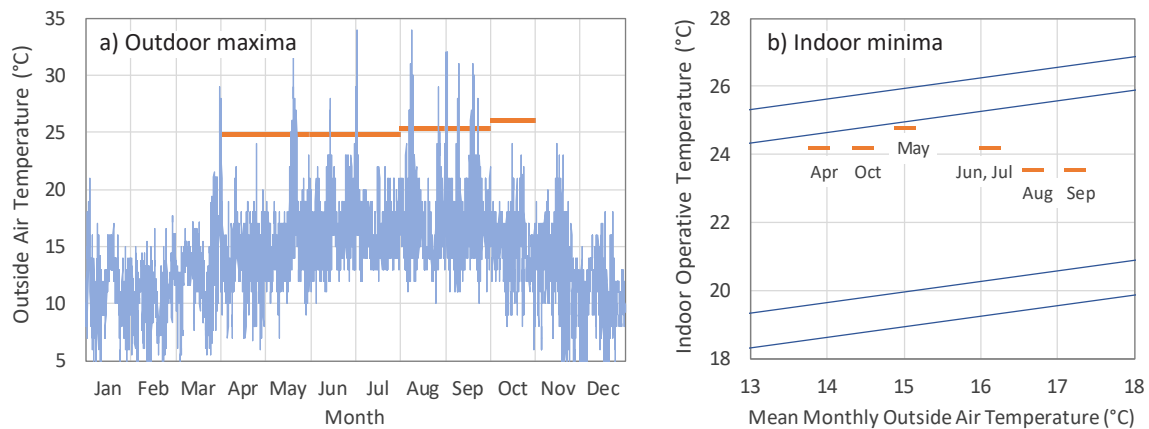


Figure 6. **Optimal temperature thresholds for natural ventilation control.** (a) Typical outdoor temperatures (blue; Oakland CA TMY3) and maximum values above which vents should be closed to avoid overheating (orange); (b) Adaptive thermal comfort zone (blue) and minimum indoor temperatures below which vents should be closed to avoid overcooling (orange).

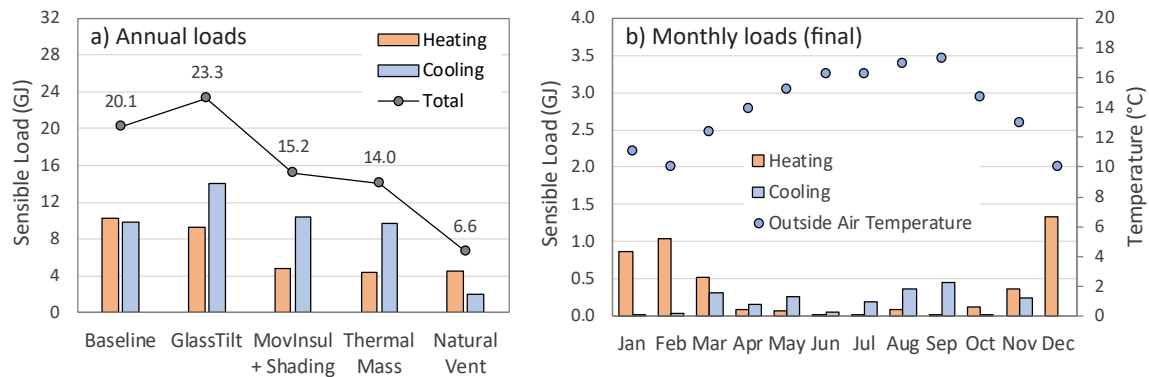


Figure 7. **Final loads with optimized controls.** (a) Annual loads at each stage, with final reductions of 56% (heating), 79% (cooling), and 67% (total); (b) Final loads by month (see Fig. 2b).

CONCLUSIONS

Together, the results above show the striking potential for well-controlled passive strategies to diminish space conditioning loads, even in a building with minimal insulation in a cloudy winter climate. In reducing the heating load by >50% and cooling load by ~80%, while maintaining adaptive comfort, the strategies that were identified challenge the perception that passive systems are difficult to control and, as a result, cannot contribute reliably to comfort. Instead, they suggest the opposite. While the load offsets found are specific to the building and climate studied, the value of well-operated elements is likely to be widespread in climates with significant diurnal and seasonal temperature variation, and the method for finding control thresholds is valid in general. Because the U.S. contributes disproportionately to the world's greenhouse gas emissions, the potential for well-controlled passive systems to meet such large fractions of heating and cooling demand, in a vital population center, is worth intense investigation and further development.

REFERENCES

- ASHRAE Standard 55-2017. Thermal environmental conditions for human occupancy. Atlanta GA.
- Chan H, Riffat S, Zhu J. 2010. Review of passive solar heating and cooling technologies. *Renew Sustain Energ Rev* 14:781-9.
- Garrett, V. and Koontz, T.M., 2008. Breaking the cycle: Producer and consumer perspectives on the non-adoption of passive solar housing in the US. *Energy Policy* 36:1551-66.
- Givoni, B. 1969. *Man, climate, and architecture*. Elsevier Science Ltd., Amsterdam.
- Nejat P, Jomehzadeh F, Taheri M, Gohari M, Majid M, 2015. A global review of energy consumption, CO₂ emissions and policy in the residential sector. *Renew Sustain Energ Rev* 43:843-62.
- Ochoa, C.E., Capeluto, I.G. 2008. Strategic decision-making for intelligent buildings: Comparative impact of passive design strategies and active features in a hot climate. *Build Environ* 43:1829-39.
- Olgay, V. 1963. *Design with climate*. Princeton University Press, Princeton NJ.
- Perez R, Ineichen, P, Seals R, Michalsky J, Stewart, R. 1990. Modeling daylight availability and irradiance components from direct and global irradiance. *Solar Energy* 44:271-89.
- Rempel AR, Remington SJ. 2015. Optimization of passive cooling control thresholds with GenOpt and EnergyPlus. *Proc Symp Simulation Arch Urban Des*:103-110.
- Rempel AR, Rempel AW et al. 2013. Interpretation of passive solar field data with EnergyPlus models: Un-conventional wisdom from four sunspaces in Eugene, Oregon. *Build Environ* 60:158-72.
- Santamouris M, Sfakianaki A, Pavlou K. 2010. On the efficiency of night ventilation techniques applied to residential buildings. *Energ Build* 42:1309-13.
- Schulze T, Eicker U. 2013. Controlled natural ventilation for energy efficient buildings. *Energ Build* 56: 221-32.
- Stevanović S. 2013. Optimization of passive solar design strategies. *Renew Sustain Energ Rev* 25:177-96.
- U.S. Energy Information Agency, 2018. Consumption by Sector. www.eia.gov/totalenergy/data/monthly/.
- van Moeseke G, Bruyère I, DeHerde A. 2007. Impact of control rules on the efficiency of shading devices and free cooling for office buildings. *Build Environ* 42:784-93.

Sensing and Information Technologies for the Environment (SITE); Hardware and Software Innovations in Mobile Sensing Technologies

ABSTRACT

This research focuses on the development and integration of low-cost Mobile Urban Sensing Technologies (MUST) and immersive environmental data exploration mechanisms with the ambition to inform citizens about their environments and aid scientists in uncovering the relations between the surface attributes and the urban environment. We propose to use 3D immersive environmental visualization techniques to enable a user-centered interactive analysis and rationalization of the available urban environmental data in relation to further urban attributes. With this ambition, we have developed three mobile apps that explore three strategies of Augmented Reality (AR) 3D visualizations of urban environmental data. While some data could be acquired from urban Geographic Information System (GIS) and existing sensor networks, we also developed an urban sensing kit specifically designed for deployment on mobile platforms such as buses or cars.

KEYWORDS

Urban Microclimate, Urban Sensing, Mobile Sensing, Augmented Reality, Environmental Visualization.

INTRODUCTION

Big data is changing urban science. Digitalization of information and ubiquitous sensing in cities are enabling the collection of data at unprecedentedly high temporal and spatial resolutions. This is most true in regard to urban environmental data. Sensor networks, remote sensing, thermal imaging, and crowd-sourced environmental monitoring are rapidly growing the availability of urban environmental data.

While high spatio-temporal resolution urban microclimate data are continuously becoming easier to collect, these data are not always analyzed in relation to further urban properties. We are generally only aware about city scale mean pollutant concentration values, and fail to understand the variable environmental quality conditions present in the urban fabric. One of the reasons for the persistence of this challenge is that while the study of urban sensing tools and strategies has been a consistent focus of research within the environmental and earth science communities, little attention has been placed on the development of data compilation and visualization techniques and methods for interactive exploration of environmental data for urban analysis, both from the scientist's and the interested citizen's perspectives. The result is that urban environmental data fail to reach wide audiences. The hypothesis of this research is that immersive and interactive urban environmental visualizations will enable the engagement of a broad team of stakeholders including scientists, citizens, policy makers and urban planners to reshape the discussion and analysis of contemporary urban environments, and the planning of future cities. This can be achieved through user-centered interactive analysis and rationalization of urban data which 3D immersive visualization techniques enable, thus removing some of the barriers that current tabular data or 2D plots engender. Specifically, we outline the development of novel 3D immersive Augmented Reality (AR) visualizations of urban air quality data. Such visualization strategies, which are currently lacking, aim for the

analysis of environmental data in relation to further urban parameters to enable the participation of a wide audience of users. The scientist would use them to understand how urban attributes modulate environmental quality, while citizens would use them to better understand their city and how to navigate while minimizing their exposure to adverse air quality or heat. However, since current sensor networks in cities mostly consist of fixed stations that cannot provide the spatial information needed to support such visualization of the entire city, we also develop a low-cost sensing kit designed specifically for mobile deployment over cars or buses, for example.

2. URBAN SENSING AND VISUALIZATION METHODS

When the access to environmental data of a site under study is limited, the use of mobile weather stations can be an effective low-cost technology to capture high spatial resolution urban air quality data. Mobile weather station studies can enable a fast response and site specific data acquisition methodology to understand parameters such as pollution sources or temperature gradients (Mahoney et al. 2010, Zwack et al. 2011, Kolb et al. 2004, Li et al. 2012). However the deployment of mobile sensing technologies specially so in urban environments still lags behind fixed sensors due to various challenges. The reliance on power sources, deployment constraints, security concerns, and the difficulty to access the kits for maintenance and calibration purposes, are amongst some of the main reasons why urban sensing technologies are not more widespread. Aiming to address these challenges, a robust and low-cost sensing kit has been developed to enable the acquisition of a high spatial resolution urban microclimate data (see Fig.1). This mobile sensing tool is essential to support the visualization techniques described next, which require high spatial resolution data (for further details on the MUST sensing kit see must.princeton.edu).

Immersive 3D visualization techniques have not yet been explored for urban environmental data representations. However urban data visualization strategies have recently been experiencing a rapid transformation with the arrival of Augmented Reality (AR) (also referred to as Mixed Reality (MR)) technologies. Urban augmented reality applications are changing the way we navigate the city. Apps such as ARCity or Yelp aid citizens to navigate the city based on the information of traffic, road conditions or amenities. Apps such as England's Historic Cities add historic layers to the city also enable citizens to navigate the city while traveling in time. However while various weather apps are available both in iOS and Android, augmented reality technologies have not yet been explored for the visualization of urban environmental data. In this context, this research explores AR technologies for environmental visualization aiming to encourage the engagement of wide communities including scientist and citizens in the discussion and management of urban environments. With this ambition three 3D immersive AR environmental visualization apps are being developed. These apps utilize the acquired mobile sensing data from the MUST sensing kits and visualize it following 3 strategies. The Navigating Urban Environments (NUE) app targeted for wide audiences, uses a mobile phone to explore a 3D urban navigation strategy where environmental data is spatially represented in relation to the physical structures of the city to enable a first person and on site exploration of the environmental data in relation to the visible urban

properties. The Virtual Urban Environments (VUE) app introduces a 3D immersive off site map visualization strategy to explore the environmental data over a city map marker deployable in interiors and exteriors; it typically uses a tablet and is aimed at very engaged citizens or city managers and policy makers. Finally the Holographic Urban Environments (HUE) app uses augmented reality smart glasses to enable further degrees of interactivity with the environmental data through spatial user hand textures or voice activation; it is designed for scientists and urban planners who want to interact with various scenarios to gage their impact on urban environmental quality.



Figure 1. MUST Sensing Kit

2.1 NUE

Despite the increasing availability of 2D and 3D urban navigation apps, urban navigation has not yet been explored to enable on site environmental visualization. Environmental navigation in cities could however transform the way citizens travel across cities. The Navigating Urban Environments (NUE) app is an augmented reality mobile app that aims to aid citizens navigate the city informed by environmental data. The app operates in two modes, i) the first-person view, and ii) the map view. In the first-person view, locational services of the user's mobile device are accessed, and the geo-tagged environmental data are overlaid on the camera view as graphic filters (see Fig.2). The map view is developed using Google Map API services over which environmental gradients are overlaid. The app queries data from the online server where the MUST sensing kit data are stored, as well as from other online web services such as OpenWeatherMap and AQICN. Through these combined sources, data on temperature, humidity and air quality are compiled. Furthermore, through GeoNames geocoding, the location for the different urban intersections is stored. This setup enables that when a geocoded user points the smartphone towards a nearby intersection, the app draws a marker over the intersection to show the street names as well as the relevant environmental data for that given intersection. Thus the app allows the user to decide on the most favorable path towards their destination, as well as to associate certain temperatures or AQI values with the urban fabric.



Figure 2. NUE app.

2.2 VUE

Not only the average citizen, but also city managers and policy makers can benefit from AR visualizations to understand their urban domain. Virtual Urban Environments (VUE) is a marker based augmented reality mobile app that aims to enable off-site environmental data visualization and analysis. To test the app, environmental data on the city of Seoul have been collected. The app recognizes a marker composed by the map of the city of Seoul and scales the environmental data over it. Historical air quality data from 1986 to 2016 can be viewed through interacting with a slider and dropdown menu. Data for PM10, PM2.5, O₃, SO₂, NO₂, and CO were available. Furthermore, the app enables real time data to be visualized over the city map. The air quality data is queried from the same sources as NUE. The setup aims to encourage the user to make correlations between the historical and real-time air quality data, while viewing the complexity of urban and geographic layers. This would help urban planners or policy makers to understand what modulates urban environmental quality.

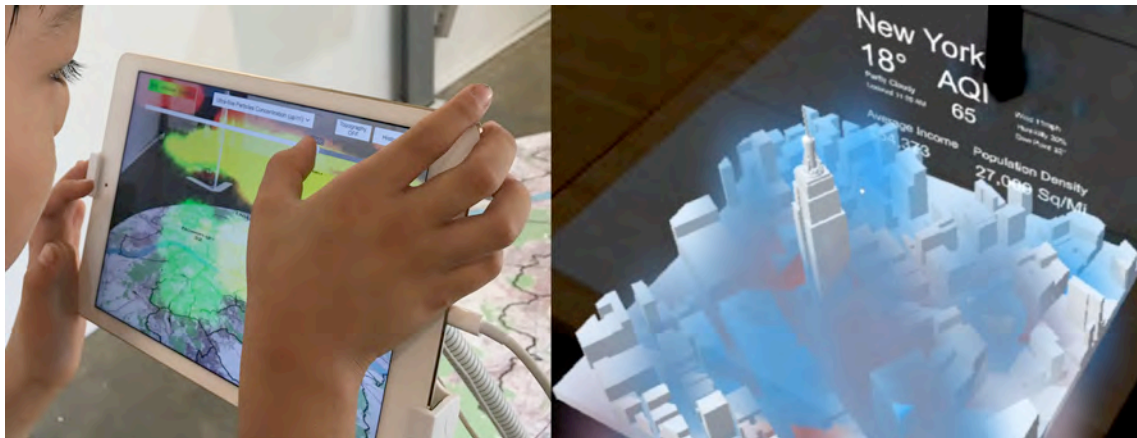


Figure 3. Left figure, VUE app. Right Figure, HUE app.

2.3 HUE

Holographic Urban Environments (HUE) is an augmented reality mobile app that utilizes a smartglass headset to enable immersive environmental data visualization and analysis. The app uses an environmental visualization platform based on the game engine Unity and the Microsoft HoloLens smartglass headset. The app queries data in real time from real-time data

is queried from online weather station databases and visualized as a particle simulation. The environmental data are mapped onto 3D physical model that the Hololens kit uses as a marker. This app is being developed aiming for a further degree of interactivity with the environmental data through spatial user hand textures or voice activation. It would allow for example, once couple to modeling tools, city planners or scientists to see what is the effect of altering the cityscape on environmental quality.

RESULTS

The MUST sensing kits and the developed AR environmental visualization applications were tested at the 2017 Seoul Architecture and Urbanism Biennale. Four MUST sensing kits were installed in the Seoul intercity bus network, collecting data from August 30th until October 4th 2017. Data on temperature, humidity, CO₂ and PM2.5 were acquired at time intervals of 30 s. Given that the sensing kits were powered by a solar panel, the battery was only charged when the weather conditions were good, thus from the time the kits were installed, only 26 days of data were acquired. The data was initially compared against a nearby Seoul city weather station and it was found in agreement with the weather station observations. In Figure 4b the averaged CO₂ and temperature data for the 31st of August are shown. With the ambition to relate the acquired environmental data with the urban spatial differences present in this area of the city, a district scale analysis has been developed. The buses travelled through 9 different districts in the city of Seoul. The Kolmogorov-Smirnov test with a 5% significance level was tested for every pair of these 9 districts (in Fig.4a the pdf distributions for temperature and for all 9 districts are shown); it showed that data from neighboring district are likely to be related (drawn from the same distribution), as expected.

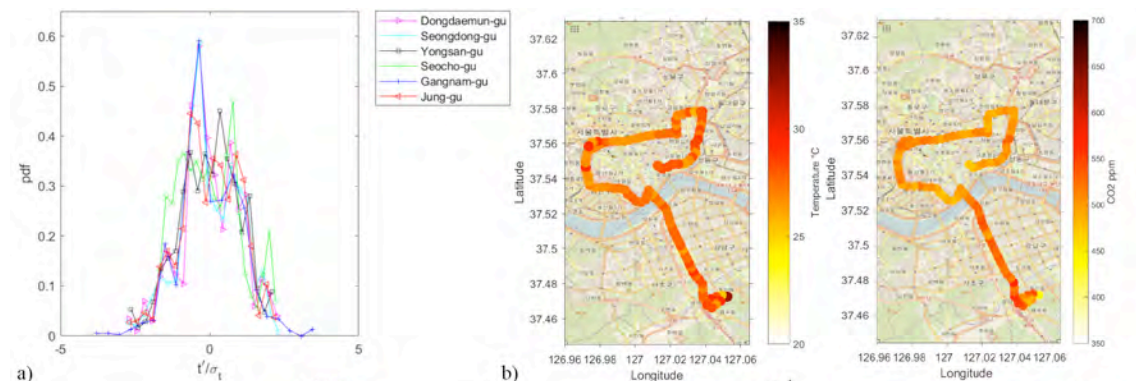


Figure 4 a) PDF of the acquired temperature for the different districts in Seoul. b) Spatial map for temperature and CO₂ collected on the 31st of August.

Two of the developed augmented reality applications were displayed in the Seoul architecture and urbanism biennale in an exhibition with the title Seoul On-Air. For the VUE app, a 2.5m diameter map of the city of Seoul was installed on the exhibition floor around which 5 iPads displayed the app enabling visitors to experience real time and historical air quality data of the city of Seoul. The NUE app was also displayed in the exhibition space. Given that this app is to be used for outdoor urban environmental navigation purposes, it was only included as a video recording for the visitors to become familiar with the functionalities of the application.

Both apps accessed the real time data collected from the MUST sensing kits and local weather stations.

CONCLUSIONS

Aiming for the acquisition of low-cost and high spatial resolution urban environmental data, a mobile urban sensing technology has been developed. The prepared sensing kits were mounted over the Seoul intercity network, and environmental data was acquired for 26 days. The data collected from the sensing kits was utilized to communicate the real time high spatiotemporal resolution air quality data to the Seoul Citizens through 2 augmented reality applications. These apps were launched at the 2017 Seoul architecture and urbanism biennale to motivate an inclusive discussion between the different stakeholders that can affect how our cities are and will be designed in the future, including scientists, urban planners, architects, policy makers and citizens. The apps were made available in an exhibition space where city planning authorities and the citizens of Seoul interacted with the applications and provided very positive feedback about their experience. A third application has also been presented which utilizes immersive smartglasses for immersive environmental visualizations. A field experimental campaign for the city of New York is currently under development where the MUST sensing kits in combination with the three AR applications will be tested. We are also currently working on an updated version of the AR apps, aiming to introduce features that make them more immersive and interactive.

REFERENCES

ARCity app: <https://itunes.apple.com/us/app/arcity-ar-navigation/id1282527727?mt=8>
England's Historic Cities app store link: <https://itunes.apple.com/us/app/englands-historic-cities/id1215745809?mt=8>
Fitness AR app: <https://itunes.apple.com/us/app/fitness-ar/id1274233318?mt=8>
Monument Valley app: <https://itunes.apple.com/us/app/monument-valley/id728293409?mt=8>
Morpholio Trace app: <https://itunes.apple.com/us/app/morpholio-trace-sketch-cad/id547274918?mt=8>
Pokemon Go app: <https://itunes.apple.com/us/app/pok%C3%A9mon-go/id1094591345?mt=8>
Yelp app: <https://itunes.apple.com/us/app/yelp-discover-local-favorites/id284910350?mt=8>

J. J. Li, B. Faltings, O. Saukh, D. Hasenfratz, J. Beutel, "Sensing the air we breathe: The opensense zurich dataset", *Proceedings of the Twenty-Sixth AAAI Conference on Artificial Intelligence ser. AAAI'12*, AAAI Press, pp. 323-325, 2012.

Kolb, C.E., S.C. Herndon, B.J. McManus, J.H. Shorter, M.S. Zahniser, D.D. Nelson, J.T. Jayne, M.R. Canagaratna, and D.R. Worsnop. 2004. "Mobile Laboratory with Rapid Response Instruments for Real-Time Measurements of Urban and Regional Trace Gas and Particulate Distributions and Emission Source Characteristics."

Mahoney, B., S. Drobot, P. Pisano, B. MacKeever, and J. O'Sullivan. 2010. "Vehicles as Mobile Weather Observation Systems." *Metereological Society* 91:1179-1182.

Zwack, L.M., C.J. Paciorek, J.D. Spengler, and J.I. Levy. 2011. "Characterizing Local Traffic Contributions to Particulate Air Pollution in Street Canyons Using Mobile Monitoring Techniques." *Atmospheric Environment* 45 (15):2507-2514.

Experimental study on the stomatal resistance of green roof vegetation of semiarid climates for building energy simulations

Rocío Arriola-Cepeda¹, Sergio Vera², Francisco Albornoz¹ and Ursula Steinfert^{1*}

¹ Facultad de Agronomía e Ingeniería Forestal, Pontificia Universidad Católica de Chile, Vicuña Mackenna 4860, Macul, Santiago, Chile.

² School of Engineering, Department of Construction Engineering and Management, Pontificia Universidad Católica de Chile, Vicuña Mackenna 4860, Macul, Santiago, Chile.

**ustefinfo@uc.cl*

ABSTRACT

Current modelling approaches for energy simulations in green roofs use a range of values for parameters such as stomatal resistance (r_s) of the vegetation. r_s reflects the capability of a plant to transpire, thus it has a direct relation to the cooling potential of green roofs in buildings. Therefore, r_s values need to be revised based on differences among species and contrasting environmental conditions, considering anatomical and physiological characteristics among species and their changes throughout the day. In order to provide real data on species commonly used for green roofs in semiarid climates, this paper aims to evaluate the stomatal resistance of nine species of groundcovers and to compare this data with current models. r_s was measured for each species at 8:00 h, 12:00 h, 16:00 h and 20:00 h during day and night-time in winter in a leaf located at the middle of the stem. The results of this study showed that r_s varies significantly among species, throughout the day and between the side of the leaf (adaxial or abaxial). The lowest r_s values for species was at noon ranging from 264 to 807 s m⁻¹ and the highest r_s was at night ranging from 568 to 973 s m⁻¹. *Sedum spurium* red, *Sedum* hybrid, and white and pink *Verbena sp.* had the largest r_s variation in the day-night cycle. The results of r_s are higher than those values recommended for some energy simulation models.

KEYWORDS

Cooling potential, plant physiology, *Sedum*, stomatal conductance,

INTRODUCTION

As a component of green infrastructure, green roofs have become more relevant in recent years because of the ecosystem services they provide, including the reduction of energy consumption in buildings (Tabares-Velasco and Srebric 2011; Zhao et al. 2014) and Urban Heat Island (UHI) (Gill et al. 2007). The cooling service of green roof vegetation relies on the abilities of different species to transpire, provide shade, reflect radiation back to the atmosphere or absorb it through photosynthesis (Cook-Patton and Bauerle 2012; Blanus et al. 2013; Vaz Monteiro et al. 2017). Transpiration relates to the water vapour movement from the plant to the atmosphere through stomata, which are pores distributed in the epidermis of leaves that allows CO₂ and O₂ exchange. The stomatal resistance (r_s) corresponds to the rate of transpiration of water vapour by the leaves through opening and closing of stomata based on the environmental conditions. In nature r_s relates to the species, their morphology and anatomy of the leaves, such as stomatal density on the adaxial and abaxial side and also temperature, water availability and photosynthetic active radiation (PAR) present, among other characteristics. In models of heat and mass transfer from green roofs to buildings, r_s is one of the most relevant parameters that defines them (Jaffal et. al, 2012; Sailor, 2008) and although its importance, r_s information comes mainly from research performed in agricultural

crops, but not from species commonly used in green roofs (Cook-Patton and Bauerle, 2012). That is why in green roof modelling, selected r_s values come from the literature available and the researcher's criteria and not from empirical data that acknowledges species variability. In this study, r_s values were obtained throughout the day in nine species of groundcovers commonly used in green roofs, to check for interspecific variation. Secondly, these r_s values were compared to those ranges proposed in the heat and mass transfer models from green roofs to buildings, to check whether these values were under or over estimating the true cooling potential of a green roof, according to a species.

METHODS

Seven succulent species *Aptenia cordifolia*, *Basella sp.*, *Sedum* hybrid, *Sedum palmeri*, *Sedum spurium* red, *Sedum spurium* green, *Sedum spurium* variegated and two herbaceous species *Verbena sp.* white and *Verbena sp.* pink grown in a heated greenhouse were used in this study. The experiment consisted in a completely randomized design (DCA), with three replicates, each consisting of four pots with one plant. The parent plant material was obtained from commercial nurseries and then propagated using four cm long cuttings, with three to four leaves, dipped in a mixture of indole butyric acid (IBA) plus Captan (Anasac Garden ®). Cuttings were placed in a greenhouse for four weeks until transplant into 1.4 L pots filled with a mixture of peat and perlite 2:3 (v:v). Plants were irrigated to container capacity, every two days and five weeks after transplant, r_s was measured with a calibrated Leaf Porometer (model SC-1, Decagon Devices, USA) throughout the day at 8:00, 12:00, 16:00 and 20:00 hours during the fall. Measurements were taken in a marked leaf located in the middle of the stem, on its adaxial and abaxial side during six consecutive days with sky clear conditions. PAR and temperature were recorded. Data was analysed by ANOVA and mean separation was carried out by Fisher's Least Significance Test (LSD) when differences were significant.

The minimum and maximum r_s values obtained in this study were compared to those reported by Sailor (2008) and Zhao et al. (2014). In Sailor (2008), the user can choose an r_s value between 50 to 300 s m^{-1} , which are values found in different plant species. On the other hand, r_s values proposed by Zhao et al. (2014) ranged from 225 to 1125 s m^{-1} and were derived from studies on desert plants by Tabares-Velasco and Srebric (2011).

RESULTS

Stomatal resistance (r_s)

Stomatal resistance (r_s) was significantly higher ($P < 0.01$) in five species at the adaxial side compared to the abaxial side of leaves. In addition, the mean r_s was species dependent ($P < 0.01$) (Fig. 1). Herbaceous species such as white and pink *Verbena sp.* had on average, an r_s value of 417 s m^{-1} , while succulent species, such as *Basella sp.* had the highest r_s with 880 s m^{-1} . On the other hand, *Sedum* species r_s ranged between 536 to 692 s m^{-1} .

r_s changed within the species across the day ($P < 0.001$) and was lower at 12:00, compared to 20:00 h, with the exception of *S. spurium* var. that had no significant differences. *S. spurium* red, for example had a 71% higher value of r_s at 20:00 than at 12:00, while *Basella sp.* had the lowest variations of r_s across the day (15%). Although PAR radiation was highest at noon, all species showed their lowest r_s values at midday while the highest values were found at night (PAR values of 0.0 $\mu\text{mol m}^{-2} \text{s}^{-1}$). In general, r_s values at 8:00 h and 16:00 h were similar across species.

Stomatal resistance (r_s) comparison with current models

When comparing the r_s values obtained on this study (Table 1) with those proposed in the heat and mass transfer models from green roofs to buildings of Sailor (2008), only the mean r_s values at 20:00 of the herbaceous White and Pink *Verbena sp.* and *S. spurium* red were within the range. On the other hand when comparing the r_s values obtained with the ones proposed for desert plants by Zhao et al., (2014), all species had values within that range.

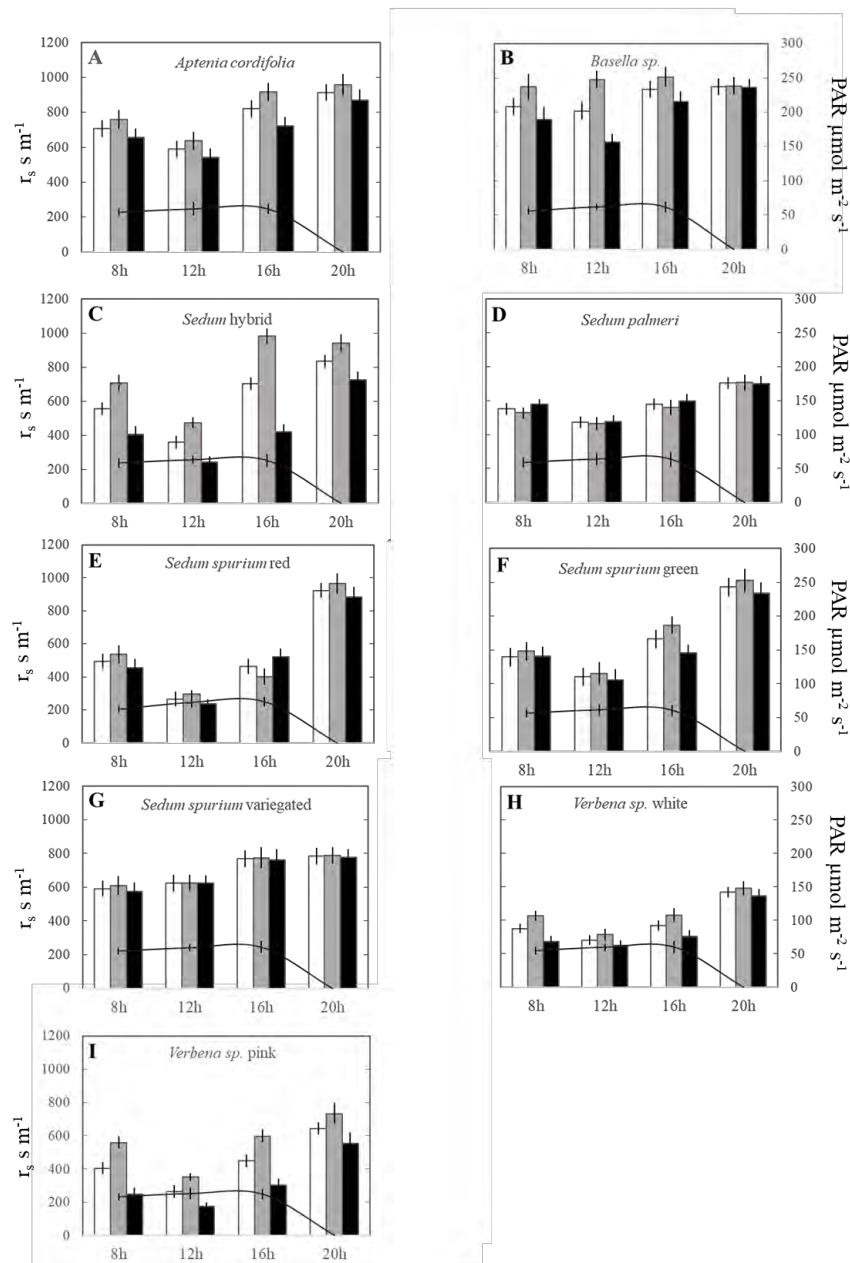


Figure 1. Photosynthetic active radiation (PAR) ($\mu\text{mol}\ m^{-2}\ s^{-1}$) and mean (white), adaxial (grey) and abaxial (black) stomatal resistance (r_s) ($s\ m^{-1}$) on of (A) *Aptenia cordifolia*, (B) *Basella sp.*, (C) *Sedum hybrid*, (D) *Sedum palmeri*, (E) *Sedum spurium* red, (F) *Sedum spurium* green, (G) *Sedum spurium* variegated (H) *Verbena sp.* White and (I) *Verbena sp.* Pink, at 8:00 h, 12:00 h, 16:00 h and 20:00 h.

Minimum and maximum r_s values obtained in this study were higher than the ones proposed by Sailor (2008), and they were closer to the r_s values proposed by Zhao et al. (2014) (Table 1).

Table 1. Minimum (min) and maximum (max) stomatal resistance (r_s) ($s\ m^{-1}$) of the nine species of groundcovers of this study and r_s values proposed by the simulation models of Sailor (2008) and Zhao et al. (2014).

Species	r_s ($s\ m^{-1}$)	
	r_s min	r_s max
<i>Aptenia cordifolia</i>	589	914
<i>Basella sp.</i>	807	948
<i>Sedum</i> hybrid	358	834
<i>Sedum palmeri</i>	471	703
<i>Sedum spurium</i> red	266	923
<i>Sedum spurium</i> green	440	973
<i>Sedum spurium</i> var.	624	784
<i>Verbena sp.</i> white	282	568
<i>Verbena sp.</i> pink	264	643
Sailor (2008)	50	300
Zhao et al. (2014)	225	1125

DISCUSSIONS

In nature, most species have hipo-stomatic leaves, meaning that stomatal density is higher on the abaxial compared to the adaxial side of the leaf (Lallana, 2003), which is also related to differences on cells of inner tissues on both sides (Fukushima and Hasebe, 2014). This anatomical and morphological characteristic of leaves is considered to be part of the plant adaptive response to avoid water loss through excessive transpiration on the adaxial side, which is directly exposed to solar radiation (Clements, 1905). In the case of the nine species evaluated in this study, stomatal density on the abaxial versus the adaxial side of the leaves was also higher (unpublished data) in line with previous information, which could be responsible for the lower r_s values on the abaxial side. It is also possible that the stomatal size, could increase or decrease r_s values together with the characteristics of the epidermis and accessory elements in leaves.

In this study, succulent species commonly grown in green roofs showed higher r_s values compared to non-succulents. Succulent species have fewer stomata per unit of area (Sayed, 1998). The opening and closing of stomata relates not only to r_s , but also with CO_2 assimilation for photosynthesis and environmental limiting factors such as vapour pressure, radiation, relative humidity, water availability and temperature (Farquhar and Sharkey, 1982), which explains the broad variability of r_s during the day, between species and in the same species. Succulents species adapted to open their stomata for CO_2 uptake during night times and close them during the day to limit water loss, do not showed crassulacean acid metabolism performance in their r_s behaviour through the day. All this morphological and anatomical traits have evolved in succulents as an adaptive response to water deficit and high temperatures, leading to higher r_s values in these species.

Irrigated plants, usually have higher transpiration rates due to the opening of stomata and, therefore, r_s is lower compared to plants under water stress. In this study though, r_s was higher compared to the values proposed in the heat and mass transfer models from green roofs to buildings of Sailor (2008) and were within the range proposed by Zhao et al. (2014). Sailor (2008) is overestimating the cooling potential of the species, by means of using r_s values commonly found in agricultural crops, while the values proposed by Zhao et al. (2014) are based on desert plants (Tabares-Velasco & Srebric, 2011), similar to the ones used in this study. Nevertheless, it is worth mentioning that r_s measurements were carried out at the end of fall under irrigated conditions, when r_s values are naturally lower, however, the cooling potential of plants and r_s values are more important over summer, when temperatures are higher. This information could be useful in green roof design, where the principal consideration should be to maximize transpiration in plants with low levels of irrigation. In addition, we think that specifically in the case of *Sedum spurium* red, the lowest r_s at noon could be related with the red pigmentation in both sides of the leaves, could be increasing the capacity to transpire even in hours with high temperature and irradiation.

CONCLUSIONS

This study has denoted a broad variability of r_s , both within species across the day and between species of common use in green roofs. Also, the results showed that the values currently used in heat and mass transfer models of green roofs are in some cases underestimating r_s . This emphasizes the need of empirical data to support species selection in green roofs in order to maximize the energy savings in buildings by means of supporting greater transpiration of plants, with the use of species with lower r_s values especially at noon, when temperatures outside buildings are higher.

It is essential to create a biological database of species commonly used in green roofs and their parameters values, such as r_s , that will support designers and modellers to improve species selection to maximize energy savings in buildings. On the other hand, a common criteria, that includes the species natural variation and their behaviour across the day is relevant to design methodologies that will aid to standardize the data collection. Also, we expect that this results will raise awareness on the biological diversity that exists in green roof vegetation, in order to identify further parameters that are currently used in green roofs from data extracted from agricultural crops which would bring greater benefits to the area of sustainable construction.

ACKNOWLEDGEMENT

We would like to thank the Department of Plant Science of the Faculty of Agriculture and Forestry from the Pontificia Universidad Católica de Chile, for partially providing the resources to develop this research. Also, this project was partially funded by research grants FONDECYT 1150675 and FONDECYT 1181610. We thank professor Jorge Gironás from the Department of Hydraulic and Environmental Engineering for facilitating the Leaf Porometer used in this research.

REFERENCES

- Blanusa T, Vaz Monteiro M, Fantozzi F, Vysini E, Li Y, and Cameron R. 2013. Alternatives to *Sedum* on green roofs: Can broad leaf perennial plants offer better 'cooling service'?. *Building and Environment*, (59), 99-106.
- Cook-Patton S. and Bauerle T. 2012. Potencial benefits of plant diversity on vegetated roofs: a literature review. *Journal of Environmental Management*, (106), 85-92.

- Clements, E. S. 1905. The relation of leaf structure to physical factors. *Trans. Am. Microsc. Soc.* (26), 19–102.
- Farquhar G. and Sharkey T. 1982. Stomatal Conductance and Photosynthesis. Annual review. *Plant Physiology*, (33), 317-345.
- Fukushima K. and Hasebe M. 2014. Adaxial-Abaxial Polarity: The Developmental Basis of Leaf Shape Diversity. *Genesis*, (52), 1-18.
- Gill, S.E., J.F. Handley, A.R. Ennos, and S. Pauleit. (2007). Adapting Cities for Climate Change: The Role of the Green Infrastructure. *Built Environment*, (33) 1: 115–33. <https://doi.org/10.2148/benv.33.1.115>.
- Jaffal I., Ouldboukhitine S.E., and Belarbi R. 2012. A comprehensive study of the impact of green roofs on building energy performance. *Renewable Energy*, (43), 157-164.
- Lallana V. and Lallana M. 2003. Manual de prácticas de fisiología vegetal. Facultad de ciencia agropecuaria-UNER, 32-35.
- Sailor D. 2008. A green roof model for building energy simulation programs. *Energy and building*, (40), 1466-1478.
- Sayed O.H. 1998. Phenomorphology and ecophysiology of desert succulents in eastern Arabia. *Journal of Arid Environments*. (40), 177-189.
- Tabares-Velasco, P.C., and J. Srebric. (2011). Experimental Quantification of Heat and Mass Transfer Process through Vegetated Roof Samples in a New Laboratory Setup. *International Journal of Heat and Mass Transfer* (54): 5149–62. <https://doi.org/10.1016/j.ijheatmasstransfer.2011.08.034>.
- Vaz Monteiro, M., T. Blanuša, A. Verhoef, M. Richardson, P. Hadley, and R. W. F. Cameron. (2017). Functional Green Roofs: Importance of Plant Choice in Maximising Summertime Environmental Cooling and Substrate Insulation Potential. *Energy and Buildings*, (141): 56–68. <https://doi.org/10.1016/j.enbuild.2017.02.011>.
- Zhao M., Tabares-Velasco P., Srebric J., Komarneni S., and Berghage R. 2014. Effects of plant and substrate selection on thermal performance of green roofs during the summer. *Building and Environment*, (78), 199-211.

Greening rooftops to reduce heat islands: How large is large enough?

Jiachuan Yang*, Elie Bou-Zeid

Department of Civil and Environmental Engineering, Princeton University, NJ

*Corresponding email: jiachuan@princeton.edu

ABSTRACT

Green roofs, with adequate water supply, have been proven as effective measures to reduce urban environmental temperature. The benefits of large-scale deployment of green roofs have been studied mainly through numerical simulations with unrealistic high penetration scenarios, where all rooftops across the entire metropolis is assumed to be retrofitted. In this study, the scale dependence of the cooling effect of green roofs is investigated with a coverage of 25% over buildings at local, city, or regional scales. We compared results at 6 major U.S. cities to assess the response of the scale dependence to geoclimatic conditions. High-resolution weather simulations reveal that the cooling of near-surface air temperature by green roofs increases non-linearly with the scale of deployment. The shape and geoclimatic setting (geographic and climatic characteristics) of metropolitan areas control the scaling that some city centers are not able to achieve a significant cooling by greening their own rooftops. Uniform deployment of green roofs at the regional scale, on the other hand, provides a substantial temperature reduction with a very low cooling efficiency per intervention area. Cities should carefully revisit the scale dependences of cooling benefit and efficiency of green roofs to develop resilient plans meeting their expectations.

KEYWORDS

Cooling efficiency; Green roof; Heat island mitigation; Urban planning

INTRODUCTION

Urban heat island (UHI), a phenomenon that urban areas are significantly warmer than surrounding rural areas, is a big sustainability challenge that has been documented in global cities (Peng et al. 2011). Elevated temperatures adversely affect energy demand, water resource, and resident health in urban environment that cities have recognized the need to mitigate heat island effects under the changing climate (Grimm et al. 2008). Among the proposed strategies in the literature, green roof has gained increasing popularity due to its environmental benefits including temperature reduction, storm water retention, aesthetic improvement and habitat provision (Carter and Fowler, 2008).

In-situ measurements reported that replacing conventional roofs with green roofs can reduce daily maximum surface temperature by up to 30 °C (Wong et al. 2003). Consequently, reduced diurnal temperature variation substantially cut building heat gain and increase energy efficiency (Parizotto and Lamberts 2011). These measurements are consistent with building-scale numerical simulations (Sailor et al. 2012). At the large scale, however, the benefits of green roofs to the whole city can only be evaluated through simulations because no urban region has yet achieved a sufficiently extensive intervention. Recent developments allow accurate simulations of green roofs in climate models (Yang et al. 2015). Nevertheless, existing studies have focused on the maximum potential benefit of green roofs, i.e., 100% coverage uniformly over the entire metropolitan area (Georgescu et al. 2014).

In reality, land use development, economic activity and government structure diverge vastly among districts and communities at the sub-city scale as well as between different metropolitan areas that execution of mitigation policies can vary extensively. Take the New York metropolitan area for example, green roofs can be implemented by the city for its dense urban core (Manhattan), for the whole New York city, or in cooperation with surrounding counties in the state of New Jersey. Temperatures in cities are closely related to the fraction and spatial configuration of urban green space (Jin and Dickinson 2010), yet the quantitative scaling laws of cooling benefits from green roofs remain unknown. This study provides a first attempt to bridge this gap by simulating green roofs in different cities to address the following questions: How large does green roof need to be to produce a considerable cooling for city centers? How do the cooling benefits from green roofs scale with their spatial extent? Will the scale dependence change with geoclimatic conditions?

METHODS

In this study, we used the Weather Research and Forecasting (WRF) model, a non-hydrostatic regional climate model developed by the National Center for Atmospheric Research (Skamarock and Klemp 2008), to simulate the effects of green roofs on regional climate. The WRF model has successful applications over major metropolitan areas around the world (Chen et al. 2011), whose parameterization of green roofs was developed and tested based on field measurements (Sun et al. 2013). Six metropolitan areas across the United States were selected for high-resolution weather simulation in this study, including Los Angeles (LA), New York City (NYC), Miami, Chicago, Phoenix and Pittsburgh. For each studied region, the fine-resolution domain (see Figure 1) has 160 by 160 grid cells covering the entire metropolitan area. Each grid is 1 km long and 1 km wide. To assess the performance of green roofs in a “typical” summer, we referred to the 1981-2010 climate normal released by the National Centers for Environmental Information for different metropolis. As a result, Pittsburgh and Chicago were simulated for year 2013, and LA, Miami, Phoenix, and NYC were simulated for year 2014. All simulations were run from 0000 UTC on 10 July to 0000 UTC on 14 August.

Metropolitan areas in this study have developed sustainability plan to mitigate climate change. Though the primary goal of these actions is to reduce greenhouse gas emissions, the need of mitigating urban heat islands is explicitly outlined and the use of green roofs is recognized by Chicago, NYC, and Pittsburgh. To obtain plausible scenarios of green roofs, we went through the land use planning and development map for each studied metropolitan area and identified three (local, city, and regional, Figure 1) levels of implementation. A set of three simulations was then carried out to estimate the cooling benefit of green roofs at three levels, assuming a 25% areal coverage on building rooftops. To focus on the effect of geoclimatic conditions and to exclude the impact of water availability, green roofs were well irrigated in all runs such that soil moisture maintained evapotranspiration at 75% of the potential evapotranspiration rate. Following previous studies (Sun et al. 2013), thermal properties of roofs were (1) conventional roof: albedo (a) = 0.3, thermal conductivity (k) = 1.0 W m⁻¹ K⁻¹, heat capacity (C) = 2.0 MJ m⁻³ K⁻¹; (2) green roof: a = 0.3, k = 1.1 W m⁻¹ K⁻¹, C = 1.9 MJ m⁻³ K⁻¹.

RESULTS

Figure 2 shows the reductions in average T_2 (air temperature at 2 m above the surface) over the local-scale planning area (red areas in Figure 1) with different levels of green roof implementation. We focus on these areas because they are the urban cores with the highest population density within the city. Temperature reductions among studied regions are found to scale with green roof areas differently. In the first group of metropolitan areas, including

NYC, LA and Pittsburgh, the cooling benefit increases considerably with the area of green roofs. Upscaling the deployment of green roofs from the local scale to the regional scale, daytime mean T_2 reduction increases from 0.03 °C to 0.21 °C for NYC, from 0.03 °C to 0.12 °C for Pittsburgh, and from 0.05 °C to 0.18 °C for LA. In the second group of cities (Chicago, Miami, and Phoenix), however, temperature reductions over urban cores by green roofs are largely independent of the intervention scale. Daytime mean T_2 over Chicago center decreases by an additional 0.02 °C after increasing green roof areas from 0.52 km² in the local plan to 679.19 km² in the regional plan. The scale dependence of nighttime cooling for individual metropolitan areas is consistent with the daytime trend.

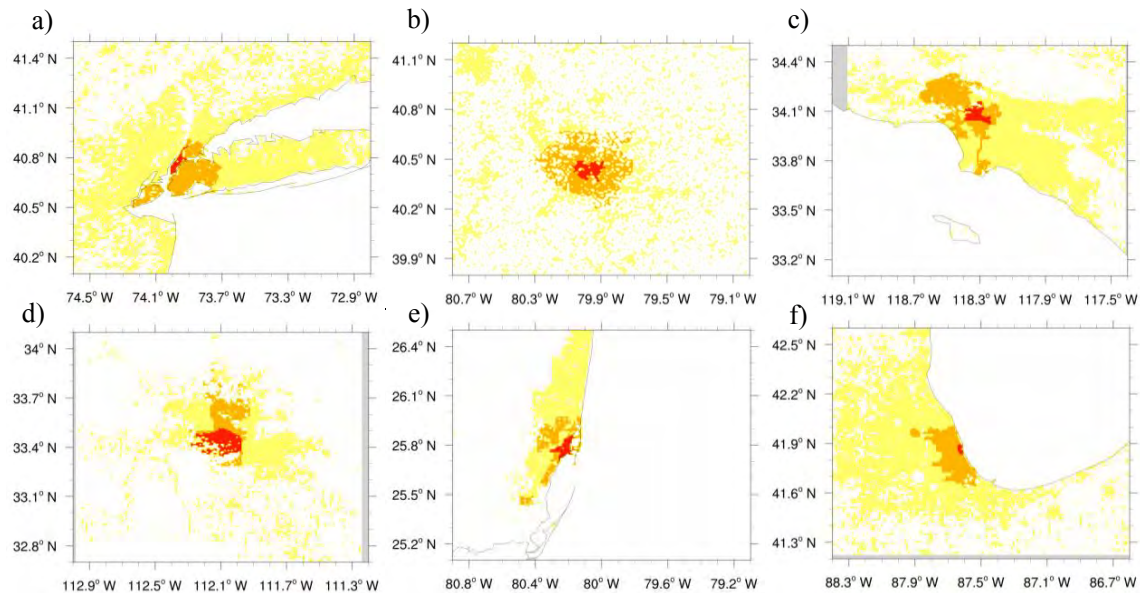


Figure 1. Spatial extent of green roofs at local (red), city (orange), and regional (yellow) scales. a) NYC, b) Pittsburgh, c) LA, d) Phoenix, e) Miami, f) Chicago.

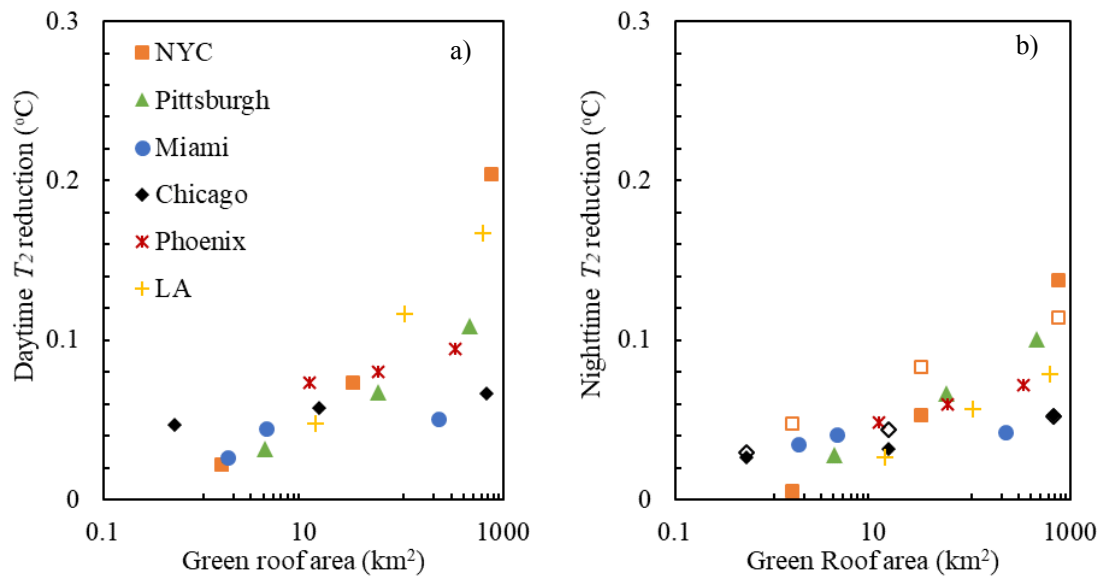


Figure 2. Scale dependence of simulated reductions in 2-m air temperature over the local planning areas by green roofs. a) daytime (0700-2000), b) nighttime (2100-0600).

Spatial distribution of the cooling by different green roof plans is plotted in Figure 3. Chicago and NYC are shown as examples to explain the dissimilar scale dependence between the two groups of cities. Greening 25% of Manhattan's rooftops leads to a negligible cooling over Manhattan and causes a small cooling downwind to the west and to the north of NYC. Adopting green roofs at the city scale creates surface cooling in upwind areas, consequently Manhattan is able to achieve a reduction of about 0.15 °C in T_2 at 1400 local time. And a uniform implementation of green roofs over the entire metropolitan area can reduce T_2 over Manhattan by about 0.36 °C at 1400 local time. Due to the existence of sea breeze, city and regional plans provide cooling benefits for Manhattan by greening its upwind areas. Similarly, strong scale dependences of the cooling benefit in LA and Pittsburgh are caused by implementing green roofs over buildings in upwind areas.

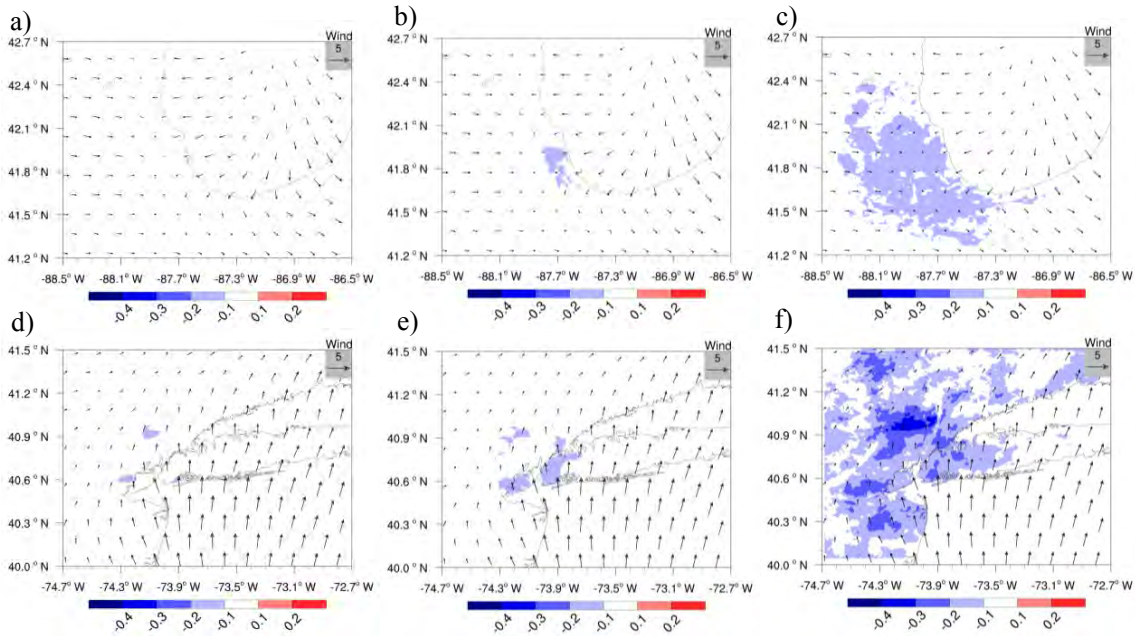


Figure 3. Simulated reductions in 2-m air temperature at 1400 local time with 10-m wind overlaid from deploying green roofs. a), b), c) local, city, and regional scales in Chicago; d), e), f) local, city, and regional scales in NYC.

The cooling effect of green roofs is more local and homogeneous in Chicago. At all levels, urban areas with green roofs are able to receive a noticeable temperature reduction. Nevertheless, a weak scale dependence is found because upscaling the mitigation plan for Chicago mainly involves altering downwind built areas. The comparison between results in Chicago and NYC demonstrates that both the geography of the metropolitan area and the climatic conditions play important roles in regulating the regional benefits of green roofs.

The scale dependence of cooling benefits in different metropolitan areas is very useful, but it is expected that larger green roof areas result in stronger temperature reductions. Cooling efficiency is a key factor if green roofs are to be implemented as a city-scale plan or regional policy. Here we estimated the cooling efficiency per unit area of green roofs at different scales in the studied metropolitan areas. The reductions of 2-m air temperature over the entire fine-resolution domain is considered to account for cooling benefits in downwind areas:

$$CE = \int \frac{\sum_{x=1}^{N_x} \sum_{y=1}^{N_y} \Delta T_{x,y}(z) A_{grid}}{A_{int}} dz, \quad (1)$$

where N_x and N_y are the number of grid cells in x and y directions, $\Delta T_{x,y}(z)$ is the temperature drop of each grid cell in the fine-resolution domain relative to the baseline without green roofs, A_{grid} and A_{int} denote the area of model grid and green roofs, respectively. In this study, we focused on a 1m thick slab centred at 2m and used T_2 to represent $\Delta T_{x,y}(z)$. Note that the integration over depth in equation 1 is necessary for obtaining a cooling efficiency over a physical volume. Figure 4 shows that cooling efficiency per unit area of green roofs decreases rapidly with the implementation scale. Different from the trend in Figure 2, geoclimate conditions are found to play a negligible role in determining the cooling efficiency over the fine-resolution domain. With an area of about 1.6 km² (e.g., local plans in NYC), daytime T_2 cooling efficiencies is about 30 °C m. At the regional scale, the daytime and night maximum efficiencies of about 2.8 and 2.5 °C m are found at NYC.

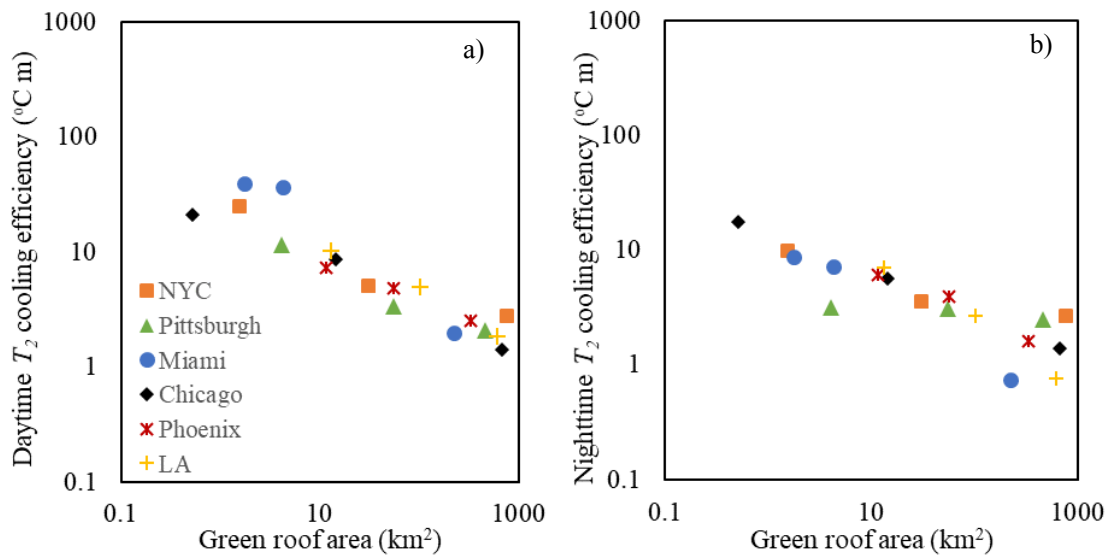


Figure 4. Scale dependence of the cooling efficiency of green roofs. a) daytime (0700-2000), b) nighttime (2100-0600).

DISCUSSIONS

Modelling results with a uniform 100% penetration intervention are at present the best available resource to guide green roof policy in context of long-term environmental adaptation. The 25% areal coverage used in this study is at the lower end of previous studies (Yang et al. 2015), but is still beyond the practical implementation potential in the foreseeable future. Using plausible scenarios based on cities' land use development map, this study provides new insight into effective green roof planning as mitigation strategies of heat island. We find that the scale dependence of T_2 reduction over urban cores is controlled by the geography of metropolitan area and its climatic conditions. To maximize the regional cooling benefits, deployment of green roofs should therefore focus on upwind areas. These upwind areas are critical to the thermal environment in the city during windy periods. Although wind direction varies continuously, planners should be able to identify the most probable wind directions. On the other hand, during periods of calm weather, the benefits of green roofs are more local.

CONCLUSIONS

This paper quantitatively examines and compares the scale dependence of cooling benefit and efficiency of green roofs for mitigating urban heat islands in six major U.S. metropolitan

areas. Increasing the spatial extent of green roofs is usually treated as an effective way to mitigate heat islands. Our finding in this study, however, suggests that green roofs at city and regional scales may or may not provide significant additional benefits for urban cores. Green roofs have a direct impact on energy consumption of the building. Nevertheless, in terms of cooling the city, the effect is more indirect and cities should account for this scale dependence and for their unique geoclimatic setting.

ACKNOWLEDGEMENT

This work was supported by the US National Science Foundation under grant number ICER 1664091 and under the UWIN Sustainability Research Network Cooperative Agreement 1444758. The simulations were performed on the supercomputing clusters of the National Center for Atmospheric Research through project P36861020 and UPRI0007.

REFERENCES

- Carter T. and Fowler L. 2008. Establishing green roof infrastructure through environmental policy instruments. *Environmental management*, 42(1), 151-164.
- Chen F., Kusaka H., Bornstein R., Ching J., Grimmond C., Grossman-Clarke S., Loridan T., Manning K.W., Martilli A., and Miao S. 2011. The integrated WRF/urban modelling system: development, evaluation, and applications to urban environmental problems. *International Journal of Climatology*, 31(2), 273-288.
- Georgescu M., Morefield P.E., Bierwagen B.G., and Weaver C.P. 2014. Urban adaptation can roll back warming of emerging megapolitan regions. *Proceedings of the National Academy of Sciences*, 111(8), 2909-2914.
- Grimm N.B., Faeth S.H., Golubiewski N.E., Redman C.L., Wu J., Bai X., and Briggs J.M. 2008. Global change and the ecology of cities. *Science*, 319(5864), 756-760.
- Jin M. and Dickinson R.E. 2010. Land surface skin temperature climatology: benefitting from the strengths of satellite observations. *Environmental Research Letters*, 5(4), 044004.
- Li D., Bou-Zeid E., and Oppenheimer M. 2014. The effectiveness of cool and green roofs as urban heat island mitigation strategies. *Environmental Research Letters*, 9(5), 055002.
- Parizotto S. and Lamberts R. 2011. Investigation of green roof thermal performance in temperate climate: A case study of an experimental building in Florianópolis city, Southern Brazil. *Energy and Buildings*, 43(7), 1712-1722.
- Peng S., Piao S., Ciais P., Friedlingstein P., Ottle C., Bréon F.M., Nan H., Zhou L., and Myneni R.B. 2011. Surface urban heat island across 419 global big cities. *Environmental science & technology*, 46(2), 696-703.
- Sailor D.J., Elley T.B., and Gibson M. 2012. Exploring the building energy impacts of green roof design decisions—a modeling study of buildings in four distinct climates. *Journal of Building Physics*, 35(4), 372-391.
- Skamarock W.C. and Klemp J.B. 2008. A time-split nonhydrostatic atmospheric model for weather research and forecasting applications. *Journal of Computational Physics*, 227(7), 3465-3485.
- Sun T., Bou-Zeid E., Wang Z.-H., Zerba E., and Ni G.-H. 2013. Hydrometeorological determinants of green roof performance via a vertically-resolved model for heat and water transport. *Building and Environment*, 60, 211-224.
- Wong N.H., Chen Y., Ong C.L., and Sia A. 2003. Investigation of thermal benefits of rooftop garden in the tropical environment. *Building and environment*, 38(2), 261-270.
- Yang J., Wang Z.-H., Chen F., Miao S., Tewari M., Voogt J.A., and Myint S. 2015. Enhancing hydrologic modelling in the coupled weather research and forecasting—urban modelling system. *Boundary-Layer Meteorology*, 155(1), 87-109.e

Integrated vegetation model for studying the cooling potential of trees in urban street canyons

Lento Manickathan^{1,2,*}, Aytaç Kubilay^{1,2}, Thijs Defraeye^{1,3}, Jonas Allegrini^{1,2}, Dominique Derome², Jan Carmeliet^{1,2}

¹ Chair of Building Physics, ETH Zurich, 8093 Zürich, Switzerland

² Empa, Laboratory of Multiscale Studies in Building Physics, 8600 Dübendorf, Switzerland

³ Empa, Laboratory for Biomimetic Membranes and Textiles, 9014 St. Gallen, Switzerland

**Corresponding email: mlento@ethz.ch*

ABSTRACT

Vegetation in cities provides natural cooling of the climate and is therefore increasingly integrated as an essential part of Urban Heat Island (UHI) mitigation strategies. In the present study, the influence of trees on the local climate in a street canyon is studied using an integrated vegetation model in OpenFOAM. Vegetation is modeled as porous medium providing the necessary source terms for the heat, mass and momentum fluxes. Additionally, a radiation model is developed to model the short-wave and long-wave radiative heat flux exchanges between vegetation and the surroundings. The study investigates the influence of transpirative and shaded cooling due to vegetation on the pedestrian comfort inside a street canyon. The study shows that both shading and transpiration have a direct positive influence on the temperatures measured in the street canyon. Moreover, the cooling due to shading is seen to be larger than the transpirative cooling, especially under the tree.

KEYWORDS

CFD, transpirative cooling, shading, vegetation, UHI

INTRODUCTION

Vegetation in urban environments has a natural cooling effect on the urban climate and can mitigate Urban Heat Islands (UHI). The natural cooling is provided through heat extraction during transpiration and through shading from vegetation on the surrounding buildings and the ground below. However, trees can also negatively influence the ventilation characteristics in cities as the foliage obstructs air movement. This effect can further deteriorate the airflow characteristics at the pedestrian level and may reduce pedestrian thermal comfort. Thus, vegetation can have non-trivial impact on the comfort in cities and numerical models are needed to assess the influence of vegetation in cities.

The interaction between vegetation and the environment is a multi-physical phenomenon. Vegetation exchanges momentum, heat and mass with the air and undergoes radiative exchanges. A computational fluid dynamics (CFD) approach (Hiraoka, 2005; Liang et al., 2006; Boulard et al., 2008) can be used to identify the interactions between vegetation and environment, where the vegetation is modeled using a porous medium approach. Such an approach is shown to provide a good estimation of the thermal impact of vegetation and was used to study the influence of vegetation in urban areas (Bruse and Fleer, 1998; Gromke et al., 2014; Robitu et al., 2006). An urban microclimate model that can model the airflow and radiation in an integrated approach provides the means to accurately assess the environmental impact of vegetation for a given complex urban topology.

In the present study, the influence of vegetation, namely trees, on the microclimate of a street canyon is studied using a CFD model in OpenFOAM. Vegetation is modeled as a porous medium, providing the source/sink terms for heat, mass and momentum fluxes. A radiation model is developed to model the short-wave and long-wave radiative heat fluxes between the leaf surfaces and the surrounding environment. The radiation model enables to model the impact of the diurnal variations of solar intensity and direction, and the long-wave radiative fluxes between vegetation and nearby urban surfaces. Using the developed model, we investigate the cooling potential of vegetation on the microclimate of a street canyon exposed to a moderate wind in June. The influence of transpirative cooling and shading due to vegetation on pedestrian thermal comfort inside a street canyon is studied. The thermal comfort for pedestrians is evaluated using the Universal Thermal Climate Index (UTCI) (Fiala et al., 2001).

MATERIALS AND METHODS

Numerical method

The mean flow field in the street canyon with vegetation is modeled using the Reynolds-Averaged Navier-Stokes (RANS) equations,

$$\frac{\partial \rho \bar{u}_j}{\partial x_j} = 0, \quad (1)$$

$$\frac{\partial \rho \bar{u}_i \bar{u}_j}{\partial x_j} = \frac{\partial}{\partial x_j} \left[-\tilde{p} \delta_{ij} + \mu_{eff} \left(\frac{\partial \bar{u}_i}{\partial x_j} + \frac{\partial \bar{u}_j}{\partial x_i} - \frac{2}{3} \frac{\partial \bar{u}_k}{\partial x_k} \delta_{ij} \right) \right] + \rho g_i + s_{u_i}, \quad (2)$$

$$\frac{\partial \rho \bar{e} \bar{u}_j}{\partial x_j} = \frac{\partial}{\partial x_j} \left(k_{eff} \frac{\partial \bar{T}}{\partial x_j} \right) + s_h, \quad (3)$$

$$\frac{\partial \rho k}{\partial x_j} = \frac{\partial}{\partial x_j} \left(\rho D_k \frac{\partial k}{\partial x_j} \right) + \rho G - \frac{2}{3} \rho \frac{\partial \bar{u}_k}{\partial x_k} k - \rho \varepsilon + s_k, \quad (4)$$

$$\frac{\partial \rho \varepsilon}{\partial x_j} = \frac{\partial}{\partial x_j} \left(\rho D_\varepsilon \frac{\partial \varepsilon}{\partial x_j} \right) + C_{1,\varepsilon} |S_{ij}| \varepsilon - C_{2,\varepsilon} \rho \frac{\varepsilon^2}{k + \sqrt{\nu \varepsilon}} + s_\varepsilon, \quad (5)$$

$$\frac{\partial \bar{w}}{\partial x_j} = \frac{\partial}{\partial x_j} \left(D_{eff} \frac{\partial \bar{w}}{\partial x_j} \right) + s_w, \quad (6)$$

where s_{u_i} , s_h , s_k , s_ε , s_w are the source terms of vegetation for momentum, energy, turbulent kinetic energy (TKE), TKE dissipation rate and humidity ratio (Manickathan et al., 2018a). The Reynolds stresses are closed using Boussinesq eddy-viscosity hypothesis where the eddy-viscosity is determined from the realizable $k - \varepsilon$ model. The air domain is coupled with the ground and building facades to model the transport of heat and moisture therein, to take in account of dynamics of the thermal and hygric storage in the street canyon (Kubilay et al. 2017).

Simulation setup

The simulations are performed for a street canyon with a vegetation zone of $2 \times 10 \times 4 \text{ m}^3$, representing a row of trees which are surrounded by two buildings of $10 \times 50 \times 10 \text{ m}^3$ ($x \times y \times z$), as shown in Figure 1. This vegetation zone has a foliage height of 4 m (with $z_{min} = 4$ m), leaf area density $LAD = 10 \text{ m}^2 \text{ m}^{-3}$, leaf drag coefficient $c_d = 0.2$ and leaf size $l = 0.1$ m. The meteorological data are based on a typical meteorological year and the total solar radiation intensity is for a clear sky on the 21st of June in the city of Zurich, Switzerland (Kubilay et al. 2017). The wind speed at the building height is $U_{ref} = 5 \text{ m s}^{-1}$, the ambient temperature varies between 11°C and 19 °C with solar noon at 13:28 and the relative humidity

varies between 62% and 86% RH. These are the boundary conditions applied at the inlet. A slip, symmetry and pressure outlet boundary conditions are applied at the top wall, side walls, and at the outlet, respectively. The ground outside the street canyon is defined to be adiabatic. Whereas, the wall temperatures inside the street-canyon is determined from the heat and moisture transport equations.

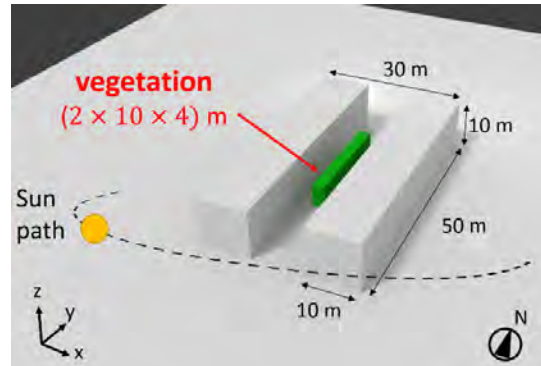
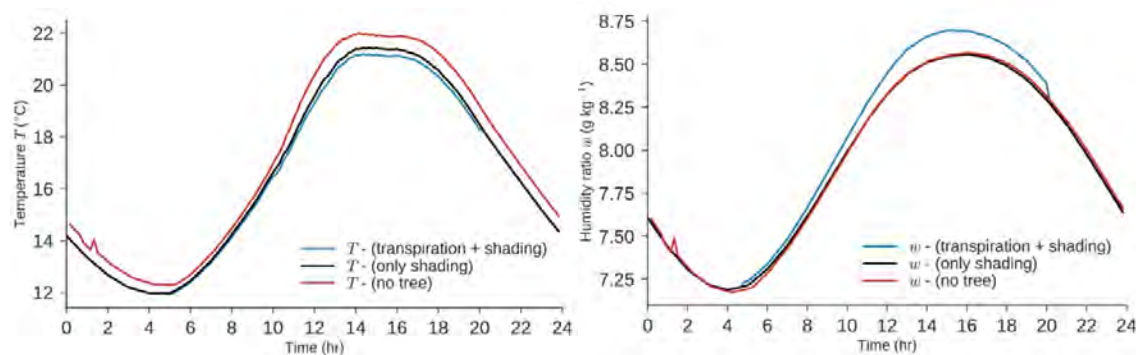


Figure 1. Simulation setup of a street canyon composed of two buildings with a vegetation band in the middle, representing a row of trees (Manickathan et al. 2018b).

RESULTS AND DISCUSSION

The cooling potential of trees in the street canyon is quantified by studying the diurnal variations of air temperature and humidity for three distinctly different configurations: street canyon without tree, street canyon with trees but only providing shading and, finally, street canyon with trees providing both transpirative cooling and cooling due to shading. The configuration of trees that only provide shading in the street canyon is achieved by artificially closing the stomata in the model. Figure 2 shows the diurnal variation of air temperature and humidity ratio below the tree at $z = 2$ m (point at the middle of the street canyon) for these three configurations. The figure shows that, without the trees, the air temperature is quantifiably higher throughout both day and night. However, once the trees are present, both shading and transpiration provide cooling in the street canyon, with an average decrease of 0.5°C in presence of shading and of an additional 0.2°C , when transpiration is added to shading. The cooling due to shading is seen to be higher than the cooling provided from transpiration. The study on the diurnal variation of humidity ratio inside the street canyon, Figure 2b, shows that the humidity in the street canyon is increased when the trees transpire. This could potentially negatively affect the pedestrian comfort below the tree.



a) Air temperature T ($^{\circ}\text{C}$)

b) humidity ratio w (g kg^{-1})

Figure 2. Diurnal variation of a) air temperature T ($^{\circ}\text{C}$) b) humidity ratio w (g kg^{-1}) below the tree at ($z = 2$ m) for three configurations: no tree, with shading and with transpiration and shading.

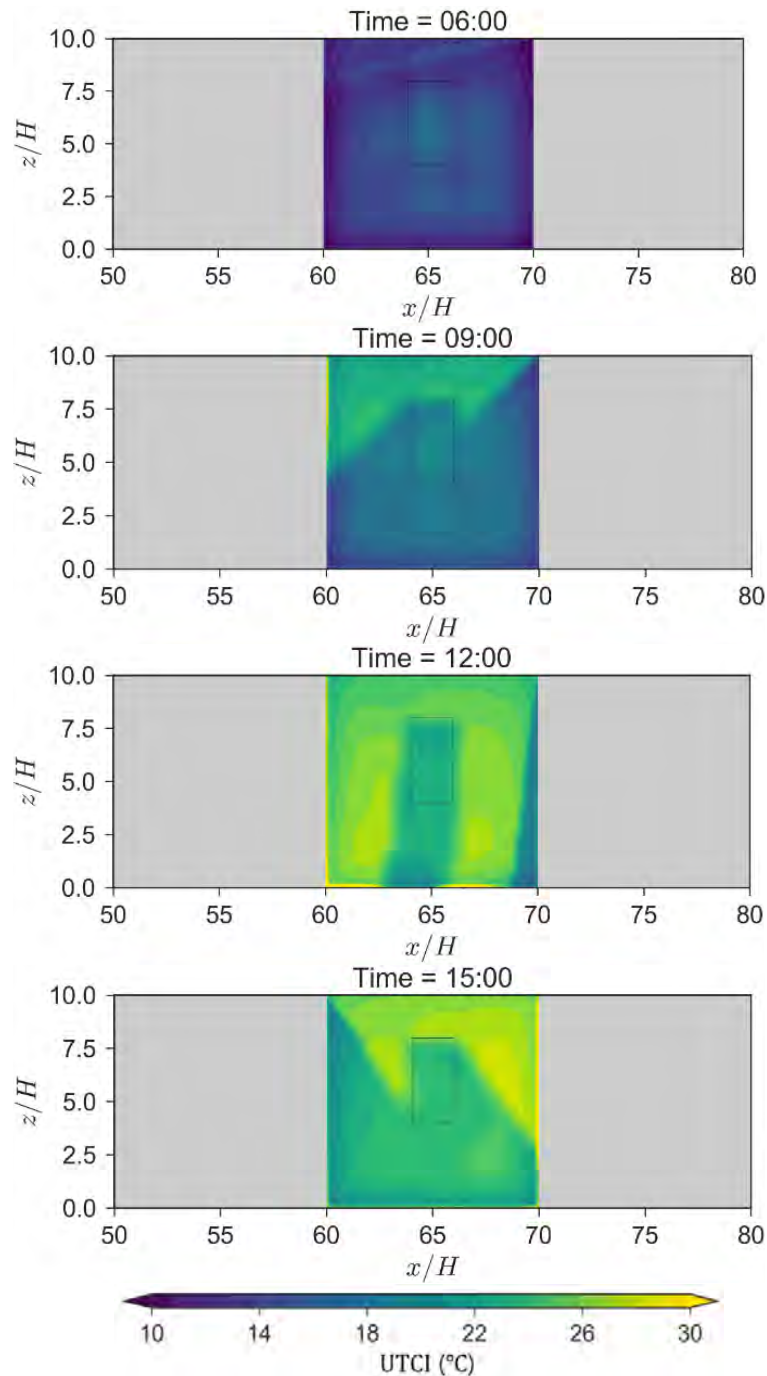


Figure 3. Spatial distribution of the universal thermal climate index (UTCI) ($^{\circ}\text{C}$) at the vertical centre-plane of the street canyon with vegetation at 06:00, 09:00, 12:00 and 15:00 local time. The buildings are indicated by the grey zones and the vegetation inside the street canyon is indicated by the outlined rectangle.

The universal thermal climate index (UTCI) is employed to study the influence of vegetation on pedestrian comfort inside the street canyon. Figure 3 shows UTCI distribution at the vertical centre-plane of the street canyon at four distinct local times: 06:00, 09:00, 12:00 and 15:00. It

is apparent that the pedestrian comfort is significantly compromised due to the exposure to solar radiation at noon. However, inside the shaded zone of the trees, the thermal comfort is substantially improved, as indicated by the reduced UTCI values. In contrast, the impact of humidity generated from the trees is not discernible in the UTCI distribution. This means the transpiration of the trees does not negatively affect pedestrian comfort in the case studied, although an increase in relative humidity could reduce the thermal comfort.

CONCLUSIONS

The integrated model is used to study the influence of transpirative cooling and cooling due to shading of trees inside a street canyon. From this case study, both transpirative cooling and cooling through shading are seen to reduce the temperatures. Furthermore, the transpiration from the vegetation is seen to increase the humidity inside the street canyon. Although, this additional humidity is seen not to have a significant impact on pedestrian comfort, measured through universal thermal climate index (UTCI), as the comfort provided by the tree shading is substantially higher and counters the negative impacts of increased humidity. However, factors such as leaf area density (LAD), vegetation position, vegetation size, ambient conditions, etc. can have an influence on the outcome. Therefore, the influence of these parameters should be investigated to accurately estimate the impact of the vegetation in urban area.

ACKNOWLEDGEMENT

The project is funded by the Chair of Building Physics, ETHZ.

REFERENCES

- Boulard T., Fatnassi H., Majdoubi H. and Bouirden L. 2008. Airflow and microclimate patterns in a one-hectare canary type greenhouse: An experimental and CFD assisted study. *Acta Horticulturae*, VOLUME: 837–845.
- Bruse M. and Fleer M. 1998. Simulating surface-plant-air interactions inside urban environments with a three dimensional numerical model. *Environmental Modelling & Software*, VOLUME: 373-384.
- Fiala D., Lomas K. J. and Stohrer M. 2001. Computer prediction of human thermoregulatory and temperature responses to a wide range of environmental conditions. *International Journal of Biometeorology*, VOLUME: 143–159.
- Gromke C., Blocken B., Janssen W., Merema B., van Hooff T. and Timmermans H. 2014. CFD analysis of transpirational cooling by vegetation: Case study for specific meteorological conditions during a heat wave in Arnhem, Netherlands. *Building and Environment*, VOLUME: 11–26.
- Hiraoka H. 2005. An investigation of the effect of environmental factors on the budgets of heat, water vapor, and carbon dioxide within a tree. *Energy*, VOLUME: 281-298.
- Kubilay A., Derome D., Carmeliet J. 2017. Coupling of physical phenomena in urban microclimate: A model integrating air flow, wind-driven rain, radiation and transport in building materials. *Urban Climate*.
- Liang, L., Xiaofeng, L., Borong, L., & Yingxin, Z. 2006. Improved k-ε two-equation turbulence model for canopy flow. *Atmospheric Environment*, 40(4), VOLUME: 762–770.
- Manickathan L., Defraeye T., Allegrini J., Derome D., Carmeliet J. 2018a. Parametric study of the influence of environmental factors and tree properties on the transpirative cooling effect of trees. *Agricultural and Forest Meteorology*, VOLUME: 259-274.
- Manickathan L., Kubilay A., Defraeye T., Allegrini J., Derome D., Carmeliet J. 2018b. Influence of vegetation on pedestrian thermal comfort in a street canyon, In: *Proceedings of 1st International Conference on New Horizons in Green Civil Engineering (NHICE-01)*, Victoria, BC, Canada, April 25 – 27.

Robitu M., Musy M., Inard C., Groleau D. 2006. Modeling the influence of vegetation and water pond on urban microclimate. *Solar Energy*, VOLUME: 435–447.

The Use of a Large, Extensive Green Roof for Multiple Research Objectives

Cliff I. Davidson^{1,2*}, Carli D. Flynn³, Charitha Gunawardana¹, Alexander J. Johnson¹, Mallory N. Squier¹, Lucie L. Worthen¹, and Yige Yang¹

¹Department of Civil and Environ. Engineering, Syracuse University, Syracuse, NY 13244

²Center of Excellence in Environ. & Energy Systems, Syracuse University, Syracuse, NY 13244

³Golisano Institute of Sustainability, Rochester Institute of Technology, Rochester, NY 14623

*Corresponding email: davidson@syr.edu

ABSTRACT

The Green Roof on the Onondaga County Convention Center in Syracuse, NY is planted with several varieties of sedum over an area of 0.56 hectares. The roof was constructed in 2011, and has been instrumented with sensors to enable research and education over an extended period. The purpose of the current work on this roof is to quantify its performance with respect to water storage and energy transfer, and to identify chemical constituents in the runoff that might be contributed by the growth medium. The scope of the project also includes a number of measurements on traditional roofs in the vicinity of the Convention Center as controls. Experimental methods include measurements with temperature probes installed in different layers of the green roof, a meteorological station, soil moisture sensors positioned around the roof, and an electromagnetic flowmeter connected to the roof drains. Chemical analysis of incoming precipitation and stormwater runoff is conducted by ion chromatography.

Besides the research underway, an educational website is under construction that shows real-time data from many of the instruments. The website includes explanations of the energy flow through the roof layers, water flow and water storage in the growth medium, and runoff through the roof drains. The website is designed for use by teachers of K-12 and undergraduate courses to enable students to learn about green roofs as a tool for managing urban stormwater.

Results of the research show that heat flow through the roof is largely controlled by extruded polystyrene insulation below the growth medium, and that the growth medium is not a major barrier to heat flow. Substantial amounts of stormwater can be stored by the roof, as long as the growth medium is able to dry somewhat between storms. Precipitation events in close succession may cause the growth medium to stay saturated, preventing the roof from storing additional stormwater. The results of this work are important for assisting designers and engineers to improve the performance of green roofs.

KEYWORDS

Green roof, water balance, evapotranspiration, soil moisture, stormwater, runoff chemistry

INTRODUCTION

Green roofs can benefit urban areas in many ways. Much has been written about urban heat islands, where densely populated cities experience higher air temperatures compared with vegetated landscapes just outside the city (e.g., Golden et al., 2004); green roofs can help reduce high urban temperatures. In climates where heating in winter or air conditioning in summer is needed, a green roof may offer some additional insulation to reduce heating or

cooling costs (Zhang et al., 2017). Furthermore, green roofs can provide wildlife habitat, e.g., for birds, and vegetation on a green roof can reduce concentrations of certain air pollutants.

Especially important is the role of green roofs in reducing flooding and combined sewer overflow. In this regard, many studies have investigated the hydrologic performance of green roofs. For example, Stovin et al. (2017) present data from several green roofs on metrics to define stormwater detention, such as time delay between peak rainfall and peak runoff, time delay between 50% cumulative rainfall and 50% cumulative runoff, and attenuation of peak runoff flowrate compared with peak rainfall flowrate. Elliott et al. (2016) examine the hydrologic performance of a green roof with thick growth medium (100 mm) and a green roof with thin growth medium (31 mm) in different seasons in New York City. Cipolla et al. (2016) report on the total amount of stormwater runoff prevented by a green roof in Bologna, Italy during 69 storms over a full year. They compare their experimental data with predictions from the commercial software SWMM 5.1, and conclude that SWMM results show reasonable agreement with data under certain conditions.

In this paper, we report on preliminary results on the performance of the green roof on the Onondaga County Convention Center in Syracuse, New York. This facility offers opportunities to expand green roof research in new directions. The climate of Syracuse includes more extremes of temperature and precipitation compared with other instrumented green roof sites. For example, according to the National Weather Service, the average accumulated snow depth for the season over the past 66 years in Syracuse is 299.5 cm, making it one of the snowiest cities in the country. The green roof measures 50 meters by 111 meters and is fully instrumented to enable energy flow as well as hydrologic studies.

There are three objectives of the research described in this paper. First, the hydrologic behavior of the roof is studied to examine factors influencing the amount of water the roof can store. Second, the benefit of the green roof in reducing heat loss from the building in winter is considered. Finally, the role of the green roof in altering the chemistry of incoming rain is examined. Besides these research goals, there is an educational goal, namely to use the green roof as an educational tool to help students learn about the benefits and challenges of using green roofs for urban stormwater management.

METHODS

The temperatures in the various layers of roof are measured using Campbell Scientific T109 probes, while the air temperature and relative humidity are measured using a Vaisala HMP-155 sensor. Windspeed and wind direction data are obtained using an R.M. Young 03-002 anemometer and wind vane set. Precipitation is measured with a Texas Electronics TE-525 tipping bucket as well as a Belfort AEPG-1000 weighing gauge for rain and snow using a double alter-shield to reduce the influence of wind. Soil moisture is measured using Campbell Scientific CS-616 reflectometers calibrated in our laboratories using samples of growth medium taken from the green roof. Runoff through the roof drains is measured with an M-2000 Badger electromagnetic flow meter calibrated on-site. All of the instruments are connected to CR-1000 Campbell dataloggers, and the data are subjected to quality assurance/quality control procedures.

Fresh rain samples are collected on the roof of the Biological Research Laboratory building at Syracuse University, about 1.6 km east of the green roof, simultaneous with collection of runoff samples from the roof drains on the green roof. Sampling during rain events usually takes place over several hours, hence the distance between the University site and the green

roof is expected to be negligible compared with the movement of rain clouds during the sampling intervals. Both sets of samples are analysed using a Dionex DX-500 ion chromatography system with anion columns to enable analysis of Cl^- , SO_4^{2-} , and NO_3^- . Field and lab blanks are collected during every experiment to estimate uncertainties in the concentrations. Additional experiments are conducted to estimate dry deposition of these chemical species onto the green roof during periods of dry weather.

The experiments related to the chemistry of precipitation, runoff, and dry deposition are conducted as the weather permits. Weather and hydrology data are collected continuously, allowing interpretation of data for any periods of interest.

Modeling of the hydrology is underway using the U.S. Environmental Protection Agency Stormwater Management Model (SWMM). Modeling of heat flow through the roof makes use of the model Combined Heat, Air, Moisture and Pollutant Simulations in Building Envelope Systems (CHAMPS-BES).

RESULTS

Hydrology of the Green Roof

For each rain event, the tipping bucket and weighing gauge are used to determine the intensity as well as the total amount of precipitation. Using the magmeter data, it is also possible to determine the partitioning of the precipitation between storage in the growth medium and runoff exiting the roof via the drainage system. Figure 1 shows an example of this type of data.

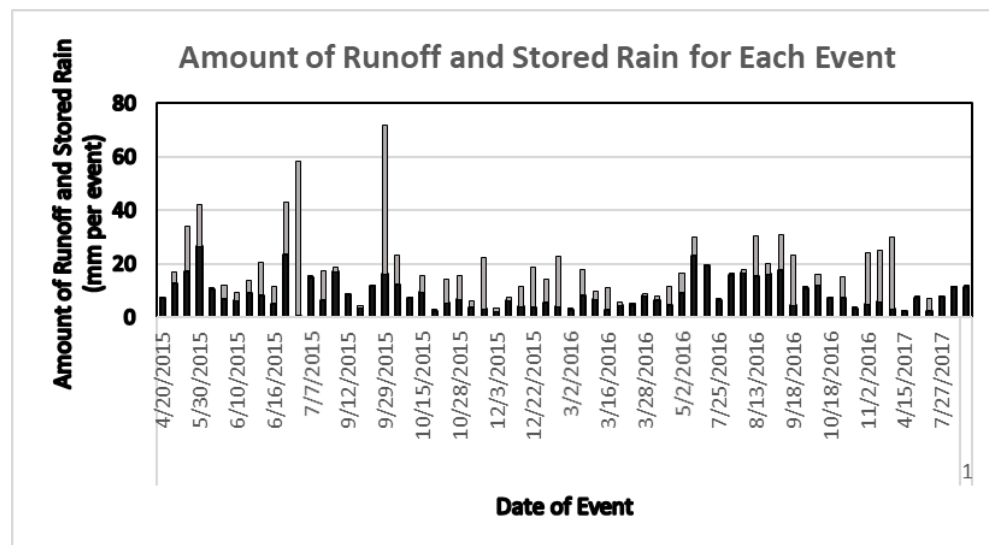


Figure 1. Partitioning of rain between runoff and storage in the growth medium of the green roof between April 20, 2015 and July 31, 2017. Events with snow are excluded. Black portion of each bar represents amount stored in the growth medium, while the gray portion indicates amount of runoff flowing into the roof drains.

Energy Flow through the Green Roof

Temperature data from various layers of the roof are used to estimate the performance of the roof in providing a barrier for energy flow from indoors to outdoors during cold weather. A cross section of the roof with locations of the temperature probes is shown in Figure 2. The layer providing the greatest barrier to heat flow is the 7.6 cm thick extruded polystyrene

insulation with a value of $R = 2.6 \text{ m}^2 \text{ K per watt}$, as given by the manufacturer. If we choose a time period when the heat flow is in quasi steady state, we can assume the heat flow in watts/m^2 is constant through the roof and thus use the temperature data to estimate values of R for the other roof layers.

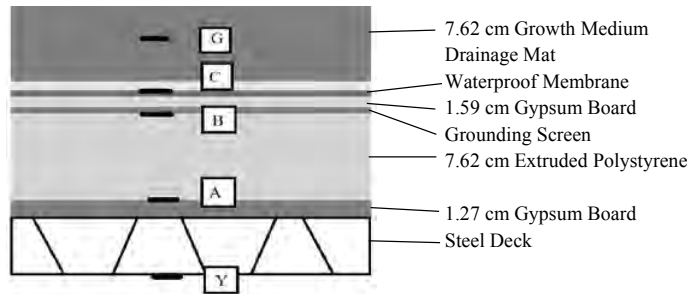


Figure 2. Cross section of the green roof, showing locations of temperature probes installed at A, B, C, and G. This sequence of 4 probes was installed at 5 locations across the roof. Three more widely spaced probes were affixed to the ceiling below the roof at Y.

Preliminary data for this roof reported by Squier and Davidson (2016) show that the total thermal resistance across all layers of roof is about $3.1 \text{ m}^2 \text{ K per watt}$, including the extruded polystyrene. Data obtained during the winter of 2017-2018 confirm this value based on a larger dataset. The R values of the other roof layers are in the range 0.14 to $0.3 \text{ m}^2 \text{ K per watt}$, which is very low compared with the extruded polystyrene. This suggests that the growth medium does not provide a significant barrier to heat loss in cold weather.

Chemistry of Green Roof Runoff

Concentrations of several anions have been measured in fresh precipitation and runoff from the green roof during measurement campaigns over the past few years. Results show that chloride and sulfate concentrations are generally much greater in green roof runoff than in the incident rain. Nitrate in runoff, on the other hand, can be either greater than or less than the levels in the rain.

Examples of concentration data for sulfate are shown in Figure 3 for 2014 and 2017. The levels in rain are small compared with the runoff draining from the growth medium of the green roof.

DISCUSSION

Figure 1 shows that the fraction of rain stored in the roof for each event varies between 0% and nearly 100%, depending on the intensity and total amount of rain in the storm. The fraction of rain stored also depends on the timing of the previous rainstorm and whether the growth medium had a chance to regenerate its storage capacity through evapotranspiration. The overall average storage per event is 51% over this time period, although many of the larger storms have much lower storage capability.

The wide range of values for the fraction of rain stored in the roof agrees with prior studies, and the overall average value of 51% is also within the range of prior work. Analysis is underway to compare values for specific events with results of modeling which accounts for the timing of successive rain events, evapotranspiration during dry periods between storms, and characteristics of the growth medium and vegetation on the roof.

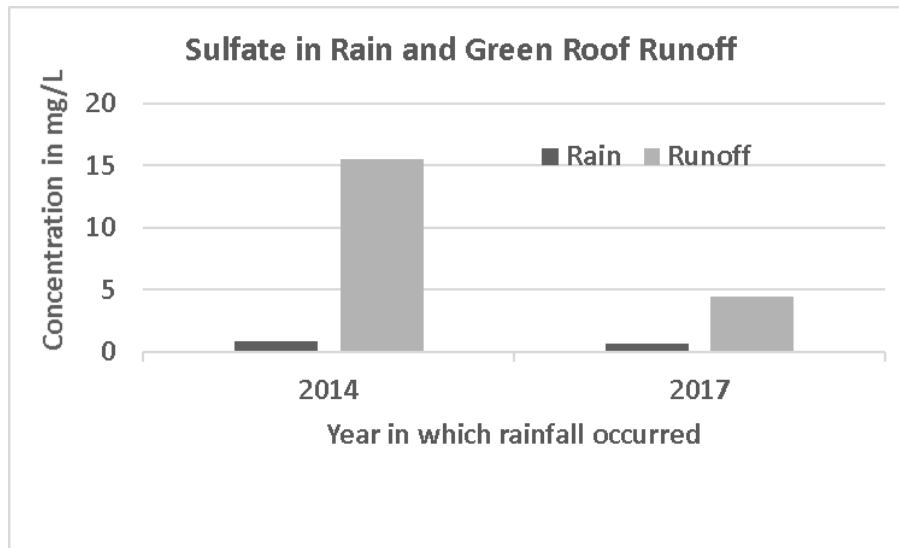


Figure 3. Average concentration of sulfate in fresh rain and in runoff from the growth medium of the green roof for storms sampled in 2014 and in 2017. Measurement campaigns included four storms in 2014 and ten storms in 2017.

The studies of energy flow using temperature data from layers of the roof show that the presence of a snowpack can serve as insulation when air temperatures drop below freezing. Data from the past three winters show that the temperature of the growth medium remains at or near 0° C when a snowpack is present, even when the air temperatures fall to minus 20° C.

Although not significant as an insulator in winter, the growth medium and vegetation of the green roof can prevent temperatures from reaching high values in bright daylight conditions in summer, relative to a traditional roof surface such as asphalt. This can result in reduced space cooling demand during the short air conditioning season in summer in Syracuse.

The CHAMPS-BES model is being used to estimate heat flow through the green roof under different conditions. Results of this modeling agree with estimated heat flow based on the temperature data from the roof layers for certain conditions.

Finally, the chemistry data in Figure 3 suggests a source of sulfate associated with the green roof. Todorov et al. (2018) report higher concentrations of sulfate in runoff from a different green roof compared with incident precipitation in Syracuse. The source of this sulfate is currently being investigated. Other researchers have reported high concentrations of phosphate and nitrate in green roof runoff, e.g., Hathaway et al. (2008) and Gregoire and Clausen (2011). These nutrients are often in fertilizer added to the growth medium when a green roof is first installed to assist growth of the vegetation on the roof. High levels of nitrate were measured in runoff from a few storms in the current study, although phosphate was not observed at detectable levels in any of the samples from the Convention Center green roof.

CONCLUSIONS

The green roof on the Onondaga County Convention Center in Syracuse, NY can store incident rain at times when the growth medium is not saturated. The stored rainwater can then evapotranspire to the atmosphere rather than contributing runoff to the combined sewers. Given the amounts of rain per event, its intensity, and the timing of rain events, the fraction of rain in each event that was stored in the roof averaged 51% over the period April 2015 to July

2017. Small events generally had most of their rain stored, but large storms had smaller fractions. The factors that influence this fraction are under investigation, and the results are expected to help designers of green roofs achieve greater amounts of rainwater storage. The growth medium and vegetation of this green roof are not observed to be significant barriers to heat loss from the building in cold weather. The extruded polystyrene insulation has a greater capacity to reduce heat loss. The chemistry of the runoff from this roof is different from the chemistry of the incident precipitation. Consistently higher levels of chloride and sulfate in the runoff compared with incoming rain are observed; the results for nitrate are mixed, with some events showing higher concentration in runoff but others showing lower concentrations. This work is important in assessing which contaminants can be contributed to runoff by a green roof, and which contaminants in incoming rain can be removed by a green roof.

ACKNOWLEDGMENT

This work was supported in part by NSF grant #1444755, Urban Resilience to Extremes Sustainability Research Network (UREx SRN), by the NSF EMPOWER NRT program, and by Syracuse University Water Fellowships. The authors acknowledge Onondaga County Department of Facilities Management, especially Han Phan and Archie Wixson, for the use of the Convention Center green roof. The authors also acknowledge the help of many undergraduate students at Syracuse University for assistance in different parts of this project.

REFERENCES

- Cipolla, S.S., Maglionico, M., and Stojkov, I. 2016. A long-term hydrological modeling of an extensive green roof by means of SWMM, *Ecological Engineering* 95, 876-887.
- Elliott, R.M., Gibson, R.A., Carson, T.B., Marasco, D.E., Culligan, P.J., and McGillis, W.R. 2016. Green roof seasonal variation: Comparison of the hydrologic behavior of a thick and a thin extensive system in New York City, *Environmental Research Letters* 11. doi.org/10.1088/1748-9326/11/7/074020
- Golden, Jay S. 2004. The built environment induced urban heat island effect in rapidly urbanizing arid regions: A sustainable urban engineering complexity, *J. Environ. Sci.* 1(4), 321-349. doi.org/10.1080/15693430412331291698.
- Gregoire, B.G., and Clausen, J.C. 2011. Effect of a modular extensive green roof on stormwater runoff and water quality, *Ecol. Eng.*, 37 (6), 963-969.
- Hathaway, A.M., Hunt W.F., and Jennings, G.D. 2008. A field study of green roof hydrologic and water quality performance, *Trans. ASABE*, 51 (1), 37-44.
- Squier, M.N. and Davidson, C.I. 2016. Heat flux and seasonal thermal performance of an extensive green roof, *Building and Environment*, 107, 235-244.
- Stovin, V., Vesuviano, G., and De-Ville, S. 2017. Defining green roof detention performance, *Urban Water Journal* 14(6), 574-588. doi.org/10.1080/1573062X.2015.1049279
- Todorov, D., Driscoll, C.T., Todorova, S., and Montesdeoca, M. 2018. Water quality function of an extensive vegetated roof, *Sci. of the Total Environ.*, 625, 928-939.
- Zhang L., Jin M., Liu J., and Zhang L. 2017. Simulated study on the potential of building energy saving using the green roof, *Procedia Engineering*, Vol. 205, pp. 1469-1476.

Thermal performance of a green roof based on CHAMPS model and experimental data during cold climatic weather

Yige Yang^{1*}, Cliff I. Davidson^{1,2}

¹ Department of Civil and Environmental Engineering, Syracuse University

² Center of Excellence in Environmental and Energy Systems, Syracuse University

*Corresponding email: yyang71@syr.edu

ABSTRACT

Green roofs are increasingly implemented in cities around the world. They have the potential to improve thermal performance of building systems through evapotranspiration, thermal mass, insulation and shading. Several studies have analyzed the heat flow impact of green roofs in hot weather, but few studies have examined the thermal performance during cold conditions. Roof membranes are known to fail in cold climates due to stress caused by large temperature fluctuations. A green roof can reduce the daily membrane temperature fluctuations ($T_{max} - T_{min}$) by an average of 7°C. This study presents an experimental investigation of a large extensive green roof on the Onondaga County Convention Center in Syracuse, NY from November 2017 to March 2018. The model known as CHAMPS has been applied to simulate the temperature profile through the layers of the green roof. In early winter without snow, the temperatures of the growth medium and roof membrane follow the diurnal cycle of ambient air temperatures with smaller amplitude. An average seven hour peak delay is observed. Under extremely cold weather, snow acts as an insulator. The temperature of the growth medium on the Convention Center remains slightly above freezing and is relatively steady when there is significant snow, even during extremely cold temperatures. Heat flux is dominated by the temperature gradient between interior space and the snow layer. On the basis of this work, it is shown that the CHAMPS model can play a valuable role in informing green roof design decisions.

KEYWORDS

Green roof; temperature fluctuation; snow; CHAMPS; roof membrane

INTRODUCTION

Green roofs normally consist of multiple layers, for example, vegetation, growth medium, drainage, waterproof membrane, and roof surface. They can vary from one design to another based on regional climates. While green roofs have been implemented in cities for years, the interest in installing green roofs in both retrofit and new construction is still increasing. Thermal benefits of green roofs include saving energy for space heating and cooling, and mitigating urban heat island effects due to evapotranspiration, direct foliage shading, the insulation effect of the soil and other factors. Another benefit is that the green roof can block solar radiation, thus protecting the base roof membrane from temperature fluctuations. In winter, a green roof can shield the roof membrane from extreme cold and from sudden changes in ambient air temperatures. Daily temperature fluctuations create thermal stress in the roof membrane and reduce its longevity (Teemusk and Mander, 2010).

The need for tools that designers and architects can use to assess the potential thermal benefits of green roofs is growing. Some studies investigate numerical models in DesignBuilder, PHPENICS, and EnergyPlus for green roof energy consumption simulations (Ran and Tang, 2017; Zhang et al. 2017; Lazzarin et al. 2005). In this paper, we present a new platform to inform the design process, the CHAMPS-BES model (Combined heat, air, moisture and pollutant simulations in building envelope systems). This model is used to assess the long-term energy and durability performance of building envelop systems.

Snow cover may provide a natural insulation layer in winter, which affects the cold weather performance of green roofs. There are two objectives of this study, both related to minimizing temperature variations that can damage the waterproof membrane on a roof. The first objective is to determine the impact of adding a green roof as a retrofit to a traditional roof on a large building in a cold climate. The second objective is to determine the impact of a significant snowpack on the retrofitted green roof.

METHODS

Study Site

This project focuses on the green roof on the Onondaga County Convention Center in Syracuse, NY. Syracuse is located at the northeast corner of the Finger Lakes region. It is known for its snowfall, in part due to the lake effect from nearby Lake Ontario. Based on the data from the weather station at Hancock International Airport (National Weather Service, 1938-2016), there are on average 65.2 days with snow per year. Total yearly snowfall depth is increasing (Fig. 1). Snow mainly falls between the months of November and March. January is the coldest month and also has the most snowfall (Fig. 2).

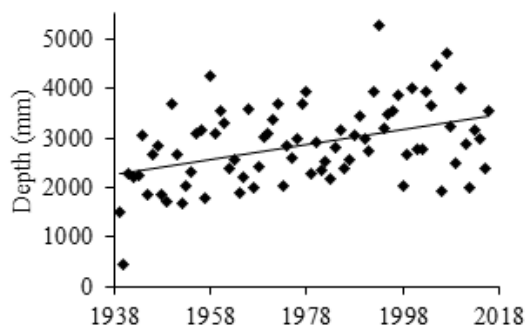


Figure 1. Yearly snowfall depth (1938-2016)

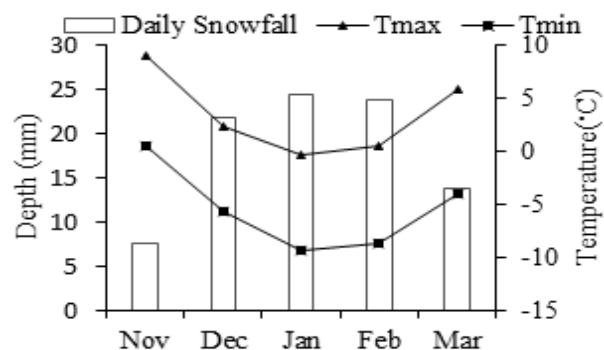


Figure 2. Daily snowfall and daily minimum and maximum air temperature (1938-2016)

The Convention Center green roof was retrofitted in 2011. The roof consists of the following layers: a steel deck, a gypsum board, extruded polystyrene insulation, a second gypsum board, a drainage mat, a waterproof membrane and a coarse growth medium layer (Fig. 3). The insulation layer and layers below are original to the building. Table 1 summarizes the main thermal properties of the layers of the green roof. The total area of the green roof is 5600 m². Plant species on the roof include *Sedum album*, *Sedum sexangulare*, *Sedum rupestre*, *Sedum floriferum*, and *Phedimus taksimense* (Squier and Davidson, 2016).

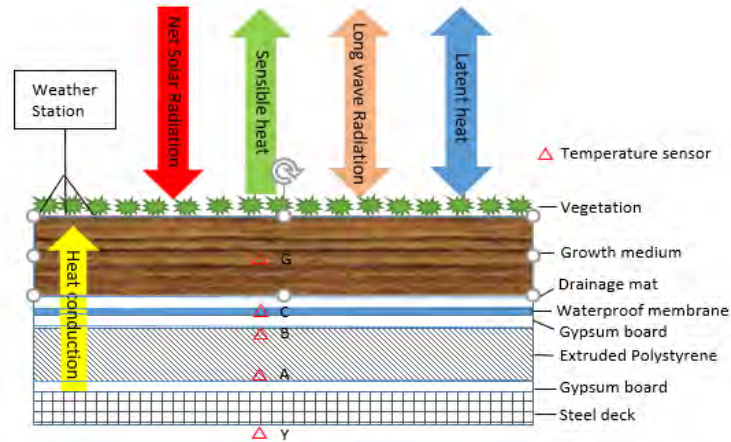


Figure 3. Schematic drawing of the Conventional Center green roof

Table 1. Thermal properties of the Conventional Center green roof

Layers	Thickness (cm)	Density (kg m ⁻³)	Thermal conductivity (W m ⁻¹ K ⁻¹)	Specific heat capacity (J kg ⁻¹ K ⁻¹)
Growth medium	7.62	790	0.36	1000
Drainage mat	0.63	1000	0.92	1000
Waterproof membrane	0.12	1400	0.43	1000
Gypsum board 2	1.59	700	0.16	870
Extruded polystyrene insulation	7.62	100	0.03	1300
Gypsum board 1	1.27	700	0.16	870
Steel deck	7.62	3600	20	700

Instrumentation and measurement

The thermal monitoring system of the green roof has been equipped with CR1000 Dataloggers and AM 16/32B Multiplexers (Campbell Scientific). A weather station on the roof includes air temperature, relative humidity, wind direction and windspeed. T109 temperature sensors (Campbell Scientific) are positioned at five different heights within the green roof (Fig. 3). This temperature profile is measured at five locations on the roof; only one location (station1) is used in this study. Temperature data are averaged and reported at hourly intervals. Interior temperatures are controlled by an HVAC system. Temperature sensor Y is mounted on the ceiling of the Exhibit Hall of the Convention Center to measure the indoor temperature. Solar radiation data are obtained from Syracuse University Weather Station, which is 1.9 kilometers from the green roof. The measuring period used for thermal analysis of the green roof is November 2017 to March 2018. Manual snow depth measurements have also been conducted.

CHAMPS simulation

Several input parameters are needed in the CHAMPS model. The weather data discussed above are used as inputs. Properties for the layers of the green roof are taken from manufacturer specifications. Snow cover is not considered in the simulation. The exchange coefficient of heat transfer is taken as 15 W/m²K, due to the large surface area of sedum plants. To assure the validity of the simulation results of CHAMPS, the model is validated using parameters for the green roof with experimental data from early November (11/1/2017-11/7/2017). After the validation, two case studies are performed based on the objectives:

- To determine the impact of the retrofit, CHAMPS is run for the case of the Convention Center traditional roof before the retrofit. The output of CHAMPS is compared with the experimental data from the green roof.
- To determine the impact of a snowpack on the green roof, CHAMPS is run for the green roof without snow. The output of CHAMPS is compared with experimental data from the green roof with a significant snowpack.

RESULT

Winter thermal performance

During the experimental campaign period, there were 87 days with snowfall in Syracuse. The average ambient temperature on the roof was -0.24°C . Temperature profiles for nine days in early November and early January are shown in Fig. 4. The extruded polystyrene layer contributes most to the effective insulation across the roof layers, where the largest temperature difference is between sensor A and sensor B. Early November represents typical early winter without snow in Syracuse. The temperatures of layers above the extruded polystyrene insulation (B, C, and G) follow the diurnal pattern of ambient air but with slightly smaller diurnal variation. An average of 7 hours delay in peak temperature is observed based on the temperature in the growth medium (G), compared to the ambient temperature. Early January represents a typical snowy winter period in Syracuse with a significant snowpack over the full nine-day period. Snow depth along the roof from west to east measured on January 9, 2018 is highly variable (Fig. 5). The snow depth on top of station 1 was 0.1 m. Figure 4 shows that the temperature of the growth medium was roughly constant at around 0°C . This is true even when the ambient air temperature was -20°C on occasion. This shows that the impact of snow accumulation on roof temperature is significant. A similar finding was reported by Getter et al (2011).

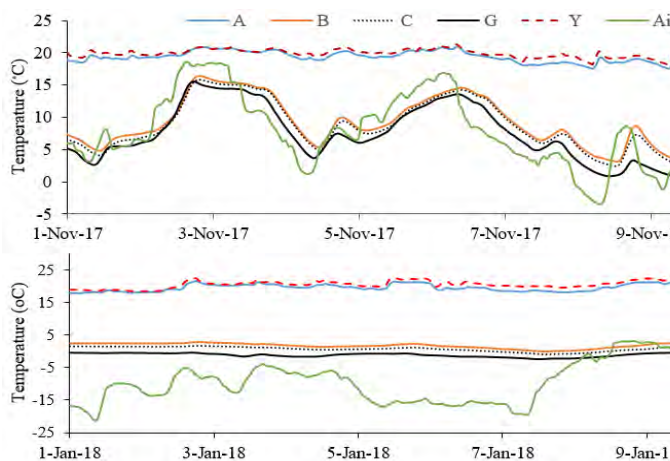


Figure 4. Temperature profiles in early November (no snow) and January (snow cover)

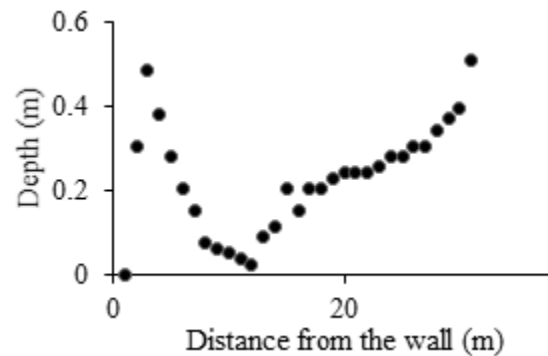


Figure 5. Snow depth measurement on Jan-9-2018

Model validation

The developed green roof model in CHAMPS has been validated using the data of the first week in November. The simulated growth medium temperature is compared with the measured data (temperature sensor G) in Fig. 6. On average, the CHAMPS model overpredicts the measured

temperature by only 17%. The simulated green roof model appears to be reliable and can be used to simulate the traditional roof and green roof without snow cover.

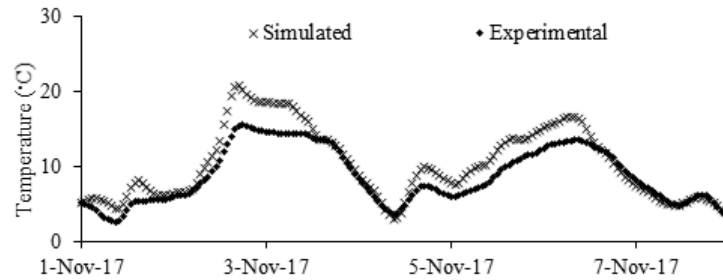


Figure 6. The validation of the CHAMPS model using experimental data for layer G

Temperature fluctuations on the membrane

The daily fluctuation is defined as the difference between daily maximum temperature and daily minimum temperature. A traditional roof model was developed in CHAMPS by deleting the growth medium and drainage mat layers. The temperature fluctuations of membrane on the traditional roof are far greater than those measured on the green roof in early winter (Fig. 7). The growth medium and drainage mat clearly play an important role in reducing temperature fluctuations on the membrane.

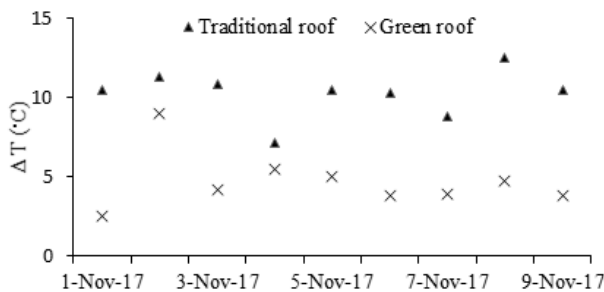


Figure 7. Temperature fluctuations at the membrane of the simulated traditional roof and measured on the green roof

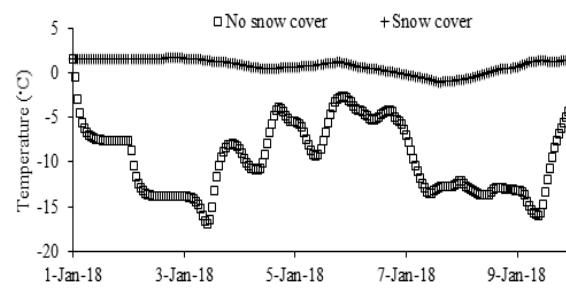


Figure 8. Temperature of the membrane for two conditions: simulated result with no snow cover and measurements with snow cover

Insulation effect of the snow cover

The green roof is simulated without a snow cover using early January meteorological data in CHAMPS. The membrane temperatures without a snow cover are compared with the measured membrane temperatures under snow (Fig. 8). The role of snow accumulation in reducing temperature fluctuations is significant. Without snow cover, under the same weather conditions, the membrane temperature could range from -18°C to 0°C . Under the accumulation of snow, the protection provided by the growth medium becomes negligible compared with the protection provided by the snow. The benefit of having a green roof is decreased in cold weather. This result has been reported in other studies (Lundholm et al. 2014).

DISCUSSIONS

Green roofs modify membrane temperature fluctuations in the winter. During times without snow cover, those membranes absorb solar radiation and are subjected to moderate temperatures. At night, exposed membranes re-radiate the heat and their temperatures drop (Liu & Baskaran, 2003).

Extreme temperature fluctuations are a major cause of membrane failure. Vegetation and growth media of green roofs improve the insulation properties of buildings and decrease the absorption of solar radiation, protecting the membranes. During snowy winter periods, snow cover promotes higher survival of perennial plants due to warmer soil temperatures. The snow cover also decreases temperature fluctuation at the membrane. In this study, a simulation using CHAMPS has been based on an energy balance through layers. Wind effects and moisture properties have not been considered due to lack of data, although those are crucial factors in assessing the overall energy performance of green roofs. Next, moisture and wind effects will be added to the simulation.

CONCLUSIONS

In this study, a large extensive green roof in Syracuse, NY was monitored during the winter months to understand its thermal performance. Furthermore, a green roof model was developed and verified by CHAMPS software. During early winter months, the plants and growth medium add thermal mass to decrease the membrane temperature fluctuations. In very cold weather, snow accumulation acts as effective natural insulation, isolating the roof from the ambient environment. CHAMPS software enables the user to add a green roof to any roof design. It is a systems model accounting for heat, air, and moisture. CHAMPS is a useful tool to the quantitative evaluation of the energy benefits of green roofs under regional climates, and can be of value to designers when considering retrofit additions of green roofs on buildings.

ACKNOWLEDGMENT

This work was supported in part by NSF grant #1444755, Urban Resilience to Extremes Sustainability Research Network, by the NSF EMPOWER NRT program, and by a Syracuse University Water Fellowship. The authors thank the Onondaga County Department of Facilities Management for their assistance and permission to work at the Convention Center.

REFERENCES

- Getter, K. L., Rowe, D. B., Andresen, J. A., & Wichman, I. S. (2011). Seasonal heat flux properties of an extensive green roof in a Midwestern U.S. climate. *Energy and Buildings*, 43(12), 3548–3557.
- Lazzarin, R. M., Castellotti, F., & Busato, F. (2005). Experimental measurements and numerical modelling of a green roof. *Energy and Buildings*, 37(12), 1260–1267.
- Liu, K., & Baskaran, B. (2003). Thermal performance of green roofs through field evaluation. *Proceedings of the First Annual International Green Roofs Conference: Greening Rooftops for Sustainable Communities.*, 10.
- Lundholm, J. T., Weddle, B. M., & Macivor, J. S. (2014). Snow depth and vegetation type affect green roof thermal performance in winter. *Energy and Buildings*, 84, 299–307.
- Ran, J., & Tang, M. (2017). Effect of Green Roofs Combined with Ventilation on Indoor Cooling and Energy Consumption. *Energy Procedia*, 141, 260–266.
- Squier, M., & Davidson, C. I. (2016). Heat flux and seasonal thermal performance of an extensive green roof. *Building and Environment*, 107, 235–244.
- Teemusk, A., & Mander, Ü. (2010). Temperature regime of planted roofs compared with conventional roofing systems. *Ecological Engineering*, 36(1), 91–95. <https://doi.org/10.1016/j.ecoleng.2009.09.009>
- Zhang, L., Jin, M., Liu, J., & Zhang, L. (2017). Simulated study on the potential of building energy saving using the green roof. *Procedia Engineering*, 205, 1469–1476.

Using rain and vegetation to improve thermal comfort in a hot street canyon with fully-integrated urban climate modeling

Aytaç Kubilay^{1,*}, Jan Carmeliet^{1,2} and Dominique Derome¹

¹Laboratory of Multiscale Studies in Building Physics, Empa, 8600 Dübendorf, Switzerland

²Chair of Building Physics, ETH Zurich, 8092 Zürich, Switzerland

*Corresponding email: aytac.kubilay@empa.ch

ABSTRACT

Building materials that are commonly used in urban areas generally have higher sensible heat storage and radiation entrapment, while having lower moisture storage and evapotranspiration, in comparison to the materials found in rural areas. These differences play a significant role in the occurrence of the urban heat island (UHI) effect, which has adverse impacts on thermal comfort, energy use and public health. Coupled numerical simulations of computational fluid dynamics (CFD) with the heat and mass transfer (HAM) in porous urban materials are performed to estimate the evaporative-cooling potential of different pavements in a street canyon. The local thermal comfort following a rain event on different pavements is compared with the one in presence of a grass-covered surface. The results show that the grass-covered ground provides better pedestrian thermal comfort, followed by porous material with large liquid permeability.

KEYWORDS

Urban climate, Thermal comfort, Computational fluid dynamics, Porous media, Vegetation

INTRODUCTION

Pedestrian thermal comfort is influenced by mean radiant temperature and local parameters such as air temperature, relative humidity and wind speed. Urban areas generally have increased sensible heat storage and radiation entrapment while having a decreased amount of evapotranspiration. Therefore, urban materials strongly influence the outdoor thermal comfort. The present study aims to investigate the evaporative-cooling potential of various urban pavement materials, showing different thermal and moisture transport properties.

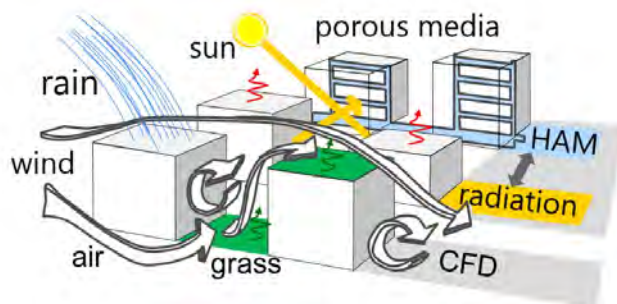


Figure 1. Schematic of the main physics implemented in the coupled urban microclimate model (CFD: Computational fluid dynamics, HAM: Heat and moisture transport).

A fully-integrated urban microclimate model is developed, where CFD simulations of wind flow around buildings are coupled with the heat and mass transport (HAM) in porous urban materials. The model solves for wind flow, transport of heat and humidity in the air and

transport of heat and moisture in building materials (Fig 1). Solar (short-wave) and thermal (long-wave) radiative heat exchange between surfaces and the sky are taken into account with multiple with diffuse reflections. Surface wetting due to wind-driven rain (WDR) is calculated based on an Eulerian multiphase model.

The proposed model is applied on a street canyon, where the three-dimensional heat and mass transport within the street-canyon ground and facades is coupled with the wind flow. The study at local scale (< 100 m) allows for parametric studies, where different contributions to thermal comfort can be evaluated in detail, such as shading, convective cooling, sensible heat transfer due to rain and evaporation. Detailed temporal and spatial analyses can be performed. The present study focuses on the drying period of different porous urban materials following a rain event. The impact of drying of pavement materials on outdoor thermal comfort is compared with the impact of evapotranspiration from a grass-covered surface. The thermal comfort for pedestrians is evaluated using the Universal Thermal Climate Index (UTCI) (Fiala et al. 2001). UTCI provides the perceived temperature based on surface temperatures, air temperature, relative humidity and wind speed.

NUMERICAL MODEL AND METHODOLOGY

Governing equations

The wind flow is solved using 3D steady Reynolds-averaged Navier-Stokes (RANS) with the standard $k-\varepsilon$ model. Additionally, transport equations for heat and moisture are solved. Heat is considered as an active scalar, where buoyancy is modeled by using a compressible formulation of the Navier-Stokes equations and calculating air density based on ideal gas law instead of the Boussinesq approximation. Moisture is modeled as a passive scalar, where the transported quantity is the humidity ratio, i.e. ratio of the mass of water vapor to the mass of dry air. Grass is modeled as a porous zone, providing the source/sink terms for heat, moisture and momentum (Manickathan et al. 2018a). Transpiration from grass blades is calculated based on leaf stomata resistance. Grass leaf temperature is calculated with an iterative energy balance calculation based on latent and sensible heat fluxes (Manickathan et al. 2018b).

Absorption, transport and storage of heat and moisture are simulated within the building materials using coupled heat and moisture transport equations for porous media. The present study uses the continuum modeling approach, where the different phases are not distinguished separately at a certain point in the material but, instead, the macroscopic behavior of the porous material is modeled. Within porous urban materials, the coupled heat and moisture transport equations are solved (Janssen et al, 2007):

$$(c_0\rho_0 + c_l w) \frac{\partial T}{\partial t} + \left(c_l T \frac{\partial w}{\partial p_c} \right) \frac{\partial p_c}{\partial t} = -\nabla(q_c + q_a) \quad (1)$$

$$\frac{\partial w}{\partial p_c} \frac{\partial p_c}{\partial t} = -\nabla(g_l + g_v) \quad (2)$$

where w denotes moisture content, p_c capillary pressure, c_0 specific heat of dry material, ρ_0 density of dry material, c_l the specific heat of liquid water, T absolute temperature. The fluxes q_c and q_a denote conductive and advective heat transfer, whereas g_l and g_v denote liquid and vapor moisture transfer including latent heat. The moisture exchange at the exterior surfaces of building materials comprises the rain flux and the convective vapor exchange, whereas the heat exchange comprises the convective heat transfer, the radiative heat transfer, the sensible

heat transfer due to rain and the latent and sensible heat transfer due to vapor exchange. Wetting due to rain on each surface in the computational domain is predicted using an Eulerian multiphase model (Kubilay et al. 2014), which solves for different sizes of raindrops and calculates the WDR intensity.

Solar and thermal radiative fluxes are calculated with separate systems of linear equations based on a radiosity approach. The direct component of incoming solar radiation is calculated with ray tracing. Multiple reflections of both solar and thermal radiation are calculated using view factors, which are calculated based on algebraic relations between surfaces. All building surfaces are assumed to be opaque to both longwave and shortwave radiation. The model further assumes that the building surfaces are grey, i.e. emissivity and absorptivity are equal and independent of wavelength. Absorption of solar radiation within the grass zone is modeled based on the Beer-Lambert law.

The numerical multi-transport model is implemented into OpenFOAM. The general framework and the detailed methodology of the model were given in an earlier paper (Kubilay et al. 2017).

Coupling algorithm

The coupling between the air and porous domains is performed by sequentially solving the steady RANS equations in the air and the unsteady heat and moisture transfer in porous building materials. This approach is valid due to the fact that the time scale of transport in building materials is larger than the time scale of transport in air. For the air domain, Dirichlet boundary conditions are used, where the values for temperature and humidity ratio are defined at the coupled boundaries. For the porous domains, Neumann boundary conditions are used, where the heat and moisture fluxes are defined at the material surfaces.

Transient heat and mass transport in porous domains are simulated using adaptive time steps (Janssen et al. 2007), during which the solution of the air domain remains constant. At each time step, internal iterations between heat and moisture equations are performed until temperature and moisture content values converge, while the thermal radiative heat fluxes are updated accordingly. Finally, the new values for temperature and moisture at the solid boundaries are used to solve the steady air flow for the next exchange time step. This information exchange between domains is repeated at each exchange time step (Saneinejad et al. 2014). In this study, an exchange time step of 10 min is chosen. For a more detailed description of the model, the reader is referred to Kubilay et al. (2017).

DESCRIPTION OF THE CASE STUDY

The case study is performed on an isolated three-dimensional street canyon, which is composed of two buildings with flat facades and horizontal roofs with a north-south orientation. Both buildings have the dimensions of height \times length \times width of $10 \times 10 \times 50 \text{ m}^3$. The computational domain is shown in Fig 2 as well as the orientation of the street canyon with respect to the wind direction and sun. For simplicity, wind speed is assumed constant at 5 m/s at the building height and wind direction is assumed perpendicular to the street canyon, i.e. from west. The variation of ambient temperature and total solar radiation intensity are based on June 21st, a typical early summer day with moderate ambient temperatures in Zurich, Switzerland. The ambient temperature varies between 11°C and 19°C, while the relative humidity (RH) varies between 62% and 86%. The simulations are run for several days with ‘dry’ conditions with no rain event until the conditions reach a daily thermal cycle that is

independent from the initial values. For 'rainy' conditions, a rain event of 1 mm/h intensity is applied for a duration of 10 hours at nighttime.

The leeward and windward facades of the street canyon are finished with an exterior layer of brick masonry with a thickness of 0.09 m. For the outer layer of the street-canyon ground, which has a thickness of 0.10 m, different materials are considered: concrete, soil and brick. Beneath this layer, an additional soil layer with a depth of 1.90 m is present for each case. Thermal properties for the dry materials are given in Table 1. For the simulations with grass, no rain event is modeled, however, transpiration rate is calculated based on the assumption that enough moisture is available in the soil at all times. Grass blades of 10 cm height are considered on the street-canyon ground (soil). Leaf area intensity (LAI) is taken as 2 and leaf drag coefficient as 0.2.

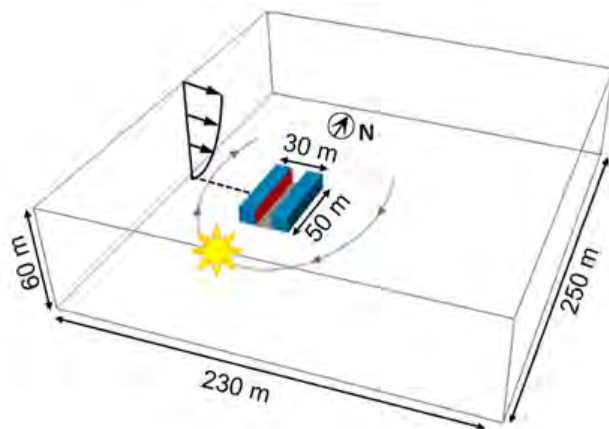


Figure 2. Computational domain and orientation of the street canyon with respect to wind direction and sun trajectory.

Table 1. Thermal properties of the dry porous media.

Material	Density [kg/m ³]	Specific heat [J/kgK]	Thermal conductivity [W/mK]
Bare soil	1150	650	1.500
Concrete	2280	800	1.500
Clay brick	1600	1000	0.682

RESULTS

Fig 3 compares the surface temperature at the center of the street-canyon ground for a duration of two days. Before the rain event, the surface temperatures for bare soil, concrete and clay brick reflect the thermal diffusivity and specific heat of the respective materials. After the rain event, due to evaporation, the maximum surface temperature decreases as much as 20°C for brick and 15°C for soil. A slightly larger reduction of temperature is observed for brick than for soil as the brick is capillary active and has a larger liquid permeability than soil in this case. For concrete, the decrease in maximum temperature is negligible as a much smaller amount of water is absorbed in concrete. Grass-covered soil temperature is in general at around the same values as concrete as it is shaded by grass, while the maximum grass leaf temperature is 26°C as a result of latent heat due to evaporation.

Fig 4 compares the conditions at pedestrian height (1.75 m) at the center of the street canyon, namely the air temperature, air relative humidity and the UTCI. Before the rain event, as a result of evapotranspiration, the lowest air temperature and the highest relative humidity are

observed for grass-covered street canyon. After the rain event, air temperature decreases by up to 1.4°C for brick. However, simultaneously, a considerable increase of relative humidity is observed as shown in Fig. 4(b). Overall, the lowest UTCI is observed for grass (Fig. 4(c)). The decrease in UTCI due to rain event is up to 2.0°C.

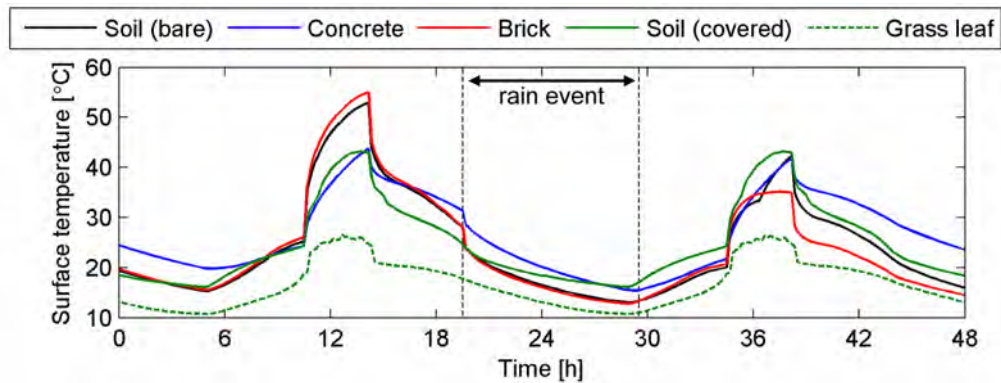


Figure 3. Variation of surface temperature at the center of the street-canyon ground for different materials.

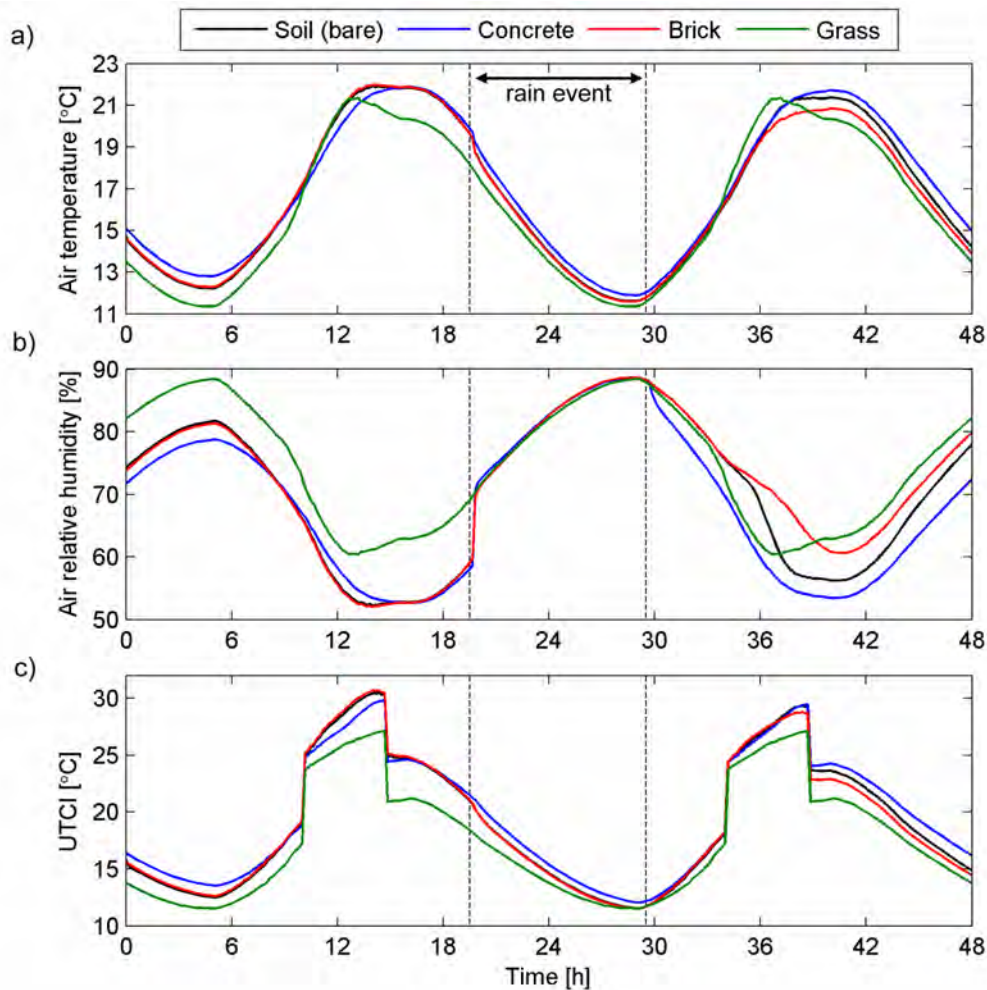


Figure 4. Variation of a) air temperature, b) air relative humidity and c) UTCI at pedestrian height at the center of the street canyon.

DISCUSSION AND CONCLUSIONS

The influence of different porous urban materials exposed to environmental loading is investigated. Evaporative-cooling potential for the materials is compared to the conditions provided by the grass-covered area. While the results obtained for the isolated street canyon cannot be generalized for complete range of urban areas, the study indicates several significant results. It is found that the effect of transpirative cooling due to grass is apparent both in terms of air temperature and of UTCI. While, the increase in relative humidity has an adverse effect on thermal comfort, overall, improved conditions are observed for the grass-covered surface. The evaporative-cooling effect due to the absorption and evaporation of rain water in porous urban materials increases as the liquid permeability of materials gets larger. We note that the conclusions depend on several factors such as total wetting amount due to rain, wetting period of the day, leaf area intensity of grass and local wind flow conditions. The transpiration from grass is also dependent on the water availability in the soil. Further work is planned on including on evaluating the local effects of heat waves, at neighborhood scale.

ACKNOWLEDGEMENT

The support through the Swiss Competence Center for Energy Research project “Future Energy Efficient Buildings and Districts”, CTI.1155000149, is gratefully acknowledged.

REFERENCES

- Fiala D., Lomas K. J., Stohrer M. 2001. Computer prediction of human thermoregulatory and temperature responses to a wide range of environmental conditions. *International Journal of Biometeorology*, 45(3):143–159.
- Janssen H., Blocken B., Carmeliet J. 2007. Conservative modelling of the moisture and heat transfer in building components under atmospheric excitation. *International Journal of Heat and Mass Transfer*, 50:1128-1140.
- Kubilay A., Derome D., Blocken B., Carmeliet J. 2014. Numerical simulations of wind-driven rain on an array of low-rise cubic buildings and validation by field measurements. *Building and Environment*, 81:283-295.
- Kubilay A., Derome D., Carmeliet J. 2017. Coupling of physical phenomena in urban microclimate: A model integrating air flow, wind-driven rain, radiation and transport in building materials. *Urban Climate*. In press.
- Manickathan L., Defraeye T., Allegrini J., Derome D., Carmeliet J. 2018a. Parametric study of the influence of environmental factors and tree properties on the transpirative cooling effect of trees. *Agricultural and Forest Meteorology*, 248:259-274.
- Manickathan L., Kubilay A., Defraeye T., Allegrini J., Derome D., Carmeliet J. 2018b. Influence of vegetation on pedestrian thermal comfort in a street canyon, In: *Proceedings of 1st International Conference on New Horizons in Green Civil Engineering (NHICE-01)*, Victoria, BC, Canada, April 25 – 27.
- Saneinejad S., Moonen P., Carmeliet J. 2014. Coupled CFD, radiation and porous media model for evaluating the micro-climate in an urban environment. *Journal of Wind Engineering and Industrial Aerodynamics*, 128:1-11.

An investigation on the quantitative correlation between urban morphology parameters and outdoor ventilation efficiency indices

Yunlong Peng, Zhi Gao, Wowo Ding*

School of Architecture and Urban Planning, Nanjing University, Nanjing, 210093, China.

*Corresponding email: dww@nju.edu.cn

ABSTRACT

Urban outdoor ventilation and pollutant dispersion have important implications for the urban planning and design of urban morphology. In this paper, two urban morphology parameters including Floor area ratio (FAR) and Building site coverage (BSC) are attempted to investigate the quantitative correlation with urban ventilation indices. Firstly, we present an idealized model including nine basic units. The FAR of model is constant 5.0, and the BSC increases from 11% to 77%, which in consequence generates 101 non-repetitive asymmetric forms. Next, the Computational Fluid Dynamics (CFD) is employed to evaluate the ventilation efficiency of pedestrian level within each model's central area. Six indicators including air flow rate (Q), mean age of air (τ_p), net escape velocity (NEV), purging flow rate (PFR), visitation frequency (VF) and resident time (TP) are used to assess the local ventilation performance. Results clearly show that when the FAR of the plot is specified, the local ventilation performance does not present an obvious linear relationship. As the BSC increases, the ventilation in the central area does not keep reducing. On the contrary, some forms with low BSC have poor ventilation and some particular forms with high BSC have better ventilation performance. This shows that for an urban, it not always exists poor local ventilation under the high-density conditions. The local ventilation performance can be effectively improved by rationally arranging the architectural arrangement within the plot. These findings suggest a preliminary way to build up the correlation between urban morphology parameters and ventilation efficiency. Even though the application of these results to the real cities require further research, but for this paper, it presents a feasible framework to the urban designers.

KEYWORDS

correlation research, urban morphology, ventilation indicators

INTRODUCTION

Past few decades the urbanization has become a global phenomenon. The urbanization process has accelerated the increase of urban density, which leads to significant differences between urban morphology and original form in natural conditions (such as the number of streets, height of buildings, void spaces, etc.). Due to the compact urban spaces, air pollutant cannot be diluted and dispersed in time and it probably causes a series of health problems.

Flow rate (Q) was used to assess the effective flow which passes through the urban canopy layer (Hang et al., 2009). The concept of mean age of air (τ_p) is a statistical measure of the time it takes for a parcel of air to reach a given point in the flow field after entering this flow field, and large mean age of air implies a poorly ventilated region. Purging flow rate (PFR), was introduced to predict the net rate of removing pollutant in the urban domain by (Bady et al., 2008), The visitation frequency (VF) is the number of times a pollutant enters the domain and passes through it. The residence time (TP) is the time a pollutant takes from once entering

or being generated in the domain until leaving the domain. The feasibility of PFR, VF and TP using to evaluate the urban ventilation has been verified by (Kato and Huang, 2009). The concept of net escape velocity (NEV) proposed by (Lim et al., 2014) represents the effective velocity at which the contaminant is transported/diluted from a target point, and a high NEV indicates fine removal efficiency of the pollutants.

Ventilation indicators abovementioned have been validated by wind tunnel measurement and numerical simulations. Nevertheless, morphological parameters associated with most of them are purely geometric parameters such as urban street aspect ratio (H/W), building height (H), building packing density (λ_p) (Cheng et al., 2007), etc. However, with the increase of urban density, the floor area ratio (FAR) within urban plots is the first key factor considered by urban designers and planners, which involves economics, policy and urban development strategies, etc. In the early planning stage, the FAR of urban plot has been determined first, so it may be of great significance to investigate the relationship between building site coverage (BSC) and ventilation performance in a specific area when the FAR is constant. Previous research (Peng et al., 2017) has preliminarily explored the relationship between FAR, BSC and ventilation performance, but only the average wind ratio was employed. In this paper, more comprehensive ventilation assessment indicators and substantial forms will be adopted for comprehensive research.

METHODS

Morphology characteristics of idealized models

During the early stage for urban planning and designing, the floor area ratio (FAR) within urban plots has been formulated, which is closely related to the cost, benefit, development strategies etc. Once the FAR of plots has been specified, it will not be easily changed. The main factors affecting the morphology of plots include the building site coverage (BSC) and the architectural arrangement within the plots. The idealized model is consisted of 9 basic units, and each unit size is a 30-meter square. The central square is the interested area which does not to be covered by building. The other eight units around the central may be covered with buildings. The FAR of all possible forms are constant 5.0, and the initial BSC is 11%, meaning that there is only one high-rise building. Meanwhile, there are five possibilities for the position of building in the plot (excluding symmetry conditions).

In order to explore the correlation between morphology and performance, all possible forms should be classified. As shown in Figure 1. according to the architectural layout around the central area, the model is divided into Form C and Form B. The Form C configuration means that the front and back directions of the central area are not blocked and there have a channelling effect. The Form B1~B3 means the number of building along the windward projection. The Form B(F1~F3) means the number of building front (in the first two rows) along the windward projection. In this study, there only one incoming wind direction ($\theta=90^\circ$) is considered. As a consequence, the symmetrical configurations along the east-west direction are exclude. When the BSC increases from 11% to 77%, a total of 101 asymmetrical forms are generated.

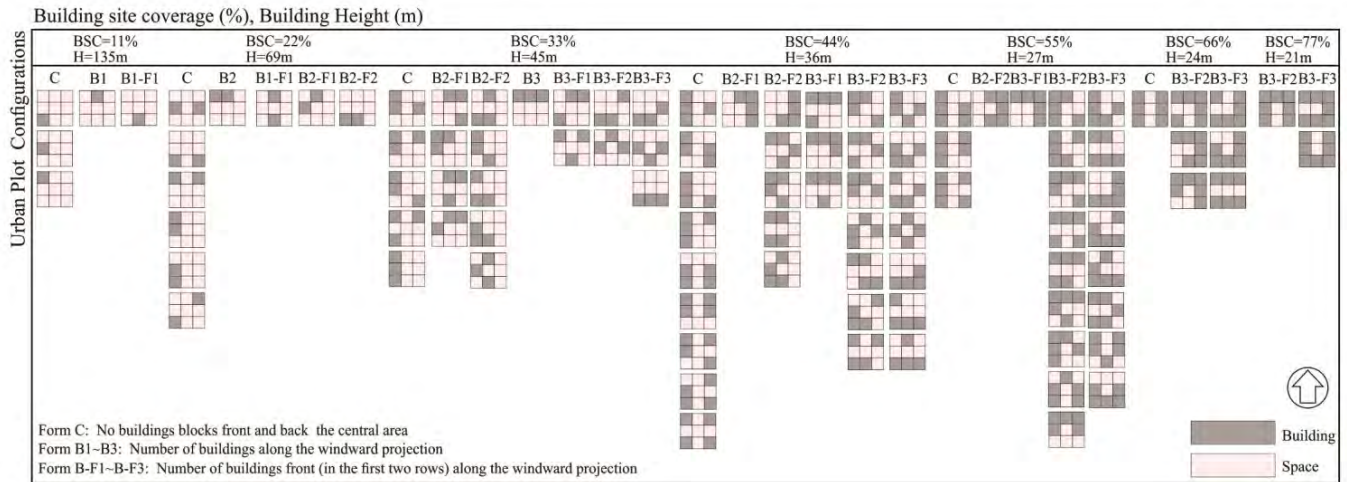


Figure 1. Idealized models with BSC increasing from 11% to 77%

CFD simulation setup

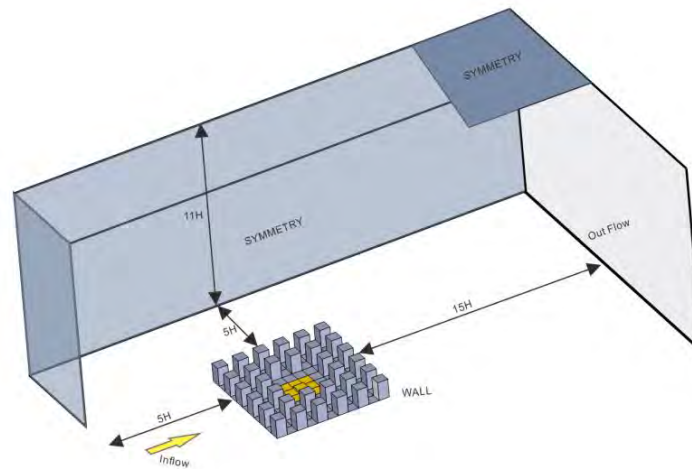


Figure 2. Schematic sketch of geometry and boundary conditions used in CFD simulations

The computational domain size is shown in Figure 2, the inflow and lateral boundaries are set 5H and away from the buildings. The outflow and the top boundaries are respectively 15H and 6H. Mesh resolution fulfils the major simulation requirements as recently recommended by (Franke et al., 2007) and by the Working Group of the Architectural Institute of Japan (AIJ). The comparison showed that the k-ε model can be used for such configurations and that there is a good agreement in terms of the essential features of the mean flow. The inlet profiles of mean wind speed U , turbulent kinetic energy k and turbulence dissipation rate ε were identical for all simulations. A logarithmic mean speed profile was fitted to the measured profile using Eq. (1) where z_0 is the aerodynamic roughness length taken as 0.2m, κ the von Karman constant equal to 0.42 and z the height coordinate. Turbulent kinetic energy profile was calculated as in Eq. (2), where I_u is the measured longitudinal turbulence intensity, and the turbulence dissipation rate ε was calculated as in Eq. (3).

$$U(z) = \frac{u_{ABL}^*}{\kappa} \ln\left(\frac{z + z_0}{z_0}\right) \quad (1)$$

$$k(z) = \frac{u_{ABL}^{*2}}{\sqrt{C_\mu}} \quad (2)$$

$$\varepsilon(z) = \frac{u_{ABL}^{*3}}{\kappa(z + z_0)} \quad (3)$$

The indicators used for correlation studies with morphological parameters in this study include flow rate (Q), local mean age of air (τ_p), net escape velocity (NEV), purging flow rate (PFR), visitation frequency (VF) and residential time (TP). Due to the limitation of pages, the calculation equations for these indicators are not listed here. Uniform release method is applied in this study (Hang et al., 2009). In this paper we used uniform tracer gas source from ground up to 2 m for ventilation analysis. The tracer gas emission rate $S_c = 10^{-7} \text{ kg/m}^3 \text{ s}$ to ensure the source release produced little disturbance to the flow.

RESULTS

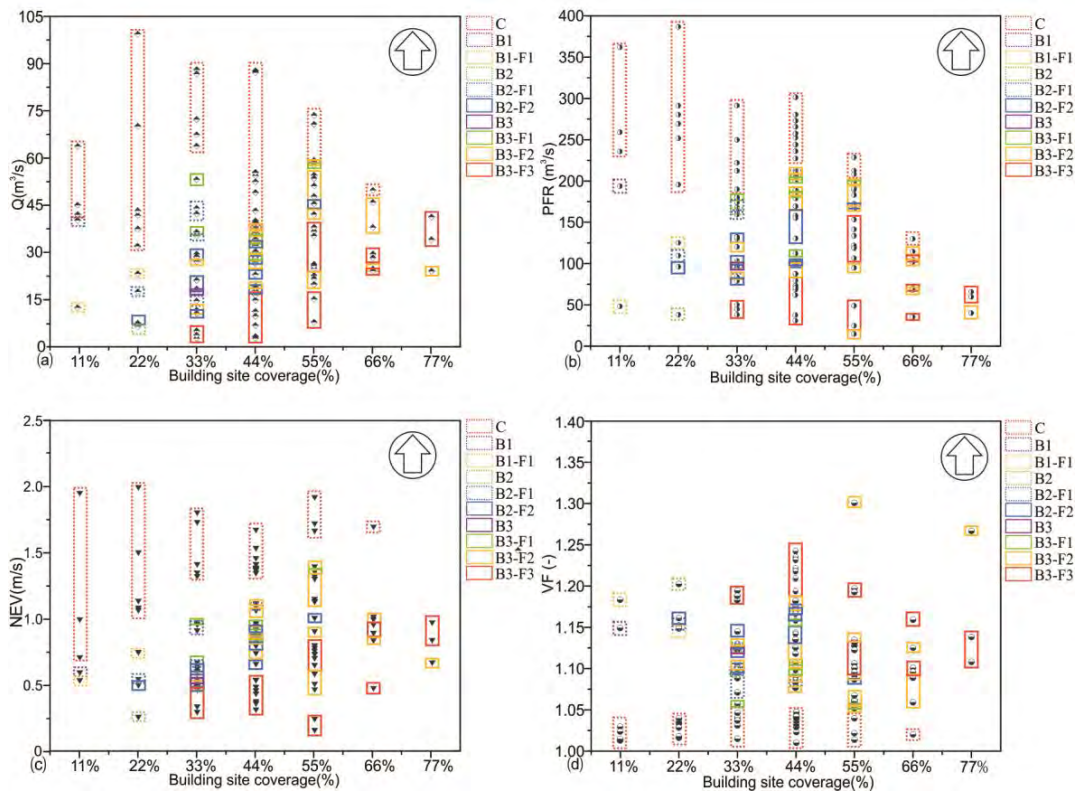


Figure 3. The value of ventilation indices within each configuration of BSC increasing from 11% to 77% (a) Q, (b) PFR, (c) NEV, (d) VF

Figure 3 shows the results within the study domain at pedestrian level for the BSC increasing from 11% to 77%. Results clearly show that the level of ventilation efficiency within the central area decreased as the BSC increased in general, due to the increase of buildings within the plot. However, it is not absolutely that with the gradual increase of the BSC, the ventilation performance of the central area is declining in particular in the calculation result of NEV and VF (Fig. 3c,3d). When the BSC continues to increase from 44% to 77%, the NEV and VF become slightly better. However, the result of each model in Figure 3 does not intuitively

reflect the relationship between ventilation indicators and morphological parameters. Also, the number of configurations corresponding to various BSC is also different and it is difficult to make comparisons. Therefore, the average value and the error are calculated for each configuration, which can reflect the intuitive relationship between the indicators and the morphology as the BSC changes.

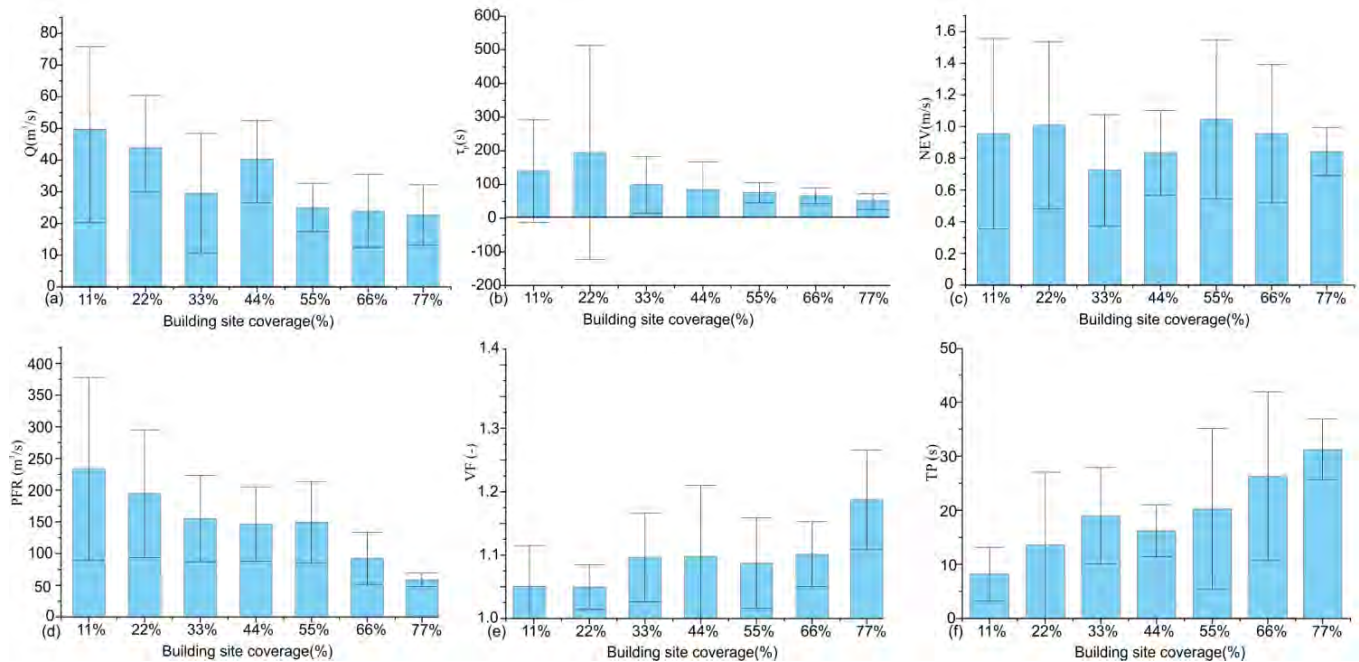


Figure 4. The average value and variance of each index corresponding to BSC increasing from 11% to 77% (a) Q , (b) τ_p , (c) NEV, (d) PFR, (e) VF, (f) TP

In Figure. 4, results of different indicators show that the ventilation performance at the pedestrian level in the central area is slightly lower as the BSC increases. In particular, when the BSC is 44%, values of six indices show that the capacity of removal pollutant obvious enhances. With the BSC ranges from 44% to 77%, although the buildings density in the plot is gradually raise, meanwhile the channeling effect is interrupted and weak. Due to the constant of FAR, the building height gradually decreases with the BSC increasing. The air flow flush the central area is mainly mean flow when the BSC is at a low level. As the BSC increases, and the building height reduces, especially the BSC is 55%, the fresh air entering the domain through the turbulent flow from the roof of building enhances obviously, which is consistent with the research results of (Hang et al., 2015), the fresh air flow flush and remove the concentration of pollutants in the central area and plays a role in improving ventilation performance.

DISCUSSIONS

It can be explained that for an urban area where the density is at a high level, the wind channeling effect is not the only and effective way to dilute or remove air pollutants. When the average building height is relatively low, the effect of turbulence flow can effectively remove the pollutants at the pedestrian level and improve the local ventilation performance. At the same time, the results also yield that the BSC is not the only factor that determines the ventilation performance within the urban plot, and the building patterns within the plot also plays a significant role on the pollutant dispersion.

CONCLUSIONS

First of all, to make constant the FAR to 5.0, the BSC gradually increases from 11% to 77%, resulting in a total of 101 asymmetrical idealized plot configurations. Second, we propose six indicators for correlation with morphological indicators. Simulation, and statistical results show that when the BSC is 11%, 22%, and 33%, the ventilation performance at pedestrian level within the domain decreased significantly, which illustrates when the BSC is below 33%, the building height is at a high level. With the increase of BSC, the fresh airflow flushes into the center area is interrupted by isolate building, resulting in an increase in the concentration of pollutants. When the BSC increased to 44%, 55%, 66%, and 77%, though the ventilation performance was slightly lower than before, due to the lower average building height, the fresh air flows into the center area which is mean flow to turbulent flow through building roof. The results in this study show that BSC and FAR are effective morphological parameters for establishing correlation studies. For high-density cities, the ventilation performance of void spaces can be effectively improved by reducing the average height of buildings.

Moreover, this study is still an idealized configuration. Subsequent research will add secondary roads within the central area, and discuss which indicators are most sensitive to morphological changes and more suitable for in-depth correlation research with BSC and FAR.

ACKNOWLEDGEMENT

The research was supported financially by the key project of the National Science Foundation of China on “Urban form - microclimate coupling mechanism and control” through Grant No. 51538005.

REFERENCES

- Bady, M., Kato, S., Huang, H., 2008. Towards the application of indoor ventilation efficiency indices to evaluate the air quality of urban areas. *Building & Environment* 43, 1991-2004.
- Cheng, H., Hayden, P., Robins, A.G., Castro, I.P., 2007. Flow over cube arrays of different packing densities. *Journal of Wind Engineering & Industrial Aerodynamics* 95, 715-740.
- Franke, J., Hellsten, A., Schlünzen, H., Carissimo, B., 2007. Best practice guideline for the CFD simulation of flows in the urban environment. *Cost Office Brussels* 732.
- Hang, J., Sandberg, M., Li, Y., 2009. Age of air and air exchange efficiency in idealized city models. *Building & Environment* 44, 1714-1723.
- Hang, J., Wang, Q., Chen, X., Sandberg, M., Zhu, W., Buccolieri, R., Sabatino, S.D., 2015. City breathability in medium density urban-like geometries evaluated through the pollutant transport rate and the net escape velocity. *Building & Environment* 94, 166-182.
- Kato, S., Huang, H., 2009. Ventilation efficiency of void space surrounded by buildings with wind blowing over built-up urban area. *Journal of Wind Engineering & Industrial Aerodynamics* 97, 358-367.
- Lim, E., Ito, K., Sandberg, M., 2014. Performance evaluation of contaminant removal and air quality control for local ventilation systems using the ventilation index Net Escape Velocity. *Building & Environment* 79, 78-89.
- Peng, Y., Gao, Z., Ding, W., 2017. An Approach on the Correlation between Urban Morphological Parameters and Ventilation Performance. *Energy Procedia* 142, 2884-2891.

Effect of Urban Texture on Building Energy Performance

Suzi Dilara Mangan^{1,*}, Irem Sozen², Gul Koclar Oral², Idil Erdemir Kocagil²

¹Istanbul Aydin University, Istanbul

²Istanbul Technical University, Istanbul

*Corresponding email: dilaramangan@yahoo.com

ABSTRACT

Today, ongoing discussions on climate change, depletion of fossil fuels and energy efficiency emphasize the need for a more sustainable built environment and thus the need to reduce energy consumption in buildings and urban textures and reduce greenhouse gas emissions. Therefore the evaluation of building energy performance with a holistic approach, taking the effect of urban textures and microclimates into consideration has become very significant in the recent years. Urban texture is a commonly accepted expression including the form and height of buildings, the width of streets, their orientation, spatial configuration and arrangement in space intersection, vegetation and so on. This study aims to develop and suggest a model which allows the evaluation of the level of effects of the design parameters which should be considered at the scale of urban textures, on the energy performance of buildings to design sustainable, energy efficient built environments. In the first stage energy performance of a reference building modeled in different urban texture alternatives was evaluated. The evaluations are performed through DesignBuilder simulation program for the location of Istanbul representing temperate-humid climatic region. The parameters of aspect ratio (H/W) and orientation were used to develop different urban texture alternatives. In the second stage, analyses of outdoor thermal comfort of the existing condition and the condition with the added effect of vegetation for the alternatives with the lowest overall energy consumption were conducted with the ENVI-Met program. The thermal comfort parameters of air temperature, mean radiant temperature, wind speed and physiological equivalent temperature (PET) index were used to evaluate outdoor thermal comfort in streets. As a result, the urban texture alternative which achieved the optimum result for energy performance and with regard to outdoor thermal comfort was determined.

KEYWORDS

Sustainable Built Environment, Urban Texture, Building Energy Performance.

INTRODUCTION

With the rapid growth of urban areas all around the world, urban textures are considered to be the main source of CO₂ emissions responsible for climate change. Therefore, urban textures and buildings in these areas should be planned, developed and used optimally in relation to energy consumption and CO₂ emissions caused by the consumed energy. On the other hand, when the relation between urban textures and climate is examined, it is possible to conclude that design parameters including layouts, building forms, building envelopes, and landscape planning have an impact on the urban climate, and urban climate has an impact on the energy performance of buildings and on the use of urban open spaces. Therefore, the correlation between urban texture and building energy consumption underlines a complex balance that includes climate parameters and urban canyons and buildings. Thus, design of urban textures and study of building energy consumption within the designed urban textures to achieve sustainable built environment have gained speed. The term “urban texture” means a territorial, planning and constructive organization, which has homogeneous characteristics from the

point of view of the historical transformation and of the formal and dimensional relationship between public and private spaces (Tiziana and Marianna, 2013). Urban texture is a commonly accepted expression including the form and height of buildings, the width of streets, their orientation, spatial configuration and arrangement in space intersection, vegetation and so on (Ratti et al. 2005). To describe and model the interaction of the urban texture with the climate and energy, the following parameters should be considered: aspect ratio, street orientation, sky view factor, local and neighborhood scale, street trees and urban parks (Oke, 1976; Golany, 1995; Sanaieian et al. 2014, Jamei et al. 2016). The most important parameter among those that are considered to define urban textures that affect outdoor comfort conditions based on climatic characteristics is the ratio of average building height (H) to average street width (W). This aspect ratio, which defines the relations among buildings in the sections of urban textures, controls solar access and wind movements with limitations of orientation and causes changes in micro-climate data. Additionally, it can affect comfort conditions of the buildings within an urban texture. Urban textures in temperate climatic regions are mostly designed based on the building requirements to have access to solar radiation during a heating period, but the level of effect of this approach on outdoor conditions is not evaluated. Therefore, the H/W ratio is taken as the primary parameter in many studies aiming to analyze outdoor thermal comfort. The orientation effect is also taken into consideration to evaluate outdoor conditions according to changing aspect ratios (Toudert and Mayer, 2006; Andreou 2013; Kariminia et al. 2015; Yang and Li, 2015). Thus, parameters such as H/W ratio, orientation and the use of green spaces that strongly affect energy performances of buildings and outdoor thermal comfort conditions should be taken into consideration during the design stage. This study aims to develop a model with which, in addition to urban texture-building interaction, outdoor thermal comfort, can also be analyzed to design sustainable, energy efficient environments. The effect of the design parameters of urban textures (building height/street width, street and façade direction, vegetation) is analyzed using the alternatives defined for this purpose. The analyses are conducted for Istanbul representing temperate-humid climate where the heating period is longer than the cooling period and the design alternatives suggested based on the findings can be applied to other regions with temperate-humid climate conditions.

METHODS

The objective of the study is to evaluate the effect of urban texture alternatives developed with the defined design parameters on the outdoor comfort conditions and energy consumption of the buildings within those urban textures. In order to evaluate the effect of urban texture alternatives on energy consumption of the buildings, a reference building is defined for each urban texture and energy consumption is calculated for this reference building. The reference buildings are given in Figure 1. Thus, the steps to be followed in this study are given below.

Defining design parameters for urban textures

In order to analyze the outdoor thermal comfort level as well as the urban texture-building interactions, first the design parameters for urban textures should be defined. For this purpose, various urban textures were created based on the H/W ratio commonly used to define urban textures, and the effects of such urban textures were analyzed. In order to develop different urban textures, the H/W ratio is taken as 1.00 for uniform canyon; 0.50 for shallow canyon and 2.00 for deep canyon (Ahmed et al. 2015). To determine street widths for the three different H/W values used in the study, a 5-story residential building representative of the residential buildings commonly used in Istanbul was evaluated. The created urban texture alternatives with different H/W ratios are oriented to north-south, east-west, northwest-

southeast, northeast-southwest in order to determine the effect of orientation on outdoor thermal conditions (Figure 1).

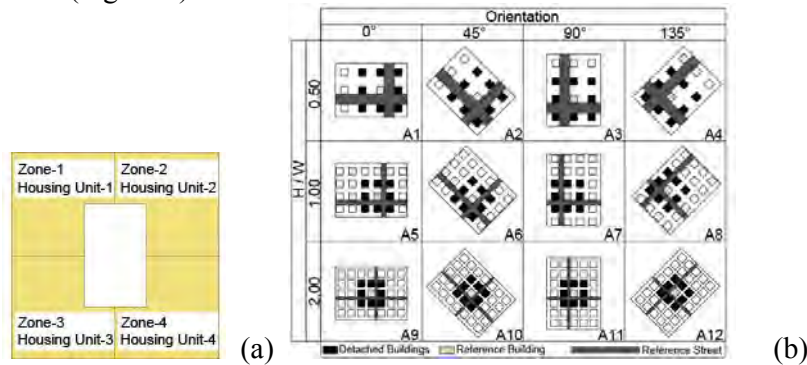


Figure 1. Floor plan of the reference building (a) and urban texture alternatives (b).

Defining design parameters for the reference buildings

In order to achieve general acceptance to define the design parameters for the reference building in the urban texture, residential building types built by TOKI (Housing Development Administration of Turkey), which plays an important role in the construction of residential buildings in Turkey, were researched and assessed. Based on the research, housing units with a building coverage of 100m^2 were chosen. The A/V ratio (total external surface / building volume) is 0.2; the total floor area of building is 400 m^2 and the total building height is 15.00 m. While developing the details for the layering of building envelope of the reference building, the building envelope sections which are commonly used in the existing mass housing projects were used and the total heat transfer coefficient values (U , $\text{W}/\text{m}^2\text{K}$) of the opaque and transparent components of the building envelope comply with the limit values set for Istanbul in TS 825 (2013) ($U_{\text{wall}}:0.57\text{ W}/\text{m}^2\text{K}$, $U_{\text{g_floor}}:0.53\text{ W}/\text{m}^2\text{K}$, $U_{\text{roof}}:0.38\text{ W}/\text{m}^2\text{K}$, $U_{\text{window}}:1.40\text{ W}/\text{m}^2\text{K}$). The transparency ratio (total transparent area / total façade area) was assumed as 30% for all façades. There are four housing units on each floor of the building and each housing unit was accepted as a single conditioned zone (area which is heated/cooled). The indoor comfort temperature was accepted as $20\text{ }^\circ\text{C}$ for the heating period and $26\text{ }^\circ\text{C}$ for the cooling period.

Development of alternatives based on the defined designed parameters

In order to evaluate energy performance of the reference building, based on the urban textures with the H/W values determined to develop alternatives for design parameters, it is assumed that the urban textures consist of detached buildings in a study area of approximately $30,000\text{ m}^2$. The number of buildings in the urban textures varies depending on the alternatives and is shown in Figure 1.

Evaluation of energy performance and outdoor thermal comfort of the alternatives

The DesignBuilder simulation program (DesignBuilder Software, 2018), which is the comprehensive interface of the EnergyPlus dynamic thermal simulation engine, was used to evaluate the energy performance of the reference building within the urban texture alternatives. Energy consumption data obtained in the calculations were reviewed and the ENVI-met program that can simulate the effects of vegetation in addition to complex urban textures based on daily micro-climatic dynamics was used to evaluate outdoor thermal comfort conditions at the street level for the developed urban texture alternatives. Annual heating, cooling and lighting energy consumption as well as overall energy consumption

(heating + cooling + lighting) of the alternatives in which the reference building is in the urban texture or as a single building are shown in Figure 2.

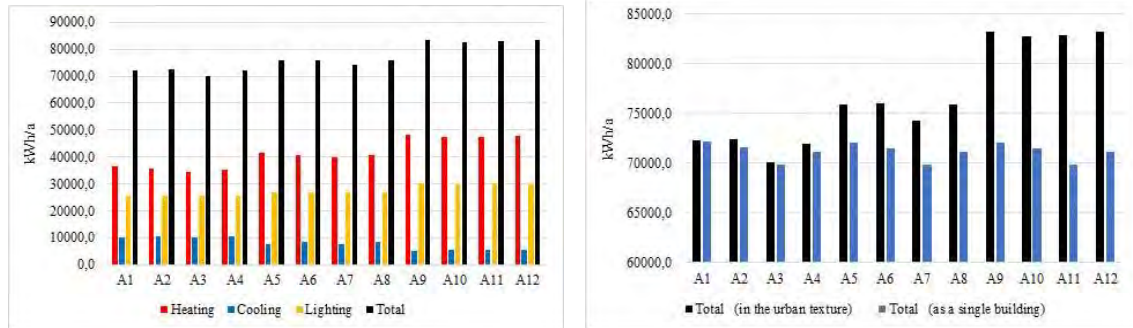


Figure 2. Energy consumption of 12 alternatives in which the reference building is located in the urban texture (a) and total energy consumption of the alternatives in which the reference building is located in the urban texture and the reference building is as a single building (b).

As seen in Figure 2, solar access of the housing units is increased with the proportional widening of street widths as the H/W ratio gets smaller, and consequently heating, lighting and total (heating + cooling + lighting) energy consumption decrease and cooling energy consumption increases. Additionally, as the heating energy consumption exceeds the cooling and lighting energy consumption, it is also determinant when the total energy consumption values are compared. When we compare total energy consumption of the alternatives in which the reference building is in the urban texture with the alternatives in which the reference building is accepted as a single building; the differences vary according to the aspect ratio. Since the streets are wider (30 m) in the four alternatives with H/W:0.50, very small differences in energy consumption are observed. However, due to the decreased street widths in 8 alternatives with H/W:1.00 and H/W:2.00 (15 m and 7.5 m respectively), the total energy consumption of the alternatives in which the reference building is modeled as single building is min. 5% and max. 16% less than the total energy consumption of the alternatives in which the reference building is in the urban texture. When the results for orientation are examined, due to the fact that the reference building in the alternatives has a symmetrical plan, it is possible to note that the percentage of change in energy consumption due to orientation is rather low. Among the 12 urban texture alternatives evaluated in this study, the highest heating and the lowest cooling energy consumption is achieved when the H/W ratio is 2.00. However, when the total energy consumption is taken into consideration, since the heating period is longer than the cooling period, heating energy consumption has more impact on the total energy consumption. Therefore, the alternatives with H/W ratio of 2.00 (A9, A10, A11 and A12) and the alternatives with the orientation angles of 0° , 45° and 135° (A1, A2, A4, A5, A6 and A8) do not give favourable results for total energy consumption. So, these alternatives are not included in the evaluation of outdoor thermal comfort in the next stage.

The outdoor thermal comfort evaluation is performed for the selected alternatives of A3 and A7 (with 90° orientation and the aspect ratios of 0.50 and 1.00 respectively) which resulted in lowest total energy consumption in the first stage. The evaluation is done at street level, through ENVI-Met microclimate simulation model for a period of 24 hours on July 21st. The meteorological inputs are entered through simple forcing method through which temperature and humidity profiles in 24 hourly values are forced onto the simulation model. The standards TS 1576 (2012) and TS 12174 (2012) were used to define street layouts in the alternatives. The surface material for sidewalks is assigned as concrete. Besides the analysis of the base cases of A3 and A7, potential improvements by the use of vegetation were evaluated through

the simulation of the urban texture alternatives A3-t (3 rows of trees) and A7-t (2 rows of trees) (Figure 3).

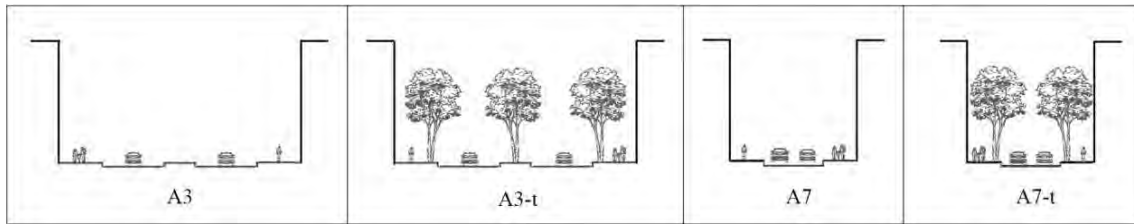


Figure 3. Street sections of alternatives for outdoor thermal comfort evaluation.

The thermal comfort parameters of air temperature (T_a), mean radiant temperature (MRT), wind speed (V_a) and physiological equivalent temperature (PET) (personal parameters based on "standard human" as defined in TS EN ISO7730 (2002) and with a summer clothing factor of 0.5 clo) were calculated at indicated street midpoints, at a height of 1.2m (z) from the ground (Figure 4).

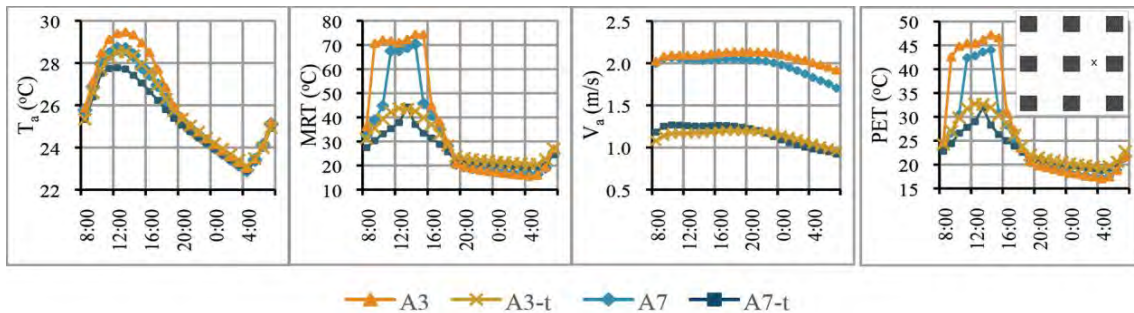


Figure 4. Temporal distribution of thermal comfort parameters.

When the hourly distribution of the thermal comfort parameters at the street midpoint are compared, the model A7 with H/W: 1.00 could have up to 16 °C higher PET values compared to A3 with H/W: 0.50 thus creating more comfortable outdoor urban spaces. The addition of trees has changed the mean radiant temperature and PET values in a similar manner. The addition of trees has reduced PET values at street midpoint up to 15 °C during day time and increased PET values slightly, up to 2 °C during the night time. During the day time, the mean radiant temperature in the streets with trees (A3-t and A7-t) is up to 32 °C lower, compared to the streets without trees (A3 and A7). On the other hand, after 19:00, the mean radiant temperature in the streets with trees gets slightly higher than the streets without trees. However, as the night time temperatures are already low, this result is not a significant drawback. Looking at the results for air temperature, the addition of trees has lowered the air temperature up to 1 °C around 13:00. Finally when the results for wind speed are compared, the addition of trees have reduced the air velocity up to 50%. Despite the reduction in air velocity and slight increase in PET values at night, the overall improvement in outdoor thermal comfort by the addition of trees is very significant.

CONCLUSIONS

Urban texture is the most important parameter that affects long term building energy consumption because an urban texture continues to exist for many years without any major change and affects the performance of the buildings that belong to that urban texture. Therefore, inclusion of the effects of urban microclimates in all evaluations of building energy performance, is critical for making correct decisions for sustainable, energy efficient buildings and urban texture design. This study aims to develop a model with which, in addition to urban texture-building interaction, outdoor thermal comfort, can also be analyzed to design sustainable, energy efficient environments. The effect of the design parameters of urban textures (building height/street width, street and façade direction, vegetation) was analyzed using the alternatives defined for this purpose for Istanbul representing a temperate-humid climatic region. The findings are compared and presented. However, similar studies using a high number of alternatives should be conducted in order to have an acceptable general conclusion.

ACKNOWLEDGEMENT

This study is supported by a grant from the Scientific Research Projects Unit of Istanbul Technical University under the Scientific Research and Development Support Program (Project No: 39956).

REFERENCES

- Ahmed K. S., Khare M. and Chaudhry K. 2005. Wind tunnel simulation studies on dispersion at urban street canyons and intersections-a review. *Jour Wind Engin Indust Aerodyn*,93,697–717.
- Andreou E.2013. Thermal comfort in outdoor spaces and urban canyon microclimate. *Renew Ener*,55,182-88.
- DesignBuilder Software. 2018. DesignBuilder 5.0.3.007 User manual, UK.
- Golany G.S. 1995. Urban design morphology and thermal performance. *Atmos Environ*, 30, 455-65.
- Jamei E. Rajagopalan P. Seyedmahmoudian M. Jamei Y. 2016. Review on the impact of urban geometry and pedestrian level greening on outdoor thermal comfort. *Renew Sustain Energy Rev*, 54, 1002-17.
- Kariminia S., Ahmada S. and Saberi A. 2015. Microclimatic conditions of an urban square: Role of built environment and geometry. *Procedia-Social Behavioral Sciences*,170,718-27.
- Oke, T.R. 1976. The distinction between canopy and boundary-layer urban heat islands. *Atmosphere*, 14, 268–77.
- Ratti C. Sabatino S. Di and Britter R. 2005. Urban texture analysis with image processing techniques: winds and dispersion. *Theor Appl Climatol*.
- Sanaieian H. Tenpierik M. Linden, K. Seraj, F.M. Shemrani, S.M.M. 2014. Review of the impact of urban block form on thermal performance, solar access and ventilation. *Renew Sustain Energy Rev*, 38, 551-60.
- Tiziana C. and Marianna C. 2013. Representation, identity and sustainable design in the urban texture. *EAEA-11 Conference*, 43-50.
- Toudert F. A. and Mayer H. 2006. Effects of asymmetry, galleries, overhanging façades and vegetation on thermal comfort in urban street canyons. *Sol Energy*, vol. 81 (6), 742-754.
- TS EN ISO7730 2002. Moderate Thermal Environments-Determination of the PMV and PPD Indices and Specification of the Conditions for Thermal Comfort. Ankara: Turkish Standards Institution.
- TSI. 2013. *TSE- 825*, Thermal Insulation Requirements for Buildings. Ankara.
- TSI. 2012. *TS- 1576*, Urban Roads-Structural Preventive and Sign Design Criteria on Accessibility in Sidewalks and Pedestrian Crossings. Ankara.
- TSI. 2012. *TS- 12174*, Urban Roads-Design Criteria on Sidewalks and Pedestrian Areas. Ankara
- Yang, X. and Li, Y. 2015. The impact of building density and building height heterogeneity on average urban albedo and street surface temperature. *Buil Environ*, vol. 90, 146-156.

New microclimate monitoring method and data process for investigating environmental conditions in complex urban contexts

Ilaria Pigliautile^{1,*}, Veronica Lucia Castaldo¹ and Anna Laura Pisello²

¹CIRIAF - Interuniversity research centre on pollution and environment Mauro Felli – Department of engineering, University of Perugia, 06125, Italy

²Department of Engineering, University of Perugia, Perugia, 06125, Italy

*Corresponding email: pigliautile@crbnet.it

ABSTRACT

The rapid urbanization of the last century coupled with local climate change imputable to anthropogenic actions triggered a huge research effort aimed at investigating urban microclimate. Typically, cities present a variety of microclimates due to the internal variation of their landscapes in terms of morphology, surfaces properties, presence of greenery, etc. Location-specific microclimate conditions affect both (i) building energy needs and (ii) citizens' quality of life. For these reasons, a small-scale analysis from the citizen perspective with high-time-resolution environmental data is required. Recent studies tried to reach that level of precision by using remote sensing, movable observational transects or dense network of weather stations located in specific points of the urban settlement. Within this framework, the current study presents a new bottom-up methodology which aims at identifying granular microclimates within the same built environment. The method consists of a cluster analysis of experimental data collected by a wearable miniaturized weather station which allows the monitoring of outdoor parameters at the pedestrian height and with high-time resolution. Experimental campaigns were conducted in five different case studies, where a planned monitoring path was repeated at different times during the day. The heterogeneity of the context demonstrates the replicability of the proposed method, suitable for clustering different areas of a same urban context characterized by variable local microclimate. The study contributes to better understand the variability of building boundary conditions for energy need prediction and indoor/outdoor environmental comfort assessment.

KEYWORDS

Urban Microclimate, Urban heat island, Outdoor thermal comfort, Monitoring, Environmental quality.

INTRODUCTION

The urban population is continuously growing, and it will reach the 60% of the world population in 2030 according to United Nation predictions (2016). The urbanization process progressively changes land usage, consequently modifying the energy balance in cities leading to the well-known phenomenon of the Urban Heat Island (Oke, 1973;). UHI negatively affects both citizens' health (Serrat et al., 2006;) and building stock energy consumption (Akbari et al., 2001). Moreover, such negative consequences are going to be exacerbated in the next decades due to climate change since extreme weather events as the heatwaves are predicted to be more intense and more frequent (Founda and Santamouris, 2017). Nevertheless, the complex and heterogeneous morphology of cities causes sensible diversification of the microclimate within the urban canopy layer. As a matter of fact, Jonsson (2004) found out an intra-urban temperature difference of the same magnitude as the detected urban-rural differences in Gaborone, Botswana. Intra-urban temperature differences up to 5°C were also detected in Wien, Austria, by Mahdavi et al. (2017). Moreover, the study

demonstrated how specific microclimate conditions affect the building thermal performance leading to a mean annual heating load variation up to 16.1 kWh/m² per year among the analysed areas.

Within the presented framework, the detection of intra-urban microclimate diversifications and how much they are related to different urban structures is a key point for the scientific community. To get this goal, high-spatial-resolution weather data are required. Nowadays, the most common implemented methodologies include: (i) remote sensing (Voogt and Oke, 2003;), (ii) permanent network of weather stations (Paolini et al., 2017), and (iii) observational mobile transects (Hart and Sailor, 2009; Parace et al., 2016). Nevertheless, an investigation procedure focused on the pedestrian perspective is still missing. This work presents a new bottom-up methodology which aims to identify different and distinctive microclimates within the same built environment from raw environmental data collected accordingly to the pedestrian perspective. An innovative monitoring wearable system is presented and the obtained outcomes are post-process through *k-means* clustering procedure. The outlined methodology is applied to five different case studies to test its validity in different urban configurations. The final findings can therefore help policymakers to select suitable mitigation strategies for the most critical areas of their cities in terms of both outdoor thermal comfort and building stock energy consumption.

METHODS

The present work proposes a bottom-up process to detect local urban microclimate conditions based on collected experimental data. The main environmental parameters are monitored by means of a miniaturized wearable weather station which can be easily worn by a pedestrian (Pigliatile and Pisello, 2018). Therefore, the perspective of the monitoring campaign is human centred, and the collected data represent what citizens are subject to, in terms of environmental forcing, air quality, and thermal overheating/overcooling. The collected data are therefore statistically analysed by means of clustering to identify the intra-urban microclimate diversification.

Monitoring campaigns

The monitoring system is a miniaturized weather station coupled with GPS tracer to link the collected environmental data to their site-specific location, i.e. latitude, longitude, altitude and attitude. The system is settled upon a common bike helmet and records all the parameters listed in (Pigliatile and Pisello, 2018) every 2 seconds, such as air temperature, relative humidity, global solar radiation, wind speed, CO₂ concentration, and geographical coordinates.

Five different monitored case studies are here presented. Every case study deals with different urban contexts as summarized in Table 1. All the monitoring pathways were planned to pass through areas characterized by different (i) geometrical configuration, (ii) orientation, (iii) amount of anthropogenic sources, and (iv) greenery. The equipped operator covers the same pathway at least twice during a day, i.e. around midday and around sunset, to have both (i) space and (ii) time daily variation of the key environmental parameters. Moreover, the length of each pathway allows to complete a single recording session in less than one hour on foot, so all the parameters fluctuation can be assumed to be space- and no time-dependent.

Table 1. Monitoring campaigns details

Case study	Typology	Start Time	Day	Length	
Knossos Palace archaeological site, Greek	Open area	9:00 a.m.	07/04/2017	1.2 km	~40 minutes
		3:00 p.m.		1.6 km	~40 minutes
		7:00 p.m.		1.3 km	~40 minutes

Gubbio historic centre, Italy	Packed, historical	8:30 a.m.	08/02/2017	2.6 km	~45 minutes
		2:30 p.m.		2.8 km	~45 minutes
		6:30 p.m.		2.7 km	~45 minutes
New York City (Soho), USA	Packed, low rise building	1:00 p.m.	11/30/2017	2.4 km	~35 minutes
		6:30 p.m.	11/28/2017	2.4 km	~35 minutes
New York City (Upper East Side), USA	Packed, high rise building	2:00 p.m.	11/29/2017	3.7 km	~45 minutes
		5:30 p.m.	12/01/2017	3.6 km	~45 minutes
New York City (Wall Street), USA	Packed, high rise building	11:45 a.m.	11/29/2017	-	~25 minutes
		5:00 p.m.	11/30/2017	3.3 km	~25 minutes

Data analysis

After having collected the abovementioned data, we grouped them adopting the k-means algorithm (Lloyd, 1982) which classifies data through a priori fixed k number of clusters. This allowed us to figure out potential relationships within the huge amount of observations derived from the monitoring sessions. The iterative grouping procedure minimizes the distance between the observations belonging to the same cluster and, in turn, maximizes the distance among observations belonging to different clusters. The algorithm minimizes the following objective function:

$$J(V) = \sum_{j=1}^k \sum_{i=1}^n \left(\|x_i^{(j)} - c_j\| \right)^2 \quad (1)$$

where, $\|x_i^{(j)} - c_j\|$ is the chosen Euclidian distance between an observation $x_i^{(j)}$ and its cluster centre c_j , i.e. its centroid. The authors assumed three different numbers of final clusters k , i.e. 2, 5, and 8, to get the sensitivity of such bottom-up approach in determining the intra-urban microclimate variation. Moreover, we grouped data considering a 3D reference space defined by three environmental parameters which are recognized as affecting the citizens well-being: (i) the global solar radiation (W/m^2), (ii) the CO_2 concentration (ppm), and (iii) the apparent temperature ($^{\circ}\text{C}$). The obtained data partitions are therefore analysed in terms of their spatial distribution linking the belonging cluster and the GPS coordinates of each observation. The length of each segment, defined by space-contiguous observations belonging to the same class, is calculated and only segments longer than 5m are considered for the analysis. Figure 1 summarizes the adopted methodology for the data analysis.

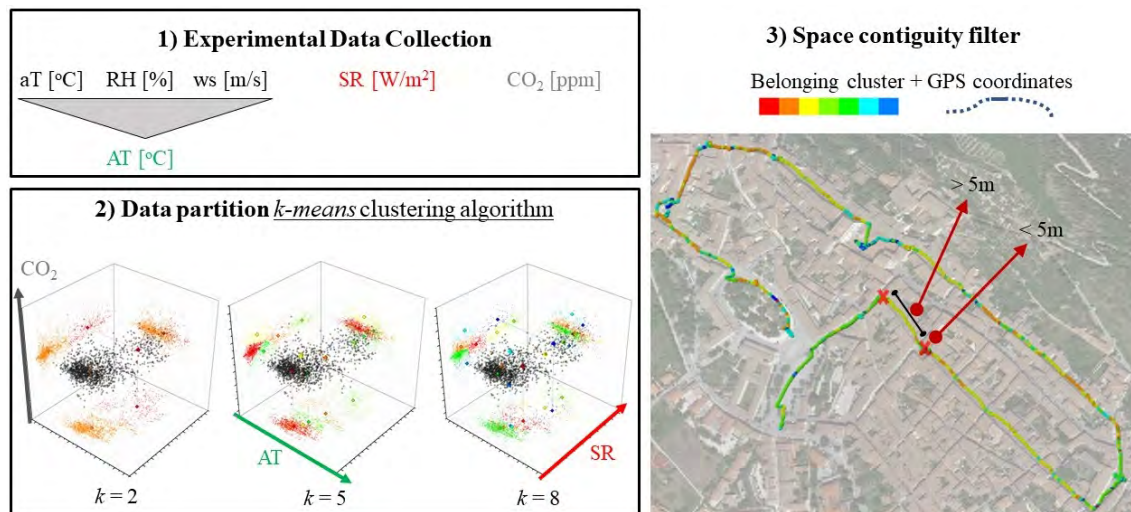


Figure 1. Scheme of the applied methodology.

RESULTS

The presented analysis aims to find out different microclimate conditions within all the considered case studies. The application of the *k-means* algorithm with a *k* value of 2 recognizes the solar radiation as the main driver of the clustering procedure. As a matter of fact, the two centroids representative of the data subgroups are mainly distinguished by their values of solar radiation. Such differences are more evident at midday and in low density urban areas, i.e. the Knossos palace archaeological site, where a maximum centroids' distance of 733.4 W/m^2 is highlighted in terms of solar radiation (Figure 2a). On the contrary, less evident is the data partitioning due to solar access at pedestrian level within the more packed urban contexts, i.e. the three monitored areas of New York City. In particular, the partition of data collected in New York City high-rise building settlement, i.e. Wall Street (Figure 2b), is driven by the CO_2 concentration which presents the widest range of collected values. Therefore, the two data sub-groups are identified by centroids which are really close in terms of apparent temperature and solar radiation, i.e. 0.6°C , 0.1°C and 4.5 W/m^2 , 6.1 W/m^2 at day- and night-time respectively but differ from each other for 130 ppm and 100 ppm of CO_2 concentration at 2:00 p.m. and 5:30 p.m. respectively.

The two data sub-groups are equally distributed in space in the open site of Knossos and in the packed historic centre of Gubbio at 2:30 p.m. The low solar radiation data in Knossos, i.e. centroid's value of solar radiation equal to 53.5 W/m^2 , 94.8 W/m^2 , and 60.3 W/m^2 at 9 a.m., 3:00 p.m., and 7:00 p.m. respectively, correspond to the areas shaded by the existing greenery. Similarly, the low and high radiation clusters in Gubbio, i.e. centroids' radiation of 101.7 W/m^2 and 776.7 W/m^2 respectively, identify urban canyons mainly characterized by different orientations, i.e. north-south and east-west oriented respectively (Figure 2c). On the other hand, low incoming solar radiation areas are prevalent in the monitored zones of New York City. Nevertheless, areas with high level of incoming radiation are mainly concentrated in north-south oriented canyons and at crossroads.

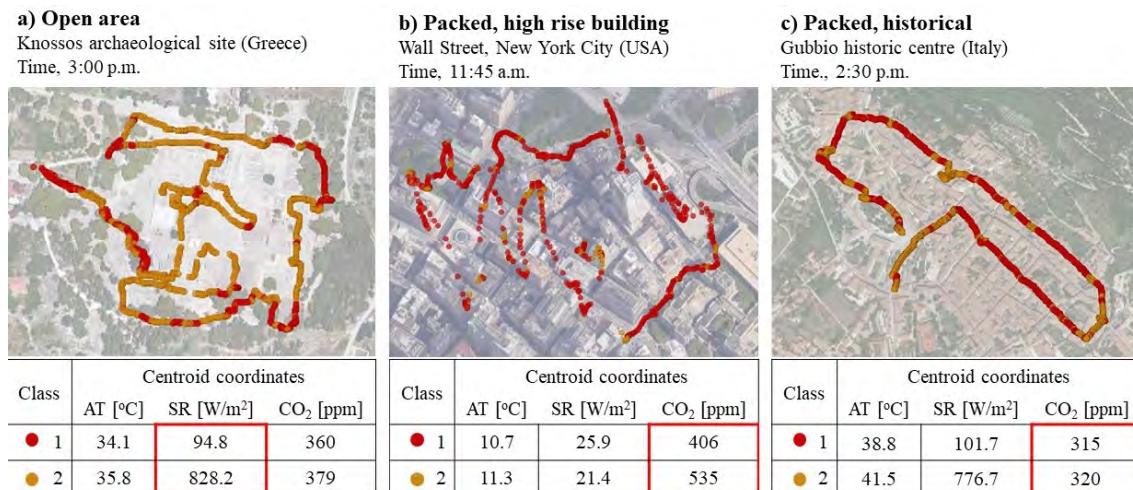


Figure 2. Spatial distribution of the two data clusters ($k=2$) obtained for the monitored open area (a), packed high rise (b), and packed historical configuration (c).

The data partition into 5 sub-groups generates diversified clusters in terms of both solar radiation and CO_2 concentration values in all the considered case studies. Therefore, such partition identifies different microclimate situations of low and high incoming solar radiation combined with less or more polluted air conditions. The generated clusters depict quite well the distinction among open areas and different typologies of urban canyons in all the packed

urban case studies, especially during day-time. Moreover, such partition highlights site-specific critical conditions in terms of CO₂ concentration level just before traffic-lights almost in all the monitored areas of New York. This condition is particularly evident in SoHo (Figure 3) where data clusters related to detected high level of CO₂ concentration, i.e. 600 ppm and 514 ppm in correspondence of low and high solar radiation values respectively, continuously cover up to a maximum of 46 m for a total amount equal to the 13.4% of the whole monitored path length.



Figure 3. Spatial distribution of the five data clusters (k=5) obtained in SoHo, New York City.

Nevertheless, not the whole 5 data sub-groups can be considered representative of site-specific conditions. The application of the minimum length filter, i.e. 5 m, reduce up to 67.1% the total amount of recorded data in the open archaeological site of Knossos. It means that the environmental parameters in mainly open and natural areas are more sensitive to temporary weather changes rather than being affected by specific spatial configurations.

Finally, the clustering procedure with 8 pre-defined number of classes does not show up further significant intra-urban variations of the monitored environmental parameters leading to redundant fragmentations of the data samples.

DISCUSSIONS

The statistical analysis of the collected data provides an intra-urban detection of specific microclimate conditions. The spatial distribution of each generated data cluster shows distinctive urban configurations along the monitored pathways during day-time and with a k of 2. The availability of incoming solar radiation at pedestrian height is depicted as the most influencing parameter for the microclimate diversification. The selection of 5 final clusters points out a relatively more detailed intra-urban microclimate detection considering also other environmental parameters, i.e. CO₂ concentration variation. Nevertheless, such high number of classes, i.e. 5, is not suitable for open areas, i.e. Knossos archaeological site, where the environmental parameters fluctuations are more time- than space-dependent. Finally, the selection of 8 final data clusters seems to be too much detailed for the detection of site-specific microclimate conditions also in high urbanized and packed contexts.

CONCLUSIONS

The presented bottom-up approach to detect the intra-urban microclimate variation shows its promising effectiveness being applied in different contexts and seasons. The statistical data analysis through *k-means* algorithm can identify those areas presenting similar configuration within each case study. The proper number of final clusters depends on the monitored context

typology in order to obtain spatially significant data sub-grouping. A further development of this work will focus on the evaluation of the right k value for each defined urban configuration typology.

Nevertheless, the outlined data clusters are associated to peculiar comfort conditions within the same urban context. Therefore, the presented methodology could help urban policymakers to figure out criticalities. A rank of risk in terms of human health or building stock energy consumption peak can be assigned to the obtained environmental data clusters. In this way, areas needing priority intervention can be easily highlighted.

ACKNOWLEDGEMENT

This work has received funding from the European Union Horizon 2020 Programme in the framework of the “HERACLES” project under grant agreement n° 700395. Additionally, the first author is supported by Ministry funding and university funding of the PhD school in Energy and Sustainable Development. Part of this research is carried out within the framework of COLO ARTE project supported by Fondazione Cassa di Risparmio di Perugia, (Grant Cod. 2016.0276.02)

REFERENCES

- Akbari H., Pomerantz M., Taha H. 2001. Cool surfaces and shade trees to reduce energy use and improve air quality in urban areas. *Solar Energy* 70, 295–310.
- Blazejczyk K., Y. Epstein, G. Jendritzky, H. Staiger, B. Tinz. Comparison of UTCI to selected thermal indices. *International Journal of Biometeorology*, 53(3), 515-535.
- Founda D., Santamouris M. 2017. Synergies between Urban Heat Island and HeatWaves in Athens (Greece), during extremely hot summer (2012). *Scientific Reports* 7, 10973.
- Hart M.A., Sailor D.J. 2009. Quantifying the influence of land-use and surface characteristics on spatial variability in the urban heat island. *Theoretical and Applied Climatology*, 95(3-4), 397–406.
- Jonsson P. 2004. Vegetation as an urban climate control in the subtropical city of Gaborone, Botswana. *International Journal of Climatolgy*, 24, 1307–1322.
- Lloyd S. 1982. Least squares quantization in PCM. *IEEE Transactions on Information Theory*, 28(2), 129-137.
- Oke T.R., 1973. City size and the urban heat island. *Atmospheric Environment*, 7(8), 769–779
- Paolini R., Zani A., Meshkinkiya M., Castaldo, V.L., Pisello A.L., Antretter F., Poli T., Cotana F. 2017. The hygrothermal performance of residential buildings at urban and rural sites: sensible and latent energy loads and indoor environmental conditions. *Energy and Buildings*, 152, 792–803.
- Parace T.E., Li J., Campbell J.B., Carrol D. 2016. Assessing urban landscape variables' contribution to microclimates. *Advanced Meteorology*, 8736263 (14 pages).
- Pigliatile I. and Pisello A.L. 2018. A new wearable monitoring system for investigating pedestrians- environmental conditions: Development of the experimental tool and start-up findings. *Science of the Total Environment*, 630, 690-706.
- Serrat C., Lemonsu A., Masson V., Guedalia D. 2006. *Impact of urban heat island on regional atmospheric pollution*. *Atmospheric Environment*, 40(10), 1743–1758.
- United Nations, Department of Economic and Social Affairs, Population Division, 2016.
- Voogt J.A., Oke T.R. 2003. Thermal remote sensing of urban climates. *Remote Sensing of Environment*, 86 (3), 370–384.

Rapid cooling of urban surfaces during rainfall: physical basis, dominant energy fluxes, and sensitivity to pavement and rainfall properties

Hamidreza Omidvar^{1,*}, Elie Bou-Zeid¹

¹Princeton University, Princeton, NJ, USA

*Corresponding email: homidvar@princeton.edu

ABSTRACT

Using model for the heat transfer between pavements and runoff during rainfall, we investigate the importance of different pavement and rainfall properties, as well as crucial energy budget terms that drive the cooling processes. The results indicate that the pavement and runoff temperature and energy fluxes are very sensitive to the rain temperature. In addition, pavement albedo has a significant effect on the simulated temperature since it modifies the initial pavement temperature before the rain starts. The results also indicated that among the different energy budget terms, evaporation and long wave radiation are the main cooling terms, while the shortwave radiation dominates energy input into the runoff-pavement system.

KEYWORDS

Pavements, rainfall, surface energy budget

INTRODUCTION

There are a variety of phenomena in the atmosphere that are affected by earth surface temperature such as urban microclimatology, turbulent transport, and surface energy budgets. In urban areas, the materials of which the pavements are made (i.e. impervious pavements with low albedo values), as well as other urban canopy properties, result in hotter surfaces than rural areas. This is the main reason for urban heat islands in metropolitan areas. However, during rainfall, hot ground surfaces cool down very fast, mainly due to the runoff advection and/or infiltration of heat. Previous investigations have proposed runoff-pavement heat transfer models to predict the surface and runoff temperature during rainfall [*Van Buren et al.*, 2000; *Herb et al.*, 2009; *Janke et al.*, 2009; *Kertesz and Sansalone*, 2014]. A few of these studies have reported the sensitivity of the cooling to the input and model parameters; however, these analysis either were conducted on limited ranges of target parameter or were not extended to indicate the influence of model inputs on the energy budgets of pavement-runoff [*Herb et al.*, 2009]. Therefore, a lack of extensive analysis still hinders the understanding of how different input parameters, especially the pavements properties, alter the heat transfer between the runoff and pavement during rainfall, and what is their effects on surface temperature and on the driving energy budget terms (such as evaporation and sensible heat) before, during and after rainfall. A more detailed sensitivity analysis of the runoff-pavement heat transfer model helps us to determine, which input parameters need to be carefully measured. In addition, determining the influence of different energy budget terms on key model outputs (such as ground surface temperature) would allow the identification of the dominant heat transfer processes in the problem, and can lead to the development of simpler and more computationally efficient models. Such reduced models would be more suitable for implementation in coarser geophysical models, such as Urban Canopy Models (UCMs), or Weather Research Forecast (WRF) models.

In this paper, we use a runoff-pavement heat transfer model to investigate the sensitivity of different temperatures and fluxes to various pavement and rain properties. In addition, we evaluate the effects of various energy flux terms on the ground surface temperature. First the model is briefly explained, and then a metric for comparing the model sensitivity to different input parameters is introduced. Finally, we present the results, and conclude the paper with a discussion and future directions.

METHODS

Model description

The model used in this paper is a 2D heat transfer model (validated by experimental data) to solve for the runoff and pavement temperature and energy fluxes during rainfall [Omidvar *et al.*, 2018]. In this section, we summarize the main model elements. The model has two parts:

1- The runoff dynamics part, which solves for the runoff velocity and depth by combining the shallow water continuity equation and the kinematic wave approach for laminar flows [Brutsaert, 2005]. With a boundary condition of zero velocity at the upstream boundary, and an initial condition of dry ground, the solution of the horizontal (u) and vertical (v) velocities inside the runoff, and of the runoff depth (h) are as follows:

$$u(x, y, t) = \frac{gs_0}{\nu} (hy - y^2 / 2) ; \quad v(x, y) = \begin{cases} 0 & \text{for } x \geq \frac{t^3 s_0 g i^2}{3\nu} \\ -\frac{s_0 g h y^2}{6\nu x} & \text{for } 0 < x < \frac{t^3 s_0 g i^2}{3\nu} \end{cases} \quad (1)$$

$$h(x, t) = \begin{cases} it & \text{for } x \geq \frac{t^3 s_0 g i^2}{3\nu} \\ \left(\frac{3x\nu i}{s_0 g} \right)^{\frac{1}{3}} & \text{for } x < \frac{t^3 s_0 g i^2}{3\nu} \end{cases} \quad (2)$$

where in equations (1) and (2), s_0 is pavement slope; ν is runoff kinematic molecular viscosity ($\text{m}^2 \text{s}^{-1}$); h is runoff depth (m); i is the rain intensity (m s^{-1}); and t is time (s).

2- The heat transfer part, which uses the advection- diffusion equation in order to solve for the runoff temperature (T_w), and a 2D conduction equation (assuming no infiltration) for solving the temperature of subsurface (T_g) as follows:

$$\frac{\partial T_w}{\partial t} = D_w \frac{\partial^2 T_w}{\partial y^2} - \left(u \frac{\partial T_w}{\partial x} + v \frac{\partial T_w}{\partial y} \right) ; \quad \frac{\partial T_g}{\partial t} = D_g \left(\frac{\partial^2 T_g}{\partial y^2} + \frac{\partial^2 T_g}{\partial x^2} \right) \quad (3)$$

In equations (3), D_w ($\text{m}^2 \text{s}^{-1}$) is the heat diffusivity of the runoff, which is modified from the molecular diffusivity to take into account the excess mixing due to the penetration of rain droplet into the runoff (an optimum value of $4 \times$ molecular diffusivity is obtained from the experimental data); D_g ($\text{m}^2 \text{s}^{-1}$) is the thermal diffusivity of the subsurface; and x and y are the horizontal and vertical distances. Surface energy budget equations are solved to get the temperature of the interfaces between the ground surface and the runoff (equation (4), left), and the interface between the runoff surface and the air (equation (4), right):

$$R_{sw} + Q_{wb} + G = 0 ; \quad R_{lw} + LE + Q_r + H + Q_{wt} = 0. \quad (4)$$

where R_{sw} and R_{lw} are net shortwave and longwave radiation fluxes respectively; Q_{wb} is heat exchange flux between ground surface and runoff; G is ground heat flux; LE is latent heat

flux; Q_r is net rain heat flux; H is sensible heat flux; and Q_{wr} is heat exchange flux between runoff and its surface (all in W m^{-2}). Among these energy terms, downwelling shortwave and longwave are the inputs of the model, and the rest are solved for.

A zero-heat flux boundary condition is considered for the bottom boundary of the subsurface, while a constant diffusive heat fluxes at the right and left of the subsurface domain are imposed. Equations (3) and (4) in conjunction with the discussed boundary conditions are solved numerically to obtain the ground surface and runoff temperatures as well as the energy budget fluxes during rainfall.

The downwelling radiative fluxes and other meteorological inputs of the model (i.e. air humidity, temperature, and pressure, wind speed) are obtained from an eddy covariance station at Princeton University (coordinates: 40°20'46.9"N, 74°38'36.5"W). A rainfall event starting from 2 PM local time on 30 of July 2016, with a duration of 3 hours, is chosen. The rain temperature is assumed to be equal to the air temperature. In addition, to get the ground surface temperature before and after rain, surface energy budget with similar terms as equation (4) are solved without any runoff model. The model for the dry surface is run for 12 hours before start of the rain (assuming a dry surface and no evaporation), then for 3 hours during rainfall, and, after rainfall stops, the model is run for an additional 2 hours and 20 minutes (until the downwelling shortwave radiation becomes zero).

Sensitivity analysis method

The model that we described in the previous section is used to conduct a set of sensitivity analyses with different pavement and rain properties. For an input (r) and output (z) of the model, we use the following metric in order to compare the sensitivity of the model to different inputs and outputs:

$$\gamma = \frac{\delta z}{\partial r / r}, \quad (5)$$

In this equation, the dimension of γ is as same as the dimension of the output (z), and indicates how much the output z changes for a 100 % change of input r . The model inputs we choose to conduct the sensitivity analysis are: (1) pavement thermal conductivity, k for the range of 0.3 - 3.1 ($\text{W m}^{-1} \text{K}^{-1}$) [Côté and Konrad, 2005; Kodide, 2010], (2) pavement albedo, α for the range of 0.01 - 0.23 [Li et al., 2013; Wang, 2015], (3) rain intensity, i for the range of 5 - 105 (mm h^{-1}), and (4) rain temperature, T_{rain} for the range of $T_{air} - 5$ °C to $T_{air} + 5$ °C (as its deviation from equilibrium with air temperature (T_{air}), which is the baseline assumption). The average T_{air} during the rainfall is 23.3 °C in the input data). The input ranges chosen represent the typical value of each input in the urban areas. Finally, γ values for each of the inputs are calculated for 8 model outputs: time averaged temperature of the ground surface during (T_{gs}^r) and after (T_{gs}^{ar}) rainfall, time averaged temperature of runoff during rainfall (T_w), initial temperature of ground surface temperature before rain starts (T_{gs}^i), time averaged latent heat flux during (LE^r) and after (LE^{ar}) rainfall, and time averaged sensible heat flux during (H^r) and after (H^{ar}) rainfall. All the output variables are averaged along the pavement except T_w , which is averaged both vertically and along the pavement. For each input, γ is averaged over the input range and the average value is reported ($\langle \gamma \rangle$).

RESULTS

Figure 1a shows the comparison of $\langle \gamma \rangle$ for different model inputs, and for the temperature outputs. Note that rain intensity and rain temperature do not affect the initial temperature of the ground surface, so their $\langle \gamma \rangle$ values are zero in the plot. As can be noted from this figure, except for T_{gs}^i , all other temperature outputs are strongly sensitive to the rain temperature such that with $\langle \gamma \rangle$ values for T_{gs}^r , T_w , and T_{gs}^{ar} are 11.0, 11.1, and 4.4 °C respectively. This emphasizes the importance of determining the rain temperature accurately. The reason that T_{gs}^{ar} is less sensitive in comparison to the temperature outputs during the rainfall is that this temperature output is modified indirectly by the rain temperature because the final ground surface temperature during rainfall is the initial condition of the simulation after rainfall ends where T_{gs}^{ar} is solved for (similar justification can be made for the rain intensity as the input).

The second input that the model outputs are most sensitive to is the pavement albedo. T_{gs}^i is the most sensitive temperature output to the pavement albedo in comparison to others because in the data we used in the model, the downwelling shortwave radiation is higher before the rainfall than during and after due to the cloudiness during and after rainfall. In addition, as we expected, the $\langle \gamma \rangle$ values corresponded to the pavement albedo are negative, meaning that if we increase of pavement albedo the temperature outputs decrease because of less available energy in the energy budget of the ground surface (which consequently leads to a cooler runoff temperature).

The $\langle \gamma \rangle$ value corresponding to the pavement heat conductivity has a negative sign for T_{gs}^i , but it is positive for other temperature output. This can be attributed to the fact that, before rainfall, while the pavement is absorbing energy, the higher the conductivity of the pavement the more heat will be transfer from the pavement surface to the deeper parts of the subsurface. Therefore, the ground surface temperature remains cooler for the pavements with higher heat conductivity. However, during and after rainfall, while the heat is still being advected away by the runoff (or evaporation for after rainfall) at the surface, the pavements with higher conductivity have more stored heat and can transfer it more rapidly to the surface. Therefore, the higher conductive pavements have higher surface temperature than the lower conductive ones during and after rainfall.

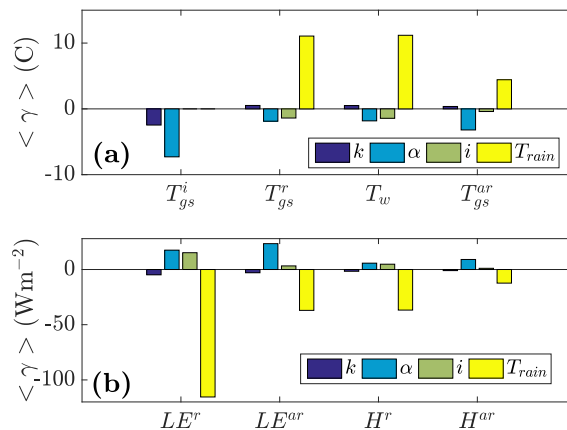


Figure 1. (a) Results of sensitivity analysis for temperature outputs, (b) for flux outputs

Figure 1b shows the sensitivity analysis for the evaporation and heat flux outputs. Similar to the temperature outputs, the flux outputs are very sensitive to the rain temperature specially the evaporation and heat fluxes during rainfall (with $\langle \gamma \rangle$ of -115 W m^{-2} and 37 W m^{-2} respectively). Although evaporation flux after rainfall is modified indirectly by the rain temperature, the $\langle \gamma \rangle$ for this flux is still comparable to the $\langle \gamma \rangle$ value for the heat flux during rainfall. Again, similar to the temperature outputs, pavement albedo rank as the second input to which the model outputs are most sensitive. The evaporation after rainfall (LE^{ar}) is the most sensitive output to the pavement albedo, then LE^r and H^{ar} , and finally H^r is the least sensitive to the pavement albedo. The sensitivity of the evaporation and sensible heat fluxes during rainfall to the rain intensity are higher than the corresponding sensitivity after the rainfall. This is expected since rain intensity directly modify the variables during rainfall, but indirectly modulates the ones after rainfall. Finally, the flux outputs are least sensitive to the thermal conductivity of the pavement among; this might be because the evaporation and heat fluxes are calculated at the interface between the runoff and air while the thermal heat conductivity of the pavement affects directly the subsurface and ground surface heat processes.

We are also interested in the effects of different surface energy budgets (here we just consider shortwave, longwave, evaporation and sensible heat fluxes) on the model outputs during rainfall. To investigate this, we choose T_{gs}^r as the target output, and evaluated how T_{gs}^r changes from its base value, $T_{gs}^{b,r}$ (the ground surface temperature during rainfall when all the energy budget terms are considered in the model), when we turn off (set to zero) a specific energy budget term in the model. Figure 2 shows the result of this analysis. It indicates that without considering the evaporation flux, the model predicts T_{gs}^r about $0.6 \text{ }^\circ\text{C}$ higher. The longwave flux is the second most important term for predicting T_{gs}^r with $T_{gs}^r - T_{gs}^{r,b} = 0.4 \text{ }^\circ\text{C}$. Without considering the shortwave flux, the model predicts T_{gs}^r $0.6 \text{ }^\circ\text{C}$ cooler than its base value. Usually the shortwave radiation has bigger impacts on the surface temperatures; however, in our application since the shortwave radiation is small during the rainfall (because of cloudiness), it has a lower effect on the energy processes of the problem. Finally, the sensible heat flux has the least impact on T_{gs}^r with $T_{gs}^r - T_{gs}^{r,b} = 0.2 \text{ }^\circ\text{C}$.

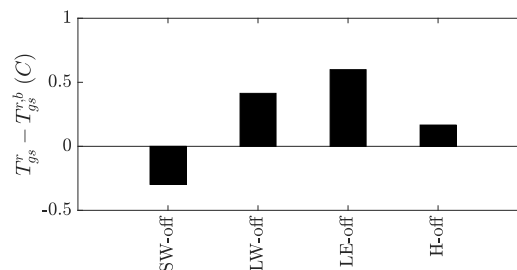


Figure 2. The effect of individual energy budget terms on the ground surface temperature

DISCUSSIONS AND CONCLUDING REMARKS

In this paper, we conducted a set of sensitivity analyses for a runoff-pavement heat transfer model in order to determine how carefully one should determine different pavement and ambient properties that are needed inputs of the model. The analysis showed that the model is very sensitive to rain temperature. It is an important result because usually the models that predicts heat processes on the pavement during rainfall assume rain temperature is equal to air temperature (or previous models that assumed a dew point temperature as the rain temperature

[Herb *et al.*, 2009]). Therefore, considering the difficulties in measuring the rain temperature, more consideration is needed when choosing the value of rain temperature as the input of the model. Another important take away from the sensitivity results is the role of the pavement albedo in modifying the surface temperature and fluxes before, during and after rainfall. The results showed that albedo of the pavement mainly affects the temperature of the pavement before the rain starts. This leads the pavement to be hotter when the rain starts, which can then lead to a hotter effluent entering the storm drainage network that ultimately joins the streams and can then have advects effect on their health [Nelson and Palmer, 2007]. Finally, we showed that among the discussed energy budgets terms in this paper, evaporation and longwave radiation play an important role in cooling the hot ground surface during the rainfall, while the shortwave radiation has an opposite role although the magnitude of the net shortwave is typically smaller during the rainfall due to clouds. Using the results of the sensitivity analysis and important energy budget terms, one can develop a reduced runoff-pavement heat transfer model that predicts the important temperature and flux outputs accurately with reduced computational demands. Such a reduced model is more suitable for implementation in coarser geophysical models.

ACKNOWLEDGEMENT

This work is supported by the Army Research Office under contract number W911NF-15-1-0003 (program Manager Julia Barzyk) and by the US National Science Foundation's Sustainability Research Network Cooperative Agreement 1444758.

REFERENCES

- Brutsaert, W. (2005), *Hydrology: An Introduction*, Cambridge University Press, New York, NY, USA.
- Van Buren, M. A., W. E. Watt, J. Marsalek, and B. C. Anderson (2000), Thermal enhancement of stormwater runoff by paved surfaces, *Water Res.*, 34(4), 1359–1371, doi:10.1016/S0043-1354(99)00244-4.
- Côté, J., and J. Konrad (2005), Thermal conductivity of base-course materials, , 78, 61–78, doi:10.1139/T04-081.
- Herb, W. R., B. Janke, O. Mohseni, and H. G. Stefan (2009), Runoff Temperature Model for Paved Surfaces, *J. Hydrol. Eng.*, 14(10), 1146–1155, doi:10.1061/(ASCE)HE.1943-5584.0000108.
- Janke, B. D., W. R. Herb, O. Mohseni, and H. G. Stefan (2009), Simulation of heat export by rainfall-runoff from a paved surface, *J. Hydrol.*, 365(3–4), 195–212, doi:10.1016/j.jhydrol.2008.11.019.
- Kertesz, R., and J. Sansalone (2014), Hydrologic Transport of Thermal Energy from Pavement, *J. Environ. Eng.*, 140(8), 4014028, doi:10.1061/(ASCE)EE.1943-7870.0000831.
- Kodide, U. (2010), Thermal conductivity and its effects on the performance of PCC pavements in MEPDG,
- Li, H., J. Harvey, and A. Kendall (2013), Field measurement of albedo for different land cover materials and effects on thermal performance, , 59, 536–546, doi:10.1016/j.buildenv.2012.10.014.
- Nelson, K. C., and M. A. Palmer (2007), Stream temperature surges under urbanization and climate change: Data, models, and responses, *J. Am. Water Resour. Assoc.*, 43(2), 440–452, doi:10.1111/j.1752-1688.2007.00034.x.
- Omidvar, H., J. Song, J. Yang, G. Arwatz, Z. Wang, K. Kaloush, and E. Bou-zeid (2018), Rapid Modification of Urban Land Surface Temperature during Rainfall, *Water Resour. Res.*, doi:10.1029/2017WR022241.
- Wang, S. (2015), Pavement albedo assessment : methods , aspects , and implication,

Using advanced Urban Canopy Models to investigate the potential of thermochromic materials as urban heat island mitigation strategies

Claudia Fabiani^{1,*}, Anna Laura Pisello^{1,2}, Elie Bou-Zeid³ and Jiachuan Yang³

¹CIRIAF–Interuniversity Research Center on Pollution and Environment “Mauro Felli”, Italy.

²Department of Engineering – University of Perugia, Italy.

³Department of Civil and Environmental Engineering, Princeton University, NJ, USA.

*Corresponding email: fabiani@crbnet.it

ABSTRACT

Recent trends in urbanization processes are causing serious threats at both local and global environmental scale. Greenhouse gas emissions, heat waves, and the heat island effect are constantly growing in intensity and produce increasing discomfort and health impacts in urban populations. In this context, the building sector is currently developing advanced and adaptive materials for building envelope and paving surface applications characterized by high energy performance and low embodied energy. Most of these innovative materials are firstly analysed at the component scale by means of laboratory investigations, while their effect on the built environment is generally assessed at a later stage, by means of advanced computer simulations in buildings and urban microclimate monitoring or modelling. In this context, this work focuses on the evaluation of the UHI modulation potential of materials with advanced dynamic optical properties, i.e. variable surface albedo, for surface urban canyon applications. Specifically, the Princeton Urban Canopy Model (PUCM) is applied with the aim of investigating the potential of advanced urban roofing material to modulate the urban heat island. The aim is to minimize the heat island in the summer but to let it develop in the winter, using roofing applications characterized by a dynamic temperature-dependent optical behavior. In particular, the effect of thermochromic materials on local energy transport phenomena is assessed and benchmarked against more common cool roof solutions. Results show that the modified UCM can effectively be implemented to represent temperature-dependent albedo variations. Additionally, this study demonstrates that using thermochromic materials produces a smart optical response to local environmental stimuli and allows enhanced short wave solar reflection in summer conditions, reduced reflected solar fraction in winter, and adaptive properties during transition periods.

KEYWORDS

Urban Canopy Model, Urban Heat Island, Building Envelope, Roof Albedo, Urban Canyon, Thermochromic materials.

INTRODUCTION

An urban heat island (UHI) is a metropolitan area that is much warmer than its rural surroundings, where the maximum temperatures occur within its densest parts (Kolokotroni and Giridharan, 2008; Giannopoulou et al., 2011). Recent research contributions suggest that even relatively small cities, i.e. of just over 200,000 people, could be affected by this detrimental phenomenon, which consequently could be more common than expected (Borbora and Das, 2014; O’Malley et al. 2015). All this considered, a deeper understanding of the main causes and effects of the UHI is nowadays of paramount importance, together with the development of ever more effective mitigation strategies and solutions. The existing literature acknowledges several mitigation strategies such as air ventilation, shading of buildings,

expansion of green surfaces, use of water and use of high albedo materials on buildings' surfaces (O'Malley et al. 2015). In particular, using cool roofing materials has been found to be highly effective in reducing both surface and air temperature peaks in the urban environment in summer (Takebayashi and Moriyama, 2012). However, they were also found to negatively affect the same parameters in winter conditions, were a roof with a low albedo value allows to increase the solar gains through the building walls, and consequently, reduce the building energy use (Hosseini and Akbari 2014; Pisello et al., 2016). All this considered, some researchers have investigated the possibility of using thermochromic pigments, i.e. parcels that respond to the surrounding environment by reversibly changing their colour from darker to lighter tones as the temperature rises (Ma et al., 2001), to produce innovative building coatings (Karlessi et al., 2008).

In this work, the Princeton Urban Canopy Model (PUCM) (Li et al. 2014; Yang and Wang 2015) is used to investigate the potential of such dynamic albedo materials as UHI mitigation strategies in the summer, while also investigating their possible countereffect in winter.

METHODS

The Princeton UCM adopts the single-layer "big-canyon" representation for urban areas, and uses an advanced surface exchange scheme, coupling the transport of energy and water inside urban canopies. It considers the one-dimensional energy balance for an infinitesimally-thin surface layer of each considered i -th surface ($i =$ ground, wall and roof), at the surface-air interface, which can be expressed as:

$$R_n = H + LE + G \quad (1)$$

where R_n is the net radiation, H is the sensible heat flux, LE is the latent heat flux (from soil evapotranspiration and/or plant transpiration) and G is the heat storage term (flux into the surface). The net radiation R_n is defined as the sum of the net shortwave and longwave radiation from each considered surface i ($i =$ ground, wall and roof), S_i^{net} and L_i^{net} , respectively. The shortwave component is defined based on the multiple reflection scheme (up to 2 reflections) according to equation 2:

$$S_i^{net} = (1 - \alpha_i)S_i^{total} + \sum_j \alpha_j S_j^{total} \frac{A_j}{A_i} \psi_{j \rightarrow i} (1 - \alpha_i) + \sum_j \alpha_j S_j^{total} \sum_k \frac{A_j}{A_k} \psi_{j \rightarrow k} \alpha_k \frac{A_k}{A_i} \psi_{k \rightarrow i} \quad (2)$$

where α_i is the albedo, $\psi_{j \rightarrow i}$ is the view factor from surface j to surface i , S_i^{total} is the total shortwave radiation per unit area incident on surface i , and A_i is the area of surface i relative to the canyon width or sky area in two dimensions (W).

While the longwave component is defined as:

$$L_i^{net} = \sum_j \varepsilon_j L_j \frac{A_j}{A_i} \psi_{j \rightarrow i} + \sum_j L_j \sum_k \frac{A_j}{A_k} \psi_{j \rightarrow k} (1 - \varepsilon_k) \frac{A_k}{A_i} \psi_{k \rightarrow i} - \varepsilon_i \sigma T_i^4 \quad (3)$$

where ε is the emissivity, σ is the Stephan–Boltzmann constant, T_i is the surface temperature of the i th surface, and L is the flux of longwave radiation emitted from each surface or the downward longwave radiation from the sky. Here, the j index denotes ground, walls, trees, or sky, and the k index denotes ground, walls, or trees only.

The Princeton UCM implements an explicit resolution for sub-facet heterogeneity in building walls, rooftops and ground facet, each of which is independently modeled by using unique

physical and thermal attributes. Consequently, the thermo-optical properties of every single surface introduced in the model may be separately controlled. In this work, the albedo of the roof is dynamically defined as a function of the roof temperature at the outermost layer that responds in a finite time (not instantly) to temperature changes according to:

$$\alpha(T) = \alpha_{dark} + \frac{\alpha_{cool} - \alpha_{dark}}{2} (1 + \operatorname{erf}(t_{norm}(T))) \quad (4)$$

where $\alpha(T)$ is the albedo at temperature T , α_{dark} is the albedo for temperatures below the thermochromic transition temperature ($T_{tc} = 30^{\circ}\text{C}$), α_{cool} is the albedo for temperatures above the thermochromic transition temperature, $\operatorname{erf}(t_{norm})$ is the error function, and t_{norm} is the normalized time, defined as a function of the thermochromic transition interval t_{TC} and, consequently, of the roof surface temperature. The thermochromic transition interval was selected to be 20 minutes based of previous researches (Karlessi et al., 2008).

Three different roof configurations where considered and compared in this work: dark roof ($\alpha=0.15$), thermochromic roof ($\alpha=0.15 \rightarrow 0.75$), and cool roof ($\alpha=0.75$). Each configuration was simulated for 4 different months: May, July, October 2011, and January 2012, and finally average day profiles where defined for each of them.

The simulations were carried out considering an urban canyon located in Princeton (NJ), characterized by an aspect ratio (building height over street width) of 0.80 and a built-up area fraction equal to 0.84. Local environmental boundary conditions obtained from a dedicated weather station, with a sampling rate of 30 minutes also placed in Princeton were used as forcing constraints in each of the three-considered scenario. More in detail, the model was driven by air temperature, specific humidity, atmospheric pressure, wind speed, shortwave radiation, longwave radiation and precipitation values, which were interpolated from the original weather data to fit the simulation time interval (10 seconds), throughout the simulation.

RESULTS AND DISCUSSIONS

Results for the four months simulations are shown in Figure 1; depicted are the roof surface temperature (TR), sensible heat flux (HR) and latent heat flux (LER) of the three considered roof configurations. As can be seen, the dark roof always presents the highest values for all the considered months, while the cool roof is always associated with the lowest surface temperature and heat fluxes. This behavior is good in terms of UHI mitigation potential during the hottest months, but inevitably reduces the heat gains during winter, causing a more intense energy consumption for heating purposes in this period of the year and negating some of the winter-time benefits of the UHI at the city scale. The thermochromic roof, on the other hand, shows the interesting ability to dampen the heat gains during summer, producing a more stable temperature profile during the average day of the month in May and July, while preserving the beneficial behavior of the dark roof in October and January, when the thermochromic transition temperature is almost never reached, and consequently the roof keeps a lower albedo and is able to absorb heat from the incident incoming radiation.

Table 1 summarizes the maximum and minimum temperature and heat flux values observed in the three considered configurations for the four simulated months. As expected, the thermochromic roof is characterized by an intermediate behavior that allows it to closely approach the cool roof profile during the hottest months (34.0 vs 33.5°C of maximum temperature for the thermochromic and the cool configuration, respectively), and reproduce the dark roof behavior in the cooler months ($TR_{min} = -1.8^{\circ}\text{C}$ in both cases).

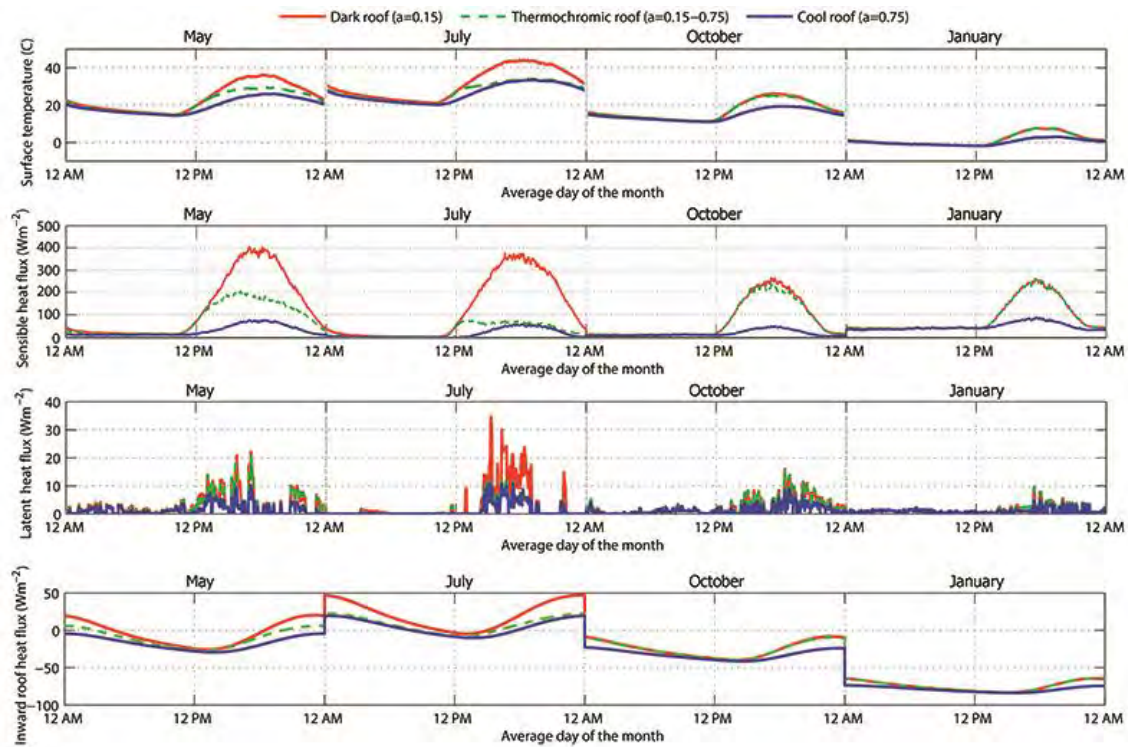


Figure 1. Roof surface temperature, sensible and latent heat flux, and inward heat flux for the three considered roof configurations, i.e. dark, thermo-chromic and cool roof.

Large differences can also be observed when the roof sensible (HR) and the latent (LER) heat fluxes are considered. More in detail, the thermo-chromic roof reduces the maximum sensible heat flux released in the atmosphere from 430.4 to 288.1 Wm^{-2} when compared to the dark roof configuration, which is a significant reduction in terms of UHI mitigation potential, although lower than the one obtained in the cool roof configuration, i.e. 86.7 Wm^{-2} . As for the latent heat flux, of course the minimum value is not different from one configuration to the other, but the maximum one was found to be equal to 38.3, 20.7 and 11.8 Wm^{-2} for the dark, the thermo-chromic and the cool roof configuration, respectively.

Finally, the heat flux at the interface between the indoor air domain and the internal roof surface is reduced from 47.2 Wm^{-2} in the dark roof configuration to 22.5 Wm^{-2} in the thermo-chromic roof, and to 19.6 Wm^{-2} in the cool roof one. In winter conditions, on the other hand, the introduction of the dynamic albedo reduces the outward heat losses obtained using the cool roof configuration only from -83.8 to -83.1 Wm^{-2} (in this case the minus sign denotes that the heat flux is transferred from the inside towards the outer environment). This ability to absorb heat in the winter is a beneficial advantage of the thermo-chromic roof.

The atypical temperature and heat fluxes profiles obtained for the thermo-chromic roof is a consequence of its dynamic nature that allows it to adjust its ability to reflect the incoming radiation as a function of the local surface temperature. Figure 2 shows the albedo variation profile obtained for the thermo-chromic roof during a representative week in May. As can be seen, each time the roof temperature overcomes the thermo-chromic transition temperature T_{TC} , the albedo starts to increase, and finally reaches the cool roof limit value of 0.75.

Table 1. Considered scenarios with the respective albedo values and the obtained maximum and minimum roof temperature (TR), sensible heat flux (HR), latent heat flux (LER) at the outer surface, and the heat flux at the inner surface (Qin) values.

	Dark roof (DR)	Thermochromic roof (TCR)	Cool roof (CR)
Albedo (-)	0.15	0.15→0.75	0.75
TRmax (°C)	44.2	34.0	33.5
TRmin (°C)	-1.8	-1.8	-1.8
HRmax (Wm ⁻²)	430.4	288.1	86.7
HRmin (Wm ⁻²)	-0.03	-0.46	-1.06
LERmax (Wm ⁻²)	38.3	20.7	11.8
LERmin (Wm ⁻²)	0	0	0
QinRmax (Wm ⁻²)	-83.1	-83.1	-83.8
QinRmin (Wm ⁻²)	47.2	22.5	19.6

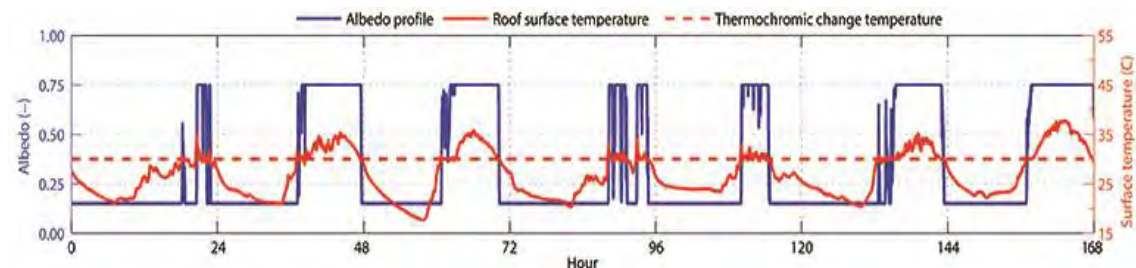


Figure 2. Albedo profile and roof surface temperature during a typical week in May for the thermochromic roof.

CONCLUSIONS

In this work, the UHI mitigation potential of an innovative thermochromic roof, capable of dynamically changing its albedo between 0.15 and 0.75 was investigated and compared to more common solutions such as a classic dark roof ($\alpha=0.15$) and a high performance cool roof ($\alpha=0.75$). The three roof configurations were investigated considering four different month-long simulations in order to evaluate the performance of the roofs in summer and winter conditions (July 2011 and January 2012), as well as during transition periods (May and October 2011). Results confirm that the thermochromic roof's ability to dynamically change its albedo to reflect the incoming solar radiation in response to the surface roof temperature has beneficial impacts. More in detail, when the roof surface is characterized by temperatures below the transition threshold, the thermochromic configuration behaves as a classic dark roof, allowing the overall urban surface to absorb heat in the form of solar heat gains. This reduces the winter penalty of the high performance cool roof and reproduces the temperature and heat flux profiles of the more convenient dark roof configuration during cooler periods.

Every time the roof surface overcomes the transition threshold temperature, on the other hand, the thermochromic roof starts to change its albedo, and within a maximum time of 20 minutes (coloring or decoloring time interval) behaves as a high albedo roof with high solar reflectance capability. Consequently, the thermochromic coating allows to reduce the heat gains during warmer months and reduces both the roof surface temperature and heat fluxes, which will positively affect the UHI effect in its surroundings.

In conclusion, the use of thermochromic coatings in building roofs can indeed be considered as an interesting solution to mitigate the increase of air temperatures in the urban environment during summer, while maintaining the positive absorption of solar radiation in winter. Future research should, however, be conducted in order to investigate the effect of thermochromic materials with different transition temperatures and albedo variation profiles. Additionally, it

would be interesting to quantify the benefits associated with this innovative roof configuration in terms of resulting building energy loads and consumption, and also to quantify its consequences on the overall urban microclimate.

ACKNOWLEDGEMENT

The authors thank the PhD school in Energy and Sustainable development and COLO ARTE project. Additionally, the first author is supported by Ministry funding and university funding of the PhD school in Energy and Sustainable Development. Part of this research is carried out within the framework of COLO ARTE project supported by Fondazione Cassa di Risparmio di Perugia, (Grant Cod. 2016.0276.02). The last two authors are supported by the US National Science Foundation under grant number ICER 1664091 and under the UWIN Sustainability Research Network Cooperative Agreement 1444758.

REFERENCES

- Borbora J., and Das A.K. 2014. Summertime Urban Heat Island study for Guwahati City India. *Sustainable Cities and Society*, 11, 61-66.
- Giannopoulou K., Livada I., Santamouris M., Saliari M., Assimakopoulos M., Caouris Y.G. 2011. On the characteristics of the summer urban heat island in Athens, Greece. *Sustainable Cities and Society*, 1(1) (2011), 16-28.
- Hosseini M. and Akbari H. 2014. Heating energy penalties of cool roofs: the effect of snow accumulation on roofs. *Advances in Building Energy Research*, 8(1), 1-13.
- Karlessi T., Santamouris M., Apostolakis K., Synnefa A., Livada I. 2008. Development and testing of thermochromic coatings for buildings and urban structures. *Solar Energy*, 83, 538-551.
- Kolokotroni M. and Giridharan R. 2008. Urban heat island intensity in London: An investigation of the impact of physical characteristics on changes in outdoor air temperature during summer. *Solar Energy*, 82(11), 986-998.
- Li D., Bou-Zeid E, Oppenheimer M. 2014. The effectiveness of cool and green roofs as urban heat island mitigation strategies. *Environmental Research Letters*, 9(5), 055002.
- Ma Y., Zhu B., Wu K. 2001. Preparation and solar reflectance spectra of chameleon-type building coatings. *Journal of Solar Energy*, 70, 417-422.
- O'Malley C., Piroozfar P., Farr E.R.P., Pomponi F. 2015. Urban Heat Island (UHI) mitigating strategies: A case-based comparative analysis, *Sustainable Cities and Society*, 19, 222-235.
- Pisello A.L., Castaldo V.L., Fabiani C., Cotana F. 2016. Investigation on the effect of innovative cool tiles on local indoor thermal conditions: Finite element modeling and continuous monitoring. *Building and Environment*, 97, 55-68.
- Takebayashi, H. and Moriyama M. 2012. Relationships between the properties of an urban street canyon and its radiant environment: Introduction of appropriate urban heat island mitigation technologies. *Solar Energy*, 86(9), 2255-2262.
- Yang J. and Wang Z.H. 2015. Optimizing urban irrigation schemes for the trade-off between energy and water consumption. *Energy and Buildings*, 107, 335-344.

A picture is worth a thousand words: Smartphone photograph-based surveys for collecting data on office occupant adaptive opportunities

William O'Brien^{1*}, Anthony Fuller¹, Marcel Schweiker², and Julia Day³

¹Carleton University, Canada

²Karlsruhe Institute of Technology, Germany

³Washington State University, USA

*Corresponding email: liam.obrien@carleton.ca

ABSTRACT

In the past several decades, psychological aspects have become important to holistic building occupant comfort and satisfaction evaluations. Psychological dimensions of comfort include occupants' opportunities to interact with their indoor environment and perceived control over the indoor environment. Current post-occupancy evaluations tend to focus on collecting quantitative data, despite overwhelming evidence that contextual factors can profoundly impact occupant comfort. This paper proposes and tests a novel method for data collection to study adaptive comfort opportunities. A smartphone-based survey was developed to concurrently collect office occupants' subjective evaluations of usability and comfort of spaces, in addition to photographs of all key building interfaces. The photos were coded to obtain quantitative characteristics of offices, such as whether the interface is obstructed. With a sample of 39 office workers, this paper reveals the effectiveness of this novel photograph-based survey method, while also providing some initial quantitative and qualitative results.

KEYWORDS

Adaptive comfort, building usability, post-occupancy evaluation, photographs

INTRODUCTION

Building designers and operators should strive to provide comfortable spaces for two reasons: (1) occupant comfort is a desirable property and because it is closely linked to occupant productivity (Leaman & Bordass, 2000), and (2) comfortable occupants are less inclined to take energy-intensive actions (e.g., opening windows when mechanical heating is on and closing blinds and turning on lights during and after periods of daylight glare). The study of occupants' thermal perception is rooted in studies addressing the relationship between physical indoor thermal conditions, physiological responses, and the perception of these conditions by humans (Fanger, 1970). ASHRAE Standard 55 (ASHRAE, 2017) defines thermal comfort as "that condition of mind which expresses satisfaction with the thermal environment and is assessed by subjective evaluation." Psychological and behavioral influences on perception have been recognized as being critical aspects of thermal comfort for over four decades (Humphreys, 1976). Indeed, non-physiological metrics can have a significant impact on occupants' reported satisfaction with indoor environmental quality (IEQ) (Kim & de Dear, 2012).

One of the non-physiological factors is perceived control. Through their extensive post-occupancy evaluation experience, Leaman and Bordass (2000) stated that "In study after study, people say that lack of environmental control is their single most important concern...". Laboratory studies have also shown a positive relationship between perception of thermal conditions and perceived control (Schweiker & Wagner, 2016). While adaptive thermal

comfort models used in standards (e.g., Standard 55 (ASHRAE, 2017)) implicitly recognize that providing adaptive opportunities to occupants (namely operable windows) improves occupant tolerance for a wider range of indoor temperatures, Standard 55 does not explicitly quantify the effect of differences in perceived control. Approaches towards such quantification are scarce and still lack generalizability (Schweiker and Wagner, 2015). Moreover, research on building usability is still in its infancy (Day and Heschong, 2016). More critically, there continues to be a trend towards greater automation under the false premise that taking control away from occupants improves comfort (Leaman and Bordass, 2000).

The theme of perceived control links human comfort with occupant behavior. Research on occupant comfort and occupant behavior—be it related to thermal, visual, or acoustic aspects—is typically performed in either a controlled laboratory environment or *in situ* (Parsons, 2014). Common quantitative research methods use one or both of: 1) surveys that ask occupants about their perceived level of comfort and control and the available and exercised controls, and 2) sensor measurements to collect data about environmental and/or physiological conditions. However, contextual factors such as workplace cleanliness, flexibility to move furniture, presence of other occupants, and ease of use of building systems, all play a critical role in occupants' likelihood to exercise adaptive opportunities (Kim and de Dear, 2012; O'Brien and Gunay, 2014). Traditional surveys are typically not capable of capturing these complex and subtle predictors of perceived opportunities for adaptive control. Moreover, surveys rely on self-reporting, which can yield significant error. Pritoni, Meier, Aragon, Perry, and Peffer (2015) performed a survey on thermostat-related behavior, including a request for participants to upload a photograph of their thermostat. They found that only 50% of occupants who claimed that they use programmable features of their thermostat were actually using them, according to the photographs. In general, participants may not possess the insight required to identify phenomena of interest and significance.

To understand contextual factors, researcher walk-throughs are frequently used, whereby the researcher takes notes and photographs. Such qualitative data can help explain anomalies in quantitative data and can serve as exploratory research to guide future research directions (Day, Theodorson, et al. 2012). However, walk-throughs are time-consuming, may jeopardize the safety of the researcher, and are subject to the Hawthorne effect (O'Brien, Gilani, et al. 2018).

This paper proposes a new survey-based research method to yield new insights about the relationships between perceived comfort and availability of adaptive opportunities and usability of building systems and interior design elements. The aim is also to continue collecting convincing anecdotal evidence to support the philosophies and design implications of providing adaptive opportunities to building occupants. To achieve this, the researchers sought to develop a method that could yield many of the benefits of field studies and obtain large datasets about comfort and building usability without a requirement for researchers to visit properties. This paper presents the survey and then briefly provides initial analysis and discussion.

METHODOLOGY

A number of research questions were posed for this research; this paper only briefly explores these questions using the current survey campaign and resulting sample of 41 participants. The questions are fundamental (e.g., what is the correlation between presence of adaptive opportunities and perceived control?); application (e.g., what lessons can be learned for future building design?); and, methodological (e.g., are the photographs as effective as researcher

walk-throughs?). The short length of this paper limits the amount of analysis to illustrative purposes.

Stemming from the primary research objectives of this study, a survey was developed and piloted. For brevity, the survey is not included in this paper. Survey sections include questions on: (1) confirmation that the participants are currently in their primary office space (and in Canada for the current study); (2) perceived level of comfort; (3) occupants' ability to improve indoor environmental quality; (4) availability of, distance to, ease of use of, concern about disturbing fellow occupants if using, and frequency of using: *window shading devices, operable windows, desk fans, thermostats, space heaters, overhead lighting, and task lighting*; (5) nature of furniture; (6) opportunities to reorient or relocate in the event of discomfort; and, (7) general features or characteristics of offices that they like or do not like. Fundamental to the survey, participants were asked to take and upload a photo of the adaptive opportunities listed in item 4 (if applicable) and item 7; up to nine photos were uploaded per participant. Depending on whether the above seven main adaptive opportunities were available, the participants were required to respond to between 41 to 83 questions, though many were repetitive (e.g., asking about many aspects of comfort). LimeSurvey (Figure 1) was selected because of its suitability for smartphone applications and ability of participants to upload their photographs.

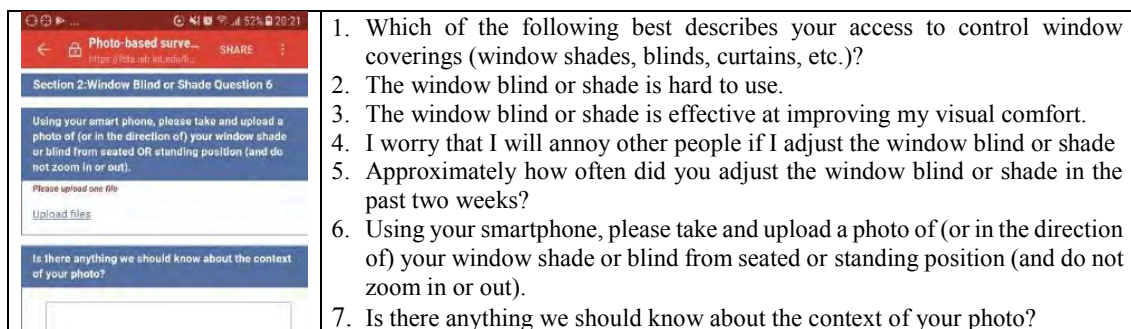


Figure 1. Sample screenshot of survey and sample questions for window shading devices.

Ethics clearance was obtained from the university research ethics board; the ethics documentation had particular focus on ensuring that occupants, buildings, and organizations could not be identified in photographs and that the photographs would be securely stored. To encourage participation, a \$10 Amazon gift card was offered to all participants who completed the survey with valid responses. Participants were recruited via three separate postings over two months on the lead author's Facebook wall. A posting on a local Reddit group yielded many incomplete and invalid responses. Survey responses were manually validated for completion and to confirm that conditions for participation were complied with, where possible. For instance, several participants responded from inside a vehicle and one participant uploaded a photo of their desk behind which a tropical plant could be seen outside (an unlikely circumstance in the Canadian winter). Approximately 50% of prospective participants who answered at least one question did not complete the survey, while approximately 20% of surveys that were completed were considered invalid (see Discussion). For valid responses, the mean and standard deviation for the completion times were 16.4 and 9.0 minutes. Despite considerable effort in recruitment and a relatively generous incentive, 41 valid responses were obtained out of the targeted 100. The responses occurred between December and February; thus, results were studied within the context of winter conditions (e.g., responses about operable windows have limited meaning). The results include between five and 33 photos uploaded for each of the seven categories of adaptive opportunities.

ANALYSIS AND RESULTS

This section describes the analysis approach and results for selected questions that were posed in the Methodology. Figure 2 shows the overall availability and proximity of adaptive opportunities.

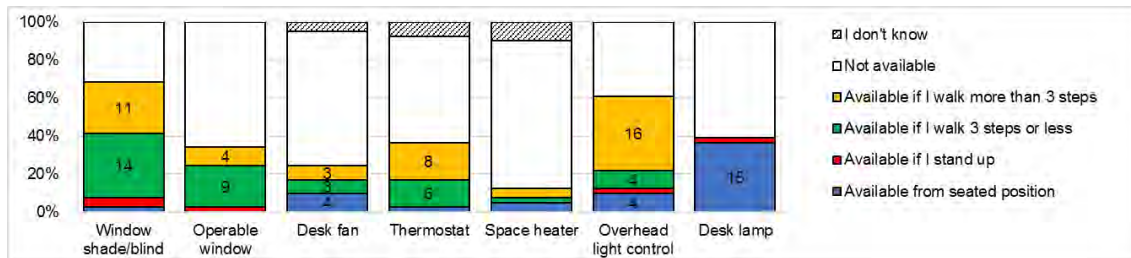


Figure 2. Availability of adaptive opportunities

Next, the influence of office type on participants' reported ability to improve comfort through adaptive actions on a five-point scale from very poor (1) to excellent (5) was explored. Given that the data are generally not normally distributed, a non-parametric test (the Kruskal Wallis test) was used to assess differences in responses between office types, as annotated in Figure 3.

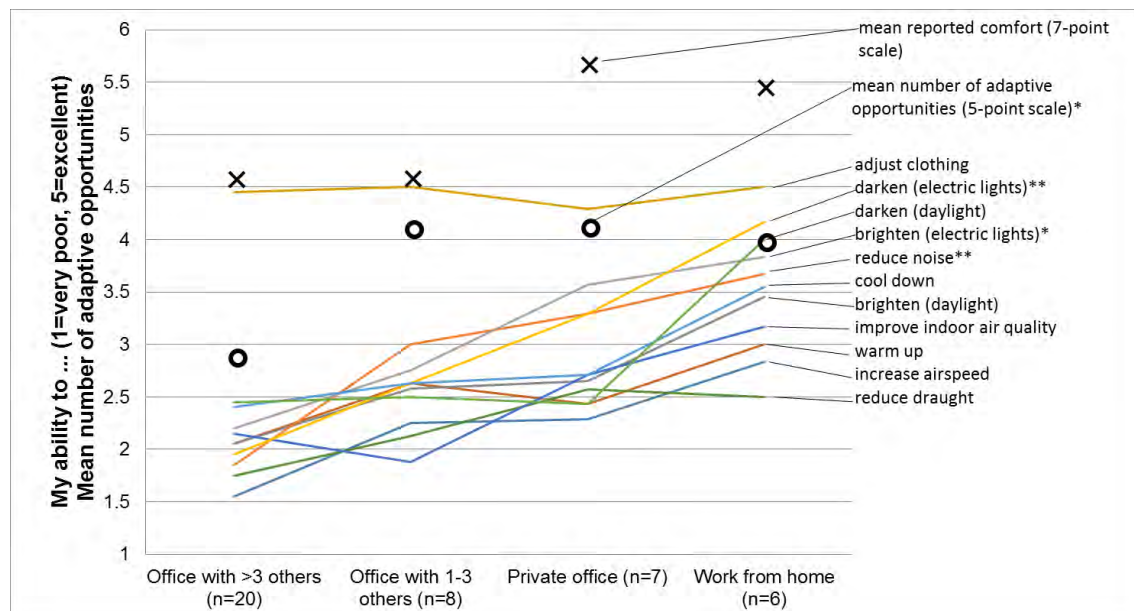


Figure 3. Relationship between office type and adaptive opportunities and comfort. The * and ** denote significance of <0.05 and <0.01 , respectively. Note: mean values on the y-axis assume the Likert scale responses are equally-spaced.

To illustrate the power of photographic data to help explain outliers, the relationship between participants' rated availability of blinds/shades and ability to reduce daylight was explored (Figure 4). A best-fit line, under the assumption that the data can be converted to into equally-spaced categories, is shown on the plot. In general, the presence and proximity of a shading device is a moderately good predictor of occupants' ability to reduce daylight levels. Six outliers were examined to reveal new insights about how the participants interpreted the questions and responded. The two photos for points below the best-fit line show that although the shading devices were nearby, they were obstructed (as explicitly written by the participant).

Notably, the occupants who took the top four photographs appear to be seated quite far away from the windows, in general, and may not be subject to chronic daylight glare. These results, which cover only a small part of the collected data, demonstrate that important contextual factors are necessary to understand the quantitative responses. Moreover, they provide anecdotal evidence to support previous research that indicated the importance of minimizing obstruction of blind interfaces (Day et al., 2012). Meanwhile, Figure 3 suggests that occupants have a greater sense of control, more adaptive opportunities, and greater comfort in private spaces.

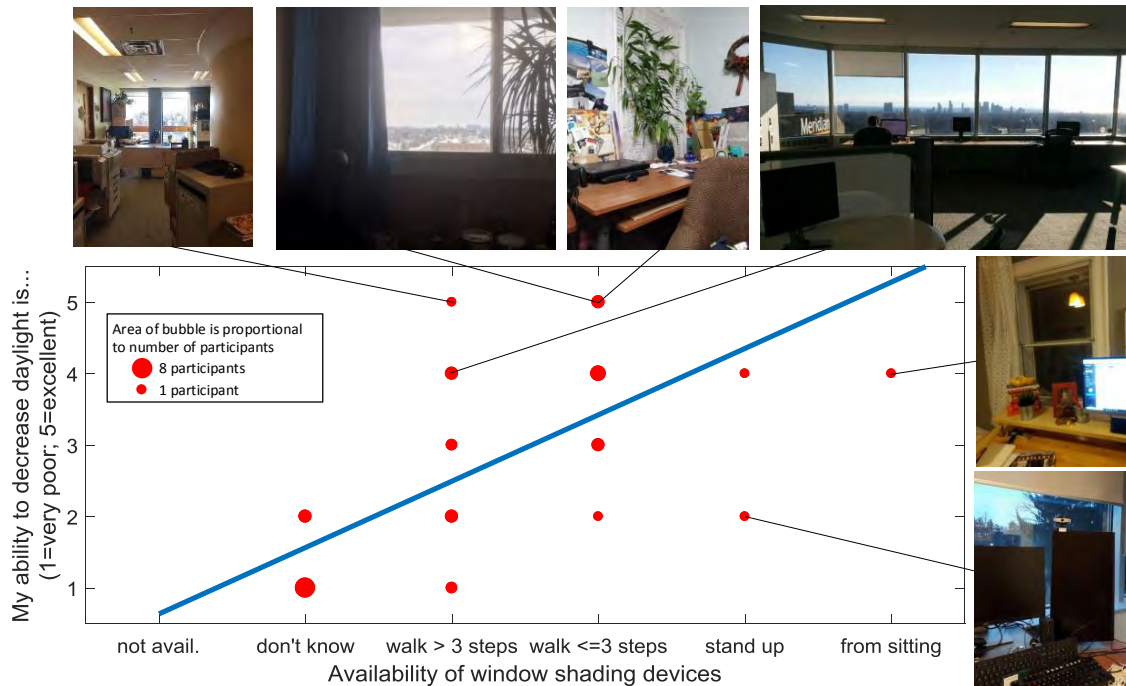


Figure 4. Example of using photographs to explain outliers in a simple correlation.

DISCUSSION

Briefly, this section provides some lessons learned and comments about the effectiveness of the photograph-based survey. The photographs were effective at providing contextual information about why a participant responded a certain way. However, this was limited to visual evidence unless the participant also provided comments to describe the photo (as was done for 109 out of 131 photos). In many cases, cases where the participant responded unexpectedly (e.g., outliers of Figure 4), interpretation of the photograph provided otherwise-missing explanation. However, in some cases photographs did not explain unexpected quantitative results. A study with walk-throughs and in-person interviews could largely resolve this limitation because the researcher could inquire about anomalies. However, on the balance, the current approach yielded significant explanatory power along with the aforementioned benefits. Recruitment of participants was significantly more difficult than expected. The researchers' acquaintances seemed to feel more responsible for supporting this project than unknown participants. However, the researchers' professional networks were avoided because of their tendency to have subject expertise (e.g., knowledge of comfort theory). One participant exited the survey early, noting that government workers cannot take photos of their workplace. In retrospect, the survey should have been slightly more specific about what to capture in photographs. There was minor confusion for overhead lights about whether to capture the luminaires or the interface. The survey specified that all photos should be taken from the

primary location of work, regardless of whether the interface was visible from this location in order to assess whether there was a clear view.

CONCLUSIONS

This paper introduced a novel post-occupancy evaluation survey that required participants to capture and upload photographs of building interfaces, adaptive opportunities, and other comfort-related items. The paper provides analysis of an initial sample of 41 participants who are office workers in Canada. Whereas previous POE surveys did not have the ability to capture contextual information about office spaces (e.g. obstruction of interfaces or presence of other occupants), the qualitative data provided by the photographs can help explain outliers and other anomalies. Future work is needed to further analyze the data, refine the survey, and expand deployment.

REFERENCES

- ASHRAE. 2017. Standard 55: Thermal environmental conditions for human occupancy. Atlanta, GA.
- Day, J., & Heschong, L. 2016 *Understanding Behavior Potential: the Role of Building Interfaces* Julia Day, Kansas State University. Paper presented at the ACEEE Summer Study on Energy Efficiency in Buildings, Pacific Grove, CA.
- Day, J., Theodorson, J., & Van Den Wymelenberg, K. (2012). Understanding controls, behaviors and satisfaction in the daylight perimeter office: a daylight design case study. *Journal of Interior Design*, 37(1), 17-34.
- Fanger, P. O. 1970. *Thermal comfort: Analysis and applications in environmental engineering*. Berkeley, CA: McGraw-Hill.
- Humphreys, M. A. 1976. Field studies of thermal comfort compared and applied. *Building Services Engineer*, 44, 5-27.
- Kim, J., & de Dear, R. 2012. Nonlinear relationships between individual IEQ factors and overall workspace satisfaction. *Building and Environment*, 49, 33-40.
- Leaman, A., & Bordass, B. 2000. Productivity in buildings: the 'killer' variables. *Building Research & Information*, 27(1), 4-19.
- O'Brien, W., & Gunay, H. B. 2014. The contextual factors contributing to occupants' adaptive comfort behaviors in offices—A review and proposed modeling framework. *Building and Environment*, 77, 77-87.
- O'Brien, W., Gilani, S., & Gunay, H. B. 2018. In Situ Approaches to Studying Occupants *Exploring Occupant Behavior in Buildings* (pp. 129-167): Springer.
- Parsons, K. 2014. *Human thermal environments: the effects of hot, moderate, and cold environments on human health, comfort, and performance*: CRC press.
- Pritoni, M., Meier, A. K., Aragon, C., Perry, D., & Peffer, T. 2015. Energy efficiency and the misuse of programmable thermostats: The effectiveness of crowdsourcing for understanding household behavior. *Energy Research & Social Science*, 8, 190-197.
- Schweiker, M., & Wagner, A. 2015. A framework for an adaptive thermal heat balance model (ATHB). *Building and Environment*, 94, 252-262.
- Schweiker, M., & Wagner, A. (2016). The effect of occupancy on perceived control, neutral temperature, and behavioral patterns. *Energy and Buildings*, 117(1), 246–259.

Benchmarking the energy efficiency of office buildings in Belo Horizonte, Brazil

Ana Carolina de Oliveira Veloso^{1,*}, Roberta Vieira Gonçalves de Souza¹

¹Federal University of Minas Gerais, Brazil

*Corresponding email: acoveloso@gmail.com

ABSTRACT

In countries in which energy efficiency regulations are already consolidated or in the process of being consolidated, an important parameter to be verified is the relative consumption of electric energy of existing buildings in accordance with established ranges of consumption for different types of buildings. In the present paper ISO 52003-1 methodology was applied to create a benchmarking for office buildings for the city of Belo Horizonte, Brazil and the work discusses the implications of using the standard's methodology for the Brazilian scenario. To fulfill this objective, it was necessary to gather electric energy consumption data for this type of buildings as well to survey for building constructive data. For the classification of buildings according to their consumption, a methodology was developed to isolate the annual consumption per area of the towers from EUI data for the whole building. Besides, information such as garages existence, lighting power density of the garages and the number of lifts was collected in loco as in many cases there was not access to the building projects. The results showed that due to the large variation in consumption data, the use of the average EUI instead of the median EUI value results in a better distribution for the towers energy consumption classification. This precaution can prevent excessive resistance in the market if a public benchmarking policy is established. Therefore, it's concluded that the understanding of the consumption of electrical energy of the buildings plays a fundamental role in the establishment of goals for the new buildings.

KEYWORDS

Energy use benchmark; energy consumption; office buildings; sensitivity analysis.

INTRODUCTION

Energy is a major factor in global efforts to achieve sustainable development (Vera and Langlois, 2007) and buildings can be the key to achieving this goal (Rey et al., 2007), because they account for about 40% of the world's energy consumption (IEA, 2008). Thus, it is estimated that there is great potential to mitigate consumption in this sector. In Brazil, the energy matrix of buildings is closely linked to the use of electric energy, and buildings in the residential, commercial and public sectors account for 42.5% of this consumption (BRASIL, 2017).

Due to economic growth, developing countries have experienced a large increase in their energy consumption (Iwaro and Mwashu, 2010). According to the National Energy Plan 2030 (MME, 2007), the energy consumption of buildings in Brazil is projected to grow 3.7% per year by 2030. Lamberts et al. (2014) point out that every decision made during the design process can influence the buildings' thermal and luminous performance. Therefore, the understanding of the influential factors in the consumption of electrical energy of the buildings will have a fundamental role in the establishment of goals for the new buildings to be constructed.

According to Lamberts et al. (2014), a building is more energy efficient than another when it provides the same environmental conditions of comfort to its user, with lower power

consumption. In countries which energy efficiency regulations are already consolidated or under consolidation, an important parameter to consider is the relative consumption of electricity according to the building typologies. This type of survey is called benchmarking, which is a method used to compare the energy and/or efficiency of a building with a reference value (Perez-Lombard et al., 2009; Signor, 1999; U.S.D.E.C.B.I, 2009). From a collected database, it is possible to propose new criteria for the construction, as well as to evaluate existing criteria and improve the management of buildings of different performances (Chung et al., 2006). The information on the building performance and the indicators implemented in the regulations should be clear and detailed so that the user knows the level reached by the building (Nikolaou et al., 2015).

In July 2009, the Technical Regulation of Quality for Energy Efficiency Levels of Commercial, Services and Public Buildings (INMETRO Directive No. 163) was launched in Brazil. The purpose of this regulation is to "create conditions for the labeling of the energy efficiency level of commercial, service and public buildings" (BRASIL, 2010). In this regulation the classification of buildings varies according to five levels, with "A" being the most efficient and "E" being the least efficient. The first benchmarking initiative in Brazil was made for bank branches in a study developed by the Brazilian Council for Sustainable Construction (CBCS). The benchmarking methodology for this typology was developed through linear regression analysis using data on electricity consumption, energy audits, and climate corrections (Borgstein and Lamberts, 2014).

ISO 52003-1- Indicators, requirements, ratings and certificates - Part 1: General aspects and application to the overall energy performance (ISO 52003-1:2017), launched in 2017, defines the ways of calculating the energy performance of buildings and procedures for setting reference values. Several European Union countries such as France, Germany, Italy, Portugal, United Kingdom are required to implement this standard.

Veloso et al (2017) article served as a basis for the present benchmarking study. The authors analyzed seven design features that influence the electricity consumption in office buildings for Belo Horizonte. According to the study, the air conditioning mode showed to be the most important feature with up to 58% impact in the electricity consumption prediction (the studied building modes were: unconditioned, mixed mode air conditioning and central air conditioning). For each air conditioning mode WWR, façade solar absorptance and SHGC also showed to be relevant design features in the consumption prediction of office buildings. The presence of glazed façade, the presence of solar shading devices and building age were also tested but with no significant results.

In view of the above, the objective of this article the application of ISO 52003-1 in the Brazilian scenario and the implications of proposed changes in the standard methodology in the establishment of a benchmarking for office buildings. It is important to emphasize that in Brazil the access to the data of electric energy consumption and characteristics of the buildings is restricted and for the most part stealthy and for that reason, it was necessary to develop a methodology for the buildings characterization.

METHODS

Experimental Design

For the present study a sample of buildings in the city of Belo Horizonte – Brazil was used. According to the climatic classification of Köppen, Belo Horizonte is classified as a Cwa climate, a hot and temperate climate with mild winter, 18 °C average temperatures in winter

and 22 °C in summer. The mild climate explains a high occurrence of mixed air conditioning in office buildings, that is, natural ventilation is used most of the time and only on hot days the air conditioning system is turned on. The number of office buildings in the city was accessed from a database provided by the City Hall. This database contains information from the IPTU (Urban Land and Territorial Tax) of all the existing buildings in the city approved until 2011. It was identified that until 2011, there were 568 buildings for commercial use and/or services from three to twenty-five floors and a gross floor area of more than 1,000 m².

Consumption data

For the analysis of the electric energy consumption, the consumption data of the 568 buildings were requested and the consumption data of 101 buildings were made available by the electric energy company of the city. Electricity consumption data available is from 2012 to 2014, divided monthly, and with no identification of this measuring unit in the building due to privacy State policies. In the received database, it was not possible then to discriminate the electricity consumption of the floor or room or the common use areas of the building, which led to the need for an on-site survey. Once EUI is quite different in office areas and garages of office buildings the aim of this survey was to separate the electricity consumption of the tower from the building garages. The decision to divide the building in these two parts (garage area and tower) was done because in the city the garage area varies greatly, from office buildings presenting no garage from buildings which present garages that represent up to 1/3 of the total constructed area.

It's important to emphasize that it was not possible to access the internal loads of the studied buildings as access usually is granted only to the common areas of the buildings.

Survey of building areas

From the 101 buildings in which electricity consumption data was obtained, only 50 complete projects were made available by City Hall of Belo Horizonte. For the building sample to be larger, the other 51 buildings were visited to verify the existence or not of a garage. It was then possible to identify that 13.7% of the buildings visited did not have garages. For those buildings the building area provided by the IPTU or the by the architectural plans was considered as being the tower area. For the other buildings the tower areas were obtained by the architectural plans or by on-site visits.

On-site survey of the garages electricity consumption

To obtain the electricity consumption of the towers it was necessary to estimate the electricity consumption of the garages. This was done through a survey of the installed lighting system (number of lamps, lamp and ballast power and use hours) and the number of elevators of the sample buildings. The installed power multiplied by the number of hours of use was used to define the electricity consumption of lighting and elevators, considered to be the electricity consumption of the garages. To estimate the electricity consumption of the towers, the average electricity consumption data provided by the energy company was used and the electricity consumption of the garages was withdrawn.

Building Classification

For the building EUI estimation, only the electricity consumption of the building towers was used, divided by the corresponding area. The methodology of ISO 52003-1:2017 to determine the benchmark scales then was applied to the defined EUI. This standard presents a methodology for establishing a certificate of energy efficiency for buildings, including energy performance indicators. It allows the indication of the energy class of a certain building in comparison to the benchmark. ISO 52003-1:2017 establishes seven levels of efficiency - from

A to G. In Brazil, for commercial, service, public and residential buildings, this index varies from A to E. For the classification to be on the same scale used in buildings in Brazil, the highest limits established in ISO 52003-1:2017 were not used to determine the classification of buildings in the present work.

RESULTS

Figure 1 (a) shows the Energy Use Intensity - EUI ($\text{kWh}/\text{m}^2/\text{year}$) of the sample buildings. The graph (a) in the figure allows the verification of the significant differences between the EUI when the whole building is considered and when towers' and garages' EUI are considered separately. The upper and lower absolute variations are represented by the points, and the lower and upper part of the box represents the percentiles of 25 and 75% of EUI variations. The center line displays the data median and the upper asterisks the outlier values. The symbol inside the box shows the average value of the sample. It is observed in the Figure 1 (b) that in the tower there is a significant variation in the tower EUIs and that 75% of the buildings consume up to 100 $\text{kWh}/\text{m}^2/\text{year}$. It's also important to stress that if only centrally air-conditioned building towers were considered the mean EUI would be of 173 $\text{kWh}/\text{m}^2/\text{year}$.

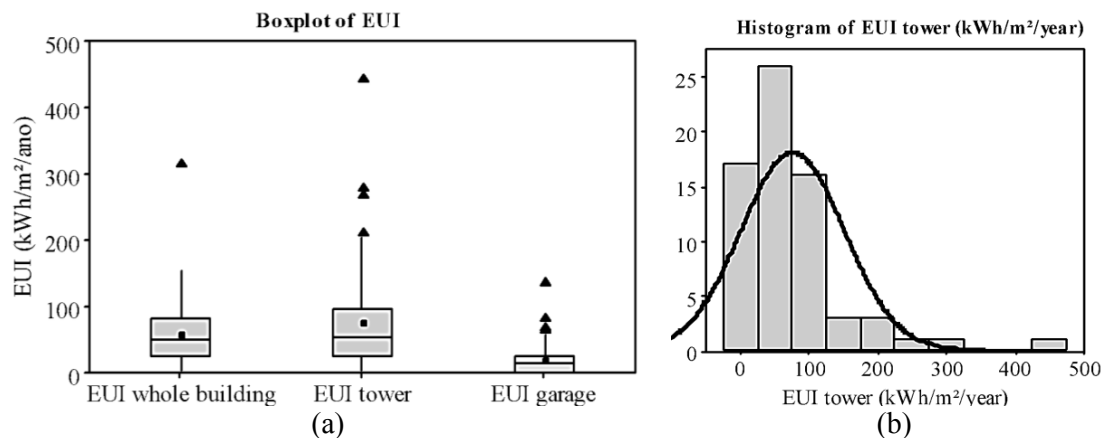


Figure 1. (a) Boxplot with the variation of total, tower and garage EUI; (b) Histogram of the towers EUI.

It is noticed that since the mean and median are not equal, the distribution is not normal, the mean value being greater than the median value. The standard deviations show that there is a great data variability. The average tower EUI is 30% higher than the whole building EUI and the highest electricity consumption found in the tower is an unusual value in the sample.

The EUI limit values using the EUIs with the median EUI value according to the ISO 52003-1:2017 methodology, can be seen in Table 1. It can be observed that 50% of the towers were rated D and E. Based on these results, the mean value in place of the median was also tested and what can be verified is that there was a better distribution of the buildings among the classifications. The increase in the consumption limit for each classification was of 38.5%.

Table 1. Table of EUI electricity consumption limits of buildings and percentage per item.

		A	B	C	D	E
Median	EUI [$\text{kWh}/\text{m}^2/\text{year}$]	27.48	39.02	54.95	77.48	
Value	Percentage of buildings	27%	6%	18%	13%	36%
Average	EUI [$\text{kWh}/\text{m}^2/\text{year}$]	38.05	54.03	76.10	107.30	
Value	Percentage of buildings	32%	17%	14%	14%	23%

DISCUSSIONS

After the implementation of energy efficiency regulations in buildings it is necessary to understand how efficient buildings are in relation to their energy consumption. Therefore, the role of benchmarking is to create reference values. The discussion of the benchmarking of electricity consumption of buildings is recent in Brazil, and there are just a few studies on this subject in the country. A major obstacle is the lack of accessible data in Brazil, which led to the need of creating a methodology to extract data from both the building projects when accessible and from on-site visits when not.

It's important to stress that the present study considered both mixed mode and centrally conditioned mode and divided the electricity consumption of garages and building towers. This decision along with the peculiarities of a continental tropical mild climate makes it difficult to compare EUI values with other studies in the literature.

It was found that there is a great variation in the electricity consumption among the sample buildings. The electricity consumption of the towers showed to be 418% higher than the garages consumption, which justified the separation of this electricity consumption. Still there was great variation of electricity consumption among the building towers due to the fact that there is diversity in the air conditioning mode. The building towers that use central air conditioning in their entirety being the largest consumers, should be studied separately for a better understanding of the specificities of their energy consumption, but once the sample available for the present study could be considered small, this was not done.

A higher number of samples might generate a better distribution using the median EUI value as proposed in ISO 52003-1: 2017 but what is perceived in Figure 1 and confirmed in Table 1 is that the mean EUI is always greater than the median EUI in the samples, showing that the EUI does not follow a normal distribution. Thus, due to the large variation in the EUI, as shown in Figure 1 (b), the use of the average in the value of the EUIs presented a better distribution in the classification of the towers. So as a suggestion for a possible public policy it is believed that the use of the average EUI would generate less resistance in the market given the available sample.

CONCLUSIONS

The construction, operation and use of buildings represent an important part of the country's energy consumption and therefore also present a great potential for energy conservation. The understanding of the buildings' consumption plays a fundamental role in the establishment of goals for the new buildings to be constructed and for retrofit policies for the existing buildings. The methodology of ISO 52003-1:2017 was important to create the ratings in this work and being slightly modified, presented a good distribution of the buildings in each level.

It is important to emphasize that this work is one of the first steps in the development of energy benchmarking for Brazil. As government, stakeholders, building owners and energy companies realize the importance of understanding the energy consumption of buildings for the country's economy, data might become more accessible and thus, it is expected that the analysis conducted in this work can be done for other types of buildings and even repeated for the same typology with a greater sample size.

The results presented in this work are a first picture of the situation of the energy consumption of office building towers with an area above 1,000 m² in the city of Belo Horizonte. It's believed that this data can serve as a basis for future work in which major design features and occupancy

patterns can be analyzed to get a better understanding of the major influencing factors in electricity consumption of this typology.

ACKNOWLEDGEMENT

The work reported in this paper was supported by the National Council of Research, CNPq.

REFERENCES

- Borgstein E.H. and Lamberts R. 2014. Developing energy consumption benchmarks for buildings: Bank branches in Brazil. *Energy and Buildings*, 82, 82–91.
- Brasil, Ministério das Minas e Energia. BEN - Balanço Energético Nacional. Brasília, disponível em: <http://www.epe.gov.br>, acessado em: novembro, 2017.
- Chung W., Hui Y.V., Lam Y.M. 2006. Benchmarking the energy efficiency of commercial buildings. *Applied Energy*, 83(1),1–14.
- International Energy Agency. Total energy use in buildings: Analysis and evaluation methods, 2013.
- ISO. Energy performance of buildings - Indicators, requirements, ratings and certificates - Part 1: General aspects and application to the overall energy performance, ISO 52003-1:2017. Geneva, Switzerland: International Organization for Standardization, 2017.
- Iwaro J., Mwashia A. 2010. A review of buildings energy regulation and policy for energy conservation in developing countries. *Energy Policy*, 38,7744-7755.
- Lamberts R., Pereira F.O.R., Dutra L. Eficiência Energética na Arquitetura. 3a edição ed. Rio de Janeiro: 2014.
- Ministério de Minas e Energia (MME). Empresa de Pesquisa Energética. Plano Nacional de Energia 2030. Rio de Janeiro: EPE, 2007. 408 p. ISSN: 978-85-60025-02-2, available in: <http://www.epe.gov.br>.
- Nikolaou, T., Kolokotsa, D., Stavrakakis, G., Apostolou, A., Munteanu, C. 2015. Managing Indoor Environments and Energy in Buildings with Integrated Intelligent Systems. *Green Energy and Technology*, p. 261.
- Pérez-Lombard L., Ortiz J., González, R., Maestre I.R. 2009. A review of benchmarking, rating and labelling concepts within the framework of building energy certification schemes. *Energy and Buildings*, 41(3), 272–278.
- Rey F.J., Velasco E., Varela F. 2007. Building Energy Analysis (BEA): A methodology to assess building energy labelling. *Energy and Buildings*, 39(6), 709–716.
- Signor R. 1999. Análise de regressão do consumo de energia elétrica frente a variáveis arquitetônicas para edifícios comerciais climatizados em 14 capitais brasileiras. *Ph.D. Thesis*. Universidade Federal de Santa Catarina, (Brazil), 314 pages.
- U.S. Department of Energy's Commercial Building Initiative. Buildings Performance Metrics Terminology. Available et: <http://energy.gov/sites/prod/files/2013/12/f5/metrics_terminology_20090203.pdf>.
- Veloso A.C.O, Souza R.V.G, Koury R.N.N. 2017. Research of design features that influence energy consumption in office buildings in Belo Horizonte, Brazil. *Energy Procedia*, 111, 101-110.
- Vera I., Langlois L. 2007. Energy indicators for sustainable development. *Energy*, 32(6) 875–882.

Exploring occupants' impact at different spatial scales

Sara Gilani^{1,*}, William O'Brien¹, H. Burak Gunay¹

¹Carleton University, Ottawa, Canada

*Corresponding email: SaraGilani@cmail.carleton.ca

ABSTRACT

Buildings' users have widely been accepted as a source of uncertainty in building energy performance predictions. However, it is not evident that the diversity of occupants' presence and behavior at the building level is as important as at the room level. The questions are: How should occupants be modeled at different spatial scales? At the various scales of interest, how much difference does it make if: (1) industry standard assumptions or a dynamic occupant modeling approach is used in a simulation-based analysis, and (2) probabilistic or deterministic models are used for the dynamic modeling of occupants? This paper explores the reliability of building energy predictions and the ability to quantify uncertainty associated with occupant modeling at different scales. To this end, the impacts of occupancy and occupants' use of lighting and window shades on the predicted building lighting energy performance at the room and building level are studied. The simulation results showed that the inter-occupant variation at larger scales is not as important as at the room level. At larger scales (about 100 offices), the rule-based model, custom schedule model, and stochastic lighting use model compared closely for predicting mean annual lighting energy use.

KEYWORDS

Occupant modeling approaches; Spatial resolution; Custom schedules; Rule-based models; Building performance simulation.

INTRODUCTION

Occupants have widely been considered as a source of the gap between the predicted and measured energy performance of buildings (Menezes et al., 2012; de Wilde, 2014). Likewise, previous studies indicated that occupants' impact on the energy performance of buildings varies between occupants (Haldi and Robinson, 2011; Saldanha and Beausoleil-Morrison, 2012; Clevenger et al., 2014). This variation in occupants' presence and behavior may begin to cancel out their impacts on the energy use for larger buildings. Therefore, the stochastic nature of occupants' presence and behavior at the building level may not be as important as at smaller scales. A few studies challenged the notion of simulating the whole building's energy performance using the probabilistic modeling approach (Parys et al., 2011; Evins et al., 2016). This modeling approach has been widely used in studying occupants in a simulation-based analysis. However, it is not evident whether using this modeling approach at larger scales yields the wide range of occupants' impacts on the energy performance of a building as that at the room level. To address the gaps in the literature, the main objective of this paper is to systematically assess the impact of occupants on the energy performance of buildings at different spatial scales. The focus of this paper is on the domain of lighting use, though the general conclusions are expected to apply to other occupant-related domains. The methodology of this paper is to implement four occupant model forms for the lighting use in a simulation-based analysis, while occupancy and window shade use domains are simulated using the probabilistic modeling approach. Simulation-based analysis of the impact of

occupant modeling approaches for occupancy and window shade use domains at different spatial scales has been previously presented (Gilani et al., 2018).

OCCUPANT MODELING

For the analysis of the impact of occupants at different spatial scales, a simulation-based analysis methodology was implemented. As there is little consensus on which occupant modeling approach best represents occupants' impacts on the energy performance of buildings in a simulation-based analysis (Mahdavi and Tahmasebi, 2015), four modeling approaches have been used in the current study for the domain of lighting use. Occupant modeling approaches can be categorized as: (1) static versus dynamic, and (2) deterministic versus probabilistic. Dynamic models represent the two-way impact that occupants and building can have on each other, whereas static models neglect this impact. Parameters of probabilistic models and generated numbers in Monte Carlo simulation method (Gilks et al., 1996) are chosen randomly for each simulated occupant and/or at each timestep. Therefore, outputs of probabilistic models may alter at each simulation run while results of deterministic models do not change every time they are simulated. The resulting four model types are shown in Figure 1. In this paper, both static/dynamic and deterministic/probabilistic approaches were implemented in simulation for the lighting use domain, however occupancy was modeled with the static-probabilistic modeling approach and window shade use was modeled using the dynamic-probabilistic modeling approach. For the static modeling of lighting use, standard and custom schedules were incorporated; whereas for the dynamic modeling of lighting use, stochastic and rule-based models were used. A brief description of the model forms which were implemented in simulation in this paper is provided in the following sections.

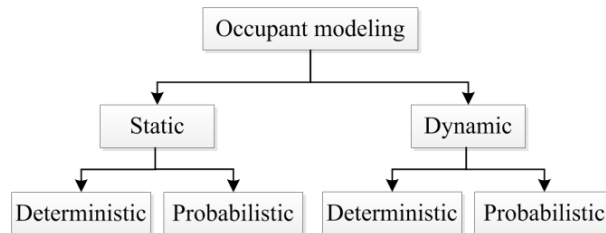


Figure 1. General categories of occupant modeling approaches.

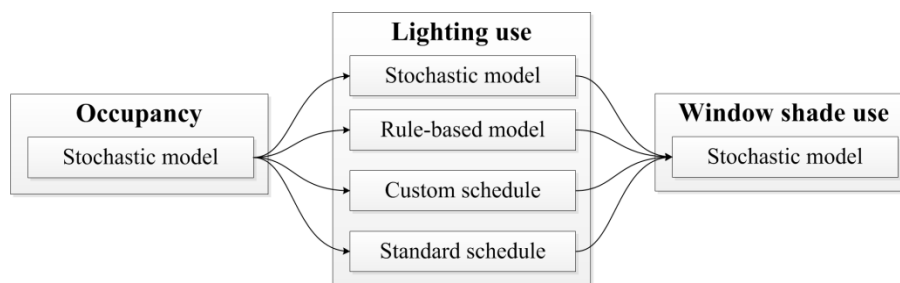


Figure 2. Four combinations of occupant model forms for occupancy and lighting and window shade use domains.

Standard schedule

For the static-deterministic modeling of lighting use, the standard schedule from National Energy Code of Canada for Buildings (NECB) (National Research Council Canada, 2015), was used (Figure 3). NECB's (2015) lighting schedule is almost identical to the lighting schedule in ANSI/ASHRAE/USGBC/IES Standard 189.1 (2014).

Custom schedule

Custom schedule was the other model form that was used for the static-deterministic modeling of lighting use. To develop custom lighting use schedules, 100 annual run periods of the stochastic models (as described later) were simulated using the Monte Carlo simulation method (Gilks et al., 1996). The hourly ratio profiles of lights-on during occupied or unoccupied periods on weekdays were generated based on the outputs of the 100 simulation run periods. To this end, the hourly lights-on ratios during occupied or unoccupied periods were calculated for each of the 100 annual run periods. The mean hourly lights-on ratios during occupied or unoccupied periods were computed using the weighting method based on the total occupied or unoccupied hours of each simulated office (Figure 3).

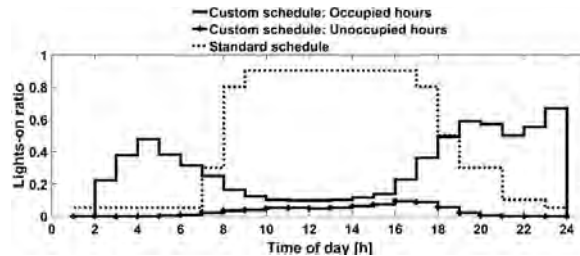


Figure 3. Hourly custom schedules for lights-on ratio during occupied and unoccupied hours and standard schedule.

Rule-based model

A rule-based model, which consists of thresholds to trigger occupants' manual light switch-on actions, was developed for the dynamic-deterministic modeling of light switch-on actions. Lights were set to be turned off automatically with a 30-minute time delay. The workplane illuminance (E_{in}) was considered as the predictor for the light switch-on actions (Hunt, 1979; Reinhart and Voss, 2003; Haldi and Robinson, 2010; Gunay et al., 2017). The thresholds for light switch-on actions were calculated based on the outputs of the 100 annual run periods of the stochastic models (as described next). To this end, a wide range of plausible values were systematically set for thresholds until the annual lighting energy use of 100 annual simulations were almost identical to the results of 100 simulations using the stochastic models. E_{in} was obtained 500 and 950 lx for light switch-on actions upon arrival and during intermediate periods, respectively.

Stochastic model

For the probabilistic modeling of the considered domains in this paper, three existing stochastic models were implemented: (1) Page et al.'s (2008) occupancy algorithm, (2) Gunay et al.'s (2017) light switch-on model, and (3) Haldi et al.'s (2016) window shade use model. For the occupancy domain, daily presence profiles and mobility parameters, which are required inputs for Page et al.'s (2008) occupancy algorithm, were generated using 17 months' worth of data collected in 24 offices in an academic building. Similar to O'Brien et al.'s (2016) study, a three-mode Gaussian mixture model (GMM) was fit to the profiles of daily occupied ratio for each monitored office. The probabilities of turning on lights and opening or closing window shades were estimated using the generalized linear model (GLM). Lights were assumed to be turned off automatically with a 30-minute time delay.

SIMULATION

For each of the four combinations of the model forms (see Figure 2), 150 annual run periods were simulated. This number was determined as the results of a sensitivity analysis of 1000 annual simulation runs showed that the coefficient of variation of the lighting electricity use

on the sample sizes of larger than 150 offices was less than 10%. The parameters of the occupancy and light switch-on models were generated randomly from the normal distribution of the required variables with the mean value and the covariance of the variables. The diversity approach proposed by O'Brien et al. (2016), which is based on keeping the joint variability between each pair of parameters, was used to address the variations in occupants' presence and lighting use. To consider the diversity in window shade use, Haldi et al.'s (2016) approach on using generalized linear mixed model (GLMM), was implemented.

A typical office space located in Ottawa, Canada, was simulated in RADIANCE-based daylighting tool DAYSIM (Reinhart, 2001) to calculate the workplane and ceiling illuminance in the simulated office for a typical year. To simulate indoor illuminance at partial shade movements using Haldi et al.'s (2016) window shade use model, five shade positions were simulated: fully open, quarter closed, half open, quarter open, and fully closed. Occupant models were implemented in MATLAB, where the DAYSIM daylighting simulation outputs were used as inputs. The timestep for the simulation in DAYSIM and MATLAB was set as 5 minutes. The office space had the dimensions of $W \times L \times H = 4.0 \times 4.0 \times 3.0$ m. The exterior south-facing window of the office had the width of 2.4 m and the height of 2.0 m with the sill height of 0.8 m. The reflectance of the floor, walls, and ceiling were set as 0.2, 0.5, and 0.8, respectively. The window glazing was assumed to have the visible transmittance of 0.44 and the visible transmittance of the window shade was assumed to be 0.2.

RESULTS AND DISCUSSION

Figure 4 shows the mean of the annual lighting electricity use for when the stochastic models were implemented for occupancy and window shade use, whereas four light switch-on models were implemented for lighting use (see Figure 2). Figure 4 also shows the coefficient of variation (CV) of the annual lighting electricity use, which is the ratio of the standard deviation to the mean annual lighting electricity use. For each of the considered number of offices, samples of offices were chosen randomly with replacement and with the size equal to the corresponding number of offices from the 150 offices. Figure 4 indicates that the annual lighting energy use averaged across the 150 simulated offices was predicted to be about 2.3 kWh/m² when the stochastic and rule-based models and custom schedule were used for light switch-on events. With the standard lighting schedule, which does not give credit for daylight, the lighting use was predicted to be about three times as much as the stochastic light switch-on model. Figure 4 shows that the average annual lighting energy use in random sampling of different numbers of offices gives similar values after a given number of offices. The standard deviation of the annual lighting energy use did not change significantly after a given number of offices as well. These observations follow the *Central Limit Theorem*. Note that since the stochastic occupancy model was used, the lighting energy use varied when the static-deterministic lighting use models were used.

To find the number of offices at which the mean annual lighting energy use approached a consistent value, the CV was calculated. The obtained CV indicated that the occupant modeling approach highly influences the office building size at which the standard deviation fell below 10% of the mean lighting energy use. The rule-based model and custom schedule for lighting use provided a similar prediction of the annual lighting energy use to the stochastic model. However, they require a smaller number of offices to provide a good approximation of the lighting use of a larger office building (Table 1).

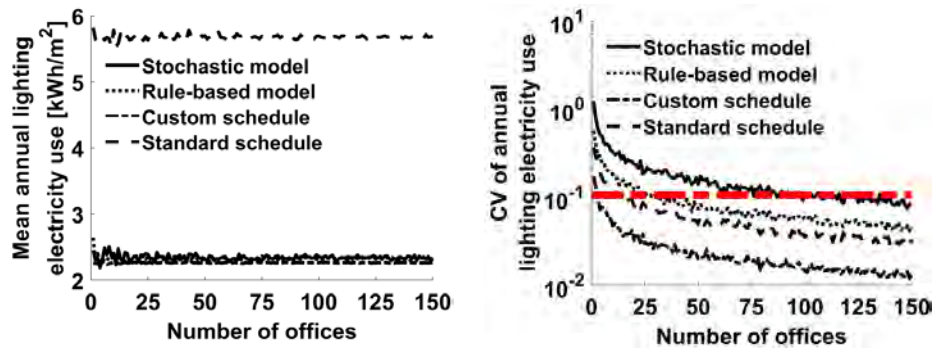


Figure 4. Annual lighting electricity use of samples with different sizes based on the simulation results of 150 annual run periods. Red dashed line represents CV of 10%.

Table 1. Number of offices at which lighting electricity use approached a consistent value with different modeling approaches for occupants' lighting use.

Lighting use model	Number of offices	Mean lighting electricity use of 150 offices (kWh/m ²)
Stochastic model	87	2.3
Rule-based model	30	2.3
Custom schedule	3	2.3
Standard schedule	17	5.7

CONCLUSION AND FUTURE WORK

This paper evaluated how the variations in occupants' presence and behavior can affect the predicted lighting electricity use at different spatial scales under different occupant modeling approaches for lighting use.

The results indicated that while occupants have been considered as an uncertainty source in the prediction of building energy performance, the inter-occupant variations at larger scales is not as important as at the room level. Therefore, building engineers may not need to be concerned about inter-occupant diversity in large office buildings if their objective of simulating buildings is to reliably predict the average annual lighting energy use of buildings. However, stochastic models still play an important role in a simulation-based design, such as evaluation of the robustness of a particular design. The results of this paper indicated that rule-based lighting use model and custom lighting use schedules can reasonably represent occupants' impact on the energy performance of buildings at larger scales. For an office building which is comprised of more than 100 private offices, rule-based lighting use model and custom lighting use schedules can be used instead of stochastic models to provide a good approximation of the lighting electricity use of the office building.

This research assumed that the lighting use of each office was controlled independently. However, one control system may be used for a group of offices. Future research on the impact of the number of offices which are controlled together is necessary. Impact of variation in occupants' characteristics, such as occupants' age, gender, and profession, at different spatial scales should also be studied.

ACKNOWLEDGEMENT

The authors acknowledge the Natural Resources Canada Energy Innovation Program for financial support and project partners: RWDI, Autodesk, and National Research Council of Canada.

REFERENCES

- ANSI/ASHRAE/USGBC/IES Standard 189.1. 2014. ANSI/ASHRAE/USGBC/IES Standard 189.1: American Society of Heating, Refrigeration and Air-Conditioning Engineers.
- Clevenger CM, Haymaker JR, Jalili M. 2014. Demonstrating the Impact of the Occupant on Building Performance. *Journal of Computing in Civil Engineering* 28:99-102.
- de Wilde P. 2014. The gap between predicted and measured energy performance of buildings: A framework for investigation. *Automation in Construction* 41:40-49.
- Evins R, Orehounig K, Dorer V. 2016. Variability between domestic buildings: the impact on energy use. *Journal of Building Performance Simulation* 9:162-175.
- Gilani S, O'Brien W, Gunay HB. 2018. Simulating occupants' impact on building energy performance at different spatial scales. *Building and Environment* 132:327-337.
- Gilks WR, Richardson S, Spiegelhalter DJ. 1996. Introducing Markov Chain Monte Carlo. In: Gilks WR, Richardson S, Spiegelhalter DJ, editors. *Markov Chain Monte Carlo in Practice*. London, UK: Chapman & Hall.
- Gunay HB, O'Brien W, Beausoleil-Morrison I, Gilani S. 2017. Development and implementation of an adaptive lighting and blinds control algorithm. *Building and Environment* 113:185-199.
- Haldi F, Cali D, Andersen RK, Wesseling M, Müller D. 2016. Modelling diversity in building occupant behaviour: a novel statistical approach. *Journal of Building Performance Simulation*:1-18.
- Haldi F, Robinson D. 2010. Adaptive actions on shading devices in response to local visual stimuli. *Journal of Building Performance Simulation* 3:135-153.
- Haldi F, Robinson D. 2011. The impact of occupants' behaviour on building energy demand. *Journal of Building Performance Simulation* 4:323-338.
- Hunt DRG. 1979. The use of artificial lighting in relation to daylight levels and occupancy. *Building and Environment* 14:21-33.
- Mahdavi A, Tahmasebi F. 2015. Predicting people's presence in buildings: An empirically based model performance analysis. *Energy and Buildings* 86:349-355.
- Menezes AC, Cripps A, Bouchlaghem D, Buswell R. 2012. Predicted vs. actual energy performance of non-domestic buildings: Using post-occupancy evaluation data to reduce the performance gap. *Applied Energy* 97:355-364.
- National Research Council Canada. 2015. *National Energy Code of Canada for Buildings 2015*.
- O'Brien W, Gunay HB, Tahmasebi F, Mahdavi A. 2016. A preliminary study of representing the inter-occupant diversity in occupant modelling. *Journal of Building Performance Simulation*:1-18.
- Page J, Robinson D, Morel N, Scartezzini JL. 2008. A generalised stochastic model for the simulation of occupant presence. *Energy and Buildings* 40:83-98.
- Parys W, Saelens D, Hens H. 2011. Coupling of dynamic building simulation with stochastic modelling of occupant behaviour in offices – a review-based integrated methodology. *Journal of Building Performance Simulation* 4:339-358.
- Reinhart CF. 2001. Daylight availability and manual lighting control in office buildings: Simulation studies and analysis of measurement. In: *Architecture*. Karlsruhe: University of Karlsruhe.
- Reinhart CF, Voss K. 2003. Monitoring manual control of electric lighting and blinds. *Lighting Research and Technology* 35:243-258.
- Saldanha N, Beausoleil-Morrison I. 2012. Measured end-use electric load profiles for 12 Canadian houses at high temporal resolution. *Energy and Buildings* 49:519-530.

Neural Network Models Using Thermal Sensations and Occupants' Behavior for Predicting Thermal Comfort

Zhipeng Deng¹, Qingyan Chen^{1,2,*}

¹Center for High Performance Buildings (CHPB), School of Mechanical Engineering, Purdue University, 585 Purdue Mall, West Lafayette, IN 47907, USA

²Tianjin Key Laboratory of Indoor Air Environmental Quality Control, School of Environmental Science and Engineering, Tianjin University, Tianjin 300072, China

*Corresponding email: yanchen@purdue.edu

ABSTRACT

It is important to create comfortable indoor environments for building occupants. This study developed neural network (NN) models for predicting thermal comfort in indoor environments by using thermal sensations and occupants' behavior. The models were trained by data on air temperature, relative humidity, clothing insulation, metabolic rate, thermal sensations, and occupants' behavior collected in ten offices. The models were able to predict similar acceptable air temperature ranges in offices, from 20.6°C to 25°C in winter and from 20.6°C to 25.6°C in summer. The comfort zone obtained by the NN model using thermal sensations in the ten offices was narrower than the comfort zone in ASHRAE Standard 55, but that obtained by the NN model using behaviors was wider than the ASHRAE comfort zone. This investigation demonstrates alternative approaches to the prediction of thermal comfort.

KEYWORDS

Indoor environment, Model training, Data collection, Air temperature, Relative humidity

INTRODUCTION

Currently, people in North America spend roughly 90% of their time indoors. Therefore, it is important to create comfortable, healthy, and productive indoor environments for the occupants. To improve an indoor environment for building occupants, one would need a good method for evaluating the environment. Current evaluation methods for thermal comfort can be divided into two categories: using questionnaires under controlled indoor environments (Fanger, 1970; Chow et al, 1994; Cheong et al, 2006) and without varying controlled parameters (De Dear, 1998; Mishra et al, 2013). However, the two types of thermal comfort model do not consider the influence of occupants' behavior on thermal comfort. Therefore, the two categories of evaluation methods may not be ideal for evaluating the thermal comfort in actual environments.

Evaluation of thermal comfort should be based on thermal sensations in actual environments rather than in controlled environments. In an actual environment such as an office, occupants go about their daily activities in surroundings with which they are familiar. However, numerous studies (Langevin et al, 2015; Luo et al, 2014) have found that occupants' behavior changes their thermal sensations, because the behavior impacts their expectations of thermal comfort. Therefore, it is necessary to develop an evaluation method for indoor thermal comfort that considers occupants' thermal sensations and behavior in actual environments. The purpose of this study is to develop methods for evaluating thermal comfort in actual environments by using thermal sensations and occupants' behavior.

METHODS

Data collection

This investigation collected data on air temperatures, relative humidity, clothing levels, thermal sensations, thermostat set points, and room occupancy in ten offices in the Ray W. Herrick Laboratories at Purdue University, Indiana, USA. Among the ten offices, half of them were multi-occupant student offices, and the rest were single-occupant faculty offices. Five faculty members and more than fifteen students participated in the data collection. This study collected thermostat set point data from the building automation system (BAS) every five minutes. Each office had a thermostat that enabled the BAS to control the air temperature set point within the range of 18.3°C to 26.7°C. We used data loggers (Sper Scientific 800049) in each office to collect air temperature and relative humidity every five minutes. We used a questionnaire to collect the thermal sensation (-3 for cold, -2 for cool, -1 for slightly cool, 0 for neutral, +1 for slightly warm, +2 for warm, and +3 for hot) and clothing level from the occupants when they were inside the offices as well as their behaviors in adjusting the thermostat set point or their clothing level, arriving at the office, and leaving the office. This study assumed that occupants actively adjusted the thermostat set point for their comfort, because the cost of maintaining a comfortable environment is typically not on their minds. Note that all data collection in this study was approved by Purdue University Institutional Review Board Protocol # 1704019079.

Neural network models

With the collected data, this study used neural network models to correlate the indoor environmental data with occupants' thermal sensation and behavior. As this investigation sought to correlate occupants' thermal sensation and behavior with indoor environmental parameters, it was necessary to identify two separate NN models. As shown in Figure 1, an NN model has a layered structure usually comprised of three layers: an input layer, a hidden layer and an output layer.

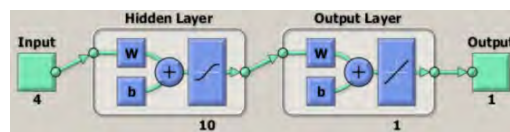


Figure 1. Structure of the NN models, with four input parameters in the input layer, ten neurons in the hidden layer, and one output parameter in the output layer. The “w” and “b” in the hidden layer and output layer represent weight matrix and bias, respectively. The transfer function in the hidden layer was a logistic function

This investigation used an NN model to predict thermal comfort. According to the PMV thermal comfort model (Fanger, 1970), six parameters have an impact on thermal comfort: air temperature, relative humidity, clothing insulation, air velocity, metabolic rate, and mean radiant temperature. Our study assumed that the mean radiant temperature was the same as the room air temperature. Our measurements showed that the air velocity in the offices was less than 0.2 m/s, and thus the impact of air velocity on thermal comfort can be neglected. To predict thermal comfort, the NN model requires only four input parameters. According to the ASHRAE Handbook – Fundamentals (ASHRAE, 2017), the occupants could sit or walk inside their offices, and the corresponding metabolic rates were 60 W/m² and 115 W/m², respectively. The insulation values for different clothing ensembles worn by participants in this study was also based on ASHRAE Handbook - Fundamentals.

This investigation used another NN model to predict occupants' behavior. We assumed that the input parameters of this NN model were again air temperature, relative humidity, metabolic rate, and clothing insulation. The output of the behavioral NN model is the occupants' behavior.

We used “-1” for raising the thermostat set point or adding clothes when occupants feel cool, “0” for no behavior when the occupants feel that the environment is acceptable, and “1” for lowering the thermostat set point or reducing the clothing level when they feel warm.

This study used Matlab Neural Network Toolbox to build and train the two NN models. The training process entailed finding the weight matrix and bias in the NN models that would minimize the error between the model outputs and targets. The targets were the actual thermal sensation and behavior occurrences that had been collected. We used the Levenberg-Marquardt algorithm to train the two NN models.

RESULTS

Data collection

Data were collected in all four seasons of 2017. In each season, we collected the data for more than one month in every office. Table 1 shows the percentage of occupants’ behavior occurrences at different thermal sensations in the offices. When the occupants felt hot (+3) or cold (-3), they always adjusted the thermostat set point or their clothing level. However, if the occupants felt warm (+2) or cool (-2), the percentages of behavior occurrences were only 72.2% and 53.3%, respectively. When they felt slightly warm (+1) or slightly cool (-1), the percentages of behavior occurrences dropped further to 17.6% and 26.4%, respectively. According to the collected data, there were several cases in which occupants felt uncomfortable, but no behavior occurred. For example, when feeling uncomfortable immediately after entering the office, some occupants preferred to adjust the thermostat set point after some time had passed. In other cases, the HVAC system may not have responded quickly to the latest adjustment, yet the occupant waited for a while even though he/she may have felt uncomfortable. There are several possible reasons. First, sometimes the control of the HVAC system had some time delay. Second, if the occupant raised or lowered the set point a lot, it would take more time to respond. Third, the room air temperature was hard to respond the low set point if the office was occupied with many occupants and their computers were on, or because of the sunlight in exterior zone. In these cases, the occupants’ behavior did not reflect their true desires in regard to controlling the indoor environment. For multi-occupant offices, meanwhile, an acceptable indoor environment may have been a compromise among several occupants. Some occupants may have felt uncomfortable, but they did not adjust the thermostat set point because the other occupants were not complaining about the comfort level, or they were unsure whether others would feel the same way. Table 1 correlates occupants’ behavior occurrences with their thermal sensations.

Table 1. Percentages of behavior occurrences under different thermal sensations in the offices

<i>Thermal sensation</i>	<i>Behavior occurrences</i>		
	-1	0	1
-3	0%	0%	100%
-2	0%	46.7%	53.3%
-1	0%	73.6%	26.4%
0	0%	100%	0%
1	17.6%	82.4%	0%
2	72.2%	27.8%	0%
3	100%	0%	0%

Comfort zones predicted by the two NN models

Figure 2 illustrates the comfort zones for the office environment in winter and summer obtained by the NN model using thermal sensations. The default clothing level was 1.0 Clo and 0.5 Clo in winter and summer in ASHRAE Standard 55 (ASHRAE, 2013), respectively. We assumed that the office occupants were sitting, and thus their metabolic rate was 1.0 MET. For the

comfort zone outlined in green in the figure from slightly cool to slightly warm, the air temperature ranged from about 20.6°C to 25°C in winter and from about 20.6°C to 25.6°C in summer. The lower and upper bounds of the absolute humidity in the comfort zones were the minimum and maximum of the absolute humidity found in the data, which may not be equivalent to the comfort boundaries. Within the range of the data, humidity does not seem to have been a key thermal comfort parameter in the offices.

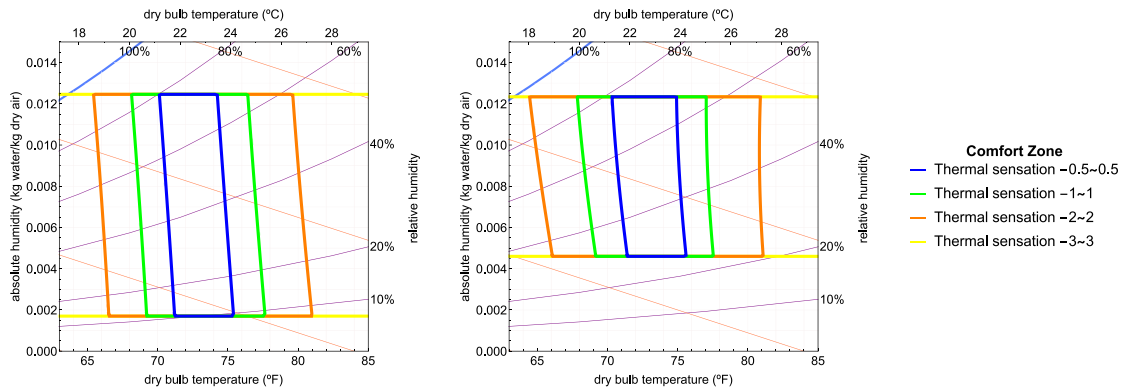


Figure 2. Comfort zones for office environments in winter (left) and summer (right) obtained by the NN model with the use of thermal sensations.

Figure 3 illustrates the acceptable zones for an office environment in the winter and summer seasons obtained by the NN model using behavior. An acceptable environment is one in which occupants can work without adjusting their behavior, although they may feel slightly uncomfortable. An unacceptable environment is one in which occupants have to adjust the thermostat set point or their clothing level. This study used the information in Table 1 to define the acceptable zones for various percentages of the occupants. The blue, green and orange zones in Figure 3 represent the humidity and temperature ranges within which 88%, 76% and 15% of the occupants did not adjust the thermostat set point or their clothing level. Under the assumption that “no behavior” signifies an acceptable environment, the acceptable indoor air temperature for 76% of the occupants ranged from 21.1°C to 25.6°C in winter and 20.6°C to 25°C in summer. The results of the behavior NN model also indicate that the humidity had little impact on behavior in the offices in different seasons. This was because our data were collected within a narrow humidity range. Furthermore, office occupants could not signify their humidity preferences by any of the adjustment actions that were recorded.

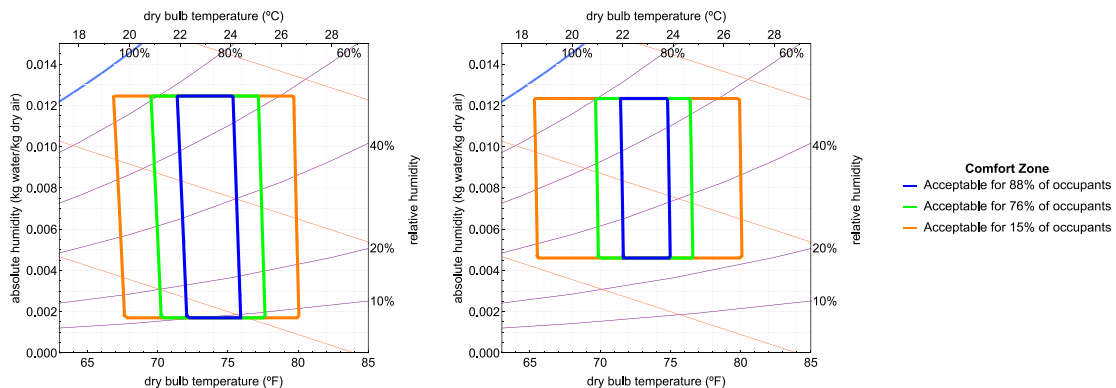


Figure 3. Acceptable zones for office environments in winter (left) and summer (right) obtained by the NN model using behavior.

The acceptable zones obtained by the NN model with the use of behavior, shown in Figure 3, are similar to the comfort zones obtained by the NN model using thermal sensations, displayed in Figure 2. The good correlation between the two sets of results implies that one may evaluate the indoor environment in offices by using either of the NN models.

Comparison of the comfort zones with the ASHRAE comfort zones

Figure 4 compares the comfort zones obtained by the two NN models with the ASHRAE comfort zones. The blue outlines indicate the ASHRAE zones, which uses a PMV range from -0.5 to 0.5 and an acceptability of 80% for the occupants. The comfort zones obtained by the NN model using thermal sensations are narrower than the ASHRAE comfort zone. This implies that the office occupants were pickier than the occupants participated in the study of obtaining ASHRAE comfort zone. However, the comfort zone obtained by the NN model using behaviors was wider than the ASHRAE comfort zone, especially in summer. This is because we assumed that the absence of behavior signified an acceptable environment. However, in some situations as stated before, the occupants may have felt that the environment was unacceptable, yet they exhibited no behavior. Thus, these situations led to a higher acceptability of the indoor environment in the offices.

In addition, the comfortable room air temperature predicted by the two NN models in summer was about 2.2°C lower than the temperature of the ASHRAE comfort zone. One possible reason is that the office occupants were not responsible for the electricity bill and often set the temperature lower than would be desirable in the comfort zone in order to cool the room more quickly. Actually, setting a lower temperature does not cause faster cooling but over cooling.

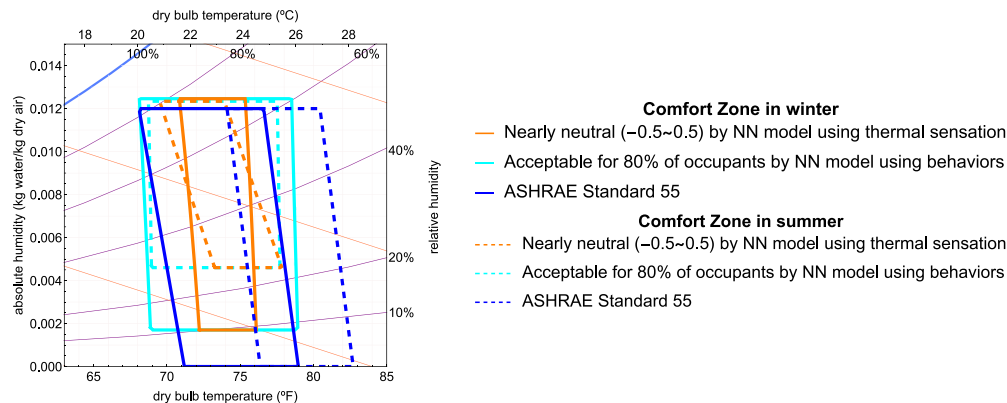


Figure 4. Comparison of the comfort zones obtained by the two NN models and the ASHRAE comfort zones in winter and summer.

DISCUSSIONS

The NN models have been developed to determine the relationship between the adjustment of thermostat set point and clothing level or thermal sensations, and air temperature and relative humidity. High-quality data were necessary for training the models. However, we used a questionnaire to collect clothing level data. The choices on the questionnaire were limited, but an overly long list might have confused the participants. In addition, we used metabolic rates for sitting and walking without accounting for differences in gender or age. Furthermore, the actual activities of the occupants were not limited to sitting and walking. Any discrepancies may have significantly impacted the robustness of the training process and thus the prediction accuracy of the NN models. In addition, since humidity was not controlled in the offices, the models may not be appropriate when the humidity level exceeds the range of the study.

CONCLUSIONS

In this study, we collected data in ten offices in Indiana, USA and built two NN models to determine the relationship between air temperature and relative humidity, and occupants' thermal sensations and behavior. This investigation led to the following conclusions:

(1) Under the assumption that a slightly cool to slightly warm environment is comfortable for occupants, the air temperature should be between 20.6°C and 25°C in winter and between 20.6°C and 25.6°C in summer. For a 76% acceptance rate, the corresponding indoor air temperature should be between 21.1°C and 25.6°C in winter and between 20.6°C and 25°C in summer. The two NN models provided similar results. Hence, we can use the behavior of occupants to evaluate the acceptability of an indoor environment in the same way that we use thermal sensations.

(2) The comfort zone obtained by the NN model using thermal sensations in the ten offices was narrower than the comfort zone in ASHRAE Standard 55, but the comfort zone obtained by the NN model using behavior was wider than the ASHRAE zone.

ACKNOWLEDGEMENT

The authors would like to thank Dr. Orkan Kurtulus of CHPB at Purdue University for his kind assistance in setting the BAS in the Herrick Laboratories building. We would also like to thank all the occupants of the offices for their participation and assistance in obtaining the data reported in this study. The research presented in this paper was partially supported by the national key R&D project of the Ministry of Science and Technology, China, on "Green Buildings and Building Industrialization" through Grant No. 2016YFC0700500, in addition to the main support from CHPB at Purdue University.

REFERENCES

- ASHRAE. 2013. *ASHRAE Standard 55-2013*, Thermal Environmental Conditions for Human Occupancy. Atlanta.
- ASHRAE. 2017. *Handbook Fundamentals*, Atlanta
- Chow W.K. and Fung W. Y. 1994. Investigation of the subjective response to elevated air velocities: Climate chamber experiments in Hong Kong. *Energy and Buildings*, 20.3, 187-192.
- Cheong K.W.D, Yu W.J, Kosonen R, Tham K.W, Sekhar S.C. 2006. Assessment of thermal environment using a thermal manikin in a field environment chamber served by displacement ventilation system. *Building and Environment*, 41.12, 1661-1670.
- De Dear R. J. 1998 A global database of thermal comfort field experiments. *ASHRAE Transactions*, 104, 1141.
- Fanger P.O. 1970. *Thermal Comfort*. Copenhagen: Danish Technical Press.
- Langevin J, Gurian P. L, Wen J. 2015. Tracking the human-building interaction: A longitudinal field study of occupant behavior in air-conditioned offices. *Journal of Environmental Psychology*, 42, 94-115.
- Luo M, Cao B, Zhou X, Li M, Zhang J, Ouyang Q, and Zhu Y. 2014. Can personal control influence human thermal comfort? A field study in residential buildings in China in winter. *Energy and Buildings*, 72, 411-418.
- Mishra A.K, Ramgopal M. 2013. Field studies on human thermal comfort-an overview. *Building and Environment*, 64, 94-106.

Quantification of building energy performance uncertainty associated with building occupants and operators

Sara Gilani^{1,*}, William O'Brien¹

¹Carleton University, Ottawa, Canada

*Corresponding email: SaraGilani@cmail.carleton.ca

ABSTRACT

Occupants play an important role in building energy performance, while building operators are the other side of the coin. This research quantifies the relative impact of probabilistic versus standard occupant models on building energy use. Energy performance of a high-performance reference small office building in Ottawa, Canada, is investigated using a simulation-based analysis. The impact of building users is studied by systematically altering occupant and operator-related domains, including occupants' presence and use of lights, window shades, operable windows, plug-in appliances, and thermostats. The results showed that the predicted natural gas energy use increased by a factor of about two compared to the reference occupant models. The predicted electricity energy use decreased about 49% compared to the reference occupant models. This deviation for the gas use resulted from modeling all six domains and for the electricity use resulted from simulating all six domains except for the window shade and operable window use using probabilistic models and operators' adjusted thermostat setpoints with the air handling unit scheduling to be on all day. The maximum deviation of the predicted electricity energy use with occupants' adjusted thermostat setpoints caused by the simultaneous probabilistic modeling of the four domains of occupants' presence and use of lighting, plug-in appliances, and thermostat. The lighting use domain showed the highest main effect on the energy use. The findings of the examination of occupant and operator-related modeling assumptions emphasizes the necessity to consider both operators' and occupants' impact on the predicted energy performance of the small building-scale model.

KEYWORDS

Building occupants and operators; Uncertainty; Building energy performance; Simulation-based analysis; Probabilistic models.

INTRODUCTION

Building engineers are required to design buildings that comply with building standards in the design phase of new constructions. However, constructed buildings which were designed to be energy-efficient may not meet building engineers' expectations due to the uncertainties associated with the predicted energy performance in a simulation-aided design process (Macdonald and Clarke, 2007). One of the widely-recognized sources of uncertainty in the predicted energy performance of buildings is how buildings are used in reality (Menezes et al., 2012; de Wilde, 2014). Occupants are perceived as the main users of buildings; however, operators are the hidden users who may divert real energy performance of buildings from what were expected. Consequently, the degree of uncertainty associated with buildings' operators may rival the uncertainty caused by buildings' occupants. The great degree of uncertainty from buildings' users on building energy performance and the corresponding importance of improving modeling practice have been repeatedly emphasized by the occupant behavior research community. For instance, Clevenger and Haymaker (2006) quantified

occupants' impact on the energy use of two typical buildings in the USA by changing different ranges for the occupant-related schedules, loads, and densities, individually and in a combination of all the considered occupant behaviours. Similarly, Hopfe and Hensen (2011) performed an uncertainty analysis of various occupant-related loads and densities. In contrast to Clevenger and Haymaker's (2006) approach of implementing discrete ranges, Hopfe and Hensen (2011) used the Monte Carlo analysis within a continuous distribution of the considered parameters (Macdonald, 2002). Furthermore, Hong and Lin (2013) incorporated a similar approach to Clevenger and Haymaker's (2006) study and compared the energy use of a typical office room for the two extreme ranges of using energy to a standard energy usage. While the aforementioned studies evaluated the impact of different building users' behaviours on the energy use of a room or building-scale model, there is still the gap in the literature with respect to the relative impact of occupants and operators on the energy use of buildings.

To address this gap, the current research performed an assessment of uncertainty associated with occupants and operators on the annual energy use of a building-scale model. The main objective of this paper is to quantify the relative impact of buildings' occupants and operators on the energy performance of buildings. Occupant and operator-related domains which were studied in this paper include: occupants' presence and use of lights, window shades, operable windows, plug-in appliances, and thermostats. Probabilistic models for each of these domains were applied systematically one at a time as well as with different numbers of domain combinations to quantify the impact of each domain and differently sized groups of domains with two sets of air handling unit (AHU) schedules and two thermostat adjustment models. The main research questions of the current study are: (1) What is the relative effect of different occupant and operator-related domains on the energy performance of buildings? (2) Among the considered domains in the current research, which domain causes the highest main effect on the energy use? (3) Relevant to the previous question, the interaction of which domains causes the highest effect on the energy use?

METHODOLOGY

This section describes the building model, occupant and operator models which were implemented in simulation, and the simulation process.

Building model description

The office building was modeled in SketchUp and OpenStudio on the basis of ANSI/ASHRAE/USGBC/IES Standard 189.1 (2014) for a high-performance small office building in climate zone 6A (Figure 1). Thermal energy demand of each office was delivered by independently controlled variable air volume boxes with reheat coil. Independently controlled hot water baseboard heaters delivered supplementary heating to each office. Each perimeter office had an operable window with the opening area of 0.1 m^2 . The heating demand of the simulated model, which was located in a heating-dominated climate, was delivered by a gas boiler.

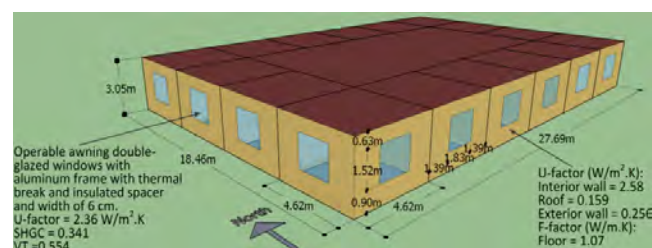


Figure 1. Geometry and envelope specifications of the office building model.

Occupant and operator models

A one-storey office building model was simulated in this study. The building consisted of one core open-plan office and 16 perimeter private offices. Standard schedule-based and probabilistic occupant models were incorporated in simulation (Table 1). Probabilistic models were implemented in the EMS application of EnergyPlus. The case study building was assumed vacant on weekends. Lights were assumed to be turned off automatically with 30-minute time delay after occupants left their offices. A daylight sensor to serve as an input to the occupant's manual light and shade adjustments was located at a height of 0.8 m in the center of each perimeter office. For the corner offices, it was assumed that once occupants took action to use operable windows and/or shades, they adjusted both operable windows and/or shades.

To perform a relative comparison between occupants and operators' impact, based on an informal study of numerous Canadian commercial buildings energy audits, two AHU modes were implemented to represent one major aspect of operator behavior: (1) always on, and (2) from 6am to 6pm on. To investigate the operators and occupants' impact, two thermostat adjustment models were implemented: (1) occupant agent, and (2) operator agent. Heating and cooling setpoints were set 21 and 24°C from 6am to midnight and were set back to 15.6 and 26.7°C the rest of the day. This setpoint adjustment was set when Gunay et al.'s (2018) model of occupant-agent thermostat adjustment was implemented. Heating and cooling setpoints were set to 21 and 24°C at the beginning of each annual run time for when Gunay et al.'s (2018) model of operator-agent thermostat adjustment was implemented. This thermostat setpoint setting follows Gunay et al.'s (2018) study, as once an operator changed thermostat setpoints, changes were kept fixed unless occupants requested another adjustment. The upper cooling setpoint was confined to 30°C. It was assumed that operators only adjusted thermostats between 7am and 4pm.

Table 1. Occupant and operator models.

Domain	Models		
	Probabilistic models		Standard-based schedule
	Private offices	Open-plan office	
Occupancy	Page et al.'s (2008) occupancy algorithm	O'Brien et al.'s (2018) model	ANSI/ASHRAE/USGBC/IES Standard 189.1 (2014)
Lighting use	Reinhart's (2004) light switch-on model		
Window shade use	Haldi et al.'s (2016) model	-	Always open
Operable window use	Haldi and Robinson's (2009) model	-	Always closed
Electric equipment use	Gunay et al.'s (2016) model	O'Brien et al.'s (2018) model	
Thermostat adjustment	Gunay et al.'s (2018) model of occupant or operator thermostat adjustment	Gunay et al.'s (2018) model of operator thermostat adjustment	ANSI/ASHRAE/USGBC/IES Standard 189.1 (2014)

Simulation

The timestep was set as five minutes. To quantify the impact of the occupant and operator-related domains, probabilistic models for each domain were used: (1) one at a time, and (2) different numbers of domain combinations. The domain(s) that was (were) not chosen to be simulated using the probabilistic model, was (were) simulated using the standard-based schedules. The results of a study involving 100 annual simulations showed that 20 annual

simulation runs was adequate that the difference between the minimum and maximum standard deviation to the average gas and electricity energy use fell below 10%. Since incorporating probabilistic occupant models for all the domains resulted in the highest uncertainty compared to when all the domains are not simulated using the probabilistic models, the required simulations for each domain combination was determined as 20.

RESULTS AND DISCUSSION

The reference small office building using the default occupant and operator-related values (i.e. base case) was simulated for one annual run period. The energy performance of the simulated building model was compared to the reference occupant models based on two performance measures: (1) total natural gas use for heating demands, and (2) total electricity use for cooling demands, lights, electric equipment, the fan, and pumps. To present results in this section, occupants' presence and use of lights, blinds, operable windows, plug-in appliances, and thermostats are hereafter referred to as: "O", "L", "B", "W", "P", and "T".

Figure 2 shows the results of implementing probabilistic models for the considered domain(s) on the energy use. Note that occupants' thermostat adjustment model was implemented in these cases. This figure shows that, generally, the interaction between a larger numbers of domains which were simulated using probabilistic models caused the predicted energy use to deviate from the base case more than those using probabilistic models for only a portion of the considered domains. The maximum effect on the electricity use was when the probabilistic models for the domains of occupants' presence and use of lights and plug-in appliances were incorporated in simulation. Figure 2 indicates that generally, AHU mode 1 caused higher deviation of the predicted natural gas energy use from the base case (with AHU mode 1) compared to AHU mode 2, while AHU mode 2 caused higher deviation of the predicted electricity energy use from the base case (with AHU mode 1). For example, the gas energy use increased by 70% with AHU mode 1, while it increased by 41% with AHU mode 2 when all considered domains were simulated using probabilistic models. On the other hand, the electricity energy use decreased by 40% with AHU mode 1, while it decreased by 52% with AHU mode 2 when all considered domains were simulated using probabilistic models.

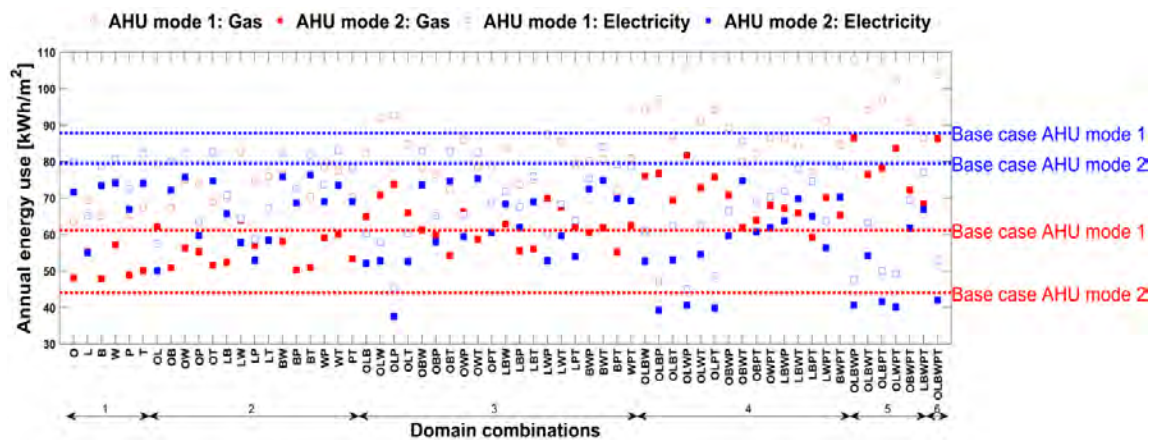


Figure 2. Comparing impact of various domain combinations with two AHU schedules.

Figure 3 compares the energy use when operators or occupants adjusted thermostat setpoints. This figure shows that adjustment of temperature setpoint by operators resulted in higher deviations in the predicted energy use from the base case compared to when occupants adjusted thermostat setpoints. Figure 3 indicates that generally the maximum deviation of the predicted electricity energy use from the base case was when occupants' presence and use of

lights, plug-in appliances, and thermostat adjustment were implemented. The three most influential domains whose modeling assumptions significantly affected the natural gas energy use were lighting, operable windows, and thermostat adjustment.

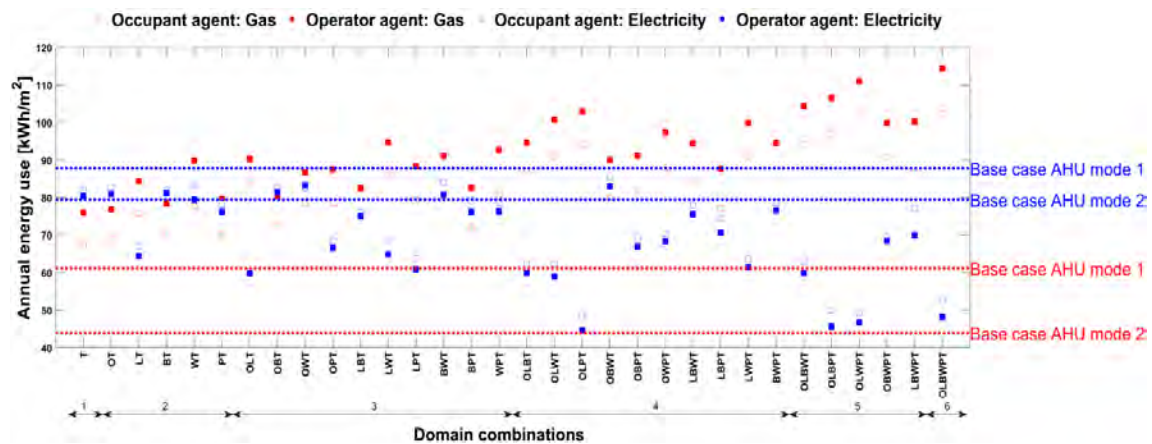


Figure 3. Comparing impact of various domain combinations with two models for thermostat adjustment and AHU mode 1.

To quantify the impact of simulating each domain using the corresponding probabilistic model on the energy use, the main effect of simulating each domain using the probabilistic model was investigated (Figure 4). To this end, the average and standard deviation of the energy use of all the possible domain combinations with either AHU mode 1 or 2 (see Figure 2) were calculated when each of the six domains was simulated using: (1) standard-based schedule, and (2) probabilistic model, whereas all the other domains were simulated using either standard-based schedules or probabilistic models. Figure 4 indicates that modeling assumptions of all the six domains had a main effect on the predicted energy use. Among the considered domains, lights had the highest effect on the total energy use. Blinds and operable windows had the lowest impact on the gas and electricity energy use, respectively. Additionally, Figure 4 shows the main effect of the two considered AHU modes. The results indicate that the AHU mode had a main effect on the energy use.

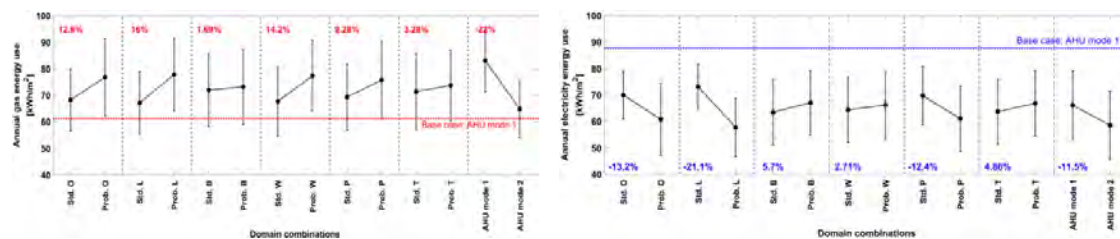


Figure 4. Comparing main effect of each domain using standard-based schedule ("Std.") and probabilistic model ("Prob.") and AHU modes.

CONCLUSION AND FUTURE WORK

The findings of this research showed that modeling assumptions of occupants' use of lights had the highest main effect on the total energy use. In general, the larger the number of the occupant and operator-related domains whose modeling assumptions were altered, the larger the impact of the interaction between the domains. The maximum deviation of the predicted electricity use resulted from the simultaneous probabilistic modeling of occupants' presence and use of lights and plug-in appliances. This study indicated that considering operators' role in building energy performance is imperative. This research was focused on a building-scale

model in a heating-dominated climate zone. The relationship between the current results and different climates is necessary future work.

ACKNOWLEDGEMENT

The authors acknowledge the Natural Resources Canada Energy Innovation Program for financial support and project partners: RWDI, Autodesk, and National Research Council of Canada.

REFERENCES

- ANSI/ASHRAE/USGBC/IES Standard 189.1. 2014. ANSI/ASHRAE/USGBC/IES Standard 189.1: American Society of Heating, Refrigeration and Air-Conditioning Engineers.
- Clevenger CM, Haymaker J. 2006. The impact of the building occupant on energy modeling simulations. In: Joint International Conference on Computing and Decision Making in Civil and Building Engineering, Montreal, Canada. p 1-10.
- de Wilde P. 2014. The gap between predicted and measured energy performance of buildings: A framework for investigation. *Automation in Construction* 41:40-49.
- Gunay HB, O'Brien W, Beausoleil-Morrison I, Gilani S. 2016. Modeling plug-in equipment load patterns in private office spaces. *Energy and Buildings* 121:234-249.
- Gunay HB, Shen W, Newsham G, Ashouri A. 2018. Modelling and analysis of unsolicited temperature setpoint change requests in office buildings. *Building and Environment* 133:203-212.
- Haldi F, Cali D, Andersen RK, Wesseling M, Müller D. 2016. Modelling diversity in building occupant behaviour: a novel statistical approach. *Journal of Building Performance Simulation*:1-18.
- Haldi F, Robinson D. 2009. Interactions with window openings by office occupants. *Building and Environment* 44:2378-2395.
- Hong T, Lin H-W. 2013. Occupant behavior: impact on energy use of private offices. In: Ernest Orlando Lawrence Berkeley National Laboratory, Berkeley, CA (US).
- Hopfe CJ, Hensen JLM. 2011. Uncertainty analysis in building performance simulation for design support. *Energy and Buildings* 43:2798-2805.
- Macdonald I. 2002. Quantifying the effects of uncertainty in building simulation. In: University of Strathclyde.
- Macdonald IA, Clarke JA. 2007. Applying uncertainty considerations to energy conservation equations. *Energy and Buildings* 39:1019-1026.
- Menezes AC, Cripps A, Bouchlaghem D, Buswell R. 2012. Predicted vs. actual energy performance of non-domestic buildings: Using post-occupancy evaluation data to reduce the performance gap. *Applied Energy* 97:355-364.
- O'Brien W, Abdelalim A, Gunay HB. 2018. Development of an office tenant electricity use model and its application for right-sizing HVAC equipment. *Journal of Building Performance Simulation*.
- Page J, Robinson D, Morel N, Scartezzini JL. 2008. A generalised stochastic model for the simulation of occupant presence. *Energy and Buildings* 40:83-98.
- Reinhart CF. 2004. Lightswitch-2002: a model for manual and automated control of electric lighting and blinds. *Solar Energy* 77:15-28.

Towards a New Way of Capturing Occupant Well-being

Mark Allen^{1,*} and Mauro Overend¹

¹University of Cambridge, United Kingdom

*Corresponding email: mca41@cam.ac.uk

ABSTRACT

Occupant well-being is undergoing a surge of interest in both the research community and industry, as the potential benefits of increased levels of well-being become better quantified and understood. Well-being science itself is also constantly evolving, moving from the traditional negative view of depression and mental disorders as markers of well-being, towards the more positive notion of flourishing, which is feeling good and functioning well. This paper first sets out the key elements of well-being, as found in psychology literature. Surveys and interviews are the main methods used to capture the well-being of individuals and populations, yet completion rates can be low, occupants distracted or irritated by requests to complete surveys and the data infrequent or irregular. Instead, cameras emerge as a potential economic way to gain information about occupants. Their comfort, health and well-being can be monitored with a high frequency, low intrusion and low cost through the use of facial emotions and movements. To this end, a small pilot study is carried out to examine the effectiveness and practicality of data capture by cameras. Data from a new naturally ventilated office building in Cambridge, United Kingdom, is inspected alongside more traditional well-being assessment techniques. It finds that occupants quickly forget that they are being monitored by the cameras and are very engaged with the research, keen to see if it can help improve their workspace. The results and experience from this pilot study form the basis of a more extensive programme of investigations that are described at the end of this paper. The aspiration is to develop this method so that it can be deployed as part of a wider toolkit to holistically capture high quality information about the comfort, health, and well-being levels of building occupants.

KEYWORDS

well-being, occupant satisfaction, smart buildings, comfort, smart sensing

INTRODUCTION

Levels of depression, stress, and anxiety have risen drastically since 2012, with 50% more incidents being reported in workplaces worldwide (Weiner, 2015). Further, the number of people living and working in urban areas is increasing significantly, a further 2.5 billion from today's figure by 2050 (United Nations, Department of Economic and Social Affairs, 2014). With urban areas becoming more dense and green spaces disappearing (CPRE, 2017), the health and well-being of people living in these areas could suffer (Maller *et al.*, 2006). However, people are beginning to take a greater interest in their own health and well-being, with the global wellness market now being three times larger than the pharmaceutical industry (Yeung and Johnston, 2014). This is mirrored in the current explosion of interest in health and well-being in the built environment, with companies such as WELL and Fitwell creating standards to promote good design and improved building control strategies. Further, through creativity and productivity improvements, research is starting to understand and put a value on the effect of increased levels of comfort, health, and well-being on businesses. While historically the construction sector has focused a lot on reducing the energy use of buildings, around 90% of a typical businesses expenditure can be attributed to people, as opposed to only 1% to end-use

energy costs (WGBC, 2014). This reinforces the need to focus on people when designing, controlling or refurbishing buildings, particularly as energy gets cheaper and cleaner, as renewables take over from fossil fuels (Renewable Energy Agency, 2017).

Health and well-being have many definitions (Dodge *et al.*, 2012) but perhaps the most commonly used is that enshrined in the constitution of the World Health Organisation (WHO) which states: '[health is] a state of complete physical, mental and social well-being and not merely the absence of disease or infirmity' (WHO, 1948). This positive focus is also mirrored in new well-being research, where flourishing, (a high level of well-being) is defined by Huppert & So (2013) as '(...) the experience of life going well. It is a combination of feeling good and functioning effectively'. The extent of the built environments contribution (or lack thereof) to an occupant's level of well-being, and how this interrelates with the nature of work and interactions at work is complex.

This paper sets out the background and initial work done on the development of a new type of sensor, which may be able to provide high quality data on the comfort, health, and well-being of building occupants. This sensor could stand alone or form part of a wider toolkit to holistically monitor occupants, helping us better our understanding in this area. The name 'well-being sensor' is purposely optimistic, particularly considering that experts in psychology cannot agree as to exactly how well-being should be measured or defined (Huppert, 2014). The initial idea is therefore to ascertain what information can be gathered about occupants' interaction with the environment from their facial expressions and movements. This moves away from the more traditional Fanger (1973) type approach, which measures environmental characteristics with average levels of activity and clothing levels and infers occupant comfort from those metrics (Figure 1). There exist several sensors for measuring the individual environmental characteristics (temperature, CO₂, etc.), however, the underlying research question in this study is: could a sensor be developed to measure 'well-being' from people directly?

AFFECTIVE COMPUTING

Affective computing is 'computing that relates to, arises from, or influences emotions' (Picard, 1995). This study takes advantage of recent improvements in this area of research, specifically emotion and action unit recognition software, such as OpenFace (Baltrusaitis *et al.*, 2016), to establish whether and how they could be used to gauge

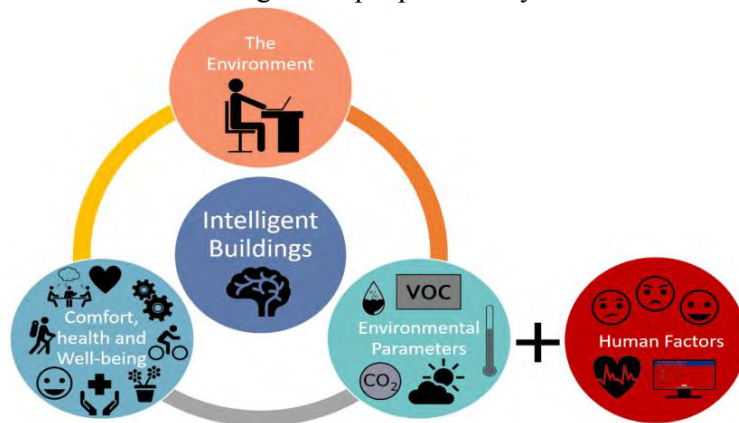


Figure 1 – Intelligent buildings need to include human factors

in order to maximise occupant comfort, health and well-being.

elements of the comfort, health, and well-being of building occupants. These softwares are quite prevalent now and, with the incorporation of artificial intelligence and machine learning, some can even recognise emotions better than humans (Bartlett *et al.*, 2014). Further, OpenFace, which uses non-verbal facial behaviours, has been shown to identify differences between suicidal and non-suicidal groups (Laksana *et al.*, 2017). Using these programs to gauge occupant comfort, health, and well-being could enable the Building Management System (BMS) to proactively change environmental conditions within a building (such as temperature or air quality) with the objective of maximising occupant comfort, health and well-being.

WELL-BEING

There exists an ongoing, lively debate as to what elements make up overall levels of well-being and on the relative contribution of each individual element. For this study, the Warwick-Edinburgh Mental Well-being Scale (WEMWBS) was chosen as the survey to measure mental well-being as it is one of the most popular and proven scale available. It is generally used to track levels of well-being in populations, but it is suitable for tracking well-being on an individual level, thus making it appropriate for studies and interventions at a local scale (Stewart-Brown *et al.*, 2011). THE WEMWBS survey used for this study consists of fourteen statements, asking the participant to describe on a scale of 1 to 5 how often they have experienced those thoughts or feelings over the last 2 weeks. The questions are as follows: • I've been feeling optimistic about the future • I've been feeling useful • I've been feeling relaxed • I've been feeling interested in other people • I've had energy to spare • I've been dealing with problems well • I've been thinking clearly • I've been feeling good about myself • I've been feeling close to other people • I've been feeling confident • I've been able to make up my own mind about things • I've been feeling loved • I've been interested in new things • I've been feeling cheerful. Similar to populations, there exists a distribution of levels of well-being in buildings as set out in Figure 2. If these levels can be measured more frequently, we can fine tune the design and control of buildings to shift this entire distribution to the right. Improving well-being levels, which may bring productivity and creativity benefits as by-products.

OBJECTIVES

The key objectives of this research are:

- Review and understand well-being from a 'Psychology' perspective and how this relates to buildings.
- Review existing well-being capture methods and the current state of the art.
- Develop a method to continuously capture elements of occupant well-being from video data.
- Deploy this in several offices to test using a mixed-methods approach.
- Consider future applications.

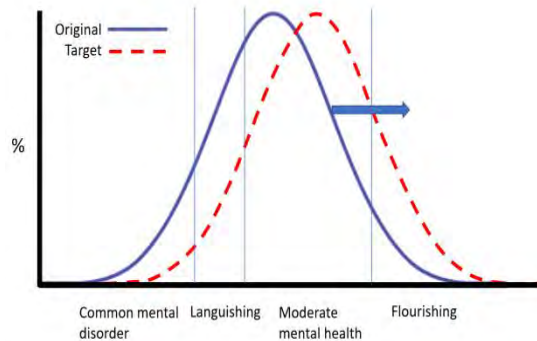


Figure 2 – The well-being distribution in a population and target to shift this further right.

METHOD

The methodology used for this study is similar to that used by the Cambridge Computer Lab in their studies using OpenFace (Baltrusaitis *et al.*, 2016). Their method is as follows:

- First, they discuss with a psychologist how they might go about diagnosing a particular condition, e.g. psychosis.
- They then use their software on two groups of people, one with and one without psychosis.
- When analysing their data, they see if there are any statistically significant differences between the two groups, enabling a 'diagnosis' from their software.

This research will take a similar approach. By combining the established method of occupant surveys with cameras and Microsoft's Emotion software, it will be possible to analyse the data and find correlations which infer the same result from survey and camera data sets. Further, from the literature it is clear that there is not a vast body of knowledge about this topic in engineering journals. Rather, most publications tend to be found in computer science, medical and psychology journals. This is a challenge, as the methodologies used by different disciplines can differ substantially. This research will attempt to move towards a methodology more suited

to the study of wellbeing (Giddings, 2012). Known as a ‘mixed-methods’ approach, it is an ‘intellectual and practical synthesis based on qualitative and quantitative research’ (Johnson *et al.*, 2007). This approach was also used by Anderson *et al.*, (2016) with surveys and observations complimenting each other in a natural experiment on well-being in a public space.

Two distinct types of experiment will be undertaken. The first set, referred to as ‘natural experiments’, include monitoring people in their offices as they go about their daily routine. This will then go on to observe how their ‘well-being’ changes as the environment changes significantly, such as when an office is refurbished or hydroponic plants are introduced. The second type of experiment will look at shorter term changes and will take place in an ‘environmental room’. In this room, people will work in isolation whilst various parameters (such as the facade type) are changed and monitored. Throughout the course of both types of experiments, regular, detailed surveys are given whilst occupants are also monitored by a camera. A small-scale proof of concept pilot study was conducted, and is discussed herein. This allowed for many lessons to be learned, ranging from the practicalities of the process of monitoring itself to the analysis of the data.

PILOT STUDY AND CONCEPT

The James Dyson Building is a mechanically assisted naturally ventilated office building located in Cambridge, United Kingdom. It consists of 4 almost identical floors, each with large open plan offices for PhD students and several cellular offices along the west side for administrators and academics. Six participants took part in the pilot study. They were each filmed every day for 2 months in the summer of 2017 from 9am until 5pm via a webcam connected to a laptop. This created over 500GB of data, which was then processed to assess the emotions of the occupants using Microsoft Emotion Recognition API in 100MB chunks. This process will be automated in future studies to save time. It also highlighted the fact that a lot of data was captured when people weren’t in the office, with the Microsoft API indicating that it could find no faces. The six participants were also given surveys to measure well-being (WEMWBS) and satisfaction with the office environment (Center for the Built Environment (CBE), Berkley).

RESULTS

The results are limited due to both the small sample size and the limits of Microsoft’s API on data size. Further, Microsoft stopped supporting the emotion from video API halfway through the study. Figure 3 shows the

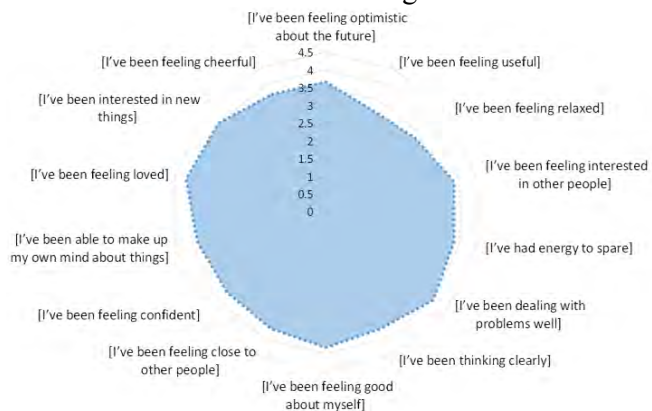


Figure 3 - WEMWS survey, average occupant response to each question



Figure 4 – Average occupant response to the CBE survey on satisfaction with the office environment.

average occupant response to the WEMWBS questionnaire. Figure 4 shows the average response to the CBE survey, showing that the office performed well when compared to buildings in the CBE database and similar to mixed-mode buildings, although the lighting could be improved. Figure 5 plots these two survey results against each other. While there are too few points to find a definitive connection, there does appear to be a link between occupant satisfaction and mental well-being. Figure 6 incorporates results from the Microsoft Emotion API, again there are too few points to find clear correlation between variables.

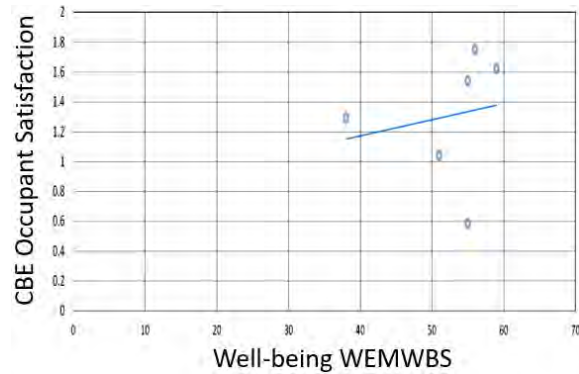


Figure 5 - CBE occupant satisfaction (left) plotted against WEMWBS (bottom).

DISCUSSIONS

Interpreting this data is difficult due to the small number of participants and the labour and computer intensive data analysis method chosen for this pilot study. It is however quite clear that occupants lie on a spectrum of well-being, even in this small study. There is insufficient data to support a correlation or indeed a relationship between occupant satisfaction and well-being. The pilot study did

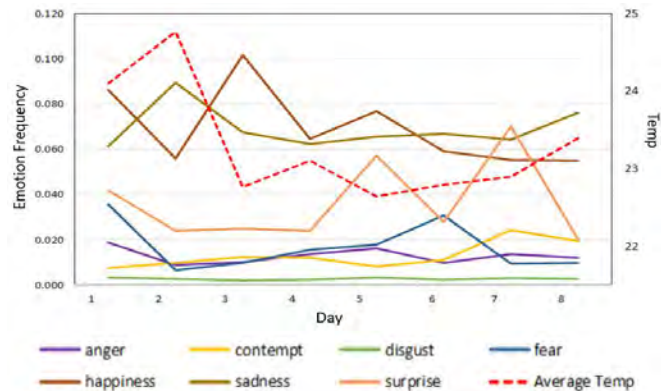


Figure 6 – Average group emotions and average office temperature on the same graph over 8 days.

however provide important lessons for future experiments. Online surveys proved to be simple to create and complete, providing data in an easy to use format. Further, the method of monitoring via web-cams atop occupant's computer monitor was also successful.

CONCLUSIONS AND FUTURE WORK

A lot was learned in the course of this pilot study, particularly in how to better acquire data. The data is really too large to be post-processed and so, in future experiments, it will have to be processed in real time. The lessons from this pilot study form the basis of a newly-developed data capture method which uses a Raspberry Pi and camera in a user-friendly case which enables data to be captured and processed onboard, or on the cloud. Further, they can be placed either on top of monitors or simply as desk decoration. They are currently being deployed in a much larger experiment which will cover the entire four floors of the James Dyson Building, as well as MATElab (a living laboratory based in Cambridge) and several other offices. We hope that this new, larger dataset will allow us to find any statistically significant correlations between the facial action units or emotions and the level of comfort, health and well-being of the occupants. This could then be used to control building elements, such as adaptive facades (Loonen *et al.*, 2017), in a more intelligent, occupant centred manner, providing a very useful input into future building management systems.

ACKNOWLEDGEMENTS

I would like to thank the EPSRC, Trimble, BRE and Microsoft for enabling this research. Further to my supervisor and colleagues in the gFT and FIBE research groups for their support.

REFERENCES

- Anderson, J. *et al.* (2016) ‘Lively Social Space, Well-Being Activity, and Urban Design: Findings From a Low-Cost Community-Led Public Space Intervention’, *Environment and Behavior*, pp. 1–5.
- Baltrusaitis, T., Robinson, P. and Morency, L. P. (2016) ‘OpenFace: An open source facial behavior analysis toolkit’, *2016 IEEE Winter Conference on Applications of Computer Vision*.
- Bartlett, M. S. *et al.* (2014) ‘Automatic decoding of facial movements reveals deceptive pain expressions’, *Current Biology*. Elsevier Ltd, 24(7), pp. 738–743.
- CPRE (2017) ‘Green Belt Under Siege : 2017’, (4302973), pp. 0–11.
- Dodge, R. *et al.* (2012) ‘The challenge of defining wellbeing’, *International Journal of Wellbeing*, 2, pp. 222–235.
- Fanger, P. O. (1973) ‘Assessment of thermal comfort practice’, *Occupational and Environmental Medicine*, 30, pp. 313–324.
- Giddings, L. (2012) ‘Mixed-methods research’, pp. 263–284.
- Huppert, F. (2014) *Measuring Wellbeing Symposium: Professor Felicia Huppert - National Measurement and Flourishing - YouTube*.
- Huppert, F. A. and So, T. T. C. (2013) ‘Flourishing Across Europe: Application of a New Conceptual Framework for Defining Well-Being’, *Social Indicators Research*, 110(3), pp. 837–861.
- Johnson, R. B. B., Onwuegbuzie, A. J. A. J. and Turner, L. A. L. A. (2007) ‘Toward a Definition of Mixed Methods Research’, *Journal of Mixed Methods Research*, 1(2), pp. 112–133.
- Laksana, E. *et al.* (2017) ‘Investigating Facial Behavior Indicators of Suicidal Ideation’, *Proceedings - 12th IEEE International Conference on Automatic Face and Gesture Recognition*.
- Loonen, R. C. G. M. *et al.* (2017) ‘Review of current status, requirements and opportunities for building performance simulation of adaptive facades†’, *Journal of Building Performance Simulation*, 10(2), pp. 205–223.
- Maller, C. *et al.* (2006) ‘Healthy nature healthy people: “contact with nature” as an upstream health promotion intervention for populations’, *Health Promotion International*, 21(1), pp. 45–54.
- Picard, R. W. (1995) ‘Affective Computing’, *MIT press*, (321), pp. 1–16.
- Renewable Energy Agency, I. (2017) ‘Renewable power generation costs in 2017: Key findings and executive summary’.
- Stewart-Brown, S. L. *et al.* (2011) ‘Plenary session : the Warwick-Edinburgh Mental Well-being Scale (WEMWBS)’, *Journal of Epidemiology and Community Health*, 65, pp. 38–39.
- United Nations, Department of Economic and Social Affairs, P. D. (2014) ‘World Urbanization Prospects’, *United Nations*, 12, p. 32.
- Weiner, J. (2015) ‘Analysis of Global EAP Data Reveals Huge Rise in Depression , Stress , and Anxiety Over Past Three Years Review of global EAP case data shows increase of nearly 50 percent in total depression , stress , and anxiety cases’, pp. 2013–2015.
- WGBC (2014) ‘Health, Wellbeing & Productivity in Offices. The next chapter for green building.’, (September), p. 88.
- WHO (1948) *Constitution of WHO: principles*.
- Yeung, O. and Johnston, K. (2014) ‘Global spa & wellness economy monitor’, p. 46.

Conserving Energy, Conserving Buildings: Airtightness Testing in Historic New England Homes

David Fannon^{1,2,*}, Jamaica Reese-Julian¹

¹School of Architecture, Northeastern University. Boston, MA.

²Department of Civil & Environmental Engineering, Northeastern University. Boston, MA.

*Corresponding email: david.fannon@northeastern.edu

ABSTRACT

As a location of early European settlement, New England enjoys a wealth of historic buildings, which represent a rich cultural heritage and insight into New England life. Their longevity also offers the opportunity to identify the characteristics of long-lasting buildings, and to guide design for the historic buildings of the future. Old buildings are inherently *sustainable*; both because of abstract ideas like “embodied energy” but also by sustaining history and culture over time. This study combines field methods from *vernacular architecture* (a branch of material culture studies) and *building science* (which exists between architecture and engineering) to conduct detailed investigations buildings representing four centuries of New England residential construction. Methods include detailed physical measurements of each building, interior and exterior photography, as well as air leakage measurement with a blower door. Buildings are contextualized from the historical literature, and scientific measurements are compared to the literature of both contemporary and other past buildings. Applying these methods to everyday buildings reconnects the study of building performance to its material, technical and cultural context, as well as the behavior of the occupants whose shelter and comfort it is meant to provide. At the same time, the information about the environment created by the building adds depth and nuance to the understanding of the cultural attitudes and activities of generations of occupants and supports the continued stewardship of these shared cultural resources. This research enriches the narrative of historic human and building interaction: infusing scientific questions of *how* buildings work with the cultural context and human intentions that dictate *why*. Understanding and preserving old buildings includes environmental as well as cultural conservation, prompts us to think of reversible interventions, and militates against the hubris of present thinking that assumes current knowledge and approaches are optimal, and therefore eternal.

KEYWORDS

Blower Door; Vernacular; Historic Buildings; New England; Building Conservation

INTRODUCTION

Pressurization testing using blower doors is a direct, and relatively inexpensive method for quantifying the airtightness of buildings (ASHRAE, 2013). Sherman concisely recounts the history, principles, and applications of blower door pressurization in buildings (1995). For detached homes—which tend to rely on uncontrolled infiltration through the envelope for ventilation—airtightness has important influence on energy conservation, indoor air quality, and identifying deficiencies for repair (Chan, Joh, & Sherman, 2013). These concerns are perhaps even more critical in historic structures, particularly those being maintained by non-profit stewardship organizations as house museums, given the tangle of preservation, maintenance, repair, alteration, cultural and economic considerations. In this context, airtightness testing may be a valuable tool. Beyond the benefit to individual buildings,

“understanding the magnitude of leakage in the building stock is important for prioritizing both research efforts and conservation measures” (M. Sherman, 2007). It is clear from the context that he means *energy* conservation, however, the same statement could equally apply to the practice of *building* conservation, particularly of vernacular buildings, both as a pragmatic measure, and as a tool for historical analysis. It may be surprising then how little data are available regarding the airtightness of historic—or even particularly old—buildings.

Sherman and Dickerhoff compiled the results of 1,492 residential airtightness tests from across the United States. to characterize the existing building stock. The data was used to investigate five building criteria that could impact leakage, including year of construction. While acknowledging the potential selection bias (much of the data came from weatherization programs) the authors found a positive relationship between leakiness and age for buildings prior to 1980 (M. H. Sherman & Dickerhoff, 1998). To address the overrepresentation of older buildings in previous data—the feature of greatest value for the present study—a subsequent database compiled blower door results from some 73,000 buildings, many shortly after construction, to yield a set only slightly older than the American Housing Survey dataset (M. H. Sherman & Matson, 2002). Using that data, an exhaustive 2003 study found that older homes are generally leakier than newer homes and described a roughly lognormal distribution. However, the authors went on to identify complex interactions among year built, floor area, and occupant income, with older, smaller and lower-income homes showing higher leakage rates (Chan, Price, Sohn, & Gadgil, 2003). It is difficult to apply these findings directly to the historic homes considered here, but these results do illustrate a similar situation in which building science is complicated by—while simultaneously offering insight about—social, cultural and economic issues. Finally, a 2013 study expanded that database to include results from blower door testing some 134,000 detached homes, and conducted regression analysis to explain the substantial variation among buildings. Limitations in the available data required the authors to categorize year of construction, with the oldest grouping including all buildings built before 1960. However age was identified as one of the most influential parameters, increasing Normalized Leakage by a factor of 2.2 (Chan et al., 2013).

METHODS

This study conducted air pressurization tests with a blower door in historic New England homes following ASTM-E1827-11 (2017) and ASTM-E779-10 (2010). Ten properties were tested in June and July 2015. Multi-point tests, typically at intervals of 10 Pa, were used in all buildings. Additional points (smaller pressure intervals) were used when building size, leakiness, or equipment limitations made it impossible to achieve a 50 Pa pressure difference. Except where curatorial concerns (e.g. intrusion of chimney soot) dictated otherwise, the results of pressurization or depressurization tests were combined to calculate results. Mechanical and plumbing systems were sealed prior to testing to ensure air leakage across the exterior envelope.

Equipment

Tests were conducted using a Retrotec Model 1000 calibrated fan, with accuracy of $\pm 3\%$ of flow. For larger and leaker properties requiring a two-fan setup, a model 3 fan from The Energy Conservancy (TEC) with accuracy of $\pm 3\%$ of flow when used with the corresponding gauge. Measurements were taken using a Retrotec Model DM32 5A WiFi gauge, running then-current firmware version 2.3.62, accurate to $\pm 1\%$ of pressure reading or ± 0.50 Pa (whichever is greater). When needed, the second fan was paired with a TEC model DG-700 gauge, with a stated accuracy of 1% of the reading, or ± 0.15 Pa, whichever is greater.

External pressure taps were split with a tee and located a minimum of 5m from the testing door, near the midpoints of two walls to balance local pressure differentials. Internal readings were taken at the gauge. All tubes were checked for leaks with the manometer, and manufacturer-recommended field calibrations conducted at the start of each test. Baseline pressure corrections were taken for a minimum of 60 seconds, and retaken whenever testing was interrupted. After stabilization, pressure and flow measurements were recorded with time-averaging of at least 5 seconds, and up to 60 seconds on windy days. A Kestrel 3500 pocket weather station, with a 0.1°C resolution, and $\pm 0.5^\circ\text{C}$ accuracy, was used to record indoor and outdoor temperatures.



Figure 1: Test Locations

Sample Buildings

The historic buildings presented in this report are managed by Historic New England, generally as house museums, and represent a broad range of sizes, ages, locations, construction types, and levels of restoration (Historic New England, 2017). Table 1 summarizes key attributes about the sample buildings, including the year of construction (although many were later modified) and primary structural material drawn from HNE records.

Table 1: Attributes of the Sample Buildings

Name	Construction Type	Year	Floors	Envl. Area (m ²)	Vol. (m ³)
Pierce House	Timber Frame	1683	3	438	585
SPL Stone House	Stone & Brick	c.1690	2	1463	2,745
Arnold House	Stone, Heavy timber	1693	2.5	404	503
Cogswell's Grant	Wood Frame	1728	2	850	1,597
Casey Farm	Timber Frame	c.1750	2	720	1,183
Langdon House	Wood Frame	1784	3	910	1,614
Lyman Carriage House	Heavy Timber	c.1793	2	823	1,309
Phillips House	Wood Frame	1820	3	1126	2,355
SPL Carriage Barn	Heavy Timber	c.1850	2	453	526
Gropius House	Wood Frame	1938	2	533	632

Buildings are located throughout New England, as shown in Figure 1. In addition to the blower door testing, each building was documented through field measurement and photography to confirm existing drawings and/or develop drawings for the area, volume and surface-area.

RESULTS

Summary results for each historic property are presented in Table 2 using several metrics. Air Changes Per Hour at 50 Pa pressure difference (ACH50), is a popular, single parameter based on the airflow measurements and building volume. Alternatively, dividing the volumetric flow by the surface area of the enclosure yields envelope flow; which is useful for envelope studies, particularly on geometrically-complex buildings like some in the sample. Effective Leakage Area (ELA) is sometimes characterized for lay readers as the size of the hole if all the leaks were combined and offers a seemingly direct metric that belies the complexity of measurement.

Table 2: Summary results from air-tightness testing sample buildings

Name	ACH50	Envelope Flow (L/s·m ²)	ELA (m ²)	NL
Pierce House	17.9	6.60	0.278	2.42
SPL Stone House	11.6	6.05	0.576	1.92
Arnold House	30.4	10.52	0.348	1.99
Cogswell's Grant	10.4	5.45	0.321	1.10
Casey Farm	14.4	6.55	0.415	1.58
Langdon House	10.9	5.38	0.453	0.82
Lyman Carriage House	13.5	5.96	0.376	1.14
Phillips House	10.8	6.29	0.479	0.95
SPL Carriage Barn	33.9	2.84	0.136	1.18
Gropius House	9.1	2.99	0.122	0.85

For context, the testing results are also presented in terms of Normalized Leakage (NL)—a metric commonly used by ASHRAE—and plotted in Figure 2 along with airtightness data for a sample of U.S. homes drawn from the literature (M. H. Sherman & Dickerhoff, 1998).

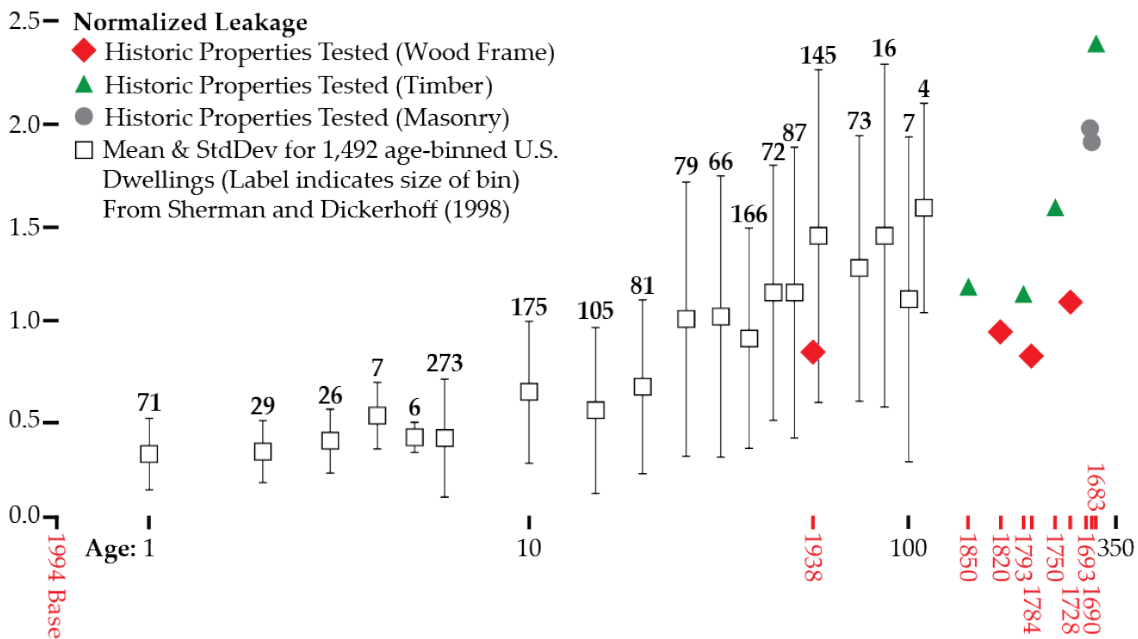


Figure 2. Plot of normalized air leakage as a function of age¹. Historic buildings from this study are noted with color-filled shapes based on primary structural material: diamonds (wood) circles (masonry) and triangles (timber). Hollow squares indicate reference averages and standard deviations for irregular age-based bins drawn from Sherman & Dickerhoff (1998).

DISCUSSION

As shown in Figure 2, older buildings are generally less air-tight than newer buildings, but even the oldest properties tested exhibit leakage rates broadly aligned with those in the pre-1980 historic record. While only a small sample, extending the historical record by approximately

¹ The testing for this study took place over 2 months; however not all houses in the reference set were tested at the same time, so as in the reference, “Age” is calculated with a base year of 1994. It is important to note that “age” cannot distinguish the effect of improvements in construction from the effect of deterioration over time.

two centuries suggests that the positive relationship identified in the literature (M. H. Sherman & Dickerhoff, 1998; Chan et al., 2003) continues, but the nature of the relationship may be complex. Naturally, the scarcity of U.S. buildings from this time, and each building's unique circumstances and history of change, necessarily complicate any generalization. While the collective results offer some general insight, these data also afford only a limited view of each unique home. Understanding the interaction of airtightness with complexities of changes over time are a bridge to a deeper and richer understanding of each building's performance, from the thermal comfort of the occupants to the labour and economic costs of fuel. These curatorial and historical interpretations require a case-study approach and are not presented here; however, they do point to a didactic function of performance testing old buildings. It is tempting to seek lessons in resilience from the sample buildings as among the most durable buildings of their era (the others having not survived), for example based on the suggestive link between leakage and construction material. Yet even putting aside the countless other factors that affect building durability, the sample buildings' status as house-museums complicates any suggestion that these structures offer direct strategies for long-term durability and performance in the New England climate. Belonging to an organization focused on the stewardship of historic buildings and landscapes, these homes are more carefully maintained and more thoughtfully modified than other buildings. Likely their longevity is both a product of care and the impetus for it, so better understanding how to care for them, and how they work demands humility and nuance.

The homes in the sample tend toward vernacular rather than monumental architecture; built for living and having endured long histories of occupation and adaptation prior to becoming museums. Now that they are owned by Historic New England, and preserved as significant examples of historic building, each has undergone various degrees of restoration, both to ensure the physical persistence of the structure into the future, as well as to represent—or interpret—cultural history as an artifact of a time and place. The homes in the sample exhibit a range of curatorial approaches. At one extreme, repairing leaks and openings in the enclosure with period-appropriate materials and techniques restores the performance of the envelope as well as the appearance, with all the associated advantages and liabilities. On the other extreme, modern interventions—albeit usually invisible—may be desirable or essential, particularly to control moisture in liquid and vapor form. For example, one of the projects in this sample required substantial envelope renovations to correct deficiencies in the roof-edge detail and to install flashing under the windows. These details intentionally altered the performance of the original design, although the appearance is all but indistinguishable (Bronski & Gabby, 2013). In another example, bronze weather stripping at windows is an essentially invisible modern intervention when the windows are closed yet provides a seal against air and moisture necessary for the economical operation of modern environmental controls quite unlike the original construction. This reality also reflects a significant challenge for house museums: the buildings in the sample must persist and ensure suitable interior environments for the artifacts inside, such as furniture and decorative arts, without continuous occupancy or the original environmental technologies. The homes in the sample are no longer heated primarily by wood burning fireplaces, and so a common intervention consists of removeable, plastic-wrapped foam plugs to seal the unused chimney flues, thereby dramatically reducing what would have been a major path for air movement out of these buildings. Since none of these buildings are “original” it is fair to wonder whether modern testing reveals anything about the historical reality, however, regardless of changes, to the extent these old buildings are “really” old, the results describe “real” old buildings. As with all history, the measurements of airtightness presented here incorporate both historical facts, and our modern reinterpretation of them.

CONCLUSIONS

As expected from the literature, blower-door testing a sample of historic, primarily vernacular New England homes built between 1683 and 1938 revealed increased leakage with increased age. Although a numerically small sample, the buildings in this group extend the record of airtightness data in U.S. homes by nearly two centuries, to a period from which there are relatively few existent structures to test. The variation in the data demonstrate that buildings particularly very old buildings, exhibit a range of performance, and militate for specific and nuanced investigations to the history of change over time. Such investigations—while perhaps prompted by and valuable for preservation and curatorial activities—also illuminate the homes performance as shelter: adding a directly human dimension to the study of vernacular history. The persistence and resilience of these vernacular buildings offer buildings scientists examples to study and from which to learn the behavior of structures which have endured—or more precisely, have been *made* to endure—in a specific climate for a long time.

ACKNOWLEDGEMENTS

The authors gratefully acknowledge Historic New England, especially Ben Haavik and his team of property managers. Thanks also to colleagues Peter Wiederspahn and Mardges Bacon, and to students Sarah Solomon, Leah Solomon, and Isadora Leal. This work is based on research supported by the College of Arts, Media and Design, the Provost's Tier One Research program, and the Brazilian Scientific Mobility Program.

REFERENCES

- ASHRAE. (2013). *ASHRAE handbook: fundamentals*. (2013th ed.). Atlanta, GA. Retrieved from <http://app.knovel.com/hotlink/toc/id:kpASHRAEC1/2013-ashrae-handbook>
- ASTM. (2010). *Standard Test Method for Determining Air Leakage Rate by Fan Pressurization* (No. E779-10). West Conshohocken, PA: ASTM International.
- ASTM. (2017). *Standard Test Methods for Determining Airtightness of Buildings Using an Orifice Blower Door* (No. E1827). West Conshohocken, PA: ASTM International.
- Bronski, M., & Gabby, B. (2013, Summer). WWGD? Restoring a Modernist Icon. *Architecture Boston*, 10(2), 46–49.
- Chan, W. R., Joh, J., & Sherman, M. H. (2013). Analysis of air leakage measurements of US houses. *Energy and Buildings*, 66, 616–625. <https://doi.org/10.1016/j.enbuild.2013.07.047>
- Chan, W. R., Price, P. N., Sohn, M. D., & Gadgil, A. J. (2003). *Analysis of U.S. residential air leakage database* (No. 53367). Retrieved from <http://escholarship.org/uc/item/6pk6r4gs>
- Historic New England. (2017). Homes, Farms & Landscapes | Historic New England. Retrieved March 25, 2018, from <https://www.historicnewengland.org/visit/homes-farms-landscapes>
- Sherman, M. (1995). The Use of Blower-Door Data. *Indoor Air*, 5(3), 215–224. <https://doi.org/10.1111/j.1600-0668.1995.t01-1-00008.x>
- Sherman, M. (2007). Air Leakage of US Homes: Model Prediction (p. 10). Presented at the Buildings X: International conference on Thermal Performance of Exterior Envelopes of Whole Buildings, Clearwater Beach, FL: ASHRAE.
- Sherman, M. H., & Dickerhoff, D. J. (1998). Airtightness of US dwellings/Discussion. *ASHRAE Transactions*, 104, 1359.
- Sherman, M. H., & Matson, N. (2002). *Air Tightness of New U.S. Houses: A Preliminary Report* (No. LBNL-48671). Berkeley, CA: Lawrence Berkeley National Laboratory.

Field occupants' behavior monitoring integrated to prediction models: impact on building energy performance

Cristina Piselli^{1,*}, Ilaria Pigliautile¹ and Anna Laura Pisello^{1,2}

¹CIRIAF – Interuniversity Research Centre, Perugia, Italy

²Department of Engineering, University of Perugia, Italy

*Corresponding email: piselli@crbnet.it

ABSTRACT

Given the massive scientific progress on passive and active solutions to reach near-zero-energy targets, the necessity to consider occupants' behavior as a key variable affecting field energy performance of buildings has become a crucial issue to face. In this panorama, a variety of deterministic and stochastic models, also supported by experimental investigations have been developed in the last decade. This paper builds upon previous contributions to analyze the real occupancy of an office building populated by peers' offices monitored for 2 years by means of microclimate and energy-need field stations. After demonstrating that the peers do not behave the same and do not control in equivalent ways indoors microclimate parameters (e.g. air temperature, desk illuminance, etc.), internationally acknowledged models and field-collected data are compared through dynamic simulation. The estimation of final energy need of different considered scenarios is calculated and the relative difference is highlighted as a possible indicator about the role of building occupancy profiles in affecting energy need prediction. Additionally, EEG experimental test are used to assess the correlation of workers' subjective emotions with external thermal stimuli. Results of final energy need estimation showed to vary by about 20% by only selecting the occupancy simulation scheme, and non-consistent prediction trends are found out while investigating lighting and electric appliances needs. Accordingly, as concerns the human psychological response to the variation of thermal conditions, negligible emotional reactions are found among the different tested workers when suddenly altering comfort conditions indoors.

KEYWORDS

Occupant behavior; Dynamic thermal-energy simulation; Continuous monitoring; Behavior modeling; Scientific Contextual EEG.

INTRODUCTION

Given the acknowledged primary influence of building occupants' behavior on indoor microclimate and energy needs, the understanding of energy related occupant behavior in buildings is a key issue for performance evaluation and optimization at the design stage (Brown and Cole, 2009). In this view, researchers have been working on the understanding and modeling of occupants' behavior in buildings to enable more reliable predictions of building performance (Hong et al. 2016). With the aim of comparing pre- and post-performance of building, Gupta and Gregg (2016) evaluated the actual performance of two low-energy retrofitted buildings in UK. In both buildings, measured annual gas consumption were lower than expected, while electricity consumption was higher as compared to predictions made by energy models, due to occupancy pattern and occupant behavior. In order to face standardized occupancy modeling approach, different stochastic models have been proposed. Such models aim at realistically describing general (Diao et al. 2017) and single energy-related occupancy behaviors, such as people's presence (Mahdavi and Tahmasebi,

2015), windows opening (Fabi et al. 2015), natural ventilation control, and appliances power loads (Zhao et al. 2014). Furthermore, adaptive thermal comfort behaviors have to be understood and taken into account. O'Brien et al. (2016) suggested that the necessary sample size to simulate and exploit occupant diversity between building occupants and uncertainty is dependent on the uniformity of the monitored population. Accordingly, occupants' behavior prediction may become particularly hard in those buildings occupied by a wide variety of users. On the other hand, peer occupants are usually assumed to have identical response to similar environmental conditions and in determining building thermal-energy performance. However, different peer occupants' personal attitudes and habits were found to differently affect the indoor environmental behavior of buildings (Pisello et al. 2016). Therefore, peers' actions homogeneity assumption can involve significant discrepancies in the thermal-energy performance of different areas situated even in the same building position (Kim et al. 2016). In fact, occupants' actions in buildings are related not only to physical stimuli, but also to multi-physics and non-measurable stimuli, in terms of thermal, acoustics, lighting, air quality issues. In this view, further research efforts, in terms of methodologies and simulation tools, are required to elaborate reliable predictive models integrating people energy needy actions into building energy modeling programs (Yan et al. 2015).

In this panorama, the purpose of the present study is to assess the capability of different existing deterministic and stochastic occupancy models for office buildings, usually considered in building dynamic simulation, to comprehensively depict occupants' behavior. To this aim, simulations are compared against real occupancy data continuously monitored in a research office building. Moreover, the discrepancy in terms of final building energy requirements is verified when considering two static standard models, a recent stochastic model, and case-specific models developed based on real monitored data. Additionally, the correlation between occupant's subjective emotions and comfort conditions variation is assessed through neural response tests. Considering the existing literature, the innovative contribution of this research is to compare the performance of different occupancy models in simulating the influence of real offices occupants on total building energy consumption by taking into account the mutual dependence of various occupants' actions. Therefore, different energy-related parameters affected by personal attitudes in office buildings are taken into account. This work builds upon a previous study by the same authors (Pisello et al. 2016) where energy-related peer occupants' behaviors were investigated through field monitoring and peers were found to behave differently based on personal habits and cultural background. Therefore, the capability of a tool based on EEG (Electroencephalography) to assess human perception of discomfort conditions and associated emotional states is evaluated.

METHODS

The research procedure implemented in this study consists of the following steps:

- Experimental continuous monitoring campaign of equivalent office rooms of a building occupied by peer occupants. Analysis of occupancy-related parameters such as energy need, indoor air temperature, illuminance over the working plane, appliances electricity consumption, and windows and door operation;
- Development of the building model and dynamic simulation when considering various occupancy schedules, i.e. static standard, stochastic, real monitored data-based;
- Data analysis and comparison of thermal-energy dynamic simulation results for the different occupancy scenarios in terms of daily trends of occupant related parameters and building total energy consumption;
- Evaluation of models representing the occupants' behavior in the five monitored office rooms against additional monitored data;

- EEG experimental test of selected occupants under different comfort conditions to assess the correlation of workers' emotional response and external thermal stimuli.

Experimental campaign

The experimental monitoring campaign has been carried out in the case study office building, located in Perugia (central Italy) from late spring 2015. The behavior of a group of peer employees working in 5 office rooms has been continuously monitored through dedicated monitoring stations constituting a Wireless Sensors Network (WSN) system. The selected office rooms presents the same characteristics in terms of geometry, energy systems, and each one is equipped with two/three computers according to the number of workers. The monitoring campaign investigates the main parameters related to (i) indoor microclimate and (ii) occupants' activity inside each office room. A more detailed description of the monitoring campaign, setup, and sensors is reported in (Pisello et al. 2016).

Dynamic simulation and occupancy scenarios

Building modeling and thermal-energy dynamic simulation is carried out through EnergyPlus v8.1 simulation engine (Crawley et al. 2000). Different occupancy models are considered for dynamic simulations: two static models, conventionally implemented in building dynamic simulation, i.e. the UK NCM (National Calculation Method for Non Domestic Buildings) standard (UK DCLG, 2004) ("standard" scenario) and the ASHRAE model based on Standard 62.1-2007 and Standard 90.1-2016 ("ASHRAE" scenario); and the stochastic model obtained from the "Occupancy Simulator" tool (LBNL 2011; Luo et al. 2017) ("occ_sim" scenario). Moreover, continuously monitored data in the five offices from June 2015 to January 2016 are considered to develop seasonal, i.e. warm and cold season, occupancy schedules to model five scenarios representative of the different offices occupants ("office_1", "office_2", "office_3", "office_4", and "office_5" scenarios). In particular, heating and cooling set-points, lighting use, and appliances energy use are taken into account. Simulation results with the three reference occupancy scenarios are compared with real monitored occupants' behaviors in terms of daily trend of occupancy-related physical parameters affecting building energy consumption in summer (July) and winter (January). Additionally, the simulation of the five experimental data-based occupancy scenarios is carried out to evaluate the discrepancy with the reference scenarios in terms of total annual building energy requirement (including HVAC, lighting, and appliances). Moreover, occupants' behavior data monitored in the office rooms during summer 2016 and winter 2016/2017, are used for the evaluation of the developed occupancy schedules. Therefore, the developed models are evaluated when compared against the additional experimental data.

EEG experimental tests

To assess the neural response of workers to external thermal stimuli, the EMOTIV EPOC+ neuroheadset (Figure 1) and software are used. In fact, this tool is capable, among other things, to report the real time changes in the subjective emotions experienced by the user, thanks to the *Affectiv* detection tab of the Xavier ControlPanel software. More in detail, the neuroheadset allows to acquire the user's EEG, which is then post-processed through the supplied software. Therefore, the tool is tested to assess the correlation between human emotions and the variation of external physical stimuli. To this aim, tests are performed to the same peer occupants working in similar office rooms ("user_1" to "user_5") when exposed to different thermal conditions, while working at the computer. More in detail, the effect of short-term alteration of the thermal comfort, i.e. by increasing the internal heat gains and, therefore, the air temperature, on the different occupants' emotions is evaluated. Therefore, each occupant is subjected to three test sessions when varying the discomfort time:

- “base”: 30 minutes in a thermally comfortable environment;
- “1/2”: 15 minutes in a thermally comfortable and 15 in a discomfortable environment;
- “1”: 30 minutes in a thermally discomfortable environment.



Figure 1. EEG experimental test. Left) Test example, Right) Neuroheadset.

RESULTS

Comparison of occupancy models

Firstly, the trend of occupancy-related simulated parameters in the “standard” and “ASHRAE” scenarios with respect to the monitored data during a summer and a winter day, show that the standardized implemented procedures are neither representative of occupants’ individual attitudes nor of their average behavior and tends to overestimate (“standard”) and underestimate (“ASHRAE”) occupants’ energy needs. As concerns the “occ_sim”, since only the occupancy presence schedule is changed in this scenario, with respect to the “standard”, negligible differences are found in a single-day-term. Switching to the total annual energy consumption for the eight occupancy scenarios, i.e. the three reference and the five experimental data-based, simulation results confirm the high variability of building energy consumption depending on the considered occupancy scenario. In fact, the monitoring-based occupancy scenarios present lower HVAC annual energy consumption with respect to the reference “standard” scenario, up to 19.7% for “office_2”. Concerning annual lighting use, all monitoring-based scenarios present lower energy consumption with respect to the three reference scenarios, up to about 13.2 kWh/m² per year (“office_4”). Additionally, although considered as peers, the occupants of the five office rooms show notably different electricity energy use and indoor thermal preference, especially in summer. Finally, the simplified occupancy models developed according to the data monitored during year 2015/2016 were evaluated when compared against the experimental data collected during the following year. Figure 2 depicts the trend of simulated parameters with respect to measured data for an average day in summer. The comparison of measured and simulated parameters stresses the higher, yet still not adequate representativeness of experimental data-based occupancy models, compared to standard and stochastic models. However, relevant discrepancies are still noticed, since occupants’ behavior is inconstant and influenced by multi-physical and multi-dimensional parameters to be more deeply investigated. Similar results are obtained in winter.

EEG tests results

EEG tests are performed to verify the possibility to correlate the variation of external physical stimuli with worker’s subjective emotions. Results (Table 1) show that the analyzed feelings are generally not affected by alteration of thermal conditions. However, some exceptions are noticed: one of the tested occupants experiences focus and excitement reduction in thermally discomfortable conditions, while another one shows excitement increase when increasing the time of exposure to discomfortable conditions. Nevertheless, this singular results cannot be considered representative. Instead, results generally show that non-physical factors, i.e. focus and involvement in the performed tasks, are more significant drivers of personal emotions and behaviors than physical factors, i.e. thermal conditions. In this view, it has to be considered the short test period and the moderate thermal alteration, which may have affected such result.

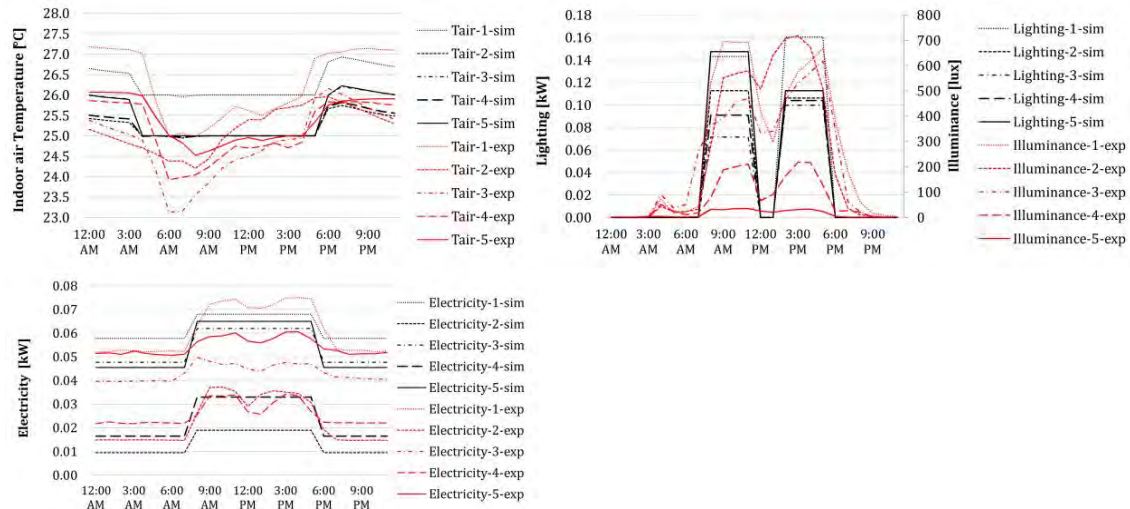


Figure 2. Average trend of data monitored in the five office room with respect to simulated data in a summer day. Up left) Indoor air temperature, Up right) Illuminance over the work plane vs. lighting energy use, Bottom) Appliances electricity use.

Table 1. Variation of occupants' subjective emotions level in different thermal conditions.

		Engagement	Excitement	Interest	Relaxation	Stress	Focus
base	User_1	61%	17%	58%	30%	99%	51%
	User_2	58%	28%	61%	33%	51%	38%
	User_3	57%	8%	55%	30%	54%	26%
	User_4	62%	26%	61%	32%	52%	38%
	User_5	58%	28%	65%	30%	50%	39%
1/2	User_1	61%	24%	60%	31%	99%	55%
	User_2	48%	24%	62%	39%	53%	35%
	User_3	56%	8%	56%	30%	53%	24%
	User_4	62%	25%	60%	30%	52%	41%
	User_5	58%	16%	64%	30%	51%	33%
1	User_1	56%	53%	56%	27%	59%	70%
	User_2	59%	29%	59%	31%	47%	39%
	User_3	56%	8%	62%	30%	59%	31%
	User_4	64%	26%	59%	32%	42%	37%
	User_5	58%	10%	64%	29%	54%	26%

CONCLUSIONS

The purpose of the present study is to verify the capability of different standard static and stochastic occupancy models to predict the behavior of real occupants of an office building. To this aim, occupancy behavior-related environmental and energy parameters were monitored in five rooms of a office building to develop experimental data-based occupancy models. Moreover, an EEG based tool is tested as complementary tool to improve occupant behavior understanding and prediction. Results show that the standard occupancy models are neither representative of specific occupants' preferences and peak energy demand nor of their averaged behavior, both in the short-term and in the long-term. In fact, the standardized existing procedures do not take into account the adaptability of human comfort and energy-saving or -wasting habits of office occupants. Conversely, the occupancy scenarios developed based on the experimental data showed to better represent the real daily occupants' attitudes, yet discrepancies are still noticed, due to inconstant human behavior affected by multi-

physical and non-physical stimuli. In this view, neural response tests are demonstrated to be a reliable tool to improve this multidisciplinary analysis. However, this method requires further investigations, by performing several tests, to provide outstanding results that strengthen the first findings obtained in terms of correlation between subjective emotions and environmental conditions.

ACKNOWLEDGEMENT

This work is part of the case-study research activity of the IEA-EBC program Annex 66: Definition and Simulation of Occupant Behavior in Buildings. Part of this research is carried out within the framework of COLO ARTE by Fondazione Cassa di Risparmio di Perugia, (Grant Cod. 2016.0276.02). The authors' acknowledgements are due to the European Union's Horizon 2020 program under grant agreement No 678407 (ZERO-PLUS).

REFERENCES

- Brown Z. and Cole R.J. 2009. Influence of occupants' knowledge on comfort expectations and behaviour. *Building Research & Information*, 37(3), 227–245.
- Crawley D.B, Pedersen C.O, Lawrie L.K, and Winkelmann F.C. 2000. Energy plus: Energy simulation program, *ASHRAE Journal*, 42, 49–56.
- Diao L, Sun Y, Chen Z, and Chen J. 2017. Modeling energy consumption in residential buildings: A bottom-up analysis based on occupant behavior pattern clustering and stochastic simulation. *Energy and Buildings*, 147, 47–66.
- Gupta R. and Gregg M. 2016. Do deep low carbon domestic retrofits actually work? *Energy and Buildings*, 129, 330–343.
- Hong T, Sun H, Chen Y, Taylor-Lange S.C, and Yan D. 2016. An occupant behavior modeling tool for co-simulation. *Energy and Buildings*, 117, 272–281.
- Kim J, de Dear R, Parkinson T, and Candido C. 2017. Understanding patterns of adaptive comfort behaviour in the Sydney mixed-mode residential context. *Energy and Buildings*, 141, 274–283.
- LBNL. 2011. Occupancy Simulator. <http://occupancysimulator.lbl.gov/> (accessed March 29, 2018).
- Luo X, Lam K.P, Chen Y, and Hong T. 2017. Performance evaluation of an agent-based occupancy simulation model. *Building and Environment*, 115, 42–53.
- Mahdavi A. and Tahmasebi F. 2015. Predicting people's presence in buildings: An empirically based model performance analysis. *Energy and Buildings*, 86, 349–355.
- O'Brien W, Gunay H.B, Tahmasebi F, and Mahdavi A. 2017. A preliminary study of representing the inter-occupant diversity in occupant modelling. *Journal of Building Performance Simulation*, 10(5-6), 1–18.
- Pisello A.L, Castaldo V.L, Piselli C, Fabiani C, and Cotana F. 2016. How peers' personal attitudes affect indoor microclimate and energy need in an institutional building: Results from a continuous monitoring campaign in summer and winter conditions. *Energy and Buildings*, 126, 485–497.
- UK Department for Communities and Local Government (DCLG). 2004. UK's National Calculation Method for Non Domestic Buildings. <http://www.uk-ncm.org.uk/> (accessed February 19, 2018).
- Yan D, O'Brien W, Hong T, Feng X, Burak Gunay H, Tahmasebi F, and Mahdavi A. 2015. Occupant behavior modeling for building performance simulation: Current state and future challenges. *Energy and Buildings*, 107, 264–278.
- Zhao J, Lasternas B, Lam K.P, Yun R, and Loftness V. 2014. Occupant behavior and schedule modeling for building energy simulation through office appliance power consumption data mining. *Energy and Buildings*, 82, 341–355.

Modeling and spatial visualization of indoor micro-climates for personalized thermal comfort

Berardo Matalucci^{1*}, Joshua Draper² and Anna Dyson³

¹ SHoP Architects, New York, NY

² Center for Architecture Science and Ecology, Rensselaer Polytechnic Institute, Troy, NY

³ Yale Center for Ecosystems in Architecture, Yale University, CT

**Corresponding email: berardo.matalucci@gmail.com*

ABSTRACT

The indoor thermal environment is conventionally considered homogeneous as anchored on a universal thermal comfort paradigm, although occupants' experience is often diversified and influenced by several physio-cognitive factors. Personal comfort devices aim to enhance thermal comfort acceptance through localized heating and cooling while reducing overall energy consumption as temperature set-points of centralized HVAC systems can be relaxed. To further incentivize the adoption of distributed HVAC systems, it is critical to examine the energy benefits and the spatial characteristics of heterogeneous thermal environments.

Here we developed a parametric framework based on building energy modeling coupled with a spatial visualization of micro-climatic thermal fields, which respond to a variable space occupation. HVAC system loads and indoor environmental conditions, extracted from the energy model, are integrated with an analysis of the human thermal balance. As a case study, a thermoelectric-based system for personalized thermal comfort was considered in an office space, based on a specific layout of workstations and meeting rooms. The contribution of distributed heating and cooling systems to the overall HVAC energy consumption was analyzed for the office, and the micro-climatic variability was visualized based on transient occupation patterns.

Understanding the impact of variable occupation for the building energy balance is significant for developing performative metrics for next-generation distributed HVAC systems. At the same time, it can inform novel design strategies based on micro-climatic controls to maximize personalized thermal comfort and enhance the quality of indoor environments.

KEYWORDS

indoor micro-climates, energy modeling, responsive environments, personalized thermal comfort, thermal field visualization.

INTRODUCTION

Expanding the temperature set-points of Heating, Ventilation and Air Conditioning (HVAC) systems may unravel new strategies to reduce building energy consumption and incentivize the adoption of distributed systems for enhanced thermal comfort. Energy savings up to 73% were projected when extending the temperature setpoints of conventional Variable Air Volume (VAV) system to near 30°C for cooling and 17°C for heating (Hoyt, Arens, & Zhang, 2015). Under these conditions, Personalized Comfort Systems (PCS) may provide maximum thermal comfort to occupants and hypothetically utilize less energy than centralized HVAC systems (Amai, Tanabe, Akimoto, & Genma, 2007; Bauman et al., 2015; Kong, Dang, Zhang, & Khalifa, 2017). However, the relationship between PCS and ambient conditions is still largely unexplored, particularly throughout an entire year. The objective of this study is to examine the potential benefits of localized heating and cooling systems for energy savings and

occupants' comfort, and provide means of spatial visualization of micro-climatic conditions indoors. As post-occupancy evaluation shows, thermal comfort acceptance in office spaces is a critical aspect to be considered because it has an impact on building operational energy and indoor environmental quality (Huizenga, Abbaszadeh, Zagreus, & Arens, 2006). Providing means of modeling and visualization of indoor micro-climates has the potential to facilitate the adoption of distributed HVAC systems beyond the strive for system efficiency for a more human-centric design approach.

METHODS

An energy model was developed to examine HVAC system loads, indoor environmental conditions, and determine human heat balance within an occupied space. An 800m² multi-zoned office space with 75% window-to-wall ratio was modeled in *OpenStudio*, a validated energy modeling software. The New York City typical meteorological year was utilized for calculations under ASHRAE 90.1 2013 construction assemblies, schedules, and internal loads. A Variable Air Volume (VAV) HVAC system type was considered for the simulation for typical baseline and expanded temperature set-point ranges. Ladybug plugin allowed for a direct integration of energy modeling from *OpenStudio* into the *Rhinoceros-Grasshopper* environment (Roudsari, Pak, & Smith, 2013). In this study, indoor air temperature, relative humidity, air flow rates, surface temperatures, and HVAC energy loads were examined in *Rhinoceros-Grasshopper* to determine the human energy balance and energy consumption parameters. Finally, the efficacy of the supplemental heating and cooling was assumed at 0.5, implying that for example, 50W of power would provide 25W of active localized heating or cooling to each occupant (Kong et al., 2017). A Coefficient Of Performance (COP) of 2.5 was also assumed for the supplemental HVAC system, which refers to current targets aimed by the authors on a solid-state HVAC system under research. The *Modular Indoor Micro-Climate* (MIMiC) system is based on a modular thermoelectric heat pump coupled with a temperature-optimized thermal storage for reversible, localized heating and cooling which may also be deployed in office environments. The detailed workflow, including the variables and procedural steps described in this study, is illustrated in Figure 1.

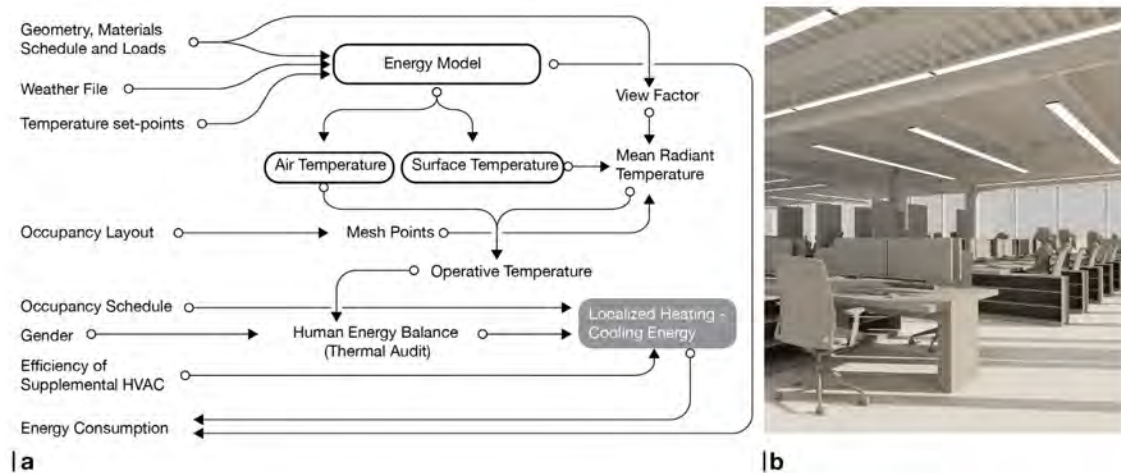


Figure 1. Diagram of the energy model workflow (left) and partial rendering of the office space considered for energy modeling (right).

Human Heat Balance

In current standards, thermal comfort is primarily assessed using the Predicted Mean Vote or the Adaptive Comfort ranges, for which there is no explicit gender differentiation (ASHRAE, 2004; Kingma & van Marken Lichtenbelt, 2015). Thereby, the thermal audit process was utilized to determine the human heat balance with the environment (Parsons, 2014). Assuming a relaxed temperature set-point, it is possible to characterize the resulting heat to be supplied or removed (S) using the following equation:

$$S = (M - W) - ((C + R + E_{sk}) + (C_{res} + E_{res})) \quad (1)$$

Where M represents the rate of heat generated by the body or metabolic activity, W is the rate of any mechanical work, R is radiation, C is convection, E_{sk} is the rate of total evaporative heat losses from the skin, C_{res} is the rate of convective heat losses from respiration, and E_{res} is the rate of evaporative heat losses from respiration. In this study, beside the radiant portion of the thermal balance, the environmental conditions are assumed to be homogeneous within the thermal zones but varying over time. The mechanical work (W) component was considered null and thermal conduction neglected. The metabolic activity (M), a critical factor in the determination of the energy balance, was gender-specific (Kingma & van Marken Lichtenbelt, 2015). In particular, the female metabolic rate was considered as 48 Wm^{-2} when performing light work. Male metabolic activity was derived from ASHRAE (2004), being at 60 Wm^{-2} under light work in office environments.

Mean Radiant Temperature

As radiant thermal exchanges constitute a large component of the human thermal balance (Parsons, 2014), this studied focused on calculating the Mean Radiant Temperature (MRT) for a specific occupation layout within an office space. The equation for the MRT is assumed as (La Gennusa, Nucara, Rizzo, & Scaccianoce, 2005):

$$T_r = \sqrt[4]{\sum_{i=1}^N F_{S \rightarrow i} T_i^4} \quad (2)$$

Where $F_{S \rightarrow i}$ represents the view factor between the receiving geometry, here a person, and a building internal enclosure (i), for which the surface temperature (T_i) is derived from the energy model. Although the calculation of the view factor is computationally expensive, this study utilized the following, validated approximation (Walton, 2002):

$$F_{S \rightarrow i} \approx \frac{-1}{\pi A_S} \sum_S \sum_i \frac{(\vec{r} \cdot \vec{n}_S)(\vec{r} \cdot \vec{n}_i)}{(\vec{r} \cdot \vec{r})} \Delta A_S \Delta A_i \quad (3)$$

Where \vec{r} is the vector connecting the centers of the finite areas ΔA_S and ΔA_i ; \vec{n}_S and \vec{n}_i are their normal vectors at the center point, and the dot product indicated scalar multiplication between vectors. A recursive calculation was coded in Python within the Grasshopper platform, to better interface with the results coming from the energy model as depicted in Figure 2.

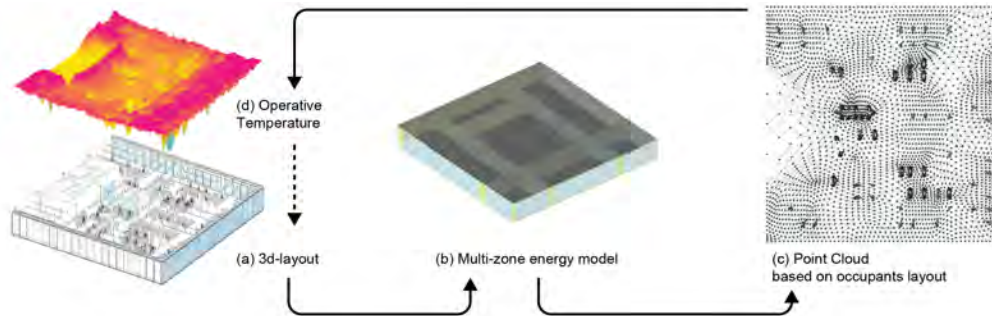


Figure 2. Approach for calculation of MRT and micro-climatic visualization: (a) office layout determining occupants position in space; (b) multi-zone energy model provides surface temperatures on hourly basis; (c) point cloud definition for view factor; (d) visualization of the operative temperature.

RESULTS

The overall HVAC energy saving are projected in 14% relative to baseline conditions when the temperature set-points are extended from 22°C to 26°C for cooling and from 21°C to 19°C for heating (Table 1). The HVAC energy savings account for the supplemental heating and cooling for each occupant based on the satisfaction of their specific human thermal balance. The energy expenditure for the MIMiC supplemental system accounts for about 1/5 of the overall energy consumption under expanded temperature set-points. However, different behaviors were observed when considering heat loads on an hourly basis. For a typical summer day such as June 21st (Figure 3, a), the energy expenditure associated with expanded temperature set-points and the supplemental system were consistently lower than baseline condition. Conversely, for a typical winter day, such as December 21st (Figure 3, b), no substantial energy savings during heating demands were observed. Also, the energy expenditures for regaining comfort almost nullified the benefits given by expanded heating temperature set-point. Mainly, from mid-morning to early afternoon, the expansion of temperature set-point did not produce any energy savings particularly in the later afternoon. The extreme peaks in heating demand around 5AM (Figure 3,b) were observed only for some days and not consistent in terms of intensity, although a more detailed investigation is required.

Table 1. Summary of the HVAC energy consumption for baseline and experimental conditions.

	a. Baseline	b. Relaxed Temp. Set-Pt	c. MIMiC	Total (b+c)	Energy Savings (%)
HVAC Energy Consumption (kWh/yr)	64,069	46,547	8,288	54,835	-14%
HVAC Energy Density (kWh/m ² - yr)	80.2	58.3	10.4	68.7	

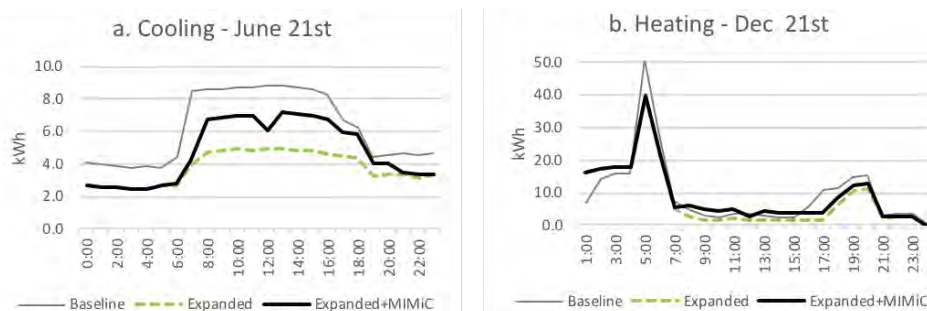


Figure 3. HVAC energy consumption for a typical cooling (a) and typical heating (b) day.

The micro-climatic maps of the operative temperature are represented for a typical summer and winter day at 1PM (Figure 4). The maps, resulting from the integrated computation of the mean radiant temperature and heat balance, suggest that the operative temperature is generally higher than relative air-temperature set-points. Such discrepancy is more pronounced during the summer day (Figure 4,a) where occupants closer to the envelope and the core may experience higher operative temperature than near the core. Instead, on winter time (Figure 4,b), the benefit of the solar exposure can be inferred from the micro-climatic map, for which south-west portion of the floor plate has 2°C higher operative temperature than central and north-east exposed spaces. Finally, gender differences in operative temperatures can be observed from the micro-climatic maps, where blue-colored areas are indicative of males with typical preferences for colder air temperature set-points (Kingma & van Marken Lichtenbelt, 2015).

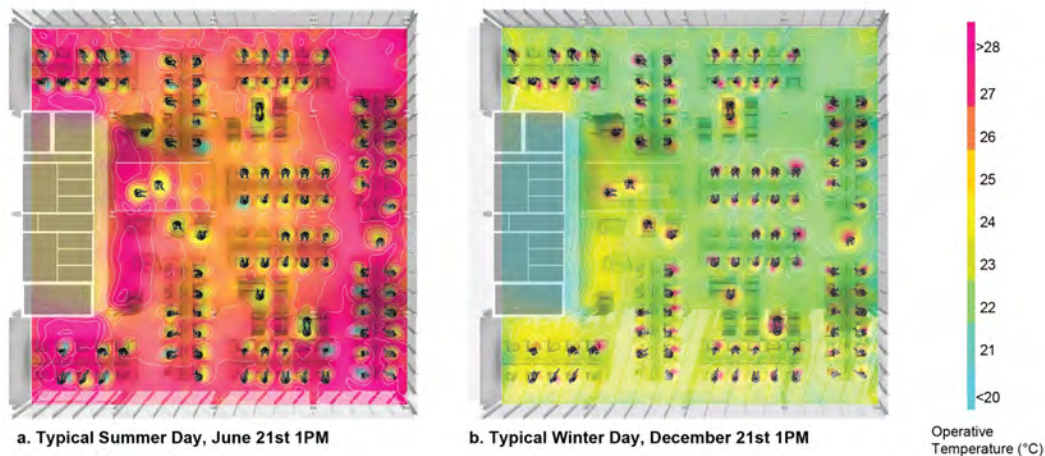


Figure 4. Synthetic visualization of localized cooling (a) and heating (b), and associated energy consumptions for a typical summer day

DISCUSSIONS

The energy savings observed herein align with previous studies on the expansions of temperature set-points, although this study project less generous savings (Hoyt et al., 2015). While the energy consumption of the supplemental system for heating and cooling is minimal, it cannot be ignored from the overall building energy balance. The integrated energy model also allows to evaluate the economic feasibility of the supplemental systems for specific cases. In fact, for this study, the simple payback of the MIMiC systems is 8.3 years for a commercial application under NYS energy rate and assuming \$80 per system installed in each occupied space. Different paybacks may be obtained when considering the benefits of productivity, however further studies are required. The operative temperature has larger swings than air temperature set-point offset, which may be associated with large glazed areas and their effects on mean radiant temperature. The impact of glazing and partitions on the operative temperature is more pronounced in areas closer to vertical envelopes as shown by the micro-climatic maps. The ability to model and visualize the operative temperature through the refined calculation of the MRT to determine the view factor, represents a key contribution of this study. Two limitations are given by not considering the furniture from the MRT calculation and the uniform distribution of air temperature in the different thermal zones. Future studies can incorporate the methodology presented herein and introduce means to model air temperature and occupation patterns with finer resolution. At the early stage of the design process, which this study targeted, practitioners and architectural scientists may utilize this methodology to evaluate both energy savings, thermal comfort implications, and economic feasibility for different primary and supplemental HVAC options.

CONCLUSIONS

The ability to provide personalized thermal comfort may unleash novel strategies for reducing building energy consumption and address raising concerns on indoor environmental quality, such as gender-specific thermal comfort preferences. This study reported on an integrated modeling and visualization framework for predicting energy savings from expanded temperature set-points and supplemental heating and cooling systems to equalize thermal balance based on different metabolic rates. The application of the modeling approach on a largely-glazed office space showed annual energy savings of 14% relative to a baseline condition. Also, different micro-climatic conditions were observed when calculating the operative temperature using a fine point could as representation of the floorplate occupancy. Integrating energy modeling and spatial visualization may provide useful insights for early-stage decision-making process on HVAC systems and sub-systems, and occupant comfort.

ACKNOWLEDGEMENT

The work was primarily conducted at the Rensselaer Polytechnic Institute. The authors would like to thank Dr. Theodorian Borca-Tasciuc for his support on heat transfer and energy balance equations. The work was supported by NYSTAR.

REFERENCES

- Amai, H., Tanabe, S. I., Akimoto, T., & Genma, T. (2007). Thermal sensation and comfort with different task conditioning systems. *Building and Environment*, 42, 3955-3964.
- ASHRAE. (2004). *ANSI/ASHRAE standard 55-2004: Thermal environmental conditions for human occupancy*
- Bauman, F., Zhang, H., Arens, E., Raftery, P., Karmann, C., Feng, J. D., . . . Zhou, X. (2015). *Advanced integrated systems technology development: Personal comfort systems and radiant slab systems*.
- Hoyt, T., Arens, E., & Zhang, H. (2015). Extending air temperature setpoints: Simulated energy savings and design considerations for new and retrofit buildings. *Building and Environment*, 88, 89-96.
- Huizenga, C., Abbaszadeh, S., Zagreus, L., & Arens, E. A. (2006, June). *Air quality and thermal comfort in office buildings: results of a large indoor environmental quality survey*. Paper presented at the Proceeding of Healthy Buildings 2006, Lisbon, PT.
- Kingma, B., & van Marken Lichtenbelt, W. (2015). Energy consumption in buildings and female thermal demand. *Nature Climate Change*, 5(12), 1054-1056.
- Kong, M., Dang, T. Q., Zhang, J., & Khalifa, H. E. (2017). Micro-environmental control for efficient local cooling. *Building and Environment*, 118, 300-312.
- La Gennusa, M., Nucara, A., Rizzo, G., & Scaccianoce, G. (2005). The calculation of the mean radiant temperature of a subject exposed to the solar radiation - a generalised algorithm. *Building and Environment*, 40(3), 367-375.
- Parsons, K. (2014). *Human thermal environments the effects of hot, moderate, and cold environments on human health, comfort, and performance*. Boca Raton, FL: CRC Press/Taylor & Francis.
- Roudsari, M. S., Pak, M., & Smith, A. (2013, August 26-28). *Ladybug: a parametric environmental plugin for grasshopper to help designers create an environmentally-conscious design*. Paper presented at the Proceedings of the 13th International IBPSA Conference, Chambéry, FR.
- Walton, G. N. (2002). *Calculation of obstructed view factors by adaptive integration*. Retrieved from Gaithersburg, MD: <http://ws680.nist.gov/>

Occupants' perception of historical buildings' indoor environment. Two case studies.

Giorgia Spigliantini^{1,2*}, Valentina Fabi¹, Marcel Schweiker² and Stefano Paolo Corgnati¹

¹Politecnico di Torino, Italy

²Karlsruhe Institute of Technology, Germany

*Corresponding email: giorgia.spigliantini@polito.it

ABSTRACT

In Europe, some historical cities have more than 50% of buildings dated from before 1920. Nowadays, these buildings faces challenges when adapted to the current necessities of livability, environmental and economical sustainability. Literature demonstrates that occupants' comfort perception and consequent behavior affect buildings' energy efficiency and are influenced also by the building configuration. Despite a large number of studies in literature investigating occupants' behavior and comfort in different situations, there is a lack of such studies for historical buildings. Therefore, the objective of this paper was to characterize occupants' thermal and comfort perception in two historical buildings during summer season. In these terms, results of objective measures were compared to occupants' evaluations of the indoor environment. Results showed that, for both case studies, despite the good thermal performances of the building fabrics and the fact that almost all of the occupants like to work in a historical building (they would also choose it instead of a modern one), most of them didn't rate the building as comfortable from a thermal point of view.

KEYWORDS

Thermal comfort, Historical buildings, Heritage preservation, Energy retrofit.

INTRODUCTION

These days, a great amount historical heritage buildings are reconverted for activities that differ from the originals, involving a complex processes of building adaptation and energy retrofit (Martínez-Molina, Tort-Ausina, Cho, & Vivancos, 2016). In this field, many studies recognized the positive role played by traditional materials and historic building configurations in mitigating outdoor conditions (Belpoliti *et al.*, 2017). However, two aspects should be considered carefully in the energy retrofit process. First, the implementation of new HVAC systems, because being designed for different technological contexts their installation entail an unavoidable duress on the historic fabric (Filippi, 2015). The second aspect is the so-called "human factor". According to Fouseki and Cassar (2014), the tension between heritage preservation and the need for occupants' thermal comfort is a bigger challenge then finding aesthetic-suitable solutions for historical buildings' energy retrofit. The same authors reported a lack of knowledge regarding occupants' perception of historical buildings and the necessity to do researches on how people feel and behave towards these buildings. Also Agbota (2014) highlights the importance of studying the unintended consequences of energy retrofit interventions for historical buildings' occupants. In this field, Anderson and Robinson's study (2011) showed that despite people appreciation of their home's historical evidence, their main concern was to enhance their thermal comfort in winter. In these terms, Crockford (2014) highlighted the central role of educating occupants in being aware of how the historic building functions and could be exploited in order to host a "twenty-first-century lifestyle".

The objective of this research is to investigate the relationship between occupants' thermal and comfort perception and indoor environmental conditions in two case studies of the same historic period and geographical area. The study was conducted in summer season. .

METHODS

This study is embedded in a larger research investigating different aspects of energy efficiency, indoor environmental quality and occupants' comfort and behavior in historic buildings. This research combined objective field measurements of temperature and subjective data obtained through a questionnaire survey. For this paper data from two case studies were chosen considering the availability of indoor environmental monitoring, historic period of the buildings, occupants' activity and geographical area.

Case studies

The two case studies are both located in the suburban territory of Turin (Italy). The first is the Rivoli castle, which is the product of a reconstruction of XVIII Century and a restoration of XX Century, finished with the opening of the current Contemporary Art Museum in 1984. Today the museum is registering more than 100,000 visitors per year and is listed in the UNESCO World Heritage List. The building, in which the last restoration maintained the original configuration and distribution, has a floor area of about 10,000 m². The surface hosts expositive areas and offices. From a constructive point of view, the Castle is a massive masonry building. During the summer season the building is passively cooled. Two types of occupants performing comparable metabolic activities were taken into account in this building: office workers and security staff of the expositive area. For the analyses, an existing network of eight Data Loggers (DLs) (model testo 175 H1), homogeneously distributed in the first and second floor of the building, was exploited. The second case study, the Centro di Conservazione e Restauro La Venaria Reale (CCR), founded in 2005, is a research, restoration and education center in which conservators, art historians and scientists work within laboratories, offices and classrooms. The CCR is based in the XVIII Century "La Venaria Reale" complex, a royal residence listed in the UNESCO World Heritage list. From a constructive point of view, the building is quite similar to Rivoli Castle; the only big difference is that the internal structure of the building was refurbished to host classrooms, offices and laboratories. For this research only offices were considered. During summer, offices are conditioned with a cooling system with a general set point of 24°C during working hours. However, in each room users are able to regulate indoor temperature with a range of +3°C/-3°C or even turn off fan coils. Regarding windows, only a part of occupants have the possibility to operate them. In both case studies, a monitoring campaign was carried out from June to September 2017. At CCR the monitoring data, consisting on the air temperature of six offices, were extracted from the temperature probes (Sauter EYB250F201) located on offices' walls, near the fan coils.

Analyses

The data were analyzed with the following procedure. First, for both cases analyses were made in order to assess DLs' measurements differences and calculate the daily fluctuation of temperature as an average of those in the same range. Second, mean daily temperatures were calculated for the whole summer season and compared with mean daily outdoor temperature of the nearest meteorological station, for both cases located in Turin. Third, the thermal indoor environmental quality was evaluated according to ASHRAE 55 (2004) and EN 15251 (2008) standards. For ASHRAE 55, analyses were done according to the prescriptions for "Naturally conditioned spaces". While for Rivoli Castle this would have been the only choice, being a passively conditioned building, for CCR the choice was partly due to the necessity of comparing it with the other building and partly due to the absence of data regarding humidity ratio, mean radiant temperature and air speed. For these analyses, indoor operative temperature was assimilated to average air temperature because all the conditions of

ASHRAE 55 Appendix A-Case 1 were met. Regarding EN 15251 standard, evaluations of indoor environmental conditions were made following Annex A “Recommended criteria for the thermal environment” indications. While for Rivoli Castle the evaluations were made only according to the second section, dedicated to buildings without mechanical cooling systems, CCR was evaluated according to both first section (dedicated to mechanical heated and cooled buildings) and second section. Fourth, subjective perception of indoor environment was evaluated basing on data from a questionnaire. In particular, authors took into account one part of the third section (Comfort conditions and preferences) and the second section (Cultural background, habits and changing attitude). The two aspects taken into account from the third section were:

- Thermal sensation vote (TSV), according to ASHRAE 55’s seven point scale (-3=cold, -2=cool, -1=slightly cool, 0=neutral, 1=slightly warm, 2=warm, 3=hot);
- Comfort evaluation according to a 5 point scale (-2=very uncomfortable,-1=moderately uncomfortable, 0=neutral, 1=moderately comfortable and 2=comfortable).

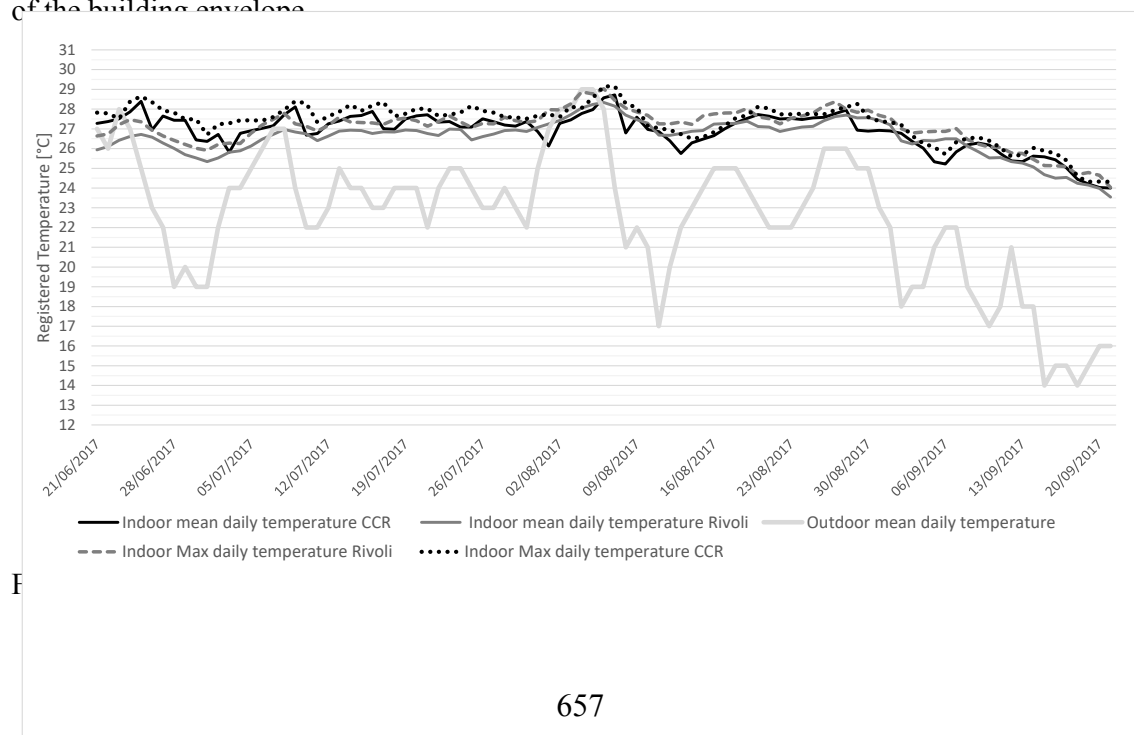
The questionnaire took place only once at the end of the season, so the evaluations were referred to the whole just-ended summer. The two considered questions of the second section were:

- If occupants like working in a historical building (yes, no, I don’t care);
- If occupants would choose to work in a modern or in a historical building.

For both case studies, the response rate was sufficient to consider occupants’ sample as representative of the building according to ASHRAE 55 “Survey of Occupant responses to Environment” section (22 respondents out of 35 for Rivoli Castle and 16 out of 19 for CCR).

RESULTS

Figure 1 shows mean indoor daily temperature and maximum indoor daily temperature of both case studies compared with the outdoor mean daily temperature data of the nearest meteorological station. Indoor mean daily temperatures of the case studies were not very different despite the presence of a cooling system in CCR (which actually had, in general, higher indoor temperature). The only noticeable difference is in the shape of profiles, which is more jagged for CCR, probably due to a fluctuating use of the cooling system. The maximum and average indoor temperature profiles show that there is not much fluctuation between day and night, because of the high thermal mass of both buildings. For both cases, indoor temperature profiles follow outdoor conditions, confirming a typical high-massive behaviour of the building envelope.



Regarding the indoor environment evaluation, Figure 2 and Figure 3 present the results of the application of ASHRAE 55 and EN 15251 standards for not mechanically cooled buildings. The graphs show the monitored average daily operative temperature compared to the prevailing mean outdoor temperature. Based on the results shown in Figure 1, at CCR there could be a high amount of users turning off their fan coils or regulating it with the highest temperature available (27°C). As a general comment, both buildings seem to behave quite well from a thermal point of view. In fact, considering ASHRAE 55 standard, in both cases almost all daily average temperature fall in the 80% acceptability interval. Regarding the 90% acceptability interval, which is not a normative requirement, 92% of values registered at Rivoli castle fall in this interval, while the equivalent percentage of CCR is 71%. Regarding the EN15251 standard, Figure 3 shows that both cases would be classified in Category I. Of course it should be noticed that for CCR these results would be relevant to the standard only assuming that the cooling system is not used.

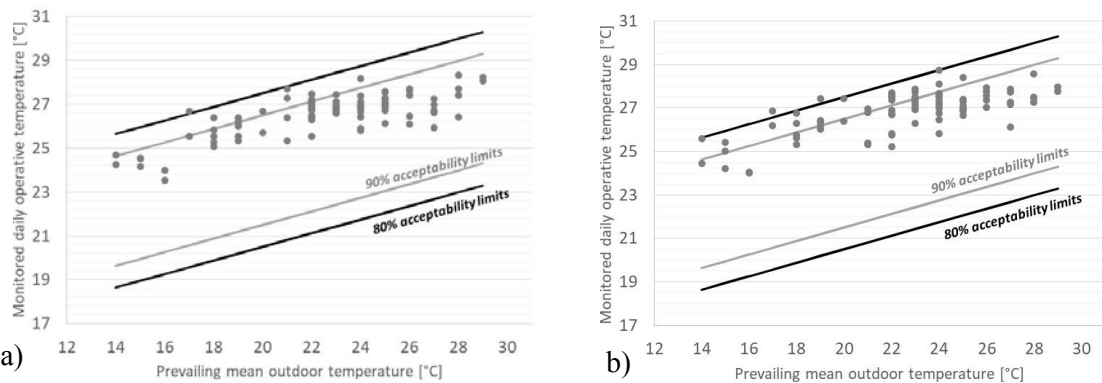


Figure 2. Indoor environment analysis - ASHRAE 55 standard. a) Rivoli Castle b) CCR.

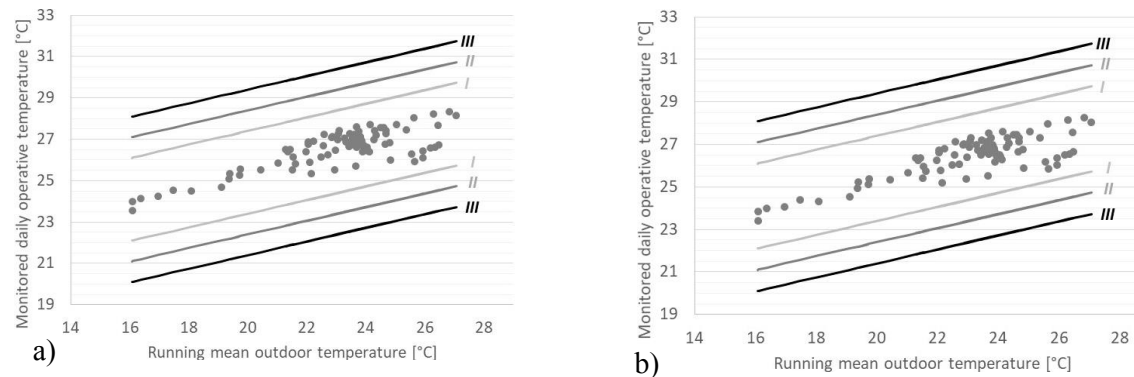


Figure 3. Indoor environment analysis - EN 15251. a) Rivoli Castle b) CCR.

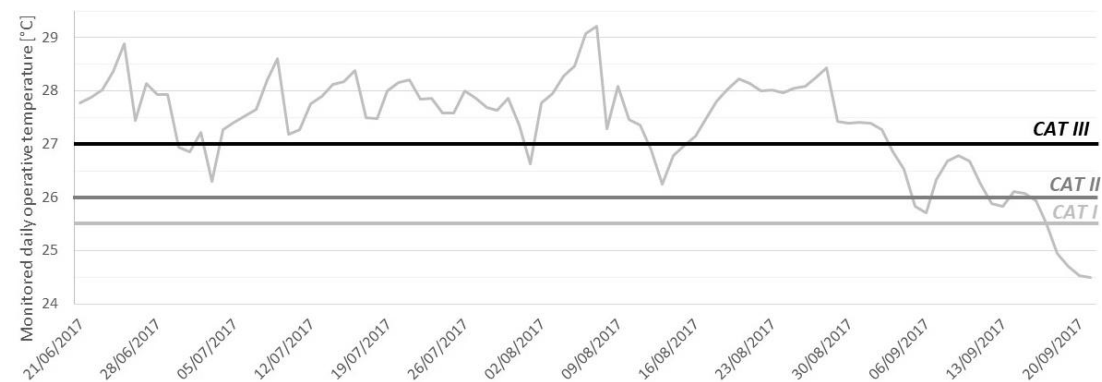


Figure 4. Indoor environment analysis (buildings with mechanical cooling) – EN 15251. CCR

Figure 4 presents CCR's indoor temperature profile evaluation with respect to the guidelines for mechanically cooled buildings according to EN 15251 standard. The figure shows that until the beginning of September the building does not comply even with Category III.

Figure 5 shows occupants' TSV and comfort evaluation. For Rivoli Castle the graph shows the combination of the two types of occupants considered. Referring to Figure 5.a, less than 70% of Rivoli Castle occupants voted between -1 (slightly cool) and +1 (slightly hot), with a quite homogeneous distribution of votes in the "warm" sensation part of the scale. About CCR occupants' TSV, percentages show a quite homogeneous distribution across all the scale, but only 57% of occupants voted between -1 and +1. Referring to Figure 5.b, two approaches could be used to describe results. The first is that only 19% of Rivoli castle and 14% of CCR occupants are comfortable (voted 1 or 2), the second is that 62% of Rivoli castle and 28% of CCR occupants are not uncomfortable (voted between 0 and 2). In the following, Table 1 describes Rivoli Castle's votes dividing office and exhibition part workers.

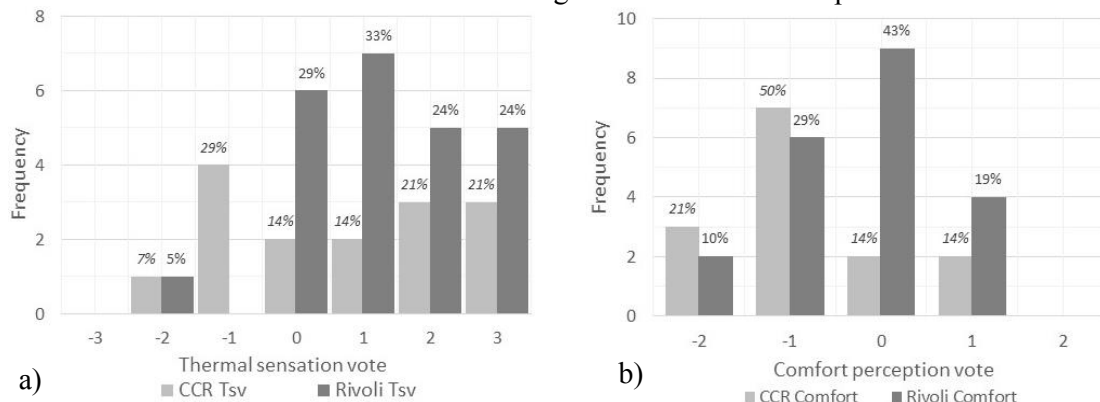


Figure 5. a) Thermal sensation vote and b) Comfort perception vote in the two case studies.

Table 1. Rivoli TSV and comfort votes (Comf) among office (Off.) and exhibition staff at Rivoli Castle.

Off.	Exb.	Off.	Exb.	Off.	Exb.
$-1 < \text{TSV} < +1$	$-1 < \text{TSV} < +1$	$\text{Comf} \geq 0$	$\text{Comf} \geq 0$	$\text{Comf} \geq 1$	$\text{Comf} \geq 1$
88%	46%	75%	54%	13%	23%

The answers related to the general attitudes towards historical buildings mentioned in method section showed that 95% of Rivoli Castle's and 93% of CCR's occupants like to work in a historical building. Moreover, 95% of Rivoli Castle's and 86% of CCR's occupants would choose to work in a historical building instead of a modern one.

DISCUSSIONS

The case studies investigated for this research offered the opportunity to have an idea of occupants' thermal comfort perception within the historical building in which they work. In general, occupants' evaluations were different from what it was expected looking at the indoor environment analyses performed according to the standards. Considering the CCR for example, referring to the analysis represented in Figure 4, it was expected that a large majority of people would have expressed a TSV between 1 and 3, but instead the percentage is about 56%, with also 30% of people feeling slightly cool. In this frame it is also curious that with a temperature set-point of 24°C the temperature profiles is quite stable around 27°C. A possibility could be that people felt too cold so they decided either to increase the set-point to 27°C or turn off the fan coils. Having this large opportunity of configuring their environment, a good comfort rate would be expected. Instead, only 28% of CCR occupants feel not uncomfortable (which is surprising in comparison to 62% of Rivoli Castle, which is passively

cooled). Two reasons could be identified: either people turn off fan coils because of punctual discomfort (e.g. disturbing position of the cool air flow) or they don't know how to properly use their control opportunities. It should be also noticed that a certain amount of occupants at CCR don't have access to windows. Further analyses should be done to see if this group of occupants have a specific pattern. Regarding Rivoli Castle, the two analyses represented in Figure 2 and 3 did not predicted very well occupants' evaluation of thermal perception and comfort. For these analyses two groups of occupants were considered. Among the groups, it should be noticed that in general workers of the exposition part were less satisfied with their environment. A possible explanation is that they are not allowed to personally open windows (they have to ask to a person in charge) so their control opportunities are lower.

CONCLUSIONS

This paper investigated the relation between human thermal comfort and indoor environment in two historical buildings in Italy during summer season. Results showed quite different results of occupants' evaluations from what it would have been expected in modern buildings with similar indoor conditions. Most occupants don't feel thermally comfortable in the two case studies. However, their thermal comfort seems not influencing their pleasure of working in a historical building. In conclusion, even if strategies to ameliorate indoor environmental conditions are necessary, it seems fundamental to educate users to adequately manage their working environment, especially when a cooling system is present.

ACKNOWLEDGEMENTS

Authors would like to thank the two institutions presented as case studies for sharing their data, actively participating to the research and being partner of the project.

REFERENCES

- Agbota, H. (2014). Anticipating the Unintended Consequences of the Decarbonisation of the Historic Built Environment in the UK. *The Historic Environment: Policy & Practice*, 5(2), 101–115.
- Anderson, W., Robinson, J., & Energy, B. P. T. and the C. for S. (2011). *Warmer Bath: A guide to improving the energy efficiency of traditional homes in the city of Bath*.
- Ansi/Ashrae. (2004). ANSI/ASHRAE 55:2004 Thermal Environmental Conditions for Human Occupancy. *Ashrae*, 2004, 30.
- Belpoliti, V., Bizzarri, G., Boarin, P., Calzolari, M., & Davoli, P. (2017). A parametric method to assess the energy performance of historical urban settlements. Evaluation of the current energy performance and simulation of retrofit strategies for an Italian case study. *Journal of Cultural Heritage*, 30, 155–167.
- Crockford, D. (2014). Sustaining Our Heritage: The Way Forward for Energy-Efficient Historic Housing Stock. *The Historic Environment: Policy & Practice*, 5(2), 196–209.
- EN. (2008). European Standard EN 15251, Criteria for the Indoor Environmental Including Thermal, Indoor Air Quality, Light and Noise. Brussels, Belgium.
- Filippi, M. (2015). Remarks on the green retrofitting of historic buildings in Italy. *Energy and Buildings*, 95, 15–22.
- Fouseki, K., & Cassar, M. (2014). Energy Efficiency in Heritage Buildings — Future Challenges and Research Needs. *The Historic Environment: Policy & Practice*, 5(2), 95–100.
- Martínez-Molina, A., Tort-Ausina, I., Cho, S., & Vivancos, J. L. (2016). Energy efficiency and thermal comfort in historic buildings: A review. *Renewable and Sustainable Energy Reviews*, 61, 70–85.

Towards human-centred intelligent envelopes: A framework for capturing the holistic effect of smart façades on occupant comfort and satisfaction

Alessandra Luna-Navarro^{1*}, Mauro Overend¹

¹University of Cambridge, Cambridge, UK

* *Corresponding email: al786@cam.ac.uk*

ABSTRACT

Intelligent buildings have the potential to simultaneously revolutionise the way humans live and reduce energy demand in buildings. In particular, the so-called, smart / dynamic / adaptive building envelope can selectively modulate the energy transfer between the building and its environment in response to transient outdoor conditions and indoor requirements, thereby providing a low-carbon means of achieving occupant satisfaction and well-being. However, the effect of smart façades on holistic occupant comfort and satisfaction with the environment is yet to be fully captured and quantified. This information is essential for evidence-based design and control of smart building envelopes. In this paper, the smart façade characteristics that underpin satisfactory environmental conditions are identified and metrics for their transient and holistic assessment are discussed. A methodology to capture the effect of smart façades on the holistic occupant comfort and satisfaction is then proposed together with its implementation into an early stage design tool. Finally, a ranking system is suggested to assess and compare alternative smart façade technologies according to their overall effect on user satisfaction and productivity for a UK climate.

KEYWORDS

occupant comfort, user satisfaction, intelligent, dynamic façades, human factors

INTRODUCTION

Although human-centred design in architecture is not a new concept, occupants are often dissatisfied with their environment (Frontczak and Wargocki 2011), regardless of the large amount of energy consumed to condition them (IEA, 2017). Novel façade technologies are often able to minimise energy consumption but they are also often the strongest drivers of occupant discomfort or dissatisfaction (Huizenga et al., 2006). Façades are the multi-sensorial skin of buildings, a boundary between indoors and outdoors, which is responsible for filtering light, heat, air and water vapour to maximise the health, well-being and productivity of occupants. Hence, façades have the potential to holistically affect occupants on different sensorial and psychological levels, such as aesthetic or personal control satisfaction, and, thus, actual occupant satisfaction requires a unified balance between all environmental comfort features. For instance, a strong dissatisfaction or “dissonance” (Clements-Croome, 2013) in any of these single comfort features would imply overall discomfort, even if greater satisfaction levels are achieved in the remaining features (Humphreys, 2005). Among all the multi-objective requirements of façades (Favoino et al., 2014), façades primary objective should be to sustain healthy and satisfactory environmental condition for occupants. A human-centred façades should be able to provide and regulate daylight and heat transfer, protecting occupants from overheating and preventing large heat losses, maintaining healthy levels of air quality. Potentially, human-centred façades should be “dynamic”, able to change their performance and characteristics according to the changing indoor and outdoor demands. Beyond this, a human-centred façade should have an “artificial intelligence” (Clements-

Croome, 2013) to allow them to be adaptive, able to capture real-time actual occupant demands and learn from past experiences to adapt and sustain optimal environmental conditions. The combination of current façade technologies with accurate control strategies and artificial intelligence provides unprecedented opportunities to create optimal human-centred façades. However, there is a need for new simulative, experimental and theoretical methodologies to capture actual occupant demand and response, and trigger responsive behaviours of intelligent façades that maximise occupant satisfaction. A fundamental distinction is made in this paper between two forms of environmental comfort: satisfaction and preference. In this research, environmental satisfaction is considered as the condition of mind where occupants express satisfaction with overall environment (Figure 1), including satisfaction with view and personal control or interaction strategies. Satisfaction is considered as the condition whereby the occupant might not be in a neutral condition, but expresses the willingness of remaining in the same condition. Environmental preference is instead defined as the desired environmental condition thriven by the occupant. This paper adopts the unified framework of personal comfort model, as defined by Kim et al. (2018), where the individual comfort response is predicted or assessed instead of the average response of a large population, and applies it to the assessment and control of dynamic façade technologies.

This paper attempts to provide initial methodological results of ongoing research at the University of Cambridge on novel methods for capturing the transient and holistic effect of intelligent façades on occupant satisfaction. A framework to capture the transient and holistic effect on personal occupant satisfaction is proposed and its future implementation in early design stage tools or ranking is discussed.

THEORETICAL BACKGROUND AND PROPOSED FRAMEWORK

The proposed framework endeavours to capture the overall holistic occupant response to and preferences for façade environmental effects. The façade effect on occupant holistic environmental satisfaction has been framed conceptually as shown in the diagram in **Error! Reference source not found.** Holistic satisfaction or preference considers the overall satisfaction with the visual, thermal, aesthetic, view, air quality, acoustic and interactive environment and their mutual interrelationships or conflicts (shown in Figure 1 as linking lines between each single comfort feature). In the diagram, the façade is considered as an interface that modulates the energy and mass flows (so called “primary inputs”) from outdoors and transfers them to indoors. Hence, alternative façades technologies have the potential to filter and modulate these flows in a different manner and according to their physical components or characteristics (such as type of glass, glass thickness, type of cavity, shading devices, coating characteristics, etc.), labelled in the framework as “Façade physical characteristics”. Consequently, the effect of a façade on occupants depends on the joint value in time of all façade properties, such as surface temperature or light transmitted, that directly affect the environment as result of the energy and mass flow across the façade. For the purposes of this framework, these façade properties will be named as “Façade comfort variables” and are considered to be the main drivers of the façade effect on occupant comfort. The façade comfort variables are directly related to “Façade physical characteristics”. However, alternative façade characteristics can result in the same comfort façade variables. For instance, different types for shading devices can produce the same value of light transmittance and different U-values could result in similar values of mean surface temperature. A literature review was conducted to identify the main façade comfort variables that affect occupant environmental satisfaction and the results are summarised in Table 1. The local environmental conditions in the vicinity of the occupant is affected by the transient value of the façade comfort properties and the non-façade input effect of environmental services or

other contextual conditions, such as space layout or furniture, that are identified in this framework as “Not-façade inputs”. The local environmental characteristics that affect occupant environmental satisfaction are labelled “Local comfort variables”. The final output of this process is the holistic response of the occupant to the local environmental conditions, and the façade comfort properties (which includes also the interaction strategies). This final output depends on the “human filter”, which is the ensemble

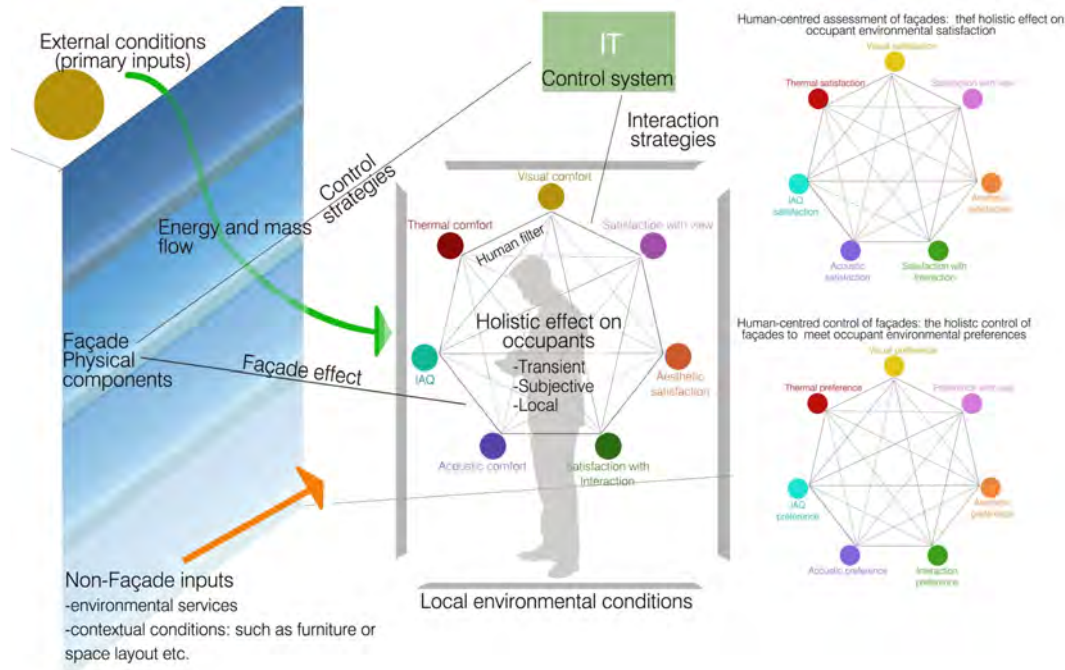


Figure 1 Diagram of the façade effect on occupants

of all individual and collective psychological features that affect human perception of the environment. Figure 2 illustrates the overall conceptual model described above. The variables and parameters of this framework are then grouped as follows: External conditions, Façade physical component, Façade comfort variables, Local comfort variables, Contextual variables, Human filter variables and Occupant response. The framework identifies all groups of variables involved in the problem of capturing the façade effect on occupant satisfaction. The research project endeavours to find a correlation between the façade comfort variables and occupant response through direct or indirect collection of occupant feedback. The correlations that will be investigated in the course of this research project are highlighted in green. As above mentioned, all these variables are time and location dependent. In order to identify a correlation between façade comfort variables and physical properties with occupant response (in terms of preferences or satisfaction) it is essential to monitor them locally and transiently, with particular attention to their rate, velocity and frequency of change and, simultaneously, gather high frequency feedback from occupants.

DISCUSSION, EXPECTED RESULTS AND FUTURE WORK

The proposed framework offers a methodology to gather valuable information on occupant levels of dissatisfaction or satisfaction with alternative façades technologies or controls. This could be useful for two purposes (Figure 3): 1) Assessing the façade quality and performance in terms of personal occupant environmental satisfaction and its effect; 2) Informing intelligent façades control strategies on actual personal occupant preferences and on the correlation between façade physical properties and comfort variable with occupant. The post-process of the data through machine learning techniques could also help to predict occupant

preferences and create personalized comfort models to be used for controlling jointly intelligent façades and BMS.

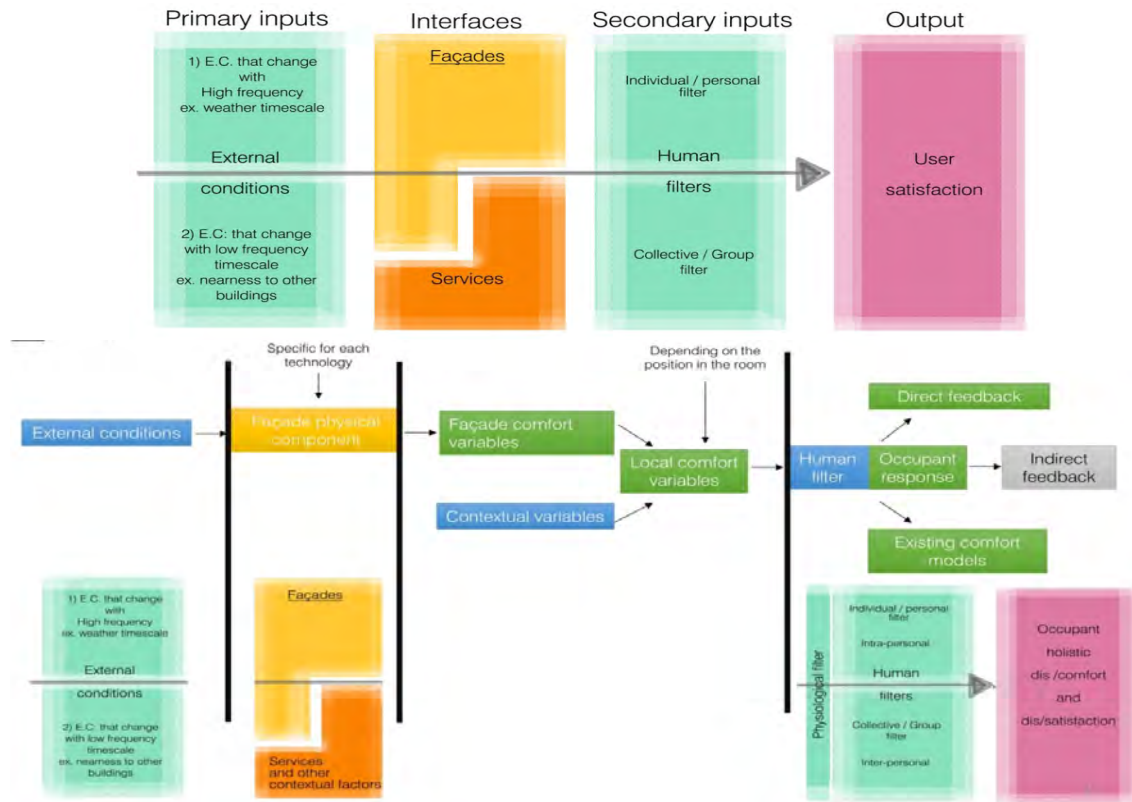


Figure 2 Concept map of the research problem: how to capture the façade effect on occupants

Table 1 Results from a literature review on the main façade comfort properties

Façade comfort variable	Unit of measure	Key reference
Surface temperature	°C	(Huizenga, 2006)
Draft: air velocity, air temperature, humidity	m/s, °C, gr/m ³	(Huizenga, 2006)
Solar radiation transmitted (Irradiance and direction)	W / m ² ; degree	(Huizenga, 2006)
Luminance	Cd/m ²	(Wienold & Christoffersen, 2006)
Light transmitted (intensity, direction, colour)	Lux; degree, ζ	(Nabil & Mardaljevic, 2006);
View extension		(Carmody et al., 2004)
View clarity		(Ko & Schiavon, 2017) (Konstantzos et al., 2015)
Sound absorbed and transmitted	dB	(Carmody et al., 2004)
User friendliness OR Ease of use	-	To be defined by follow-up research

The comfort and satisfaction assessment of façades, particularly intelligent façades, is challenging since there is a lack of holistic and transient metrics to identify occupant response. This is even more challenging considering the strong influence of occupant location on the

perceptible effect of façades and the differences in the type of sensorial perception affected with distances from the façade. The data gathered from this framework could be used to identify the main triggers of occupant satisfaction with façades and, potentially, the thresholds of occupant dissatisfaction and discomfort. More importantly, the data from façade comfort properties and occupant response would allow to assess the human-centred performance of alternative intelligent façade technologies. This would also provide the platform to compare façades and understand which façade and control strategy is more appropriate in different contexts, space layouts and building typology.

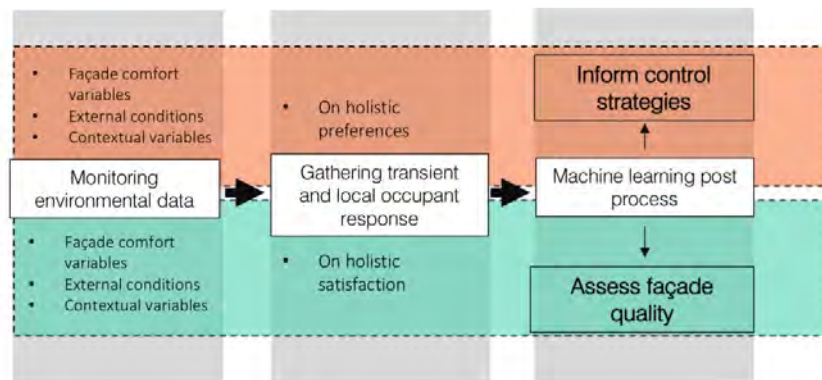


Figure 2 Diagram of the potential applications of the framework

Implementation of the new metrics in early design stage tools

A potential façade comfort scale is then proposed in Figure 3 to assess and measure the level of environmental personal comfort or, conversely, discomfort that a façade and its control strategy is associated with. Since façades need to be assessed transiently and locally, the scale in Figure 3 provides a holistic, local and transient assessment of occupant response for each category of holistic occupant satisfaction. Firstly, each category is assessed holistically considering the potential conflicts and inter-effects with other satisfaction categories, since occupants response is gathered experimentally and exposing them to the overall holistic effect of façades. Secondly, the scale indicates a value of occupant satisfaction regarding three different occupant positions with respect to the façades (1, 3 and 5 metres from the facade) in order to show the different effect of façades with distance on non-uniformity tendency. Lastly, façades are assessed according to 5 classes of occupant response and satisfaction. Each category is an indication of the percentage of time in a year when an occupant is satisfied with the dynamic performances of façades or, in other words, the proportion of time in which a façade has successfully interpreted occupant preferences and personal satisfaction criteria and has adapted with an appropriate frequency and velocity. This comfort assessment tool could average occupant response in time or weight a group of occupant responses according to specific design criteria or motivations (such as importance of task to be performed or health sensitivity). This draft comfort scale tool is highly dependent of the type of building, space layout and all the variables that affect environmental occupant responses, such as cultural and geographic context. Eventually, the scale has the potential to be implemented in an early-design stage tool to rank alternative façade technologies and inform early-design decision on façade physical components and control strategies.

CONCLUSIONS

This paper was conceived to frame the transient changes in façade properties, including frequency, level and velocity of change, to occupant holistic levels of comfort and satisfaction. The short-term experimental work will aim to validate the framework and

provide quantitative data to inform the draft comfort scale and gain a better understanding of how to implement the transient and holistic effect of façades in early-design stage tools.

ACKNOWLEDGEMENT

The authors acknowledge the valuable contribution and support from EPSRC, Ove Arup and Permasteelisa.

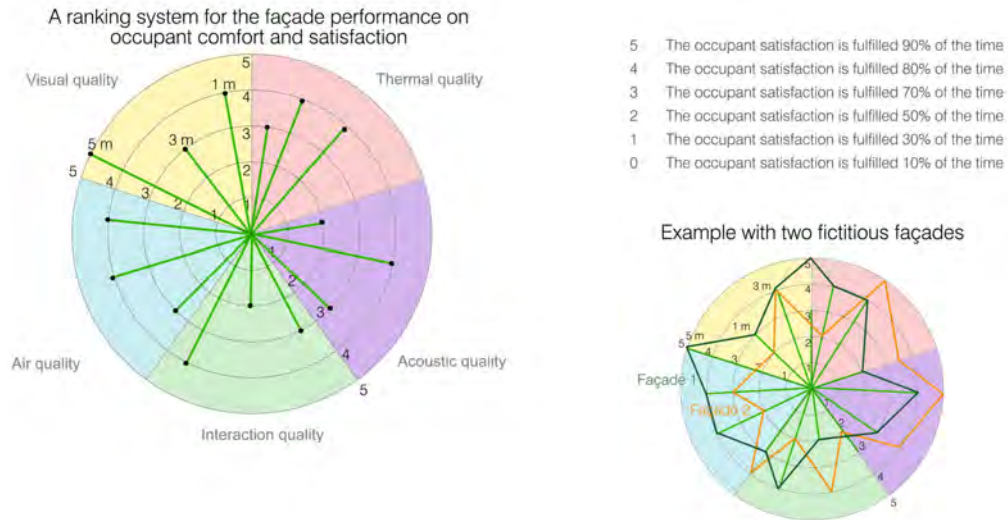


Figure 3 Draft structure of the comfort model tool

REFERENCES

- Carmody, J., Selkowitz, S., Lee, E., Arasteh, D., & Willmert, T. (2004). *Window systems for high performance buildings* (First). New York: Norton.
- Clements-Croome, D. (2013). *Intelligent buildings: An introduction. Intelligent Buildings: An Introduction* (Vol. 9780203737). <http://doi.org/10.4324/9780203737712>
- Favoino, F., Jin, Q., & Overend, M. (2014). Towards an ideal adaptive glazed façade for office buildings. In *Energy Procedia* (Vol. 62, pp. 289–298). <http://doi.org/10.1016/j.egypro.2014.12.390>
- Frontczak, M., & Wargocki, P. (2011). Literature survey on how different factors influence human comfort in indoor environments. *Building and Environment*, 46(4), 922–937. <http://doi.org/10.1016/j.buildenv.2010.10.021>
- Huizenga, C., Zhang, H., Mattelaer, P., Yu, T., Arens, E., & Lyons, P. (2006). *Window Performance for Human Thermal Comfort. Final report to the National Fenestration Rating Council.*
- Humphreys, M. A. (2005). Quantifying occupant comfort: Are combined indices of the indoor environment practicable? *Building Research and Information*, 33(4), 317–325. <http://doi.org/10.1080/09613210500161950>
- IEA. (2017). World Energy Outlook 2017. *International Energy Agency*. [http://doi.org/10.1016/0301-4215\(73\)90024-4](http://doi.org/10.1016/0301-4215(73)90024-4)
- Ko, W. H., & Schiavon, S. (2017). Balancing Thermal and Luminous Autonomy in the Assessment of Building Performance. In *Proceedings of Building Simulation Conference 2017*.
- Konstantzos, I., Chan, Y.-C., Seibold, J. C., Tzempelikos, A., Proctor, R. W., & Protzman, J. B. (2015). View clarity index: A new metric to evaluate clarity of view through window shades. *Building and Environment*, 90, 206–214. <http://doi.org/10.1016/j.buildenv.2015.04.005>
- Nabil, A., & Mardaljevic, J. (2006). Useful daylight illuminances: A replacement for daylight factors. *Energy and Buildings*, 38(7), 905–913. <http://doi.org/10.1016/j.enbuild.2006.03.013>
- Wienold, J., & Christoffersen, J. (2006). Evaluation methods and development of a new glare prediction model for daylight environments with the use of CCD cameras. *Energy and Buildings*, 38(7), 743–757. <http://doi.org/10.1016/j.enbuild.2006.03.017>

Energy Flexibility of Building Cluster – Part I: Occupancy Modelling

Rongling Li^{1*}, Andong Wang², Carsten Rode¹, Shi You³

¹Department of Civil Engineering, Technical University of Denmark, Denmark

²Department of Building Science, School of Architecture, Tsinghua University, China

³Department of Electrical Engineering, Technical University of Denmark, Denmark

*Corresponding email: liron@byg.dtu.dk

ABSTRACT

With the growing application of renewable energy, the stability of power systems can be seriously affected due to the fluctuations in the instantaneous generated power. As one of the potential solutions for this upcoming challenge, energy flexibility of buildings has received attention for research and technology development. Demand response and energy flexibility should be implemented at a large scale to have the accumulated energy flexibility to a magnitude, which can be meaningful for energy sectors. Studies have shown that the energy flexibility of a building is greatly influenced by both building physical characteristics and occupancy pattern of residents. To the best knowledge of authors, occupancy has not been considered in the study of building cluster. The aim of this paper is to present the modelling process of occupancy/vacancy of Danish households based on Danish Time Use Survey (DTUS) 2008/09 data. In this paper, we present a data-driven approach to generate occupancy/vacancy models for different types of household and for building cluster of different scales. As the result, vacancy profile and vacancy duration models are developed. The stochasticity of occupancy is also unveiled. The next step is to apply these models to quantify energy flexibility of building cluster and the uncertainty of energy flexibility due to the stochastic occupancy.

KEYWORDS

Occupancy; Stochastic; Building cluster; Energy demand flexibility

INTRODUCTION

The penetration of renewable energy resources is increasing rapidly. In EU countries, at least 20% of total energy demand must come from renewables by 2020 (EU, 2009). Denmark plans to be fossil-fuel free by 2050 (The Danish Government, 2013). High penetration of intermittent renewables will affect the stability of energy grid and energy flexibility in the grid will be more crucial. Buildings account for one third of total energy consumption in Denmark and most other developed countries, which amounts to considerable potential for activating flexible energy demand in buildings. In future smart cities, demand response and energy (demand) flexibility of buildings are likely to play a significant role.

Demand response and energy flexibility should be implemented at a large scale to have the accumulated energy flexibility to a magnitude, which can be meaningful for energy sectors. To the best knowledge of the authors, there are only a few publications about demand response or energy flexibility at building cluster level. Vigna et al. (2018) presented an overview of the concept of building cluster and its relevant concepts. A definition to Building Cluster was defined from the perspective of building and energy grid interaction. In this definition, the building cluster is an aggregation of buildings which can be managed by a common agent such as a utility company to exploit the energy flexibility of the building cluster.

Studies have shown that the energy flexibility of a building is greatly influenced by both building physical characteristics and occupancy pattern of residents (Masy et al., 2015), (Li et al., 2017). A review of large scale demand response estimation (Goy and Finn 2015) conducted in 2015 concluded that studies by then commonly oversimplified building models without considering different building types nor various building characteristics such as thermal characteristics and occupants behavior. There are only a few studies done after 2015 (Li et al., 2016), (Ma et al., 2016), (Georges et al., 2017), but none of the studies included the influence from occupancy and occupant behavior. The lack of data support and multidisciplinary knowledge together with the requirement on computational efficiency are among the main reasons for achieving better investigations.

In this study, we aim to model the stochastic occupancy to quantify its influence on energy flexibility of building cluster with different scales of occupants and quantify the uncertainty of flexibility. The value of the uncertainty quantification is in the planning of energy services.

METHODS

Occupancy models are developed based on data from Danish Time Use Survey (DTUS) 2008/09 (Bonke and Fallesen, 2010). The data consists of 9640 individuals and 4679 households. Individuals' daily activities were logged in two diaries, one for a weekday and another for a weekend day with 10 min time interval starting at 4:00 and ending at 3:50 the next day (Bonke and Fallesen, 2010), (Barthelmes et al., 2018). In this study, only weekday is considered, as on weekend vacancy time is much shorter for residential buildings and the pressure on the energy grids could be less in comparison with weekdays.

Based on the Statistics Denmark (2017), 84% of the households living in apartment buildings consist of no more than three members. The data of household with one to three persons from the DTUS are used in this study. The data consists of 1641 one-person households, 1980 two-person households and 448 three-person households, which is generated from the same data source presented in (Barthelmes et al., 2018).

Occupancy modelling includes three steps: 1) data resampling, 2) occupancy/vacancy profiling and 3) occupancy/vacancy duration estimation.

1) Occupancy data resampling

We resampled the data by randomly divide N households into X samples with each sample contains Y (**n, 2n, 3n ...**) households using Bootstrapping method. Limited by the total number of each type of household, we predefined n=100 for one-person household, n=50 for two-person household and n=33 for three-person household. For example, in the case of 1641 one-person households, the data processing steps are as follows.

- a) Sample size: 100 households.
- b) Randomly divide 1641 households into 16 groups with each group contains 100 households.
- c) Repeat the above process for several times (In this study, 10 times).
- d) Obtain 160 samples.
- e) Change sample size to 200, 300, 400 ...

2) Vacancy profiling based on Normal Distribution Probability

Each data sample is a 3D matrix as shown in Equation (1) with 1 indicates occupancy and 0 indicates vacancy.

$$OccupancyData(\text{household serial number}, \text{timeline}, \text{sample serial number}) = \begin{pmatrix} \text{house}_1 & \begin{matrix} s_1^1 & \dots & s_1^{144} \\ \vdots & \ddots & \vdots \\ s_n^1 & \dots & s_n^{144} \end{matrix} \end{pmatrix} (s_i^t = 1 \text{ or } 0), \text{sample serial number} \quad (1)$$

Taking the case of the 160 samples of 100 one-person households as an example to explain the processing in detail. The size of the 3D matrix is 100×144×160 (households: 100, the length of timeline: 144, samples: 160). As the time interval is 10 min, there are thus 144 states for one day. For every state, vacancy percentage of 100 households are calculated. As for every state, there are 160 different samples; there are thus 160 vacancy percentages. A Normality Test (95% confidence) is carried out on these 160 vacancy percentages. The result can be expressed in equation (2).

$$VacancyPercentage_t \sim N(\mu, \sigma^2) \quad (2)$$

Where μ : mean, also the mathematical expectation; $\mu + 1.96\sigma$: upper limit of 95% confidence interval, $\mu - 1.96\sigma$: lower limit of 95% confidence interval.

The result of probability distribution of vacancy is a 3×144 matrix as shown in Equation (3).

$$Probability\ distribution\ of\ vacancy = \begin{matrix} \mu \\ \mu + 1.96\sigma \\ \mu - 1.96\sigma \end{matrix} \begin{matrix} \text{timeline} \\ \begin{bmatrix} \mu_1 & \dots & \mu_{144} \\ \vdots & \ddots & \vdots \\ (\mu - 1.96\sigma)_1 & \dots & (\mu - 1.96\sigma)_{144} \end{bmatrix} \end{matrix} \quad (3)$$

The above data processing is applied to all three household types. This results with probability distribution of vacancy matrices for every sample size and every type of household.

To assign the above probability distribution of vacancy to Danish households, we used the data from Statistics Denmark (2017). Among the households living in apartment buildings, 38% are one-person household, 33.7% are two-person household and 11.9% are three-person household. Only 16% of Danish households living in apartment buildings consist of more than three residents. Therefore, households of four people and above are not included in this study. Taking these three household sizes as a whole, one-person household accounts for 45.5%, two-person household accounts for 40.3% and three-person household accounts for 14.2%. Vacancy matrices for every sample size and every type of household are aggregated according to these three percentages as shown in Equation (4).

$$Probability\ distribution\ of\ vacancy_{aggregated} = [45.5\% \quad 40.3\% \quad 14.2\%] \begin{bmatrix} Probability\ distribution\ of\ vacancy_{1\ person} \\ Probability\ distribution\ of\ vacancy_{2\ persons} \\ Probability\ distribution\ of\ vacancy_{3\ persons} \end{bmatrix} \quad (4)$$

3) Vacancy duration based on Kaplan-Meier estimator

Survival analysis (Kaplan-Meier estimator) is applied to estimate vacancy duration, which is the time duration occupants are away from home. The Kaplan-Meier estimator, also known as the product limit estimator, is a non-parametric statistic to compute probabilities of occurrence of an event from a certain moment (Goel et al. 2010). The estimator is given by:

$$S(t) = \prod_{i:t_i} \left(\frac{n_i - d_i}{n_i} \right) \quad (5)$$

Where n_i is the number of activates on-going at time t_i and d_i is the number of actions ended. The followings are the steps of survival analysis.

- a) The initial matrix (InitialOccupancyData) shown in Equation (6) is used for survival analysis.

$$\begin{aligned}
 & \text{InitialOccupancyData}(\text{household serial number}, \text{timeline}) \\
 & = \begin{matrix} \text{house}_1 \\ \vdots \\ \text{house}_n \end{matrix} \begin{matrix} \text{timeline} \\ \left[\begin{matrix} s_1^1 & \cdots & s_1^{144} \\ \vdots & \ddots & \vdots \\ s_n^1 & \cdots & s_n^{144} \end{matrix} \right] \end{matrix} (s_i^t = 1 \text{ or } 0) \quad (6)
 \end{aligned}$$

b) There are 144 observation states in the timeline. For each state, all the vacant households is identified and then the vacancy duration of these households is calculate from this moment to the future. Then the matrix of SurvivalTimeLength is generated as shown in Equation (7).

$$\text{SurvivalTimeLength} = \begin{matrix} \text{house}_1 \\ \vdots \\ \text{house}_n \end{matrix} \begin{matrix} \text{timeline} \\ \left[\begin{matrix} d_1^1 & \cdots & d_1^{144} \\ \vdots & \ddots & \vdots \\ d_n^1 & \cdots & d_n^{144} \end{matrix} \right] \end{matrix} \quad (7)$$

Where d_i^t is the vacancy duration at time t of house_i , $d = 0$ means occupancy.

c) For every state (1~144), Kaplan-Meier Estimator is used to estimate the probability of vacancy duration as shown in Equation (8).

$$(\text{timelen}_t, P_t) = \text{Kaplan} - \text{Meier} \left(\begin{matrix} \text{house}_1 \\ \vdots \\ \text{house}_n \end{matrix} \begin{matrix} t \\ \left[\begin{matrix} d_1^t \\ \vdots \\ d_n^t \end{matrix} \right] \end{matrix} \right) \quad (8)$$

RESULTS

With the aggregation of the probability distribution of vacancy of different types of household, vacancy matrix becomes a 3D matrix where the first two dimensions are shown in Equation (3) and the third dimension is the sample size. This vacancy matrix is generated for cluster of households consisting of one person, two persons and three persons. Fig. 1 shows three different sample sizes of the matrix. With number of residents and number of households specified, sample size of occupancy model is determined and thus the occupancy model can be chosen. In the timeline of one day, there are 144 states with 10-minute interval between each state. For each state, the mathematical expectation, $\mu + 1.96\sigma$ and $\mu - 1.96\sigma$ of vacancy percentage are determined as it is shown in Fig. 1. For example, for a building cluster with 1000 residents and 643 households, the right diagram in Fig. 1 is the vacancy profile can be used.

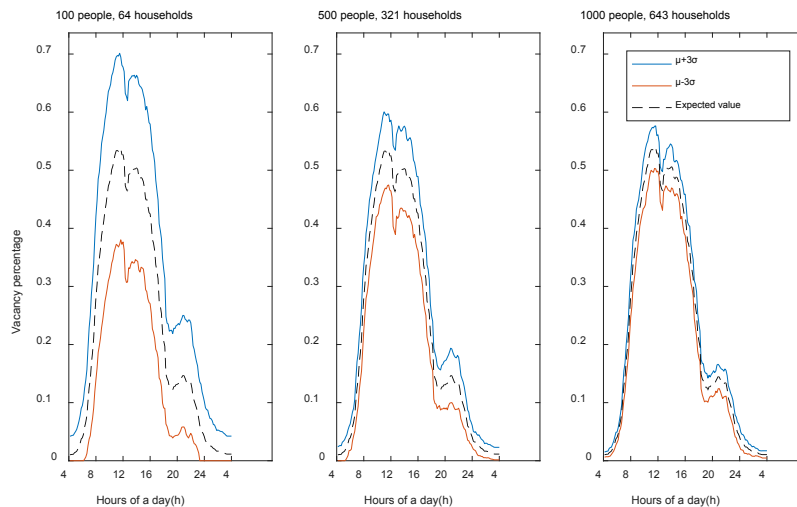


Fig. 1 Vacancy profile of clusters with different number of people and households

As it is shown in Fig.1, expected value of vacancy percentage does not change with the number of residents. However, σ becomes smaller with more residents aggregated. In other words, uncertainty of vacant percentage decreases with the size of residents increases.

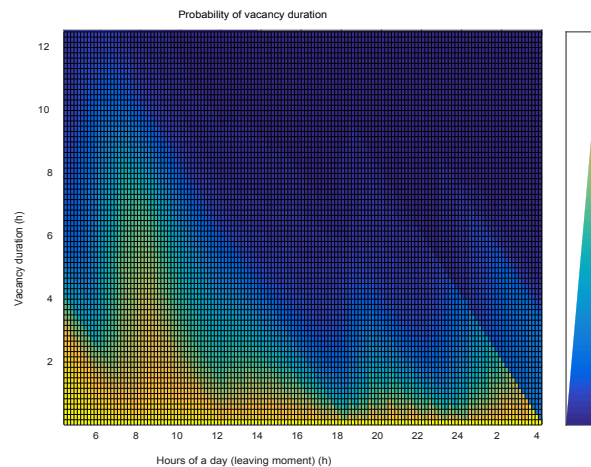


Fig. 2 Survival analysis of vacancy for all 144 states.

The probability of vacancy duration is shown in Fig. 2. It is the aggregation of results from all 144 states. This figure shows the probability a house is vacant from any states onwards. For example, if a house is unoccupied at 8:00 (see x-axis), the probability it is still unoccupied after two hours (see y-axis) is around 80% (color bar) and after six hours is around 60%.

DISCUSSIONS

In this study, using a data-driving approach, statistical occupancy models were developed for the investigation of the uncertainty of energy flexibility due to the stochastic nature of occupancy using TUS data. Some existing studies showed that TUS data was a valuable resource by validating their TUS-based approaches against field measurements. Fischer et al. (2015) modelled household electricity load profiles based on German TUS. The models were validated against measurement data from 430 households with good accuracy. Widén et al. (2009) modelled household electricity load profile based on Swedish TUS data. The profile was validated with electricity measurements in a few households. It revealed that the models captured important features of the measured data. Although there is no measured data from Danish households available for the authors now, model validation is planned for further work. Nevertheless, the models developed in our study can be a tool for the simulation of energy flexibility of buildings for district energy planning under the background of mass application of renewable energy in the future. In addition, this method can be used in other geographical areas if TUS data of these areas are available. The vacancy percentage, vacancy duration, household size, etc. might be different due to different geographical and demographical conditions. This method can also be used to capture seasonal differences in vacancy using TUS data collected during specific seasons, such as heating/winter season.

CONCLUSIONS

In this paper, we presented a data-driven approach to generate occupancy/vacancy models for different types of household and for different scales of building cluster using Danish Time User Survey 2008/09 data. Using this approach, vacancy profile and vacancy duration of any building cluster can be generated. The stochasticity of occupancy is also unveiled. The next step is to apply these models in the quantification of energy flexibility of building cluster and the uncertainty of the quantification due to the stochastic occupancy. The value of the uncertainty

quantification is in the planning of energy services. A typical case is that a grid operator will have information on the reliability of deploying a certain amount of households and buildings for using demand flexibility to balance the grid.

ACKNOWLEDGEMENT

This study was made possible with the financial support of two Danish pilot projects: EnergyLab Nordhavn: New Urban Energy Infrastructures and CITIES: Centre for IT-Intelligent Energy Systems in cities. This work partially receives the support from Tsinghua University Initiative Scientific Research Program. The authors would also like to acknowledge IEA EBC Annex67 – Energy Flexible Buildings for providing excellent research networking.

REFERENCES

- EU, 2009. Directive 2009/28/EC of the European Parliament and of the Council of 23 April 2009 on the Promotion of the Use of Energy from Renewable Sources and Amending and Subsequently Repealing Directives 2001/77/EC and 2003/30/EC. <http://eur.europa.eu/eli/dir/2009/28/oj>.
- The Danish Government. 2013. The Danish Climate Policy Plan – Towards a Low Carbon Society.
- I. Vigna, R. Perneti, W. Pasut, and R. Lollini. 2018. New Domain for Promoting Energy Efficiency: Energy Flexible Building Cluster. *Sustainable Cities and Society* 38: 526–33.
- R. Li, F. Wei, Y. Zhao, and W. Zeiler. 2017. Implementing Occupant Behaviour in the Simulation of Building Energy Performance and Energy Flexibility : Development of Co-Simulation Framework and Case Study. *Proceedings of Building Simulation 2017*: 1339–46.
- G. Masy, E. Georges, C. Verhelst, V. Lemort & P. André. 2015. Smart grid energy flexible buildings through the use of heat pumps and building thermal mass as energy storage in the Belgian context. *Science and Technology for the Built Environment* 21: 800-811
- S. Goy, D. Finn. 2015. Estimating Demand Response Potential in Building Clusters. *Energy Procedia* 78.
- X. Li, J. Wen, and A. Malkawi. 2016. An Operation Optimization and Decision Framework for a Building Cluster with Distributed Energy Systems. *Applied Energy* 178: 98–109.
- E. Georges, et al. 2017. Residential Heat Pump as Flexible Load for Direct Control Service with Parametrized Duration and Rebound Effect. *Applied Energy* 187: 140–53.
- L. Ma, N. Liu, L. Wang, J. Zhang, J. Lei, Z. Zeng, C. Wang, M. Cheng. 2016. Multi-Party Energy Management for Smart Building Cluster with PV Systems Using Automatic Demand Response. *Energy and Buildings* 121: 11–21.
- J. Bonke and P. Fallesen. 2010. The impact of incentives and interview methods on response quantity and quality in diary- and booklet-based surveys. *Surv. Res. Methods*, vol. 4, no. 2, pp. 91–101.
- V. Barthelmes, R. Li, R. K. Andersen, W. Bahnfleth, S. P. Corgnati, and C. Rode. 2018 Profiling Occupant Behaviour in Danish Dwellings using Time Use Survey. Submitted to *Energy and Buildings*, under review.
- Statistics Denmark, 2017. <http://www.statistikbanken.dk/statbank5a/default.asp?w=1280>
- M. Goel, K. Pardeep and J. Kishore. 2010. Understanding survival analysis: Kaplan-Meier estimate. *International journal of Ayurveda research* 1, no. 4: 274.
- D. Fischer, A. Härtl, and B. Wille-Hausmann. 2015. Model for electric load profiles with high time resolution for German households. *Energy and Buildings* 92:170–179.
- J. Widén, M. Lundh, I. Vassileva, E. Dahlquist, K. Ellegård, and E. Wäckelgård. 2009. Constructing load profiles for household electricity and hot water from time-use data-Modelling approach and validation. *Energy and Buildings* 7:753–768.

HOUSE: Building energy efficiency understanding through an enabled boundary object

Deborah Adkins^{1,*} and Peter R.N. Childs¹

¹Imperial College London, United Kingdom

*Corresponding email: drdadkins@gmail.com

ABSTRACT

We report the results of an empirical study on an enabled application's ability to act as a boundary object and build understanding of energy efficiency solutions. Combining digital and tangible technology with radio-frequency identification (RFID) tags, we have created an interactive, digitally enabled device and application called HOUSE (Home User and Stakeholder Environment). The HOUSE tool and application have been designed and developed to support interaction and collaboration in the exploration of domestic energy efficiency solutions.

HOUSE allows users to associate information with physical representations, and to explore this information through manipulation of enabled objects. The interactive application consists of a 24:1 scale representation of an archetypal UK home and thirteen model energy efficiency interventions integrated with a digital application. Each energy efficiency intervention is enabled with RFID tagging and detection, to allow participants to physically interact with the HOUSE application. The app detects when a model energy efficiency intervention is placed in the model HOUSE. Participants then receive real-time feedback on their energy efficiency selection and the implication of their retrofit decisions.

We explore the role of HOUSE acting as a boundary object, in facilitating the transfer of knowledge across domains. The application was evaluated in academic non-expert and industry (expert) stakeholder workshops. Results showed there is a self-reported increase in collaboration and consensus amongst non-experts (Group A) using the HOUSE interactive application. There is also a self-reported difference in the decision-making process surrounding retrofit selection for experts (Group D) using the HOUSE interactive application. Moreover, there is evidence from experts to conclude that the HOUSE can assist in transmitting findings in meaningful ways to non-experts in the field.

KEYWORDS Boundary Object, Energy Efficiency, Exploratory Study, Tangible User Interface.

INTRODUCTION

The decision-making process surrounding domestic energy use and retrofit is complex, dynamic, multidimensional and involves multiple stakeholders and information asymmetry. However how to enable the transfer of knowledge between stakeholders has received little attention. As a society, we are facing complex challenges such as climate change, energy transition and adaptation that require large numbers of multidisciplinary stakeholders to interact and quickly navigate elaborate data sets. Stakeholders need to rapidly access a wide range of scenarios, build understanding and decide on an appropriate set of actions.

New technologies have made it possible to create new ways for stakeholders to interact. Innovations allow us to enable objects with digital information and allow us to interact with this information through tactile interaction with radio-frequency identification (RFID) enabled

(tangible) media. Enabled media can be combined with technologies to provide instantaneous feedback on a wide range of different scenarios.

Despite wide-ranging policies for encouraging and supporting energy efficiency, there remains a persistent gap between the technological and economic potential and actual market behaviour (Jaffe & Stavins 1994). Two of the most crucial retrofit decision-making barriers identified are firstly the 'cognitive burden' regarding the difficulty of taking complex and permanent decisions (Phillips 2012) and secondly the 'hassle factor', i.e. the anticipation of the inconvenience provided by the retrofit operations (Roy et al. 2007). It is widely accepted that interventions to reduce the energy efficiency gap need to address these and other behavioural factors (Whitmarsh 2009). This article introduces a combined physical and digital application to assist stakeholders' decision-making process in selecting retrofit technologies. To do this, we have developed the HOUSE (HOMe User and Stakeholder Environment) tool which provides a tangible representation of an average UK home and allows stakeholders to interact with energy efficiency interventions.

TANGIBLE BOUNDARY OBJECTS

The exchanges of knowledge between organisations and stakeholders throughout the retrofit process take place along multidisciplinary boundaries between specialist and non-specialist, as shown in Figure 1a. A boundary object can link retrofit stakeholders together via 'collaboration on a common task' (Star & Griesemer 1989).

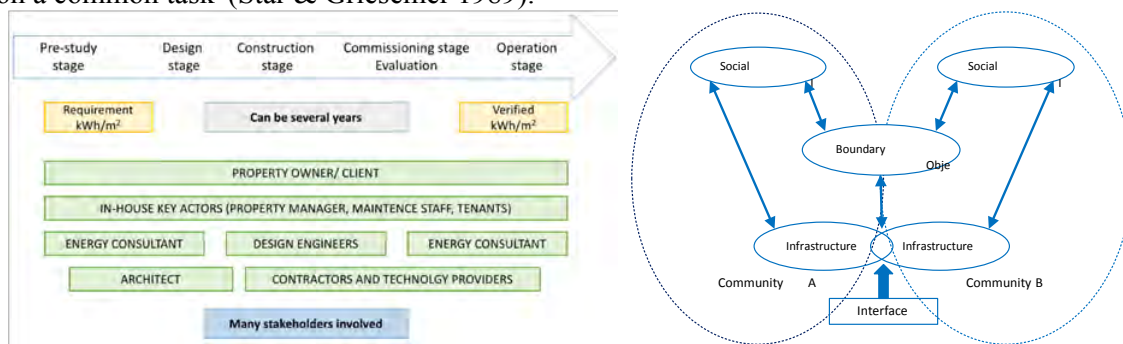


Figure 1a. (Left) Some of the stakeholders throughout the retrofit process adapted from Moseley (2016) Figure 1b. (Right) Representation of a boundary object.

Boundary objects (Figure 1b) are mediating artefacts that have interpretive flexibility and can be a means of achieving collaboration and promoting the sharing of knowledge among diverse groups (Sapsed & Salter 2004). The practice of reducing and managing domestic energy consumption, as well as upgrading or retrofitting a house, incorporates numerous objects (interventions) including requirements (specifications) and user behaviour methodologies. By combining elements with an architectural model, we seek to bridge and overcome knowledge boundaries between those with technical knowledge (e.g. an engineer) and others with domainspecific knowledge (e.g. home users with knowledge of their individual needs and requirements) (Tiwana & Mclean 2005).

Ishii & Ullmer (1997) define a tangible user interface (TUI), as a device that "augments the real physical world by coupling digital information to everyday physical objects and environments." Fishkin's (2004) taxonomy for tangible interfaces defined them as a device which allows "the user to use their hands to manipulate some physical object(s) via physical gestures, and a computer detects this and alters its state and gives feedback accordingly." Some researchers have demonstrated the advantages of TUIs, regarding a more natural, intuitive, user-friendly experience with the potential to promote stronger and long-lasting engagement with

stakeholders. In this paper, we define an enabled Boundary Object (BO) as a TUI realised as a boundary object.

HOUSE: A NEW MEDIUM TO EXPLORE ENERGY EFFICIENCY

One of the most common UK residential typologies is the semi-detached house built in the 1930's. There are currently 1,731,000 semi-detached dwellings in England built between 1919 and 1944, equating to approximately 1 in 6 UK homes. Because of its prevalence, the 1930's semi-detached house can be defined as "the average UK dwelling" (Beizaee et al. 2015). We used a plan of a 1930's house situated in London as a reference for the development of the scale model. The floor plan of the house and the elements relevant to energy efficiency interventions such as suspended floor and cavity walls were integrated into the scale model. The final model of the case study dwelling is shown in Figure 3. Table 1 provides a list of the interventions considered in the study. The interventions were exemplified as physical objects that could be manipulated by users and added and removed from the model to represent the process of retrofitting.

Table 1. Energy efficiency interventions

1	Internal wall insulation	7	Draught stripping
2	Cavity wall insulation	8	Low energy lights
3	External wall insulation	9	Replacement gas boiler
4	Floor Insulation	10	Upgrading heating controls
5	Loft insulation	11	1 kW Solar Photovoltaic Panels
6	Replacement windows and doors	12	3 kW Solar Photovoltaic Panels
		13	Solar hot water heating

A digital application, developed in Objective-C in Xcode 8.2 and displayed on an iPad, was designed to provide a visualisation of the model HOUSE status. When an intervention was applied to the model (input), the digital application senses this input event and alters its state. The digital application provides feedback (output event) to show the impact of the addition or removal of an intervention. The digital application displays a series of properties such as total installation cost, annual savings on bills and annual CO₂ savings based on the interventions currently added to the property. The costs and savings were calculated based on straightforward calculations and were therefore provided instantaneously on the iPad. The final HOUSE tool, as shown in Figure 3 was an interactive tool of enabled interventions allowing customers to 'play' with a representation of their home.



Figure 3 The Model of the case study dwelling

METHOD

This exploratory study aimed to understand the contribution of the HOUSE application. To design the HOUSE tool a mix of literature review and stakeholder input through interviews and discussions were used to develop the initial HOUSE prototype. In the descriptive study, firstly, a non-expert (academic) workshop was held to provide an evaluation of the tool and the workshop design. Secondly, an expert (industrial) workshop was held to provide an assessment of the prototype and to gather suggestions for improvements. An identical design exercise took place in each workshop; participants were split into three groups and using three different tool sets (c.f. Table 2) were asked to address the same design brief. The design exercise was designed to compare the effect of the various tool sets on the behaviour (e.g. interactions, collaboration, discussions, manipulations, solutions and intervention selections) of participants.

Table 2. Schematic setup of the tool sets provided to each workshop group

Group	HOUSE model	Digital Application	Pens and Paper
A non-expert	Yes	Yes	Yes
B non-expert	No	Yes	Yes
C non-expert	No	No	Yes
D expert	Yes	Yes	Yes
E expert	No	Yes	Yes
F expert	No	No	Yes

RESULTS

The initial academic (non-expert) workshop was conducted with 12 non-specialists, during a one-hour session, to evaluate the functionality of the device and its impact on the group. The non-specialists were split into three groups A, B & C with four participants in each group. The groups were asked on a Likert scale if they felt the tool set provided (Table 2) increased collaboration and improved consensus. To compare participants' subjective experience while using the three different tool sets, we conducted several two-way analyses of variance (ANOVA) with the format of presenting tool sets as independent variables. The ANOVA (Table 3) was significant for collaboration (question 1): $F(2, 9) = 13.286, p < .05$ ($p = .002$) and consensus (question 2): $F(2, 9) = 6.643, p < .05$ ($p = .017$). Thus, there is evidence to reject the null hypothesis and conclude there is a self-reported increase in the collaboration and consensus for Group A conducting the same task using the HOUSE interactive application tool set. [Table 3. Academic workshop one-way between groups ANOVA for each domain and group](#)

ANOVA		Sum of squares	df	Mean Square	F	Sig.
1) Do you feel HOUSE provided increased collaboration amongst your group?	Between Groups	5.167	2	2.583	13.286 ^a	.002 ^b
	Within Groups	1.750	9	.194		
	Total	6.917	11			
2) Do you feel HOUSE provided improved consensus?	Between Groups	5.167	2	2.583	6.643 ^a	.017 ^b
	Within Groups	3.500	9	.389		
	Total	8.667	11			

^aCritical Value 4.26, ^bStatistical significance testing ($p > .05$).

The industry (expert) workshop was conducted with 18 specialists, during a longer three-hour session, to further evaluate the functionality of the device and its impact on decision making. The specialists were split into three groups D, E & F with six participants in each group. During this workshop participants were given a longer questionnaire and were asked additional questions on a Likert scale to investigate if they felt the tool set provided improved the decisionmaking process and if they thought the tool set provided could assist in transmitting findings.

The ANOVA (Table 4) was significant for decision-making (question 3): $F(2, 15) = 4.239$ $p = .035$ and transmitting findings to non-experts in the field (question 4): $F(2, 15) = 5.648$ $p = .015$. Thus, there is evidence to reject the null hypothesis for question 3 and conclude there is a self-reported difference in the decision-making process surrounding retrofit selection for Group A using the HOUSE. There is also evidence to reject the null hypothesis for question 4 and conclude there is self-reported evidence that the HOUSE can assist in transmitting findings in meaningful ways to those (non-experts in the field). However, the actual difference in mean score between groups was quite small based on Cohen's (1992) conventions for interpreting effect size.

Table 4. Industry workshop one-way between groups ANOVA for each domain and group

ANOVA		Sum of squares	df	Mean Square	F	Sig.
1) Do you feel HOUSE provided increased collaboration amongst your group?	Between Groups	.778	2	.389	.530	.599
	Within Groups	11.00	15	.733		
	Total	11.778	17			
2) Do you feel HOUSE provided improved consensus?	Between Groups	2.778	2	1.389	3.378	.061
	Within Groups	6.167	15	.411		
	Total	8.944	17			
3) I feel HOUSE improved the decisionmaking process surrounding retrofit selection.	Between Groups	4.333	2	2.167	4.239 ^a	.035 ^b
	Within Groups	7.667	15	.511		
	Total	12.000	17			
4) I feel HOUSE could assist in transmitting findings in meaningful ways to non-experts in the field.	Between Groups	6.778	2	3.389	5.648 ^a	.015 ^b
	Within Groups	9.000	15	.600		
	Total	15.778	17			

^aCritical Value 3.68, ^bStatistical significance testing ($p > 0.05$).

DISCUSSION

As boundaries pose difficulties in knowledge flows, we aimed to reduce the influence of boundaries on multi-stakeholder and multi-domain collaboration by finding a way to communicate across them. There is a need for a comprehensive but easy to use tool to allow interaction amongst stakeholders during retrofit selection. Current retrofit selection tools are complex methodologies and software tools, requiring extensive training and guidance. These tools do not utilise tangible representations or allow for stakeholder interaction.

The evidence from the non-expert workshop suggests that participants felt that the HOUSE tool provided increased collaboration amongst the group of participants and improved consensus. The evidence from the industry workshop suggests that the participants perceived that the HOUSE tool improved the decision-making process surrounding retrofit selection and that the HOUSE tool could assist in transmitting findings in meaningful ways to non-experts in the field. The HOUSE concept was found to have the potential to act as a transdisciplinary boundary object, engaging non-scientists in shaping and achieving societal goals.

It is interesting to note there was no significant self-reported increase in the collaboration and consensus amongst the experts (Group D) conducting the same task using the HOUSE interactive application tool set. This lack of significance may be as a result of the group's dynamic and requires further exploration. It would have been ideal to have asked the first workshop groups the longer questionnaire, to investigate if they felt the tool set provided improved the decision-making process surrounding retrofit selection and if they thought it could be used to assist in transmitting findings in meaningful ways to non-experts in the field.

CONCLUSION

This article has introduced the HOUSE tangible application. Although this presents a preliminary study, the workshops yielded important insights and show that a tool such as HOUSE can support collaboration, consensus, improve decision making and transmit findings in meaningful ways. The results of the stakeholder workshops also demonstrate that the HOUSE tool has the potential for further development and implementation as part of a user-centred engagement process. Because participants were taking part in a theoretical design exercise rather than real-world selection and implementation – there are some limitations to this study although the initial results are promising. The tool should adapt to answer the questions and priorities that emerged from stakeholder engagement. The authors agree with the proposition given by Underkoffler & Ishii (1999) when outlining areas for future work “the proposition of giving additional meaning and animate life to ordinary inert objects is a cognitively powerful and intriguing one.”

ACKNOWLEDGEMENT

We gratefully acknowledge funding from the Engineering and Physical Sciences Research Council (EPSRC) for the Design the Future ‘HOUSE’ Grant no EP/N009835/1. We would like to thank Dr Shayan Sharifi and Dr Weston Baxter for acting as workshop facilitators. We are also grateful to all the workshop participants for their input and insight.

REFERENCES

- Beizaee A. et al. 2015. Measuring the potential of zonal space heating controls to reduce energy use in UK homes. *Energy and Buildings*, 92, pp. 29–44.
- Cohen J. 1992. A power primer. *Psychological Bulletin*, 112(1), p.155.
- Fishkin K.P. 2004. A taxonomy for and analysis of tangible interfaces. *Personal and Ubiquitous Computing*, 8(5), pp. 347–358.
- Ishii H. and Ullmer B. 1997. Tangible bits: towards seamless interfaces between people, bits and atoms. In *Proceedings of the ACM SIGCHI Conference*, pp. 234–241.
- Jaffe A.B. and Stavins R.N. 1994. The energy-efficiency gap What does it mean? *Energy policy*, 22(10), pp. 804–810
- Moseley P. 2016. *Practical Approaches to the Building Renovation Challenge*.
- Phillips Y. 2012. Landlords versus tenants: Information asymmetry and mismatched preferences for home energy efficiency. *Energy Policy*, 45(11), pp.112–121.
- Rock I.A. and MacMillan, I.R. 2005. *The 1930s House Manual*, Haynes.
- Roy R., Caird S. and Potter S., 2007. *People-centred eco-design: consumer adoption of low and zero carbon products and systems*,
- Sapsed J. and Salter A. 2004. Postcards from the edge: local communities, global programs and boundary objects. *Organization Studies*, 25(9), pp. 1515–1534.
- Star S.L. and Griesemer J.R. 1989. Institutional ecology, translations’ and boundary objects, 1907-39. *Social studies of science*, 19(3), pp. 387–420.
- Tiwana A. and Mclean E.R., 2005. Expertise integration and creativity in information systems development. *Journal of Management Information Systems*, 22(1), pp. 13–43.
- Underkoffler J. and Ishii H., 1999. Urp: A luminous-tangible workbench for urban planning and design. *Proceedings of the SIGCHI conference*, pp. 386–393.
- Whitmarsh L. 2009. Behavioural responses to climate change: Asymmetry of intentions and impacts. *Journal of Environmental Psychology*, 29(1), pp.13–23.

Inter-ActiveHouse: users-driven building performances for Nearly Zero Energy Buildings in Mediterranean climates

Federica Brunone¹, Arianna Brambilla^{*2,5}, Alberto Sangiorgio³ and Marco Imperadori^{1,5}

¹ ABC Department, Politecnico di Milano, Milano, Italy

² School of Architecture, Design and Planning, The University of Sydney, Sydney, Australia

³ Grimshaw Architects, Sydney, Australia

⁵ Active House Alliance

**Corresponding email: arianna.brambilla@sydney.edu.au*

ABSTRACT

Building simulations rely on fixed assumptions and mathematical models to describe a specific building scenario, overlooking the building occupants' component. Almost 40% of in-home energy use is due occupants interacts with the building systems. The goal of this paper is to understand the magnitude of the performance gap when applied to two case studies in a Mediterranean climate. A set of scenarios are simulated assuming both a typical building usage and possible variations given by the users' interactions with shading, ventilation and cooling systems. Results show that the magnitude of the effects with a negative impact is bigger if compared to actions that might have a positive influence, this means that simulated results with standard usage assumptions are not an average of the possible effects but they reflect an optimistic outcome given by the optimal equipment usage.

KEYWORDS

Users interactions, energy efficiency, occupants behaviour, building simulation.

INTRODUCTION

Buildings sustainability standards usually focus on passive strategies to reduce the energy consumption by improving the envelope and system performances (Rodriguez-Ubinas et al., 2014). Considering the operational phase, several studies (Fabi et al., 2013; Shuqin et al., 2015; Martinaitis et al., 2015) attest a deep performance gap between simulated/predicted and real data, quantifiable towards, e.g.: the 56% offices' electrical request for lighting during non-working hours (Masoso and Grobler, 2010); the 200% increase in energy bills (Fabi et al., 2012). This gap clearly relates buildings' performances to the occupants' misuse of buildings systems that often does not follow the designed assumptions (Hale, 2018). Actually, virtual simulations take into account standard conditions of use, neglecting the big influence of users and reducing their interactions to a fixed system of defined schedules. Whereas some software integrate users-related variables, often their predictions fail because the working hypotheses do not properly reflect real conditions. The real human action drivers can contribute to model a reliable algorithm of interaction between users and buildings. A driver is anything that pushes an occupant to perform either an action or an interaction with the building system, affecting also the energy consumptions. The interactions between occupants and the construction system could be related to a combination of several drivers, both external and internal (Schweiker and Shukuya, 2009; Boerstra et. Al, 2013, Hellwig, 2015; Lou et al., 2016). The main objective of the study is to assess the magnitude of the users' impact on buildings behaviour in relation to outstanding examples of sustainable architecture. The analysis is performed on certified case studies of Mediterranean Active House, in order to exclude any possible bias of non-optimised design. Active House (AH) is a holistic approach

to building design aimed at promoting sustainability. AH is supported by a network of research centres and construction companies (namely AH Alliance), among which Politecnico di Milano is delegated to adapt the vision to Mediterranean climate. This analysis is part of the preliminary research done in this field. The analysis concerns the cooling season, since a hot-warm climate characterises the weather clusters of the Mediterranean region (Peel et al., 2007). Here, winter is a mild season, while summer offers a large daily range of temperature (Causone et. Al, 2014), requiring a dynamic approach and proving to be more relevant to the definition of the design resilience in Mediterranean region.

METHOD

The proposed analysis performs several sets of dynamic simulation scenarios in the software tool TRNSYS17 (<http://www.trnsys.com/>), starting from the typical usage assumptions, and implementing possible interactions with (i) cooling, (ii) shading and (iii) ventilation systems.

Case studies

The dynamic simulations are performed on two outstanding examples of sustainable and high energy-efficient buildings, designed and validated according the AH principles (www.activehouse.info): SVEVAH and VELUXlab¹. While SVEVAH virtual model represent an example of applied design strategies for a Mediterranean building project, VELUXlab is a real building prototype, whose virtual model has been set and calibrated according to the real use and measured energy consumption (Imperadori et al., 2013).

Table 1. Main features and technical characteristics of the two case studies.

		VELUXlab	SVEVAH
Project data	Location	Milan	Rome
Roof	Transmittance (W/m ² K)	0,133	0,117
	Damp effect (h)	10,5	10
Envelope	Transmittance (W/m ² K)	0,124	0,137
	Average FLD (%)	5,7	5
Transparency	Transmittance (W/m ² K)	1,1	1,1

Baseline scenario

The buildings are equipped with a fully automated system that controls heating and cooling, as well as natural ventilation and shading systems. It operates as follows: i) cooling is switched on only when the indoor temperature T_i is above the AH overheating thresholds²; ii) natural ventilation is allowed when outdoor temperature T_e is above 22°C and $T_i > T_e$; iii) windows facing north are never shaded; iv) windows are shaded when outdoor temperature is above 24°C, $T_i > T_e$, and the irradiance on the glass overcomes 140W/m² (Reinhart, 2001); v) East and West facing windows are shaded only if the condition in iv) is met during morning/afternoon time. Following the performance rating method of ASHRAE 90.1 §G1.2, these assumptions have been used to create a baseline scenario, within which the simulated performances represent the baseline for further results from different user-driven scenarios.

¹ Designed as the demo-house ATIKA, by ACXT/IDOM studio for VELUX, in 2011; retrofitted by Atelier2 – Valentina Gallotti and Prof. Marco Imperadori – Politecnico di Milano

² According to the AH Specifications, 2nd edition (2013) (www.activehouse.info), the maximum operative temperature limits follow the AH ranking: 1. $T_{i,o} < 25.5^\circ\text{C}$; 2. $T_{i,o} < 26^\circ\text{C}$; 3. $T_{i,o} < 27^\circ\text{C}$; 4. $T_{i,o} < 28^\circ\text{C}$, with an outside $T_m \geq 12^\circ\text{C}$. Beyond the set threshold of 26°C, the automated control system activates the floor cooling system.

Cooling set point variation scenarios

The set of simulation scenarios (Table 2) compares the several static set point (a) with a complex modulation (b, c) that reflects the real conditions of use, and an adaptive setup (d), which assures the lowest adaptive category of comfort (UNI EN 15251:2008). Only for this analysis, the reference scenario adopted is the one with cooling system set at 26°C, as it reflects the standard cooling set point temperature in Mediterranean climate.

Table 2. Set of scenarios defining the users' action of changing the cooling set point

SCENARIO		TIME	SET POINT (°C)
Sp_(set point)	(a) Static set point	0-24	from 24 to 28 with 1°C step
sp_night	(b) Night set back	8-20 (20-8)	26 (28)
sp_c	(c) Daily combination	8-20 (20-23) 23-6.30 (6.30-8)	26 (28) off (28)
sp_a	(d) Adaptive opportunity	8-23 (23-8)	$0,33T_{rm}^3 + 20,8^{\circ}C$ (off)

Shading system variation scenarios

Buildings users interact with the shading system as a reaction to sun position and solar radiation intensity and depth (Reinhart, 2001), even if indoor daylight supply is lower than the comfort threshold. In order to represent the effect of different drivers, several scenarios are scheduled (Table 3), differing in duration (all day, AM, PM) and interaction between users and MAS (Multi Agent Systems).

Table 3. Set of actions scenarios for the interactions with the shading system.

SCENARIO	MAS ON	MAS OFF (time) control modification
Base_s	-	(0-24) 80% shading (no ref. on external conditions)
Base_n	-	(0-24) Not shaded
PM_i	0-13 and 18-24	(13-18) 80% shading if irradiance > 250W/m ²
PM_s	0-13 and 18-24	(13-18) 80% shading (no ref. on external conditions)
PM_n	0-13 and 18-24	(13-18) Not shaded
AM_i	0-8 and 13-24	(8-13) 80% shading if irradiance > 250W/m ²
AM_s	0-8 and 13-24	(8-13) 80% shading (no ref. on external conditions)
AM_n	0-8 and 13-24	(8-13) Not shaded

Ventilation scenarios

Ventilation interactions are set according to different time schedule of natural ventilation. (Herkel et al., 2009). Scenarios are shown in Table 4. Ceiling fans are not considered, since the prime design strategies of the buildings did not account them.

Table 4. Actions scenarios for the interactions with the ventilation system.

SCENARIO	MAS ⁴ ON	MAS OFF (time) control modification
Base_o	-	(0-24) open
Base_c	-	(0-24) close
PM_o	0-13 and 18-24	(13-18) open
PM_c	0-13 and 18-24	(13-18) close
AM_o	0-8 and 13-24	(8-13) open
AM_c	0-8 and 13-24	(8-13) close
Day_o	0-8 and 18-24	(8 and 18) open
Day_c	0-8 and 18-24	(8 and 18) close

³ Trm is the running mean external temperature, as defined by UNI EN 15251:2008

⁴ MAS (Multi Agent Systems) applied to ventilation systems manages natural ventilation through the automatic opening/closing of windows, according to the external and internal temperatures and CO₂ concentration.

Night_o	8-18	(0-8 and 18-24) open
Night_c	8-18	(0-8 and 18-24) close

RESULTS

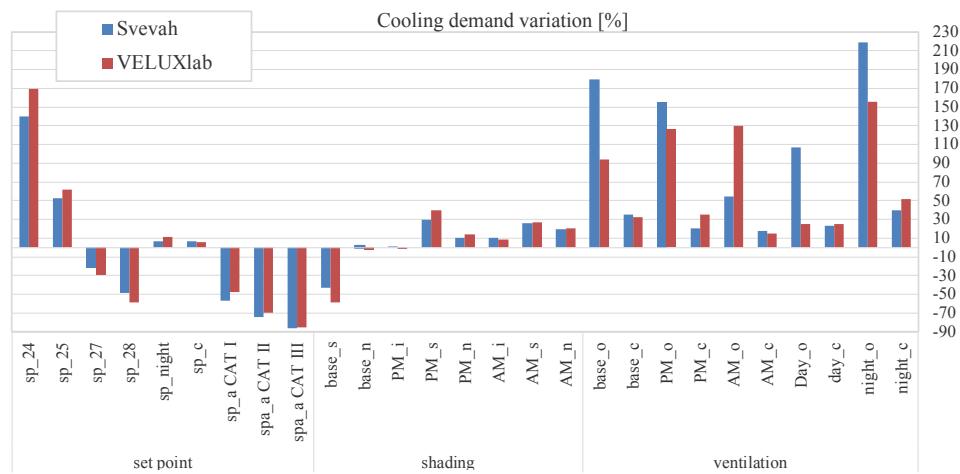


Figure 1. Variation of cooling demand in the different scenarios compared to the baseline, expressed as percentage.

Figure 1 shows that some scenarios improve the final energy performance up to 90% less; others instead increase it up to almost 230%. The first important observation concerns the asymmetry of the variations: this is particularly clear in the cooling set up scenarios, where a 1°C variation in the setpoint temperature causes different effects on energy consumption. In fact, a 1°C reduction in setpoint temperature increases the cooling demand by approximately 60% above the baseline, while a 1°C increase in setpoint temperature reduces cooling demand of 20% below baseline. This tendency is even clearer when a 2°C variation is taken into account. This means that the cooling demand variation and the set point variation are not proportional and, therefore, the energy efficiency can drastically change if lower setpoint temperatures are considered (SP 24°C 150% more in cooling demand if compared to SP 26°C). Generally, it is possible to notice that the set of scenarios with shading interactions has less influence on the energy demand. This is due to the resilient design of the case studies, which integrate architectural features to prevent summer overheating, such as enclosed shape and internal shaded patio (VELUXlab) and smaller openings to South (SVEVAH). Another interesting consideration involves the influence of different outside scenarios, between the two case studies: although the observed tendency is the same, VELUXlab prove to be more sensible to setpoint changes, while it is more resilient to variations in the ventilation management system. The background reason stands in the different climate: Rome is a warmer city if compared to Milan, meaning that natural ventilation and external air infiltration are more critical. On the opposite side, when cooling is relying only on mechanical air conditioning, the relative influence is lower, due to the already higher cooling demand.

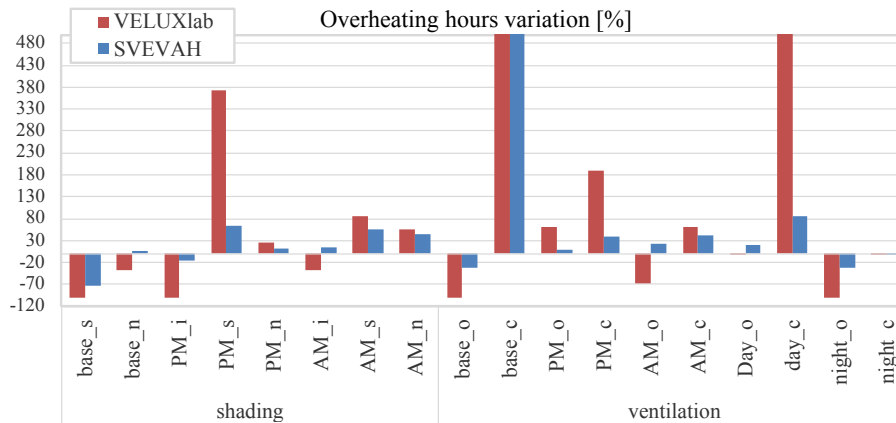


Figure 2. Variation of overheating hours in percentage, calculated according to AH Specifications, 2nd edition (2013) (www.activehouse.info) and compared to baseline scenario.

Figure 2 shows the overheating hours for the scenarios with interaction on the shading and ventilation systems. Similar ventilation and shading scenarios have comparable effects on the comfort point of view -in contrast with previous results. The highest number of overheating hours is detected when no ventilation is allowed, this means that the buildings are unable to dissipate the internal heat gains and the overheating is mainly internally driven. These results confirm that modern efficient buildings are less sensitive to external stress, due to their engineered envelope with optimized performance, but also less resilient to indoor increasing heat gains.

DISCUSSIONS

The results clearly attest the outcomes of experimental and monitored experiences in literature (Fabi et al., 2013; Shuqin et al., 2015; Martinaitis et al., 2015): the users interaction with the building systems could create a significant gap between predicted and real performance.

The presented case studies are supposed to be at the forefront of a sustainability. However, final performances change completely when the simulation assumptions and parameters are modified. This result indicates that the actual energy efficiency standard should account for the criticism related to users' interactions, allowing a better calibration of the design strategies. At last, the simplified scenarios could represent a limitation of the study, which does not account for more complex interactions. However, this simplified approach, based on the one-at-a-time method, helps to separate possible correlations and to quantify the criticisms of each system in the Mediterranean climate. According to this approach, users' influence represents a big source of uncertainty in the final energy performance of Mediterranean sustainable buildings. Sometimes also positive: shading scenarios are controlled by irradiance (Reinhart, 2001) and decrease the energy consumption of the building: less irradiance would mean less solar gain, and thus, a reduction of overheating effect and cooling demand. These outcomes represent a first step towards a proposal for modification of the thresholds on efficiency in regulations and standards, which should clearly account for usage behavior.

CONCLUSIONS

The analysis is a preliminary step into the investigation of the interaction between users and building automation systems. According to the achieved results, the actual sustainability certification scheme can lead to biased conclusion on buildings final energy performance. The analysis in this paper is an additional contribution to the research on this issue and the case studies analysed show that the criticisms is not related only to low-performing buildings, but it is extended also to ambitious projects that claim outstanding performances.

Future

investigations of the presented project aim at defining a threshold acceptance boundary to account for misuse and interaction between MAS and users to be integrated into the future generation of sustainability standards.

ACKNOWLEDGMENT

The work was partially supported by VELUX Group and Active House Alliance, as a part of the ongoing research collaborations with Politecnico di Milano.

Conflict of interest: The authors declare no conflict of interest.

REFERENCES

- Boerstra A., Beuker T., Loomans M., Hensen J. 2013. Impact of available and perceived control on comfort and health in European offices, *Architectural Science Review*, vol. 56:1, 30-41.
- Causone, F., Carlucci, S., Pagliano, L., & Pietrobon, M. 2014. A zero energy concept building for the Mediterranean climate. *Energy Procedia*, vol. 62, 280–288.
- Fabi, V., Andersen, R.V., Corgnati, S.P. et al. 2013. A methodology for modelling energy-related human behaviour: Application to window opening behaviour in residential buildings. *Building Simulation*, vol. 6, 415.
- Fabi V., Andersen R.V., Corgnati S., Olsen B.W. 2012. Occupant's window opening behaviour: a literature review of factors influencing occupant behavior and models, *Building and Environment*, vol. 58, 188-198.
- Hale, L.A. 2018. At Home with Sustainability: From Green Default Rules to Sustainable Consumption. In *Sustainability*, vol. 10, 249.
- Hellwig R.T. 2015. Perceived control in indoor environments: a conceptual approach. In: *Building Research & Information*, vol. 43:3, 302-315.
- Herkel S., Knapp U., Pfafferoth J. 2005. A preliminary model of users' behaviour regarding the manual control of windows in office buildings, 9th International IBPSA Conference, *Building Simulation*, Canada.
- Imperadori M., Sauchelli M., Brambilla A., Falcone N., Zanella C. and Zorzi V. 2013. Comfort and Energy Assessment of the First Italian Nearly Zero Energy Building in a University Campus. In proceedings of PLEA. Munich, Germany.
- Luo M., Cao B., Ji W., Ouyang Q., Lin B., Zhu Y. 2016. The underlying linkage between personal control and thermal comfort: Psychological or physical effects?, *Energy and Buildings*, vol 111, 56-63.
- Martinaitis V., Zavadskas E. K., Motuzienė v., Vilutienė T. 2015. Importance of occupancy information when simulating energy demand of energy efficient house: A case study. In: *Energy and Buildings*, vol 101, 64-75.
- Masoso O.T. and Grobler L.J. 2010. The dark side of occupants' behaviour on building energy use, *Energy and Buildings*, vol. 42, 173-177.
- Peel, M. C., Finlayson, B. L., & McMahon, T. A. 2007. Updated world map of the Köppen-Geiger climate classification. *Hydrology and Earth System Sciences*, 11(5), 1633–1644.
- Reinhart C. 2001. Daylight availability and manual lighting control in office buildings - simulation studies and analysis of measurements, University of Karlsruhe, Germany
- Rodriguez-Ubinas, E., Montero, C., Porteros, M., et al. 2014. Passive design strategies and performance of Net Energy Plus Houses. *Energy and Buildings*, 83, 10–22.
- Schweiker M. and Shukuya M. 2009. Comparison of theoretical and statistical models of air-conditioning-unit usage behaviour in a residential setting under Japanese climatic conditions, *Building and Environment*, vol. 44, 2137–2149.
- Shuqin C., Weiwei Y., Hiroshi Y., Mark D. L., Katy N., Adam H., 2015. Definition of occupant behavior in residential buildings and its application to behavior analysis in case studies. In: *Energy and Buildings*, vol. 104, 1-13

www.activehouse.info

The influence of window opening habits on the residential energy use in nearly zero energy buildings

Silke Verbruggen^{1,*}, Marc Delghust¹, Jelle Laverge¹, Arnold Janssens¹

¹University of Ghent, Department of Architecture and Urban planning, Ghent, Belgium

**Corresponding email: Silke.verbruggen@Ugent.be*

ABSTRACT

In this paper, we discuss the presence of habits in the window opening behaviour of social housing tenants in a nearly zero-energy development in Belgium. A window opening habit can be defined as an action with a window that is repeated daily around the same time independently of the prevailing weather conditions. A carbon neutral social housing estate (106 apartments and 90 single family dwellings) was used as a test case. Questionnaires, window opening logging with a building monitoring system and cross-sectional surveys were used to collect window opening data. A method to identify window opening habits is determined. Up to 45% of the occupants act on some sort of habit in wintertime, predominantly in the bedrooms and in the morning. In summer these habits dissipate due to very long window openings. Weather variables and indoor climate parameters, traditionally used as the basis for window opening behaviour models, are rather poor predictors of opening behaviour in winter. The incorporation of habits in window opening models can lead to more reliable predictions of window opening behaviour.

KEYWORDS

Habits, Windows, Occupant behaviour, Residential energy use, NZEB

INTRODUCTION

The occupants' window opening behaviour can have a substantial influence on the indoor climate and the energy use in a dwelling. In order to implement this behaviour in energy simulation tools, window opening models have been developed. In literature, most window opening models are based on outdoor and/or indoor climate variables (Brundrett and Poultney, 1982; Conan, 1982; Erhorn, 1988; Fabi et al. 2013; Lyberg, 1983; Maeyens and Janssens, 2000; Rijal et al. 2007). However, the study of Verbruggen et al. (2017) on the window opening behaviour of social housing tenants in a Belgian case study revealed that weather variables cannot accurately predict the window opening behaviour in winter time. The weather variables have a significant influence on the window opening behaviour when yearly data are considered, nevertheless the influence is not significant when only winter data are analysed. It was revealed that most occupants who opened their windows in wintertime either could not define an explanation for their actions or linked it to the need to 'air' the dwelling. A recent study (Clarysse, 2018) did not reveal any performance issues with the heat recovery ventilation system. The lack of (accurate) motivation to perform these window openings leads to the hypothesis that the occupants interact with the windows out of habit.

A habit can be defined as an automatic action carried out without conscious effort that is the consequence of frequently repeating this action in a stable context (Ouellette and Wood, 1998). Consequently, a window opening habit is an action with a window that is repeated daily around the same time independently of the prevailing weather conditions. Habits have been elaborately researched in the field of sociology and psychology (Ajzen, 2002; Ouellette and Wood, 1998; Verplanken et al. 1998); however, little research has been carried out in the building sciences.

In several window opening studies, occupant characteristics have been reviewed, such as age, income, sex and household size, but the habits of the occupants have not been considered. Habits are very personal and vary greatly among the different occupants. It is consequently difficult to incorporate them into a window opening model. Nonetheless, it is interesting to investigate these habits, since window opening actions can considerably influence the ventilation rate and accompanying energy losses.

This paper first explains how the presence of window opening habits is determined in a case study. Subsequently, the observed habits are discussed and their influence on the energy use is assessed.

METHODS

Case study

The research is based on data collected in a nearly zero-energy social housing development in Belgium (Himpe et al. 2015). The housing project is equipped with a building monitoring system which is directly linked to a university server. The project, built between 2010 and 2015, consists of 106 apartments and 90 single family houses. All apartments and 39 houses are fitted with a balanced mechanical ventilation system with heat recovery, while the other dwellings have demand controlled exhaust ventilation with trickle vents.

Data-acquisition

In 14 apartments and 16 houses, window sensors were installed which provided direct measurements on the window opening actions. The time and state of the windows were registered when a window is opened or closed. Only one sensor was installed on each window; therefore, it was not possible to differentiate between turning and tilting actions. In the apartments, the signals of the sensors were combined into one signal per apartment. Consequently, the individual actions with a single window were not registered. The window sensor data were analysed for the years 2015 and 2016 for the apartments, but only for the year 2016 for the houses since they were inhabited later. In four apartments, the data was corrupted so these were discarded from the analysis. To broaden the window opening data, a logbook study was carried out between 20 January and 27 February 2017. The occupants were asked to write down when the windows were opened and closed, and to mention whether those were opened completely or tilted. A total of 47 occupants filled in a logbook. However, the motivation of occupants to participate dropped considerably after a few weeks. The validity of the logbooks was checked by visual observations carried out during the same period, and compared with window sensor data if available. In total, 62% (20 apartments, 9 houses) of the logbooks were evaluated as correct. Additionally, the occupants were queried on the reasons for opening and closing the windows, the family composition, the presence in the house and the occupants' satisfaction with the ventilation system. In Himpe et al. (2015) and Verbruggen et al. (2017) respectively, the case study is discussed in more detail and a summary is provided of the observed window opening behaviour.

Determining Habits

The data of the logbook study was used to determine which occupants perform habitual actions. Indications of a habit can be observed when examining the opening percentage per hour, this is the fraction of the hour that the window is opened. When the opening percentage approximates a value of 1 (100%), it indicates that the window is always opened at that time (independently of e.g. indoor and/or outdoor climate); consequently, the presence of an opening habit is very likely. This was visually checked by plotting the average opening percentages per hour over the measuring period (Jan-Feb 2017) for every hour of the day (Figure 1). When a clear peak in

opening percentages was observed, but the 100% mark was not reached, an opening habit could still be present. This can indicate an opening habit that occurred a limited number of times per week (e.g. only on weekdays), a habit that has slightly shifted in time throughout the days or a habit with a duration shorter than one hour. For example, clear habits could be observed in apartments 6 and 21 (Figure 1), while the opening percentages of apartments 20 and 22 merely suggest a habit. Additionally, indications of habits were derived from conversations with the occupants.

Next, these habits were more precisely determined by examining the exact data of the logbook papers. In all dwellings with an indication of a habit, it was checked if the windows were actually opened every day at that time. First, an average starting-time of the habit was determined, as well as an average end-time. Subsequently, it was checked if this habit is present every day during the measuring period. A deviation of the starting- and end-time of one hour was allowed to compensate for incorrect clock-setting and the lack of accuracy in time notation. Generally, the habit will not be present every single day at the exact time-slot; therefore, it was also determined on how many days the habit was present. This value was corrected when a habit was only performed on specific days of the week (e.g. only on Mondays), for the number of these specific days present in the measuring period. The analysis was repeated for the data of the window sensors, considering the same winter period as the logbook study (Jan-Feb 2017).

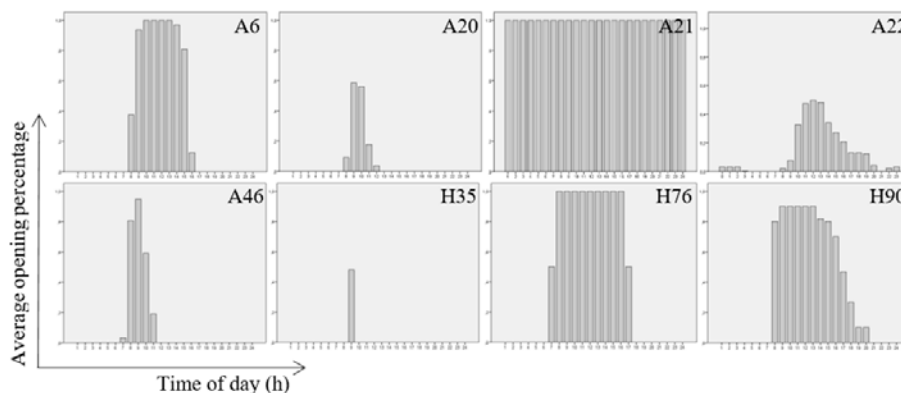


Figure 1. Average opening percentages per hour – Dwellings with a window opening habit.

RESULTS & DISCUSSION

Habits in winter

In 17 of the 47 dwellings (36 %) that participated in the logbook study, at least one opening habit was registered. This percentage rose to 45% when not all logbooks were considered, but only those that were assumed to be correct. When assessing the window sensor data, only in 5 of the 26 dwellings (19 %) a habit could be observed. This habit presence is lower than observed from the logbook data. However, 4 from the 5 dwellings where habits were observed are apartments which leads to a habit presence of 40% in the apartments, while in merely 1 out of 16 houses (6%) a habit is present. In Table 1, the dwellings that exhibited a window opening habit are presented with the corresponding percentage of the day that the habit occurred. The table also shows in which rooms and on which days of the week the habit was carried out. Even if no habits were found in certain dwellings, they may still be present. The presence of a habit can be missed by the determination method when the habit is performed on varying times during the day or is repeated on only a few days in the week/month. The difference in the number of detected habits between the logbook-data and sensor-data may be attributed to the occupants' participation in the survey. Most participants of the logbook-study partook in the survey, wherein some mentioned specific habits that could have been missed by the determination

Table 1. Dwellings with window opening habits: logbooks (underlined) & window sensors (*).

ID	Room	Habit	Day	Habit presence	Reason
<u>A6</u>	Master Bedroom	07:30 – 14:30	Always	87%	-
<u>A20</u>	Master Bedroom	08:00 - 09:30	Always	72%	-
<u>A21*</u>	Master Bedroom	00:00 - 24:00	Always	100%	-
<u>A22*</u>	All	09:45 - 14:30	Weekdays	69%	-
<u>A46*</u>	Master Bedroom	07:30 - 10:00	Always	91%	-
<u>A49</u>	Master Bedroom	14:00 - 17:00	Always	87%	-
<u>A51*</u>	Master Bedroom	08:30 - 09:30	Always	86%	-
	Living room	08:30 - 09:30	Always	86%	-
<u>A54</u>	Master Bedroom	07:30 - 08:00	Always	93%	-
<u>A75</u>	Master Bedroom	08:00 - 12:00	Thursday	100%	Cleaning
<u>H26*</u>	Second Bedroom	00:00 - 24:00	Always	100%	-
<u>H35</u>	Master Bedroom	08:00 - 08:30	Always	100%	-
	Second Bedroom	07:30 - 08:00	Always	100%	-
<u>H40</u>	Master Bedroom	12:00 - 14:00	Always	59%	-
	Living room	12:00 - 12:30	Always	100%	-
<u>H76</u>	Second Bedroom	06:30 - 16:30	Always	100%	-
<u>H90</u>	Master Bedroom	07:30 - 17:00	Always	100%	-
	Second Bedroom	07:30 - 17:00	Always	56%	-
	Third Bedroom	07:30 - 17:00	Always	56%	-
	Bathroom	08:30 - 12:00	Always	44%	-
	Living room	08:00 - 12:00	Always	67%	-
	Kitchen	08:00 - 11:00	Always	44%	-
<u>H97</u>	Living room	07:40 - 07:50	Weekdays	84%	-

method (e.g. cleaning every Thursday). Of the dwellings with window sensors, only a few occupants participated in the survey consequently lowering the probability of detecting habits. Accordingly the substantial difference between apartments and houses may be attributed as well to the limitations of the determination method or the small data sample. However, it may also be due to a better understanding of the working of the ventilation system by the inhabitants of the houses. Further research is needed on the occupants' knowledge of the ventilation system and the corresponding relationship with the presence of habits.

Most habits occurred in the bedrooms in the morning (Table 1). This observation corresponds to the findings of Fabi et al. (2013) that the probability of opening a window is the highest in the morning. However, they attribute the opening actions to the presence of high CO₂-levels, while it is more likely that occupants open their windows when they wake up, as a habit. The windows will not necessarily be opened due to high CO₂-levels, rather due to the fact that occupants are only able to interact with the windows when they are awake and because the CO₂-levels will only decrease as a result of the opening of the windows. In merely four dwellings a living room opening habit was observed. Other habits were present when a recurring activity took place every week that demanded the opening of windows or doors. For example, cleaning personnel may clean the dwelling every week at the exact same time and open the windows while doing so. On average, the habits were present during more than 80% of the measuring period, so on more than 80% of the days the habits were executed. Some dwellings showed just a 50% presence of habits; in these dwellings the hours at which the opening actions occurred were shifted. This may indicate that the habits are linked to a certain activity rather than to a certain time-slot. For example, the opening of the bedroom windows in the morning will be closely linked to the waking-up event, which may not happen every day at exact the same time. Other dwellings revealed a 100% habit-presence; in these dwellings the habit was punctually repeated every day.

Habits in summer

The discussed habits are the results of a winter study; additionally, it was checked if these habits were similarly present in summer. No logbook study has been performed in summer,

consequently solely the window sensor data could be used. The month August in 2016 was selected since in June and July the monitoring system was not working properly and in previous years the sensors in the houses were not yet operational. It was observed that the winter-habits were not present anymore in summer, as visualised in Figure 2. The majority of the windows were continuously opened in summer, which leads to the dissipation of the winter-habits. This may evidently be a habit as well. It is necessary to do more research on the ‘survival time’ of these habits, this is the time that the context is stable and habits are executed (Ouellette and Wood, 1998), in order to examine in which period the winter-habits and summer-habits are present and to develop a window opening model accordingly. There may be spring- and autumn-habits as well, but this needs to be analysed further.

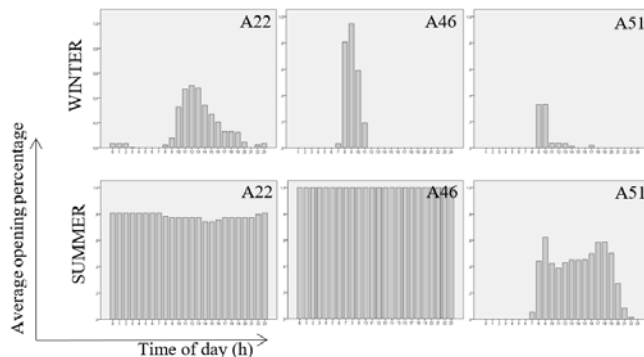


Figure 2. Average opening percentages per hour in winter and summer

Influence of window opening habits on opening percentages and energy use

The average window opening percentages per day in winter were higher for dwellings where a habit was present, compared to dwellings without a habit. In the master bedrooms the average opening percentages for dwellings with a habit was 19%, while for dwellings without habits it was 9%. In the living room the opening percentages were lower, but the difference was still present with respectively 3% and 1% for dwellings with and without habits. Consequently, a large part of the opening actions happened independently of any weather variables. This demonstrates why the window opening models based on weather variables were not able to correctly predict the opening behaviour in winter. There is a potential large effect on the energy use when the opening percentages increase. Nevertheless, no significant correlation was found between the monitored energy use and the presence of a habit, which could be caused by the limited number of cases or the multitude of other factors that simultaneously influence the energy use.

CONCLUSION

Using logbook and window sensor data the presence of habits in winter was determined for the residents of a nearly zero-energy social housing neighbourhood. In 45% of the dwellings a habit was performed with an average presence of 80% during the measuring period. A 100% habit-presence could not be observed in all dwellings since the habitual opening actions could differ slightly in time. Consequently, it is assumed that the window openings are rather linked to an activity which is performed consistently every day than to an exact time-slot. Most habits occurred in the morning in the bedrooms, this may be closely linked to the waking-up event. Other habits were present due to repeated activities during the week such as cleaning. In summertime these winter-habits dissipated due to the extended duration of the window openings. Further research is needed to determine the presence of summer-habits and the ‘survival time’ of these habits. The winter-habits have an important influence on the opening percentage of the windows. With the window opening models based on weather variables

lacking accuracy in winter time, developing a model that includes these habits may lead to more precise predictions of the window opening behaviour.

ACKNOWLEDGEMENT

We gratefully acknowledge the financial support received for this work from the Fund for Scientific Research (FWO) in the frame of the strategic basic research (SBO) project “NEPBC: Next generation building energy assessment methods towards a carbon neutral building stock” (S009617N). The authors would also like to thank the social housing company ‘Goedkope Woning’ and the occupants who willingly participated in this project.

REFERENCES

- Ajzen I. 2002. Residual Effects of Past on Later Behavior: Habituation and Reasoned Action Perspectives. *Personality and Social Psychology Review*, 6(2), 107-122.
- Brundrett G. W. and Poultney G. H. 1982. Use of natural ventilation. in: *3rd AIC Conference: Energy Efficient domestic ventilation systems For Achieving Acceptable Indoor Air Quality*, London, Paper 2.
- Clarysse G., Laverge J., Verbruggen S., and Janssens A. 2018. Performance review of balanced ventilation systems in a CO₂-neutral residential area. *Master thesis*, University of Ghent (Belgium), 116 pages.
- Conan G. 1982. Variations in householders’ window opening patterns. in: *3rd AIC Conference: Energy Efficient domestic ventilation systems For Achieving Acceptable Indoor Air Quality*, London, Paper 3.
- Dubrul C., Wouters P., Trepte L., Roux M., de Gids W.C., Phaff J.C., Van Dongen JEF, Jackman P., and Warren P.R. 1988. Technical Note AIVC 23: Inhabitant Behaviour with Respect to Ventilation, *IEA Annex VIII. Air Infiltration and Ventilation Centre*.
- Erhorn H. 1988. Influence of meteorological conditions on inhabitants’ behaviour in dwellings with mechanical ventilation. *Energy and Buildings*, 11(1-3), pp. 267-275.
- Fabi V., Andersen R.V., Corngati S.P., and Olesen B.W. 2013. A methodology for modelling energy-related human behaviour: Application to window opening behaviour in residential buildings. *Building Simulation*, 6(4), 415-427.
- Himpe E., Janssens A., Vaillant Rebollar J.E. 2015. Energy and comfort performance assessment of monitored low energy buildings connected to low-temperature district heating. *Energy Procedia*, 78 (2015), 3465-3470.
- Lyberg M. D. 1983. Residents and windows: Airing. *Meddelande/Bulletin*, M83 (21), pp. 1-20.
- Maeyens J. and Janssens A. 2000. A stochastic ventilation model regarding leakage and user behaviour. In: *Proceedings of the Second International Conference on Building Physics*, Leuven, pp.737-748.
- Ouellette J.A. and Wood W. 1998. Habit and intention in everyday life: The multiple processes by which past behavior predicts future behavior. *Psychological Bulletin*, 124(1), 54-74.
- Rijal H. B., Tuohy P., Humphreys M.A., Nicol, J.F., Samuel A. and Clarke J. 2007. Using results from field surveys to predict the effect of open windows on thermal comfort and energy use in buildings. *Energy and Buildings*, 39(7), pp. 823-836.
- Verbruggen S., Laverge J., Delghust M. and Janssens A. 2017. Window opening in relation with residential energy use and indoor climate. *Master thesis*, University of Ghent (Belgium), 137 pages.
- Verplanken B., Aarts H., Van Knippenberg A., and Moonen A. 1998. Habit versus planned behaviour: A field experiment. *British Journal of Social Psychology*, 37(1), 111-128.
- Wouters, P. and De Baets, D. 1986. A detailed statistical analysis of window use and its effect on the ventilation rate in 2400 Belgian social houses. In: *Proceedings of the 7th AIC Conference*, Stratford-upon-Avon, pp. 33-53.

Utilization of heat recovery ventilation: steady-state two-zone heat loss analysis and field studies

Arnold Janssens, Wolf Bracke, Marc Delghust, Eline Himpe, Silke Verbruggen, Jelle Laverge

Research group Building Physics, Construction and Services, Faculty of Engineering and Architecture, Ghent University, Belgium

**Corresponding email: arnold.janssens@ugent.be*

ABSTRACT

In new houses in Europe the share of mechanical ventilation with heat recovery is increasing as a result of more severe energy performance requirements and of energy labelling for residential ventilation units. The methods used to assess the influence of heat recovery ventilation on the heating energy use in energy labelling and certification are typically based on single zone energy balance equations, although heating behaviour and set-points differ in different rooms of a dwelling. As a result of this the energy savings of heat recovery ventilation as assessed with single zone methods may be larger than when the spatial variations in dwellings are taken into account. This is related to the fact that the recovered heat supplied to the dwelling through the ventilation system is not 'useful' to reduce space heating and cooling demand at all time and in every room.

A two-zone steady-state heat loss analysis was conducted to investigate the relation between spatial variations in a dwelling and the utilization of heat recovery. One zone represents the rooms in a house which are regularly heated and are typically equipped with heat emitters and local controls. The other zone represents the rooms which are rarely heated or have no individual heat emitters or controls.

The results show the differences between a single zone and two-zone approach in terms of the effects of heat recovery ventilation on building heat loss, and define the main influencing parameters for the utilization of heat recovery in residential ventilation systems.

The analysis is supported by results of a field study where energy use in 114 low-energy houses was monitored. Half of the houses had mechanical ventilation systems with heat recovery, while the other half had demand-controlled mechanical extract ventilation. Apart from the differences in ventilation systems, the houses were largely identical.

KEYWORDS

Heat recovery ventilation, Building heat loss, Temperature zoning, Energy performance

INTRODUCTION

The European market for residential ventilation is highly driven by energy performance regulations. In new buildings the share of mechanical ventilation with heat recovery (MVHR) is increasing as a result of more severe energy performance requirements. For instance in Belgium the share of MVHR in new single family houses has increased in 10 years' time from 25% to almost 50% since the introduction of the energy performance regulation in 2006 (VEA, 2015). The energy labelling for residential ventilation units and the ecodesign requirements for ventilation units may further contribute to the wide-spread application of MVHR in new buildings (EC, 2014).

However, at the same time research reveals a performance gap between the rated energy performance of residential buildings and the actual energy use. The effect of energy saving

measures is typically overrated compared to reality. Majcen et al. (2016) found that in 280 houses where mechanical exhaust ventilation was replaced by MVHR the actual reduction in gas use was less than a quarter than what was expected based on the EPC-rating. One possible cause of the discrepancy is a poor installation quality of the ventilation unit, resulting in shortcuts and leakage that may decrease dramatically the efficiency of heat recovery (Roulet et al. 2001). Another cause of the discrepancy is the simple model used in rating methods to calculate the ventilation heat loss, perhaps not sufficiently accurate to reflect the actual influence of the heat recovery system (HRS).

Indeed, the methods used to assess the influence of heat recovery ventilation on the energy use of buildings in energy labelling and certification are typically based on single zone steady-state energy balance equations, using the thermal efficiency or heat exchange effectiveness of the HRS as an input. The single zone approach assumes that all rooms are heated to the same set-point temperature and that the extract air temperature equals room temperature. Intermittency and multi-zoning is not considered although heating behaviour and set-points may differ in different rooms of a dwelling. In a typical lay-out of MVHR air is extracted from wet rooms with lower set-point temperatures than the main living areas and recovered heat is also supplied to unheated habitable rooms (eg bed rooms), unnecessarily increasing the indoor temperature and heat loss in the latter rooms. As a result of this the energy savings of heat recovery ventilation as assessed with single zone methods may be larger than when the spatial variations in dwellings are taken into account.

Faes et al. (2017) assessed the influence of MVHR on the space heating demand of a detached dwelling using dynamic simulations with a 10-zone-model and defined different 'use factors' to take temporal and spatial variations in temperature into account. Their results show that less than 50% of the heat recovered from the extraction air is actually supplied usefully to the rooms of the dwelling, in the sense that the recovered heat contributes to the reduction of yearly heating demand. Furthermore the relative influence of MVHR on the heating demand increases with higher thermal resistance and airtightness of the building envelope. A high performance building envelope causes the temperature throughout the dwelling to be more constant over time and uniform with respect to the different spaces. As a result the single zone assumption is valid and the thermal efficiency of the HRS better reflects the energy savings of MVHR. However, as Berge et al. (2016) observed in field studies in Norway, inhabitants of highly insulated dwellings with heat recovery tend to apply extensive window ventilation in bedrooms to compensate for the undesired oversupply of heat to these rooms. This leads to an increased space-heating demand, and again reduces the potential energy savings of MVHR, and the validity of the single zone assumption.

In this work, a two-zone steady-state heat loss analysis is conducted to investigate the relation between spatial variations in a dwelling and the utilization of heat recovery to reduce the building heat loss. A definition of the 'useful' efficiency of MVHR is proposed and compared to the thermal efficiency of the HRS. The results show the differences between a single zone and two-zone approach in terms of the effects of heat recovery ventilation on building heat loss, and define the main influencing parameters for the utilization of heat recovery in residential ventilation systems. The analysis is supported by results of a field study where energy use in 114 low-energy houses in a carbon neutral social housing district was monitored (Janssens et al. 2017). Half of the houses had mechanical ventilation systems with heat recovery, while the other half had demand-controlled mechanical extract ventilation. Apart from the differences in ventilation systems, the houses were largely identical.

METHODS

Heat loss analysis

In order to take spatial temperature variations within a dwelling into account different methodologies exist, ranging from correction factors introduced in a single zone model to a coupled multi-zone representation of a house (Delghust et al. 2015). Here a two-zone approach is chosen as a first order improvement of the single zone assumption. One zone represents the rooms in a house which are regularly heated and are typically equipped with heat emitters and local controls, such as living room and kitchen. The other zone represents the rooms which are rarely heated or have no individual heat emitters or controls, for instance bedrooms, bath rooms and hallway. Figure 1 shows the model parameters in a single-zone and two-zone representation of a dwelling with MVHR.

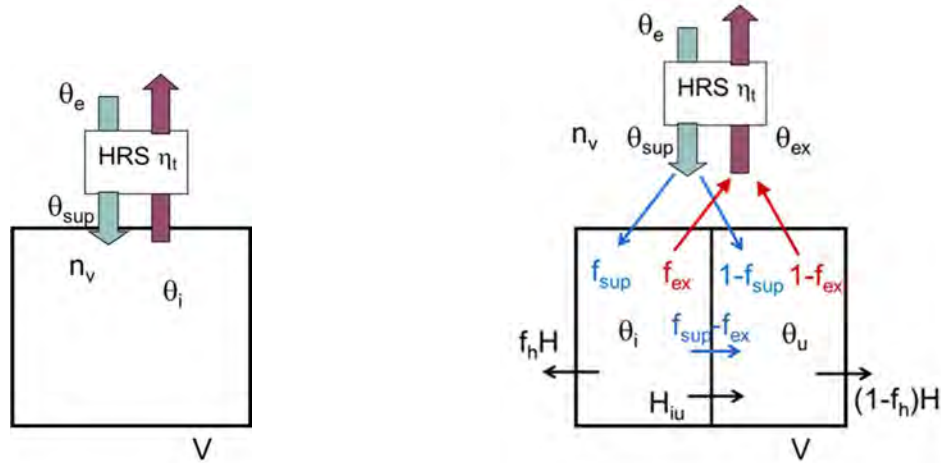


Figure 1. Single-zone model (left) and two-zone model (right) of a dwelling with MVHR, with indication of model parameters: η_t , thermal efficiency of HRS (-); V , building volume (m^3); n_v , ventilation air change rate (h^{-1}); θ_e , exterior temperature ($^{\circ}\text{C}$); θ_i , set-point temperature in heated zone ($^{\circ}\text{C}$); θ_{sup} , supply air temperature ($^{\circ}\text{C}$); θ_{ex} , extraction air temperature ($^{\circ}\text{C}$); θ_u , balance temperature in unheated zone ($^{\circ}\text{C}$); H , heat loss coefficient of building envelope (W/K); H_{iu} , heat loss coefficient of partition walls between heated and unheated zone (W/K); f_h , fraction of building envelope heat loss related to heated zone (-); f_{sup} , fraction of supply air supplied to heated zone (-); f_{ex} , fraction of extraction air extracted from heated zone (-).

The overall steady-state heat loss Φ_L (W) of the heated zone is defined by Eq. 1 and Eq. 2 in the single-zone and two-zone model, respectively:

$$\Phi_{L,1z} = [H + 0.34n_vV(1 - \eta_t)](\theta_i - \theta_e) \quad (1)$$

$$\Phi_{L,2z} = f_h H(\theta_i - \theta_e) + H_{iu}(\theta_i - \theta_u) + 0.34f_{sup}n_vV(\theta_i - \theta_{sup}) \quad (2)$$

The heat loss equation of the two-zone model may be solved using the heat balance equation of the unheated zone to find θ_u (Eq. 3) and the heat transfer and mixing equation of the supply and extraction air to find θ_{sup} (Eq. 4).

$$[H_{iu} + 0.34(f_{sup} - f_{ex})n_vV](\theta_i - \theta_u) = (1 - f_h)H(\theta_u - \theta_e) + 0.34(1 - f_{sup})n_vV(\theta_u - \theta_{sup}) \quad (3)$$

$$\theta_{sup} = (1 - \eta_t)\theta_e + \eta_t[f_{ex}\theta_i + (1 - f_{ex})\theta_u] \quad (4)$$

Expression of results

The heat loss calculation is applied for different values of the heat loss coefficient H of the building envelope, using typical values for the other model parameters (Laverge et al. 2013): $V = 500 \text{ m}^3$, $n_v = 0.5 \text{ h}^{-1}$, $H_{iu} = 200 \text{ W/K}$, $f_h = 0.5$, $f_{sup} = 0.45$, $f_{ex} = 0.30$ and $\eta_t = 0.80$.

The overall heat loss of the heated zone of the dwelling with MHRV is compared to the heat loss of the dwelling with a ventilation system without HRS, eg mechanical exhaust ventilation (MEV) or mechanical ventilation with $\eta_t = 0$. The difference between both defines to what extent the overall heat loss is reduced by the application of MVHR. The ratio between this difference and the extra heat loss incurred by adding ventilation defines the specific heat loss reduction or ‘useful’ efficiency of the HRS in Eq. 5 (called ‘use factor’ by Faes et al. 2017) :

$$\eta' = \frac{\Phi_{L,MEV} - \Phi_{L,MVHR}}{0.34n_v V (\theta_i - \theta_e)} \quad (5)$$

When applying the single-zone model, the useful efficiency η' is equal to the temperature efficiency η_t of the HRS, independent of other parameters.

RESULTS

Calculated useful efficiency

Figure 2 shows the results of the two-zone heat loss analysis for the parameter values given in the previous paragraph. The dimensionless temperature in the unheated zone and the useful efficiency are depicted as a function of the volumetric heat loss coefficient of the building envelope H/V . The right hand side of the x-axis corresponds to poorly insulated envelopes, the left hand side to highly insulated envelopes. The temperature in the unheated zone decreases with higher values of heat loss coefficient. In the dwelling with MVHR the unheated zone is slightly warmer than with MEV since air preheated by the HRS is supplied to the unheated zone. Since the supply air temperature of MVHR depends on the temperature of the extraction air and a large share of the extraction is taken from the unheated zone, the supply air temperature also decreases with higher values of heat loss coefficient, thus diminishing the heat loss reduction provided by MVHR. This effect is reflected in the calculated useful efficiency, which remains substantially lower than the value of the thermal efficiency of the HRS (equal to the useful efficiency in the single-zone approach). With better insulation of the building envelope and lower ventilation rates, the useful efficiency predicted by the two-zone model increases towards the result of the single-zone model.

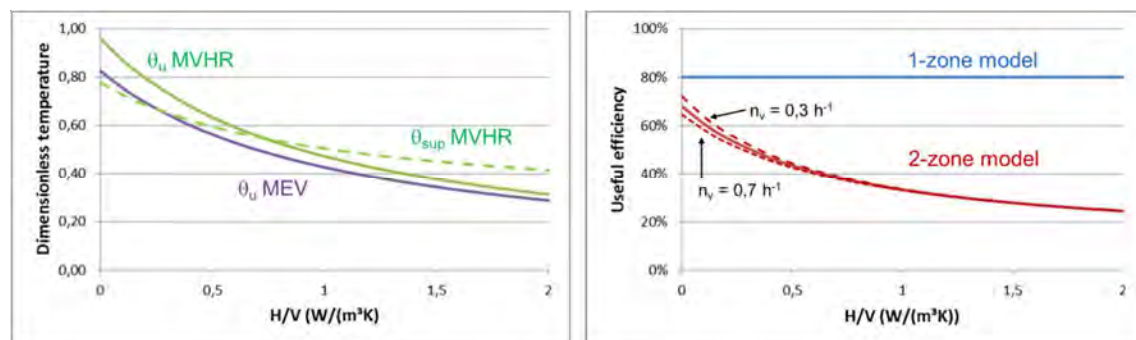


Figure 2: Results of two-zone heat loss analysis: dimensionless temperature in unheated zone with MEV and MVHR and supply air temperature with MVHR (left) and useful efficiency η' following from two-zone model compared to single zone model (right).

Field study

The heat loss analysis shows that the energy performance of MVHR largely depends on modelling assumptions. Still, both the 1-zone and 2-zone model remain simplifications; in reality the spatial variations in temperature in dwellings are in between both modelling extremes. To put the results of the theoretical analysis into perspective monitoring results of a field study are now discussed, where the total metered heat use (space heating and sanitary hot water) in the dwellings of a carbon neutral housing district was compared to the heat use rated in the energy performance certificates. In Belgium the energy performance of new and renovated buildings needs to be assessed at the moment of completion of the works by an EPB-assessor, who collects the as-built information, creates the input in the EPB-software, and evaluates whether the building meets the requirements. Half of the houses had MVHR with a rotary HRS ($\eta_t = 80\%$), while the other half had demand-controlled MEV. The volumetric heat loss coefficient of the building envelope was about $0.15 \text{ W}/(\text{m}^3\text{K})$. In total 90 houses (41 MVHR, 49 MEV) had complete metering data to perform the comparison. More information about the district and the monitoring method is given by Janssens et al. (2017).

As Figure 3 shows, the rated heat use in houses with MEV was significantly higher than that in houses with MVHR, on average 32%. However, this is not reflected in the results of the monitoring where the metered heat use shows no significant difference between both types of houses. Apart from the ventilation system the houses were largely identical. Also the user behaviour in both groups of houses was similar according to the monitored living room temperatures, with average values in winter months $23.0 \pm 1.5^\circ\text{C}$ for MEV and $22.7 \pm 1.5^\circ\text{C}$ for MVHR. Temperatures in bedrooms were on average 3 to 4°C lower in both types of houses. Therefore differences in heating behaviour are no explanation for the deviation between rated and metered performance of the houses with MVHR.

An analysis based on the EPB input-files of the rated houses shows that the heat use in the houses with MVHR strongly depends on the input value of the thermal efficiency of the HRS (Figure 3, right). So the reduced useful efficiency of MVHR as a result of temperature differences between rooms may partly explain the underperformance of MVHR in terms of metered heat use. Furthermore large differences were measured between day zone temperatures and extract air temperatures in some houses, possibly related to window opening in wet rooms. This still needs to be investigated in more detail.

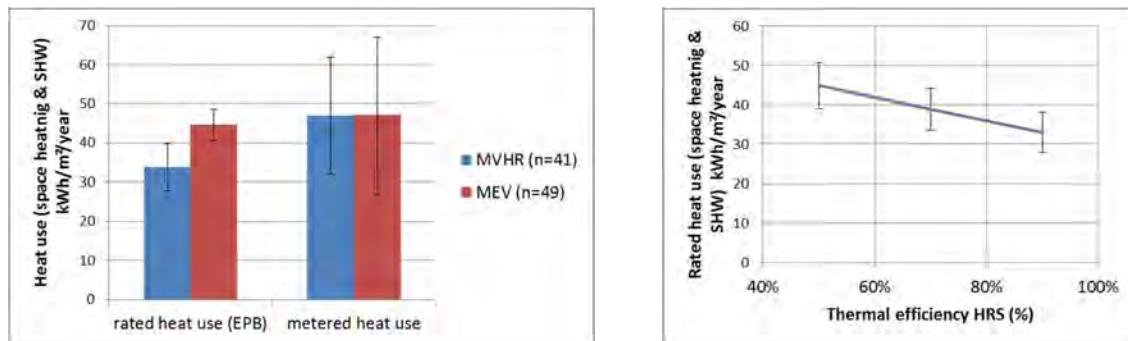


Figure 3: Comparison between the rated and metered (1/5/2015-30/4/2016) heat use of low-energy dwellings with MVHR and MEV (left) and relation between rated heat use of houses with MVHR and thermal efficiency of HRS, with specified thermal efficiency of 80% (right).

CONCLUSIONS

A two-zone steady-state heat loss analysis was conducted to investigate the relation between spatial variations in a dwelling and the utilization of heat recovery in mechanical ventilation. The results show that the building heat loss reduction of MVHR assessed by single zone methods typically used in energy labelling and certification is optimistic compared to the assessment of a two-zone model. When temperature differences between heated and unheated rooms are taken into account, the building heat loss reduction of MVHR is influenced not only by the thermal efficiency of the HRS but also by building envelope heat loss, flow rates and lay-out of the ventilation system, and size of day and night zone. Field studies show evidence that the positive influence of MVHR on heating energy use as predicted by single zone rating methods, is not confirmed by the metered heat use. A definition of the 'useful' efficiency of MVHR is proposed as a metric to take heat recovery ventilation into account in a more correct way in energy performance rating methods. With better insulation of the building envelope and lower ventilation rates, the useful efficiency predicted by the two-zone model increases towards the result of the single-zone model.

ACKNOWLEDGEMENT

This work was supported by the EU Concerto initiative, 'Sustainable Zero Carbon ECO-Town Developments Improving Quality of Life across EU' (ECO-Life) (TREN/FP7EN/239497/"ECO-Life"), <http://www.ecolife-project.eu/index.html>, project leader COWI, and by the Fund for Scientific Research (FWO) in the frame of the strategic basic research (SBO) project "NEPBC: Next generation building energy assessment methods towards a carbon neutral building stock" (S009617N). The support is gratefully acknowledged.

REFERENCES

- Berge M., Georges L. and Mathisen H.M. 2016. On the oversupply of heat to bedrooms during winter in highly insulated dwellings with heat recovery ventilation. In: *Building and Environment*, 106, 389-401.
- Delghust M., De Weerd Y. and Janssens A. 2015. Zoning and Intermittency Simplifications in Quasi-steady State Models. In: *Energy Procedia*, 78, 2995-3000.
- EC (European Commission). 2014. Commission regulation (EU) No 1253/2014 implementing Directive 2009/125/EC of the European Parliament and of the Council with regard to eco-design requirements for ventilation units. In: *Official Journal of the European Union*, 25.11.2014, L 337/8-44
- Faes, W., Monteyne H., De Paepe M. and Laverge J. 2017. A 'use factor' for HRV in intermittently heated dwellings. In: *Proceedings of the 38th AIVC-conference: Ventilating healthy low-energy buildings*, Nottingham, UK, 337-341.
- Janssens A., Vaillant Rebollar J., Himpe E. and Delghust M. 2017. Transforming social housing neighbourhoods into sustainable carbon neutral districts. In: *Energy Procedia*, 132, 549-554.
- Laverge J., Pattyn X. and Janssens A. 2013. Performance assessment of residential mechanical exhaust ventilation systems dimensioned in accordance with Belgian, British, Dutch, French and ASHRAE standards; In: *Building and Environment*, 59, 177-186.
- Majcen D., Itard L. and Visscher H. 2016. Actual heating energy savings in thermally renovated Dutch dwellings. In: *Energy Policy*, 97, 82-92.
- Roulet C.-A., Heidt F.D., Foradini F. and Pibiri M.-C. 2001. Real heat recovery with air handling units. In: *Energy and Buildings*, 33, 495-502.
- VEA (Flemish Energy Agency). 2015. *EPB-cijfers en statistieken 2006-2014* (in Dutch: EPB-figures and statistics), <http://www.energiesparen.be/bouwen-en-verbouwen/epb-pedia>

Application of C-SVM Classification Algorithm to the Lighting Visual Comfort of University Classrooms

Rui Dang¹, Qingchen Wang¹, Yanhui Bu¹, Gang Liu¹

¹ Department of Architecture, Tianjin University

*Corresponding email: hendy_wqc@126.com

ABSTRACT

Considering the quality of the classroom light-environment will directly affect students' eye health and learning efficiency, it is a problem to be solved that how to evaluate the visual comfort levels of the classroom light-environment and save lighting energy on the premise of necessary visual comfort. Aiming at these problems above, this study restored the classroom scene through adjustable full-size light-environment simulation laboratory, in which 135 subjects participated in the visual comfort evaluation experiment of the indoor light-environment. After features (illuminance and correlated color temperature) and labels (comfort levels) preprocessed, we trained and visualized the visual comfort classification models of desktop reading and blackboard reading using the algorithms of C-Support Vector Machine (C-SVM). Through the contour map and the scatter diagram, we get the classification boundary of different comfort levels and the relationship between visual comfort and lighting parameters, which has guiding significance to classroom lighting design and evaluation.

KEYWORDS: Classroom lighting; Visual comfort; Lighting energy efficiency; Subjective evaluation experiment; C-SVM

INTRODUCTION

The quality of indoor artificial light-environment has important influence on the indoor space user's psychological feeling, visual effect, visual fatigue, physiological rhythm and so on. Classrooms are the main venues for students to study in, the pros and cons of the light-environment will directly affect not only the students' eyesight health, but also the student's psychological feeling and learning efficiency (Gao, 2013). Considering the variable classroom usage patterns, it is necessary to verify the comfort range of light parameter of desktop reading, blackboard reading and PPT reading. Only in this way can we guide the light-environment design of classrooms according to the actual usage patterns.

The A.A.Kruithof's lighting comfort curve, which is considered the classic research on spatial light-environment visual comfort, roughly shows the corresponding relationship among the visual comfort, color temperature and illuminance (Kruithof, 1941). After that, visual comfort of light-environment research mainly divided into two directions: one is to further explore the relationship among the visual comfort, illuminance and correlated color temperature (CCT) under different space types based on Kruithof's curve; The other one is to use the methods of fuzzy comprehensive evaluation, linear regression or some other mathematical methods to find the mathematical relationship among the visual comfort, illuminance, CCT and other explanatory variables.

However, most research results are controversial or difficult to apply to practical applications. As an important algorithms in the fields of pattern recognition and machine learning, support

vector machine (SVM) which is based on the theory of VC (Vapnik-Chervonenkis) dimension theory and structural risk minimization principle performs well on the nonlinear and small sample classification or regression problems, which causes scholars' continuous exploration on the optimization of this model and the practical application in recent years (Ben et al, 2012; Kaya et al, 2012; Huo and Duan, 2011). This research tries to develop a classification model using the algorithm of C-support vector machine (C-SVM) with features of illuminant parameters and labels of subjects' visual comfort level. The results can be visualized on 2d contour plots which can estimate the quality of light-environment easily and guide the lighting design of the same space type.

METHODS

Experiment Platform

The experiment was carried out in the experimental module of variable building space designed and constructed independently by Tianjin university. The length and width of the experimental module are both 24 m, which can be divided into any space by partitions. The ceiling is composed by the 16 pieces of 6 m * 6 m lift alone LED lighting modules with individual lift range of 3 m to 9 m. Each lighting module deploys 12 LED tube lights which can be adjusted within a certain range of luminous flux and CCT. Therefore, it can stimulate real light-environment of any regular space with proper scene decoration. The experiment cabin exterior and interior view are shown in Figure 1.

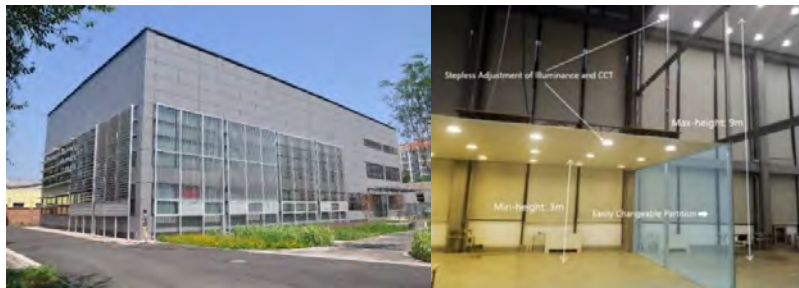


Figure 1. Exterior and interior view of the experiment cabin.

Working Condition

This experiment was carried out in a 12 m * 6 m * 9 m stimulated classroom through space adjusting device. As shown in Figure 2, The outer windows were covered with opaque grey curtain and 18 sets of desks (size: 1.2 m * 0.6 m) and chairs and a blackboard (size: 2 m * 1 m) were put properly.

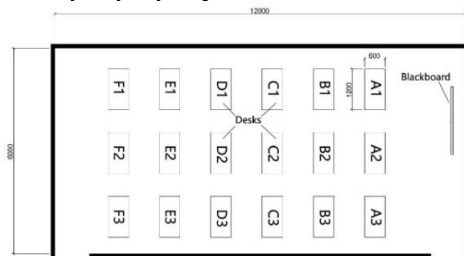


Figure 2. Stimulated classroom setting.

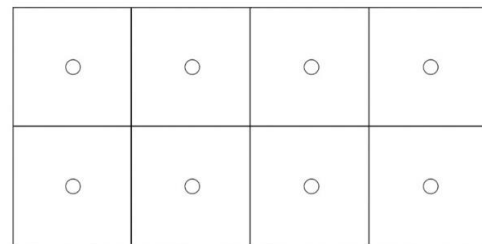


Figure 3. Measuring points on blackboard.

In this experiment, the visual comfort of desktop reading and blackboard reading was taken as the evaluation object. The experiment set up 74 working conditions with only general lighting, making sure that the illuminance parameters of the two lighting modules were consistent. With adjustment of lighting parameters under different working conditions, the 0.75 m horizontal illuminance and CCT covered 20-1100 lx and 2670-6700 K respectively, and

making sure the color rendering index was above 80 in any case. The illuminance and CCT of each measuring point in each working condition was measured by the spectrophotometer (KONICA MINOLTA CL-500A). The layout of measuring points on the blackboard is shown in Figure 3, and the measuring points on desktops were the subjects' visual center of reading. The average value of two-time measurement of each point was taken as the final measured value. The measuring time was chosen after 20 o'clock to minimize the effect of natural light.

For the blackboard surface, the arithmetic mean value of all measurement points was taken as the average illuminance of current working condition. The formula is as follows:

$$E_{av} = \frac{1}{M \cdot N} \sum E_i \quad (1)$$

In this formula: E_{av} is the average illuminance and the unit is lux (lx); E_i is the illuminance of the i th measure point, and the unit is lux (lx); M and N are respectively the longitudinal and transverse measurement points. The measurement results are shown in Table 1 and Table 2:

Table 1. Measurement values of light-environment parameters on desktop.

Condition No.	Percentage of maximum power of white light	Percentage of maximum power of yellow light	Measuring point	Average illuminance (lx)	CCT (K)
1	0%	80%	A1	582.60	2729
		
			F3	682.45	2750
...
74	20%	80%	A1	704.20	3075
		
			F3	835.80	3129

Table 2. Measurement values of light-environment parameters on blackboard.

Condition No.	Percentage of maximum power of white light	Percentage of maximum power of yellow light	Average illuminance (lx)	CCT (K)
1	0%	80%	361.05	2711
2	80%	0%	378.84	6506
3	50%	50%	393.01	4030
...
74	20%	80%	436.18	3054

Subjective evaluation experiment of visual comfort in light-environment.

As shown in Fig. 4, 8 group experiments were carried out in which 16 to 18 undergraduates or postgraduates aged 20 to 26 evaluated the visual comfort of desktop reading and blackboard reading under 74 sets of lighting conditions. The whole subjects were consists of 135 students with a roughly equivalent sex ratio.



Figure 4. Subjective evaluation experiment of visual comfort in classroom light-environment.

After taking 1-minute rest with eye masks on between adjacent sets of working conditions, the subjects can minimize the influence of the former light-environment. Each question on the subjective evaluation questionnaire, with an evaluation standard of "If it is conducive to learning or not", must be chosen one number among 0 to 10 as the visual comfort score of the current conditions. The questionnaire is as Table 3:

Table 3. Subjective evaluation questionnaire

Condition No.										
1. Which do you think is the visual comfort score of current desktop reading?										
0	1	2	3	4	5	6	7	8	9	10
2. Which do you think is the visual comfort score of current blackboard reading?										
0	1	2	3	4	5	6	7	8	9	10

RESULTS

Data preprocessing

We removed the outliers of visual comfort evaluation scores according to the quartile of 8 group experiments. Then we get mean value of the visual comfort evaluation scores of the same seat position, and discretized the average of normal values into 4 range: $0 < \text{comfort average} \leq 2.5$, $2.5 < \text{comfort average} \leq 5$, $5 < \text{comfort average} \leq 7.5$ and $7.5 < \text{comfort average} \leq 10$, representing "awful", "uncomfortable", "good" and "excellent". For visual comfort of blackboard reading, we still need to take arithmetic mean value of 18 subjects in the same group of experiment as the overall comfort value of each condition. Finally, the label of each lighting condition is expressed as integer 0~3, which corresponding to "awful", "uncomfortable", "good" and "excellent" visual comfort level. The data prepared for modeling are shown in table 4 and table 5.

Table 4. Desktop reading data.

No.	Illuminance	CCT	Evaluation
1	582.60	2729	2
2	664.95	2727	2
3	637.55	2723	2
4	612.55	2730	1
5	701.60	2726	1
...
1332	835.80	3129	2

Table 5. Blackboard reading data.

No.	Illuminance	CCT	Evaluation
1	361.05000	2711	2
2	378.84375	6506	2
3	393.00625	4030	2
4	115.60000	6355	1
5	137.02500	4045	2
...
74	436.17500	3054	2

Light-environment evaluation modeling based on C-SVM

Support vector machine (SVM) is a machine learning algorithm based on VC dimension theory and the principle of structural risk minimization (Breerton and Lloyd, 2010), and can improve the generalization ability of the models as far as possible, even to the limited training set. So the SVM model has a good performance on small sample data. By using Python3.6 and its extension packages, we built C-SVM light-environment quality evaluation models of desktop reading and blackboard reading with the kernel of radial basis function (RBF). The specific modeling process is shown as follows:

(1) Divide training set and test set: in this study the blackboard reading visual comfort experiment has 74 groups of data samples, while desktop reading comfort experiment 1332

ones. They were divided into training set and test set randomly according to the proportion of 4:1 respectively, which prepared to train and test the C-SVM model.

(2) Parameter adjustment and model training: C-SVM models were trained for desktop reading and blackboard reading respectively with features of average illuminance and CCT and labels of visual comfort level pre-processed; Through adjusting the parameter by grid search and K-fold cross-validation, we get the optimal C and gamma value (the penalty factor C for error, gamma for parameter of RBF kernel function), and prevent model overfitting by observing the training set prediction accuracy.

(3) Then we got the C-SVM light-environment evaluation model by training on the whole training set with the optimal combination of C and gamma obtained in the previous step.

(4) At last we can evaluate the performance of the trained C-SVM model by predicting accuracy on test sets.

Eventually we got the C-SVM model for desktop reading and blackboard reading as shown in Figure 4, and “x” means “awful”, “●” means “uncomfortable”, “▲” means “good”, “■” means “excellent”:

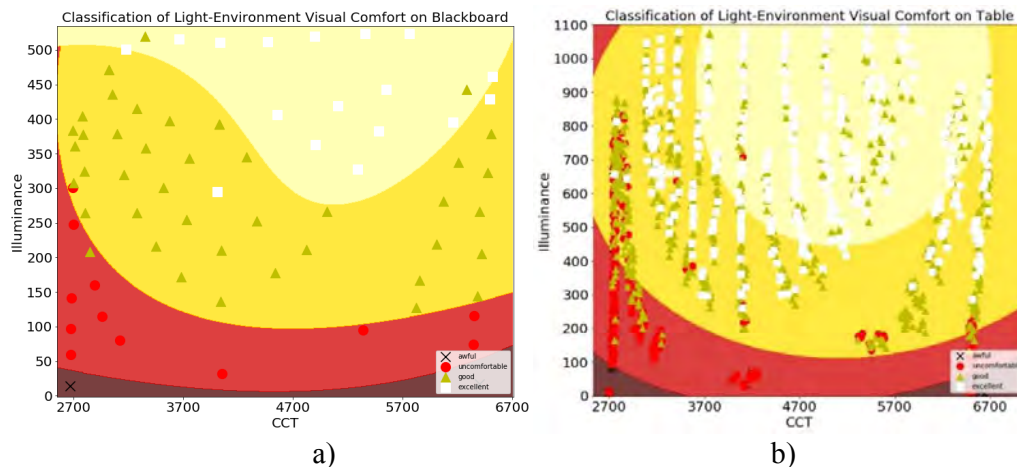


Figure 4. Visual comfort C-SVM model. a) For blackboard reading (accuracy on test set and training set are 0.933 and 0.898), b) For desktop reading (accuracy on test set and training set are 0.667 and 0.663).

DISCUSSIONS

As shown in Fig.4, the horizontal axis represents CCT, the vertical axis represents the illuminance, yellow and white areas are for good and excellent combinations of illuminance and CCT, red and dark red area are for uncomfortable and awful ones. The following conclusions can be drawn from the two graphs:

For blackboard reading:

a) The light yellow area is the best for blackboard reading visual comfort and should be as a priority for teaching mode. The lowest vertical illuminance of blackboard is required to be 290 lx in the goal of achieving “excellent” visual comfort with a CCT of 5000 K at the same time. When the CCT is adjusted lower or higher than 5000 K, we must increase the illuminance to maintain the same level of visual comfort at the price of higher lighting power density (LPD). Even if there are special requests for the CCT of light source, try not to make CCT lower than 4000 K or higher than 6000 K, or we need above 400 lx of illuminance to achieve the same visual comfort level, which is not conducive to energy saving.

b) The yellow area is recommended as a good or acceptable area for non-teaching mode. In this area, the lowest vertical illuminance of blackboard should be limited to 100 lx with a CCT

of 4000-5500 K at the same time. Similarly, CCT lower than 4000 K is not recommended.

c) Red and dark red area are uncomfortable and awful area respectively. If the vertical illuminance of blackboard is lower than 100 lx, no matter what CCT can meet the requirement of visual comfort. Therefore, the vertical illuminance of blackboard should be higher than 100lx.

For desktop reading:

a) The light yellow area is the best for desktop reading visual comfort and should be as a priority for self-study or reading mode. Similarly, the lowest vertical illuminance of desktop is required to be 450 lx in the goal of achieving “excellent” visual comfort with a CCT of 5000 K at the same time, but we cannot achieve “excellent” area if the CCT is lower than 3700 K or higher than 6500 K. Even if there are special requests for the CCT of light source, try not to make CCT lower than 4200 K or higher than 6000 K for the sake of energy saving.

b) The yellow area is recommended as a good or acceptable area when there is less use of desktop. In this area, the lowest vertical illuminance of desktop should be limited to 140 lx with a CCT of 5200 K at the same time. Similarly, CCT lower than 3700 K or higher than 6500 K is not recommended for energy efficiency.

c) Red and dark red area are uncomfortable and awful area respectively. If the vertical illuminance of blackboard is lower than 140 lx, no matter what CCT can meet the requirement of visual comfort. Therefore, the vertical illuminance of desktop should be higher than 140 lx.

CONCLUSIONS

The quality of indoor light-environment is often difficult to evaluate directly. The research results of lighting-environment visual comfort experiment show that the light-environment quality evaluation model based on C-SVM has good interpretability, strong generalization capacity and low risk of wrong classification in the limited sample space. It can effectively identify the visual comfort level of classroom light-environment, which is also a guide to other research of light-environment quality in different space types.

REFERENCES

- Gao S. 2013. A research review of classroom light environment. *China illuminating engineering journal*, 2013(s1), pp. 94-100.
- Kruithof A. 1941. Tubular Luminescence Lamps for General Illumination. *Philips Technical Review*, 6(3), pp. 65–96.
- Ben S.S., Bacha K., and Chaari A. 2012. Support vector machine based decision for mechanical fault condition monitoring in induction motor using an advanced Hilbert-Park transform. *Isa Transactions*, 51(5), pp. 566.
- Kaya B., Oysu C., Ertunc H.M., et al. 2012. A support vector machine-based online tool condition monitoring for milling using sensor fusion and a genetic algorithm. *Proceedings of the Institution of Mechanical Engineers Part B Journal of Engineering Manufacture*, 226(11), pp. 1808-1818.
- Huo Y.T. and Duan Z.X. 2011. Soft-sensing of optical environmental quality in tunnel space based on support vector machine. *Modern electronics technique*, 34(8), pp. 167-169.
- Brereton R.G. and Lloyd G.R. 2010. Support vector machines for classification and regression. *Analyst*, 135(2), pp. 230.

Developing and Testing Visual Privacy Metrics

Noor Alkhalili^{1*}, Ted Kesik¹, William O'Brien² and Terri Peters³

¹ University of Toronto, Toronto, Ontario, Canada

² Carleton University, Ottawa, Ontario, Canada

³ Ryerson University, Toronto, Ontario, Canada

*Corresponding email: noor.alkhalili@mail.utoronto.ca

ABSTRACT

The dense redevelopment of inner cities (intensification) has been accompanied by a dramatic surge in the development of multi-unit residential buildings (MURBs) within ever shrinking proximities to one another. Modern multi-unit residential building design often embodies conflicting desires for daylighting and visual privacy, or designers simply do not consider collective occupant discomfort factors. Thus, the focus of this project was to develop and validate conceptual and quantitative variables influencing visual privacy, such that future and existing residential designs can be analyzed from a visual privacy perspective. This paper formulates an approach that combines building physics (visual angles and relative brightness) with social and psychological factors to avoid conflicts between competing aspirations for sustainable and resilient buildings that promote occupant wellbeing.

KEYWORDS

Visual privacy, occupant discomfort, visual angles, relative brightness, occupant wellbeing.

INTRODUCTION

Visual privacy is a common perception that is influenced by different cultural, psychological and physiological experiences (Kennedy and Buys, 2015). It is a perceptual progression that occurs between an individual and 'others'. Studies show that visual privacy can be a major influence on a building inhabitant's awareness of comfort (Kang and Kim, Lee et al Lee, 2014). Practically speaking, this means that perceptions of privacy differ among cultures, age groups and sexes, and all variables should be considered in the design-appropriate levels of privacy. Globalization, urban intensification and the trend to larger glass areas in residential buildings are making visual privacy an increasingly critical consideration. Canada is a suitable "living laboratory" for examining visual privacy because it has among the highest percentage of foreign-born citizens who hold diverse perceptions of privacy due to their various religious, cultural and psychological backgrounds (Roy, 2013). Combined with a growing trend toward the use of large windows and glazed facades around the world, visual privacy is being recognized as a major problem in dense urban environments, such as the large cities in Canada where multi-unit residential buildings predominate. Architects and developers put little to no attention towards visual privacy when designing these residential buildings because the metrics of visual privacy are not part of their design vocabulary.

Theoretical approaches to privacy consider the human psychology, culture, and behaviour. Privacy has been split into different categories by theorists, where each defines the comfort level of a person with regards to being observed or touched. Since most individuals seek more privacy at home than anywhere else, the meaning of "solitude" (being free from the observation of others), defines a major need for visual privacy metrics in residential designs (Lang, 1987). When the achieved privacy is less than the desired privacy, a situation known as crowding, adaptive solutions are implemented to counteract the discomfort (Lang, 1987).

The optimum privacy can be difficult to achieve as the desired privacy from one individual to another may differ, causing the achieved privacy to result in social isolation or crowding (Altman and Grove, 1978). Meanwhile, prioritizing privacy through architectural design (e.g., small or translucent windows and moveable shading systems) may compromise views, daylight, and sense of spaciousness. The theoretical privacy mechanism mentioned by Altman is the nonverbal privacy mechanism (1978, pp.34). It suggests that body language reflects upon the level of comfort from non-verbal intrusion to one's privacy (through seeing or touching). The delinquency for someone's ability to visually step into another's private space can have no limitations. People may look into others' houses intentionally or unintentionally; but to the occupant, intention is irrelevant and still results in discomfort for the occupant. An essential factor of living in a multi-story apartment is the amount to which everyday routines are affected by "proxemics and sharing" (Kennedy and Buys, at el Miller, 2015). The connection between proxemics and privacy in housing raises the concern for personal space and the longing for a place that is acknowledged as one's own (Deasy and Lasswell, 1985). People often seek privacy and connection to the community, which creates a challenge for designers, as limits differ from one person to another. However, the connecting base-line to privacy for the occupants is usually their ability to control the privacy.

This research takes a conceptual and quantitative approach to visual privacy in multi-unit residential buildings and analyses the perception of privacy through a series of survey questions of real-life privacy related situations.

METHODS

This research is focused heavily on peoples' perceptions of privacy which is influenced by their lifestyle and background. Therefore, this research focused exclusively on field data, and initiated the process by conducting a survey to facilitate the quantification of visual privacy comfort levels. The survey consisted of 32 questions where respondents evaluated real-life visual privacy-related scenarios. The aim of the survey was to produce a realistic setting (based on photographs and renderings) where responders were able to rate the privacy feeling with a scale value. Some of these images were taken of existing residential units in downtown Toronto. These images were then used as part of the questions in the survey to guide the responses to a personal level. Each question from the survey was defined by two visual privacy metrics that were identified to affect the visual privacy rating. These metrics are the visual angle and the brightness level. Visual angle is the viewpoint at which an object spans at the eye of an observer (COSMOS, 2003). It is the angle at which our eyes perceive the size of an object in real life, by incorporating the size of the object and its distance from the observer (see Figure 1 below). Using the equation below considers a small angle approximation.

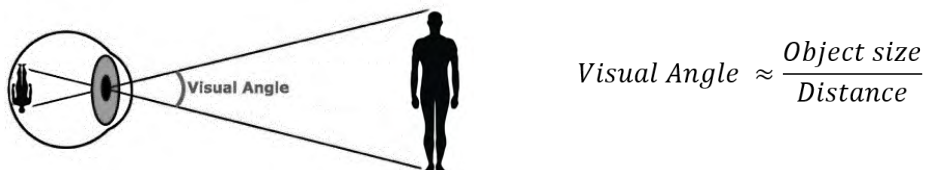


Figure 1: Visual Angle

The farther away a human is, the more private that human/occupant feels. Thus, distance is a variable that is considered in this calculation. Visual angles were chosen as the initial metric used to determine the equation for optimum visual privacy level, since it is dependent on the distance and the angle at which it is viewed. Multiple visual angles can be determined for

each window in a unit, but in this research the highest visual angle value has been utilized and ascribed to each scenario.

The brightness level is another crucial metric that defines the visibility of inside and outside. Figure 2 consists of two pictures of the same condominium, in Vancouver, in the morning and at night. In the morning, views into the condominium are very limited, whereas at night one can clearly see well into the condominium.

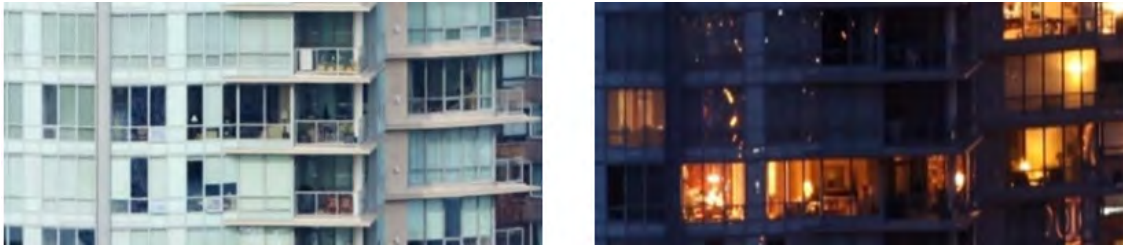


Figure 2: Appearance of condominium in Vancouver in the morning and at night (Gigapixel)

A brightness factor defines the light conditions that affect the privacy rating of housing design. This brightness factor is determined from a range of 1 to 5 which is applied to both the inside and outside conditions simultaneously to obtain a brightness ratio (see Figure 3). The brightness level outside and inside is dependent. For example, the sight conditions when it is bright inside and outside differ greatly compared to bright inside and dark outside. Hence, both conditions were applied as a factor, and then the ratio of what is observed inside to outside was identified.

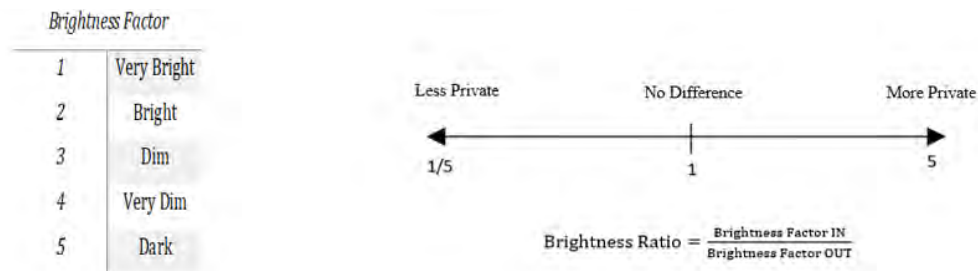


Figure 3: Brightness factor rating from 1 to 5 and brightness ratio calculation.

When the brightness ratio approaches a value of 1/5 (very bright inside and dark outside) the occupied space is considered less private, and when the ratio approaches 5 (dark inside and very bright outside) the occupied space is considered more private. This method for estimating the brightness ratio has been created in support of this research and there are no known prior studies that calculate such factors.

The survey has been created upon the consideration of both the visual angles and brightness levels. Various scenarios were created in SketchUp and from images taken of the field study in Toronto, for the different views at which people would feel comfortable or uncomfortable in. Observers were placed in a hypothetical real-life setting (pedestrian walking, neighbour's balcony, etc.) at different distances away from occupants for visual angles to be calculated at diverse configurations. Figure 4 shows one observer looking at an occupant's window from two different horizontal distances.

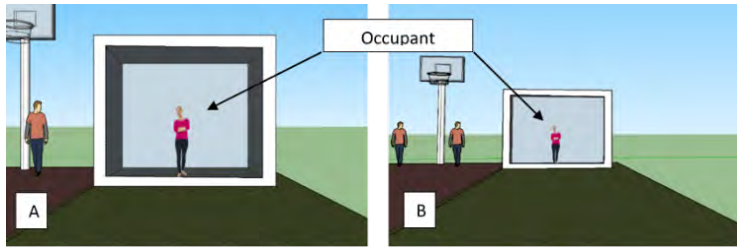


Figure 4: SketchUp model. “A” from observer 5m away and “B” from observer 15 m away.

Most of the questions are scalar, meaning that pictures (like those in Figures 2 and 4) were presented and participants were asked to rate the situation by a scale of 1 (not very private) to 10 (very private). A sample question can be seen in Figure 5.

Q25) On a scale of 1 (not private) to 10 (very private), how private would you feel if you lived in this condominium at this time of day?
Mark only one oval.

	1	2	3	4	5	6	7	8	9	10	
Not Very Private	<input type="radio"/>	Very Private									



Figure 5. Sample question from online survey.

Overall, the survey consisted of 32 questions of this type. It was presented to a variety of age groups, genders and persons from different cultures to enhance the understanding of visual privacy in relation to identity and background. A relationship between visual privacy rating (dependent variable) and visual angles and brightness levels (independent variables) can then be established from survey answers, by graphing the results of the three variables together.

RESULTS

Numerous relationships have been interrogated through the 32 survey questions to examine the relationships between the visual privacy metrics and age, gender, and culture. The survey was completed by 214 people varying in age, gender, background. The results were processed and modelled, using MATLAB and Excel, aiming to create an equation for visual privacy rating. To confirm the affiliation and viability of the privacy metrics, a graph was created for both the brightness levels and visual angles against privacy ratings.

Figure 6 below shows the relationship between brightness ratio levels and participant-rated privacy ratings. As seen in the graph, the hypothesis based in Figure 3 earlier is confirmed: perceived privacy decreases as the brightness ratio decreases (it is brighter indoors than out) – particularly below 1. The most critical values lie where the brightness ratios are lower than 0.5. This is where it is bright inside and dark outside, which is considered the high stakes of visual privacy issues as so much detail can be seen inside. Brightness ratio is primarily dependent on weather conditions and indoor electric lighting intensity.

Unlike brightness ratios, visual angles are influenced by geometric factors such as window size, orientation, balcony size, etc. Nonetheless, the affiliation of the visual angles with privacy ratings, from the conducted survey, shows a relatively linear relationship (see right side of Figure 6) – beyond certain angles privacy is not affected.

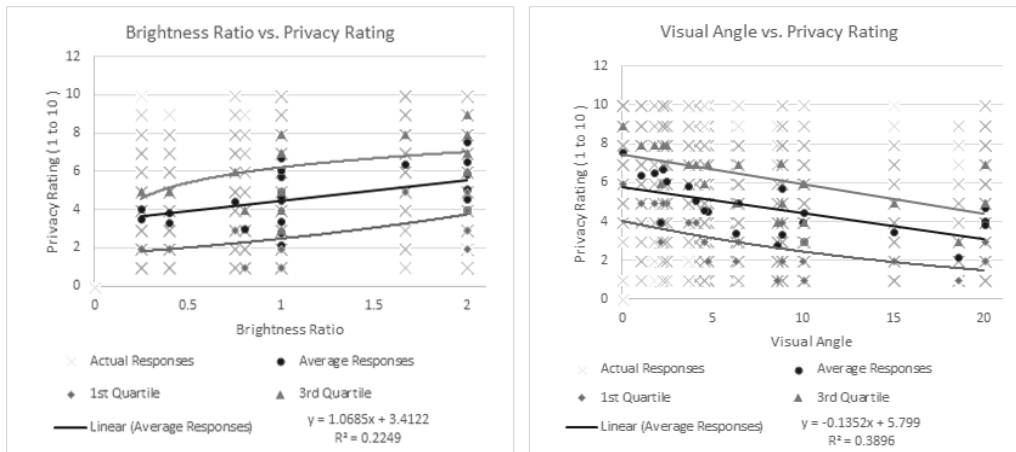
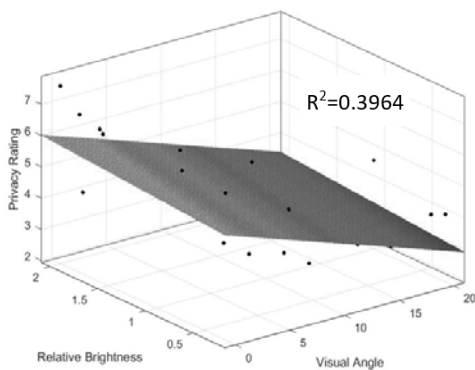


Figure 6. Comparison of relationship between Brightness Ratios and Privacy Ratings versus Visual Angles and Privacy Ratings.

The first and third quartiles in the graphs above lie within reasonable distance to the mean, meaning that generally the privacy is favoured under most circumstances. The quantity at which the amount of visibility (visual angle) is considered acceptable from one person to another is mutable. Cultural influence, for example, plays a key role in the value of privacy and explains the divergence between the data from one person to another, which is discussed later. Thus, the distribution of data in Figure 6 implies a combination of two observations. The first is that people feel differently about privacy and hence answer differently, while the second is that people interpreted the survey questions inconsistently. Further analysis is required understand the variability of responses.

Through MATLAB, the linear relationship between Visual Angle, Relative Brightness, and Privacy Rating was obtained (see Figure 7). Visual angles and relative brightness values can be used to estimate the privacy ratings for any room or unit in residential buildings.



$$PR = 5.375 - 0.1195 (VA) + 0.2471 (RB)$$

Where: PR: Privacy Rating = ranges 1: Not Very Private to 10: Very Private

$$RB: \text{Relative Brightness} = \frac{\text{Brightness Factor In}}{\text{Brightness Factor Out}}$$

$$VA: \text{Visual Angle [0 to 32]} = 2 \arctan \left(\frac{\text{Object Size}}{2 \times \text{Distance}} \right)$$

Figure 7. Graph and equation for visual privacy rating as a function of visual angle and relative brightness.

DISCUSSIONS

One of the aims of this research was to compare the visual privacy rankings between the different genders, age groups, and cultural standards. The limited length of this paper does not permit presenting the statistics, however several relationships were found. First, culture plays a significant part in privacy ratings, hence in multi-cultural and densely developed urban regions designers should address the full range of cultural values. Second, age was

also found to be a determining factor for visual privacy standards. In this research, perceptions of privacy were more closely correlated for two age cohorts, ages 18-29 and 50+, while a difference in response was reported for the age group of 30-50 years. Young people, and especially females, demand higher levels of visual privacy to feel comfortable. The relationship between room types (e.g., bedroom/bathroom versus living room and clothing levels (e.g., fully dressed versus sleep wear) was not surveyed, but it is reasonable to assume different expectations of privacy based on these parameters. The multi-unit residential building design challenge is to recognize the importance of daylighting and views for occupant wellbeing (Veitch and Galasiu, 2012), while still providing acceptable visual privacy.

CONCLUSIONS

Visual privacy in residential design has been an issue in various countries for many years (Kennedy, Buys and Miller, 2015). However, there has been very minimal research to develop practical design metrics for visual privacy. This paper indicates that both relative brightness and visual angle are important predictors for visual privacy. However, the large spread in the data indicate two possibilities: 1) that there are many other predictors for privacy (as preliminary examination on demographics has revealed); or 2) that there were multiple interpretations of survey questions. Field studies are needed to confirm the visual privacy metrics advanced in this paper are effective in predicting the need for mitigating measures such as plantings, screens or blinds, frosted glass, etc., and to help determine the potential tradeoffs between daylighting, views and visual privacy. In the future, a visual privacy metric could be incorporated into architectural design software tools as well as building standards (e.g., WELL™ Building Standard).

REFERENCES

- Altman, I. and Gove, W. 1978. *Contemporary Sociology*, Vol.7, no.5, pp.638.
- Angular Diameter | COSMOS. 2003. *Centre for Astrophysics and Supercomputing*. Available at: [http://astronomy.swin.edu.au/cosmos/A/Angular Diameter](http://astronomy.swin.edu.au/cosmos/A/Angular_Diameter). (Accessed: 3rd January 2018)
- Deasy, C. M. and Lasswell, T. E. Whitney Library of Design, 1985. *Designing places for people: a handbook on human behavior for architects, designers, and facility managers*.
- Kang, N. N., Kim, J. T. and Lee, T. K. 2014. A Study on the Healthy Housing Quality of Multi-family Attached House According to Dwelling Unit Age. *Energy Procedia*, 62, 595–602.
- Kennedy, R. and Buys, L. The Impact of Private and Shared Open Space on Livability in Subtropical Apartment Buildings. (2015).
- Kennedy, R., Buys, L. and Miller, E. 2015. Residents' Experiences of Privacy and Comfort in Multi-Storey Apartment Dwellings in Subtropical Brisbane. *Sustainability*, Vol.7, pp.7741–7761.
- Lang, J. *Privacy, Territoriality, and Personal Space - Proxemic Theory*. 1987, pp.145-156
- Roy, B. Diversity in Canada: an overview. *Canadian Immigrant* (2013). Available at: <http://canadianimmigrant.ca/guides/moving-to-canada/diversity-in-canada-an-overview>. (Accessed: 2nd January 2018)
- Vancouver Gigapixel Panorama Photography. *gigapixel.com*. Available at: <http://www.gigapixel.com/>. (Accessed: 5th January 2018)
- Veitch, J and Galasiu A. 2012. The Physiological and Psychological Effects of Windows, Daylight, and View at Home: Review and Research Agenda. National Research Council of Canada Institute for Research in Construction NRC-IRC Research Report RR-325.

Environmental Conditions and Occupant Satisfaction in the Workplace: A Controlled Study in a Living Lab

Jennifer Nguyen^{1,*}, Stephanie Huynh¹, Anja Jamrozik^{1,2}, Nicholas Clements^{1,2,3}, Christian Ramos^{1,2,3}, Brent Bauer^{2,4}, Jie Zhao^{1,2,3}

¹Delos Living LLC, New York, NY, USA

²Well Living Lab, Rochester, MN, USA

³General Internal Medicine, Mayo Clinic, Rochester, MN, USA

⁴Complementary and Integrative Medicine Program, Mayo Clinic, Rochester, MN, USA

*Corresponding email: jennifer.nguyen@delos.com

ABSTRACT

Living labs offer a powerful, new way to measure human-building interactions. In addition to having the advantages of a traditional controlled laboratory setting, living labs facilitate the study of how combinations of environmental factors directly affect human health and satisfaction in a real-world setting. The aim of this experimental study was to characterize the relationship between individual-level exposure to environmental conditions and reported satisfaction with environmental quality in a simulated open-office workspace created in a living lab. Eight office workers were exposed to six different week-long combinations of light (natural and electric), sound, and thermal conditions over 18 weeks in a living lab. We assigned exposure to temperature, relative humidity, and light, specifically illuminance, to each participant using measurements from the environmental sensor in closest proximity to the participant. Sound measurements were collected by only one device, so all participants were assigned the same sound exposure. Participants also completed daily questionnaires in which they rated their level of satisfaction with the overall quality of the workplace and with specific environmental parameters in the simulated workspace. Using ordinal response mixed effects models, we found that temperature, noise, and light — individually and in combination — were significant predictors of self-reported occupant satisfaction. Our results contribute to a better understanding of the relative importance of environmental parameters to employee satisfaction in a real-world context, which may be useful for guiding and optimizing building design and management decisions to best serve its occupants.

KEYWORDS

Controlled-study, IEQ, Living lab, Satisfaction, Workplace

INTRODUCTION

An active area of research at the intersection of building sciences, health sciences, and behavioural sciences is understanding the relative impact of different environmental conditions on satisfaction with the indoor environment. This is important because environmental conditions are key determinants of occupant comfort and satisfaction, as well as health, well-being, and performance (Wargocki et al. 2000; Veitch et al. 2008; Lan et al. 2012; Al Horr et al. 2016; MacNaughton et al. 2017; Tanabe et al. 2014; Geng et al. 2017; Küller et al. 2006). Living labs, defined as research settings in which study participants occupy a simulated environment for an extended period of time, are well-positioned to collect this information. Living labs enable the delivery of combinations of environmental conditions, while providing the scientific rigor of an experimental study and the real-world applicability of an observational study.

The aim of this study was to examine the association between exposure to environmental conditions and reported satisfaction with environmental quality in a simulated open-office workspace created in a living lab. This study is also an extension of a proof-of-concept study previously reported by Jamrozik (2018) that found that changes in environmental office conditions affected occupants' experiences inside and outside of the space. In contrast to Jamrozik et al.'s scale of analysis at the level of weeklong "scenes" – combinations of acoustic, lighting, and thermal conditions, this study examined the daily-level relationship between individual exposure to these combinations of environmental conditions and reported satisfaction with office environmental quality. This approach was undertaken for two reasons: 1) doing so enabled an analysis at increased temporal granularity (i.e., from the average response over multiple weeks to the daily scale), and 2) actual exposure values may differ day-to-day and between weeks despite having identical scene conditions and setpoints.

METHODS

Study design

The Well Living Lab is a research facility consisting of six experimental modules that can be configured to simulate real-world indoor environments (Jamrozik et al. 2018). In this study, three of the fabric modules (Modules D, E, and F) were combined to form a 124 m² open office (Figure 1), which served as the experimental setting for six environmental "scenes" made up of combinations of acoustic, lighting, and thermal conditions. A baseline condition (scene 1) was designed based on existing research and the participants' previous office in order to simulate environmental conditions commonly found in an average office setting.

Figure 1 shows the layout of the modules where eight office workers sat at desks 1-4 and 6-9 and worked in the simulated office, where they were exposed to week-long combinations of natural light (three levels), electric light (four levels), sound (five levels), and temperature (three levels) (Table 1). A nine-week sequence of scenes (order: 1, 2, 3, 4, 1, 2, 5, 6, 2) was repeated twice over a period of eighteen weeks, from May 31, 2016 to September 30, 2016.

Acoustic, lighting, and thermal conditions

Using the Center for the Built Environment Thermal Comfort tool, assuming a mean radiant temperature of 26.0°C, a wind speed of 0.1 m/s, relative humidity (RH) of 45%, a metabolic rate of 1.1 met, and a clothing level of 0.7 clo (Hoyt et al. 2017), three temperature setpoints were chosen for this experimental study: 21.7°C (cool-neutral temperature), 23.9°C (neutral-warm), and 19.4°C (uncomfortably cold). Additionally, study participants were exposed to five acoustic conditions including sound masking via white noise (two conditions), sound masking via simulated speech (two conditions), and no sound masking.

To vary participant exposure to natural light, windows were equipped with electrochromic (EC) glass (VIEW Dynamic Glass, Inc.) which provided controllable window tinting. Sheer shades (Phifer SheerWeave 4100, 10%, Alabaster – motorized by Lutron) provided occupants a means of controlling natural light via wall switches next to windows, and blackout shades (Mermet Blackout-White – motorized by Lutron) were used to simulate a windowless office. The EC glass tint varied between clear (visible transmittance 58%), dark (visible transmittance 1%), and intelligence mode, in which tint level is automated and varied over four levels throughout the day to limit glare and reduce solar heating. For electrical lighting (S30, Ketra), the following color correlated temperature (CCT) setpoints were used: 2700°K (warm colour), 3500°K (warm-neutral white), 4200°K (cool-neutral white), and 6500°K (cool white).

Participants

The eight participants recruited for this study were employees of the Mayo Clinic in Rochester, Minnesota, all of whom were adults between the ages of 18 and 65 years, able to conduct current work duties from a remote location (i.e., the living lab), and able to work 20-40 hours per week. Full inclusion and exclusion criteria for study participants have been previously described in detail by Jamrozik (2018). One participant (located at desk 4) was removed from the data set due to sensor connection issues, leaving a total of seven participants for inclusion in the data analysis (mean age = 46.9 years, standard deviation (SD) = 13.1). The study was approved by the Mayo Clinic Institutional Review Board.

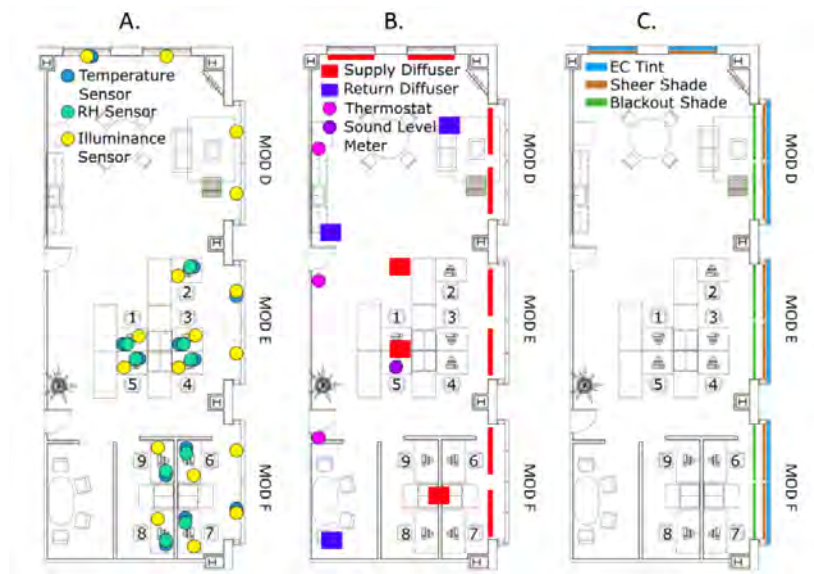


Figure 1. Layout of the experiment space and locations of a) temperature, relative humidity (RH), and illuminance sensors, b) thermostats, sound level meter, and ventilation diffusers, and c) electrochromic (EC) tint glass, sheer shades, and blackout shades. Participants were located at desks 1-4 and 6-9.

Survey design

At the start of the study, participants completed a baseline survey asking about demographics, work, and health behaviors. At the end of each day, participants completed questionnaires asking about satisfaction with environmental conditions and their overall work experience for the day, as well as their mood and health behaviors. In this study, we focused our analysis on daily ratings of overall workplace quality (How much did your work environment make it easy for you to get your work done? 1-5 scale; 1: Not at all, 5: Very much) and satisfaction with the noise level, lighting, and temperature (Today, how satisfied are you with the ___ in the work environment? 1-5 scale; 1: Very dissatisfied; 5: Very satisfied).

Data collection, processing and analysis

At desk-level, wireless temperature and humidity sensors (Wireless Humidity Sensor, Monnit Corp.) collected data at five-minute intervals, and wireless horizontal illuminance sensors (Lux1000 Light Level Sensor, Wovyn LLC) collected data at ten-minute intervals. Sound level was measured every ten seconds by a single sound level meter (XL2 Audio and Acoustic Analyzer with M2211 Microphone, NTi Audio Inc.) located at desk 5. Because of connection issues for the temperature and RH sensor located at desk 4, which resulted in missing data, all information collected from the participant located at desk 4 was excluded from the analysis.

The calculation of average daily exposure was restricted to measurements collected between 7:00 and 17:00 CDT because participants' usual working hours were 6:30 to 17:30 CDT. We performed ordinal mixed effects regression analyses using the 'ordinal' package in R (Version 3.4.0). Day of the week, calendar date, and study week were assessed for confounding and not included in the final models. Final models included sound level, illuminance, temperature, and RH (all as continuous variables), an indicator for study scene, and a random intercept for study participant. The number of quadrature points in the adaptive Gauss-Hermite approximation was set to 10 to improve the accuracy of maximum likelihood estimates. To facilitate direct comparison across environmental conditions, odds ratios (ORs) and 95% confidence intervals (CIs) are reported for a normalized unit of exposure, i.e., a one standard deviation (SD) change in estimated exposure, assuming a linear exposure-response function.

RESULTS

Overall (across the six experimental scenes), mean (\pm SD) desk-level temperature and RH was 24.1°C (\pm 1.7) and 42.9% (\pm 5.8), respectively, and mean illuminance was 778.2 lx (\pm 692.8). Measured desk-level temperatures were, on average, higher than setpoints by 1.2 to 3.1°C. Mean RH across different scenes ranged from 37.6% (\pm 3.0) to 48.6% (\pm 4.5). Substantial variation was observed in mean illuminance between and within scenes, with estimates ranging from 413.1 lx (\pm 495.0) to 1001.8 lx (\pm 622.5). The mean sound level was 47.1 dBA (\pm 1.0) and showed little variation between scenes, although measured sound levels were loudest for the two scenes in which sound masking was white noise (Table 1).

Workplace quality satisfaction

Using ordinal response mixed effects models, we found that lower measured illuminance was significantly associated with greater workplace quality satisfaction and greater satisfaction with sound levels (Table 2). Additionally, greater measured overall volume was significantly predictive of increased satisfaction with overall workplace quality, sound levels, and temperature. Higher measured temperature was also significantly associated with increased satisfaction with temperature. We did not observe any significant associations for reported satisfaction with lighting. Although convergence criteria for all models were met, the condition number of the Hessian exceeded 10^7 , which indicates that models were not well-defined and should be interpreted with caution. The large variability in illuminance in this study likely contributed to the observed lack of empirical identifiability (e.g., scaling issues).

DISCUSSION

Utilizing a living lab designed to simulate an open office workspace, we found that measured illuminance and sound were significantly predictive of satisfaction with overall workplace quality, and that this pattern was also true for satisfaction with sound levels. However, in contrast to these results, none of the four examined environmental parameters were associated with reported satisfaction with lighting. Additionally, we found that measured temperature and sound were significantly associated with satisfaction with temperature.

As reported previously by Jamrozik (2018), when participants were asked whether they were more sensitive to certain environmental conditions than to others, they most frequently reported that cold temperatures were the most noticeable and unpleasant conditions, followed by noise, and then lack of daylight. This analysis complements the previous qualitative findings, by quantifying the link between individual-level exposure to environmental conditions and reported satisfaction with environmental quality. However, based on model performance metrics, the magnitude and direction of our results should not be interpreted as indicative of the relative importance of environmental conditions nor of the direction of the

Table 1. Description of building system set points and mean (\pm SD) environmental conditions, by study scene (weekdays from 7:00 to 17:00 CDT).

Scene No.	Total Days	EC Glass (Tint No.)	Sheer Shades (Blackout Shades)	Light CCT ($^{\circ}$ K)	Light Illuminance (Lx)	Relative Humidity (%)	Temperature ($^{\circ}$ C)	Sound Masking (dBA)		
					<i>Measured</i>	<i>Measured</i>	<i>Setpoint</i>	<i>Measured</i>	<i>Setting</i>	<i>Measured</i>
1 (Baseline)	19	Clear (Tint 1)	Open, Controllable (Open)	3500	999.6 (\pm 690.4)	40.3 (\pm 3.7)	21.7	24.8 (\pm 1.2)	Off	46.9 (\pm 0.9)
2	28	Intelligence (Tints 1-4)	Open, Controllable (Open)	4200	703.0 (\pm 675.4)	43.0 (\pm 6.2)	21.7	23.9 (\pm 1.4)	Off	47.0 (\pm 0.9)
3	10	Dark (Tint 4)	Closed, Inoperable (Closed)	2700	413.1 (\pm 495.0)	48.1 (\pm 3.8)	19.4	22.4 (\pm 1.4)	White Noise (Low)	47.2 (\pm 0.8)
4	10	Clear (Tint 1)	Open, Controllable (Open)	2700	1001.8 (\pm 622.5)	37.6 (\pm 3.0)	23.9	26.0 (\pm 1.2)	Simulated Speaking I	47.1 (\pm 1.0)
5	10	Dark (Tint 4)	Closed, Inoperable (Closed)	6500	695.0 (\pm 801.4)	48.6 (\pm 4.5)	19.4	22.3 (\pm 1.1)	White Noise (High)	47.6 (\pm 1.3)
6	10	Intelligence (Tints 1-4)	Open, Controllable (Open)	6500	752.3 (\pm 654.8)	40.8 (\pm 3.4)	23.9	25.1 (\pm 0.9)	Simulated Speaking II	46.7 (\pm 0.9)

Table 2. Odds ratios (OR) and 95% confidence intervals (CI) of reporting higher satisfaction associated with a 1 SD change* in environmental conditions.

Environmental Parameters in Model	Satisfaction with Workplace Quality OR (95% CI)	Satisfaction with Acoustics OR (95% CI)	Satisfaction with Temperature OR (95% CI)	Satisfaction with Lighting OR (95% CI)
Light (Illuminance)	6.3 (1.5, 26.0)†	4.7 (1.7, 13.2)‡	1.6 (0.6, 4.1)	1.4 (0.5, 3.7)
Sound	1.4 (1.1, 1.9)†	1.3 (1.03, 1.7)†	1.4 (1.1, 1.7)‡	0.9 (0.7, 1.2)
Temperature	1.2 (0.8, 1.8)	1.4 (0.9, 2.0)	1.5 (1.05, 2.0)†	0.9 (0.7, 1.3)
Relative Humidity	1.04 (0.96, 1.1)	1.0 (0.94, 1.1)	1.1 (0.99, 1.12)	1.0 (0.95, 1.1)

* +1 SD change for sound, temperature, and relative humidity. -1 SD change for light.

† P-value < 0.05; ‡ P-value < 0.01

relationships. Accordingly, although we observed interesting associations between environmental parameters and satisfaction with other parameters (e.g., light was predictive of satisfaction with acoustics; sound was predictive of satisfaction with temperature), these findings may be due to multi-collinearity since exposure was experimentally delivered in scene combinations. Nonetheless, our results support a link between temperature, noise, and light and satisfaction with workplace quality and/or indoor environmental conditions.

CONCLUSIONS

In this study we demonstrate that living labs can be used to identify the environmental conditions predictive of higher self-reported satisfaction with overall workplace quality, and with specific workplace ambient conditions. We found that temperature, noise, and light are important, predictive factors of occupant satisfaction, consistent with prior studies. Future studies should examine more combinations of environmental parameters in a real-world setting, in order to generate evidence that may guide and optimize building design and management decisions to best serve occupants.

ACKNOWLEDGEMENT

We sincerely thank the participants for their time and participation in this study. We especially thank the staff of the Well Living Lab who kept everything running, and the staff and leadership teams of Delos Living LLC, Mayo Clinic, the Well Living Lab (WLL), and the WLL's Joint Steering Committee, Scientific Advisory Council, and Alliance members.

REFERENCES

- Al Horr Y., Arif M., Kaushik A., Mazroei A., Katafygiotou M., and Elsarrag E. 2016. Occupant productivity and office indoor environment quality: A review of the literature. *Building and Environment*, 105, 369-389.
- Hoyt T., Schiavon S., Piccioli A., Cheung T., Moon D., and Steinfeld K. 2017. CBRE Thermal Comfort Tool for ASHRAE-55. Center for the Built Environment, University of California Berkeley. <http://comfort.cbe.berkeley.edu/>
- Geng, Y., Ji W., Lin B., and Zhu Y. 2017. The impact of thermal environment on occupant IEQ perception and productivity. *Building and Environment*, 121, 158-167.
- Jamrozik A., Ramos C., Zhao J., Bernau J., Clements N., Wolf T. V., and Bauer B. 2018. A novel methodology to realistically monitor office occupant reactions and environmental conditions using a living lab. *Building and Environment*, 130, 190-199.
- Küller R., Ballal S., Laike T., Mikellides B., and Tonello G. 2006. The impact of light and colour on psychological mood: a cross-cultural study of indoor work environments. *Ergonomics*, 49(14), 1496-1507.
- Lan L., Wargoocki P., and Lian Z. 2012. Optimal thermal environment improves performance of office work. *REHVA Journal*, 49(1), 12-17.
- MacNaughton P., Satish U., Laurent J.G.C., Flanigan S., Vallarino J., Coull B., Spengler J.D., and Allen J.G. 2017. The impact of working in a green certified building on cognitive function and health. *Building and Environment*, 114, 178-186.
- Tanabe S.I., Haneda M., Nishihara N. 2014. Workplace productivity and individual thermal satisfaction. *Building and Environment*, 91, 42-50.
- Veitch J.A., Charles K.E., Farley K.M., and Newsham G.R. 2007. A model of satisfaction with open-plan office conditions: COPE field findings. *Journal of Environmental Psychology*, 27(3), 177-189.
- Wargoocki P., Wyon D.P., Sundell J., Clausen G., and Fanger, P. 2000. The effects of outdoor air supply rate in an office on perceived air quality, sick building syndrome (SBS) symptoms and productivity. *Indoor Air*, 10(4), 222-236.

Generating design-sensitive occupant-related schedules for building performance simulations

Mohamed Ouf^{1,*}, William O'Brien¹ and Burak Gunay¹

¹Carleton University, Ottawa, ON, Canada

*Corresponding email: mohamedouf@cunet.carleton.ca

ABSTRACT

Despite the benefits of occupant behavior (OB) models in simulating the effect of design factors on OB, there are challenges associated with their use in the building simulation industry due to extensive time and computational requirements. To this end, we present a novel method to incorporate these models in building performance simulations (BPS) as design-sensitive schedules. Over 2,900 design alternatives of an office were generated by varying orientation, window to wall ratio (WWR), the optical characteristics of windows and blinds, as well as indoor surfaces' reflectance. By using daylight simulations and stochastic OB modeling, unique light use schedules were generated for each design alternative. A decision tree was then developed to be used by building designers to select light use schedules based on design parameters. These findings are relevant for building energy codes as they provide an approach to incorporate design-sensitive operational schedules for use as BPS inputs by practitioners. These design-sensitive schedules are expected to be superior to default ones currently specified in codes and standards, which ignore the effect of design factors on OB, and ultimately on energy consumption.

KEYWORDS

occupant behavior modeling; light use schedules; building performance simulation; decision trees; office buildings

INTRODUCTION

Occupant behavior (OB) is recognized as one of the sources of uncertainty in building performance simulations (BPS) (Delzendeh et al., 2017; Haldi and Robinson, 2010; Parys et al., 2011). It is often represented in BPS based on default assumptions rather than measured observations or predictive models (Virote and Neves-Silva, 2012), which could lead to a performance gap between estimated and measured energy consumption (Menezes et al., 2012). Default schedules, specified in building energy codes and standards, do not necessarily reflect the way buildings are occupied and used today, given new societal and technological trends (O'Brien et al., 2017). For example, default schedules assume 90 – 95% occupancy for office buildings during regular business hours. However, previous studies showed that peak occupancy rarely exceeds 50% in private offices (Duarte et al., 2015). The current schedule-based occupant modeling approach also assumes occupants are passive recipients of indoor environmental conditions and do not react to discomfort (Hong et al., 2015). However, the relationship between occupants and buildings is a two-way process, in which occupants' actions that influence energy consumption, are in turn influenced by building design and indoor environmental conditions (Gaetani et al., 2016; Haldi and Robinson, 2010; Yan et al., 2015). Therefore, default schedules that are currently prescribed in building energy codes and standards do not incentivize designers to explore the effect of design decisions on OB.

To partially address this issue, previous studies introduced stochastic models to represent OB more accurately in BPS based on monitoring of existing buildings (e.g. Haldi and Robinson,

2010; Page et al., 2008; Reinhart, 2004). These models can simulate occupants' presence or actions when triggered by environmental or situational conditions (Hong et al., 2016; Parys et al., 2011). Actions may include the use of lights, blinds, windows, thermostats or other building systems. Despite the advances in OB modeling research in the past decade, several issues remain unresolved such as these models' transferability and validation on a wider scale (Lindner et al., 2017). Similarly, the significant computation time required to run these models in BPS hinders their use in the building simulation industry, which is the main issue we address in this paper.

Quantifying the effect of OB on buildings' energy consumption requires integrating OB models in BPS tools. Several approaches can be used to achieve this, depending on the specific tool being used, its capabilities, and the available information about the model (Hong et al., 2017). Regardless of which approach to follow, one of the main challenges facing OB models' implementation in the building simulation industry is the extensive time and computational requirements for integrating them in BPS tools (Yan et al., 2015). As an alternative approach, we present a workflow to generate design-sensitive schedules that can be readily used as BPS inputs. Generating these design-sensitive schedules is based on parametric simulations of building design alternatives and using data-mining techniques to establish the relationship between design parameters and operational schedules. The process of generating these schedules which entails modeling OB needs to be performed only once, while its results can be used by building simulation practitioners to select design-sensitive schedules for their proposed designs.

The main goal of this paper is to provide a proof of concept application of the proposed workflow. However, undertaking this workflow on a larger scale to include other design factors, end-uses, and locations is a necessary step before results can be used by building simulation practitioners. Specific objectives of this study focused on generating light use schedules for 2,916 unique design alternatives of an office in Ottawa, ON. For each design alternative, parameters that influence workplane illuminance, and consequently the way occupants use lights were changed. These design parameters included, building orientation, WWR, windows and blinds' visible transmittance, wall, floor, and ceiling materials' reflectance. The second objective focused on developing a decision tree classification model to help in selecting light use schedules based on design parameters.

METHOD

The RADIANCE-based simulation program DAYSIM was used to calculate workplane illuminance in an office room during the whole year. The shoe-box office model, shown in Figure 1, had a floor area of 15 m² and height of 3 m², and was simulated in Ottawa, ON.

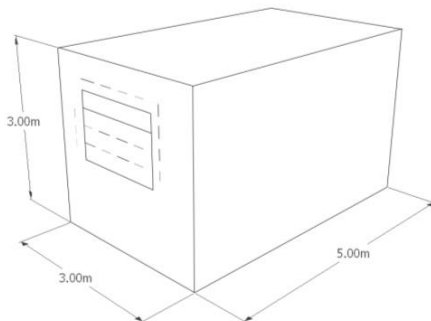


Figure 1 Three-dimensional diagram of the modeled shoe-box office

All possible combinations of the design parameters shown in Table 1 were modeled, resulting in 2,916 design alternatives. A window was modeled on one façade, whose dimensions were calculated to correspond to the proposed WWR for each design alternative. Since workplane illuminance, which triggers the use of lights is also influenced by blinds' position, five whole-year simulations were performed with the blind position in five equal increments: fully open, 1/4, 1/2, 3/4, and fully closed, resulting in a total of 14,580 simulations.

Table 1 Design parameters used to model different design alternatives of the shoe-box office model

Design parameters	Variations			
	South - 0°	West - 90°	North - 180°	East - 270°
Building Orientation	South - 0°	West - 90°	North - 180°	East - 270°
WWR	20%	40%	60%	
Glazing Visible Transmittance	0.5	0.6	0.7	
Blinds Visible Transmittance	0.05	0.1	0.15	
Ceiling Reflectance	0.6	0.7	0.8	
Floor Reflectance	0.2	0.3	0.4	
Wall Reflectance	0.4	0.5	0.6	

The next step entailed generating light use schedules for each design alternative based on modeling OB. An occupancy model developed by Page et al. (2008), a blind use model developed by Haldi and Robinson (2010), and a light use model developed by Reinhart (2004) were implemented in MATLAB for each design alternative. Details about these models' parameters and their implementation process can be found in Gunay et al. (2016), and Lindner et al. (2017). Results were used to calculate an average daily light use schedule for each design alternative, based on their annual light use profile.

A decision tree classification model, developed using the Classification and Regression Trees (CART) algorithm by Breiman et al. (1984), was then implemented in MATLAB to predict daily light use based on design parameters. This algorithm generates a flowchart tree structure to categorize data into various subsets and is applicable for predicting categorical responses. Therefore, the average daily light use schedules which represent the target response were first transformed into a categorical variable. For each design alternative, the duration of light use per day was calculated from its daily light use schedule generated earlier. The duration of light use was then categorized as High, Medium, or Low by splitting the dataset equally over these three categories. Results of this equal split indicated that light use durations below 5.7 hours/day were classified as low, durations between 5.7 and 6.7 hours/day were classified as medium, and durations above 6.7 hours/day were classified as high. Therefore, three categories of light use schedules were used to build the decision tree classification model, by assigning each of the 2,916 design alternatives to one of these categories.

To provide a practical application for the developed decision tree classification model, three distinct light use schedules were specified that correspond to the three categories of light use durations. These schedules can be used as inputs in BPS tools, and have the same shape profile as the average light use schedule calculated from the entire dataset for all design alternatives. They were generated by normalizing the average light use schedule for all design alternatives, and multiplying it by the average light use duration of each category (5.15, 6.2, 7.4 hours/day for low, medium and high categories, respectively).

Developing the decision tree was a two-step process, where the dataset was split into two subsets; a training subset randomly populated using 80% of the data, and a validation subset populated using the remaining 20%. Readers can refer to (Breiman et al., 1984) for more

details on the methodology of developing decision tree classification models. The training subset was then used to generate the model, while its accuracy was evaluated by making predictions against the validation subset. Accuracy was measured by comparing the predicted categorical response from the model to the original category of each data-point in the validation subset. Furthermore, the relationship between original values of light use duration in the validation subset (prior to categorization), and the average light use duration of its predicted category was assessed using the coefficient of determination R^2 .

RESULTS

Using the CART algorithm, a classification decision tree, shown in Figure 2, was developed. Post-pruning the decision tree with a confidence factor of 0.01 resulted in a total of seven decision tree nodes, of which eight were leaf nodes, representing low, medium, or high light use durations. The confusion matrix, shown in Table 2, evaluated the decision tree's classification accuracy. It indicated that 61% of the validation dataset, were correctly classified. However, only 1.9% of the dataset was incorrectly classified by more than one profile away from the correct one (e.g. High light use duration being classified as low). As shown in Table 2, the number of correctly classified records is given in the main diagonal, i.e. upper-left to lower-right diagonal; while others were incorrectly classified. Using the 584 records in the validation subset, and comparing their daily light use durations to the average light use duration of their predicted classes, R^2 was 0.66.

Despite the relatively low accuracy of this decision tree, one of its main advantages is the ease of use for practical applications by following the path from the root node to any of the leaf nodes. For example, if WWR is less than 0.3, building orientation is higher than 225° , and glazing visible transmittance is higher than 0.5, then medium light use duration and its corresponding schedule should be used in BPS. Changes to the parameters of the decision tree algorithm, the cross-validation method or the classification method used to split target variables can improve its accuracy. However, the main goal of this paper is demonstrating the workflow to generate design-sensitive schedules, and not improving the accuracy of the specific data-mining techniques used.

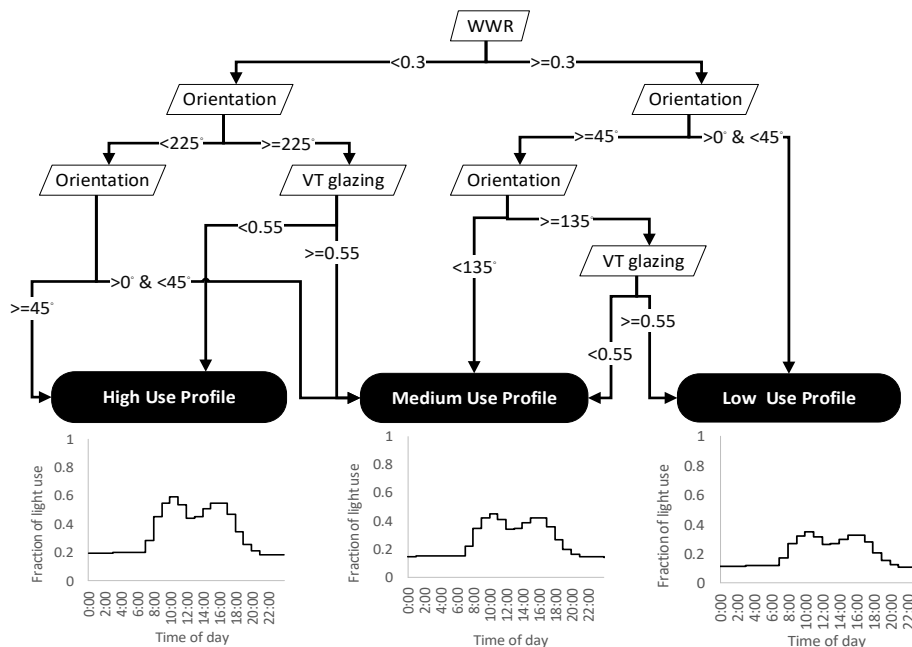


Figure 2 Decision tree diagram for selecting light use profiles

Table 2 Decision tree confusion matrix

Classified as →	Low light use profile	Medium light use profile	High light use profile
Low light use profile	137	49	4
Medium light use profile	78	116	50
High light use profile	7	39	103

DISCUSSION

Decision trees can help designers and building simulation practitioners select approximate light use schedules based on their design. Instead of using one default light use schedule that does not consider the effect of design parameters on OB, the proposed method provides three potential schedules that correspond to different building designs. Given the modeled office location in Ottawa, ON, future research should include other locations which can be treated as an additional parameter in the decision tree to select location-specific light use schedules.

It is important to note that the specific daily light use durations and schedules reported in this study were a function of the OB models used, and the design parameters investigated. However, more robust OB models and other parameters that influence OB such as clothing, and the decision to sit or stand at modern workstations should be investigated in future research. The presented workflow only focused on showing a methodology to eliminate the extensive time requirements for running OB models by providing design-sensitive schedules, but it did not address these models' transferability or validation in other buildings.

CONCLUSION

This paper demonstrated a novel method for generating design-sensitive schedules that can be used in BPS. For proof of concept, a decision tree was developed for selecting light use schedules based on design parameters. These design-sensitive schedules represent an improvement over the default schedules provided in current codes and standards, which do not match actual building operations. One approach to improve the accuracy of default schedules could be updating them based on data from a statistically representative sample of existing buildings, taking their design parameters into consideration. However, given the extensive logistical requirements for data collection at such large scale, the method presented in this paper relies on data-mining and parametric building simulations to account for the effect of building design on OB. This method only addresses the time and computational barriers to OB modeling, by providing ready-to-use design-sensitive schedules that can be used as BPS inputs. It does not address other issues related to OB modeling such as models' validation, which was outside the scope of this paper. Incorporating these schedules in building codes and standards would require extending the workflow on a larger scale for different locations and building archetypes.

ACKNOWLEDGEMENT

The generous financial support of Natural Resources Canada through the Clean Energy Innovation Program is acknowledged. The authors have greatly benefited from discussion with project partners RWDI, Autodesk, and National Research Council Canada, and would like to acknowledge their generous support for this research.

REFERENCES

- Breiman, L., Friedman, J., Stone, C.J., Olshen, R.A., 1984. Classification and Regression Trees. Chapman and Hall/CRC.
- Delzendeh, E., Wu, S., Lee, A., Zhou, Y., 2017. The impact of occupants' behaviours on

- building energy analysis: A research review. *Renew. Sustain. Energy Rev.* 80, 1061–1071. doi:10.1016/j.rser.2017.05.264
- Duarte, C., Budwig, R., Van Den Wymelenberg, K., 2015. Energy and demand implication of using recommended practice occupancy diversity factors compared to real occupancy data in whole building energy simulation. *J. Build. Perform. Simul.* 8, 408–423. doi:10.1080/19401493.2014.966275
- Gaetani, I., Hoes, P.J., Hensen, J.L.M., 2016. Occupant behavior in building energy simulation: Towards a fit-for-purpose modeling strategy. *Energy Build.* 121, 188–204. doi:10.1016/j.enbuild.2016.03.038
- Gunay, H.B., O'Brien, W., Beausoleil-Morrison, I., 2016. Implementation and comparison of existing occupant behaviour models in EnergyPlus. *J. Build. Perform. Simul.* 9, 567–588. doi:10.1080/19401493.2015.1102969
- Haldi, F., Robinson, D., 2010. Adaptive actions on shading devices in response to local visual stimuli. *J. Build. Perform. Simul.* 3, 135–153. doi:10.1080/19401490903580759
- Hong, T., Chen, Y., Belafi, Z., D'Oca, S., 2017. Occupant behavior models: Implementation and representation in building performance simulation programs. *Build. Simul.* doi:10.1007/s12273-017-0396-6
- Hong, T., D'Oca, S., Taylor-Lange, S.C., Turner, W.J.N., Chen, Y., Corgnati, S.P., 2015. An ontology to represent energy-related occupant behavior in buildings. Part I: Introduction to the DNAs framework. *Build. Environ.* 94, 196–205. doi:10.1016/j.buildenv.2015.08.006
- Hong, T., Taylor-Lange, S.C., D'Oca, S., Yan, D., Corgnati, S.P., 2016. Advances in research and applications of energy-related occupant behavior in buildings. *Energy Build.* 116, 694–702. doi:10.1016/j.enbuild.2015.11.052
- Lindner, A.J.M., Park, S., Mitterhofer, M., 2017. Determination of requirements on occupant behavior models for the use in building performance simulations. *Build. Simul.* 1–14. doi:10.1007/s12273-017-0394-8
- Menezes, A.C., Cripps, A., Bouchlaghem, D., Buswell, R., 2012. Predicted vs. actual energy performance of non-domestic buildings: Using post-occupancy evaluation data to reduce the performance gap. *Appl. Energy* 97, 355–364. doi:10.1016/j.apenergy.2011.11.075
- O'Brien, Gaetani, I., Gilani, S., Carlucci, S., Hoes, P.-J., Hensen, J.L.M., 2017. International survey on current occupant modelling approaches in building performance simulation? *J. Build. Perform. Simul.* doi:10.1080/19401493.2016.1243731
- Page, J., Robinson, D., Morel, N., Scartezzini, J., 2008. A generalised stochastic model for the simulation of occupant presence 40, 83–98. doi:10.1016/j.enbuild.2007.01.018
- Parys, W., Saelens, D., Hens, H., 2011. Coupling of dynamic building simulation with stochastic modelling of occupant behaviour in offices - a review-based integrated methodology. *J. Build. Perform. Simul.* 4, 339–358. doi:10.1080/19401493.2010.524711
- Reinhart, C.F., 2004. Lightswitch-2002: A model for manual and automated control of electric lighting and blinds. *Sol. Energy* 77, 15–28. doi:10.1016/j.solener.2004.04.003
- Virote, J., Neves-Silva, R., 2012. Stochastic models for building energy prediction based on occupant behavior assessment. *Energy Build.* 53, 183–193. doi:10.1016/j.enbuild.2012.06.001
- Wang, D., Federspiel, C.C., Rubinstein, F., 2005. Modeling occupancy in single person offices 37, 121–126. doi:10.1016/j.enbuild.2004.06.015
- Yan, D., O'Brien, W., Hong, T., Feng, X., Burak Gunay, H., Tahmasebi, F., Mahdavi, A., 2015. Occupant behavior modeling for building performance simulation: Current state and future challenges. *Energy Build.* 107, 264–278. doi:10.1016/j.enbuild.2015.08.032

Lighting systems and users interactions in classrooms and laboratory rooms

Camila Novais^{1,2,3*}, Roberta Souza¹ and Andrea Pereira¹

¹Universidade Federal de Minas Gerais, Brasil

²Centro Universitário UNA, Brasil

³Universidade de Itaúna, Brasil

*Corresponding email: arq.camilacampos@gmail.com

ABSTRACT

In Brazil, there has been an increase in the use of certifications designed to assess and improve building performance. Despite these advances, there is still little knowledge concerning the buildings' post-occupancy. Thus, the present work aimed to evaluate the occupants' behaviour regarding the use of lighting and internal shading devices. Classrooms and laboratories at UFMG Architecture and Design School were used as case study. The main objective was to analyse how a cycle of influences works: how occupants influence energy consumption and act in relation to the buildings systems, as well as how the building and the internal systems influence the occupants' behaviour. Firstly, daylighting and artificial lighting conditions of the rooms were diagnosed. As for the occupants' behaviour analysis in loco, observations were made to evaluate barriers and potentials in the systems use. Afterwards, changes were made in the lighting circuits division, in the curtain types and informative posters were installed in the studied rooms. The results showed that there is a hierarchy in the use of classroom systems, in which professors are the main controllers and that in laboratories the systems use is well distributed among occupants. It was considered that the original evaluated systems did not meet the occupants' expectations in general, so changes were proposed. The changes proved to be efficient once the interaction of users to the systems improved in quality and in number. This research allowed to infer that a more occupant-centered design leads to a more efficient use of spaces.

KEYWORDS

Occupants' behaviour, Energy Efficiency, Buildings performance, School Building.

INTRODUCTION

Buildings account for approximately 40% of the world energy consumption (IEA, 2013) and for 50.8% of all the electricity consumed in Brazil (EPE, 2016). According to PROCEL (2005), lighting represents 22% of this consumption to commercial buildings and 23% to public buildings. The emergence of building certifications and the effort that has been observed nowadays regarding this issue, in Brazil and in the world, points to visible advances for more efficient buildings. However, little is known about the operation of a cycle of influences that is essential for the buildings energy efficiency: how occupants influence the efficiency and comfort of buildings and how buildings as proposed influence the occupants' behaviour.

Lindelof and Morel (2006) described the results of an analysis carried out in Switzerland. They concluded that after the occupants' arrival and departure periods in the office the lighting system was only turned on again in cases of extreme discomfort. The authors believe that this behaviour was a consequence of the position of the light switches, which were located near the offices entrance door and not near the workers' tables. Mahdavi et al (2008) described a empirical study of occupant's operation of lighting and shading systems in Austria office

buildings. They concluded that patterns of user control behaviour depends on indoor and outdoor environmental parameters, as the illuminance and the solar radiation incidence. They also realized that there is a relationship between occupancy and lighting operation. Based on a literature survey on drivers and models, Fabi, Andersen and Corgnati (2015) reinforced that the probability of light-switching is highly related to people's arrival or departure in the offices. They also concluded that it is essential to consider the occupants' individuality in order to understand different behaviours, as some individuals consider daylighting when switching on the lights, whereas other occupants switch on the lights independently of daylighting. Reinhart and Voss (2003), while conducting a survey at an office building where one or two people worked, in Germany, concluded that groups of individuals follow a very similar behaviour, whereas isolated individuals follow more diverse patterns. The authors verified that all building occupants considered daylight, which could confirm the influence of architectural conception and lighting system proposed for the building on the differentiated occupants' behaviour.

Jennings et al (1999), after testing different lighting control technologies in an office building in San Francisco, concluded that the lighting requirements of occupants depend on their type of work. Daylight dimming, as an example, showed to be more adequate for workers who stay at their desks all day. Moore, Carter and Slater (2003) also concluded, after a long-term study which monitored the switching behaviour in offices where occupants could vary the level of illuminance on their working areas, that user controlled lighting systems could save energy, keeping the occupant's comfort. LEED Reference Guide for Green Building Design and Construction (USGREEN BUILDING COUNCIL, 2009) indicates that independent lighting controls should ensure occupants' autonomy in changing them in order to promote comfort, productivity and well-being. It also indicates that windows must be treated in order to allow appropriate levels of illumination without disrupting projections.

Gyberg and Palm (2009), in a study carried out on residential buildings, concluded that to change people's behaviour, it is necessary to ensure that the choices can be made by the individual, by the provision of design alternatives that do not affect their lifestyle. On the other hand, after analysing the use of curtains, windows and lamps in offices in Austria, Mahdavi and Proglhof (2009) verified how difficult it is to estimate a single individual's behaviour. Norman (2010) argues that bad projects, created for people the way designers would like them to be and not as they really are, constitute the real causes of design inefficiency. On the other hand, ISO 50.001 (2011) presents a methodology based on a continuous improvement model - "Plan-Do-Check-Act" - which points out the need for constant checks on installed systems to guarantee their quality, efficiency and understanding by their users.

Therefore, the present research aimed to verify the occupants' behaviour regarding artificial and daylighting systems, by identifying the barriers and potentialities of installed systems and proposing changes to enhance lighting and daylighting systems use.

METHODS

Case Study: Architecture and Design School - UFMG

For the present research, three classrooms and three laboratory rooms of the Environmental Comfort and Energy Efficiency in the Built Environment Laboratory (LABCON) of the Architecture and Design School of the Federal University of Minas Gerais (EAD-UFMG) were investigated. The rooms presented windows faced to different orientations and solar control elements. Classroom A has windows facing the North and South façade, translucent curtains in all windows and external shading devices to the North (Belo Horizonte is in the South hemisphere). Classroom B has windows oriented East façade and presented blackout curtains.

Classroom C windows faced West and besides blackout curtains presented the windows painted in white which indicated extreme user discomfort. The three rooms of the Laboratory face West and presented white metallic horizontal venetian blinds (Figure 1). All studied rooms presented internal controls for the artificial lighting switching, located next to the doors.



Figure1 – Classrooms A, B e C and laboratory rooms 01, 02 e 03, respectively.

In loco Observation and daylighting analysis

The occupants' behaviour was investigated by a group of 3 *shadow observers* (an observer was always present in each of the studied rooms but not identified) during a total period of 161 days divided according to the classes schedule and the Laboratory occupation hours in the mornings and afternoons. Classroom A was observed in 31 classes (totalizing 136 hours); Classroom B in 34 classes (totalizing 111 hours); Classroom C in 21 classes (totalizing 56 hours); Room 1 was observed for 24 periods (totalizing 129 hours); Room 2 for 27 periods (totalizing 145 hours); Room 3 for 24 periods (totalizing 136 hours). For the data collection, checklists were fulfilled by each observer, that covered six aspects: General Characteristics of the room; Visual activities; Occupation; Lighting system status; Solar Incidence in the work plane; control systems and Use of windows. The observations were divided into four parts: a) rooms as originally configured, b) after changes were made in the lighting circuits, c) after the substitution of the solar shading devices and d) after the insertion of informative posters.

The daylight autonomy (DA) was analysed through simulations in Daysim software to help analyse the potential use of daylighting in the studied rooms.

Changes carried out in the lighting control systems and in the window shading devices

The observations allowed the researches to point out barriers and potentialities of the existing systems. After that, changes were made in three stages: 1) Lighting system: circuit division modifications to allow the integrated use of daylighting and artificial lighting and light switches reorganization to better express the spatial distribution of the luminaires. 2) Solar shading devices: replacement of the blackout curtains for venetian blinds. The purpose of this change was to allow greater availability of daylight and to broaden the possibilities of user interaction with the system by changing the fins position. 3) Insertion of informative posters: this step was intended to fill up the lack of readability of the existing systems and to test the effectiveness of graphic representations of the ambient systems in informing users how to better use the venetian blinds and lighting switches. At each change, a new diagnosis was made to verify the effectiveness of the changes and the need for further modifications in the systems.

RESULTS

In the first stage, when rooms were observed as originally configured, Classroom A and the laboratory rooms presented solar shading devices considered to be effective in controlling the

sun incidence indoors and the artificial lighting was adequately integrated with daylighting. On the other hand, classrooms B and C presented no integration with daylighting; besides that, the blackout curtains obstructed from 30 to 50% the window area. Daylight simulations showed that in classroom A the luminaires located near the windows could be turned off during the whole morning and part of the afternoon. Computer simulations also showed that if the blackout curtains were substituted by internal venetian blinds, in Classrooms B and C, the Daylight Autonomy near the window would be superior to 80% in all classrooms when there was no sunlight incidence in the façade.

For the laboratory offices, the use of integrated daylighting and artificial lighting systems showed greater potential in the morning during the first stage of the observations. In the afternoon, the venetian blinds tended to remain closed or partially closed in order to control sunlight radiation incidence once their windows face West. The observations pointed out that the professors were the main controllers of the lighting systems in the classrooms and that changes occurred mainly upon arriving and leaving the rooms. Changes during classes occurred only when the lack of lighting was noticed or when a change in the visual task was necessary (mainly for data-show use). In the laboratory rooms, there was no pre-defined controller and more changes were noticed in the lighting systems associated with the arrival of new occupants.

In the second stage of observations, after the changes to enhance the systems operation in classrooms B and C were made, it was found that the use of integrated daylighting and artificial lighting became more significant in both classrooms. The luminaires located near the windows remained turned off in 50% and in 67% of the observed classes in classrooms B and C.

Finally, after informative posters were fixed, luminaires association with daylighting enhanced and luminaires located near the windows remained turned off in 87% and in 67% of the observations in classrooms B and C, respectively. As for the LABCON rooms, luminaires located near the window were turned off in 34% of the observed days and the position of venetian blinds was modified in more than 50% of all observations. For classroom A considered to be the better daylit room in the study, on the other hand, the occupant behaviour was not significantly altered.

Regarding the use of solar shading devices, a tendency to preferably open the venetian blinds or curtains positioned on the movable parts of the windows was observed. This was mainly due to ventilation needs than to the intention of enhancing daylighting. After the substitution of blackout curtains to venetian blinds, an increase of difficulties in using this system was noticed. There was also an increase in the number of changes made in the venetian blinds especially during the classes where the data-show was used. The difficulties in the use of the blinds were reduced after the informative posters installation.

DISCUSSIONS

The observations made reinforced the conclusions drawn by Lindelof and Morel (2006), who claimed that occupants tend to act in lighting systems upon arriving and leaving the rooms and that during this interval they only act on these systems when they feel disturbed or when there are changes in the visual task.

The lack of a user behaviour pattern in LABCON rooms confirmed the findings of Reinhart and Voss (2003), who observed that behaviours of groups of individuals are standardized, whereas isolated individuals follow a more diverse pattern of behaviour. While in the classrooms the use of the lighting system was mostly associated with the type of class that took

place and data-show use, in the laboratory rooms the use of the lighting systems was more related to the room occupation.

It was verified that, accordingly to the LEED Reference Guide, when the room presents different control options for the lighting systems, usage is enhanced. This finding also confirms the conclusions by Gyberg and Palm (2009) that individuals should have choices. The alterations made in the original systems enhanced occupants' behaviour, reinforcing Norman's (2010) conclusion that the inefficient use is a consequence of project failures. The significant increase in the number of observed cases in which the occupants had difficulty in using the venetian blinds, after they substituted blackout curtains, showed that the installed system was not intuitive enough to its users, confirming once again Norman's (2010) conclusions.

Lindelof and Morel (2006) statement in that users of rooms act on systems when they are disturbed was confirmed in all analysed rooms, once curtains and venetian blinds were closed when there was incidence of direct solar radiation in the work planes or desks. In this way, it was verified that in favourable orientations or when external shading devices were present, there were fewer actions in the solar incidence control system.

Observations also reinforced the validity of the model of continuous improvement proposed in ISO 50.001 (2011), as it was verified that each system change was correspondent to a change in user behaviour.

The study also showed the importance of detailing systems. The use of venetian blinds was an interesting alternative to encourage the use of daylight integrated with artificial lighting. As observed, the modifications in the curtains were made only to enable the opening of the windows for ventilation and not to improve daylighting. So, testing venetian blinds divided in 2 parts and not in 4 parts, as the original venetian blinds, could be a great alternative, as when they were opened for ventilation purposes, daylighting would automatically enhanced as the fixed parts of the windows would also be uncovered. This new system would probably work well in rooms with lower problems of direct sun incidence in the work planes.

CONCLUSIONS

The present study showed that the usage efficiency of the buildings depends greatly in the architectural and interior systems design. If users tend to act on existing systems either when arriving or leaving internal spaces or when they are disturbed, it is concluded that the best designs are those which demand the minimum number of changes by users, especially when entering the rooms. Therefore, designers should be aware of the many factors that may influence the user behaviour and pay special attention to the first occupancy hours as they may determine if lighting systems will need to be turned on. The correct choice of room orientation and proposition of an adequate solar control system, consistent with the activities that will be carried out, is a point that must be observed. External elements that guarantee visual and thermal comfort showed to be preferable than internal shading devices that require special handling by the occupants.

In the study case, LEED recommendations contributed to the improvement of the use of the lighting system, confirming that not only the occupants influence the efficiency of the proposed system, but the way the system is proposed also influences the behaviour of the occupants.

It was observed, from the methodology applied in this work – which consisted in performing changes and re-evaluating the space use after the changes – that the process of working in a

cycle of continuous improvement is fundamental to improve the quality of existing systems. Working in a cycle of continuous improvement is also essential to understand the relations between systems' use and user behaviour.

Finally, it is recognized that projects are not static, as the needs change and since users of each space are different. When retrofitting a space, the decisions made must contemplate the resulting quality of the space and especially the users' well-being. It is only by observing the occupants' behaviour that patterns can be understood and it is only after understanding them that good projects can be designed. The way the design is thought influences greatly how users act in a particular building.

ACKNOWLEDGEMENT

The work reported in this paper was supported by the National Council of Research, CNPQ.

REFERENCES

- ABNT. 2011. *NBR ISO 50.001: Sistemas de Gestão de Energia: Requisitos com orientação para uso*. Rio de Janeiro, 24 pages.
- EPE. 2016. Balanço energético Nacional. Available in: <https://ben.epe.gov.br/downloads/Relatorio_Final_BEN_2016.pdf>.
- Fabi, V., Andersen, R. K. and Corgnati, S. 2016. Accounting for the Uncertainty Related to Building Occupants with Regards to Visual Comfort: A Literature Survey on Drivers and Models. In: *Buildings*, 6 (5), 17 pages.
- Gyberg, P., and Palm, J. 2009. Influencing households' energy behaviour – how is this done and on what premises? In: *Energy Policy*, Vol. 37, no. 7, pp. 2807-2813.
- International Energy Agency. 2013. Total energy use in buildings: Analysis and evaluation methods, 17 pages.
- Jennings, J.; Rubinstein, F.; DiBartolomeo, D.; Blanc, S. 1999. Comparison of control options in private offices in an advanced lighting control testbed. In: *Proceedings of the IESNA 1999 Annual Conference*, New Orleans, LA, USA, 26 pages.
- Lindelof, D., and Morel, N. 2006. A field investigation of the intermediate light switching by users. In: *Energy and Buildings*. Vol. 38, n° 7, pp. 790-801.
- Mahdavi, A.; Mohammadi, A.; Kabir, E.; Lambeva, L. 2008. Occupants' operation of lighting and shading systems in office buildings. In: *J. Build. Perform. Simulation*. 1, pp. 57–65.
- Mahdavi, A.; Proglhof, C. 2009. *User Behavior and energy performance in buildings*. IEWT.: pp. 1-13. Available in: <http://eeg.tuwien.ac.at/eeg.tuwien.ac.at_pages/events/iewt/iewt2009/papers/4E_1_MAHDAVI_A_P.pdf>.
- Moore, T.; Carter, D.J.; Slater, A.I. 2003. Long-term patterns of use of occupant controlled office lighting. In: *Lighting Res. Technol.* 35, pp. 43–59.
- Norman, D. A. 2010. *O design do futuro*. Rio de Janeiro: Rocco, 191 pages.
- PROCEL. 2005. *Avaliação do Mercado de Eficiência Energética do Brasil*. 77 pages. Available in: <<http://www.procelinfo.com.br>>.
- Reinhart, C. F., and Voss, K. 2003. Monitoring manual control of electric lighting and blinds. In: *International Journal Lighting Research & Technology*, Vol.35, n° 3, pp. 243-260.
- U.S.GREEN BUILDING COUNCIL. 2009. *LEED Reference Guide for Green Building Design and Construction*. Washington, 645pages.

Visual Comfort Assessment of Different Shading Strategies in a Commercial Office Building in the Southeastern US

Armin Amirazar¹, Mona Azarbayjani¹, Ben Futrell¹, Amir Hosseinzadeh Zarrabi¹, and Roshanak Ashrafi¹

¹University of North Carolina at Charlotte, USA

*Corresponding email: aamiraza@uncc.edu

ABSTRACT

It is challenging to design buildings that simultaneously consider both the dynamic nature of daylight and specific occupant preferences. The authors have investigated this problem by studying the performance of four specific shading strategies using quantitative measurements of occupants visual comfort: discomfort glare and daylight availability. This paper specifically evaluates the performance of four shading strategies, two types of electrochromic (EC) glass, an automated fabric roller shade, and a venetian blind in a building located in the Southeastern United States. This paper examines how these technologies impact occupant visual comfort and it also examines how the buildings perform relative to the two metrics outlined in IES LM-83-12. Horizontal illuminance and high dynamic range images were recorded to assess the existing luminous environment in order to better understand the potential of various shading strategies. Calibrated daylighting models were also constructed in DIVA. Our results suggest that perimeter-zone occupants benefits from EC glass as it can reduce more than 40% of glare annually in this zone. Findings from the interior zones are shown that all four shading strategies perform quite similarly in regards to reducing the glare. This study suggest that by providing a designer at early-design-stage with direct information related to the level of daylight availability and glare condition within a space will lead to improve occupant's visual comfort.

KEYWORDS

Visual comfort; Shading strategies; Office building; Daylight Glare Probability (DGP)

INTRODUCTION

Designing a well-daylit space requires to satisfy both qualitative and quantitative aspects of daylight by balancing daylight provision with occupant visual comfort in both core and perimeter zones of the work environment. Over the past two decades, much of the available literature on visual comfort deals with glare and the amount of light as the two most reliable metrics. Similarly, Carlucci (2015) reviewed the literature of several studies and highlighted that over 75% of metrics employed glare and amount of light to assess the visual comfort. Daylight Autonomy (DA) is one of the most common used approach to assess the annual amount of daylight in a space (Reinhart and Wienold, 2011). Results of various studies showed while DGP performs better than the other metrics in predicting discomfort glare when the direct sun is present, the DGP isn't effective at predicting contrast-based discomfort glare (Van Den Wymelenberg et al., 2010; Pierson et al., 2018; Jakubiec and Reinhart, 2012; Kleindienst and Andersen, 2009). This view is supported by Konis (2014) who found that simple contrast ratios predicted discomfort best in 'core' zones of buildings further than 6m from the facade. Together, in all the studies

reviewed here, DGP is recognized as the most robust glare metric as it is least likely to produce inaccurate glare prediction and also has a stronger correlation with vertical illuminance on the eye when bright, direct sunlight is generally associated with glare such as perimeter zone. In modern office spaces with large glazing facades, natural light coming in through the window can increase the visual comfort of occupants by providing the access to views, treating sleep disorder, and improving concentration and productivity of the working environment (Andersen, 2015; Keis et al., 2014). However, direct sunlight can cause visual discomfort in the form of glare. Therefore, the goal of shading technologies is to control the direct entry of sunlight from the windows in order to prevent severe glare. In order to avoid glare related problem which is the main cause of visual discomfort within office spaces, the direct sunlight should be blocked by using advanced glazings and innovative shading systems (Tzempelikos and Athienitis, 2007). Unlike the conventional shading strategies, the dynamic shading strategies, such as electrochromic glass, prevent severe glare, while also maintaining access to daylight and outdoor views. Electrochromic glass as an active device respond to various sensors (illumination and temperature) and the voltage causing the change in transmission. Following those works, this paper aim to investigate the visual comfort using the simulation-based visual comfort to evaluate the performance of various shading strategies in an open-office space. The objective of this paper is to assess the ability of four different shading strategies to reduce excessive glare while maintaining sufficient daylight through the space.

METHODOLOGY

This study was conducted on the southwest side at the upper floor of a side-lit open office located in Charlotte, NC. The Southwest side of the office is chosen due to extreme condition related to sun exposure. The building form is square shape with a 22m deep floor plate. It is important to note that the core of the building (length 26.5m and width 22m) including stairs, elevators, and bathrooms, is excluded from the analysis. To analyse daylight sufficiency of the space, annual illuminance is used to quantify Spatial Daylight Autonomy (sDA) and Annual Sun Exposure (ASE) on horizontal surface for window without shading. $sDA_{300lux50\%}$ expressing the percentage of analysed floor area that meet or exceed a threshold of 300 lx for more than 50% of occupied hours. Then, DA is used to compare the daylight availability for four shading strategies. 1534 sensors are distributed with 0.5m spacing on a horizontal measurement grid 76cm above the floor to assess daylight availability for different scenarios. In addition, annual glare and point-in-time glare were investigated to analyse the appearance of discomfort glare across two locations (Loc a and Loc b), positioned 1.2m above the floor to represent occupant's seated eye-height. For analysing point-in-time glare, the CIE clear sky was selected as direct sunlight reported the most important cause of discomfort for building occupants in modern spaces with large windows (Jakubiec and Reinhart, 2012) and simulation can predict discomfort glare of real lighting environments more accurately on sunny days than overcast sky (Kong et al., 2015). The method of this study consists of two steps. In the first step, an office without shading device is assessed using HDR image technique and compared with Radiance model to determine the accuracy of the model as a substitution tool. In this step, two HDR cameras are placed at Loc b, one towards southwest window and the other one facing southeast side, at the seated eye height level of 1.2m to collect data related to discomfort glare. Figure 1 shows the location and directions of the two HDR cameras. An office space is modeled based upon a real office space in Rhinoceros 3D modeling software where room geometry and orientation are assigned to the model. After

that, Radiance materials are assigned to all surfaces using the open-source plugin DIVA 4.0. The model properties and Radiance simulation parameters are presented in Table 1 and Table 2, respectively. It is important to note that the HDR images were taken on a sunny day, January 14th, 2016 from 8 AM to 6 PM in fifteen minute time intervals. Evaglare developed by (Wienold et al., 2004) is used in this study to calculate the results of DGP to compare the HDR images with simulated scenes. Second, Radiance model is used to evaluate the performance of the four proposed shading strategies (see Table 3) to control glare and provide sufficient daylight within the space in comparison with the base case scenario. The yearly hour-by-hour glare for both Loc a and Loc b for view direction perpendicular to southwest window is analysed for all proposed alternatives to identify intolerable and disturbing glare appearance for entire year. Moreover, automated glare control as a dynamic shading strategies applied in DIVA to avoid excessive interior daylighting levels and also block direct sunlight as a main cause of discomfort glare.

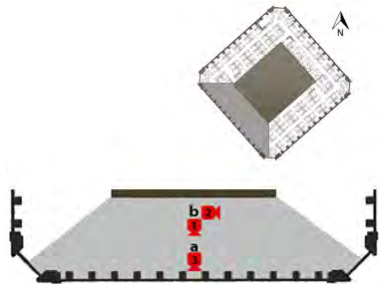


Figure 1: Plan view of the office building model presenting two different seating positions (loc a and loc b) across view 1-3 at the Southwest side.

Window to wall ratio	76%
Climate	Charlotte, NC
Analysis grid spacing	0.5 m
Number of view vectors per grid point	12
Ceiling height	3 m
Surface reflectance (interior floor)	20%
Surface reflectance (interior wall)	50%
Surface reflectance (interior ceiling)	80%
Surface reflectance (mullion)	90%
Glazing visible light transmittance (VLT)	65%
Floor plate length (NW-SE)	48.5 m
Floor plate length (NE-SW)	48.5 m
Location a distance from southwest window	1.5 m
Location b distance from southwest window	6 m

Table 1: Model properties.

Table 2: Model radiance parameters.

Parameters					
aa = 0.1	ab = 4	ad = 1024	sj= 1	Ir =6	dj=0
ar= 256	dr= 2	ds=0.2	st= 0.15	Lw =0.004	

Table 3: Main characteristics of various shading strategies.

Strategies	Shading system	Control strategy	Visible light transmittance (%)
1	Electrochromic glazing	Clear state	58
		Intermediate state	40
		Intermediate state	6
		Fully tinted	1
2	Electrochromic glazing	Clear state	60
		Intermediate state	18
		Intermediate state	6
		Fully tinted	1
3	Roller Shade	Half down	0.04
		Quarter down	0.04
		Fully down	0.04
4	Venetian blind	Horizontal	-
		30 degree	-
		60 degree	-

RESULTS

Comparison between the captured HDR images and simulated scenes

In order to have consistency with captured images, the same 82 scenes were recreated in DIVA to simulate time of the day of each captured HDR image. The results of DGP scores for view 1 and view 2 are plotted in Figure 3 according to four glare levels, with imperceptible glare in green ($DGP < 0.35$), perceptible glare ($0.4 > DGP \geq 0.35$) in yellow, disturbing

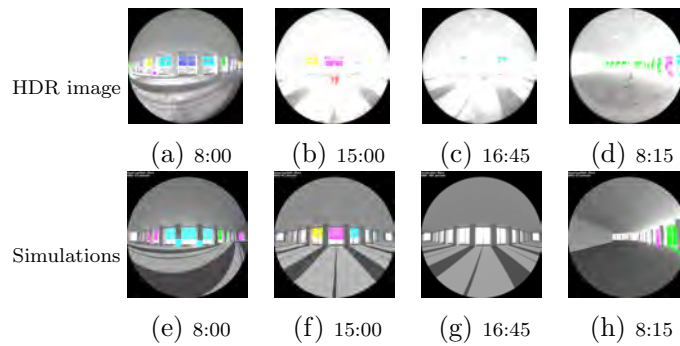


Figure 2: The HDR images and the simulations for different glare levels across view 1 and 2.

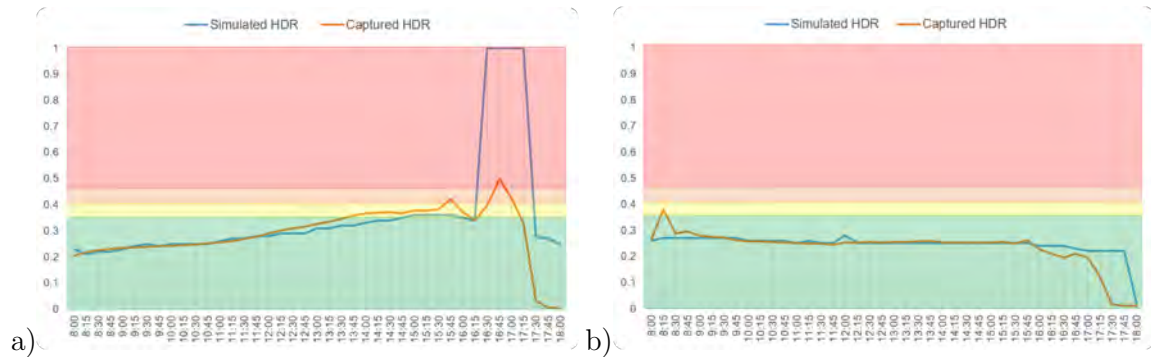


Figure 3: DGP score comparison between captured HDR image and simulated HDR scenes of a) view 1 and b) view 2 at Loc b.

glare in orange ($0.45 > \text{DGP} \geq 0.4$), and intolerable glare in red ($\text{DGP} \geq 0.45$) (Jakubiec and Reinhart, 2010). The captured HDR images and simulations can be compared visually for different glare levels in Figure 2. In view 2, more than 98% of HDR images and 100% of simulations generated DGP values were in the range of imperceptible glare (see Figure 3b). The only exception is at 8:15am, where the DGP value of the HDR image was higher than the simulation one. In contrast, for view 1, although 10% of simulated HDR scenes were fell into the range of intolerable glare, only 2% of captured HDR image were fell within this range (see Figure 3a). Although the amount of DGP for simulations were higher than captured HDR images between 16:15 to 18:00, but for the rest of the time the DGP value for both captured HDR images and simulated HDR scenes are comparable. As the simulated model has no light-shelf that allows considerable amount of direct sunlight hit the sensor in view 1 from 16:15 to 18 which may be the cause of deviation between simulated and HDR images generated DGP values during this period. Taken together, the difference between HDR images and simulations for all 82 scenes are about 16%, these results are in line with those of previous studies and confirm the association between HDR images and simulations which indicate that simulation can accurately predict real lighting spaces in terms of glare analysis, even though, the results of HDR images and simulations may not exactly match together (Rushmeier et al., 1995; Kong et al., 2015).

Assessment of various shading strategies

In order to improve the visual comfort of the common space, four shading strategies have been proposed to provide a comprehensive annual glare analysis within the space (see Table 3). The total annual hours of occupancy of 3650 is assumed for the purpose of this study. The view 1 and view 3 at loc b are used to analyze the performance of all shading strategies as the view point with extreme amount of sunlight in comparison with

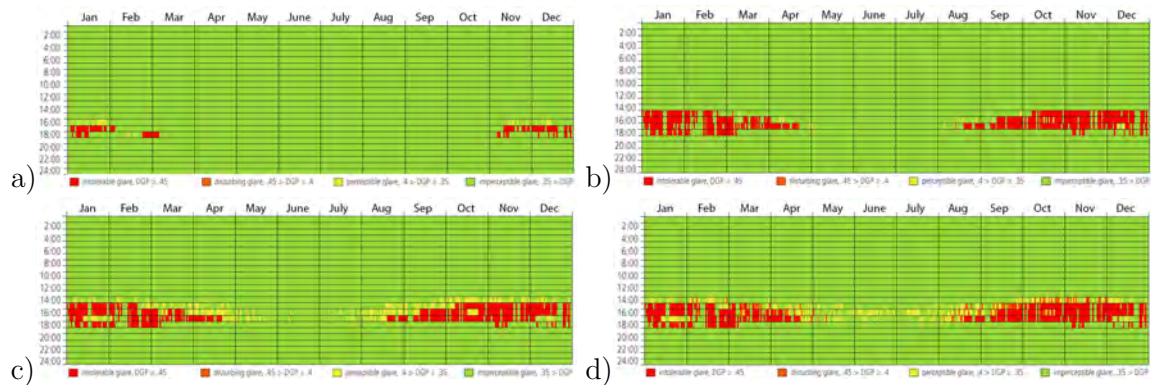


Figure 4: Annual glare calculations of view 3 at Loc a for strategies a)1, b)2, c)3, and d)4

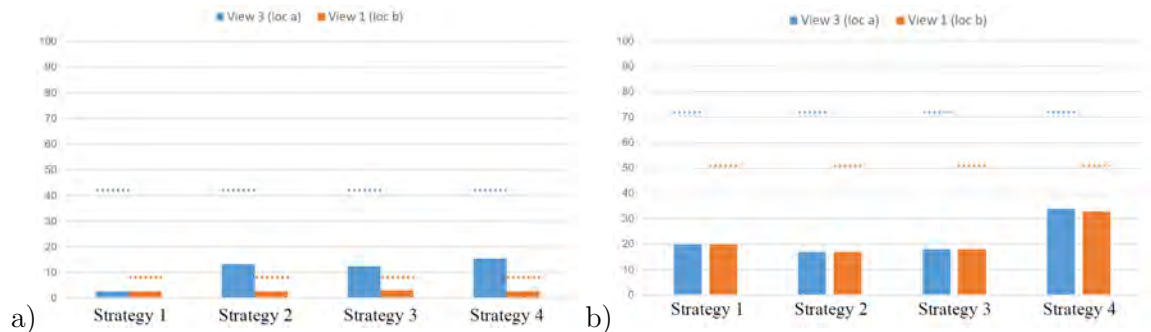


Figure 5: Reduction of a) Annual glare and b) DA of four shading strategies for view 1 and 3.

other view directions. The disturbing and intolerable glare ($DGP \geq 0.4$) as a worse glare condition is reported 47.5% for view 3 and 10.2% for view 1 without a shading device. In addition, sDA and ASE were calculated for the southwest side of the model to analyse daylight sufficiency. The results show that 42.4% of the southwest side has sDA 300lux value for more than 50% of occupied hours, and 34.5% of the space has an ASE greater than 250 hours. As the accuracy of Radiance model is demonstrated, this model is used to investigate the performance of different shading strategies. The results of these four shading strategies for view 3 are presented in Figure 4. The same colours green, yellow, orange, and red represent the four different levels of glare as Figure 2. Vertical axis represents the hours of the day and 365 days in a year are shown in horizontal axis. As the worst glare condition ($DGP \geq 0.4$) occurred during winter when the sun is in the low angles, Strategy 1 performs significantly better in controlling annual glare rather than other strategies for view 3 (see Figure 4). Figure 5a indicates the annual glare reduction of each shading strategies for view 3 and view 1. The results shows that the level of annual glare for location a is significantly higher than location b due to excessive amount of direct sunlight. Strategy 1 has the best potential for controlling glare as it reduces over 40% of glare annually, but the other three strategies can decrease between 27% and 31% of the annual glare in location a. In location b, all the four strategies have the same performance by reducing around 6% of the annual glare. Figure 5b shows the reduction in the percentage of the occupied hours of the year when a minimum illuminance threshold is met by daylit alone. The results indicate that strategy 4 caused the lowest reduction (about 40%) of DA through the space followed by strategy 1. Overall, comparing four shading strategies reveal that Strategy 1 performed better in terms of balancing between daylight provision and control discomfort glare than other strategies.

DISCUSSION AND CONCLUSION

This study was conducted in an office space as an example to show the importance of considering different shading strategies to control discomfort glare as the most cause of visual discomfort reported by office occupants. For the purpose of this study, four shading strategies were applied to evaluate their potential in controlling discomfort glare and daylight sufficiency. Dynamic electrochromic window which can be switched from 58% visible transmittance (T_{vis}) to a fully tinted state with 1% T_{vis} had a better performance in comparison with other shading alternatives by reducing over 40% of glare annually when excessive amount of sunlight is present. While Venetian blind shows the better performance in terms of DA than other strategies, it allows entering considerable amount of direct sunlight into the interior space. Therefore, Electrochromic glazing had a better performance than other strategies in this study by considering the ability to control glare and provide view to the outside as two important criteria for assessing visual comfort. In addition, the accuracy of simulation tool is determined and can be used by designers in early-stage design process to better understand the performance of various shading strategies by combining both annual glare and point-in-time lighting simulations of the space. A reliable prediction of glare with metrics is an important challenges among designers as visual comfort strongly depends on both daylight availability and the observer's position. Therefore, providing a designer at early-design-stage with direct information related to the level of daylight availability and glare condition within a space will lead to improve occupant's visual comfort. As the quality of the luminous environment produced by EC glazing is considered as an important factor for user acceptance, future research might investigate the non-visual effect of different Electrochromic windows on occupant's health and well-being.

References

- Andersen, M. (2015). Unweaving the human response in daylighting design. *Building and Environment*, 91:101–117.
- Jakubiec, A. and Reinhart, C. (2010). The use of glare metrics in the design of daylit spaces: recommendations for practice. In *9th international Radiance workshop*, pages 20–21.
- Jakubiec, J. A. and Reinhart, C. F. (2012). The 'adaptive zone'—a concept for assessing discomfort glare throughout daylit spaces. *Lighting Research & Technology*, 44(2):149–170.
- Keis, O., Helbig, H., Streb, J., and Hille, K. (2014). Influence of blue-enriched classroom lighting on students cognitive performance. *Trends in Neuroscience and Education*, 3(3-4):86–92.
- Kleindienst, S. and Andersen, M. (2009). The adaptation of daylight glare probability to dynamic metrics in a computational setting. In *Proceedings of the Lux Europa 2009 Conference. Lausanne, September 9e11*.
- Kong, Z., Utzinger, M., and Liu, L. (2015). Solving glare problems in architecture through integration of hdr image technique and modeling with diva. In *Proceedings of BS2015*, pages 1221–1228.
- Pierson, C., Wienold, J., and Bodart, M. (2018). Review of factors influencing discomfort glare perception from daylight. *Leukos*, pages 1–37.
- Reinhart, C. F. and Wienold, J. (2011). The daylighting dashboard—a simulation-based design analysis for daylit spaces. *Building and environment*, 46(2):386–396.
- Rushmeier, H., Ward, G., Piatko, C., Sanders, P., and Rust, B. (1995). Comparing real and synthetic images: Some ideas about metrics. In *Rendering Techniques' 95*, pages 82–91. Springer.
- Tzempelikos, A. and Athienitis, A. K. (2007). The impact of shading design and control on building cooling and lighting demand. *Solar energy*, 81(3):369–382.
- Van Den Wymelenberg, K., Inanici, M., and Johnson, P. (2010). The effect of luminance distribution patterns on occupant preference in a daylit office environment. *Leukos*, 7(2):103–122.
- Wienold, J. et al. (2004). Evalglare—a new radiance-based tool to evaluate daylight glare in office spaces. In *3rd International RADIANCE workshop 2004*.

A method for an effective microclimate management in historical buildings combining monitoring and dynamic simulation: the case of “Museo Archeologico di Priverno”

Francesca Frasca^{1,*}, Cristina Cornaro² and Anna Maria Siani³

¹ Sapienza Università di Roma, Dept. of Earth Sciences, Rome, Italy

² Università degli Studi di Roma “Tor Vergata”, Dept. of Enterprise Engineering, Rome, Italy

³ Sapienza Università di Roma, Dept. of Physics, Rome, Italy

*Corresponding email: f.frasca@uniroma1.it

ABSTRACT

In this work a method is proposed to estimate the effect of indoor microclimate on the risk of degradation of ancient materials stored in historical buildings. The method, which combines microclimate observations and dynamic simulation, has shown to be strategic in preventive conservation of historical buildings. Indeed, once the building model is calibrated, it can be effectively used for evaluating the microclimate control solutions on the conservation reducing general degradation risks. The method has been applied to a historical building close to Rome, where deteriorations in ceilings occurred and visitors complain about thermal discomfort. First, the HVAC system in the model has set in order to guarantee both thermal comfort and adequate condition for the conservation of the material. Then, the crack width of wooden ceiling has been estimated by means of an empirical model based on indoor temperature and relative humidity data and validated with the measurements of the crack width. It was found a reduction of annual variation from 0.4 mm to 0.2 mm, experimented by panels, and an improvement of maximum daily variation, especially in winter and summer (less than 0.01 mm on average).

KEYWORDS

Historical building, microclimate, conservation strategy, dynamic simulation.

INTRODUCTION

In the last years, an increasing attention has been paid to the energy refurbishment of the existing buildings (Mazzarella 2015), both modern and historical buildings, which belong to public institutions (Ascione et al. 2017; Cornaro et al. 2016; Semprini et al. 2016). Even though in Italy the energy retrofit for the historical buildings is not mandatory due to the priority of conservation heritage, several studies about this issue have been conducted by combining experimental data and whole-building dynamic simulation (Bellia et al. 2015; Dalla Mora et al. 2015; Lucchi 2016; Roberti et al. 2017). However, to take advantages of simulations, the calibration of building model is necessary. Currently, most of the calibration methodologies focuses on matching of measured and modelled energy consumptions instead of hourly measured indoor climate data (Paliouras et al. 2015), especially the relative humidity data. Moreover, the optimization of retrofitting solutions (including new control strategies) mainly concerns the energy saving and the conservation of the aesthetic aspect of buildings, while the control of the indoor climate with respect to its interaction with objects is little considered. Among climatic parameters, the relative humidity plays a key role in the degradation and the durability of building components, especially organic and hygroscopic materials. This is very important when valuable artworks and/or building components made of material sensitive to hygrometric variables are within the building.

This paper aims at showing a methodological approach which uses indoor microclimate measurements and simulations for addressing a climate control solution adequate both for the conservation of the valuable wooden ceilings and for the thermal comfort of visitors.

MATERIALS AND METHODS

A flow chart of the methodology proposed in this study is displayed in Figure 1. First, the calibration of the building model is carried out following two steps: a) the Sensitivity Analysis (SA) for the identification of the most affected input parameters on the building model and b) the genetic algorithms, by means of GenOpt® (Genetic Optimization), for the minimization of the discrepancy between measured and simulated data. Then, the calibrated building model can be used to analyse retrofit/control solutions taking also into account the degradation risk of the materials to preserve and the thermal comfort of the visitors. The workflow can be generally applied to other historical buildings that need for refurbishment or novel control strategies and where the conservation of artworks has the priority. It is worth to note that the methodology takes advantages only if a comprehensive knowledge of the indoor climate and its interaction with the objects is reached.

For this study, the building model was calibrated by using hourly measured data of indoor temperature (T) and relative humidity (RH) and surface temperature (T_s). Then, the temporal behaviour of the width cracks (C) in wooden panels was modelled by means of an empirical model based on T_s and RH data to predict the effect of the estimated indoor climate on C .

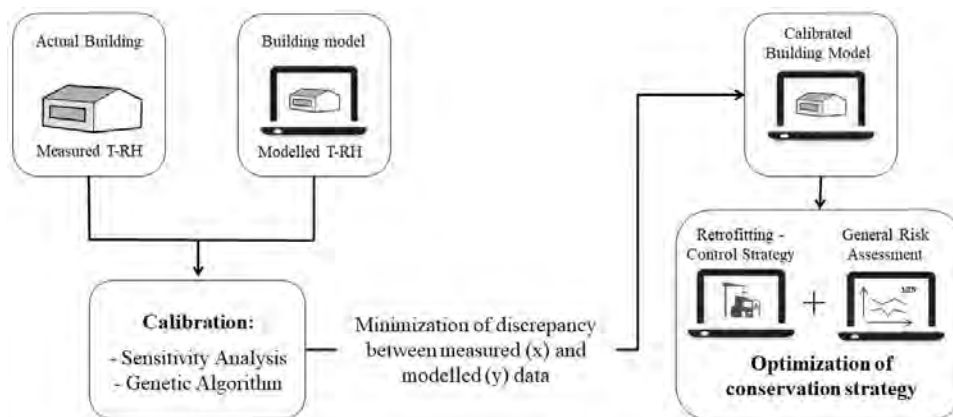


Figure 1 Schematic workflow of methodology.

The building under study and the field campaign

The “Museo Archeologico di Priverno” is housed in the Palazzo Valeriani-Guarini-Antonelli, in the central Italy at about 70 km SE far away from Rome (Lat. 41.5 and Long. 13.2). It is a three-storey building, built between 13th and 16th century and restored in 1924-1926. The HVAC is switched on during opening hours both in winter and summer and consists in one or more convection heating/cooling systems with only temperature control in each room. The study is focused on the conservation of wooden ceilings Liberty decorated by Pietro Campeggi (Figure 2a), that suffer from cracks and deformations especially in summer, when high temperatures are experienced in the room. Visitors complain about thermal discomfort due to rigid temperatures in winter and unpleasant warm in summer.

Sensors to measure indoor and outdoor temperature (T_{in} and T_{out}) and relative humidity (RH_{in} and RH_{out}) were installed as shown in Figure 2a and indicated as ‘*’. Moreover, a sensor for surface temperature (T_s) and a crack width meter (C) were installed on a wooden panel in room 9, indicated as ‘o’ in Figure 2b. These measurements have allowed to monitor the

stress/strain behaviour of panel (mechanical degradation). For this study the acquisition time was set to 30 min and the monitoring campaign lasted from August 2016 till November 2017.

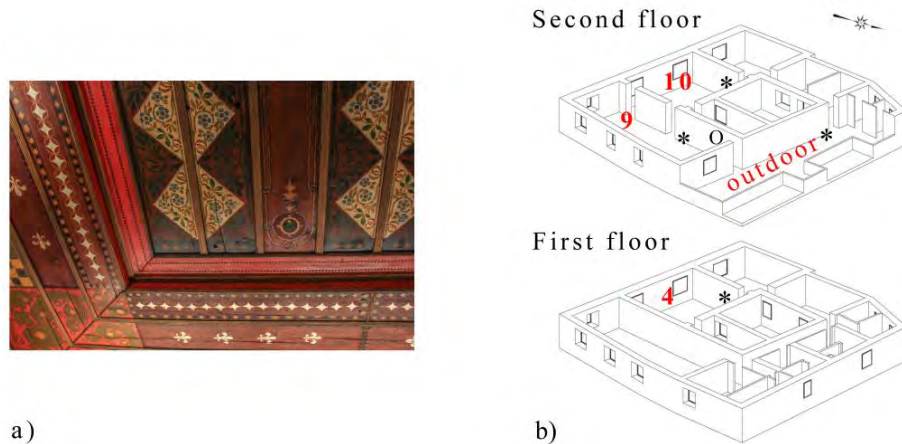


Figure 2 a) An example of wooden panels with cracks and deformations at the second floor. b) The axonometric cross section of first and second floor of the Museum. Numbers individuate the rooms where sensors were installed: ‘*’ for T and RH and ‘o’ for T_s and C.

Building dynamic simulation model

Dynamic building simulation for indoor climate analysis was performed using the IDA Indoor Climate and Energy (IDA ICE) 4.8 developed and distributed by EQUA simulation AB.

The geometry of the building model of the Museum was created starting from the architectural survey provided by Arch. Lucia Di Noto and using the hygrothermal properties reported in *MASEA Datenbank* for opaque components. The wall stratigraphy was gathered from literature referred to construction techniques in lower Latium in the Middle Age and was assumed to be unchanged over time except for ceilings. The building model consisted in sixteen zones, but only the zones with sensors were calibrated.

The climate file used to run the model was determined from T_{out} and RH_{out} measurements. Wind variables and solar radiation, measured at Maenza station (Lat. 41.5° , Long. 13.2°) belonging to the ARSIAL (Agenzia Regionale per lo Sviluppo e l'Innovazione dell'Agricoltura del Lazio), were also included in the climate file.

The calibration of the envelope of the building model was carried out using hourly T-RH data collecting in two different periods (May and September 2017), when the HVAC was off and no visits occurred. The calibration consisted in two steps through a semi-automatic procedure, as shown in the scheme in Figure 1. The agreement between measured and modelled data was evaluated by using the Mean Absolute Error (MAE), the Root Mean Square Error (RMSE) and the Coefficient of Variation of RMSE (CV-RMSE) (Fabrizio and Monetti 2015).

Optimization of conservation strategy

Wood panels can be damaged if directly exposed to fast fluctuations of indoor RH and T (Bratasz et al. 2007), which are responsible of changes in the moisture content (MC) of hygroscopic materials. This might cause stresses in terms of shrinkage and/or swelling of fibres with a following deformation up to a definitive fracture if the strain is not elastic. The relationship between the measured crack width (C) and indoor T-RH data has been assessed by using Spearman's rank-order correlation (ρ). It was found that C and T_s are well positive correlated ($\rho = 0.67$), whereas C and RH are highly anti-correlated ($\rho = -0.81$).

From the above outcomes, we have defined an empirical relationship (eq. 1) between crack width (C_{sim}) in wooden panel and $T_s - RH$ data:

$$C_{sim} = a \cdot RH^b \cdot T_s^c \quad (1)$$

The coefficients a , b , and c were computed by a non-linear multiple regression over the whole period of measurements. They are 6.4343, -0.0575 and 0.0057, respectively. The agreement between C and C_{sim} is less than instrumental accuracy. In this study, the eq. 1 is used with modelled indoor variables, as a predictive conservation target, i.e. C_{sim} will allow knowing in advance if the novel control strategy is addressed in such a way the mechanical degradation risk of wooden panel is minimized.

The optimization of control strategy of indoor climate was addressed to update the set-point controller of the existing HVAC system without any modification of the plant. The HVAC was designed in the simulation environment as simple fan coils. The new control strategy of the indoor climate was tested using a dynamic set-point for T and RH (Kramer et al. 2017). First, T was set according to the Adaptive Temperature Limits (ATL) for thermal comfort requirements (Nicol and Humphreys 2002) leaving RH in free-floating. Then, for assessing conservation risks, these T limits were compared with T limits computed from the class of control As , as recommended in ASHRAE (2011), updating the T dynamic set-point and leaving RH in free-floating. Finally, the modelled RH values were compared with limits recommended in the guidelines to check if the system also guarantees the RH control. The class of control As provides a seasonal adjustment for T set point of $+5/-10$ K and $\pm 10\%$ for RH with respect to the annual mean and short-term fluctuations of ± 2 K and $\pm 5\%$, respectively. For each step, the estimated indoor variables were replaced in the eq. 1 to analyse the effect of the new control strategy on the crack width with respect to no control strategy, i.e. the free-floating indoor climate. For the novel control strategies in the rooms with wooden ceiling, the peak demand is 8.7 kW in heating hours and 1.5 kW in cooling hours, whereas the annual energy consumption is 21026 kWh and 917 kWh, respectively.

RESULTS

The results from the Sensitivity Analysis (SA), carried out by means of 18 general input parameters, have demonstrated that the indoor RH of building model is strongly affected by the rate of infiltration, whereas the indoor T by the thermal bridges. Starting from these outcomes, the building model was calibrated with the most affecting input parameters by using a genetic algorithm. The MAE is, on average, 0.3°C for T , 1.6% for RH and 0.2°C for T_s . The RMSE is, on average, 0.4 for T , 2.1% for RH and 0.2 for T_s . Finally, the CV-RMSE is less than 2.0% for T , less than 1.0% for T_s and less than 5.0% for RH .

Figure 3 shows the histogram plot with the percentage of occurrences (%) of C when the indoor climate is free-floating (red bars) and is controlled (blue bars). In free-floating indoor climate, about 40% of data corresponds to the bin limits 5.00-5.05 mm, i.e. when, in cold period, T is low ($T < 14^\circ\text{C}$) and RH is high ($RH > 85\%$); about 16% of data is in the bin limits 5.25-5.30 mm, i.e. when, in warm period, T is up to 31°C and RH is down to 35%. In both cases, the thermal comfort requirement of people is not reached. No significant difference has been detected among the three climate controls described in the previous paragraph. However, the control of the indoor climate allows a minor annual variation between minimum and maximum width of wooden cracks: 0.20 mm instead of 0.40 mm in free floating. This means that, when thermal comfort needs and the assessment of material risks according to ASHRAE (2011) are met, wooden panels would test less stresses and, consequently, strains.

Looking at the histograms of daily span (difference between the maximum and the minimum value) of C (Figure 4), the free-floating strategy might provoke additional daily stresses and

consequently strains to the wooden fibres over the year. If a control of indoor climate is considered, the daily span is in about 80% of the occurrences less than 0.010 mm. It is worth to notice that the T control, so as designed, guarantees the control of RH as recommended in ASHRAE (2011). This means that the current system can be used, as it is, just updating the set-point controller.

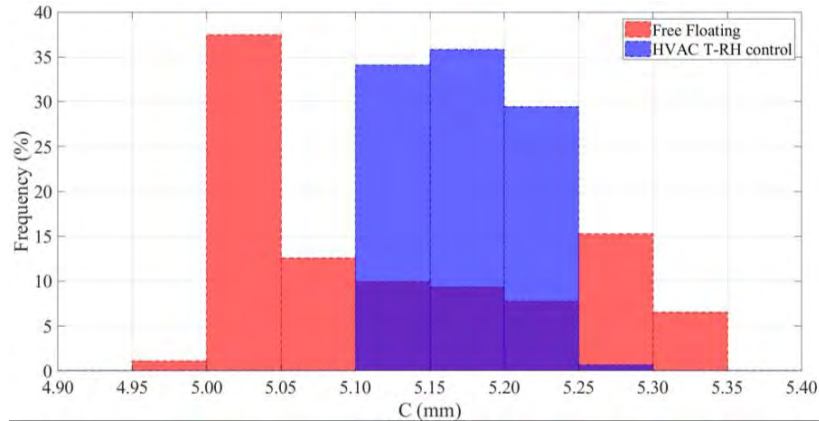


Figure 3 Histogram plot with the percentage of occurrences (%) of crack width when the indoor climate is free-floating (red bars) and is controlled by a dynamic T and RH set-points (blue bars).

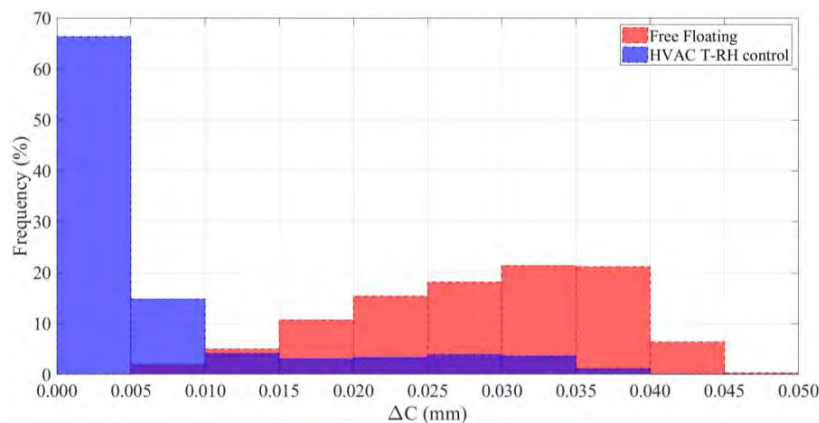


Figure 4 Daily span (ΔC) of crack width when the indoor climate is free-floating (red bars) and is controlled by a dynamic T and RH set-points (blue bars).

CONCLUSIONS AND DISCUSSIONS

The management of historical buildings in Italy is strongly related to the priority of preservation of architectural components. So, the control of the indoor climate should mainly concern the optimization of the current system with respect to the degradation phenomena. This study has revealed that the semi-automatization of calibration methods using hourly measurements of climate variables might be very useful to design a building model as representative as possible of the indoor climate of the actual case. Moreover, it has demonstrated that long-term indoor climate monitoring campaign coupled with the monitoring of crack width of wood might be essential in addressing the optimization of indoor climate control with respect to mechanical degradation of valuable wooden ceilings. Indeed, the indoor climate control, designed so at ensuring both the thermal comfort and the minimization of general degradation risks for objects, seems beneficial also for the peculiar case of the mechanical degradation of wooden panels.

Further simulations will be addressed to investigate the heat and moisture transport inside the wooden panels for modeling the evolution of degradation in the internal layers.

ACKNOWLEDGEMENT

We thank Sapienza University of Rome for funding the multidisciplinary project “*Preservation, conservation and valorisation of archaeological sites: The case of the ancient site Privernum*”. This research has been carried out within the “*Renovation of existing buildings in NZEB vision (nearly Zero Energy Buildings)*” Project of National Interest (Progetto di Ricerca di Interesse Nazionale - PRIN) funded by the Italian Ministry of Education, Universities and Research (MIUR).

REFERENCES

- ASHRAE. 2011. *ASHRAE handbook—HVAC applications*. Chapter 23: museums, galleries, archives, and libraries. Atlanta: American Society of Heating, Refrigerating and Air-Conditioning Engineers, Inc.
- Ascione F., De Masi R.F., De Rossi F., Ruggiero S., Vanoli G.P. 2017. NZEB target for existing buildings: Case study of historical educational building in Mediterranean climate. *Energy Procedia*, 140, 194–206.
- Bellia L., Alfano F.R.D.A., Giordano J., Ianniello E., Riccio G. 2015. Energy requalification of a historical building: A case study. *Energy and Buildings*, 95, 184–189.
- Bratasz L., Camuffo D. and Kozłowski R. 2007. Target microclimate for preservation derived from past indoor conditions. In: Padfield T, Borchersen K (eds) *Museum Microclimates Contributions to the Copenhagen conference 19–23 November 2007, Copenhagen, 2007*. The National Museum of Denmark, Copenhagen, 129–134.
- Cornaro C., Puggioni V. and Strollo R. 2016. Dynamic simulation and on-site measurements for energy retrofit of complex historic buildings: Villa Mondragone case study. *Journal of Building Engineering*, 6, 17–28.
- Dalla Mora T., Cappelletti F., Peron F., Romagnoni P., Bauman F. 2015. Retrofit of an historical building toward NZEB. *Energy Procedia*, 78, 1359–1364.
- Fabrizio E. and Monetti V. 2015. Methodologies and advancements in the calibration of building energy models. *Energies*, 8(4), 2548–2574.
- Kramer R., van Schijndel J., Schellen H. 2017. Dynamic setpoint control for museum indoor climate conditioning integrating collection and comfort requirements: Development and energy impact for Europe. *Building and Environment*, 118, 14–31.
- Lucchi E. 2016. Multidisciplinary risk-based analysis for supporting the decision-making process on conservation, energy efficiency, and human comfort in museum buildings. *Journal of Cultural Heritage*, 22, 1079–1089.
- Mazzarella L. 2015. Energy retrofit of historic and existing buildings. The legislative and regulatory point of view. *Energy and Buildings*, 95, 23–31.
- Nicol J.F. and Humphreys M.A. 2002. Adaptive thermal comfort and sustainable thermal standards for buildings. *Energy and buildings*, 34(6), 563–572.
- Paliouras P., Matzaflaras N., Peuhkuri R.H., Kolarik, J. 2015. Using measured indoor environment parameters for calibration of building simulation model—a passive house case study. *Energy Procedia*, 78, 1227–1232.
- Roberti F., Oberegger U.F., Lucchi E., Troi A. 2017. Energy retrofit and conservation of a historic building using multi-objective optimization and an analytic hierarchy process. *Energy and Buildings*, 138, 1–10.
- Semprini G., Marinosci C., Ferrante A., Predari G., Mochi G., Garai M., Gulli R. 2016. Energy management in public institutional and educational buildings: The case of the school of engineering and architecture in Bologna. *Energy and Buildings*, 126, 365–374.

Description Method of Outdoor Climate Characteristics Considering the Comprehensive Effect on Indoor Climate

Xinying Fan¹, Bin Chen^{1,*}, Meiling Sun¹ and Tongke Zhao¹

¹ Dalian University of Technology, China

*Corresponding email: chenbin@dlut.edu.cn

ABSTRACT

What human and buildings perceived the environmental information is comprehensive information. However, existing indoor environment design methods are often simplified to single parameters for indoor and outdoor environmental prediction and indoor environment design. In order to describe the indoor climate characteristics of the comprehensive impact of outdoor climate, this study uses the ensemble empirical mode decomposition (EEMD) method to establish a multi-parameter integrated outdoor comprehensive environmental information description method based on the information-response theory. The outdoor climate feature description method is applied to the analysis of the amplitude and frequency characteristics of outdoor comprehensive information, which provides a research basis for further exploring the indoor and outdoor environmental response under the multi-parameters interaction.

KEYWORDS

Feature extraction; natural information; information-response; comprehensive parameters.

INTRODUCTION

Indoor and outdoor environmental status points are formed under the influence of multiple parameters. Due to the limitations of the test instrument, we can only test a single parameter, but can't acquire a comprehensive environmental parameter. Under this condition, the information transfer process between the indoor and outdoor environments is described by constructing the heat and mass transfer equations. However, it is difficult to simulate building information response combined heat, air, moisture and pollutant simulation environment for whole-building performance analysis (Tariku F et al. 2010). This paper put forward building environment information analysis method transformation from single parameter to comprehensive parameters. In order to build a comprehensive parameter, this paper attempted to combine multi-parameters by EEMD for feature extraction.

BUILDING ENVIRONMENT INFORMATION ANALYSIS METHOD TRANSFORMATION

All of the orderly linear transfer laws of heat, mass, and fluid can be described using Fourier's law. Based on the above rules, the heat conduction equation, mass diffusion equation, etc. can be derived. However, these linear conduction laws are only correct when the mass and energy transfer processes are not strong. When the transfer process is very strong, it is necessary to consider the interaction between mass and heat transfer. However, the building mass and heat transfer process is actually a strong transfer process. When the steady-state solution equation is used to solve the mass and heat transfer process of a building, it often brings about a large error in simulation calculation. Onsager (1931) put forward the fluxes as linear combinations of the forces, in analogy to Stokes law where the velocity of a body pulled in a viscous fluid is proportional to the drag force. According to Onsager, a thermodynamic system can then be described by a set of linear equations, as shown in Eq. (1).

$$\begin{aligned}
 I_1 &= L_{11}X_1 + L_{12}X_2 + L_{13}X_3 + L_{14}X_4 \\
 I_2 &= L_{21}X_1 + L_{22}X_2 + L_{23}X_3 + L_{24}X_4 \\
 I_3 &= L_{31}X_1 + L_{32}X_2 + L_{33}X_3 + L_{34}X_4 \\
 I_4 &= L_{41}X_1 + L_{42}X_2 + L_{43}X_3 + L_{44}X_4
 \end{aligned}
 \tag{1}$$

where I_i is the conjugated thermodynamic fluxes, L_{ij} is symmetric matrix, X_i is the different force.

The above equation has showed that the state point of the outdoor environment was formed by the coupling of multiple factors. The same process exists in human thermal comfort and free-running building. Because of the complexity of solving the above equation, we generally use the theory of reductionism to decompose the overall information transfer process of the building into a single parameter response process. Under such a theoretical system, we have established a series of prediction model for the building thermal transfer, moisture migration, pollutant diffusion and so on. However, some researchers (Hens 2015; Zhang et al. 2017) found that the single parameter transfer process was influenced by other parameters. Therefore, researchers began to try to establish a coupled prediction model with two or three parameters (Kumaran et al. 2008). Due to the influence of factors such as multi-parameter interactions, personnel behaviour, cultural background, and architectural control methods during the actual operation of the building, it is difficult to couple multiple parameters to solve the problem (Zhang & Qin 2011). Therefore, this study proposed that if the outdoor multiple parameters could be converted into a single comprehensive information, the information transmission process of the building can be simulated, as shown in Figure 1.

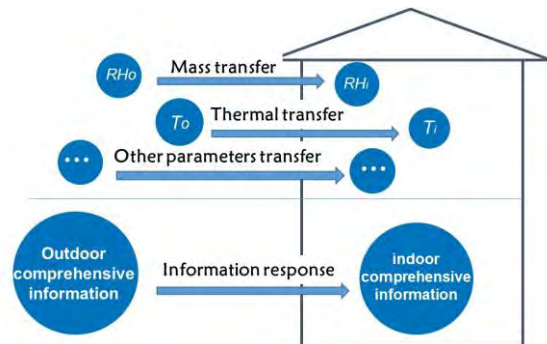


Figure 1. A schematic diagram of the information response of a building.

INFORMATION FEATURE EXTRACTION METHOD

The outdoor comprehensive information contains multiple parameters such as temperature, relative humidity, solar radiation, wind speed, dew point temperature, vapour pressure, etc. The existing integrated information theory description model mainly establishes the integration of several parameters, such as the PMV index and Universal Thermal Climate Index (UTCI) (Fiala et al. 2012). In addition to the theoretical model, there are some relational models in Chinese traditional culture to analysis the outdoor environment and human health, such as Jiugong Bafeng (Xinying Fan et al. 2017). However, it is difficult to establish a comprehensive information description method for the above model. Chinese people have always believed that there are certain differences in outdoor comprehensive information at different times. The 24 Solar Terms have been formed under the special climatic conditions in China, which is reflected in the basic necessities of life. It means the small-scale climate directly affects people's feelings. Meehl et al. (2001) proposed a conceptual model of multi-time scale coupling of outdoor climate, which means outdoor weather data could be decomposed into different time-scale information for analysis. It provided a certain theoretical

basis for the Chinese to experience climate change on a small time scale. Due to the different time scale characteristics of the outdoor environment parameters, it is very important to choose an appropriate feature extraction method. Norden E. Huang et al. systematically compared several common information decomposition methods, as shown in Table 1.

Table 1. Comparison between Fourier, Wavelet, and EEMD analysis

Characteristic	Fourier	Wavelet	EEMD
Basis	a priori	a priori	a posteriori adaptive
Nonlinearity	×	×	√
Non stationarity	×	√	√
Feature extraction	×	discrete, continuous, yes	no; √
Theoretical base	complete mathematical theory	complete mathematical theory	empirical

Compared with wavelet and Fourier analysis method, EEMD can not only analyze nonlinear problems, but also extract the features of information, such as climate data. Due to the advantages of EEMD in the feature extraction of outdoor meteorological parameters, it was used to analysis the feature of outdoor meteorological information in this study. The original single using the EEMD method can be decomposed into the sum from the high frequency to the low frequency components and the residual sequence. The residual sequence represents the trend of the original sequence, as shown in Eq. (2).

$$x(t) = \sum_{i=1}^n IMF_i(t) + r_n(t) \quad (2)$$

where $x(t)$ is the original single; $IMF_i(t)$ is the different frequency components; $r_n(t)$ is residual sequence (RES).

SINGAL ENVIRONMENT PARAMETER DESCRIPTION

The feature description process of a single meteorological parameter information mainly consists of three steps. This article takes the outdoor temperature in Zhengzhou, China, from 2014 to 2016 as an example.

(1) First, the outdoor air temperature in Zhengzhou was decomposed using the EEMD method to obtain 12 IMF and one residual sequence. Accumulation of IMF 1~IMF 5 below the time scale of the year gives the high-frequency component of outdoor temperature, ie, high-frequency (HF); Accumulation of IMF 6~IMF 12 at the time scale and above can produce the low frequency component of the outdoor temperature, ie, the periodic change sequence (PCS); summing the PCS and RES to obtain the annual low-frequency cycle (ALC), as shown in Figure 2.

(2) Second, by calculating the same day average of the ALC of meteorological parameters for the period 2014-2016, a 365-day smooth annual average cycle sequence ALC_{avg} is formed.

(3) Then, by fitting the annual average cycle sequence ALC_{avg} , Zhengzhou outdoor temperature information feature description model can be obtained, as shown in Eq. (3).

$$y = 13.694 + 14.05 * \sin\left(\frac{\pi(n-96.131)}{199.234}\right) \quad (3)$$

where y is the temperature, °C; n is the number of the day starting from January 1 (e.g. for the 1st January, $n = 1$ and for the 31st December, $n = 365$); 13.694 was average temperature of Zhengzhou, °C; 14.05 is the amplitude of temperature, °C.

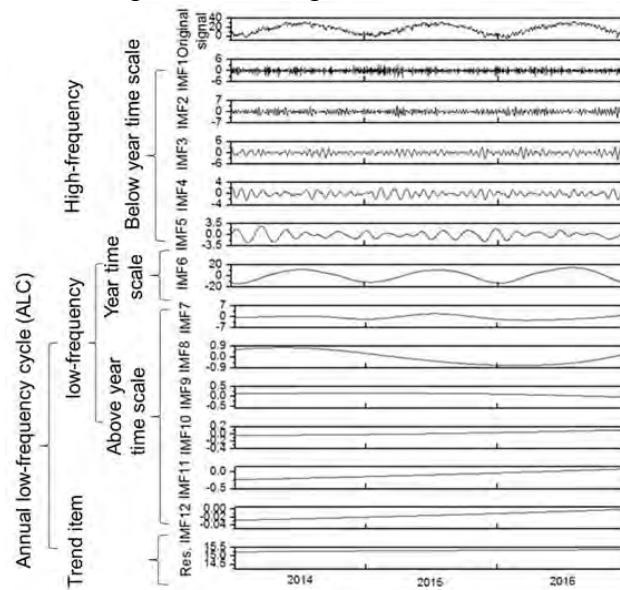


Figure 2. Feature extraction of outdoor temperature in Zhengzhou.

In addition to temperature, any other outdoor weather parameters can also be described as the above model. Through literature research, it is difficult to find the expression of outdoor climate parameters that represent a region. In order to obtain solar radiation mathematical formulas for use in computer software, several mathematical models are given below. Bulut (2007) presented a simple model using sine wave equation (SW) below to predict global solar radiation, as shown in Eq. (4). Kaplanis (2007) suggested the following cosine wave (CW) relationship, as shown in Eq. (5). Some researchers (Zang et al. 2012) presented a daily global solar radiation model in connection with a sine and cosine wave (SCW) correlation which is developed to simulate the long-term measured data as shown in Eq. (6). In the present study, we get solar radiation model by EEMD method in Zhengzhou, as shown in Eq. (7).

$$I = a + b \left| \sin\left(\frac{\pi}{365}(n+5)\right) \right|^{1.5} \quad (4)$$

$$I = a + b \cos\left(\frac{2\pi}{364}n + c\right) \quad (5)$$

$$I = a + b \sin\left(\frac{2\pi c}{365}n\right) + d \cos\left(\frac{2\pi e}{365}n\right) \quad (6)$$

$$I = 12.71 + 5.59 * \sin\left(\frac{\pi(n-72.48)}{187.97}\right) \quad (7)$$

where I is the daily global solar radiation; n is the number of the day starting from January 1 (e.g. for the 1st January, $n = 1$ and for the 31st December, $n = 365$); a , b , c , d and e are regression coefficients of Zhengzhou, as shown in Table 2.

Table 2. The regression coefficients of different solar model in Zhengzhou

Model	a	b	c	d	e
SW	6.4235	11.678			
CW	12.9363	-5.7068	0.2944		
SCW	12.0955	4.1152	0.9500	-5.8501	0.8580

In this study, the Pearson correlation coefficient was used to analysis the relationship between predicted solar radiation and original data, as shown in Figure 3. The result showed that the EEMD model almost same as other models. However, the EEMD method could be used to other environmental parameters ie, outdoor temperature. Therefore, this study selected the indoor and outdoor temperature of a tested building in Zhengzhou to analyze the frequency characteristics. The testing time is February 12-19, 2015. Figure 4 shows that the building filters outdoor high frequency information (IMF1-IMF5). Low-frequency information (IMF6-IMF9) has a certain influence on the indoor environment. It means the building envelope filter many outdoor environment information which may be benefit for people.

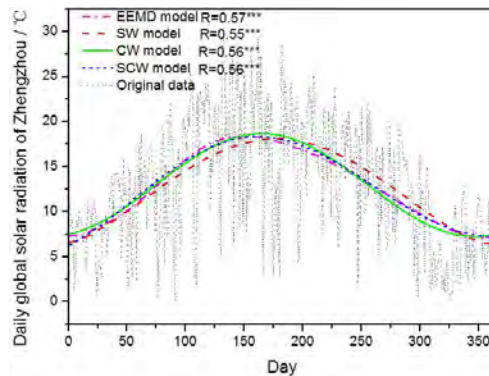


Figure 3. Comparison of several solar radiation models of Zhengzhou.

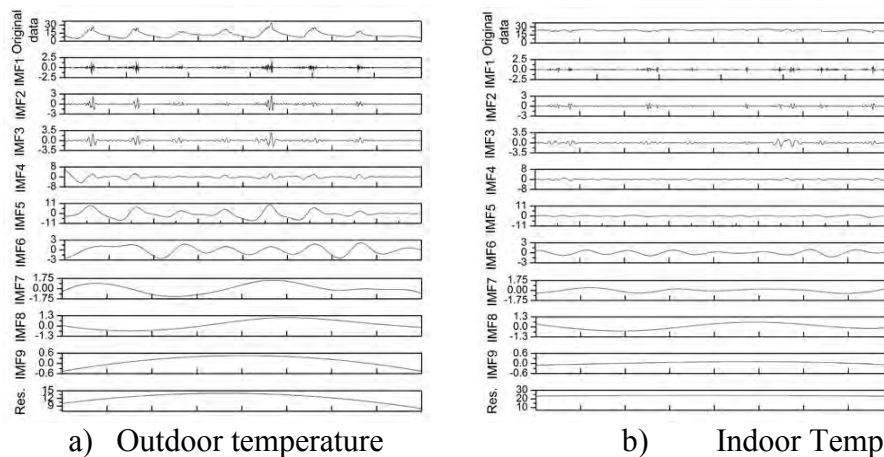


Figure 4. Comparison of indoor environmental information differences about temperature.

OUTDOOR ENVIRONMENT COMPRESIVE INFORMATION DESCRIPTION

The existing outdoor environment comprehensive parameters are generally described by establishing an equivalent temperature for people and buildings as objects. The environmental parameters considered are often limited. For example, the UTCI index takes into account four outdoor environmental parameters, and the outdoor integrated air temperature takes into account three outdoor environmental parameters. However, the outdoor environment parameters has more than four parameters. In order to describe the comprehensive parameters, this paper build a simple described formula by EEMD method, as shown in Figure 5. The weighting factors of the comprehensive environmental parameters refer to the weights of the meteorological factors during the typical meteorological year of TMY3. This formula expressed the frequency characteristics of the comprehensive information of the outdoor environment. This study uses the EEMD method to attempt to describe the comprehensive information of the outdoor environment. It also needs further discussion. This study provides the basis for further research on environmental comprehensive information - response.

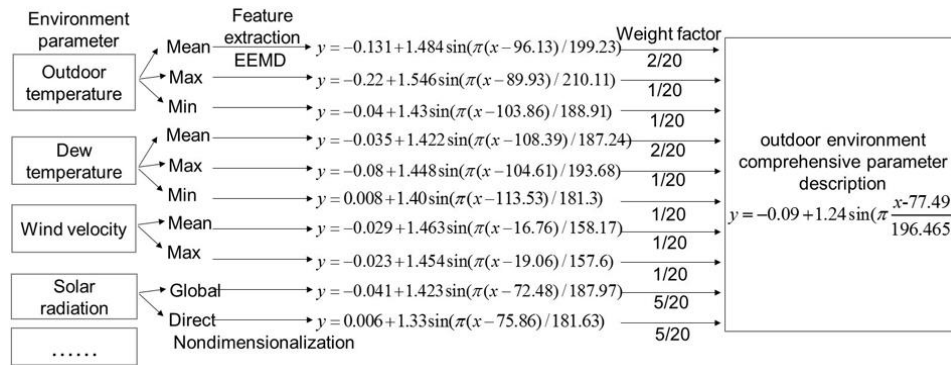


Figure 5. The outdoor environment comprehensive parameters formed process with EEMD.

CONCLUSIONS

This study proposed analysis method transformation of building environment information from single parameter to comprehensive parameters. Based on the conceptual model of multi-time scale, the described method of single outdoor meteorological parameter was put forward. This study has attempted to obtain the description method of outdoor comprehensive parameters considered weight factor in Zhengzhou region by EEMD.

ACKNOWLEDGEMENT

The authors would like to thank the research funding from the National Natural Science Foundation of China (NSFC, No. 51178073, No. 51578103).

REFERENCES

- Bulut, Hüsametlin, and Orhan Büyükalaca. 2007. Simple model for the generation of daily global solar-radiation data in Turkey. *Applied Energy*, 84(5):477-491.
- Fiala D, Havenith G, Bröde P, et al. 2012. UCI-Fiala multi-node model of human heat transfer and temperature regulation. *International Journal of Biometeorology*, 56(3):429-441.
- Hens, Hugo L. S. C. 2015. Combined heat, air, moisture modelling: A look back, how, of help? *Building & Environment*, 91(9):138-151.
- Kaplanis, S., and E. Kaplani. 2007. A model to predict expected mean and stochastic hourly global solar radiation values. *Renewable Energy*, 32(8):1414-1425.
- Meehl, G. A., R. Lukas, G. N. Kiladis, et al. 2001. A conceptual framework for time and space scale interactions in the climate system. *Climate Dynamics*, 17(10):753-775.
- Norden E. Huang and Zhaohua Wu. A review on Hilbert-Huang transform: Method and its applications to geophysical studies[C]// Rev. Geophys. 2008.
- Onsager, Lars. 1931. Reciprocal Relations in Irreversible Processes. I. *Physical Review*, 38(37):405-426.
- Tariku F, Kumaran K, Fazio P. 2010. Integrated analysis of whole building heat, air and moisture transfer. *International Journal of Heat & Mass Transfer*, 53(15):3111-3120.
- Xinying Fan, Bin Chen, Yu Chen et al. 2017. Relationship between seasonal variation and occupant health based on nine-palaces and eight-winds theory. *Healthy Buildings 2017 Europe*, Lublin, Vol. 3, pp. 63-68.
- Zang, Haixiang, Qingshan Xu, and Haihong Bian. 2012. Generation of typical solar radiation data for different climates of China. *Energy*, 38(1):236-248.
- Zhang J J, Qin M. 2011. Combined heat, air moisture and pollutant simulations (CHAMPS) for buildings. *Building Simulation*, 4(4):279-282.
- Zhang M, Qin M, Rode C, et al. 2017. Moisture buffering phenomenon and its impact on building energy consumption. *Applied Thermal Engineering*, 124(9):337-345.

IEQ measurement and assessment tools for Plug-and-Play deep renovation in buildings

Marco Arnesano^{1,*}, Lorenzo Zampetti¹, Gian Marco Revel¹, Rizal Sebastian², Anna Gralka², Carlo Macciò³, Eva Raggi³ and Michele Mililli³

¹ Dipartimento di Ingegneria Industriale e Scienze Matematiche, Università Politecnica delle Marche, Ancona, Italy

² Demo Consultants BV, Delft, Netherlands

³ RINA Consulting, Genova, Italy

*Corresponding email: m.arnesano@univpm.it

ABSTRACT

This paper presents the approach developed for the monitoring and assessment of Indoor Environmental Quality (IEQ) in the whole deep renovation process aimed at reducing energy consumptions and improving comfort. The research was performed by the P2Endure project, that aims to provide scalable, adaptable and ready-to-implement prefabricated Plug-and-Play systems for deep renovation of building envelopes and technical systems. The idea is to use IEQ as one of the design criteria supporting the decision-making process, included into the holistic renovation process developed by P2Endure and called “4M: Mapping-Modelling-Making-Monitoring”. For this reason, a set of Key Performance Indicators (KPI) was selected, with the consequent measurement and calculation methodologies. The KPIs are collected and showed together with the analysis of the different IEQ dimensions (thermal and indoor air quality). The data collection has been investigated extensively, taking into account all possible data sources, measurements and surveys (e.g. special questionnaires for children in schools). In addition to traditional devices, the innovative Comfort Eye sensor is used in the proposed framework. This is a low-cost sensing system capable of measuring thermal comfort together with IAQ, applicable for permanent or periodic monitoring and with low disturbance for inhabitants. The overall procedure is presented, also in relation with the deep renovation process. Then, the application of the measurement and assessment tools in real demonstration cases is illustrated with initial results from the monitoring campaign.

KEYWORDS

Measurement, Comfort, IEQ, Deep renovation, Plug-and-Play

INTRODUCTION

The existing building stock counts 210 million buildings in Europe and 75-90% of these buildings are estimated to still be standing in 2050. Most of Europe’s existing building stock – over 90% of the total – has yet to be affected by energy performance requirements¹. Therefore, the majority of the existing stock is composed by low-performance buildings in terms of energy consumption and IEQ (Indoor Environmental Quality), that will be subjects of renovation in the near future to accomplish 2030 EU targets. Considering that people spend about 90% of their time in indoor environments where microclimatic conditions greatly affect health, well-being and productivity, the renovation approach has to deal with the challenge of reducing the energy use but guaranteeing the optimal comfort. In fact, existing buildings are not able to keep the required comfort conditions because of the poor performance of their envelope and heating/cooling systems (Roaf et al. 2015). Although the renovation is the

¹ BPIE factsheet: 97% of buildings in the EU need to be upgraded

solution to the problem of performance, major attention is provided to the final energy performance and it is very usual that passive buildings design could lead to very tight environments suffering of Sick Building Syndrome. (Yousef et al. 2016) concluded that green building designs don't automatically guarantee that the building designed will be comfortable and will ensure occupants' well-being. Experts recognized and demonstrated that the environmental conditions have a significant effect on building occupants' health, although the general public has only recently started to understand the effect that this relationship can have on their everyday lives and well-being (Sappanen and Fisk, 2006). Detailed analysis and monitoring of building performance during its operations are necessary. In this framework, the EU project P2Endure proposes an innovative approach to buildings renovation, where a set of Plug-and-Play (PnP) technologies are provided within a holistic renovation approach that entails a set of KPIs (Key Performance Indicators) to assess the overall performance under different domains. The IEQ is one of them, and P2Endure developed a dedicated approach for the IEQ measurement and assessment, based on the innovative system called Comfort Eye in conjunction with standard surveying and measurement techniques.

METHODS

P2Endure approach for deep renovation

The P2Endure project is based on a holistic strategy for buildings deep renovation, structured on the 4M approach. The 4M modular process is a stepwise approach for preparing and implementing the deep renovation of buildings making use of PnP based innovative deep renovation products, followed by real monitoring of the resulting performance. The 4M correspond to 4 stages of the renovation process: Mapping, Modelling, Making, Monitoring. In this context, the data collection and monitoring before and after the renovation plays a pivotal role to: i) capture the actual real performance of the building and feed the design; ii) verify the compliance with renovation goals with deep Post Occupancy Evaluation. This paper presents the work done to implement tools for the IEQ mapping and monitoring.

IEQ monitoring and assessment protocol

The IEQ monitoring and assessment protocol has been developed starting from the standard EN 15251 (CEN, 2007), as already performed in the previous experience of (Zangheri et al. 2011). The proposed methodology is based on the evaluation of KPIs and benchmarks according to the buildings classification provided by EN 15251 (Categories I, II, III, IV). Different comfort domains are investigated (thermal comfort, IAQ and acoustic comfort) and for each domain a KPI, expressed as percentage of fulfillment of the criteria according to the targeted Category, is used. According to EN 15251, an acceptable amount of deviation is 5% of occupied hours. The best performance is achieved when there are no deviations outside the design limit. To define an assessment scale, a linear interpolation between the minimum (5%) and best performance (0%) is used. In this way the KPI assigned to each domain is normalized on a 0-100% scale. In addition, a detailed analysis of each domain is performed on measured data to provide insight on building performance and potential pathologies. The scope is the support of the renovation design (before intervention) and verification of renovation results (after intervention).

Comfort Eye

Thermal Comfort is assessed using the predictive (PMV) model. The Comfort Eye is a sensor capable of measuring the PMV for multiple positions in a room. The measuring concept is based on the thermal scanning of indoor room surfaces to calculate the mean radiant temperature with the angle factors method, according to ISO 7726, in function of the room geometry and occupants location. The detailed description of the methodology is presented in

(Revel et al. 2014). The mean radiant temperature is merged with the data (air temperature and relative humidity) acquired by a second sensing node that is placed in the most representative zone of the room. Embedded algorithms allow the calculation of comfort indexes, applying subjective parameters (occupants' activity and clothing insulation) in function of the typical end-use of the building. Furthermore, the second sensing node integrates a CO₂ sensor to provide IAQ monitoring.



Figure 1 The IR scanning device of the Comfort Eye

In the proposed framework, the Comfort Eye is used to measure the IEQ before the renovation to assess the building performance and potential pathologies to be solved in the design phase. In fact, together with comfort and IAQ indexes, information about the thermal performance of building envelope can be extracted from IR thermal maps. The same device is used after the renovation to evaluate if renovation design goal is met.

Surveys

The P2Endure protocol includes the investigation based on surveys to complement the monitoring data collection. This is particularly important in the case of occupants with characteristics that could differ from generic adults (e.g. office worker). In particular, a survey to investigate the thermal sensation of children was specifically created because of the presence of 3 nurseries within the project demonstration cases. Given the age of the interviewed persons (from 3 to 5 years old), traditional questionnaires could not be used. Thus, a graphical questionnaire, based on previous researches in this field (Fabbri 2013; Vasquez et al. 2014), was prepared together with the teachers. The questions asked to children were related to their feeling (hot/neutral/cold), sensation (happy/sad), thermal preference (colder/neutral/warmer), weather (sunny/cloudy/rainy) and clothing. Each question was asked with a set of images, drawn in function of how children could associate the reply with a representative image (Figure 2).



Figure 2 Graphical questions for children interviews

Description of the case studies

The IEQ monitoring protocol has been applied in two real demonstration projects where renovation will be applied. A nursery in Genova, located on the second floor of a two-level building, built in 1930s with concrete structure and non-structural brick walls. A nursery in Warsaw, built in 1983. It is in the southern part of the city and is one of 55 municipal nurseries in Warsaw.

RESULTS

Results from the monitoring in Genova

The thermal comfort and CO₂ have been measured with standard sensors (Deltaohm Microclima HD 32.3A and Deltaohm IAQ Datalogger HD21ABE), compliant with ISO7730 and ISO7726, located in two different rooms. Winter and summer monitoring was one month long each, with an acquisition time of 5 minutes.

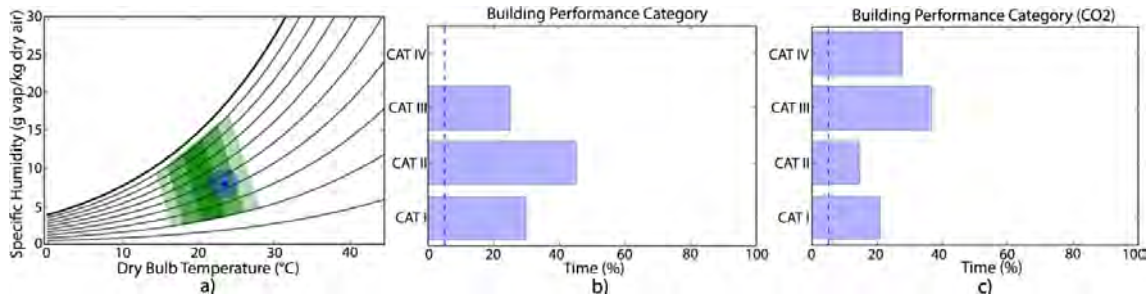


Figure 3 Winter comfort analysis: average operating conditions within comfort zones (a) category compliance of occupied hours for thermal comfort (b) and CO₂ (c)

The detailed analysis of comfort conditions in winter, is reported in Figure 3 a), where the average thermal condition (dark blue dot) is located with respect to comfort zones calculated according to EN15251. The deviation from the average condition (variability) is represented with the transparent blue circle, calculated with Monte Carlo analysis applied to input parameters according to their fluctuation in the time domain. The PMV was calculated with a clothing insulation of 0.9 clo and metabolic rate equal to 1.2 met. The monitoring campaign registered an average PMV of 0.3. The overall thermal sensation is within the optimal comfort range, slightly unbalanced toward warm sensation. The calculation of the percentage of time of building operation within the different Categories is presented in Figure 3 b). For about the 23% the time, the building operated a Category III, which indicates a poor condition. The KPI calculated as weighted average of all the monitored rooms turned out to be equal to 0% for Category II. The indoor air quality has been measured and assessed according to the P2Endure protocol. During winter, windows were mostly kept closed to ensure thermal comfort and the indoor air quality turned out to be poor, the nursery operated mostly as Category III and IV (Figure 3 c). During summer season, both measurements and surveying were performed. Questionnaires were compiled according to the presented methodology, with the support of teachers. A total number of 127 questionnaires were collected presenting a general warm sensation as reported in Table 1.

Table 1 Recap of children surveys in summer

Question	Q1: How do you think is the classroom today?			Q2: When the classroom is (Q1 answ.) how do you feel?		Q3: At this moment you like to feel...		
	Hot	Not hot neither cold	Cold	Sad	Happy	Warmer	No change	Cooler
Number	87	38	3	57	70	20	50	58
Percentage	69%	30%	2%	45%	55%	16%	39%	46%

From the interviews, the warm sensation is prevalent with 69% of replies. This is also confirmed by the higher percentage of children preferring a cooler feeling. At the same time the environmental data were acquired to assess thermal comfort using adaptive model for

naturally ventilated buildings, according to EN15251. Measured data turned out to provide averaged operating conditions in the Category III comfort zone, with a variability that brought the building outside that category (Figure 4 a and b). Concerning the IAQ, in summer, the windows were opened and the building presented a very high performance (Figure 4 c).

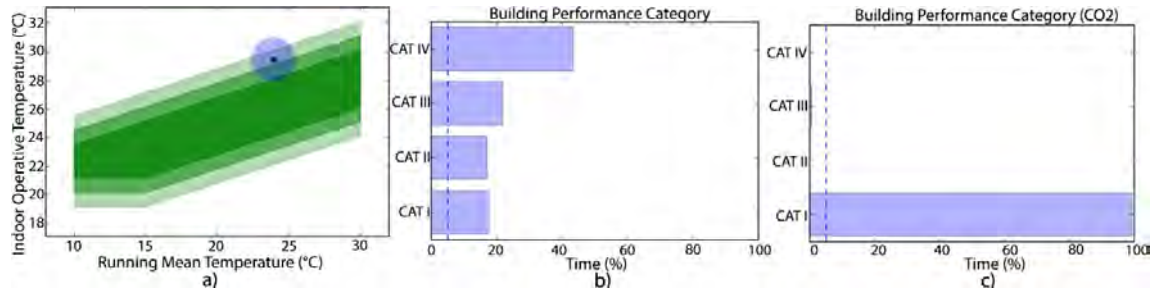


Figure 4 Summer comfort analysis: average operating conditions within comfort zones (a) category compliance of occupied hours for thermal comfort (b) and CO₂ (c)

Results from the monitoring in Warsaw

The Comfort Eye system was applied to Warsaw demo case for testing the first prototype. The installation was performed in March 2018 for 2 days, with an acquisition time of 5 minutes.

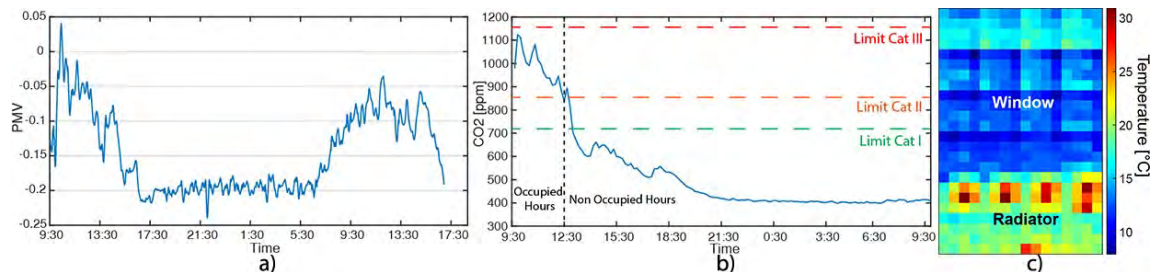


Figure 5 Comfort Eye measurement in Warsaw: Thermal comfort a) CO₂ b) Thermal map c)

Figure 5 a) shows the PMV measured in the room during the test, which turned out to provide an average value of -0.15. The comfort is maintained within the acceptable range, providing a KPI of 100% with the fulfilment of Category II criteria. The CO₂ was measured during the two days of testing, but the room was occupied only during the first day. Figure 5 b) shows the CO₂ trend during the occupied and non-occupied period of the first day. The monitoring turned out to provide a poor level of IAQ during the occupied hours with CO₂ concentrations always within the Category III, leading to a KPI equal to 0%. Figure 5 c) shows an example of thermal map, provided by the Comfort Eye, where the elements composing the outer wall of the room are measured. The window area is distinguished by a lower temperature (average of 10°C) with respect to the other parts. The opaque element of the wall registered an average temperature of 16°C, providing a strong deviation from the average room air temperature (22.8°C). This deviation, together with the low window temperature, had an impact in terms of radiant temperature. In fact, a mean radiant temperature of 17.8°C was measured near the wall (50cm of distance, not in front of the radiator). This initial investigation suggests a non-efficient building performance since, although thermal comfort is kept within requirements, the air temperature is kept high to balance the cooling effect of the building envelope.

DISCUSSIONS

The presented results reveal the importance of the IEQ measurement in buildings renovation process. The demo cases presented issues that need to be addressed by the renovation design.

In both cases, the indoor air quality is poor, especially in winter, suggesting the inclusion of mechanical ventilation systems. Moreover, the envelope performance monitoring is important to highlight masked pathologies, as the low wall and window temperature that can provide discomfort conditions by strong deviations from the air temperature, or, despite the almost optimal PMV, non-efficient use of energy to keep the building comfortable because of the low envelope thermal performance.

CONCLUSIONS

The proposed paper presents the initial results from the application of innovative IEQ measurement systems in the renovation process. The use of dedicated tools, as the Comfort Eye, can be useful to bring IEQ issues to the attention of the design team. In P2Endure, the monitoring results are going to feed the design of dedicated PnP renovation solutions, as multifunctional panels with embedded ventilation systems. The overall design will thus address not only energy, but also IEQ criteria. After the renovation, the same measurements will be applied to verify the final IEQ result. Finally, the possibility of integrating the measurements all in a unique device, the Comfort Eye, will make easier and less intrusive the monitoring.

ACKNOWLEDGMENT

This research has received founding from the P2Endure (Plug-and-Play product and process innovation for Energy-efficient building deep renovation) project (<https://www.p2endure-project.eu/en>) under the Horizon 2020 research and innovation programme (Grant Agreement no. 723391). The authors wish to thank the partners for the useful discussions.

REFERENCES

- CEN. 2007. EN Standard 15251, Indoor environmental input parameters for design and assessment of energy performance of buildings addressing indoor air quality, thermal environment, lighting and acoustics. Brussels: CEN.
- Fabbri K. 2013. Thermal comfort evaluation in kindergarten: PMV and PPD measurement through datalogger and questionnaire. *Building and Environment*, Vol. 68, pp. 202-214
- Yousef A.H., Arif M., Katafygiotou M., Mazroei A., Kaushik A. and Elsarrag E. 2016. Impact of indoor environmental quality on occupant well-being and comfort: A review of the literature. *International Journal of Sustainable Built Environment*, Vol. 5, pp. 1-11.
- Revel G.M., Arnesano M. and F. Pietroni. 2014. Development and validation of a low-cost infrared measurement system for real-time monitoring of indoor thermal comfort. *Measurement Science and Technology*, Vol. 25 (085101), 10pp.
- Roaf A., Brota L. and Nicol F. 2015. Counting the costs of comfort. *Building Research -and- Information*, Vol. 43, pp. 269-273.
- Sappanen O.A. and Fisk W. 2006. Some Quantitative Relations between Indoor Environmental Quality and Work Performance or Health. *HVAC-and-R Research*, Vol. 12, pp. 957-973.
- Vasquez N.G., Rupp R.F., Diaz L.A., Cardona A.G. and Arenas D.M. 2014. Testing a Method to Assess the Thermal Sensation and Preference of Children in Kindergartens. In: *Proceedings of 30th International PLEA Conference*, Ahmedabad.
- Zangheri P., Pagliano L and Armani R. 2011. How the comfort requirements can be used to assess and design low energy buildings: testing the EN 15251 comfort evaluation procedure in 4 buildings. In: *Proceedings of the ECEE 2011 Summer study – Energy Efficiency First: The Foundation of a Low-Carbon Society*, Belambra Presqu'île de Giens, pp. 1569-1579.

Influence of Illumination on Paper and Silk used in Chinese Traditional Painting and Calligraphy Based on Raman Spectroscopy in Museum

Rui Dang^{1*}, Huijiao Tan, Gang Liu^{2*} and Nan Wang

School of Architecture, Tianjin University, Tianjin Key Laboratory of Architectural Physics and Environmental Technology, Tianjin, 300072.

^{1*}*Corresponding email: dr_tju@163.com*

^{2*}*Corresponding email: LGLGMIKE@163.com*

ABSTRACT

As the substrate of Chinese traditional painting and calligraphy, the paper and silk are susceptible to optical radiation in the museum illumination and appear mechanical damage such as brittleness, chalking, deformation, etc. However, there is no effective method now of quantitatively evaluating the mechanical damage of cultural relics caused by illumination. In this paper, Raman spectroscopy used in the analytical chemistry field was introduced into the illumination research of the cultural relics in museum. The four light sources with different center wavelengths of 450nm, 510nm, 583nm, and 650nm, which constitute the spectra of the white light-emitting-diode (LED), were used as the light sources. As experimental specimens, the paper and silk specimens were illuminated by the above light sources for half of a year. Raman spectra of specimens before and after illumination were detected. By analyzing the variations of Raman characteristic peak intensity, the relative damage coefficients of four light sources on the microscopic molecular structure of the paper and silk specimens were studied, respectively. Finally, white LED illumination, namely the spectral irradiance distribution (SPD) of white LED, for the paper and silk should be designed according to the corresponding relative damage coefficients, respectively. Simultaneously, the paper proposed a new research method of studying mechanical damage of cultural relics based on Raman spectroscopy.

KEYWORDS

Museum illumination, paper and silk, Raman spectroscopy, illumination damage

INTRODUCTION

Chinese traditional painting and calligraphy (CTPC) are recognized as the treasures of oriental art in the world (Dang et al. 2013). However, according to the photochemical stability grading standard of museum exhibits formulated by the Commission Internationale de L'Eclairage (CIE) (2004), CTPC belong to the highest level of light sensitivity. The paper consisting of plant fibres and silk consisting of protein molecules are used as the substrates of CTPC, both of which are natural organic substances with unstable properties (Proniewicz et al. 2001; Shao et al. 2005). At present, the illumination damage research mainly uses the color difference to evaluate the influence of museum illumination on color fading and discoloration of cultural relics (Dang et al. 2017, 2018; Pinilla et al. 2016; Farke et al. 2016). As non-staining organic substrates, the illumination damage to the substrates is mainly mechanical damage caused by the microscopic molecular structure changes, which cannot be evaluated by the color difference. Therefore, there is an urgent need for a method to study microscopic molecular structure damage of the paper and silk substrates under illumination of museum light sources.

Raman spectroscopy is an analytical method based on Raman scattering principle and an effective method of accurately evaluating the microscopic damage to substances. Like human fingerprints, each substance has its Raman spectral characteristic bands, namely Raman

characteristic peaks, which correspond to the major molecular functional groups of the substance. When the substance is irradiated with the incident light with energy E ($E = h\nu$, where h is Planck's constant and ν is the frequency of light), energy exchange between the substance and the light occurs when photons of the incident light collide with molecules inside the substance, which is manifested as changes of photon frequency and characteristic peak intensity. Huang (Huang et al. 2016) analyzed the content of unsaturated fatty acids in different edible oils by calculating the peak intensity of different Raman spectra. According to Alves (Alves et al. 2016), Raman peak intensities of cellulose's spectral peaks were used to characterize the fibre structure and its changes in different acid and alkali environments. Monti (Monti et al. 2001) evaluated the amount of silk I form in the silk specimens by calculating the Raman intensity ratio. It can be seen that changes in the microscopic molecular structure inside the substance can be further quantified by Raman peak intensity.

The white light-emitting-diode (LED) spectra currently meeting the requirements of low correlated color temperature ($CCT \leq 4000K$) and high color rendering ($Ra \geq 90$) formulated by the lighting code of Museum (2009) mainly include four monochromatic light spectra of red, yellow, green and blue. By adjusting the ratios of them, Red, Yellow, Green and Blue (RYGB) type white LED with low CCT and high Ra can be achieved, which was defined by Dang et al. (2017). Therefore, determining the quantified damage of four monochromatic light spectra on the paper and silk substrates is of great significance for obtaining new white LED spectra suitable for illuminating CTPC.

In this research, Raman spectroscopy was innovatively introduced into the illumination study of museum cultural relics. The four monochromatic light spectra were used as experimental light sources. The peak intensity of the Raman spectra was used as an evaluation index. The change of microscopic molecular structure inside the paper and silk specimens before and after illumination was characterized by the variations of Raman peak intensity. By analyzing the degree of microscopic damage to the paper and silk specimens caused by four monochromatic light spectra, the problem that cannot quantitatively studying the mechanical damage to the paper and silk substrates at present could be solved.

EXPERIMENT PROCESS

Experimental specimens

In accordance with traditional techniques, the paper and silk specimens used in CTPC were prepared by the National Museum of China. Then two specimens were cut into the same size and combined together, as shown in Figure 1(a).

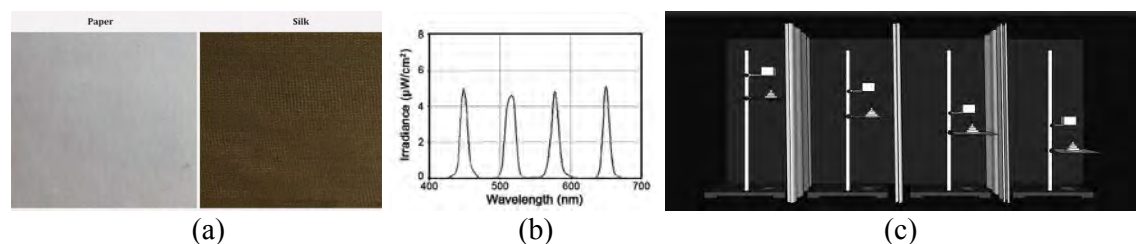


Figure 1. (a)The paper and silk specimens. (b) The SPDs of four monochromatic light sources used in illumination experiment. (c) The illumination experiment scene.

Experimental light sources

Four light sources with different center wavelengths of 450nm, 510nm, 583nm, and 650nm

were fabricated by using a museum-specific tungsten halogen lamp combined with a 20nm wide narrowband filter and an infrared filter. By using a spectrophotometer, the SPDs of four monochromatic light sources were detected, as shown in Figure 1(b).

Illumination methodology

The illumination methodology was in accordance with the previous study, which was clearly defined by Dang et al. (2017). The experimental scene is shown in Figure 1(c).

Experiment program

The analytical process was as follows. First, before the illumination experiment, Raman shift and Raman peak intensity of specimens as a control group was detected by Raman spectrometer, whose resolution was set at 1.496 cm^{-1} . The specimens were excited with the 780nm line of a diode laser. After illumination experiment, the Raman data of the illuminated specimens were detected again as the experimental group. Then Raman spectrogram of Raman peak intensity varying with Raman shift was plotted. Raman characteristic peaks of the specimens were selected. Then, the peak intensity values of the selected peak before and after illumination were read by the Origin software. By using Eq. (1), the difference ΔI of Raman peak intensities before and after the illumination experiment were obtained.

$$\Delta I = |I_1 - I_0| \quad (1)$$

Where I_0 and I_1 are the peak intensity values of the selected peak before and after illumination, respectively. The smaller the ΔI , the lower the microscopic damage degree of specimens. By comparing microscopic damage degree caused by different monochromatic light sources to the paper and silk specimens, the relative damage coefficients of different light sources on the microscopic molecular structure of the paper and silk specimens were obtained.

EXPERIMENT RESULT

Paper

Paper consists of mostly bonded cellulose fibres that are held together by strong intramolecular hydrogen bonds that promote aggregation of single chains into highly oriented structure. These aggregates are ordered up to even 80% 'crystalline forms'. The unordered rest is called 'amorphous form', which was defined by Proniewicz et al. (2001). Owing to the influence of illumination environment and its own characteristics, the microscopic molecular structure of the paper can be easily damaged. Therefore, Raman spectroscopy was introduced to evaluate microscopic damage of different monochromatic light sources to the paper.

Raman spectra of the paper specimens before and after illumination experiment are shown in Figure 2. The abscissa represents Raman shift, that is, the frequency shift of the scattered light relative to the incident light after the incident light is scattered by the substrate specimens. Raman shift is recorded in wavenumbers, which is commonly expressed by inverse centimetres (cm^{-1}) in Raman spectra; the vertical axis represents the intensity of Raman scattered light. The solid Raman spectral line represents the Raman spectra before illumination and the dotted one represents the Raman spectra after illumination. The Raman peaks in the dotted Raman spectral line were obtained by the redshift of the Raman peaks in solid Raman spectral line. Taking the Raman spectra of the paper specimens illuminated by the 510nm light source as an example, the Raman peak at 895 cm^{-1} in solid spectral line was red-shifted to 897 cm^{-1} in dotted spectral line. The following Figure 3 is analogous.

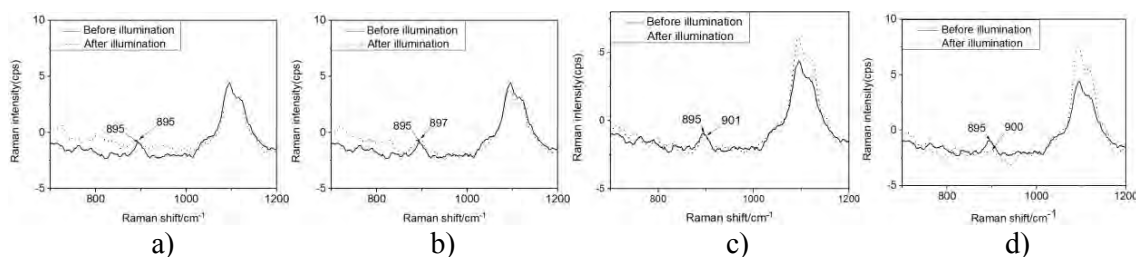


Figure 2. Raman spectra of the paper specimens under illumination of (a) 450 nm monochromatic light spectrum, (b) 510 nm monochromatic light spectrum, (c) 583 nm monochromatic light spectrum, and (d) 650 nm monochromatic light spectrum.

It could be seen from the solid spectral line in Figure 2, the Raman peak with medium intensity is 895 cm^{-1} . According to Proniewicz et al. (2001), they found that the intensity of 900 cm^{-1} peak was sensitive to the amount of crystalline versus amorphous structure of cellulose. It was also found I_{900} was proportional to the amount of disorder in the cellulose (Wiley and Atalla, 1987). Therefore, Raman peak intensity I_{895} was selected to characterize the microscopic damage of different monochromatic light sources to the paper specimens.

The variations in Raman peak intensity of the paper under four light sources were analyzed. As shown in Figure 2(b), the paper illuminated by 510 nm light source was taken as an example. According to the solid Raman spectral line obtained before illumination, the Raman peak intensity of 895 cm^{-1} was read by the Origin software as I_0 ; according to the dotted Raman spectral line obtained after illumination, the intensity of Raman band at 897 cm^{-1} was read as I_1 . By using Eq. (1), Raman peak intensity difference ΔI could be obtained. Similarly, the ΔI of the paper specimens illuminated by the rest light sources were calculated. By defining ΔI 0.4278 of the paper specimens illuminated by 450 nm light source was 1.0000, through conversion the relative damage coefficient of four light sources to the paper specimens was 1.0000: 0.9093: 0.3714: 1.9780. The calculation results are shown in Table 1.

Table 1. The comparison of the paper's Raman peak intensity differences under illumination of four types of monochromatic light sources

Measure Light sources	Before illumination	After illumination	Calculation	Through conversion
	I_0	I_1	$\Delta I = I_1 - I_0 $	
450nm	-0.9361	-0.5083	0.4278	1.0000
510nm		-0.5471	0.3890	0.9093
583nm		-1.0950	0.1589	0.3714
650nm		-1.7823	0.8462	1.9780

Silk

Silk fibroin contained in silk is natural polymer fibre protein, which was defined by Shao et al. (2005). Exposure to light will cause significant changes in these organic components of silk.

Raman spectrum changes of the silk specimens before and after the illumination are shown in Figure 3. In solid Raman spectral line, the strongest peak is 1230 cm^{-1} and medium Raman peak is 1082 cm^{-1} . According to Shao et al. (2005), the peak intensities at 1232 and 1087 cm^{-1} corresponding to C-N bond decreased after UV/ozone irradiation, indicating that UV/ozone irradiation causes peptide chain breaks and confirming that photodegradation occurs at the C-N bond. Silk phototendering is caused by peptide fission initially at the weaker C-N bond,

which leads to loss of fibre strength (Setoyama, 1982). We selected *I*₁₀₈₂ and *I*₁₂₃₀ to comprehensive characterize the microscopic damage of light sources to the silk specimens.

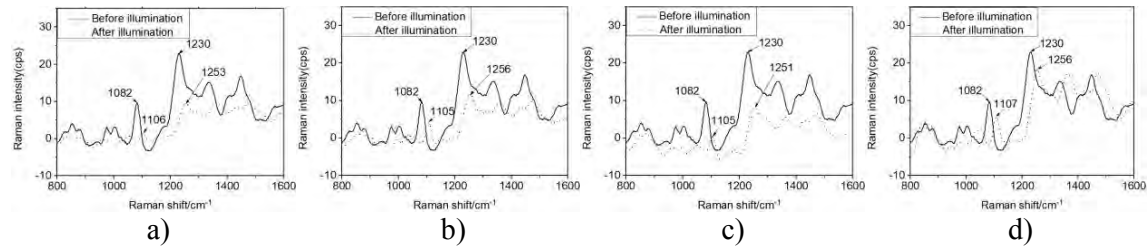


Figure 3. Raman spectra of the silk specimens under illumination of (a) 450 nm monochromatic light spectrum, (b) 510 nm monochromatic light spectrum, (c) 583 nm monochromatic light spectrum, and (d) 650 nm monochromatic light spectrum.

The variations of Raman peak intensities under illumination of four light sources were analyzed. Silk specimen illuminated by 510 nm light source was taken as an example. According to solid Raman spectral line detected before illumination, the intensity values of 1082 and 1230 cm^{-1} Raman peaks were read as I_0 and I_0' , respectively; according to the dotted Raman spectral line detected after illumination, the intensity values of the Raman peaks at 1105 and 1256 cm^{-1} were read as I_1 and I_1' , respectively. By using Eq. (1), based on I_0 and I_1 , Raman peak intensity difference ΔI was calculated; based on I_0' and I_1' , $\Delta I'$ was calculated. Then, $\Delta I''$ was obtained by calculating the average value of ΔI and $\Delta I'$. Similarly, the $\Delta I''$ of the silk specimens illuminated by the rest light sources were calculated. By defining $\Delta I''$ 10.8402 of the silk specimens under illumination of the 450nm light source was 1.0000, through conversion the relative damage coefficient of four light sources to the silk specimens was 1.0000: 0.7740: 1.1046: 0.3846. The calculation results are shown in Table 2.

Table 2. The comparison of the silk's Raman peak intensity differences under illumination of four types of monochromatic light sources

Measure Light sources	Before illumination		After illumination		Calculation		Average	Through conversion
	I_0	I_0'	I_1	I_1'	ΔI	$\Delta I'$	$\Delta I''$	
450nm	9.6050	22.9035	1.4985	9.3297	8.1065	13.5738	10.8402	1.0000
510nm			4.1123	11.6151	5.4927	11.2884	8.3906	0.7740
583nm			0.3696	8.1909	9.2354	14.7126	11.9740	1,1046
650nm			5.7272	18.	3.8778	4.4593	4.1686	0.3846
				4442				

DISCUSSIONS

There are different damage degrees caused by light sources with different center wavelengths of 450nm, 510nm, 583nm, and 650nm. According to Table 1, the ratio of four light spectra constituting white LED used in illuminating the paper, namely the SPD of white LED, should be based on the relative damage coefficient of 450nm: 510nm: 583nm: 650nm = 1.0000: 0.9093: 0.3714: 1.9780. According to Table 2, the ratio of four light spectra constituting white LED used in illuminating the silk, namely the SPD of white LED, should be based on the relative damage coefficient of 450nm: 510nm: 583nm: 650nm = 1.0000: 0.7740: 1.1046: 0.3846. The larger the influence coefficient value, the greater the damage caused by the monochromatic light to the paper and silk substrates. The coefficients can be used as selection

criteria for WLEDs that are suitable for illumination in museum paper and silk relics

CONCLUSION

The research method of studying illumination damage based on Raman spectroscopy proposed in this paper can evaluate the mechanical damage to substrates from the microscopic level.

ACKNOWLEDGEMENT

This work was supported by the <National Key Research and Development Program of China #1> under Grant <number 2016YFB0601700>; <Natural Science Fund of Tianjin #2> under Grant <number 17JCYBJC22400>; <Peiyang scholar Program #3> under Grant <number 1801>.

REFERENCES

- Alves A.P.P, Oliveira L.P.Z, Castro A.A.N, Neumann R, Oliveira L.F.C, Edwards H.G.M, Sant'Ana A.C. 2016. The structure of different cellulosic fibres characterized by Raman spectroscopy. *Vibrational Spectroscopy*, 86, 324-330.
- China National Standardization Administration. 2009. *GB/T 23863-2009*, Code for Lighting Design of Museum. Beijing: China Standard Press.
- Dang R, Zhang M.Y, Liu G, Yu J, Hou D. 2013. Research on the Lighting of Museum Exhibition Chen Lighting Based on Cultural Relics Protection. *China Illuminating Engineering Journal*, 24(3), 18-23.
- Dang R, Yuan Y, Liu G, Luo C, Liu J. 2017. White LED spectrum for minimising damage to Chinese traditional heavy colour paintings. *Lighting Research and Technology*. doi: 10.1177/1477153517707996.
- Dang R, Yuan Y, Liu G, Liu J. 2018. Chromaticity changes of inorganic pigments in Chinese traditional paintings due to the illumination of frequently-used light sources in museum. *Color Research and Application*. doi: 10.1002/col.22215.
- Farke M, Binetti M, Hahn O. 2016. Light damage to selected organic materials in display cases: A study of different light sources. *Studies in Conservation*, 61(Suppl 1), 83-93.
- Huang F.R, Li Y.P, Guo H.X, Xu J, Chen Z, Zhang J, Wang Y. Identification of waste cooking oil and vegetable oil via Raman spectroscopy. *Journal of Raman Spectroscopy*, 47(7), 860-864.
- International Commission on Illumination. 2014. *CIE 157-2004*, Control of damage to museum objects by optical radiation.
- Monti P, Taddei P, Freddi G, Asakura T, Tsukada M. 2001. Raman spectroscopic characterization of bombyx mori silk fibroin: Raman spectrum of silk I. *Journal of Raman Spectroscopy*, 32(2), 103-107.
- Pinilla S.M, Vazquez D, Fernandez-Balbuena A.A, Muro C, Munoz J. 2016. Spectral damage model for lighted museum paintings: Oil, acrylic and gouache. *Journal of Cultural Heritage*, 22, 931-939.
- Proniewicz L.M, Paluszkiwicz C, Weselucha-Birczynska A, Majcherczyk H, Baranski A, Konieczna A. 2001. FT-IR and FT-Raman study of hydrothermally degraded cellulose. *Journal of Molecular Spectroscopy*, 596(Special), 163-169.
- Setoyama K.J. 1982. *The journal of sericultural science of Japan*, 51, 271.
- Shao J.Z, Zheng J.H, Liu J.Q, Carr C.M. 2005. Fourier Transform Raman and Fourier Transform Infrared Spectroscopy Studies of Silk Fibroin. *Journal of Applied Polymer Science*, 96(6), 1999-2004.
- Wiley J.H, Atalla R.H. 1987. Band assignments in the Raman spectra of celluloses. *Carbohydrate Research*, 160, 113-129.

Impact of Indoor Temperature and CO₂ Levels on Occupant Thermal Perception and Cognitive Performance of Adult Female Students in Saudi Arabia

Ahmed, Riham Jaber*; Mumovic, Dejan; Ucci, Marcella

UCL Institute for Environmental Design and Engineering, The Bartlett, University College London, 14 Upper Woburn, WC1H 0NN London, UK

**Corresponding email: riham.ahmed.10@alumni.ucl.ac.uk*

ABSTRACT

Due to hot arid climate in Jeddah, Saudi Arabia, occupants rely on air conditioning (AC) to provide both ventilation requirements and thermal comfort. It is believed that this total reliance on AC have also a significant effect on thermal sensation as well as cognitive performance of building occupants. Using a multi-variable multilevel statistical analysis, the effects of classroom temperature and CO₂ levels on cognitive performance were estimated. Eight neurobehavioral cognitive tests were used to evaluate cognitive performance of 499 female students (16-20 years old). In addition, thermal sensation votes were collected. All participants were exposed to nine different environmental conditions, a combination of three temperature levels 20°C, 23°C and 25°C, and three CO₂ levels: 600 ppm, 1000 ppm and 1800 ppm. The baseline condition levels were set at 20°C and 600 ppm. In this paper the interrelationships between the thermal sensation votes and effects of classroom temperature and CO₂ levels on vigilance (Simple Reaction Test, SRT) and memory tasks (Reversal Learning, RL) are presented. The results suggested that the ‘cold’ thermal sensations have been linked to significant increase in ‘percentage of errors’ for both memory and vigilance tasks. Also, the exposure to higher CO₂ levels of 1800 ppm and 1000 ppm have led to a significant increase in the ‘percentage of errors’ for both cognitive performance tasks compared to the baseline conditions. The study has also confirmed that the significant influence of acclimatization should not be overlooked when setting up the environmental design criteria for buildings in hot arid climates.

KEYWORDS

thermal sensation, temperature, ventilation, cognitive performance, hot arid climate

INTRODUCTION

This study was conducted in Jeddah, which unlike other cities in Saudi Arabia retains its warm climate even in winter. This has consequently led to the total reliance of occupants on air conditioning (AC) for both achieving thermal comfort and providing the prescribed ventilation requirements. Furthermore, due to changing climate an increase in temperature by ~2.5°C is estimated according to regional climate model projections of the average temperature changes (°C) across the Gulf region by 2050 (Alpert et al., 2008). It is also believed that the total reliance on AC for cooling has a significant effect on thermal sensation of buildings’ occupants. All these factors have been some of the key drivers of ever increasing energy demand in the Gulf region and a major barrier to adoption of carbon reduction strategies in buildings. For example, it has been shown that only 1°C rise in set AC

temperature could significantly reduce energy consumption by ~6% (e.g. Yamtraipat et al., 2005).

Equally important when it comes to design and operation of educational buildings is the consideration of ventilation rates in classrooms and lecture theatres. However, a limited data is available on actual ventilation rates in educational buildings in Saudi Arabia. AlSubaie (2014) provided evidence based on data collected from 36 primary schools, indicating that classroom ventilation rates in educational buildings in Saudi Arabia do not meet the ASHRAE ventilation rates requirements. What might be the impact of lower ventilation rates on cognitive performance of students in hot arid climates is yet to be determined.

Finally, only recently the government in Saudi Arabia, started to promote gender equality to empower women's education and eliminate gender disparity at all levels of education (AlMunajjed, 1997). This has culminated in the last 10 years which has led to the increase in female enrolments at the university level and capital investment in university sector targeting female students. This specific cultural and behavioral context also offers an opportunity to reflect on design of interdisciplinary studies such as this one combining building science and cognitive performance.

METHODS

Only temperature and CO₂ concentration levels (no attempt was made to establish if the CO₂ is a pollutant on its own right) were the independent variables which were investigated in the study whilst the other parameters were kept within constant ranges during the exposure conditions (namely: sound levels, lighting intensity, air velocity, and relative humidity). Based on a pilot study which was conducted prior to the intervention study reported in this paper we obtain some evidence on the base line temperature conditions in the case study building, the maximum operative temperature the participants were able to tolerate was 25°C. Furthermore, according to a facility management questionnaire which was disseminated to the educational buildings in Jeddah, the most common set temperature is 20°C. Therefore, the indoor temperatures set during the conditions of exposures were 20°C, 23°C and 25°C.

The intervention study was carried out in a teaching room with a CAV AC system with no direct access to sunlight. CO₂ levels ~1800 ppm were the maximum achieved and ~600 ppm were the minimum achieved. Therefore, the CO₂ levels set during the exposure conditions were 600, 1000, and 1800 ppm. Therefore, nine different exposure conditions combining temperatures (20°C, 23°C and 25°C) and CO₂ levels (600 ppm, 1000 ppm and 1800 ppm) were investigated in this study (Table 1).

Within-subjects design was adopted where the same participants were exposed to the same exposure conditions. Participants performed eight different cognitive tests (only two of which are discussed in this paper, namely: Simple Reaction test (SRT) as a reference to the vigilance tasks involved and Reversal Learning (RL) is a reference to the memory tasks involved). In parallel, the participants evaluated their thermal comfort sensations during the exposures. The actual mean votes (AMV) were collected. The rating scale used for the thermal sensation vote was based on the ASHRAE/ISO seven-point thermal sensation scale, defined as: hot (3), warm (2), slightly warm (1), neutral (0), slightly cool (-1), cool (-2) and cold (-3).

Table 1. The exposure conditions investigated in the study.

Conditions of exposure	Ambient temperature	CO2 concentration level
Condition 1: Temp: 20°C, CO2: 600 ppm	T1: 20°C	CO2: 600 ppm
Condition 2: Temp: 20°C, CO2: 1000 ppm	T2: 20°C	CO2: 1000 ppm
Condition 3: Temp: 20°C, CO2: 1800 ppm	T3: 20°C	CO2: 1800 ppm
Condition 4: Temp: 23°C, CO2: 600 ppm	T1: 23°C	CO2: 600 ppm
Condition 5: Temp: 23°C, CO2: 1000 ppm	T2: 23°C	CO2: 1000 ppm
Condition 6: Temp: 25°C, CO2: 1800 ppm	T3: 23°C	CO2: 1800 ppm
Condition 7: Temp: 25°C, CO2: 600 ppm	T1: 25°C	CO2: 600 ppm
Condition 8: Temp: 25°C, CO2: 1000 ppm	T2: 25°C	CO2: 1000 ppm
Condition 9: Temp: 25°C, CO2: 1800 ppm	T3: 25°C	CO2: 1800 ppm

The analysis of data was based on multivariable multilevel analysis approach which takes into consideration the confounding factors' effect including: thermal comfort sensations, age, physical activity, clothing levels, stress, caffeine intake, sleeping hours, noise levels, set air conditioning (AC) temperature at home, as well as the ethnic background and the number of years spent in the country for non-Saudi participants, as well as the detected symptoms related to the inability to focus. Almost no relevant studies have adopted the multilevel modelling approach except for one recent study by Haverinen-Shaughnessy and Shaughnessy (2015), which employed the multilevel modelling approach to find the association between ventilation rates and indoor temperature with mathematics test scores. However, no statistically significant interactions were found because of the limited sample size. The study was designed to have 90–95% power at 95 percent level of significance. Using this information the sample size was calculated using the following formula, (Daniel, 1999):

$$n = \frac{Z^2 P (1 - P)}{d^2} \quad (1)$$

Where; n = sample size, Z = statistic for a level of confidence (95% level of confidence used, therefore Z value is 1.96), P = expected prevalence or proportion, and d = precision (In a standard situation, d is considered 0.05 to produce good precision and smaller error of estimate). The calculated sample size was 385. However, the size was over-estimated since the duration of the experiment was long (over one year) and many withdrawals were expected, and particularly in this context of study where research consciousness is absent. Finally, 499 female subjects participated in all nine exposure conditions investigated in the study. The data analysis was carried out in three steps, as follows:

- Step 1: a descriptive analysis was performed to check for any patterns due to intra-individual differences by comparing an individuals' performance pattern of across intervention measures. If all performances fall within the mildly to moderately impaired range, the multilevel mixed effect models can be performed. However, if a significant variability in performances across domains is observed, then a specific pattern of impairment may be indicated.
- Step 2: univariable multilevel mixed effect models were then performed to check whether any association is found between the confounders of this study with the outcomes of interest including: age, ethnicity, physical activity, number of years spent in Saudi Arabia (for non-Saudis), trend of use and temperature of AC used at home, the effect of caffeine, sleeping hours, thermal comfort sensation votes, clothing levels, the effect of ambient noise, and the effect of stress owing to personal reasons not related to the exposure conditions, and/or any

other reported symptoms by the participants which impaired their focusing ability including un-tolerable thermal stress sensation.

- Step 3: multivariable multilevel mixed effect models were applied according to the results of the univariable multilevel mixed effect models, which adjusted for the confounders which were found associated with the accuracy and speed of performance. Two models, one for accuracy (i.e. percentage of error), and the other for speed (i.e. time needed to complete a task) were executed to determine the estimated effect sizes of the exposure conditions relative to the base-line condition (Condition 1) for all the cognitive tasks considered in the study after adding the confounders.

RESULTS

According to the analysis of data, the accuracy (percentages of errors) of the cognitive tasks increased at the different exposure conditions, relative to the baseline condition (Condition 1), after adding the estimated effect sizes of the confounding variables to the zero model and the estimated effect sizes derived from the multivariable multilevel statistical model. The estimated effect sizes are listed in Table 2. For instance, the percentages of errors increased significantly from 2.4% for the SRT test (at the zero model where no confounding variables were added at this stage) to become 5.4% at Condition 2 versus Condition 1 (when CO₂ increased from ranges of 600 ppm to 1000 ppm, while temperature remained constant at 20°C). The increase in the percentage of errors was almost doubled (from 5% to become 9%) at Condition 3 versus Condition 1 (when CO₂ increased from ranges of 600 ppm to 1800 ppm, while temperature remained constant at 20°C), where all reported results were highly significant, $p < 0.001$. This trend has continued during all exposure conditions when CO₂ increased from ranges of 600 ppm to 1000 ppm and 1800 ppm, and temperature remained at 20, 23 and 25°C, and particularly when the temperature was set at 25°C. In addition, it is indicated from the Table 2 that significant effects occurred when the variables of ethnicity, number of years spent in the country for the non-Saudi participants, AC temperature set at home in the range between 18 and 24°C, thermal comfort sensations, the reported intolerable thermal discomfort which leads to inability to focus, and other symptoms reported that impaired the focusing ability, were added to the model. By doing simple arithmetic calculations, it was found that the estimated effect size caused by the effects of thermal sensations are the ones responsible for significant amount of the caused effects. With regard to the speed of performance, it was found that the speed of reaction increased significantly during exposure to all the investigated conditions relative to Condition 1.

It is indicated from Table 2 that Saudi participants had significant lower percentages of errors by ~1.5% for the vigilance tasks and ~2.5% for memory and learning tasks relative to the non-Saudis. Also, the inclusion of the confounder of set AC temperature at home in the final model resulted in a significant increase in the percentages of errors for every unit decrease in temperature from 24 to 24°C by an average of ~1%. According to participants' subjective questionnaire responses, the mean AC temperature set by the Saudi participants at home was lower by 2°C, relative to that reported by the non-Saudi participants. An average of ~15% for all tasks was noted for those who reported the symptoms of intolerable thermal discomfort versus which distracted their focusing ability as well as other symptoms like headache, blur eye, heaviness on head for those who did not. With regards to the thermal sensations, it was noted that they account for a considerable amount of the attributed effects. Negative associations for the thermal sensations of cool, slightly cool and slightly warm, relative to neutral, with the percentages of errors for all tasks (higher percentages of errors). However, positive associations with the percentages of errors were observed for perceiving the thermal environment as cold, warm and hot relative to neutral (lower percentages of errors).

Table 2. Changes in percentage of errors for two cognitive performance tasks before and after adding the confounding variables compared to the baseline condition (Condition 1).

The confounding variables considered	Zero model SRT accuracy (error%) estimate (95% CI)	SRT accuracy (error%) estimate (95% CI)	Zero model RL accuracy (error%) estimate (95% CI)	RL accuracy (error%) estimate (95% CI)
Condition 2 vs. 1	2.4 (1.4, 3.4)	5.4 (3.6, 7.1)	3.9 (2.6, 5.4)	7.6 (5.8, 10.4)
Condition 3 vs. 1	5.4 (4.9, 6.8)	9.1 (7.5, 11.6)	8.9 (7.6, 9.3)	16.9 (14.6, 19.4)
Condition 4 vs. 1	3.9 (3.5, 4.2)	7.70 (5.9, 9.5)	-1.9 (-2.4, -1.3)	-5.2 (-6.7, -4.7)
Condition 5 vs. 1	9.7 (9.3, 10.1)	20.6 (15.5, 19.6)	9.7 (9.3, 10.1)	18.1 (15.6, 19.6)
Condition 6 vs. 1	12.1 (11.7, 12.4)	29.1 (26.3, 32.6)	15.1 (14.7, 16.5)	30.8 (27.3, 33.3)
Condition 7 vs. 1	4.4 (3.0, 5.8)	8.4 (6.4, 10.5)	8.8 (8.4, 9.2)	13.9 (11.36, 15.4)
Condition 8 vs. 1	13.9 (13.5, 14.2)	30.3 (27.0, 32.6)	17.3 (16.9, 17.7)	32.4 (29.9, 35.9)
Condition 9 vs. 1	22.1 (21.8, 22.5)	46.1 (43.7, 47.4)	21.6 (20.0, 22.1)	47.6 (43.0, 49.1)
Ethnicity (Saudi vs. other)		-2.2 (-3.4, -1.4)		-2.3 (-3.5, -1.4)
Cold vs. neutral		10.6 (5.1, 7.0)		10.7 (9.1, 11.4)
Cool vs. neutral		-1.5 (-2.2, -0.3)		-0.9 (-1.5, -0.4)
Slightly cool vs. neutral		-2.5 (-3.6, -1.0)		-1.8 (-2.6, -0.1)
Slightly warm vs. neutral		7.0 (4.5, 6.6)		-0.5 (-0.3, -0.8)
Warm vs. neutral		9.1 (5.5, 7.7)		12.2 (7.1, 9.9)
Hot vs. neutral		14.5 (8.3, 10.3)		18.0 (13.0, 15.9)
AC temperature at home (per unit between 18°C-24°C)		-0.9 (-1.1, -0.7)		-0.9 (-1.1, 0.73)
Detected intolerable thermal discomfort vs. not		14.5 (8.3, 10.3)		18.0 (13.0, 15.9)
Other symptoms reported vs. not		16.6 (12.6, 20.8)		17.0 (14.7, 21.8)

DISCUSSIONS

The aforementioned results indicated that the exposure to CO₂ of 1800 ppm and 1000 ppm have led to a significant increase in the percentage of errors for all tasks, versus 600 ppm. These results agree with Twardella et al. (2012) who reported a significant increase in the percentage of errors when CO₂ levels were 2000 ppm, relative to 1000 ppm in their field study, in assessing the effect of IAQ as indicated by the median CO₂ level effect on the concentration performance of students. Also, Allen et al. (2015) observed that several domains of the decision-making tests decreased significantly and by a very high degree during exposure to CO₂ at 945 and 1400 ppm compared with the levels of 550 ppm. It is worth noting that in this present study that CO₂ is not considered to be a pollutant but an indicator of the efficiency of ventilation. In this regard, numerous studies like Bako-Baro et al. (2012) and Coley et al. (2007) provided evidence that poor ventilation rates in classrooms significantly impair students' attention and vigilance. Moreover, interestingly the inclusion of the confounder of set AC temperature at home in the final model resulted in a significant decrease in the percentages of errors for every unit increase in temperature in the range between 18 and 24°C. Correspondingly, it was found that the subjective ratings of the TSVs of the participants varied considerably by ethnicity. For the Saudi participants, exposure to 23°C reduced their thermal sensations to slightly warm from cool and/or slightly cool at 20°C, while at 25°C

almost all participants perceived the ambient thermal environment as uncomfortably hot. However, the non-Saudi participants perceived the thermal environment as slightly cool and/or neutral at 23°C while more participants reported feeling cold, cool and slightly cool at 20°C. Fewer participants reported feeling hot at 25°C relative to the Saudi participants. According to de-Dear and Brager (1998), human adaptation to the thermal environment, physiological and one's past thermal exposure experience plays a crucial role in human's thermal comfort sensation. Thus, this could be interpreted as the effect of home acclimatization of the most prevailing set AC temperature on mean comfort sensations. It was noted that the thermal sensation votes were very much influenced by the AC set temperature at home. Yamtraipat et al. (2005) supports this suggestion, and indicated that acclimatization to using home ACs could affect thermal comfort sensation considerably.

CONCLUSIONS

- Temperature setting leading to sensation of cold, warm and hot are suggested to be linked to a significant decrease in accuracy for both memory and vigilance tasks, and also the exposure to higher CO₂ levels of 1800 ppm and 1000 ppm compared to 600 ppm.
- It is of a great importance to consider the effects of acclimatization, AC set temperature at home, and the associated intolerable thermal discomfort and other symptoms that may be caused when developing the thermal comfort standards in this climatic context.

REFERENCES

- Allen J. G., MacNaughton, P., Satish, S., Santanam, S., et al. 2015. Associations of Cognitive Function Scores with CO₂, Ventilation, and Volatile Organic Compound Exposures in Office Workers. *Environ Health Perspective*, 124(6), 805-812.
- AlMunajjed M. 1997. Women in Saudi Arabia Today. United States: St. Martins Press.
- Alpert P., Krichak S.O., Shafir, H., Haim, D., Osetinsky, I. 2008. Climatic trends to extremes employing regional modelling and statistical interpretation over the E. Mediterranean', *Global Planetary Change*, Volume 63, Issue 2-3.
- Alsubaie R. 2014. Indoor Air Ventilation in Primary Schools in Eastern Province, Saudi Arabia. *International Journal of Current Research*, 6 (5), 6552-6557.
- Bakó-Biró Z., Clements-Croome D. J., Kochhar N., Awbi H. B. Williams M. J. 2012. 'Ventilation rates in schools and pupils' performance'. In: *Build Environ* 48, 215-223.
- Coley D.A., Greeves R.; Saxby B.K. 2007. The effect of low ventilation rates on the cognitive functions of a primary school class. *International journal of ventilation*, 6(2), 107-112.
- Daniel W.W. 1999. Biostatistics: A Foundation for Analysis in the Health Sciences. 7th edition. New York: John Wiley & Sons.
- De-Dear R., Brager G. 1998. 'Developing an adaptive model of thermal comfort and preference'. *ASHRAE Trans* 104(1), 145-167.
- Haverinen-Shaughnessy U., Shaughnessy R.J. 2015. Effects of Classroom Ventilation Rate and Temperature on Students' Test Scores. *PLoS ONE* 10(8), 136-165.
- Twardella D, Matzen W, Lahrz T, Burghardt R, et al. 2012. Effect of classroom air quality on students' concentration: results of a cluster-randomized cross-over experimental study. *Indoor Air*;12, 378-387.
- Yamtraipat N., Khedari J., Hirunlabh J. 2005. 'Thermal comfort standards for air-conditioned buildings in hot and Humid Thailand considering additional factors of acclimatization and education level'. *Solar Energy*,78, 504-517.

Thermal and mycological active protection of historic buildings on the example of the baroque residence of Polish kings in Wilanów

Robert Wójcik¹, Piotr Kosiński^{1,*}

¹University of Warmia and Mazury in Olsztyn, Olsztyn, Poland

*Corresponding email: piotr.kosinski@uwm.edu.pl

ABSTRACT

Protection of the external partitions of historic buildings is a broad topic due to the limited possibilities of interfering with the structure. Restoration restrictions on prevention in the mycological protection of historic buildings are so large that, from the broad list of possible protective measures, practically only the heating of the nodes and the control of air parameters are practically safe. The reason for restrictions is the lack of possibility of introducing architectural changes and the limited possibility of interfering into the structure of external partitions.

A fast method that uses fluorescence was used for quantitative assessment of the mycelium development during the research and design work preceding the revalorization of the baroque seat of Polish kings in Wilanów (Warsaw). Mould mycelium were found mainly in the areas of increased humidity of the substrates. The use of an innovative method of local reheating of thermal bridge areas has been proposed there. Systems for reheating with halogen radiators using various infrared radiation (IR) bands were analyzed. There was also designed an anti-condensation system consisting on electric heating cables. The proposed solutions prevent the development of mould mycelium to a satisfactory degree. Finally, the interior of the palace regained its beautiful appearance and healthy microclimate.

KEYWORDS

Historical buildings, mycological protection, thermal bridges, anti-condensation systems, infrared heating.

INTRODUCTION

Historical buildings, especially those from the Baroque period, are often exposed to moisture and mycological problems. The baroque style developed mainly in Italy, where, due to the warm climate, the departure from the massive Gothic architecture did not result in the mould mycelium growth. Significantly lighter construction, with numerous niches intended for extended architectural details, may result in moisture degradation of the building in less than favourable Central European climate conditions. Mycological problems were found in the royal palace in Wilanów in Warsaw. The building was erected for Polish King Jan III Sobieski in the years 1681-1696, according to the design of Augustyn Locci, stylized on Italian styles. The problems were mainly concerned the surface of thermal bridges within the connection of external walls and ceiling, where in the winter time, condensation of water vapour occurs. An intervention was needed, due to the indoor environment deterioration and threats to the valuable interior design of painting and sculpting. Despite the numerous reconstruction changes resulting from the destruction that occurred during World War II, the architecture of the palace is original and required full protection. It is a particularly valuable combination of European art and the old Polish tradition of construction. One of the most important and difficult problems requiring an urgent solutions in the palace, was the necessity

to increase the surface vapour condensation resistance of the palace enclosure. It is a complicated issue which should be considered individually for each building. (Bomberg et al. 2016, Wójcik et al. 2017). Figure 1 presents the building and its interior designs.



Figure 1. Baroque palace in Wilanów. The façade and ceilings.

In the Baroque historical facilities, the thermal and moisture problems of the external partitions usually concern roofs in the zone of attic walls and cornices. Due to the valuable design of both external and internal façades, the classic procedure of implementation additional thermal insulation was unacceptable in the analyzed case. On the example of the palace in Wilanów it was possible to present the scope of research and computational analyzes that were used to develop innovative solutions in the field of thermomodernization of museum rooms, using local heating of thermal bridges.

ASSESSING THE MYCOLOGICAL CONDITION OF THE SURFACE

A non-destructive method, based on fluorimetry detection of the enzyme in filamentous mycelium was used (Rylander et al. 2010). A total of 47 surface sampling points were selected. Each sample was taken using sterile cotton swabs from a surface of 9 cm². The selected positions of samplings were characterized with visible surface changes.

The fluorimetry method, a quantitative method, is based on the determination of the mycelium mass density on the tested surface using a fluorocarbon substrate that releases a fluorescence fluorophore under the influence of division process. The intensity of the light emission phenomenon by a substrate excited by electromagnetic radiation depends on the mycelium biomass density. The method serves both to diagnose areas of mycelial growth as well as to control the effectiveness of cleaning the mould, which is particularly important in facilities requiring urgent intervention.

The mycelium density is categorized into three levels:

- category A - up to 25 units - normal level of mycelium- typical for clean surfaces,
- category B - 25÷450 units - level of mycelium above normal - indicates the growth of mycelium,
- category C - more than 450 units - very high mould level - high density of biomass.

Amongst 47 tested samples. 18 were classified in category A, 13 in category B and 16 in category C. The results presented in the Figure 2 clearly indicates that there was a serious mycological problem in palace and it required urgent intervention. It concerned not only the elements of the roof construction, but also the internal surfaces and external walls. Mould growth were closely related to the level of moisture content in the substrate material.

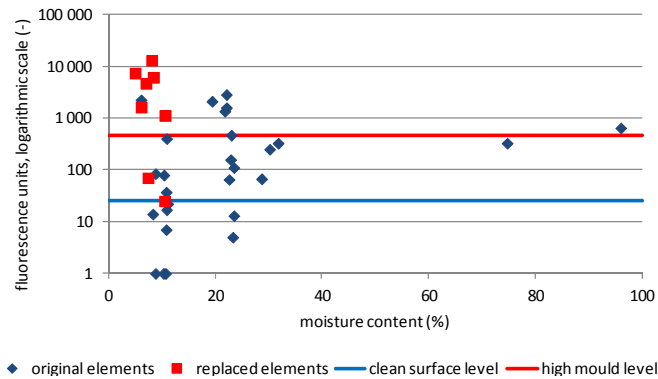


Figure 2. Illustration of the results of the mycelium density as a function of the moisture content in substrate of wooden elements.

An analysis of mycelium distribution, combined with measurements of moisture contents in substrates and with IR detection, clearly indicated that excessive cooling of the surface during the low outside temperature periods caused growth of mould. At first, the hygrothermal state of attics over the endangered museum rooms was analyzed. Unfortunately, two of required conditions for mould growth were fulfilled there: periodically an air temperature over 25°C and wood moisture content over 8%, theoretically it corresponds to relative air humidity around 40%. It was found during the investigation, that the air humidity in the closed zones of roof trusses exceeded 76% at 19°C. The moisture content in wood elements reached 90%. Poorly ventilated attics underwent heating during the insolation of the roof, while night cooling of the roof sheet caused 'morning dew' of the inner surfaces of the not insulated roof covering. Thus favoured the wetting of the timber roof construction. Fortunately, the protection of the roof truss zone was relatively an easy task. The problem can be solved by improving ventilation and by using chemical protection of elements. More complicated and difficult was to solve the problem of ventilated and full roofs, where the risk of excessive cooling occurred in the joints of ceiling and attic walls.

HYGROTHERMAL SIMULATIONS OF THE AREAS OF THERMAL BRIDGES

When it is impossible to avoid thermal bridges in the renovated building, their impact on additional heat demand for heating the facility ought to be calculated as well as the risk of condensation and mould growth in areas of lowering temperatures on internal surfaces. Particularly endangered, during insulation, areas of roof and wall joints are those adjacent to geometrical type thermal bridges.

Temperature field analyzes were performed using the Finite Element Method in Autodesk Simulation Multiphysics 2013 software. The heat flow distribution is presented in the form of coloured diagrams. Calculations of thermal bridges include two or three dimensional heat flow analyzes. The sample calculation results of wall-roof joints are shown in Figure 3. Boundary conditions: standard conditions (based on ISO 6946), $t_i=20^{\circ}\text{C}$, $t_e = -20^{\circ}\text{C}$, indoor air relative humidity 55%. The calculated dew point 10.7°C. Figure 3a presents the first corner. The computational calculated temperature in the corner was 12.12°C, what indicated on no water vaporization on the inner surface, but IR measurements indicated that the risk was present. Much more serious situation is presented in Figure 3b where the computational temperature was 5.85°C. The interior insulation of such knee wall will cause the movement of the temperature front into the wall and cooling the ceiling-wall joint (Figure 3c). Even, if the interior insulation layer was implemented, full protection against condensation would not be obtained (8.73°C). The periodically condensation of water vapor during the lower outside

temperature periods can be eliminated by installing infrared radiators or by performing an anti-condensation installation consisting of heating cables or mats and control automation.

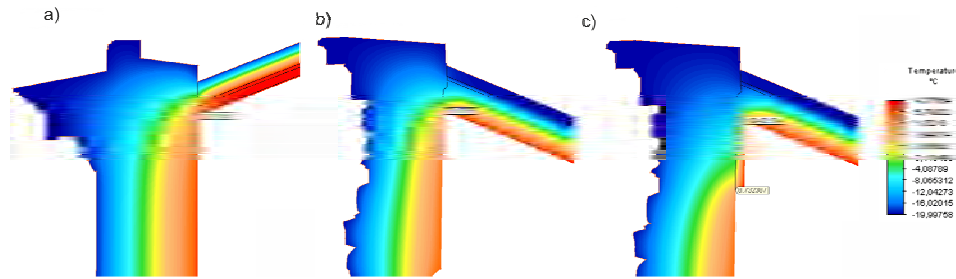


Figure 3. Temperature distribution in the flat roof section. a) roof corners, b) roof corners, c) interior insulation of the corner – incorrect solution due to the dew point.

SELECTION OF THE METHOD FOR HEATING OF THE NODES

The IR radiators were investigated as the periodically solution to increase the temperature of the excessively cooled internal surfaces of the partitions. Generally, wave emission in the range $0.76\div 1000\ \mu\text{m}$ can be used to increase the surface temperature of partition. However, the most effective radiators that can be used to heat the surface operate in one of the IR range:

- IRS (Infrared Short) - shortwave radiation, IR wavelength $1.2\ \mu\text{m}$
- IRM (Infrared Medium) - medium wavelength radiation, IR wavelength $3\ \mu\text{m}$,
- IRL (Infrared Long) - long wave radiation, IR wavelength $5\ \mu\text{m}$.

The division is contractual, because the ranges of emitted spectra waves overlap.

Originally, convection was the basic form of energy exchange in the palace rooms, only partially it was radiation. The use of additional radiators means that the transfer of heat to the partition surfaces will depend mainly on the temperature difference between the emitter and the partition surface. Thus, the length of emitted wave plays the main role. In the analyzed case, IR should be absorbed mainly by water vapor molecules. This is possible only when the energy of intra-particle vibrations is on the same level as the energy of the quanta of IR. The phenomenon of IR absorption by moisture should bring significant benefits. Infrared radiator, depending on the temperature, emit an energy wave length in the range $1.2\text{-}5.6\ \mu\text{m}$. Due to the drying properties, quartz-halogen heaters with a temperature of wolfram fiber of about $2\ 000^\circ\text{C}$ give the best results. On the other hand, in museum conditions (gilded surfaces), other aspects of IR emission should be taken into account. An important role is played by the effect of reflecting radiation – changing the direction of the wave propagation at the boundary of the surface with the internal environment. In practice, surfaces requiring heating to a safe level are very diverse. Thus, there is simultaneous almost perfect reflection, reflection scattering and absorption on such surfaces. The surface can thus absorb energy in a very diversified range depending on the reflective properties and the ratio of surface roughness to wavelength. So, the longer the wave and the smoother surface, the weaker the scattering. From this point of view, longer waves have the significant advantages of evenly heating the surface. Quartz-halogen, which emit the highest energy, but in the range of shorter reflected waves pose a threat to the polychrome. The share of radiation in the total energy balance would be too diverse in the case of valuable decorations, so it should be considered as disadvantageous phenomenon.

For the sake of problems related to one-side cooling of the partition joints, it is recommended to use the anti-condensation installation, for example the author's IN method (Polish patent nr

212791 – the method of insulation building partition from the inside). Positive results of the first implementations of the method in the historic town hall in Mrągowo and Social Security building in Bartoszyce influenced the choice of the IN method for the palace. In this case, the heating cables were designed from the attic side. Local reheating of excessively cooled areas prevents condensation due to local energy transfer. The method is easy to install, and what is more, it does not pose a threat to polychrome. The heating system may be constructed of the intelligent cables that detect other heat sources such as solar radiation and automatically adjust their heating power to receive the heat by environment (Figure 4). More heat is generated in cooler areas (e.g. window covers), less in warmer areas (e.g. the heater zone). Two parallel supply wires are embedded in a conductive polymer core. With decreasing the ambient temperature, the core of the conductor shrinks microscopically and the number of electric paths in the core increase, thus results in increased heat generation. Due to the variable power of the heating cables, the system is high efficient, because it only slightly increases heating costs. The system can be implemented in various insulation and finishing material solutions.



Figure 4 A self-regulating heating cable with possibility of adapting heating power to ambient temperature. 1-power supply cables, 2-conductive polymer, 3-insulation cover, 4-screen, 5-outer cover.

According to the patent description, in order to eliminate the negative impact of excessive cooling of the thermal bridges zones, the thermal insulation material should be placed leaving gaps for the heating conductors and temperature sensor. The heating system is initiated by the small controller located in a flush-mounted box (diameter of 60 mm). The thermal insulation layer can be covered with tight vapor barrier (e.g. in accordance with the principles of the single-sided internal barrier method) or panels separated by specially shaped joints with the function of linear reverse capillarity. The heating cable installed in critical heating areas can be treated as a supplement to the existing heating system, however, due to the small and variable power of 5 to 20 W/m, depending on the ambient temperature, the range of influence is limited to the most cooled zone of the thermal bridge. This sufficiently eliminates harmful phenomena associated with the cooling of the partition surface, condensation of water vapor and the development of mould. During warmer spring and autumn days, external partitions can be effectively protected when the basic heating is turned off, because the temperature in the connector is regulated by the automatically activated anti-condensation system. The areas exposed to surface moisture condensation of the water vapor remain dry, making the rooms hygienic and clean, as dust does not settle as on the wet surfaces.

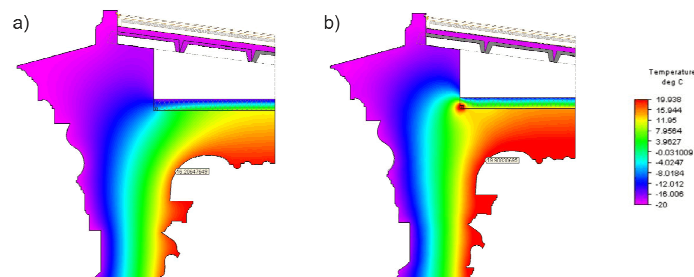


Figure 5 Temperature distribution in the heated node in winter. a) no heating b) heating

Positive thermal effects were obtained by placing the heating cable in the decorated attic of the palace (presented in Figure 1). The cable was placed on the outside, invisible to users. Thanks to this, it was possible to preserve historical matter without any interference in its structure. The obtained results for winter season (same boundary conditions as for Figure 3) are shown as false-color temperature distributions in Figure 5.

DISCUSSION

An implementation of the anti-condensation system was examined also on the thermal bridges presented in the Figure 3. Under the same boundary conditions as the 1st simulation ($t_i=20^{\circ}\text{C}$, $t_e = -20^{\circ}\text{C}$), in case of the corner 3b, the 5W power of heating cables resulted in rising the corner temperature up to 18.01°C (12.16°C more). While in case of the internal insulation layer (Figure 3c), the temperature of the contact point insulation-wall raised up to 13.09°C (4.36°C more). Both results are above the dew point.

CONCLUSIONS

The following conclusions can be made on the basis of mycological studies, analyzes and calculations:

1. The fluorescence method used to determine the mass of mycelium allows a full quantitative assessment of the mycological risk of the building.
2. Placing the insulation in the roof slope layers does not solve the problem of excessive cooling of internal surfaces in the areas of thermal bridges occurrence.
3. Good effects are achieved in the case of full roof by the introduction of heating of the attic zones with ventilation ensuring that the attics maintain a temperature of not less than 20°C , and humidity up to 55%.
4. In the case of flat and ventilated flat roofs, adequate protection against condensation in the thermal bridge zone can be achieved by introducing linear heating with self-regulating heating cables.
5. The hygrothermal calculations showed the correctness of the designed solutions, while maintaining the appropriate materials and proper ventilation performance of individual layers. Not insulated alcove knee wall require additional thermal energy supply. The use of shortwave radiation to avoid periodic condensation of moisture on their internal surfaces can be dangerous for the durability of polychrome.
6. The optimal solution seems to be performing the air heating of the attic with the air nozzles directed partly to the knee walls and the implementation of an intelligent anti-condensation installation consisting of heating cables and control automation.

REFERENCES

- Bomberg M., Wójcik R., Piotrowski J. 2016. A concept of integrated environmental approach, part 2: Integrated approach to rehabilitation. *Journal of Building Physics* 39(6), 482-502.
- Rylander R, Reeslev M and Hulander T. 2010. Airborne enzyme measurements to detect indoor mould exposure. *Journal of Environmental Monitoring* 11.
- Wójcik R. 2017. *Internal thermal insulation of buildings* (Pol. *Docieplanie budynków od wewnątrz*). Medium, 199 pages.
- Wójcik R, Kosiński P. 2017. On rehabilitation of buildings with historical façades. *Energy Procedia* 132, 927-932.

Classification of the indoor environment in a high-school building by means of subjective responses

Lorenza Pistore^{1,*}, Ilaria Pittana², Francesca Cappelletti², Andrea Gasparella¹, Piercarlo Romagnoni²

¹ Faculty of Science and Technology, Free University of Bozen-Bolzano, piazza Università 5, 39100 Bolzano, Italy

² University Iuav of Venice, Dept. of Design and Planning of Complex Environments, Dorsoduro 2206, 30123 Venezia, Italy

**Corresponding email: lorenza.pistore@natec.unibz.it*

ABSTRACT

In this paper the subjective evaluation of the indoor environment of a secondary school in Treviso (Italy) is presented. Field campaigns have been carried out during the winter season in order to assess people overall satisfaction about the environment, their behavior towards discomfort and their interactions with the building and the systems. A specific questionnaire has been elaborated, paying particular attention to the occupants target and to the questions needed to grasp not only the comfort feedbacks, but also the dynamics and the individual students' attitudes that can influence the building energy performance. A first general evaluation has been elaborated for all the comfort areas (i.e. thermal, visual, acoustic and air quality) applying the method proposed by the EN 15251 for thermal comfort to all the comfort aspects. Then, further analyses have been implemented focusing on thermal conditions, in order to integrate the results and to check if an average comfort evaluation can be significant and representative of all the spaces in the building. Results show that specific classrooms conditions seem not to match completely the overall general analysis, even if representative differentiated spaces were selected for the analysis.

KEYWORDS

IEQ, School buildings, Thermal comfort, Acoustic comfort, Visual comfort, Indoor Air Quality.

INTRODUCTION

In the last decade, many works on Indoor Environmental Quality (IEQ) and Post-Occupancy Evaluations (POEs) in educational buildings have been performed on primary schools, secondary schools, and universities, aiming at a better understanding of the indoor conditions, especially focusing on thermal comfort. Nevertheless, beyond the thermal aspects, recent studies have also investigated the overall environmental comfort by considering various indoor aspects (Ricciardi and Buratti, 2018; Jamaludin et al. 2017). These works are based on field measurements, occupants' surveys, or a combination of them (Corgnati et al. 2007). Generally, POE is applied for a better understanding of occupants' comfort perception as well as for the estimation of students' thermal comfort ranges in comparison with the European standards (EN 15251,2007, ASHRAE,2017) however, integrating both the objective and subjective approaches, allows quantifying both the physical phenomena and the occupants' experience (Peretti and Schiavon, 2011). The two methods have been used together for analyzing the subjective parameters most correlated with quantitative results (Ricciardi and Buratti, 2018), as well as to investigate the impact of the IEQ on students' performance (Mishra and Ramgopal, 2015; Liu et al. 2015; Mongkolsawat et al. 2014). Personal perception has been also used to find the energy management strategies most suitable to ensure both energy efficiency and indoor quality (Kolokotsa et al. 2005; Zinzi et al. 2016). However, only few works focus on the behavioral response of students (Wong and Khoo, 2003; De Dear et al. 2015; Kim and De Dear,

2018) or try to investigate people preference in different environment and ventilation conditions (Dias et al. 2011, Chen et al, 2014).

This paper presents the results of subjective survey campaigns carried out on an educational building during the winter season of the scholastic years 2016-17 and 2017-18, with the aim of investigating the overall indoor environmental quality as perceived by students along with their opinions on the causes of discomfort and their reactions towards it.

METHOD

The selected building is a secondary school in the Municipality of Treviso, in the North-East of Italy. It has been chosen as reference among a set of 41 educational buildings using the approach presented in Pistore et al. (2016). Built in 1985, it hosts about 1150 students aged 14 to 18, and consists of 4 floors plus a basement, for a total floor area of 12,605 m², a heated volume of 50,845 m³ and a compactness ratio of 0.35. Four main wings compose the building (Figure 1): offices and administration face North-West, while the classrooms are located all around the building, with a transparent envelope area of about 2,074 m². The conditioning system consists of two different types: an all air system for the most part of the school, and radiators in a small classrooms area. Seven classrooms located on different floors and with different exposures have been selected, because of their representativeness according to EN 15251 (2007).

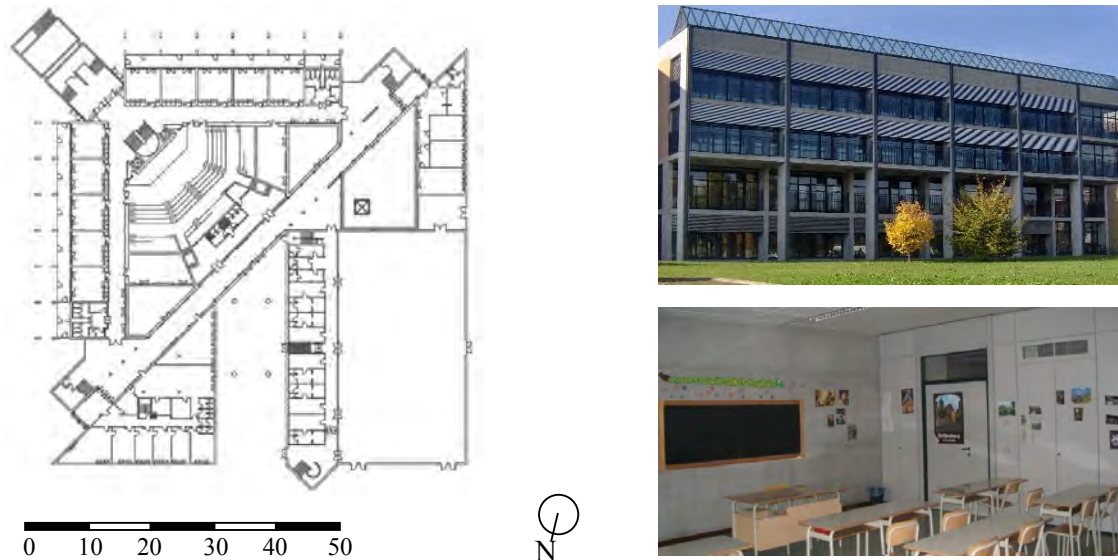


Figure 1. School ground floor map (left) and classrooms external and internal view (right).

A specific questionnaire has been elaborated and administered to 168 students during the regular classes. Five field campaigns have been carried out, from December 2016 to February 2018, only in the winter period with the heating system turned on. Subjective comfort responses have been assessed in seven selected representative classrooms, located on different floors and different areas of the building, in order to obtain a significant mapping of the environmental conditions inside the whole school as prescribed by EN 15251 (2007). An application on tablet devices has been used to administer the questionnaires, consisting of six different sections: general student information, general comments, lighting and visual environment, thermal environment and air quality, acoustic environment. The sections about the comfort areas have been structured consistently and, in order to make comparison analysis more homogeneous, with the same evaluating scales. In more details, a sensation vote scale, according to (EN ISO 10551,2002), (ASHRAE, 2012) and Annex H of EN 15251 (2007), rated from the lowest (-3) to the highest (+3) level a specific aspect, with 0 being the neutral condition. A Likert scale was

used for assessing occupants' satisfaction, in ascending order of satisfaction from 1 to 7 according to (EN ISO 10551,2002) and (ASHRAE,2012). Finally, the survey included a scale of preference, according to Annex H of EN 15251. In order to investigate the causes for discomfort, multi-choice questions have been introduced along with some specific questions about their habits when actions to modify the environmental conditions are required. Questions did not include technical terms (for instance lighting level was used instead of illuminance, air temperature for thermal environment, etc.) to be more understandable to pupils.

RESULTS

In order to evaluate the overall indoor environmental quality inside the school, the method prescribed in EN 15251 – Annex I.4 (2007) has been applied. Although it is proposed only for thermal comfort and air quality, it has been extended to the other comfort areas. Likert 7-points scale answers have mainly been taken into consideration for the assessment of the satisfaction (votes larger than or equal to 4 have been considered as satisfied). In addition, for the visual and thermal comfort, some more detailed information have been reported, such as the percentage of answers in the sensation votes and in the preference vote scales.

Although 44 % of them report high lighting levels (Table 1), this does not cause much discomfort to the students: almost 84 % are satisfied, 71 % do not prefer any change and the remaining are almost equally preferring lighter and darker conditions. This is a very interesting outcome, which suggests how comfort is not always associated with a condition of neutrality. Also in terms of thermal comfort, only 27.4 % of students perceive a sensation of neutrality, but, also in this case, 51 % are satisfied and 41 % would not have any change. Since satisfaction is lower and almost half of the population would prefer warmer temperatures, this aspect will be further investigated in the discussion section.

Also air quality raises some concern, with only 55 % people satisfied, despite the fact that most of the building is served by an all air system.

Finally, students seem to be very satisfied with both the acoustics (89 %) and the acoustic insulation of the building towards the outdoor noises (71 %).

DISCUSSION

Figure 2 shows an overview of the declared causes of discomfort and the behavior of students when annoyed by the environment.

Concerning the lighting environment, part of the occupants reports high lighting conditions, but only 10 % of the students take action towards it, whereas 44 % and 38 % rely on schoolmates and on the teacher to operate shades (Figure 2a), revealing a certain inertia.

Regarding the thermal conditions, the majority of the students (62 %) generally feel thermal discomfort during the first hours, from 8 a.m. until about 10 a.m., suggesting inefficiencies in the heating system operation. Occupants themselves relate this to the system regulation, but also to draughts and to surface temperatures (Figure 2b) and, in order to enhance their thermal sensation, 53 % of the students declared to take action to modify their clothing level.

In terms of air quality, 64 % of the occupants perceive unpleasant odours, with the result that windows are opened from 2 to 5 times per day, usually during intervals. This is confirmed also by the behavioural report: 42 % use to act towards discomfort, but still a great share rely on schoolmates and teachers (Figure 2c).

Regarding the acoustics, even if satisfaction is high, occupants report being annoyed by noises from adjacent spaces: this may indicate an issue in the acoustic insulation of internal walls and floors. Also in this case, students reveal to be very passive users: half rely on teacher's help to close doors and windows, and a quarter of them does not act against discomfort.

However, when a large building is considered, satisfaction and preference votes could hide some specific problems related to different spaces and conditions in the building.

Table 1. Classification of the environment based on occupants responses

Lighting	Satisfaction (≥ 4)	83.9%						
	Sensation	-3 (Low) 1.2%	-2 0.6%	-1 7.1%	0 47.0%	1 13.1%	2 26.2%	3 (High) 4.8%
	Preference	Lighter 12.5%		Unchanged 71.4%			Darker 14.3%	
Temperature	Satisfaction (≥ 4)	51.2%						
	Sensation	-3 3.6%	-2 13.1%	-1 20.2%	0 27.4%	1 23.2%	2 10.1%	3 1.2%
	Preference	Warmer 49.4%		Unchanged 41.1%			Colder 8.3%	
Air quality	Satisfaction (≥ 4)	54.8%						
Acoustics and insulation	Satisfaction (≥ 4) acoustics	88.7%						
	Satisfaction (≥ 4) insulation	70.8%						

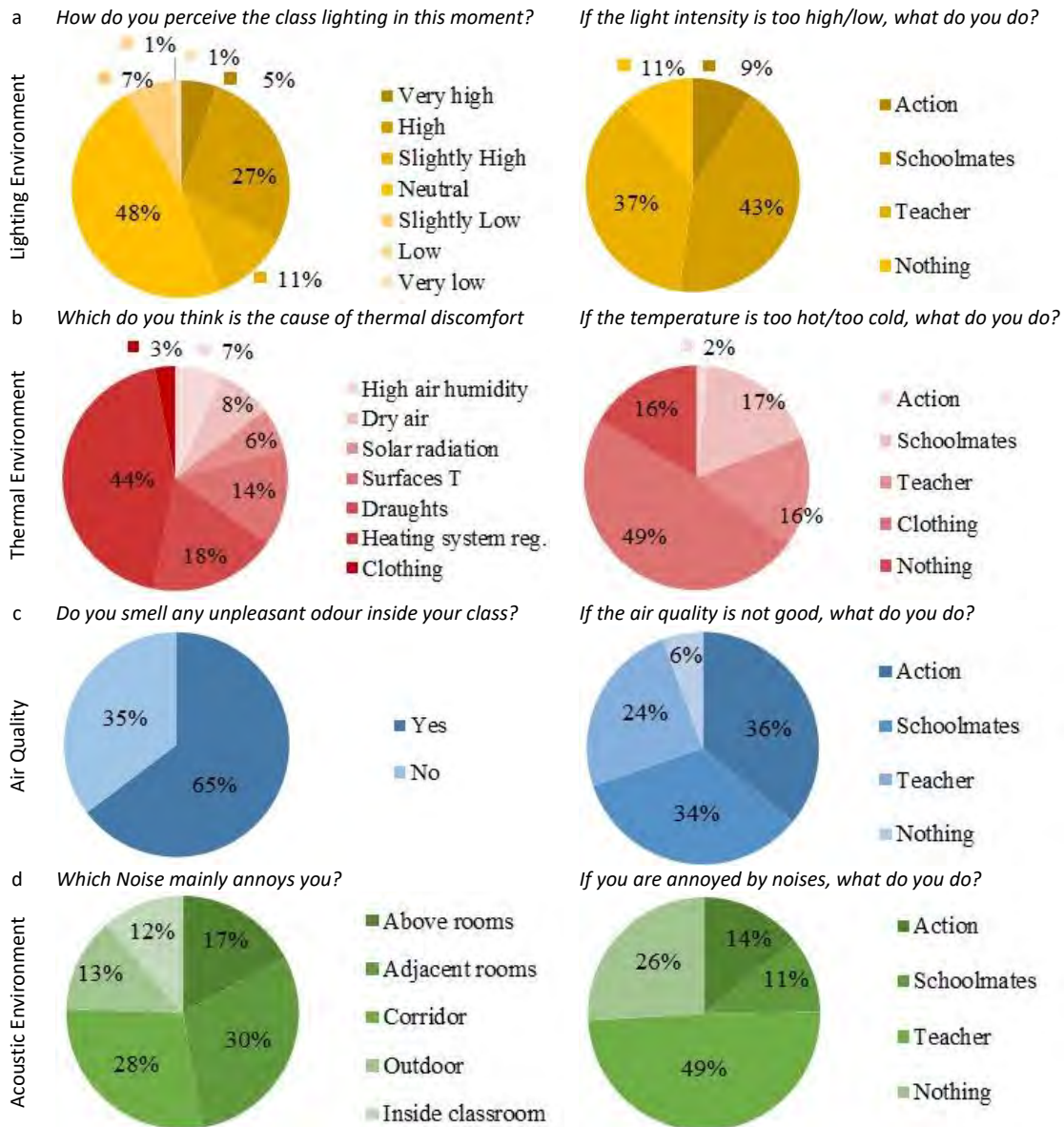


Figure 2. Causes of discomfort (left) and students behavior towards discomfort (right)

Considering the lower satisfaction for thermal conditions, a deeper analysis has been devoted to specific features of the classrooms, namely the different floor and the different heating

system. In particular (Figure 3), the satisfaction with air temperature increases from 44 % on the ground level, to 82 % on the 3rd floor. On the ground floor, 45 % of the students perceive a temperature from slightly cool to cold, contrarily to the 3rd floor spaces, where discomfort is caused by temperatures slightly warm (50 %). Focusing on the ground floor, where discomfort is higher, it appears that classrooms heated by different systems perform very differently. Occupants in spaces with an air system declared much greater dissatisfaction with the thermal environment (54 %), due more often to cool temperatures. In rooms with radiators, on the contrary, students reveal to be more satisfied (78 %) and, in case of discomfort, this is caused by warmth, consistently with what happens on the 3rd floor.

This shows that, sometimes, an overall evaluation of a building is not an easy task. In fact, as in this case, an average of the sensation votes, as reported in Table 1, could not be representative of every room in the building.

How much are you satisfied with the air temperature in your classroom?

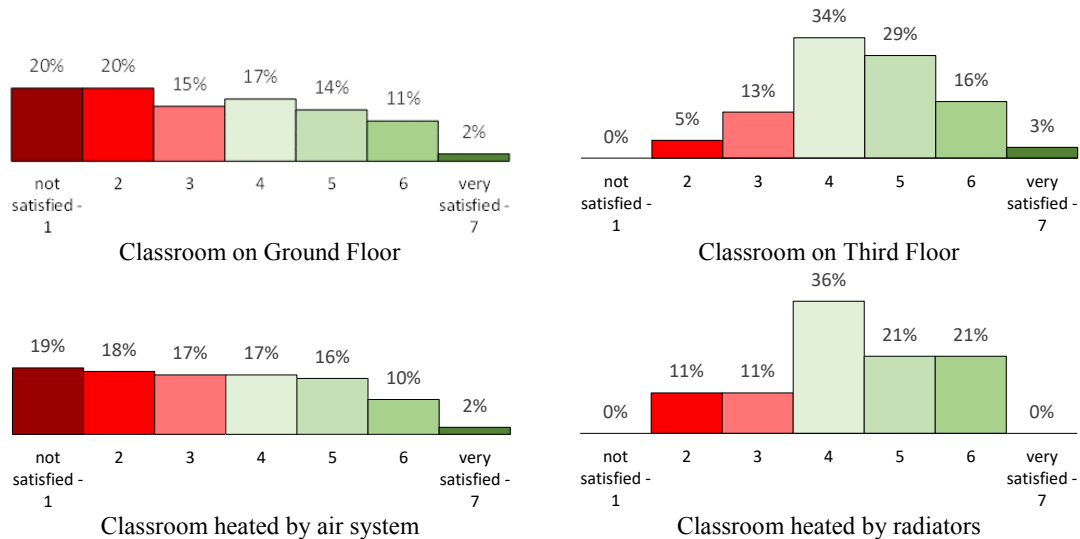


Figure 3. Comparison of subjective thermal perception in different classrooms

CONCLUSIONS

In this paper, the evaluation of the indoor environment of a secondary school building is reported. An average evaluation has been elaborated for all the comfort areas, with an attempt to extend the prescriptions of Annex I.4 about thermal comfort also to the other areas. A further analysis has been implemented focusing on thermal conditions, in order to check if an overall comfort evaluation can be significant and representative of all the spaces in the building. Results show that the use of all the occupants' answers sometimes does not reflect the peculiarities of some parts of the building even if representative differentiated spaces are selected, thus compromising the potentiality of surveys in detecting problems about the building operation. Moreover, the study reveals that young students aged from 14 to 19 are very passive towards discomfort: this is an important aspect to be further investigated, especially in a shared environment, as school is, and considering all the factors involved in a peculiar young environment with its own internal dynamics. Understanding and recognizing patterns in occupants' behavior would surely be a step forward in grasping information useful for energy consumptions evaluations and for adopting new strategies.

ACKNOWLEDGMENT

The authors would like to thank the Municipality of Treviso, the Head and the members of ISS Da Collo of Conegliano for making the school available for this research.

REFERENCES

- ASHRAE. 2012. Performance Measurement Protocols for Commercial Buildings: Best Practices Guide. Atlanta: American Society of Heating, Refrigerating, and Air-Conditioning Engineers, Inc.
- ASHRAE. 2017. ANSI/ASHRAE Standard 55-2017, Thermal Environmental Conditions for Human Occupancy. Atlanta: American Society of Heating, Refrigerating, and Air-Conditioning Engineers, Inc.
- EN ISO 10551. Ergonomics of the thermal environment - Assessment of the influence of the thermal environment using subjective scales. European Committee for Standardization, Brussels, Belgium, 2002.
- EN 15251. Indoor environmental input parameters for design and assessment of energy performance of buildings addressing indoor quality, thermal environment, lighting and acoustics. European Committee for Standardization, Brussels, Belgium, 2007
- Chen C.P., Hwang R.L., Liu W., Shih W.M., Chang S.Y. 2014. The influence of air-conditioning managerial scheme in hybrid-ventilated classrooms on students' thermal perception. *Indoor and Built Environment*, 24(6), 761-770.
- Corgnati S.P., Filippi M., Viazzo S. 2007. Perception of the thermal environment in high school and university classrooms: Subjective preferences and thermal comfort. *Building and Environment*, 42(2), 951-959.
- De Dear R., Kim J., Candido C., Deuble M. 2015. Thermal comfort expectations and adaptive behavioural characteristics of primary and secondary school students. *Building Research and Information*, 43, 23-36.
- Dias M., Bernardo H., Ramos J., Egidio M. 2011. Indoor Environment and Energy Efficiency in School Buildings - Part 1: Indoor Air Quality. In: Proceedings of the 2011 3rd International Youth Conference on Energetics (IYCE).
- Jamaludin N.M., Mahyuddin N., Akashah N.M. 2017. Assessment on indoor environmental quality (IEQ) with the application of potted plants in the classroom: Case of university Malaya. *Journal of Design and Built Environment*, 17(2), 1-15.
- Kim J., De Dear R. 2018. Thermal comfort expectations and adaptive behavioural characteristics of primary and secondary school students. *Building and Environment*, 127, 13-22.
- Kolokotsa D., Niachoub K., Gerosb V., Kalaitzakisc K., Stavarakakisc G.S., Santamourisb M. 2005. Implementation of an integrated indoor environment and energy management system. *Energy and Buildings*, 37 (1), 93-99.
- Liu Y., Jiang J., Wang D., Liu J. 2016. The indoor thermal environment of rural school classrooms in Northwestern China. *Indoor and Built Environment*, 26 (5), 662-679.
- Mishra AK, Ramgopal M. 2015. A comparison of student performance between conditioned and naturally ventilated classrooms. *Building and Environment*, 84, 181-188.
- Mongkolsawata D., Alexi Marmota A., Uccia M. 2014. A comparison of perceived learning performance of Thai university students in fan-assisted naturally ventilated and air-conditioned classrooms. *Intelligent Buildings International*, 6 (2), 93-111.
- Pistore L., Pernigotto G., Cappelletti F., Gasparella A., & Romagnoni P. 2016. From energy signature to cluster analysis: an integrated approach. 4th International High Performance Buildings Conference at Purdue.
- Ricciardi P., Buratti C. 2018. Environmental quality of university classrooms: Subjective and objective evaluation of the thermal, acoustic, and lighting comfort conditions. *Building and Environment*, 127, 23-36.
- Wong N.H., Khoo S.S. 2003. Thermal comfort in classrooms in the tropics. *Energy Building*, 35, 337-51.
- Zinzi M., Agnolia S., Battistini G., Bernabini G. 2016. Deep energy retrofit of the T. M. Plauto School in Italy—A five years experience. *Energy and Buildings*, 126, 239-251.

Comparison between qualitative and quantitative measurement in assessing thermal comfort in an elementary school

Boyu Li^{1,*}, Ming Hu² and Greg Goldstein²

¹Torti Gallas and Partner, Silver Spring

²University of Maryland, College Park, MD, USA, School of Architecture, Planning and Preservation

*Corresponding email: boyu0920@gmail.com

ABSTRACT

We compare qualitative and quantitative measurements to assess an elementary school building's thermal comfort. Quantitative measurements of the physical environment are useful but not sufficient, since different people respond differently in the same indoor environment. A qualitative survey of the school employees shows the thermal comfort level has a 3.73 out of 7 score and 40% of subjects rated it unsatisfactory, even though the temperature and humidity level are measured within the comfort range recommended by ASHRA 90.1 – 2004. This gap occurs because human metabolism is not taken into account in current design guidelines, even though there is a clear correlation between human metabolic level and perceived thermal comfort. The gap between design guidelines and occupants' thermal comfort presents an opportunity to improve indoor environmental quality. School buildings are especially challenging because they have a mix of adult and child occupants with widely varying metabolic rates. Therefore, an elementary school was used as a case study to compare differences between quantitative and qualitative measurement. We conducted a series of simulations to compare the thermal comfort in relation to adult and children's metabolism and their thermal responses. We demonstrate that the negligence of occupants' metabolism can lead to inaccurate design guidelines for the physical environment's thermal comfort. Our results could potentially improve design manuals to accommodate buildings with mixed occupants to maximize comfort levels.

KEYWORDS

Thermal comfort, metabolic rate, qualitative and quantitative, elementary school, adaptive model

INTRODUCTION

Most elementary schools in United States were built during the 1950s to 1970s and are in need of renovation, modernization and repairs (Sheryl, et. Al, 2017). One of the most critical issues among those public schools that were built prior to active mechanical systems is the lack of control of thermal comfort of the interior environment (U.S.ED, 2012). As the design standard evolves, new buildings optimize indoor environment comfort, especially thermal comfort via active mechanical systems. However old facilities are designed with passive strategies which try to create a steady singular environment. Maintaining a comfortable indoor environment while simultaneously preserving energy will be a major challenge for both designers and school administrations.

Clients are usually given three options for old school buildings: demolishing, renovating, and retrofitting. To get a better understanding of existing school buildings and to understand the targeted area of improvement through retrofitting, we took a case study that focuses on an elementary school built prior to active mechanical systems. We measured an elementary school facility in Maryland, USA, which is in climate zone 4 according to IEC (International

Energy Code). The building is a 44,200 square foot educational facility approaching the end of its expected life cycle. Constructed in 1968, the building envelope consists primarily of CMU block with a single layer of brick veneer, gypsum roof assembly, and a hollow core concrete slab finished with terrazzo over a plenum space for gas furnace duct system. The primary massing of the building is one story with partial double height at the gymnasium. School classrooms are installed with a water-based heating system, which are non-adjustable, and with window-mount air conditioners.

The assessment of thermal comfort in elementary school is challenging because both adults and children use the space relatively equally. Many people have conducted research focusing on regional climate and indoor environment and its impact to students' health and learning process (Sheryl. et.Al. 2017). Research shows that thermal comfort may have a direct impact on working efficiency and learning ability in an enclosed environment. Even though the current ASHRAE considers an adaptive model when measuring thermal comfort, assessing thermal comfort in buildings that are built with passive strategies requires an additional evaluation to gain the users' responses.

METHODS

Qualitative

The first step of evaluating the building performance was to take qualitative data, which helps to understand which part of the building needs to be improved. We distributed an occupancy survey among 19 faculty and staff. The survey had 11 questions, covering comfort and satisfaction ratings on lighting, daylighting, thermal, acoustic and air quality. Survey respondents were provided the opportunity to respond on a scale of 1-7 for each question; responses measured as 3 or under were regarded as "dissatisfied." Survey results were anonymous and unbiased regardless of staff occupation and working locations.

In the thermal comfort portion, we asked the participants two questions. The first was to identify whether they could adjust the thermal comfort level of the rooms, and the second was to evaluate the overall thermal comfort of their work environment.

Part 1 - Indoor Environmental Quality

Room number	
Temperature	
Humidity	
PPM	
Dimension	
Lighting Level	
Sound level	

Part 2 - Indoor Environmental Quality
The following section of the survey focuses on your satisfaction with indoor environmental quality in your workplace. How important is each of the following items to doing your job well?

Thermal Comfort

1. Which of the following do you personally adjust or control in your workspace? (check all that apply)

<input type="checkbox"/>	Window blinds or shades	<input type="checkbox"/>	Operable window
<input type="checkbox"/>	Thermostat	<input type="checkbox"/>	Portable heater
<input type="checkbox"/>	Permanent heater	<input type="checkbox"/>	Room air-conditioning unit
<input type="checkbox"/>	Portable fan	<input type="checkbox"/>	Ceiling fan
<input type="checkbox"/>	Adjustable air vent in wall or ceiling	<input type="checkbox"/>	Adjustable air vent in floor (diffuser)
<input type="checkbox"/>	Door to interior space	<input type="checkbox"/>	Door to exterior space
<input type="checkbox"/>	None of the above	<input type="checkbox"/>	other

a)

2. How satisfied are you with your access to a window view?

Very Satisfied Very Dissatisfied

7 6 5 4 3 2 1

Acoustic Quality

1. How satisfied are you with the noise level in your workspace?

Very Satisfied Very Dissatisfied

7 6 5 4 3 2 1

2. How satisfied are you with the speech privacy in your workspace (ability to have conversations without your neighbors overhearing and vice versa)?

Very Satisfied Very Dissatisfied

7 6 5 4 3 2 1

Cleanliness and Maintenance

1. How satisfied are you with the cleanliness and maintenance of the building?

Very Satisfied Very Dissatisfied

7 6 5 4 3 2 1

Please describe any other issues related to Indoor Environmental Quality that are important to you.

b)

Figure 1. Survey questions regarding thermal comfort. a) thermal comfort questions 1: Which of the following do you personally adjust or control on your work space. b) question 2: how satisfied are you with your access to a window view.

Quantitative

In this survey, measurements included CO₂ levels in parts per million, decibel levels, lux levels, humidity percentages, and air temperature. Instruments used included portable digital CO₂ meters, digital sound level meters, digital light meters, and digital psychrometers. We split into three groups, and measurements were acquired from all locations of the school at approximately 1:30 pm on February 7th, 2017.

Psychrometers graph is one of the best way to represent temperature and humidity as the parameter of thermal comfort. To further expand our data analysis we utilized the CBE thermal comfort tool developed by Center for the Built Environment in UC Berkeley. The model is based off Gail and Brager's original research ASHRAE RP-884, now the new ASHRAE 2004 standard hypothesized a thermal conform model called 5h3 adaptive model. This model accounts for behavioral adjustment, physiological and psychological adaptation within a built environment. (Richard and Gail, 1998) The fundamental principal of adaptive model for thermal comfort is to acknowledge human behavioral adjustment, physiological and psychological adaptation within a built environment. (Richard and Gail, 1998)

Thermal comfort in buildings built before active mechanical control is achieved by passive strategies and natural ventilation. Constructing active control in these buildings would be expensive and require significant maintenance, therefore retrofitting is one of the best options for minimal energy consumption.

RESULTS

Existing Conditions

We found an average thermal comfort satisfaction level of 3.9 out of 7. Of 19 responses, 40% ranked 3 or lower. (*fig 1*) Surveyed occupants had access to operable blinds/shades, permanent heaters, doors to interior space, operable windows, and room air conditioning units. Occupants did not, however, have access to customizable thermostats, portable fans, adjustable vents in wall or ceiling, portable heaters, or ceiling fans. (*fig 1b*). In other words, humidity of 33.5%. Recorded temperatures ranged from 22 °C to 26 °C and humidity ranged from 27.7% to 38%. (*fig 2*). We used this data to generate a psychrometric chart, applying the metabolic rate of a seated adult with average summer clothing (given the outdoor conditions on February 7th were quite temperate). The result was outside the noted range of accepted thermal comfort. (*fig 3*)

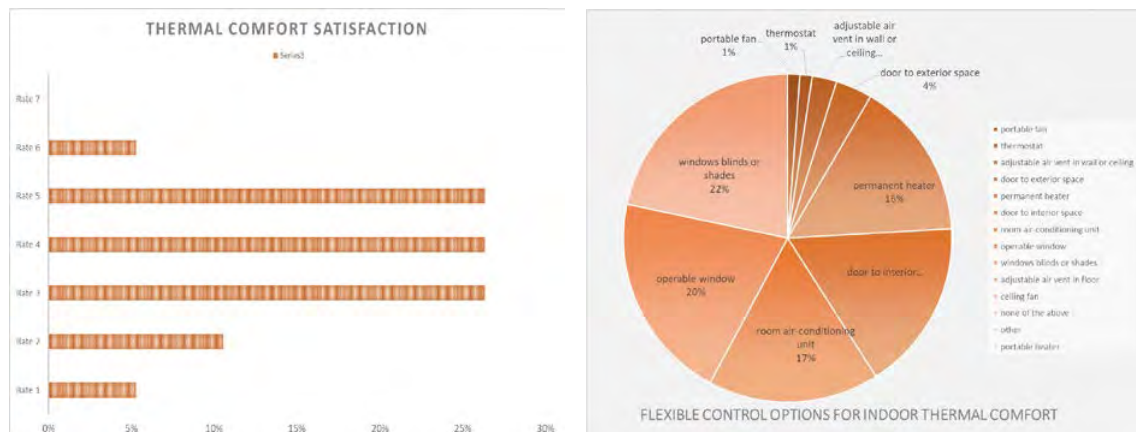


Figure - 1.a) Thermal comfort satisfaction. b) Thermal comfort control flexibility

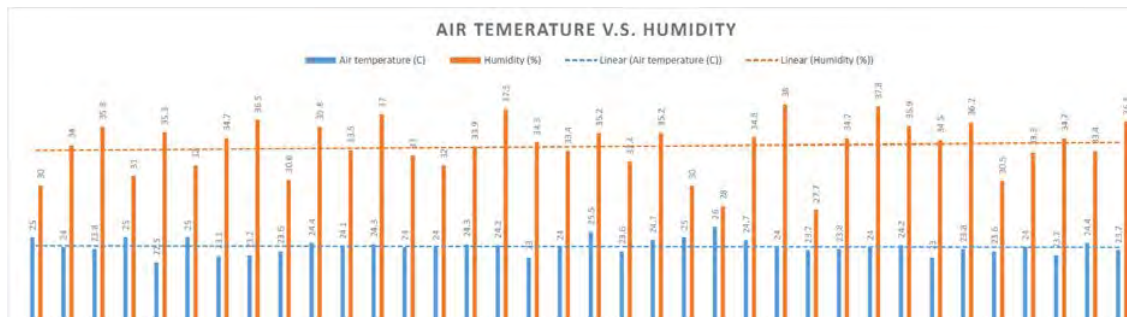


Figure - 2. - Air temperature vs humidity

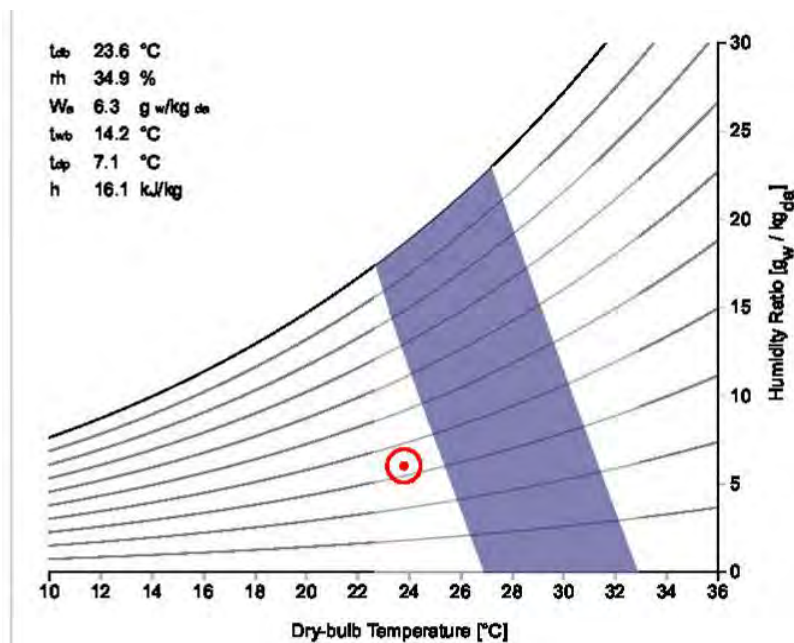


Figure - 3. Psychrometric chart based on a seated adult

We concluded from the qualitative and quantitative data that the thermal comfort in the building under study was unsatisfactory for adults. We next simulated the children's thermal comfort using the same physical environment. The two most prevalent methods for determining the thermal comfort of individuals are the adaptive method, and the rational method. The adaptive method involves surveying the occupants to determine the most comfortable conditions for users. Problems with this method include environmental variability and inaccuracy of survey reports in terms of reproduction. A key stipulation of the adaptive approach is *"if a change occurs such as to produce discomfort, people react in ways which tend to restore comfort."* (Nicol and Humphreys, 2002) According to De Dear's research on adaptive model, the adaptive process also predicts that persons in warmer climates will prefer warmer temperatures indoors, whereas persons in colder climates will prefer cooler temperatures indoors (1998).

The rational method, according to Nicol and Humphreys (2002), involves an index which develops a model for thermal comfort based on variables listed above such as metabolic rate and clothing insulation. We used both the rational and the adaptive method when analyzing our case study school in Maryland.

Simulation comparison of thermal comforts

Interestingly, the resting metabolic rate is reduced from infancy to adulthood by 1.5-2 times according to Son'kin and Tambovtseva (2012). Taking this fact into account, we produced a series of psychometric charts using CBE comfort simulation analyzing isolated variables between persons with a metabolic rate of 1 (adults) 2 (children), assuming an indoor temperature of 23.8 °C and a relative humidity level of 50%. The variables included high air speed, low air speed, and varying clothing. We found each variable tested made either the adult control or child control uncomfortable. However, we produced a chart overlaying child comfort over adult comfort, where airspeed was adjusted for children and clothing insulation was adjusted for adults.

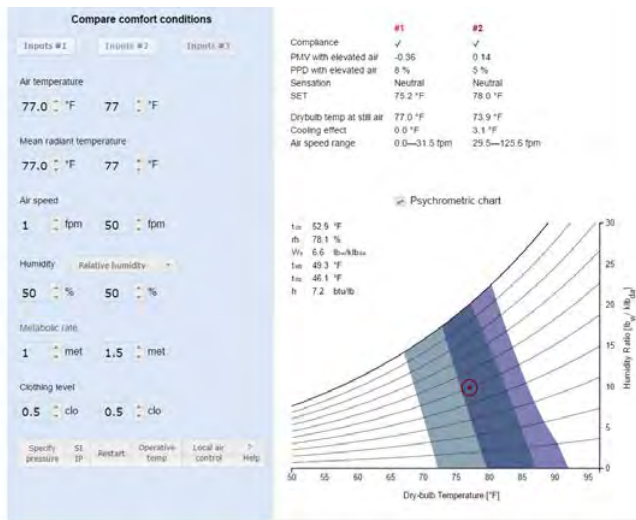


Figure.4 - Simulated thermal comfort comparison of pupils and adults in the same environment due to different metabolic rate.

DISCUSSIONS

This research produces thermal comfort for both adults and children via the rational index. The overlaying result shows that using the adaptive model could produce a comfortable condition for everyone, which would require either one of the occupancy group adjust clothing level or activity level (direct relative to MET rate).

To adjust air speed, a building could either upgrade the HVAC system to be active or zoned to cater to either students or faculty. Another option which reflects the survey is to increase the use of portable devices that allows the faculty to control the ventilation rate. Elementary school usually tend to have a student-teacher ratio between 15:1 and 20:1. Priority of improving thermal comfort would be given to students. Faculty and staff in classrooms would adjust their clothing levels to adapt to the higher air speed conditions.

Taking both qualitative and quantitative data into account mitigates some of the limitations of both data sets. However, neither rational nor adaptive methods provide accurate thermal comfort for students (Zahra, et al 2017). One of the concerns for conducting pupil-focused qualitative surveys is that students have not yet developed a complete and comprehensive perception of thermal comfort. To minimize the potential impact on the qualitative data, we

decided to adopt the simulation result to generalize the possible thermal comfort responses from pupils. Surveys for children, especially 5th-grade and below, may require a different writing style to be properly understood than surveys for adults. The school administration may consider providing thermal comfort education to allow the students to express their feelings accurately and respond to indoor environments properly.

CONCLUSIONS

As many school facilities approach the end of their life cycle, it is critical to reconsider the design of the school facilities. Because implementing an active HVAC system for a whole building might be too economically challenging to be feasible, it is useful to learn and assess occupants' thermal comfort from multiple perspectives. Having a comprehensive assessment for a school facility that in need of future repair and renovation will help the school administrators identify potential problems, minimizing the discrepancy between design and end product of the architect. More importantly, better assessments of school facilities will enable more accurate responses to occupants' sick-building syndrome and eventually create better and healthier environments for both young and adult occupants.

REFERENCES

- ASHRAE,2016. *Standard 90.1-2016, Energy Standards for Buildings except Low Rise Residential Buildings*. Atlanta, GA: ASHRAE Research, Print.
- ASHRAE 2016. *Standard 62.1-2016 user's manual: Ventilation for Acceptable Indoor Air Quality*. Atlanta, GA: ASHRAE Research, 2016. Print
- Department of Education. U.S. Condition of America's Public School Facilities: 2012–13. 2014 *Fanger P.O. 1970*.
- De Dear, Richard, and G. S. Brager. *Developing an Adaptive Model of Thermal Comfort and Preference*. 1st ed. Vol. 104. N.p.: ASHRAE transactions, 1998. Print.
- Sheryl M. et. Al. 2017. A Multidisciplinary Research Framework on Green Schools: Infrastructure, Social Environment, Occupant Health, and Performance *Journal of School Health*. American School Health Association. Vol. 87, No. 5
- Nicol, J. F., and M. A. Humphreys. *Adaptive Thermal Comfort and Sustainable Thermal Standards for Buildings*. Oxford: Elsevier Science, 2002. Print.
- Son'kin, V, and Ritta. T. *Energy Metabolism in Children and Adolescents*. N.p.: INTECH Open Access Publisher, 2012. Print.
- Zahra S.Z., Mohammad T. and Mohammadreza H. 2016. Thermal Comfort in educational building: A review article. *Renewable and Sustainable Energy Reviews* 59, 895–906

Empirical assessment of summertime overheating risk in new, retrofitted and existing UK dwellings

Rajat Gupta* Matt Gregg, and Robert Irving

Low Carbon Building Research Group, Oxford Brookes University, Oxford, UK

*Corresponding email: rgupta@brookes.ac.uk

ABSTRACT

This paper statistically assesses the hourly internal summertime temperature datasets gathered during the summer of 2013 (May to September), from 63 dwellings across the UK. The sample consisted of unmodified dwellings (existing); dwellings with varying levels of fabric improvements (retrofitted) and dwellings constructed to higher levels of the Code for Sustainable Homes (new). Indoor and outdoor temperature data from bedrooms and living rooms from these homes were collected at five-minute intervals using temperature sensors. These data were processed and analysed for summertime overheating, using both static criteria (CIBSE Guide A) and the criteria associated with the EN15251 adaptive thermal comfort model (CIBSE TM52). The results show that despite a relatively cool summer, sufficiently high temperatures were found in a high proportion of dwellings, which were found to be overheated according to the CIBSE static temperature criteria, although the prevalence of overheating was found to be much lower when assessed by the adaptive method. Considerably higher temperatures were found in bedrooms, much higher than living rooms. Interestingly, dwellings with higher levels of insulation experienced overheating twice as frequently as uninsulated dwellings. Given the prevalence of overheating found across the sample, it is necessary to carefully consider this risk during the design and retrofit of homes, to avoid the growth of domestic air-conditioning in future.

KEYWORDS

Dwellings, overheating, UK housing, adaptive thermal comfort, indoor air quality

INTRODUCTION

Despite the relatively mild climate of the UK, concern has increased about summertime temperatures in dwellings due to the effects on occupant health of high temperatures and the possibility that these may occur more frequently with the forecast rise in global temperatures. Though overheating may be prevented by the use of air-conditioning, this will add, undesirably, to greenhouse gas emissions through increased energy use and refrigerant emissions. As most UK householders turn their heating off in the summer even when temperatures are comparatively cool, the fabric of the dwelling can provide a cool buffer against hotter weather. It is therefore important to study internal temperatures in dwellings to observe the relationship to construction, dwelling type and occupant characteristics.

With the implementation of the higher level of fabric efficiency under current UK Building Regulations, overheating in newly-constructed dwellings has become a concern, particularly due to the perception that it is caused by the 'excessive' levels of insulation required to reduce heat energy consumption and hence CO₂e emissions to meet the requirements of the UK Climate Change Act. With the focus on overheating has come a realisation that both the definition of, and the criteria for assessing overheating in naturally-ventilated residential buildings are inadequate (CIBSE, 2013).

Previous studies examining summer temperatures in UK dwellings have included Lomas and Kane (2013) who found, in a study of 230 dwellings in Leicester, that a sizeable proportion had temperatures outside the ranges anticipated by the BS EN 15251 model. Beizaee et al. (2013) performed a similar study based on 207 dwellings across the UK. This study found that a large proportion of living rooms and bedrooms had more than 5% of their occupied hours above the CIBSE recommended temperature thresholds of 25°C and 24°C respectively. Across the regions of the UK, warmer homes were found in the South East, the East, East and West Midlands, with cooler homes in the North East, North West and Yorkshire. The oldest dwellings (pre-1919) were found to be significantly cooler than more modern homes, solid wall houses cooler than those with cavity wall construction and detached homes cooler than those of other built-form types. This study also found that dwelling temperatures in cooler UK regions were correspondingly cooler than those in warmer regions, inferring from this that a further level of adaptation, dependent on region, is required.

The objective of this paper is to combine data collected from several studies to examine the variations between the different methods of assessing overheating and to examine the relationships between temperature and other environmental variables. The study is significant in that it contains data gathered from existing houses, both with retrofit energy efficiency improvements and without, and new houses built to the highest energy efficiency levels under the UK standards current at this time (DCLG, 2006). This allows the examination of the differing effects of built-in and retrofit energy efficiency measures and unimproved housing, whereas the previous studies lack the ability to make these distinctions.

METHOD

This study is based on data collected between 1 May and 30 September 2013 in nine different locations in the UK, ranging from Swansea in the west to Tyneside in the north and west London in the south. The data analysed for this paper come from one large-scale monitoring study and three smaller studies. The large-scale study, known as EVALOC, covered 57 existing dwellings in six locations across the UK. The dwellings in these locations include a mix of existing (unchanged) and retrofitted dwellings. For EVALOC, temperature data were collected via sensors linked to a wireless network within the house, from which it was transmitted to a webserver for accumulation and download as required for analysis. In some dwellings data were also acquired by individual 'button' loggers for direct download to a PC.

The three smaller studies each consisted of two new-built dwellings and were carried out as Building Performance Evaluation (BPE) studies, being accompanied by a detailed survey of the occupant satisfaction with the dwellings and a comparison dwelling as built with the original design. Because of the higher level of air-tightness enforced by Code for Sustainable Homes, all these houses have mechanical ventilation with heat recovery (MVHR) installed to provide ventilation and prevent condensation from excess humidity. Temperature data for the BPE studies were collected every five minutes from wireless sensors transmitted to a data-hub and uploaded over Global System for Mobile Communications network to a website for acquisition. The environmental data were limited to a period of between three and nine months with some gaps in the data due to the limitations of the data loggers. Sufficient data were collected over the summer period to assess overheating.

In all the studies, external temperature and RH were also collected by the same methods for all dwellings with the exception of C3 and C8 where external temperatures had to be extracted from nearby weather stations due to equipment failures. Table 1 lists the communities of dwellings and their relevant characteristics.

Table 1. Characteristics of study dwellings

	Location (Code) / setting	No. of dwellings: Date of construction mix
EVALOC	Community 1, South Wales (C1) / rural elevated	Total 11: pre-1919, 1919-44, 1965-80, 1981-90, post-1990
	Community 2, Merseyside (C2) / suburban sheltered	Total 12: 1919-44, 1945-64, 1965-80, 1981-90
	Community 3, North East (C3) / suburban sheltered	Total 10: 1919-44, 1945-64, 1965-80
	Community 4, Oxfordshire (C4) / rural elevated	Total 10: pre-1919, 1945-64, 1965-80, 1981-90
	Community 5, Yorkshire (C5) / urban elevated	Total 5: pre-1919
	Community 6, Midlands (C6) / urban sheltered	Total 9: pre-1919, 1919-44, 1965-80, 1981-90
BPE	Community 7, Wilts (C7) / urban sheltered	Total 2: new-build BPE
	Community 8, London (C8) / urban sheltered	Total 2: new-build BPE
	Community 9, Midlands (C9) / urban sheltered	Total 2: new-build BPE

Overheating assessment

Research on overheating in dwellings commonly employs two different methods of assessment published by the Chartered Institution of Building Services Engineers (CIBSE). For overheating criteria in non-air-conditioned buildings, CIBSE's Environmental Design Guide A (CIBSE, 2006) suggests that values for indoor comfort temperatures should be 25°C for living areas and 23°C for bedrooms. CIBSE notes that temperatures are expected to be lower at night with people finding that sleeping in warm conditions is difficult, particularly above 24°C. Environmental Design Guide A provides static benchmark summer peak temperatures and overheating criteria:

- 1% of annual occupied hours over 28°C in living rooms
- 1% of annual occupied hours over 26°C in bedrooms

For adaptive thermal comfort, the BS EN 15251 (BSI, 2008) criteria were developed taking the outdoor conditions and human adaptation into account by identifying comfort limits based on a running mean of external temperature and the quality of the thermal comfort required. Based on this, the CIBSE TM52 (CIBSE, 2013) document suggests a series of criteria by which the risk of overheating can be assessed or identified. The first criterion suggests that the number of hours during which the internal temperatures are 1 K higher or equal to the upper comfort limit during the period from May to September should not exceed 3% of occupied hours. For the adaptive assessment, the 'running mean' comfort temperature range was calculated using the external temperatures acquired for each locality.

For both methods of assessing overheating, priority is given to those hours during which each room is occupied. For this study, it is assumed that living rooms are occupied between 7 am and 11 pm and bedrooms are occupied for the remaining hours from 11 pm till 7 am. Treating only these periods as significant for overheating could be considered somewhat restrictive since a considerable proportion of the population work shifts and will need to sleep during the day at times of higher outside noise levels, precluding window opening etc.

RESULTS

Regarding external temperatures, localities in the north (including urban) and those in the rural localities of the south had the lower temperatures. Those in the urban areas of the south had the highest temperatures. Overall the analysis illustrated a fairly mild climate with only short intervals of high temperatures and comparatively low minima, which should enable householders to use night-time cooling if necessary. From cooling degree day (CDD) analysis it would appear that localities C1 and C5 had considerably warmer summers than usual, C3 and C7 somewhat warmer, C2, C8 and C9 were, more or less, as would be expected and C4 and C6 considerably cooler.

Overheating in bedrooms and living rooms

The most significant result from static overheating analysis for bedrooms is that only one dwelling, C3-H06, out of 63 dwellings in the dataset, does not exceed the 26°C limit. Five dwellings out of 34 with cavity wall insulation and two out of 24 dwellings without wall insulation experienced significant periods of >30°C temperatures. Of the modern houses in the BPE studies, only one, C7-H02, maintains temperatures close to the CIBSE requirement. *Note that the dwellings in C7 were unique in that they are constructed of heavy-weight hempcrete, whereas the other BPE dwellings are light weight timber construction.* Results for overheating assessment using the adaptive method indicates that far fewer houses are judged to overheat under these criteria, six out of the 34 with cavity wall insulation and three out of the 24 with no insulation. Similarly, fewer instances of overheating were found using the adaptive vs. static method in Gupta and Gregg (2017). In contrast to bedrooms there are considerably lower levels of overheating in the living rooms, indicated by the fact that only two houses, C4-H02 and C8-H01 were judged to experience any significant proportion of the summer period >30°C and only a further two, C1-H03 and C8-H02 had periods >28°C. There is also a similar lower level of overheating according to the adaptive method, with an identical list of dwellings being identified in the cavity wall insulation category plus only one in C4-H04 in the uninsulated category.

Adaptive overheating analysis by dwelling characteristics

For dwelling types, the variation across built form is comparatively small, apart from a small sample of flats (n=2) where overheating durations are at least twice to four times the others. For the house types, the variations do not entirely reflect that expected from the differences in exposed outside walls. Mid-terrace houses, with the least exposed area have, as might be expected, the highest degree of overheating in as far as bedrooms are concerned. However, semi-detached houses, which would have been expected to have similar characteristics to end-terraces, are much warmer in bedrooms, but similar in living rooms; and end-terraces have the lowest values of all, at 25% of the semi-detached values. For dwelling age analysis, the most obvious group suffering from comparatively higher levels of overheating are those built between 1981 and 1990, where bedrooms exhibit twice the overheating as the next highest group and where living rooms are also significantly affected. The new-builds have highest level of overheating in living rooms.

The results of the insulation analysis show the insulated dwellings experience overheating approximately twice as frequently as those without; more dwellings with a percentage of occupied hours above comfort temperatures by the adaptive method (Figure 1). The analysis also considered whether the insulation was included in the house as-built or was the subject of a subsequent improvement, either before or after 2008 (pre-2008 insulation standards were lower). Again, dwellings with the highest standard of insulation installed as part of the build, post-2008, were assessed as experiencing the highest level of overheating and those with no

insulation as the lowest. The results of the analysis by UK region show little connection between the relative warmth of the 2013 summer and that of the 20-year average, since the dwellings in Wales, where 55.8% higher CDDs were experienced, were almost entirely devoid of overheating and the highest degree of overheating was experienced in London where the actual CDD showed little difference from the 20-year average.

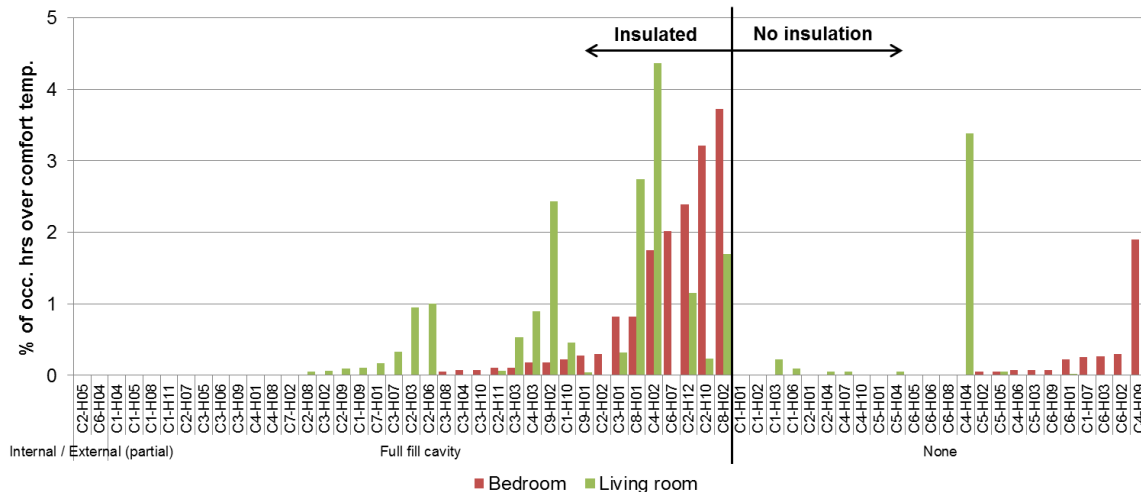


Figure 1. Percentage of hours over comfort temperature (EN BS 15251) by wall insulation. *Note: dwellings are ordered by lowest to highest percentage for bedrooms in each category.*

DISCUSSION

Of the 63 dwellings, only two were found to have bedrooms not exceeding the recommended temperature of 26°C and 17 (27%) were found to have bedrooms exceeded 30°C. Conversely, only three (4.7%) of the living rooms exceeded 30°C, and 22 (34%) had temperatures less than 26°C. In addition, considerably higher temperatures were found in bedrooms than in living rooms. There are wide variations in temperatures between bedrooms and living rooms even in the same dwelling. Overall, it was found that about 74% (42) of bedrooms had higher maximum temperatures than the living room, with this variation being about 1.5°C, whilst, across the remaining 26% (15), the difference was about 0.5°C. It is considered that the higher bedroom temperatures are attributable to the greater exposure to solar irradiance than living rooms since these are largely located at ground floor level rather than bedrooms which are located on the first floor. Given these findings it is important to consider for new-build and retrofit opportunities that bedrooms are equipped to adaptively cool the space, e.g. daytime shading devices designed for seasonal use.

Dwellings with insulated walls appear more prone to overheating than those without, particularly those built to the most modern specifications. However, it would appear that this tendency is moderated in high thermal mass dwellings such as C7-H01 and C7-H02. The coupling of high thermal mass and progressive insulation standards would benefit from further research as a potential solution to this apparent problem which is projected to be more problematic as the climate changes.

The adaptive method assessed far fewer rooms in the dwellings as overheating compared with the fixed temperature criteria of the static method. It could be argued from these results that the adaptive method adjusts better to changes in external temperature since it will adjust the assessment of overheating to correspond to the occupants' perception. However, it is important to note that the adaptive method was designed within the non-domestic context and

would benefit from a domestic counterpart as there is currently no dynamic overheating assessment method designed specifically for UK dwellings.

A *domestic* overheating method will need to be tested in all dwellings types, forms and ages since it is likely that any methods used to assess overheating will, in the future, be incorporated into UK government policy and, hence regulations affecting the design of and provision of cooling systems in, social housing, the efficacy of such methods are economically significant. If the required method over-estimates overheating and causes excessive rates of cooling system installation, this will lead to increase in initial building costs and, once such equipment is installed, it will inevitably be used, resulting in increased energy use (and costs) for cooling. If overheating is simultaneously associated with high levels of insulation, then this may lead to a reduction in insulation levels, resulting in excessive energy use for space heating. Conversely, if the method employed underestimates the extent of overheating, this is likely to result in higher levels of health problems, particularly for the elderly, with consequent cost increases for the health services, as well as the distress for the occupants.

CONCLUSION

This study, based on data collected during the summer of 2013 in nine different locations across the UK assessed the prevalence of summertime overheating in bedrooms and living rooms in existing, retrofitted and new-build dwellings. The overheating levels in the dwellings, which were all deemed to be ‘free-running’, i.e. unheated during the period, were assessed using both static and adaptive thermal comfort criteria. Examined from the point of view of the occupants’ health, the significance of the accurate assessment of overheating in dwellings is fairly obvious. However, its significance for the policy and practice of designing new, low-energy homes and energy-efficiency retrofit measures is more subtle. Inaccurate assessment of overheating may leave occupants with houses that are uninhabitable during the hotter days of the year, if underestimated, but if overestimated may cause the installation of many unnecessary air-conditioning units. Moreover, if the causes of overheating were to be wrongly attributed, for example, to high levels of insulation, then many opportunities for energy saving in the heating season might be lost through under-insulation. This is particularly relevant for UK social housing where standards are more rigorously applied.

REFERENCES

- Beizaee, A., Lomas, K. J., & Firth, S. K. 2013. National survey of summertime temperatures and overheating risk in English homes. *Building and Environment*, 65(0), pp. 1-17.
- BSI. 2008. BS EN 15251:2007 Indoor environmental input parameters for design and assessment of energy performance of buildings addressing indoor air quality, thermal environment, lighting and acoustics.
- CIBSE. 2006. *Environmental Design Guide A*. London, UK
- CIBSE. 2013. *TM52 The limits of thermal comfort: avoiding overheating in European buildings*: CIBSE.
- DCLG. 2006. *Code for Sustainable Homes : A step-change in sustainable home building practice*. London: Communities and Local Government Publications, Retrieved from http://www.planningportal.gov.uk/uploads/code_for_sust_homes.pdf.
- Gupta, R., & Gregg, M. 2017. Care provision fit for a warming climate. *Architectural Science Review*, 60(4), pp. 275-285.
- Lomas, K. J., & Kane, T. 2013. Summertime temperatures and thermal comfort in UK homes. *Building Research & Information*, 41(3), pp. 259-280.

Indoor air quality and thermal comfort for elderly residents in Houston TX—a case study

Amir Baniassadi^{1*}, David J Sailor², Cassandra R. Olenick³

¹ School of Sustainable Engineering and the Built Environment, Arizona State University, Tempe, Arizona

² School of Geographical Sciences and Urban Planning, Arizona State University, Tempe, Arizona

³ National Center for Atmospheric Research, Boulder, Colorado

*Corresponding email: amir.baniassadi@asu.edu

ABSTRACT

The elderly population is more vulnerable to poor indoor environmental quality. They also spend a larger portion of their time indoors than the general public, further exacerbating the associated health risks. As part of a larger study which aims to understand the health risks for the elderly population resulting from extreme heat events in Houston, TX, this study gathered empirical data on thermal comfort and air quality in existing assisted living facilities and in individual homes of the elderly. We made continuous measurements of indoor dry-bulb temperature, relative humidity, carbon dioxide (CO₂) levels and occupancy status in 25 buildings during summer months in 2016 and 2017. Then, using the measured data, we calculated the percentage of hours in which the thermal discomfort index or CO₂ levels were above healthy thresholds for each site. Our results show that the indoor discomfort index and/or CO₂ level exceeded the safe thresholds for at least 5% of the time in two-thirds of the buildings tested. Considering that research suggests more extreme summer weather in this region in the future, the results of this study highlight the need to consider changes in building management and occupant behavior as well as targeted improvements in the building stock to minimise adverse health impacts. In addition, the results also highlight a potential trade-off between thermal comfort and air quality in these building; air-tightening of the buildings will result in better thermal comfort at the expense of higher CO₂ levels, especially in buildings with a higher number of occupants.

KEYWORDS

Indoor air quality; Carbon Dioxide; Thermal Comfort; Senior Living Facilities; Warm Humid Climates

INTRODUCTION

In the United States, the majority of people, especially older Americans, spend ~90% of their time indoors (Klepeis et al., 2001). As a result, there is a growing awareness that much of the exposure to unhealthy environmental conditions may occur indoors. For example, Chan et al. found that a healthy person in a poorly ventilated indoor environment was 3.8 times more likely to suffer from a heat-related condition compared to outdoors (Chan et al., 2001). Sensitivity to heat and air pollution is equally important. Older adults are more sensitive than the general population to heat because the ability to regulate body temperature and physiologically adapt to the heat lessens with age (Kim et al., 2012; Luber and McGeehin, 2008). Likewise, older adults may experience more adverse health effects than the general population to air pollution as respiratory function declines with age (Wang et al., 2010). For

example, exposure to moderate to high levels of carbon dioxide (CO₂), with its well-documented negative impacts on cognitive function (Allen et al., 2016; Satish et al., 2012), may be more detrimental to the elderly than other age groups. Therefore, considering the population ageing in the U.S (Wiener and Tilly, 2002), there is a growing interest in understanding the indoor environmental quality to which the elderly are exposed. Hence, this study focuses on indoor CO₂ levels and thermal comfort in a sample of buildings with elderly occupants in Houston, TX, the largest city in Texas and the fourth largest city in the United States. We performed continuous measurements of CO₂, dry-bulb temperature, and relative humidity in a sample of homes over summer months of 2016, and 2017. Post-processing the data and interpreting it using applicable metrics revealed a general picture of the indoor environment in the sample homes.

METHODS

Measuring indoor environment variables

We had ongoing measurements of CO₂, dry-bulb temperature, relative humidity, and occupancy status in a sample of 25 buildings during summers of 2016 (6 buildings) and 2017 (19 buildings). These buildings were either individual homes, or small assisted living facilities and were selected to represent different locations and income levels. In each building, a set of two to four HOBO MX1102 loggers (Figure 1) were installed at various locations to record environmental parameters. The measured variables were recorded in at least two rooms (namely, a bedroom and the living room) in each building. We made regular visits to each site to calibrate CO₂ sensors to outdoor conditions (~400 ppm). As demonstrated in Figure 1, to the extent possible, we tried to avoid placing sensors near non-human sources of CO₂ (e.g., plants) or heat sources (e.g., electric appliances). Occupancy status was recorded via HOBO UX90-005 Occupancy/Light Data Loggers and was used to filter out the unoccupied hours during which no exposure took place.

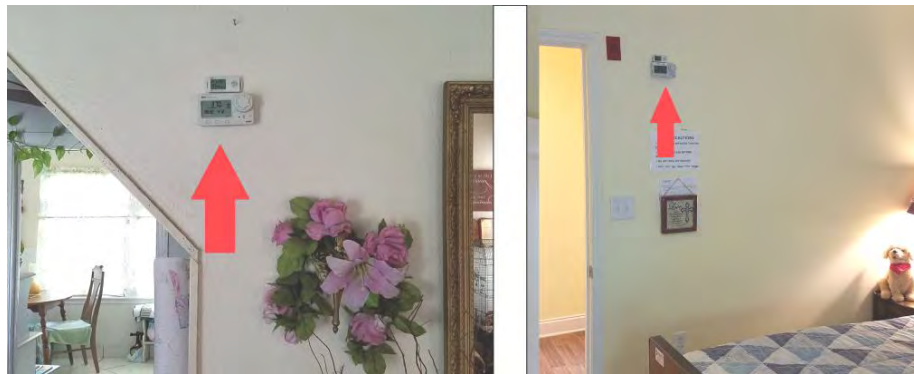


Figure 1. Sensor installation in sample buildings. Photo credit: Peter Chen, Houston Health Department

Post-processing the data

To better represent the data from long-term measurements, we calculated metrics for each site based on available thresholds. While there are numerous studies, guidelines, and thresholds for assessing indoor thermal comfort, most of them are not applicable for our purpose. The reason is that the zone of homeothermy (within which body can maintain constant core temperatures) is broader than the zone of thermal comfort (within which individuals report satisfaction with the thermal environment (Bianca, 1968). From the limited available guidance

for generating suitable metrics of indoor overheating in residential settings, we selected the Discomfort Index (DI), the average of dry-bulb and wet-bulb temperatures. The DI metric has been suggested as a potential surrogate for overheating by Epstein and Moran (2006), and Holmes et al. (2016). We used the following equation to calculate the wet-bulb temperature which is needed to derive DI (Stull, 2011):

$$T_{wb} = T_a \operatorname{atan}[0.151977 (RH\% + 18.313659)^{1/2}] + \operatorname{atan}(T_a + RH\%) - \operatorname{atan}(RH\% - 1.676331) + 0.00391838(RH\%)^{3/2} \operatorname{atan}(0.023101RH\%) - 4.686035 \quad (1)$$

Here, T_{wb} is the wet-bulb temperature ($^{\circ}\text{C}$), T_a is the dry-bulb temperature ($^{\circ}\text{C}$), and RH is the relative humidity. Regarding the overheating threshold, we assumed a DI index of 24°C , over which “the heat load is moderately heavy and individuals would feel very hot” (Epstein and Moran, 2006). At two extremes of relative humidity, a DI of 24°C is associated with dry-bulb temperatures of 36.5°C (at $\text{RH}=0\%$) and 24°C (at $\text{RH}=100\%$), exceeding almost all thermal comfort thresholds commonly used. This shows that a DI threshold of 24°C is considered as an upper limit for the zone of homeothermy instead of the zone of thermal comfort. For CO_2 levels, we considered a threshold of 1200 ppm. According to Allen et al. (2016) the decline in cognitive ability (even under typical activity levels) is easily observed above this threshold. It should be mentioned that for both parameters, the thresholds we selected are reported for the general public. The fact that elderly are more vulnerable to heat and CO_2 will make the results presented here conservative.

RESULTS

We calculated the total number of hours that DI or CO_2 were above the defined thresholds. An important consideration is that we did not have sensors logging data at all sites simultaneously. However, since all measurements took place over summer months (for at least one month in each location), the general outdoor conditions were similar enough that a side by side comparison of all buildings is still valid. Figure 2 shows the percentage of hours above thresholds for both DI and CO_2 for all 25 buildings.

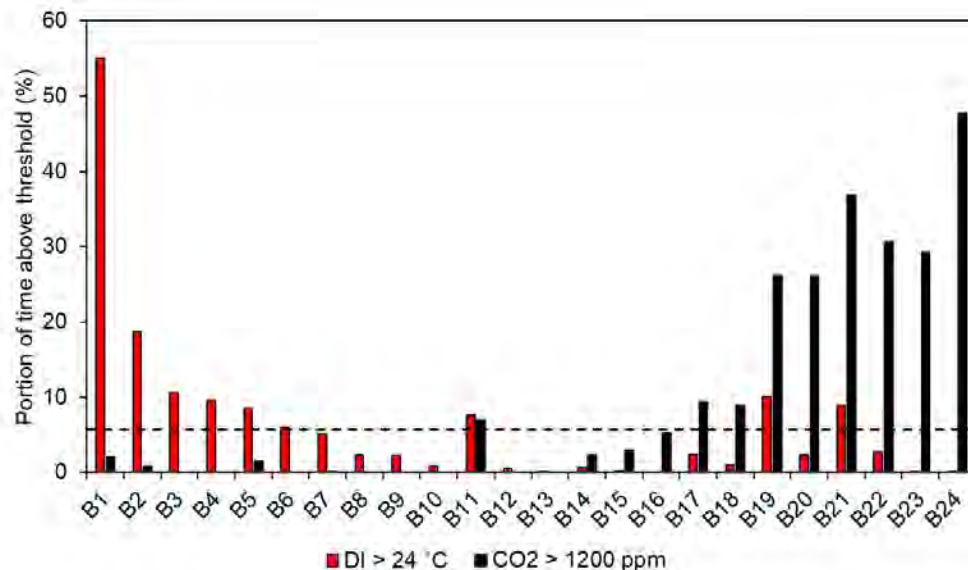


Figure 2. Summertime DI and CO_2 levels inside sample buildings. Data from authors' measurements over the summer months of 2016 and 2017. Dotted, horizontal line indicates that safe thresholds were exceeded 5% of the time.

According to the Chartered Institute of Building Service Engineers (McLeod et al., 2013), buildings are considered to experience long-term overheating if they exceed the safe thresholds for more than 5% of the time. As the data suggests, DI and/or CO₂ exceed the safe thresholds for more than 5% of the recorded period in 15 out of the 25 buildings. Notably, in this graph, an inverse relationship is observable between high CO₂ levels and overheating. Generally, homes with high DI values seem to have low CO₂ levels and vice versa.

DISCUSSION

The results presented here highlight the fact that a considerable portion (almost a third) of the sample buildings of elderly residents in Houston, TX are overheating during summer months. Considering the health implications of heat, especially for the elderly, as well as the predicted warming in Houston due to local (urban heat island effect) or global (climate change) signals (Georgescu et al., 2014), the observed conditions could be regarded as a significant public health issue. Notably, all these buildings had air conditioning. According to the U.S. Census Bureau, more than 99% percent of buildings constructed over the last three decades in the southern U.S. were equipped with AC. Hence, our sample represents the general building stock of the region with respect to AC prevalence. However, existence of AC equipment does not guarantee its effective operation. For example, building #1, the building with most overheated hours in our sample, had AC. However, based on our post-measurement surveys, the AC system was not functioning well, and the residents do not have the financial resources to properly maintain or repair it. In addition to this, the loss of power during outages is another mechanism that can lead to severe overheating. Hurricane Harvey, which happened during our measurement campaign, caused at least 5 of our sample buildings to lose power. While in this instance, the relatively low outdoor temperatures during and subsequent to Hurricane Harvey (a maximum outdoor temperature of 24 °C), as well as completely overcast skies, helped maintain indoor conditions below overheat levels, the outcome could have been different if the power outage occurred under a different scenario. A recent example of this happened during Hurricane Irma in Florida where 8 senior citizens died in a nursing home because of the resulting power outage and AC loss (Reisner et al., 2017). We believe that this is mostly due to the overdependence of the current building stock on AC technology. Lightweight construction with minimum regard for passive mitigation strategies lead to buildings that are highly vulnerable to extreme heat, power outages, and climate change (Baniassadi and Sailor, 2018; Nahlik et al., 2016; Sailor, 2014). The other important aspect, emphasized by the measurements, is the role of ventilation, namely, window-opening. As seen in Figure 2, there is an observable inverse relation between overheating and CO₂. In general, residents of buildings that have difficulty maintaining thermal comfort, would resort to ventilation by opening the windows. However, while this mitigates indoor CO₂ levels which are largely controlled indoor sources, it can increase exposure to outdoor pollutants such as ozone, its secondary bi-products, and particulate matter. Therefore, not having proper running AC not only leads to overheating, but can also indirectly increase exposure to outdoor pollutants. On the other hand, more air-tight buildings in our study with functioning AC, exhibited consistently comfortable indoor thermal conditions, but in some instances experienced high CO₂ levels. Building number 24 is an extreme example of this. This building was a senior living facility with 10 elderly residents and full-time staff. This led to very high CO₂ levels as the managing personnel did not operate the windows. Notably, this building was categorized as a facility whose residents are cognitively impaired (e.g., diagnosed with Dementia-Related Disorders).

CONCLUSIONS

In this study, we used long term measurements of CO₂ levels and thermal comfort conditions in 25 buildings with elderly residents in Houston, TX. Our post-processing of the measured data showed that at least a two-thirds of sample buildings exceeded the CO₂ threshold of 1200 ppm or were overheated for at least 5% of the measurement period. These results suggest that many elderly citizens, in particular, those with limited financial resources, are exposed to indoor environments that potentially adversely affect their health and well-being. In addition, the observed inverse relation between overheating and high CO₂ levels suggests that window opening is a strategy consistently used by occupants in overheated homes. While this helps curb indoor CO₂ levels, it exposes occupants to more outdoor pollutants. Considering predictions that suggest a more extreme climate in Houston in the coming decades, and a building stock that is highly dependent on AC, the situation is likely to worsen. Future research should focus on developing easy-to-implement and market-ready building construction and operation strategies to reduce the dependency of buildings on AC and increase indoor air quality.

ACKNOWLEDGEMENT

This research was supported in part by Assistance Agreement No. 83575401 awarded by the U.S. Environmental Protection Agency. It has not been formally reviewed by the EPA. The views expressed in this document are solely those of the authors and do not necessarily reflect those of the Agency. EPA does not endorse any products or commercial services mentioned in this publication.

In addition, the authors would like to thank Mr. Peter Chen and Mr. Youjun Qin from Houston Health Department for their help in installing and calibrating sensors during summer 2017.

REFERENCES

- Allen, J.G., MacNaughton, P., Satish, U., Santanam, S., Vallarino, J., Spengler, J.D., 2016. Associations of cognitive function scores with carbon dioxide, ventilation, and volatile organic compound exposures in office workers: a controlled exposure study of green and conventional office environments. *Environmental health perspectives* 124, 805.
- Baniassadi, A., Sailor, D.J., 2018. Synergies and trade-offs between energy efficiency and resiliency to extreme heat—A case study. *Building and Environment*.
- Bianca, W., 1968. Thermoregulation. *Adaptation of Domestic Animals*. Lea & Febiger, Philadelphia, USA, 97-118.
- Chan, N.Y., Stacey, M.T., Smith, A.E., Ebi, K.L., Wilson, T.F., 2001. An empirical mechanistic framework for heat-related illness. *Climate Research* 16, 133-143.
- Epstein, Y., Moran, D.S., 2006. Thermal comfort and the heat stress indices. *Industrial health* 44, 388-398.
- Georgescu, M., Morefield, P.E., Bierwagen, B.G., Weaver, C.P., 2014. Urban adaptation can roll back warming of emerging megapolitan regions. *Proceedings of the National Academy of Sciences* 111, 2909-2914.
- Holmes, S.H., Phillips, T., Wilson, A., 2016. Overheating and passive habitability: indoor health and heat indices. *Building Research & Information* 44, 1-19.
- Kim, Y.-M., Kim, S., Cheong, H.-K., Ahn, B., Choi, K., 2012. Effects of heat wave on body temperature and blood pressure in the poor and elderly. *Environmental health and toxicology* 27.

- Klepeis, N.E., Nelson, W.C., Ott, W.R., Robinson, J.P., Tsang, A.M., Switzer, P., Behar, J.V., Hern, S.C., Engelmann, W.H., 2001. The National Human Activity Pattern Survey (NHAPS): a resource for assessing exposure to environmental pollutants. *Journal of exposure analysis and environmental epidemiology* 11.
- Luber, G., McGeehin, M., 2008. Climate change and extreme heat events. *American journal of preventive medicine* 35, 429-435.
- McLeod, R.S., Hopfe, C.J., Kwan, A., 2013. An investigation into future performance and overheating risks in Passivhaus dwellings. *Building and Environment* 70, 189-209.
- Nahlik, M.J., Chester, M.V., Pincetl, S.S., Eisenman, D., Sivaraman, D., English, P., 2016. Building Thermal Performance, Extreme Heat, and Climate Change. *Journal of Infrastructure Systems*, 04016043.
- Reisner, N., Fink, S., Yee, V., 2017. Eight Dead From Sweltering Nursing Home as Florida Struggles After Irma, *The New York Times*.
- Sailor, D.J., 2014. Risks of summertime extreme thermal conditions in buildings as a result of climate change and exacerbation of urban heat islands. *Building and Environment* 78, 81-88.
- Satish, U., Mendell, M.J., Shekhar, K., Hotchi, T., Sullivan, D., Streufert, S., Fisk, W.J., 2012. Is CO₂ an indoor pollutant? Direct effects of low-to-moderate CO₂ concentrations on human decision-making performance. *Environmental health perspectives* 120, 1671.
- Stull, R., 2011. Wet-bulb temperature from relative humidity and air temperature. *Journal of applied meteorology and climatology* 50, 2267-2269.
- Wang, L., Green, F.H., Smiley-Jewell, S.M., Pinkerton, K.E., 2010. Susceptibility of the aging lung to environmental injury, *Seminars in respiratory and critical care medicine*. NIH Public Access, p. 539.
- Wiener, J.M., Tilly, J., 2002. Population ageing in the United States of America: implications for public programmes. *International journal of epidemiology* 31, 776-781.

Method for Detecting Contaminant Transport through Leakages in a Condemned School

Fredrik Domhagen*, Paula Wahlgren¹ and Carl-Eric Hagentoft¹

¹Chalmers University of Technology, Sweden

*Corresponding email: fredrik.domhagen@chalmers.se

ABSTRACT

Many schools in Sweden, have problems with the indoor air, affecting the wellbeing and health of both pupil and teachers. Contaminants in the air, such as mold spores, radon, odors, and VOC, cause problems and it can be difficult to find the contaminant source, in particular if it is within the building construction. The aim of this project is to investigate air leakage paths and pressure differences in a school building with IAQ problems and to analyze how these parameters are related to contaminant transport. An increased knowledge of how contaminants are transported will then form the base for an improved strategy for dealing with renovations of schools with IAQ issues. The main method of investigation in this initial part of the project is blower door measurements and leakage paths detection. A method to use CO₂ from dry ice as tracer gas for leakage detection is under development and tested in a condemned school building. Results presented in this paper show that it is possible to use this method to determine whether air leakages are coming from the crawlspace or from elsewhere.

KEYWORDS

air infiltration, tracer gas, air leakage detection, dry ice, contaminant transport

INTRODUCTION

There are several types of contaminants in indoor air, such as mold spores, radon, VOC (volatile organic compounds) and odors. The sources for these contaminants are both located in the rooms, in the building envelope and outdoor. The contaminants sometimes result from excessive moisture levels in the building envelope, which can cause increased emissions and mold growth. There are several studies showing possible contaminant sources that are connected to the building envelope and to moisture (for example Bornehag, 2005; Täubel, 2011, Cai G-H et al, 2011). In an investigation covering 220 schools and pre-schools, Hilling (1998) found that there are large deficiencies in maintenance, moisture safety, building airtightness and air treatment in Swedish schools.

The current work focus on the contaminant transport by air that moves through leakages in the thermal envelope. This requires a pressure difference (by wind, stack effect or ventilation) and a leakage path. Commonly, the pressure distribution is such that air infiltrates from a crawlspace, to the indoor air, bringing contaminants. The pressure at ceiling level often cause moist air to infiltrate attics, causing mold problems. However, in 10 % of the time, the pressure difference is adverse, such that mold contaminated attic air infiltrates into the indoor air (Sasic, 2007). The amount of air that passes through the building envelope and the origin of the air entering the building depends on the overall airtightness of the building and on the leakage path distribution (Sikander et al. 2009). The contaminant transport in the current work is investigated by numerical simulations, by tracer gas measurements (CO₂) and by measuring pressure distributions in a school building. Both field measurements and laboratory measurements have been performed to develop the measurement equipment and procedure.

METHODS

There are several ways to detect leakages in buildings, for example tracer gas, smoke, thermography (in combination with pressure differences), acoustic methods etc. However, in this work thermography in combination with CO₂ as a tracer gas is used. CO₂ is present in the atmosphere (at levels of approximately 400 ppm) and is produced in the building by occupants, from gas cylinders or from sublimation of dry ice.

CO₂ is chosen for several reasons, it does not easily react with other gases and it mixes well with air since its density is of similar order of magnitude as for air (slightly higher). CO₂ meters to use for measuring the CO₂ concentrations are easily found on the market and are often cheaper compared to other gas meters. CO₂ can be purchased as dry ice (CO₂-ice) which is used in the following experiments. Dry ice sublimates (in atmospheric pressure) at a temperature of -78.5 °C and has therefore to be handled with care in order to prevent frost damage.

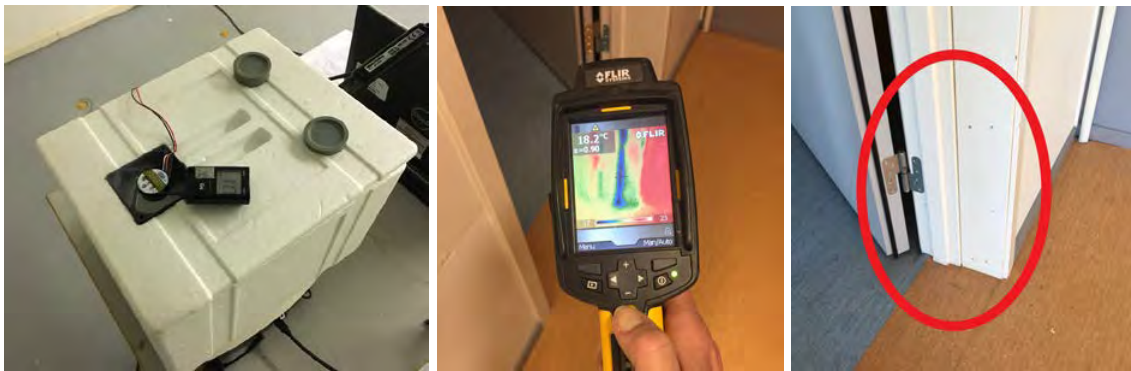


Figure 1. To the left: Icebox with dry ice, fan and heater. In the middle: Thermographic image of leakage at location L4. To the right: Image of leakage at location L4.

In this project, dry ice is used in an attempt to design a test methodology that is easy to use and inexpensive. The dry ice is placed in an insulated box, called icebox see Figure 1, with a fan to produce a steady air flow and on a scale to determine production rate. An electric heater is covered by the ice inside the box in order to increase the rate of sublimation. The advantages of dry ice compared to a gas bottle is that a higher production rate is achievable, a bottle can produce about 0.5 g/s (Konder 2008). The icebox used in this paper has a production rate of about 0.7 g/s, something which can be increased by using a higher power output on the heater. Initial tests are performed in laboratory to study production rates and distribution of CO₂ in a room. Laboratory tests of the ice box showed some stratification of the CO₂ in the room, which is why the icebox is complemented with two desktop fans, placed at some distance from the icebox, with the purpose of improve the mixing of air and CO₂ to prevent stratification. Other ways of dispersing CO₂ as dry ice were tested to estimate the sublimation rate, ease of use and repeatability. Spreading out 0.5 kg dry ice on the floor in a room with an air temperature of 20 °C had an average sublimation rate of 0.7 g/s. Interestingly, using a fan to blow air over the ice decreased the sublimation rate to 0.4 g/s. The reason to this is thought to be that more water condensates on the dry ice and works as thermal insulation. Submerging dry ice in boiling water had the highest average sublimation rate, 3.0 g/s. However, this method was the most inconvenient. If room tempered water was used, ice formed around the dry ice which stopped the sublimation. Field tests are performed in a school building in order to study real leakage paths. The principle of the field tests is to introduce CO₂ to one volume of the test building and measure change in CO₂ concentrations in adjacent volumes, in most cases in combination with applied pressures.

Field measurements

The method is tested in a condemned school with IAQ problems. The school is situated in Gothenburg, on the west coast of Sweden, and has gone through a number of renovations in an attempt to improve the IAQ but none have been successful and the school now awaits deconstruction. The school has a crawlspace and after investigations it was concluded that the main problem originated from the crawl space and that emissions from wood preservatives is a contaminant source. Measures that has been taken to improve the IAQ is constructing ventilated floors on top of the original floor, exhaust ventilation in the crawlspace that draws air out from the crawlspace causing a negative pressure, and installing an air cleaning system. The ventilated floor is ventilated through small ducts exhausting air at roof level. Additional ventilation systems have also been installed in addition to the original ventilation system.

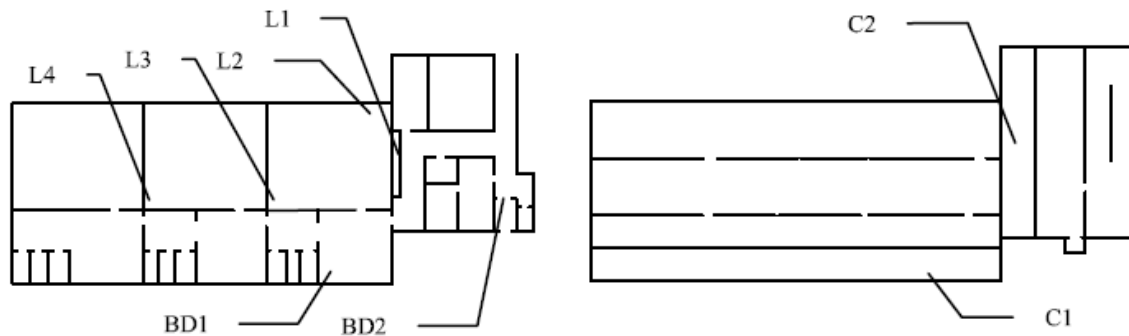


Figure 2. The figure to the left shows the floor plan with locations of CO₂ meters (L) and locations of blower door (BD1 and BD2). The figure to the right shows the crawlspace together with locations of the icebox and CO₂ meters (C1 and C2).

CO₂ meters are placed at positions L1 to L4, see Figure 2. L1 is inside a cupboard (with open doors) that contains electrical wiring from the crawlspace. L2 is close to the corner between an interior wall and the exterior wall. L3 is located by a crack in an internal wall-to-floor connection in the corner of one of the classrooms. L4 is beside one of the interior door-frames that has large cracks in the door framing.

The test procedure to detect leakages consisted of releasing CO₂ in the crawl space and detecting it at leakage positions (L1 to L4) in the classrooms. Different pressure situations were investigated (each during approximately one hour), but during the tests the crawlspace had a higher pressure than the classrooms. Pressures differences were created using blower door equipment placed either in a hatch between the indoor and the crawlspace (BD1), referred to as Case 1, or in an exterior door (BD2), referred to as Case 2. To ensure that there was an over pressure in the crawlspace, the pressure difference was measured and the fan speed of the blower door adjusted accordingly. The CO₂ was released at two different locations in the crawlspace and measured at 1-2 locations in the crawlspace, and 3-4 locations in the class rooms next to leakage positions. Leakages were found both in the middle of the building, where all incoming air is from the crawlspace, and close to external wall where some of the incoming air is outdoor air. An initial scan of leakage points was made by ocular inspection and thermography. Thermography reveals the leakage positions but not if the air is clean air from the outside or contaminated air from the crawlspace. The measurements were made during wintertime so the temperature of the crawlspace was approximately 8 °C, outdoor temperature 0 °C and the indoor temperature 20 °C.

The aim of the field measurement was to investigate **a.** the influence of the location of the CO₂ source (icebox) on the CO₂ distribution in the building, **b.** the effect of different locations of the blower door, **c.** how the pressure difference across the floor construction affects the CO₂ concentration at the leakage positions.

RESULTS OF THE FIELD INVESTIGATION

Two cases are investigated, Case 1 when the blower door is placed in the hatch down to the crawlspace (BD1, Figure 2) and Case 2 when the blower door is situated in an exterior door (BD2, Figure 2). The principle airflow paths for each case are illustrated in Figure 3.

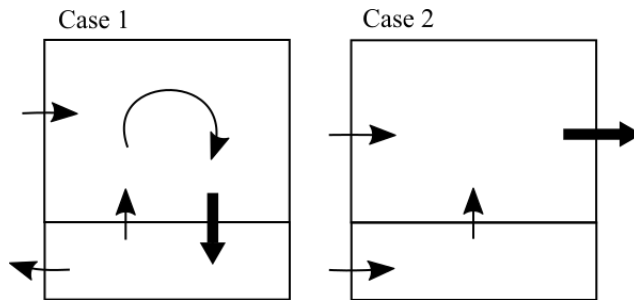


Figure 3. Shows the principle airflow paths dependent on the location of the blower door (thick arrow) where the lower rectangle represents the crawlspace and the upper rectangle represents the classrooms.

Figure 4 shows measured CO₂ concentrations for Case 1. Note that at the end of the measurement period the CO₂ meter is moved from position L3 to position L4. The results show that the concentration levels at L1 and L4 are affected by leaking air from the crawlspace (to a high degree in the cupboard at L1) whereas no significant change in concentration can be seen at L2 and L3. In Case 1 the pressure difference over the floor construction was about 35 Pa throughout the entire measurement period.

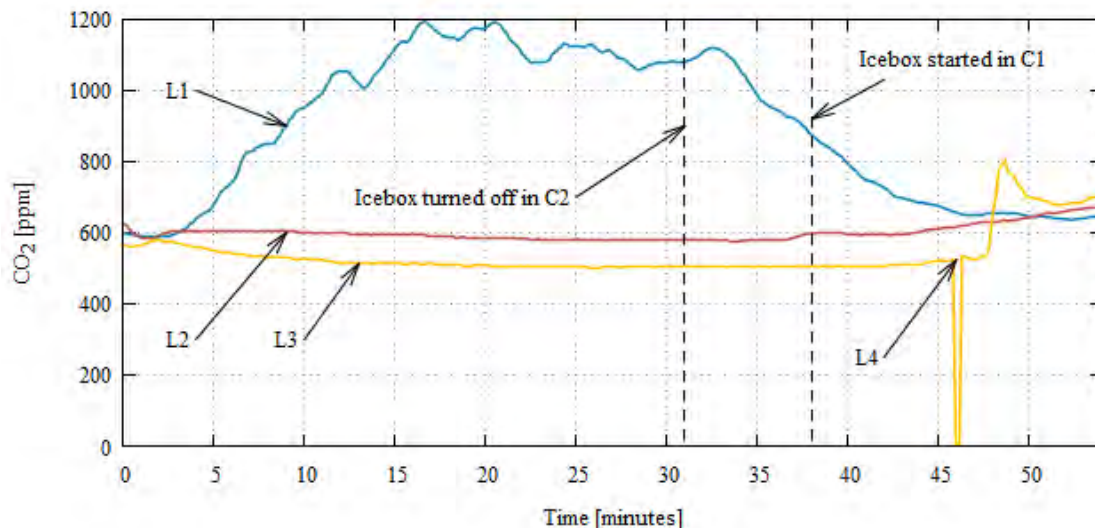


Figure 4. CO₂ concentrations measured at different locations in Case 1 (blower door in crawlspace hatch). New location for one meter at 46 minutes (from L3 to L4).

Figure 5 shows measured CO₂ concentrations for Case 2. After 21 minutes the pressure difference across the floor construction was changed from 5.7 Pa to 4.4 Pa (by decreasing the blower door fan speed), which resulted in an increase in CO₂ concentration in L1 from 1500 ppm to 2300 ppm. Concentration levels at L1 are affected by leaking air from the crawlspace, similar to Case 1. However, L2 is reaching higher concentration levels than in Case 1. One possible explanation could be that the air leakage path inside the construction is affected by the relations in pressure between indoor, crawlspace and outdoor, which will be further investigated. Measurements also showed that CO₂ concentrations were higher when the icebox was placed in the air volume directly beneath the cupboard with L1, i.e. in location C2 compared to location C1 further away.

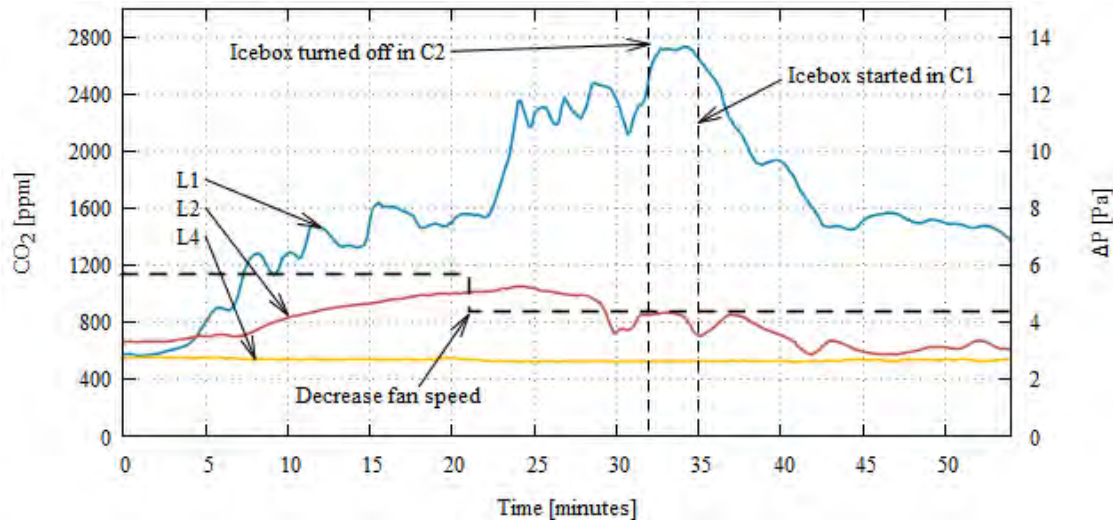


Figure 5. CO₂ concentrations measured at different locations together with the pressure difference over the floor construction in Case 2 (blower door in exterior door frame).

Different pressure differences across the floor construction will result in different CO₂ concentrations in the classrooms. A higher fan speed will then result in higher air flow rate upward through the floor but also to an under pressure in the classrooms and more outdoor air entering the building which dilutes the CO₂ concentration. It may therefore be difficult to anticipate if it is better to have a high or low pressure difference over the floor construction in order to maximize the concentrations levels at the measurement points. However, in this study it became clear that a lower pressure difference gave higher CO₂ concentrations in Case 2 with pressure difference of approximately 5 Pa (Figure 5) compared to Case 1, pressure difference 35 Pa (Figure 4). The outcome of these effects has also been confirmed in numerical simulations.

When investigating the correlation between changes such as CO₂ production, icebox location and pressure difference, the delay in response in the CO₂ concentrations at the different leakage points is a few minutes, typically three minutes. This corresponds to a leakage path of 10 m in length, 5 mm in height and at a pressure difference of 5 Pa. If the height is decreased to 4 and 3 mm, the time increases to 4 and 8 minutes respectively. This effect will be further studied in future measurements.

The method for detecting air leakages will be improved with the goal of making quantification of leakages possible. This could be done by creating a steady CO₂ production

and measure the change of the mean concentration in the air volumes inside a building. Methods of dispersing CO₂ will also be investigated to make leakage detection more efficient.

CONCLUSIONS

Tracer gas measurements, using CO₂ from dry ice is used in combination with forced pressure differences in order to investigate contaminant transport in a school building. The measurements showed that:

- For the investigated cases, a lower pressure difference over the floor construction (with overpressure in the crawlspace) results in higher concentrations at measurement locations. The reason is that the crawlspace becomes less ventilated when the pressure difference is lower and therefore the leaking air has a higher concentration of CO₂.
- It is possible, with the described icebox method, to determine if the leaking air is coming from the crawlspace or from elsewhere. This method is cheaper and simpler compared to conventional tracer gas methods.

Suggested procedure for detecting air leakages from a crawlspace to the indoor environment

1. Use blower door to either pressurize the crawlspace or depressurize the indoor space.
2. Performing a leakage search to find leakages in the construction. This can for instance be done using a thermal camera.
3. Measure CO₂ background concentration prior to starting the CO₂ production in the crawlspace.
4. Add CO₂ to the crawlspace, for instance by using the icebox method presented earlier in this paper.
5. Measure CO₂ concentration at locations that in step 1 proved to have air leakage.
6. Locations with CO₂ levels high above CO₂ background concentrations will have air coming from the crawl space.

Each test step is preferably performed until steady-state conditions are reached, and at least for 15 minutes.

ACKNOWLEDGEMENT

The research is financed by Formas, the Swedish research council for sustainable development.

REFERENCES

- Bornehag C-G., Lundgren B., Weschler C. J., Sigsgaard T., Hagerhed-Engman L., Sundell J., 2005. Phthalates in Indoor Dust and Their Association with Building Characteristics, *Environmental Health Perspectives*, Vol. 113, No. 10.
- Cai G-H., Mälarstig B., Kumlin A., Johansson I., Janson C., Norbäck D., 2011. Fungal DNA and pet allergen levels in Swedish day care centers and associations with building characteristics, *Journal of Environmental Monitoring*, 13.
- Hilling R. [Swedish] 220 skolor: skador och fel i skolbyggnader, SP Rapport 1998:34
- Konder H., Bednar T., 2008. Estimation of air flow rates in large buildings based on measurements, *Building Physics 2008 – 8th Symposium*.
- Sasic, A., 2007. Simulations as the way of bridging the gaps between desired and actual hygrothermal performance of buildings. In *IBPSA 2007-International Building Performance Simulation Association 2007* (pp. 1712-1719).
- Sikander E., Wahlgren P., Åhman P., 2009. [Swedish] Lufttätetens kontroll - tidig läckagesökning, *Sveriges Byggindustrier FoU-Väst*.

The impact of physical environments in satisfaction in shopping centers

Rui Dang^{1,2}, Lai Wei^{1,2}, Ye Yuan^{1,2} and Gang Liu^{1,2*}

¹School of Architecture, Tianjin University, Tianjin, China

²Tianjin Key Laboratory of Architectural Physics and Environmental Technology, Tianjin, China

*Corresponding email: lglgmike@163.com

ABSTRACT

Lighting, thermal and acoustic are three main components of indoor physical environments affecting people's satisfaction, productivity and health. Good physical environments in shopping centers not only improve the environment atmosphere but also increase the customers' satisfaction. This study aims to find correlations between the physical environments and the satisfaction levels. Firstly, an objective measurement of physical environments had been carried out in four shopping centers. Then, a subjective evaluation was carried out in a real scene laboratory by changing four kinds of illuminance and three types of Correlated Color Temperatures (CCTs), which aims to find the relationship between the lighting environment and people's lighting, thermal and acoustic satisfaction. Moreover, the interaction of satisfaction levels were also explored. The results of field study showed that lighting and acoustic environments have a wide fluctuate range in four shopping centers. The experiment found that illuminance has a significant effect on lighting satisfaction and is best at 1000 lux (lx). The thermal and acoustic satisfaction were not directly influenced by lighting parameters; however, they had the interactions with lighting satisfaction, which showed that lighting environment would enhance the satisfaction levels of thermal and acoustic environments when it was satisfied.

KEYWORDS

Shopping centers; Physical environments; Satisfaction level; Interaction

INTRODUCTION

With the improvement of people's demand for shopping, indoor environment quality (IEQ) is more and more important for shopping centers. As a part of the indoor environment, physical environments- lighting, thermal and acoustic- greatly affect consumers' satisfaction levels (Zhao et al. 2015; Jin et al. 2017).

For satisfaction evaluations, several studies have attempted to find the relationship among lighting, thermal and acoustic environments. Huebner et al. (2016) confirmed that CCT can affect people's thermal comfort. Ma and Nie (2014) found improving lighting environment quality reduced the noise annoyance and increased the acoustic comfort. Geng et al. (2017) indicated that when the thermal environment was satisfying, it raised the "comfort expectation" of lighting and acoustic factors. Above studies showed that physical environments will strengthen or weaken each other. However, most of the studies focused on residential, office, campus buildings, etc. (Ma and Nie, 2014; Geng et al. 2017; Ricciardi and Buratti, 2017), and seldom refers to shopping centers. Therefore, it's necessary to explore the physical environment satisfaction for shopping centers.

As for the research method, field study is frequently used in shopping centers (Zhao et al. 2015; Jin et al. 2017). Through field study, physical environments can be measured accurately, however, satisfaction levels of customers are usually influenced by many nonphysical factors like spatial and social parameters (Meng et al. 2013), which influenced

the accuracy of physical environment evaluation. Therefore, a new method should be provided to improve the evaluation accuracy.

In summary, this study combined the methods of field measurement and experimental evaluation, aiming to quantitatively and accurately reveal the correlations between indoor physical environment and satisfaction in shopping centers. In addition, the interactions among different factors were explored. And the research results can be utilized to improve the physical environment and consumers' satisfactory in shopping centers.

METHODS

Field measurement

Field measurement were conducted in four shopping centers in winter and summer of 2017, and the buildings' information was shown in Table 1. The field measurement parameters included the illuminance, CCT, air temperature and sound pressure level. Testing time were selected in business hours (10:00 AM to 10:00 PM) and the test information was shown in Table 2.

Table 1. Information of the four shopping centers.

Shopping Center	Built year	Total area (thousand m ²)	Total numbers of floor
H-S	2016	125	5
F-S	2016	92	6
S-S	2011	150	6
D-S	2014	113	7

Table 2. Test information.

Indoor environment	Parameter	Measurement instrument	Measuring range/ accuracy
Lighting	Illuminance	CL-500A	0.1-100,000 lx / $\pm 2\%$
	CCT	CL-500A	>5 lx / -
Thermal	Temperature	TSI model 9545	-10-60°C / $\pm 0.3^\circ\text{C}$
Acoustic	Sound pressure level	Nor140	15-140 dB A / -

Experimental evaluation

Overview of experiment

In order to find the correlations between physical environments and their satisfaction levels, a series of experiments were carried out in a laboratory with variable space and environment during January 2018 at Tianjin University (see Fig. 1 a)). A typical clothing store (see Fig. 1 b)) was simulated by an actual space, which total area was 48 m² and 4 meters high. During the experiments, illuminance and CCT were set as the variables and other physical parameters were the control variables. The range of illuminance and CCT were respectively 200 lx, 500 lx, 1000 lx, 1500 lx and 3000 Kelvin (K), 4500 K, 6000 K, and the air temperature and sound pressure level were set to 23°C and 75 dB A, which based on the previous field measurement in four shopping centers.

Participant and questionnaire

A total of 27 students from Tianjin University took part in the experiment and Table 3 shows the information of participants. To ensure the experimental results not affected by other factors, participants were instructed to wear the same type of clothing for each test. The information of the questionnaire consisted the satisfaction of lighting, thermal and acoustic environments. Satisfaction votes were used the ASHRAE (2013) 7-point scale as follows: strongly dissatisfied (-3), dissatisfied (-2), slightly dissatisfied (-1), neutral (0), slightly satisfied (1), satisfied (2), and strongly satisfied (3).

Table 3. The information of participants (mean value \pm standard deviation).

Gender	Sample size	Age(y)	Height(cm)	Weight(kg)
Male	13	21.2 \pm 3.26	177.2 \pm 4.54	67.7 \pm 7.35
Female	14	20.2 \pm 3.38	162.2 \pm 7.53	53.4 \pm 6.50
Total	27	20.7 \pm 3.29	169.4 \pm 9.78	60.3 \pm 9.97

Experimental procedure

The satisfaction experiment lasted three weeks and the time was from 19:30 to 21:30 each day. Twelve types of lighting environments were selected in the experiment, and each environment condition lasted 20 minutes, including 9 minutes' adaptation time and 11 minutes' testing time (see Fig. 1 b) and c)). In adaptation time, participants were required to sit in a preparation room (500 lx; 4000 K) whose overall environment was constant. Meanwhile, the illuminance and CCT of the clothing store were changed through the controllable lighting system. In testing time, participants were asked to move around in the clothing store, and the first 10 minutes were utilized to experience the shopping environment and the last 1 minute to fill in the evaluation questionnaire. The experimental procedure for each day was shown in Fig. 1 d).

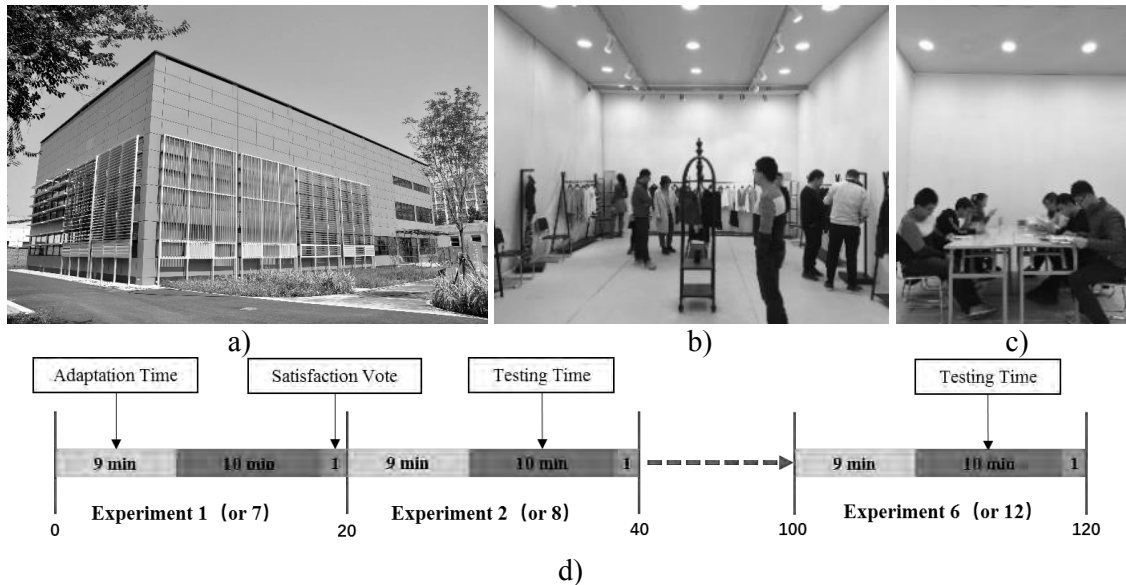


Figure 1. a) Variable space and environment laboratory, b) Testing time, c) Adaptation time, d) Experimental procedure.

RESULTS AND DISCUSSIONS

Objective environmental measurement

Fig. 2 shows the objective measurement results of illuminance, CCT, air temperature and sound pressure level of the 4 shopping centers. For lighting parameters, building H-S has the largest illuminance fluctuation between 431.8 lx and 2512.4 lx, and the average illuminance of the other three is between 224.9 lx to 1587.5 lx, which is mostly controlled above the lower limit of illuminance (300 lx) in Chinese standard GB50034 (2014) (see Fig. 2 a)). The result of CCT shows that building D-S has the largest fluctuation between 2828 K and 6398 K, and others are concentrated between 3000 K and 4000 K (see Fig. 2 b)).

The air temperature was respectively measured in summer and winter (see Fig. 2 c)). Through the comparison of measured levels and the thermal comfort standard GB50736 (2012) in

China, it is found that all shopping centers have a qualification rate above 70%, respectively H-S (72%), F-S (84%), S-S (91%), D-S (96%). In terms of indoor acoustic environment, S-S building has the smallest fluctuation between 68 dB(A) and 77 dB(A), while others stay at a high level and mostly fluctuate between 65 dB(A) and 85 dB(A) (see Fig. 2 d). Through further analysis, the high noise level is mainly due to the background music and personal talking.

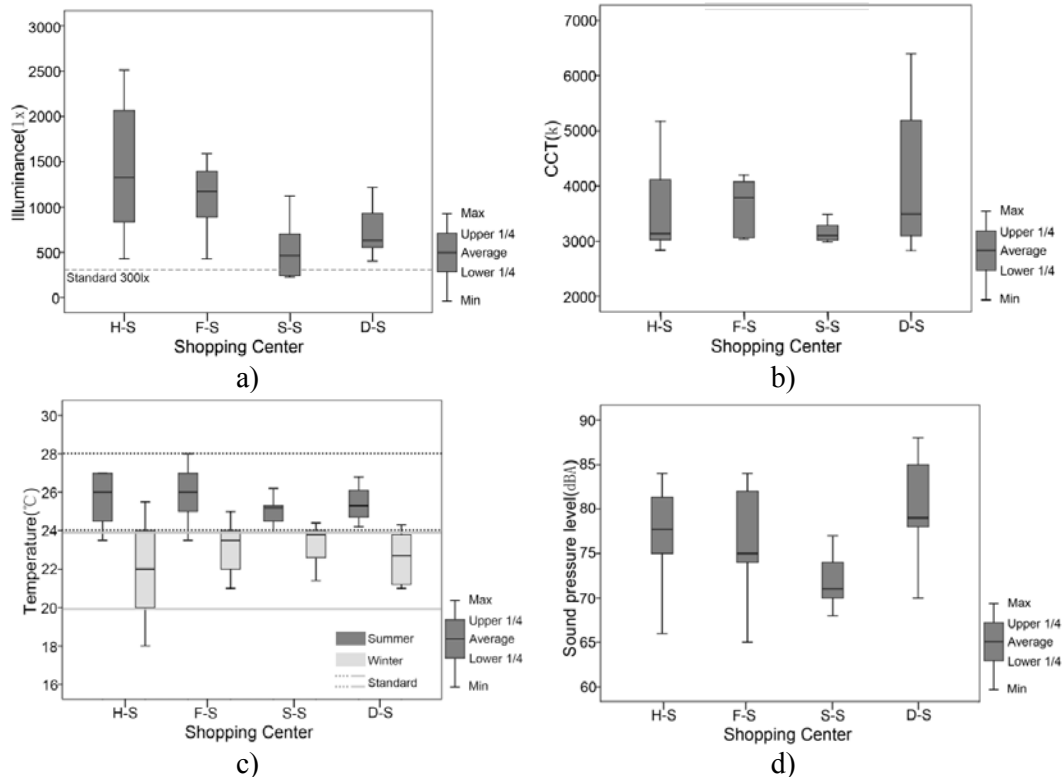


Figure 2. Objective measurements of indoor a) Illuminance, b) CCT, c) Temperature, d) Sound pressure level.

The impact of lighting parameters to satisfaction

The correlation analysis between lighting environment (illuminance, CCT) and people's satisfaction of lighting, thermal and acoustic environments is shown in Table 4. The correlation R value between illuminance and lighting satisfaction ranges from 0.532 to 0.648 ($p < 0.01$), while the correlation R value between CCT and lighting satisfaction ranges from 0.204 to 0.292 ($p < 0.01$ or $p < 0.05$) in two illuminance environments (200 lx, 500 lx). However, there is no significant difference in the correlation of thermal and acoustic satisfaction with lighting environment (illuminance, CCT).

Fig. 3 shows the relationship between the illuminance parameter and satisfaction level in three different CCT environments. Each point represents the mean value of the satisfaction level in the same illuminance and CCT environment. When the satisfaction level is larger than 0, it indicates that subjects are satisfied with the environment. Fig. 3 a) shows subjects are satisfied when the illuminance isn't lower than 500 lx, and the highest evaluation level occurs when the illuminance is 1000 lx and CCT is 4500 K. Moreover, between 200 lx and 1000 lx, participants feel more satisfied under the light of 6000 K and 4500 K than 3000 K. These result shows that Kruthof's rule (1941) of lighting comfort maybe not applied to the lighting environment preference for Chinese consumers. Fig. 3 b) and c) show that both thermal and

acoustic evaluation are satisfied and have small fluctuations in different lighting environments. The range of thermal satisfaction is from 0.39 to 0.87, and the acoustic satisfaction is from 0.69 to 1.13.

Table 4. Relationships between Lighting parameters and evaluation of satisfaction.

Lighting parameters	Conditions	Lighting	Thermal	Acoustic
Illuminance	3000 K	0.648**	0.003	-0.072
	4500 K	0.606**	-0.070	-0.103
	6000 K	0.532**	0.042	0.044
CCT	200 lx	0.292**	-0.044	-0.045
	500 lx	0.204*	0.045	-0.132
	1000 lx	0.146	-0.102	0.019
	1500 lx	-0.164	0.124	0.045

* $p < 0.05$; ** $p < 0.01$

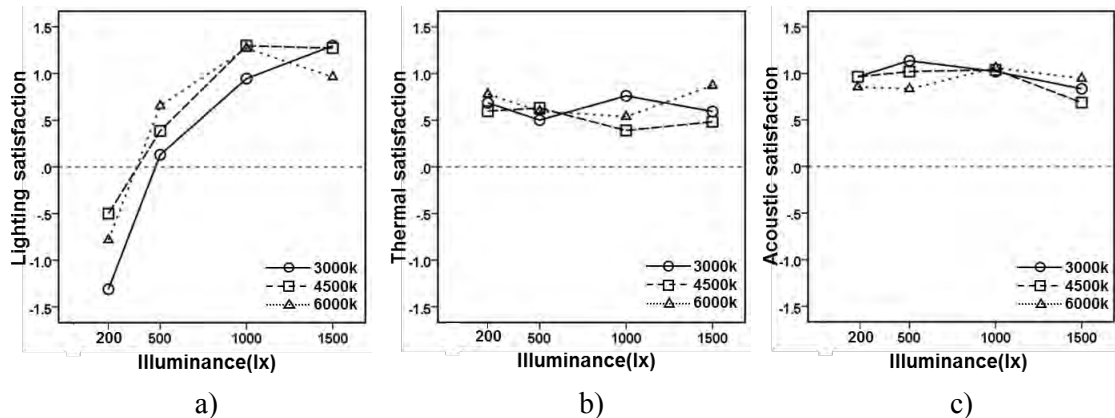


Figure 3. Relationships between illuminance and a) Lighting satisfaction, b) Thermal satisfaction, c) Acoustic satisfaction.

The interaction of satisfaction level

Pearson correlation between lighting evaluation and satisfaction of thermal and acoustic environments is shown to be significant ($p < 0.01$), and the correlation coefficient R is 0.250 and 0.219 respectively. Fig. 4 shows the voting results of thermal and acoustic environment at different lighting satisfaction level. When the lighting evaluation changing from “dissatisfied” to “satisfied”, the dissatisfaction rate of thermal and acoustic is reduced by 34.47% and 17.74% respectively. The result shows that good lighting satisfaction can raise people’s evaluation of thermal and acoustic environment in shopping centers.

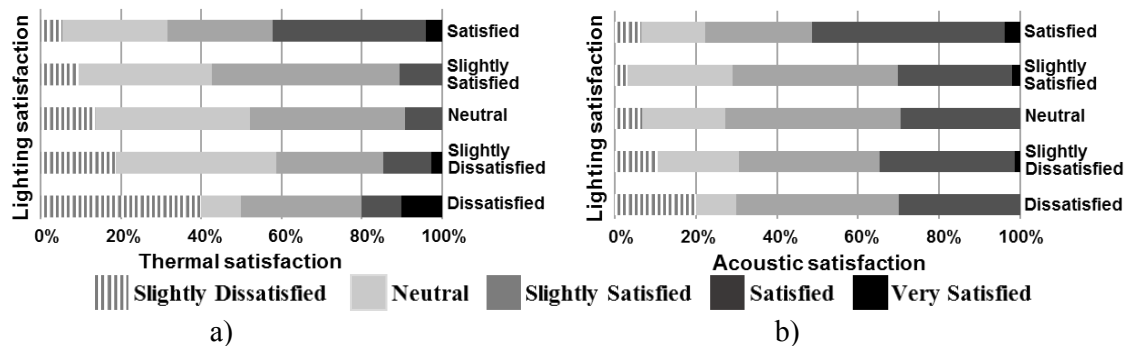


Figure 4. Satisfaction votes of a) thermal environment, b) acoustic environment under different lighting satisfaction votes.

CONCLUSIONS

On-site measurement shows that the range of illuminance was mostly from 500 lx to 1500 lx and the CCT was from 3000 K to 4000 K, the temperature qualification rate above 70% and the range of sound pressure level mainly from 65 dB A to 85 dB A. Satisfaction level experiment found the highest level of lighting satisfaction occurred when the illuminance was 1000 lx. From 200 lx to 1000 lx, subjects prefer the lighting environment with middle and high CCT. Moreover, the thermal and acoustic satisfaction were not directly influenced by lighting parameters; however, they had the interactions with lighting satisfaction, which showed that lighting environment would enhance the satisfaction levels of thermal and acoustic environments when it was satisfied.

ACKNOWLEDGEMENT

The authors disclosed receipt of the following financial support for the research, authorship, and/or publication of this article: This work was funded by National Key Research and Development Program (2016YFC0700200), National Natural Science Fund of China (51338006).

REFERENCES

- ASHRAE. 2013. *ANSI/ASHRAE Standard 55-2013*, Thermal Environmental Conditions for Human Occupancy. Atlanta: American Society of Heating, Refrigerating, and Air-Conditioning Engineers, Inc.
- GB. 2012. *GB50736-2012*, Design code for heating ventilation and air conditioning of civil buildings. China Academy of Building Research etc. (in Chinese)
- GB. 2014. *GB50034-2013*, Standard for lighting design of buildings. China Academy of Building Research etc. (in Chinese)
- Geng, Y., Ji, W., Lin, B., and Zhu, Y. 2017. The impact of thermal environment on occupant ieq perception and productivity. *Building & Environment*.
- Huebner, G. M., Shipworth, D. T., Gauthier, S., Witzel, C., Raynham, P., and Chan, W. 2016. Saving energy with light? experimental studies assessing the impact of colour temperature on thermal comfort. *Energy Research & Social Science*, 15, 45-57.
- Jin, H., Li, X., Kang, J., and Kong, Z. 2017. An evaluation of the lighting environment in the public space of shopping centres. *Building & Environment*, 115, 228-235.
- Kruithof, A. A. 1941. Tubular iluminescence lamps for general illumination. *Philips Tech. Review*, 6.
- Ma, H., and Nie, W. 2014. Influence of visual factors on noise annoyance evaluation caused by road traffic noise in indoor environment.
- Meng, Q., & Kang, J. 2013. Influence of social and behavioural characteristics of users on their evaluation of subjective loudness and acoustic comfort in shopping malls. *Plos One*, 8(1), e54497.
- Meng, Q., Kang, J., & Jin, H. 2013. Field study on the influence of spatial and environmental characteristics on the evaluation of subjective loudness and acoustic comfort in underground shopping streets. *Applied Acoustics*, 74(8), 1001-1009.
- Ricciardi, P., and Buratti, C. 2017. Environmental quality of university classrooms: subjective and objective evaluation of the thermal, acoustic and lighting comfort conditions. *Building & Environment*.
- Zhao, M., Kim, Y. S., and Srebric, J. 2015. Occupant perceptions and a health outcome in retail stores. *Building & Environment*, 93, 385-394.

A novel methodology to spatially evaluate DGP classes by means of vertical illuminances. Preliminary results.

Luigi Giovannini^{1,*}, Fabio Favoino², Valerio R.M. Lo Verso¹, Anna Pellegrino¹ and Valentina Serra¹

¹Politecnico di Torino, Italy

²Eckersley O'Callaghan Ltd., United Kingdom

*Corresponding email: luigi.giovannini@polito.it

ABSTRACT

A novel methodology to overcome the main limit of the Daylight Glare Probability DGP (i.e. the heavy computational time for an annual analysis of the DGP profile in one point) is presented. This uses a proxy based on the vertical illuminance (E_v) at the eye level. To do so, the most suitable value of E_v , to substitute DGP, is found by means of a comparison to the corresponding DGP value through a fault-detection diagnosis technique.

The methodology was applied to a representative enclosed office with one South-facing window (Window-to-Wall Ratio of 50%) located in Turin. The glazing was assumed to have different transmission properties (specular and scattering) with different visible transmittances (in the range 3%-66%). The error in the estimation of the DGP classes calculated through the eye vertical illuminance was evaluated, for an analysis period of a whole year.

The main advantages of the methodology proposed lie (i) in a significant reduction of the computational time required for its application and (ii) in the possibility of evaluating glare conditions not only for one or few points, but for a grid of points across a considered space. Its main limitation lies on its inability to quantify the exact DGP value, returning instead, at every time-step, the DGP class of performance.

KEYWORDS

Daylight simulation; Daylight Glare; DGP spatial resolution.

INTRODUCTION

Glare sensation is one of the most important aspects to control when dealing with visual comfort related to daylight. Daylight Glare can be caused either by a too high solar radiation in the occupants' visual field or by the presence of objects whose luminance is considerably higher than the background average luminance. Currently, the most widespread and validated metric to numerically assess daylight glare condition is the Daylight Glare Probability (DGP) (Wienold and Christoffersen, 2006), which expresses the percentage of people dissatisfied with the visual environment. The DGP is view-dependant, which means that its validity applies only to a specific point in the space and to a specific direction of observation. Moreover, due to its calculation algorithm, evaluating DGP on a yearly basis requires a heavy and time-consuming computation (Carlucci et al., 2015).

An attempt to simplify the DGP algorithm was made by Wienold (2007) to reduce the computation time required, by devising a simplified algorithm accounting for vertical illuminance (E_v) hitting the eye only. This metric, called DGPs (simplified DGP) showed a strong correlation to DGP for situations in which no direct sunlight hits the eye only, making thus its application unsuitable for a wide range of situations.

Kleindienst and Andersen (2012) developed a different simplified algorithm to evaluate DGP, the DGPm: this considers the apertures (windows, skylights, etc...) as the only luminance

sources in the scene, not accounting thus for the light reflected by internal surfaces. Despite its advantages (a more efficient computation algorithm than DGP, a better correlation to DGP than DGPs, possibility of a spatial glare evaluation), the application of DGPm remained limited as it was implemented on a non Radiance-based simulation software only. Another attempt to simplify the evaluation of DGP was made by Torres and Lo Verso (2015): they correlated the DGP to the cylindrical illuminance in the same point. Even though they obtained a good correlation to DGP, their approach is limited to the specific calculation point. In this framework, the paper presents a novel methodology to assess DGP by means of a proxy based on vertical illuminance values measured at eye level only. Such a methodology is able to significantly reduce the computation time, as the annual DGP profile for one point only needs to be calculated. Moreover, it allows the glare sensation to be assessed not only for a point in the space, but for the whole space analysed.

STEP-BY STEP DESCRIPTION OF THE NOVEL METHODOLOGY

The novel methodology proposed is presented for a representative case-study, which is an enclosed office located in Turin (45.06°N, 7.68°E), 3.6 m large, 4.5 m deep and 2.7 m high. A 3.3 m large and 1.5 m high window (Window-to-Wall Ratio = 50%) is located in one of the short walls, oriented South. The window was assumed to be alternatively equipped with 13 different glazing types, each with a specific transmission property (specular or scattering) and different visible transmittance (T_{vis}). The glazing features are summarised in Table 1.

Table 1. Glazing types considered in the study.

	Scattering glazing					Specular glazing								
$T_{vis, diffuse}$	12%	15%	23%	34%	45%	$T_{vis, specular}$	3%	12%	15%	23%	34%	45%	55%	66%

Three points in the office were identified to be representative of the different glare conditions occurring in the different parts of the room. They are all located 1.2 m above the floor, i.e. the height of the eyes of a seated person. For all the points, the observation direction was assumed perpendicular to the window, so as to evaluate the worst-case scenario (see Fig. 1).

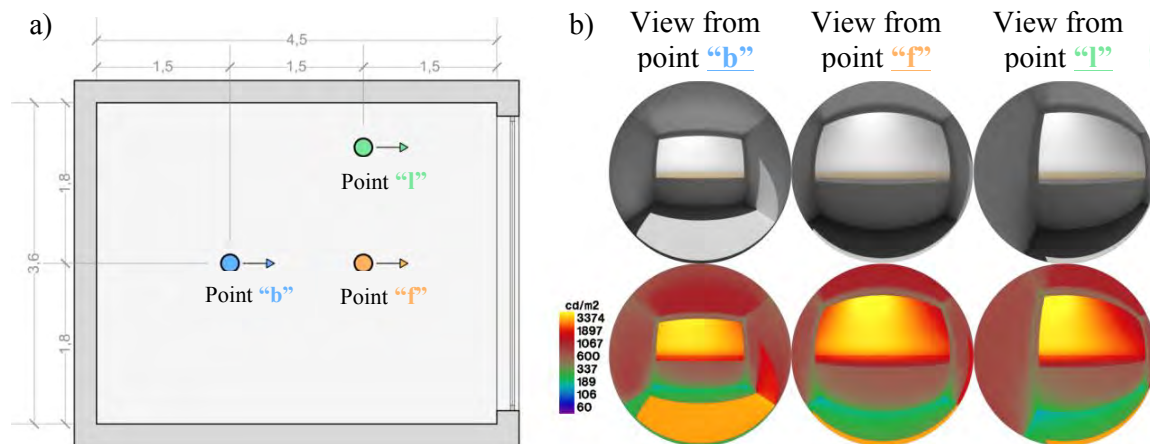


Figure 1. a) office plan with the locations and observation directions of the three points selected, b) example images and luminance images illustrating the view from each point.

For each point, DGP and E_v values at eyes were calculated through DAYSIM simulations during the course of a year (time-step: 1 hour) whenever daylight was present (night hours were not considered). This operation was repeated for each glazing type. As a result, an

annual database for each glazing type was built, containing a pair of values for each time-step: a DGP value and an E_v value. The procedure is then structured in three steps.

Step 1. The goal of this phase was to define the most suitable E_v values to be used as threshold for each DGP comfort class, defined by Wienold (2009). Table 2 summarises the DGP classes with the relative DGP thresholds (DGP_{thr}).

Table 2. Daylight glare comfort classes with relative DGP threshold values.

Daylight glare comfort class	DGP thresholds
Imperceptible	$DGP < 35\%$
Perceptible	$35\% \leq DGP < 40\%$
Disturbing	$40\% \leq DGP < 45\%$
Intolerable	$DGP \geq 45\%$

Practically speaking, E_v and DGP were compared for each time-step as metrics to identify a glare/non glare condition, using the DGP thresholds as validation reference. For each DGP threshold (DGP_{thr}), the optimal E_v threshold ($E_{v,thr}$) was found by means of a fault-detection diagnosis technique. Four sceneries were possible:

- True Positive (TP): a condition in which $E_v > E_{v,thr}$ is associated to $DGP > DGP_{thr}$
- True Negative (TN): a condition in which $E_v < E_{v,thr}$ is associated $DGP < DGP_{thr}$
- False Positive (FP): a condition in which $E_v > E_{v,thr}$ associated to $DGP < DGP_{thr}$
- False Negative (FN): a condition in which $E_v < E_{v,thr}$ is associated to $DGP > DGP_{thr}$.

The fault-detection diagnosis technique was applied to every annual database previously determined (each relative to a specific glazing type and a single point). Being the *faults* represented by FP and FN cases, the E_v value minimising the FP+FN value was assumed as threshold for each DGP class. The result of this analysis was a triplet of $E_{v,thr}$ (one for each DGP_{thr}) for each of the three points in the space selected and for every glazing type. A total number of 39 $E_{v,thr}$ triplets was obtained in this phase.

Step 2. The calculation of the annual DGP for a single point in the room is a necessary assumption to reduce the computational time. Therefore, to be able to perform a simplified spatial evaluation of glare throughout the room, the $E_{v,thr}$ triplet for one point in the space was used as thresholds to assess glare for the other points. This needs to be repeated for each point of the room, i.e. applying its specific triplet of $E_{v,thr}$ as thresholds for all the other point. The goal of this phase is to determine the errors that are committed when applying this procedure. The error committed in the estimation of DGP was quantified again in terms of FP+FN. This was evaluated for every $E_{v,thr}$ and for every glazing type considered. Output of this phase are, for every glazing type, three triplets of errors for each point selected (one for DGP_{thr} of 35%, one for DGP_{thr} of 40% and one for DGP_{thr} of 45%).

Step 3. Aim of this phase is to identify the most suitable point in the space, among the three considered, to be used to determine the only annual DGP profile and hence the $E_{v,thr}$ values. To do so, for every point, the average error committed for all the glazing types was calculated for each DGP_{thr} . The optimal $E_{v,thr}$ triplet was eventually found to be the one minimising the average error committed.

RESULTS

The results of each of the three steps exposed above are shown in the following sub-sections.

Step 1. Figure 2 shows the results relative to Step 1, i.e. the $E_{v,thr}$ values obtained in correspondence of the DGP_{thr} values for every glazing type and for each of the three points in the room. As one could expect, the results show that the $E_{v,thr}$ values obtained for a DGP_{thr} of 35% are nearly always lower than the ones obtained for a DGP_{thr} of 40%, which are in turn lower than those obtained for a DGP_{thr} of 45%. It is also possible to observe a common trend for the three DGP_{thr} : $E_{v,thr}$ values tend to grow as T_{vis} increases, either for specular or scattering glazing types, up to a maximum T_{vis} value (which varies depending on the DGP_{thr} considered). Over this T_{vis} , the $E_{v,thr}$ values fluctuate around nearly the same value. For all the DGP_{thr} , a huge difference in the $E_{v,thr}$ values was observed for the three calculation points for lower T_{vis} values (considering the same glazing), while as T_{vis} grows, this difference becomes almost negligible. The error committed when assessing glare with the $E_{v,thr}$ values found, calculated as $FP+FN$, is in the range 0.33% - 7.24% for DGP_{thr} of 35%, 0.33% - 6.50% for DGP_{thr} of 40% and 0.29% - 5.01% for DGP_{thr} of 45%.

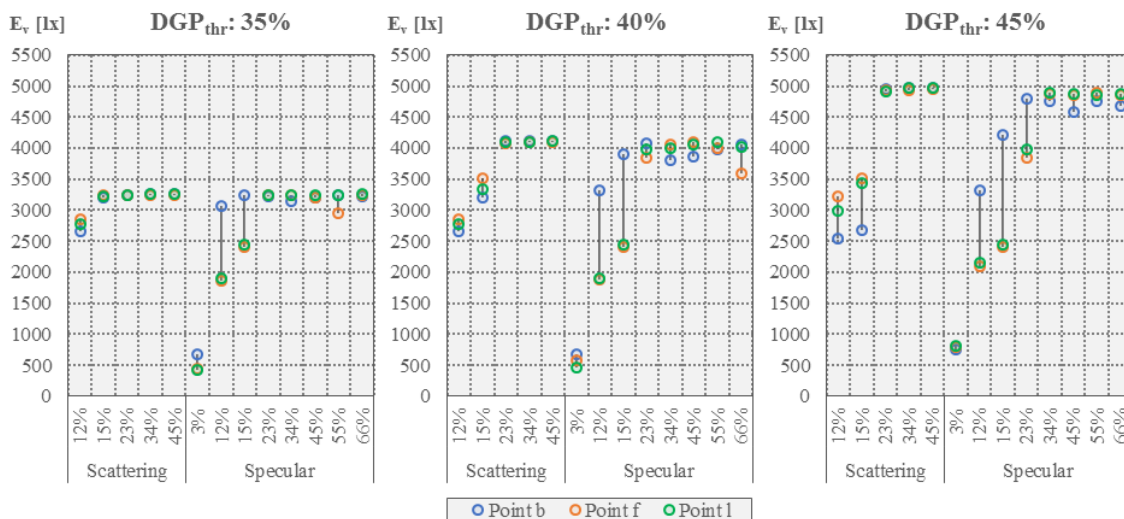


Figure 2. $E_{v,thr}$ values obtained, for every glazing type considered, for each DGP threshold

Step 2. Figure 3 shows the results relative to Step 2, i.e. the error committed when estimating the DGP class (error computed as $FP+FN$) by using the $E_{v,th}$ values found for a given point for all the three points. The results show that, for each DGP threshold and for every point, higher errors are committed for glazing, either specular or scattering, with lower T_{vis} . As T_{vis} grows, lower errors are committed. Analysing then the errors committed for the three calculation points, it is possible to observe that point b (located in the back part of the room) shows the most cases with higher errors. For most of the other cases instead, the errors obtained for the three points are similar.

Step 3. Figure 4 shows the average error committed for all the glazing types when estimating DGP by means of the $E_{v,thr}$ obtained for each of the 3 points in the room. For every DGP_{thr} , the results confirm that the average error committed when assessing glare by means of $E_{v,th}$ triplets relative to point b are higher than the ones relative to the other points. Similar average errors were instead obtained for point f and point l. In more detail, it is possible to observe that average errors committed for DGP_{thr} of 35% and 40% are lower for point l, while the average error relative to DGP_{thr} of 45% is lower for point f.

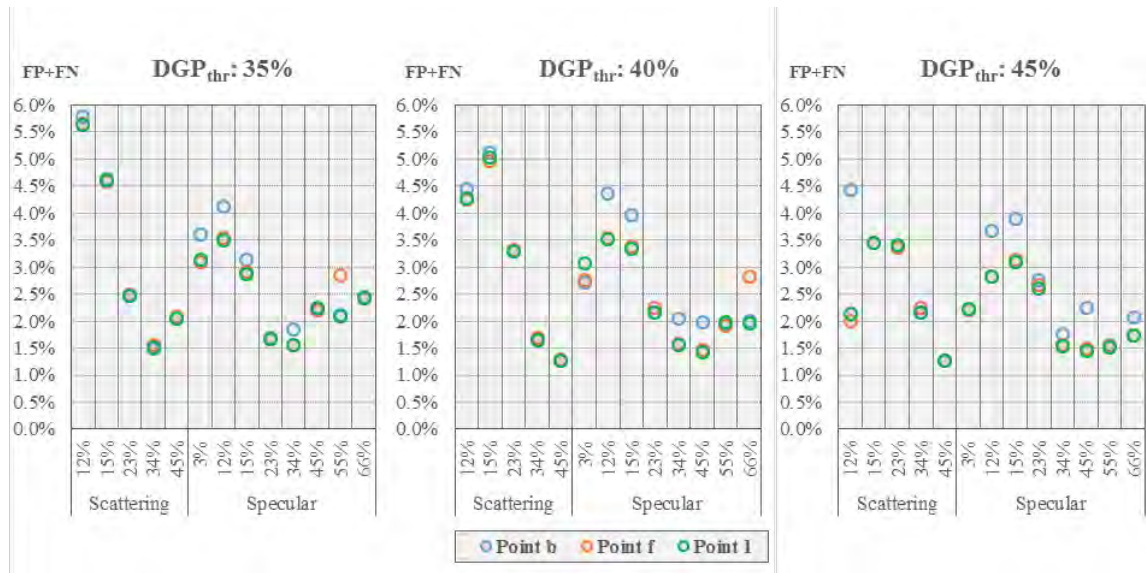


Figure 3. Error committed in the estimation of the DGP classes, for every glazing type, using the $E_{v,thr}$ values relative to each point in the room.

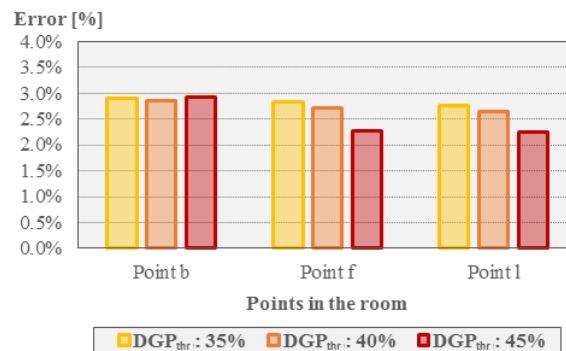


Figure 4. Average error committed, for every point, for each DGP_{thr} .

DISCUSSION

The novel methodology proposed allows the DGP to be assessed in a simplified way by means of a proxy based on vertical illuminance hitting the eye. Being a simplified methodology, it only allows the glare comfort class for DGP, and not the exact value, to be determined for a given E_v value.

Using a proxy based on vertical illuminance implies an average error in the estimation of the glare comfort class, which was quantified to be, for every DGP_{thr} , lower than 3% of the cases analysed. Such a value is considered acceptable by the Authors. The advantage of the present methodology lies in the reduction of the computation time necessary for the calculation of the annual DGP values in a grid of points across a space. In fact, the DGP for all the points in the space is assessed by means of one annual DGP computation for a single point in the room; for this point the triplet of $E_{v,thr}$ corresponding to the three DGP_{thr} is calculated and used to estimate DGP for all the space. As an example, for an office such as the case-study used in this study, the computation of spatial DGP for a grid of points with a mesh of 0.5m x 0.5m (48 points) would require a computational time 48 times higher than that necessary to apply the novel methodology presented. Assuming to use an i7 processor (8 cores), the evaluation of full DGP would require 12 hours, against the 15 minutes necessary for the proposed methodology. The difference in the computation time would of course even grow as the size of the room (and the number of calculation points) increases.

CONCLUSIONS

The paper presented a novel methodology for the estimation of DGP across a space by means of a proxy based on vertical illuminance hitting the eye appears. The methodology proved to be robust, with an average error committed below 3% for all the cases considered. Its main advantage consists in its ability to significantly reduce the computation time required for the calculation of DGP for a whole space. It may therefore be used to improve the visual comfort assessment, evaluating glare sensation not only for a few points in a space, which is currently the common practice, but for a grid of points across the whole space considered.

Future work consists in an extensive validation of the proposed methodology for different directions of observation, different geometrical features of the space analysed (depth, width, Window-to-Wall Ratio, etc...) and different orientations and climates.

ACKNOWLEDGEMENT

The authors would like to thank Eckersley O'Callaghan Ltd. and the Glass & Façade Technology Research Group (University of Cambridge) for their support in the present research. The authors would like to thank the COST Action TU1403 as well for providing financial support to allow the present research to be carried out.

REFERENCES

- Carlucci S., Causone F., De Rosa F. and Pagliano L. 2015. A review of indices for assessing visual comfort with a view to their use in optimization processes to support building integrated design. *Renewable and Sustainable Energy Reviews*, 47, 1016-1033.
- Kleindienst S. and Andersen M. 2012. Comprehensive annual daylight design through a goal-based approach. *Building Research and Information*, 40(2), 154-173.
- Torres S. and Lo Verso V. R. M. 2015. Comparative Analysis of Simplified Daylight Glare Methods and Proposal of a new Method Based on the Cylindrical Illuminance. *Energy Procedia*, 78, 699-704.
- Wienold J. and Christoffersen J. 2006. Evaluation methods and development of a new glare prediction model for daylight environments with the use of CCD cameras. *Energy and Buildings*, 38(3), 743-757.
- Wienold J. 2009. Dynamic daylight glare evaluation. In: *Proceedings of the 11th International IBPSA (International Building Performance Simulation Association) Conference – Building Simulation 2009*, Glasgow, Scotland, Vol. 11, pp. 944-951.
- Wienold J. 2007. Dynamic simulation of blind control strategies for visual comfort and energy balance analysis. In: *Proceedings of the 11th International IBPSA (International Building Performance Simulation Association) Conference – Building Simulation 2007*, Beijing, China, Vol. 10, pp. 1197-1204.

Comparative Study of Different Design Configurations Based on the Daylight and Visual Comfort Performance of Electrochromic Glass in a side-lit Office building

Amir Hosseinzadeh Zarrabi*, Mona Azarbayjani¹, Armin Amirazar¹, Roshanak Asharafi¹

KEYWORDS

Daylighting; Shading strategies; Workstation; Electrochromic Glass; office building; glare; Furniture layout; Daylight simulation

ABSTRACT

The objective of this research is to demonstrate the application of an optimization framework to assess and improve the impacts of workstation properties in relation to the performance of electrochromic glass regarding daylight and visual comfort. This framework is executed through a simulation-based parametric modeling workflow of an open-plan office to optimize partition layout, height, direction to windows, and materiality in response to annual glare probability (DGP) and climate-based daylighting metrics. In this paper, different office layouts equipped with Electrochromic glass, located in a mixed-humid climate has been simulated with DIVA plug-in for Rhinoceros/grasshopper software to maximize the daylight and reduce the visual discomfort.

The results of the optimization study show that the visual comfort and daylighting can be increased from 17 % to 36 UDI (100–2000 lx) while maintaining the percentage of occupied hours glare between 3.1 and 4.1. Considering these two aspects, the workstation with opaque 42” partition height in perimeter and 60” in Interior (“Pre 42_Int 60”) layout in 10° oriented towards the south perform the best with the Electrochromic user-based schedule.

INTRODUCTION

According to a broad range of studies, the quality of office environment is influenced by office layout, furnishing, and lighting quality (Kim & de Dear, 2013; Lee & Guerin, 2009). Although the previous studies believe that partitions in an open plan office spaces provide privacy for employees as the first objective in the design process, the robust role of partition layouts in the better distribution of daylight into the space and occupant visual comfort can not be undermined (Paper, Carolina, Modaresnezhad, & Nezamdoost, 2017). Lighting has a significant direct impact on office workspace, as the studies show daylight offices increase employees’ comfort, productivity, satisfaction, health, and well-being (Kelly, Painter, Mardaljevic, & Irvine, 2013). However, overlit spaces can cause glare and visual discomfort, especially with sunlight penetration when the amount of daylight is not sufficiently controlled. There are internal and external design strategies to control the daylight. The electrochromic glass as a dynamic shading device is used to both prevent and control undesirable daylight and solar radiation (Sbar, Podbelski, Yang, & Pease, 2012).

Recently, by allowing the occupants to control the stage of tinting in glazing through a timed override, the window can be darkened only when the occupants are exposed to excessive daylight and the presents of glare, otherwise, it permits daylight penetration in the space (Arnold, 2010). In this case, the attributions of occupant locations (office layout properties, partition’s height, materiality and direction to windows) become crucial to provide visual comfort (Modaresnezhad, M Nezamdoost, 2017). Nevertheless, daylight buildings are rarely studied in terms of the impact of interior design strategies on the user-based performance of electrochromic glass. This study outlines the daylight performance of workstation strategies based on the user- based control of electrochromic glass to 1. Maximize daylight illuminance while minimizing visual discomfort and 2. Find the optimum solution for the future office layout refurbishment.

METHOD

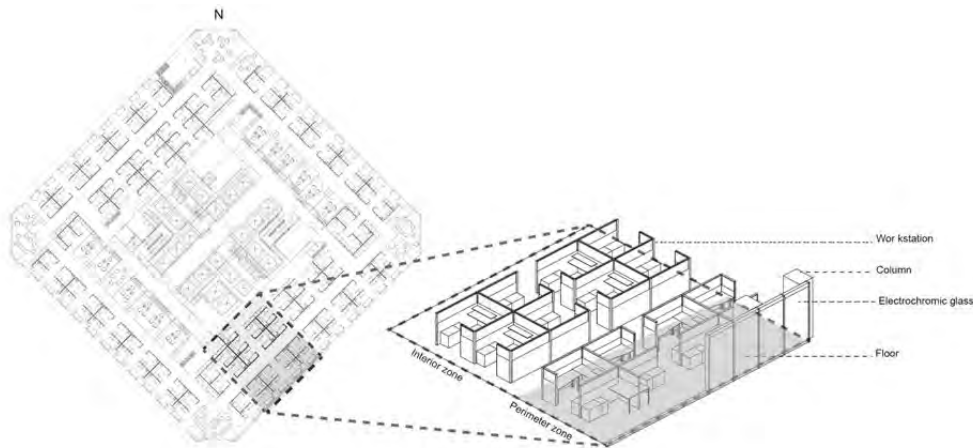
In order to study the daylight performance and visual comfort of multiple workstation designs scenarios, a simulation-based design workflow was developed in grasshopper. The workflow consists of modeling the existing workstation and the façade in an office building and analysing different scenarios of workstation attributions based on the annual climate-based daylight. In the optimization process, the occupant comfort feedback (levels of comfort) is used to find the optimum attributions of the workstation model that will provide the optimum daylight and visual comfort. An overview of each step is as follows:

1. Geometry Creation

Building the base case

For the purposes of this study, one section of an office building in warm and humid climate was modeled as illustrated in Figure 1. The office layout is divided into a core, interior (6 to 14m) and perimeter (1 am to 5 am) zones to represent the typical floor plan of high rise office building that is rotated 45° clockwise from the north axis. In order to examine daylighting and visual comfort of the occupants, the south-east orientation in the 20th floor (without exterior obstruction) is chosen as a critical orientation that receives a significant amount of morning exposure.

Figure 1. Office plan with workstation layout



2. Modelling the Shading Device

The exterior envelopes are modeled with switchable Electrochromic windows with the same window position and size illustrated in Figure 1, the Electrochromic window is switched based on user preference level into three tinted states as stated in table 1, based on their visual comfort (manual glare control). In this case, occupants can activate shading systems as their visual discomfort increases ($DGP > 0.4$).

Table 1. Workstation design scenarios

	65 EC Clear state	60%
Electrochromic Glass	EC Tinted state 1	30%
	EC Tinted State 2	2%

3. Defining the Workstations properties

The 56 alternative workstation partition designs are modeled based on the four variables including partitions' height, material, and direction to the window and layouts as indicated in Table 2. The layouts consist of three configurations: 1. "Pre 42_Int 60": 42" partition in perimeter zone and 60" partition height in the interior zone. 2. "Pre 40, 48_In 60": the partition height gradually increased from perimeter zone to the interior zone (40" to 60"). 3. "Pre 60_Ver: 60" partition in the vertical (y-axis) of the workstation in the perimeter zone.

Table 2. Workstation design scenarios

Layout	Pre 42 Int 60	Pre 40,48 In 60	Pre 60 Ver
Height	W 42"	W 48"	W 60"
Material	Translucent Ref .4 Trn 20	Transparent 88 Trn	Opaque 88 Ref
Orientation	Perpendicular to window	10° to the south	10° to the North

4. Simulation

Annual glare simulation is conducted to calculate the Daylight Glare Probability (DGP) for multiple camera views based on the occupants' view directions. As the occupants of perimeter zones are exposed to daylighting, the shading device (EC) assumed to be tinted by occupants when glare becomes uncomfortable. This value is calculated for the location of occupants at the eye level (1.2m) that points directly at the screen of the monitor.

An annual climate-based daylighting simulation is executed utilizing the plug-in DIVA-for-Rhino 5.0 to quantify the annual daylighting performance of each scenario, the "Useful Daylight Illuminance" or UDI (Nabil & Mardaljevic, 2006) is used to measure the annual percentage of time that a sensor point receives an amount of daylight that is sufficient for office work while avoiding glare.

5. Optimization

In the last phase of the workflow, the outcomes are examined relative to one or more performance goals. The best trades between designed daylighting objectives; visual comfort and interior design strategies are explored to reach a series of possible optimum solutions.

As the quality of daylight and avoidance of glare are equally important, subtracting percentage of occupied hours DGP (g) from the percentage of the space with a UDI<100-2000lux larger than 50% (u) yields a single maximization objective (both UDI and DGP are in the range [0, 100]). It turned this result into a minimization objective by subtracting it from 100.

$$\min f(x) = 100 - \bar{u}(x) + \bar{g}(x)$$

RESULTS

The following section, first, compares the results of 56 scenarios of workstation designs based on the following variables and second, the best optimized solutions are analysed and compare with the base case scenario.

Height

The highest UDI values were recorded for 42" height partition, in perpendicular orientation to windows (28 %) that in comparison to base case scenario 11% was improved. As it was expected, by increasing the partition height, the amount of daylight that enters into the space reduces, which consequently decreases the percentage of the UDI<100-2000lux during occupied hours. The lowest percentage of occupied hours glare is recorded for the 60" height partition according to base case layout (3.7%). The percentage of occupied hours that occupants are exposed to glare are (3.7 %, 4.1%) for the 42" and 48" respectively and

unexpectedly the value for the 48" slightly is more than 42" due to the reflection of partition surfaces.

Material

The UDI value in figure 2a, implementing transparent material, brings more daylight into the study space. As it was expected, UDI values were reported higher in transparent partitions (with 88% visual transmittance) in comparison to the 20% visual transmittance in translucent partitions (base case), while the percentage of glare for both materials have quite similar values (2.9% and 3.1%). In opaque partitions (85% Reflection), the UDI value is less than the transparent material (20 to 25), however, it is slightly more than the translucent material (20% to 17%) and even the high glare value and more hours shading did not make significant differences.

Orientation

The orientation investigation of daylighting's impacts on translucent materials with 30% and 50% VLT was conducted and illustrated in figure 2 c) respectively. It shows that the UDI values for workstations with perpendicular partitions to the window (base case) are relatively low (17 %). Regardless of rotation direction, the UDI values of rotated partition are higher than in the partitions with orientations perpendicular to the windows. In the workstation with 10° rotated towards the south and north directions, UDI values are more than the base case (22% and 19%). Although the workstation with 10° rotation towards the south has higher UDI value in comparison with others, the percentage hours of visual discomfort is considerably high (6.4%). The workstation with 10° rotation towards north are not exposed to daylight and the percentage of glare hours and shading hours in all states are significantly lower than the base case and other. This led to higher UDI value for the workstation with direction towards north even in comparison with perpendicular partitions to the window (19%)

Layout

As the plots illustrated in figure 2 d) the UDI and Glare values reveal that in the translucent partitions all alternatives have the better performance in comparison with the base case scenario. The highest useful daylight illuminance (UDI) belongs to the workstation with 60" vertical partitions oriented perpendicular to the windows (Pre 60_Ver) and the workstation layout with 42" partitions in perimeter zone and 60" partitions in interior zone (Pre 42_Int 60) that both are almost identical (28%). The lowest values were recorded 2.9% in a layout with 60" partition in the vertical axis of the workstation in perimeter zone (Pre 60_Ver) that prevent excessive daylight into the space and where the occupants are located. The UDI value of "42, 48 PR_ 60 In" workstation layout is more than base case scenario (24%) but the glare value is quite similar to "Pre 42_Int 60" workstation layout (3.7%).

Overall

Based on the simulated plots illustrated (Figure 3), the base case scenario has good performance regarding the visual comfort and low occupied hours of glare (3.1%). However, the daylight in the base case scenario is the lowest ranked value (17%) that is recorded in which the 60" partitions block the daylight and reduce the UDI significantly. The best scenarios belong to a workstation with opaque partition layout in 10° oriented towards the south ("Pre 42_Int 60") illustrated in Figure 4. The hours which the EC is fully shaded, is low and the reflected diffuse light of surfaces in perimeter zones are also low due to the absence of high reflective partitions. Therefore the 4.1% hour of glare provide the more unshaded hours that led to more daylight entering the space and recorded the highest value of useful daylight illuminance (36%). According to the ranking, the workstation with 60" vertical opaque partition in the perimeter zones for the case rotated 10° towards the south (Pre 60_Ver) could provide a balance between daylight and glare (32 UDI and 4.1 DGP). This scenario would be considered as a good alternative for the first ranked scenario if the level of privacy considered.

Figure 2. a) Height, b) Material, c) Direction to windows, d) Layout

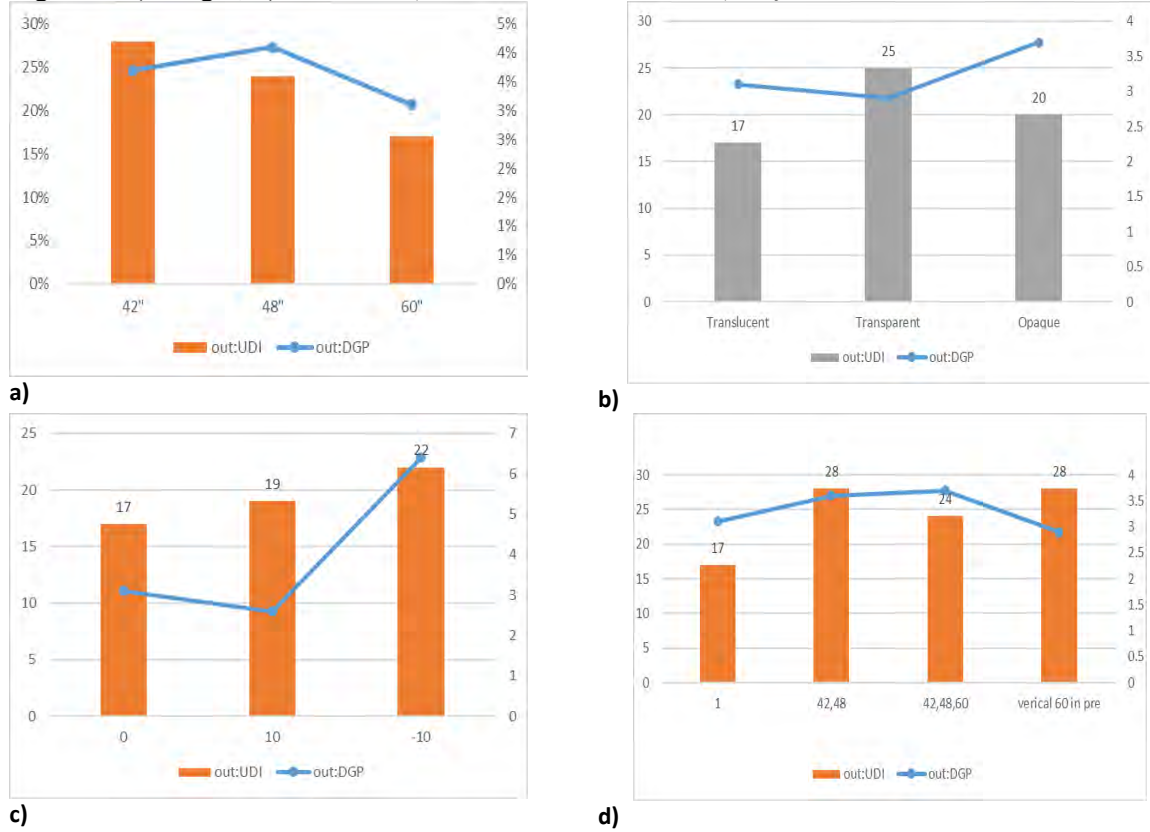


Figure 3. Parallel coordination of all variables Red: Worst case scenario, Blue: Best case scenario

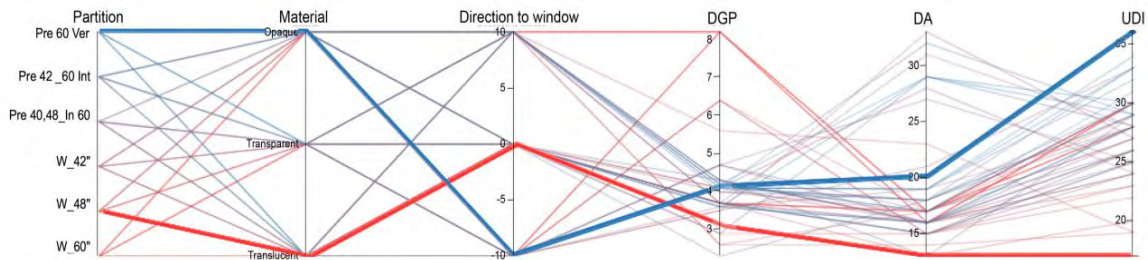
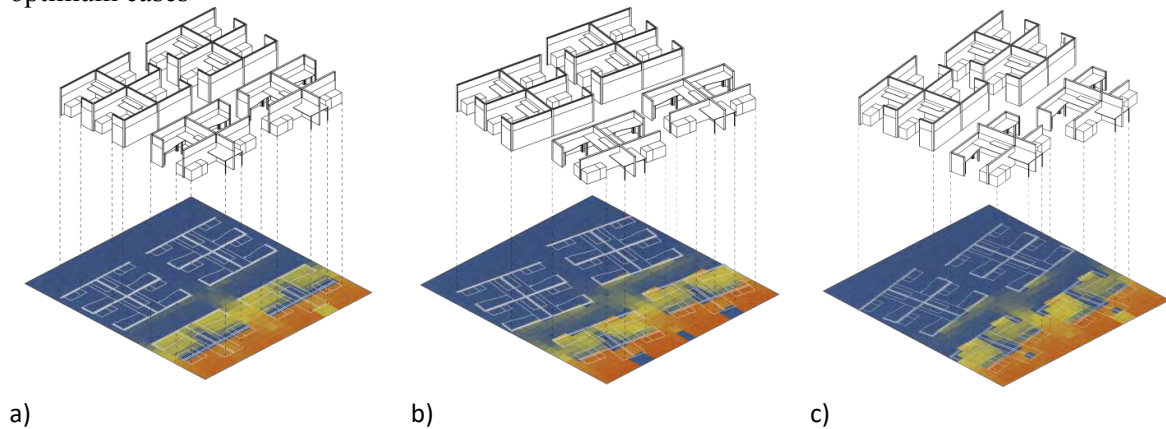


Figure 4. The layout and The Daylight Autonomy. a) Worst case (Base case), b and c. optimum cases



Discussion

Generally, the ranges of workstation properties are limited to certain degrees and materials and they could be expanded to different choices. For instance, because of the high reflectivity of selected opaque surfaces, the reflection of defuse light can cause more glare and lead to more shading time while the other opaque material with lower range of reflectivity could produce less glare that reduce the shading time.

Electrochromic glass works with different schedules beside the visual comfort. The energy and thermal schedules in some cases are in contrast with daylighting and visual comfort and their impact on the occupants' visual comfort at workstation needs to be studied and explored for the possible trade-off among all other parameters.

Conclusion

This paper presented an optimization method, used multi objective workflow with visual comfort and daylight simulation, and applied them to selected optimal values of design parameters associated with workstations (partition height, layout, direction to windows and materials) in an office building equipped with EC (user-based schedule) to deliver optimum daylight values while minimizing Glare Probability in the course of the year.

Considering the workstation design layouts into the simulation of dynamic shading (EC glass) makes the relation of UDI and Glare interdependent so that the daylight depends on the glare value. For instance, although the lower percentage of glare in high partition (60") reduces the shading hours and allows more daylighting that enter into the space, however, the high partition height prevent the penetrations of daylight.

The result of optimized scenarios show improvements of UDI ranging from (65% to 100%) across a diverse range of layouts and partition properties while simultaneously reducing visual discomfort varying degrees (between 4% and 17%) depending on variables. For instance the workstation with opaque ("Pre 42_Int 60") partition layout in 10° oriented towards the south is one of the optimum scenario that increase the performance of EC regarding daylight and comfort. This study tries to raise the awareness and attention of manufacturers and designers to the performance of workstation in relation to the user-based scheduled EC.

REFERENCES

- Arnold, D. L. (2010). Performance Assessment of C - T Ech. *City, I*(Appendix 4), 35–35.
- Kelly, R., Painter, B., Mardaljevic, J., & Irvine, K. (2013). Capturing the User Experience of Electrochromic Glazing in an Open Plan Office. *CIE Midterm Conference -- Towards a New Century of Light*, 12 April.
- Kim, J., & de Dear, R. (2013). Workspace satisfaction: The privacy-communication trade-off in open-plan offices. *Journal of Environmental Psychology*, 36, 18–26. <https://doi.org/10.1016/j.jenvp.2013.06.0071>
- Lee, Y. S., & Guerin, D. A. (2009). Indoor Environmental Quality Related to Occupant Satisfaction and Performance in LEED-certified Buildings. *Indoor and Built Environment*, 18(4), 293–300. <https://doi.org/10.1177/1420326X09105455>
- Nabil, A., & Mardaljevic, J. (2006). Useful daylight illuminances: A replacement for daylight factors. *Energy and Buildings*, 38(7), 905–913. <https://doi.org/10.1016/j.enbuild.2006.03.013>
- Paper, C., Carolina, N., Modaresnezhad, M., & Nezamdoost, A. (2017). Daylight-based Partition Design in Side-lit Open Plan Offices, (August). Retrieved from https://www.researchgate.net/profile/Amir_Nezamdoost/publication/319182979_Daylight-based_Partition_Design_in_Side-lit_Open_Plan_Offices/links/59c16ef00f7e9b21a8265bbf/Daylight-based-Partition-Design-in-Side-lit-Open-Plan-Offices.pdf
- Sbar, N. L., Podbelski, L., Yang, H. M., & Pease, B. (2012). Electrochromic dynamic windows for office buildings. *International Journal of Sustainable Built Environment*, 1(1), 125–139. <https://doi.org/10.1016/j.ijbsbe.2012.09.001>

Daylight availability in a room equipped with PCM window

Dominika Knera^{1,*}, Dariusz Heim¹

¹Department of Environmental Engineering, Lodz University of Technology, Poland

*Corresponding email: dominika.knera@p.lodz.pl

ABSTRACT

The increase in building energy performance mainly focused on the improvement of physical properties (thermal and optical) of individual components of building envelope. Very good isolation parameters can be easily achieved for opaque elements like walls and roofs. However, improvement of glazed component parameters is still required. Improving thermo-physical properties of window can be achieved using phase change material (PCM). Presented work is a part of extensive research project including the analysis and experimental investigation of window integrated with PCM layer. This modification changes the thermal properties of glass unit and effects on visible light transmission through the window.

The main purpose of the presented work is numerical analysis of the daylight conditions in the office room equipped with PCM window. The research was done for two geometrically identical indoor spaces varying by the window orientations: eastern and western respectively. Simulation was performed using a coupled validated simulation tools: ESP-r and Radiance. First software was used to model analyzed rooms then using second computational environment the illuminance and daylight factors in selected points were determined. Optical data of glazing unit equipped with PCM were appointed experimentally and adjusted to the numerical model. Simulations were carried out for characteristic sky conditions and selected days of year. Assessment of daylight availability in each room was done based on obtained values of illuminance and daylight factor in selected points. Five cases of the triple glazed window were considered: standard one and equipped with PCM layer positioned in the inner or outer cavity in liquid or solid state. Obtained results show that window with PCM in liquid state does not significantly reduce the daylight availability in room regardless the PCM position. However, window with PCM in solid state significantly decrease the light transmission through the window consequent in insufficient daylight conditions in analyzed rooms.

KEYWORDS

daylighting, PCM layer, light transmission, ESP-r, Radiance.

INTRODUCTION

Visually comfortable environment in building provide good ability to work and health of occupants. Appropriate visual conditions can be achieved by ensuring required lighting levels, illuminance uniformity and access to daylight. In traditional building the daylight availability is provided by the windows. However, glazing components are commonly the weakest building envelope element considering thermo-physical properties. One of the ways to improve the thermal capacity properties of window is integration of phase change materials (PCM) with glazing unit. Recently many studies about application of PCM in glazed elements of building envelope were published. The first article presenting parametric study of PCM glass system describes numerical and experimental investigation of window with PCM (Ismail and Henriquez, 2002). During last few years, many PCM technologies for the translucent and transparent building envelope, such as windows, shutters and other shading

devices (Silva et al., 2016) as well as roof glazing (Liu et al., 2018) were developed. Majority of the available researchers focuses on the analysis of thermal and optical parameters of PCM included into double glazing window on a laboratory scale (Gowreesunkera et al., 2013; Goia et al., 2014). Some of the studies consider adding of the additional container with PCM to double glazing window (Weinlader et al., 2005). Lastly, Giovannini et al. (2017) presents the analysis of impact of a double glazed unit with PCM layer in solid phase on the luminous environment and on the visual comfort in room equipped with such glazed unit.

Presented work is part of wider research project SOLTREN concerning the extensive analysis and experimental investigation of triple glazed window integrated with PCM layer considering effect of proposed solution on energy performance and visual comfort in experimental room. Double glazed windows have insufficient thermal properties in moderate and cold climatic conditions, therefore analysis of triple glazed window equipped with PCM layer is performed. Research described in this paper provides preliminary studies of impact of PCM layer on daylight availability in analyzed office room. Impact of PCM state, position in triple glazing unit and orientation of the window is considered.

METHODOLOGY

Analysis was performed using coupled ESP-r and Radiance tool. ESP-r, a modelling tool for building performance simulation, was chosen for energy analysis of proposed PCM window. Whole geometry and material properties was defined using ESP-r program. Subsequently, the simulation of daylighting was made by Radiance engine. Connection of ESP-r and Radiance allow calculating energy performance and illuminance simultaneously for one geometry model of analysed zone. However, ESP-r and Radiance coupling permit only for limited lighting analysis such as visualisation or calculation of illuminance and daylight factors for defined grid points. Glare can be calculated using only UGR coefficient which is not suitable to large-area light sources like windows (Carlucci et al., 2015). Therefore, in presented paper the daylight availability assessment will be made based on obtained illuminance and daylight factors.

Analysis was performed for 4 characteristic days of spring equinox, summer solstice, autumn equinox and winter solstice which occur respectively in March, June, September and December. In each selected day simulations were made for 3 characteristic hours during typical work profile for office: 9 a.m., 12 p.m. and 3 p.m.. In further part of paper each simulation step will be named by month and hour: III 9, III 12, III 15, VI 9, VI 12, VI 15, IX 9, IX 12, IX 15, XII 9, XII 12, XII 15. Furthermore, analysis was performed for two identical office rooms differentiated by the window orientation: eastern and western. Two standard sky conditions: CIE clear sunny and overcast sky was taken into account for all cases. The following 5 window types were considered:

- A - standard triple glazed window,
- B - triple glazed window filled with PCM in liquid state positioned in the outer cavity,
- C - triple glazed window filled with PCM in liquid state positioned in the inner cavity,
- D - triple glazed window filled with PCM in solid state positioned in the outer cavity,
- E - triple glazed window filled with PCM in solid state positioned in the inner cavity.

Window cavity filled with PCM was 16 mm depth. The characteristic of each glazed unit type were determined based on the previously performed measurements with experimental window component and artificial sun (Table 1). Cases A, B and C were modelled as glass material when cases D and E were introduced as translucent material.

Table 1. The characteristics of modelled types of windows

window case	A	B	C	D	E
light transmission [-]	0.71	0.64	0.55	0.06	0.03

Simulations for all described cases were made for 0.5 m density grid points filling the whole room and located at the height of working plane at the level of 0.75 m. Daylight factor and illuminance in all points for the clear sunny and overcast sky were calculated. Analysis of obtained results with particular attention on points located at the position of occupants working plane was performed.

CASE STUDY

Analysis was conducted for individual office cells representing the existing experimental office rooms. Dimensions of analysed zone are respectively width, length and height: 2.6 m, 4.4 m and 2.6 m. Window is situated in a centre of the exterior wall at the height of 0.7 m and dimensions of the glazed unit are 1.1 m of width and 1.1 m of height. Each office room is occupied by two workers. Both occupants working plane are located in the middle axis of the office room and at the distance of 1.5 m (1st working plane) and 3.0 m (2nd working plane) from the window. The RGB values of the interior surfaces of walls, floor and ceiling were determined based on the measurements using spectrophotometer Konica Minolta CM-2500d.

Analysis was performed for the location of the office rooms in the Central Europe under the temperate climatic conditions. Furthermore, analysed office rooms were located at the level of 4th floor which corresponds with real location of the experimental rooms.

RESULTS

Analysis of the obtained results was divided into three parts: comparison of the effect of PCM layer position on daylight conditions at first working plane, investigation of the illuminance distribution in whole room and detailed assessment of daylight availability in all considered simulation steps. Obtained results were named with two letters, first describe orientation and second type of window.

Daylight conditions at working plane for different position of PCM layer

Two positions of PCM layer were considered: in outer and inner window cavity. In Figure 1 are presented graphs of illuminance at 1st working plane obtained for windows with PCM in liquid and solid state positioned in outer and inner cavities of eastern oriented window for clear and overcast sky conditions.

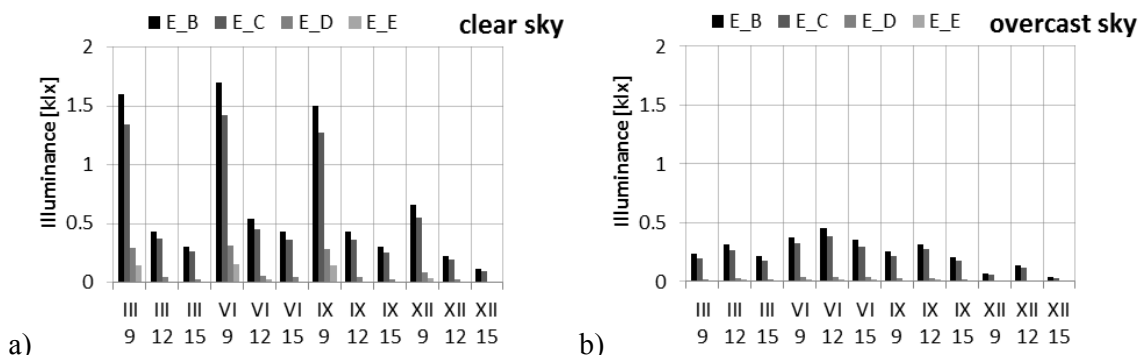


Figure 1. Illuminance at 1st working plane for eastern oriented window for a) clear, b) overcast sky conditions

It can be noticed that position of PCM layer has impact on illuminance calculated at working plane. Illuminance for cases with PCM located in outer cavity (B, D) is higher than for cases with PCM located in inner cavity (C, E) regardless the state of PCM. Described differences are the highest for clear sky conditions at 9 a.m. for all presented cases, which is caused by the solar beam radiation incident directly through the eastern oriented window. The same dependence was noticed for western oriented window at 3 p.m. For the other cases the divergences between illuminance calculated for both position of PCM layer is lower because of operation under only diffused solar radiation.

Illuminance distribution in analyzed office room

In Figure 2 were presented illuminance distribution in analysed office room with eastern orientated window (cases E_A, E_B, E_D) in spring equinox at 9 a.m. for CIE clear sunny sky. It can be noticed that illuminance distributions for cases A and B have a similar shape and only a level of illuminance for window with liquid PCM is slightly lower. However, distribution of illuminance in these cases is uneven, level of illuminance is very high near the window and significantly lower in further part of room, which may cause visual discomfort of occupants. On the other hand, illuminance distribution for case D is more uniform, however level of light at both working planes is too low considering minimal requirements of 500 lx for office work.

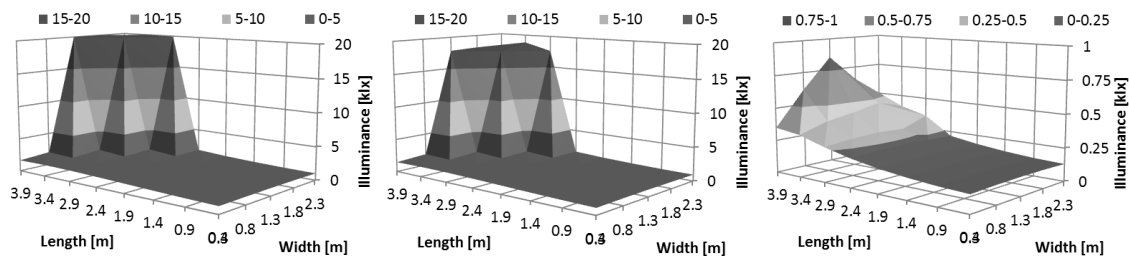


Figure 2. Illuminance distribution in analysed office rooms with a) A, b) B, c) D type of eastern oriented window in spring equinox at 9 a.m. and for CIE clear sunny sky.

Daylight availability at working plane

In last part of the paper the results of illuminance and daylight factors at 1st working plane were presented for the A, B, D type of window and both orientation: eastern and western (Figure 3). It can be seen that for clear sky conditions maximum levels of illuminance for eastern and western oriented windows occurs respectively at 9 a.m. and 3 p.m. according to operation of direct solar radiation. Nevertheless, maximum values of illuminance for cases with western oriented window are higher than for cases with eastern oriented window. Level of illuminance for other cases, when only diffused solar radiation operates, is comparable between eastern and western cases.

Considering illuminance requirements for office space at the level of minimum 500lx, it can be noticed that sufficient illuminance is reached only for clear sunny sky conditions (at 9 a.m. for eastern oriented window, at 3 p.m. for western oriented window and at 12 p.m. in summer solstice for both orientations) for cases of standard window and window with liquid PCM. Implementation of liquid PCM decrease illuminance in all cases, however it does not influence the number of cases meeting the requirements of 500 lx. Whereas cases with PCM layer in solid state influence significantly on illuminance level, in all cases below required 500 lx.

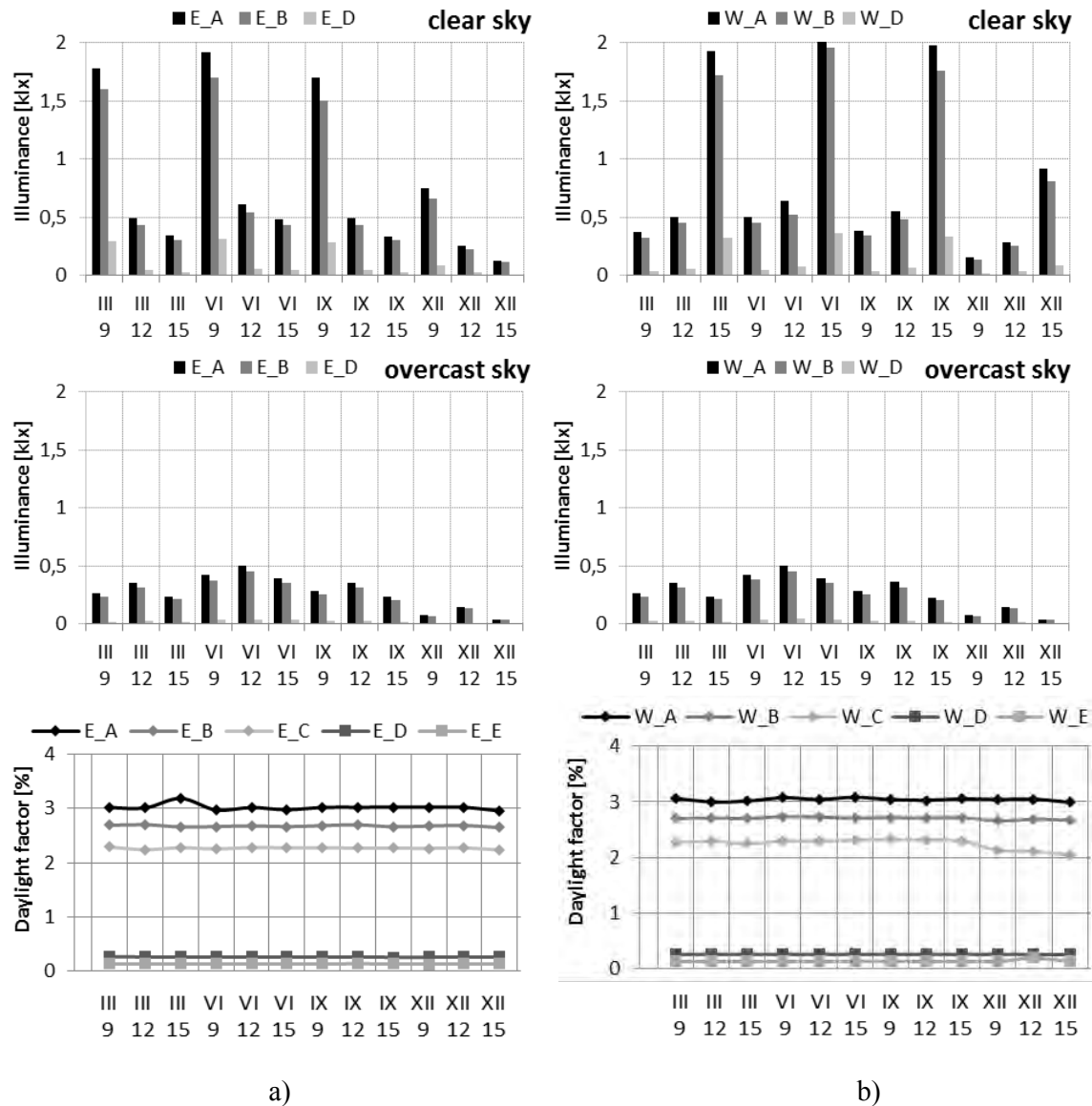


Figure 3. Illuminance and daylight factor and at 1st working plane for a) eastern, b) western oriented window.

Levels of daylight factors are constant during all analyzed days and hours with only slight fluctuations. Differences for eastern and western oriented window are insignificant. The daylight factor level for basic case with standard window reached averagely 3% for both orientations. Subsequently, daylight factor for cases with liquid PCM window are slightly lower – averagely 2.7% and 2.3% for window with PCM layer positioned in the outer and inner cavity respectively. Such level of daylight factors meets the requirements of minimum 2% at the working plane in the office area. Nevertheless, level of daylight factors for cases with solid PCM layer are significantly lower and not complete required level.

DISCUSSIONS AND CONCLUSIONS

Presented analysis focus on the assessment of daylight availability in a room with triple glazed window integrated with PCM layer. The application of PCM in window increases its thermal capacity but simultaneously decrease the light transmission through the window. Therefore, the analysis of the PCM application in glazing unit need to include the visual

comfort assessment in area connected with modified unit. This topic was studied so far only by Giovannini et al. (2017), analysing impact of double glazed unit with PCM layer in solid phase on the luminous environment and the visual comfort in room under a clear sky and with the façade facing south. Considering different assumptions of presented study and mentioned Giovannini et al. (2017) research, results obtained from them are incomparable.

In presented research the daylighting availability in the office room were presented considering different types of triple glazed window: standard and filled with liquid/solid PCM positioned in interior/exterior cavity. It was observed that application of PCM layer into triple glazed window decrease the daylight transmittance of glazing unit causing reduction in the illuminance and DF in room. For liquid phase of PCM this reduction is small and not influences significantly the daylight distribution in interior. However, PCM in solid phase highly decrease the daylight transmittance and hence the illuminance distribution. Furthermore, analysis of PCM position indicates that position of the PCM layer in the outer cavity for both liquid and solid phase influence higher daylight availability than position of the PCM in inner cavity. In conclusion, application of PCM layer in glazing unit decrease the daylight availability in room equipped with such window. However, PCM window has high potential to improve the thermal capacity properties with insignificant influence on the visual comfort when it will be design to be melted during a day to ensure visual comfort in room.

ACKNOWLEDGEMENT

This work was funded in a framework of ERANet-LAC 2nd Joint Call on Research and Innovation by NCBiR as part of the project entitled: Solar hybrid translucent component for thermal energy storage in buildings (acronym: SOLTREN).

REFERENCES

- Carlucci S., Causone F., De Rosa F., Pagliano L. 2015 A review of indices for assessing visual comfort with a view to their use in optimization processes to support building integrated design. *Renewable and Sustainable Energy Reviews*, 47, 1016–1033
- Giovannini L., Goia F., Verso V.R.M., Serra V. 2017 Phase Change Materials in glazing: implications on light distribution and visual comfort. Preliminary results. *Energy Procedia*, 111, 357 – 366
- Goia F., Perino M., Serra V. 2014 Experimental analysis of the energy performance of a full-scale PCM glazing prototype. *Solar Energy*, 100, 217–233
- Gowreesunkera B.L., Stankovic S.B., Tassou S.A., Kyriacou P.A. 2013 Experimental and numerical investigations of the optical and thermal aspects of a PCM-glazed unit. *Energy and Buildings*, 61, 239-249
- Ismail K.A.R., Henriquez J.R. 2002 Parametric study on composite and PCM glass systems. *Energy Conversion and Management*, 43, 973-993
- Liu C., Wu Y., Bian J., Li D., Liu X. 2018 Influence of PCM design parameters on thermal and optical performance of multi-layer glazed roof. *Applied Energy*, 212, 151–161
- Silva T., Vicente R., Rodrigues F. 2016 Literature review on the use of phase change materials in glazing and shading solutions. *Renewable and Sustainable Energy Reviews*, 53, 515–535
- Weinlader H., Beck A., Fricke J. 2005 PCM-facade-panel for daylighting and room heating. *Solar Energy*, 78, 177–186

Development of an Electric-Driven Smart Window Model for Visual Comfort Assessment

Michelangelo Scorpio¹, Giuseppina Iuliano¹, Antonio Rosato¹, Sergio Sibilio^{1,*}, Luigi Maffei¹, Giuseppe Peter Vanoli² and Manuela Almeida³

¹University of Campania “Luigi Vanvitelli”, Department of Architecture and Industrial, Aversa (CE), Italy

²University of Molise, Department of Medicine and Health Sciences “Vincenzo Tiberio”, Campobasso, Italy

³CTAC, School of Engineering of University of Minho (UMinho), Guimarães, Portugal

*Corresponding email: sergio.sibilio@unicampania.it

ABSTRACT

Smart windows, especially those electric-driven, represent one of the most advanced technologies for controlling solar radiation. For a correct use, it is necessary to understand their real behaviour through in-situ measurements on full-scale application as well as calibrating and validating visual simulation models capable of predicting their performances. In this paper, the preliminary results of current research activities aimed at developing simulation models of electric-driven full-scale glazing are presented. The research activities started with the assessment of the visible solar transmittance as a function of light incident angle through in-situ measurements; different models, with related values, of the visible solar transmittance were considered. For each simulation model, the corresponding transmittance value was set in the RADIANCE “*trans*” material model and the simulated illuminance values, for a defined acquisition point of a test-facility, were then compared with the experimental data. Finally, for each model, indoor luminance distributions were reported considering a typical office seating position. Preliminary results, based on the in-situ measurements approach, highlighted a sufficient accuracy for one of the models adopted; further analyses are needed in order to upgrade the simulation models available and assess the effective performances of these windows.

KEYWORDS

Electric driven window, Experimental measurements, Visual Comfort, Daylight simulation, Radiance.

INTRODUCTION

The correct use of daylight allows to reduce energy use for lighting in buildings as well as improve visual comfort (Ciampi et al., 2015a; Ciampi et al., 2015b). In this scenario, smart windows, especially those electrically driven, can play an important role in controlling the visual and thermal conditions inside a room. Differently from conventional windows, these new typologies of glazing allow to vary their visible and thermal characteristics by applying an electric field to active layers. With the aim of controlling solar radiation and improving indoor conditions, more and more new electric-driven types of smart materials and systems are being developed. Nevertheless, for the best use of these new technologies, in-situ assessments on full-scale devices are necessary to understand their real behaviour upon varying internal and external conditions as well as to develop simulation models capable of predicting their performance under different operating conditions. For these reasons, experimental and theoretical studies have been performed to evaluate the visual and thermal

performances of different full-scale devices as: electrochromic windows (Piccolo et al., 2009), Suspended Particle Device (SPD) (Ghosh et al., 2016) or gasochromic windows (Feng et al., 2016). In this paper, the preliminary results of experimental research aimed at evaluating the visual behaviour and developing simulation models of an Electric-Driven (ED) glazing are presented. The analysed electrically driven glazing can be switched from an opaque white (milky) to a transparent (clear) state in the presence of an electric field. A preliminary and simplified optical characterization of the electric-driven glazing was performed to evaluate the visible solar transmittance as a function of sunlight incident angle, through simultaneous on-site measurement of the vertical illuminance values on the external and internal surfaces of the window; the measurements were collected on a full-scale ED device by using a test facility. Experimental data were then used to calibrate and validate simulation models of the two states of the ED glazing using a RADIANCE “trans” material model as first approach; the calibration/validation was carried out by using models of glazing solar transmittance presented in previous researches. Finally, it has been performed a preliminary comparison among different simulation models for ED glasses in terms of illuminance distributions as well as Discomfort Glare Probability (DGP) inside the facility.

TEST FACILITY AND MEASUREMENTS SET UP

In order to allow for experimental studies to assess the in-situ visual performances of full-scale smart windows, an experimental station was designed and set-up at the Department of Engineering of the University of Sannio (Ascione et al., 2016; Sibilio et al., 2016). The station consists of a steel structure placed on a turntable, with external size of 6.00 m x 6.00 m and height of 5.50 m. The facility is equipped with a double-hang wood frame window with a total size of 2.000 m x 1.200 m, a ratio between glass area and total window area equal to 0.59; each hang has a glazing with size of 0.785 m x 0.900 m. In this paper, the first results of the in-situ visual characterization of the two full-scale double ED glazings, manufactured by Gesimat (GESIMAT), were presented. The ED glazing was composed, from outside to inside, of a 4 mm uncoated float glass, a 16 mm gap filled with Argon and an electric-driven layer between two 4 mm uncoated glasses. According to the technical data declared by the manufacturer, the ED glazing is switched from milky to clear state by applying an electric field of about 115 V, within about 1 s. In the clear state, ED glazing was characterized by a visible solar transmittance (τ_{vis}) equal to 72.5%, a thermal transmittance (U_g) equal to 2.5 W/m²K, a solar factor (g) equal to 0.72 and a power demand of about 10 W/m². In the milky state, the ED glazing was characterized by a visible solar transmittance (τ_{vis}) equal to 60.7%, a thermal transmittance (U_g) equal to 2.5 W/m²K and a solar factor (g) equal to 0.67. The in-situ visual characterization was carried out in two steps: (1) evaluation of the visible solar transmittance as a function of light incident angle and (2) evaluation of vertical internal daylight illuminance on a specific measurement point.

Evaluation of the visible solar transmittance as a function of light incident angle

The first set-up was realized to evaluate the variations of visible solar transmittance as a function of the sunlight incident angle. With this aim, the vertical illuminance values on the external surface of the window E_v^{ext} and just behind the internal surface of each ED glazing E_v^{int} were acquired during different days with completely clear sky conditions. In this step, measurements were performed with i) window west oriented and ii) left ED glazing in clear and right ED glazing in milky state. The illuminance values were acquired every 20 s by three Konica Minolta T-10 (accuracy of $\pm 2\%$) when direct sun light strikes on lux-meters, from around 2 pm (incident angle of direct light about 65°) to the sunset (incident angle about 5°).

Figure 2a shows the experimental visible solar transmittance values, calculated as E_v^{int} / E_v^{ext} for clear state, while Figure 2b shows those for milky state.

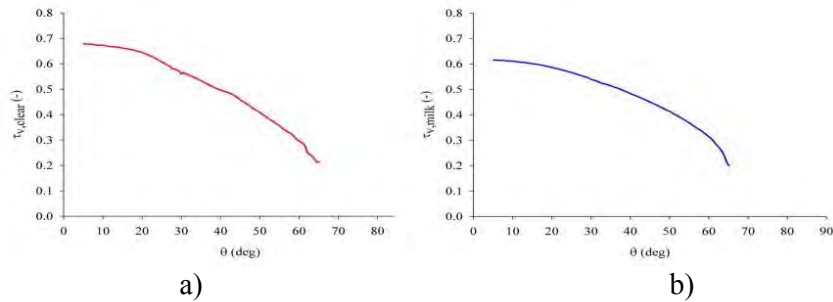


Figure 1. Experimental visible solar transmittance values as a function of the sunlight incident angle for a) clear and b) milky state.

The experimental data were then compared with 3 simulation models:

- 1) **#1 (τ_{maker})**: value of the visible transmittance constant for different sunlight incident angles and equal to the value declared by manufacturer;
- 2) **#2 ($\tau_{dif-dif,fit}$)**: value of the visible transmittance constant for different sunlight incident angles and equal to the diffuse-diffuse transmittance $\tau_{dif-dif,fit}$ of the glazing, defined as

$$\tau_{dif-dif,fit} = \int_0^{\pi/2} \tau_v(\theta) \sin(2\theta) d\theta \quad \text{where } \theta \text{ is the incident angle and } \tau_v(\theta) \text{ is the}$$

empirical angular function $\tau_v(\theta) = \tau_0 \cdot (1 - \tan^x(\theta/2))$ (Reinhart and Andersen, 2006); these models are reported as dash lines in Figure 2a for clear and Figure 2b for milky state. The calculated values of $\tau_{dif-dif,fit}$ are equal to 43.8% for clear and 42.7% for milky state;

- 3) **#3 (τ_{fit})**: value of the visible transmittance variable with the sunlight incident angle and equal to value predicted by the empirical angular function $\tau_v(\theta) = \tau_0 \cdot (1 - \tan^x(\theta/2))$ (dash lines in Figure 2a and Figure 2b).

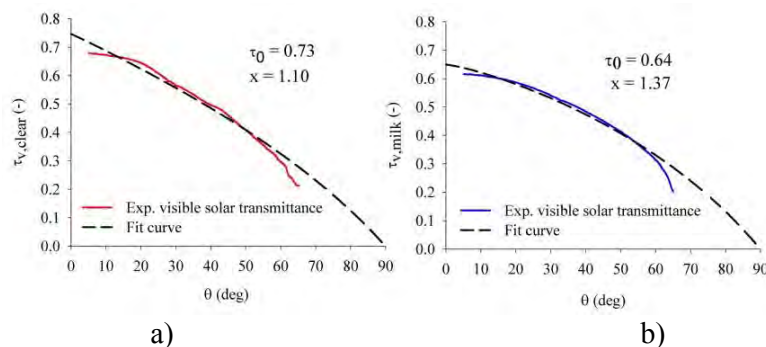


Figure 2. Curve fitting for a) clear and b) milky state (model #2 and #3).

Later, as first approach, the ED glazing was modelled through the RADIANCE “*trans*” material. The “*trans*” material model considers the glass as a perfect Lambertian diffuser and assumes the solar visible transmittance constant for different light incident angles. The two states of ED glasses were simulated setting the amount of light transmitted as totally direct for clear and totally diffuse for milky state.

Evaluation of vertical internal daylight illuminance on a specific measurement point

The external daylight availability as well as the internal illuminance daylight distributions were acquired at the same time, with the test room south oriented. The measurements were collected on sunny days from 9:00 to 18:00 local time with a time step of 1 hour, on 12th, 13th and 18th July in the milky state and on 11th, 15th and 16th July in the clear state. The external daylight availability was evaluated acquiring the horizontal global and diffuse illuminance values on the roof of the facility, by using two illuminance-meters LP PHOT 03 (DELTA-OHM), with accuracy <4%. For the horizontal diffuse illuminance, a black painted shadow-ring, with a diameter of 0.574 m and thickness equal to 0.052 m were used. The simulation results were compared with the experimental data acquired by an illuminance-meters Konica Minolta T-10 placed in vertical position just behind the glass (V1, as reported in the Figure 3a). Figure 3b shows the window equipped with the ED glasses in the clear (left pane) and milky (right pane) states. In this paper, only the sensor V1 was considered because it was not affected by internal light reflections, allowing to evaluate the behaviour of the glazing alone.

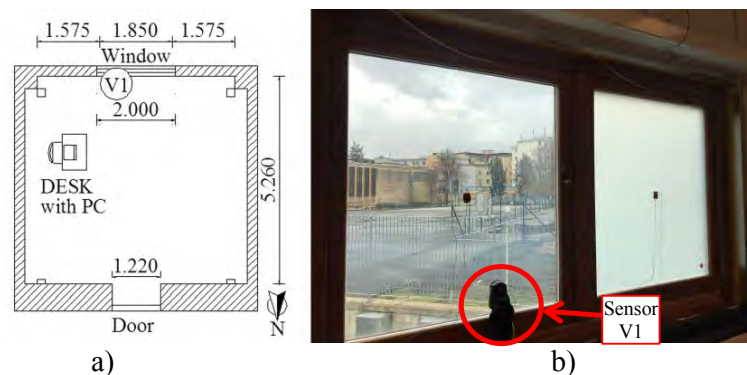


Figure 3. a) Layout of the room with position of the sensor and b) the ED device in the two states.

RESULTS AND DISCUSSION

Figure 4 the comparison among the experimental illuminance values acquired behind the ED device (measurement point V1), the simulation results obtained setting the visible transmittance equal to τ_{maker} , $\tau_{\text{dif-dif,fit}}$ and τ_{fit} as well as the external horizontal global illuminance values. In the figure, the connecting lines between the dots are only guidelines for the eye to connect data points. The values are plotted as a function of both the hour of the day and the light incident angle. The Figure 4 shows that:

- whatever the glazing state is, the simulation performed using τ_{maker} overestimates the experimental data, while τ_{fit} underestimates the experimental data;
- for both the clear and milky state, the simulations performed using $\tau_{\text{dif-dif,fit}}$ allow to achieve the best prediction of experimental data;
- whatever the glazing state is, the simulation performed using $\tau_{\text{dif-dif,fit}}$ overestimates the experimental data in the morning, while underestimates the measured values in the afternoon;
- the average relative percentage error values with respect to the measurements are equal to about 73.0% for τ_{maker} , -2.6% for $\tau_{\text{dif-dif,fit}}$ and -59.0% for τ_{fit} in clear state, while in the milky state are equal to about 59.0%, -2.0% and -52.0%, respectively;
- for $\tau_{\text{dif-dif,fit}}$ in the clear state, the smallest illuminance difference between the experimental and simulated data is observed on 16th July at 16:00 (with values of about 5287 lux and

5243 lux, respectively); in milky state, it is observed on 12th July at 17:00, (with values of about 4900 lux and 4861 lux, respectively).

In Figure 5, the simulated luminance distributions inside the facility, using the three simulation models described above, were reported. With the aim of reproducing a typical seating position, the luminance distributions, with associated DGP values, were calculated from a point placed at the eye level of a person considered as seated at the desk, facing and looking at the screen of a notebook computer (Figure 3a). The simulations were carried out at midday of a conventional sunny sky with sun.

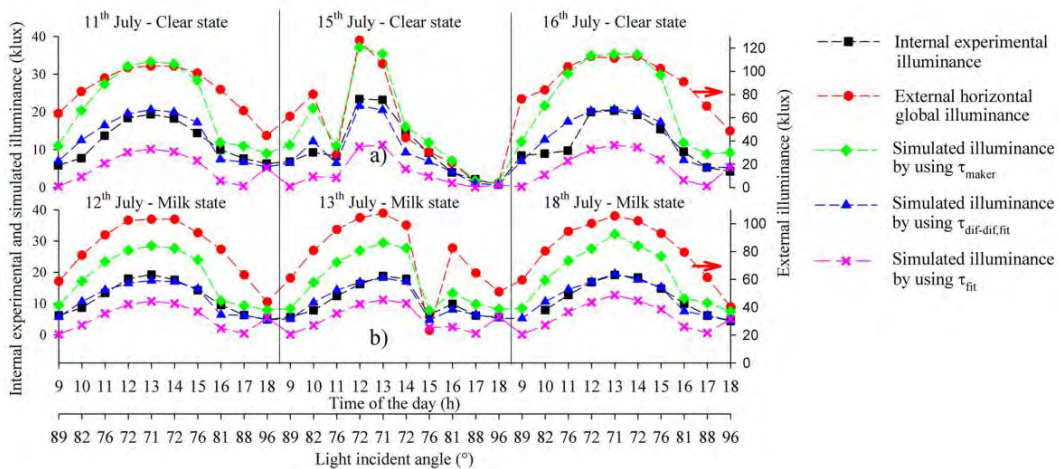


Figure 4. Measured and simulated illuminance values on the measuring point V1 for a) clear and b) milky states as well as the external horizontal global illuminance values.

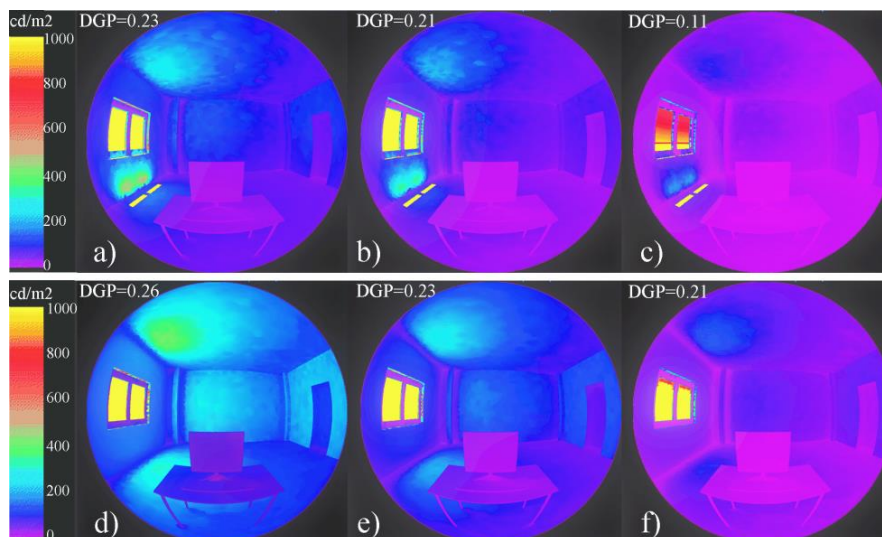


Figure 5. Simulated daylight luminance distributions for a) τ_{maker} , b) $\tau_{\text{dif-dif,fit}}$ and c) τ_{fit} in clear state as well as d) τ_{maker} , e) $\tau_{\text{dif-dif,fit}}$ and f) τ_{fit} in milky state.

The preliminary investigation allows to provide some models for the simulation of the ED glasses and define, among them, the more accurate one for utilization within software for indoor daylighting analysis. The research, even if performed with a preliminary approach based upon on-site measures, highlighted differences in outcome among the different considered models of ED windows. In particular it should be noted that the data provided by

the manufacturer do not always provide an accurate assessment of the transmission of sunlight and its value nearby the window. The same results were obtained considering the model τ_{fit} that always underestimate experimental data. Through preliminary on-site measurements it was defined a more reliable sunlight visible transmittance factor that took into account the influence of the incidence angle of solar radiation. The availability of models with a good accuracy represent the starting point to perform detailed analyses for evaluating the ability of these ED glasses to reduce energy consumption and improve visual and thermal comfort in comparison with more conventional design solutions. In addition, for these types of glasses there are other issues to consider, such as: (i) the way in which the light is transmitted inside the room and (ii) the fact that the milky state prevents exterior view. An example of these last effects can be viewed in Figure 5, where ED milky state prevents reflections of direct sunlight on internal surfaces but at the same time lead to higher DGP values with respect to the clear state. Finally, it is important to highlight that the progress in the use of innovative materials raises the issue to have reliable simulation models able to correctly describe their behaviour.

CONCLUSIONS

In this paper, the preliminary results of research activities aimed at calibrating and validating visual simulation models for ED glazing were presented. The RADIANCE “trans” material model was used as a first approach to simulate the behavior of the two states of the ED glazing. Starting from the manufacturer data and in-situ measurements, three different values of the visible solar transmittance, for each ED state, were deduced to be set in the “trans” material model. The results of the three simulation models show that the simulation model #2 is the best way to predict the experimental data, for both the clear and milky states. The results also suggest that internal daylight distribution, in addition to the weather conditions, is strongly correlated to the simulation models applied for the same smart glazing. In the next research step the ability of other simulation models will be considered to provide a suitable tool for predicting the real performance of these systems.

REFERENCES

- ASCIONE F. et al. 2016. MATRIX, a multi activity test-room for evaluating the energy performances of ‘building/HVAC’ systems in Mediterranean climate: Experimental set-up and CFD/BPS numerical modelling. *Energy and Buildings*, 126, 424–446.
- CIAMPI G. et al. 2015a. Daylighting Contribution for Energy Saving in a Historical Building. *Energy Procedia*, 78, 1257–1262.
- CIAMPI G. et al. 2015b. Daylighting Measurements and Evaluation of the Energy Saving in an Historical Building. In: *Proc. Heritage and Technology focus on Mind Knowledge Experience Le Vie dei Mercanti XIII*. Aversa-Capri, pp. 1977-1986.
- DELTA-OHM. <<http://www.deltaohm.com/ver2012/>>.
- FENG et al. 2016. Gasochromic smart window: optical and thermal properties, energy simulation and feasibility analysis. *Solar Energy Materials & Solar Cells*, 144, 316-323.
- GESIMAT. <<http://www.gesimat.de/elektrotrop.html>>.
- GHOSH A. et al. 2016. Daylighting performance and glare calculation of a suspended particle device switchable glazing. *Solar Energy*, 132, 114–128.
- PICCOLO A. et al. 2009. Daylighting performance of an electrochromic window in a small scale test-cell. *Solar Energy*, 83, 832–844.
- RADIANCE. <<http://radsite.lbl.gov/radiance/framework.html>>.
- REINHART C.F. and ANDERSEN M. 2006. Development and validation of a Radiance model for a translucent panel. *Energy and Buildings*, 38, 890–904.
- SIBILIO, S. et al. 2016. A Review of Electrochromic Windows for Residential Applications. *International Journal of Heat and Technology*, 34(2), S481-S488.

Lighting Quality Study of Shopping Malls in China Based on the Evaluation Experiment

Rui Dang^{1,*}, Yanhui Bu¹, Qingchen Wang¹, Gang Liu^{1,*}

¹ School of Architecture Tianjin University, Tianjin Key Laboratory of Architectural Physics and Environmental Technology, 92 Weijin Road, Tianjin, China.

*Corresponding email 1: dr_tju@163.com

*Corresponding email 2: LGLGMIKE@163.com

ABSTRACT

The lighting environment of the shopping malls will greatly influence the customer's visual comfort and product sales. This experiment studied the lighting environment of jewelry stores with the highest lighting energy consumption in shopping malls. The jewelry store scene which was built in the Key Laboratory of Building Environment Simulation had a total of 150 lighting conditions. Then, we measured lighting parameters, and subjective evaluation of lighting quality (including lighting comfort and commodities display effect) with 30 participants were carried out. We analyzed the experimental data to get the influence law of lighting parameters on lighting quality. Finally, this paper introduces an emerging ensemble learning algorithm XGBoost (extreme gradient boosting) to construct evaluation models of multiple lighting parameters for lighting quality in jewelry stores, which were verified to have good accuracy. It is of great significance to save energy on the basis of ensuring the lighting quality of the shopping malls.

KEYWORDS

Jewellery stores, Lighting quality, Experimental study, XGBoost, Evaluation model

INTRODUCTION

With the development of economy in China, the increasing number of shopping malls have very high requirements for visual comfort of the indoor light environment, resulting in high energy consumption (Hou et al. 2016). However, visual comfort of shopping malls is poor due to incomplete lighting design standards (MOHURD 2013); lighting in shopping malls accounts for 30%-40% of total energy consumption, so energy conservation has become an urgent problem (Xu et al. 2013; Lowry 2016). Because the establishment of the light environment index system is based on human subjective feelings, the impact mechanism of different spatial and lighting parameters on visual comfort is studied through evaluation experiments and parameter analysis. And to build the lighting evaluation model is the main means to solve the above problems, but there are still some problems in the current studies:

(1) In the aspect of evaluation experiments, there are mainly three kinds of research methods: a) The evaluation experiment in real buildings can not change lighting parameters. Therefore, it is difficult to obtain the influence rules to establish an index system (Jin et al. 2017; Ricciardi and Buratti 2018); b) Constrained by the laboratory environment, evaluation experiments in the laboratories can not study the impact of spatial parameters (Ampenberger et al. 2018); c) There is some controversy over using virtual reality technology to study lighting environment (Heydarian et al. 2015; Natephra et al. 2017). (2) In the aspect of lighting parameters analysis, regression equations were used to fit the visual comfort formula which continuous number could be predicted. However, the sample size was usually limited,

and the existing methods greatly reduced the accuracy of the evaluation formula (Deng et al. 2018; Jin et al. 2017).

In order to solve the above problems, the real store scene was built in the Key Laboratory of Building Environment Simulation to conduct an evaluation experiment; XGBoost (Hassan et al. 2017; Urraca et al. 2017) was used to solve the classification problem of big data. Based on this, the impact of lighting parameters on the lighting quality were studied, and lighting evaluation models were established to ensure visual health, to improve visual comfort, and to save lighting energy consumption, while satisfying the functions of lighting. It has important scientific and practical significance for achieving a healthy, comfortable and energy-saving light environment of shopping malls.

METHODS

Experimental setup

We designed and built the Key Laboratory for building light environment simulation in Tianjin University, which is biggest and high performance in Asia (Figure 1). The plan, the height and all the luminaires of the laboratory can be adjusted. Therefore, the light environment of various architectural spaces can be restored and monitored in the laboratory.

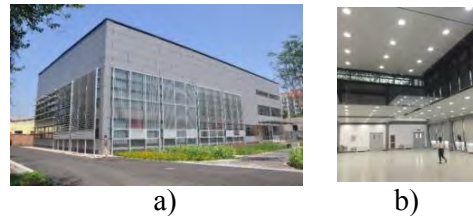


Figure 1. Key Laboratory of Building Environment Simulation. a) Exterior, b) Interior.

The jewelry stores with the highest lighting energy consumption in the shopping malls were selected as the research object, and the jewelry store experiment scene was set up in the laboratory (Figures 2). 12 downlights (Dimension: ϕ 282*H130; Beam angle: 120° ; Power: 60w) embedded in the ceiling were as ambient lighting; 12 spotlights (Dimension: ϕ 158*H100mm; Light source: LED; Beam angle: 24° ; Power: 30w) embedded in the crane span structure and the strip light (Dimension: W39*H9mm; Light source: LED (SMT 2835); Beam angle: 110° ; Power: 12w) in the counters were as accent lighting. The luminous flux and CCT (correlated color temperature) of all luminaires can be adjusted intelligently which can constitute a large number of lighting conditions.

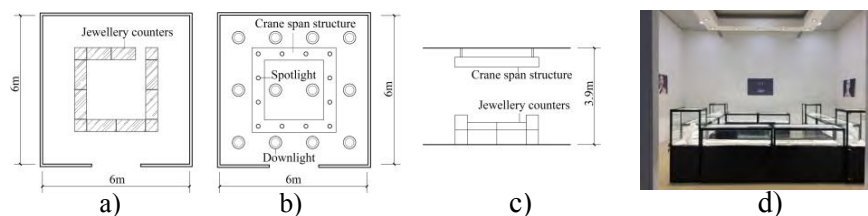


Figure 2. The simulated jewelry store. a) Store plan, b) Luminaire plan, c) Elevation, d) Photo.

Lighting variable setting and measurement methods

According to the standards and the field investigation, we determined the extreme values of the variables of lighting conditions to cover most of actual conditions. In the experiment, all luminaires were intelligently controlled to set up a total of 150 lighting conditions (Table 1).

Using the center-distribution method, measurement points are shown in Figure 3. And the measurement height was 0.75m (SAC 2009). The measurement instrument was CL-500A spectroradiometer. The stores scene without windows avoided the effect of natural light while measuring.

Table 1. Lighting variable setting.

Lighting system	Variable	Number of levels	Value
Ambient lighting	illuminance	3	500 lx, 1000 lx, 1500 lx
			1000 lx, 1500 lx, 2000 lx, 3000 lx, 4000 lx,
Accent lighting	illuminance	10	5500 lx, 7000 lx, 8500 lx, 10000 lx, 12000 lx
	CCT	5	3500 K, 4000 K, 4500 K, 5000 K, 5500 K

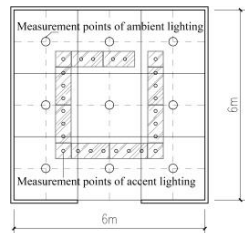


Figure 3. Measurement points plan. Figure 4. The process of the experiment.

Subjective lighting quality assessment

In the experimental scene of jewelry stores, a questionnaire survey (Table 2) was conducted to subjectively evaluate 150 lighting conditions. Thirty research participants who aged 22 to 26 years (15 female and 15 male subjects) were divided into 6 groups to evaluate the randomly disturbed lighting conditions in 5 days. In the experiment scene, participants simulated the shopping process, fully experienced the light environment and then subjectively evaluated the lighting quality. The experimental process is shown in Figure 4. Participants were asked to wear eye masks to avoid interference between two lighting conditions. After evaluating every 10 lighting conditions, participants rested for 20 minutes to eliminate the effect of fatigue experiment on the experiment results.

Table 2. Lighting quality questionnaire.

Lighting condition number	Visual comfort	Very bad		Bad		Good		Excellent			
		1	2	3	4	5	6	7	8	9	10
	Effects of commodities presentation	Very bad		Bad		Good		Excellent			
		1	2	3	4	5	6	7	8	9	10

RESULTS

Processed experimental data and conducted preliminary analysis. 150 lighting conditions were discussed separately in accordance with three ambient lighting conditions. In each ambient lighting scene, CCT of the accent lighting was set in five levels. But in the actual measurement, CCT changed due to the change of the illumination. In order to analyze the results, the average number of CCT was obtained from the CCT which were set up as same.

The influence of lighting parameters on lighting quality

Figure 5 describes the influence of illuminance and CCT of accent lighting on visual comfort when ambient CCT is 4000 K which is the most commonly used and ambient illuminance is in three levels. The abscissa is horizontal illuminance of accent lighting, and the ordinate is

the value of visual comfort. The different colored lines represent different CCT of accent lighting. The question of visual comfort had a scale value from 1(very bad) to 10(excellent) which greater values indicated more comfort.

As shown in Figure 5, within the range of experimental values, (1) When the ambient illuminance is different: visual comfort increases with the increased ambient illuminance. With the increase of ambient illuminance, visual comfort increases smaller and smaller with increased accent illuminance. When ambient illuminance increases to more than 8000 lx, visual comfort of some conditions begin to decrease. (2) When the ambient illuminance is the same: visual comfort increases with the increase of illuminance, and the increase tends to be smaller and smaller. When the accent CCT is about 4000K (medium color temperature), the jewelry store has better visual comfort. (3) As shown in Figure 5-c, when the ambient illuminance is 1500 lx, the reason for the special point is: the sequence of lighting conditions to evaluate was random. The lighting condition of special point (Accentuated CCT is 5290.8K, and accent illuminance is 10000 lx) was evaluated after the condition (Ambient illuminance is 500 lx, and the accent illuminance is 576 lx). The difference in illuminance between the two lighting conditions is too large, causing visual discomfort.

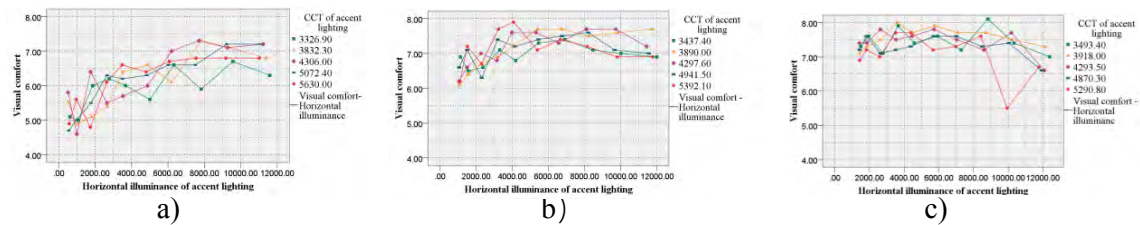


Figure 5. Influence of lighting parameters on visual comfort. a) Illuminance of ambient lighting is 500 lx, b) Illuminance of ambient lighting is 1000 lx, c) Illuminance of ambient lighting is 1500 lx.

Fig. 6 describes the lighting parameters on the presentation effect of the commodities when the ambient CCT is 4000K. The abscissa is horizontal illuminance of accent lighting, and the ordinate is effect of commodities presentation. The scale value of presentation effect is from 1(very bad) to 10(excellent), and larger values indicate better presentation.

As shown in Figure 6, within the range of the experiment values, (1) When the ambient illuminance is different: the ambient illuminance has small effect on the presentation effect. (2) When the ambient illuminance is the same: the effect of commodity presentation increases with the increased accent illumination. When the accent illuminance is greater than 10000 lx, the presentation effect decreases or stays the same. When the accent CCT is medium CCT(4000K) or high CCT(4000K-5600K), the presentation effect is better. Accent lighting in low CCT in the jewelry store has poorer presentation effect.

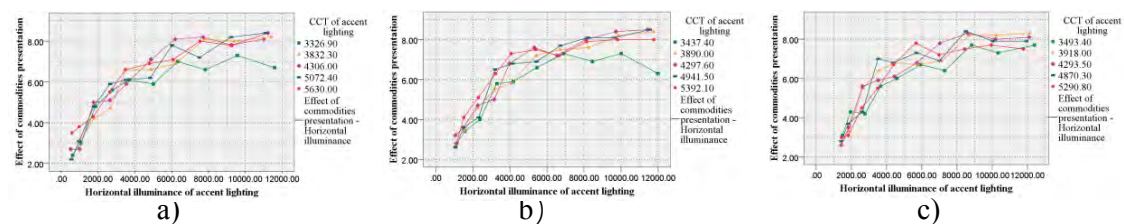


Figure 6. Influence of lighting parameters on effects of commodities presentation. a) Ambient illuminance is 500 lx, b) Ambient illuminance is 1000 lx, b) Ambient illuminance is 1500 lx.

Evaluation model

XGBoost is an extension of the Gradient Boosting Machine. The Boosting classifier belongs to the ensemble learning model (Hassan et al. 2017; Urraca et al. 2017). XGBoost is widely used in energy consumption prediction (Touzani et al. 2018; Robinson et al. 2017) and power distribution due to its high efficiency and accuracy. This paper introduces XGBoost into the evaluation of lighting quality in shopping malls and establishes a multi-parameter evaluation model.

Evaluation model of visual comfort in the jewelry store

Data preprocessing was performed, the outliers of visual comfort experiment data were removed by using an interquartile range method, and then the end points of the interval were used as the comfort label values. We obtained the visual comfort distribution of all lighting conditions of the jewelry store.

We used python to build an evaluation model of visual comfort in the jewelry store based on the XGBoost ensemble learning classification algorithm. Experimental data was randomly divided into training sets and test sets in a ratio of 4:1. And we built XGBoost classification models on the training sets and adjusted parameters according to the classification prediction accuracy rate of the test sets. Finally, the optimal combination of parameters are as follows: max_depth=3, n_estimators=50, learning_rate=0.1, subsample=0.95. The prediction accuracy rate of the model on the test sets is 0.9, which shows that the model has good generalization ability, and the accuracy rate of the training sets is 0.942, which can effectively prevent the model from overfitting. According to the weights, the order of features of well-trained XGBoost model is: accent illuminance (0.3483), accent CCT (0.2780), Ra (general color rendering index) of accent lighting (0.2161), ambient illuminance (0.1573) (Figure 7).

Evaluation model of commodities presentation effect in the jewelry store

Similarly, an evaluation model of product presentation effect in jewelry store was obtained. When ambient CCT is approximately 4000K, the order of the features is: accent illuminance (0.5244), accent CCT (0.2502), Ra of accent lighting (0.1934) and ambient illuminance (0.0319) according to the weights (Figure 8).



Figure 7. Weights of the features that affect visual comfort of the jewelry store. Figure 8. Weights of the features that affect commodity presentation effect of the jewelry store.

DISCUSSIONS

In the aspect of illuminance, visual comfort and commodity display effect increase with the increase of illuminance, but the increasing trend gradually flattens. And for the effect of commodities display, the accent illuminance has a greater influence, and the influence of the ambient illuminance is smaller (Figure 8). However, when the accent illuminance is greater than 8000 lx, most of the visual comfort and display effect begin to decrease. In the aspect of CCT, when accent CCT is about 4000K, the jewelry store has better visual comfort and product display effect. Store lighting design should consider both sides.

When the ambient CCT is about 4000K, the well-trained XGBoost model can be used to predict the visual comfort and the commodities display effect to guide the lighting design of the jewelry stores. The evaluation model has the following limitation: In order to avoid the fatigue test of participants from affecting the results, the ambient CCT is unified to the

commonly used value (4000 K) according to the field investigation. Therefore, this evaluation model can not evaluate other lighting conditions except that the ambient CCT is 4000K.

CONCLUSIONS

This study proposes the influence laws of lighting parameters on lighting quality of jewelry stores in shopping malls, and obtains an evaluation model of lighting environment in jewelry stores. Based on advanced machine learning algorithms, the proposed model can predict and evaluate lighting quality (visual comfort and effect of commodity display) through multiple lighting parameters (illuminance of ambient lighting, illuminance of accent lighting, CCT of accent lighting, and Ra of accent lighting). The results show that the model achieves an ideal predicting accuracy. This method can be extended to lighting design in shopping malls to improve lighting quality and to achieve energy saving.

ACKNOWLEDGEMENT

This work is funded by the National Key Research and Development Program of China (2016YFB0601700), The National Natural Science Foundation of China (51338006); Peiyang scholar program (1801).

REFERENCES

- Hou J, et al. 2016. Comparative study of commercial building energy-efficiency retrofit policies in four pilot cities in China. *Energy Policy*, Vol. 88, pp. 204-215.
- MOHURD. 2013. *Standard for lighting design of buildings (GB 50034-2013)*. Beijing: Ministry of housing and Urban-Rural Development of the People's Republic of China.
- Xu P, et al. 2013. Commercial building energy use in six cities in Southern China. *Energy Policy*, Vol. 53, pp. 76-89.
- Lowry, G. 2016. Energy saving claims for lighting controls in commercial buildings. *Energy and Buildings*, Vol. 133, pp. 489-497.
- Jin H, et al. 2017. An evaluation of the lighting environment in the public space of shopping centres. *Energy and Buildings*, Vol. 115, pp. 228-235.
- Ricciardi P. and Buratti C. 2018. Environmental quality of university classrooms: Subjective and objective evaluation of the thermal, acoustic, and lighting comfort conditions. *Energy and Buildings*, Vol. 127, pp. 23-36.
- Ampenberger A, Staggl S, and Pohl W. 2017. Attention Guidance, Perceived Brightness and Energy Demand in Retail Lighting. *Energy Procedia*, Vol. 111, pp. 658-668.
- Heydarian A, et al. 2015. Immersive virtual environments, understanding the impact of design features and occupant choice upon lighting for building performance. *Building and Environment*, Vol. 89, pp. 217-228.
- Deng H, Fannon D, and Eckelman M.J. 2018. Predictive modeling for US commercial building energy use: A comparison of existing statistical and machine learning algorithms using CBECS microdata. *Energy and Buildings*, Vol. 163, pp. 34-43.
- SAC. 2009. *Measurement methods for lighting (GB/T 5700-2008)*. Beijing: Standardization and Ministration of the People's Republic of China
- Hassan M.A., et al. 2017. Exploring the potential of tree-based ensemble methods in solar radiation modeling. *Applied Energy*, Vol. 203, pp. 897-916.
- Urraca R, et al. 2017. Estimation methods for global solar radiation: Case study evaluation of five different approaches in central Spain. *Renewable and Sustainable Energy Reviews*, Vol. 77, pp. 1098-1113.
- Touzani S, et al. 2018. Gradient boosting machine for modeling the energy consumption of commercial buildings. *Energy and Buildings*, Vol. 158, pp. 1533-1543.
- Robinson C, et al. 2017. Machine learning approaches for estimating commercial building energy consumption. *Reviews Applied Energy*, Vol. 208, pp. 889-904.

Thermal Performance of an Electric-Driven Smart Window: Experiments in a Full-Scale Test Room and Simulation Model

Giovanni Ciampi¹, Antonio Rosato¹, Sergio Sibilio^{1,*}, Giuseppe Peter Vanoli², Manuela Almeida³ and Luigi Maffei¹

¹University of Campania “Luigi Vanvitelli”, Department of Architecture and Industrial Design, Built Environment Control Laboratory, Aversa (CE), Italy

²University of Molise, Department of Medicine and Health Sciences “Vincenzo Tiberio”, Campobasso (CB), Italy

³CTAC, School of Engineering of University of Minho (UMinho), Guimarães, Portugal

*Corresponding email: sergio.sibilio@unicampania.it

ABSTRACT

This paper reports the results of experimental tests and numerical simulations aimed at evaluating the performance of an electric-driven smart window with respect to solar control in buildings. The experimental performances of the electric-driven smart window were evaluated using a south oriented full scale experimental facility designed and realized. The tests were carried out during the summer under real sky conditions upon varying the state of the electric-driven smart window (clear and milky). In the first part of the paper, the experimental results are discussed in terms of surface temperature of glazings as well as indoor air temperature in order to highlight the potential benefits on thermal comfort associated to the application of electric-driven smart windows. In the second part of this paper, the experimental data are compared to the numerical results generated through a simulation model of the electric-driven smart window in order to assess its reliability under different operating scenarios. Finally, the simulation model is used to quantify the potential cooling load reduction deriving from the integration of electric-driven smart windows in an office façade located in Naples (Italy).

KEYWORDS

Smart windows, Electric-driven smart windows, Thermal comfort, Solar control, TRNSYS

INTRODUCTION

A significant portion of the total worldwide energy demand (around 40%) can be attributed to heating and cooling of the building sector (European Commission, 2015). In this context, the Electric-Driven (ED) smart window technology, especially for the buildings with a large glazed surface, can help to significantly reduce the energy consumption as well as to improve the indoor thermal comfort. Indeed, these new typologies of glazings allow to vary their visible solar transmission and solar factor by applying an electric field. A large number of studies are currently in progress about electric-driven smart windows (Baetens R. et al. 2010, Fernandes et al. 2013, Niklasson and Granqvist 2006, Piccolo 2010, Piccolo et al. 2009, Piccolo and Simone 2009, Sibilio et al. 2017). The literature review reveals the need to perform further experimental analysis to evaluate the on-site performances of these type of smart windows taking into account that: (i) the most analyzed electric-driven smart windows typology has been the electrochromic window, (ii) the visual comfort as well as the electric energy savings for lighting have been the most investigated aspects and (iii) the experimental performances of small-scale smart windows prototypes have been generally investigated. However, it can be noticed that the benefits in terms of reduction of cooling energy demand as well as capability in maintaining the thermal comfort by the application of the smart windows have been rarely investigated.

In this paper, the results of experimental tests and computer simulation modelling aimed at evaluating the thermal performance of a full-scale ED windows with respect to solar control in buildings are reported. The experimental thermal performances of the ED window were evaluated by using a south oriented full-scale experimental station during the summer and under real sky conditions. In the first part of the paper, the experimental results are discussed in terms of surface temperature of glazings as well as indoor air temperature. The ED window is modelled by means of the software (WINDOW 7.5) and then imported into the software (TRNSYS 17). In the second part of the work, the numerical results are compared to the experimental data in order to assess the model reliability. Finally, the ED window model is used to quantify the cooling energy demand reduction deriving from the use of ED windows into an office façade located in Naples (Italy).

FULL-SCALE TEST-ROOM

The experimental facility is a full-scale outdoor test-room (Ascione F. et al. 2016) designed and set-up at the Department of Engineering of the University of Sannio, Benevento (latitude: $41^{\circ}7' N$; longitude: $14^{\circ}47' E$). The test room has a floor area of 36.0 m^2 ($6.0 \text{ m} \times 6.0 \text{ m}$) with a height of 5.5 m . The test-room is able to rotate 360° on the horizontal thanks to a motorized steel support that allows to modify the orientation. The envelope of the experimental station consists of three removable vertical test walls ($U=0.43 \text{ W/m}^2$), one unremovable vertical technical wall ($U=0.05 \text{ W/m}^2$), a floor ($U=0.05 \text{ W/m}^2$) and a roof ($U=0.06 \text{ W/m}^2$) (Ascione F. et al. 2016). The total size of the window is $2.00 \text{ m} \times 1.20 \text{ m}$; two ED double glazings (each with size of $0.785 \text{ m} \times 0.900 \text{ m}$), produced by (GESIMAT), were installed. This typology of electric-driven smart window consists of three layers as reported in Figure 1a. In particular, the ED glazing is a polymer with dispersed Liquid Crystal (LC) between two float glass substrates. This third layer allows the ED window to switch quickly (1 second) from transparent to opaque state, and vice versa. The switching is possible thanks to a potential difference across the glazing; in particular, when the voltage is equal to 0 V the smart window is opaque (milky), while when the voltage is equal to 115 V the ED window is transparent (clear). Figure 1b reports an indoor view of the ED window installed in the test-room with the left window pane in the clear state and the one on the right in the milky state.

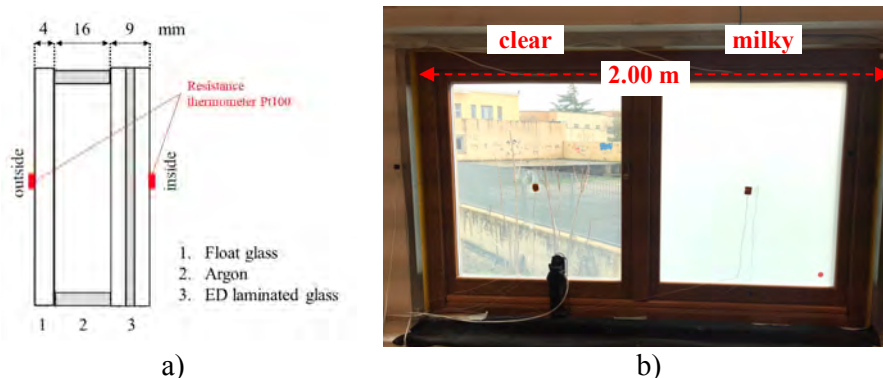


Figure 1. a) Schematic layout of the ED double glazed unit, b) indoor view of the ED window installed in the test-room.

In clear state, ED glazing is characterized by a visible solar transmittance (τ_{vis}) equal to 72.5%, a thermal transmittance (U_g) equal to $2.5 \text{ W/m}^2\text{K}$, a solar factor (g) equal to 0.72 and a power demand of about 10 W/m^2 . In milk state, the ED glazing is characterized by τ_{vis} equal to 60.7%, U_g equal to $2.5 \text{ W/m}^2\text{K}$ and g equal to 0.67.

The outdoor boundary conditions were monitored by means of a weather station. In particular, the test-room is well equipped (Ascione F. et al. 2016) in order to measure the following parameters: air temperature, relative humidity, rainfall, wind-speed, wind-direction, diffuse and global solar radiations. The technical specifications of the outdoor sensors are reported in (Ascione F. et al. 2016). In addition, external daylight availability is evaluated by measuring the horizontal global and diffuse illuminance values on the roof of the test-room by means of two illuminance-meters LP PHOT 03 of (DELTA-OHM) and with an accuracy $< 4 \%$. In order to highlight the potential benefit on thermal comfort associated to the use of the ED windows, the surface temperature of glazings as well as the indoor air temperature are also measured. The temperatures are monitored by using a resistance thermometer Pt100 with a range of $-40 \div 80 \text{ }^\circ\text{C}$ and an accuracy equal to $\pm 0.1 \text{ }^\circ\text{C}$ at $0 \text{ }^\circ\text{C}$. The sensors on the surface of glazings are installed with appropriate shielding to consider the effect of direct solar radiation. Each parameter is logged every 10 seconds by means of a Fluke NetDAQ Data Logger.

SIMULATION MODELS

The whole ED window was modelled by means of the software WINDOW 7.5, considering the schematic layout of the ED double glazed unit reported in Figure 1a. In particular, two different window models were realized, one for the ED window in the clear state and another one for the ED window in the milky state. The output file of the software WINDOW 7.5 was then used in software platform TRNSYS 17 by means of the Type 56 to compare the experimental thermal performances with those obtained through simulations. However, in order to take into account the thermo-physical characteristics of the building envelope of the facility (Ascione F. et al. 2016), the test-room was firstly modelled in TRNSYS 17.

A simulation time step equal to 10 seconds was used. During the simulations, the same outdoor boundary conditions measured during the experimental tests were considered.

Finally, the two simulation models of ED window were used to quantify the cooling energy demand reduction associated to a typical office building located in Naples by replacing the conventional double-glazing windows with the same thermal transmittance.

RESULTS AND DISCUSSION

Experimental results

Measurements were carried out for about 1 month during the summer of 2017 from 29th June up to 20th July (for a total of 22 days) from 9:00 up to 18:00 by using the above-described facility located in Benevento (latitude: $41^\circ 7' \text{ N}$; longitude: $14^\circ 47' \text{ E}$). The experimental tests were carried out under real sky conditions with the ED window south orientated. The ED window was manually switched from clear to milky state and vice versa. During the experimental tests the indoor air temperature was monitored, but not controlled, in order to estimate the influence of solar gains upon varying the state of the ED window. Taking into account that only one test-room was available, a first comparison between the boundary conditions during the days with the ED window in clear state and those with the ED window in milky state was carried out. This comparison is mandatory, in order to verify that the experimental tests for both states were conducted in the same outdoor condition. This comparison was performed in terms of percentage difference of external air temperature (ΔT_{amb}), percentage difference of global solar radiation on the horizontal (ΔI) and wind velocity. The comparative test was considered acceptable in the cases of the difference in the outdoor environmental variables never exceeded 5%. Figure 2a reports the values of ΔT_{amb} and ΔI as a function of the hour of the day for July 8th (clear ED window) versus July 12th (milky ED window). No significant differences in terms of wind velocity were observed for this two days. This figure highlights how the values of both ΔT_{amb} and ΔI_{mean} never exceeded

5%; in particular, ΔT_{amb} ranges between -1.77% and 4.58%, while the values of ΔI range from a minimum of 0.46% up to a maximum of 4.41%. This means that the same outdoor conditions for both July 8th and July 12th can be assumed. With respect to these two days, the measured values of the internal surface temperature of the glazing (T_{int}) and the measured values of the indoor air temperature (T_{indoor}) are reported in Figure 2b. In particular, Figure 2b shows, on left axis, the difference between the internal surface temperature of the glazing with the ED transparent window ($T_{int,clear}$) and the internal surface temperature of the glazing with the ED opaque window ($T_{int,milky}$) and, on right axis, the difference between the measured values of the indoor air temperature with the ED transparent window ($T_{indoor,clear}$) and the measured values of the indoor air temperature with the ED opaque window ($T_{indoor,milky}$), both as a function of the time. This figure highlights how the differences are always positive: this means that (i) the values of the internal surface temperature of the glazing associated to the clear window are greater than those of the milky window and (ii) using the ED window in the clear state, the indoor air temperature is greater than that one of the ED window in the milky state. In particular it can be noticed how using the ED window in the milky state during the summer the indoor air temperature can be reduced by a value between 0.65°C and 1.10°C.

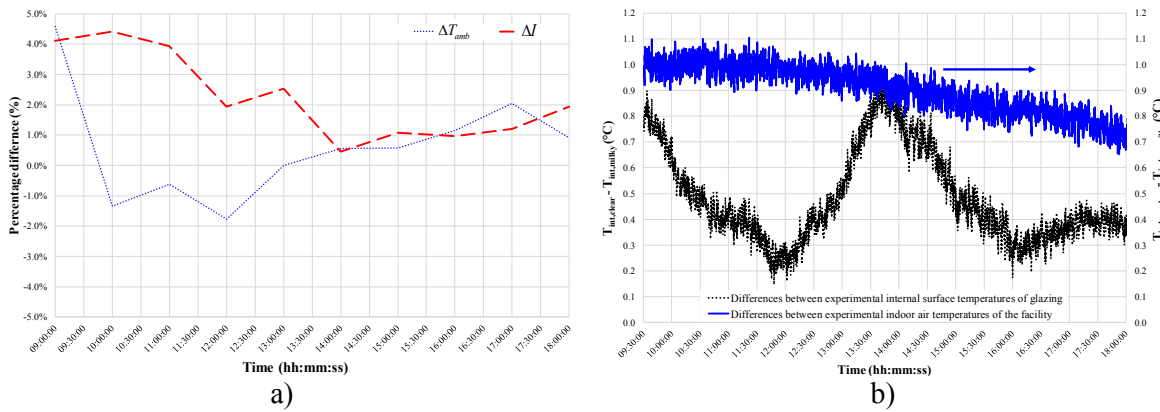


Figure 2. a) Values of ΔT_{amb} and ΔI , b) differences between $T_{int,clear}$ and $T_{int,milky}$ as well as between $T_{indoor,clear}$ and $T_{indoor,milky}$ as a function of the time.

Numerical results

The simulation results were compared to the experimental data in order to assess the model reliability. The comparison was performed in terms of internal surface temperature of the glazing as well as indoor air temperature for both July 8th (ED window in clear state) as well as July 12th (ED window in milky state). In order to verify the accuracy of the modelled ED window, the following percentage differences were calculated:

$$\Delta T_{int} = \frac{T_{int,exp} - T_{int,sim}}{T_{int,exp}} \quad (1)$$

$$\Delta T_{indoor} = \frac{T_{indoor,exp} - T_{indoor,sim}}{T_{indoor,exp}} \quad (2)$$

where $T_{int,exp}$ and $T_{int,sim}$ are the experimental and simulated internal surface temperature of the glazing, respectively; $T_{indoor,exp}$ and $T_{indoor,sim}$ are the experimental and simulated indoor air temperature of the test-room, respectively.

Figures 3a and 3b compare the simulation results with the experimental data in terms of T_{int} and T_{indoor} as a function of the time for the clear state (July 8th). These figures highlight how the modelled clear ED window predicts quite well the measured values. In particular, the values of ΔT_{int} range from -1.13% to 4.14%, while the values ΔT_{indoor} during July 8th range from -3.67% to 0.82%. Figures 4a and 4b compare the simulation results with the experimental data in terms of T_{int} and T_{indoor} as a function of the time for the milky state (July 12th). These figures highlight a good model reliability. In particular, the values of ΔT_{int} range from -1.79% to 2.19%, while the values of ΔT_{indoor} range between -4.14% and 1.08%.

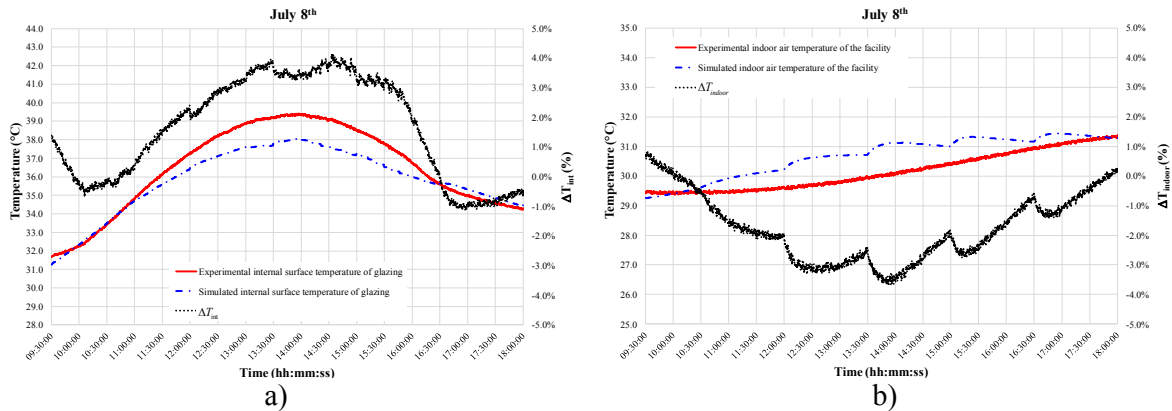


Figure 3. Comparison between simulation results and experimental data in terms of: a) internal surface temperature of the glazing, b) indoor air temperature.

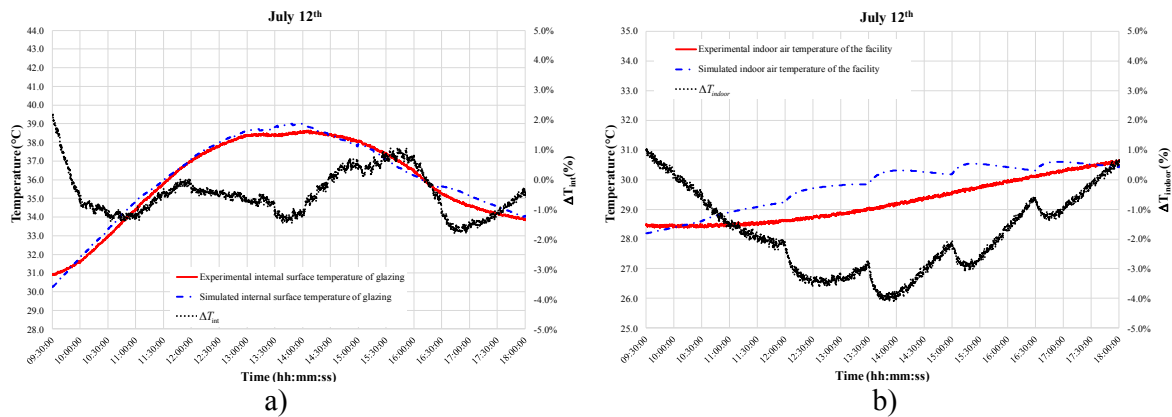


Figure 4. Comparison between simulation results and experimental data in terms of: a) internal surface temperature of the glazing, b) indoor air temperature.

Finally, the two simulation models of ED window were used to quantify the cooling energy demand reduction associated to a typical office building located in Naples (latitude = 40°51'46"80 N; longitude = 14°16'36"12 E) by replacing the conventional double-glazing windows with the same thermal transmittance. In particular, an office building with 200 m² as floor area and 600 m³ as volume with a total window area ($A_{w,total}$) of 36.02 m² ($A_{w,South}$ =27.02 m², $A_{w,East}$ = 4.5 m², $A_{w,West}$ = 4.5 m²) was modelled in TRNSYS 17 by means of the Type 56. Thermal transmittance of the building envelope has been equated to the threshold values specified by the Italian Law (Italian Decree 2015). A preliminary ON/OFF control logic for the ED window was used; in particular two hours before and two hours after the maximum

global solar radiation on the horizontal (from 10:00 up to 14:00) the ED window was switched in milky state, while it was switched in clear state in the rest part of the day. The cooling plant was considered ON from 8:00–18:00 in weekdays with an indoor target temperature equal to 26°C. Performing a simulation during the summer time (from June 1st to August 31st) with a simulation time step equal to 1 minute, a cooling energy demand reduction of about 26% was achieved.

CONCLUSIONS

In this paper the results of experimental tests and computer simulation modelling aimed at evaluating the thermal performance of a full-scale ED window with respect to solar control in buildings were reported. The experimental analysis showed how switching the ED window to the milky state can reduce the indoor air temperature of about 1°C. The ED window was modelled by means of the software WINDOW 7.5 and the comparison between numerical and experimental data showed a good reliability of the developed ED model.

Finally, a cooling energy demand reduction deriving from the integration of ED windows in a typical office façade located in Naples of about 26% was assessed by means of the software TRNSYS 17. In future works, the modelled ED smart window will be used to study and predict the performance of these windows under different operating scenarios.

REFERENCES

- Ascione F., De Masi R.F., de Rossi F., Ruggiero S. and Vanoli G.P., MATRIX, a multi activity test-room for evaluating the energy performances of ‘building/HVAC’ systems in Mediterranean climate: Experimental set-up and CFD/BPS numerical modeling, *Energy and Buildings* 126 (2016) 424–446.
- Baetens R., Jelle B.P. and Gustavsen A., Properties, requirements and possibilities of smart windows for dynamic daylight and solar energy control in buildings: a state-of-the-art review, *Sol. Energy Mater. Sol. Cell.* 94 (2010) 87–105.
- DELTA-OHM, <http://www.deltaohm.com/ver2012/>
- European Commission, Buildings, 2015, June 2015, <http://ec.europa.eu/energy/en/topics/energy-efficiency/buildings>
- Fernandes L.L., Lee E.S. and Ward G., Lighting energy savings potential of split-pane electrochromic windows controlled for daylighting with visual comfort. *Energy and Buildings* 61 (2013) 8–20
- GESIMAT, <http://www.gesimat.de/elektrotrop.html>
- Italian Decree, DM 26/06/2015, http://www.sviluppoeconomico.gov.it/images/stories/normativa/DM_requisiti_minimi.pdf
- Niklasson G.A. and Granqvist C.G., Electrochromics for smart windows: thin film of tungsten oxide and nickel oxide, and devices based on these, *Journal of Materials Chemistry* 17 (2006) 127–156.
- Piccolo A., Thermal performance of an electrochromic smart window tested in an environmental test cell, *Energy and Buildings* 42 (2010) 1409–1417
- Piccolo A., Pennisi A. and Simone F., Daylighting performance of an electrochromic window in a small scale test-cell, *Solar Energy* 83 (2009) 832–844.
- Piccolo A. and Simone F., Effect of switchable glazing on discomfort glare from windows, *Building and Environment* 44 (2009) 1171–1180.
- Sibilio S., Rosato A., Iuliano G., Scorpio M., Vanoli G. P. and de Rossi F., Preliminary experimental evaluation of electrochromic windows in a full scale test facility, in: Lux Europa 2017, Ljubljana, September 18-20, 2017, pp. 584-588.
- TRNSYS 17, <http://www.trnsys.com/>
- WINDOW 7.5, <https://windows.lbl.gov/tools/window/software-download>

A Novel Approach to Near-Real Time Monitoring of Ventilation Rate and Indoor Air Quality in Residential Houses

Achalu Tirfe^{*1}, and Jianshun Zhang¹

¹Syracuse University, Syracuse, USA

**Corresponding email: Achalu.Tirfe@gmail.com*

ABSTRACT

Physics-based infiltration models, like Lawrence Berkeley Laboratory (LBL) and Alberta Infiltration Model (AIM-2), have been used to predict infiltration rate in near-real time. These models are derived from the driving forces of wind and temperature difference across the building enclosure system, both of which cause pressure differences across the enclosure system for infiltration. The model incorporates other major factors like building leakage characteristics, distributions of openings, microenvironment conditions around the building enclosure as affected by building shields, topography and building shape. The accuracy of the models depends on getting these factors right. However, these factors are specific for individual buildings and measuring these factors in occupied buildings is difficult. In theory, these can be determined by using generalized table and blower door test but it requires heavy equipment and skilled work force, which is difficult to implement in occupied houses.

In this paper, a methodology is developed to determine the air change rate (ACH) and Indoor air quality (IAQ) in near-real time by combining a physics-based infiltration model with a tracer gas decay test method. The methodology is applicable to naturally ventilated houses. Existing infiltration models are modified explicitly to include the impact of the wind direction. The input data for the models also include indoor air temperature and weather data. Tracer gas method is used to determine the infiltration model parameters using multi variable nonlinear regression. Once these parameters are obtained, it is able to predict the ACH with 10% and 16% error for AIM-2 and LBL models, respectively

KEYWORDS

Infiltration, ACH, AIM2 model, LBL Model, Tracer Gas method

INTRODUCTION

For many residential houses in the U.S, infiltration is the main source of ventilation. Airtight buildings raise concern in indoor air quality (IAQ) unless mechanical ventilation is used (Skon et al., 2011). It requires measuring or predicting the ACH in better accuracy. The two standard methods to measure ACH are the building pressurization method and tracer gas method (ASTM E779-10, 2010; ASTM E741-11, 2011). Building pressurization method uses to compare infiltration between buildings and to measure building leakage characteristic. However, it is not applicable to near-real time infiltration measurement. Tracer gas method is the most accurate infiltration measurement near-real time. The choices of the tracer gas are limited. The presence of the occupant in test site could affect the measurement for tracer gas like carbon dioxide. Therefore, tracer gas methods are also not applicable at occupant presence.

Infiltration models are an alternative way to determine the infiltration rate in the building. The most common infiltration models are Reduction Pressurization Test, Regression Technique, ASHRAE Model, Building Research Establishment (BRE) model, Lawrence Berkley

Laboratory (LBL) model, and Alberta Infiltration model (AIM-2) (Awbi, 2003). All the infiltration models required blower door test to determine building leakage characteristics. Physics based models, LBL and AIM-2, gives a better prediction than the other models. These models derives base on the infiltration driving forces: wind and stack effect induced pressure differences across the building enclosure. They also include all of the important parameters like neutral pressure level, wind shield effect and building leakage characteristics. The accuracy of these models heavily depends on quantifying these factors. However, these factors are specific to individual buildings.

The objective of this paper is to combine the infiltration model, LBL or AIM-2, with tracer gas decay method to predict the ACH in near-real time for occupied naturally ventilated houses with a better accuracy.

METHODS

A methodology is developed to combine infiltration model (AIM-2 or LBL) with tracer gas method. As it is shown in Figure 1 below, the methodology has two parts: building calibration and monitoring. Steps only needed for building calibration are indicated by dotted line.

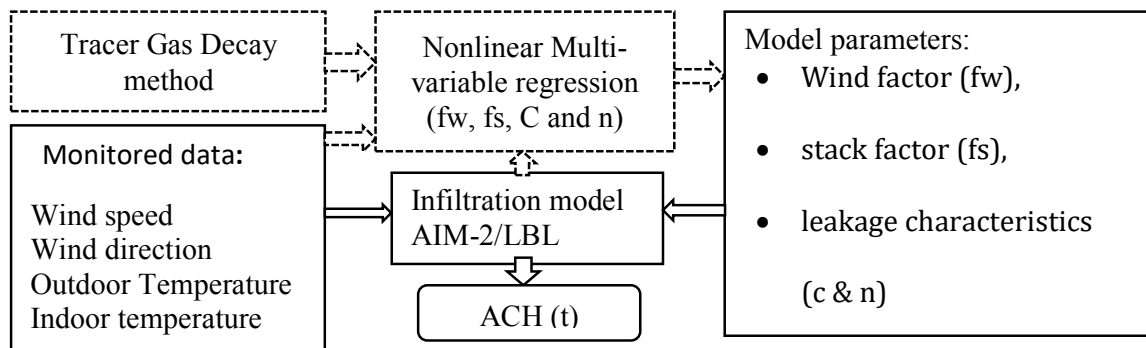


Figure 1. Methodology to determine ACH near-real time using tracer gas and weather data in the infiltration model

To determine the infiltration model parameter, preparing the house for a tracer gas decay test is the starting point. The calibration should be done in the absence of occupants. All door and windows should be closed. The indoor air temperature is set to 75°F and measured every minute. The weather data (temperature, wind speed and wind direction) for every minute is obtained from the nearby weather station. For this study, the National Oceanic and Atmospheric Administration (NOAA) weather data collected at Syracuse airport was used. A well mix condition is created inside the house by running the circulation fan continuously. The next step is to apply tracer gas method to determine the infiltration rate. The detail of the tracer gas technique was described in detail in (Sherman, M.H. 1990). CO₂ is injected until it reaches 1200 ppm. Occupant generated CO₂ can be used as the tracer gas for easier implementation of the method. This tracer gas concentration limit is set based on CO₂ sensor capacity. It can be injected in the return duct or after the circulation fan. The CO₂ concentration is measured in every minute. For leaky house the infiltration rate is higher. The tracer gas decays faster and reaches the outdoor CO₂ concentration before collecting enough data to do the regression. For this kind of situation, the tracer gas is injected again when the room CO₂ level reaches 600 ppm. The data collected from the BEST laboratory indicates that the outdoor CO₂ concentration is between 360 to 380 ppm. It is important to note that the presence of CO₂ in

the background would affect the ACH measurement. From the CO₂ concentration data, ACH is determined for every minute.

Once the weather data, the infiltration rate and the room temperature are known for every minute, nonlinear multi-variable regression technique is used to determine the infiltration model parameters. The regression variables, which are also the infiltration model parameters, are building leakage characteristics, building leakage exponent, wind factor and stack factor. To get valid results from the regression test, it is important to use the following the reasonable constraints:

1. Building exponent is between 0.5 and 1.
2. The building leakage coefficient is always greater than 0.
3. The combined shield and wind factor is between 0 and 1.
4. The stack factor is between 0 and 1.

Once the infiltration model parameters are determined from the regression, the infiltration of the house is calculated more accurately from the monitored wind speed, wind direction, the indoor temperature and the outdoor temperature.

Modified Infiltration Models

AIM-2 and LBL models are discussed in detail in (Walker and Wilson 1990) and (Sherman and Grimsrud, 1980) respectively.

In this paper, a discrete function is used to determine the wind factor and to capture the effect of the terrain and building microclimate as a function of wind direction. The wind factor function is given as:

$$f_w = \begin{cases} f1 & \text{where } 0 \leq \phi < 30 \\ f2 & \text{where } 30 \leq \phi < 60 \\ f3 & \text{where } 60 \leq \phi < 90 \\ \vdots & \\ \vdots & \\ f12 & \text{where } 330 \leq \phi < 360 \end{cases} \quad (1)$$

where f_w is the wind factor and ϕ is the wind direction. Wind angles 0, 90, 180 and 270 indicate wind blows from north, east, south and west respectively.

Error calculation

The absolute percentage error was used to compare the AIM2-Regression and LBL-Regression results. The error is calculated using the following equation:

$$|Error\%| = \frac{|(ACH_{measured} - ACH_{predicted})|}{ACH_{measured}} * 100 \quad (2)$$

where $|Error\%|$ is the percentage error, $ACH_{measured}$ is the air change rate measured using tracer gas method, and $ACH_{predicted}$ is the air change rate calculated using AIM-2 or LBL model.

Test House and location

The experiment was performed in Building Enclosure System Technology (BEST) laboratory located at Sky top Rd, Syracuse NY. The BEST laboratory is a two story building constructed in 2009 with the collaboration of Oakridge National Lab, Air Barrier Association of America, NYSERDA, and Syracuse University. The building has 41ft length, 33ft width and 21ft height. It has no internal partitions. The first story and the second story of the building are connected with a stairway opening. The building has central air system to cool and heat the house. The circulation system fan can set to run continuously. The building is also equipped with blower door test equipment. INNOVA gas monitoring system is used for tracer gas methods. The building east side is shielded by trees. An office building is located in the west side the test house. The south side has no shield. There is a hill on the south west side of the BEST laboratory building. The elevation difference is around 120 feet.

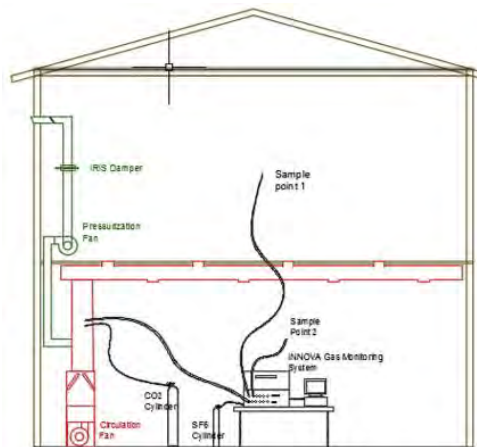


Figure 2. BEST lab equipment and arrangement

RESULTS

A non-linear multi-variable regression was used to determine the model parameters for both AIM2 and LBL models with a ten day data. Figure 3 presents the comparison between the measured and predicted ACH for AIM-2-Regression and LBL-Regression models respectively.

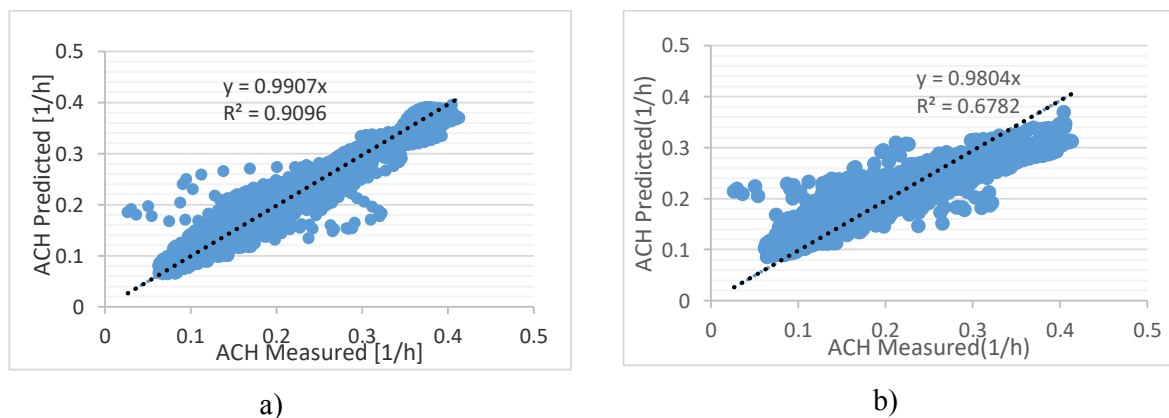


Figure 3. Comparison between measured and predicted ACH results. a) AIM-2 model, b) LBL model

Table 1 indicates the AIM2 regression result has average error of 9.7 % with the standard deviation of 9.2%. On other hand LBL regression result indicates an average error of 15.6% with a standard deviation of 14.1%.

Table 1: Average error in percent for LBL and AIM2 model

	AIM2-Regression	LBL-Regression
 Error% 	9.7%	15.6%
Standard deviation	9.2%	14.1%

AIM-2 regression model captures the entire measured infiltration spectrum better than LBL-Regression model. LBL-Regression tends to underestimate the infiltration rate due to the wind effect and overestimate infiltration rate cause by stack effect. The main difference between the AIM-2 regression and LBL regression equation that AIM-2 model considers the interaction between the wind effect and the stack effect. It is also important to notice that the wind effect of the AIM-2 model is as a function of wind velocity square.

Table 2: Comparison of AIM-2 regression with AIM 2 model done in other studies

	AIM2-Regression (BEST Lab)	Standard AIM2 model prediction (BEST Lab)			Francisco and Palmiter, 1996	Wang et al., 2009
Leakage Distribution	Not Applicable	X=R=0.6	X=R=0.5	X=R=0.37	X=R	X=0 & R=0.5
Error %	9.7	17.3	24	35	16.2	46
Standard Deviation (%)	9.2	12.7	18.6	22.6		16

Table 2 shows the percentage error of AIM2 model for BEST laboratory and work done in previous studies. We can see that the AIM-2-Regression is the only method able to predict the ACH with an average absolute value error less than 10 %.

DISCUSSIONS

The AIM-2 Regression and LBL Regression model wind factor was expressed in a discrete function. This capture the impact of the building shape and the building surrounding to improve the accuracy of the model. The model parameters are unique for each building and its surrounding. The nonlinear multivariable regression for each building give a better result.

The author likes to mention the following two assumptions were validated. First a well-mix condition was maintained when the circulation fan was running continuously. Second, Decay tracer gas method can be used to estimate near-real time ACH, if the decay process is capture in a minute interval and the CO₂ level is high enough from the background level. The minimum CO₂ level for decay test was set to 600 while the background level was around 360ppm.

CONCLUSIONS

The findings are summarized as followed:

- Weather data, IAQ monitoring and decay method can be used to predict the building leakage characterizes wind factor and stack factor.
- AIM2-Regression method predicts ACH better than LBL-Regression
- The accuracy of the new methodology is depending on the number of records obtained for regression.
- AIM-2-Regression predicts the ACH with an average absolute value error less than 10 %.

REFERENCES

- ASTM E741-11, 2011. Test Method for Determining Air Change in a Single Zone by Means of a Tracer Gas Dilution. ASTM International.
- ASTM E779-10, 2010. Test Method for Determining Air Leakage Rate by Fan Pressurization. ASTM International.
- Awbi, H.B., 2003. Ventilation of buildings, 2nd ed. ed. Spon Press, London ; New York.
- Franciso, P.W., Palmiter, L., 1996. Modeled and Measured Infiltration in Ten Single-Family Homes. American Council for Energy and Economy, Washington DC, USA.
- Hayati, A., Mattsson, M., Sandberg, M., 2014. Evaluation of the LBL and AIM-2 air infiltration models on large single zones: Three historical churches. *Build. Environ.* 81, 365–379.
- Palmiter, L., Bond, T., 1991. Modeled and Measured Infiltration : A Detailed Case Study of Four Electrically Heated Homes. *Electr. Power Res. Inst.*
- Sherman, M., Modera, M., 1986. Comparison of Measured and Predicted Infiltration Using the LBL Infiltration Model, in: Trechsel, H., Lagus, P. (Eds.), *Measured Air Leakage of Buildings*. ASTM International, 100 Barr Harbor Drive, PO Box C700, West Conshohocken, PA 19428-2959, pp. 325-325–23.
- Sherman, M.H., 1990. Tracer-gas techniques for measuring ventilation in a single zone. *Build. Environ.* 25, 365–374.
- Sherman, M.H., Grimsrud, D., 1980a. Measurement of infiltration using fan pressurization and weather data. Lawrence Berkely Labratory.
- Sherman, M.H., Matson, N.E., 2002. Air tightness of new houses in the U.S.: A preliminary report (LBNL report 48671). Lawrence Berkeley National Laboratory.
- Skon, J., Kauhanen, O., Kolehmainen, M., 2011. Energy consumption and air quality monitoring system, in: 2011 Seventh International Conference on Intelligent Sensors, Sensor Networks and Information Processing (ISSNIP). Presented at the 2011 Seventh International Conference on Intelligent Sensors, Sensor Networks and Information Processing (ISSNIP), pp. 163–167.
- Walker, I.S., Wilson, D.J., 1998. Field Validation of Algebraic Equations for Stack and Wind Driven Air Infiltration Calculations. *ASHRAE HVACR Res. J.* 4.
- Walker, Wilson, D.J., 1990. The Alberta Air Infiltraion Model. The University of Alberta, Department of Mechanical Engineering, Alberta.
- Wang, W., Beausoleil-Morrison, I., Reardon, J., 2009. Evaluation of the Alberta air infiltration model using measurements and inter-model comparisons. *Build. Environ.* 44, 309–318
- Wilson, D.J., Walker, I.S., 1991. Wind shelter effects on air infiltration for a row of houses. *12 AIVC Conf. 1*, 335–346.

Design and operational strategies for good Indoor Air Quality in low-energy dwellings: performance evaluation of two apartment blocks in East London, UK

Esfand Burman*, Clive Shrubsole, Samuel Stamp, Dejan Mumovic, Michael Davies

Institute for Environmental Design and Engineering, University College London (UCL), Central House, 14 Upper Woburn Place, London, WC1H 0NN, UK

*Corresponding email: esfand.burman@ucl.ac.uk

ABSTRACT

To achieve stringent energy objectives, new dwellings are subject to energy conservation measures including low air permeability and high levels of insulation. Mechanical Ventilation with Heat Recovery (MVHR) can be used to control the balance between energy efficiency and Indoor Air Quality (IAQ) in these buildings. This paper evaluates the effectiveness of the design and operational strategies adopted in a new development comprising two apartment blocks in East London. The findings point to significant gaps in operational energy use compared against design projections, and high concentrations in benzene and formaldehyde three years after construction. It is suggested that a combination of internal source control measures at design stage and building fine-tuning in early stages of post-occupancy is necessary to close the performance gap in energy and IAQ.

KEYWORDS

Low-energy dwellings, IAQ, MVHR, Performance gap

INTRODUCTION

In pursuing energy objectives such as the nearly zero-energy target in Europe, the existing standards for building air tightness and fabric heat loss are reaching their technical and economic limits. There is thus a risk that the focus may be shifting to save energy by reducing ventilation demand with potential adverse impacts on health and wellbeing. Annex 68 of the Energy in Buildings and Communities Programme of the International Energy Agency (IEA EBC Annex 68) aims to address this issue by finding design solutions and operational strategies that help achieve low energy and good IAQ in new dwellings. A review of empirical evidence carried out as part of the on-going activities in IEA EBC Annex 68 found that concentrations of pollutants such as toluene, ethylbenzene, trichloroethylene and styrene in new low energy dwellings were up to 10 times higher than in old dwellings (Salis, et al., 2017). Another driver for a focus on IAQ is heavy traffic and high outdoor pollution (e.g. micro particles and NO₂) in cities such as London and Beijing (Walton, et al., 2015).

The work presented in this paper is part of a wider research programme entitled 'Total Operational Performance of Low Carbon Buildings in China and the UK (TOP)', which covers the energy and environmental performance of a large cross section of non-domestic buildings and apartment blocks. The aim of this paper is to evaluate the Energy and IAQ performance of a new residential development. The specific objectives are to: 1) compare operational energy against design projections, 2) monitor the concentration level of major outdoor and indoor driven air-borne pollutants, and 3) identify the improvement opportunities to close the performance gaps in energy and IAQ in the context of the case study, and more generally suggest improvements for future projects.

OVERVIEW OF THE CASE STUDY

To investigate IAQ in low energy residential buildings, two recently built apartment blocks constructed as part of a regeneration scheme in East London were selected as a case study.

Apartment blocks A and B were completed in December 2014 and January 2015 respectively. Block A is a 13-storey building; Block B has 9 floors. They are located next to each other and close to two main roads in the London Borough of Tower Hamlets in East London. There are 97 flats and maisonettes (two-storey apartments) in these blocks. Building fabric U values are around 40% better than the limits prescribed by the 2013 edition of the Building Regulations. The buildings were also designed with target air permeability of 2-3 m³/hr./m² at 50 Pa pressure difference which is significantly lower than 10 m³/hr./m² limit set out in the Building Regulations (HM Government, 2013). Consequently, mechanical ventilation with heat recovery (MVHR) was specified to ensure adequate background ventilation is provided to these apartments. Heating is provided by a community heating scheme that is currently gas fired with provisions for integration of a combined heat and power (CHP) plant in future. There is no mechanical cooling. Table 1 provides background information about the sample apartments included in this study. The air permeabilities reported are based on pressure test results carried out on these apartments after building completion.

Table 1. Background information about sample apartments

Dwelling	Type	Gross Floor Area (m ²)	Floor level	Orientation	Bedroom no.	Occupant no. (steady mode)	Air tightness (m ³ /hr/m ² @ 50 Pa)
Apt. 1	Flat	100	Block A, 7 th floor	South/West	3	3	3.3
Apt. 2	Flat	100	Block A, 8 th floor	South/West	3	5	2.2
Apt. 3	Flat	100	Block A, 9 th floor	North/West	3	5	2.0
Apt. 4	Maisonette	127	Block B, Ground floor	South/East	5	7	3.8
Apt. 5	Maisonette	106	Block B, 8 th floor	East	3	4	2.9

METHOD

The following activities were planned with relevant methods adopted:

- 1) **Energy monitoring:** A review of the annual energy performance of the apartments that were fully occupied during the monitoring period and had reliable energy data was carried out. Heating demands of these apartments were compared against the projections made in the respective Energy Performance Certificates produced after completion in accordance with the Standard Assessment Procedure (BRE, 2012). Available data for the community heating scheme serving the blocks were sourced from its Energy Service Company (ESCO) to evaluate the supply side. Electricity use of five sample apartments sourced from the electrical meters were also compared against the benchmarks.
- 2) **Active monitoring of IAQ:** Five sample apartments were selected for detailed analysis of IAQ to meet the minimum sampling requirement of 5% of zones in large buildings in BS EN 15251 (BSI, 2007). IAQ sensors were installed to measure the concentration levels of CO₂, PM_{2.5} and NO₂ in living rooms and kitchens of the apartments during typical weeks

in the heating season (February-March 2018) with 5-minute frequency.¹ CO₂ levels were also monitored in one bedroom. CO₂ concentrations are often used as a proxy for IAQ in the UK construction sector. PM_{2.5} and NO₂ were identified as pollutants with risk of high concentration in new low energy buildings in the IEA EBC Annex 68 programme with significant health impacts, and are also of great interest in London due to major outdoor sources for these pollutants. Concentrations of these pollutants were compared against the recommended limits provided in BS EN 15251 and WHO guidelines (WHO, 2006).

- 3) **Passive Sampling for IAQ:** the diffusive sampling method, in accordance with ISO 16017, was used to measure the average concentrations of volatile organic compounds (VOCs) with risk of concentrations higher than long-term/chronic exposure limit values (ELVs) in new low energy dwellings (Salis, et al., 2017). Concentration levels of benzene, formaldehyde, trichloroethylene, styrene, naphthalene, toluene, and tetrachloroethylene were measured in living room, kitchen and one bedroom of the sample apartments during the same weeks active monitoring took place. Passive tubes and absorbent pads were also installed outdoors to identify the indoor/outdoor trends and sources. Finally, to give context to IAQ monitoring results, a perfluorocarbon tracer (PFT) gas method (Persily, 2016) was used to infer the average air exchange rates in the monitored zones of the sample apartment.

RESULTS

Energy: Figure 1 compares the actual heating demand of 40 apartments in the case study against the design projections. Actual heating demand in 30 apartments is higher than expected and in the worst case is around three times more than the design performance. Figure 1 also shows a snapshot of a thermographic survey of the case study which did not reveal any significant defects or thermal bridges within the external envelope. These observations, combined with the variation in heating demand across different apartments, suggests the overall increase in heating demand is predominantly driven by occupant behaviour (e.g. heating set points and heating schedules), and is reminiscent of the rebound effect seen in new dwellings built to meet energy efficiency requirements (Kelly, 2011).

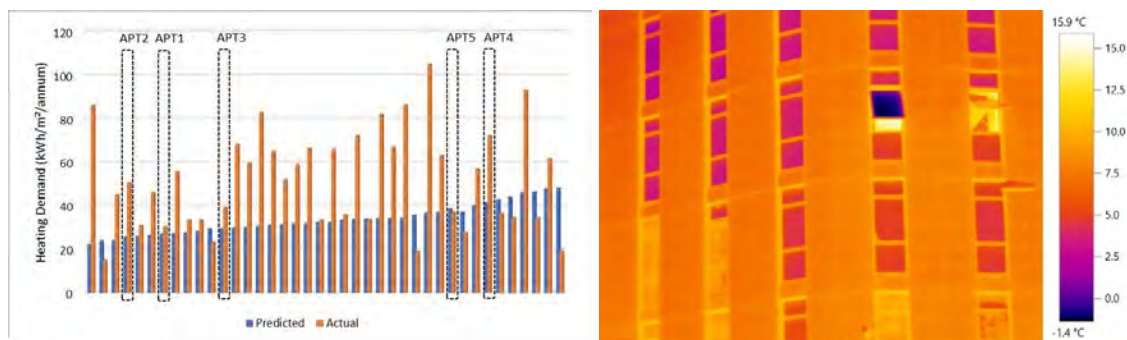


Figure 1. Actual vs. design heating demand, and external envelope thermographic survey

The annual gas use data and the data for delivered heat to the apartments released by the ESCO running the community heating scheme show an average annual heating efficiency of 50%, significantly lower than the design specification of 87%. This exacerbates the performance gap between actual operation and design intent.

¹ Measurement accuracies: CO₂: ± 50 ppm, PM_{2.5}: 0.84 coincidence probability at 10⁶ particles/L; 0.24 coincidence probability at 500 particles/L, NO₂: $< \pm 0.5$ ppm

Annual electricity use of all sample dwelling is higher than design intent with a maximum 53% deviation in Apartment 3.

Active monitoring of IAQ: Figure 2 shows the boxplots for indoor concentration levels of CO₂, and indoor and outdoor concentrations of PM_{2.5}, and NO₂.²

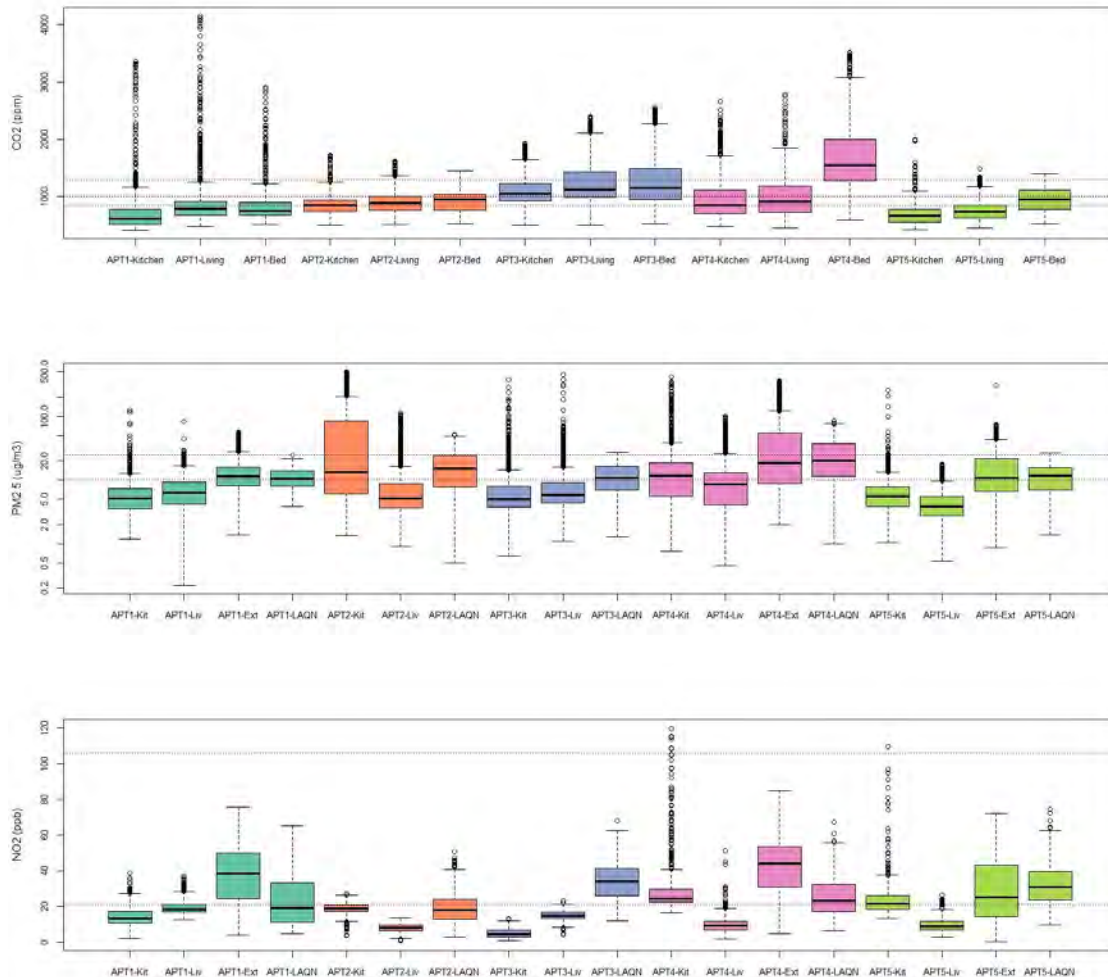


Figure 2. Concentrations of CO₂, PM_{2.5}, and NO₂ during typical weeks in heating season

The dotted horizontal lines on the CO₂ graph represent 350, 500, and 800 ppm above external CO₂ concentrations in keeping with the classification provided in BS EN 15251. Apartments 3 and 4 show CO₂ concentration levels above the other apartments and the most lenient guideline limit, which could be indicative of inadequate ventilation. The guideline limits for PM_{2.5} are the WHO annual and daily means of 10 µg/m³ and 25 µg/m³ respectively. It is notable that the outdoor PM_{2.5} levels are often higher than WHO guideline for annual mean. However, indoor concentrations in most spaces are kept below the guideline limit most of the time, which could be indicative of the effectiveness of the air filtration installed in the MVHR system. Whilst outdoor levels are again often higher than the WHO annual mean (40 µg/m³, 21 ppb), indoor NO₂ levels are generally lower than this limit, except in the kitchens of Apartments 4 and 5. Indoor NO₂ levels are generally well below the WHO hourly guideline

² Ext: external air quality kit installed onsite, LAQN: closest weather station to the site

limit of 200 $\mu\text{g}/\text{m}^3$ (105 ppb). In addition to the effect of outdoor sources, $\text{PM}_{2.5}$ and NO_2 levels in apartments could be increased by internal sources especially in the kitchens.

Passive Sampling for IAQ: Table 2 reports the results of passive sampling for Apartments 3 and 4. These apartments were selected for reporting in this paper as the active monitoring results pointed to potential ventilation issues in these apartments. Furthermore, this selection allows a cross comparison of the dispersion of pollutants in the lowest (ground floor) and highest (9th floor) height in the sample and between different building orientations.

Table 2. Passive sampling results for Apartments 3 and 4 (typical weeks in heating season)

VOC concentration ($\mu\text{g}/\text{m}^3$) & Air Change rates per Hour for each zone	APT. 3 (Block A, 9th Floor)			APT. 4 (Block B, Ground Floor)			IEA EBC Annex 68 Long Term ELV
	Living room	Kitchen	Sample bedroom	Living room	Kitchen	Sample bedroom	
Benzene	1.3	1.0	1.2	1.5	2.1	1.6	0.2
Formaldehyde	29.25	26.87	29.53	21.23	31.35	27.44	9
Trichloroethylene	<0.5	<0.5	<0.5	<0.5	<0.5	<0.5	2
Styrene	1.5	2.2	3.0	0.8	0.7	1.7	30
Naphthalene	5.4	5.4	5.0	0.9	0.9	1.3	2
Toluene	2.7	2.9	3.1	2.2	2.6	2.4	250
Tetrachloroethylene	0.6	<0.6	<0.6	1.5	1.2	1.8	100
ACH (PFT measurements)	0.50	0.52	0.76	1.02	1.14	0.6	n/a

The VOCs with concentration levels higher than the recommended long-term ELVs are highlighted in bold. While high concentrations of Naphthalene could be a specific problem in Apartment 3 related to occupant behaviour (e.g. smoking or use of chemical insecticides/pest control), concentrations of Benzene and Formaldehyde in both apartments are significantly higher than the respective ELVs. Measurement of outdoor concentrations confirm benzene is driven by outdoor sources, whereas formaldehyde levels are driven by internal sources.

DISCUSSION

The outcomes of this study point to the challenge of achieving a ‘low energy’ building in practice. People’s expectation of comfort in new dwellings may be different than their previous older accommodation. This case study represented a social housing scheme. An appropriate system of incentives and effective behavioural strategies may be developed in parallel with design processes and implemented post-occupancy to address potential rebound effects. From a supply point of view, the existing operational efficiency of the community heating scheme is a key driver of the performance gap. This is however not a unique case. Detailed studies of community heating schemes have found operational efficiencies as low as 37% (Wingfield, et al., 2013). The existing plant room in the case study is currently not running at full capacity, as the second phase of the development has not yet been completed and part load performance compromises efficiency. Distribution losses are also a major issue and significantly higher than the default factor of 5% assumed for new developments in the Standard Assessment Procedure (BRE, 2012). Better understanding of inefficiencies in energy generation and distribution can help narrow the energy performance gap. If the operational issues are addressed, a community heating scheme provides ample opportunities for further improvements including decarbonisation by integrating CHP plant with other technologies. Air filtration in the installed MVHR units appear to be effective. The ventilation rates inferred from PFT measurements are also generally consistent with the minimum ventilation

requirements set out in the UK Building Regulations (HM Government, 2010), although the MVHR system is only partially responsible for air exchange, and other factors such as natural ventilation (via window opening) are also effective. Enhanced ventilation beyond the regulatory requirements by adjusting the fan speed in the MVHR to its boost or maximum flow rate can help reduce formaldehyde levels, although this can also increase the concentrations of outdoor driven pollutants such as benzene as well as energy use. A trade-off based on an assessment of health impact of these pollutants may inform the ventilation strategy. However, a more fundamental solution in future projects is to improve source control of materials used in the building and furniture to keep formaldehyde levels below the limits. The fact that after three years of building handover formaldehyde levels are higher than three times the chronic ELV points to significant IAQ issues and potential health impacts. This problem can be addressed by a combination of source control and enhanced/boost ventilation in the early stages of post-occupancy with seasonal commissioning to reduce fan speed after the off-gassing period and when measurements confirm concentrations of formaldehyde and other critical pollutants are acceptable.

CONCLUSIONS

This study uncovered significant gaps in energy performance and concentration levels of benzene and formaldehyde in dwellings more than 3 years after construction. The gap between actual building performance and design intents is currently not adequately addressed in energy efficiency policies. The intricate relation between energy efficiency requirements and IAQ may also lead to unintended consequences for IAQ where sources of pollution are not effectively controlled and ventilation is not adequate. Building performance evaluation and fine-tuning in the early stages of post-occupancy should be an integral part of building procurement process to ensure low energy and good levels of IAQ are delivered in practice.

ACKNOWLEDGEMENT

The authors wish to thank building occupants for their support and participation in research. This research was funded by the EPSRC ('TOP' project, Grant Code: EP/N009703/1).

REFERENCES

- BRE, 2012. *The Government's Standard Assessment Procedure for Energy Rating of Dwellings*, Watford: BRE.
- BSI, 2007. *BS EN 15251:2007, Indoor Environmental Input Parameters for Design and Assessment of Energy Performance of Buildings Addressing Indoor Air Quality, Thermal Environment, Lighting and Acoustics*, London: BSI.
- HM Government, 2010. *Approved Document Part F, Means of ventilation*, s.l.: NBS.
- Kelly, S., 2011. Do homes that are more energy efficient consume less energy?: A structural equation model of the English residential sector. *Energy*, Volume 36, pp. 5610-5620.
- Persily, A., 2016. Field measurement of ventilation rates. *Indoor Air*, 26(1), pp. 97-111.
- Salis, L. C. R., Abadie, M., Wargocki, P. & Rode, C., 2017. Towards the definition of indicators for assessment of indoor air quality and energy performance in low-energy residential buildings. *Energy and Buildings*, Volume 152, pp. 492-502.
- Walton, H. et al., 2015. *Understanding Health Impacts of Air Pollution in London*, London: King's College London.
- WHO, 2006. *WHO Air quality guidelines for particulate matter, ozone, nitrogen dioxide and sulfur dioxide*, Geneva: The World Health Organization (WHO).
- Wingfield, J. et al., 2013. *Centenary Quay Fabric and District Heating Performance Study*, London: Innovate UK Building Performance Evaluation programme.

Effects of Semi-Open Space on Micro-Environmental Control

Meng Kong^{1,*} and Jianshun Zhang¹

¹Department of Mechanical and Aerospace Engineering, Syracuse University, NY, USA

*Corresponding email: mkong01@syr.edu

ABSTRACT

Semi-open space (SOS) is defined as a space semi-confined by partitions in an open space environment. Most of the previous indoor environmental researches were focused on the open space environment, while only a few of them looked into the performance of the SOS. The existence of the SOS is for providing a certain level of privacy to the occupant, but it has been reported that it significantly affects the room air distribution, hence the thermal environment and indoor air quality. The micro-environment control system is defined as a system which provides heating, cooling or ventilation to the occupant locally. In this study, we evaluated the performance of a cubicle, as an SOS in the office, with different configurations, including opening size and orientation, and the combination of the micro-environmental control system and SOS in providing improved indoor air quality. The work included the computational fluid dynamics (CFD) simulation representing a typical office space with one cubicle. The results showed that the cubicle “protects” the occupants from background air flow but this protection may not always be favored, and the location of the pollutant source significantly influenced the performance of the cubicle. The combination of the micro-environmental control system helped create an independent micro-environment as well as offset the effect of the cubicle.

KEYWORDS

Semi-open space, micro-environmental control system, air quality, computational fluid dynamics, cubicle.

INTRODUCTION

Semi-open Space (SOS) is defined as a subspace created by semi-enclosed partitions in a larger open space. A semi-open space, on the one hand, is a partially open space with connections between one SOS and the others as well as the outside space. On the other hand, SOS also provides a relatively independent space. So far most of the ventilation studies are focused on the air distribution in open spaces.

Only a few studies have been conducted to investigate the performance of SOS (Zhang et al. 2007; Demetriou et al. 2008). Jiang et al. (1997) numerically studied two kinds of office configurations with five ventilation strategies and found that the use of partitions significantly affects the uniformity of the supply air distribution. Bauman (Bauman et al. 1991; Bauman et al. 1992) did a very comprehensive work to look into the influence of a series of partition configurations and environmental parameters in a ceiling-ventilated room regarding the thermal environment and ventilation efficiency. After this study, another work (Shaw et al. 1993; Shaw et al. 1993) investigated the effect of the cubicle partition on the air quality. It was concluded that the existence of a cubicle could cause a dead air space inside the cubicle and, hence, an increase of mean age of air. Nevertheless, due to the non-uniformity of the mixing ventilation, different configurations of the workstation and different air supply conditions, the effects of the partitions cannot be generalized.

The micro-environment control system (μ X) or personal environmental control (PEC) system is defined as a system which provides heating, cooling or ventilation to the occupant locally. Integrated with an SOS, the μ X has a big potential of saving energy while improving thermal comfort level and air quality around occupants as well as providing sound, light, and spatial privacy. This study is focused on investigating how the Semi-Open Space, equipped with or without a μ X, would affect the air quality by using the Computational Fluid Dynamics (CFD) model.

METHODS

A CFD model based on the guidelines given by Russo's validated CFD case (Russo, 2011) was developed and further validated by the experimental work (Kong et al. 2017). A 1.8 m \times 1.8 m cubicle placed in a typical office space was built in the CFD model (Figure 1). The air quality in all regions in the room was compared for scenarios with and without a cubicle. The effect of the openness of the cubicle was also investigated as well as the opening direction. This work also included the studies on the effects of the cubicle as an SOS in combination with a μ X with local air purification.

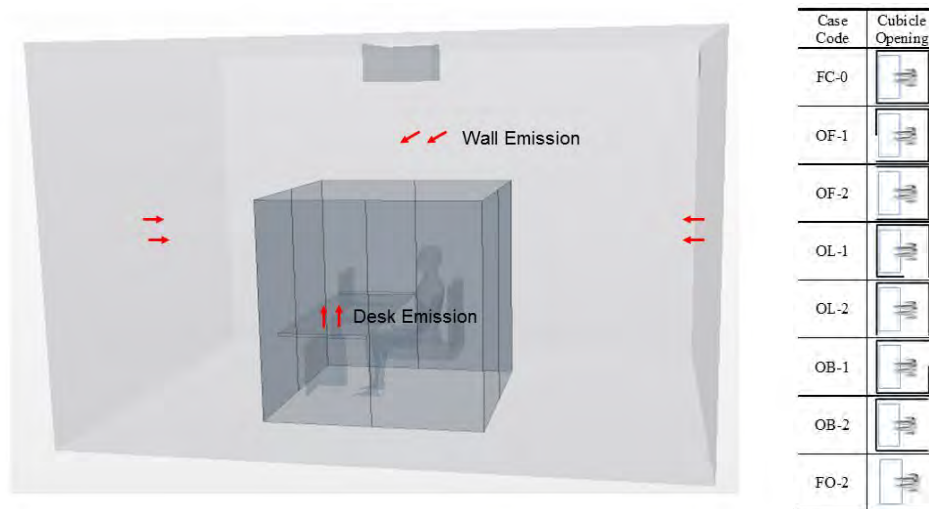


Figure 1 Computational domain and cubicle opening condition

The room modeled is the same as those used in the previous work (Kong et al. 2017). The cubicle was created symmetrically around the desk and seated occupant. The height of the cubicle partition was 1.8 m. All the four sides of the cubicle could be half or fully opened. The boundary condition of each segment of the manikin was set to be constant heat flux. The heat flux value came from the experimental results. The room wall was set to be the same with the indoor temperature set-point (return air temperature) – 26.1 °C for the cases with the μ X (because the μ X was designed to provide local cooling for elevated room temperature) and 23.9 °C for the case without the μ X. The supply air temperature from the μ X was set to be 23.0 °C at a flow rate of 0.014 m³/s. Since this work focuses on how the cubicle configuration, as well as the μ X, affects the indoor air quality instead of the actual distribution of specific contaminant, a tracer gas (sulfur hexafluoride, SF₆) was used to represent the pollutant emission. Two emission sources, the wall, and the desk, were simulated in this work (Figure 1). The emission from the wall is used to present the case in which pollutant sources are outside the cubicle and that from the desk to represent the sources inside the cubicle. The μ X placed under the table has a supply duct attached to the bottom side of the table and two

suction openings on both sides of the box (Kong et al. 2017). When the μX is on, the air purification starts to work by taking in contaminated air and supplying clean air.

In the current work, the Contaminant Removal Efficiency (also called Ventilation Efficiency, ε) and Blocking Coefficient (β), were used to quantify the performance of the ventilation strategies and SOS. The Contaminant Removal Efficiency or Ventilation Efficiency was calculated using Eqn. 1 where C_e is the pollutant concentration in the exhaust, C_s is the pollutant concentration in the supply and C_p is the pollutant concentration in the breathing zone, which is conventionally defined as the zone within a 0.3 m radius of a worker's nose and mouth (OJIMA 2012). Blocking Coefficient was calculated using Eqn. 2 where C_{SOS} is represented by the volume averaged SF6 concentration in the cubicle.

$$e = \frac{C_e - C_s}{C_p - C_s} \quad (1)$$

$$\beta = \frac{C_e - C_s}{C_{SOS} - C_s} \quad (2)$$

RESULTS AND DISCUSSIONS

The partitions around the workstation changes the airflow pattern around it, hence the contaminant distribution. However, the performance of the cubicle is dependent on many factors, including the opening direction and size, the location of the contaminant source, as well as whether the μX is on or off.

Pollutant mass fraction level in the breathing zone

Pollutant mass fraction in the occupied space is a direct indication of the air quality. Figure 2a shows the mass fraction level of the SF6 when the pollutant was emitted from the desk. When the μX is off, FC gave the highest pollutant mass fraction in the breathing zone, and the pollutant concentration in the breathing zone was reduced with opened cubicles. After turning on the μX , the effect of the local purification was obvious regardless whether there was a cubicle even though the clean air was not supplied to the breathing zone directly. Figure 2b shows the mass fraction level of the SF6 in the breathing zone when the pollutant was emitted from the wall. Different from the cases of desk source, the pollutant mass fraction in the breathing zone was quite close to each other among the cases without local purification. This is because when the emission was from the walls, the distribution of the pollutant was very uniform, and the air was well mixed before it entered the cubicle. When the μX was turned on with local purification, regardless how the cubicle was arranged, the mass fraction was reduced by almost the same amount.

Contaminant Removal Efficiency

In order to examine the performance of the ventilation system under different configurations of the cubicle, Contaminant Removal Efficiency (e) was calculated in the breathing zone (Figure 3). The results show that when the pollutant was emitted from the desk, the air quality in the breathing zone was not better than the well-mixed condition for any of the cases with or without the μX . The worst efficiency was given by the FC case. The use of the μX could improve the efficiency by more than 20 percent when there was a fully closed cubicle or no cubicle at all. When the cubicle was opened partially the advantage of using the μX became unclear and sometimes negative. This means that when the cubicle was partially opened, adding a local purification in the μX is not necessarily better than adding purification process in the background mixing ventilation. When the pollutant was emitted from the wall, as

mentioned before, a well-mixed condition was established in the room including the cubicle, so the e in the breathing zone of any cases was around 100%. However, different from the case of the desk source, the use of the μ X with local purification always brought an improvement of the air quality in the breathing zone.

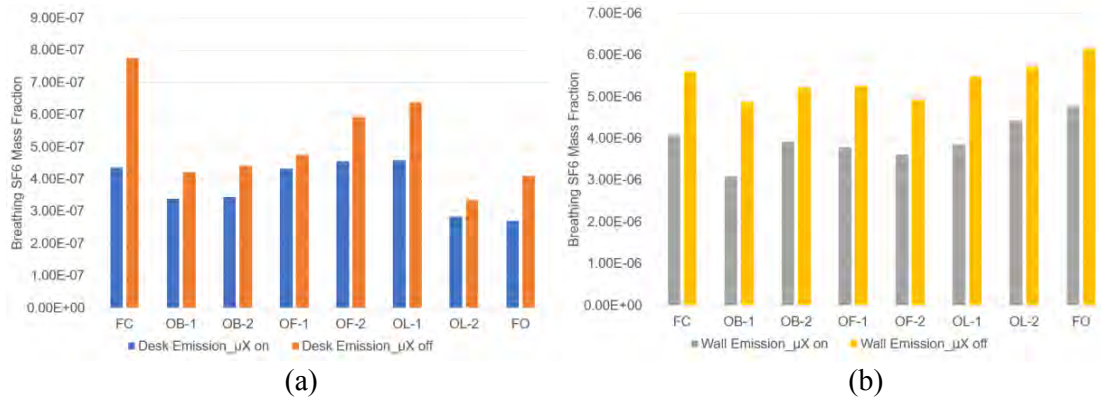


Figure 2 SF6 mass fraction in the breathing zone (a. desk emission; b. wall emission)

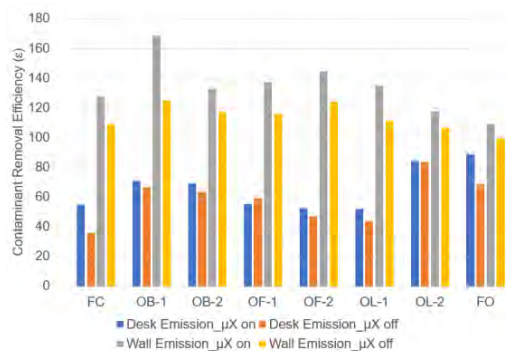


Figure 3 Contaminant Removal Efficiency in the breathing zone

Figure 4a shows the Contaminant Removal Efficiency contours for the cases with desk emission. It was demonstrated that the pollutant distribution in the cubicle was highly non-uniform, especially in the region close to the desk. The dirty air carrying the pollutant from the desk was mixed with the surrounding air in the cubicle and then was pulled out of the cubicle due to the entrainment of the supply jet of the background mixing ventilation. The make-up air entered the cubicle in different ways depending on the opening direction and size and diluted the air in the breathing zone. A local jet of clean air was observed when the μ X was turned on. However, since the local supply air was maintained at a lower temperature than the ambient room air, most of the local clean air, instead of entered the breathing zone, was transported downward to the lower region and mixed with the dirty air carrying the pollutant from the bottom side of the desk. This should be the reason why the μ X brought little improvement of the contaminant removal efficiency in the breathing zone. Figure 4b shows the Contaminant Removal Efficiency contours for the cases with wall emission. Different from the cases of desk emission, the pollutant distribution of the wall emission cases was much more uniform and well-mixed. When the μ X was turned on, a clean jet, as well as a clean region, showed up around the occupant. This clean region effectively reduced pollutant concentration in the breathing zone and increased the contaminant removal efficiency. Comparing these cases with the cases of desk emission, the reason why the μ X could improve the air quality more effectively is that in the lower region of the cubicle there was no pollutant

source and therefore the cooler clean air remained clean before it was taken by the thermal plume to the breathing zone.

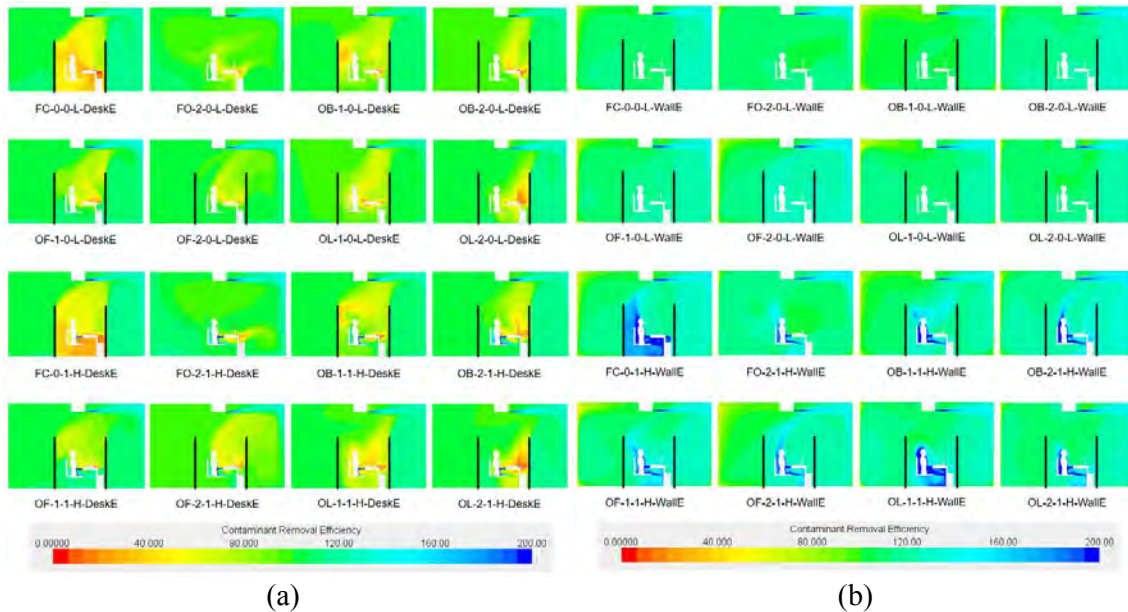


Figure 4 Contaminant Removal Efficiency (a. desk emission; b. wall emission)

Blocking Coefficient

Blocking Coefficient (β) is an index to quantify the performance of the SOS. It is a ratio between the exhaust pollutant concentration and the pollutant concentration in the SOS. Figure 5 illustrates the blocking coefficient of the cubicle. When there was no cubicle, the blocking coefficient was around 100% regardless where the emission source was. When the pollutant was emitted from the desk, β was always less than 100%. A fully closed cubicle (FC) gave a blocking coefficient less than 40%, and a partially opened cubicle gave a blocking coefficient between 60% and 80%. In this case, the μX did not make a big difference because it reduced the pollutant level in the cubicle as well as the pollutant level in the exhaust. When the pollutant was emitted from the wall, the β was always higher than 100%. Without the μX , β was a little higher than 100% with a maximum of around 120%. Turning on the μX could significantly improve the blocking coefficient, and the most improvement was given by the fully closed cubicle in which the blocking coefficient was increased by 30%. This is because the fully closed cubicle could hold most of the clean air made by the μX inside the cubicle.

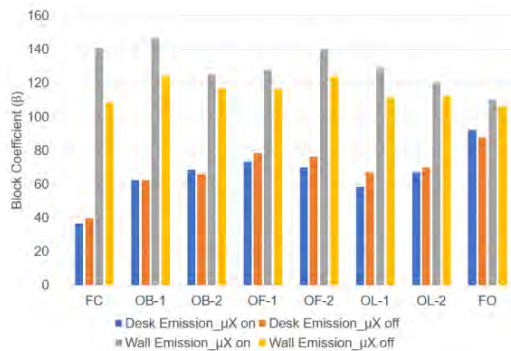


Figure 5 Blocking Coefficient of the cubicle

CONCLUSIONS

The effects of the cubicle and the combination of the μX with air purification in the cubicle on the air quality were evaluated using CFD simulation. The results indicate that the performance of the cubicle that defines the semi-open space was highly sensitive to the location of the emission location and it should be used and designed with caution. When the pollutant was emitted inside the cubicle, the use of the cubicle was unfavoured since it prevented the contaminant from being diluted by the mixing ventilation. However, when the pollutant was emitted from outside cubicle, the use of it should be encouraged since it helps prevent the contaminant from entering the cubicle. The use of the μX with local air purification could always improve the air quality in the breathing zone, and especially when the emission source was outside the cubicle, it demonstrated a big advantage. However, this combination might not be more efficient than adding the same amount of purified return air to the background mixing ventilation system when the emission source was inside the cubicle. In general, the use of the μX with local air purification is beneficial for improving the air quality in the breathing zone and the cubicle, reducing the pollutant concentrations by 10 to 44%.

ACKNOWLEDGEMENT

The work presented herein was partially supported by a project funded the Advanced Research Projects Agency-Energy (ARPA-E), U.S. Department of Energy, under Award Number **DE-AR0000526** and Syracuse University. The views and opinions of authors expressed herein do not necessarily state or reflect those of the United States Government or any agency thereof.

REFERENCES

- Bauman, F. S., D. Faulkner, E. a. Arens, W. J. Fisk, L. P. Johnston, P. J. McNeel, D. Pih, and H. Zhang. 1992. Air movement, ventilation, and comfort in a partitioned office space. *ASHRAE Transaction: Symposia*, 98(1):0–13.
- Bauman, F. S., D. Faulkner, E. A. Arens, W. J. Fisk, L. P. Johnston, P. J. McNeel, D. Pih, and H. Zhang. 1991. *Air movement, comfort and ventilation in workstations*. Berkeley.
- Demetriou, D., O. Ozdemir, H. E. Khalifa, and C. Isik. 2008. Distributed demand controlled ventilation for improving IAQ. In *11th International Conference on Indoor Air Quality and Climate. Copenhagen, Denmark*.
- Jiang, Z., F. Haghghat, and Q. Chen. 1997. Ventilation Performance and Indoor Air Quality in Workstations under Different Supply Air Systems: A Numerical Approach. *Indoor and Built Environment*, 6(3):160–167.
- Kong, M., T. Q. Dang, J. Zhang, and H. E. Khalifa. 2017. Micro-environmental control for efficient local cooling. *Building and Environment*, 118:300–312.
- OJIMA, J. 2012. Gaseous Contaminant Distribution in the Breathing Zone. *Industrial Health*, 50(3):236–238.
- Russo, J. 2011. A Detailed and Systematic Investigation of Personal Ventilation Systems.
- Shaw, C. Y., F. Vaculik, J. S. Zhang, R. J. Magee, and M. N. Said. 1993. Effect of air diffuser layout on the ventilation conditions of a workstation. Part II: Air change efficiency and ventilation efficiency. *ASHRAE Transactions*, 99(2):133–143.
- Shaw, C. Y., J. S. Zhang, M. N. Said, F. Vaculik, and R. J. Magee. 1993. Effect of air diffuser layout on the ventilation conditions of a workstation. Part I: Air distribution patterns. *ASHRAE Transactions*, 99(2):125–132.
- Zhang, S., H. E. Khalifa, and J. F. Dannenhoffer. 2007. Flow between adjacent cubicles due to occupant-controlled floor diffusers. In *Roomvent 2007 Conference, Helsinki, Finland*.

Numerical investigation of a diffuse ventilation ceiling system for buildings with natural and hybrid ventilation

Alessandro Nocente^{1,*}, Francesco Goia¹ and Steinar Grynning²

¹Norwegian University of Science and Technology (NTNU), Trondheim, Norway

² Sintef Byggforsk, Trondheim, Norway

**Corresponding email: alessandro.nocente@ntnu.no*

ABSTRACT

The need to meet requirements, both in terms of ventilation and thermal comfort in modern buildings, has led to the development of different concepts for ventilation, among which the so-called Diffuse Ceiling Ventilation (DCV). This system makes use of the space between the ceiling slabs and the suspended ceiling as a plenum for fresh air, while the suspended ceiling itself becomes an air diffuser element. If compared to traditional solutions, this allows a higher amount of ventilation air to be injected in the room at lower speed, and a more even distribution of the fresh air within the room. Furthermore, it allows an easy integration with sound-absorbing perforated ceiling panels, since their typical design makes them particularly fit to be used as air diffusers.

This paper builds upon a previous work by the authors where CFD simulations were used to optimise the dimension and the distribution of the perforation pattern in the panels to achieve an even air speed distribution. In this work, the performance of the perforated ceiling is investigated in a more comprehensive way, evaluating the thermal comfort in the room when varying the outdoor temperature. This solution is in fact meant to work in combination with natural or hybrid ventilation strategies, where the fresh air flow is supplied from the façade.

Numerical simulations were performed on a typical office room, considering both the winter and the summer season, for different inlet air temperatures. This solution demonstrated a positive impact on the indoor conditions and on the thermal comfort inside the room in most of the cases but the most extreme ones. The thermal stratification in the room demonstrated to remain within a satisfactory level.

KEYWORDS

CFD, Diffuse Ceiling Ventilation (DCV), Sound absorbing perforated panels, Natural and hybrid ventilation, Thermal comfort.

INTRODUCTION

Diffuse Ceiling Ventilation (DCV) is a novel air distribution concept for ventilation in low and plus energy buildings. The volume between the ceiling slabs and the suspended ceiling constitutes a plenum where the ventilation air is injected, and the dropped ceiling acts as an air diffuser. This way a large amount of ventilation air can be provided to the room at lower speed, and with a more even distribution compared to conventional inlet solutions realized through ceiling/wall/duct diffusers. According to previous researches, this concept provides several advantages, such as a low pressure loss, low investment cost and higher thermal comfort if compared to traditional ventilation systems (Zhang et al. 2016).

First proposed in livestock buildings (Van Wagenberg and Smolders 2002), it was presented as a suitable solution to improve the air quality in classrooms by Jacobs et al. (2008). Several scholars investigated the effect of the suspended ceiling characteristics on the ventilation quality (Fan, et al. 2013; Petersen et al. 2014). Zhang et al. (2015) performed hot-box

measurements to evaluate the possibility to couple the DCV with water based thermal elements in the plenum while Hviid and Svendsen (2013) evaluated the performances and excluded DCV as source of possible thermal discomfort by means of experiments in a real size test chamber. The last two works both considered the dropped ceiling as realised with sound-absorbing perforated panel. The presence of these panels is quite common, especially in office buildings, and their constructive characteristics make them particularly fit to act as air diffuser without particular design modification, even if their use as air diffuser could slightly affect the sound absorbing capacity – an aspect not herewith investigated, though.

One of the known limitation of the DCV concerns the possible unevenness in the air distribution in the room. In fact, the injection of air ventilation in the plenum typically takes place through a surface of the plenum or via duct works. This creates an uneven pressure distribution in the plenum, therefore the air exiting the diffuser will present a highly non-uniform velocity profile. A proper design of the suspended ceiling considering the use of different panels perforation size and rate in different zones, could partially solve this issue.

In the last years, CFD as a tool to evaluate the performance of DCV appeared in research works (Mikeska and Fan 2015; Zhang et al. 2017). In those cases, the perforated panels were modeled as porous media, not focusing on the different influence that different perforation patterns can have on the fluid dynamics of the ventilation and the air circulation in the room.

In Figure 1, a comparison between injecting the air directly through the façade ((a) and (b)) or through the dropped ceiling plenum is shown. This first illustration previews how a direct inlet leads to potential discomfort (a) due to low air temperature (below 10 °C in most of the room) and an uneven distribution of the fresh air (b), especially if compared to a solution where the air is (much more evenly) distributed through the plenum of the dropped ceiling (c). The present investigation builds up on a previous work by the authors (Nocente et al. 2018) in which CFD calculations were used to evaluate an optimal panel distribution for a typical office room which ensures a more even velocity distribution out of the perforated ceiling. The previous work focused only on the fluid-mechanical aspects, but neglected the thermal domain of the problem.

The objective of the analysis presented in this paper is instead to take into consideration the thermal environment derived by the direct injection of ventilation air from the façade through the dropped ceiling. For this reason, simulations have been carried out parametrizing the inlet temperature (and the airflow rate) with the aim of assessing the performance of DCV in a more comprehensive way, and evaluating the risk of incurring in thermal discomfort conditions in the room under different outdoor air temperature conditions.

The investigation is however limited by the fact that the entire thermal balance of the room is not considered, i.e. the effect of the ventilation air on the heating and cooling load of the room is not assessed in this work.

METHODS

Numerical Model

In a previous work (Nocente et al. 2018) three models (with different perforation size and distribution) of commercially available sound-absorbing panels were taken into account for the suspended ceiling. Two optimal combination were found in that study, and one of those was chosen to realise the numerical analysis presented in this work.

The computational domain, in order to reduce the simulation time, is a room section, which is representative of the entire room geometry. The width is that of one dropped ceiling panel (0.6 m), while all other dimensions are typical of an office room: length 3.6 m and height 3.0 m. The height of the plenum is 0.35 m. The air inlet is the whole surface of the plenum directed towards the façade, while the outlet is placed on the opposite surface and it is modelled as a rectangular opening with dimensions (WxH) 0.6 m x 0.05 m.

The computational mesh is structured hexahedral and counts 22 million cells. The high number of cells was necessary to calculate with sufficient precision the flow conditions past the panel perforation. This also required a high computational effort, which was reduced considering a section of the room, and by setting a non-conformal mesh interface between the suspended ceiling and the room volume. The commercial code Ansys Fluent was used, especially because of the ease of handling of non-conformal interfaces.

Boundary Conditions

Two typical seasonal conditions were taken into account. In both cases the temperature of the plenum ceiling, room floor, and the vertical wall which contains the ventilation outlet, were set constant at the internal room temperature. The wall below the ceiling inlet was considered part of the façade. Therefore, the wall temperature was calculated considering an ideal thermal transmittance in steady state conditions for the façade equal to $0.8 \text{ W/m}^2\text{K}$. Both the side walls ($3.6 \times 3.0 \text{ m}$) are treated as internal air and not as walls.

The calculations were performed in steady state imposing atmospheric pressure at the room outlet and a constant velocity at the plenum inlet. Two conditions were tested, calculated to provide an amount of ventilation air of $1.2 \text{ m}^3/\text{h}$ and of $2.7 \text{ m}^3/\text{h}$ per square meter of room floor area. The lowest value is meant to represent a baseline ventilation, while the highest one is representative of a fresh airflow that satisfies the requirements for ventilation in a low-polluting office, reaching an IEQ category III.

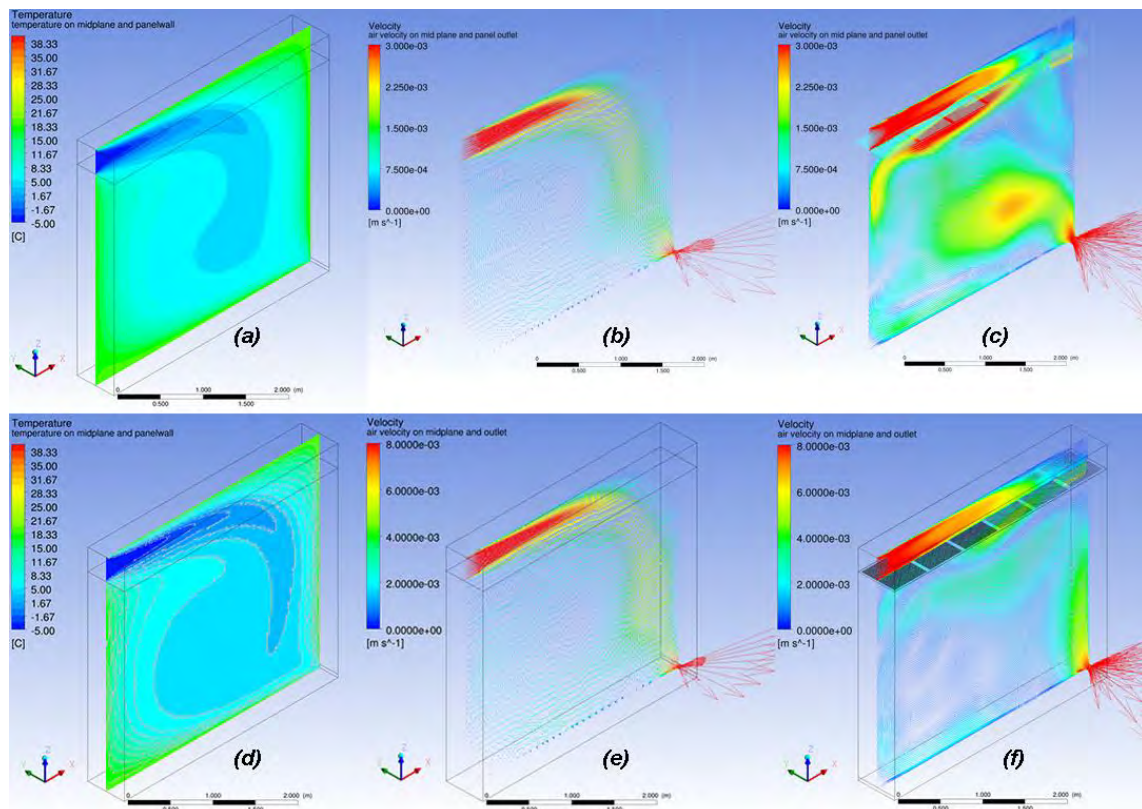


Figure 1. Comparison between inlet design without (a, b and d, e) and with (c, d) a dropped ceiling. (a) temperature profile with inlet temperature equal to $-5 \text{ }^\circ\text{C}$, airflow: $1.2 \text{ m}^3/\text{h m}^2$; (b) velocity field with airflow: $1.2 \text{ m}^3/\text{h m}^2$; (c) velocity field with airflow: $1.2 \text{ m}^3/\text{h m}^2$; (d) temperature profile with inlet temperature equal to $-5 \text{ }^\circ\text{C}$, airflow: $2.7 \text{ m}^3/\text{h m}^2$; (e) velocity field with airflow: $2.7 \text{ m}^3/\text{h m}^2$; (f) velocity field with airflow: $2.7 \text{ m}^3/\text{h m}^2$.

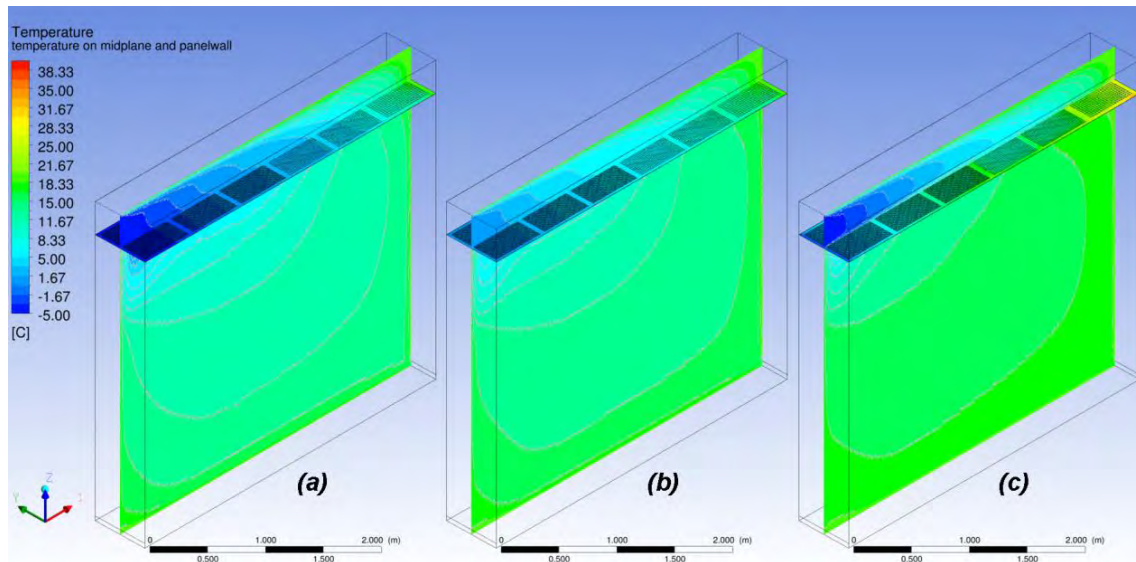


Figure 2. Temperature profile on midplane and dropped ceiling panels for inlet temperature equal to: (a): $-5\text{ }^{\circ}\text{C}$; (b): $0\text{ }^{\circ}\text{C}$; (c): $-5\text{ }^{\circ}\text{C}$ and imposed heat flux 10 W/m^2 .

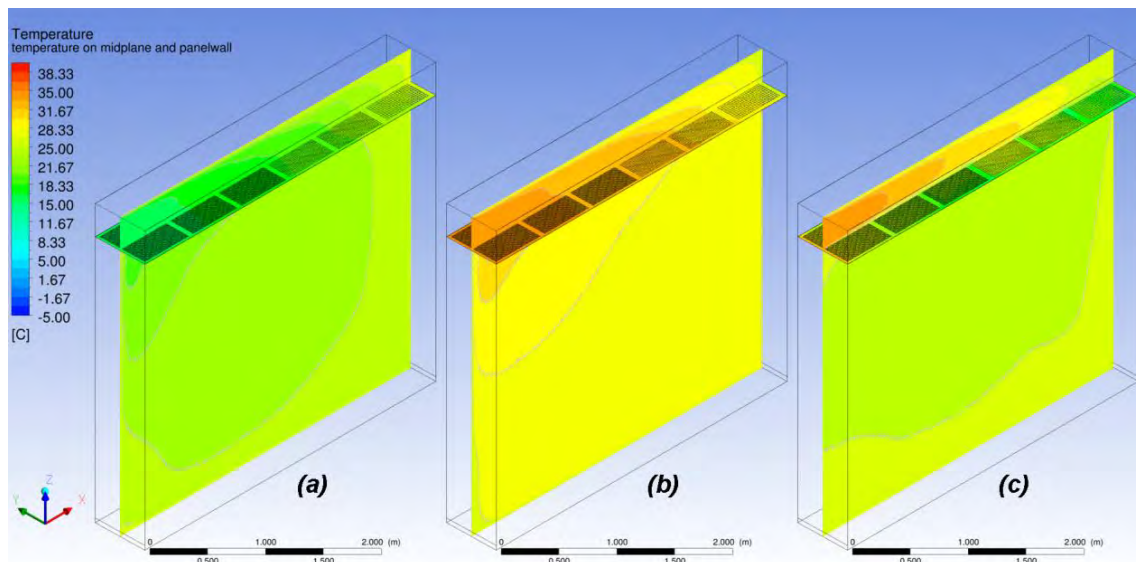


Figure 3. Temperature profile on midplane and dropped ceiling panels for inlet temperature equal to: (a): $15\text{ }^{\circ}\text{C}$; (b): $35\text{ }^{\circ}\text{C}$; and (c): $35\text{ }^{\circ}\text{C}$ and imposed heat flux -10 W/m^2 .

RESULTS

Winter case

For the winter case, the temperature of the room surfaces (with the exception of the façade and of the dropped ceiling) was considered $20\text{ }^{\circ}\text{C}$. The outdoor air temperature was set as a variable, and a parametric analysis was carried out to assess the impact of this variable on the system's performance. Simulations were repeated for the following values of the outdoor air temperature: -5 , 0 , 5 and $10\text{ }^{\circ}\text{C}$. The ventilation air enters the plenum with conditions equal to that of the outdoor air temperature. Figure 2 reports the temperature distribution in the plenum, the room and the ceiling panel surface for the most extreme cases ($-5\text{ }^{\circ}\text{C}$ and $0\text{ }^{\circ}\text{C}$). In the cases where the inlet temperature is greater than case $0\text{ }^{\circ}\text{C}$, the injection of air at outdoor temperature does not cause a substantial deviation from the comfort temperature except for

the part of volume directly in contact with the ceiling and the façade. Conversely, the internal comfort can be affected in case of an outdoor temperature ≤ -5 °C.

Summer case

In the summer case, the temperature of the room surfaces (with the exception of the façade and of the dropped ceiling) was set at 26 °C. The outdoor air temperature was imposed at 15 °C, 20 °C, 30 °C and 35 °C. The case with outdoor temperature 25°C was not investigated since, as obvious, it does not lead to any significant variation to the internal temperature field being the difference only 1°C.

The case with outdoor air temperature equal to 15°C was instead selected to represent early morning situation with an outdoor air temperature relatively low. The temperature distribution on the mid-plane and the suspended ceiling surface for the summer case is reported in Fig.3, for the most extreme conditions (cold and warm air). Here it is possible to verify that only under the most extreme conditions (inlet air temperature of 35°C, Fig. 3 b)), the indoor air in the room is outside the comfort range.

DISCUSSION

In both winter and summer situation, the use of a DCV coupled with natural or hybrid ventilation, does not entail particular problems for the thermal comfort, both in terms of temperature and air velocity, with the exception of the most extreme conditions.

Under the most extreme (investigated) winter conditions (namely, case (a)), the indoor air reaches a too low temperature in the volume immediately close to the dropped ceiling – i.e. a volume of air that is not usually occupied by the user. However, even under these conditions, the performance of the system is better than a competing solution where the air intake is performed directly through the façade (see Fig. 1). The temperature of the dropped ceiling surface is also low, and this might negatively affect the indoor environment, even if problems related to radiant asymmetry discomfort are probably avoided due to the very small surface at low temperature. The lack of surface condensation was also verified (with the assumption of a relative humidity of the air immediately closed to the surface of 90%).

Under the most extreme (investigated) summer conditions (namely, case (d)), the indoor air reaches a too high temperature in the entire room volume. However, a similar condition would occur also with direct inlet through the façade without the dropped ceiling plenum.

In both the extreme winter and summer conditions, a strategy to minimize discomfort is by locally treating the ventilation air right before it enters the room. An interesting solution could be the use of the dropped ceiling as the terminal of a water based cooling/heating system. Two simulations to assess the performance under this configurations were performed, imposing a constant heat flux of 10 W/m² in winter (Fig. 2 c) and of -10 W/m² in summer (Fig. 3 c), to the entire dropped ceiling, thus turning it into an active conditioning surface.

The temperature of the suspended ceiling shows in both cases a non-uniform distribution, and this is due both to the temperature distribution in the plenum and the different air velocity through the perforation. In the winter situation, the solution seems to accomplish the objective with no particular problems. In the back section of the dropped ceiling may reach surface temperatures as high as 30 °C, which is still an acceptable surface temperature, even if in the proximity with the head of the users.

In the summer case instead, a more evident thermal stratification in the room is shown, and the temperature of the section of the suspended ceiling at the rear of the room (far away from the façade) reaches values as low as in the range 15-16 °C. Limiting the area of the dropped ceiling's panels equipped with hydronic system to the first two panels next to the façade would probably assure a suitable air temperature and an optimal surface temperature of the dropped ceiling.

CONCLUSIONS

The DCV ventilation system, object of the present work, demonstrates to have a positive impact on the comfort inside a typical office room. A sufficient amount of ventilation air is provided at low velocity and ensuring the absence of draft according to the values recommended by ISO 7730(7730:2005). In case of coupling between DCV and natural and hybrid ventilation, the system ensures the thermal comfort except in case of extremely high or low outdoor temperature. The use of the suspended ceiling as terminal of a water based heating/cooling system can be taken into account. According to preliminary simulations, the water based system should be capable of proving a thermal flux of $\pm 10 \text{ W/m}^2$, depending on the seasons. This eventuality demonstrated both in the winter and in the summer case a good influence on the comfort conditions. The portion of the dropped ceiling to be equipped with a water based heating/cooling system could be limited to the area closest to the façade and provide an adequate surface temperature of the DCV while conditioning the airflow under the most critical boundary conditions.

ACKNOWLEDGEMENT

This work has been supported by the Research Council of Norway and several partners through the project "Advanced facades with integrated technology – SkinTech" (nr. 255252).

REFERENCES

- Fan, J., C. A. Hviid, and H. Yang. 2013. "Performance Analysis of a New Design of Office Diffuse Ceiling Ventilation System." *Energy and Buildings* 59:73–81
- Hviid, C. A. and S. Svendsen. 2013. "Experimental Study of Perforated Suspended Ceilings as Diffuse Ventilation Air Inlets." *Energy and Buildings* 56:160–68.
- ISO-EN 7730:2005 *Ergonomics of the Thermal Environment-Analytical Determination and Interpretation of Thermal Comfort Using Calculation of the PMV and PPD Indices and Local Thermal Comfort Criteria.*
- Jacobs, P., E. van Oeffelen, and B. Knoll. 2008. "Diffuse Ceiling Ventilation, a New Concept for Healthy and Productive Classrooms." in *Proceedings of Indoor Air, paperID*, vol. 3.
- Mikeska, T. and J. Fan. 2015. "Full Scale Measurements and CFD Simulations of Diffuse Ceiling Inlet for Ventilation and Cooling of Densely Occupied Rooms." *Energy and Buildings* 107:59–67.
- Nocente, A., S. Grynning, H. M. Mathisen, and F. Goia. 2018. "Computational Fluid Dynamics Study of a Diffuse Ceiling Ventilation System through Perforated Sound Absorbing Ceiling Panels." in *Roomvent&Ventilation 2018: Excellent Indoor Climate and High Performing Ventilation*, p: 899-904.
- Petersen, S., N. Christensen, C. Heinsen, and A. Hansen. 2014. "Investigation of the Displacement Effect of a Diffuse Ceiling Ventilation System." *Energy and Buildings* 85:265–74.
- Van Wagenberg, A. V. and M. Smolders. 2002. "Contaminant and Heat Removal Effectiveness of Three Ventilation Systems in Nursery Rooms for Pigs." *Transactions of the ASAE* 45(6):1985.
- Zhang, C., P. K. Heiselberg, Q. Chen, and M. Pomianowski. 2017. "Numerical Analysis of Diffuse Ceiling Ventilation and Its Integration with a Radiant Ceiling System." *Building Simulation* 10(2):203–18
- Zhang, C., P. K. Heiselberg, M. Pomianowski, T. Yu, and R. L. Jensen. 2015. "Experimental Study of Diffuse Ceiling Ventilation Coupled with a Thermally Activated Building Construction in an Office Room." *Energy and Buildings* 105:60–70.
- Zhang, C., T. Yu, P. K. Heiselberg, M. Z. Pomianowski, and P. V. Nielsen. 2016. "Diffuse Ceiling Ventilation-Design Guide."

Research for the Optimization of Air Conditioner Sensor Position Based on the Room Spatial Parameter

Kuixing Liu¹, Gang Liu^{1,*}, and Yueqiang Di¹

¹School of Architecture, Tianjin University, China

*Corresponding email: diyueqiang@tju.edu.cn

ABSTRACT

The indoor temperature measured by the sensor is an important basis of air conditioner control strategy. Accordingly, the position of the sensor influences power consumption and the stability of indoor temperature control. This paper aims to study the influence of different sensor positions on air conditioner power consumption and indoor temperature stability. An experiment is conducted, which has 20-position circumstances, including different height, horizontal distance, and vertical distance from the air conditioner. Furthermore, Fluent is used to simulate the situation that sensor is in rooms with different sizes and air conditioner direction. An optimal sensor position searching model is developed, and an ideal position is proposed. A correction parameter is presented to adjust the sensor in original position. This study provides theoretical and practical support for improvement of the operation of air conditioners.

KEYWORDS

Air conditioner; Thermal comfort; Indoor temperature; Temperature sensor

INTRODUCTION

With the advancement of science and technology, the living condition of people is becoming increasingly comfortable, and the air conditioner plays an important role in creating such a comfortable condition. As the demand for indoor comfort continues to increase, higher requirements have been placed on the air conditioner (Jani et al. 2017). Moreover, efficient operation of an air conditioner is necessary under the energy conservation trend.

One study focuses on the heat pump inside the air conditioner (Waheed et al. 2014). However, as a key input for the operation of the air conditioner, the temperature measured by temperature sensor cannot be neglected. The temperature of the sensor position directly affects the air conditioner start-stop control, which eventually affects energy consumption and indoor temperature. If comfort and efficiency can be improved by optimizing this input, then low-cost optimization can be achieved. The conventional air conditioner contains a temperature sensor positioned on the return air grill, which measures the temperature of the return air. This is due to the closed control link of the air conditioner. However, as technology advances, information interconnection makes it possible for an open control link of the air conditioner operation. The temperature data from other sensors, and even the humidity and velocity, could be the input of the air conditioner. When the sensor position is not confined inside the air conditioner, it is necessary to study the ideal position of the sensor. In this paper, cool mode, rather than dehumidification mode or others, will be focused on, thus only temperature would be used as an input.

Yang (2009) put forward a method to find a proper position that can represent the sectional environment of the air conditioner. Liu et al. (2013) studied the influence of three different sensor positions on an indoor PMV. These studies focus on the indoor average temperature, which is affected by the average temperature of the position of the sensor. But the initiative of

people could eliminate the bias of the average temperature because people can change the target temperature of the air conditioner. Meanwhile, Nevins (1971) found that people are sensitive to the fluctuation of temperature, and the fluctuation cannot be directly controlled by changing the target temperature.

In this article, the domestic air conditioner is chosen as the experiment object, and the stability of indoor temperature and power consumption are the criteria to evaluate the air conditioner operation. By analyzing the characteristic of the temperature of different position using clustering and classification method, an ideal measurement position could be indicated.

METHODS

Experiment

The experiment is in a 5 m x 3.5 m room on the fourth floor of a six-story residential building in Tianjin, China (as shown in Figure 1). The air conditioner is located 2.7 m high at the southwest corner, which faces east. The temperature monitor device is a HOBO thermocouple data logger. Several pre-experiments are conducted and show that when the distance between two HOBO loggers is bigger than 1.5 m, the measurement error would be insignificant.

The measurement positions fill the room with a 1.5 m interval distance, and there are 20 measurement positions in total, including one at the return air grill. Except for the return air position, all 19 positions are distributed in a grid that has 2 layers (0.3 m high and 1.8 m high), 3 rows with a 1.5 m interval in an east–west direction, and 4 columns with a 1.5 m interval in a north–south direction. In the grid, 5 positions in a 0.3 m high layer are unreachable because of furniture and thus are ignored. HOBO loggers are placed at all 20 positions to monitor the temperature change (as shown in Figure 2).

There is only one adjacent room with an exterior wall, which is installed using a smart heater to be constant 30° C, according to the local summer outdoor design temperature. The air conditioner mode is cool, and the target temperature is set at 24° C, which is accordant with the adjacent room to avoid external factors. Other settings are set at default. By modifying the circuit, the sensor inside air conditioner is extended to reach all the positions. During the experiment, the sensor will be at one of the 20 positions, and the air conditioner will operate using the temperature of that position. The moving of the air conditioner temperature sensor only happens during the stopped period of the air conditioner's intermittent operation.

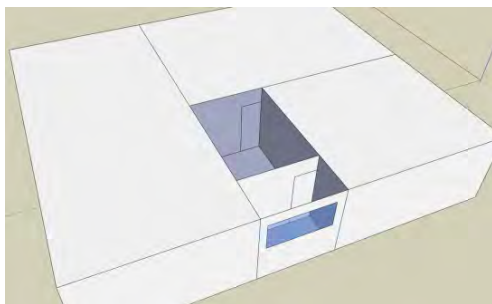


Figure 1. Experiment environment

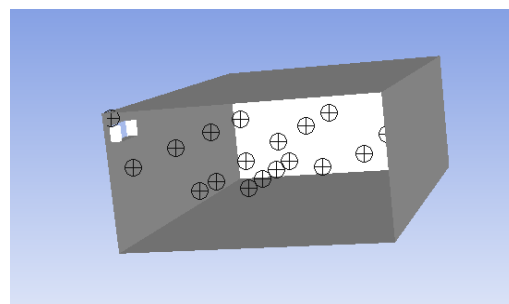


Figure 2. Measurement positions

Data analysis outline

The 20-position temperature is clustered using two key factors, and the influence of sensors located at positions of different cluster is analyzed. Thus, the clustering result and the cluster to which the ideal sensor measurement position belongs are obtained. The clustering result would be used to train a classifier. Afterwards, ANSYS is used to simulate the indoor temperature of rooms with different parameters, and the trained classifier is used to classify the temperature. Then, the recommended measurement position for rooms with different

parameters could be drawn. In this project, clustering and classification algorithms run in the Ubuntu operating system, and the algorithm program is written in Python.

Simulation

ANSYS is used to simulate three different conditions, including a verification condition and two generalization conditions (GCs). In the verification condition, all parameters are accordant with the experiment to verify. In GC I, the room is changed to 10 m x 7 m. In GC II, the room is changed to 10 m x 7 m, and the air conditioner direction is changed to northeast. DesignModeler is used to build models, and ICEM-CFD is used to generate the mesh. Fluent is used to perform the transient simulation calculation, and the time step is set to 2 s.

Data analysis method

Min–Max Normalization is used before the analysis algorithm to normalize the data with different ranges or units. The clustering method is K-means, which has better performance (Milligan and Cooper, 1980), and the silhouette coefficient is used to select the clustering number. The Bayesian classifier is used for classification, which is not sensitive to data deficiency. The temperature of the 20 positions is recorded using a time–domain curve, which is not compatible with the clustering or classification methods. Therefore, two key factors—temperature fluctuation amplitude and delay—are extracted from the original data to represent the characteristic of the temperature curve. Because the average indoor temperature is not the evaluation quota, the average temperature is not chosen to be the key factor.

RESULTS

Experiment and clustering result

Figure 3 show a 20-position temperature curve controlled by the air conditioner from one day of the experiment. It is obvious that the temperature of every position fluctuates together but has different amplitudes. For the following discussion, a position named α position is defined as the position that is 2 m high, along the same wall as the air conditioner but 1 m away from the air conditioner. In the experiment, α position is position 2. The experiment lasted for 19 days, and all the data is used for following analysis. When the clustering number is 3, the silhouette coefficient reaches best, which indicates the proper clustering number. By using amplitude and delay, the clustering result could be calculated (as shown in the Table 1).

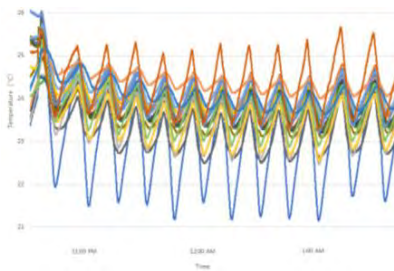


Figure 3. 20-position temperature

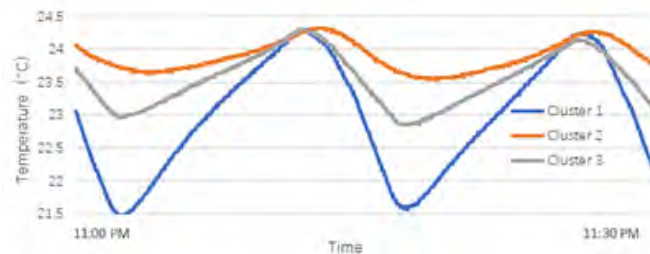


Figure 4. Typical curves

Table 1. Clustering result: experiment

Cluster	Measurement Position
Cluster 1	5, 9, 10, 13, 20
Cluster 2	4, 7, 8, 12, 14, 17, 19
Cluster 3	1, 2(α), 3, 6, 11, 15, 16, 18

Difference between clusters

The typical temperature curves of three clusters are shown in Figure 4. It is obvious that the temperature of positions in cluster 1 fluctuates significantly, of which the amplitude is the

largest. In cluster 2, it fluctuates softly with an obvious delay. Cluster 3 performances between two other clusters. The average parameter of three clusters is shown in Table 2.

Table 2. Parameter of three clusters

Cluster	Average Temperature (°C)	Amplitude (°C)	Delay (s)
Cluster 1	23.54	2.43	32
Cluster 2	23.93	1.13	81
Cluster 3	23.79	1.6	55

Runtime difference

The temperature of the different clusters behaves variously, which will cause diversity in the air conditioner operation if the sensor is placed at positions of different clusters. When the sensor is changed from one cluster to another one, the air conditioner will perform differently, which leads to the change of both indoor temperature and power consumption. By using 20-position temperature to represent the indoor temperature, the alteration is clear. It can be seen in Figure 5 that when the sensor is changed to the position in cluster 1, the indoor temperature fluctuates gently and is more agglomerative. The period of air conditioner operation shortens obviously but the temperature changes as almost straight lines. In Figure 6, compared with that of cluster 3, the period is stretched and the temperature in cluster 2 changes in a bent way.

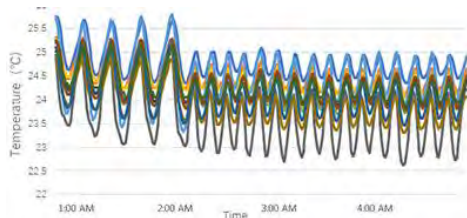


Figure 5. Cluster 3 to 1

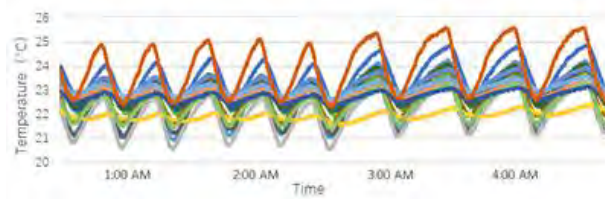


Figure 6. Cluster 3 to 2

Three parameters are used to evaluate the air conditioner operation caused by different sensor position. Temperature fluctuation variance is the temporal variance. Temperature distribution variance is the spatial variance. Power consumption is the electricity used in a unit time. The former two represent the stability of indoor temperature, which is directly related to indoor comfort. For better comparison, three parameters are converted to three indexes: temperature fluctuation variance index (TTVI), temperature distribution variance index (TDVI), and power consumption index (PCI). These three indexes are three parameters divided by the respective average value. For example, the TTVI is the temperature fluctuation variance divided by the 20-position average value. A comparison is shown in Table 3.

Table 3. Run-time difference of the three clusters.

Cluster	TTVI	TDVI	PCI
Cluster 1	0.88	0.93	1.14
Cluster 2	1.37	1.19	0.81
Cluster 3	0.99	1.02	0.98

Simulation

Figure 7 is the temperature distribution of a 2 m high layer in vilification condition; the general boundary of three clusters at 2 m high is also shown by blue lines: the left part is cluster 2, the middle part is cluster 3, and the right part is cluster 1. In Figure 8, the normalized value of the temperature fluctuation amplitude is shown, where the average

temperature is 23.8° C, and the min/max value of temperature fluctuation is 0.9/2.6° C. In verification condition, though there is a visible bias from position 13 to position 19, which is because of the unconsidered furniture in simulation, the simulation result shows a high accordance with the experiment. In two GCs, by using the classifier trained by the clustering result, the positions could be classified as the previous three clusters according to their temperature amplitude and delay. The classification result is shown in Table 4. As the size of room becomes larger, the airflow has a weaker return trend, which leads to a weak response for every position. Because the characteristic of positions changes, the clustering result alters.

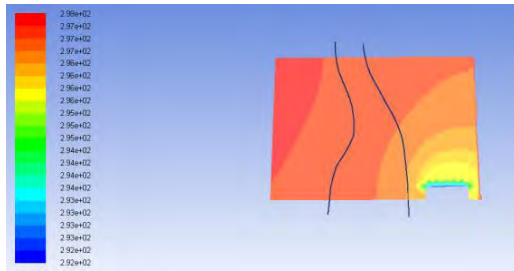


Figure 7. Temperature distribution

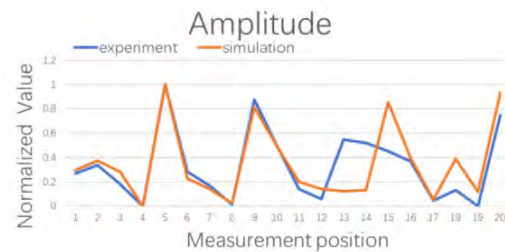


Figure 8. Verification

Table 4. Clustering result: simulation.

Cluster	Measurement Position-GC 1	Measurement Position-GC 2
Cluster 1	1, 5, 20	5, 20
Cluster 2	3, 4, 6, 7, 8, 11, 12, 14, 15, 16, 17, 18, 19	3, 4, 7, 8, 10, 11, 12, 14, 15, 16, 17, 18, 19
Cluster 3	2(α), 9, 10, 13	1, 2(α), 6, 9, 13

DISCUSSIONS

Evaluation index

To compare the performance of the air conditioner operation, an evaluation index (EI), as a comprehensive consideration of indoor comfort and power consumption, is defined as:

$$EI = \frac{2}{\frac{2}{TTVI + TDVI} + \frac{1}{PCI}} \quad (1)$$

where *TTVI* is the temperature fluctuation variance index, *TDVI* is the temperature distribution variance index, and *PCI* is the power consumption index. A lower EI is better. As shown in Table 5, cluster 3 shows a better performance than the two other clusters.

Table 5. EI of three clusters

Cluster	EI (lower is better)
Cluster 1	0.981
Cluster 2	0.986
Cluster 3	0.973

Suggested position

After analyzing the characteristics of the three clusters, it can be drawn that three clusters can be named as Direct Zone, Inert Zone, and Reasonable Zone, respectively.

Direct Zone: The positions are close to the air conditioner, and are directly blown by the air conditioner, so the temperature fluctuates greatly; the response is quick; and the feedback to

the air conditioner is intense. In general, this zone is within 3.2 m of the wind path of the air conditioner, and the boundary varies around 3 m when the wind speed or room size changes.

Inert Zone: The positions are located far away from the air conditioner or in the corner of the room. Obviously, due to the stagnant airflow, the temperature fluctuation is weak, and the feedback to the air conditioner is weak. The boundary of this zone varies significantly.

Reasonable Zone: The measurement points in this cluster are in the middle of two other clusters. They are in a relatively open position with moderate temperature fluctuations. The reasonable zone is an ideal choice of air conditioner sensor measurement position, which considers both indoor comfort and energy conservation. The clustering stability, the accordance in different condition clustering, of the position should also be considered. The distance from the center of the cluster represents the clustering stability, and positions that are closer to the center would be clustered in the same cluster and perform more like the expect performance. The location of air conditioner temperature sensor recommended in this paper is position α , defined previously as located on the same wall as the air conditioner, 1.8 m high and 1 m away from the air conditioner. This measurement position is not only good in theoretical performance but also in application because it is located on the wall surface, which is convenient for placement. It is not in the center of the room or in the place where people pass by, which is less influenced by human activities, ensuring stable and efficient operation.

Sensor correction

The original position of the temperature sensor is at the return air grill, which belongs to the Direct Zone. By analyzing and comparing the characteristic of the temperature curve of the recommended measuring position and that of the original position, which is the fluctuation amplitude and delay, it can be found that the delay is 25 s shorter and the fluctuation amplitude is 35% higher. It can be adjusted simply by adding an RC circuit.

CONCLUSIONS

This paper proposes the following method to find the ideal air conditioner sensor position of different parameters of the room: by clustering and classification after simulation to obtain the proper and stable position. This method does not require the actual measurement of different rooms, as different circumstances can be achieved through simulation. Therefore, it is applicable not only to the actual construction but also to the design stage. Meanwhile, this article gives the recommended air conditioner temperature sensor position, α position, which can make the air conditioner run at the balance point of energy-saving and indoor comfort.

More kinds of room conditions, including different return air forms and room shapes, may produce different ideal measuring positions, which could be studied in the future. Moreover, due to the distance between measuring points, the precise α position needs further study.

REFERENCES

- Jani DB, Mishra M, Sahoo PK. A critical review on solid desiccant-based hybrid cooling systems. *Int J Air-Cond Refrig*. 2017;25(3):1730002.
- Waheed MA, Oni AO, Adejuyigbe SB, Adewumi BA, Fadare DA. Performance enhancement of vapor recompression heat pump. *Appl Energy*. 2014;114:69-79.
- Yang B. The analysis of improving the comfortable performance of multi A/C from sensor's position design and fan speed design. *Chin Assoc of Refrig*. 2009:4.
- Liu Q-l, Du Z-m, Jin X-q. A study on the effect of location of indoor temperature sensor's of VAV air conditioning system. *Build Energy & Environ*. 2013;32(01):11-14.
- Nevins RG. Thermal comfort and draughts. *J Physiol*. 1971;13:356-358.
- Milligan GW, Cooper MC. An examination of the effect of six types of error perturbation on fifteen clustering algorithms. *Psychometrika*. 1980;45(3): 159-179.

The impact of ventilation strategy on overheating resilience and energy performance of schools against climate change: the evidence from two UK secondary schools

Esfand Burman* and Dejan Mumovic

Institute for Environmental Design and Engineering, University College London (UCL), Central House, 14 Upper Woburn Place, London, WC1H 0NN, UK

*Corresponding email: esfand.burman@ucl.ac.uk

ABSTRACT

The indoor environmental quality and energy performance of two modern secondary schools in the UK which have fundamentally different environmental strategies were investigated during building performance evaluations. The performances of these buildings against the projected weather data for future were also analysed. The results point to significant risk of future overheating as a result of climate change in the naturally ventilated building with passive measures that go well beyond the existing guidelines for schools. The other school with mechanical ventilation shows resilience to future overheating. However, shortcomings in building procurement and operation have severely compromised its energy performance. It is suggested to carry out integrated life-cycle assessment of energy performance and overheating resilience in the context of climate change during design stages and identify the corresponding risks and mitigation measures required to ensure design intents will be met in practice.

KEYWORDS

Overheating, Energy Performance, Climate Change, Schools, UK

INTRODUCTION

Average global temperatures are rising due to climate change. This has serious repercussions for the risk of overheating in buildings. Our understanding of human response to high ambient temperatures is also evolving and has led to adaptive overheating criteria for free-running buildings and overheating thresholds for mechanically conditioned buildings defined in BS EN 15251 (BSI, 2007) and CIBSE TM52 (CIBSE, 2013). This necessitates revisiting the performance of the existing buildings that were designed in accordance with different sets of overheating criteria and climatic conditions. Furthermore, while resilience against overheating is a key objective in climate change adaptation, improving the energy performance of buildings is also significantly important in the context of climate change mitigation to limit the increase in average global temperatures. Reconciling these competing objectives is therefore essential. This paper adopts a case study approach to investigate how energy efficiency and overheating control measures are being implemented in the UK construction industry. Two educational buildings have been selected for this purpose. Both buildings were constructed in England over the period 2008-2010 under the Building Schools for the Future (BSF) programme, which led to renewal or replacement of one fifth of English secondary schools. These buildings represent fundamentally different environmental strategies and were subject to post-occupancy investigations as part of a wider programme of building performance evaluation (BPE) instigated by the Innovate UK, the UK government innovation agency. The BPE programme, however, was focused on the current performance, and did not consider the potential response of these cases to future climate change. The aim of this paper is thus to adopt a long-term perspective in the context of a changing climate. The key

objectives are: 1) to review the performance of the case studies against outdoor temperatures experienced during monitoring along with their energy use, 2) investigate the likely response of the existing design strategies and operational regime to future climate change, and 3) review the potential measures to enhance buildings' resilience against future climate change and the implications of the research for wider building stock.

OVERVIEW OF THE CASE STUDIES

School A: School A is a secondary school in London that was completed in 2010. Total useful floor area of the building is around 14,600 square meters. It was designed as a 2,000-pupil facility. The building is predominantly naturally ventilated and mechanical ventilation is only provided to the core spaces that do not have access to external facades and the ICT enhanced spaces with high internal gain. In total, around 80% of the building area is naturally ventilated. The external skin is formed from pre-cast concrete panels finished with brick tiles to achieve air permeability less than $5 \text{ m}^3/(\text{m}^2.\text{hr})$ at 50 Pa. The reported air permeability following the pressure test on completion of the building was $4.36 \text{ m}^3/(\text{m}^2.\text{hr})$. The main facades of the building are east and west oriented. Previous studies found the risks of such a layout for overheating (Pegg, 2007). The design team specified several measures to mitigate overheating: 1) vertical fins are positioned on east and west elevations to provide solar shading; 2) Glazing g values are relatively low between 0.45-0.5; 3) typical classrooms have opening areas at around 7% of the floor area for single-sided ventilation. This is significantly higher than the existing guideline for opening area required for single-sided ventilation in schools which is 5% (DfES, 2006); 4) the facility for cross or stack ventilation has been provided for most classrooms by means of motorised vents controlled by the building management system (BMS). These vents are meant to open in response to poor indoor air quality or high temperatures. 5) the exposed thermal mass of the building can help regulate indoor temperatures; 6) Secure louvered windows facilitate night-time ventilation in summer.

School B: School B is located in Greater Manchester and was completed in 2008. Total useful floor area of the building is around 10,400 square meters. It was designed as a 1,150-pupil facility. The school is a steel frame building with brick facades and cavity wall insulation that was designed to comply with the regulatory air tightness requirement of $10 \text{ m}^3/(\text{m}^2.\text{hr})$ at 50 Pa. The building is located under the flight path of Manchester airport. Therefore, mechanical ventilation strategy was adopted to meet acoustic requirements. Classrooms facing external facades have at least one operable top-hung window. Glazing g values are between 0.68-0.75, reduced to 0.36 on the south, southeast and southwest elevations by applying solar film after completion. A Ground Sourced Heat Pump (GSHP) system is installed as the lead heating system and is also capable of providing cooling to ICT enhanced spaces of the school that have chilled beams installed for cooling. Other classrooms do not have cooling terminals. However, the main air handling units (AHUs) serving classrooms and labs have cooling coils that are fed by the GSHP system. While the building is not fully air-conditioned, the GSHP system and AHU cooling coils can provide limited cooling when outdoor temperatures are high.

Figure 1 shows the external views of the case studies.

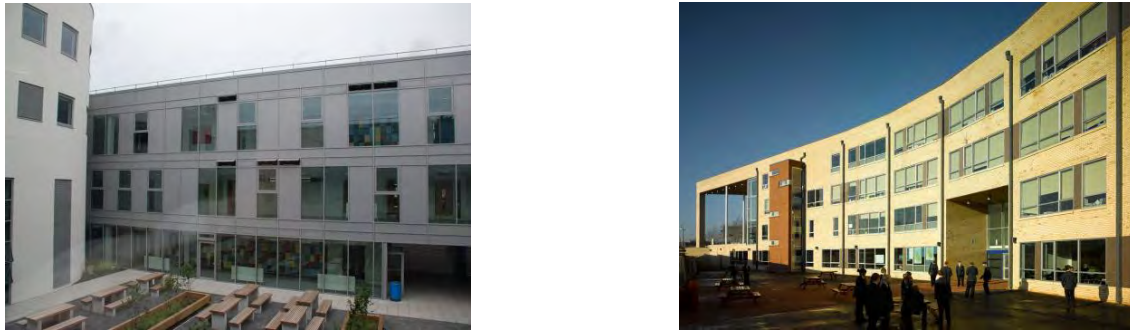


Figure 1. External view from the courtyard of School A (left), and southside of School B

METHODS

Occupants' perception of the current conditions: The Building Use Studies (BUS) questionnaire survey (Leaman & Bordass, 2001) was used to assess the satisfaction of teaching and support staff with the current performance. The response rate in both schools was 75%. The results for comfort variables are presented in this paper.

Overheating analysis and simulation under current climate conditions: Calibrated Type T copper-constantan thermocouple data loggers were used to record air temperatures every 10 minutes for one full year (measurement accuracy: ± 0.35 °C). At least 10% of teaching zones, representatively chosen, were covered. The results were compared against the overheating criteria for schools which were prevalent at the time the buildings were designed (DfES, 2006). Actual measurements were also compared with the outcomes of building simulations carried out with IES software (using current Test Reference Year weather file for London) to ensure a reasonable base model is available for future climate scenario analysis.

Energy Performance: the actual annual energy performances of the schools were established through regular recording of all main meters and submeters. Annual energy performances were then compared against the median of secondary schools in the UK to evaluate the success of energy efficiency measures adopted.

Projections for performance under future climate scenarios: The IES models developed based on the current performance were used to investigate the effects of the expected changes in weather conditions in future. It is envisaged that the buildings will be subject to major refurbishment within the next 20-30 years, the usual life-expectancy of most building services. This sets out a reasonable time horizon for investigating the effects of future climate change (CIBSE, 2014). Prometheus weather files developed by the Exeter University were used for this investigation. The current Design Summer Year (DSY), and the central estimate (50th percentile) for the effects of the medium carbon emissions scenarios in 2030 and 2050 were used to consider the effect of current climate change mitigation policies. The results for two classrooms in each school, which according to the technical measurements are prone to high temperatures, are presented against the new overheating assessment criteria set out in CIBSE TM52. Where a classroom fails 2 criteria (i.e. is overheated according to CIBSE TM52 criteria), the findings of building performance evaluations are used to identify improvement opportunities within the existing environmental strategies or suggest low cost interventions that may be used to improve overheating resilience.

RESULTS

Figure 2 shows the BUS survey comfort variables generally score higher than the median benchmarks which represent the results of the last 50 survey in the database. However, the score for temperature in summer is the lowest among variables for both case studies and the benchmark. This is indicative of challenges of achieving occupant satisfaction in summer.

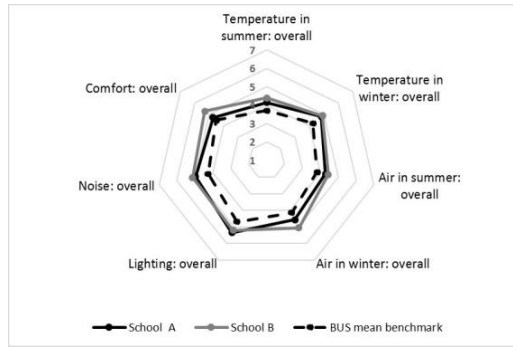


Figure 2. BUS results for comfort variables in the case studies

Figure 3 shows the measured and simulated air temperatures under ambient conditions close to Test Reference Years which are representative of the current climatic conditions. All sample classrooms comply with the overheating criteria prevalent at the time of design (DfES, 2006). Uncertainties in occupancy pattern, internal heat gains, and window positions can explain the discrepancies observed between measured data and simulation. Overall, the models appear to be reasonable representations of the thermal performance of the schools to be used for future climate scenario analysis. Classrooms with significant discrepancies between measurement and simulation were discounted from future climate analysis.

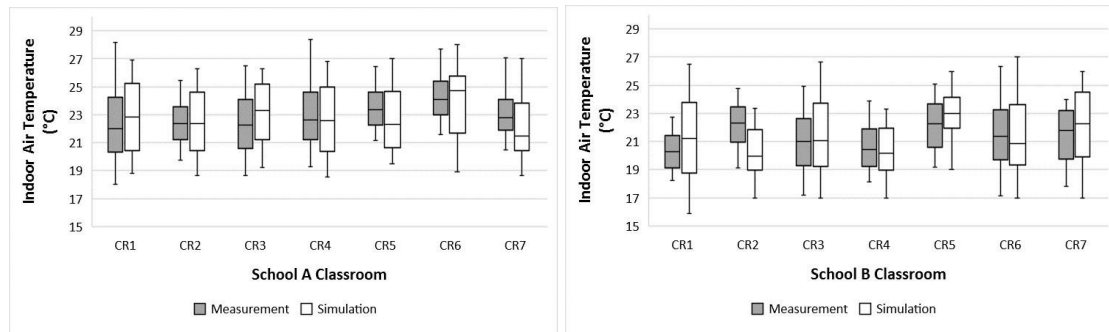


Figure 3. Whisker plots of current summertime air temperatures (May-September, 9:00-15:30)

Figure 4 compares the CO₂ emissions associated with operational energy use in these schools against the median stock (typical benchmark for schools in the UK).

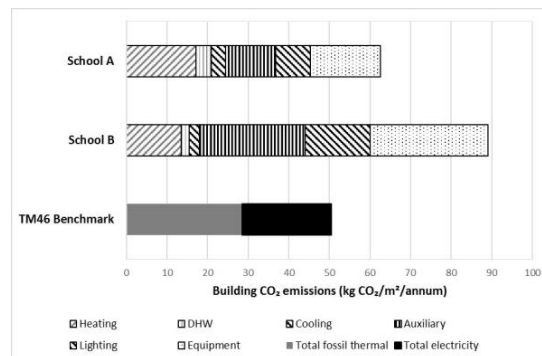


Figure 4. Carbon dioxide emissions associated with operational energy use

Table 1 reports the results of future climate change analysis (grey color indicates failure to meet the overheating criterion). The following additional passive measures were considered for School A that showed risk of overheating with the existing environmental strategies: 1) increasing the window opening from the design value of 250 mm to 400 mm, 2) applying solar films to glazing to reduce the g value to 0.15.

Table 1. Overheating risk assessment (CIBSE TM52/ BS EN 15251 method)

School Classroom	Internal gain of people, lighting, and small power (W/m ²)	Simulation scenario	Current Design Summer Years (DSY): more extreme dataset than TRY			2030 DSY for medium emissions scenario (50 th percentile)			2050 DSY for medium emissions scenario (50 th percentile)		
			Exceedance (%)	Degree-hours above limit	Max Δ T (°C)	Exceedance (%)	Degree-hours	Max Δ T (°C)	Exceedance (%)	Degree-hours	Max Δ T (°C)
A CR 3	Min: 29 (current 'average' use of the space)	Single-sided ventilation	14 (fail)	27	6	38	37	7	39	43	8
		As-designed: cross & night-time ventilation	2 (ok)	8	3	8	17	5	10	25	6
		Additional passive measures	1	5	2	3	10	4	4	19	5
	Max: 42 (full load mode for internal gain)	Single-sided ventilation	20	31	6	45	41	8	45	46	9
		As-designed: cross & night-time ventilation	3	9	3	10	19	5	13	27	6
		Additional passive measures	2	6	3	5	13	4	6	21	5
A CR 5	Min: 30	Single-sided ventilation	7	14	4	25	27	6	28	32	7
		As-designed: stack & night-time ventilation	1	4	2	3	9	4	4	17	5
		Additional passive measures	1	4	2	1	7	3	2	15	5
	Max: 42	Single-sided ventilation	13	20	5	36	33	7	37	38	8
		As-designed: stack & night-time ventilation	2	6	3	4	6	4	4	11	6
		Additional passive measures	1	4	2	2	9	3	3	16	5
B CR5	Min: 30	Existing building	0	0	0	0	0	0	0	0	0
	Max: 42	Existing building	0	0	0	0.3	0	0	0	0	0
B CR6	Min: 31	Existing building	0	0	0	0	0	0	0	0	0
	Max: 43	Existing building	0	0	0	0.2	0	0	0.4	0	0

DISCUSSION

Both case studies had been designed to comply with the requirements set out in the Schools Building Bulletin 101 (DfES, 2006) when exposed to a weather file representative of

‘average’ weather conditions. Applying the new overheating criteria and the more stringent DSY weather conditions (representative of ‘extremes’ for overheating analysis) shows the resilience of the environmental strategies adopted for these buildings to more extreme conditions. School A would comply with the overheating criteria under the current DSY conditions if the design strategy is followed in practice. However, a number of interventions would be required to mitigate the risk of overheating over the coming years. Table 1 shows that overheating is not merely a result of exceeding certain threshold temperature (Exceedance criterion), but the severity of it also exceeds the 6 degree-hours limit set out by CIBSE TM52. School B, on the other hand, is quite resilient to the current and future weather conditions even under the new overheating criteria set out for mechanically conditioned buildings that specify fixed threshold and upper limit temperatures lower than Building Bulletin 101. Figure 4 shows that this resilience comes at a huge price in terms of energy use and specifically auxiliary energy that includes the energy used by air handling units. However, building performance evaluations revealed significant shortcomings in the procurement of School B that compromised its operational energy, notably failure of demand-controlled ventilation and specific fan powers being much worse than the design intents.

CONCLUSIONS

The future overheating risk in new school buildings in the UK is currently not adequately addressed at design stage. This can have implications for capital expenditure on the necessary interventions across the school estate in future that are not quite transparent.

This study found that a naturally ventilated school with several measures to protect the building against overheating in current climate will almost certainly experience severe overheating during teaching hours over the expected life cycle of its environmental strategy unless additional measures are specified to enhance its resilience. Mechanical measures to improve overheating resilience, on the other hand, can increase energy use and carbon emissions of schools. It is therefore recommended to carry out integrated life-cycle assessment for both energy performance and overheating resilience at design stage and identify major risks and mitigation measures to ensure design intents will be met in practice.

ACKNOWLEDGEMENT

This study was supported by the EPSRC (Grant Reference Code: EP/G037698/1) and Innovate UK (Project Numbers.: 1798-16365 & 1281-16183).

REFERENCES

- BSI. (2007). *BS EN 15251:2007: Indoor Environmental Input Parameters for Design and Assessment of Energy Performance of Buildings Addressing Indoor Air Quality, Thermal Environment, Lighting and Acoustics*. London: BSI.
- CIBSE. (2013). *CIBSE TM52, The limits of thermal comfort: avoiding overheating in European buildings*. London: CIBSE.
- CIBSE. (2014). *CIBSE Guide M, Maintenance engineering and management*. London: The Chartered Institution of Building Services Engineers (CIBSE).
- DfES. (2006). *Building Bulletin 101, Ventilation of school buildings*. London: Department for Education and Skills, The Stationary Office.
- Leaman, A., & Bordass, B. (2001). Assessing building performance in use 4: the Probe occupant surveys and their implications. *Building Research & Information*, 29(2), 129-143.
- Pegg, I. (2007). *Assessing the Role of Post-occupancy Evaluation in the Design Environment - A Case Study Approach*. London: Brunel University: EngD Environmental Technology Dissertation.

Analysis of Dynamic Variation Characteristics and Influential Factors of PM_{2.5} on Subway Platforms under Air-Conditioning Condition and Ventilation Condition

Lihui Wang^{1,*}, Jihua Zhang¹, Tianwei Hu¹, Meng Kong², Jensen Zhang², Jie Song³ and Yi Zheng³

¹ University of Shanghai for science and technology, Shanghai, China

² Department of Mechanical and Aerospace Engineering, Syracuse University, NY, USA

³ Shanghai Shentong metro company of technology center, Shanghai, China

*Corresponding email: 66amy99@126.com

ABSTRACT

The purpose of this study is to investigate the main influential factors of the subway Particulate Matter (PM) pollutants under the air-conditioning condition and ventilation condition, by an on-site field measurement in a subway station in Shanghai. It is found that the dust accumulation at fresh air shaft was the secondary dusting action under the influence of fresh air flow, leading to a higher concentration of the PM in the subway station than in the outdoor air even when the outdoor air quality was good. In addition, in the morning rush hour the PM 2.5 value near the platform screen door our is highest of the day.

KEYWORDS

Subway platform, PM 2.5 concentration, air-conditioning conditions, ventilation conditions

INTRODUCTION

The air quality of the subway station such as the PM concentration affects the health and comfort of a larger number of passengers and staffs. On the one hand, the friction on the rails during the operation of the train generates a large number of particles (Wen Zhengjiang et al.2012), on the other hand, ventilation shafts bring the outdoor particles into the tunnels, leading to the higher PM concentration in the tunnels. Furthermore, the suspended particles caused by the trains' operation may cause the increasing of the PM concentration on the platform during the opening of the platform screen door (Chang Jingjing and Sun Jian, 2014). Therefore, The variation of the PM concentration on the platform is relevant to the health of the passengers and staffs and arouses extensive attention from the researchers.

At present, researches on pollutants' control of the subway platform are mostly conducted through on-site measurements. For example, Zhao et al. used this method to study the concentration of particulates in subway platforms and train compartments, and observed their changes with the subway operation (Zhao et al., 2016). Kim et al. found that the concentration of PM₁₀ and PM_{2.5} in the passenger compartment of the subway was lower than that in the station (Kim et al., 2010). Liu et al. measured and analyzed the concentration of the PM in the subway station and obtained a clear spatial-temporal distribution of the PM concentration in each area. It was found the concentration of the PM in the transition zone of the station was significantly higher than that of the PM on the platform and in ticket hall (Lu et al., 2015). There is no research or analysis on the influential factors of the PM_{2.5} on subway station platform and its significance. Therefore, the research on the influential factors of the PM_{2.5} on the station platform is urgently needed.

In this work, the dynamic PM 2.5 concentration on the subway platforms was measured on-site under the real-time inspection, aiming at finding the influential factors of the PM 2.5 on the platform.

Methods and Methodology

Characteristics of the PM2.5 concentration on the platform were measured at varied locations during several periods of the day with systematical field-monitoring of the carbon dioxide concentration, air temperature, and humidity. The measurement was conducted under the ventilation condition and air-conditioning condition. The pollutants' distribution characteristics were analyzed regarding the concentration and the heat pressure differences between the tunnel and the station platform during the opening process of the screen doors.

The field-measurements were conducted in the Caobao Road station of Shanghai Metro Line 12 on September 27th, 2017. The ventilation condition was from the starting points of train's operation in the morning to the noon, and the air-conditioning condition was from the noon to the midnight. In order to avoid interfering with the subway operation, two types of on-site measurement methods were developed including long-term and short-term monitoring. During the long-term monitoring, the equipment was fixed for a whole day, recording the data once a minute; during the short-term monitoring, the removable cart is utilized to collect the data at 1.5 m height dynamically.

The traditional ventilation and air conditioning system is used in Caobao Road subway station with the supply air pipe and the return air pipe on the two sides of the platforms (Figure 1). The platform is about 120 m long. Both the supply air pipe and the return air pipe are extended from the two ends to the middle of the platform. The locations of measuring points are shown in Figure 1 with the detailed descriptions in Table 1. The key parameters of the instruments used in the field-measurements are shown in Table 2. Figure 2 presents the photos of the measurement sites.

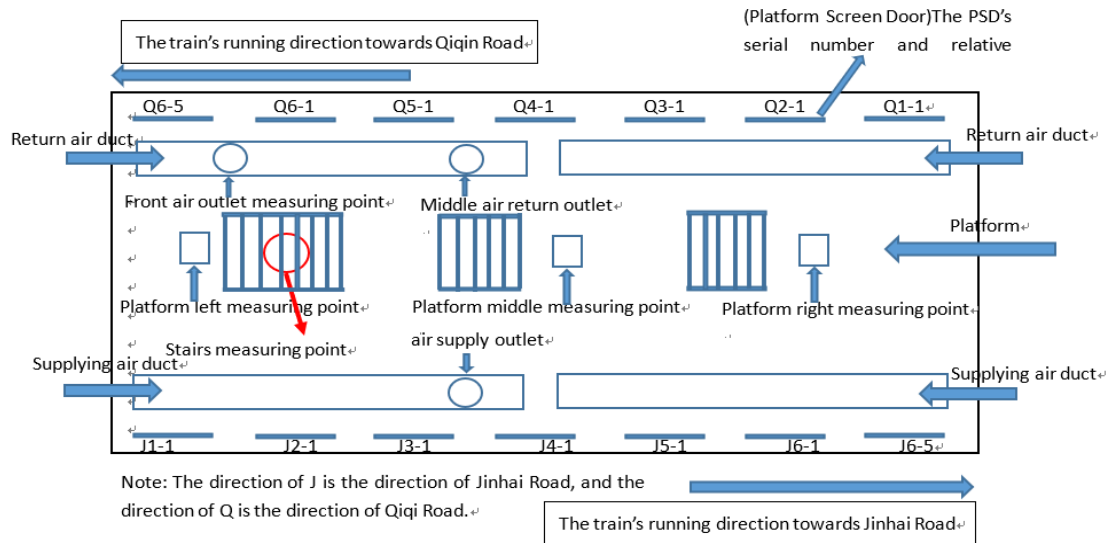


Figure 1 The locations of measuring points

Table 1 On-site measurement methods and object description

Detection method	Objects and measuring location	Number	Data collection method
Real-time inspection	Points on the platform left, middle, right, at 1.5m height	3	All day, 1 data per minute
	Supply air vents closed to the middle of the platform	1	

	Return air vents at the end and in the center of the platform		2	
	Fresh air shaft		1	
	Outdoor air		1	
On-site inspection	near the platform screen door in upline direction	1.5m height near the platform screen door	3-7	Morning rush, off-peak and evening rush hour period
	near the platform screen door in downline direction	1.5m height near the platform screen door	3-7	
	In the train, in the tunnel	the carriage, near the terminals of the platform	4	Off-peak period

Table 2 Measurement instrument parameters

Number	Name	Measuring range	Accuracy
1	Huayun GXH-3010E1CO2 Tester	0~1.000%	0.001%
2	HOBE thermometer	Temperature range : 30□ ~ 70□ Humidity range : 0 ~ 100%	Temperature accuracy : ±0.2□ Humidity accuracy : ±3%
3	BYWF2001 Anemometer	0 ~ 10m/s	0.05 ~ 5m/s± (reading×2%+0.1m/s)
4	Multifunctional dust measuring instrument	(0.01 ~ 100)mg/m3	±10%



(a)



(b)

Figure 2 Measurement sites a) On-site inspection sites b) Real-time inspection sites

RESULTS

Dynamic variation of PM2.5 concentration on the platform and related influential factors under air-conditioning condition

Figure 3 shows the dynamic monitoring results of the PM_{2.5} concentration in the supply air and return air vents, fresh air shaft, and outdoor air during the long-term monitoring. The PM_{2.5} concentration in the supply air was affected by both the concentrations in both the fresh air and return air. The supplying air parameters are relevant to those of the fresh air shaft and the outdoor environment.

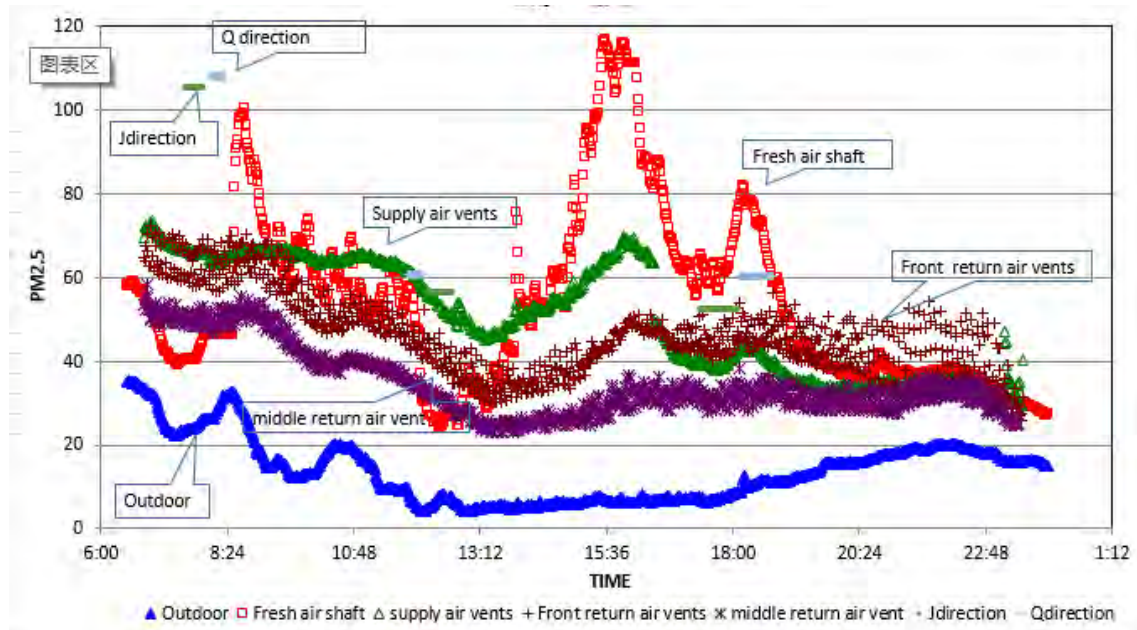


Figure 3 Monitoring results of the PM_{2.5} concentration in the supply air and return air vents, fresh air shaft, and outdoor air during the long-term monitoring

It can be seen from Figure 3 that the PM_{2.5} concentration in the return air vents was lower and correlated with the one in the supply air vents. The return air seemed not the main reason for the high PM concentration in the supply air under the air-conditioning condition. However, the fresh air was likely to contribute to the peaks of PM concentration in the supply. The PM level of the outdoor air was the lowest and much lower than that in the fresh air shafts. One explanation is that there was lots of dust accumulated in the fresh air shaft. It can be concluded that the secondary dusting action by the fresh air shaft led to the higher PM concentration in the fresh air intake even though the outdoor air was fairly clean. The PM concentration in the supply air was lower than that in the fresh air shaft and return air during most of the time, demonstrating that the filtration equipment in the air-conditioning system of the subway station did provide certain purification.

Dynamic variation of PM value on the platform under ventilation condition

Figure 4 shows the dynamic monitored PM_{2.5} concentration in the supply air, fresh air shaft and outdoor air under the ventilation condition. As shown in Figure 4, the PM_{2.5} concentration in the fresh air shaft was higher than that in the outdoor air, confirming that the dusting action in the air shaft was the main reason for the high PM_{2.5} concentration in the supply air. To avoid that, the supply air shaft of the subway station needs to be maintained and cleaned. On the other hand, the filtration system is critical for maintaining the PM concentration in the subway.

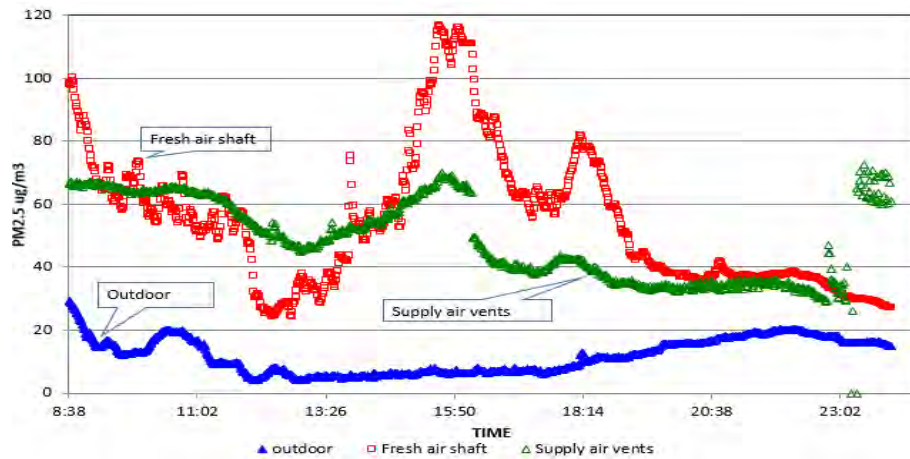


Figure 4 Variation of PM_{2.5} Concentration in Ventilation, New Ventilation Well, Outdoor Air under air conditioning condition and all-fresh-air condition

Dynamic characteristics of PM_{2.5} on the platform, return air and influential factors

Figure 5 shows the relationship between the concentration of PM_{2.5} in the return air and that of some typical locations on the station platform under both ventilation condition (from morning to noon) and air-conditioning condition (from noon to evening). The PM_{2.5} concentration in the return air correlated with the concentrations on the platform. The PM level both on the platform and in the return air vent reached the peak of the day during the rush hour in the morning. It can be concluded that the accumulation dust in the tunnel and in the fresh air shaft at night are secondary-dusting generated by the trains' operation during the rush hour in the morning. Besides, the PM levels of the typical locations and in the return air vent were also high from the evening rush hour to the end of the day. It can be attributed to the PM continuously escaping from the tunnel through platform screen doors (PSDs) during the operation hour, with the help of the passengers' movement on the platform.

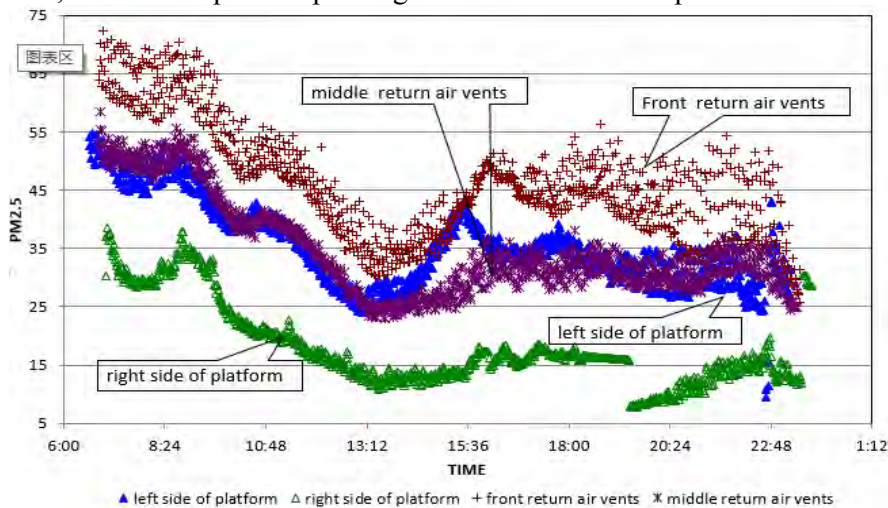


Figure 5 Variation of PM_{2.5} at different locations over time

The variation of the PM concentration near the platform

Figure 6 shows the data at the two typical measurement locations at 1.5m height on the platform, as well as the average values near the PSDs obtained during the rush hour in the morning, off-peak periods and rush hour in the evening. It can be seen that the PM_{2.5} concentration near the PSDs during the rush hour in the morning was significantly higher than

that on the platform. Besides during the non-rush and rush hour in the evening, the PM_{2.5} concentration during the door opening process was slightly higher than that of the typical locations on the platform.

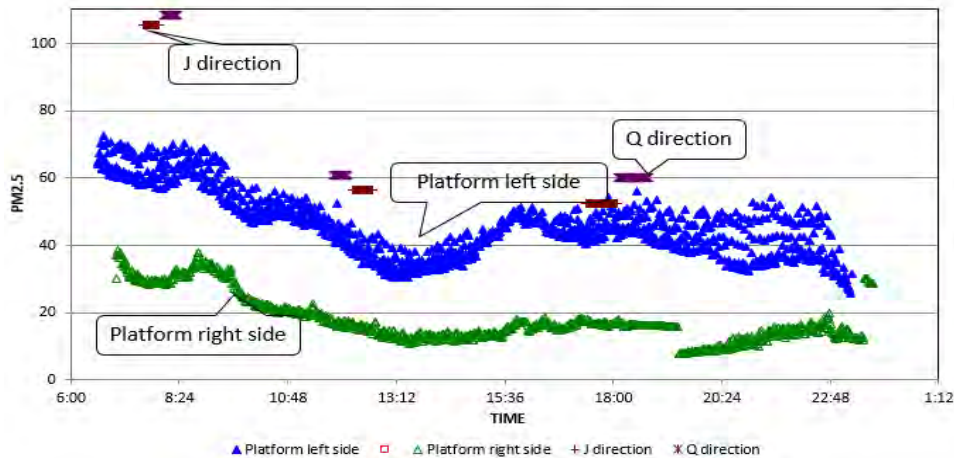


Figure 6 Comparison between PM_{2.5} concentration on the platform and near the PSDs

CONCLUSIONS

The conclusions of this current work are as follows:

1. The dusting action in the fresh air shaft led to the higher PM_{2.5} concentration in the fresh air vents even though the outdoor air was fairly clean.
2. The PM_{2.5} concentration in the return air correlated with the ones on the platform.
3. The PM_{2.5} concentrations during the rush hour in the morning were obviously higher than that of the off-peak hour and the rush hour in the evening.
4. The dusting action in the tunnel caused by the train in the morning is remarkable, resulting in that the PM_{2.5} concentrations on the platform near PSDs were always higher than that on the platform.
5. In order to avoid the dusting action in the fresh air, the fresh air shafts should be cleaned in a regular schedule.

ACKNOWLEDGEMENT

Funding from the Shanghai Shentong metro company of technology center and Shanghai Association for the promotion of Science is gratefully acknowledged. Thanks to National Natural Science Organizational support. Special appreciate of the help of the Syracuse University.

REFERENCES

- Chang Jingjing and Sun Jian. 2014. Spatio-temporal analysis and assessment of CO and PM_{2.5} exposure concentrations under traffic micro-environment in Shanghai [D]. *Shanghai Jiaotong University*: 1-97.
- Wen Zhengjiang, Han Xu, Liu Yingxin. 2012. Experimental Study and Source Analysis of Air Pollutants in Underground Buildings. *Cleansing and Air Conditioning* (1), 4-8
- Zhao Jingde, Wang Jinlong, Yan Guoqing. 2016. Research on Measurement of Particle Concentration in Environmental Control System of Urban Rail Transit. *Journal of Safety and Environment*, (4): 342-347.
- Yong Su Kim a, MinJung Kim a, JungJin Lim et al. 2010. Predictive monitoring and diagnosis of periodic air pollution in a subway station. *Journal of Hazardous Materials*, 183:448-459.
- [5] Senlin Lu, Dingyu Liu, Wenchao Zhang et al. 2015. Physico-chemical characterization of PM_{2.5} in the microenvironment of Shanghai subway. *Atmospheric Research*, 153:543-552.

Assessing the Performance of Photocatalytic Oxidation of Volatile Organic Compounds in Three Different Scaled Set-ups

Zahra Shayegan¹, Chang-Seo Lee¹, Ali Bahloul², Melanie Huard², and Fariborz Haghighat^{1,*}

¹Department of Building, Civil and Environmental Engineering, Concordia University, Montreal, Quebec, Canada

²Institut de recherche Robert-Sauvé en santé et en sécurité du travail, Montreal, Quebec

*Corresponding email: Fariborz.Haghighat@Concordia.ca

ABSTRACT

Volatile organic compounds (VOCs) are considered a major group of indoor air contaminants with several proven adverse health effects. Ultraviolet photocatalytic oxidation process (UV-PCO) is a promising technology for the removal of VOC contaminants in indoor air environments. In addition, adequate efficiency of PCO has been proven in laboratory conditions. However, when PCO is scaled up and applied in real conditions, there are some limitations that need to be addressed. Several factors are involved in the efficiency of the PCO process such as humidity, flow rate (residence time), inlet of contaminant concentration, light source, etc. To the best of our knowledge, most of the research conducted in this area has been performed in a bench-scale reactor with long residence times of several minutes and at high VOCs concentrations (hundreds ppm level), which are far from being real indoor conditions. The main objective of this research is to study the scaling effect on isobutanol removal efficiency under the conditions relevant to real indoor applications. For this purpose, full-scale (0.6 m × 0.6 m), pilot-scale (four parallel ducts, 0.3 m × 0.3 m each) and bench-scale (9 cm × 7 cm) test set-ups were used to study the VOCs removal efficiencies via PCO in the gas phase. First, three experimental set-ups for testing TiO₂ photocatalyst are described. Then, the isobutanol removal efficiency is evaluated in the condition, which is close to the real application, considering the low-level contaminant concentration and high flow rate. The relative humidity in this study is kept in the comfort zone (RH ~ 50±5 %). The performance of UVC-PCO of the three scales is compared and discussed. For isobutanol with 0.003 mg/m³ inlet contaminant concentration, around 24%, 56%, and 68% removal efficiencies were achieved in the full, pilot, and bench-scale systems, respectively.

KEYWORDS

Photocatalytic oxidation (PCO), Volatile organic compound, Indoor air quality, Scale-up, Titanium dioxide (TiO₂)

INTRODUCTION

Volatile organic compounds (VOCs) are considered major contributors to air pollution and a cause of adverse health effects in humans. VOCs are found in the indoor air of residential and commercial buildings; they are released from building materials, consumer products, and occupant-related activity (Vildoza et al. 2011, Weon et al. 2017). Various techniques have been studied to remove VOCs, including adsorption, non-thermal plasma, catalytic oxidation, etc. (Huang et al. 2017a). However, these methods may have several drawbacks, such as generation of secondary pollutants, high energy consumption and high cost, which are obstacles when dealing with low VOCs concentration ranges (Ji et al. 2017).

Photocatalytic oxidation (PCO) is a promising technique, which can degrade various types of VOCs at low concentration levels (Huang et al. 2017b, Lyulyukin et al. 2018). Among different photocatalysts, TiO₂ is considered as one of the most efficient, because of its low cost, abundance, strong photo-oxidation power, and high chemical and photochemical stability (Ji et al. 2017, Weon et al. 2018). Our previous work summarized the PCO of several types of contaminants on TiO₂ photocatalyst surface (Shayegan et al. 2018). Accordingly, most of the published papers are based on bench-scale applications in laboratory conditions, whereas there is limited research on pilot or full-scale, which are applicable to real indoor application (Zhong et al. 2013). Small-scale investigations have often considered a high level of contaminant concentration and a low amount of flow rate with long residence time. Their results are not suitable for scaling up since they do not resemble real indoor air conditions (Shu et al. 2018).

This paper focuses on the effects of scaling up on the PCO process of a commercial filter. PCO of isobutanol at three different scales—including bench, pilot, and full-scale set-ups—are studied to determine the possible obstacles in scaling up the air purification process.

METHODS

Materials

In this study isobutanol (99.9%, ACS grade, Fisher Scientific, Canada) was used as the target contaminant. A commercial PCO filter was purchased from Saint Gobain Quartz Company. The 2,4-dinitro-phenylhydrazine (DNPH) cartridge and acetonitrile (HPLC grade) were purchased from Sigma Aldrich and Fisher Scientific, respectively for HPLC analysis.

Experimental set-ups

In this work, three experimental set-ups are used to investigate the effect of scaling up on the removal efficiency of the PCO process. Table 1 shows the operational parameters of these set-ups.

Bench-scale. The first experiment was carried out using a bench-scale duct. Fig. 1a shows the schematic diagram of the bench-scale set-up. The apparatus was made from an aluminum duct which had been anodized to have the highest reflectance to UV, with 7 cm × 9 cm cross-sectional area, 100 cm length, and 6.3×10⁻³ m³ volume. All the fitting and tubing used in the system were stainless steel or PTFE. For this set-up, two separate compressed air streams were used as the carrier gas and passed through the mass flow controller (MFC, OMEGA, FMA5442ST). The total flow rate of the duct was adjusted at 1.8 m³/h. Relative humidity of the system was controlled by passing one of the air streams through a vessel of distilled water. The second air stream was used to adjust the specific flow rate. The specified amount of isobutanol (see Table 1) was automatically injected by a syringe pump (KD Scientific, KDS-210, USA) into the duct. GC/MS (Agilent) and HPLC (Perkin Elmer) were used to analyze the contaminant concentration. Accordingly, GC and HPLC samples were collected to measure the isobutanol concentrations at the points upstream and downstream of the duct.

Pilot-scale. The second test apparatus used in this work is made of four parallel aluminum ducts, each with a 31 cm × 31 cm inner cross-sectional area. Fig. 1b depicts the schematic diagram of the test rig. As shown, the dimension of the closed part of the set-up is 3.6 m long and 1.2 m wide, with a total volume of 1.7 m³. The length of each duct is long enough to assume the air is following the ideal plug flow pattern. By using a radial fan, the system was able to control the speed of air and provide the flow rates up to 340 m³/h (200 cfm). Due to the size of the set-up, the laboratory air was used as the carrier air. The laboratory air, which

had passed through the filter, mixed with the air containing the evaporated isobutanol, was introduced into the system. The experimental set-up is an open duct system; therefore three humidifiers were used near the entrance of set-up to keep the relative humidity at a specified amount. The relative humidity and temperature at upstream and downstream of each duct were monitored by sensors (HMT 100, Vaisala) and recorded. The sensors were installed in two locations: at the center for upstream and past each duct's reactor sections for downstream. The cross-shaped sampling tubes were mounted at the beginning and at the end of the reactors to collect the upstream and downstream samples. GC and HPLC samples were collected to analyze the isobutanol concentrations at the upstream and downstream of each duct. Two pressure taps were installed, at the beginning and at the end of the PCO reactors for each duct. All of the probes and tubing used in the system were stainless steel or PTFE. The reactor was designed to be able to accommodate the various geometric shapes of the in-duct UV-PCO filters available on the market. Moreover, the design of these reactors allow for the changing of the number of lamps and catalysts. In this study, two layers of PCO filters and two UVC lamps were installed. The distance between the surfaces of catalyst and UV lamps was approximately 5 cm. In addition, the distance between each of the two lamps and the distance from each lamp to the reactor's wall were 13.3 cm and 8.6 cm, respectively. At the end of each duct, the clean-up section containing activated carbon, activated aluminum, and MnO₂ scrubbing filters was installed to capture the residual VOCs and any potentially generated by-products. The adequate numbers of MnO₂ layer post-filters were installed to control the exhaust ozone concentrations, less than 50 ppb.

Full-scale. The third set of experiments was carried out with a full-scale set-up, as presented in Fig. 1c. The duct was designed based on the ASHRAE standard 145.2 (ASHRAE 2016). The full-scale set-up has a 61 cm by 61 cm cross-sectional area, 11.5 m length, and 10 m³ volume. It is constructed of stainless steel with a smooth interior finish to minimize the absorption of contaminants on the internal surface of the duct. The design of the reactor offers the ability to test different types and sizes of air cleaning systems. As depicted in Fig. 1c, a radial fan with speed control (Rosenburg America, DKNB-355) is utilized which can provide an airflow rate up to 3400 m³/h (2000 cfm). A clean-up bed followed by a HEPA filter are installed, just past the fan, to filter out the possible particulate matter and aerosol from the carrier air. To reduce air leakage through the inlet or outlet dampers, ultra-low leakage positive pressure dampers (M&I Air Systems Engineering) were utilized in the system. The final clean-up bed was installed to adsorb possible by-products or unreacted contaminants before the exhaust is directly vented through the laboratory exhaust duct (Bastani et al. 2010).

Table 1: The operating parameters in the bench, pilot, and full-scale set-ups.

Parameter	Value		
	Bench-scale	Pilot-scale	Full-scale
Temperature	23.5 ± 0.5 °C	21 ± 0.5 °C	23.5 ± 1 °C
Relative humidity	50 ± 1 %	47 ± 3 %	48 ± 2 %
Air velocity	0.5 and 1.25 m/s	0.5 m/s	1.25 m/s
Inlet concentration	0.003 and 3.03 mg/m ³	0.003 and 3.03 mg/m ³	0.003 and 3.03 mg/m ³

RESULTS

The performance of commercial PCO filter for isobutanol degradation was evaluated under UV irradiation. The experimental data obtained from upstream and downstream of each set-up is employed to calculate the removal efficiency, η (%), as follow:

$$\eta(\%) = \frac{(C_{up} - C_{down})}{C_{up}} \times 100 \quad (1)$$

where $\eta(\%)$ is the single-pass removal efficiency and C_{up} and C_{down} (mg/m^3) are the contaminant concentrations at upstream and downstream of each set-up.

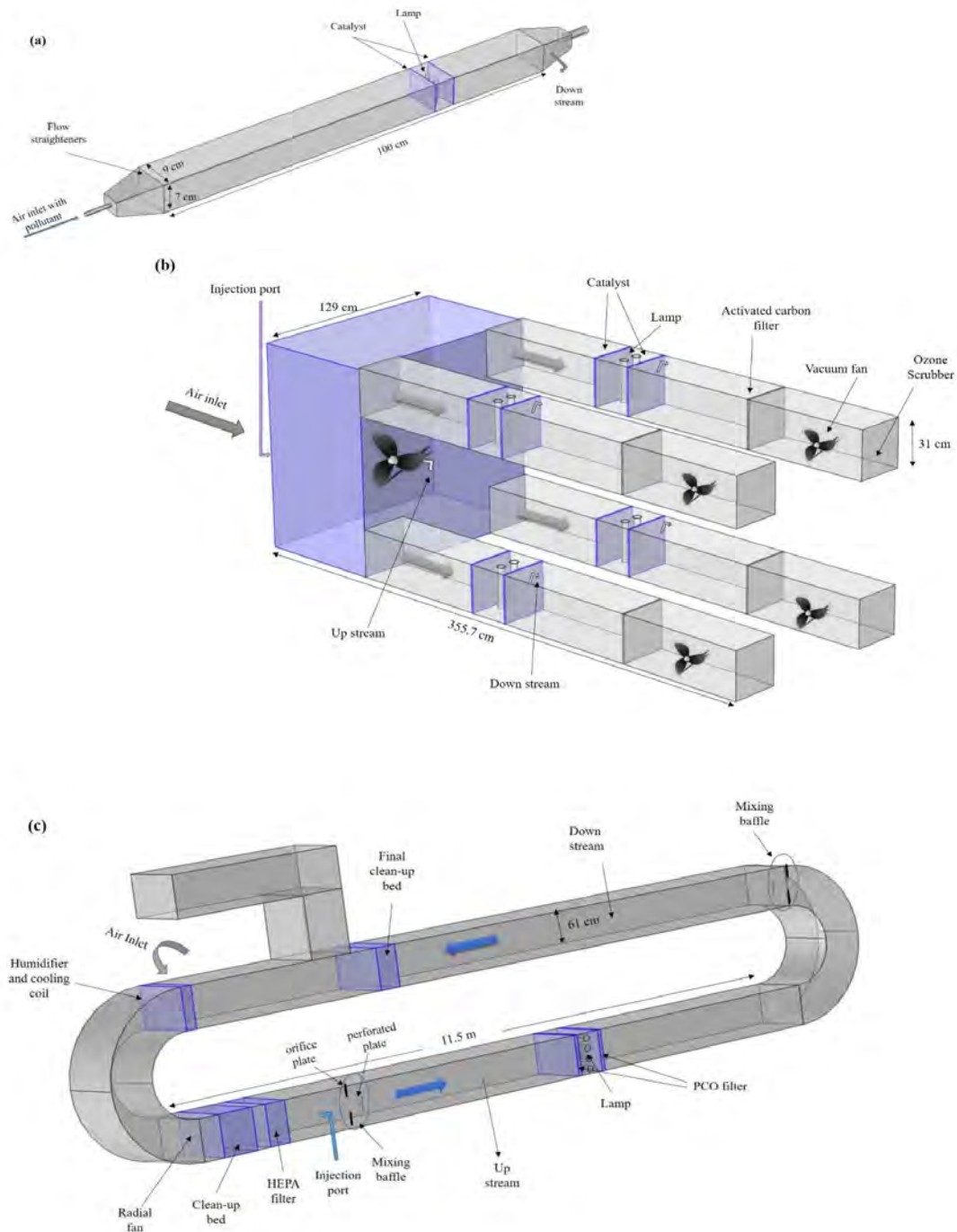


Figure 1. Schematic diagram of a) bench-scale, b) pilot-scale, c) full-scale set-ups.

Fig. 2a and b depict the removal efficiency of isobutanol at 0.003 mg/m^3 and 3.03 mg/m^3 , respectively, for bench, pilot, and full-scale set-ups. The velocity of air flow for pilot and full-scale was adjusted at 0.5 m/s and 1.25 m/s , respectively. In order to compare the results with bench-scale, two sets of experiments were conducted at 0.5 m/s and 1.25 m/s . As presented in Fig. 2a and b, the removal efficiency of isobutanol in low concentration is higher than in high concentration. Moreover, the removal efficiency of isobutanol decreased as the scale of set-up increased. The difference in results between setups of the same velocity may be a result of the effect of the light source. It is also observed that by increasing the air velocity, the removal efficiency was decreased, either in comparing two sets of bench-scale results or by comparing the pilot and full-scale ones. This is a result of the high air velocity, whereby the residence time is decreased and contaminant molecules have less chance to decompose in the shorter reaction time.

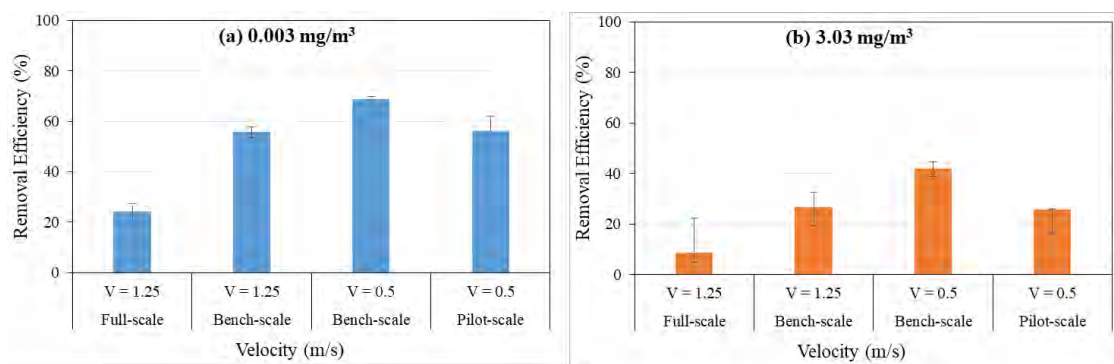


Figure 2. Removal efficiency of isobutanol a) 0.003 mg/m^3 , b) 3.03 mg/m^3 at three scale of set-ups.

DISCUSSIONS

The main problem in scaling up the photocatalytic reactor in large-scale applications is in having a uniform distribution of light irradiation for the entire photocatalyst's surface. The evaluation of light distribution inside the reactor is crucial for the extrapolation of laboratory scale results to pilot or full-scale operations. As mentioned in the results section, the lower inlet contaminant concentration showed higher removal efficiency. This occurs because the fixed active sites of the catalyst have limited adsorption capacity. Moreover, at high inlet concentration, the surface of the photocatalyst becomes saturated and quantum yield decreases due to the shielding effect of contaminants on the catalyst surface. In addition, increasing the airflow rate velocity causes a) the reduction in residence time of PCO process followed by decrease of removal efficiency, b) the increase of the mass transfer rate of contaminants to the surface of the catalysts, improving the PCO removal efficiency. It is obvious that laboratory-scale results are not sufficiently accurate and reliable for use in designing the UV-PCO system for indoor contaminants on a large-scale. Further studies need to be conducted to evaluate the effects of scaling up combined with indoor real conditions (e.g. multi-component mixtures) on by-product generation and catalyst deactivation.

CONCLUSIONS

Three scales of experimental set-ups were designed and constructed to study the UV-PCO performance of the commercial filter. In order to compare pilot and bench-scale set-ups, the experiments in bench-scale were conducted at 0.5 m/s velocity. The results showed that the removal efficiency in the bench-scale setup was higher than that of the pilot in both considered inlet concentrations. Additional experiments were performed at 1.25 m/s in bench-

scale in order to compare the results of the bench with full-scale. It is concluded that by increasing the air velocity and the size of the system, the removal efficiency of isobutanol was decreased.

ACKNOWLEDGEMENT

The authors gratefully acknowledge the financial support from the Institut de recherche Robert-Sauvé en santé et en sécurité du travail (IRSSST). We also appreciate Ms. Lucie Rene for performing the GC experiments.

REFERENCES

- Vildoza D., Portela R., Ferronato C., and Chovelon J.-M. 2011. Photocatalytic oxidation of 2-propanol/toluene binary mixtures at indoor air concentration levels. In: *Applied Catalysis B: Environmental*, 107(3), pp. 347-354.
- Weon S., Choi J., Park T., and Choi W. 2017. Freestanding doubly open-ended TiO₂ nanotubes for efficient photocatalytic degradation of volatile organic compounds. In: *Applied Catalysis B: Environmental*, Vol. 205, pp. 386-392.
- Huang H., Lu H., Zhan Y., Liu G., Feng Q., Huang H., Wu M., and Ye X. 2017a. VUV photo-oxidation of gaseous benzene combined with ozone-assisted catalytic oxidation: Effect on transition metal catalyst. In: *Applied Surface Science*, Vol. 391, pp. 662-667.
- Ji J., Xu Y., Huang H., He M., Liu S., Liu G., Xie R., Feng Q., Shu Y., Zhan Y., Fang R., Ye X., and Leung D.Y.C. 2017. Mesoporous TiO₂ under VUV irradiation: Enhanced photocatalytic oxidation for VOCs degradation at room temperature. In: *Chemical Engineering Journal*, Vol. 327, pp. 490-499.
- Huang H., Huang H., Feng Q., Liu G., Zhan Y., Wu M., Lu H., Shu Y., and Leung D.Y.C. 2017b. Catalytic oxidation of benzene over Mn modified TiO₂/ZSM-5 under vacuum UV irradiation. In: *Applied Catalysis B: Environmental*, Vol. 203, pp. 870-878.
- Lyulyukin M.N., Kolinko P.A., Selishchev D.S., and Kozlov D.V. 2018. Hygienic aspects of TiO₂-mediated photocatalytic oxidation of volatile organic compounds: Air purification analysis using a total hazard index. In: *Applied Catalysis B: Environmental*, Vol. 220, pp. 386-396.
- Weon S., Kim J., and Choi W. 2018. Dual-components modified TiO₂ with Pt and fluoride as deactivation-resistant photocatalyst for the degradation of volatile organic compound. In: *Applied Catalysis B: Environmental*, Vol. 220, pp. 1-8.
- Shayegan Z., Lee C.-S., and Haghghat F. 2018. TiO₂ photocatalyst for removal of volatile organic compounds in gas phase – A review. In: *Chemical Engineering Journal*, Vol. 334, pp. 2408-2439.
- Zhong L., Haghghat F., Lee C.-S., and Lakdawala N. 2013. Performance of ultraviolet photocatalytic oxidation for indoor air applications: Systematic experimental evaluation. In: *Journal of Hazardous Materials*, Vol. 261, pp. 130-138.
- Shu Y., Ji J., Xu Y., Deng J., Huang H., He M., Leung D.Y.C., Wu M., Liu S., Liu S., Liu G., Xie R., Feng Q., Zhan Y., Fang R., and Ye X. 2018. Promotional role of Mn doping on catalytic oxidation of VOCs over mesoporous TiO₂ under vacuum ultraviolet (VUV) irradiation. In: *Applied Catalysis B: Environmental*, Vol. 220, pp. 78-87.
- ASHRAE .2016. *ANSI/ASHRAE Standard 145.2*, Laboratory Test Method for Assessing the Performance of Gas-Phase Air-Cleaning Systems: Air-Cleaning Devices. Atlanta: American Society of Heating Refrigeration and Air Conditioning Engineers, Inc.
- Bastani A., Lee C.-S., Haghghat F., Flaherty C., and Lakdawala N. 2010. Assessing the performance of air cleaning devices – A full-scale test method. In: *Building and Environment* 45(1), pp. 143-149.

Fate of particles released by a puff–dispersion with different air distributions

Shichao Liu^{1,*}, Atila Novoselac²

¹Department of Civil and Environmental Engineering, Worcester Polytechnic Institute, USA

²Department of Civil, Architectural and Environmental Engineering, The University of Texas at Austin, TX, USA

*Corresponding email: sliu8@wpi.edu

ABSTRACT

Well-mixed assumption normally has flaws in the space with continuous-releasing particle sources. For transient point or puff sources, however, particle concentration might vary differently among locations during emission periods and afterwards. This study measures whether and how rapidly ventilation systems can distribute particles emitted from puff-like sources in an indoor space. The impact of ventilation pattern (over-head mixing ventilation and displacement ventilation), particle size (0.77, 2.5 and 7 μm) and source location are also examined. The results show that particles with sizes of 0.77 μm and 2.5 μm can be distributed uniformly by both mixing ventilation and displace ventilation shortly (within a few minutes) after particle injection is terminated, regardless of particle source locations with the absence of obstructed airflow. This paper validates the well-mixed assumption when assessing long-term human exposure to puff-generated particles in the indoor environment. With regard to puff sources, the spatial concentration enhancement in human microenvironment/breathing zone might not be as significant as continuous-releasing particle sources.

KEYWORDS

well-mixed assumption, puff, mixing time, displacement ventilation (DV), mixing ventilation (MV)

INTRODUCTION

The assessment of human exposure to indoor particles relies on the information of particle concentration and spatial distribution. The well-mixed assumption is a convenient approximation in the human exposure analysis (Mosley et al., 2001). In many situations, however, particle size and source location affect indoor fate and lead to spatial variability of particle concentration (Bouilly et al., 2005). Rim and Novoselac (2009) found that thermal plume of a sedentary manikin caused up to four times higher concentration in the breathing zone than room concentration with stratified airflow patterns in the room. Air distribution patterns or ventilation systems also cause inhomogeneity of spatial distribution (Zhao and Wu, 2009). These findings on the inadequacy of the well-mixed assumption presume that indoor particles are released from stationary and continuous injecting sources.

Indoor particle sources are often transient, mobile, and in the form of puff-dispersion. Intermittent human activities such as folding clothing, walking around and sitting on upholstered furniture resuspend substantial particles smaller than 5 μm (Ferro et al., 2004). During particle releasing, spatial concentration is greater near the source than other regions. The non-uniformity decays after the particle releasing finishes. The well-mixed condition can be achieved when the standard deviation of the concentration at all locations to be within 10% of the spatial average (Gadgil et al., 2003).

Since human activities release substantial indoor particles near a human body, this study investigates the fate of particles (0.77, 2.5 and 7 μm) released from a puff-like source in the feet region of an occupant, which simulates particle resuspended from the floor or shed from clothing (pants). Injecting a blast puff of particles in the supply air, we also examine the influence of source location on the mixing time of indoor particles.

The primary objective of this study is to re-visit the well-mixed assumption for indoor particles released from puff-like sources. In addition, this study aims to investigate particle mixing time when considering different indoor ventilation systems (overhead mixing and displacement ventilation), particle sizes and source locations.

METHODS

Test chamber and setups

The test chamber for all particle experiments consisted of a precisely controlled HVAC system and a water-heating wall. The chamber had a geometry of 6 m \times 4.5 m \times 2.7 m. It is able to create displacement ventilation and mixing ventilation by using different air diffusers (Figure 1). Both overhead mixing ventilation (MV) and displacement ventilation (DV) provided an air change rate per hour (ACH) of 3.2 hr⁻¹ that represented a typical office environment. The supply air temperature and turbulence intensities were approximately 17.4 °C and 5%, respectively, which were measured by a hot sphere anemometer (HT-400, SENSOR) with a sampling frequency of 0.5 Hz. This study considered a relatively low-occupation-density office that consisted of two thermal dummies (90W each), two table-boxes (0 W) and one heated wall (320W) representing warm windows or façade in the summer time (Figure 1). An embedded HEPA (high-efficiency particulate arrestment) filter in the HVAC system enabled background particle concentration without indoor sources three order of magnitudes lower than that with such sources.

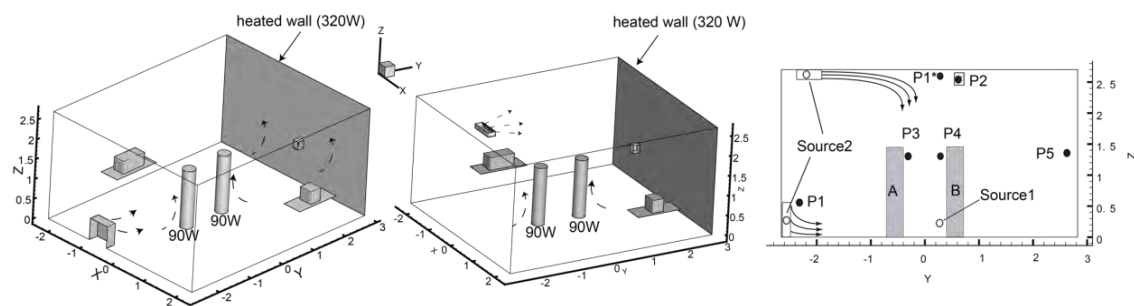


Figure 1. Schematic of experimental setups. Left) displacement ventilation, Middle) mixing ventilation, Right) particle sampling positions.

Particle seeding and measurements

Outdoor particles and indoor human activities contribute to indoor particles. Particle sources described in Figure 1 represents resuspended particles (Source 1) from the floor or shed particles from clothing because of human activities and unfiltered outdoor particles entering indoors via supply air (Source 2). We tracked the fates of particles with three different sizes, 0.77, 2.5 and 7 μm considering particle and airflow dynamics (Liu and Novoselac, 2014).

For both DV and MV, particles were released close to body proximity (Source1) (0.02 m from a dummy and 0.3 m above the floor) or in the duct before diffusers (Source 2). Coarse particles (7 μm) were released only in the duct due to the strong flow disturbance of the generator. The generation period was 100 seconds for 0.77 and 2.5 μm particles, while 30 seconds for 7 μm

particles. We measured particle time-serial concentration at five locations (Figure 1) for 1200 seconds across the chamber using Optical Particle Counters (Aerotraks 9306, TSI, Inc). All experiments were repeated three times and measurements uncertainty is represented by standard deviation among the three repeats in this study.

In order to facilitate concentration comparison at the different sampling locations, this study normalized particle concentration by a reference value. For 0.77 and 2.5 μm particles, we used the average concentration over the entire sampling period (1200 seconds) at the chamber exhaust (P2 in Figure 1) as the reference (C_{ref}). Nevertheless, particle deposition loss becomes significant for 7 μm particles. As such, we normalized particle concentration for 7 μm based on the instantaneous average concentration over the five sampling locations, C_{ref}^* . This study focuses on the instantaneous comparison of particle concentration at different locations. The reference value does not affect the comparison of spatial concentration.

RESULTS

Mixing ventilation

Supply air diffusers for MV typically create high-momentum jets that entrain air and particles from surroundings and blend them inside the whole room. The concentration of submicron particles that transport similarly to gaseous pollutants tends to be uniformly distributed in the room with MV. Figure 2 shows the measured time-serial concentration of particles (0.77, 2.5 and 7 μm) released from two sources. When the particle source (Source1) resides in the vicinity of thermal dummy B, convective boundary flow of the thermal dummy spreads particles during the injection period. In Figure 2, the concentration right above the particle source (P4) is approximately two orders of magnitude higher than at other locations for 0.77 and 2.5 μm particles during injection. Nevertheless, this difference disappears a few minutes after particle injection finishes, rendering all concentration curves collapsing onto one. When particles were released into supply duct (Source 2), on the other hand, the concentrations at five locations show a very similar trend for both 0.77 and 2.5 μm particles. With regard to 7 μm particles, the gravitational force becomes competing with drag force, leading to increased deposition loss and decayed concentration with height.

The results for MV indicate that particle source locations only affect $\text{PM}_{2.5}$ transport during the injection period and the relatively short period (**2 min**) afterward. The well-mixed assumption concentration is valid for transient puff-like particle sources in the typical office environments when considering particle distribution and human exposure for a long term. However, the assumption does not hold for coarse (e.g. 7 μm) particles.

Displacement ventilation

Particles take a longer time to transport across the chamber with DV than MV, because DV supplies air at the floor level at a low air speed. In Figure 2, particles (0.77 and 2.5 μm) emitted at the feet region (Source 1) of the thermal dummy B are transported by the plume to the breathing zone of thermal dummy A (P4) where concentration is one order of magnitude greater than that at room exhaust during particle injection. Compared to the concentration at P4 for MV, DV reduces considerably the peak concentration in the breathing zone. This reduction is attributed to the enhanced airflow disturbance on Source 1 (feet region) when supply air is provided at the floor level.

When outdoor or room-recirculated particles enter the room with DV via supply air diffusers (Source 2), particles transport along the floor and then upwards with thermal plumes when encountering heat sources. Figure 2 shows that particle concentration in the locations close to

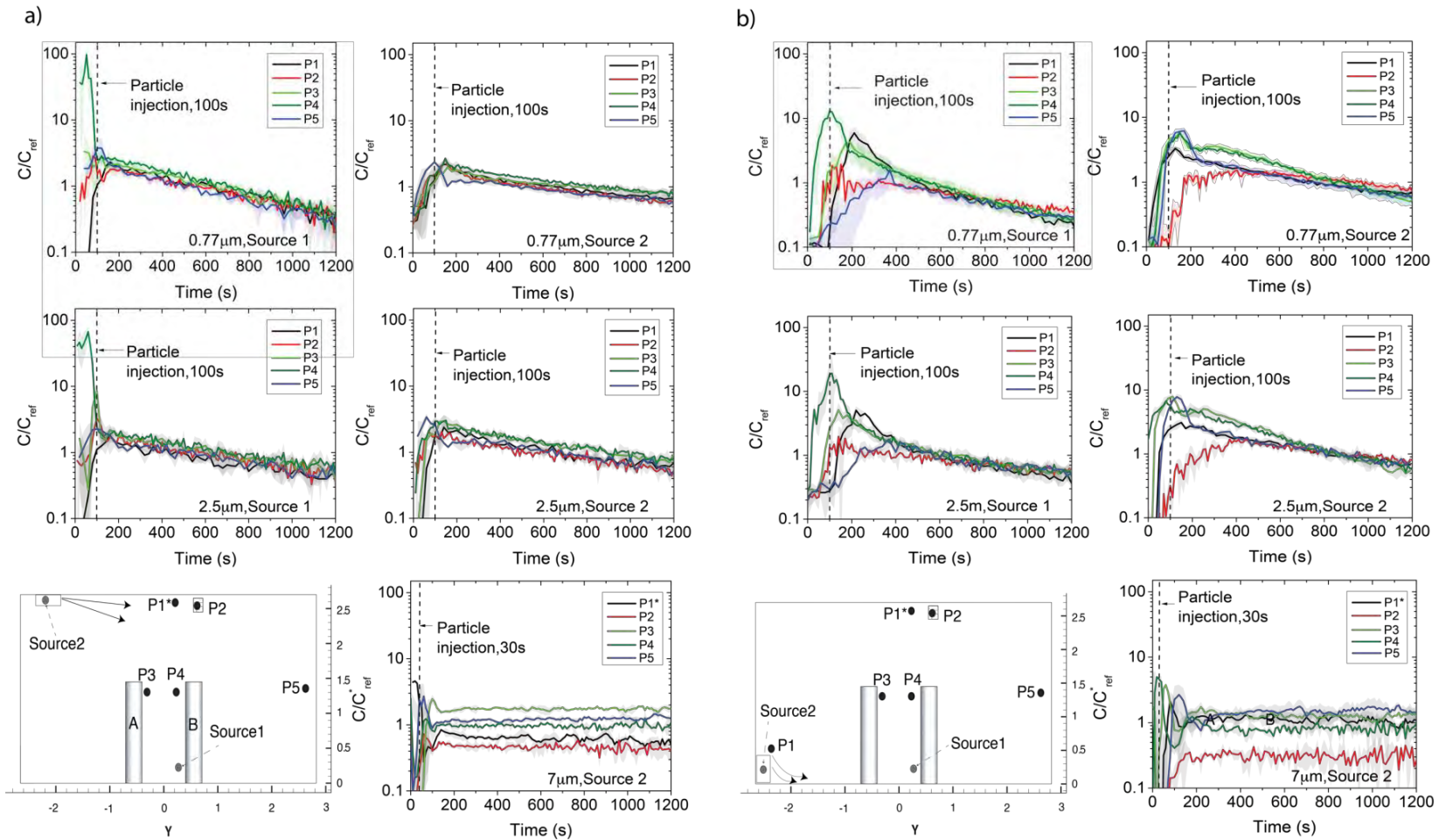


Figure 2. The variation of particle concentration in the room. a) mixing ventilation, b) displace ventilation (cooling condition, $ACH=3.2 \text{ hr}^{-1}$, exhaust: P2; curve shades represent uncertainty). Note: P2 is the exhaust on a chamber wall, and all other locations are at the central plane of the room

thermal plume such as P3, P4, and P5 are higher than other measured locations during and in the short period after particle injection finishes.

Unlike creating thermal stratification, DV fails to generate stratified concentration for 0.77 and 2.5 μm particles. It is observed in Figure 2 that particle concentrations for the two sizes at all the measured locations decay to the same level in 10 min after particle injection ends. The results suggest that puff-like sources transport $\text{PM}_{2.5}$ uniformly across a typical office environment shortly after the particle-releasing period, even for thermally stratified systems. Source locations have little effect on the well-mixed assumption for $\text{PM}_{2.5}$.

We also measured particle concentration at P1* that is near the room ceiling and right above the breathing zone (P4) of thermal dummy B. Figure 2 shows that particle (7 μm) concentration at P1* is at the same magnitude of that at breathing zones (P3 and P4). The observation implies human thermal plume is able to transport coarse particles (7 μm) from the floor up to the ceiling level. Again, coarse particles (7 μm) settle down easily in the indoor environment, and well-mixed assumption is unjustified.

DISCUSSIONS

Airflow in a typical office with MV distributes uniformly $\text{PM}_{2.5}$ that constitutes most indoor particles shortly (2 min) after particle injection period. As a stratified system, DV spreads particles generated by puff-like sources and is able to homogenize particle distribution in 10 min after particle generation finishes. The location of particle sources has insignificant influence on the mixing time. However, such phenomena are not observed in the similar indoor environments for continuously releasing sources. For instance, when particles are continuously released in the vicinity of a human manikin, exposure increases significantly compared to other particle sources (Rim and Novoselac, 2009, 2010; Salmanzadeh et al., 2012). These findings assuming continuous particle sources propose a scrutinized investigation in the spatial difference of particle concentration for further exposure analysis. In a real office environment, however, intermittent and short-term puff-like sources, such as walking, body shedding and printing, are much more common than stationary continuous particle sources. The findings from this study imply that $\text{PM}_{2.5}$ is likely to be uniformly distributed if considering long-term exposure. The findings for $\text{PM}_{2.5}$ also justify the well-mixed assumption shortly after particle injection ends, regardless of particle location.

In addition, spatial variability of particle concentration occurs during particle injection and only a few minutes afterwards. Such short period makes source-localization that applies inverse tracking techniques more challenging to identify puff-like sources of $\text{PM}_{2.5}$ or gaseous pollutants (Zhang et al., 2012).

We measured particle transport in a test chamber where interior surfaces might be different in surface roughness and area from offices in reality (Thatcher et al., 2002). In addition, the study considered no furnishing obstructing airflow around particle sources. The findings from this study might be generalized to other short-term puff-like particles sources, such as coughing and sneezing rather than intermittent repeatable sources including breathing and chatting. Other factors such as air change rate per hour, heating source intensity and the number of particle sources might affect particle fate. These factors should be investigated in future.

CONCLUSIONS

We investigated the fate of particles generated by transient puff-like sources in a test chamber that simulated a typical office environment. We also examined how ventilation pattern, particle size and source location affected particle transport across the room.

This study concludes that both MV and DV can distribute uniformly PM_{2.5} released by a puff-like source in the entire room shortly after particle generation finishes. In specific, particle concentration varies insignificantly among different locations in 2 min and 10 min after particle source terminated for MV and DV, respectively. However, gravitational settling generates concentration stratification for coarse particles (7 µm) in the room.

The study justifies the well-mixed assumption for PM_{2.5} related to puff-like sources in the indoor environment if considering long-term exposure. In such conditions, long-term human exposure in the microenvironment might not be significantly different from other room space.

REFERENCES

- Bouilly J., Limam, K., Béghein, C. and Allard, F. 2005. Effect of ventilation strategies on particle decay rates indoors: An experimental and modelling study. *Atmospheric Environment*, 39(27), 4885–4892.
- Ferro, A.R., Kopperud, R.J. and Hildemann, L.M. 2004. Source Strengths for Indoor Human Activities that Resuspend Particulate Matter, *Environmental Science and Technology*, 38(6), 1759–1764.
- Gadgil, A.J., Lobscheid, C., Abadie, M.O. and Finlayson, E.U. 2003. Indoor pollutant mixing time in an isothermal closed room: an investigation using CFD, *Atmospheric Environment, Indoor Air Chemistry and Physics: Papers from Indoor Air 2002*, 37, 5577–5586.
- Liu, S. and Novoselac, A. 2014. Lagrangian particle modeling in the indoor environment: A comparison of RANS and LES turbulence methods (RP-1512), *HVAC&R*, 20(4), 480–495.
- Mosley, R.B., Greenwell, D.J., Sparks, L.E., Guo, Z., Tucker, W.G., Fortmann, R. and Whitfield, C. 2001. Penetration of Ambient Fine Particles into the Indoor Environment, *Aerosol Science Technology*, 34(1), 127–136.
- Mundt, E. 2001. Non-buoyant pollutant sources and particles in displacement ventilation, *Building and Environment*, 36(7), 829–836.
- Rim, D. and Novoselac, A. 2009. Transport of particulate and gaseous pollutants in the vicinity of a human body, *Building and Environment*, 44(9), 1840–1849.
- Rim, D. and Novoselac, A. (2010) Occupational Exposure to Hazardous Airborne Pollutants: Effects of Air Mixing and Source Location, *Journal of occupational and environmental hygiene*, 7(12), 683–692.
- Salmanzadeh, M., Zahedi, G., Ahmadi, G., Marr, D. and Glauser, M. 2012. Computational modeling of effects of thermal plume adjacent to the body on the indoor airflow and particle transport, *Journal of Aerosol Science*, 53, 29–39.
- Thatcher, T.L., Lai, A.C., Moreno-Jackson, R., Sextro, R.G. and Nazaroff, W.W. 2002. Effects of room furnishings and air speed on particle deposition rates indoors, *Atmospheric Environment*, 36(11), 1811–1819.
- Zhang, T.T., Li, H. and Wang, S. 2012. Inversely tracking indoor airborne particles to locate their release sources, *Atmospheric Environment*, 55, 328–338.
- Zhao, B. and Wu, J. 2009. Effect of particle spatial distribution on particle deposition in ventilation rooms, *Journal of hazardous materials*, 170(1), 449–456.

Radon levels in rented accommodation

Torben Valdbjørn Rasmussen^{1,*}

¹ Danish Building Research Institute at Aalborg University, Denmark

*Corresponding email: tvr@SBI.AAU.dk

ABSTRACT

Indoor radon levels were measured in 221 homes located in 53 buildings, including 28 multi-occupant houses and 25 single-family terraced houses. The homes consisted of rented accommodation located in buildings recorded as being constructed before 2010 and after the year 1850. In addition, the radon level was measured in the basement in 9 of the buildings.

The mean year value of the indoor radon level was 30.7 (1–250) Bq/m³. The indoor radon level exceeded 100 Bq/m³ in 5.9% of the homes, all located in single-family terraced houses. The variable single-family terraced houses explained 5.9% of the variation in indoor radon levels, and although associations were positive, none of these, besides homes in single-family terraced houses, were statistically significant. Approx. 75% of homes exceeding 100 Bq/m³ indoor radon level had levels between 100 and 200 Bq/m³ and 25% had indoor radon levels exceeding 200 Bq/m³. Significant differences in indoor radon levels were found in homes located in multi-occupant houses. Additionally, the risk of indoor radon levels exceeding 100 Bq/m³ in homes in multi-occupant houses was found to be very low, but the risk was highest on the ground floor in a building constructed with slab on ground.

KEYWORDS

Radon, measurements, homes, rented accommodation, mean year value.

INTRODUCTION

Radon-222 develops from the radioactive decay of radium-226 and has a half-life of 3.8 days. This noble gas seeps through soil into buildings, and if it is not evacuated, there can be much higher exposure levels indoors than outdoors (Nazaroff, 1992), which is where human exposure occurs (Brunekreef and Holgate, 2002). In this way, radon affects occupants through the indoor climate.

The World Health Organization recommends states to introduce requirements for the maximum concentration of radiation from natural sources in the indoor air. These recommendations are the result of the World Health Organization's evaluation of radon as being responsible for 3-14% of lung cancer incidents, depending on the average radon exposure in different countries (Zeeb and Shannoun, 2009). Results show radon to be the second-largest cause of lung cancer (tobacco smoking is still the primary cause). Radon exposure must be taken seriously in the struggle against radon-induced lung cancer due to the large number of people who are exposed daily in buildings and especially in residential buildings (Zeeb and Shannoun, 2009). If people spend their whole life in a house with an average radon concentration in the indoor air that exceeds 200 Bq/m³, their risk of getting lung cancer is higher than 1%. This is far too high and higher than what in other contexts is acceptable for a single-factor risk (Andersen et al., 1997). Therefore, it is crucial to ensure a low radon level in the indoor air and to prevent radon from infiltrating into buildings.

Since 2010, Danish buildings must be constructed so as to ensure indoor radon levels below 100 Bq/m^3 as the mean year value (Danish Enterprise and Construction Authority, 2010). For all other buildings including homes it is recommended that the mean year value for the indoor radon levels should be below 100 Bq/m^3 .

In this study, radon levels in rented accommodation were measured in the winter of 2013/14 and again in the winter of 2014/15. The paper shows how well 221 homes for rented accommodation perform, with respect to the Danish Building Regulations for homes constructed after 2010 and with respect to the recommendations for older homes, with regard to radon and to identifying the association between indoor radon in these homes and floor level, multi-occupant houses, single-family terraced houses, and basements. The number of homes with radon levels exceeding 100 and 200 Bq/m^3 was determined.

MEASUREMENTS

Measurements were carried out in 221 homes for rented accommodation and in 9 basements. Families and building owners were invited to participate in a radon monitoring programme. The programme took place in the heating periods of 2013/2014 and 2014/2015 between November and May. 196 homes were located in 28 multi-occupant houses and 25 homes were located in single-family terraced houses. Homes were selected from regions where other studies have shown a 1-30% chance of finding detached single-family houses with radon levels exceeding 200 Bq/m^3 , (Andersen et al., 2001a). Three detectors were distributed to each participant by mail in sealed aluminum-coated envelopes and returned after the integration period in a pre-stamped envelope. Each participant was asked to fill in a questionnaire regarding the date when exposure started and ended, as well as type of room in which the detector was placed. Participants were instructed regarding placement of the detectors (>25 cm from a wall and away from strong draughts and heat) and also instructed to clean and ventilate their homes as they usually would, so that representative levels were obtained. Information regarding year of construction, basement, crawl space, and building and roof materials was gathered from the Danish Building and Housing Register (Christensen, 2011). Information gathered from the Danish Building and Housing Register was used to make sure that homes represented typical rented accommodation in Denmark. In accordance with Danish recommendations for radon measurements in private homes, the simplest assessment of radon concentrations is based on direct integrated measurements (Rasmussen and Wraber, 2011a, Wraber and Rasmussen, 2011b), thus no indirect measurements (geological samples, soil gas measurements, external gamma radiation, etc.) were performed in this study.

DWELLINGS

Homes were either rented accommodation located in buildings privately owned by landlords or social housing owned by the Danish association of non-profit rented accommodation. Buildings were multi-occupant houses and single-family terraced houses. The buildings represented the building technique and commonly used building materials used in Denmark from 1850 until today. Buildings from this period can be grouped into three types:

- Multi-occupant house built between 1850 and 1920. The buildings were constructed with a solid brick wall founded on masonry foundations. Sometimes single natural stones might be included in the foundations and outer walls. Suspended floors were timber floor constructions. Suspended floors were horizontal partitions and included timber beams. They were traditionally constructed from the top with floor boards, clay infill, wooden boards, empty space, wooden boards and a layer of plaster on straw. The timber beams were usually of good quality with the dimensions approximately

200 mm by 200 mm, see Figure 1. Solid floor against the ground were made of concrete, asphalt or soil.

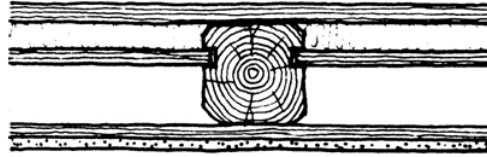


Figure 1. Suspended floors include from top floor boards, clay infill, wooden boards, empty space, wooden boards and a layer of plaster on straw.

- Multi-occupant house built between 1920 and 1960. The buildings were constructed with solid brick walls or cavity walls founded on cast-on-site concrete foundations. Suspended floors were timber floor constructions, see Figure 1 or reinforced concrete suspended floors cast on site. Solid floors against the ground were made of concrete.
- Multi-occupant house or single-family terraced house built in the period from 1960. The buildings were constructed with load-bearing concrete constructions as prefabricated elements above the ground. Foundations and load-bearing basement walls were made of concrete cast on site. Suspended floors were made of reinforced concrete usually as prefabricated concrete elements. Solid floors against the ground were of concrete cast on site.

EQUIPMENT

The detectors used were closed passive etched track detectors, made from CR39 plastic film placed inside an antistatic holder. Analysis were carried out by an ISO 17025 and ISO 14001 certified as well as EMAS (European Eco-Management and Audit Scheme) registered laboratory. Measurement methods are accredited according to standards of SWEDAC (Swedish board of Accreditation and Conformity Assessment) and accepted in 18 European countries by the European Cooperation for Accreditation of Laboratories (EAL).

RESULTS

Radon was measured for a median duration of 90 days (min–max: 60 – 194 days). A single representative indoor radon concentration for each home was calculated as the arithmetic average of the three measurements and used in all statistical analyses.

Table 1 shows the distribution of the determined mean year values of the radon concentration grouped according to floor level in intervals of 50 Bq/m^3 . The minimum value was 1 Bq/m^3 , the maximum value was 250 Bq/m^3 . The standard variation was 38.3 Bq/m^3 , the median value was 18 Bq/m^3 and the mean value was 30.7 Bq/m^3 . The ratio of homes with a mean year value of the radon concentration ranging between 100 Bq/m^3 and 200 Bq/m^3 was 4.5%. The ratio of homes with a mean year value of the radon concentration exceeding 200 Bq/m^3 was 1.4%. The ratio of homes with a mean year value of the radon concentration exceeding 100 Bq/m^3 was 5.9%.

Table 2 shows the distribution of the determined mean year value of the radon concentration in homes, with a basement or a crawlspace as the lowest level facing the ground, grouped by floor level and in intervals of 50 Bq/m^3 . The minimum value was 1 Bq/m^3 , the maximum

value was 206 Bq/m³, the standard variation was 32.3 Bq/m³, the median value was 17 Bq/m³ and the mean value was 26.2 Bq/m³.

Table 1. The number of homes grouped according to the determined mean year values of the radon concentration is shown by their location, as the floor number, and in intervals of 50 Bq/m³.

	0-50	51-100	101-150	151-200	>200	Number of homes
Ground floor	58	18	7	3	3	88
1st Floor	50	0	0	0	0	51
2nd Floor	38	0	0	0	0	38
3rd Floor	30	0	0	0	0	30
4th Floor	6	0	0	0	0	6
5th Floor	8	0	0	0	0	8
Number of homes	190	18	7	3	3	221
Ratio in %	86.0	8.1	3.1	1.4	1.4	100

Table 2. The number of homes, grouped by the determined mean year value of the radon concentration shown by their location and in intervals of 50 Bq/m³, in a building with a basement or a crawlspace at the lowest level facing the ground.

Location (floor number)	0-50	51-100	101-150	151-200	>200	Number of homes
Ground floor	42	9	6	2	1	60
1st Floor	43	0	0	0	0	43
2nd Floor	34	0	0	0	0	34
3rd Floor	28	0	0	0	0	28
4th Floor	5	0	0	0	0	5
5th Floor	6	0	0	0	0	6
Number of homes	158	9	6	2	1	176
Ratio in %	89.8	5.1	3.4	1.1	0.6	100

For homes in a building with a slab on ground in the accommodation on the lowest level facing the ground, the minimum value was 10 Bq/m³, the maximum value was 250 Bq/m³, the standard variation was 53 Bq/m³, the median value was 33 Bq/m³ and the mean value was 50 Bq/m³.

Table 3 shows the distribution of the determined mean year value of the radon concentration in homes grouped in intervals of 50 Bq/m³ for homes located on the ground floor in multi-occupant houses.

Table 3. The number of homes grouped by the determined mean year value of the radon concentration in intervals of 50 Bq/m³. Homes were located on the ground floor in multi-occupant houses.

	0-50	51-100	101-150	151-200	>200	Number of homes
Home over basement/crawlspace	42	5	0	0	0	47
Ratio i %	89.4	10.6	0	0	0	100
Home with floor on ground	9	7	0	0	0	16
Ratio in %	56.3	43.7	0	0	0	100

Figure 2 shows the mean year value of the radon concentration in homes measured in the winter of 2013/2014 and in the winter of 2014/2015. Results are shown for homes where the

first measurements showed results exceeding the recommended radon level for homes. Homes were located in single-family terraced houses. The mean year value of the radon concentration was determined with an accuracy of 20 Bq/m³ to 40 Bq/m³.

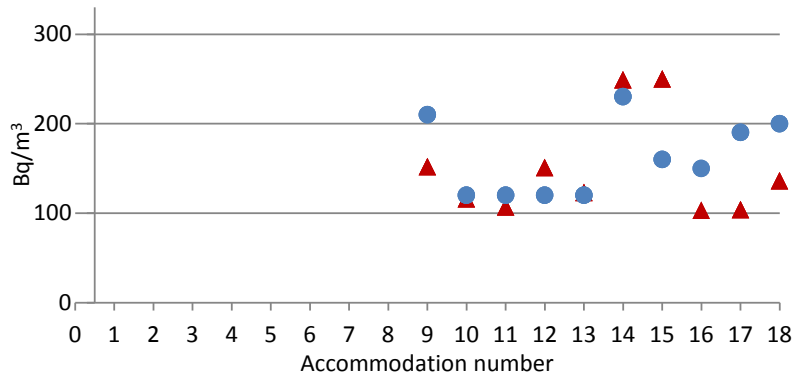


Figure 2. Mean year value of the radon concentration in homes measured in the winter of 2013/2014 (Red Δ) and again in the winter of 2014/2015 (Blue o). Each accommodation is given a number.

DISCUSSION

This study found a mean year value of the indoor radon level of 30.7 Bq/m³ ranging between 1 and 250 Bq/m³. In total, 5.9% (13 of the 221) homes had indoor radon levels exceeding 100 Bq/m³, all located in single-family terraced houses. The variable single-family terraced houses were statistically significant and explained 5.9% of the variation in indoor radon levels.

The mean year value of the radon level of 30.7 Bq/m³ is somewhat lower than the population-weighted average annual radon concentration of 59 Bq/m³ for all Danish homes (Andersen et al., 2001a, b). The population-weighted average annual radon concentration of 59 Bq/m³ was based on 1-year measurements in 3012 single-family homes and 101 multifamily (apartment buildings) in Denmark.

The present study found the indoor radon level exceeded 100 and 200 Bq/m³ in 10 (4.5%) and 3 (1.4%) homes, respectively. Approx. 75% of homes with indoor radon levels exceeding 100 Bq/m³ had levels between 100 and 200 Bq/m³ and 25% had indoor radon levels exceeding 200 Bq/m³. Significant differences in indoor radon levels were found in homes located in multi-occupant houses. The risk of indoor radon levels exceeding 100 Bq/m³ in homes in multi-occupant houses is very low, but if there is a risk, it is most likely to be found in the lowest accommodation in a building with a slab on ground. A risk of indoor radon levels exceeding 100 Bq/m³ was found in homes in single-family terraced houses.

The municipalities selected in the present study were previously characterised as having the highest levels of residential radon concentration indoors in Denmark (1–30% of homes with levels over 200 Bq/m³) (Andersen et al., 2001a). Measurements showed that the soil type was the main determinant of indoor radon levels (Andersen et al., 2001a, b). The present study did not include measuring radon levels in soil. The homes in this study were located on clayey/sandy to clayey soil, with 2–18% sand and gravel content (Andersen et al., 2001b; Greve and Breuning-Madsen, 1999), and although radon variation in these soils can be expected, this is not described at each specific home location.

The mean year value of the radon concentration in homes was measured in the winter of 2013/2014 and again in the winter of 2014/2015. Measurements were carried out twice in homes where the first measurements showed results exceeding the advised radon level for buildings of 100 Bq/m³. These homes were all located in single-family terraced houses. Results from the first measuring period correspond with the results from the second measuring period. However, results show that the radon concentration indoors is affected by seasonal variations and the use of the home.

CONCLUSION

This study found a mean year value of the indoor radon level of 30.7 Bq/m³ ranging between 1 and 250 Bq/m³ in homes in rented accommodation. In total, 5.9% (13 of the 221) homes had indoor radon levels exceeding 100 Bq/m³, all located in single-family terraced houses. Approx. 75% of homes exceeding 100 Bq/m³ indoor radon level had levels between 100 and 200 Bq/m³ and 25% had indoor radon levels exceeding 200 Bq/m³. Significant differences in indoor radon levels were found in homes located in multi-occupant houses. The risk of indoor radon levels exceeding 100 Bq/m³ in homes in multi-occupant houses is very low, but if there is a risk, it is most likely to be found in the lowest accommodation in a building with a slab on ground. A risk of indoor radon levels exceeding 100 Bq/m³ was found in homes in single-family terraced houses.

ACKNOWLEDGEMENT

This study was supported by the Danish association of private landlords of multi-occupant houses and the Danish association of non-profit rented accommodation.

REFERENCES

- Andersen, C.E., Ulbak, K., Damkjaer, A. and Gravesen, P. (2001a). *Radon in Danish Dwellings*. Copenhagen. National Institute of Radiation Hygiene.
- Andersen, C.E., Ulbak, K., Damkjaer, A., Kirkegaard, P. and Gravesen, P. (2001b). *Mapping indoor radon-222 in Denmark: design and test of the statistical model used in the second nationwide survey*. *Sci. Total Environ.* 272 p. 231–241.
- Andersen, C.E., Bergsøe, N.C., Brendstrup, J., Damkjær, A., Gravesen, P. og Ulbak, K. (1997). *Radon-95: En undersøgelse af metoder til reduktion af radonkoncentrationen i danske enfamiliehuse* (Methods to reduce radon indoors i Danish single-family terraced houses). In Danish. Forskningscenter Risø, Risø-R-979(DA), 108 sider, www.risoe.dk
- Brunekreef, B. and Holgate, S.T. (2002). *Air pollution and health*. *The Lancet*. 360p. 1233–1242.
- Christensen, G., (2011). *The Building and Housing Register*. *Scand. J. Public Health*. 39 p. 106–108.
- Danish Enterprise and Construction Authority, (2010). *Danish Building Regulations 2010*.
- Greve, M.H. and Breuning-Madsen, H., (1999). *Soil mapping in Denmark*. European Soil bureau. Research Report No. 9.
- Nazaroff, W.W., (1992). *Radon transport from soil to air*. *Rev. Geophys.* 30 p. 137–160.
- Rasmussen, T.V. and Wraber, I., (2011a). *Radon - kilder og maling* (Radon - sources and measurements). In Danish. SBI-Anvisning 232.
- Wraber, I. and Rasmussen, T.V. (2011b). *How to ensure low radon concentrations in indoor environments*. 9th Nordic Symposium on Building physics - NSB 2011. Vol. 1: 105–112.
- Zeeb, H., Shannoun, F. (ed). (2009). *WHO Handbook on indoor radon – a public health perspective*. World Health Organization. Geneva. 94 p.

Condensation-free radiant cooling using infrared-transparent enclosures of chilled panels

Eric Teitelbaum^{1,*}, Adam Rysanek², Jovan Pantelic³, Dorit Aviv¹, Simon Obelz⁴, Alexander Buff⁴, Yongqiang Luo⁵, Brian Poirier⁵, Forrest Meggers^{1,5}

¹Princeton University, School of Architecture, USA

²University of British Columbia, Vancouver, School of Architecture, CAN

³University of California, Berkeley, Center for the Build Environment, USA

⁴Interpanel GmbH, Germany

⁵Princeton University, Andlinger Center for Energy and the Environment, USA

*Corresponding email: eteitelb@princeton.edu

ABSTRACT

Radiant cooling power in the humid climates is inherently limited by condensation. This research investigates a type of radiant cooling methodology whereby the cold temperature source is convectively and conductively isolated from the environment with a membrane transparent to visible radiation to allow supply temperatures to be decreased for radiant cooling systems in humid climates. We conduct an FTIR analysis on three candidate membrane materials and fabricate a prototype experimental test panel that allows for thermal performance evaluation at different panel orientation and depths. Our study shows that for a 5 °C chilled panel temperature, the exterior membrane surface temperature reaches 26 °C in a 32 °C / 70% RH environment resulting in an effective panel temperature of 15.8 °C. Such a panel construction would avoid condensation in many humid environments and allow for radiant cooling without any latent load handling.

INTRODUCTION

Radiant cooling environmental systems are a class of measures and technologies for space cooling in the built environment. They involve exposing building occupants to mechanically-cooled indoor enclosures, or parts of entire enclosures, allowing for a greater degree of heat to be rejected radiatively by the human body to the ambient environment than would otherwise occur. While thermal comfort models demonstrate the potential for radiant cooling systems to provide comfortable conditions in spaces with high indoor air temperatures (de Dear et al. 1996; Arens et al. 2006), in practice generating large air-to-panel temperature differences is hard to achieve without risking condensation occurring on chilled surfaces (Teitelbaum and Meggers, 2017; Feng, 2014). It is for this reason that radiant cooling systems are nearly always combined with mechanical ventilation systems that supply dehumidified air to interior spaces, ensuring indoor air dew point temperatures are sufficiently low to prevent condensation arising on cooled surfaces.

An alternative solution to mitigating the risk of condensation can be found through a more focused investigation of the specific radiant heat transfer and convection processes occurring within and around radiant panel assemblies. In 1963, Morse (Morse, 1963) described a new type

of radiant cooling panel for the tropical environments of Australia, whereby a membrane transparent to long wave infrared radiation is used to enclose, or isolate, the cold panel from the warm, humid ambient air as shown in figure 1a. Since the radiant panel and humans emit in the longwave regime, typically defined as wavelengths between 2.5 and 50 microns, their radiation is able to exchange proportionally to the transmissivity of the membrane. If the enclosure volume would be sufficiently large, and filled with dry air, internal convection would not be significant enough to lower the surface temperature of the membrane below the ambient dewpoint temperature of the interior space, thereby preventing condensation.

Today, whilst there are some emerging commercial applications of Morse's original idea (interpanel, 2018), there remains a lack of understanding of the spectral quality of potential membrane materials and how different material and geometric configurations of such panel assemblies affect overall radiant cooling flux and condensation risks. This paper presents an empirical study which expands on Morse's original chilled panel design by carrying out: 1) Fourier Transfer Infrared (FTIR) Spectroscopy analysis of infrared transparent materials to select the most suitable, common building material for a future panel membrane; and 2) an experimental study of the radiant flux achieved with a prototype radiant cooling panel against varying geometric parameters such as the distance between the membrane and chilled panel, and the vertical/horizontal orientation of the panel itself.

The objective of the overall study is to identify a potentially *optimal* radiant cooling panel design which would provide the greatest cooling flux in a very hot and humid environment without condensation occurring.

MATERIALS AND METHODS

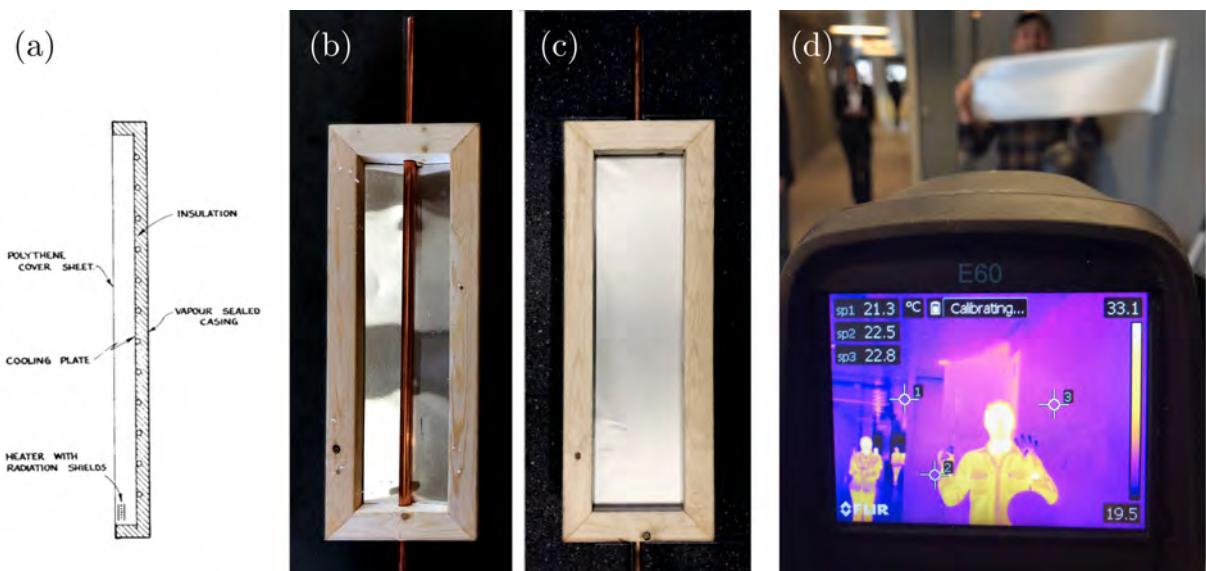


Figure 1: (a) Original infrared transparent radiant cooling panel (Morse, 1963). (b) Test panel prior to black paint. (c) Finished panel with the PP membrane. (d) Visible image of the author holding a sample PP membrane sheet (background) in comparison to the equivalent infrared image of the scene (foreground)

FTIR Analysis

Many common household materials are transparent to longwave infrared radiation, such as high density polyethylene (HDPE) trash bags and low density polyethylene (LDPE) or polypropylene (PP) bottles. However, the comparatively large wavelengths for infrared radiation and correspondingly low frequencies contribute to faster extinction and absorption of the radiation in materials, so it becomes difficult to select these materials for a potential infrared transparent membrane without a detailed representation of their individual spectral properties. Three specific types of prototype LDPE, PP, and HDPE panels were procured for this research, respectively United States Plastic, 1/32" LDPE #42568; United States Plastic, 1/8" HDPE #42587 and a 50 micron-thick polypropylene panel produced proprietarily for interpanel GmbH, FTIR spectroscopy was conducted using a Nicolet i10 infrared spectrophotometer to measure the wavelength-based transmission spectra for each material between 2.5 and 15 microns. The FTIR transmission spectra was overlaid with a true black body emission curve to visualize the ability of each membrane to transmit radiation between the panel and a human. The resulting curve is a true spectral radiance diagram providing radiant power per steradian per micron. Integrating the curve numerically between the measured wavelengths provides a panel radiance value, in units $W/m^2/sr$. Assuming a Lambertian emission function over an arbitrary hemisphere about any point on the panel provides the integration constant for converting radiance to radiant exitance as π , providing a panel radiant power in W/m^2 . This number is calculated for a panel of a known temperature through each candidate membrane. Dividing this number by the radiant exitance of a true black body provided the hemispherical transmissivity, τ .

Panel Evaluation

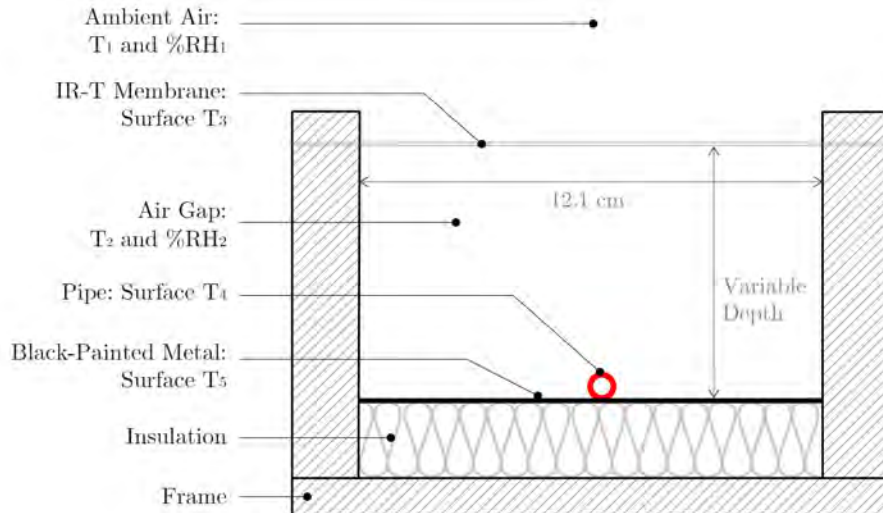


Figure 2: Schematic of panel and sensor layout on cross section up “upwards” facing panel.

Radiant panel frames were constructed with plywood, foam insulation, copper tubing, and aluminum. Douglas fir lumber was fashioned into a 53 by 20 cm open-face box, 7 cm deep with a 1.3 cm plywood back. The framing wood was 3.9cm thick, providing interior panel dimensions of 45.7 by 12.1 cm. Inside the open faced box, 3 cm foam insulation was cut to fit flush along the back of the frame, followed by a piece of 0.8 mm thick aluminum cut to fit flush against the pink insulation. This provided a base panel depth of 3.5 cm from the front face to the aluminum. A straight through copper pipe was then inserted through the top of the frame into the box,

shown in figure 1. This copper pipe contains the chilled flowing fluid. The interior of the box was then spray painted black to make the metallic surfaces emissive ($\epsilon = 0.95$). A schematic of the cross section of the panel is shown in figure 2.

The performance evaluation of the panel was carried in a 1.5 x 2 x 2 meter room at the Embodied Computation Lab of Princeton University. Ultrasonic humidifiers, steam, and the building's in-floor radiant heat were used to generate indoor conditions in the room that would emulate a hot, tropical environment - maintaining an air temperature of 30 to 32 °C and 70 to 80 %RH. Temperature and humidity were continuously monitored with Sensirion's SHT75 temperature and relative humidity sensor (± 0.3 °C; ± 1.8 %RH) and were recorded at 5 second intervals during experimentation.

The radiant panel frames were then outfitted with either HDPE, LDPE, or PP across the top, sealed in a dry environment to minimize humidity inside the dry air gap. The depth between the membrane and panel backing was varied with wooden spacers to allow for 4 different depths: 3.5 cm, 7.8 cm, 9.9 cm, and 12.4 cm. The panels were outfitted with 4 Omega ® Precision Surface Temperature Thermistors (± 0.1 °C), one place on the copper pipe, another inside the panel on the metal heat spreader midway between the copper pipe and the panel wall, and two more on the surface above the two inside. In addition, air temperature and relative humidity were measured inside the panel with an SHT75. Measurements were taken for 4 different panel configurations, facing "upwards" towards the ceiling, "downwards" towards the floor, "horizontally" facing a wall with the long dimension parallel to the floor, and "tilted" angled 30° towards the floor.

RESULTS AND DISCUSSION

Spectral Analysis

The calculated hemispherical transmissivity at 278 K for LDPE, HDPE, and PP was found to be 0.247, 0.298 and 0.597, respectively. Additionally, their respective thicknesses were 0.76, 3.4, and 0.05 mm. The values for τ were then used through the remaining 15-50 microns in the panel's emission spectrum, estimating the full range of thermal radiation transmission at wavelengths above 15 microns. Spectral radiance curves of each membrane material are shown in figure 3, demonstrating, for each candidate membrane material, the predicted radiant heat transfer between a idealized human body at 30 °C and a chilled panel cooled to 5 °C. Blue represents radiation transmitted through the panel, and is replotted below for comparison. Gray area represents absorbed radiation. In the HDPE plot, radiation above the black body line is caused by a measurement error, with random reflection in the laboratory pushing transmission above 100%.

Panel Evaluation

Despite initial promising images with a thermal camera measuring reasonably low temperatures of a cold source behind each panel (see figure 1c), it was found after the FTIR analysis that, in comparison to PP, LDPE and HDPE are relatively poor transmitters of infrared heat at temperature ranges of 5°C to 30°C. This was an unfortunate finding, as otherwise the LDPE and HDPE materials could be advantageous in being structurally rigid and able to support dual role as both a membrane and part of the structural housing of an entire cooling panel assembly membrane.

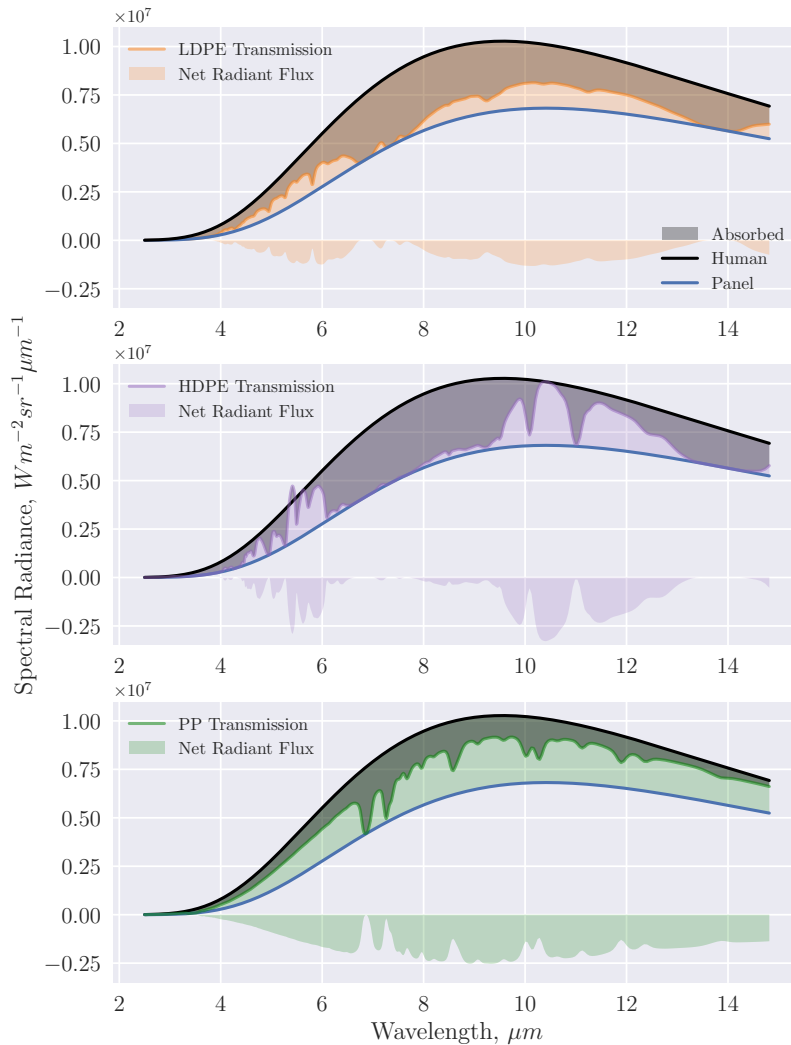


Figure 3: (a-c) FTIR transmission data for each membrane material, LDPE, HDPE, and PP top to bottom, modifying the spectral radiance for a 5 °C panel radiantly exchanging with a 30 °C surface.

The thin PP membrane was therefore the only tested material that was viewed to be able to provide a sufficiently transparent barrier between the chilled panel and ambient environment, and was subsequently used as the membrane for the assembled experimental test panel. Figure 4a shows the temperature profile within the panel at each measurement location for three panel orientations of a 124 mm deep panel outfitted with the PP membrane. The height of each point represents +/- one standard deviation calculated over 60 sampled points. The outer surface of the membrane always remains above the dew point, confirmed visually and through touch during the course of the experiment that no condensation occurred. Data in figure 4b shows the dependence of the membrane's outer surface temperature on both panel orientation and depth, important design information. There is a rough equivalence between membrane surface temperatures at 99 mm panel depth, implying at this point orientation is a non-contributor. Additionally, horizontally positioned panels do not show much membrane temperature variation. Also on figure 4b is the effective panel temperature of 15.8°C which represents fictitious panel temperature with which a body exchanges. The low value is exciting not only for observing no

condensation at this effective temperature, but it represents a 14 °C gradient from the ambient air temperature, a gradient difficult to sustain with existing technology.

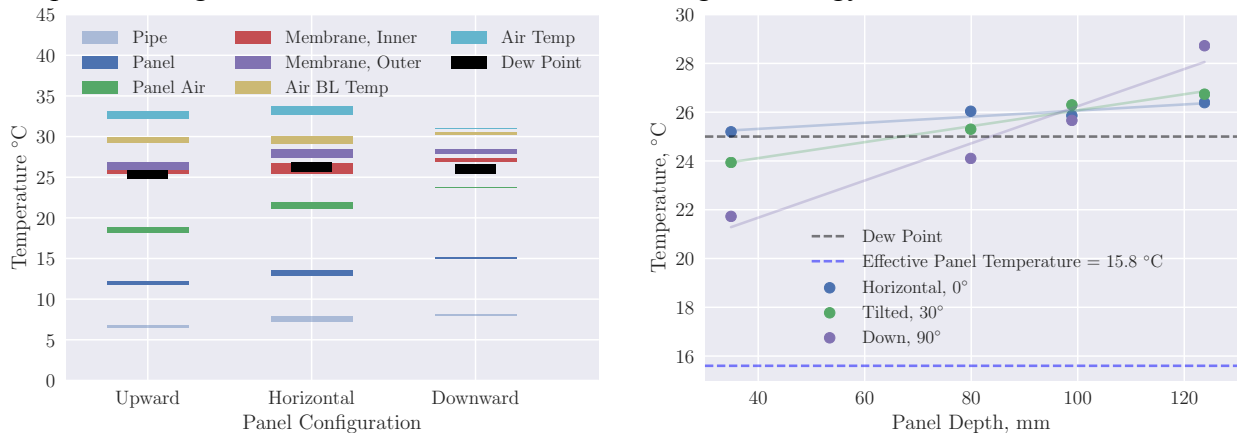


Figure 4: (a, left) Temperature profile within a 124 mm deep panel. The height of each measurement represents +/- one standard deviation of 60 measurements at steady state for each configuration. (b, right) Membrane outer surface temperature measurements for three panel orientations against panel depth.

CONCLUSIONS

This study was particularly successful at demonstrating required design considerations for increased radiant cooling power through an IR-T membrane in warm and also humid environments. Starting with fundamental understanding about how each membrane influences a body's radiant exchange with a panel with a 5 °C supplied water temperature, and building an applied knowledge base about how to design and operate the type of radiant cooling panel described herein to maximize cooling power while avoiding condensation was achieved. A major result indicates there exist equivalence points between radiation, conduction, and convection, such as the one observed at a 9.9 cm panel depth, whereby membrane outer surface temperatures are the same across all orientations. Future work should seek to further parametrize the data, in particular for panel slenderness ratio of the panel to further improve design guidance. Eventually, a model incorporating FTIR data into CFD analysis, for example, would be worthwhile to create.

REFERENCES

- Arens, E.A., Zhang, H., and Huizenga, C. "Partial- and Whole-Body Thermal Sensation and Comfort—Part II: Non-Uniform Environmental Conditions." *Journal of Thermal Biology* 31, no. 1–2 (January 2006): 60–66.
- de Dear, R.J., Arens, E.A., Zhang, H., Oguro, M. "Convective and Radiative Heat Transfer Coefficients for Individual Human Body Segments." *Center for the Built Environment*, November 27, 1996.
- Feng, J.D. Design and control of hydronic radiant cooling systems. Dissertation, University of California, Berkeley, 2014.
- Interpanel GmbH. Sub dew point radiant cooling, 2017.
- Morse, R.N. "Radiant cooling." *Architectural Science Review*, 6(2):50–53, 1963.
- Teitelbaum, E., Meggers, F. "Expanded Psychrometric Landscapes for Radiant Cooling and Natural Ventilation System Design and Optimization." *Energy Procedia*, CISBAT 2017 International Conference Future Buildings & Districts – Energy Efficiency from Nano to Urban Scale, 122 (September 1, 2017): 1129–34.

Experimental Study on the Impact of Passive Chilled Beam in a Room with Displacement Ventilation

Zhu Shi¹, Vishal Anand¹ and Qingyan Chen^{1,*}

¹School of Mechanical Engineering, Purdue University, West Lafayette, IN 47907, USA

*Corresponding email: yanchen@purdue.edu

ABSTRACT

Previous studies have demonstrated that displacement ventilation (DV) can provide better air quality than mixing ventilation (MV), and may save energy in buildings. However, since DV introduces supply air to the occupied zone directly, the temperature of supply air it provides is normally higher than in a MV system, so the ability to remove cooling load is limited with the same amount of air. On the other hand, passive chilled beam (PCB) systems have been shown to be able to remove a large cooling load while saving energy. Therefore, this research studied a coupled configuration that combined DV and PCB, and examined its thermal and ventilation performances through the measurements of airflow velocity, temperature, and contaminant (simulated by sulfur hexafluoride, or SF₆) concentration at various locations. Measurement results were compared with those in the same room but with only DV system. A third set of measurements was also conducted to test how sensitive the results were to room layout and ratio of heat removed by PCB.

Experimental results showed that PCB increased the overall air flow velocity in occupied zone, although the maximum airflow velocity was still observed at floor level, which was similar as in a DV only system. When both PCB and DV systems were used, temperature gradient was observed in most locations of the room. Meanwhile, contaminant concentration stratification was seen to be destroyed by PCB in this experiment. Similar trend was observed in the third set of measurement which had a different room layout and a lower ratio of heat removed by PCB.

KEYWORDS

Passive Chilled Beams, Displacement Ventilation, Coupled System, Indoor Environment

INTRODUCTION

Starting from 1980s, displacement ventilation (DV) has been increasingly commonly used in both Europe and U.S. buildings, especially in industrial and office applications (Svensson, 1989; Burt, 2007). Although this ventilation method demonstrated stronger capability in improving air quality and saving energy, when compared with mixing ventilation (MV), one limitation it has is its relatively low ability to remove cooling load, since it supplies fresh air to occupied zone directly. To remedy this weakness, suggestions were made in previous literatures (Riffat et al., 2004; Schiavon et al., 2012) to conjugate DV with other systems. Among the different possible systems to combine DV with, passive chilled beam (PCB) seems to be a very potential option, due to its shown ability to remove large cooling loads (Kosonen et al., 2010). Hence, there needs an investigation on a conjugate system of DV and PCB, to explore how well the merits of these two methods could be integrated.

In the study of indoor environment design, experimentation has always been an important and necessary method for us to understand the physics inside a room, as well as to appraise the

design. For example, to evaluate thermal comfort levels using two well recognized empirical models, PMV (predicted mean vote) (Fanger, 1970) and PD (percentage dissatisfied people due to draft) (ASHRAE, 2013), information on airflow velocity, temperature and turbulence intensity is needed as input. Also, to quantify the air quality via contaminant removal effectiveness, it needs contaminant concentration data at various locations of the room, which could be measured through experiment. Moreover, accurate experimental measurements can provide high-quality data for boundary condition specifications in simulations (such as computational fluid dynamics, or CFD simulations) and model validations.

Therefore, this investigation used experimental methods to measure the airflow velocity, temperature and contaminant (simulated by sulfur hexafluoride, SF₆) concentration in an indoor air quality (IAQ) chamber which was equipped with the conjugate system of DV and PCB. In the measurement of each type of data, experimental data was collected at 35 locations which were evenly distributed in the chamber that had an office layout. For comparison, a corresponding experiment was performed in the same chamber but with only DV system. This study also explored how sensitive the measured results were to the room layout and PCB cooling power by performing measurements in a third case that had a classroom layout. Through comparing results in the three measurement cases, this study summarized the impacts that PCB made on a DV system in several aspects.

METHODS

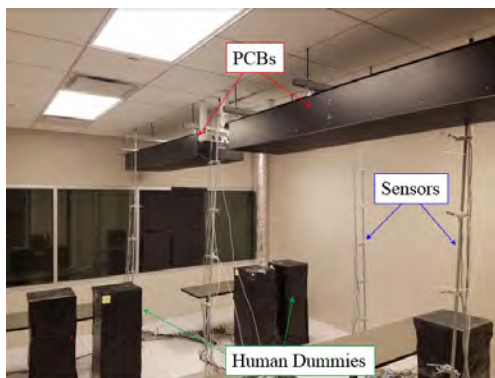
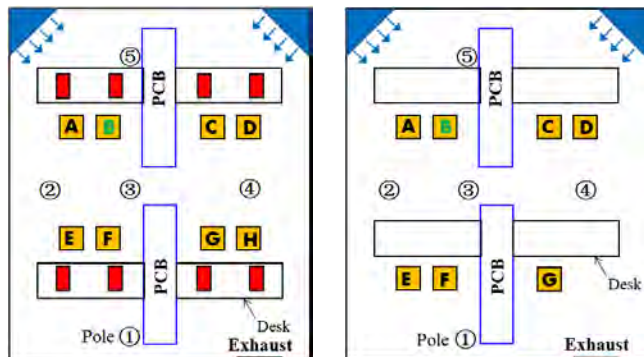


Figure 1. Inside view of IAQ chamber



(a) Office Case_0 and Office Case_1

(b) Classroom Case

Figure 2. Room layouts in 3 measured cases (Red box: PC; Yellow box: humman dummy)

Figure 1 shows the IAQ chamber where experiments were performed. In the chamber, two displacement ventilation diffusers were installed next to the floor, while the exhaust was placed near ceiling. Two pieces of PCBs were suspended on the central plane of the room, near the ceiling. Heated boxes were used to simulate occupants and computers in the room (Figure 2). Table 1 specifies the total cooling loads, number of heated items, and PCB utilizations in all three measured cases.

Table 1. Cooling loads and PCB utilizations in three cases

Case Name	Total Cooling Load	Cooling load breakdowns (Number of items)			Ratio of Heat Removed By PCB
		Light	Human Dummy	PC	

Office Case_0	61 W/m ²	4	8	8	0 (PCB not used)
Office Case_1	61 W/m ²	4	8	8	60%
Classroom Case	30 W/m ²	4	7	0	40%

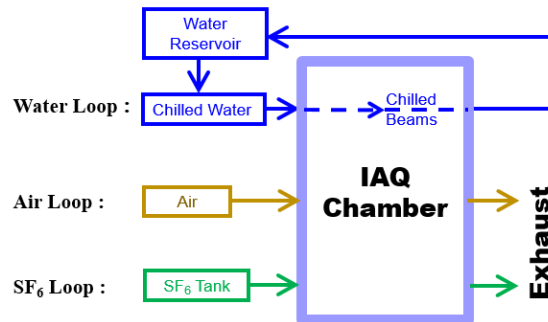


Figure 3. Three “loops” that run through the chamber

This experiment designed three loops that ran through the IAQ chamber, which is illustrated in Figure 3. Chilled water was supplied from water reservoir, and after travelling through pipes inside PCB’s, it still returned to water reservoir. Air was discharged into the room via displacement ventilation diffusers. With a developed LabView program, the air flow rate and temperature could be well controlled. Lastly, SF₆ was provided from an SF₆ tank outside of the chamber, and was discharged in the chamber on top of one human dummy (at a height of about 1.1m). All the operations of the three loops could be performed outside of IAQ chamber.

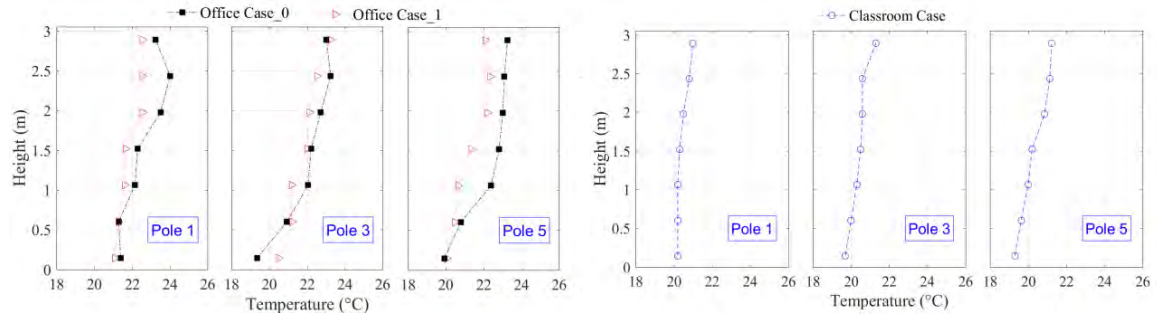
To obtain airflow velocity and temperature data, this experiment employed hot-sphere anemometer probes, whose temperature measurement accuracy is ± 0.3 °C and velocity measurement accuracy is ± 0.01 m/s. In addition, a multi-gas sampler, monitor and analyser system was utilized to measure SF₆ concentration at desired sampling points. In each measurement case, data was collected on 5 poles in the room, with 7 heights at each pole.

RESULTS

This section illustrates and compares the results from the three measurement cases described in the above section. Due to the limit of space in this paper, results from only 3 of the 5 measured poles are demonstrated. However, three locations are sufficient to indicate the air flow characteristics and contaminant distributions in the three measured cases. Results from more measurement locations could be found in Shi and Chen (2018).

Temperature results

Figure 4(a) shows the temperature distributions in “Office Case_0” and “Office Case_1”. “Office Case_0” demonstrated a very typical temperature distribution in a displacement ventilation case, where a clear temperature gradient could be observed at various locations of the room. Temperature gradient was seen to be largest at near-floor region, especially when the measured locations were relatively close to displacement ventilation diffuser (like Pole 3 and 5), and gradually decreased as the height increased. Meanwhile, in “Office Case_1”, although PCB was turned on and was removing 60% of heat in the room, temperature gradient was observed as well in three measured locations. This indicated that the cold downward jet PCB generated was pretty local. In addition, it could be noticed that PCB was able to decrease the temperature gradient when “Office Case_0” and “Office Case_1” were compared.



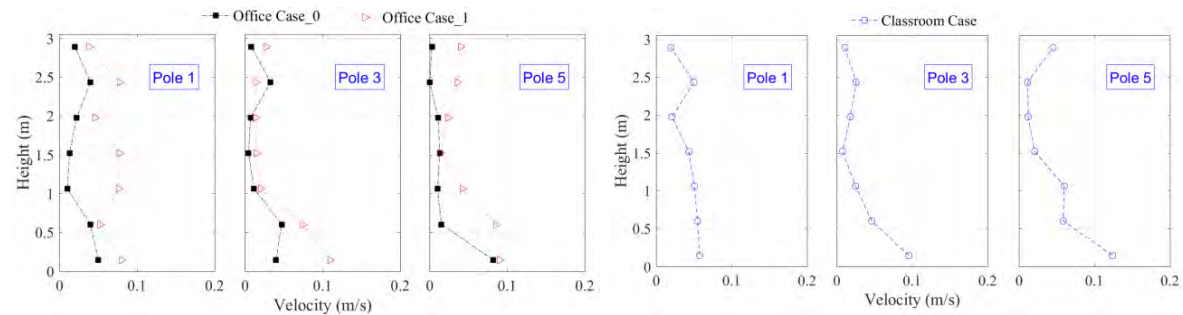
(a) “Office Case_0” and “Office Case_1”

(b) “Classroom Case”

Figure 4. Temperature measurement results

“Classroom Case” also showed similar temperature distribution trend, as can be seen from Figure 4(b), although it had a different room layout and a different ratio of heat removed by PCB.

Velocity Results



(a) “Office Case_0” and “Office Case_1”

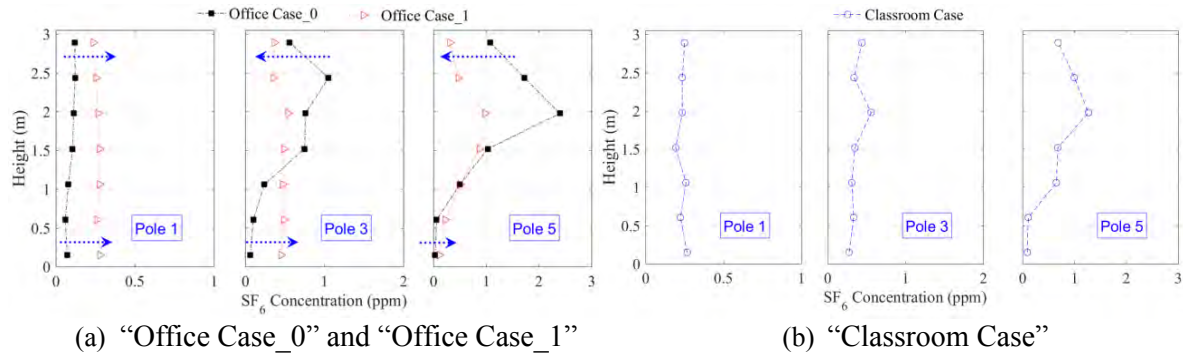
(b) “Classroom Case”

Figure 5. Velocity measurement results

Figure 5 illustrates velocity distributions in three measured cases. Again, results in “Office Case_0” showed a typical velocity distribution in a displacement ventilation, in which airflow velocity was largest near floor, and became very small as the height enters occupied zone. However, when PCB was turned on, although largest airflow velocity was still observed at floor level, PCB seemed to increase the airflow velocity in occupied zone, as could be observed in the comparison in Figure 5(a). This could be because the air movement was intensified by entrainment induced by PCB downward jet, which could also explain why airflow velocity was seen to have increased more at poles placed close to PCB than poles placed further away from PCB.

Airflow velocity distribution in “Classroom Case” showed a similar trend as “Office Case_1”, and its airflow velocity magnitude in occupied zone was seen to be between “Office Case_0” and “Office Case_1”.

Contaminant Concentration Results

Figure 6. SF₆ measurement results

Contaminant concentration distributions are demonstrated in Figure 6 (Note that scales in plots of three poles are different.). Results showed that in “Office Case_0”, there was a clear contaminant stratification at locations (e.g. Pole 3 and Pole 5) close to where SF₆ was released. At locations that were relatively far away from SF₆ release location, SF₆ concentration was seen to be always low from floor to ceiling levels. This could be explained by the fact that in a DV system, contaminant is lifted to the upper part of a room until leaving the room through exhaust, which verified the satisfying contaminant removal effectiveness of DV.

When PCB was turned on, however, the contaminant stratification seemed to be weakened, as observed at Pole 5. Meanwhile, at locations that were further away from PCB, overall SF₆ concentration was seen to be increased, although the concentration level was still quite similar from floor to ceiling. This was because PCB, while turned on, generated downward jet and pushed SF₆ from top region to the lower region of the room. As a result, the SF₆ that was pushed down could re-distribute itself after it hit the floor or desk, and moved horizontally to other locations. In “Classroom Case”, the SF₆ distribution was seen to be similar as “Office Case_1”, The concentration levels at different locations, though, were about in between “Office Case_0” and “Office Case_1”, which could be due to that the ratio of heat removed by PCB (40%) in “Classroom Case” was in between of 0 and 60%.

DISCUSSIONS

This investigation reported detailed measurement results of airflow velocity, temperature and SF₆ concentrations at three experimental cases, which was valuable for improving the understanding of ventilation and thermal performances of a combined system of DV and PCB. To better evaluate an indoor environmental design, however, there might need more analysis of the measured data by employing indices for appraising thermal comfort and indoor air quality, such as PMV and contaminant removal efficiency. Besides, although measurements took place at as many as 35 locations in each of the measured cases, the resolution of data obtained from measurements was relatively low as compared to a validated CFD simulation. Therefore, at a later stage, adopting indoor environmental appraisal indices and employing CFD method would yield an even more comprehensive study to the current research.

CONCLUSIONS

This research leads to the following conclusions:

- (1) With the experimental apparatus that was set up in this research, detailed measurements could be performed to obtain airflow velocity, temperature, contaminant concentration

data in the IAQ chamber. Results from “Office Case_0” showed a typical airflow and contaminant distribution in a DV only system.

- (2) While PCB was used together with DV system, large temperature stratification was observed in most regions of the room, although PCB could produce a local downward jet. Besides, the downward cold jet was able to entrain ambient air, which resulted in slightly increased airflow velocity in occupied zone.
- (3) Experimental results showed that PCB, while turned on, could weaken or even destroy the contaminant stratification built up by DV. The higher percentage of heat was removed by PCB, the more the contaminant stratification appeared to be destroyed.
- (4) This research demonstrated that the observed impacts of PCB made in an office layout was also seen in a room with a different room layout, as could be observed in “Classroom Case”. Therefore, conclusions (2) and (3) could still apply when room layout changes.

ACKNOWLEDGEMENT

The authors would like to thank ASHRAE for funding this research project via ASHRAE RP-1666.

REFERENCES

- ASHRAE. 2013. *ANSI/ASHRAE Standard 55-2013*, Thermal Environmental Conditions for Human Occupancy. Atlanta: American Society of Heating, Ventilating and Air-conditioning Engineers, Inc.
- Burt L. W. 2007. Life cycle cost of displacement ventilation in an office building with a hot and humid climate. *Ph.D. Dissertation*, University of Florida.
- Fanger P.O. 1970. *Thermal Comfort*. Copenhagen: Danish Technical Press.
- Kosonen R., Saarinen P., Koskela H., and Hole A. 2010. Impact of heat load location and strength on air flow pattern with a passive chilled beam system. *Energy and Buildings*, 42(1), 34-42.
- Riffat S. B., Zhao X., and Doherty P. S. 2004. Review of research into and application of chilled ceilings and displacement ventilation systems in Europe. *International Journal of Energy Research*, 28(3), 257-286.
- Schiavon S., Bauman F., Tully B., and Rimmer J. 2012. Room air stratification in combined chilled ceiling and displacement ventilation systems. *HVAC&R Research*, 18(1-2), 147-159.
- Shi Z. and Chen Q. 2018. Thermal comfort analysis of displacement ventilation system coupled with passive chilled beams. Accepted by: *5th International High Performance Buildings Conference at Purdue*.
- Svensson A. G. L. 1989. Nordic experience of displacement ventilation system. *ASHRAE Transaction*, 95(2), 1013-1017.

Liquid Desiccant-Polymeric Membrane Dehumidification System for Improved Cooling Efficiency in Built Environments

Michael Bozlar^{1*}, Eric Teitelbaum² and Forrest Meggers^{1,2}

¹Andlinger Center for Energy and the Environment, Princeton University, Princeton, NJ 08544 USA

²School of Architecture, Princeton University, Princeton, NJ 08544 USA

**Corresponding email: mbozlar@princeton.edu*

ABSTRACT

We have recently demonstrated a new type of moisture absorber using a silicone-based liquid desiccant and a nonporous hydrophilic membrane. The setup consists of a core-shell structure where the desiccant flows inside the hydrophilic membrane (core) surrounded with humid air and confined inside a larger diameter tube (shell). In this work, we propose to extend the capabilities of this moisture absorber prototype by addressing two additional characteristics in order to fully validate its capabilities in the built environment. In the first section of this study, we developed a new setup to demonstrate the regeneration process of the liquid desiccant. The regeneration process takes into account the following parameters: (i) air temperature and relative humidity level, (ii) desiccant temperature and water saturation amount, (iii) air/desiccant contact length, (iv) air and liquid desiccant flow rates. In the second part of this paper, we extend our earlier work with this absorber and propose to further improve its performance. We investigate in detail the water absorption kinetics to favor water access to the bulk liquid desiccant surface through efficient mixing inside a confined volume.

KEYWORDS

Liquid desiccant; hydrophilic nonporous membrane; dehumidification; absorption/desorption kinetics.

INTRODUCTION

The global demand for air conditioning is expected to increase drastically over the next 30 years according to recent studies conducted (Shah et al., 2015). This is predominantly attributed to the rapid economical growth of developing countries in Latin America (e.g. Brazil, Mexico), and Asia (e.g. China, India), which are located in hot and humid climate zones (Shah et al., 2015). To effectively cool buildings using existing Heating, Ventilation, and Air Conditioning (HVAC) systems, a major requisite is controlling the humidity level, commonly known as latent loads. In highly-populated geographical zones, excluding desert climates, latent loads require several times larger energy amounts than sensible loads (Harriman et al., 1997). Nevertheless, conventional HVAC technologies address both loads within the same system using a sub dew point vapor compression air conditioner (Meggers et al. 2013). Overall, this process is energy intensive, and better suited for climates with high latent loads. A promising alternative for dehumidification in the built environment is the use of liquid desiccant technologies which present several advantages over traditional solid desiccant wheel systems available on the market (Lowenstein, 2008; Pantelic et al., 2018). Due to their physical and chemical properties, liquid desiccants have the unique capability of being adaptable to the host environment, and can therefore be easily deployed. Another

important characteristics of liquid desiccant is their ability to be regenerated at a different location from where dehumidification takes place.

In a recent study, we have demonstrated the capabilities and advantages of a liquid desiccant absorber prototype where the two key components are: (i) a noncorrosive alkoxyated siloxane liquid desiccant, (ii) a nonporous hydrophilic membrane to contain the desiccant (Ahn et al., 2013; Pantelic et al., 2018). We have demonstrated that such a system can effectively remove moisture from the air, while also solving carryover problems and eliminating the need for noble metal parts. However, we also pointed out the need to investigate the direct regeneration capabilities of the desiccant after exposure to moisture. In addition, we have mentioned the possibility to further improve the kinetics of water absorption into the desiccant by analyzing the different diffusion mechanisms taking place in the system.

In this work, our objective is to address these two remaining aspects that are required for a successful and complete implementation of this new generation of liquid desiccant absorber. In the first part of this paper, we demonstrate preliminary experimental results that support the regeneration potential of the liquid desiccant under easily achievable experimental conditions. Then, we discuss the remaining improvements and future work required to determine the ideal parameters for the water desorption process. In the second part of this manuscript, we describe a new manifold concept that will be tested to improve the kinetics of water absorption into the desiccant, and improve the dehumidification performances of the device.

METHODS

The liquid desiccant regeneration setup shown in Fig. 1 consists of the following main components: (i) alkoxyated siloxane liquid desiccant, XX-8810 (Dow), (ii) commercially available nonporous hydrophilic tube, Pebax® 1074 (noted Pebax in the following sections) (Foster Corporation) with 1.50 mm outer diameter, (iii) clear Polyvinyl Chloride (PVC) tube (Advanced Technology Products) with 6.35 mm outer diameter, and inside which the Pebax tube is located.

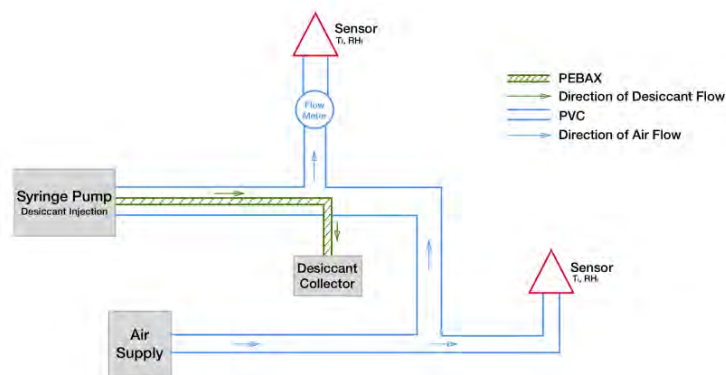


Figure 1. Diagram of the experimental setup used for the desiccant regeneration.

The liquid desiccant was fed through the Pebax membrane at controllable flow rates using a syringe pump (Harvard Apparatus). The air flow was measured with a gas flow meter (Sensirion SFM 4100), and the temperature (T), relative humidity (RH) of the air were acquired with Sensirion SHT75 type sensors. All raw data were recorded through an Arduino Uno board interface for subsequent analysis.

The desiccant regeneration experiments were carried out by feeding supply air around the Pebax tube which was confined inside a PVC tubes (Fig. 1). The liquid desiccant at room temperature, and saturated with 3 wt.% deionized water was flowing inside the Pebax at various flow rates. The supply air was directly taken from the in-house laboratory system and

subsequently heated through a hot water bath prior to contacting the Pebax membrane. During the desiccant regeneration experiments, we recorded the T and RH of the air before (T_i , RH_i) and after (T_f , RH_f) contacting the Pebax membrane across a defined contact length. For all experiments, the supply air and desiccant flows were in counter flow configuration. We let at least about a 15 minute gap between each experiment to ensure that the system was at equilibrium. The air flow rates were determined such that they would be within the range of rates previously used for dehumidification (Pantelic et al., 2018). Two air/desiccant contact lengths of 10 and 30 cm were studied. All experiments were carried out inside a fume hood where the T was near 20 °C and RH fluctuating between 2 and 6%.

RESULTS & DISCUSSIONS

Desiccant regeneration experiment with 10 cm air/desiccant contact length

In Table 1, we summarize the first series of the results collected using the setup described in Fig. 1. Experiment A corresponds to the baseline T and RH measurements in the absence of air and desiccant flow. The high humidity value of RH_f is simply due to the location of the sensor inside the fume hood, i.e. closer to the higher RH indoor environment of the laboratory. In experiment B, no change in RH_f is observed after running the desiccant (with 3 wt.% water) through the Pebax tube, and in the presence of air flow around it. This clearly indicates no desorption of the water (absorbed in the desiccant) through the hydrophilic membrane. Therefore, in the subsequent experiments, B-E, the liquid desiccant flow rate was progressively decreased by a factor of 2, while maintaining the air flow constant. Despite lower desiccant flow rates, experiments B-E do not result in any obvious water desorption. Therefore, in experiments F and G, we further increased the air flow rate by a factor of 2 to reach higher Reynolds numbers. Yet, higher air flow rates combined with low desiccant flow rates do not result in a water desorption mechanism. All results obtained with 10 cm contact length appear to indicate that the region of air/desiccant contact is insufficient to allow the desorption process to take place.

Table 1. Summary of experiments for 10 cm air/desiccant contact length.

Experiment	Desiccant Flow Rate (L/s)	Air Flow Rate (L/s)	T_i (°C)	RH_i (%)	Desiccant Injection Time (s)	T_f (°C)	RH_f (%)	Duration of Experiment (s)
A	0	0	20.98	2.40	N/A	20.88	6.48	5
B	$1.30 \cdot 10^{-5}$	16.67	43.99	1.66	105	22.24	0.83	260
C	$0.65 \cdot 10^{-5}$	16.67	43.47	1.64	105	22.33	0.90	250
D	$1.67 \cdot 10^{-6}$	16.67	43.49	1.64	105	22.33	1.04	215
E	$0.84 \cdot 10^{-6}$	16.67	43.32	1.63	105	22.35	1.13	220
F	$0.65 \cdot 10^{-5}$	33.40	43.75	1.56	105	21.67	0.27	380
G	$0.84 \cdot 10^{-6}$	33.40	45.15	1.53	105	21.5	0.15	330

Desiccant regeneration experiment with 30 cm air/desiccant contact length

In these series of experiments, we maintained the desiccant flow rate as low as $0.84 \cdot 10^{-6}$ L/s and studied the effect of 33.40 and 16.67 L/s air flow rates. The Reynolds number corresponding to the flow rates of 33.40 and 16.67 L/s are $4.3 \cdot 10^5$ and $8.6 \cdot 10^5$, respectively. These results are shown in Fig. 2. When the air flow rate is as low as 16.67 L/s, there is a possible water desorption process taken place, as confirmed by the higher RH_f values. In this case, the increase in absolute humidity is about 23.10 mg/m^3 . Although the difference between RH_i and RH_f is about 10%, we acknowledge that this RH range is within the domain where readings from the sensor can reach up to 4% error. Nevertheless, in all experiments,

including the first series with 10 cm contact length, we have obtained consistent and reproducible data. Therefore, we expect the results obtained with 30 cm contact length to support an effective water desorption process which tends to support the possible regeneration of the alkoxyated siloxane desiccant.

In the next series of ongoing experiments, we plan to investigate the effect of larger air/desiccant contact lengths to confirm these preliminary results. In addition, we will also increase the RH value of the air to reach 10% or more RH. This will ensure that we are in the range where the sensors are the most accurate.

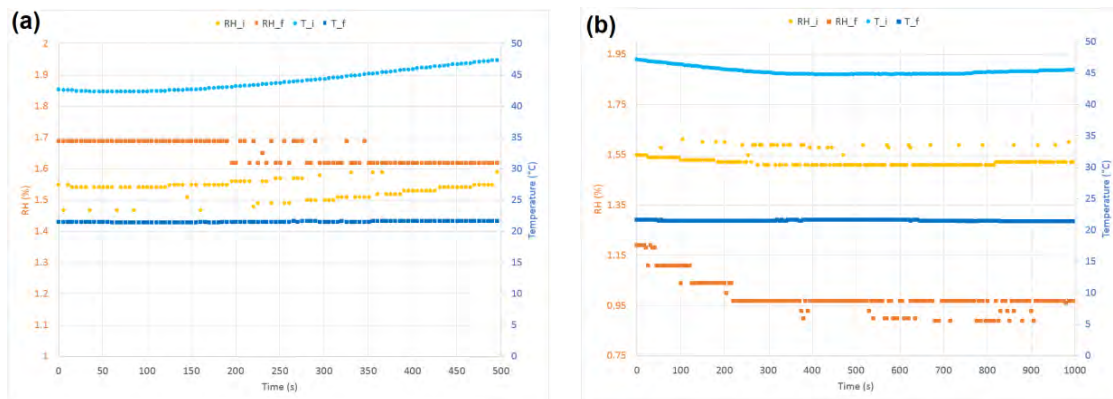


Figure 2. Water desorption experiments for 30 cm air/desiccant contact length. Air flow rate of (a) 16.67 L/s, and (b) 33.40 L/s.

Improving the performance of the dehumidification prototype

In parallel to the desiccant regeneration experiments, we are currently exploring solutions to enhance the overall performance of the dehumidification system described in our previous study (Pantelic et al., 2018). To achieve this goal, we propose to improve the kinetics of water absorption into the desiccant by designing a chamber to enhance the mixing of the desiccant, and thus to effectively use its total volume for water absorption. The new desiccant mixing chamber is represented in Fig. 3. This initial design includes four inlets for the Pebax and PVC tubes. In our ongoing experiments, our objective is to test the dehumidification performance of the absorber under similar conditions to our earlier study (Pantelic et al., 2018), and directly evaluate the anticipated advantages of the mixing chamber.

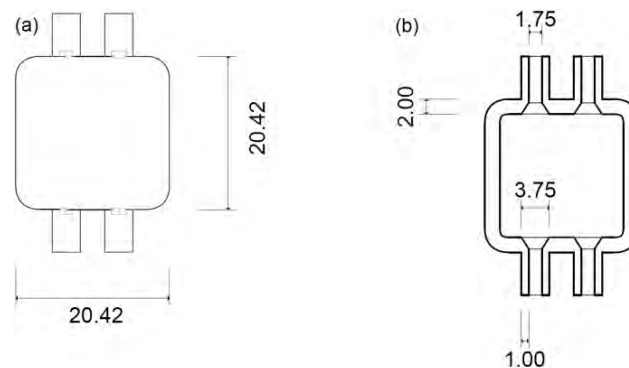


Figure 3. Technical drawing of the 3D printed manifold, with dimensions in mm. (a) Top view, (b) Cross-sectional view of the chamber showing the 1.75 mm inlets for the Pebax tubes.

CONCLUSIONS

In this study, we have covered two fundamental characteristics of the liquid desiccant-based dehumidification prototype. In the first part, we have demonstrated preliminary and ongoing experiments to investigate the regeneration process of the alkoxyated siloxane liquid desiccant in the presence of 3 wt.% water. The preliminary results appear to confirm that at least a 30 cm air/desiccant contact length is necessary to effectively evidence the water desorption. We are currently in the process of evaluating the effect of larger contact lengths on the water desorption from the desiccant.

In the second part of this work, we presented the potential of a new mixing chamber for the liquid desiccant. This chamber is expected to improve the water absorption kinetics by favoring water access to the bulk liquid desiccant surface through mixing. The initial results presented in this paper are still the subject of ongoing research. We expect to complete the two research directions described here and successfully demonstrate the dehumidification and regeneration capabilities of this new generation of liquid desiccant prototype.

ACKNOWLEDGEMENT

This project is supported by the Intellectual Property Accelerator Fund of the Office of Technology Licensing at Princeton University.

REFERENCES

- Ahn D., Greiner A., Hrabal J., and Lichtor A. 2013. Method of Separating a Gas Using at Least One Membrane in Contact with an Organosilicon Fluid. *US Patent App.*, 14/413,231.
- Harriman III L.G., Plager D., and Kosar D. 1997. Dehumidification and cooling loads from ventilation air. *ASHRAE J.*, 39(11), 37.
- Lowenstein A. 2008. Review of Liquid Desiccant Technology for HVAC Applications. *HVAC&R Research*, 14(6), 819-839.
- Meggers F., Pantelic J., Baldini L, Saber E.M., and Kim M.K. 2013. Evaluating and Adapting Low Exergy Systems with Decentralized Ventilation for Tropical Climates. *Energy Build.*, 67, 559-567.
- Pantelic J., Teitelbaum E., Bozlar M., Kim S., and Meggers F. 2018. Development of Moisture Absorber Based on Hydrophilic Nonporous Membrane Mass Exchanger and Alkoxyated Siloxane Liquid Desiccant. *Energy Build.*, 160, 34-43.
- Shah N., Wei M., Letschert V., and Phadke A. 2015. Benefits of Leapfrogging to Superefficiency and Low Global Warming Potential Refrigerants in Room Air Conditioning. Energy Technologies Area, LBNL-1003671, Lawrence Berkeley National Laboratory (USA).

Simulation-based Approach to Optimize Courtyard Form Concerning Climatic Comfort in Hot and Humid Climate

Mehmet Bekar^{1,*}, Gülten Manioğlu²

¹ Graduate School of Science Engineering and Technology, Istanbul Technical University, Istanbul, Turkey

² Department of Architecture, Istanbul Technical University, Istanbul, Turkey

*Corresponding email: bekarm@itu.edu.tr

ABSTRACT

In hot and humid regions, in order to provide indoor thermal comfort conditions, most important design strategies are to maximize shady areas and natural ventilation. Courtyard building form was developed mainly in response to climatic requirements especially in hot climates. A courtyard is an unroofed area that is completely or partially enclosed by walls or building spaces. The function of the courtyard is to improve comfort conditions by modifying the microclimate around the building. The proportion of the courtyard affects considerably the shadows produced on the building envelope, and consequently the received solar radiation and the comfort conditions in the building. Moreover, courtyards are claimed to be highly effective in enhancing the ventilation and decreasing humidity level. This study intends to investigate variations in indoor thermal conditions according to different design configurations and scenarios. All calculations are made for a surrounded space of the courtyard. Thermal comfort conditions of this space are evaluated according to its orientation, ventilation type and courtyard configuration. In the study, different courtyard proportions, orientations and ventilation types are developed. Indoor comfort conditions of the selected space are calculated for Antalya which is a representative city of hot and humid region of Turkey. The software EnergyPlus, is used as a tool for simulating the thermal performance of the selected space. Operative temperatures, indoor humidity, and solar gains are calculated by using this dynamic thermal simulation program and a comprehensive evaluation on the aspects of thermal comfort conditions is carried out. In conclusion, the importance of the systematic approach in order to optimize the decisions taken during the design stage of thermally comfortable and conservative buildings is discussed.

KEYWORDS

Courtyard building, hot-humid climate, thermal comfort conditions, orientation

1. INTRODUCTION

The number of new residential buildings has been growing steadily in the southern coastline of Turkey with hot and humid climate conditions due to increasing population. However, contrary to traditional buildings, construction of new buildings without due consideration of energy efficiency and climate responsive criteria increases energy costs and presents itself as an important consequence. Since most of the energy in buildings is used for heating and cooling, reducing consumptions in this area and achieving energy efficiency in buildings have become a priority (Yılmaz, 2007; Manioğlu and Oral, 2015). Reducing energy consumption in residential buildings is possible through taking correct decisions about energy efficient design variables (Kocagil and Oral, 2015).

One of the most effective ways to have thermal comfort conditions in buildings is to design climate responsive buildings according to existing climate conditions for each climatic region (Lechner, 2014). Protection from the heating effect of sunlight and mitigating the effect of excessive humidity in hot-humid climatic regions play an important role in ensuring comfort conditions. In this climatic region, buildings with courtyards are frequently preferred to reduce the area of façades which are affected by solar radiation. It is possible to create shades in the courtyard during the day with spaces surrounding the courtyard and high walls that separate the courtyard from the street. Courtyard dimensions and courtyard orientation are determinant factors to locate shades within the courtyard. When courtyard dimensions change, heat loss and gain through courtyard walls and thus indoor comfort conditions will also change (Muhaisen, 2006; Muhaisen and Gadi, 2006).

The courtyard form has a configuration that also supports natural ventilation (Ghaffarianhoseini et al. 2015). The process of daily changes in temperature and humidity in summer in hot-humid climate regions can be studied in three phases. In the first phase, during the night cool air descends into the courtyard and into surrounding rooms. The courtyard loses heat by radiation. In the second phase, at midday direct sunlight affects the courtyard floor. Some of the cool air begins to rise and leaks out of the rooms. This induces convective currents in rooms. At this phase, the courtyard acts as a chimney depending on its size. In the third phase, the courtyard floor is warmer than interiors and convective currents occur in the late afternoon. After sunset, the air temperature falls rapidly and the courtyard radiates heat and cool air begins to flow to the courtyard and from there to interiors (Gallo et al. 1988; Talib, 1984). During this entire process, due to their effect on solar radiation gain and air movements, courtyard dimensions and sizes of the windows and ventilation types preferred in surrounding spaces have a direct impact on interior thermal comfort conditions (Ok et al. 2007). Therefore, this study evaluates with a parametric approach, indoor comfort conditions of a building with a courtyard in hot-humid climatic region, which are affected and changed according to different courtyard dimensions, different orientation and different ventilation types. Building form and courtyard dimension alternatives evaluated in this study are taken from the author's master's thesis (Bekar, 2018).

2. METHODOLOGY

This study intends to have an approach to evaluate the effects of orientation and ventilation options of a building with varying courtyard dimensions on the thermal comfort conditions in the building. A total of 72 building energy simulations have made by shifting the orientation of the courtyard facing space of 6 building forms with the same courtyard width but different depths to north, east, south and west and by using different ventilation alternatives.

2.1 Determining building and climate related variables

Buildings included in the study are situated on a level land in Antalya with the following coordinates: 30°73'(E) and 36°87'(N). Calculations are made based on the assumption that there are no other buildings that can cast a shade on these buildings and that the buildings are located in the countryside. In the evaluation there are 6 building forms with different courtyards with the same width (400 cm.) but with different depths (50 cm., 100cm., 150cm., 200cm., 250cm., 300cm.). The interior space facing the courtyard with the dimensions 400x400 cm. is the same in every building form. The dimensions of the model created for the study are shown in Figure 1. The transparency ratio on the wall facing the courtyard and the opposing wall is set at 12%. No transparent material is used in other façades in the model. Recommended (TS 825) and existing overall heat transfer coefficients (U values) for Antalya are shown in Table 1.

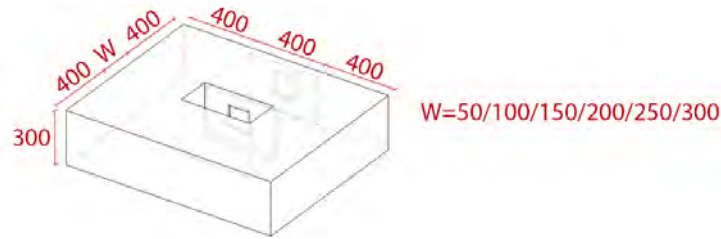


Figure 1: Dimensions of the building with courtyard model (cm)

Table 1. Recommended (TS 825) and existing U values for Antalya

	U_{wall} (W/m ² K)	U_{ceiling} (W/m ² K)	U_{floor} (W/m ² K)	U_{window} (W/m ² K)
U_{TS825}	0.66	0.43	0.66	1.8
U_{existing}	0.633	0.399	0.646	1.5

2.2 Determining variables in calculations

The change in comfort conditions when the orientation of this space facing the courtyard is north, east, south and west are analysed. The indoor comfort conditions for 6 different courtyard dimensions and for all orientations (S, W, N, E) when there is one window each on the wall facing the courtyard and the opposing wall (cross ventilation) are evaluated. In the study three different ventilation types are defined: windows are open all day (open between 00:00-24:00); windows are closed all day (closed between 00:00-24:00); and windows are closed during the day and open during night (open between 00:00-09:00, closed between 09:00-21:00, open between 21:00-24:00). There assumed to be 2 occupants in the building and one occupant was present between 08:00 - 19:00 and two occupants were present between 19:00 - 08:00 both during week days and on weekends. Lighting level is set 8 W/m² per space.

Calculations of indoor comfort conditions of building models with courtyards with different courtyard dimensions, orientation types and ventilation options were done with EnergyPlus 8.3.0. This is a building energy simulation program with high calculation capacity which uses algorithms such as transfer function, finite difference method and finite elements and with which heating, cooling, lighting, ventilation and other energy flow system can be modelled. Climate data in epw format for Antalya was used in calculations. Operative temperature, relative humidity and solar radiation values on July 21st which represents the hottest day of the year were calculated separately to evaluate the performance of the selected space. Relative humidity and operative temperature values in the spaces with cross ventilation are shown in Figure 2 and total transmitted solar radiation values through windows of the buildings are shown in Figure 3.

3. RESULTS

When the courtyard depth changes, operative temperature values in the space depending on whether the window facing the courtyard has a south or north orientation show similarities for all ventilation types. When the courtyard window of the space is east or west oriented and when windows are closed all day and night ventilation is done, operative temperatures increase with the increasing courtyard depth. When the window facing the courtyard is east and west oriented in the models with the same courtyard depth, operative temperature values are higher than those obtained when window is south and north oriented (Figure 2).

The lowest operative temperature values are obtained in the alternatives with night ventilation and the highest operative temperature values are obtained in the alternatives with windows open all day for the models with the same courtyard depth (Figure 2).

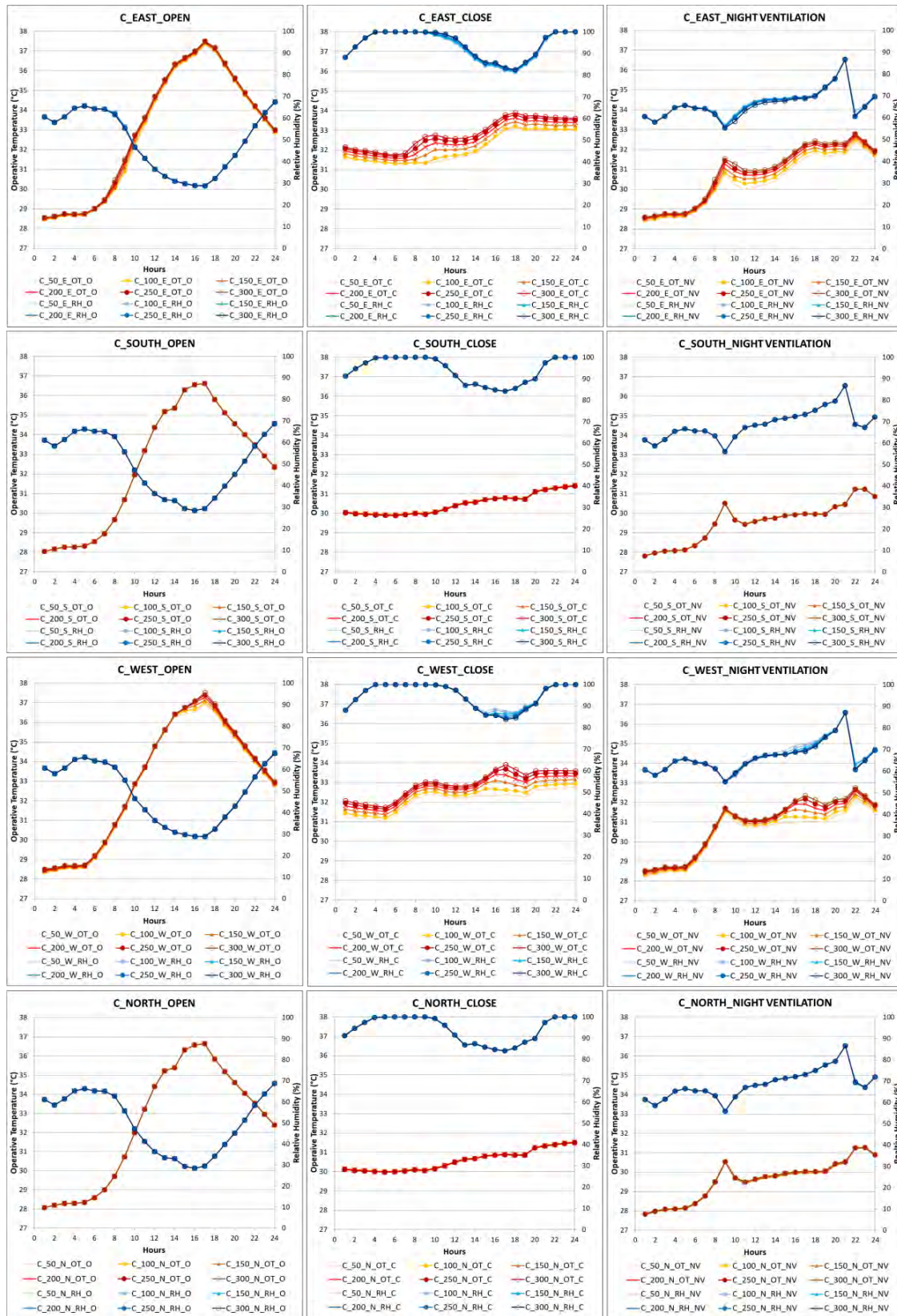


Figure 2. Relative humidity and operative temperature values when windows are open all day (open), closed all day (closed) and with night ventilation

However when a comparison is made for orientation; when courtyard window is west oriented, even if there is night ventilation, lower operative temperature values are obtained between 07:00 - 24:00 hours in all alternatives where courtyard window is north or south oriented and windows are closed all day. The alternative with the lowest operative temperature values is the alternative where courtyard window is south oriented, courtyard depth is 300 cm and night ventilation is used (C_300_S_NV). The alternative with the highest operative temperature values is the alternative where courtyard window is west and east oriented, courtyard depth is 300 cm and windows are kept open all day (C_300_E_O, C_300_W_O) (Figure 2).

When the courtyard depth changes, the relative humidity values in the space, in the case the window facing the courtyard has a south or north orientation, show similarities within themselves when all ventilation types are considered separately. For spaces with east and west oriented courtyard windows; a similar trend continues in the alternative where the window is open all day however in the alternatives where windows are closed all day and night ventilation is done, as the courtyard depth changes, relative humidity values in the space also change albeit small. Relative humidity values in spaces are the lowest in the alternatives where windows are kept open all day and the highest in the alternatives where windows are closed all day (Figure 2).

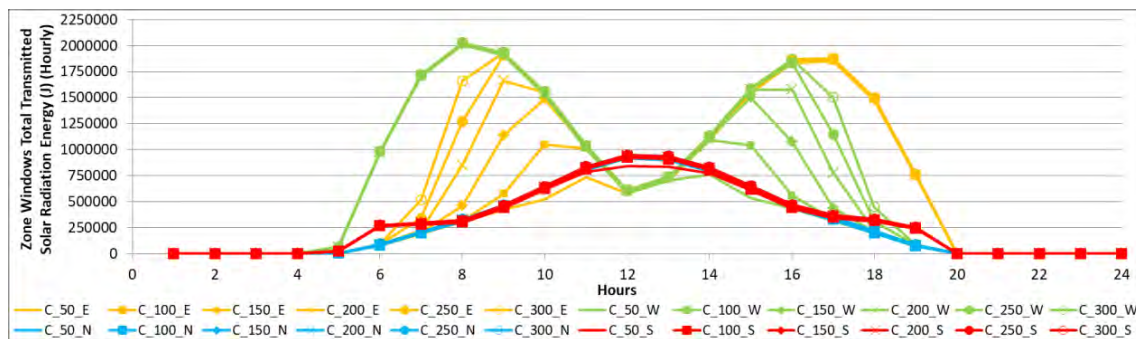


Figure 3. Total solar radiation values transmitted through windows according to orientation of the windows

When courtyard depth is 50 cm, higher solar radiation values are obtained with south and north oriented windows than with east and west oriented windows. When courtyard depth is 100, 150, 200, 250 and 300 cm., higher solar radiation values are obtained with east and west oriented windows than with north and south oriented windows. Solar radiation values decrease before noon in the alternatives with east facing courtyard window and afternoon in the alternatives with west facing courtyard window and with the decreasing courtyard depth as the opposing courtyard wall casts a shadow. In all models, as the courtyard depth increases, solar radiation transmittance through windows increases. The lowest values are achieved when the courtyard depth is 50 cm and the highest values are achieved when the courtyard depth is 300 cm (Figure 3).

4. CONCLUSIONS

This study examined 72 different alternatives to evaluate the effects of orientation and types of ventilation of a building with varying courtyard dimensions on the thermal comfort conditions in the space. When operative temperature and relative humidity values are evaluated together, the optimum result for indoor comfort conditions is achieved with the alternative C_300_S_NV. The findings of the study are;

- Courtyard dimensions, orientation of spaces facing the courtyard and ventilation alternatives of spaces have a direct impact on the indoor climate conditions and consequently on the energy consumption for cooling.
- Courtyard dimensions in the east and west oriented spaces facing the courtyard have more effect on the change of indoor operative temperature values. Orientation of the space has more effect compared to ventilation options for spaces facing the courtyard.
- When different ventilation types should be selected depending on the building function (office or residential building etc.), the most suitable alternative can be created using different courtyard dimensions and orientation options.
- When the building is used in different times of the day depending on the building function (day or night use) the most suitable alternative can be created using different courtyard dimensions and orientation options.
- Courtyard dimensions affect operative temperature and transmitted solar radiation values through windows depending on the orientation of the space facing the courtyard.

It is possible to identify the most efficient building form alternative, orientation and ventilation option which provide the optimum comfort conditions and minimum cooling loads using the parametric evaluation method discussed in this study. In future studies, designs that provide optimum comfort conditions with minimum cooling energy consumption will be possible by also analysing air movements in building forms using computational fluid dynamic methods.

REFERENCES

- Bekar M., An evaluation of the effects of courtyard dimensions on thermal comfort conditions in buildings in hot-humid climatic regions. *Master's Thesis*, ITU, Graduate School of Science Engineering and Technology, May 2018.
- Gallo C., Sala M., and Sayigh A.A.M. 1988. *Architecture: Comfort and Energy*. Oxford, UK: Elsevier Science.
- Ghaffarianhoseini A., Berardi U., and Ghaffarianhoseini A. 2015. Thermal performance characteristics of unshaded courtyards in hot and humid climates. *Building and Environment*, 87, 154-168.
- Kocagil İ.E. and Oral G.K. 2015. The effect of building form and settlement texture on energy efficiency for hot dry climate zone in Turkey. *Energy Procedia*, 78, 1835-1840.
- Lechner N. 2014. *Heating, cooling, lighting: sustainable design methods for architects* (4th ed.). New Jersey: John Wiley & Sons.
- Manioğlu G. and Oral G. 2015. Effect of courtyard shape factor on heating and cooling energy loads in hot-dry climatic zone. *Energy Procedia*, 78, 2100-2105.
- Muhaisen A. 2006. Shading simulation of the courtyard form in different climatic regions. *Building and Environment*, 41, 1731-1741.
- Muhaisen A.S. and Gadi M.B. 2006. Shading performance of polygonal courtyard forms. *Building and Environment*, 41, 1050-1059.
- Ok V., Yaşa E., and Özgünler M. 2008. An experimental study of the effects of surface openings on air flow caused by wind in courtyard buildings. *Architectural Science Review*, 51, 263-268.
- Talib K. 1984. *Shelter in Saudi Arabia*, New York: St. Martin's Press
- TSE. 2013. *TS 825*, Thermal insulation requirements for buildings, Turkish Standards Institution, Ankara.
- Yılmaz Z. 2007. Evaluation of energy efficient design strategies for different climatic zones: Comparison of thermal performance of building in temperate-humid and hot-dry climate. *Energy and Buildings*, 39, 306-316.

The effect of the position and temperature difference of local radiant asymmetry on thermal comfort: an experimental investigation

Stijn Van Craenendonck^{1,*}, Leen Lauriks¹, Cedric Vuye¹, Jarl Kampen^{2,3}

¹ EMIB research group, University of Antwerp, Antwerp, Belgium

² Department of Epidemiology and Social Medicine, University of Antwerp, Antwerp, Belgium

³ Biometris, Wageningen University, Wageningen, The Netherlands

**Corresponding email: Stijn.vancraenendonck@uantwerpen.be*

ABSTRACT

In cold and moderate climates, poorly designed construction joints can lead to local low surface temperatures, which entails local radiant asymmetry. An experiment was set up to test the hypothesis that overall and local thermal sensation is influenced by temperature difference, and position and distance of local radiant asymmetry. In the experiment, 18 subjects participated where they were introduced in a room at 21°C and 45% relative humidity. The subjects were exposed to local radiant asymmetry created by a cooling plate. This plate was positioned at three different heights, and controlled for temperatures at 3, 6 or 10°C below room air temperature. The data was analyzed using general linear modelling.

The results show that thermal sensation is not influenced by local radiant asymmetry directly, but that the deviation from base comfort level is linked to height and temperature of the cold plate, as well as distance of the plate to the subject. This last effect proved to be the strongest. Contrary to what was expected however, participants felt warmer when exposed to local radiant cooling, compared to when not exposed to it. Further research is needed to determine the cause of this effect.

KEYWORDS

Thermal comfort, thermal sensation, radiant asymmetry, experiment.

INTRODUCTION

While renovating existing buildings, planar parts of the building shell are often insulated without proper care for the joints connecting these parts. In cold and moderate climates, poorly designed construction joints can lead to local wall areas with a low surface temperature. These local colder areas lead, next to a higher risk for surface condensation, to radiant temperature asymmetry and can influence thermal comfort of the residents.

McNall and Biddison started the research into radiant asymmetry by placing subjects in a test chamber of which they cooled and heated one wall or the ceiling. They concluded that no significant discomfort could be attributed to radiant temperature asymmetry due to a wall with view factor 0.2 at 11°C colder than the environment. (McNall & Biddison, 1970) Olesen et al. discovered that subjects could sense small degrees of radiant temperature asymmetry, but much larger asymmetry was needed to cause discomfort. (Olesen et al., 1972) Research by Fanger et al. (Fanger et al., 1985) found that cool walls have the largest influence on thermal comfort compared to floors and ceilings. This influence however was relatively limited: if the surface temperature of the cool wall was less than 10 °C under average air temperature, the percentage of people dissatisfied with the environments was less than 5%.

In all these experiments, the asymmetric environment was realized by cooling entire walls. For construction joints, lower surface temperature is only a local effect which can influence only a specific body region. Research has proven that different body regions have different thermal sensitivities. Cooling of the trunk areas of the body (chest, back) strongly affects overall thermal sensation, while the effect is much less noticeable in the bodies' extremities. (Arens et al., 2006) Nakamura et al showed that different parts of the body not only have different thermal sensation, but also have different influences on overall thermal comfort. (Nakamura et al., 2013)

In this paper, a thermal comfort experiment in a semi-controlled environment is reported to test our hypothesis: overall and local thermal sensation are influenced by temperature difference, position and distance of local radiant cooling.

METHODS

Subjects

18 subjects (16 men, 2 women) participated in the experiment. Mean subject age (\pm Standard deviation) was 28.2 (\pm 13.5) years. Average length and weight were 181 (\pm 8) cm and 77.4 (\pm 11.1) kg respectively. Clothing was prescribed for all subjects: short-sleeve T-shirt, non-ripped long pants, underwear, socks and closed shoes. Together with the office chair, the total clothing value was 0.52 according to ISO 9920. (Bureau voor Normalisatie, 2009) During conditioning and testing, subjects had to sit at a desk and perform office work on a computer. This corresponds with 1.2 met according to ISO 8996. (Bureau voor Normalisatie, 2004)

Conditions

Experiments took place in a 6.4 m x 4.7 m x 4.1 m room with concrete walls at the University of Antwerp, Belgium (test setup in Fig. 1). The building management system controlled air temperature and relative humidity in the room. Average (\pm standard deviation) air temperature and relative humidity were 21.7 (\pm 0.4) °C and 44.9 (\pm 4.3) %. Radiant temperature was ensured to be equal to air temperature. Air velocity was less than 0.1 m/s at all points.

Plate temperature was based on thermal simulations of typical Belgian construction joints. Setpoints for plate temperature were 0, 3, 6 and 10°C below ambient room temperature.



Fig. 1: Test setup

Experimental procedure

The experimental procedure is displayed in Fig. 2. Before subjects entered the test chamber, they filled out a preliminary survey in an anteroom. The temperature and humidity in the anteroom was the same as the test room. After this preconditioning, subjects took place in the test room and started their office work. The first 30 minutes in the test room, no test conditions were applied to let subjects acclimatize to the environment. Afterwards, each subject experienced 3 test phase with 1 randomly selected test condition each. A test condition consisted of a set plate temperature, plate position and distance to subject.

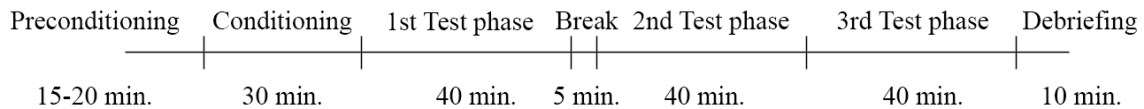


Fig. 2: Experimental procedure

Questionnaire

Subjects were asked to fill out a preliminary survey during preconditioning. In this survey, subjects were asked about age, length, weight, caffeine and alcohol consumption, sleep duration and quality and whether subjects were often warm or often cold.

Subjects had to fill out a questionnaire every 15 minutes, and at 10 and 25 minutes in the conditioning phase. A 5-level scale was used to rate overall and local thermal sensation (TSV) and change preference. A 7-level scale was employed to rate overall thermal comfort (TCV). Overall and local draft perception was noted as yes-no choice, just as acceptability. Local TSV and draft perception had to be rated for 9 different body regions (head, neck, chest, upper arm, lower arm, hand, upper leg, lower leg, foot). These scales were selected because of their widespread use in similar experiments. (Van Craenendonck et al., 2018)

Analysis Methods

Linear regression (McDonald, 2015, pp. 190–208) and chi-square tests (McDonald, 2015, pp. 59–67) were used to determine the influence of demographic data of the sample, such as age and sleep quality, and on general and local thermal sensation votes (TSV) (IBM, 2015). Post-hoc analysis of the standard residuals as proposed by Sharpe (Du Bois & Du Bois, 1989) was employed when the Chi-square test yielded significant results.

The relation between temperature of the cooling plates and local TSV-scores of the subjects was examined using general linear modelling. Temperature of the plate, height of the plate and distance between plate and subject were used as fixed effects.

Analysis was performed in SPSS version 24 (IBM, 2015). A full factorial model was used as a starting point, excluding variables that were not significant for further analysis. Main effects were always included in the model if they were included in a significant second-order effect. Adjusted R^2 (Frost, 2013) was used to assess goodness of fit of the models, and partial η^2 ($p\eta^2$) (Levine & Hullett, 2002) was used to compare effect sizes.

RESULTS

All analysis was performed on the scores each subject gave in the last 5 minutes of each test phase, i.e. at 25 minutes in the conditioning phase, and at 35 minutes in each test phase. Previous research has shown that full adaptation to the thermal environment has occurred at this point. (Van Craenendonck et al., 2018).

First analysis showed that alcohol consumption in the 24 hours prior to the experiment had a significant effect on all thermal sensation scores. It should be noted however that there was only one person who did consume alcohol in the 24 hours prior to the experiment. This person was excluded from further analysis. Age also had a significant effect on TSV-values in the legs (upper legs, lower legs and feet), with people over 60 years old feeling significantly colder. People who self-indicate that they often feel cold, signaled that their head, neck and chest felt significantly warmer than people who don't indicate often feeling cold. All further analysis was performed with the respective influencing groups once included and once excluded to determine their effect on the conclusions of this paper.

When looking at the TSV-scores nominatively, whole-body ($p = 0.011$), neck ($p = 0.050$), chest ($p = 0.022$), upper arm ($p = 0.003$) and upper leg TSV ($p = 0.029$) are all significantly influenced by distance between cold plate and subject. Subjects exposed to the cold plate at

1,5 m mark thermal sensation for these regions lower than subjects exposed to the plate at 0,75 m. Whole-body ($p = 0.004$) and hand TSV ($p = 0.041$) are influenced by the height of the cooling plate, with subjects exposed to the plate at chest height being significantly colder than subject exposed to the plate at feet height in both cases. Excluding people who self-indicate that they often feel cold from the analysis does not influence these results, and neither does excluding people over 60.

Because different subjects may have different base comfort levels in the ambient conditions of the test room, a new analysis was performed on the change in TSV-values under test conditions compared with the TSV-scores after conditioning. The strongest main effect in each of the models and adjusted R^2 -values are displayed in Table 1.

Table 1: Summary of the models for change in thermal sensation

	aR ²	Strongest predictor ($p\eta^2$)		aR ²	Strongest predictor ($p\eta^2$)
Whole-body TSV	0.37	Height (0.26)	Lower arm TSV	0.20	Distance (0.20)
Head TSV	0.19	Height (0.17)	Hand TSV	0.08	Distance (0.10)
Neck TSV	0.35	Distance (0.28)	Upper leg TSV	0.47	Distance (0.23)
Chest TSV	0.32	Distance (0.28)	Lower leg TSV	0.40	Height (0.18)
Upper arm TSV	0.23	Temperature (0.20)	Foot TSV	0.23	Height (0.14)

Temperature of the cooling plate is a significant effect in whole-body thermal sensation ($p = 0.025$), as well as neck ($p < 0.001$), chest ($p = 0.004$), upper arm ($p = 0.004$) and lower arm TSV ($p = 0.017$). In all cases, the change in TSV-values indicated that subjects felt warmer as the temperature of the cold plate was lower. In almost all cases, subjects felt warmer than they did after conditioning. Excluding people who often feel cold from the analysis made the effect of temperature on neck TSV insignificant.

Distance between cooling plate and subject had a significant effect on all TSV-values. As can be seen in Fig. 3, the difference in all cases was greater than zero for participants exposed to the plate at 0.75 m, indicating that they felt warmer than after conditioning. Furthermore, in all cases, subjects exposed to the plate at 0.75 m felt warmer than those exposed to the plate at 1.5 m. Participants subjected to a cooling plate at 0,75 m in all cases felt warmer than after conditioning.

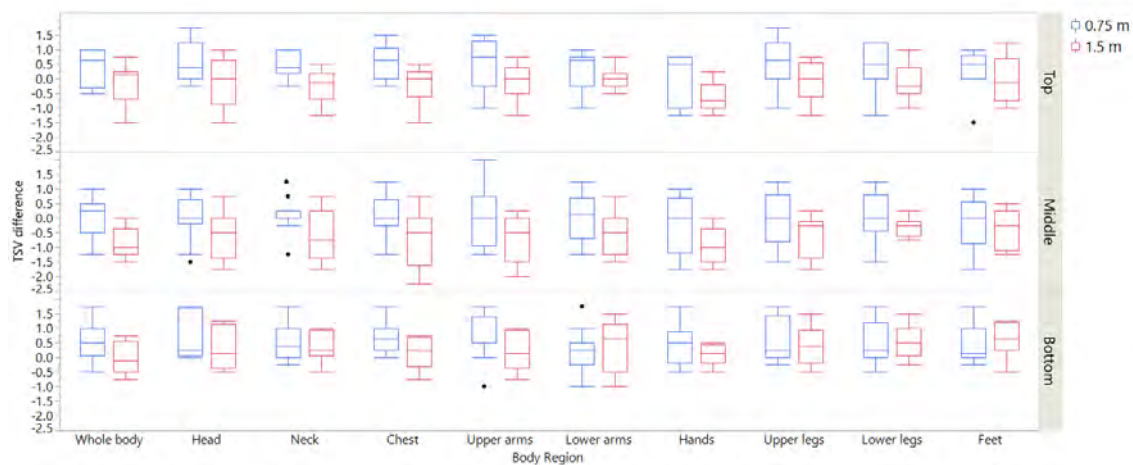


Fig. 3: Difference of TSV value during testing and after conditioning, split by distance between cold plate and subject and by plate height. (Positive indicates warmer during testing)

Plate height had an effect on whole-body TSV ($p < 0.001$), as well as thermal sensation in the head ($p = 0.013$) and leg region (upper legs ($p = 0.006$), lower legs ($p = 0.006$) and feet ($p = 0.021$)). The effect was the same in all cases: difference in TSV between during test and after conditioning was significantly higher for the people exposed to the plate at feet level than those exposed to the plate at chest level, as seen in Fig. 3. People exposed to the plate at chest level always felt colder than after conditioning, while people exposed to the plate at feet level always felt warmer. Removing people over 60 from the analysis made the effect of height of the cold plate on thermal sensation in the feet insignificant.

DISCUSSION

From the results of the whole-body and local TSV-score analysis, it is clear that neither temperature of the cooling plate, nor position (height and distance to subject) have a strong effect on thermal sensation. Even when a statistically significant effect is found, adjusted R^2 -values show that only a very small amount of variance in the thermal sensation can be explained by parameters related to local radiant asymmetry.

When looking at the change in thermal sensation during testing vs after conditioning, the parameters related to local radiant asymmetry have a stronger effect. Nevertheless the predictive powers of the models for hand TSV remained very low, as shown by R^2 -value in Table 1. The significant effect of plate temperature on neck TSV and height of the cold plate on foot TSV occur to be linked to an uneven distribution of people with different demographics across the test conditions, rather than to local radiant asymmetry.

Distance between cooling plate and subject is often the most important effect in the models for predicting change in thermal sensation. Examining the details, almost all TSV-values are higher during testing than after conditioning, meaning that, on average, subjects feel warmer when subjected to local radiant cooling. These results are counter intuitive: e.g. subjects tend to feel warmer in the leg region when the cold plate at feet level is active. It is also remarkable that all participants subjected to a cooling plate at 0,75 m felt warmer, while the results for participants subjected to a cooling plate at 1,5 m were mixed, with some feeling warmer and some feeling colder than after conditioning. No significant rise in ambient temperature or relative humidity, nor radiant temperature from other parts in the test setup were discovered. Further research will be necessary to determine the cause for this effect.

The results as such confirm previous research by McNall & Biddison and Fanger, in that small radiant temperature asymmetry causes almost no change in thermal sensation in people. Most significant effects are found for bodies' extremities, which suggest that those are more strongly affected by local radiant cooling. However, no logical link existed between the height of the cooling plate and the location of the affected body region. Because results are this unexpected, further validation of the experimental setup will be performed by thermographic imaging with view factor correction to quantify radiant temperature asymmetry at the subjects' position. The results of this validation will provide additional information to explain the results of this experiment. The questionnaire will be validated by running short experiment series in more extreme conditions to test whether it is an adequate instrument to assess the thermal environment.

It should be noted that these results are based on an experiment with 18 subjects. The number of participants is lower than the average of 25 found in literature. (Van Craenendonck et al., 2018) Within these 18 participants, only 2 were female. Schellen et al found evidence for a significant difference in thermal response between men and women. (Schellen et al. 2012) No influence of gender was found in these results, but this may be due to the small amount of females. Further experiments will be conducted to correct for the skewed gender distribution.

CONCLUSIONS

From the experiments, it can be concluded that the temperature difference and position of local radiant asymmetry does not strongly affect thermal sensation directly, but does have an impact on the base comfort level. The effects however are not as expected, with subjects who are exposed to local radiant cooling indicating that they feel warmer. This effect is noticeable for whole-body thermal sensation, as well as local thermal sensation, except in the head.

REFERENCES

- Arens, E., Zhang, H., & Huizenga, C. (2006). Partial- and whole-body thermal sensation and comfort - Part II: Non-uniform environmental conditions. *Journal of Thermal, 31*(1–2), 60–66.
- Bureau voor Normalisatie. (2004). *NBN EN ISO 8996: Bepaling van het energiemetabolisme*.
- Bureau voor Normalisatie. (2009). *NBN EN ISO 9920: Bepaling van de thermische isolatie en verdampingsweerstand van kleding*.
- Du Bois, D., & Du Bois, E. F. (1989). A formula to estimate the approximate surface area if height and weight be known. 1916. *Nutrition (Burbank, Los Angeles County, Calif.)*, 5(5). <https://doi.org/10.1001/archinte.1916.00080130010002>
- Fanger, P. O., Ipsen, B. M., Langkilde, G., Olesen, B. W., Christensen, N. K., & Tanabe, S. (1985). Comfort Limits for Asymmetric Thermal Radiation, 8, 225–236.
- Frost, J. (2013). Multiple Regression Analysis: Use Adjusted R-Squared and Predicted R-Squared to Include the Correct Number of Variables.
- IBM. (2015). SPSS Statistics. Retrieved from <https://www-01.ibm.com/software/be/analytics/spss/>
- Levine, T. R., & Hullett, C. R. (2002). Eta Squared, Partial Eta Squared, and Misreporting of Effect Size in Communication Research. *Human Communication Research, 28*(4), 612–625. <https://doi.org/10.1093/hcr/28.4.612>
- McDonald, J. H. (2015). *Handbook of Biological Statistics* (3rd ed.). Baltimore, Maryland. Retrieved from <http://www.biostathandbook.com/kruskalwallis.html>
- McNall, P. E. J., & Biddison, R. E. (1970). Thermal and comfort sensations of sedentary persons exposed to asymmetric radiant fields.
- Nakamura, M., Yoda, T., Crawshaw, L. I., Kasuga, M., Uchida, Y., Tokizawa, K., ... Kanosue, K. (2013). Relative importance of different surface regions for thermal comfort in humans. *European Journal of Applied Physiology, 113*(1), 63–76. <https://doi.org/10.1007/s00421-012-2406-9>
- Olesen, S., Fanger, P. O., Jensen, P. B., & Nielsen, O. J. (1972). Comfort limits for man exposed to asymmetric thermal radiation. In *Thermal comfort and moderate heat stress* (pp. 133–148). London.
- Schellen, L., Loomans, M. G. L. C., de Wit, M. H., Olesen, B. W., & Lichtenbelt, W. D. V. M. (2012). The influence of local effects on thermal sensation under non-uniform environmental conditions - Gender differences in thermophysiology, thermal comfort and productivity during convective and radiant cooling. *Physiology and Behavior, 107*(2), 252–261. <https://doi.org/10.1016/j.physbeh.2012.07.008>
- Van Craenendonck, S., Lauriks, L., Vuye, C., & Kampen, J. (2018). A review of human thermal comfort experiments in controlled and semi-controlled environments. *Renewable and Sustainable Energy Reviews, 82*(December 2016), 3365–3378. <https://doi.org/10.1016/j.rser.2017.10.053>

Thermal Effect of Metal Fin inside Elevated Radiant Floor Based on the Thermal Utilization of a Burning Cave

Xueyan Zhang*, Bin Chen, Jiayi Zhao.

Dalian University of Technology, China

*Corresponding email: zxychenggong2008@126.com

ABSTRACT

A rural house integrated with an elevated floor heating system based on the thermal utilization of a burning cave has been established to provide a more comfortable and clear indoor environment. Inside the elevated floor heating system, air is taken as the heat transfer medium and tin layer is designed as metal fin in the middle layer of the elevated floor to enhance heat transfer. In this study, heat transfer process and thermal performance of the inner metal fin were analyzed by theoretical calculations and field measurements. The results show that while the heat flux of the burning cave is decreased from 460 W/m^2 to 200 W/m^2 , the convection heat intensity of the hot air inside the elevated floor under each room is from 2 W/m^2 to 9 W/m^2 . Finally, it confirms that the effective length of the metal layer should be less than 0.4 m . All the above results show that appropriate design parameters can lead to an optimum heat transfer process.

KEYWORDS

Elevated floor heating, Effective length, Heat transfer performance

INTRODUCTION

In order to solve existing problems, such as larger indoor temperature fluctuation, poorer indoor air quality, lower thermal efficiency in a rural house (shown in Figure 1(a)), the model house integrated with an elevated radiant floor heating system based on the thermal utilization of a burning cave was presented (shown in Figure 1(b)). The heat is released from the burning cave to each heating room through the raised floor. The thermal efficiency was increased from 30% to 56.7% (Zhang, 2014).

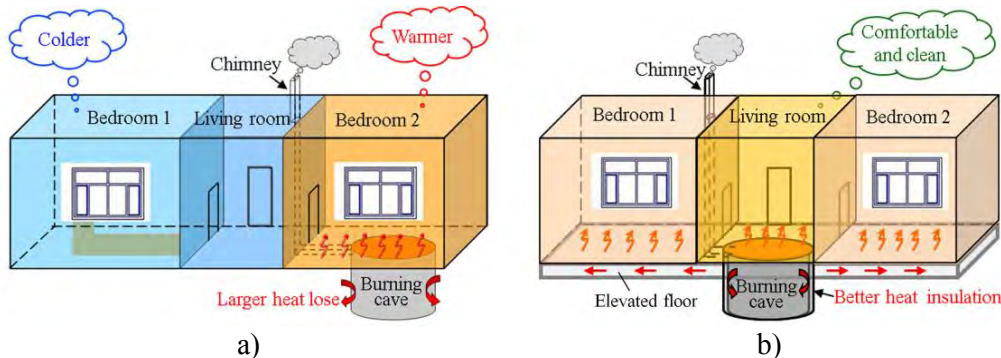


Figure 1. Optimization of a burning cave for residential heating. a) Burning cave is used to heat a room, b) Burning cave is used to heat the whole house.

As a result of lower heat storage coefficient and lower specific heat of the air, an enhanced heat transfer mode was taken into account for improving heat distribution inside the raised

floor. Natural convection in a differentially heated inclined square enclosure with a fin attached to the solar collector for reducing heat losses has been studied numerically (Frederick, 1989). The fin position inside a differentially heated cavity is a major role in heat transfer inside the cavity, the effect of fin position on the heat transfer rate is strongly affected by Rayleigh number and the fin length (Bilgen 2005). The steady laminar natural convection within a differentially heated by square cavity with a thin fin was found that for high Rayleigh numbers, heat transfer can be enhanced regardless of the position or the length of the fin (Shi and Khodadadi, 2003.). Natural convection inside an enclosure with three thick cold walls and a hot thin vertical left wall was studied numerically (Abdullatif and Chamkha, 2007). For the case of highly conductive fin, it was found that the Nusselt number on the cold wall increased compared to the case with no fin (Nag, Sarkar, et al, 1993). Laminar flow regime was found while turbulent flow regime starts to be formed for higher values of Rayleigh number (Bilgen, 2002). Natural convection inside cavities was examined extensively for different boundary conditions, aspect ratios and Rayleigh numbers (Du and Bilgen, 1992.). In this paper, the fin efficiency of the thin metal plate in the middle layer inside the elevated floor can be discussed, and the optimum length of the metal layer can be determined.

METHODS

In the whole heating house, some parameters are including: air temperature, surface temperature, heat flux. The detailed structure information inside the elevated floor is shown in Figure 2. The measured parameters and test error of test instruments are shown in Table 1 respectively. The record interval of all the analyzers was 10 mins.

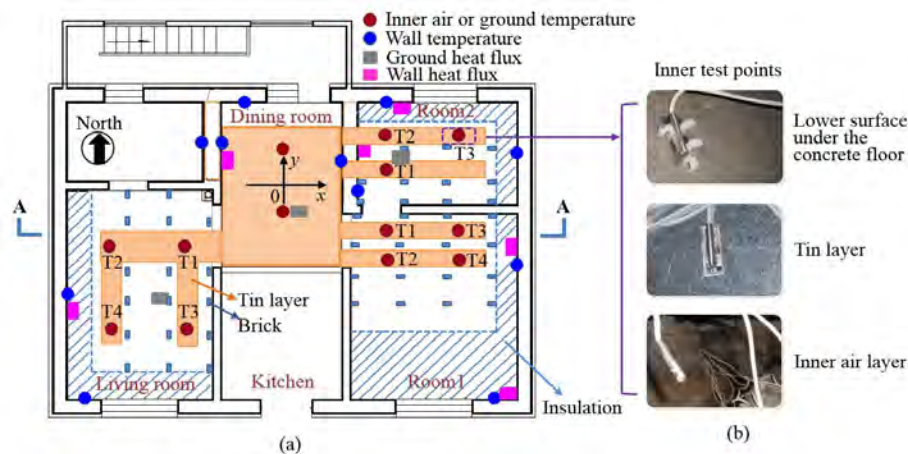


Figure 2. Test points and construction. a) Test points in the whole house, b) Test points in each layer inside the elevated floor.

Table 1. The measured parameters and test instruments

Measuring parameters	Name of instruments	Measuring accuracy
The quality of fuels	Desk type electronic scale	$\pm 0.1g$
Thermal parameter of the building envelops and heating surfaces	Multi-channel heat flow tester JTNT-A/C (SWP-L816)	$\pm 0.1^{\circ}C$ $\pm 1\sim 2 W/m^2$
Indoor/outdoor air temperatures and relative humidity	Digital thermo recorder TR-72U	$\pm 0.1^{\circ}C$
Inner temperature inside the burning cave	High temperature thermocouple	$\pm 1^{\circ}C$
Recording system	Automatic communication and recording system	$\pm 0.1\%$

According to the fin efficiency calculation method of heat transfer in reference (Rohsenow, Hartnett, et al, 1998), the heat distribution transferred by metal layer is equal to the heat gained from the basis of metal layer. The equation that applies to this case is:

$$\frac{d\theta}{dx^2} = m_t^2 \theta \tag{1}$$

Where, $\theta = T - T_\infty$ is the temperature excess, x is the axial coordinate.

$$L_e = \lambda_t A_L m_t \theta_t \left[m_t \left(l_t + \frac{\delta_t}{2} \right) \right] + \frac{2\pi}{\sqrt{5}} \varepsilon \delta_t \theta_t m_t, \quad m_t = \sqrt{\frac{l_t U_t}{(\lambda_t + \varepsilon \sigma) A_L}} \tag{2}$$

Where, L_e is heat changed from metal surface to the air layer at steady state, W . l_t is the effective length of metal layer, m . A_L is the effective area of metal layer, m^2 . λ_t is thermal conductivity coefficient, $W/(m \cdot K)$. U_t is the total length of metal layer, m . δ_t is the thickness of metal layer, m . θ_t is temperature excess, $^\circ C$. m_t is the metal layer performance factor.

$$\eta = \frac{Q_a}{Q_{a,max}} \tag{3}$$

Where, η is the fin efficiency of metal layer; Q_a is the actual heat transfer, including radiation and convection heat transfer inside the elevated floor, W ; $Q_{a,max}$ is the theoretically maximum heat transfer that can be diffused by the metal layer, under the assuming condition is that the entire area of the metal layer is at the maximum temperature.

RESULTS

Temperatures inside the burning cave

During the heating period, temperature field inside the burning cave is shown in Figure 3. After igniting the fuels for 12h, the temperature of test point BN1 (at the height of 1.1m) in Part I is reached to 300 $^\circ C$, but the temperature of test point BS1 (at 1.1m height in Part II) is 100 $^\circ C$ lower than BN1. In part II, the burning time for reaching to the highest temperature is 6h longer than which in part I. Because the air inlet was on the wall of Part I. Through calculation, average burning velocity is about 1.31 mm/h, 1.34mm/h respectively in part I and Part II, which is larger than the results in reference (Beijing civil construction society, 2008.), because the moisture of mixed biomass fuels is 3.36% lower than which in reference.

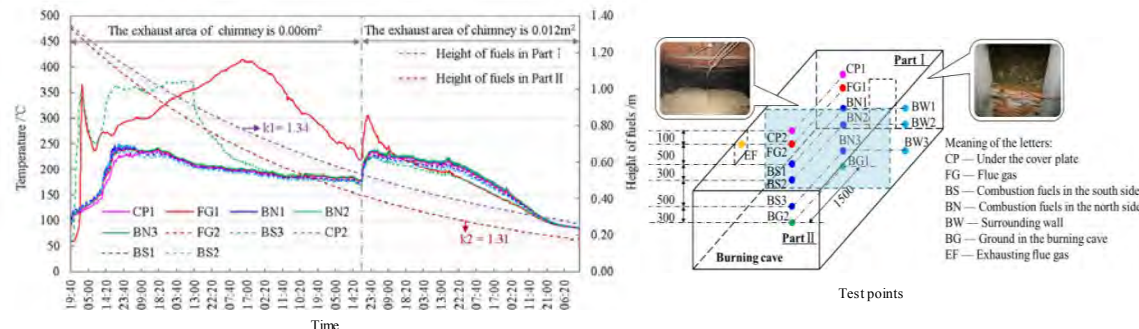


Figure 3. Temperature variations inside the burning cave

Indoor Air Temperatures in the whole house

Temperature variations of the elevated radiant floor heating system and indoor air temperatures during the heating period are shown in Figure 4. While the outdoor air

temperature is between -15°C and 2°C , the average indoor air temperature is about 3°C higher than a room heated by traditional Kang. The temperature difference between adjacent rooms is only about 2.0°C . The results show that using the elevated floor heating system is effect for reducing temperature difference between different rooms in the whole house.

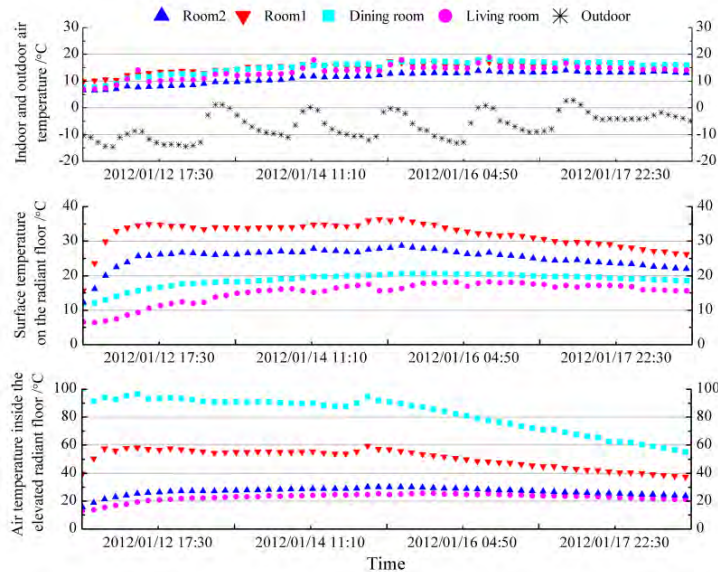


Figure 4. Temperature variation inside the elevated floor and in the house

DISCUSSIONS

As shown in Figure 5(a), the radiation heat is about two to six times more than convection heat. The value of radiation heat on test point 3 in each room is nearly close to zero, and the value of radiation heat on test point 4 in each room is negative. It shows that the effect of the metal plate is heat absorption, and convection is the main heat transfer method. It illustrates that inner heat transferred from heat source to room1 facing south is the best. So that the effective length of the metal layer should be determined to reach the optimum state.

Through comparison in Figure 5(b), the fin efficiency of the metal plate is decreasing as its length was increasing. In order to take the fin efficiency of metal plate maintain at 50%, the effective length of metal plate is determined to be no more than 0.4m by calculation.

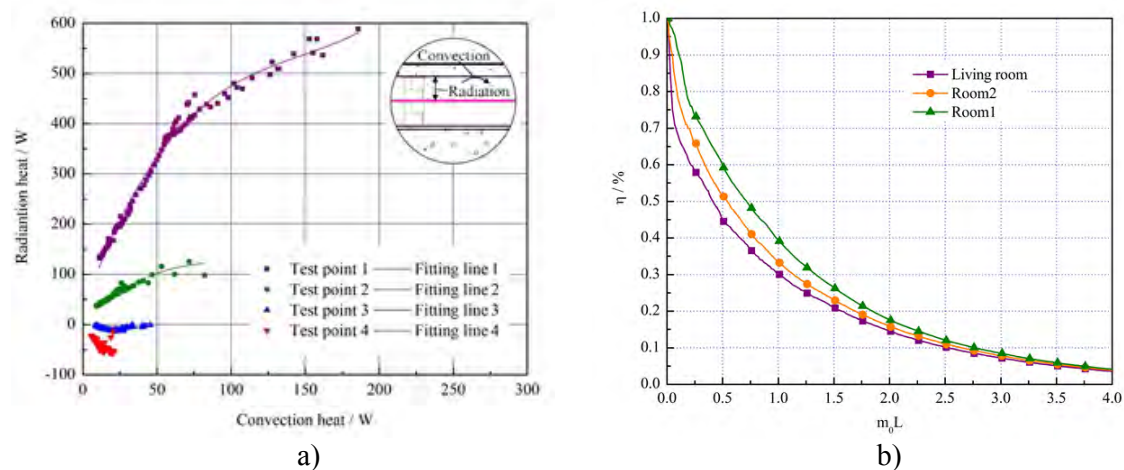


Figure 5. Heat transfer comparison inside the elevated floor. a) Heat transfer analysis, b) The length of metal layer impact on the fin efficiency

CONCLUSIONS

Some significant conclusions are described as follows: (1) In this elevated radiant floor heating house, the temperature difference between adjacent rooms is only about 2.0°C. It illustrates that the heating environment can be more comfortable than using traditional Kang, and the heating time can be maintained for twenty days with once filling by biomass fuels. (2) The temperature drop rates of inner hot air inside the elevated floor under different function rooms were between 0.3°C/m and 0.9°C/m. (3) To maintain the higher fin efficiency, though thermodynamic criterion analysis on the heat transfer performance of the elevated floor, the effective length of inner metal plate was confirmed and should be no more than 0.4m. The optimized method is enhancing convection heat transfer inside the elevated floor heating system to get a more comfort indoor heating environment.

ACKNOWLEDGEMENT

The work was supported by a NSFC (No. 51608092), a China Postdoctoral Science Foundation (No. 2015M571306), and the Fundamental Research Funds for the Central Universities (DUT16RC(3)092).

REFERENCES

- Zhang X.Y. 2014. Study on Heat Source Characteristics and Heat Transfer Process of Burning Cave Heating System, Doctorate dissertation from Dalian University of technology, 25-40. (in Chinese)
- Frederick R. L. 1989. Natural convection in an inclined square enclosure with a partition attached to its cold wall, *International Journal of Heat and Mass Transfer* 32(1), 87-94.
- Bilgen E. 2005. Natural convection in cavities with a thin fin on the hot wall, *International Journal of Heat and Mass Transfer* 48(17), 3493-3505.
- Shi X.D., Khodadadi J.M. 2003. Laminar natural convection heat transfer in a differentially heated square cavity due to a thin fin on the hot wall, *Journal of heat transfer* 125(4), 624-634.
- Abdullatif B.N., Chamkha A. J. 2007. Conjugate natural convection in a square enclosure with inclined thin fin of arbitrary length, *International Journal of Thermal Sciences* 46(5), 467-478.
- Nag A., Sarkar A., Sastri V.M.K. 1993. Natural convection in a differentially heated square cavity with horizontal partition plate on the hot wall, *Computer Methods in Applied Mechanics and Engineering* 110(1-2), 143-156.
- Bilgen E. 2002. Natural convection in enclosures with partial partitions, *Renewable Energy* 26(2), 257-270.
- Du Z.G., Bilgen E. 1992. Coupling of wall conduction with natural convection in a rectangular enclosure, *International Journal of Heat and Mass Transfer* 35(8), 1969-1975.
- Rohsenow W.M., Hartnett J.P., Cho Y.I., et al. 1998. *Hand Book of Heat Transfer*, Third ed., McGraw-Hill Professional publishing, New York, United States of America, 198 pages.
- Beijing civil construction society. 2008. *Building a new socialist countryside based on biomass energy utilization*, China electric power press, First ed., Beijing, China, 56 pages. (in Chinese)

Implementation of integrated wireless sensors technology in renovation of social housing buildings. A Danish case study.

Hagar Elarga^{1,*}, Danai Alifragki^{1,2} and Carsten Rode¹

¹Department of Civil Engineering, Technical University of Denmark.

²Democritus University of Thrace, Civil Engineering Department.

*Corresponding email: Hagel@byg.dtu.dk

ABSTRACT

Social housing units built in the 1960s and 1970s make up one-fifth of all housing units in Denmark. Their renovation is an important step towards meeting the goals of the national energy road map. Sensors based on wireless technology could be considered a feasible solution to increase occupant's awareness towards their indoor climate and their energy consumption. In the present experimental study, a framework implementing wireless sensors to monitor energy and indoor climate before and after renovation has been applied in two apartments of a Danish social housing site. In the first phase of the study, the accuracy of some commercially available wireless systems was investigated. This was followed by installation in the field, where occupant behavior (e.g. window opening status) was also monitored. Heating energy data monitored before and after renovation indicated savings of up to 34%.

KEYWORDS

Social housing, buildings renovation, data collection, integrated wireless sensors.

INTRODUCTION

Measurement and verification are effective ways of documenting energy savings achieved as a result of buildings renovation, while most of current renovation assessment are based on numerical simulations (Ma et al., 2012). On the other hand and in Denmark, one of the current barriers of energy renovation decision making is the lack of sufficient information about energy consumption and accordingly cost and possible savings (Bjørneboe et al.2018). Wireless sensor technology offers new potential for monitoring energy consumption and indoor environmental parameters such as temperature, relative humidity and CO₂ with less invasive nature to occupants comparing to wired systems (Stojkoska et al., 2014). The idea of using wireless sensors in the built environment is not new, but applications are limited despite the recognized potential of this technology and more research in the domain is needed to lift the barriers (Noye et al. 2018). While, it can be implemented in either new or renovated buildings with means for internal and external communication (Loboccaro et al., 2017), but particularly applying the technology at building renovation projects can help to comprehend the performance of existing systems and to evaluate the improvements after the completion of the renovation (Noye et al. 2018). Another advantage is that it communicates with end-user through user-friendly app's where direct interaction is a priority. On the other hand, very few studies has focused on accuracy checking of these wireless sensors. Petersen et al. (2018) have investigated two commercial indoor climate monitoring systems (IC-METERS and NETATMO) through an experimental campaign. Results showed that the accuracy of latter system to measure the CO₂

concentrations was highly dependent on the air temperature. For the study reported in this paper, two particular systems (IC-METERS and WIRELESS- TAGS) have been investigated for use in a project for social housing in Aalborg, Denmark to monitor performance before and after renovation. These two WSN systems have been applied in previous projects in Denmark and have shown good reliability to monitor the indoor climate and occupant behavior, (Henriksen and Olsen, 2018) and (Azouz, 2017). The monitored parameters included heating consumption, electricity use measured by SMAPPEE's, air temperature, relative humidity, CO₂, occupancy with PIR sensors, and window opening. The measuring campaign in the field started with a lab test of the sensors to determine their accuracy and determine the sensibility of CO₂ measurements to temperature variations.

METHODOLOGY

The experimental based study is subdivided into two main steps, the first is calibrating the IC meters and wireless tags, checking how to save and retrieve the collected data on lab level. Followed by the field site installation phase, which included two groups of apartments, renovated and non-renovated cases.

Calibration of the wireless sensors

IC meters and wire-less tags systems were investigated in climatic chambers of the Technical University of Denmark. The IC METER (version 4.3) communicates through a GSM based module and has accuracy of the CO₂ measurements of ± 30 ppm or $\pm 3\%$. The WIRELESS TAGS are square tags with dimension 4.0 x 4.0 x 0.2 cm, which can be distributed over indoor zones and connected to a data router that is connected to the internet via a LAN cable. These tags are capable of measuring air temperature and RH with accuracy of ± 0.4 °C and ± 2 % respectively, in addition to being able to track the motion of windows and doors. Both systems have shown good reliability in many projects (Henriksen and Olsen, 2018) and (Azouz, 2017).

The climate chamber has a volume of 22 m³ and it is well insulated preventing outside factors to influence the temperature stability inside the chamber, see Figure 1a. The CO₂ concentration was measured by a Photoacoustic Gas Monitor "INNOVA 1412i" (LumaSense Technologies Inc., Figure 1b) with a detection limit of ± 1.5 ppm for CO₂. Two gas flow meters were used to control the dosing of CO₂, see Figure 1c.

Testing in the field

The measurements were carried out in two non-renovated and renovated apartments, which were selected in a social housing site (Figures 2a and 2b). Thermal characteristics of the building envelope were different for the two types of apartments. The measured heat transfer coefficients for the external walls of the renovated and non-renovated apartments were 0.12 and 1.4 W/m²K, respectively, and 0.85 and 2.6 W/m²K for the windows. The heat transfer coefficients were measured by a wireless heat flow meter (GREENTEG) with accuracy of $\pm 3\%$ for a continuous 3 days in compliance with ISO 9869.

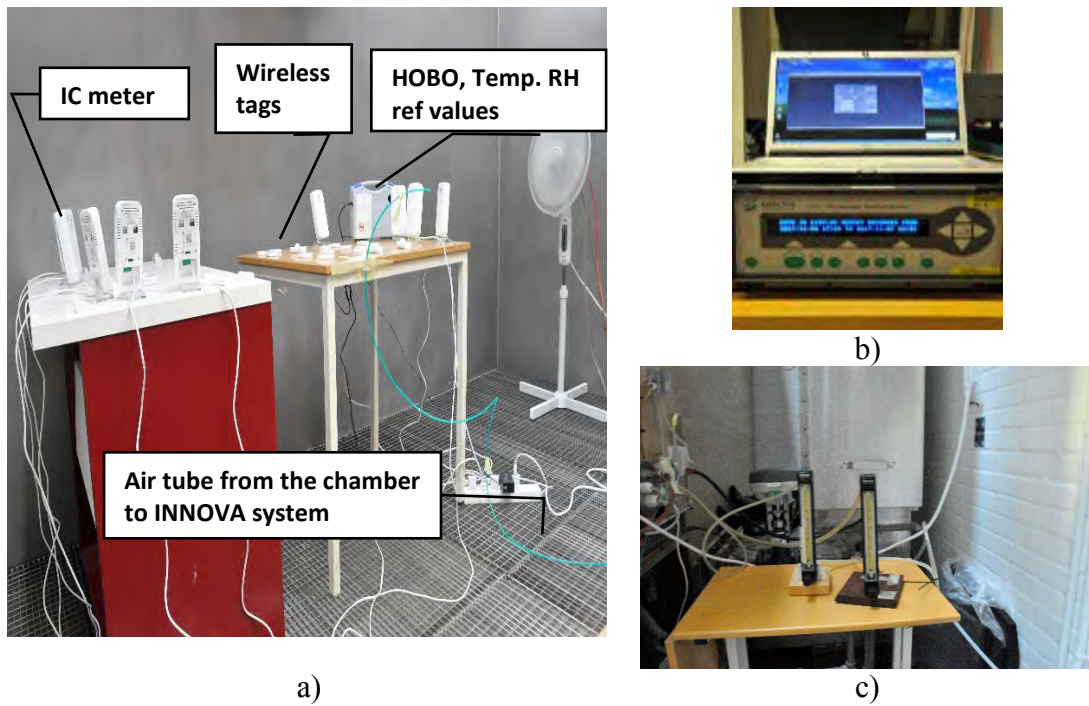


Figure 1. Calibration of the sensors. a) Climatic chamber, b) Photoacoustic Gas Monitor, c) CO₂ flow meters

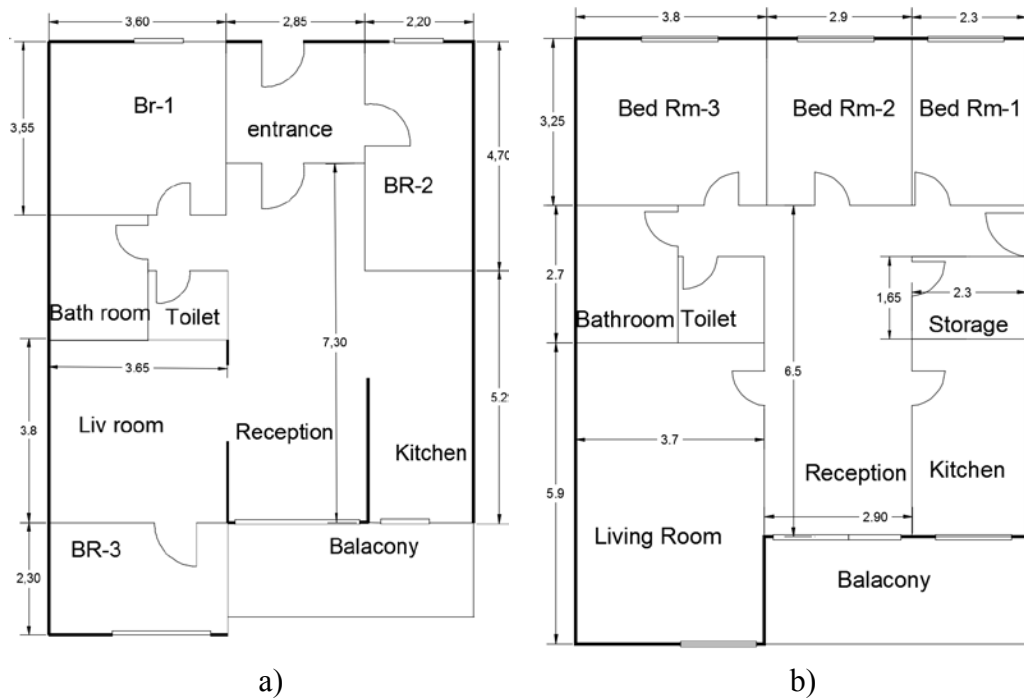


Figure 2. Apartments under investigation. a) Non-renovated apartment, b) Renovated apartment

Both types of apartments have been equipped with wireless sensors to collect dynamic energy and indoor climatic performance data. Time step for the data collection is 5 minutes. The

measurements of heating flowrates and energy has been carried out through an ultrasonic heating meter. The meter is implemented with a wireless M-Bus function, which enables the communication with a stationary multi utility controller, and it supports the open metering system through compliant data transfer

RESULTS

The results are subdivided into three parts, the lab level experiments that included *i)* the IW sensors calibration. Followed by analysis of the site level monitored data, which included *ii)* the indoor climate and *iii)* heating consumption.

Accuracy check and calibration of instruments

The performance of the sensors was compared for different levels of CO₂ concentrations, relative humidity and air temperature. Calibration profiles are shown in Figures 3a and 3b. The IC meters Root Mean Square Error (RMSE) values ranged from 0.1 to 0.3°C, 0.6 to 1.5 % RH, and 25 to 50 ppm, for temperature, RH and CO₂, respectively. For the sensor tags, RMSE values ranged from 0.3 to 0.7°C for temperature readings, and 2.5 to 3% for RH readings.

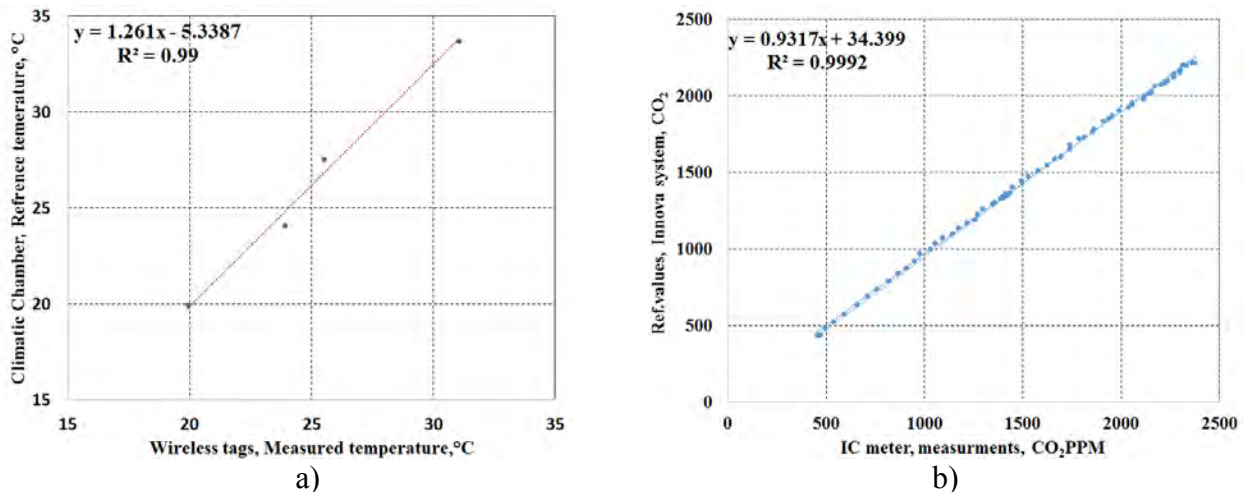


Figure 3. Sensor calibrations. a) Wireless tag- Air temperature, b) IC meter- CO₂ levels

Indoor climate profiles

Figure 4 illustrates weekly temperature and RH profiles for the entrance area of the two apartments. The data were retrieved from the IC meter and wireless tag data cloud. The decreasing air temperature between the 22nd and 24th of February in the non-renovated apartment reflects a reduction in the control setting of the radiator's thermostat by the occupants due to their absence (winter vacation).

Heating energy profiles

Heating profiles for a renovated and a non-renovated apartment are shown in Figures 5a and 5b. For the non-renovated apartment, the heating consumption was 462 Wh/m² per day, while it was 304 Wh/m² per day for the renovated apartment.

DISCUSSION

The measured data has shown that by improving the thermal characteristics of the building-envelope, the overall heating consumption has decreased the about 35%. The monitored air temperature in the entrance and living areas, which are shared by all family members, was between 20 and 22 °C. However, in the bedrooms, where individual preferences are dominating, opening the windows all night caused a drop of air temperature to 10 °C.

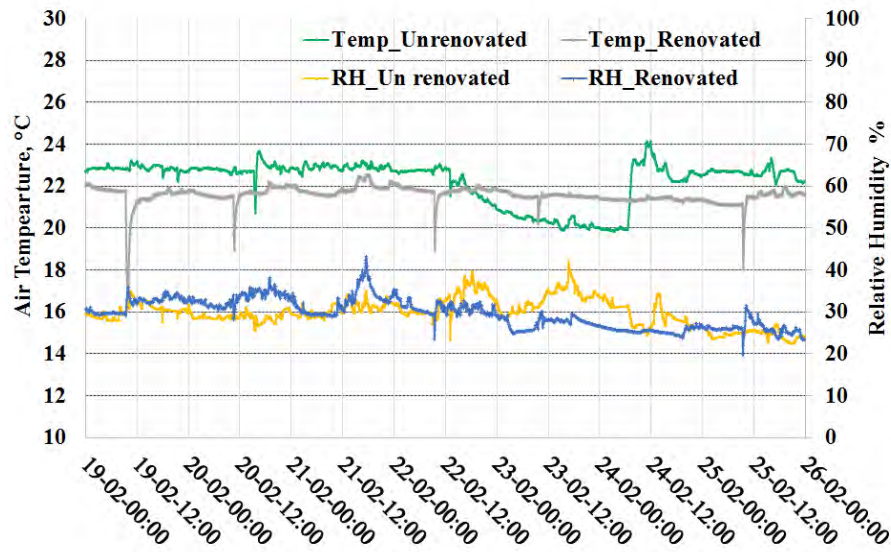


Figure 4. Indoor air temperature and Relative humidity profiles

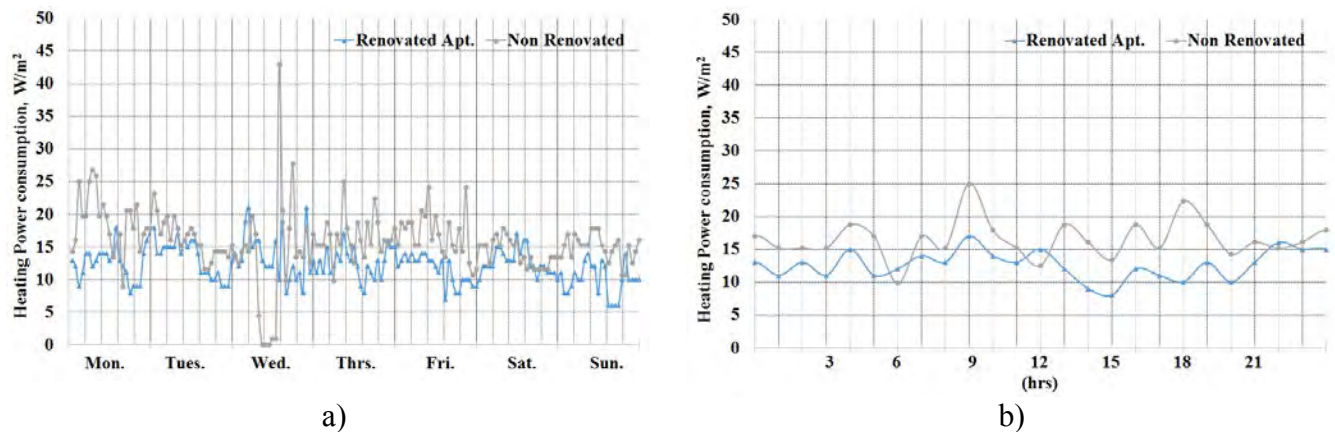


Figure 5. Heating consumption profiles for both apartments. a) a weekly profile, b) a day profile

CONCLUSIONS

Continuous measuring of the building performance provides opportunity for better design and operative improvements. Integration of wireless sensors as a non-invasive measuring system could be considered an applicable solution for both the tenants and the social housing company to monitor and analyze building performance through the renovation and operation phase. Implementation of a wireless system saves time and installation efforts, and facilitates distance monitoring of all measured data. The increasing availability of user-friendly monitoring and feedback systems will facilitate the involvement of occupants in their energy use and quality of

the indoor environment. However, further investigations of the accuracy and reliability of the wireless sensor systems under different boundary conditions have to be carried out. In addition, it will be desired to have all the different sensors collected in a single data cloud to ease the retrieving and analysis of the saved data.

ACKNOWLEDGEMENT

This study was carried out under the framework of the REBUS project, *Renovating Buildings Sustainably*, www.rebus.nu, funded by the *Innovation Fund Denmark*, *Realdania*, *Grundejernes Investeringsfond*, and companies involved in the project.

REFERENCES

- Azouz T. 2017. Energy use, indoor environment and occupant behavior in dwellings, M.Sc. Thesis. Technical University of Denmark, 71 pages
- Bjørneboe M. G., Svendsen S., Heller A., 2018, Initiatives for the energy renovation of single-family houses in Denmark evaluated on the basis of barriers and motivators, *Energy and Buildings* Vol 167, pp. 347-358,
- GreenTEG AG: <https://www.greenteg.com/> Accessed 06/2018.
- Henriksen N. and Olsen B. 2018. Modelling of occupant behavior in relation to window operations. M.Sc. Thesis. Technical University of Denmark), 253 pages.
- Henriksen N. and Olsen B. 2018. Modelling of occupant behavior in relation to window operations. M.Sc. Thesis. Technical University of Denmark), 253 pages
- IC-Meter. <http://www.ic-meter.com/> Accessed 06/2018.
- ISO 9869-1:2014. Thermal insulation building elements Part 1: Heat flow meter method. International Organization for Standardization. pp.36.
- Loboccaro G, Carlucci S., Lofstrom E., 2016. A review of Systems and Technologies for Smart Homes and Smart Grids, *Energies*, Vol.9.
- Ma Z., Cooper P., Daly D., Ledo L. 2012. Existing building retrofits: methodology and state-of-the-art, *Energy and Buildings*. Vol 55, pp. 889–902.
- Noye S, North R, Fisk D. 2018. A wireless sensor network prototype for post-occupancy troubleshooting of building systems, *Automation in Construction* Vol.89, pp. 225–234.
- Netatmo. <https://www.netatmo.com/> Accessed 06/2018
- Petersen J., Kristensen J., Elarga H., Andersen R. and Midtstraum A. 2018. Accuracy and air temperature dependency of commercial low-cost NDIR CO₂ sensors: An experimental investigation. In proceedings of 4th International Conference on Building Energy, Environment, Melbourne.
- Stojkoska B, Avramova A and Chatzimisios P, 2014. Application of Wireless Sensor Networks for indoor temperature regulation, *International Journal of Distributed Sensor Networks* Vol. 10.
- Smappee: <https://www.smappee.com/> Accessed 06/2018.
- Wireless tags: <http://wirelesstag.net/> Accessed 06/2018.

LightLearn: Occupant centered lighting controller using reinforcement learning to adapt systems to humans

June Young Park, Thomas Dougherty, Hagen Fritz and Zoltan Nagy*

Intelligent Environments Laboratory,
Department of Civil, Architectural and Environmental Engineering,
The University of Texas at Austin, Austin, TX, USA

*Corresponding email: nagy@utexas.edu

ABSTRACT

Humans spend up to 90% of their time indoors, thus building systems should maintain the indoor environment within the comfort range. In this paper, we present LightLearn, a reinforcement learning based occupant centered lighting controller. The control agent interacts with the occupant non-intrusively, learns her/his preferences, and determines actions for achieving both human comfort and energy saving. We present system hardware, control algorithm, and experimental results of LightLearn for an office space. Compared to the full (9am-5pm) and occupancy based control, LightLearn reduced 83% and 63% of operation time, respectively, by adapting to the occupant.

KEYWORDS

building retrofit, occupant behavior, adaptive control, reinforcement learning

INTRODUCTION

Lighting accounts for approximately 20% of the total commercial building energy consumption (DoE 2011). One promising energy efficient strategy is a daylight linked automatic lighting control system, which switches lights on/off depending on the amount of natural lighting. The challenge for this automatic control system, however, is that typically control set-points are not driven by occupant preference but set to a uniform value. In other words, even though different people may have different preference on their comfort, the conventional automatic control uses fixed threshold values for operation. As a result, occupants often either override control settings indicating their discomfort, or in the worst case, they deactivate their control system (Gunay et al. 2013). Note that if occupant comfort is not satisfied, it could have serious repercussions on not only work productivity but also both physical and mental health for humans (Loftness et al. 2003). To put this in a more general perspective, beyond lighting: the objective of building environmental systems should be to provide comfort for the occupants, who spend up to 90% of their time indoors. However, building control research has largely neglected occupant satisfaction (Park and Nagy, 2018).

The occupant centered control system (OCC) has been introduced to address this discrepancy between building control and occupant comfort (Nagy et al. 2015; Nagy et al. 2016). There are two components of occupant comfort, one of which is the actual physical comfort, i.e., the absence of the feeling of pain, and the other is the perception of control over their indoor environment (Nagy et al. 2016). To accomplish the two parts of comfort, the building control system should be focused, or centered, on the characteristics of the occupant. An ideal system should learn the unique preferences of the occupant, and adapt the control set-points to these preferences to balance the decisions of the occupant with the calculated decision for energy

savings. There are several experimental results indicating that OCC approach can save energy without sacrificing occupant comfort (Nagy et al. 2015; Nagy et al. 2016).

In this paper, we introduce LightLearn, a reinforcement learning (RL) controller for lighting in the OCC framework. We describe RL and the OCC framework in general, as well as the specific hardware and control algorithm of LightLearn in the next Section. Finally, we present experimental results and conclude the paper.

METHODOLOGY

Reinforcement learning

RL is a machine learning technique (Sutton & Barto, 1998), in which the learning agent interacts with its environment, and uses feedback from the environment to determine the best possible action given the current state (Figure 1a). RL is formalized as a Markov Decision Process (MDP): It is a tuple of states (S), actions (A), transition probabilities (P), and rewards (R: $S \times A \rightarrow R$). Each state has a value $V^\pi(s)$ which is the expected return for the agent when starting in that state and following the policy, where the policy $\pi : S \rightarrow A$ maps states to actions. The agent's objective is to calculate the optimal policy, i.e., the one that leads to maximum expected return (Nagy et al. 2018a). We used model based RL for LightLearn, where P and R are determined from experimental data, and the MDP is solved for the optimal policy using value iteration (Sutton & Barto, 1998).

RL based Occupant centered building control

The general RL-OCC framework acquires two types of data (Figure 1b): 1) Indoor environment, e.g., temperature, humidity, and luminance. 2) Interaction of the occupant with the building systems, which is directly related to occupant satisfaction, e.g., thermostat, blind, and switch usage. For the RL agent, type 1 data is used for states, and type 2 data is the feedback/reward signal. Ultimately, the RL agent determines the optimal action based on states and reward. This action is then used as e.g., set-point for the building control system.

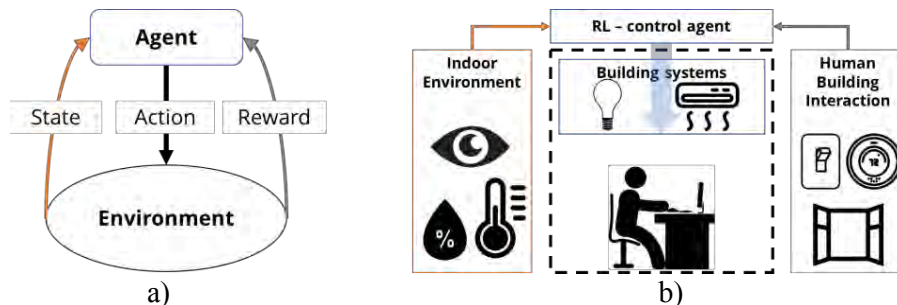


Figure 1. a) Reinforcement learning b) general concept of the RL-OCC framework

LightLearn: An RL-OCC Case Study

Hardware configuration

The hardware of LightLearn consists of low-cost off-the-shelf components to allow retrofitting any manual on/off light switch (Figure 2a). The controller itself is implemented in Python on a Raspberry Pi Zero W (RPi). The gathered environments are 1) luminance (TSL 2561). 2) A personal BT enabled device (mobile phone, watch, etc) paired with the RPi serves as proxy for occupancy (Nagy et al. 2018b). 3) For both sensing and actuating the light switch, we used a product called Switchmate. It uses a DC motor to move the light switch (on/off), while the occupant can switch the lights via a push button. We also designed a custom printed circuit board to interface and control the Switchmate with the RPi.

Table 1. Data acquisition summary

Variable	Type	Values	Unit	Logging Frequency
Switch position	binary	0/1	-	1 minute
Occupancy	binary	0/1	-	1 minute
Room light level	integer	0-10,000	lux	1 minute

The controller has the three components (Figure 2b): 1) Data acquisition of switch position, occupancy, and light level on the wall each minute (Table 1). 2) Learning process by building the MDP and determining the optimal policy once a day at midnight. (see next section) 3) Live control of the lighting system with the most recent learning results. Each minute, the controller determines the states and actuates the action when new state is different from previous state. A LightLearn was installed in a south facing, one person office, retrofitting the previously manual light switch, and an experiment was conducted for three weeks (3/19 – 4/5).

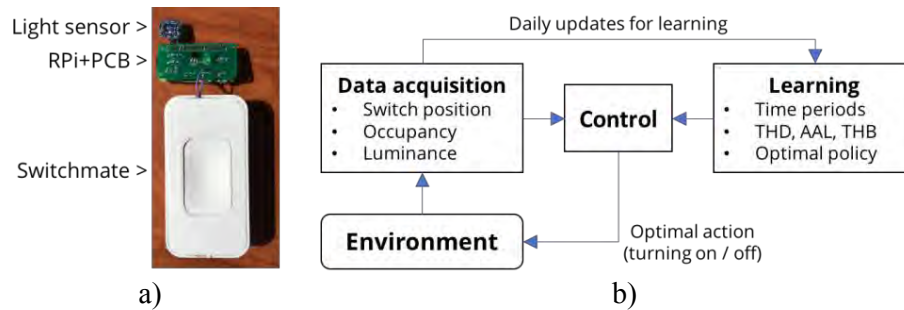


Figure 2. a) LightLearn hardware

b) Control algorithm flow chart

State-action Space Design and Learning process

The key when developing a robust RL controller is the design of the state-action space for the MDP. For LightLearn, the possible actions (A) are turning on/off. The states (S) are defined by four parameters: 1) Each day is split into four periods according to the trends of increasing (P1), midday (P2), decreasing (P3), and low ambient light (P4). These periods were identified using the gradient between two consecutive luminance data points. P4 is defined when the gradient is constant. If the majority (>80%) of the gradients are positive or negative, the time periods are set to P1 and P3, respectively. P2 is assigned in between P1 and P3. 2) Occupancy, and 3) switch position (on/off) are additional considerations for the states. 4) The indoor light levels that correspond to the cutoffs between Dark, Comfort, and Bright: if the occupant switches the lights on, we assume that he/she feels dark. Thus, the light level at that moment is the threshold for darkness (THD). If the light levels are below THD, it is considered Dark. Typically, the occupant can switch the light multiple times. Then we average the values to obtain THD. The artificial light level (AAL) is measured by the lux level difference between switch off & on. A last threshold value is the threshold for brightness (THB=THD+AAL), which indicates that it is bright enough for occupant. Light levels above THB are considered to be Bright. Light levels between THD and THB are regarded as Comfort.

Figure 3 shows all possible states for the control agent. For example, when the room is occupied during P1, P2, and P3, the agent can be in the Bright or Comfort state if the lights are on or off, and in the Dark state when the lights are off. In brief, each day can be split into, e.g., at most 26 states, and the objective of the agent is to determine the best action for each of those states. Once states and actions are defined, the probabilities of transitioning from one state to any other state are calculated by historical data. For each state, all the state transitions are counted and divided by the total number of state transitions. Finally, we use the reward

values shown in Figure 3. We set negative rewards (-1) for energy wasting, positive rewards (+1) for using energy for occupant comfort, and larger rewards (+2) for energy savings.

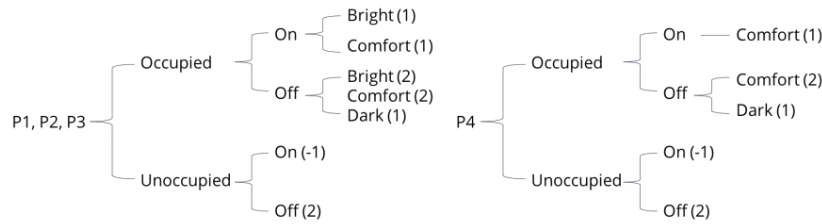


Figure 3. State-Action definition by time periods, occupancy, switch position, and light level; Rewards on each state are annotated in parenthesis.

RESULTS

To illustrate how the controller worked, we show the MDP and the data collection result on March 27th (Figure 4). Historic data (3/19-26) was used to build the MDP (Figure 4a). The controller solved it for the optimal policy for the following day. Specifically, there are 7 states (circles), the transition probabilities are calculated between two states (arrows), and the calculated optimal policy (values) is mapped on each state.

With this optimal policy, the controller actuated the switch to maximize the value based on its current state. For example, the controller determined its state based on the three sensor values (i.e., lux level, occupancy, switch position) in Figure 4b. Based on state transition, the associated values were changed. On March 27th, there were the two control actions: 1) The controller read the current state as S17 (occ-on-bright) and switched off to transition to the state with maximum value (S14, occ-off-comfort) around 13:30. 2) Similarly, the controller read S9 (occ-on-bright) and turned off, transitioning into state S7 (occ-off-comfort) at 10:51 in P1. We emphasize that both actions were taken because the controller transitioned into “Comfort” states.

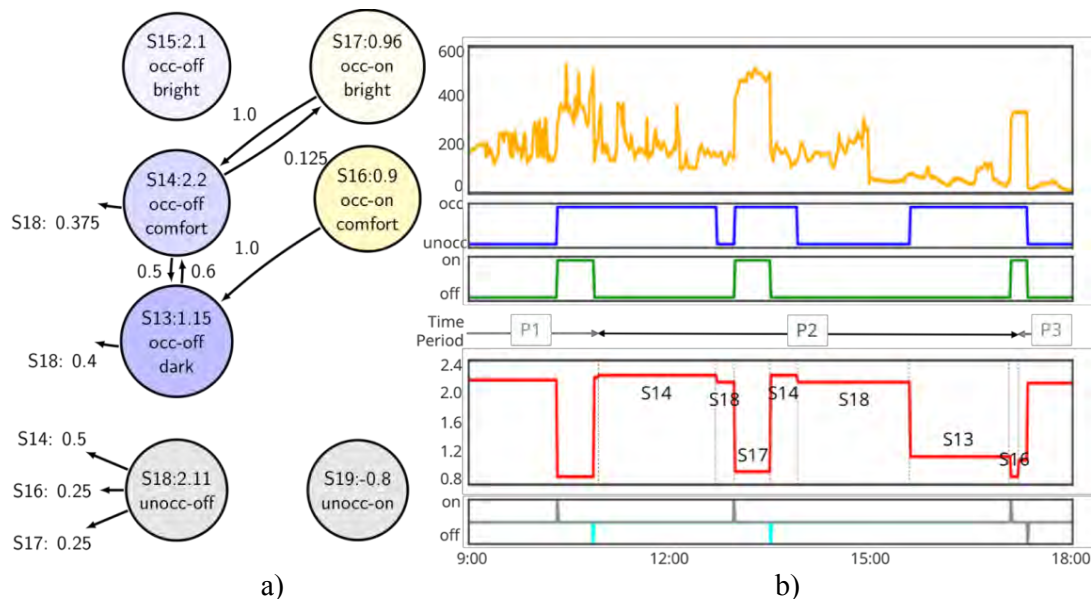


Figure 4. March 27th: a) MDP during P2 b) Data: lux level (yellow), occupancy (blue), switch position (green), value with states (red), and control actions (human-gray, controller-cyan)

The controller calculates the learning outputs every midnight. With these daily outputs, we investigate the evolutions of control parameters: Figure 5a shows how the time period varied by day: the start times of P1 and P4 were relatively constant, because sunrise and sunset time did not significantly change during the experiment. The duration of P2 increased while the durations of P1 and P3 decreased. Because there were no clear patterns for both daylight increasing and decreasing due to the weather condition (cloudy). In figure 5b, we also observe that the THD is around 280 lux until the 7th day. Then, it drops to around 190 lux. This is because the occupant turned on the switch with lower ambient light levels on the cloudy days (7th–10th). This shows how LightLearn adapts its set-points based on occupant interaction.

Similarly, the evolution of the values for states S6, S9, and S10 in Figure 5c demonstrate the adaptation capabilities of LightLearn. Each state has same value (1) on the first day, yet the values of S9 is the lowest until the 8th day, because there was no state transition into S9. However, after the 7th day, the occupant turned on the light often due to cloudy weather, which increased the transition probabilities to the S9 state.

To evaluate energy savings of LightLearn, we calculated the total light-on time and compared with other scenarios (Table 2). Essentially, the operation time serves as proxy for energy consumption. The full operation is the worst-case scenario, assuming the light is on during the normal office schedule (9am-5pm) on weekdays. In addition, the occupancy-based operation was compared. In this case, we assumed that the occupant turns on the light whenever she/he occupies the room. Compared to the full operation and the occupancy-based case, LightLearn reduced the operation time by 83% and 63%, respectively. In brief, the controller successfully saved energy consumption by learning the occupant behavior and the room environment.

Table 2. Operation time (light-on) of each scenario

Scenario	Full operation (9am-5pm)	Occupancy-based	LightLearn
Operation time (hrs)	104	48.8	17.6

DISCUSSIONS

The learning process can be tuned by varying the RL parameters. First, the controller determines the importance of future reward by discount factor (γ). Typically, lighting control requires a very small value ($\cong \gamma 0$): If excess weight is given to future energy saving, the controller might keep the switch off in a morning and expect to have sufficient daylight level later. This would cause discomfort situation for the occupant. However, in other types of building control problems, i.e., HVAC, higher discount factors might be required (Vazquez-Canteli et al. 2017). Also, the reward assignment can initialize the objective of controller. For the sake of energy saving, we assigned higher rewards ($r=2$) for the off states (Figure 3). Thus, those states have relatively higher values, and lead the controller to primarily switch off.

CONCLUSION

This paper introduced RL based OCC framework. As a case study, we implemented LightLearn in an office. LightLearn was successfully deployed and collected occupant related data. Ultimately, the controller generated the MDP and calculated the optimal policy every midnight for the operation on the following day. The results indicate that the controller reduced unnecessary operation time by learning unique characteristics of the occupant behavior and the room environment. For future studies, RL-OCC approach should be further evaluated by different building systems (i.e., dimmable lighting, HVAC), environments (i.e., visual and thermal), more occupants, and for longer periods.

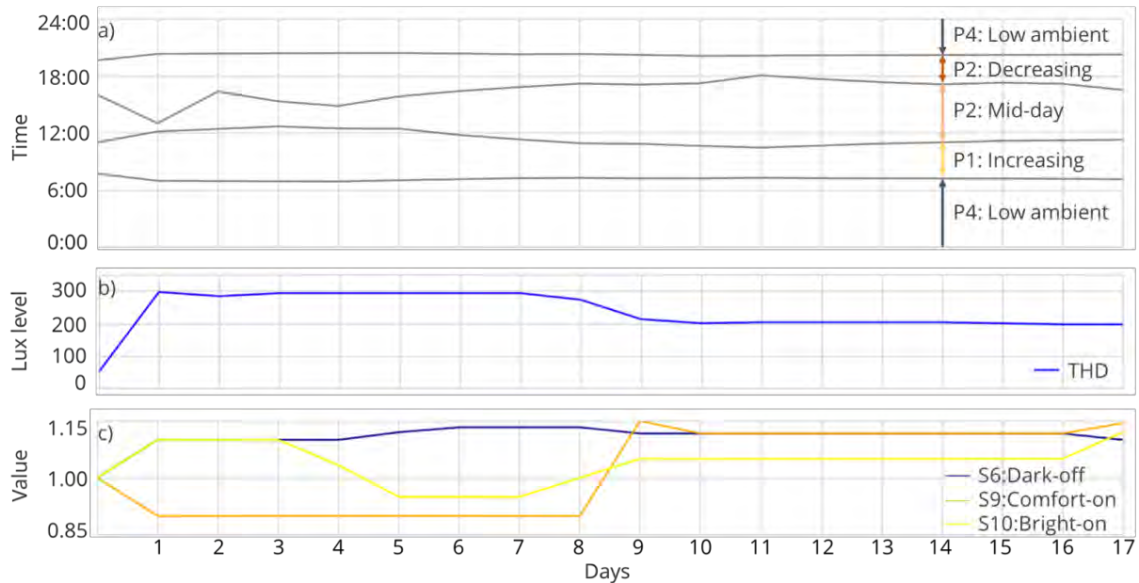


Figure 5. Evolutions of a) time period b) threshold darkness level, and c) values of S6,S9,S10

ACKNOWLEDGEMENT

This research is supported by UT Austin through a Green Fee Award.

REFERENCES

- DoE, 2011. Buildings energy databook. *Energy Efficiency & Renewable Energy Department*.
- Gunay H.B., O'Brien W. and Beausoleil-Morrison I. 2013. A critical review of observation studies, modeling, and simulation of adaptive occupant behaviors in offices. *Building and Environment*. Vol. 70, pp. 31-47.
- Loftness V., Hartkopf V., Gurtekin B., Hansen D., and Hitchcock R. 2003. Linking energy to health and productivity in the built environment. In: *Proceedings of the 2003 Greenbuild Conference*.
- Nagy Z, Park J.Y., and Vazquez-Canteli J. 2018 Reinforcement learning for intelligent environments: A tutorial. in press.
- Nagy Z, Vazquez-Canteli J., and Park J.Y. 2018. Using Bluetooth Based Occupancy Estimation for HVAC Set-Back to Reduce Energy Consumption in Buildings. In: *Proceedings of the 2018 ASHRAE Annual Conference*.
- Nagy Z., Yong F. Y., Frei M., and Schlueter A. 2015. Occupant centered lighting control for comfort and energy efficient building operation. *Energy and Buildings*, Vol. 94, pp. 100-108.
- Nagy Z., Yong F. Y., and Schlueter A. 2016. Occupant centered lighting control: a user study on balancing comfort, acceptance, and energy consumption. *Energy and Buildings*, Vol. 126, pp. 310-322.
- Park J.Y. and Nagy Z. 2018. Comprehensive analysis of the relationship between thermal comfort and building control research-A data-driven literature review. *Renewable and Sustainable Energy Reviews*. Vol. 82, pp. 2664-2679.
- Sutton R. S., and Barto A. G. 1998. *Reinforcement learning: An introduction* (Vol. 1, No. 1). Cambridge: MIT press.
- Vazquez-Canteli J., Kampf J., and Nagy Z. 2017. Balancing comfort and energy consumption of a heat pump using batch reinforcement learning with fitted Q-iteration. *Energy Procedia*. Vol. 122, pp. 415-420.

Sequential Monte Carlo for on-line estimation of the heat loss coefficient

Simon Rouchier^{1*}, Maria José Jiménez², Sergio Castaño²

¹Univ. Grenoble Alpes, Univ. Savoie Mont Blanc, CNRS, LOCIE, 73000 Chambéry, France

²CIEMAT, Department of Energy, Energy Efficiency in Buildings Unit, Av. Complutense 22, E28040 Madrid, Spain

*Corresponding email: simon.rouchier@univ-smb.fr

ABSTRACT

The calibration of building energy models based on in-situ sensor information is generally performed after the measurement period, using all data in a single batch. Alternatively, on-line parameter estimation proposes updating a model every time a new data point is available: this allows observing a direct relation between external events and the identifiability of parameters. The present study uses the Sequential Monte Carlo method to train a RC model, and thus estimate a Heat Loss Coefficient, and other parameters, sequentially. Results show the direct impact of solicitations (solar irradiance and indoor heat input) on this estimation, in real time. The method is validated by comparing its results with the Metropolis-Hastings algorithm for off-line estimation.

KEYWORDS

Bayesian inference; on-line; SMC

INTRODUCTION

The calibration of simplified building energy models using in-situ measurements is now a widespread research topic (Rouchier, 2018). It is commonly performed for two general types of applications: the characterisation of intrinsic building performance (Heo et al. 2012; Bauwens and Roels, 2014), and the identification of a model for predictive purposes, for instance in the aim of model predictive control. State-space models, which include the simplified resistor-capacitor (RC) model structures, are a popular choice for both applications. When written as a set of Stochastic Differential Equations, they allow accounting for modelling approximations (Madsen and Holst, 1995) and offer a more reliable parameter estimation than deterministic models (Rouchier et al. 2018).

Parameter estimation is typically performed *off-line*: measurements of indoor and outdoor conditions are first carried in a test building, and data is processed after the experiment in a single batch. An interesting challenge is to carry parameter estimation *on-line*, during the observation period: starting from an initial guess for parameter values, these estimates are updated sequentially, every time a new observation becomes available. The motivation is twofold: first, it would allow using the measurement period for computations, thus reducing the total time of the procedure (Raillon and Ghiaus, 2017). Second and foremost, it would allow directly observing which phenomena “bring information” to the parameters, by correlating the reduction in their estimation uncertainty with observed events.

Bayesian inference offers the possibility of on-line estimation with Sequential Monte-Carlo (SMC) methods (Doucet et al. 2000). Originally developed for the sequential estimation of states (Handschin 1970), SMC was later adapted to state and parameter estimation (Kantas et al. 2015). Building physics applications are scarce and very recent (Raillon and Ghiaus, 2017), but may become more common due to the motivations listed above. The present paper

applies SMC for the on-line estimation of the heat loss coefficient (HLC) of a test building. Starting from a highly uncertain prior knowledge of HLC, the target is to dynamically observe what leads its estimation to narrow down to a more precise value. The identifiability of HLC regarding available data is then discussed.

CASE STUDY

Test case

This study uses measurements that were carried in the Round Robin Test Box (RRTB), within the framework of the IEA EBC Annex 58 (Jimenez et al. 2016). This experimental test cell has a cubic form with dimensions of one cubic meter, identical wall components on all sides and one window with dimensions 60x60cm². It was installed outdoors, in the LECE laboratory at Plataforma Solar de Almeria, in the South East of Spain. Experiments were carried during a 43 days period in the winter of 2013-2014. More information on the conditions of the test is available in the Annex 58 report (Jimenez et al. 2016).

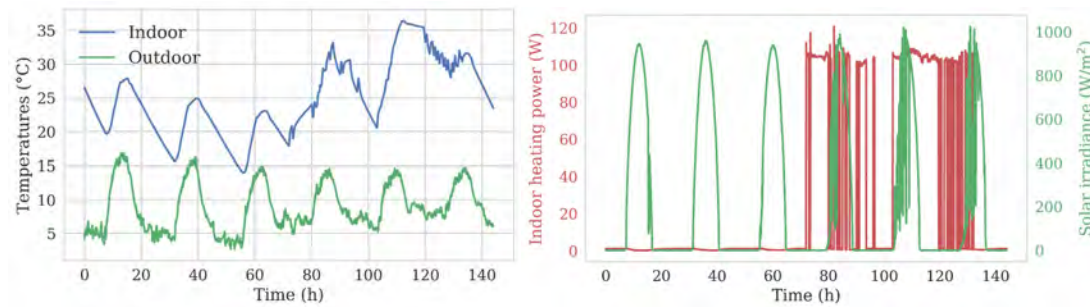


Figure 1. Measured indoor and outdoor temperature, heating power and solar irradiance

A period of six days was chosen for the present investigation, shown on Fig. 1. The indoor temperature is left free floating during the first three days, although it is impacted by daily peaks of solar irradiance. Then, a ROLBS heating signal was imposed inside the test box during the remaining three days. The motivation behind the choice for this sequence of measurements is that these boundary conditions are not very informative at first, then become more informative: we expect to witness their effects on the evolution of the estimation of the heat loss coefficient.

Model

The test box is represented by a 2R2C model described by:

$$\begin{bmatrix} \dot{T}_e(t) \\ \dot{T}_i(t) \end{bmatrix} = \begin{bmatrix} -\frac{1}{R_1 C_1} & \frac{1}{R_2 C_1} \\ \frac{1}{R_2 C_2} & -\frac{1}{R_2 C_2} \end{bmatrix} \begin{bmatrix} T_e(t) \\ T_i(t) \end{bmatrix} + \begin{bmatrix} \frac{1}{R_1 C_1} & 0 \\ 0 & \frac{1}{C_2} \end{bmatrix} \begin{bmatrix} T_a(t) \\ q(t) \\ I_{sol}(t) \end{bmatrix} + w(t) \quad (1)$$

$$y(t) = \begin{bmatrix} 0 & 1 \end{bmatrix} \begin{bmatrix} T_e(t) \\ T_i(t) \end{bmatrix} + v(t) \quad (2)$$

where T_i , T_a and T_e are the indoor, ambient (outdoor) and envelope temperatures. The model has two states T_e (unobserved) and T_i (observed); q (W) is the indoor heating power; I_{sol} (W/m²) is the solar irradiance on a southern vertical plane; R_1 and R_2 (m².K/W) are two thermal resistances, C_1 and C_2 (J/K) are thermal capacities, and k_1 and k_2 (m²) are two solar

aperture coefficients, one for each state of the model. $\mathbf{w}(t)$ denotes a Wiener process that represents modelling errors with an incremental covariance \mathbf{Q}_c (Madsen and Holst, 1995), and $\mathbf{v}(t)$ is the measurement error of the indoor temperature, normally distributed white noise with zero mean and variance \mathbf{R}_c . Both are considered unknown and will be estimated along with the other static parameters of the model, which are all denoted by a single vector θ .

The stochastic model described by Eq. 1 and 2 must be discretized to specify its evolution between discrete time coordinates.

$$\begin{aligned} x_t &= F x_{t-1} + G u_t + w_t & (3) \\ y_t &= H x_t + v_t & (4) \end{aligned}$$

where \mathbf{x}_t denotes the vector of states at the time coordinate t , and \mathbf{y}_t denotes the observations. The reader is referred to (Madsen and Holst, 1995) and (Rouchier 2018) for more details regarding the discretization steps.

Given a state transition probability $p(x_t \vee \theta, x_{t-1}, u_t)$ (Eq. 3) and an observation probability $p(y_t \vee x_t)$ (Eq. 4), filtering produces $p(x_t \vee y_{1:t}, \theta)$, the probability distribution function of each state given measurements and parameter values, and the marginal likelihood function $L_y(\theta) = p(y_{1:T} \vee \theta)$. The Kalman filter algorithm is not described here for the sake of concision, but has been described by many authors including (Madsen and Holst, 1995; Rouchier 2018).

BAYESIAN PARAMETER ESTIMATION

The target of the on-line parameter estimation exercise is to assess the value of all static parameters of the model, at each time coordinate of the measurement period: the expected output is a sequence of posterior distributions $\{p(\theta \vee y_{1:t}), t \in 1 \dots T\}$, where T is the number of data points in the measurement period. This sequential estimation is performed by the SMC algorithm. For the sake of validation, the estimation has also been carried in a “traditional” off-line fashion with the Metropolis-Hastings algorithm. Both methods are described below.

Off-line estimation: Marginal Metropolis Hastings

The Marginal Metropolis Hastings (MMH) algorithm is part of the family of Markov Chain Monte Carlo (MCMC) methods. Given one batch of data $y_{1:T}$, a parameter prior $p(\theta)$ and a model specification (Eq. 3 and 4), the MMH algorithm returns a finite sequence of samples $\{\theta_n, n \in 1 \dots N\}$ approximating the posterior distribution $p(\theta \vee y_{1:T})$. Examples of applications to the calibration of building energy models include (Heo et al. 2012; Rouchier et al. 2018).

The algorithm employs a Kalman filter to compute the states $p(x_{1:T} \vee \theta, y_{1:T})$ and likelihood $L_y(\theta)$ associated to each proposal for θ . If the state-space model (Eq. 3) is non-linear, this filter can be replaced by a particle filter: this approach is known as Particle Markov Chain Monte Carlo (PMCMC).

On-line estimation: Sequential Monte Carlo

The SMC algorithm for parameter estimation is an adaptation of particle filtering for state variables. The foundation of this method is the Importance Sampling paradigm as described by (Cappé et al. 2007): simulating samples under an instrumental distribution and then approximating the target distributions by weighting these samples using appropriately defined importance weights. The reader is referred to (Cappé et al. 2007) and (Kantas et al. 2015) for a deeper explanation of SMC and its application to parameter estimation. The method used

here is inspired from the Iterated Batch Importance Sampling algorithm (Chopin 2002). It is described on Fig. 2.

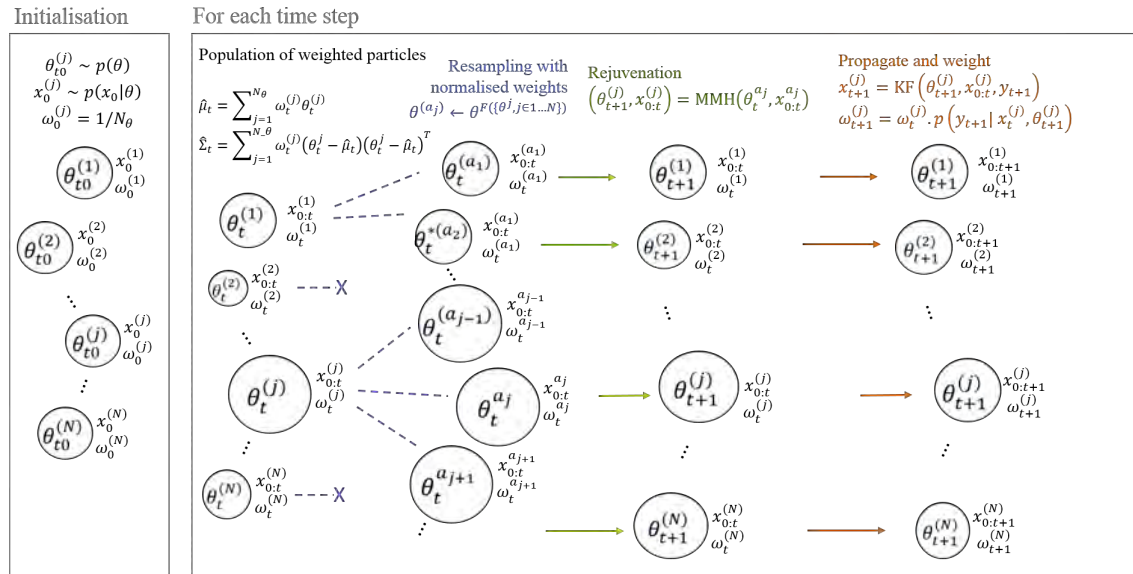


Figure 2. Principle of the Sequential Monte Carlo algorithm

The algorithm starts with the generation of a population of N_θ particles drawn from a prior distribution $p(\theta)$. Each parameter is assigned an initial state \mathbf{x}_0 and weight. At each time step t , a Kalman filter computes the states $x_t^{(j)}$ and likelihood $L_t^{(j)}$ associated to each particle $\theta_t^{(j)}$. By this operation, the population of particles is updated so that at each time t they are a properly weighted sample from $p(\theta \vee y_{1:t})$. After several time steps, there is a risk that only a few of the initial particles are significantly more likely than the others and concentrate most of the total weight: a resampling step is then performed to generate a new population of particles from the most influential ones, and a MCMC rejuvenation step then restores the diversity of particles (Murray 2013).

Resampling does not occur every time a new observation becomes available, but only when required: this is measured by the effective number of particles that significantly contribute to the total weight of all particles (Murray 2013). This operation decreases the number of unique particles, hence the subsequent MCMC rejuvenation step that restores diversity. The choice of the proposal distribution for the MCMC rejuvenation step was proposed by (Chopin 2002) and ensures a reasonable acceptance ratio while leaving $p(\theta \vee y_{1:t})$ invariant. The rejuvenation step makes the algorithm quite computationally expensive, since the total likelihood of all particles must be recalculated every time resampling occurs. This problem is mitigated by the fact that particles can be resampled independently, making this effort parallelizable.

RESULTS

The MMH and SMC algorithms were used to estimate the parameter vector θ , either off-line or on-line, using the batch of measurements shown on Fig. 1 from the RRTB test cell represented by a 2R2C model (Eq. 1). First, the sufficiency of the 2R2C model to recreate the indoor temperature time series in checked. This is ensured by the autocorrelation function of the residuals after parameter estimation shown on Fig. 3.

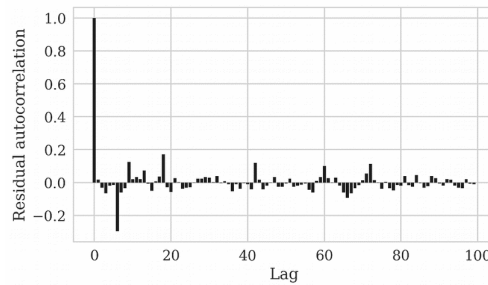


Figure 3. Autocorrelation of one-step prediction residuals

As pointed out by (Madsen and Holst, 1995), the low value of this function ensures that residuals are uncorrelated and thus are close to white noise, in accordance with the hypothesis is the model. This observation allows us to analyze the parameter estimation results. All estimation results from both MMH and SMC are assembled into Fig. 4.

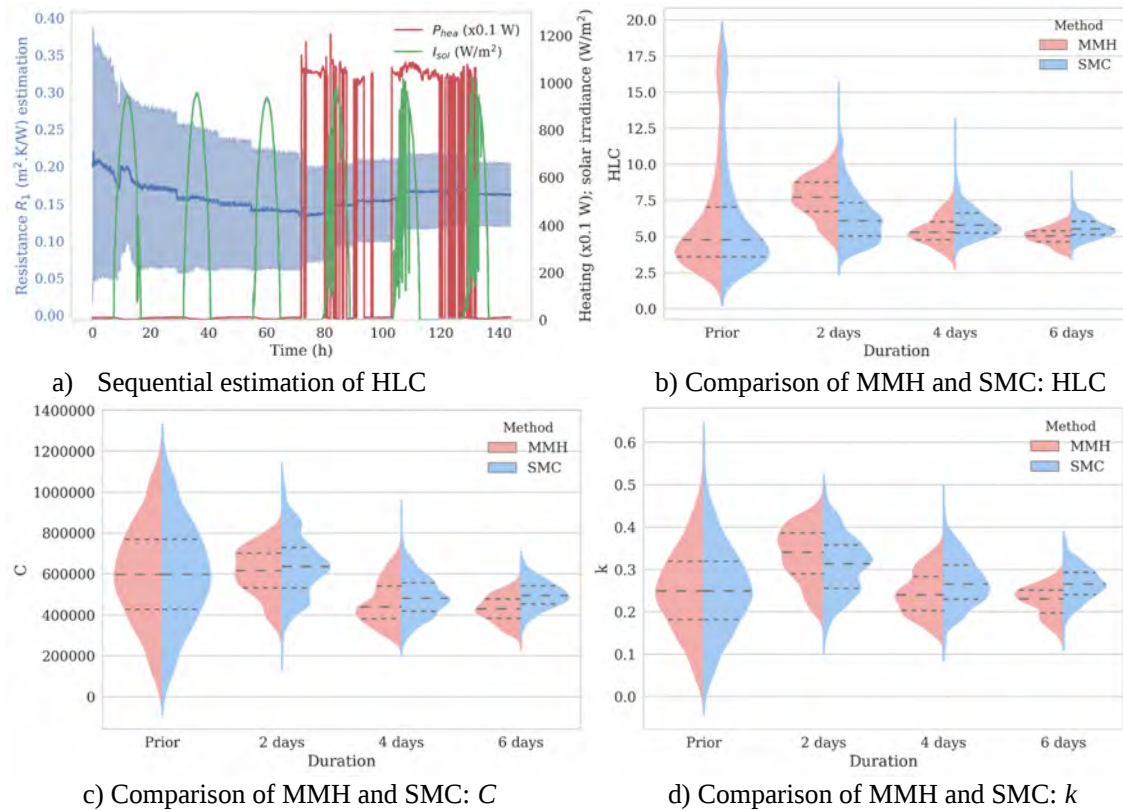


Figure 4. Parameter identification results

First, Fig. 4(a) shows the progression of the estimation of the parameter R_1 by SMC during the six days of measurements. The blue area denotes the mean and the 95% confidence region of R_1 at each time coordinate. The indoor heating power and solar irradiance are superimposed over it and allows the interpretation of the estimation. During the first three days of measurements, the value of R_1 can be seen to narrow down to a more confident estimation during the day, when the solar irradiance is positive. An important uncertainty however remains on this parameter. The heating is then turned on inside the test box, which causes the estimation to narrow down more abruptly. These results are consistent with the general knowledge that some indoor solicitations are necessary to make a building energy model identifiable. The originality of the present study is that we can observe the information brought to the parameter estimates in real time.

The performance of SMC is then compared to the MMH algorithm, which estimates parameters from a single batch of data at once. Fig. 4(a), 4(b) and 4(c) respectively show estimates of the heat loss coefficient $HLC=1/(R_1+R_2)$, the total heat capacity $C=C_1+C_2$ and the total solar aperture $k=k_1+k_2$. Each plot shows the prior distribution of these properties, and their estimation after 2 days, 4 days and 6 days of measurements. The MMH algorithm had to be run separately with each measurement length, while the SMC algorithm only had to run once to return all results. Starting from vague Gaussian prior distributions for each parameter, both methods resulted in mostly matching results.

CONCLUSION

The present study uses the Sequential Monte Carlo method to train a RC model, and thus estimate a Heat Loss Coefficient, and other parameters, sequentially. Results show the direct impact of solicitations (solar irradiance and indoor heat input) on this estimation, in real time. The method is validated by comparing its results with the Metropolis-Hastings algorithm for off-line estimation.

ACKNOWLEDGEMENTS

The author would like to thank the French National Research Agency (ANR) for funding this work through the BAYREB research project (ANR-15-CE22-0003).

REFERENCES

- Bauwens G., Roels S. 2014. Co-heating test: a state-of-the-art. *Energy and Buildings*, 82, 163-172
- Cappé O., Godsill S. and Moulines E. 2007. An overview of existing methods and recent advances in Sequential Monte Carlo. In: *Proceedings of the IEEE*, 95 (5), 899-924
- Chopin N. 2002. A sequential particle filter method for static models. *Biometrika*, 89, 539-552
- Doucet A., Godsill S. and Andrieu C. 2000. On sequential Monte Carlo sampling methods for Bayesian filtering. *Statistics and Computing*, 10(3), 197-208
- Handschin J.E. 1970. Monte Carlo techniques for prediction and filtering of non-linear stochastic processes. *Automatica*, 6(4), 555-563
- Heo Y., Choudhary R. and Augenbroe G.A. 2012. Calibration of building energy models for retrofit analysis under uncertainty. *Energy and Buildings*, 47, 550-560
- Jimenez M.J. et al. 2016. Report of subtask 3a: Thermal performance characterization based on full scale testing - description of the common exercises and physical guidelines. In: *IEA EBC Annex 58*
- Kantas N., Doucet A., Singh S.S., Maciejowski J. and Chopin N. 2015. On particle methods for parameter estimation in state-space models. *Statistical Science*, 30(3), 318-351
- Madsen H. and Holst J. 1995. Estimation of continuous-time models for the heat dynamics of a building. *Energy and Buildings*, 22, 67-79
- Murray, L. M. 2013. Bayesian state-space modelling on high-performance hardware using LibBi. *arXiv preprint arXiv:1306.3277*.
- Raillon L. and Ghiaus C. 2017 Sequential Monte-Carlo for states and parameter estimation in dynamic thermal models. In: *Proceedings of the Building Simulation 2017 conference*, San Francisco, USA
- Rouchier S. 2018. Solving inverse problems in building physics: an overview of guidelines for a careful and optimal use of data. *Energy and Buildings*, 166, 178-195
- Rouchier S., Rabouille M., Oberlé P. 2018. Calibration of simplified building energy models for parameter estimation and forecasting: stochastic versus deterministic modelling. *Building and Environment*, 134, 181-190

The co-heating test as a means to evaluate the efficiency of thermal retrofit measures applied on residential buildings

Evi Lambie^{1,2,*}, Marieline Senave^{1,2,3} and Dirk Saelens^{1,2}

¹KU Leuven, Department of Civil Engineering, Building Physics Section, Kasteelpark Arenberg 40 – box 2447, BE-3001 Heverlee, Belgium

²Energyville, Thorpark 8310, BE-3600 Genk, Belgium

³VITO NV, Boeretang 200, BE-2400 Mol, Belgium

*Corresponding email: Evi.Lambie@kuleuven.be

ABSTRACT

In order to reduce the energy use of residential buildings, regional governments in Belgium established, amongst others, mandatory criteria for the energy performance to be achieved after retrofitting. However, due to construction deficiencies, deviating boundary conditions, and non-modeled physical phenomena and interactions, the actual energy performance may differ significantly from theoretical design value. Several studies indicate this as the performance gap. This paper focuses on analyzing the actual impact of the refurbishment measures applied to a single-family home in Belgium. Hereto, in-situ measurements assessing the building envelope's thermal performance, described by the overall heat loss coefficient HLC [W/K], are performed both before and after the retrofit. To analyze this HLC, a quasi-steady state test, the so-called co-heating test, has been performed before and after renovation of a single-family home in Belgium, renovated to the nearly Zero Energy Building (nZEB) level.

As a result, the HLC determined with linear regression and an Auto-Regressive model with eXogenous inputs (ARX) show similar estimates, except for a smaller confidence interval for the ARX. Furthermore, it is shown that data set lengths shorter than 10 days are quite sensitive to sample times. For our case study, the gap between the theoretical and measured HLC enlarges after retrofit. Finally, the influence of a unheated neighboring zone on the HLC is assessed.

KEYWORDS

Heat loss coefficient – In-situ measurement – Renovation – Residential buildings – Regression techniques

INTRODUCTION

Since households have a 25 % share in the total energy use in Europe (Eurostat 2017), and a large share of the buildings has a poor energy performance (Cyx et.a al 2011), there is a high need to renovate existing buildings in order to increase energy savings. However, several studies indicate discrepancies between the theoretical and the actual energy use after renovation, a phenomena most-commonly known as the 'performance gap'. (Hens 2007 & Bell 2010)

This paper aims to assess the building envelope performance and identify the performance gap before and after retrofit by evaluating the overall heat loss coefficient (HLC) using a co-heating test (Bauwens 2015). Three aspects of the HLC estimation are evaluated for a single-family, terraced house. First, different sample times and data set lengths are evaluated for HLC estimation with linear regression and ARX models. Secondly, the performance gap of the pre-retrofit and post-retrofit dwelling state is assessed. Thirdly, the influence of the garage as a neighboring unheated room is evaluated for the post-retrofit HLC.

The methodology section consists of three parts: first the test case is described, then the heat loss coefficient is calculated from theory and finally the two data assessment models for HLC identification are presented. The results section discusses the HLCs and the performance gap.

METHODOLOGY

Test case

The case study is a terraced dwelling in Belgium, which has been renovated in the framework of the 'Ecoren'-project, one of the Flemish pilot projects for renovation. The characteristics of this dwelling before and after renovation are presented in Table 1. The table distinguishes between the situation with and without the garage enclosed in the protected volume, which enables to evaluate the garage's influence on the HLC, since the walls between the dwelling and its garage are uninsulated. As the attic floor was already insulated before renovation, the attic is assumed to be a neighboring unheated zone. The envelope renovation was realised by replacing the outer cavity leaf of the original uninsulated wall by a prefabricated building component. The air permeability and the air change rate at 50 Pa shown in Table 1 represent the resulting values of the blower door tests performed according to NBN EN 13829:2001.

Table 1. Characteristics of the dwelling case

	Pre-retrofit With garage	Pre-retrofit Without garage	Post-retrofit With garage	Post-retrofit Without garage
Protected volume [m ³]	467	408	467	408
Building envelope [m ²]	261	261	261	261
Air permeability at 50 Pa V_{50} [m ³ /(hm ²)]	18.11	9.03	24.49	21.63
Air change rate at 50 Pa n_{50} [1/h]	15.95	9.59	21.57	22.98

A quasi steady-state co-heating test, as elaborated by Bauwens (2015), was carried out on the last three dwelling scenarios in Table 1. The co-heating tests of the protected volume without garage enables to compare the HLC of the same volume before and after renovation, while the tests of the two different volumes of the post-retrofit state can be used to estimate the heat losses through the garage. Before renovation, the protected volume without garage was kept at a constant indoor temperature of 20 °C for a period of 34 days in January 2016. After renovation, in February 2018, the indoor set temperature was 22 °C. During the first 20 days the protected volume included the garage, and secondly for 14 days the garage was excluded from the protected volume by closing the door. During these co-heating tests, the heating power was monitored, together with the outdoor climate, and the indoor air temperatures (accuracy ± 0.4 °C) in all rooms of the protected volume and neighboring zones, i.e. the attic, the garage and the two neighboring dwellings. The mean indoor temperature of the tested volume, used to estimate the HLC, was calculated as the volume-weighted average temperature $T_{i,avg}$ of all rooms enclosed by the protected volume. Additionally, the heat flux in between the protected volume and neighboring zones was measured using Hukseflux HFP01 sensors (3 % accuracy).

Theoretical heat loss coefficient

The HLC, composed by ventilation heat losses H_v and transmission heat losses H_{tr} , is calculated using equation (3) based on the approach of Bauwens (2015):

$$HLC = H_v + H_{tr} \quad (3)$$

With $H_v = c_a \rho_a n_{actual} V_i$ & $H_{tr} = \sum_{j=1}^c U_j A_j$

First, for ventilation heat losses H_v the following parameters are used: specific heat capacity of air c_a ($\text{Jkg}^{-1}\text{K}^{-1}$), air density ρ_a (kg/m^3), actual air change rate per hour n_{actual} (1/h), and the net air volume V_i enclosed by the building envelope (m^3). The actual air change rate per hour is estimated by dividing the air change rate at 50 Pa by 20 (Kronvall 1978) or by a tracer gas test.

Second, H_{tr} is calculated using the thermal transmittance U ($\text{Wm}^{-2}\text{K}^{-1}$) and the surface area A (m^2) of all building envelope components. As the original U -values cannot be identified exactly, H_{tr} is defined as a range to incorporate uncertainties. Therefore, for the original dwelling the thermal resistances of the building components are based on the national standard NBN B 62-002 2008, while for the renovated state an accuracy band of $\pm 5\%$ was set to the designed H_{tr} -value. In these H_{tr} -calculations, an equivalent, increased thermal resistance is determined for the floor addressed to the unheated attic following the national standard. (NBN B 62-002 2008).

Table 2 shows the resulting HLC calculated with equation (3) and the intermediate results of the actual air change rates n_{actual} and the heat losses H_v and H_{tr} . First, for all dwelling states n_{actual} -values in Table 2 were calculated from the n_{50} -values divided by 20. Additionally a tracer gas test was carried out for the full protected volume of the renovated dwelling, which resulted in a n_{actual} -value of 0.31 using the decay regression method (Sherman 1990). This is about three times lower than the resulting value based on the n_{50} -value, which was 1.08 1/h (Table 2). Therefore, the ventilation heat losses H_v of the post-retrofit dwelling are given as a range, of which the minimum is based on the tracer gas test and the maximum is based on the n_{50} -values. Finally, the resulting values of the HLC indicate an influence of 26 % to 31 % of excluding the garage from the pre-retrofit dwelling and 6 % to 10 % for the post-retrofit dwelling.

Table 2. Theoretic overall heat loss coefficient and its components

	Pre-retrofit With garage	Pre-retrofit Without garage	Post-retrofit With garage	Post-retrofit Without garage
Actual air change rate n_{actual} [1/h]	0.80	0.48	1.08	1.15
Ventilation heat loss H_v [W/K]	83	41	32 – 112	32 – 99
Transmission heat loss H_t [W/K]	310 – 366	260 – 314	114 – 126	105 – 116
HLC [W/K]	393 – 449	301 – 355	146 – 238	137 – 215

Data assessment models

In this work, the HLC is estimated using both a linear regression model and an Auto-Regressive model with eXogenous inputs (ARX). Using linear regression, the HLC can be estimated from equation (1) as the regression parameter ω_i , following the recommendations of Bauwens (2015):

$$\phi_h^h - \phi_{tr}^n = \omega_i T_{i,avg} + \omega_e T_e + \omega_{sol} I_{sol} + \epsilon \quad (1)$$

with ϕ_h^h the heating power, ϕ_{tr}^n the heat losses towards the neighboring zones, T_i the volume-weighted average of the indoor temperature, T_e the outdoor temperature, I_{sol} the global horizontal solar radiation, ϵ the residuals and ω_x the estimated regression parameters. Note that the intercept of equation (1) is equal to zero. The heat losses ϕ_{tr}^n , calculated from the heat flux signals, depend on the two tested volumes. When the garage is included in the protected volume, ϕ_{tr}^n consists only of the heat losses towards the neighboring dwellings, else the heat losses towards the garage are also accounted for.

The research of Bauwens (2015) assessed that one disadvantage of the linear regression model is that it tends to underestimate the confidence interval, and that the result is often less robust.

The ARX model however, leads to a more reliable confidence interval. Therefore, the second model used is the ARX model, represented by a similar equation as the linear regression model:

$$\Phi(B) [\phi_h^h - \phi_{tr}^n] = \omega_i(B)T_{i,avg,j} + \omega_e(B)T_{e,j} + \omega_{sol}(B) I_{sol} + \epsilon_j \quad (2)$$

However, in this model backshift operators are applied to the inputs and output of the model ($\Phi(B), \omega_i(B), \omega_e(B), \omega_{sol}(B)$), each of them being a polynomial of a different order. (Madsen et al. 2015) The overall HLC is now estimated as $\frac{\omega_i(1)}{\Phi(1)}$. The order of each backshift operator is determined by backward elimination: a 12-order model is reduced eliminating insignificant high-order parameters stepwise.

Following the statistical guidelines from IEA EBC Annex 58 (Madsen et al. 2015), the models are validated performing different tests: (1) testing for white noise residuals by autocorrelation plots or cumulative periodograms, (2) testing for uncorrelated inputs by cross-correlation functions between the residuals and their inputs, but also in between the inputs (3) testing for high parameter significance, and (4) testing for similar results using different data subsets and sample times. This fourth test is quite important, since the results of both models might be varying for different data subsets and sample times. Since cross-correlations might be affected by autocorrelations, an ARIMA(1,1,0) model is used to pre-whiten the inputs. (Bauwens 2015)

RESULTS

HLC estimation using linear regression models

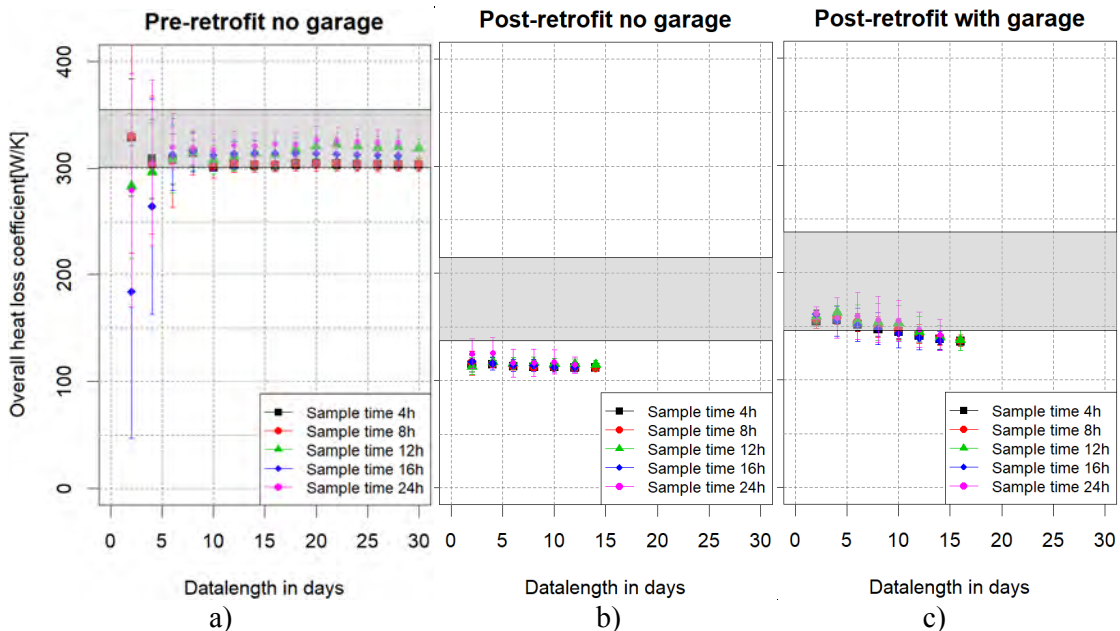


Figure 1. HLC estimated by linear regression a) pre-retrofit state without the garage enclosed in the tested volume, b) post-retrofit without garage, c) post-retrofit with garage.

Figure 1 shows the resulting overall heat loss coefficients and the related confidence intervals (2 times the standard deviation, 2σ), estimated by linear regression using different sample times and data set lengths. The grey band presents the theoretical HLC (Table 2). For the original dwelling (pre-retrofit Figure 1.a) the estimated overall heat loss coefficient (HLC_{estim}) in general

corresponds to the theoretical value (HLC_{theo}). The HLC_{estim} values for data set lengths of more than ten days are quite similar. The sample time, however, seems to influence the estimates: for small sample times (4h and 8h) HLC_{estim} is ca. 10 % lower than for large sample times (24 h). Validation plots in Figure 2.a and 2.b show that the estimates of larger sample times are more reliable, although these results are less robust (i.e. more susceptible to the input) since less data points are involved. Therefore, a 12h sample time was selected to compare the linear regression model to the ARX model (further in Table 3), being more reliable than short sample times and more robust than long sample times. (see Figure 2.c)

For the post-retrofit dwelling scenarios, the gap between HLC_{estim} and HLC_{theo} has increased: HLC_{estim} is now lower than HLC_{theo} , although this discrepancy diminishes if the garage is enclosed in the protected volume (Figure 1.b and 1.c). Next, compared to the pre-retrofit state, the influence of sample time has decreased: HLC_{estim} of the first post-retrofit state is quite constant for a dataset length of more than ten days. The results for the second post-retrofit state, however, are more scattered and also less reliable (Figure 1.d and 1.e).

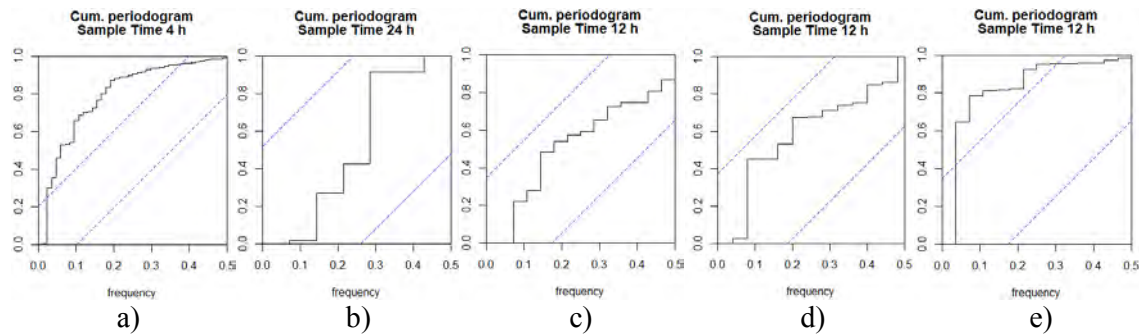


Figure 2. Validation plots of the linear regression model of a 14 day data set, first for the pre-retrofit dwelling scenario for a sample time of a) 4 h b) 24 h and c) 12 h, second for the post-retrofit dwelling scenario for a sample time of 12 h d) without garage and e) with garage

Performance analysis using different models

The dynamic ARX model was the second model from which the HLC was estimated. Since this model type can incorporate dynamic effects like the influence of solar radiation and thermal inertia of a building, the sample time can be reduced considerably. Out of four sample time models – 15, 30, 60 or 120 minutes – a 30 minute model was selected as the most reliable, based on the validation plots. The resulting HLC_{estim} for this model are compared to the theoretical values and the estimates of the linear regression model in Table 3. This table shows quite similar estimates of the HLC for both models, but with smaller confidence intervals for the ARX model.

Table 3. HLC values and confidence intervals ($\pm 2\sigma$) using the different models, for a 14 days dataset length. Linear regression: 12 hours sample time. ARX model: 30 minutes sample time.

Dwelling state	Theoretical	Linear regression	ARX
	HLC_{theo} [W/K]	HLC_{estim} [W/K]	HLC_{estim} [W/K]
Pre-retrofit no garage	301 ~ 335	313 ± 12.31	308 ± 6.68
Post-retrofit no garage	137 ~ 215	115 ± 4.61	115 ± 3.66
Post-retrofit with garage	146 ~ 238	139 ± 11.04	142 ± 10.21

As a result, table 3 shows a quite small performance gap for the pre-retrofit state, since HLC_{estim} is identified in the range of HLC_{theo} . Conversely, the HLC_{estim} -value for the first post-retrofit dwelling scenario deviates ca. 20 % from the theoretical lower boundary. However, the

discrepancy decreases for the second post-retrofit scenario to ca. 5 %, although here a larger confidence interval was found. Altogether, the measured HLC increases by 20 % if the garage is included in the protected volume, which is higher than the theoretical influence (10 %).

CONCLUSIONS

In this paper, the building envelope performance of a terraced single-family dwelling was assessed before and after renovation by means of the overall heat loss coefficient (HLC), identified from co-heating tests. First, for linear regression analysis, the estimated HLC is quite constant for a data set length of more than 10 days, although the pre-retrofit results are varying with about 10 % for different sample times. Using ARX models results in similar estimates albeit with a smaller confidence interval. Hence, a co-heating test of 10 days should suffice to estimate a quite reliable HLC of a dwelling. Second, the measured HLC corresponds quite well to the theoretical HLC for the original dwelling state, but deviates ca. 20 % for the post-retrofit dwelling state without garage. Third, the garage's influence on the HLC is theoretically lower (10 %) than was measured (20 %), indicating the need for further assessment on the influence of an unheated neighboring zone on a dwelling's HLC.

ACKNOWLEDGEMENT

This research has been conducted as part of the pilot project 'Ecoren', supported by 'Vlaams Agentschap innoveren en ondernemen' (VLAIO). It contributes to Annex 71 "Building energy performance assessment based on optimized in-situ measurements".

REFERENCES

- Bauwens G. 2015. In situ testing of a building's overall heat loss coefficient. Embedding quasi-stationary and dynamic tests in a building physical and statistical framework. *Ph.D. Thesis*, KU Leuven (Belgium), 194 pages
- Bell M., Wingfield J., Miles-Shenton D. and Seavers J. 2010 Low carbon housing. Lessons from Elm Tree Mews. Joseph Rowntree Foundation.
- Cyx W., Renders N., Van Holm M. and Verbeke S. 2011. IEE TABULA – Typology approach for building stock energy assessment. VITO scientific report.
- Eurostat - Statistics Explained. 2017. *Consumption of energy*. Consulted December 23 2017. http://ec.europa.eu/eurostat/statistics-explained/index.php/Consumption_of_energy
- Hens H., Janssens A., Depraetere W., Carmeliet J. and Lecompte J. 2007. Brick cavity walls: a performance analysis based on measurements and simulations. *Journal of Building Physics*, Vol. 31, No 2, pp. 95-124
- Hukseflux Thermal Sensors. 2018. *HFP01 Heat flux plate*. Consulted February 28 2018. https://www.hukseflux.com/product/hfp01?referrer=/product_group/heat-flux-sensors
- Kronvall J. 1978. Testing of houses for air leakage using a pressure method. *ASHRAE Transactions* 84(1): 72-9
- Madsen H., Bacher P., Bauwens G., Deconinck A., Reynders G., Roels S., Himpe E. and Lethé G. 2015. Thermal performance characterization using time series data - IEA EBC Annex 58 Guidelines. *Technical University of Denmark (DTU)*. (DTU Compute-Technical Report-2015; No. 8) 83 pages.
- NBN B 62-002. 2008. Belgian national standard. Thermal performance of buildings – Calculation of thermal transmittances of building components and building elements – Calculation of transmission and ventilation heat transfer coefficients.
- NBN EN 13829:2001. Belgian national standard. Thermal performance of buildings – Determination of air permeability of buildings – Fan pressurization method
- Sherman M. H. 1990. Tracer-Gas Techniques for Measuring Ventilation in a Single Zone. *Building and Environment*, Vol. 25, No. 4, pp. 365-374

The thermal resistance of retrofitted building components based on in-situ measurements

Evi Lambie^{1,2,*} and Dirk Saelens^{1,2}

¹KU Leuven, Department of Civil Engineering, Building Physics Section, Kasteelpark Arenberg 40 – box 2447, BE-3001 Heverlee, Belgium

² Energyville, Thorpark 8310, BE-3600 Genk, Belgium

*Corresponding email: Evi.Lambie@kuleuven.be

ABSTRACT

Buildings are responsible for a large share of the worldwide energy use. For new buildings very strict objectives for the energy performance of buildings are set. The main energy use however occurs in existing buildings emphasizing the need for renovation of the older building stock. In order to detect deviations from the theoretical performance, in-situ measurements of the envelope performance after renovation can give insight in the workmanship and issues with different renovation techniques. Therefore, the focus of this paper is to determine the thermal resistance of building components from in-situ measurements, before and after renovation.

Different methods were applied to examine the thermal resistance of the building components: the average method, linear regression, Anderlinds' method, ARX modelling (Auto-Regressive models with eXogenous inputs) and Grey Box Modelling. All of these methods seem to lead to similar results with only a small variation in confidence intervals, except for linear regression, which couldn't capture dynamic heat flows due to solar radiation.

For the assessed exterior walls, different phenomena influencing the thermal resistance were noted. The measured thermal resistance answers the estimated theoretical value of the building components quite well before renovation, but after renovation the difference is varying due to cavity air flows.

KEYWORDS

Thermal resistance – In-situ measurement – Renovation – Building components – Characterization techniques

INTRODUCTION

Being responsible for ca. 25 % of the total energy consumption (Eurostat 2017), the residential sector holds a large opportunity to increase energy savings. However, for each renovated dwelling, the resulting energy savings can deviate from the theoretically designed energy savings, amongst others because of poor workmanship for instance causing short circuiting of the insulation layers (Hens 2007 & Baker 2011). Several phenomena can be distinguished: wind-washing (air cavity flows due to wind pressure), rotational air flows (air flow loop around the cavity insulation), inside air washing (caused by air leaks in the interior cavity leaf), etc.

Therefore, the focus of this paper is to assess discrepancies between the actual and the designed renovated building envelope, by thermal resistance characterization based on in-situ measurements. Besides the most commonly used average method (EN ISO 9869-1:2014), four other characterization methods are compared. In the methodology section, first the case study and the performed measurement campaign are explained, followed by an overview of the used characterization methods. Subsequently, the estimated thermal resistances and the discrepancies with the theoretical values will be discussed both before and after renovation of the dwelling.

METHODOLOGY

Case study

The analysed case is part of the 'Ecoren' project, one of the Flemish VLAIO renovation pilot projects. It concerns a terraced house that is chosen from a block of four single-family dwellings, originally constructed in 1975 and renovated in 2017.

Table 1 shows the theoretical thermal resistances of the exterior walls, calculated following the national standard (NBN B 62-002 2008). The wall before renovation is an uninsulated wall that consists of an outer leaf made out of bricks, an air cavity of which it is unknown whether it has a (partly) ventilated air cavity or not and an inner brick leaf finished with a gypsum layer. During renovation, the outer brick layer was replaced by an insulated prefabricated element, constructed of a timber frame construction. For both dwelling states, the thermal resistance is shown for non-ventilated and ventilated walls: The thermal resistance of the original ventilated cavity wall is calculated as the thermal resistance of only the inner cavity leaf and its finishing (NBN EN ISO 6946:2007), while the thermal resistance of the renovated structure is decreased by 50 %, based on findings of Maroy (2017) and Deconinck (2016).

Table 1. Range of theoretical thermal resistance of the exterior wall of the case study before and after renovation

	Before renovation			After renovation		
	λ (W/mK)	d (m)	R (m ² K/W)	λ (W/mK)	d (m)	R (m ² K/W)
Outer cavity leaf	0.61 - 1.24	0.09	0.07 - 0.15	0.053	0.21	3.87
Non-ventilated air cavity		0.05	0.18		0.03	0.18
Inner cavity leaf	0.30 - 0.64	0.14	0.22 - 0.47	0.30 - 0.64	0.14	0.22 - 0.47
Gypsum layer	0.52	0.01	0.02	0.52	0.01	0.02
$R_{\text{non-ventilated}}$ (m ² K/W)			0.49 - 0.81			4.29 - 4.54
$R_{\text{ventilated}}$ (m ² K/W)			0.24 - 0.49			2.15 - 2.27

Measurement campaign

Several in-situ measurements are carried out on the dwelling. First, the air permeability of the dwelling in both states was measured using a blower door test (NBN EN 13829:2000), and an infrared scan was performed. Second, the heat flow meter method was carried out, for which the surface temperatures at both sides of the building component and the heat flux through the component must be measured (EN ISO 9869-1:2014). The surface temperatures are measured with thermocouples, having an accuracy of ± 0.50 °C, which corresponds with ± 7 % for a mean temperature difference of 15 °C. The Hukseflux HFP01 sensors, used to measure the heat flux, have an accuracy of ± 3 %, and are attached with silicone as recommended by the manufacturer (Hukseflux Thermal Sensors 2018). Hence, the overall measurement accuracy is ± 10 %.

The heat flow meter method was performed before and after renovation of the dwelling. As this method is a local assessment, multiple locations of the exterior wall were carefully chosen, aiming to minimize the influence of thermal bridges. Before renovation, two exterior façade locations were monitored, namely the back and the front façade of the dwelling. Subsequently, after renovation, four locations were monitored: the back façade at the ground floor and first floor, and the front façade at the first floor at two locations. Since the dwelling was uninhabited, a constant indoor temperature could be maintained, which is preferable since the research of Deconinck (2016) showed that a free-floating indoor temperature complicates the thermal resistance estimation. The measurement campaigns are summarized in Table 2, with T_{int} the interior set temperature, T_{ext} the outdoor temperature and I_{sol} the global horizontal irradiation,

of which first the variation during daytime is given in W/m² and second the hours in % for which I_{sol} exceeds 100 W/m².

Table 2. Measurement campaign boundary conditions

Campaign	Period	Duration	T _{int} °C	T _{ext} °C	I _{sol} W/m ²	I _{sol} % hours
Before renovation	05/Jan/2016 - 09/Feb/2016	35 days	20	Min. -7.67	Min. 0.42	11.2 %
				Mean 5.84	Mean 85.84	
				Max. 16.22	Max. 405.4	
After renovation	07/Feb/2018 - 22/Feb/2018	15 days	22	Min. -6.62	Min. 0.45	26.3 %
				Mean 1.85	Mean 164.5	
				Max. 10.4	Max. 486.5	

Data assessment models

Consecutively, five data processing models are applied to estimate the thermal resistance: two semi-stationary models, i.e. the average method and linear regression, and three dynamic models, i.e. Anderlind's regression, ARX modelling (Auto-Regressive models with eXogenous inputs) and Grey Box Modelling (GB modelling). Semi-stationary models are quite easy to use, but they rely on steady state boundary conditions, which are never encountered on site. The dynamic models, on the other hand, capture dynamic building behavior more accurately, although they are more complex in usage. (Madsen et al 2015 & Deconinck 2016)

First, the average method assumes that the thermal resistance R can be calculated by dividing the mean temperature difference by the mean heat flux q over a period of time n. This method results in a single value (equation (1)), without further knowledge of the reliability of the estimated value. The second semi-stationary model is simple linear regression, for which the estimated slope is the inverse of the thermal resistance (equation (2)).

$$R = \frac{\sum_{j=1}^n (T_{si,j} - T_{se,j})}{\sum_{j=1}^n q_j} \quad (1)$$

$$q_j = \frac{1}{R} (T_{si,j} - T_{se,j}) + \epsilon_j \quad (2)$$

The first dynamic model is the Anderlind's regression method, which assumes that the heat flux q at given time j is a function of the temperature difference over the building component, but also of the interior and exterior surface temperature changes in the past. A 24-hour time lag is applied here, following the recommendations of Deconinck (2016), leading to equation (3):

$$q_j = \frac{1}{R} (T_{si,j} - T_{se,j}) + \sum_{l=j-p}^{j-1} A_l (T_{si,l+1} - T_{si,l}) + \sum_{l=j-p}^{k-1} B_l (T_{se,l+1} - T_{se,l}) \quad (3)$$

For the ARX model, a backshift operator B is applied to the input and output, using the polynomials of which the order (n_q, n_i and n_e) indicates how many data points from the past are taken into account (equation (4.1)). For this model type, the thermal resistance is calculated using minimum variance weighting of the first-order polynomials (equation (4.2)).

$$\begin{cases} Q(B)q_j = \omega_{si}(B)T_{si,j} + \omega_{se}(B)T_{se,j} + \epsilon_j & (4.1) \\ \frac{1}{R} = \lambda \frac{\omega_{si}(1)}{Q(1)} - (1 - \lambda) \frac{\omega_{se}(1)}{Q(1)} & (4.2) \end{cases}$$

The used Grey Box model belongs to the class of stochastic state space models, existing of a system equation (5.1) and a measurement equation (5.2), with C the thermal capacitance. Since

in this paper a one order model is used, there is only one system equation. For this model, the total thermal resistance of the component is the sum of R_1 and R_2 .

$$\begin{cases} dT_1 = \frac{1}{c_1 R_1} (T_{si} - T_1) dt + \frac{1}{c_1 R_2} (T_{se} - T_1) dt + \sigma_i d\omega_i & (5.1) \\ Q_{hfm,j} = \frac{1}{R_1} (T_{si} - T_1) + \epsilon & (5.2) \end{cases}$$

All five characterization methods are applied to the collected data, which was averaged to hourly data sets. The models were validated by two major checks, following the guidelines of Annex 58 (Madsen et al 2015): (1) the parameters and related model orders were selected on their significance (p-value) and (2) the residuals were tested to be white noise by plotting the AutoCorrelation Function (ACF), the QQ plot and the time series plot of the residuals.

RESULTS

Air tightness of the renovated dwelling

As a result of the blower door test of the dwelling, air permeability at 50 Pa was identified to be $18.11 \text{ m}^3/(\text{hm}^2)$ before renovation, and $24.49 \text{ m}^3/(\text{hm}^2)$ after renovation. Hence, the air tightness is decreased, indicating the presence of air leaks. In addition, the infrared scan also visualized air leaks after renovation. Figure 1.a) shows low interior temperatures at the bottom of the back façade, caused by cold air infiltrating the cavity from the outside at the bottom of the prefabricated element. Figure 1.b) shows high temperatures at the top of the back façade, indicating rising warm air that infiltrated the cavity from the inside.

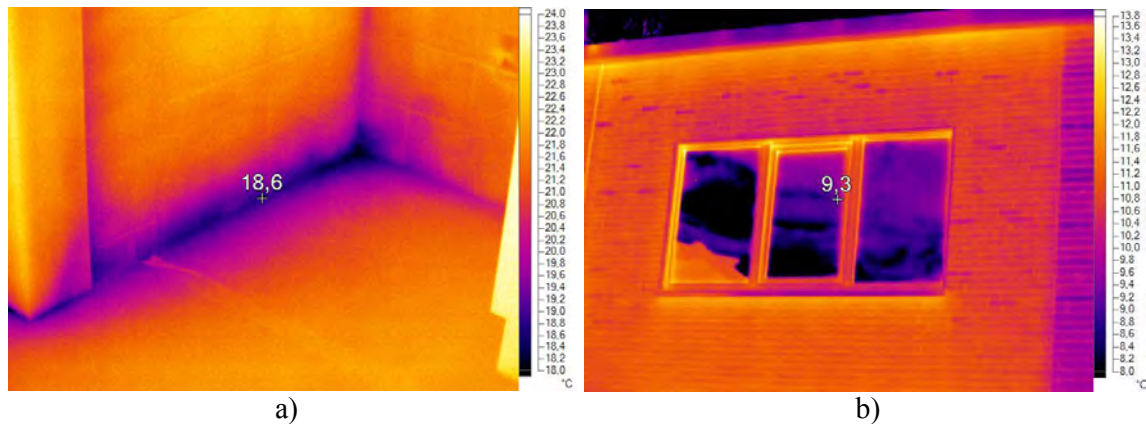


Figure 1. Infrared scan of the renovated dwelling. a) Inside view: Cold air infiltration at the bottom of the back façade b) Outside view: Warm air exfiltration at the top of the back façade

Thermal resistance estimation

The thermal resistances estimated by the five prediction models with usage of the complete dataset are shown in Figure 2; Note the different vertical scales for Figure 2.a and 2.b. First, Figure 2.a) shows that the calculated thermal resistances correspond to the unventilated reference value for the original façades. For both façades, the results of the five different models differ by maximum 5 % which is within each other's confidence interval. Comparing front and back, it is observed that the thermal resistance of the front façade is about 10 % higher than for the back façade. This may be caused by solar radiation, as the front façade is southeast oriented and thus influenced by solar radiation. However, linear regression of both night-time and daily-averaged values resulted in similar results, so different air cavity behavior is more plausible. Still, it can also be a measurement error, since the accuracy is about 10 %.

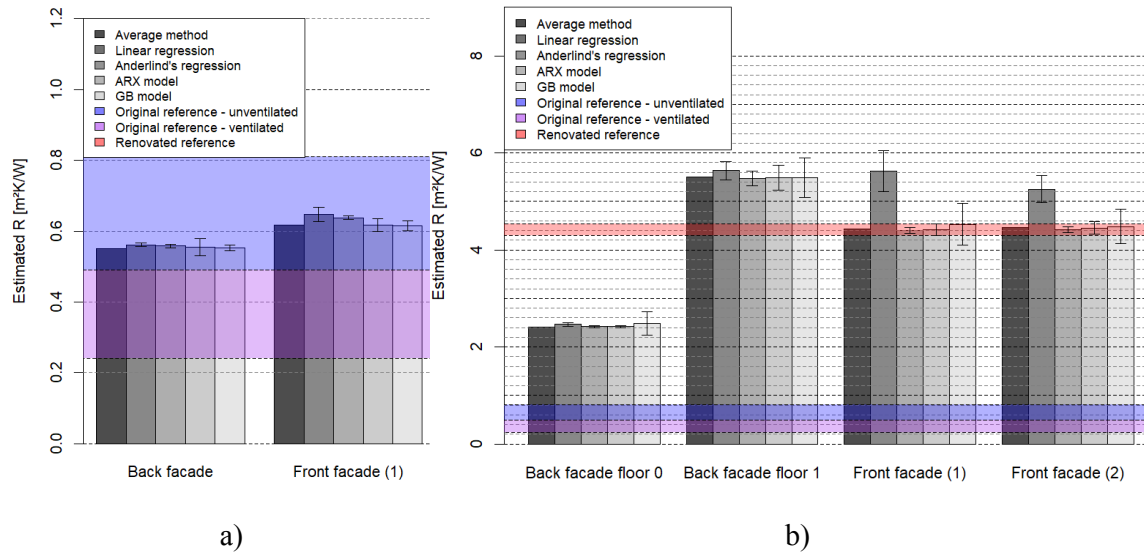


Figure 2. Estimated thermal resistances using the five analysis methods of (a) the original terraced dwelling (b) the renovated terraced dwelling. Note the different vertical scale.

Subsequently, Figure 2.b) shows the results for the renovated dwelling. Firstly, it can be noted that both measured resistances of the back façade do not correspond to the reference value. The measured thermal resistance on the ground floor is only 50 % of the reference value here, while on the first floor the result is about 20 % higher than the reference value. These findings can be explained by the influence of the air leaks shown in Figure 1, causing natural convection. As Lecompte (1989) and Maroy (2017) assessed in their numerical analysis of cavity walls, the measured thermal resistance of a building component will be lower if air infiltration from the outside decreases the temperature in the cavity. Hence, the temperature difference increases and the thermal resistance will decrease (see equation (2)). Inversely, at the top, air cavity temperature will increase due to interior air leaks, resulting in a higher thermal resistance.

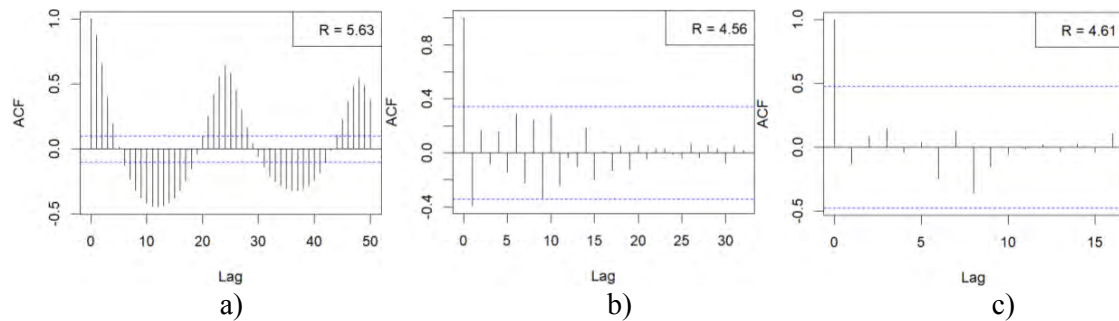


Figure 3. AutoCorrelation Function (ACF) of the linear regression for the renovated state of the front façade (1) with a) 1 hour sample time b) 12 hour sample time and c) 24 hour sample time

A second observation from Figure 2.b) is that the five models result in similar values for the back façade, while linear regression is an outlier for the front façade. Since linear regression is a semi-stationary model, here applied to a one hour data set, the model fails to capture the dynamic heat flows through the wall due to solar radiation. (Deconinck 2016) However, linear regression with an increased sample time estimates a thermal resistance similar to the results of

the other models. Hence, if the sample time of the data set is increased, the linear regression model is more reliable, as can be observed in the ACF-plots of the residuals in Figure 3, because now the dynamics are averaged out. This also explains why the average method estimates a similar thermal resistance as the dynamic methods, as the dynamic effects are also averaged out for this model. Still, this method does not give any information on the reliability of the estimate.

CONCLUSIONS

First of all, quite similar thermal resistances of the exterior façades were estimated by five characterization methods, besides a varying confidence interval size. Only the linear regression model failed to capture dynamic building behaviour for a 1 hour data set. Hence, longer sample times should be used here. Secondly, only one of the two exterior facades of the renovated dwelling corresponded to the reference value, despite the fact that the same renovation measure was performed. Discrepancies were caused by different cavity behaviour and the air leaks.

ACKNOWLEDGEMENT

This research has been conducted as part of the pilot project ‘Ecoren’, supported by ‘Vlaams Agentschap innoveren en ondernemen’ (VLAIO). It contributes to Annex 71 “Building energy performance assessment based on optimized in-situ measurements”.

REFERENCES

- Baker P. 2011. U-values and traditional buildings. In-situ measurements and their comparisons to calculated values. Glasgow Caledonian University.
- Deconinck A. 2016. Reliable thermal resistance estimation of building components from on-site measurements. *Ph.D. Thesis*, KU Leuven (Belgium), 215 pages
- EN ISO 9869-1:2014. European international Standard. Thermal insulation – Building elements – In-situ measurement of thermal resistance and thermal transmittance – Part 1: Heat flow meter method.
- Eurostat - Statistics Explained. 2017. *Consumption of energy*. http://ec.europa.eu/eurostat/statistics-explained/index.php/Consumption_of_energy
- Hens H., Janssens A., Depreterre W., Carmeliet J. and Lecompte J. 2007. Brick cavity walls: a performance analysis based on measurements and simulations. *Journal of Building Physics*, Vol. 31, No 2, pp. 95-124
- Hukseflux Thermal Sensors. 2018. *HFP01 Heat flux plate*. https://www.hukseflux.com/product/hfp01?referrer=/product_group/heat-flux-sensors consulted February 28 2018.
- Lecompte J. 1989. De invloed van natuurlijke convectie op de thermische kwaliteit van geïsoleerde spouwconstructies. *Ph.D. Thesis*, KU Leuven (Belgium), 206 pages (in Dutch)
- Madsen H., Bacher P., Bauwens G., Deconinck A., Reynders G., Roels S., Himpe E. and Lethé G. 2015. Thermal performance characterization using time series data - IEA EBC Annex 58 Guidelines. *Technical University of Denmark (DTU)*. (DTU Compute-Technical Report-2015; No. 8) 83 pages.
- Maroy K., Steeman M., Van Den Bossche N. 2017. Air flows between prefabricated insulation modules and the existing façade: a numerical analysis of the adaptation layer. *Nordic Symposium on Building Physics 11-14 June 2017, Trondheim, Norway. Energy Procedia*, 132 (2017), pp.885-890
- NBN B 62-002. 2008. Belgian national standard. Thermal performance of buildings – Calculation of thermal transmittances of building components and building elements – Calculation of transmission and ventilation heat transfer coefficients.
- NBN EN ISO 6946:2007. Belgian national standard. Building components and building elements – Thermal resistance and thermal transmittance – Calculation method.

Wireless Sensor System for Intelligent Facades

Ayman Bishara and Helge Kramberger^{1,*}, Andreas Weder and Marcus Pietzsch²

¹Dr. Robert-Murjahn-Institute (RMI), Ober-Ramstadt, Germany

²Fraunhofer Institute (IPMS), Dresden, Germany

*Corresponding email: ayman.bishara@dr-rmi.de

ABSTRACT

The integration of a wireless-transponder system into building components (“intelligent building materials”) with built-in relative humidity and temperature sensors (RH, T) allows for a cost-efficient and non-destructive measurement of data regarding the current hygro-thermal conditions of a building. Even during long-term use, quality assurance of the building system can be achieved by “looking into” the component. This supports the sustainability of the building from both a technical and an ecological point of view. In this paper, the development, the functionality and the exemplary application of Radio Frequency (RF), as well as an hygro-thermal analysis for solving the challenges of building-climatology planning is presented. Built on the measurement data of a real case study, the results of hygrothermal simulation tools are confirmed. Based on this, the use of thermal insulation in buildings for energy saving has been verified and the implementation into a hygrothermal simulation tool is shown. For the verification of results, a case study in Berlin was chosen, in which interior and exterior temperature and relative humidity values were recorded. Even with the peculiarity of irregular user behaviour of the building, good accordance between measured and calculated values could be achieved. Based on the analysis and evaluation of measurement data, as well as the implementation of hygrothermal simulations, the presented study provides a guideline for planning of ETICS with particular respect to extremely climate conditions.

KEYWORDS

hygrothermal, ETICS, intelligent façade, ultra-low power sensor system, wireless sensor node

INTRODUCTION

External thermal insulation composite systems (ETICS) on energy efficient façades are widely used under cold and hot climate conditions. However, the construction in both cases should be investigated in order to ensure avoidance of moisture damage. By an integration of wireless transponders into the installed insulation systems, it is possible to obtain information about the hygrothermal (temperature and relative humidity) condition of the system. In the case of critical measured values, concrete measures for the avoidance of damage (e.g. condensation within the construction, mold growth, algae) can be developed and implemented timely. In addition, the measured data can be compared with the results obtained from hygrothermal simulation tools that are used for verification and calibration of the data for further hygrothermal planning tasks. The wireless technology used here is a new transponder system with integrated humidity and temperature sensors. This system has been developed in order to check the material conditions in components such as exterior walls, ceilings or roofs, and to evaluate their structural-physical quality during the construction process. It allows for a non-destructive measurement data acquisition (cost effective, minimal effort) and an early detection of hygrothermally critical points within an insulated building structure, and thus contributes significantly to the prevention of structural damage. Traditional wired systems are cost intensive and always come with a high on-site installation effort (see figure 1). Moreover,

extra imperfections (thermal bridges) are introduced into the construction due to the wiring of the sensor and can bias the result. In addition, wired system could be installed only if power connection is available in situ. Wireless system can be installed also in inaccessible places.



Figure 1 a) Traditional wired sensor system, b) Wireless sensor system in the adhesive layer

WIRELESS SENSOR SYSTEM

The main challenge for long-term monitoring systems is to provide energy for the operation for a long period of time. Traditionally, batteries are used to provide the energy for such a system. For the mentioned application of intelligent facades, size does matter: only small and low height electronic systems can be embedded into the facade in a simple way. This means that the energy supply cannot be enlarged indefinitely - only coin cell batteries can be used. This results in additional technical challenges, such as limited maximum discharge currents and self-discharges. These challenges have to be addressed when designing the wireless sensor system. The system is sourced from a pair of low leakage lithium manganese dioxide coin cells. Since it is difficult to change the batteries, the main focus of development of such a sensor system is the energy optimization of the whole system. This starts with the component selection, the hardware design, goes over to specific energy management and sleep strategies and optimized filter algorithms, and ends with an energy enhanced wireless protocol.

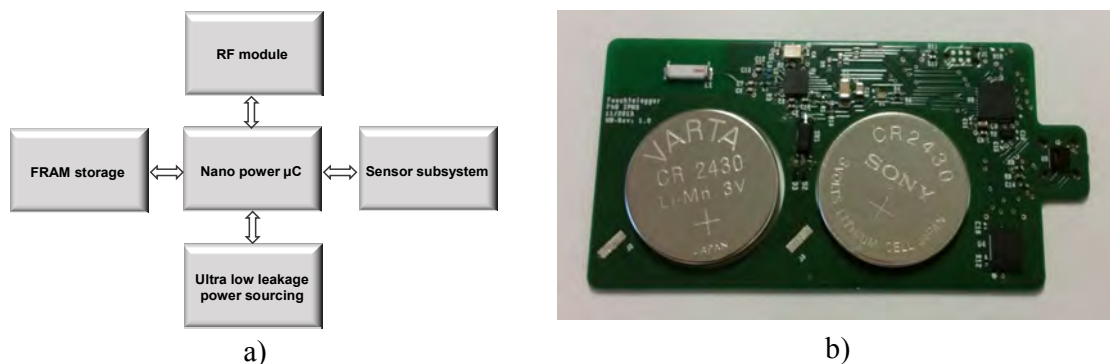


Figure 2. a) Block diagram of the wireless sensor system, b) Wireless node of the system.

Figure 2 (a) shows the block diagram of the wireless sensor node hardware. To enable the intended operation duration of more than 3 years, the system uses two ferroelectric-random-access-memory blocks (FRAM). One of these blocks holds the program execution context for the microcontroller. This enables the implementation of a programming model, utilizing an ultra-deep sleep mode without active RAM retention while significantly reducing the system

boot time and thus the energy consumption. The second memory block is for long-time storage of the recorded data, which is stored in a proprietary format. By choosing a FRAM technology, a non-volatile random access memory alternative to flash memory, the required energy for data storage is reduced by more than one order of magnitude, still guaranteeing the data retention for more than a decade and reducing the write/read times, which in turn reduces the energy consumption (Fujitsu, 2013). Figure 2(b) shows the final sensor node hardware before encapsulation. For wireless sensor systems, it is typical that the actual wireless transmission consumes the most energy in the system (Heinzelmann, 2000). Therefore, the design and optimization of the radio frequency sub-system is essential, and results in a large benefit for the operational time of the sensor system. For the described sensor system, a 2.4 GHz ultra-low power transceiver circuit has been selected. This circuit enables the design and implementation of custom wireless transmission protocols. The energy consumption of the transmitter circuit has been measured. Based on the measurements, an energetic model has been derived. Using this model, an energy optimized proprietary wireless communication protocol has been implemented. The protocol uses a net data rate of 2 Mbit/s with an automatic acknowledgement (ACK) packet generation and automatic retransmission of lost RF frames to ensure reliable wireless data transmission. The range has been limited to around 10 meters in indoor environments to reduce the energy consumption of the RF transmission. The sensor hardware uses an integrated humidity and temperature sensor circuit, which is connected to the microcontroller unit via the Inter Integrated Circuit (I²C) bus (NXP, 2014), a standard bus to connect peripheral ICs to microcontrollers. The sensor itself is factory calibrated. The accuracy of the sensor system has been evaluated using several experiments in a climatic chamber and with long term measurements. At the time of writing, this evaluation test has run for 30 months, and will be continued until the battery stops supplying power. The measurement of the battery voltage does not show any sign of wear-out for the near future.

APPLICATIONS OF WIRELESS TECHNOLOGY IN BUILDING CONSTRUCTION

Digitization of building materials and components, by means of the above described innovative transponder system with integrated temperature and humidity sensors (e.g. insulation board, façade elements) is important to carry out non-destructive monitoring of components for further physical investigations of the buildings, and thus preventing structural damage. For this purpose, a digital temperature and relative humidity sensor, embedded in a wireless-transponder, is installed in a wall structure. SHT21 sensor was chosen for the case study described below. It provides calibrated, linearized sensor signals in digital format. It contains a capacitive type humidity sensor, a band gap temperature sensor and specialized analog and digital integrated circuits. This yields an unmatched sensor performance in terms of accuracy and stability as well as minimal power consumption. Every sensor is individually calibrated and tested. Also the resolution of SHT21 can be changed on command from 8/12bit (0,7/0,04%) up to 12/14bit (0,04/0,1°C) for RH/T. Accuracy tolerance are $\pm 2\%$, $\pm 0,03^\circ\text{C}$, hysteresis is $\pm 1\%$, and operation range are 0% to 100%, -40°C to 125°C (Sensirion, 2014).

APPLICATION OF WIRELESS SENSOR SYSTEM IN A CASE STUDY IN BERLIN

With the goal of investigating the functionality of different ETICS by the use of a wireless measurement system and hygrothermal simulation tools, a case study in Berlin (Maerkische Scholle) was chosen. Five multi-story residential buildings are located in the same street, identical in terms of general dimensions, area, function, construction and direction. They were insulated with different insulation materials (EPS, hemp, wood fibre and mineral wool), and equipped with the newly developed measuring system as follows: Two measuring points were set up in each test house, points A and B (northeast façade, southwest facade). Each measuring point contains 3 sensors (RH, T), resulting in a total of 60 sensors. The reading out

of the sensor systems takes place via a read-out station with a reading distance of 10 meter (see figure 3). The temperature and relative humidity are recorded within the construction, as well as inside and outside. This examines the moisture absorption of the plaster and the change of the insulating effect of the five ETICS under changing daily and seasonal conditions, with regard to their protective effect against summer heat, winter cold and rain.

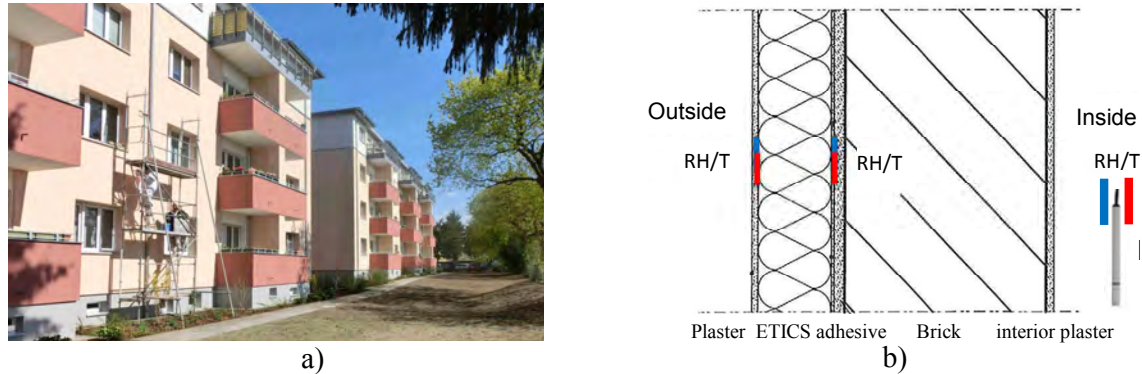


Figure 3. a) The case study in Berlin, b) location of the RH/T Sensors in the building

MEASUREMENT RESULTS AND HYGROTHERMAL ASSESSMENT

In addition to the functionality of ETICS for reducing energy consumption, the hygrothermal situation and the indoor air quality should be examined for damage-free construction. For a hygrothermal performance assessment of the walls, the temperature and humidity measurements, recorded by above described innovative wireless sensors, were evaluated for buildings 1 to 5 at both sides of the insulation boards as well as indoors in each measurement section. The measurements of the test houses are shown in the sample below. Figure 4 (a) presents the measured temperature and relative humidity on hemp (measurements started October 17, 2016) under the plaster level as well as in the adhesive layer (between insulation and solid wall). At the beginning, the moisture in the adhesive layer is relatively high, which can be related to residual construction moisture, in addition to the fact that the apartment was not inhabited until mid-December. After that, the humidity drops significantly, remaining between 40 and 50% from December until the end of April, and raising to about 60% starting in May. The moisture under the plaster layer, in contrast to the moisture in the adhesive layer, rises significantly in winter and reaches the max. value of 100%, then beginning to decrease in March. The hemp moisture is also evaluated here according to the data-sheet of Scientific-Technical Association for Building Preservation (WTA). It defines a limit curve for the relation of temperature and relative humidity in the wood-pore to keep wood non-destructive (WTA 2002). For the evaluation the daily average values of temperature and humidity were used. Only in two days, at the beginning of the measurement, the hemp moisture slightly exceeded the limit; this is normal, because the flat was not heated and the building moisture had not dried out yet (see figure 4 (b)). Figure 5 shows the temperature profile on both sides of the hemp as well as of the mineral wool for comparison. We see that both systems keep the room-temperature relatively constant in summer as well as in winter. More precisely, the temperature on the inner side of the mineral wool is about 2 K higher than that on the inner side of hemp or wood fibre mainly in the summer. Hemp reacts slowly to the outside temperature, compared to mineral wool. It has a temperature time shift of about 4-6 hours. This is due to the high heat storage capacity of hemp and wood fibre, and provides also a positive feature for the summer heat protection. The temperature time-shift between that of hemp und that of mineral wool can be seen clearly in figure 5 (b), which presents the temperature curves on both sides of insulation board during a 3- days period in a bigger scale.

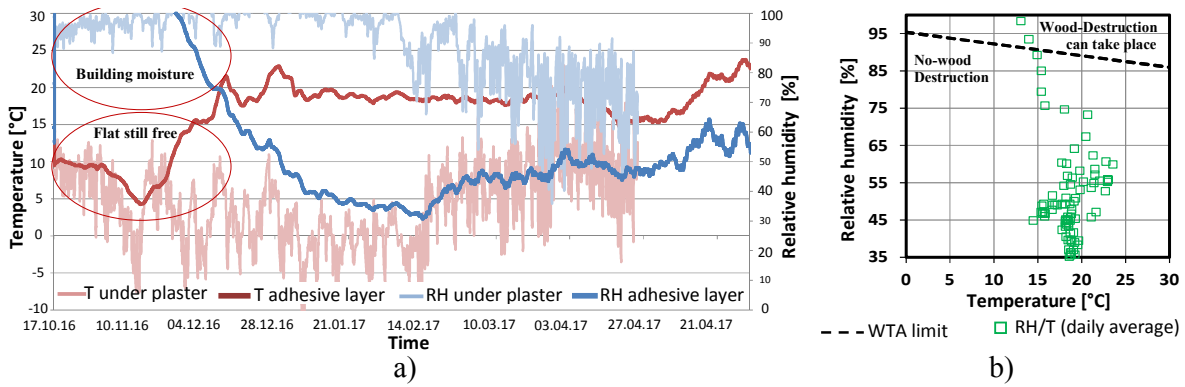


Figure 4. a) Measured RH/T on both sides of hemp, b) Evaluation of hemp RH/T by WTA

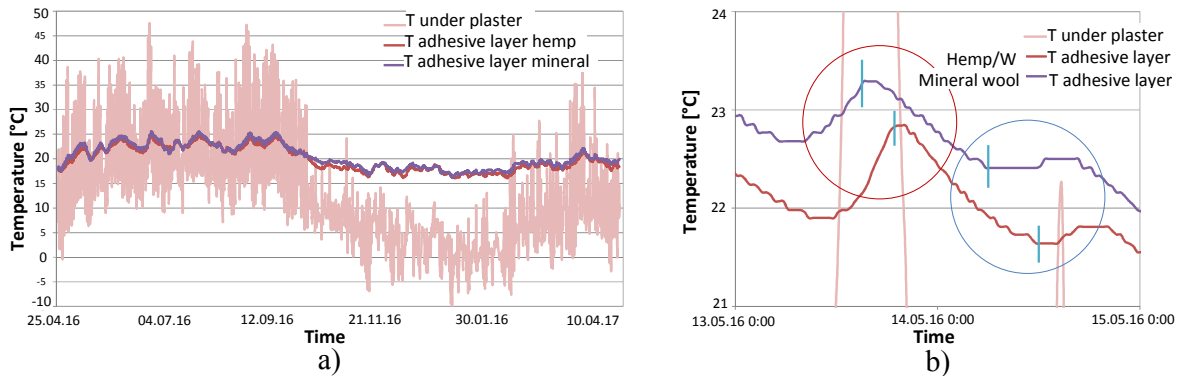


Figure 5. a) Measured temperature on both sides of the wood fibre, hemp and mineral wool, b) The same measurements in bigger scale during a period of three days

The conditions for mold growth on the inner wall surface depending on the indoor climate are also evaluated according to ISO 15026/13788 in all five buildings with four different ETICS. Here the daily average of absolute indoor humidity is assessed (calculated as a function of measured indoor relative humidity and temperature). Figure 6 shows the evaluations of buildings insulated with hemp (a) and with mineral wool (b) in comparison. All values of the building insulated with hemp are below the limit for normal occupancy (conditions for mold growth not given). For the building insulated with mineral wool few values exceed the limit for normal occupancy, and in about 7- days the values exceed even the limit for high occupancy.

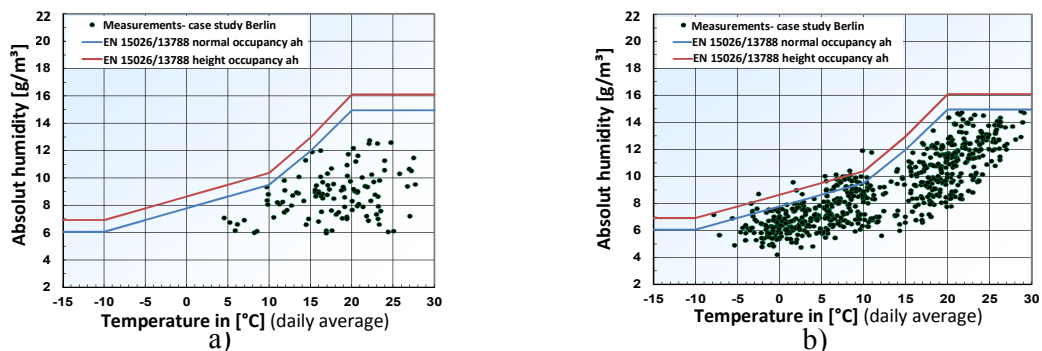


Figure 6. a) Relationship between outdoor air temperature and indoor absolute humidity for the building insulated with hemp, b) the same for the building insulated with mineral wool

COMPARISON OF THE MEASUREMENT AND SIMULATION RESULTS

For the comparison of the measurement and simulation results the hygrothermal model WUFI® is used (WUFI-Manual, 2015). For the calculation, the real outdoor climate conditions of Berlin and a constant indoor climate (20°C, 50%) according to ASHRAE 160 as well as the all hygrothermal material parameters, determined in laboratory (thermal conductivity, vapour division resistance, water absorption coefficient, thermal capacity, porosity) are considered. Figure 7 shows an exemplary comparison of measured and simulated relative humidity and temperature between hemp and massive wall. The results of calculated and measured RH/T are in good agreement. Little deviation is seen on occasion, which can be attributed to user behaviour (inconstant indoor climate). However, both results indicate moderate moisture values between hemp and massive wall. Since the calculation results using WUFI® are in good agreement with the measured one, the simulation model could be used for hygrothermal calculations, which could be needed for further analysis considering real climatic conditions.

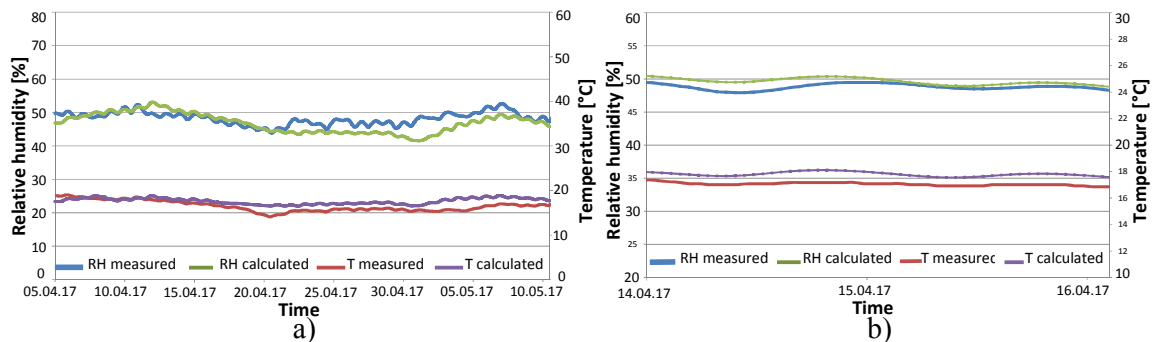


Figure 7. a) Measured and calculated (RH, T) between wall and hemp, b) The same in 4 days

CONCLUSIONS

On the basis of wireless technology an innovative sensor system for the humidity and temperature measurements (RH, T) has been developed. For ensuring a long-lasting, energy-efficient and performing measuring system an energy model has been derived from lab measurements and thus an optimized wireless protocol was implemented. Using this developed wireless technology, non-destructive effective measurement and diagnosis about the current state of building component were recorded and evaluated. Additionally to the fact that insulation does have a big effect of significantly reducing the heat flow through the wall, the results of the wireless system show that measuring after two years, no damage and no rain penetration were found in all variants. The moisture content of hemp/wood fibre ranged between 8 - 12M%. Hemp and wood fibre have a positive effect on summer heat protection. The indoor climate in both buildings, insulated with hemp and wood fibre, is comparable to other systems. So the conditions for mold growth on the inner wall surface are not given. This study proves that, an intelligent façade with integrated wireless- sensors (RH/T) guarantees a long-term, damage-free construction, during building use, by “looking into” the construction.

REFERENCES

- Fujitsu. 2013. <http://www.elecfans.com/topic/seminar/industrial/Fujitsu.pdf>
- Heinzelmann W. R.2000. Energy-efficient communication protocol for wireless microsensor networks, 33rd Annual Hawaii International
- NXP. 2014. UM10204 I2C bus specification and user manual, Rev. 6, <https://www.nxp.com>
- Sensirion. 2014. Datasheet SHT21, Humidity/Temperature Sensor IC, www.sensirion.com
- WTA. 2002. Leitfaden für hygrothermische Simulationsberechnungen, WTA
- WUFI-Manual. 2015, https://wufi.de/download/WUFI_Pro_4_Manual.pdf

A resilient refurbishment project for an Italian large sports hall

Renata Morbiducci^{1,*}, Andrea Morini², Alberto Messico¹ and Clara Vite¹

¹University of Genoa, Dept. Architecture and Design (DAD), Genoa, Italy

² University of Genoa, Dept. of Electrical, Electronic, Telecommunications Engineering and Naval Architecture (DITEN), Genoa, Italy

**Corresponding email: Renata.morbiducci@unige.it*

ABSTRACT

In Europe the management costs and lack of flexibility of the sports halls, built in the second half of the '900, brought to the progressive abandonment of many structures. In this context the environmental, social and economic sustainable aspects of a refurbishment project of an Italian large sports hall, named "Palasport", are presented. It was designed by a group of architects and engineers and completed in 1962. It is located in the expo area of Genoa, a north Italian city, called "Fiera del Mare" and it plays a strategic role in the social community.

In the past it hosted several international events such as concerts, fairs, exhibitions and sporting events. Today the building is completely unused for several reasons, including the obsolescence of the mechanical and technological systems, the high operating costs, the lack of versatility and adaptability of the structure. For these reasons, it has been developed a project in the name of environmental, social and economic sustainability for a building that could attract different types of users during the day. The project is realized with the support of Building Information Modelling (BIM) methodology. The BIM is used to execute various simulations and scenarios to obtain the best possible results, to analyze functional, social, energetic and economic aspects. Furthermore, it is used to simulate Palasport in dynamic condition to understand its real behavior with dedicated applications (Equest, ElumTools). In the presented refurbishment project renewable energies are used: from the sun for the production of electrical energy, from the seawater to improve the performance of the Heat Ventilation and Air Conditioning (HVAC) system and from the wind to refresh the pavilion. This project makes the Palasport a flexible and resilient construction and adapt it to the future needs of society.

KEYWORDS

Resilient refurbishment, BIM applications, dynamic lighting simulations, thermal behavior.

INTRODUCTION

The urban fabric, mostly in Europe, is saturated and therefore it is increasingly the need to optimize existing heritage, improving its qualities and transforming the criticalities in new strengths. In the European cities often there are disused buildings because they are no longer able to meet the functions for which they were designed and the needs of the urban context in which they are located. The Genoa "Palasport" is certainly one of this kind of buildings, despite the historical importance it represented.

The Palasport, also known as "Pavilion S", stands in the Sea Fair of Genoa (Figure 1), whose urban design is attributed to the engineer Luigi Carlo Daneri. Today the fairground is developed among the following buildings: Pavilion B (designed by Jean Nouvel), Pavilion D (old place of University of Genoa), Pavilion C (exhibition places with historical and "experimental" tensile structures). The actual project of the Municipality of Genoa to transform the entire area offers an opportunity to return a sea view to the city and to relocate

the recreational activities in areas suitable for the performance of sports and nautical activities. This reconversion follows the design of the New Waterfront of Levante (masterplan by Renzo Piano) and combines the development needs of one of the most important industrial sectors of the city (naval repairs) with the process of modifying one of the most delicate and precious stretches of the entire urban coastline. The new places thus released will host, in addition to the navigable canals of the new marinas for pleasure boats, residential/receptive, directional, sporting and commercial functions; places and opportunities for meeting, exhibition, development and enhancement in the areas of leisure, sport and culture, with the relative parking spaces.

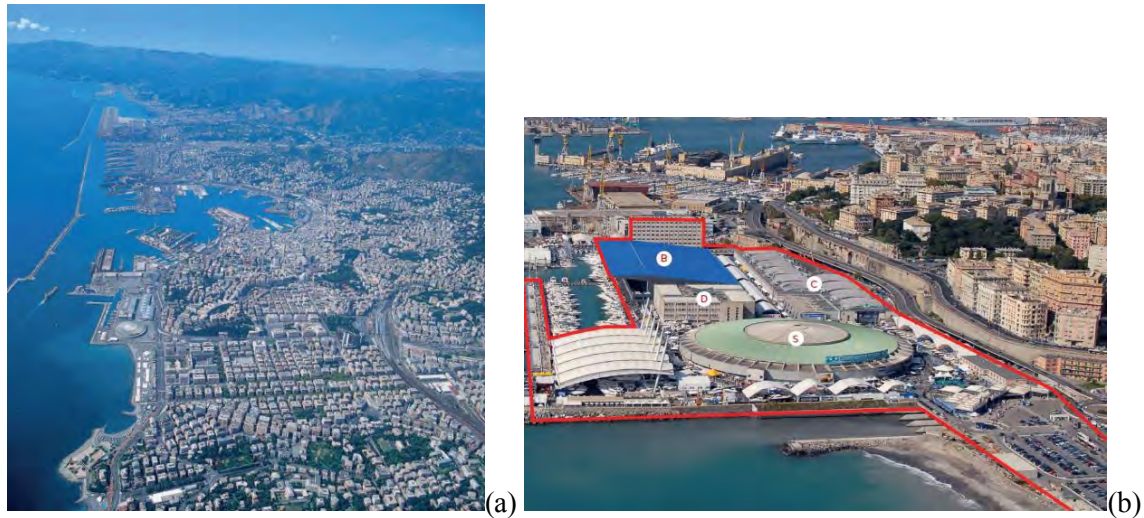


Figure 1. (a) The coast of Genoa; (b) The pavilions of Sea Fair of Genoa: S (Palasport), B (designed by Jean Nouvel), D (old place of University of Genoa), C (exhibition places with historical and “experimental” tensile structures) (Cenci, 2018).

The Palasport, object of this writing, has an area of 30.000 m², split in three different levels: the ground floor, just below the external reference quote, has a diameter of 160 meters and it's surmounted by two concentric ring galleries. The central zone with two grandstands with 2.000 seats has a large space at full height. From the inauguration, the Palasport is characterized by its great multi-functionality, hosting international sport events, concerts, exhibitions with great success. However, with time, the previous events were too sporadic to justify the high running costs; this aspect, with the age of the technological systems, has brought to a progressive inactivity of the pavilion. The project of the new functions and consequence design for the Palasport regeneration was based on the resolution of these problems and took advantage from the inclusion of different activities inside and outside, because inserted in the masterplan by Renzo Piano.

METHODS

The requalification project of the Palasport wants to give back the building to Genoa, making it the pivot of sports agonistic and amateur activities. So it was chosen to make a project table with CONI Liguria to understand the real needs of the sports federations, located in the Ligurian territory. This collaboration has brought to an optimization of the internal spaces in order to host the large number of sports activities, like as basketball, volleyball, tennis, boxe, rhythmic gymnastics, football, ping pong, badminton, etc. To cover the operating costs is necessary to include other collateral activities, for example commercial establishments, restaurants, conference rooms and entertainment spaces.

Thanks to the collaboration with sports federations it's born the need for a sport medicine center, agreement with CONI, to be included in the Genoese urban context. Therefore the project includes a large space dedicated to sports medicine in the building, that could become a landmark for all of Liguria.

The careful study of the spaces has allowed to insert a large number of activities, without precluding the possibility of hosting large sports events, exhibitions and concerts (Figure 2).

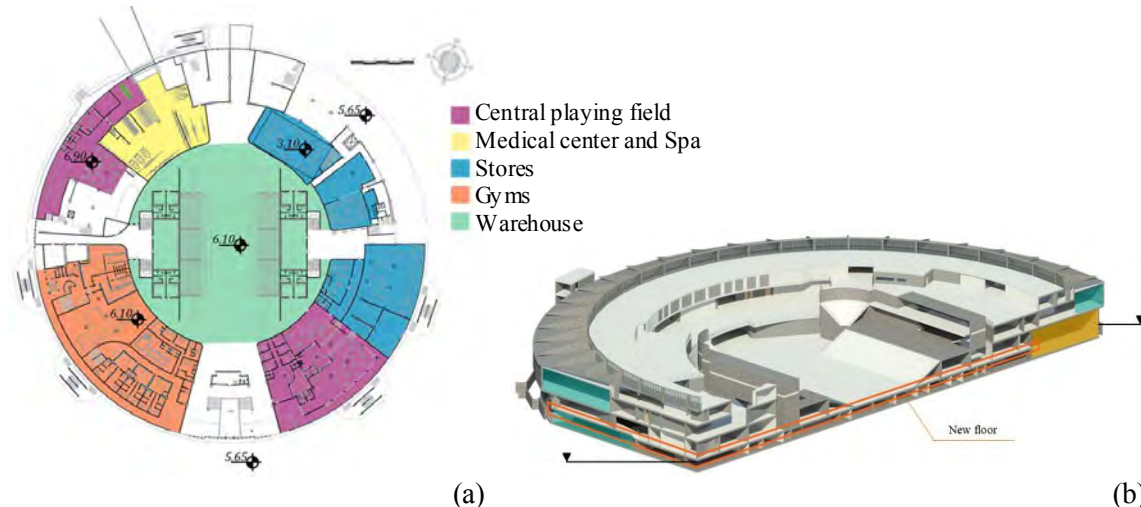


Figure 2. The requalification project of Palasport, examples of project development in BIM mode: (a) first floor; (b) the new floor.

Thanks to the new floor at the same elevation of outside, the Palasport has four floor, so there was the necessity to design some new side stands, that can host 4.000 spectators. As previously stated, one of the standards on which this design is based is the versatility of the interior spaces; this has been achieved with the use of slight prefabricated walls to give greater freedom to the interior arrangement, that could change according to the needs of users. The independence of the rooms hasn't pursued only at the planimetric level, but also from the plan engineering point of view, especially under the thermal and lighting aspects.

For the outer casing only some interventions are necessary in order to keep the original characteristics of the Palasport as much as possible; furthermore, insulating and compartmentalizing the rooms it wasn't necessary to modify the roof and the vertical curtain walls to obtain good thermal insulation values.

The plant engineering aspects were addressed to minimize consumption; in particular, the lighting and thermal conditioning systems, incorporating renewable energies: infact the heat generation system was granted to seawater heat pumps, while the electrical requirements were partially satisfied by the use of photovoltaic panels.

All the simulations of this project have been performed with BIM technology. This type of design is based on a parametric modelling, born in the '80s, whose innovative aspect is the ability to report the changes made on an element, or some of its features, throughout the model, keeping it continuously updated, in function of the context changes too. Through BIM technology you can do a lot of operations, such as architectural, structural, plant engineering simulations, controlling temporal and economic variables too. For these reasons Building Information Modelling is considered a 5D technology.

RESULTS

In the BIM's mode several dynamics simulations are used to verify the project hypotheses for energy efficiency and comfort conditions. In particular, are conducted: lighting simulations,

thermal-hygrometric simulations (for energy efficiency and indoor thermal-hygrometric comfort); irradiation analyses (for renewable energies production) and wind flow analyses (for indoor thermal-hygrometric comfort).

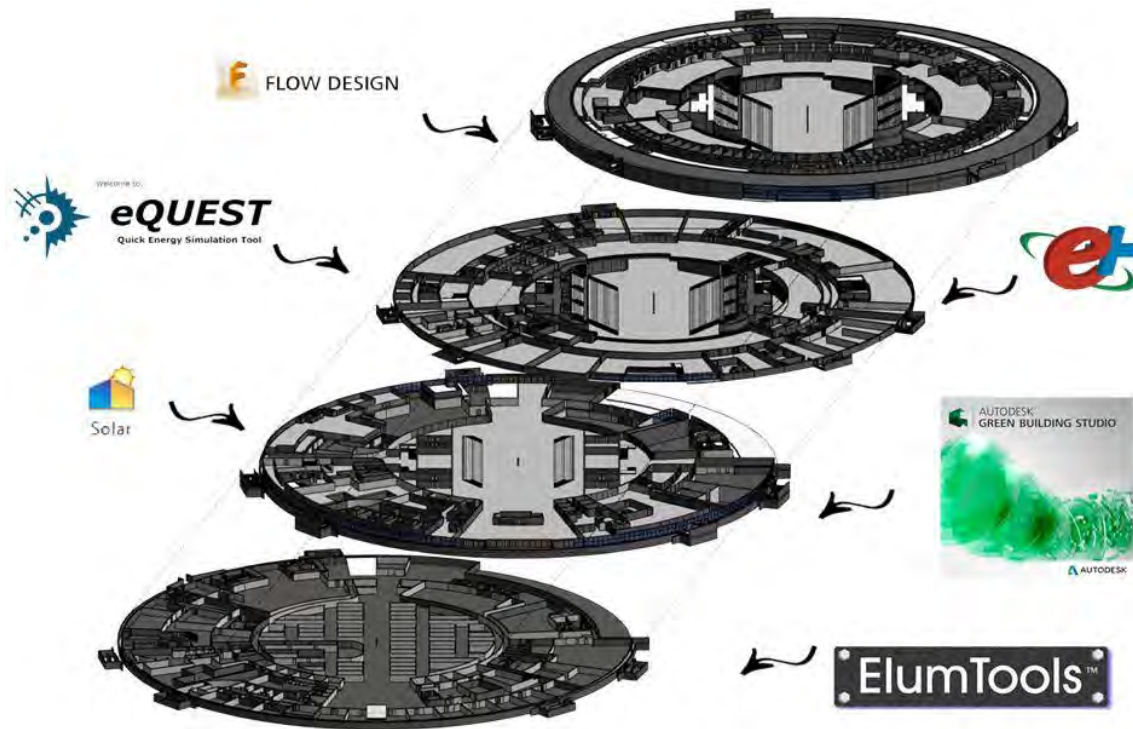


Figure 3. Used tools for dynamic simulations: lighting simulations (ElumTools, EnergyPlus), thermal-hygrometric simulations (Green Building Studio, Equest), irradiation analyses (Solar-Autodesk) and wind flow analyses (FlowDesign-Autodesk).

The first topic was the lighting project, with the purpose of obtaining the maximum illuminance value, respecting the quality parameters required by current legislation (UNI EN 12464-1:2011), namely: general uniformity, glare, color rendering and color temperature.

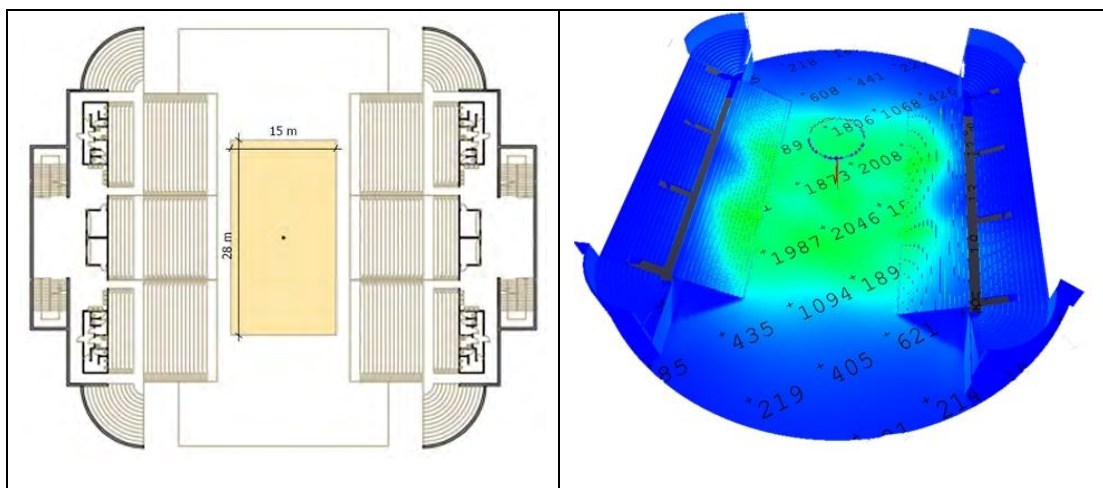


Figure 4. Examples of results for lighting simulations in lux.

The next step was the insertion of a control system for many applications: to optimize the luminous flux of the luminaires, according to the specific requirements of the regulations for the different activities, to keep the best visual comfort, to have, overall, the greatest energy savings possible.

The thermal-hygrometric project was studied using dynamic energy simulations, in order to analyze in detail the Palasport behavior and needs. As an example of the conducted dynamic analyses, the hourly values of the energy demand are shown (Table 1). In this case the dynamic simulation permitted to determine the exact peak load for heating and cooling through which the heat pump was sized.

Table 1 - Peak load values.

Peak loads	
Heating peak load [kW]	-1896.6
Peak cooling load [kW]	2926.7

Consequently, a seawater source heat pump (SWHP) was chosen which harnesses the Mediterranean sea thermal energy as a means of generating renewable energy. Three modular SWHP were, therefore, assumed to be used (Table 2).

Table 2 – SWHP Specification.

Heating		Cooling	
Rated Heating Output [kW]	1188	Rated Cooling Capacity [kW]	1061
Power Consumption [kW]	242	Power Consumption [kW]	204
Coefficient of performance (COP)	4.89	Energy efficiency ratio (EER)	5.21
Evaporator water flow [m ³ /h]	205	Evaporator water flow [m ³ /h]	185

In this way, the winter requirement is satisfied thanks to the use of only two SWHP, achieving savings in terms of electricity consumption. The third, therefore, would be used during the cooling season or in case of failure of one of the other two.

BIM simulations were used to sizing the renewable energy systems too; in particular, for the photovoltaic systems it has been planned the use of CIS panels, composed with copper, indium and selenium. These panels have an excellent efficiency, so we can ensure a greater production than the use of traditional photovoltaic panels maintaining the aesthetics of the Genoese roofs.

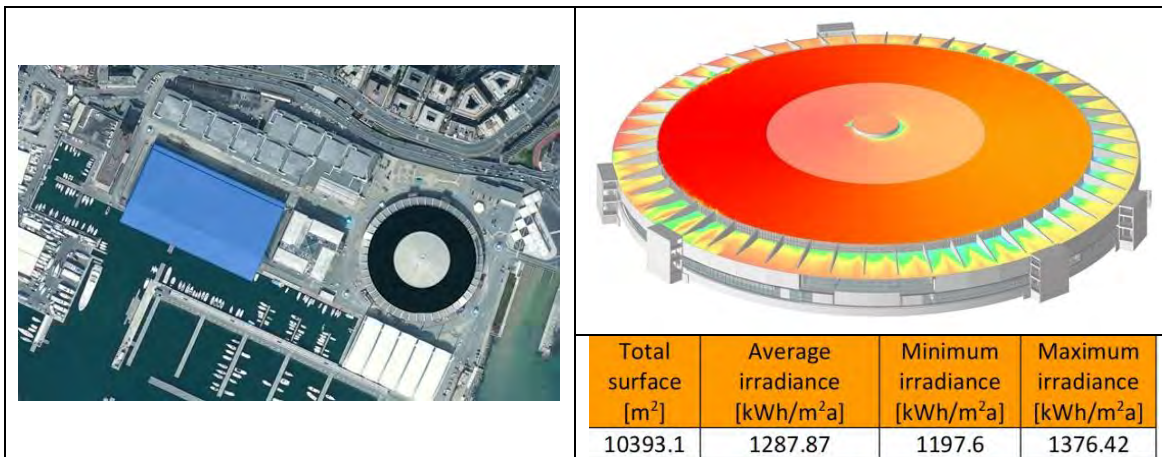


Figure 6. Photo insertion of photovoltaic panels and annual irradiance on Genoa "Palasport".

To fully exploit the context in which the building is located, it was decided to use natural ventilation to condition the premises during summer, checking beforehand the intensity and the direction of the prevailing winds. The natural ventilation takes place through the opening and closing of windows controlled by a Building Automation system that conveys the air inside the building, in function of outdoor and indoor temperatures and wind's characteristics.

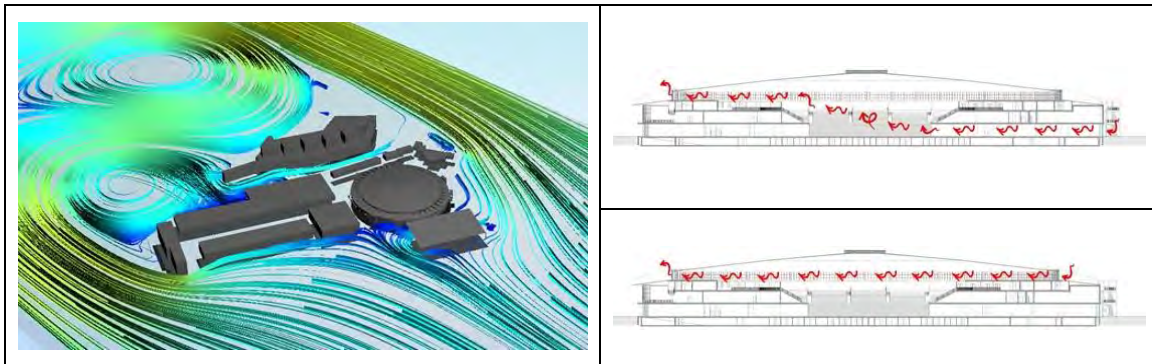


Figure 7. Analysis of the summer wind regime and the schematic dynamic natural ventilation.

DISCUSSIONS

Building automation is a fundamental element in this project: thanks to it, it's possible to control the ventilation, the heating system, according to the individual indoor use destinations, monitoring the thermal-hygrometric conditions of each rooms, the lighting requirements with presence and twilight sensors and the optimization of photovoltaic panels.

CONCLUSIONS

In the end we can say that the design solutions chosen in the project, such as the subdivision of the rooms, the plant engineering independence, the use of sea water to refrigerate the heating system, the use of LED technology for lighting, natural ventilation to counteract the heating in summer and the Building Automation, have led to an important reduction in operating costs, that are equal to about 200.000 €/year. This amount is in particular due to electricity consumption which is further reduced by 40% thanks to the use of photovoltaic panels, making the Palasport sustainable from an environmental and economic point of view.

REFERENCES

- Cenci S. (edited by) 2018. Genova Meravigliosa, rigenerare Genova, "Genova Fronteamare". Comune di Genova (Italy), Ante Prima Consultants, Paris (France).
- Dassori E. and Morbiducci R. 2010. Costruire l'architettura: tecniche e tecnologie per il progetto, Tecniche Nuove, Milano, ISBN 978-88-481-2298-6.
- Barengli G. and Franza F. 2016. Analisi in regime dinamico per il benessere e la sostenibilità ambientale: la cittadella dello sport di Genova", Università di Genova.
- Merz H., Hansemann T. and Hübner C. 2009. Building Automation - Communication systems with EIB/KNX, LON und BACnet", Springer, ISBN 978-3-540-88828-4.
- Eastman C., Teicholz P., Sacks R., Liston K. 2011. BIM Handbook: A Guide to Building Information Modeling for Owners, Managers, Designers, Engineers and Contractors", 2nd Edition, Wiley, ISBN: 978-0-470-54137-1.
- Dassori E. and Morbiducci R. 2013. Requalification Pilot projects of Nearly Zero Energy Building for "smart" district and cities", *TECHNE* 6, 2013, pp. 48-54, ISSN online: 2239-0243 | ISSN print 2240-7391.

Dynamic Life Cycle Assessment Integrating Cultural Value

Ming HU*

University of Maryland
College Park, Maryland

*Corresponding email: mhu2008@umd.edu

ABSTRACT

Lack of spatial and temporal flexibility is a well-known limitation of current life cycle assessment (LCA). Exclusion of human and time consideration in LCA can also limit the potential of results. This paper explicitly proposes a dynamic life cycle framework and assessment model and demonstrated the potential importance of the method by integrating the cultural theory of risk. Cultural theory (CT) of risk was developed by anthropologist Mary Douglas and is originally a societal social anthropology approach based on the structure and functioning of groups within societies. Different society produces its own selected view of the natural environment, a view which influences its choice of danger worth attention. Applying the set of views of natural environment helps us to understand how occupants behave and make important decisions that produce substantial environmental impacts during the building use phase. Cultural theory results in five archetypes of people: the individualist, hierarchist, egalitarian, hermit, and fatalist. Each archetype reflects a composition of ideologies, cultural biases, social relationships, moral beliefs, and concerns of interest. One of the reasons to apply CT in this LCA research is the fact that the different archetypes can be considered as theoretical constructs that facilitate a comprehensive classification of decision makers in LCA. A case study of an elementary school is used to illustrate the importance of the method and demonstrate the differences between conventional static LCA and dynamic LCA. The results showed a noticeable difference and illustrated some unique environmental impact trends by integrating value choice and human factors in the LCA model. The findings suggest changes during a building's lifetime can influence the analysis results to a greater degree, and that long-term indicators and short-term indicators have different impacts on results. Therefore, adapting a dynamic framework could increase the applicability of LCA in decision-making and policymaking.

KEYWORDS

Dynamic life cycle assessment, school building, value choice

INTRODUCTION

As designers, engineers and building industry practitioners become increasingly aware of the environmental impact caused by building products, building systems and early design decisions, accurate environmental assessment has become important for the building and construction industry to achieve a more sustainable future. Life cycle assessment (LCA) can aid in quantifying the environmental impacts of whole buildings by evaluating materials, construction, operation, and end of life stages, with the goal of identifying areas of potential improvement (Junnilla et al. 2006; Scheuer et al. 2003; Kofoworola and Gheewala 2008; Wu et al. 2011). Effective improvement and utilization of life cycle assessment in building industry, particularly design phase, hinge upon identifying current barriers that burden LCA. One of the critical barriers is the integration of ever changing factors during the entire life span of a building. Unlike other commercial products, a building has a much longer life span, 50-75

years, and the use phase can have large environmental impacts with multiple renovations and building upgrades related to building technology developments. Variations (such as multiple renovations) within the use phase can sometimes be greater impact than the total impacts of materials, construction, or end-of life phases (Collinge et al. 2013), and the variations are often caused by the users' choice and decisions, human factors. The proposed dynamic LCA framework and model allow the integration of value choice in the LCA of building.

CULTURAL THEORY

Cultural theory (CT) was developed originally as a societal social anthropology approach based on the structure and functioning of groups within societies. Any form of society produces its own selected views of the natural environment, a view which influences its choice of danger worth attention (Douglas 1982). Applying this set of views of the natural environment will help us to understand how people behave and make important decisions that produce substantial environmental impacts during a building's entire life cycle. Douglas argues that the variety within an individual's social life can be adequately captured by the two dimensions of sociality: group and grid. Group is the extent to which an individual is incorporated into bounded units, and grid denotes the degree to which an individual's life is circumscribed by externally imposed prescriptions (Mamadouh 1999, Hofstetter et al 2000). The two dimensions together define an archetype: strong group boundaries along with minimal prescriptions produce *egalitarian*; *hierarchist* is characterized by strong group boundaries and prescriptions; *fatalist* is excluded from group decisions coupled with binding prescriptions; *individualist* is defined by neither group incorporation nor prescribed social roles; *hermit* is the individual completely withdrawn from social involvement. These five archetypes could be understood as perspectives that are taken to view and manage the system, dealing with risks presented from natural disasters or man-made catastrophes. Among the five archetypes, "*fatalist*" will not take long-term or life cycle perspective and take no active role in decision making, and "*hermits*" withdraw from social involvement altogether (Hofstetter et al 2000), therefore, only three are active in public decision-making: the *individualist*, *hierarchist*, and *egalitarian*. Using CT could help us understand and predict the decisions made by a group of people, a community, or a society. *Egalitarians* have the longest time horizon for building life. They would argue that exposure in the distant future is at least as important as exposure today and society should adjust its needs to limit the exposure of future disasters or risks (Frischknecht et al 2001). The *individualist* views humans as having a high adaptability through technological and economic advancement; therefore, their decision-making will be based on known damage or threats. They concentrate on the present effects over future loss and gain, and their time horizon for a building's service life span is the shortest. The *hierarchist* considers nature to be in equilibrium. They view the present and future as equally important. They seek proper management to avoid future risk and search for a balance between manageability and precautionary principles. Their time horizon for a building's service life span falls in between the *egalitarian* and *individualist* and typically coincides with the current life span used among the building industry which is 60-70 years (De Schryver 2011; Hofstetter 1999). Collectively, the different social groups' views on building longevity and impact are reflected in their approach of pursuing energy efficiency while reducing environmental impact. The *Individualist* group focuses on short-term payback and result, thus site net zero energy is their interest. The *hierarchist* group focus on long-term energy balance and impact reduction, so source energy is their main concern. We could assume different countries could be viewed as collective social groups. For instance, we assume United States is an *Individualist* dominated group, and China is a *hierarchist* dominated group. The different views of the natural environment could result in different, localized approaches to energy conservation and environmental reduction. The understanding

of each groups' decision-making mechanism and their view of the built environment could eventually feed into policy making, particularly the policies and regulations in the building industry, since building industry has a profound impact on the natural environment.

METHODS

Figure 1 represents this dynamic LCA framework. Compared to the static method, this proposed framework counts character change along with the time horizon (CT horizon) analysis, which is also discounted based on choice value. Time is influential when a life cycle assessment method is used to estimate the environmental impact of an object. An impact rarely occurs instantaneously but rather occurs over an indefinite period of time. In the proposed framework, instead of allowing only one time horizon, we used a finite time horizon to define the system evolution through the entire life span. To incorporate the human factor to LCA decision-making, user value choice based on the archetype and the discount rate were used to rank the importance of different parts of multiple objectives. An existing elementary school in the state of Maryland was used as the case study to test the framework and model. Quarterfield Elementary School is a one-story masonry building about 44,000 square feet.

Proposed Life Cycle Assessment Framework

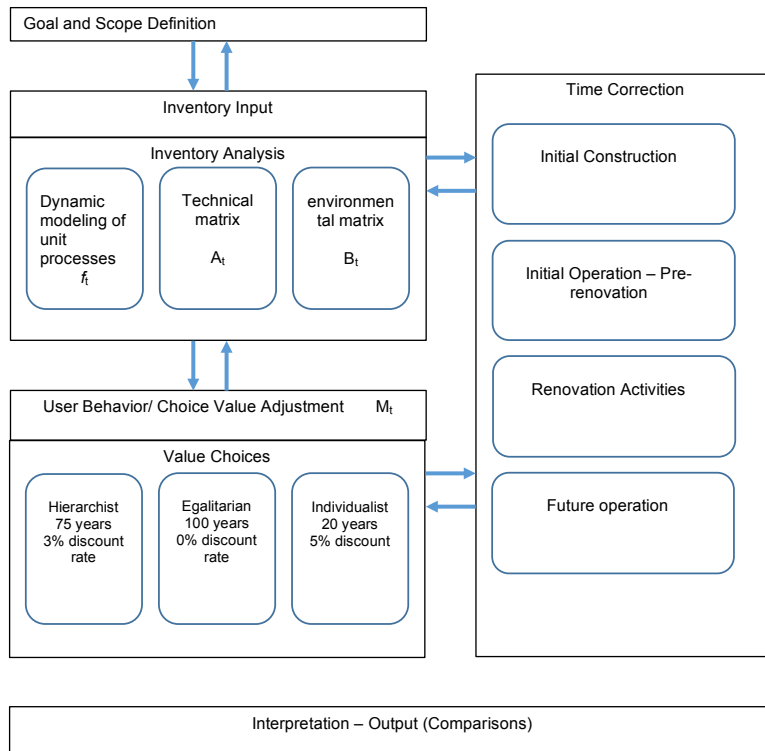


Figure 1 Dynamic framework and model

The major difference between the static model and proposed model is (1) the use of time sequence tables to simulate dynamic variation in matrix coefficients representing modeled relationships. If there is no particular time sequence assigned to variables, then we assume to use a constant value for all time steps; the same as what is used in the static model. The full lifetime in the dynamic model encompasses four time sequences/steps that are explained in Table 1. The future operation includes potential renovation, future operational repair, and

maintenance. The second major difference between the models is (2) the adjustment of results through the user's value choice to predicate different scenarios.

Table 1 Time sequence/adjustment included dynamic model

Time Sequences/Steps	Duration	Timeline	Annual Average Energy Usage
Initial Construction (DY-IC)	1 year	1968	
Initial Operation – Pre-renovation (Dy-PA)	23 years	1969-1992	375,400KWh (electricity) 2,4 Million ft ³ (gas)
Renovation Activities (DY-RA)	16 years	1992-2008	319,090KWh (electricity) 2,0 Million ft ³ (gas)
Future Operation (Dy-FO)	35 years	2008-2043	225,240KWh (electricity) 1,4 Million ft ³ (gas)

RESULTS

The results have been normalized to the final static LCA results for each environmental impact category. The categories included in this study are global warming potential, acidification potential, Particular Matter effect on human health (HH Particulate) impact, and ozone depletion potential. The static LCA model was set up based on the original construction documents without any renovation and modification and with a life span of 75 years, which includes the embodied energy and operational energy consumption. The dynamic model was created based on the four time steps explained in table1.: initial construction (year 1), initial operation (before the first major renovation), renovation activities (including multiple renovations across a 16-year life span), and future operation. Figure 2 illustrates the results before integrating the users' value choice. The static model results are higher than the results from the dynamic model in all categories. The largest difference is in the ozone depletion category with the static model projecting more than an 8% higher impact. For the rest of the categories, the acidification potential is 1% higher, human health particulate potential is 2% higher, and global warming potential is less than 1% higher.

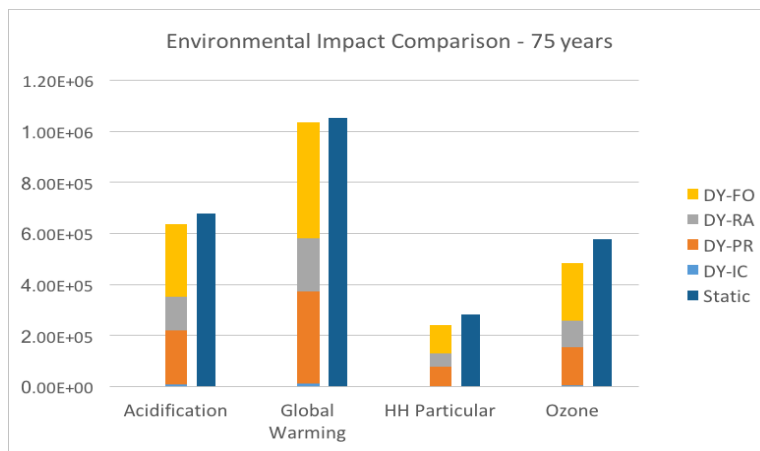


Figure 2 Environmental impact comparison between static model and dynamic model

Three different archetypes have been analyzed and compared. The actual values have been normalized and compared as annual impacts. For egalitarians, the global warming impact takes higher priority. The second and third impacts are the human health particulate potential and smog potential, which could be due to the long-term view of egalitarians and long-term service life span of the building. Those three categories are influenced by long-lived impact

indicators, especially those factors particularly related to human health that are embedded in building materials and assemblies, lasting the entire building life. Without discount, the time compounding effect shows a big difference. Hierarchists and individualists have similar impact profiles, with the ozone depletion potential being the primary concern. Most ozone depletion indicators have a relatively short-lived term. Both hierarchists and individualists have shorter building lives with discount; therefore, those short-lived indicators illustrate a bigger impact. Overall, the egalitarian has very different trends from the individualist and hierarchist, which indicate that the discount rate factor has a higher impact than life span, meaning the integrating users' preferences and value choices could create very different results from those using the existing static model. For a society or community who holds a long-term vision and an enduring perspective of its future development, paying attention to those long-lived environmental indicators is imperative. If we translate the perspective of building design and construction for building types such as institution, health care, and civic buildings, whose owners and operators are usually the same, then the categories that will contribute the most to environmental impacts would be global warming and human health particulate impact potential.

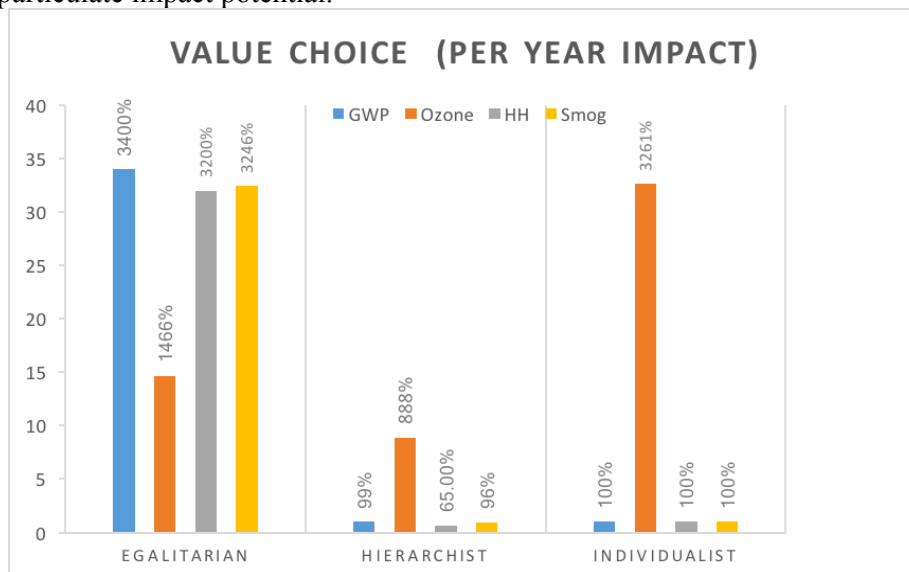


Figure 3 Value choice comparison

CONCLUSION

Therefore, adopting a more dynamic LCA approach, as demonstrated herein, seems likely to provide a more detailed and project-specific projection and equip policymakers and decision-makers with a more accurate and holistic estimation. More importantly, using the cultural theory demonstrated, that the user's choice and cultural context will play a critical part in the LCA of the same building, and the results could vary largely due to the community's and group's perception of building use and tolerance of the risk. In order to fully account for all necessary uncertainties in the LCA study, future research needs to include users and cultural factors, and additional exploration of the interactions with dynamic, temporal, or cultural variables will be very useful to fully understand the environmental impact of individual buildings.

REFERENCE

- Collinge, William O., Amy E. Landis, Alex K. Jones, Laura A. Schaefer, and Melissa M. Bilec. "Dynamic life cycle assessment: framework and application to an institutional building." *The International Journal of Life Cycle Assessment* 18, no. 3 (2013): 538-552.
- De Schryver, A. M. (2011). *Value choices in life cycle impact assessment*. [Sl: sn].
- Douglas, Mary, and Aaron Wildavsky. *Risk and culture: An essay on the selection of technological and environmental dangers*. Univ. of California Press (1982).
- Frischknecht, R., Braunschweig, A., Hofstetter, P., & Suter, P. (2000). Human health damages due to ionising radiation in life cycle impact assessment. *Environmental impact assessment Review*, 20(2), 159-189.
- Hofstetter, P. (1999). Top-down arguments for a goal-oriented assessment structure. *Global LCA Village*.
- Heijungs, Reinout, and Sangwon Suh. *The computational structure of life cycle assessment*. Vol. 11. Springer Science & Business Media, 2013.
- Junnila S, Horvath A, Guggemos AA (2006) Life-cycle assessment of office buildings in Europe and the United States. *J Infrastruct Syst* 12(1):10–17
- Scheuer, Chris, Gregory A. Keoleian, and Peter Reppe. "Life cycle energy and environmental performance of a new university building:
- Kofoworola, Oyeshola F., and Shabbir H. Gheewala. "Environmental life cycle assessment of a commercial office building in Thailand." *The International Journal of Life Cycle Assessment* 13, no. 6 (2008): 498.
- Mamadouh, Virginie. "Grid-group cultural theory: an introduction." *GeoJournal* 47, no. 3 (1999): 395-409.
- Wu, Huijun J., Zengwei W. Yuan, Ling Zhang, and Jun Bi. "Life cycle energy consumption and CO2 emission of an office building in China." *The international journal of life cycle assessment* 17, no. 2 (2012): 105-118.

Investigation of Energy Modelling Methods of Multiple Fidelities: A Case Study

Naveen Kumar Muthumanickam¹, Vaclav Hasik^{2*}, Mehmet Unal¹, Simon W. Miller¹, Tina Unwalla¹, Melissa M. Bilec², Lisa D. Iulo¹, and Gordon P. Warn¹

¹Pennsylvania State University

²University of Pittsburgh

*Corresponding email: vah16@pitt.edu

ABSTRACT

Building energy modelling has become an integral part of building design due to energy consumption concerns in sustainable buildings. As such, energy modelling methods have evolved to the point of including higher-order physics, complex interconnected components and sub-systems. Despite advances in computer capacity, the cost of generating and running complex energy simulations makes it impractical to rely exclusively on such higher fidelity energy modelling for exploring a large set of design alternatives. This challenge of exploring a large set of alternatives efficiently might be overcome by using surrogate models to generalize across the large design space from an evaluation of a sparse subset of design alternatives by higher fidelity energy modelling or by using a set of multi-fidelity models in combination to efficiently evaluate the design space. Given there exists a variety of building energy modelling methods for energy estimation, multi-fidelity modelling could be a promising approach for broad exploration of design spaces to identify sustainable building designs. Hence, this study investigates energy estimates from three energy modelling methods (modified bin, degree day, EnergyPlus) over a range of design variables and climatic regions. The goal is to better understand how their outputs compare to each other and whether they might be suitable for a multi-fidelity modelling approach. The results show that modified bin and degree day methods yield energy use estimates of similar magnitude to each other but are typically higher than results from EnergyPlus. The differences in the results were traced, as expected, to the heating and cooling end-uses, and specifically to the heat gain and heat loss through opaque (i.e., walls, floors, roofs) and window surfaces. The observed trends show the potential for these methods to be used for multi-fidelity modelling, thereby allowing building designers to broadly consider and compare more design alternatives earlier in the design process.

KEYWORDS

Building energy modelling, multi-fidelity, modified bin, degree day, dynamic simulation

INTRODUCTION

Advancements in building energy modelling methods have helped building designers to gain more insights into the energy use of prospective building designs (Lam et al., 2014). However, the increased complexity of these methods has often hindered their use to broadly explore and compare design alternatives early in the design process. In various fields of engineering design, some of the approaches to resolving this issue have included fitting a surrogate model to data from high fidelity (i.e. expensive) model evaluation of a sparse subset of the design space (for example Forrester, 2007, Unal et al., 1996), or through multi-fidelity modelling approaches (Jin, 2001; Simpson et al., 2001). One method in particular, uses a set of multi-fidelity models in sequence to evaluate the design space whereby low-fidelity models are used to remove non-optimal designs prior to evaluation by higher fidelity models (Miller et al., 2017). In the building

design field, prior efforts have been taken to review and categorize load estimation methods such as ASHRAE's Cooling Load Transfer Function (CLTD), Radiant Time Series (RTS), Transfer function methods and Heat Balance Method (HBM) based on their increasing levels of complexity and accuracy (ASHRAE 2009). However, such efforts were focused on comparing the differences of the underlying calculation procedures and to our knowledge, there is a limited number of studies comparing the outputs of the various energy modelling methods in the context of a *multi-fidelity modelling approach*. Given that the building design community possesses many energy modelling methods ranging from simple spreadsheets utilizing temperature-bin methods to simulation-based energy modelling tools such as EnergyPlus (Mao et al., 2013; Crawley et al., 2008), a multi-fidelity modelling approach could be a viable solution to the issue of exploring large sets of design alternatives. Here we investigate energy estimates from three candidate energy modelling methods to assess how they compare to each other, if there are any general trends across the methods, and whether they may be suitable for a multi-fidelity modelling framework.

METHODS

Selection of energy modelling methods

Annual building energy use can be estimated using three types of energy modelling methods: (1) *forward or classical methods* - based on a building model and engineering calculation methods (ASHRAE, 2009); (2) *data-driven methods* - based on building system parameters from actual measured data (ASHRAE, 2009); and (3) *simulations* - that estimate energy requirements using differential equation solvers for transient simulations and time-stepping weather data (Mao et al., 2013). Forward methods include the thermal response factor method (Mitalas & Stephenson, 1967), weighting factor method (ASHRAE, 1981) and the heat balance method (Buchberg, 1958; Kusuda, 1999) for annual heating/cooling load estimation and degree day method, equivalent full load hour method, bin method (Ayres and Stamper, 1995) and modified bin method (Knebel, 1983) for annual energy use calculation. Simulation methods used in the United States typically include whole building dynamic simulation tools such as DOE-2, eQuest, EnergyPlus, TRNSYS, TRACE, HAP, and others (Mao et al., 2013; Crawley et al., 2008). Forward and simulation methods have also been categorized based on varying complexities into benchmarking, degree day, bin, quasi steady-state, lumped parameter, and dynamic simulation methods (CIBSE, 2015). Each of the methods may require different time steps of climate data, such as annual, seasonal, monthly, daily, hourly, and even sub-hourly intervals. This study investigated forward and simulation methods only, since data-driven methods rely on actual data from buildings. A comprehensive review of energy modelling methods and tools can be found in the papers by Mao et al. (2013) and Crawley et al. (2008). From the above methods three modelling methods were selected, namely the modified bin method, degree day method (manual calculation methods under the forward method category) and dynamic simulation method (EnergyPlus), as potential candidate energy modelling methods to be used in the multi-fidelity modelling approach.

Case study design scenario

The three candidate energy modelling methods were used to estimate the energy consumption of a set of sixteen design alternatives for a hypothetical generic office building in four locations with a mix of hot, mild, cold, humid, and dry climates. The locations included Fairbanks, AK, Philadelphia, PA, Phoenix, AZ and Sydney, Australia. The building's fixed parameters included: gross area of 932 m²; commercial office type; serving 50 people; lighting intensity 9.69 W/m²; plug load intensity 14.42 W/m². Additionally, all of the sixteen design alternatives had the same slab on grade and roof construction as well as requirements for interior climate (e.g., interior temperature setpoints). Four variables namely wall type, window type, window-

to-wall ratio and building shape (i.e., number of floors and their dimensions) with two options per variable were considered, resulting in sixteen total design combinations. Table 1 shows the variables, options, descriptions, and main attributes; Table 2 shows all the design option combination with associated numbers to identify each (ids). Note that the options were selected to represent reasonable higher or lower technical possibilities. This study's goal was not to create a code-compliant design, but rather to investigate the energy modelling methods' ability to simulate different conditions.

Table 1: Varied parameters for 16 building designs.

Variables	Options	Description	Attributes
Wall Type	Option A	Plaster, brick, plaster	U-value: 1.57 W/m ² K
	Option B	Brick, EPS, CMU, plaster	U-value: 0.44 W/m ² K
Window Type	Option A	Single glazing, 1/4 in pane	U-value: 3.19 W/m ² K; SHGC: 0.86
	Option B	Triple glazing, 1/4 in panes	U-value: 1.53 W/m ² K; SHGC: 0.56
Window-to-Wall Ratio (WWR)	Option A	Small window area	WWR: 0.2
	Option B	Large window area	WWR: 0.8
Building Shape	Option A	1 level	Dimensions: 3.7x45.7x20.4 m
	Option B	3 level	Dimensions: 11.0x10.2x30.5 m

Table 2: Building design options with corresponding variables.

Design id	Wall assembly	Glazing	WWR	Floors
1	Plaster, Brick, Plaster	Single	0.2	1
2	Brick, EPS, CMU	Single	0.2	1
3	Plaster, Brick, Plaster	Triple	0.2	1
4	Brick, EPS, CMU	Triple	0.2	1
5	Plaster, Brick, Plaster	Single	0.8	1
6	Brick, EPS, CMU	Single	0.8	1
7	Plaster, Brick, Plaster	Triple	0.8	1
8	Brick, EPS, CMU	Triple	0.8	1
9	Plaster, Brick, Plaster	Single	0.2	3
10	Brick, EPS, CMU	Single	0.2	3
11	Plaster, Brick, Plaster	Triple	0.2	3
12	Brick, EPS, CMU	Triple	0.2	3
13	Plaster, Brick, Plaster	Single	0.8	3
14	Brick, EPS, CMU	Single	0.8	3
15	Plaster, Brick, Plaster	Triple	0.8	3
16	Brick, EPS, CMU	Triple	0.8	3

Calculation and simulation setup

The calculation procedures for the modified bin (MB) and degree day (DD) methods were followed as prescribed by Knebel (1983) and ASHRAE (2009) respectively and computationally executed using Microsoft Excel. The histogram function in Microsoft Excel was used to convert TMY-3 weather data into 5-degree interval temperature bins to be used in the modified bin calculations. The same hourly temperature data was used to estimate the annual heating and cooling degree days to be used in the degree day method. The EnergyPlus™ (EP) simulations were run for four time-steps per hour, using the TARP and DOE-2 surface convection algorithms and the conduction transfer function heat balance algorithm. Zone and system sizing was auto-calculated for each weather file and design. The buildings were modelled using Revit 2017 and then exported into an EP input data file (IDF) format using Autodesk® Green Building Studio. The HVAC system setup did not export from Green Building Studio, and a default packaged variable-air-volume template in EP was used instead. HVAC system efficiency details from the same template were used in the system sizing

calculations of modified bin and degree day methods as well. The annual energy use intensity (EUI) in kWh/m²/year was calculated for the sixteen design alternatives using the above modelling methods. Subsequently, to gain better insight on the differences in energy estimates, results were then disaggregated in two categories, following EP's categorization schemes: by end-use (i.e., heating, cooling, lighting, equipment, and fans) and by loads (i.e., heat gains and losses associated with opaque surfaces, windows, infiltration, people, lighting, and equipment).

RESULTS

In our empirical study, MB and DD methods consistently yielded higher annual building energy use estimates than EP, although they showed similar trends for design-to-design comparisons. The results in Figure 1 show the total energy use intensity of each building design using the three methods for one of the four locations, Philadelphia, Pennsylvania, USA. The results are also disaggregated into individual end-uses as defined in the methods section. The results for this location show the predominant energy use for climate control, i.e. heating, cooling, and fans. The same trend was seen in other locations, although its contribution in warmer climates was smaller than in colder climates. The differences between individual methods generally show higher cooling demands in MB and DD results than EP, and this trend was even more evident in warmer climates. The calculated cooling demands were 275-699% higher using MB and DD methods for the design ids 1 through 12, and 171-266% in the 3 story, high window-to-wall ratio designs (ids 13 through 16). Heating demands were relatively similar between methods, although EP values were slightly higher (by 1 to 25% in Philadelphia) in most design scenarios across all locations. The overall energy demand estimated by MB and DD methods were 3-26% and 7-27% higher than that of the EP estimates, respectively, except for design id 14, where the MB estimate was 1.5% lower than EP.

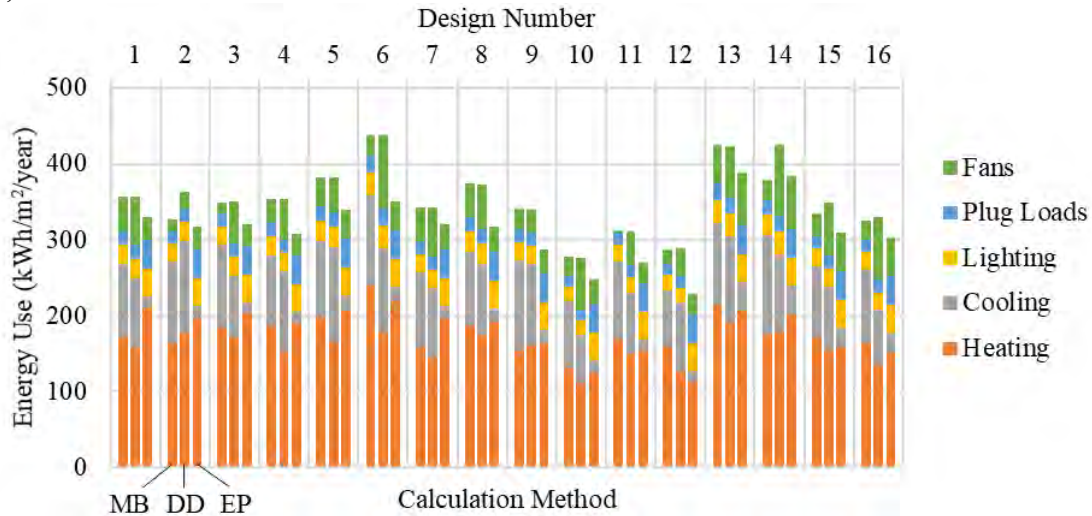


Figure 1. Example end-use results for Philadelphia, PA using three methods. Each design shows results from modified bin method (MB, left), degree day method (DD, middle), and EnergyPlus (EP, right).

Sample results for Philadelphia, PA disaggregated into individual loads are shown in Figure 2. Building designs and modelling methods are presented in the same order as in Figure 1. The results show that window heat gains and opaque surface heat losses are the primary contributors to heating and cooling demands in most design cases across all methods. The opaque surface heat transfer as well as heat gains from people, lights, and equipment (i.e., plug loads) are similar across the three methods, with sometimes slightly lower values from EP. The most noticeable difference is in the window gain values, which are 30-60% higher in MB and DD methods than in EP, especially in designs with high window-to-wall ratios. This trend is even more pronounced in the warmer climates of Phoenix and Sydney.

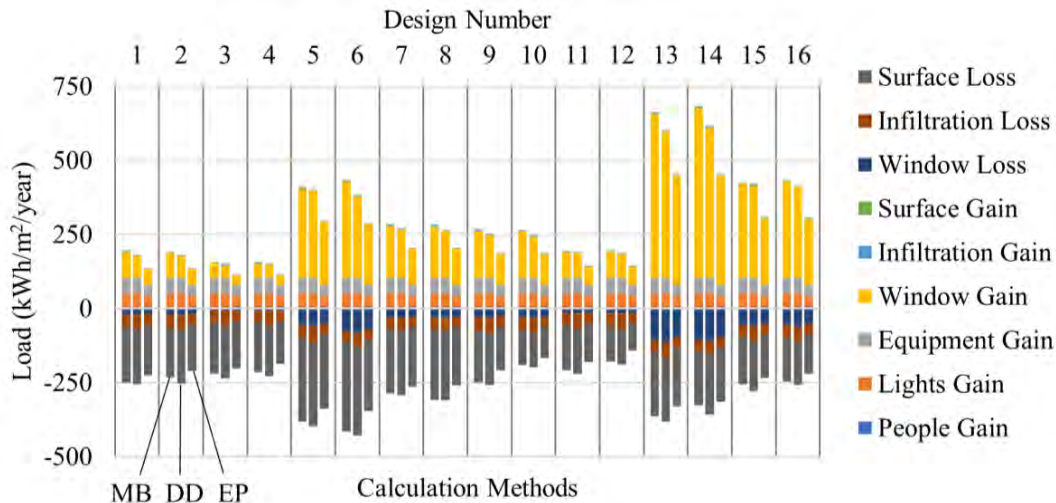


Figure 2. Example load results for Philadelphia, PA using three methods. Each design shows results from modified bin method (MB, left), degree day method (DD, middle), and EnergyPlus (EP, right).

DISCUSSION

Empirical results show that modified bin and degree day methods yield energy use intensity estimates of similar magnitude to each other but are relatively higher than results from the dynamic simulation method (EnergyPlus). Predictably, the differences in the results were traced to the heating and cooling end-uses, and specifically to the heat gain and heat loss through opaque (i.e., walls, floors, roofs) and window surfaces. It should be noted that the findings are specific to the medium office use type, default schedules and HVAC setup, and that the findings may not be applicable to all other design scenarios. It is also important to note that the temperature interval used for binning (5°C in our case) might impact the performance of the method by increasing or decreasing the load estimates. Future research may investigate other design scenarios and bin discretisations.

Plausible explanations for the differences in surface heat gains and losses could be due to each method's underlying treatment of convection, conduction and radiation. For example, degree day and modified bin methods assume steady-state heat transfer in their calculations, whereas EnergyPlus considers transient heat transfer in its calculations. Furthermore, our investigation revealed, although not presented here for brevity, that radiation contributes significantly to the heat gains/losses and that modified bin and degree day method use approximate calculation methods to account for radiation whereas EnergyPlus utilizes advanced calculation methods that account for long wave and shortwave radiation effects. Understanding the effects of the varying heat transfer methods on the energy estimates is part of our ongoing efforts.

CONCLUSIONS

Our empirical results showed trends in differentiation between methods that could be utilized in a multi-fidelity energy modelling design framework. Ongoing research is focusing on a more theoretical explanation of the methods' differences in the underlying heat transfer calculations (i.e., steady state and transient) as it pertains to the surface heat gains and losses. An in-depth understanding of these differences is necessary to determine how to sequence these energy modelling methods in terms of fidelity and how lower fidelity models will inform higher fidelity models. For example, using the approach of Miller et al. (2017), bounding mechanisms (i.e., a method for the lower-fidelity models to bound the more precise estimate from the higher fidelity model over the entire design space) will be required to eliminate non-optimal building designs from large sets of early design alternatives efficiently.

ACKNOWLEDGEMENT

This research is supported by NSF grant CMMI-1455424 and CMMI-1455444, RSB/Collaborative Research: A Sequential Decision Framework to Support Trade Space Exploration of Multi-Hazard Resilient and Sustainable Building Designs. All opinions, findings, conclusions or recommendations expressed in this paper are those of the authors and do not necessarily reflect the views of the National Science Foundation.

REFERENCES

- ASHRAE. (2009). 2009 ASHRAE Handbook: Fundamentals. Atlanta, GA: American Society of Heating, Refrigerating and Air-Conditioning Engineers, Inc.
- Ayres, J.M., and Stamper, E. (1995). Historical Development of Building Energy Calculations. ASHRAE Transactions, 101, Pt.1, 841-849.
- Buchberg, H. (1958). Cooling Load from Thermal Network Solutions. ASHRAE Transactions, 64, 111-128.
- CIBSE. (2015). AM11: 2015, Building Performance Modelling (pp. 221). London, UK: Chartered Institution of Building Services Engineers.
- Crawley, D. B., Hand, J. W., Kummert, M., & Griffith, B. T. (2008). Contrasting the capabilities of building energy performance simulation programs. Building and environment, 43(4), 661-673.
- Forrester, A. I. J., Sóbester, A., & Keane, A. J. (2007). Multi-fidelity optimization via surrogate modelling. Proceedings of the Royal Society A: Mathematical, Physical and Engineering Science, 463(2088), 3251 LP-3269.
- Jin, R., Chen, W. & Simpson, T. Structural and Multidisciplinary Optimization (2001) 23:1.
- Knebel, D.E. (1983). Simplified Energy Analysis using the Modified Bin Method. Atlanta, GA: American Society of Heating, Refrigerating and Air-Conditioning Engineers, Inc.
- Kusuda, T. (1999). Early History and Future Prospects of Building System Simulation. Proceedings of the Sixth International IBPSA Conference, Kyoto, 3-15.
- Lam, K. P., Zhao, J., Ydstie, B. E., Wirick, J., Qi, M., & Park, J. (2014). An EnergyPlus whole building energy model calibration method for office buildings using occupant behavior data mining and empirical data. Center for Building Performance and Diagnostics, Carnegie Mellon University, Pittsburgh, PA Department of Chemical Engineering, Carnegie Mellon University, Pittsburgh, PA Phipps Conservatory and Botanical Gardens, Pittsburgh, PA, 160–167.
- Mao, Chunliu., Haberl, Jeff S, Baltazar, Juan-Carlos. (2013). Literature review on the history of building peak load and annual energy use calculation methods in the U.S. Energy Systems Laboratory Transactions, Texas Engineering Experiment Station, The Texas A&M University.
- Miller, Simon W, Michael A Yukish, and Timothy W Simpson. 2017. “Design as a Sequential Decision Process: A Method for Reducing Design Set Space Using Models to Bound Objectives.” Structural and Multidisciplinary Optimization, 1–20.
- Mitalas, G.P., & Stephenson, D.G. (1967). Room Thermal Response Factors. ASHRAE Transactions, 73, Pt.1.
- Simpson, T. W., Peplinski, J. D., Koch, P. N., & Allen, J. K. (2001). Metamodels for Computer-based Engineering Design: Survey and recommendations, 129–150.
- Unal, R.; Lepsch, R.A.; Englund, W.; Stanley, D.O. 1996: Approximation model building and multidisciplinary design optimization using response surface methods. Proc. 6th AIAA/USAF/NASA/ISSMO Symp. on Multidisciplinary Analysis and Optimization (held in Bellevue, WA), Vol. 1, 592–597. AIAA.

Optimal passive design strategies for nearly zero-energy dwellings in different Chilean climates using multi-objective genetic algorithms

Daniela Besser^{1,*} and Frank U. Vogdt¹

¹Technische Universität Berlin, Berlin

*Corresponding email: d.besserjelves@campus.tu-berlin.de

ABSTRACT

At present, most developed countries attempt to highly diminish the energy consumption of buildings towards nearly zero-energy performances. This study assesses passive design strategies by means of multi-objective optimizations with genetic algorithms, aiming to minimize the heating and cooling demand of typical single-family dwellings in Chile. The results show that the thermal transmittance and airtightness of the whole building envelope should be highly improved from the current limiting values in all assessed locations. Complementarily, strategies for managing overheating would be crucial for avoiding to shift the heating demand into cooling. With this regard, the use of thermal mass, natural ventilation and shading devices in the east and west façades would be highly determining for achieving a balance between the two conflicting objectives throughout climatic zones in Chile.

KEYWORDS

Low energy dwellings, passive design, energy performance, multi-objective optimizations.

INTRODUCTION

The Chilean government aims to highly improve the energy-environmental quality of new Chilean dwellings to comparable standards with the OECD countries by 2035 (Ministerio de Energía, 2015). However, the current Chilean Thermal Regulation (TR) only limits the thermal transmittance of the major building envelope components of residential buildings, being its levels usually not enough for achieving low energy, high quality homes, as demonstrated by several studies (Bustamante et al., 2009; OECD, 2012). Complementarily, a ‘Code for Sustainable Homes’ (CSH) was published in 2014 and recently amended in 2018 by MINVU, highly tightening the energy-environmental requirements of dwellings when compared with the compulsory ones. This standard might set the path towards the necessary update of the TR, imperative for achieving low energy dwellings by 2035. Consequently, this study assesses its impact and explores the remaining gap for achieving nearly zero-energy demands in Chile, using multi-objective optimizations with evolutionary genetic algorithms, which is a probabilistic search technique based on nature that assumes that in a random initial population of individuals (being here each individual a certain combination of design variables), natural selection would foster the survival of the fittest. Their reproduction by recombination (i.e. crossover), together with mutations, would convey robustness and diversity to the new population, evolving until a solution is found (Eiben and Smith 2003). Having more than one objective to optimize would lead to a set of optimal solutions, i.e. Pareto front, being all of them equally suitable when no other objective or constraint exists (Deb et al., 2002).

METHODS

The research uses Design Builder v5 software to perform multi-objective optimizations to a Case Study (CS) in four climatic zones (Z) of Chile (See Figure 1). The CS is a 114m² single-family, detached, two-story dwelling, which is one of the most built housing typologies in the

country according to the National Statistics Institute (www.ine.cl). For the external walls, both brickwork (CS-A) and timber-frame (CS-B), the most used building systems for single-family dwellings, were assessed. The new CSH requests minimum heat capacity levels per m² of building element for each climatic zone, calculated according to ISO 13786:2007 (Annex A) and classified into light, medium and heavyweight. Accordingly, a typical 140mm brickwork wall represents a medium weight solution and a typical timber-frame wall a lightweight one. In both cases a lightweight timber-frame roof and a medium weight concrete slab-on-ground were used. With regards to the simulations, the software optimizes with a non-dominated sorting genetic algorithm (NSGA-II) developed by Deb et al. (2002). Two objective functions were used: to minimize the heating demand and to minimize the cooling demand of the CS; simulating with ideal loads, at 20°C and 26°C (25°C in ZI) operative temperature respectively, whenever when demand. Each story was considered a single thermal zone with constant internal gains of 4.8 W/m². As design variables, ten passive design strategies were simultaneously tested, each of them ranging between two to four levels, which are summarized in Table 1 and briefly described below. The levels in bold in Table 1 were used for the ‘reference cases SH’, that assess the U-values and airtightness suggested by the CSH, whereas the ‘reference cases TR’ evaluate the CS when minimally complying with the TR. The optimizations were set to a maximum of 200 generations, with an initial population of 20 individuals and a maximum of 50 per generation, and crossover and mutation rates of 0.9 and 0.5 respectively.

- Opaque envelope (**Env**): this parameter varies the U-value of the external walls, roofs and suspended floors in four levels, progressively increasing them from the CSH values.
- Floor-on-ground (**FGr**): its insulation level was separately assessed, since it is not regulated by the TR and since the perimeter vertical insulation proposed by the CSH would have a low impact according to a previous study (Besser and Vogdt, 2017). Instead, horizontal insulation under the slab was assessed in three levels, together with a non-insulated option.
- Windows (**Win**): the CSH levels plus three more options that are currently available on the market were tested, varying both the U- and g-values of windows. Since the TR still allows single-glazing along the country when small windows’ proportion, the reference cases TR were simulated using O1 in all locations (See Table 3).
- Window-to-wall ratio (WWR) on the North (**wwN**) and on the East-West façades (**wwE**): Both the TR and the CSH limit the WWR according to the windows’ U-value, the former for the whole building and the latter for each façade. Generally speaking, the colder the climate, the smaller the WWR that is allowed in both standards. This parameter was separately assessed for the North and for the East-West façades, assuming the lowest tested values for the reference cases TR and SH, and a constant 5.5% WWR on the South façade.
- Overhang Nord (**OvN**): It assesses the suitability of a fixed horizontal shading device above the North windows to help seasonally regulating solar access.
- Temporary shades on the East and West facades (**ShE**): Evaluates using external blinds on the East and West windows when internal temperatures are above 23°C (22.5°C in ZI).
- Infiltration rate (**n50**): The limiting airtightness levels proposed by the CSH and two further levels were tested for each location. The values were normalized according to the DIN V 18599-2:2016-10 procedure, and 1 h⁻¹ (14.28 h⁻¹ at 50Pa) was assumed for the TR cases.
- Ventilation for cooling (**VfC**): All cases consider natural ventilation for air quality purposes that seasonally varies according to DIN V 18599-2:2016-10. In addition, ventilation for cooling was assessed, increasing in 3 h⁻¹ the ventilation rate when internal temperatures are above 23°C (22.5°C in ZI) and they are not below the external one.
- Internal thermal mass (**ThM**): In CS-A, two types of internal partitions were assessed: lightweight timber-frame (L) and medium weight 140mm brickwork partitions (M), while a 120mm concrete slab remained constant. In CS-B, the timber-frame internal partitions

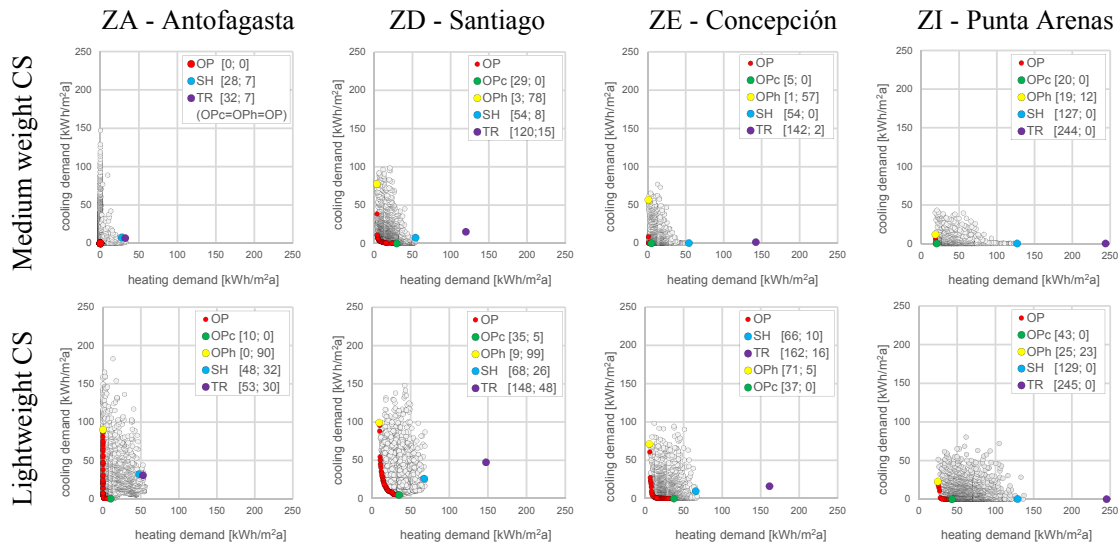


Figure 2. Optimization results plus reference performances TR and SH

Consequently, each Pareto front was analysed, aiming to identify those parameter combinations and levels that would lead to the optimal energy performances in each location. Since the Pareto front is the set of solutions not dominated by other solutions (Deb et al. 2002), and since minimizing the heating and the cooling demand are conflicting objectives, the lower the heating, the higher the cooling and vice versa for every Pareto point, which makes possible to simultaneously list the solutions by ascending heating and descending cooling demand. The outcomes are summarized in Tables 4 to 11, conveying the average heating (AvH) and cooling (AvC) demand of groups of solutions that achieve similar performances and showing the relationship between the ten design variables and the respective levels that would lead to Pareto solutions. In addition, the amount of Pareto points in every group of solutions is given by its frequency (Freq), being 100% the total amount of points within the Pareto front. The set of points with the lowest heating are located on the top of each table, the solutions with the lowest cooling at the bottom, and the trade-offs points are located in between. The highlighted level when grouped conveyed corresponds to the OP_h and OP_c point accordingly. It is worth mentioning that not all combinations among the grouped levels would lead to Pareto solutions.

When looking at Tables 4 to 11, it becomes clear that tightening the envelope thermal transmittance to the best levels together with increasing thermal mass are determining strategies to drastically reduce both the heating and the cooling demand in all locations and for both constructive systems, since these levels are present in 100% of the points forming the Pareto fronts. The OP_h points had additionally in common not considering ventilation for cooling, nor shading devices or overhang, plus the highest wwN, windows with the best U-values, the best n50 rate and the highest or middle floor insulation level, but they resulted in extremely high cooling loads when compared with the TR reference cases in all locations, in spite of reducing heating by 90 to 100%. On the contrary, the OP_c points had in common to allow VfC, to consider the lowest wwE with shading devices, plus windows with the lowest g-values and either a short or a large overhang, in addition to the previously mentioned levels of Env and ThM. These cases would eliminate the need of cooling in all locations, except for the lightweight CS-B in ZD, where nonetheless a 90% reduction would be achieved when compared with the TR performance. Moreover, the resulting heating demands would be 75 to 100% lower than in the TR reference cases in all locations. In ZA it would even be possible to achieve zero energy demands for space conditioning when enough levels of thermal mass, as in CS-A. Finally, the trade-off Pareto points attempt a balance between the two conflicting objectives. Here, most

Table 4. Optimal combinations in Antofagasta for Case Study A (17 points = 100%)

Env	ThM	Win	VfC	ShE	wwN	wwE	OvN	n50	FGr	AvH	AvC	Freq
E7	M	O5	Y	Y	40	10	0.4/0.8	4/6/8	0.3/0.6/1.2/3.6	0	0	59%
						40	0.8	4/6/8	1.2/3.6	0	0	29%
						10	40	-0.4	4	0.3/0.6	0	0

Table 5. Optimal combinations in Antofagasta for Case Study B (78 points = 100%)

Env	ThM	Win	VfC	wwN	wwE	ShE	n50	OvN	FGr	AvH	AvC	Freq				
E7	M	O5	N	Y	70	10	N/Y	4	-0.4	0.3/0.6/1.2/3.6	0	69	14%			
					40	10	Y	4	-0.4	0.3/0.6/1.2	0	34	12%			
					70	10	Y	4	0.4	0.6/3.6	0	20	3%			
					40	10	N	4	-	0.3/0.6	0	14	3%			
					10	10	Y	4/6	-0.4/0.8	0.3/0.6/1.2/3.6	0	4	18%			
			O2	Y	10	10	Y	40	Y	4	0.4/0.8	0.3/0.6/1.2/3.6	1	2	9%	
								10	Y	4/6/8	-0.4/0.8	0.3/0.6/1.2/3.6	3	0	22%	
								10	10	Y	4/6/8	-0.4/0.8	0.3/0.6/1.2/3.6	7	0	21%

Table 6. Optimal combinations in Santiago for Case Study A (40 points = 100%)

Env	ThM	n50	VfC	ShE	Win	wwN-wwE	OvN	FGr	AvH	AvC	Freq			
E8	M	3	Y	Y	O7	N/Y	N	O7	70-40	-	0.3/0.6	3	58	5%
						70-40	-0.4/0.8	0.3/0.6/1.2/3.6	5	7	20%			
						70-10/40-40	0.4/0.8	0.3/0.6/1.2/3.6	8	3	25%			
						40-10	-0.4/0.8	0.3/0.6/1.2/3.6	13	1	23%			
						O6/O7	10-10	-0.4/0.8	0.3/0.6/1.2/3.6	26	0	28%		

Table 7. Optimal combinations in Santiago for Case Study B (51 points = 100%)

Env	ThM	Win	ShE	VfC	wwN-wwE	n50	FGr	OvN	AvH	AvC	Freq		
E8	M	O7	Y	Y	N	N	70-40/70-10	3	0.3	-	10	84	8%
					N/Y	70-40/70-10/40-40	3	0.3	-0.4/0.8	12	35	18%	
					70-10/40-40	3/4	0.3/0.6	-0.4/0.8	16	20	31%		
					40-10	3/4	0.3/0.6	-0.4/0.8	19	13	31%		
					10-40/10-10	3/4	0.3/0.6/1.2/3.6	-0.4/0.8	27	7	43%		

Table 8. Optimal combinations in Concepción for Case Study A (13 points = 100%)

Env	ThM	Win	VfC	ShE	wwN-wwE	n50	FGr	OvN	AvH	AvC	Freq		
E10	M	O7	Y	Y	N	N	70-40	3	0.3	-	1	57	8%
					N	70-40	3	0.3	-	1	8	8%	
					70-40	3/4	0.3/0.6/1.2	-0.4/0.8	3	0	69%		
					70-10/40-40	3	0.3	-0.8	5	0	15%		

Table 9. Optimal combinations in Concepción for Case Study B (47 points = 100%)

Env	ThM	Win	ShE	VfC	wwN-wwE	FGr	n50	OvN	AvH	AvC	Freq		
E10	M	O7	Y	Y	N	N	70-40	0.3	3/4	-0.4	6	67	6%
					N	70-40/70-10	0.3	3	-0.4	7	21	9%	
					70-40/70-10	0.3	3/4	-0.4/0.8	10	5	15%		
					40-40/40-40	0.3/0.6	3/4/5	-0.4/0.8	14	1	21%		
					10-40/10-10	0.3/0.6/1.2/3.6	3/4/5	-0.4/0.8	26	0	49%		

Table 10. Optimal combinations in Punta Arenas for Case Study A (7 points = 100%)

Env	ThM	Win	n50	FGr	wwN	VfC	wwE	OvN	ShE	AvH	AvC	Freq
E12	M	O7	2	0.3	70	N	10	-	Y/N	19	6	29%
						Y	10/40	-0.4	Y/N	20	0	71%

Table 11. Optimal combinations in Punta Arenas for Case Study B (17 points = 100%)

Env	ThM	Win	n50	FGr	VfC	wwN	wwE	OvN	ShE	AvH	AvC	Freq
E12	M	O7	2	0.3	N	70	10	-/0.4	Y/N	26	17	24%
					Y	70	10-40	-/0.4/0.8	Y/N	31	1	41%
						40	10-40	-/0.4/0.8	Y/N	39	0	35%

combinations have additionally in common to allow VfC, windows with the lowest U- and g-values, the best n50 levels and ShE. The WWR on the North and on the East-West façades varies depending on the case and location, highly determining the degree of compromise between the objectives. The final election of a best case among each Pareto front would depend on a complementary factor, such as the heating and cooling systems to be used, their efficiency, their energy source, its price, its primary energy factor, the costs of the design strategies, etc.

CONCLUSIONS

It would be possible to highly diminish the heating and cooling demand of Chilean dwellings when tightening the envelope thermal transmittance and n50 values as the CSH proposes. Moreover, a high improvement potential remains beyond. In fact, the energy demand for space conditioning could approach to zero in all assessed locations when properly combining passive design strategies as the ones assessed in this study. However, attempting to minimize both demands are conflicting objectives and therefore, care should be taken to avoid shifting the heating savings into cooling demands or vice versa. Since some strategies attempt minimizing heating and others pursuit cooling reductions, a balance should be aimed and thus the interaction among strategies becomes highly relevant, which confirms the appropriateness of multi-objective analyses when searching for zero-energy buildings and the importance of the interaction between the design strategies when optimizing buildings' energy performance.

ACKNOWLEDGEMENT

This study was undertaken as part of a doctoral study in the Building Physics Department of the Technische Universität Berlin, financed by the German Academic Exchange Office DAAD.

REFERENCES

- Besser, D. and Vogdt, F.U. 2017. First steps towards low energy buildings. How far are Chilean dwellings from nearly zero-energy performances?. *Energy Procedia*, 132, 81-86.
- Bustamante, W., Rozas, Y., Cepeda, R., Encinas, F. and Martinez, P. 2009. *Guía de diseño para la eficiencia energética en la vivienda social*. Santiago: MINVU & CNE.
- Deb, K., Pratap, A., Agarwal, S. & Meyarivan, T. 2002. A fast and elitist multiobjective genetic algorithm: NSGA-II. *IEEE Transactions on evolutionary computation*, 6(2), 182–197.
- Eiben, A.E. and Smith, J.E. 2003. *Introduction to evolutionary computing*. New York: Springer.
- DIN. 2016. *Prestandard DIN V 18599-2:2016-10*, Energy efficiency of buildings - Calculation of the net, final and primary energy demand for heating, cooling, ventilation, domestic hot water and lighting - Part 2: Net energy demand for heating and cooling of building zones. Berlin: Beuth Verlag.
- ISO. 2007. *Standard ISO 13786:2007*, Thermal performance of building components - Dynamic thermal characteristics - Calculation methods. Switzerland: International Organization for Standardization.
- Ministerio de Energía. 2015. *Energy 2050. Chile's energy policy*. Santiago: Ministerio de Energía.
- MINVU. 2018. *Estándares de construcción sustentable para viviendas de Chile*. Santiago: Ministerio de Vivienda y Urbanismo.
- OECD. 2012. *OECD Economic Surveys: Chile 2012*. Paris: OECD Publishing.

Pareto Optimality Analysis for Evaluating the Tradeoff between Visual Comfort and Energy Efficiency

Maryam Hamidpour^{1*}, Vincent Blouin¹

¹Clemson University, Clemson, SC

**mhamidp@g.clemson.edu*

ABSTRACT

Architectural designs are increasingly driven by both sustainability and health, which requires evaluating the tradeoff between visual comfort and energy consumption. Lack of daylight leads to poor visual comfort and health issues but reduces heat gains, while excessive daylight may lead to over-illumination, glare, and high heat gains. Identifying the tradeoff between multiple criteria is an intricate process that requires skill and experience, especially when dealing with complex phenomena such as visual comfort. In order to facilitate this process, this paper provides two contributions: (1) the description of a new single-valued visual comfort measure, and (2) the application of the Pareto optimality analysis method. Pareto optimality analysis consists of comparing different design options in terms of the tradeoff between multiple criteria, which is a method that is rarely used in architectural design albeit its many advantages. For the Pareto optimality analysis, single-valued performance metrics are required. The energy performance metrics such as annual heating and cooling loads are single-valued quantities that, nowadays, can be calculated and measured easily. Daylight performance, however, is a complex multi-dimensional phenomenon. While previously developed daylight and glare performance metrics have their merits, they are not readily applicable to Pareto analysis. In this work, a new light metric called Effective Glare and Light Measure (EGLM) is developed to address the current limitations. The EGLM metric is defined as a weighted sum of several normalized performance metrics to end up with a single-valued measure of visual comfort. Two software programs, DIVA-for-Rhino and EnergyPlusTM, are used to calculate the time-dependent visual performance data and energy consumption, respectively. A script is then used to post-process the data. Several case studies are presented to illustrate the method with various building orientations, window-to-wall ratios, overhang depths, and glass visibility transmittance.

KEYWORDS

Pareto Optimality, Daylighting Analysis, Glare, Energy Efficiency

INTRODUCTION

Daylight has consistently been an essential component of architecture and the primary source for illuminating the interior environment. The benefits of using daylight in buildings range from savings in energy consumption and enhancing occupant health and comfort to improving outside views, and design aesthetics (Reinhart, 2014). While admitting daylight within a building has many known benefits, there are some disadvantages associated with transferring too much light into a space. These problems include occupants' visual and thermal discomfort and waste of cooling energy. Careful design is required to adjust these effects. As such, it is beneficial to apply methods helping designers to predict the tradeoff between criteria as much as possible during early design stages. Using Pareto optimality analysis is a quantitative and rigorous way of predicting this tradeoff (Hunt et al., 2007). However, this method requires single-valued metrics for all design criteria. This explains why this method is extensively used in engineering design, which generally involves design criteria that are easily quantifiable.

Architectural design is a discipline that involves qualitative metrics, one of them being aesthetics, which explains the unpopular use of Pareto optimality analysis. The premise of this paper is to demonstrate that Pareto optimality analysis can be used in architectural design when dealing with quantifiable criteria such as visual comfort and energy consumption. The method is used to compare the performance of different design alternatives corresponding to variations of several design parameters including building orientation, window-to-wall ratio, overhang depth, and glass visibility transmittance.

Energy performance metrics are generally straightforward since they are based on annual heating and cooling loads, which can be added to provide the annual energy consumption as a single-valued quantity. Visual comfort, however, is a complex phenomenon quantified using various intricate performance metrics that evaluate the level of illuminance and glare (Reinhart, 2014). A number of metrics have been adapted to evaluate the sufficiency of illuminance within a space, including, Daylight Factor, Daylight Autonomy, and Useful Daylight Illuminance (Reinhart, 2014). These metrics, however, have a number of drawbacks as they are either climate-independent, excessively simple, or multi-valued. As for glare, a number of metrics have been developed, including, CIE Glare Index, Unified Glare Rating System, Daylight Glare Index, and Daylight Glare Probability (Wienold and Christoffersen, 2006). These metrics, however, are either only applicable to artificial lighting or are metrics that measure glare at a given time as opposed to during a period of time such as the whole year. Therefore, a new visual comfort metric, called the Effective Glare and Light Measure (EGLM) is developed specifically for the purpose of architectural design driven by the tradeoff between visual comfort and energy consumption.

Most studies that evaluate the performance of daylighting systems and shading devices such as blinds, overhangs, louvers, light shelves, and dynamic glass fall short of providing an effective approach to the tradeoff analysis when evaluating the building performance with multiple criteria. For instance many studies have evaluated the performance of electrochromic glass (Lee and Tavit, 2007) without quantitatively analyzing the tradeoff between light levels and energy efficiency. Similar work that focus on glazing and shading devices have the same limitation (Ochoa et al., 2012).

The paper includes three sections. The first section describes the development of the new visual comfort metric, some of its variations, and its application in the Pareto optimality analysis method using a single office room with a window on the South façade as a case study. The performance of a given design in terms of visual comfort and energy consumption is quantified using the simulation software DIVA-for-Rhino (Solemma, 2017) and EnergyPlus™ (DOE and NREL, 2017). The second section presents results of practical applications of the method on the case study problem for various design alternatives corresponding to various values of building orientation, window-to-wall ratio, overhang depth, and visibility transmittance. The method is compared to the traditional way of comparing alternatives without the Pareto optimality analysis to illustrate its practicality. The third section includes a discussion of the method, its limitations, and the design opportunities that it provides.

METHODS

The Pareto optimality analysis method consists of visualizing the performance criteria of different design alternatives on a two- or three-dimensional graph when dealing with two or three criteria, respectively. In this paper, the first criterion consists of minimizing the annual energy consumption of the building of interest as the annual heating and cooling loads. The

annual energy consumption is a single-valued quantity measured in mega-Joules (MJ). The second criterion consists of maximizing visual comfort in a room of interest.

Development of the Effective Glare and Light Measure (EGLM)

The EGLM metric is defined as a weighted sum of two additional metrics. i.e., the Effective Light Measure (ELM) and the Effective Glare Measure (EGM), as follows:

$$\text{EGLM} = \beta \text{ELM} + (1 - \beta)\text{EGM}$$

where β is a user-defined weight between 0 and 1.

Development of the Effective Light Measure (ELM)

Illuminance, measured in lux, is the amount of light that falls on a given surface area (Lechner, 2008). The Illuminating Engineering Society of North America (IESNA) recommends target values of illuminance for various tasks, including for instance, an average of 400 lux for office tasks and 1000 lux for laboratory work (Rea and IESNA, 2000). These target values are then converted into target ranges, such as 300 to 500 lux for office tasks. An illuminance below or above these recommended ranges puts unnecessary strain on the eyes and induces fatigue, among other issues. Unlike artificial lighting, daylighting varies constantly during the day as it depends significantly on the climate, seasons, and the weather. As a result, maintaining the desired illuminance level at all times is virtually impossible, and the goal is then to maximize the number of hours in the recommended range. In this paper, the illuminance spectrum is divided into five ranges defined as follows: Range 1 between 0 and 100 lux is undesirable, Range 2 between 100 and 300 lux is acceptable, Range 3 between 300 and 500 lux is desirable, Range 4 between 500 and 1000 lux is acceptable, and Range 5 above 1000 lux is undesirable. Using five ranges, as opposed to only three, provides the increased resolution needed to capture the difference between architectural design alternatives. Using five ranges, the Effective Light Measure (ELM) is defined as a weighted sum of the normalized numbers of hours when the illuminance is within a predefined range, which can be written as follows: $\text{ELM} = \sum_{i=1}^5 \alpha_i \frac{N_i}{N_{\text{total}}}$,

where α_i is a user-defined weight for range i , with $\sum_{i=1}^5 \alpha_i = 1$, N_i is the number of hours in range i , and N_{total} is the total number of working hours in a year. The user-defined weights, α_i , are subjective and are currently defined as 0.1, 0.2, 0.4, 0.2, and 0.1 for ranges 1 to 5, respectively.

Development of the Effective Glare Measure (EGM)

Glare depicts the contrast in brightness between different objects in one's field of vision and one way to quantify it is with the instantaneous measure called the Daylight Glare Probability (DGP). The DGP defines the probability that a person is disturbed by brightness distribution throughout the space (Wienold and Christoffersen, 2006). The DGP is a number between 0 and 1 to be minimized. Wienold (2009) proposes several ranges as follows. Range 1 corresponds to imperceptible glare with a DGP below 0.35, Range 2 is perceptible glare between 0.35 and 0.40, Range 3 is disturbing glare between 0.40 and 0.45, and Range 4 is intolerable glare above 0.45. The Effective Glare Measure (EGM) is defined as a weighted sum of the normalized numbers of hours when the DGP is within a predefined range, which can be written as follows: $\text{EGM} = \sum_{j=1}^4 \gamma_j \frac{N_j}{N_{\text{total}}}$ where γ_j is a user-defined weight for range j , with $\sum_{j=1}^4 \gamma_j = 1$, N_j is the number of hours in range j , and N_{total} is the total number of working hours in a year. The user-defined weights, γ_j , are subjective and are currently defined as 0.5, 0.3, 0.15, and 0.05 for ranges 1 to 4, respectively.

Pareto optimality analysis

It is assumed that a set of design alternatives are analyzed in terms of visual comfort and energy consumption. The Pareto optimality analysis corresponds to plotting the corresponding values of all design alternatives on the two-dimensional graph. In this paper, the horizontal axis is the annual energy consumption to be minimized and the vertical axis is visual comfort to be maximized. As a result, the best design alternatives are those closest to the top-left corner of the graph.

Case study

As shown in Figure 1, the room of interest is a rectangular office, 4.26-m long, 3.35-m wide, and 3.00-m floor-to-ceiling height with a window. The work table is placed at the middle of the room such that the user is facing the window. The baseline design of the office has the window on the South façade, a window-to-wall ratio of 50%, no overhang, and a glass visibility transmittance of 80%. The point where horizontal illuminance is simulated is at the center of the table. The glare sensor is located 1.4 meters from the floor facing the window to represent the position and orientation of the person sitting at the desk. The weather of Anderson, South Carolina is used for all simulations, which corresponds to a mild climate with approximately equal heating and cooling loads. A standard heat-pump HVAC system is considered for heating and cooling the building with lower and upper setpoint temperatures of 24°C and 22°C. The R-values of the exterior wall and window are 17 and 3.5, respectively, and the interior walls, floor, and ceiling are considered adiabatic to represent the effect of an interior office of a multi-story building. DIVA-for-Rhino and EnergyPlus™ are used to simulate the illuminance, glare, and energy consumption over the entire year, 10 hours per day from 8:00AM to 6:00PM.

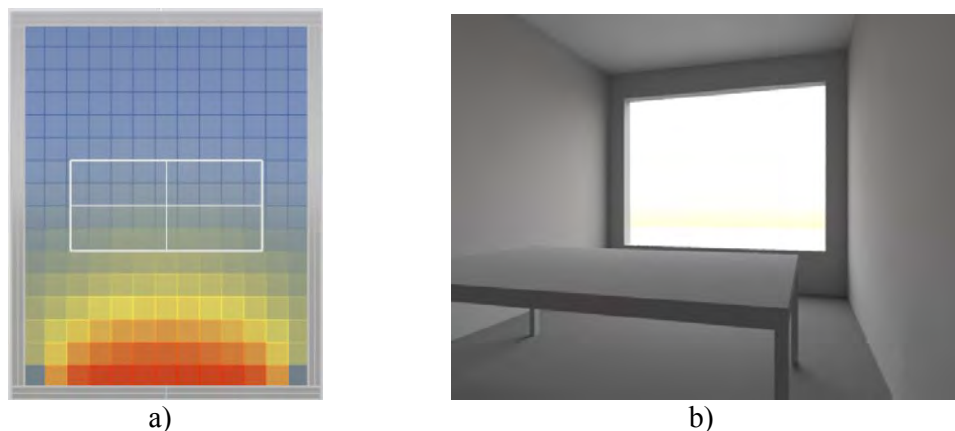


Figure 1. a) Plan of view of the room of interest with window oriented towards South, table at the center of the room, b) Rendering of the room as simulated by DIVA-for-Rhino.

RESULTS

Effect of building orientation

Five different building orientations are considered, i.e., East, South-East, South, South-West, and West. Figure 2 shows the results using the traditional method of visualization with three histograms, namely, the number of hours of illuminance in each of the five ranges, number of hours of glare in each of the four ranges, and energy consumption. The graphs include all necessary information to compare the five design alternatives. However, this method is fairly confusing and analyzing the tradeoff between alternatives in terms of visual comfort and energy consumption is virtually impossible.

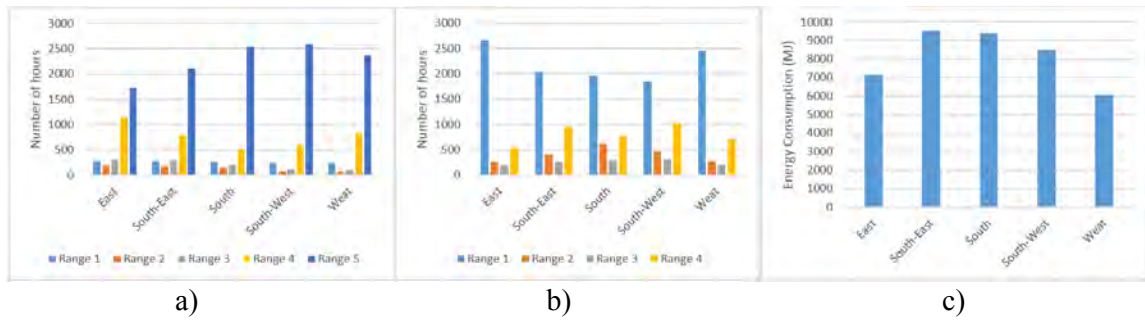


Figure 2. a) Number of hours of illuminance in each of the five ranges for each building orientation, b) Number of hours of glare in each of the five ranges for each building orientation, and c) Energy consumption for each building orientation.

Figure 3.a) shows the same results in a more compact manner by plotting the visual comfort metrics ELM, EGM, EGLM, and Energy on the same histogram. The information is easier to understand. However, the tradeoff is still difficult to extract. Finally, the same results are shown in Figure 3.b) using the Pareto optimality analysis method with the visual comfort metrics on the vertical axis and the energy consumption on the horizontal axis. Using this method, the tradeoff between the design alternatives can be easily identified since the best designs are those closest to the top left corner of the graph. Focusing on EGLM (grey curve), it is clear that the East and West orientation are significantly better than the other three building orientations. The selection of the final design alternative (either East or West) depends on the designer's preferences. The East orientation is best if visual comfort is preferred. The West orientation is best if energy consumption is preferred.

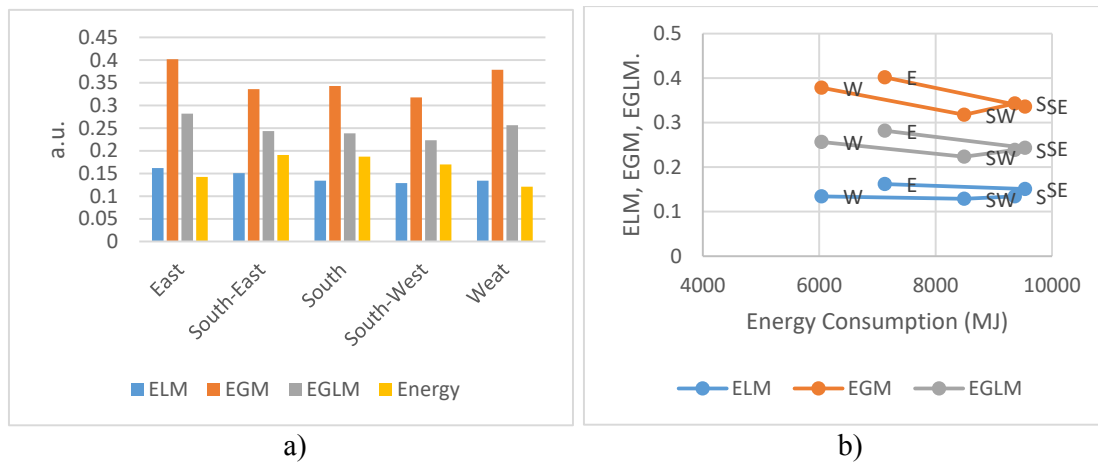


Figure 3. a) ELM, EGM, EGLM, and Energy (in MJ divided by 50,000 for scaling), b) ELM, EGM, EGLM versus Energy (MJ)

Figure 4 shows the Pareto curves corresponding to the variations of three other design parameters, i.e., window-to-wall ratio, dimension of overhang, and glass visibility transmittance. Analysing each curve allows identifying the best design in terms of tradeoff between criteria.

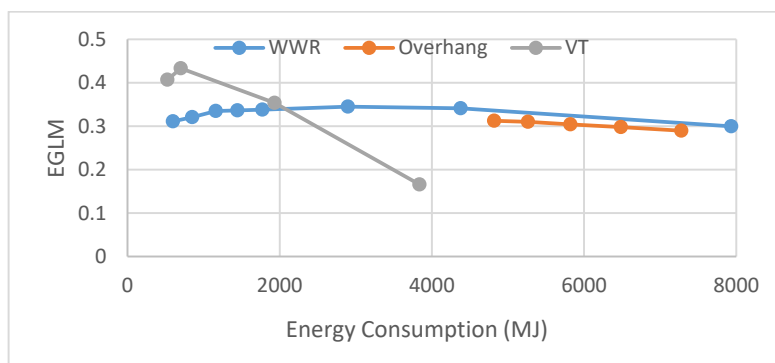


Figure 4. Pareto curves of three parametric studies: blue curve: WWR varies between 6% (lowest energy) and 40% (highest energy), orange curve: overhang depth varies between 0.5m (highest energy) and 1.4m (lowest energy), grey curve: glass visibility transmittance varies between 1% (lowest energy) and 60% (highest energy).

CONCLUSIONS

This paper shows the advantages of using the Pareto optimality analysis method to identify the tradeoff between multiple criteria in architectural design. This method, however, requires the use of single-valued quantities. Since visual comfort is a complex phenomenon that is generally quantified using multi-valued quantities, a new single-valued metric was developed in order to be readily usable in Pareto optimality analysis. Several case studies are presented to illustrate the benefits of the method. The single-valued metric is based on a weighted sum of additional metric, which are also based on subjective user-defined weights. The effect of the subjectivity of these weights will be studied as future work. However, this disadvantage is somewhat negligible compared to the benefits of using the Pareto optimality analysis method.

REFERENCES

- DOE & NREL (2017). EnergyPlus (version 8.7.0) [computer software]. Available from <https://energyplus.net>.
- Hunt B. J., Blouin V. Y., & Wiecek M. M. (2007). Modeling relative importance of design criteria with a modified Pareto preference. *ASME. J. Mech. Des.*, 129(9), 907-914.
- Lechner, N. (2008). *Heating, cooling, lighting: Sustainable design methods for architects*. Wiley, Inc. Hoboken: New Jersey.
- Lee, E. S., & Tavit, A. (2007). Energy and visual comfort performance of electrochromic windows with overhangs. *Building and Environment*, 42, 2439-2449.
- Ochoa, C. E., Aries, M. B., Loenen, E. J., & Hensen, J. L. (2012). Considerations on design optimization criteria for windows providing low energy consumption and high visual comfort. *Applied Energy*, 95, 238-245.
- Rea, M. S., & IESNA (2000). *The IESNA lighting handbook: Reference & application*. New York, NY: Illuminating Engineering Society of North America.
- Reinhart, C. (2014). *Daylighting Handbook, Volume I*. United States: Christoph Reinhart. ISBN: 9780692203637.
- Solemma, LLC. (2017). DIVA-for-Rhino (version 4.0) [computer software]. Available from: <http://diva4rhino.com>.
- Wienold, J. (2009). Dynamic daylight glare evaluation. *Proceedings of the Eleventh International Building Simulation Conference*. Glasgow, Scotland.
- Wienold, J., & Christoffersen, J. (2006). Evaluation methods and development of a new glare prediction model for daylight environments with the use of CCD cameras. *Energy and Buildings*, 38(7), 743-757.

Passive Survivability in Residential Buildings during Heat Waves under Dynamic Exterior Conditions

Timothy Aduralere¹, Jacqueline Isaacs¹, David Fannon^{2,3*}

¹ Department of Mechanical Engineering, Northeastern University, Boston, MA

² Department of Civil and Environmental Engineering, Northeastern University, Boston, MA

³ School of Architecture, Northeastern University, Boston, MA

**Corresponding email: d.fannon@northeastern.edu*

ABSTRACT

The increased frequency of heat waves around the world has prompted numerous studies to improve building resilience and maintain thermal comfort in the face of extreme conditions. However, previous studies rely on the assumption of steady-state conditions, including external temperature, which limits real-world applicability, demanding a more practical perspective. This paper presents the use of recorded heat wave temperatures for a specified location to simulate the effect of extreme temperatures on the interior temperature of buildings when air conditioning is not used. The objective of this study is to determine how a building becomes uninhabitable during extreme heat and to effectively compare the changes in internal temperature of different building types during heat waves and standard climatic conditions. Residential buildings were modeled using OpenStudio and simulated using EnergyPlus 8.7.0. for modified weather data files using recorded historical heat wave events. The results obtained provide a method for dynamic simulation of extreme events, establish a framework for policies supporting passive survivability in construction and consequently, reduce heat-related mortality.

KEYWORDS

Heat waves, Passive survivability, Energy Simulation, Thermal Comfort

INTRODUCTION

Heat waves are sometimes described as silent killers (Carroll, 2002) that often disproportionately affect vulnerable populations. To better understand and respond to such disasters, modeling and numerical simulations promise to identify critical thresholds, formulate parameters to estimate the damage, and evaluate possible design responses. In order to analyze the effect of a heat wave duration in the simulations carried out in this research, a heat wave will be defined as a period of at least three days, where the daily maximum temperature exceeds a threshold of the 97.5th percentile of the distribution of maximum temperatures observed in a given location (Meehl and Tebaldi, 2004).

Climate Change and Heat Waves

Nearly all extreme weather events are exacerbated by climate change. A 2016 report notes that “If an extreme event truly is rare in the current climate, then almost by definition it required some unusual meteorological situation to be present, and the effect of climate change is a contributing factor (National Academies of Sciences, 2016).” The influence of global warming on heat waves is particularly direct. It is very likely that human influence has contributed to observed global scale changes in the frequency and intensity of daily temperature extremes since the mid-20th century, and likely that human influence has more than doubled the probability of occurrence of heat waves in some locations

(Intergovernmental Panel on Climate Change (IPCC), 2013). Heatwaves are a dangerous natural hazard, and one that requires increased attention (World Meteorological Organization and WHO, 2015), therefore a diverse body of prior research on heat waves includes exploring the risk and damage, providing recommendations for community adaptation, and identifying personal safety practices.

Overheating in Buildings

Building HVAC systems are designed to provide conditions of acceptable human comfort. While a complex and nuanced field, indoor human thermal comfort is generally held to occur in a range of operative temperatures from 67°F (19°C) to 82°F (28°C), assuming low air velocities, < 40 fpm (0.2032 m/s), and moderate relative humidity (<65%) for sedentary subjects wearing western-style clothing (ASHRAE, 2017; ASHRAE, 2016). In older people, however, this range is narrower because their responses to changes in body temperature are altered (Güneş and Zaybak, 2008). Regardless of these standards, in buildings without mechanical cooling, or where systems are not functioning, indoor conditions can significantly exceed comfort conditions, rendering survivability—rather than comfort—the objective.

Researchers and policymakers are turning to energy simulation to understand the performance of buildings in extreme conditions, for example, to estimate how quickly indoor air temperature of buildings increase during extreme heat. Nahlik et al. (2017) simulated 39 building prototypes in Los Angeles and Phoenix and found that older buildings are more vulnerable to extreme heat than newer buildings because their interiors warm the fastest. Based on these data, the researchers proposed a new metric for building vulnerability to extreme outdoor heat called Building Heat Performance Index (BHPI). However, these results used a constant outdoor air temperature, which is not a good representation of actual exterior conditions. Using EnergyPlus to simulate the effectiveness building modifications to terrace houses in Greater London, UK, Porritt et al. (2012) showed that investments like insulation, solar controls, and ventilation could help reduce building overheating during heat waves.

METHODS

This study uses dynamic meteorological conditions of Fresno, CA during a major historic heat wave as a case study to determine their impact on the interior temperature of buildings. Two typical, residential building prototypes were simulated with the EnergyPlus software. Clear differences were found between the effect of heat wave weather data and typical meteorological conditions on interior temperatures without air conditioning.

Software

Simulations were carried out using the EnergyPlus v8.7.0 (EnergyPlus, 2018)—an open-source, whole-building energy modeling engine developed by the US Department of Energy. Widely-used in research and practice, EnergyPlus performs dynamic thermal and building energy simulations to yield hourly results for a whole year or period thereof, in this case a heat wave. EnergyPlus simulates sub-hourly timesteps through an iterative calculation procedure to improve the accuracy of its results. Simulations were controlled, and input files were edited using the Open-studio plugin (OpenStudio, 2018) for Trimble SketchUp® (Trimble Sketchup, 2018) and the EnergyPlus IDF editor (EnergyPlus, 2018).

Building Prototype

To support replication, this study adapted residential prototype building models developed by the Pacific Northwest National Laboratory (PNNL) under the Department of Energy's

Building Energy Codes Program. The present study considers the single-family detached house (SF), and the multi-family (MF) low-rise apartment building, both illustrated in Figure 1.

The prototype building models are intended to be representative of homes in the state of California (PNNL, 2006). The material properties of the SF and MF buildings were defined with the assumption that the existing buildings during the 2006 heat wave considered in this research satisfies the 2006 version of the International Energy Conservation Code (IECC). Consequently, the minimum requirements given by the IECC for Fresno, located in Climate Zone 3B, were employed as the building construction properties in its entirety. Major features and characteristics are summarized in table 1.

Table 1. Comparison of major features of the building prototypes.

Feature	Single-Family	Multi-Family
Total floor area	148.6 m ²	204.9 m ²
Stories	1	2
Bedrooms	3	3
Wall R-Value	13 (hr °F ft ²)/BTU	13 (hr °F ft ²)/BTU
Ceiling R-Value	30 (hr °F ft ²)/BTU	30 (hr °F ft ²)/BTU
Window U-Value	0.65 BTU/(hr °F ft ²)	0.65 BTU/(hr °F ft ²)
HVAC	NA (turned off for study)	NA (turned off for study)

To support this research, the available prototype models were upgraded from EnergyPlus version 5.0.0 to version 8.7.0, and associated errors and warnings corrected. Finally, to represent the performance of a building without air conditioning during a heat-wave, HVAC schedules were set to prevent the equipment from operating.

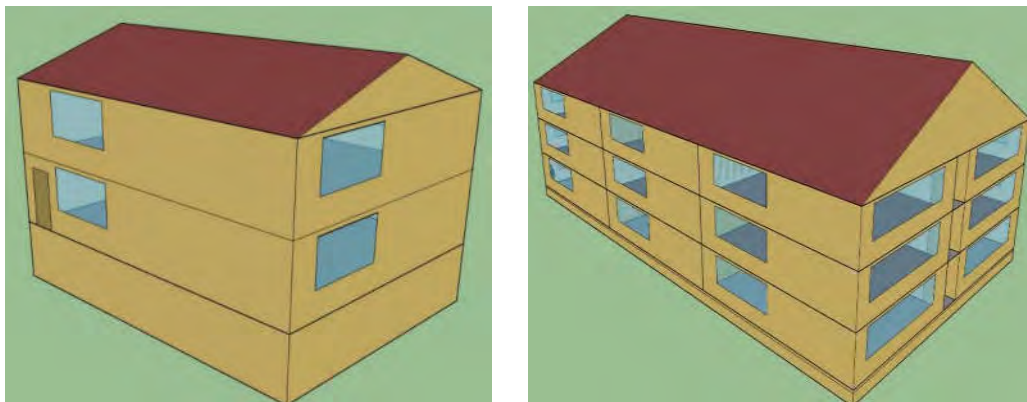


Figure 1. 3D representations of the Single-family (SF) detached residential prototype (left) and the Multi-family (MF) low-rise apartment residential prototype (right).

Location and Climate data

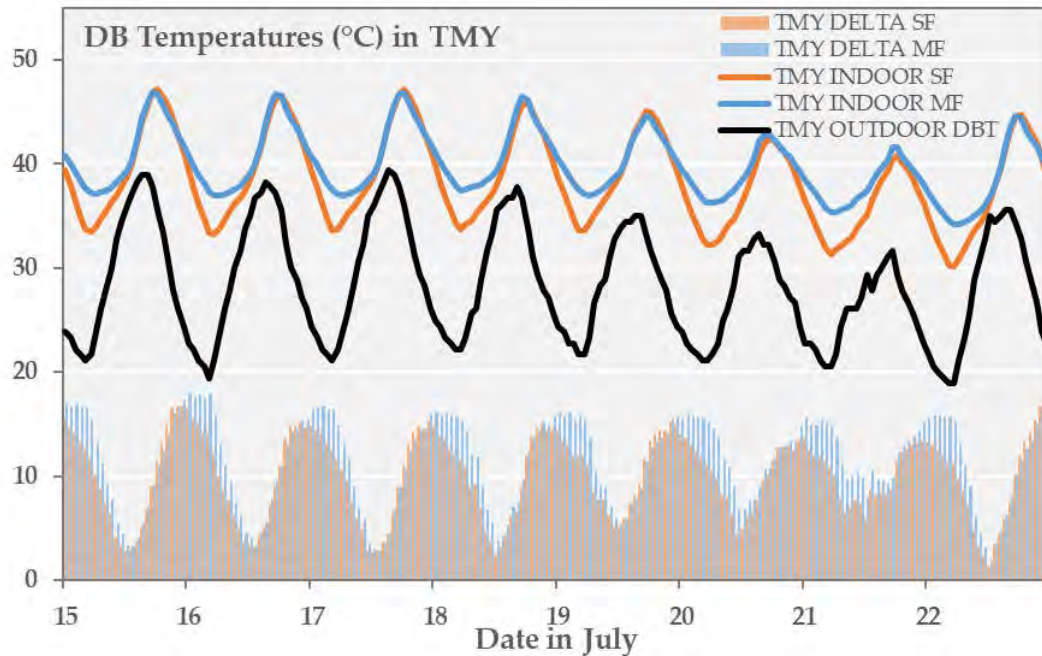
This study uses Fresno California, and the 2006 heatwave, as a case study. Located in California's central valley, Fresno experiences a semi-arid climate (ASHRAE Zone 3B, CA climate zone 13). Climate data from Fresno Yosemite International Airport (36.7758° N, 119.7181° W, elevation 102 meters) was used. Energy plus uses data files in the EnergyPlus Weather (EPW) file format to represent exterior conditions. Each prototype was simulated with two different weather files: one representing the Typical Meteorological Year (TMY) for Fresno; and the second based one consisting of measured extreme weather in this location. The base TMY weather file was produced by the National Renewable Energy Laboratory's

(NREL's) Analytic Studies Division for the TMY3 process, using selected hourly data to represent standard climatic conditions. The second weather file contains the record of meteorological data for 2006, a year when this area experienced a major, multi-day heat event, and was purchased from White Box Technologies. Of interest is the 2006 summer heat wave, covered using a run period of July 15th – 22nd.

RESULTS

Dynamic thermal simulations were carried out for the two cases considered.

a)



b)

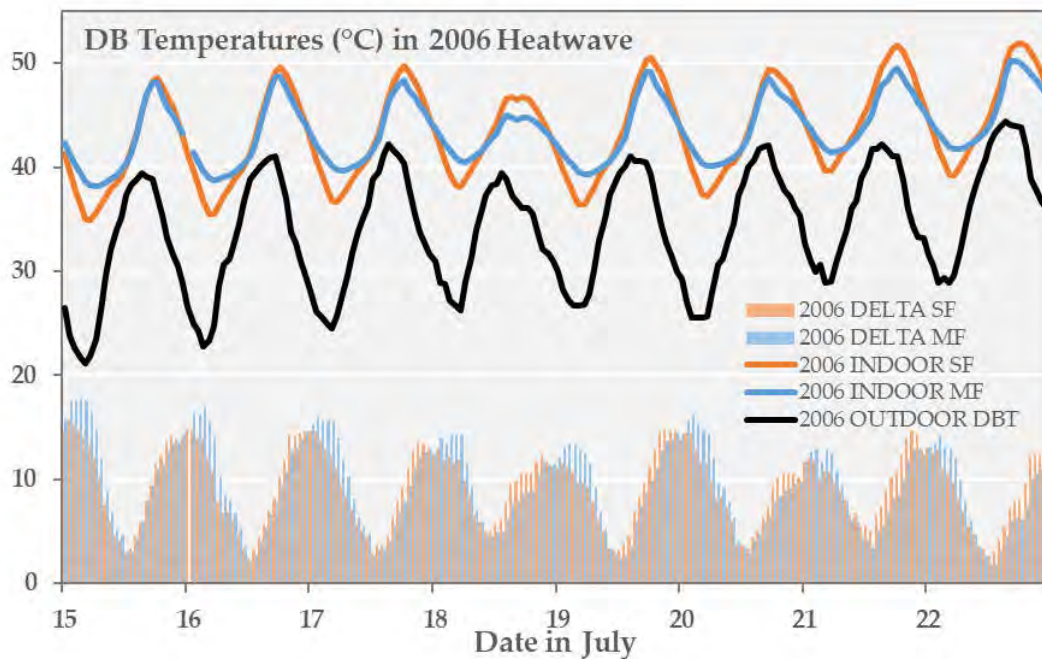


Figure 2. Outdoor Air Temperature and simulated indoor dry-bulb temperatures and deltas for the dates of the study period considering a) Typical conditions (TMY), and b) the 2006 heat wave. Diurnal patterns in absolute temperature are visible, as is the clear trend of increasing temperature in the heatwave, and the declining delta-T.

Figure 2 shows the effect of an extreme heat period lasting 8 days (July 15th – 22nd) on a single-family and multi-family residential building.

DISCUSSION

Figure 2 shows that the natural, diurnal variation of outdoor air temperature is approximately 15°C in July from warmest (midday) to coolest (predawn). This is apparent and similar in magnitude in both the typical year and under a heat wave. Notably, the indoor temperature closely follows the pattern of varying outdoor dry bulb temperature. All windows were treated as non-operable, therefore the indoor temperature always remains above the outdoor dry bulb temperature, suggesting that skin conduction is always a neat heat loss, while internal and especially solar gains are responsible for the increased temperature. Further, the relatively low-mass of the prototype buildings does little to damp the diurnal oscillation from dynamic thermal simulation. The MF building exhibits longer lags and less variation, due to higher mass and a lower surface-to-volume ratio. In both cases, the rate of conductive heat loss to the exterior is of course dependent on the magnitude of the temperature difference between interior and exterior temperature. These behaviors are not well represented by assuming a constant/steady state outdoor temperature.

In both the TMY and 2006 extreme heat data, the largest magnitude of difference between interior and exterior temperatures (ΔT) typically occurs at night, because the outdoors cools down after sunset, but the house retains some heat. In the heat wave, that difference is smaller, in part because the nights are not cooling off as much, and because the entire system is warmer. The smaller ΔT reduces the loss through envelope convection, so the home cannot shed heat as quickly and continues to grow warmer. Consequently, as the outdoor DB temperature increases with increasing severity of the heat wave, the 2006 Indoor SF and MF increases with decreasing ΔT . This indicates that a more severe heat wave, produces a more uninhabitable building in the absence of mechanical cooling or other strategies.

While not primarily focused on the human physiological consequences, these temperatures are dangerous. The highest temperature observed was 51.96°C, in the Single-Family residential building under the 2006 heat wave, compared to a maximum of 47.15°C in a typical year. Both these thermal conditions are hazardous and potentially fatal to occupants because they exceed body temperature, precluding the body from shedding heat and leading to heat stroke or other heat-related illnesses. It is therefore necessary to have a method that presents an analysis of the indoor conditions of buildings using dynamic exterior conditions.

There are other system-scale effects that can affect heat gain and loss, such as urban heat island effect and the cooling effect from neighborhood vegetation, as well as other cooling strategies such as operable windows that would complicate these models and increase the accuracy of this approach.

CONCLUSIONS

This paper applied dynamic building energy simulation techniques to analyze heat wave effects on the indoor thermal conditions of residential buildings. This is not a complete representation of the scope of the analysis, as site-scale conditions, possible window

operation, and other physiological factors such as relative humidity are not included. Additional work is needed to characterize the vulnerability of a building occupants to extreme heat in dynamic conditions, however, thanks to the widespread availability of recorded actual meteorological data, the approach demonstrated here can be applied to a study using dynamic simulation of extreme heat events in any city of interest.

REFERENCES

- ASHRAE. 2017. *ANSI/ASHRAE Standard 55-2017*, Thermal Environment Conditions for Human Occupancy. Atlanta: American Society of Heating, Refrigerating, and Air-Conditioning Engineers, Inc.
- ASHRAE. 2016. *ANSI/ASHRAE Standard 62.1-2016*, Ventilation for Acceptable Indoor Air Quality. Atlanta: American Society of Heating, Refrigerating, and Air-Conditioning Engineers, Inc.
- Carroll, P. 2002. The Heat Is On: Protecting Your Patients From Nature's Silent Killer. *Home Healthcare Now*, 20, no. 6, 376.
- Güneş, U.Y., and Zaybak, A. 2008. Does the body temperature change in older people? *Journal of Clinical Nursing*, 17, pp. 2284–2287.
- Intergovernmental Panel on Climate Change (IPCC). 2013. Contribution of Working Group I to the Fifth Assessment Report - Climate Change 2013, 1552 pages.
- Meehl, G.A., Tebaldi, C., 2004. More Intense, More Frequent, and Longer Lasting Heat Waves in the 21st Century. *Science* 305, 994–997.
<https://doi.org/10.1126/science.1098704>
- Nahlik, J., Chester, V., Pincetl, S., Eisenman, D., Sivaraman, D., and English, P. 2017. Building Thermal Performance, Extreme Heat, and Climate Change. *Journal of Infrastructure Systems*, 23, no. 3, 04016043.
- National Academies of Sciences, Engineering and Medicine. 2016. *Attribution of Extreme Weather Events in the Context of Climate Change*.
- OpenStudio SketchUp Plug-in. Available from <https://www.openstudio.net/>
- Pacific Northwest National Laboratory (PNNL). IECC residential code 2006. Available from: https://www.energycodes.gov/development/residential/iecc_models
- Porritt, M., Cropper, C., Shao, L., and Goodier, I. 2012. Ranking of interventions to reduce dwelling overheating during heat waves. *Energy and Buildings*, 55 (Suppl. C), pp. 16–27.
- Trimble Sketchup, 2018. Available from: <http://www.sketchup.com>.
- U.S. Department of Energy, Energy Efficiency and Renewable Energy Office, Building Technology Program, EnergyPlus. Available from: <https://energyplus.net/>.
- World Meteorological Organization, WHO, 2015. WHO | Heatwaves and health: guidance on warning-system development, 114 pages.

Comparison of daylighting simulation workflows and results using plugins for BIM and 3D Modeling programs: application on early phases of design process

Marina da Silva Garcia^{1*}, Maíra Louise Martins de Freitas¹, Roberta Vieira Gonçalves de Souza¹ and Ana Carolina de Oliveira Veloso¹

¹Federal University of Minas Gerais, Brazil

*Corresponding email: marinagarcia.arq@gmail.com

ABSTRACT

The present paper investigated the application of the daylighting analysis features of the Insight BIM plugin, comparatively to DIVA, a plugin for a 3D Nurbs modeling software. Considering the early phases of the design process, workflows, simulation results and processing times were analyzed, focusing on the prediction of static (illuminance level) and dynamic (sDA_{300,50%}) metrics. Simulations on both tools were performed in the context of analyzing the daylight behavior in a deep office room model, with and without light shelves. Results indicate that Insight has limitations compared to DIVA, especially concerning input data configuration flexibility. Simulation results presented significant similarity between Insight and DIVA in most cases, being the direct sun case the one in which illuminance levels differed the most. Insight presented longer processing time for the static metric and similar average time for the dynamic metric. Work findings indicate that Insight has important potential to contribute to daylighting analysis on early phases of design process, and points out to barriers to its adoption and correct use. Authors expect this paper to benefit architects, engineers and students on the comprehension of both tools.

KEYWORDS

Daylighting simulation; Building Information Modeling; Insight; DIVA; design process.

INTRODUCTION

Different work indicates the need for a highly skilled and experienced workforce in the field of high complexity software to have reliability on the results obtained through computational simulation, besides the great financial and time investment (Korolija and Zhang, 2013). Such difficulties reflect on the habit pointed by Dogan and Reinhart (2013) in which computational simulation occurs mainly for code compliance evaluations on final phases of design process. The authors also cite the potential benefit of using simplified easy to use simulation tools at early stages of design process, in which computational analysis exert a great impact on the project's qualification. Furthermore, with the current emphasis on sustainability, including building's energy performance, the multi-disciplinary design solution became more important in initial design stages (Negendahl, 2015).

In this context, Building Information Modeling (BIM) is recognized as a collaborative and information exchange methodology that generates integrated computer models, providing a reliable basis for decision-making regarding the building's design, construction, maintenance and disassemble (Santos et al, 2017). Recent research approaches the use of BIM tools to perform energy and environmental analysis (Chong et al, 2017). According to USGA (2015) these tools have the ability to generate analytical models in an automated or semi-automated

way, creating a simpler process, as simulations can be conducted directly on the modeling program interface. Thus, it can be less prone to errors and demand minimized time and financial investments if compared to current practices.

Insight is a daylighting analysis plugin for Revit, that uses A360 cloud-based rendering service. The tool was designed to be operated by non-daylighting simulation experts professionals (Autodesk, 2015). It presents automated settings for some study types and for others there are customizable input options. Possible analysis includes illuminance levels, daylight autonomy – spatial daylight autonomy ($sDA_{300,50\%}$), studies for LEED credits, and solar access. A360 uses bidirectional ray tracing with multidimensional light cuts algorithm along with secret/patented extensions. The simulation engine has been validated in comparison with Radiance results and measured data (Autodesk, 2017). Such technology has the potential to contribute to the greater adoption of computational simulation, considering that tools difficulty level is a factor of great influence for its adoption (Rogers, 1995). However, although it is possible to increase the accessibility to computational simulations, there is still little research regarding the workflow, results quality and processing time of simulations performed through this methodology, comparable with notably known engines.

Regarding the most used daylighting predictions tools, Radiance, a backward ray tracer simulation engine "enjoys the status of a *gold standard*" (Reinhart and Breton, 2009, p. 1514), being widely validated comparatively to measured data under different sky conditions and complexity of models. Radiance simulates daylighting conditions under one sky condition at a time, and the Radiance-based simulation tool Daysim allows the processing of dynamic simulations under various sky conditions. It is a freeware also extensively used and validated comparatively to measured data (Reinhart and Breton, 2009). Several works that developed Radiance validation studies since 1995 are presented in Reinhart and Anderson (2006).

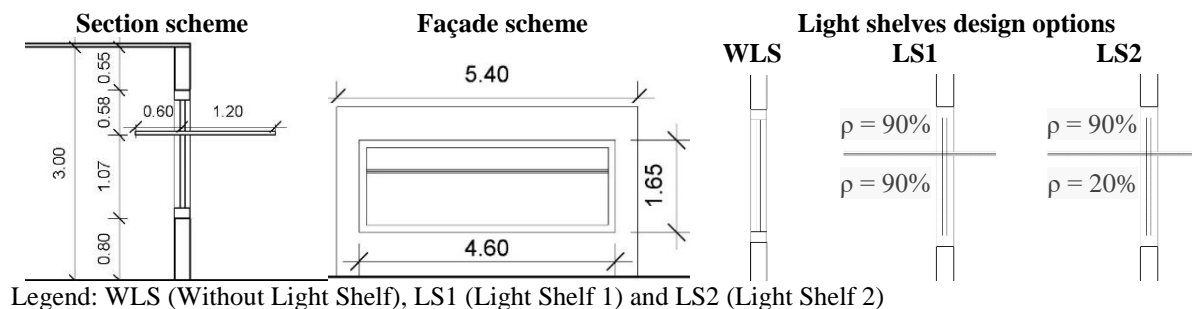
Over the last years, the adoption of DIVA, a plugin that incorporates Radiance and Daysim into the 3D Nurbs modeling program Rhinoceros has been noticed. From this plug-in, it is possible to analyze the performance of different design options without manually exporting the architectural model to another software. International researches have been using DIVA for daylighting and energy consumption studies (Sharma et al. 2017, Tabadkan et al. 2018 and Villalba et al., 2018). DIVA was initially developed at the Graduate School of Harvard University and is now distributed and developed by Solemma LLC. Free use is available through educational licenses for students and educators (Solemma LCC, 2018). Due to its validated simulation engines and acceptance among the academic community, DIVA will be considered in this study as a reference program.

In the search for a better distribution of daylight in laterally daylit rooms, light redistribution elements such as light shelves and daylight harvesting louvers have been widely studied (Berardi et al. 2018, Villalba et al. 2018 and Tabadkan et al. 2018). This article aims then to investigate the plugin Insight, focusing on its application on daylighting simulations analysis during the early phases of a design process. For that, the daylight behavior in a deep office room model with a 1:2 proportion with and without light shelves was analyzed. Workflows, static (illuminance levels) and dynamic ($sDA_{300,50\%}$) results and processing time were studied comparatively to DIVA.

METHODS

The study was developed in two phases. In the first phase Insight and DIVA workflows were apprehended, and in the second one, the study focused on simulation results and processing

time. A design process was assumed within the context of analyzing daylight behavior in a deep office room model with a 1:2 proportion with and without light shelves. The model is not obstructed by neighbouring building and has a depth which corresponds to nearly 4 times the aperture height. Its internal dimensions are 5.0m x 9.9m; 3.0m height, with a 15° Azimuth. This office configuration is commonly found in commercial buildings in Belo Horizonte, Brazil as stated by Alves et al. (2017). Three design options were tested: the basic model (without light shelf) and two models with light shelves with varied inferior surface reflectance (ρ) (Figure 1). A 0.2m wall thickness was assumed and the reflectance of interior walls, interior ceiling, interior floor and exterior ground was 50%, 80%, 20% and 20%, respectively. The outer frame represented a framing factor of 20% of the rough opening area of the window, which included a single glazing with a 90% direct visual transmittance.



Legend: WLS (Without Light Shelf), LS1 (Light Shelf 1) and LS2 (Light Shelf 2)
Figure 1. Schematic models description.

Daylighting simulations were performed with Insight (v. 3.0.0.1 for Revit 2018) and DIVA (v. 4.0 for Rhinoceros5.0) for Belo Horizonte (lat.: -19.85, long.: -43.95). Simulated metrics and parameters were: illuminance levels for winter solstice at 12:00h with analysis plan height of 0.75m and nodes distance of 0.35m; and sDA_{300,50%} with 0.8m plan height and 0.6m node distance. For illuminance analysis the Perez sky model was used in both software, using weather data as sources for sky condition information. The one considered for Insight simulations was automatically assigned from the project location indication through a default city list, and for DIVA simulations a SWERA file was considered (Table 1). Table 2 presents DIVA advanced simulation parameters - at Insight, it is not possible to access such settings.

Table 1. Sky condition information.

	GHI ¹	DNI ¹	DHI ¹	Sky cover	Weather file
Insight	890Wh/m ²	810Wh/m ²	93Wh/m ²	0%	GBS_04R20_299004
DIVA	623Wh/m ²	616Wh/m ²	179Wh/m ²	5%	Belo Horizonte/Pampulha-SWERA

¹GHI: Global Horizontal Irradiance, DNI: Direct Normal Irradiance, DHI: Diffuse Horizontal Irradiance.

Table 2. Advanced Radiance simulation parameters used in DIVA.

Model	ab	ad	as	ar	dt	ds
Without light shelf	5	1000	20	300	0	0
With light shelves (1 and 2)	7	1500	100	300	0	0

RESULTS

Figure 2 displays workflows schemes of Insight and DIVA. Key aspects of Insight operation mode involve the use of a BIM model to perform cloud-based daylighting analysis and having the option to configure or not analysis parameters, as the tool presents default values for material, nodes and analysis information. DIVA uses a scene modeled in Rhinoceros and processes simulations on user's computer. There are also default parameters for numerous daylighting analysis, but nodes and materials properties must be configured manually.

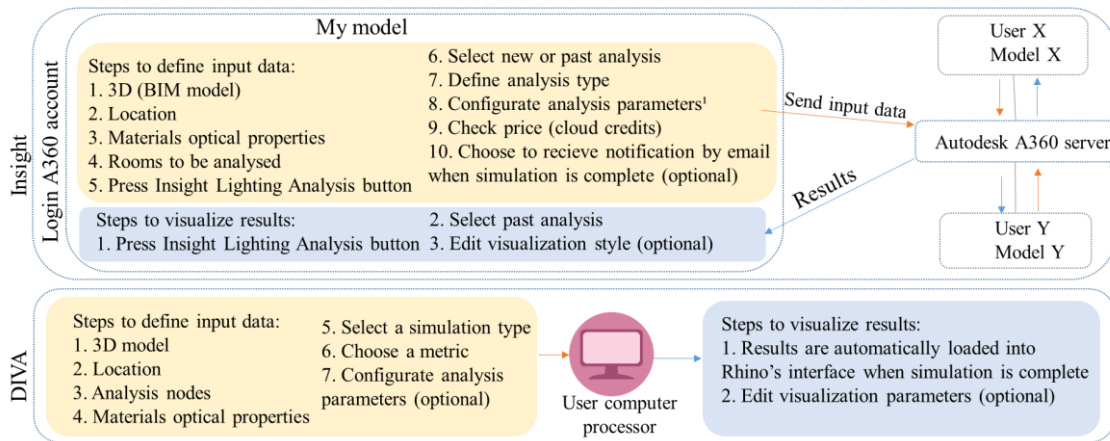


Figure 2. Schematic operating mode of Insight and DIVA.

Important workflow differences rely on material's optical properties configuration: on Insight it is set by color or by specific Red, Green and Blue (RGB) values, defined by equations presented in Autodesk (2017); while in DIVA it is set by a default list, which can be altered in a .rad file. In Insight it is viable to load past simulation results, as a simulation historic is stored in the A360 user account. Also, it provides users with design tips for lighting performance improvement. Both tools allow configuring result scale appearance, an important aspect of comparing design options. In Insight users can manually change color schemes and define intervals between the maximum and minimum thresholds, which are fixed on the scale; while in DIVA it is viable to choose between three color schemes and to define scale's maximum and minimum thresholds, but quantity and value of intermediate intervals are automatically set. Figure 3 presents both tools results and its processing time.

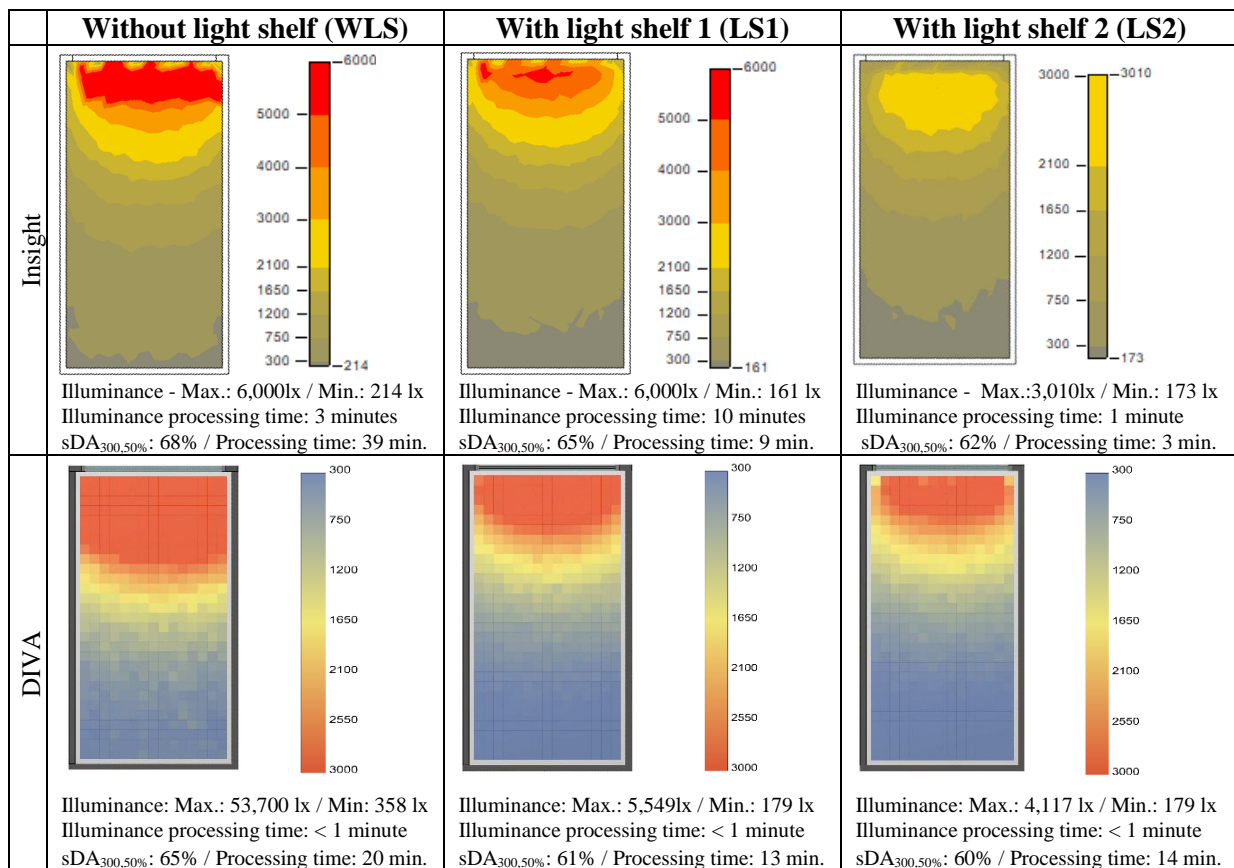


Figure 3. Results and processing time of Insight and DIVA simulations.

Maximum and minimum resulting illuminance levels were similar on both tools in the cases of light shelves use (LS1 and LS2). Most discrepant illuminance result was in the case with direct sun exposure (WLS), being the maximum level in DIVA approximately 9 times higher than in Insight. In what concerns the three design options, both tools demonstrated decreasing illuminance levels in the area next to the opening and more uniform daylight distribution when WLS, LS1 and LS2 were tested, respectively. Medium illuminance simulation time in Insight was 4.7 minutes, while in DIVA it was less than 1 minute. In what concerns the $sDA_{300,50\%}$, both tools presented similar results in all cases, being the bigger difference in case LS1 (4%). Medium $sDA_{300,50\%}$ simulation time was 17 minutes for Insight and 15.7 minutes for DIVA. Authors point out that there were occasions when Insight simulations were impaired due to connection problems with Autodesk's server.

DISCUSSIONS

With the workflows study, characteristics that can favour Insight adoption on early phases of design process were noticed. Firstly, there is the possibility to use a BIM model to perform daylighting analysis, for all benefits of BIM design process cited by Santos et al (2017). Secondly, the indication of design tips can assist the development of project solutions. Thirdly, default values configured for material properties, analysis nodes and metrics parameters enables simulations execution by nonexperts professionals, in congruence with Insight developers objectives, as stated in Autodesk (2015). As indicated by Rogers (1995) those simplifications can contribute to the tools higher adoption. Also, the storage of simulation historic facilitates results comparison between design options. On the other hand, with the experience of this work, authors encountered aspects that can be considered barriers to Insights adoption and correct use. Among them, there is the occurrence of errors with Autodesk's server connection. Also, when consulting the design tips, which was based on studies developed in the USA, users should attempt to their specific project climate characteristics. Further, fixed input values encountered in Insight may represent an obstacle for more detailed analysis. An example is the impossibility to specify the desired weather file and although it is possible to inform GHI, DNI and DHI values for illuminance analysis, it is not viable to inform a sky cover percentage. Additionally, the configuration process of the desired material reflectivity or visible transmittance is unintuitive compared to DIVA's, due to the necessity of informing the RGB values. Since calculated values presented in Autodesk (2017) are not available in Revit or Insight interfaces, users must search for this reference.

Illuminance levels and $sDA_{300,50\%}$ results of both tools presented similarity, mostly in cases with a predominance of diffuse light, when LS1 and LS2 were used. The case with direct sun exposure (WLS) presented illuminance significant discrepancy among both tools, and based on weather files sky condition information, authors infer this was due to Insight's maximum threshold specification. Authors could not confirm this hypothesis because this configuration could not be accessed. Still, transposing this results to a design process practice, such difference may not imply great prejudice, for illuminance levels in both cases were above comfortable desired levels if a 3,000lx limit is considered - so both of them indicated the necessity to develop sun protection solutions. In this study, illuminance simulation processing time was notably shorter when using DIVA than when using Insight, and this may be caused by the low computing capacity necessary for such static metric along with the low complexity of the model. The average processing time for $sDA_{300,50\%}$, in its turn, was similar in both tools.

CONCLUSIONS

This work investigated the application of Insight daylighting features on design process, comparatively to DIVA. Workflows, simulation results and processing time were analyzed.

Results indicate that Insight has limitations, mostly on what concerns input data configuration flexibility, but it still has significant similarity in results with DIVA, mainly in cases with a predominance of diffuse daylighting. Findings demonstrate Insight has important potential for contributing to daylighting analysis on early phases of design process, assisting A&E professionals on developing more based solutions in conjunction with the use of a BIM platform. Authors intend this paper to benefit architects, engineers and students on the better comprehension of both studied tools. Future research could approach simulations with other metrics, model complexities, and the use of DIVA along with Rhinoceros BIM plugins.

ACKNOWLEDGEMENT

The work reported in this paper was supported by Capes and CNPq.

REFERENCES

- Alves T, Machado L, Souza R.G, De Wilde P.2017. A methodology for estimating office building energy use baselines by means of land use legislation and reference buildings. *Energy and Buildings*,143,100-113.
- Autodesk. 2015. *Light Analysis for Revit*.Autodesk, Inc.
- Autodesk. 2017. *Insight Lighting Analysis Help*.Autodesk, Inc.
- Berardi U, Anaraki H. 2018. The benefits of light shelves over the daylight illuminance in office buildings in Toronto. *Indoor and Built Environment*, 27, 244-262.
- Chong H-Y, Wang X, Lee C-Y. 2017. A mixed review of the adoption of Building Information Modelling (BIM) for sustainability. *Journal of Cleaner Production*, 142, 4114-4126.
- Dogan T, Reinhart C. 2013. Atmosphères: proof of concept for web-based 3D energy modeling for designers with WebGL/html5 and modern event-driven, asynchronous server systems. In: *Proceedings of the 13th Conference of International Building Performance Simulation Association (IBPSA)*, Chambéry, pp. 1039-1044.
- Korolija I, Zhang I. 2013. Impact of model simplification on energy and comfort analysis for dwellings. In: *Proceedings of the 13th Conference of International Building Performance Simulation Association (IBPSA)*, Chambéry, pp. 1184-1192.
- NegendahlK. 2015. Building performance simulation in the early design stage: An introduction to integrated dynamic models. *Automation in Construction*, 54, 39-53.
- Reinhart C, Anderson M. 2006. Development and validation of a Radiance model for a translucent panel. *Energy and Buildings*, 38, 890-904.
- Reinhart C, Breton P. 2009. Experimental validation of 3DS max® design 2009 and Daysim 3.0. In: *Proceedings of the 11th Conference of International Building Performance Simulation Association (IBPSA)*, Glasgow, pp. 1514-1521
- Rogers E M. 1995. *Diffusion of Innovations*. 3° Ed. New York. The Free Press.
- Santos R, Costa A, Grilo A. 2017. Bibliometric analysis and review of Building Information Modelling literature published between 2005 and 2015. *Automation in Construction*, 80, 118-136.
- Sharma L, Lal K, Rakshit D. 2017. Evaluation of impact of passive design measures with energy saving potential through estimation of shading control for visual comfort. *Journal of Building Physics*, 1-19.
- SOLEMMA LCC. *Diva-for-Rhino*. 2018.
- Tabadkan A, Banihashemi S, Hosseini M. 2018. Daylighting and visual comfort of oriental sun responsive skins: A parametric analysis. *Building Simulation*, 11, 663-676.
- U. S. General Services Administration (USGSA). 2015. GSA BIM Guide 05 - Energy Performance.
- Villalba A, Monteoliva J, Rodríguez R. 2018. A dynamic performance analysis of passive sunlight control strategies in a neonatal intensive care unit. *Lighting Research & Technology*, 50, 191-204.

Existing Energy Performance and The Potential of Simulation in School Buildings – A Review

Ming Hu¹

¹University of Maryland, College Park, Maryland

*Corresponding email: mhu2008@umd.edu

Abstract:

The objective of this paper is to present finding of existing building performance assessment for educational buildings and related energy simulation tools with a focus on K-12 buildings. First, the paper examines the current status of energy performance in educational buildings and existing simulation tools used in building energy retrofit. Then, the paper summarizes the obstacles to conducting energy simulation for school buildings, gaps and weaknesses in existing tools will be summarized, and potential opportunities for a comprehensive tool will be outlined. Last, the paper identifies the particular needs of educational buildings, and a set of criteria and requirements for future tools will be proposed based on the particular needs for educational building.

KEYWORD

educational buildings, K-12, energy simulation tools

INTRODUCTION

In the United States, educational buildings account for 12% of total commercial building energy consumption, with K-12 schools accounting for 8% (EIA 2012). All together, educational buildings are the third largest energy consumers in the commercial building sector, following office buildings and mercantile buildings. K-12 schools account for 10% of total commercial building floor area and other educational buildings account for 4% (EIA 2012).

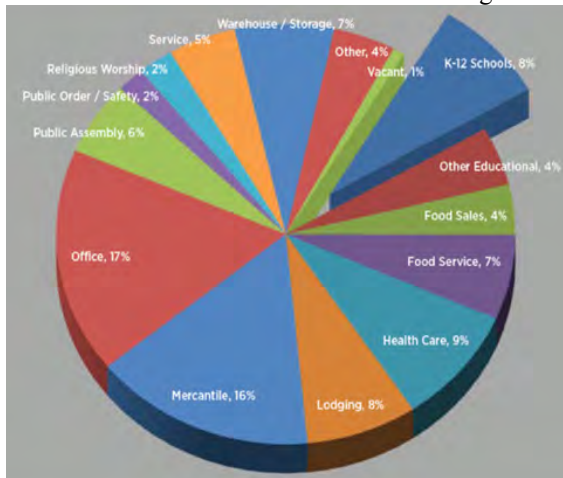


Figure 1 commercial building energy use

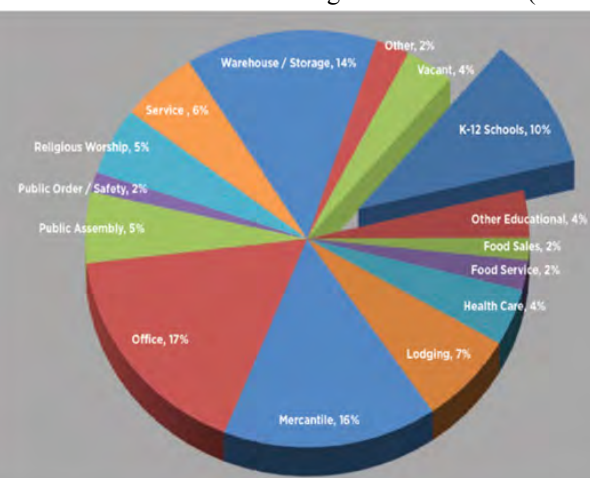


Figure 2 commercial building floor area

K-12 school buildings in U.S spend more than \$8 billion each year on energy—more than they spend on computers and textbooks combined (EPA 2011). Most occupy older buildings that often have poor operational performance—more than 30% of schools were built before 1960. 53% of public schools need to spend money on repairs, renovations, and modernization to ensure that the schools buildings are in good overall condition. And among public schools with permanent buildings, the environmental factors in these permanent buildings have been rated as unsatisfactory or very unsatisfactory in 5% to 17% of schools (DOE 2012). The average age of a school is about 42 years—which is nearly the expected serviceable lifespan of the building (McGraw Hill 2011).

Improving the energy performance of school buildings could result in the direct benefit of reduced utility costs, and

improving the indoor quality could improve the learning environment for students. Research also suggests that aging school facilities and inefficient equipment have a detrimental effect on academic performance that can be reversed when schools are upgraded. Several studies have linked better lighting, thermal comfort, and air quality to higher test scores (Chan et al, 1979; Earthman et al. 1998; Phillips et al. 1997). Another benefit of improving the energy efficiency of education buildings is the potential increase in market value through recognition of green building practice and labelling such as that of a net zero energy building. In addition, because of their educational function, high-performance or energy-efficient buildings are particularly valuable for institution clients and local government. More and more high-performance buildings, net zero energy buildings, and positive energy buildings serve as living laboratories for educational purposes. Currently, educational/institutional buildings represent the largest portion of NZE (Net Zero Energy) projects. Educational buildings comprise 36% of all net zero buildings, according to a 2014 National New Building Institute report. Of the 58 net zero energy educational buildings, 32 are used for kindergarten through 12th grade (K-12), 21 for higher education, and five for general education (NBI 2014).

EXISTING ENERGY PERFORMANCE OF K-12 BUILDING

For this study, first author compared three different database: Building Performance Database, EIA's (Energy Information Administration) Commercial Building Energy Consumption Survey (CBECS), and Building Energy Data Book. BPD was chosen because of its size and non-biased sources. BPD is the United States largest dataset of information about the energy-related characteristics of commercial and residential buildings. This database is sponsored by Department of Energy and raw data come from variety sources includes federal, state and local government data, as well as utility companies and other energy efficiency programs. In BPD, there are 8883 school buildings. In the CBECS, there are 389 education buildings include elementary, middle school, high school, college and other types of adult education and vocational training facilities. CBECS is much smaller dataset than BPD. Building Energy Data Book does not list the original raw data quantity, so it is hard evaluating its' reliability.

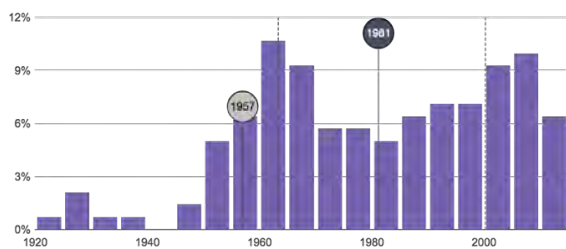


Figure 3 Age of school buildings in U.S.

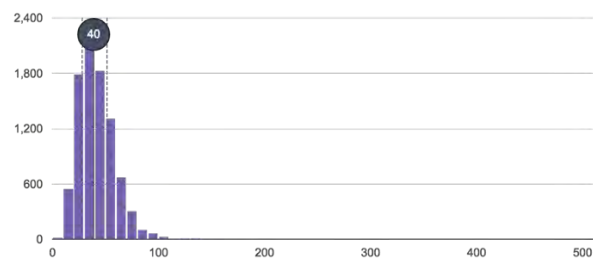


Figure 4 Current energy performance (EUI) of school

Among the 8883 school buildings in BPD, 10.71% was built between 1960-1965, 10% was built between 2005-2010, 9.29% was built between 1965-1970, and 2000-2005 (refer to figure 3). 545 buildings have site EUI of 10-20KBtu/sf/yr, 1791 buildings have site EUI of 20-30KBtu/sf/yr, 2151 buildings have site EUI of 30-40KBtu/sf/yr, 1828 buildings have site EUI of 40-50KBtu/sf/yr, 1314 buildings have site EUI of 50-60KBtu/sf/yr, 673 buildings have site EUI of 60-70KBtu/sf/yr. Majority K-12 school buildings have a site EUI between 30-40 KBtu/sf/yr which is indeed smaller than what is extracted from CBECS and later on used in Energy Start Portfolio Manager tool (refer to figure 4).

The energy performance of K-12 buildings is primarily affected by three impact factors: site/climate condition; building total area; and very significantly by occupancy rate. *The first impact factor* in education building energy performance is the external environment conditions. In the U.S., based on BPD data there is a clear correlation between cold climate zone and overall energy consumption. Buildings in hot climate zone have better performance than those in cold climate, as illustrated in Figure 5. From data obtained in Europe, studies also indicated that the energy usage intensity (EUI) is typically higher in regions with a harsh and cold climate than in those with relatively pleasant climate conditions.

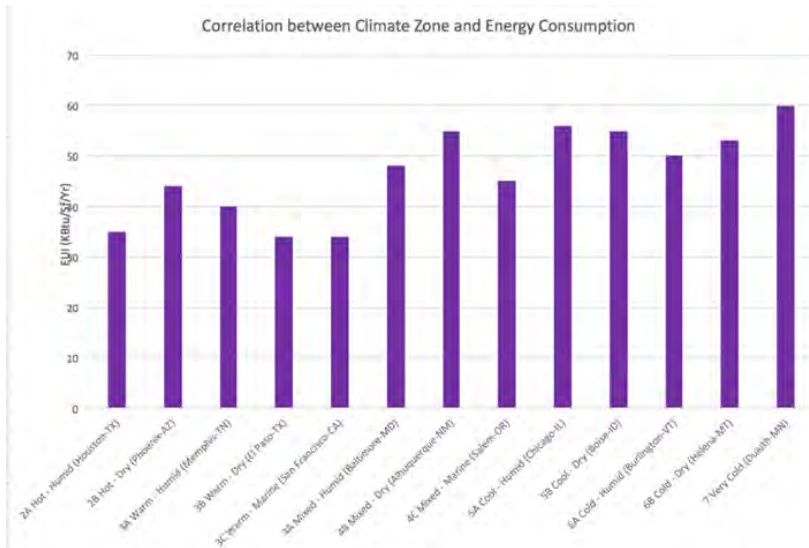


Figure 5 Correlation between climate zone and energy efficiency

The second factor is the overall area of the buildings. First, author has ruled out the impact from construction year. Building ages is not the key issue affecting the energy performance, the newer buildings particularly built around 1990s to 2000s have higher EUJ number than those built before 1980s. This could be due to the larger plug load in newer schools. When we look at the building total area, smaller buildings tend to have higher energy intensity compared to larger buildings which is the same across different climate zones and building ages (refer to figure 6).

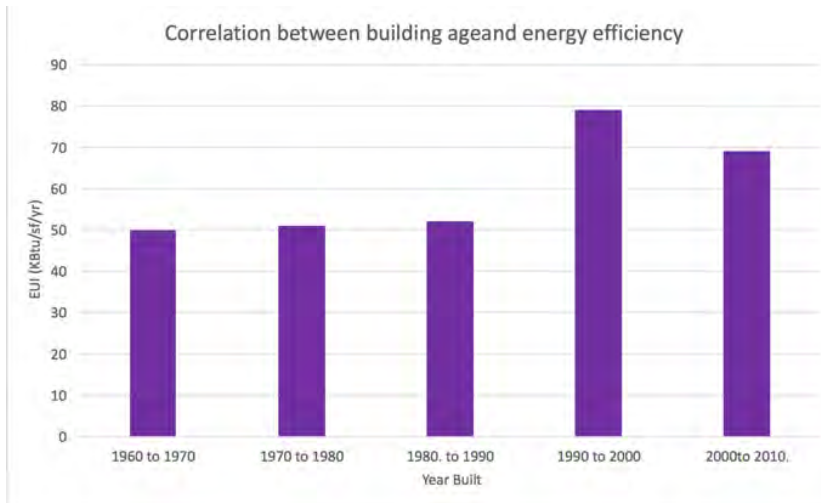


Figure 7 Correlation between building area and energy efficiency

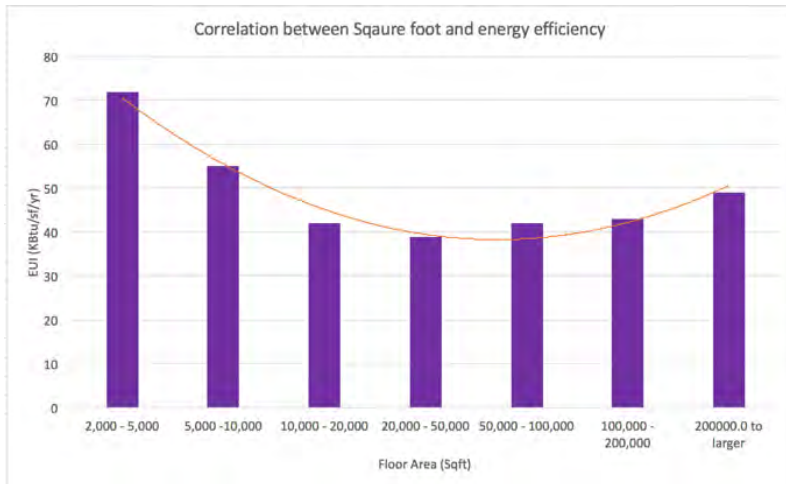


Figure 6 Correlation between building age and energy efficiency

The third factor is occupancy rate. Data shows lower occupancy density is correlated to the higher EUI (refer to figure 8), which suggest fewer people consume more energy due to the behavior change. This could be interpreted by the occupant's behaviors. In the United States, historically low energy prices have contributed to building occupants engaging in relatively energy-intensive behaviors (Climate Policy Initiative Report 2013). In other countries due to the conscious mind of energy conservation, we have seen close correlation between building operational characteristic of the buildings as a result of how they affect the actions taken by students or teachers to control their internal environment (Theodosiou et al 2014).

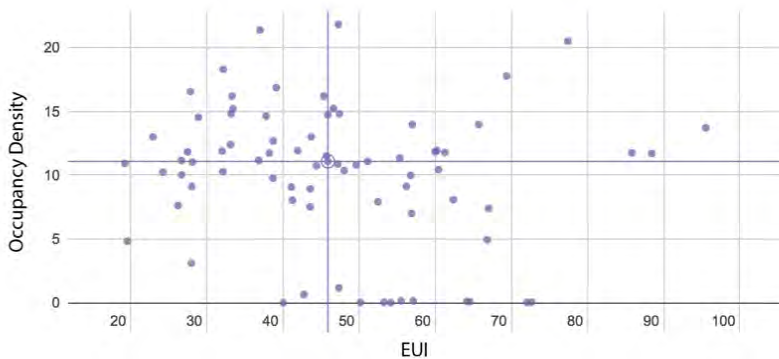


Figure 8 Correlation between occupancy density and energy efficiency

EXISTING SIMULATION TOOLS USED IN BUILDING ENERGY ANALYSIS

Realizing the energy efficient design is a two-steps concept: first is to reduce energy consumption, and the second is to increase the energy generated on site through renewable energy. The different steps require different simulation tools. The first set of tools (energy consumption simulation tool) is utilized to predict the future energy consumption based on sufficient parameters with the aim to make sure the energy demand could be reduced to minimal. This type of tool has been in development since the past 50 years, and typically requires experienced professionals from the building community. The second set of tools (energy generation simulation tool) is used to predict the energy generated onsite, which could depend on the site and geographic condition. Most tools also require certain professional training and knowledge in the utilization of these tools. More and more whole building simulation software is starting to include the potential energy generation on-site combined with predicted energy consumption on-site so that the design team can view the energy balance result in one interface.

In energy consumption simulation tools, the core tools in the building energy efficiency field are the whole-building energy simulation programs. Those programs can take a large number of building parameters into consideration such as building geometry, massing, orientation, wall-window ratio, temperature, humidity, energy use and demand, and costs. Large bodies of research and surveys have been conducted to compare different energy simulation tools.

Among those surveys and studies, two research projects have the most impact. In 2006, a team of research from U.S DOE and Scotland studied twenty major building energy consumption simulation programs and concluded that even among the ‘mature’ tools, there was not a common language to describe what the tools could do, and solely relying on a single tool might not be productive (Crawley et al 2008). In 2010, researchers from Ireland and Denmark studied 37 tools in collaboration with the tool developers or recommended points of contact. This study provides a review of different computer tools that can be used to analyse the integration of renewable energy generation (Connolly et al 2010). Among the 37 tools studied, four programs are applicable to single-building, group of buildings, or a community. Those four programs are BChP Screening Tool, HOMER, and TRNSYS16. Between those two studies, there is only one overlap (Trnsys16). In this session, the author chose 10 of the most used and most invested whole-building simulation programs and illustrated their characteristics based on a high number of users from the previous studies. Table 1 illustrate those major tools.

Table 1 Major Characteristic of Energy Simulation Tools

Tool	Year	Free Use	Country	Zone	Building Envelope	Ventilation / Infiltration	HVAC	Whole Building Simulation	Scenario development	Integration of Renewable energy
Trnsys 18	1975	no	USA	yes	yes	yes	yes	yes	yes	yes
BChP Screening Tool	2003	yes	USA	yes	no	yes	yes			yes
HOMER	1992	Yes/no	USA	no	no	no	no	No	yes	yes
RETScreen	1996	yes	Canada	no	no	no	no	No	no	yes
DOE-2.2		yes	USA	Y	Y	Y	Y	Y	Y	Y
IES	1994	no	UK	Y	Y	Y	Y	Y	Y	Y
EnergyPlus	2001	yes	USA	Y	Y	Y	Y	Y	Y	Y
IDA	1998	no	SW	Y	Y	Y	Y	Y	Y	Y
ESP-R	1974	yes	UK	Y	Y	Y	Y	Y	Y	Y
CBES		yes	USA	Y	Y	Y	Y	Y	Y	Y
Bsim		no	DK	Y	Y	Y	Y	Y	Y	Y

GAPS AND POTENTIAL OPPORTUNITIES FOR EDUCATIONAL BUILDING ENERGY SIMULATION

Currently, most whole-building simulation tools generally focus on commercial and residential buildings. According to the most recent Commercial Building Energy Consumption Survey (CBECS), conducted in 2012, space heating demanded the greatest overall energy use (25%), followed by lighting, refrigeration, ventilation, and cooling. In residential buildings, space heating demanded the greatest overall energy use (45%), followed by water heating (18%) and space cooling (9%). School buildings have a unique energy profile that does not align with that of typical commercial buildings. In school buildings, space heating accounts for 47% of the overall energy consumption, followed by lighting (14%) and cooling (10%). The energy behavior of schools is more similar to that of a residential building than that of a commercial building. This could be due to the operational schedule of schools; in particular, primary and secondary schools are largely different from regular commercial buildings that operate on a 12 months per year schedule. Further research could be conducted to obtain a better understanding of school building energy behavior. Using a typical commercial energy simulation model setting for school buildings could create inaccurate results. There is a potential gap and need for integrated simulation tools that are created and suitable for school building design. In most existing schools, the building system does not have smart sensors that can automatically control the lighting, so one can often observe that sun shades and blinds are pulled down during the day to avoid glare while the electric lights are all turned on because of the reduced daylight level. Hence, the users’ energy behavior management requires a cultural shift, which could take a long time, and we should simulate the energy consumption caused by the relatively high-intensity energy behavior in schools. A future energy simulation tool should accommodate a wide range of operation schedules and users’ behavior could lead to more accurate results. Illustrating the direct savings from behavior change could create a positive environment to expedite the behavior paradigm shift.

CONCLUSION

Educational buildings in the U.S. consume large amounts of energy, representing immense opportunities for energy savings. K-12 schools offer unique opportunities for deep, cost-effective energy-efficiency improvements. According to the EPA, the modification of a pre-existing school building for energy efficiency can save a typical 100,000-square-foot school building between \$10,000 and \$16,000 annually. Future building performance will not be generic and will vary according to the buildings' operational character, local context, and user behaviors. The overall goal of future buildings, including educational buildings, may be "net zero" or "net positive". The intent of reviewing the current energy performance status of K-12 buildings is to identify the gaps and opportunities for improvement of K-12 building performance.

Reference

- Energy Information Administration. Commercial Building Energy Survey 2012.
- Environment Protection Agency, Energy Efficiency Programs in K-12 Schools: A Guide to Developing and Implementing Greenhouse Gas Reduction Programs, 2011.
- Department of Education. U.S. Condition of America's Public School Facilities: 2012–13. 2014
- Schneider, Mar. "Do School Facilities Affect Academic Outcomes?" National Clearinghouse for Educational Facilities, 2002.
- Chan, T. The impact of school building age on pupil achievement. Greenville, S.C.: Office of School Facilities Planning, Greenville School District. 1979.
- Earthman, G. I., and L. Lemasters. Where children learn: A discussion of how a facility affects learning. Paper presented at the annual meeting of Virginia Educational Facility Planners. Blacksburg, Va., February 1998.
- Phillips, R. Educational facility age and the academic achievement of upper elementary school students. D. Ed. diss., University of Georgia. 1997
- National New building institute. 2014 Getting to Zero Status Updates: A look at the projects, policies and programs driving zero net energy performance in commercial buildings. 2014
- Climate Policy Initiative Report. Buildings Energy Efficiency in China, Germany, and the United States. 2013
- Theodosiou, T.G., and K.T. Ordoumpozanis. "Energy, comfort and indoor air quality in nursery and elementary school buildings in the cold climatic zone of Greece." *Energy and Buildings* 40, no. 12 (2008): 2207-214.
- Crawley, Drury B., Jon W. Hand, Michaël Kummert, and Brent T. Griffith. "Contrasting the capabilities of building energy performance simulation programs." *Building and environment* 43, no. 4 (2008): 661-673.
- Connolly, David, Henrik Lund, Brian Vad Mathiesen, and Martin Leahy. "A review of computer tools for analysing the integration of renewable energy into various energy systems." *Applied energy* 87, no. 4 (2010): 1059-1082.
- Oak Ridge National Laboratory. Whole-Building and Community Integration Program. <<http://www.coolingheatingpower.org/about/bchp-screening-tool.php>> [accessed 26.05.09].
- Connolly, David, Henrik Lund, Brian Vad Mathiesen, and M. Leahy. "Developing a model of the Irish energy-system." Proceedings of the Joint Action on Climate Change. Aalborg (2009) <http://sel.me.wisc.edu/trnsys/features/features.html>
- Murray, M., Neil Finlayson, Michaël Kummert, and John Macbeth. "Live energy TRNSYS–TRNSYS simulation within google SketchUp." In Eleventh International IBPSA Conference, Glasgow, Scotland. pp1389-1396. 2009.
- U.S. Environmental Protection Agency. 2011. "Energy Efficiency Programs in K-12 Schools: A guide to developing and implementing greenhouse gas reduction programs."
- Deng, S., Y.I. Dai, R.Z. Wang, and X.Q. Zhai. "Case study of green energy system design for a multi-function building in campus." *Sustainable Cities and Society* 1, no. 3 (2011): 152-63.

Lighting simulation for External Venetian blinds based on BTDF and HDR sky luminance monitoring

Yujie Wu^a, Jérôme Henri Kämpf^b, Jean-Louis Scartezzini^a

^aSolar Energy and Building Physics Laboratory (LESO-PB), École polytechnique fédérale de Lausanne (EPFL), CH-1015, Lausanne, Switzerland

^bHaute école d'ingénierie et d'architecture Fribourg (HEIA-FR), University of Applied Sciences Western Switzerland, CH-1700, Fribourg, Switzerland

**Corresponding email: yujie.wu@epfl.ch*

ABSTRACT

The precise daylighting simulation in buildings can potentially contribute to designers' and occupants' smart utilization of it. The traditional method of employing sky models was indicated with noticeable errors in transient lighting simulation for complex fenestration systems (CFS), due to the mismatch between the real sky and standard sky models. This paper evaluates the performance of a calibrated embedded photometric device based on sky luminance monitoring, capable of real-time on-board lighting computing. Daylighting experiments for external Venetian blinds (EVB) were conducted in a lighting test module to demonstrate its accuracy in the simulation of horizontal work-plane illuminance. The BTDF of the EVB was generated for two different tilt angles of slats respectively. With partly cloudy skies, the photometric device was validated with improved accuracy in simulating the work-plane illuminance distribution compared with a common practice employing the Perez all-weather sky model.

KEYWORDS

BTDF, HDR, Workplane illuminance, Venetian blinds, Transient Simulation

INTRODUCTION

Lighting constitutes about 15 - 30% energy consumption in non-residential buildings (ul Haq et al., 2014). The utilization of daylight, as a free source, can potentially mitigate the energy consumption of buildings at a considerable scale and, at the same time, contributes to occupants' health condition and working performance (Mills et al., 2007). However, excessive penetration of daylight into buildings can increase the cooling load and glare probability for occupants. To overcome this issue, shading devices or electrochromic glazing is commonly applied in commercial and residential buildings for the regulation of daylight provision and the prevention of glare. Despite of their merits in tuning daylighting, the complexity of their architecture, with curved profile or micro structures, makes it difficult for designers to pre-plan the room or to dynamically control the daylight precisely.

The bi-directional transmittance distribution function (BTDF) describes the light transmittance behaviour of a certain material or a complex fenestration system (CFS). The function is defined by the ratio of directional exiting radiance over the incident irradiance on a surface (Dereniak et al., 1982). The BTDF is a five-dimensional quantity, with two sets of spherical coordinates for incident and exiting directions respectively as well as the wavelength of light. In the context

of photometric scope, the variable of wavelength can be cancelled by the integration with the luminosity function $V(\lambda)$ over the wavelength. Over the past decades, multiple angular basis has been defined, which discretize the BTDF with a finite number of incident and exiting directions, including the Tregenza and Klems basis (Tregenza, 1987; Klems and Warner, 1995). Together with the ray-tracing techniques, the BTDF of a CFS can be used to calculate the daylight provisions and assess glare risks in buildings, however, the BTDF of a CFS is limited by a number of factors in daylighting application: firstly, the approximated BTDF commonly neglects the spatial variation over different positions on the incident surface plane, which takes the average over a periodic section; secondly, although the BTDF can be either generated by using simulation software, with the defined surface properties and geometry, or monitored by a Gonio-photometer, the cost and time can be considerable for a CFS with multiple states; last but not the least, the resolution of the BTDF has to balance between the computation load and accuracy in lighting simulation.

For dynamic regulation of daylighting, the accuracy of transient lighting simulation is constrained by the mismatch between the standard sky models and the real sky. The standard sky models can hardly reproduce the real sky for a specific location and moment, because they are based on averages over a range of sky types, including the CIE standard sky model and Perez all-weather sky model (Perez et al., 1993). In addition, a limited number of input weather data is not sufficient to reconstruct the reality, since the sampling frequency of inputs were not over two times the maximum spatial frequency of the sky, according to the Shannon sampling theory (Shannon, 1949). Especially for partly cloudy skies with scattered high contrast sky patches, the discrepancy between the standard sky models, with smooth luminance distribution, and the reality can be pronounced, contributing to substantial error in transient lighting simulation from the simplified source of daylighting.

In this paper, an embedded photometric device (Wu et al., 2017b,a), integrating the sky luminance monitoring and on-board lighting computing, is validated experimentally in the horizontal work-plane illuminance simulation for external Venetian blinds (EVB) in a daylighting testbed. The device, employing high dynamic range (HDR) imaging techniques, is able to monitor the luminance of the sun orb, the sky and landscape during the day with high resolution mapping, which can potentially reproduce the real sky more accurately than the standard sky models. The BTDF was generated for the EVB at various tilt angles and employed in the daylighting simulation.

METHODOLOGY AND EXPERIMENTS

One EVB, with a sinusoidal profile, was installed in a lighting test module, as illustrated in Figure 1 a). The profile of the EVB was modelled with the identical geometry in RADIANCE (Larson and Shakespeare, 2004), an open source lighting simulation software employing ray-tracing techniques. To improve the accuracy in lighting simulation, the reflectance of the surface material of the EVB at both sides were measured by a chromameter (MINOLTA CR-220) and its specularity was monitored by a gloss meter (MINOLTA GM-060), characterizing the specular component at 60° incident angle to approximate the specularity. As various tilt angles of its slats correspond to different light transmittance properties, a group of BTDF for the EVB was computed by the 'genBSDF', a sub-program of RADIANCE, at 5° interval of tilt angles respectively. In the scope of this paper, two tilt angles were evaluated at 72° and 32° respectively to the vertical plane, directing downward. Their BTDF was generated employing the Klems angu-

lar basis, with 145 incident and exiting directions respectively. During the lighting simulation, the EVB was defined as the 'BSDF material' with proxy geometry in the RADIANCE. In this way, the direct tracing rays interact with the modelled geometry of the EVB, while the indirect rays, with multi-reflections, use the BTDF to compute lighting, reducing the computation load for ambient calculation.

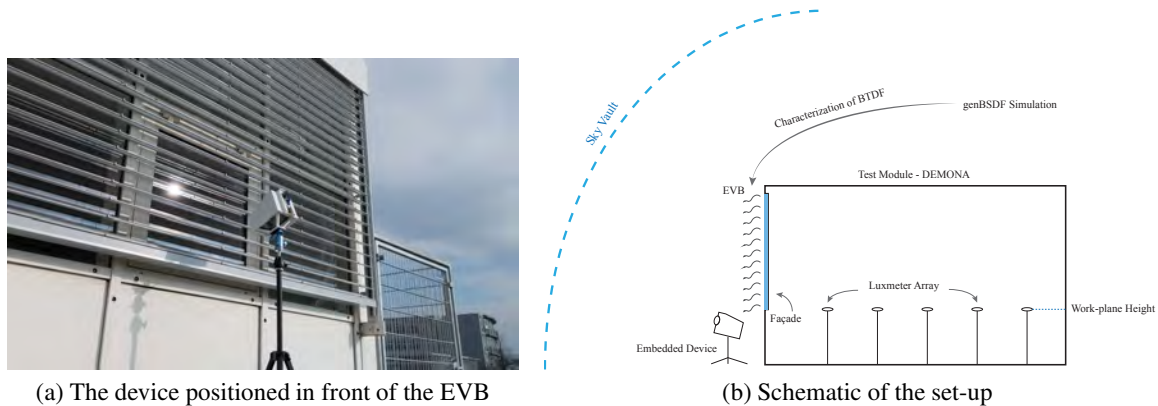


Fig. 1. The experimental set-up for testing the embedded photometric device

To validate the daylighting simulation of the embedded photometric device, 'in situ' experiments were conducted in a retrofitted test module (interior size: $6.4 \times 2.9 \times 2.6 \text{ m}^3$), equipped with a unilateral façade reaching a 0.62 window-to-wall ratio and with the EVB. This module was modelled at 1:1 scale with surface material properties monitored by the chromameter and gloss meter, including the wall, ceiling, floor, and surfaces of each furniture. The photometric device was positioned in front of the EVB with its lens targeting toward the sky vault, as shown in Figure 1 a). The modelled scene was embedded into the device with its on-board RADIANCE software operating for quasi real-time lighting simulation. The embedded photometric device, as a compact platform, calculated the horizontal work-plane illuminance distribution at 1 m, 2 m, 3 m, 3.9 m, and 4.7 m distance to the façade. To assess its accuracy, an array of lux-meters was positioned at identical positions inside the module to monitor the work-plane illuminance as reference, illustrated in Figure 1 b). Each lux-meter was connected to a data logger, recording the illuminance simultaneously. For comparison, both the embedded device and lux-meters were synchronized to simulate and monitor the work-plane illuminance respectively every 15 min. Furthermore, the direct normal and diffuse horizontal irradiance were monitored by a pyranometer at the rooftop for contrasting the performance employing the Perez all-weather sky model.

RESULTS

For a partly cloudy day, the slats of the EVB were fully stretched and directed downward at 32° to the vertical plane. The horizontal work-plane illuminance simulated by the embedded photometric device from 9:00 to 18:00, based on HDR imaging techniques, is illustrated in Figure 2 a), with green data points and curves. The five curves stacked from up to bottom represent the five sensors at different distance to the façade respectively. The monitored illuminance values by using the lux-meters are denoted by grey dotted lines stacked similarly as reference. In comparison, the illuminance simulated by using the Perez all-weather model was illustrated in Figure 2 b) by stacked green lines. According to the two figures, the simulated illuminance by

using the embedded device is closer to the monitored value than that employing the Perez all-weather sky model. The relative error, as shown in Figure 3, further illustrates the merits of the HDR imaging techniques in reconstructing the sky. The Perez sky model is not well performing in simulating relatively dim skies and tend to have pronounced error, when the sky has scattered high contrast patches. The average relative error for work-plane illuminance by the embedded device at the five positions is 18.7%, 19.1%, 22.7%, 24.7%, and 27.2% respectively, while that by employing the Perez all-weather model is 169.1%, 166.0%, 144.1%, 133.4%, and 134.1% respectively.

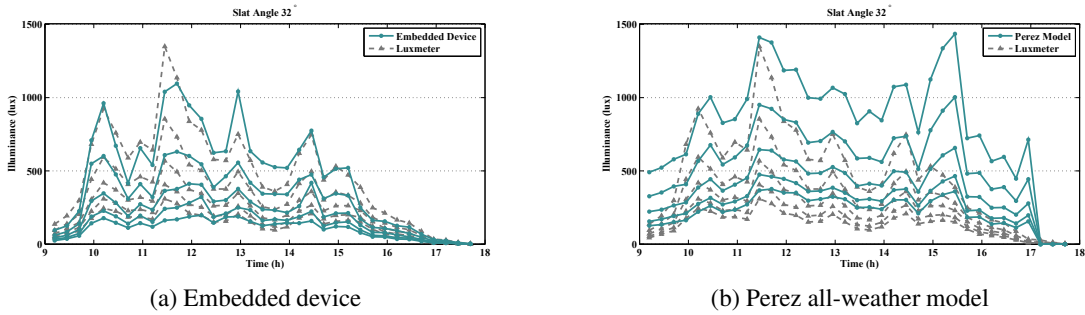


Fig. 2. Simulated horizontal work-plane illuminance by using the two approaches to reproduce the sky (32° tilt angle)

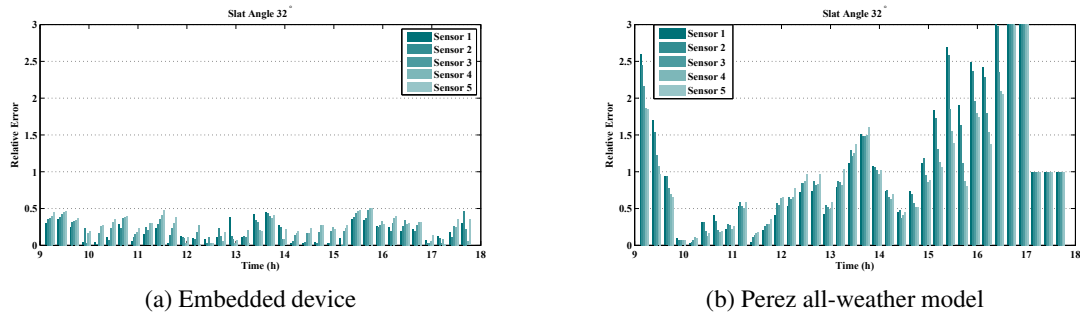


Fig. 3. Relative error in the simulated horizontal work-plane illuminance by using the two approaches (32° tilt angle)

For the tilt angle of slats at 72° to the vertical plane, the simulated work-plane illuminance and its relative error are illustrated in Figure 4 and Figure 5 respectively. The embedded photometric device out-performs the Perez sky model in transient simulation, especially for relatively dim skies with thick clouds and with high contrast sky patches. The spikes of error bars at mid-day were possibly due to the exposure of the lux-meters to the sun disk through the spacing of the EVB slats. For clear illustration and comparison, the error bar is not scaled to include the maximum peaks. The average relative error at the five positions through out the day for the embedded device is 35.8%, 33.8%, 42.1%, 34.9% , and 24.8%, while that for the common practice employing Perez all-weather model is 659.6%, 538.7%, 401.2%, 378.9%, and 400.0%.

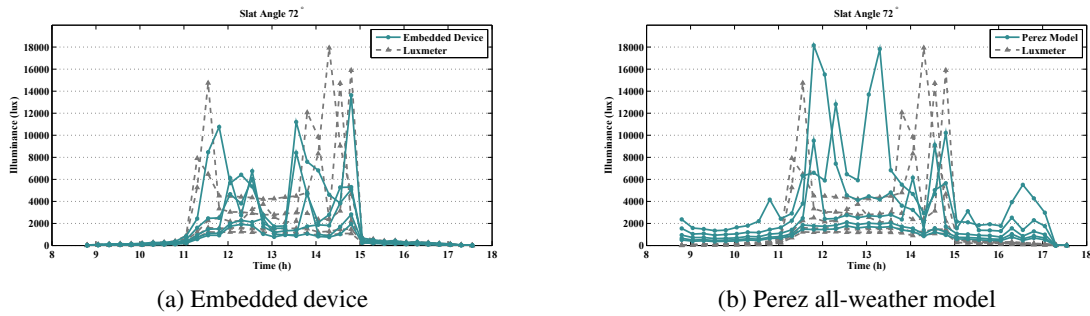


Fig. 4. Simulated horizontal work-plane illuminance by using the two approaches to reproduce the sky (72° tilt angle)

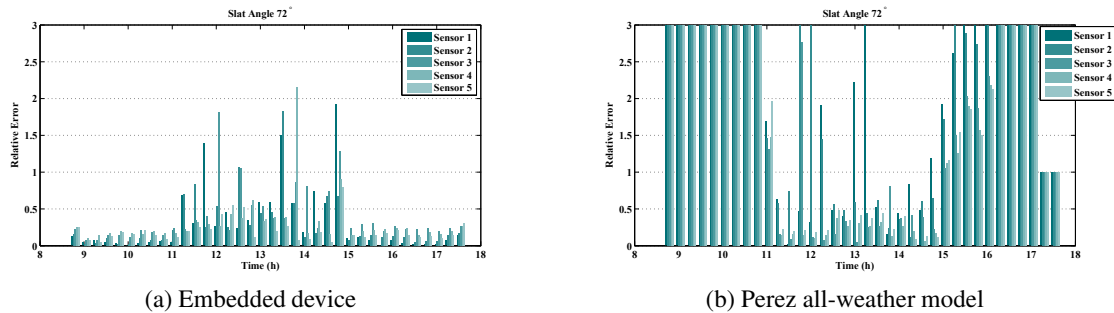


Fig. 5. Relative error in the simulated horizontal work-plane illuminance by using the two approaches (72° tilt angle)

CONCLUSIONS

Daylighting simulation is contingent on the mismatch between the modelled sky and real sky particularly for transient analysis. This paper demonstrates an embedded photometric device, integrating the HDR sky luminance monitoring and on-board lighting computing, in the daylighting simulation of horizontal work-plane illuminance for an EVB with a sinusoidal profile. Experiments were conducted for the EVB in a lighting test module. The BTDF of the EVB at tilt angle 32° and 72° was generated by the genBSDF program respectively. Employing the BTDF and geometry of EVB in the daylighting simulation, the experimental results show the embedded photometric device, based on HDR sky luminance monitoring, improves the accuracy in simulating the transient work-plane illuminance than the common practice employing the Perez all-weather sky model, especially for partly cloudy skies with high contrast sky patches. Despite of its merits in annual lighting analysis, the Perez model may have pronounced mismatch with the real sky for a specific location and moment.

Although the embedded photometric device, based on HDR sky luminance mapping, reproduces the sky more accurately than sky models, its computation load and bulky input data can limit its application in annual daylighting analysis, including daylight autonomy. The device is advantageous in applications sensitive to the accuracy of daylighting simulation, including dynamic shading control and building retrofitting. Its accuracy can be potentially improved further by the BTDF with higher resolution, which will be studied in the future.

ACKNOWLEDGEMENT

The authors would like to thank the Commission for Technology and Innovation of Switzerland for funding Swiss Competence Center for Energy Research (SCCER), Future Energy Efficiency Buildings and District (FEEB&D).

REFERENCES

- Dereniak, E. L., Brod, L. G., and Hubbs, J. E. (1982). Bidirectional transmittance distribution function measurements on ZnSe. *Applied optics*, 21(24):4421–4425.
- Klems, J. H. and Warner, J. L. (1995). Measurement of bidirectional optical properties of complex shading devices.
- Larson, G. W. and Shakespeare, R. (2004). *Rendering with Radiance: the art and science of lighting visualization*. Booksurge Llc.
- Mills, P. R., Tomkins, S. C., and Schlangen, L. J. (2007). The effect of high correlated colour temperature office lighting on employee wellbeing and work performance. *Journal of circadian rhythms*, 5(1):2.
- Perez, R., Seals, R., and Michalsky, J. (1993). All-weather model for sky luminance distribution preliminary configuration and validation. *Solar energy*, 50(3):235–245.
- Shannon, C. E. (1949). Communication in the presence of noise. *Proceedings of the IRE*, 37(1):10–21.
- Tregenza, P. R. (1987). Subdivision of the sky hemisphere for luminance measurements. *Lighting Research & Technology*, 19(1):13–14.
- ul Haq, M. A., Hassan, M. Y., Abdullah, H., Rahman, H. A., Abdullah, M. P., Hussin, F., and Said, D. M. (2014). A review on lighting control technologies in commercial buildings, their performance and affecting factors. *Renewable and Sustainable Energy Reviews*, 33:268–279.
- Wu, Y., Kämpf, J. H., and Scartezzini, J.-L. (2017a). Characterization of a quasi-real-time lighting computation system based on HDR imaging. In *CISBAT 2017*, Lausanne, Switzerland.
- Wu, Y., Kämpf, J. H., and Scartezzini, J.-L. (2017b). An embedded system for quasi real-time lighting computation based on sky monitoring. In *15th IBPSA Building Simulation 2017*, San Francisco, USA.

Modelling of a naturally ventilated BIPV system for building energy simulations

Juliana Gonçalves^{1,2*}, Glenn Reynders^{1,2}, Jonathan Lehmann^{1,2}, Dirk Saelens^{1,2}

¹Department of Civil Engineering, KU Leuven, Building Physics Section, Heverlee, Belgium

²EnergyVille, Genk, Belgium

*Corresponding email: juliana.goncalves@kuleuven.be

ABSTRACT

Two major causes of energy yield reduction in PV systems are partial shading and high operating temperatures. Both issues are particularly critical for BIPV systems. The correct assessment of the BIPV contribution to the built environment depends, therefore, on the accurate prediction of PV temperature and on the possibility of simulating shading effects. This paper describes the development of a multi-physics model for a naturally ventilated façade BIPV system within the openIDEAS environment for building and district energy simulations. The PV electrical model used here follows a physics-based approach that takes into account solar intensity and temperature spatial variations within the PV module, enabling the simulation of shading effects both at cell and module level. A detailed thermal model has been developed and coupled to the electrical model to estimate the PV temperature. Four case studies illustrate the importance of temperature and shading effects on the PV power output. The model has been validated using data from an experimental BIPV setup deployed in Belgium. The results indicate that the model is able to predict both the PV surface temperature and the power production, given the correct boundary conditions are applied.

KEYWORDS

Building Integrated PhotoVoltaics (BIPV), partial shading, Building Energy Simulation (BES), Modelica, openIDEAS.

INTRODUCTION

The effort to mitigate climate change is driving a revolutionary transformation in the energy system. Worldwide, nations have established strategic plans aiming at the reduction of greenhouse gas emissions. Responsible for a large percent of energy consumption and CO₂ emissions, the building sector is key to comply with such challenging guidelines. In view of the potential to increase the share of renewable energy in the built environment and reduce the related CO₂ emissions, building integrated photovoltaics (BIPV) systems have currently been considered the backbone of the 2020 zero energy buildings target in the European Union.

Building energy simulation (BES) tools can be used to assess the BIPV performance at building level. This paper addresses three main aspects regarding BIPV modelling in BES programs. TRNSYS, EnergyPlus and ESPr are considered here. The first aspect concerns the limited range of BIPV applications currently available in these programs. TRNSYS only offers a mechanically ventilated BIPV component (TRNSYS, 2018), while in EnergyPlus only a naturally ventilated variant is available (EnergyPlus Documentation, 2017). The development and validation of a mechanically ventilated façade BIPV model in ESPr has been reported by Clarke et al. (1997).

Secondly, the traditional BES tools, including the three considered here, are typically based on imperative language, which makes the code hard to maintain and restricts the inclusion of

new models (Wetter et al., 2016). Integrating new models in these tools requires not only a great effort from the user but also a high level of specific knowledge that may not be equally shared by all BIPV stakeholders. The ability of such tools to follow the development of new technologies and support the implementation of new systems is consequently limited, which is a major drawback for building and district energy simulation programs.

Finally, the third aspect focuses on the PV electrical model. All three tools considered here assume that (1) the performance of an array of identical modules is linear with the number of modules in series and parallel, and (2) all modules within the array operate always at maximum power point (MPP). This means that module and cell mismatch losses are not taken into account. While the assumption that all PV modules operate at the same conditions might be representative for roof installations, where partial shading effects are less important, this is not the case for façade BIPV applications. To allow the simulation of shading events, this work follows a physics-based approach that takes into account solar intensity and temperature spatial variations within the PV module. Although this approach has been extensively validated for different PV module topologies and varying weather conditions (Goverde et al., 2017; Goverde, 2016), to the best of the authors' knowledge, it has not been applied to BIPV systems, nor implemented in BES tools.

The following section introduces the methodology. First, the modelling approach is described. Next, four case studies are defined to illustrate the impact of the PV temperature and shading effects on the PV power output. An overview of the experimental BIPV setup used for the models validation is then presented. The third section brings the results. Finally, the last two sections discuss and elaborate on the results, and indicate the direction of future work.

METHODOLOGY

Modelling approach

The BIPV model was developed within the IDEAS environment, an open-source framework for building and district energy simulations based on Modelica language (Jorissen et al., 2018). Modelica is a general-purpose language for modelling complex and multi-domain systems. In particular, its equation-based object-oriented nature brings on the flexibility required to cover the wide range of BIPV applications and provides autonomy to the user to include new models or modify existing ones.

Figure 1 (left) illustrates the object-oriented approach: the PV elements represent the electrical model while the BIPV elements represent the thermal model. Each PV element corresponds to one PV cell, and has a different temperature and solar irradiation intensity as input, allowing for temperature and shading spatial variations. The temperature-dependent one-diode model based on Goverde (2016) represents the PV electrical behaviour at cell level. Each PV element is combined to one thermal element (explained below). The airflow circulating inside the BIPV element interconnects the thermal elements. The electric-thermal coupling between PV and thermal elements is achieved by using the PV temperature obtained from the thermal model to calculate the power output in the electrical model, which is in turn imposed as a heat sink to the PV thermal layer. A multi-step solver with a tolerance of 0.0001 resolves the equations iteratively. The PV controller limits the maximum time step to 10 s.

The thermal model is detailed in Figure 1 (right). The airflow rate results from the balance between the local and friction losses (calculated as in Langmans et al., 2015) and the driving pressure (wind and buoyancy). Buoyancy-driven pressure depends on the density difference

between the air inside the cavity and the ambient air. The wind-driven pressure is calculated according to Saelens and Hens (2011). Correlations available in the literature are used to model the convective heat transfer inside the cavity and at the exterior BIPV surface (Churchill and Chu, 1975; Montazeri and Blocken, 2017). Radiative heat transfer follows the Stefan Boltzmann's law. Long-wave losses to the ground and the sky are modelled separately.

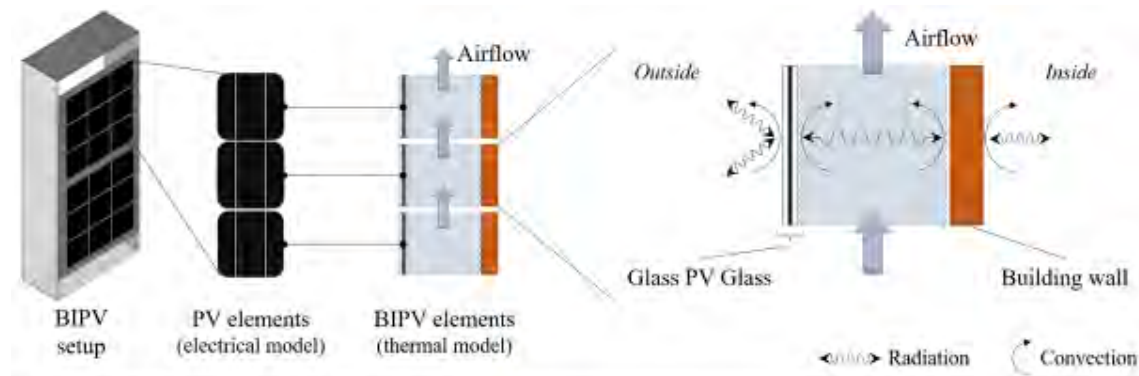


Figure 1. Schematics of (left) electric-thermal couplings, and (right) thermal model.

PV electrical model: case studies

To demonstrate the effect of temperature and shading on the PV power production, four cases were simulated. In Case 1, the temperature of all PV cells within the module was taken equal to 25 °C, which represent the standard test conditions (STC) for PV systems. Case 2 uses the surface temperature measured at cell level as an input to the model. Cases 1 and 2 are compared to the measured PV power output. In Case 3, shading is simulated at cell level, with 3 out of 9 cells within the PV module receiving 50% less irradiation. Case 4 represents the shading at module level, where all 9 cells receive the same amount of equivalent solar irradiation (83.3%). Case 3 characterizes the spatial approach used in this work while Case 4 represents the approach available in TRNSYS and EnergyPlus (spatial variations within the PV module are not included). Cases 3 and 4 are compared to non-shading conditions.

Experimental setup: overview

A schematic representation of the BIPV experimental setup used in this work is presented in Figure 1 (left). Lehmann et al. (2017) and Goverde et al. (2017) provide detailed information and experimental results for this setup. The BIPV element (1.3 x 0.6 x 0.14 m) is composed of two PV modules connected to a naturally ventilated cavity (width: 0.14 m; openings: 0.05 x 0.6 m). Each module consists of nine monocrystalline silicon PV cells connected in series and assembled in a glass-glass panel. The setup was integrated into the south-west façade of the Vliet test building in Leuven, Belgium. The instrumentation provides the BIPV surface and air temperature at relevant locations, PV power generation, and weather conditions, including the solar irradiation on the façade.

RESULTS

PV electrical model: case studies

The results presented here focus on two consecutive sunny days in May 2017. Weather conditions recorded on-site and measured PV surface temperatures are inputs to the simulations. On the left side of Figure 2, the comparison of Cases 1 and 2 against the measured values demonstrates the effect of the PV temperature on the power output. Assuming that the PV cells are at 25 °C overestimates the PV output by 14% at peak solar

irradiation. Provide the temperature of each PV cell is correct (Case 2), the results also indicate that the one-diode electrical model is able to predict the PV power output. Slightly larger deviations are observed in the beginning of the day. The right side of Figure 2 focuses on shading events. Case 3 shows that considering solar intensity variation at cell level leads to power reduction of more than 40% at peak solar irradiation compared to non-shading situations. The difference of 32% at peak solar conditions between cases 3 and 4 corresponds to the impact of the PV electrical modelling approach used in this work compared to the existing implementation in BES tools.

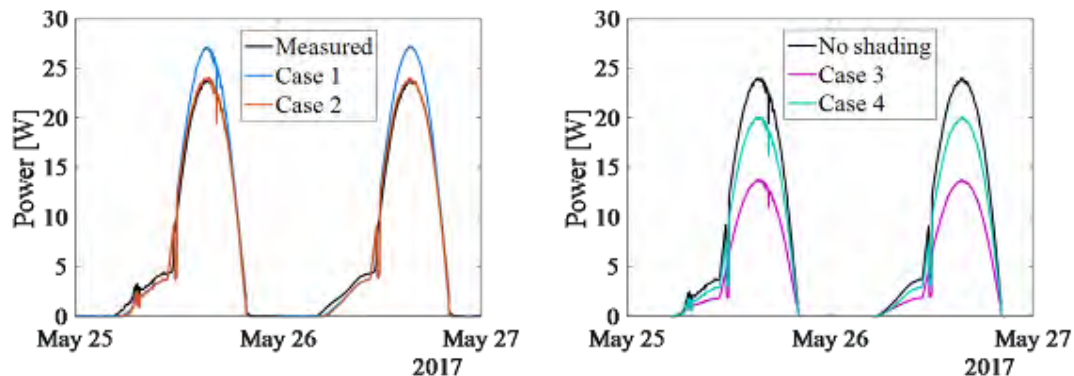


Figure 2. Results for two sunny days in May 2017: (left) Cases 1 and 2 are compared to measured power production, (right) Cases 2 and 3 compared to no shading conditions.

Experimental validation: multi-physics BIPV model

Simulations were performed for the fully coupled multi-physics model using weather data measured on-site from June to August 2017. Saelens et al. (2004) demonstrate that the assumption of an inlet air temperature equal to the exterior temperature may not be valid for ventilated façades. Thus, the air temperature measured at the cavity bottom is used as inlet temperature in the model. The heat flux through the building wall was measured at the middle of the wall and imposed to all thermal elements in the model as a boundary condition. Now, the coupled model predicts the PV temperature, instead of using measured PV temperatures as input to the model, as done previously for the case studies.

In Figure 3, on the left side, the results are presented for the same two days in May 2017. It has been demonstrated previously (Cases 1 and 2) that the PV electrical behavior is highly dependent on the PV temperature. Figure 3 (left) shows that the coupled model is capable of well predicting the average PV temperature and, therefore, is equally able to estimate the power output accurately. The absolute monthly energy yield error shown in Figure 3 (right) varies from less than 2.5% in June to 4% in July. The error has been calculated for power output above 2 W, which corresponds approximately to the period between 7h30-20h.

DISCUSSION

This paper has demonstrated the importance of considering temperature and shading effects to model BIPV systems. For the monocrystalline silicon cells used in this work, the power temperature coefficient is about $-0.5\%/K$ (Goverde, 2016), which leads to a power reduction of 15% for a temperature 30K above STC. Such temperature conditions are observed in Figure 3 (left). Note that the BIPV configuration investigated in this paper corresponds to a fairly well ventilated system. The temperature influence is expected to be more important for BIPV concepts with limited heat dissipation. These results indicate that assessing BIPV systems based on the temperature at STC may not be a suitable approximation, which corroborates the need for more detailed BIPV thermal models.

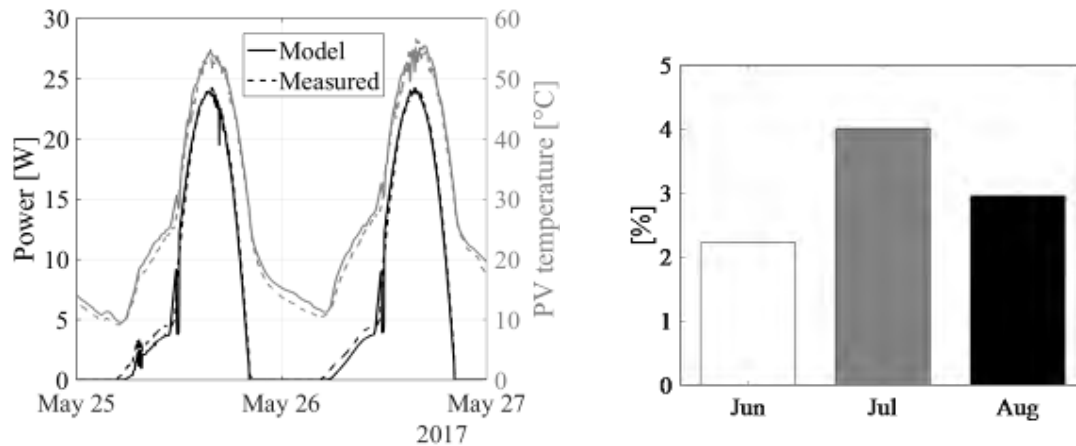


Figure 3. Left: results for two sunny days in May 2017. Right: monthly energy yield error.

As for shading effects, the results show that including solar intensity spatial variation at cell level within the PV module leads to a significant power reduction. This occurs because the PV module performance is bounded to the worst performing cell, a consequence of current mismatch between cells connected in series. The same applies to an array of PV modules in series, in which the worst performing module will dictate the array overall performance. Although a constant shading profile (throughout the day) might not represent real conditions, the results presented here are also quantitatively valid if shading occurs during peak solar irradiation, since larger differences in power production occur at high irradiation conditions.

The fully coupled BIPV model described in this paper is able to predict the BIPV temperature and, therefore, its power production. Possible causes for the power deviations in the beginning of the day are the following: 1) different pyranometer and PV response to the solar irradiation; 2) use of parameters not optimized for low irradiation conditions (Goverde, 2016); 3) use of one-diode model at low irradiation conditions (Chin et al., 2015). These aspects will be investigated in the future. Finally, the error difference from one month to the other indicates that the model is sensitive to weather conditions, in agreement with Goverde (2016).

Although this paper focused on naturally ventilated BIPV systems, which is more challenging from the modelling point-of-view, the flexibility of object-oriented models allows for easily adapting the model to a mechanically ventilated or unventilated variant. Validating the model for different BIPV concepts, including unventilated and real-size setups, is part of ongoing effort. Modelling the airflow behind the PV modules has also proven to be a challenging task. Future work will focus on computational flow dynamic methods and experimental techniques to better understand the airflow inside the cavity and improve the model accordingly.

CONCLUSIONS

This paper focused on the experimental validation of a naturally ventilated façade BIPV model. The modelling approach proposed here comprehends (1) a detailed multi-physics BIPV model; (2) the use of the equation-based object-oriented Modelica language; (3) the use of hydraulic network to model the airflow; (4) the individual modelling of wind and buoyancy effects; (4) a physics-based model to represent the PV electrical behaviour under non-uniform spatial conditions (temperature and solar irradiation). Thereby, mismatch losses between cells and modules are taken into account, and both shading and temperature effects can be simulated. This approach further provides detailed BIPV and building models within the same simulation environment.

This paper has demonstrated that, for a BIPV system, temperature effects may reduce the PV power output by 15% at peak solar irradiation compared to STC. Shading effects may be even more important with power reduction up to 40%. Although the air temperature measured at the bottom of the cavity was taken as the air inlet temperature for validation purposes, the authors recognize the importance of accurately modelling the inlet conditions. Nevertheless, provide that correct cavity flow characteristics and boundary conditions are used, the model presented in this paper is able to predict the performance of naturally ventilated BIPV systems with monthly energy yield error inferior to 4%.

ACKNOWLEDGEMENT

This work has been conducted within the EFRO SALK project, which receives the support of the European Union, the European Regional Development Fund (ERDF), Flanders Innovation & Entrepreneurship and the Province of Limburg.

REFERENCES

- Chin, V.J., Salam, Z., and Ishaque, K. 2015. Cell modelling and model parameters estimation techniques for photovoltaic simulator application: A review. *Applied Energy*, 154, 500-519.
- Churchill, S.W., and Chu, H.H. 1975. Correlating equations for laminar and turbulent free convection from a vertical plate. *International Journal of Heat and Mass Transfer*, 18(11), 1323-1329.
- Clarke, J. A., Johnstone, C., Kelly, N., and Strachan, P. A. 1997. The simulation of photovoltaic-integrated building facades. *Building Simulation*, 97, 189-195.
- EnergyPlus Documentation. 2017. *Engineering Reference*. U.S. Department of Energy.
- Goverde, J. 2016. Understanding and Increasing the Energy Yield of Crystalline Silicon Photovoltaic Modules. *Ph.D. Thesis*, KU Leuven, Belgium.
- Goverde, J., Anagnostos, D., Govaerts, J., Manganiello, P., Voroshazi, E., Szlufcik, J., Catthoor, F., Poortmans, J. and Driesen, J. 2017. Accurately simulating PV energy production: exploring the impact of module build up. In *34th EUPVSEC*, 1643-1646.
- Jorissen, F., Reynders, G., Baetens, R., Picard, D., Saelens, D. and Helsen, L. 2018. Implementation and verification of the IDEAS building energy simulation library. *Journal of Building Performance Simulation*, 1-20.
- Langmans, J., and Roels, S. 2015. Experimental analysis of cavity ventilation behind rainscreen cladding systems: A comparison of four measuring techniques. *Building and Environment*, 87, 177-192.
- Lehmann, J., Parys, W., Goncalves, J., Govaerts, J., Goverde, J., Baert, K., and Saelens, D. 2017. An in-depth comparison of PV modules in a BIPV facade test setup. In *34th EUPVSEC*.
- Montazeri, H., and Blocken, B. 2017. New generalized expressions for forced convective heat transfer coefficients at building facades and roofs. *Building & Environment*, 119, 153-168.
- Saelens, D., and Hens, H. 2001. Experimental evaluation of airflow in naturally ventilated active envelopes. *Journal of Thermal Envelope and Building Science*, 25(2), 101-127.
- Saelens, D., Roels, S., and Hens, H. 2004. The inlet temperature as a boundary condition for multiple-skin facade modelling. *Energy and Buildings*, 36(8), 825-835.
- TRNSYS. 2018. [online] Available at: <http://www.trnsys.com/>.
- Wetter, M., Bonvini, M., and Nouidui, T.S. 2016. Equation-based languages—A new paradigm for building energy modeling, simulation and optimization. *Energy and Buildings*, 117, 290-300.

Numerical analysis of the influencing factors on the performance of a pipe-embedded window operated in summer

Sihang Jiang, Chong Shen and Xianting Li*

Tsinghua University, Beijing, China

*Corresponding email: xtingli@tsinghua.edu.cn

ABSTRACT

The pipe-embedded window is a double window structure with pipes embedded inside the cavity to adjust the temperature. The preliminary studies showed that it can significantly reduce the cooling load of buildings with natural cooling sources such as the water from cooling towers in summer. However, the research on the influencing factors of the pipe-embedded window is insufficient. In this paper, the numerical calculation models are established for a pipe-embedded window and a traditional window. The influence of climatic factors, such as the natural cooling source temperature and outdoor air temperature on the thermal performance of the pipe-embedded window are studied. Based on these, the building energy efficiency is analysed. The results show that the thermal resistance of the pipe-embedded window is basically constant. A linear relationship has been found between the inner surface heat flux, pipe heat flux, interlayer mean air temperature and the outdoor air temperature, mean water temperature or solar radiation intensity. The solar radiation intensity, water temperature, outdoor air temperature is ranked from most to least influence. The location of pipe has little effect on the temperature field and heat transfer of a pipe-embedded window. In summer, the difference between inner-glass and outer-glass insulation is small.

KEYWORDS

Space cooling, Pipe-embedded window, CFD, Cooling load, Building energy efficiency

INTRODUCTION

It is crucial to reduce the cooling load caused by glass envelope. Double Skin Façade (DSF) is able to utilize the dry bulb temperature of outdoor air to improve its own thermal performance, so it has a very large energy-saving potential. However, some problems of the DSF have been exposed with the research and application going in deep. As the two main problems, under summer solar radiation, it is prone to the interlayer greenhouse effect because of the interlayer overheat (Gratia and De Herde, 2007); in winter, strengthening insulation can only be achieved by closing the passageway. The external environment is underutilized in regulating temperature as in summer.

To further reduce the cooling load from window, Shen and Li (2016a) proposed a system that embedding water pipes in the venetian blinds of a double glass window utilizing cooling water and studied the system performance under the design condition. Their results showed the effectiveness of the pipe-embedded window. However, the system performance under different weather conditions and water temperatures wasn't studied; Shen and Li (2016b) also studied the performance of the pipe-embedded window they proposed applying it to different regions and orientations. It showed that the above pipe-embedded window had a great energy saving potential in most climatic regions of China. However, the influence of different types of window structures wasn't considered. Overall, at present, the influencing factors on the heat transfer of this kind of window are rarely studied. The analysis of the relevant energy

efficiency and heat transfer mechanism is also insufficient, which also restricts the popularization and application of this kind of window to a certain extent.

In this paper, a numerical model is built for a pipe-embedded window. The influences of the climatic influencing parameters, such as the natural cooling source temperature, outdoor air temperature and solar radiation intensity, as well as the geometrical influencing parameters, such as the pipe and insulating layer location on the thermal performance of this kind of window are systematically studied in order to provide reference for engineering practice.

METHODS

Physical model

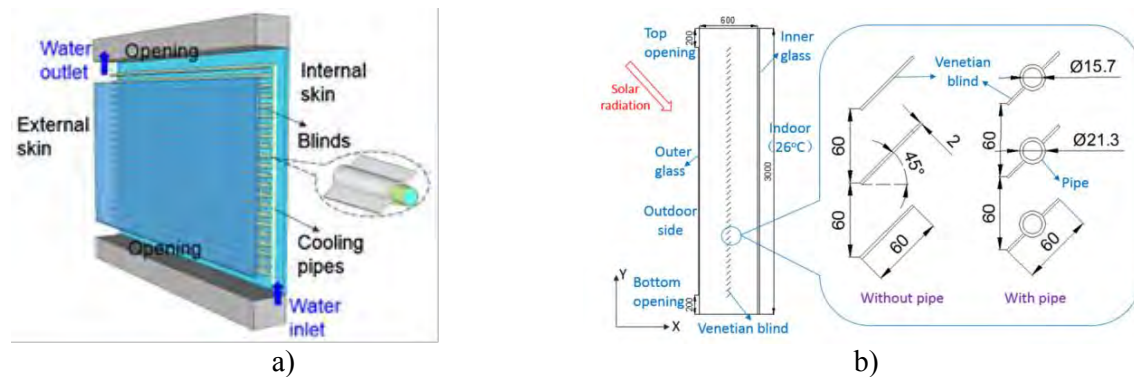


Figure 1. Pipe-embedded double window system. a) Structures, b) Dimensions

Fig. 1 provides the structures and dimensions of a pipe-embedded double window system. Water pipes are embedded into the venetian blinds of the double window. Actually, the differences between the traditional window and the pipe-embedded window only exist in sunshade structures. The dimensions of the studied pipe-embedded window are 3 m (height, Y) \times 0.6 m (width, X). In total, 44 cooling pipes are embedded into the venetian blinds with an interval of 60 mm. The outside diameter of each cooling pipe is 21.3 mm. The thermal parameters of materials are determined by referring to the references (Iyi et al. 2014; Zeng et al. 2012). The working conditions about the climatic influencing factors in this paper are divided into three groups: Different water temperatures (A); Different outdoor air temperatures (B); Different solar radiation intensities (C). The working conditions about the geometrical influencing factors are divided into two groups: Different pipe locations (D); Different insulating layer locations (E). The details are summarized in Table 1 and Table 2.

Table 1. The settings of the working conditions (Climatic influencing factors)

Working condition	Water temperature(°C)	Outdoor temperature(°C)	Solar radiation(W/m ²)
A	24/26/28/30	34	500
B	28	32/34/36/38	500
C	28	34	125/250/375/500

*The pipes are located in the middle of interlayer. The insulating layer closes to the indoor side.

Table 2. The settings of the working conditions (Geometrical influencing factors)

Working Condition	Water temperature(°C)	Pipe location	Insulating layer location
D	28	left/middle/right	right
E	22/26/30	middle	left/right

*The outdoor air temperature is 34 °C. The solar radiation intensity is 500W/m².

Numerical method

A CFD model is established in this paper. The κ - ε turbulence model is adopted in this paper (Iyi et al, 2014). A two-dimensional simplification is adopted in this paper (Manz, 2004; Saelens et al, 2008). The heat transfer is considered to be a steady process. Discrete ordinate (DO) method is adopted for simulating the radiation heat transfer. The commercial CFD software ANSYS Fluent is employed to solve all the numerical equations in this paper. Structured quadratic meshes are divided in the main domain except for a small part near venetian blinds; the mesh with 35,000 cells is eventually employed. The numerical simulation methods in this section have been validated successfully (Shen and Li, 2016b).

Energy efficiency analysis method

The electricity consumption of delivery for a pipe-embedded window system (P_{pipe} , W/m²) is made up of the electricity consumption of indoor pumps and outdoor heat rejection equipment (such as cooling tower), it can be calculated as:

$$P_{pipe} = \frac{Q_{pipe}}{WTF_{pipe}} + \frac{Q_{pipe}}{EER_{out}} \quad (1)$$

where Q_{pipe} is the heat flux of water pipes, W/m². WTF_{pipe} is the transport factor (ratio of transferred heat energy to the electricity consumption of pumps) of the pipe-embedded water system. EER_{out} is the energy efficiency ratio of outdoor unit, the NDRC (2008) recommends the values.

The electricity consumption of delivery for a traditional air conditioning system (P_{room} , W/m²) is made up of the electricity consumption of indoor pumps, outdoor heat rejection equipment and indoor heat exchangers (such as fan-coil unit), it can be calculated as:

$$P_{room} = \frac{Q_{room}}{WTF_{room}} + \frac{Q_{room}}{EER_{in}} + \frac{Q_{room}}{EER_{out}} \quad (2)$$

where Q_{room} is the indoor air conditioning load caused by the window (equal to the inner surface heat flux), W/m². WTF_{room} is the transport factor of the indoor air conditioning water system. EER_{in} is the energy efficiency ratio of indoor unit, the NDRC (2008) recommends the values.

The electricity consumption of the traditional air conditioning system (E_{trad} , W/m²) can be calculated as:

$$E_{trad} = \frac{Q_{room}}{COP} + P_{room} \quad (3)$$

where COP is the coefficient of performance of the chiller system.

RESULTS AND DISCUSSIONS

Influences of the climatic influencing factors

By calculating the inner surface heat flux, pipe heat flux, interlayer mean air temperature in every case, the relevant fitting formulas can be obtained ($R^2 \approx 1$):

$$Q_{room} = 0.9964 \cdot t_{air} + 3.3456 \cdot t_{water} + 0.07889 \cdot R_{solar} - 86.25 \quad (4)$$

$$Q_{pipe} = 4.7091 \cdot t_{air} - 9.5898 \cdot t_{water} + 0.60877 \cdot R_{solar} + 60.22 \quad (5)$$

$$t_{aver} = 0.1954 \cdot t_{air} + 0.6761 \cdot t_{water} + 0.00413 \cdot R_{solar} + 3.18 \quad (6)$$

where T_{aver} is the interlayer mean air temperature, °C. t_{air} is the outdoor air temperature, °C, and t_{water} is the water temperature, °C. R_{solar} is the solar radiation intensity, W/m².

The above formulas with a very high linearity show that the thermal resistance of the pipe-embedded window will be basically constant if the structure of a pipe-embedded is defined. The convective and radiant heat transfer coefficients are basically unaffected by the climatic influencing parameters such as outdoor air temperature. The influence of the water temperature on the inner surface heat flux is significantly higher than that of the outdoor air temperature. However, the pipe heat flux will increase by 50 W/m^2 if the solar radiation intensity increases by 60 W/m^2 . The fluctuation range of the solar radiation intensity in one day is often at the order of several hundred W/m^2 , so the solar radiation intensity is the most significant influencing factor. The water with a higher temperature can also take away effectively solar radiation heat energy because of the solar radiation heating source with a very high temperature, so the influence of the water temperature is slightly smaller.

Fig 2 and Fig 3 show the influences of the outdoor air temperature, water temperature and solar radiation intensity on the cooling load reduction rate of the embedded window (compared with the traditional DSF) and electricity consumption.

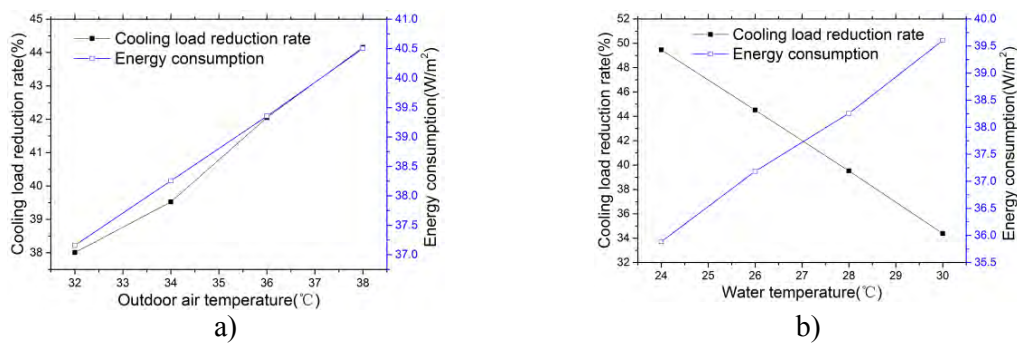


Figure 2. Influences of outdoor air and water temperature. a) Outdoor air temperature, b) Water temperature

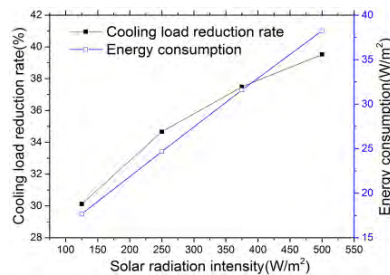


Figure 3. Influence of solar radiation intensity

It can be seen that all the influence relations are approximately linear. The load reduction rate increases with the outdoor temperature and solar radiation intensity, decreases with the water temperature. The water temperature has a greater influence than the outdoor air temperature. It shows that when the outdoor air temperature or solar radiation intensity rise or the water temperature reduces, the pipes can take away not only more heat energy but also a greater proportion of heat energy because of the increase of difference between the water temperature and solar-air temperature. When the outdoor air temperature is $38 \text{ }^{\circ}\text{C}$, the inner surface heat flux is 84.7 W/m^2 and the load reduction rate is up to 44%; when the water temperature is $24 \text{ }^{\circ}\text{C}$, the inner surface heat flux is 67.4 W/m^2 and the load reduction rate is up to 49%; when the

solar radiation intensity is 125 W/m^2 , the inner surface heat flux is 80.7 W/m^2 and the load reduction rate is up to 40%. The electricity consumption increases with the outdoor air temperature, water temperature and solar radiation intensity. However, it doesn't change much around 38 W/m^2 when the outdoor air temperature and water temperature change. The solar radiation intensity has the most significant impact on electricity consumption. When the solar radiation intensity is 125 W/m^2 , the electricity consumption reduction rate is up to 25%.

Influences of the geometrical influencing factors

Fig 4 shows the comparison of the temperature fields with different pipe locations. It can be seen that the temperature fields are basically the same. When the pipes are near the indoor side, the overall air temperature between the pipes and outer glass is slightly higher because of more direct radiation hitting the bottom surface. The pipe location almost has no effect on the electricity consumption (around 39 W/m^2) and the heat transfer of the window.

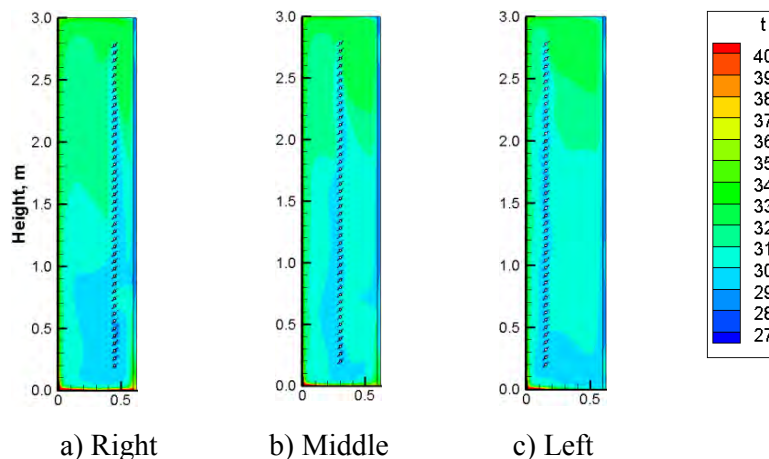


Figure 4. Comparison of the temperature fields with different pipe locations (The left boundary direct contacts with the outdoor environment). a) Right, b) Middle, c) Left

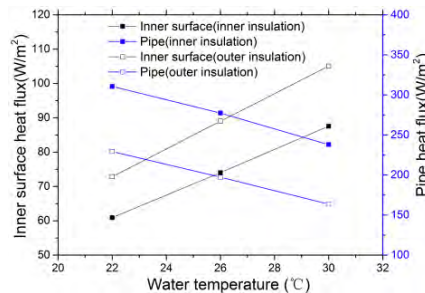


Figure 5. Influences of insulating layer with different locations

Figure 5 shows the influences of insulating layer with different locations. It can be seen that the weights between the inner surface and pipe heat flux with different insulating layer locations are different. When the insulating layer is located near the indoor side, the heat flux passing the inner surface is very little but the heat flux passing the pipe wall is very much. On the contrary, when the insulating layer is located near the outdoor side, the no-water interlayer air temperature is higher, the inner surface heat flux will increase and pipe heat flux will decrease with the decrease of the difference between the interlayer air temperature and water temperature. When the insulating layer location changes, the change range of the pipe heat

flux is about 2.5 times that of the inner surface heat flux. In other words, if the cooling efficiency of the pipes is 2.5 times higher than that of indoor heat exchangers, the way of inner-glass insulation will be more energy-saving. However, the pipes are mainly used to remove the solar radiation energy instead of the thermal conduction and convection in summer. Besides, the difference between the water temperature and outdoor air temperature is usually little, so the difference of the electricity consumption between the inner-glass and outer-glass insulation is very small.

CONCLUSIONS

A linear relationship was found between the inner surface heat flux, pipe heat flux, interlayer mean air temperature and the outdoor air temperature, mean water temperature or solar radiation intensity. The solar radiation intensity, water temperature, outdoor air temperature is ranked from most to least influence.

The cooling effect of the pipe-embedded window is significant even if the water temperature is higher than the indoor air temperature. For example, When the water temperature is 28 °C, the interlayer mean air temperature of the pipe-embedded window is 5.5 °C lower than that of traditional DSF. The inner surface heat flux of the pipe-embedded window is 52.7 W/m² lower than that of tradition DSF, the load reduction rate is nearly 40%; when the water temperature is equal to the indoor air temperature, the load reduction rate can be up to 45%.

In summer, the pipe location almost has no effect on the temperature field and heat transfer of the pipe-embedded window. The performance of glass is not the decisive factor in the overall performance of the pipe-embedded window. The difference between inner-glass and outer-glass insulation is small.

ACKNOWLEDGEMENT

This study is supported by the China National Natural Science Foundation (Grant No. 51638010 and No. 51578306).

REFERENCES

- Gratia E and De Herde A. 2007. Greenhouse effect in double-skin facade. *Energy and Buildings*, 39(2), 199-211.
- Iyi D, Hasan R, Penlington R, et al. 2014. Double skin façade: Modelling technique and influence of venetian blinds on the airflow and heat transfer. *Applied Thermal Engineering*, 71(1), 219-229.
- Manz H. 2004. Total solar energy transmittance of glass double façades with free convection. *Energy and Buildings*, 36(2), 127-136.
- National Development and Reform Commission. 2008. *GB/T 17981-2007*, Economic operation of air conditioning systems. Beijing, People's Republic of China.
- Saelens D, Roels S and Hens H. 2004. The inlet temperature as a boundary condition for multiple-skin facade modelling. *Energy and Buildings*, 36(8), 825-835.
- Shen C and Li X. 2016. Solar heat gain reduction of double glazing window with cooling pipes embedded in venetian blinds by utilizing natural cooling. *Energy and Buildings*, 112, 173–183.
- Shen C and Li X. 2016. Energy saving potential of pipe-embedded building envelope utilizing low-temperature hot water in the heating season. *Energy & Buildings*, 138.
- Zeng Z, Li X, Li C, et al. 2012. Modeling ventilation in naturally ventilated double-skin facade with a venetian blind. *Building and Environment*. 57, 1–6.

Validation of the EN 15193:2017 calculation method to estimate the daylight supply in a building: comparison with dynamic climate-based simulations

Valerio Roberto Maria Lo Verso¹, Argun Paragamyan¹ and Anna Pellegrino^{1*}

¹Politecnico di Torino, Energy Department, TEBE Research Group, Turin, Italy

*Corresponding email: anna.pellegrino@polito.it

ABSTRACT

This paper compares a simplified method to calculate the daylight factor and the annual daylight contribution in a space to the output of dynamic daylighting simulations. The simplified calculation method is the one implemented in the European Standard EN 15193 for the calculation of the energy demand for lighting in buildings, while the tool for dynamic simulations is Daysim (managed through DIVA-for-Rhino). The analysis was carried out by applying the two approaches to a reference office room, which was assumed to be located in different sites and having different window areas, with different orientations, both in the absence and in the presence of a mobile shade. The presence of an obstructing building was also considered. A total number of 108 cases was considered for the comparison.

The results showed a very good correlation between the analytical method and the Daysim simulations to calculate the daylight factor ($R^2=0.99$, with an absolute average difference of 11%). The correlation was lower for the calculation of the annual daylight contribution ($R^2=0.86$, with an absolute average difference of 35%), due to the complexity of variables included (climate, orientation, presence of a moveable shade). Among the variables, the higher differences between the analytical and simulation results were observed for the climate and the absence/presence of a shade.

KEYWORDS

Daylight supply estimation, simplified calculation method, Daylight Factor, DIVA-for-Rhino simulations, EN15193-1 standard.

INTRODUCTION

The standard EN 15193-1 (2017) belongs to a set of standards that were developed to support the implementation of the Energy Performance of Buildings Directives. In the standard, the metric LENI (Lighting Energy Numeric Indicator) was introduced to quantify the energy demand for lighting for a building. Consistently, an analytical calculation method was also supplied. This includes all the main factors that affect the energy consumption for electric lighting: power of the lighting systems, daylight contribution into an indoor space, type of lighting control and building usage. The “core” of the calculation method is the estimation of the daylight contribution through the daylight dependency factor (F_D). This depends on other two factors: the *daylight supply factor*, $F_{D,S}$, to estimate the “daylight autonomy” of the space under consideration; the *lighting control factor*, $F_{D,C}$, to account for the effectiveness of the type of lighting control system in exploiting daylight. To calculate F_D , the building is divided into ‘Daylit Areas - A_D ’, which receive daylight, and ‘Non-Daylit Areas - A_{ND} ’ for which F_D is assumed equal to 1 (no significant daylight contribution).

The calculation method introduced in the original standard (2007) was deeply revised in the present version (2017), with regard to both $F_{D,S}$ and $F_{D,C}$. The analytical procedure adopted in the new version of the standard relies on a parametric study, whose basic principles are described in the EN 15193-2 (2017) and in the ISO 10916 (2014).

Focusing on $F_{D,S}$, this is the result of a two-step calculation. Firstly the daylight factor for the opening (D) is calculated as a function of external obstructions, room sizes and characteristics of the apertures (such as window size, glazing visible transmittance and maintenance, and frame factor). Secondly, the annual daylight supply factor of the considered space ($F_{D,S}$) is determined as a function of D , of the climate, of the orientation of the windows, of the absence/presence of a shading system for thermal and/or glare control, and of the target illuminance. Except for the illuminance, the other factors of step *two* of the calculation method were not included in the original version of the standard (2007). In the new standard, the climate is taken into account through the *luminous exposure* H_{dir}/H_{glob} , i.e. the ratio of the direct horizontal illuminance to the global horizontal illuminance, each being calculated by summing up the illuminances in the hour range 8-17 throughout a year. To account for the presence of mobile shading systems, $F_{D,S}$ is determined with reference to two different façade states, i.e. with systems activated ($F_{D,S,SA}$) and with systems non-activated ($F_{D,S,SNA}$). $F_{D,S}$ is calculated as a weighted average of $F_{D,S,SA}$ and $F_{D,S,SNA}$, using the annual relative time of usage or non-usage of the shading system as weighting factors.

Figure 1 shows a schematic representation of the flow chart to calculate F_D and of the space segmentation into Daylit and Non-Daylit Areas.

More information about the calculation method of the EN15193 standard can be found in Tian and Su (2014), Zinzi and Mangione (2015), and in Aghemo et al. (2016).

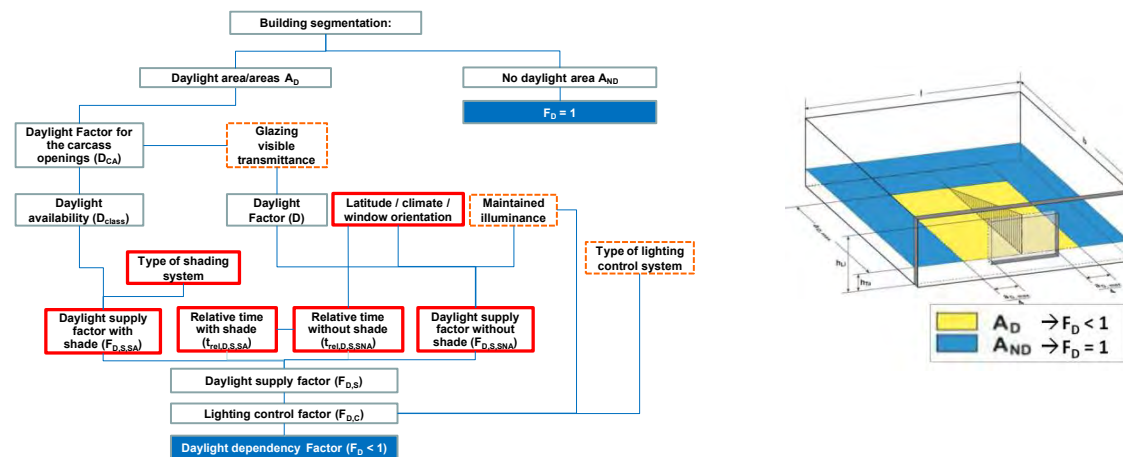


Figure 1. Flow chart to calculate the daylight dependency factor F_D for A_D and A_{ND} .

With the new standard, building practitioners are supplied with an analytical method, which accounts also for climate conditions, orientations and movable shadings, to calculate the daylight contribution in a space and therefore the LENI, without any simulations. The method is tabular, and the influencing factors are considered in a simplified way through discrete ranges. Compared to a dynamic simulation, the analytical method has a lower level of detail. Within this frame, this paper presents a comparison of the daylight contribution in a space as calculated through the analytical method of the standard and through a dynamic simulation tool. The validated Radiance-based daylight simulation method DAYSIM was used for this purpose (Reinhart and Walkenhorst, 2001). This combines the concept of the daylight coefficients and the Perez sky model to run annual simulations to determine the daylighting and the energy demand for lighting in a space.

METHODS

A set of case studies was defined for the analysis of the daylight supplied in a room, calculated both through the analytical method and advanced simulation. The analytical

method was carried out in accordance with the Standard EN 15193-1 through a purpose-developed Excel spreadsheet, while the program DIVA-for-Rhino was used to manage Daysim annual daylighting simulations (a time-step of 1h was used). The Energy Plus climate files were used, both as input for the Daysim simulations and to calculate the *luminous exposure* H_{dir}/H_{glob} , which in turn was then used as input for the analytical calculation of $F_{D,S}$. A reference room was chosen, whose plan sizes are 6 m x 6 m, with a floor-to-ceiling distance of 3 m. The room has a single vertical opening (with a lintel height of 2.70 m and a sill height of 1 m above the floor), equipped with a glazing with a visible transmittance of 0.70. The room was meant to be used as a cellular office, with a target illuminance of 500 lx and with an occupancy profile 8:00 through 17:00, Monday through Friday, as specified in Standard EN 15193-1. A series of variables were parametrically modified to obtain a meaningful number of cases for which to compare the daylight contribution determined analytically and from simulations. The cases were defined so as to determine different daylight amounts in the room (poor, medium, high) under different climates to test the two methods.

For each case, D and $F_{D,S}$ values were calculated analytically following the standard, while through the Daysim simulations two climate-based daylight metrics were determined: the continuous Daylight Autonomy DA_{con} and the Daylight Autonomy DA . Conceptually, the DA_{con} appears as the most consistent metric to be compared to $F_{D,S}$, based on how $F_{D,S}$ is defined and calculated in the EN 15193-2 (2017). Considering that the DA is a more widely used metric to calculate the daylighting in a space, this was also determined and compared to the $F_{D,S}$. For the simulations, a grid of sensors was positioned over the workplane (0.8 m above the floor), with a spacing of 50 cm, covering the whole room area except a peripheral stripe of 50 cm. Annual DA and DA_{con} values were calculated for each point of the grid, then computing their average value to be compared to $F_{D,S}$.

The parameters that were modified were: site (3), size of the openings (3), type of shading (2), presence of a building ahead that produces a frontal obstruction (obstruction angle of 45°) (2), and orientation (3) (see Table 1). Each variable was parametrically combined with all the other variables, resulting in a database of 108 cases for the comparative analyses.

Table 1. Variables of the reference room that were changed for the comparative analysis.

Position (3)	London - L = 52.3°N ($H_{dir}/H_{glob} = 0.37$)	Turin - L = 51.5°N ($H_{dir}/H_{glob} = 0.43$)	Palermo - L = 38.1°N ($H_{dir}/H_{glob} = 0.50$)
Window area (3)	1 m x 1.7 m (WWR = 0.09) (carcass area 1.70 m ²)	6 m x 1.7 m (WWR = 0.57) (carcass area 10.2 m ²)	6 m x 3 m (WWR = 1) (carcass area 18 m ²)
Shading (2)	No glare protection	Blind for glare protection	
Obstruction angle (2)	0°	45° (Building with a visible reflectance of 25%)	
Orientation (3)	South	West	North

RESULTS

Comparison of the daylight factor calculated analytically and through simulations

Figure 2 shows the daylight factor results (analytical and from simulations) for the entire database. For the analytical method, the D value is the area weighted average value of the two D values for A_D and A_{ND} . Plotting the analytical D values (standard) versus the DF values from Daysim simulations (Fig. 2a) shows a robust correlation ($R^2=0.99$). In spite of this, a difference in the estimate is observed: the relative difference between the daylight factor values through the two approaches for all the cases analyzed is in the range -18.7% ÷ +9.9%, with an average difference of -5.2% (Fig. 2b). It seems therefore that the analytical method on average tends to underestimate the daylight amount compared to the simulation results.

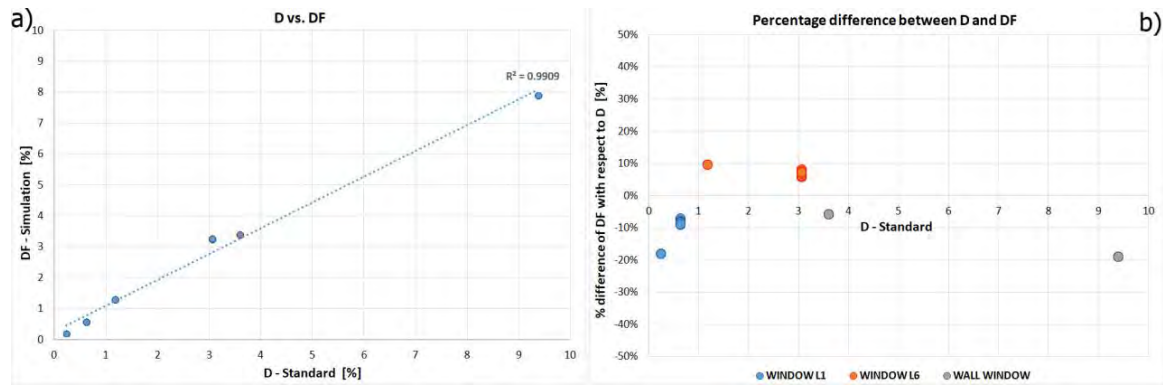


Figure 2. D values (analytical method of the standard) versus DF values from simulations: a) absolute values, b) relative percent difference.

Comparison of the *daylight supply* calculated analytically and through simulations

The daylight contribution in the spaces analyzed through the analytical method ($F_{D,S}$) was compared to two climate-based daylight metrics from DIVA simulations (Fig. 3): the continuous Daylight Autonomy DA_{con} (Fig. 3a) and the Daylight Autonomy DA (Fig. 3b). $F_{D,S}$ is calculated as area weighted average value of the two $F_{D,S}$ values for A_D and A_{ND} .

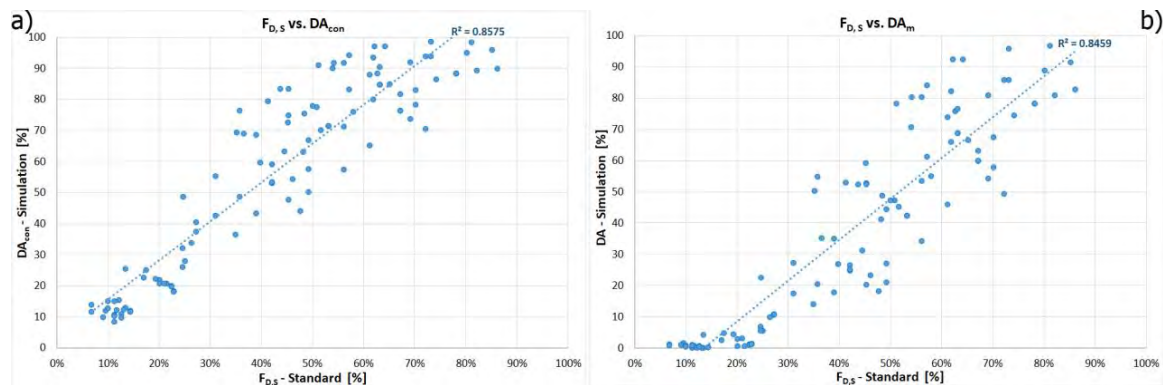


Figure 3. Comparison of the daylight supply: a) $F_{D,S}$ vs. DA_{con} , b) $F_{D,S}$ vs. DA .

The correlation between analytical and simulation results is similar when using the DA_{con} metric ($R^2=0.86$) or the DA metric ($R^2=0.85$). In spite of this, the comparison $F_{D,S}$ - DA shows a gap for the lower values, in a way that $F_{D,S}$ values in the range 7%-23% correspond to a DA of around 0% (such gap was not observed using the DA_{con}).

Figure 4 shows the relative percent differences between analytical and simulation results.

Based on the results shown in Figure 4, the following considerations can be drawn:

- *range of relative differences*: the range was $-115\% \div +22\%$, with an average difference of -32.4% . Consistently with what observed for the daylight factor but to a greater extent, the comparison between DA_{con} and $F_{D,S}$ values shows that the analytical method on average tends to underestimate the daylight supply in a room compared to Daysim simulations
- *effect of climate*: the highest differences between analytical and simulation results were observed for Palermo, then for Turin and for London (average difference: -60% , -29% , and -17% , respectively). The way the climate is taken into consideration in the standard approach and in simulations plays therefore a crucial role on the final result: the standard accounts for the climate through the *luminous exposure* H_{dir}/H_{glob} , which synthetizes the climatic variation during the course of a year through a single value that expresses the annual presence of direct radiation compared to the global radiation. Differently, an annual

- simulation calculates the daylighting into a space with a time-step of 1 hour, i.e. accounting for a specific sky condition that takes place every hour
- *effect of obstruction*: the relative difference values between the analytical and the simulations results for cases without and cases with obstruction were found to be of the same magnitude (average difference: -35.4% and -28.8%, respectively)
 - *effect of orientation*: the three orientations considered showed differences between analytical and simulations results of the same magnitude (average difference: -37.2% for South, -29.1% for West, and -30.1% for North; again, the analytical results tend to underestimate the simulation results). Another aspect to mention is that the analytical approach assumes the same tabular coefficients for East and West orientations, which means that the same D and $F_{D,S}$ values are obtained for the same space facing East or West. Besides, in the presence of the blinds, the DA_{con} values obtained with DIVA for the same space with the window West and East oriented were quite different: the relative differences of DA_{con_W} and DA_{con_E} values were in the range $-56\% \div +8\%$. These differences are due to the calculation algorithm implemented in Daysim to model the blinds: once glare is detected, the blind is pulled down and left in that position for the rest of day, so an East-facing space remains shaded for longer periods compared to the same space facing West.

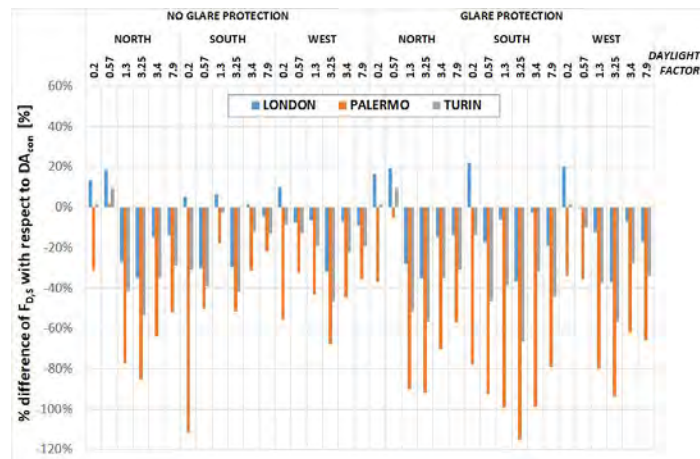


Figure 4. Relative percent differences of the results for the daylight supply.

DISCUSSIONS

The paper presented the results of a study on the effectiveness of a simplified analytical method, adopted in the European standard EN 15193-1, to calculate the daylight supply in buildings, compared to the results from dynamic simulations with a commercially available tool (DIVA-for-Rhino, which uses Daysim). The study was focused on the analysis of two of the parameters included in the simplified calculation procedure: the daylight factor (D) and the daylight supply factor ($F_{D,S}$). The first one is representative of the daylight provision under an overcast sky condition and in the absence of shading devices; the second one is descriptive of the daylight supply calculated taking into account the actual climate conditions, the window orientation, the presence of movable shadings and the required target illuminance.

The results of the study demonstrated that there is a very good correlation between the analytical method and the dynamic simulations with Daysim for what concerns the calculation of D ($R^2 = 0.99$, with an absolute average percent difference of 11%), while the correlation is lower when $F_{D,S}$ is considered ($R^2 = 0.86$). The daylight supply factor $F_{D,S}$ was compared to the DA_{con} , as these two parameters have the same conceptual meaning. The results showed an average difference of -32.4%, ranging between -115% and +22%. Such lower correspondence for the global daylight supply ($F_{D,S}$ and DA_{con}) with respect to the daylight factors is in line

with the greater complexity of the factors affecting $F_{D,S}$ and DA_{con} . The way the climate and movable shading systems are considered in the two estimation approaches particularly seem to be responsible for the greatest gaps observed between the results: the average difference is higher for Palermo (-60%), intermediate for Torino (-29%) and lower for London (-17%), and it is higher for cases with moveable shading devices than without shadings (-41% vs. -29%). The great difference between $F_{D,S}$ and DA_{con} for Palermo is probably due to the very simplified approach used in the standard to account for climate conditions. Very few climate conditions (expressed in terms of H_{dir}/H_{glob}) are reported in the tables of the standard and, while Torino and London show a H_{dir}/H_{glob} very close to the values used in the tables, the H_{dir}/H_{glob} for Palermo is almost halfway through the values reported in the standard. A linear interpolation was used to calculate the daylight supply factor to overcome this problem.

CONCLUSIONS

The evaluation of the daylight contribution to indoor lighting is a key factor for the estimation of the energy performance of buildings. The availability of simplified calculation methods could be of help to take this aspect into account since the beginning of the design process.

The results of this study confirmed a good correlation between the parameters to estimate the daylight supply in buildings used in the simplified calculation method proposed by the European standard EN 15193 and in the dynamic simulation software DIVA-for-Rhino (which uses Daysim). Nonetheless, the differences between the results, especially for what concerns the $F_{D,S}$ compared to the DA_{con} , are sometimes relevant, particularly for climate conditions that deviate from the data reported in the standard.

As a future work, the database will be expanded (new weather conditions and types of shading) and the energy demand for lighting will be calculated. The study shall provide useful information and data to optimize and implement the standard, particularly for what concerns the impact of climate and movable shading devices.

ACKNOWLEDGEMENT

The research for this paper was financially supported by the Italian National Agency for new technologies, energy and sustainable economic development (ENEA).

REFERENCES

- Aghemo C., Blaso L., Fumagalli S., Lo Verso V.R.M., Pellegrino A. 2016. The new prEN 15193-1 to calculate the energy requirements for lighting in buildings: comparison to the previous standard and sensitivity analysis on the new influencing factors. *Energy Procedia*, 101, 232 – 239.
- CEN. 2017. EN 15193-1:2017, Energy performance of buildings - Energy requirements for lighting - Part 1: Specifications. Brussels: Comité Européen de Normalisation.
- CEN. 2017. EN 15193-2:2017. Energy performance of buildings - Energy requirements for lighting - Part 2: Explanation and justification of EN 15193-1, Module M9. Brussels: Comité Européen de Normalisation.
- ISO. 2014. ISO 10916:2014. Calculation of the impact of daylight utilization on the net and final energy demand for lighting. Geneva: International Standard Organization
- Reinhart C.F., Walkenhorst O. 2001. Validation of dynamic RADIANCE-based daylight simulations for a test office of external blinds. *Energy and Buildings* 33, 683-697.
- Tian M, Su Y. 2014. An Improvement to calculation of lighting energy requirement in the European Standard EN 15193:2007. *Journal of Daylighting* 1, 16–28.
- Zinzi M, Mangione A. 2015. The daylighting contribution in the electric lighting energy uses: EN standard and alternative method comparison. *Energy Procedia*, 78, 2663 – 2668.

Assessment of Cumulative Damage of Selected Building Envelopes Exposed to Various Environmental Effects

Václav Kočí^{1,*}, Jiří Maděra¹ and Robert Černý¹

¹Czech Technical University in Prague, Czech Republic

*Corresponding email: vaclav.koci@fsv.cvut.cz

ABSTRACT

Hygrothermal performance of building envelopes based on three different building materials (solid brick, high performance concrete, aerated autoclaved concrete) is assessed under climatic conditions of Prague and Atlantic City. Main objective of the paper is to evaluate the influence of cumulative damage, which was induced by means of natural weathering in 2012-2015 period, on the long-term performance. The performance is assessed using various measures, namely time-of-wetness function, number of freeze/thaw cycles, and annual amount of energy transmitted through the envelope. The results show that thermal performance of the envelopes gets mostly better after weathering as the annual amount of energy is decreased by ~3.5% in average. On the other hand, time-of-wetness function and number of freeze/thaw cycles increase by ~24.1% and ~22.0%, respectively. Based on the results summary it can be concluded, that cumulative damage of materials has an indisputable influence on the hygrothermal performance of building envelopes which might be either negative or positive. A detailed computational assessment is therefore necessary, incorporating not only reference, but also weather-affected material properties.

KEYWORDS

Cumulative damage, computational modelling, hygrothermal performance, weathering, building envelope.

INTRODUCTION

Possibilities of predicting hygrothermal performance of building envelopes are generally known, exploiting capabilities of computational techniques (Oladokun *et al.*, 2017). Such an approach provides relatively fast results without necessity of a construction to be built. Therefore, it is mostly used by building designers or building material producers. However, all computational models are strongly dependent on the quality of input data, the material properties in particular (Goffart *et al.*, 2017). An acquisition of material characteristics is therefore essential and advanced experimental techniques have been developed for this purpose so far, being more or less precise and demanding on time or costs. Unfortunately, it has been mostly ignored that material properties may change upon exposure to environmental conditions. The reason of ignoring this phenomenon, even if it is clear, might be found in the fact that such a kind of experimental investigations is extremely time-demanding and requires considerable storage space which makes it inconceivable for many research groups or departments. The vast majority of computational simulations in the field of building physics is therefore performed using reference material data that remain unchanged during the simulated period (Lakatos, 2017). However, having an indisputable impact on hygrothermal performance of materials, these changes should be included in all serious damage assessment analyses or simulations of hygrothermal performance.

The main objective of this research is to point at the differences in hygrothermal performance of building materials/envelopes that might occur when reference or weather affected data is used within the computational simulations. For this purpose, solid brick, high performance concrete, and autoclaved aerated concrete have been selected as representative load-bearing materials. They had been exposed to natural weathering and induced changes of their hygric and thermal transport and storage parameters were studied. Using computational modelling of coupled heat and moisture transport, subsequent long-term analyses of hygrothermal performance of building envelopes were carried out using reference and weather-affected material parameters in order to emphasize the possible differences.

MATERIALS AND METHODS

Materials

Solid brick (SB), high performance concrete (HPC), and autoclaved aerated concrete (AAC) have been selected as objects of study, representing typical building materials. The material characterization was carried out in the reference state and then after three years of natural weathering between 2012 and 2015. The weather characteristics of this period were continuously recorded using Davis Vantage Pro 2 weather station. The summary of selected weather parameters is given in Table 1, being compared to reference weather parameters of Prague, Czech Republic and Atlantic City, NJ. Climatic conditions of these locations were further considered as the exterior boundary conditions of the simulated walls. The abbreviations used in Table 1 have following meanings: Nov – November, Dec – December, Jan – January, Feb – February, Real – real weather data that were the materials exposed to, TRY – Test Reference Year, PRG – Prague (Czech Republic), ATC – Atlantic City (NJ).

Table 1. Comparison of selected weather parameters.

	Temperature (°C)					Relative humidity (%)					Rainfalls (mm)				
	Real		TRY			Real		TRY			Real		TRY		
	12/13	13/14	14/15	PRG	ATC	12/13	13/14	14/15	PRG	ATC	12/13	13/14	14/15	PRG	ATC
Nov	6.53	6.01	7.93	5.62	7.99	83.22	86.82	79.96	78.19	71.93	27.6	0.4	54.2	24.9	74.1
Dec	0.98	3.25	4.14	1.56	3.47	84.42	81.59	83.62	77.64	71.60	7.2	5.2	24.2	21.3	88.0
Jan	0.34	1.95	3.51	1.83	0.78	84.54	86.89	81.07	77.20	71.01	34.5	16.2	47.2	5.4	69.1
Feb	0.80	4.15	2.01	2.53	2.41	83.07	78.44	77.76	72.44	68.16	40.9	5.4	14.6	16.9	51.3

Table 2. Material characteristics of studied samples.

	SB		HPC		AAC	
	reference	3y-weathering	reference	3y-weathering	reference	3y-weathering
ρ (kg·m ⁻³)	1831	1860	2273	2330	289	305
ψ (%)	27.9	30.9	12.1	9.6	86.9	87.5
$\mu_{\text{dry cup}}$ (-)	22.1	11.4	106.2	108.3	6.17	5.57
$\mu_{\text{wet cup}}$ (-)	8.8	8.3	86.4	86.8	15.61	15.18
κ_{app} (m ² ·s ⁻¹)	1.08·10 ⁻⁶	7.23·10 ⁻⁷	2.53·10 ⁻⁹	4.02·10 ⁻⁹	7.02·10 ⁻⁸	3.35·10 ⁻⁸
c_{dry} (J·kg ⁻¹ ·K ⁻¹)	825	813	780	661	1090	1127
c_{sat} (J·kg ⁻¹ ·K ⁻¹)	1254	1287	929	772	2813	3032
λ_{dry} (W·m ⁻¹ ·K ⁻¹)	0.590	0.541	1.724	2.083	0.071	0.068
λ_{sat} (W·m ⁻¹ ·K ⁻¹)	1.735	1.896	2.817	2.754	0.548	0.536
w_{hvg} (m ³ ·m ⁻³)	0.00360	0.00896		0.01566		0.00755

The material characteristics of the studied materials were determined following the procedure described by Černý (2013). The results are summarized in Table 2 (Maděra *et al.*, 2017; Kočí *et al.*, 2017; Kočí *et al.*, 2018b). The meaning of used symbols is as follows: ρ – bulk density

($\text{kg}\cdot\text{m}^{-3}$), ψ – total porosity (%), μ - water vapor diffusion resistance factor (measured using dry cup and wet cup methods) (-), κ_{app} – apparent moisture diffusivity ($\text{m}^2\cdot\text{s}^{-1}$), c – specific heat capacity (in dry and water saturated state) ($\text{J}\cdot\text{kg}^{-1}\cdot\text{K}^{-1}$), λ – thermal conductivity (in dry and water saturated state) ($\text{W}\cdot\text{m}^{-1}\cdot\text{K}^{-1}$).

Computational modelling

The computational modelling of one-dimensional heat and moisture transport was applied to assess the hygrothermal performance of studied materials when exposed to different weather conditions. Comparing the results obtained using reference and weather-affected material properties, one can evaluate the influence of weathering on long-term hygrothermal performance of the investigated building materials.

The computations were performed using the computer code HM Transport (Kočí *et al.*, 2018a) which works on the basis of the general finite element package SIFEL (Kruis *et al.*, 2010). The coupled transport processes were described using a diffusion type mathematical model derived from the Kunzel's original formulation (Madera *et al.*, 2017), as it requires only a tight set of input parameters while sufficiently precise results are provided. Besides the mathematical model and material properties, also boundary conditions, discretization mesh and time controller of the simulations are required. Within this paper, a 500 mm thick wall was assumed being exposed to dynamic climatic conditions of Prague and Atlantic City from the exterior side and to constant conditions (21 °C, 55 % RH) from the interior side (see Fig. 1). While Prague is typical with its continental climate, Atlantic City has the oceanic climate as it is located on the east coast of the USA. The weather conditions were applied in the form of TRY which contains long-term average hourly values of temperature, relative humidity, rainfalls, wind direction and orientation, and several kinds of sun radiation. The simulations took 10 years which is long enough to reach a certain kind of dynamic equilibrium.

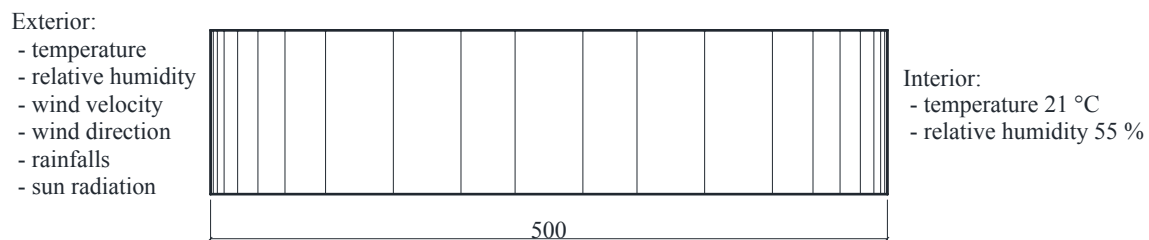


Figure 1. Scheme of the analysed construction detail.

The hygrothermal performance of the wall was assessed by means of time-of-wetness function (ToW) and the number of freeze/thaw (FT) cycles (Koci *et al.*, 2014). These measures were applied to the whole construction detail. Additionally, thermal performance was evaluated by means of quantification of the annual amount of energy transported through 1 m^2 of the particular envelopes (further denoted as Annual EB). It was calculated as

$$Q = \int_{1.\text{Jan}}^{31.\text{Dec}} q(t) dt, \quad (1)$$

where

$$q(t) = \lambda(w,t) \frac{\Delta T(t)}{\Delta x} \quad (2)$$

In Eq. (2), $\lambda(w,t)$ is the moisture dependent thermal conductivity as a function of time ($\text{W}\cdot\text{m}^{-1}\cdot\text{K}^{-1}$), $\Delta T(t)$ the temperature difference (K) between two nodes defining the boundary element and Δx is their distance (m). The hourly values of $\lambda(w,t)$ and $T(t)$ were obtained as the results of computational modelling.

RESULTS AND DISCUSSION

The results of computational simulations revealed that the hygrothermal performance of studied materials is definitely affected by their weathering. However, the influence may be positive as well as negative, depending on the material, climatic data and the measure investigated. The summary of hygric and hygrothermal performance is given in Table 3.

Table 3. Summary of hygric/hygrothermal performance.

		Prague		Atlantic City	
		ToW (h)	FT cycles (-)	ToW (h)	FT cycles (-)
SB	reference	350.02	30	3380.64	38
	3y-weathering	406.22	35	3478.49	42
HPC	reference	155.06	8	850.70	7
	3y-weathering	197.06	14	1240.70	8
AAC	reference	76.08	9	651.74	13
	3y-weathering	93.10	9	847.73	15

The hygric performance measure, ToW function, determines the sum of time when liquid moisture is present in any of nodes of the computational mesh (see Fig. 1). For this sake, the decisive value of relative humidity was considered to be 95 %. Approximately 8 times higher values in average were obtained when the weather conditions of Atlantic City were assumed. This finding agrees with the weather parameters presented in Table 1 showing much higher amount of rainfalls in Atlantic City than in Prague. However, more interesting is the fact that ToW values got higher after weathering in all the investigated cases. For instance, ToW of solid brick increased by ~16 % under climatic conditions of Prague and by ~27 % and ~22 % in case of high performance concrete and aerated autoclaved concrete, respectively. Except for solid brick, the relative increase of ToW was even higher under Atlantic City weather conditions. In case of high performance concrete, the ToW changed from 850.70 to 1240.7 h which represented an increase of about 45 %.

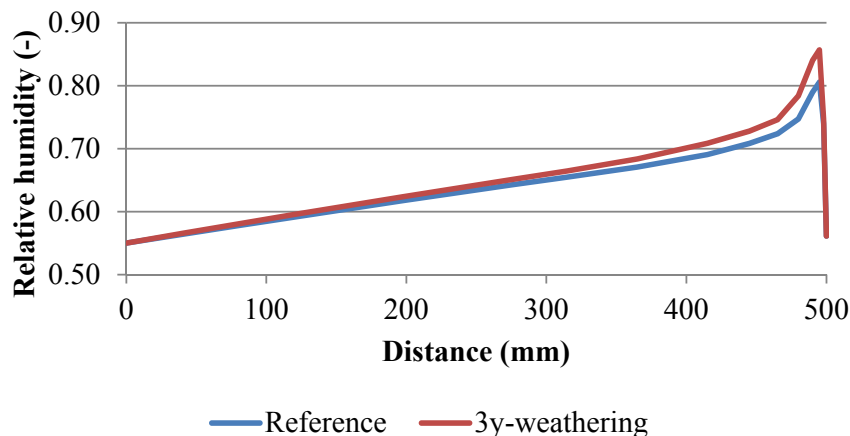


Figure 2. Comparison of moisture profiles: HPC, Atlantic City, Aug 10, 15:00

These changes can be explained mostly by the decrease of moisture diffusivity of studied materials, which led to retaining moisture for longer periods. The changes of hygric performance can also be demonstrated by a comparison of moisture profile before and after weathering. In Fig. 2 the moisture profiles of HPC under Atlantic City's climatic conditions as of August 10 are captured. The differences in this case reached more than 5 % of RH.

Closely related to hygric performance of materials is a risk of creation of freeze/thaw cycles that might cause a serious damage. The possibility of creation of FT cycles appears only when moisture is contained in the liquid phase and, at the same time, the temperature drops below zero. The principles of ice formation in real porous structures are, of course, more complex, incorporating other aspects such as pore characteristic, freezing temperature and duration, mechanical straining, or presence of chemical compounds. However, this measure serves well as a comparative indicator. Alongside with worsening of ToW values, also the number of FT cycles increased as it is shown in Table 3. It can be therefore concluded, that weathering of materials negatively affects their hygrothermal performance and thus might have also a negative impact on their durability. The rate of worsening depends on the type of material, as well as on specifics of the climatic conditions.

Table 4. Summary of thermal performance.

		Prague		Atlantic City	
		Average thermal conductivity ($\text{W}\cdot\text{m}^{-1}\cdot\text{K}^{-1}$)	Annual energy balance ($\text{kWh}\cdot\text{m}^{-2}$)	Average thermal conductivity ($\text{W}\cdot\text{m}^{-1}\cdot\text{K}^{-1}$)	Annual energy balance ($\text{kWh}\cdot\text{m}^{-2}$)
SB	reference	0.59253	98.66	0.59309	81.78
	3y-weathering	0.54811	92.34	0.54932	76.60
HPC	reference	2.12483	250.55	2.12764	207.41
	3y-weathering	2.15129	253.05	2.15426	209.49
AAC	reference	0.07276	13.98	0.07359	11.72
	3y-weathering	0.06908	13.29	0.06983	11.12

Unlike hygric performance, the thermal performance of studied materials got mostly better after weathering. It can be ascribed to the increase of porosity due to formation of microcracks which subsequently contribute to decrease of thermal conductivity. The opposite phenomenon can be observed in the case of high performance concrete, of which porosity decreased most likely due to secondary hydration processes. However, more sophisticated method such as SEM or XRD would be necessary to provide a detailed explanation. The summary of thermal conductivity changes is provided in Table 4: the annual energy balance of brick and aerated concrete was improved by $\sim 6.4\%$ and by $\sim 5.0\%$, respectively. On the other hand, the energy transmitted through 1 m^2 of high performance concrete got higher by $\sim 1.0\%$. All these findings correlate with the changes of thermal conductivity.

CONCLUSIONS

A study of the influence of weathering on the hygrothermal performance of selected building envelopes was presented in this paper. In the first step, the samples made of solid brick, high performance concrete, and aerated autoclaved concrete were exposed to natural weathering and the weather-induced changes of their material properties were investigated. Subsequently, computational analyses of coupled heat and moisture transport of walls made of these materials were carried out in order to assess the impact of weathering on their long-term hygrothermal performance.

The natural weathering of materials led to changes in microstructure which was reflected also in their transport and storage parameters and thus in their hygrothermal performance. While the hygric performance got worse, being proved by an increase of ToW and FT values, the thermal performance got slightly better. As the formation of microcracks contributed to the increase of porosity, the lower thermal conductivity resulted in better thermal insulating properties of the studied materials except for HPC of which porosity decreased due to secondary hydration processes.

Based on the results presented in this paper it can be concluded, that weathering of materials and cumulative damage of theirs have indisputable influence on their long-term hygrothermal performance. Since the effects can be positive as well as negative, depending on the specific measure and climatic conditions, the cumulative damage should be included in computational simulations that are supposed to provide precise results.

ACKNOWLEDGEMENT

This research has been supported by the Czech Science Foundation, under project No P105/12/G059.

REFERENCES

- Černý R. 2013 *Complex system of methods for directed design and assessment of functional properties of building materials and its applications* (Prague: Czech Technical University)
- Goffart J, Rabouille M, and Mendes N. 2017. Uncertainty and sensitivity analysis applied to hygrothermal simulation of a brick building in a hot and humid climate. *Journal of Building Performance Simulation*, 10, 37-57.
- Kočí J, Maděra J, and Černý R. 2014. Generation of a critical weather year for hygrothermal simulations using partial weather data sets. *Building and Environment*, 76, 54-61.
- Kočí V, Kočí J, Maděra J, Pavlík Z, Gu X, Zhang W, and Černý R. 2018a. Thermal and hygric assessment of an inside-insulated brick wall: 2D critical experiment and computational analysis. *Journal of Building Physics*, in press.
- Kočí V, Čáchová M, Koňáková D, Vejmelková E, Jerman M, Keppert M, Maděra J, and Černý R. 2018b. Heat and moisture transport and storage parameters of bricks affected by the environment *International Journal of Thermophysics*, in press.
- Kočí V, Čáchová M, Vejmelková E, and Černý R. 2017. Cumulative damage assessment of concrete exposed to environmental effects. *AIP Conference Proceedings*, in press.
- Kruis J, Koudelka T, and Krejčí T. 2010. Efficient computer implementation of coupled hydro-thermo-mechanical analysis. *Mathematics and Computers in Simulation*, 80, 1578-1588.
- Lakatos A. 2017. Investigation of the moisture induced degradation of the thermal properties of aerogel blankets: Measurements, calculations, simulations. *Energy and Buildings*, 139, 506-516.
- Maděra J, Kočí J, Kočí V, and Kruis J. 2017. Parallel modeling of hygrothermal performance of external wall made of highly perforated bricks. *Advances in Engineering Software*, 113, 47-53.
- Maděra J, Kočí V, Doleželová M, Čáchová M, Jerman M, and Černý R. 2017. Influence of weather-affected material characteristics on appearance of freeze/thaw cycles in building envelopes. *AIP Conference Proceedings*, in press.
- Oladokun M.O, Ali M, Osman S.B, and Lin Z. 2017. Indoor mould growth prediction using coupled computational fluid dynamics and mould growth model. *Building Simulation*, 10, 551-562.

Impact of the substrate thermal inertia on the thermal behaviour of an extensive vegetative roof in a semiarid climate

Sergio Vera^{1,3,*}, Gilles Flamant^{1,3}, Germán Molina¹, Camilo Pinto^{1,3}, Paulo Tabares-Velasco², Nicholas Kincaid², Waldo Bustamante^{3,4},

¹ Department of Construction Engineering and Management, School of Engineering, Pontificia Universidad Católica de Chile, Santiago, Chile

² Department of Mechanical Engineering, Colorado School of Mines, Golden (CO), USA

³ Center for Sustainable Urban Development, Pontificia Universidad Católica de Chile, Santiago, Chile

⁴ School of Architecture, Pontificia Universidad Católica de Chile, Santiago, Chile

*Corresponding author email: svera@ing.puc.cl

ABSTRACT

The aim of this paper is to evaluate the impact of thermal inertia of the substrate of a vegetative roof on its thermal behaviour. Thermal inertia of the substrate was incorporated in two existing thermal models of vegetative (green) roof systems, the Sailor (2008) and Tabares and Srebric (2012) models. The predicted temperatures across the substrate, with and without inertia, were compared with experimental data obtained on a real vegetated roof located in a semiarid climate. The study shows the absolute need to consider the thermal inertia of the substrate to accurately predict the temperatures within the substrate and thus the heat flux through the roof. When taking into consideration the thermal mass, substrate temperatures predicted by both models agree well with experimental data, with a Root-Mean-Square Deviation of about 1°C at a depth of 10 cm. For the analysed period and investigated vegetative roof, the Tabares and Srebric model outperforms the Sailor model.

KEYWORDS

Vegetative roof substrate, thermal inertia, thermal models, substrate temperature.

INTRODUCTION

At global level, buildings are responsible for one third of greenhouse gases and around 32% of energy consumption. Consequently, the energy efficiency of buildings represents a key factor in limiting global warming and mitigating the impacts of climate change. Therefore, improving the energy performance of the building envelope is one of the main objectives to achieve. In this context, vegetative roofs (VRs), usually called green roofs, offer a technological solution that contributes, through an appropriate design, to the reduction of the energy consumption of buildings (Berardi et al. 2014; Castleton et al. 2010; Fioretti et al. 2010; Tabares-Velasco, 2009; Vera et al. 2017).

The impacts of VRs on the energy performance of buildings have been widely studied. Table 1 summarizes the main heat and mass transfer mechanisms occurring in the VRs that might contribute to the reduction of the building energy consumption. Several heat and mass transfer models of VRs have been developed since 1982. Currently, Sailor model (2008) is the only one incorporated in the building simulation tool *EnergyPlus*, whereas Tabares and Srebric model (2012) is currently being included in the same tool. However, none of these two VR models incorporates thermal inertia of the substrate, which can influence the heat transfer through the roof and the energy consumption of buildings.

The objective of this study is to incorporate thermal inertia of the substrate in the vegetative roofs models developed by Sailor (2008) and Tabares and Srebric (2012) in order to evaluate

its impact on the predictions of both models. These two thermal models were first programmed in Matlab without any substrate thermal inertia and then thermal inertia was incorporated by finite differences method. The predicted temperatures across the substrate with and without thermal inertia were compared with experimental data of a real vegetated roof located in Santiago of Chile at the Laboratory of Vegetated Infrastructure of Buildings at Pontificia Universidad Católica de Chile, location that is characterized by a semiarid climate.

Table 1. Heat and mass transfer mechanisms in VRs (Vera et al. 2015).

Heat and mass transfer mechanisms	Description
Substrate evaporation and vegetation transpiration	This is known as evapotranspiration or latent heat transfer. It is a combined effect of water evaporation from the substrate and transpiration of plants. Evapotranspiration is the main contributor to counterbalance the incident solar radiation on the roof.
Shading provided by the canopy	The foliage reduces the amount of solar radiation that reaches the outer roof surface. This reduces the roof surface temperature in comparison with a traditional roof. Thus, heat flux into the roof also decreases.
Thermal inertia provided by substrate	The growing media contributes with thermal mass that helps to stabilize indoor temperature.
Additional insulation provided by substrate	The substrate adds thermal resistance to the roof, which helps to reduce heat losses through the roof and heat gains into the roof.

METHODS

Brief description of the Sailor (2008) and Tabares and Srebric (2012) vegetative roof models

The VR model developed by Sailor (2008) is based on the Fast All-season Soil STrenght (Frankenstein and Koenig, 2004a, 2004b), the Biosphere Atmosphere Transfer Scheme (Dickinson et al. 1993) and the Simple Biosphere (Sellers et al. 1986) models. This model is currently the only model implemented in the building energy simulation tool *EnergyPlus* (Crawley et al. 2001, 2004). The VR model developed by Tabares and Srebric (2012) can consider partially-covered VRs. This model has been validated using laboratory and field data (Tabares-Velasco et al. 2012).

Both VR models are similar in the way they present the energy balance and the components they consider and neglect. In fact, both models assume one-dimensional heat transfer, a single vegetation layer located above the surface of the substrate layer. The differences that exist are only evidenced in the way both models calculate each of the components of the energy balance. For both the substrate and foliage layers, the energy balances equations consider the absorbed short-wave solar radiation ($R_{sh,abs}$), the absorbed infrared radiation from the sky (Q_{ir}), the radiation heat transfer between the foliage and substrate surface layers ($Q_{ir,s-f}$), the latent (L) and sensible (H) heat transfer and the conduction heat transfer from the substrate surface going downwards (Q_{cond}) (only for the substrate layer). The net heat fluxes to the foliage F_f and to the substrate F_s are given by Equations 1 and 2, respectively:

$$F_f = R_{sh,abs,f} + Q_{ir,f} + Q_{ir,s-f} + H_f + L_f \quad (1)$$

$$F_s = R_{sh,abs,s} + Q_{ir,s} - Q_{ir,s-f} + H_s + L_s - Q_{cond} \quad (2)$$

Implementation of the thermal inertia in the models

Both VR models were implemented in Matlab, including the thermal inertia of the substrate. While some simulation tools use conduction transfer functions to propagate the heat fluxes to the interior of the building, the VR models in Matlab use the finite difference approach. The original assumption that says that the canopy has a neglectable thermal mass was maintained. Assuming a vertical direction for the heat flux through the roof, the thermal behaviour of the VR can be approximated using the finite difference method with a discretization of the layers as shown in Figure 1, and can be represented by Equation 3.

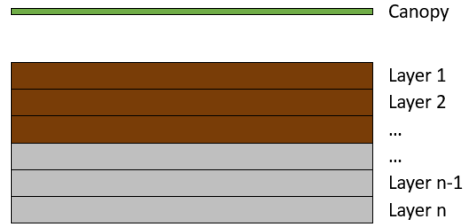


Figure 1. Discretization of the different layers of the VR (Brown and grey layers correspond to the substrate and concrete slab structure, respectively)

$$C_p \rho \Delta x \frac{T_i^{j+1} - T_i^j}{\Delta t} = k_{i+1} \frac{(T_{i+1}^{j+1} - T_i^{j+1})}{\Delta x} + k_{i-1} \frac{(T_{i-1}^{j+1} - T_i^{j+1})}{\Delta x} \quad (3)$$

where $k_i = k(T_i^{j+1}, VWC_i^{j+1})$ is the thermal conductivity that depends on the temperature T and volumetric water content VWC ; T_i^j the temperature of node i at time j ; Δt the time step; Δx the finite-difference layer thickness; and C_p and ρ the specific heat and the density of the material.

In this study, 16 layers were defined (8 for substrate and 8 for concrete slab). To model the substrate without thermal inertia, parameters C_p and ρ were set to very negligible values, leading to a steady state solution to the energy balance.

Experimental dataset

The experimental data was collected in the city of Santiago, Chile (33°26'S, 70°39'W) and corresponds to measurements performed on a real vegetated roof system installed in a test facility called 'Laboratory of Vegetative Infrastructure of Buildings' (LIVE, for its acronym in Spanish). The experimental data considered in this study was measured during 10 days in September 2017 (end of the winter period). Santiago is characterized by a typical dry Mediterranean climate (semiarid) and has a warm temperate climate with dry summers (Peel et al. 2007). The average annual temperature is 14.6°C and the mean annual precipitation is 313 mm, with 25-30 rainy days per year (DGAC, 2015). The LIVE consists of 4 testing modules of 2 m height, with high level of thermal insulation in their walls and floors. Three of the modules are 25 m² each while one is 35 m². This facility allows testing up to 18 different specimens of VRs, each of one has an area of about 1.8m x 1.8m (see Figure 2) (Reyes et al. 2016).

This paper presents the results obtained on only one vegetated roof installed on one of the four testing modules. It is composed by the following layers (from top to bottom): (1) a vegetation layer (grass); (2) a 15 cm thick substrate composed by 1/3 part of humus, 1/3 part of garden soil and 1/3 part of perlite (measures in volume); (3) a filter layer; (4) a root barrier; (5) a drainage layer; (6) a waterproofing layer and (6) a support structure (a 15 cm thick concrete slab).

Measured data included the weather data conditions, the temperatures at different depths in the substrate (at the surface and at a depth of 5 cm and 10 cm), the heat flux across the substrate, the vegetation and substrate properties and the volumetric water content of the substrate.



Figure 2. Photo of the four specimens of the investigated vegetated roof in the LIVE.

Analysis method

In order to assess the level of agreement between the model results and the measured data, the metric ‘Root-mean-square deviation’ (RMSD) was used. It is a measure of the average value of the absolute deviation between the simulation results and the experimental data, and it is calculated according to Equation 4.

$$RMSD = \sqrt{\frac{\sum_{t=1}^n (x_{1,t} - x_{2,t})^2}{n}} \quad (4)$$

where $x_{1,t}$ is the simulated substrate temperature (°C) at time step t , $x_{2,t}$ is the measured substrate temperature (°C) at time step t and n is the quantity of data compared.

RESULTS AND DISCUSSIONS

Figures 3 and 4 shows the comparison of the simulated and measured values of the surface temperature and at 10 cm depth of the VR substrate for the Sailor and Tabares models, with and without thermal mass. All data points that were measured and simulated during the considered period (10 days in September 2017), with a time step of 5 minutes, are plotted in the graphs. Table 2 shows the RMSD-values between the simulated and measured temperatures at different.

	With Thermal Inertia		Without thermal inertia	
	Tabares	Sailor	Tabares	Sailor
Surface	1.12	2.18	1.41	4.38
5 cm depth	1.13	1.74	1.88	4.19
10 cm depth	0.76	1.25	1.80	3.39

These results evidence vegetative roof models that consider thermal inertia perform significantly better than the same models without thermal inertia. These results show a good agreement between the measured temperatures at different depths in the substrate and the ones predicted with both models – the Tabares model and the Sailor model – when thermal mass is taken into account. For the considered period and investigated vegetative roof, the Tabares and Srebric model is performing slightly better, showing lower RMSD-values around 1°C when thermal inertia is considered.

On the other hand, models that do not consider thermal inertia significantly overpredict the temperatures within the substrate. They present RMSD-values of 1.3 to 2.7 times higher than those that do consider thermal inertia. In particular the Sailor model without thermal inertia shows very high RMSD-values around 4°C, which is not acceptable for a correct estimation of the heat flow through the roof.

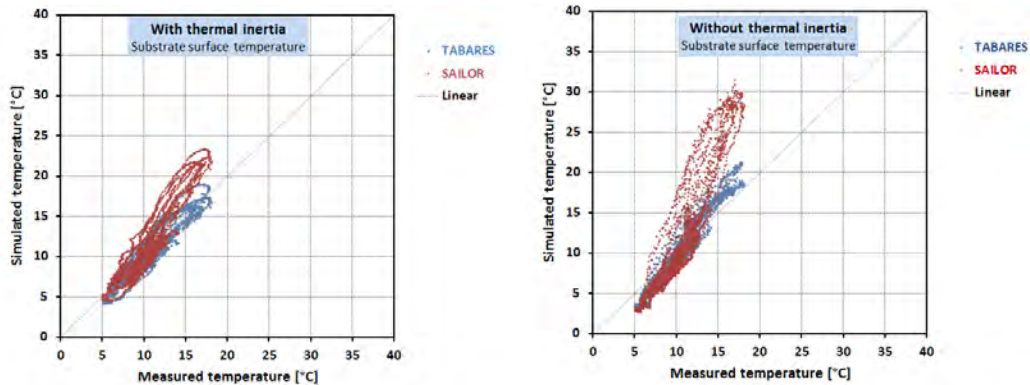


Figure 3. Simulated vs Measured surface temperatures of the substrate for models with and without thermal mass.

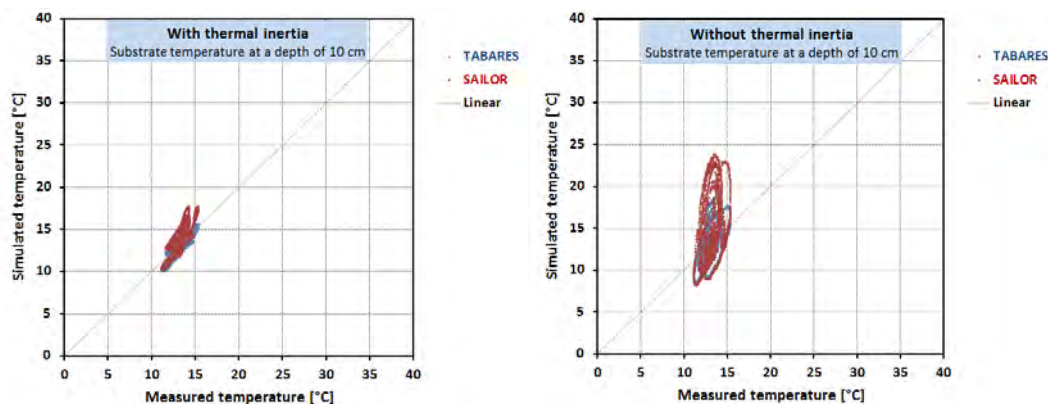


Figure 4. Simulated vs Measured substrate temperatures at a depth of 10 cm for models with and without thermal mass.

CONCLUSIONS

This paper discusses the impact of the thermal inertia of the substrate on the thermal behaviour of a vegetative (green) roof system. Two thermal models – the Sailor (2008) and the Tabares and Srebric (2012) models - were implemented in Matlab and the thermal inertia was implemented in them by using the finite difference approach. Substrate temperatures simulated by the two models were then compared with experimental data during 10 days at the end of the winter period, first without considering the thermal inertia of the substrate and secondly by taking it into account. The results clearly evidence the importance of considering thermal inertia of the substrate to accurately predict the temperatures within the substrate. When thermal mass of the substrate is taken into consideration, both investigated VR models are capable of accurately predicting the substrate temperature, with a RMSD about 1°C at 10 cm of depth. For the analysed period and investigated vegetative roof, the Tabares model outperforms the Sailor model. The future work of this study should include other periods of evaluation such as summer and mid-seasons and different climates and vegetation species.

ACKNOWLEDGEMENT

The authors acknowledge funding from research grants FONDECYT N°1150675 and FONDECYT N°1181610. Also, this study was supported by the Center of Sustainable Urban Development (CEDEUS) (CEDEUS – CONICYT/FONDAP/15110020).

REFERENCES

- Berardi U., GhaffarianHoseini A., and GhaffarianHoseini A. 2014. State-of-the-art analysis of the environmental benefits of green roofs. *Applied Energy*, 115, 411–428.
- Castleton H.F., Stovin V., Beck S.B., and Davison J.B. 2010. Green roofs; building energy savings and the potential for retrofit. *Energy and Buildings*, 42(10), 1582–1591.
- Crawley D.B., Lawrie L.K., Winkelmann F., Buhl W.F., Huang Y.J., Pedersen C.O., ... Glazer J. 2001. EnergyPlus: creating a new-generation building energy simulation program. *Energy and Buildings*, 33, 319–331.
- Crawley D.B., Pedersen C.O., Winkelmann F., Witte M.J., Strand R.K., Liesen R.J., and Buhl W.F. 2004. EnergyPlus: New, capable and linked. In *Proceedings of the SimBuild* (Vol. 21). Boulder, CO. Retrieved from http://gundog.lbl.gov/dirpubs/epl_austin.pdf
- Dickinson E., Henderson-Sellers A., and Kennedy J. 1993. Biosphere-atmosphere Transfer Scheme (BATS) Version 1e as Coupled to the NCAR Community Climate Model. *NCAR Tech. Rep. NCAR/TN-3871STR*, 72, (August), 77.
- Dirección General de Aeronáutica Civil (DGAC). Dirección Meteorológica de Chile. Available online: <http://www.meteochile.cl> (accessed on 23 July 2015).
- Fioretti R., Palla A., Lanza L.G., and Principi P. 2010. Green roof energy and water related performance in the Mediterranean climate. *Building and Environment*, 45(8), 1890–1904.
- Frankenstein S. and Koenig G.G. 2004a. FASST Vegetation Models. *Cold Regions Research and Engineering Laboratory*, (December), 56.
- Frankenstein S. and Koenig G.G. 2004b. Fast All-season Soil STrength (FASST) Cold Regions Research, (September).
- Peel M.C., Finlayson B.L. and McMahon T.A. 2007. Updated world map of the Köppen-Geiger climate classification. *Hydrol. Earth Syst. Sci.*, 11, 1633–1644.
- Reyes R., Bustamante W., Gironás J., Pastén P.A., Rojas V., Suárez F., Vera S., Victorero F. and Bonilla C.A. 2016. Effect of substrate depth and roof layers on green roof temperature and water requirements in a semi-arid climate. *Ecol. Eng.*, 97, 624–632.
- Sailor D.J. 2008. A green roof model for building energy simulation programs. *Energy and Buildings*, 40(8), 1466–1478.
- Sellers P.J., Mintz Y., Sud, Y.C., and Dalcher A. 1986. A simple biosphere model (SiB) for use within general circulation models. *Journal of Atmosphere Science*.
- Tabares-Velasco P.C. 2009. Predictive heat and mass transfer model of plant-based roofing materials for assessment of energy savings. Pennsylvania State University.
- Tabares-Velasco P.C., and Srebric J. 2012. A heat transfer model for assessment of plant based roofing systems in summer conditions. *Building and Environment*, 49(1), 310–323.
- Tabares-Velasco P.C., Zhao M., Peterson N., Srebric J., and Berghage, R. 2012. Validation of predictive heat and mass transfer green roof model with extensive green roof field data. *Ecological Engineering*, 47, 165–173.
- Vera S., Pinto C., Tabares-Velasco P.C., Bustamante W., Victorero F., Gironás J. and Bonilla C.A. 2017. Influence of vegetation, substrate, and thermal insulation of an extensive vegetated roof on the thermal performance of retail stores in semiarid and marine climates. *Energy and Buildings*, Vol. 146, 312-321.
- Vera S., Pinto C., Victorero F., Bustamante W., Bonilla C., Gironás J. and Rojas V. 2015. Influence of plant and substrate characteristics of vegetated roofs on a supermarket energy performance located in a semiarid climate. *Energy Procedia*, Vol 78, p. 1171-1176.

New algorithm for water leakages flow through rain screen deficiencies

Lars Olsson^{1,2,*}, Carl-Eric Hagentoft²

¹RISE Research Institute of Sweden, Division Built Environment, Sweden

²Chalmers University of Technology, Division of Building Technology, Sweden

*Corresponding email: lars.olsson@ri.se

ABSTRACT

There is a need of more knowledge about the mechanisms of water leakage through façades exposed to driving rain to make reliable risk analyses. Therefore, we have studied it in more detail and the outcome include inter alia a new algorithm. The algorithm is developed for calculation of water leakages through rain screen deficiencies. The algorithm is based on empirical values from many measurements according to standardized test method and validation. Even though the leakage process is very complicated, simple correlations have been shown. The leakages flow rate through deficiencies are mainly limited by the runoff rate and the catch area above the hole and around the hole with dam. Apart from wind pressure as a driving force, the inlet of the holes is often on a higher level than the outlet at the rear of the façade, which creates significant hydrostatic pressure, which can be elevated by impoundment at the obstacle. This is the main reasons to comprehensive water leakages through façades without any wind pressure (pressure equalized façades).

If precise information about defects data is not available, there are extensive measurements supporting the following assumption – a realistic leakage flow for a small or invisible spot leakage at a façade detail is presumed to be 0.5 to 2% of the runoff rate per meter of façade width. If there are multiple penetrations or obvious defects in the façade design in combination with the dams, a significantly higher proportion of the runoff flow can leak in.

KEYWORDS

Rain intrusion, runoff, catch area, mechanisms of water leakage, façade details

INTRODUCTION

The latest research in Sweden confirms the statements in ASHRAE Standard 160, which state that façades are normally not completely rainproof (ASHRAE, 2016) and should be considered in moisture calculations (Olsson, 2017b). In addition, there is no reliable theoretical risk analysis tool to assess the moisture resistance of new façade solutions and of renovation solutions (Bednar & Hagentoft, 2015). If you rely solely on today's theoretical analyses, you end up underestimating water intrusion with consequences such as moisture-related damage, interior environment problems, and failure to meet energy efficiency requirements. Among other things, there is a lack of input data for driving rain intrusion to enable sufficiently relevant analyses. Several studies have therefore been conducted in recent years to investigate rain resistance due to driving rain and leakage flow in full scale with different solutions and different mounted details in Sweden (Olsson, 2017a).

One significant conclusion from the studies is that leakage at cracks and joints between façades and façade details and details are more the rule than the exception, regardless of façade type, material, ventilated vs unventilated, etc. Similar conclusions are drawn in other similar studies (Lacasse, 2003, Straube, 1998). Furthermore, (Olsson, 2016) has shown that significant leakage can be expected even in extremely small and invisible penetrations,

making it difficult or practically impossible to visually assess whether attachment details have been mounted tight. It is a matter of spot leakage flows of 0.01–0.05 l/min,m during a heavy driving rain load for rain-exposed multi story façades or 0.5–2% of the runoff rate per meter of façade width (Olsson, 2017a) for small or invisible penetrations. These results correlate well with an earlier study (Sahal & Lacasse, 2004), where a function was developed to describe the connection between applied quantity and leakage flow. The percentage of leakage in the study was 1.2–2.5% of the runoff rate per meter of façade width. It penetrated via a 50 mm elastic joint that was missing sealant between a mounting plate and the façade (in connection to a ventilation lead-through in the façade with a 15 mm protrusion). A study of a field experiment that was published relatively recently (Ngudjiharto, 2015) showed that the percentage of leakage flow was 1.5% of the runoff rate at a window detail with a 90 mm long penetration (without dam). Naturally, greater leakage can occur with noticeable penetrations, multiple penetrations in close proximity, façade details that both dam and lead in water, and extreme loads (Van Den Bossche, 2013, Lacasse, 2003).

The outcome of several of these studies and a newly study, (Olsson & Hagentoft, 2018) to be submitted 2018, which this paper is mainly based on has increased the understanding, both practical and theoretical, of driving rain intrusion and its mechanisms, and to present a modelling theory.

METHODS

Many targeted experiments with different vertical surfaces (fibre cement and polycarbonate board) and different hole geometry and dam sizes were conducted. The results of the measurement and linear regression analysis serve as the basis for the empirically-determined values. As in previous studies (Olsson, 2017a), a standardized method, EN 12865, (SIS, 2001) was used. Additionally, theory from literature and simple phenomenological experiments performed prior served as the basis for describing the water's behaviour on a vertical surface and with different types of defects.

THEORY

A theoretical description of the most dominated factors and forces involved that are of practical significance to the inward leakage process follows.

Amount of water that can reach the defect

If the façade is capillary saturated or non-moisture-absorbing, then all the driving rain that lands on the façade surface will run downwards and be added along the vertical façade surface. The greatest runoff rate thus occurs at the bottom of the façade provided there are no water-diverting details. The water quantity that loads a penetration, G_{max} (kg/s), is based on the area (catch area) above the penetration, defined by height, H , (m) and width, D or W , (m), see equation (1) and Figure 1(a). The width of the catch area is made up of either the width of the hole (D) or the width of the dam (W). The dam can direct in more water from surfaces next to and above the hole. Designations for the geometry of the dam are also provided in Figure 1(a) and (b). The driving rain intensity is denoted g_{DR} (kg/(m²s))

$$G_{max} = H \cdot D \cdot g_{DR} \quad \text{or} \quad H \cdot W \cdot g_{DR} \quad (1)$$

The water leakage rate through the defect is denoted G (kg/s). We define a factor η (-) describing how efficiently the caught water is actually leaking in through the façade layer, see equation (2).

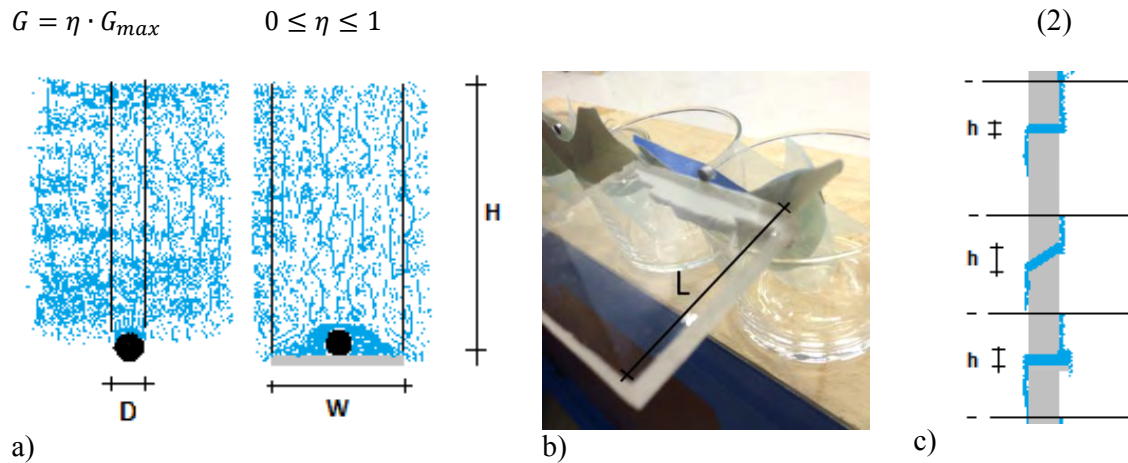


Figure 1. (a) Catch area as regards hole width (D) or dam width (W) plus façade height (H). The assumed catch area is shown within the two vertical lines. (b) The figure shows a dam located at the bottom edge of a hole in a polycarbonate board. The dimension of the protrusion is given by (L). (c) Wall section with spraying water with different holes and a dam. The height difference (h) between the highest and the lowest point of the water across the hole constitutes the hydrostatic pressure. The figure shows how the water penetrates through a horizontal hole, downward-sloping hole and a hole with underlying dam.

Hydrostatic pressure

The hydrostatic pressure P_h (Pa) is determined by water depth h (m), gravity g (m/s^2) and the water's density ρ (kg/m^3); see equation (3) and Figure 1 (c). The highest pressure thus occurs at the bottom of a pool of water or at the bottom edge of a hole filled with water. Increased hydrostatic pressure may therefore occur at protruding details in façades that cause dams.

$$P_h = \rho \cdot g \cdot h \quad (3)$$

Wind pressure

In addition to the hydrostatic pressure described earlier, wind pressure is an essential driver for water leakage into façades due to air pressure difference across the façade layer. Assuming that the façade constitutes the dominant air pressure differences across the wall, the façade is subjected to the current wind pressure. The wind pressure P_w (Pa) across the façade layer can be estimated using the following formula, where wind velocity is denoted v (m/s) and f (-) is a form factor with a value somewhere between 0 and 1 depending primarily on wind direction in relation to the façade:

$$P_w = f \cdot \frac{\rho \cdot v^2}{2} \quad (4)$$

Capillarity and surface tension

The surface properties of the materials have a bearing on how water acts on material surfaces. Even if the material is not capillary absorbing, the water may act differently on a surface depending on the surface energy of the material, or as it is also called the surface tension. Water has a lower surface tension than e.g. hydrophilic materials like steel, aluminium, glass and stone. For this reason, the water tends to flow out over such material surfaces (De Gennes et al., 2004). Conversely, water has a higher surface tension than hydrophobic materials, such as many plastics. The water surface tension coefficient is denoted γ , for water at 20 °C is

equal to 72,8 mN/m. The meniscus that is formed on the backside of the rain screen is resulting in a counteracting pressure, with a radius r (m) and contact angle θ we get:

$$P_{men} = \frac{2\pi \cdot r \cdot \gamma}{\pi \cdot r^2} = \frac{2\gamma}{r} \quad (5)$$

MODEL

We assume that the total pressure will be an important factor to include in an algorithm for estimated leakage flow. Thus, the estimated value of the leakage factor can be expressed as:

$$\eta_{est} = f(P_{tot}) \quad (6)$$

The total pressure for a non-absorbing surface is obtained through:

$$P_{tot} = P_w + P_h - P_{men} \quad (7)$$

The counterpressure in the meniscus that forms on the rear counteracts leakage, while the pressure from the water column and the wind helps to increase the leakage. For an absorbing surface, a counteracting meniscus does not form on the rear in the same systematic way and P_{men} is set to zero otherwise given by (5).

VALIDATION OF MODEL

The measured leakage flow was examined in relation to the hole width or dam width and the actual runoff rate as per equation (2). We found that the dam width has a significant impact. If the hole is small in relation to the dam, maximal leakage efficiency of $\eta=0.5$ is obtained as a rough target value. The maximal leakage efficiency of $\eta=1$ is obtained at higher wind pressure as a rough target value.

The following formula, with linear relation to the total pressure, for leakage factor η_{est} was adopted:

$$\eta_{est} = \eta_0 + \alpha \cdot P_{tot} + \beta \cdot \frac{D}{W} + \gamma \cdot \frac{D}{L} \quad (8)$$

A large number of measurements were performed (Olsson&Hagentoft to be submitted 2018) and the constants in equation (8) were determined using linear regression, see Table 1. The wind pressure used in equation (4) relates to the maximum pressure that occurs under each wind pressure cycle. According to method EN 12865, the wind pressure during one-third of each cycle is zero, $P_w/2$ and P_w respectively. The average pressure over the cycle is thus $P_w/2$. The total pressure P_{tot} , used in equation (8) is set to zero if negative. η_{est} is limited to stay in the range of zero to one.

Table 1. Constants determined for equation (8) for a number of experimental cases. R^2 is a determination coefficient. The table applies for different runoff rates see column Runoff and different D width, see column Case.

Case	η_0	α	β	γ	R^2	Runoff (l/min,m)
Fiber cem. with hole (2/4/8 mm)	0.19	0.0011	-	-	0.71	2.9
(-//-)	0.16	0.0010	-	-	0.69	1.1
Fiber cem.-hole with dam (1/4 mm)	-0.039	0.00035	1.36	-0.044	0.85	2.9
(-//-)	0.012	0.00044	0.92	-0.055	0.71	1.1
Polycarbonate with hole (4 mm)	0.065	0.0013	-	-	0.88	2.9
(-//-)	0.19	0.0014	-	-	0.36	1.1
Polycarb. hole with dam (1/4 mm)	-0.011	0.00054	1.30	0.040	0.73	2.9
(-//-)	0.029	0.00042	0.77	-0.043	0.47	1.1

Comments for validation

The results of linear regression in Table 1 show in most cases $R^2 > 0.7$, which indicates that there are more or less clear correlations even though the water forms stochastically on surfaces to varying degrees. In some cases with low runoff rate, rivulets or small hole equal to 1 mm, there were no clear correlations for holes without dam.

We can establish that constants was not changed very much with different runoff rates, see Table 1. This indicates that the algorithm is applicable for different runoff rates with moisture-absorbing façades. Accordingly, equation (8) suits this best as a uniform water film is formed on the façade surface, resulting in a smaller spread in the repeated experiments. For non-absorbing materials, rivulets instead occur, particularly at low runoff rates, which move more stochastically across the surface.

USE OF ALGORITHM – AN EXAMPLE

An example of how the algorithm, equation (2), can be used is presented here. The driving rain load in, for example, Gothenburg for the most exposed compass direction is assumed to be 250 liters/year, m^2 . For a pressure-equalized façade with a three-meter high façade (capillary saturated), the runoff rate that can strike a hole in the lower part of the façade is 750 liters/year,m. For a small, downward-sloping ($h=60$ mm) hole with e.g. a 3 mm diameter and with a dam of 60 mm (W) and 30 mm (L), ($\eta_{est} = 0.24$) as per equation (8) based on the constants for fibercement board (holes with dam) indicates a spot leakage of 11 liters/year (equivalent to 1.5% of the total runoff rate per meter of façade width), which is significant.

DISCUSSION AND COMMENTS

The algorithm was based on our own newly made studies and validated against measurement results from our own earlier studies and the studies of others (Olsson & Hagetoft, 2018), and seems to fall relatively well in line.

If precise data is not available, there are extensive measurements supporting the following assumption – a realistic leakage flow for a small or invisible spot leakage at a façade detail is presumed to be up to a few percent of the flow rate per meter of façade width. If there are multiple penetrations or obvious defects in the façade design in combination with the dams, a significantly higher proportion of the runoff rate can leak in. Exactly how the spread of the leakage in the wall appears, needs to be known or investigated, alternatively that the worst case scenario (the whole leakage is placed concentrated and in the most critical point) is applied.

CONCLUSION

A new calculation algorithm, using equation (2) and (8) was developed as an expression based on runoff rates that strike the width of the hole or dam, plus a factor η_{est} . The constants in equation (8) are based on empirical values. The new knowledge increases the ability to make more accurate calculations of expected leakage flows. However, there must be exact data on factors such as geometry and the dimensions of holes and dams. Furthermore, the constants in Table 1 must be selected with respect to representative of the façade material.

ACKNOWLEDGEMENT

The support provided by the Swedish Energy Agency and SBUF (the Swedish construction industry's organization for research and development) is gratefully acknowledged.

REFERENCES

- ASHRAE 2016. ASHRAE Standard 160-2016 *Criteria for Moisture-Control Design Analysis in Buildings*. ASHRAE website (www.ashrae.org): ASHRAE.
- BEDNAR, T. & HAGENTOFT, C.-E. 2015. Annex 55-Reliability of Energy Efficient Building Retrofitting- Probability Assessment of Performance and Cost (RAP-RETRO), Report 2015:7. *International Energy Agency (IEA) och Energy in Buildings and Communities Programme (EBC)*. Gothenburg: Chalmers University of Technology.
- DE GENNES, P.-G., BROCHARD-WYART, F. & QUÉRÉ, D. 2004. *Capillarity and wetting phenomena: drops, bubbles, pearls, waves*. New York: Springer Science & Business Media.
- LACASSE, M. 2003. Recent studies on the control of rain penetration in exterior wood-frame walls. National Research Council Canada.
- NGUDJIHARTO, E. 2015. *Field Study of Wind Driven Rain Penetration into Vinyl Siding and Stucco-Clad Wood-Frame Wall Systems at Window Sill*. Master, Master of Applied Science (Building engineering) at Concordia University.
- OLSSON, L. 2016. Laboratory study of driving rain resistance of four facade systems with window fittings-Experimental results of leakage flows. *CESB16-Central Europe toward Sustainable Building 2016*. Prague: Grada Publishing a.s. Czech Technical University in Prague.
- OLSSON, L. 2017a. Rain intrusion rates at facade details - a summary of results from four laboratory studies. *11th Symposium on Building Physics, 11-14 June*. Trondheim, Norway: NTNU.
- OLSSON, L. 2017b. Rain resistance of façades with façade details: A summary of three field and laboratory studies. *Journal of Building Physics*, Article first published online: June 13, 2017
- OLSSON, L. & HAGENTOFT, C.-E. 2018. Driving rain induced water leakage through rain screen defects in façades. *To be submitted 2018*.
- SAHAL, N. & LACASSE, M. 2004. Water entry function of a hardboard siding-clad wood stud wall. *Building and Environment*, 40, 1479-1491.
- SIS 2001. SS-EN 12865 Hygrothermal performance of building components and building elements-Determination of the resistance of external wall systems to driving rain under pulsating air pressure. *The European Standard EN 12865:2001 has the status of a Swedish Standard*. Stockholm: SIS, Swedish Standards Institute.
- STRAUBE, J. F. 1998. *Moisture control and enclosure wall systems*. Doctoral thesis, University of Waterloo.
- VAN DEN BOSSCHE, N. 2013. *Watertightness of Building Components: Principles, Testing and Design Guidelines*. Doctoral thesis, University Ghent, Belgium.

PV-PCM system integrated into a double skin façade. A Genetic optimization based study for the PCM type selection.

Hagar Elarga^{1*}, Andrea Dal Monte², Francesco Goia³, Ernesto Benini²

¹Denmark Technical University-DTU, Denmark

²University of Padova, Italy

³Norwegian University of Science and Technology, NTNU, Trondheim, Norway

*Corresponding email: Hagel@byg.dtu.dk

ABSTRACT

This paper reports the results of a genetic optimisation based numerical analysis of a PV-PCM system integrated into a double skin façade. The aim of the research activity was to develop and test the performance of a proposed simulation approach to identify the optimal configuration of the PCM layer, in terms of temperature transition range, and thickness, to assure the best energy performance of the façade system.

Furthermore, because of the intimate relationship between the PCM's features and the ventilated cavity to define the performance of the façade system, the domain of exploration included as variable the airflow rate and ventilation schedule.

The evaluation of the performances of the PV-PCM glazed facade is carried through an on-purpose developed, transient 1-D (with finite difference method) heat transfer model, which integrates a suitable representation of the PCM's system (through the so-called enthalpy method) to include the thermophysical behaviour of such a type of materials. This numerical model is implemented in MATLAB and coupled to TRNSYS in order to calculate the dynamic thermal energy profiles of a fictitious building equipped with such a façade.

The subsequent single objective optimization is based on a genetic algorithm, which looks for the best PCM type and schedule of ventilation in order to optimize the summer thermal energy performance in two case-study cities, Venice and Chicago.

The results show how the proposed genetic optimisation algorithm is capable of identifying the most suitable configuration (that differs in each climate) after a relatively small number of generations (ca. 25). Furthermore, the optimisation approach used in this study leads to the identification of configurations capable of assuring a reduction in the cooling energy need (objective function) in the range 28% to 19 %, when compared to non-optimal configurations, for the two case-study cities.

KEYWORDS

Simulation based optimization, PV-PCM modules, PCM type, Buildings energy savings.

INTRODUCTION

Designers often use dynamic thermal simulation programs to analyse thermal and energy behaviours of a building and to achieve specific targets, e.g. reducing energy consumption, environmental impacts or improving indoor thermal environment (Garber, 2009). Two approaches are commonly considered at the simulation process. The first is the parametric method, which consists of changing the input of one variable at a time to evaluate the effect on the design objectives, while all other variables are kept unchanged. It is often time-consuming and it only results in partial improvement because such an approach cannot fully consider the complex and non-linear interactions of different variables in the simulation (Nguyen et al,

2014). The second approach is the simulation-based optimization and it usually achieved through iterative methods, which construct infinite sequences of progressively better approximations to an “optimal” solution, i.e. a point in the domain of possible values that satisfies an optimality condition (Wetter, 2009). The optimization of Phase change materials (PCMs) technology implementation has been the centre of attention of many researchers due to its exclusive assets for thermal regulation of buildings (Cascone et al. 2018 and Soares et al., 2014). Huang et al. (2014) performed an optimisation of the thermal properties of an envelope in an energy-saving renovation of existing public buildings. They concluded that the performance parameters for the renovation of existing buildings should be determined for each orientation. Ascione et al. (2014) carried out a study on the retrofitting of an office building in which they added a PCM plasterboard to the inner side of its exterior envelope. It was found that a refurbishment, by means of PCM wallboards, seemed to be more appropriate for a semi-arid climate. Ramakrishnan et al. (2016) performed a parametric optimization for the retrofitting of a typical Australian residential building by installing bio-PCM mats on the ceiling. The investigated variables included, the phase transition temperature, the thickness of the PCM layer and the night ventilation rate that guaranteed the best indoor thermal comfort. It was found that depending on the climatic condition, the optimal phase change temperature was about 3–5 °C higher than the average outdoor air temperature. Furthermore, selection of a proper PCM thickness and night ventilation are important to maximise PCM efficiency and minimise costs. Saffari et al. (2017) have investigated optimum PCM melting temperature of a wallboard integrated into a residential building envelope. It has been concluded that the proper selection of PCM enhanced gypsum technology as integrated passive system into the building envelopes. Soares et al. (2014) have concluded that 10% to 62% savings in energy consumption can be achieved utilizing PCM passive technology through building prototypes located in warm temperate climates. However, few of the available modelling studies concerning the implementation of PCM-PV systems make use of simulation-based optimization.

The present simulation based optimization is an extension of previous works (Elarga et al., 2017). Optimizations were automated by coupling between the dynamic building simulation model, the PV-PCM façade module and the optimization engine. A library of 18 PCM types containing the specifications and thermal characteristics of these materials (obtained from Rubitherm) has been integrated in the algorithm and the optimization has run for two cities Venice and Chicago.

METHODS

The optimization numerical approach consists of two steps: the pre-processing phases and the optimization phases.

- The Pre-processing step included the following elements.

The definition of a fictitious double skin façade that integrates a PV-PCM system where the façade consists of outer clear glass layer (g_1) with a thickness of 8 mm and U value of 5.3(W/m²K), middle and inner glass layers (g_2 & g_3) with a thickness of 4mm and U value of 5.6(W/m²K). The applied Cavity ventilation technique is outside to outside and the considered PV-PCM area equals 70m² which is 100% from the overall façade area, a future study will address the optimum façade composition percentage, scheme is illustrated in Figure 1a.

- The modelling and the definition of the design conditions of a double glazed skin, ventilated facade office zone area of 80m² was carried out with TRNSYS software (Klien et al. 2004).
- Since TRNSYS does not include a defined TYPE to model a glazed PV-PCM facades, it was necessary to separately model the PV-PCM façade in MATLAB. This model is based on a finite difference method scheme (based on a grid with 15 fixed nodes grid as shown in Figure 1b. Each glass layer has been represented by 2 nodes and for the PCM layer a sensitivity analysis has been carried out to estimate the required nodes number i.e. 5 nodes, combined

with the enthalpy method (Voller, 1997) in order to model the non-linear behaviour of the PCM layer. For more details, refer to (Elarga et al., 2016). The governing equations are:

$$C^A = \frac{dH}{dT} = \begin{cases} c_s & T \leq T_{m-\epsilon} \\ \left[\frac{c_s + c_l}{2} + \frac{L}{2\epsilon} \right] & T_{m+\epsilon} < T < T_{m-\epsilon} \\ c_l & T \geq T_{m+\epsilon} \end{cases} \quad (1)$$

Where:

ϵ : is an arbitrarily small value representing half the phase change temperature interval.

c_s : Solid specific heat capacity

c_l : Liquid specific heat capacity

H : Enthalpy

$$\sum a_{nb} T_{nb} - (a_p + \rho C^A) T_p^n = a_p \rho C^A T_p^{n-1} - \rho \cdot \frac{v}{\Delta\tau} [H_p^\circ - H_p^{n-1}] \quad (2)$$

Where:

H_p° : Enthalpy node value of the previous time step

H_p^{n-1} : Enthalpy node value of iteration n-1

T_p : Nodal temperature value

a_{nb} : Nodal coefficients of neighbor nodes to control volume P

τ : Time Step

T_{nb} : Nodal Temperature of neighbour nodes to control volume P

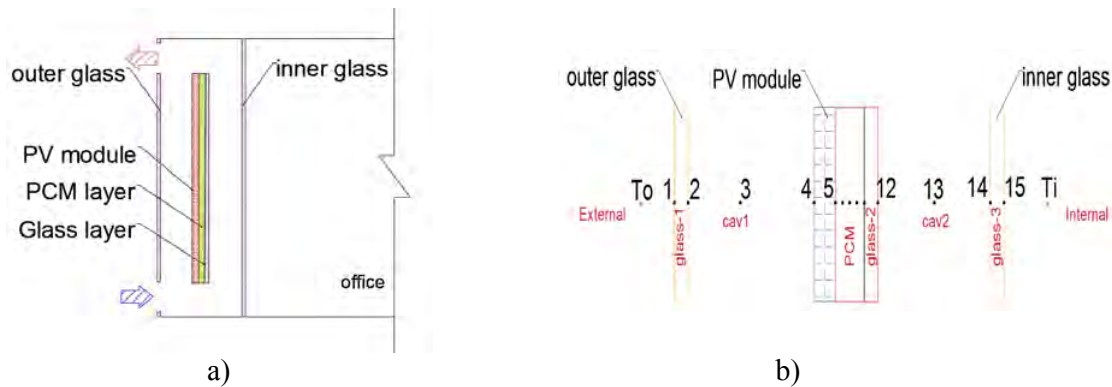


Figure 1: a) Sketch of the glazed PV-PCM façade; b) PV-PCM façade with fixed nodal grid

The integration between the MATLAB model and the TRNSYS model has been carried out using TYPE155 from TRNYS library, which reads external codes executed by MATLAB. The numerical algorithm starts by linking the required weather condition from TYPE16 to both the MATLAB and the zone built in TRNblD TYPE-56. Generally, it is mandatory to link the weather to TYPE-56 in order to operate the simulation model. On the other hand, for each listed inner zone on TYPE-56, there is availability to set its input data and boundary conditions as a user defined option. The PV-PCM 1D numerical code estimates the temperature and transmitted solar radiation for each of the fixed grid nodes including the last node which represents the inner surface layer temperature i.e. node 15. However, the transient interface between TRNSYS and MATLAB models occurs in air node 13. Climatic data of the Test Reference Year (TRY) are then used. For the case study presented in this paper, TMY for Chicago and Venice were adopted. The Optimization step included the following elements:

- Setting the objective function: the objective function is the reduction of required thermal energy for cooling purpose during summer season. However, in the present study, the simulation has run for the entire year to assure PCM thermal storage and transition consistency.
- Selecting and setting independent (design) variables that are part of the domain of search: *i)* PCM layer thickness, *ii)* schedule and starting hour of cavity ventilation, *iii)* PCM type selected from the integrated 18 PCM types library on-purpose developed for this study. The technical data of the PCM list are shown in Table1:

Table 1 List of properties of 18 commercial-grade PCMs (source: Rubitherm GmbH)

Type	temp/ storage cap.	Type	temp/ storage cap.	Type	temp/ storage cap.
PCM-1	21°C /155kJ/Kg	PCM-7	25°C /180kJ/Kg	PCM-13	43°C /250kJ/Kg
PCM-2	21°C / 190kJ/Kg	PCM-8	28°C /250kJ/Kg	PCM-14	46°C /165kJ/Kg
PCM-3	22 °C/190kJ/Kg	PCM-9	31°C /165kJ/Kg	PCM-15	49°C /160kJ/Kg
PCM-4	24°C /160kJ/Kg	PCM-10	33°C /160kJ/Kg	PCM-16	54°C/200kJ/Kg
PCM-5	25 °C/170kJ/Kg	PCM-11	35°C /240kJ/Kg	PCM-17	55°C /170kJ/Kg
PCM-6	25°C /230kJ/Kg	PCM-12	41°C/165kJ/Kg	PCM-18	60 °C/160kJ/Kg

- Selecting an appropriate optimization algorithm and its settings: the adopted optimization algorithm was the mono-objective (MATLAB-GA) and it was set to consider 6 design variables (mass flows of cavity 1 and 2, PCM type, PCM thickness and ventilation schedule in terms of starting hour and duration). The imposed lower and upper boundaries represent the space of exploration of the design variables, as reported in Table 2. The population consists of 20 individuals and the analysis run for 50 generations.

RESULTS

Optimization solutions evolution through generations

The mono-objective optimizations ran for 50 generation and succeeded in archiving an improvement for both the considered cities. The convergence trends show some similarities, with an important decrease of thermal load approx. (-16% for Chicago, -40% for Venice) reached around the 5th generation. After this, the optimization further improves the thermal performances by small steps. Finally, the overall decrease in thermal load is 17% for Chicago and about 43% for Venice.

Analysis of best solution

The best solution for each city is defined by the set of variables that led the minimum required thermal loads. For Venice city, the best individual was: PCM type-16 with melting temperature of 54°C and a storage capacity of 200 kJ/Kg; a PCM thickness of 0.03m; a ventilation duration of 18 hrs. The ventilation schedule has allowed an efficient PCM melting/solidification cycle to be exploited in order to take advantage of higher values of the material heat storage capacity occurred only during this transition. Seasonal cooling thermal loads have reached in this case 2793 kW h. Optimization of PCM dimensions was important to be investigated: the expected weight for this PCM layer in Venice case is about 0.072kg for a PV module area of (2m x 1.5m). On the other hand, in Chicago, the optimum solution was found to be: PCM Type 17 of 55°C melting temperature and 170 kJ/Kg storage capacity; PCM thickness of 5mm. With a ventilation

schedule of 18 hrs, cooling thermal loads have reached 2622 kW h and the layer weight equals 0.012kg for PV module area of (2m x 1.5m).

Table 2: Optimization upper and lower bounds

	cav1 kg/s	cav2 kg/s	PCM type	PCM thick m	Vent. start hr	Vent. duration hrs
Lb	60	60	1	0.001	12:00am	0
Ub	360	360	18	0.1	11:45am	5

Table 3: Best solution of variables

City	cav1 kg/s	cav2 kg/s	PCM type	PCM thick m	Vent. start hr	Vent. duration hrs
Venice	0.2	0.09	16	0.03	9:00am	10
Chicago	0.15	0.10	17	0.005	10:00am	9

DISCUSSIONS

The influence of the PCM type on the building configuration has been highlighted through a parametric study its only variable is the PCM type. While, the best solutions achieved through the optimization process remains constant (Table 2). In Venice, for the same indoor air operative temperature, seasonal thermal loads of the best configuration, 2.0 kW h m^{-2} (PCM-16), are increased up to 2.6 kW h m^{-2} by implementing a non-optimized type (PCM- 8), see Figure 3a. Furthermore, the energy savings for the overall season is 28% if the optimized (PCM-16) and non-optimized solution (PCM-8) are compared. In a similar way, the daily cooling energy consumption in Chicago (1.5 kW h m^{-2} in the best case) is increased up to 1.8 kW h m^{-2} when a different type is adopted (PCM-6) (Figure 3b) and the seasonal energy savings are 19% when the optimal solution is compared to a non-optimal one.

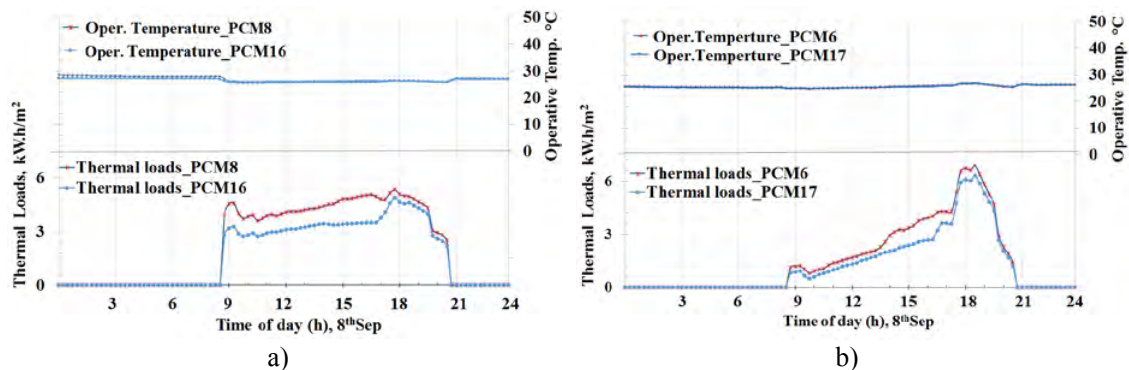


Figure 2: Daily thermal loads and operative air temperature profile a) Venice, b) Chicago

CONCLUSIONS

The ventilation schedule, proper selection of the type and layer thickness of PCM are among the fundamental design parameters to achieve an efficient implementation of the latent heat storage technology in buildings. The present mono objective algorithm has focused on minimizing the cooling energy requirements of an office building at Venice and Chicago. The

optimized solutions have been analysed varying only the PCM type through a parametric study. It has been shown that thermal energy savings could be achieved by selecting the proper PCM type. However, designers may also need to evaluate different trade-off settings, taking into consideration multidisciplinary aspects and their interactions in order to identify the best, suitable, solutions. Accordingly, the present optimization algorithm might be increased in comprehensiveness to include more objectives such as the indoor comfort, the PV electrical performance, the cost of the material and the electrical consumption of the ventilation system; façade composition leading to a multi-objective optimisation process, where the complexity lies in the definition of the optimisation function.

REFERENCES

- Ascione F, Bianco N, De Masi RF, de Rossi F, Vanoli GP.2014. Energy refurbishment of existing buildings through the use of phase change materials: energy savings and indoor comfort in the cooling season. *Applied Energy*, Vol.113, pp. 990–1007.
- Cascone Y., Capozzoli A., Perino M, 2018. Optimisation analysis of PCM-enhanced opaque building envelope components for the energy retrofitting of office buildings in Mediterranean climates. *Applied energy*, Vol.211, pp. 929–953.
- Elarga H., Goia F. and Benini E., 2017. PV-PCM integration in glazed buildings. Numerical study through MATLAB/TRNSYS linked model" in *Building Simulation Application conference, Bolzano Italy*, vol. 3, <https://www.researchgate.net/publication/313572061>.
- Elarga H, Goia F., Zarrella A., Dal Monte A., and Benini E., 2016. Thermal and electrical performance of an integrated PV-PCM system in double skin facades: A numerical study, *Solar Energy*, Vol. 136, pp.112-124.
- Elarga H., Monte A.D., Andersen R. K, Benini E., 2017. PV-PCM integration in glazed building. Co-simulation and genetic optimization study, *Building and Environment* Vol 126, pp. 161-175
- Garber R. 2009. Optimization stories: the impact of building information modelling on contemporary design practice. *Architectural Design*, Vol. 79, pp. 6–13.
- Huang J, Lv H, Gao T, Feng W, Chen Y, Zhou T. 2014. Thermal properties optimization of envelope in energy-saving renovation of existing public buildings. *Energy and Buildings* Vol.75, pp.504–510.
<http://www.rubitherm/>
- Klien S., Beckman W., Mitchell J., Due J., DueN., Freeman T., Mitchell J., Braun J., Evans B., Kummer J., 2004. "Trnsys 16, a transient system simulation program, user manual", *Solar Energy Laboratory. Madison, WI: University of Wisconsin-Madison*
- Nguyen A., Reiter S., Rigo P., 2014. A review on simulation-based optimization methods applied to building performance analysis, *Applied Energy*, Vol. 113, pp. 1043–1058.
- Ramakrishnan S, Wang X, Alam M, Sanjayan J, Wilson J. 2016. Parametric analysis for performance enhancement of phase change materials in naturally ventilated buildings. *Energy and buildings*, Vol.124, pp. 35–45.
- Saffari M., Gracia A.D., Fernández C., Cabeza L.F., 2017. Simulation-based optimization of PCM melting temperature to improve the energy performance in buildings, *Applied Energy*, Vol. 202, pp. 420–434.
- Soares N, Gaspar AR, Santos P, Costa JJ, 2014. Multi-dimensional optimization of the incorporation of PCM-drywalls in lightweight steel-framed residential buildings in different climates. *Energy and Buildings*, Vol. 70, pp. 411–421.
- Voller V. 1997. An overview of numerical methods for solving phase change problems, *Advances in numerical heat transfer*, Vol. 1, pp. 341-380.
- Wetter M. 2009. Generic optimization program – user manual. Technical report LBNL-5419, *Lawrence Berkeley National Laboratory*, Vol. 3.

Stochastic modelling of hygrothermal performance of highly insulated wood framed walls

Lin Wang^{1,*}, Hua Ge¹

¹Concordia University, Montreal, Canada

*Corresponding email: forestwang2013@gmail.com

ABSTRACT

Recent years, the majority of building codes in North America require an energy efficient envelope to improve the building energy efficiency. There are different design strategies to achieve a higher insulation level of the wood framed building envelope, such as increasing the depth of stud cavity to accommodate thicker insulation or adding an exterior insulation while keeping the depth of stud cavity unchanged. However, the highly insulated walls may lead to a higher risk of moisture problems. The deep cavity walls will reduce the temperature of the wood sheathing, which may increase the potential for condensation and mold growth. The exterior insulated walls may result in a low drying capacity of the wood sheathing if the exterior insulation has a low vapour permeance. Although hygrothermal simulations have been widely used to investigate the moisture performance of wood framed walls, the uncertainty of the input parameters may lead to discrepancies between simulation results and real performance of the walls. This paper investigates the hygrothermal performance of highly insulated wood framed walls- deep cavity wall and exterior insulated wall using a stochastic simulation approach. The uncertainties of the input parameters including the material properties, air leakage and rain leakage rates are taken into account in stochastic modelling. The mold growth risks of the walls are evaluated based on the stochastic simulation results.

KEYWORDS

Highly Insulated Wood Framed Wall, Hygrothermal Simulation, Stochastic Modelling

INTRODUCTION

Recent years, the majority of building codes in North America require an energy efficient envelope to improve the building energy efficiency. There are different design strategies to achieve a higher insulation level of wood framed building envelope, such as increasing the depth of the stud cavity to accommodate a thicker insulation or adding an exterior insulation while keeping the depth of stud cavity unchanged. However, the highly insulated walls may lead to a higher risk of moisture problems. Hygrothermal simulations have been widely used to investigate the hygrothermal performance of highly insulated walls (Maref et al., 2010; Arena et al., 2013; Parsons and Lieburn, 2013; Smegal et al., 2013; Craven and Garber-Slaght, 2014; Glass et al., 2015). However, the uncertainties of the input parameters may lead to discrepancies between simulation results and real performance of the walls. Stochastic approach has been applied to investigate the uncertainties of the input parameters and their influence, but the stochastic variables were often limited to material properties and surface transfer coefficients (Salonvaara et al., 2001; Holm and Kunzel, 2002; Zhao et al., 2011; Defraeye et al., 2013). The moisture loads such as air leakage and rain leakage were not taken into account in previous studies.

To investigate the air leakage effect on the hygrothermal performance of highly insulated wood framed walls, field measurements were conducted for three types of walls: 2x6 framed wall with fiber glass insulation, deep cavity walls and exterior insulated walls in Southern

Ontario Canada (Fox, 2014). Hygrothermal models using the mean values of the input parameters have been created and validated with the field measurements (Fox, 2014). In this paper, a stochastic approach is applied to investigate the influence of the uncertainties of input parameters including material properties, air leakage and rain leakage rates. Stochastic simulations are carried out using DELPHIN on four walls tested: 2x6 framed wall with fiberglass insulation, I-joist framed deep cavity wall with cellulose fiber insulation, polyisocyanurate exterior insulated wall and mineral wool exterior insulated wall. The mold growth risks are evaluated under the air leakage and rain leakage based on the stochastic results.

STOCHASTIC MODELING

Material properties and boundary conditions

Figure 1 shows the configuration of the walls under investigation. The material properties and their uncertainties are determined from several sources (Kumaran et al., 2003; Mukhopadhyaya et al., 2007). The hygric properties (saturation water content, vapor resistance factor and moisture diffusivity) of the OSB sheathing and insulations are considered as stochastic variables since the moisture content of OSB is used for performance evaluation.

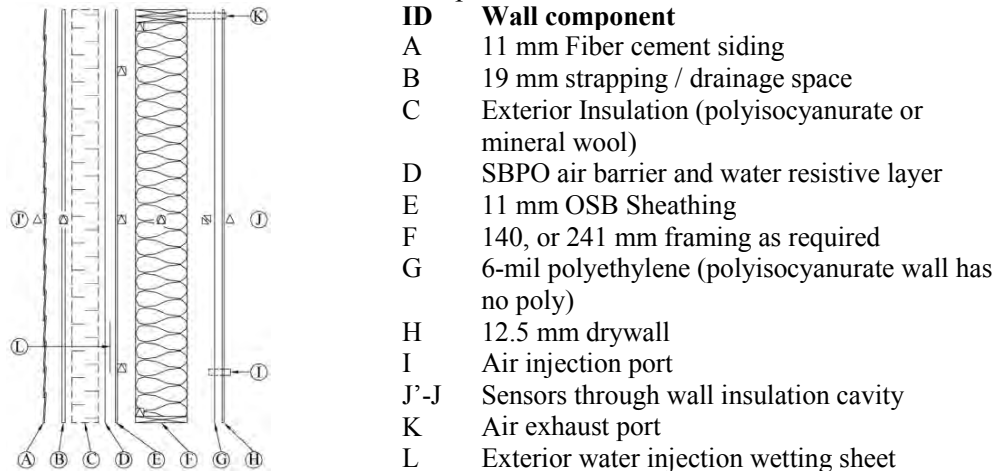


Figure 1 General section view of the highly insulated walls and the wall components (adapted from Fox, 2014)

The surface transfer coefficients are considered as deterministic parameters since these parameters have no significant influence on hygrothermal performance of wood framed walls (Zhao et al., 2011). The rain deposition factor is considered as stochastic variable to reflect the variability of wind-driven rain load on façade, thus, rain leakage rate. The monitored on-site weather data is used to generate the customized weather data files for DELPHIN. The indoor climate file is also generated based on the monitored indoor temperature and relative humidity, which was maintained at 20°C and 40%RH.

Air leakage and rain leakage

The impact of air leakage is simulated using the air infiltration method (Kunzel, 2012). By using this method, a moisture source that is equivalent to the condensing rate caused by air leakage is deposited on the interior surface of OSB sheathing. The air leakage rate ($5.0 \pm 3.7 \text{ m}^3/\text{h}\cdot\text{m}^2$ under 75Pa pressure difference for walls with air barrier) is determined based on the air leakage database developed by Emmerich and Persily (2014), and converted to those under 5Pa pressure difference. Details of modeling air leakage can be found in (Wang and Ge, 2017). The rain leakage is simulated by depositing 1% of wind-driven rain on the exterior surface of OSB sheathing. The rain deposition factor is from 0.35 to 1 as prescribed in ASHRAE 160 (2016).

Generation of stochastic models

The material properties and air leakage rate are assumed to follow normal distribution to obtain the stochastic values, while the rain deposition factor is assumed to follow a uniform distribution. The stochastic models are generated for three scenarios: 1) only material properties are considered as stochastic variables; 2) material properties and air leakage rate are considered as stochastic variables; and 3) material properties and rain deposition factor are considered as stochastic variables. For each scenario, 100 stochastic models are generated using Latin Hypercube Sampling technique. Simulations are performed for five years starting from Oct. 2012.

STOCHASTIC RESULTS

Influence of material properties

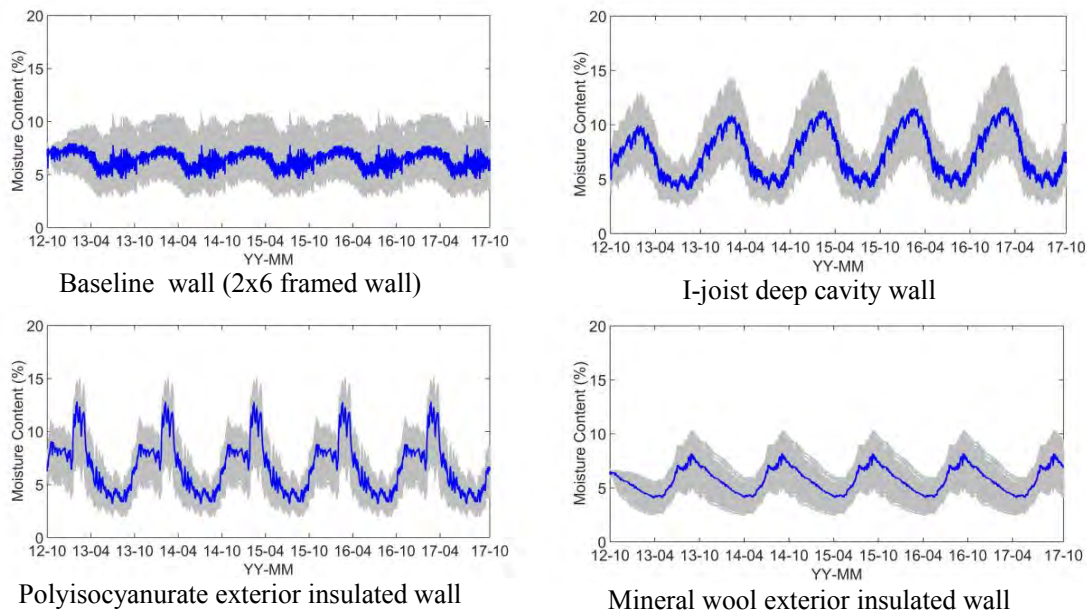


Figure 2 Stochastic results of MC with variation of material properties_south

Figure 2 shows the stochastic results of OSB moisture content of the south-facing walls with only the material properties are treated as stochastic variables. The blue curve is the base case, which uses the mean values of the input parameters. The grey curves are the stochastic results. The highly insulated walls generally have higher MC level and more significant seasonal variation (increasing in winter and decreasing in summer) than the baseline wall except for mineral wool exterior insulated wall, which has similar MC level to the baseline wall but different seasonal variations (increasing from spring to summer but decreasing starting from fall to winter). The MC of I-joint wall has an upward trend with a highest value of $12 \pm 4\%$, which is slightly higher than the polyisocyanurate insulated wall. The highest MC of the baseline wall is $8 \pm 3\%$, which is similar to the mineral wool exterior insulated wall. The highest moisture content is below 20% for all the walls.

Influence of air leakage

There is no condensation caused by air leakage for the exterior insulated walls and the MC profiles of OSB are the same as those presented in Figure 2, therefore, only the results of south facing baseline wall and I-joint wall are presented. It can be observed from Figure 3 that the influence of air leakage is more significant for the baseline wall than for the I-joint wall. The highest MC of baseline wall is $23 \pm 17\%$, which is much higher than that of I-joint wall $17 \pm 8\%$.

For the baseline wall, 75% of the stochastic cases have highest MC exceeding 20%, but only 35% of stochastic cases of I-joint wall have highest MC exceeding 20%. The I-joint wall performs better than the baseline wall because the cellulose fiber in I-joint wall has a higher moisture storage capacity than fiberglass in the baseline wall, and the cellulose fiber is able to absorb the moisture carried by the air leakage and reduces the amount of moisture reached the OSB sheathing.

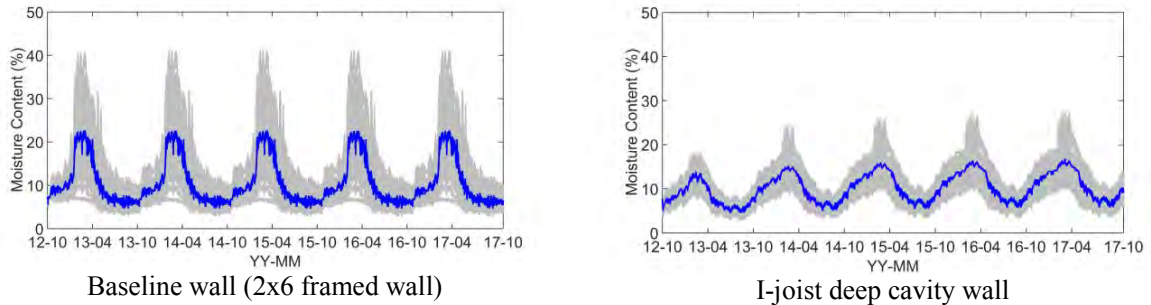


Figure 3 Stochastic results of MC with variation of material properties and air leakage rate_south

Influence of rain leakage

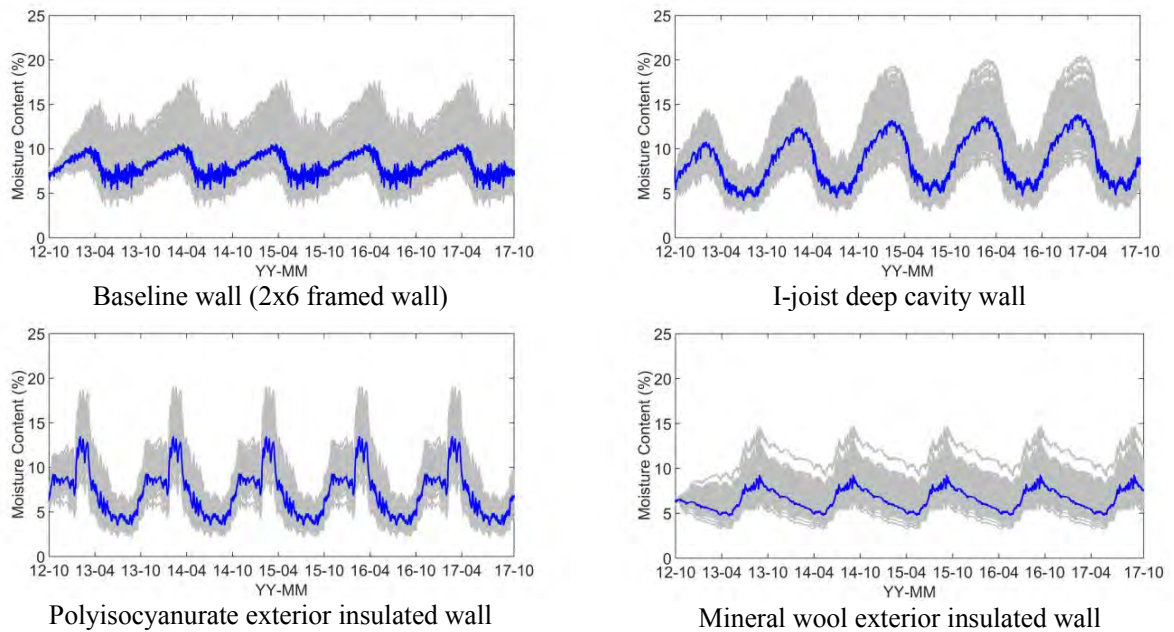


Figure 4 Stochastic results of MC with variation of material properties and rain factor_south

Since the south orientation receives higher wind-driven rain than the north orientation, the results for south oriented walls are presented in Figure 4. It can be seen that the impact of rain leakage is less significant than air leakage. The highest MC of the baseline wall is $12 \pm 5\%$, the base case is lower than average because the rain deposition factor in base case is 0.35, which is lower than the average value. The highest MC of I-joint wall is $15 \pm 5\%$, which is slightly higher than the baseline wall. The MC level of polyisocyanurate wall is similar to I-joint wall, but has no upward trend. The mineral wool wall has the lowest MC level, which is $10 \pm 4\%$. All the walls under rain leakage scenario have moisture content lower than 20%.

Mold growth index

Figure 5 shows the mold growth index over 5 years and probability density function of the 5 years' highest mold growth index for the baseline wall and I-joint wall under air leakage scenario. It can be found that the mold growth index for the baseline wall increases gradually from 0 up to 1.6 ± 1.6 . The 5 years' highest mold growth index has 1.5% probability higher than 3, which exceeds the threshold (visually detectable mold growth) prescribed in ASHRAE 160 (2016). For the I-joint wall the highest mold growth index is about 1.2, which indicates there is no risk of detectable mold growth.

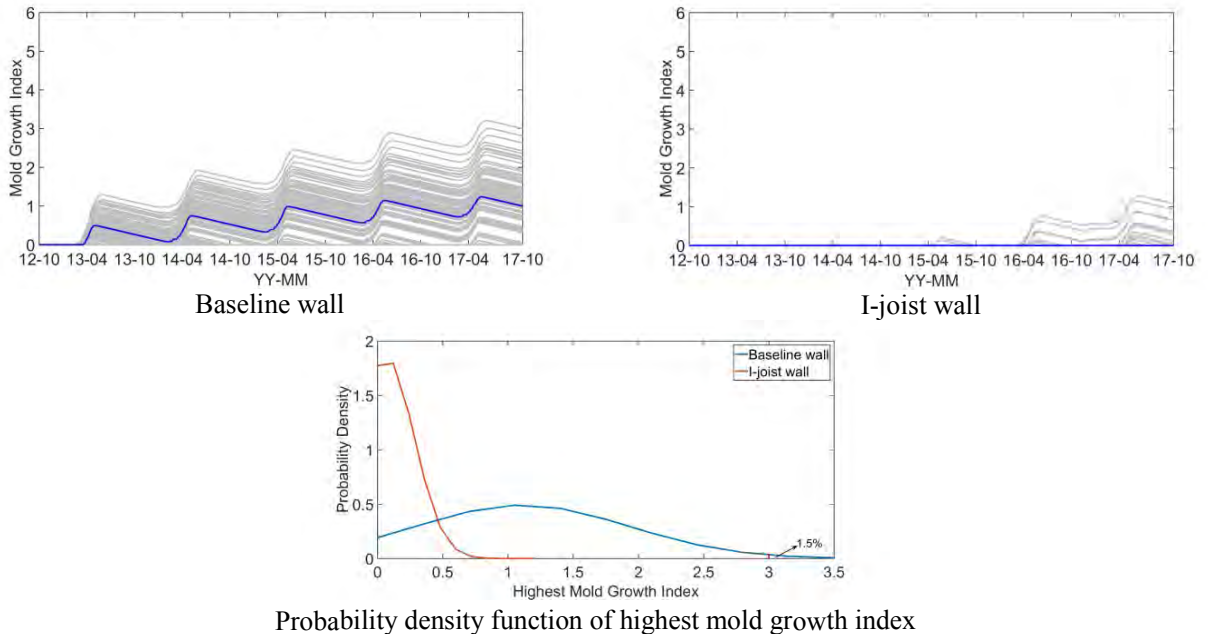


Figure 5 Mold growth index of baseline wall and I-joint wall under air leakage

CONCLUSION

This paper investigates the hygrothermal performance of highly insulated walls, i.e. I-joint framed deep cavity wall and exterior insulated walls, compared to a conventional 2x6 framed wall with fiberglass insulation (baseline wall) through stochastic approach with consideration of the uncertainties of material properties, air leakage and rain leakage rates. The main findings of this paper are:

- The uncertainties of material properties in I-joint wall and polyisocyanurate exterior insulated wall (low exterior vapour permeance) lead to greater variations of MC of OSB than that in the baseline wall and mineral wool exterior insulated wall (high exterior vapour permeance). Without air leakage or rain leakage, the uncertainty of material properties does not lead to mould growth risk in the walls investigated.
- The air leakage has no influence on the exterior insulated walls using air infiltration simulation method. The MC of OSB in the baseline wall is more sensitive to air leakage than that in the I-joint wall with cellulose fiber. The mold growth risk of the baseline wall is higher than the I-joint wall under air leakage.
- Under climatic condition of South Ontario, the influence of rain leakage is less significant than air leakage for the baseline wall and I-joint wall, while the influence of rain leakage is more significant than air leakage for the exterior insulated walls. The MC of OSB in polyisocyanurate wall has higher uncertainty than that in mineral wool wall under simulated rain leakage, while all the walls studied do not have mold growth risks under simulated rain leakage.

REFERENCES

- Arena, L., Owens, D., & Mantha, P. (2013). Measured performance of an R-40 double-stud wall in climate zone 5A. Paper presented at the *Thermal Performance of the Exterior Envelopes of Whole Buildings XII International Conference*. Florida, USA.
- ASHRAE. (2016). *ASHRAE standard 160-2016 Criteria for moisture-control design analysis in buildings*. Atlanta, GA: ASHRAE.
- Craven, C., & Garber-Slaght, R. (2014). Exterior insulation envelope retrofits in cold climates: Implications for moisture control. *HVAC&R Research*, 20(4), 384-394.
- Defraeye, T., Blocken, B., & Carmeliet, J. (2013). Influence of uncertainty in heat-moisture transport properties on convective drying of porous materials by numerical modelling. *Chemical Engineering Research and Design*, 91, 36-42.
- Emmerich, S., & Persily, A. (2014). Analysis of U.S. commercial building envelope air leakage database to support sustainable building design. *International Journal of Ventilation*, 12(4), 331-344.
- Fox, M. J. (2014). *Hygrothermal performance of highly insulated wood frame walls with air leakage: Field measurements and simulations*. (Master's Thesis). Ryerson University, Toronto, Canada.
- Glass, S. V., Kochkin, V., Drumheller, S. C., & Barta, L. (2015). Moisture performance of energy-efficient and conventional wood-frame wall assemblies in a mixed-humid climate. *Buildings*, 5, 759-782.
- Holm, A. H., & Kuenzel, H. M. (2002). Practical application of an uncertainty approach for hygrothermal building simulations-drying of an AAC flat roof. *Building and Environment*, 37(8-9), 883-889.
- Kumaran, M. K., Lackey, J. C., Normandin, N., Tariku, F., & van Reenen, D. (2003). Variation in hygrothermal properties of several wood-based building products. Paper presented at the *Second International Building Physics Conference*. Leuven, Belgium. 35-42.
- Maref, W., Armstrong, M., Rousseau, M., & Lei, W. (2010). A field monitoring investigation of the effect of adding different exterior thermal insulation materials on the hygrothermal response of wood-frame walls in a cold climate. Paper presented at the *BEST2 Conference (Building Enclosure Science & Technology)*, Portland, USA. 1-15.
- Mukhopadhyaya, P., Kumaran, M. K., Lackey, J. C., van Reenen, D., & Tariku, F. (2007). *Hygrothermal properties of exterior claddings, sheathing boards, membranes and insulation materials for building envelope design*. (NRCC-50287). Ottawa, Canada: National Research Council Canada.
- Parsons, G., & Lieburn, B. (2013). Comparative energy and wall performance of twelve residential houses constructed in cold climate. Paper presented at the *Thermal Performance of the Exterior Envelopes of Whole Buildings XII International Conference*. Florida, USA.
- Salonvaara, M., Karagiozis, A., & Holm, A. (2002). Stochastic building envelope modelling-the influence of material properties. Paper presented at the *Proceedings for Performance of Exterior Envelope of Whole Building VIII: Integration of Building Envelope*, Clearwater Beach, Florida, USA.
- Smegal, J., Lstiburek, J., Straube, J., & Grin, A. (2013). Moisture-related durability of walls with exterior insulation in the pacificnorthwest. Paper presented at the *Thermal Performance of the Exterior Envelope of Whole Building XII International Conference*, Florida, USA.
- Wang, L., & Ge, H. (2017). Effect of air leakage on the hygrothermal performance of highly insulated wood frame walls: Comparison of air leakage modelling methods. *Building and Environment*, 123, 363-377.
- Zhao, J., Plagge, R., Nicolai, A., Grunewald, J., & Zhang, J. S. (2011). Stochastic study of hygrothermal performance of a wall assembly-the influence of material properties and boundary coefficients. *HVAC&R Research*, 17(4), 591-601.

Thermal Insulation of Radon Systems to Avoid Freezing

Mehdi Ghobadi^{1,*}, Liang Zhou¹

¹National Research Council Canada, Ottawa

*Corresponding email: mehdi.ghobadi@nrc-cnrc.gc.ca

ABSTRACT

Radon (Rn) stacks, with or without an inline Rn fan, are designed to extract damp soil gas from under basement concrete slabs of homes. Along with Rn gas, moisture vapor also travels up through the Rn stacks. The amount of moisture in the vent pipes can, depending on the circumstances, be significant. In extremely cold weather, this moisture can condense, freeze, form ice and clog the vent pipe at the exit point. In this study, COMSOL Multiphysics was used to examine the amount of insulation required to avoid ice build-up in the Rn vent pipe located in unheated attic space under different outdoor weather conditions. The effects of different parameters on the air temperature in a Rn stack were studied; specifically, (i) air velocities in the vent pipe, (ii) thermal insulations, (iii) different lengths of vent pipe in unheated attic space. The boundary conditions for the model, including the relative humidity, inlet air velocity, and the inlet air temperature in the stack, as well as the temperature in the attic and outdoors were determined based on the data from the Canadian Centre for Housing Technology. Based on the results obtained from numerical simulations, recommendations for insulation to avoid freezing of Rn stack at the exit were proposed. Thereafter, a Rn mitigation system was designed and installed in a home in Ottawa, based on the recommendations. Data was collected from the in-situ experiment during the winter of 2017. This stack was then modeled using the hypothesis used in the predictive simulations, and the model was benchmarked against the data collected from the experiment. The benchmarking results indicated that no freezing was observed using the recommended level of insulation on the Rn vent pipe in an unheated attic and above roof.

KEYWORDS

Radon Stacks, COMSOL Multiphysics, Numerical Simulations, In-situ Measurements

INTRODUCTION

Radon (Rn, atomic weight 222) is a naturally occurring radioactive colorless and odorless gas, which can be found in varying amounts in all types of soil and bedrock. Recent research by Health Canada estimates that 16 per cent of lung cancer deaths among Canadians are attributable to indoor Rn exposure (HC, 2010; HC 2014). Since December 2014, provisions in the British Columbia Building Code have required the installation of a full size passive vent pipe (i.e. passive stack) that extends through the building and terminates outside, in high Rn risk areas. A schematic of such a system is depicted in Figure 1.

Seasonal variation of external and indoor environmental conditions (e.g. temperature, RH, air pressure, wind speed and wind direction) may significantly influence the effectiveness of a passive stack. Previous experimental data from the Canadian Centre for Housing Technology demonstrated that the Relative Humidity (RH) of soil gas within the Rn stacks was close to 100%. The amount of moisture being extracted from under a home can be very significant. At lower temperatures air loses its capacity to retain moisture. In cold climates, condensation within an uninsulated vent pipe is inevitable. However, condensation within the pipe can freeze if the temperature inside the stack remains consistently below the freezing point.

Hence, the clogging of Rn stacks due to the formation of ice in the vent pipe can occur in extreme cold climates.

This paper provides a description of numerical simulations using a COMSOL Multiphysics software platform to predict the temperatures and relative humidity of air along the length of a Polyvinyl chloride (PVC) vertical stack used to exhaust Rn gas from beneath a typical Canadian home with an attic, a main floor, and a basement. Different scenarios for insulation thicknesses, insulation material, in-stack air speed, vent lengths in attic and outdoor temperatures were investigated. Based on the numerical results, a suggestion for required insulation was made for an in-situ test to avoid freezing. The results from tests then were compared with the results from the simulations.

METHODS

A 2D axis-symmetric COMSOL Multiphysics model was employed to examine the temperature profile of soil gas inside a PVC pipe having an outer diameter of 11.43 cm and inner diameter of 10.16 cm (4 inches). Soil gas at 18 °C with the RH of 50%-100% enters the pipe and rises vertically from the basement through the building, into the unheated attic and thereafter is expelled to the exterior atmosphere beyond the roof line. The building other than the attic is generally conditioned and the temperature maintains approximately at 20 °C, which does not appear to affect the temperature in the stack significantly. Therefore, this portion of the stack is not considered in this study. The exposed length of the pipe to outdoor temperature was 30 cm. Different lengths (1 m, 1.5 m, 2 m and 2.7 m) of the part in the attic were studied. Ambient exterior temperatures of -25 °C and -30 °C with the corresponding attic temperatures of -13 °C and -17 °C were considered. Two insulation materials with the thermal conductivities of 0.02 W/(m•K) and 0.04 W/(m•K) were used in the simulations to achieve R7 and R14 insulation. On the outer wall of the pipe located in the attic, natural convection heat transfer coefficient of $h = 10$ [W/(m²•K)] was considered; whereas, the convective heat transfer coefficients on the outer surface of the pipe above the roof were calculated using an average wind speed of 21.5 km/h (6 m/s) and an insulation thickness of 2.54 cm (1 inch), resulting in a forced convection heat transfer coefficient of 30.9 [W/(m²•K)] based on the equations from Incropera et al. (2011).

There was also a need to account for the condensation that occurs on the inner surface of the pipe. To simplify the problem, condensation was modelled as a surface heat source at the wall. Both the exit temperature and the condensation amount were unknown but correlated. Hence, an iterative approach was taken to determine both these values. For the first iteration, the heat release from the heat source was assumed to be zero and a simulation was conducted. Based on the outlet temperature, the amount of heat source was calculated as the input for the second iteration. This procedure was continued until the values from two consecutive simulations converged; this usually occurred after three to four iterations.

In order To find the amount of water vapour at each temperature, there was first a need to calculate the saturation vapour pressure of water in air. Monteith and Unsworth (2008) provided Tetens' correlation for temperatures above 0 °C and Murray (1967) provided Tetens' equation for temperatures below 0 °C:

$$P = 0.61078 \exp\left(\frac{17.27T}{T+237.3}\right) \quad T > 0 \text{ °C} \quad (1)$$

$$P = 0.61078 \exp\left(\frac{21.875T}{T+265.5}\right) \quad T < 0 \text{ °C} \quad (2)$$



Figure 1. The schematic of system modeled (Left), Temperature sensor in the stack in the attic (Middle), and insulation around the stack in the attic (right).

Where T is the temperature in degrees Celsius. P is the saturation pressure in kilopascals (kPa). The humidity ratio, ω , is defined as the ratio of the mass of the water vapor, m_v , to the mass of dry air, m_a , and can be calculated knowing the air pressure and saturation:

$$\omega = 0.622 \frac{P_v}{P - P_v} \quad (3)$$

Hence, given the average air temperature at each cross section, the saturation pressure and water vapor pressure could be calculated in relation to the RH and humidity ratio. Calculating the mass flow rate of the inlet air, the water vapor content at the inlet and outlet of the pipe could then be determined. The difference in the water vapor content between the inlet and the outlet of the pipe determined the amount of condensation. Using the latent heat of condensation, the heat source term could be established. Figure 2 shows the Control Volume (CV) that was analyzed.

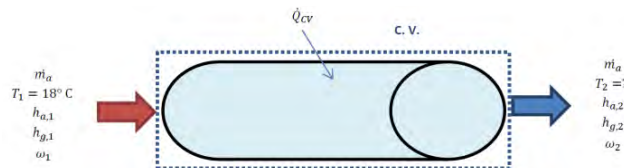


Figure 2. Thermodynamics analysis of the control volume

This analysis can be written as:

$$\dot{Q}_{CV} + \dot{m}_a [(h_{a,1} - h_{a,2}) + \omega_1 h_{g,1} + (\omega_2 - \omega_1) h_w - \omega_2 h_{g,2}] = 0 \quad (4)$$

Where \dot{Q}_{CV} accounts for heat transfer to the surrounding cold environment; $\dot{m}_a (h_{a,1} - h_{a,2})$ represents the sensible heat carried by the air, which can be written as $C_p (T_1 - T_2)$; $\dot{m}_a (\omega_2 - \omega_1) h_w$ accounts for the sensible heat released by the condensed water; and $\dot{m}_a (\omega_1 h_{g,1} - \omega_2 h_{g,2})$ is the amount of water that condensed. The first two terms in the bracket were calculated in the simulations, whereas the last two terms were calculated after the aforementioned source heat term was established. An excel sheet was created to input the corresponding heat being transferred to the surrounding for each outlet condition.

RESULTS

Numerical simulations — Extensive simulations were conducted to determine the insulation requirement to minimize the risk of stack ice clogging. Two RH levels in the soil gas were

considered, 100% and 50%. It was found that the worst case scenario when freezing is the most likely to occur near the pipe outlet is the case with 50% RH at the inlet. When the RH of the air at the inlet is 50%, condensation is delayed until the air reaches a temperature where the air becomes saturated with moist. The air velocities at the pipe inlet were assumed to be 0.05 m/s, 0.1 m/s and 0.15 m/s. It has been observed that the heat source term decreases as the velocity of the soil gas reduces, and the risk for freezing will thus increase in these instances. Using insulating materials with greater thermal resistances around vent pipe can reduce the overall diameter of the pipe and consequently reduce the overall area exposed to cold temperature, which is preferred.

In order to better determine a threshold for the ice accretion at the end of the pipe, the average temperature at the end cross section was calculated. If the average temperature is above 0 °C, it can be assumed that ice accretion or blockage at the end of the pipe is unlikely to occur. The average air temperatures at the end of the pipe for each case were calculated when outdoor temperature was -25 °C, and the results are shown in Figure 3 (a) and (b), corresponding to $k = 0.04 \text{ W/(m}\cdot\text{K)}$ and $k = 0.02 \text{ W/(m}\cdot\text{K)}$ respectively. It can be seen when R7 insulation is used along the entire length of pipe, the average temperature at the end of the pipe can reach below the freezing point when the inlet velocity is 0.05 m/s regardless of the insulation material. As mentioned before, this is the worst case scenario where the vent stack air velocity is minimal (0.05 m/s) and the RH is only 50%; hence, the minimum amount of heat from condensation is added to the control volume. The results also showed that using R14 insulation all along the entire length of pipe is more than sufficient to avoid freezing, however it is also more costly.

Figure 4 depicts the temperature contours along the pipe for the case when R7 was applied to the outer perimeter of the stack in the unheated attic and R14 was used around stack above the roof. We used $k = 0.02 \text{ W/(m}\cdot\text{K)}$, $V=0.05 \text{ m/s}$, inlet RH= 50% and the length in attic = 2 m in our simulation and the outdoor temperature was -25 °C. It can be seen that, with the R7/R14 insulation combination, the core of the air flow is still warm at the pipe end and freezing is unlikely to occur. Hence, it is recommended that R7 insulation be used along the pipe section located in the attic and R14 insulation for that section exposed to outdoor conditions.

Validation of simulation using experimental results — The recommendations for Rn vent stacks insulation based on simulation results have been taken by a field study conducted between December 2017 and February 2018 in the National Capital Region of Canada. An outdoor temperature of -26 °C occurred on 28 December, 2017, which was chosen to benchmark the simulation results. The velocity of the vent stack was measured as 0.15 m/s and the RH was 100% at the pipe inlet. The 150 cm of the stack was located in the attic and having R7 insulation. 40 cm of pipe, insulated with R14 insulation, was above the roof line. The air temperature was measured at 86 cm from the pipe inlet and was used to benchmark the simulation. The average temperature derived from the simulation was 13.4 °C, and an average temperature of 13.25 °C was measured from the test. These results confirm that the method used to model the condensation as the surface heat source was rational. The temperature contours for the simulation are shown in Figure 5. It can be seen that the soil gas remains warmer than 0 °C even at the end of the pipe using the suggested insulation. The in-situ observations also confirmed that no freezing developed at the pipe exit.

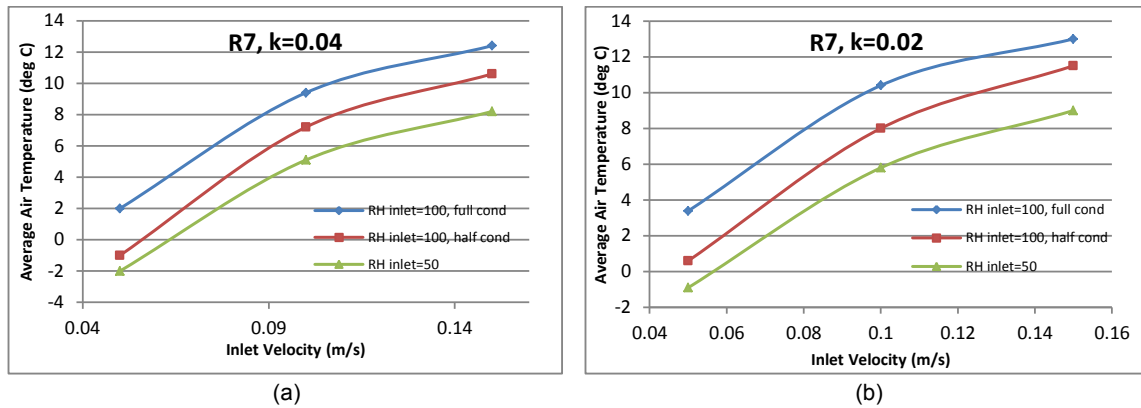


Figure 3. Average temperature at the outlet cross section of the pipe for R7 and (a) $k=0.04$ W/(m.K) insulation, (b) $k=0.02$ W/(m.K) insulation with an outdoor temperature of -25 °C

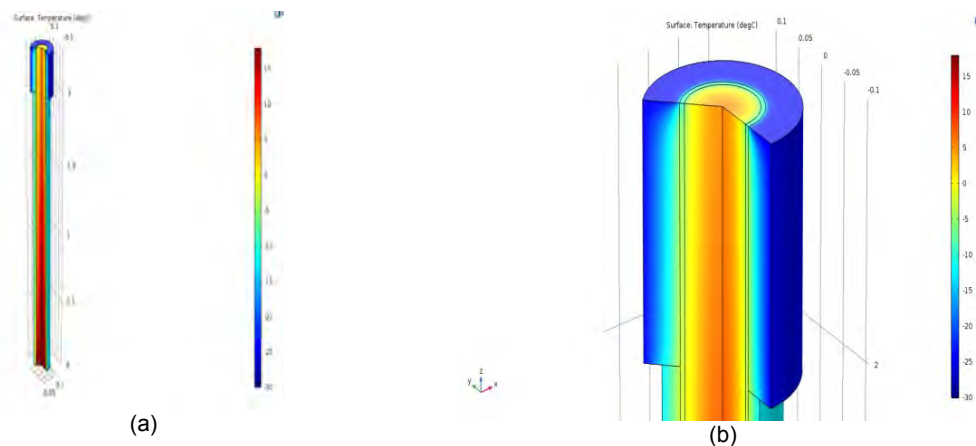


Figure 4. Temperature contours for the combined R7/R14 insulation using $K=0.02$ W/(m.K), $V=0.05$ m/s, inlet RH= 50% and the length in attic= 2 m (a) along the pipe (b) at the end of the pipe

DISCUSSIONS

Using the COMSOL Multiphysics package, a study was undertaken to determine the level of insulation required to avoid freezing and ice clogging of Rn stacks in Canadian winters. Different air velocities in the pipe, lengths of vent pipe, insulation level and thickness, and outdoor conditions were investigated. The following outcomes were derived from the simulations:

- Soil gas flow in the stack was found to be vulnerable to freezing; the lower the air velocity is in the pipe, the more likely freezing occurs.
- Using insulation materials with lower thermal conductivity for the same thermal resistance can reduce the surface area exposed to the cold temperature and thereby reduce the freezing risk.
- Minimizing the length of pipe located in the attic and outdoors can reduce the exposure to low temperatures and hence reduce the freezing risk.
- A Rn stack was installed in a Canadian home by applying R7 insulation around the pipe in the attic and R14 insulation around pipe above roof line, as suggested by the simulation results. The combined insulation appeared to avoid freezing of the Rn stack vent effectively, even when the outdoor temperature dropped to -26 °C.

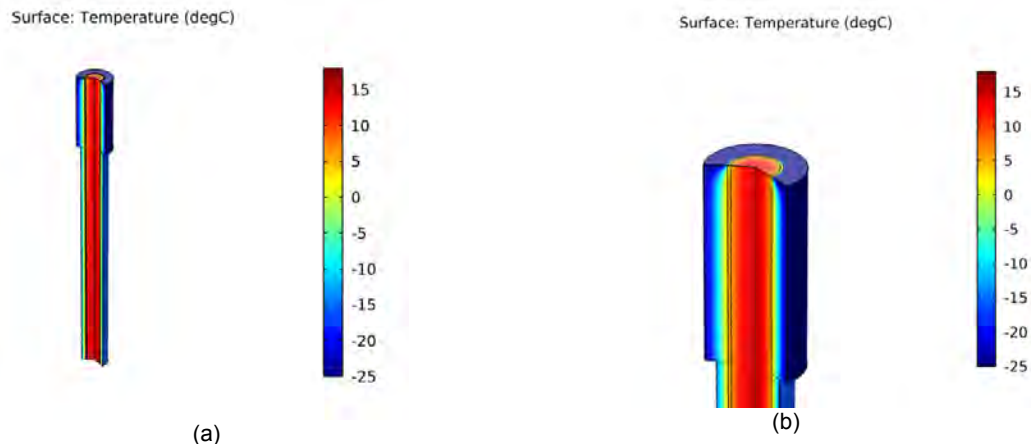


Figure 5. Temperature contours for the combined R7/R14 insulation using $K=0.02$ W/(m.K), $V=0.15$ m/s, inlet RH= 100% and the pipe length in attic= 1.5 m (a) along the pipe (b) at the end of the pipe

CONCLUSIONS

This study presents a numerical model to determine the required insulation level around Rn stacks in unheated attic space and above roof, in order to minimize the risk of ice blockage at the exit of the stack. Simulation results provided guidance on insulating a stack in a field study home in cold climate. The soil gas temperature measured from one point in the pipe was compared with the results from simulation. The difference is only 1.2%. This demonstrates the model benchmarking is successful. These results confirm the validity of the assumptions made for the numerical model as well as the recommendations for the insulation level. No freezing in the Rn stack occurred during the coldest days of the test period using the R7/R14 insulation combination. Future field testing from other regions of Canada will demonstrate further whether the combined R7/R14 insulation suggested by simulation work described in this paper is sufficient for Rn stacks to avoid ice blockage at the exit, in cold Canadian winter.

ACKNOWLEDGEMENT

This work was supported by the Canadian Federal Government Taking Action on Air Pollution funding.

REFERENCES

- Bergman, T., Lavine, A., Incropera, F., DeWitt, D. 2011, Fundamentals of Heat and Mass Transfer, 7th Ed., New York: J. Wiley.
- Health Canada (2010): Reducing Radon Levels in Existing Homes: A Canadian Guide for Professional Contractors [Online]. http://www.radonleaders.org/sites/default/files/HC%20Rn%20Mitigation%20Guide%20English_0.pdf
- Health Canada (2014): Radon Frequently Asked Questions [Online]. http://www.hc-sc.gc.ca/ewh-semt/radiation/radon/faq_fq-eng.php
- Monteith, J.L., and Unsworth, M.H. 2008. *Principles of Environmental Physics*. 3rd Ed. AP, Amsterdam.
- Murray, F.W. 1967. On the computation of saturation vapour pressure. *J. Applied Meteorology*, Vol. 6, pp. 203-204.
- Tetens, O. 1930. Über einige meteorologische Begriffe. *Z. Geophys*, Vol. 6, pp. 207-309.
- World Health Organization (2009): WHO Handbook on Indoor Radon [Online]. http://whqlibdoc.who.int/publications/2009/9789241547673_eng.pdf

A GIS based methodology to support multi-criteria decision making for the retrofitting process of residential buildings

Kristina Orehounig^{1,2*}, Emmanouil Thrampoulidis^{1,2}, Georgios Mavromatidis^{1,2} and Jan Carmeliet^{2,3}

¹Laboratory for Urban Energy Systems, Empa Duebendorf, Switzerland

²Chair of Building Physics, ETH Zurich, Switzerland

³Laboratory for Multiscale Studies in Building Physics, Empa Duebendorf, Switzerland

**Corresponding email: kristina.orehounig@empa.ch*

ABSTRACT

This paper presents a workflow to support the decision making for building retrofit and building systems update at urban scale. The workflow includes *i*) a method to extract information from a geographical information system including information on building characteristics, building systems and building typology, *ii*) a method to evaluate the current and future energy demand of buildings using a dynamic building simulation tool, and *iii*) an updated version of the energy hub approach to evaluate best performing options in terms of energy systems update. The developed method is applied to the city of Zurich to evaluate the optimal energy system update for all existing buildings within the city. Modelling results include best performing options in terms of CO₂ emissions, renewable energy share, or energy efficiency while minimizing resulting costs for possible system and retrofitting solutions.

KEYWORDS

Urban energy, energy system optimization, retrofitting of buildings, energy hub.

INTRODUCTION

Buildings and urban energy systems have an important potential to reduce energy consumption and greenhouse gas emissions to meet future energy strategy targets. A combination of measures are usually required to achieve the envisaged targets, which include replacing current fossil fuel based heating systems with more sustainable solutions, to integrate decentralized energy systems, and retrofitting the existing building envelopes. To support the decision making process, optimization tools are required, which allow for a multi-criteria assessment of an optimal combination of measures within urban energy systems. Finding suitable solutions for already existing neighbourhoods depends thereby strongly on the buildings and their installed systems. Questions such as which buildings need to be updated first in order to meet the targets as soon as possible, or which measures are more important compared to others play thereby a critical role.

This paper presents a workflow which builds on simulation and optimization techniques to support the decision making for building retrofit and building systems update at urban scale. Thereby information which is retrieved from Geographic Information Systems (GIS) about the current situation of the buildings (such as layout, U-values, occupancy, etc.) and their systems is integrated in the model. The method can be used to evaluate best performing options in terms of CO₂ emissions, renewable energy share, or energy efficiency while minimizing resulting costs for possible system and retrofitting solutions. In this paper the developed method is applied to 12802 residential buildings of the city of Zurich.

METHODS

The workflow which was developed, shall support the decision making for identifying optimal building retrofitting measures at urban scale. It includes: *i)* A method to extract geo-spatial information, including information on building characteristics and building energy systems, based on building and census data, *ii)* A method to evaluate current and future energy demands of buildings using an automated process developed in Matlab to deploy EnergyPlus at urban scale, that includes a connection to geo-spatial information and facilitates the computation of energy demand profiles for different scenarios at individual building level, and *iii)* an optimization model to evaluate best performing options in terms of retrofitting and energy system updates, based on multi-criteria decision making. As a result, input information on existing buildings, including their system state, is integrated into the modelling methodology. The tool allows for the evaluation of individual building level solutions, and is additionally able to take renewable energy potentials and boundary conditions of the neighborhood into account.

Geo-spatial information

To describe the current situation of buildings within a neighbourhood GIS based building information is required such as building layout, building characteristics and environmental information. Relevant input information is collected from different sources, such as census data from Switzerland (BFS, 2013), 3D building information (Swisstopo, 2016), weather information (Meteotest, 2016), etc. This information is further processed in a database structure and connected to the different models presented below.

Buildings energy demand modelling

Modelling of current energy demand of buildings

To represent the current situation in terms of energy demand pertaining to heating, cooling, electricity and domestic hot water the bottom up modelling tool CESAR is deployed (Wang et al., 2018). The tool allows for calculation of hourly energy demand profiles for multiple buildings within a neighbourhood. Thereby geo-spatial information pertaining to building floorplans, their height (2.5D shape) and a set of additional input information to derive relevant building characteristics are used as model input. The CESAR tool utilizes the building simulation engine EnergyPlus (U.S. Department of Energy, 2015) to compute for each building heating, cooling and electricity loads separately. Neighbouring buildings are considered as shading objects.

Modelling of building envelope retrofitting potential

The model can be used to evaluate different envelope retrofitting options. In case of a retrofit of the building envelope, additional insulation is added to the original constructions until required U-Values for retrofitted constructions according to SIA 380/1 are met (SIA, 2009). Additional envelope retrofitting options include replacement of windows, partial retrofitting of individual constructions, such as roofs or facades, and whole building retrofitting solutions which combines all the different measures. The resulting retrofit constructions are structured in a database similar to the non-retrofitted constructions and linked with the model.

Modelling of solar potential

For calculating the building integrated renewable potential pertaining to the utilization of the solar resource also the tool EnergyPlus is used. The variation of different roof inclinations, and orientations was evaluated. Thereby values between 0 and 60 degrees, with 5 degrees step

for roof inclinations, while the roof orientation could take discrete values from East (90 degrees) to South (270 degrees) with a step of 45 degrees. In total 65 solar simulations were performed to calculate the annual solar profiles for the selected combinations of roof slopes and orientations stored in a solar database. For each building the total roof area was calculated and based on the building orientation and slope of the roof a respective solar profile was assigned to the building.

Simulation results

Results are computed for individual buildings at an hourly resolution, including actual and future demand for heating, domestic hot water, cooling and electricity, as well as solar potential on roof surfaces. Additionally, annual primary energy consumption and GHG emissions for operation of the buildings, as well as operational energy, embodied energy and economical aspects of retrofit measures are analyzed in detail.

Optimization model for optimal retrofitting option

For selecting the optimal retrofitting strategy for each building an optimization tool based on the energy hub approach is utilized. The model takes a combination of both building envelope retrofitting options and energy supply systems to provide electricity, space heating and DHW into account. The approach is based on a Mixed Integer Linear Programming (MILP) optimization framework (Wu et al., 2017, Mavromatidis et al., 2014). To evaluate multiple objectives the epsilon constraint method is deployed. In this study, the two objective functions for annualized costs and life cycle environmental impacts are considered. The generated energy demand profiles together with the solar potential profiles of individual buildings are taken as input to the model. The demand profiles are further processed to extract typical days, which are then used for the optimizations. A representation of the current system based on the above mentioned database (BFS, 2013) is included in the model. Additionally the following system options are implemented into the optimization framework which pertain to: air source heat-pumps (ASHP), ground source heat-pumps (GSHP), biomass boilers, photovoltaic panels (PV), solar thermal collectors (ST), oil boilers and gas boilers as conversion technologies and hot water thermal storage tanks and batteries as storage technologies. The building envelope retrofitting scenario is implemented as an additional decision variable within the optimization framework.

CASE STUDY

The city of Zurich in Switzerland is taken as a case study. The city has about 400 000 inhabitants, who live in around 35000 residential buildings. Zürich has a heating dominated climate, with an average outside temperature of 9.5°C. From about 20 800 buildings were input information was available, about 12800 buildings were selected for the analysis. Characteristics such as building type, existing building energy carrier, age of building, size of ground floor and building height of the sample set is summarized in Figure 1. As can be seen from this figure, the majority of the buildings are multi-family houses, equipped with a gas or oil heating system and built before 1960.

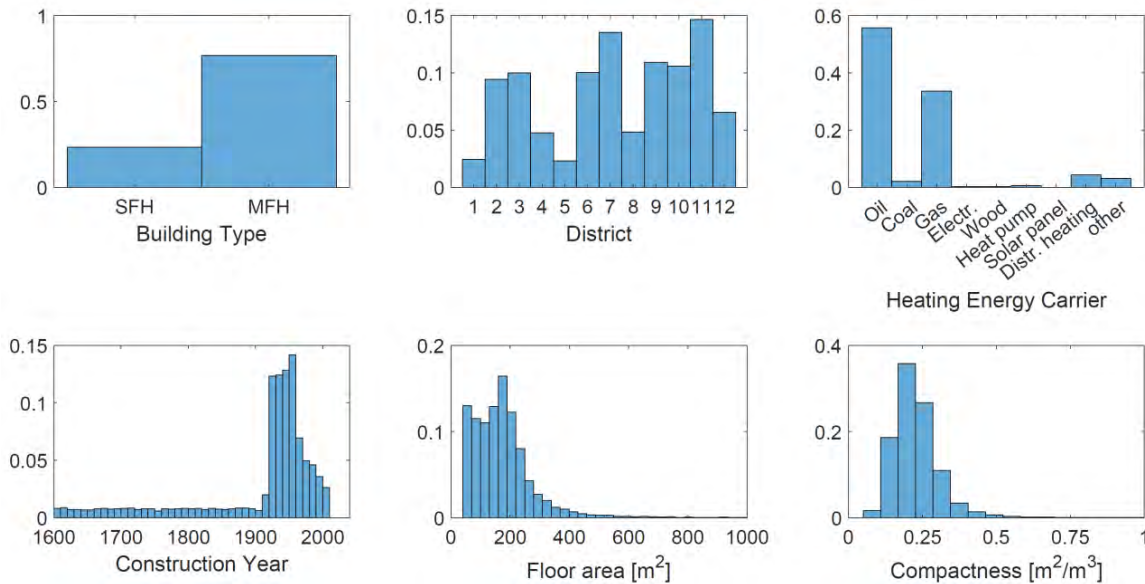


Figure 1. Distribution of building characteristics of all 20863 residential buildings.

RESULTS AND DISCUSSION

Results were retrieved for the 12802 selected buildings. In a first step the current energy demand of the sample set was calculated with the CESAR tool, as described above. Energy demand of buildings pertain to space heating, domestic hot water and electricity demand. Results are computed for each individual building, Figure 2 shows a histogram of mean annual space heating demand distribution of all buildings. The space heating demand varies between 30 to 280 kWh.m⁻².a⁻¹. In a next step, different envelope retrofitting strategies are calculated. Retrofit options considered vary between no retrofit, roof, wall, window retrofit and combinations between them. Additionally, the building integrated maximum solar potential is calculated. Results of the current building characteristics, current energy demand, and potential options for retrofitting as well as the solar potential act as input information for the optimization framework. In a final step, the optimization tool is deployed to evaluate the most cost and CO₂ friendly retrofitting solution. Thereby building envelope retrofitting options together with building system solutions are taken into account. Results are given as pareto optimal solutions for each individual building. Pareto optimal solutions are the set of solutions for which no criterion can be improved without making another criterion worse off. Figure 3 shows Pareto fronts of 3 different buildings in Zurich.

Results of the 3 different buildings show that the shape of the Pareto curve and the selection of retrofitting interventions can vary considerable between buildings. However, results also show that the best performing option in terms of CO₂ is usually a biomass based heating system, which is due to very low CO₂ emissions of biomass. Results also show that the set of Pareto-optimal transformation strategies are depend on the original heating system, while age and size of the building influence the achievable GHG emissions and related costs. The retrofitting of the building envelope option varies considerable between the different buildings. While for some buildings no retrofitting of the envelope was selected, buildings like the one shown in Figure 3a have a wall and window retrofit, and only a few a full retrofitting of the envelope. Figure 4 shows the distribution of optimal solutions for system selection (a) and retrofitting (b) for all Pareto points. As can be seen from these figures the majority of optimal solutions are distributed between no retrofitting, which are clearly the cost

optimal solutions and partly retrofitting of single elements such as roof or wall insulation. A full retrofit of windows, walls roofs and floor construction is only selected for a minority of buildings. This is mainly due to very high costs for retrofitting in Switzerland. At the system side, it can be seen that for the majority of solutions an ASHP is selected, followed by biomass boilers and GSHP.

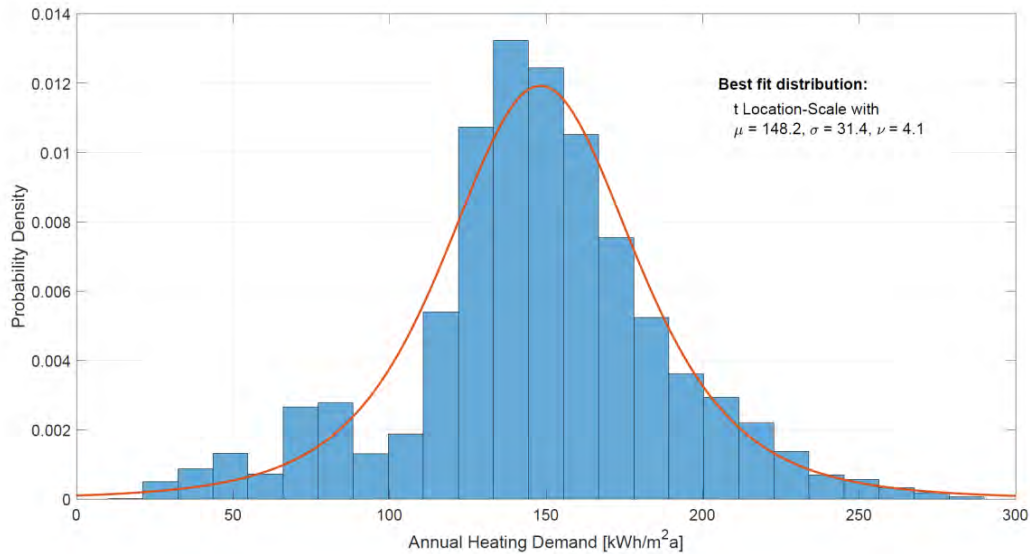


Figure 2. Histogram of current heating demand of the sample set of buildings.

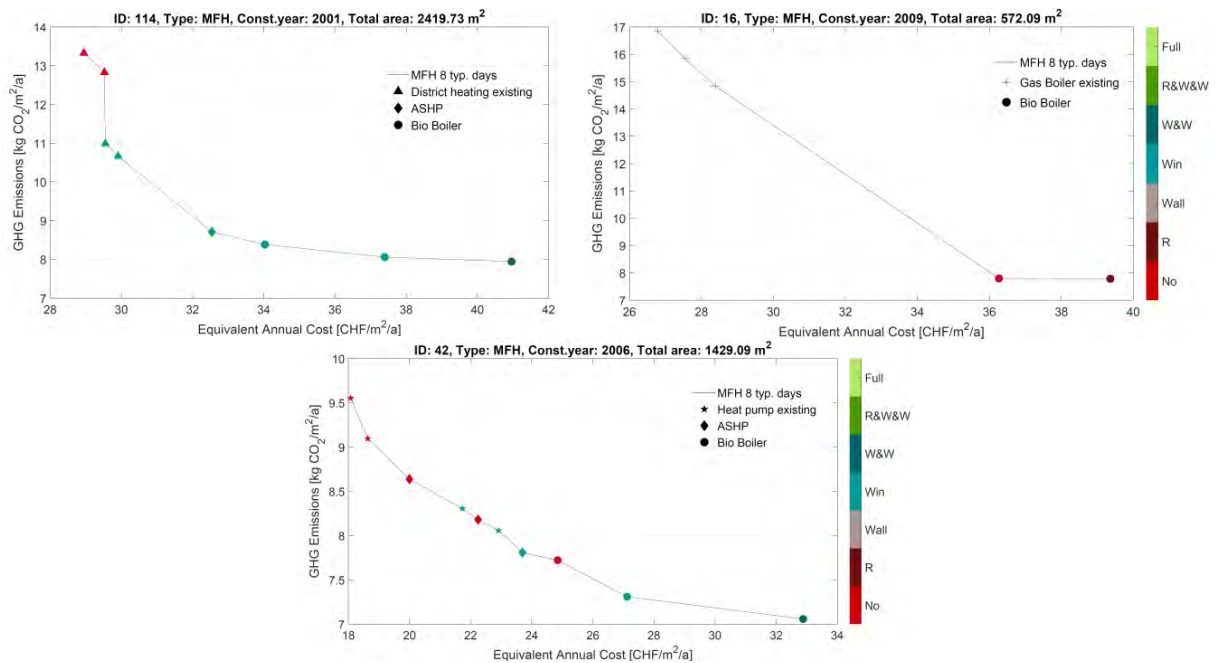


Figure 3. Example of Pareto fronts

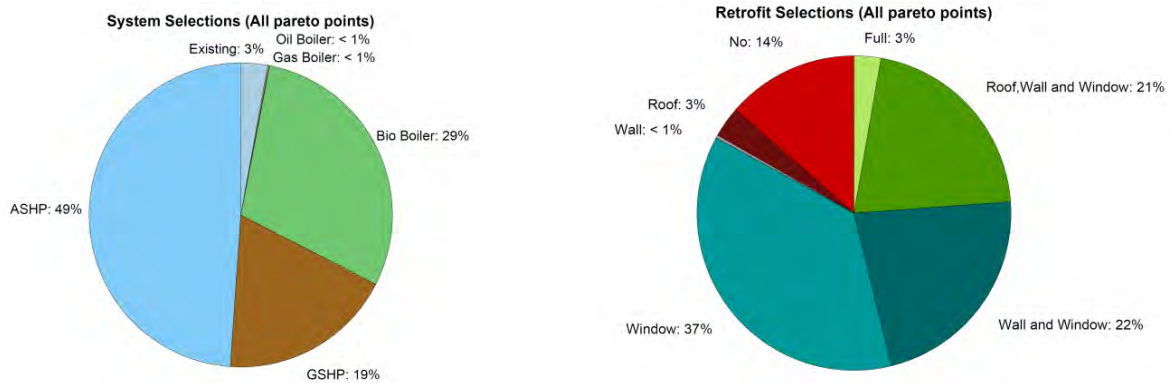


Figure 4. Retrofit and system selection shares of the sample set of buildings

CONCLUSIONS

This paper presents a workflow for evaluating sustainable retrofitting options for buildings at an urban scale. The workflow consists of a combination of a GIS based data collection which is connected to different tools to identify building energy consumption, retrofitting options and finally to evaluate the CO₂ and cost optimal solutions for buildings within a city. The approach can be easily applied to residential buildings in Switzerland. As a case study, 12802 buildings of the city of Zurich are selected. Results of the case study show that solutions vary considerable between the buildings. As a conclusion, it can be summarized that the optimal transformation strategies depend on the original heating system, while age and size of the building influence the achievable GHG emissions and related costs.

ACKNOWLEDGEMENT

This research has been financially supported by CTI within the SCCER FEED&D (CTI.1155000149), by SNF within the NFP 70 program "Energiewende" project IMES (407040_153890) and SNF project RePoDH.

REFERENCES

- BFS 2013. "Eid. Gebäude- und Wohnungsregister (GWR)," Federal Office of Statistics, Switzerland, Zurich.
- Mavromatidis, G., Evins, R., Orehounig, K., Dorer, V., Carmeliet, J., 2014. Multi-objective optimization to simultaneously address energy hub layout, sizing and scheduling using a linear formulation, in: Engineering Optimization IV. Presented at the International Conference on Engineering Optimization, CRC Press/Balkema, Lisbon, pp. 609–614.
- Meteotest, 2016. "Meteonorm," [Online]. Available: <http://www.meteonorm.com/de/downloads>.
- U.S. Department of Energy 2015. Energy Plus Simulation Software V8-3-0. Available at <https://energyplus.net/>, Accessed 18 March 2015.
- SIA 2009. SIA 380/1: Thermische Energie im Hochbau. Zürich: SIA.
- Swisstopo 2016. "swisstopo-swisstopo homepage," [Online]. Available: <http://www.swisstopo.admin.ch/internet/swisstopo/en/home.html>.
- Wang, D., Landolt, J., Mavromatidis, G., Orehounig, K., Carmeliet, J., 2018. CESAR: A bottom-up building stock modelling tool for Switzerland to address sustainable energy transformation strategies. Energy and Buildings 169, 9–26.
- Wu, R., Mavromatidis, G., Orehounig, K., Carmeliet, J. 2017. Multi-objective optimisation of energy systems and building envelope retrofit in a residential community, Applied Energy 190, 634-649.

A New Normative Workflow for Integrated Life-Cycle Assessment

Karen Angeles¹, Dimitrios Patsialis², Tracy Kijewski-Correa³, Alexandros Taflanidis⁴, Charles F. Vardeman II⁵, Aimee Buccellato^{6*}

¹⁻⁶University of Notre Dame, Indiana

**ABuccellato@nd.edu*

ABSTRACT

In order to curtail energy use by the building sector, consideration of how a "sustainable" building is constructed is paramount, in many respects, to how efficiently it operates over its lifetime. A typical building must be in use for decades before the energy expended in its daily operations surpasses the energy embodied within its initial construction, as a result of the materials used. More vitally: every building has specific vulnerabilities, particularly to hazards (e.g., earthquakes, wind, flooding) whose effects on sustainability are not explicitly considered alongside other aspects of sustainability in the design process – despite the significant environmental impact of damage and repairs after a disaster. Unfortunately, the joint consideration of resilience and sustainability in design is far from trivial, requiring various interdisciplinary perspectives involved in the delivery of building projects. These perspectives each contribute the models and data necessary for integrated evaluation, leading to the notorious challenges of BIM and data interoperability. In response, this paper presents a new end-to-end workflow for life-cycle assessment (LCA) of buildings that captures the dependencies between multi-hazard resilience and sustainability, across multiple dimensions of environmental impact. An illustrative example reveals how consideration of hazards during design and material selection influence embodied energy, ultimately revealing design choices that best achieve joint resiliency and sustainability.

KEYWORDS

Life Cycle Analysis, Natural Hazards, Resilience, Sustainability, Embodied Energy

INTRODUCTION

Buildings account for 40% of annual CO₂ emissions in the United States, placing the building industry at the forefront of the growing international mandate to better steward our environment (Dixit et al., 2012). This has prompted the mainstreaming of sustainability assessments into project workflows, with efforts focused on optimizing operating energy. However, a typical building must be in use for decades before its operating energy surpasses the energy embodied in the extraction, processing, manufacture, delivery, repair and disposal of its constitutive materials (Sartori and Hestnes, 2007; Dixit et al., 2012). Additionally, energy expended in material and system repairs due to damage by natural hazards is often not explicitly considered in the design process. However, this evaluation is critical when one recognizes that each building's hazard vulnerabilities are driven by the unique choices of material assemblies that form the building's systems, components, and finishes. This demands an integrated approach to Life Cycle Assessment (LCA) wherein the vulnerabilities that drive hazard resilience can be included in a holistic environmental impact assessment.

Historically, the numerous disciplines involved in building projects have partitioned the analyses central to delivering such integrated LCAs, with each developing unique abstractions of the structure to simplify modeling requirements and fulfill design objectives. This limits

interoperability between modeling environments and discipline-specific data sources, creating barriers in the joint evaluation of resilience and sustainability. However, by leveraging semantic data perspectives from computer science, one is able to efficiently bridge data structures and maintain the vocabularies normative to each domain's tools so they can interoperate. This research adopts such an approach, developing an automated framework for integrated LCAs. This framework is capable of capturing the dependencies between multi-hazard resilience and sustainability, across multiple dimensions of environmental impact, while maintaining the native modeling environments common to building practice. This paper presents a schematic representation of the resulting end-to-end workflow, including methodologies used to conduct its various analyses. An illustrative example building is presented to demonstrate the initial joint evaluation of resilience and sustainability, including the assessment of design alternatives.

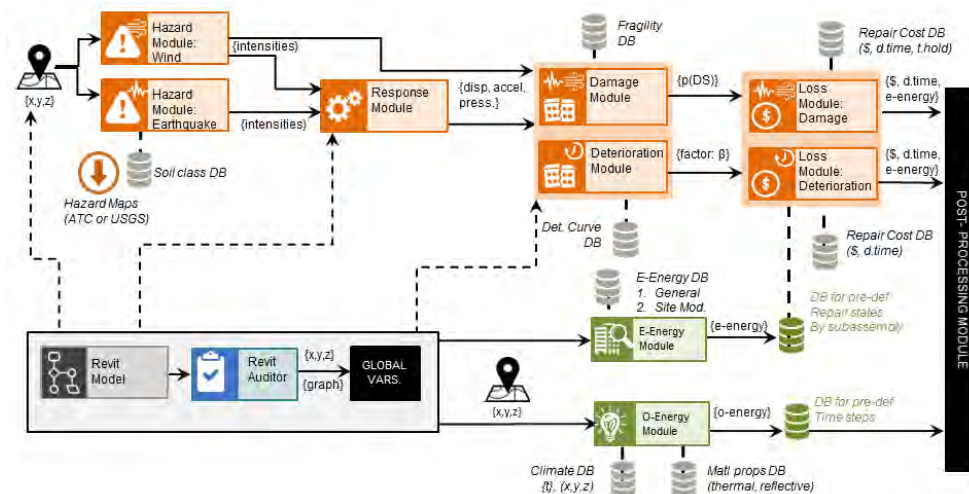


Figure 1. Schematic representation of proposed integrated life cycle analysis framework.

METHODOLOGY

The proposed integrated LCA (depicted in Figure 1) adopts a modularized approach to enable “best of breed” tools to be incorporated as they become available. The sequencing of operations in the LCA framework is now introduced for each of the integrated modules. While the framework conducts multi-hazard evaluations, specific focus is placed upon seismic hazards in the following description and subsequent example for brevity.

1. Primary user interfacing adopts the commercial software Revit©, due to its popularity in practice. The Revit model and building location are circulated into the **Revit Auditor**, which characterizes relevant geometries and creates an inventory of components using ontology-based data patterns (Ferguson et al., 2016a). This provides a queryable semantic “knowledge graph” of building information enabling the extraction of features and data required by subsequent modules.
2. The building location and dynamic properties are retrieved by the **Hazard Module**, which identifies the intensities for each natural hazard at different return periods, (e.g. 500-year event). For seismic hazards, spectral acceleration (e.g., 0.5 g) is used as the intensity measure to construct a hazard curve describing the degree of exposure (return period) at each intensity level (USGS, 2018). In this study, intensity selection effectively partitions the hazard curve into eight intervals.
3. These intensity measures and the corresponding building properties (e.g., floor to floor height and natural period) are utilized in the **Response Module** to calculate the building’s engineering demand parameters (EDPs) over the building’s intended service life (e.g., 50

years). For seismic hazards, EDPs (such as drift ratios and accelerations) are determined through a linear-elastic finite element analysis and FEMA (Federal Emergency Management Agency) P-58's Simplified Analysis Procedure (ATC, 2012).

4. The resulting EDPs are fed to the **Damage Module** to evaluate the vulnerabilities of building components due to hazard exposure. By explicitly representing each building assembly, those most driving resilience or sustainability performance can be identified, providing designers with insight about the broader impact of their design decisions. This is made possible through an assembly-based vulnerability approach (Porter et al., 2001), in which each assembly is comprised of a group of building components that share common vulnerability and cost characteristics. Vulnerabilities are defined using fragility curves, obtained from FEMA's Performance Assessment Calculation Tool (PACT), defined as the probability that an EDP will exceed a threshold defining acceptable structural performance. This provides a detailed damage assessment for each assembly. A parallel physics-based Deterioration Module (see Figure 1) considers service-induced wear, but is beyond the scope of this paper.
5. The **Loss Module** correlates these damages due to hazard exposure to a set of consequences (emphasis herein is on monetary costs, though downtime can also be determined) for various service lives. For this study, the direct seismic losses are evaluated considering the probability of incurring damage and relating this to the corresponding repair cost for each assembly (ATC, 2012; Cardone and Perrone, 2015). For consistency, initial cost of construction is based upon total replacement cost.
6. The embodied energy in the building's initial construction (EE:IC) and its operating energy are evaluated within the **Environmental Impact Module**. Operating energy is calculated through a lumped capacitance model which evaluates the heat flux using material and spatial properties (Ferguson et al., 2016b). It should be noted that plug loads are not included in operating energy calculations, though these can be easily accommodated in the future. Site-specific assessment of the building's operating energy is informed by climatology data from EnergyPlus (DOE, 2018). To determine the EE:IC, material volumes are calculated using the Revit Auditor and multiplied by each material's respective cradle-to-gate embodied energy and density (Hammond and Jones, 2011). Energy embodied in the repair materials (EE:RM) necessitated by hazard exposure is calculated by expressing the monetary cost of each assembly's repair as a percentage of the initial cost and multiplying that by the EE:IC of the assembly for a cradle-to-gate estimate.
7. These results are aggregated by the **Post-Processing Module**, which outputs embodied and operating energy as well as monetary losses by assembly as standard visualizations for different service lives. These assembly-based visualizations provide greater insight into the design choices that are most likely to improve the building's resilience and sustainability over different service lives.

ILLUSTRATIVE EXAMPLE

The integrated LCA framework is next applied to a building in Los Angeles employing a two-story reinforced concrete (RC) frame with concrete floor and roof slabs. The building consists of a regular floor plan, measuring 7 by 9 meters, with top-of-slab elevations at of 4.15 and 7.65 meters. The structural system of the building is a special moment resisting frame, as required for regions of high seismicity. The envelope consists of infill concrete masonry units (CMU) with a brick veneer. There are two interior partitions at each floor: gypsum wall board on metal stud. The following section presents the evaluation of this Initial Design from the joint perspective of sustainability and resilience using the proposed end-to-end LCA workflow. All results are described by assembly to reveal those which may warrant design revisions. To

further demonstrate how such assembly-based insights can be used, two design alternatives are respectively evaluated: increasing the size of the columns in the special moment frame (termed Frame Upgrade) and selecting an Alternate Envelope using precast RC panels.



Figure 2. Annotated visualization of embodied energy (sequence 1), total energy (sequence 2) and total monetary costs (sequence 3), at inception (1 Year) and as a result of hazard exposure over service lives of 10 and 50 years, for Initial Design and two design alternatives.

RESULTS

Figure 2 presents a three-panel visualization using images from the post-processing module (annotated in three sequences to facilitate discussion). Each numbered sequence illustrates the increases in the building's embodied energy (sequence 1), total energy (sequence 2) and monetary costs (sequence 3) due to repairs resulting from hazard exposure for service lives of 10 and 50 years. Each bar chart is further discretized to illustrate the relative contributions of different building assemblies (sequences 1 and 3) or energy measures (sequence 2). An examination of the embodied energy (per square meter) (sequence 1) reveals that the building envelope chosen for the Initial Design is the primary contributor to embodied energy. As a result, the choice of the Alternate Envelope significantly reduces the EE:IC (see results shaded in blue in sequence 1, Year 1), as well as the EE:RM over its service life (see results shaded in blue in sequence 1, Year 50). Figure 2's first sequence also illustrates that the Frame Upgrade results in a higher EE:IC (see Year 1 in sequence 1); though over a service life of 50 years, this

choice ultimately results in a lower overall embodied energy due to the reduction of drifts and thereby earthquake-induced repairs over time (see Year 50 in sequence 1). While the Alternate Envelope outperforms other designs from the perspective of embodied energy, this is not the case once operating energy is considered (see sequence 2). The consideration of operating energy reveals that the Frame Upgrade is actually a superior option, due to the Alternate Envelope's larger energy expenditure in operations (see results shaded in blue in sequence 2, Year 1 vs. Year 50). Meanwhile, the monetary costs of each of these options (see sequence 3), considering both construction costs (Year 1), as well as the accumulated cost of hazard-induced repairs over service lives of 10 and 50 years, are driven significantly by the frame and envelope (see results shaded in blue in sequence 3, Year 1 vs. Year 50). As such, while the two design alternatives respectively improve total energy and embodied energy expenditures, the Initial Design requires less up-front investment. Note that the repair costs are not exorbitant, a result of using a highly resilient special moment frame, and these would increase for a more seismically-vulnerable typology. Though difficult to discern in the total costs visualized in sequence 3 due to the high construction cost of the frame, seismic vulnerability was dominated by the envelope, which drove approximately 80% of the annual repair costs in the Initial Design. The selection of an Alternate Envelope reduces annual repair costs by nearly 70%. This illustrative example demonstrates how a more data-informed and comparative conceptual design process could unfold with newfound access to critical resilience and sustainability performance metrics for the building's assemblies.

DISCUSSIONS

Integrating the tools and data from the professions surrounding the design process into a single workflow is challenging, admittedly necessitating simplifications in the models and even examples used herein to vet this workflow. This paper constitutes an important first step to be followed by more faithful case studies sourced from practice. Nonetheless, this illustrative example demonstrates the importance of material choice in design, as embodied energy can be a key driver of environmental impact, particularly over shorter service lives. Moreover, as advances in energy-efficient building systems and non-grid-based energy sources are outpacing advances in efficient material extraction, manufacturing, transportation, and assembly, material embodied energy will be an increasingly larger portion of the total energy balance for the foreseeable future. As such, embodied energy data, and in particular that associated with the repair of hazard-induced damages, will require continued attention within the community. It is anticipated that embodied energy will routinely surpass operating energy once a more complete accounting is possible. Recent studies further suggest that hazard-induced repairs may consume considerably more energy than that embodied in the repair materials themselves (Simonen et al., 2018). While much work remains to truly quantify these impacts, this at minimum underscores the importance of considering not only embodied energy but also its dependence upon hazard exposure in any sustainability evaluation.

CONCLUSIONS

This paper reiterates that a parceled approach, where each discipline optimizes a single performance objective/metric in isolation, does not effectively capture the interrelated concerns of resilience and sustainability. It is worth noting that while these independent concerns may be qualified, their reconciliation is hampered by the lack of a universal metric for comparison, given that sustainability and resilience are quantified in far different "currencies," including even the potential loss of human life. Nonetheless, the integrated LCA presented herein enables a data-informed approach to navigating the inevitable trade-offs between monetary cost, resilience and environmental impact. However, it is important to note that while the Revit-compatible workflow herein is, in and of itself, a significant contribution, its utility will remain

dependent on the quality and completeness of the data it relies upon, as well as the ongoing commitment to widely sharing these as linked, open data. The use of semantic data perspectives in the proposed workflow will not only enable the seamless integration of such machine-readable data when it becomes available, but enable a more rigorous geospatial accounting of the life-cycle costs related to the transportation of materials to and from the site. Until that day, the environmental impact of design choices will remain largely speculative. As such, the propagation of uncertainties associated with this source data, as well as those created by the site-specific future hazard/climate exposure and assumptions/simplifications of the wider design process, will be a critical next stage for the authors.

ACKNOWLEDGEMENT

The authors gratefully acknowledge the support of the National Science Foundation (CMMI-1537652). Any opinions, findings, and conclusions or recommendations expressed in this material are those of the authors and do not necessarily reflect the views of the National Science Foundation. The authors further thank Notre Dame's Center for Research Computing for its support and recognize the contributions of former graduate student Holly Ferguson and undergraduate Alexandria Gordon. The first author also recognizes the financial support of her Dean's Fellowship from the Notre Dame College of Engineering.

REFERENCES

- ATC. 2012. Seismic performance assessment of buildings. FEMA P-58, Applied Technology Council, Redwood City, CA.
- Cardone D. and Perrone G. 2015. Developing fragility curves and loss functions for masonry infill walls, Article in Earthquakes and Structures.
- Dixit, M.K., Fernández-Solís J.L., Lavy S., and Culp C.H. 2012. Need for an embodied energy measurement protocol for buildings: a review paper. *Renewable and Sustainable Energy Reviews*. 16, 3730-3743.
- DOE. 2018. Weather Data for Simulation. *Department of Energy*. <https://energyplus.net/weather/simulation>. Accessed 3/27/2018.
- Ferguson H., Vardeman C., and Nabrzyski J. 2016a. Linked data view methodology and application to BIM alignment and interoperability. *2016 IEEE International Conference on Big Data (Big Data)*, Washington, DC. 2626-2635.
- Ferguson, H.T., Buccellato, A.P.C., Paolucci, S., Yu, N., and Vardeman II, C.F. 2016b. Green Scale Research Tool for Multi-Criteria and Multi-Metric Energy Analysis Performed During the Architectural Design Process. CoRR, abs/1602.0. Retrieved from <http://arxiv.org/abs/1602.08463>. doi: 10.1109/BigData.2016.7840905.
- Hammond, G.P. and Jones, C.I. 2011. Inventory of Carbon and Energy (ICE), Version 2.0, Department of Mechanical Engineering, University of Bath. <http://www.bath.ac.uk/mech-eng/ser/embodied/>. Accessed 3/27/2018.
- Porter K.A., Kiremidjian A.S., and LeGrue, J.S. 2001. Assembly-based vulnerability of buildings and its use in performance evaluation. *Earthquake Spectra*. 18(2), 291-312.
- Sartori I. and Hestnes A.G. 2007. Energy use in the life cycle of conventional and low-energy buildings: a review article. *Journal of Energy and Buildings*. 39, 249-257.
- Simonen, K., Huang, M., Aicher, C., and Morris, P. 2018. Embodied carbon as a proxy for the environmental impact of earthquake damage repair. *Journal of Energy and Buildings*. 164, 131-139.
- USGS. (2018). Unified Hazard Tool. United States Geological Survey. <https://earthquake.usgs.gov/hazards/interactive/> Accessed 4/4/2018.

Big-open-real-BIM Data Model - Proof of Concept

Galina Paskaleva^{1,*}, Sabine Wolny¹ and Thomas Bednar¹

¹Research Division of Building Physics and Sound Protection, Institute of Building Construction and Technology, TU Wien, Vienna

*Corresponding email: galina.paskaleva@tuwien.ac.at

ABSTRACT

The goal of Building Information Modeling (BIM) is the continuous use of digital construction models from the planning stage onwards. The affected processes are iterative and involve multiple stakeholders who work at varying pace and in varying levels of detail. These stakeholders require highly specific tools based on diverging data models. To satisfy all those requirements one of the best known Open BIM implementations – IFC – offers a data model containing more than one thousand different types – from basic to highly specific. Due to its complexity, potential users must undergo prolonged training. The even bigger challenge for IFC, however, is keeping up with the updates of building regulations or with the ever expanding state of the art in simulation tools. Our approach, SIMULTAN, in contrast to IFC, consist of 26 different basic types. They can be combined to increasingly complex models, which can themselves be used as types for other models. This enables each domain expert to create a custom data structure for any specific task, which is automatically compatible with the data structure of any other domain expert using the same basic types. It shortens the training time and facilitates the loss-, corruption-, and conflict-free exchange of information between domain experts, which is a key aspect of BIM. As a use case, we present the calculation of the U-Value of a multi-layered wall. We compare number, complexity and adequacy of the necessary data modelling steps in IFC4 and in SIMULTAN. The result shows that the flexible data model of SIMULTAN can be better adapted to the task. Another significant advantage of SIMULTAN is its inbuilt separation of responsibilities at the level of the most basic types, which, when combined with secure transaction technologies, can enable safe, effective and easily traceable interaction among stakeholders.

KEYWORDS

data model, BIM, information exchange, multidisciplinary

INTRODUCTION

The idea of the *Building Information Modeling (BIM)* is the consistent use of digital building models from planning to realization, from the operational phase to demolition. Already in the 70s, Eastman (1975) published a concept for the construction and the use of virtual building models. In 1992, van Needervan and Tolman (1992) first used the term BIM. One huge advantage of digital building models is the lossless information exchange. However, to ensure this exchange, the whole model must be interoperable, including all information such as climate data, usage information, variants, etc.

The interoperability of BIM models is present to varying degrees depending on the type of BIM. *Little BIM* refers to the use of a specific BIM software by a single planner. In this case, BIM is used without external communication (Jernigan, 2008). *Big BIM* refers to consistent model-based communication between all stakeholders involved in all phases of a building's

life cycle. In addition, a distinction is made between *closed* and *open BIM*, depending on whether vendor-neutral data exchange formats are used or not (Borrmann 2015).

An existing and already widely used standard for BIM is the Industry Foundation Classes (IFC) (buildingSMART, 2018) definition. The IFC models hold geometric data as well as metadata about building objects and are designed to support interoperability. Steel et al. (2012) investigate various issues of model-based interoperability in exchanging building information models between different tools, with particular focus on the use IFC. The authors pointed out that one of the greatest challenges with regard to interoperability is the inconsistency of modelling styles. The modeling language should clearly describe all possibilities so that unexpected alternatives are not possible. The authors Polit-Casillas and Howe (2013) also take up the issue of complex systems and the synchronization of different types of information. In their work, they combine BIM with a systems engineering approach to obtain a model based engineering approach. Thereby, they focus on the interoperability and validation of information in different planning phases, from requirements modelled in a modelling language such as the systems modeling language (SysML) to models drawn in, e.g., Computer Aided Design (CAD) tools.

In this paper, we move towards a big open BIM data model where the information is available at the level of detail at which it is required. This means that general information or information placeholders can be defined at the beginning of planning and later on be refined to become a realistic model that depicts the system behaviour. Our approach has the advantage that the complexity of the data model itself does not increase with the complexity of the represented buildings.

MOTIVATING EXAMPLE

Let us consider the case of a wall that consists of material layers and has a geometry, which sets an upper limit to its total thickness. The wall, the material layers and their respective materials have properties that are necessary for various calculations (e.g. of the U-Value). Fig. 1 displays an excerpt of the IFC4 data model (buildingSMART, 2013) in Universal Modelling Language (UML) notation (OMG, 2017) that enables the storage of that information. The coloured paths show all types and associations involved in establishing various relationships between objects. In the case of linking a wall with a property set we have just two objects that require the maintenance of 13 types and 3 associations (path 2 in Fig. 1). It must be taken into account that type and object are not synonyms. The distinction between a type *material* and an object *m1* of type *material*, for example, is as follows: The type *material* requires all objects conforming to it to have a text parameter *Name*. Object *m1* conforms to type *material* and therefore has a specific text value (e.g. *Wood*) associated with the parameter *Name*. In other words, the type can be regarded as a template for the creation of (an unlimited number of) objects and the associations between types – as information exchange contracts between the corresponding objects. Fig. 1 contains only types.

Our objective is to decrease complexity by minimizing the number of types and associations required for the production of any object.

MULTI-LEVEL DATA MODEL

The complete data model of IFC4 contains a total of 1167 type definitions and tens of thousands of associations among them (see Fig. 1). This data model has to be implemented and maintained in each software that manipulates IFC4 object models. Partial implementations carry the risk of loss of information across software boundaries.

PROOF OF CONCEPT

As demonstration case for our proof of concept, we use the calculation of the U-Value of a multi-layered wall according to EN ISO 6946:2017. As shown in Fig. 1, the association of a wall with a material in IFC4 involves 14 types and 5 associations. For the same purpose in SIMULTAN we need a component *wall* referencing a component *wall construction* (see path 1 in Fig. 1, Fig. 2 and Table 1). Table 1 summarizes the difference in complexity of the IFC4 and SIMULTAN data models and their limitations.

Table 1. Quantitative comparison between the IFC4 and the SIMULTAN data models.

Comparison Criteria	IFC4 Data Model	SIMULTAN Data Model
total no of type definitions	776 entities and 391 types, including 206 enumerations and 59 select types: 1167 in total	19 classes and 7 enumerations: 26 in total
total no of pre-defined parameter collections	408 property sets and 91 quantity sets: 499 in total (not contained in the formal IFC4 specification)	-
total no of user-defined parameter collections	unlimited	unlimited
total no of user-defined calculations	-	unlimited
min. no of types, objects and associations included in path 1	14 types, 2 objects, 5 associations	1 type, 2 objects, 1 association
min. no of types, objects and associations included in path 2	13 types, 2 objects, 3 associations	2 types, 2 objects, 1 association

For the U-Value calculation we now need the following parameters – the external and internal surface resistance R_{se} and R_{si} , and, for each homogenous material layer, the thickness d and the design thermal conductivity λ . In IFC4, this calculation requires the association of a material object with the property set *8.10.5.10 Pset_MaterialThermal*, containing a *ThermalConductivity* property in addition to *BoilingPoint*, *FreezingPoint* and *SpecificHeatCapacity*. The wall object also needs to be associated with *6.1.4.23 Pset_WallCommon*, containing a *ThermalTransmittance* property (according to the documentation, corresponding to the U-Value) in addition to 10 others (buildingSMART, 2013). The thickness of each material layer is a direct attribute of the type *IfcMaterialLayer* (see Fig.1). IFC4 has a type *IfcThermalResistanceMeasure* but no pre-defined property or quantity set containing a property corresponding to R_{se} or R_{si} , which necessitates the definition of a custom property set. In summary, in order to depict the calculation of the U-Value in IFC4, we need two pre-defined and one user-defined property set, we need to maintain 14 redundant entries in these property sets, and any calculation method using this structure has to read and write both to object values (material layer thickness, total wall thickness) and to parameter sets.

The SIMULTAN data model, on the other hand, allows the user to define exactly the parameters needed for the specified calculation, since additional parameters or calculations can be added later. One possible expression of such data structure can consist of the following: A component *wall construction* contains parameters R_{se} , R_{si} and *U-Value*. Each material layer is a sub-component of it, with parameters d and the thermal resistance of the layer R , references a component carrying the material properties, in this case only λ , and calculates R on its own. The component *wall construction* gathers the information from its

sub-components into its own calculation(s) and determines its own *U-Value*. In this way, SIMULTAN enables not just the efficient storage of information but also manages its flow.

CONCLUSION AND OUTLOOK

In order to be able to incorporate new methods and technologies data models need flexibility. IFC4 has already made the first step by decoupling data structure from data content. SIMULTAN takes the next step and introduces an adaptable data structure that can define any domain-specific ontology (e.g. building physics) in addition to the traditional numeric and textual parameters and can act as a universal translator. However, with a greater flexibility comes also a greater responsibility for the domain experts defining new data structures. Therefore, SIMULTAN incorporates an access tracking system (see *ComponentAccessProfile* in Fig. 2) as the mandatory equivalent of IFC4's *IfcActorResource*, where each component has an owner solely responsible for its development. Other actors (or stakeholders) can have supervision or publication rights. Thus, our data structure enables the stakeholders to view and modify all necessary information within their workflow. Applications using this data structure adapt to the user's workflow instead of forcing the user to adapt to the application. In a future development step, this system can be coupled with secure transaction technologies, such as BlockChains (Puthal et al. 2018), to provide a solid foundation for reliable and effective interactive work in real time.

ACKNOWLEDGEMENT

The Austrian Ministry for Transport, Innovation and Technology (bmvit) supported this work.

REFERENCES

- Borrmann A., König M., Koch C. and Beetz J. 2015. Building Information Modeling. Technologische Grundlagen und industrielle Praxis. Wiesbaden: Springer Vieweg.
- buildingSMART 2018. <http://www.buildingsmart-tech.org/specifications/ifc-overview>
- buildingSMART 2013. <http://www.buildingsmart-tech.org/specifications/ifc-releases/ifc4-release>
- Eastmann C. 1975. The Use of Computers Instead of Drawings. AIA Journal, Volume 63, Number 3, pp 46-50.
- Jernigan F. E. 2008. BIG BIM little bim - The practical approach to Building Information Modeling - Integrated practice done the right way! 2nd ed., 4 Site Press, Salisbury (MD), USA.
- Laakso M. and Kiviniemi A. 2012. The IFC Standard - A Review of History, Development, and Standardization. Information Technology in Construction, Volume 17, pp 134-161.
- Liu J. N. K., He Y. L., Lim E. H. Y. and Wang X. Z. 2013. A New Method for Knowledge and Information Management Domain Ontology Graph Model. IEEE Transactions on Systems, Man, and Cybernetics: Systems, Volume 43, Number 1, pp 115-127.
- OMG 2017. <https://www.omg.org/spec/UML>
- Polit-Casillas R. and Howe A.S. 2013. Virtual Construction of Space Habitats: Connecting Building Information Models (BIM) and SysML. In: *Proceedings of the AIAA Space 2013 Conference and Exposition*, San Diego, (AIAA 2013-5508).
- Puthal D., Malik N., Mohanty S. P., Kougianos E. and Yang C. 2018. The Blockchain as a Decentralized Security Framework. IEEE Consumer Electronics Magazine, Volume 7, Number 2, pp 18-21.
- Steel J., Drogemuller R. and Toth B. 2012. Model Interoperability in Building Information Modelling. *Software and Systems Modeling*, 11(1), 99-109.
- van Nederveen G. and Tolman F.P. 1992. Modelling multiple views on buildings. *Automation in Construction*, Volume 1, Number 3, pp 215-224.

BIM and Game Engine Integration for Operational Data Monitoring in Buildings

Yunjie Xiong*, Tanyel Bulbul and Georg Reichard¹

¹ Department of Building Construction, Virginia Tech, VA, US

**Corresponding email: yunjie8@vt.edu*

ABSTRACT

Building Information Modelling (BIM), as a new approach to the digital representation of the whole building lifecycle, including design, construction, building operation and maintenance, increases the efficiency and productivity of the architecture, engineering, and construction (AEC) industries. Because of complicated and comprehensive building information, BIM by itself is not able to provide an interactive visual environment for stakeholders and mobile access to the building information model is limited too. This paper aims to integrate BIM and 3D game engines to provide a real-time monitoring, mobile and interactive model. We've developed this building model as a serious game, capable of running on both Windows and IOS platforms. Players go through a virtual building, check enclosure materials, MEP systems, and real-time operating data in the game. A case study has been developed to show the benefits of integrating BIM and 3D game engines for modern building management.

KEYWORDS

BIM, Game Engine, Revit, Database

INTRODUCTION

Building Information Modelling (BIM) is “a new approach to design, construction, and facilities management, in which a digital representation of the building process is used to facilitate the exchange and interoperability of information in digital format” (Eastman, Teicholz, Sacks, & Liston, 2011). A building information model supports all digital building information, such as geometry data, MEP data, and real-time monitoring data.

Building geometry information enables architectural visualization, which is one of the important areas in current Virtual Reality (VR) research into the AEC area. Many BIM tools provide basic architectural visual functions for building design and construction but lack an interactive building environment for users. 3D game engines, however, are considered to provide a real-time, interactive visualization, using first or third person perspectives (Kumar, Hedrick, Wiacek, & Messner, 2011; Yan, Culp, & Graf, 2011). The main area of research into the integration of BIM and 3D game engines involves implementing a real-time and interactive architectural visualization for various goals, such as design review, construction management, fire simulation, construction safety, training and education, etc. Yan and Culp developed a 3D game with BIM to support an innovative Design-Play review in which designers can play their own designed environments and run a simulation of user activities and physical dynamics. Kumar and Hedrick developed a 3D game for reviewing a scenario-based design approach for healthcare facilities. Olofsson and Lee conducted research and found that using BIM/VDC tools saved 20-30% of the labour cost involved in the coordination of MEP systems (Olofsson, Lee, Eastman, & Reed, 2007). A 3D web-based game environment based on a hospital BIM model was developed for the virtual on-site visiting of building HVAC systems. It was then later implemented on an IOS mobile platform later (Shen, Jiang, Grosskopf, & Berryman, 2012). Edwards developed a two-way data transferring channel between BIM and game engines for structural design (Edwards, Li, &

Wang, 2015). A 3D game environment of an existing whole-building HVAC system was developed to enable students to interactively visualize and operate typical HVAC systems on computer monitors (Nandam, 2015). Furthermore, game engines could utilize networking features that enable real-time data exchange for potential data management. A game engine with a query interface connected an architectural semantic web to support calculations and simulations for the design stage (Pauwels, De Meyer, & Van Campenhout, 2011).

METHODS

The aim of the research is to seek a possible BIM and 3D game engine integration to support the building visualization and the actual building operation process. A framework of a BIM and a 3D game engine integration with an online database was developed, and a small-scale case study was implemented to validate the framework and investigate its potential to assist architectural visualizations and support the building operation processes.

Framework

A general framework encompassing a BIM, a game engine and a database was developed, demonstrated in Figure 1. Building information from the BIM model was exported into the game engine. Then, a virtual building with the necessary game functions was developed using the 3D game engine to develop an interactive and virtual serious game. Real-time sensor data are collected onsite and uploaded onto the online database for data management. The game engine connects to the online database to show these sensor data and their sensor location on the virtual building in real time.

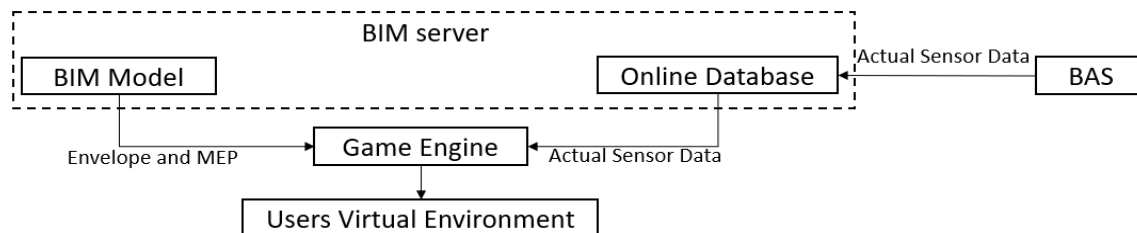


Figure 1. Framework of the Integrated Platform

Case study

The case study named ‘Classroom Building’ is a three-story, 73,275-square-foot building located on Virginia Tech’s north campus in Blacksburg, VA. It includes study rooms, group spaces, an auditorium, and laboratories for about 1500 students.

The BIM and game engine integration and its networking features were tested in this case study. Autodesk Revit was used to develop a building information model. Figure 2 shows the actual building and the Revit model. The game engine Unity 3D was used to create the 3D game. Unity 3D provides a visual editor, full and robust scripting and an animation system, and supports multiple platforms, therefore fulfilling the requirements of developing simple game functions and easily running the game on multiple platforms (Unity3D, 2005). The Revit model is exported as an .FBX file and Unity 3D imports these .FBX files to develop assets in the game. The .FBX file is complex because it contains all detailed building components. To reduce the file size, we split the Revit models (Architectural and MEP models) into different parts, e.g. Arch_1st floor, which is the first level of architectural model. 3Ds Max is applied to optimize the original .FBX file and reduce the number of polygons of the model. For example, the number of polygons of the original Arch_1st floor.FBX in 3Ds Max was 902,667. 3Ds Max can reduce about 30% of the number of polygons while keeping

a satisfiable performance. Simple textures were added to the assets in the Unity 3D engine to save the system resources. Room temperature data measured by sensors were uploaded onto a MySQL server and saved manually. Unity 3D provides a scripting API to connect the MySQL server and generate form data. Figure 3 shows the process and method of exchanging building information among the BIM, online database and game engine.



Figure 2. Classroom Building. a) Real project, b) Revit model.

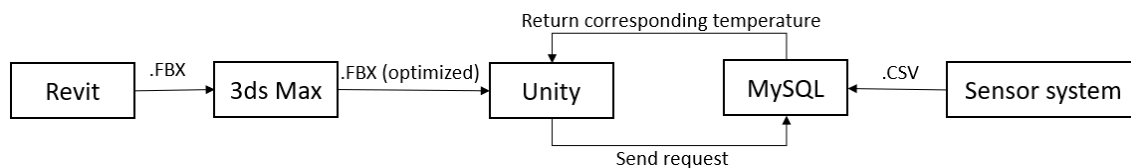


Figure 3. Flowchart: BIM Tools/Systems to Game Engine

The basic functions of the serious game are to visualize the architecture and MEP systems and connect to the online database for better building management. Therefore, the whole virtual Classroom Building, including architecture and HVAC systems, were created in Unity 3D. Figure 4 shows the building envelope and HVAC system model in Unity. Related game functions were developed to help the players understand the building materials and MEP systems. In addition, a link between the online database and the virtual building was developed for checking real-time operational data in the virtual building.

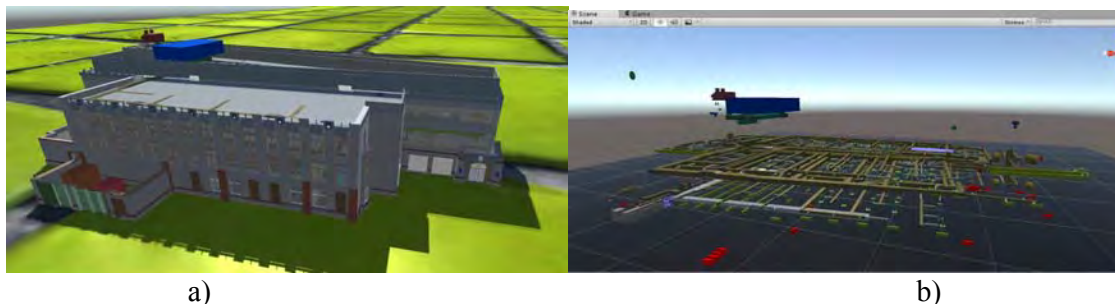


Figure 4. Unity 3D Model. a) Building envelope, b) HVAC system.

Table 1 shows the basic functions of this game. The players walk through and around the whole virtual building, identify the function of HVAC ducts or building envelope materials,

connect to the online database and get the current sensor reading of the room temperature. A mini map helps the player to find their location in the building. For the mobile version, we plan to add location function. When the players come into the actual building, their location will automatically be read and shown in the game to enable accurate loading of the surrounding environment. This function which is currently under development, will help players compare the actual building and the virtual building in a simple way.

Table 1. Game Functions

Function	Game Controls	Comments
Walk through/Mini Map	WASD keys	Navigating inside building
Building envelope	Click the related elements	Show building envelope material
MEP system	Click the related elements/ F1 turn off the Building envelope	Show HVAC system
Identify location(ongoing)	-	Identify user's Location
Sensor data show	Click the Virtual Sensor	Return on-site temperature data
Multiply Platform	-	Windows and IOS

RESULTS

A virtual building was developed on the Unity 3D platform. Players can walk around and enter the building to check the whole interior space. Figure 5 shows the indoor environment. The player can see the interior space and HVAC ducts from a third person perspective. A mini map was developed to locate the players position in the building. The building envelope and MEP system were imported. When clicking on a building component, such as an interior wall or a duct, the related component information was shown. It is like a virtual tour of the actual building. System components that have a similar function are the same colour, e.g. all equipment used for exhausting air is dark red.

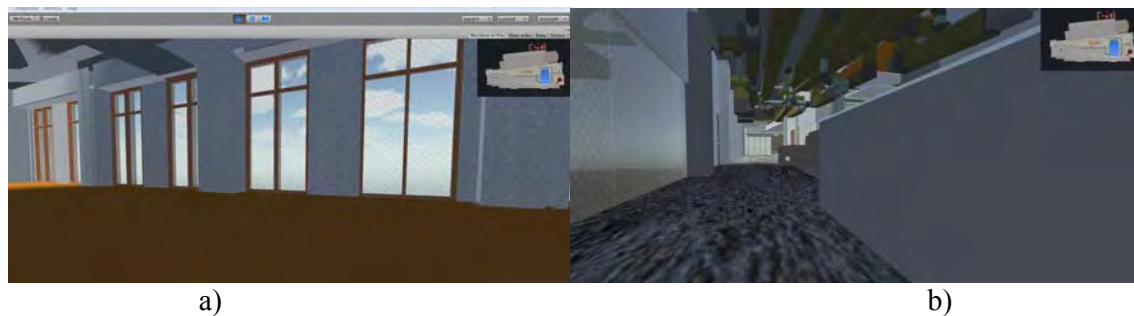


Figure 5. Third person Perspectives. a) Interior space, b) HVAC system.

The player can click on a building element to check the related material or MEP information. Figure 6a shows how, when the player clicks on an interior wall, the game shows the element information as “Basic wall” and its structural information from the Revit model. Temperature data were collected and uploaded onto a local MySQL server. Every room has a special table to save the time and temperature data in the online database. By clicking on the “Temp” button, the game sends the current player’s location as a room number and current time to the database, and then gets the related temperature data from the database. Figure 6b shows the process.



Figure 6. Game Function. a) Material Information, b) Read Temperature.

The whole game was initially run on a Windows platform and was then moved onto an IOS platform in test mode. For the windows platform, the computer configuration is shown in Table 2. The FPS in game is about 30 FPS which is an average speed for RPG.

Table 2. Computer Configuration

Type	Exposed
Operating System	Windows 10
Processor	Intel(R) Core(TM) i7-6700HQ
Video	NVIDIA GeForce GTX 970M with 3GB GDDR5
Memory	32 GB DDR4 2133MHz
Resolution	1920 x1080

The new identify location function will be added for the mobile version. The players can scan the Quick Response (QR) code using the mobile device in the real building and load their actual location (e.g. classroom or lobby) with the surrounding virtual environment in the game automatically. This function should help the players compare the virtual building to the real building, gain a better understanding of the real building and can be used as an educational tool embedded into course work such assignments.

DISCUSSIONS

Building information models remain a challenge for a 3D game engine. When importing the BIM model into the 3D game engine, all building components will be imported as numerous detailed objects, which is unusual for a common commercial game. Even with only basic functions, the high quality of architectural visualization consumes a huge amount of system resources. However, considering the wide application of portable devices during building construction and management, the virtual building game should support portable devices.

The case study works as a small-scale project without high resolution architectural details and complex gaming functions. More available and efficient methods of optimizing the building product model and importing it into 3D game engines with reasonable architectural details should be considered, as all unnecessary details will have an impact on game performance. The case study has shown that a virtual game can get on-site sensor data. The main challenge in this case was that the real building operation process is complex and numerous sensors work all day and produce a huge data set. It is possible to develop a series of special game functions to work as a basic data management tool, which helps the building managers' routine work, e.g. selecting a series of temperature values within a time range. This means the game developer should have a deep understanding of the game's goal and develop special functions to fulfil the user requirements. In this case study, the sensor data were directly uploaded onto an online database from the data logger, but the BIM can represent the sensor

information. To simplify the whole process, it would be possible to use a BIM server connected to a 3D game engine and the on-site building automation system, and to save and exchange all the BIM related data based on this server, but the research related to making this a reality is currently very limited.

CONCLUSIONS

This paper provides a framework for integrating BIM and game engines and uses a case study to identify the benefits. The research shows that it is possible to utilize the benefits of both BIM and game engines to create an interactive and virtual building, which can return on-site sensor data from the online database for modern visual and interactive building operation management. A more advanced game could help building managers understand their buildings more intuitively. The data exchange process between BIM tools and game engines work, but the main challenge are the geometric complexities in architectural models and the building scale involved. The prototype game can achieve real-time data, but it is still a very early attempt at using the game to manage a multitude of building operation data.

Future work includes the optimization of network connections for huge amounts of data and the development of proper functions to match the virtual sensors in the building and sensor data from the online database. We envision this virtual building game to help building managers to check on-site indoor air conditioners more visually and conveniently. Furthermore, augmented reality (AR) equipment could probably be applied to this virtual building game as a building management tool. Another typical benefit is that we can use the virtual building in AR and go to the real building to verify if the actual construction matches the design in the virtual building.

REFERENCES

- Eastman, C., Teicholz, P., Sacks, R., & Liston, K. (2011). *BIM handbook: A guide to building information modeling for owners, managers, designers, engineers and contractors*: John Wiley & Sons.
- Edwards, G., Li, H., & Wang, B. (2015). BIM based collaborative and interactive design process using computer game engine for general end-users. *Visualization in Engineering*, 3(1), 4.
- Kumar, S., Hedrick, M., Wiacek, C., & Messner, J. I. (2011). Developing an experienced-based design review application for healthcare facilities using a 3D game engine. *Journal of Information Technology in Construction (ITcon)*, 16(6), 85-104.
- Nandam, L. D. (2015). Evaluate Students' Learning Effectiveness of HVAC System Using 3D Game Animation.
- Olofsson, T., Lee, G., Eastman, C., & Reed, D. (2007). Benefits and lessons learned of implementing building virtual design and construction (VDC) technologies for coordination of mechanical, electrical, and plumbing.
- Pauwels, P., De Meyer, R., & Van Campenhout, J. (2011). Linking a game engine environment to architectural information on the semantic web. *Journal of Civil Engineering and Architecture*, 5(9).
- Shen, Z., Jiang, L., Grosskopf, K., & Berryman, C. (2012). *Creating 3D web-based game environment using BIM models for virtual on-site visiting of building HVAC systems*. Paper presented at the Construction Research Congress 2012: Construction Challenges in a Flat World.
- Unity3D. (2005). Retrieved from <https://unity3d.com/>
- Yan, W., Culp, C., & Graf, R. (2011). Integrating BIM and gaming for real-time interactive architectural visualization. *Automation in Construction*, 20(4), 446-458.

Cross-platform, Public Domain Simulation Tools for Performing Parametric IAQ and Energy Analysis

W. Stuart Dols^{1,*} and Lindsay J. Underhill²

¹National Institute of Standards and Technology, Gaithersburg, MD, U.S.A.

²Boston University School of Public Health, Boston, MA, U.S.A.

*Corresponding email: stuart.dols@nist.gov

ABSTRACT: As building design is being driven towards lower energy use, the relationship between indoor air quality (IAQ) and energy becomes more important due in large part to reduced building envelope leakage, which can lead to higher indoor pollutant levels. Simulation tools that can analyze building design measures that aim to improve IAQ and energy use are necessary for evaluating potential trade-offs involving such measures. This paper will present the use of CONTAM and EnergyPlus, coupled using co-simulation, to perform parametric analysis of IAQ and energy impacts. Both of these tools are available in the public domain and provide cross-platform methods to evaluate both IAQ and energy use. Applications and workflow using these tools and available building models will be presented, including various energy and IAQ related measures that can be addressed with them. In particular, we present a framework for addressing energy measures (envelope tightening, insulation, and mechanical ventilation) and IAQ-related parameters (indoor/outdoor sources, ventilation rate, and filtration) in multi-family housing and effects on occupant exposure via a cohesive simulation environment that minimizes inter-domain coupling issues.

KEYWORDS

CONTAM, co-simulation, energy, EnergyPlus, indoor air quality, whole building simulation

INTRODUCTION

Building energy and indoor air quality (IAQ) are intertwined due to the interdependence of heat transfer, airflow, and contaminant transport. Often the same mechanical systems are utilized to maintain the thermal properties of air, e.g. temperature and relative humidity, and to dilute and/or remove pollutants that exist in the indoor environment, e.g., via outdoor air ventilation and filtration. As such, tools are needed to simulate these transport phenomena and associated systems to enable consideration of the interactions of these domains that are important to the health and comfort of building occupants. These tools will support the design and economic considerations of various stakeholders in the building community, including community planners, standards developers, designers and equipment manufacturers.

As highlighted by [Teichman et al. \(2015\)](#), activities related to design and construction of high-performance buildings (HPB) tend to focus heavily on energy-related concerns, and IAQ is often not addressed in a comprehensive and consistent manner. This is also borne out in the common use of building energy simulation, but not IAQ, in HPB design and analysis. However, recent activities by those evaluating HPBs from an IAQ perspective are bringing to bear building simulation methods that address both the energy and IAQ.

Building simulation is often employed to evaluate the impact of various building properties on building performance metrics ([Azimi et al., 2016](#); [M. P. Fabian et al., 2016](#)). For example, improving building envelope airtightness can affect energy use, indoor contaminant concentrations, and occupant exposure. The ability to evaluate the myriad building types;

heating, ventilating, air-conditioning (HVAC) systems; and climate zones, can provide information to those making decisions related to community-level energy use and contaminant exposure ([Levy et al., 2016](#)). To this end, two widely-used, public domain software tools, CONTAM and EnergyPlus, have been coupled to enable more complete evaluations of building performance ([Dols et al., 2016](#)). On their own, each tool is limited in its ability to account for transport processes upon which building IAQ, airflow and energy may be dependent.

EnergyPlus is a whole building energy simulation program with multizone heat balance as its underlying calculation method. EnergyPlus determines zone thermal loads and the energy used by HVAC systems to meet those loads. It calculates zone air temperatures based on current system and plant capacity, including system airflow rates. Generally, infiltration and interzone airflows are user-specified, i.e., not pressure-dependent as in CONTAM, and are not required to be in balance with system airflow rates. Typically, infiltration is modelled based on correlations associated with rectangular, low-rise residential buildings or may be assumed to be constant, but better methods are available ([Lisa C. Ng et al., 2018](#)).

CONTAM predicts airflows, contaminant concentrations, and airborne occupant exposures in multizone representations of whole buildings. In this paper, CONTAM will be used to assess IAQ while estimating infiltration airflows that impact building energy use. The CONTAM mass transport model treats a building as a system of interdependent zones or nodes (e.g., rooms, plenums and duct junctions) that store air and contaminant mass, and airflow paths (e.g., openings, cracks and duct segments) that transport air and contaminants between the nodes. Interzone airflows (including flows between the indoors and outdoors) are determined by calculating the node pressures that satisfy mass balance in each node based on driving forces and boundary conditions that include HVAC system airflows as well as wind and stack pressures exerted on the building envelope. CONTAM does not implement heat transfer calculations, so it requires indoor temperatures as inputs, which are often assumed to be ideally met thermostatic set-points.

The fact that CONTAM, when utilized on its own, requires the user to input zone temperature schedules, makes co-simulation with EnergyPlus an improved analysis approach. This is especially important for those who require analysis of both IAQ and energy related building performance.

METHODS

The National Institute of Standards and Technology (NIST) has been working with the Boston University School of Public Health to utilize co-simulation between CONTAM and EnergyPlus to evaluate the impact of energy retrofit programs in multi-family apartment buildings on energy savings and occupant exposure. Co-simulation is being used to evaluate multiple types of building energy retrofits, contaminant sources, and building ventilation systems.

Building Model Overview

The focus of the work to date has been on a four-story, mid-rise apartment building in Boston, Massachusetts. The Mid-Rise Apartment building model is based on the EnergyPlus representation selected from the set of U.S. Department of Energy (DOE) Commercial Reference Building models developed by the National Renewable Energy Laboratory (NREL). NIST developed a corresponding CONTAM representation of this building ([Lisa C Ng et al., 2012](#)) to be compatible with the co-simulation approach outlined in [Dols et al. \(2016\)](#). Both models were modified to include stair and elevator shafts that enable simulation of stack flows that can be particularly important to infiltration, energy use and contaminant transport in multi-story buildings.

The base building model, shown in Figure 1, consists of eight apartments on each floor separated by a central hallway with a stair and elevator shaft located at opposite ends of the hallway. Each apartment is served by a dedicated unitary HVAC system with a direct expansion cooling coil, a natural gas heating coil, and a constant volume supply fan. Each apartment is served by a dedicated exhaust system that is scheduled according to the ventilation system type: infiltration only, balanced outdoor air intake, or continuous exhaust ventilation.

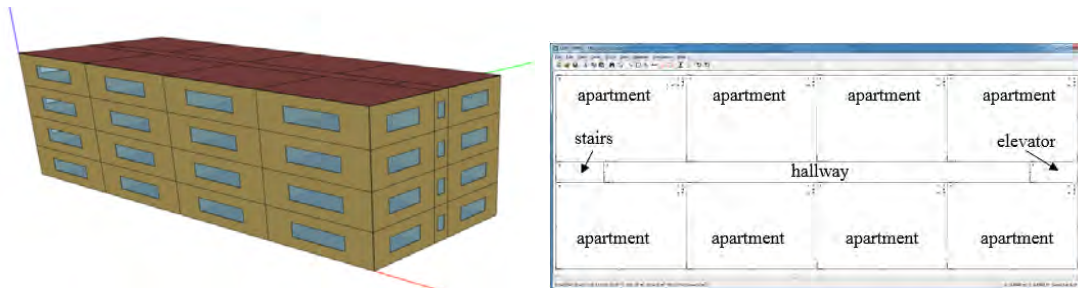


Figure 1. Mid-rise Apartment Building geometry (left) and floor plan in CONTAM (right)

Simulation Tools Development

The EnergyPlus/CONTAM co-simulation capabilities were previously developed as described in [Dols et al. \(2016\)](#). Coupling was implemented based on the Functional Mock-up Interface (FMI) for Co-Simulation specification according to which EnergyPlus was modified to enable the control of coupled simulations ([Nouidui et al., 2013](#)). However, the CONTAM co-simulation capability was originally implemented to execute only within the Windows operating system. To run a large set of parametric simulations, we required that the co-simulation capability be ported for execution on a high-performance, Linux cluster maintained by Boston University. EnergyPlus and the CONTAM simulation engine (ContamX) were already Linux compatible, so it was necessary to port the component that facilitates the FMI capability between EnergyPlus and CONTAM referred to as the ContamFMU dynamic link library (DLL). Modifications were made to enable the same source code to be used to build the Windows DLL (ContamFMU.dll) and the Linux equivalent referred to as a *shared object* (ContamFMU.so). Modifications were also required to address the methods used to spawn the ContamX process and enable socket communications to perform within the Linux, multi-core processing environment.

Simulation Setup

The simulation process and associated input files are illustrated in Figure 2. Base building models (template files) were developed for both EnergyPlus (IDF file) and CONTAM (PRJ file). Each of these templates was modified using a text editor to flag relevant values for replacement via a *Factorial Generator Tool* that reads both the flagged input file and a variable parameter file (*PRJ Parameters* and *IDF Parameters*) to create a full set of simulation input files. For the purposes of this demonstration case, Table 1 presents the set of parameters that were varied for a total of 810 simulations. However, these methods can be applied in an almost limitless number of combinations.

The IDF files and PRJ files were generated by the *Factorial Generator Tool* prior to simulation. Scripts were then used to submit jobs to the process manager on the Linux cluster, after packaging files together as required for execution by EnergyPlus using co-simulation. The script then called EnergyPlus and CONTAM post-processing software (ReadVarsESO and simread3, respectively) to glean data from results files for further statistical evaluation.

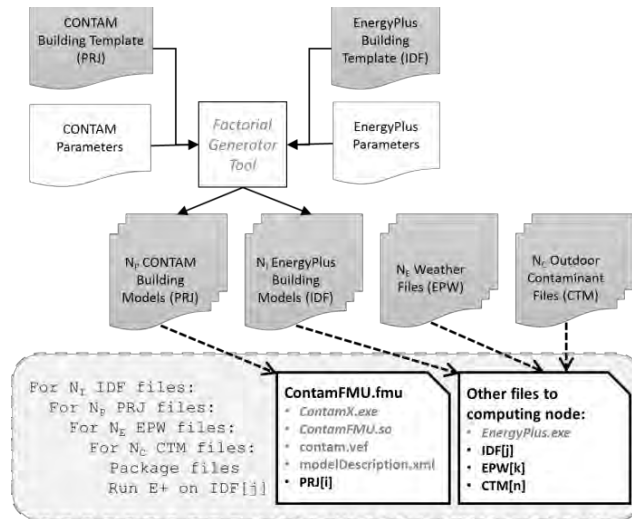


Figure 2. Schematic of parametric simulation process. N_P , N_I , N_E and N_C indicate number of respective file types: CONTAM building model (PRJ), EnergyPlus building model (IDF), weather (EPW), and outdoor contaminants (CTM).

Table 1. Set of Values for Parametric Simulations

Program	Parameter	Values
EnergyPlus (IDF file)	Ventilation Type	Infiltration only, Balanced supply, Exhaust
	Insulation (Walls/Roof)	R12/R13, R16/R30, R21/R35
CONTAM (PRJ file)	Envelope Leakage Rate ($L/s \cdot m^2$ @75 Pa, exponent 0.65)	10.19, 5.42, 1.25
	Cooking Source	None, Low Cooking, High Cooking, Low Cooking w/ Local Exhaust, High Cooking w/ Local Exhaust
	Smoking Source	Non-Smoking, Smoking
	Filtration - Minimum Efficiency Reporting Value (MERV)	4, 8, 12

RESULTS

Results presented here are based on simulations performed using Boston, MA weather and outdoor $PM_{2.5}$ data as described in [P. Fabian et al. \(2012\)](#), i.e., EnergyPlus weather (EPW) and CONTAM contaminant (CTM) files respectively. Detailed analysis of these results will be presented in future publications, but we present a subset of results to demonstrate the capabilities. The first case is a building with indoor particle sources of high-cooking activity and smoking, and outdoor particles, an indoor formaldehyde source, a MERV 4 filter in each air handler, and a relatively leaky building envelope. The second case is the same building with no indoor particle sources, MERV 12 filters, and a relatively tight building envelope. Each case was modelled with three types of ventilation systems: infiltration only, exhaust only, and balanced outdoor air. Figure 3 presents box-whisker data generated by CONTAM and show the average (line inside the boxes), standard deviation, and maximum and minimum air change rates and energy use (Figure 3a) and concentrations averaged across all occupied zones (Figure 3b).

Figure 3a shows whole-building air change rates and total annual energy use. In terms of energy use, all the buildings have the same insulation levels, so they only differ by envelope leakage and ventilation system type. As shown in Figure 3a, the tighter buildings have reduced infiltration rates and lower total energy use for the respective ventilation systems.

Figure 3b shows indoor particle concentrations (grey boxes) and formaldehyde concentrations (yellow boxes). As expected, there are significant differences between indoor particle levels

when source control and filtration are implemented. However, the indoor formaldehyde source leads to elevated concentrations in the tighter buildings especially when no mechanical ventilation is provided. Conversely, from the perspective of improving IAQ, increasing dilution by ventilation may reduce contaminant levels of indoor sources but could lead to increased levels of outdoor pollutants and increased energy use. This is demonstrated in the second case, which shows that exhaust only ventilation, when compared to infiltration only, has lower formaldehyde concentrations but slightly higher particle concentrations due to particles being drawn in through the building envelope, along with a higher total annual energy use. These examples highlight the need for an integrated approach to building design and analysis ([ASHRAE, 2017](#)).

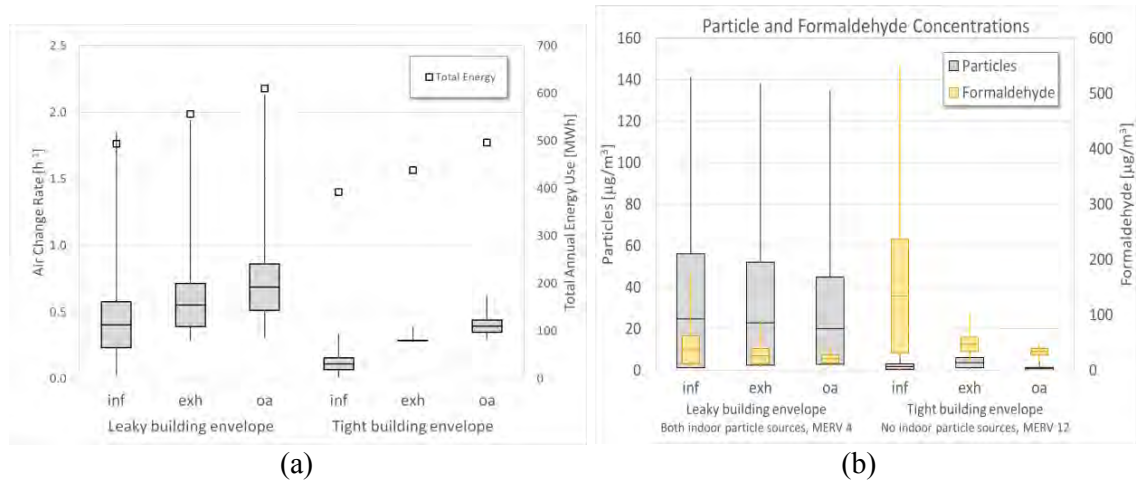


Figure 3. (a) Simulated whole building air change rates and total energy use of a Mid-rise Apartment Building with relatively leaky and tight building envelopes and three different ventilation systems: infiltration only (inf), exhaust only (exh), and balance outdoor air (oa). (b) Simulated particle and formaldehyde concentrations averaged over all occupied zones of a Mid-rise Apartment Building for two cases of envelope air-tightness and source emissions scenarios with same three ventilation systems.

CONCLUSIONS

Co-simulation between whole-building IAQ, airflow, and energy simulation programs provides a comprehensive tool to evaluate the interactions between IAQ and energy when considering building energy retrofits. This paper highlighted the development and application of cross-platform, parametric simulation tools that provide the foundation to an integrated approach to building design and analysis to address energy and IAQ. The benefits of this integrated approach were demonstrated with an example from a case study carried out by Boston University and NIST. This example showed the interactions between building energy measures and IAQ parameters and their effects on whole-building energy use and occupant exposures, including reduced energy levels from envelope tightening and occupant exposure commensurate with source location and ventilation.

While these tools and parametric analysis methods are useful in their current state, there is also much work to be done to explore and improve them. For example, the coordination of CONTAM and EnergyPlus models is critical to success, and current methods rely on detailed knowledge of both simulation tools. Tools and associated workflows are available to minimize the redundancy and errors associated with coordinating the building representations, but modifications of existing building models can be quite cumbersome. Therefore, one of the goals of this work is to develop a set of coupled building models to be made publicly available. Output

of the simulation tools can be voluminous and difficult to manage. However, they can also provide much greater insight into the interaction among the input parameters and building performance metrics than was presented herein. Work could also be done to provide outputs of desired metrics either directly or by enabling output to be easily manipulated by data processing utilities or scripts.

ACKNOWLEDGEMENTS

The authors would like to thank Charles A. Jahnke of Boston University (BU) for his invaluable assistance in setting up the simulation platform on the BU shared computing cluster.

DISCLAIMER

Certain trade names and company products are mentioned in the text or identified in an illustration in order to adequately specify the equipment used. In no case does such an identification imply recommendation or endorsement by the National Institute of Standards and Technology, nor does it imply that the products are necessarily the best available for the purpose.

REFERENCES

- ASHRAE. (2017). *ASHRAE Position Document on Indoor Air Quality*. Atlanta, GA.
- Azimi, P., Zhao, D., & Stephens, B. (2016). Modeling the impact of residential HVAC filtration on indoor particles of outdoor origin (RP-1691). *Science and Technology for the Built Environment*, 1-32. doi:10.1080/23744731.2016.1163239
- Dols, W. S., Emmerich, S. J., & Polidoro, B. J. (2016). Coupling the Multizone Airflow and Contaminant Transport Software CONTAM with EnergyPlus using Co-simulation. *Building Simulation*, 9, 469-479. doi:10.1007/s12273-016-0279-2
- Fabian, M. P., Lee, S. K., Underhill, L. J., Vermeer, K., Adamkiewicz, G., & Levy, J. I. (2016). Modeling Environmental Tobacco Smoke (ETS) Infiltration in Low-Income Multifamily Housing before and after Building Energy Retrofits. *International journal of environmental research and public health*, 13(3), 327.
- Fabian, P., Adamkiewicz, G., & Levy, J. I. (2012). Simulating indoor concentrations of NO₂ and PM_{2.5} in multifamily housing for use in health-based intervention modeling. *Indoor Air*, 22(1), 12-23.
- Levy, J. I., Woo, M. K., & Tambouret, Y. (2016). Energy savings and emissions reductions associated with increased insulation for new homes in the United States. *Building and Environment*, 96, 72-79. doi:10.1016/j.buildenv.2015.11.008
- Ng, L. C., Musser, A., Persily, A. K., & Emmerich, S. J. (2012). *Airflow and Indoor Air Quality Models of DOE Reference Commercial Buildings* (NIST Technical Note 1734). Retrieved from Gaithersburg, MD:
- Ng, L. C., Ojeda Quiles, N., Dols, W. S., & Emmerich, S. J. (2018). Weather correlations to calculate infiltration rates for U. S. commercial building energy models. *Building and Environment*, 127(Supplement C), 47-57. doi:<https://doi.org/10.1016/j.buildenv.2017.10.029>
- Nouidui, T., Wetter, M., & Zuo, W. (2013). Functional mock-up unit for co-simulation import in EnergyPlus. *Journal of Building Performance Simulation*, 7(3), 192-202. doi:10.1080/19401493.2013.808265
- Teichman, K. Y., Persily, A. K., & Emmerich, S. J. (2015). Indoor air quality in high-performing building case studies: Got data? *Science and Technology for the Built Environment*, 21(1), 91-98. doi:10.1080/10789669.2014.976509

Optimization of four-primary white LEDs based on protective effect and color quality-a solution for museum illumination

Rui Dang^{1,*}, Nan Wang, Gang Liu^{2,*} and Huijiao Tan

School of Architecture, Tianjin University, Tianjin Key Laboratory of Architectural Physics and Environmental Technology, Tianjin, 300072.

^{1*}*Corresponding email: dr_tju@163.com*

^{2*}*Corresponding email: LGLGMIKE@163.com*

ABSTRACT

A solution was proposed for obtaining white light-emitting-diodes (LEDs) which are suitable for illuminating traditional Chinese paintings painted with inorganic pigments (iop-TCPs) based on the requirements of protective illumination and color quality. The damage laws and degrees of 450nm, 510nm, 583nm, and 650nm monochromatic lights which can construct four-primary white LEDs on the iop-TCPs were obtained through long-term illumination experiment and data analysis by converting color coordinates into CIE DE2000 color difference values. Then we obtained the damage formula of the constructed white LEDs, which can be used to evaluate damage degree. Spectral power distributions (SPDs) of the white LEDs, which can be iterated by brute-force algorithm, were simulated by the Gaussian formula. Constructed SPDs were evaluated by the damage formula and color quality formulas. The color quality eligible white LEDs with higher correlated color temperatures (CCTs) damage less to iop-TCPs. And the lowest damage SPDs satisfying color quality requirements in CCT ranges from 2700K to 4000K were obtained. Achievements can provide the theory and application basis for manufacturing white LEDs suitable for illuminating iop-TCPs; and the method can be further used in preparing white LEDs applicable to other cultural relics.

KEYWORDS

Inorganic pigments; protective illumination; color quality; white LEDs; spectral optimization.

INTRODUCTION

Numerous traditional Chinese paintings (TCPs) in museum suffer irreversible damage in various degrees. Among all the influencing factors, illumination cannot be eliminated for the need of visual effect (Dang et al. 2013). And the TCPs were classified as high responsivity to light by a technical report (CIE, 2004) and code (CNSA, 2009). Thus, the protective effect must be considered in museum illumination. Meanwhile, color quality is also an important element because exhibit paintings is a crucial function of the museum. Accordingly, it is urgent to develop museum light sources meeting both the need of the protective illumination and visual effect. The existing traditional Chinese paintings painted with inorganic pigments (iop-TCPs) are old and delicate. Therefore, we aim at solving the museum illumination problems for iop-TCPs which mainly contain natural mineral material made and easy fading, discoloration, color vanishing pigments-ancient graphite, clam shell powder, azurite, cinnabar, and orpiment-based on protective effect and color quality (Wu, 2011).

White LEDs which feature spectrum adjustable (Schubert and Kim, 2005), no infrared and ultraviolet radiation have the potential to form the desired light sources in museum. First, exhibits suffer seriously damage by infrared and ultraviolet radiation. Second, by adjusting the SPDs of the white LEDs, different wishes are made realizable to accomplish optimization

(Lin et al. 2017). At present, SPDs of the white LEDs satisfying the prerequisites of color quality mostly contain primary of red, yellow, green, and blue (Oh et al. 2012, 2014), namely red/yellow/green/blue (RYGB) four-primary white LEDs. Thus, we choose 450nm, 510nm, 583nm, 650nm waveband monochromatic lights as the deputies of the blue, green, yellow, and red monochromatic lights to construct the desired light sources by framing and evaluating the corresponding SPDs. Some researches explored for the influence of visible radiation on paintings, silks and so on (Farke et al. 2016). However, for our purpose to appraise the damage degree of the RYGB type white LEDs, it is indispensable to quantify the various influence of the corresponding monochromatic lights on the iop-TCPs.

It has been a prevalence to simulate SPDs by Gaussian distribution and iterate SPDs for evaluating figures of merit like the color quality, visual performance, circadian effect by algorithms (Wu et al. 2016). Among them, brute-force method which can cycle all the conditions in given ranges and steps provides accurate iterative results (Robinson et al. 2018).

Herein, we conducted a long-term experiment illuminating specimens of the iop-TCPs by the four monochromatic lights, test color parameters of specimens periodically, and calculated CIE DE2000 color differences; then we obtained relative color damage values of the monochromatic lights through data analysis, and based on which we deduced the relative color damage formula of the corresponding four-primary white LEDs to the iop-TCPs. In addition, we optimized the SPDs of the white LEDs by evaluating simulated spectra based on the obtained damage formula and the formulas about color quality parameters-color rendering index R_a and R_9 (CIE,1995; Hayashida et al. 2017), correlated color temperature (CCT), the distance from the Planckian locus (Duv) (Ohno, 2013).

METHODS

Models of specimens and experimental light sources

One of four groups of the iop-TCPs specimens (Dang et al. 2017), is shown in Figure 1a. And four monochromatic lights with the peak wavelengths of 450nm, 510nm, 583nm, and 650nm were produced by museum tungsten halogen lamp cooperating with infrared cut-off filters and 20 nm narrow band-pass filters. The irradiance of each light source was kept the same and constant during the long-term experiment, spectra are illustrated in Figure 1b.

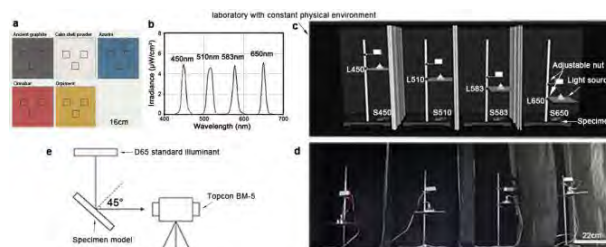


Figure 1. (a) One of four specimen illuminated by light sources. (b) Irradiance distribution of four monochromatic lights on the surface of the specimens. (c) Model of the experimental device, L represents the monochromatic light source, S represents specimen. (d) The realistic experimental device. (e) Diagrammatic sketch of the test environment.

Experimental methodology

The long-term illumination experiment was conducted in the Optical Laboratory. Detail has been depicted by Dang (2017). The experimental scheme is illustrated in Figure 1c-d.

Test of the parameters

After each cycle of illumination, the specimens were moved under the D65 standard light source; and color parameters of the specimens were measured by the standard color test method of CIE (1999), method shows as Figure 1e. The CIE LAB chromaticity coordinates (a^* , b^*) and metric brightness value L^* of four specimens were measured before and each cycle after the illumination, at test points marked in Figure 1b, achieved by Luminance Colorimeter. Color parameters of one pigment in one specimen were determined by the average value of the three test points to minimize the measurement error. Color differences of the five pigments were calculated using the CIE DE2000 formula (Farke et al. 2016).

RESULTS

Changing curves of CIE DE2000 color differences

The damage law and the influence degree of different light sources can be seen in figure 2. We conclude from the figure that monochromatic lights with various peak wavelength impact at different degrees on pigments with distinct colors. It also implies that the monochromatic lights differently affect the iop-TCPs.

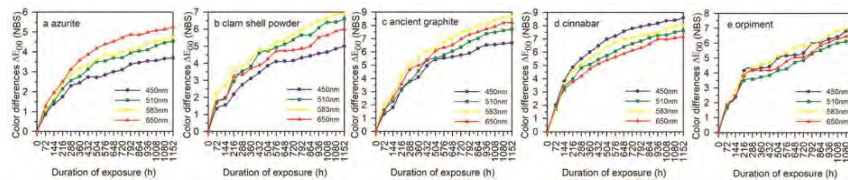


Figure 2. The changing curve of CIE DE2000 color differences of pigments (a) Azurite, (b) Clam shell powder, (c) Ancient graphite, (d) Cinnabar, and (e) Orpiment.

Relative damage values of the monochromatic lights

To express the relative damage of different monochromatic lights to the iop-TCPs whose color can be basically represented by the five pigments, the average damage value of the 450nm light to the five pigments is defined as 1.00, to which other values are normalized, detail is given in Table 1. Accordingly, relative damage values (D) of the monochromatic lights to the iop-TCPs is $D(450): D(510): D(583): D(650)=1.00: 1.03: 1.14: 1.06$.

Table 1. Relative damage values of monochromatic lights on inorganic pigments.

	450nm	510nm	583nm	650nm
Ancient graphite	1.08	1.19	1.38	1.29
Calm shell powder	0.79	1.02	1.10	0.93
Azurite	0.60	0.71	0.76	0.87
Orpiment	1.09	0.97	1.13	1.03
Cinnabar	1.45	1.25	1.34	1.17
Average	1.00	1.03	1.14	1.06

Damage formula of RYGB four-primary white LEDs

The damage degree to the exposed object is determined by the power of the incident light, the relative spectral responsivity of materials to incident radiation, and the illumination hours (CIE, 2004). The relative damage values we obtain can represent the relative responsivity of the iop-TCPs to the incident radiations; and for one white LED, the four monochromatic light sources constructing it share the same illumination hours; as for the power of the incident light, it is determined by the addition of the spectral power of every wavelength in the waveband. E.g. the power of the 450nm monochromatic light is expressed by Equation 1, and the power of 510nm, 583nm, and 650nm can be calculated in the same way.

$$W(450) = \int_{450-\Delta\lambda_l}^{450+\Delta\lambda_r} S_{450}(\lambda) \cdot d\lambda \tag{1}$$

Where $\Delta\lambda_{ll}$ and $\Delta\lambda_{lr}$ represent left and right half spectral width of the spectrum, respectively; S_{450} is the SPD of the 450 nm monochromatic light.

After confirming the damage factors of the light sources, the relative damage formula for the RYGB four-primary white LED is deduced according to Equation 1, where, the total power of the white LED is divided for eliminating the influence of various energy input:

$$D^*(\lambda) = \frac{1.00W(450)+1.03W(510)+1.14W(583)+1.06W(650)}{W(450)+W(510)+W(583)+W(650)} \tag{2}$$

DISCUSSIONS

Spectral simulation and construction

All of the figures of merit which we want to optimize for the white LEDs-Ra, R₉, CCT, Duv, D*-are determined by the SPDs. And the SPDs of the white LEDs, which are the determinant factor can be theoretically constructed by the addition of monochromatic lights (Ohno, 2005) as the Figure 3e shows, before practical production to avoid waste and unnecessary preparation. And the monochromatic lights can be simulated by the Gaussian distribution, the model of which we select is an accurate modified Gaussian model (Ohno, 2005). Accordingly, the monochromatic spectra are determined by the main parameters of the Gaussian distribution-peak wavelength λ , relative intensities of the peak wavelength V , and full width at half maximum $\Delta\lambda$ (FWHM)-depicted in Figure. 3a-d. Peak wavelengths of the constructing lights are confirmed to be 450nm, 510nm, 583nm, and 650nm. While, the other two parameters need iterating to form various spectra for further research and optimization.

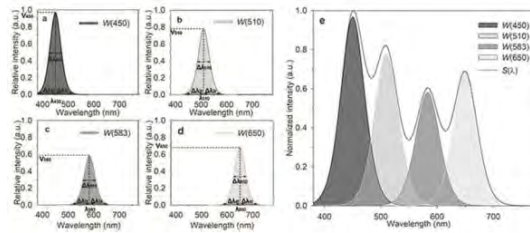


Figure 3. The S-model simulated spectral of monochromatic lights with peak wavelength of (a) 450 nm, (b) 510 nm, (c) 583 nm, and (d) 650 nm, W means the spectral power of the light. (e) spectral diagram of RYGB four-primary WLED, here, S represents the SPD of the WLED.

For overall scanning of the possible spectra, brute-force method is used. For circulation, relative intensities of the four monochromatic lights are set from zero to one with a step of 0.01 and the FWHM cycled from thirty to fifty with a step of five. After obtaining the spectra, values of figures of merit are calculated for further research.

Results of optimization

A total of 9150625 pieces of spectra are simulated. Eliminating unsatisfied spectra according to the color quality requirements for light sources illuminating op-TCPs-Ra \geq 90, R₉ \geq 90, |Duv| \leq 0.005, 2700K \leq CCT \leq 4000K (CNSA, 2009; ANSI, 2015)-6742 pieces remain.

Then we analyze the relative damage values $D^*(\lambda)_1$ - $D^*(\lambda)_{6742}$ of the satisfied SPDs, which were normalized to the range 0-100 for better comparison. The relationship among $D^*(\lambda)$

values, the amount of the satisfied SPDs, and the relative average damage values in different ranges of CCTs (the ranges of CCTs are divided by the interval of 100, e.g., 2650 K-2750 K represents the range of 2700 K) is displayed in Figure 4.

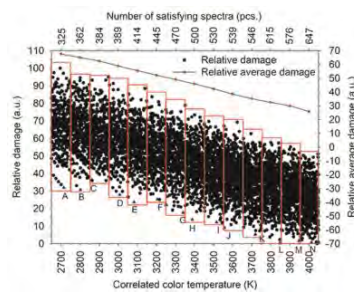


Figure 4. A diagram of $D^*(\lambda)$ values, the amount of satisfied SPDs, and the relative average damage in different ranges of CCT, the points of SPD with the same CCT range are enclosed by the red rectangle. The lowest damage points in the CCT ranges are marked with triangle.

We can see from the Figure 4 that: First, with the increase of the CCTs, relative average damage values in 2700K-4000K ranges appear an overall decrease trend (the black line), mains damage less to the iop-TCPs; second, the amount of SPDs satisfying requirements of color quality increases with the rise of CCTs (shown in the upper axis of Figure 4). e.g., the amount of qualified SPDs in the range of 2700 K is 325, while 647 for the 4000 K; third, when producing white LEDs, from the consideration of cultural relics protection, SPDs in high CCT ranges should be selected preferentially for lower damage, that means SPDs in the range of 4000 K are preferable. For further selection in the selected range, choosing SPDs with the damaged order of low to high in the selected range of CCTs, e.g., for 647 SPDs in the range of 4000 K, the SPD of point N in Figure 4 is firstly developed, but, if the SPD of the point N cannot be manufactured due to technical restrictions, other points in the range of 4000 K will be developed from low to high of the damage degree; fourth, if low CCT light sources are indispensable for reasons like the need of exhibition effect or some others which need further researching, the development should choose SPDs from the low damage to high damage in the target range.

CONCLUSIONS

Different monochromatic lights influence variously on different color pigments. Among all the painting types, the iop-TCPs suffer the damage of 450nm, 510nm, 583nm, and 650nm monochromatic lights by the damage proportion of 1.00: 1.03: 1.14: 1.06, by which a damage formula for the corresponding white LEDs is developed. The specific influence law is illustrated in Figure 2. Then the corresponding RYGB four-primary white LEDs can be evaluated protection effect by our damage formula.

By further analyzing the parameters of the constructed RYGB white LEDs, we conclude that the damage of the RYGB white LEDs to iop-TCPs decrease with the CCT ranges increase. When satisfying the requirements of color quality, the “CCTs,” “spectra amount in different ranges of CCTs,” and “relative damage of each spectrum to iop-TCPs” of the four-primary white LEDs have clear relationships, demonstrated in Figure 4. And in the realistic production of new type white LEDs, method for choosing SPDs is introduced.

The method flow of the illumination experiment, the data analysis, and the optimization of the spectra can be extended to develop and evaluate spectra of white LEDs using for other high-

responsivity cultural relics like lacquerwares, frescos, folding screens, dyed silks and so on. In addition, the white LED spectra we obtain by the method flow, which are applicable for different kinds of cultural relics, can be manufactured by the lighting systems due to the tunable characteristics of white LEDs, for which fundamentally solved the problem of protective illumination for cultural relics in museums.

ACKNOWLEDGEMENT

This work was supported by the National Key Research and Development Program of China under Grant number 2016YFB0601700; Natural Science Fund of Tianjin under Grant number 17JCYBJC22400; Peiyang scholar Program under Grant number 1801.

REFERENCES

- American national standards institute. 2015. Electric lamps specifications for the chromaticity of solid-state lighting products (ANSI C78.377-2015).
- China National Standardization Administration. 2009. Code for Lighting Design of Museum (GB/T 23863-2009), Beijing: China Standard Press.
- Dang R, Zhang MY, Liu G, Yu J, Hou D. 2013. Investigation and research on display lighting in museum based on protected historical relics. *China illumination engineering journal*, 24(3), 18-23.
- Dang R, Yuan Y, Liu G, Luo C, Liu J. 2017. White LED spectrum for minimising damage to Chinese traditional heavy colour paintings. *Lighting Research and Technology*. doi: 10.1177/1477153517707996.
- Farke M, Binetti M, Hahn O. 2016. Light damage to selected organic materials in display cases: A study of different light sources. *Studies in Conservation*, 61, S83-S93.
- Hayashida T, Iwasaki H, Masaoka K, Shimizu M, Yamashita T, Iwai W. 2017. Appropriate indices for color rendition and their recommended values for UHD TV production using white LED lighting. *Optics Express*, 25(13), 15010-15027.
- International Commission on Illumination Publication 13.3. 1995. Method of measuring and specifying colour rendering of light sources. Vienna.
- International Commission on Illumination. 2004. CIE 157: Control of damage to museum objects by optical radiation.
- Lin DY, Zhong P, He GX. 2017. Color temperature tunable white LED cluster with color rendering index above 98. *Ieee Photonics Technology Letters*, 29(12), 1050-1053.
- Ohno Y. 2005. Spectral design considerations for white LED color rendering. *Optical Engineering*, 44(11).
- Ohno Y. 2013. Practical use and calculation of CCT and Duv. *Leukos*, 10(1), 47-55.
- Oh JH, Yang SJ, Sung YG, Do YR. 2012. Excellent color rendering indexes of multi-package white LEDs. *Optics Express*, 20(18), 20276-20285.
- Oh JH, Yang SJ, Do YR. 2014. Healthy, natural, efficient and tunable lighting: four-package white LEDs for optimizing the circadian effect, color quality and vision performance. *Light science and application*, 3.
- Robinson AC, Quinn SD. 2018. A brute force method for spatially-enhanced multivariate facet analysis. *Computers, Environment and Urban Systems*, 69.
- Schubert EF and Kim JK. 2005. Solid-state light sources getting smart. *Science*, 308(5726), 1274-1278.
- Wu J. 2011. Research of pigments in the pre-Qin and Han dynasties. *Ph.D. thesis*, Tianjin University.
- Wu TZ, Lin Y, Zhu HH, Guo ZQ, Zheng LL, Lu YJ, Shih MS, Chen Z. 2016. Multi-function indoor light sources based on light-emitting diodes—a solution for healthy lighting. *Optics Express*, 24(21), 24401-24412.

Analytical and Numerical Investigation on Depth and Pipe Configuration for Coaxial Borehole Heat Exchanger, A Preliminary Study

Hongshan Guo¹, Forrest Meggers^{1,*}

¹ Princeton University, Princeton, NJ, United States

² Andlinger Center for Energy and the Environment, Princeton, NJ, United States

**Corresponding email: fmeggers@princeton.edu*

ABSTRACT

Existing research on the performance of shallow geothermal systems are prone to investigate the ground as a large thermal mass at a constant temperature despite possible temperature increase at depths - otherwise commonly known as the geothermal gradient. Most of the existing analytical models that predict the heat exchange between a borehole heat exchanger with the soil does not allow for the geothermal gradients to be accounted for. The few models that actually does account for the geothermal gradients, on the other hand, does so by enforcing a pre-existing temperature gradient only. We are presenting a bottom up approach in this paper to solve the temperature distribution by accounting for both the convective heat transfer from the working fluid and the conductive heat transfer through both the pipe and the soil. Assuming the heat transfer is entirely axisymmetric, we approach the problem by solving the Navier-stokes equation and energy equation with a finite difference solver that calculates the temporal change of temperature with given diameter, depth of borehole and geothermal gradient. The heat transfer through the pipe and into the ground can therefore be further calculated. We were able to determine a CBHE configuration that allows maximized thermal output by assuming a synthetic heating/cooling load for year-round production of heat.

KEYWORDS

geothermal gradient; CBHE; geothermal energy; ground-source heat pump

INTRODUCTION

Existing research on the harvesting geothermal energy categorizes the harvesting process with respect to the depth of the ground roughly into shallow geothermal systems and deep use systems. The prior are often associated with harvesting the energy solely for thermal purposes, in particularly exploiting the benefits from geothermal energy as a source of large thermal mass where energy can be deposited and/or extracted while the source maintains relatively consistent temperatures (Lund, 1999). The deep use systems, on the other hand, are usually associated with geothermal basins and highly pressurized steams that can be used for power generation. For the shallow geothermal system, the temperature of the working fluid extracted from the boreholes commonly rises up to 25 degree Celsius, while for the deeper geothermal systems, this temperature could go up to 225 degree Celsius (Lu, 2018). Obtaining the working fluid at a temperature in-between is a much less practiced approach.

This would have been made possible by exploiting the geothermal gradient that was known to be at 25 to 50 K/km for different types of geological conditions. According to data released from NGDS where the temperature at the bottom of 17,462 boreholes were made public, the temperatures at the bottom of deeper boreholes could go up to 75 degree Celsius since some

of the boreholes went as deep as 2.4 km. Admittedly, these boreholes were neither designed to be delivery heat to households, nor were they to ever be connected to municipal district heating networks. Yet the temperatures alone could cast questions as to whether spending much more money to drill deeper boreholes could in fact repay such investments with higher quality of energy coming out from the boreholes. To fully appreciate the scope of this questions, we are presenting a numerical study that we are currently investigating in this paper as we try to determine the most optimized design for a coaxial borehole heat exchanger (CBHE) since it provides the maximized amount of surface area for heat exchange comparing to other alternatives.

METHODS

We have created a three-step solver to investigate the flow regime within a CBHE with a set of known design parameters so that the temperature inside the borehole, at the casing and outside of the borehole can all be calculated. At every single time step, the temperature distribution and velocity field within the borehole heat exchanger will first be solved. The temperature at the wall and pipe interface are then used to calculate the temperature within the pipe and casing. The resulting temperature at the outside of the casing will then be used to compute the temperature distribution at the end of this time step.

Assuming water to be the main working fluid, the flow that is being modelled should be considered incompressible. Solving the hydraulic performance of a CBHE while considering the convective heat exchange between the water and the borehole casing, we are essentially solving the flow conditions with respect to the following three equations:

$$\nabla \cdot u = 0 \quad (1)$$

$$\frac{\partial u}{\partial t} + u \cdot \nabla u = -\frac{1}{\rho} \nabla p + \nu \nabla^2 u + g\alpha \Delta T \quad (2)$$

$$\frac{\partial T}{\partial t} + u \cdot \nabla T = \kappa \nabla^2 T \quad (3)$$

Equation 1 denotes the continuity of an inviscid fluid, Equation 2 is the Navier-Stokes equation which can be solved to understand the fluid condition for an inviscid fluid, while Equation 3 is the Boussinesq approximation that can be used to solve for temperature distribution. For the in-pipe fluid flow, we solve the N-S equation for an incompressible flow condition. The incompressibility acts as a constraint for the pressure. Within the borehole, for every single time step, the velocity profile will be imported, following which the pressure field can be updated with the new velocities. The further influence of the boundary conditions can then be used to further constraint the new pressure condition within the heat exchanger, creating new pressure conditions, leading to an updated velocity profile, thus updating the temperature profiles in Equation 3.

Since we are working with an axisymmetric coordinate system, it is possible to assume Equation 2 can be further simplified into a 2D form, with an exception of its final term .

$$\rho \left(\frac{\partial u}{\partial t} + u \frac{\partial u}{\partial x} + v \frac{\partial u}{\partial y} \right) = -\frac{\partial P}{\partial x} + \mu \left[\frac{\partial^2 u}{\partial x^2} + \frac{\partial^2 u}{\partial y^2} \right] \quad (4)$$

$$\rho \left(\frac{\partial v}{\partial t} + u \frac{\partial v}{\partial x} + v \frac{\partial v}{\partial y} \right) = -\frac{\partial P}{\partial z} + \rho g \alpha \Delta T + \mu \left[\frac{\partial^2 v}{\partial x^2} + \frac{\partial^2 v}{\partial y^2} \right] \quad (5)$$

To solve for the pressure term, we took divergence of Equation 4 and 5, adding them up, and simplified with the continuity constraint Equation 1, it is possible to arrive at a Pressure Poisson Equation of

$$\frac{1}{\rho} \left(\frac{\partial^2 P}{\partial x^2} + \frac{\partial^2 P}{\partial y^2} \right) + \frac{g\alpha\Delta T}{\rho C} = \left(\frac{\partial u}{\partial x} \right)^2 + \frac{\partial v}{\partial x} \frac{\partial u}{\partial y} + \left(\frac{\partial u}{\partial x} \right)^2 \quad (4)$$

After updating the temperature for the fluid is determined, the temperature of the fluid that is most adjacent to the casing and inner pipe can then be introduced Equation 5, where the conduction within the casing. The ρ stands for the pipe density, C stands for their specific heat capacity ($J/kg \cdot K$), while k stands for the pipe's thermal conductivity.

$$\rho C \frac{\partial T(x,t)}{\partial t} = \nabla \cdot [k \nabla T(x,t)] \quad (5)$$

As we are solving energy equation for a incompressible fluid in an internal space before moving on to the heat conduction happening in the soil, it is also necessary to non-dimensionalize both the momentum equation and the energy equations. The non-dimensionalize terms that will be used are the following:

$$\begin{aligned} u &= \frac{u^*}{U_\infty}, \quad v = \frac{v^*}{U_\infty}, \quad \theta = \frac{T - T_\infty}{T_w - T_\infty}, \\ x &= \frac{x^*}{L}, \quad y = \frac{y^*}{L}, \quad t = \frac{t^*}{L/U_\infty} \end{aligned} \quad (6)$$

such that Equation 5 can be re-written in the form of non-dimensionalized form as

$$\frac{\partial \theta}{\partial t} + u \frac{\partial \theta}{\partial x} + v \frac{\partial \theta}{\partial y} = \frac{1}{Pe} \left[\frac{\partial^2 \theta}{\partial x^2} + \frac{\partial^2 \theta}{\partial y^2} \right] + \frac{Ec}{Re} \Phi \quad (7)$$

Since the flow velocity is very small ($M \rightarrow 0$), Ec also disappear so that the last term on the right hand side disappears, the temperature can therefore be fully written as a function that can be obtained from the u and v velocity components with the help of the Peclet number which we can obtain with Equation 8.

$$Pe = Pr \cdot Re = \frac{Lu}{\alpha} = \frac{Lu\rho c_p}{k} \quad (8)$$

where L represents the characteristic length, u is the local velocity, ρ is the density, c_p is the specific heat capacity, and k is the thermal conductivity of water. We will be using the depth of the borehole as the characteristic length hence $L = H$. The resulting temperature distribution, specifically the temperature at the outside of the casing resulting from the calculations were then introduced into Equation 4 again, with different set of parameters, where ρ stands for the soil density, C stands for soil specific heat capacity ($J/kg \cdot K$), while k stands for the soil thermal conductivity. As all the computation were resulted from discretized analytical modeling, we were able to construct this solver in a light-weight, easy-to-interpret Python module that takes in only diameter of borehole, depth of borehole as inputs to produce the geothermal energy. The parameters this study was subjected to are as the following in Table 1:

Table 1. Parameters used in the numerical simulation

Material	Density, (kg/m^3)	Specific heat capacity ($kJ/kg \cdot K$)	Thermal conductivity ($W/m \cdot K$)
Soil	1.8×10^3	0.8	1.59
Pipe	0.95×10^3	1.9	0.5
Casing	7.9×10^3	0.47	14.9
Water	1.0×10^3	4.1844	0.609

To further decrease the computational costs, both the control equations and inputs were further non-dimensionalized in both the vertical and axial directions, more specifically with

respect to $2H$, where H stands for the depth of the proposed borehole depth designs. This nondimensionalization method is consistent with a few existing studies. The parameters from Table 1 were then used to run a series of iterations of simulations to simulate the temperature out at different flow velocities. The pseudocode for the algorithm used can be found in Table 2 as is shown below.

Table 2. Algorithm used to calculate the temperature field inside and around CBHE

Input: CBHE Diameter (D), Depth (H), Mass Velocity(\dot{m}), Length of Time for simulation (T)

Initialize grid network ($j = [1, J]$, $k = [1, K]$) within, inside and outside of the CBHE shell

mass velocity converted to linearized velocity for inlet and outlet u_{in} and u_{out} from \dot{m} and T_{ij}

Start of Simulation for a total of N time steps where $N = T/dt$

For i to N :

While $T_i - T_{i+1} > 0.001$ do

Velocity ($u_{j,k}, v_{j,k}$) and Temperatures($t_{j,k}$) inside the CBHE solved by N-S & Energy Equations;

Temperature inside the inner and outer tube solved by heat conduction equations;

Temperature outside of the outer tube and inside the soil solved from heat conduction equations;

$t = t + dt$

Output Velocity fields U, V and Temperature fields T

End

Assigning the time of simulation (T) to be 1 h and the size of time step at 0.005s for the simulation, the temperature distribution inside and outside of the borehole can be simulated. We will be assuming a constant temperature of 10°C within the scope of this paper, but could switch to a varying $Q(t)$ since the temperature development was strictly temporal hence can handle varying heating/cooling demand. This is a placeholder for variable heat input that can better simulate the load coming from actual buildings in the future. It is also important to point out that we will be assuming a geothermal gradient of 30 K/km, and no underground water flow that interacts with the CBHE within the context of this study. We will be modeling the analytical problem with the central difference approximation scheme as it provides a much better smoothness and could serve our purpose better. Due to the page limit imposed on this paper, the actual discretization expressions will be omitted.

RESULTS

The proposed solver was very time consuming to develop, and was very time-consuming to develop. We were able to determine the flow pattern using the 2D solver we developed. For every time step, the velocity and temperature can be computed by solving the Navier-Stokes equation with the Boussinesq Approximation. At every step in time, the pressure term is first solved from the velocity and temperature profile of the last time step. Velocity and temperature profile are then calculated and developed over time, as is being shown in Figure 1.

The in-borehole temperature distribution development within the borehole can be qualitatively captured over time. Since we used $dt = 5.4\text{e-}6\text{s}$ for the simulation, a fully developed flow pattern at the 1st hour requires a total of 61 minutes to compute. This was computationally very expensive comparing to similar solvers in TRNSYS and COMSOL.

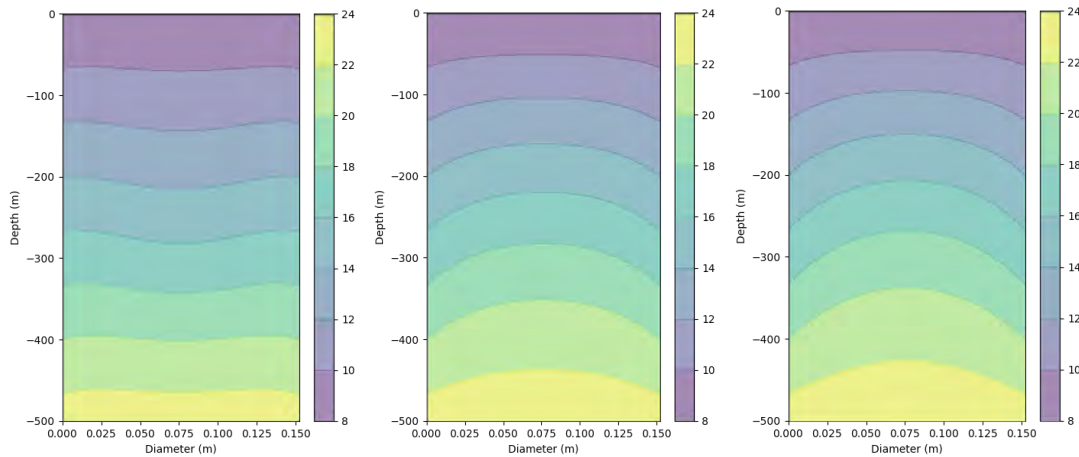


Figure 1. Temporal change of the temperature distribution within the in-bore model from the solver as time steps forward $t = 0.1s$ (left), $0.5s$ (middle), $0.7s$ (right).

DISCUSSIONS

To save computation time and avoid excessive read/write to the hard drive, we did not store the temporal change of the temperature field. What was stored, was rather only data at the end of calculation, i.e. by the end of the 1st hour of hypothetical borehole operation. Understanding the temporal change of temperature was not of significant interest for this paper, but we would like to acknowledge its importance with follow-up studies, since the temporal response of the borehole is of major research interests to many preliminary borehole assessment simulations where thermodynamic properties can be compared against simulation results. We believe the first step to further this investigation is to compare their performances both in terms of computation time and the resulting temperature and velocity profiles. A clear benefit of our method would be the simplification of creating meshes as it'd be fully automated for any given diameter and depth of borehole, while any change in the geometry of a CBHE requires a new mesh generated to be calculated. Also highly simplified is the geotechnical conditions around the borehole. As we assumed homogeneous soil condition for this study, the actual soil conditions are often observed to vary significantly and needs to be described with an entire set of thermodynamic properties instead of the one set that was used in this study. As this study is, again, purely numerical, it might be possible to further customize the soil conditions through assigning different soil properties that exist by layers but is off the focus of this research and are hence not pursued within the scope of this paper.

Additionally, there is a missing link that this solver does not provide information for, but could prove helpful to further analyze: stress/strain on the borehole wall, in particular the stress and strain on the outer tube/casing interface. Better characterization of the temperature increases' influence on the harvestation of geothermal energy may very likely increase the awareness of how to better quantify the heat exchange with the ground in other modeling practices, i.e. helix geothermal heat exchanger, single and double U-tube geothermal heat exchanger as well as multiple inlet/outlet energy pile systems. There are currently no existing research that quantitatively compare the differences in between their performances, which we are also very interested in quantifying in the near future.

Last but not the least, it is important to stress that existing commercial softwares does not achieve the similar level of resolution during design-stage analysis. In short, refined solution

of the temperature profile within a CBHE is relevant to harvest the most amount of thermal energy to ground level, but cannot be achieved without fine grids in numerical simulations - which is impossible when the depth of a CBHE is yet to be determined through parametric analysis. The proposed method, on the other hand, will allow such analysis at the expense of computational time but has its own merits in the ease of use as steady-state results after prolonged periods of operation can be calculated and compared against another - as well as using variable insulation levels for the inner pipe of the annulus. We believe this is research that is crucial to further the current understanding of borehole heat exchangers and could be brought further by putting additional attention to rewrite the algorithm in compiled language to reduce the computational time in the near future.

CONCLUSIONS

We have devised the very basics of fluid mechanics in conjunction with the heat exchange by solving the hydraulic condition within the CBHE. Working with the basic assumption that the flow inside a CBHE can be assumed to be axisymmetric, we based our model on the fundamentally solving the Navier-Stokes equation with the boundary constraints of a CBHE with known inlet and outlet information, we demonstrated that it is possible to use a simple 2D model to predict the temperature distribution within and outside of the borehole. Admittedly, the result we reached can also be completed with commercially available softwares, we believe our method is much more simplified to run parametric studies and/or for further optimization.

REFERENCES

- Wagner, Valentin, Peter Bayer, Markus Kübert, and Philipp Blum. "Numerical Sensitivity Study of Thermal Response Tests." *Renewable Energy* 41 (May 1, 2012): 245–53.
- Rybach, Ladislaus. "Design and Performance of Borehole Heat Exchanger/Heat Pump Systems." *Proc. European Summer School of Geothermal Energy Applications*, 2001.
- John Lund. "Examples-of-United-States-Geothermal-District-Heating-Systems.Pdf." *Bulletin d'Hydrogiologie* 17 (1999).
- Shyi-Min Lu. "A Global Review of Enhanced Geothermal System (EGS)." *Renewable and Sustainable Energy Reviews* 81 (January 1, 2018): 2902–21.

Comparison of Lattice Boltzmann Method and Finite Volume Method with Large Eddy Simulation in Isothermal Room Flow

Mengtao Han^{1,*}, Ryoza Ooka² and Hideki Kikumoto²

¹ JSPS Research Fellow, School of Engineering, the University of Tokyo, Japan

² Institute of Industrial Science, the University of Tokyo, Japan

*Corresponding email: hanmt@iis.u-tokyo.ac.jp

ABSTRACT

Lattice Boltzmann method (LBM), as a new computational fluid simulation method, has aroused widespread attention in recent decades within engineering practice. LBM with large eddy simulation (LBM-LES) model is commonly used in predicting high Reynolds flow, and is considered to have a prediction accuracy similar to traditional finite volume method (FVM-LES). Nonetheless, a systematic discussion on the accuracy of LBM-LES, and its consistency with FVM-LES, in indoor turbulent flow situations, is still insufficient. In this study, simulations of an indoor isothermal forced convection benchmark case (from IEA Annex 20) are implemented by using both LBM-LES and FVM-LES, with the aim of comparing the accuracies of LBM-LES and FVM-LES, in indoor turbulent flow situations. A comparison of their relative computation speeds, and parallel computation performances, is also implemented. The results show that LBM-LES can achieve the same level of accuracy as FVM-LES, in indoor turbulent flow situations; however, more refined meshes are required. Compared with FVM-LES, half size grids are required for LBM-LES to approach similar levels of accuracy, meaning that the meshes of LBM-LES are approximately eight times as large as FVM-LES. The computation speeds of both LBM-LES and FVM-LES scale well, with the increase in the number of computation cores in one node. Their computation speeds (with the same accuracy) approach a similar level; however, the parallel computation speed of the LBM-LES speed can be larger than FVM, owing to its superior parallel speedup performance.

KEYWORDS

Lattice Boltzmann method, Finite volume method, Large-eddy simulation, Indoor turbulent flow

INTRODUCTION

The lattice Boltzmann method (LBM) has recently been applied in indoor turbulent flows (Sajjadi et al. 2016), in place of the conventional finite volume method (FVM). Based on the lattice Boltzmann equation, the LBM simulates the fluid motion process by assuming a collection of particles colliding, and a stream behavior for their distribution functions (Chen and Doolen 1998). When solving turbulent flow problems with a high Reynolds number, the LBM can be used with a large eddy simulation (LBM-LES) model, as in the FVM (FVM-LES). As it is necessary to solve the Poisson equation in the FVM, there is an obvious disadvantage in that the calculation load and time cost are tremendous. However, the LBM shows more promise in high-speed LES simulations for complex and large-scale urban flows, owing to its simpler algorithm, and it is also more appropriate for parallel calculations.

Although the LBM has been applied in the flow simulation of indoor turbulence, a systematic comparison of its accuracy, consistency, and computation speed with the FVM is still insufficient. Therefore, in this research, simulations of an indoor turbulent flow benchmark case from IEA Annex 20 (Lemaire et al. 1993) are implemented by using both the LBM-LES and

FVM-LES, to verify the accuracy of the LBM-LES and to compare this accuracy with that of FVM-LES. The computation speeds and parallel computation performances are also determined.

OUTLINE OF LBM

Lattice Boltzmann equation

Instead of the Navier-Stokes equation, the LBM in this research simulates the fluid using the lattice Boltzmann equation, with the BGK approximation (Bhatnagar, Gross, and Krook 1954). The non-external-force lattice Boltzmann-BGK equation is expressed as Equation (1), where Δt is the discrete time, \mathbf{e}_a is the discrete speed in the a -direction, $f_a(\mathbf{r}, t)$ is particle a s distribution function, $f_a^{eq}(\mathbf{r}, t)$ is the equilibrium function, and τ is the relaxation time.

$$f_a(\mathbf{r} + \mathbf{e}_a \Delta t, t + \Delta t) - f_a(\mathbf{r}, t) = \frac{1}{\tau} [f_a^{eq}(\mathbf{r}, t) - f_a(\mathbf{r}, t)] \quad (1)$$

Discrete velocity scheme

The DdQq (d = spatial dimension, q = discrete particle speed) discrete velocity scheme (Qian, D Humières, and Lallemand 1992) is widely accepted for the LBM. In this research, the D3Q19 scheme was employed, as shown in Figure 1. Cubic lattices are used in this scheme, with 18 adjacent points for every lattice point. The particles only exist on the points, and move to an adjacent point, or just rest, during each time step. Therefore, the D3Q19 scheme has three types of particles, with motion speeds indicated in Table 1, where e is the particle speed, $e = \Delta x / \Delta t$, and Δx is the lattice length.

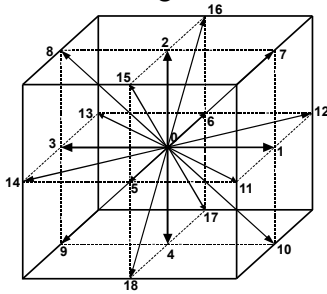


Figure 1. Lattice system of the D3Q19 scheme

Table 1. Discrete velocity of each particle

Particle No.	Discrete velocity	Motion paths
0	0	rest
1-6	e	along the normal axis
7-18	$\sqrt{2} e$	along the diagonal

LES model in LBM

In this study, the LES (using the standard Smagorinsky SGS model) is implemented. According to the LES theory, the total viscosity ν_{total} is composed of the molecular viscosity ν and the eddy viscosity ν_t . The ν_{total} and ν_t are given by Equation (2).

$$\nu_{total} = \nu + \nu_t, \quad \nu_t = (C_s \Delta)^2 |\bar{s}| \quad (2)$$

where C_s is the Smagorinsky constant, Δ is the filter, and \bar{s} is the strain rate tensor. This is as same as the LES theory of the FVM.

Furthermore, the total viscosity can be calculated using Equation (3) by the LBM s theory.

$$\nu_{total} = e_s^2 (\tau_{total} - 0.5) \Delta t \quad (3)$$

where e_s is the speed of sound of the particles, and τ_{total} is the total relaxation time. Therefore, the total relaxation time τ_{total} is obtained from ν_{total} , and it substitutes the original relaxation time τ in Equation (1), to implement the LBM-LES simulation.

OUTLINE OF SIMULATION TARGET AND SIMULATION CONDITIONS

The LBM-LES and FVM-LES (abbreviated to LBM and FVM below) approach was conducted for the indoor isothermal forced flow. The room model and simulation boundary conditions are shown in Figure 2 and Table 2, respectively. The room characteristics are $L/H = 3$, $h/H = 0.056$, $t/H = 0.16$, and $Re = 5000$, where L, H, h, t and Re represent the room length, room height, slot inlet height, outlet height, and the Reynolds number (refer to the inlet height and velocity), respectively. Since the inlet turbulence intensity of the experimental data is only 4% according to the IEA report, it can be considered to have a very small impact on the velocity, and thus, the inlet turbulence intensity was ignored in this simulation. A set of various uniform grid resolutions were employed, as illustrated in Table 3.

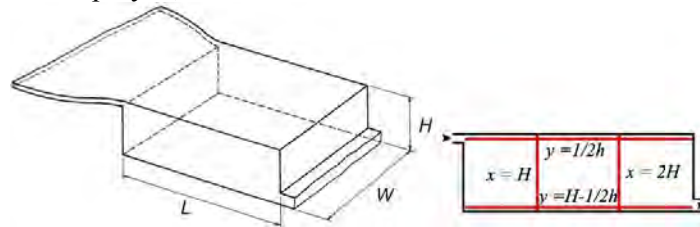


Figure 2. Sketch of the simulation target (from IEA Annex 20)

Table 2. Boundary conditions (B.C.)

Item	FVM-LES	LBM-LES
Sub-grid scale model	Standard Smagorinsky model ($C_s = 0.12$)	
Damping function	Van Driest-style	
Simulation domain	9.0 m (L) \times 3.0 m (W) \times 3.0 m (H)	
Time discretization	Euler-implicit	-
Space discretization	2 nd -order central difference	-
Simulation Period	Preparatory: 18 min, average: 6 min (air change rate: 0.172 min ⁻¹)	
Inlet B.C.	Uniform velocity boundary, $U_{in} = 0.455$ m/s, (no fluctuations)	
Outlet B.C.	Gradient-zero	
Other B.C.	Wall function (Spalding s law)	No-slip (Bounce-back)

Table 3. Case study

Case Name	Simulation Method	Grid size	Mesh quantity
LBM_004	LBM-LES	0.04 m (1/75 H)	1.6 M
LBM_002		0.02 m (1/150 H)	10.1 M
LBM_001		0.01 m (1/300 H)	81 M
FVM_004	FVM-LES	0.04 m (1/75 H)	1.6 M
FVM_002		0.02 m (1/150 H)	10.1 M

RESULTS AND DISCUSSIONS

Time-averaged scalar velocity

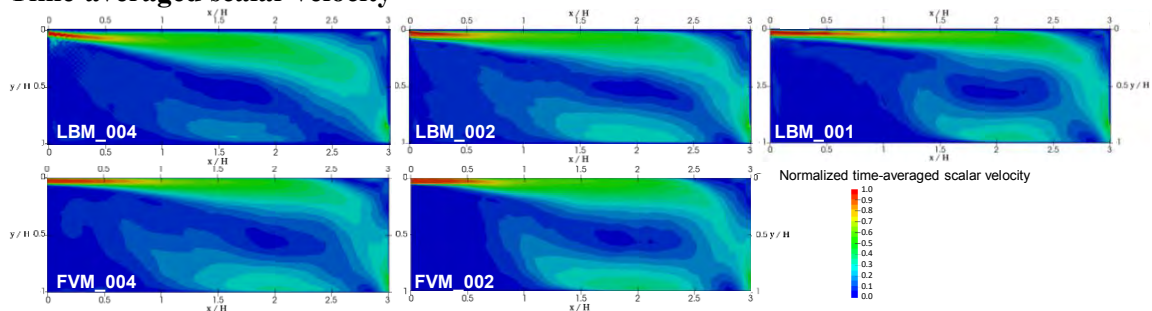


Figure 3. Normalized time-averaged scalar velocity of each cases

Figure 3 shows the normalized time-averaged scalar velocity of the central vertical section for the different cases. A large air circulation flow, which was equivalent to the room size, occurred

from the inlet, with a region-stagnated air flow in the center of the room. The LBM represented the flow features as well as the FVM. Nonetheless, a tendency of moving lower away from the ceiling, for the airflow from the inlet, could be observed clearly in LBM_004. This is most probably because the LBM employed the standard bounce-back boundary condition, which excludes a wall function (such as the Spalding rule) for calculating the eddy viscous drag at the wall layer. Also, the damping function (such as the Van Driest style) is absent from the LBM, causing an overestimation of the eddy viscosity adjacent to the ceiling compared with the FVM, and it weakened as the LBM's grids became finer. This phenomenon did not occur in the FVM, regardless of grid resolutions, since the wall function and the damping function was employed.

Comparison of the accuracy of LBM and FVM

The experimental data (Nielsen, Rong, and Olmedo 2010) was used to validate the accuracy. As shown in Figure 4, both LBM and FVM were generally able to represent the distribution tendency of $\langle U \rangle$ (the mainstream direction component of the time-averaged mean velocity), except for LBM_004, which demonstrated the most unacceptable accuracy. The LBM's accuracy improved as the grid resolutions improved in each region. For $x = H$, the velocities of all the LBM cases were under-predicted in the jet, most probably due to the absence of the damping function, while the FVM agreed well. Further, both LBM and FVM slightly underestimated the velocity on the height of the inlet at $x = 2H$, and the same was true along $y = 1/2h$. Along $y = H - 1/2h$, LBM cases agreed well with the experiment, as did the FVM.

Figure 4 shows the comparison of the RMS profiles of the horizontal velocity component ($\text{RMS} = \sqrt{\langle u'^2 \rangle}$). Near the ceiling, at $x = H$, FVM overestimated the RMS, while the accuracy of the LBM was higher (especially LBM_001). Along $y = 1/2h$, the FVM also over-predicted the RMS, and the LBM achieved a higher accuracy. On the other hand, both the LBM and FVM underestimated the RMS at the lower area, at $x = 2H$ and along $y = H - 1/2h$. This underestimation of the RMS also appeared in the FVM-LES implemented by Davidson (Davidson and Nielsen 1996). In addition, because both the LBM and FVM demonstrated an underestimation at these areas, it may not be not an inherent problem of the LBM, but rather due to a difference between the simulations and experimental conditions.

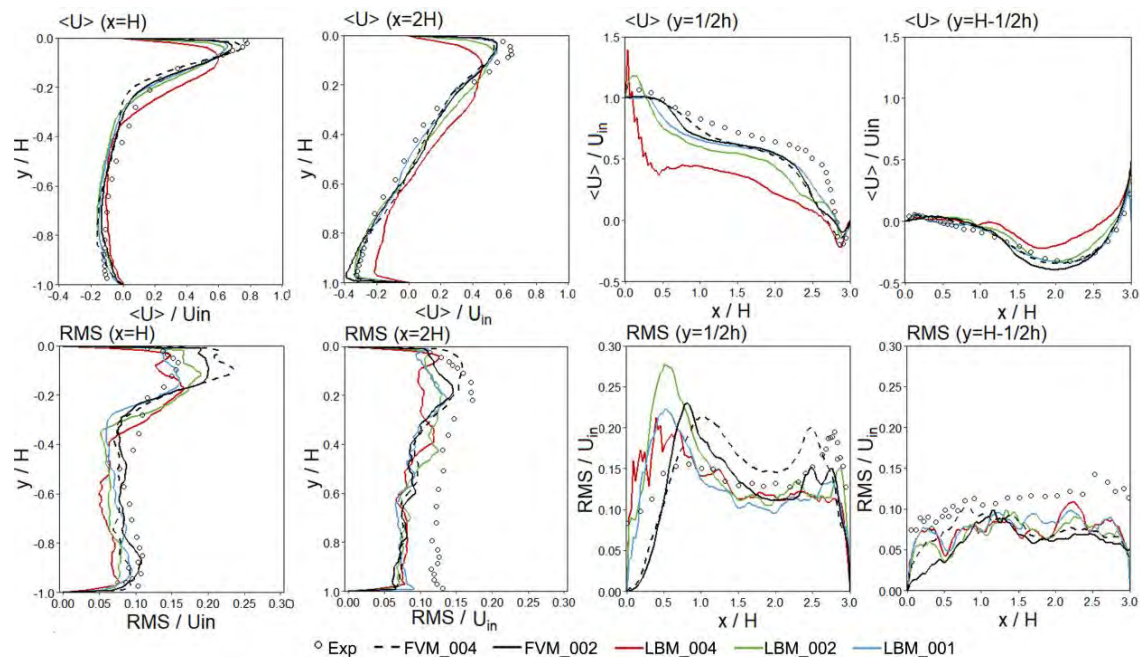


Figure 4. Distribution of $\langle U \rangle$ (top row) and RMS (bottom row)

The accuracy of simulations is quantitatively evaluated by considering all the experimental and predicted data of the corresponding spots, using the mean error (ME) defined by Equation (4), where $V_{EXP(i)}$ and $V_{LBM \text{ or } FVM(i)}$ are the experimental or predicted data of corresponding spots.

$$ME = \frac{1}{M} \sum_{i=1}^M |V_{LBM \text{ or } FVM(i)} - V_{EXP(i)}| \quad (4)$$

Figure 5 shows the ME of the measurement points at all the points (All Data), the points adjacent to the ceiling ($y = 1/2h$), the ground ($y = H - 1/2h$), and points far away from walls ($x = H, 2H$). Generally, among all the LBM cases, the accuracy of $\langle U \rangle$ was markedly improved when the grid resolution was changed from 0.04 m to 0.02 m, but only slightly improved when it was changed from 0.02 m to 0.01 m. The accuracy of the FVM cases was between that of LBM_002 and LBM_001. With respect to RMS, the accuracy of the LBM was almost the same at any grid resolution and was slightly better than the FVM. Whether for all points, or sub-regional points, the previous tendency was clearly observed. With regard to the sub-regional points MEs (for $\langle U \rangle$), the maximum and minimum MEs appeared adjacent to the ceiling ($y = 1/2h$) and to the ground ($y = H - 1/2h$), respectively, regardless of simulation methods and grid resolutions. The difference in RMS among different sub-regions was small.

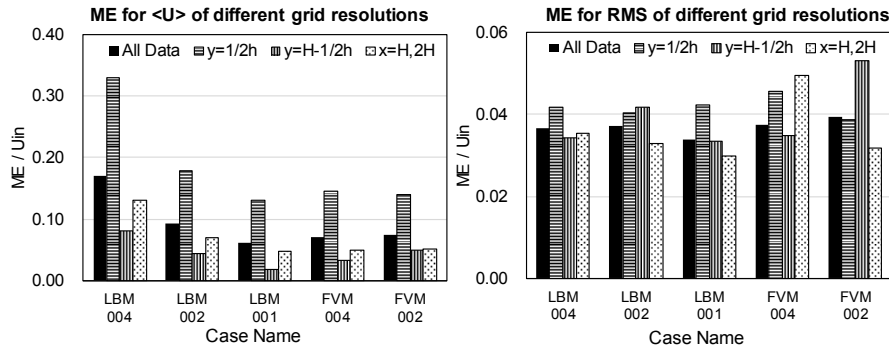


Figure 5. Mean Error (ME) of different grid resolutions

In conclusion, the same grid resolution of the LBM and FVM led to different accuracy levels in this study. More refined grids were required for the LBM to achieve the same accuracy than the FVM. The accuracy of LBM_002 and LBM_001 approximated that of FVM_004 and FVM_002, respectively, showing that the LBM required half the grid width of the FVM.

COMPUTATION SPEED AND PARALLEL COMPUTATION PERFORMANCE

The computation speeds, and parallel computation performances attained using the two methods, were compared using one node including two Intel (R) Xeon (R) E5-2667v4 @ 3.20 GHz (8 cores) CPUs, and the simulations were performed with different core utilization situations (1, 2, 4, 8, and 16). The elapsed computation time was normalized by the physical time for the flow motion (24 min), as shown in Figure 6. The computation times of both the LBM and FVM linearly decreased (approximately) with the increase in the cores, indicating that their speeds scaled well. The computation times of LBM_002 and LBM_001 were of almost the same order as those of FVM_004 and FVM_002, respectively, signifying that for the same accuracy, LBM and FVM used the same amount of computation time.

Figure 7 shows the LBM's computation speed ratio of the FVM of LBM and FVM with different core usage situations, and parallel efficiency for both the FVM and LBM. The computation speed of the LBM using one core was only 0.4 times that of the FVM, but it increased with increase in the number of cores, and finally became about 1.2 when the number

of cores approached 16. Although the parallel efficiency of both the LBM and FVM had initial values of 2-3, the parallel efficiency of the LBM increased to 24, whereas that of the increased only to 9. This signified that the parallel efficiency of the LBM responded much better to an increase in the number of cores.

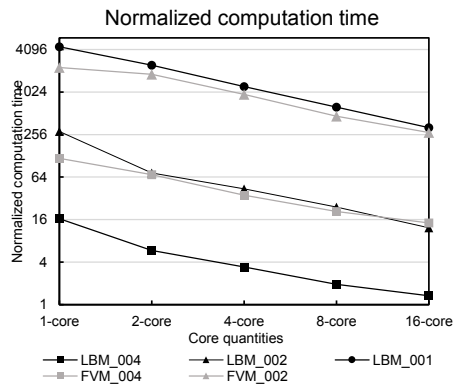


Figure 6. Normalized computation time

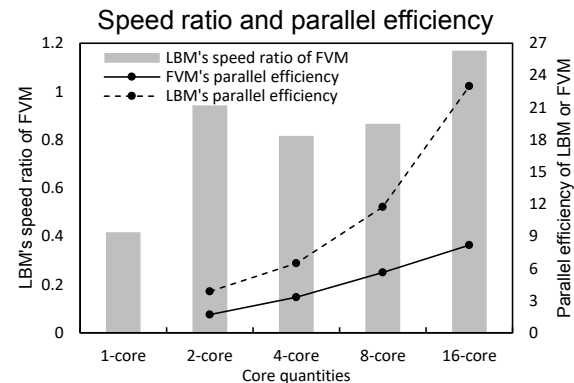


Figure 7. Parallel computation efficiency

CONCLUSIONS

In the indoor turbulent flow situation, the LBM can accurately represent the physical flow structure, and this accuracy improves as the grid resolution becomes higher. The grid width needed for the LBM is approximately half that of the FVM, to achieve the same level of accuracy, partly due to the absence of the wall function in the LBM. Regarding the computation speeds, the speeds of both the LBM and FVM scaled well with an increase in cores quantity in one node. The speeds of LBM and FVM were on approximately the same level for the same degree of accuracy, even though the LBM's mesh was 8 times that of the FVM's. The speed of the LBM corresponding to 1-core is much slower than the FVM, while the speeds corresponding to 16-core became faster due to the better parallel simulation performance of the LBM. Furthermore, the LBM parallel speedup scales well with the increase in the cores, whereas FVM suffers from an upper limitation. Therefore, the speed of the LBM may be further increased by employing more cores (for e.g., in supercomputers); this will be considered in future research.

ACKNOWLEDGEMENT

This research was partially supported by the Research Fellowships program of the JSPS for Young Scientists (KAKENHI Grant Number 18J13607, general manager: Mengtao Han).

REFERENCES

- Bhatnagar, P. L., E. P. Gross, and M. Krook. 1954. "A Model for Collision Processes in Gases. I. Small Amplitude Processes in Charged and Neutral One-Component Systems." *Physical Review* 94 (3): 511–25.
- Chen, Shiyi, and Gary D Doolen. 1998. "Lattice Boltzmann Method for Fluid Flows." *Annual Rev. Fluid Mechanics* 30 (Kadanoff 1986): 329–64. doi:10.1146/annurev.fluid.30.1.329.
- Davidson, Lars, and Peter V Nielsen. 1996. "Large Eddy Simulations of the Flow in a Three-Dimensional Ventilated Room." *5th Int. Conf. on Air Distributions in Rooms ROOMVENT '96* 2: 161–68.
- Lemaire, A.D., Qingyan Chen, M. Ewert, Jorma Heikkinen, C. Inard, Alfred Moser, Peter Vilhelm Nielsen, and G. Whittle. 1993. "Room Air and Contaminant Flow, Evaluation of Computational Methods, Subtask-1 Summary Report." *IEA Annex 20: Air Flow Patterns within Buildings*, 82.
- Nielsen, Peter V, Li Rong, and Inés Olmedo. 2010. "The IEA Annex 20 Two-Dimensional Benchmark Test for CFD Predictions." *Clima 2010, 10th REHVA World Congress*, 978-975-6907-14–16.
- Qian, Y. H., D. D. Humières, and P. Lallemand. 1992. "Lattice Bgk Models for Navier-Stokes Equation." *Epl* 17 (6): 479–84.
- Sajjadi, H, M Salmazadeh, G Ahmadi, and S Jafari. 2016. "Simulations of Indoor Airflow and Particle Dispersion and Deposition by the Lattice Boltzmann Method Using LES and RANS Approaches." *Building and Environment* 102. Elsevier Ltd: 1–12.

Development of a Supermarket Prototype Building Model

Piljae Im^{1,*}, Brian A. Fricke¹, Joshua R. New¹, and Mark B. Adams¹

¹Oak Ridge National Laboratory, Oak Ridge, TN. U.S.A.

*Corresponding email: impl@ornl.gov

ABSTRACT

The U.S. Department of Energy supports the development of commercial building energy codes and standards by participating in industry reviews, update processes, and providing technical analyses to support both published model codes and potential changes. In support of ANSI/ASHRAE/IES Standard 90.1 and the International Energy Conservation Code, 16 commercial prototype building models were developed that cover 80% of the commercial building floor area in the United States for new construction, including both commercial buildings and mid- to high-rise residential buildings, across all U.S. climate zones. However, the current set of commercial prototype building models does not include a supermarket building type, which is one of major building types defined in the Energy Information Administration's Commercial Building Energy Consumption Survey. As part of an ongoing effort to expand the current Commercial Building Prototype Model suite, this paper presents the procedure used to develop the prototype supermarket building model based on multiple studies as well as a previously developed reference building model. The final set of prototype models includes 68 models for different vintages of ASHRAE Standard 90.1 (i.e., 2004, 2007, 2010, and 2013) and for 17 ASHRAE climate zones.

KEYWORDS

Commercial Building Prototype Model, EnergyPlus, OpenStudio, Supermarket

INTRODUCTION

The U.S. Department of Energy (DOE) supports the development of commercial building energy codes and standards by participating in industry reviews and update processes, and provides technical analyses to support both published model codes and potential changes. DOE publishes its findings to ensure transparency and to make its analysis available for public use. In conjunction with this effort, DOE's flagship building energy modeling (BEM) tools consist of the open-source EnergyPlus simulation engine and the OpenStudio software development kit. These tools allow a user to modify a building and estimate energy use. New releases of these tools are typically downloaded by over 40,000 users.

As part of DOE's support for ANSI/ASHRAE/IES Standard 90.1 (ASHRAE, 2016a) and the International Energy Conservation Code (IECC) (ICC, 2015), researchers at Pacific Northwest National Laboratory (PNNL) apply a suite of prototype buildings covering approximately 80% of the U.S. commercial building floor area (Goel et al., 2014; Deru et al., 2011). These buildings include new and existing construction, mid- to high-rise residential buildings and span all U.S. climate zones. These prototype buildings—derived from DOE's Commercial Reference Building Models¹—cover all Reference Building types except for supermarkets, and an additional prototype representing high-rise apartment buildings. Since Standard 90.1 and IECC are updated every three years, PNNL modifies the commercial

¹ Available in <https://www.energy.gov/eere/buildings/commercial-reference-buildings>

prototype building models with extensive input from ASHRAE 90.1 Standing Standards Project Committee (SSPC) members and other building industry experts.

The prototype models include 16 commercial building types in 17 climate locations (across all 8 U.S. climate zones) for recent editions of Standard 90.1 and IECC. The combinations result in an overall set of 2,176 total building models (in EnergyPlus Version 8.0). The supermarket model was excluded from the original prototype suite for the following reasons: 1) the building type covers a relatively small percentage of total commercial floor area (EIA, 2003), 2) the refrigeration equipment/system was not regulated by earlier versions of ASHRAE Standard 90.1, and 3) there was insufficient data regarding common design practice. Newer versions of ASHRAE Standard 90.1 include regulations for refrigeration systems, and more data is now available for supermarket building characteristics (especially for refrigeration systems). This study leveraged multiple sources to develop the OpenStudio supermarket prototype building model. This paper presents the research conducted to define the building and system characteristics for prototype supermarkets, and the final prototype building energy models for supermarkets.

METHODS

The new supermarket prototype building model was developed based on extensive review of existing literature and resources as well as the original, post-1980 supermarket reference model. The basic building size, shape, and window distribution of the new prototype follows the original reference model, consisting of a one-story building, 4,181 m² floor area, floor-to-floor height of 6.10 meters, and window area of 130 m². This building form was originally defined based on the *2003 Commercial Buildings Energy Consumption Survey (CBECS)* and DOE Benchmark documents (EIA, 2003; DOE, 2008). Subsequently, the space types and their internal layout were updated based on the *Grocery Store 50% Energy Savings Technical Support Document* (Leach et al., 2009). The updated space types in this report were also used in the development of the baseline model found in ASHRAE's *Advanced Energy Design Guide (AEDG) for Grocery Stores* (ASHRAE, 2015). Figure 1 shows allocated floor area for each space type in the newly-developed prototype building model. The original reference model consists of 6 space types, whereas the updated prototype building consists of 13 space types. With the additional space types, the model more accurately reflects actual supermarket buildings. In addition, the corresponding space attributes (including occupancy density, lighting power density, plug load and ventilation rate) are defined for each space type to represent properties based on surveys of supermarket buildings. These space attributes are in alignment with the requirements from each vintage of ASHRAE Standard 90.1 and ASHRAE Standard 62.1 (ASHRAE, 2016b). The operating hours for the prototype supermarket are 6:00

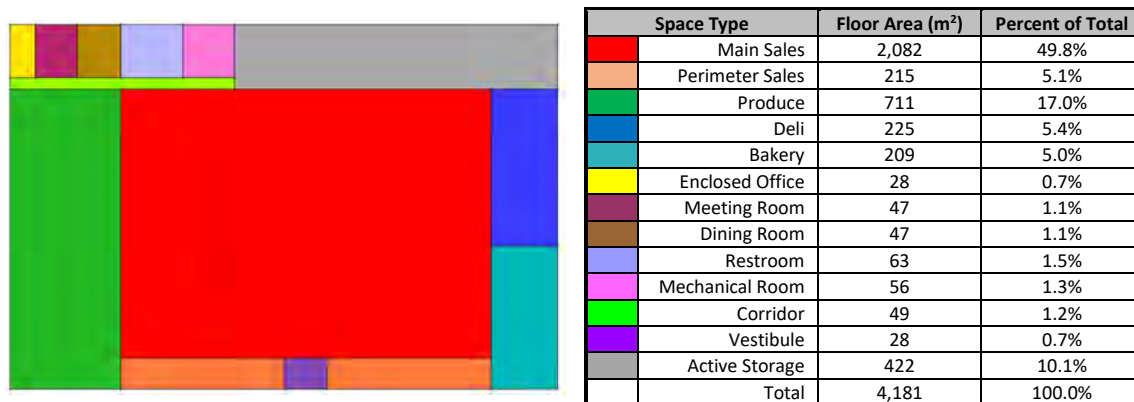


Figure 1. Supermarket space layout and floor area per space type

am through 10:00 pm, Monday through Sunday, with occupancy and lighting schedules defined in accordance with ASHRE 90.1-1989. The dominant wall type is mass (e.g., brick, stone, or concrete) (EIA, 2003) and the roof type is all insulated above deck (ASHRAE, 2016a).

The heating, ventilation, and air conditioning (HVAC) system for the new model consists of a unitary rooftop unit with direct expansion (DX) coils and natural gas heating, as defined by CBECS (EIA, 2003). The supply fans are constant volume. The efficiency of the cooling and heating units, including economizers, are defined per ASHRAE 90.1 requirements.

Major updates were made to the refrigeration system in the new prototype building model. Since there were no regulations for the refrigeration system in ASHRAE Standard 90.1-2004, the requirements for the refrigeration system were assumed to be the average of nationwide standard design practice in the corresponding year. In updating the refrigeration system, first, based on the AEDG project committee's feedback, the original refrigeration system in the reference model was modified with longer display cases and increased walk-in cooler/freezer space. The original reference model has 6 refrigerated display cases, 5 refrigerated walk-ins, and 4 compressor racks, while the updated model has 26 refrigerated display cases of 7 different types, 10 refrigerated walk-ins, and 4 refrigeration systems. The low-temperature (LT) display case models include specifications for coffin ice cream, coffin frozen food, reach-in ice cream and reach-in frozen food cases, while the medium-temperature (MT) display case models include coffin, vertical open, service and reach-in cases. For "old" systems (ASHRAE 90.1-2004, 2007 and 2010) and "new" systems (ASHRAE 90.1-2013), typical values for the rated capacity, fan power, lighting power, anti-sweat heater power, defrost type and power, and evaporator temperature of these display case types (for both "old" and "new" vintage cases) were defined, based on statistical analysis of refrigeration system manufacturers' data. A summary of the display case types and their specifications are given in Table 1. Furthermore, walk-in cooler/freezer cooling capacity was defined in terms of walk-in floor area, based on a least-squares fit of walk-in manufacturers' performance data. In the prototype supermarket models, the total length of the display cases is 225.2 m, and the total insulated floor area for the walk-ins is 321 m².

Table 1. Summary of selected display case performance parameters.

Case Type	Rated Cooling Capacity (W/m)		Defrost Type		Evaporator Temperature (°C)	
	Old	New	Old	New	Old	New
LT Cases						
Coffin Ice Cream	695	521	Electric	Electric	-28.9	-32.2
Coffin Frozen Food	589	436	Electric	Electric	-25.6	-26.7
Reach-in Ice Cream	618	462	Electric	Electric	-28.3	-27.4
Reach-in Frozen Food	584	425	Electric	Electric	-23.9	-23.3
MT Cases						
Coffin	1250	303	Off cycle	Electric	-6.1	-6.4
Vertical Open	1438	1143	Off cycle	Off cycle	-6.1	-3.1
Service	404	599	Off cycle	Off cycle	-7.8	-6.4
Reach-In	--	309	--	Off cycle	--	-0.8

Generic compressor performance maps are provided for modeling “old” compressor racks (using reciprocating compressors) and “new” compressor racks (using scroll compressors). Compressor racks utilize air-cooled condensers, and condenser fan power has been fit to compressor heat rejection capacity based on condenser manufacturers’ data. To simplify the model development, only limited number of inputs value were entered, and other required input parameters were automatically calculated based on further study from refrigeration system manufacturers’ data and statistical analysis.

Once all the building characteristics for the prototype supermarket building were defined, the prototype building model was generated in an automated fashion. An OpenStudio Measure was used to automatically generate the supermarket prototype building for 16 climate locations and 4 building standards (Roth et al., 2016). This measure, OpenStudio-Standards, provides mechanisms to add new building types, such as the supermarket, and its building characteristics. Additionally, the measure automatically assigns and models all 90.1 building standard requirements. By using an OpenStudio Measure, the OpenStudio-Standards can be used to generate OpenStudio Prototype Buildings using all OpenStudio workflows.

RESULTS

Based on the procedure described above, the final set of 68 prototype supermarket models were created covering different vintages of ASHRAE Standard 90.1 (i.e., 2004, 2007, 2010, and 2013) and for 17 ASHRAE climate zones. We compared the models for ASHRAE Standard 90.1-2004 to the original, post-1980 vintage reference building. Figure 2 presents the annual site energy by end use for the prototype building models and the post-1980 reference building models. The comparison shows that the overall refrigeration system energy use increased for the new prototype models in all climate zones since there were major updates to the refrigeration system, and the size (e.g., linear length of case) of the refrigeration system increased. The reduction in cooling energy use in warmer climates and heating energy use in colder climates is primarily due to improved building envelope systems and reduced infiltration rates. Other end uses such as interior/exterior lighting and interior equipment are nearly identical. The difference in total site energy use between the new prototype model and the original referent model ranged from -13% to 11%.

Total simulated energy use was also compared with real-world surveys of energy use data from EIA’s CBECS (EIA, 2003). According to CBECS, the national average energy use per unit floor area for the building type “food sales” is 630.2 kWh/m². The simulated energy use intensity (EUI) across climate zones for the new supermarket model are between 610 and 902 kWh/m². These simulation results appear reasonable given that CBECS includes all (i.e., old and new) existing supermarket buildings. The largest energy use within the supermarket is attributed to “Refrigeration”, and CBECS shows the EUI for refrigeration energy use is about 299 kWh/m², close to the simulated refrigeration use, which ranges from 233 to 298 kWh/m².

Figure 3 shows the total site energy use of the prototype supermarket model for different climate zones and different ASHRAE 90.1 vintages. As shown, the total energy use decreases for newer vintages, but there is a larger decrease for the 2013 vintage. This is primarily due to the reduced refrigeration energy use since the refrigeration system in 2004, 2007, and 2010 was defined as an “old system”, while the system for 2013 model was defined as a “new system”. The total energy use for the 2013 model is about 29 to 36% lower than the 2004 model.

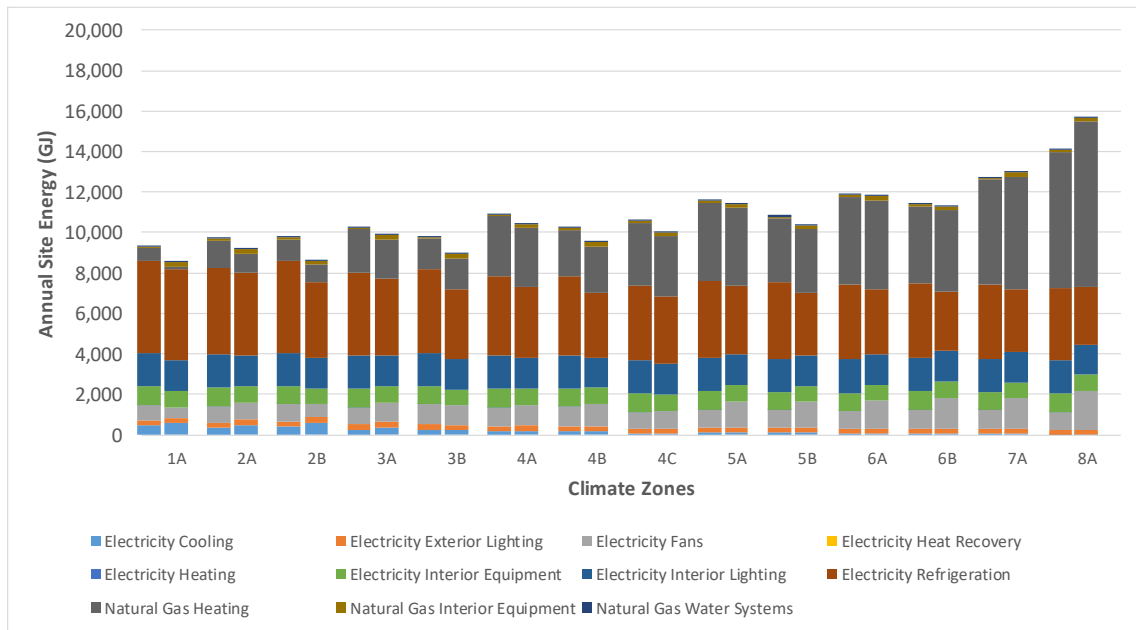


Figure 2. Annual site energy for the 2004 prototype supermarket models (left) vs. the post-1980 reference supermarket models (right)

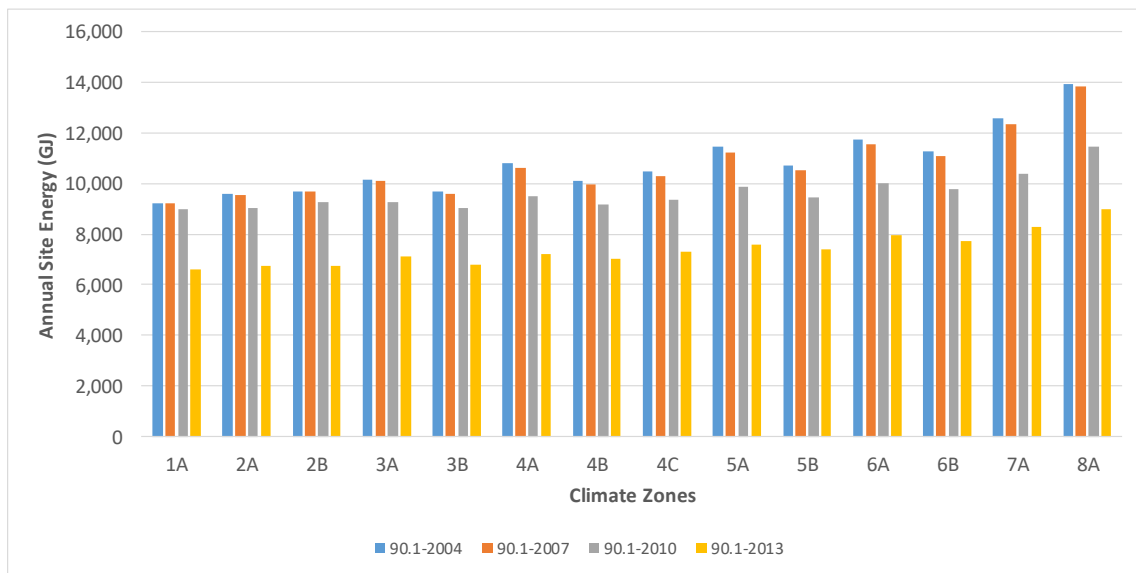


Figure 3. Annual site energy for the supermarket models corresponding to ASHRAE 90.1-2004, 2007, 2010, and 2013.

DISCUSSIONS AND CONCLUSIONS

As an effort to expand the current Commercial Building Prototype Model suite, this paper presents the procedure and results of developing a prototype supermarket building model. The final set of prototype models includes 68 models for different vintages of ASHRAE Standard 90.1 (i.e., 2004, 2007, 2010, and 2013) and for 17 ASHRAE climate zones, and the modelled energy uses are consistent with existing data from multiple sources.

ACKNOWLEDGEMENT

This work was funded by field work proposal CEBT105 under the Department of Energy Building Technology Activity Number BT0305000. The authors would like to thank Amir Roth for his support and review of this project.

DISCLAIMER

Oak Ridge National Laboratory is managed by UT-Battelle, LLC, for the U.S. Dept. of Energy under contract DE-AC05-00OR22725. This manuscript has been authored by UT-Battelle, LLC, under Contract Number DE-AC05-00OR22725 with the U.S. Department of Energy. The United States Government retains and the publisher, by accepting the article for publication, acknowledges that the United States Government retains a non-exclusive, paid-up, irrevocable, world-wide license to publish or reproduce the published form of this manuscript, or allow others to do so, for United States Government purposes.

REFERENCES

- ASHRAE. 2015. *Advanced Energy Design Guide (AEDG) for Grocery Stores*. Atlanta, GA: American Society of Heating, Refrigerating and Air-Conditioning Engineers, Inc. (ASHRAE).
- ASHRAE. 2016a. *ANSI/ASHRAE/IES Standard 90.1-2016*, Energy Standard for Buildings Except Low-Rise Residential Buildings. Atlanta, GA: American Society of Heating, Refrigerating and Air-Conditioning Engineers, Inc. (ASHRAE).
- ASHRAE. 2016b. *ASHRAE Standard 62.1-2016*, Ventilation for Acceptable Indoor Air Quality. Atlanta, GA: American Society of Heating, Refrigerating and Air-Conditioning Engineers, Inc. (ASHRAE).
- Deru M, Field K, Studer D, Benne K, Griffith B, Tocellini P, Liu B, Halverson M, Winiarski D, Yazdani M, Huang J, and Crawley D. 2011. *U.S. Department of Energy Commercial Reference Building Models of the National Building Stock*. NREL/TP-5500-46861, Golden, CO: National Renewable Energy Laboratory (NREL).
- DOE. 2008. *Commercial Building Benchmark Energy Simulation Models*. Washington, D.C.: U.S. Department of Energy (DOE).
- EIA. 2003. *Commercial Buildings Energy Consumption Survey*. Washington, D.C.: U.S. Energy Information Administration (EIA).
- Goel S, Athalye R, Wang W, Zhang J, Rosenberg M, Xie Y, Hart R, Mendon V. 2014. *Enhancements to ASHRAE Standard 90.1 Prototype Building Models*. PNNL-23269, Richland, WA: Pacific Northwest National Laboratory (PNNL).
- ICC. 2015. *2015 International Energy Conservation Code (IECC)*. Falls Church, VA: International Code Council, Inc. (ICC).
- Leach, M., E. Hale, A. Hirsch, and P. Torcellini (2009). *Grocery Store 50% Energy Savings Technical Support Document*, Technical Report, NREL/TP-550-46101.
- Roth A, Goldwasser D, and Parker A. 2016. There's a measure for that! *Energy and Buildings*, 117, 321-331.

Improving the representation of convective heat transfer in an urban canopy model

Qi Li^{1,*}, Jiachuan Yang², Zhi-Hua Wang³ and Elie Bou-Zeid²

¹School of Civil and Environmental Engineering, Cornell University, Ithaca, NY

²Civil and Environmental Engineering, Princeton University, NJ

³School of Sustainable Engineering and the Built Environment, Arizona State University, AZ

*Corresponding email: ql56@cornell.edu

ABSTRACT

The urban street canyon has been widely recognized as a basic surface unit in urban micrometeorological studies. Urban canopy models (UCMs), which quantify the exchange of energy and momentum between the urban surface and the overlying atmosphere, often adopt this type of street canyon representation as the fundamental surface element. Since UCMs can be coupled to regional-scale weather and climate models such as the Weather Forecast and Research Model (WRF), parametrizations of the surface momentum and scalar fluxes in UCM are of paramount importance. However, many current single-layer UCMs rely on empirical relations that were obtained over 80 years ago and often invoke the exponential wind profile derived from the existing literature for vegetation canopy. In this study, we conducted wall-modeled large-eddy simulations (LES) to study the forced (very weak buoyancy) convective heat transfer over idealized two-dimensional street canyons. It shows that the transfer efficiency computed following commonly applied resistance formulations can be one order of magnitude lower than LES results. The main reasons for the deviation include inaccurate wind speed parameterization and the use of a log-law based formulation for turbulent heat exchange between canyon air and the flow above.

KEYWORDS

Large-eddy simulation, convective heat transfer, urban canopy model

INTRODUCTION

Buildings do not exist as isolated objects. Their energy consumptions are subject to their external environment and especially the climatic factors such as wind speed, temperature and moisture (Li and Sailor, 1995). To represent this impact of urban climate on building performance, various building energy models have been implemented into urban canopy models (UCMs) (Kikegawa et al. 2003; Salamanca et al. 2010; Bueno et al. 2011). A UCM is one type of urban land-surface model that accounts for the surface heat balance using the street canyon as the prototypical element for the surface. Different UCMs of different degrees of complexity exist in the literature, e.g. (Masson, 2000; Ryu et al. 2011; Wang et al. 2013). Buildings exchange energy with the surrounding environment via conductive, radiative, and convective heat transfer processes. While the two former processes are captured relatively well by current UCMs, convective transfer poses significant challenges.

Nevertheless, accurate modelling of convective heat transfer is essential for building energy simulation (Mirsadeghi et al. 2013). For example, as summarized by Palyvos (2008), the wall convective heat transfer coefficient (CHTC), often denoted by h , could lead to errors in energy demand calculation of 20-40% if set improperly. The convective heat transfer due to turbulent air motions around the building envelopes has been parameterized in UCMs using empirical relations derived in the 1920s, such as the so-called Jürges formula (Rowley et al.

1930). One way to obtain better estimates of h is to use computational fluid dynamics (CFD) modelling to calculate the rate of convective heat transfer, with the CFD model coupled to the building energy model (Zhai et al. 2002; Zhai and Chen, 2004; Defraeye et al. 2010). However, this is not feasible for more than a few buildings and thus not applicable directly in a UCM. However, CFD results could be used to develop reduced parametrizations of convective heat transfer in UCMs, which have not been analyzed in detail. Therefore, this study conducts large-eddy simulations (LES) to assess the current formulation of convective heat transfer, as well as to propose possible reasons for its success or failure.

METHODS

LES is one type of computational fluid dynamics models, in which the large-scale fluid motions are explicitly resolved and appropriate subgrid-scale models are implemented for turbulence closure. We use a research code, which shares many commonalities with the open-source code LESGO (<https://github.com/lesgo-jhu/lesgo>). Details of the current LES code, validations of the turbulent quantities and convective heat transfer coefficients for two-dimensional roughness elements can be found in previous studies (Bou-Zeid et al. 2005; Chester et al. 2007; Li et al. 2016a,b). A surface of two-dimensional street canyons of various height-to-width aspect ratios H/W are considered in this study. The boundary conditions are horizontally periodic and free-slip for velocity at the top of the domain (Figure 1a). The net radiation on all surfaces (i.e., roof, wall, and road) is kept at 800 W/m^2 , and the wall-model is coupled to a conduction model with a constant indoor temperature at $25 \text{ }^\circ\text{C}$, similar to the setup in Li and Wang (2017). 16 points are used to represent the obstacle height H at 12.5 m. The total number of points in each direction is shown in Fig. 1a and grid resolution is the same in all three directions.

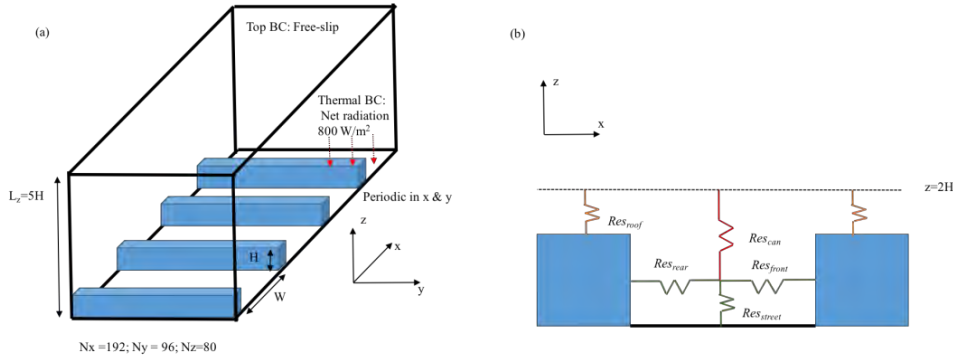


Figure 1. Sketch showing domain setup of LES in (a) for $H/W=1/2$ and (b) schematic diagram of resistance, the dotted line denotes the ‘reference height’ at $z=2H$, which is not shown to scale.

RESULTS

The exchange of energy between building facets with canyon air and canyon air with the flow above is often conceptualized as a resistance network (Fig. 1b), such as in previous UCMs and those coupled with EnergyPlus (Bueno et al. 2011). Resistance is related to h by $R = (h/\rho C_p)^{-1}$, where ρC_p is the volumetric heat capacity. Since h is the heat flux divided by the wall-fluid temperature difference, the normalized canyon resistance is computed as

$$R_{can} = \frac{\langle T_{can} - T(z=2H) \rangle}{\langle Q_H \rangle / \rho C_p}, \quad (1)$$

where $\langle \rangle$ denotes averaging over the canyon width for all canyons in the computational domain; T_{can} is the air temperature averaged over the entire canyon; $T(z=2H)$ denotes air

temperature at $z=2H$; Q_H is the sensible heat flux from the resolved and subgrid-scale contributions. Values of the canyon resistance span almost two orders of magnitude for the five different cases of canyon aspect ratios considered in this study (Fig. 2).

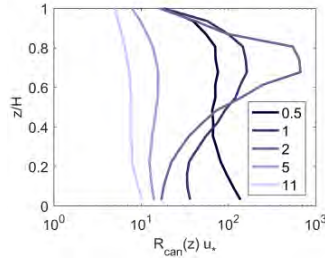


Figure 2. The canyon resistance R_{can} normalized by u_* , the friction velocity, for different values of W/H indicated by the legend.

Figure 3 shows the height averaged canyons resistance, $\langle Res_{can} \rangle_z$ plotted as a function of the difference between U_a , the horizontally averaged mean streamwise velocity at $z=2H$, and U_{can} , which is defined as the average magnitude of the vector sum of the horizontal and vertical components of velocity averaged over all non-solid grids for $z \leq H$ (Fig. 3a). All velocities in subsequent analyses are normalized by u_* . The square symbols denote modelled values based on the log-law and constant momentum and heat roughness lengths (e.g. Masson 2000). $\langle Res_{can} \rangle_z$ is also plotted as a function of the streamwise velocity averaged over the canyon space, $\langle U \rangle_z$, in Fig. 3b.

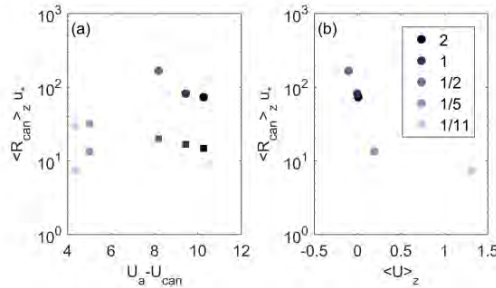


Figure 3. The averaged canyons resistance plotted as a function of U_{can}^2 in (a) and $\langle U \rangle$ in (b). Square: model in (Masson 2000), where $Res_{can} \sim \log(z/z_{0m})\log(z/z_{0h}) / (U_a - U_{can})$; circles are LES results.

The wall resistance R_{facet} is computed as the average over the facet of

$$R_{facet} = \frac{T_{facet} - T_{canyon}}{\langle Q_{Hwall} \rangle / \rho C_p} \quad (\text{rear, street and front facets}), \quad R_{roof} = \frac{T_{roof} - T(z=2H)}{\langle Q_{Hwall} \rangle / \rho C_p}, \quad (2)$$

where T_{air} is the air temperature at the closest grid to the wall surface; T_{canyon} is the air temperature averaged over the canyon space (for all rear, front and street facets) or T_{air} at $z=2H$; $\langle Q_{Hwall} \rangle$ is the facet-averaged sensible heat flux computed from the wall model in LES. Figure 4 shows the spatial variability of $u_*(h/\rho C_p)^{-1}$ for different facets of the two-dimensional obstacles, where h is the CHTC computed from the LES wall-model averaged over y . Cases with $H/W=2$ and 1 have similar roof resistances (Fig 4a), but a wider street canyon, especially $W/H=5$, has approximately 25% higher resistances than those in $H/W=2, 1$ and $1/2$. It is also interesting to note that the rear surface resistance is higher for smaller aspect ratio (i.e. $H/W < 1/2$), which could lead to overall smaller average wall resistance as demonstrated in Figure 5. The wall resistance averaged over different facets as a function

U_{can}^2 and comparisons to some of the convective heat transfer formulations defined as $\rho C_p(11.8+4.2U_{can}^2)^{-1}$ (Rowley et al. 1930) in UCMs are plotted in Fig. 5.

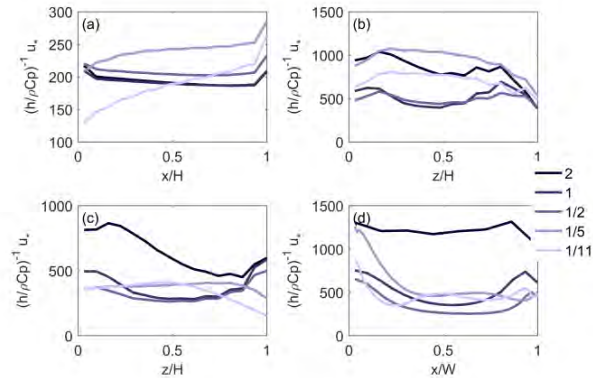


Figure 4. The wall resistance normalized by u^* for different facets of the street canyon for W/H indicated by the legend. a) roof, b) rear surface, c) front surface, d) ground.

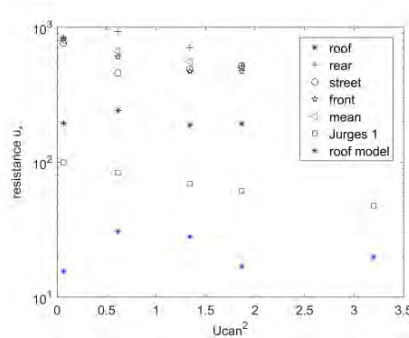


Figure 5. Res_{facet} averaged over different facets as a function of U_{can}^2 . The mean of Res_{facet} is the average over rear, ground and front surfaces. From low to high U_{can}^2 corresponds to $H/W = 2, 1/5, 1/11, 1$ and $1/2$ respectively.

DISCUSSION

The spatial variation of canyon resistance demonstrates some commonalities for canyons of different aspect ratios. The most pronounced peak in Res_{can} is observed for $H/W = 1/2$ at around $z/H = 0.6 - 0.8$ in Fig 2. Although other cases also show similar peaks, the pronounced peak is associated with street canyons that are categorized as ‘wake interference’ flow regime (Oke 1987), where the recirculation regions behind the two-dimensional obstacles impinge on the obstacle downstream. For regions $z/H < 0.5$, R_{can} decreases with aspect ratio as shown in Fig. 2. Street canyons with $H/W < 1/2$ have a smaller resistance, leading to higher turbulent heat fluxes given a constant temperature difference between the canyon air temperature and surface temperature. However, the canyon averaged R_{can} as shown in Fig. 3 is predominantly affected by the maximum values of R_{can} . The recirculation region, where the mean streamwise velocity becomes negative, is evident for $H/W > 1/2$. The case of $H/W = 1/2$ features the most negative canyon averaged streamwise velocity and the highest $\langle R_{can} \rangle_z$, which is the R_{can} averaged over the entire street canyon. $\langle R_{can} \rangle_z$ decreases monotonically with the canyon averaged wind speed. Notice that the simulations only consider the canyon axis perpendicular to the streamwise direction, which facilitates the formation of strong recirculation bubble. The ubiquitously adopted exponential wind profile for the canopy layer in UCMs (Masson 2006; Ryu et al. 2011; Wang et al. 2013) are usually considered as an average over all wind directions. Future studies of variable wind directions can be included in LES and investigate

how the canyon wind speed can be used as the key dependent variable for parameterization of the canyon resistance.

The canyon wall resistance is important to quantify the turbulent heat transfer between individual facet and the canyon air for the rear, front and ground faces in particular. The Jürges formula (Rowley et al. 1930) applied with the canyon wind speed computed from LES (Jürges 2) has almost one order of magnitude difference compared to the LES results, although the decreasing trend with higher U_{can} is consistent. Results using the parameterized canyon wind speed according to Masson (2000) (not shown here) show over prediction of the canyon wind speed. This demonstrates that the importance of improving the accuracy of the canyon wind speed when the Jürges formulation is invoked, such as using a CFD model to parameterize U_{can} for different wind directions as propose by Ryu et al. (2011). The empirical Jürges formula in the form of $(a+bU_{can}^2)^{-1}$, where a and b are both tuneable parameters, could still be a valid formulation.

On the other hand, the roof resistance in Fig. 4 shows both inconsistent trend and large bias in magnitude compared to the formulation based on the log-law wind profile over a rough surface. Alternative parameterization of the roof resistance assuming the flow is a free shear layer (Harman et al. 2004) gives rise to $R_{roof}=(U_{ref}-U_{roof})/u_*^2$. We also tested plotting R_{roof} as a function of $\Delta U=U(z=2H)-U_{roof}$, where U_{roof} is taken as the velocity at $z=1.06H$ averaged over points directly above the roof surfaces (not shown here). A monotonic change in R_{roof} with ΔU suggests that the free shear layer could be a more appropriate conceptual model to parameterize the roof resistance, instead of using the parameterization based on log-law, which assumes that the boundary layer is in equilibrium with the roof surface. More investigations of how the free shear layer impacts the roof resistance will be carried out.

CONCLUSIONS

We applied the LES model to study the convective heat transfer coefficient for idealized two-dimensional street canyons of different aspect ratios. The canyon and surface resistance were computed and compared with the Jürges formula (for rear, front and ground surfaces) and log-law based formulation (for canyon and roof surface). It was found that the current formulation, on average, predicts resistances one order of magnitude smaller than results from LES. Although the Jürges formula appears capable of capturing the trend of surface resistance as a function of the canyon wind speed, it is essential to obtain more accurate estimates of the canyon wind speed. Canyon wind speed computed from the exponential relation has been shown by Castro (2017) to be inappropriate for roughness canopy and alternative wind speed parameterizations need to be formulated for better representation of forced convective heat transfer. Our preliminary results also show that the canyon and roof resistances could be improved by considering a free shear surface and using the difference in mean velocity as the dependent variable. Future work includes simulations of multiple wind directions, expanding the range of canyon aspect ratio and testing the resistance parameterizations in UCMs.

ACKNOWLEDGEMENT

This work is supported by the US National Science Foundation's Sustainability Research Network Cooperative Agreement 1444758. The simulations were performed on the supercomputing clusters of the National Centre for Atmospheric Research through projects P36861020 and UPRI0007.

REFERENCES

Bou-Zeid, E., C. Meneveau, and M. Parlange, 2005: A scale-dependent Lagrangian dynamic

- model for large eddy simulation of complex turbulent flows. *Phys. Fluids*, **17**, 1–18.
- Bueno, B., L. Norford, G. Pigeon, and R. Britter, 2011: Combining a Detailed Building Energy Model with a Physically-Based Urban Canopy Model. *Boundary-Layer Meteorol.*, **140**, 471–489.
- Castro, I. P., 2017: Are Urban-Canopy Velocity Profiles Exponential? *Boundary-Layer Meteorol.*, **164**, 337–351.
- Chester, S., C. Meneveau, and M. B. Parlange, 2007: Modeling turbulent flow over fractal trees with renormalized numerical simulation. *J. Comput. Phys.*, **225**, 427–448.
- Defraeye, T., B. Blocken, and J. Carmeliet, 2010: CFD analysis of convective heat transfer at the surfaces of a cube immersed in a turbulent boundary layer. *Int. J. Heat Mass Transf.*, **53**, 297–308.
- Harman, I. N., J. F. Barlow, and S. E. Belcher, 2004: Scalar Fluxes from Urban Street Canyons Part II: Model. *Boundary-Layer Meteorol.*, **113**, 387–410.
- Kikegawa, Y., Y. Genchi, H. Yoshikado, and H. Kondo, 2003: Development of a numerical simulation system toward comprehensive assessments of urban warming countermeasures including their impacts upon the urban buildings' energy-demands. *Appl. Energy*, **76**, 449–466.
- Li, Q., E. Bou-Zeid, and W. Anderson, 2016a: The impact and treatment of the Gibbs phenomenon in immersed boundary method simulations of momentum and scalar transport. *J. Comput. Phys.*, **310**, 237–251.
- , ———, ———, S. Grimmond, and M. Hultmark, 2016b: Quality and reliability of LES of convective scalar transfer at high Reynolds numbers. *Int. J. Heat Mass Transf.*, **102**, 959.
- Li, X., and D. J. Sailor, 1995: Electricity use sensitivity to climate and climate change. *World Resour. Rev.*, **7**.
- Masson, V., 2000: A physically-based scheme for the urban energy budget in atmospheric models. *Boundary-Layer Meteorol.*, **94**, 357–397.
- Masson, V., 2006: Urban surface modeling and the meso-scale impact of cities. *Theor. Appl. Climatol.*, **84**, 35–45.
- Mirsadeghi, M., D. Cóstola, B. Blocken, and J. L. M. Hensen, 2013: Review of external convective heat transfer coefficient models in building energy simulation programs: Implementation and uncertainty. *Appl. Therm. Eng.*, **56**, 134–151.
- Oke, T. R., 1987: *Boundary layer climates, Second edition*. 435 pp.
- Palyvos, J. A., 2008: A survey of wind convection coefficient correlations for building envelope energy systems' modeling. *Appl. Therm. Eng.*, **28**, 801–808.
- Rowley, F. B., A. B. Algren, and J. L. Blackshaw, 1930: Surface conductances as affected by air velocity, temperature and character of surface. *ASHRAE Trans*, **36**, 429–446.
- Ryu, Y. H., J. J. Baik, and S. H. Lee, 2011: A new single-layer urban canopy model for use in mesoscale atmospheric models. *J. Appl. Meteorol.* **46**, 1067–1079.
- Salamanca, F., A. Krpo, A. Martilli, and A. Clappier, 2010: A new building energy model coupled with an urban canopy parameterization for urban climate simulations-part I. formulation, verification, and sensitivity analysis of the model. *Theor. Appl. Climatol.*, **99**, 331–344.
- Wang, Z.-H. H., E. Bou-Zeid, and J. a Smith, 2013: A coupled energy transport and hydrological model for urban canopies evaluated using a wireless sensor network. *Q. J. R. Meteorol. Soc.*, **139**, 1643–1657.
- Zhai, Z., and Q. Chen, 2004: Numerical determination and treatment of convective heat transfer coefficient in the coupled building energy and CFD simulation. *Build. Environ.*, **39**, 1001–1009.
- , ———, P. Haves, and J. H. Klems, 2002: On approaches to couple energy simulation and computational fluid dynamics programs. *Build. Environ.*, **37**, 857–864.

Streamlined CFD Simulation Framework to Generate Wind-Pressure Coefficients on Building Facades for Airflow Network Simulations

Timur Dogan^{1,*}, Patrick Kastner¹

¹Cornell University, Department of Architecture, Environmental Systems Laboratory

*Corresponding email: tkdogan@cornell.edu

ABSTRACT

Energy modeling packages such as EnergyPlus and TRNSYS come with capable airflow network solvers for natural ventilation evaluation in multi-zone building energy models. These approaches rely on pressure coefficient arrays of different wind directions based on simple box-shaped buildings without contextual obstructions. For specific sites, however, further attention is needed to avoid geometric oversimplification. In this study, we present an automated and easy-to-use simulation workflow for exterior airflow simulation based on OpenFOAM to generate pressure coefficient arrays for arbitrary building shapes and contextual situations. The workflow is compared to other methods commonly used to obtain pressure coefficients for natural ventilation simulation.

KEYWORDS

Natural Ventilation, Airflow Networks, Pressure Coefficients, Computational Fluid Dynamics.

INTRODUCTION

Due to urbanization and population growth, the United Nations expects a construction demand that is equivalent to 750 times the size of Rome (Heilig, 2012). This may be a unique opportunity to improve the built environment and quality of life through an integrated design process that utilizes Building Energy Modeling (BEM) to create high-comfort habitats with low carbon footprints. The majority of the construction volume is expected to take place in warmer, subtropical and tropical climates. Here, studies have shown that natural ventilation (NV) can be an effective method for space cooling and can lead to significant energy savings compared to mechanical ventilation (Cardinale, Micucci, & Ruggiero, 2003; Oropeza-Perez & Ostergaard, 2014). BEM packages like *Energy Plus* and *TRNSYS* come with capable airflow network (AFN) solvers for NV evaluation in multi-zone BEMs. These solutions rely on pressure coefficient (c_p) arrays of different wind directions and exterior simulation nodes. For simple, box-shaped buildings without contextual obstructions, lookup tables and fast methods for surface-averaged pressure coefficient generation exist, such as the work of Swami and Chandra (Swami & Chandra, 1988) now implemented in *EnergyPlus*, or the wind-pressure distribution model *CpCalc+* developed for *COMIS* (Grosso, 1992). Since then, many attempts have been made to deal with air flow sheltering effects for simplified urban geometries and there is an evolving literature about pressure coefficients for sheltered buildings that are summarized by (Costola, Blocken, & Hensen, 2009). However, for specific sites such as dense urban environments, further attention is needed to avoid geometric oversimplification (Cheung & Liu, 2011). In such cases, computational fluid dynamics (CFD) analyses are required. CFD is a numerical method to calculate the desired flow variables on a number of grid points within a simulation domain by solving discretized Navier-Stokes equations (NSE).

However, the expertise, the modeling effort, and simulation overhead required to perform such analyses often hinder a wider dissemination of AFN-based NV studies. To facilitate modeling of NV in early design processes at urban and complex architectural scale, the authors introduce

Eddy, an easy-to-use tool, that utilizes OpenFOAM to conduct isothermal exterior airflow simulations to generate pressure coefficient (c_p) arrays for the AFNs. The framework is fully automated and generates c_p arrays for arbitrary building shapes and contextual situations using a novel cylindrical domain approach to avoid expensive re-meshing of the domain for different wind directions. Further, a case study for an urban building is presented to compare CFD-based c_p values against the wind pressure distribution model of *CpCalc+* and *EnergyPlus*' internal c_p calculation method called "Average-Surface Calculation" (Swami & Chandra, 1988). The c_p results of each method are subsequently passed on to an *EnergyPlus* BEM with an AFN to evaluate the differences in NV potential using the different NV simulation modes provided by *EnergyPlus*.

METHODS

Overview: Usually, five steps are required to compute c_p arrays for AFN simulations: (1) modeling the building geometry and context with CAD software; (2) defining the simulation domain and meshing of the building geometry and topography; (3) conducting isothermal airflow simulations for a set of wind directions using appropriately assigned boundary conditions; (4) post-processing the CFD data and extracting pressure values on openings for multiple directions and (5) setup of energy model and AFN while providing c_p arrays for all openings in the model. In most cases, these steps are conducted manually and tend to be tedious and error-prone, especially when they have to be repeated multiple times. For step 2 and 3, several best practice guidelines propose adequate domain dimensions, convergence criteria, and relaxation factors. For basic urban CFD simulations, it is considered best practice to construct a box-shaped virtual wind tunnel with predefined dimensions with respect to the building geometry that shall be simulated. A widely used best practice proposed by (Tominaga et al., 2008) suggests the size of the simulation domain to be $z = 6H_{max}$, $l = 20H_{max}$ and w given by a blocking ratio of $\leq 3\%$, where z , l , and w are the dimensions of the domain and H_{max} is the height of the tallest building in the building agglomeration. The blocking ratio is defined as the ratio of building area perpendicular to the inlet to the total area of the inlet. A visual representation of those suggestions is illustrated in Figure 1 (A). For cases where symmetry cannot be exploited and where the weather does not have strongly pronounced predominant wind directions, the steps 2-4 would have to be repeated at least eight times to cover approaching wind in 45° increments. However, interpolating the remaining in-between directions often results in significant errors (Cheung & Liu, 2011). This can only be overcome by further increasing the wind direction increments, resulting in greater meshing, simulation, and post-processing time.

Cylindrical simulation domain: To circumvent re-meshing of the simulation domain for every wind direction and to reduce manual and computational overhead, a cylindrical mesh is used to facilitate the simulation of arbitrary wind directions, see Figure 1 (B). The modeling approach has been validated against three cases with measured data showing insignificant differences compared to the best practice box-domain approach (Kastner & Dogan, 2018). Furthermore, the proposed method automates the setup of boundary conditions so that a significant amount of time will be saved to change the boundary conditions in case of an annual wind analysis. More specifically, every lateral cylinder patch represents an adjustable and therefore sufficiently small circular sector and can be assigned to either inlet (blue) or outlet (red) conditions depending on the wind direction of interest, see Figure 1 (B).

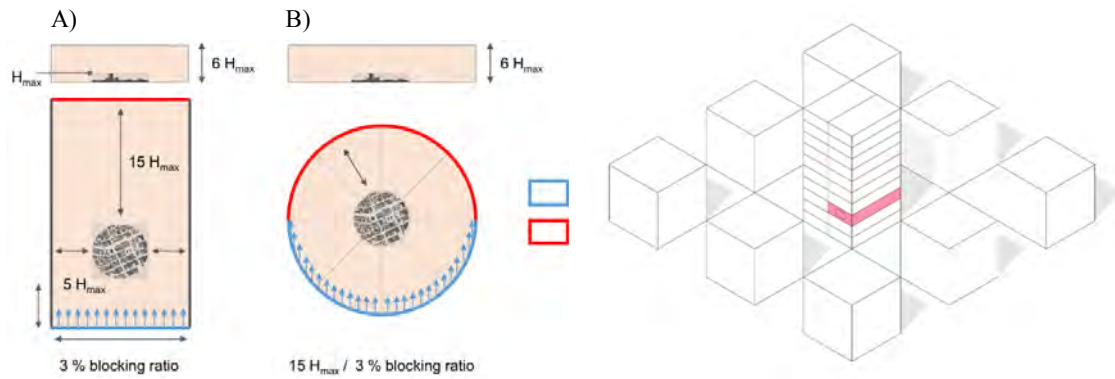


Figure 1: Top view of the (A) of a typical simulation domain for an arbitrary urban area; (B) top view of proposed cylindrical simulation domain accounting for the same best practice requirements.

Figure 2: CAD model of the test case. Case one is simulated without contextual obstructions. Case two is simulated as depicted. Red highlights the zone that was modeled in EnergyPlus.

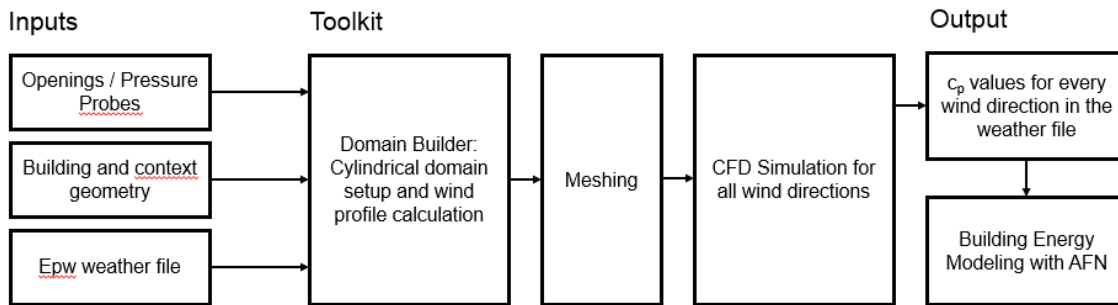


Figure 3: Flow-chart for proposed c_p generation methodology

Implementation: The procedure above has been fully automated and implemented in C# as a plugin for Rhino v5 (Robert McNeel & Associates, 2016b) and Grasshopper (Robert McNeel & Associates, 2016a) for seamless design workflow integration. The developed tool, called *Eddy*, consists of the following main components: (1) the Domain-Builder sets up the cylindrical simulation domain by analyzing the input geometry and applying best practice rules. The Domain-Builder organizes geometric and non-geometric input data and manages the setup of all cases required to model different wind directions (2). The Meshing-Component creates one circular domain mesh that can be used for all wind directions. (3) The CFD-simulation component executes the simulations and encapsulates the result processing routines and probes data for a given slice, envelope or point (figure 4). c_p values are then automatically calculated for all façade openings. A coupling to the Archsim interface for *Energy Plus* (Dogan, 2018) is provided. All simulation framework components and the flow of inputs and outputs are illustrated in Figure 3. Numerical simulations are based on the open source CFD library *OpenFOAM*, using its steady-state RANS models and solvers in combination with a $k-w-SST$ turbulence model. Pressure and velocity were coupled with the SIMPLE algorithm using three non-orthogonal correctors. Buoyancy effects were neglected due to the domain-decoupled approach and the given air velocities that are well above 1.8 m/s (Ramponi & Blocken, 2012; Tecle, Bitsuamlak, & Jiru, 2013). The framework uses a combination of a logarithmic, exponential or uniform profile as introduced by (Bueno, Roth, Norford, & Li, 2014). Further, we assumed that convergence was obtained when reaching residuals of $1e-4$ for p and $1e-5$ for the remaining parameters. The relaxation factors were chosen to be 0.7 for p and 0.3 for U , k , and ω . Relative wind pressure coefficients (c_p^*) are defined as the difference of the wind pressure coefficient with respect to the inlet condition as given in equation (1) (ASHRAE,

2013). The subscript (*i*) labels the inlet condition. The pressures c_p and $c_{p,i}$ are obtained from CFD simulation results. The reference velocity ($u_{ref,nv}$) is mainly used to normalize the nodal pressure, and can therefore be set as the largest freestream velocity at the top of the modeling domain. Further, (ρ) is the density of air given in kg·m⁻³. Those pressure differences can be utilized to calculate flow rates and air changes per hour, thus in turn estimating the NV potential.

$$c_p^* = c_p - c_{p,i} = \frac{p-p_{atm}}{\frac{1}{2}\rho u_{ref,nv}^2} - \frac{p_i-p_{atm}}{\frac{1}{2}\rho u_{ref,nv}^2} = \frac{p-p_i}{\frac{1}{2}\rho u_{ref,nv}^2} \quad (1)$$

Case study: Figure 2 shows the case study (Architectural Institute of Japan, 2003) used for the coupling of CFD-based c_p values with an *EnergyPlus* energy model using an AFN. The scale ratio used for the simulations in this paper is 100:1. The c_p values generated with the proposed CFD workflow are compared to *CpCalc+* and the Swami & Chandra model implemented in *EnergyPlus*. The latter only calculates surface-averaged c_p values for orifices with respect to the incident wind angle. The obstructed case shown in Figure 2 is compared to an unobstructed case for which all eight surrounding buildings have been removed. Further, a single zone on the third floor with two opposing orifices (red) is modeled in *EnergyPlus* to compute indoor temperatures, air change rates, cooling loads, and the ASHRAE 55 Adaptive Comfort model. For this zone, a hybrid NV system is assumed that switches to full mechanical cooling if the outdoor air temperature increases beyond 28°C. For each variant, the zone is modeled based on either a residential, classroom or office setting using SIA space templates (SIA, 2006) as well as based on heavy mass or lightweight structure with an average envelope U-Value of 0.4 [W/m²K]. Using weather data from Darwin, Cairo, Hyderabad, Mumbai, New Delhi, Nairobi, Mexico City, Karachi, Manila, Bangkok, Tunis, Izmir, Taipei, Caracas, Cape Town, Melbourne, and Singapore — each variant was further tested yielding a total 102 simulation variants.

RESULTS

Figure 4 compares the c_p values retrieved from the CFD simulation and *CpCalc+*. Without the surrounding buildings, both methods are in good agreement. With surrounding obstructions, *CpCalc+* exceeds its confidence interval and is neither able to estimate c_p distributions nor pressure differences between facades. A comparison of the c_p values of all three methods for eight wind directions is given in Figure 5. The results show that both *CpCalc+* and Swami & Chandra consistently overestimate the c_p arrays. This overestimation leads to significantly deviating air change rates calculated by the AFN in *EnergyPlus* as shown in Figure 6 (left and middle). However, this influence is less significant with respect to the comfort hours where the majority of predictions fall within a $\pm 5\%$ interval (Figure 6 (right)). Nonetheless, significant outliers exist when the cooling potential of NV reaches its limit and is thus more dependent on high flow rates.

DISCUSSION AND CONCLUSION

The study has shown that it is possible to automate and streamline CFD-based c_p generation and the coupling with AFN workflows. The juxtaposition of c_p values calculated with different methods reveals that NV modeling is still subject to great uncertainty. Especially in denser environments where contextual building geometries change wind patterns, the current user-friendly tools significantly overestimate wind-induced air flow rates and NV potential. It should be noted that a fairly simple building geometry was used for the case study. It is therefore likely that the performance of the methods by *CpCalc+* and Swami & Chandra will be worse for geometries for which symmetries cannot be exploited. Thus, they are not recommended for (1) geometries that differ from cuboids, (2) projects that are sited in hilly topography (3) buildings with significant contextual obstructions such as urban areas. For such cases, the tool introduced provides a viable alternative that may be used for NV analysis in case of complex building

geometries and dense urban sites. It is worth noting that both the setup of the presented study as well as the coupling with the annual AFN simulation took less than 10 minutes. Further, the CFD simulations converged in less than one hour on consumer hardware. As such, it is the authors' hope that the presented tool facilitates the use of CFD-based NV analysis for sustainable and passive design strategies.

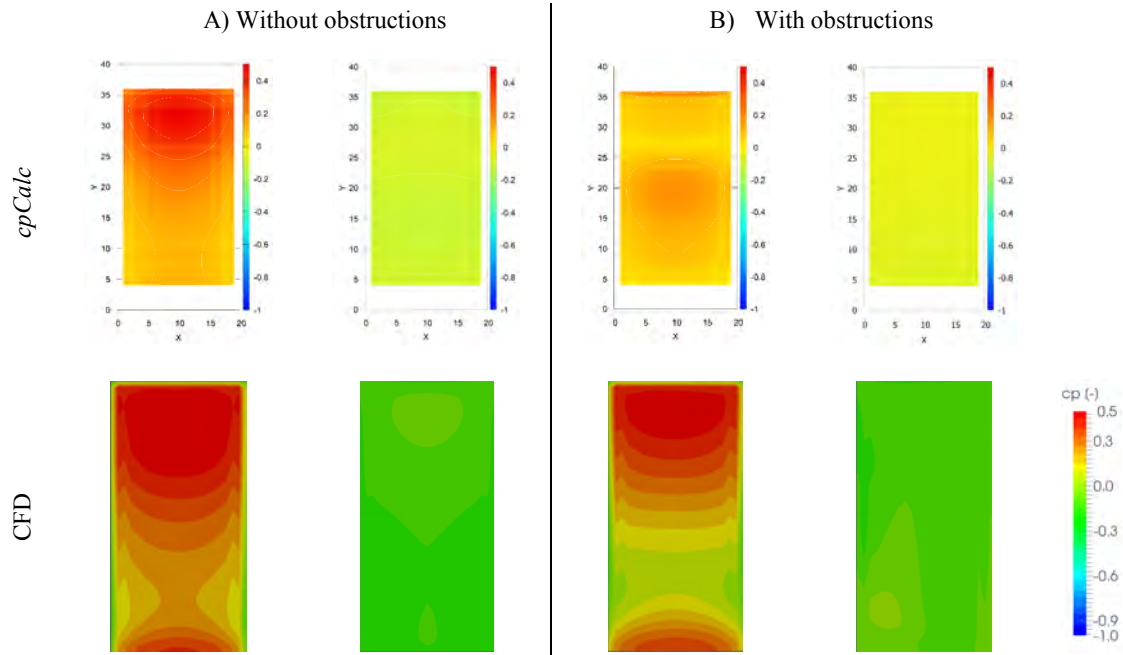


Figure 4: Pressure coefficients at wind-ward (left) and lee-ward (right) façade calculated with CpCalc+ and CFD. The left plots refer to the simulation without obstructions (single building), the right plots to the simulation with obstructions (10 buildings).

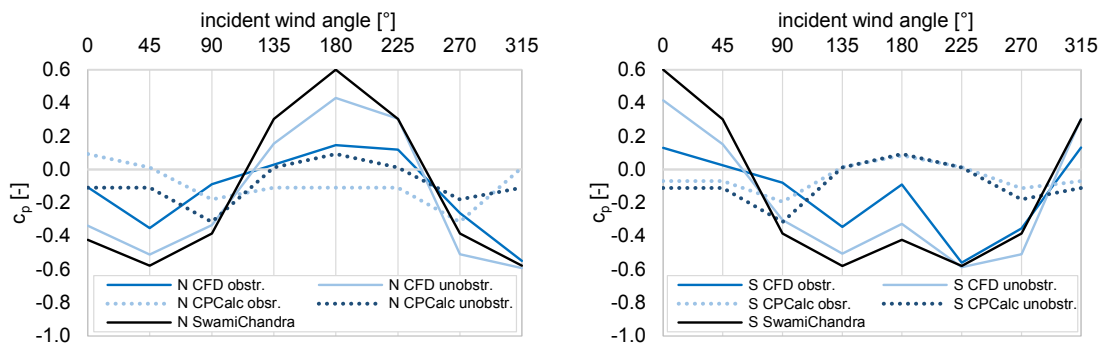


Figure 5: c_p arrays by method for window 1 (left) and window 2 (right).

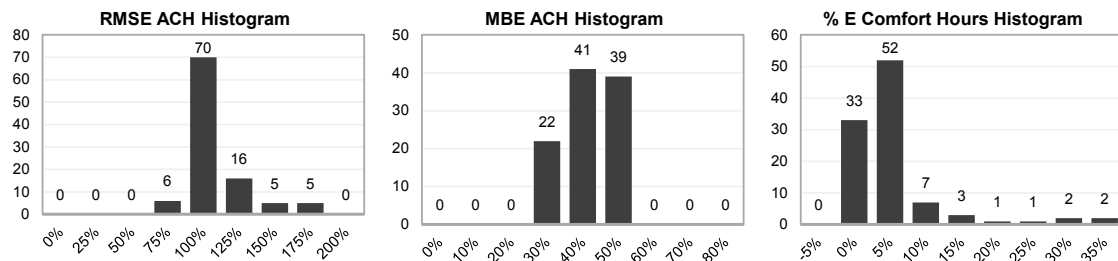


Figure 6: Histograms quantifying the RMSE (left), mean bias error and the difference between c_p values generated by EnergyPlus (auto-calculation) and the CFD simulation (right).

ACKNOWLEDGEMENTS

The authors would like to acknowledge the financial support by the Cornell University David R. Atkinson Center for a Sustainable Future for funding this research.

REFERENCES

- Architectural Institute of Japan. (2003). Guidebook for Practical Applications of CFD to Pedestrian Wind Environment around Buildings: C Simple Building blocks. Retrieved from https://www.aij.or.jp/jpn/publish/cfdguide/index_e.htm
- ASHRAE. (2013). *ASHRAE Handbook—Fundamentals (SI)*. ASHRAE Atlanta.
- Bueno, B., Roth, M., Norford, L., & Li, R. (2014). Computationally efficient prediction of canopy level urban air temperature at the neighbourhood scale. *Urban Climate*, 9, 35–53.
- Cardinale, N., Micucci, M., & Ruggiero, F. (2003). Analysis of energy saving using natural ventilation in a traditional Italian building. *Energy and Buildings*, 35(2), 153–159.
- Cheung, J. O., & Liu, C.-H. (2011). CFD simulations of natural ventilation behaviour in high-rise buildings in regular and staggered arrangements at various spacings. *Energy and Buildings*, 43(5), 1149–1158.
- Costola, D., Blocken, B., & Hensen, J. (2009). Overview of pressure coefficient data in building energy simulation and airflow network programs. *Building and Environment*, 44(10), 2027–2036.
- Dogan, T. (2018). *Archsim energy modeling software*. Retrieved from www.solemma.net
- Grosso, M. (1992). Wind pressure distribution around buildings: a parametrical model. *Energy and Buildings*, 18(2), 101–131.
- Heilig, G. K. (2012). World urbanization prospects: the 2011 revision. *United Nations, Department of Economic and Social Affairs (DESA), Population Division, Population Estimates and Projections Section, New York*, 14.
- Kastner, P., & Dogan, T. (2018). Optimization of meshing methodologies for annual urban CFD simulations. In *ESIM Canada 2018*. Montreal, Canada: IBPSA Canada.
- Oropeza-Perez, I., & Ostergaard, P. A. (2014). Energy saving potential of utilizing natural ventilation under warm conditions—a case study of Mexico. *Applied Energy*, 130, 20–32.
- Ramponi, R., & Blocken, B. (2012). CFD simulation of cross-ventilation for a generic isolated building: Impact of computational parameters. *Building and Environment*, 53, 34–48. <https://doi.org/10.1016/j.buildenv.2012.01.004>
- Robert McNeel & Associates. (2016a). *Grasshopper*. Retrieved from <http://www.grasshopper3d.com/>
- Robert McNeel & Associates. (2016b). *Rhinoceros (Version 5)*. Retrieved from <https://www.rhino3d.com/>
- SIA. (2006). 2024: Standard-Nutzungsbedingungen für die Energie-und Gebäudetechnik. *Zürich: Swiss Society of Engineers and Architects*.
- Swami, M., & Chandra, S. (1988). Correlations for pressure distribution on buildings and calculation of natural-ventilation airflow. *ASHRAE Transactions*, 94(3112), 243–266.
- Tecle, A., Bitsuamlak, G. T., & Jiru, T. E. (2013). Wind-driven natural ventilation in a low-rise building: A Boundary Layer Wind Tunnel study. *Building and Environment*, 59, 275–289.
- Tominaga, Y., Mochida, A., Yoshie, R., Kataoka, H., Nozu, T., Yoshikawa, M., & Shirasawa, T. (2008). AIJ guidelines for practical applications of CFD to pedestrian wind environment around buildings. *Journal of Wind Engineering and Industrial Aerodynamics*, 96(10–11), 1749–1761.

Unsteady-state exergy analysis on two types of building envelopes under time-varying boundary condition

Wonjun Choi^{1,*}, Ryoza Ooka¹ and Masanori Shukuya²

¹Institute of Industrial Science, The University of Tokyo

²Department of Restoration Ecology and Built Environment, Tokyo City University

**Corresponding email: wonjun@iis.u-tokyo.ac.jp*

ABSTRACT

In the built environment, the thermal exergy behavior is very sensitive to the change of environmental temperature, because the temperature difference between the reservoir and a system of interest is small. Moreover, the transient characteristics become very important for the building envelope, which is primarily affected by the environmental temperature changes and has a relatively large heat capacity. Most of the exergy analyses have been performed under steady-state assumption. However, it may miss some important details of the transient process. Thus, when the transient transfer process becomes important, the unsteady-state exergy analysis should be conducted. In this study, we propose complete energy, entropy, and exergy equations in their partial differential forms. By solving them numerically, we examined the transient exergy process inside the building envelope composed of concrete and insulation layers under time-varying boundary condition. Using this new methodology, we can improve the temporal and spatial resolution of the exergy analysis and thus provide more complete information about exergetic behavior.

KEYWORDS

Unsteady-state heat conduction; Thermodynamics; Numerical exergy analysis; Warm and cool exergy; Building envelope

INTRODUCTION

Applying exergy analysis method to a system of interest, we can quantify the part of the energy supplied that is not converted into work and the one that is converted (Shukuya, 2013). Here, we want to focus more on the temporal change of system state and discuss it in more detail. This transient exergetic process has not been well understood yet, because the majority of the exergy analyses have been conducted under steady-state assumption.

Consider building envelope as the system of interest, which is primarily affected by the dynamic change of the environmental temperature. In general, the building envelope has low thermal conductivity and large thermal capacity. Thus, when there is a temperature difference between the boundaries, the temperature distribution inside the envelope is not uniform. With respect to the environmental temperature, a very complex exergy process occurs that is dependent on the outer and inner surface temperatures, temperature distribution inside the envelope, and indoor air temperature. In other words, if we consider the building envelope as several discretized subsystems, the direction of heat flow changes dynamically with time due to the relationship between the temperatures of the adjacent subsystems. Consequently, the state and flow of warm or cool exergy and consumption change dynamically as well. For such a system, applying steady-state assumption could overlook some important details of the transient processes. Thus, when the transient exergy transfer process becomes important, an unsteady-state exergy analysis should be conducted.

Recently, we have proposed a complete form of unsteady-state exergy analysis which can be applied to any heat conduction problem (Choi, Ooka, & Shukuya, 2018). The governing equations for the energy, entropy, and exergy were presented in the differential form. Moreover, the numerical solution approach was described in detail and the numerical integrity of proposed methodology was verified by comparing the numerical result with the steady-state analytical solution. In this study, based on the developed method for unsteady-state exergy analysis, we studied transient exergy process in building envelopes.

GOVERNING EQUATIONS FOR UNSTEADY-STATE EXERGY ANALYSIS

Partial differential forms for energy, entropy and exergy equations

The governing equations for one-dimensional energy, entropy, and exergy transfers are given by Eqs. (1), (2), and (3), respectively. The details can be found in (Choi et al., 2018).

$$\frac{\partial Q}{\partial t} = -\frac{\partial q}{\partial x} \quad (1)$$

$$\frac{\partial S_{st}}{\partial t} = -\frac{\partial}{\partial x}\left(\frac{q}{T}\right) + q\frac{\partial}{\partial x}\left(\frac{1}{T}\right) \quad (2)$$

$$\frac{\partial X_{st}}{\partial t} = -\frac{\partial}{\partial x}\left(q - T_0\frac{q}{T}\right) - q\frac{\partial}{\partial x}\left(\frac{1}{T}\right)T_0 \quad (3)$$

Here, the infinitesimal change of thermal energy stored in a unit volume and the rate of heat flux are defined as $\partial Q = C\partial T$ and $q = -k(\partial T/\partial x)$, respectively. Additionally, $\partial S_{st}(= \partial Q/T)$ is the stored entropy, $X_{st}(= Q - T_0S_{st})$ is the stored exergy, C is the volumetric thermal capacity, T is temperature, t is time, x is the space coordinate, k is the thermal conductivity and T_0 is the environmental temperature. It should be noted that the temperature used in the entropy and exergy equations is the absolute temperature and has the units of Kelvin.

Discretized form of energy, entropy, and exergy equations

Using finite difference method, the governing equations can be solved. We used a central difference scheme and the hybrid Crank-Nicolson scheme for the temporal and spatial discretization, respectively. The discretized forms of the energy, entropy, and exergy equations are given by Eqs. (4), (5), and (6), respectively. The entropy and exergy equations are written in the form of [inflow] - [entropy generation or exergy consumption] = [stored] + [outflow] to explicitly represent the balance within the system.

$$\frac{T_i^{n+1} - T_i^n}{\Delta t} = \frac{1}{2C_i\Delta x_i} \{-q_{i+}^n + q_{i-}^n - q_{i+}^{n+1} + q_{i-}^{n+1}\} \quad (4)$$

$$\sigma_{fi,i} + \sigma_{g,i} = \sigma_{st,i} + \sigma_{fo,i} \quad (5)$$

$$\chi_{fi,i} - \chi_{c,i} = \chi_{st,i} + \chi_{fo,i} \quad (6)$$

It should be noted that each term in Eqs. (2) and (3) has the units of $W/(m^3 \cdot K)$ and W/m^3 , respectively, but Eqs. (5) and (6) have the units of $W/(m^2 \cdot K)$ and W/m^2 , respectively. Each term in Eqs. (5) and (6) has the following forms: entropy inflow, $\sigma_{fi,i} = (q_{i-}/T_{i-})|^{n+0.5}$, entropy generation, $\sigma_{g,i} = (\Delta x_i/k_i)(q_i^2/T_i^2)|^{n+0.5}$, entropy stored, $\sigma_{st,i} = \Delta x_i C_i (T_i^{n+1} - T_i^n)/\Delta t (T_i)|^{n+0.5}$,

entropy outflow, $\sigma_{fo,i} = (q_{i+}/T_{i+})|^{n+0.5}$, exergy inflow, $\chi_{fi,i} = \{q_{i-}(1 - T_0/T_{i-})\}^{n+0.5}$, exergy consumption, $\chi_{c,i} = (\Delta x_i/k_i)(q_i^2 T_0/T_i^2)|^{n+0.5}$, exergy stored, $\chi_{st,i} = \Delta x_i C_i (1 - T_0/(T_i))^{n+0.5} ((T_i^{n+1} - T_i^n)/\Delta t)$, and exergy outflow, $\chi_{fo,i} = \{q_{i+}(1 - T_0/T_{i+})\}^{n+0.5}$. Additionally, the subscript i is the i -th node, i_+ and i_- are the quantities defined between the nodes i and $i + 1$, and $i - 1$ and i , respectively, superscript n is the time step and $n + 0.5$ is the time step required for the Crank-Nicolson scheme. The detailed definition of each quantity and numerical scheme used can be found in (Choi et al., 2018).

PROBLEM SETTING

Concrete and insulation layers which have a thickness of 10 cm and 6 cm, respectively, were considered. Its thermal properties are listed in Table 1. To examine the difference in exergetic behavior depending on the location of insulation, two different envelope configurations were used. From the outside, the wall composition in the order of insulation–concrete or concrete–insulation is referred to as IC or CI, respectively (Figure 1).

The envelope was discretized at the uniform intervals of 1 cm as shown in Figure 1. The calculation conditions are summarized in Table 2. The total calculation period was 180 h, but the first 120 h were considered as the warm-up period. Thus, we only present the results of the last 60 h. Time-varying Dirichlet boundary condition (BC) using 24-h period sine curve was assigned for the outer surface BC, T_{os} and regarded as the environmental temperature, T_0 . For the inner surface BC, T_{is} , the constant temperature of 20 °C was assigned.

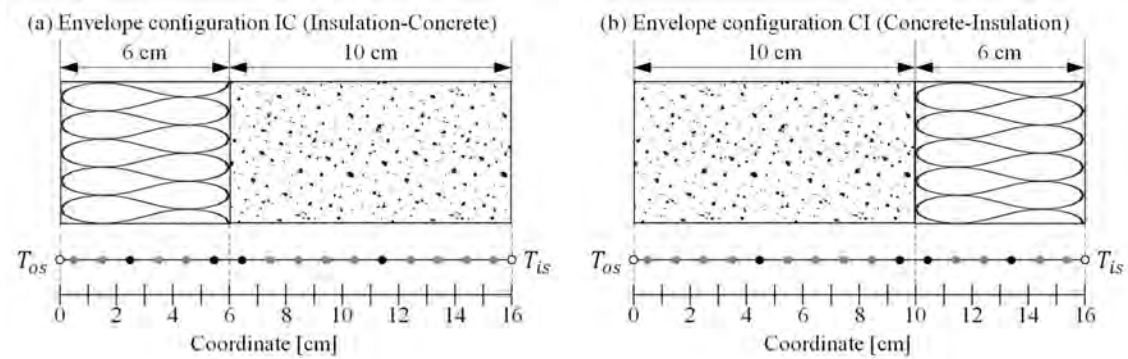


Figure 1. Schematic of two envelope configurations and nodes (T_{os} : outer surface boundary temperature, T_{is} : inner surface boundary temperature).

Table 1. Thermal properties of concrete and insulation.

Material	Thermal conductivity	Specific thermal capacity	Density
Concrete	1.5 W/(m·K)	2000 J/(kg·K)	1000 kg/m ³
Insulation	0.04 W/(m·K)	1500 J/(kg·K)	30 kg/m ³

Table 2. Calculation conditions (T_{ini} : initial temperature of calculation domain).

Time step	Calculation period	T_{ini} [°C]	$T_{os} = T_0$ [°C]	T_{is} [°C]
20 s	180 h (120 h warm up)	20	$T_{os} = 20 + 10 \sin\left(\frac{2\pi t}{24 \cdot 3600}\right)$	20

RESULTS

Energy results

The temperature variations obtained by solving the energy equation are shown in Figure 2 (a) and (b). In IC, the effect of time-varying outer BC reduces significantly through the insulation layer. As a result, the temperature near the interface between two material layers (near $x = 6$ cm) does not change a lot from the inner BC of 20 °C, and consequently the change of the external BC does not have a significant influence on the concrete layer. On contrary, CI has the concrete layer with low thermal resistance of the outer side, and thus the effect of time-varying T_{os} is transmitted through the concrete layer to the outer surface of the insulation layer without significant attenuation. Therefore, the interface temperature (near $x = 10$ cm) in CI is affected more by the change of T_{os} compared to that in IC.

In the plots of heat flux (Figure 2 (c) and (d)), we can observe a large difference between two cases. It should be noted that the direction of q from the outer to inner surface is defined as the positive value. The maximum magnitude of q in IC occurs at the outermost surface (approximately ± 6.5 W/m²) and there is no significant difference between the insulation and concrete layers (Figure 2 (c)). In contrast, in CI, the difference in q between the layers is significant. In concrete layer, the maximum q of $\sim \pm 130$ W/m² is generated at the outermost surface, but the one in the insulation layer is $\sim \pm 6$ W/m² only, that is almost of the same magnitude as the maximum q in IC (Figure 2 (d)).

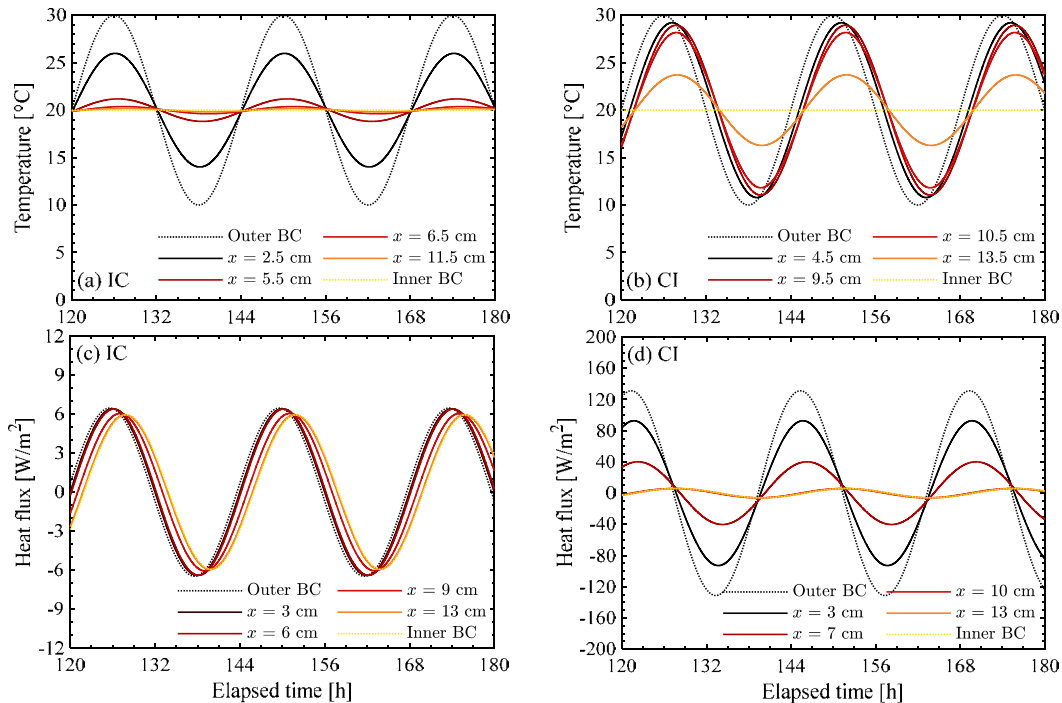


Figure 2. Node temperatures and heat flux at the interfaces: (a) temperature in IC; (b) temperature in CI; (c) heat flux in IC; and (d) heat flux in CI

Exergy results

Based on the results for the temperature and heat flux, entropy and exergy calculations are performed. Because the entropy is considered in the exergy equation, only the results of the exergy are presented. Figure 3 shows the exergy consumption rate, χ_c , stored rate, χ_{st} , and flow, χ_f , for some nodes and at the interfaces in the computational domain. The dashed and solid lines represent the values in insulation and concrete layers, respectively.

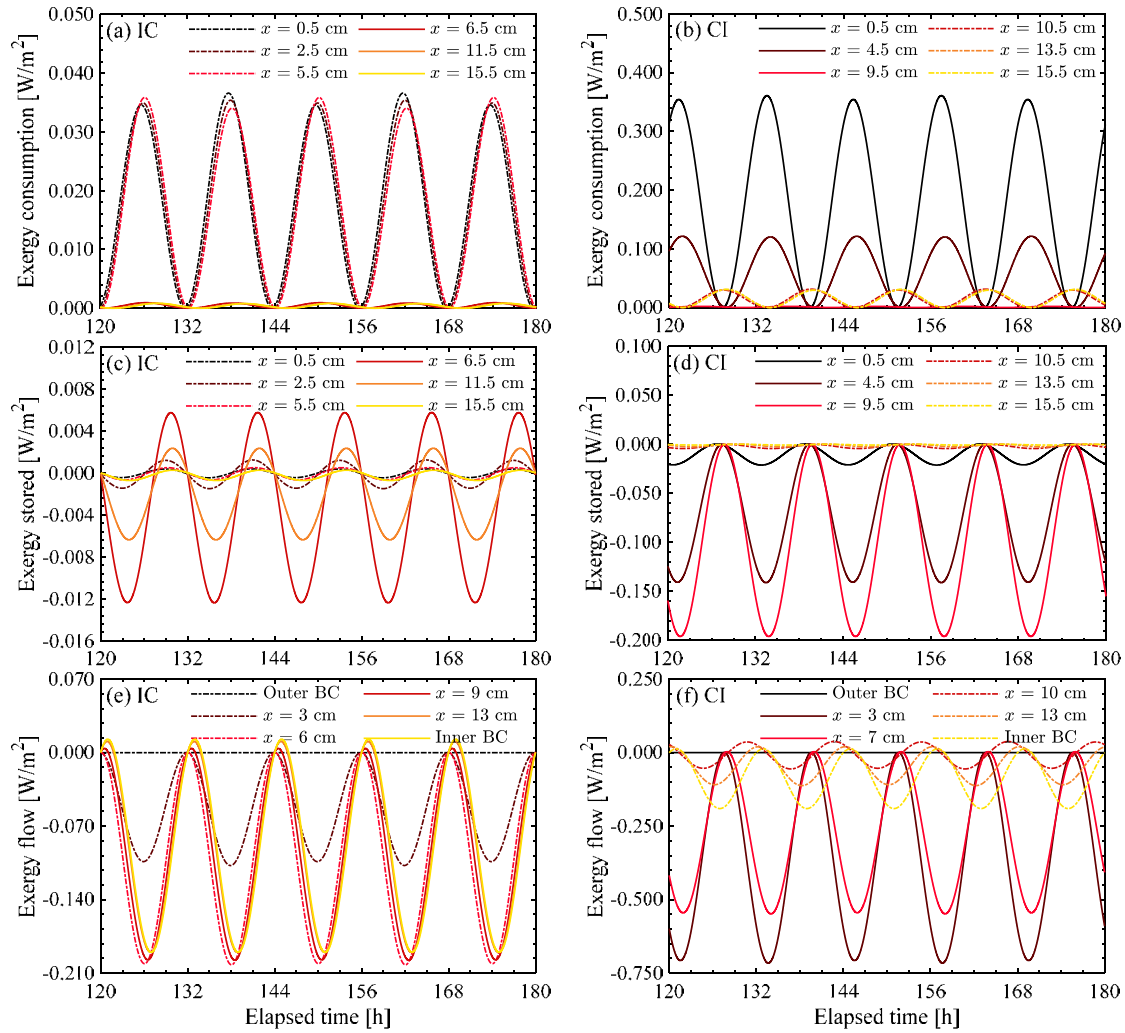


Figure 3. Exergy consumption rate, exergy stored rate, and exergy flow: (a) exergy consumption in IC; (b) exergy consumption in CI; (c) exergy stored in IC; (d) exergy stored in CI; (e) exergy flow in IC; and (f) exergy flow in CI.

Figure 3 (a) and (b) show that the maximum χ_c in CI is 10 times larger than that in IC (Note the difference in scales of vertical axes). This is because the heat flux, q , presented in Figure 2 is the dominant factor influencing χ_c . If the magnitude of q is similar, the larger the resistance, the greater the exergy consumption. It can be confirmed when we compare the magnitudes of χ_c in the insulation and concrete layers of IC.

The exergy stored rate, χ_{st} , is determined by Carnot coefficient $(1 - T_0/T_i)$ at the node, the time derivative of the node temperature $\partial T_i/\partial t$, and the volumetric heat capacity, C_i . Whether it becomes cool or warm is dependent on the sign of the node Carnot coefficient, and the increase or decrease of exergy stored rate is determined by the sign of χ_{st} . Because C_i of concrete is ~ 44 times larger than that of insulations (Table 2), we can observe large χ_{st} in the concrete layer for both cases (Figure 3 (c) and (d)). In addition, in terms of the time derivative of temperature, $\partial T_i/\partial t$ of the concrete layer in CI is larger than that in IC, because the effect of time-varying T_{os} is significantly reduced by the insulation layer placed at the outer side. Therefore, we can observe a large difference in χ_{st} for the concrete layer for IC and CI cases. Moreover, the behavior of χ_{st} changes depending on the location of the insulation. CI has

negative χ_{st} value for most times, which means that it moves only in a decreasing direction, whereas IC has a certain range of positive χ_{st} values.

The exergy flow, χ_f , is determined by the product of Carnot coefficient and heat flux. Because of the nature of the problem, that assumes the outer surface boundary as the environmental temperature, T_0 , the exergy inflow at the outer surface is zero, because the Carnot coefficient is always zero at the outer surface (Figure 3 (e) and (f)). As shown in Figure 2 (c), IC has very small spatial variations in the magnitude of q . Thus, there is no significant spatial variations in χ_f (Figure 3 (e)). However, in CI, a large attenuation of q from the outer to inner surface is observed (Figure 2 (d)) and it leads to the large spatial variations of χ_f (Figure 3 (f)). As mentioned previously, the heat flux from the outer to inner surface was defined to be positive. Thus, if the exergy flow has a negative value with the associated heat flux to be positive, then it is a cool exergy flow and its direction is opposite to the heat flux (i.e., the flow is from the cell interface to the outer surface).

We further analyzed the effects of insulation location on χ_c for the entire envelope. The total χ_c for two configurations and χ_c in each material layer are shown in Figure 4 (a) and (b), respectively. In the insulation layer, χ_c in IC is slightly larger than that of CI. In contrast, in the concrete layer, there is a significant difference in χ_c between two cases. The maximum χ_c in concrete layer are $\sim 0.008 \text{ W/m}^2$ and $\sim 1.33 \text{ W/m}^2$ for IC and CI, respectively. This significant difference is because χ_c increases quadratically with the heat flux q_i^2 . Therefore, the difference in q is further amplified in the results of χ_c . As a result, the total χ_c for the period of 120–180 h (i.e., $\chi_c \Delta t$) for IC and CI is 11.8 and 76.4 kJ/m², respectively.

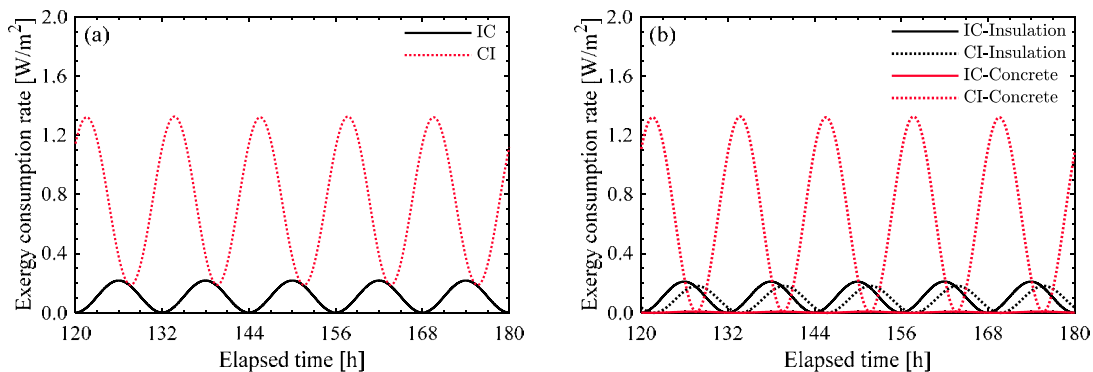


Figure 4. (a) total exergy consumption rate for two cases and (b) exergy consumption rate in insulation and concrete layers.

CONCLUSIONS

In this study, we have conducted an unsteady-state exergy analysis for two different building envelopes under time-varying boundary condition. This methodology provides insight into the transient exergetic behavior that is missing in the steady-state analysis. Moreover, it can provide higher temporal and spatial resolutions for the system of interest. In future, the studies will be conducted with more realistic problem setting considering radiative and convective exergy transfers.

REFERENCES

- Choi, W., Ooka, R., & Shukuya, M. (2018). Exergy analysis for unsteady-state heat conduction. *International Journal of Heat and Mass Transfer*, 116, 1124–1142.
- Shukuya, M. (2013). *Exergy: Theory and Applications in the Built Environment*. Springer.

Achieving Faster Building Energy Model Optimization through Selective Zone Elimination

Zixiao Shi, Scott Bucking, William O'Brien

Carleton University, Ottawa Canada

**Corresponding email: zixiao.shi@carleton.ca*

ABSTRACT

Optimization in building performance simulation (BPS) has become increasingly important due to the growing need for high-performance building design and operation. Numerous research efforts have been dedicated to decreasing optimization runtime by introducing improved optimization algorithms and advanced sampling techniques. This paper presents a novel model order reduction (MOR) algorithm tailored for speeding up building energy simulation. The algorithm identifies archetype zones simplifying the needless repetition of thermal zones. For an entire optimization process, this MOR method can be repeated recursively to reproduce reduced models. The proposed method can be used to speed up large-scale simulations including optimization, uncertainty analysis and model predictive controls. Preliminary results with parametric simulations show a runtime reduction of about 76% reduction for 15 simulations while still maintaining the predicted total annual energy consumption within a 10% margin. Further research will be conducted to compare the optimization results when applying the proposed MOR algorithm and determine if the reduced model produces the same optimal design. The proposed method may significantly improve the optimization runtime with a minor effect on optimization accuracy, thus increasing the overall usability of BPS optimizations.

KEYWORDS

building performance simulation, EnergyPlus, optimization, model reduction

INTRODUCTION

With the growth of interest in a sustainable built environment, the need for building performance simulation (BPS) has been accelerating (Infiniti Research Limited, 2015). Optimization in BPS has been used to find the optimal building energy performance within a considerable number of design variations. The recent development of generative community and building design have also led to the broader use of optimization in BPS. Furthermore, BPS optimization has also been applied in model predictive control to come up with optimal control strategies. While optimization is a powerful tool, the requirement for computational power and lengthy simulation time have been noted in many previous research, which hinders the practical usage of such technologies.

Reducing computation complexity and speeding up BPS optimization have been investigated by numerous researchers in the past. The following paragraphs will discuss three main approaches to this problem.

The first approach is to improve existing optimization algorithms. Many researchers have looked into improving the efficiency of commonly used optimization algorithms used for BPS (Christensen, Anderson, Horowitz, Courtney, & Spencer, 2006; Hamdy & Sirén, 2016; Nguyen, Reiter, & Rigo, 2014). A faster optimization process decreases the number of simulations

needed to obtain the optimal outcome, but it does not reduce the runtime of individual simulations.

Some researchers have also proposed the use of surrogate models. Surrogate models, or meta-models, are statistical models or machine learning models used to imitate BPS outputs based on different parameter changes. Examples of this approach include the use of support vector regression (Eisenhower, O'Neill, Narayanan, Fonoberov, & Mezić, 2012) for BPS optimization. The resulting surrogate models can produce outputs significantly faster than individual simulation runs. The shortcomings of this approach include the requirement of a large simulated dataset, as well as accuracy run-off when the inputs go outside of the trained parameter space. This approach is more reliable when the parameter space remains constrained, which makes it more suitable for model predictive control applications.

Finally, it is possible to reduce BPS model complexity. This approach aims to directly reduce the complexity of the BPS model to cut down simulation time. A mixture of physics-based abstraction and machine learning methods can be used for this purpose. The reduced model can be generated by simplifying the original model, or by building up a template model to approximate the original model. Van Treeck and Rank (2007) demonstrated reduction of building geometry by using graph theory. Georgescu and Mezić (2015) used a Koopman operator to merge similar adjacent zones into a single joint zone. The main disadvantage of this approach is that the reduced model can no longer be transformed back into the original model after the reduction process (Schilders, 2008).

This paper focuses on the building energy simulation (BES) aspect of the BPS. It is an extension of a previously published BPS MOR method called Model-Cluster-Reduce (Shi & O'Brien, 2017). The goal is to achieve faster BES optimization by integrating the MOR method with conventional iterative BES optimization. Unlike surrogate models, this MOR method only requires one simulation to obtain the reduced model. The reduced model is still a standard BPS model capable of accepting parameter changes beyond its trained parameter space. The reduced model can be opened up for troubleshooting. Throughout this paper, the original BES model is called original model, and the simplified BES model is called reduced model.

METHODOLOGY

In this paper faster optimization is achieved through the reducing the original model from one simulation run, then use it to partially or entirely replace further optimization steps. An overview of this process is shown in Table 1.

For a serial optimization process, multiple optimization steps can be carried out with the reduced model. Then the newly optimized parameters can be validated by a direct comparison between the reduced model and the original model. If the accuracy of the reduced model is confirmed, the optimization path based on the reduced model is accepted, and the optimization process will carry on. For an optimization process using a population, such as evolution algorithm, the reduced model can be used to replace a subpopulation of the models to speed up optimization. After a certain number of optimization steps, the newly updated reduced models need to be validated by the updated original models with the same parameter inputs, similar to the previous serial optimization process.

Table 1. Pseudo code for the proposed optimization procedure

1. Simulate original model
2. Create reduced model through selective zone elimination
3. Simulate reduced model
4. **If** results from the reduced model agrees well with the original model:
5. Optimize reduced model until parameters deviates too much or a certain number of iterations is reached
6. Update original model
7. **Else:**
8. Follow normal optimization procedures

The central philosophy behind this model reduction process is to selectively eliminate redundant thermal zones inside a BPS model and replace them with their archetypes. There are three main steps called model-cluster-reduce for this model reduction process:

The model step captures the characteristics of the original thermal zones by parameterizing a physics-based or statistically-driven model. This step produces a reduced number of parameters from the original model. Parameters estimated from inverse modelling and area normalized heating/cooling profile can be used to represent the zone characteristics. The normalized heating/cooling time series is selected to represent each zone in this paper, and the reduced parameter p is calculated as below:

$$p = \frac{\text{zone hourly heating/cooling load}}{\text{zone floor area}}$$

The cluster step uses the parameters obtained from the previous step to group thermal zones automatically using clustering techniques. Then the resulting centres of each clustered group become archetype zones needed for model reduction. Affinity Propagation (AP) is used in this research to form zone clusters and identify archetype zones. AP splits thermal zones into two categories: archetypes and zones belonging to their archetypes. This clustering process is achieved by iterating messages (availability and responsibility) between thermal zones until the similarity distance between the zones and their archetypes are minimized. For details about AP, the original paper by Frey & Dueck (2007). In this application, the similarity distance s is calculated by the Euclidean distance between the thermal zones:

$$s(\beta, \alpha) = -\|p_\beta - p_\alpha\|^2$$

As its name suggests, s represents how similar zone β is to its archetype zone α . The availability and responsibility are the same from the original AP paper by Frey & Dueck (2007).

The archetype zones are then used to produce the reduced model with a scale factor. All other zones except the archetype zones are removed from the model. The scale factors are calculated from attributes such as floor area and volume. If the boundary condition of the archetype zones' surfaces is not exterior or another archetype zone, it will be converted to adiabatic. In this application the scale factor is calculated from floor area:

$$\lambda_\alpha = \frac{\sum A_{\beta\alpha}}{A_\alpha}$$

Where λ is the scale factor, A is the zone floor area. More details about the model reduction process can be referred to the original paper by the authors (Shi & O'Brien, 2017).

RESULTS

A calibrated mixed-used building model is created in EnergyPlus (Crawley et al., 2001) and used as a proof of concept demonstration for this paper. The modelled building is located at London, Ontario, Canada. The model contains a total number of 51 zones with a mixture of retail and office space. The reduced model created from the reference design consists of 6 zones in total, resulting in an 86% reduction in computation time for each simulation run on an Intel® i5-7600 processor. For the whole optimization process using the proposed procedure, the total computation time is cut down by about 76%, from 44 minutes to 11.5 minutes.

Figure 1 shows a comparison of the predicted annual consumption from the original model and the reduced model. The difference in total energy consumption is approximately 10%, though with a significant difference in interior lighting. This discrepancy can be explained by the model reduction process being only focused on the heating/cooling response of the thermal zones while overlooking the internal load components. The implications of this will be further commented in the discussion section.

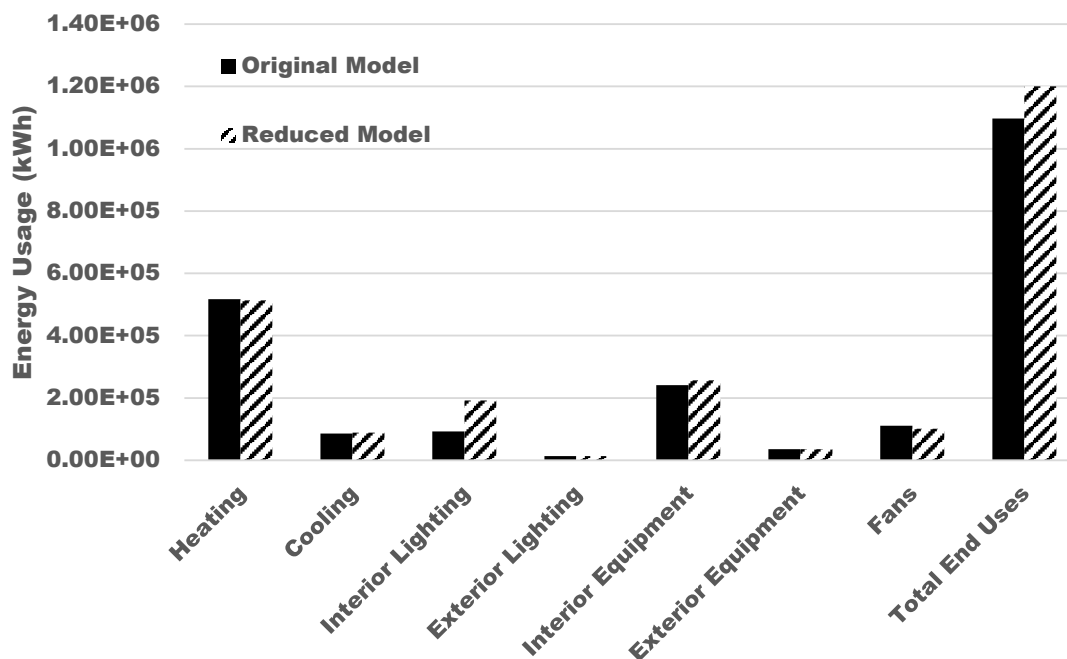


Figure 1. Comparison of the reference models

The reduced model and the original model were further tested in a series of parametric simulations to imitate an optimization process. Insulation levels, infiltration rate and south-facing window type were varied randomly to create 16 samples for each model. The results of these simulation runs are summarized in Figure 2 in the form of energy usage intensity (EUI) in kWh/m². EUI of the baseline model is approximately 220 kWh/m². As seen in the figure, as the parameter variations become larger and the EUI reduction from the reference model increases, the deviations of the energy savings predicted between the original model and the reduced model becomes larger. To alleviate this deviation inside the reduced model, after the initial ten simulations, the original model was updated with the new parameters, and a new

reduced model regenerated. The refreshed reduced model was able to provide closer simulation results to the reduced model, thus making the overall optimization process more reliable.

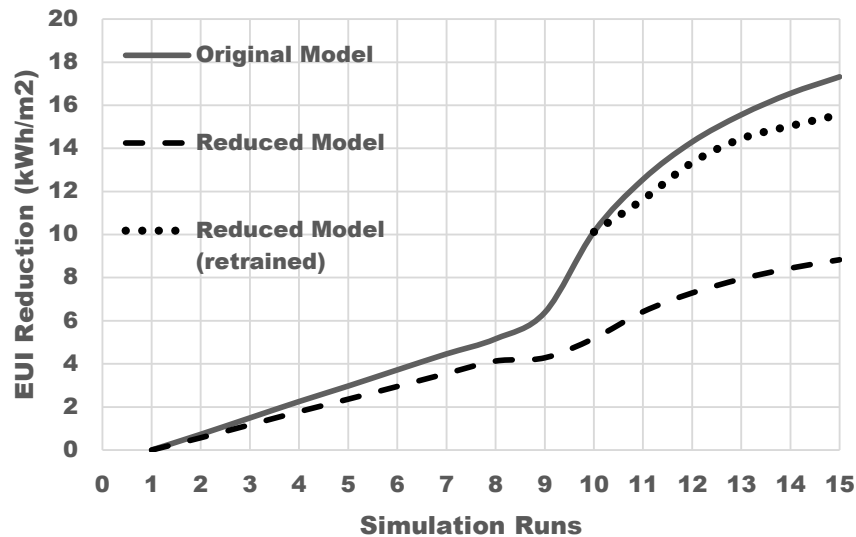


Figure 2. Comparison of the predicted EUI reduction between the original model and the reduced model over 15 simulations

DISCUSSIONS

Overall the proposed model reduction method shows potential to reduce the optimization time of large-scale BES. It also requires much less training data when compared to surrogate models. However, discrepancies in lighting loads were still identified, possibly due to the model reduction process only focused on heating/cooling characteristics. Fortunately, in this case study these loads are less significant than the other components, making the reduced model still reasonably accurate when used for parameter optimization. Other inverse modelling techniques can be tested to determine if this issue could be resolved.

As for the parametric simulation part, the first ten simulation runs performed quite well but the reduced model starts to diverge as its parameters deviate more from the values it was trained from. This mandates an iterative reduced model validation and retraining process inside an actual optimization process. This validation process can be designed to perform intermittently on a determinant number of optimization steps or based on the divergence of parameters from reference values. Even though new reduced models need to be regenerated intermittently, this model reduction process could still significantly reduce the overall simulation time.

Currently, the proposed model reduction process is not yet fully integrated with the existing BES optimization tools; part of the future work would be integrating it as part of a BES optimization package to provide a complete toolkit to the users. More simulation studies are also needed to further validate the proposed model reduction method.

CONCLUSIONS

This paper introduces a novel model order reduction method based on selective zone elimination to achieve faster building energy simulations. This method could significantly reduce the run time of large-scale simulation by providing approximations of best optimization path. Compared to surrogate models based on machine learning methods, this model reduction process still provides a first-principle BES model and requiring fewer simulations to generate

training data. The case study used in this paper shows a 76% reduction in total optimization time while still providing reasonable accuracy. The authors are planning to integrate this process with existing BES optimization packages and make it available as an open-source project.

ACKNOWLEDGEMENT

The authors would like to acknowledge the support they received from Autodesk Research and Natural Science and Engineering Research Council of Canada for implementing this work. The authors would also like to thank the valuable insights and advice provided by Dr. Ian Beausoleil-Morrison on this topic.

REFERENCES

- Christensen, C., Anderson, R., Horowitz, S., Courtney, A., & Spencer, J. (2006). *BEopt™ Software for Building Energy Optimization : Features and Capabilities*. Golden, CO.
- Crawley, D., Lawrie, L., Winkelmann, F., Buhl, W., Huang, Y., Pedersen, C., ... Glazer, J. (2001). EnergyPlus: creating a new-generation building energy simulation program. *Energy & Buildings*, 33(4), 319–331.
- Eisenhower, B., O'Neill, Z., Narayanan, S., Fonoberov, V.A., & Mezić, I. (2012). A methodology for meta-model based optimization in building energy models. *Energy and Buildings*, 47(April), 292–301.
- Frey, B. J., & Dueck, D. (2007). Clustering by passing messages between data points. *Science*, 315(5864), 972–977.
- Georgescu, M., & Mezić, I. (2015). Building energy modeling: A systematic approach to zoning and model reduction using Koopman Mode Analysis. *Energy and Buildings*, 86, 794–802.
- Hamdy, M., & Sirén, K. (2016). A multi-aid optimization scheme for large-scale investigation of cost-optimality and energy performance of buildings. *Journal of Building Performance Simulation*, 9(4), 411–430.
- Infiniti Research Limited. (2015). *Global Building Energy Software Market 2015-2019*.
- Nguyen, A.T., Reiter, S., & Rigo, P. (2014). A review on simulation-based optimization methods applied to building performance analysis. *Applied Energy*, 113, 1043–1058.
- Schilders, W. (2008). *Introduction to Model Order Reduction*.
- Shi, Z., & O'Brien, W. (2017). Building energy model reduction using model-cluster-reduce pipeline. *Journal of Building Performance Simulation*.

Comparison of data-driven building energy use models for retrofit impact evaluation

Yujie Xu^{1,*}, Azizan Aziz¹, Bertrand Lasternas¹, Vivian Loftness¹

¹Carnegie Mellon University

*Corresponding email: yujiex@andrew.cmu.edu

ABSTRACT

A change-point (piecewise linear regression) model fitted to the pre-retrofit data as the counterfactual for the savings calculation, is considered to be the best approach to evaluating the energy savings of building retrofits (ASHRAE Guideline 14). However, when applied to a large portfolio savings analysis with substantial multi-year data, the change-point model does not fit the data well in some cases. The study thus aims to improve the accuracy of the change-point model by: 1) using more advanced non-linear models, 2) incorporating additional input features, and 3) increasing the time resolution of input variables. We found that random forest regression (RF) models with an array of climate (humidity, wind, solar radiation, etc.), time (day of the week, season, holiday), and energy consumption of the immediate past 1-4 hours (energy lag terms) outperformed the change-point model, shallow neural networks, and support vector machine regression (SVR). Our result implies that high resolution smart meter data should be used in place of monthly utility bills to more accurately evaluate retrofit savings. We further explored the relative contribution of the input variables to the random forest regression model using Shapley Value, a game theoretic variable importance metric. We found that the most important input feature is the energy consumption of the immediate past (or energy lag terms). We also found that solar radiation and weekend day indicators are more important than outdoor temperature. The improved model could provide better insights to portfolio managers in planning future energy retrofits. Policy makers could also use such models to evaluate the average energy saving potential for energy policy changes, such as the requirement of minimum insulation level, and lighting equipment efficiency.

KEYWORDS

Energy Performance Prediction, Random Forest Regression, Inverse Modelling, Comparison

INTRODUCTION

In the U.S., buildings account for 40% of the nation's energy consumption (EIA 2018). Reducing the energy consumption of the building sector is critical to mitigating the global climate change. Energy efficiency upgrades could save 5% to 50% of energy consumption in buildings (DOE 2018). However, in order to accurately evaluate the impact of these upgrades, differences in weather, operating schedules and modes, occupant behavior, and other unobserved factors between pre and post retrofit needs to be accounted for. This will require a counterfactual energy model that accurately describes the potential energy consumption had the upgrade not have happened, or the counterfactual.

In ASHRAE guideline 14, the counterfactual is estimated with a change-point regression model (ASHRAE 2014). The saving is calculated as the difference between the model estimated consumption and the measured post-retrofit consumption. We, and many studies aimed to compare and improve the prediction accuracy of such counterfactual energy models (Zhang et al. 2015; Brown et al. 2012). Unlike most existing studies with only a handful of case studies,

this study evaluates models on a larger sample size of 65 buildings. We tested hypothesis about whether the following three strategies improve on model accuracy: 1) advanced models using only the temperature input, 2) adding more input features, and 3) increasing the time resolution from monthly to hourly.

METHODOLOGY

The input energy data consists of 2014 to 2016 15-min interval electricity consumption data of 65 commercial buildings (24 office, 14 courthouses, 11 courthouse/office, 11 unknown) in the General Service Administration (GSA) portfolio. The climate data is retrieved from the national solar radiation database (NRSDB) Physical Solar Model (PSM).

Model evaluation procedure and metric

For each building, the input features are aligned by their timestamps. The aligned data set is then randomly split into a training set and a test set using year-month index, the first 70% of the year-months is the training data, and the rest is the validation data. The error is evaluated in Coefficient of Root-Mean-Square Error (CV-RMSE). CV-RMSE is root-mean-square error divided by mean electricity consumption (Equation 1, \bar{y} is the sample mean of the energy data, n is the number of data points, y_i is the i th observed electricity consumption, \hat{y}_i is the corresponding predicted electricity consumption, $(n - p)$ is the degree of freedom). However, the degree of freedom may not be well defined for models other than linear regression, for example, the effective degree of freedom for Neural Network models is changing through the training process (Anzai 2012). We believe the degree of freedom could be left out as we evaluated the model on a held-out test set. Thus, we used the adjusted CV-RMSE (Equation 2) in the evaluation.

$$CV - RMSE = \sqrt{\sum_i \frac{(y_i - \hat{y}_i)^2}{n - p}} / \bar{y} \quad (1)$$

$$CV - RMSE_{adj} = \sqrt{\sum_i \frac{(y_i - \hat{y}_i)^2}{n}} / \bar{y} \quad (2)$$

Models

We compared the prediction accuracy of the following five models: 3-parameter change-point model (baseline algorithm), neural network with one hidden layer, neural network with two hidden layers, kernelized support vector machine regression (SVR), and random forest regression. The Change-point model is implemented using Python scipy optimize package, and the other models are implemented using Python scikit-learn package (Pedregosa et al. 2011).

Change-point model splits the range of temperature into 2 to 3 different segments and fits a separate linear regression model in each segment, with continuity requirement at the boundaries of segments. The method is adopted by ASHRAE Guideline 14 (ASHRAE 2014) and IPMVP (Efficiency Valuation Organisation 2012). In this study the change-point model is implemented with a grid search over the temperature range from 40F to 80F according to (Kissock et al. 2003).

Neural network is a popular predictive method applied in a variety of fields. A neural network consists of inter-connected neurons and non-linear activation functions. Most commonly, neurons form a layered directed acyclic graph (DAG) structure with one input layer, some hidden layers, and one output layer. Directed links are formed between layers, and assigned

weights using the backpropagation algorithm. Two shallow network structures are tested in this study: one with one hidden layer, and one with two hidden layers. We used the tanh activation, following the choice of (MacKay 1996; Dodier and Henze 2004). A grid-search method is applied to find the optimal number of hidden units per layer.

The support vector machine algorithm is developed by Vapnik and Chervonenkis in 1963, as a “nonlinear generalization of the Generalized Portrait algorithm” (Sewell n.d.). It can be applied to both classification and regression tasks. Support vector machine regression (SVR) tries to find a function as flat as possible that is at most ϵ from training data (Smola and Schölkopf 2004). C and ϵ are two hyper-parameters to be optimized. A grid search of the optimal C is performed in the range of 1 to 1000 with step size 100. ϵ is left as default.

Random Forest Regression is an ensemble method which constructs many regression trees at the training time, and forms predictions by taking a weighted average of the output of individual trees. In the study, the tuning parameter, maximum tree depth, is set as default 30.

RESULTS

Hypothesis 1: advanced models have better accuracy using only temperature input.

We tested whether applying more advanced nonlinear models could directly reduce the prediction error by using just temperature as the input. Our result suggests that advanced models (NN, SVM, RF) perform similarly to simple change-point model using only temperature input.

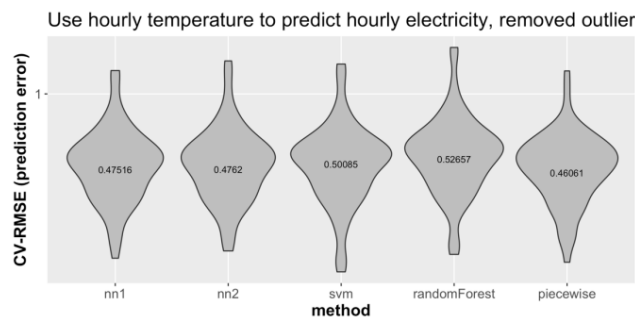


Figure 1. Violin plot, showing distribution of CV-RMSE (the prediction error) across buildings, for each method. All methods appear to have similar error distributions.

Hypothesis 2: Additional input features improves model performance.

By adding the following input variables (Table 1), in addition to temperature, we saw substantial reduction in CV-RMSE (prediction error) using random forest regression (Figure 2).

Table 1. Additional input variables.

Climate	Humidity	Dew Point
		Relative Humidity
	Solar Radiation	Diffuse Horizontal Irradiance (DHI)
		Direct Normal Irradiance (DNI)
		Global Horizontal Radiation (GHI)
		Solar Zenith Angle (Z)
	Pressure	
	Precipitable Water	
	Wind	Wind Direction
		Wind Speed
Time	Season	

	Day of the Week
	If a Day Is Federal Holiday
Energy	Energy lag term (Energy Consumption in Previous 4 Steps)

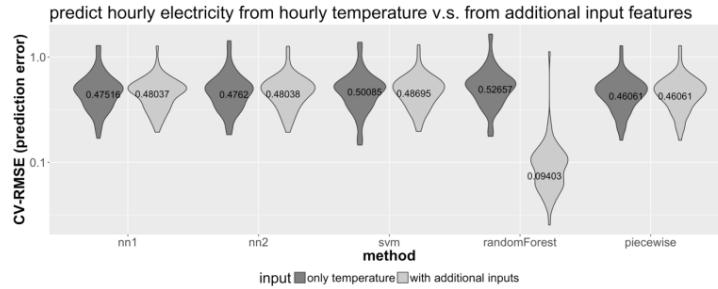


Figure 2. Violin plot, showing distribution of CV-RMSE (prediction error) across buildings, for each method: light grey uses only temperature input, dark grey is using all features in Table 1.

To compare the relative importance of these variables for prediction accuracy in random forest regression, we applied a game-theory metric, the Shapley Value imputation (Lipovetsky and Conklin 2001). The Shapley Value for the i th variable is shown in Equation 3. n is the number of input features. v is a function from feature subsets to real numbers. $v(S)$ represents the “expected sum of payoffs” (“Shapley Value” 2018) using the feature set S . In our case, $v(S)$ is CV-RMSE. R is a permutation, P_i^R is the list of features before the i th one. Computing the exact Shapley Value is #p complete (Fatima et al. 2008), i.e. intractable, so we computed an estimated Shapley Value using a random sample of permutations. The estimated Shapley Value is shown in Figure 4. The variables with lower Shapley Value are more important. The energy lag terms are the most important. A series of solar radiation related factors (GHI, DHI, etc.) ranked second, and the indicators for weekends ranked third.

$$\phi_i(v) = \frac{1}{n!} \sum_R v(P_i^R \cup \{i\}) - v(P_i^R) \tag{3}$$

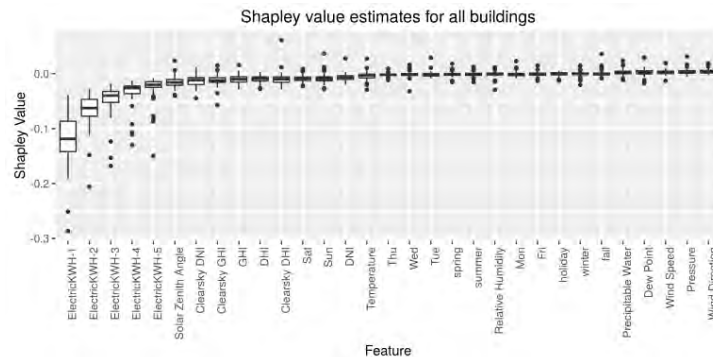


Figure 4. Shapley Value estimates for all input features

Hypothesis 3: Higher resolution input improves model performance

For each modelling method, we compared the following two approaches: 1) use monthly average of the input features in hypothesis 2 to predict monthly electricity consumption; 2) use hourly input to predict hourly electricity and aggregate the result to monthly. With higher resolution hourly input, Random Forest Regression achieved significantly better performance than using monthly average inputs (Figure 3).

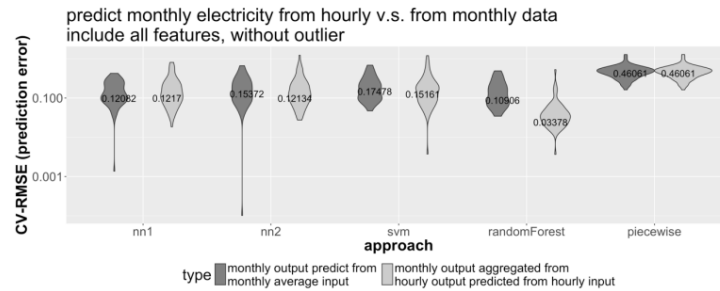


Figure 3. Violin plot, showing distribution of CV-RMSE across buildings, for each method: dark grey is using monthly average input to predict monthly electricity, light grey is using hourly input to predict hourly output then aggregate to monthly.

DISCUSSIONS

Findings

All models perform similarly when only using temperature as the input variable. Random forest regression model with an array of climate and time variables outperformed our implementation of shallow neural networks, SVR, and change-point models in terms of lowest CV-RMSE. For the random forest regression model, the most effective predictors for the hourly energy consumption are the energy lag terms, followed by solar radiation, then indicator variables for weekends.

Limitations and next stage work

We observed outliers in the 15-min electricity data that are: negative records, a large positive immediately followed a large negative record, and extremely large values followed by a data gap. A simple outlier removal rule is applied for the analysis: 1) remove negative entries 2) remove data points greater than 1.5 times the 97th percentile of the positive records. Further research into the reasons for the outliers, and more advanced outlier detection routine might help improve the model accuracy. In the Shapley Value computation, we used a sample of 100 random permutations to construct an initial estimate. The number of permutations here is chosen arbitrarily. Analyzing the convergence rate of the Shapley Value estimate, i.e. how many samples are needed to achieve certain approximation accuracy, would be a next step of the study. All the counterfactual models in this paper and many other papers under the ASHRAE Guideline 14 framework are based on the assumption of no un-measured confounding factors. In this sense, adding more covariates to the models, other than just temperature, could make the model prediction more accurate, and make it more viable to draw causal conclusions.

CONCLUSIONS

The paper compared the prediction accuracy of five data-driven energy counterfactual models under three conditions: 1) using only temperature input 2) using an array of climate and energy inputs, and 3) using higher resolution hourly inputs to predict monthly energy. We found that random forest regression model ensures the best performance when supplied with additional inputs with higher temporal resolution. The most important input features for Random Forest Regression are energy lag terms and solar radiation.

The predictive power of the energy counterfactual model determines the accuracy of the ECM savings evaluation. The result could assist ESCO companies to better predict the potential savings for implementing certain retrofit. In addition, our improvement of such energy

counterfactual models could also be useful in system fault detection, and development of new control strategies (Zhang et al. 2015).

ACKNOWLEDGEMENT

This research is made possible through a collaboration with the General Service Administration to evaluate their portfolio-wide energy retrofit impact (contract PR201508040012). The author also wishes to thank Professor Matt Gormley for recommending the machine learning methods.

REFERENCES

- Anzai, Yuichiro. 2012. *Pattern Recognition and Machine Learning*. Elsevier.
- ASHRAE. 2014. *Ashrae Guideline 14-2014: Measurement of Energy, Demand and Water Savings*. Ashrae. <https://books.google.com/books?id=zLJkQAACAAJ>.
- Brown, Matthew, Chris Barrington-Leigh, and Zosia Brown. 2012. “Kernel Regression for Real-Time Building Energy Analysis.” *Journal of Building Performance Simulation* 5 (4): 263–76. <https://doi.org/10.1080/19401493.2011.577539>.
- Dodier, Robert H., and Gregor P. Henze. 2004. “Statistical Analysis of Neural Networks as Applied to Building Energy Prediction.” *Journal of Solar Energy Engineering* 126 (1): 592–600.
- DOE. 2018. “Why Energy Efficiency Upgrades.” June 5, 2018. <https://www.energy.gov/eere/why-energy-efficiency-upgrades>.
- Efficiency Valuation Organisation. 2012. “International Performance Measurement and Verification Protocol. Concepts and Options for Determining Energy and Water Savings.” *Efficiency Valuation Organisation, Toronto*.
- EIA. 2018. “How Much Energy Is Consumed in U.S. Residential and Commercial Buildings?” May 3, 2018. <https://www.eia.gov/tools/faqs/faq.php?id=86&t=1>.
- Fatima, Shaheen S., Michael Wooldridge, and Nicholas R. Jennings. 2008. “A Linear Approximation Method for the Shapley Value.” *Artificial Intelligence* 172 (14): 1673–99. <https://doi.org/10.1016/j.artint.2008.05.003>.
- Kissock, J. K., J. S. Haberl, and D. E. Claridge. 2003. “Inverse Modeling Toolkit: Numerical Algorithms for Best-Fit Variable-Base Degree Day and Change Point Models,” July. <http://oaktrust.library.tamu.edu/handle/1969.1/153708>.
- Lipovetsky, Stan, and Michael Conklin. 2001. “Analysis of Regression in Game Theory Approach.” *Applied Stochastic Models in Business and Industry* 17 (4): 319–30. <https://doi.org/10.1002/asmb.446>.
- MacKay, David J. C. 1996. “Bayesian Non-Linear Modeling for the Prediction Competition.” In *Maximum Entropy and Bayesian Methods*, edited by Glenn R. Heidbreder, 221–34. Fundamental Theories of Physics 62. Springer Netherlands. https://doi.org/10.1007/978-94-015-8729-7_18.
- Pedregosa, Fabian, Gaël Varoquaux, Alexandre Gramfort, Vincent Michel, Bertrand Thirion, Olivier Grisel, Mathieu Blondel, et al. 2011. “Scikit-Learn: Machine Learning in Python.” *Journal of Machine Learning Research* 12 (October): 2825–2830.
- Sewell, Martin. n.d. “History of Support Vector Machines.” Support Vector Machines (SVMs). n.d. <http://www.svms.org/history.html>.
- “Shapley Value.” 2018. *Wikipedia*. https://en.wikipedia.org/w/index.php?title=Shapley_value&oldid=840058989.
- Smola, Alex J., and Bernhard Schölkopf. 2004. “A Tutorial on Support Vector Regression.” *Statistics and Computing* 14 (3): 199–222.
- Zhang, Yuna, Zheng O’Neill, Bing Dong, and Godfried Augenbroe. 2015. “Comparisons of Inverse Modeling Approaches for Predicting Building Energy Performance.” *Building and Environment* 86 (April): 177–90. <https://doi.org/10.1016/j.buildenv.2014.12.023>.

Modeling and model calibration for model predictive occupants comfort control in buildings

Shiyu Yang^{1, 2}, Man Pun Wan^{1*}, Bing Feng Ng¹, Zhe Zhang², Adrian S. Lamano², Wanyu Chen².

¹School of Mechanical and Aerospace Engineering, Nanyang Technological University, Singapore

²Energy Research Institute at NTU (ERI@N), Nanyang Technological University, Singapore

*Corresponding email: mpwan@ntu.edu.sg

ABSTRACT

Mathematical models are essential in Model-Predictive Control (MPC) for building automation and control (BAC) application, which must be precise and computationally efficient for real-time optimization and control. However, building models are of high complexity because of the nonlinearities of heat and mass transfer processes in buildings and their air-conditioning and mechanical ventilation (ACMV) systems. This paper proposes a method to develop an integrated linear model for indoor air temperature, humidity and Predicted Mean Vote (PMV) index suitable for fast real-time multiple objectives optimization. A linear dynamic model is developed using SIMSCAPE language based on the BCA SkyLab test bed facility in Singapore as a case study. Experimental data is used to calibrate the model using trust-region-reflective least squares optimization method. The results show that the mean absolute percentage errors (MAPE) of predicted room temperature and humidity ratio are 1.25% and 4.98%, compared to measurement, respectively.

KEYWORDS

Model predictive control; modeling; model calibration; linearization.

INTRODUCTION

Developing an appropriate building mathematical model has been a major challenge of MPC implementation for building automation and control (BAC) application (Cigler et al., 2013). Henze (2013) pointed out that about 70% of project costs were consumed by model development and calibration for MPC in buildings. Cigler et al. (2013) also found more than 55% of project time spent on modeling work for implementing MPC in different two buildings. The mathematical model of the building must be sufficiently accurate in predicting building dynamics and computationally efficient for real-time control and optimization in MPC. A viable solution is to develop linear models of buildings that are of medium to high fidelity and is computationally more efficient (Cigler et al., 2013). Currently, two modeling methods, thermal resistance-capacitance (RC) model (Sturzenegger et al., 2012) and system identification (Cole et al., 2014) have been adopted to develop linear building models for control purpose. However, most of the previous studies focus on the prediction of indoor temperature whereas the indoor humidity and human thermal comfort are seldom covered (Kramer et al., 2012). To improve indoor thermal comfort and building energy performance with MPC further, it is necessary to include humidity and thermal comfort index in the prediction model of MPC.

This work aims to develop a general methodology for constructing a linear model for indoor thermal comfort and energy optimization with MPC. A building model is developed based on the BCA SkyLab test bed facility in Singapore, as a case study, to predict indoor temperature,

humidity, and thermal comfort. The thermal and humidity dynamic models are created using the RC network. A linear approximation method is proposed to linearize the nonlinearities in the ACMV cooling coil model and PMV calculation model. A model calibration procedure is also adopted to refine the proposed linear model.

METHODS

Room space model

For air-conditioned room spaces, the heat and moisture balance could be modeled by equations (1) and (2),

$$m_{air,z} \frac{d\psi_z}{dt} = \dot{m}_{occ} + \dot{m}_{ACMV}, \quad (1)$$

$$m_{air,z} C_{air} \frac{dT_z}{dt} = Q_{inte} + Q_{env} + Q_{ACMV}, \quad (2)$$

where Q is heat flow rate (W), \dot{m} is mass flow rate (kg/s), m is mass (kg), T is temperature (K) and ψ is humidity ratio (kg/kg). The subscript *inte* refers to internal, *z* refers to thermal zone, and *env* refers to envelope.

RC models of walls, ceiling and floor

Figure 1 shows the lumped parameter and RC representations of a building wall model. The wall is virtually split into two aggregates and only heat conduction in the normal direction is considered. The RC model is a 5R2C model, which includes two thermal capacitances of the two aggregates, three thermal conduction resistances of aggregates and two surface thermal resistances between surface and air (outer and inner surfaces).

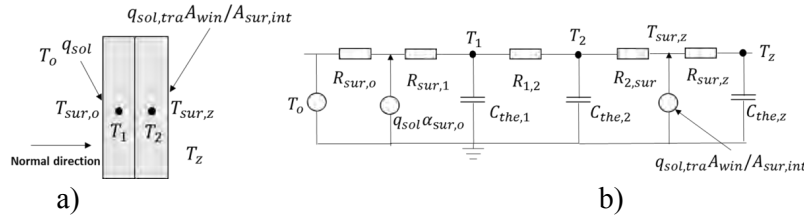


Figure 1 a) lumped parameter and b) RC representations of a building wall model

In Figure 1, the symbols R , C , and q refer to thermal resistance (K-m/W), thermal capacity (J/K) and heat flux (W/m^2), respectively. Subscripts *sur*, *o*, *1*, *the*, *sol*, *z*, *tra*, and *int* refer to surface, outside, aggregate number, thermal, solar radiation, thermal zone, transmission, and interior respectively. The same model treatment is applied to the roof and the floor.

Linearized cooling coil model

When the ACMV system is in operation, the supply air relative humidity (RH) is assumed 100% and the heat/mass transfer between the mixed air and the cooling coil can be described by,

$$Q_{cc} = \dot{m}_{ma}(C_{air} + C_{vap}\psi_{ma})(T_{ma} - T_{sa}) + \dot{m}_{ma}L_{vap}(\psi_{ma} - \psi_{sa}), \quad (3)$$

$$\psi_{sa} = 0.62198p_{vap,sat}/(p_z - p_{vap,sat}), \quad (4)$$

$$p_{vap,sat} = e^{(77.345+0.0057T_z-7235/T_z)/T_z^{8.2}}, \quad (5)$$

where the subscripts *ma*, *vap*, *sat* and *cc* refer to the mixed air in FCU, water vapor, saturation and cooling coil, respectively. L refers to the specific latent heat (J/kg) of water condensation.

For temperature between 283.15K – 293.15K (covering the typical range of supply air temperatures), nonlinear equations (4) and (5) can be approximated by the linear equation,

$$\psi_{sa} = 7.014 \times 10^{-4}T_{sa} - 0.1913. \quad (6)$$

With this assumption, the indoor moisture and sensible heat load removed by ACMV system can be calculated by,

$$\dot{m}_{ACMV} = 2.58 \times 10^{-4} \dot{m}_{fa} T_{fa} + 2.58 \times 10^{-4} \dot{m}_{ra} T_{ra} - 2.57 \times 10^7 Q_{cc} + 0.633 \dot{m}_{fa} \psi_{fa} - (\dot{m}_{fa} + 0.368 \dot{m}_{ra}) \psi_{ra} - 0.0703 \dot{m}_{fa} - 0.0703 \dot{m}_{ra}, \quad (7)$$

$$Q_{ACMV} = 369.4 \dot{m}_{fa} T_{fa} - (1005 \dot{m}_{fa} + 635.6 \dot{m}_{ra}) T_{ra} - 0.368 Q_{cc} + 9.062 \times 10^5 (\dot{m}_{fa} \psi_{fa} + \dot{m}_{ra} \psi_{ra}) + 1.734 \times 10^5 \dot{m}_{fa} + 1.734 \times 10^5 \dot{m}_{ra}, \quad (8)$$

where the subscripts *fa* and *ra* refer to fresh air and return air. When the supply air flow rate and fresh air flow rate are constant, the equations become linear. The equations are valid under the conditions of $RH_{sa} = 100\%$, $283.15\text{K} < T_{sa} < 293.15\text{K}$ according to the assumptions in the modeling procedure.

Linearized PMV calculation model

Predicted Mean Vote index (Fanger, 1970) is calculated according to the equation,

$$PMV = (0.303e^{-0.036M} + 0.028)Q_{diff}. \quad (9)$$

The difference between the internal heat production and loss, Q_{diff} , that occurs in a human body is calculated by,

$$Q_{diff} = M - Q_{work} - Q_{res} - Q_{sens} - Q_{evap}, \quad (10)$$

$$Q_{res} = 0.0014M(307.15 - T_{air}) + 1.72 * 10^{-5}M(5867 - p_{vap}), \quad (11)$$

$$Q_{sens} = 39.6 * 10^{-9}f_{clo}(T_{clo}^4 - T_{mr}^4) + f_{clo}h_{conv}(T_{clo} - T_{air}), \quad (12)$$

$$Q_{evap} = 0.42(M - Q_{work} - 58.15) + 3 * 10^{-3}[5733 - 6.99(M - Q_{work}) - p_{vap}] \quad (13)$$

$$T_{clo} = T_{skin} - R_{clo}[f_{clo}h_{conv}(T_{clo} - T_{air})] - Ins_{clo}[39.6 * 10^{-9}f_{clo}(T_{clo}^4 - T_{mr}^4)] \quad (14)$$

In the equation (9) – (14), M is the metabolic rate of a human being (W), p is air pressure (Pa), f_{clo} is clothing factor, and Ins_{clo} is clothing insulation (1 clo = 0.155 m²-K/W). The subscripts *clo*, *mr*, *vap*, *conv*, *sens*, *evap*, *res*, *skin* and *work* refer to clothing, mean radiant, water vapor, convection, sensible, evaporation from occupant skin, respiration of occupant, skin surface, and external work.

There are two nonlinear items, radiative heat transfer $39.6 * 10^{-9}f_{clo}(T_{clo}^4 - T_{mr}^4)$ and water vapour pressure, p_{vap} , in the PMV model. The radiative heat transfer term can be linearized by (Park, 2013),

$$Q_{rad} = 39.6 * 10^{-9}f_{clo}(T_{clo} + T_{mr})(T_{clo}^2 + T_{mr}^2)(T_{clo} - T_{mr}) = h_{rad}f_{clo}(T_{clo} - T_{mr}). \quad (15)$$

The water vapor pressure can also be calculated by the following equation, for air temperatures within 293.15 - 303.15 K covering the range of typical room temperatures,

$$p_{vap} = \psi_z p_z / (\psi_z + 0.622) \cong 1.598 \times 10^5 \psi_z. \quad (16)$$

In a scenario that the cloth factor, metabolic rate of the occupants, external work of the occupants and room pressure can be assumed constant, likely so in a typical office environment, the PMV equation can be reduced to one linear equation,

$$PMV = \left[\frac{(0.68h_{conv} + 0.0051h_{rad} + 0.06)T_{air} + 0.68h_{rad}T_{mr} + (35.7h_{conv} + 35.7h_{rad} + 419)\psi_z + 7.3 - 208h_{rad} - 208h_{conv}}{(h_{conv} + h_{rad} + 11.73)} \right] / \quad (17)$$

The equation is valid for a common office environment with air conditioning where room temperature is within 293.15 - 303.15 K.

MPC formulation

A MPC controller for future study of building energy and indoor thermal comfort optimization with MPC could be modeled as

$$J = \text{Minimize}(\sum_{i=0}^M \sum_{k=0}^N Q_{i,t+k|t}^2 + \sum_{k=0}^N (W_{PMV} PMV_{t+k|t})^2 + \sum_{k=0}^N W_{\epsilon} (\epsilon_{t+k|t})^2), \quad (18)$$

where Q , PMV , W and ϵ refer to normalized cooling power, normalized thermal comfort, weighting factor and slack variable. M and N refer to the number of cooling system and prediction horizon.

The objective function subjects to the building dynamics modelled in this section, limits of cooling power and acceptable indoor thermal comfort zone ($-0.5 < PMV < 0.5$). In this study, the building dynamic model is linearized. This results into a convex optimization problem, which can be more efficiently solved compared to a nonlinear optimization problem with a nonlinear building model, for finding the optimal control strategies for building control (Cigler et al., 2013).

CASE STUDY AND RESULTS DISCUSSION

The physical building studied in this work is the BCA SkyLab located in the BCA Academy in Singapore. SkyLab has two side-by-side identical experimental cells with full-height window façade on one side, as shown in Figure 2. The properties of the building envelope are described by Lamano et al., (2018), and Yang et al., (2018).

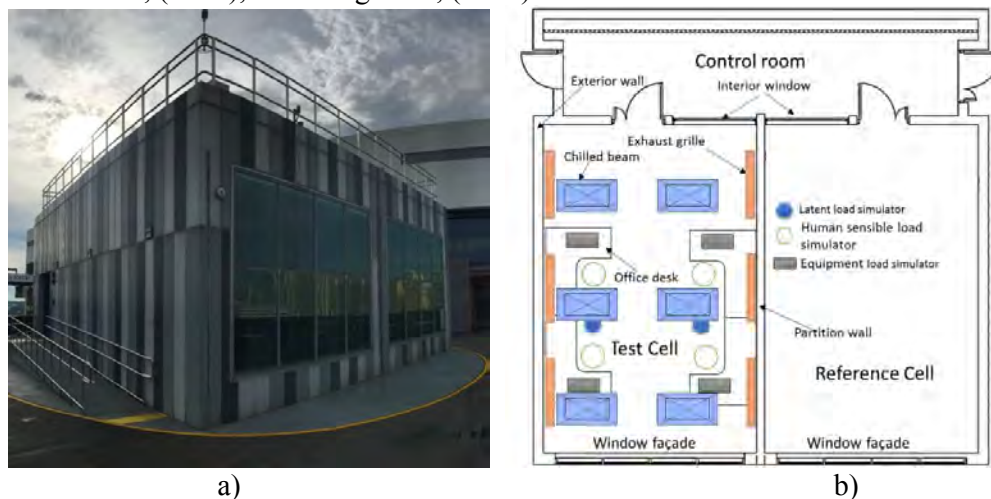


Figure 2 a) exterior view of BCA SkyLab, b) Schematic drawing of BCA SkyLab

An ACMV system that consists of one fan coil unit (FCU) and six active chilled beam (ACB) units was installed in the Test Cell of SkyLab, as shown in **Error! Reference source not found.** The chilled water valve in FCU was controlled by a thermostat according to pre-cooled air set point temperature. The pre-cooled air from FCU was supplied into the ACB units, meanwhile, induced some room air into the ACB units. The sensible load in the induced air was removed by the cooling coils in ACB. The conditioned induced air mixed with pre-cooled air and was distributed into the room space. A heat exchanger was installed to regulate the supplied chilled water temperature of ACB higher than dew point in the room space to avoid condensation. Thus, FCU is capable of dealing with all the latent load and partial sensible load and the rest sensible is removed by the ACB.

The Test Cell operates at a design condition during office hours (9 am – 6 pm of weekday). The design occupancy density, internal plug load and internal lighting load are 0.092 person/m², 16 W/m² and 8.22 W/m² floor area, respectively. The ACMV system supplies constant 33 l/s fresh air and 147 l/s supply air into the room space.

Based on the modeling methods described earlier, an integrated linear model the Test Cell is developed in the MATLAB/Simulink environment. The RC models and heat/mass balance of

room air model are developed using SIMSCAPE language, which is an object-oriented physical modeling method (Miller & Wendlandt, 2010). The thermal comfort in SkyLab Test Cell is modeled with Equation (17) and measured three-day average velocity (0.09 m/s) in the occupied zone during office hours. The FCU in the ACMV system is modeled with Equations (7) and (8) under design conditions. The cooling coils in ACB system are treated as negative heat sources. The developed model is calibrated and refined using measurement data obtained in SkyLab. Fourteen days (8th to 21st January 2018) of experiment was conducted to measure the room temperature and humidity responses to different conditions.

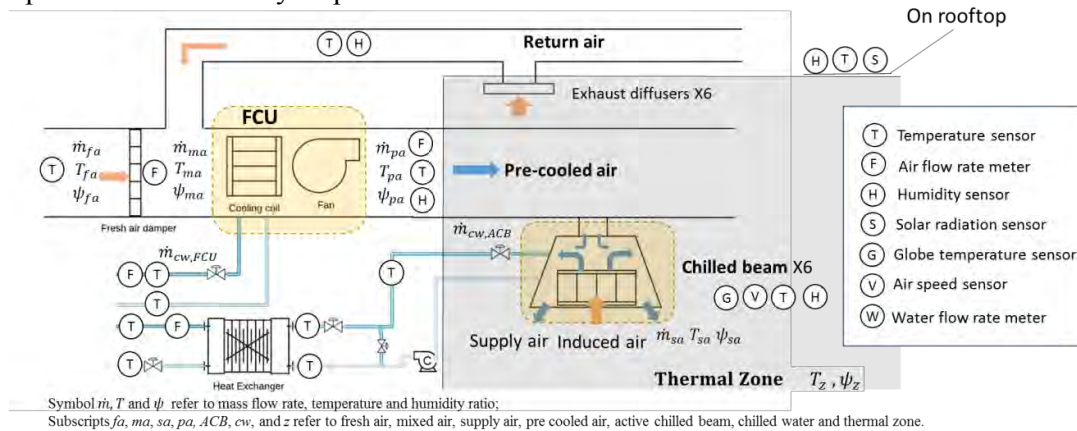


Figure 3 Schematic drawing of the ACMV system in SkyLab Test Cell

In the Test Cell, there are some thermal masses (such as ducts, furniture and steel beams) inside the ceiling space, raised floor space and room space that are not included in the RC model. Thus, the R and C parameters of roof, floor and internal thermal mass are tuned in the calibration procedure. The thermal mass in room space is represented by a 1R1C node, separately, which is only connected to room air temperature node. The Trust-Region-Reflective Least Squares optimization method (Coleman & Li, 1996) is then employed to tune the RC model parameters in MATLAB environment to minimize the sum-squared error of room temperature as. After calibration, the parameter values of the SkyLab Test Cell are listed in Table 1.

Table 1 Tuned parameter values of liner model of SkyLab Test Cell

Envelope	Initial U value (W/m ² K)	Initial C value (kJ/m ² K)	Tuned U value (W/m ² K)	Tuned C value (kJ/m ² K)
Internal thermal mass	1.6	100	32	485
Roof	0.25	308.4	0.67	391.67
Floor	0.25	77.6	0.43	85.7

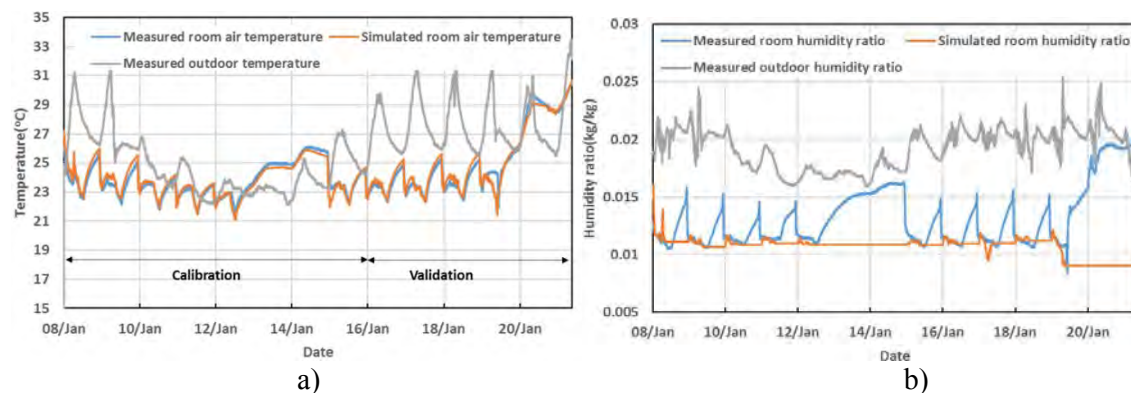


Figure 4 Comparison of simulated a) temperature and b) humidity ratio with measured data

Figure shows that there is good agreement between the simulated and measured results after the model calibration. The mean absolute percentage error (MAPE) of room temperature is 1.25% for the entire fourteen-day period. The MAPE of room humidity is 4.98% during office hours. The deviation of the humidity ratio prediction in non-office hours is because the model does not consider the moisture penetration from the ambient into room space.

CONCLUSIONS

Methods to build a linear building model, which can be used to predict indoor temperature, humidity and thermal comfort for indoor environment control with linear MPC, are proposed. The RC model is adopted to represent the heat and moisture dynamic in the building. The heat transfer and dehumidification process in the ACMV system and PMV index calculation models are linearized by linear approximation of the nonlinear items in the theoretical models. A case study is conducted based on the BCA SkyLab in Singapore. After calibration, the developed linear model has high accuracy and the MAPE of predicted room temperature and humidity ratio are 1.25% and 4.98% compared to measured data, respectively.

ACKNOWLEDGEMENT

This research is supported by the National Research Foundation (NRF) of Singapore through the Building and Construction Authority (BCA) under the Green Buildings Innovation Cluster (GBIC) grant nos. NRF2015ENC-GBICRD001-020 and GBIC-R&D/DCP02. Technical support from the Simulation Group of ERI@N and scientific inputs by Prof Gregor Henze, University of Colorado Boulder are appreciated.

REFERENCES

- Cigler, J., Gyalistras, D., Široky, J., Tiet, V., & Ferkl, L. (2013, June). Beyond theory: the challenge of implementing model predictive control in buildings. In Proceedings of 11th Rehva World Congress, Clima (Vol. 250).
- Cole, W. J., Powell, K. M., Hale, E. T., & Edgar, T. F. (2014). Reduced-order residential home modeling for model predictive control. *Energy and Buildings*, 74, 69-77.
- Coleman, T. F., & Li, Y. (1996). An interior trust region approach for nonlinear minimization subject to bounds. *SIAM Journal on optimization*, 6(2), 418-445.
- Fanger, P. O. (1970). *Thermal comfort Analysis and applications in environmental engineering*. Thermal comfort. Analysis and applications in environmental engineering.
- Henze, G. P. (2013). Model predictive control for buildings: A quantum leap? *Journal of Building Performance Simulation*, 6(3), 157-158.
- Lamano A.S., Yang S, Wan M.P. et al. (2018). Energy Performance of an Integrated Automated Blinds and Dimmable Lighting System with Model-Predictive Control (MPC). COBEE2018.
- Miller, S., & Wendlandt, J. (2010). Real-time simulation of physical systems using Simscape. *MATLAB News and Notes*, 1-13.
- Park, H. (2013). *Dynamic thermal modeling of electrical appliances for energy management of low energy buildings* (Doctoral dissertation). Université de Cergy Pontoise.
- Sturzenegger, D., Gyalistras, D., Morari, M., & Smith, R. S. (2012, November). Semi-automated modular modeling of buildings for model predictive control. In Proceedings of the Fourth ACM Workshop on Embedded Sensing Systems for Energy-Efficiency in Buildings (pp. 99-106).
- Yang, S., Wan, M.P., Ng, B.F., Zhang, T., Babu, S., Zhang, Z., Chen, W. and Dubey, S. (2018). A state-space thermal model incorporating humidity and thermal comfort for model predictive control in buildings. *Energy and Buildings*, 170, 25-39.

Neural networks to predict the hygrothermal response of building components in a probabilistic framework

Astrid Tijskens^{1,*}, Staf Roels¹ and Hans Janssen¹

¹KU Leuven, Department of Civil Engineering, Building Physics Section, Kasteelpark Arenberg 40, 3001 Leuven, Belgium

*Corresponding email: Astrid.Tijskens@kuleuven.be

ABSTRACT

In recent years, probabilistic assessment of hygrothermal performance of building components has received increasing attention. Given the many uncertainties involved in the hygrothermal behaviour of building components, a probabilistic assessment enables to assess the damage risk more reliably. However, this typically involves thousands of simulations, which easily becomes computationally inhibitive. To overcome this time-efficiency issue, this paper proposes the use of much faster metamodels. This paper focusses on neural networks, as they have proven to be successful in other non-linear and non-stationary research applications. Two types of networks are considered: the traditional multilayer perceptron (with and without a time window) and memory neural networks (LSTM, GRU). Both are used for predicting the hygrothermal behaviour of a massive wall. The results showed that all networks are capable to predict the temperature profiles accurately, but only the LSTM and GRU networks could predict the slow responses of relative humidity and moisture content. Furthermore, the LSTM and GRU network were found to have almost equal predicting accuracy, though the GRU converged faster.

KEYWORDS

Internal insulation, hygrothermal performance, metamodel, neural networks, LSTM

INTRODUCTION

In recent years, traditional deterministic assessments in building physics have evolved towards a probabilistic framework (Annex 55, 2015; Vereecken et al. 2015). When evaluating the hygrothermal behaviour of a building component, there are many inherently uncertain parameters, such as the exterior climate, geometry, material... A probabilistic simulation enables taking into account these uncertainties, which allows evaluating the hygrothermal behaviour and the related damage risks more reliably. However, this often involves thousands of simulations, which easily becomes computationally inhibitive, especially when analysing more-dimensional component connection details. To overcome this time-efficiency issue, this paper proposes the use of metamodels, which aim at imitating the original hygrothermal model with a strongly reduced calculation time. Many different metamodeling strategies exist, of which multiple linear regression (MLR) or polynomial linear regression might be the most frequently used. MLR attempts to model the relationship between multiple input variables and an output variable by fitting a linear equation. It often performs well when predicting aggregated values such as the total heat loss (Van Gelder et al. 2014). On the other hand, many damage criteria, such as wood decay or mould growth, require evaluation over time, as such damage often has a long incubation time, whereafter it accumulates. Hence, more advanced metamodeling strategies that can handle time series prediction are needed. Furthermore, the model must be able to capture the highly non-linear and non-stationary pattern of the hygrothermal response of building components. Hence, this paper focusses on neural networks, as they have proven successful in other non-linear and non-stationary research applications.

The multilayer perceptron (MLP) is the most known artificial neural network. It has a feed-forward structure with one input layer, one output layer, and at least one hidden layer in between. Because the MLP can perform a non-linear mapping, it is a widely used (meta-)modelling method. In time-series prediction, it is sometimes used for predicting the next time step based on the current step (Soleimani-Mohseni et al. 2006). However, the MLP is static and has no memory of past time steps; hence, it cannot model input-output relations that span multiple time steps. When these temporal dependencies are short-term, often a time window is added (MLP TW), i.e. the current time step as well as a number of past time steps are used as input to the network (Kemajou et al. 2012). However, the MLP TW fails to capture patterns outside of this time window. Since the time window needs to be determined beforehand, a considerable number of experiments is required to identify the optimum time window.

Recurrent neural networks (RNN) overcome this problem by introducing memory. A simple RNN has a cyclic structure that feeds the output from previous time steps into the current time step as input. Hence, RNNs can model temporal contextual information along time series data. The simple RNN easily suffers from the vanishing or exploding gradient problem though, which makes it difficult for the network to learn correlations between temporally distant events. To deal with this problem, the long-short memory network (LSTM) was proposed by Hochreiter (1998). The LSTM model changes the structure of the hidden units to memory cells with gates. Via these gates, the LSTM unit is able to decide what information to keep from its existing memory, while the simple recurrent unit overwrites its content at each time-step. Hence, if the LSTM unit detects an important feature from an input sequence at early stage, it easily carries this information over a long distance, thus capturing potential long-term dependencies (Chung et al. 2014). Consequently, the LSTM has been widely used for many time-series forecasting and sequence-to-sequence modelling tasks. More recently, the gated recurrent unit (GRU) was proposed by Cho et al. (2014) to make each recurrent unit adaptively capture dependencies of different time scales. Similarly to the LSTM, the GRU has gating units that modulate the flow of information inside the unit, but without having separate memory cells. Both the LSTM unit and the GRU keep their existing memory and add the new content on top of it.

In this paper, the LSTM and GRU, as well as the MLP and MLP TW, are applied for predicting the hygrothermal behaviour of a massive masonry wall, as an explorative study. All network types are compared based on their prediction performance and training time.

DATA AND METHODS

Data description

As an example of predicting more complicated damage patterns, the hygrothermal performance of a massive masonry wall is evaluated for frost damage, wood decay of embedded wooden beam ends and mould growth. To estimate whether these damage patterns will occur, the temperature (T), relative humidity (RH) and moisture content (MC) are monitored at the associated positions for a period of 6 years (see Table 1). In this explorative study, the probabilistic aspect of the influencing parameters was not yet taken into account fully, as this allows for a more efficient exploring of several network architectures on a smaller dataset. The data was obtained via hygrothermal simulations in Delphin 5.8. The used input parameters are shown in Table 2; the brick material properties are given in Table 3. To account for variability in boundary conditions, different years of the external climate were used, as well as different wall orientations. Since the interior climate is calculated based on the exterior climate, this variability is also included. In total, 24 samples were simulated, of which 18 samples were used for training and 6 for testing. The neural networks are trained to predict the T, RH and MC time-series, given the time-series of the external temperature and relative humidity, the wind-driven-rain load, the short-wave radiation and the internal temperature and relative humidity.

Table 1. The monitored quantities for the damage patterns at different positions in the wall.

Damage pattern	Position	Quantity
Frost damage	0.5 cm from exterior surface	T, RH, MC
Decay of wooden beam ends	5 cm from interior brick surface	T, RH
Mould growth	Interior surface	T, RH

Table 2. Used input parameters for hygrothermal simulations of brick wall.

Input parameter	Value
Brick wall thickness	360 mm
External climate	Gaasbeek, Belgium
Internal climate	cfr. EN 15026 A
Wall orientation	U(0,360)
Rain exposure factor	1
Solar absorption	0.4

* U(a,b): uniform distribution between a and b

Table 3. Properties of the used brick type.

Material property	Value
Dry thermal conductivity (W/m ² K)	0.87
Dry vapour resistance factor (-)	14
Capillary absorption coefficient (kg/m ² s ^{0.5})	0.277
Capillary moisture content (m ³ /m ³)	0.25
Saturation moisture content (m ³ /m ³)	0.35

Network architecture

Several hyper-parameters should be pre-set before building and training the networks, including the number of hidden layers and the number of neurons in these hidden layers. In this paper, all constructed networks have a single hidden layer, as comparative experiments showed no benefits using multiple hidden layers. Furthermore, networks with 32, 64, 128 and 256 hidden units were tested. In case of the MLP TW, a time window of 24 hours was explored. A larger time window, which would be required to capture long-term dependencies, resulted in an extensive input dataset which became too memory intensive. The networks are trained by minimising the mean squared error (MSE) via backpropagation (MLP and MPL TW) or backpropagation-through-time (LSTM, GRU). Based on the results of comparative experiments, the LSTM and GRU networks were trained using the RMSprop learning algorithm (Hinton, 2012) with a learning rate of 0.002. The MLP and MLP TW networks were trained using the Adam learning algorithm (Kingma and Ba, 2015) with a learning rate of 0.001. In general, before presenting data to the network, the data is standardised (zero mean, unit variance) to overcome influences from parameter units. In this paper, both the input and output data are standardised, as this was found to improve training speed and accuracy. The network's accuracy is evaluated by three indicators: the normalised root mean square error (NRMSE), normalised mean absolute error (NMAE), and coefficient of determination (R2), formulated as follows:

$$NRMSE = \frac{\sqrt{\frac{1}{n} \sum (y - y^*)^2}}{y_{max} - y_{min}} \quad NMAE = \frac{\frac{1}{n} \sum |y - y^*|}{y_{max} - y_{min}} \quad R2 = 1 - \frac{\sum (y - y^*)^2}{\sum (y - \bar{y})^2} \quad (1)$$

where y is the true output, y^* is the predicted output, \bar{y} is the mean of the true output and n is the total number of time steps. The RMSE and the MAE are normalised to remove the scale differences between the different outputs. Although the networks are trained to predict all outputs simultaneously, these performance indicators are calculated for each output separately. This allows assessing which outputs are more difficult to predict and which ones are easy.

RESULTS AND DISCUSSION

Figure 1 presents the three performance indicators (rows) for all outputs (columns) and each network type. This graph shows that some outputs are easier to predict than others; all networks are capable to predict the temperature accurately, as well as the interior surface relative humidity. Since the wall temperature and surface relative humidity respond almost immediately to a change in boundary conditions, not much memory is needed to accurately predict these profiles; for these outputs, the MLP with a time window of 24 hours is about as accurate as the more complicated LSTM or GRU. The relative humidity and moisture content at 0.5 cm from the exterior surface (frost damage) and the relative humidity at the wooden beam ends (wood decay) appear less evident to model. As moisture is transported inwards only slowly, there is a large delay between a change in boundary conditions (e.g. a heavy rain shower) and the response in relative humidity in the wall. At the wooden beam ends, this response delay can go up to several months. Hence, the MLP and MLP TW, which have no or only limited memory, are incapable to capture these long-term temporal dependencies and perform poorly. The LSTM and GRU, on the other hand, are able to capture these complex long-term patterns because of their connections to information from long-past time-steps. Figure 2 shows the temperature and relative humidity at the wooden beam ends predicted by the GRU network with 256 hidden units, compared with the true value. The residuals ε_t show that that the error is very small.

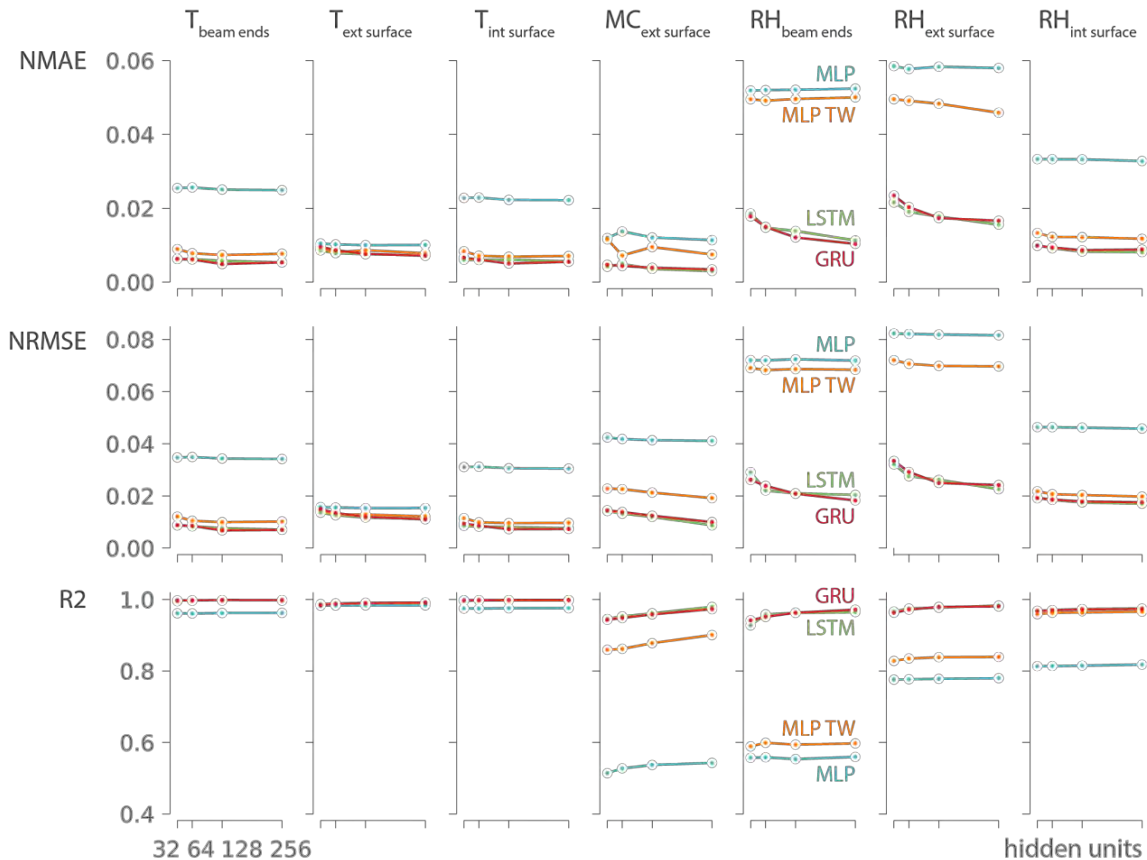


Figure 1. The performance indicators show that the temperature patterns are easy to model, while only the memory networks types (LSTM, GRU) are able to model the moisture content and relative humidity patterns accurately.

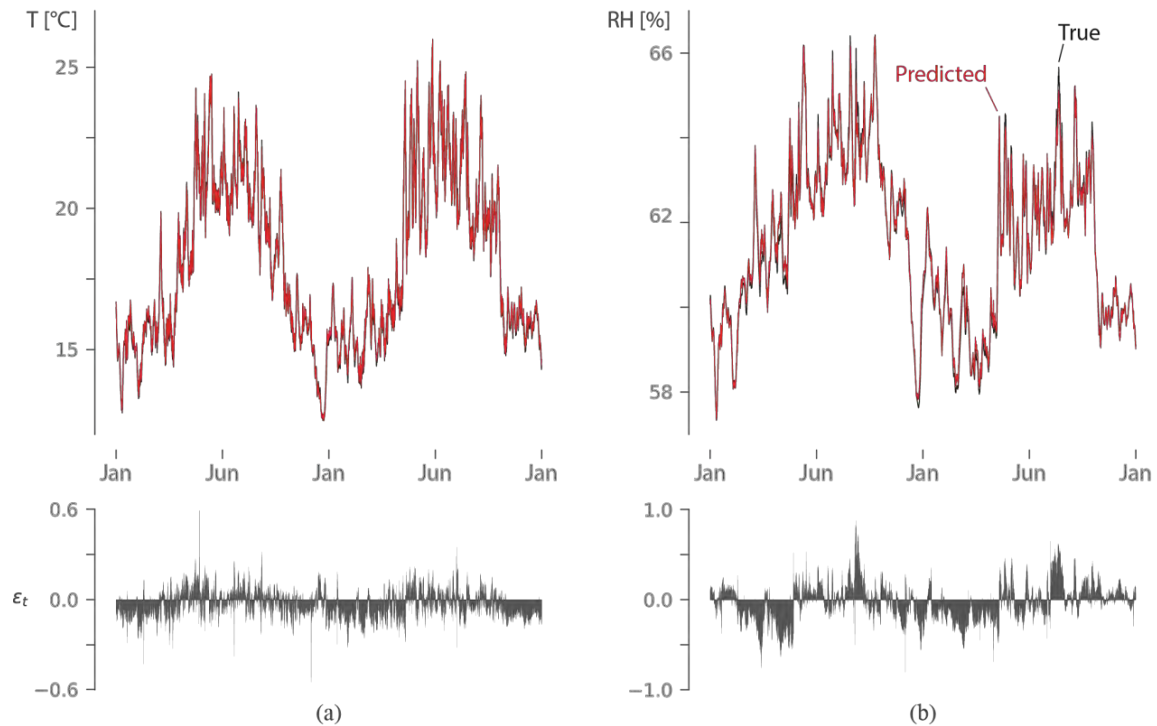


Figure 2. The temperature (a) and relative humidity (b) at the wooden beam ends, predicted by the GRU network with 256 hidden units. The residuals ϵ_t show that that the error is small.

Furthermore, it was found that the number of hidden units appears to have limited effect on the prediction performance in case of the MLP and MLP TW, though it increased the training time (Figure 3). In case of the LSTM and GRU on the other hand, more hidden units resulted in an improved prediction performance and a decrease in training time. It appears that the memory networks converge faster when they have more hidden units. Though prediction accuracy is very similar for both the LSTM and the GRU, the latter required less training time as it has fewer network parameters.

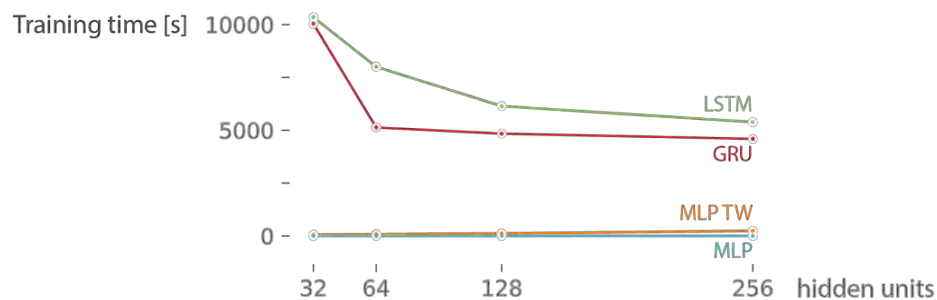


Figure 3. The training time for the memory network types (LSTM, GRU) decreases with increasing number of hidden units. The simulation time for one sample is 1 s for all network types. The reference simulation time for one sample in the original hygrothermal model is about 720 s.

CONCLUSIONS

In this paper, the hygrothermal simulation model for a massive masonry wall is replaced by a much faster metamodel. Four different types of neural networks were considered as metamodel:

a traditional multilayer perceptron (MLP), a multilayer perceptron with a pre-defined time window (MLP TW), a long-short term memory network (LSTM) and a gated recurrent unit network (GRU). Only the last two types have dynamic memory. The MLP TW has only access to the past time steps within the pre-defined time window, and the MLP tries to predict based on the current time step only. It was found that all network types were capable to predict the temperature accurately. Since the temperature responds almost immediately to a change in boundary conditions, not much memory is needed to capture these patterns. By contrast, only the LSTM and the GRU were able to accurately capture the long-term dependencies needed to predict the relative humidity and moisture content, as these respond much slower to a change in boundary conditions. Both types of memory networks were found to have almost equal predicting accuracy, though the GRU converged faster and thus required less training time.

ACKNOWLEDGEMENT

This research is part of the EU project RIBuild, which has received funding from the European Union's Horizon 2020 research and innovation program under grant agreement No 637268. This financial support is gratefully acknowledged.

REFERENCES

- Cho K., Van Merriënboer B., Bahdanau D. and Bengio Y. 2014. On the properties of neural machine translation: Encoder-decoder approaches. *arXiv preprint* arXiv:1409.1259.
- Chung J., Gulcehre C., Cho K. and Bengio Y. 2014. Empirical Evaluation of Gated Recurrent Neural Networks on Sequence Modeling. *arXiv preprint* arXiv:1412.3555.
- Hinton G., Srivastava N. and Swersky K. 2012. Lecture 6.5-rmsprop: divide the gradient by a running average of its recent magnitude. *COURSERA: Neural Networks for Machine Learning*.
- Hochreiter S. 1998. The vanishing gradient problem during learning recurrent neural nets and problem solutions. *International Journal of Uncertainty, Fuzziness and Knowledge-Based Systems*, 6(02), 107–116.
- Janssen H., Roels S., Van Gelder L. and Das P. 2015. Annex 55 - Reliability of Energy Efficient Building Retrofitting, Probability Assessment of Performance and Cost. Final Report. Chalmers University Of Technology Gothenburg (SE), 152 pages.
- Kemajou A., Mba L. and Meukam P. 2012. Application of artificial neural network for predicting the indoor air temperature in modern building in humid region, *British Journal of Applied Science and Technology*, 2(1), 23–34.
- Kingma D.P. and Ba L.J. 2015. Adam: A Method for Stochastic Optimization. *In: Proceedings of International Conference on Learning Representations*. arXiv:1412.6980
- Soleimani-Mohseni M., Thomas B. and Fahlén P. 2006. Estimation of operative temperature in buildings using artificial neural networks. *Energy and Buildings*, 38(6), 365-640.
- Van Gelder L., Das P., Janssen H. and Roels S. 2014. Comparative study of metamodelling techniques in building energy simulation: Guidelines for practitioners. *Simulation Modelling Practice and Theory*, 49, 245–257.
- Vereecken E., Van Gelder L., Janssen H., and Roels S. 2015. Interior insulation for wall retrofitting – A probabilistic analysis of energy savings and hygrothermal risks, *Energy and Buildings*, 89, 231–244.

Optimization of Night Cooling of Commercial Premises Using Genetic Algorithms and Neural Networks

Emmy Dahlström¹, Linus Rönn² and Angela Sasic Kalagasidis³

¹NCC Construction, Sweden

²Integra Engineering, Sweden

³Chalmers University of Technology, Sweden

Corresponding email: emmy.dahlstrom@ncc.se, linus.ronn@integra.se, angela.sasic@chalmers.se

ABSTRACT

This paper investigates if it is possible to optimize night cooling control setpoints and ventilation schedule regarding energy consumption and indoor climate. A retail store, located in Gothenburg, was used as a case study. The investigation was done by numerical modelling and simulations. It started with development and calibration of a building energy model for the store with data collected from the field. Afterwards, the calibrated model was used in the optimization of the night cooling. Initially, a genetic algorithm was applied to find the global minimum of the problem and further refined with a local search algorithm. The optimization speed was increased by neural networks, as they can approximate results faster than the building energy model.

The study suggests that the cooling and fan energy consumption can be reduced by 16% in the studied facility, compared to the currently used trial-and-error schemes. The project concludes that the use of logged control data in combination with genetic algorithms and neural networks are an efficient way for both calibration and optimization of building energy models. The industry moves towards an increase of available logged control data. As such, it is important to be able to properly utilize the data, for improving the accuracy of building energy simulations and improving the results.

KEYWORDS

Night Cooling, Building Energy Modelling, Genetic Algorithms, Neural Networks and Optimization.

INTRODUCTION

Cooling load has significant impact on energy cost in commercial premises in Sweden mainly due to the peaks in cooling power demand thus increasing the need for power generation. Ventilation at night with cool outdoor air is a wide-spread strategy for reducing and shifting the cooling peaks. Due to complex relations between the building's response to night cooling, the requirements on the thermal comfort and the weather, control setpoints for night cooling are often established on site, through trial-and-error methods. Hence, the opportunity for further optimization of night cooling is missed.

Monitoring of building performance in real time is becoming a wide-spread praxis due to reliable and affordable data acquisition techniques. Indoor parameters, electricity, heat and air flows are recorded continuously, on minute basis. Big data sets that are generated thereby can be used to identify opportunities for energy savings in buildings.

The purpose of the paper is to evaluate the use of genetic algorithms and neural networks with post-processed data from a building to improve the building energy simulations and to

optimize the control settings for night cooling. A store from a real commercial building is used as a case study to allow verification of the modelling results against the measured data. The building in question has a SCADA data logging system of control data such as; indoor temperatures, ventilation temperatures and ventilation air-flow rates. The data are saved every third minute. The records from the SCADA-system worked as a base for calibration of a building energy simulation.

OPTIMIZATION METHODS AND SCHEMES

The work is conducted in several steps. Firstly, a building energy model of the store was created by using MATLAB (MATLAB, 2017). It is a dynamic model that considers the building's capacity to store heat, and where indoor temperature and cooling loads are calculated based on time-varying outdoor conditions, as well as ventilation, comfort and occupancy schemes (Dahlström & Rönn, 2017). This initial model was calibrated to better simulate the reality with the help of logged data from the actual building as shown in the next section. In addition, an optimization strategy was developed and used to improve the model calibration and the settings for the night cooling. This was done by means of genetic algorithms and neural networks as described below.

Genetic algorithm

The optimization method for this analysis needs to be robust as the problems that are optimized can have a number of local minima. This makes a deterministic approach for the general optimization an unsuitable choice. Instead, a genetic algorithm is used as it is better suited to find a global minimum.

Genetic Algorithms (GAs) operate in a way that can be described similar to evolution (Aria, 2015) because they involve random inputs and stochastic search. A genetic algorithm uses a pool of variable-sets that makes it possible to search for the global minimum instead of a local one as multiple potential solutions are kept in the pool. A variable-set contains individual values for all the parameters that are being optimized. Each variable-set is tested by an objective function and gets an associated fitness value produced by the objective function. The objective function is the function for which the global minimum is searched and the fitness value is a measure of the variable-sets suitability as a solution.

Neural network

Neural networks can be used to approximate the results of functions that are relatively unknown and dependent on large numbers of input (Aria, 2015). So, called shallow neural networks (MATLAB, 2018) are used in the analysis as they can approximate the fitness value for a variable-set much faster than the building energy model, thus allowing the use of a much broader genetic function with larger pools and more iterations. One simulation by building energy model took 10 seconds, which was 1500 times slower than the neural network.

Shallow neural networks need to be trained to do a specific job. The training is done by providing the network with examples of input variables and their respective outputs. It will then learn the relation between the inputs and the outputs and can then be used to approximate outputs with new inputs.

Optimization scheme

Two optimization schemes were developed and used in the analyses, each employing a genetic algorithm as illustrated in Figure 1. The objective function for the first genetic algorithm is running the building simulation in MATLAB and calculating the fitness value.

All the variable-sets that are tested by the first GA with their respective fitness value are used as inputs and outputs to train a neural network. This trained neural network can then approximate the fitness value based on new input. The second genetic algorithm uses the neural network as its operative function.

The last step in the scheme is a local search algorithm that starts from the most optimized variable-set in Step 2. The purpose of it is to check if the minimum that was found could be further improved. A local search is used, as the genetic algorithm has very likely found a result close to the global minimum. For this purpose, a deterministic gradient-based method is used, as it will quickly converge to a minimum.

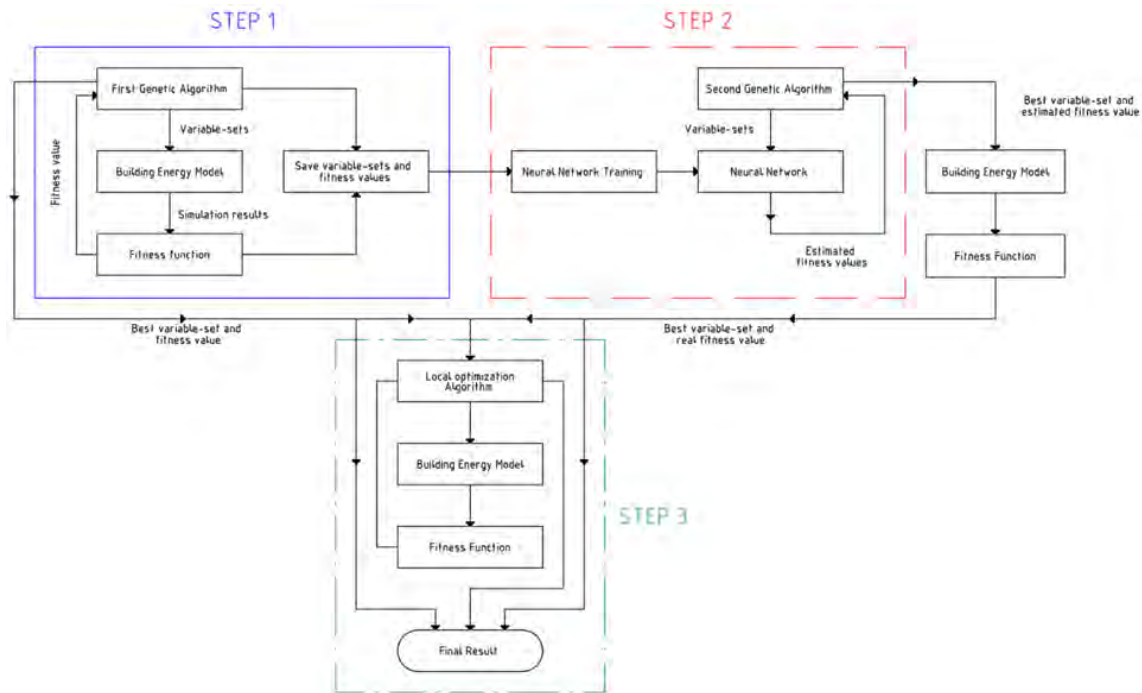


Figure 1: The optimization and calibration scheme used for the analysis.

THE BUILDING MODEL CALIBRATION

The genetic algorithms are used to calibrate different building constants such as thermal masses of interest, heat transfer coefficients between the indoor air and the interior surfaces, magnitude of internal heat loads and how they are divided between the thermal masses. The aim of the calibration is to achieve as small difference as possible between the measured indoor temperature and the simulated temperature. The model was calibrated for the entire cooling season, from May 1 to September 30, 2016. With this long calibration period, most weather conditions are accounted for.

Variable-sets and Fitness values

The calibration of the building energy model was done by making minor changes to the parameters that were initially either assumed or estimated by calculations, as the thermal masses and U-values of building envelope components, intensity of heat gains, occupancy schemes, etc. In the calibration, the fitness value is defined as a difference between the time integral of the measured indoor temperature and the simulated one, and presented in degree hours. By minimizing the difference in degree hours, the calibrated model more closely correlates with reality as the integral average between the real temperature and the simulated becomes smaller.

In the optimization of night cooling, new variable-sets, such as air flow rates, indoor and outdoor temperatures, are used instead of the building parameters that were found in the calibration. The fitness value is changed to represent the amount of energy used in the system instead of the difference between measured and simulated temperature. The energy use in the model considers the fan energy, cooling energy and the penalties, if the indoor temperature becomes too low, as described below.

To prevent the optimization to cool the facility below comfort levels in the morning, temperature requirements were inserted in the model. This was done by adding a penalty that starts if the temperature is below a thresholds value at specific times in the morning. The penalty is in form of an added energy usage. It is described as the temperature difference between the optimized indoor temperature and the threshold value, multiplied by a factor. The purpose of this is to train the system to not fall below these requirements.

Simulation of ventilation

To calibrate the building parameters the measured ventilation data was used. This made sure that the ventilation was not a changing variable in the calibration, thus providing the same conditions for each simulation. However, for the optimization of night cooling, a simulated ventilation scheme was used in order to be able to change the ventilation set-points.

RESULTS

The calibration results show that a decrease of the degree hours between the simulated and the measured temperature is possible. Table 1 and Figure 2a shows the improvements of the calibrations.

Table 1. Mean temperature and temperature difference for the simulation before and after the calibration for the period May 1 – September 30

	Measured	Uncalibrated Model	Calibrated Model
Mean Temperature	22.71 °C	22.94 °C	22.35 °C
Percentile error	-	1.03%	0.34%
Degree hour difference	-	2207 °Ch	1740°Ch
Average temperature difference		0.6°C	0.47°C

Figure 2b shows the difference in indoor temperatures between the original setpoints, taken from the SCADA-system, and the optimized setpoints.

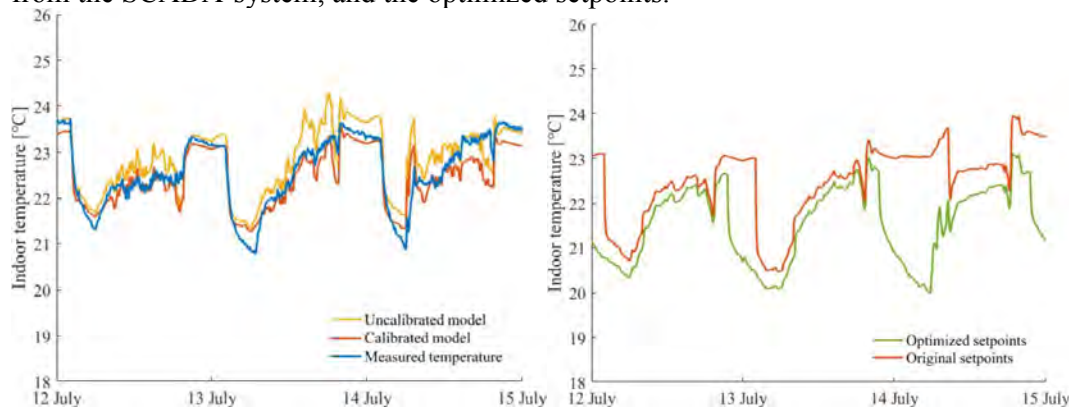


Figure 2a: To the left a comparison between the uncalibrated model, calibrated and the measured temperature for 72 hours in mid-July. Figure 2b: To the right the temperature for the facility with optimized night cooling setpoints and the original setpoints.

The main differences between the optimized and the original setpoints are; 1) the optimized night cooling is allowed to start earlier, e.g. before business hours, 2) the longer active hours of night cooling make it possible for the indoor temperature to reach lower temperatures, 3) night cooling can be active during weekends.

The optimization reduced the total energy demand for the store by 16%, but only resulted in a daytime temperature decrease of 0.22 °C. Without night cooling the energy demand and temperature increases as shown by Table 2. The original setpoints taken from the SCADA-system.

Table 2. The energy demand for the case study.

	Original night cooling setpoints	No night cooling	Optimized night cooling setpoints
Mean Temperature	22.34°C	23.08°C	21.40°C
Day 08:00-20:00	22.32°C	22.77°C	22.10°C
Night 20:00-08:00	22.37°C	23.58°C	21.32°C
Cooling Energy	19.22 kWh/m ²	22.58 kWh/m ²	15.55 kWh/m ²
Difference	-	17.4 %	-19.3%
Fan Energy	9.51 kWh/m ²	10.49 kWh/m ²	8.55 kWh/m ²
Difference	-	10.3%	-9.7%
Total Energy	28.74 kWh/m ²	33.06 kWh/m ²	24.10 kWh/m ²
Difference	-	15.1%	-16.1%
Average Ventilation Flow	1.19 m ³ /s	1.11 m ³ /s	1.33 m ³ /s
Day 08:00-20:00	1.80 m ³ /s	2.09 m ³ /s	1.41 m ³ /s
Night 20:00-08:00	0.59 m ³ /s	0.09 m ³ /s	1.27 m ³ /s

An increased ventilation during night leads to a decreased daytime ventilation as shown by the table above. This also leads to an overall increase in ventilation flow. An increase of total ventilation flow does not lead to an increase in fan energy due to the quadratic specific fan power (SFP) curve. A consequence of its polynomial shape is that peak flows have a significant increase in energy use. These peak flows are reduced with night ventilation as shown in the decrease of average ventilation flow during daytime. The temperature for the three results behave as expected, the overall mean temperature decreases with increased night-cooling but most of that decrease comes from the decrease in temperature during the night. Without night cooling the mean- and night temperature increase.

DISCUSSIONS

In the study, the use of neural network is applied in the calibration of the building energy model and the optimization of night cooling, but not tested as a control system. To use a dynamic control system such as a neural network for controlling the ventilation could be an option. However, this would increase the "black box" effect of night cooling. Maintenance technicians and technical managers would have a harder time understanding and changing it and that would decrease its usefulness and flexibility. To train such a control system a genetic algorithm or another algorithm could be used to optimize the weights and transfer functions of the neural network. It would then optimize towards a goal of good indoor climate and less energy use. A neural network can also potentially be used instead of a building simulation model, if sufficient measured data would be available to train the network. However, this would require a complex network and a large number of examples to train it and, thereby, making it impractical to use.

During the analysis, we discovered some limitations and inaccuracies of the neural network. It was very useful and worked with good accuracy for the calibration of the building simulation. But when implementing the penalties for the optimization, the neural network had issues with accuracy. Without the penalty, the neural network would make an accurate prediction but the optimization would lead to an indoor climate that would be unacceptable. Testing showed that reducing the penalty would result in a better accuracy but colder indoor climate. Therefore, for our purpose the penalty was kept high to ensure a better indoor climate even though it counter act the results from the neural network and led to less optimization and testing.

Our reason behind the inaccuracies is that introducing the penalties leads to unexpected behavior. An example of this is a prolonged ventilation that leads to lower energy use until the system gets penalties, which would then quickly result in a larger energy use and a discontinuity in the results. Other configurations of the neural network and more examples to train the network could be a solution that could handle this behavior but it is not included in the scope of this analysis.

CONCLUSIONS

The results show that genetic algorithms can be used for calibration and optimization of building energy simulations but with some limitations regarding both. For example, the genetic algorithm will always favor an increase in thermal mass and because of that, it would be better to only use it for thermal load calibration. The neural network has also proved to be useful for increasing the speed of the calibration but it had problems with the optimization due to the penalties from the temperature requirements.

ACKNOWLEDGEMENT

We would like to thank Eric Eliasson and Jörgen Greek at Vasakronan for the support and the technical knowledge. Furthermore, the economic support provide by Torsten Janssons Stipendiefond was appreciated and used to further our research.

REFERENCES

- Aria, H. (2015). *A systematic approach of integrated building control for optimization of energy and cost* (Doctoral dissertation).
- Dahlström, E. Rönn, L. (2017). *Optimization of Night Cooling in Commercial Buildings - Using Genetic Algorithms and Neural Networks* (Master Thesis).
- MATLAB. (2017). Release 2017a. (2017). The MathWorks, Inc., Natick, Massachusetts, United States.
- MATLAB. (2018) *Fit data with a neural network*. Retrieved March 25, 2018, from <https://se.mathworks.com/help/nnet/gs/fit-data-with-a-neural-network.html>

Use of calibrated building simulation to investigate comfort conditions in a healthcare facility

Luca Zaniboni^{1,*}, Giovanni Pernigotto¹, Matthias Schuß², Kristina Kiesel², Andrea Gasparella¹ and Ardeshir Mahdavi²

¹Free University of Bozen-Bolzano, Italy

²TU Wien, Austria

**Luca.Zaniboni@natec.unibz.it*

ABSTRACT

Design activity regarding healthcare buildings must not only address the energy efficiency aspects but also account for the indoor thermal comfort conditions. Indeed, the occupants of this category of buildings are affected by different kinds of health issues. Thus, particular efforts are required in order to ensure conditions adequate for therapies and medical treatments. Simulation can be a helpful tool in designing new buildings, particularly in case of complex clinics and hospitals. When analyzing existing facilities, a proper calibration is a necessary step to reduce discrepancies between simulated and measured performance. This improves the reliability of the model itself and allows its use for many purposes, from the assessment of energy performance to the evaluation of indoor thermal comfort, under a broader range of operating conditions and use patterns. In the present contribution, a calibrated model of a healthcare facility in Vienna, Austria, was developed for the assessment of both thermal performance and comfort conditions. The facility, built in the early '90s with later expansions, consists of different rooms and spaces in which several therapeutic activities are performed. Long-term measurements of the air temperature were conducted every 10 minutes for the period between March and June 2015 and used for calibrating the model. During the same period, occupants were interviewed concerning their thermal comfort sensations and detailed short-term measurements were collected to calculate thermal comfort indicators, including Fanger's Predicted Mean Vote and Predicted Percentages of Dissatisfied. The same indices were also calculated through the calibrated simulation model and compared to experimental results and subjective evaluations. The resulting model is finally used to extrapolate the assessment of thermal comfort conditions beyond the measurement period.

KEYWORDS

Building simulation calibration

Thermal comfort

Healthcare facility

INTRODUCTION

Ensuring high levels of indoor comfort to all occupants of healthcare facilities can be particularly critical since employees' and patients' comfort perceptions can differ significantly (Hwang *et al.*, 2007; Khodakarami *et al.*, 2012; Skoog *et al.*, 2005; Verheyen *et al.*, 2011). To this extent, building energy simulation, *BES*, can support designers' activity, but when it comes to existing buildings, calibration is required. As reported by Fabrizio and Monetti (2015), among *manual calibration methods based on iterative approach* and *automated techniques based on analytical and mathematical approaches*, also *optimization-based methods* can be

included. For example, Arambula Lara *et al.* (2017) exploited the genetic algorithm implemented in jEPlus+EA to calibrate an EnergyPlus model of an Italian school building. In this work, a portion of a healthcare facility in Vienna was analyzed. After collecting short and long-term measurements, global comfort according to Fanger's model (ASHRAE, 2013; ISO, 2005) was assessed and contrasted with the results by interviews submitted to occupants. An EnergyPlus model was developed and calibrated by means of two steps: first, by comparison with the collected air temperature measurements, and then against the calculated Fanger's indexes - predicted mean votes, *PMV*, and predicted percentages of dissatisfied, *PPD*. After calibration, the developed model was used to predict the comfort in the facility during the whole year, highlighting the extent of the discrepancies between the different occupants' perceptions. Further developments will focus on redesign tasks, based on the analysis of scenarios for long-term thermal comfort optimization, able to manage effectively the discrepancies among the different occupants' perceptions and to minimize overall energy costs.

METHODS

Case study and measurements The study was conducted on the Physikalisches Institut Leopoldau, a private physiotherapy center located at the ground floor of a 20-year old building in Vienna. The analysed area, about 103 m², includes 22 therapy rooms, where therapies are performed from 7:00 am until 8:00 pm, from Monday to Friday. Further details of the case-study, as well as the collected measurements and outcome of the survey on thermal comfort, are reported in a previous research (Zaniboni *et al.*, 2017), in which a new approach for calibration of TRNSYS energy model and cross-validation against calculated and measured Fanger's indexes was proposed.

Simulation model definition Since the technical details of the heating system (primary air system integrated with radiators) are largely unknown, it was decided to adopt a simplified model of an ideal air system active only during the occupancy time, with a simple control of air flow rate and temperature, the latter ranging from 22 °C to a 40 °C. EnergyPlus was chosen as simulation code, while the calibration was made partially manually and by means of jEPlus brute-force approach. The analysis included only one thermal zone and the 3D model was prepared using Rhinoceros and the Grasshopper plugin Honeybee. The same initial values and weather data, provided by ZAMG (Zentralstalt für Meteorologie und Geodynamik), used in Zaniboni *et al.* (2017), were set. The average daily occupational profile was calculated from the occupancy data, known from July 2nd 2014 to January 20th 2015. Shading devices, covering only part of the windows' areas, were simulated as a shading factor equal to 0.6. The EnergyPlus default specific infiltration rate for square meter of façade, equal to 0.0006 m³/(s m²) and representative of leaky buildings, was selected. Since it was observed that windows were quite often opened in the facility, a dynamic control for natural ventilation was modelled.

Simulation model calibration 14 variables were identified for calibration. The initial simulated air temperature profile resulted quite far from the measured one, therefore a first attempt manual calibration was made, considering a different interval of variation for each variable. A sensitivity analysis on *RMSD* (Figure 1) was performed to reduce the number of variables to calibrate in a second step, based on both manual and automatic brute-force calibration with jEPlus.

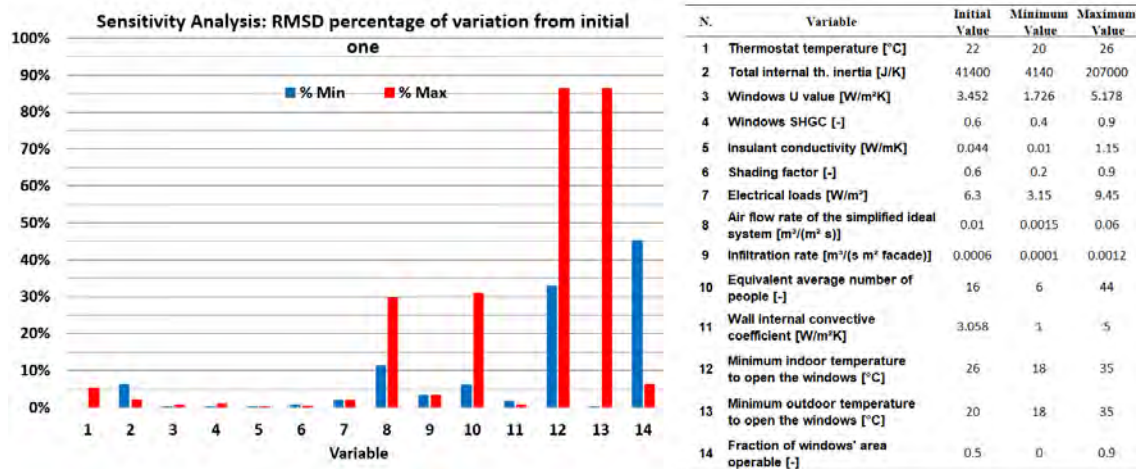


Figure 1. The sensitivity analysis results: percentages of variation of the *RMSD* in comparison with the initial value, using the maximum and the minimum limit values for each parameter reported on the right.

All the variables affecting the *RMSD* of more than the 5 % were considered. A manual calibration was made on these ones, i.e., thermostat setpoint temperature, the minimum outdoor temperature to open the window and the fraction of windows' area operable. At this point, a brute force calibration using jEPlus was applied to the internal thermal inertia, the air flow rate of the simplified ideal system and the equivalent average number of people present in the structure, the latter used to represent the thermal load by the occupants considering a load of 104 W per person, corresponding to the average between patients' and employees' metabolic rate. For each variable, new ranges were defined with a discrete number of levels from 5 to 7, and a total number of 175 simulations.

Comfort indexes *PMV* and *PPD* were derived from both measured and simulated data during occupancy time in order to validate the calibrated model. Considering the indexes determined from simulations, EnergyPlus air and mean radiant temperature outputs were used in calculations, together with average humidity and air speed by measurements. Finally, in both cases, the *PMV* evaluated at the same time in which votes were collected, were compared for both patients and employees.

Prediction of the thermal comfort during the whole year The calibrated model was used to calculate the indexes at each hour during the measurement period of three month, and also during the whole year. To do this last step, the Vienna typical year downloaded from the EnergyPlus Website (2018) was used.

RESULTS

Calibration The first attempt of manual calibration halved the *RMSD* from 2.67 to 1.28 °C. The second attempt of manual and automated calibration made it furtherly decrease to 0.21 °C. The values of the variables after the first attempt manual calibration and at the end of the process are reported in Table 1.

The profile of the measured and simulated air temperature inside the thermal zone are reported in Figure 2, during the whole period and for the last month as an example. As it can be observed, the two profiles get along very well.

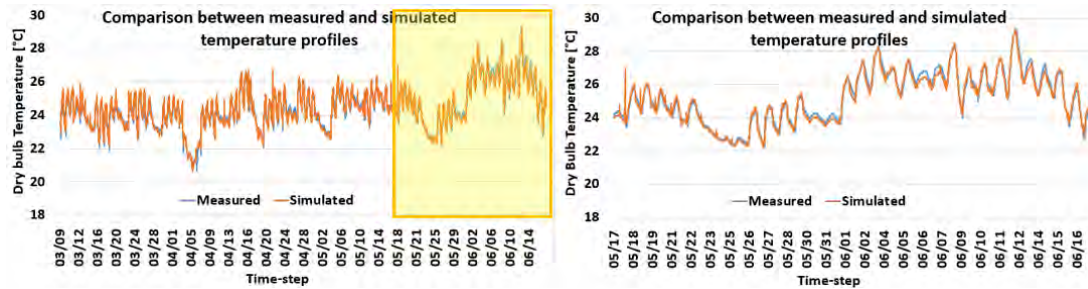


Figure 2. The comparison between the air temperature profiles (measured and simulated) during the whole period and for the last 20 days of March 2015.

Table 1. List of the variables varied in the second attempt manual and automated calibration

Variable	Initial	Final
Thermostat Setpoint Temperature [°C]	22	22
Internal Thermal Inertia [J/K]	20700	41400
Air flow rate of the simplified ideal system [m ³ /(m ² s)]	0.0022	0.04
Equivalent average number of people [-]	22	13
Minimum Indoor Temperature to open the window [°C]	26	18
Minimum Outdoor Temperature to open the window [°C]	24	20
Fraction of window operable area [-]	0.5	0.5

PMV and PPD indexes The comparison between the *PMV* indexes at the time in which questionnaires were filled out by the occupants and the corresponding votes is reported in box and whiskers charts in Figure 3. Considering the patients, there is a good agreement between the average values of comfort indexes evaluated from measurements and votes collected by questionnaires and indexes calculated from the simulated model. On the contrary, the average *PMV* calculated from measurements and simulations overestimate the real employees' votes and dissatisfied percentage, which show also larger interquartile ranges. The wider dispersion of comfort sensation of employees can be explained by the large range of clothes and activities made. Figure 4 reports a comparison between average hourly *PMV* and *PPD* indexes calculated by measured and simulated data. The values are the hourly averages during the three months at which the measurements were taken, during the occupational time. In this case, the indexes do not refer to the time in which questionnaires were compiled by employees and patients but to the whole occupancy time. Also in this case, the two groups of indexes are similar, even if a slight underestimation of *PMV* and *PPD* calculated by simulation data can be registered.

The annual simulation results in Figure 6 show very low *PMV* for the patients. The image reports also a second solution, with a higher temperature thermostat setting. The too low *PMV* and *PPD* during the annual simulation are due to the fact that the period of measurements at which the model was calibrated, was a particular year, hotter than usually. This could be solved by the regulation of the thermostat. The lowest peaks are due to the fact that the plant is switched on at 7:00. A solution can clearly be to anticipate it, but at 7:00 not many patients are present in the structure.

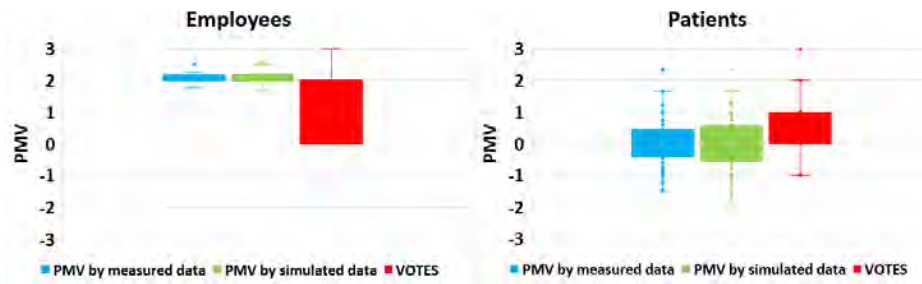


Figure 3. Comparison among PMV indexes obtained by measured and simulated internal temperatures and real votes – box and whiskers chart.

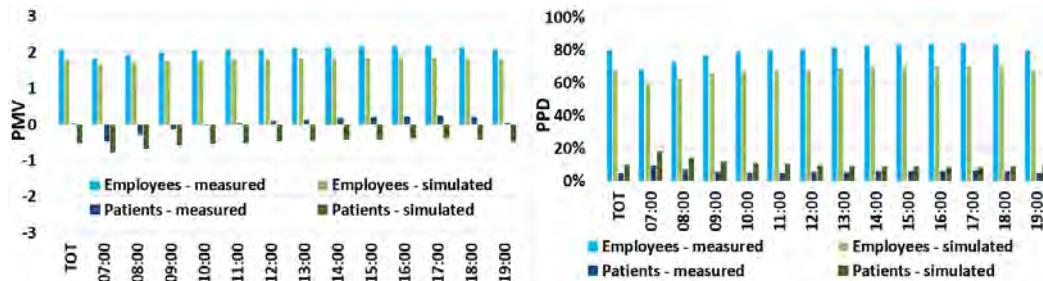


Figure 4. Hourly and daily comparison between PMV and PPD indexes obtained by measured and simulated internal temperatures.

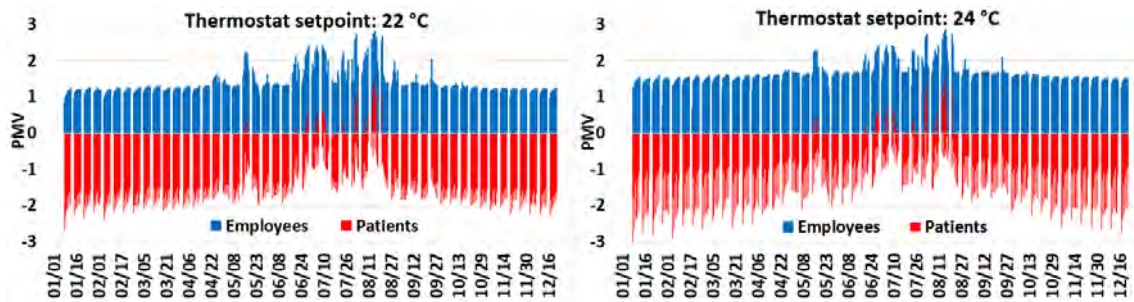


Figure 5. PMV calculated during the whole year, hour by hour, regulating the thermostat with 22 °C and 24 °C.

DISCUSSION AND CONCLUSIONS

In this work, an EnergyPlus model of a thermal zone of a healthcare building in Vienna, Austria, was calibrated for the assessment of both thermal behavior and comfort conditions. Many properties of the building envelope and system were unknown and initial values were assumed from direct inspections and documentation on technical standards. Air temperature measurements taken from March to June 2015 were used for calibrating the model. During the same period, occupants were interviewed about their thermal comfort sensations and detailed short-term measurements were collected to calculate Fanger's Predicted Mean Votes and Predicted Percentages of Dissatisfies. Simulated air and mean radiant temperature profiles from the calibrated model were used to evaluate the same indexes, which were compared to the ones calculated from the short term measured data and people's votes for cross-validation purposes. With the calibrated and cross validated model, an annual simulation was made using the typical year. Thanks to these analyses, we observed that:

- Even starting with a limited number of monitored variables, it is possible to calibrate a simplified model able to simulate, with sufficient accuracy, the comfort indexes for the considered thermal zone.

- With a good synergy of manual and automated calibration, the calibration time can be significantly reduced. This is particularly true when, as in this case, the sensitivity analysis shows a strong dependence of the model on some variables, and also gives some clear indications on how to change these variables in order to minimize the objective function.
- The validated and calibrated model permits to extend the comfort analysis in the structure to time periods which are different from the one in which the measurements were taken for building management purposes. In this case, this allowed to observe that, using a typical year instead of 2015 data as weather file, a different building management is required to ensure proper thermal comfort to patients.

Possible further developments on this case study will be based on the calibrated model and deal with optimization techniques and solutions of model predictive controls. As a final consideration, the proposed method is expected to be applicable also to similar buildings, with the aim to assess the building management in order to optimize thermal comfort for occupants in various seasons and years.

ACKNOWLEDGEMENT

This study has been funded by the project “Klimahouse and Energy Production” in the framework of the programmatic–financial agreement with the Autonomous Province of Bozen-Bolzano of Research Capacity Building. The authors kindly thank the Zentralanstalt für Meteorologie und Geodynamik (ZAMG) for providing the meteorological data.

REFERENCES

- Arambula Lara R., Naboni E., Pernigotto G., Cappelletti F., Zhang Y., Barzon F., Gasparella A., and Romagnoni P. 2017. Optimization Tools for Building Energy Model Calibration. In: *Energy Procedia* 111:1060-1069.
- ASHRAE. 2013. *ASHRAE Standard 55*, Thermal Environmental Conditions for Human Occupancy. Atlanta: American Society of Heating, Refrigerating, and Air-Conditioning Engineers, Inc.
- CEN. 2005. *EN ISO 7730:2005*. Ergonomics of the thermal environment -- Analytical determination and interpretation of thermal comfort using calculation of the PMV and PPD indices and local thermal comfort criteria. Brussels, Belgium: CEN.
- Energy Plus. 2018. Accessed March 2018. <https://energyplus.net/>
- Fabrizio E., Monetti V. 2015. Methodologies and advancements in the calibration of building energy models. In: *Energies*, vol. 8, no. 4, pp. 2548–2574.
- Hwang R. L., Lin T. P., Cheng M. J., Chien J. H. 2007. Patient thermal comfort requirement for hospital environments in Taiwan. In: *Building and Environment* 42: 2980–2987.
- ISO. 2001. *ISO 10551*. Ergonomics of the thermal environment - Assessment of the influence of the thermal environment using subjective judgement scales. Geneva, Switzerland: ISO.
- Khodakarami J., and Nasrollahi N. 2012. Thermal comfort in hospitals – A literature review. In: *Renewable and Sustainable Energy Reviews* 16: 4071– 4077.
- Skoog J., Fransson N., Jagemar L. 2005. Thermal environment in Swedish hospitals: summer and winter measurements. In: *Energy and Buildings* 37: 872-877.
- Verheyen J., Theys N., Allonsius L., Descamps F. 2011. Thermal comfort of patients: Objective and subjective measurements in patient rooms of a Belgian healthcare facility. In: *Building and Environment* 46: 1195-1204.
- Zaniboni L., Kiesel K., Schuß M., Pernigotto G., Gasparella A., Mahdavi A. 2016. Calibrated simulation models for indoor comfort assessment: the case of a healthcare facility in Vienna. In: 3rd Building Simulation Applications Conference BSA 2017 at Bolzano, Italy February 8-10.

An Experimental and Modelling Study on the Adsorption Characteristics of Activated Carbon under Different Challenge Concentration Levels

Chuan He^{1,*}, Jingjing Pei² and Jensen Zhang¹

¹Syracuse University, USA

²Tianjin University, China

*Corresponding email: chhe@syr.edu

ABSTRACT

Applying air cleaning devices is an effective approach to control targeted indoor gaseous pollutants. It is important to understand the adsorption characteristics of filter media (e.g. activated carbon) at typical indoor application conditions as well as standard test conditions. Tests per ASHRAE Standard 145.1 for filter media performance evaluation can provide a relative comparison among different media. However, as the tests are conducted at elevated gas concentrations (1~100 ppm), they do not represent the media performance under lower concentrations typical of indoor applications (<0.1 ppm). Data are currently lacking for describing the correlation between the gas-phase filter media performance and the challenge concentration levels. In this study, single-pass adsorption tests were performed with smaller bed depth and pellet size than that specified in ASHRAE std 145.1 test protocol at four different concentration levels (50 ppb, 500 ppb, 5 ppm and 50 ppm). The data were used to determine the sorption isotherm and suggest a correlation between the partition coefficient and challenge concentration. Results revealed for the first time a linear correlation at log-log scale between the partition coefficient and the challenge concentration. Incorporation of this new correlation in a sorbent bed simulation model enabled the prediction of filter performance at low concentration based on the test data obtained from high concentration tests.

KEYWORDS

Indoor air quality, adsorption, partition coefficient, activated carbon.

INTRODUCTION

Poor indoor air quality has been statistically associated with occupants' health and performance (Seppänen & Fisk, 2006). Volatile organic compounds (VOCs) are found to be one of the major risk factors that are responsible for poor indoor air quality (Gallego et al, 2009). Ventilations, as a dilution method, has limitation in practice for removing targeted pollutants of interest because of its energy consumption and dependency on outdoor air quality. Thus, filtration through sorbent media (e.g., activated carbon) is considered as an effective alternative to reduce specific VOC concentration in an energy efficient manner (Fisk, 2008). Understanding and evaluating the performance of sorbent media become very important for designing a filtration system. ASHRAE standard 145.1-2015 has provided a laboratory test method to evaluate the performance of granular sorbent media (ASHRAE, 2008). However, the challenge concentration described in the test method is at 100±10 ppm, which is far above typical indoor concentration. Consequently, the results of the standard test cannot represent the actual performance of the sorbent media in the indoor environment. The goal of this study is to 1) investigate the performance of sorbent media at different concentration levels, from 100 pm down to 100 ppb (close to typical indoor concentration level of less than 50 ppb), and 2) develop a mechanistic model to simulate the sorbent media at real operation conditions.

METHODS

An air-cleaning technology test system (ACTTS) was used to investigate the performance of sorbent media at different challenge concentration levels. The design of the test system is illustrated in **Figure 1**. The ACTTS could control and provide the same test conditions, e.g., flow rate, temperature, humidity and challenge concentration to each test column (Figure 2). The diameter of the test column was consistent with ASHRAE 145.1 standard test but the height of sorbent media was reduced to $L=1$ cm to shorten the test period. Two test columns (sorbent column) were packed with sorbent media, and another one (reference column) was empty for inlet concentration monitoring.

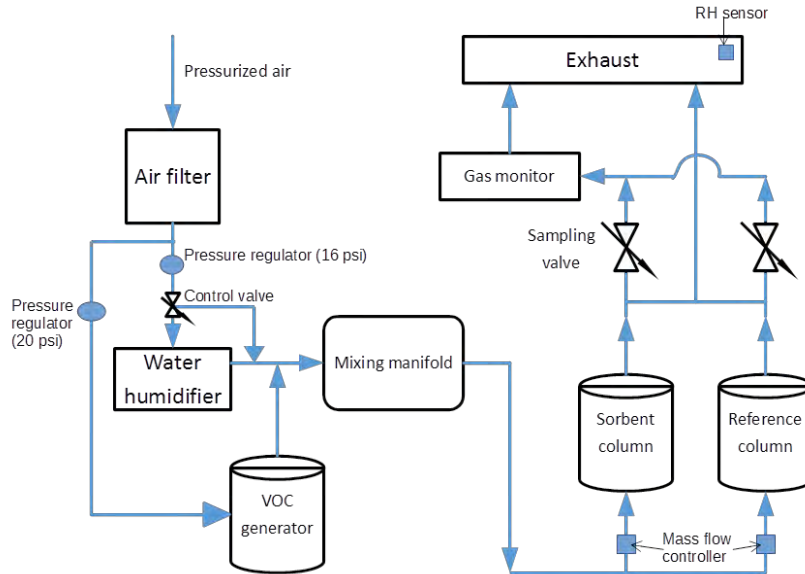


Figure 1 Schematics of the ACTTS

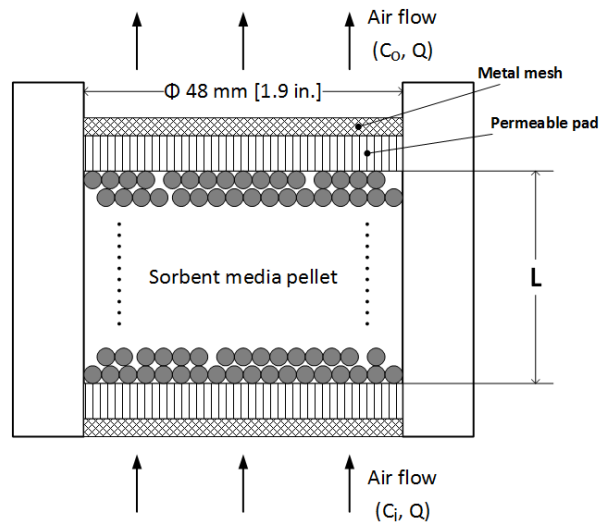


Figure 2 Schematic of the test column

Activated carbon is a widely used sorbent media in practice due to its high surface area and porous structure. Two types of virgin activated carbon were selected to test. The sorbent media were grounded into the particle size of 1 mm through ball-milling. The purpose of the

grounding procedure is to ensure the packing of the sorbent bed is uniform. The specifications of the selected media are listed in Table 1.

Table 1 Specifications of test media

Media ID	M#1	M#2
Material	Coconut base virgin activated carbon	Coal base virgin activated carbon
Apparent density*	0.45 g/cc	0.49 g/cc
Pellet porosity*	0.3	0.4

* provided by manufactures

Toluene is one of the typical VOCs commonly found in the indoor environment. It has been widely used as a reference compound for total volatile organic compounds (TVOCs) in many studies. Bubbling method and heated permission tubes were used to generate high (≥ 5 ppm) and low concentrations of toluene, respectively. A portable device, ppbRAE 3000 (1ppb resolution; $\pm 3\%$ accuracy at calibration point), is used for toluene measurement. During the test, both the inlet concentration, C_i and outlet concentration C_o were monitored. The ratio between the adsorbed phase concentration and the gas-phase VOC concentration at equilibrium is defined as partition coefficient and used to represent the capacity of the activated carbon. The partition coefficient can be calculated through Eq-1.

$$K_{ma} = \frac{C_s}{C_i} = \frac{Q \cdot \int_0^t (C_i - C_o) dt}{\pi \cdot \frac{\phi^2}{4} \cdot L \cdot (1 - \varepsilon_b)} / C_i \quad (1)$$

where K_{ma} is the partition coefficient, C_s is the sorbent phase concentration, ε_b is the bed porosity, L is the height of the sorbent bed, and ϕ is the diameter of the sorbent bed. Tests were conducted in this study to provide the partition coefficients of the two types of activated carbon under 4 different concentration levels ranging from 100 ppb to 50 ppm.

MODELING AND SIMULATION

The mass transfer of VOC in the packed bed system includes: external convective mass transfer at the outer surface of sorbent particle, internal diffusion inside the pellet (within the pore air and on the internal surface) and adsorption of VOCs on the solid matrix of the sorbent, such as activated carbon. A mechanistic model has been developed to describe the mass transfer process in the sorbent bed in the previous study (He et al., 2014; Pei & Zhang, 2010). The same model was applied but a new method to determine the partition coefficient was used in the present study. Instead of using a constant partition coefficient gained from each experiment, the partition coefficient is considered as a variable that depends on the gas-phase concentration. The correlation between the partition coefficient and the gas-phase concentration, namely, P-C correlation, was found to follow the form of:

$$K_{ma} = a(C_p)^b \quad (2)$$

where C_p is the gas-phase VOC concentration, which is equal to the inlet concentration at 100% breakthrough.

The parameters used in the simulation are listed in Table 2. The methods to determine the mass transfer coefficient and diffusion coefficient were introduced in the previous study (Pei & Zhang, 2012).

Table 2 Summary of the simulation parameters

Packed-bed	Bed diameter, D , cm	4.8	Measured
	Particle diameter, d_p , mm	1	
	Bed length, L , cm	1	
	bed porosity, ε_b	0.3	
	Pellet porosity, ε_p	0.3 (M#1), 0.4(M#2)	
	mass transfer coefficient, h_m , m/s	0.076	Sh, Re, Sc
Environment	Inlet concentration, C_i , ppm	42, 5, 0.58, 0.1	Measured
	Flow rate, Q , m ³ /h	1.699	
	Superficial velocity, u_s , m/s	0.26	
Media	Pore diffusivity, D_p , m ² /s	8e-6	Literature (Do, 2011; Khazraei, 2014; Pei, 2011)
	Surface diffusivity, D_s , m ² /s	5e-10	
		P-C correlation	$K_{ma}=2121.5 \cdot C_p^{-0.728}$ (M#1) $K_{ma}=1880.7 \cdot C_p^{-0.70}$ (M#2)

RESULTS AND DISCUSSIONS

According to the experimental data from the breakthrough tests, the partition coefficient for two activated carbon at 4 different toluene concentration levels were obtained for Test M#1 and Test M#2 (**Figure 4**). The correlation of the partition coefficient and the corresponding challenge concentration was established by regression using Eq-2 (Figure 3). These two correlations for M#1 and M#2 were then used for determining the partition coefficient in each control volume in the simulation.

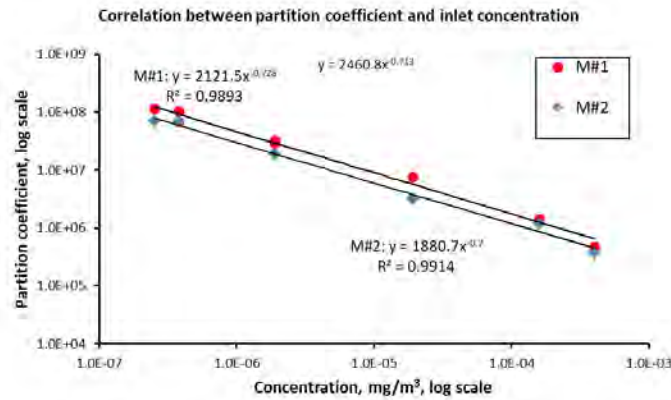


Figure 3 Correlation between the partition coefficient and the challenge concentration

In **Figure 4**, the simulation results were compared with the experimental data at 4 different concentration levels. The mechanistic model with the partition coefficient determined from the tests could generate results that have good agreement with the test data ($R^2 > 0.9$). The P-C correlation for each activated carbon media could be used to simulate the tests at both high concentration and low concentration.

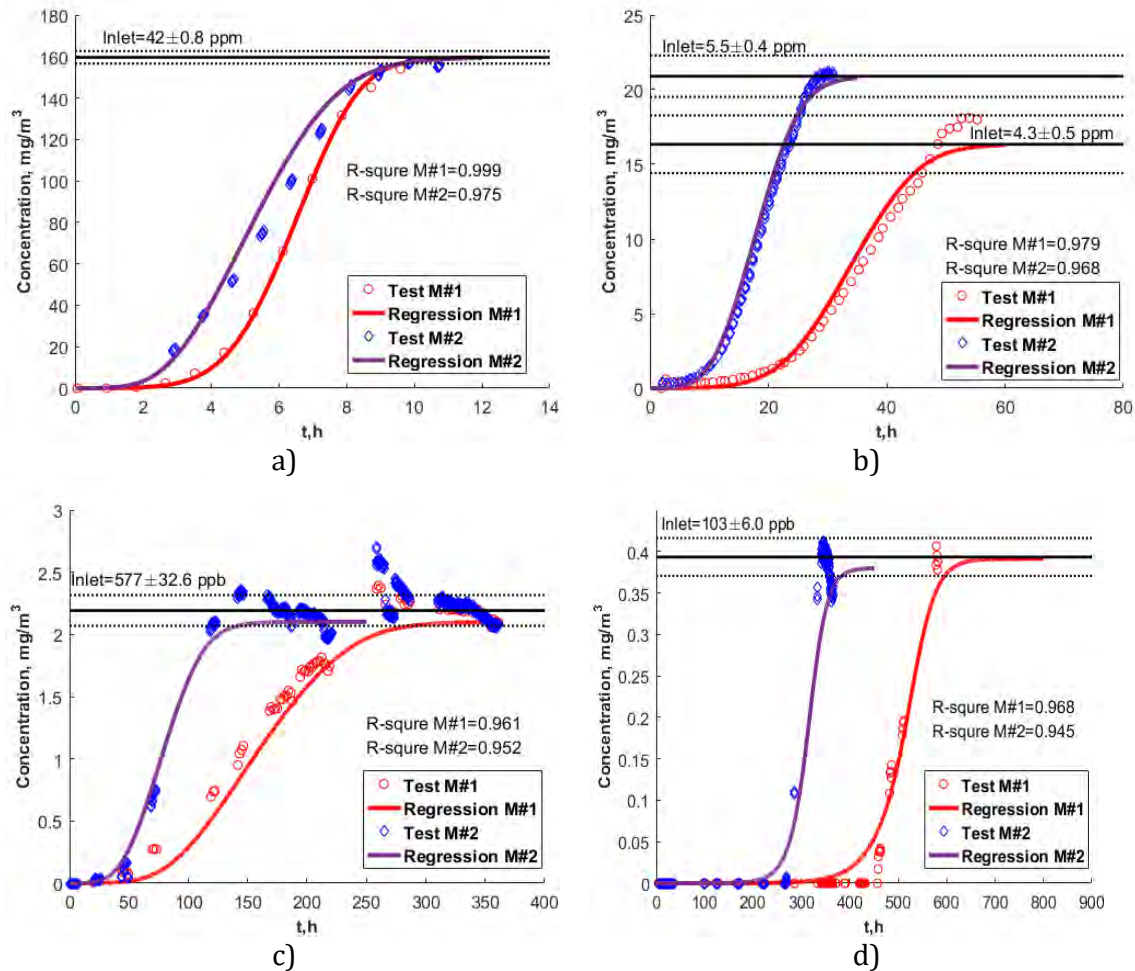


Figure 4 Breakthrough curve of toluene in activated carbon (M#1 and M#2) at four concentration levels

CONCLUSIONS

Based on the experimental investigation, the removal capacity at 100% breakthrough depends on the challenge concentration significantly. Tests of two types of activated carbon at 4 different concentration levels of toluene show that the partition coefficient increases with decreasing inlet concentration. The correlation between the partition coefficient and the concentration can be represented by a power-law empirical equation (i.e., a linear relationship in the log-log scale). The empirical equation can be used to determine the partition coefficient in the sorbent bed and applied in the mechanistic model to simulate performance of the activated carbon at both high and low concentration of toluene. As a result, it would enable the prediction of the filter performance at low concentration levels typical of indoor environment based on the standard accelerated tests at high concentration levels.

REFERENCES

- ASHRAE, B. S. R. (2008). ASHRAE standard 145.1 P, laboratory test method for assessing the performance of gas-phase air cleaning systems: loose granular media. *American Society of Heating, Refrigerating and Air-Conditioning Engineers, Inc., Atlanta*.
- Fisk, W., & Fisk, W. J. (2007). Can Sorbent-Based Gas Phase Air Cleaning for VOCs Substitute for Ventilation in Commercial Buildings? (No. LBNL-255E). *Ernest Orlando Lawrence Berkeley National Laboratory, Berkeley, CA (US)*.
- Gallego, E., Roca, X., Perales, J. F., & Guardino, X. (2009). Determining indoor air quality and identifying the origin of odour episodes in indoor environments. *Journal of Environmental Sciences*, 21(3), 333–339.
- He, C., Chen, W., Han, K., Guo, B., Pei, J., & Zhang, J. S. (2014). Evaluation of filter media performance: Correlation between high and low challenge concentration tests for toluene and formaldehyde (ASHRAE RP-1557). *HVAC&R Research*, 20(5), 508–521. <https://doi.org/10.1080/10789669.2014.907096>
- Pei, J., & Zhang, J. (2010). Modeling of sorbent-based gas filters: Development, verification and experimental validation. *Building Simulation*, 3(1), 75–86. <https://doi.org/10.1007/s12273-010-0309-4>
- Pei, J., & Zhang, J. S. (2012). Determination of adsorption isotherm and diffusion coefficient of toluene on activated carbon at low concentrations. *Building and Environment*, 48, 66–76. <https://doi.org/10.1016/j.buildenv.2011.08.005>
- Seppänen, O. A., & Fisk, W. (2006). Some quantitative relations between indoor environmental quality and work performance or health. *Hvac&R Research*, 12(4), 957–973.

Development of a Procedure for Estimating the Parameters of Mechanistic Emission Source Models from Chamber Testing Data

Zhenlei Liu^{1,*}, Andreas Nicolai², Marc Abadie³, Menghao Qin⁴ and Jensen Zhang¹

¹Syracuse University, Syracuse, USA;

²Dresden University of Technology, Dresden, Germany

³University of La Rochelle, La Rochelle, France

⁴Technical University of Denmark, Lyngby, Denmark

*Corresponding email: zliu138@syr.edu

ABSTRACT

In order to evaluate the impacts of volatile organic compounds (VOCs) emissions from building materials on the indoor pollution load and indoor air quality beyond the standard chamber test conditions and test period, mechanistic emission source models have been developed in the past. However, very limited data are available for the required model parameters including the initial concentration (C_{m0}), in-material diffusion coefficient (D_m), partition coefficient (K_{ma}), and convective mass transfer coefficient (k_m). In this study, a procedure is developed for estimating the model parameters by using VOC emission data from standard small chamber tests. Multivariate regression analysis on the experimental data are used to determine the parameters. The Least Square and Global search algorithm with multi-starting points are used to achieve a good agreement in the normalized VOC concentrations between the model prediction and experimental data. To verify the procedure and estimate its uncertainty, simulated chamber test data are first generated by superposition of different levels of “experimental uncertainties” on the theoretical curve of the analytical solution to a mechanistic model, and then the procedure is used to estimate the model parameters from these data and determine how well the estimates converged to the original parameter values used for the data generation. Results indicated that the mean value of the estimated model parameters C_{m0} was within -0.04%/+2.47% of the true values if the “experimental uncertainty” were within +/-10% (a typical uncertainty present in small-scale chamber testing). The procedure was further demonstrated by applying it to estimate the model parameters from real chamber test data. Wide applications of the procedure will result in a database of mechanistic source model parameters for assessing the impact of VOC emissions on indoor pollution load, and for evaluating the effectiveness of various IAQ design and control strategies.

KEYWORDS

Building materials, Volatile organic compounds (VOCs), Emission source model, Indoor air quality.

INTRODUCTION

Indoor air quality (IAQ) plays an important role in human health because people typically spend 80-90% of their time indoors. To evaluate the effects of volatile organic compounds (VOCs) emissions from building materials, a physical mechanistic model was developed by Little and Hodgson (1994) and improved by Yang (2001), Huang and Haghghat (2002), Zhang and Xu (2003) with their specific assumptions and solutions. Deng and Kim (2004) successfully derived the analytical solution to the model that considering the convective mass transfer resistance across the boundary layer. The model in theory can be used to evaluate and predict the emissions of VOCs from dry building materials beyond the standard chamber test condition and test period. However, very limited data are available for the required model parameters including the initial concentration (C_{m0}), in-material diffusion coefficient (D_m), partition coefficient (K_{ma}), and convective mass transfer coefficient (k_m).

Little and Hodgson (1994) also performed a series of emission test for four kinds of carpets. Bodalal et al. (1999) tested three types of VOCs through typical dry materials. The correlation

for predicting D_m and K_{ma} based on molecular weight and vapor pressure were developed for each product and type of VOCs. These correlations were later verified and improved by Zhang et al. (2003) in the sorption and desorption experiments. Xu et al. (2011) implemented a Dual-chamber test that can measure D_m and K_{ma} directly. Xu's data were used for developing and verifying the method that can predict D_m and K_{ma} based on the similarity between water vapor and VOC transport in porous media. Cox (2001) measured the D_m and K_{ma} in vinyl flooring. Zhou et al. (2018) developed an alternately airtight/ventilated emission method for efficient determination of the key parameters from building materials. The measured D_m ranged across six orders of magnitudes from $1E-14$ to $1E-8$ m^2/s and K_{ma} ranged from 1 to 450,000 (as shown in Figure 1), depending on the Media (materials)-Environment (T and RH)-Species (VOCs) combinations.

The objective of the present study is to develop a procedure for estimating the model parameters by using gas-phase VOC concentration data from standard small chamber emission tests and explore the feasibility of using the estimated parameters in the mechanistic diffusion model to analyse and predict the long-term emissions from building materials and their impact on indoor air quality.

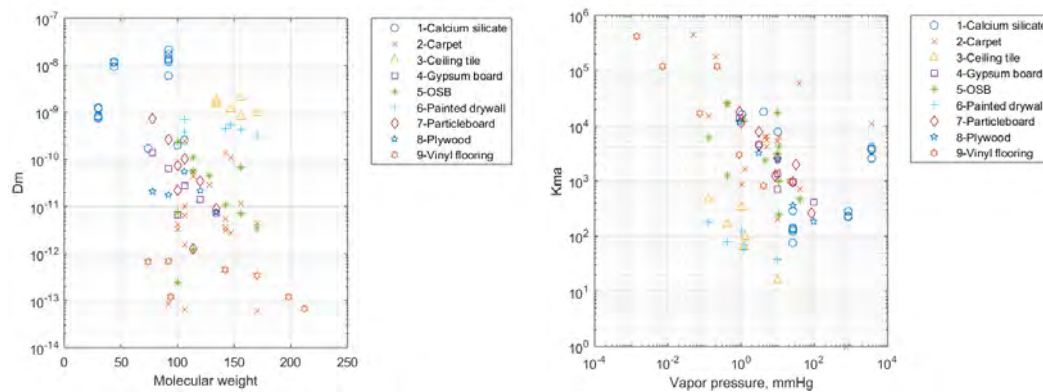


Figure 1 Summary of D_m (left) and K_{ma} (right) values from the literature

METHODS

Mathematical model

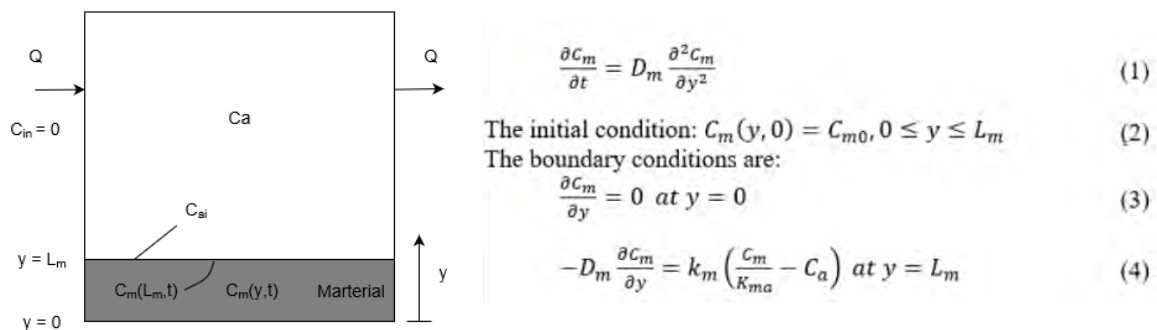


Figure 2 Schematic of VOC emission in a test chamber and the governing equations

A schematic of emission testing and the equations governing the material diffusion process of a dry material in a ventilated chamber is shown in Figure 2, assuming that (1) the material is homogenous with a uniform initial concentration; (2) The diffusion process is one dimensional in the material; (3) The pollutant in the chamber air is perfect mixed; and (4) the interactions between different VOCs are negligible.

For the concentration in the chamber air, the governing equation can be represented as:

$$V \frac{dC_a}{dt} = -QC_a - AD_m \left. \frac{\partial C_m}{\partial x} \right|_{y=L_m} \quad (5)$$

$$\text{Initial condition: } C_a = 0 \text{ at } t = 0 \quad (6)$$

Where, V is the volume of the chamber, m³. A is the top surface area of the material, m². Q is the air flow rate, m³/s.

Analytical solution

Deng and Kim (2004) derived an analytical solution derived the following analytical solutions to Eqs. 1-6:

Concentration in the material:

$$C_{m(y,t)} = 2C_{m0} \sum_{n=1}^{\infty} \frac{(\alpha - q_n^2)}{A_n} \cos\left(\frac{y}{\delta} q_n\right) e^{-D_m L_m^{-2} q_n^2 t} \quad (7)$$

Concentration in the gas-phase:

$$C_a(t) = 2C_{m0} \beta \sum_{n=1}^{\infty} \frac{q_n \sin q_n}{A_n} e^{-D_m L_m^{-2} q_n^2 t} \quad (8)$$

$$A_n = [K_{ma} \beta + (\alpha - q_n) K_{ma} Bi_m^{-1} + 2] q_n^2 \cos q_n + q_n \sin q_n [K_{ma} \beta + (\alpha - 3q_n^2) K_{ma} Bi_m^{-1} + \alpha - q_n^2] \quad (9)$$

$$Bi_m = k_m L_m / D_m \quad (10)$$

$$\alpha = N L_m^2 / D_m \quad (11)$$

$$\beta = L \cdot L_m \quad (12)$$

Where, Bi_m is termed as the Biot number for mass transfer, which represents the ratio of in-material to on-surface mass transfer resistance. α is the dimensionless air exchange rate, which show the ratio of dilution rate in the chamber air to the in-material diffusion rate. L is loading ratio, area of material / volume of chamber. β is the ratio of the chamber air to the volume of the material.

$$\text{The } q_n \text{ are the positive roots of: } q_n \tan q_n = \frac{\alpha - q_n^2}{K_{ma} \beta + (\alpha - q_n^2) K_{ma} Bi_m^{-1}} \quad (13)$$

Approach to the determination of the model parameters

The present model has four key parameters: k_m , K_{ma} , D_m , and C_{m0} . Due to the consistent flow patterns in the standard chamber test condition, the k_m can be pre-determined as part of the chamber characterization measurements. For example, the k_m of the small scale environmental chambers used to establish the material emission database (MEDB-IAQ) at the National Research Council Canada (NRC) were measured to be 1.0 and 1.5 m/h, respectively (Zhang et al., 1999). Some empirical relations were also adopted for the gas-phase mass transfer coefficient (Huang and Haghightat 2002). For laminar flow, there exists (White, 1988)

$$Sh = 0.644 Sc^{1/3} Re^{1/2} \quad (14)$$

Where, Sh is Sherwood number ($Sh = \frac{k_m l}{D_m}$). Sc is Schmidt number ($Sc = \frac{\nu}{D_m}$), ν is the kinematic viscosity, m²/s. Re is Reynolds number ($Re = \frac{v \cdot l}{\nu}$), v is the velocity of the fluid, m/s, l is the characteristic dimension, m.

The remaining three key parameters (C_{m0} , D_m and K_{ma}) need to be obtained from the emission test data. From Deng's analytical solution of gas-phase concentration (Eq.8), C_{m0} does not affect the shape of concentration curve $C_a(t)$, though it affects the magnitude of $C_a(t)$. So we first

estimated the initial value of C_{m0} ($C_{m0,ini}$) by using a first-order evaporation model (Zhang et al, 1999) and then use it in the regression analysis of normalized concentration to estimate D_m and K_{ma} . Since the gas-phase concentration is proportional to C_{m0} for the same D_m and K_{ma} , the final value of C_{m0} can be obtained by:

$$C_{m0} = C_{m0,ini} \frac{\int_0^{t_n} C_{a,data} dt}{\int_0^{t_n} C_{a,sim} dt} \quad (05)$$

Where, $C_{m0,ini}$ is the initial guess of C_{m0} . t_n is the time of the last data point. $C_{a,data}$ is the measured gas-phase concentration from chamber test data. $C_{a,sim}$ is the simulated gas-phase concentration calculated by the analytical solution with D_m and K_{ma} from the regression analysis with initial guess of C_{m0} ($C_{m0,ini}$).

Procedure for the determination of the model parameters

The chamber data are first pre-processed by curve fitting with a power law model, which is then used to generate the data with the same “sampling” time interval. The initial guesses of the three key parameters are obtained from the generated data. To minimize the distortion of normalized curve due to measurement error of maximum concentration, we used the average concentration over the test period ($C_{a,avg}$) to normalize the measured concentrations in the chamber. Then the regression analysis with global minimum algorithm that could find the minimum least square of error in the concentration (target function: $F(D_m, K_{ma}) = \sum (C_{a,estimate}(t) - C_{a,data}(t))^2$) is performed on the normalized data ($C_a/C_{a,avg}$), which is followed by the re-calculation of the C_{m0} by Eq.15. If the results of D_m and K_{ma} are in the range of K_{ma} dominated state (i.e., K_{ma} is so large that there is abundant VOC mass on the surface that the in-material diffusion resistance is inconsequential comparing to the convective mass transfer resistance over the surface), the upper limit of D_m were accepted as final estimation of D_m as the conservative estimate. Otherwise, the results of the regression are used as the parameter estimates.

RESULTS

Verification of the procedure from measured parameters

A reference emission test with 840 hours of experimental data for a particleboard (PB1) obtained by NRC (1999) are used to examine the effect of the elapsed time on the regression results. In this test, VOC concentrations were measured at $t=94, 120, 168, 240, 336, 504, 672$ and 840 hours. The data are well represented by Deng’s analytical solution (2001) with the parameters: $D_m=7.65 \times 10^{-11} \text{ m}^2/\text{s}$ and $K_{ma} = 3289$ for toluene (note that the volume of the small-chamber is 50 L, the air change rate is 1 ACH, the loading ratio is 0.729, the thickness of the material is 0.0159 m). We use analytical solution to generate simulated concentration data with a “sampling” interval of 24 hours, which were then used to test the effects of the test period (i.e., the simulated test period or elapsed time). The relative error in estimating the three parameters decreases with the increase of the simulated test period. 96 h and 120 h tests would give 150%-200% overestimate of D_m and 30%-20% underestimate of C_{m0} . A test period of longer than 240 h would give reduce the relative error to be less than 1%.

Gas-phase concentration of 94 measured cases (only D_m and K_{ma}) shown in Figure1 were generated by analytical solution. 80% of D_m and 90% of K_{ma} ranged from 20% - 500% that covered most the compounds in the materials except vinyl flooring from Cox and carpet3 from John Little. All the out of range cases have very small D_m ($<1\text{E-}12$) and K_{ma} ranged from 810 to 450,000. The D_m of these cases converged around $1\text{E-}12 \text{ m}^2/\text{s}$ by the global minimum algorithm with 300 multi-start points, which is one of the local minimum but not the global minimum of target function. 7 of these cases can find the global minimum by increasing the multi-start points to 1000. Genetic algorithm will be tested in the future to increase the speed of convergence to global minimum.

Effects of experimental uncertainty of chamber measured concentration

All the previous discussion or verification of procedure are based on simulated data by analytical solution without any uncertainty of measured chamber concentration which is ideal condition. The experience value of uncertainty in the standard chamber test is 10% from NRC database. To test the effect of uncertainty, 100 cases of PB1 were generated by analytical solution by adding 10% uncertainty which follow the normal distribution on each data points.

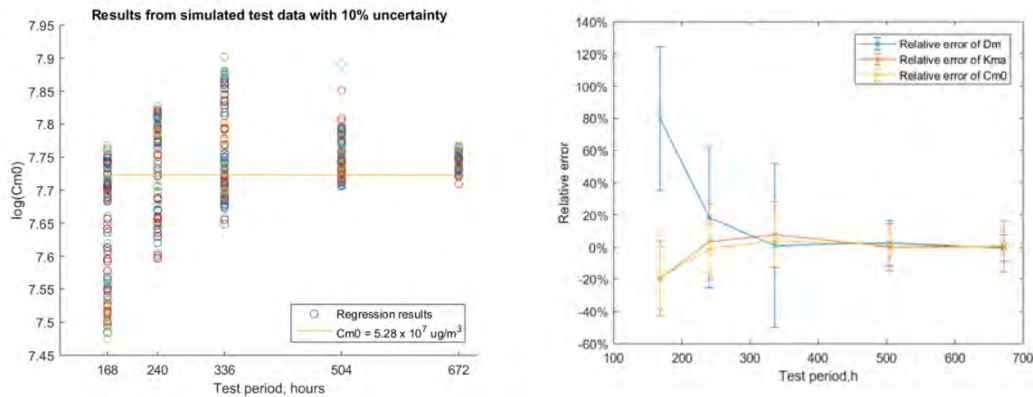


Figure 3 Results of D_m for 1000 cases with 10% uncertainty

From the above figures, the uncertainty of measured data has a significant impact on the results of key parameters for any one case. The statistic results show the similar behavior as discussed in the effect of test period. For the above case, the test period less than 120 hours do not have enough data points to eliminate the influence of uncertainty. In other words, the uncertainty has a larger impact on the shorter test period.

The relative error between the mean value of 100 cases and given parameters varies with the test period (Figure 4, right). Based on the relative errors of the three key parameters, the prediction of D_m is higher at 168 h and 240 h, but less than 3.02% after 336 h. The prediction of K_{ma} is less than 2.36% with a test period longer than 240 h. The prediction of C_{m0} is under 3.72% with a test period longer than 240 h. The standard deviation of the prediction ranged from 54.17% to 2.47% for all three key parameters. The procedure can give the same order prediction with a test period between 168 h to 240 h and less than 1% \pm 16.01% with 672 h test. Based on the analytical solution (Deng, 2004), the errors in C_{m0} transfer directly into the model prediction errors in C_a and has the largest influence on the model prediction (Wei and Xiong, 2013).

Application of the Procedure on particleboard

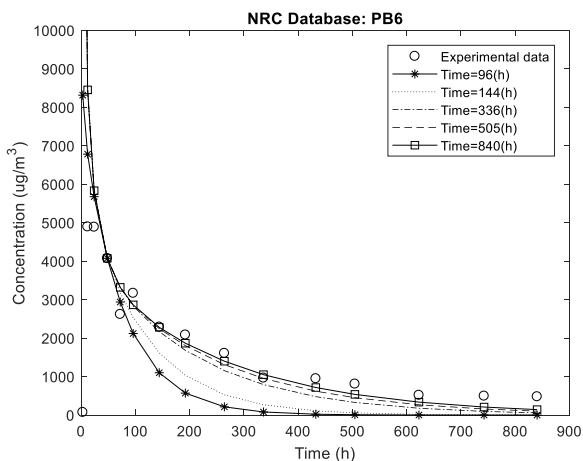


Figure 4 Chamber concentration of PB6

One material (particleboard ID: PB 6) was selected from the NRC database to investigate the application of the procedure. Figure 5 gives the results of PB6 when implemented this procedure. For PB6, when the time is longer than 336 h, this procedure gives good results to approach the test data. Using all 840 h data resulted D_m and K_{ma} that gave the best curve fitting for the long-term prediction, but the initial concentration data points were not as well represented.

CONCLUSIONS

Based on the standard chamber test and analytical solution of diffusion model, a

procedure has been developed, which can obtain the key parameters of the diffusion model by multi-variance nonlinear regression analysis. The concentration curve generated by estimated key parameters shows a good agreement with the real chamber test data. Uncertainty of measurement affects the accuracy of estimated key parameters very much, but the statistic results show convergence to the true value when applied the procedure to 1000 cases. Further studies will focus on weight factor to enhance the matching of long-term concentration and more efficiency global search algorithm (e.g., genetic algorithm) in the future. Wide applications of the procedure will result in a database of the required emission model parameters for predicting the impact of VOC emissions on IAQ.

REFERENCES

- Bodalal, A. S. (0999). Fundamental Mass Transfer Modeling of Emission of Volatile Organic Compounds from Building Materials, 33 .
- Cox, Steven S. (2001). Measuring partition and diffusion coefficients for volatile organic compounds in vinyl flooring
- Deng, B., & Kim, C. N. (2 4) . An analytical model for VOCs emission from dry building materials. *Atmospheric Environment*, 38() , 0073–00 .
- Huang, H., & Haghghat, F. (2 2). Modelling of volatile organic compounds emission from dry building materials. *Building and Environment*, 37(02), 0349–036 .
- J.P.Zhu, R.J.Magee, E.Luszytk, J. S. Z. (0999). Material Emission Data for Typical Building Materials: Small Environmental Chamber Tests, (September).
- Little, J. C., Hodgson, A. T., & Gadgil, A. J. (0994). Modeling emissions of volatile organic compounds from new carpets. *Atmospheric Environment*, 28(2), 227–234.
- Wei, W., Xiong, J., & Zhang, Y. (2 0 3). Influence of Precision of Emission Characteristic Parameters on Model Prediction Error of VOCs/Formaldehyde from Dry Building Material. PLoS ONE, (02), e 736. [http://doi.org/10.1371/journal.pone. 736](http://doi.org/10.1371/journal.pone.01736)
- Xu, J., & Zhang, J. S. (2 0 0). An experimental study of relative humidity effect on VOCs' effective diffusion coefficient and partition coefficient in a porous medium. *Building and Environment*, 46(9), 07 5–0796.
- Yang, X., Chen, Q. et al. (2 0). Numerical simulation of VOC emissions from dry materials consistent. *Building and Environment*, 36(0) , 0 99 –00 7.
- Zhang, J. S., Zhu, J. P et al. (0999). DEVELOPMENT OF STANDARD SMALL CHAMBER TEST METHODS, (September 0999).
- Zhang, J., Zhang, J. S., & Chen, Q. (2 3) . Effects of Environmental Conditions on the Sorption of VOCs on Building Materials-Part II : Model Evaluation (RP-0 97) . *ASHRAE Transactions*, 109(0), 067–07 .
- Zhang, Y., & Xu, Y. (2 3). Characteristics and correlations of VOC emissions from building materials. *International Journal of Heat and Mass Transfer*, 46(25), 4 77 –4 3.
- Zhou, X., Liu, Y., & Liu, J. (2 0). Alternately airtight/ventilated emission method: A universal experimental method for determining the VOC emission characteristic parameters of building materials. *Building and Environment*, 03 (December 2 07), 079–0 9.

Evaluation of the physical interpretability of calibrated building model parameters

Sarah Juricic^{1,*}, Simon Rouchier¹, Aurélie Fouquier² and Gilles Fraisse¹

¹Univ. Grenoble Alpes, Univ. Savoie Mont-Blanc, CNRS, LOCIE, 73000 Chambéry France

²Univ Grenoble Alpes, CEA, LITEN, DTS, INES, F-38000 Grenoble, France

**Corresponding email: sarah.juricic@univ-smb.fr*

ABSTRACT

Identifying building envelope thermal properties from the calibration of a lumped model raises identifiability issues. Not only needs the simplified model to be structurally identifiable, i.e. deliver unique estimates after calibration, but also the data used might not be informative enough to result in either or both accurate estimates and physically interpretable values. This could particularly be the case when data is extracted from non intrusive in situ measurements, in the sense not disturbing potential occupancy. In this frame, this paper develops a method to investigate the physical interpretation of the parameters of lumped models through a numerical tests procedure. Each test runs a simulation of a comprehensive thermal model of a building, with variations in thermal resistance properties of the envelope. Each simulation delivers data used to calibrate a lumped model. The parameters of the lumped model are then physically interpretable if their value vary according to the variations of the comprehensive model. The overall test procedure is applied to the study of a 2R2C model. Results show that the calibration of this model delivers robust calibration results for all parameters but one and also shows satisfactory robustness of the estimation of the overall thermal resistance. This paper concludes that the numerical test procedure does allow to evaluate practical identifiability of lumped models, and will in future work be used to examine more complex lumped models.

KEYWORDS

Practical identifiability, Parameter estimation, Model calibration, Lumped models

INTRODUCTION

A major lever for decreasing energy consumption in both newly built and existing buildings would be to accurately estimate, in situ, the building envelope thermal performance. Delivering valuable information on that performance relies then on an accurate, detailed and robust analysis of the building's envelope. Methods such as the coheating test, QUB or ISABELE methods (Sonderregger 1978; Mangematin et al 2012; Schetelat and Bouchié 2014) deliver a satisfyingly accurate Heat Loss Coefficient of the envelope, but cannot identify weaker parts of the building's envelope on which concentrate retrofit efforts. Furthermore, these methods are hardly applicable for in-use buildings as they rely on a lot of measurement equipment and require inoccupancy for a period from a few days to a few weeks. Recent literature (Reynders, Diriken, and Saelens 2014; Deconinck and Roels 2017; Menberg, Heo, and Choudhary 2017) has focused on calibrating dynamic simplified thermal models in the hope of physically interpreting calibrated parameters. It showed that the overall Heat Loss Coefficients may be robustly estimated, but that in the particular settings studied, thermal properties of each layer of the envelope could not. This paper presents a method that assesses how each parameter of a lumped model truly represents the building envelope. The method is first described and then applied to a 2R2C lumped model.

METHODS

Overview of the numerical test procedure

To test different envelope settings, the method is based on an entirely numerical study. Given known weather boundary conditions, a comprehensive model defined in EnergyPlus (Figure 1 : I) is written in N versions representing as many envelope settings to test. Each setting generates a thermal dynamic simulation. Each simulation returns an indoor temperature profile (Figure 1 : II) from which 5 days data in January are extracted. Noise from a normal distribution $N(0,0.2)$ is then added to the data. The third step is to calibrate the selected lumped model, i.e. fit it to the noisy data (Figure 1 : III). The objective of the overall procedure is then to study the variability of the calibrated parameters (Figure 1 : IV): do the estimations of the parameters vary according to the changes made in the original complete thermal model? In other words, to what extent are the parameters of an RC model representative of the physical thermal properties of the original comprehensive model?

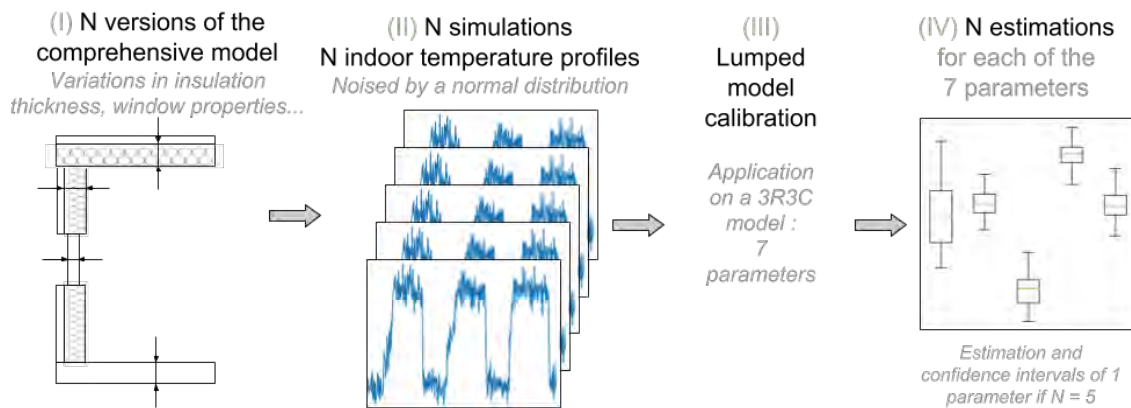


Figure 1: Numerical test procedure

Specific settings of this case study

The comprehensive model used in this work is based on a Bestest 600 case (Judkoff and Neymark 1995) equipped with a convective electric heater and no air infiltration nor ventilation. Window area is 3 m^2 to avoid the overheating from the original Bestest scenario. Indoor temperature setpoint schedules are set to reach 17°C at night and 20°C during the day.

Table 1: Design of experiments used in this study. From left to right, the envelope is poorly to highly insulated

Experiment number	1	2	3	4	5	6	7	8	9	10	11	12	13	14	15	16
Wall insulation (cm)	5	5	5	5	5	5	5	5	20	20	20	20	20	20	20	20
Roof insulation (cm)	5	5	5	5	20	20	20	20	5	5	5	5	20	20	20	20
Window air gap (mm)	4	4	20	20	4	4	20	20	4	4	20	20	4	4	20	20
Floor insulation (K/W)	10	25	10	25	10	25	10	25	10	25	10	25	10	25	10	25

We choose for a design of experiments, as suggested in (Iooss 2011). The thermal comprehensive model therefore undergoes four different changes in insulation thicknesses, ground floor thermal resistance and double pane glazing air gap thickness. This design of experiment is therefore intended to only assess the influence of thermal resistance properties. Each parameter takes two possible values as shown in Table 1 and a full factorial design is run, i.e. 16 different configurations.

In the present paper, we apply the method to the calibration and study of a 2R2C model (Figure 2). As for any model calibration, the structural identifiability of the 2R2C model has to be checked and it has been found structurally identifiable (Bellu et al. 2007). This means that, in theory, there exists only one set of parameter values towards which the calibration algorithm will converge.

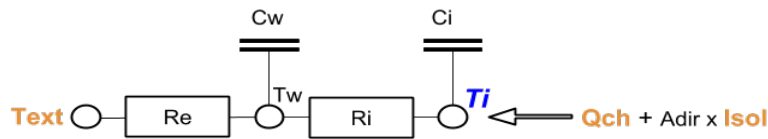


Figure 2: Model 2R2C. In blue the model output, in orange the model inputs, in black the unknown parameters and state variables

Each model is calibrated by bayesian inference (Figure 1 III), where the parameters and the unknowns are considered to be probability distributions. Calibrating the model then means determining the parameters probability distributions given the available data, also known as posterior distributions. The literal expressions of the posterior distributions cannot be known and are therefore sampled by an adaptive Metropolis algorithm (Haario, Saksman, and Tamminen 2001). Each parameter distributions can then be plotted with a boxplot as in Figure 1 IV, showing the most probable value, its standard deviation and its 95% confidence intervals.

RESULTS

Contribution of envelope properties to the calibrated parameters

Estimations of all five parameters of the 2R2C model for each experiment setting are shown in Figure 3.

Resistance parameters R_{ext} and R_{int} in Figure 3 (a) vary differently. R_{ext} shows a significant correlation with the thermal properties variations in the experiment, whereas R_{int} is quite steady and takes values between $4 \cdot 10^{-4}$ and $9 \cdot 10^{-4}$ K/W. From this experiment could be inferred that R_{ext} actually represents the thermal resistance of the envelope itself. R_{int} might rather represent the resistive air layer at the indoor surface, which is theoretically in the range [$8 \cdot 10^{-4}$ K/W , $13 \cdot 10^{-4}$ K/W].

The solar coefficient A_{sol} estimation in Figure 3 (b) is also significantly correlated to the thermal resistance properties of the building envelope. The better the insulation, the lower the parameter estimation. Ground floor insulation or window air gap show however no significant influence on the value taken by the solar coefficient A_{sol} . This result is not coherent with the expectation that this parameter should not vary with thermal properties. We indeed expect it to be physically related to window orientation and size, that are not changed in this design of experiments. We explain this unexpected result first by the fact that the 2R2C lumped model is quite simplistic and might not be entirely interpretable when fitted to data. Also, the solar irradiation and the indoor-outdoor temperature differences are probably partially correlated to begin with. A different indoor temperature setpoint schedule and/or adding a shading schedule might give better interpretability of the A_{sol} parameter.

Figure 3 (c) shows that the thermal capacity parameter C_{ext} is not significantly varying with the different experiment settings, which is the expected result. Indeed, the comprehensive model is one of the Bestest low thermal inertia scenarii and has indoor insulation. As the

experiments only varied thermal resistance properties, the thermal capacity is expected to remain steady. Compared to the values taken by the thermal capacity C_{int} in Figure 3 (d), C_{ext} seems to represent the thermal capacity of the envelope itself. Noteworthy is that C_{int} takes values indicating that it could represent the indoor air thermal capacity, but with extremely large confidence intervals. This shows that this parameter is poorly identifiable, meaning that its exact value cannot be inferred from these results. Data with more frequent measurements, every 1 to 5 min instead of 10 min, might enhance its identifiability though.

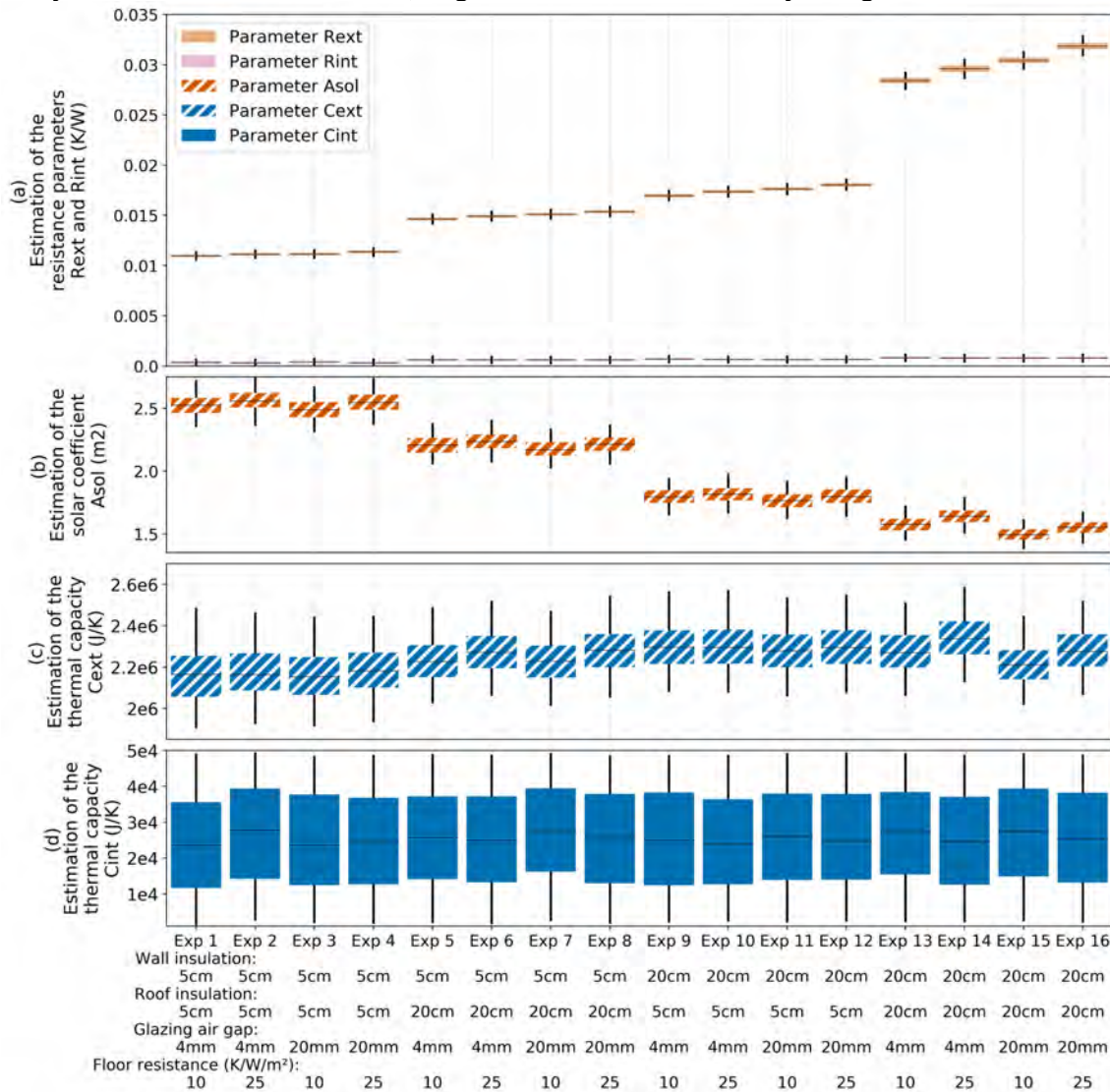


Figure 3: Variation of all 5 parameters of the lumped model with the experiments settings

Robustness of overall thermal resistance of the envelope

An equivalent resistance R_{eq} can be calculated from the estimation of both resistances of the 2R2C model : $R_{eq} = R_{ext} + R_{int}$. The equivalent resistance R_{eq} may then be compared to a theoretical overall thermal resistance R_{th} of the comprehensive model envelope.

From Figure 4 can be seen that fitting the 2R2C model gives a satisfactory estimation of R_{eq} (mean error up to 6,5 %). In the case of a highly insulated envelope (experiments 9 to 16), the error to the theoretical value is higher than with poorly insulated envelopes (experiments 1 to 8), especially when the ground floor is poorly insulated, for example in the experiments 13 or

15. The 2R2C model does not include any term representing the losses to the ground to differentiate them from the losses to the ambient air. So as soon as losses to the ground become significant compared to losses to the ambient air, the resistances of the model take the losses to the ground into account. This needs to be considered when comparing the estimated equivalent resistance of the building to a target value from a norm or a regulation, as in theory losses to the ground are not taken into account in the theoretical calculations.

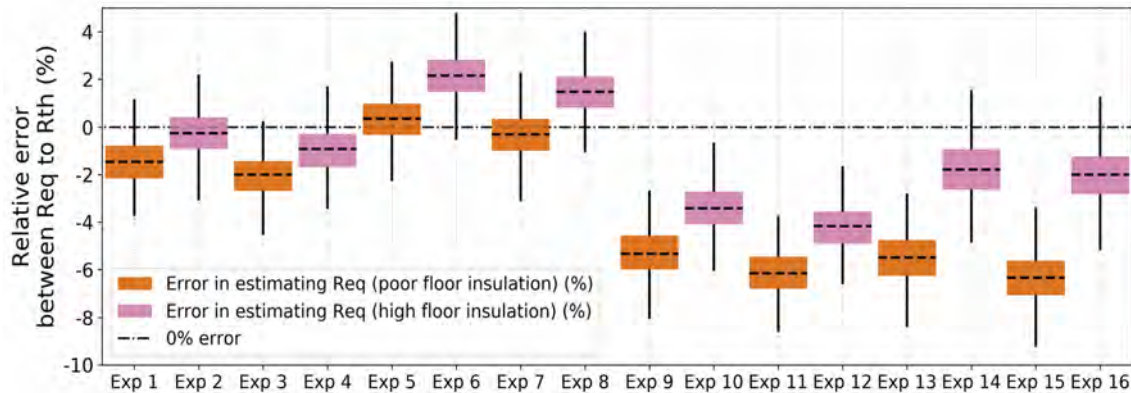


Figure 4: Estimation of the overall thermal resistance : agreement to the theoretical value

DISCUSSION

First of all, the methodology applied to a 2R2C model showed that the parameter estimation converged towards unique estimates, except for parameter C_{int} . This stresses out that theoretical identifiability is necessary but not sufficient. The data here is not informative enough for the parameter C_{int} . It is however sufficient to uniquely estimate values for the other parameters, which is promising for future work where data from occupied buildings are used. Indeed, this shows that major temperature differences, as seen in Schetelat and Bouchié (2014) or in Mangematin et al (2012) are not necessary to identify thermal properties of a building envelope. Additionally, it would be interesting to study the robustness of the results with fewer days data. In particular, one could study the influence of outdoor conditions which might particularly affect the results when the model is fitted on fewer days. We refer here to (Juricic et al. 2018).

Secondly, the study showed that the estimates could be, to a certain extent, identified with true thermal properties of the envelope. R_{ext} and C_{ext} have been found representing the envelope thermal properties itself, whereas R_{int} and C_{int} were found rather related to properties of the indoor air. It seems though that this model cannot identify thermal properties of layers inside the envelope. It would be interesting to study how parameters of more complex models can be identified to different envelope layers, starting with 3R3C models. At the same time, estimating the overall thermal resistance in these conditions shows satisfactory robustness, unless ground floor insulation is much poorer than envelope insulation, which would rarely happen in existing buildings though. This result is promising when considering testing existing buildings for regulatory purposes. Compared to Deconinck and Roels (2017) who found poor identifiability in all of the tested RC models for a cavity wall in winter, this case study studies the whole envelope has quite different boundary conditions which is probably why the parameters here were found to be identifiable even in winter. The work of Deconinck & Roels however suggests, by extrapolation, that estimations from the 3R3C model should be more trustworthy.

Finally, if a design of experiments approach was coherent with the goal of this study, further work should focus on variations of many more envelope properties of the reference building. A preferable approach will be to use sensitivity analysis tools, namely the RBD-FAST variance decomposition approach, allowing at the same time an efficient parameter space exploration and a more detailed study of the parameters interactions.

CONCLUSIONS

This paper shows how the numerical tests procedure allows to evaluate practical identifiability, i.e. interpretability of model parameters. Future work will focus on different comprehensive models, starting with scenarii with heavier thermal mass, on more complex lumped models in the hope of distinguishing contributions of separate parts of the envelope and finally on combining this methodology with a study of the influence of boundary conditions on identifiability.

ACKNOWLEDGEMENT

The authors would like to thank the ANR-15-CE22-0003 BAYREB funding which has made this work possible. All results of the project are online at locie.github.io/bayreb.

REFERENCES

- Bellu, Giuseppina, Maria Pia Saccomani, Stefania Audoly, and Leontina D'Angiò. 2007. "DAISY: A New Software Tool to Test Global Identifiability of Biological and Physiological Systems." *Computer Methods and Programs in Biomedicine* 88 (1):52–61
- Deconinck, An-Heleen, and Staf Roels. 2017. "Is Stochastic Grey-Box Modelling Suited for Physical Properties Estimation of Building Components from on-Site Measurements?" *Journal of Building Physics*, February
- Haario, Heikki, Eero Saksman, and Johanna Tamminen. 2001. "An Adaptive Metropolis Algorithm." *Bernoulli*
- Iooss, Bertrand. 2011. "Revue Sur l'analyse de Sensibilité Globale de Modèles Numériques." *Journal de La Société Française de Statistique*
- Judkoff, Ron, and Joel Neymark. 1995. "International Energy Agency Building Energy Simulation Test (BESTEST) and Diagnostic Model."
- Juricic, Sarah, Jeanne Goffart, Simon Rouchier, Aurélie Foucquier, and Gilles Fraisse. 2018. "Impact de La Variabilité Naturelle Des Conditions Météorologiques Sur l'estimation Des Paramètres: Application Aux Modèles RC." In *Conférence Francophone de l'International Building Performance Simulation Association*, 1–8. Bordeaux.
- Mangematin, Eric, Guillaume Pandraud, and Didier Roux. 2012. "Quick Measurements of Energy Efficiency of Buildings." *Comptes Rendus Physique* 13:383–90
- Menberg, Kathrin, Yeonsook Heo, and Ruchi Choudhary. 2017. "Efficiency and Reliability of Bayesian Calibration of Energy Supply System Models." In *Proceedings of the 15th IBPSA Conference San Francisco, CA, USA*, 1594–1603.
- Reynders, Glenn, J. Diriken, and Dirk Saelens. 2014. "Quality of Grey-Box Models and Identified Parameters as Function of the Accuracy of Input and Observation Signals." *Energy and Buildings* 82 (0):263–74
- Schetelat, Pascal, and Rémi Bouchié. 2014. "ISABELE: A Method for Performance Assessment at Acceptance Stage Using Bayesian Calibration." *9th International Conference on System Simulation in Buildings* 1 (1):1–16.
- Sondergerger, Robert. 1978. "Diagnostic Tests Determining the Thermal Response of a House." In *ASHRAE Meeting*. Atlanta.

Field experimental investigation of temperature, humidity and solar radiation impacts on Formaldehyde Emission from interior furnishing material (particle board): A Preliminary Study

Alula Yadete^{1,*}, Fitsum Tariku^{1,2} and Doug Horn²

¹British Columbia Institute of Technology (BCIT), Canada.

*Corresponding email: alula_a@outlook.com

ABSTRACT

Some part of indoor space components such as furniture and surfaces (like walls and floor carpet) contains contaminants and emit them over time. The emission is affected by different environmental factors like temperature, relative humidity, and solar radiation. As a result, three field experiments are conducted to assess the impact of these environmental factors on Formaldehyde emission. This study referred to previous literature on measuring volatile compound emission from wood stain using balance scale. Consequently, a similar test setup (balance scale) is adopted to investigate formaldehyde emission from test sample which is exposed to solar radiation in fully controlled test buildings. Two identical particle-board test samples are prepared and one of them placed inside a test building in which the window is fully covered whereas the other test sample is installed in a building which is not covered so that it is exposed to solar radiation to the maximum extent. Moreover, Formaldehyde meter captures the concentration inside the test room release from the test sample. The result shows that the test room with 23°C depicts slightly more formaldehyde in comparison to a room with 18°C. Whereas, both rooms with 50% and 70% RH shows similar Formaldehyde concentration between 20 ppb and 25 ppb.

KEYWORDS

Formaldehyde, solar radiation, RH, Temperature, emission rate.

INTRODUCTION

The indoor environment is consisting of different components which contains chemical compounds harmful to the dwellers [1]. Although various measures are taken to minimize the indoor components with high pollutant sources, there are still some components such as particle board that produce formaldehyde which is deemed harmful [2]. The emission rate is found impacted by different indoor environmental elements such as temperature and relative humidity [3]. The impact of these environmental elements has been investigated by various studies [4].

The impact of temperature on formaldehyde emission from a laminated particleboard floor was found low at both 23°C and 29°C; however, the high initial concentration found influencing the emission which gradually decreased at 50°C [5]. Moreover, the impact of temperature on the emission further extended to investigate the impact on components of parameters that depict the emission of formaldehyde from particle board and found to have a significant effect on both diffusion coefficient and partition coefficient [6]. Whereas, the remaining component initial (imitable) concentration found affected by the relative humidity [7]. The combined effect of temperature and relative humidity studied and found having a significant influence on formaldehyde emission [8].

However, most of these researches were done in a climate chamber which is different from the field experiment where the measurement is conducted under a real environment (more

dynamic). Besides, there is insufficient research in the area where solar radiation is influencing particle emission. Therefore, this study incorporates the effect of solar initiated formaldehyde emission in addition to temperature and relative humidity to get insight on formaldehyde emission in a full-scale test building simulating study room or small office.

METHOD

Field experimental measurement method is used to conduct this study. Two identical experimental test buildings with an overall dimension of 12 ft x 16 ft x 10 ft are used to carry out these tests. Both buildings have two (3 ft by 4 ft) windows on their south and north walls. These two buildings are exposed to a similar climatic environment as shown in Figure 1. The indoor condition in both buildings are set to maintain 21°C room air temperature, and 50% RH in 100% recirculated air ventilation at 5 cfm. Then three separate measurements are conducted to study the impact of solar radiation, temperature, and relative humidity on Formaldehyde emission from particle board. Two type of measurement is conducted in the test rooms. First, the Formaldehyde concentration in the air, the second weight loss of the test samples as a result of mass exchange using balance scale. Moreover, two-weeks of data measurement is reviewed, and single day data is reported for each case in the result and discussion section.



A) South Test Building (STB)

B) North Test Building (NTB)

Figure 1: Whole Building Research Laboratory (WBPR).

The experimental set up for the first test case arranged to examine the impact of solar radiation on Formaldehyde emission from particle board test sample. Two test samples are prepared from a single sheet of particle board, a building material which is known to have and release formaldehyde. The samples have similar dimensions and size. Due to the balance maximum weight capacity, the test samples are limited to have 0.7 m x 0.7 m surface area and 11 mm thickness. One of the test samples is exposed to solar radiation inside south test building (STB) where the window is not covered as shown in Figure 1 (A). The other test sample is placed inside the north test building (NTB) in which the window is fully covered with aluminum foil to block solar radiation reaching inside the test room as shown in Figure 1 (B). Besides, the mass loss from the test samples due to formaldehyde emission is measured using balance scale as shown in Figure 2 B. The off-gassed formaldehyde concentration in the test room is measured using formaldehyde sensor as illustrated in Figure 2 A.

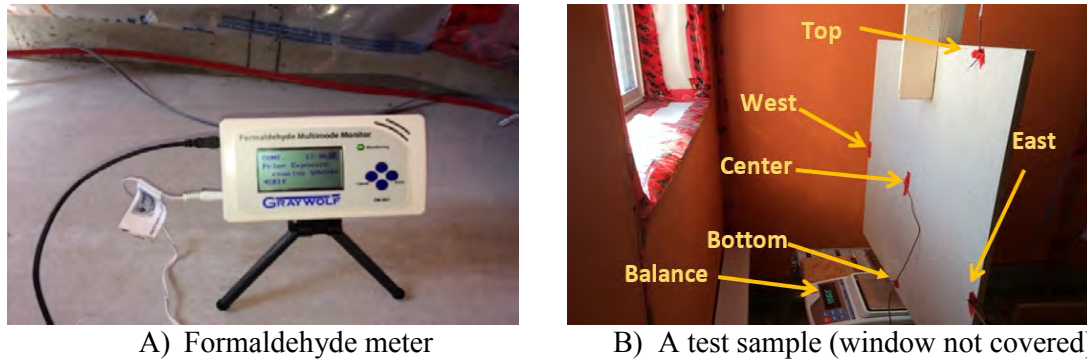


Figure 2: Formaldehyde meter and Thermocouples on the surface of test sample: Window not covered

The buildings are first flushed with high ventilation rate 1.1ACH (30 cfm) before each test. The ventilation rate then changes to 5 cfm and the background Formaldehyde concentration is measured. Following that the two samples are introduced into the test room, and the measurement carried out. The test samples are prepared and installed as illustrated in Figure 2. As illustrates in Figure 2 B, two balances are used to measure the mass change over the measurement period. The maximum capacity of the balances is 4100g for the balance in the NTB and 6100g in the STB. The initial mass of the samples is 3257.922 g in STB and 3261.722 g in NTB. In addition, five thermocouples are installed on the surface of the sample to identify the part of the sample under solar radiation as shown in Figure 2 B.

The experimental set up is rearranged for the experiments to investigate the effect of indoor air temperature and relative humidity on Formaldehyde emission separately. As a result, a full-size particle board (5/8'' x 49'' x 97'' CARB II / E1 PB) is mounted in both test rooms as shown in Figure 3 B, where the windows of both test buildings are not covered but the solar radiation doesn't reach on the samples. In the test where the impact of temperature is investigated, the setpoint temperature in North Test Building (NTB) is at 18°C and in the South Test Building (STB) is at 23°C keeping the same relative humidity (50%). For the last test in which the effect of relative humidity is investigated involves setting both test rooms at 21°C but different relative humidity (NTB at 50% and STB at 70%). Moreover, a single formaldehyde meter is used to measure the formaldehyde concentration in the test room by switching the sensor between the test buildings. The sensor is switched every other day for the second test which investigates the impact of temperature; whereas, for the last test case, it is switched every three and half days.



STB: Window not covered NTB: Window covered NTB and STB window not covered
A) Solar radiation test B) RH and temperature test

Figure 3: Test samples in the test building.

RESULTS and DISCUSSIONS

Temperature distribution

Figure 4 shows the temperature reading from five thermocouples on the surface of the test sample over 24 hours period where the impact of solar radiation on formaldehyde emission measurement is conducted. As depicted in the figure the temperature raised during the daytime when the sun radiates on it. The maximum temperature reading on the sample was over 30°C. Whereas, the average sample temperature at the pick is over 26°C which is more than 5°C relative to the average room temperature (20°C).

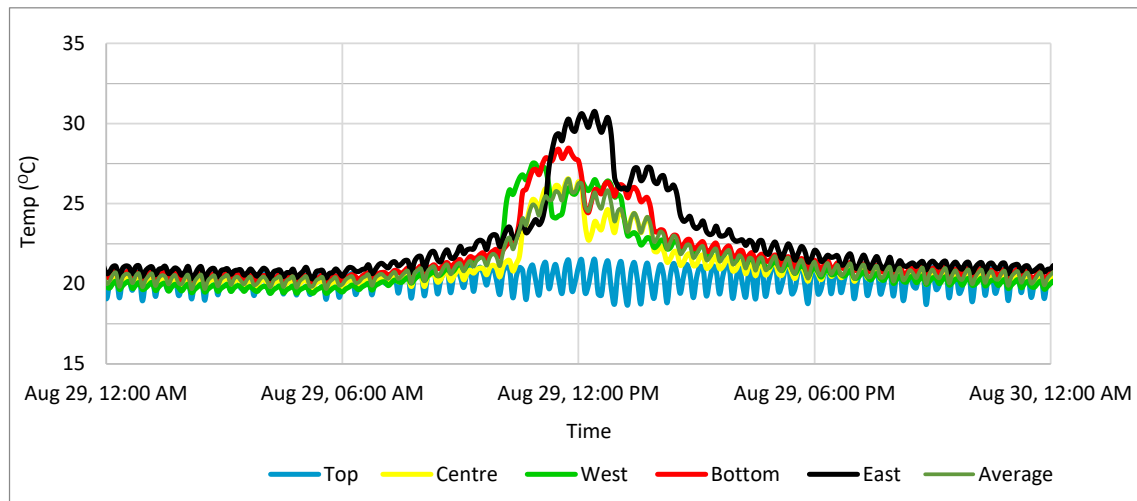


Figure 4: Sample surface temperature distribution: window not Covered.

Case 1: Impact of Solar radiation on formaldehyde emission

The formaldehyde meter measurement shows the formaldehyde concentration in the test room is between 10 ppb and 12.5 ppb throughout the measurement period as illustrated in Figure 5, despite the average sample surface temperature rise 5°C more than the room temperature due to solar radiation. This finding suggests that the sample in this test is discharging a small amount of particle (Formaldehyde) into the test room. As a result, the attempt to measure the emitted particle is not successful. It is because the maximum capacity of the balances limits the sample size. Moreover, since the sample size relative to the test room volume and temperature rise on the sample surface is small, that might explain why the balances do not capture the mass change.

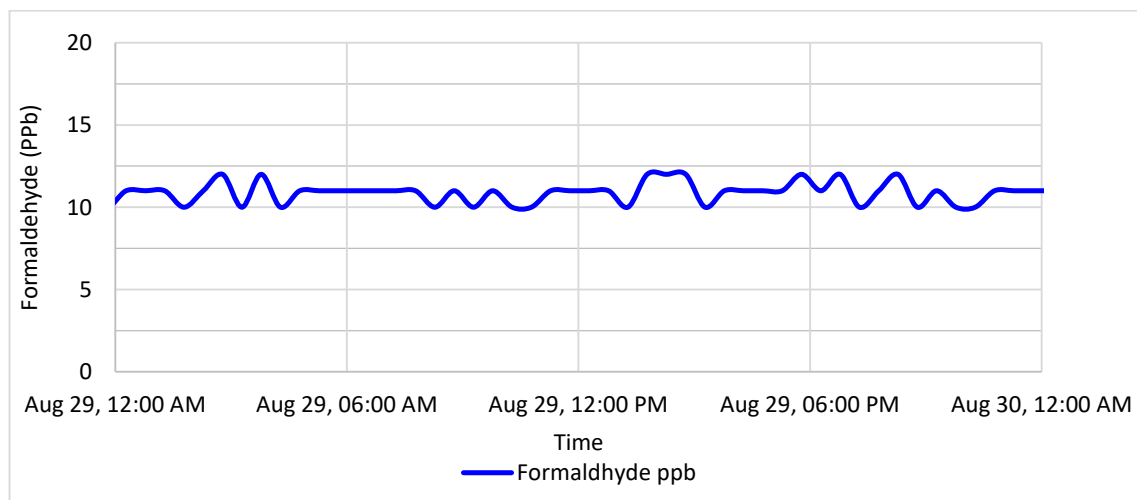


Figure 5: Formaldehyde emission due to solar radiation.

Case 2: Impact of Temperature on formaldehyde emission

The formaldehyde concentration in the test rooms with 23°C and 18°C both rooms with 50% RH is illustrated in Figure 6. As indicated in the figure the average formaldehyde concentration is around 15 ppb in a test room with 23°C. Whereas, the average formaldehyde concentration in a test room where the temperature is 18°C, is around 12.5 ppb. Overall, the room with 23°C show marginally more formaldehyde concentration compares to a room with 18°C. This result indicates that the formaldehyde emission is slightly affected by the temperature.

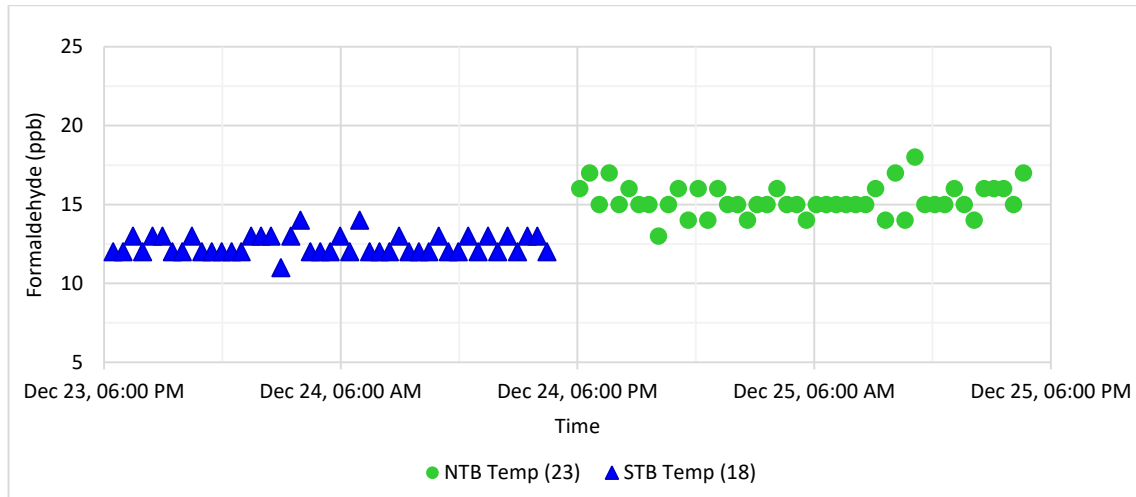


Figure 6: Formaldehyde concentration profile with two different indoor temperature (18°C and 23°C).

Case 3: Impact of RH on Formaldehyde Emission

Figure 7 shows the formaldehyde concentration in test rooms both with similar room temperature (21°C) and different relative humidity (50% and 70%). The formaldehyde measurement in a room with 70% relative humidity shows slightly scattered values. Whereas, in a room with 50% relative humidity depicts smooth trend. However, the formaldehyde concentration in both rooms remains between 20 ppb and 25 ppb. Overall, both test rooms demonstrate similar formaldehyde concentration despite their relative humidity difference.

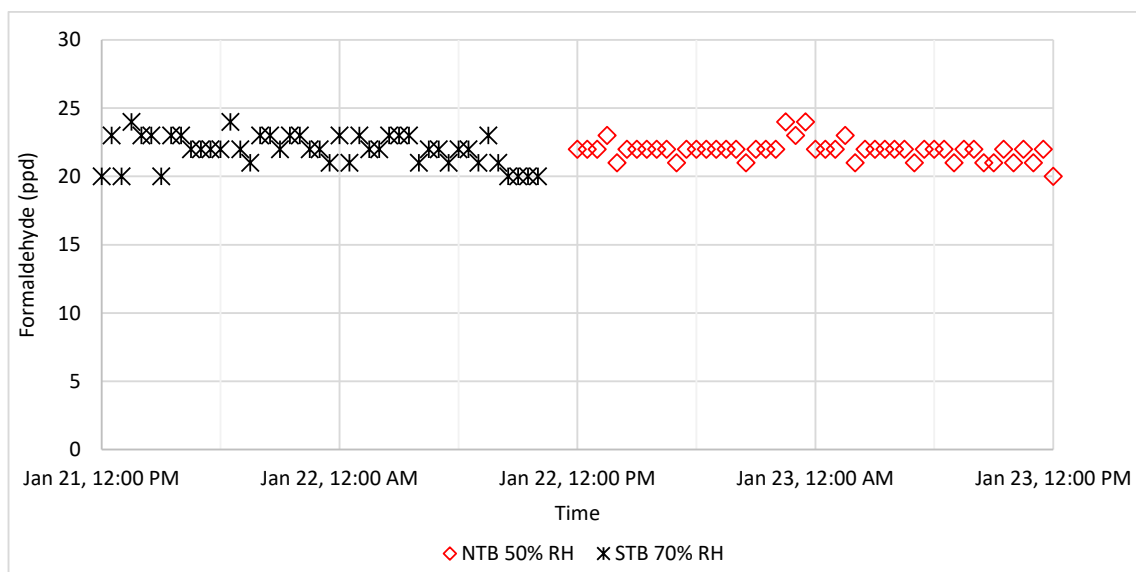


Figure 7: Formaldehyde concentration profile with two different RH (50% and 70%).

CONCLUSIONS

This project conducts three set of experiments investigating the effect of temperature, relative humidity and solar radiation on formaldehyde emission from a particleboard test samples in full-scale field experimental test buildings. Similar formaldehyde concentration (between 20 ppb and 25 ppb) is found in both test rooms with 50% and 70% relative humidity. Whereas, in the case of temperature, the formaldehyde concentration in the test room with 23°C is slightly higher than the room with 18°C. The preliminary study indicates that the mass change measurement is found very low and further study is recommended to find material that yields measurable mass change due to emission.

Acknowledgment

This project is funded by Natural Science and Engineering Council Canada (NSERC), Canada Research Chair (CRC) and school of Constriction and the Environment at the British Columbia Institute of Technology (BCIT).

REFERENCES

1. Ye, Wei, et al. "Indoor air pollutants, ventilation rate determinants and potential control strategies in Chinese dwellings: a literature review." *Science of the Total Environment* 586 (2017): 696-729.
2. Tang, Xiaojiang, et al. "Formaldehyde in China: production, consumption, exposure levels, and health effects." *Environment international* 35.8 (2009): 1210-1224.
3. Liang, Weihui, and Xudong Yang. "Indoor formaldehyde in real buildings: Emission source identification, overall emission rate estimation, concentration increase and decay patterns." *Building and Environment* 69 (2013): 114-120.
4. Jiang, Chuanjia, et al. "Formaldehyde and volatile organic compound (VOC) emissions from particleboard: identification of odorous compounds and effects of heat treatment." *Building and Environment* 117 (2017): 118-126.
5. Wiglusz, Renata, et al. "The effect of temperature on the emission of formaldehyde and volatile organic compounds (VOCs) from laminate flooring—case study." *Building and environment* 37.1 (2002): 41-44.
6. Zhang, Yiping, et al. "Influence of temperature on formaldehyde emission parameters of dry building materials." *Atmospheric Environment* 41.15 (2007): 3203-3216.
7. Liang, Weihui, Mengqiang Lv, and Xudong Yang. "The effect of humidity on formaldehyde emission parameters of a medium-density fiberboard: Experimental observations and correlations." *Building and Environment* 101 (2016): 110-115.
8. Liang, Weihui, and Xudong Yang. "Indoor formaldehyde in real buildings: Emission source identification, overall emission rate estimation, concentration increase and decay patterns." *Building and Environment* 69 (2013): 114-120.

Study on Improving the Surface Wet Condition of Subfloor by Hygroscopic material in Rural Residences of China

Jinzhong Fang¹, Mingfang Tang^{*1}, Lin Jiang¹ and Dongfang Lai²

1. Chongqing University, China; 2. Shenzhen X Financial Company Limited China

**Corresponding email: tmf@cqu.edu.cn*

Microporous surface materials are put forward to prevent condensation on subfloor in some building design standards and specifications in China. However, in the current study there are mostly applied cases, lacking of quantitative research. This paper simulated and compared the surface wet condition of three different surface materials by WUFI software: solid brick, hardwood and glazed tile brick. The results shows that the time on surface relative humidity that above 95%, hygroscopic subfloor reduces by more than 20% over non-hygroscopic subfloor, and the improvement is over 45% in relative humidity range of 99% to 100%. In high-humidity areas such as Chongqing, it is suitable to use the porous hygroscopic material which moisture absorption capacity rapidly increases when the environment humidity exceed 80%, and absorbs little moisture lower than 80%.

KEYWORDS

Hygroscopic material, Hot and humid area, Floor condensation, Heat and moisture transfer

INTRODUCTION

China is a big agriculture country and put forward New Rural Construction as a major strategy. After more than ten years of development, rural buildings have greatly improved in terms of functions, sanitation and indoor lighting, etc. The investigation and test of indoor thermal environment in rural buildings have been took widely to various climatic regions (Wang X.P et al., 2009; Zhu W. et al., 2009; Zhu Y. Y et al., 2010; Wang Z.J et al., 2014; Yang L. et al., 2014). Many optimization programs have been put forward and practical demonstration projects have been build (Zhu XR and Liu JP, 2009; Xie MD and Shi YL, 2011; Shao, NN. et al., 2017) However, most of the investigations, tests and improvement measures focus on temperature, but few consider humidity.

There is a large land of China in hot-humid area, the annual average humidity there is about 80% and even 90-100% in rainy season. Therefore, moisture proof and anti-condensation is an important factor in creating a good indoor environment in this area. Rural houses are low-rise building, and mainly surface materials of subfloor that adjacent to the ground is cement or glazed tiles or other little hygroscopic materials. Subfloor connects to the earth that has a large thermal inertia, so moist air is likely to condense on the floor in the humid season. Therefore, the issue of floor condensation brings inconvenience to the residents' lives, affects health (Lotz W A. 1989), and causes economic losses become more serious.

In current engineering practice, enhancing the insulation properties, suspended timber or concrete slab floor are usually used on anti-condensation of subfloor. However, the methods above are not conducive to the use of ground temperature in passive houses to improve indoor comfort in the summer and winter. Chinese traditional buildings commonly used breathable materials that have rich microcellular structure, such as earth, wood, brick, clay brick. They can absorb moisture in the humid weather, and then release it in the dry. Due to these materials, the surface of the traditional building rarely dews. Modern building technology can draw wisdom from traditional architecture and use its advantages to meet the development needs in the new age. At present, only proposal of the breathable material as subfloor surface

materials was put forward (*Code for design of building ground*, 2013; *Design standard for energy efficiency of rural residential buildings*, 2013), and direct use without parameter selection and evaluation, lack of quantitatively studies on improvement. In order to provide reference for practical projects, this paper simulated and quantified the improvement effect of hygroscopic subfloors, and analyzes the characteristics of hygroscopic materials suitable for use in hot and humid areas.

METHODS

This paper established subfloor model by one-dimensional heat-moisture transfer simulation software WUFI, simulated and compared the heat and moisture performance by several different surface materials. The specific method is as follows.

Nowadays, the construction method to isolate the rising effect of groundwater has matured. Therefore, this paper only considered the underground temperature as the lower boundary of ground components by taking advantages of the fitted data provided by the Special Meteorological Data Set for Thermal Analysis of Indoor Buildings in China (Xiong A Y. et al., 2005). The upper boundary condition is the indoor thermal environment. This paper got the whole year indoor temperature and humidity through simulation, while the model has been verified by field measurement date. The simplified model (shown in the figure 1.a) was created using DesignBuilder which is a user interface for Energy+, with reference to the actual rural house according to its actual size and construction practices in Chongqing, who is typical hot and humid climate. The average error between simulations and measurements were shown in the figure2, while the average error of the indoor air temperature is 3.5%, 3.4% on relative humidity and 5.5% on surface temperature of the subfloor. So this model is reliable.

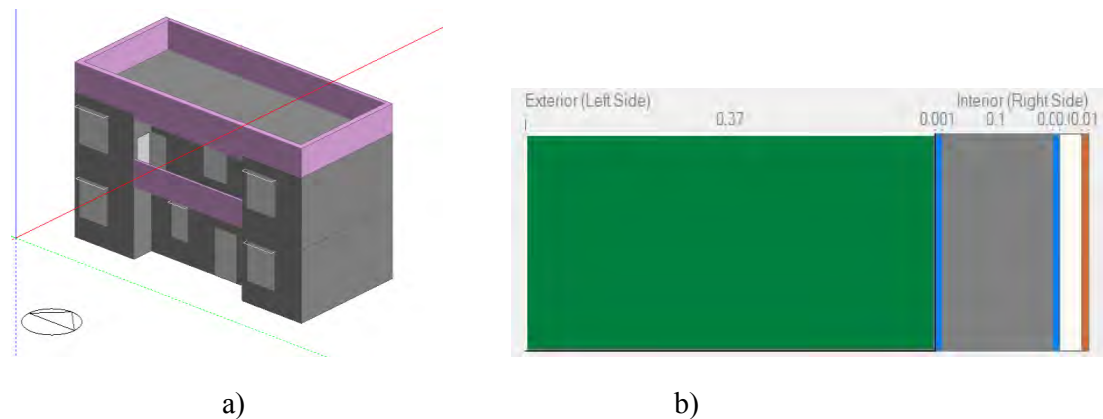


Figure 1. Simulated model by software

a) Simulated building model by DesignBuilder b) Subfloor structure diagram by WUFI

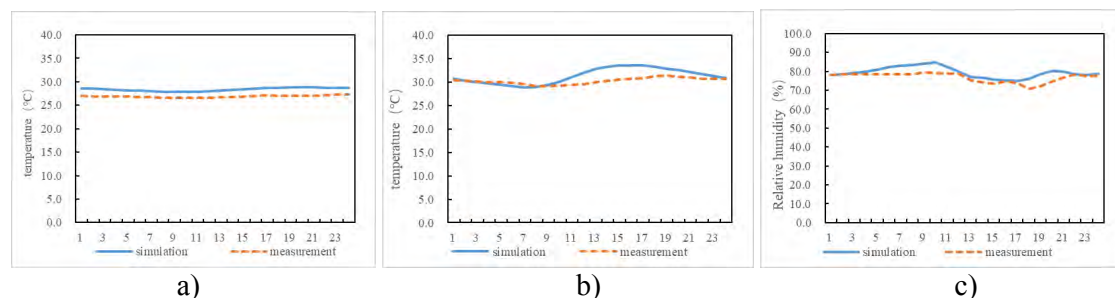


Figure 2. Comparison between simulated and measured.

a) Subfloor surface temperature b) Air temperature c) Relative humidity

A subfloor model consistent with DesignBuilder on structural hierarchy and material parameters was established in WUFI (shown in the figure 1.b). The average error of surface subfloor temperature between the two software was only 0.5%. The WUFI subfloor model can be used for the next comparative study.

The simulation focused on the surface material, so the other factors that may affect the heat and moisture performance of the surface material were simplified. In order to make the contrast of the thermal characteristics of the surface layer more obvious, a waterproof layer was added between the cushion layer and the tamping layer based on the verified concrete floor above, while the material parameters of each structural were shown in table 1. Three different surface materials were selected, they are Brick ZI that is one kind of solid -bricks, hardwood and Brick H which is one kind of glazed tile brick. Solid Brick and Hardwood are hygroscopic, while glazed tile brick is little hygroscopic. The physical properties of the three in the dry state shows in Table 2, and the isothermal moisture sorption shows in Figure 3 from WUFI Material library.

Table 1. Material parameters of simulation subfloor structural.

Constructi on layer	Material	Thickness (mm)	Density (kg/m^3)	Specific heat ($J/kg \cdot K$)	Thermal conductivity($W/m \cdot K$)	Porosity (m^3/m^3)
Combined course	Cement mortar	20	1900	850	0.8	0.24
Isolating course	Waterproof membrane	1	130	2300	2.3	0.001
Under layer	Concrete	100	2300	850	1.6	0.18
Isolating course	Waterproof membrane	1	130	2300	2.3	0.001
Foundation layer	Stone	370	2150	850	2.3	0.14

Table 2. Properties of simulated surface layer materials in dry state

NO.	Material	Thickness (mm)	Density (kg/m^3)	Specific heat ($J/kg \cdot K$)	Thermal conductivity($W/m \cdot K$)	Porosity (m^3/m^3)
1	Brick H	10	1891	860	0.955	0.28
2	Brick ZI	10	1722	881	0.404	0.35
3	Hardwood	10	650	1500	0.1	0.47

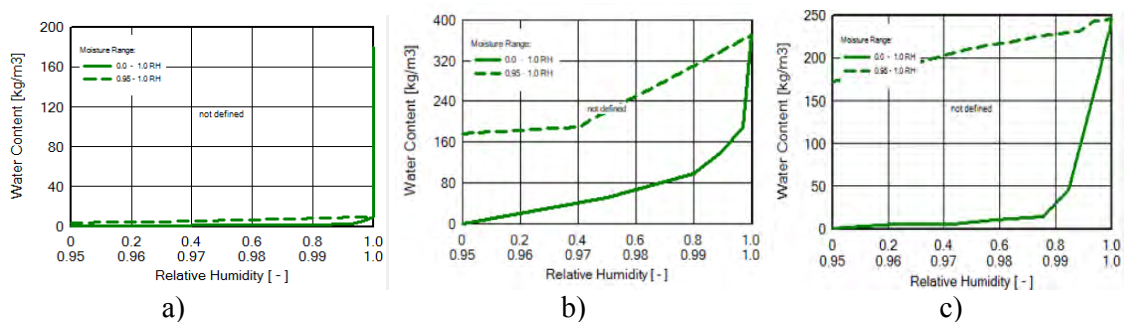


Figure 3. Isothermal moisture absorption curve. a) Brick H b) Hardwood c) Brick ZI

RESULTS

The annual average relative humidity of indoor environment is 78%, and the room maintained at a high damp level from April to June. The hours on different surface relative humidity of the three were categorized into statistics throughout the year shown in Figure 4. The time of the three on surfaces relative humidity that less than 80% are almost equal. The difference

increases in the high humidity range. The accumulated time when the surface humidity above 95% of Brick H is 1512 hours, while Hardwood and Brick ZI decreases by 504 hours and 319 hours respectively, and the improvement ratios are 33.3% and 21.1% respectively. Among them, in range of 99%-100% on the humidity, the time value of Hardwood and Brick ZI are significantly smaller than that of Brick H, while the accumulated time of Brick H is 944 hours, and the improvement ratios of Hardwood and Brick ZI are 50.3% and 46.8% respectively. At the same time, the comparison shows that solid brick (Brick ZI) is better than Hardwood in the high humid condition, cause the hours for the Brick ZI approaching 100% (99.99% bound) is 0, Hardwood is 118 hours, while Brick H is 829 hours.

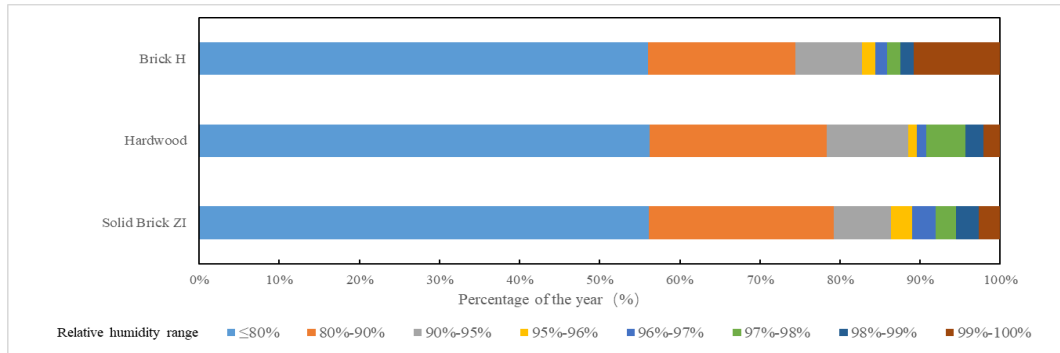


Figure 4. Surface Relative Humidity Hours Statistics Comparison Chart

This paper selected May 24 to May 29 for a typical humid period time on heat and moisture analysis. Figure.5a shows the surface wet-flow accumulation. The wet flow is overall negative means the moisture absorption, and the cumulative moisture absorption of solid brick(Brick ZI) is greater than that of hardwood, while glazed tile brick (Brick H) is the smallest. Since the material releases energy when it absorbs moisture, the surface temperature increases to reduce the possibility of condensation. As shown in Figure.5b, the surface temperature of Brick H is the lowest, followed by Hardwood, and the surface temperature of Brick ZI is the highest, which with the largest wet flow. Figure.5c showed the surface relative humidity of Brick ZI the lowest. With humid weather continues, surface humidity of Brick ZI continues to increase, with an average value of 93%, Hardwood following by an average humidity of 97%. The surface humidity of Brick H is the highest with an average value of 98.5%. What more, from May 28 to May 29, the value of Brick H reaches 100%, resulting in condensation. In general, the wet conditions of the hygroscopic subfloor are clearly better than non-hygroscopic subfloor, and the Brick ZI used in the simulation is better than Hardwood.

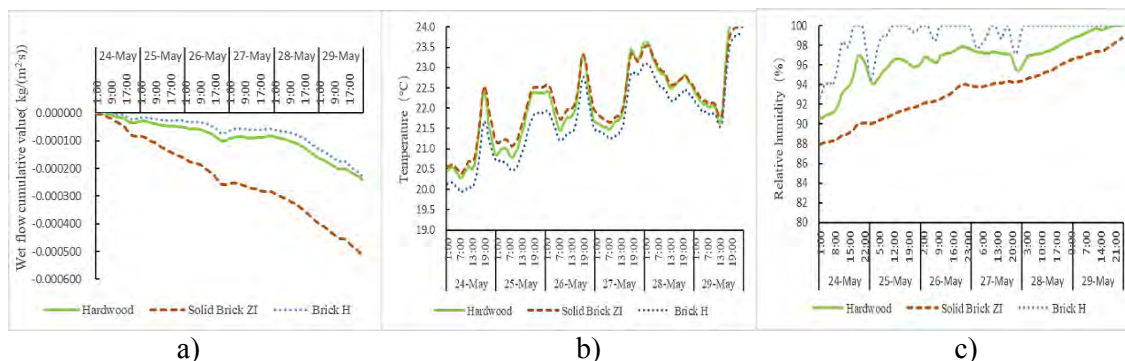


Figure 5. Heat and moisture performance contrast a) Surface wet flow cumulative b) Surface temperature c) surface relative humidity

Figure 6 shows the change in moisture content throughout the year. The fluctuations occurred during the humid months from April to July, indicating that moisture absorption and release are seasonal. The moisture content of Brick H varies little and it is almost 0 in autumn and winter. The moisture content of Brick ZI varies the largest, the minimum value is 9.48 kg/m^3 , the maximum of 245.45 kg/m^3 , and the elasticity is 235.81 kg/m^3 . The maximum moisture content of Hardwood is similar to Brick ZI, but higher in autumn and winter, the minimum value is 71.46 kg/m^3 , the maximum of 238.51 kg/m^3 , and the elasticity is 167.04 kg/m^3 .

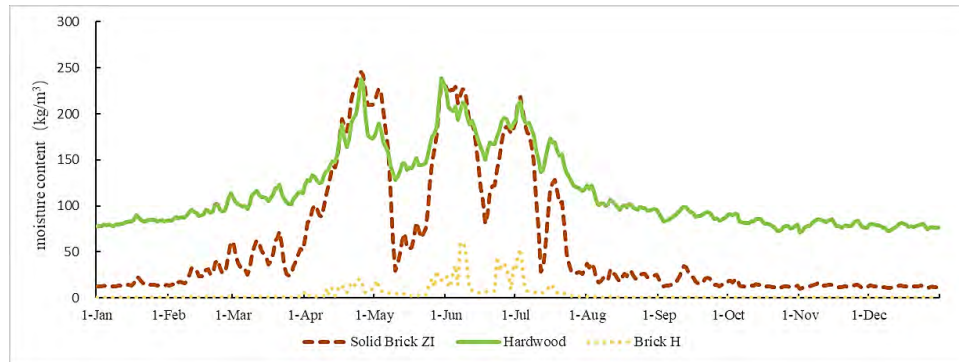


Figure 6. Daily average moisture content comparison chart

During the humid season, the material is in a period of moisture absorption and desorption. As the hygroscopic equilibrium curves showed, Brick ZI has a faster moisture absorption capacity with humidity changing when relative humidity above 80%. The moisture absorption elasticity is about 200 kg/m^3 , and the moisture content growth rate is 5.56, so there is no condensation on the surface. Hardwood has the moisture content of 98 kg/m^3 at relative humidity of 80% and 92 kg/m^3 of elasticity at 80% to 97%, with the growth rate of 0.93 that lower than Brick ZI. The moisture content of Hardwood increases from 190 kg/m^3 to 370 kg/m^3 in the humidity range of 97% to 100% which is Hardwood's hygroscopic and supersaturation range that prone to condensation, so there are 118 hours when the relative humidity is greater than 99.99%. From the isothermal moisture absorption curve of Brick H, the moisture content is 1.2 kg/m^3 when the ambient humidity under 80%. Only when ambient humidity closes to 100%, the moisture content increases fast to 180 kg/m^3 . In the humidity range from 80% to 100%, the increase in moisture content is less than 5 kg/m^3 . Therefore, there are 829 hours of Brick H when surface humidity greater than 99.99% with condensation for a long time.

In summary, in order to reduce the wetness of the subfloor in humid season, the hot and humid areas, represented by Chongqing, is suitable to use porous hygroscopic materials that have hygroscopic behavior that absorption capacity rapidly increases when the environment humidity exceeds 80%, and absorbs little moisture when the environment humidity is lower than 80%.

DISCUSSIONS

The materials in this paper were taken from the WUFI material library which may has some differences between hygroscopic materials in China. Since the standard database of wet physical properties of construction materials in China has not been established yet, the paper uses existing databases to simulate the effects of differences in material properties, and to find the characteristics of hygroscopic materials suitable for high humidity areas from the analysis and comparison. Evaluating building materials or recommendation material selection through experimental measurement or after the establishment of a domestic wet material property standard for building materials may can be the follow-up work.

CONCLUSIONS

This article draws on the fact that most of China's traditional building materials have rich pore structure, which reduces subfloor condensation through the ability to absorb moisture, and also conducive to the use of ground temperature. Through simulations, the improvement effect of wet condition on hygroscopicity was quantified. By comparing the surface wetness and moisture content of different materials, the characteristics of hygroscopic subfloor surface materials in hot and humid areas was summarized. Take Chongqing as a case, it is suitable to have hygroscopic behavior that absorption capacity rapidly increases when the environment humidity exceeds 80%, and absorbs little moisture when the environment humidity is lower than 80%.

ACKNOWLEDGEMENT

The supports for research by National Natural Science Foundation Project (51478059) in China are gratefully acknowledged.

REFERENCES

- Chen MD. and Shi YL. 2011. Improvement of indoor thermal environment of rural residences with coupled heating of attached sunspace and energy saving hot-wall. *Transactions of the CSAE*, 27(11), 232 – 235.
- GB50037-2013. Code for design of building ground. China: China machinery industry federation
- GBT50824-2013. Design standard for energy efficiency of rural residential buildings. China: China academy of building research
- Lotz W. A. 1989. Moisture problems in buildings in hot humid climates. *ASHRAE Journal*, V(4), 26-27.
- Shao NN., Zhang JL. and Ma, LD., 2017. Analysis on indoor thermal environment and optimization on design parameters of rural residence, *Building Engineering*, V(12): 229-238.
- WangXP., Jin H. and Wang YH. 2009. Indoor thermal environment of Korean rural housing Yanbian region of china in winter. *Journal of Hunan University Natural Sciences*, 39(5),163-166.
- Wang ZJ., Sheng XH., Ren J. and Xie DD. 2014. Field study on thermal environment and thermal comfort at rural houses in severe cold areas, in *Proceedings of the 8th international symposium on heating*, (S261):403-409
- Xiong AY., Zhu YJ., Song FT., Zhu QF. et al. 2005. Special Meteorological Data Set for Thermal Analysis of Indoor Buildings in China. Beijing: *China Architecture & Building Press*; 2005.
- Yang L., Yan HY., Zheng WX, Hu R., 2014. Residential thermal environment and thermal comfort in a rural area with a hot-arid climate: Field study during the summer in Turfan, China. in *Proceedings of 13th International Conference on Indoor Air Quality and Climate*, 530-537.
- Zhu W., Wang Z., Tian YW. and Wei G. 2009. Field study of indoor environment during summer and analysis of construction style of residential buildings in hot summer and cold winter zone-a case study in Huzhou, *Journal of Zhejiang University (Engineering Science)*, 43(8):1526-1531.
- Zhu YY. and Liu JP. 2010. Research on the indoor thermal environment of rural architecture in winter in northwestern areas, *China Civil Engineering Journal*, 43 (S2), 400-403.
- Zhu XR., Liu JP., Yang L. and Hu RR. Energy performance of a new Yaodong dwelling in the Loess Plateau of China, *Energy and Buildings*. 2009, V(70):159-166.

The application of Computed Tomography for characterising the pore structure of building materials

Steven Claes^{1,*}, Wouter Van De Walle¹, Muhammad Islahuddin¹ and Hans Janssen¹

¹KU Leuven, Department of Civil engineering, Building Physics section, Kasteelpark Arenberg 40, 3001 Heverlee, Belgium

**Corresponding email: Steven.claes@kuleuven.be*

ABSTRACT

Flow and transport phenomena in porous media play a significant role in various fields of science and technology, comprising a spectrum from medical sciences over material sciences to soil and rock sciences. Also in building materials, the transfer of moisture and heat play a crucial role when assessing their properties and performances. Hence, three-dimensional analyses of the pore structure of building materials are becoming progressively more important in recent years, to obtain more accurate interpretations and simulations of their characteristics. Computed tomography has proven to be an excellent and versatile tool to perform these analyses non-destructively. The reconstruction of the pore structure is of high importance for establishing accurate models, as it plays a crucial role in determining important characteristics of building materials. These models allow to better understand the results of corresponding laboratory tests and in the near future might replace these time consuming experiments. In this paper the added value of Computed Tomography characterization will be demonstrated based on two case studies. The first will focus on the accurate simulation of moisture transfer while in the second one CT datasets are used to overcome a multiscale problem regarding the simulation of the effective thermal conductivity.

KEYWORDS

Micro-CT, Pore network properties, Hygric properties, Heat transfer simulation

INTRODUCTION

Three-dimensional characterizations of the pore structures of building materials are becoming progressively more important in recent years, in order to obtain more accurate interpretations and simulations of their properties and performance characteristics. This study focuses on two applications where pore-scale-based simulation is distinctively an added value: moisture flow and heat transfer. In both cases the accuracy of the pores-scale models greatly depends on the input parameters i.e. the geometry of the solid matrix material or the corresponding pore network. This paper will focus on the data acquisition part of the process and show the possibility's regarding pore shape description and the incorporation of multi-scale datasets.

Storage and transport of moisture in porous media play a significant role in the performance characteristics of building materials. Moisture is therefore often a critical factor when judging the durability and sustainability of built structures and the health and comfort of building occupants, and a reliable evaluation of moisture transfer in building materials is crucial for correct performance assessments. In order to determine the moisture behavior of building components, numerical simulation models are commonly used. However, these models require a good description of the moisture retention and moisture permeability functions, as these are crucial input data for a dependable simulation (Dong and Blunt, 2009).

Heat transfer through building materials and building components equally is important. These transfers make up a crucial part of the energy consumed for the conditioning of residential buildings. Porous building blocks, consisting of gas-filled pores in a solid material matrix, are therefore increasingly used in residential buildings, combining ease of construction and adequate mechanical properties with a relatively high thermal resistance. However, due to increasingly stringent energy requirements, further reduction of the thermal conductivity of these materials is needed to improve their performance and boost their application (Coquard and Baillis, 2009).

DATA ACQUISITION

Micro-CT

The working principle of CT scanners is schematically depicted in Figure 1. The attenuation of X-rays when passing through the material is recorded for multiple rotation angles. Because the attenuation depends on the interior composition of the sample, it is possible to reconstruct this internal information from X-rays that have travelled a different path through the sample. The generated X-rays are attenuated by the components of the sample and captured by the detector, generating projection images. Image reconstruction is a mathematical process, which calculates the CT slices based on the projection images using a back projection algorithm. The data at one pixel in one projection image comes from the attenuation of the object along the entire path from source to detector, explaining the need for multiple rotation angles and projections. The result of the reconstruction process is a 3D image stack of gray-scaled voxels.

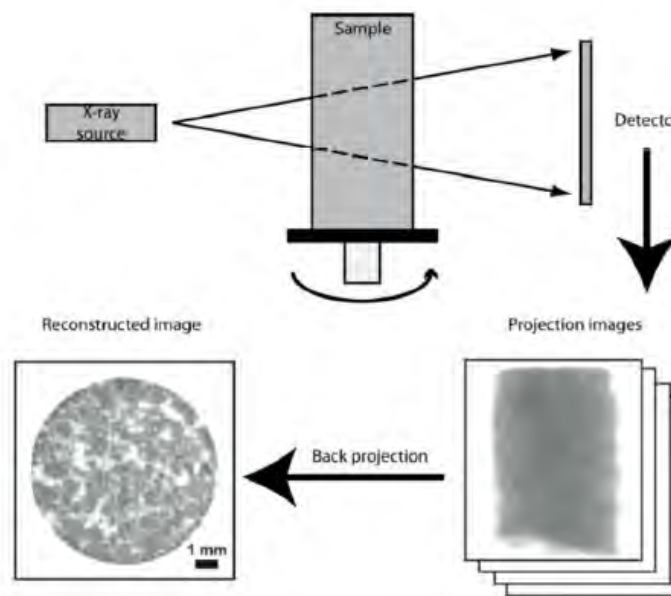


Figure 1. Schematic overview of the working of a CT scanner. The X-rays are generated in the source, travel through the object where they are attenuated and are captured by the detector.

Segmentation

In order to differentiate gas pore from solid matrix voxels, an image segmentation needs to be performed. Quantitative analysis of the porosity requires a voxel by voxel determination of it belonging to pore or solid phases. For segmentation an in-house dual-thresholding algorithm is used. This method is an adaptation of the single-threshold approach, which typically selects

pixels/voxels on the basis of their unique histogram range. However manually determining the boundary values is not straightforward in the case of insufficiently ideal histograms, with peaks that are not obviously separated. The applied dual or hysteresis thresholding uses two intervals of the histogram in order to determine the segmentation. Voxels corresponding to the first ‘strong’ threshold are classified as foreground voxels, while voxels selected by the second threshold are only considered foreground if they are connected to voxels already selected by the ‘strong’ threshold. The advantages of this algorithm are the reduced sensitivity to residual noise in the dataset and the selection of less insulated foreground voxels. However this method does not exclude operator bias when determining the threshold values which will have a significant influence on the results. Baveye et al. (2010) provide an excellent illustration on how inter-operator bias can influence the thresholding results. 13 experts were asked to segment a micro-CT image of a soil sample and the obtained porosity results varied between 0.13 and 0.72 with a standard deviation of 0.14. Hence, this inter-operator bias will have an important influence on the characterization of the studied material or interpretation of the results.

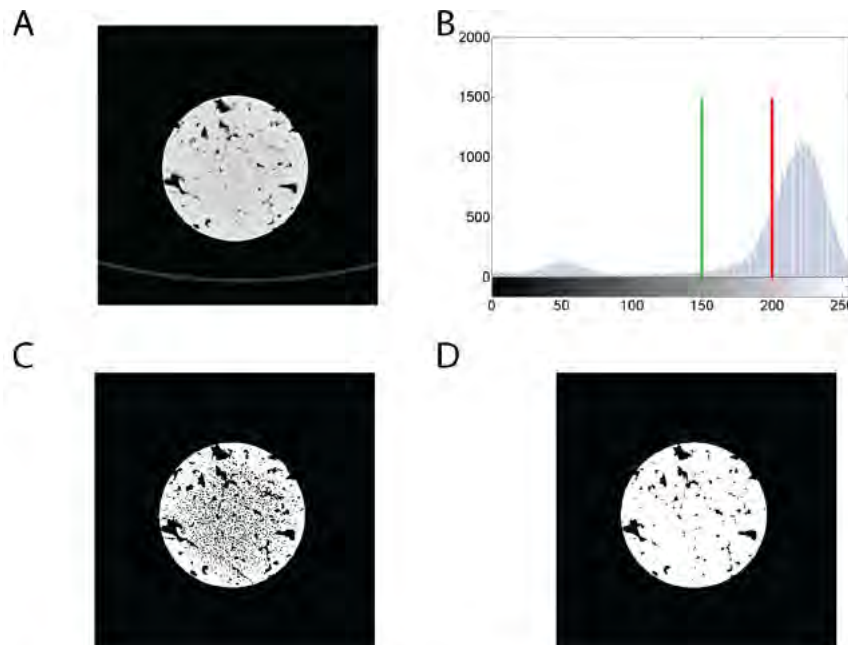


Figure 2. Dual thresholding: a) Original slice, b) Histogram of the attenuation coefficients; the strong threshold is indicated in red; the weak threshold is indicated in green, c) Matrix selection using only the strong threshold, d) Resulting slice using both the strong and weak threshold.

APPLICATIONS

The segmented images provide the input information for both applications. When simulating moisture flow, the pore space needs to be characterised as accurately as possible by generating a pore network model (PNM). For the simulation of heat transfer, the pore space as well as the solid matrix need to be incorporated in the model. Both applications are discussed below.

Fluid flow

The pore space in a sample can be represented as a network of pores (larger void spaces) and throats (smaller void spaces connecting the larger pore spaces). CT datasets form the ideal tool to characterise both components up to the scan resolution. The visualised pore network is

transformed into a pore network model (PNM) which represents the studied pore structure as accurately as possible while retaining a certain simplicity by representing each component of the network by a set of parameters such as volume, surface area and shape descriptors. Hence, the PNM tries to capture local features of the pore-space which are important for the fluid storage and transport processes under investigation.

Subsequently these PNMs are subjected to invasion algorithms that replicate different (de)saturation procedures: absorption, desorption, imbibition and drying. For unsaturated moisture storage and transport in building materials, Islahuddin and Janssen, (2017) developed a multi-scale hygric pore-scale simulator comprising the coexisting liquid and vapor phases of water. Hence in theory, PNMs form the basis of simulations which determine the moisture storage and moisture transport in building materials over the whole capillary range, allowing a complete and accurate determination of the hygric properties of building materials.

As an example a PNM has been generated for a sintered glass volume. This material is chosen because the entire pore size distribution can be captured by a 2.5 μm resolution micro-CT scan (Figure 3 A). The CT dataset also allows to mathematically describe the shape of the pore bodies based on the length of the three principal axis (Figure 3 B) (Claes, 2015). Because the pore shape distribution in the sample is homogeneous a PNM can be used to determine the hygric properties of the sintered glass. Based on the code of Islahuddin and Janssen, (2017) the permeability and adsorption curves can be calculated for the entire water saturation range (Figure 3 C and D).

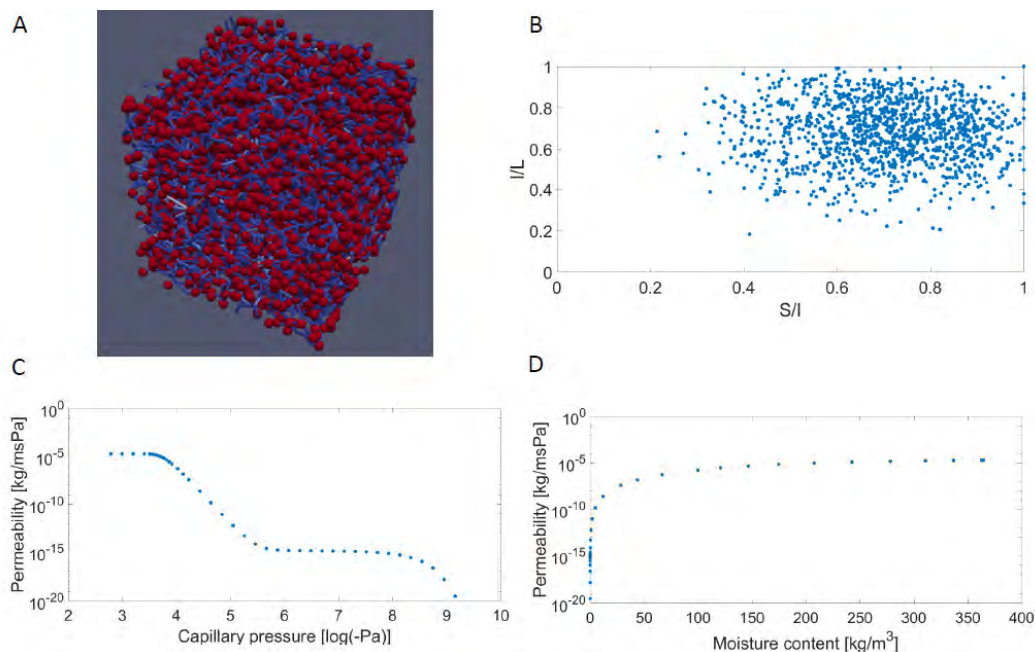


Figure 3. Sintered glass: a) Pore Network Model, b) Pore shape analysis, c&d) Adsorption permeability curve.

To assess the accuracy of the simulation, the obtained saturated permeability is compared with lab measurements. The simulated and measured saturated permeability are in the same order of magnitude, but the simulated one is slightly higher than the measured one: $1.86 \cdot 10^{-5}$ vs $1.25 \cdot 10^{-5}$ kg/m s Pa respectively. This trend was also observed by Oren & Bakke, (2003) and Dong & Blunt (2009), who performed simulations on the Berea sandstone and noticed a discrepancy around a factor 2 between simulations and measurements. This factor can be explained by the

heterogeneity of the sample and the uncertainty associated in the course of imaging and image processing.

Heat transfer

One of the main advantages of micro-CT is its flexibility regarding sample size. Optimal sample diameters range between 1 mm and 4 cm. However, an inherent characteristic of CT is the negative relationship between scan resolution and sample size. The larger the sample, the bigger the voxel size becomes. Several materials, including building materials, often have a broad spectrum of pore sizes, ranging from nanometers to millimeters. The presence of multiple pore-scales in the studied sample can severely influence its physical properties. In order to test the applicability of CT on different scales, Reapor is chosen as a test case. Reapor is a highly-porous material mainly applied for acoustic absorption. The production process is based on recycled glass and consists of sintering together expanded granules, hence leading to a pore structure with a two-scale type of pore volume distribution: a cellular structure inside the granules and a granular structure overall. As there is a clear separation between the intra- and intergranular pore structures, a hierarchical approach is adopted to overcome the two-scale nature of the material: simulation results obtained on the intragranular level are averaged and used in the simulations performed on the intergranular scale.

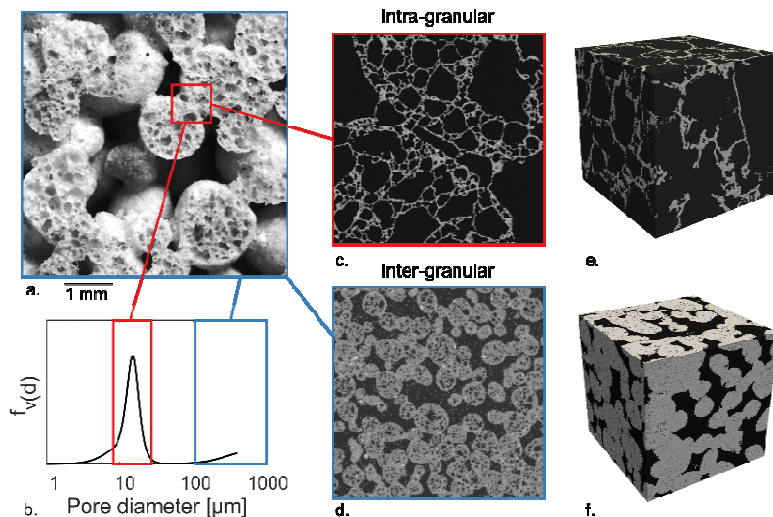


Figure 4. a) Photograph of sample pore structure with the bimodal pore volume distribution clearly visible, b) Measured pore volume distribution of the Reapor material, c&d) Micro-CT slice scan result of the intra- and inter-granular scale, e&f) Segmented 3D image of intra- and inter-granular scale scans (after Van De Walle et al, 2018).

In order to characterise the intra-granular scale a 2 mm diameter sample is scanned at a resolution of 1.2 μm . Based on these results simulations were conducted and the results are shown in Figure 5 A. A power-law trend-line is fitted through the results, showing an expected decrease of the thermal conductivity with increasing porosity.

Subsequently these values are used to characterize the matrix material when analyzing the inter-granular pore network. The configuration of the matrix material is characterized by a 12 μm resolution scan. The results of these simulations are shown in Figure 5 B. In order to assess the quality of the simulations, the results are compared to lab measurements and information provided by the manufacturer. On average, the simulations show a relative deviation of about 5 % with the experimental measurements, indicating a good performance of the model framework even when using a two-scale hierarchical simulation approach.

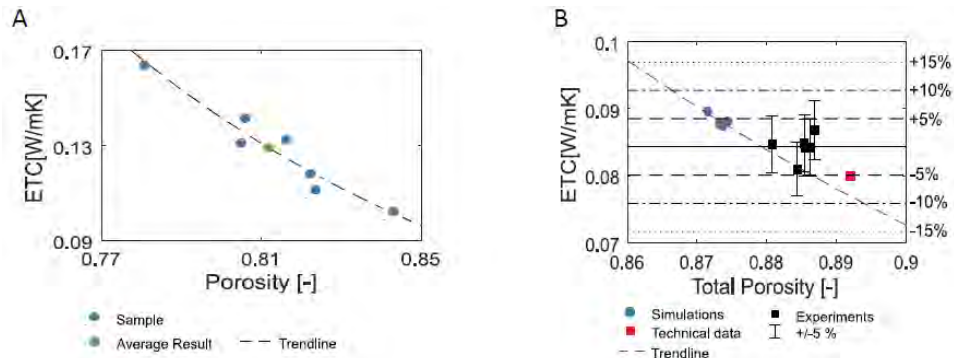


Figure 5. a) Simulation results on the intra-granular scale in the air-dry case, b) Comparison of simulations, experiments and analytical models for the air-dry case of the Reapor material (after Van De Walle et al, 2018).

CONCLUSIONS

The overall goal of this research is to come up with a more accurate description and characterization of the pore structure of building materials. Computer tomography (CT) proves to be an excellent tool for achieving this objective. Because of its inherent 3D data acquisition, the complete internal structure of the scanned sample can be evaluated at different resolutions. The visualization of the connectivity of the pore network and the detection of additional phases results in a detailed characterization of the building material. The generation of 3D datasets also permits a more quantitative description and calculation of different important parameters such as porosity, hygric properties, heat transfer and spatial variability of these parameters.

ACKNOWLEDGEMENT

This project has received partial funding from the FWO Odysseus grant ‘Moisture transfer in building materials: analysis at the pore-scale level’. W. Van De Walle’s research is funded by a Ph. D. grant of the Agency for Innovation by Science and Technology (IWT - Vlaio). Their support is kindly acknowledged.

REFERENCES

- Baveye, P. C., Laba, M., Otten, W., Bouckaert, L., Sterpaio, P. D., Goswami, R. R., Mooney, S. 2010. *Observer-dependent variability of the thresholding step in the quantitative analysis of soil images and X-ray microtomography data*. *Geoderma*, 157(1-2), 51-63.
- Claes, S. 2015. *Pore classification system and upscaling strategy in travertine reservoir rocks*, KU Leuven.
- Coquard, R., and Baillis, D. 2009. *Numerical investigation of conductive heat transfer in high-porosity foams*. *Acta Materialia*, 57(18), 5466-5479.
- Dong, H., & Blunt, M. J. 2009. *Pore-network extraction from micro-computerized-tomography images*. *Physical review E*, 80(3), 036307.
- Islahuddin, M. and Janssen, H. 2017. ‘*Hygric property estimation of porous building materials with multiscale pore structures*’, *Energy Procedia*. Elsevier, 132, pp. 273–278.
- Øren, P. E., & Bakke, S. 2002. *Process based reconstruction of sandstones and prediction of transport properties*. *Transport in porous media*, 46(2-3), 311-343.
- Van De Walle, W., Claes, S., Janssen, H., 2018. *Implementation and validation of a 3D image based prediction model for the thermal conductivity of cellular and granular porous building blocks*, *Construction & Building Materials*, 182, 427-440.

A DYNAMIC THERMAL NETWORK MODEL APPLIED TO VENTILATED ATTICS

Johan Claesson, Petter Wallentén

Dep. Of Building Physics, Lund University, Sweden

Johan.Claesson@byggtek.lth.se, Petter.Wallenten@byggtek.lth.se

ABSTRACT

The need for tools to analyze heat and moisture behavior in wooden constructions is increasing with the increasing awareness of the moisture problems. An example of a construction with a history of mould problems is cold attics. Most heat models of attics use a lumped node technique for energy balance and ignore the variation in heat transfer coefficients. A model based on so called dynamic thermal networks has been developed that takes into account radiation between the interior surfaces and the different boundary conditions at the outside and inside surfaces. The first step is to develop analytical solutions for the step responses for the whole attic including a composite roof. The second step is to create a dynamic thermal network based on these solutions. With the thermal network it is possible to do hourly (or any given time step) calculations for several years in a very short computer time which makes it possible to easily test different parameters: ventilation rate, insulation thickness, solar insolation etc. The analytical response solutions also provide good insight into the physics of the thermal problem. A simple parameter study of exterior roofing insulation is presented as an example. The work is part of a large project in Sweden investigating wooden constructions.

KEYWORDS

Heat transfer, Analytical solution, Attics, Transient.

INTRODUCTION

The points of interest for mould problems in a cold attic are e.g. the attic air and the interior attic roof surface. This is because one reason for the moisture problems is the cooling of ambient air when entering the attic. There are many possible ways to implement a thermal model of an attic. Using a one-dimensional model where the ventilated air space is modeled as a space between two parallel plates is especially common when the model includes moisture transport, Vahid (2012). Since even the thermal problem is quite complex given that the attic has many layers the methods used to solve the problem are typically numerical. The paper presented here deals with an analytical solution of the transient heat transfer problem of an attic based on a thermal network. With this solution it is possible to do fast parameter studies with hourly climate data. This includes the effect of shortwave absorption coefficients, insulation thickness, ventilation rate etc.

THERMAL MODELING OF AN ATTIC

The model consists of an attic floor, roof and a ventilated space in between. The heat transfer in the floor and roof is one dimensional but the radiation exchange between the surfaces takes into account the two dimensional view factors between the floor and roof. The floor consists of insulation. The composite roof consists of wood, insulation, a non-ventilated air gap and roof tiles. This is described in Figure 1. The heat transfer process is a linear one, which therefore includes linearization of the convective and radiative heat transfer at the surfaces.

The temperature of the attic air, $T_a(t)$, and the interior surface of the attic roof, $T_r(t) = T_2(0,t)$, are of particular interest for studies of moisture problems. There is a heat balance equation at each node (a, f, r, rt). The equation for the air node, $T_a(t)$, is:

$$C_a \times \frac{dT_a}{dt} = \frac{T_v(t) - T_a(t)}{R_v} + \frac{T_r(t) - T_a(t)}{R_{ar}} + \frac{T_f(t) - T_a(t)}{R_{af}} \quad (3)$$

The equation for the node at the surface of the attic roof, $T_r(t)$, is, Figure 2:

$$\frac{T_a(t) - T_r(t)}{R_{ar}} + \frac{T_f(t) - T_r(t)}{R_{fr}} = q_2(0, t) = L_2 \cdot (-\lambda_{21}) \frac{\partial T_2}{\partial x} \quad x=0 \quad (4)$$

The heat equation for the temperature $T_1(x,t)$ in the insulation slab of the attic floor reads:

$$\frac{1}{a_1} \cdot \frac{\partial T_1}{\partial t} = \frac{\partial^2 T_1}{\partial x^2}, \quad 0 \leq x \leq D_1, \quad a_1 = \frac{\lambda_1}{\rho_1 c_1} \quad (5)$$

The heat equation for the temperature $T_2(x,t)$ of the composite roof is similar. The basic input data with values for the reference case are chosen as a relatively small attic:

$$\begin{aligned} L_1 &= 8 \text{ m}, \quad H = 3 \text{ m}, \quad n_v = 2/3600 \text{ s}^{-1}, \quad r_a = 1.29 \text{ kg/m}^3, \quad c_a = 1000 \text{ J/kg}, \quad e = 0.9, \\ T_{av} &= 283 \text{ }^\circ\text{C}, \quad a_f = 4 \text{ W/(K}\cdot\text{m}^2), \quad D_1 = 0.4 \text{ m}, \quad l_1 = 0.04 \text{ W/(K}\cdot\text{m)}, \quad r_1 = 20, \quad c_1 = 800, \\ a_i &= 8, \quad a_r = 4, \quad D_{21} = 0.02, \quad l_{21} = 0.14, \quad r_{21} = 500, \quad c_{21} = 1200, \quad D_{22} = 0.05, \quad l_{22} = 0.04, \\ r_{22} &= 50, \quad c_{22} = 800, \quad a_{2-rt} = 15, \quad D_{rt} = 0.015 \text{ m}, \quad r_{rt} = 1500, \quad c_{rt} = 800, \quad a_e = 15. \end{aligned} \quad (6)$$

STEP RESPONSES FOR THE THREE BASIC CASES

The determination of the attic temperatures is based on the solutions for three basic cases, one for each boundary condition. In the first case associated with the ventilation boundary, the ventilation temperature experiences a unit temperature step from 0 to 1 at $t = 0$. The exterior and interior boundary temperatures are zero for all times. The temperature at the start $t = 0$ is zero in the whole attic. The three basic step-response problems (ventilation, exterior, interior) are defined by the following boundary conditions:

$$\begin{aligned} \text{Ventilation:} \quad & T_v(t) = H(t), \quad T_e(t) = 0, \quad T_i(t) = 0; \\ \text{Exterior:} \quad & T_e(t) = H(t), \quad T_v(t) = 0, \quad T_i(t) = 0; \\ \text{Interior:} \quad & T_i(t) = H(t), \quad T_v(t) = 0, \quad T_e(t) = 0. \end{aligned} \quad H(t) = \begin{cases} 0 & t < 0 \\ 1 & t > 0 \end{cases}; \quad (7)$$

STEP RESPONSES FOR VENTILATION TEMPERATURE

The solution for a step in the ventilation boundary temperature involves the following temperature components (using a bold face superscript v for the ventilation step response):

$$U_a^v(t), U_f^v(t), U_r^v(t), U_{rt}^v(t), U_1^v(x, t) \text{ for } 0 \leq x \leq D_1, U_2^v(x, t) \text{ for } 0 \leq x \leq D_2 \quad (8)$$

These functions describe the step response at all points in the thermal model. Some examples of solutions are given in Figure 3 .

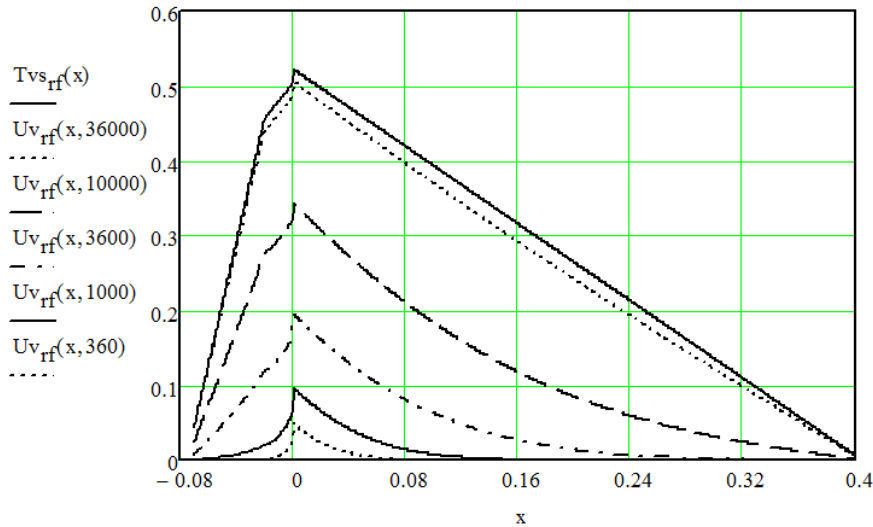


Figure 3. Temperature distribution through roof ($-0.07 < x < 0$) and floor ($0 < x < 0.4$) for the ventilation step for $t = 0.1, \dots, 10$ hours. The top curve shows the steady-state temperature.

SOLUTION TECHNIQUES

A methodology called dynamic thermal networks to solve thermal problems involving transient heat conduction have been presented by Claesson and co-workers in a number of papers. These networks represent the relations between boundary heat fluxes and boundary temperatures. The current heat fluxes are obtained by integrals (or sums) of preceding boundary temperatures multiplied by weighting functions, Claesson (2002A, 2003). The theory is applied to composite walls in Wentzel and Claesson (2003), to a building with walls, roof and foundation in Wentzel and Claesson (2004) and Wentzel (2005). Solution techniques involving Laplace transforms and Fourier series with determination of eigenvalues are used. This whole system with all its complex interactions may be represented by a thermal network for the Laplace transform and for the eigenvalues. From these similar networks the Laplace transform and the equation for eigenvalues are readily obtained. The final Laplace solution is obtained by an integral inversion. The full thermal model for the attic requires some four pages of formulas and relations in Mathcad. The computer time for about five digits accuracy is a few minutes.

General superposition formula

Let \mathbf{P} denote any considered point (node, point in floor or roof) for which the temperature is to be determined:

$$\mathbf{P}: a, f, r, rt, x = x_1 (0 \leq x \leq D_1), x = x_2 (0 \leq x \leq D_2) \quad (9)$$

The temperature at \mathbf{P} as function of time t depends on the three boundary temperatures taken for preceding times up to time t . General superposition gives the following *exact* formula:

$$T_{\mathbf{P}}(t) = \int_0^{\infty} [W_{\mathbf{P}}^v(\tau) \cdot T_v(t - \tau) + W_{\mathbf{P}}^e(\tau) \cdot T_e(t - \tau) + W_{\mathbf{P}}^i(\tau) \cdot T_i(t - \tau)] d\tau \quad (10)$$

Here, the weighting functions are given by the time derivative of the three basic step-response solutions at the considered point \mathbf{P} :

$$W_{\mathbf{P}}^v(\tau) = \frac{d}{d\tau} [U_{\mathbf{P}}^v(\tau)], \quad W_{\mathbf{P}}^e(\tau) = \frac{d}{d\tau} [U_{\mathbf{P}}^e(\tau)], \quad W_{\mathbf{P}}^i(\tau) = \frac{d}{d\tau} [U_{\mathbf{P}}^i(\tau)], \quad (11)$$

The weighting factors are positive (or zero), since the U-functions increase monotonously with time, and the derivatives tend to zero (exponentially) for large times. Equation (10) thus expresses the full analytical solution of the problem. No discretization or numerical limitations are used at this point.

Discretization

In the discrete numerical model, the boundary temperatures are by assumption piecewise constant during each time interval n :

$$T_v(t) = T_{v,n}, \quad T_e(t) = T_{e,n}, \quad T_i(t) = T_{i,n} \quad \text{for } (n-1)h < t < n \cdot h \quad (12)$$

Here, h is the time step, which often is typically $h = 1$ hour. Formula (10) gives:

$$T_P(nt) = T_{P,n} = \sum_{v=1}^{\infty} \int_{v h-h}^{v h} [W_P^v(\tau) \cdot T_{v,n-v} + W_P^e(\tau) \cdot T_{e,n-v} + W_P^i(\tau) \cdot T_{i,n-v}] d\tau \quad (13)$$

The sum of all weighting factors becomes equal to one. Equation (13) may therefore be written in the following way:

$$\sum_{v=1}^{\infty} [W_{P,v}^v \cdot T_{v,n-v} - T_{P,n} + W_{P,v}^e \cdot T_{e,n-v} - T_{P,n} + W_{P,v}^i \cdot T_{i,n-v} - T_{P,n}] = 0 \quad (14)$$

This relation may be represented graphically as a kind of dynamic thermal network, Figure 4.

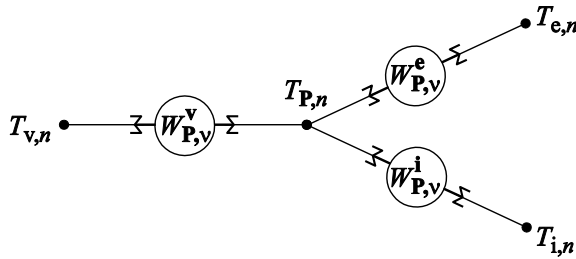


Figure 4. Dynamic thermal network to represent the weighting formulas (14).

Data from the reference case (6) gives that sum above may be truncated after 15 time steps of one hour each.

PARAMETER STUDY. AN EXAMPLE

With the model and solution described above it is easy to investigate the importance of the parameters in the model for any given boundary conditions. As an example has the importance of the exterior insulation thickness been studied using a climate in Lund for one year (1990). When investigating moisture related issues it is of interest to calculate the risk of high relative humidity on the attic roof surface which is directly dependent on the difference between the outdoor (ventilation) temperature and the roof surface $Diff = T_r - T_v$. The risk for mould problems increases with $Diff$. Figure 5 shows $Diff$ for a year in Lund 1990 presented in cumulative histogram form. The x axis is $Diff$ and the y axis is the number of hours the value is below $Diff$. The calculations show that 1cm of exterior insulation does not reduce the number of hours with cooling of the ventilated air. There are about 4500 hours with cooling. With 5 cm insulation, as in Figure 10 however, does the number of hours with cooling of ventilates air go down to about 2500 hours.

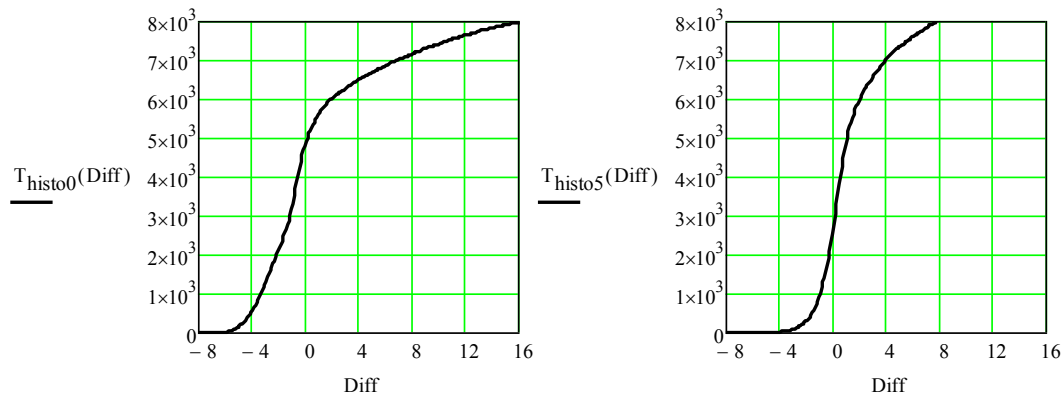


Figure 5 Cumulative histogram of *Diff* from hourly simulation of year 1990 in Lund, Sweden. Left: Exterior insulation thickness 0cm. Right: Exterior insulation thickness 5cm.

CONCLUSION

The paper presents an analytical solution method based on dynamic thermal networks for the heat transfer problem in an attic with a pitched roof. Although there exists a number of numerical approaches to solve this problem (Energy+, IDA-ICE etc), no analytical solution has as far as the authors know been presented before. The solution shows the physical behavior of the different components in a very clear way. It is also easy to investigate the effect of the included parameters. The temperature at any point can be calculated using about 15 preceding boundary temperatures. A few examples of possible parameter studies are presented.

ACKNOWLEDGEMENTS

This project is part of WoodBuild, a research programme within the Sectoral R&D Programme 2006-2012 for the Swedish forest-based industry.

REFERENCES

- Claesson J. (2002A). Dynamic Thermal Networks. Outlines of a General Theory. 6th Symposium on Building Physics in the Nordic Countries, June 2002, Trondheim, Norway.
- Claesson J. (2003). Dynamic Thermal Networks. A Methodology to Account for Time-dependent Heat Conduction. Sec. Int. Building Physics Conference, Sept. 2003, Leuven, Belgium.
- Wentzel E.-L., Claesson J. (2003). Heat Loss Dynamics of Walls. Analysis and Optimizing Based on the Theory of Dynamic Thermal Networks. Sec. Int. Building Physics Conference, Sept. 2003, Leuven, Belgium.
- Wentzel E.-L., Claesson J. (2004). Heat Loss to Building Foundations. An Analyses Based on a Theory of Dynamic Thermal Networks. Performance of Exterior of Whole Buildings. Ninth Int. Conf., Florida, Dec. 2004.
- Wentzel E.-L. (2005). Thermal Modelling of Walls, Foundations and Whole Buildings Using Dynamic Thermal Networks. Thesis, Dept. of Civil and Env. Eng., Div. of Building Technology, Chalmers Univ. of Technology, Gothenburg, Sweden.
- Vahid M. N., Sasic Kalagasidis A., Kjellström E. (2012) Energy and Buildings Assessment of hygrothermal performance and mould growth risk in ventilated attics in respect to possible climate changes in Sweden, Building and Environment 55 (2012) 96-109

A Holistic Decision Support Tool for Façade Design

Sinem Kultur^{1,*}, Nil Turkeri² and Ulrich Knaack³

¹Bahcesehir University, Istanbul, Turkey

²Istanbul Technical University, Istanbul, Turkey

³Delft University of Technology, Delft, Netherlands

**Corresponding email: sinemkultur@gmail.com*

ABSTRACT

The aim of this paper is to present a tool which will support decision-makers of façade design process while giving decisions on façade parameters to consider their interactions with functional performance issues. The tool is believed to contribute the holistic design of facades which is lacking in existing literature. The functional performance aspects included in the tool are structural, fire, water related, air permeability related, thermal, moisture related, daylighting, and acoustic performances. Façade parameters that are taken as the main decision subjects within the tool are orientation, transparency ratio, façade type, window type, glazing, framing, solar control, wall configuration, finishing, and detailing. First, for each façade parameter, design options are generated to keep the tool relatively simple and comprehensible. Then, matrices having design options in rows and performance aspects in columns are established. To support the decision-making, each intersecting cell in matrices proposes a rating. The proposed rating bases on comparisons and indicates for that façade parameter how superior is that design option when compared to the others in terms of that specific performance aspect. The tool not only proposes strict ratings, but also gives prescriptions that describe how to rate the options in various environmental and/ or spatial conditions. Consequently, the tool is composed of separate rating charts (matrices) designed for each predefined façade parameter. The proposed tool is in the form of spreadsheet designed via Microsoft Office software. The information provided in the tool is based upon an extensive literature review. The tool is believed to provide insight about the entire façade performance while addressing the interactions, conflicting issues among separate performance aspects and their relationships with design decisions. Thus, it will enable the decision-makers to give the decisions in a transparent way by highlighting the compromises in design and will support the communication among stakeholders.

KEYWORDS

Façade design, façade performance, decision-making, decision support tool, holistic design.

INTRODUCTION

Façade design is a significant sub-process of building design. This process is driven by a substantial number of factors such as user requirements (and performance requirements accordingly), environmental conditions, building/ space features, project conditions (various constraints, time/ budget limitations, feasibility issues, etc.), legislation, and stakeholders from different disciplines. Moreover, limitless variety of today's material and technology opportunities, changing conditions in time, designers' working trends (sense of aesthetics which is hard to assess) have influences on façade design (Knaack, et al., 2007, Klein, 2013). All these necessitate a holistic approach for façade design not to skip any significant factor and to make an optimization.

Although there are a few researches (Jin, 2013, Ramachandran, 2004, Hendriks & Hens, 2000, Aksamija, 2013, Oliveira & Melhado, 2011, Rivard, et al., 1999) in literature, there is a lack of a holistic point of view in façade design. It is believed that there is a need for an approach through which all factors, variables, conditions, constraints, and interactions can be seen/ addressed together.

A guide focusing the whole, rather than the fragments may have a positive contribution to both the product (façade) and the process (design). Instead of testing and evaluating a considerable number of alternatives via simulation tools or field studies in real conditions, to follow a model having holistic point of view in line with design goals and to reduce the number of design alternatives in early stages of design process to a lesser amount and near-ideal options and thereafter to carry out the evaluation accordingly may have a significant contribution to the facade design process.

Being within different disciplines' area of interest make it essential to design this building system (the façade) in a systematic way. There is not any single resource which guide the stakeholders for all these subjects. The stakeholders need to apply for separate resources during the facade design process.

Nevertheless, it is possible to provide a holistic support in the early stages of facade design process by organizing all the information/ knowledge in the literature from various researches conducted by different disciplines with different points of view and by establishing the relationships in-between to constitute a meaningful whole.

Main objectives of the study are to develop a systematic/ methodology for design process based on functional performance issues, and to propose a user-friendly tool for the usage of stakeholders of façade design process. To achieve these goals, a tool is developed which provides insight/ gives impression about façade performance as a whole. The tool highlights the interacting, conflicting issues of the process in order to see the whole with a holistic point of view.

In this way, both time/ cost savings and quality improvement are expected. Through the use of the proposed design decision support tool, the stakeholders of facade design process may give faster and more proper decisions and make more efficient collaborations.

It will support transparent and integrated façade design process, by doing so, strengthen the dialogue and collaboration among the participants, in turn it will ensure/ improve the product (façade) quality. It will assist design decision-making process and optimization in design, enable the stakeholders gain holistic point of view, and contribute to/ support the design of well-performing facades today and in future.

METHODOLOGY

The method followed in the study is illustrated in Figure 1. In the first part of the study, an extensive literature review regarding façade design and façade performance is conducted. The review of the existing literature covers all the relevant publications including books, e-books, journal articles, conference proceedings, theses, seminar/ course notes, standards, codes, regulations, commercial publications, encyclopaedias, dictionaries, etc. In the second part, during the development of the design decision support tool, the knowledge is organized by resolving, filtering, and relating the literature. In addition to this, expert opinions are gathered for rating the design options and weighting the relationships.

Functional performance aspects that are associated with biological/ physiological and social/ psychological requirements of the user are taken as the focus of the tool. The key performance aspects included in the tool are structural, fire, water related, air permeability related, thermal, moisture related, daylighting, and acoustic performances (Rich & Dean, 1999, Herzog, 2008, Boswell, 2013, Jin, 2013, ITU Seminar, 2013, Oraklıbel, 2014). On the other hand, façade

parameters that are taken as the main decision subjects within the tool are orientation, transparency ratio, façade type, window type, glazing, framing, solar control, wall configuration, finishing, and detailing.

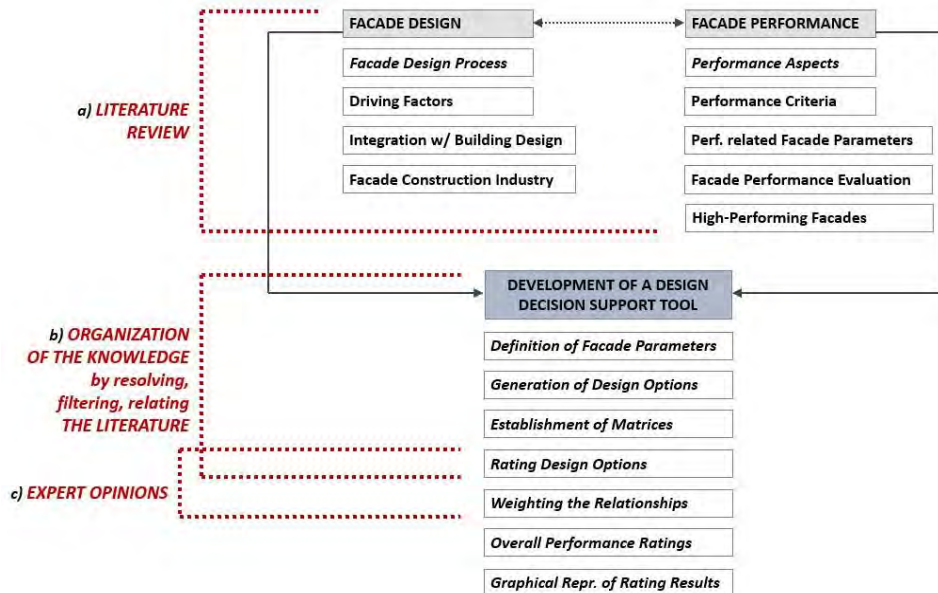


Figure 1. Methodology of the study

The proposed tool is in the form of spreadsheet designed via Microsoft Office software. First, for each façade parameter, design options are generated to keep the tool relatively simple and comprehensible. The design options are generated in accordance with the existing façade industry and knowledge. The options are not for limiting the flexibility in design, they are for guiding the tool users (façade design decision-makers) by indicating the consequences of various design decisions. So, the tool user can make deductions for their specific conditions. Then, matrices having design options in rows and performance aspects in columns are established. To support the decision-making, each intersecting cell in matrices proposes a rating (++, +, 0, -, --) or a rating prescription having conditional sentences. So, the tool user is expected to rate each option in terms of each performance in accordance with the prescriptions. The tool not only proposes strict ratings, but also gives prescriptions that describes how to rate the options in various environmental and/ or spatial conditions. These conditions may totally change the rating. Within the context of the study, environmental conditions represent location, climate, and surrounding (e.g. buildings, landscape, noise sources) while spatial conditions are for function of the building/ space, building height, spatial features of the room (e.g. room proportions, surface colours, heating, cooling, ventilation, and lighting systems). Some other significant factors as budget, feasibility, aesthetics, etc. are kept out of the tool and left to the user to make decision regarding these issues according to the project conditions, architectural intentions, etc.

The rating proposed in the tool bases on comparisons and indicates how superior is that design option (for that façade parameter) when compared to the others in terms of that specific performance aspect. If the option has direct advantage for that performance when compared to the other options, it can be given +. Here, the 'direct advantage' means if the option is chosen instead of other ones, the performance of the façade will be affected positively. On the other hand, if it has direct disadvantage for that performance, it can be rated as -. If it has no direct effect, or negligible difference which means there is no superiority among the options, it can be given 0. Besides, degree of superiority/ inferiority among options may increase for some environmental and/ or spatial conditions, then the values can be multiplied by 2 and become ++, --, and 0. Consequently, the tool is composed of separate but interlinked rating charts

designed for each predefined façade parameter. Some given decisions inevitably limit the options to be selected for the other decision subjects. These are prescribed within the charts, as well.

Moreover, an individual performance aspect is affected by more than one design decision. But, each design decision may have different weighted impacts on that performance. So, for each performance aspect, each design decision is weighted according to the strength of relationships (6 for a strong relationship, 3 for a medium-strength relationship, 1 for a weak relationship). The tool gives the ideal design option(s) for each decision subject based on the rates and weights. It is not always possible to choose the ideal option proposed by the tool. It may be due to space organization, land settlement, etc. Under these circumstances, the tool implicitly recommends paying attention to the inferior performances in other design decisions. For the assessment of each single performance of a façade design; firstly, each rate given by the tool users is multiplied by its weight (the strength of the relationship between the decision subject and the performance aspect), secondly, these multiplied scores are accumulated with the assumption that the sum total of the design decisions composes the façade design.

RESULTS

The results of the study are the separate but interlinked rating charts (matrices) prepared for each predefined key decision subject. The rating charts/ prescriptions which belong to orientation are presented in this paper. Screenshots from rating charts are given in Table 1. The chart on the left (assume it without any rating) is the one that appears when the user clicks on the orientation decision subject on the tool’s home page. Then, if the ‘rate !’ button under the thermal performance is clicked on, the chart on the right side appears. In this page, the user is expected to rate the options according to the given prescriptions. As soon as the options are rated, on the left chart, the empty cells are updated, and the tool highlights the ideal and worst options with a holistic point of view (based on the weights and the user’s rates). Ultimately, the user is expected to make a choice by clicking on ‘choose !’ button. When the option is selected, the scores of that option is taken into account for evaluation.

Table 1. Screenshots from rating charts (tool interface, and sample rating)

RATING FOR ORIENTATION		EVALUATION				HOME				
		P1	P2	P3	P4	P5	P6	P7	P8	
ORIENTATION	North					-				
	South					+				
	East					0				
	West					0				
	North East					-				
	North West					-				
	South East					+				
	South West					+				
	SELECTED OPTION	CHOOSE !								

Options & How to Rate		PS		
		RATING	THERMAL PERFORMANCE	
		<i>to balance solar heat gain with solar shading</i>		
North		In N hemisphere, for heating dominated climates, give (+) for S, SE, SW, (0) for E, W, (-) for N, NE, NW, for cooling dominated climates, give (+) for N, NE, NW, - for the rest. In S hemisphere, vice versa, however, in N hemisphere, for cooling dominated climates, in spaces having need to direct sunlight (esp. for health reasons), give (0) for S, SE, SW.		
South		the above rating is for spaces occupied throughout the all day.		
East		if it is mostly occupied in the mornings, in N hemisphere, for heating dominated climates, give (+) for E, S, SE, (-) for the rest. for cooling dominated climates, give (+) for N, NW, W, (-) for the rest. in S hemisphere, vice versa.		
West		if it is mostly occupied in the afternoons, in N hemisphere, for heating dominated climates, in N hemisphere, for heating dominated climates, give (+) for W, S, SW, (-) for the rest. for cooling dominated climates, give (+) for N, NE, E, (-) for the rest. in S hemisphere, vice versa.		
North East		plus all the above, change the rating to protect or utilize (for hot & humid climates) from the predominant wind.		
North West		if the space mostly occupied in certain seasons like Winter or Summer, the rating changes as well. S, SE, SW are again advantageous in Winters, while N, NE, NW can be superior options for spaces mostly occupied in Summers.		
South East		for spaces rarely occupied, there is no need to rate the options.		
South West				
rate after checking these issues...		location (Northern or Southern hemisphere) and predominant wind direction (& intensity)	climate (heating or cooling dominated, or mixed based on heating degree days)	function of the space (use period (daily & seasonal))

The rating prescriptions for the orientation is given in Table 2. All the prescriptions in the chart are grounded on the information/ knowledge deduced from the literature. The options for the orientation are North (N), South (S), East (E), West (W), Northeast (NE), Northwest (NW), Southeast (SE), and Southwest (SW).

Table 2. Rating prescriptions for the orientation

Options for the Design Decision & How to Rate Them		P1	P2	P3	P4	P5		P6	P7		P8
DESIGN DECISION	Options	STRUCTURAL PERFORMANCE	FIRE PERFORMANCE	WATER related PERFORMANCE	AIR PERMEABILITY related PERFORMANCE	THERMAL PERFORMANCE		MOISTURE related PERFORMANCE	DAYLIGHTING PERFORMANCE		ACOUSTIC PERFORMANCE
ORIENTATION	North	give (-) for the options exposed to predominant wind directions (due to pressure & suction forces), (+) for the perpendicular directions, and (0) for the rest.	give (-) for the options exposed to the predominant wind directions, (+) for the most wind protected ones, and (0) for the rest.	give (-) for the options exposed to predominant wind directions, (+) for the most wind protected ones, and (0) for the rest.	give (-) for the options exposed to predominant wind directions, (+) for the most wind protected ones, and (0) for the rest.	in N hemisphere, for heating dominated climates, give (+) for S, SE, SW, (0) for E, W, (-) for N, NE, NW. for cooling dominated climates, give (+) for N, NE, NW, - for the rest. in S hemisphere, vice versa. however, in N hemisphere, for cooling dominated climates, in spaces having need to direct sunlight (esp. for health reasons), give (0) for S, SE, SW.		give (-) for the options exposed to predominant wind directions, (+) for the most wind protected ones (except N orientations in N hemisphere and S orientations in S hemisphere due to low solar radiation that reduces the drying potential), and (0) for the rest.	according to the function of the space, define which of the following is desirable: diffuse & homogeneous skylight (a) or direct sunlight (b). for a, in N hemisphere, give (+) for N, NE, NW, (-) for the rest (high glare potential). in S hemisphere, do the rating reversely.		give (-) for the options in the direction of noise sources, (+) for the most noise protected directions, and (0) for the rest.
	South	if building function has high importance in terms of fire protection, then multiply the rating values by (2).	if it is high-rise building and wind intensity is high, multiply the rating values by (2).	if it is high-rise building and wind intensity is high, multiply the rating values by (2).	if it is high-rise building and wind intensity is high, multiply the rating values by (2).	the above rating is for spaces occupied throughout the all day.		if it is high-rise building and wind intensity is high, multiply the rating values by (2).	if it has mainly winter and cloudy conditions during the year, then for some space functions, sky illumination may not be sufficient in N orientations in N hemisphere. check the latitude & climate and make the relevant adjustments (e.g. give (0) for N, and (+) for NE, NW), for b, give (+) for S since it provides direct sunlight and relatively easier to control. give (0) for E, W, SE, SW for providing low-angle direct sunlight which is hard to control in terms of glare. give (-) for the rest.		if the space is highly noise-sensitive, then multiply the rating values by (2).
	East	if there is no predominance among the winds of different orientations, then there is no need for rating.	if there is no predominance among the winds of different orientations, then there is no need for rating.	if there is no predominance among the winds of different orientations, then there is no need for rating.	if there is no predominance among the winds of different orientations, then there is no need for rating.	if it is mostly occupied in the mornings, in N hemisphere, for heating dominated climates, give (+) for E, S, SE, (-) for the rest. for cooling dominated climates, give (+) for N, NW, W, (-) for the rest. in S hemisphere, vice versa.		if it is high-rise building and wind intensity is high, multiply the rating values by (2).	plus all above conditions, surrounding obstacles (buildings, trees, etc.) or view change the rating. highly reflective surrounding surfaces (including the ground) may contribute to the illumination levels or a pleasing view may be a desire. adjust the above ratings accordingly.		if the space is rarely used, there is no need for rating.
	West	if there is no predominance among the winds of different orientations, then there is no need for rating.	if there is no predominance among the winds of different orientations, then there is no need for rating.	if there is no predominance among the winds of different orientations, then there is no need for rating.	if there is no predominance among the winds of different orientations, then there is no need for rating.	if it is mostly occupied in the afternoons, in N hemisphere, for heating dominated climates, give (+) for W, S, SW, (-) for the rest. for cooling dominated climates, give (+) for N, NE, E, (-) for the rest. in S hemisphere, vice versa.		if there is no predominance among the winds of different orientations, then there is no need for rating.	for spaces rarely occupied, there is no need to rate.		
	North East	if stack effect dominates the air infiltration (in cold climates), there is no need to rate the options according to wind directions.				plus all the above, change the rating to protect or utilize (for hot & humid climates) from the predominant wind.			for spaces rarely occupied, there is no need to rate.		
	North West					if the space mostly occupied in certain seasons like Winter or Summer, the rating changes as well. S, SE, SW are again advantageous in Winters, while N, NE, NW can be superior options for spaces mostly occupied in Summers.					
	South East					for spaces rarely occupied, there is no need to rate the options.					
	South West										
rate after checking these issues...	predominant wind direction (& intensity) / building height (as high or low-rise)	predominant wind direction (& intensity) / building function	predominant wind direction (& speed) / building height (as high or low-rise)	predominant wind direction (& speed) / building height (as high or low-rise) climate	location (Northern or Southern hemisphere) and predominant wind direction (& intensity)	climate (heating or cooling dominated, or mixed based on heating degree days)	function of the space (use period (daily & seasonal)	predominant wind direction (& intensity) / building height (as high or low-rise)	location (Northern or Southern hemisphere, latitude) / view climate	surrounding noise sources and function of the space (type of activity)	surrounding noise sources and function of the space (use period, noise sensitivity)

The scores obtained from separate charts are accumulated (the sum of + and - is 0, one advantage plus one disadvantage make the design neutral) for the overall performance evaluation of façade design. Then the results are illustrated by a spiderweb chart (the format is given in Figure 2). The final spiderweb graphic, which includes separate sections for each performance aspect, gives the opportunity to compare the façade design alternative with the tool's ideal. The tool does not give real performance values, instead it gives the opportunity to relatively compare alternative designs in terms of performance aspects and to see the overall performance footprint.

DISCUSSIONS AND CONCLUSION

The tool is believed to provide insight about the entire façade performance while addressing the interactions, conflicting issues among separate performance aspects and their relationships with design decisions. Thus, it will lead to a holistic façade design, better trade-offs, and transparency in decision-making, especially in early stages of façade design process. Design is a process of limiting possible alternatives and here the tool may function as a supportive

guidance. By having the potential to prevent negative iterations in the design process, it will be time-saving, as well. Although the decisions need to be finalized by integrating some other issues like costs, and aesthetic features of the design alternatives, by means of the tool, options can be compared in terms of their functional performances. Besides, the tool provides the notion of how (by changing which design decision(s)) to improve the performance of the final design.

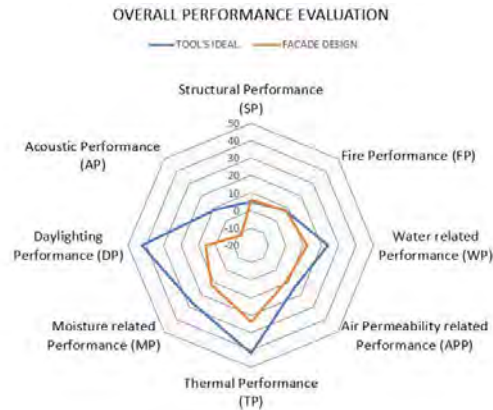


Figure 2. A representative spiderweb chart

Project conditions may vary, so the importance factors of the performance aspects. In that case, design decisions can be given accordingly which makes the tool flexible to changing priorities/ conditions. In future studies, design options within the scope of the tool can be expanded and rated by following the similar logic. Furthermore, the tool can be customized for specific climatic conditions, or building/ façade types. It may evolve in future, as new knowledge is incorporated into the tool.

REFERENCES

- Aksamija, A. 2013. *Sustainable Facades: Design Methods for High-Performance Building Envelopes*. Wiley.
- Boswell, C. K. 2013. *Exterior Building Enclosures. Design Process and Composition for Innovative Facades*. Wiley.
- ITU: Çelik, O. C., Özgünler, M., Köknel Yener, A., Türkeri, N., Tamer Bayazıt, N., Koçlar Oral, G., Altun, C. 2013. *Facade Seminar Notes*. Istanbul Technical University.
- Hendriks, L. and Hens, H. 2000. *Building Envelopes in a Holistic Perspective*. Amsterdam, Netherlands: Laboratorium Bouwfysica.
- Herzog, T. 2008. *Facade Constructional Manual*. Birkhauser Architecture, Germany.
- Jin, Q. 2013. A Whole-life Value Optimization Model for Facade Design. *PhD Thesis*, University of Cambridge, Department of Engineering.
- Klein, T. 2013. Integral Facade Construction. Towards a New Product Architecture for Curtain Walls. *PhD Thesis*, TU Delft, Architectural Engineering + Technology Department.
- Knaack, U., et al. 2007. *Facades Principles of Construction*. Birkhauser.
- Oliveira, L. A., and Melhado, S. B. 2011. Conceptual model for the integrated design of building facades. *Architectural Engineering and Design Management*, 7, 190-204.
- Oraklıbel, A. 2014. Giydirme Cephe Sistemlerinin Bina ile Bütünlenmesinde Kullanılabilecek Performans Ölçütlerinin ve Bağlı Önemlerinin Belirlenmesi. *Yüksek Lisans Tezi*, İstanbul Teknik Üniversitesi Fen Bilimleri Enstitüsü.
- Rich, P. & Dean, Y. 1999. Principles of Element Design. Butterworth-Heinemann.
- Rivard, H., Bedard, C., Ha, K. H., & Fazio, P. 1999. Shared conceptual model for the building envelope design process. *Building and Environment*, 34, 175-187.

Considerations on the Thermal Modelling of Insulated Metal Panel Systems

Ligia Moga^{1,*} and Ioan Moga¹

¹Technical University of Cluj-Napoca, Romania

*Corresponding email: ligia.moga@ccm.utcluj.ro

ABSTRACT

The very strict regulations imposed by the European directives regarding low energy consumptions of buildings imposes the availability of thermal and energy efficient solutions for the building envelope. One common solution is given by insulated metal panel systems, which are typically used for industrial buildings but lately also used for other types of buildings (e.g. residential buildings, hotels, hospitals). These types of solutions must be properly addressed from the thermal modelling and simulation point of view considering a different thermal behaviour due to its detail components. For insulated metal panel systems the typical calculations are done by considering only the current field area without the impact of the thermal bridges. This means that the value used in calculations is just a 1D, and not a 2D or a 3D simulation which are closer to the real heat transfer phenomena for this types of constructive details. Thus, the paper addresses a study regarding the manner by which metallic building components can be thermally evaluated and optimized in order to improve their thermal performance and reach the imposed thermal transmittances-U values imposed for the market of high performant energy efficient buildings. The paper brings a complex approach in evaluating the thermal performance of insulated metal panel systems.

KEYWORDS

Metal panels, thermal bridges, heat transfer, modelling, simulation

INTRODUCTION

On an international level the development of high performance buildings (i.e. nearly Zero Energy Buildings – nZEB, passive buildings) is one of the main focuses aimed on achieving important decreases of the energy consumptions and greenhouse gas emissions. On a European level a decrease in the energy consumptions level of 20% is expected by 2020 (2020 Energy Strategy) and of 27% by 2030 (2030 Energy Strategy). Thus, the construction of new buildings offers the best opportunity to implement thermally optimised solution for the building envelope components, solutions that are able to meet the European targets regarding energy consumptions.

The building envelope plays a very important role in establishing both the energy demand for heating or cooling the building and also the interior comfort level of that building. The construction market offers several solutions described as optimal solutions for meeting the nZEB target imposed by the European directive (Directive 2010/31/UE). Among traditional solutions, the insulated metal panel systems (i.e. sandwich panels) typically used for industrial buildings are becoming popular among builders as an alternative solution for other types of buildings (e.g. office buildings, hospitals, residential buildings). Although that the metal panel has an interior layer of thermal insulation, this is covered on both sides by a corrugated metal sheet, thus decreasing the thermal performance of the ensemble. Also, several thermal bridges occur in the joints area, thermal bridges that must be addressed with at least a 2D calculation approach.

In many situations the calculations are done by a 1D approach, without considering the negative effect of the thermal bridges. Thus, an inaccurate thermal assessment can lead to code compliance issues and a poor thermal performance in the operating phase of the building. The study aims to analyse the thermal performance of insulated metal panel systems by approaching 3D calculations with the help of CIMPSPAT program. The adjusted thermal resistance R' (i.e. thermal resistance that considers the effect of the thermal bridges) and the adjusted thermal transmittance U' are calculated and compared with the standard values for traditional and values for nZEB.

METHODS

A heat transfer computing software called CIMPSPAT is used for the numerical modelling and simulation of the 3D heat transfer phenomena that takes place in insulated metal panel systems. The CIMPSPAT computing software is similar to other tools like THERM, Physibel, Antherm and others. Similar to mentioned tools, CIMPSPAT was developed in the last 35 years by our research staff. The finite-differences method is used for solving the third order heat transfer differential equations. The boundary conditions for the simulated cases are set in accordance to national and European standards. The program does 3D calculations by employing the heat conduction equation in a stationary thermal regime:

$$\frac{\partial}{\partial x} \left(\lambda(x, y, z) \cdot \frac{\partial \theta(x, y, z)}{\partial x} \right) + \frac{\partial}{\partial y} \left(\lambda(x, y, z) \cdot \frac{\partial \theta(x, y, z)}{\partial y} \right) + \frac{\partial}{\partial z} \left(\lambda(x, y, z) \cdot \frac{\partial \theta(x, y, z)}{\partial z} \right) = 0 \quad (1)$$

where: θ is the temperature variable in time, in the (x,y,z) node, λ is the thermal conductivity of the body [W/(m·K)]

The geometry of the panel was discretized using a discretisation network in accordance with the stipulations of the standard EN ISO 10211. The digitization network is done automatically by the program, until the conditions for the heat flow between the inner and outer surfaces of the wall give a difference under 0.001W and in each node of the spatial mesh the obtained differences are under 0.000001 W (EN ISO 10211).

The input of data is done with the help of a graphical module. The required data is the spatial geometry of the component, the physical characteristics of each material that is forming the building component, the boundary conditions, the ambient temperatures, the exterior temperature, and the interior and exterior air humidity. The library of the program contains climatic data in accordance with the SR EN ISO 13790 standard and other specific standards.

The analysed components are specific details for walls made with insulated metal panel systems existing in the construction market. The component is described by three layers: i.e. an exterior and an interior profiled sheeting and an inner layer of thermal insulation having a thermal conductivity $\lambda=0.04$ [W/(m·K)].

The simulated case scenarios are described as it follows: in current field area without the purlin (1) and in the area with the purlin (2). Thus, results are given considering both areas of a metallic component. Two hypotheses were simulated for each studied case:

- hypothesis (a): an air layer exists between the two thermal insulation layers that are in contact with the interior and exterior sheeting;
- hypothesis (b): a thermal insulation layer is placed between the two thermal insulation layers in contact with the interior and exterior sheeting.

For case scenario I is presented a wall with a thickness of 150 mm in two variants, the first in the current field area (a) and the second in the purlin area (see figure 1), the Z purlin having a length equal to 150 mm. For case scenario II is presented a wall with a thickness of 250 mm with an interior layer of thermal insulation between the existing thermal insulations (b), in the current field area (i.e. 1.II.b) and in the Z purlin area, purlin with a length of 200 mm (i.e. 2.II.b). For case scenario III is presented a wall with a thickness of 300 mm with an interior layer of thermal insulation between the existing thermal insulations (b), in the current field area (i.e. 1.III.b) and in the Z purlin area, purlin with a length of 250 mm (i.e. 2.III.b). The Z, C and U purlins have a thickness equal to 1.5 mm, while the profiled sheeting has a thickness equal to 0.5 mm. The mentioned case scenarios are briefly described in table 1. Also, the geometrical model of the constructive details is presented in figure 1.

Table 1. Studied case scenarios

	Case Scenario					
	(1)			(2)		
	150 mm	200 mm	250 mm	150 mm	200 mm	250 mm
Hypotheses	I	II	IV	I	II	III
a.	1.I.a	1.II.a	1.III.a	2.I.a	2.II.a	2.III.a
b.	1.I.b	1.II.b	1.III.b	2.I.b	2.II.b	2.III.b

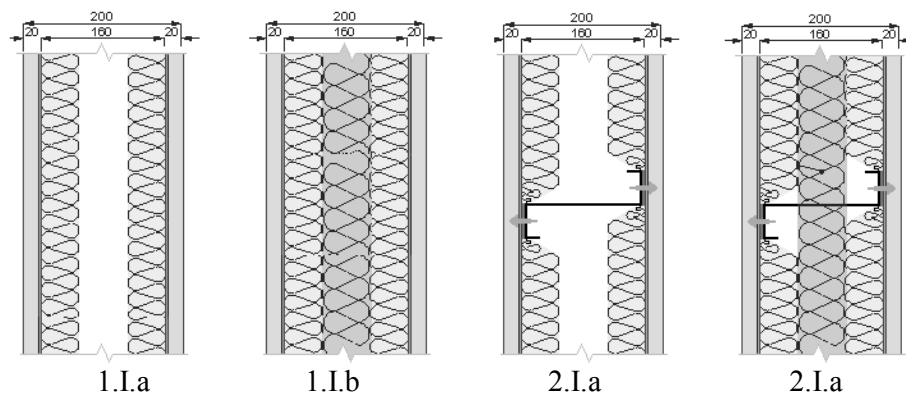


Figure 1. Extract from the analysed case scenarios

RESULTS

As mentioned before the European Directive 31/UE/2010 defines new types of energy efficient buildings starting by 31 December 2021. The nZEB require significantly improve thermal performances that will lead to higher thermal resistances (i.e. lower thermal transmittances) in accordance to what a building envelope can be described as having nearly zero energy consumptions. Although that the term of “nearly zero” is understood as more related to building systems than the building envelope, the reality is that the envelope still plays a key role in reaching that zero level.

The Romanian Governmental Order (GO 2641/2017) that came into force in April 2017 imposes more strict requirements for reaching the nZEB levels. Minimum adjusted required values for thermal resistances of building envelope components are given for both of residential and other types of buildings. The adjusted thermal resistances values refer to the ones obtained by applying the thermal bridges effect described by the linear and punctual thermal transmittance coefficients. In the case of an exterior wall for residential building the minimum adjusted required values is $R' = 1.80 \text{ [m}^2\text{K/W]}$, that being an adjusted thermal

transmittance $U' \leq 0.56$ [W/(m²K)]. For other types of buildings the values for exterior walls are not higher but even smaller than the one mentioned for residential buildings, e.g. for category I of building going from $R'=1.10$ to 1.8 [m²K/W] while for category II of buildings going from $R'=1.0$ to 1.7 [m²K/W], category being defined based on the main usage of the building. Unfortunately, the minimum required values for both residential or other types of buildings, do not meet the values defined for a nZEB that should be around $R' \geq 6,67$ [m²K/W], which means an $U' \leq 0,15$ [W/(m²K)].

Thus, the values obtained through 3D calculations were compared to the above mentioned values in order to evaluate if the analysed case scenarios comply with them. It is good to mention that in current design practice thermal performance of metal insulated panels is evaluated mainly in the current field area and not in the area purlins area.

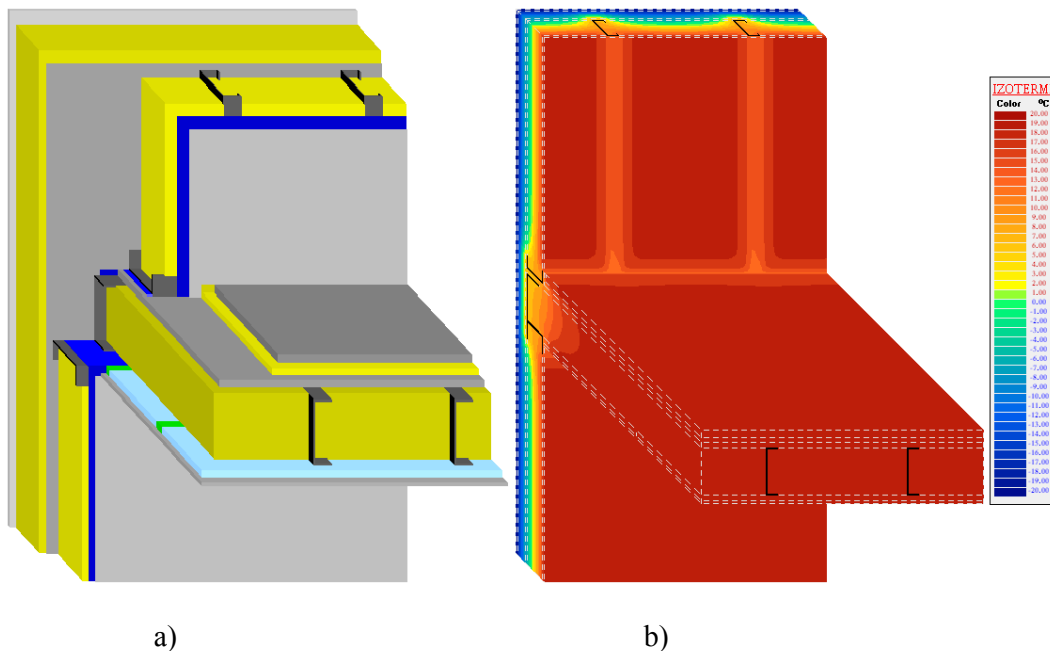


Figure 2. The 3D geometrical model (a) and the spatial temperature field (b)

Table 2. Simulation results and compliance to design norms

	Values	Calculation		GO 2641/2017	nZEB	
		R'	U'	U'	U'	
		[m ² K/W]	[W/(m ² K)]	[m ² K/W]	[W/(m ² K)]	
Studied Cases	I	1.I.a	2.647	0.378	yes	no
		1.I.b	3.930	0.254	yes	no
		2.I.a	1.921	0.520	yes	no
		2.I.b	2.487	0.402	yes	no
	II	1.II.b	5.125	0.195	yes	no
		2.II.b	2.844	0.352	yes	no
	III	1.III.b	6.331	0.158	yes	no
		2.III.b	3.329	0.300	yes	no
	Fig.2		2.835	0.353	yes	no

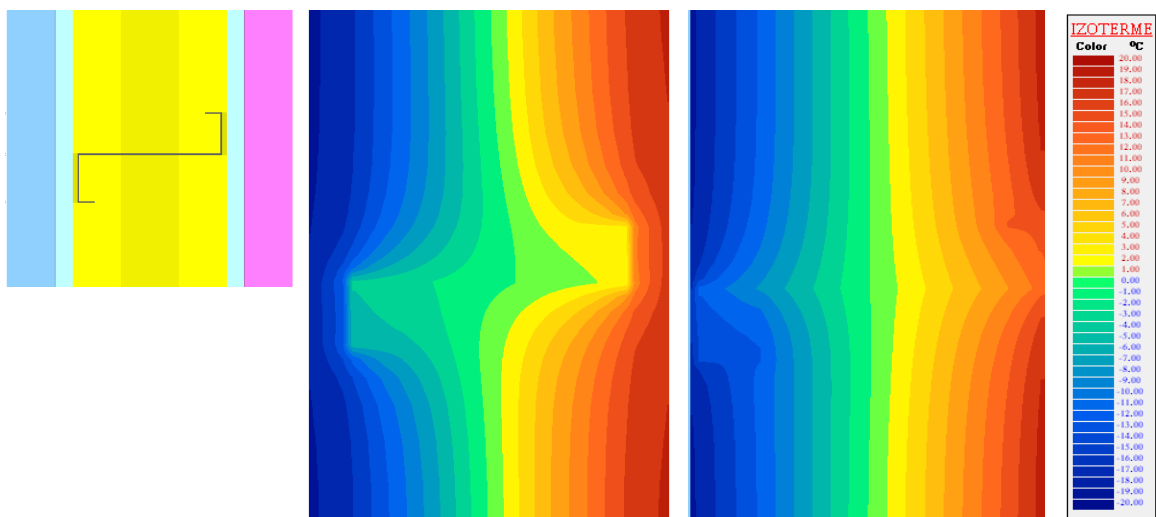
DISCUSSIONS

Table 2 gives an accurate image of the thermal behaviour of the studied cases. As it can be observed for all examined cases the adjusted thermal transmittances U' have lower values

compared to national norms (GO 2641/2017) but much higher values compared to the ones described by the nZEB targets. When 1D calculations are done for the presented details, the results obtained, without considering the negative effect of the thermal bridges, is somewhere equal to a thermal resistance of 4 [m²K/W] for case scenarios I, value higher than all results (see table 2) obtained by implementing complex calculations (i.e. 2D or 3D). A 1D calculation approach does not consider the negative effect of the thermal bridges, thus giving a thermal performance even two times better than the actual (i.e. real) performance of a component. Therefore, such complex details should always be analysed by a 3D approach, using a spatial discretization network associated with the analysed case. Thus, the mesh will describe the exact shape of the corrugated sheet (i.e. the spatial shape), and also the presence of the steel purlins and of the fixing elements.

An example of the geometrical model and the spatial temperature field for an exterior wall in connection with an intermediate metallic thermal insulated flooring, is presented in figure 2. Such complex details that beside the material layers have several metallic elements (i.e. purlins) in its structure, placed in various positions (e.g. horizontal or vertical) and orientations, impose a 3D calculation procedure that can evaluate the spatial volume of the analysed detail. The metallic purlins give a spatial thermal effect of the heat flows that are passing through the building component. Doing 2D calculations for several defined areas of the geometrical model and overlapping the plane effects will not lead to accurate results for these type of complex details. The results will be overestimated compared to the actual thermal behaviour of the building envelope.

The simulated model and the temperature field for case 2.I.b and case 2.III.b are presented in figure 3. All simulated models started from the geometrical model presented in figure 1, that was described and modelled based on the real dimensions for each constructive detail. Figure 3 presents (a) the generic modelling in the purlin area.



a) Case 2 b) 2.I.b 2.III.b
Figure 3. The geometrical model (a) and the spatial temperature field (b) - with purlin

CONCLUSIONS

Meeting the required energy efficiency targets imposed by the European Union is a very hard task considering that even nowadays, some of the solutions offered on the construction market are not able to fulfil the thermal performance values imposed by design norms. When

calculating complex details (e.g. insulated metal panels), the approach is usually done 1D instead of a 2D or more accurate a 3D calculation procedure. Therefore, the final thermal and energy performance of a building is quite different than the performance obtained during the operation phase of the building, case usually met in current practice at metallic structures. This has significant economical implication for the owners or operators of that building, from the energy consumption point of view. Even for the case of thermally optimized details (i.e. case scenario for all studied dimensions)) the thermal performance still does not comply with required values for nZEB. That means that several solutions could be employed to improve their thermal performance: thicker thermal insulation layer, an extra thermal insulation system on the exterior side of the panel, or better thermal performing materials (e.g. nanoinsulating materials) (Lakatos, 2014, 2017) and fasteners made of non-super conductive materials.

To conclude, beside the reduction of the energy consumption also a reduction of the greenhouse gas emission must be obtained, which means a low CO₂ emission index for the analysed building. With building envelope components with a thermal performance far worse than the modelled scenario in design phase, will set a trend opposite to what is needed, not only on a European but also on a worldwide level. The “A” energy class buildings or nZEB obtained on “paper” must behave likewise in operating phase. A 3D complex approach of the calculations for the insulated metal panel systems is able to offer accurate results for what means a real operation of a building.

ACKNOWLEDGEMENT

This research was supported through funding from the Technical University of Cluj-Napoca and RCPPB research group.

REFERENCES

- 2020 Energy Strategy accessed at <https://ec.europa.eu/energy/en/topics/energy-strategy-and-energy-union/2020-energy-strategy>
- 2030 Energy Strategy accessed at <https://ec.europa.eu/energy/en/topics/energy-strategy-and-energy-union/2030-energy-strategy>
- Directive 2010/31/EU of the European Parliament and Of the Council of 19 May 2010 on the energy performance of buildings (recast)
- CÎMPSPAT. 2017 Computer program for 3D steady –state heat transfer calculation, Building Physics Research Team, Cluj-Napoca, Romania.
- EN ISO 10211. 2007. Thermal bridges in building construction- Heat flows and surface temperatures- Detailed calculation.
- SR EN ISO 13790. 2005. Thermal performance of buildings. Calculation of the energy necessary for heating, Romania.
- Governmental Order 2641/2017 for the modification and addition of the technical regulation “Calculation methodology of the energy performance of buildings”
- Lakatos A. 2014. Comparison of the Thermal Properties of Different Insulating Materials, *Advanced Materials Research*, Vol. 899, pp. 381-386.
- Lakatos, Á. 2017. Comprehensive thermal transmittance investigations carried out on opaque aerogel insulation blanket, *Materials and Structures*, Vol. 50: 2. <https://doi.org/10.1617/s11527-016-0876-7>
- Zabcik R.A. 2014. Thermal Performance of Insulated Metal Panels per ASHRAE 90.1-2010, Research and Development NCI Group Inc., 6 pages.
- Jung-Min Oh et al. 2016. Analysis of building energy savings potential for metal panel curtain wall building by reducing thermal bridges at joints between panels, *Energy Procedia*, vol. 96 , pp. 696 – 709.

Numerical thermal model of a double-glazed window filled with phase change materials

Daniel Uribe^{1,3}, Nicolás Benavente⁴, Waldo Bustamante^{2,3}, Sergio Vera^{1,3,*}

¹ Department of Construction Engineering and Management, School of Engineering, Pontificia Universidad Católica de Chile

² School of Architecture, Pontificia Universidad Católica de Chile

³ Centre for Sustainable Urban Development, Pontificia Universidad Católica de Chile

⁴ Faculty of Physical and Mathematical Sciences, Universidad de Chile

*Corresponding author email: svera@ing.puc.cl

ABSTRACT

Phase change materials (PCMs) glazing systems might be able to improve the building energy performance because of controlling solar heat gains and peak heating and cooling loads. EnergyPlus, a state-of-the-art energy simulation tool, allows simulating the heat transfer through opaque elements that incorporate PCMs. However, EnergyPlus does not allow this for transparent elements with PCMs. As consequence, the main objective of this research is to develop a numerical thermal model of double glazing windows with PCM in the cavity to be coupled with EnergyPlus in the future. To develop the numerical heat transfer model, the sensible and latent heat of the PCM is numerically modelled in MATLAB. This model is used to evaluate the impact of PCM on the inner surface temperature of the window and the Predicted Mean Vote (PMV) in Santiago of Chile. The PCM RT25HC of Rubitherm® shows the better performance because it keeps the internal surface temperature of the window near of the comfort range for more time and the Predicted Mean Vote (PMV) below 1.0.

KEYWORDS

PCM glazing, thermal model, office buildings, PMV.

INTRODUCTION

Central Chile shows a semiarid climate (Bsk according Köppen-Geiger classification) which is characterized by high solar radiation and outdoor temperature during 6 to 8 months. On the other hand, most of office buildings are fully glazed façade office buildings that have very high cooling energy consumption due to high solar heat gains even tough in winter (Bustamante, Vera, Prieto, & Vásquez, 2014).

Phase change materials (PCMs) are able to reduce building cooling loads when incorporated to opaque building envelopes (Ilaria, Lorenza, Goia, & Serra, 2018). However, open floor buildings have low percentage of opaque surfaces. Therefore, there is the opportunity to use windows with PCM to control solar heat gains, daylighting transmission and cooling loads (Giovannini, Goia, Verso, & Serra, 2017; Silva, Vicente, & Rodrigues, 2016). EnergyPlus, a state-of-the-art energy simulation tool, does not include the heat transfer modelling through transparent elements that incorporate PCMs. Otherwise, the heat transfer through opaque elements is well supported by EnergyPlus (Tabares-Velasco, Christensen, & Bianchi, 2012).

Different heat transfer models of the state-of-the-art has the potential to be coupled to an energy modelling software. In particular, Goia et al. (2012) developed a 1D model for heat transfer considering shortwave and longwave radiation heat exchange, conduction and convection. On

the other hand, Liu et al. (2016) developed a model considering absorption of the different layers, conduction, convection and radiation of shortwave and longwave transfer. They validated the model with measurements of temperatures.

As consequence, the main objective of this paper is to develop a numerical thermal model of double glazing windows with PCM, which is incorporated in the window's cavity. This numerical model is based on: the main heat transfer equations of Goia et al. (2012) and their nodal distribution to use Crank-Nicolson finite differences method; border conditions according to Liu et al. (2016); PCM's solar properties of Goia et al. (2015); and Tabares-Velasco et al. (2012), where is explained the specific heat calculation of opaque walls based on the relationship between enthalpy and temperature of PCM. To develop the numerical heat transfer model, window properties and the sensible and latent heat of the PCM are numerically modelled in MATLAB. The model is used to determine the best PCM to improve the window's thermal behaviour and thermal comfort of an office space located in Santiago of Chile.

METHODOLOGY

Overall

The process to get the best PCM to improve thermal comfort in an office building in Santiago is carried out in three steps: (i) selection of PCM to be evaluated, (ii) calculation of the mean radiant temperature of the office space using PCM and without PCM by means of a numerical thermal model of heat transfer introduced in this paper, and, (iii) evaluation of the thermal comfort using Predicted Mean Vote (PMV). In the following sections, the building model, climate of Santiago and the heat transfer model are presented.

Building model

The space to be studied corresponds to an office of 6.0 m x 8.0 m x 3.0 m, as shown in Figure 1. A window of 3.0 x 2.0 is oriented north or west. The walls, ceiling and floor are considered adiabatic. Thus, heat transfer only occurs through the glazed façade. The HVAC system consists of an ideal system with heating and cooling thermostat setpoints of 20°C and 25°C, respectively. The internal heat gains are not considered in this case because this study is focused on the heat transfer through the window.

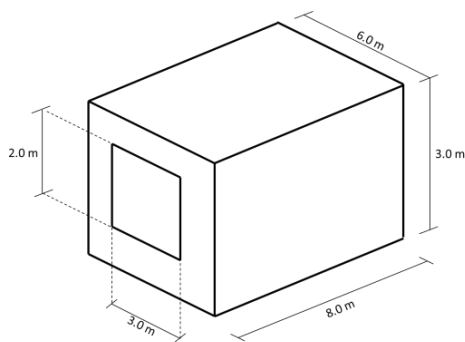


Figure 1. Office space building.

Climate

In Santiago, the highest temperature is 33.2°C, which occurs in December, and the lowest temperature is in August (-6°C). The mean outdoor temperature is 14.4°C. Figure 2a shows the annual air temperature in Santiago. Analysis of solar radiation in Santiago revealed that direct and diffuse solar irradiation are 1632.09 kWh/m² and 649.48 kWh/m², respectively. Figures 2b and 2c shows the diffuse and direct solar radiation respectively.

Selection of PCM

PCMs selected are paraffin of the RT Line of Rubitherm company. The melting temperature varies between 12°C and 35°C based on the Internal Report of SOLTREN project (Shipkovs et al., 2018). The detailed information about each PCM is presented in Table 1.

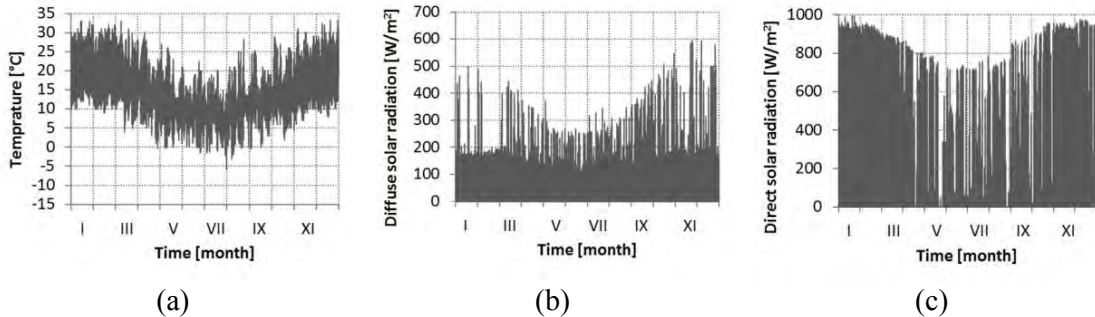


Figure 2. (a) Annual temperature in Santiago. (b) Annual diffuse solar radiation in Santiago. (c) Annual direct solar radiation in Santiago.

Table 1. PCM from Rubitherm® to be studied

PCM	Melting temperature [°C]	Heat capacity storage [kJ kg ⁻¹]
RT12	12	155
RT25	25	170
RT25HC	25	230
RT28HC	28	250
RT31	31	165
RT35	35	160

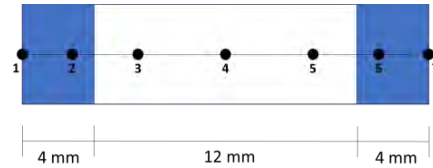


Figure 3. Discretization of thermal model.

Numerical heat transfer model

The heat transfer model has been developed based on model of Goia et al. (2012), Liu et al. (2016), Goia et al. (2015) and Tabares-Velasco et al. (2012). The model consists of a 1D nodal heat transfer of shortwave and longwave radiation, conduction and convection. In this model, 2 nodes are in each glass and 4 nodes in the gap (air or PCM). The discretization scheme is presented in Figure 3.

The model considers the following assumptions: (1) Convection is considered in the air gap cavity; (2) convection is neglected when the window cavity is filled with PCM; and (3) the absorption through the different layers is considered. Ec. 1 represents the heat transfer through the PCM:

$$\rho C_p \frac{\partial T}{\partial t} = k \frac{\partial^2 T}{\partial x^2} + \phi \quad (1)$$

where, t is the time (s), T is the temperature (K), ρ is the density (kg/m³) and C_p is the specific heat (J/(kg·K)), k is the thermal conductivity, and ϕ is the radiation source term. To solve the equation, Crank-Nicolson finite differences method has been used. The following equations represents the discretization:

$$\frac{\partial T}{\partial t} = \frac{T_i^{n+1} - T_i^n}{\Delta t} \quad (2)$$

$$\frac{\partial^2 T}{\partial x^2} = \frac{T_{i-1}^{n+1} - 2T_i^{n+1} + T_{i+1}^{n+1}}{\Delta x^2} \quad (3)$$

where, Δt is the time step, 1 minute in this paper, Δx is the spatial step (m), T_i^n is the temperature in the node i and time n . To this discretization is added the generated radiation. Finally, following is presented the matrix form of the equation to be solved.

$$(I - rA)T^{n+1} = (I + rA)T^n + r(b^n + b^{n+1}) + \phi' \quad (4)$$

Where, I is the identity matrix, A is a matrix of Eq. (5) and b are the remains of the boundary condition also presented in Eq. (5).

$$A = \begin{pmatrix} -2 & 1 & 0 & 0 & 0 & 0 & 0 \\ 1 & -2 & 1 & 0 & 0 & 0 & 0 \\ 0 & 1 & -2 & 1 & 0 & 0 & 0 \\ \vdots & \vdots & \vdots & \vdots & \ddots & \vdots & \vdots \\ 0 & 0 & 0 & 0 & 1 & -2 & 1 \\ 0 & 0 & 0 & 0 & 0 & 1 & -2 \end{pmatrix}, \quad b = \begin{pmatrix} q_1 \\ 0 \\ \vdots \\ 0 \\ q_2 \end{pmatrix} \quad (5)$$

The numerical thermal model of the heat transfer of the window was implemented in MATLAB. Also, a model of the office space in EnergyPlus was used for calculating the inputs for the MATLAB model. The inputs are the interior mean air temperature, exterior air temperature, the interior and exterior surfaces temperatures of the window, solar radiation and convection parameters.

Thermal comfort evaluation

Thermal comfort is evaluated in terms of the Predicted Mean Vote (PMV) (ISO-7730:2005), a mathematical model of a thermal scale that runs from Cold (-3) to Hot (+3) which describe the thermal sensation of occupants.

RESULTS

Figure 3 shows the interior surface temperature of the window oriented north and west in a representative summer and winter week, respectively, for all the PCMs evaluated as well as for the window cavity filled with air. Firstly, these results show all peaks of internal window surface temperatures filled with PCM are delayed in comparison with the window filled with air. This effect is due to the difference between the specific heat of the air and PCM. RT12 paraffin is always in liquid state because the temperature in the window is at least 20°C approximately. When RT25, RT25HC and RT28 paraffin are used in both, north or west façade, they change phase every day, keeping the internal surface temperature constant near to the melting temperature during all working hours. During winter, these three PCMs in north façade are able to keep the internal temperature near to the melting temperature. However, only RT25 and RT25HC are able to change phase in west façade case. The difference of heat storage between RT25 and RT25HC has no relevant effect in this case. Finally, RT31 paraffin changes phase only in summer for both window orientations, and RT35 paraffin never changes phase.

Also, the PCM has a night effect. During summer in the west façade case, the phase change is able to keep the internal surface temperature by two days. To ensure the correct behavior of the PCM glazing, it is needed that the phase change occurs every day. In the morning, the PCM must change to liquid state, and at night must change to solid state. In this case, on day 2, the

heat storage is over at the end of the working hours, then, the internal temperature increases, and the thermal comfort of occupants is affected. Due to this, in summer, RT31 and RT35 paraffin have the ability to change phase every day, and in winter, RT25 and RT25HC paraffin show this ability.

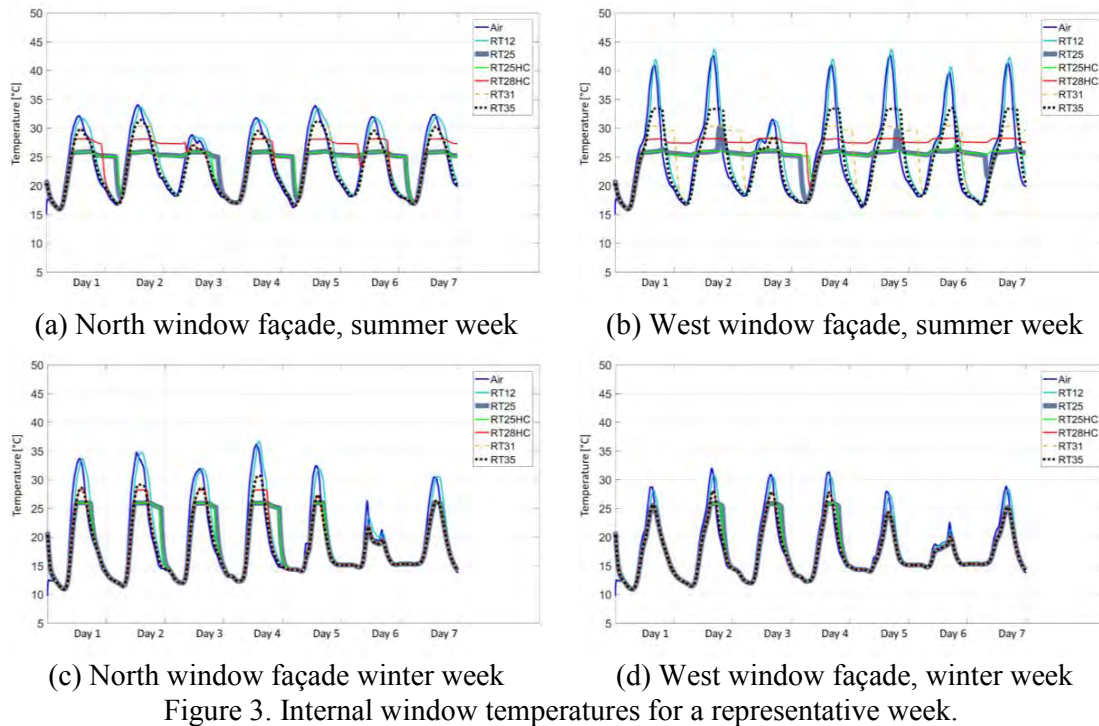


Table 2. Mean PMV results for each case

Cavity filling	Summer		Winter	
	North	West	North	West
Air	1.0	1.5	1.1	0.9
RT12	0.9	1.6	1.1	0.9
RT25	0.7	0.9	0.9	0.8
RT25HC	0.7	0.9	0.9	0.8
RT28HC	0.8	1.0	0.9	0.8
RT31	0.8	1.0	1.0	0.8
RT35	0.9	1.1	1.0	0.8

Table 2 shows the mean PMV for the temperature peaks of each day for the representative week of winter and summer. It shows that the PMV for the window filled with air is above or very close to 1.0, which means the indoor environment is slightly hot. On the other hand, PMV value less than 1.0 indicates a comfortable environment. In the north façade for summer, all the PCMs evaluated decrease the PMV below 1.0, but in the west façade, only RT25 and RT25HC decrease the PMV below 1.0. In winter, all PCMs evaluated show PMV values near to 1.0.

CONCLUSIONS

This study developed a heat transfer model of a double-glazed window filled with PCM. The PCMs RT25 and RT25HC have better behavior than the other PCMs because they reduce the inner surface temperature of the windows between 0°C and 10°C. As consequences, RT25 and RT25HC allows achieving a comfortable office indoor environment because PMV values are below 1.0. Also, it was found that RT25 and RT25HC does not change phase during summer

for 2 days or more, thus the benefits of PCMs are not obtained during these days. Further studies are needed in order to evaluate other climates, whereas future work consists on integrating this model to EnergyPlus to evaluate the impact of windows with PCM on the building energy performance.

ACKNOWLEDGEMENT

This work was funded by the National Commission for Scientific and Technological Research (CONICYT) under research grant ELAC2015/T06-0462 and CONICYT/FONDAP/15110020 (CEDEUS).

REFERENCES

- Bustamante, W., Vera, S., Prieto, A., & Vásquez, C. (2014). Solar and Lighting Transmission through Complex Fenestration Systems of Office Buildings in a Warm and Dry Climate of Chile. *Sustainability*, 6(5). doi:10.3390/su6052786
- Giovannini, L., Goia, F., Verso, V. R. M. L., & Serra, V. (2017). Phase Change Materials in Glazing: Implications on Light Distribution and Visual Comfort. Preliminary Results. *Energy Procedia*, 111(Supplement C), 357-366. doi:<https://doi.org/10.1016/j.egypro.2017.03.197>
- Goia, F., Perino, M., & Haase, M. (2012). A numerical model to evaluate the thermal behaviour of PCM glazing system configurations. *Energy and Buildings*, 54(Supplement C), 141-153. doi:<https://doi.org/10.1016/j.enbuild.2012.07.036>
- Goia, F., Zinzi, M., Carnielo, E., & Serra, V. (2015). Spectral and angular solar properties of a PCM-filled double glazing unit. *Energy and Buildings*, 87, 302-312. doi:<https://doi.org/10.1016/j.enbuild.2014.11.019>
- Ilaria, V., Lorenza, B., Goia, F., & Serra, V. (2018). Phase Change Materials in Transparent Building Envelopes: A Strengths, Weakness, Opportunities and Threats (SWOT) Analysis. *Energies*, 11(1), 1-19. doi:10.3390/en11010111
- ISO-7730:2005. Ergonomics of the thermal environment - Analytical determination and interpretation of thermal comfort using calculation of the PMV and PPD indices and local thermal comfort criteria.
- Liu, C., Zheng, Y., Li, D., Qi, H., & Liu, X. (2016). A Model to Determine Thermal Performance of a Non-ventilated Double Glazing Unit with PCM and Experimental Validation. *Procedia Engineering*, 157, 293-300. doi:<https://doi.org/10.1016/j.proeng.2016.08.369>
- Shipkovs, P., Lebedeva, K., Vanags, M., Snegirjovs, A., Kashkarova, G., Franco, J., . . . Knera, D. (2018). *Internal Report Workpackage 1 Project SOLTREN. PCM selections. Investigation of thermophysical properties of PCMs. Experimental study on solar transmittance using spectrophotometric techniques*. Retrieved from
- Silva, T., Vicente, R., & Rodrigues, F. (2016). Literature review on the use of phase change materials in glazing and shading solutions. *Renewable and Sustainable Energy Reviews*, 53, 515-535. doi:<https://doi.org/10.1016/j.rser.2015.07.201>
- Tabares-Velasco, P. C., Christensen, C., & Bianchi, M. (2012). Verification and validation of EnergyPlus phase change material model for opaque wall assemblies. *Building and Environment*, 54, 186-196. doi:<https://doi.org/10.1016/j.buildenv.2012.02.019>

On the compliance of thermal performance requirements for highly insulated building units

Giovanni Murano^{1,*}, Ilaria Ballarini¹, Giovanna De Luca¹, Domenico Dirutigliano¹, Elisa Primo¹ and Vincenzo Corrado¹

¹Department of Energy, Politecnico di Torino, Italy

*Corresponding email: giovanni.murano@polito.it

ABSTRACT

The target of the nearly zero-energy building (nZEB), stated by the European Union, represents one of the most strenuous challenges to reduce energy consumptions and greenhouse gas emissions in the building sector. In Italy, the nZEB concept refers to a set of energy performance requirements, fixed at national level and establishing a maximum allowable mean thermal transmittance value of the building envelope, as a function of the heating degree-days and of the shape factor. The building envelope is becoming more and more thermally insulated; this determines the reduction of the energy need for heating, but on the other hand it can cause the indoor overheating and the resulting increase of the energy need for cooling. In the design of highly energy efficient buildings, the different energy needs should be kept in balance as to increase the overall energy performance.

The article aims to investigate the conditions and extent for which the envelope insulation is beneficial for containing overall energy needs. A sensitivity analysis that involves different insulation levels of the building envelope is performed on some apartments of a typical residential building, located in three different Italian climatic zones. The energy performance calculations are carried out by means of a detailed dynamic simulation tool (*EnergyPlus*). The results point out that, whereas the effect of increasing the thermal insulation causes a stable reduction of the energy need for heating, the energy need for cooling is very sensitive to the apartment storey; specifically, it increases in ground-floor apartments, and decreases for top-floor building units. Its reduction becomes progressively more consistent at the decrease of the heating degree-days. Considering the annual imbalances between the energy needs for cooling and heating due to the hyper-insulated envelope, reference values of thermal transmittance can be derived as to maximise the overall energy performance of the building.

KEYWORDS

Nearly zero-energy building; thermal insulation; building energy performance; building envelope; dynamic simulation.

INTRODUCTION

Directive 2010/31/EU (European Union, 2010) promotes the energy performance improvement of buildings and enforces the Member States to draw up national plans for increasing the number of nearly zero-energy buildings (nZEBs). In Italy, the detailed application of the definition of nZEB has been specified by the Ministerial Decree (M.D.) 26/06/2015 (Italian Republic, 2015): a set of provisions concerning the building envelope, the technical building systems and the use of renewable energy sources must be complied with to achieve the nZEB target. In particular, the national strategy focuses on the building envelope (Zinzi et al., 2017), enforcing restrictive mean thermal transmittance values. In addition, the adoption of adequate insulation thickness as to meet winter energy requirements could lead to indoor overheating and, consequently, to an increase of the energy need for space cooling. Guaranteeing the best

trade-off between energy performance for heating and cooling is of crucial importance to minimize the overall energy needs.

Several studies investigated the role of the building envelope in achieving the nZEB target and demonstrate the discrepancy between the envelope requirements and the building energy behaviour in summer. Ballarini and Corrado (2012) proposed a methodology to investigate the effect of thermal insulation in summer. They underlined that transparent envelope and shading devices have a greater influence on summer energy needs than the opaque envelope. Murano et al. (2017) demonstrate the imbalance of nZEB energy need for heating and cooling by evaluating the effects of the reduction of the U -values of the envelope components and of the improvement of solar shadings on the energy needs of three reference buildings. Applying the two measures simultaneously, they proved that the influence of the thermal insulation on the energy needs for heating is greater than the effect of solar shading on the energy needs for cooling. Chvatal and Corvacho (2009) and Chvatal et al. (2005) investigated the summer overheating in buildings as a consequence of thermal insulation and thermal inertia of the building envelope; when solar and internal gains are not adequately controlled, there is a tendency towards more discomfort as the envelope insulation increases. Sameni et al. (2015) highlighted the risk of overheating in a hyper-insulated social housing, identifying the most critical flats on the basis of both occupants' behaviour and geometrical characteristics.

Within this framework, the choice of an optimal insulation level would prevent overheating and ensure the lowest overall energy consumption. The present research focuses on a typical Italian residential building and carries out a sensitivity analysis including different insulation levels and climatic zones. The imbalance of the energy needs and its effect on the overall primary energy for heating and cooling are discussed for four representative apartments, highlighting the different behaviour for storey location and climatic condition.

METHODS

Theory

The dynamic numerical simulation of the building was performed by means of *Energy Plus*. Each apartment has been modelled as a single thermal zone. The code solves a convective heat balance equation on the internal air node of the building thermal zone. As the analysis of technical building systems is out of the scope of the work, an infinite heating and cooling capacity was adopted to determine the net energy needs for space heating and space cooling. The overall energy performance (EP_{gl}), expressed as the ratio of the annual non-renewable primary energy for space heating and space cooling to the net conditioned floor area, was determined as the weighted sum of the thermal energy needs for heating and for cooling:

$$EP_{gl} = \frac{EP_{H,nd} \cdot f_{p,nren,gas}}{\eta_{H,u} \cdot \eta_{H,g}} + \frac{EP_{C,nd} \cdot f_{p,nren,el}}{\eta_{C,u} \cdot \eta_{C,g}} \quad (1)$$

where $EP_{H/C,nd}$ is the annual energy need for space heating/cooling, $f_{p,nren,gas/el}$ is the non-renewable primary energy conversion factor for natural gas (1.05) and electricity (1.95) respectively, $\eta_{H/C,u}$ is the mean seasonal efficiency of the heating/cooling utilisation subsystems (i.e. heat emission, control and distribution, equal to 0.81) and $\eta_{H/C,g}$ is the mean seasonal efficiency of the heating (0.95) and the cooling (2.50) generation subsystem, respectively. The reference mean seasonal efficiency values of the thermal subsystems were assumed in compliance with M.D., and the most used energy carriers in Italy were adopted. Gas condensing boiler and chiller were used as reference generators for heating and cooling.

Case study

The case study is a 4-storey multi-family house, studied in a previous work (Murano et al.,

2016). It is not a real building but an “archetype”, which is a “virtual” building characterised by a set of properties detected through statistical analysis of a large building sample. It is supposed to be located in Palermo (Southern Italy), Rome (Central Italy), and Turin (Northern Italy). The main climatic data (UNI, 2016) are listed in Table 1. The building consists of 12 units; its main facades are North-South oriented. Four representative apartments were chosen as to cover a wide range of the shape factor values (i.e. ratio of the envelope surface to the conditioned volume) and kinds of adjacent spaces (e.g. ground, conditioned spaces). The main geometric data are reported in Table 2. The sensitivity analysis took into account six levels of thermal insulation, from highly (level no. 1) to scarcely insulated (level no. 6). Each level is a combination of the U -values of the opaque and transparent envelope components (Table 3); the same U -value is assumed for each opaque component (walls, roof and ground floor) and the insulating material is placed on the exterior side. The areal thermal mass is about $270 \text{ kg}\cdot\text{m}^{-2}$ for the external walls and the ground floor, and $400 \text{ kg}\cdot\text{m}^{-2}$ for the roof. For each insulation level, the U -value of windows varies accordingly, while the total solar energy transmittance of glazing at normal incidence is kept constant ($g_{gl,n}=\text{SHGC}_n=0.67$). A solar shading ($\tau=0.15$, $\rho=0.70$) is supposed to be placed on the external side of all windows. The external opaque surfaces are intermediate coloured (solar absorption coefficient equal to 0.6).

Table 1. Main climatic data of the analysed locations.

Cities	Heating period		Cooling period		$H_{\text{sol,gl,hor,C}}$
	Duration [h]	HDD _{20 °C}	Duration [h]	CDD _{26 °C}	
Palermo (PA)	5 034	1 121	1 446	166	3 830
Rome (RM)	5 789	1 643	1 084	143	4 004
Turin (TO)	6 604	2 648	809	84	3 511

HDD = heating degree-days [$^{\circ}\text{C}\cdot\text{d}$], CDD = cooling degree-days [$^{\circ}\text{C}\cdot\text{d}$], $H_{\text{sol,gl,hor,C}}$ = global solar irradiation on a horizontal surface in the cooling period [$\text{MJ}\cdot\text{m}^{-2}$]

Table 2. Main geometric characteristics of the building and of the analysed units.

Pictures	Building unit code	Storey	Building unit	V_g	V_n	A_f	A_{env}	A_w	A_{env}/V_g	WWR
	BU0C	0	C	389	320	118	246	18.0	0.63	0.18
	BU1C	1	C	389	320	118	116	18.0	0.30	0.18
	BU3A	3	A	285	230	85	201	11.1	0.71	0.14
	BU3B	3	B	184	153	57	108	8.7	0.58	0.29
	Building	-	-	-	3 401	2 788	1 033	1 653	151	0.49

V_g = gross conditioned volume [m^3], V_n = net conditioned volume [m^3], A_f = net conditioned floor area [m^2], A_{env} = envelope area [m^2], A_w = windows area [m^2], WWR = windows-to-wall ratio [-]

Table 3. Thermal properties of the building envelope components.

Insulation level	External walls			Flat roof			Ground floor			Windows
	U	κ_i	$ Y_{\text{ic}} $	U	κ_i	$ Y_{\text{ic}} $	U	κ_i	$ Y_{\text{ic}} $	U
1	0.10	48.9	0.009	0.10	64.8	0.006	0.10	56.6	0.015	1.00
2	0.20	49.3	0.031	0.20	65.1	0.021	0.20	56.9	0.049	1.50
3	0.30	49.6	0.053	0.30	65.3	0.034	0.30	56.7	0.081	2.00
4	0.40	50.0	0.076	0.40	65.5	0.048	0.40	56.6	0.115	2.50
5	0.50	50.4	0.104	0.50	65.7	0.064	0.50	56.5	0.151	3.00
6	0.60	50.9	0.138	0.60	66.0	0.081	0.60	56.5	0.191	3.50

U = thermal transmittance [$\text{W}\cdot\text{m}^{-2}\text{K}^{-1}$], κ_i = internal areal effective heat capacity [$\text{kJ}\cdot\text{m}^{-2}\text{K}^{-1}$],

Y_{ic} = periodic thermal transmittance [$\text{W}\cdot\text{m}^{-2}\text{K}^{-1}$]

The weather data were derived from the CTI database (CTI, 2017). Hourly profiles of the

internal heat sources and the ventilation flow rate were determined according to UNI/TS 11300-1 (UNI, 2014). As specified by the Italian regulations, a continuous thermal system operation is considered during the heating and cooling seasons. The set-point temperature was fixed at 20 °C and 26 °C for heating and cooling, respectively. The solar shading devices are considered in function when the hourly value of solar irradiance exceeds 300 W·m⁻².

RESULTS AND DISCUSSION

The results of the sensitivity analysis are reported in Figures 1-2. For each location, Figure 1-a) shows annual cooling energy need vs. annual heating energy need of the whole building for different insulation levels. Figure 1-b) shows cooling peak power vs. heating peak power for the same insulation levels. Figure 2 shows the same outcomes both for the whole building and for each building unit. In addition, Figures 2-a), 2-c) and 2-e), for different location, also show the annual overall primary energy vs. the annual energy needs for heating and cooling. The dotted grey lines represent the *iso-EP_{gl}* lines, calculated as described in “Methods” section.

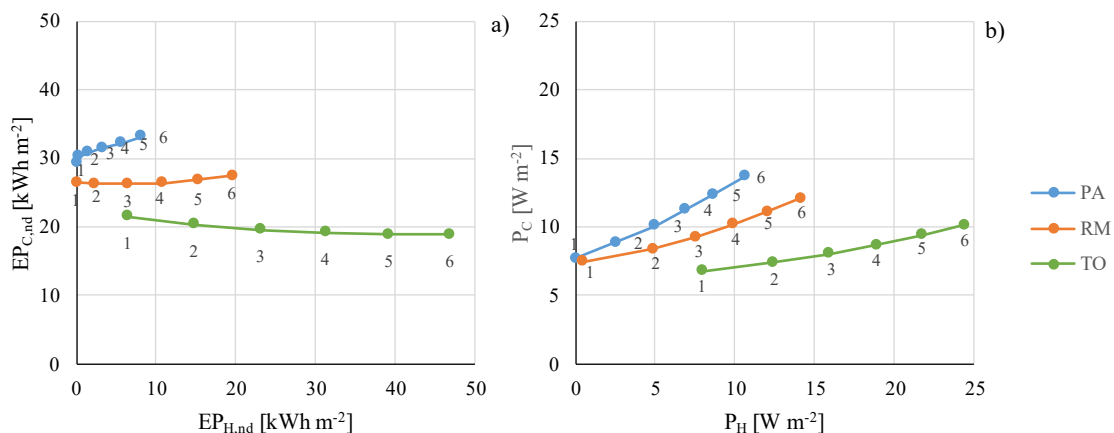


Figure 1. Net energy need (EP_{nd}) and peak power (P) for heating (H) vs. cooling (C) for the whole building and for six insulation levels.

Analysing the whole building (Figure 1), the sensitivity of the heating energy need to the insulation level is higher in the zones with higher HDD, like Turin, and generally it is more sensitive than the cooling energy need. Anyway, in Turin a reduction of heating energy need by progressively reducing the U -values corresponds to an increase of need for cooling.

Differences in the energy behaviour between the apartments are noticeable, above all in Rome and Palermo (Figure 2). In Palermo, where the CDD are higher, the influence of thermal insulation is more evident in summer than in winter and an opposite effect is revealed between the units at ground floor and those at the highest floor. Specifically, by reducing the thermal transmittance of the envelope, at ground floor the reduction of heating corresponds to an increase of the energy need for cooling, while at the highest floor the reduction of cooling is higher than the reduction of the energy need for heating.

The difference between apartments is less evident moving from Palermo to Turin, even if the hyper-insulation of the ground floor units always determines a higher energy need for cooling regardless of the climatic zone. For instance, considering a medium insulation level (level no. 4) in Turin, the difference between the cooling energy needs of the ground floor and the third floor units is greater by 68% than the difference between the respective heating needs. In Palermo, switching from insulation level no. 6 to no. 1, the cooling need is reduced by 31% for BU3B and increases by 32% for BU0C. This is due to a greater value of the solar-air temperature on the upper units, where a high level of insulation has a favourable effect. On the

other hand, the hyper-insulation of the ground floor does not allow the discharge of the accumulated heat, thus leading to an increase of the cooling need. For intermediate floors above all in Palermo, the sensitivity to the insulation level is negligible, due to a very low shape factor.

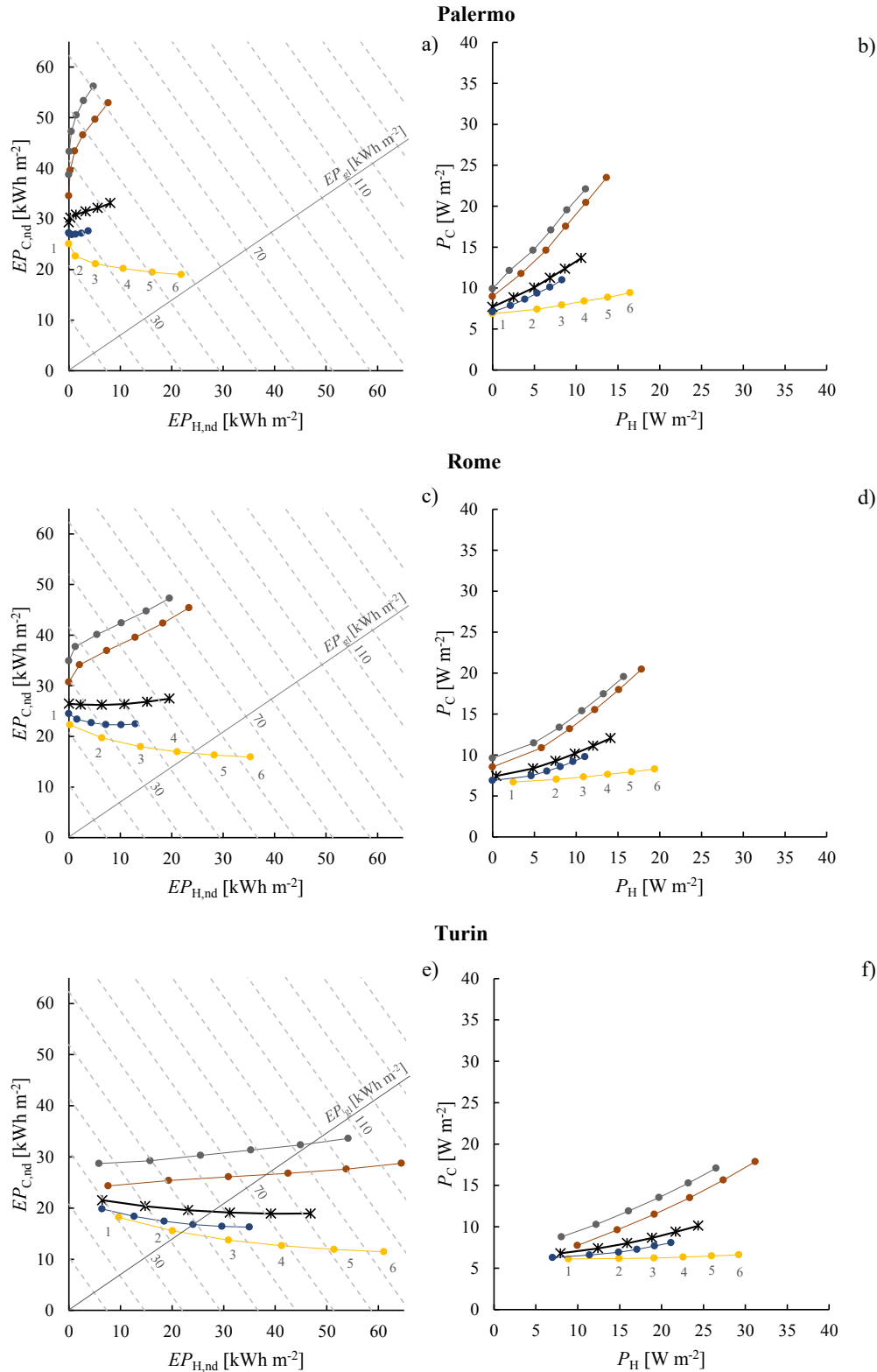


Figure 2. Net energy need (EP_{nd}) for heating vs. cooling, and overall primary energy for the whole building and for different building units, for six insulation levels.

The high differences of the energy needs between units at different storeys are also evident in the overall primary energy (EP_{gl}), so that the same EP_{gl} can be achieved by insulating the units differently. For instance in Palermo, BU3B and BU0C have the same EP_{gl} with $U = 0.1 \text{ W}\cdot\text{m}^{-2}\text{K}^{-1}$ in the former case and $U = 0.4\div 0.5 \text{ W}\cdot\text{m}^{-2}\text{K}^{-1}$ in the latter case.

Due to the imbalances between annual energy needs for heating and cooling and in the ground floor units, it would be possible to identify limit U -values below which EP_{gl} tends to increase. An example is BU0C in Palermo; by switching from level no.2 to level no.1, the same EP_{gl} is obtained ($24 \text{ kWh}\cdot\text{m}^{-2}$). Level no.2 would consist in a limit U -value for this unit.

The thermal transmittance decrease generally causes the reduction both of heating and cooling peak powers. A higher power for heating than for cooling occurs in Turin rather than in Palermo, where in addition the cooling peak power is more sensitive to the insulation level.

CONCLUSIONS

To improve the energy design of buildings, the findings of the work pointed out that, where possible, it would be desirable to differentiate the envelope requirements for each building unit in function of the geometrical properties, storey location and exposure. In such a way, the imbalances between energy needs for heating and cooling on the building energy performance due to the hyper-insulation of the envelope can be controlled and the overall EP minimised.

The analysis will be widened by investigating more use categories, glazing properties and shading positions, and assessing the primary energy through detailed models of the technical building systems, as to take into account the temporal variability of system efficiencies.

REFERENCES

- Ballarini I. and Corrado V. 2012. Analysis of the building energy balance to investigate the effect of thermal insulation in summer conditions. *Energy and Buildings*, 52, 168-180.
- Chvatal K.M.S. and Corvacho M.H.P. 2009. The impact of increasing the building envelope insulation upon the risk of overheating in summer and an increased energy consumption. *Journal of Building Performance Simulation*, 4, 267-282.
- Chvatal K.M.S., Maldonado E.A.B. and Corvacho M.H.P. 2005. The impact of envelope insulation and ventilation on summer performance. In: *Proc. of International Conference "Passive and Low Energy Cooling for the Built Environment"*, Santorini, pp. 823-828.
- European Union. 2010. Directive 2010/31/EU of the European Parliament and of the Council on the energy performance of buildings (recast).
- Italian Organisation for Standardisation (UNI). 2014. *UNI/TS 11300-1*, Energy performance of buildings, Part 1: Evaluation of energy need for space heating and cooling. (In Italian).
- Italian Organisation for Standardisation (UNI). 2016. *UNI 10349-3*, Heating and cooling of buildings – Climatic data, Part 3 (In Italian).
- Italian Republic. 2015. Ministerial Decree 26/06/2015 – Calculation methodologies of the building energy performance and minimum energy performance requirements. (In Italian).
- Italian Thermotechnical Committee (CTI). 2017. Test reference years (<http://try.cti2000.it/>).
- Murano G., Ballarini I., Dirutigliano D., Primo E. and Corrado V. 2017. The significant imbalance of nZEB energy need for heating and cooling in Italian climatic zones. *Energy Procedia*, 126, 258-265.
- Murano G., Nidasio R., Panvini A., and Terrinoni L. 2016. Le criticità nella progettazione e realizzazione di interventi di riqualificazione a nZEB: implicazioni pratiche, normative e legislative. *ENEA RdS/2016/127*, Roma. (In Italian).
- Sameni S.M.T., Gaterell M., Montazami A. and Ahmed A. 2015. Overheating investigation in UK social housing flats built to the Passivhaus standard. *Building and Environment*, 92, 222-235.
- U.S. Department of Energy's (DOE). *Energy Plus* software, v. 8.5 (<https://energyplus.net/>).
- Zinzi M., Pagliaro F., Agnoli S., Bisegna F. and Iatauro D. 2017. Assessing the overheating risks in Italian existing school buildings renovated with nZEB targets. *Energy Procedia*, 142, 2517-2524.

The effect of ambient moisture conditions on heat flux time shift and decrement factor of multi-layered walls

Nadja Bishara^{1, 2*} and Andrea Gasparella¹

¹Free University of Bozen, Italy

²KREBS+KIEFER Ingenieure GmbH, Germany

*Corresponding email: bishara.nadja@kuk.de

ABSTRACT

Thermal properties of the opaque building envelope components are crucial for limiting the energy needs of a building. In particular, dynamic thermal properties of envelope components can significantly contribute to the minimization of heat transfer through the envelope and to the appropriate utilization of the internal and solar gains. This is particularly important in the cooling operation, especially in hot climates. Previous experimental and numerical studies on the determination of dynamic thermal parameters of opaque building components neglected the influence of moisture conditions prevailing within the ambient climate. This paper utilizes a calibrated and validated dynamic heat and mass transfer model to analyse the impact of ambient moisture conditions on the determination of dynamic thermal parameters. Time shift and decrement factor are determined for different wall structures (internally insulated or externally insulated) with regard to different outdoor climatic conditions (dry and humid climate). The impact of moisture conditions on the results is analysed and assessed. The results of this study clearly show that the effect of ambient moisture conditions on time shift and decrement factor can be significant and that an application of purely thermal models will lead to inaccurate predictions of the dynamic thermal behaviour of building components.

KEYWORDS

Building envelope, moisture dependent response, heat flux time shift, decrement factor

1) INTRODUCTION

The thermal quality of opaque building envelope is a key factor in buildings whole energy performance. In order to reduce the energy consumption in the building sector and to preserve comfortable indoor conditions, heat losses and gains have to be controlled in both, new and rehabilitated buildings, which are particularly incline to overheating problems. Especially for climates with important annual cooling season, Dynamic Thermal Properties (DTP) are determined to assess the thermal performance of a building envelope and its ability to damp and delay externally impinging heat waves with respect to the building's interior. In this context, the DTP are also important indicators to prescribe efficient solutions for building envelopes.

Some researchers have already shown that, besides thermal conditions, further boundary conditions have an effect on the DTP of building components. For example Kontoleon and Bikas (2007) showed that solar absorptivity is affecting time shift and decrement factor. Moreover, a study conducted by Bishara (2017) showed that internally applied convective heat transfer conditions have a non-negligible impact on the DTP of a wooden wall structure. With regard to material moisture content, Kontoleon and Giarma (2016) showed that a certain impact of a single layer wall's moisture content on its thermal inertia parameters exists. However, the effect of hygrothermal boundary conditions on the DTP of an opaque envelope component has not been extensively investigated yet. In particular, it is not known to which extend relative humidity (RH) conditions are affecting the DTP of multi-layered envelope components.

This paper aims at a preliminary analysis of the influence of hygrothermal boundary conditions on the dynamic thermal behaviour of both, insulated and non-insulated, multi-layer walls, considering different materials and layer order.

2) METHODS

2.1) Wall structures and climatic boundary conditions

The wall structures studied in this work (see Figure 1) are similar to those analyzed with respect to thermal insulation performance by Ozel (Ozel, 2011) and Al-Sanea et.al (Sanea et.al, 2011). Case (a) is a concrete wall, 25 cm thick with external (2 cm) and internal (1.5 cm) plaster layer. In case (b), an external EPS insulation layer of 10 cm thickness is applied to the same concrete wall. Case (c) considers the same EPS insulation layer as well as an OSB layer of 1 cm thickness, installed at the internal side of the concrete wall. In a further step, two further insulation materials, namely wood fiber (WF) and mineral wool (MW) are applied, instead of the previously considered EPS layer (externally and internally, respectively).

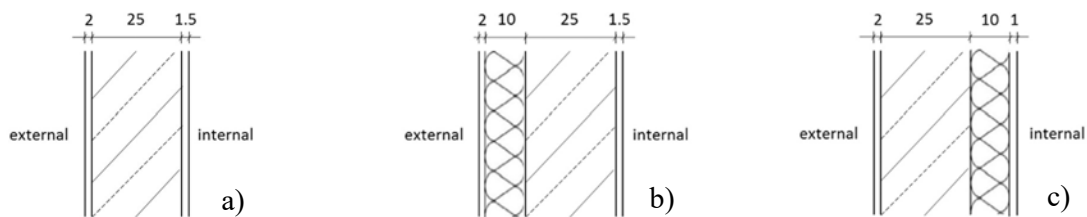


Figure 1. Investigated wall structures a) concrete wall with plaster, b) concrete wall with external EPS insulation layer, c) concrete wall with internal EPS insulation layer.

The external boundary conditions considered in this study are intended to depict summer conditions within a warm-humid (e.g. Nice, France) and a warm-dry (e.g. Madrid, Spain) European climate. The influence of radiation was neglected at this point. Internally, constant hygrothermal boundary conditions are applied (25°C, 45%RH). Both climates, climate1 (warm-humid), and climate2 (warm-dry), are shown in Figure 2a.

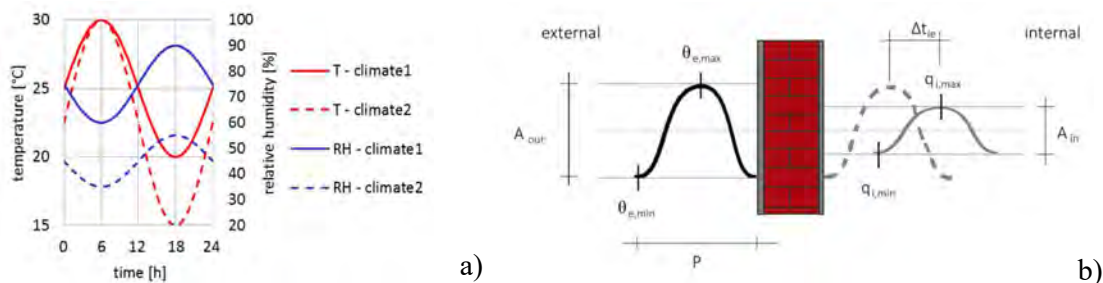


Figure 2. a) External climatic boundary conditions, b) Principal of dynamic heat wave propagation through an opaque building envelope component.

2.2) Calculation of decrement factor and time shift

The dynamic thermal behaviour of an opaque building envelope is induced by an external temperature solicitation with a period P of 24 h. This heat wave can be approximated with a harmonic function (in black in Figure 2b), which ranges from a temperature minimum ($\theta_{e,min}$) to a maximum ($\theta_{e,max}$) that define the solicitation amplitude (A_{out}). Due to storage effects that dependent upon the thermal mass of the building component, the internal response to an external temperature signal is damped and delayed. The resulting heat flux profile exhibits maximums

($q_{i,max}$) and minimums ($q_{i,min}$) with a decreasing amplitude moving to the internal surface heat flux amplitude (A_{in}). Moreover, the temporal occurrence of minimum and maximum is shifted with respect to the external original signal. This temporal shift between external and internal peak values occurrence time is the time shift (Δt_{ie}).

For the analysis of DTPs, the values of internal heat flux and external temperature are needed. They are used to determine decrement factor and time shift according to EN ISO 13786 (European Committee for Standardization, 2007), for each analysed day.

The decrement factor f is calculated by correlating periodic thermal transmittance and steady state thermal conductance:

$$f = \frac{|\hat{q}_i|}{|\hat{\theta}_e| \cdot C_s} = \frac{Y_{ie}}{C_s} \quad \text{with} \quad C_s = \frac{\phi}{(T_1 - T_2) \cdot A} \quad (1, 2)$$

The time shift Δt_{ie} is calculated as the difference of phase displacements of the first harmonics, which are φ for the external surface temperature and ψ for the internal heat flux respectively:

$$\varphi_e = \bar{\theta}_e + \theta_{e,1} \cdot \cos(\omega \cdot t + \varphi) \quad \text{and} \quad \psi_i = \bar{\phi}_i + \phi_{i,1} \cdot \cos(\omega \cdot t + \psi) \quad (3, 4)$$

$$\Delta t_{ie} = \frac{(\psi - \varphi)}{(2\pi)} \cdot 24 \quad (5)$$

2.3) Numerical simulation model

For each wall structure presented in 2.1., a two-dimensional numerical thermal simulation as well as a simulation considering heat, air, and mass (HAM) transport processes are conducted. The numerical models (thermal and HAM) are implemented within the software tool Delphin which provides a validated tool set for the representation of hygrothermal transport processes (Nicolai, 2011). This software has been applied in previous studies for analyzing decrement factor and time shift of different wall structures and under various hygrothermal boundary conditions, whereas a very good correlation with laboratory measurement results could be achieved (Bishara, 2017). For climate1, initial conditions are set to 25°C and 80% RH. In case of climate2, initial conditions are 22.5°C and 80% RH. Since the initial moisture content may also affect the calculation results, the same value was chosen for both climates in order to ensure comparable calculation conditions. The material data are taken from the extensive Delphin material database. Output values of temperature and heat flux are generated each minute of calculation, for a simulation period of 10 days. In total, a set of 28 simulation cases is analysed.

3) RESULTS AND DISCUSSION

Decrement factors are calculated, considering the steady thermal conductances, which are provided in Table 1. Time shifts and decrement factors are calculated for each day of the analysis and the results are evaluated for the 10th day, when steady periodic conditions have been reached for each of the analysed cases.

Table 1. Steady state thermal conductances.

	concrete	EPS ext.	EPS int.	WF ext.	WF int.	MW ext.	MW int.
C_s [W/m ² K]	5.46	0.339	0.333	0.391	0.384	0.374	0.367

The decrement factor results for climate1 are shown in Figure 4a. Each of the three wall structures show deviations between thermal and hygrothermal simulation results. In case of the concrete wall, the thermal simulation leads to a decrement factor overestimation of 2.5%. In case of the EPS insulated walls, the thermal values are underestimated (external 7.1%, internal

1.8%). With regard to time shift, differences between thermal and hygrothermal results are visible, as well. They are lowest for the concrete wall without insulation (thermal overestimation of 0.5%), and highest for the case of external insulation (thermal underestimation of 1.6%).

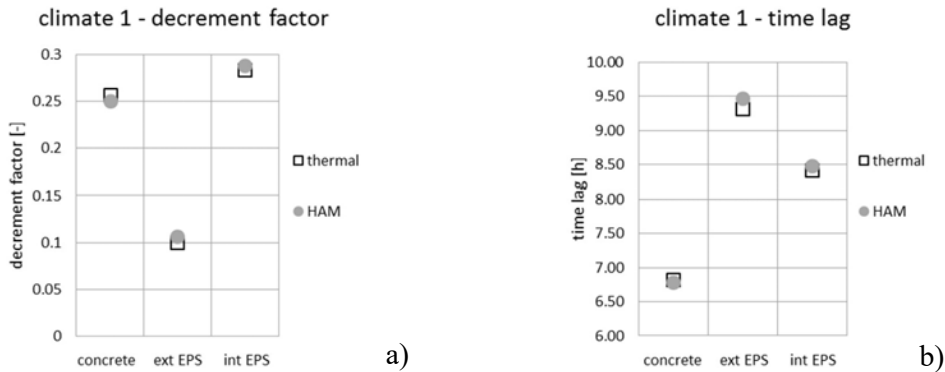


Figure 4. Results for climate 1: a) decrement factor, b) time shift

The moisture gradient, which induces through over the wall components due to the different ambient humidity conditions, affects the energy transport. Therefore, the concrete wall's internal surface heat flux is reduced, whereas the insulated wall variants show increased heat flux values. It is well known that porous materials show a relation between material moisture content and thermal conductivity, which is rising with increasing moisture content. Initial material moisture contents for both simulations, thermal and hygrothermal, is set to 80% RH. The Delphin software automatically scales the initial thermal conductivity of all materials to the given humidity reference value. Consequently, the initial thermal conductivities applied to the thermal numerical model remain at a high level, whereas they decrease during the HAM simulations due to the lower ambient humidity values. As a result, time shift values of the hygrothermal simulation are higher than those of the thermal analysis.

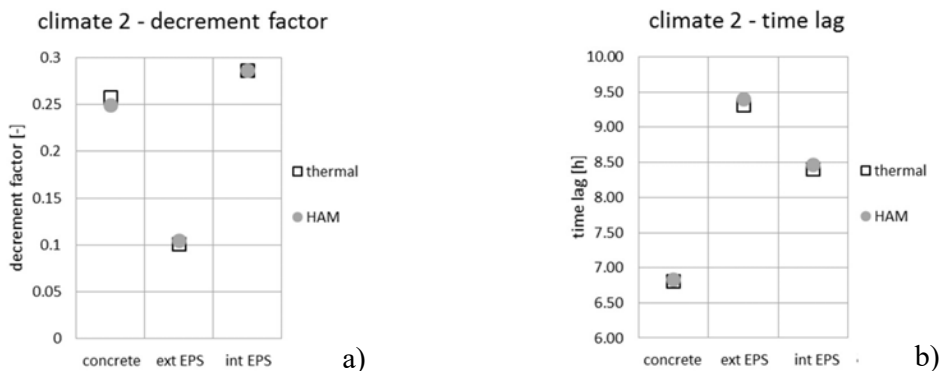


Figure 5. Results climate 2: a) decrement factor, b) time shift

With regard to climate 2 external conditions, the difference between thermally and hygrothermally determined decrement factor is about 3.3% for the concrete wall. Moreover, the thermal and hygrothermal time shift values are in accordance with each other.

For both insulation variants, the deviations are minimized compared to the climate1 results. The decrement factor deviation for an external insulation variant is about 3%, and for an internal insulation variant 0.2%. The deviation is small too, in case of time shift (<1%).

With climate2, the partial pressure difference between indoors and outdoors is less than with climate1 ambient conditions. Therefore, the differences between thermal and hygrothermal calculation of decrement factor and time shift are also smaller.

Figure 6 shows the thermally and hygrothermally determined decrement factors and time shifts for the different insulation materials and in dependence of different insulation layer positions. It can be seen from Figure 6a, that for all considered insulation materials under climate1 conditions, external insulation is promoting lower decrement factors, and thus a better heat insulation capability, than internal insulation. At the same time, installing EPS insulation leads to the smallest difference between thermal and HAM simulation results. Differences in case of wood fiber are 48.8% for external and 39.3% for internal installation. Deviation is highest for externally installed mineral wool, reaching 63.9%, and lowest for internal installation (32.0%). Also with regard to time shift, external insulation promotes better results than internal insulation (see Figure 6b). Again, deviations between thermal and hygrothermal values are lowest for EPS. They are higher in case of wood fiber (external 8.1%, internal 8.3%) and highest in case of mineral wool (external 12.7%, internal 13.3%).

Differences between thermal and hygrothermal values are relatively low for a wall being insulated with EPS. The major differences between thermal and hygrothermal results in case of a wall being insulated with wood fiber or mineral wool are due to a higher material porosity of these insulating materials, compared to EPS. Thus, moisture diffusion is higher and leads to higher moisture contents and thus to increased thermal conductivity and thermal diffusivity values. Consequently, energy transport is enhanced, which raises decrement factor and minimizes time shift.

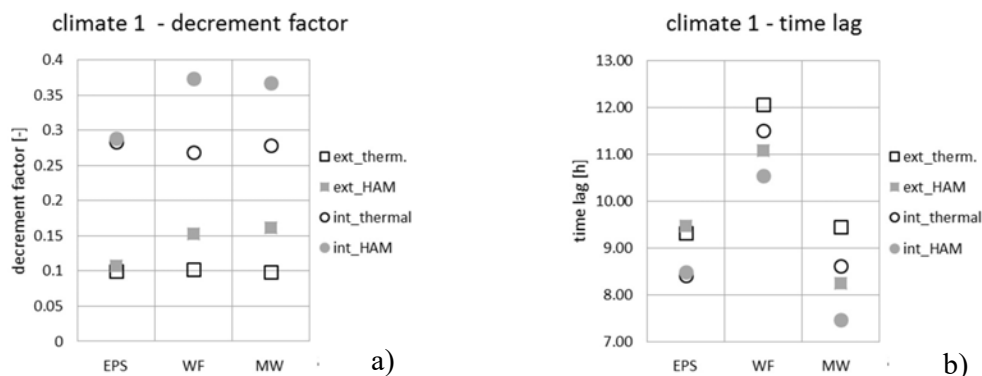


Figure 6. Climate 1 – Results for different insulation materials and layer position.

External insulation achieves preferable results under climate2 conditions too, as can be seen from Figures 7a and 7b. Differences between thermal and hygrothermal simulation are lowest for the wall structure with EPS insulation. In case of wood fiber insulation, the difference between thermally and hygrothermally determined decrement factor is 35.7% in case of external insulation, and 36.9% in case of internal insulation. For the external application of mineral wool, the decrement factor difference is even higher, being 67.9%, whereas internally applied mineral wool leads to a difference of 17.2%.

The time shift analysis under climate2 external conditions also reveal differences between thermal and hygrothermal values. They are low for the concrete wall and higher in case of wood

fiber insulation (external 7.6%, internal 8.0%). In case of the mineral wool insulation, deviations are highest (external 11.4%, internal 9.5%).

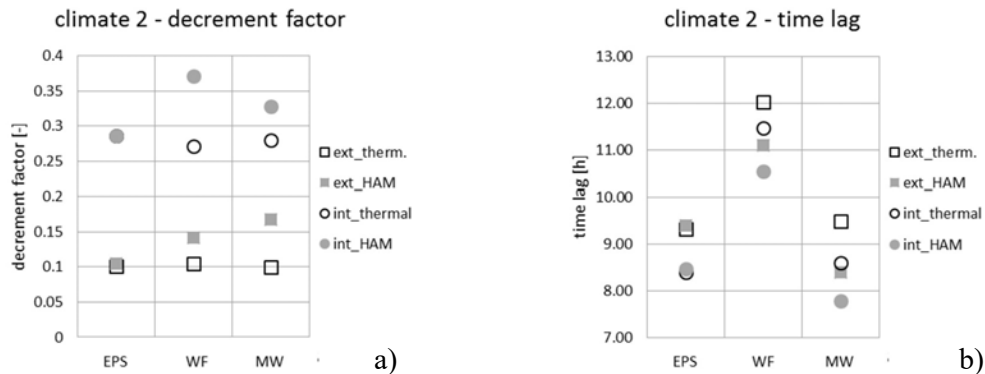


Figure 7. Climate 2 – Results for different insulation materials and arrangement.

4) CONCLUSIONS

In the present work, the influence of ambient moisture conditions on the determination of decrement factor (DF) and time shift (TS) was analyzed. In this context, various multi-layered wall structures were investigated by means of thermal and hygrothermal numerical simulations. The results clearly showed that ambient relative humidity affects dynamic thermal characteristics of the analyzed wall structures. Especially when porous materials are considered, a purely thermal determination of DF and TS leads to erroneous results. The errors in these cases were up to 68% in terms of DF, and up to 13% in case of TS. As a result, this can have a negative effect on the predicted cooling demand of a building. Future research will focus on an analysis of real ambient moisture conditions and their impact on dynamic thermal characteristics of various wall structures. In this context, also the initial material moisture content will be varied in order to determine its impact on the hygrothermal solutions. Moreover, different insulation thicknesses and the impact of external radiation will be regarded.

REFERENCES

- Bishara N (2017) Measurement of dynamic properties of building envelope materials and components - methods, tools, instruments and application. *PhD Thesis*, Free University of Bozen (Italy), 162 pages.
- European Committee for Standardization (2007). *EN ISO 13786*: Thermal performance of building components - Dynamic thermal characteristics - Calculation methods.
- Kontoleon KJ and Bikas DK (2007) The effect of south wall's outdoor absorption coefficient on time shift, decrement factor and temperature variations. *Energy and Buildings* 39(9): 1011–1018.
- Kontoleon KJ and Giarma C (2016) Dynamic thermal response of building material layers in aspect of their moisture content. *Applied Energy* 170: 76–91.
- Nicolai A (2011) Towards a Semi-Generic Simulation Framework for Mass and Energy Transport in Porous Materials. In: *Proceedings of the 9th Nordic Symposium on Building Physics*, Tampere, p. 559–66.
- Ozel M (2011) Thermal performance and optimum insulation thickness of building walls with different structure materials. *Applied Thermal Engineering* 31: 3854–3863
- Al-Sanea SA and Zedan MF (2011) Improving thermal performance of building walls by optimizing insulation layer distribution and thickness for same thermal mass. *Applied Energy* 88: 3113–3124

Conceptual framework for improved management of risks and uncertainties associated with the performance of the building enclosure

Ivar Björnsson^{1,*} and Miklós Molnár²

¹Division of Structural Engineering, Lund University, Sweden

*Corresponding email: ivar.bjornsson@kstr.lth.se

ABSTRACT

The building enclosure has a substantial impact on the overall performance of a building, especially in relation to moisture safety, energy use, environmental footprint and economy. Although the introduction of novel building technology can increase the risk of failures in terms of reduced building performance, failures can also result from the recurrence of past mistakes while using well established building technologies. This indicates that the dissemination of existing knowledge, often documented in project reports, handbooks or experience databases, is not always carried out in an efficient way. One way of addressing the issue is by increasing awareness concerning potential risks and uncertainties in the building process. The current paper presents a conceptual framework which has the broader aim of promoting risk awareness, improving the treatment of uncertainties and ultimately facilitating risk informed decision making during the modern design and construction process. The framework incorporates risk treatment with BIM based design and construction and could be supported by existing failure/damage and/or experience databases or knowledge systems.

KEYWORDS

Building performance, risk management, BIM, conceptual framework.

INTRODUCTION

There is currently an imbalance with respect to the treatment of risks and uncertainties in the design and construction of our built environment. While safety formats that aim at ensuring, and assuring, adequate safety against structural failures and malfunction are in place (e.g. CEN 2002), the treatment of risks and uncertainties related to the performance of the building envelope, indoor climate energy use, etc., lags behind. One important factor is that there are less severe consequences associated with building performance failures compared with structural failures. On the other hand, building performance risks are more long term and have a clear negative impact on durability, environment and the end users' economy. In addition, the predicted performance of a building, determined during design or through simulation, may in some cases deviate significantly from the actual observed behaviour of the building; e.g. the deviation of observed and predicted performance of so called green rated buildings (Lee & Hensen, 2015). These deviations highlight the underlying uncertainties which will require consideration in order to more appropriately treat building performance risks.

Building information modelling (BIM) is widely used by the architectural, engineering and construction (AEC) industry. There are a number of ongoing efforts to extend the traditional use of BIM to cover other aspects of building design and construction including engineering risk management (Zou et al., 2017) and building performance (El-Diraby et al., 2017). BIM is considered as having the potential to generate more design alternatives, enabling an optimization of, e.g., a building's energy performance (Habibi, 2017; Li et al., 2017). Another

area of focus for research and development efforts is quantification of the sustainability or robustness of building design (Jelle et al 2013).

Efforts have been made to integrate a risk aware approach into the analysis of building life cycle aspects using BIM (Pruvost and Scherer, 2017). Design alternatives can be re-analyzed in the light of identified uncertainties and simulation results. Analysis of risks is often carried out by development of ontologies and the use of semantic web technology for representation of the risks (Ding et al., 2016). Main difficulties associated with an ontology and semantic representation approach are, however, that the complexity of the semantic representation of risk knowledge. There is a need for collaboration between the experts creating the BIM models and those working with risk interpretation; these types of approaches are often time-demanding.

This paper presents a conceptual framework for the treatment of building performance risks, with focus on the durability of the building envelope, using BIM. The framework has been developed taking into consideration the following aspects:

- Existing knowledge base concerning risks of conventional building solutions is vast.
- The dissemination of this knowledge to avoid failures may be poor or lacking.
- Risk awareness among AEC professionals may not be adequate in all cases.
- Uncertainties concerning building performance may be difficult to treat numerically.

To help address these issues, the framework aims to promote critical reflection rather than delivering detailed answers or metrics; provide support through all phases of the design and construction process, and; improve transparency and traceability of the risk management process in practice. In the current paper, theoretical aspects are highlighted while some discussions concerning the practical implementation of BIM risk management are provided.

INTEGRATING BIM & RISK MANAGEMENT

There is significant interest by researchers to integrate risk management in AEC through BIM and BIM-related technologies. A survey by Zou et al. (2017) reviewed a number of these efforts and identified some common approaches including the use of BIM to implicitly improve risk management, automatic rule checking as well as reactive and proactive IT-based systems to manage safety risks. In terms of application, a vast majority of the existing approaches focus on construction personnel safety risks (e.g. Ding et al., 2016). There are some exceptions, however, including Pruvost and Scherer (2017) who investigated risks in the building life cycle through an explicit consideration of uncertainties in energy simulations; i.e. quantified uncertainty modelling. A difficulty with applying this type of approach in practical cases is that it requires a stochastic model representation; i.e., a statistical description of the model parameters. Realizing such representations for all relevant risk scenarios may be difficult in practice due to a lack of reliable data and the nature of the uncertainties involved (e.g. the prediction of human behaviour in dwellings). Furthermore, the evaluation of the resulting quantified risk metric will require an objective risk based acceptance criteria and it is unclear how one can be obtained which is generally applicable for all building performance risks.

Although there is a great deal interest towards using BIM or BIM-related technologies to facilitate risk management, there are limitations of existing approaches to consider building performance risks. To start, unlike construction safety risks, which are the focus of many existing efforts, there is a discontinuity in the process of managing building performance

risks. The former is often conducted by a dedicated team of practitioners while the latter is affected in varying degrees by the different process actors (architects, structural designers, HVAC engineers, etc) and can also be influenced by the end-users. There is nothing to ensure an effective knowledge transfer between process actors in terms of addressing these risks. In addition, design and construction decisions that affect building performance risks are not necessarily made in light of these risks. This may be due to a lack of knowledge or simply that they are overlooked or neglected as a result of focus on other integral aspects of the construction process; e.g. time pressure or economic constraints.

CONCEPTUAL FRAMEWORK

In reviewing building failures it is common that the unfavourable influences leading to failure were avoidable. Failures – generally defined as any unwanted deviation from design expectations – can often result from such influences being subjectively unknown, inadequately treated or overlooked during the design or construction process (Schneider, 1997; Breyse, 2012). This highlights a need for more effective knowledge transfer and management within the AEC community. In light of this, a conceptual framework for improving the management of building performance risks is considered which integrates risk relevant information from existing sources with BIM tools. The primary aim is to increase the awareness of risks by the process actors (architects, engineers, constructors) throughout the building process, especially during the early design stages, and facilitate the treatment of potential building performance risks during the entire design process. It is proposed that the framework should facilitate risk informed decision making through a cognitive loop as shown in Figure 1. Focus is on building performance risks resulting from poor or uninformed decisions made during the design and construction; a treatment of risks related to e.g. human behaviour in dwellings requires special attention.

The proposed framework intends on making information concerning technical solutions with long term risks available in BIM-software in order to provide decision support for improved risk management. The following objectives are highlighted:

- Improve risk awareness and promote critical reflection.
- Provide access to existing risk relevant knowledge *throughout all project phases*.
- Improve transparency and traceability.
- Improve risk communication & knowledge transfer *throughout all project phases*.

It is envisioned that the framework shall be integrated with existing BIM platforms as an add-on or independent application. Design decisions concerning building solutions (facade materials, drainage, etc) shall consider potential building performance risks and this requires feedback to the process actors. A risk filter is thus required which can review construction objects within the BIM software and provide output, while citing source materials that describe potential risks, present possible causes and consequences, and describe suitable mitigation and avoidance measures. To enable this filtration, an IT database could be constructed which utilizes existing experience and knowledge concerning performance failures; i.e. a database containing relevant risk information. In contrast with earlier attempts (Ding et al., 2016) risk information shall be made available to construction objects structured according to existing, commercially available, building classification system(s) such as BSAB (<https://bsab.byggjtjanst.se/>) or Uniclass (<https://toolkit.thenbs.com/articles/classification>).

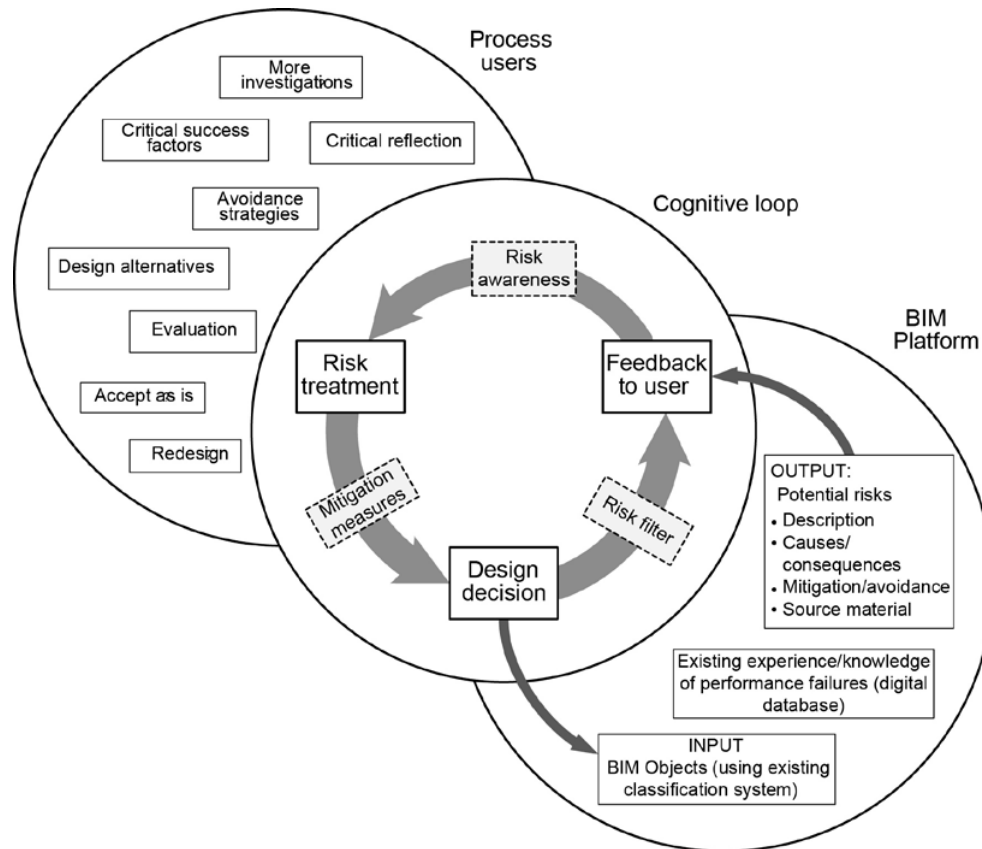


Figure 1. Illustration of Conceptual Framework showing a cognitive loop connecting the BIM platform with process users for integrated risk informed decision making

Commonly, risk relevant information is contained within textbooks or published papers (e.g. Douglas and Ransom, 2013; Molnár et al, 2016) although online or electronic databases may also be available (e.g. Imhof 2004). The relevance and reliability of information to be used as a basis for risk informed decision making has to be secured. In some cases, this type of data may be management by dedicated agencies with integrated quality control processes. One example from the Nordic region includes BYG-ERFA in Denmark (www.byg-erfa.dk), which is an independent organization collecting and disseminating quality controlled knowledge concerning building technology failures through traditional information channels such as print and pdf.

Feedback to the user shall be presented in terms of identified risk scenarios providing information concerning the following aspects:

- Description of potential risk (e.g. damage type)
- Potential causes and factors influencing initiation
- Possible consequences of the identified risk
- Possibilities for risk avoidance and mitigation strategies
- Link to source material and reliability of information

The proposed risk analysis steps might also serve as a structure enabling integration of the risk information into a digital knowledge database.

ILLUSTRATIVE EXAMPLE

In what follows, an illustrative example is provided which highlights the type of risk information that could be useful for improving the treatment of risks in the design of masonry veneers, see Table 1. The specific risk concerns frost damage of the bricks, that might occur due to the combined effects of high exposure to wind driven rain, frequent freeze-thaw cycles and poor frost resistance of the bricks.

Table 1. Risk relevant information for case: Frost Damage in Masonry Facades

Description	Clay brick veneer with frost damage. Brick exhibiting exfoliation & spalling.
Potential causes	High exposure to wind driven rain in combination with frost-thaw cycles. Poor frost resistance of the clay bricks.
Mitigation/ avoidance	Moulded bricks more frost resistant than extruded bricks; extrusion causes lamination parallel to external surface constituting zones of weakness. Deep-fired bricks more frost resistant than low-fired bricks Recommended to choose brick type considering intended conditions of usage.
Potential consequences	Degradation on large scale. Impaired aesthetics. Demolition of veneer followed by replacement with more suitable bricks or another type of facade.
Additional relevant information	The upper parts of facades are more exposed than lower parts. Current European standards concerning frost resistance of clay brick EN 771-1 requires that veneers exposed to driving rain are built with bricks with high frost resistance (class F2); conforming to the provisions of this standard do however not guaranty complete security against frost damage.
Source material	<i>Damage atlas. Expert system for the evaluation of the deterioration of ancient brick masonry structures.</i> ISBN 3-8167-4702-7. <i>Avoid mistakes in masonry and render</i> (Molnár et al 2016).
Reliability of source data: High	

Typically, the architect will decide the brick type to be used in a brick veneer. Thus, the risk management system can issue a warning to the architect concerning the potential risk for frost damage. The architect is provided an opportunity to investigate whether the selected brick type, under the given exposure conditions, is prone to frost damage and determine whether the original design decision should be altered. A similar assessment can be carried out by the contractor or a building physics expert, if involved in the project.

CONCLUSIONS & DISCUSSIONS

The current paper presents a conceptual framework for the treatment of risks related to poor building performance considering modern building applications and specifically integration with digital tools such as BIM. The framework aims to improve the treatment of these types of risks to reduce potential impacts to facility owners and end users in general and the environment in special.

Although the framework from this paper addresses issues of improved risk management in building design on a theoretical level, an implementation plan is underway which has identified important issues concerning practical applications. These issues include the establishment and management of the risk relevant knowledge base, the classification of BIM objects to enable risk filtration, as well as the evaluation of the approach in practical cases. One important aspect of implementing the framework in practice is quality control. This is

significant both in relation to the information which will provide the basis for risk management as well as the process of risk treatment in itself. The former could be achieved by having in place a technical review of risk information by experts within relevant fields of engineering. The latter should provide some mitigation concerning the risk of gross human error in whatever form. Further development of the framework shall assess the effectiveness of the framework in practical application and this process should highlight inherent factors for improved quality control in relation to risk management in the building process.

One anticipated difficulty associated with the implementation of the framework is related to cases of innovative, complex or uncertain (ICU) solutions; as strong focus on risk issues might have an inhibiting effect on introduction of ICU solutions. Thus, some opposition is expected from material suppliers, constructors, etc., if these parties/actors feel that the framework will hinder effectivization of the construction process. The issue of how risks associated with ICU solutions can be introduced with acceptable risk levels and under full transparency for all stakeholders must be considered explicitly. As a direct consequence, possibilities should be created for continuous updating of the risk relevant knowledge base while a risk neutral perspective may be initially taken with regards to ICU solutions until more data and experience are available.

ACKNOWLEDGEMENT

Financial support from the Swedish research and innovation programme Smart Built Environment (www.smartbuilt.se) is acknowledged.

REFERENCES

- Breysse D. 2012. Forensic engineering and collapse databases. *Forensic Eng.*, 165(FE2), 63-75.
- CEN. 2002. *EN 1990, Eurocode – Basis of structural design*. European Committee for Standardization.
- Ding L.Y., Zhong B.T., Wub S., et al. 2016. Construction risk knowledge management in BIM using ontology and semantic web technology. *Safety Science*, 87, 202–213.
- Douglas J. and Ransom B. 2013. *Understanding building failures*. 4th Ed. Routledge.
- El-Diraby T., Krijnen T., and Papagelis M. 2017. BIM-based collaborative design and socio-technical analytics of green buildings. *Automation in Construction*, 82, 59-74.
- Imhof, D. 2004. Risk assessment of existing bridge structures. *PhD Thesis*: University of Cambridge, UK.
- Jelle B.P., Sveipe E., Wegger E., et al. 2013. Robustness classification of materials, assemblies and buildings. *Journal of Building Physics*, 0(0), 1-33.
- Lee B. and Hensen J.L.M. 2015. Developing a risk indicator to quantify robust building design. *IBPC 2015, Energy Procedia*, 78, 1895-1900.
- Li X., Wu P., Qiping Shen G., et al. 2017. Mapping the knowledge domains of Building Information Modeling: A bibliometric approach. *Automation in Constr.*, 84, 195-206.
- Molnár, M., Jönsson, J. Sandin, K., Gustavsson, T. 2016. Avoid mistakes in masonry construction (in Swedish). The Swedish Construction Industry's Research Fond.
- Pruvost H. and Scherer R.J. 2017. Analysis of risk in building life cycle coupling BIM-based energy simulation and semantic modeling. *Creative Construction Conf. 2017, Primosten, Croatia*.
- Schneider J. 1997. *Introduction to safety and reliability of structures*. International Association for Bridge and Structural Engineering.
- Zou Y., Kiviniemi A., and Jones S.W. 2017. A review of risk management through BIM and BIM-related technologies. *Safety Science*, 97, 88-98.

Effect of Economic Indicators on Cost-Optimal Energy Performance Levels of Residential Buildings Retrofits in the Mediterranean Region of Turkey

Neşe Ganiç Sağlam^{1,*}, A. Zerrin Yılmaz² and Stefano P. Corgnati³

¹Ozyegin University, Turkey

²Istanbul Technical University, Turkey

³Politecnico di Torino, Italy

*Corresponding email: nesegetic@gmail.org

ABSTRACT

This study aims to analyse the effect of economic indicators on cost-optimal levels of residential building retrofits in Mediterranean region of Turkey. Sensitivity analyses were applied on the cost-optimality calculation results for the residential reference building. The sensitivity analyses address discount rate and potential investment cost decreases. Results reveal that 6% variation in the discount rate corresponds to more than 30 kWh/m²y difference in the primary energy consumption of the cost-optimal solutions. Potential investment cost decreases for certain retrofit measures are also effective on identified cost-optimal levels and subsidy opportunities appear as an effective tool to achieve higher energy efficiency in existing buildings and to stimulate building energy retrofits.

KEYWORDS

Residential building retrofits, Building energy efficiency, Cost-optimal analysis, Economic indicators, Subsidy opportunities.

INTRODUCTION

Cost-optimality concept, introduced by the European Commission (EC), is one of the key determinants driving policy and targets related to energy efficiency of European building stock (2016). By means of this concept, the Commission expects gradual progress in building energy performance requirements towards nearly-zero energy building (NZEB) target (2013).

The cost-optimality concept mainly assesses energy consumption levels of buildings by associating them with the corresponding costs occurred as a consequence of energy consumption and other expenses linked with components and systems influencing the energy performance of buildings. Having regard to Directive 2010/31/EU (EPBD Recast), EC introduced a methodology framework representing this assessment procedure in 2012 (The European Parliament and the Council of the European Union, 2010; The European Parliament and the Council of the European Union, 2012). This methodology framework requires to couple energy performance and cost calculations to identify the cost-optimal level for Reference Buildings (RBs) representing the building stock. Sensitivity analysis is an important stage of this methodology since it has the potential to reveal outcomes contributing further policy and targets. It displays the alteration in cost-optimal solutions under different economic situations and options.

The specific focus of this study is on the sensitivity analyses directed to the effect of economic indicators and possible investment cost decreases on cost-optimal energy performance level of building retrofits. Towards this aim, retrofit alternatives for a high-rise residential reference building in Mediterranean region of Turkey was analysed. Since the main focus is on the sensitivity analyses, previous stages of cost-optimality calculations are

explained briefly in order to keep entirety. A detailed information about the analysed reference building and initial stages of cost-optimal calculation procedure for this building can be found in research of Ganiç Sağlam et al. (2017).

The procedure presented in this study responds challenges faced in consequence of unsteady economic indicators that extend the range of aspects required to be considered in determination of future energy efficiency targets. It also considers energy retrofit of identical high-rise residential buildings constructed without considering the character of Mediterranean climate they face with. The adapted cost-optimality calculation procedure is presented below together with the sample implementation and policy implication.

METHOD

This study mainly follows the perspective of cost-optimal methodology framework and implements it for residential reference building retrofit actions.

The Reference Building

The analysed reference building (RB) represents high-rise apartments constructed between 1985 and 1999 in Turkey. As shown in Figure 1, it has an unconditioned basement and 12 superior floors. Overall heat transfer coefficients of building envelope components are $1.04 \text{ W/m}^2\text{K}$ and $1.09 \text{ W/m}^2\text{K}$ for external wall types, $1.25 \text{ W/m}^2\text{K}$ for basement ceiling and $0.71 \text{ W/m}^2\text{K}$ for attic slab. The windows consist of double glazing with polyvinyl chloride frame. Overall heat transfer coefficient of the window glazing (U_{window}) is $2.9 \text{ W/m}^2\text{K}$, visible transmittance (T_{vis}) is 0.80 and solar heat gain coefficient (SHGC) is 0.75. Internal heat gains including occupancy, activity level and appliances were set to represent recent Turkish family structure surveys and accordingly, it is assumed as each apartment flat accommodates a family consisting parents and two children.

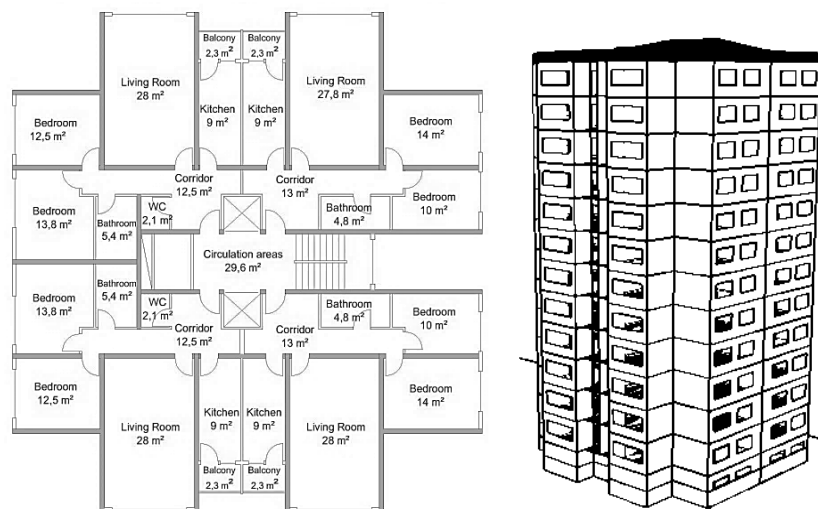


Figure 1. Typical floor plan and the geometry of the reference building.

The RB has a central natural gas boiler and radiators. The nominal thermal efficiency of the boiler is 80%. The cooling energy demand is met by individual split air conditioners using electricity. Seasonal energy efficiency ratio of the split air conditioners are 5.8. Domestic hot water (DHW) system of each flat is individual electric water heater with 80% efficiency. The heating and cooling systems were assumed as being operated continuously with 20°C and 26°C set points respectively. Air change rate is assumed as 0.5 h^{-1} (Yilmaz et. al, 2015).

Lighting system provides 200 lux illuminance level for kitchen, 300 lux for children bedroom and 100lux for living room, bedroom, corridor and bathroom with compact fluorescent lamps.

Energy efficiency measures

Various energy efficiency measures referring to building envelope and building energy systems were applied on the RB. The retrofit measures shown in Table 1 were applied to the RB both as individual retrofit measures and as packages of measures combining these individual retrofits. 472 retrofit scenarios were analysed in total.

Table 1. Retrofit measures applied to the RB.

	Definition of the retrofit measure
IN	Thermal insulation applied on external walls (W), floor (F), roof (R) or on the whole envelope (E). Different levels of thermal insulation result in following overall heat transfer coefficients: IN1: $U_{\text{wall}}=0.60 \text{ W/m}^2\text{K}$, $U_{\text{roof}}=0.39 \text{ W/m}^2\text{K}$, $U_{\text{floor}}=0.66 \text{ W/m}^2\text{K}$ IN2: $U_{\text{wall}}=0.48 \text{ W/m}^2\text{K}$, $U_{\text{roof}}=0.32 \text{ W/m}^2\text{K}$, $U_{\text{floor}}=0.48 \text{ W/m}^2\text{K}$ IN3: $U_{\text{wall}}=0.31 \text{ W/m}^2\text{K}$, $U_{\text{roof}}=0.18 \text{ W/m}^2\text{K}$, $U_{\text{floor}}=0.29 \text{ W/m}^2\text{K}$ IN4: $U_{\text{wall}}=0.16 \text{ W/m}^2\text{K}$, $U_{\text{roof}}=0.11 \text{ W/m}^2\text{K}$, $U_{\text{floor}}=0.17 \text{ W/m}^2\text{K}$
GL	Window glass replacement. Following glass alternatives were considered: GL1: $U_{\text{window}}=1.8 \text{ W/m}^2\text{K}$, $T_{\text{vis}}=0.79$, $\text{SHGC}=0.56$ GL2: $U_{\text{window}}=1.6 \text{ W/m}^2\text{K}$, $T_{\text{vis}}=0.79$, $\text{SHGC}=0.56$ GL3: $U_{\text{window}}=1.6 \text{ W/m}^2\text{K}$, $T_{\text{vis}}=0.71$, $\text{SHGC}=0.44$ GL4: $U_{\text{window}}=1.3 \text{ W/m}^2\text{K}$, $T_{\text{vis}}=0.71$, $\text{SHGC}=0.44$ GL5: $U_{\text{window}}=1.1 \text{ W/m}^2\text{K}$, $T_{\text{vis}}=0.71$, $\text{SHGC}=0.44$ GL6: $U_{\text{window}}=0.9 \text{ W/m}^2\text{K}$, $T_{\text{vis}}=0.69$, $\text{SHGC}=0.48$ GL7: $U_{\text{window}}=0.9 \text{ W/m}^2\text{K}$, $T_{\text{vis}}=0.63$, $\text{SHGC}=0.39$
SHD	SHD1: Fixed aluminium shading device installation: 60cm width overhang or fins. SHD2: Installation of external semi-transparent textile blinds.
BOI	Central boiler replacement with a condensing boiler having 95% thermal efficiency.
RF	Replacement of the existing heating system with radiators to radiant floor system
CHW	Change of the individual domestic hot water systems to the central hot water system.
AC	Upgrade SEER value of split type air conditioners to 8.5 kWh/kWh by replacement.
VRV	Installation of a central variable refrigerant volume (VRV) system in substitution for split air conditioners. Gross rated cooling coefficient of performance (COP) is equal to 3.1.
LED	Installation of LED lamps to provide same illuminance levels in the spaces.
SP	Installation of 48 solar thermal panel at roof with 120m ² total gross area.
PV	Installation of photovoltaic system at roof with 11 kW rated power

Energy performance calculations

Energy performance of the RB under the retrofit scenarios were calculated using conduction transfer function algorithm in EnergyPlus building energy simulation tool. The thermal model constituted for the calculations regards each flat as a thermal zone and the common circulation areas as different thermal zones at each floor. Energy consumptions were calculated for space heating and cooling, lighting and DHW. In order to obtain results in primary energy, national primary energy conversion factors, 1 for natural gas and 2.36 for electricity, were used. Calculated primary energy consumption of the RB is 7.7 kWh/m²y for space heating, 92kWh/m²y for space cooling, 30.6 kWh/m²y for domestic hot water, 28.8 kWh/m²y for lighting and 1.9 kWh/m²y for fans and pumps.

Global cost calculations

Global cost reflects the present value of the sum of investment, replacement, maintenance and operation costs and residual value of the building. The calculations were made using Net Present Value Method (NPV) according to EN15459 standard (CEN, 2007). The fixed

expenses and the costs related to the building elements that does not affect the energy performance of the building were not included in the cost calculations. Initial investment costs of retrofit measures can be found in research of Ganiç Sağlam et al. (2017) as indicated above.

Since the calculation beginning year is 2015, prices of that year were considered in this study. Market costs were used for investment costs of the system and components. For energy costs, average unit prices of the year were used. Tax included prices are 0.1213 €/kWh for electricity and 0.0368 €/kWh for natural gas in Antalya. For the economic rates, averages of the last five years were considered. In this context, inflation rate (R_i) is 8.054% and market interest rate (R) is 14.3%. Using these average economic rates and Equation 1, real discount rate (R_R) was calculated as 5.78. Calculated global cost of the RB is 114.9 €/m².

$$R_R = \frac{R - R_i}{1 + R_i} \quad (1)$$

Determination of cost-optimal energy performance level

Cost-optimal level, the energy performance level which results in minimum global cost for the RB, is determined by comparing the primary energy consumption and global cost results obtained for RB retrofit scenarios. Findings are presented in Results section below.

Sensitivity Analyses

Effects of the alterations in the discount rate and potential investment cost decreases on the cost-optimal results were examined within the sensitivity analyses. Besides the calculated discount rate (5.78%), the sensitivity analyses focused on two different discount rate alternatives: 3% as required by EU regulation and 9%.

Sensitivity analyses on investment cost decrease focused on a discount which is equal to value added tax (VAT) of the retrofit investments. Although the analyse seems as focusing on tax exemption, the same amount of investment cost decrease may also be obtained by autogenous decrease in the cost or as the result of technological development or may be triggered by other subsidy and incentives. In the analyses, effect of investment cost decreases for VRV (installation of central variable refrigerant volume system) and SP (installation of solar thermal system) measures were analysed since these measures were seen as the opportunity for decreasing the global cost of the retrofit scenarios which were slightly higher in comparison to the cost-optimal scenario. These options were also analysed under different discount rates.

RESULTS

Results obtained by the cost-optimality calculations are presented in Figure 2. The cost-optimal result was achieved by the retrofit package combining GL7, CHW, LED and PV retrofits. This package results with 96.4 kWh/m²y primary energy consumption and 97.8 €/m² global cost. This package provides 40% energy saving and 26% cost saving with 4.3 years payback period. By 4.6 €/m² higher global cost afforded for VRV and SP measures, 52.6 kWh/m²y primary energy consumption level can be achieved. Further retrofit measure addition in the package results in rapid increase in global cost with unsatisfactory energy performance improvement.

Results of sensitivity analyses show that cost-optimal results for the RB retrofits are sensitive to the changes in discount rate as displayed with Figure 3 below. Decrease in the discount rate enables moving towards 61.8 kWh/m²y cost-optimally by adding VRV retrofit within the retrofit package. Another opportunity to achieve more ambitious cost-optimal energy

performance level is to ensure investment cost decrease around VAT for VRV and SP retrofits. With this cost decrease, 52.6 kWh/m²y primary energy consumption level is achievable in case the discount rate is equal to 3%. In order to achieve this level, SP retrofit should also be included in the retrofit package.

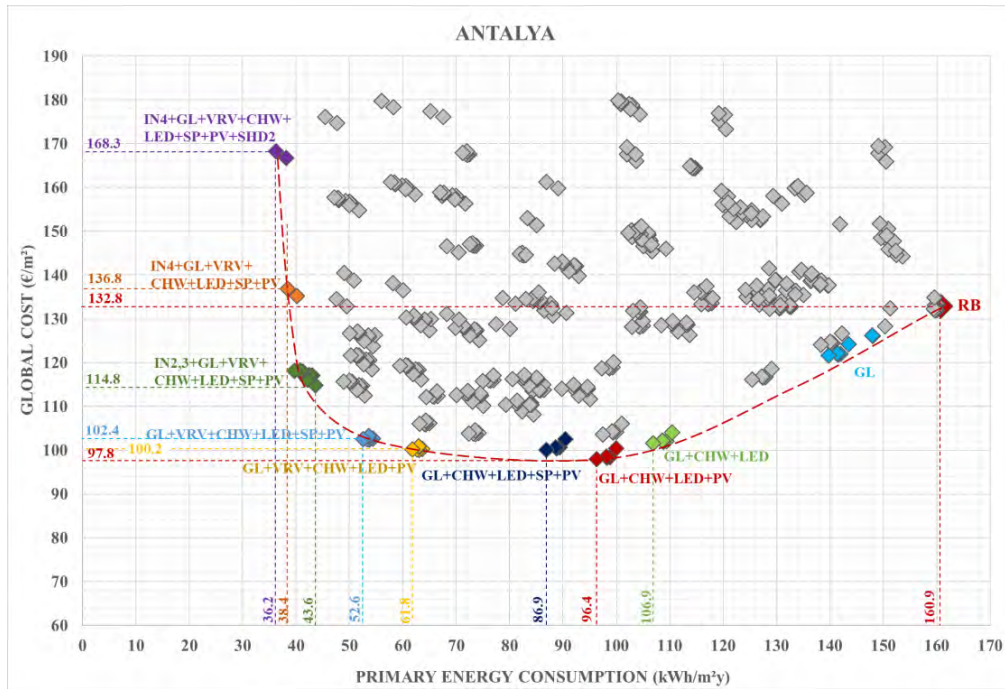


Figure 2. Results of cost-optimality analyses performed for the RB retrofits.

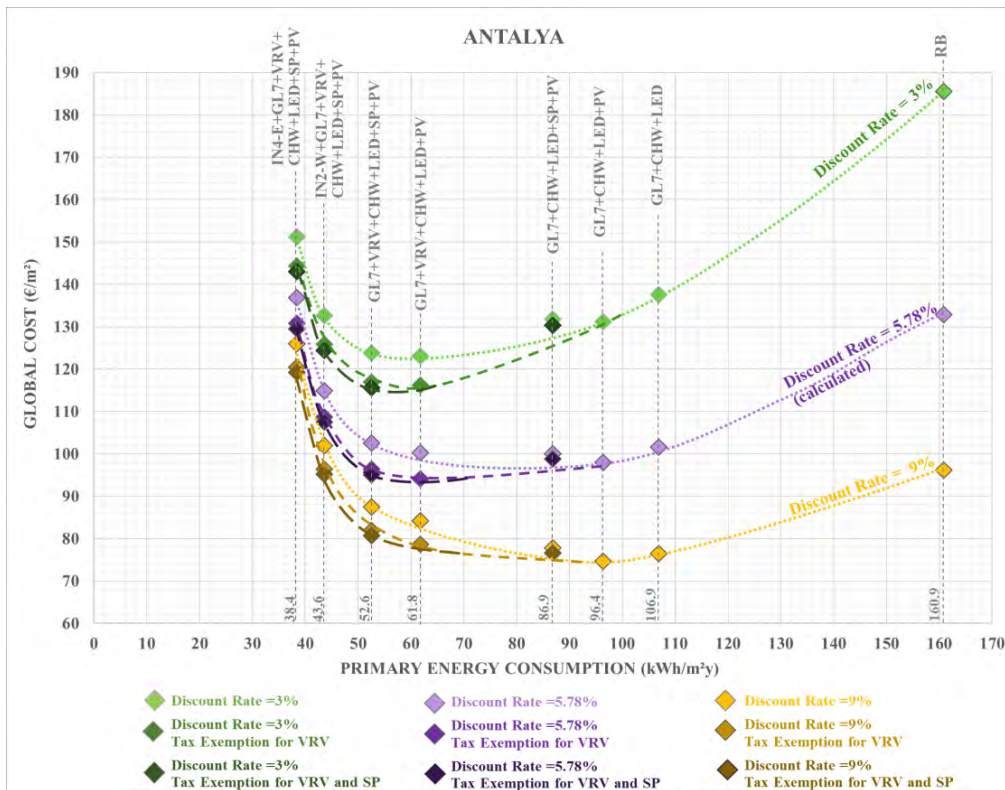


Figure 3. Results of sensitivity analyses.

When the discount rate is equal to reference assumption (5.78%), cost-optimal level remains at 61.8 kWh/m²y even an investment cost decrease is provided. However, only with 1 €/m² higher global cost, SP retrofit can be included in the retrofit package in order to achieve 52.6 kWh/m²y primary energy consumption level cost-optimally in case of an investment cost decrease in SP and VRV. Moreover, the payback period of this retrofit package (including GL7, VRV, CHW, LED, PV retrofits) decreases from 8.3 years to 7.5 years.

DISCUSSION AND CONCLUSION

Results reveal that 6% variation in the discount rate corresponds to more than 30 kWh/m²y difference in the cost-optimally achieved primary energy consumption level. Therefore, strong forecasts on the economic indicators are required to point reliable targets for cost-optimal and NZEB levels.

Specific to Mediterranean climate, VRV and SP measures have a critical role to move towards higher energy performance level. In order to move towards 52.6 kWh/m²y primary energy consumption level cost-optimally, cost decreases for solar thermal system and VRV system should be provided for high-rise apartments. If an investment cost decrease is not expected naturally in time or as the result of technological development, it may be triggered by some subsidy and incentives put forward by policy-makers. Climate responsive tax exemption appears as an effective tool to stimulate building retrofits in Mediterranean building market.

ACKNOWLEDGEMENT

This work was supported by The Scientific and Technological Research Council of Turkey (TUBITAK) with a PhD researcher grant.

REFERENCES

- CEN Standard *EN 15459:2007*, Energy performance of buildings – Economic evaluation procedure for energy systems in buildings, Brussels.
- Ganiç Sağlam N, Yılmaz A. Z, Becchio C, Corgnati, S. P, A Comprehensive Cost-Optimal Approach for Energy Retrofit of Existing Multi-Family Buildings: Application to Apartment Blocks in Turkey, *Energy and Buildings*, 150, 224-238.
- The Commission to the European Parliament and the Council, 2013. Progress by Member States Towards Nearly Zero-Energy Buildings, 7.10.2013, COM (2013) 483 final/2.
- The European Commission. 2016. Commission Recommendation (EU) 2016/1318 of 29 July 2016 on guidelines for the promotion of nearly zero-energy buildings and best practices to ensure that, by 2020, all new buildings are nearly zero-energy buildings, Official Journal of the European Union, 2.8.2016, L208/46.
- The European Parliament and the Council of the European Union (2010). Directive 2010/31/EU of The European Parliament and of the Council of 19 May 2010 on the energy performance of buildings (recast), Official Journal of the European Union, 18.6.2010, L153/13.
- The European Parliament and the Council of the European Union (2012). Directive 2012/27/EU of the European Parliament and of the Council of 25 October 2012 on energy efficiency, amending Directives 2009/125/EC and 2010/30/EU and repealing Directives 2004/8/EC and 2006/32/EC, Official Journal of the European Union, 14.11.2012, L315/1.
- Yılmaz A.Z, Ganiç Sağlam N, Gali G., Ashrafiyan T, Akguc A, Determination of Turkish Reference Residential Buildings and National Method for Defining Cost Optimum Energy Efficiency Level of Buildings, Scientific and Technological Research Council of Turkey (TUBITAK), 2015, Project no:113M596.

Evaluation of Efficiency and Renewable Energy Measures Considering the Future Energy Mix

Fabian Ochs^{1,*}, Georgios Dermentzis¹

¹University of Innsbruck, Innsbruck

*Corresponding email: Fabian.Ochs@uibk.ac.at

ABSTRACT

Sustainable and responsible use of resources is required in order to mitigate climate change. Micro-economic goals usually consider the capitalized investment costs and/or the purchased energy but disregard environmental impacts. However, on macro-economic scale, the aim must be the reduction of the (non-renewable) primary energy (PE) use and of CO₂-emissions. There is need for an appropriate evaluation method for comparing and ranking different passive and active building technologies, e.g. according to their impact on the PE consumption. National conversion factors for PE/CO₂ differ significantly between different countries and are subject to change. Seasonal variations are not considered at all.

The electricity mix is and will be influenced to a higher extend in future by the available renewable energy sources, which are hydropower, wind energy and PV with strong differences in daily and seasonal availability. Without presence of seasonal storage, fossil fuels will predominantly cover the winter load. The electricity mix is also influenced by the load: buildings, have a high demand in winter, and lower in summer. The share of electricity for heating is still relatively low, but will increase with the more widely use of heat pumps and electric heating. Hence, savings in winter will have higher value.

This paper discusses - using a realized NZE multi-family building as an example - a PE evaluation method, that allows to include future development of the load (i.e. building stock) and electricity mix (share of REs) with seasonal variations and shows the impact on the ranking of different passive and active technologies.

KEYWORDS

Renewable Energy and Efficiency in Buildings, Primary Energetic Evaluation, Monthly Primary Energy Factors

INTRODUCTION

Sustainable and responsible use of resources is required in order to mitigate climate change. Micro-economic goals usually consider the capitalized investment costs and/or the purchased energy but the disregard environmental impact. However, on macro-economic scale, the (non-RE) primary energy (PE) use and CO₂-emissions must be reduced. The potential of the energetic use of biomass for buildings is limited. A significant further increased use of biomass for buildings will not be possible as high density energy will be also required for processes and mobility in a future sustainable energy system (see also Feist 2014).

The electricity mix is influenced by both, the (seasonal and daily) availability of renewable energy (RE) sources such as hydropower, wind and PV and by the load (i.e. the building stock).

Available energy sources: hydro power availability is relative homogeneous (slightly lower in winter), wind energy is volatile and slightly higher in winter and PV features very strong differences in daily and seasonal availability.

Load: buildings have a high demand in winter and lower in summer. The share of electricity for heating is still relatively low (e.g. in the range of below 5 % in Germany (D) acc. to BEDW 2016 and also in Austria (At) acc. to Statistik Austria 2016). It will increase with the

more widely use of heat pumps and electric heating in nZEBs/NZEBs (see below for a definition). This will result in a stronger seasonal variation of the electricity load. Without presence of seasonal storage, the winter load will be covered predominantly by fossil resources. Hence, savings in winter have higher value.

PREDICTING MONTHLY PRIMARY ENERGY CONVERSION FACTORS

There is a need for an appropriate evaluation method for comparing and ranking different passive and active technologies on micro- and macro- economic scale. National conversion factors for PE/CO₂ differ significantly between different countries and also between the EU member states and are subject to change. For example, the PE factor for electricity is 1.8 in Germany (ENeV) since 2016 (2.4 before), in Austria 1.91 since 2015 (2.62 before) (OIB-6, 2015, OIB-6, 2011). Seasonal variations are not considered at all.

For the electricity mix, the share of renewables within the time frame of consideration (e.g. 20 years) should be included and not as usually done the current (or past) status. A significantly increased share of RE electricity can be expected in the near future in particular in summer (PV), while in winter only a moderate increase is likely, unless there is a significant further extension of wind power or seasonal storage capacities are strongly build up.

If a large number of buildings use heat pumps (HP) for space heating and DHW preparation and produce electricity with on-site PV, both, the purchased electric energy and the share of renewables in the electricity mix depend on each other. Electricity that is used on site is not available in the grid and an increased share of fossil fuels in the energy mix have to be considered. PV electricity sold to the grid will replace fossil fuels more likely in winter, spring and autumn than in summer. Thus, a model for the PE/CO₂ conversion factor of the electricity mix needs to consider RE availability and the load curve. A possible approach of balancing PE demand (and CO₂ emissions) of a building with onsite RE generation is shown schematically in Fig. 1. Solar thermal (ST) energy is used to reduce the energy demand (heating, DHW + storage and distribution losses) that has to be covered by e.g. a heat pump (HP). Onsite PV can be used directly for appliances and auxiliary energies or to drive the HP. For higher own consumption, a (battery) storage is required, which is subject to losses.

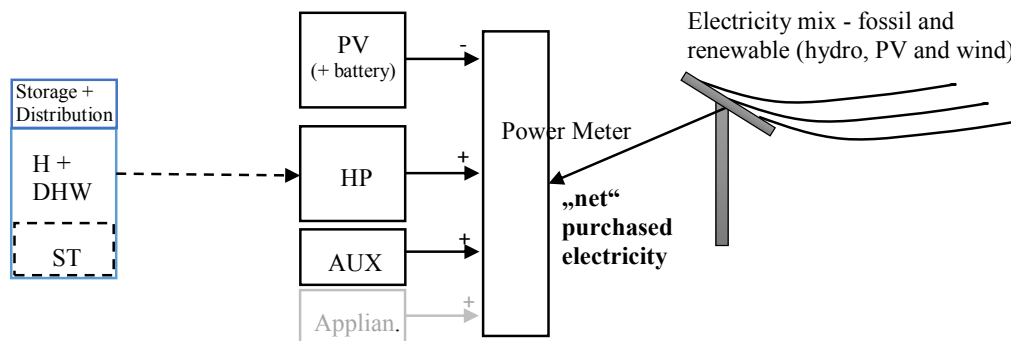


Figure 1 Possible approach for the calculation of the monthly net energy balance with heating (H) and domestic hot water (DHW) demand covered partly by ST; the remaining demand is covered by a heat pump (HP), which is partly powered by onsite PV, the remaining electricity demand for the HP, auxiliary energies (and appliances) is covered by the grid with volatile shares of renewable electricity

A monthly evaluation based on monthly primary energy factors is proposed, which can be used to calculate a more representative environmental impact of different efficiency and RE measures. The specific primary energy e_{PE} is calculated for each month (i)

$$e_{PE} = \sum f_{PE,i} \cdot w_{el,i} \quad (\text{eq. 1})$$

where $f_{PE,i}$ is the primary energy conversion factor for each month (i) considering the energy mix in each month and $w_{el,i}$ is the specific electric energy purchased in each month, see Fig. 2.

In two scenarios (A and B) with different shares of hydro, wind, PV and fossil energy, the PE conversion factor were calculated on monthly basis using e.g. the PE conversion factors shown in Fig. 2 and Table 1.

$$f_{PE} = f_{PE,hyd} \cdot W_{el,hyd} / W_{el} + f_{PE,wind} \cdot W_{el,wind} / W_{el} + f_{PE,PV} \cdot W_{el,PV} / W_{el} + f_{PE,fos} \cdot W_{el,fos} / W_{el} \quad (eq. 2)$$

Table 1. CO₂-emissions and primary energy (PE) conversion factors of fossil and renewable electric energy sources, acc. to DVGW 2016

Source	CO ₂ / [g/kWh]	f _{PE} / [kWh _{PE} /kWh _{el}]
Electricity Mix Germany	520	
Electricity from Gas	432	2.4
Hydro		0.01*
Wind	9	0.05
PV (off-site)	56	0.1

*assumptions

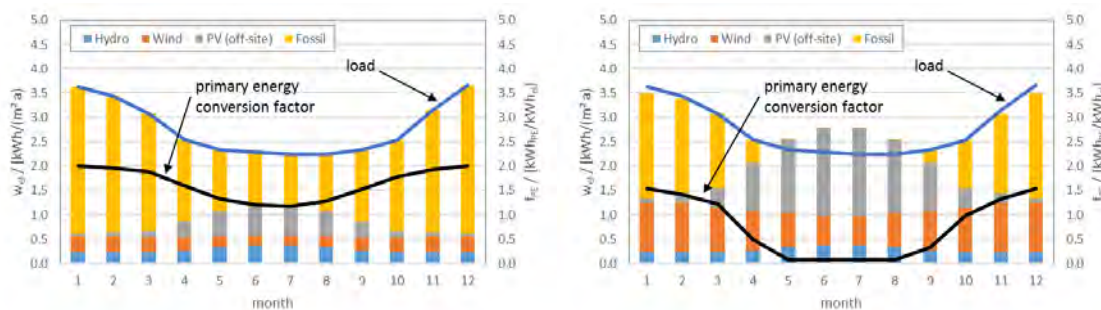


Figure 2 Monthly share of renewables (hydro, wind, PV, fossil) and corresponding PE conversion factor, example of a PH with a HP for heating and DHW supply with (A) a share of 10 % hydro, 10 % wind, 10 % PV and 70 % fossil, and (B) a share of 10 % hydro, 30 % wind, 30 % PV and 30 % fossil in the electricity mix

Table 2: Monthly PE conversion factors see Fig. 5 and PE conversion factors acc. to Tab. 1

	Jan	Feb	Mar	Apr	May	Jun	Jul	Aug	Sep	Oct	Nov	Dec	av.
A: 10-10-10	2.01	1.96	1.89	1.60	1.33	1.20	1.18	1.28	1.53	1.78	1.92	2.01	1.6
B: 10-30-30	1.53	1.42	1.23	0.50	0.08	0.08	0.08	0.08	0.33	0.98	1.33	1.54	0.8

CASE STUDY: NZEB Innsbruck Vögelebichl

The Passive House (PH) project Vögelebichl in Innsbruck, two multi-family houses (MFH) with together 26 flats of the social housing company NHT (see Fig. 3) was designed such that the optimum share of PV and Solar Thermal (ST) should enable a NZE balance for heating, DHW preparation and aux. energies. One roof of the MFH is covered by PV (99.8 m²), the other is partly used for PV (52.5 m²) and partly for ST (73.6 m²). Fig. 4 shows a simplified hydraulic scheme including the GW heat pump (two stage), solar thermal collector (SC) field as well as the low temperature heat distribution and the separate decentral fresh water preparation (DHW plate HX). The double stage heat pump is equipped with hot gas (HG) de-superheating. Depending on the operation mode (heating or DHW preparation), the flow of the heat pump enters the buffer store (BS) at the top or at 1/3 of the height from the top. The combined return of the heating and DHW loop enters the large 6 m³ buffer store depending on the temperature level either at the bottom or at about 1/3 of the height of the store in order to enhance stratification. The electric backup heater (BH) is currently not used.

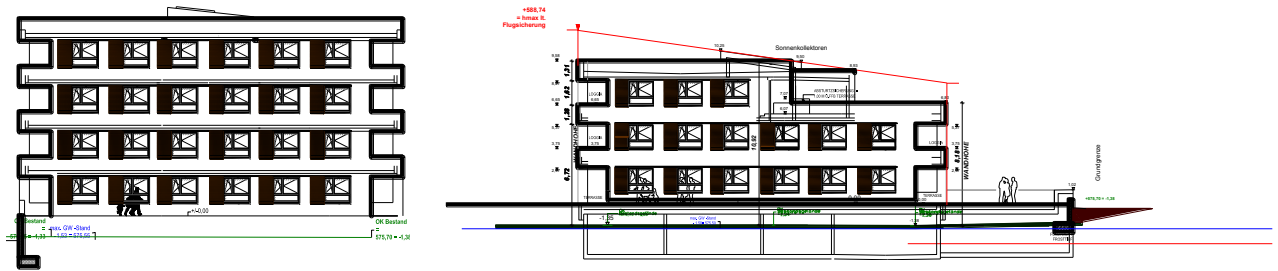


Figure 3 West view of the two MFHs in Innsbruck Vögelebichl, NHT Tirol; PHs with 4-pipe low temperature distribution system and fresh water modules in each flat

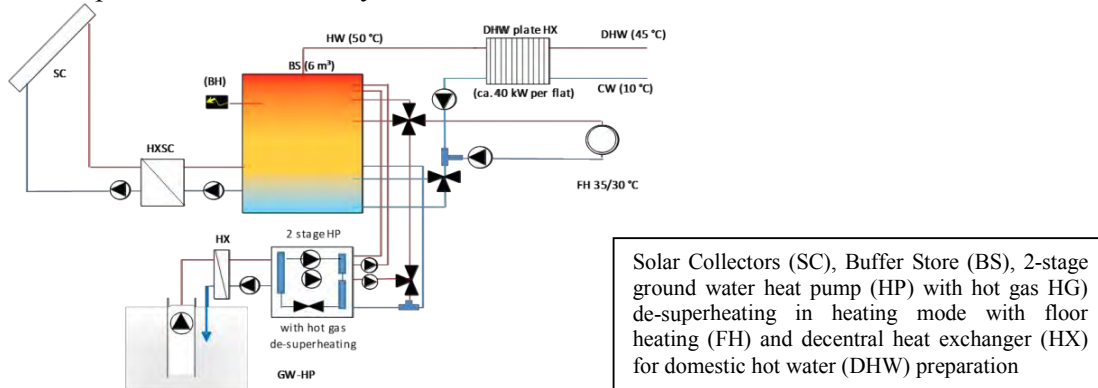


Figure 4 Simplified hydraulic scheme of the two NZEBs, project NHT Vögelebichl

nZEB vs. NZEB

nZEBs and NZEBs are comparable in the sense that both aim at minimizing CO₂-emissions and non-RE primary energy, nevertheless, their definitions differ quite much in detail and thus, their performance might eventually be quite different.

nZEB: nearly zero Energy Building according to EPBD, 2010. Each member state has a national definition with significant differences with respect to the energy use considered (heating, cooling, DHW, auxiliary, appliances), the maximum limits, the conversion factors etc. (see BPIE, 2016).

NZEB: Net Zero Energy Building. Generally an NZEB is a "grid-connected building which produces the same amount of energy on-site by renewable energy sources as it consumes on annual basis." (IEA SHC T40/HPT A40). There is a fuzziness in this definition regarding the interpretation of the system boundary, the energy flows, the weighting/conversion factors etc. Usually, Net Zero includes heating (and cooling), DHW supply and aux. energies (HRV, pumps, control, etc.) but excludes appliances. Even though, appliances have a large contribution to the overall electricity consumption (1500 kWh/a to 4500 kWh/a depending on the number of persons per household for a typical central European household, Statistik Austria 2016, BEDW 2013). According to this definition, a NZEB can consume relative high amount of (electric) energy in winter, when correspondingly a large PV area produces this amount as excess electricity in summer. This means, that according to the NZEB concept, the electric grid is considered as a loss-free seasonal storage, which is obviously not the case. In order to account for this weakness in this concept, additional performance indicators such as the load match factor or fraction of PV own consumption were suggested (see IEA SHC T40/HPT A40).

Remark: „net-zero“ as a goal can be a misleading concept, since optimization for net-zero may lead to one storey buildings, because reaching the net zero balance is more difficult compared to a multi-storey building (with smaller roof and façade area related to treated area). However, MFHs, which are more compact, are favorable from the overall energetic and macro-economic point of view (compare also Feist et al. 2014).

SIMULATION AND MONITORING RESULTS

In Ochs et al. 2017, detailed monitoring results of the buildings (heating and DHW demand) and of the system (distribution losses, performance factors, solar thermal and PV yield) are reported and improvements after the first year of operation were discussed and design recommendations based on monitoring data and simulation results were given. It has to be noticed that the first year of operation is not representative (construction moisture, partial occupation, adjustment of control/set points, etc.) and should not be used for the analysis. After the initial phase and after implementing some first optimization measures (adapted set points, etc.), an operation of the buildings and the HVAC system with net zero energy balance can be expected. Fig. 5 (a) gives the simulated monthly energy balance with the introduction of the improvements. Fig. 5 (b) gives the resulting electric energy balance that is used for further analysis of the data. Net energy balance for heating, DHW and auxiliary energy is achieved with PV on the roof. PV on the façade is required, if appliances are considered, too.

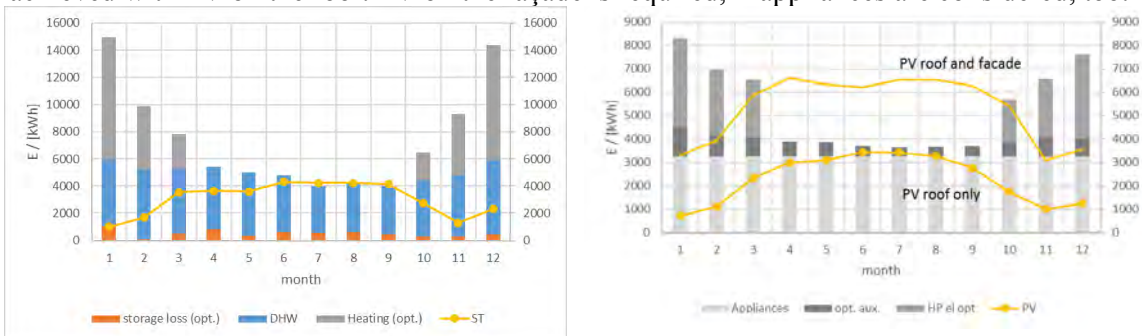


Figure 5 (a) simulated monthly thermal energy balance and (b) simulated monthly electric energy balance with PV on roof (as realized) and PV on roof and south façade (not realized)

RESULTS and DISCUSSIONS

The specific PE (e_{PE}) for heating and DHW production including the HP (after introduction of improvements, i.e. NZEB is achieved), appliances and with or without 300 m² of PV in south façade is calculated for the two scenarios (Fig. 2). It can be seen in Fig. 6 that in scenario B with higher share of renewables in the grid (all together 70 %), the additional PV in the façade yields less PE savings than in the scenario A (all renewables 30 %).

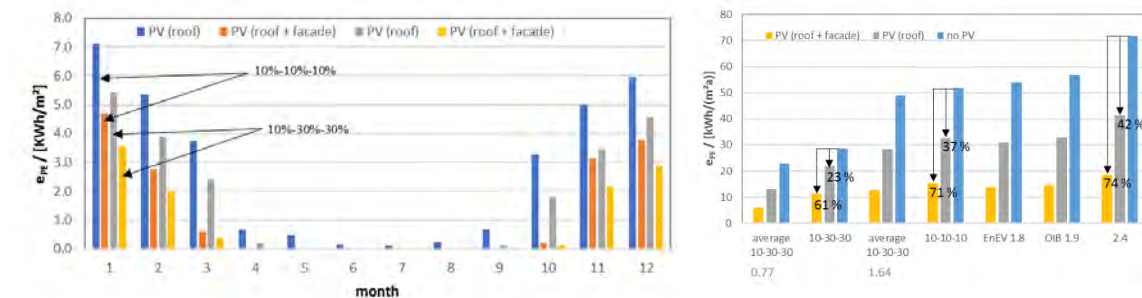


Figure 6 Specific PE (e_{PE}) for heating and DHW supply including the improved HP, appliances and with or without 300 m² of PV in south façades for scenario A (10 % hydro, 10 % wind and 10 % PV) and scenario B (10 % hydro, 30 % wind and 30 % PV); monthly balance.

In scenario A, the additional PV in the façade reduces the annual specific PE demand from 32.7 kWh_{PE}/(m² a) to 15.2 kWh_{PE}/(m² a), or by 53.5 % while in scenario B, it reduces from 21.9 kWh_{PE}/(m² a) to 11.2 kWh_{PE}/(m² a) or by 49.2 %.

State of the art is to use a constant PE conversion factor, e.g. 1.8 in Germany and 1.9 in At. PE savings with a constant PE conversion factor are 42 % without and 74 % with PV in the façade compared to the case without any onsite PV). In scenario A, savings reduce to 37 % without and 71 % with PV in the façade and to 23 % (without) and 61 % (with) in scenario B. With constant (i.e. average) PE conversion factor, savings are accounted for with the same weighting independent of the season. Thus, savings in summer are overrated. Measures such as (even) better insulation level, reduced storage and distribution losses or (even) better HPs would further reduce the winter load and are favourable compared to more PV.

CONCLUSIONS

Two MFHs in PH Standard with ST and HP system and onsite PV to achieve maximum PE savings were realized in Innsbruck and monitored for a period of more than two years. Net zero energy balance (for heating and DHW and auxiliary energies) could not be achieved during the first year of monitoring (2016), but predictions based on results after introduction of improvements show that Net Zero can be achieved. PH standard is key for achieving NZEB level for heating, DHW and aux. energies. If electricity consumption of appliances is included in the energy balance, additional PV on the south façade would be required.

NZEB do not significantly reduce winter grid load. The mismatch between (electricity) demand and PV yield has to be considered, e.g. by means of different electricity prices for purchase and sell or by seasonal/monthly PE conversion factors. A method is discussed allowing to compare different nZEB/NZEB concepts considering the time (season) of the electricity purchase from the grid in order to be able to optimize concepts towards reduced non-RE PE demand or CO₂-emissions in winter when renewable electricity is rare. The future development of the electricity mix and the load (building stock) can be considered and possible scenarios can be evaluated.

ACKNOWLEDGEMENT

This project is financially supported by NHT, Innsbruck, Austria. PHPP calculations and PH certification was done by PHI Innsbruck. The financial supports from the Austrian Ministry for Transport, Innovation and Technology and the Austrian Research Promotion Agency (FFG) through the IEA Research Cooperation to this work are gratefully acknowledged.

REFERENCES

- BPIE, *Nearly Zero Energy Buildings Definitions Across Europe*, EPISCOPE project (IEE/12/695/SI2.644739), 2016
- BEDW (2016), *Wie heizt Deutschland*, BEDW-Studie zum Heizungsmarkt, Juli, 2016.
- BEDW (2013), *Energie-Info*, Stromverbrauch im Haushalt, Berlin, 2013.
- DVGW 2016, Weiterentwicklung der Primärenergiefaktoren im neuen Energiesparrecht für Gebäude, Endbericht 7.4.2016
- Feist, Wolfgang (2014), Passivhaus – das nächste Jahrzehnt. In: Tagungsband zur 18. Internationalen Passivhaustagung, Aachen, April 2014.
- OIB-6 Richtlinie 6, *Energieeinsparung und Wärmeschutz*, Österreichisches Institut für Bautechnik, 2011, update 2015
- Ochs Fabian, Dermentzis Georgios, Feist Wolfgang (2014), Minimization of the Residual Energy Demand of Multi-storey Passive Houses – Energetic and Economic Analysis of Solar Thermal and PV in Combination with a Heat Pump, Energy Procedia Volume 48
- Ochs Fabian, Dermentzis Georgios, Aleksandra Ksiezyk (2018), Simulation and Monitoring Results of two MFHs in PH Standard with Heat Pump, Solar Thermal and PV, Solar Works Congress, 2018, Abu Dhabi, UAE, 2018
- Statistik Austria, Bundesanstalt Statistik Österreich, 2016

Optimization of government subsidization strategies for building stock energy refurbishment

Alessandro Prada¹, Francesca Cappelletti² and Andrea Gasparella^{3,*}

¹University of Trento, Italy

²IUAV University of Venice, Italy

³Free University of Bozen-Bolzano, Italy

**Corresponding email: andrea.gasparella@unibz.it*

ABSTRACT

The high initial investment required in existing building refurbishment can limit the initiative of the building owners and prevent the full exploitation of a huge energy saving potential. Public incentives can play an essential role in fostering the energy retrofitting of the existing buildings and in increasing the renovation rate of the building stock, effectively reducing the energy final uses, the dependence on the fossil fuels, and helping meet the national efficiency targets. Public subsidization are intended to enhance the economic performance in terms of global cost of the energy efficiency measures for the owner, in order to induce positive actions and move optimality from low to high energy efficient solution. In contrast, the overall economic efficiency is obtained with combinations of interventions, able to achieve a certain energy saving target for the entire building stock at the minimum initial Investment Costs (IC).

This paper tries to identify the overall economic efficiency in reducing the energy consumption of the existing stock and compares it with the efficiency of solutions optimal from the owner's perspective, in order to support more efficient subsidization strategies. Different mixes of three reference building archetypes, representative of the existing buildings, are considered to define different possible stocks, in order to analyse their impact on the efficiency of energy renovation solutions. Four groups of energy efficiency measures (EEMs) dealing with respectively the opaque envelope insulation, the windows substitution, the heat generating system replacement, and the mechanical ventilation introduction are defined and their combinations considered.

KEYWORDS

Government subsidies optimization

Stock Retrofit

Multi-objective optimization

INTRODUCTION

Buildings, including households and services, are responsible for more than 30 % of world Total Final Consumption (TFC) (IEA, 2017), and an even larger share of 41 % (Eurostat, 2016) in the European Union (EU). Conversely, a largest share of the existing buildings is considered to be energy inefficient. In EU, 75 % of the buildings have been built before 1990 (i.e. before any EU building regulation) and over 97 % are in class B or worse (BPIE, 2017), so not ready to meet the challenging 2050 decarbonisation target, i.e. a reduction of greenhouse gas by 90 % with respect to 1990 (EU Commission, 2011). This can be obtained only through energy efficiency measures, aimed at a direct reduction in the use of fossil fuels, and at a deeper penetration of renewable energy sources. For these reasons, EU aims at increasing the current rate of renovation, close to 1% (BPIE, 2011), through new policies and

market tools. Government financial incentives play a crucial role to promote the energy retrofitting of existing buildings since they should remove the barriers due to the high up-front initial Investment Costs IC (Amstalden et al. 2007; Gamtessa 2013; Higgins et al. 2014). Incentives able to change the consumer's behaviour and investment convenience, such as financial (penalizing or rewarding) or non financial (as for instance on-site advice by experts) are required, together with stricter performance targets for new and renovated buildings. In Europe, a wide variety of financial incentives is applied to support the enhancement of buildings energy performance such as grants, subsidies, preferential loans, tax reduction and tax credit (BPIE, 2012). Besides their effectiveness in driving the decision maker toward the best solution, which can be affected by different factors that make it uncertain, their efficiency should be accounted for, in order to maximize their impact and limit their societal cost. For instance, Di Pilla et al (2016) analysed the incentives in the Italian context, investigating the optimal regional distribution of subsidies through linear programming.

In this work, the economic efficiency of possible incentives policies is analysed through a multi-objective optimization approach. For a given percentage energy saving target, the public authority perspective, aiming at minimizing the overall initial IC is compared with the owner's one, which aims at minimizing the global cost of each single building over its lifespan. Several stock compositions are defined as a mix of three archetypical residential building modules. Four groups of energy efficiency measures (EEMs) dealing with respectively the opaque envelope insulation, the windows substitution, the heat generating system replacement, and the mechanical ventilation introduction are defined and their combinations considered. No cooling system is considered, since the existing stock is assumed not to be conditioned, as is usually the case in Italy (STRATEGO, 2016), and the EEMs with an appropriate operation strategy of natural ventilation and shading systems have been recognized to be effective in limiting overheating occurrences below the initial conditions. The initial IC in the two optimization approaches is then compared as representative of the social cost for achieving the same savings target, and of the possible financial incentive required, which is generally defined as a percentage of the IC.

METHODS

Building Archetypes

The analysis focuses on the economic efficiency of the renovation of a residential building stock as a function of its characteristics. For this reason, different building stocks have been defined starting from three archetypical buildings described in Penna et al (2015). These represent a semi-detached house with a compactness ratio of 0.97, a penthouse with a compactness ratio of 0.63 and an intermediate flat in an apartment building, with a compactness ratio of 0.30. Concerning the building envelope and heating system components they represent a typical configuration of Italian households built prior to the first energy legislation. Hence, a non-insulated envelope, with single pane glazing system and a hydronic system with a standard gas boiler coupled with radiators and on-off control system define the initial configuration for all the archetypes. Before renovation, the semi-detached house has an energy demand for heating of $269.17 \text{ kWh m}^{-2} \text{ yr}^{-1}$, the penthouse needs about $190.30 \text{ kWh m}^{-2} \text{ yr}^{-1}$ and the intermediate flat about $113.81 \text{ kWh m}^{-2} \text{ yr}^{-1}$.

Three different energy saving targets are considered for the stock, that are the reduction of 50%, 60% and 70% compared to the original primary energy demand.

Six off the shelf energy efficiency measures (EEMs) categories are considered:

- external insulation of the external opaque envelope with an expanded polystyrene layer. The insulation thickness is optimized independently for vertical walls, roof and floor in the range 0 to 20 cm and in steps of 1 cm;

- windows replacement with double or triple pane with either high or low solar heat gain coefficient;
- boiler replacement with either a modulating or condensing boiler with an outside temperature reset control;
- mechanical ventilation system installation with a heat recovery system.

The IC is derived from regional price list (Penna et al. 2015) for all the EEMs, and contributes to the global cost expressed by the Net Present Value (NPV), together with the annual energy cost, the maintenance cost, the replacement cost and the residual value for the pieces of equipment with longer lifespan. The simulations of the energy performance of the building stock are carried out in Trnsys considering the weather conditions of Milan (Latitude 45°27'51'' N, Longitude 9°11'22'' E), a city with a 4A climate according to Ashrae 90.1 classification (Ashrae, 2007). Sixty-six building stock configurations were considered by varying the share of each archetype in the range from 0 to 100% in steps of 10 %.

Optimization Algorithm

A large number of optimization algorithms have been developed for solving multi-objective optimization problems however, according to Wetter and Wright (2004) the gradient-based optimization and the linear programming methods are not suitable to Building Performance Optimization (BPO). Evolutionary algorithms are the most popular optimization methods, and non-dominated sorting genetic algorithm (NSGA-II) is one of the most implemented in BPO (Nguyen et al., 2014). The NSGA-II, firstly developed by Deb et al, (2002), uses elitism by maintaining the current and the previous population. Then, after the population mating, the populations are sorted according to the non-domination concept and the best ranking solutions are selected as the next parent population.

In this research, we implemented the NSGA-II with some customizations such as sampling, external data-set and convergence criterion. Firstly, the code included a Sobol sequence sampling to overcome the clustering that can occur with other sampling techniques. Besides, an external data-set of the simulation runs is saved in order to avoid repeating expensive simulation runs during the BPO. Finally, the hypervolume measure (Zitzler and Thiele, 1999) was used as a stopping criterion.

Optimization with the authority's or with the owner's perspective

In the Italian scenario, incentives are provided for energy refurbishment investment in the form of tax credit calculated as a percentage of the IC. This is independent of the energy saving actually achieved, provided the law minimum requisites are fulfilled, so that the economic efficiency of the intervention and most importantly of the action on the entire building stock is left to the owners' decision. However, the optimum of the building stock does not necessarily coincide with the individual optima of all the buildings. First, the building owner convenience is typically expressed by the global cost in the lifespan, while the social cost, in presence of incentives, is better represented by the IC. Second, when optimizing the interventions over the entire stock, the marginal return of an investment on a building can be very different from that on another, making it possible to prioritize the interventions on the different buildings according to criteria of overall efficiency.

For the above reasons, a first optimization considers the minimization of primary energy for heating (EP_H) and, simultaneously, the initial IC for the entire building stock. These two indices are calculated by summing the energy performance and the IC of all the buildings renovation in the stock, and then dividing them by the total floor area of the building stock, in order to normalize the indicators independently of the stock size.

Each owner aims at achieving a given energy saving target in such a way to maximize the economic benefit during the building lifespan. Either energy efficiency requisites or public

incentives recognized to interventions able to overcome a minimum law target, will therefore foster the individual optimization of the EEMs for each building. This perspective does not necessarily lead to the most effective solutions from the point of view of the public authority. A second optimization run has then been conducted, with the optimal refurbishment of each building is evaluated by optimizing the energy and cost savings following the cost-optimal approach. The first objective is the reduction of the primary energy for heating (EP_H) in order to reach the requested target. Moreover, the minimization of the global cost of the building, the total cost of the building over a 30-year lifespan, quantified through the NPV, is pursued. The energy savings and the total IC for the building stock is subsequently quantified as the sum of the values obtained for the optimal solutions of each individual building, and compared with those of the first optimization in order to understand the extent to which the individual point of view produces suboptimal results for the community.

RESULTS AND DISCUSSION

Figure 1 (left) show on three-coordinate diagrams the absolute difference between the IC needed for the optimal solution of the two optimizations, ΔIC , considering three specified targets for energy saving (e.g., 50%, 60% and 70%). Each side of the triangular plots reports the percentage of buildings with the same compactness ratio, S/V (e.g. 0.30, 0.63, 0.97), so the position of each point represents a different percentage composition of the building stock. The colour of the points follows from blue (no difference) to red (highest difference) highlights the difference in the IC (ΔIC) between the owner's and authority point of views. It should be noticed that the larger the difference, the more the retrofit measures in the optimal solution and the performance itself of each single type of buildings will differ in the two perspectives. For instance, for the target 50% the high values of ΔIC (up to 1322 EUR/ 100 m^2) imply that it is possible to reach the target energy saving applying retrofit actions very different from the ones that optimize the NPV for the single building. Thus the target is reached by saving more energy in some types of buildings and less in others. Comparing the results of the three targets it is evident that the suggested approach is more convenient for the target of 50% and 70%, than for 60%. In the first case, it is possible to obtain a saving of more than 670 EUR/100 m^2 in 75 % of the reference stocks, and more than 922 EUR in 50 %. The largest benefits are when the building stock tends to have a smaller share of buildings with $S/V=0.3$ and medium to high with $S/V=0.63$. In the last case, the NPV optimization or the IC optimization give similar results and savings are higher than 100 EUR/100 m^2 in 75 % of the reference stocks, and more than 159 EUR/100 m^2 in 50 %, with maximum savings lower than 400 EUR. The best performance of the whole stock optimization (authority point of view) is for 10 % of $S/V=0.3$ buildings, 20 % of 0.63 and 70 % of 0.97. The best performance when target is 70 %, is for 10 % of $S/V=0.3$ buildings, 30 % of 0.63 and 60 % of 0.97.

As regards percentage savings, (Figure 1, right), it can be seen that the impact of a whole stock optimization is quite high when the smallest target is considered. Savings are up to 22 %, with 75 % of the building stocks saving more than 14.8 %, and 50 % more than 18.7 %. Very low in percentage terms is the advantage for 60 and 70 % EP_H saving targets, reaching at most 4 %. With 50 % savings target it is also clear a trend, showing the maximum percentage saving at a similar value for many stock configurations up to a maximum share of $S/V=0.3$ buildings of 40 %. Larger shares of compact buildings ($S/V=0.3$) reduces the maximum advantage of the authority perspective approach. Trends get less clear when larger saving targets are considered.

CONCLUSIONS

In this work the overall economic efficiency, in terms of IC, in reducing the energy consumption of the existing stock (authority point of view) has been assessed and

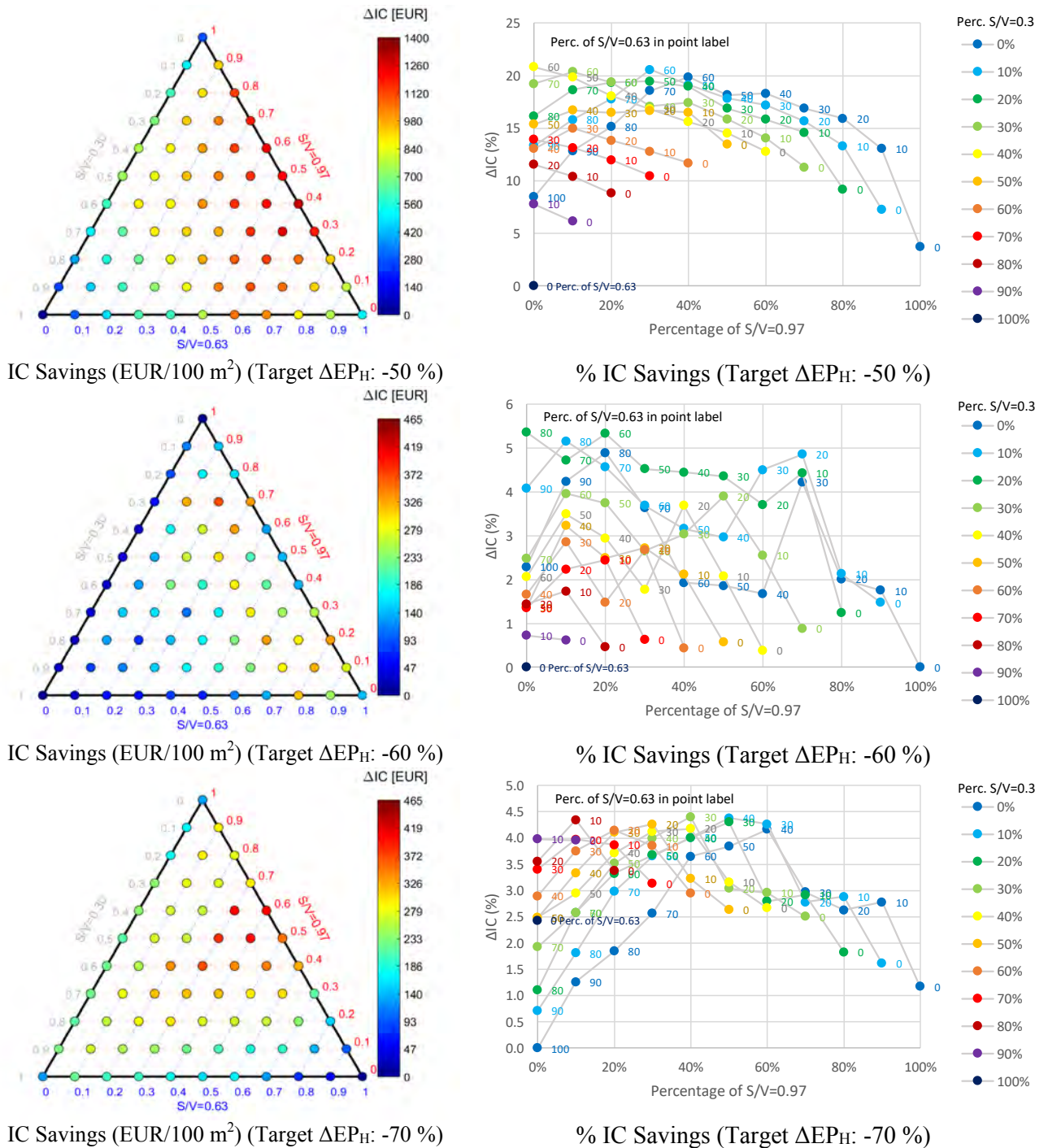


Figure 1: Absolute and percentage IC savings of the authority vs owner optimization perspective with the three EP_H savings (50, 60, and 70 %).

compared with that of solutions optimal from the owner's perspective. Different mixes of three reference building archetypes have been considered to define different possible stocks, in order to analyse their impact on the efficiency of energy renovation solutions. Four groups of energy efficiency measures (EEMs) have been defined and their combinations considered. Three target energy savings have been considered, namely 50, 60 and 70 % with respect to the initial building stock performance.

The main findings show that in some cases the optimal solutions at a stock level do not coincide with those at an individual level. Depending on the target, the stock optimization (authority point of view) is always preferable to individual optimization (owner's point of view). Very large savings on the IC are obtained when optimizing the intervention on the entire stock for the lower target performance (50 %).

REFERENCES

- Amstalden R.W., Kost M., Nathani C., Imboden D.M. 2007. Economic potential of energy-efficient retrofitting in the Swiss residential building sector: The effects of policy instruments and energy price expectations. *Energy Policy*, 35, 1819–1829
- ASHRAE 2007. *ASHRAE Standard 90.1-2007, Energy standard for buildings except low-rise residential buildings*. American Society of Heating, Refrigerating, and Air-Conditioning Engineers, Inc. Atlanta, Georgia, USA.
- BPIE. 2011. *Europe's Building under the Microscope, A country-by-country review of the energy performance of buildings*. Brussels, Belgium.
- BPIE. 2012. *Energy efficiency policies in buildings – The use of financial instruments at member state level*. Brussels, Belgium.
- BPIE. 2017. *97 % of buildings in the EU need to be upgraded - Factsheet*. Brussels, Belgium.
- Deb K. Pratap A. Agarwal S. and Meyarivan T.A.M.T. 2002. A fast and elitist multiobjective genetic algorithm: NSGA-II, *IEEE Transaction on Evolutionary Computation*, 6, 182–197
- Di Pilla L., Desogus G., Mura S., Ricciu R, Di Francesco M. 2016. Optimizing the distribution of Italian building energy retrofit incentives with Linear Programming. *Energy and Buildings*, 112, 21-27.
- EU Commission. 2011. *Communication from the commission to the European parliament, the council, the European economic and social committee and the committee of the regions Energy Roadmap 2050*, COM/2011/0885 final, Brussels, Belgium
- Eurostat. 2016. *Energy Balance Sheet, 2014 Data*. Luxembourg.
- Gamtesa, S.F. 2013. An explanation of residential energy-efficiency retrofit behavior in Canada. *Energy and Building*, 57, 155–164.
- Higgins A., Syme M., McGregor J., Marquez L., Seo S. 2014. Forecasting uptake of retrofit packages in office building stock under government incentives. *Energy Policy*, 65, 501–511.
- IEA. 2017. *Energy Technology Perspectives 2017. Data visualization* (<http://www.iea.org/etp/explore/>). Paris, France.
- Nguyen A.T. Reiter S. and Rigo P. A review on simulation-based optimization methods applied to building performance analysis. *Applied Energy*, 113, 1043-1058
- Penna P. Prada A. Cappelletti F. and Gasparella A. 2015. Multi-objective optimization for existing buildings retrofitting under government subsidization, *Science and Technology for the Built Environment*, 21, 847–861.
- STRATEGO. 2016. *Enhanced Heating and Cooling Plans to Quantify the Impact of Increased Energy Efficiency in EU Member States*. Aalborg University, Denmark.
- Zitzler E. and Thiele L. Multiobjective evolutionary algorithms: A comparative case study and the strength Pareto approach. *IEEE Transactions on evolutionary computation*, 3, 257–271.

Techno economic analysis of individual building renovation roadmaps as an instrument to achieve national energy performance targets

Iná Maia^{1*}, Andreas Müller¹, Lukas Kranzl¹, Michael Hartner¹, Sebastian Forthuber¹

¹ Technische Universität Wien (TU Wien), Institute of Energy Systems and Electrical Drives, Energy Economics Group

**maia@eeg.tuwien.ac.at*

ABSTRACT

In order to achieve the Paris COP21 agreement, retrofitting activities in the building stock have to be strongly enhanced, therefore individual building renovation roadmaps (IBRR) can be an instrument for guiding building owners through this process. The research question of this paper is: how ambitious should individual building renovation roadmaps be to achieve consistency with future scenarios of the building stock's energy performance? The methodology applied follows these steps: first, the bottom-up discrete choice building stock model Invert/EE-Lab (www.invert.at) is applied to develop a scenario of building stock related energy demand, CO₂-emissions and costs until the year 2050. The scenario is based on the assumption of current or only slightly strengthened policies and results in 77% CO₂-emission reductions of the building stock from 2012 to 2050. In the second step, we selected representative building types from the Invert/EE-Lab model scenarios. For these building types, we developed IBRR (individual building renovation roadmaps) based on previous experience and literature research. Further, we calculated the building's new energy performance after the renovation measures defined in the IBRR. Finally, we analysed to which extent the energy saving through IBRR measures are in line with the simulated scenario. We carried out this study for the case of Germany. Moreover, we restrict the analysis to single-family houses. The results showed that - based on the approach of the IBRR - it would be required that annually about 4-6% of the buildings apply at least one refurbishment measure (change windows or insulate the roof, change heating system, etc.) in order to achieve a scenario, such as the one simulated by the model Invert/EE-Lab.

KEYWORDS

Deep renovation, Individual Renovation Roadmap, Bottom-up modelling, Energy Performance for Buildings Directive (EPBD), Energy performance targets.

INTRODUCTION

The building sector has been identified as one of the key sectors for achieving the energy and climate policy targets of the EU, as buildings are responsible for 40% of energy consumption and 36% of CO₂ emissions in the EU. In light of single family houses, they represent across the EU between 59,4% (in Slovakia) to 89% (in Italy) of the total building floor area (EU Buildings Datamapper, 2013). In this context, the recast of the Energy Performance of Buildings Directive 2010/31/EU (revised in 26.04.2018)(European Parliament, 2018) is an important legislative instrument at EU level, which supports deep renovation of existing buildings. Here, it is necessary to highlight the necessity of deep renovation (retrofitting), instead of esthetical or maintenance renovation. In a study on renovation rates of energy performance activities in the residential building stock in the Netherlands (Filippidou et al., 2017), the authors pointed out the need of packages for deep renovation measures, rather than single refurbishment measures. A study on the success for energy efficient renovation of dwellings in Norway emphasizes the importance of private homeowners to have access to

relevant and reliable advices, to make energy efficient choices in the process of renovation, as a role player in the process of increasing building renovation rates (Risholt and Berker, 2013). Fabbri et al., 2018 identified the lack of engagement and knowledge of the homeowners with energy efficiency issues as main barrier to increase energy performance of single-family houses, stressing the relevance of developing individual building renovation roadmaps (IBRR), which foresee the renovation measures over a period, according to building owner's desire. In Europe, there are already some demonstration projects, which focus on the key concept of IBRR, as an initiative to increase awareness about building's energy performance, and to encourage homeowners to deep renovate their houses. One of these are: in Germany, the concept of renovation roadmap (*Sanierungsfahrplan – SFP*), and in France, the low energy roadmap *Passeport Efficacité Énergétique (P2E)*. In this context, the iBRoad EU-funded project works on eliminating the barriers between house owner and building energy performance, by developing an Individual Building Renovation Roadmap (iBRoad) tool for single-family houses. This study aims to understand the role of these IBRR in the German case as an instrument to achieve national decarbonisation targets until 2050 for the energy performance of single-family houses.

METHODS

To analyse on how ambitious IBRR (individual building renovation roadmaps) should be, in order to achieve national decarbonisation targets in the building stock, first, the dynamic bottom-up discrete choice building stock simulation model Invert/EE-Lab was used to simulate the a “current policy scenario” for the German building stock. Secondly, a norm based monthly energy balance calculation model was applied to calculate the energy savings resulting from the measures suggested in IBRR for reference buildings. As cooling energy demand in Germany's single family houses are low: 0.07 TWh (Olonscheck et al., 2011), the present study focused on space heating energy demand. Finally, we compared and aligned both results, by extrapolating the results of the selected reference buildings on Germany's single-family building stock.

1. Techno-economic bottom-up modelling of energy demand and CO₂ emissions for the building stock

Invert/EE-Lab is a dynamic bottom-up discrete choice building stock simulation tool. In particular, Invert/EE-Lab is designed to simulate the impact of policies and other side conditions in different techno-economic scenarios. These scenarios drawn with this tool build on much disaggregated representation of the national building stock by a large number of reference buildings. Based on several parameters such as the age distribution of the building components; heat supply; distribution technologies in the building stock; and the ratio between the total costs of purchase of new components and the energy-consumption related annual costs using the installed component, the share of buildings and components is determined, carrying out a renovation measure. For more information see www.invert.at (Müller, 2015), (Kranzl et al., 2013) and (Steinbach, 2016). By setting the model with the current policy instruments, a scenario study developed for the European Project SET-Nav showed that 77 % CO₂-Emission from the building stock during the analysed period 2012 to 2050 can be achieved (Hartner et al., 2018).

2. Choice of reference buildings and their individual building renovation roadmaps

In order to select representative reference buildings, Germany's single family house building stock was mainly classified according to building construction vintage, building geometry, gross and heated floor area, envelope quality and heating systems (Pfluger et al., 2017). For this, from the mentioned database of the German building stock, six reference buildings,

which together represent 33% of total energy demand of single-family houses, were chosen. Table 1 below shows the building characteristics and the relation between construction vintages and envelope's quality of the selected reference buildings B1-B6:

Table 1: Reference buildings characteristics selected from Invert/EE-Lab building stock typology database

Reference building	Construction vintage	Heated area [m ²]	U-value Exterior walls [W/m ² K]	U-value windows [W/m ² K]	U-value roof [W/m ² K]	U-value floor [W/m ² K]	Heating system
B1	1949 - 1957	139	0.93	2.57	1.11	1.01	Oil boiler
B2	1958 - 1968	140	1.44	2.90	0.92	0.97	Oil boiler
B3	1969 - 1978	147	1.21	2.57	0.63	0.85	Oil boiler
B4	1979 - 1983	148	0.80	4.30	0.43	0.81	Oil boiler
B5	1984 - 1994	146	0.68	2.57	0.30	0.55	Oil boiler
B6	1995 - 2001	142	0.50	1.60	0.22	0.34	Oil boiler

The renovation roadmap measures for the reference buildings listed above were defined based on literature (Hoier et al., 2013) and considering the achievement of national building code standards (EnEV,2014). Table 2 shows the stepwise renovation measures:

Table 2: Individual building renovation roadmap

Renovation step	Renovation measures	
1	Roof insulation	A survey within the iBRoad Project scope, which aimed understanding potential users, showed that a time horizon of individual building renovation roadmaps between 5 and 10 years is most favorable for
2	Walls, floor insulation and air tightness increase	
3	Window replacement	
4	Insulation heat distribution system	
5	Heating system replacement	

building owners (Fabbri et al., 2018). Because of that, in the present study assumes a total of 10 years renovation period with two years renovation time-step (period between renovation measures are made). Building elements present different renovation cycles, opaque envelope elements have renovation cycle of 50 years, while window's renovation cycle are about 36 years and heating systems 30 years (Hoier et al., 2013). In the assumed 10 years renovation period, only one renovation cycle was considered.

3. Building Energy Performance Calculation Model and Extrapolation

The energy performance of the reference buildings due IBBR was assessed using a norm based monthly energy balance calculation model. This multi-zone model was developed in Matlab and calculates the monthly balance of energy performance of buildings. Energy need, delivered energy and primary energy demand for heating, cooling, ventilation, domestic hot water and lighting are assessed based on the calculation methodology specified on the DIN V 18599, which is a an aggregation of the norms (DIN V 4108-6/ DIN V 4701-10 und -12, EN 832, ISO 13790) (Garcia, 2017). After assessing building's new energy performance for the IBBR, a linear extrapolation method was applied, where the calculated energy demand [kWh/m²a] was multiplied by the number of existing buildings of each reference building according to the building stock typology database from Invert/EE-Lab, also into consideration, the percentage of reference building on the total single-family houses construction vintages, as showed in **Fehler! Ungültiger Eigenverweis auf Textmarke.** below.

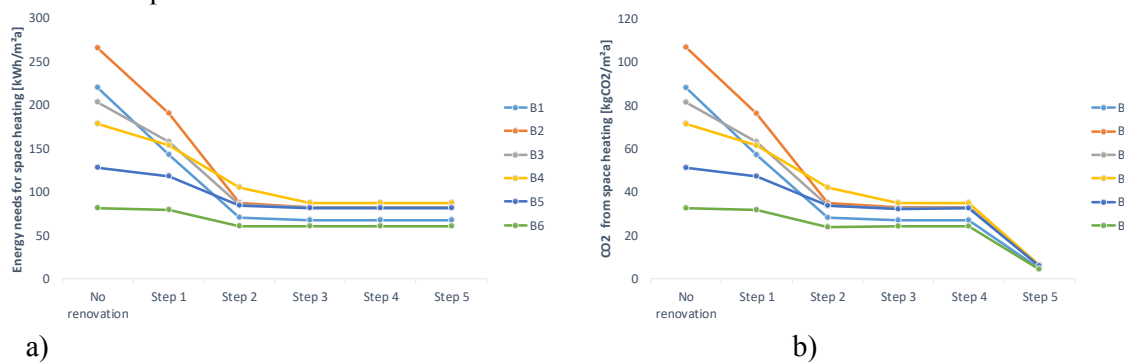
Table 3: Reference Buildings and its representativeness in the building stock for the base year 2012

Construction vintage	Number of buildings per Construction vintage [Tds]	Reference building for the Construction Vintage	Percentage of Reference building's on the Building Vintage	Percentage of Reference building's on Reference building the SFH building stock
1949 -1957	162	B1	26%	2%
1958 -1968	407	B2	36%	7%
1969 -1978	451	B3	39%	6%
1979 -1983	518	B4	80%	7%
1984 -1994	743	B5	79%	7%
1995 -2001	962	B6	94%	5%

This method allowed obtaining an estimation of the total energy needs for space heating, aligning them with the scenario estimated by the techno-economic bottom-up modelling with Invert/EE-Lab.

RESULTS

The graph 2 illustrates the energy needs and CO₂-emissions caused by space heating of each reference building (B1 until B6) and their effects due to the five steps IBRR, according to the renovation steps and measures described in Table 2 above.



Graph 1: Effects on the a) energy needs, on the b) CO₂ emissions, for space heating due to the individual renovation roadmap (IBRR)

The results show a wide range on energy needs for space heating between the reference buildings in the status quo (base year 2012). Reference building B2 has the highest energy need (266 kWh/m²a) while reference building B6 the lowest (81 kWh/m²a), which can be expected since envelope quality differs according to the building construction vintages. Renovation measures on the envelope quality (renovation steps 1 until 3) lead to 25% until 70% energy needs reduction, in reference buildings B6 and B2 respectively. The effects of the renovation measures “insulation of the heat distribution system” and “heating system change” are better observed on the final energy and on primary energy. In step 5, we considered a roadmap, where the oil boiler is substituted by a biomass boiler, which has a lower thermal efficiency, but has significantly lower CO₂ emission factors. As a result from the individual renovation roadmaps, CO₂ emissions are reduced to 5 until 6 kgCO₂/m² depending on the building. The current policy scenario calculated with Invert/EE-Lab, which only considers single-step major renovation of buildings, resulted a reduction from 260 TWh to 132 TWh on the total energy needs for single-family houses space heating. The extrapolation of the IBRR results indicates that such a scenario is also achievable with the approach of stepwise renovation, guided through IBRR. **Fehler! Verweisquelle konnte nicht gefunden werden.** depicts the comparison of energy needs for space heating between Invert/EE-Lab model and the IBRR extrapolation, for each building construction vintage:



Graph 2: Comparison between Invert/EE-Lab and the individual renovation roadmap (IBRR) extrapolation

The graph shows the energy needs for space heating according to the building construction vintages in both years, 2012 (base year) and 2050, for both approaches (Invert-EE/Lab and IBRR). For the base year (2012), Invert/EE-Lab and IBRR present similar energy needs for space heating, exceptionally for the construction vintage 1958-1968, where a difference of

8.140 GWh can be seen. Regarding the trend of the energy needs, between 2012 and 2050 occurs a significant decrease on the energy needs in all building construction vintages, especially on the buildings constructed in 1850-1918, 1958-1968 and 1969-1978. In the Invert-EE/Lab model, buildings constructed after 2012 did not carry out any renovation measures, as the model prioritizes building renovation in buildings with higher specific energy need (kWh/m²), which is the case of older building construction vintage. Finally, the graph shows that for the analysed building construction vintages represented by the reference buildings B1 until B6, Invert/EE-Lab current scenario's can be achieved, as the points representing scenario for 2050 Invert/EE-Lab (in blue) and IBRR (in red) are overlapped.

DISCUSSIONS

The results showed that - based on the approach of the IBRR – it would be required that annually about 4-6% of the single-family building stock, according to the building construction vintage, need to apply at least one retrofitting measure (change windows or insulate the roof, change heating system, etc.), in order to achieve the scenario simulated by the model Invert/EE-Lab. This annual building stock renovation rate results deliver from a static calculation, as the extrapolation considers the same number of buildings from 2012 until 2050, meaning no demolition of old buildings. The definition of a 10-years IBRR period is a significant parameter for the obtained results, rather than the time step between the measures. Concerning the IBRR concept, it should consider national, regional and cultural particularities, political incentives and available technology and therefore it is specific for each country. Especially by the renovation measure “change of heating system”, the analysis should be extended and study a mix of different measures as connecting to district heating net or installing a heat pump. In the present study, only one possibility by changing the oil boiler to biomass boiler was considered. Also, when developing IBRR to buildings situated in hotter climate zones as Germany, measures related to the cooling energy demand should also be considered, as well as cooling energy demand scenario analysis. In regard to the ambitiousness of IBRR, this paper considers renovation standards according to the national building codes. However, if ambitious CO₂-reductions were aimed (>90% CO₂-Emission) not only more energy efficient IBRR would be needed, but also higher annual percentage of at least one retrofitting measure.

CONCLUSIONS

Results show that for the analysed construction vintage (1949-2001), annually about 4-6% of the single-family building stock need to apply at least one retrofitting measure, in order to achieve CO₂-Emission reduction according to the current policy scenario. Uncertainties are related to the calibration of the base year (2012) between both approaches Invert-EE/Lab and IBRR. More accuracy on the results can be assured by extending the reference buildings to all

construction vintages provided by the single-family houses building stock of Invert-EE/Lab, in a way that each building construction vintage from 1850 until 2012 has at least one reference building. Also, the chosen reference buildings for the vintages 1949-1958, 1959-1968 and 1969-1978 represent less than 50% of percentage of energy needs on the building construction vintage. This means, choosing more than one reference buildings for these groups can increase accuracy. In all, IBRR can become an important instrument to achieve national targets, as it reduces some barriers for renovation activities in single-family houses, by increasing the application of annual deep renovation measures in the existing single-family houses.

ACKNOWLEDGEMENT

This work was supported by the European Union's Horizon 2020 Framework Programme (iBRoad project –<http://ibroad-project.eu/>).

REFERENCES

- EU Buildings Datamapper, 2013. EU Buildings Datamapper - Energy - European Commission [WWW Document]. Energy. URL [/energy/en/eu-buildings-datamapper](#) (accessed 6.21.18).
- European Parliament, 2018. Directive of the European Parliament and of the Council - amending Directive 2010/31/EU on the energy performance of buildings and Directive 2012/27/EU on energy efficiency [WWW Document]. URL <http://data.consilium.europa.eu/doc/document/PE-4-2018-INIT/en/pdf> (accessed 6.12.18).
- Fabbri, M., Volt, J., de Groote, M., 2018. iBRoad_D.2.2 The Concept of the Individual Building Renovation Roadmap.pdf.
- Filippidou, F., Nieboer, N., Visscher, H., 2017. Are we moving fast enough? The energy renovation rate of the Dutch non-profit housing using the national energy labelling database. *Energy Policy* 109, 488–498. <https://doi.org/10.1016/j.enpol.2017.07.025>
- Garcia, J., 2017. Nearly Zero Energy Buildings (nZEB): definition and comparative analysis in selected EU countries. Master Thesis.
- Hartner, M., Forthuber, S., Kranzl, L., Fritz, S., Müller, A., Bernath, C., Sensfuß, F., Maranon-Ledesma, H., 2018. D5.3 SET-Nav: Summary report on case study - Energy demand and supply in buildings and the role for RES market integration.
- Hoier, A., Erhorn, H., Hauser, G., Sedlbauer, K., 2013. Energetische Gebäudesanierung in Deutschland, Studie Teil 1: Entwicklung und energetische Bewertung alternativer Sanierungsfahrpläne.
- Kranzl, L., Hummel, M., Müller, A., Steinbach, J., 2013. Renewable heating: Perspectives and the impact of policy instruments. *Energy Policy*. <https://doi.org/10.1016/j.enpol.2013.03.050>
- Müller, A., 2015. Energy Demand Assessment for Space Conditioning and Domestic Hot Water: A Case Study for the Austrian Building Stock 285.
- Olonscheck, M., Holsten, A., Kropp, J.P., 2011. Heating and cooling energy demand and related emissions of the German residential building stock under climate change. *Energy Policy* 39, 4795–4806. <https://doi.org/10.1016/j.enpol.2011.06.041>
- Pfluger, B., Bernath, C., Bosmann, T., Elsland, R., 2017. Langfristszenarien für die Transformation des Energiesystems in Deutschland [WWW Document]. URL https://www.bmwi.de/Redaktion/DE/Downloads/B/berichtsmodul-0-zentrale-ergebnisse-und-schlussfolgerungen.pdf?__blob=publicationFile&v=6 (accessed 6.12.18).
- Risholt, B., Berker, T., 2013. Success for energy efficient renovation of dwellings—Learning from private homeowners. *Energy Policy* 61, 1022–1030. <https://doi.org/10.1016/j.enpol.2013.06.011>
- Steinbach, J., 2016. Modellbasierte Untersuchung von Politikinstrumenten zur Förderung erneuerbarer Energien und Energieeffizienz im Gebäudebereich. FRAUNHOFER VERLAG, Stuttgart.

Impact of an Energy Efficiency Regulation in Northern Canada

Asok Thirunavukarasu^{1,*}, Hua Ge¹ and Andreas Athienitis¹

¹Concordia University, Montreal, Quebec, Canada

*Corresponding email: asok.thiruna@gmail.com

ABSTRACT

Extreme cold climates and Canada's sparsely populated Northern regions have limited human and infrastructural capacity making it difficult to build energy-efficient homes. Despite such differences, homes are built based on codes and standards developed for Canada's South. In 2008, a by-law was passed in Yellowknife, Canada requiring a minimum EnerGuide Housing (EGH) rating of 80 for all new single-family and two-family residential buildings. The EnerGuide's Energy Rating Service (ERS) program is an energy assessment program for residential housing formerly known as the EnerGuide Rating for Houses (EGH). Homes are rated between 0 to 100; lower numbers represent homes that are less efficient and 100 represents an airtight and well-insulated house that is net-zero energy. 1002 homes from the City of Yellowknife evaluated since 1950s were studied from the ERS database, Performance metrics studied include energy intensity, EGH rating, ACH rating, window types, the thermal resistance of the building envelope, primary heating and hot water heating equipment's efficiencies, total electricity used, and total energy used. The analysis identified the current state of housing in Yellowknife, past and present housing trends, and determined the effect of the city of Yellowknife's new building by-law had on housing performance. The preliminary finding shows a pathway to significantly improve the energy efficiency of the housing stock in Yellowknife. This regulation shows other municipalities in Canada that legislations pushing energy efficient buildings can be very effective.

KEYWORDS

Remote Communities, Extreme Cold Climates, Energy Efficient Housing, Policy

INTRODUCTION

The Canadian northern region is remote with limited human and infrastructural capital, little demand for private housing and small incentives for suitable northern building products. Temperatures drop to -50°C for extended periods; homes must have high performing building envelope with minimized thermal bridges and air leakage. There are housing standards adopted in northern regions that were developed for Southern regions of Canada with warmer climates. With growing concerns about climate change and the region's desire to become less dependent on fossil fuels, governments have identified new housing standards as urgent (Government of Nunavut, 2007). As part of a research program, a protocol for low energy homes for northern Canadian regions was developed (Thirunavukarasu et al., 2016). This paper outlines a section of the research, which examined the impact of the city of Yellowknife's building by-law no. 4469 had on the energy performance of housing. The by-law, adopted in 2008, required a minimum EnerGuide Housing (EGH) rating of 80 for all low-rise residential buildings. This paper presents the impact of by-law no. 4469 on the housing performance to show methods that improve significantly the energy efficient of homes.

METHODS

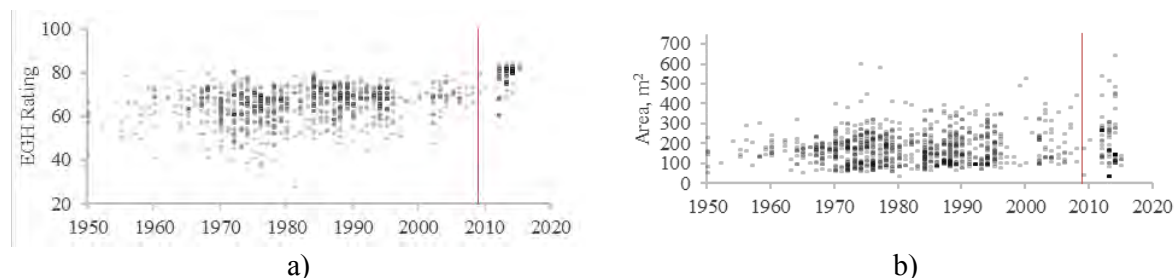
The EnerGuide's Energy Rating Service (ERS) or the EnerGuide Rating for Houses (EGH) program, developed by Natural Resource Canada (NRCan), is an energy assessment program for residential housing. The program evaluates the housing size, location, orientation of the home, building envelope (area, average insulations levels in walls, ceiling, floors,) window types, air leakage (measured), mechanical systems (heating, domestic hot water and ventilation), occupant behaviors, appliances, and lighting loads (Parekh et al., 2000). The total energy consumption is estimated based on the above inputs into HOT2000 software platform, validated by Natural Resource Canada (NRCAN). The program assumes, for single family homes, 2 adults and 2 children occupancy, 225 liters/day hot water load and an electric load of 24kWh/day.

The EGH rating is calculated as the ratio of estimated total energy consumption to benchmarked total energy consumption of the building. The benchmarked values are based on heating degree days for the location. Homes are rated between 0, indicating high energy consumption, and 100 indicating a net-zero energy home. Homes rated EGH 80 represent home built to ENERGY STAR standards. The EGH rating allows a standardized energy labels for homes. Data collected through certified evaluators upload information into the ERS database. The database is a comprehensive tool to track and manage residential energy evaluations and allows for identification of trends over time and region. 1002 homes evaluated for EGH rating from the City of Yellowknife were data mined from the ERS database – the last evaluated home included in this study was built on July 1st, 2015.

By-law no. 4469 required a minimum EGH rating of 80 for low-rise residential units. Pre-drywall blower door testing for air leakage and submission of construction plans to city for recommendations. The study compares performance metrics of 225 homes built from 1990 to 2009 to 102 homes built between 2010 and 2015. The parameters include ACH rates obtained through blower door testing, thermal resistance levels of building envelope, and mechanical systems efficiencies obtained through on-site verification, EGH rating, energy intensity (kWh/m^2), total annual electricity use (kWh/m^2), and total annual energy consumption (kWh/m^2) calculated using software.

RESULTS

102 homes evaluated are built after 2009 when by-law no. 4469 took effect. Figures 1a to 1g plot performance metrics based on construction dates from 1950 to 2015. There is a gradual improvement in the air leakage rate, thermal efficiency of the building envelope, and the annual energy consumption. Primary heating and hot water equipment's efficiencies remained constant 2009, then improved by 5 to 10%. After 2008, there is a 'clustering effect' as seen in Figure 1a, 1b, 1c, 1d, 1e and 1g.



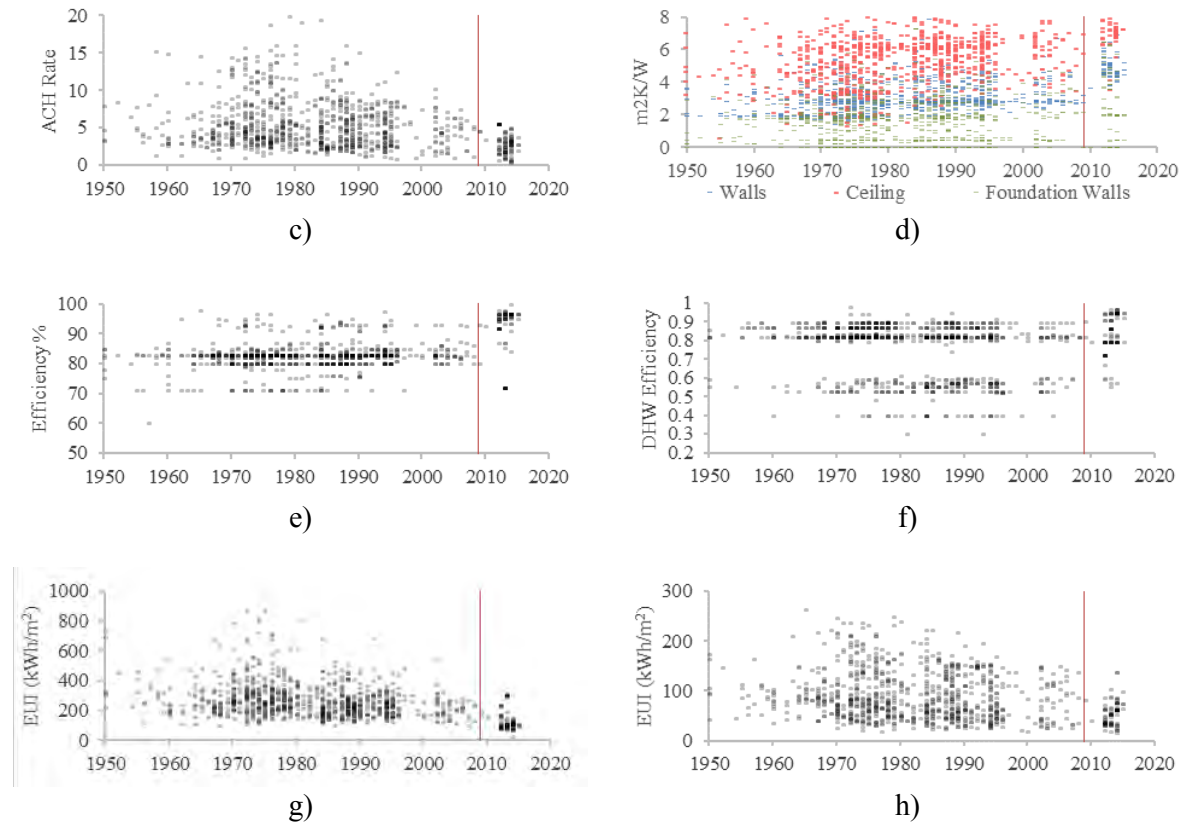


Figure 1. Performance metrics for homes since 1950 to 2015 (a) EGH rating, (b) home footprint (m²), (c) ACH Rate @ 50 pa, (d) Thermal resistance for walls, ceiling and foundations, e). primary heating equipment efficiency, (f) primary DHW equipment efficiency, (g) annual energy use intensity, (h) Annual electricity use.

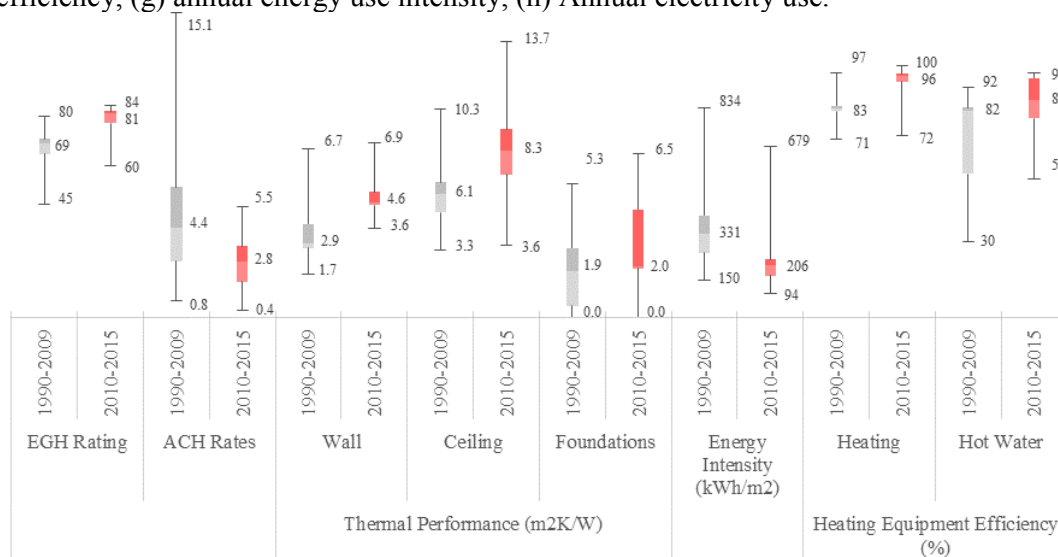


Figure 2. Percentage box plot shows minimum, 25% percentile, median, 75% percentile and maximum values for performance parameters between 1990 to 2015. Values for minimum, median and maximum are labelled on the graph.

Figure 2 presents the percentage box plot comparing 225 homes built in 1990 to 2009 and 103 homes built in 2010 to 2015. Impact of by-law no. 4469 is further evident in Figure 2. The median EGH rating rose from 69 to 81, the median ACH rate reduced by 36% from 4.4 to 2.8.

Primary heating and hot water equipment efficiency increased by 10% and 5% to 96% and 87%, respectively. Higher efficiencies were achieved by installing condensing boilers for heating and switching to instantaneous condensing hot water heaters from conventional storage-type water heaters. Thermal performance of the exterior walls increased from 2.9 m²K/W to 4.6 m²K/W. The minimum thermal performance of the exterior wall in homes built after 2009 was 3.6 m²K/W, greater than the median for homes built between 1990 and 2010. Median thermal performance of the ceiling increase by 35% (2.2 m²K/W). Median energy intensity is reduced by 37% after the by-law was adopted. Newer homes used 10% less total annual electricity than homes built between 1990 to 2009. EnerGuide’s rating systems has a standard assumption for household lighting and plug loads – so, this research did not assess any energy efficiency steps to reduce lighting and plug loads.

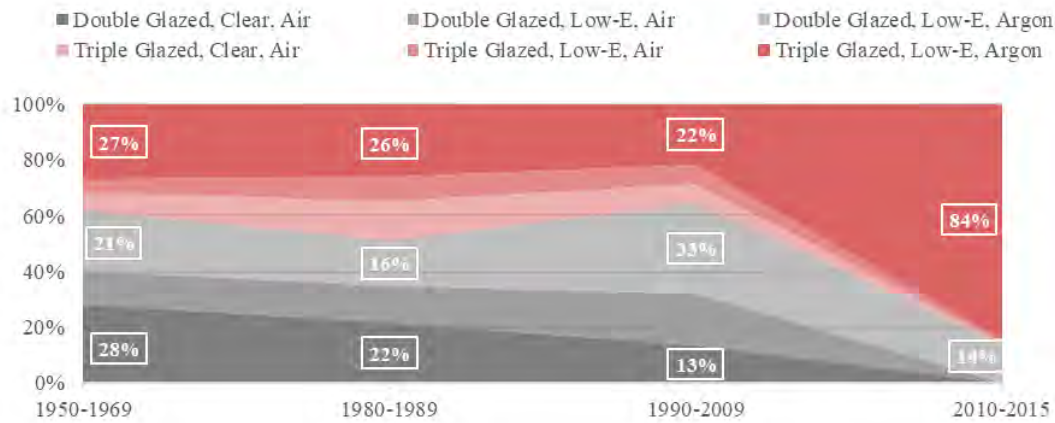


Figure 3. Distribution of window types as a percentage between 1950 to 2015

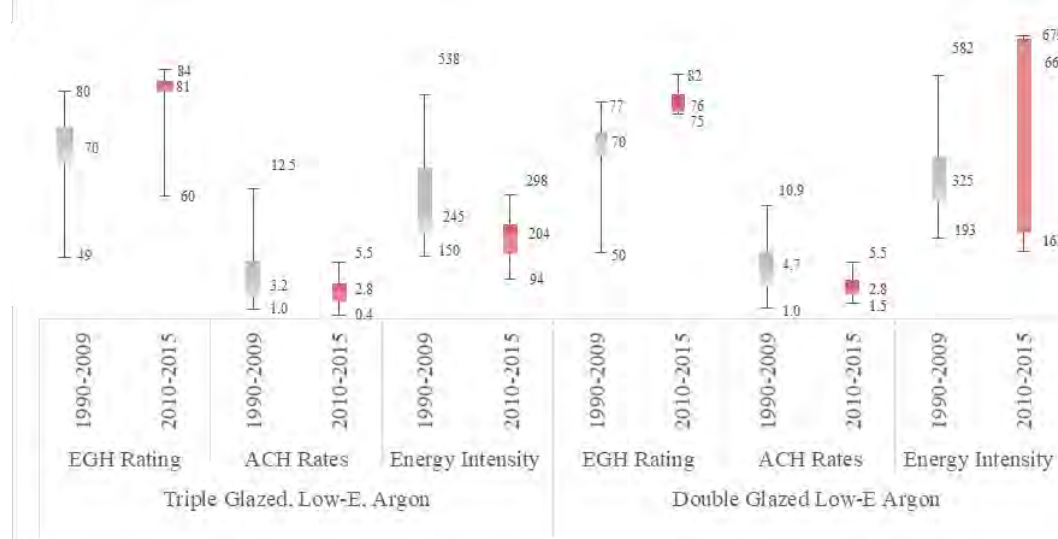


Figure 4. Percentage box plot shows minimum, 25% percentile, median, 75% percentile and maximum values for performance parameters between 1990 to 2015 comparing triple glazed to double glazed windows. Values for minimum, median and maximum are labelled on the graph.

After 2009, shares of triple-glazed, low-E, argon windows (TG) installed in homes increased from 22% to 84%. Between 1990 and 2009, double-glazed, low-E, argon windows (DG) were most common – although, notice a greater variation in windows install between 1950 to 2009. Between 2010 and 2015, 98% of all windows install were either DG or TG. Figure 4 evaluates

EGH, ACH rates, and energy intensity of homes using TG and DG for homes built from 1990 to 2009 and from 2010 to 2015. First, homes built after 2009 had higher EGH rating and lower ACH rating for both window types. Energy intensity reduced only for TG after 2009. 14 homes built after 2009 installed DG; which may explain the higher variance in energy intensity for DG. Homes built from 1990 to 2009 had similar EGH rating, ACH rating and energy intensity levels regardless of window type used.

DISCUSSION

The data shows a clear pathway to increase energy efficient homes for the North with 75% of homes built after 2010 reaching ENERGY STAR performance (Figure 2.) Although cost was not considered in this study, as fuel is imported in the northern regions of Canada, electricity cost per kilowatt-hour (kWh) can be up to 10 times as much as in southern cities (Northwest Territories Power Corporation, 2015). Significant energy savings can be achieved for little added cost by building high performing envelope systems, performing pre-drywall blower door testing and installing triple pane windows. Energy savings through the building envelope can reduce size of the mechanical systems and more efficient mechanical systems such as condensing boilers and instantaneous hot water heaters is chosen. Further optimization of solar design parameters (Thirunavukarasu et al., 2016) can further reduce energy consumption for little added cost.

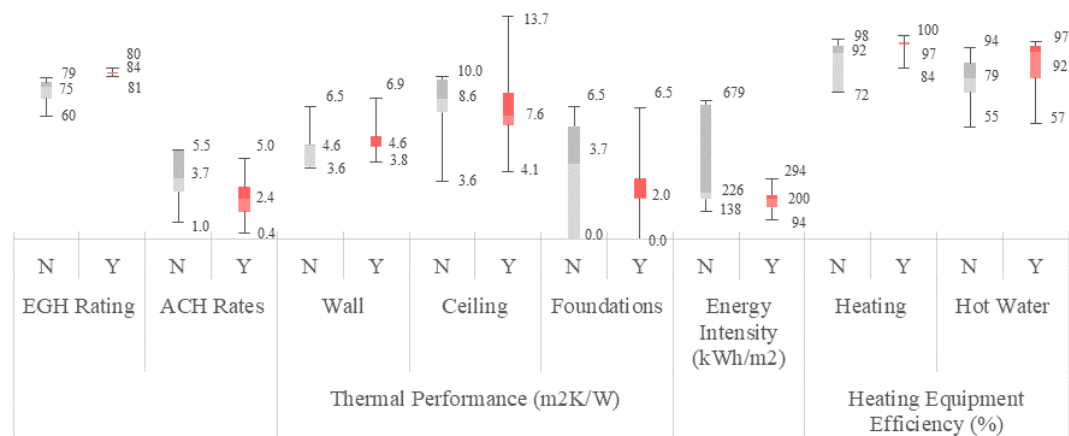


Figure 5. Percentage box plot showing performance of homes in non-compliance (N) and compliance (Y) with by-law.

This study shows that since by-law no. 4469 was passed, 84% of homes used triple glazed, low-e, argon windows, reduced air leakage, and increased thermal efficiency of the building envelope. Although the by-law faced resistances from local builders, general opinions of builders in 2015 were supportive (Thirunavukarasu et al., 2016). Of the 102 homes evaluated since 2010 to July 1st, 2015, 69 homes built met the by-law requirements.

Homes not in compliance with the by-law either had twice the average ACH rate of homes in compliance with the by-law (see Figure 5) and/or used less efficient conventional hot water heaters and/or had little to no insulation levels on foundation walls.

CONCLUSION

This paper presents the results analyzed for 1002 houses from the EnerGuide's Energy Rating Service (ERS) for Yellowknife, Northwest Territories and the impact of by-law no. 4469 by

evaluating 225 homes built from 1990 to 2009 and comparing to 102 homes built between 2010 and 2015. By-law no. 4469 required a minimum EGH rating of 80 and city offered pre-drywall blower door testing for air leakage, and pre-construction submission of plans for recommendations from the city.

This by-law shows other municipalities in Canada that legislation for more energy efficient buildings can be very effective when combined with verification methods such as blower door testing.

ACKNOWLEDGEMENT

The authors would like to acknowledge the following organizations for their support: Arctic Energy Alliance, NSERC Smart Net-Zero Energy Buildings Strategic Research Network (SNEBRN), Natural Sciences and Engineering Research Council of Canada (NSERC), Natural Resources Canada (NRCan) and the Northern Scientific Training Program by Canadian Polar Commission.

REFERENCES

- Thirunavukarasu et al. 2016, Protocol for Low Energy Houses for Northern Canadian Regions, MAsc. thesis, Concordia University.
- Parekh et al. 2000, Residential Buildings: Program Design, Implementation, and Evaluation, American Council for an Energy-Efficient Economy.
- Government of Nunavut, 2007, Report: Ikummatiit: The Government of Nunavut Energy Strategy. Retrieved 2016 from <https://www.gov.nu.ca/files/Ikummatiit>
- Northwest Territories Power Corporation. (2015), Residential Electric Rates, Retrieved January 2016 from <https://www.ntpc.com/customer-service/residential-service/what-is-my-power-rate>

A comparison of model order reduction methods for the simulation of wall heat transfer

¹Tianfeng Hou*, ¹Staf Roels and ¹Hans Janssen

¹KU Leuven, Department of Civil Engineering, Building Physics Section, Kasteelpark Arenberg 40, 3001 Leuven, Belgium

*Corresponding email: tianfeng.hou@kuleuven.be

ABSTRACT

In this paper, the potential of model order reduction for simulating building performance is assessed, via a case study of modelling heat transfer through a massive masonry wall. Two model order reduction techniques – proper orthogonal decomposition and proper generalized decomposition – are investigated and compared. Moreover, to illustrate the performance of model order reduction techniques, the accuracies of the two model order reduction techniques are respectively compared with a standard finite element method. The outcomes show that both of the two model order reduction techniques are able to provide an accurate result, and the proper generalized decomposition tends to be more versatile than the proper orthogonal decomposition method.

KEYWORDS

Model order reduction, proper generalized decomposition, proper orthogonal decomposition, finite element method, heat transfer

INTRODUCTION

Today, 30% of the European building stock consists of ‘historic’ buildings built prior to World War II (Ribuild.eu, 2018). These buildings are typically far less energy-efficient than new buildings, and they hence account for a large share of the total energy consumption of buildings. One important measure to reduce their energy consumption is to install internal insulation. However, internal insulation is often associated with moisture damage, and much care should be taken when applying this solution. This paper is part of the EU H2020 RIBuild project, which aims at developing effective and comprehensive guidelines for internal insulation in historic buildings. Given that a multitude of scenarios and factors can be easily evaluated with numerical analyses, the use of numerical simulations for hygrothermal performance assessment tends to be the best option. However, the standard numerical methods for space and time discretization are usually very time consuming due to the high non-linearity of the equations, the multi-dimensional spatial domains and the long simulation time intervals required, in order to reduce the computation time as much as possible, an efficient solver for modelling the hygrothermal behavior of the wall is needed. Therefore, a faster surrogate model is highly desired.

Instead of using the standard numerical models, Van Gelder et al. (2014) employed statistical regression and interpolation based surrogate models (such as polynomial regression, Kriging etc.) to reduce the simulation time. However, these statistical surrogate models can only deliver static results: for the heat transfer through a wall, they may predict the yearly total heat loss, but not the temperature profile at each moment in time. Hence, to obtain the dynamic behavior with a simplifying surrogate model, model order reduction techniques as alternatives of the statistical surrogate modelling are investigated. In this paper, two model order reduction methods (proper orthogonal decomposition (POD) and proper generalized decomposition (PGD)) are

investigated and compared. The first method belongs to a family of a posteriori methods - it is built based on the preliminary results of the original time-consuming model. The second method is an a priori method which can be established by a suitable iterative process. Instead of the standard finite element method (FEM), we will use both POD and PGD to simulate the building thermal performance, exemplified through a case study of modelling the heat transfer through a massive masonry wall.

Below, first a brief introduction of POD and PGD are put forward, with focus on the potential use for the modelling of wall heat transfer. Subsequently, the calculation object and the case study with its input parameters are introduced, as that forms the central application in this study. Next, the results of using POD and PGD for simulating the wall heat transfer are presented and a discussion with respect to the interpretation of their accuracies follows. Finally, conclusions on which method is considered most optimal are formulated.

POD AND PGD FOR MODELLING WALL HEAT TRANSFER

The thermal performance of a building component can be assessed by analyzing the transfer of heat through building materials. Heat transfer is mainly related to the normal flows of heat conduction, convection, radiation and advection. Thus, assessing the thermal performance of a building component requires to get numerical simulation results of the heat transport equation based on the component geometry, the boundary conditions and the material properties. The conventional thermal simulation models are mainly based on numerical simulation methods for space and time discretization, for instance, the FEM. As mentioned before, these standard numerical methods can be very time consuming due to the high number of degrees of freedom after the spatial and temporal discretization. Therefore, in this paper we investigate two model order reduction methods (POD and PGD) which reduce the degrees of freedom of the complex system and still mimic the dynamic behavior (such as time evolution of temperatures,...).

Proper orthogonal decomposition

The POD method was first proposed by Kosambi (1943), and has been successfully applied in a variety of engineering fields, such as image processing, signal analysis, data compression and recently in building physical engineering (Tallet et al., 2017). POD is also known as Karhunen - Loeve decomposition, principal component analysis, or singular value decomposition, and the connections of these three methods are provided by Liang et al. (2002). A brief tutorial of POD can be found in (Chatterjee, 2000), a detailed introduction of its theory and related application for modelling heat transfer process are respectively presented by Liang et al. (2002) and Fic et al. (2005). The basic idea of POD is approximating a high dimensional process by its ‘most relevant information’. In this paper, we extract the ‘most relevant information’ by making use of principal component analysis (PCA). After the PCA, the POD modes are constructed by selecting the most important k components, here $k \ll m$, where m is the number of the mesh elements. As a result, these POD modes can be used to construct a reduced model for simulating different problems (for instance, variations in the boundary conditions or material properties or longer simulation period).

Proper generalized decomposition

Despite the POD method being able to provide a reduced basis and save the computational time when simulating similar problems, this method has an important drawback: to construct a POD, ‘a priori knowledge’ – the snapshots of the large original model – is needed. This disadvantage in turn leads to an extra computational cost and limits its application to ‘different but similar problems’. On the contrary, Ladeveze (1985) proposed a different strategy, called ‘radial

approximation'. This method is based on the hypothesis that the solution of the considered problem is given by a finite sum representation:

$$u(\mathbf{x}, t) = \sum_{i=1}^N \mathbf{X}_i(\mathbf{x}) \cdot T_i(t) \quad (1)$$

Here, u is the solution of the target problem, \mathbf{X}_i usually stands for the spatial parameters, T_i represents the temporal parameter. Next, injecting equation (1) into the weak formulation of the differential equation and starting from an initial point based on the related initial and boundary conditions, the solution $u(\mathbf{x}, t)$ can be constructed by successive iterative enrichment methods. The procedure is stopped when the convergence criteria are reached. As a result, this strategy allows to approximate the solution without any 'a priori knowledge'. Inspired by this strategy, Ammar et al. (2006) generalized this method to the multidimensional situation and named it proper generalized decomposition (PGD). A detailed tutorial of PGD is proposed by Chinesta et al. (2013), and an application of PGD for simulating thermal processes is provided by Pruliere et al. (2013). In addition, two reviews of PGD are provided by Chinesta et al. (2010) and Berger et al. (2016), with attention for general and physical engineering applications respectively.

CALCULATION OBJECT AND CASE STUDY

For investigating the performance of POD and PGD for hygrothermal simulations, a calculation object hence needs to be formulated. Since the reference situation prior to retrofit is often a massive masonry wall, and that configuration is adopted here as calculation object. In order to judge the feasibility of internal insulation in historic buildings, the hygrothermal performances of internally insulated massive walls – heat loss, mould growth, wood rot, ... – need to be investigated (Vereecken et al. 2015). To simplify the calculation complexity in this study, this paper limits that performance assessment to the transmission of heat loss through the wall. Since quantifying the heat loss requires solution of the temperature profiles of the wall, both the temperature profiles and heat losses over the entire year are taken as the targeted outputs. To do so, the thermal behavior of the wall is simulated with FEM, POD and PGD, wherein the conductive heat transfer equation is solved under the relevant interior and exterior boundary conditions. The simulation result of the FEM is taken here as the reference solution: more specifically, this reference solution is calculated by the FEM with 200 mesh elements and a fixed time step of one hour.

As mentioned before, since POD is constructed for simulating different problems, in this paper, several POD models are constructed by using snapshots of different time intervals (one year, one month, one day, half day, six hours and three hours). Except for the time interval of one year, all the other scenarios are performed 12 times: once for every month. In addition, each of the one day, half day, six hours and three hours are taken at the start of each month. In order to evaluate the performance of different model order reduction methods as a function of the number of modes, both of the POD and PGD models are calculated with 1 to 15 modes.

For the comparison case study of PGD and POD, the detailed information of the input parameters is mentioned here. For the material properties, the density, thermal capacity and conductivity of the wall are 2087 kg/m^3 , 870 J/kgK and 1.07 W/mK . The boundary conditions are kept restricted to combined convection and radiation, governed by climate data of Gaasbeek (Belgium) at the exterior surface, and by the indoor air temperature as described in (EN 15026) at the interior surface. The related interior and exterior surface transfer

coefficient are $8 \text{ W/m}^2\text{K}$ and $25 \text{ W/m}^2\text{K}$, respectively. In relation to the component geometry, the thickness of the wall is 0.2 m .

RESULTS

To compare the accuracies of PGD and different POD models, the average temperature difference between the FEM solution and different model order reduction models, as a function of the number of modes, is shown in Figure 1. For getting a more direct view of the performance of POD and PGD methods, different profiles of temperature are compared at different moments, and the result is presented in Figure 2. In addition, since in practice the cumulated heat loss is usually considered as an indicator of the thermal performance of the wall, the relative deviation of heat losses between the reference solution and different model order reduction models are shown in Figure 3.

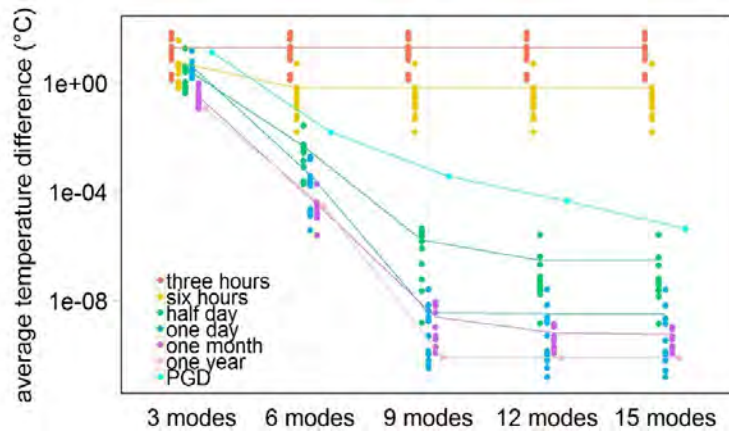


Figure 1. Average temperature differences between reference solution and different model order reduction approximations.

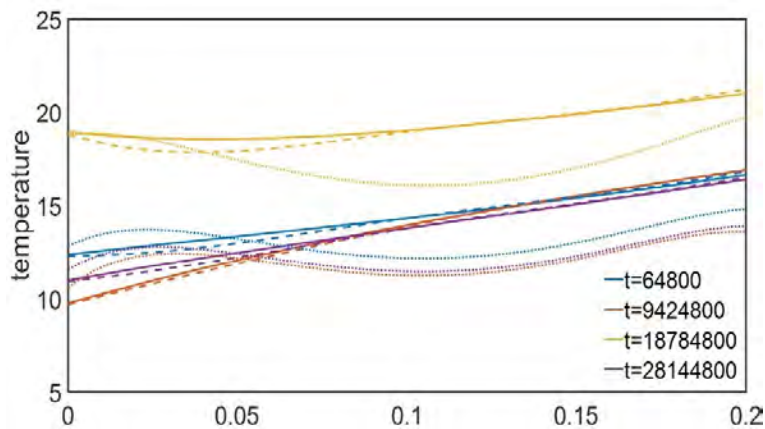


Figure 2. Temperature profiles of the reference solution and PGD solution (solid lines), POD solution constructed from 6 hours' snapshots (dashed lines) and from 3 hours' snapshots (dotted lines). All the reduced models are constructed by 15 modes.

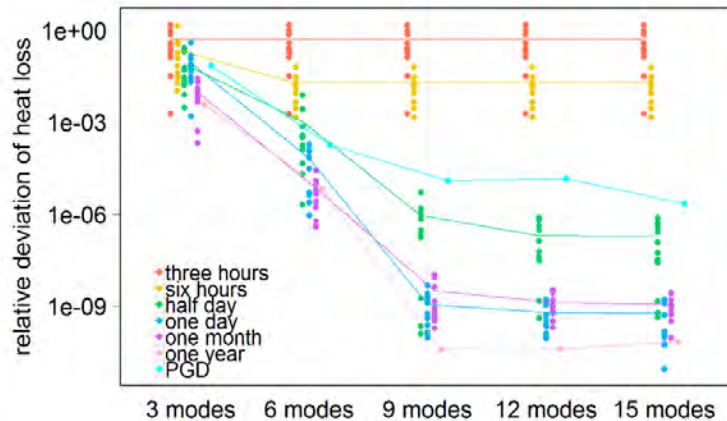


Figure 3. Relative deviation of heat loss between reference solution and different model order reduction approximations.

DISCUSSIONS

Figure 1 illustrates that, except for the POD constructed from the 3 and 6 hours' snapshots, the accuracy of the other reduced order models increases as the number of their construction modes raises. However for the POD, after 9 modes this improvement becomes negligible. In addition, one can see that the accuracy of the POD increases as the time duration of its snapshots raises. In relation to the PGD, one can see that a relatively accurate result can be reached with a sufficient number of construction modes. Figure 2 confirms the result of Figure 1, it is shown that visually there is no difference between the reference solution and PGD approximation. On the other hand, larger differences can be respectively found between the reference solution and the solution calculated by the POD with the 6 and 3 hours snapshots. Furthermore, compared with Figure 1, a very similar result can be found in Figure 3 - except for the POD constructed from the 3 and 6 hours' snapshots, the relative errors of the other reduced order models decreases as the number of their construction modes increases and these relative errors can be reached below 1% with a very limited number of modes. These findings indicate that the performance of all the model order reduction methods do not vary much for quantifying the heat loss instead of calculating the temperature profile.

In summary, combined the results of all the Figures, we can conclude that, with enough number of modes the PGD method can provide a relatively accurate result. In relation to the POD, only when the number of snapshots is really insufficient (three and six hours), an inaccurate result may be obtained. As a consequence, for using the POD method to obtain an accurate result with the smallest size of snapshot, an error estimation method is thus needed. On the other hand, since the PGD model is constructed based on a suitable iterative method, an error controller is naturally embedded in this method. Therefore, together with the advantage that the PGD model is constructed without any 'prior knowledge', this method tends to be more versatile than the POD.

CONCLUSIONS

In this paper, we investigated the performance of two model order reduction methods (POD and PGD), based on a case study of modelling heat transfer through a massive masonry wall. It is shown that, both of the two methods can provide a very accurate result. In addition, since the construction of PGD does not rely on any 'a priori information', this method tends to be more versatile than the POD and should be preferred.

ACKNOWLEDGEMENT

This work has been supported by the H2020 RIBuild project, their support is gratefully acknowledged.

REFERENCES

- Ammar A., Mokdad B., Chinesta F., and Keunings R. 2006. A new family of solvers for some classes of multidimensional partial differential equations encountered in kinetic theory modeling of complex fluids. *Journal of non-Newtonian fluid Mechanics*, 139(3), pp.153-176.
- Berger J., Mendes N., Guernouti S., Woloszyn M., and Chinesta F. 2017. Review of Reduced Order Models for Heat and Moisture Transfer in Building Physics with Emphasis in PGD Approaches. *Archives of Computational Methods in Engineering*, 24(3), pp.655-667.
- Chatterjee A. 2000. An introduction to the proper orthogonal decomposition. *Current science*, pp.808-817.
- Chinesta F., Ammar A., and Cueto E. 2010. Recent advances and new challenges in the use of the proper generalized decomposition for solving multidimensional models. *Archives of Computational methods in Engineering*, 17(4), pp.327-350.
- Chinesta F., Keunings R., and Leygue A. 2013. *The proper generalized decomposition for advanced numerical simulations: a primer*. Springer Science & Business Media.
- EN B., 2007. 15026: 2007: Hygrothermal performance of building components and building elements-Assessment of moisture transfer by numerical simulation. German version DIN EN, 15026.
- Fic A., Białecki R.A., and Kassab A.J. 2005. Solving transient nonlinear heat conduction problems by proper orthogonal decomposition and the finite-element method. *Numerical Heat Transfer, Part B: Fundamentals*, 48(2), pp.103-124.
- Kosambi D.D. 2016. *Statistics in function space*. In DD Kosambi (pp. 115-123). Springer, New Delhi.
- Ladeveze P. 1985. On a family of algorithms for structural mechanics. *Comptes rendus de l'Académie des Sciences*, 300(2), pp.41-44.
- Liang Y.C., Lee H.P., Lim S.P., Lin W.Z., Lee K.H., and Wu C.G. 2002. Proper orthogonal decomposition and its applications—Part I: Theory. *Journal of Sound and vibration*, 252(3), pp.527-544.
- Pruliere E., Chinesta F., Ammar A., Leygue A., and Poitou A. 2013. On the solution of the heat equation in very thin tapes. *International Journal of Thermal Sciences*, 65, pp.148-157.
- Ribuild.eu. (2018). about RIBuild. [online] Available at: <http://ribuild.eu/about>.
- Tallet A., Liberge E., and Inard C. 2017, February. Fast POD method to evaluate infiltration heat recovery in building walls. *Building Simulation*.
- Van Gelder L., Das P., Janssen H., and Roels S. 2014. Comparative study of metamodelling techniques in building energy simulation: Guidelines for practitioners. *Simulation Modelling Practice and Theory*, 49, pp.245-257.
- Vereecken E., Van Gelder L., Janssen H., and Roels S. 2015. Interior insulation for wall retrofitting—A probabilistic analysis of energy savings and hygrothermal risks. *Energy and Buildings*, 89, pp.231-244.

A framework for comfort assessment in buildings and districts retrofit process

Marco Arnesano^{1,*}, Federica Naspi¹, Livia Claudi¹ and Gian Marco Revel¹

¹Dipartimento di Ingegneria Industriale e Scienze Matematiche, Università Politecnica delle Marche, via Brecce Bianche, Ancona 60131, Italy

**Corresponding email: m.arnesano@univpm.it*

ABSTRACT

The retrofit design of buildings and districts cannot exclude the occupants' perspective if comfortable and healthy conditions have to be obtained. For this reason, the NewTREND¹ project developed a collaborative platform for the energy efficient buildings and districts retrofit that includes the users' perspective. Three modules have been developed for thermal comfort, acoustic comfort and behavioural assessment. These modules are integrated into a Simulation and Design Hub that, after gathering data from on-site measurements, builds a simulation model of the district, calculates yearly results and exposes them to the design team through a dedicated District Information Model server and user interfaces. These modules perform deep investigations on the occupants' sensation and behaviour, based on both measured and simulated datasets and provide comparisons of comfort performances, considering different retrofit scenarios and related uncertainties. In details, the thermal comfort module performs analysis according to both predictive and adaptive models, evaluates the variability around the design conditions together with sensitivity analysis that highlights which parameters are the most critical for the retrofit design. The acoustic module provides a complete tool to predict and assess the indoor acoustic comfort, taking into account the performance of building envelope and the impact of district noise. Finally, the behavioural module empowers the building energy simulation with co-simulation capabilities that reproduces the real occupants' behaviours in relation to comfort conditions. The final goal of the framework is to support the decision-making process in selecting the optimal retrofit option that achieves the targeted energy efficiency without infringing the occupant's expectation in terms of comfort and well-being.

KEYWORDS

Thermal Comfort, Acoustic Comfort, Behavioural Modelling, Monitoring, Simulation.

INTRODUCTION

Buildings have the main goal of providing comfortable conditions for the occupants. The lower is the comfort sensation the higher will be the probability that occupants occur in non-efficient behaviours and low productivity because of the degraded well-being. Thus, maintaining the optimal thermal conditions in all occupied spaces is a key feature. On the other side buildings account for the 40% of the total energy consumption and they have to become as much efficient as possible so to use the minimum energy to provide comfortable conditions. Considering that, more than the 35% of European buildings have been built before the 60's and more than the 80% before the 90's (BPIE, 2011), they do not include materials and technologies capable of high performance or they have degraded with. In this context, the renovation and retrofit interventions are to be considered as priority to achieve the objective

¹ <http://newtrend-project.eu/>

of reducing the global energy consumption and striving to the resilience required for facing climate changes. Comfort plays an important role in buildings renovation. In fact, the recent report “Feel Good, Live Well - The UK home, health and wellbeing report”² points out that over 95% of homeowners and renters make some effort to look after their health and wellbeing and health and wellbeing issues in their existing homes they would like to change are in the first position. In this context, the NewTREND project proposes a Collaborative Design Platform to enable wide retrofit actions of buildings and districts, including comfort and well-being into the multicriteria assessment framework. This paper presents the platform and three tools dedicated investigate the occupants’ perspective.

METHODS

The NewTREND cloud platform

The main aim of the NewTREND cloud-based platform is to support the collaborative design and to promote the dialogue between the different subjects involved in a retrofit project. In this perspective, a District Information Model (DIM) server has been developed to store data and to make them available for the designers. In parallel, a Simulation & Design Hub (SDH), creating a simulation model of the district, allows effective comparisons between retrofit options at both building and district level and guide the decision makers in choosing the best strategy. These targets are achieved using dynamic simulations (IESVE software) which provide yearly energy assessments and calculations of Key Performance Indicators (KPIs). These components are merged in a Collaborative Design Platform, which provides the access to all the embedded tools and the visualization of the results through an intuitive Graphical User Interface. Figure 1 reports a scheme of the platform.

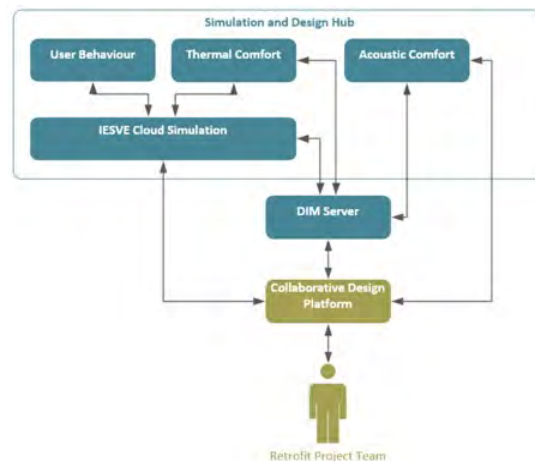


Figure 1. Scheme of the NewTREND platform.

A key improvement of this methodology concerns the inclusion of the occupants’ perspective in the decision-making process. In fact, the evaluation of different retrofit scenarios is investigated considering both users’ comfort (thermal and acoustic) preferences and the human-building interaction. According to this people-centred perspective, three modules have been developed. The thermal comfort and acoustic comfort modules perform a post-processing analysis on the simulation data to provide simple comfort indicators for the different design alternatives. The behavioural module includes the human component inside the simulation process since it is directly coupled with the IESVE engine.

² <https://www.multicomfort.co.uk/media/1096/saint-gobain-uk-home-health-and-wellbeing-report-summary.pdf>

Thermal Comfort Module

Thermal comfort is a subjective quantity which has to be measured and assessed using a statistical approach. The tool offers an evaluation of the thermal comfort conditions for each room of the studied building. The algorithms post-process the data provided by the IESVE simulation or measurements, according to the user selection both in terms of comfort model (i.e. predictive and adaptive) and season (i.e. heating, cooling). The tool displays KPIs related to the thermal comfort assessment for each investigated retrofit scenario, calculated as the percentage of occupied hours out of the optimal ranges provided by predictive and adaptive comfort models according to EN 15251 (2007). It receives the input data from the IESVE cloud energy simulation and, after the post-processing analysis, stores the results in the DIM server. In addition, this module provides a sensitivity analysis, based on Monte Carlo method, to determine which parameter has the highest impact of thermal comfort. In this way the designer has the possibility to address specific issues to be solved with the retrofit. The tool has been tested simulating a room of a monitored building to guarantee the reliability of the obtained results (Naspi et al. 2018a). After simulating the actual thermal condition, two retrofit configurations have been selected and applied. The KPIs related to the three different scenarios are illustrated and compared to investigate which solution is to be preferred.

Acoustic Comfort Module

The acoustic comfort module is composed of algorithms for the assessment of indoor acoustic comfort at building level, according to equations of EN 12354-3 (2017). The improvement of the acoustic comfort is obtained by applying building envelope interventions on the basis of the evaluation of district noise levels (through measurements - EN 16283-3 (2016) - or predictive calculation models³). After simulating the current building condition, the tool performs post-retrofit simulations according to the retrofit interventions selected by the user. The output of each simulation process is a specific KPI, calculated by assignment of a score according to the measured/calculated indoor sound pressure level, which allows the assessment of the indoor acoustic comfort and the comparison between the pre and post retrofit configurations. The KPI provides to the designers a clear identification of the best retrofit option on the building envelope to improve the indoor acoustic comfort. The tool, integrated in the SDH, communicates with the DIM server to receive the required input data. The investigation of the potentialities of the tool occurred following several steps. At first, an extensive data collection by acoustic measurements has been performed in a residential building, settled in Ancona (Italy), to evaluate the actual comfort condition calculating the acoustic KPI. Then, applying different retrofit scenarios, the tool simulates the post-retrofit conditions and offers a comparison of pre and post scenarios through the KPIs.

The Behavioural Module

The module consists of two behavioural functions that predict occupants' interaction with windows and electric lights in offices. The algorithms have been developed using experimental data acquired for a full year in a University building in Italy. People presence, environmental parameters and the status of the devices have been continuously recorded (10 min sampling time) in three offices equipped with sensor networks (Naspi et al. 2018a). Following the approach proposed by (Wang et al. 2016), the influence of environmental variables and time-related events on users' behaviours has been investigated. Window adjustments are driven by both indoor and outdoor temperature; while the lights are switched on and off in relation to the decreasing of the work-plane illuminance and to the users' departure, respectively. Identified the triggers, the coefficients of the equations have been

³ Directive 2002/49/EC. Directive of the European Parliament and of the Council of 25 June 2002 relating to the assessment and management of environmental noise. Official J Eur Communities 2002; L189: 12-25.

tuned using regression methods. The co-simulation approach between the module and the IESVE engine allows the data exchanges during the simulation run-time. This approach offers a considerable modelling improvement since the operational schedules are dynamically defined at each time step, according to the module outputs. The integration and the predicting capabilities of the module have been tested simulating a portion of the case study. Ventilation and lighting profiles are stochastically defined; while heating and occupancy ones are set according to ASHRAE standards (2004). The results obtained using the behavioural module have been compared to those related to a standard simulation (i.e. deterministic results). Then, both of them have been evaluated in relation to the monitored data to assess which approach would have made the best predictions.

RESULTS

To demonstrate the functionalities of the tools, they have been applied to assess different retrofit scenarios to a building of the UNIVPM campus, located in Ancona (centre of Italy), and built in the seventies.

Thermal Comfort

Thermal comfort module was applied to heating season. Figure 2 shows that, before retrofit, the building is uncomfortable since the average operation is at the limit of the lowest comfort zone. This is also confirmed by the KPI, which is for more than the 60% of the time in “cold” conditions, calculated considering the category II as reference (± 0.5 PMV as boundaries). The first retrofit configuration (Retrofit 1), concerning the application of envelope thermal insulation, moves the building to category II. This intervention produces only a partial improvement of the comfort conditions since the KPI is not sufficiently high. The second retrofit scenario (Retrofit 2) concerns the windows replacement and the improvement of the heating system. The design condition and its deviation reach the higher building category (± 0.2 PMV). Also, the KPI shows a number of cold hours lower than the 2% of the total building operation.

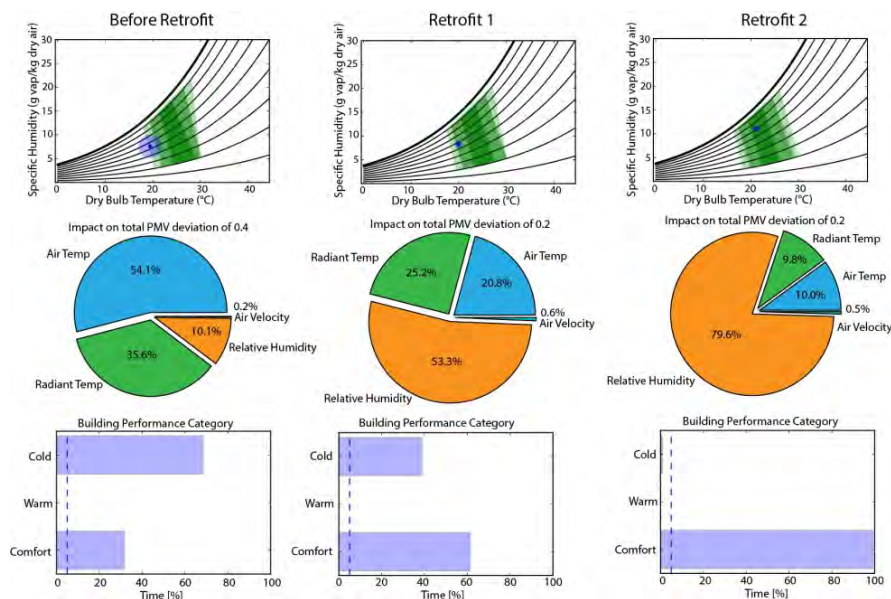


Figure 2. Results from thermal comfort analysis for heating season with predictive model.

Acoustic Comfort

The main outcomes of the acoustic comfort tool are the comparisons both between actual and retrofitted conditions and between different retrofit designs, using KPIs. Figure 3 shows the

influence of four types of interventions, with increasing impact. The first two scenarios concern only one action: the addition of an external insulation layer (case 1) and the substitution of the windows (case 2). The last two retrofit options are connected to concurrent operations: addition of an external insulation layer, substitution of windows and small elements. The key difference between case 3 and case 4 regards the features of the windows, which are much more performing in the second instance.

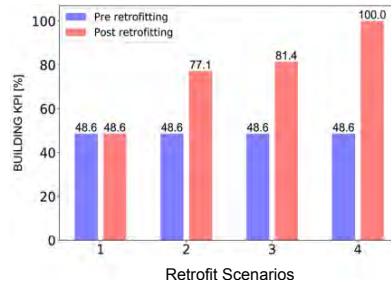


Figure 3 KPIs comparison of pre and post scenarios.

The analysis highlights that the external insulation has no impact on improving the acoustic condition while changing the type of windows provides an increase of 28.5% in the KPI value. The preferred comfort assessment is reached in case 4. In fact, combining several interventions and enhancing the features of the components, the KPI raises of 51.4%. Such assessment, clearly identifying the most effective acoustic retrofit solution, aids the users in selecting the design strategy and in avoiding time and money wastes.

Behavioural Module

The lighting and ventilation profiles obtained applying the behavioural module are compared both to standard profiles and to real users' behaviours. To perform the comparison, a sample of 14 days during the non-heating season has been selected (to avoid the influence of fixed heating profiles on the results). Figure 4 presents the lighting and ventilation profiles during two representative days. The real users' behaviours (blue dashed line) have been examined in relation to the behavioural (red solid line) and standard (grey dotted line) profiles.

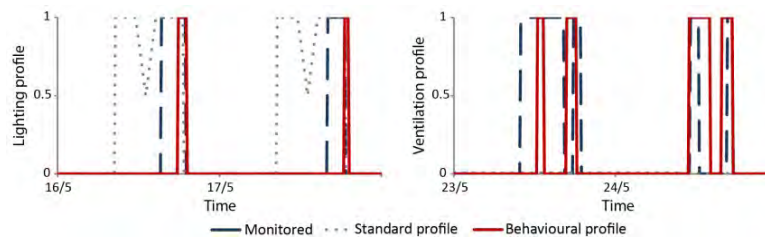


Figure 4. A two-day comparison of lighting and ventilation profiles.

Table 1 summarises the analysis for all the 14 days, reporting the percentage of time with lights on and windows open and the percentage difference (i.e. error) between simulated and real actions. The outcomes highlight that both the simulation approaches tend to overestimate the lighting use and to underestimate the window openings. However, the behavioural module minimises the discrepancy with actual data, especially for the lighting use ($\Delta=+5.1\%$), with a consequent deviation of 10% on the prediction of energy consumption, compared to standard profiles (Naspi et al. 2018b).

Table 1. Errors of Standard and Behavioural profiles in relation to the real data.

Lighting Profile	% of time lights ON	$\Delta\%$ with real	Ventilation Profile	% of time windows OPEN	$\Delta\%$ with real
Real	8.5	--	Real	24.9	--
Standard	42.4	+33.9	Standard	1.9	-23
Behavioural	13.6	+5.1	Behavioural	8.2	-16.7

DISCUSSIONS

The tools presented in this work are useful to support the retrofit design with deep investigations of comfort issues. Acoustic and thermal comfort modules can be a support for the selection of the optimal retrofit solution, addressing buildings pathologies. Also, the behavioural module provides a substantial empower to the simulation results since it reproduces the human-building interaction more accurately than standard profiles.

CONCLUSIONS

The paper presents the framework of the NewTREND cloud platform and, in particular, three embedded tools. The thermal comfort and acoustic comfort tools provide clear and effective evaluations between different retrofit scenarios using KPIs. The behavioural module reproduces the human-building interaction during the simulation, overwriting standard schedules. These tools, including the human component under different perspectives, support the decision-making process and aid the design team in selecting the optimal retrofit option in terms of energy efficiency and occupant's comfort expectations.

ACKNOWLEDGMENT

This research has received funding from the NewTREND (New integrated methodology and Tools for Retrofit design towards a next generation of Energy efficient and sustainable buildings and Districts) project (<http://newtrend-project.eu/>) under the Horizon 2020 research and innovation programme (GA no. 680474).

REFERENCES

- ASHRAE. 2004. ANSI/ASHRAE Standard 90.1, Energy standard for buildings except low-rise residential buildings. Atlanta: American Society of Heating, Refrigerating, and Air-Conditioning Engineers, Inc.
- BPIE. 2011. Europe's Buildings Under the Microscope. Brussel: Buildings Performance Institute Europe.
- CEN. 2007. EN Standard 15251, Indoor environmental input parameters for design and assessment of energy performance of buildings addressing indoor air quality, thermal environment, lighting and acoustics. Brussels: CEN.
- CEN. 2016. EN Standard 16283 part 3, Acoustics — Field measurement of sound insulation in buildings and of building elements — Façade sound insulation. Brussels: CEN.
- CEN. 2017. EN Standard 12354 part 3, Building acoustics — Estimation of acoustic performance of buildings from the performance of elements — Airborne sound insulation against outdoor sound. Brussels: CEN.
- Naspi F., Arnesano M., Zampetti L., Stazi F., Revel G. M., and D'Orazio M. 2018a. Experimental study on occupants' interaction with windows and lights in Mediterranean offices during the non-heating season. *Building and Environment*, 127, 221–238.
- Naspi F., Arnesano M., Revel G. M., Klebow B. and Aird G. 2018b. Data-driven Behavioural Modelling for Building Energy Simulation Based on Scripted Profiles. Submitted to *BSO2018*.
- Wang C., Yan D., Sun H., and Jiang Y. 2016. A generalized probabilistic formula relating occupant behavior to environmental conditions. *Building and Environment*, 95, 53–62.

A Rain Simulator to Examine Green Roof and Soil Moisture Sensor Performance

Endla S. Feustel^{1,*}, Yige Yang¹ and Cliff I. Davidson^{1,2}

¹Department of Civil and Environmental Engineering, Syracuse University, 151 Link Hall, Syracuse, NY 13244

²Center of Excellence in Environmental and Energy Systems, Syracuse University, Syracuse, NY 13244

**Corresponding email: esfeuste@syr.edu*

ABSTRACT

Green roof technology plays a large role managing stormwater runoff in urban areas, where impervious surfaces cause substantial amounts of stormwater runoff to enter combined sewer systems. If the stormwater flow exceeds the capacity of treatment plants, this often results in the discharge of raw sewage into nearby bodies of water. Green roofs can reduce the occurrence of raw sewage discharge by decreasing the amount of mixed wastewater and stormwater flowing into combined sewers. Engineers and designers are looking for ways to improve the performance of green roofs and to understand parameters such as field capacity and time to onset of runoff. A better understanding of field capacity could be used to test hydrologic models that predict how much water a green roof could store under different conditions and to estimate how much runoff could be reduced.

In this project, a drip-type rain simulator is used to estimate field capacity of a plot of soil and sedum taken from the green roof on the Onondaga County Convention Center in Syracuse, NY. Three soil moisture sensors placed into the plot are used with different rain intensities to track the increase in soil water content during rain and the decrease following the end of the rain. The experimental results show that the field capacity of the Convention Center green roof is about 0.081 m³water / m³soil. This value is lower than expected and additional testing is underway. It is also shown that as rain intensity increases, time to onset of runoff decreases. With additional experiments to be conducted in Summer 2018, results of this work can be used by engineers to design and install green roofs with field capacities that complement average rain intensities and peak rain intensities and effectively reduce runoff.

KEYWORDS

Rain Simulator, Green Roof, Field Capacity, Runoff

INTRODUCTION

Green roofs play a significant role in urban stormwater management. They can store incoming precipitation, which reduces the amount of stormwater runoff flowing to combined sewers (Mentens et al. 2006). It is important to determine how much water a green roof can store during rain events in order to estimate how much runoff can be reduced. This information is important for developing improved engineered soil as well as to further advance hydrologic models like USEPA SWMM.

Rain simulators are used to produce different intensities of rain in well-controlled laboratory experiments. Operating a rain simulator with a small plot from a green roof can help

determine the performance of the green roof under various rain intensities. A drip-type rain simulator is used in these experiments to control rain intensity, drop size, and field conditions, such as slope of the roof (Bowyer-Bower and Burt, 1989).

Field capacity is an important parameter in hydrologic modeling and can be useful for simulating infiltration and evapotranspiration. The field capacity depends on soil texture, soil structure, and organic content and is measured in units of $\text{m}^3 \text{water} / \text{m}^3 \text{soil}$ (Narasimhan, 2009). There are many definitions of field capacity, but for the purpose of this paper it can be described as the maximum volumetric soil water content held against the force of gravity after all excess water has been drained (Fazackerley and Lawrence, 2011). According to Veihmeyer and Hendrickson (1931), this value can be measured two days after a rain event in pervious soils.

This project utilizes soil moisture sensors that are inserted into a plot of the full depth of soil with vegetation (7.6 cm soil depth, plot area 35 cm x 58 cm) taken from the green roof on the Onondaga County Convention Center in Syracuse, NY. The plot is used with a drip-type rain simulator to determine field capacity of the green roof soil under three different rain intensities.

There are two main objectives of this project. The first is to determine the field capacity of a large, extensive green roof in a four-season climate in the Northeastern US using a rain simulator in a laboratory setting. This experimental result is compared to a theoretical value based on fundamental characteristics of the soil. The second objective is to determine how different rain intensities affect the time to onset of runoff. This research is important in preparing to use computer models to predict the hydrologic performance of this green roof in both cold and hot weather. The roof is well-instrumented to provide experimental data over a wide range of conditions for comparison with computer model results to improve our understanding of the hydrology of green roofs.

METHODS

How rain intensities were chosen

Rain event data were collected from the Convention Center green roof tipping bucket from 2015 to 2017 in order to determine the range in rain intensities to simulate. As seen in Figure 1, four mm/hr was chosen because it represents a peak rain intensity in the 50th percentile. Fourteen mm/hr was chosen because it is a relatively high peak intensity (80th percentile). Finally, an intensity of 81 mm/hr was chosen to examine the effects of extreme peak intensities (98th percentile).

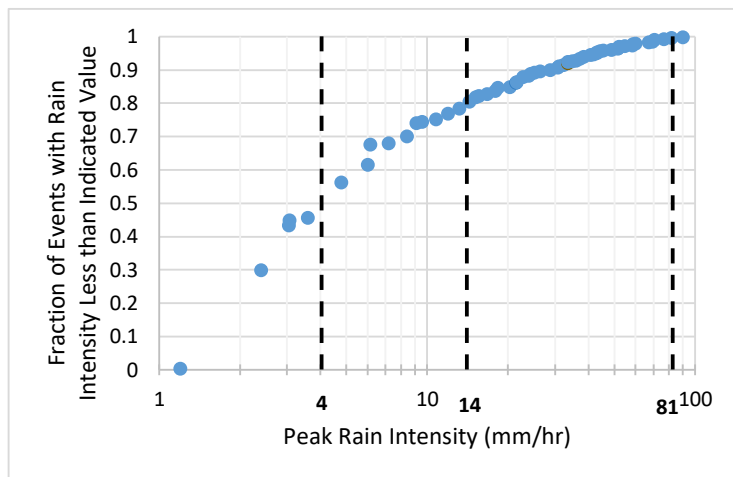


Figure 1: Fraction of rain events on the Convention Center green roof from 2015 – 2017 with peak rain intensities less than the indicated value (N=373). Each rain event has a total accumulation of 0.1 mm or greater.

Rain simulator and experimental setup

As seen in Figure 2, the rain simulator consists of a water source that feeds into a drip former box. There are small holes in the box for droplets to fall through. The plot from the green roof is placed underneath the box.

The rain simulator is calibrated directly before each experiment to ensure a constant and accurately measurable rain intensity. The first step in calibrating the rain simulator is to place a known volume of water in the drip former box and then allow additional water to flow into the box to exactly balance the droplets falling out below the box. A bucket is used to collect the droplets while the water in the box is monitored to ensure a constant volume. A specific intensity is attained by maintaining a calibrated constant volume in the drip former box. A greater water volume and thus greater height of water in the box will result in higher intensities. Smaller intensities are obtained by inserting small pieces of fish line into the holes in the bottom of the box.

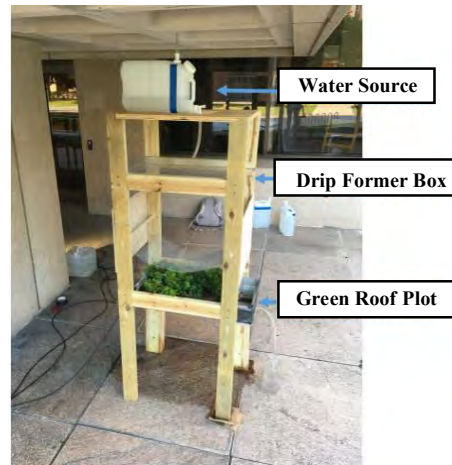


Figure 2: Drip-type rain simulator with plot from Convention Center Green Roof in Syracuse, NY

Before the green roof plot is placed under the simulated rain, three soil moisture sensors are inserted at equal depths into the side of the plot. For two experiments (reaching 4 mm/hr and 81 mm/hr intensities), Campbell Scientific 615 soil moisture sensors were used. These sensors were calibrated with one new CS655 sensor, which has a $\pm 3\%$ volumetric water content accuracy with manufacturer calibration. The 14 mm/hr experiment used three CS655 sensors. After a desired rain intensity is reached, the green roof plot is placed at a fixed distance below the drip former box at a 1% slope to mimic the slope of the green roof, and volumetric water content data are collected.

As the experiment continues, it is noted when runoff occurs. The plot is kept under a constant rain intensity until runoff becomes steady and volumetric water content has reached a constant value. At this point, the rain is stopped and the soil moisture sensors continue to collect data for 48 hours so that field capacity is determined. Evapotranspiration is assumed to be negligible because the plot is left in a dark basement laboratory, where relative humidity is expected to be high, while data are being collected.

Calculation of field capacity based on soil characteristics

Dingman (2002) provides the following equation for field capacity:

$$\theta_{fc} = \phi * \left(\frac{|\psi_{ae}|}{340}\right)^{\frac{1}{b}} \quad (1)$$

where θ_{fc} is the soil field capacity, ϕ is the porosity, ψ_{ae} is the air-entry tension in cm, and b is the exponent describing the moisture characteristic curve. The data collected in the rain simulation experiments can be compared to this model.

RESULTS

Figure 3 shows volumetric soil water content measured during a period of 48 hours for three rain intensities: 4 mm/hr, 14 mm/hr, and 81 mm/hr. The point shown in the first 5-hour period represents when runoff is first observed for each experiment. During each test, the water content increases during the simulated rain event, levels out once soil is saturated and rain is stopped, then gradually decreases until the decline can be considered negligible and field capacity is measured. The results of Figure 3 show that the water content in all three experiments reaches a maximum of around 0.12 when the soil is fully saturated and that the field capacity reached is about the same for the three intensities, as shown by the dashed lines, at 48 hours.

The findings presented in Table 1 show that the field capacities reached for the three intensities range from 0.069 to 0.088, averaging 0.081. Table 1 also indicates that as rain intensity increases, time to onset of runoff decreases.

Table 1: Field Capacity and Time to Onset of Runoff for Different Rain Intensities

Rain Intensities	4 mm/hr	14 mm/hr	81 mm/hr
Field Capacity	$0.086 \frac{m^3}{m^3}$	$0.088 \frac{m^3}{m^3}$	$0.069 \frac{m^3}{m^3}$
Time to Onset of Runoff	2 hours 42 minutes	1 hour 30 minutes	14 minutes

DISCUSSION

As seen in Figure 3, there is a noticeable increase in soil water content during each simulated rain event. A greater rain intensity gives a sharper increase in water content. Figure 3 shows that after water content has reached a maximum value of 0.12, the curve remains at this value for a short time and rain is stopped. At this point, a gradual decrease in water content can be noted in the three graphs. All three plots show an initial steeper decrease directly after the rain is stopped followed by a more gradual decrease. At the time when the curve becomes less steep, percolation occurs and the water begins moving out of the large soil pores and is being replaced by air (Zotarelli, 2010). The water content curves continue to decrease as water slowly drains from the soil. After 48 hours, the drainage rate becomes negligible and field capacity is determined (Dingman, 2002). At this point, the large soil pores are filled with both air and water, and the smaller pores are still full of water (Brouwer et al. 1985). In general, green roof soil is made up of mostly large pore spaces rather than the small pore spaces that contribute to water retention at field capacity (Stovin et al. 2015). The mass median diameter of the soil particles at the Convention Center green roof is 4.0 mm, suggesting a similar size for pore spaces (Wu, 1987). The soil porosity is $0.512 \frac{m^3}{m^3}$.

The results in Table 1 show that the rain intensity does not seem to have an impact on field capacity. A particle size analysis of the green roof soil indicates the soil texture to be similar to sand, which provides parameter values used in Equation 1. From this equation, the predicted field capacity of the Convention Center green roof is 0.17. This value is also smaller than the typical value of 0.3 noted by Jarrett (2009), although roughly double the value measured in the current work. There is some uncertainty in the value generated by the equation. Further analysis of the green roof soil texture will be completed in future work.

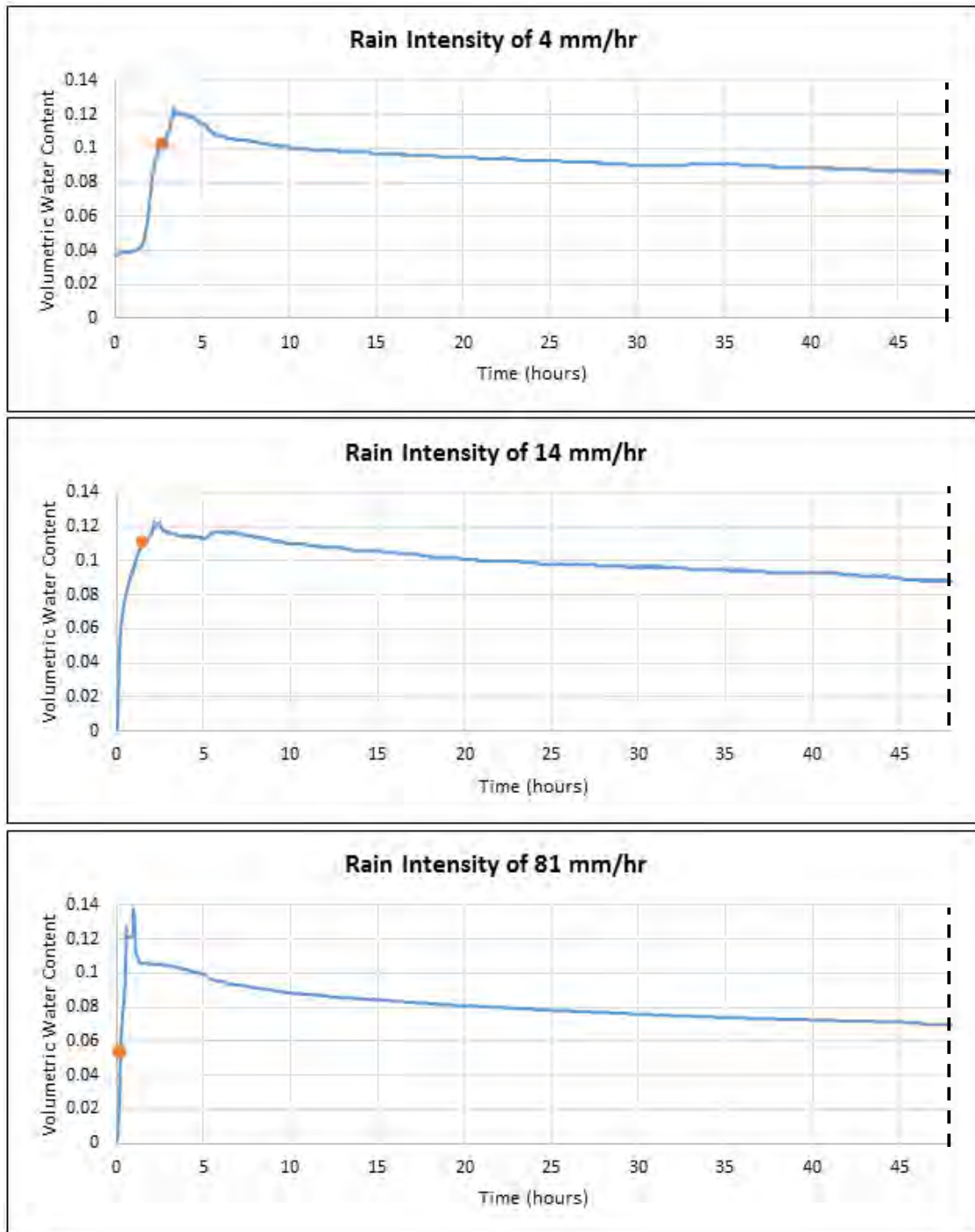


Figure 3: Volumetric Water Content vs. Time for Rain Intensities of (a) 4 mm/hr (b) 14 mm/hr, and (c) 81 mm/hr

The average field capacity of a green roof is said to be about 0.3 (Jarrett, 2009). Therefore, the field capacity measured in this project is low. Experiments are currently underway to investigate this low value.

CONCLUSIONS

A critical parameter of green roof models is the estimation of field capacity. The findings of this work indicate that the field capacity for the green roof on the Convention Center in Syracuse, NY is about 0.081. This result can be incorporated into green roof models to predict maximum soil storage capacity under various conditions. The results of this project also show that the time to onset of runoff decreases as rain intensity increases. This information will help green roof designers improve the performance of engineered soil and estimate how much runoff can be reduced. In addition, the use of a rain simulator and soil moisture sensors can be valuable for collecting data on a small scale for a green roof that does not have a monitoring system installed. This can be valuable for modeling green roof performance in a variety of climates.

ACKNOWLEDGMENT

This work was supported in part by NSF grant #1444755, Urban Resilience to Extremes Sustainability Research Network (UREx SRN), by the NSF EMPOWER NRT program, and by the Syracuse University Water Fellowship. The authors acknowledge Onondaga County Department of Facilities Management, especially Han Phan and Archie Wixson, for the use of the Convention Center green roof. The authors also acknowledge the help of Joshua Saxton and Yang Hu at Syracuse University.

REFERENCES

- Bowyer-Bower T.A.S. and Burt T.P. 1989. Rainfall simulators for investigating soil response to rainfall. *Soil Technology*, Vol. 2, pp. 1-16.
- Brouwer C., Goffeau A., and Heibloem M. 1985. Soil moisture conditions. *Introduction to Irrigation*, Food and Agriculture Organization of the United Nations.
- Dingman S. Lawrence. 2002. *Physical Hydrology*, Long Grove, Illinois: Waveland Press, pp. 235.
- Fazackerley S. and Lawrence R. 2011. Automatic in situ determination of field capacity using soil moisture sensors. *Irrigation and Drainage*, Vol. 61, pp. 416-424. DOI: 10.1002/ird.646
- Jarrett A. 2009. Green roofs for stormwater. *Penn State Extension*. <https://extension.psu.edu/green-roofs-for-stormwater>.
- Mentens J., Raes D., and Hermy M. 2006. Green roofs as a tool for solving the rainwater runoff problem in the urbanized 21st century? *Landscape and Urban Planning*, Vol. 77, pp. 217-226. DOI: 10.1016/j.landurbplan.2005.02.010
- Narasimhan T.N. 2009. Hydrological cycle and water budgets. *Encyclopedia of Inland Waters*, pp. 714-720. DOI: 10.1016/B978-012370626-3.00010-7
- Stovin V., Poe S., De-Ville S., and Berretta C. 2015. The influence of substrate and vegetation configuration on green roof hydrological performance. *Ecological Engineering*, Vol. 85, pp. 159-172. <http://dx.doi.org/10.1016/j.ecoleng.2015.09.076>
- Veihmeyer F.J. and Hendrickson A.H. 1931. The moisture equivalent as a measure of the field capacity of soils. *Soil Science*, Vol. 32, pp. 181-194.
- Wu, L. 1987. Relationship between pore size, particle size, aggregate size and water characteristics. (Unpublished master's thesis). Oregon State University, Corvallis, OR.

A Study on Natural Lighting Design Strategies for Teaching Buildings in Hot-summer and Cold-winter Zone of China—A case of the Arts and Sciences Building of Xinyang Normal University

Xinyue Yang¹, Jiehui Wang^{1,*}, Juanli Guo¹

¹School of Architecture, Tianjin University, China

*Corresponding email:645896526@qq.com

ABSTRACT

The natural lighting of buildings plays an important role in creating a comfortable indoor light environment and reducing the energy consumption of artificial lighting. Teaching buildings have special requirements for the indoor light environment. Classroom glare, corridor backlit, and low natural illumination in corridor are light pollution problems easily appear in teaching building, which cannot be ignored in the design of teaching building. Regarding the issues above, the paper took the Arts and Sciences Building of Xinyang Normal University as an example, through the architectural modeling, space forms, facade effects and other features, used VELUX simulation software to simulate the illuminance and daylighting parameters of different sunroofs and provided solutions for classroom glare and corridor lighting. Ultimately, the paper analyzed the building lighting energy saving schemes based on regional climate and environment, and found out the best balance point for the energy saving design of lighting and thermal environment, meanwhile, provided valuable and practical reference for lighting design of corridor skylights in the region.

KEYWORDS

Teaching building, Natural lighting, Design strategy, Hot-summer and Cold-winter

INTRODUCTION

The architect Ludwig Mies Van der Rohe said: "The history of architecture is the history of human struggle for light, the history of the window." The lighting discussed in the article refers to the use of direct, reflective or other aids to provide natural light to the interior of a building.

It is an important energy-saving means to optimize the design of lighting and shading for public buildings with different functions. A good architectural light environment can improve the visual comfort of indoor personnel, which also has a very important influence on people's physical and mental health. The teaching buildings have many problems in natural lighting, such as large lighting power consumption and glare which greatly reduce the quality of indoor light environment.

For the study of the top lighting of public buildings, most of them are concentrated in the skylight design for the space with large depth. It also has many research methods and design strategies on indoor glare. In specific climate such as hot-summer and cold-winter area, for the special lighting issues of teaching building including corridor skylight design, glare of side windows and corridors lack of systematic research and solutions. Computer simulation is been used to analyse the influence of inner corridor various factors on the natural lighting (Zhifang Zhang, 2011). Hao Xie summarized several design points of the public building skylight. How to put forward the corresponding design technology strategy for the special needs of education building in light environment is the key to solve the indoor natural lighting problem.

METHODS

Educational building lighting standards

Architectural lighting design standards (GB50033-2013) stipulated that the corridor lighting of the teaching building should not be lower than the standard value of the lighting level V. In this project, the illuminance of the area with roof lighting shall be 75lx, and the lighting factor shall be 0.5%.

Description of project

The comprehensive building for liberal arts and sciences to be built is in Xinyang Normal University, including the roof skylight of Building A1, the corridors of Buildings D and F, and the side windows of the classroom. The Building A1 has 12 floors, and the corridors are illuminated by both sides of the windows. To achieve the Architectural Lighting Standard, increase indoor comfort, 10-12 layers will add the skylight to meet the indoor light environment requirements through the reasonable design of natural lighting. The side windows in classrooms and corridors glare easily when it's sunny. Therefore, effective shading equipment is needed to avoid glare and create a good learning environment for students.



Figure 1. The model of Arts and Sciences Building

Specific design content

Simulation software selection and parameter setting

The solar radiation conditions are determined according to the location of the area. In the corridor lighting simulation, set the height of the reference surface to 1.5m, and the selected weather conditions for the winter solstice cloudy day. VELUX natural lighting simulation software is used to simulate the illuminance, daylighting factor and other parameters of different skylights, in order to compare their lighting effects.

Corridor skylight design

The design of the skylight is based on the building lighting standards in the area, and considering the balance of skylight lighting and heat collecting effects. Through simulation optimization, the skylight design schemes suitable for the teaching corridor of the area are analysed showed in Table 2.

Table 1. Advantages and disadvantages on skylights

Type of top light	Advantages	Disadvantages
Flat skylight	High lighting efficiency	Easy to glare, higher heating load
Rectangular skylight	Uniform daylighting, easy on ventilation	Complex roof structure
zigzag skylight	No glare	Low lighting efficiency in winter

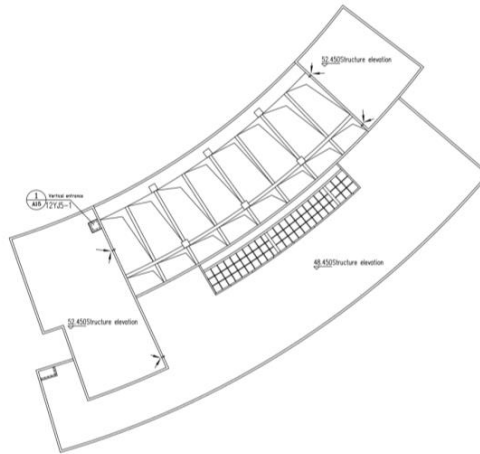
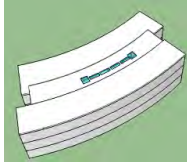
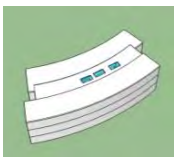
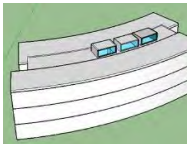
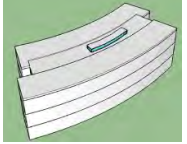
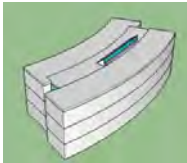
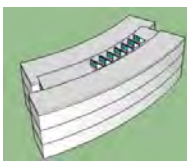


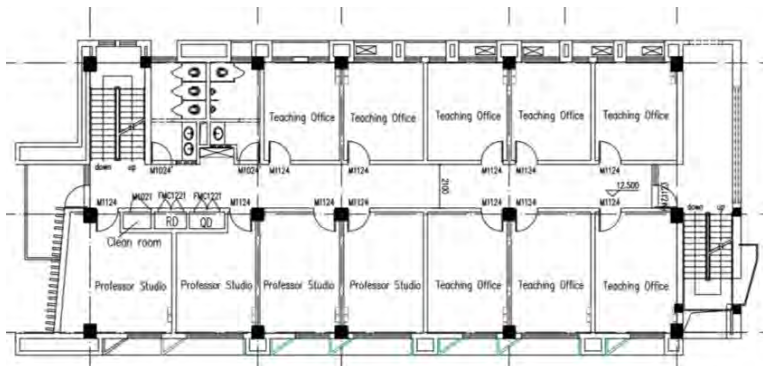
Figure 2. Position of corridor skylight

Table 2. Design of the corridor skylight.

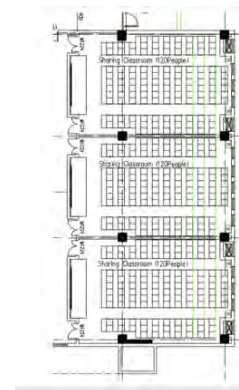
Type of skylight	Design 1		Design 2	
	Graphic	Design parameter	Graphic	Design parameter
Flat skylight		Total area: 20 m ² Two pieces 2×2 m ² Four pieces 1×3 m ² Area ratio of window to floor: 1/23		Total area: 24 m ² Three pieces 2×2 m ² Area ratio of window to floor: 1/19
Rectangular skylight		North and south Total area: 52.3 m ² Area ratio of window to floor: 1/8.8		Window all around Total area: 32.42 m ² Area ratio of window to floor: 1/14.3
zigzag skylight		Total area: 28.42 m ² Incline: 40° Interior surface: White latex paint		Total area: 24.71 m ² Incline: 40° Interior surface: White latex paint

Corridor glare design research

Due to the climate characteristics of the hot-summer and cold-winter areas, shading facilities are required to not only cover the sun radiation in the summer, but also allow the solar radiation to enter the interior as much as possible in winter. Therefore, The selection of shade strategies should be based on the climate characteristics of the area.



a)



b)

Figure 3. a) Corridor plan in Building D , b) Classroom plan in Building F

RESULTS

Simulation result of corridor skylight

The VELUX simulation software was used to simulate the mentioned skylight design scheme, and the minimum illuminance during the day and daylighting factor values under different skylight forms were obtained. The simulation results are shown in the Table 3.

Table 3. Corridor skylight lighting parameters simulation results

Type of skylight		Flat skylight	Rectangular skylight	zigzag skylight
Plan 1	Minimum illuminance during the day (lx)	65.1	17.0	31.0
	Lighting factor (%)	1.1	0.2	0.6
Plan 2	Minimum illuminance during the day (lx)	84.6	13.8	21.4
	Lighting factor (%)	1.3	0.2	0.4

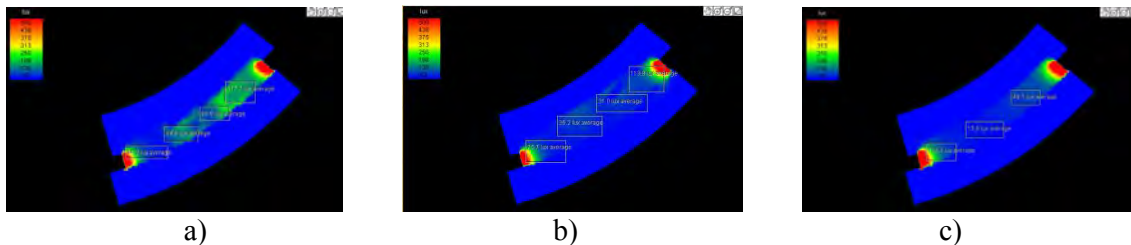


Figure 4. Illuminance during cloudy winter solstice. a) Plan 2 of Flat skylight, b) Plan 1 of zigzag skylight, c) Plan 2 of Rectangular skylight

Shading measures

After simulating the natural illumination in classrooms and corridors, it is found that the classroom relies on one side window to light has different illuminance values. The area close to side window is brighter. On the contrary, the area farther from the side windows is darker. The indoor light environment is not ideal. It is clear that corridor will generate backlight without shading measures. The simulation results are shown in the Figure 5.

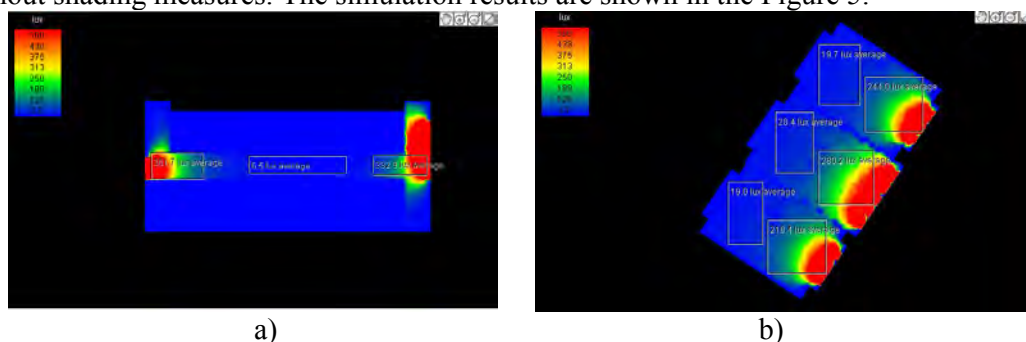


Figure 5. Illuminance during summer solstice day. a) Corridor, b) Classroom

According to the characteristics of building space, several applicable shading strategies are selected and optimized.

Higher lighting side window

It is the side window set above the sight line that can be used in corridors and classrooms to improve the illumination inside. According to *Architectural lighting design standards(GB50033-2013)*, The total area of the windows on both sides in corridors is

determined to be 6.3 m², The size of each side window is 2m×1.6m, and 1.9 meters above the ground.

Reflector

It can provide more natural light for the interior space while preventing excessive direct light from entering the room which may create glare. The addition of reflectors can significantly improve the uniformity of reference surface illumination. Indoor illumination uniformity from small to large is arranged as: non-reflective plate < internal reflector < external reflector < internal and external reflector.

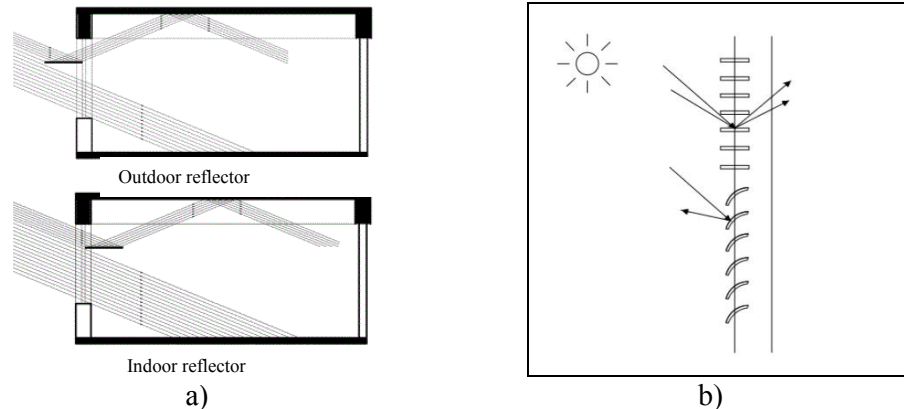


Figure 6. a) The principle of reflector, b) Separately controlled venetian blinds.

Venetian blinds

The user adjusts the appropriate blade angle according to different seasons to maximize the sunlight, so that the interior space of the classroom gets sufficient diffuse light. For buildings that do not have separate lighting windows and landscape windows, separately controlled blinds can be used to maximize the advantages of the upper and lower windows. Blinds used for outdoor shading are usually made of galvanized steel, anodized aluminum or colored steel, anodized aluminum and plastic (PVC). For ease of adjustment, the width of the external shading blade is usually about 100mm, and the pitch of the blade is set to 90mm (Wei Yu, 2012).

Venetian blinds are mainly horizontal and vertical. Research test findings shows venetian blinds of different rotation angles can block sunlight at different height angles and directions.

Table 4. The commonly setting method of venetian blinds

Venetian from	Rotation method
Horizontal blinds	Parallel to normal (Level 0°)
	Rotate 45° counterclockwise (Level 45°)
Vertical blinds	Parallel to normal (Vertical 0°)
	Rotate 45° counterclockwise (Vertical 45°)
	Rotate 45° clockwise (Vertical -45°)

DISCUSSIONS

From the above simulation results, it is found that when choosing plan 2 of plat skylight whose area is 24m², the natural illumination of the corridor can meet the requirements of the lighting of the whole year. Both rectangular skylight designs are unable to meet the requirements of natural light throughout the year for the three-tier walkway. However, their windows open around to avoid glaring, moreover, they are easy to open that promote natural ventilation and reduce mechanical ventilation and cooling energy consumption. The skylight area used in the two designs of the zigzag skylight is the smallest area, and the simulation

results do not meet the requirements. Due to the limitation of the skylight design position, it is difficult to increase its area. The zigzag skylight design with a window angle of 40° and interior surface of white latex paint is slightly lower than the requirement. The winter illumination may be slightly lower, but the zigzag skylight is easy to open that can improve indoor ventilation.

For some public buildings such as office and teaching buildings, the choice and design of shading measures, if the main consideration is summer shade, an outdoor reflector is generally installed to block the light with high solar elevation angle in summer and reduce building cooling load. At the same time, it reflects light to interior ceiling and enhances secondary reflections. When using a reflector to introduce light, it can also be used together with a reflective ceiling to form a light guide system.

Through the analysis of corridor skylight design and the side window shading measures of the project, the application technology of the teaching building light environment in the hot-summer and cold-winter area can be obtained and is summarized as follows.

- a) The flat skylight has the best lighting effect. If the natural ventilation in the corridor is good, the skylight can be selected. The rectangular skylight and the serrated skylight can be selected to improve the natural ventilation in the corridor.
- b) It is more suitable to adopt higher side lighting window and vertical blinds in order to solve the problem of backlighting in corridors. For the east side window of the corridor, it can be set with vertical blinds rotated at a certain angle to avoid direct sunlight in the morning which may generate backlighting, and to make the corridor brighter.
- c) In order to solve the problem of classroom glare, you can choose high side windows, reflectors and venetian blinds.

CONCLUSIONS

Improve the natural lighting quality of teaching buildings is the key to creating a good learning environment and improving people's visual comfort. Through the rational use of auxiliary equipment for daylight and sunshade, natural light can be effectively used and controlled, which can not only achieve the purpose of energy conservation, but also can produce distinctive architectural lighting effects. The paper took the Arts and Sciences Building of Xinyang Normal University as an example, with the method of computer software simulation, analysed the lighting design strategy of the corridor in teaching building and shading measures applied to avoiding glare of the corridors and classrooms, ultimately concluded the light environment design technology strategy suitable for the teaching building in the hot-summer and cold-winter area which supported the light design of teaching building in that area.

REFERENCES

- Hao Xie. 2008. Public building sunroof design strategy. *Energy Saving Technology*, 26(4), 353-357
- Liuqing Pan. 2016. Optimization of light environment in typical teaching buildings, Nanjing University(China),137 pages.
- Wei Yu. 2012. The study on the shading of the east and west Windows of building in hot-summer and cold-winter area, Huazhong University of Science and Technology(China), 79 pages.
- William O'Brien, Konstantinos Kapsis, Andreas K. 2103. Athienitis. Manually-operated window shade patterns in office buildings: A critical review. *Building and Environment*, 60, 319-338
- Zhifang Zhang. 2011. Study on Natural Lighting Optimization Strategy of Interior Gallery with Single Interior Gallery, Hebei University of Engineering(China), 93 pages.

Analysis of thermal bridges in insulated masonry walls: a comparison between vacuum insulated panels and expanded polystyrene

Adrian Bucur¹, Ligia Moga¹

¹Faculty of Civil Engineering/Technical University of Cluj-Napoca, Romania

*Corresponding emails: bucuradrian90@yahoo.com, ligia.moga@ccm.utcluj.ro

ABSTRACT

The paper presents a comparative study between the thermal performances of a couple of masonry walls with no insulation and then insulated with vacuum insulation panels and expanded polystyrene. The research purpose is to demonstrate the superior thermal performance of the vacuum insulation panels compared to common thermal insulation, in initial state and even after 25 years in service. It also provides the steps to determine the effective thermal resistance of the buildings elements insulated with vacuum insulation panels, considering both local and geometric thermal bridges. Results emphasize that even after 25 years in use, the walls insulated with vacuum insulation panels with reduced thickness possess a greater thermal performance than that of the walls insulated with expanded polystyrene with common thickness. This is one of the reasons for which this material should be improved and developed further for the future buildings envelopes.

KEYWORDS

vacuum insulation panels, thermal bridges, steady-state, effective thermal resistance

INTRODUCTION

Vacuum insulation panels are composite nano insulation materials, consisting of a nanoporous core encapsulated by a sealing envelope with multiple functions such as airproofing, waterproofing and radiation thermal transfer blocking. Their thermal conductivity in initial state is 4 mW/(mK), about 8-10 times lower than those of the common thermal insulation materials such as expanded polystyrene or mineral wool. Also, even if the envelope is damaged and the panel is filled with air, its thermal conductivity is the same as for the core material, i.e. 20 mW/mK for fumed silica, which is still approximately half of that of the expanded polystyrene.

In this paper, a comparative study is made between the thermal performances of several brick masonry walls without insulation and then thermally insulated with expanded polystyrene (EPS) and vacuum insulation panels (VIP), in different thicknesses. For each situation there are determined the effective thermal resistances, taking into account the walls thermal bridges by computing the related linear heat transfer coefficients. There are considered two types of thermal bridges given by the walls corner intersection with a concrete column (see Figure 1) and also by the walls intersection with a balcony slab (see Figure 2). At the same time, there are computed the effective thermal conductivities of the VIP, considering the local thermal bridges developed on their edges. These thermal bridges are analysed and computed in several other studies (i.e. Tenpierik and Cauberg, 2010; Sprengard and Holm, 2014).

The layers of the analysed elements may be observed in the following figures. A levelling rendering is applied on the masonry walls and then the VIP are installed. The panels are protected on their exterior side by a layer of EPS and a decorative rendering. The mounting of

the panels on the levelling layer and of the EPS on the panels is made by adhesion. The balcony slab has a width of 1.00 m and is insulated both at its inferior and superior side.

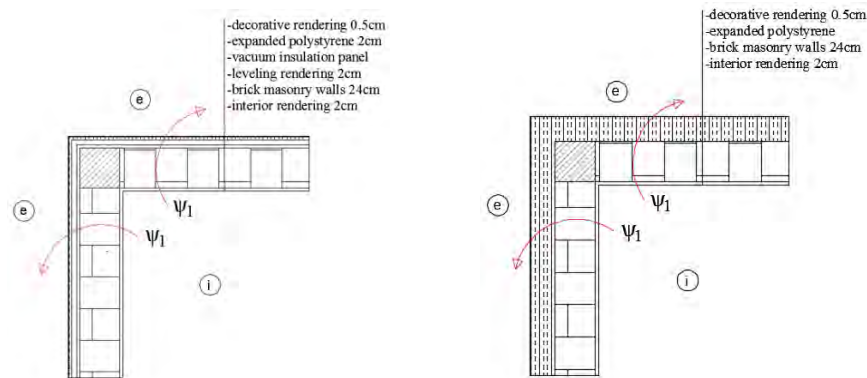


Figure 1. Wall corner intersection - i) insulated with EPS, ii) insulated with VIP

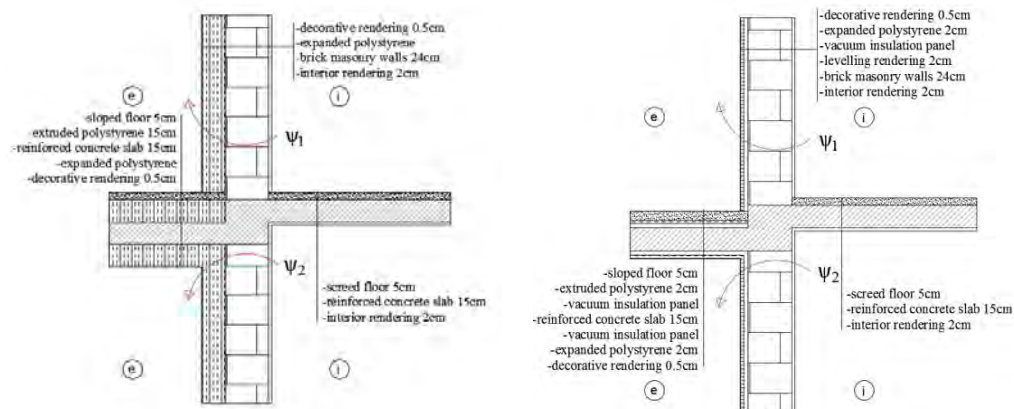


Figure 2. Balcony slab-wall intersection - i) insulated with EPS, ii) insulated with VIP

The analysis is made for the following situations: the walls and balcony slab without thermal insulation, insulated with EPS having a thickness of 10 cm, 20 cm and 30 cm and insulated with VIP of 2 cm, 3 cm and 4 cm, the latter being analysed both in initial state and also after 25 years in service. The maximum chosen thickness of the vacuum insulation panels is the highest one for the adhesion procedure. For larger thicknesses, the material requires a mounting system which develops supplementary local thermal bridges. In the case of balcony slab - exterior wall intersection where EPS is the analysed insulation, on the superior side of the exterior cantilever slab it is considered a layer of extruded polystyrene with a thickness of 15 cm.

METHODS

First of all, there is computed a mean effective thermal conductivity of the VIP. The determination considers the thermal bridges developed on the panel edges using a method from literature (Tenperik and Cauberg, 2007).

The design value of the centre-of-panel thermal conductivity is $\lambda_{cop}=4$ mW/(mK) in initial state after production and $\lambda_{cop}=8$ mW/(mK) after 25 years in service, for the panels with envelopes consisting in metallised polymer films (MF) (Heinemann et al, 2010). The difference is given by an inherent decrease of the material thermal performance in time due to the increase of the water content and internal pressure. Two types of panel envelope are considered in analysis: MF2 having a thickness of $t_f=84\mu\text{m}$ and a thermal conductivity of $\lambda_f=0.54$ W/(mK) and MF3

having a thickness of $t_f=97\mu\text{m}$ and a thermal conductivity of $\lambda_f=0.39 \text{ W/(mK)}$ (Berge and Johansson, 2012). The panels have no gaps or seams between them, therefore their possible influence on the edge thermal bridge is not considered. Having this data, there are computed the linear thermal transfer coefficients ψ_{VIP} related to the thermal bridges developed on the panel edges. Then, there are determined the effective thermal conductivities of the VIP having the following dimensions: $300\times 600 \text{ mm}$, $600\times 600 \text{ mm}$ and $600\times 1500 \text{ mm}$ and an average value is calculated. The computation is made with the following formula:

$$\lambda_{VIP.eff} = \lambda_{cop} + \frac{\psi_{VIP} \times d \times P}{A} \quad [\text{W/(mK)}] \quad (1)$$

where: $\lambda_{VIP.cop} [\text{W/(mK)}]$ is the design value of the centre-of-panel thermal conductivity, $\psi_{VIP} [\text{W/(mK)}]$ is the linear thermal transfer coefficient developed on the panel contour, $d [m]$ is the panel thickness, $P [m]$ is the panel perimeter and $A [m^2]$ is the panel area.

A next step in the analysis is the determination of the linear thermal transfer coefficients ψ related to the considered walls thermal bridges: walls corner and wall-balcony slab intersection. First of all, the unidirectional thermal resistance of the wall is determined:

$$R_{unidir} = \frac{1}{\alpha_{int}} + \sum_i \frac{d_i}{\lambda_i} + \frac{1}{\alpha_{ext}} \quad [m^2 \cdot K/W] \quad (2)$$

where: $d_i [m]$ is the layer i thickness, $\lambda_i [W/K]$ is the layer i thermal conductivity, α_{int} and $\alpha_{ext} [W/m^2K]$ are the superficial heat transfer coefficients at the interior and exterior surface of the wall

Table 1. Thermal conductivities of the materials used (C107/3, 2008)

Material	λ [W/(mK)]
Brick masonry	0.55
Reinforced concrete	1.74
Renderings: interior, exterior, leveling, protection	0.93
Screed floor, sloped floor	0.93
Decorative rendering	0.7
Expanded polystyrene	0.044
Extruded polystyrene	0.04

The determination of the linear heat transfer coefficients ψ is based on a two-dimensional steady-state modelling in Therm software in accordance with EN ISO 6946:2017. The geometric models were designed according to the details presented in Figure 1 and Figure 2, for each layer being given its corresponding thermal conductivity. Also, the models were built taking into account the recommendations of the C107/3 standard which states that the cross section limits have to be placed at minimum 1.20 m relative to the central element. The interior temperature is considered $T_i=20^\circ\text{C}$ and the external one $T_e=-18^\circ\text{C}$. The walls superficial heat transfer coefficients are $\alpha_{ext}=24 \text{ W/m}^2\text{K}$ (exterior side) and $\alpha_{int}=8 \text{ W/m}^2\text{K}$ (interior side). The limits of the cross-sectioned elements (wall, interior slab) are considered to be adiabatic. After the input data is introduced, the software generates the discretization mesh, computing the temperature and thermal flow values in each of its elements, using the Finite Element Method. The model computation is characterised by the following parameters: the maximum dimension of the grid elements is 25 mm, the maximum number of iterations is 50 and the maximum computation error is 1%. Using the program output data, the linear thermal transfer coefficients are computed with the following formula:

$$\psi = \frac{l_{therm}}{R_{therm}} \frac{B}{R_{unidir}} [W/mK] \quad (3)$$

where: l_{therm} [m] is the thermal bridge length, R_{therm} [m^2K/W] is the output R -value from Therm, B [m] is the effective dimension of the linear thermal transfer coefficients ψ and R_{unidir} [m^2K/W] is the unidirectional thermal resistance

Finally, using the computed linear heat transfer coefficients, the effective thermal resistances of the walls are calculated for a 2 story building in accordance with EN ISO 10211:2017. Each level is composed of four walls having the same geometrical characteristics: two walls of $3m \times 3m$ and two walls of $3m \times 6m$. Also, the two stories are separated by a reinforced concrete slab with a balcony cantilever on the building contour, having a width of 1m. The balcony slab is at an inferior level compared to the interior slab, according to the analysed details. The layers and thicknesses of the walls and slabs correspond to the ones presented before (see Figure 1 and Figure 2). The analysis is made for two inferior level walls and two superior level walls, the other four walls of the system having the same characteristics. Each wall has a corner thermal bridge for each of their lateral margins. The inferior level walls have a thermal bridge at their superior edge given by the intersection with the balcony slab. In the same way, the superior level walls have a thermal bridge at their inferior edge. The free margins (section margins) of the walls are considered to be adiabatic.

RESULTS

Table 2. Linear heat transfer coefficients ψ related to the panel edges thermal bridges. Effective thermal conductivities λ of the panels considering these thermal bridges

Panel dimensions [mm]	Envelope type	ψ_{VIP}	ψ_{VIP}	$\lambda_{VIP,eff}$	$\lambda_{VIP,eff}$
		-initial- [mW/(mK)]	-25 years- [mW/(mK)]	-initial- [mW/(mK)]	-25 years- [mW/(mK)]
300 x 600 x 20	MF2	1.33	1.25	4.265	8.250
300 x 600 x 20	MF3	2.05	1.93	4.409	8.386
300 x 600 x 30	MF2	0.95	0.91	4.284	8.273
300 x 600 x 30	MF3	1.47	1.41	4.442	8.423
300 x 600 x 40	MF2	0.73	0.71	4.294	8.284
300 x 600 x 40	MF3	1.15	1.12	4.461	8.448
600 x 600 x 20	MF2	1.33	1.25	4.177	8.167
600 x 600 x 20	MF3	2.05	1.93	4.273	8.257
600 x 600 x 30	MF2	0.95	0.91	4.189	8.182
600 x 600 x 30	MF3	1.47	1.41	4.295	8.282
600 x 600 x 40	MF2	0.73	0.71	4.196	8.189
600 x 600 x 40	MF3	1.15	1.12	4.307	8.299
600 x 1500 x 20	MF2	1.33	1.25	4.124	8.117
600 x 1500 x 20	MF3	2.05	1.93	4.191	8.180
600 x 1500 x 30	MF2	0.95	0.91	4.132	8.127
600 x 1500 x 30	MF3	1.47	1.41	4.206	8.197
600 x 1500 x 40	MF2	0.73	0.71	4.137	8.133
600 x 1500 x 40	MF3	1.15	1.12	4.215	8.209

According to these results, in the following computations a mean effective thermal conductivity is considered: $\lambda_{VIP,eff,0} = 4.25$ mW/(mK) – for initial state; $\lambda_{VIP,eff,25} = 8.25$ mW/(mK) – after 25 years in use.

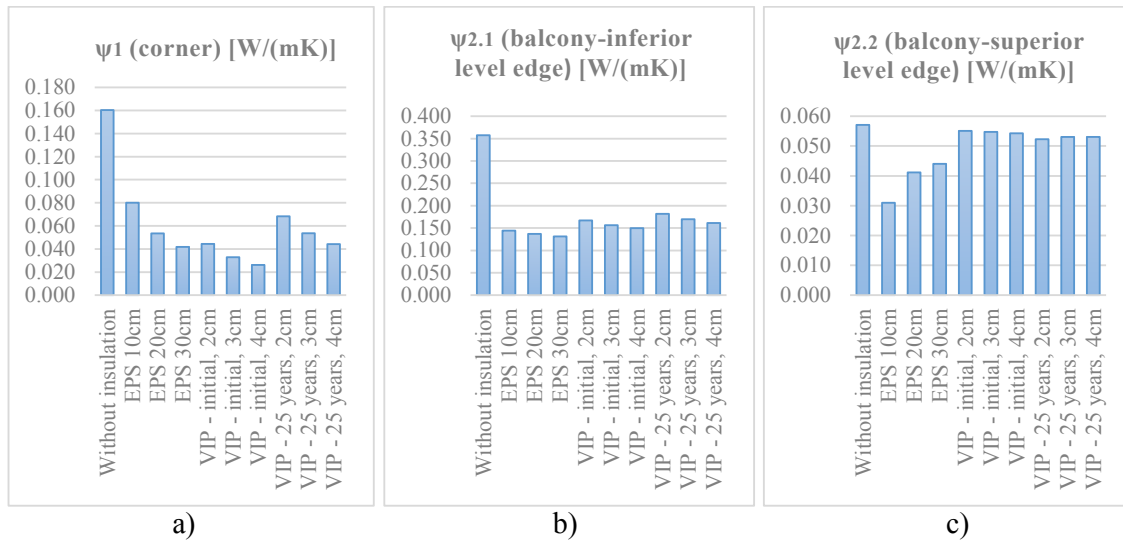


Figure 3. Linear thermal transfer coefficients of the analysed details
 a) wall corner intersection, b) balcony slab-wall intersection – inferior level edge
 c) balcony slab-wall intersection – superior level edge

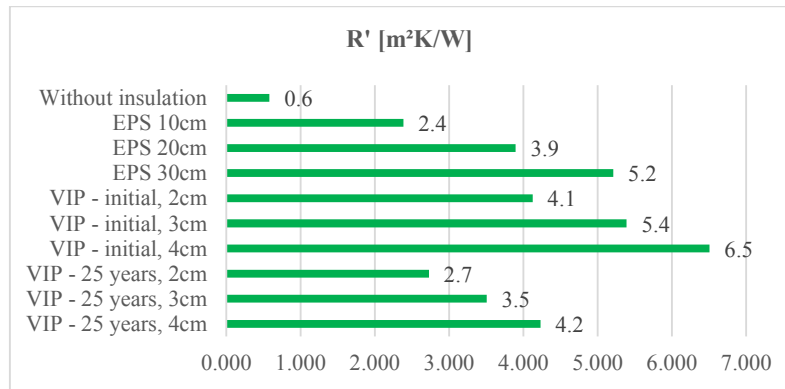


Figure 4. Average effective thermal resistance of the analysed walls

DISCUSSIONS

The results regarding the thermal bridges developed on the panel contour ψ_{VIP} validate the findings from another studies (Tenpierik and Cauberg, 2007; Sprengard and Holm, 2014), for the panels having $\lambda_{cop}=4$ mW/(mK), with MF type envelope and with no gaps or seams between them. One may observe that the thermal bridges developed on the VIP edges after 25 years in service are slightly lower (between 2.60%-6.40%) than those of the new panels, a phenomenon which is more prominent as its thicknesses are lower (see Table 2). At the same time, the envelope type influence the panel thermal performance. Between two panels with same geometrical characteristics, the one with MF2 type foil has a lower linear thermal transfer coefficient with about 54-58% than the one with MF3 type foil. Another aspect revealed by the results is that the linear heat transfer coefficients related to the panels edges decrease with the increase of its thickness.

As a consequence of these local thermal bridges, the panels effective thermal conductivity is greater for those with MF3 type foil, compared to that of those with MF2 type (see Table 2). The difference raises with the increase of the panel thickness and decrease with the increase of the panel 2D dimensions: for 300×600mm – difference of 1.5-2%, for 600×600mm – difference of 1-1.5% and for 600×1500mm – difference of 0.8-1%. At the same time, the panel effective

thermal conductivity is greater than the centre-of-panel thermal conductivity with 0.124-0.461 mW/(mK) for the new panels and with 0.117-0.448 mW/(mK) after 25 years in service.

The thermal bridges of the analysed details are lowered by the use of thermal insulation (see Table 3). In most cases, the thermal bridges of the wall corner detail (ψ_1) with VIP are lower than those of the same detail with EPS. Also, the thermal bridges at the inferior level edge of the balcony detail ($\psi_{2.1}$) with VIP have similar values to those with EPS. At the same time, the thermal bridges at the superior level edge of the balcony detail ($\psi_{2.2}$) with VIP have a rather constant value, regardless of their thickness or age and they have higher values compared to the details insulated EPS.

The effective thermal resistance of the walls insulated with VIP decrease with about 35% after 25 years in use, compared to their initial state, as shown in figure 4. However, one should note that even in this situation, the thermal performance of VIP is comparable to that of the EPS, but for a reduced insulation thickness of approximately 80%. The walls insulated with the panels having a thickness of 4 cm develop an increased effective thermal resistance which recommend this solution for the higher thermal efficiency building systems.

CONCLUSIONS

One of the directions in this research field is the continuous improvement of the existing thermal insulation solutions and the development of new ones in order to increase the overall thermal performance of the buildings. In this regard, the VIP may represent a leap forward, considering its superior thermal performances.

The study reveals that even the VIP develop larger thermal bridges and their performance decrease over time, the building elements insulated with this solution have a superior effective thermal resistance compared to common solutions such as EPS. Therefore, the VIP may be a suitable replacement for the traditional insulations, especially when there is required a reduced insulation thickness.

REFERENCES

- Berge A. and Johansson P. 2012 - Literature Review of High Performance Thermal Insulation. Report in building physics, Chalmers University of Technology, Gothenburg, 28 pages
- C107. 2008. *C107 Standard 3-2008*, Romanian Standard for the thermotechnical computation of the buildings components
- EN ISO. 2007. *EN ISO Standard 6946-2017*, Building components and building elements. Thermal resistance and thermal transmittance. Calculation methods
- EN ISO. 2017. *EN ISO Standard 10211-2017*, Thermal bridges in building construction. Heat flows and surface temperatures. Detailed calculations
- Heinemann U., Schwab H., Simmler H., Brunner S., Ghazi K., Bundi R., Kumaran K., Mukhopadhyaya P., Quénard D., Salée H., Noller K., Küçükpinar-Niarchos E., Stramm C., Tenpierik M., Cauberg H., Binz. A., Steinke G., Moosman A. and Erb M. 2010. Vacuum Insulation Panel Properties & Building Applications, ECBCS Annex 39 Project Summary Report, 32 pages
- Sprengard, C., Holm, A. H. 2014. Numerical examination of thermal bridging effects at the edges of vacuum-insulation-panels (VIP) in various constructions. *Energy and Buildings*, Vol. 85, pp. 638-643
- Tenpierik M. and Cauberg H. 2007. Analytical Models for Calculating Thermal Bridge Effects Caused by Thin High Barrier Envelopes around Vacuum Insulation Panels, *Journal of Building Physics*, Vol. 30, No. 3, pp. 185-215

PCM-to-Air Heat Exchangers for Free Cooling Applications

Mohamed Dardir^{1,*}, Mohamed El Mankibi², Fariborz Haghighat¹

¹Department of Building, Civil and Environmental Engineering, Concordia University, Montreal, Canada

²Ecole Nationale des Travaux Publics de l'Etat (ENTPE), Lyon, France

*Corresponding email: mo_m@encs.concordia.ca

ABSTRACT

Applications of PCM-to-air heat exchangers (PAHXs) were discussed in literature for free cooling application due to their latent thermal storage abilities. This paper aims to justify the generalization of a numerical model of PAHX and to compare the thermal performance of two different configurations of PAHX system. A generalized numerical model is developed and validated based on general apparent heat capacity method. The validation results show good agreement of the generalized approach in terms of averaged error with the experimental data. Model potential and limitations are discussed, and further recommendations are proposed to improve model accuracy. The paper ensures the significant potential of a PAHX ventilated façade configuration in free cooling applications.

KEYWORDS

Latent thermal storage, PCM-to-air heat exchangers, phase change materials, free cooling.

INTRODUCTION

The general awareness of using latent heat thermal energy storage (LHTES) systems has been growing widely due to their increased storage capacity, system efficiency and durability. Phase Change Materials (PCMs) are being used in building applications due to their latent thermal storage abilities. One of the efficient passive cooling concepts is utilizing night cold energy to be re-supplied at hot period of the next day; this needs involving a thermal storage process. Integrating this free cooling concept with a LHTES system can provide an acceptable indoor environment for building occupants. Applications of PCM-to-air heat exchangers (PAHXs) have been widely discussed in literature for free cooling applications. Those applications can be classified into two main configurations: system equipment as a part of ventilation systems, and ventilated facades as improved building envelopes. Both types involve convective heat transfer process between air and PCM.

It can be inferred from literature of integrated PAHX ventilation system configuration that maintaining supplied air temperature that achieves indoor thermal comfort is a current system limitation. Several studies reported that insufficient difference between phase change temperature (PCT) range and inlet temperature during charging affects system storage abilities and overall thermal performance (De Gracia et al. 2015; Waqas and Kumar, 2011). Using a hybrid system of PAHX and a direct evaporative cooling unit, Panchabikesan et al. (2017) experimentally found that the hybrid system increased the cooling potential by reducing the inlet air temperature during PCM solidification. Some studies confirmed the potential of using multiple PCMs in free cooling systems to satisfy workability under high inlet temperatures (Mosaffa et al. 2013). Regarding long-term applications, applying same PCM affects the annual system performance due to changing of ambient temperature profiles in various seasons, consequently, standalone PAHX system cannot maintain indoor thermal comfort all year-round; thermal management is required in such cases (Osterman et al. 2015). On the

other hand, PAHX ventilated envelope configuration showed some achievements in free cooling applications, De Gracia et al. (2013) showed that direct free cooling had a high potential in reducing the cooling loads, however, insufficient difference between night temperature and PCT during solidification results in low system energy storage. Some other studies assured the system cooling potential when combined with night ventilation strategy (Jaworski, 2014; Evola et al. 2014, El-Sawi, et al 2013).

It can be inferred from the literature that PAHX ventilated façade configuration has lower performance than the ventilation system configuration. This paper investigates the performance of the two configurations of PAHXs. By monitoring system outlet air temperature, the current work investigates PAHX system parameters of both configurations that achieve same thermal performance. The main goal of this paper is the justification of a general numerical model of PAHX to be used efficiently in both configurations by designers and building developers. Also, this paper investigates the effect of numerical model generalization on the overall PAHX thermal behavior.

METHODS

In this study, a generalized numerical model for PAHX is proposed and validated based on developments of an earlier version of the model. The model proposes an energy balance approach over number of control volumes to represent the system three media of heat transfer: air flow, encapsulation material and PCM. Full model nodal discretization and heat balance equations are described in detail in (Stathopoulos et al. 2016). Expression of latent heat storage during the phase change of the PCM is achieved by monitoring the change of heat capacity (c_p) values over the temperature range for each control volume. This apparent c_p method assumes fixed rate of heating/cooling during the latent heat transfer process. An earlier version of the numerical model was proposed by Stathopoulos et al. (2016) based on an improved apparent c_p method that proposes multiple values of c_p due to different heating/cooling rates. This method is based on measurements data using Differential Scanning Calorimetry (DSC). Using a developed version of model, this study is performing a comparison between general apparent c_p model and improved apparent c_p model proposed by Stathopoulos et al. (2016) to test the thermal performance of the two configurations of PAHXs: integrated ventilation system configuration, and ventilated envelope configuration.

Model potential and limitations

The model has good potential in terms of predicting the outlet air temperature due to the accurate evolution of c_p values over temperature. PCM thermal conductivity, density and volume are interpolated over temperature through phase change range. The model can auto-generate air density value according to air temperature. However, the early version of model discussed by Stathopoulos et al. (2017; 2016) showed some limitations in terms of its dependency on experimental data. Inlet air temperature and volume flow rate were represented to model every time step; these values were obtained from experimental data. Also, both cooling and heating curves for c_p were determined based on different cooling/heating rates of DSC measurements. Although these procedures provided better model accuracy, the dependency on experimental data obstructed the model applicability for broad investigations instead of single case study. Moreover, the model used a fixed input value for convective heat transfer coefficient, h . As mentioned by authors, the model also neglected the natural convection inside PCM, and long-wave radiation heat transfer between PCM plates. In this paper, further developments are made in terms of generalization of the model to be applicable for broad investigations. Also, the developed model promotes the applications of different PAHX configurations.

Justification of general apparent heat capacity method

Heat capacity value is a key factor in model accuracy. Stathopoulos et al. (2017) proposed the improved apparent c_p model using the experimentally obtained values of c_p , shown in figure 1-a, as model input. They also divided the system to three consequent parts (inlet, middle and outlet) assigning different cooling/heating curve for each part. Towards model generalization, the c_p values are reconsidered as average values for each curve maintaining the same approach of multiple curves for c_p , as presented in figure 1-b. In this case, an average value of c_p is introduced for each curve. Moreover, this approach still requires knowledge and access to the measured values of c_p to calculate the average values. Towards tackling the model limitation of obstructing the broad applications, current model developments assume having two curves for heating and cooling, as shown in figure 1-c. This approach assumes one fixed rate for cooling/heating along the system, which is the original assumption of apparent heat capacity method. This assumption was previously discussed by Stathopoulos et al. (2017) and was claimed to have less accuracy than the improved apparent c_p method due to the differences in heat transfer rate along the PCM plate. Despite the expected less accuracy, this approach can be beneficial to formulate a platform for system designers based on data sheets of c_p cooling and heating curves provided by PCM suppliers. In this paper, investigations for the general apparent c_p approach will be conducted to justify its acceptability and validity with experimental data.

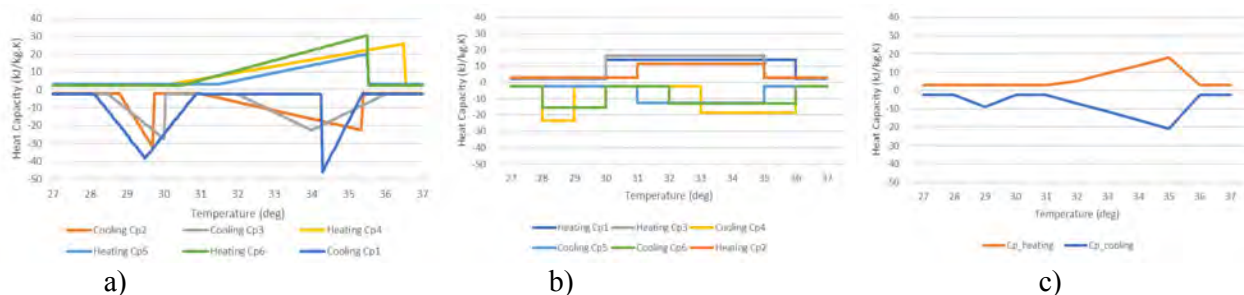


Figure 1. Heat capacity heating and cooling curves for PCM Microtek 37D a) improved apparent c_p method, b) c_p average values, c) general apparent c_p method

Experimental installation

The experimental investigation of PAHX ventilation system type (configuration 1) was illustrated in-detail in (Stathopoulos et al. 2016). A flat plated encapsulation of 16 aluminum PCM plates were investigated under various airflow rates. Microtek 37D paraffin was used as PCM (melting temperature 37.0°C and latent heat of 230 kJ/kg). The total dimensions of the heat exchanger were 1.05m in length, 0.75m in width and 0.25m in height; it contained 31.8kg of PCM. Airflow and air temperature were actively regulated and controlled to the desired velocity and temperature. Inlet temperature varied from around 44.0°C during melting phase and 26.0°C during solidification phase. The available experimental data are for around 15 hours (1.0 hour introductory – 9.0 hours for melting – 5.0 hours for solidification). Sensors were installed within the heat exchanger to measure: PCM and encapsulation surface temperatures in three locations (inlet, mid, and outlet parts), inlet and outlet air temperatures, and airflow rate.

RESULTS

Figure 2 presents the results of the validation for different numerical models with the experimental results. The results show the evolution of system outlet air temperature under volume airflow rate of around 300 m³/h during both melting (discharging) and solidification

(charging). There are three presented numerical models based on the different $c_{p,v}$ values discussed earlier: 1- the improved apparent $c_{p,v}$ model tested by Stathopoulos et al. (2016) with experimentally obtained values of $c_{p,v}$, 2- the model that is based on developed average values of $c_{p,v}$, and 3- the generalized apparent $c_{p,v}$ model that is based on simplified $c_{p,v}$ values. The results show that considering an average value for each $c_{p,v}$ curve is very close to the improved apparent $c_{p,v}$ model. The generalized apparent $c_{p,v}$ model shows some discrepancy with the original model and experimental results due to the simplified approach of $c_{p,v}$. For investigating the discrepancy level of the generalized model, a percent error test is performed for both improved and generalized apparent $c_{p,v}$ models. Figure 3-a shows the percentage of error of both models compared to experimental data. The results show that both models exceed 10% of error percentage with the experimental data only at the start of each phase changing. Otherwise, the error for both models remains below 10% with the experimental data. In terms of the average error, improved apparent $c_{p,v}$ model shows average errors of 3.2% and 3.7% during melting and solidification respectively with the experimental data. While the general apparent $c_{p,v}$ model shows average errors of 3.9% and 4.6% during melting and solidification respectively with the experimental results. In comparison with the improved model, the generalized apparent $c_{p,v}$ model shows up to 7% of percent error.

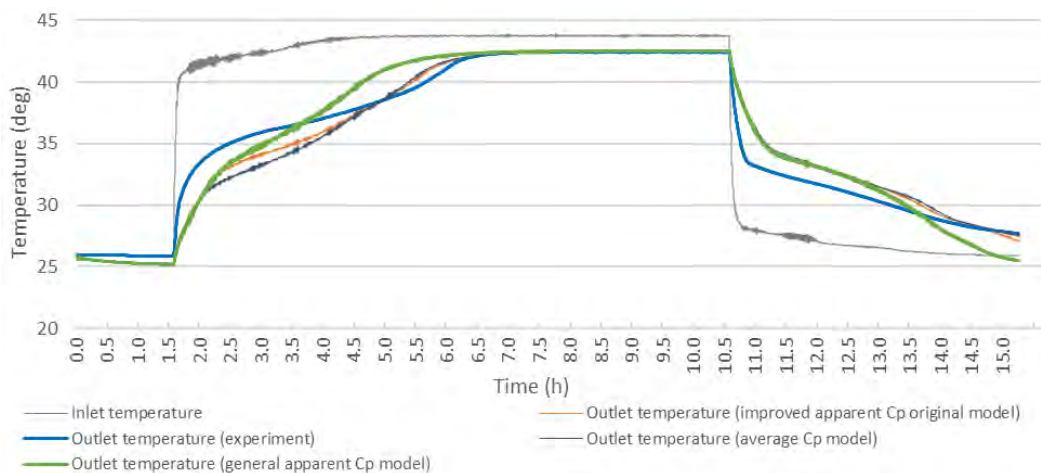


Figure 2. Validation of different models with experimental data

Comparison to ventilated envelope configuration

Using the generalized apparent $c_{p,v}$ model, a comparison between the previous investigated PAHX ventilation system unit (configuration 1) and a ventilated envelope PAHX type (configuration 2), shown in figure 4, is held to monitor the thermal performance of the two configurations. In both configurations, inlet air temperature is fixed to two values: 44.0°C during melting and 26.0°C during solidification. Airflow rate is fixed to 300 m³/h. RUBITHERM RT35 is used as a storage medium with thermal properties mentioned in table 1. Two curves for heating and cooling for $c_{p,v}$ values are applied and presented at figure 5. The total PCM volume is 0.052 m³. PAHX ventilated façade configuration variables are mentioned in figure 4, with total PCM volume of 0.064 m³. It is worth mentioning that the objective of this investigation is the comparison between the two configurations and not obtaining the best thermal performance of the system. The results, shown in figure 3-b, prove that with almost the same volume of PCM, both configurations show significant conformity with values of outlet air temperature profile.

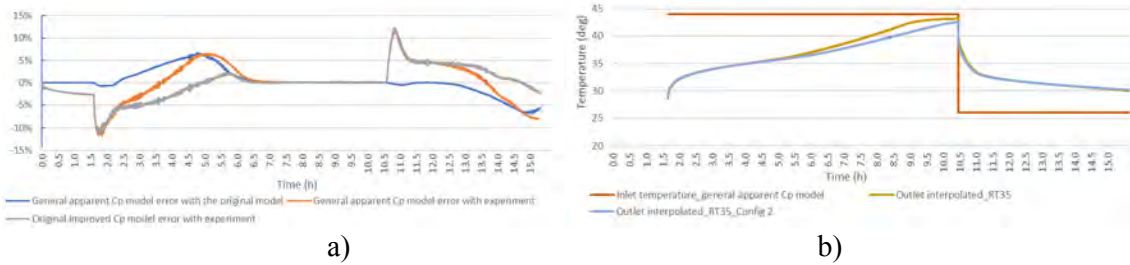


Figure 3. a) Percent error analysis of original and generalized models b) Outlet air temperature of PAHX different configurations

Table 1. Thermal properties of PCM RUBITHERM RT35

Melting range	Solidification range	Heat Storage Capacity	Specific heat capacity	Density	Thermal conductivity	Volume expansion
29-36 °C	36-31 °C	160 kJ/kg	2.0 kJ/kg.K	0.86 solid / 0.77 liquid	0.2 W/m.K	12.5%

A complementary study is conducted to test the indoor thermal performance of a ventilated façade PAHX type with the given configuration using TRNSYS. A standalone test unit of volume 27.0m³ (3.0*3.0*3.0) is proposed with a northern window of 1.0m² and a heavy construction of stone walls (0.3m thick) and concrete roof slabs (0.25m thick). Two systems are compared: the PAHX ventilated façade system, and a conventional ventilation system with the same airflow and inlet temperature as the numerical model. The results show that 4.6% of the cooling loads can be saved during 5.0 hours of PAHX system operation.

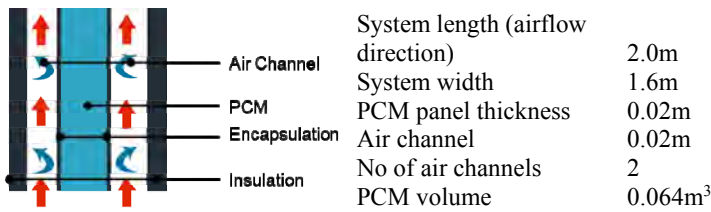


Figure 4. Ventilated envelope PAHX configuration

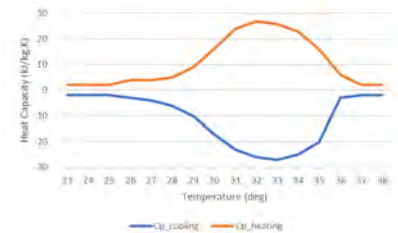


Figure 5. RT35 apparent c_p curves

DISCUSSIONS

With the validation of the general apparent c_p model, the discrepancy at the end of each phase change process is noticed. It means that with the simplified c_p approach the system tends to consume its storage capacity faster than the actual behavior. Accordingly, it can be noticed from the percent error analysis that the general apparent c_p model shows up to 10% as a level of discrepancy, and 3.9% and 4.6% as average errors during melting and solidification respectively with the experimental data due to consideration of system storage capacity. However, one of the advantages of the general model is its in-dependence of the spatial time constrains. Time step, discretization length and investigation duration can be adapted to desired conditions. Regarding general model limitations, the model still uses a fixed input value for convective heat transfer coefficient. Also, the natural convection inside PCM during melting and liquid phase is still neglected. It is expected that model accuracy can be enhanced when heat transfer coefficient is calculated according to airflow conditions. Also, it can be inferred from the results of comparison between the two configurations of PAHX system that the governing parameter in determining PAHX thermal performance is the volume of PCM. Both configurations have almost the same PCM volume and, as reported in results, the both outlet temperature profiles show the same behavior with great level of consistency, especially during solidification process. PAHX ventilated façade configuration shows promising

potential for free cooling applications; it is recommended to improve the model by developing the convective and radiative heat transfer boundaries.

CONCLUSIONS

A generalized numerical model of PCM-to-air heat exchangers is developed and validated in this paper based on general apparent heat capacity method. A simplified approach for implementing heat capacity cooling and heating curves is presented and validated with experimental data. The general approach showed some discrepancies with experimental data. Using a percent error test, the average error of the general model was 3.9% and 4.6% during melting and solidification processes respectively. Referring to its ability of broad applications, the developed general model is very beneficial to building designers due to its in-dependence from experimental data as model inputs. Using the developed general model, a comparative analysis between PAHX ventilation system configuration and a ventilated envelope PAHX configuration is conducted. The study proved that PAHX ventilated façade type has promising potential for free cooling applications.

ACKNOWLEDGEMENT

The authors would like to express their gratitude to Concordia University for the support through the Concordia Research Chair – Energy & Environment, and to Egyptian missions' sector.

REFERENCES

- De Gracia, A. et al., 2013. Experimental study of a ventilated facade with PCM during winter period. *Energy and Buildings*, Issue 58, pp. 324-332.
- El-Sawi, A., Haghghat, F., Akbari, H., 2013, Centralized latent heat thermal energy storage system: model development and validation, *Energy and Buildings* 65, 260-271
- Evola, G., Marletta, L. & Sicurella, F., 2014. Simulation of a ventilated cavity to enhance the effectiveness of PCM wallboards for summer thermal comfort in buildings. *Energy and Buildings*, Volume 70, pp. 480-489.
- Jaworski, M., 2014. Thermal performance of building element containing phase change material (PCM) integrated with ventilation system – An experimental study. *Applied Thermal Engineering*, 70(1), pp. 665-674.
- Mosaffa, A., Ferreira, C. I., Talati, F. & Rosen, M., 2013. Thermal performance of a multiple PCM thermal storage unit for free cooling. *Energy Conversion and Management*, Issue 67, pp. 1-7.
- Osterman, E., Butala, V. & Stritih, U., 2015. PCM thermal storage system for 'free' heating and cooling of buildings. *Energy and Buildings*, Issue 106, pp. 125-133.
- Panchabikesan, K. et al., 2017. Effect of direct evaporative cooling during the charging process of phase change material-based storage system for building free cooling application - A real time experimental investigation. *Energy and Buildings*, Volume 152, pp. 250-263.
- Stathopoulos, N. et al., 2016. Air-PCM heat exchanger for peak load management: Experimental and simulation. *Solar Energy*, Issue 132, pp. 453-466.
- Stathopoulos, N., El Mankibi, M. & Santamouris, M., 2017. Numerical calibration and experimental validation of a PCM-Air heat exchanger model. *Applied Thermal Engineering*, Issue 114, pp. 1064-1072.
- Waqas, A. & Kumar, S., 2011. Thermal performance of latent heat storage for free cooling of buildings in a dry and hot climate: An experimental study. *Energy and Buildings*, Issue 43, pp. 2621-2630.

Assessment of the BIPV potential at the city of Prague and their effect on the built environment

Nikolaos Skandalos^{1,*}, Jan Tywoniak^{1,2}, Kamil Stanek^{1,2}, Lenka Maierova^{1,2}

¹University Centre for Energy Efficient Buildings, Czech Technical University in Prague
Trinecká 1024, 273 43 Buštěhrad, Czech Republic

²Faculty of Civil Engineering, Czech Technical University in Prague, Thákurova 7, 166 29
Prague 6, Czech Republic

*Corresponding email: Nikolaos.Skandalos@cvut.cz

ABSTRACT

This work highlights the BIPV potential in two urban areas with different characteristics at the city of Prague. Representative building blocks were selected and CitySim software tool was used for the assessment of the hourly irradiation profiles on each surface over one year period. Considering appropriate irradiation thresholds, suitable surfaces were then quantified. Integration criteria are discussed and suitable BIPV applications are proposed considering not only energy performance but also their impact on the quality of built environment. Results indicated that only 5.5% of the total area can be used in Vinohrady and 13.7% in Jizni Mesto contributing on average by 32% and 31% on the hourly electricity demand respectively.

KEYWORDS

Building-integrated photovoltaics, solar potential, architecture, load matching

INTRODUCTION

The building sector is the major consumer of energy, accounting for around 40% of the worldwide consumption (UNEP, 2012). On the road towards Low or Zero Energy Buildings, renewable energy harvesting becomes compulsory and thus photovoltaic systems are expected to be the main technology to generate on-site electricity. PV systems have great potential to be used in the city context through various BIPV products (Shukla et al., 2017). Rooftop PVs are so far considered to be the most common application since it provides the best annual energy harvesting. However, due to significant decrease in prices and technological improvements in PV industry, building facades now represent good potential especially for high-rise buildings. Successful integration of PVs into a building requires both technical and architectural knowledge.

In this context, a suitable procedure is needed to assess the solar potential and propose PV concepts based on the characteristics and cultural aspects of the location. This paper aims to analyse the PV potential of two locations within the city of Prague. Considering the solar availability and shadings for the surrounding buildings, the available area for installation is determined and suitable PV applications are proposed considering all the constraints imposed from the locations and building morphologies. Finally, suitable index is used to investigate the interaction between on-site generation and building's electricity demand on hourly basis.

METHODS

Location characteristics

Two urban areas in the city of Prague with different characteristics were selected and used for analysis and comparison. A representative building block, constitute of residential buildings,

was selected for each location as presented in Fig.1. Case one, Vinohrady, is within a high dense area of the city centre with considerable architectural and cultural value. Houses built around 1900 are characterized by sloped roofs in different shapes and heights. Case two, Jizni Mesto, is a suburban area built in 1970es. Prefabricated high rise buildings are characterized by simple shape, flat roofs and big vertical facades with balconies on South and West orientation.



Figure 1. Aerial view of the selected locations in a) Vinohrady and b) Jizni Mesto.

Solar PV potential

Appropriate 3D models for each building block were prepared based on the geometry of the buildings, including dimensions and shape of the roof superstructures (dormer, chimney, etc.). Building surfaces were divided according the floor level, excluding areas that for some reason cannot be considered for PV integration (e.g. north facade). Radiation on building surfaces is commonly influenced by the near environment and thus were the heights of the surrounding buildings, trees and elements in each direction were considered in the model for the evaluation of shading. Afterwards, the 3D model was imported to CitySim Pro, an urban energy modelling tool developed at LESO-PB/EPFL, for further analysis. Incoming solar radiation was calculated in hourly values, according to the type of the building surface and the climate data collected by a nearby meteo station. For each building surface was defined by its area, orientation and tilt angle. Finally, percentage of solar obstruction were calculated as the ratio of the solar radiation within the surrounding context to the one without the surrounding obstacles. Hourly values were solar weighted, annual shading index (SI) was derived according to Eq.1, where $F_{sh,i}$ is the hourly shading factor of each building surface, G_i is the hourly and G_t the annual solar radiation respectively.

$$SI = \frac{\sum_{i=1}^{N=8760} F_{sh,i} G_i}{G_t} \quad (1)$$

Once the radiation values on each surface are available, they can be analyzed to assess the PV potential. For this purpose, an irradiation threshold was used indicating the minimum amount of annual radiation required for PV system to be beneficial. Such thresholds are somewhat arbitrary; conservative value of 800 kWh/m²annually is proposed by many authors (Li et al., 2015), while others define it as a percentage of the horizontal insolation (Vulkan et al., 2018). Considering the technological progress and enormous decline of PV costs within last decade, approximately 58% according to (Maturi et al., 2017), lower values such as 650 kWh/m² (Kanters et al., 2014) are still reasonable. To this end, PV potential calculated as the relative fraction (percentage) of the roofs and facades of the buildings that can be used for PV integration. Based on the area of the suitable surfaces a simple model was applied to quantify the annual energy output (E_{PV}) of each building block according to Eq.2:

$$E_{PV} = \eta * PR * \sum_{i=1}^{n_{threshold}} (I_i * A_i) \quad (2)$$

,where η is the PV conversion efficiency, PR is the performance ratio representing all system losses (mismatch, inverter..), $n_{threshold}$ is the number of surfaces exceeding irradiation threshold, I_i is the cumulative insolation ($\text{kWh}/\text{m}^2 \cdot \text{year}$) and A_i the relative area (m^2) of surface i .

Afterwards, data for the annual electricity consumption of representative buildings in each location, were collected and analyzed in hourly basis according to the occupants (REMODECE, 2008) and typical user profiles (Staněk, 2012). Based on the peak loads and the selection criteria that apply in each location, PV systems were sized properly, while load match index (Voss et al., 2010) was used as indicator of the hourly self-consumption of the PV generated energy.

BIPV integration criteria

It is evident that excessive use of PV systems can often have an adverse effect on the build environment and thus criteria and recommendations about dimensioning and positioning are needed. In order to select an appropriate BIPV application, both technical, architectural and economical aspects should be included. In case of Jizni Mesto, there is no limitations arising from the near environment and thus several scenarios and PV technologies can be considered (Fig.2). High performance modules can be installed on flat roof of the buildings horizontally to camouflage the installation or tilted to optimize performance. On vertical facades, PV modules should be grouped together in an ordered way creating unique textures (e.g. horizontal stripes). In this context, ceramic panels or solar glazing in various colours (Jolissaint et al., 2017) could be a solution, providing good durability and aesthetic quality. Finally, complementary building elements such as windows and existing balconies are well suited to support PV integration representing good compromise in terms of energy performance and aesthetics. In addition, optimized semi-transparent PV elements could be used as shading devices to increase indoor thermal comfort by mitigation of overheating during summer, but still to provide daylighting and to make use of passive heating during winter (Skandalos et al., 2018).



Figure 2. Examples of architecturally integrated PV systems in the two building blocks: (1) PV balconies. Source: Etsprojects; (2) Coloured PV-façade. Source: Swissinsol; (3) Roof-added PVs. Source: Cromwellsolar; (4) PV tiles. Source: Tradeford; (5) PV shutter and PV blinds. Source: COLT international, Solargaps; (6) PV terrace. Source: (López and Frontini, 2014).

On the other hand, BIPV integration in the sensitive built environment such as Vinohrady district, is a more challenging task. Applicability of conventional PV modules in buildings with strong architectural or cultural value is limited. Since the full integration and imperceptibility of the technical elements from the public domain is the most important criteria for the acceptance of the BIPV within the historical context (Munari Probst and Roecker, 2015), small scale highly innovative PV products are needed. Suitable surfaces are limited to the sloped roof, flat terraces and vertical facades facing to the courtyard. Based on the geometry of each surface, BIPV applications such as solar glazing or PV tiles, balustrades and PV shutters (Fig.2) constitute effective practices of integration in the building envelope providing a balanced solution between technical and architectural standards as defined in (Frontini et al., 2012).

RESULTS & DISCUSSION

Solar PV potential

Results from solar analysis in both locations are presented in form of annual irradiation colour map (Fig.3). As expected, best solar resources were observed for sloped roofs facing south (Vinohrady), exceeding the 1200kWh/m^2 annually. However, different roof typologies were recognised and thus solar potential varies according to its slope and orientation. Relative results for the flat roofs of Jizni Mesto were slightly lower (around 10%), but still exceed the irradiation thresholds. Conversely, facades in both locations found to receive significantly lower level of irradiation, especially the ones on East and West façade. This is also explained from the increased shading factors. Average solar obstruction can reach up to 57% for a building in Vinohrady (high density) and 22% in Jizni Mesto respectively. Consequently, only a small portion of the total building area can be considered as suitable for PV integration. Percentages for buildings in each location vary between 5-18% in Vinohrady and 15-27% in Jizni Mesto respectively.

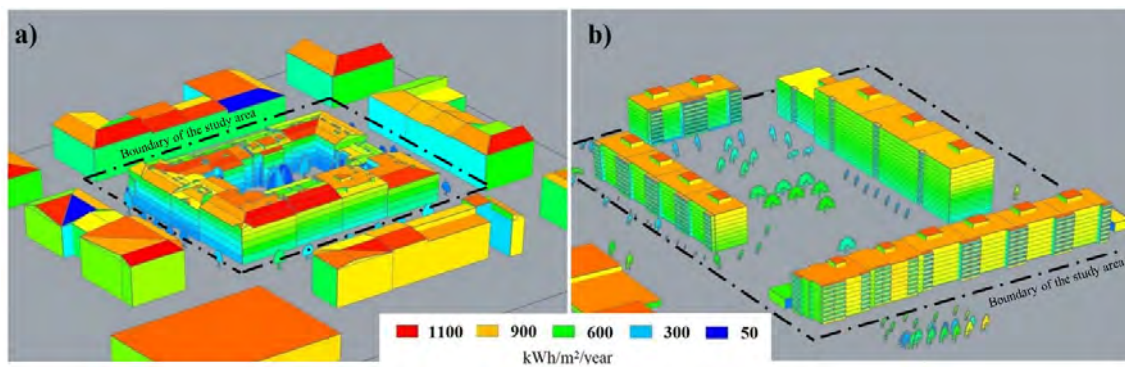


Figure 3. Annual solar irradiation map for each building block in a) Vinohrady and b) Jizni Mesto.

With respect to the hourly irradiation profiles, maximum PV potential in each location was calculated and presented in Fig.4. PV modules were assumed to be installed at the same plane with the building surface considering typical values for the conversion efficiency (η) according to the BIPV application ($\eta=15\%$ for roofs and $\eta=8\%$ for facades/balconies/glazing). For Vinohrady, annual PV generation could be up to 440MWh with peak generation in July (62 MWh). However, 58% of that energy is related to the building surfaces facing streets and thus could not be considered according to the criteria discussed in previous section (Fig.4a). Similar results for the Jizni Mesto revealed 2.7 times higher PV potential (1100 MWh/annually) with relative contribution from roof, façades and balconies by 49%, 45% and 6% respectively (Fig. 4b).

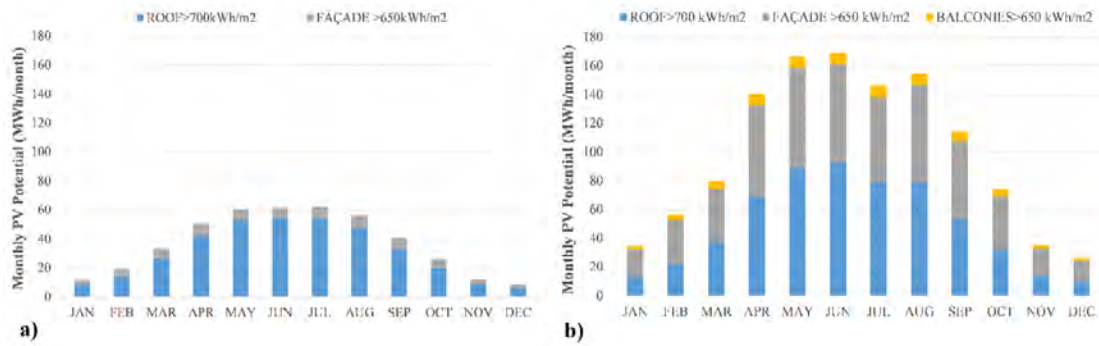


Figure 4: Monthly PV potential for the building block in a) Vinohrady and b) Jizni Mesto based on the selected irradiation thresholds.

System evaluation

Hourly peak loads were calculated and used as indicator, together with the criteria discussed in previous section, to size properly the PV systems in each building. Consequently, suitable PV systems were considered and results regarding the interaction between electricity consumption and generation are presented in Fig.5 for both locations. Despite the PV potential in Vinohrady, available space is limited to only 5.5% of the total building area due to the integration criteria applied. It is obvious that the generated energy is not enough to cover the loads of the building block (Fig.5a). However, almost all the generated PV energy can locally be used within the building block and it is enough to compensate on average by 38% (max value of 49% per building) the hourly electricity demand. In case of Jizni Mesto, there is no such limitations and thus 19% of the area can be used according to the irradiation thresholds. In that case, PV generation is enough to cover the electricity demand during the summer period, but also leads to excess of energy for 35% of the PV operation time (hourly). Therefore, better interaction between generated and consumed electricity is needed to increase the self-consumption of the buildings providing more efficient performance. If maximum load matching is taken into account, integration will be limited to only 13.7% of the total building area leading to lower PV generation (Fig.5b). Alternatively, excess of energy can be used for cooling purposes since peak production coincides with peak cooling demand. Analytical results, regarding maximum load match index (hourly intervals) between the buildings in Jizni Mesto found to be 43%.

CONCLUSIONS

Two representative building blocks, with different characteristics and level of preservation in the urban context of Prague, were selected and analysed for their hourly solar radiation per unit area according to the local weather data. As expected, most of the potential is intrinsically related to roofs, while façades suffer more the shadowing effect caused by the surroundings. According to the integration criteria and energy consumption applied in each location, suitable PV systems were proposed. Only small part of the building area can be used, varying from 5.5% for Vinohrady and 13.7% for Jizni Mesto. Interaction between electricity demand and consumption revealed that proposed PV systems could compensate on average by 32% the hourly energy demand in Vinohrady and by 31% in Jizni Mesto. It is evident that even in areas with sensitive built environment adoption of solar energy is still possible for balancing local electricity needs. Further work is needed to assess the indirect effect (thermal, daylighting) of the proposed solutions. Also economic assessment based on the actual market conditions (BIPV prices, installation costs and electricity tariffs) will also reveal the profitability of the proposed solutions.

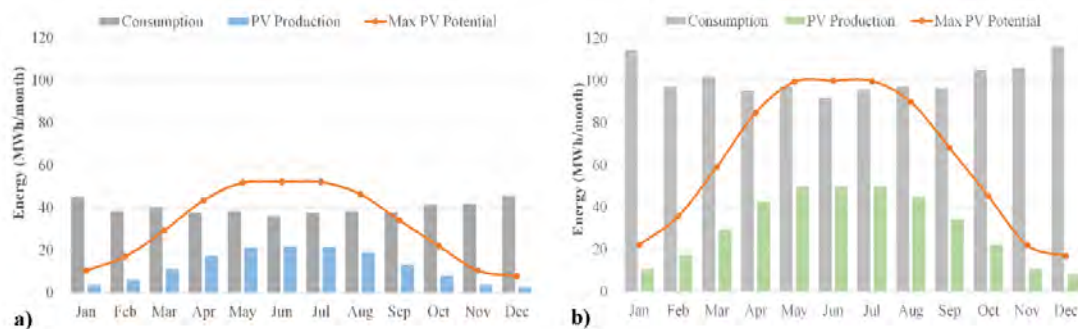


Figure 5: Annual electricity consumption and generation of the proposed PV system together with maximum potential according to irradiation threshold (800kWh/m^2 year) based on monthly data for a) Vinohrady and b) Jizni Mesto.

ACKNOWLEDGEMENT

This work has been supported by the Operational Programme Research, Development and Education of the European Structural and Investment Funds, project CZ.02.1.01/0.0/0.0/15_003/ 0000464 Centre for Advanced Photovoltaics. The authors would also like to acknowledge Solar Energy and Building Physics Laboratory (LESO-PB) of EPFL to provide the software CitySim.

REFERENCES

- Frontini F., Manfren M. & Tagliabue L.C. 2012. A Case Study of Solar Technologies Adoption: Criteria for BIPV Integration in Sensitive Built Environment. *Energy Procedia*, 30, 1006-1015.
- Jolissaint N., Hanbali R., Hadorn J.C. & Schuler A. 2017. Colored solar façades for buildings. *Energy Procedia*, 122, 175-180.
- Kanters J., Wall M. & Dubois M.C. 2014. Typical Values for Active Solar Energy in Urban Planning. *Energy Procedia*, 48, 1607-1616.
- Li, D., Liu G. & Liao S. 2015. Solar potential in urban residential buildings. *Solar Energy*, 111, 225-235.
- Lopez C.S.P. & Frontini F. 2014. Energy Efficiency and Renewable Solar Energy Integration in Heritage Historic Buildings. *Energy Procedia*, 48, 1493-1502.
- Maturi L., Adami J., Lovati M., Tilli F. & Moser D. 2017. BIPV Affordability. *33rd European Photovoltaic Solar Energy Conference and Exhibition*. Amsterdam, the Netherlands.
- Munari Probst M.C. & Roecker C. 2015. Solar Energy Promotion & Urban Context Protection : Lesoqsv (quality- Site-visibility) Method. *31th PLEA Conference*, Bologna, Italy.
- REMODECE 2008. Residential Monitoring to Decrease Energy Use and Carbon Emissions in Europe. *Annual electricity use in the Czech Republic*. Available at: <http://remodece.isr.uc.pt>.
- Shukla A.K., Sudhakar K. & Baredar P. 2017. Recent advancement in BIPV product technologies: A review. *Energy and Buildings*, 140, 188-195.
- Skandalos N., Karamanis D., Peng J. & Yang H. 2018. Overall energy assessment and integration optimization process of semitransparent PV glazing technologies. *Progress in Photovoltaics: Research and Applications*, 26, 473-490.
- Stanek, K. 2012. Photovoltaics for buildings, Grada for the Department of Building Structures at the Faculty of Civil Engineering of the Czech Technical University in Prague.
- UNEP 2012. Building Design and Construction: Forging Resource Efficiency and Sustainable Development.
- Voss K., Sartori I., Napolitano A., Geier S., Gonzalves H., Hall M., Heiselberg P., Widen J., Candanedo J.A., Musall E., Karlsson B. & Torcellin P. 2010. Load Mating and Grid Interaction of Net Zero Energy Buildings. *EuroSun Conference*. Graz, Austria.
- Vulkan A., Kloog I., Dorman M. & Erell E. 2018. Modeling the potential for PV installation in residential buildings in dense urban areas. *Energy and Buildings*, 169, 97-109.

Bio-inspired outdoor systems for enhancing citizens thermal comfort in public spaces by learning from nature

Marta Chafer^{1,2}, Cristina Piselli^{2,*}, Anna Laura Pisello^{2,3}, Ilaria Pigliautile², Gabriel Perez¹, Luisa F. Cabeza¹

¹GREiA Research Group, INSPIRES Research Centre, University of Lleida, Lleida, Spain

²CIRIAF - Interuniversity Research Centre, Perugia, Italy

³Department of Engineering, University of Perugia, Perugia, Italy

* *Corresponding email: piselli@crbnet.it*

ABSTRACT

In the last decades a variety of high-energy efficient solutions for building envelopes were developed and tested for enhancing indoor thermal comfort and improving indoor environmental quality of private spaces by learning from nature. To this aim, adaptive solutions, conceived thanks to green and bio inspiration, were designed and constructed in various climate conditions and for a variety of building uses. Given the huge population flow toward urban areas, well-being conditions in the public spaces of such dense built environment are being compromised, also due to anthropogenic actions responsible for massive environmental pollution, local overheating, urban heat island, etc. Moreover, this process is exacerbated by temporary phenomena such as heat waves. Therefore, outdoor spaces are becoming increasingly less comfortable and even dangerous for citizens, especially if they are affected by general energy poverty, with no chance for active systems management for air conditioning, or health vulnerability. In this view, this study concerns the first concept for the development of a simple and adaptive nature-inspired solution for outdoor thermal comfort enhancement and local overheating mitigation for pedestrians. The system will be evaluated in terms of the cradle-to-cradle approach and the initial performance assessment is carried out via thermal-energy dynamic simulation. The final purpose will be to design outdoor “alive” shading system to be applied in open public spaces, with evident physical and social benefits.

KEYWORDS

Bio-inspired solutions; Biomimetics; Biophilic cities; Outdoor thermal comfort; Thermal-energy dynamic simulation.

INTRODUCTION

Nowadays, a topic with increasing relevance is how an exterior space affects physical, physiological, and psychological well-being. The achievement of comfortable outdoor spaces and microclimate in urban environments is, indeed, fundamental since those spaces are where social activities happen, people gather/socialise, but also connect the indoors with nature (sun/green spaces). Architects and designers were inspired by nature since long before the term biomimicry (biometrics or bio-inspired architecture) was introduced. In the past, architecture featured ornamental design influenced by nature, and this tendency was accentuated by turn-of-the century Catalan Modernism (Spain) or Art Nouveau (Belgium) as examples. Nowadays, a methodological approach to assess innovation was developed through merging bio-inspiration and sustainability based on the reintegration of basic bio-inspired principles into material systems of humankind (Horn et al. 2018). Biomimetics is a rapidly growing discipline in engineering, and an emerging design field in architecture. In

biomimetics, solutions are obtained by emulating strategies, mechanisms, and principles found in nature (Badarnah 2017). Therefore, the study of green infrastructures providing benefits not only in terms of outdoor thermal comfort, but also for the built environment located in their close proximity may represent a further mitigation and wellbeing opportunity.

In this context, plants have also the capability to transform global solar radiation that reaches their surfaces into biomass, oxygen, air humidity, etc. (Pacheco-Torgal et al. 2015). Furthermore, biophilic spaces, those that learn from nature and emulate natural systems, must be considered for the development of cities. In fact, a biophilic city is a city in which residents are actively involved in experiencing nature (Beatley & Newman 2013). Moreover, biophilic urbanism can complement urban greening efforts to enable a holistic approach, which is conducive to comprehensive, intentional, and strategic urban greening (Revee et al. 2015). Different studies about outdoor thermal comfort showed that the sun sensation coming from solar radiation has the most significant influence on human thermal sensation in outdoor spaces (Yang et al. 2013). On the other hand, pedestrians usually inclined to green areas within the urban environment. This increase of vegetation, combined to other solutions, showed the most significant impact in summer overheating mitigation and urban resilience to anthropogenic climate change (Piselli et al. 2018).

Within this background, there is a lack of information about how greenery shading systems can influence outdoor thermal comfort in the inter-building space. Therefore, the purpose of this work is to study a simple and adaptive system of bio-inspired architecture connected to the building for the improvement of thermal comfort in the outdoor inter-building space. Therefore, this strategy is able to mitigate the build environment and the urban heat island phenomenon (UHI) as bottom-up approach. The other aim of the paper is to simulate the outdoor thermal comfort with greenery, since there are no previous studies concerning that. Moreover, the selected materials are meant to produce the minimum impact in terms of cradle-to-cradle vision.

METHODS

Description of the concept

The design was created with different spaces that can provide thermal comfort to outdoor users (Figure 1). Two main objectives were pursued: (i) to reduce the incidence of the direct solar radiation to achieve higher visual comfort, and (ii) to mitigate surface temperatures of the connected buildings and the air temperature in the inter-building space to achieve thermal comfort. In fact, the system did not seek to create a stand-alone piece at the outdoor. On the contrary, the intervention tried to strengthen the key assets of surrounding buildings, creating an extension of the existing buildings that it may be.



Figure 1. The shading system proposed.

The shading system was composed of two interwoven systems of ropes running freely between the two buildings. The ropes connected on the middle creating a bench where people

could sit. The new three-dimensional surfaces created shadings of varying densities that reconfigure the original outdoor space into a more confined and enclosed space. The confined space changed constantly with shadows produced by the rope and greenery systems (using deciduous plants) depending on the season since the solar irradiance is different for each one. Thus, the inter-building space became an ever-changing stage that responded to the movement of the visitor, the changing patterns of light through the day, and the outdoor thermal comfort depending on the season. The selected specie, i.e. Boston Ivy (*Parthenocissus Tricuspidata*), is a deciduous specie well adapted to the Mediterranean Continental climate.

The performance of the system was simulated in this study to demonstrate its potential in sites requiring context-specific real-time responses. The system was modelled under the case study climate context of Lleida, Spain, with Continental-Mediterranean weather conditions, i.e. Csa (warm temperate, dry and hot summer) zone according to Köppen-Geiger climate classification (Kottek et al. 2006). To improve the efficacy of the proposed system in terms of cradle-to-cradle, the materials selected for the prototype corresponded to: (i) Wood structure to support the shadow shading system. This wood structure includes a bench integrated in the basement structure with a substrate for the climbing plants that will grow on it. (ii) Ropes made of natural fibres for the shading system. (iii) Climbing deciduous plants.

Thermal-energy dynamic simulation

For the system modelling and thermal-energy assessment, EnergyPlus v8.1 simulation engine (Crawley et al. 2000) with DesignBuilder v4.7 graphical interface (DesignBuilder software Ltd, 2016) were selected. The following steps were followed in the simulation process:

- Building geometry modelling based on the designed drawings and technical specifications.
- Characterization of the architectural elements and their thermal properties.
- Proposed shading system modelling and characterization: the rope-based shading system with greenery was modelled as a solid obstacle, characterized by rope properties. This configuration was considered an acceptable approximation due to the unavailability in the software of a model for stand-alone green infrastructures implemented in outdoor areas, i.e. not integrated in the building envelope.
- Run of hourly simulations for the hottest week in summer (i.e. July 15th to July 23rd), with the more regular outside temperatures along the season.
- Analysis and comparison of the performance of different scenarios for the outdoor shading system in terms of thermal conditions under the shading and external surface temperatures of the shaded buildings.

The statistical weather file of the city of Lleida from the EnergyPlus database (U.S. DOE BTO, 2016) was used for triggering the model in the calculations. Different scenarios were defined for the proposed system in order to evaluate the impact of shading percentage of the system, i.e. the amount of vegetation growth on the rope-based system. To this aim, the different scenarios were modelled by varying the transmittance capability of the solid obstacle. Therefore, the studied scenarios (Figure 2) were those proposed by Ng et al. (2012):

- Covered 0%: Without greenery, i.e. solar radiation transmittance equal to 1.
- Covered 33%: With greenery covering 33% of the structure, i.e. solar radiation transmittance equal to 0.67.
- Covered 67%: With greenery covering 67% of the structure, i.e. solar radiation transmittance equal to 0.33.
- Covered 100%: With greenery covering 100% of the structure, i.e. solar radiation transmittance equal to 0.

The purpose of the numerical simulation was to study the influence on the surface temperatures of the buildings connected and shaded by the system (east and west walls were selected since are those which receive more solar radiation in summer) and to study the variation of temperatures below the system depending on the coverage. To this aim, the inter-building area below the shading system was modelled as an internal thermal zone, characterized by thin air layer envelope and high air infiltration and ventilation to approximate outdoor conditions to the best.

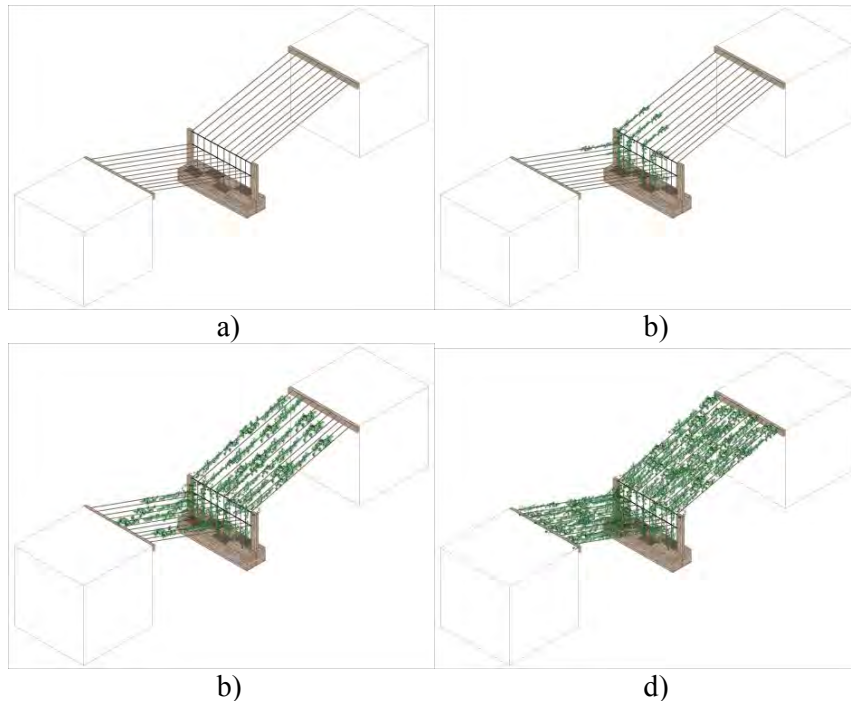


Figure 2. The four different scenarios of the shading system. a) Without greenery, b) With greenery covering 33%, c) With greenery covering 66%, d) With greenery covering 100%.

RESULTS AND DISCUSSION

As the external wall surface concerns (Figure 3), significant differences were observed between the four scenarios. More in detail, the maximum variation in the surface wall temperatures was found in the west facade, since among the considered orientations it is the one that receives the highest solar radiation in summer (Pérez et al. 2017). The peak temperatures showed significant variation depending on the shading scenario, while the minimum temperatures were similar.

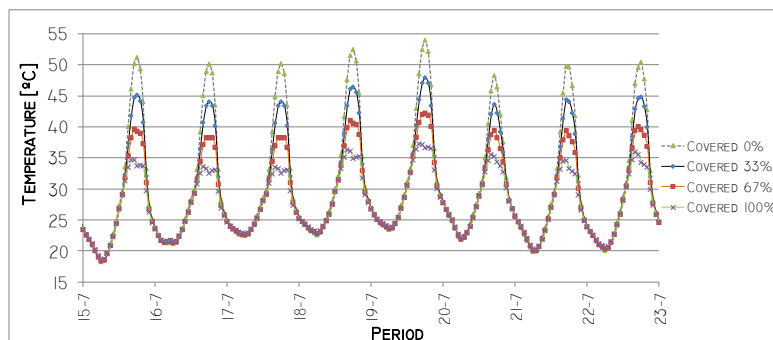


Figure 3. Daily variation of west facade temperature.

In particular, a difference of 16°C was found between the scenario without shadow (i.e. Covered 0%) and the one totally Covered (i.e. Covered 100%), where the surface temperatures reached 54°C and 38°C, respectively. Concerning the scenarios Covered 33% and Covered 67%, the maximum surface temperature reached 48°C and 42°C, respectively. These results highlight that the external temperatures of the walls of existing buildings can be reduced thanks to the implementation of the proposed shading system. Accordingly, this is expected to be associated to a significant decrease in the indoor ambient temperature.

On the other hand, in the east facade, a difference of 7°C was found between the scenario Covered 0% and the Covered 100% (with peak temperatures up to 43°C and 36°C, respectively). In this facade, each day shows two peaks, the first following the solar incidence and the second one corresponding to the maximum outside air temperature. As expected, the solar incidence has a stronger influence when no shadowing system is used (wall temperatures reaching up to 39°C), while with the system this temperature decreases up to 22.5°C. When the solar incidence decreases, the outside temperature effect is very strong, but in this case all scenarios reach similar temperatures (around 34-35.5°C).

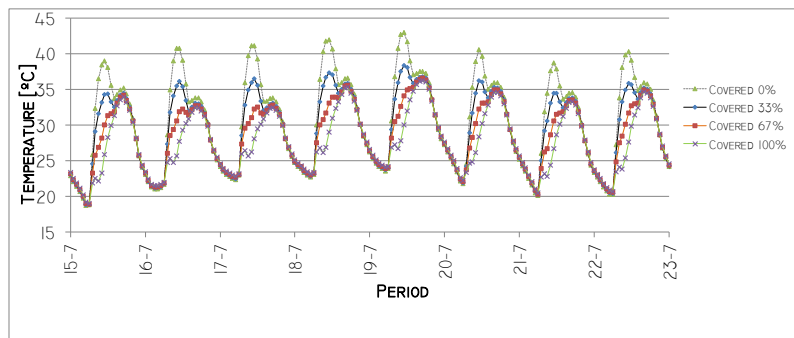


Figure 4. Daily variation of east facade temperature.

Regarding the air temperature in the inter-building space, i.e. under the shading system, the maximum temperatures ranged from 33°C for the Covered 100% scenario, to 34°C for the Covered 67%, to 36°C for the Covered 33%, up to 38°C for the system without greenery, i.e. Covered 0%. Therefore, the shading effect associated to the implementation of the greenery was able to provide an outdoor air temperature reduction up to 5°C.

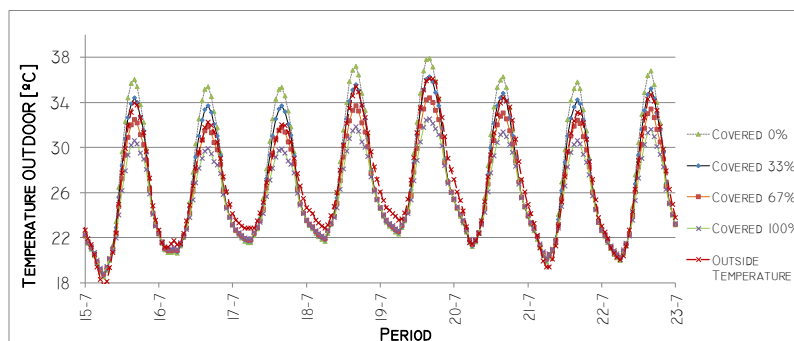


Figure 5. Daily ambient temperature under the shading system.

CONCLUSIONS AND FUTURE DEVELOPMENTS

This study presented the concept of a simple and adaptive bio-inspired vegetated shading system for inter-building spaces. The purpose of the study was to analyse the effect of varying the greening percentage on the shading system on the air temperature of the inter-building

area covered by the system and the connected buildings surfaces, through numerical modelling tools usually considered for indoor thermal-energy dynamic simulation. Simulations showed, as expected, that both the wall surface temperature and the air temperature under the shading system decreased when percentage of covering due to the greenery increased. Therefore, the theory of the benefits of a greenery system in summer is confirmed also for inter-building spaces. Since this study was carried out via numerical simulation, more exhaustive experimental research is needed to confirm these results. Therefore, reliable data will be available for architects, urban planners and engineers on the implementation of new concepts inspired by nature for both indoors and outdoors well-being.

ACKNOWLEDGEMENTS

The work is partially funded by the Spanish government ENE2015-64117-C5-1-R (MINECO/FEDER). The authors would like to thank the Catalan Government for the quality accreditation given to their research group (2017 SGR 1537). GREA is certified agent TECNIO in the category of technology developers from the Government of Catalonia. Also Marta Chàfer would like to thank the program Spanish Universities for EU Projects from Campus Iberus for the mobility scholarship. Part of this research is supported by COLO ARTE project by Fondazione Cassa di Risparmio di Perugia, (Grant Cod. 2016.0276.02).

REFERENCES

- Badarnah L. 2017. Form Follows Environment: Biomimetic Approaches to Building Envelope Design for Environmental Adaptation. *Buildings* 7 (2), 40.
- Beatley T. and Newman P. 2013. Biophilic cities are sustainable, resilient cities. *Sustainability (Switzerland)*, 5, 3328–3345.
- Crawley D.B, Pedersen C.O, Lawrie L.K, and Winkelmann F.C. 2000. Energy plus: Energy simulation program, ASHRAE Journal, 42, 49–56.
- DesignBuilder software Ltd. 2016. DesignBuilder software. <https://www.designbuilder.co.uk/> (accessed March 22, 2018).
- Horn R., Dahy H., Gantner J., Speck O., Leistner P. 2018 Bio-Inspired Sustainability Assessment for Building Product Development: Concept and Case Study. *Sustainability*, 10 (1), 130.
- Kottek M., Grieser J., Beck C., Rudolf B., Rubel F. 2006 World map of the Köppen-Geiger climate classification updated, *Meteorol. Zeitschrift*. 15, 259–263.
- Ng E., Chen L., Wang Y., Yuan C. 2012. A study on the cooling effects of greening in a high-density city: An experience from Hong Kong. *Building and Environment*, 47, 256–271.
- Pérez G., Coma J., Sol S., Cabeza L.F. 2017. Green facade for energy savings in buildings: The influence of leaf area index and facade orientation on the shadow effect. *Applied Energy*, 187, 424–437.
- Piselli C., Castaldo V., Pigliautile I., Pisello A.L., Cotana F. 2018. Outdoor comfort conditions in urban areas: on citizens' perspective about microclimate mitigation of urban transit areas. *Sustainable Cities and Society*, 39 16–36.
- Reeve A. C., Desha C., Hargreaves D. 2015. Biophilic urbanism: contributions to holistic urban greening for urban renewal. *Smart and Sustainable Built Environment*, 4(2), pp. 215-233
- U.S. Department of Energy's (DOE) Building Technologies Office (BTO). 2016. EnergyPlus - Weather Data. <https://energyplus.net/weather> (accessed March 22, 2018).
- Yang W., Wong N.H., Jusuf S.K. 2013. Thermal comfort in outdoor urban spaces in Singapore. *Building and Environment*, 59, 426–435.
- Pacheco-Torgal, F., Labrincha, J.A., Diamanti, M.V., Yu, C.-P., Lee, H.K. 2015. Biotechnologies and biomimetics for civil engineering. Springer.

Building Information Modeling (BIM) Implementation for Sustainability Analysis: A Mega Airport Project Case Study

Basak Keskin^{1*}, and Baris Salman²

¹Syracuse University, Syracuse

²Syracuse University, Syracuse

**Corresponding email: bkeskin@syr.edu*

ABSTRACT

It has been generally perceived that decision-making processes for implementing sustainable solutions to building elements should be in design and pre-construction phases. This perception hinders the transformation of current non-sustainable buildings into sustainable ones. It has been realized that retrofitting existing buildings can be more beneficial in terms of time and cost compared to new construction. This study aims to show that implementation of Building Information Modeling (BIM) for energy analysis improves the retrofit planning process. This study explains that in practice, BIM tools provide significant opportunities for creation of Building Energy Modeling (BEM); and the outputs of BEM analysis can be readily used in selection of energy efficiency measures. The case study approach is used in this study. Accordingly, 3D energy models of the Istanbul Grand Airport Project have been created. A heuristic optimization depicts a clear picture of why it is necessary to incentivize transforming BIM to BEM for decision-making processes of retrofitting. Correspondingly, the study findings show that BIM implementations can provide cost and time savings for energy analysis practices.

KEYWORDS

Building Information Modeling, Building Energy Modeling, retrofitting, heuristic model

INTRODUCTION

Energy analysis tools are integral to the process of identifying and implementing building energy savings measures (Evan, 2003). Such tools have many uses; typically, they are used for design of new building or renovation of existing ones with detailed design analysis (Sanquist & Ryan, 2012; Evan, 2003). Appropriate utilization of building energy analysis tools leads to accurate and cost-effective energy analyses, which depict the total energy use and savings opportunities. The origins of building energy software trace back to the 1970s. Before then, energy analysis was managed by hand at significant cost and time. According to Evan (2003), in the 1980s, the first-generation of simulation-based analysis and design tools emerged. From late 90s until now, rapid proliferation of tools targeted at a broader spectrum of users and the advent of web-based tools. Through web and literature searches, commonly used whole building energy simulation software tools in North America are compiled: TREAT, Sefaira Architecture, EnergyPlus, Pleiades+COMFIE, Autodesk Insight 360, EDAPT, TRNSYS, eQuest, TRACE 700, REM/Design, Open Studio, EDGE Excellence In Design, Design Builder, HA (Carrier).

Moreover, the opportunities can be magnified using recent innovations in energy management tools that provide greater access to energy use data as well as analytics and increased intelligence to optimize systems (Woo & Gleason, 2014). Additionally, typical processes of whole Building Energy Model (BEM) generation are subjective, labor intensive, time

intensive, and error prone (O'Donnell, et al., 2013). At this point, it is clear that integrating BIM and BEM generates value in terms of time, cost, and quality since BIM-based building energy models are capable of collecting and also rapidly processing real-time energy performance data. This also provides more accurate and detailed input and output for energy simulation process.

Using the aforementioned energy analysis tools for retrofitting with an optimized investment budget appears to be a viable investment tool. Such procedures can provide substantial savings in terms of energy use, energy cost, and carbon emissions. (Camlibel & Otay, 2011) Not all facility managers, building owners, and other related parties have the ability to access and use a sophisticated optimization software. There are cases in which fast and cost-efficient processes are needed. Heuristic approach can be used to calculate energy, energy cost, and CO₂ savings per invested amount for different energy efficiency measures (EEMs) (retrofit alternatives). Heuristic approach includes the following steps: calculating energy, energy cost, CO₂ savings per investment for each EEM; showing budget amount by drawing a vertical line along the budget amount; selecting EEM with the highest value of saving per USD on the left side of the vertical line; subtracting the selected EEM's investment amount from the given budget; drawing a new vertical line along the new value of the budget amount (Camlibel & Otay, 2011). This process is repeated until the budget no longer supports any other EEM. Thus, the BIM-BEM integration can improve heuristic optimization and selection of energy efficiency measures by providing fast and more accurate input data.

This study shares the energy analysis approach applied to Istanbul Grand Airport Project BIM models. The project encompasses four phases, which includes six runways, three terminals, and an annual 200 million passenger capacity. The first phase of the construction started in 2015. It was planned to make the airport operational in the first half of 2018. This timeline shows that the energy analysis results address the potential future rework that may target to meet or exceed performance guidelines set by building rating systems (e.g., ISI's Envision and the Middle East's ESTIDAMA which include energy efficiency of building envelopes, day-lighting performance, and embodied energy as the crucial part of their evaluation.)

In the literature, it is generally discussed that BIM-based energy modelling utilization leads to sustainable design, and provides easy access to energy analysis results in the early design process. However, to the authors' knowledge, there are no case studies showing that BIM can contribute to sustainability, not only in the design phase, but also throughout the life cycle of the building. Essentially, this study tries to fill the gap in the literature, via proposing BEM generation, by the use of BIM to accelerate the energy retrofitting decision making process.

METHODOLOGY

The case study shows the energy analysis procedure used for Istanbul Grand Airport (IGA) Project BIM models. These models are composed of architectural and structural Revit models. As one of the world's largest aviation projects, the IGA Project encompasses a terminal building with a total floor area of 950,000 m², and pier buildings with a total floor area of 320,000 m². The methodology used in the case study enables a holistic approach on the magnitude of future energy consumption of IGA project. In this respective order, the methodology contains a selection of the most suitable digital tools, an optimization of BIM models, and generation of an energy analysis.

According to Stumpf, Kim, & Jenicek (2009), the energy modeling process can be divided into two sub-processes. The first sub-process is a macro-level energy analysis, which focuses

on comparing building size, shape, and orientation. The second sub-process is a micro-level energy analysis, which considers building details such as wall penetrations and building system details. An energy analysis framework is obtained through the methodology presented below (See Figure 1). It contains data coming from both macro and micro level energy analysis processes.

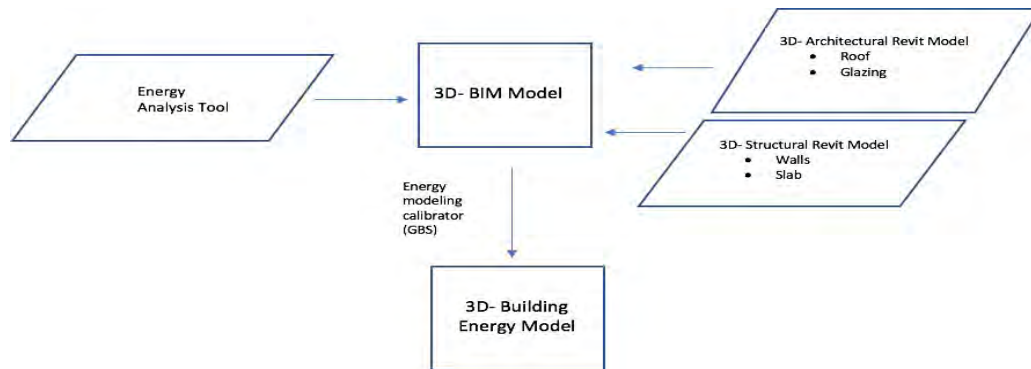


Figure 1: Energy Analysis Process Framework

At the first step of the methodology, the digital tool Insight 360 is chosen for this case study. This tool works as an add-in to Autodesk Revit and integrates existing workflows such as Revit Energy Analysis and Lighting Analysis for Revit. Insight 360 also allows visualization of solar radiation on mass or building element surfaces. Solar analysis includes a new automated workflow for understanding photovoltaic (PV) energy production. Insight 360 also provides a comparison of design scenarios to track performance of the building lifecycle, as well as, measuring the performance against Architecture 2030 and ASHRAE 90.1 benchmarks. The energy analysis results presented in this case study are limited. In essence, only visualization of solar radiation and energy production results are provided.

At the second step, optimization of BIM models, which is mainly dividing and simplifying architectural and structural Revit models, is conducted. Smaller models were extracted out of one master model (See Figure 2). Main purpose of this optimization, which requires discarding some architectural and structural elements, is to achieve the most appropriate model size and complexity for Insight 360, so that the tool can process data smoothly. Such tools have limited capabilities in terms of model size and complexity, making the model shown in Figure 2 infeasible to be analyzed as a whole. Accordingly, five different models with the most basic features (Kim & Anderson, 2011) (See Table 1) were obtained via taking reference of high level zoning plan given in Figure 3. However, it is important to keep in mind that, the number of sub-models should be kept to a minimum. Also, all sub-models should have a fully closed geometry to generate energy analytical models. Overall, the purpose is to eliminate issues including missing elements, elements that are not set to room bounding, gaps in geometry, in-place families, small spaces and surfaces, and columns that cause surfaces to be omitted from the energy model.

Table 1. List of sub-models

Sub-Models

Terminal 1 (all levels)
Terminal 2 + Terminal 3 (all levels)
Pier 1 – Pier 2 (all levels)
Pier 3- Pier 4 (all levels)
Pier 5 (all levels)

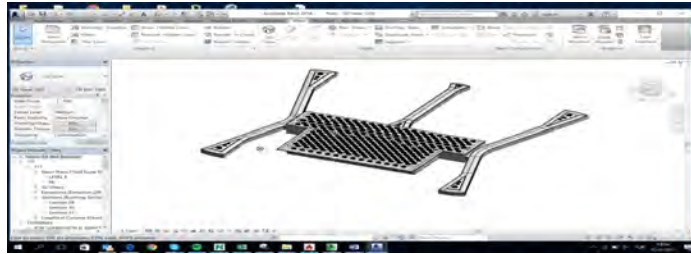


Figure 2: Master Model of the Project

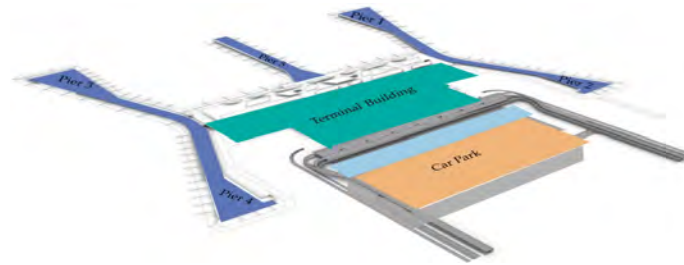


Figure 3: High Level Zoning of the Project

Furthermore, the master model is at its real-world coordinates having high accuracy in level and shape to ensure sustaining maximum accuracy in total volume of energy analytical model. As the third step, energy analysis is conducted; and for that purpose, **Generate** command (in Revit 2017) or **Generate Insight** command (Revit 2016) in **Analyze** ribbon (see Figure 4) is used. The process begins with creation of energy analytical model, followed by transmission of the model to the cloud-based Green Building Studio (GBS) server to obtain the results of energy analysis.



Figure 4: Analyze Command in Revit 2016

RESULTS & DISCUSSIONS

Visualization of solar radiation and energy production results are provided below for each sub-model developed through optimization. The results demonstrate significant total potential in solar energy generation due to the geographic coordinates of the structures, when the retrofitting solutions are applied correctly.

However, the BIM tools used in this study for energy analysis are still under development. Accordingly, it is a significant challenge to optimize models to have accurate flow of data between systems. Since, BIM modeling software market is greatly dominated by only a few companies (e.g. Autodesk Revit), sustainability practitioners are depending upon a limited extend of energy analysis plug-ins; which may otherwise result in compatibility issues.

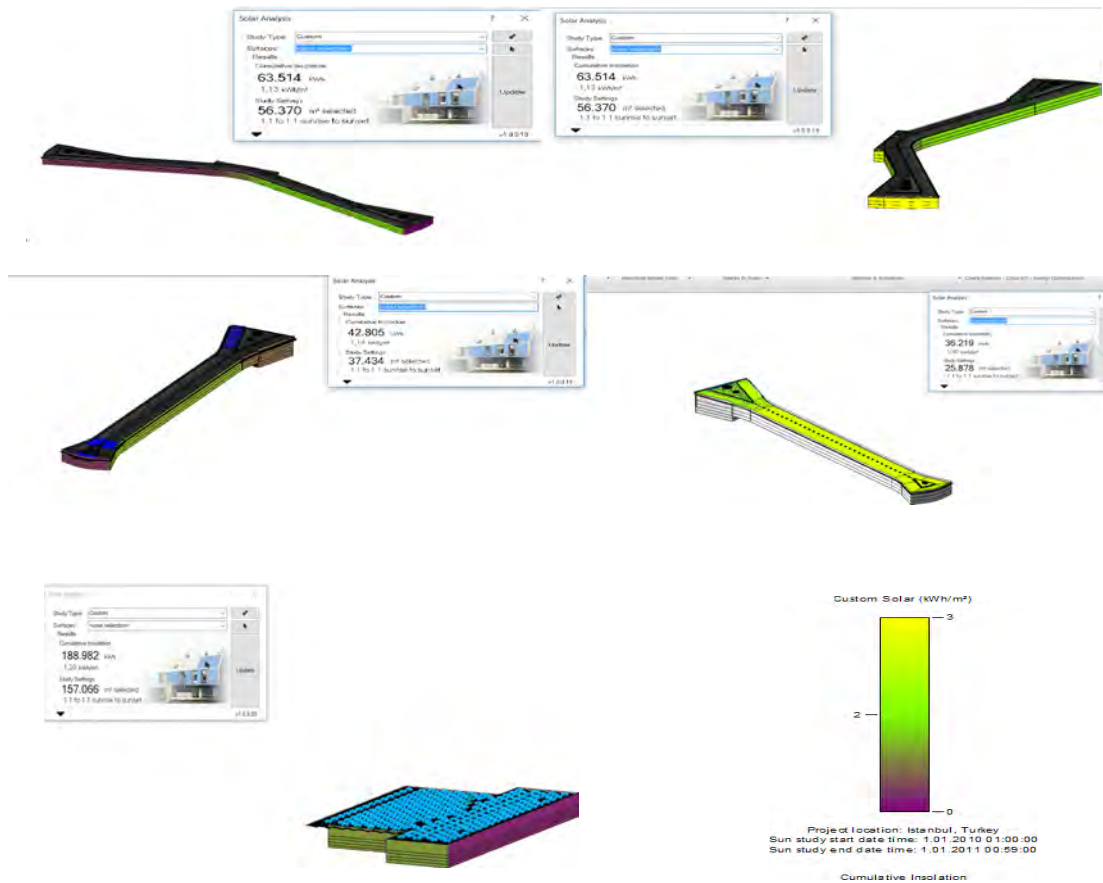


Figure 5: Solar Energy Results for Pier 1-2, Pier 3-4, Pier 5, Pier 5 Roof, Terminal Building, Custom Solar Scale on Energy Units (kWh) per Unit Area (m²)

Another problem about this BIM application is associated with the lack of guidelines and standardized workflows for right data retrieval from BIM models. Correspondingly, commercial BIM software technology market should further be evolved; and preparation of detailed BIM guidelines should be encouraged to improve the effectiveness of building retrofitting plans.

Retrofitting of existing buildings, as an evolving field of research, represents vast possibilities in increasing the energy efficiency of buildings. Façade design plays a crucial role in the retrofit of a building, and can offer additional benefits by incorporating possibilities of energy production (Bigaila, Hachem-Vermette, El-Sayed, & Athienitis, 2016).

Correspondingly, building-integrated photovoltaic (BIPV) glazing can be suggested as a retrofit solution for this case study. This is a new approach in which PV modules are integrated into the building envelope materials and components. As such, the PV system is not an added component, but rather a part of the essential building envelope. The electricity generated by the BIPV system can be stored in batteries so that the system can be used as an off-grid system. Alternatively, the system can be interfaced with the utility grid and the electricity generated can be sold back to the grid (Verboon & Laufs, 2013).

BIM implementation in the project gives many opportunities in terms of providing easy access to all project data (or one can say “big data”) – including 3D models at various levels of detail (LODs), 2D drawings, and all supplemental documents- from a single digital platform. Besides,

BIM also allows fast modification or update on data whenever needed while greatly eliminating waste in terms of time and money. As a summary, following points can be listed as benefits of BIM for sustainability;

- Energy modeling (detailed analysis of energy needs of the structure and analysis of renewable energy options such as solar energy),
- Building orientation (providing best building orientation option that leads to minimum energy cost),
- Reducing wasted time and resources for energy analysis (allowing rapid modifications in many design parameters),
- Access to current data for unit energy costs and weather via an internet server.

CONCLUSIONS

Building energy modeling tools provide an efficient, simple method in predicting the energy use of new and existing buildings. Via a decent optimization procedure and project defaults assumptions, energy analysis of all Terminal and Pier Buildings are conducted. Consequently, Autodesk Insight 360 provides annual and monthly data – both in energy units and in monetary units- of total energy consumption of the analyzed buildings. Annual and monthly monetary and energy equivalents of space heating, space cooling, area lighting, hot water supplies can also be generated graphically, which can enable the users to foresee energy consumption levels of airport buildings in future studies. However, in the context of this paper, solar analysis results are presented to articulate the simplicity in extracting data for retrofitting decision-making process. Since the tool aids in conducting iterative process by means of fast data-input, the facility owners can acknowledge the potential in PV energy production at the operational stage of the airport.

REFERENCES

- Abdalla, J. A., & Law, H. K. (2014). A Framework for Building Energy Model to Support Energy Performance Rating and Simulation. *Computing in Civil and Building Engineering*.
- Bigaila, E., Hachem-Vermette, C., El-Sayed, M., & Athienitis, A. K. (2016). Solar Energy Potential For Commercial Building Facade Retrofit. *IBPSA eSim 2016*. Hamilton: International Building Performance Simulation Association.
- Camlibel, M. E., & Otay, E. N. (2011). *An Integrated Optimization Model Towards Energy Efficiency For Existing Buildings - A Case Study For Bogazici University Kilyos Campus*. Istanbul: Bogazici University.
- Evan, M. (2003). Inter-comparison of North American residential energy analysis tools. 865-880.
- Kim, H., & Anderson, K. (2011). Energy Simulation System Using BIM (Building Information Modeling).
- O'Donnell, J. T., Maile, T., Rose, C., Mrazović, N., Morrissey, E., Regnier, C. . . . Bazjanac, V. (2013). *Transforming BIM to BEM: Generation of Building Geometry for the NASA Ames Sustainability Base BIM*. California: Lawrence Berkeley National Laboratory.
- Sanquist, T. F., & Ryan, E. M. (2012). Validation of building energy modeling tools under idealized and realistic conditions. *Energy and Buildings*, 375-382.
- Stumpf, A., Kim, H., & Jenicek, E. (2009). Early Design Energy Analysis Using BIMS (Building Information Models). *Construction Research Congress*. ASCE.
- Verboon, E., & Laufs, W. (2013). Innovative Façade Design and Products. In t. C. Engineers, *Curtain Wall Systems* (pp. 154-194). Reston: American Society of Civil Engineers.
- Woo, J.-H., & Gleason, B. (2014). Building Energy Benchmarking with Building Information Modeling and Wireless Sensor Technologies for Building Retrofits. *Computing in Civil and Building Engineering*.

Chemical Analysis of Precipitation and Stormwater Runoff from a Large Green Roof

Kimberly Fitzgerald^{1*}, Alexander Johnson¹ and Cliff I. Davidson^{1,2}

¹Department of Civil and Environmental Engineering, Syracuse, NY 13244

²Center of Excellence in Environmental and Energy Systems, Syracuse, NY 13244

**kafit100@syr.edu*

ABSTRACT

The growth medium of a green roof is likely to affect the chemistry of the rainwater passing through it, which may impact the receiving waters. Currently only limited data exist on the changes in rain chemistry caused by green roofs. The objectives of this project are to determine the differences in concentration of several contaminants in rain and in runoff from a green roof in downtown Syracuse, NY, and to explore reasons for the observed differences. A few samples were collected in 2014 and 2016, but most of the data are from 2017. Collection of precipitation uses funnels, while collection of runoff takes place using a drainpipe that connects to several roof drains. Both types of samples are analyzed by ion chromatography for chloride, sulfate, and nitrate. Preliminary tests show that chloride concentrations in the green roof runoff are generally greater than or equal to those in precipitation. Sulfate in the runoff is greatly enhanced compared with precipitation. Nitrate concentrations do not show a clear pattern. Engineered soil greatly influences the chemistry of the incoming rain, and additional research is needed to better understand this chemistry.

KEYWORDS

Green Roof, Stormwater, Ion Chromatography, Precipitation Chemistry, Runoff Chemistry

INTRODUCTION

Widespread urbanization has shown an increase in impermeable surfaces where there was once soil and plants to absorb the precipitation. The lack of area for infiltration can lead to flooding, and in cities with combined sewers, it can lead to combined sewer overflow where raw sewage enters the receiving waters. To reduce flooding and discharge of untreated sewage, green infrastructure such as green roofs can be installed to delay and store rain runoff.

Previous work has shown that rainwater flowing through the growth medium of a green roof (engineered soil) can experience changes in chemistry. For example, Vijayaraghavan et al. (2012) report higher concentrations of nitrate, phosphate, and sulfate in runoff compared to the incident rain using green roof test plots in Singapore. The plots incorporated growth medium with the trade name “universal garden soil” and were planted with sedum. Czemieli Berndtsson (2010) presents a literature review of green roof studies, some of which include chemical analysis of runoff. The data show that levels of nitrogen and phosphorus species in green roof runoff by different authors are quite variable, in part due to different roof characteristics.

The primary objective of this project is to compare the concentrations of chloride (Cl^-), sulfate (SO_4^{2-}), and nitrate (NO_3^-) in fresh precipitation and in rainwater that has passed through a large, extensive green roof. A second objective is to explore the reasons for these changes. Chemicals such as sulfate and nitrate, which contribute to acid deposition, are especially

important. Excess nitrogen in the runoff can have an adverse effect on the receiving waters by enhancing algae growth and eutrophication. The roof used in this study is on the Onondaga County Convention Center (OnCenter) in Syracuse, NY.

METHODS

The green roof, installed in 2011, is 0.56 hectares with growth medium 7.6 cm deep planted with six types of sedum. There are 25 roof drains, and samples are collected from a pipe connected to eight of these drains. Precipitation is collected on the roof of the Biological Research Laboratories on the Syracuse University campus, about 1.6 km east of the green roof. Sample bottles are secured in a wooden frame with funnels. Field blanks are obtained at each location. All samples are analyzed for chloride, sulfate, and nitrate using an ion chromatograph (IC). No fertilizer or other chemicals have been added to the roof since it was installed in 2011, although characteristics of the growth medium have undoubtedly changed over time. Only limited chemistry data from runoff were obtained prior to 2017.

RESULTS

Figure 1. a, b, c shows average net concentrations for Cl^- , SO_4^{2-} , and NO_3^- in the precipitation and green roof runoff. Each bar represents a separate rain event from 2014 to 2017.

DISCUSSION

Figure 1a shows that chloride concentrations in the runoff are usually equal to or greater than concentrations in the incoming rain. In storms 4/15/2017 and 7/20/2017, the opposite is observed, but the number of samples in these storms is small. The reason for the high chloride concentration in runoff on 6/4/2017 is unknown. This concentration is not likely due to contamination, as all three samples of runoff show similar high concentrations.

Sulfate concentrations shown in Figure 1b are consistently significantly higher in the runoff than in the precipitation. The data support the green roof being a source of sulfate. Investigations of the source of this sulfate are underway.

The nitrate concentrations from the runoff represented in Figure 1c show no dominant pattern when compared to the rain concentrations. About half of the rain events have runoff concentrations greater than precipitation, while the other half of the runoff concentrations are less than the those in precipitation.

The highest nitrate concentration in runoff occurs on 8/3-4/2017. The precipitation data shown in the graph is an average of five samples, one from an event on 8/3 and four from an event on 8/4. The storm on 8/3 had a nitrate concentration of 5.7 mg/L, while the storm on 8/4 had a concentration of 1.4 mg/L. The first storm had an intensity of 15.6 mm/hr and lasted for 10 minutes, a brief but intense cloudburst. In contrast, the second storm the next day had an intensity of 2.4 mm/hr and lasted two hours. The differences in concentrations in the precipitation from these storms is notable.

No runoff from the green roof occurred during the cloudburst on 8/3, as the total rainfall was only 2.6 mm. However, runoff occurred the next day when the total rainfall reached 4.6 mm. The concentration in the runoff averaged 5.0 mg/L, much greater than the concentration in the rain on that day. The runoff on 8/4 most likely included some of the high concentration rain on 8/3. Hence one cannot conclude that the nitrate in the growth medium was responsible for the elevated levels in runoff on 8/4.

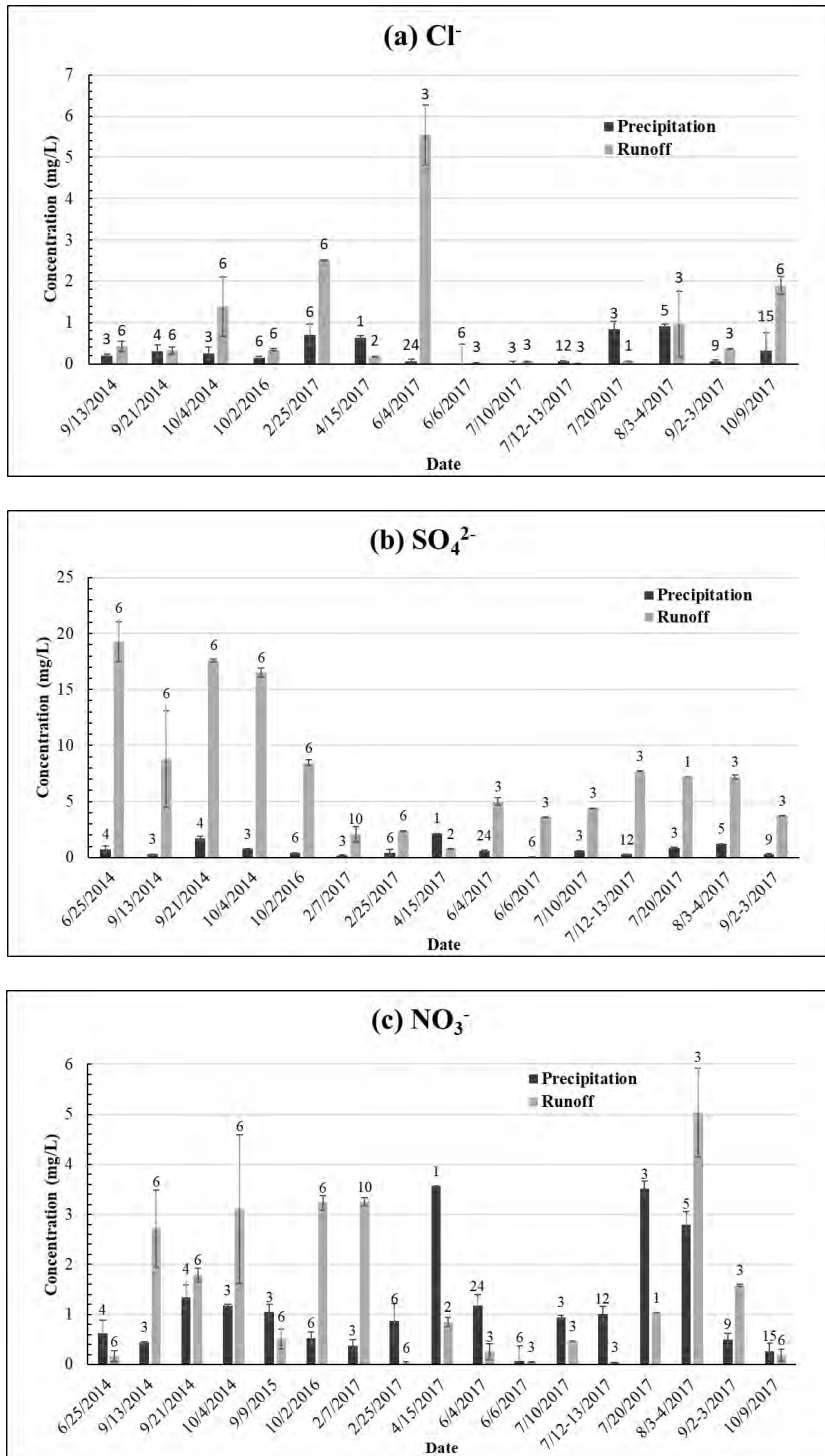


Figure 1. Average concentrations of chloride, sulfate, and nitrate, measured in precipitation and green roof runoff from selected storms. Error bars show one standard deviation from the mean. Each bar represents the average of the indicated number of samples, ranging from 1 to 24.

Johnson and Davidson (2017) note that fertilizer was applied to the green roof at the time of its installation in 2011. It is not known whether the nitrate concentrations in Figure 1c were influenced by this fertilizer. However, it is of interest that events on 6/25/14, 9/9/15, and many events in 2017 had runoff nitrate levels less than those in incoming rain. Rowe (2011) reports high nutrient concentrations in green roofs that have been fertilized. Age of green roof and vegetation type can factor in to the leeching of nitrate into the runoff (Czemieli Berndtsson, 2010).

Comparing patterns for the three analytes in Figure 1 shows that the storm on 4/15/2017 is unique in that concentrations in precipitation exceeded those in runoff for all three analytes. Further investigation of this event is underway.

Data collection is continuing and will expand to include other chemicals in future work. Arrangements are also being made to sample a nearby traditional roof as a control.

CONCLUSIONS

Concentrations of chloride, sulfate, and nitrate in fresh precipitation and runoff from a green roof in several events show a number of patterns. Concentrations of chloride in the runoff are generally equal to or greater than levels in the incoming rain. The same is true for sulfate. However, concentrations of nitrate showed more complex results: nitrate levels in runoff exceeded levels in rain for roughly half of the events, while the opposite was observed for the other half. One especially intense storm produced the highest levels of nitrate in rain observed throughout the study; runoff from a storm the next day most likely included some of the previous day's rainwater and showed similarly high concentrations. Chemical analysis of rain and runoff will continue in future work.

ACKNOWLEDGMENT

This work was supported in part by NSF grant #1444755, Urban Resilience to Extremes Sustainability Research Network, by funding from an NSF EMPOWER NRT grant, and by a Syracuse University Water Fellowship. The authors gratefully acknowledge the assistance of the Onondaga County Department of Facilities Management, especially Han Pham and Archie Wixson. The laboratory assistance of Mario Montesdeoca is also appreciated.

REFERENCES

- Czemieli Berndtsson, J. (2010). Green roof performance towards management of runoff water quantity and quality: A review. *Ecological Engineering*, 36(4), 351–360. <https://doi.org/10.1016/J.ECOLENG.2009.12.014>
- Johnson, Alex J. and Cliff I. Davidson, Chemistry of stormwater runoff from a large green roof in Syracuse, NY, Poster Presentation. *Proceedings, Third International Conference on Sustainable Infrastructure*, New York City, NY, October 26-28, 2017.
- Rowe, D. B. (2011). Green roofs as a means of pollution abatement. *Environmental Pollution*, 159(8–9), 2100–2110. <https://doi.org/10.1016/j.envpol.2010.10.029>
- Vijayaraghavan, K., Joshi, U. M., & Balasubramanian, R. (2012). A field study to evaluate runoff quality from green roofs. *Water Research*, 46(4), 1337–1345. <https://doi.org/10.1016/J.WATRES.2011.12.050>

Computational Evaluation of the Thermal Performance of Underground Bunkers: The Case of Albania

Rudina Breçani^{1,*} and Sokol Dervishi^{1,2}

¹ Epoka University, Faculty of Architecture, Tirana, Albania

² Vienna University of Technology, Institute of Architecture Science, Vienna, Austria

*Corresponding email: rbrecani12@epoka.edu.al

ABSTRACT

The present paper studies the thermal and energy performance and potential adaptive reuse of the lost underground bunkers of Kukës, Albania. The approach is exemplified using a 150-m long cross-section of the underground network selected for the parametric computational simulations. Data regarding local climate, design typology, and building materials is used to generate a finite-element simulation model of the underground tunnels. Different scenarios including insulation of the outer walls, occupancy patterns, and ventilation regimes are tested. The results show that indoor air temperature ranges from 15-18°C during winter and 23- 28°C during summer. During January, the temperatures are higher by 3-5 °C in comparison to the same structure and scenarios located above ground, whilst during July they are 5-8 °C lower. Insulation does not affect the heat flux through the outer walls. The average energy consumption oscillates around 55 KWh.m⁻².a⁻¹ for base case and 98-230 KWh.m⁻².a⁻¹ for design scenarios. The results establish the same building consumes 44-145% more energy when located above ground as opposed to underground.

KEYWORDS

Thermal performance simulation, scenarios, energy, underground nuclear bunker, adaptive reuse

INTRODUCTION

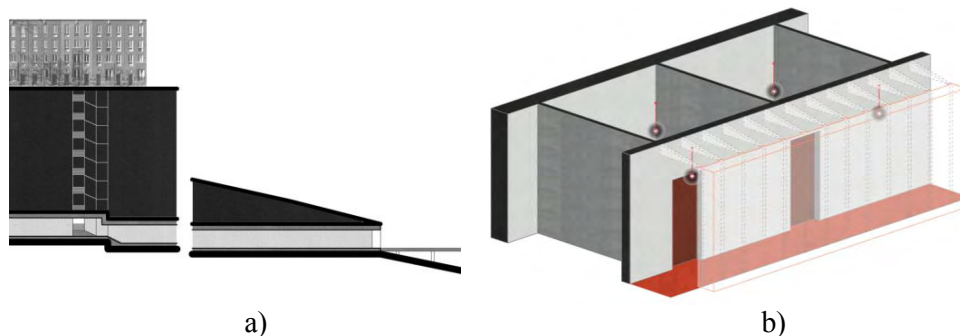


Figure 1. a) Partial section of the underground network of tunnels for Kukës, b) Close-up partial axonometric drawing of the inner construction of the tunnels.

Whilst above ground thermal comfort can be reached only via additional services, earth sheltered buildings are known for their temperature stability (Kajtar et al. 2015) and they gain benefit from the soil's quasi-stationary temperature to achieve energy conservation (Alkaff et al. 2016). Because of the high thermal inertia of the soil, the temperature fluctuations at the

surface of the ground are diminished as the depth of the ground increases (Florides and Kalogirou, 2005): the temperature of the soil changes with amplitude of 0.6 °C in the depth of 8 m and 0.2 °C in the depth of 10 m (Kajtar et al. 2015). After the depth reaches more than 20 m, the temperature becomes practically constant (Popiel et al. 2001). Popiel has concluded with the formula shown in Equation 1, where x is the depth below the ground surface, T is the temperature, k is the heat conductivity of the ground, and q the heat flux, that the heat flux of the soil is practically constant (2001). Florides depicts that due to the solar radiation and soil's relative capacity there is a 5-hour time lag a day regarding temperature distribution (2005). This explains why after reaching a specific depth the soil's temperature is always higher than the air temperature during winter and lower during summer.

$$q = -k \frac{\partial T}{\partial x} \quad (1) \text{ (Popiel et al. 2001)}$$

This knowledge has been practiced since ancient times: Samos, Greece, Cappadocia in Turkey, and the Hypogeum belong to the 6th century BC, 1900-1200 BC, and 4000 BC respectively (Nývlt et al. 2016; Debertolis et al. 2015). Living underground has become today a widely spread trend in countries such as China, Japan, and Korea where residents find comfort from the increasingly high economic pressure of living in apartments. In these countries, underground urban planning is a field study of its own (Zhao et al. 2016; Li et al. 2016) and some insist it should be an integral part of any National Regulation Plan (Tan et al., 2018). The studies on the computational evaluation of either thermal or energy performance for such spaces are fewer in number. Zhu has carried out thermal simulations on a sample of atrium plan earth sheltered buildings concluding that the buildings constitute a step forward towards low energy building design (Zhu and Tong, 2017). Another thermal performance simulation and evaluation study has been carried out by Ip, but the building in question has only one wall in contact with the earth (Ip and Miller, 2009). Tan has investigated the thermal comfort conditions in underground spaces in four major Chinese cities characterized by different climate conditions in order to assess the influence of the specific climatic variables (Tan et al. 2018). Tan however also recognizes his study as only qualitative and evaluates a building energy modeling would provide more solid data since qualitative analyzes often depend on real life restrictions (Tan et al. 2018).

In Albania, a special kind of underground shelters can be observed: nuclear bunker tunnels. A similar design typology is the subway, but it differs in many ways such as scenario, and traffic network which greatly influence the thermal and energy performance of the construction. The tunnels of Kukës are part of the ex-secret military establishments of Albania. This network is 2400 m long and composed of 30 galleries. Each gallery is composed of a corridor with a row of rooms on one side; an outer concrete shell envelops rooms and corridors, whilst the indoor walls were built with bricks. The tunnels have corridors which are 270 cm high and 120 cm wide, and rooms of an average of 3.4x3.4m. The network is located from 319 m to 336 m above the sea level (the different levels are connected by staircases), whilst the ground level of the city of Kukës is located 350 m above the sea level (Poliba, 2017; Municipality of Kukës, 1973). The outer walls of the tunnels are composed of 40 cm thick reinforced concrete. The inner walls are composed of bricks and amount to 27 cm thickness. These capillaries, which were constructed in several cities during the communist period and never used to fulfill the purpose for which they were built (refuge in case of war), constitute a large underground network of concrete leftover space. Therefore, the question on the efficiency with which they can fulfill their original purpose i.e. that of sheltering, comes out naturally. This study assesses the thermal performance and evaluates the adaptive reuse efficiency of the underground shelters via computational simulation modelling using the case study of the

tunnel network found in the city of Kukës as a starting point. Whereas previous studies have provided significant insight on different topics related to underground structures, there is a lack of quantitative studies providing close examination of thermal performance and energy consumption evaluation. Thermal and energy performance evaluation has not been explored yet on this typology of shelter in Albania or elsewhere, and the number of similar studies worldwide is limited. Furthermore, this paper suggests and tests alternatives for low energy consumption adaptive reuse functions appropriate for the design typology, and space quality of the tunnels.

METHODS

Initial simulation models were generated based on collected geometry and construction data. Assumptions were made based on in situ observations and historical documents. The simulations are conducted with Design Builder, a software tool used to perform building energy, lighting, and comfort performance. The software has been developed to simplify the process of building, modelling, and simulation for maximum productivity allowing users to rapidly compare the function and performance of building designs, different scenarios, and deliver results quickly. Meteornorm software was used to generate the local weather file for the city of Kukës. A 150 m tunnel section that serves as an extension of the existing hospital of the city, directly connected to it by its basement, is used for the simulations. A digital performance simulation model of the underground tunnel section is generated including the modelling, occupancy patterns, air humidity, and ventilation regimes. A set of five sample scenarios are established for the parametric study. The first scenario (S1) corresponds to the existing conditions. A second scenario (S2) is defined involving thermal insulation. Three additional scenarios (S3-S5) address the thermal performance of different potential reuse activities: laboratory (S3), hospital (S4), and museum (S5). Two simultaneous sets of simulations for scenarios S3-S5 are conducted to verify energy reduction potential of underground buildings with comparison to above ground buildings: S3-S5 when the building is located at 325 m above the sea level (the actual level of the tunnels), and S3.2-S5.2 when the building is located at 350 m above the sea level (the level of the city). Table 1 illustrates the data on scenarios S3-S5 and S3.2-S5.2. The thermal transmittance of the materials is as follows: 0.27, and 0.29 for inner and outer walls respectively, whilst without insulation these values are 1.42, and 2.31.

Table 1. Data pertaining to chosen scenarios for the study of activity impact on the underground tunnels' thermal load.

Code	Activity	Schedule	Density (people/m ²)	Gain (W/m ²)	Radiant fraction	Heating (20°C)	Cooling (20°C)
S3; S3.2	Laboratory	12/24 h	0.11	8.73	0.2	20	23
S4; S4.2	Hospital	24/24 h	0.10	3.58	0.2	18	25
S5; S5.2	Museum	varying	0.15	3.50	0.2	20	24

RESULTS

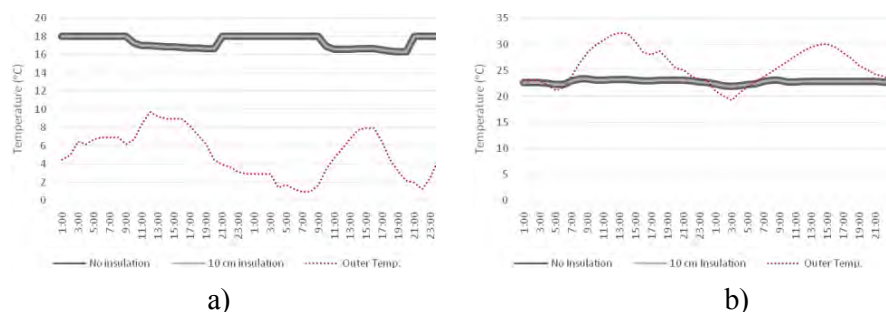


Figure 2. Simulated indoor temperatures (whole building) for S1 (base case without insulation) and S2 (base case with insulation) together with the external temperature data from the weather file. a) 15th and 16th of January, 2016, b) 15th and 16th of July, 2016.

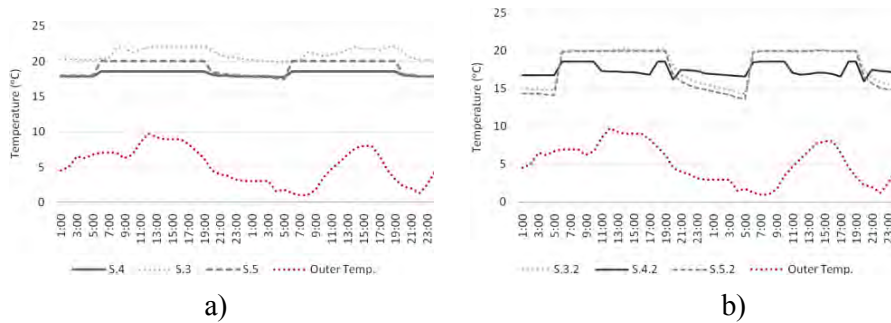


Figure 3. Comparison of the simulated indoor temperatures (whole building) of the scenarios together with the external temperature data from the weather file for the 15th and 16th of January, 2016, a) S3-S5 (underground), b) S3.2-S5.2 (above ground).

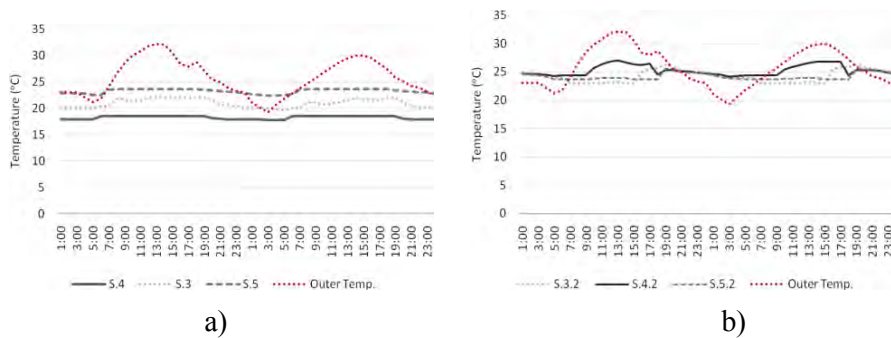


Figure 4. Comparison of the simulated indoor temperatures (whole building) of the scenarios together with the external temperature data from the weather file for the 15th and 16th of July, 2016, a) S3-S5 (underground), b) S3.2-S5.2 (above ground).

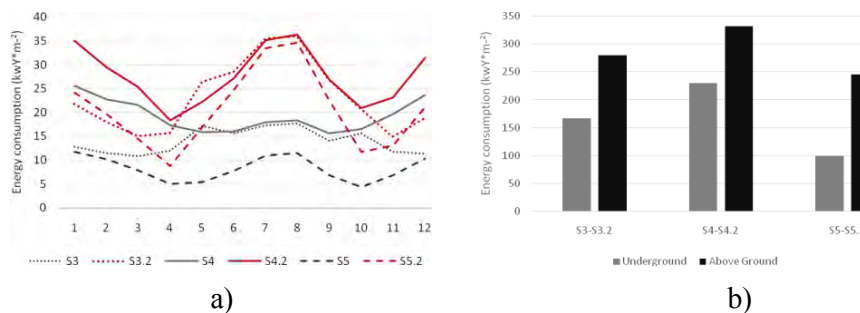


Figure 5. a) Comparison of simulated monthly energy demand ($\text{kWh}\cdot\text{m}^{-2}$) for S3-S5 and S3.2-S5.2, b) Simulated annual energy demand ($\text{kWh}\cdot\text{m}^{-2}\cdot\text{a}^{-1}$) for S1-S5.

Figure 2 illustrates the thermal performance of base case scenarios with and without insulation, S1-S2. Figures 3 and 4 provide an overview of the thermal performance in the selected scenarios (S3-S5; S3.2-S5.2) based on two reference days in January and July. Figure

5 summarizes comparative information regarding undergrounds' monthly energy use for the selected activities (S3-S5; S3.2-S5.2), as well as yearly overall energy consumption for S1-S5.

DISCUSSIONS

After comparing the theoretical background presented in the *Introduction* section and the results from the graphs in the *Results* section, conclusions are as follows:

- i. The theoretical background assesses the heat flux of the soil in the depth where the tunnels are located, 25 m underground, is almost constant and allows the spaces enveloped in it to remain cool during summer and warm during winter. This fact is proven by the graphs shown in Figure 2 where the graph lines for 10 cm and no thermal insulation temperature performance are overlapping, thus demonstrating the effect of thermal insulation on the thermal performance of the building is negligible. During January, the time lag phenomenon described in the *Introduction* can be observed: the temperature alternates between the earth and the ground, when above ground the temperatures are high, they are lower underground and vice versa. The time lag is of approximately 10 hours. However, this phenomenon cannot be observed during July because the temperatures are constantly high and do not vary.
- ii. Figures 3a and 4a compare the temperature performance of scenarios S3-S5 during two days in January and July. During January, all temperatures show an increment during the day, and cooling down after 18:00. The hospital's temperatures are more constant and 2-3°C lower. The laboratory's and museum's temperatures vary considerably during the 12/24 hours of activity, most likely due to the nature of the activities held which require more physical interaction and movement from the people involved. During July, the temperature variation lines are considerably more constant and closer in value to one another. The average temperatures during July are 23.1°C, 24.2°C, and 23.3°C for S3, S4, and S5 respectively. The average temperatures during January are 21°C, 18.3°C, and 19.1°C for S3, S4, and S5 respectively. Figures 3b and 4b compare the temperature performance of the activity scenarios when located above ground: S3.2-S5.2. During January, the temperatures are lower by 3-5°C in comparison to the same scenarios located underground, whilst during July they are 5-8°C higher.
- iii. The performance of the three scenarios regarding energy consumption varies. The average energy consumption per month is 14, 19.2, and 8.24 kWh m⁻².a⁻¹ for S3, S4, and S5 respectively. Regarding yearly energy consumption, the hospital's energy consumption results are 38% higher than the laboratory's, and 135% higher than the museum's. The results establish the same building consumes 44-145% more energy when located above ground as opposed to underground.

CONCLUSIONS

The case study of underground shelters poses an invitation for different research topics, however, the majority of information on them is provided by theoretical or qualitative studies. This paper is preoccupied with providing quantitative data on underground spaces, specifically nuclear shelters situated in the city of Kukës, Albania. The focus is on indoor thermal performance and energy consumption evaluation conducted via simulation software in order to assess the feasibility of adaptive reuse. Using the example of thermal simulation of a tunnel section, we explore the process and the recent results from the data collection. Hence, a building simulation model can be applied toward the assessment of the buildings'

performance and prediction of the consequences of alternative options for its renovation, reuse, and adaptation. Different scenarios are tested in order to assess the thermal performance of adaptive reuse alternatives for activities of 12/24 h, 24/24 h, and indefinite occupancy hours such as laboratories, hospital extensions, and museums respectively. The study concludes that a preferable scenario for adaptive reuse would be an activity held only 12/24 h, resulting in less energy consumption. In the present specific case, the 150 m section rooms can be proficiently repurposed as laboratory sectors that could serve to the hospital situated above ground. Although simulation and evaluation through software may face limitations due to the inability to make comparison with real life situations, the study represents an effective and well documented first step towards energy efficiency and possible adaptive reuse of abandoned underground or earth sheltered bunkers.

ACKNOWLEDGEMENT

This research did not receive any specific grant from funding agencies in the public, commercial, or not-for-profit sectors.

Special thanks are extended to Artan Hysa, professor at Epoka University, for his assistance during the preliminary phase of this research.

REFERENCES

- Alkaff, Saqaff A., Sim, S. C., and Ervina Efzan, M. N. 1993. A review of underground building towards thermal energy efficiency and sustainable development. In: *Renewable and Sustainable Energy Reviews*, Vol. 60, pp. 692-713.
- Debertolis, P., Coimbra, F., and Eneix L. 2015. Archaeoacoustic Analysis of the Hal Saflieni Hypogeum in Malta. In: *Journal of Anthropology and Archaeology*, Vol. 3, pp. 59-79.
- Florides, G., and Kalogirou, S. 2004. Measurements of Ground Temperature at Various Depths. In: *Proceedings of the SET 2004, 3rd International Conference on Sustainable Energy Technologies on CD-ROM*, Nottingham.
- Ip K. and Miller A. 2009. A. Thermal behaviour of an earth-sheltered autonomous building- The Brighton Earthship. In: *Renewable Energy*, Vol. 34, pp. 2037-43.
- Kajtar L, Nyers J, and Szabo J. 2015. Dynamic thermal dimensioning of underground spaces. In: *Energy*, Vol. 87, pp. 361-8.
- Li., X., Xu, H., Li, C., Sun, L., and Wang R. 2016. Study on the Demand and Driving Factors of Urban Underground Space Use. In: *Tunneling and Underground Space Technology*, Vol. 55, pp. 52-8.
- Municipality of Kukës. 1973. General Urban Plan for the New City of Kukës. 1:2000.
- Nývlt V, Musílek J, Čejka J, and Stopka O. 2016. The Study of Derinkuyu Underground City in Cappadocia Located in Pyroclastic Rock Materials. In: *Procedia Engineering*, Vol. 161, pp. 2253-58.
- Polytechnic University of Bari. 2017. *Notes on the Underground Tunnels of Kukës*.
- Popiel, C. O., Wojtkowiak, J., and Biernacka, B. 2001. Measures of Temperature Distribution in Ground. In: *Experimental Thermal and Fluid Science*, Vol. 25, pp. 301-309.
- Tan Z, Roberts AC, Christopoulos GI, Kwok KW, Car J, Li XZ, et al. 2018. Working in underground spaces: Architectural parameters, perceptions and thermal comfort measurements. In: *Tunneling and Underground Space Technology*, Vol. 71, pp. 428-39.
- Zhao, J., Peng, F., Wang, T., Zhang, X., and Jiang B. 2016. Advances in Master Planning of Urban Underground Space (UUS) in China. In: *Tunneling and Underground Space Technology*, Vol. 55, pp. 290-307.
- Zhu J and Tong L. 2017. Experimental study on the thermal performance of underground cave dwellings with coupled Yaokang. In: *Renewable Energy*, Vol. 108, pp. 156-68.

Criteria for identifying failure optimization algorithms in building energy optimization and case studies

Binghui Si¹ and Xing Shi^{1,*}

¹School of Architecture, Southeast University, Nanjing, China

*Corresponding email: shixing_seu@163.com

ABSTRACT

Optimization algorithms play a vital role in the Building Energy Optimization (BEO) technique. Although many algorithms are currently used in BEO, it is difficult to find an algorithm that performs well for all optimization problems. Some algorithms may fail in some cases. This study specifically focuses on failure algorithms in BEO and the possible causes. Several criteria are proposed for identifying failure algorithms. Four optimization problems based on the DOE small and large office buildings are developed. Three commonly used algorithms in BEO, namely, Pattern Search (PS) algorithm, Genetic Algorithm (GA) and Particle Swarm Optimization (PSO) algorithm, are applied to the four problems to investigate possible reasons for their failure. Results indicate that the effectiveness of the three selected algorithms is highly dependent on the optimization problems to be addressed. Besides, the control parameter setting of the PS algorithm appears to be a significant factor that may cause the algorithm to lose effectiveness. However, it does not seem to be the main reason for the failure of the GA and PSO algorithm. In General, the results gained from this study can deepen our understanding of optimization algorithms used in BEO. Besides, understanding the reasons why optimization algorithms are ineffective can help architects, engineers, and consultants select the appropriate optimization algorithms and set their parameters to achieve a better BEO design that is less vulnerable to failure.

KEYWORDS

Building energy optimization; failure optimization algorithm; cause of failure; algorithm parameter setting

INTRODUCTION

Building Energy Optimization (BEO) is a booming technique that combines building energy simulation engines with optimization engines. Unlike the conventional “trial-and-error” design methodology, which requires designers to manually adjust the design based on their experience and limited simulations, the BEO technique can automatically generate and simulate new designs utilizing optimization algorithms and performance simulation software and finally achieve the best design based on the predefined design objectives (Si et al. 2016). Therefore, optimization algorithms play a crucial role in the application of the BEO technique.

As shown in some important review works (Machairas et al. 2014; Shi et al. 2016), a quite number of algorithms can be used in BEO, for example, the evolutionary algorithms, direct search algorithms, hybrid algorithms, etc. However, there is in fact no universal algorithm that applies to all optimization problems, which means an algorithm may fail under certain circumstances. Thus, finding the causes for their failure and exploring the circumstances under which an algorithm may become fail can significantly help designers to choose an appropriate algorithm among the available options and help them avoid failure algorithms.

The objective of this research is to study failure optimization algorithms used in BEO and possible failure reasons. The first research task is to develop a set of criteria to recognize whether an optimization algorithm fails for a BEO problem. Then four optimization problems are developed using the DOE small and large office buildings. Three optimization algorithms are selected to investigate the possible factors that may cause them to fail for the four optimization problems.

METHODS

Criteria for identifying failure algorithms

Before defining a failure algorithm, we need to distinguish two concepts: a failure algorithm and a failure optimization run. For a specific optimization problem, an optimization algorithm fails on an optimization run does not mean it fails for the optimization problem. The reasons are stochastic optimization algorithms (e.g., GA, PSO, etc.) usually involve random operators in their optimization processes, which will result in different optimization runs when they are run repeatedly. In this case, one specific optimization run cannot reflect the performance of the algorithm. Users need to repeat the optimization test as many times as possible and then analyse all optimization runs. However, for a determined optimization algorithm, it usually has a unique optimization run which can fully reflect the performance behaviour of the algorithm when all relevant parameters and the initial solution remain unchanged. Therefore, in this study, we firstly proposed two criteria, which are the most concerned issues for designers when using optimization techniques, to identify a failure optimization run. Then the failure rate criterion was used to identify a failure algorithm. Note that this paper is particularly focuses on single-objective algorithms because about 60% of the building optimization studies used the single-objective approach (Nguyen et al. 2014). Multi-objective optimization algorithms are not covered.

In general, a successful optimization run should find the optimal solution within the desired accuracy level using a limited amount of time. It requires two criteria that should be met simultaneously, one of which is the quality of the optimal solution obtained in the optimization run should be high enough to meet the users' requirements, and the other is the computing time cannot exceed the time limit. An optimization run that violates any of the above two criteria is considered failure. In this study, to measure the quality of the optimal solution, Equation 1 can be used to calculate the relative distance between the optimal solution found in an optimization run and the true optimum of the optimization problem.

$$\delta = \frac{|f(X') - f(X^*)|}{f(X^*)} \times 100\% \quad (1)$$

where $f(X')$ is the objective value of the optimal solution found in an optimization run, and $f(X^*)$ is the objective value of the true optimum, which in some cases can be obtained through brute-force search. If the value of δ is larger than that of δ^* which is the acceptable accuracy level defined by the designer, then the optimization run is considered failure.

To define a failure optimization algorithm for a given problem, the algorithm needs to repeat the optimization process several times and then those failure runs need to be isolated to calculate the failure rate, which in essence, is the ratio of failure optimization runs to the total runs. Equation 2 provides a formula.

$$\beta = \frac{N_{failure}}{N_{total}} \times 100\% \quad (2)$$

where $N_{failure}$ is the number of failure runs and N_{total} is the total number of runs driven by the algorithm. According to the Low Probability Event (LPE) principle (McClelland et al. 1993), which is an important theorem in probability and commonly applied in practical projects and mathematical statistics, an LPE is considered will not occur in the actual environment. In practice, the value of 0.01, 0.05 or 0.1 are commonly used for an LPE which can be denoted by β^* . Users can also set other values according to their specific conditions. Consequently, in this study, an algorithm is considered failure for a given optimization problem when $\beta > \beta^*$.

Description of the standard optimization problem

Table 1. Specifications of optimization variables.

Design variables	Symbol	Unit	Step size	Range	Initial value
Building long axis azimuth	x_1	°	5	[0,180]	90
Cooling set-point temperature	x_2	°C	0.05	[22,29]	24
Heating set-point temperature	x_3	°C	0.05	[15,22]	21
Roof insulation conductivity	x_4	W/m·K	0.001	[0.03,0.06]	0.049
Roof insulation thickness	x_5	m	0.002	[0.01,0.15]	0.126
South wall insulation conductivity	x_6	W/m·K	0.001	[0.03,0.06]	0.049
East wall insulation conductivity	x_7	W/m·K	0.001	[0.03,0.06]	0.049
North wall insulation conductivity	x_8	W/m·K	0.001	[0.03,0.06]	0.049
West wall insulation conductivity	x_9	W/m·K	0.001	[0.03,0.06]	0.049
South wall insulation thickness	x_{10}	m	0.002	[0.01,0.15]	0.036
East wall insulation thickness	x_{11}	m	0.002	[0.01,0.15]	0.036
North wall insulation thickness	x_{12}	m	0.002	[0.01,0.15]	0.036
West wall insulation thickness	x_{13}	m	0.002	[0.01,0.15]	0.036
South window upper position	x_{14}	m	0.02	[1,2.7]	2.5
East window upper position	x_{15}	m	0.02	[1,2.7]	2.5
North window upper position	x_{16}	m	0.02	[1,2.7]	2.5
West window upper position	x_{17}	m	0.02	[1,2.7]	2.5
South window U-value	x_{18}	W/m ² K	0.05	[1,7]	3.25
East window U-value	x_{19}	W/m ² K	0.05	[1,7]	3.25
North window U-value	x_{20}	W/m ² K	0.05	[1,7]	3.25

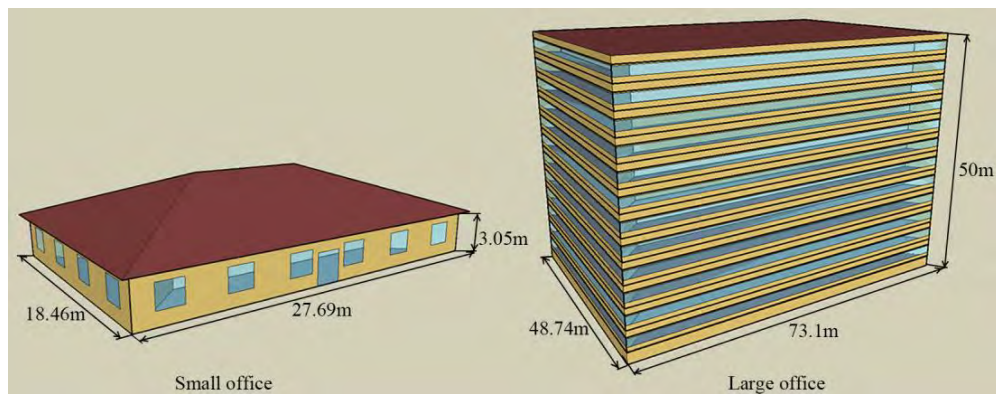


Figure. 1 Perspective views of the DOE small and large office buildings.

In this study, four optimization problems with 10 and 20 optimization variables respectively were developed following the models of the DOE small and large office buildings (Deru et al. 2011) in Baltimore, USA. They were all designed to minimize the annual energy consumption of the case buildings. Figure 1 shows the architectural schematic views of the buildings. They

all have one core thermal zone and four perimeter thermal zones on each floor. Table 1 lists the optimization variables involved in the optimization problems as well as their initial values, step sizes and range of variations. Specifically, the value for the lower window position is fixed at 0.9 m, and the windows in the same facade are of equal area. Besides, the first ten variables were used for optimization problems with 10 design variables.

RESULTS

In this section, three commonly used optimization algorithms in BEO, namely, Pattern Search (PS) algorithm, Genetic Algorithm (GA) and Particle Swarm Optimization (PSO) algorithm were assessed to find out possible factors that may cause the algorithms to fail. As shown in Table 2, four algorithm parameter settings for each algorithm are randomly generated to investigate their impacts on the effectiveness of the selected algorithms. Readers are referred to the manual book (Wetter M, 2011) for more information of the working strategies and the original development of each algorithm. Based on the two criteria proposed above about a failure optimization run, two evaluation approaches are accessible: (1) assessing the quality of the optimal solution obtained when the computing time is restricted; (2) assessing the computing time consumed when the optimization run finds the desired solution. In this study, we chosen the first approach. The maximum number of simulations for each optimization run was restricted at 300, and each optimization process was repeated 10 times to calculate the failure rate. These numbers were chosen to strike a balance between what is preferred and what is practical in terms of computing time. Specifically, the true optimum of the four optimization problems were obtained by brute-force search and were listed in Table 3. Besides, the desired accuracy level δ^* of optimal solutions was set at 1%, and the acceptable maximum failure rate β^* was 10%.

Table 2. Algorithm control parameter settings for each algorithm.

Algorithms	Parameters	Test 1	Test 2	Test 3	Test 4
PS	Expansion factor	2	3	4	5
	Contraction factor	0.2	0.4	0.6	0.8
GA	Population size	10	15	20	30
	Number of generations	30	20	15	10
	Elite count	1	2	3	4
	Crossover fraction	0.2	0.4	0.6	0.8
	Mutation rate	0.05	0.1	0.15	0.2
PSO	Population size	10	15	20	30
	Maximum number of iterations	30	20	15	10
	acceleration const 1 (local best influence)	2	3	2	3
	acceleration const 2 (global best influence)	2	2	3	3
	Initial inertia weight	0.9	0.8	0.7	0.6
	Final inertia weight	0.4	0.3	0.2	0.1

For each optimization problem, the quality variation of the optimal solution obtained by each algorithm in each test were illustrated in Figure 2. As shown, each algorithm has 4 consecutive boxplots, corresponding to the 4 tests listed in Table 2. It is noted that all optimization runs used the same initial solution listed in Table 1 to avoid the influence of different initial solutions on the evaluation results.

As shown in Figure 2, for each optimization problem, the average quality of optimal solutions found by the PS algorithm changes violently between different tests, which means the performance of the algorithm is sensitive to its parameter settings. It is further verified when the PS algorithm was use to solve Problem 1, in which it succeed in Test 1 but failed in Tests

2-4. Therefore, inappropriate parameter settings of the PS algorithm may cause it to fail. However, for the same optimization problem, the average quality of optimal solutions searched by the GA and PSO algorithm appears to be more stable between different tests. Thus, the effectiveness of the two algorithms are less sensitive to their parameter settings. Although GA and PSO algorithm failed in all four tests for Problem 1, 2 and 4, we cannot conclude if different parameter settings will cause the two algorithm to lose effective.

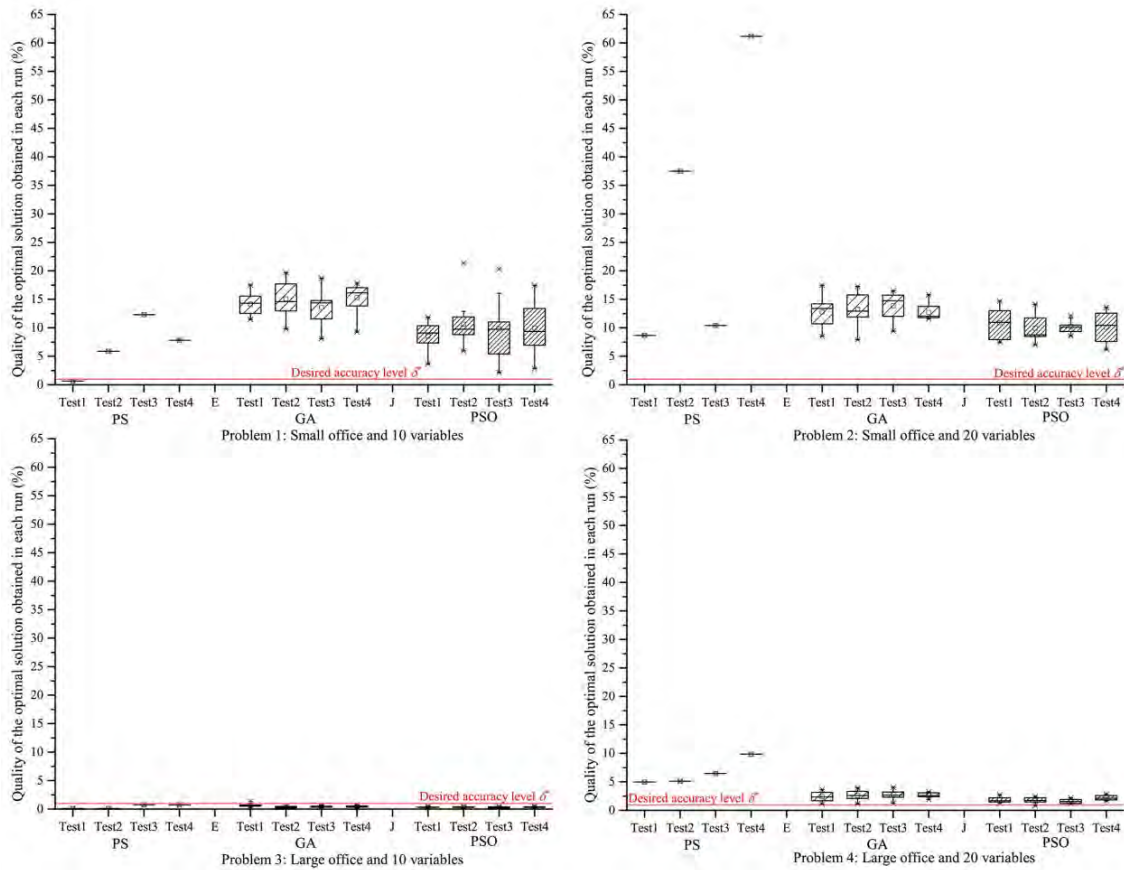


Figure. 2 Quality variability of the optimal solutions obtained by each algorithm in each test with different algorithm parameter settings.

Table 3. True optimum of each optimization problem and failure rate of each algorithm for each test.

Index	Optimization problems	True optimum (kW·h/m ² a)	Algorithms	Failure rate			
				Test 1	Test 2	Test 3	Test 4
Problem 1	Small office and 10 variables	95.532	PS	0	100%	100%	100%
			GA	100%	100%	100%	100%
			PSO	100%	100%	100%	100%
Problem 2	Small office and 20 variables	134.741	PS	100%	100%	100%	100%
			GA	100%	100%	100%	100%
			PSO	100%	100%	100%	100%
Problem 3	Large office and 10 variables	96.066	PS	0	0	0	0
			GA	10%	0	0	0
			PSO	0	0	0	0
Problem 4	Large office and 20 variables	125.355	PS	100%	100%	100%	100%
			GA	100%	100%	100%	100%
			PSO	100%	90%	100%	100%

Table 3 gives the calculated failure rate of the trial optimizations (each statistic relating 10 repeated optimization runs). It shows that for Problem 1, the PS algorithm performed well for Test 1 with a failure rate of 0, but failed for Tests 2-4 with a failure rate of 100%. The quality of the optimal solutions obtained by GA and PSO in the four tests were all beyond the desired accuracy level of Problem 1, and therefore, their failure rates were all 100%. For Problems 3 and 4, all the three algorithms failed to find desired solutions in all tests with a failure rate larger than the acceptable maximum failure rate (i.e., 10%). However, when applying the three algorithms to Problem 2, all of them could consistently find desired optimal solutions with a failure rate of no more than 10% even when they used different parameter settings. Thus, the effectiveness of the three selected algorithms highly depends on the optimization problems solved. In this study, some properties involved in the Problems 1, 2 and 4 seem to dominate the failure of the three selected algorithms.

CONCLUSIONS

Optimization algorithms play a critical role in determining the effectiveness and efficiency of BEO techniques. In this study, the criteria for helping users to detect failure optimization algorithms used for BEO problems are proposed. Four optimization problems were developed to find out possible factors that may cause three commonly used algorithms to fail. The numerical results demonstrate the following failure mechanisms of the selected algorithms: (1) algorithm control parameter setting is an important factor that may cause the PS algorithm to fail but it does not seem to be a key factor that may cause the failure of the GA and PSO algorithm. (2) Some inherent properties of optimization problems may cause the three algorithms to fail because their performance appeared to be highly dependent on the optimization problems addressed. Future research is required to examine the impacts of different properties involved in a BEO problem on the performance behaviour of different optimization algorithms.

ACKNOWLEDGEMENT

This paper was financially supported by the Scientific Research Foundation of Graduate School of Southeast University (grant number: YBJJ1702).

REFERENCES

- Si B., Tian Z., Jin X., Zhou X., Tang P. and Shi X. 2016. Performance indices and evaluation of algorithms in building energy efficient design optimization. *Energy*, 114, 100-112.
- Machairas V., Tsangrassoulis A. and Axarli K. 2014. Algorithms for optimization of building design: A review. *Renewable & Sustainable Energy Reviews*, 31(2), 101-112.
- Shi X., Tian Z., Chen W., Si B. and Jin X. 2016. A review on building energy efficient design optimization from the perspective of architects. *Renewable and Sustainable Energy Reviews*, 65, 872-84.
- Nguyen A.T., Reiter S. and Rigo P. 2014. A review on simulation-based optimization methods applied to building performance analysis. *Applied Energy*, 113, 1043-1058.
- Mcclelland G.H., Schulze W.D., and Coursey D.L. 1993. Insurance for Low-Probability Hazards: A Bimodal Response to Unlikely Events. *Making Decisions About Liability And Insurance*, Springer Netherlands.
- Deru M., Field K., Studer D., Benne K., Griffith B., Torcellini P., Liu B., Halverson M., Winiarski D., Rosenberg M. and Yazdani M. 2011. US Department of Energy commercial reference building models of the national building stock.
- Wetter M. 2011. GenOpt® Generic Optimization Program User Manual Version 3.1.0. Lawrence Berkeley National Laboratory.

Effects of Gaseous Pollution and Thermal Conditions on the Corrosion Rates of Copper and Silver in Data Centre Environment: A Literature Review

Rui Zhang^{1,*}, Roger Schmidt¹, Jeremy Gilbert² and Jensen Zhang¹

¹Syracuse University, Syracuse

²Clemson University, South Carolina

*rzhang20@syr.edu, rrschmid@syr.edu, jlgilbe@clemson.edu, jszhang@syr.edu

ABSTRACT

The objectives of the present review are to: 1) summarize the existing knowledge on the mechanisms of the corrosion, identify and analyze the major factors affecting the corrosion of copper and silver; 2) compare various measurement techniques for the study of atmospheric corrosion and models of corrosion; 3) identify knowledge gaps for atmospheric corrosion; 4) recommend “realistic worst case” pollution levels for laboratory testing of humidity and temperature effects on corrosion and assessment of datacom equipment reliability in data centers. This review focuses on the five pollutants: SO₂, NO₂, H₂S, O₃ and Cl₂. Results of the review include: the pollution levels and thermal environmental conditions in data centers; fundamental mechanisms of corrosion; current knowledge of the major factors affecting the corrosion rates of copper and silver; the techniques (QCM, Coulometric Reduction, SEM, XPS, FTIR and EIS) for the measurement of corrosion levels. It was found that the “realistic worst-case” concentrations for H₂S, NO₂, SO₂, Cl₂ and O₃ are 10 ppb, 80 ppb, 40 ppb, 2 ppb and 60 ppb, respectively. Different levels and combinations of contaminants, temperature, relative humidity and air velocity cause different corrosion on the metal. Chloride, Nitrogen dioxide and Sulfur dioxide are the common corrosive gases for the datacom equipment. Hydrogen sulfides and ozone are very important gaseous contamination in data center environment. Each of them alone can damage the equipment, and their synergistic effects with the other compounds and humidity can cause significantly more damages, but a mechanistic model is lacking for predicting the synergistic effects and better design of the thermal environment to ensure equipment reliability while improve the energy efficiency through the use of outdoor air for free cooling.

KEYWORDS

Atmospheric corrosion, copper, silver, SO₂, NO₂, H₂S, O₃ and Cl₂

INTRODUCTION

Data centers have the highest energy usage intensity among all building types and consume increasingly more energy due to the significant increase in the number of data centers worldwide. In an effort to reduce energy consumption, an increasing number of data centers have adopted air-side economizers to enable “free-cooling”. However, gaseous and particulate contaminants can enter data center when using air-side economizers, which may cause environment-related IT and Datacom equipment failures. Due to lack of data on the severity of the corrosion effects under realistic concentration levels and thermal environmental condition, gaseous contamination limits for the reliable operation of electronic equipment cannot be specified presently in terms of the concentration of gaseous contaminants in the air. ITEs can operate in a wide range of thermal environmental conditions including relative humidity levels up to 80% according to the current standards (ASHRAE, 2012c). There is clearly a need to determine the allowable gaseous concentration limits for the data center environment, especially under higher relative humidity conditions.

The objectives of the present review are to summarize the existing knowledge about the mechanisms of the corrosion, compare various measurement techniques for the study of atmospheric corrosion, identify knowledge gaps for atmospheric corrosion and recommend the “realistic worst case” pollutant levels and thermal environmental conditions for corrosion testing and assessment for data center applications.

MECHANISM OF ATMOSPHERIC CORROSION

Atmospheric corrosion is one kind of electrochemical corrosion. It occurs at the metal-solution interface with the creation of cathodic and anodic sides of the metal surface. The anode and cathode reactions in atmospheric corrosion are shown in Equation (1) and (2):

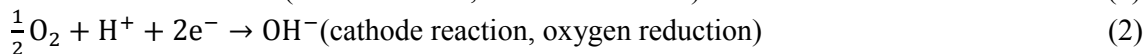
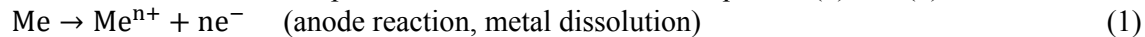


Figure 1 shows various processes involved in the atmospheric corrosion of copper based on the existing finding from the literature (T. Aastrup, 2000).

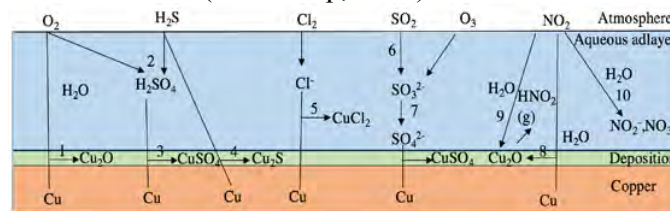


Figure 1 A schematic description of the atmospheric corrosion of copper

In the case of corrosion of ITEs, because the air is strictly controlled to have a dew point lower than the surface temperature of ITEs components to avoid apparent condensation, the aqueous layer above is likely to be only a thin layer or multi-layer of H₂O molecules adsorbed on the surface. Without the presence of contaminants, O₂ can diffuse into the aqueous layer and react with the pure copper to form a layer of copper oxide, a deposition layer that would protect the copper from corrosion. However, the gaseous pollutants, if present, can be dissolved into the adsorbed water molecules and react with O₂ to form H₂SO₄, which then reacts with copper to form copper sulfates. H₂S can also react directly with copper and O₂ to form copper sulfides (Processes 1 through 4 above).

When chlorine dissolves in the aqueous adsorption layer (adlayer), it resolves to the chloride ions. And these ions can react with the copper, which causes the copper dissolves into the liquid regime. Sulfur dioxide react with ozone in the liquid regime and ozone oxidizes the sulfur dioxide to H₂SO₄. Then H₂SO₄ combines with copper to generate the CuSO₄. NO₂ dissolves in the liquid regime and create HNO₂. And it has a reaction between HNO₂ and Cu to get the products of Cu₂O and HNO₂(gas). NO₂ also generates NO₂⁻ and NO₃⁻ after dissolving in the liquid. (Processes 5 to 10 above). While the reaction processes can be identified qualitatively, data are lacking on the reaction rate constants for the various processes identified above, and the synergistic effects of the various compounds under different relative humidity and temperature conditions cannot be readily determined from the existing literature.

FACTORS AFFECTING THE CORROSION RATES OF COPPER AND SILVER

Relative humidity

Primary, secondary and tertiary values of Critical Relative Humidity have been defined as the values of relative humidity below which no corrosion of the metal in question takes place, at which corrosion occurs rapidly, and above which further acceleration of corrosion can be

observed (if exists). The primary value of critical RH for uncorroded metals seems to be virtually independent of type of metals, which depends on the type of pollutants and moisture content (and hence the temperature for the given relative humidity level) in the atmosphere (Vernon, 1935). But the secondary and tertiary (if exists) values vary quite widely, depending on the presence and levels of gaseous pollutants and their potential synergistic effects as well as the metal type (Syed, 2006).

Air temperature

For a given moisture content (or specific humidity) in the moist air mixture, an increase in temperature reduces the level of relative humidity, resulting less water molecules being adsorbed on the material surface, and hence leads to a less amount of soluble pollutant's deposition on the surface and would likely reduce the corrosion effect (Mohan, 1991). However, on the other hand, a higher temperature tends to increase the reactivity of the ionization processes involved in the corrosion, and hence could enhance the corrosion effect (Franey, 1985). Therefore, the tradeoff between these two opposite effects needs to be evaluated for specific pollutant or pollutant mixture.

Sulfur dioxide

Sulfur dioxide is the most common corrosive gas for the Datacom equipment. Combustion of all fossil fuels can form the sulfur dioxide. Copper exposed to 80% RH, and 200 ppb SO₂ for approximately 1000 minutes formed copper sulfite, probably as a CuSO₃-xH₂O-like species, and cuprous (Cu₂O-like) oxide as major corrosion products (T. Aastrup, 2000). Similar results were also obtained by Erikson (1993).

Nitrogen Dioxide

Nitrogen dioxide source is the high-temperature combustion and biomass burning. Natural phenomenon like lightening also forms NO₂. According to Eriksson (1993), NO₂ has very small corrosive effects alone even in the ppm range. Muller (1991) also found that nitrogen dioxide had little influence on the corrosion rate of silver. The data reviewed above indicates that the NO₂ alone is not a significant factor for corrosion, but it can accelerate corrosion through synergistic effect with SO₂. Data on its possible synergistic effect with other gases of interests such as O₃, H₂S, and Cl₂ under different humidity and temperature conditions are lacking.

Hydrogen sulfide

Hydrogen sulfides is the most important gaseous contamination in the data center. It can cause the serious corrosion on the circuit board. Hydrogen sulfide is formed by the fossil fuel processing and combustion and natural processes (decay of vegetation in soils and wetlands, excess sulfur emission from vegetation and the like). There are two common modes of hardware which will be damaged if they are exposed to the sulfur-bearing gases (H₂S, SO₂): printed circuit boards (PCBs) and miniature surface-mount technology (SMT) resistors. Trana (2003) found that after the copper was exposed in this condition, copper sulfide was formed. Exposure to a higher concentration of H₂S resulted in a faster and larger increase of the thickness of Cu₂S, as expected. The data also show that there appears to be a maximum thickness of Cu₂S of 8-10 μm, beyond which further increase of exposure time had little impact on the thickness. It is possible that at this thickness, the Cu₂S layer became a significant resistance to the diffusion of ions between the adsorbed moisture layer and the pure copper, and hence slowed down the electrochemical process that was responsible for the corrosion. It is noted that even at 10 ppb (the proposed realistic worst-case level), 0.1 μm of corrosion layer was measured after 3 days of exposure (T.T.M.Trana, 2003).

Ozone

Natural and anthropogenic electrical discharge is the source of the ozone. It can increase the corrosive effect for the copper and silver (T. Aastrup, 2000). Ozone also enhanced the copper sulphadation when copper was exposed in SO₂ with ozone (T. E. Graedel, 11 May 1984).

Chloride

Chloride has limited corrosive ability to copper or silver. But it has a large influence on these metals when it combines with the hydrogen sulfide. In the study by Muller (1991), the copper and silver were exposed to 1.9 ppb of Cl_2 at 22°C and $50 \pm 5\%$ RH for one month. The results show that chloride alone had mild corrosion effect, similar to that of SO_2 tested, but significantly weaker than that of H_2S . Data are lacking on the synergistic effects of Cl_2 with other gasses, and for different RH and temperature conditions. When copper is exposed in H_2S , Cl_2 and NO_2 , the role of Cl_2 is to remove the Cu_2O then other pollutants can attack Cu directly (Abbott, 1988).

Synergistic effect

Figure 2 shows the corrosion thickness as a function of pollutant exposure amount (concentration times duration) found by previous researchers. The combined effects of different pollutants and relative humidity are very complex, and not yet well understood. Data is especially lacking under field concentration levels which are typically much lower than those used in the laboratory studies.

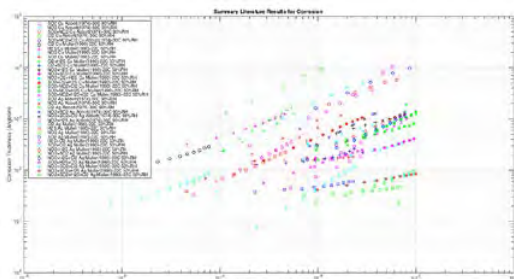


Figure 2 Summary Literature Corrosion Results

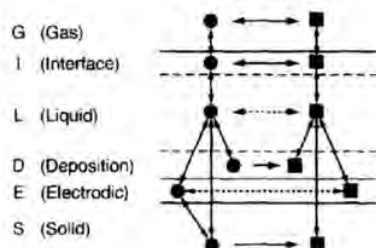
Chloride, Nitrogen dioxide and Sulfur dioxide are the common corrosive gases for the Datacom equipment. Each of them alone can cause only a small amount of corrosion on the metallic surfaces, even though some corrosion products can be detected on the surfaces of the materials. However, their co-existence can cause significant corrosion to ITEs due to synergistic effects among them Muller (1991). Cl_2 , H_2S , NO_2 and SO_2 can all cause significant damages to silver

surface. But for coppers, H_2S and Cl_2 can cause the most damage. Hydrogen sulfides and ozone are very important gaseous contamination in data center environment. Each of them alone can damage the equipment, and their synergistic effects with the other compounds can cause even more damages (T. Aastrup, 2000). The catalytic mechanism can increase the reaction speed but cannot produce additional products. It is necessary to consider the synergistic effect to assess the risk of ITE failure in a polluted environment. Such studies are lacking and need to be pursued in order to develop a reliable method for failure predictions.

MODELING OF ATMOSPHERIC CORROSION

In the data center, gaseous contaminations can include SO_2 , H_2S , NO_2 , Cl_2 , and H_2S . They can corrode the metallic materials and damage the circuit boards, connectors and various other electronic components. From the multi-regime perspective on atmospheric corrosion chemistry (Graedel, 1996), six regimes can be identified (Figure 3-1): G (gas), I (interface), L (liquid), D (deposition layer), E (electrode regime) and S (solid). Study of different layers requires knowledge of different science fields: gas layer – atmospheric chemistry; interface layer – convective and diffusive mass transfer and interface thermodynamics; liquid layer – freshwater, marine, and brine chemistry; deposition layer – colloid chemistry, surface science, and mineralogy; electrodic layer – electrochemistry; and solid layer – solid-state chemistry.

In this model, for the gas regime, pollutant gases by convection or detrainment from interface get into this regime. Then some of the gases deposit on the interface. Some species have chemical interaction with each other. When they arrive at the interface, some of them will volatilize into the gas regime and some enter into the liquid regime. In the interface regime, there are some chemical transformations among different



species. In the liquid regime, the species not only can reach the deposition regime but also can directly reach the electrodic regime and the solid regime. Chemical transformation can take

place at each regime. For the species in the solid regime, they react with species which come from the liquid regime and electrodic regime. The electrodic regime is where electrochemical reaction takes place. Copper loses its electrons and becomes the copper ions which get into the electrodic regime. Oxygen which is in the liquid regime reacts with the copper ions to generate the depositions. The circle and square symbols represent different species. When the corrosion products are generated over the surface, they will become more resistant to the corrosion process. The research of T.T.M.Tran (2003) shows that Cu_2S is an important resistance of diffusion of the ions between the liquid regime and the solid regime.

MEASUREMENT TECHNIQUES

In order to analyze the corrosion, there are many techniques for monitoring the mass change and for analyzing the geography of surface and surface compositions. Quartz crystal microbalance (QCM) is a technique to detect the mass change of the materials using the piezoelectric effect. In scanning electron microscopy (SEM), the information of topography and composition on the surface can be gained. X-ray photoelectron spectroscopy (XPS) is for the solid surface. It can be applied for the oxide thickness measurements. It can identify all elements except for hydrogen. In Fourier transform infrared spectroscopy (FTIR), it is useful for identifying the “chemical family” of a substance. An electrochemical impedance spectroscopy (EIS) is very useful for detecting the atmospheric corrosion. It measures the corrosion rate by estimating the polarization resistance, which is based on the theory of AC impedance. This technique is useful on high resistance materials and non-destructive. Coulometric Reduction is an electrochemical-based technique. This technique measures the thickness of the film by monitoring the quantity of electricity which is forming during the chemical reaction between the electrolyte and the corrosion products.

RECOMMADATION FOR THE “REALISTIC WORST-CASE CONCENTRATION LEVELS”

Table 1. Summary of Pollutant Concentrations and Recommended Limits by IEC (2002), Telcordia (2006), ISA(1985) and One Manufacturer’s Internal Standards

Gas	H_2S		SO_2		Cl_2		NO_2		O_3	
	Max	Min	Max	Min	Max	Min	Max	Min	Max	Min
Measurement (ppb)	8310008	0.101	87	0	0.58	0	152	0	174	0
Limits (ppb)	40	2	50	10	35	1	700	50	123	2

Table 1 shows the measurement data of outdoor pollutant levels and the concentration limits recommended for IT equipment protection against corrosion. The current guideline gives the recommended temperature and relative humidity envelope: the dew point is from $-9\text{ }^\circ\text{C}$ to $15\text{ }^\circ\text{C}$; The dry-bulb temperature is from $18\text{ }^\circ\text{C}$ to $27\text{ }^\circ\text{C}$ and the relative humidity is less than 60%. We propose the following as the “realistic worst- case concentration levels” for the MFG testing (Table 2)

Table 2. Proposed “Realistic Worst Case” Concentrations for Mixed Flow Gas (MFG) Testing

Pollutant	H_2S	NO_2	SO_2	Cl_2	O_3
Concentration (ppb)	10	80	40	2	60

The values in the table are consistent with the guideline limits for G2 (moderate) levels of corrosion per the ANSI/ISA Standard 71.04-2013.

SUMMARY AND CONCLUSIONS

It was found that the “realistic worst-case” concentrations for H₂S, NO₂, SO₂, Cl₂ and O₃ are 10 ppb, 80 ppb, 40 ppb, 2 ppb and 60 ppb, respectively. Chloride, Nitrogen dioxide and Sulfur dioxide are the common corrosive gases for the datacom equipment. Hydrogen sulfides and ozone are very important gaseous contamination in data center environment. But the lack of knowledge is about the synergistic effect at different thermal environmental conditions. There is lacking for a mechanistic model to predict the synergistic effects combing with various thermal environment.

REFERENCES

- Abbott, W. H. (1988). The Development and Performance Characteristics of Mixed Flowing Gas Test Environment. *IEEE Transactions on Components, Hybrids, and Manufacturing Technology VOL. 11. NO. 1. MARCH 198R*, Vol. 11, No. 1, 22-35.
- ASHRAE. (2012c). *Thermal Guidelines for Data Processing Environment, 4ed.* ASHRAE.
- Chris, M. (1991). Multiple Contaminant Gas Effects on Electronic Equipment Corrosion. *Corrosion - Houston*, 47(2), 146-151.
- D.W.Rice, P. E. (1981). Atmospheric Corrosion of Copper and Silver. *Journal of Electrochemical Society*, Vol. 128, No. 2, 275-284.
- J. P. Franey, G. W. (1985). The Corrosion of Silver by Atmospheric Sulfurous Gases. *Corrosion Science*, Vol. 25, No. 2, 133-143.
- L.Mariaca, D. I. (2008). Interaction of Copper and NO₂: Effect of Joint Presence of SO₂, Relative Humidity and Temperature. *Journal of Physics and Chmistry of Solids*, 895-904.
- P. S. Mohan, M. S. (1991). Corrosion of Metals in Sulphur Dioxide Atmosphere - A Laboratory Study. *Key Engineering Materials*, 179-184.
- Peter Eriksson, L.-G. J. (1993). Initial Stages of Copper Corrosion in Humid Air Containing SO₂ and NO₂. *Journal of the Electrochemical Society*, Vol. 140, No. 1.
- R.Wiesinger, I. C. (2013). Influence of Relative Humidity and Ozone on Atmospheric Silver Corrosion. *Corrosion Science*, 69-76.
- S. Feliu, L. M. (2003). Effect of NO₂ and/or SO₂ Atmospheric Contaminants and Relative Humidity on Copper Corrosion. *Rev. Metal. Madrid*, 279-288.
- Syed, S. (2006). Atmospheric Corrosion of Materials. *Emirates Journal for Enginerring Research*, 1-24.
- T. Aastrup, M. W. (2000). In Situ Studies of the Initial Atmospheric Corrosion of Copper Influence of Humidity, Sulfur Dioxide, Ozone and Nitrogen Dioxide. *Journal of the Electrochemical Society*, 147(7), 2543-2551.
- T. E. Graedel, J. P. (11 May 1984). Ozone- and Photon-Enhanced Atmospheric Sulfidation of Copper. *Science*, Vol. 224, Issue 4649, 599-601.
- T.T.M.Trana, C. F. (2003). The atmospheric corrosion of copper by hydrogen sulphide in underground conditions. *Corrosion Science*, Volume 45, Issue 12, 2787-2802.
- Vernon, W. H. (1935). A Laboratory Study of the Atmospheric Corrosion of Metals.

Elaboration of the decision space for an optimization of building retrofit

Yannis Merlet^{1,*}, Simon Rouchier¹ Arnaud Jay² and Monika Woloszyn¹

¹Univ. Grenoble Alpes, Univ. Savoie Mont Blanc, CNRS, LOCIE, 73000 Chambéry, France

²Univ Grenoble Alpes, CEA, LITEN, DTS, INES, F-38000 Grenoble, France

**Corresponding email: yannis.merlet@univ-smb.fr*

ABSTRACT

Multiobjective optimization is widely used in building physics but it has to face construction and regulation constraints to elaborate feasible solutions. This paper investigate how to integrate constraints in genetic optimization carried out with NSGA2 algorithm: it studies the implementation of constraints in the decision space and its impact on convergence speed and diversity in the optimization. The study was carried out on a 8 apartments building with three objective function to optimize: energy demand, comfort of the tenants and economic cost. As a result, convergence speed was improved and expert knowledge was included inside the decision space in a comprehensive way.

KEYWORDS

Multiobjective optimization, retrofit, building stocks, decision space

INTRODUCTION

In France, new buildings represent 1% of constructions each year. Decreasing the energy demand of the entire building stock will only be achieved if existing building are refurbished. On this topic social housing tenants have specific constraints and opportunities, and build their refurbishment strategies based on expert judgment. Experts try to balance constraints such as environmental impact, energy consumption, comfort of tenants to end up on a good solution and it is not possible to confirm that they are objectively the best solutions. Multi-objective optimization is an appropriate approach to efficiently suggest optimal solutions, so the expert could focus on picking a solution in the optimal ones. This work has been carried out in the scope of Reha-Parcs project which aim to apply multi-objective optimization on building stocks constituted of approximately 100 buildings owned by the same entity. Optimal solutions may then feed a decision-making tool for managers to pick the best one according to subjective needs like local policy, and funding.

Multi-objective optimization has been carried out on the design stage of new buildings to improve the shape and windows with respect to the energy demand and comfort (Tuhus-Dubrow and Krarti 2010; Diakaki, Grigoroudis, and Kolokotsa 2013) . Other work addresses the optimization of HVAC Systems in addition to the building envelope (Machairas, Tsangrassoulis, and Axarli 2014).

In multi-objective optimization, the formulation of the problem has a significant role in the success of the process, in order to get solutions that fit with construction and regulation constraints. The implementation of these constraints is mostly done at the optimization level by a penalty function (Coello Coello 2002). This approach limits the number of valid individuals in the population and consequently limits the diversity of the solutions. This seems to imply more generations to be computed in order to achieve the same diversity. This can be

time consuming depending on the computational cost of the evaluation function, especially on multiple buildings, as it limited previous works (Rivallain 2013)

A novel approach is to integrate constraints directly into the decision space, and this is the main focus in this paper. The aim of the study is to determine the impact of the integration of constraints in the decision space in term of convergence speed and diversity of the optimization.

METHODS

Optimization involve multiple parts: in this section will be detailed the evaluation function used to affect a fitness value to each retrofit strategy, the algorithm that has been chosen to carry out the optimization and the decision space of the optimization.

To evaluate the energy efficiency of a retrofit strategy, a test building has been modelled. This building is constituted of 4 floors and 8 apartments. Each apartment is 65m² large and is 2,3m high. In the model, each of those apartments is a thermal zone. The building is modelled in Modelica language using models issued from the *BuildSysPro* library, developed by EDF (Plessis et al. 2014). The model features an ideal heating generator and will be upgraded in future work with realistic systems. A TMY file is used to simulate the weather of the city of Nice (France). The objective function of the simulation are the energy needs of the building and summer comfort of the inhabitants that is presented in degrees.hours above an adaptive comfort temperature. The adaptive comfort model chosen is the revised standard 55 of ASHRAE (De Dear and Brager, 2002).

The last objective function is the economic cost of retrofit strategies. It is calculated with expert data provided in Reha-Parcs project: material price is a function of its thickness, then labour time cost is included and added to it.

First of all, the choice of an appropriate algorithm has been made with respect to the discrete nature of the problem: in order to keep only possible strategies. Indeed we had to comply with commercial solutions (eg. insulation is available for only selected thickness). In a discrete decision space, genetic programming suits better to the problem (Evins 2013). Moreover, genetic algorithm are widely used in building physics, especially NSGA2 (Deb et al. 2000) as it has proven to be both stable and efficient. In this paper, we used the implementation of NSGA2 provided in Python library DEAP (Fortin et al. 2012). The parameters used are the following:

Table 1: Settings of NSGA2 algorithm

Number of individuals	96
Number of generations	50
Probability of crossing	0,8
Probability of mutation	0,2

Those parameters were selected after a literature study (Rosenthal and Borschbach). They enable to have a good exploration of the decision space with mutation while the convergence speed towards Pareto front is not slowed down. The number of individuals has been selected to be 96 for a good diversity and to suit the 48 cores available for parallel computation.

In this paper, the main focus is on the decision space. In our case, the decision space is constituted of a series of retrofit possibilities. Those retrofit possibilities are considered for the

envelope: outer walls, top floor ceiling, bottom floor and windows. The comparison is made between a decision space that includes every retrofit possibility broken down into elementary tasks and a decision space composed of aggregated task for walls and windows operations. Both of them are described below.

Standard decision Space

The outer vertical walls, ceiling and floor have the same structure, which is 20cm of reinforced concrete. Vertical walls, ceiling and floor are independent from each other in the optimization. The insulation proposed features one of the following component:

Table 2: Insulation possibilities for outer walls in the optimization

Insulation material	Commercially available thickness (in cm)
Polyurethane	2, 4, 6, 8, 10, 12, 14, 16, 18, 20
Glasswool	6, 8, 10, 12, 14, 16, 18, 20
Polystyrene	6, 8, 10, 12, 14, 16

Another parameter of the optimization is the windows: the U coefficient for each type of window is the value that changes. Commercially available windows used in refurbishment in France where again provided by expert data within Reha-Parcs project, and are as follow:

Table 3: windows possibilities in the optimization

Windows U values	0.8, 1, 1.2, 1.4, 2
------------------	---------------------

As a result, this decision space provides 109760 possibilities of retrofit that could be applied on the building.

Constrained decision Space

The second decision space differs from the first one as windows and outer vertical walls are combined: in this problem, one gene of each individual corresponds to a facade solution which includes one type of window and one type of insulation of the vertical walls.

In order to fit construction constraints, some solutions are not possible: these solutions involve high performance wall with low performance windows or high performance windows with low performance walls. In this problem, 22 combination are forbidden. Should an individual propose on a forbidden solution, it will be mutated until it is an allowed combination. In this way, optimization avoids a costly evaluation function but can slow the convergence of the optimization. Constraints slightly reduce the decision space to 92512 possibilities offered to elaborate retrofit strategies.

RESULTS

In order to benchmark convergence speed of the optimization, we chose the Hypervolume criteria (Zitzler et al. 2002). Hypervolume is computed with a reference point chosen outside the objective space of both optimizations: depending on the shape of pareto front, the reference point can be selected from Nadir point to 150% of the values of Nadir point (Ishibuchi et al. 2017). Here, according to Ishibuchi and the shape of our Pareto fronts, the reference point should be between 120% and 150% of Nadir point's values. Whatever the value for the reference point results remain identical, hence figures for a reference point at 130% of Nadir point will be presented. Same reference point has been selected for both of hypervolumes computation.

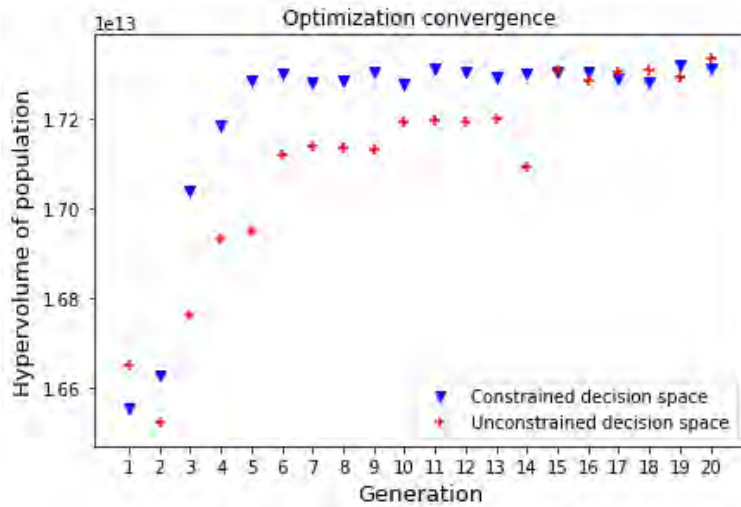


Figure 1: Convergence performance of each decision space

This figure shows a quickest convergence of the optimization when carried out with the constrained decision space. With this decision space, the best Pareto front is reached from generation 6 while with the first and unconstrained decision space, best solutions are found at generation 15. Moreover, the figure shows that with the unconstrained decision space, optimization does not reach global optimum before generation 15, while constrained decision space does reach it as soon as generation 5.

Pursuing the optimization until 50th generation shows that hypervolume does not vary significantly after generation 15, that is why only the first 20 generations are showed in Figure 1. It decreases for some generations due to mutations of individuals and get back to prior levels after two generations of selection.

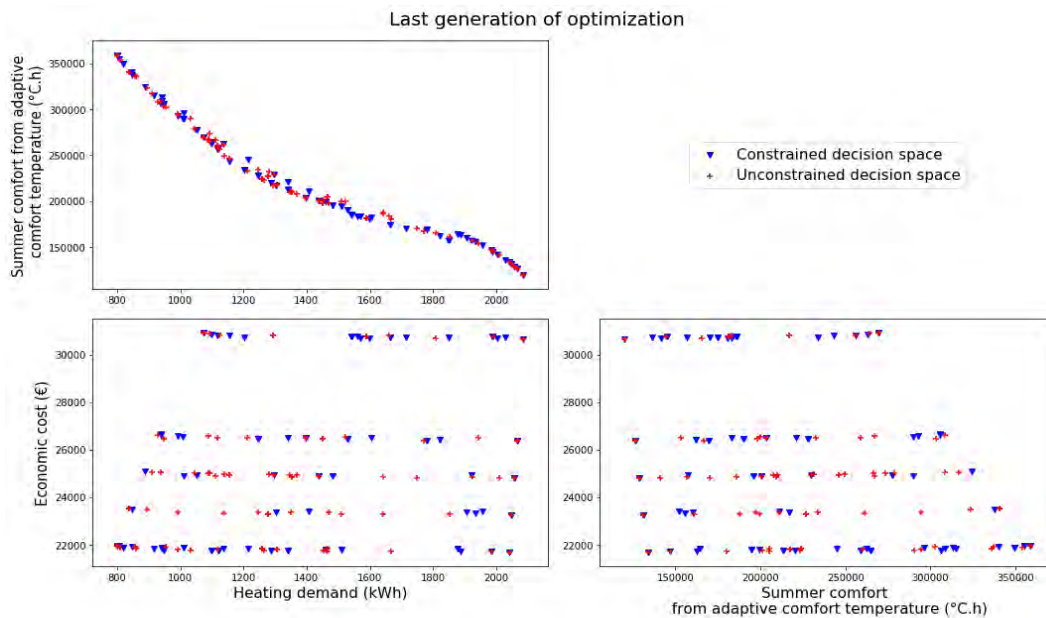


Figure 2: Pairwise plotting of last generation of optimization

Diversity of individuals is ensured with NSGA2's selection process. The diversity of proposed solutions can be checked by plotting Pareto fronts: Figure 2 shows Pareto fronts for all of the 3 objectives. A wide spread of the solution can be noticed and can sometimes be counter-intuitive regarding the performance of some of them. However, NSGA2 tends to keep only strictly non dominated solutions since it is an elitist algorithm.

DISCUSSIONS

Results support the integration of constraints in the decision space on a test case rather small with a decision space composed of around 100 000 possible combinations. It shows that optimization could be stopped 7 generations earlier with the same results if constraints are implemented in decision space, saving in our case 672 thermal simulations, which are the more costly part of the optimization calculation-wise.

This approach avoid implementing constraints by penalty function or by "death penalty" (Coello Coello 2002), but still enable to incorporate expert knowledge in the optimization problem. Moreover, it shows that adding expert knowledge in the algorithm can speed up the elaboration of retrofit strategies on this multi-family dwellings. Those results are promising since regulation and new construction solutions brought to market are generating more and more constraints, and we can implement them in a comprehensive way. Indeed it will help bringing multi-objective optimization to engineering by keeping the link between optimization constraints and practical solutions. In addition as a minor side effect, implementing constraints in the decision space saves time in post-processing to pick possible solutions and preventively clears out unrealistic solutions.

As optimization problem are quite specific, further studies will have to determine whether the impact is the same with more complex problems. First of all, the combinatorial will get bigger with the implementation of new possible retrofit tasks in the decision space. Secondly, the aim is to turn building model into a small building stock model of around 15 buildings with different shape and construction type. Finally, the application of such constraints should be verified with more than 3 objectives as NSGA2 algorithm is less efficient with more objectives (Campos Ciro et al. 2016).

CONCLUSIONS

This paper presents a method to integrate constraints in a problem of multi-objective optimization of building retrofit. A case test was studied in order to compare the performances of this approach: as a result, 25% less evaluation were needed during the optimization process in order to converge to Pareto front of optimal solutions. Some solutions proposed by the algorithm can be counter intuitive because of its performance on one objective but are still non-dominated on other objective, which illustrates that diversity is kept in the set of possible solutions.

Multi-objective optimization is a growing field when it comes to retrofitting buildings, and will get more important to develop strategies for energy conservation for buildings and building stocks. That is why we handled constraints here with a simple description that keeps the link between the decision space and the actual construction work. This method would be appropriate for an integration in an engineering tool featuring interactive decision-aid for the elaboration of optimal retrofit strategies developed by (Delhomme et al. 2017). This tool will enable designers to parse through optimal solutions for energy retrofit and to save time on

defining building stock-wide retrofit strategies and spend more time on non objective criteria such as the acceptability by users and urban integration of retrofit strategies.

ACKNOWLEDGEMENT

The authors would like to acknowledge French National Research Agency (ANR) for its funding within ANR-15-CE22-0011 Reha-Parcs project.

REFERENCES

- Campos-Ciro, Guillermo, Frédéric Dugardin, Farouk Yalaoui, and Russell Kelly. 2016. "A NSGA-II and NSGA-III Comparison for Solving an Open Shop Scheduling Problem with Resource Constraints." Elsevier: 1272–77.
- Coello Coello, Carlos A. 2002. "Theoretical and Numerical Constraint-Handling Techniques Used with Evolutionary Algorithms: A Survey of the State of the Art." *Computer Methods in Applied Mechanics and Engineering* 191 (11–12): 1245–87.
- Dear, Richard J. De, and Gail S. Brager. 2002. "Thermal Comfort in Naturally Ventilated Buildings: Revisions to ASHRAE Standard 55." *Energy and Buildings* 34 (6): 549–61.
- Deb, Kalyanmoy, Samir Agrawal, Amrit Pratap, and T. Meyarivan. 2000. "A Fast Elitist Non-Dominated Sorting Genetic Algorithm for Multi-Objective Optimization: NSGA-II." In *Proceedings of 6th International Conference on Parallel Problem Solving from Nature*
- Delhomme, Benjamin, Franck Taillandier, Irène Abi-Zeid, Rallou Thomopoulos, Cédric Baudrit, and Laurent Mora. 2017. "Designing an Argumentative Decision-Aiding Tool for Urban Planning,"
- Diakaki, Christina, Evangelos Grigoroudis, and Dionyssia Kolokotsa. 2013. "Performance Study of a Multi-Objective Mathematical Programming Modelling Approach for Energy Decision-Making in Buildings." *Energy* 59 (September): 534–42.
- Evins, Ralph. 2013. "A Review of Computational Optimisation Methods Applied to Sustainable Building Design." *Renewable and Sustainable Energy Reviews* 22: 230–45.
- Fortin, Félix-Antoine, François-Michel De Rainville, Marc-André Gardner, Marc Parizeau, and Christian Gagné. 2012. "DEAP: Evolutionary Algorithms Made Easy." *Journal of Machine Learning Research* 13: 2171–75.
- Ishibuchi, Hisao, Ryo Imada, Yu Setoguchi, and Yusuke Nojima. 2017. "Reference Point Specification in Hypervolume Calculation for Fair Comparison and Efficient Search." In *Proceedings of the Genetic and Evolutionary Computation Conference on - GECCO '17*, 585–92. New York, New York, USA: ACM Press.
- Machairas, Vasileios, Aris Tsangrassoulis, and Kleo Axarli. 2014. "Algorithms for Optimization of Building Design: A Review." *Renewable and Sustainable Energy Reviews* 31 (March): 101–12.
- Plessis, Gilles, Aurélie Kaemmerlen, and Amy Lindsay. 2014. "BuildSysPro: A Modelica Library for Modelling Buildings and Energy Systems," 1161–69.
- Rivallain, Mathieu. Étude de l'aide à la décision par optimisation multicritère des programmes de réhabilitation énergétique séquentielle des bâtiments existants. Université Paris-Est, 2013.
- Rosenthal, Susanne, and Markus Borschbach. n.d. "Impact of Population Size, Selection and Multi-Parent Recombination within a Customized NSGA-II and a Landscape Analysis for Biochemical Optimization."
- Tuhus-Dubrow, Daniel, and Moncef Krarti. 2010. "Genetic-Algorithm Based Approach to Optimize Building Envelope Design for Residential Buildings." *Building and Environment* 45 (7): 1574–81.
- Zitzler, Eckart, Lothar Thiele, Marco Laumanns, Carlos M Fonseca, Viviane Grunert, and Da Fonseca. 2002. "Performance Assessment of Multiobjective Optimizers: An Analysis and Review."

Energy Flow through the Onondaga County Convention Center Green Roof in Syracuse, NY

Alyssa Pizzi^{1,*} and Cliff I. Davidson^{1,2}

¹Department of Civil and Environmental Engineering, Syracuse University, 151 Link Hall, Syracuse, NY 13210

²Center of Excellence in Environmental and Energy Systems, Syracuse University, Syracuse, NY 13210

**Corresponding email: ampizzi@syr.edu*

ABSTRACT

Buildings in the Northeast U.S. with large interior open spaces and high ceilings require substantial amounts of energy to heat and cool the spaces. The objectives of this experiment are to model the heat flux across different layers of a green roof and to estimate the thermal resistance of the layers. The project will examine conditions in winter and summer, considering air temperature and snow cover on the roof. The scope of this study includes measurements of the transfer of energy through the green roof on the Onondaga County Convention Center in Syracuse, NY. The methods include collection of data from Campbell Scientific temperature probes at six heights through the roof layers, ranging from the Convention Center ceiling to the ambient air above the roof. The temperature data are stored in CR-1000 data loggers. Under certain conditions, the green roof is expected to be an effective barrier to energy flow across the roof. The implications of this work are a better understanding of how green roofs function as a barrier to energy loss from the building in winter and a barrier to energy gain from direct sunlight in the summer. This, in turn, can assist designers of green roofs in a variety of climates.

KEYWORDS

Green Roof, Energy Flow, Heating and Cooling, R-values

INTRODUCTION

Green roofs are sometimes used to reduce the amount of flooding and combined sewer overflow in a city caused by lack of surface area where rainwater can infiltrate into the soil. However, they can also have other benefits, such as reducing the heat loss during winter and reducing heat gain in summer, leading to reductions in energy used for heating and cooling.

For example, Jaffal et al. (2012) report a 6% reduction in annual energy demand in a simulation study with a single-family house when a green roof is added. Another simulation study by Zhang et al. (2017) shows the potential temperature reduction of the external surface of a building and subsequent energy savings with a green roof. Dahanayake and Chow (2018) have determined that green roofs and green walls reduce the surface temperature of buildings, therefore controlling the cooling load to maintain indoor temperatures.

The overall goal of this study is to determine the heat flux through the Onondaga County Convention Center green roof in different seasons, and to calculate the thermal

resistance of the roof layers. Previous work on heat flux through this roof was based on a smaller dataset and produced preliminary findings for 2014-15 (Squier and Davidson, 2016).

This study looks at temperatures in different layers of the Onondaga County Convention Center green roof from December 2016 through February 2018. Heat flux was calculated for December 2016 until June 2017. Times in winter were chosen when there was sufficient snowpack to insulate the surface from variable air temperature, creating quasi steady state conditions in which the thermal resistance (R-values) were calculated.

METHODS

During construction of the roof, Campbell Scientific T109 temperature probes were placed in 4 roof layers (A, B, C, G); this was accomplished at 5 widely separated stations on the roof. Three more probes were affixed to the ceiling below at Y (**Figure 1**).

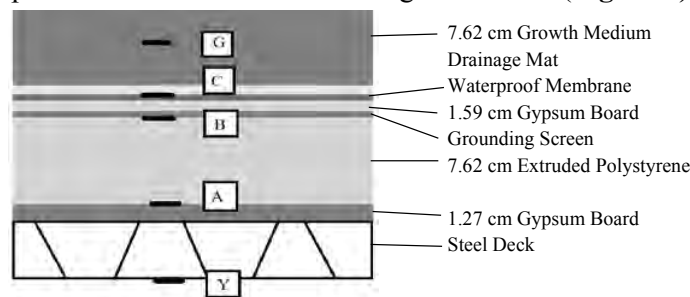


Figure 1: Layers of the roof and locations of the temperature sensors.

Because of possible malfunctioning probes, duplicate temperature sensors were placed in a number of roof layers. When analyzing the temperature data, some values from probes at stations 3 and 4 were flagged due to inconsistent temperatures for short time periods; the problematic data represent only a small fraction of the data from these sensors. Nevertheless, it was decided to exclude values from stations 3 and 4 in calculating average temperatures and R-values. Thus, data from only stations 1, 2, and 5 were used in the current study.

R-values were calculated over a period of high snow depth, 400-600 mm, which occurred over March 15-19, 2017 (**Figure 2**).

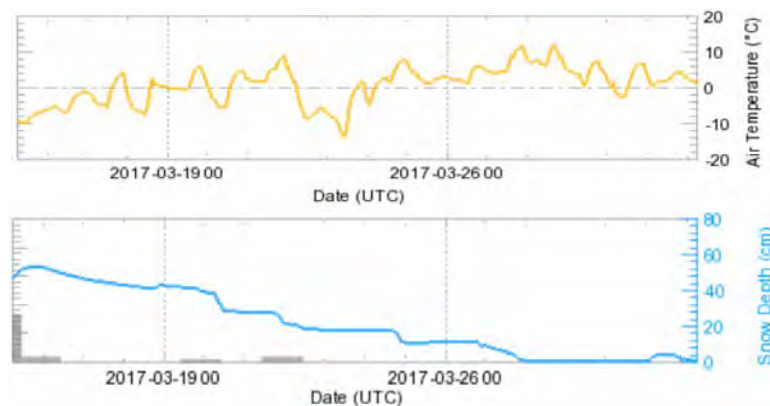


Figure 2: Air Temperature and Snow Depth as reported by the National Weather Service. The y-axis on the left side of both graphs corresponds to March 15, 2017.

The snow depth on the roof was assumed to be the same as the data collected by the National Weather Service station in Dewitt, NY, 4.1 km from the test site. This snow depth is consistent with the height of snow used by Squier and Davidson (2016) to calculate the R-values.

Fourier's equation was used for the steady state calculation of flux and resistance:

$$q = \frac{1}{R} \Delta T \quad (1)$$

where q is heat flux through the layers (W m^{-2}), R is the thermal resistance of the layers between the sensors ($\text{m}^2 \text{K W}^{-1}$), and ΔT is the difference in temperatures (degrees K) between the layers of the roof, calculated using the data from the temperature sensors. The R-values reported by the manufacturer are in **Table 1**. Additionally, the values calculated by Squier and Davidson (2016) based on limited data are in **Table 2**.

Table 1: Layers of the roof and their respective thickness and thermal resistance values as reported by the manufacturer.

Layer	Thickness (cm)	Material R-Values ($\text{m}^2 \text{K W}^{-1}$)
Growth Medium	3.81	0.211
Drainage Mat	0.63	n/a
Waterproof Membrane	0.12	0.028
Gypsum Board 2	1.59	0.118
Grounding Screen	0.102	0
Extruded Polystyrene Insulation	7.62	2.64
Gypsum Board 1	1.27	0.079

Table 2: R-values calculated by Squier and Davidson (2016) at stations 1, 3, 4, and 5 from February 1-14, 2015.

	5	1	4	3
B-C (Gypsum Board 2)	0.245	0.170	0.180	0.268
C-G (Waterproof Membrane and Growth Medium)	0.216	0.306	0.218	0.241
Overall, A-G	3.100	3.116	3.038	3.149

RESULTS AND DISCUSSION

Using Fourier's equation, the R-values across the roof layers for March 15-19, 2017 are given in **Table 3**. Based on the difference in temperature between layers B and C in both **Table 2** and **Table 3**, the R-values at station 5 are higher than the R-values at station 1. Conversely, over C-G, values at station 5 are less than the values at station 1. Values for stations 3 and 4 as presented by Squier and Davidson (2016) could not be compared for March 2017 due to malfunctioning sensors. It should be noted that station 2 reported average values in between the values of stations 1 and 5 in **Table 3**.

Table 3: R-values calculated at stations 1, 2, and 5 from March 15-19, 2017.

	5	1	2
B-C	0.246	0.139	0.174
C-G	0.214	0.327	0.278
Overall, A-G	3.100	3.106	3.092

The relationships between R-values shown in **Tables 2 and 3** are consistent. The values across different stations may be explained by the placement of sensors within the layers at each station. It is possible that some sensors rest slightly higher or lower than others at different stations, which would account for these deviations.

Figure 3 shows the temperature data for the G layer at the three stations used in this experiment from December 1, 2016 until March 31, 2017. The effect of the mid-March snowpack was to insulate the soil so that the temperature of the G layer hovered around 0° C throughout the period, despite wide variations in air temperature as shown in **Figure 2**.

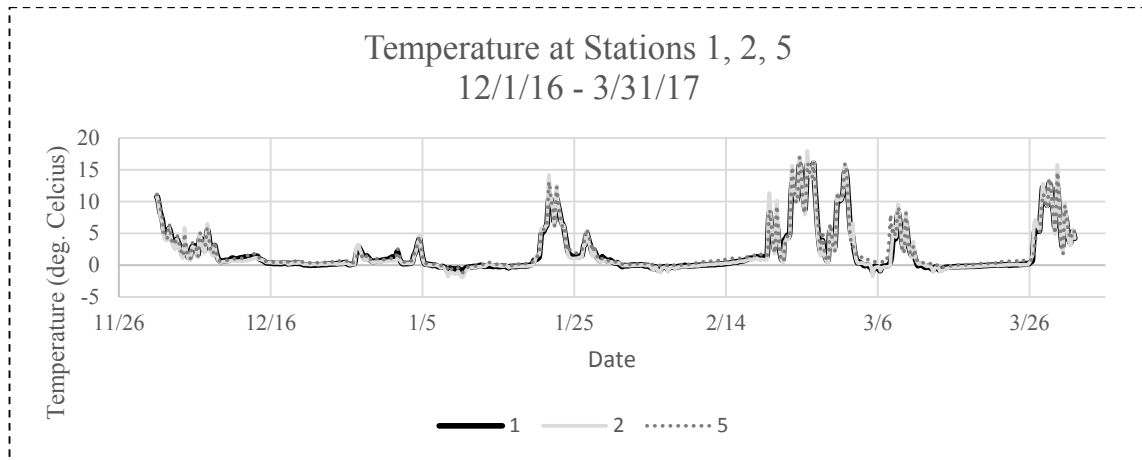


Figure 3: G-layer temperatures from three stations during Dec. 1, 2016 - March 31, 2017.

Figure 4 shows the temperatures in the different layers of the roof during 20 days of typical weather in the summer. Values shown are the averages at stations 1, 2, and 5. The temperatures at sensors G, C, and B follow the curve of the air temperature and frequently exceed the air temperature due to direct sunlight reaching the roof. The peaks at G, C, and B occur slightly later each day than the peak in air temperature, due to the time for heat conduction through the roof. Temperatures at A and Y are much lower than the air temperature and the other sensors in the roof because the Center is air conditioned. The greatest difference in temperature between adjacent sensors occurs between A and B.

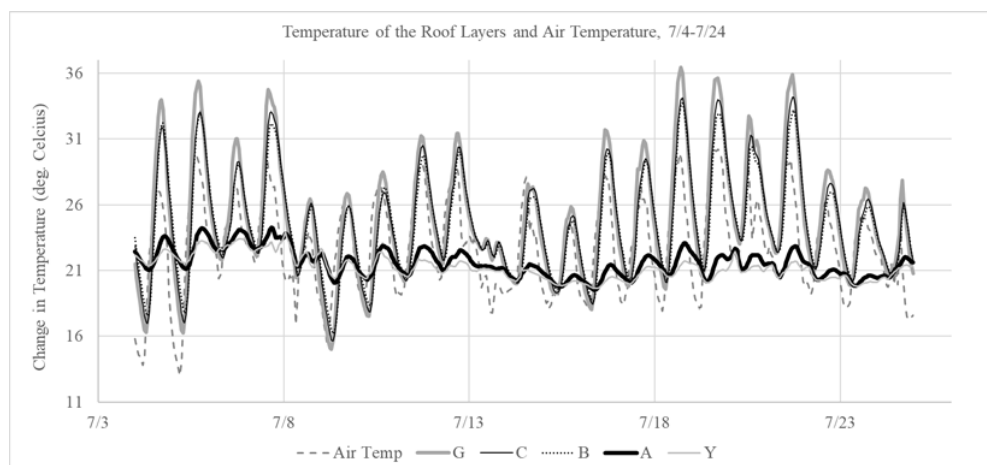


Figure 4: Temperature of each layer of the roof during July 4-24, 2017

Figure 5 shows the temperatures in the different layers of the roof during a 20-day period with typical winter weather. According to the National Weather Service there was no snow until January 24. There was significant snowpack (~100 mm) from January 24-27. From January 28-29, there is no snow on the roof, which corresponds to the small increase in temperature in the roof layers on January 28. Finally, there is significant snowpack again from January 31-February 9. The temperatures at Y and A reflect the heated interior of the building. The greatest difference in temperature between adjacent sensors again occurs over the insulation layer from sensor A to sensor B. Sensor G is closest to the air, followed by sensors C and B. The temperature at B is higher than at C, which is higher than at G, consistent with distance from the heated interior. Around January 23, there is an increase in air temperature, and the temperatures at sensors G, C, and B increase and are nearly the same over this period.

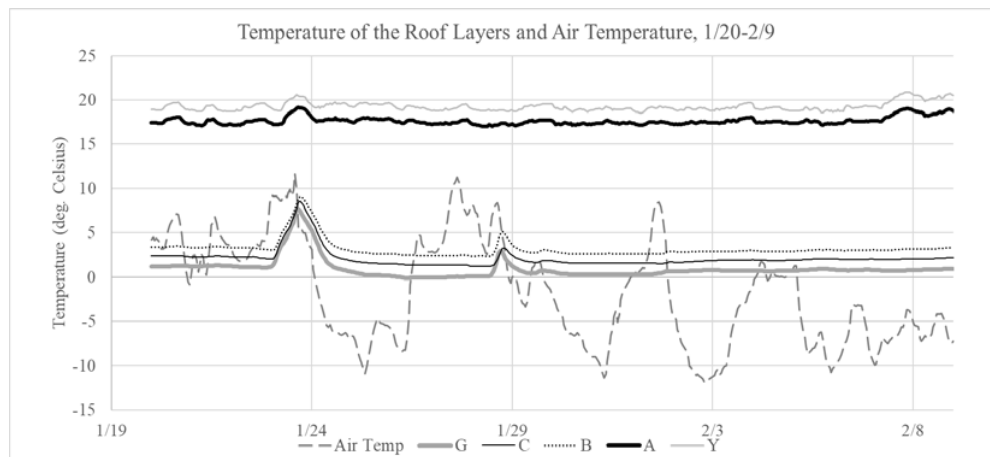


Figure 5: Temperature of each layer of the roof during January 20 - February 9, 2018.

The heat flux from A to B shows the transfer of energy across the insulation layer. **Figure 6** shows this heat flux over six months. During the winter months, there is generally a positive flux of heat escaping the building through the roof. During the summer months, the flux is negative, indicating heat entering the building. The heat flux from March 15-19 (shown by dashed lines) is positive as expected, and this time period corresponds to the period of high snowpack on the roof, as shown in Figure 2.

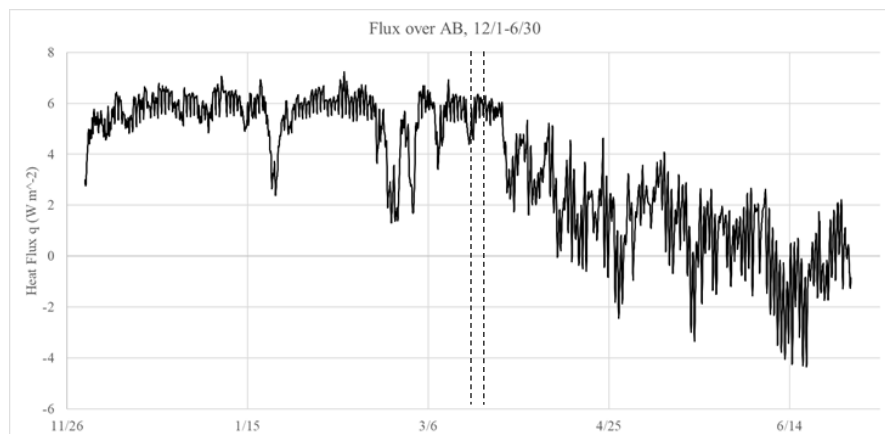


Figure 6: The heat flux through the insulation layer during Dec. 1, 2016 - June 30, 2017.

CONCLUSION

Temperatures have been measured from December 2016 to February 2018 in layers of a green roof on the Onondaga County Convention Center. The inside temperature at the ceiling, and temperatures in the lowest roof layers below the insulation, remain around 20° C in both winter and summer. The greatest difference in temperature between adjacent sensors occurs across the insulation layer (A to B). The temperatures at the top of the insulation (B), at the upper gypsum board (C), and in the growth medium (G) are closer to the air temperature. During the winter, and when there is significant snowpack on the roof, the temperature in these upper layers remains at 0-5° C despite much colder air temperatures. The insulation layer provides the main barrier to heat escaping the building during cold conditions. During the summer, the temperatures in the top layers of the roof tend to be higher than the air temperature, due to the impact of direct sunlight impinging on the roof surface.

The calculated R-values of the green roof are consistent with previously calculated R-values based on limited data. The values from stations 1, 2, and 5 show distinct differences that may be due to the precise placement of the sensors within the various roof layers. For example, the R-values overall from A to G are nearly identical at all three stations, but the R-values between sensors B and C at stations 1 and 2 are much smaller than at station 5. This indicates that sensors B and C are probably closer together at stations 1 and 2 than originally thought, providing more information on the build of the roof. Additional data collection and analysis is underway, both at the green roof and at a traditional roof nearby.

ACKNOWLEDGMENT

This work is supported in part by the National Science Foundation under grant number SES-1444755, Urban Resilience to Extreme Weather-Related Events Sustainability Research Network (URE_x SRN). The authors acknowledge the assistance of the Onondaga County Department of Facilities Management for enabling this work on the green roof. The assistance of several other members of the Green Roof Research Group at Syracuse University is greatly appreciated.

REFERENCES

- Dahanayake K.C. and Chow C.L. 2018. Comparing reduction of building cooling load through green roofs and green walls by EnergyPlus simulations, *Building Simulation*, Vol. 11, pp. 421-434.
- Jaffal I., Ouldboukhitine S.E., Belarbi R. 2011. A comprehensive study of the impact of green roofs on building energy performance, *Renewable Energy*, Vol. 43, pp 157-164.
- Squier M. and Davidson C. 2016. Heat flux and seasonal thermal performance of an extensive green roof, *Building and Environment*, Vol. 107, pp. 235-244
- Zhang L., Jin M., Liu J., and Zhang L. 2017. Simulated study on the potential of building energy saving using the green roof, *Procedia Engineering*, Vol. 205, pp. 1469-1476.

Estimating time constants for over 10,000 residential buildings in North America: towards a statistical characterization of thermal dynamics

Camille John^{1,*}, Charalampos Vallianos², José Candanedo^{1,2} and Andreas Athienitis¹

¹Concordia University, 1515 St. Catherine W., Montreal, QC, H3G 2W1, Canada

²CanmetENERGY-Varenes, 1615 Lionel-Boulet Blvd., Varennes, QC, J3X 1S6, Canada

**Corresponding email: camille.john@mail.concordia.ca*

ABSTRACT

Understanding the dynamic response of a building is essential in the design of sustainable energy-efficient buildings. Using data from over 10,000 smart thermostats, this study identifies patterns in the dynamic thermal response of residential buildings in Canada and the United States (US). The data set consists of one year of measurements recorded at 5-minute intervals for the indoor and outdoor air temperature as well as HVAC equipment run times.

This study focuses on identifying effective values of time constants for the houses by applying the following procedure. First, periods complying with the following basic criteria are identified: a) the house is under free-floating conditions (i.e. when the HVAC system is switched off) for more than three hours and b) the outdoor temperature remains approximately constant (the outdoor temperature change is smaller than or equal to 2°C). Second, for each identified period, time constant values are determined by tracking the temperature responses of the house. These values are determined assuming the characteristic exponential decay of a first-order resistance-capacitance (RC) thermal model. Finally, a statistical analysis is applied to identify a typical range of effective time constant values according to month.

Consequently, calculations show significant differences between estimated values for the summer and winter months, which may be attributed to occupant behaviour. In winter, the majority of time constants range from 15 to 55 hours. In summer, most of time constants vary between less than 1 hour and 18 hours due to occupants opening windows. In addition, the dependence of the time constant on the age of the home is investigated.

KEYWORDS

Time constant estimation; pattern recognition; dynamic thermal response; residential building; statistical analysis.

INTRODUCTION

In support of sustainable development and energy efficiency, effective energy management in buildings is increasingly recognized as a priority. In Canada and the US, the building sector accounts for approximately 28% and 40% of the national energy consumption, respectively. The residential sector is a major contributor to the energy use of both the Canadian and American building sectors, making up 62% and 53% of their total energy consumption, respectively. Moreover, in both countries, more than 40% of the total energy demand in a residential building is used to heat and cool the occupied spaces (Office of Energy Efficiency, 2016; U.S. Energy Information Administration, 2009, 2018).

With the increased adoption of the Internet-of-Things (IoT) such as smart thermostats, numerous homeowners are outfitting their residences with home automation and data acquisition systems. A recent study predicted that, by 2025, IoT applications would offer a potential economic impact of \$200-300 billion a year in relation to the residential sector (Manyika et al., 2015). In the building and urban environment, big data sources are becoming increasingly more prominent and the release of certain anonymized data sets for data science could progressively become the norm. As a result, the building industry will face a critical dilemma: how will performance data from potentially thousands—or even millions—of buildings be reasonably integrated into design and energy management? This unprecedented level of access to raw data will promote the potential of machine learning, visual analytics, and data-driven statistical modelling techniques in estimating the building's dynamic thermal response (Miller, Nagy, & Schlueter, 2017). Grey-box model approaches use operational data from numerous real buildings to calibrate a simplified physical model, in the effort of providing good approximation of a building's thermal response (Vivian, Zarrella, Emmi, & De Carli, 2017).

In this study, the operational data of real homes are analyzed to recognize patterns in their dynamic thermal response. This paper focuses on proposing a method of estimating the typical thermal time constant values for residential buildings located in Canada and the US. The estimation is based on temperature measurements and equipment runtimes acquired from smart thermostats. When limited information is available, the knowledge provided in this paper can: i) assist in the generation of simple grey-box models that could guide the preliminary design of new residential buildings (Vivian et al., 2017), and ii) assist in the development and adoption of effective load management strategies for existing buildings.

METHODOLOGY

Data Collection

Ecobee, a Canadian home automation company, has established the Donate Your Data (DYD) program for its smart thermostat users to donate measured time series data to science. The meta-data from this program are user-reported, anonymized and include details such as the geographic location, age of home, total floor area, style of home, and number of occupants. Recorded at 5-minute intervals, the Ecobee thermostats collect measurements for temperature, humidity, occupancy detection, and HVAC equipment runtimes. For the building time constant estimation, over 10,000 residential buildings were monitored between March 2016 and February 2017. The Ecobee smart thermostats control the HVAC system based on the indoor control temperature, which is an average temperature of the building based on readings from the thermostat and any additional remote sensors present.

Building Time Constant Estimation

Diurnal and seasonal variations in outdoor temperature, solar energy and occupant behaviour account for the main thermal losses and gains between the building and its surroundings. The time constant is a measure that characterizes a building's ability to retain heat. With no influence from a heating or cooling system, theoretically, the thermal time constant provides an indication of how fast the building will take to achieve a new thermal equilibrium in response to changes in its internal and external thermal conditions. As demonstrated in Figure 1, the time constant can be found by applying a step input to the building and then recording the time the building takes to realize 63.2% of the final value in the step change (Equation 1).

The first step in estimating the time constant of a building is the identification of suitable time periods for analysis. In this study, these analysis periods are selected according to following

basic criteria: a) the house is under free-floating conditions (i.e. when the HVAC system is switched off) for more than three hours, and b) the outdoor temperature remains approximately constant (the outdoor temperature change is smaller than or equal to 2°C).

The measured time series data for HVAC equipment runtimes and the outdoor temperature are used to determine if the criteria are met during each analysis period.

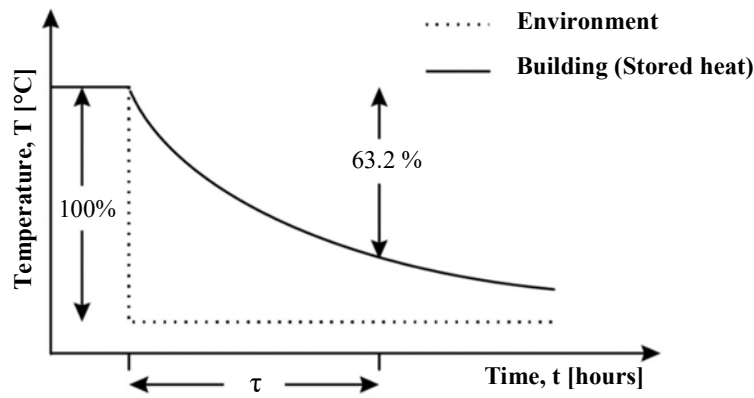


Figure 1: The time constant, τ , is the time needed for the building to realize 63% of the final value of an applied step change.

The second step is the determination of a time constant for each identified analysis period by treating the thermal space of every home as a first-order resistance-capacitance (RC) model (Vivian et al., 2017). While this is a relatively simple model, it provides a useful characterization of the dynamic behaviour of the house. Assuming the characteristic exponential decay of a first order system:

$$T(t) = T_f + (T_i - T_f)e^{-t/\tau_{bldg}} \quad (1)$$

where t represents time elapsed in hours, T_i represents the initial indoor temperature, T_f represents the long-term final temperature of the indoor space in free-floating conditions, and τ_{bldg} represents the estimated time constant value.

Considering plausible physical constraints and using the least squares method, the following parameters of a regression function are calculated according to Equation 1 and the recorded indoor temperature measurements $T(t)$: a) the long-term final indoor temperature b) the change in indoor temperature ($T_i - T_f$), and c) the time constant value to be estimated. The time constant values were estimated with the use of the programming language Python. Next, these estimated values are then filtered, retaining only those whose corresponding R-squared values are 0.7 or higher. The R-squared value of 0.7 was visually determined to be the minimum acceptable value representing an accurate fit of the regression line to the observed data.

Identification of Typical Building Time Constant Values

In the previous step, multiple time constants are found for each building and organized according to month for analysis purposes. For each residence, a monthly average of the estimated time constant values can be obtained by weighing these estimated values by their corresponding R-squared values from the previous step. Statistical learning methods, particularly visual analytics, are then used to identify typical time constant values among the weighted averages. Histograms, kernel density estimations (KDE) (a method to estimate frequency distributions), and other statistical analysis tools are used to identify patterns in the

distribution of time constant averages. Furthermore, possible correlations between the time constant averages and the age of the home have been investigated.

RESULTS

Figure 2 and 3 show typical results obtained for the time constants for the months of August and February, respectively. The time constants are plotted versus the age of the home.

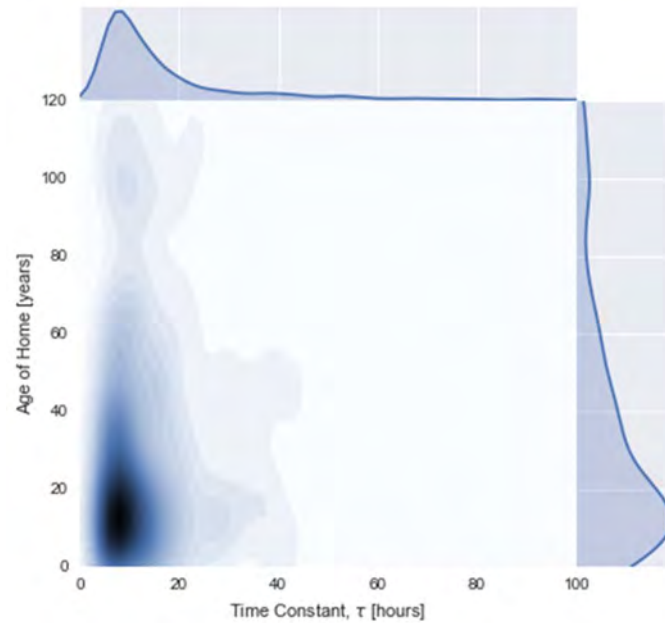


Figure 2: For August 2016, KDEs representing the building age distribution (right), time constant distribution (top), and their relationship to each other (center).

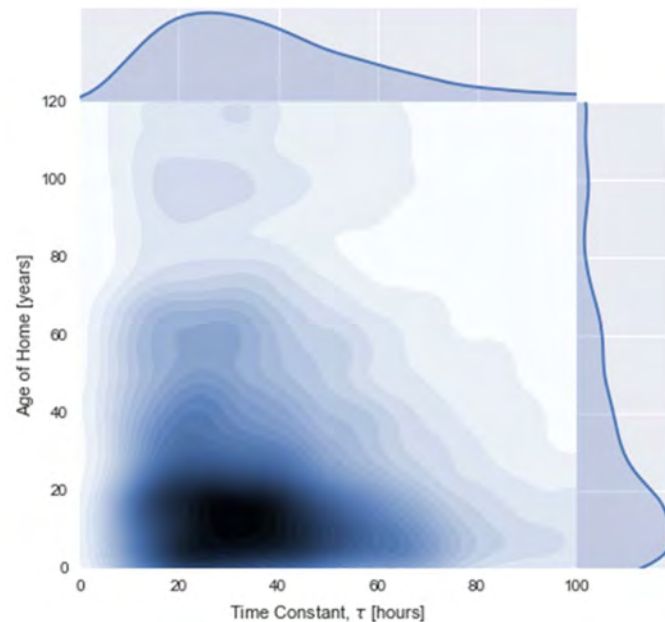


Figure 3: For February 2017, KDEs representing the building age distribution (right), time constant distribution (top), and their relationship to each other (center).

The patterns observed in August and February are very similar to time constant distributions seen throughout the rest of the warmer months and colder months, respectively. For the warmer months, specifically June through September, most of time constants fall within a range of less than 1 hour to 18 hours as seen in Figure 2. The colder months, meaning October through May, have most of their time constants varying between approximately 15 to 55 hours as demonstrated in Figure 3. As seen in both Figure 2 and Figure 3, the greater part of the buildings observed are between 0 and 35 years old.

DISCUSSION

Comparing Figure 2 and Figure 3, the warmer and colder months show significant differences between their resulting time constant averages; for the same group of homes, the warmer months have time constants that are much lower in value. The occurrence of different time constants for one building at different times of the year is an interesting phenomenon. In principle, the time constant should only depend on the materials and physical configuration of the house, which should not be expected to change. This decrease in value for the time constant averages may be linked to occupant behaviour. During the warmer months, it is reasonable to expect occupants to have their windows open and leave them open for longer periods of time due to more favorable weather conditions; open windows decrease a building's ability to resist changes in external thermal conditions thus reducing the effective resistance. Moreover, there is also a trend observed shared by both the warmer and colder months: the variance of time constants narrows with an increase in the age of home. The broad range of values for younger buildings and the narrow range of low values for older buildings suggest the introduction of a larger variety of construction methods and materials—some more energy efficient than others—over the last 120 years.

Understanding a building's natural dynamic thermal response is crucial to the design of heating, ventilation, and air conditioning (HVAC) systems, the maintenance of a comfortable environment for occupants, and the management of their electrical load profile (Palensky & Dietrich, 2011). In future studies, the proposed method will be extended to a larger data set of approximately 27,000 smart thermostats in North America to examine the relationship of the time constant to other variables. The variables to be considered include type of home (e.g. semi-detached, row house, condominium), geographical location and floor area. Considering that the age of home is user-reported, it would be interesting to see if the relationship observed between the time constant and the age of home persists in a larger sample of homes. Other considerations taken into account to select the periods of interest will include the effects of weather conditions, solar gains and occupancy which are currently not being tracked.

As we seek increasingly low-energy solutions for buildings, HVAC systems are being designed as more responsive to changes in a building's internal (e.g. occupants, appliances) and external thermal conditions (e.g. temperature, humidity, solar gain). The most commonly used software tools for building performance simulation (e.g. EnergyPlus or TRNSYS) require extensive computational power and a large number of assumptions about the building's geometry, its characteristic physical properties, its environment and its occupancy (Zawada, 2017). In addition, many of these inputs end up being assumptions based on the experience and intuition of professional experts. As a result, simple, reliable building models (e.g. grey-box models) have been receiving more attention of late, because there is often a need to model building performance when the required inputs are limited (e.g. only age, location and building type) and the energy modelers are less experienced. When limited building information is available, the knowledge acquired from this study will be used to facilitate preliminary estimations of dynamic parameters (such as RC values) in the rapid generation of control-oriented models.

CONCLUSIONS

This study presents a statistical methodology for the identification of typical time constant values of residential buildings for the heating, cooling and intermediate shoulder seasons (i.e. when houses are typically in passive mode with open windows). Preliminary results for different times of the year have been presented. Based on a simple physical model and measurement data from smart thermostats in North America, the proposed method for making preliminary estimations of the time constant offers benefits for researchers, home automation companies, utilities and homeowners who seek to reduce energy costs while maintaining occupant comfort. The advantages include facilitating the creation of simpler models for testing and control scenarios, providing a better understanding of consumer behaviour and needs, and promoting energy conservation and efficiency. A major result of the present study is the observation that time constants vary seasonally: from less than 1 hour to 18 hours during summer, to 15 to 55 hours during winter. This result is most likely due to open windows that directly couple the interior of a house to the exterior environment through a high effective thermal conductance. Future studies will focus on extending the proposed method to a larger data set and examining the relationship of the time constant values to other variables including type of home, geographical location and floor area.

ACKNOWLEDGEMENT

The financial support of both the NSERC Discovery Grant Program and the NSERC/Hydro Québec Industrial Research Chair held by Dr. Athienitis are gratefully acknowledged. The authors thank Ecobee, a Canadian home automation company, for kindly providing the data used in this study. The authors would like to thank Vasken Dermardiros and the internal reviewers at CanmetENERGY-Varenes for their valuable comments.

REFERENCES

- Manyika, J., Chui, M., Bisson, P., Woetzel, J., Dobbs, R., Bughin, J., & Aharon, D. (2015). *The Internet of Things: Mapping the value beyond the hype*. *McKinsey Global Institute*.
- Miller, C., Nagy, Z., & Schlueter, A. (2017). A review of unsupervised statistical learning and visual analytics techniques applied to performance analysis of non-residential buildings. *Renewable and Sustainable Energy Reviews*, 1–13.
- Office of Energy Efficiency. (2016). *Energy Use Data Handbook*. Ottawa, ON. Retrieved from http://oee.nrcan.gc.ca/corporate/statistics/neud/dpa/data_e/downloads/handbook/pdf/2013/HB2013e.pdf
- Palensky, P., & Dietrich, D. (2011). Demand side management: Demand response, intelligent energy systems, and smart loads. *IEEE Transactions on Industrial Informatics*, 7(3), 381–388.
- U.S. Energy Information Administration. (2009). *Residential Energy Consumption Survey*. Washington, DC. Retrieved from <https://www.eia.gov/consumption/residential/data/2009/index.php?view=consumption>
- U.S. Energy Information Administration. (2018). *February 2018 Monthly Energy Review*. Washington, DC. Retrieved from <https://www.eia.gov/totalenergy/data/monthly/pdf/mer.pdf>
- Vivian, J., Zarrella, A., Emmi, G., & De Carli, M. (2017). An evaluation of the suitability of lumped-capacitance models in calculating energy needs and thermal behaviour of buildings. *Energy and Buildings*, 150, 447–465.
- Zawada, B. (2017). Experimental determination of parameters in models of indoor air temperature response to reduction in supplied energy. *Journal of Building Physics*, 40(4), 346–371.

Experimental Investigation of the Impact of PCM Containment on Indoor Temperature Variations

Iva Rešetar^{1*}, Norbert, Palz¹

¹Berlin University of the Arts, Institute for Architecture and Urban Planning

**Corresponding email: i.resetar@udk-berlin.de*

ABSTRACT

In view of growing concerns on climate change and temperature extremes, there is a need to explore novel methods that provide thermal comfort in architecture. Latent heat thermal energy storage with phase change materials (PCM) has been widely researched in last decades in the field of energy technology and proved beneficial for reduction and shifting of the thermal loads and improving the overall thermal storage capacity of building components. Although a variety of PCM containments have been investigated for indoor cooling applications, the examples of exposed, design-oriented macro-encapsulations are rare.

This paper presents a study of visible, suspended ceiling encapsulations for passive cooling, made of glass and novel bio-based PCM. The aim is to provide an overview of correlations between basic containment geometries and their thermal behavior that serves as a base for the further design of custom-made PCM macro-encapsulations. An experimental set-up of test boxes is developed for thermal cycling and a comparative analysis of the thermal performance of varied PCM encapsulation geometries. The study concludes that the containments with the large exchange surface and the small thickness offer an optimal material distribution for the temperature reduction in the box. Based on experimental results, suggestions are made on further formal strategies for the design of cooling elements for local thermal regulation.

KEYWORDS

Phase change materials, passive cooling, containment geometry, thermal cycling, glass macro-encapsulation

INTRODUCTION

Contemporary buildings increasingly rely on centralized mechanical systems for the indoor climate control, due to the low thermal inertia and high energy gains in buildings. A promising renewable energy alternative that could decrease the dependency on high-energy consuming technologies and improve the thermal stability of buildings is the latent thermal energy storage with PCM (Kośny, 2015; Zalba et al., 2003).

Current advancements in materials science and the growing interest of designers in a material-driven performance are opening a possibility for architectural elements to take a more active role in managing thermal environments (Addington and Schodek 2005; Bechtold and Weaver 2017). PCM belong to the novel class of property-changing materials with an inherent capacity for thermoregulation, as they can dynamically exchange the energy with surroundings while changing the phase at a desirable temperature. Although the primary goal of the implementation of PCM is to achieve energy savings in buildings, PCM present yet unrealized potential for architectural design and an opportunity for new design methodologies based on their thermodynamic behavior.

PCM are substances capable to absorb, store and release a large amount of energy in the form of latent heat during melting and solidification at a certain, predictable temperature. PCM act as latent thermal energy storage due to their large phase change enthalpy or latent heat of fusion. Unlike the sensible heat storage, where the added heat results in the temperature increase of the storage medium, the latent heat storage medium remains at almost constant temperature throughout the solid-liquid phase transition. The added heat is gradually absorbed by the material till the melting is complete and released when the surrounding temperature drops, and the material starts to solidify (Mehling and Cabeza, 2008). In that way, PCM operate in thermal cycles responding to local temperature fluctuations and can be used repeatedly without material degradation.

In passive or free cooling applications, PCM takes advantage of diurnal temperature differences, releasing the coldness stored during the night when, during the day, the indoor temperature rises above the comfort zone (Raj and Velraj, 2010). Currently available PCM products for passive cooling span from micro-encapsulations integrated in different building materials to macro-encapsulated elements placed behind the suspended ceiling. However, for PCM to function efficiently and regenerate during the night, a direct contact with the cold air (heat sink) is of advantage. This study therefore proposes visible suspended glass encapsulations that support recharging of the PCM by night ventilation. Since PCM has a low thermal conductivity, the containment geometry plays an important role for managing the heat transfer between the PCM and surroundings. Thus, coupling the basic encapsulation geometries with their thermal behavior in this paper aims to widen the range of PCM encapsulations and outline their use within the design realm.

METHODS

To evaluate the impact of varied PCM encapsulations on the indoor temperature, an experimental set-up for thermal cycling with test boxes was developed. Previous experiments that used test boxes to access the thermal performance of the composite PCM wall are described in literature (Kuznik and Virgone, 2009). Similarly, in this study two identical boxes – a test box containing the PCM sample and an empty reference box – were placed next to each other in a controlled indoor environment and exposed to thermal excitation. Boxes were made of plywood 18mm, covered with 30mm insulation panels, with the glazed front that allowed irradiation by two halogen 750W lamps placed in the front (Fig. 1).

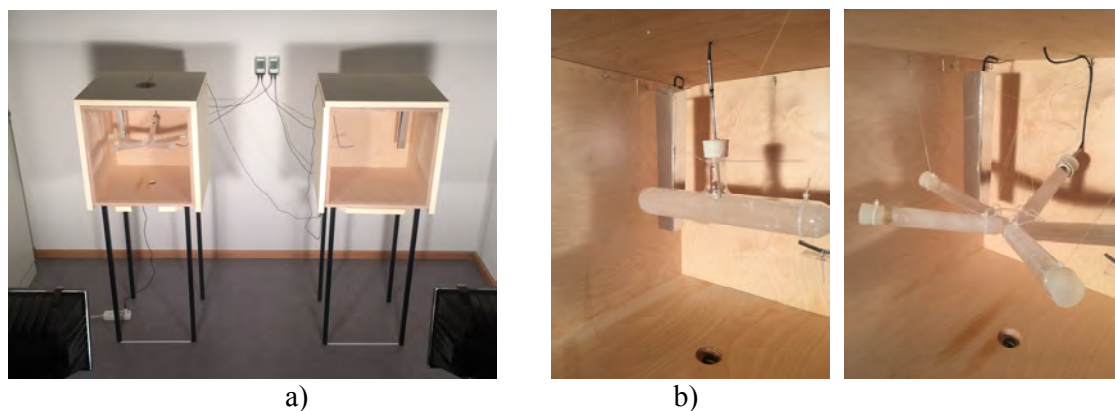


Figure 1. Experimental set-up for thermal cycling. a) Test boxes, b) Tubular encapsulations.

The temperature differences were observed during two subsequent heating (3h) and cooling (6h) cycles of total duration of 18h. During heating cycle, the temperature in the boxes

oscillated from 17°C to 30°C, with a resulting heat rate slightly above of the average due to the direct solar irradiation of buildings in the summer. The cooling cycle corresponded to the effect of night cooling needed for the PCM regeneration. The instrumental set-up consisted of two 176T2 dataloggers with four Pt-100 glass-coated probes of the class A precision, measuring air, PCM and the room temperature in the interval of 1 minute. Thermal camera was attached at the bottom of the box, capturing surface temperatures every 30 minutes. A reflective shield protected air probes from the direct irradiation. Before commencing measurements, several calibration cycles with different positions of probes were done and showed no temperature gradients in the box, and the temperature differences within tolerance values (0.2°C).

Table 1. Physical properties of bio-based PCM from the data sheet of the producer.

Property	Values
Melting / crystallization temperature	21°C / 19°C
Latent heat	190 KJ/kg
Specific heat capacity solid / liquid	2.1 kJ/(kg·°C) / 2.3 kJ/(kg·°C)
Thermal conductivity solid / liquid	0.18 W/(m·°C) / 0.15 W/(m·°C)
Density solid / liquid	891 kg/m ³ / 850 kg/m ³

The material used in the study belongs to the novel bio-based category of PCM, with a low melting temperature suitable for indoor applications (Tab. 1). The choice of the containment geometries was made according to the standard typologies described in the literature (Mehling and Cabeza, 2008; VDI, 2016). A total volume of 500ml of PCM was used in each measurement, either in a single containment or divided into five smaller units of 100ml. Encapsulations were made of borosilicate or soda-lime glass of approx. thickness 2mm in following formats: spherical containments used standard laboratory 500ml and 100ml glass flasks; multiple tubular used standard 100ml test tubes; 500ml tube was produced by lampworking technique; flat container was produced by modifying a standard petri dish \varnothing 180mm.

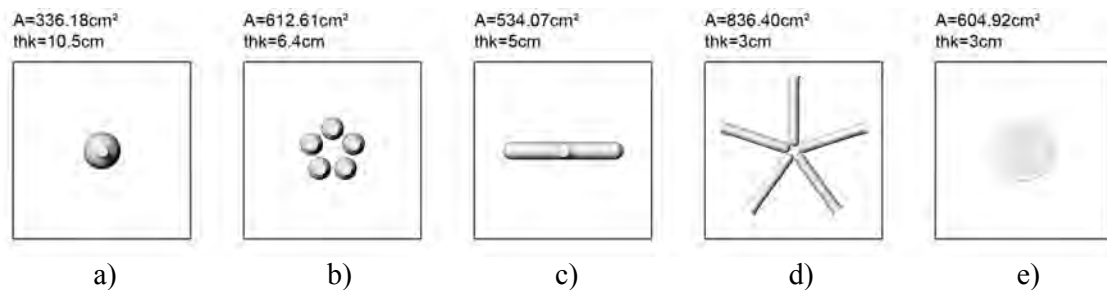


Figure 2. Ground plan of the box with containment geometries showing surface area and max. thickness. a) Sphere 500ml, b) Multiple spheres 5x100ml, c) Tube 500ml, d) Multiple tubes 5x100ml, e) Flat plate containment 500ml.

RESULTS

The graphs show a characteristic latent heat thermal storage effect with a temperature plateau during the melting phase of the material (Fig. 3). All encapsulations except the 500ml spherical and flat containments allowed the full melting of the PCM. The multiple tubular geometry caused the biggest temperature differences between the test boxes (Tab. 2 and Fig. 3) and allowed the largest portion of the material to recharge during the cooling cycle in comparison to other containments (Fig. 4).

Tables and illustrations

Table 2. Temperature differences in boxes in relation to geometry.

Encapsulation geometry	Values 1 st /2 nd cycle
a) Sphere 500ml	1.15°C / 1.13°C
b) Multiple spheres 5x100ml	1.64°C / 1.62°C
c) Tube 500ml	1.51°C / 1.48°C
d) Multiple tubes 5x100ml	2.04°C / 2.03°C
e) Flat containment 500ml	1.41°C / 1.50°C

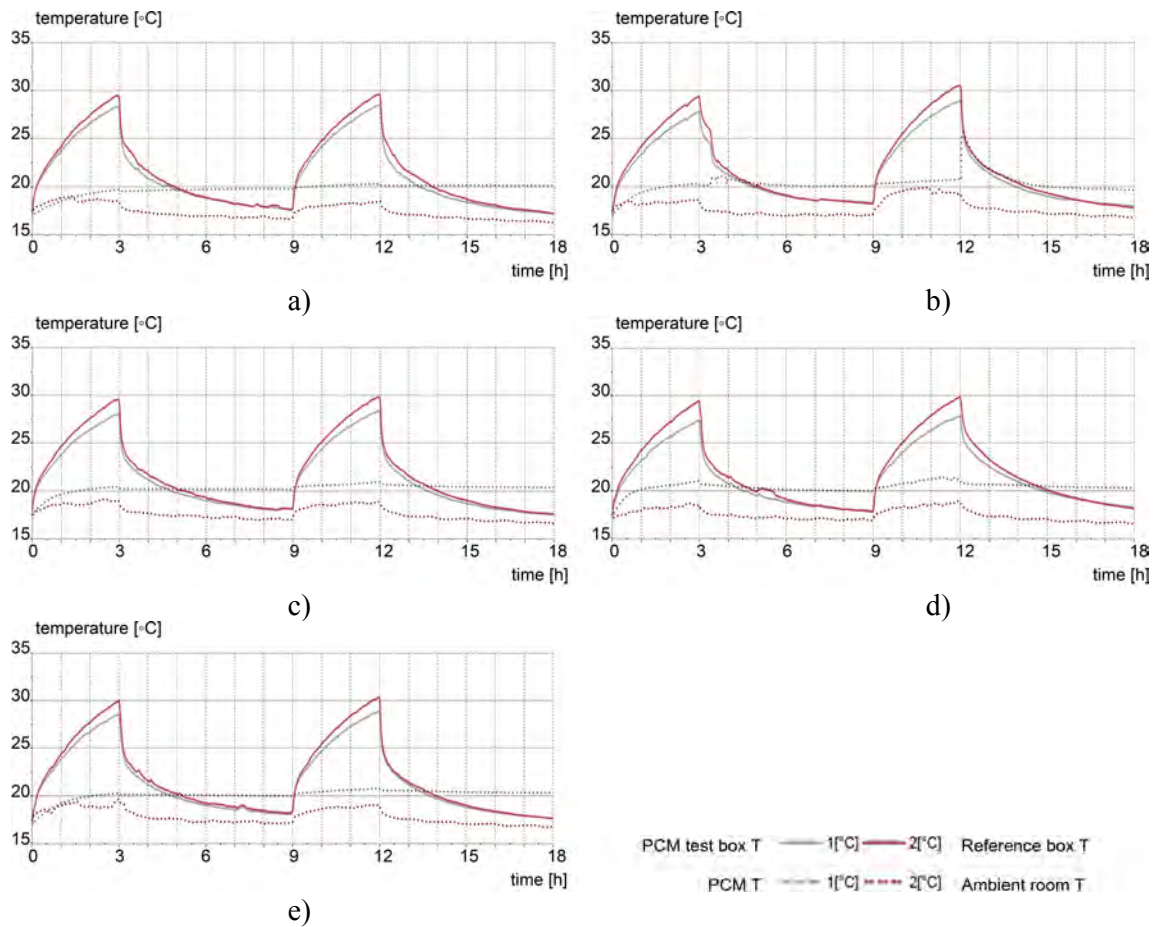


Figure 3. Impact of PCM on temperature reduction in the box. a) Spherical containment, b) Multiple spherical containment, c) Tubular containment, d) Multiple tubular containment, e) Flat plate containment.

DISCUSSIONS

Multiple containments improved the cooling effect of the single ones by 40%. The results point out to benefits of increasing and differentiating surfaces that enclose a certain volume. Although the exhibited differences of the cooling potential between PCM containments are small, it is expected that they gain on importance in the design of larger ceiling systems. Measurements in real conditions with actual thermal loads, building materials and occupant behaviour are, however, necessary to validate these findings. Regarding the orientation of encapsulations, the experiments assumed the horizontal position of tubes and flat containers optimal for the uniform temperature distribution and steadily moving melting fronts (Khan et. al, 2016).

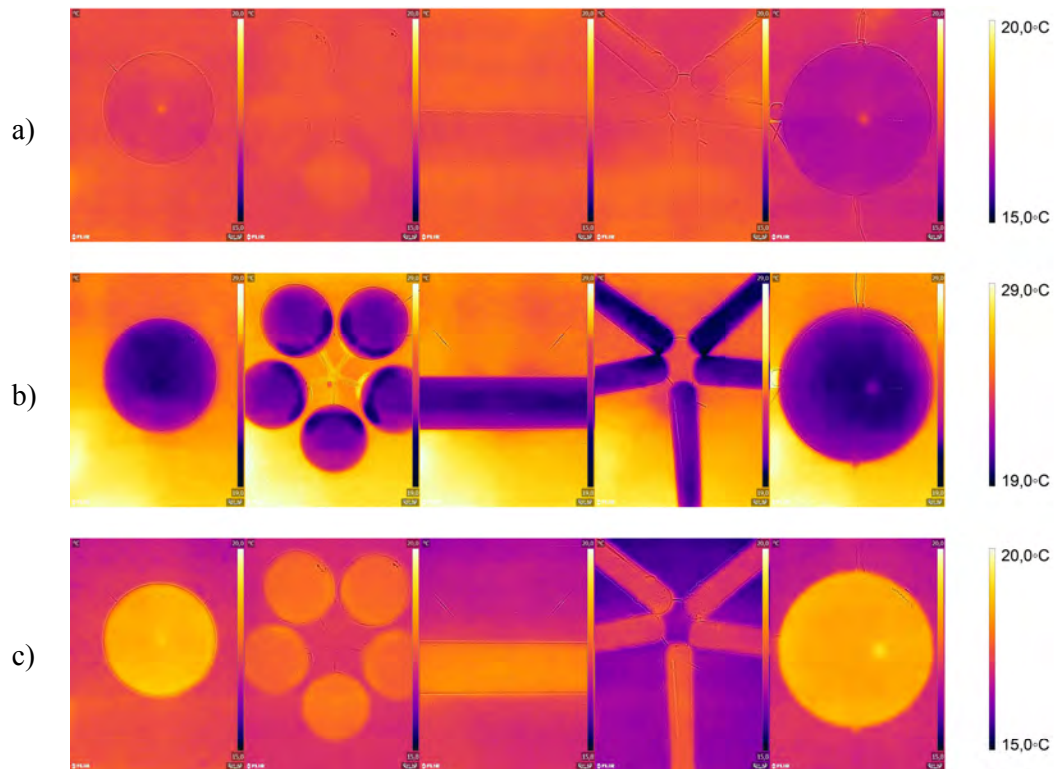


Figure 4. Thermographic images showing surface temperature at the beginning and the end of the heating and cooling cycle: a) 0h, b) 3h, c) 12h.

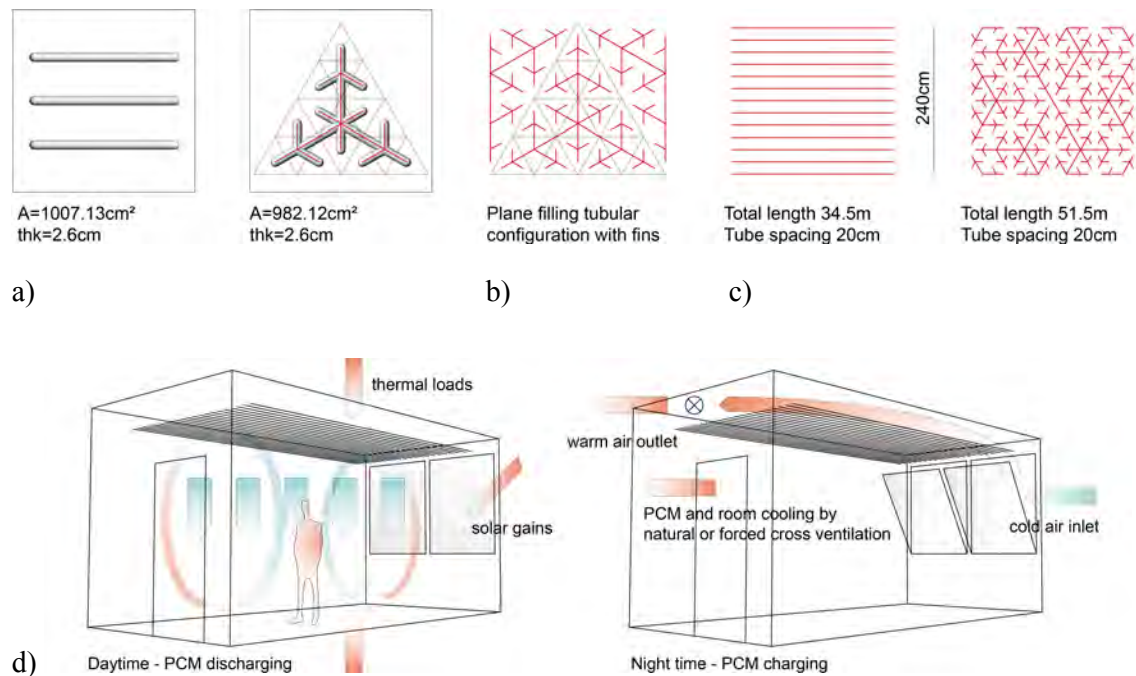


Figure 5. a) Linear and plane filling tubular elements of 2.6cm thickness and 500ml volume in the test box, b) Plane filling configuration principle, c) Difference between linear and plane filling patterns in material distribution in larger space, d) Diagram of the operating principle of the PCM cooling ceiling made of suspended glass elements.

A further increase of the surface area of tubular encapsulations could be achieved by introducing elements with fins (Fig. 5a), and by formal strategies for connecting elements into larger systems, such as plane or space filling tree configurations (Fig. 5b). Compared to linear configurations (VDI, 2016), these branching structures could provide a large and uniform material distribution with an increased element spacing (Fig. 5c) necessary for recharging the material during the night by convection and conduction (Fig. 5d).

CONCLUSIONS

This work presented investigation of thermal performance of spherical, tubular and flat plate glass encapsulations containing novel bio-based PCM. An experimental set-up of the test box was developed for the comparative analyses of the impact of the encapsulation geometry on the indoor temperature in the test box. Single and multiple units of an equal volume, but varying surface and thickness were tested, and the effect of the increased surface and reduced thickness on temperature reduction was observed. Temperature measurements reflected the differences in the volume-surface ratio of containments and showed the biggest reduction of 2°C in the box with multiple tubular PCM encapsulations. The paper concludes that new design and recharging opportunities for cooling ceilings could be afforded by the exposed glass encapsulations and suggests further formal strategies for increasing the surface area while keeping the thickness, volume and spacing of the encapsulation elements at optimum. These findings on cooling effects of glass encapsulations can inform the concept phase of the design of more elaborate custom-made ceiling elements for local thermal regulation.

ACKNOWLEDGEMENT

The project has received funding from the European Union's Horizon 2020 research and innovation programme under the Marie Skłodowska-Curie grant agreement No. 642328.

REFERENCES

- Addington M. and Schodek D. 2005. *Smart Materials and Technologies for Architecture and Design Professions*. Oxford: Elsevier Architectural Press.
- Bechthold M. and Weaver J. C. 2017. Materials science and architecture. *Nature Reviews Materials*. Vol. 2, pp. 1-20.
- Mehling H. and Cabeza L. 2008. *Heat and cold storage with PCM: An up to date introduction into basics and applications*. Berlin: Springer.
- Khan Z.; Khan Z.; Ghafoor A. 2016. A review of performance enhancement of PCM based latent heat storage system within the context of materials, thermal stability and compatibility, *Energy Conversion and Management*, 115, pp. 132–158.
- Košný, J. 2015: *PCM-Enhanced Building Components: An Application of Phase Change Materials in Building Envelopes and Internal Structures*. Springer International Publishing.
- Kuznik F. and Virgone J. 2009. Experimental Investigation of Wallboard Containing Phase Change Material: Data for Validation of Numerical Modeling. *Energy and Buildings*, 41 (5), pp. 561-570.
- Raj V. A. A. and Velraj R. 2010. Review on free cooling of buildings using phase change materials. *Renewable and Sustainable Energy Reviews*, 14, pp. 2819–2829
- VDI. 2016. *VDI Standard 2164*, PCM energy storage systems in building services. Düsseldorf: Verein Deutscher Ingenieure.
- Zalba, B.; Marin, J.M.; Cabeza F.L.; Mehling. H. 2003. Review on thermal energy storage with phase change materials, heat transfer analysis and applications. *Applied Thermal Engineering*, 23, pp. 251–283.

Hygrothermal modelling of building enclosures: reference year design for moisture accumulation and condensation risk assessment

Michele Libralato^{1,*}, Giovanni Murano², Onorio Saro¹, Alessandra De Angelis¹ and Vincenzo Corrado².

¹Università degli Studi di Udine / Università dal Friùl, Italy

² Politecnico di Torino, Italy

*Corresponding email: Libralato.michele.1@spes.uniud.it

ABSTRACT

Interstitial condensation and water accumulation risk in building envelopes could be assessed with methods and models based on moisture migration through porous media coupled to heat transfer. One of the difficulties in evaluating the boundary conditions for the heat and mass transfer model is the choice of an appropriate weather file. The most advanced models, described by the standard EN 15026:2007, require the hourly values of rain, wind, radiation, temperature and relative humidity to compute the water content in the porous materials.

In this contribution, the method described by the standard EN ISO 15927-4:2005, typically used to design Moisture Reference Years (MRY), has been extended to the design of 34 typologies of representative weather files. The generation criteria have been based on the assumption that the simulation results are influenced by rain deposition on the considered wall. The procedure has been followed considering 5 different wall exposures that lead to different MRV. The years of the climate of Turin (Italy) between 2002 and 2016 have been considered for the generation of the reference years.

Finally, the annual mean moisture contents for two common wall types have been calculated using the obtained MRV and compared to the annual mean moisture contents obtained with the measured weather data, and the effects of the selection of the weather parameters is presented.

KEYWORDS

Building enclosures, condensation risk assessment, moisture accumulation, reference year, weather file, Moisture Reference Years.

INTRODUCTION

The building envelope design process requires the risk assessment for condensation and moisture accumulation of all the enclosures and their intersections to avoid mould growth conditions and material damage due to prolonged moisture exposure. Up to now, several evaluation methods, simplified and advanced, have been developed. The simplified and most used methods are based on stationary models, they consider monthly mean weather data and are not intended to simulate the real phenomena of the heat and moisture transfer (for example the Dew-Point method or the Glaser method). When more accurate methods are needed (and a simulation of the real physical phenomena is required) it is possible to use advanced models. These models are based on transient state heat, air and moisture transfer equations and require a deep knowledge of the material properties, with weather data files that have to include additional hourly normal rain, wind and solar radiation descriptions.

The standard EN 15026:2007 describes the commonly accepted models used for the advanced moisture accumulation and interstitial condensation risk assessment and refers to the EN ISO 15927-4:2005 for the boundary conditions; this standard describes a method intended to produce hourly data for assessing the annual energy use for heating and cooling. In this paper,

following the previous works of the authors (for example Riva et al. 2010, Riva et al. 2012 and Murano et al. 2016), a modification to the standard method of reference years generation is presented. It has to be noted that the methodology produces reference years and not extreme weather years. Reference years could be used only for moisture accumulation and interstitial condensation risk assessment; if water condensation in building components is not acceptable, even for short periods, other methods are available for the generation of extreme weather years. Various approaches have been investigated in the literature. Cornick et al. (2003) have selected Reference Years using a Moisture Index approach developed for Moisture Management of Exterior Wall Systems (MMEWS). The index comprises wetting function and drying function. In this approach wet and dry years are defined as those years that deviate more than one standard deviation from the mean value on long-term. MEWS is a building-independent method. The wet year is defined as the year with highest moisture index, the dry year as the year with lowest moisture index, and the average year as the year closest to the mean Moisture Index. MEWS can be assembled for problems such as long-term performance or limit-state design. There isn't a definitive method for selecting MRY's but different sets of MRYs should be produced to evaluate different problems.

Salonvaara et al. (2010) have developed a new method that provides an approach for selecting the most critical years in terms of hygrothermal performance. Performance data is analysed using various methods to provide a ranking of the weather years in terms of severity. Damage functions (time of wetness, mould growth index, and maximum moisture content) are used to quantify the moisture related performance of the building envelope. The analysis has included 30 years of hourly weather data for 12 locations in the U.S. and Canada.

Schönerl and Zirkelbach (2016) for the selection of the months of the reference years for the hygrothermal assessment (HRY) have used median, mean, minimum, maximum value, the 25%, and the 75% quartile of air temperature and normal rain. The results of HRY was compared with the standard methodology of EN ISO 15927-4 and with measured data on long-term. The simulations have shown that the mean water content based on the HRY was slightly higher than the one based on the measured data.

Considering the effect of climatic variability on the performance of the building envelope, Zhou et al. (2016) have developed a Climatic Index that considered wind-driven rain load and potential evaporation. This index was suitable for the evaluation of the level of moisture damage risk of wall assemblies where typical moisture problems are mainly caused by rainwater uptake or ingress. The combination of Climatic Index and RHT Index has allowed the creation of MRYs that have 10% level of failure.

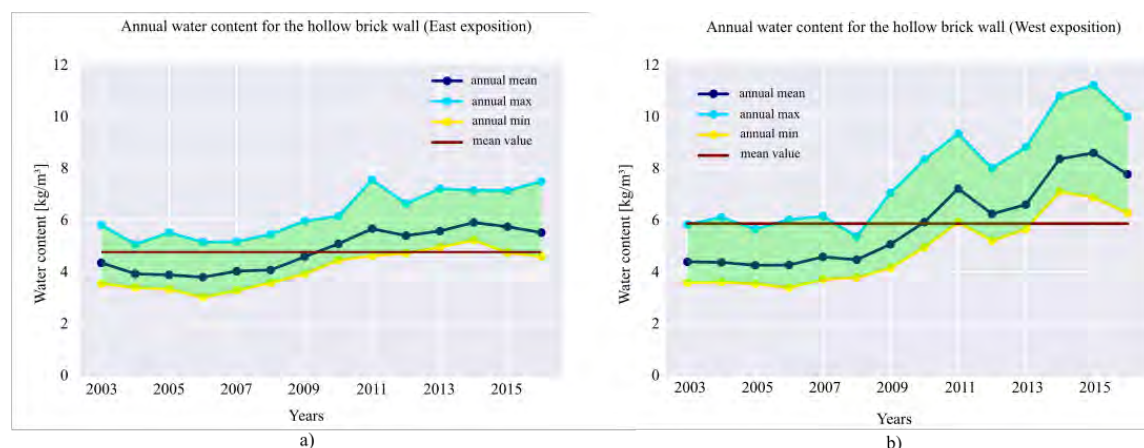


Figure 1. Annual mean water contents of the hollow brick wall for the measured weather files simulations for the East exposition (a) and the West exposition (b).

METHOD

The EN 15026 (European Committee for Standardization, 2007) refers to EN ISO 15927-4:2005 (International Organization for Standardization, 2005) for the creation of Moisture Reference Years. This method is intended for the creation of typical meteorological years and it is based on the Finkelstein-Schafer (FS) statistic method (Finkelstein and Schafer, 1971). In this research some modifications are introduced to extend the procedure to moisture migration related applications. From the observation that the total moisture content of a simulated wall depends also on the exposure of the wall itself (Figure 1) other rain related climate parameters (normal rain, driving rain) are alternatively considered to select the representative months of the reference year from the historical measured data, in addition to the standard ones (temperature, relative humidity, irradiation, wind speed). Then, the validity of the reference years generated for every combination is evaluated on two wall build-ups with a comparison in terms of the moisture contents against the historical years. The revised procedure for the generation of reference years is shown below. Let p be the generic measured parameter of the historical years required for the hygrothermal simulations. First, from at least 10 years of hourly values of p , for every day i , the daily mean \bar{p}_i is calculated; then, for each calendar month (m), the values \bar{p}_i are ordered in ascending order and 12 arrays for the whole data set are obtained. The cumulative distribution function $\Phi(p, m, i)$, associated to every \bar{p}_i over all the years in the data set, is calculated using the Eq. (1), with i the considered day in the month, from 1 to N , and N the sum of the number of days in any calendar month, $K(i)$ is the position (“rank”) in the ordered list of \bar{p}_i of the month m ;

$$\Phi(p, m, i) = \frac{K(\bar{p}_i)}{N+1} \quad (1)$$

For each year y of the data set, the cumulative distribution function of the daily means within each calendar month (using Eq. (2)), $F(p, y, m, i)$, is obtained by sorting all the values for the month m and the year y , in increasing order. 12 arrays are obtained for every year. $J(i)$ is the “rank” of the value of the daily mean \bar{p}_i for the month m and the year y , n is the number of days in the month m ;

$$F(p, y, m, i) = \frac{J(\bar{p}_i)}{n+1} \quad (2)$$

For each calendar month, for each year of the data set, the Finkelstein-Schafer statistic, $F_S(p, y, m)$, is calculated using Eq. (3):

$$F_S(p, y, m) = \sum_{i=1}^n |F(p, y, m, i) - \Phi(p, y, m, i)| \quad (3)$$

For each calendar month with the same m from all the years, the rank R is calculated for each value. Differently from the standard method, in this work the ranking is performed ordering the values ascending by the F_S , calculated from the multiyear record for the parameters selected among temperature (T), solar irradiance (I) and relative humidity (RHU) the driving rain (RDW) obtained from the wind normal to the considered wall direction and from normal rain (RIH), the wind speed (WS) and the normal rain (RIH); for each calendar month and for each year, the separated ranks (R) are summed for the climate parameters selected for the formation of MRY (the parameter selection used in this work is shown in Table I) and the total ranking $R_{\text{tot}}(y, m)$ is obtained; the month with the lowest $R_{\text{tot}}(y, m)$ is selected as the “best” month to be included in the Moisture Reference Years;

Once the months are selected, the weather file is completed substituting the unrealistic leaps between the values of adjacent months with a linear interpolation.

The validation of the proposed MRYs is carried out by comparing the hygrothermal behaviour of building components simulated with the new MRY, with the behaviour obtained with the weather conditions over the long term from the measured weather file. 34 MRYs weather files have been generated with 16 different criteria. The historic weather data series, from 2002 to 2016, are provided by the Regional Agency for the Protection of the Environment (ARPA) of the Piedmont Region (Italy).

The evaluation of the obtained reference years has been performed comparing the hygrothermal simulation results of two different building envelopes, a hollow brick wall and a timber wall. The simulations have been performed with the software WUFI Pro, based on the model presented in Künzle et al. (1996). The comparison is held evaluating the monthly mean moisture content and comparing it to the one evaluated with the historical data set.

Table I: Climate parameters selected for the formation of MRY.

ID	ISO	1	2	3	4	5	6	7	8	9	10	11	12	13	14	15	16	17	18	19	20	21	22	23	24	25	26	27	28	29	30	31	32	33	34			
<i>T</i>		x	x	x	x	x	x	x	x	x				x	x	x	x										x			x	x			x				
<i>I</i>		x	x	x	x	x													x	x	x	x							x	x					x			
<i>RHU</i>		x	x	x	x	x	x	x	x	x	x	x	x													x												
<i>WV</i>		x																									x											
<i>RIH</i>																																						
<i>RDW</i> (South)		x				x				x					x																							
<i>RDW</i> (East)			x				x				x					x																						
<i>RDW</i> (North)				x				x				x					x																					
<i>RDW</i> (West)					x				x				x					x									x											

T=Air temperature, *RHU*=Relative humidity, *I*=Solar irradiance, *RDW*=Rain deposition on vertical wall, *MRY*=Moisture Reference Years, *WS*=Wind speed, *WD*=Wind direction, *RIH*=Rainfall intensity on a horizontal surface

RESULTS

The reference years from number 1 to number 24 have been simulated considering the design orientation (for example the reference year 1, designed considering the rain deposition on vertical wall facing South has been used for the simulation of the wall build-up facing South), while the reference years from number 25 to 34 have been used for the simulations for the five expositions considered (since normal rain has a general effect on all the expositions). The walls passed the moisture accumulation assessment and the condensation risk assessment for every MRY considered and for the historical data set. For this reason the annual mean results (Figure 1) have been compared in terms of relative standard deviation from the annual mean values obtained by the measured weather data (Figure 2). The Timber wall results show better representative MRY, with lower values of the relative standard deviation, with respect to the Hollow brick wall results.

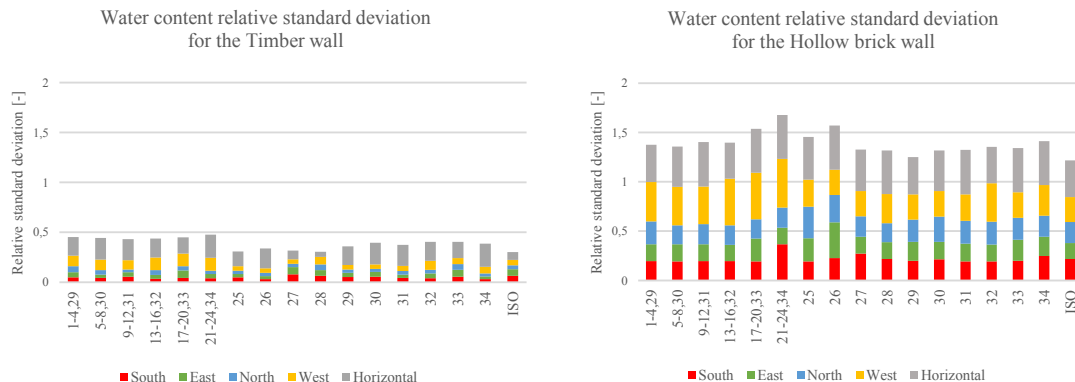


Figure 2. Relative standard deviations of the moisture contents between the simulation of the historical years and every reference year described in Table 1.

The results present exposition specific trends. For the Timber wall, the ID 34 (based on *RIH*) better represents the South, East and North expositions, while the West exposition is better described by the ID 25 (based on *RHU*) and the Horizontal by the ID 28 (based on *I*). The ID ISO and the ID 28 are the reference years better representing the walls in the five directions. The Hollow brick wall shows different exposition specific trends: the South facing exposition is better represented by the ID 34 (based on *T* and *RHI*), the East and West by the ID ISO, the North by the ID 7 (based on *T*, *RHU*, *RDW*) and the Horizontal by the ID 32 (based on *T* and *RHI*). From Figure 2 it is also possible to observe some overall results. The ID from 1 to 24, considering *RDW* are generally less representative for the most rain exposed directions (West and Horizontal). Exclusively *RDW* based years (21-24) are less representative than ID from 29 to 34, based also on *RIH*. For the Timber wall the ID from 25 to 28 and the ID ISO (not based on *RIH* or *RDW*) are better performing than the *RIH* based ones, while for the Hollow brick wall, their behaviour is similar.

DISCUSSION

The relative standard deviations of the Timber wall are lower than the Hollow brick wall. This difference is due to the different hygrothermal properties of the materials. The Hollow brick wall external layer has higher liquid transport coefficient values than the Timber wall, which has also higher moisture storage function values, and that could lead in faster responses to the rainfall (larger water content variations), with larger differences from the historical data set results.

The moisture reference years depending on rain deposition on vertical wall (obtained from wind speed, direction and normal rain) led to less representative years than the ones generated by the standard method. This result could be related to the features of the climate of Turin (Italy), whose rains are brief and quickly dried afterwards. On the other hand, one of the reasons could also be the fact that the external material layers do not respond instantly to the transient hourly rainfall excitations (slower than the heat excitations) and that the total water content of the wall is more influenced by the long term mean values of the environmental excitations, which is also been discussed in Libralato et al. (2017).

CONCLUSIONS

In this study, 34 moisture reference years (MRY, to be used for hygrothermal analysis of building structures) have been generated from a data set of measured weather files from the year 2002 to the 2016, in the city of Turin (Italy). Each MRY has been generated selecting the months from the historical data set, with a modified EN ISO 15927-4:2005 method, based on the rain deposition on vertical walls with different expositions. From the simulation of two wall types to all the 34 MRY, it has been observed that an orientation differentiation does not lead to more representative MRY for the two considered building structures in the considered climate.

The results suggest that, when the use of a single MRY is preferred, the MRYs obtained with the standard procedure EN ISO 15927-4:2005 better reproduce the results obtained with the simulation of the measured weather files and that it could be used, not only for the energy consumption simulations, but also for the moisture migration in building envelopes simulations. Considering exposition and material specific applications, that could benefit from the use of more than one MRYs, other generation methods presented in this work could be taken in consideration, depending on the building material properties and on the wall orientation.

Further work will be carried out to establish if this approach could be extended to critical weather data design for moisture accumulation risk assessments and if the proposed MRY generation method could be used proficiently for other applications, like energy simulations in

which the efficiency of the components of the systems depends on moisture related environmental conditions, such as evaporative towers (De Angelis et al. 2013), evaporative cooling systems for industrial buildings (De Angelis et al. 2017a), shopping malls (De Angelis et al. 2017b) and other heat recovery systems (Chinese et al. 2017).

REFERENCES

- Chinese D, Santin M. and Saro O. 2017. Water-energy and GHG nexus assessment of alternative heat recovery options in industry: A case study on electric steelmaking in Europe. *Energy*, 141, 2670–2687.
- Cornick S, Djebbar R, and Alan Dalglish W. 2003. Selecting moisture reference years using a Moisture Index approach. *Building and Environment*, 38(12), 1367–1379.
- De Angelis A, Saro O and Truant M. 2017a. Evaporative cooling systems to improve internal comfort in industrial buildings. In *Energy Procedia* (Vol. 126, pp. 313–320).
- De Angelis A, Chinese D and Saro, O. 2017b. Free-cooling potential in shopping mall buildings with plants equipped by dry-coolers boosted with evaporative pads. *International Journal of Heat and Technology*, 35(4).
- De Angelis A, Saro O, Lorenzoni G, D’Elia S, and Medici M. 2013. Simplified Models for Assessing Heat and Mass Transfer in Evaporative Towers. *Synthesis Lectures in Engineering*, Morgan & Claypool Publishers.
- Finkelstein J. M. and Schafer R.E, Improved goodness-of-fit tests. 1971. *Biometrika*, Volume 58, Issue 3, Pages 641–645
- Künzel H. M, and Kiessl K. 1996. Calculation of heat and moisture transfer in exposed building components. *International Journal of Heat and Mass Transfer*.
- Libralato M, Saro O, De Angelis A and Spinazzè S. 2017. Comparison between Glaser method and Heat, Air and Moisture transient model for moisture migration in building envelopes. *Proceedings of the 12th International enviBUILD 2017 Conference*, Vienna.
- Murano G, Corrado V, and Dirutigliano D. 2016. The new Italian Climatic Data and their Effect in the Calculation of the Energy Performance of Buildings. In *Energy Procedia* (Vol. 101, pp. 153–160).
- Riva G, Murano G, Corrado V, Baggio P, and Antonacci G. 2012. Aggiornamento parametri climatici nazionali e zonizzazione del clima nazionale ai fini della certificazione estiva. September 2012, *ENEA, Ministero dello Sviluppo Economico*.
- Riva G, Murano G, Corrado V, Baggio V, and Antonacci G. Definizione degli anni tipo climatici delle province di alcune regioni italiane (Emilia Romagna - Friuli Venezia Giulia – Liguria – Lombardia – Piemonte Toscana – Trentino Alto Adige Valle D’Aosta – Veneto); *ENEA, Ministero Dello Sviluppo Economico*, 2010, pp 347.
- Salonvaara M, Sedlbauer K, Holm A, and Pazera M. Effect of selected weather year for hygrothermal analyses. In: *Buildings XI, thermal performance of the exterior envelopes of whole buildings XI, CD-ROM proceedings*, Clearwater Beach, Florida. Atlanta: ASHRAE; 2010.
- Schöne T and Zirkelbach D. 2016. Development of hygrothermal reference years for Germany, *Proceedings of Central European Symposium on Buildings Physics (CESBP)*.
- Zhou X, Derome D, and Carmeliet J. 2016. Robust moisture reference year methodology for hygrothermal simulations. *Building and Environment*, 110, 23–35.

Hygrothermal performance of historic massive wall: when is 2D simulation necessary?

7th International Building Physics Conference, IBPC2018

Dario Bottino Leone^{1,2*}, Marco Larcher¹, Alexandra Troi¹ and John Grunewald²

¹Eurac research, Italy

²Technical University of Dresden, Germany

**Corresponding email: dario.bottino@eurac.edu*

ABSTRACT

Hygrothermal analysis of historical building envelopes is crucial in ensuring their durability and enhancing their performances. The use of hygrothermal dynamic simulation is the most effective approach to predict moisture related damages or risk of mould growth on ancient masonry envelopes. However, simulating the hygrothermal behaviour of a historic wall composed by stones or bricks and mortar joints, with a detailed two-dimensional (2D) model, is typically a complex and time-consuming process. For this reason, in numerical models, composite walls are often simplified with a one-dimensional (1D) layer, neglecting the mortar joints. An oversimplified numerical model could affect the evaluation of a retrofit intervention and lead to inadequate design choices. This study evaluates when the description of a historic wall as a 1D homogenous layer leads to an acceptable level of accuracy and when it is necessary the use of a more precise 2D model. We quantified the error by comparing 1D and 2D simulations of different massive walls in three Italian climate conditions. We examined a possible retrofit intervention with different internal insulation systems considering vapor tight, vapor retardant and capillary active solutions. Although simplified 1D models are reliable for thermal parameters, we have identified a different behavior regarding the hygric parameters. Whereas for a capillary active insulation system the 1D and 2D simulations show a reasonable agreement, the 1D approximation is no longer acceptable in the case of vapour closed insulation systems as it leads to large deviations. Knowing when it is possible to implement a simplified 1D model and quantifying the introduced error will support architects and energy consultants in the design process. It will guide them in the choice of the most suitable model depending on their specific requirements.

KEYWORDS

Hygrothermal simulation, Interior insulation, Performance evaluation, Moisture related issues, Historic stonewall.

INTRODUCTION

Historic buildings are highly energy-consuming parts of the city center, and their energy consumption provokes large CO₂ emissions due to the low performances of their thermal envelopes. A possible strategy to reduce this impact is to decrease the thermal transmittance of the outer walls. In the case of aesthetically valuable historic buildings, interior insulation has proven to be a reliable solution, but dynamic hygrothermal simulations are needed to avoid possible hygrothermal risks. In fact, the change of the original thermal and moisture balance could lead to a higher moisture accumulation into the wall [1] with a consequent spalling and cracking due to hygric expansion and contraction or frost-thaw cycles, or visual deterioration due to salt efflorescence [2]. A thorough understanding of the moisture transport is also primary to make an accurate choice of the correct inner insulation system. It is common practice, while performing a hygrothermal simulation, to simplify the historical wall as a homogeneous stone or brick layer. This simplification gives the user the possibility to have quicker results, but has the effect of

neglecting mortar joints, which could play a significant role in terms of moisture storage and transport; the resultant deviations are investigated in this paper. A previous study [3] analyzed the impact of the mortar joints for a massive brick wall exposed to real climate conditions showing that they have a negligible impact and concluding that typically the approximation to a homogenous brick layer is allowed. In the present work, we extend previous analysis considering a broader range of variants and situations. We analyze a historic wall that is retrofitted with the application of different types of internal insulation, we consider several materials for the composition of the historic wall, ranging from stone to bricks, and finally we examine different climates zones.

METHODS DESCRIPTION

Hygrothermal simulation tool

In order to perform a full hygrothermal assessment, the commercial software Delphin 6.0.16 is employed. We considered a full hygrothermal simulation, which includes heat transport, liquid convective transport and vapor diffusion [4].

Boundary condition: Outdoor

In this study we focus on Italian climate; in particular we selected three locations to consider North, Middle and South latitudes and cover different climate zones. The hourly climate data files were generated with Meteororm 7.0. They include hourly data of temperature, relative humidity, direct and diffuse short wave radiation, long wave radiation, wind direction, wind velocity, and rain. In Table 1, we summarize the main characteristics of the three selected climates, Udine, Ancona and Messina for a North-facing wall.

	Annual Wind Driven Rain [l/m ²]	Annual Global Radiation [kWh/m ²]	Winter T average [°C]	Summer T average [°C]	Winter RH average [%]	Summer RH average [%]
Udine	44.29	326.54	4.72	23.95	71.95	66.86
Ancona	31.53	344.76	6.51	23.22	72.69	69.24
Messina	50.14	358.08	10.07	24.75	72.22	68.49

Table 1. Environmental conditions highlights. Annual radiation is calculated on the wall.

The thermal resistance of the exterior surface was set to 0.04 m²K/W. The absorption coefficient for short wave radiation was set to 0.6 and the emissivity for long wave radiation exchange to 0.9. The rain exposure coefficient was set at 1.00 assuming no sheltering, since worst-case scenarios were assessed.

Boundary condition: Indoor

The interior climate was calculated based on external daily temperature data, according to the adaptive indoor climate model presented in the standard UNI EN 15026 [5]. The selected temperature range is between 20 and 25°C, while relative humidity varies between 35 and 65% following the recommendation of the WTA leaflet 6.2 [6]. The thermal resistance of the interior surface was set to 0.125 m²K/W.

Historical wall characterization

The construction technique chosen for the reference hygrothermal model is a traditional core masonry wall. It is a widely used technology of the ancient Italian buildings [7]. The materials for the simulations are chosen among the most commonly spread over the Italian context. Four different stones are selected: granite, limestone, sandstone and tuff. The brick masonry, generally widespread in the Center-North of the country, is also included in this study. The mortar and the plaster chosen for the reference wall are a Lime Cement Mortar and an historical Lime Plaster; their hygric characterization parameters, as for the other materials, are selected from Delphin Material Database 6.0. In Figure 1 and Table 2, we report the main hygrothermal characteristics of the chosen materials.

Table 2. Hygrothermal proprieties of the chosen materials. Density (ρ), Specific Heat capacity (C_p), Theta effective (θ_{eff}), thermal transmittance (λ_{dry}), vapor resistance (μ_{dry}), and water absorption coefficient (A_w).

Investigated outputs

The choice of the output to analyze in this assessment is based on the prescriptions of the WTA leaflet 6.5 [6]. The analysis of frost damages is neglected, since in the studied locations temperatures barely go under zero. Moreover, this study had shown a good correspondence of surface temperature and relative humidity values between 2D and 1D simulations, so the mold germination risk is not strongly influenced by this simplification. Therefore, the most interesting outputs to discuss, as proposed in WTA leaflet 6.5 [6], are relative humidity and temperature behind insulation, averaged on the first 10mm behind the insulation layer.

Error calculation

Outputs are evaluated on an hourly basis, in particular we compare the results of 1D and 2D simulations. The deviation between the two simulations is evaluated calculating the absolute error. In particular, for a given quantity X (that can be either the temperature, T , or the relative humidity behind the insulation, φ) we define the absolute error as

$$\Delta X(t) = |X_{2D}(t) - X_{1D}(t)| \quad (1)$$

where $X_{2D}(t)$ and $X_{1D}(t)$ represent the parameter X calculated as a function of time in the 2D and in the 1D simulation respectively. Then we define the absolute mean error, $\langle \Delta X \rangle$, as the time average of $\Delta X(t)$ over the last year of simulation and the maximum absolute error, ΔX_{max} as the maximum over the all simulation.

RESULTS

The thermal analysis shows a high correspondence of the simulation results between 2D and 1D case. In particular for the calculation of the temperature behind the insulation we get the following typical errors: $\langle \Delta T \rangle = 0.12^\circ\text{C}$ and $\Delta T_{max} = 1.4^\circ\text{C}$. Contrariwise, more deviations exist for the hygric behavior reaching mean absolute errors up to 7% for the relative humidity behind the insulation. Figures 3, 4 and 5 show the average relative humidity behind the insulation in the simulations of Udine for each case: Vapor Barrier, Vapor Retardant and Vapor Open insulation systems. A similar behavior is observed also for the simulation performed in Messina and Ancona.

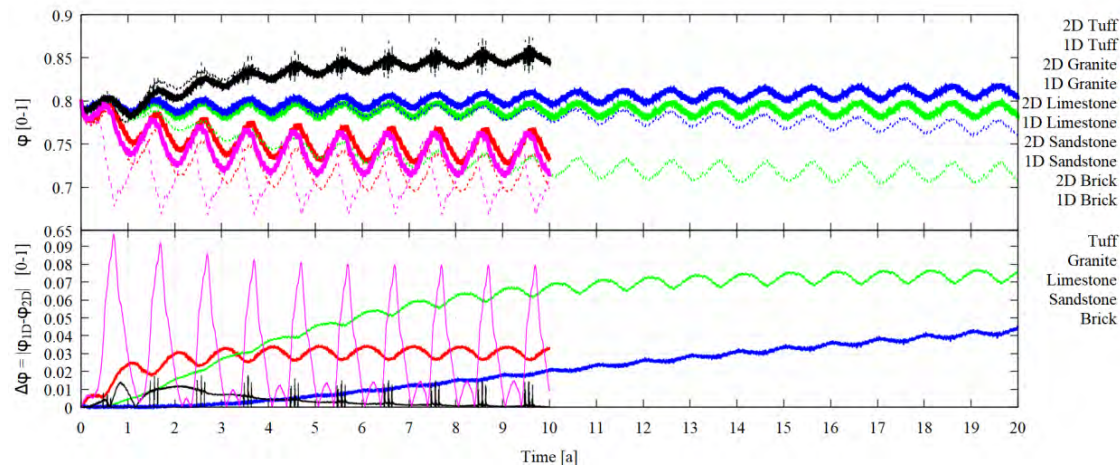


Figure 3. Relative humidity behind the insulation, φ , as a function of time (top panel) and corresponding absolute error, $\langle \Delta \varphi \rangle$, (bottom panel) for Vapor Barrier insulation system and for the climate of Udine. The different colors refer to different materials composing the historic wall.

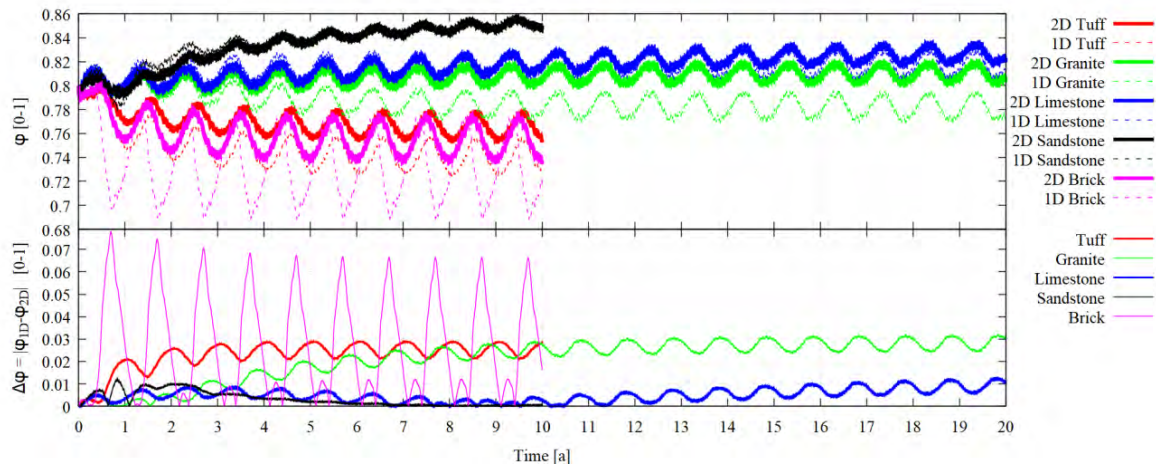


Figure 4. Same as Figure 3 but for Vapor Retardant insulation systems.

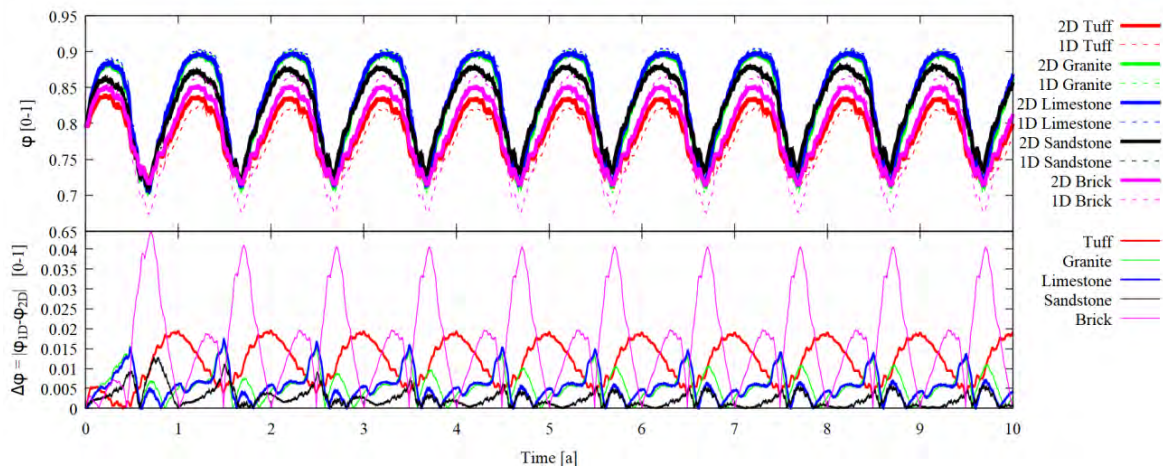
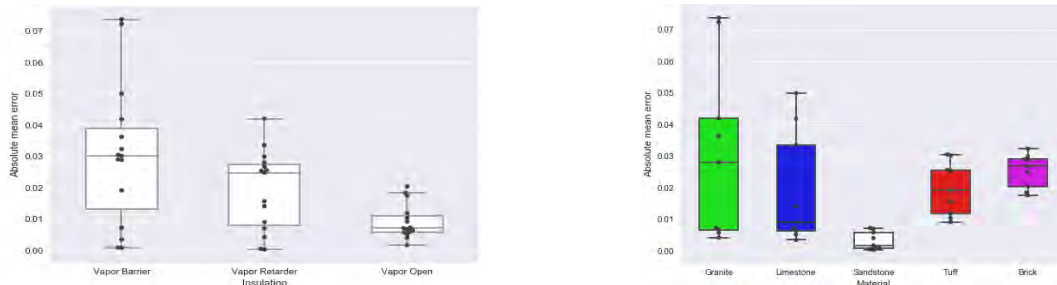


Figure 5. Same as Figure 3 but for Vapor Open Insulation system.

DISCUSSIONS

Figures 3, 4 and 5 show that depending on the insulation type and on the material that forms the historic wall we can get very different absolute errors between 1D and 2D simulations. For instance when considering the sandstone wall we always get very small errors, while the largest mean absolute errors are observed for the case of granite. Also in the case of the limestone wall we get significant deviations. In the specific case of the limestone wall with a vapor tight insulation system, the situation is particularly critical since the 1D and the 2D simulation have different behaviors. The 2D simulation reaches a quasi-stationary behavior, while the relative humidity in the 1D simulation keeps decreasing over the years. For the brick masonry wall we observe peaks up to 9% deviation. For the vapor open insulation system, we typically get small deviations while the largest errors are found in the case of vapor tight solutions. Conversely, we observe that the climate does not play a crucial role in the determination of the behavior of the absolute error. We only observe a small correlation between the quantity of wind driven rain that reaches the façade and the absolute error. In order to get a closer insight on the correlation between the observed error and the parameters varied in the simulations we represent in Figure 6 and 7 the distributions of the absolute mean error using box plots. In Figure 6 the absolute mean error distributions are grouped depending on the insulation type, while in Figure 7 according to the material of the historic wall.



Figures 6-7. Absolute mean error: Insulation system dependency, Material dependency.

Fig.6 confirms that vapour tight insulation systems lead to higher errors. In particular, decreasing the vapour tightness of the insulation system, we observe smaller mean absolute errors. For vapour open insulation systems the mean absolute error $\langle \Delta\phi \rangle$ is, for almost all the cases, smaller than 2%, while for vapour barrier insulation system we get errors of up to 7%. When using a vapour retardant solution we get an intermediate behaviour. The use of a vapour tight system on the internal side of the construction strongly reduces the interaction of the wall with the internal environment and therefore the behaviour of the wall is mainly determined by the interaction with the exterior climate. This interaction strongly depends on the way in which the wall is modelled, thus a detailed description of the wall becomes more relevant in this situation. Fig.7 confirms that the material forming the wall plays a significant role in the determination of the mean absolute error. In particular, we observe smaller errors for materials that have a liquid water conductivity close to the one of the mortar in the range 80 – 99%. These observations strongly suggest that the approximation of a masonry wall to a homogenous brick or stone layer has to be used with caution, especially when looking at hygric properties of the wall.

CONCLUSIONS

This study analyzed the effect of simplifying an historical wall with a homogeneous layer in hygrothermal assessments, comparing the results of a 1D approximated simulation with those of a detailed 2D simulation. Three Italian climates and five materials were investigated, in combination with three internal insulation systems: a Vapor Barrier, a Vapor Retardant and a Vapor Open one. Results had shown a high correspondence in thermal behavior. Contrariwise, higher deviations are found in hygric results, especially in vapor tight and retardant insulation systems, which are influenced by a moisture accumulation process. Regarding the historic wall composition, those materials that have a similar liquid water conductivity to the mortar in the relative humidity range of the simulation, lead to smaller deviations. Our results show that representing an historic wall with a homogenous 1D layer could be in some situations an oversimplified model. We identified the situations that lead to larger errors in the framework of the parameters that we varied. However, further investigation are needed to develop a systematic approach for the identification of those situations.

REFERENCES

- [1] Vereecken E., Van Gelder L., Janssen H., 2015. Interior insulation for wall retrofitting – A probabilistic analysis of energy savings and hygrothermal risks.
- [2] Janssen H., Derluyn H., Carmeliet J., 2012. Moisture transfer through mortar joints: a sharp-front analysis.
- [3] Vereecken E., Roels S., 2013. Hygric performance of a massive masonry wall: How do the mortar joints influence the moisture flux?
- [4] Sontag L., Nicolai A., Vogelsang S., 2013. Validierung der Solverimplementierung des hygrothermischen Simulationsprogramms DELPHIN.
- [5] UNI/EN15026,2008.Hygrothermal performance of building components and building elements.
- [6] WTA, 2014. Leaflet 6.2 and 6.5, Simulation of heat and moisture transfer. Interior insulation.
- [7] Pascucci M., Lucchi E. 2D-Hygrothermal simulation of historical solid walls.

Innovative composite materials with enhanced acoustic, thermal, and optical performance for urban pavements: experimental characterization

Verronica Lucia Castaldo¹, Claudia Fabiani^{2,*}, Anna Laura Pisello³ and Franco Cotana⁴

¹CIRIAF-Interuniversity Research Center, Department of Engineering, University of Perugia, Via G. Duranti 63, 06125, Perugia, Italy, castaldo@crbnet.it

²CIRIAF-Interuniversity Research Center, Department of Engineering, University of Perugia, Via G. Duranti 63, 06125, Perugia, Italy, fabiani@crbnet.it

³Department of Engineering, University of Perugia, Via G. Duranti 93, 06125, Perugia, Italy, anna.pisello@unipg.it

⁴ Department of Engineering, University of Perugia, Via G. Duranti 93, 06125, Perugia, Italy, cotana@crbnet.it

**Corresponding email: fabiani@crbnet.it*

ABSTRACT

Over the last decades, the implementation of innovative multifunctional materials for urban surfaces has produced a variety of paving solutions characterized by self-cleaning, self-healing, electricity conductive, solar reflective, sound absorbent properties and so on. Therefore, a key challenge is nowadays represented by the need for combining multi-physics properties in a single material or system for flooring. The present work concerns the development of a new outdoor paving application with enhanced acoustic, thermal, and optical performance. To this aim, eleven concrete mix-designs were tested. The composites were characterized by different aggregate size, material and additives. The aggregates included in the composite consist of (i) natural stones with different grain sizes, (ii) expanded clay aggregates, and (iii) glass fragments. Acoustic, thermal, and optical measurements were performed for each sample. Additionally, a dedicated in-field monitoring campaign was carried out to characterize the albedo under summer boundary conditions. Finally, the thermal behaviour of the samples was tested in an environmental chamber using controlled boundary conditions in terms of temperature, humidity, and radiation. The results demonstrate that bigger grain size presents the best acoustic performance in terms of absorption capability, i.e. absorption coefficient of about 0.9 and 0.8 at 1000 Hz and 500 Hz, respectively. Moreover, the thermal-optical lab and field tests confirm previous literature results demonstrating that the mix-design with the smaller grain size has the best reflectivity potential.

KEYWORDS

Paving materials; Optimized mix-design; Thermal-optical performance; Acoustic properties.

INTRODUCTION

Urban environments are often affected by microclimate phenomena such as Urban Heat Island (UHI), a local condition that can significantly harm the health and the quality of life of citizens. In particular, the UHI consists of a significant increase in temperature in the urban area compared to the surrounding rural areas (Vardoulakis, Karamanis, Fotiadi, & Mihalakakou, 2013). Such phenomenon is generally influenced by the thermal and radiative properties of the typical urban surface materials (i.e. asphalt, cement) where the absorption of solar radiation prevails over its reflection (Taha, 2008). Moreover, the human action and the buildings operation strongly contribute to the overheating of urban areas. Such contribution is (i) direct, through traffic, industrial activities and HVAC systems, and (ii) indirect, though the alteration

of the radiative properties of the atmosphere due to the high levels of associated pollution (Pisello, 2017). Over the last few decades, many techniques have been proposed for the mitigation of such phenomenon. Among the main ones there is the use of permeable surfaces in urban environment, consisting of gravels or vegetation able to generate surface cooling by means of evapotranspiration. Furthermore, "cool" materials represent another suitable solution for reducing high urban temperatures (Santamouris, Synnefa, & Karlessi, 2011). These materials are characterized by a high solar reflectance and thermal emissivity that avoids overheating of the surfaces and the air near them. The benefits achievable when installing a cool material over urban paved surfaces can be summarized as follows (Rosso et al., 2017): (i) mitigation of the urban overheating thanks to the capability to reflect most of the incoming incident solar radiation and (ii) consequent reduction of CO₂ emissions emitted in the environment. Another issue typical of urban environments relates to the high noise levels in cities and is referred to as Urban Noise Island (UNI), where depending on the road and tires characteristics and of course on the vehicles' speed, the prominent noise peak very frequently is found at 1000 Hz but it may also be shifted within the range 630-2000 Hz (Sandberg 2003). It is generated by the combination of the different and multiple sources of noise (such as traffic, industrial activities, etc.) that generate sound pollution in urbanized environments (Asdrubali et al., 2015). The study of this phenomenon, which depends on both the generation and propagation of sound, involves the environmental analysis of the external and internal sources at building level, of the control actions on the source, on the propagation path and on the receptor, as well as on the analysis of the response of the human ear to sound stress. In this case, the main mitigation techniques consist of passive type protections that act on the propagation path or on the receptor. In this sense, to reduce the problem of urban noise it is possible also to act on the shape of the buildings, i.e. mainly on the acoustic requirements of the façade (i.e. acoustic insulation). Based on the framed background, the present research work deals with the development, characterization and optimization of concrete-based materials with high-thermal and acoustic performance for urban paving applications. The aim is therefore to implement innovative materials able to mitigate both the UHI and UNI when installed over urban pavements. To this purpose, an extensive experimental laboratory and field campaign was carried out and different mix design were tested and compared in terms of their coupled thermal-acoustic behavior.

MATERIALS AND METHODS

Five different components were selected and used to produce advanced concrete mix designs with enhanced acoustic and visual performance to be used as urban pavements: sand (i.e. fine grains, 0-4 mm), pebbles (i.e. medium grains, 2-5.6 mm), chippings (i.e. large grains, 4-12.5 mm), glass fragments (4-12.5 mm) and expanded clay spheres (2-5 mm). These components were alternatively treated with titanium dioxide to maximize their capability to reflect solar radiation. The samples had a diameter of 10 cm and 2.9 cm and a thickness of 6.5 cm for the laboratory acoustic tests (i.e. for the evaluation of the acoustic absorption).

Starting from the first basic paving mix-design (i.e. traditional paving recipe chippings-based), additional samples were prepared, by varying (i) type of aggregate (sand, pebbles, chippings, expanded clay spheres, and glass fragments), (ii) TiO₂ treatment, and (iii) kind of additive (i.e. dynamon floor 20 and bt02) in the case of the pebble mix design.

Thermal-optical in-lab experimental analysis

Firstly, spectrophotometric measurements were carried out to investigate the reflectance capability of the different evaluated samples. The experimental campaign was performed by using a Shimadzu UV-VIS-NIR spectrophotometer equipped with a double-radius optical system over time and integrating sphere. Moreover, the calculation of the spectral solar reflectance in the range 300-2500 nm was carried out according to the ASTM E903-12

Standard Test Method (American Society for Testing and Materials, 2010b). Secondly, the thermal emissivity of the samples was measured by means of a portable emissometer according to the ASTM C1371 Standard Test Method (American Society for Testing and Materials, 2010a). Finally, a DM340SR (ATT) climatic chamber was used to test the thermal behavior of the samples within controlled dynamic conditions in terms of temperature, humidity and solar radiation (Fabiani & Pisello, 2017).

Acoustic in-lab experimental analysis

In order to characterize the acoustic properties of the selected materials, the impedance tube was used. To this aim, a Brüel & Kjær Kundt's tube with all the related equipment and accessories was used. The measurements were carried out according to the classic standardized procedures in materials analysis in the lab (Asdrubali et al., 2015). The test procedure involved at least three measurements for each sample to obtain an acceptable result reliability. Finally, the comparison between the absorption coefficients of the different samples was made considering the average value of the measurements carried out for each sample.

Albedo field monitoring

After the preliminary in-lab experimental campaign, the albedo of the samples was monitored in-field by means of a dedicated double pyranometer or albedometer, an instrument able to measure both the incident solar radiation and the one reflected from the surface between 300 and 2500 nm. The experimental measurement campaign was carried out according to the ASTM E1918-06 international standard (2006). The experimental campaign was performed in the period from 10 July to 10 August 2017 to characterize its reflectance potential when the climatic forcing to the boundary and the meteorological conditions vary. To this end, after the measurement of black and white reference samples (Akbari, Levinson, & Stern, 2008) the different samples were monitored on typical summer days.

RESULTS

Thermal Emissivity and Solar Reflectance

In this section, the results of the testing of the thermal-optical properties of the samples are presented. In particular, Figure 1 shows the trend of the solar reflectance of fine sand, mortar and pebbles concrete mix designs, and the obtained solar reflectance (SR), emissivity (ϵ) and solar reflectance index (SRI). It is clear how the solar reflectance increases as the grain size decreases. In fact, as can be seen by comparing the pure mortar with the mix designs produced by introducing the same amount of sand or pebbles, the sample with fine sand shows the greatest solar reflectance, followed by pebbles and the traditional mortar. In terms of thermal emissivity, the values are generally high, i.e. varying from 0.91 (mortar) to 0.99 (fine sand).

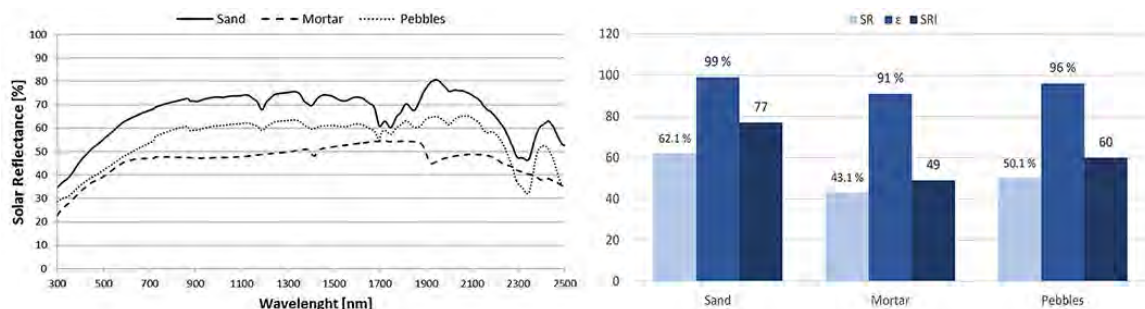


Figure 1. Solar reflectance profiles in the range 300-2500 nm, SR, ϵ and SRI of the samples.

Dynamic controlled environment: climatic chamber

This section summarizes the results of the tests carried out in the climatic chamber. The purpose of the tests was to investigate and compare the thermal behavior of the samples under the same controlled dynamic environmental conditions, i.e. a typical summer day in the Rome climate zone taken from the TMY (Typical Meteorological Year). Therefore, the surface temperatures of the upper and lower face of the samples was measured with varying air temperature, relative humidity, and incident solar radiation.

Figure 2 shows how the samples containing fine sand present the best surface thermal behaviour, followed by the mortar and the pebbles mix design with the Dynamon 20 additive, which possess the highest thermal inertia due to their highest density and the samples with TiO₂ and glass fragments, which are capable to reflect the highest amount of the incoming radiation (an average direct radiation on the horizontal surface of 820 W/m² was imposed through the halogen lamp according to data from the TMY). On the other hand, expanded clay sphere and pebbles samples with bt02 or without any additive, which are characterized by a larger grain size and lower densities, show the worst performance in terms of surface temperature, reaching up to 68°C.

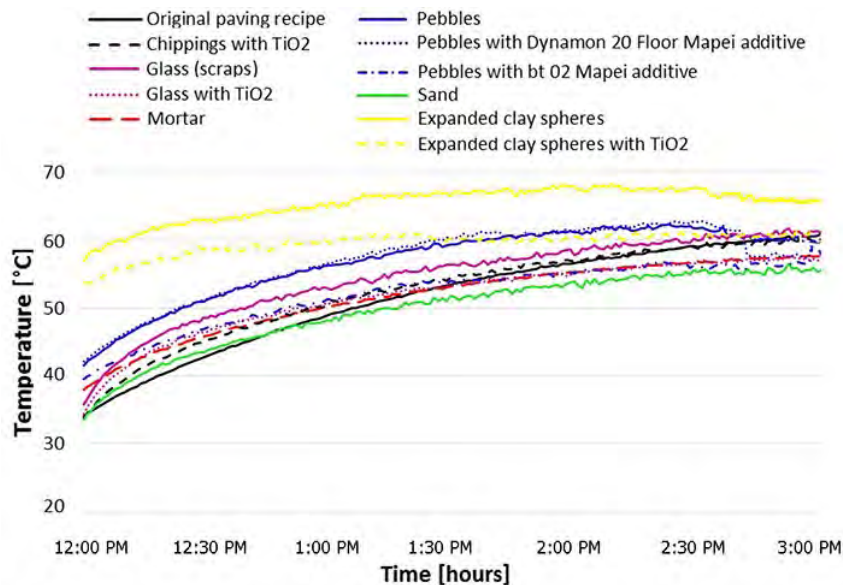


Figure 2. Average temperatures of the upper (left) and lower (right) surface of the samples.

Albedo in-field measurements

Table 2 shows the albedo values measured in the field during typical summer days (July 2017) for the different samples of paving material produced. It is evident how the paving recipe characterized by the presence of glass fragments and TiO₂ treatment present a greater albedo than all the other samples, followed by the expanded clay spheres with TiO₂ treatment. The paving samples produced using the original recipe with chippings included, and the one characterized by the presence of pebbles are those with lower potential in terms of albedo. These results are consistent with previous studies showing that albedo increases with decreasing grain size.

Table 2: Albedo test results.

Sample	Traditional asphalt	Original paving recipe	Expanded clay spheres+ TiO ₂	Glass fragments + TiO ₂	Pebbles
Albedo (12-3PM)	~7	37.9	40.8	44.4	36.8

Acoustic absorption coefficient

Figure 3 shows the trend of the acoustic absorption coefficient for the various samples tested with respect to the original paving recipe. The sample of the original pavement recipe is not very absorbent. In fact, the maximum absorption coefficient is equal to 0.2 at 450 Hz. As for the mortar sample, this has a maximum absorption coefficient equal to 0.2 at 600 and 1300/1400 Hz. As regarding the samples with aggregates of different grain sizes, the sand has a maximum absorption coefficient of 0.2 at 400 Hz, and then remains almost constant (<0.1) at the other frequencies. The sample with pebbles, on the other hand, presents a bell-shape absorption coefficient with a positive peak of 0.85 just before 600 Hz and a negative peak of less than 0.2 at about 1600 Hz. The clay sphere sample is characterized by a high absorption coefficient, with a peak of 0.9 at 600 Hz. As for the mix design with chippings and TiO_2 , a maximum absorption of 0.3 between 500 and 600 Hz is reached. Subsequently, the absorption capacity decreases at about 0.1 between 800 and 1200 Hz, then decreasing again. By adding the bt02 additive, the aforesaid sample becomes very absorbent, with a maximum absorption coefficient of 0.9 at 500 Hz. By adding a different type of additive ("Dynamon"), the absorption coefficient reaches a value of almost 0.8 at 500 Hz. The sample produced using expanded clay spheres and TiO_2 has a very high absorption capacity, up to a maximum value of 0.8 at 500 Hz. The sample with glass fragments, on the other hand, has a low absorption capacity, with a maximum of less than 0.2 at 450 Hz. By adding the TiO_2 to the present recipe, the absorption coefficient increases slightly to 0.25 at 600 Hz and then decreases at the other frequencies.

Based on such results, the mix-design showing the highest absorption coefficient is that with pebbles, with and without additives, and the expanded clay spheres one, with and without TiO_2 . All the other samples examined show absorption coefficient peaks ranging from about 0.2 to 0.3. On the other hand, samples with pebbles and expanded clay spheres reach peaks of almost 0.9 with respect to the traditional paving recipe which almost does not reach 0.2. It is also possible to notice that all the tested samples have an absorption coefficient peak between 400 and 600 Hz.

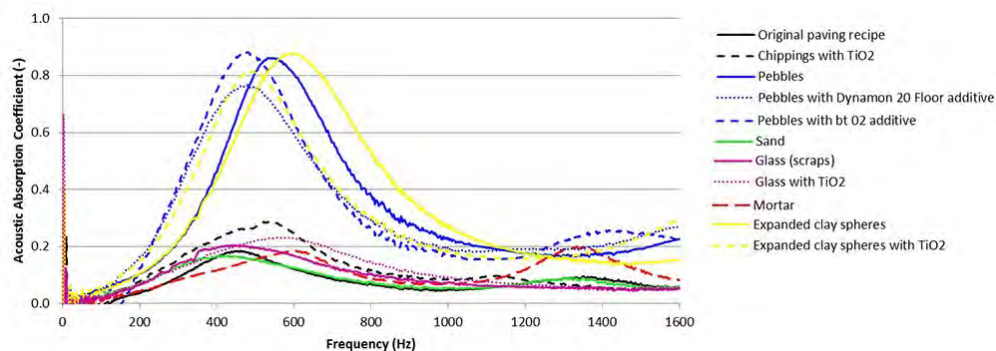


Figure 3. Comparison among the acoustic absorption coefficients of the tested samples.

CONCLUSIONS

The present work aimed at developing and experimentally characterize the thermal and acoustic performance of composite materials for external urban paving. To this purpose, samples of different materials were produced, with varying mix design, particle size, and components (i.e. natural gravel, glass fragment, expanded clay). Results from the experimental campaign allowed to identify the best recipe for urban paving application depending on the need to optimize the performance in terms of solar reflectance, thermal emissivity, albedo, surface temperature and/or absorption and sound insulation potentiality. In general, it was found that to optimize the thermo-optical performance of the paving it is necessary to reduce the grains size of the aggregates as much as possible. In fact, the solar reflectance increases as the particle size of these components decreases. As far as the albedo is concerned, the tests demonstrated that to

improve the performance of the original paving mix it is appropriate to integrate glass fragments and TiO₂ (40% enhancement of the albedo compared to the traditional base-case paving recipe). As for the optimization of the acoustic behavior, it was shown that the best absorption performances are achieved by the samples in loose configuration, due to the interstitial voids that increase the amount of sound energy dissipated by the interaction between the solid matrix and the air molecules. Furthermore, it was possible to notice how the two different configurations (i.e. low density and high density mix design) work properly at different frequencies. Therefore, to maximize the acoustic performance of urban paving materials it is necessary to select materials that work well at low frequencies. In this view, the best materials in terms of acoustic absorption potential are those ones with expanded clay balls, which allow an improvement up to 0.6 (300%) compared to the original paving.

ACKNOWLEDGEMENT

The authors' acknowledgements are due to Luigi Metelli S.p.A. for supporting the development of Regional 598 project named COOL CRETE. The authors would like to thank Dr. Antonella D'Alessandro and Dr. Emanuele Piccioni for helping them in the preparation phase.

REFERENCES

- Akbari, H., Levinson, R., & Stern, S. (2008). Procedure for measuring the solar reflectance of flat or curved roofing assemblies. *Solar Energy*, 82(7), 648–655. <https://doi.org/10.1016/J.SOLENER.2008.01.001>
- American Society for Testing and Materials. (2010a). ASTM C1371-04a, Standard Test Method for Determination of Emittance of Materials Near Room Temperature Using Portable Emissometers. West Conshohocken, PA, USA.
- American Society for Testing and Materials. (2010b). ASTM E903-96, Standard Test Method for Solar Absorptance, Reflectance, and Transmittance of Materials Using Integrating Spheres. West Conshohocken, PA, USA.
- Asdrubali, F., Cotana, F., Pisello, A. L., Mencarelli, N., D'Alessandro, F., & Schiavoni, S. (2015). Acoustic properties of stone aggregates used in cool roofs. In *22nd International Congress on Sound and Vibration, ICSV 2015*.
- Fabiani, C., & Pisello, A. L. (2017). Coupling controlled environmental forcing and Transient Plane Source method: an innovative thermal characterization procedure for building insulation materials. *Applied Thermal Engineering*, In Press. <https://doi.org/10.1016/j.applthermaleng.2017.10.155>.
- Pisello, A. L. (2017). State of the art on the development of cool coatings for buildings and cities. *Solar Energy*. <https://doi.org/10.1016/j.solener.2017.01.068>
- Rosso, F., Pisello, A. L., Castaldo, V. L., Fabiani, C., Cotana, F., Ferrero, M., & Jin, W. (2017). New cool concrete for building envelopes and urban paving: Optics-energy and thermal assessment in dynamic conditions. *Energy and Buildings*, 151. <https://doi.org/10.1016/j.enbuild.2017.06.051>
- Sandberg, U. (2003). The Multi-Coincidence Peak around 1000 Hz in Tyre/Road Noise Spectra. Euronoise Conference. Naples.
- Santamouris, M., Synnefa, A., & Karlessi, T. (2011). Using advanced cool materials in the urban built environment to mitigate heat islands and improve thermal comfort conditions. *Solar Energy*. <https://doi.org/10.1016/j.solener.2010.12.023>
- Taha, H. (2008). Meso-urban meteorological and photochemical modeling of heat island mitigation. *Atmospheric Environment*. <https://doi.org/10.1016/j.atmosenv.2008.06.036>
- Vardoulakis, E., Karamanis, D., Fotiadi, A., & Mihalakakou, G. (2013). The urban heat island effect in a small Mediterranean city of high summer temperatures and cooling energy demands. *Solar Energy*, 94, 128–144. <https://doi.org/10.1016/j.solener.2013.04.016>

Intrinsic Evaporative Cooling with Natural Ventilation and Shading for Adaptive Thermal Comfort in Tropical Buildings

Lokko, Mae-ling,^{1*} and Alexandra Rempel²

¹School of Architecture, Rensselaer Polytechnic Institute, Troy NY 12180, USA

²Environmental Studies Program, University of Oregon, Eugene OR 97403, USA

*Corresponding email: lokkom2@rpi.edu

ABSTRACT

Hygroscopic materials, including earth- and plant-based materials used in tropical vernacular architecture, often sorb significant moisture from the atmosphere during humid nighttime hours; evaporation the following day then provides a pronounced cooling effect, particularly in semi-arid regions. While such intrinsic evaporative cooling is also active in wet-tropical climates, it cannot maintain indoor comfort, and vernacular structures are highly open to facilitate air movement. Recently, new hygroscopic materials have been developed from coconut agricultural wastes that show great potential for intrinsic evaporative cooling and indoor humidity control in contemporary tropical buildings. As expected, however, they must be combined with additional cooling strategies to maintain thermal comfort. This investigation explores the integration of intrinsic evaporative cooling with natural ventilation and shading to determine the extent to which indoor thermal comfort, as evaluated by the ASHRAE 55 adaptive thermal comfort standard, may be maintained in the representative wet-tropical climate of Ghana, West Africa.

KEYWORDS

intrinsic evaporative cooling, hygroscopic, agrowaste, natural ventilation, passive cooling

INTRODUCTION

Hygroscopic materials, including adobes, grasses, fibers, and leaves used widely in tropical vernacular buildings can sorb significant moisture from the atmosphere during humid nighttime hours; evaporation the following day can then offset appreciable solar gains. This phenomenon, termed intrinsic evaporative cooling, has recently been characterized in diverse earth materials and semi-arid climates (Rempel 2016) as well as in agrowaste fibers and fiberboards in humid and subtropical climates (Lokko 2016). Intrinsic evaporative cooling in itself, however, cannot maintain indoor comfort in humid tropical climates (Lokko 2016). While moisture sorption by hygroscopic agrofiber envelope materials has previously been shown to lower indoor humidity to as little as 70% of outdoor daytime levels (Lokko 2016), indoor operative temperatures remained outside adaptive thermal comfort standards (ASHRAE 2017) and higher than outdoor conditions. The present study addresses these comfort issues by incorporating the effects of shading and natural ventilation, using window operation strategies common in tropical cities like Accra, Ghana, and evaluating results in light of the adaptive comfort standard (ACS) to reflect the relaxation of thermal expectations and higher levels of perceived control observed in naturally ventilated buildings (Brager 1998). Following natural ventilation strategies used in vernacular and contemporary buildings, which facilitate air movement through occupied zones, this work studies the impact of shading and natural ventilation on two scales of window openings. While the ACS applies to sedentary activity and may not account for the changing thermal preferences of tropical building inhabitants who have become accustomed to air-conditioning, it is used here to reflect the broad thermal adaptation typical of people living in the tropics.

METHODS

A simple gabled rectangular building with multiple window and shading configurations was

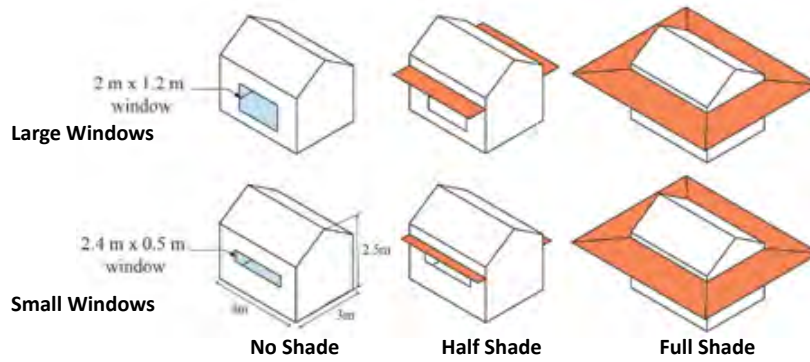


Figure 1. Study building dimensions, window configurations, and shading elements.

modeled in EnergyPlus 8.7, using Euclid 0.9.3 for geometry input (Fig. 1). Oriented along the east-west axis, the roof and walls were simulated as hygroscopically-active coconut fiberboard assemblies surrounding a tiled concrete floor in contact with the ground. Internal gains assumed a single occupant, with a sensible heat fraction of 0.3, activity level of 90-120 W/person when occupied, and 5pm-9am residential occupancy. To understand heat, air, and moisture transfer patterns, the EnergyPlus Heat and Moisture Transfer (HAMT) algorithm was used to simulate the effects of evaporation from, and condensation onto, building materials following established procedures (Rempel 2016). Infiltration and natural ventilation were simulated with airflow networks, allowing EnergyPlus to calculate wind pressure coefficients from the orientations of wall and roof surfaces with respect to wind speed and direction. Infiltration, active in all models, was governed by an air mass flow coefficient of 0.001 kg/s at reference conditions of 20°C with a cross-crack pressure difference of 1 atm, for wall and roof assemblies, and 0.01 kg/s at the same reference conditions for window perimeters, reflecting typical construction practices. Natural ventilation, in turn, assumed openable areas equal to the window areas specified (Fig. 1), with discharge coefficients estimated conservatively at 0.65. To reveal the effect of natural ventilation on indoor operative temperatures, independent of shading, models possessing either small or large windows (Fig. 1) were simulated with a baseline condition of closed windows (i.e. with infiltration only) and with two predominant ventilation control practices found in Ghana in the hottest months: one with windows open only during the day, and one with windows open both day and night. Natural ventilation was anticipated to improve thermal comfort in three ways: first, by removing warm indoor air and replacing it with cooler outdoor air; second, by cooling thermal mass; and third, by increasing indoor air velocity, thereby accelerating evaporation of moisture from skin and effectively expanding the thermal comfort zone. Because of this, building indoor operative temperatures (°C) and air velocities (m/s) were compared to adaptive comfort boundaries in each case. All simulations used the SWERA weather file for Accra, Ghana, and results were reported for one representative week in March, the warmest month of the year.

Table 1. EnergyPlus Model Parameters

Construction	Material	Density (kg/m ³)	Thickness (m)	<i>k</i> (W/m-K)	<i>c</i> (J/kg-K)
Exterior Floor	Heavyweight concrete	2240	0.1016	1.95	900
	Ceramic tile	1920	0.0127	1.59	1260
Coconut Wall	Coconut Fiberboard	1100	0.00952	0.36	4379
Coconut Roof	Coconut Fiberboard	1100	0.00952	0.36	4379
	Coconut Fiber mat	155	0.00318	0.03	4102
Window Glazing	Clear uncoated glass	-	0.003	0.90	0

RESULTS

Intrinsic evaporative cooling. Typical outdoor air temperatures in Accra, Ghana in March, the warmest month of the year, fluctuate from the high 20's to low 30's Celsius, while outdoor relative humidity typically rises above 80% overnight but falls to ~60% at mid-day (Fig. 2a). Sorption of moisture from humid nighttime air by hygroscopic coconut fiber materials is evident in latent heat transfer into wall and roof surfaces, shown by negative values. Evaporation from these surfaces, in turn, which provides cooling, is shown by positive latent heat flux values, resulting in an average daytime evaporative cooling effect of ~50 W/m² for wall and ~15 W/m² for roof surfaces. While this process effectively diminished indoor relative humidity compared to outdoor levels (Fig. 2a), indoor temperatures remained uncomfortably high (e.g. Figs. 3a, c).

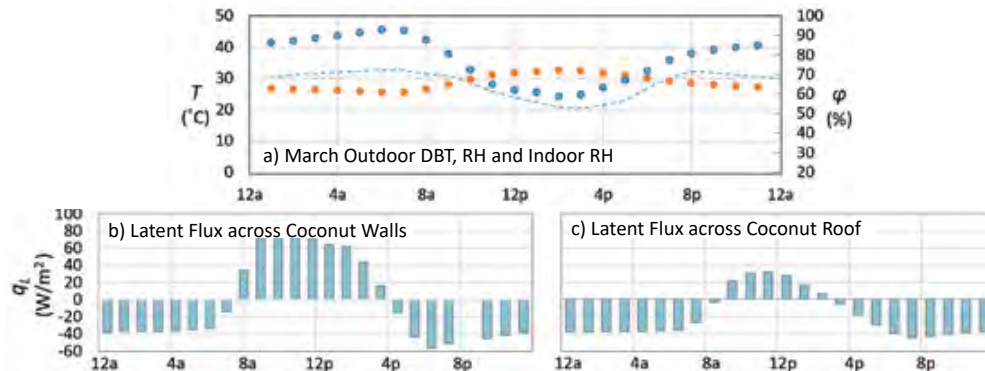


Figure 2. Intrinsic evaporative cooling in the study building, showing a) March outdoor air temperatures (orange dots) and relative humidities (blue dots) and indoor relative humidity (blue dashes), as well as latent heat fluxes across b) coconut fiberboard walls and c) roof surfaces.

Natural ventilation. Without natural ventilation, i.e. with only infiltration to exchange indoor and outdoor air, indoor operative temperatures reached ~40°C at mid-day, with small-windowed models remaining only slightly cooler than the large-windowed counterparts (Figs. 3a,c). This shows the importance of heat transfer through the lightweight, relatively conductive coconut envelope panels, which contributed more than window solar transmission or infiltration to total heat gain. At the same time, this envelope allowed “No Vent” models to cool to near-outdoor temperatures each night, such that near-comfortable conditions were predicted during most occupied hours (6pm-8am). Adding daytime ventilation (8am-8pm) diminished daytime operative temperatures dramatically, lowering peak values by about 6°C in the days shown (Fig. 4) and bringing 2-4 additional hours per day into the adaptive comfort zone, easily encompassing the occupied hours. Night operative temperatures dropped as well, though less extensively, reaching minima ~1-2°C lower than observed in “No Vent” models. This drop was associated with lower mass surface temperatures, showing that the limited mass provided (0.5cm ceramic tile over a 10cm concrete floor) was able both to sustain higher nighttime temperatures when ventilation was eliminated, and to facilitate additional cooling when it was permitted, even during the day. Adding night ventilation, i.e. opening windows for 24h daily, did not noticeably affect indoor operative temperatures in either small- or large-windowed models (Figs. 3a, c). This was unexpected, given the massive floor, but closer inspection revealed several explanations. First, March nighttime winds are typically low in Accra (≤ 3 m/s in >90% of hours), compared to daytime values of 4-6 m/s, diminishing night ventilation effectiveness. Second, infiltration exchanged sufficient air at night in the “12h Vent” model that open windows added only modest air exchange. Third, consistent with the previous two points, the mass floor did not become appreciably cooler in the “24h Vent” models, showing that the additional air exchange was not enough to lower floor mass temperatures to an extent relevant to thermal comfort.

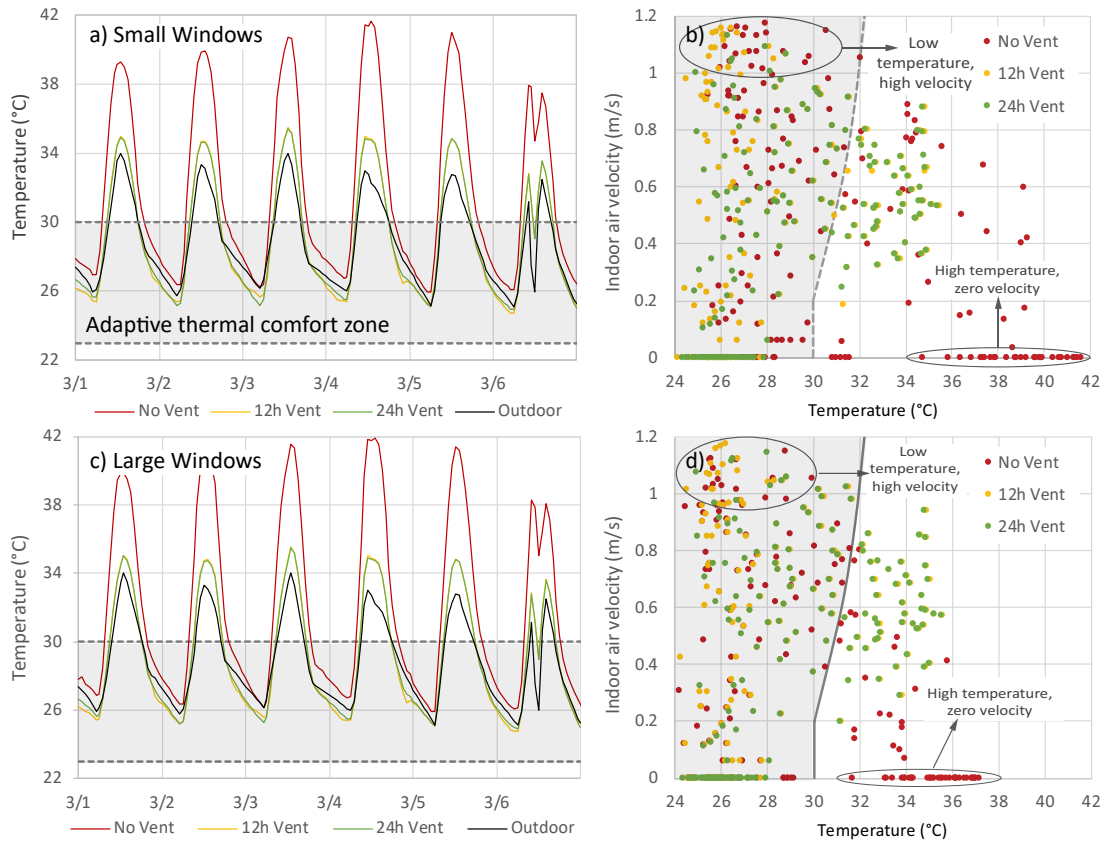


Figure 3. The predicted natural ventilation alone on indoor operative temperatures and adaptive thermal comfort (shaded areas) over six representative March days in Accra, Ghana, for dwellings with small (a, b) and large (c, d) window “Vent”: “12h Vent”: windows open 8am-8pm; “24h Vent”: windows open at all times.

To reveal whether increased air velocity brought some of the warm hours into the velocity-expanded comfort zone (ASHRAE, 2017), air velocity was next plotted against operative temperature (Figs. 3b, d). “No Vent” models predicted considerable indoor air motion from infiltration; this was calculated as a function of pressure difference across each crack, which is a function of both temperature difference and wind pressure (USDOE, 2016), with the result that high indoor air temperatures drove considerable exfiltration (coinciding with calm indoor air, shown as pronounced rows of high-temperature, zero-velocity symbols (Fig. 3). Adding daytime ventilation (“12h Vent”) replaced this hot-hour exfiltration with cooler air of considerably higher velocity, allowing thirteen hours with operative temperatures $>30^{\circ}\text{C}$ to enter the velocity-expanded comfort zone over a six-day period, or $\sim 2\text{h}$ per day. Adding all-day ventilation (“24h Vent”) had little effect on daytime conditions, as expected, but diminished the bursts of infiltration-driven high air velocity that occurred during the coolest hours of the night in the previous two models, replacing them with steadier, lower-velocity air movement.

Shading. The cooling effect of shading alone was investigated by comparing a configuration with no shade at all (“No Shade”) with two having external overhangs that shaded half or all of the south-facing wall at noon, including the entire south-facing window in both cases (“Half Shade” and “Full Shade”, respectively). As expected, shading noticeably lowered indoor temperatures: while unshaded models reached peak operative temperatures of $\sim 40^{\circ}\text{C}$ on typical March days (Fig. 4), far beyond the thermal comfort range, half-shading reduced these peaks by $1\text{-}1.5^{\circ}\text{C}$, and full shading reduced them by $2\text{-}3^{\circ}\text{C}$, providing significant cooling given the un-

shaded, relatively conductive roof. Shading alone did not, however, bring additional hours into the adaptive comfort zone (Fig. 4), showing that further cooling measures would be necessary.

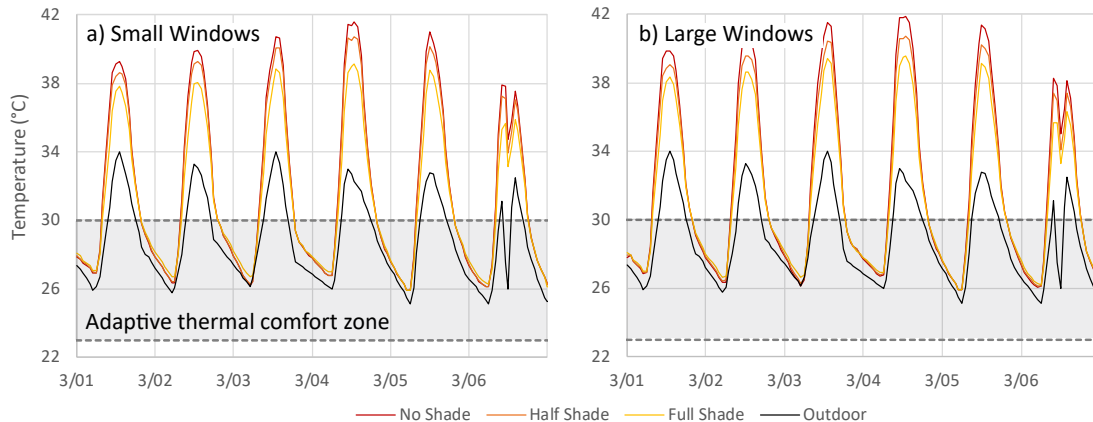


Figure 4. The predicted effect of shading alone (i.e. without natural ventilation, apart from infiltration) on indoor operative temperatures and adaptive thermal comfort (shaded areas) in six representative March days in Accra, Ghana, for dwellings with small (a) and large (b) window configurations. “No Shade”: windows are unshaded at all times; “Half Shade”: walls are half shaded at noon by exterior overhangs; “Full Shade”: walls are fully shaded at noon by exterior overhangs.

Combinations. Since shading showed cooling ability independent of natural ventilation, combinations of “12h Vent” and “24h Vent” with “Half Shade” and “Full Shade” were next investigated. As expected, these out-performed each individual strategy, reducing peak operative temperatures by $\sim 1^\circ\text{C}$ each day in both small- and large-windowed models (Figs. 5a, c) and bringing them to within 1°C of the outside air temperature. They did not, however, cool additional hours below the 30°C threshold of the adaptive comfort zone; instead, additional cooling appeared confined to the warmest hours of the day. Furthermore, shading did not improve the ability of natural ventilation to bring additional hours into the comfort zone through air velocity; 12-14 warm hours were made comfortable by air movement regardless of shading level (Figs. 5b, d).

DISCUSSION

While building simulations are vulnerable to numerous sources of error, including algorithmic simplifications (USDOE, 2016), failure to capture occupant usage patterns accurately, etc., they are invaluable for revealing priorities for subsequent investigations. In this study, the modest effect of wall and window shading, combined with high heat gains through the roof, revealed the likely importance of ventilated attics that allow roofs to shade interior ceilings in such lightweight construction. Likewise, the ability of cross ventilation to expand the hours of adaptive comfort by two per day through increased air velocity suggests a valuable resource worthy of field investigation; thermal mass configurations were similarly shown to be in need of further study in this climate, with little diurnal temperature variation, given the nearly identical results generated by 12h and 24h ventilation patterns. Finally, any interdependence among intrinsic evaporative cooling, shading, and natural ventilation remains mysterious, although interaction is likely: a shaded wall is expected to evaporate less moisture, for example, while a naturally-ventilated interior might evaporate more.

CONCLUSIONS

Together, shading and natural ventilation, in the most effective combinations, lowered predicted indoor operative temperatures in the coconut-material study building from peak levels that exceeded outdoor temperatures by $\sim 10^\circ\text{C}$ to levels approximating outdoor temperatures.

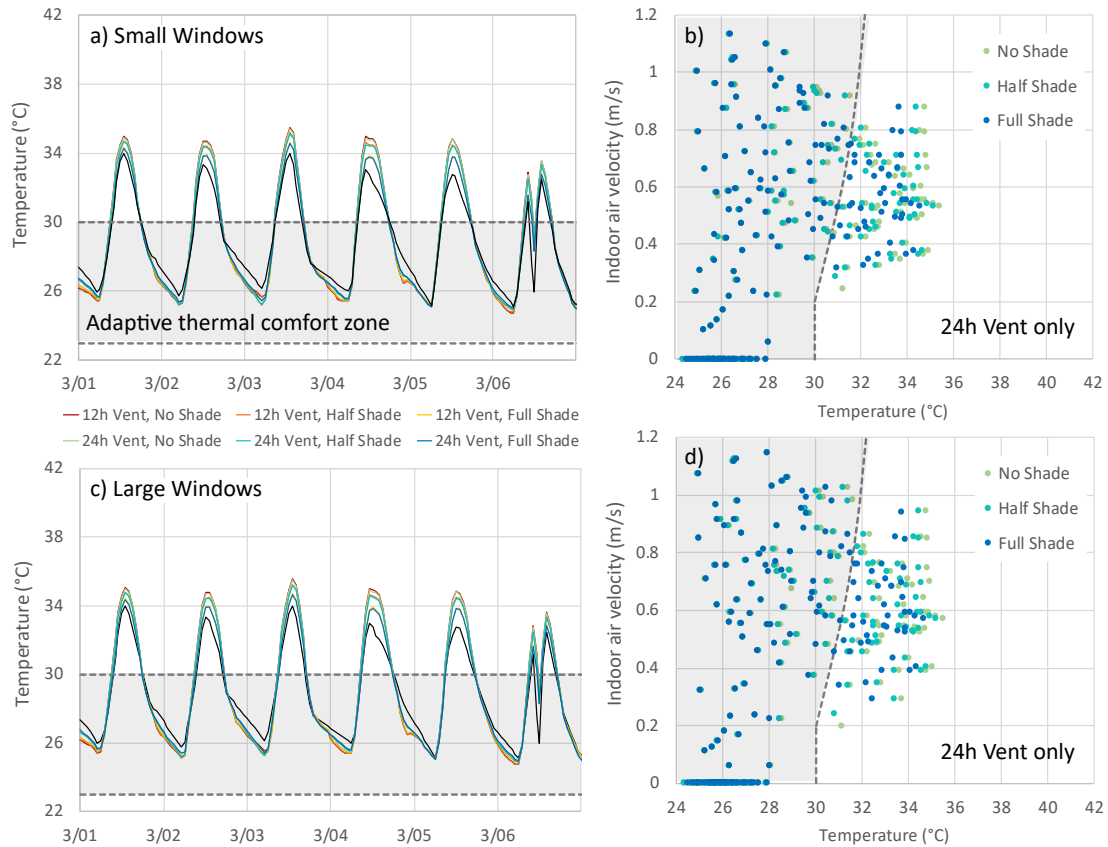


Figure 5. Predicted effects of combined shading and natural ventilation on adaptive thermal comfort (shaded) in March in Accra, Ghana, for dwellings with small (a, b) and large (c, d) window configurations. “No Shade”: unshaded at all times; “Half Shade”: walls half shaded at noon by exterior overhangs; “Full Shade”: walls fully shaded at noon by exterior overhangs; “No Vent”: infiltration only; “12h Vent”: windows open 8am–8pm; “24h Vent”: windows open at all times.

While further cooling is necessary for daytime comfort, this represents significant progress. The upcycling of local agricultural waste such as coconut husk into building materials has the potential to expand the economic value chain of coconut producers in tropical nations while producing low-embodied energy materials. Because of this, further investigations of their effective integration into buildings, allowing them to provide reliable thermal comfort without energy-intensive mechanical air conditioning, hold economic, environmental and social value.

ACKNOWLEDGEMENTS

The authors thank Alan Rempel (University of Oregon), Trevor Simmons (Rensselaer Polytechnic Institute), and Michael Rowell (e2e Materials) for their expertise and insight.

REFERENCES

- ASHRAE Standard 55. 2017. Thermal environmental conditions for human occupancy. Atlanta GA.
- De Dear, R.J., Brager, G.S., Reardon, J. and Nicol, F., 1998. Developing an adaptive model of thermal comfort and preference/discussion. *ASHRAE Transactions* 104:145.
- Lokko, M. 2016. Invention, design and performance of coconut agrowaste fiberboards for ecologically efficacious buildings (Ph.D. Thesis, Rensselaer Polytechnic Institute).
- Rempel AR, Rempel AW. 2016. Intrinsic evaporative cooling by hygroscopic earth materials. *Geosciences* 6:1-38.
- U.S. Dept. of Energy, 2016. EnergyPlus 8.7 Engineering Reference. Lawrence Berkeley National Laboratory.

Long term measurements and HAM modelling of an interior insulation solution for an office building in cold climate

Paul Klõšeiko^{1,*}, Targo Kalamees¹

¹Tallinn University of Technology, Estonia

*Corresponding email: paul.kloseiko@ttu.ee

ABSTRACT

Excessive mould damage was detected in an office building in Northern Europe and thus a renovation need was established. This paper studies a renovation solution using measurements and heat, air & moisture (HAM) modelling. Polyurethane (PUR) foam was used to fill the air gap in masonry while capillary active calcium silicate (CaSi) insulation was used on the interior surface at thermal bridges. During renovation works temperature and relative humidity (*t&RH*) and heat flux sensors were installed throughout the wall.

Nearly 3 years of measurements are presented. Average thermal transmittance (*U*) of the wall was reduced around 3 times. While the climate was probably not critical during the monitoring, the measured values stayed within hygrothermally safe limits.

The paper also compares the measurement data to 2D HAM modelling and discusses the discrepancies. Calibrated models were used to model the wall using real 42-year weather data and give a more thorough assessment of the hygrothermal performance. Although the original wall stayed fairly moist, no performance limits were exceeded and the interior surface became safer in terms of mould risk.

KEYWORDS

interior insulation, HAM modelling, capillary active, cold climate, case study

INTRODUCTION

Interior insulation has usually been disapproved in Northern Europe as a hygrothermally risky solution. However, “capillary active” insulation has gained ground in Central Europe and become a compelling choice by taking a different approach to mitigating the risks caused by insulation on the interior side (compared to traditional mineral wool + vapour barrier solution). This study took place on the last floor of an 8-storey office building (built in 1936; cultural heritage). Existing interior insulation (gypsum board, PE foil, min. wool) exhibited excessive mould damage and a renovation solution had to be found. Main challenges were: low surface temperatures, high thermal transmittance and avoidance of future biological decay. Preliminary HAM modelling showed that “closed cell” PUR foam injected into air cavities of the masonry and “capillary active” CaSi on the surface of the wall could perform well. This paper discusses the monitoring and modelling of the chosen solution.

METHODS

Measurement setup

Vertical and horizontal sections of the studied wall are given in Figure 1. The wall structure, renovation solution and sensor placement are also shown. Sensors and their positions were selected both to assess the hygrothermal situation after the insulation and to have enough reference points to calibrate the HAM models.

The following measurement devices were used: T&RH probes: Rotronic HygroClip HC2-C05 (accuracy $\pm 0.3^{\circ}\text{C}$, $\pm 1\%\text{RH}$); heat flux plates: Hukseflux HFP01 (accuracy $\pm 5\%$); data logger Grant Squirrel SQ2020 1F8 (accuracy $\pm 0.05\%$ of readings $\pm 0.025\%$ of range); temp. probes & logger: Onset Hobo UX120-006M & TMC6-HD (accuracy $\pm 0.15^{\circ}\text{C}$); T&RH data loggers: Onset Hobo U12 and UX100 (accuracy $\pm 0.21^{\circ}\text{C}$, $\pm 2.5\text{-}3.5\%\text{RH}$). Measurement interval: 1h.

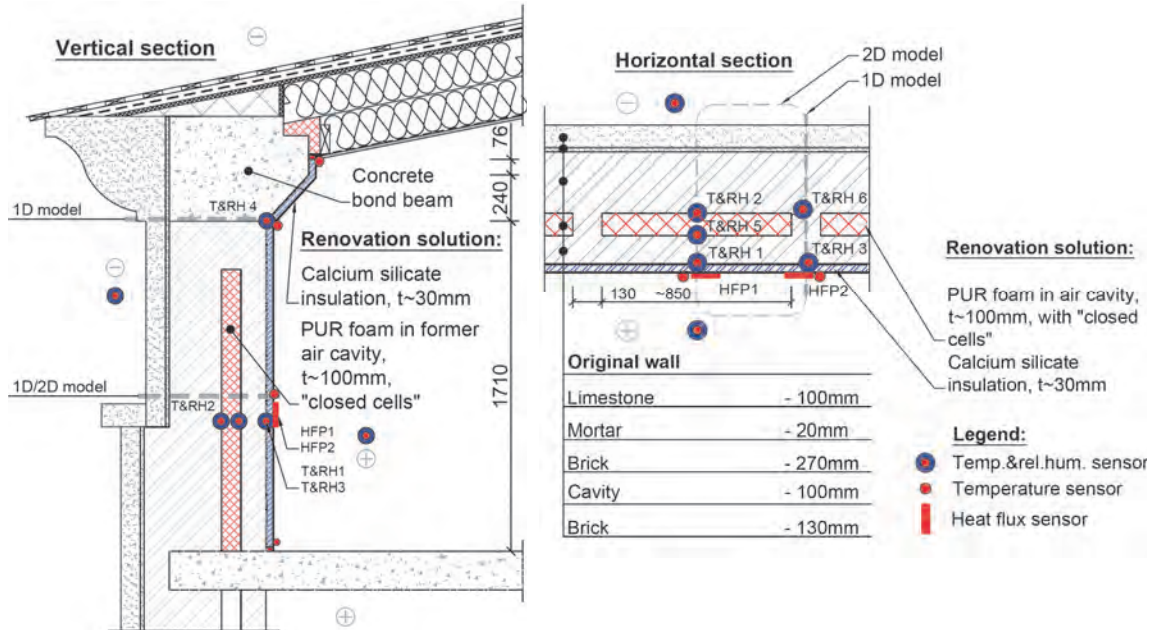


Figure 1. Vertical and horizontal sections of the wall showing sensor placement and wall layers.

Performance criteria

WTA Merkblatt 6-5 (Künzel et al. 2012) proposes to avoid frost and condensation in insulation and glue. Assessment according to saturation degree should be carried out – maximum of $30\%_{\text{sat}}$ is allowed to avoid frost damage. However, our previous research (Klůšeiko et al. 2017) showed that freeze-thaw cycling affected tensile strength of capillary active insulation material even though saturation degree stayed below the $30\%_{\text{sat}}$ limit. Therefore, slightly stricter limits of $RH_{\text{crit.}} = 95\%_{\text{RH}}$ and $t_{\text{crit.}} = -5^{\circ}\text{C}$ (Künzel 2011) are used in this study. Minimizing freeze-thaw cycles of the limestone cladding was not a criterion as conversion to ventilated façade is planned for the building.

Hygrothermal modelling

IBK Delphin 5.9.0 (Grunewald 1997; Nicolai et al. 2009) was used to model the hygrothermal performance of the exterior wall. Modelling consisted of 2 steps: 1) model calibration and 2) modelling with 42-year weather data. 1D and 2D models of the masonry section were created (while brickwork was treated as a homogenous material for both). Concrete bond beam was modelled as a 1D case. Model geometry is given in Figure 1.

During calibration, measured (t , RH (+ calculated vapour pressure), heat flux) and modelled data were compared. Then the HAM models were iteratively changed within plausible extents to achieve a better match between the two. Different bricks and concrete types from Delphin material database were tested (finally settling with ID 543 and 569 for brick and concrete respectively), PUR foam properties were fine-tuned according to limits given in its datasheet (based on ID 195; following changes were made: $\rho = 39\text{ kg/m}^3$, $\mu = 39$, $\lambda = 0.022\text{ W/(m}\cdot\text{K)}$). Rest of the material IDs from Delphin database used in models were 464, 143, 424, 21, 230.

Boundary conditions for model calibration were: t & RH (measured on site); wind, rain (measured 10km away) and solar radiation (measured 165km away). 42-year weather data (t , RH , wind, rain, solar radiation; all measured 165km away) was used to assess the performance in more critical conditions. As the indoor humidity load in the test room was very low, more critical indoor t & moisture excess profiles were used for 42-year modelling (roughly moisture class 2 given in EN ISO 13788 Table/Figure A.2). They were based on an earlier study in a similar building (Klůšeiko & Kalamees 2016).

RESULTS & DISCUSSION

Measurement results

Temperatures behind CaSi (Figure 2 top, sensors TRH1, 3, 4) were closest to limits during the winter of the first year. At sensor TRH4 (concrete section) they fell to as low as -2.5°C , but not reaching the critical -5°C . In masonry section the temperatures were higher due to PUR insulation adding further thermal resistance. Consequently, sensors on the exterior side of PUR (TRH2 shown here) measured far lower temperatures than between CaSi and concrete bond beam. Figure 2 (bottom) gives the measured relative humidities. Dryout of the built-in moisture to stable levels took about 2.5...3 months. RH values between exterior brick leaf and PUR (sensor TRH2) were quite stable (fluctuating about $5\%_{RH}$ throughout the year) after the dryout of CaSi built-in moisture.

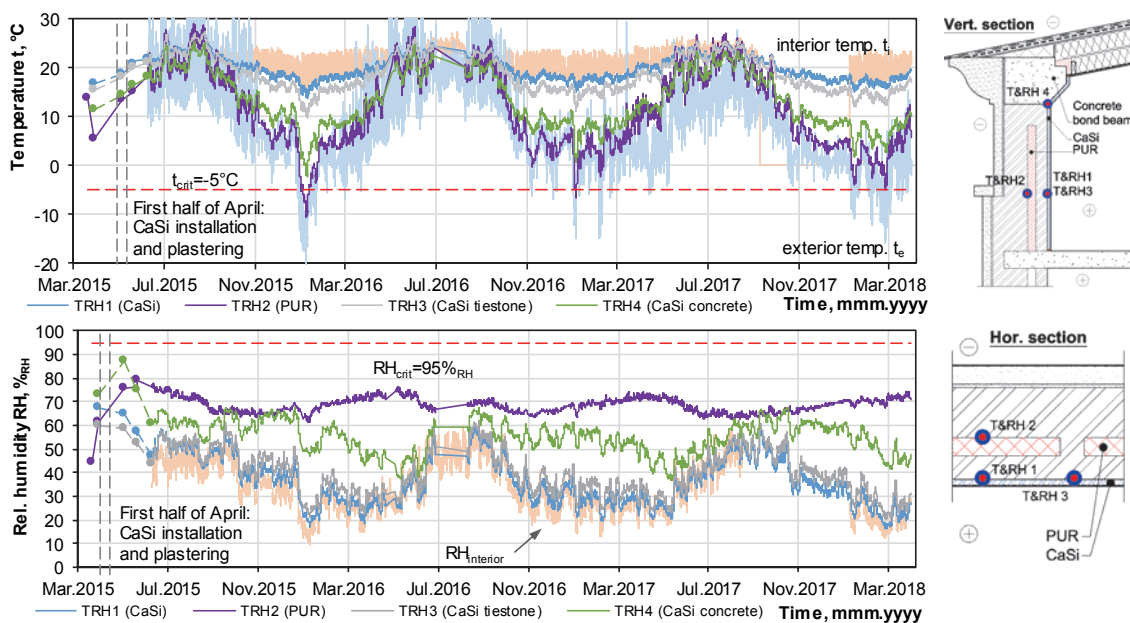


Figure 2. Measured temperatures (top) and relative humidities (bottom) throughout the monitoring period.

Moisture excess during the measurement period in the test room was very low (close to moisture class 1 according to EN-ISO 13788 A.2), as a well-functioning HVAC system was installed. Analysis of measured data hints that moisture contents of air in the pores of exterior masonry leaf are governed by outdoor climate while lagging about half a week. A $\sim 4 \text{ g/m}^3$ rise in moisture contents compared to indoor and outdoor air in autumn (mid-Aug...Oct.) is pronounced, possibly due to rain. However, moisture does not seem to be accumulating in the wall over time, which could be the case with vapour tight interior insulation and heavy wind

driven rain loads. Sensors behind CaSi insulation measured moisture contents quite close to that of the indoor air throughout the year. A lag of a couple of days was detected.

Temperature indexes (f_{Rsi}) were calculated from surface temperatures to assess mould and condensate risk on the wall surface. The worst situation was detected at wall-floor intersection ($f_{Rsi} = 0.79$) and at concrete bond beam ($f_{Rsi} = 0.83$). None of those results should indicate a risk, however, as indoor moisture load was low. f_{Rsi} values at the rest of the intersections were also considerably higher (i.e. safer).

Average heat flux and temperature data from 1. Nov. 2015... 29. Feb. 2016 was used to calculate the thermal transmittances (U) of the insulated wall (see Figure 1 for placement of the sensors). At tie bricks (HFP2) $U = 0.52 \text{ W}/(\text{m}^2 \cdot \text{K})$ was measured and between tie bricks (HFP1) the value was $U = 0.31 \text{ W}/(\text{m}^2 \cdot \text{K})$. 2D thermal transfer modelling of the insulated structure results in average thermal transmittance of $U = 0.39 \text{ W}/(\text{m}^2 \cdot \text{K})$, which is ~ 3 -fold reduction compared to the uninsulated case ($U = 1.14 \text{ W}/(\text{m}^2 \cdot \text{K})$).

Calibration of HAM models

Results from the models which achieved the best fit and positions that are most relevant to the assessment criteria are presented here. Figure 3 shows data from TRH2 (between CaSi and tie brick) and TRH4 (between CaSi concrete bond beam). Relative humidity is given as it integrates the errors in thermal and moisture calculations.

Agreement of calculated and measured temperatures (TRH3 2D model; TRH4 1D model) was within $\pm 1^\circ\text{C}$ for most of the year with overestimation of temperatures by $2 \dots 3^\circ\text{C}$ taking place in summer (possibly due to deficiencies in solar modelling of the south facing wall). TRH3 1D model exhibits too low temperatures which results in higher than measured RH . Modelled RH values exhibit less fluctuation in all cases, however, that seems to be the characteristic of the Delphin program (Klöße et al. 2015; Klöße & Kalamees 2016; Klöße et al. 2017). 24h avg. heat fluxes in masonry section achieved less than $\pm 1 \text{ W}/\text{m}^2$ ($\sim 5 \dots 10\%$) difference for most of the heating period using 2D model; in case of 1D models, the errors were 4...8 times higher. Possible sources of errors could be: material data (limestone as location specific and inhomogeneous material; only basic parameters were measured for brick), unknowns concerning the actual wall structure, wind driven rain modelling, solar radiation modelling.

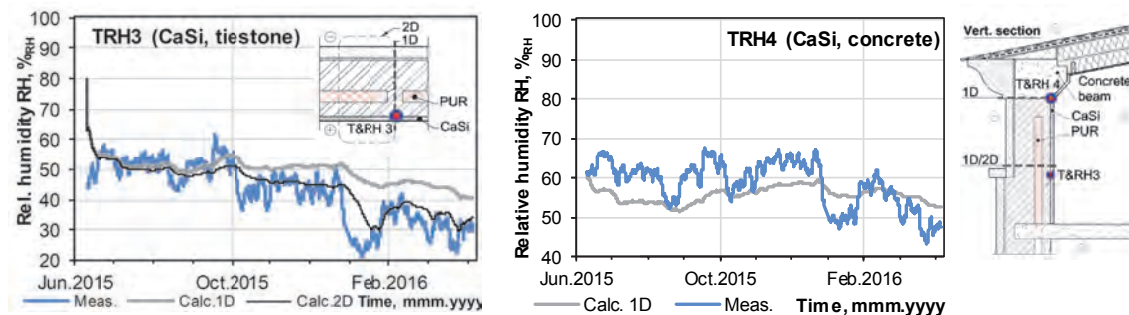


Figure 3. Comparison of measured and modelled relative humidities at TRH3 (between CaSi and tie brick; left) and TRH4 (CaSi insulation on top of concrete; right).

The correlation between measurements and modelling was deemed satisfactory. For performance assessment of CaSi insulation the 1D model of the masonry section might be good enough as the errors on that part were conservative. However, as wind driven rain could cause accumulation of moisture in the exterior masonry leaf, 2D model is also necessary.

Modelling with 42-year weather data

Due to limited space only the most critical point in the wall (TRH4 behind CaSi on concrete bond beam) is discussed here. Modelled t & RH values are given in Figure 4. Yearly minimum temperatures and maximum relative humidities are shown so the most critical year can be highlighted. In the case of TRH4, the 1986/1987 season was the harshest and is shown in Figure 4 (right). Yearly maximum relative humidities are much more stable than temperatures. “Flattening” the peaks of the RH graphs is possibly due to relatively high moisture capacity and redistribution of moisture in both concrete and CaSi.

Figure 4 also illustrates that 42-year modelled t & RH are far more critical than measured values. While lower t is largely the result of colder outdoor climate, the significantly higher modelled RH are caused by using higher indoor moisture load.

During 10 out of 42 years (~24%) t behind the insulation fell below critical -5°C . Still, RH was far below the 95% $_{RH}$ limit. Thus, according to the modelling data, frost damage in insulation system will not be a problem and the solution could be approved for use in the rest of the building. However, as previous research (Binder et al. 2013; Klůšeiko et al. 2017) has shown, the modelling results of “capillary active” materials can also be non-conservatively skewed, especially when higher moisture contents are concerned and values are closer to the performance limits. To overcome that, development of improved liquid and vapour conductivity curves for CaSi as well measurements of limestone and brick properties are in progress.

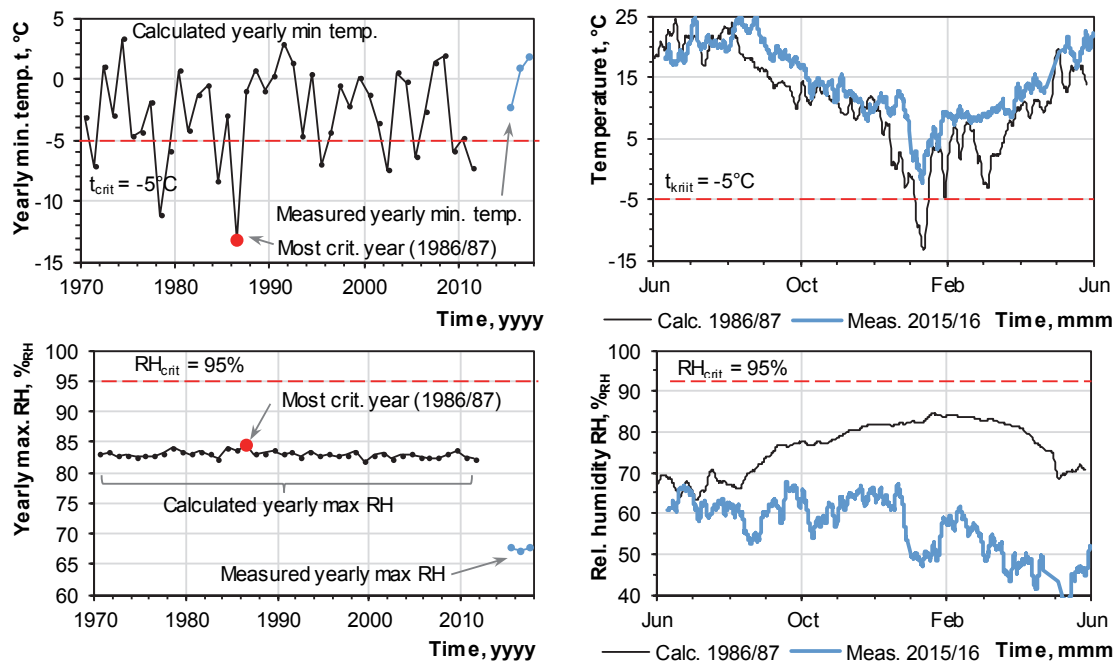


Figure 4. Most critical point in the wall (TRH4 – betw. CaSi insulation and concrete beam): yearly min. temperatures (top left) and max. rel. humidities (bottom left) of the 42-year HAM modelling and hourly values for the most critical year (right) compared to the measured values.

CONCLUSIONS

Measurements show that interior insulation can perform well at least if HVAC systems function nominally. Wind driven rain did not cause a notable accumulation of moisture on the exterior side of “vapour tight” PUR foam. Comparison of modelled and measured data shows that 2D modelling should be used for this type of structure. If interior insulation layers are thin, the HAM models can still fairly adequately portray the processes behind the insulation even if detailed material data for existing wall is unavailable.

Modelling results suggest that even in the case of increased moisture load, the CaSi boards are quite a robust solution and provide an extra layer of safety thanks to quite high moisture capacity and lack of biological decay. Modelling with long-term weather data gives an increased confidence in the results. For example, if test reference years are used, the principle of their selection might not always match that of the current modelling aim. Also, the measured data was far on non-conservative side compared to 42-year modelling results, partly due to current winters being quite mild. To test an experimental structure in more critical boundary conditions, modelling with historic data and calibrated model can be a viable option.

ACKNOWLEDGEMENT

This research was supported by the Estonian Centre of Excellence in Zero Energy and Resource Efficient Smart Buildings and Districts, ZEBE, grant TK146 funded by the European Regional Development Fund, and by the Estonian Research Council, with Institutional research funding grant IUT1-15 “Nearly-zero energy solutions and their implementation on deep renovation of buildings”. The authors wish to thank Tallinn City Government for fruitful collaboration and Estonian Weather Service for providing the weather data.

REFERENCES

- Binder, A., Künzel, H.M. & Zirkelbach, D., 2013. A new approach to measure liquid transport in capillary active interior insulation. In *Proceedings of 2nd Central European Symposium on Building Physics*. Vienna.
- Grunewald, J., 1997. *Diffusiver und konvektiver Stoff- und Energietransport in kapillarporösen Baustoffen*. TU Dresden.
- Klõšeiko, P., Arumägi, E. & Kalamees, T., 2015. Hygrothermal performance of internally insulated brick wall in cold climate: A case study in a historical school building. *Journal of Building Physics*, 38(5), pp.444–464.
- Klõšeiko, P. & Kalamees, T., 2016. Case study: In-situ testing and model calibration of interior insulation solution for an office building in cold climate. In *CESB 2016 - Central Europe Towards Sustainable Building 2016: Innovations for Sustainable Future*.
- Klõšeiko, P., Varda, K. & Kalamees, T., 2017. Effect of freezing and thawing on the performance of “capillary active” insulation systems: a comparison of results from climate chamber study to HAM modelling. *Energy Procedia*, 132, pp.525–530.
- Künzel, H. et al., 2012. Innendämmung nach WTA II: Nachweis von Innendämmsystemen mittels numerischer Berechnungsverfahren (Merkblatt 6-5).
- Künzel, H.M., 2011. Bauphysik der Innendämmung und Bewertungsverfahren. In *1. Internationaler Innendämmkongress 2011*. Dresden: TU Dresden, pp. 9–16.
- Nicolai, A. et al., 2009. An efficient numerical solution method and implementation for coupled heat, moisture and salt transport: The Delphin Simulation Program. In *Simulation of Time Dependent Degradation of Porous Materials*.

New Technology Creates New Lightscape

Jianzhen Qiu^{1,2} and Shuoxian Wu^{1,2}

¹Dept. of Architecture, South China University of Technology.

²Key state Laboratory of Subtropical Building Sciences of China

*Corresponding email: jzqiu@scut.edu.cn

ABSTRACT

Light is a key element of our world's beauty. Chinese scholar Wu Shuoxian put forward the concept of "Lightscape", and proposed its research as a parallel discipline of the "Soundscape". As a special aspect of the visual-scape, lightscape can give us a comprehensive and multi-disciplinary perspective of living environment. Many traditional lightscape cases have always been remembered as the representations of specific regional cultures. This article presents several cases of modern lightscape created with new technologies and methods. Included in these cases are: outstanding lightscape and art installments created by artists using light as a key element and fulfilled with the help of new materials; preservation of nostalgia by transforming and flourishing the traditional lightscape; multidisciplinary cooperation where artists, scientists and engineers use digital technology and biology knowledge to create intriguing lightscape.

KEYWORDS

Lightscape Lighting technology creation

INTRODUCTION

The concept of lightscape, put forward by the Chinese scholar Wu Shuoxian as a special aspect of visual-scape, refers to the special visual-scape that utilizes light source, shadow and their transformations to form landscape and to invoke strong visual impression. We advocate it as a parallel discipline of "soundscape" and "smellscape", so that it can play an important role in inheriting human culture and creating a human habitation for a better living (Wu Shuoxian, 2017) .

Since antiquity, the significance of light has gone beyond the practical level of delivering information. As a unique aspect of visual-spect, lightscape has specific records and meanings in various cultures. Historically, there was appreciation of the natural lightscape as well as the description of artificial light-based scenery. For instance, in China, the torch festival in minority areas is originated from primitive times ceremonies where the laboring people commemorated the harvest. The Lantern Festival, began at Han Dynasty, celebrates the first full moon night of the New Year. actually, the whole human-world has been creating wonderful lightscapes for thousands of years. This paper aims to tell that, with the help of new technology and its application, creative artificial lightscape will emerges constantly.

1. NEW LIGHTSCAPES AROUND THE WORLD

Human's beauty-love instinct is global. Civilization has been given new connotation by the developing science. Wonderful lightscape works supported by new technologies amaze people all over the world.



Fig.1 Light Show, Giza, Egypt
picture taken from:
<http://www.nipic.com>

1.1 Breathtaking light shows

There are light shows coming forward in well-known cities and famous scenic spots around the world. Compared to traditional performance, those emphasize more on the combination of light, shadow and other medias, with the addition of various means including music and installation art, to give a comprehensive sensory experience to live audiences.

Light and Sound Show of the Pyramids The Light and Sound Show in the Giza region, Egypt, uses dramatic narration means to present the tales of pyramids, the sphinx and influential persons. During the show, lasers are projected on the pyramids to form the shapes of inner structures, along with explanations. Accompanied by a mysterious voice that seems to come from ancient times, lights are cast on the pyramids making diversiform shadows. This hour-long show tells the story of ancient pharaohs in such a vivid way, that the audiences indulge in it as if they have taken an journey through the time.

Dame de Cœur of Notre-Dame De Paris To mark the centenary of the end of the first world war, Notre-Dame De Paris dedicated the "Dame DE Coeur" 3D sound and light show directed by Bruno Seillier in November 11, 2017. In virtue of the touching story of a soldier and a nurse, history had a dialogue with art across the time. The magnificent and eye-dazzling 850-year-old Notre Dame cathedral was granted a full-bodied sense of technology. The frontal lines, the sculptures on the exterior wall and projections were fused with each other. Classic paintings joint performance of firework were all exhibited in 3D perspective.



Fig.2 light show, Notre-Dame De Paris,



Fig.3 Artwork, Guggenheim Museum Bilbao
picture taken from:
<https://www.theguardian.com>

Artwork of Guggenheim Museum Bilbao On October 2017, Guggenheim Museum Bilbao created a 20-minute public artwork for the 20th anniversary of Frank Gehry's architectural masterpiece in Spain. This artwork combining light, music and projection were played on a loop across four evenings. 59 Productions, the world leader in projection-mapping, was commissioned to produce a 20-minute public artwork called Reflections. This special anniversary program celebrated the role this museum has been playing in making Bilbao and the Basque region a thriving artistic centre.

1.2 Famous light festivals around the world

Lyon Festival of Lights The Lyon Festival of Lights, held on December and usually lasts for four days, is a centuries-old religious tradition where people use candlelight to express gratitude toward gods.

Today, the festival does still retain the art form of candlelight: every house still places candles along the outsides of all the windows to produce the spectacular ambience throughout the streets; a romantic candle show is held in Odeon of Lyon every year. On the other hand, it also integrates modern lightscape that sparkles in this old city: there are contemporary lighting artworks in the center and dozens of other places on the periphery, where sound, light, electricity, lasers and 3D special effects are widely used. The whole city is checkered with light and shades, attracting artists from France and all over the globe to show their talent here. Among pieces of



Fig.4 Lyon Festival of Lights
picture taken from:
<http://www.sohu.com>

art equipment, we can find some amazing works of traditional culture, such as the elegant colored drawing LUMIÈRE DE VERRE, Homer's epic Odysseus, were expressed using modern techniques. A astonishing and modern light and sound show is staged annually in the front of the gothic cathedral Saint-Jean Baptistete.

In Lyon, traditional and modern lightscape coexist ideally in harmony.

Vivid Sydney Light Festival Vivid Sydney light festival, started in 2009 as the smart light festival which promoted energy conservation , has become a famous stage for universal creativity competition. During the 3 weeks from May to mid-June every year, there are tens to hundreds of exhibitions and events, including lighting sculpture, multimedia interactive works, as well as the show of water, fog, light and shadow. Most astonishing among those are the projections of landmark, including the eye-catching super light show of Sydney Opera. In Vivid Sydney, the public are guided to communicate and have a discussion on art, where they have sufficient chances to interact with unique lighting technology.

So much unprecedented lightscape has been created thanks to technology development; in correspondence, unique lightscape also shortens the distance between those technologies and human.



Fig.5 light show, Sydney opera,
Vivid Sydney
picture taken from:
<http://www.poco.cn>

2. NEW LIGHTSCAPES IN CHINA

As China grows in economy, science and technology, there have been many high-profile events held in China in recent years, including G20, Fortune Global Forum 2017 and other worldwide theme activities. Guangzhou International Light Festival has been held annually for 7 years, and in 2015 was selected to International Year of Light large-scale cultural event by UNESCO(United Nations Educational, Scientific and Cultural Organization), with a special recommendation on the website of International Year of Light.

2.1 Group of 20, 2016, Hangzhou, China.

On October 2016, Hangzhou city undertook the G20 conference. Hangzhou, located in East China, is the most beautiful landscape city of China with the world-renowned west lake scenic spot. Zhang Yimou, the chief director of the opening ceremony of 2008 Beijing Olympic Games, directed a overwater artistic performance "Enduring Memories of Hangzhou" for G20, in which the application and effect of high-tech light and shadow was unprecedented. With the stage set 3cm under water, the traditional atmosphere “ glistening wave and reflective water” of Chinese gardens was best portrayed. The show used the Pepper's ghost holographic projection technology to integrate images into the show harmoniously, where the performers were even able to interact with the lights. It was hard to tell the authenticity of bridges, lotus pond and pavilions in the view of natural lake, trees and mountain; the combination of light, music, scenery and performances brought audiences into the wonderland of Chinese classical landscape beauty.

Swan Lake ballet on water On the west lake, graceful dancers performed the classic ballet Swan Lake while shuttling through the milky way of an ancient bridge. This program uses holographic projection where real actors and virtual images interacted and completed the performance together. One of the most breath-taking scenes was: under the arched light bridge between landscape, a little swan appeared gracefully. After



Fig.6 Swan Lake ballet on water
picture taken from:
<http://www.wekeywu.com>

several challenging rotations, it split into 2 little swan, then 4, then 8... Suddenly, a group of swan girls magically appeared, and danced lightly, unanimously and gorgeously.

Piano playing “Clair de lune” Moonlight has always been an important part of the west lake scenery, evidenced by the natural lightscapes "Autumn Moon over the Calm Lake" and "Three Pools Mirroring the Moon". The performance combined the moonlight with the piano piece "Clair de lune", one of the most well-known works by French composer Debussy. When the smooth and stretched music was played craftily by the pianist, LED lights shaped the poetic hazy background atmosphere. The holographic projection of the moon entwined with the reflection of the moon in the water, coupled with the distant picturesque nightscape, composed a modern view of the west lake lunar landscape.

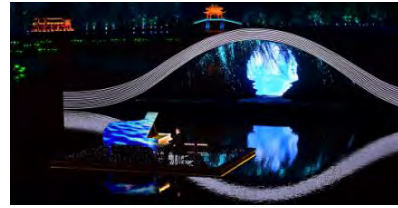


Fig.7 Piano playing "Clair de lune"
picture taken from:
<http://www.xinhuanet.com>

Play "A Beautiful Love Story" "The Butterfly Lovers" is one of the four folk love stories in ancient China, which tells the tragedy of a pair of young lovers who fell in love with each other but could not stay together, and reputedly they turned into two concomitant butterflies in their deaths. The play "A Beautiful Love Story" is based on this myth. On the performance, when two dancers danced to the waves like two chromatic butterflies flying to the center of the stage, a huge fan was slowly unfolded from the surface of water. Then, patterns on the fan transform continually between various elements of traditional Chinese realistic painting including peony, orchid, peacock, blue and white porcelain, landscape and human characters. As the story continues, the fan rotates tridimensionally following the rhythm of music until the last note gradually fades away. Finally, the giant fan submerged into the water and the lake returned to calmness.

The fan is a traditional Chinese handicraft as well as a special local product in Hangzhou. This special mechanical folding fan, believed to govern a representative temperament of Hangzhou, measures up to 20m in diameter with a total weight of 20 tons. When spread out, the fan becomes an upright screen for well-designed 3D video to project on using 3D mapping. When it is furled, it is hidden underwater. The opening and closing of the fan have achieved precise synchronization with the live music, the video projection and dance tempo of the dancers in the performance.



Fig.8 play, "A Beautiful Love Story"
picture taken from :
<http://www.wekeywu.com>

2.2. Guangzhou International Lighting Festival

Guangzhou is a diversified southern metropolis. Over 2200 years of history blesses it with a deep traditional culture as well as opening, innovative and inclusive temper.

Beginning in 2011, at the end of every year, the Guangzhou International Lighting Festival is held at Flower City Square on the "new city axis of Guangzhou". The festival revolves around different themes each year and each has its own merits; for example, in 2015, representatives from Lyon, Sydney and Singapore were invited to communicate in present, and the 3D projection work "Illusion", which had shined on Vivid Sydney, was on display, while "People Screen" connected Perth in Australia with Guangzhou via internet.

The lighting festival has now become a tourist interest in Guangzhou. The 2017 Guangzhou Lighting Festival lasted for 24 days, had served more than 8 million people; moreover, the original artwork "Rain Beating Plantain" will visit Guangzhou's sister city Lyon for its lighting festival.

3D Print Work: Butterfly-changing Canton, 2016

The annotation of metamorphosis in Chinese represents a striking change towards perfection, similar to the rapid transformation of a pupa into an butterfly. At the main venue of 2016 Guangzhou International Light Festival, two gaudily-dressed "butterflies" perched on the side pool of Guangzhou Grand Theatre, contrasting with the streamlined main building of the very



Fig.9 The Butterfly-changing Canton, picture taken from: <http://itbbs.pconline.com.cn>

dynamic Theatre. To demonstrate the connotation of another butterfly-changing of Guangzhou city as the capital of commerce for thousands years. This work is actually an experiment in the field of architecture, as a bold attempt combining 3D printing technology and architectural digital design. The big "butterfly" span up to 6.6m and is 12 meters long, with only two supporting points, but the body part is only 3.8 cm thick. Its irregular hyperbolic form and texture are like the microscopic veins of the leaves. The entire set of the thin shell weighs 500 kg and was assembled from nearly a thousand units printed by 50 3D printers.

"Rain Beating Plantain", 2017 Canton music is one of the traditional Chinese local musics, and "Rain Beating Plantain" is the most representative and well known. Plantain, also known as Chinese banana, is a common native plant in Guangdong. 《The artistic lightscape installation "Rain Beating Plantain" involves environmental elements that frequently appear in Canton music such as plantain, moonlight, mini bridges, lotus leaves and colorful cloud, with the virtual rain scene to strengthen austral atmosphere, all created with light. The main artwork is formed with LED light source; the light outlines shape of plantain leaves and their venation. The moon in the background is made up of LED light pixels, which projects changeable clouds, and the luminance changes following the rhythm of the background music. As a gesture of friendly communication, this lightscape artwork is going to attend the festival of Lyon. There will be interactive factors added at the time, making the production more interesting.



Fig.10 "Rain Beating Plantain" picture taken from: <https://mp.weixin.qq.com>

2.3 Fortune Global Forum 2017, Guangzhou, China.

Fortune Global Forum is one of the most influential financial forums in the world, and the vibrant city Guangzhou was chosen to host it in 2017. More than 1000 business leaders, politician and economists attended.

Drone Formation Performance In the evening of December 7th, a welcome cocktail party was held in Canton Tower, while 1180 unmanned aerial vehicles flew over the Pearl River, performing a 8 minute technological dance. First, the drones formed the Chinese character "财富", which means "Fortune", and then changed to "FGF". Then, the formation transformed into different patterns, in the order of ship(Since Guangzhou is an old port city), the Chinese character "开放", "创新" which means correspondingly "open" and "innovation", English letters "I LOVE GZ", and last but not least the map of China, which marked the end of the show. Only 1 computer was needed to control the total of 1180 flying drones, and the error tolerance of precise positioning was 2cm. The lighting sets carried on the drones can create 60 thousand kinds of color, and change intensity as freely as



Fig.11 the drones formed the Chinese character "财富" picture taken from: <http://gd.people.com.cn>

breathing lights, which means designers can construct almost any pattern as they wish.

River Bank Animation Show Guangzhou is close to the South China Sea. It has been the departure port of Ancient Maritime Silk Road, and was the only port open to the oversea merchants in Qing dynasty. As the Pearl River flows from west to east across the urban area of the city, the beautiful scenery on both sides is an important tourist resource of this city with intriguing history and culture.

During the 2017 Fortune Global Forum, guests took a cruise along the "Pearl River Night Tour" route to enjoy the lightscape animation that was shown on continuous facades of the 24 buildings on the north shore. The animation called "Stories of Guangzhou" is ten minutes long, divided into two parts. The first part, called "Southland Pearl, Thousand Years", depicts the prosperity of the ancient "Maritime Silk Road"; the second part, called "Amorous City of Lingnan", shows the traditional culture of porcelain, jade, tea culture, spices, embroidery, food culture, as well as characteristic Lingnan elements such as gardens, fruits, kapok, carp and lotus pond. This work utilized 210 thousand efficient LED lamps, which were coordinately controlled on the big data platform. The installation lasted for four months, involved the cooperation of as many as 1500 construction workers, including 500 steeplejacks.



Fig.13 cars play in the water
picture taken
from: <http://s.dianping.com>



Fig.12 the map of China
picture taken
from: <http://news.sina.com.cn>

EPILOGUE

This paper shows some light-works closely related to our life. Modern scientific and technological means can both create unprecedented lightscape and give traditional lightscape vitality, enabling its survival and further development. We wish, with the support of modern technology, designers would use more lightscape, soundscape, smellscape, and allow their combination with other forms of art, and more brilliant buildings, gardens and cities would turn up.

REFERENCES

- Dame de Cœur. [EB/OL].
- Fortune Global Forum 2017, Guangzhou. [EB/OL]. (in Chinese).
- Guangzhou International Lighting Festival. [EB/OL]. (in Chinese).
- Guggenheim Bilbao's 20th anniversary light show. [EB/OL].
- Lyon's festival of lights. [EB/OL].
- Qiu Jianzhen and Wu Shuoxian, Lightscape and Architecture, Architectural Journal, 2017, 09, No.588,115-118(in Chinese).
- R. Murray Schafer. Our Sonic Environment and the Turning of the World: The Soundscape [M], Destiny Books Rochester Vermont, 1994.
- Su Chao hao, Lin Kangqiang, Cui Yang, Sun Bin. "Butterfly-changing": A Visual Feast Combining Power and Beauty Presented by 3D Printing Technology[J].Southern Architecture,2018(02):120-125.
- Vivid Sydney. [EB/OL].
- Wang Xiaoyi. Deciphering the Performance for G20 by Zhang yimou: Tell the world some wonderful stories about China. (in Chinese). [EB/OL].
- Wu Shuoxian, Main points of lightscape, South Architecture, 2017,03, No.179,4-6(in Chinese).

Optical Performance of Polycarbonate Multi-Wall Panels in the form of Transparent Insulation Based on Long-Term Outdoor Measurements

Miroslav Čekon^{1,*}

¹Brno University of Technology, Brno, Czechia

*Corresponding email: cekon.m@fce.vutbr.cz

ABSTRACT

Buildings are subject to strongly time variable solar radiation impacts, which are phenomena that typically occur at a characteristic timescale resolution. Recent technologies and advances which are currently being used to produce polycarbonate-based materials may be used in applications where it is useful to activate the solar transmittance functions of building envelopes. In general, systems utilizing polycarbonate as a type of transparent insulation material exhibit the thermal performance of standard glazing systems. This study is focused on the optical characterization of several polycarbonate panels for buildings that are based on different numbers of chambers and differing geometries. The optical performance was analyzed in order to monitor the long-term solar properties of polycarbonate panels, by means of outdoor measurements in order to demonstrate the impact of year-round aspects on solar transmittance. This represented a specific methodical approach incorporating real full-scale components. Finally, the solar transmittance is evaluated with regard to the various outdoor time scales (hourly/daily, monthly and year-round). The studied multi-wall polycarbonate panels indicate that they may have very specific characterization from the solar transmittance perspective regarding the solar radiation that penetrates throughout their internal structure. The solar transmittance of polycarbonates, to which the timescales of the outdoor conditions respond, may significantly vary. Overall, the differences in total solar transmittance for laboratory, declared and outdoor test methods are very obvious; they differ by tens of percent. The study provides an initial insight into the optical behaviour of polycarbonate multi-wall panels and a very large set of data in order to make careful use of these parameters concerning their specificity and time dependent characteristics in thermal analysis of building integration.

KEYWORDS

Transparent insulation, Polycarbonate system, Outdoor testing, Solar transmittance

INTRODUCTION

Transparent Insulation Materials (TIMs) (Kaushika and Sumathy 2003) have the potential to be predominantly used in current concepts that are being put forward in an attempt to replace conventional insulating materials. However, their involvement in the building envelope is specific and so their application in building practice is currently rather rare. Several early studies described the benefits, disadvantages and options for the application of TIMs in the 1990's (e.g. Braun et al. 1992). Nevertheless, they are generally too expensive, though many cheaper materials have been diffusing such as polycarbonate sheets and panels. This represents one approach involving TIMs, which may be applied either directly as a transparent part of the building envelope, or as a part of potential solar façade concepts to obtain both transparency and thermal insulation. Various types have already been developed with different numbers of chambers and differing geometries. This development is specifically concerned with improvements from the thermal aspect. Furthermore, there could be potential in the development of polycarbonates regarding their optimal optical performance and

selective properties. Hence it is necessary to analyze in detail data for the materials which are already available, and their optical variation needs to be investigated from the spectral, angular and real outdoor perspectives. A variety of studies have been produced concerning different transparent glazing systems (e.g. Juráš et al. 2017), although some early studies aimed at measuring solar transmittance were performed on various honeycomb-type structures with an indoor solar simulator more than 25 years ago (Platzer 1992). In this relation, outdoor measurements using the sun as the source might be a good option. Overall, apart from Čekon et al (2017), there is a lack of information regarding real outdoor test in the literature dealing with solar transmittance measurements. Nevertheless, this may represent a very simple yet highly feasible way of measuring the total solar transmittance at a particular site, though Platzer (1992) pointed out that it is not an acceptable approach for Central European climates. Fundamental principles are already well implemented in the standard method of testing the solar transmittance of sheet materials using sunlight with detailed specification and procedures stated in ASTM (2015). In this relation, the key aim of this study is to investigate the optical performance of polycarbonate components that are primarily based upon multi-wall systems via real outdoor measurements. Based on the large quantity data obtained during long-term measurements, the aim of this study is to summarize these data with regard to their specificity and to provide time dependent characteristics.

MATERIALS AND METHODS

Three different polycarbonate systems were analyzed at the year-round scale. Table 1 shows all the measured components (PC10, PC25 and PC32) and their properties. The main difference between them lies in their overall thickness and the structure of their internal chambers. The analysis employs long-term measurements performed on vertical south-east (SE) oriented full-scale components located at the AdMaS centre operated by Brno University of Technology (Čekon et al. 2016) (longitude 16°34', latitude 49°14', altitude 297.23 m). Although there are many specific issues to take into account, such as inclined angular dependence, fluctuations of solar irradiation and overall solar distribution as well as cardinal point aspect, the estimation of solar transmittance via real outdoor measurements following ASTM (2015) principles was employed. This main objective is achieved via the analysis of optical performance studies carried out at different time-scale levels. The solar transmittance is then evaluated over various outdoor timescales (hourly/daily, monthly and year-round) and a comparison with values declared by the producers is provided as well.

Table 1. Description and key parameters of polycarbonate systems

Type	Thickness [mm]	Declared T_{decl} [-]	τ_{λ} * ASTM G 173	Measured** ASTM E1084-86	Geometry
PC10 Clear 2walls	10	0.82	0.74	0.63	
PC10* PC10 + prismatic glass	10+5	n/a	n/a	0.57	
PC25 Clear 3walls /diagonals	25	0.63	0.48	0.54	
PC32 Clear 6walls combined	32	0.53	0.43	0.53	

* obtained based on Čekon et al. (2017b); ** averaged values measured over 2017

Two photodiode elements were mounted in the air cavity behind each polycarbonate sample and a third additional element was left exposed to outdoor conditions. A commercial Star Pyranometer FLA 628 S was additionally used for photodiode comparison and accuracy correlations. Diode error depends on many factors and could not be directly determined. Based on the data obtained during diode circuit calibration procedures, the maximum error could be estimated at less than +/-10% of the measured value. However, a detailed analysis was conducted in relation to the measurement of solar radiant flux using a photodiode (Čekon et al 2016), its optimization and the estimation of its correction factor during measurements

(Slávik and Čekon, 2016). Finally, the ratio between the two solar intensity rates obtained by the silicon pin photodiodes represents the solar transmittance values.

RESULTS

As the focus on the long-term monitoring of real full-scale components is to demonstrate the annual progress of the total solar transmittance and passive solar gains of multi-wall panels, the fundamental principles of a standard test method an extraordinary mode was used. This section presents results from different timescales that depend for the purpose of evaluation on variables corresponding to hourly/daily, monthly and year-round progressions.

Hourly/daily-based timescale

The results presented in Figure 1 and 2 cover two different measurement days during which clear sunny and total cloud cover conditions prevailed. This corresponds to a combined hourly/diurnal time scale, where the detailed influence of polycarbonate structure can be observed. For the clear sunny period shown in Figure 1a, the results are strongly hourly sensitive due to the non-homogeneity of the tested polycarbonate systems and their internal structure (Figure 1b). This factor is demonstrated by the continuous variation in solar transmittance by several tens of percent resulting in a presence of multiple internal reflection of the incoming direct beam radiation distributed over a large-scale area towards the measurement sensor. The overall inhomogeneity and sun incident angle effect, occurring in both the parallel and perpendicular partitions over each tested structure, involve strong uniformly throughout the materials. On the other hand, very stable progressions are observed during overcast conditions (Figure 2a). For both test periods, the higher the maximum level of solar intensity, the higher the daily solar transmittance obtained.

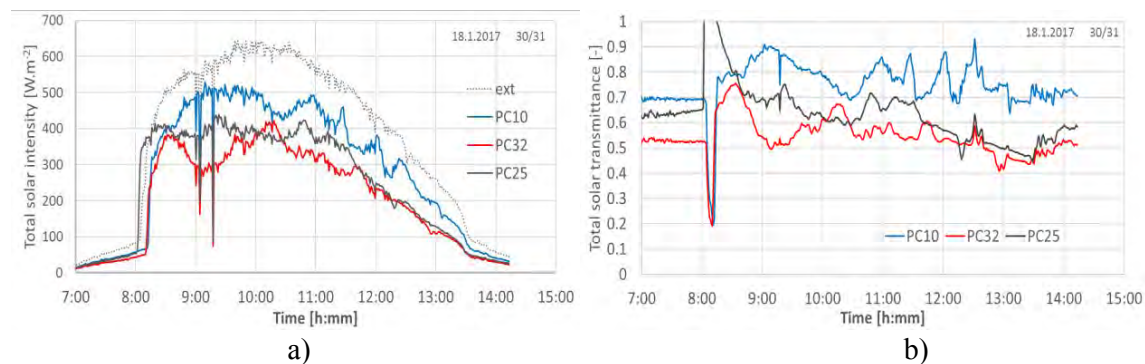


Figure 1. Measurements taken at an hourly/diurnal timescale under clear sky conditions; a) solar radiation rates measured; b) total solar transmittance derived.

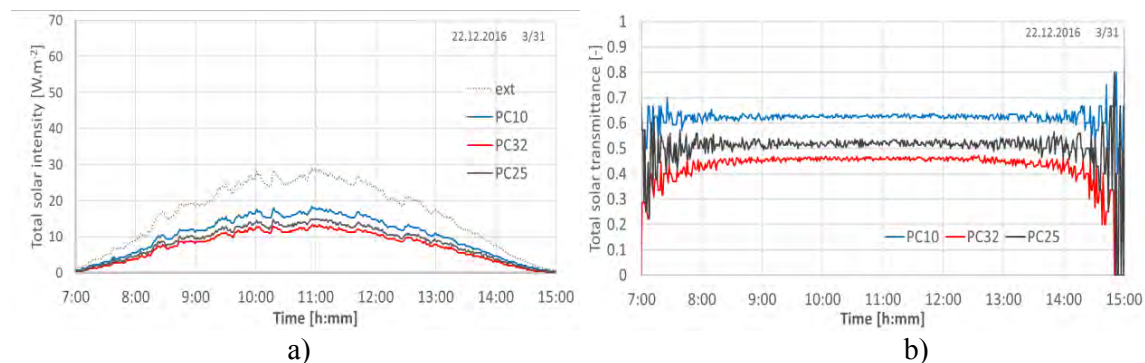


Figure 2. Measurements taken at an hourly diurnal timescale under total cloud cover; a) solar radiation rates measured; b) total solar transmittance derived.

Monthly-based timescale

The results shown in Figure 3 are an example of monthly-based result evaluation that is dependent on solar intensity rates and the relation with the angle of incidence of the sun above the horizon (altitude α). Outdoor solar intensities greater than 60W/m^2 obtained at the vertical level of test samples are included starting at 135° from the north azimuth. The results are presented using point clouds. Linear tendencies are indicated so as to generalize these strongly time variable and numerous data. In this regard, resultant linear relation is derived, and the monthly dependencies shown in Table 2 are provided for each PC panel. It should be noted that the linear functions do not represent the measured values adequately as this is first preview gained from the analyzed data; in the case of this study it provides an initial insight.

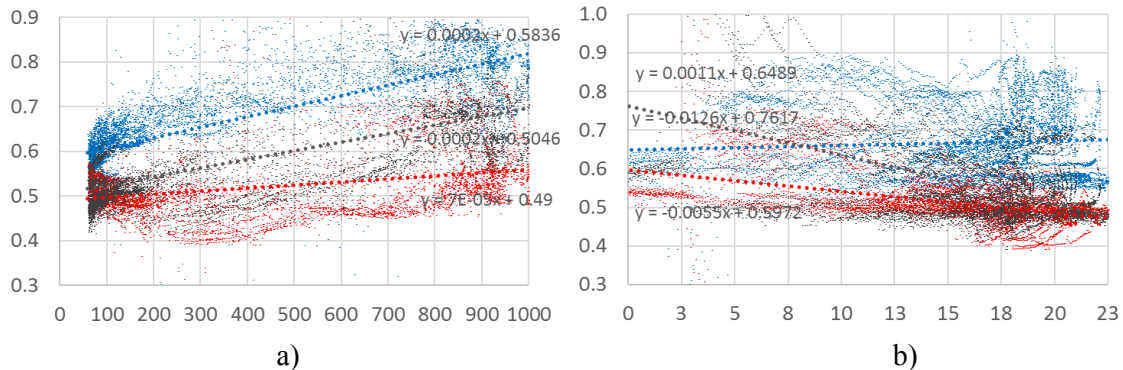


Figure 3. An example of measurements taken at a monthly-based timescale: a) the relation to the amount of total vertical solar radiation, b) the relation to the angle of incidence of the sun.

Table 2. Linear tendencies of monthly-based relations depending on solar intensity rates

2017	JANUARY	FEBRUARY	MARCH	APRIL	MAY	JUNE
max α	$17^\circ - 22^\circ$	$22^\circ - 31^\circ$	$31^\circ - 44^\circ$	$44^\circ - 54^\circ$	$54^\circ - 61^\circ$	$61^\circ - 64^\circ$
PC10	$2E-4 \cdot I + 0.58$	$7E-5 \cdot I + 0.60$	$7E-5 \cdot I + 0.60$	$8E-5 \cdot I + 0.61$	$9E-6 \cdot I + 0.62$	$9E-5 \cdot I + 0.51^*$
PC25	$2E-4 \cdot I + 0.50$	$1E-4 \cdot I + 0.50$	$1E-4 \cdot I + 0.50$	$8E-5 \cdot I + 0.54$	$-7E-6 \cdot I + 0.56$	$-4E-5 \cdot I + 0.55$
PC32	$7E-5 \cdot I + 0.49$	$2E-5 \cdot I + 0.50$	$2E-5 \cdot I + 0.50$	$2E-5 \cdot I + 0.50$	$-2E-5 \cdot I + 0.51$	$-6E-5 \cdot I + 0.53$
2017	JULY	AUGUST	SEPTEMBER	OCTOBER	NOVEMBER	DECEMBER
max α	$64^\circ - 59^\circ$	$59^\circ - 49^\circ$	$49^\circ - 37^\circ$	$37^\circ - 26^\circ$	$26^\circ - 18^\circ$	$18^\circ - 17^\circ$
PC10*	$9E-6 \cdot I + 0.55^*$	$7E-5 \cdot I + 0.55^*$	$7E-5 \cdot I + 0.56^*$	$7E-5 \cdot I + 0.55^*$	$2E-4 \cdot I + 0.54^*$	$2E-4 \cdot I + 0.54^*$
PC25	$-9E-5 \cdot I + 0.57$	$-2E-5 \cdot I + 0.56$	$4E-5 \cdot I + 0.55$	$4E-5 \cdot I + 0.57$	$1E-4 \cdot I + 0.56$	$8E-5 \cdot I + 0.57$
PC32	$-1E-4 \cdot I + 0.57$	$-6E-5 \cdot I + 0.56$	$-6E-5 \cdot I + 0.57$	$-6E-5 \cdot I + 0.56$	$-6E-5 \cdot I + 0.58$	$-4E-5 \cdot I + 0.57$

* Sample PC10 coupled with prismatic glass

Year-round time scale

Similarly, in Figure 4 and 5, year-round progressions are interpreted based on the same visualizations, and again linear relations are derived for each polycarbonate panel. The data obtained during year-round monitoring are divided into two presented periods. One corresponds to the first half of the year, and the other to the second half; during these two periods the maximum midday height of the sun above the horizon ranged from 17° to 61° and from 64° to 17° , respectively. In both periods, not surprisingly due to the angular aspects involved, the solar transmittance decreased with higher angles of incidence of the sun (see Figure 4). If Figure 5 is studied in detail, one can observe some angular selective functions of panel PC32 as well as PC10 combined with prismatic glass (PC10*). In contrast, the solar transmittance increases with increasing solar intensity rates, and vice versa, a trend that really corresponds to the height of the sun above the horizon during the whole year. This means that the differences in the behavior of the full-scale samples in relation to solar conditions become higher with increasing solar intensity, and vice versa.

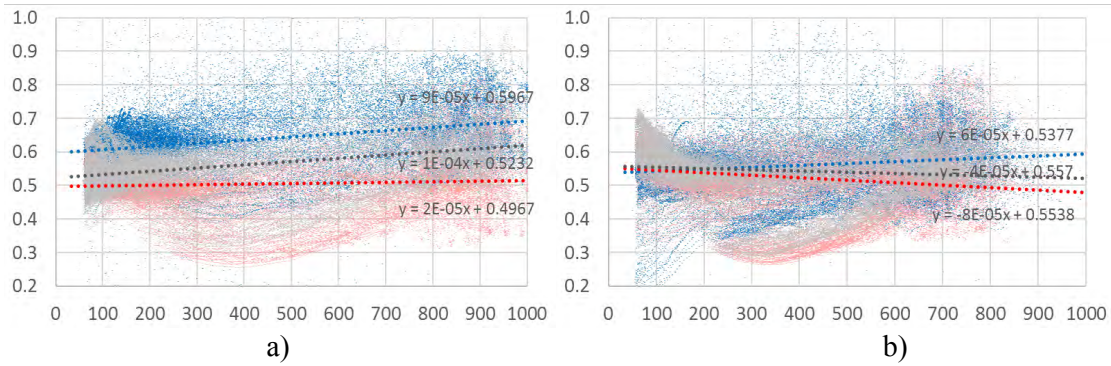


Figure 4. Measurements taken at the year-round timescale regarding the amount of total vertical solar radiation in a) the first half year before 1st June, b) the second after 1st June.

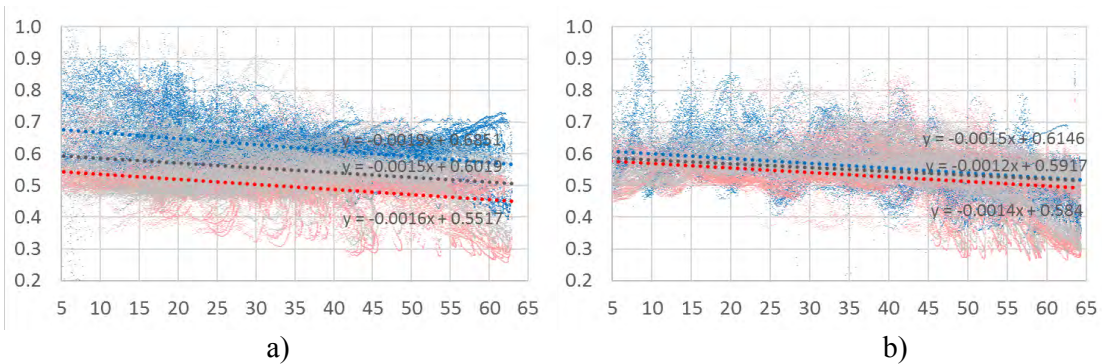


Figure 5. Measurements taken at the year-round timescale regarding the angle of incidence of the sun in a) the first half year before 1st June, b) the second half year after 1st June.

DISCUSSIONS

Based on the results presented, it can be observed that analyzed panels exhibit time-sensitive solar transmittance parameters. Looking at the hourly and/or daily scaled values, a continuous variation in solar transmittance of several tens of percent can be clearly detected. For the presented day with a clear sky, the obtained diurnal values are in the area of 0.79 (PC10), 0.53 (PC32) and 0.63 (PC25). This principally corresponds to the declared values (see Table 1). On the other hand, looking at the detailed hourly based progressions it can be seen that strong fluctuations occurred. This contrasts with overcast conditions, under which the average daily values are approximately 0.63 (PC10), 0.44 (PC32) and 0.52 (PC25). In this case the values correspond to those measured in the laboratory. Overall, the discrepancy in lab tests are that the incoming beam radiation is distributed disproportionately throughout the tested materials in range of approx. 15 nm diameter of spectrophotometer detector, while using outdoor tests, the transmittance is averaged over a large area. As regards the real outdoor measurements during longer timescale periods, the gained data concerning the influence of different solar intensity, angular and time dependent conditions on the solar transmittance is highly variable. The values obtained regarding solar intensity rates range from 0.50 to 0.55 (PC32), from 0.52 to 0.56 (PC25), from 0.60 to 0.67 (PC10) and from 0.54 to 0.60 (PC10*). Meanwhile, the values obtained regarding the angle of the sun above the horizon range from 0.59 to 0.49 (PC32), from 0.61 to 0.51 (PC25), from 0.68 to 0.57 (PC10) and from 0.61 to 0.52 (PC10*). However, the prevailing values show significant movement away from a linear tendency.

CONCLUSIONS

The paper presents the results of the long-term optical characterization of multi-wall panels utilizing co-extruded polycarbonate as a transparent insulation material (TIM). The study

evaluated the impacts of polycarbonates with different numbers of chambers and differing geometries. The experimental monitoring of full-scale components was focused on annual optical performance as a fundamental step towards understanding overall interactions influencing the solar transfer of the presented polycarbonate TIMs. Regarding the real outdoor in-situ measurements using the sun as the source, this study applied a specific methodical approach introduced by this research using long-term solar radiation rate monitoring and its evaluation with three different multi-wall panels. This indicates that the internal structures and geometry currently used to produce polycarbonate-based materials may affect the solar transmittance functions of such components. The analysis demonstrated that from this perspective, the presented panels employ selective aspects regarding the solar radiation that penetrates throughout their internal chambers. Overall, the differences in solar transmittance for all tested periods are strongly variable; they differ by tens of percent. Finally, these results may be considered in order to make careful use of the data in thermal calculation models. Further studies should be focused on the advanced statistical analysis of obtained data in order to describe their overall dependencies more adequately.

ACKNOWLEDGEMENT

This research was supported by the project GJ 16-02430Y "Contemporary concepts of climatically active solar façades integrating advanced material solutions" supported by Czech Science Found. and the No. LO1408 "Advanced Materials. Structures and Technologies".

REFERENCES

- ASTM. 2015. *ASTM E1084-86* International Standard Test Method for Solar Transmittance (Terrestrial) of Sheet Materials Using Sunlight. ASTM International: West Conshohocken, PA, USA.
- ASTM 2012. *ASTM G173-03*, Standard Tables for Reference Solar Spectral Irradiances: Direct Normal and Hemispherical on 37° Tilted Surface, ASTM International, West Conshohocken, PA, USA.
- Braun P.O., Goetzberger A., Schmid J., Stahl W. 1992. Transparent insulation of building facades - Steps from research to commercial applications, *Solar Energy*, 49(5), 413-427.
- Cekon M., Slavik R., Struhala K., and Formanek, M. 2016. Experimental Full- Scale Test Cell Optimizing for Research of Novel Concepts towards Climatically Active Solar Façade Design. *Applied Mechanics and Materials*, 861, 213-220.
- Cekon M. and Slavik R. 2017. Total Solar Transmittance Quantifying of Transparent Insulation Building Materials Based on Real Climate Outdoor Measurements. *Energy Procedia*, 132, 243-248.
- Cekon M., Slavik R. and Zach J. 2017. Experimental Analysis of Transparent Insulation Based on Poly-carbonate Multi-Wall Systems: Thermal and Optical Performance. *Energy Procedia*, 132, 502-507.
- Cekon M., Slavik R. and Juras P. 2016 Obtainable Method of Measuring the Solar Radiant Flux Based on Silicone Photodiode Element. *Applied Mech. and Materials*, 824, 477-484.
- Juras P., Staffenova D. and Durica P. 2017. Comparison of different windows for low-energy houses. *MATEC Web of Conferences*, 117
- Kaushika N. D., Sumathy K. 2003. Solar transparent insulation materials: a review. *Renewable and Sustainable Energy Reviews*, 7(4), 317-351.
- Slavik R. and Cekon M. 2016 Correction Factor Estimating of Silicon Pin Photodiode Derived from Outdoor Long-term Measurement. In Book of proceedings from ATF2016 4th International Conf. on Applied Technology, Leuven, Belgium, 262-266.
- Platzer W.J. 1992. Directional-hemispherical solar transmittance data for plastic honeycomb-type structures. *Solar Energy*, 49 (5), 359-369.

Preliminary monitoring results of ventilated heavyweight building envelope from recycled aggregate

Marina Bagarić^{1,*}, Ivana Banjad Pečur¹ and Bojan Milovanović¹

¹University of Zagreb, Faculty of Civil Engineering, Department of Materials, Croatia

*Corresponding email: mbagaric@grad.hr

ABSTRACT

Potential of recycled aggregate concrete (RAC) has already been acknowledged by many researchers, but the focus was primarily on its mechanical and durability properties at material level. If the focus is shifted to element and whole building level, then the question can be raised; how building envelopes made from RAC behave when exposed to real environment? The present paper describes an experimental set up to monitor hygrothermal behaviour of one three-storey family house built with prefabricated ventilated sandwich wall panels made from recycled concrete and recycled brick aggregate. This type of building envelope can be classified as a heavyweight envelope. In ground-floor flat a wall in the living room facing south is analysed in terms of internal temperature evolution and humidity distribution. Conditions of indoor and outdoor environment were monitored as well. Time lag and decrement of temperature extremes were observed and these benefits can be attributed to the presence of thermal mass. Ventilation of air in cavity ensured acceptable humidity level in all characteristic layers of wall panel. Summer overheating occurred due to insufficiently shaded large transparent openings. Further step is validation of numerical model and assessing the suitability of presented envelope type to different climates. This paper indicates the great potential of RAC application in energy efficient and moisture safe building envelope design.

KEYWORDS

Recycled aggregate concrete, prefabricated ventilated sandwich panels, heavyweight building envelope, field monitoring, hygrothermal behaviour

INTRODUCTION

Recycled aggregate concrete (RAC) has been identified as sustainable alternative to conventional concrete. Its mechanical and durability behaviour has already been widely acknowledged by many researchers (Behera et al. 2014; Fraile-Garcia et al. 2017; Marco 2014). Contrary to that, its hygrothermal behaviour as an important aspect of overall performance, has only been scarcely investigated. There are fragmented research findings on thermal and hygric properties of different types of RAC at material level (Banjad Pečur et al. 2015; Fenollera et al. 2015; Zhu et al. 2015). Having in mind the influence that building envelope's hygrothermal behaviour has on buildings energy needs, service performance, indoor thermal comfort and air quality which is directly related to the health of occupants (Feng and Janssen 2016), obviously there is a strong need to predict hygrothermal behaviour of RAC at component and ultimately at entire building level. To establish trustworthy numerical model, experimental results are desirable for model validation. This paper investigates transient hygrothermal behaviour of ventilated heavyweight building envelope constructed with RAC prefabricated panels under real variable climate conditions and occupants' behaviour.

DESCRIPTION OF MONITORED BUILDING AND EXPERIMENTAL SET-UP

The subject of this study is a 3-storey family house (approx. 268 m²) built within socially – supported housing program in City of Koprivnica, Republic of Croatia (Figure 1a) as very low energy (A+) standard.

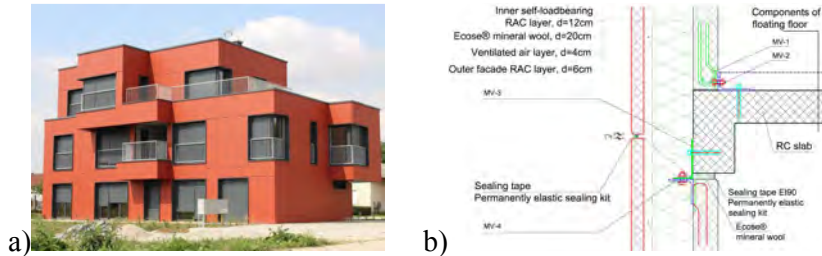


Figure 1. a) View of monitored building; b) Cross section of prefabricated ventilated RAC wall panel

Its building envelope consist of 42 cm thick prefabricated ventilated sandwich wall panels made from recycled aggregate. With surface mass of 458 kg/m², building constructed with this type of envelope system can be classified as a heavyweight building. Based on thorough research of mechanical and durability properties (Banjad Pečur et al. 2015), replacement ratio of 50 % natural aggregate with recycled one deemed as the most favourable. As shown in Figure 1b), observed panel consists of four characteristic layers: outer RAC facade layer (6 cm), ventilated air cavity (4 cm), thermal insulation (20 cm), and inner self-loadbearing RAC layer (12 cm). The thermal transmittance of panel is approx. 0.16 W/(m²K).

For production of outer RAC façade layer (RAC-B), recycled brick from waste generated during manufacturing brick process was used, while recycled aggregate from demolition of old concrete structure was used for production of inner self-loadbearing RAC layer (RAC-C). Thermal insulation is formaldehyde-free glass wool with integrated wind barrier. Air cavity is placed between thermal insulation and outer façade layer, with aim to prevent possibility of water vapour condensation. The water-repellent coating was applied on outer façade surface. Main hygrothermal properties of target recycled aggregate concrete are shown in Table 1.

Table 1. Hygrothermal properties of RAC-C and RAC-B

	RAC-C	RAC-B
Dry density [kg/m ³]	2204.96	1948.22
Open porosity [%]	16.67	19.27
Thermal conductivity $\lambda_{dry,+10^{\circ}C}$ [W/(mK)]	0.944	0.745
Water vapour resistance factor μ [-]	41	28

to approx. 44% lower λ when concrete is used and approx. 56% when brick is used as recycled aggregate. It is suggested to use μ -value for normal concrete as a constant value of 150. From Table 1, it can be seen that μ -factors for RAC-C and RAC-B concrete are up to 80% lower compared to value suggested for normal concrete. This basic hygrothermal parameters indicate that more energy efficient building design can be achieved with RAC without compromising mechanical requirements – 43.3 MPa was mean cube compressive strength of RAC-C and 38.7 MPa of RAC-B, respectively.

Conventional concrete made completely with natural aggregates with a density of 2300 kg/m³ has λ -value of approximately 1.7 W/(mK).

Replacement of 50% contributed

In ground-floor flat a wall panel in the living room facing south (marked red in Figure 2a) is analyzed in terms of internal temperature evolution and humidity distribution. Panel is 128.5×297 cm, with the first set of sensors centrally positioned 86 cm from the panel's bottom and second set of sensors 100 cm, respectively.

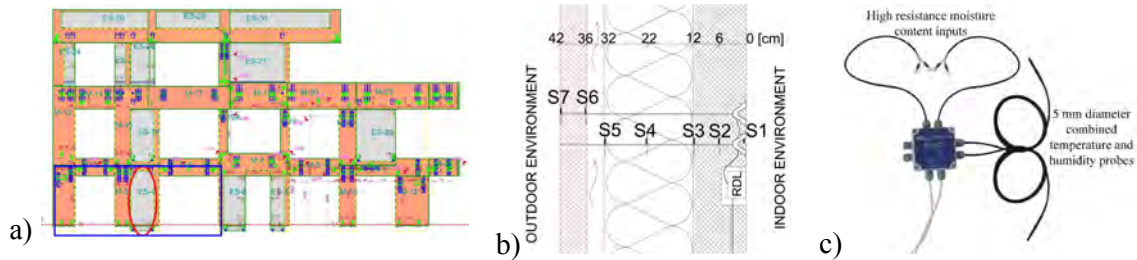


Figure 2. Measurement location: a) Position plan for southern façade; b) Arrangement of T-H sensors within panel layers; c) RDL Client-THR system

Temperature (T) and humidity (H) distribution was monitored in all four characteristic layers of presented wall panel, in total seven positions S1-S7 (Figure 2b), using the RDL Client-THR system from Caption Data Limited (Figure 2c). Installation of T-H sensors was carried out in precast factory during the moulding of panels (Figure 3). Presented monitoring system



Figure 3. Installation of T-H sensors

is a combination of wire-based and wireless measurement system. Sensors (S1-S7) at south measurement location are wired connected to

the central measurement unit in building's entrance hall, where sensors readings are recorded every hour and then sent by Internet on a dedicated server. The data can be accessed via custom Brightcore computer system. Further analysis of measured data was performed with Microsoft Excel software. Boundary conditions in terms of indoor and outdoor environment were also monitored. Indoor climate is dependent on the occupants' behaviour – young couple with small child. TFA Klimalogg Pro Thermo-Hygro-Station data logger was used for monitoring and recording the air temperature and relative humidity in living room of the house every 15 minutes. Basic meteorological data were measured every 5 min at nearest available meteorological station Herešín. These data are taken as representative for the Cfb climate of City of Koprivnica (Köppen climate classification).

RESULTS AND DISCUSSIONS

Period of almost one year was monitored (March 9, 2017 – February 28, 2018). In winter months outside temperature was occasionally under 0°C with peak of -17.3°C at the end of February 2018. Five days in a row was the longest continuous period of temperature under 0°C with mean value of -6.6°C . Max value was 38.3°C in August 2017 and its average monthly value was 22.5°C . Inside air temperature (living room) was in range from 19.5 to 29.1°C . It needs to be noted that in this paper humidity distribution will be presented only in terms of relative humidity (RH). Used moisture content sensors are electrical resistance-based sensors with readings in [kohm] and establishment of correlation curves for both type of RAC is still in process. Those results will be published elsewhere. Figure 4a) and 4b) show the measured T and RH values within the panel. While the exterior surface T (S7) vary in a wide range (from -10.8 to 55.4°C) following the pattern of outdoor climate, T variations through inner RAC layer (S1 – S3) are more stable and limited from 17.18 to max 31°C . RH sensors at positions S1 – S3 (inner RAC layer) did not send any information (Figure 4b).

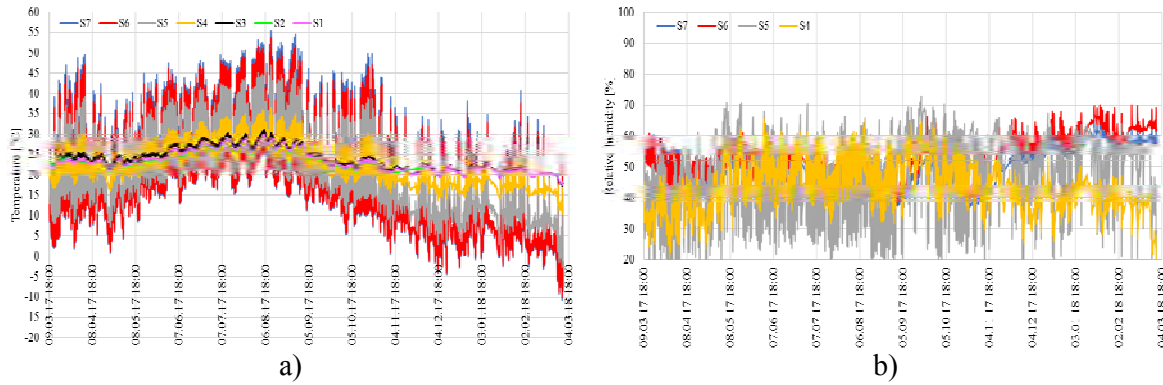


Fig 4. One-year monitoring data: a) Temperature b) Relative humidity

Figure 5 presents the measured RH in the mineral wool (MW) and RAC outer facade layer for period December 1, 2017 – February 28, 2018. MW is of big interest due to its thermal insulation function, while RAC outer facade layer presents the most humid area of the panel in winter by being directly submitted to wind driven rain. Despite high outdoor RH values (above 90%), for external surface of RAC facade layer RH oscillates mostly around 60%. This can probably be attributed to the water-repellent coating.

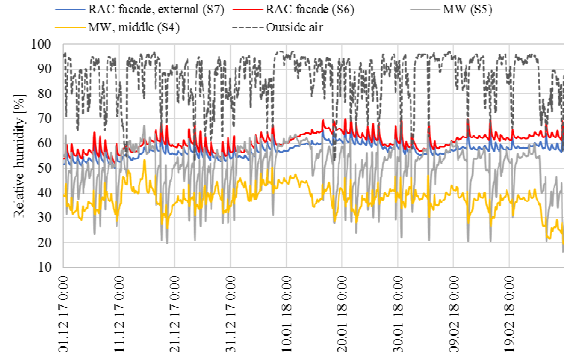


Figure 5. RH inside RAC outer facade and MW layer of monitored panel during winter

It appears that the RH is mostly, except the few occasional peaks, under 60 % at the surface of MW layer (S5). In the middle of MW (S4), RH is almost always under 50 % and mostly fluctuating around 40% which indicates the positive effect of air ventilation in cavity. To gain a deeper understanding of hygrothermal behaviour of observed south-facing panel, monitoring results are presented hereafter for the three coldest days of the winter period (February 26-28, 2018) and the three hottest days of the summer period (August 3-5, 2017), respectively.

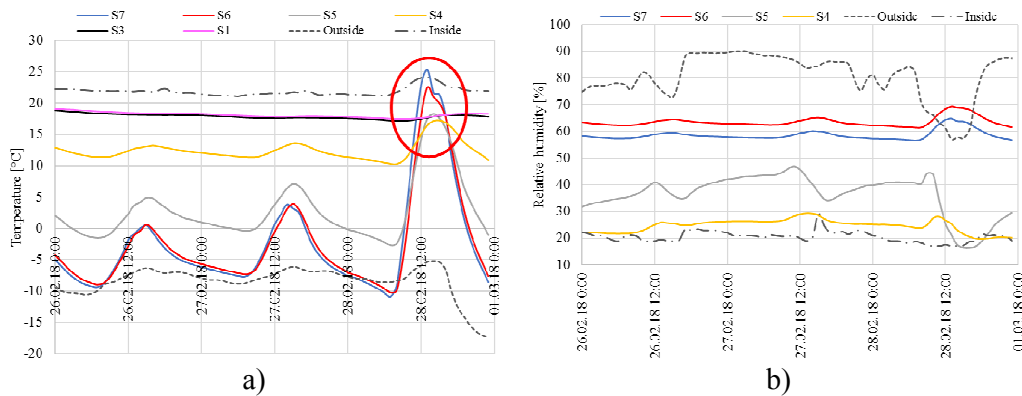


Figure 6. Hygrothermal responses within the panel for three coldest days: a) T; b) RH

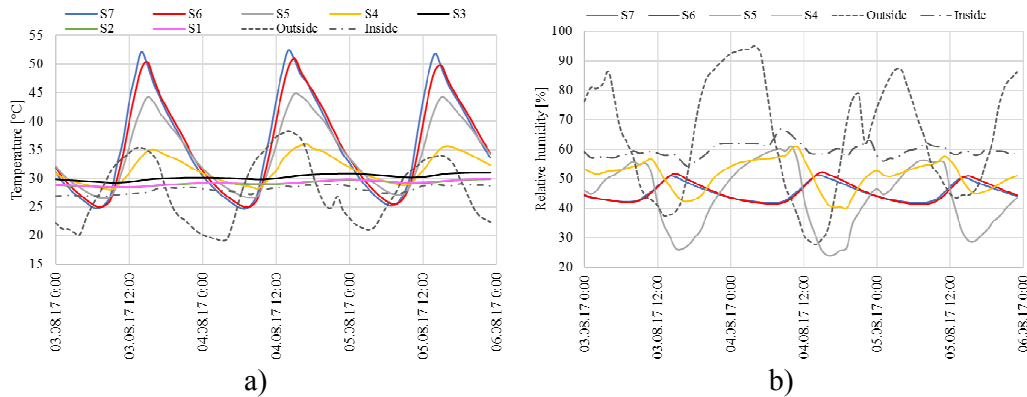


Figure 7. Hygrothermal responses within the panel for three hottest days: a) T; b) RH

In February 2018, indoor air temperature varies between 21.1 – 25.5°C with a mean of 22.9 °C. Values of RH vary between 41.3 – 71.7 % with a mean of 53.3 %. During August 2017, indoor air temperature varies in a wider range from 29.1 – 33.7°C, with a mean of 31.4°C, while values of RH vary between 69.3 – 87.3 % with a mean of 78.3 %. The fluctuations of indoor temperature are limited by heating system (mechanical ventilation with recuperation system and radiators as additional heating system in winter but without additional cooling system in summer). The exterior surface temperature (S7) of observed south-facing panel follows the pattern of behaviour of the outdoor temperature reaching a high peak at 14:00h in summer conditions due to the solar exposure. The same pattern is followed by S6 – S4 but with decreased amplitude. Further and more progressive attenuation of T amplitude is present in S3 – S1 (inner layer). In winter period, high peak occurs on February 28 reaching 25.3°C at panel's exterior surface at 13:00h. This specific peak is most likely induced by increased solar radiation at clear winter day compared to previous days (Figure 8). Unfortunately, there was occasional interruption of measurement and some hourly solar radiation data are missing.

Besides attenuation of T amplitude, a time shift between the peaks can be observed. These appearances are due to the thermal inertia of RAC panel. Thermal inertia is evaluated in terms of time lag and attenuation of heat wave amplitude while propagating from the outer surface to the inner surface. February 27, 2018 is analysed for winter conditions and August 4-5, 2017 for summer conditions, respectively. In summer conditions, between S7 – S1 a

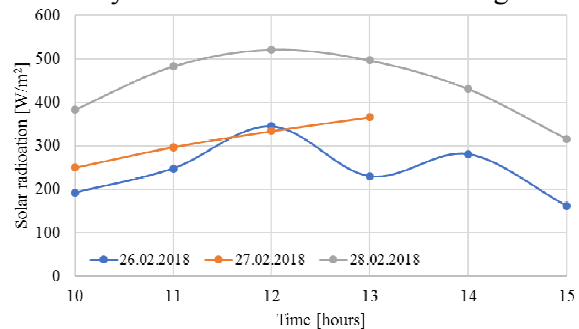


Figure 8. Solar radiation data in February 2018

damping of approx. 57 % is measured. The panel attenuates the temperature very well with a time lag of 10h over a period of 25 hours. These two observations indicate that the panel has a good thermal inertia. For completely opposite boundary conditions, i.e. winter conditions, the min exterior surface temperature (-7.7°C) and min interior surface temperature (17.8°C) are analysed. In this case, time lag is approximately 6h over a period of 24 hours. High façade surface temperatures (> 50°C) in the summer indicate there may be periods of overheating that potentially could compromise thermal comfort of occupants. Living room has large transparent openings (marked blue in Figure 2a) oriented to south which ensures considerable solar heat gains. In Figure 9 coincidence of the measured psychrometric data in living room and the summer comfort zone is presented for period of June 1 to September 1, 2018. Used summer comfort limits are the ones defined for living spaces in residential buildings, Category II (HZN 2008). During summer, T and RH were in the comfort zone 57.7% of time.

Actually, RH exceeds the upper threshold (60%) only 17.5% of the time, while T exhibited significant violation of upper threshold (26°C). This overheating is related to architectural design of building, where large transparent openings at south are not adequately shaded. To avoid installation of additional air-conditioning systems, application of adequate shading devices or/and external greenery should be considered. That would undoubtedly decrease operating temperatures in summer period.

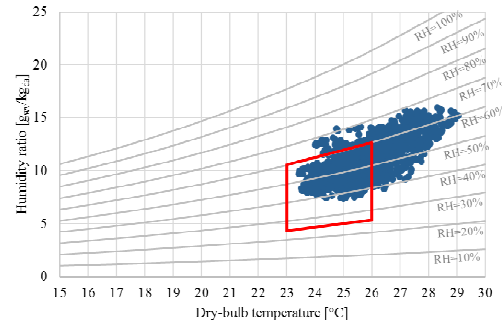


Figure 9. Internal psychrometrics data vs. HRN EN 15251 summer comfort limits

CONCLUSIONS AND FURTHER RESEARCH ACTIVITIES

The first in-situ monitoring results of family house constructed with prefabricated ventilated sandwich wall panels from recycled aggregate concrete (RAC) were analysed. Hygrothermal behaviour under real variable climate conditions and real use of occupants was experimentally monitored during one year. The south-oriented RAC panel exhibited a good thermal inertia - high damping capacity (>50 %) and time shift up to 10 hours in summer period. Air ventilation maintained relative humidity levels in mineral insulation under 60 % during winter months. Even though these results are preliminary results, they can already confirm that it is possible to upscale RAC from laboratory material experiments to full-scale construction product implementation and design sustainable, energy efficient and moisture-safe buildings. Special attention should be on preventing summer overheating. Further research steps are: i) analysis of west- and north-oriented (more shady) facades and their comparison with presented south panel; ii) numerical simulation of panels and validation with experimental results (assessing the panel's suitability for different climates); iii) continue with monitoring for at least next two years – possibility to confirm pattern of RAC's hygrothermal behaviour.

ACKNOWLEDGEMENT

The authors acknowledge the financial support from the “ECO-SANDWICH” project funded within the frame of EU CIP ECO Innovation programme (ECO/11/304438/SI2.626301).

REFERENCES

- Banjad Pečur, I., Štirmer, N., & Milovanović, B. 2015. Recycled aggregate concrete for nearly zero-energy buildings. *Magazine of Concrete Research*, 67(11), 575–584.
- Behera, M., Bhattacharyya, S. K., Minocha, A. K., Deoliya, R., & Maiti, S. 2014. Recycled aggregate from C&D waste & its use in concrete - A breakthrough towards sustainability in construction sector: A review. *Construction and Building Materials*, 68, 501–516.
- Feng, C., & Janssen, H. 2016. Hygric properties of porous building materials (II): Analysis of temperature influence. *Building and Environment*, 99(Ii), 107–118.
- Fenollera, M., Míguez, J., Goicoechea, I., & Lorenzo, J. 2015. Experimental Study on Thermal Conductivity of Self-Compacting Concrete with Recycled Aggregate. *Materials*, 8(7), 4457–
- Fraile-Garcia, E., Ferreiro-Cabello, J., López-Ochoa, L. M., & López-González, L. M. 2017. Study of the technical feasibility of increasing the amount of recycled concrete waste used in ready-mix concrete production. *Materials*, 10(7).
- HZN. 2008. *HRN EN 15251:2008 Indoor environmental input parameters for design and assessment of energy performance of buildings addressing indoor air quality, thermal environment, lighting and acoustics (EN 15251:2007)*, Zagreb: Croatian Standards Institute
- Marco, P. 2014. A conceptual model to design recycled aggregate concrete for structural applications. *Ph.D. Thesis, Springer Theses*. Springer.
- Zhu, L., Dai, J., Bai, G., & Zhang, F. 2015. Study on thermal properties of recycled aggregate concrete and recycled concrete blocks. *Construction and Building Materials*, 94, 620–628.

Review of the sky temperature and solar decomposition, and their impact on thermal modeling

Farhad Hemmati^{1,*}, Fitsum Tariku²

^{1&2}British Columbia Institute of Technology, Burnaby, BC, Canada

*Corresponding email: fhemmati@my.bcit.ca

ABSTRACT

Performing accurate hourly building energy modeling requires presence of reliable boundary conditions. The required data for energy simulation model entries are exterior air temperature, exterior air relative humidity, solar radiation, sky temperature, wind velocity and cloud cover. Unfortunately, most available measured solar energy data is in the form of global horizontal radiation. Moreover, measured night sky temperature is normally not available. Proper energy modeling of a full building requires to have accurate solar radiation intensity on angled building envelope assemblies as well as precise sky temperature data available.

In this study, among several available models, three hourly horizontal global solar radiation decomposition models, four hourly diffuse radiation on inclined surface models, and five sky temperature estimation models are studied for Vancouver climate. For solar radiation validation perspective, 2013 one-year measured total solar radiation on a south-east oriented wall located at BCIT Burnaby Campus is compared with the results from selected solar models. For both solar radiation and sky temperature models, impact of using different models on transient heat transfer results of light-weight and mass-type walls (two walls) are reviewed. Results reveal high impact of both solar and sky temperature models on hourly heat transfer simulation results.

KEYWORDS

Sky temperature, diffuse radiation on tilted surface, decomposition of global radiation, transient thermal simulation.

INTRODUCTION

From the total energy spent in 2013 within Canada, 17% was found in residential sector, and 10% in commercial and institutional sectors (Canada, 2016). Therefore, it is important to thoroughly understand the interaction between energy consuming elements within a building, which requires hourly energy simulation. Performing an accurate hourly energy simulation requires having correct input boundary conditions available. Two important boundary conditions that could highly impact the simulation results are solar radiation and sky temperature values.

Solar radiation

Most available climatic weather data only contains global value for solar radiation, while direct and diffuse components of solar radiation as well as diffuse radiation on inclined surfaces are not always available (Burlon, et al., 1991). These three components are ultimately required to calculate the total solar radiation on a tilted surface. Many decomposition models for calculation of diffuse solar radiation are developed based on the terminology first studied by Liu & Jordan (1960). Performance of several previous solar radiation models are reviewed in this study, and results are compared with the measured data for validation purposes.

Sky radiation

Measured sky radiation is not always available. Therefore, approximation models are being used to estimate the values.

There are several studies performed on sky radiation estimation. Most of the models are based on clear sky condition (Algarni & Nutter, 2015), while climates with high cloud coverage (i.e. Vancouver) require a certain correlation to account for sky condition. In this study, different models for cloudy sky temperature estimation are reviewed. Since no measured sky temperature values is available, only the impact of using different sky temperature models is reviewed on transient thermal modeling.

METHODS

In this study, total of three hourly horizontal global solar radiation decomposition models, four hourly diffuse radiation on inclined surface models, and five sky temperature estimation models are reviewed.

Solar radiation

The selected hourly horizontal global solar radiation decomposition models are Erbs, et al. (1982), Reindl, et al. (1990), and Orgill & Hollands (1977). Studied hourly diffuse radiation models on an inclined surface are Reindl, et al. (1990), Skartveit & Olseth (1986), Hay, (1979) and Perez, et al. (1990). These models are selected based on the climates that they have been developed based on, and extent of their use in energy modeling industry. Therefore, the combination of decomposition models and diffused radiation on tilted surface models would result in total of twelve models.

The above-mentioned models require extraterrestrial solar radiation, global solar radiation, cloud index, temperature and relative humidity, and sun position as inputs. Model inputs are imported from Engineering Climate Datasets (Government of Canada, n.d.). The model results (total of twelve combined models) are compared with 2013 one-year measured total solar radiation on a south-east oriented wall located at BCIT Burnaby Campus. Global solar radiation (Government of Canada, n.d.) is decomposed into direct and diffuse components using the selected three models. Fraction of diffuse solar components on south-east wall is then calculated using the four selected models. Lastly, results for total tilted solar radiation on south-east orientation wall (twelve models) are compared with 2013 measured data from BCIT Burnaby Campus.

In order to review the impact of different solar radiation models on hourly thermal modeling, solar radiation from different models are used to simulate the transient heat transfer in one-dimensional light-weight and mass-type walls (total of two walls). Errors caused by utilizing different models are presented.

Sky temperature

In this study, selected sky emissivity models are Melchor (1982b), Clark & C. Allen (1978), Dagenet (1985) (both England and Sweden), and Aubinet (1994). All these models are developed according to climates with relatively high chance of rain; therefore, they would be potential candidates for climates such as Vancouver.

The above-mentioned models require relative humidity, ambient temperature, atmospheric pressure, site elevation, sky cover and clearness index as inputs. Model inputs are imported from Engineering Climate Datasets (Government of Canada website).

Since measured data was not available for sky temperature, only impact of using different sky temperature on hourly thermal modeling is reviewed. Sky temperature results from different models are used to simulate the transient heat transfer in one-dimensional light-weight and mass-type walls (total of two walls). 2005 hourly Vancouver International Airport weather data is used for the purpose of this simulation. Deviation of the results from the reference case of “no sky temperature” is reviewed for each model.

Simulation setup

For both solar radiation and sky temperature, light weight wall consists of ½” drywall, 5 ½” of batt insulation, ½” plywood sheathing, ½” air cavity and ½” hardie-siding, and mass-type wall consists of ½” drywall, 3” of XPS insulation and 8” concrete structural wall. Material properties are selected from 2013 ASHRAE Handbook – Fundamentals. Interior air film coefficient is assumed 8.33 W/m²K and exterior air film coefficient is assumed 33 W/m²K. No sky temperature radiation is considered for solar radiation simulation cases, and no solar radiation is considered for sky temperature simulation cases. Ground reflectivity is assumed to be 0.2 (dimensionless).

For all transient numerical simulations, COMSOL Multiphysics Modelling Software has been used. The software results are validated using the four benchmark cases from ISO 10211 (10211, 2007).

RESULTS

Solar radiation

Six days of hourly results for different solar radiation models on the south-east wall are provided in Figure 1. Discrepancy of results are calculated using seasonal and total Mean Absolute Error (MAE) for each model in Table 1. Figure 2 shows percentage of hourly solar radiation results corresponding to specified range of relative error, which reveals the reliability of each model.

Table 2 is provided to review the impact of different solar models on transient heat transfer simulation for light-weight and mass-type wall assemblies. This table contains seasonal and total heat transfer Normalized Mean Absolute Error (NMAE) compare with simulation results from measured solar values. The errors are normalized by dividing MAE by the average heat transfer results corresponding to measured values for the specified period of time.

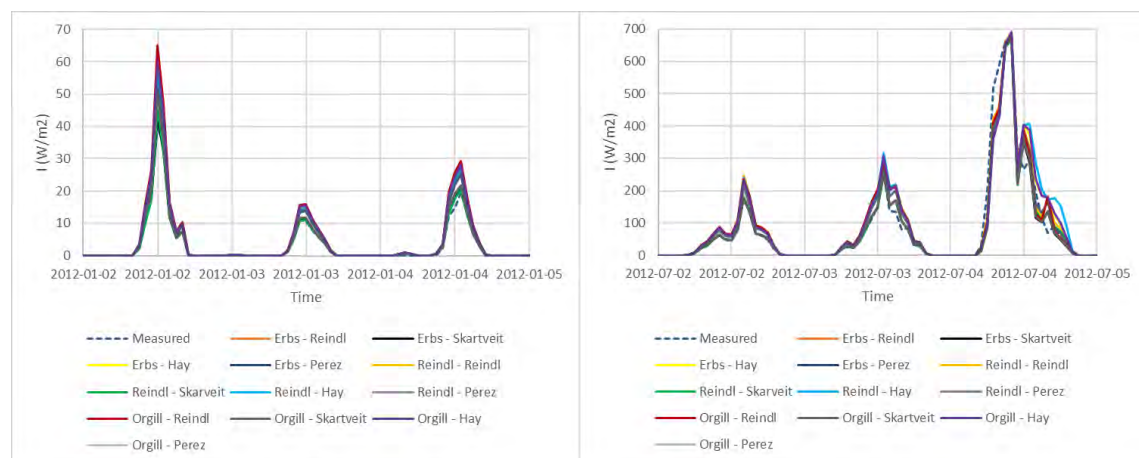


Figure 1. Solar radiation comparison for Jan 2nd-4th and July 2nd-4th.

Table 1. Solar radiation model comparison - MAE

Models	Winter	Spring	Summer	Fall	Total
Erbs - Reindl	32.7	37.8	49.6	33.4	39.6
Erbs - Skartveit	29.6	30.4	49.6	27.6	35.6
Erbs - Hay	33.5	38.5	50.0	34.7	40.3
Erbs - Perez	31.4	34.5	50.8	31.4	38.3
Reindl - Reindl	32.5	37.0	50.1	32.4	39.3
Reindl - Skartveit	29.6	29.8	48.4	26.2	34.7
Reindl - Hay	33.7	47.3	73.3	33.2	49.9
Reindl - Perez	31.4	34.4	50.8	31.5	38.3
Orgill - Reindl	33.5	38.5	50.0	34.7	40.3
Orgill - Skartveit	29.5	30.3	49.7	28.3	35.7
Orgill - Hay	34.3	44.8	66.3	35.8	47.6
Orgill - Perez	32.0	35.3	51.7	32.6	39.2

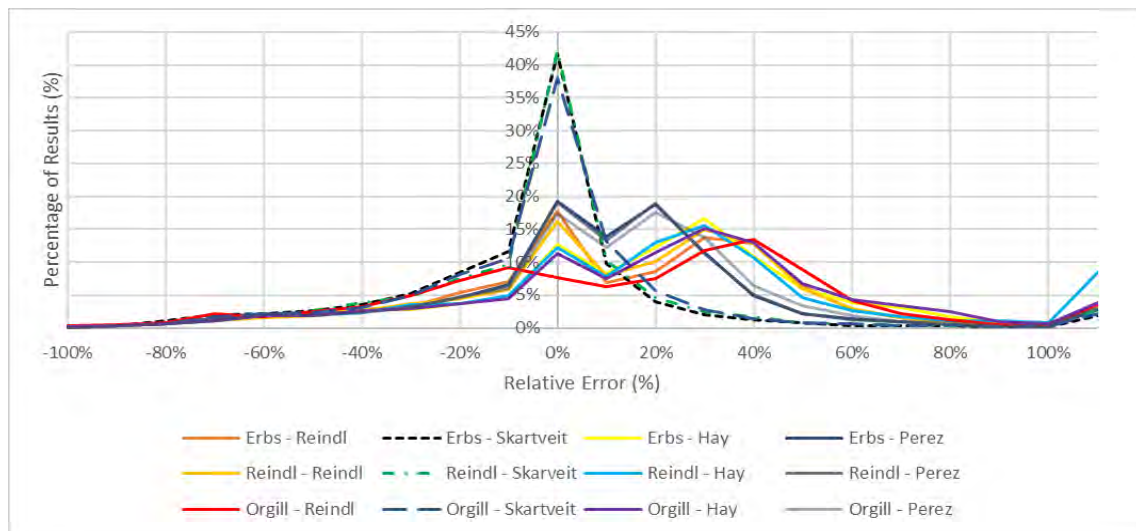


Figure 2. Percentage of results corresponding to selected range of relative error – solar model comparison

Table 2. Transient heat load comparison – Solar radiation – Light-weight and mass-type walls

Model	Light-Weight Wall					Mass-Type Wall				
	Winter	Spring	Summer	Fall	Total	Winter	Spring	Summer	Fall	Total
Erbs - Reindl	5.3%	7.2%	35.8%	2.8%	5.7%	4.3%	6.2%	30.3%	2.0%	4.6%
Erbs - Skartveit	4.8%	5.9%	36.3%	2.3%	5.2%	4.3%	5.5%	35.4%	1.5%	4.6%
Erbs - Hay	5.4%	7.3%	35.8%	2.9%	5.8%	4.4%	6.4%	30.3%	2.0%	4.7%
Erbs - Perez	5.2%	6.7%	37.1%	2.6%	5.6%	4.1%	5.4%	29.9%	1.7%	4.4%
Reindl - Reindl	5.2%	7.1%	36.2%	2.7%	5.7%	4.0%	5.7%	26.5%	1.9%	4.3%
Reindl - Skartveit	4.7%	5.7%	35.8%	2.1%	5.0%	4.0%	5.2%	31.0%	1.4%	4.3%
Reindl - Hay	6.6%	9.2%	53.7%	2.8%	7.3%	4.1%	5.8%	28.7%	1.8%	4.4%
Reindl - Perez	5.1%	6.7%	37.1%	2.5%	5.5%	4.0%	5.3%	29.3%	1.7%	4.3%
Orgill - Reindl	5.4%	7.3%	35.8%	2.9%	5.8%	4.4%	6.4%	30.3%	2.0%	4.7%
Orgill - Skartveit	4.9%	5.9%	36.5%	2.4%	5.2%	4.3%	5.5%	35.3%	1.6%	4.7%
Orgill - Hay	6.3%	8.8%	48.4%	2.9%	6.9%	4.2%	6.0%	27.9%	2.0%	4.5%
Orgill - Perez	5.3%	6.9%	37.9%	2.8%	5.7%	4.1%	5.5%	29.1%	1.9%	4.4%

Sky temperature

Fourteen days of hourly results for sky temperature are provided for each model in Figure 3. For both light-weight and mass-type walls, NMAE between calculated results from the

selected sky temperature models and reference model (no sky temperature) are shown in Table 3 in order to review the heat transfer deviation caused by different models.

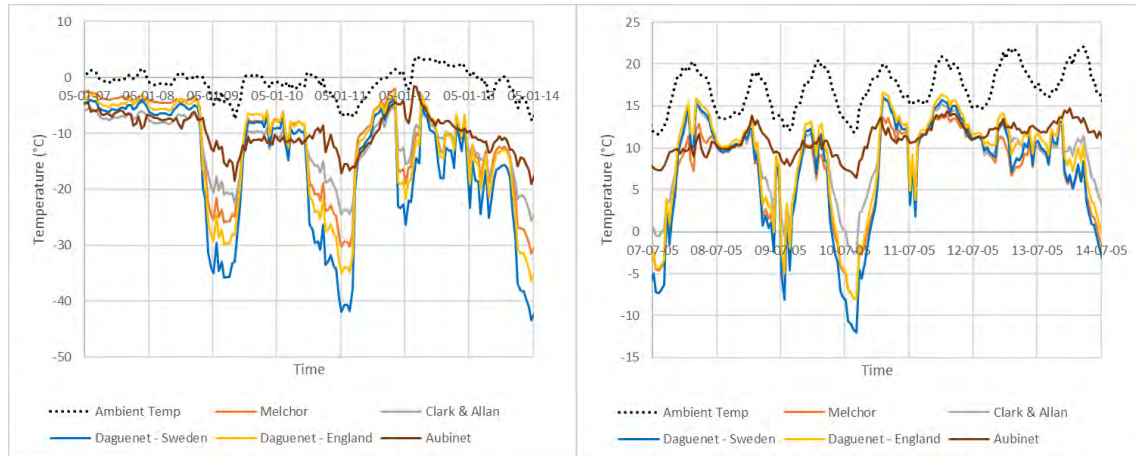


Figure 3. Night sky temperature comparison for Jan 7th-14th and July 7th-14th

Table 3. Transient heat load comparison – Sky temperature – Light-weight and mass-type walls

Model	Light-Weight Wall					Mass-Type Wall				
	Winter	Spring	Summer	Fall	Total	Winter	Spring	Summer	Fall	Total
Melchor	3.6%	7.0%	19.1%	3.4%	6.5%	7.4%	11.2%	25.0%	6.8%	10.6%
Clarke	2.7%	5.5%	14.5%	2.6%	5.0%	7.0%	10.0%	19.9%	6.9%	9.5%
England	5.3%	10.2%	15.2%	8.4%	8.8%	8.9%	14.9%	20.0%	12.8%	13.0%
Sweden	6.5%	12.6%	17.9%	10.4%	10.7%	10.5%	17.5%	23.0%	15.1%	15.3%
Aubinet	1.4%	3.1%	7.3%	1.5%	2.7%	4.4%	7.0%	11.9%	4.3%	6.0%

DISCUSSIONS

Solar radiation

Table 1 and Figure 2 reveal that Erbs - Skartveit, Reindl - Skartveit and Orgill - Skartveit models result in the closest solar radiation values to measured data. Among these three models, Reindl - Skartveit model has the best performance with 42% of the results within $\pm 10\%$ relative error, and has the lowest seasonal and total MAE (35.78 W/m²). This model also shows the least seasonal fluctuation in MAE values, which proves the stability.

Table 2 confirms the fact that Reindl - Skartveit model also results in the lowest seasonal and total NMAE (5.09% for light-weight and 4.31% for mass-type) hourly heat transfer for both light-weight and mass-type walls. Different solar models could result up to 2.26% additional discrepancy in total NMAE for the light-weight wall and 0.47% additional discrepancy in total NMAE for the mass-type wall. Similar pattern could be found for seasonal NMAE results.

Sky temperature

Significant variation between sky temperature models' results is revealed in Figure 3, which mostly occurs during days with clear sky. Using different night sky models could result in total deviation (Table 3) in the range of 2.71% to 10.77% for light-weight wall and 6.09% to 15.33% for mass-type wall from the reference case (no sky radiation). Significant seasonal deviation is also shown in Table 3 for both light-weight and mass-type walls. This shows the great impact of utilizing different sky temperature models on transient heat transfer simulations.

CONCLUSIONS

Several different horizontal global solar radiation decomposition models, hourly diffuse radiation on inclined surface models, and sky temperature estimation models are reviewed in this study. Solar radiation models' results are compared with one-year measured data from BCIT campus. With respect to solar radiation, combination of Reindl, et al. (1990) and Skartveit & Olseth (1986) models revealed the best result compare with measured values. Impact of using different solar radiation model on transient heat transfer modelling was reviewed, and 2.26% additional discrepancy on the light-weight wall and 0.47% on the mass-type wall were found. Using different sky radiation models could result in additional deviation of 8% in light-weight wall and 9.3% in mass-type wall compare with reference results.

Transient thermal simulation results reveal the fact that sky temperature models' estimation have more impact on total transient heat transfer compare to solar radiation models. Overall, in order to conduct an accurate building energy simulation, it is critical to diligently select the proper estimation model for both solar radiation and sky temperature if the measured values are not available.

REFERENCES

- 10211, I. 2007. Thermal bridges in building construction – Heat flows and surface temperatures – Detailed calculations.
- Algarni, S., & Nutter, D. 2015. Survey of sky effective temperature models applicable to building envelope radiant heat transfer. *ASHRAE Transactions*, 121, p.351.
- Aubinet, M. 1994. Longwave sky radiation parametrizations. *Solar energy*, 53(2), pp.147-154.
- Burlon, R., Bivona, S., & Leone, C. 1991. Instantaneous hourly and daily radiation on tilted surfaces. *Solar Energy*, 47(2), pp.83-89.
- Canada, N. R. 2016. *EFFICIENCY, N. R. C. S. O. O. E. Energy Efficiency Trends in Canada 1990 to 2013*. .
- Clark, G., & C. Allen. 1978. The estimation of atmospheric radiation for clear and cloudy skies. *Proceedings of 2nd National Passive Solar Conference (AS/ISES)*, 2:675–8.
- Daguenet, M. 1985. Les séchoirs solaires: théorie et pratique. *Paris: United Nations Educational, Scientific and Cultural Organization*.
- Erbs, D., Klein, S., & Duffie, J. 1982. Estimation of the diffuse radiation fraction for hourly, daily and monthly-average global radiation. *Solar energy*, 28(4), pp.293-302.
- Government of Canada. (n.d.). Retrieved from http://climate.weather.gc.ca/historical_data/search_historic_data_e.html
- Hay, J. 1979. Calculation of monthly mean solar radiation for horizontal and inclined surfaces. *Solar energy*, 23(4), pp.301-307.
- Liu, B., & Jordan, R. 1960. The interrelationship and characteristic distribution of direct, diffuse and total solar radiation. *Solar energy*, pp.1-19.
- Melchor, C. 1982b. New formula for the equivalent night sky emissivity. (model B). *Solar Energy*, 28(6), 489–98.
- Orgill, J., & Hollands, K. 1977. Correlation equation for hourly diffuse radiation on a horizontal surface. *Solar energy*, 19(4), pp.357-359.
- Perez, R., Ineichen, P., Seals, R., & Michalsky, J. 1990. Modeling daylight availability and irradiance components from direct and global irradiance. *Solar energy*, 44(5), pp.271-289.
- Reindl, D., Beckman, W., & Duffie, J. 1990. Diffuse fraction correlations. *Solar energy*, 45(1), pp.1-7.
- Reindl, D., Beckman, W., & Duffie, J. 1990. Evaluation of hourly tilted surface radiation models. *Solar energy*, 45(1), pp.9-17.
- Skartveit, A., & Olseth, J. 1986. Modelling slope irradiance at high latitudes. *Solar energy*, 36(4), pp.333-344.

Roof Windows for Passive Houses – What Can Be Improved?

Jan Tywoniak^{1,*}, Kamil Staněk¹ and Vítězslav Calta¹

¹Czech Technical University in Prague, Czech Republic

*Corresponding email: tywoniak@fsv.cvut.cz

ABSTRACT

In general, skylights and roof windows in pitched roofs can be described as the critical components of buildings concerning heat losses, risk of surface condensation, increased risk of overheating of rooms behind etc. This is very sensible task especially for passive house solutions. The paper informs about studies analyzing the importance of these relatively small areas in the building envelope and more detailed in pitched roof of a passive house. One of the key problems is the position of roof window within the pitched roof construction.

Second part of the paper comments results of detailed analysis of thermal performance for different combination of frame type and glazing. These studies are performed hand in hand with development works. It is documented that such approach can lead to promising results, reducing the thermal transmittance of roof window to 0.7 – 0.5 W/(m²K). If we consider the real roof window quality including the thermal couplings due to window installation such thermal transmittance stays safely below 0.9 W/(m²K).

KEYWORDS

roof window, pitched roof, thermal transmittance, passive house

INTRODUCTION

It is known that roof windows are the weakest components of building envelope. Therefore they are quite unpopular by passive house designers. Nevertheless, they have to be used in some cases and the resulting increased heat transmission must be compensated in order to achieve the passive house criteria. The database of components certified for passive houses (PHI, 2018a) contains only 2 products (for comparison: there are 218 products of passive house suitable vertical windows in this database). The problem with roof window quality is rather complex and starts with the non-optimal position of such window in the pitched roof: Perimeters of window frames are more or less exposed to outdoor condition (Fig.1). Typically for passive houses, no heating body below the window is placed there. This can be a critical issue for avoiding the risk of surface condensation in some details. Even if the heating body would be used its temperature is controlled according to heating demand which does not guarantee the presence of warm air movement near to window surface. From both mentioned reasons only the very best roof windows should be used, carefully checked for very low thermal transmittance and for high enough surface temperature.

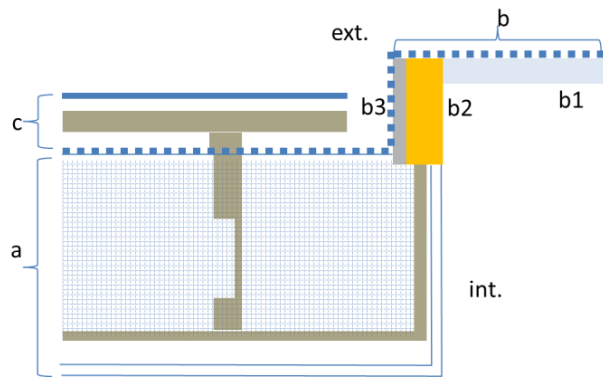


Figure 1. Schematic horizontal cross section of a typical position of roof window in a pitched roof. Dotted line represents the surfaces exposed to the exterior temperatures.

(a typical pitched roof assembly (from interior): indoor gypsum board lining, OSB boards, mineral wool thermal insulation, protective membrane open to water vapor diffusion), b roof window (simplified): b1 glazing unit, b2 frame and sash, b3 possible additional thermal insulating shield), c roof covering)

THERMAL TRANSMITTANCE

Thermal transmittance of the roof window installed in a pitched roof can be described in an extended way as follows (in accordance with PHI, 2018b):

$$U_{w,inst.} = \frac{A_g \cdot U_g + A_f \cdot U_f + \Sigma(\psi_g \cdot l_g) + \Sigma(\psi_w \cdot l_w)}{A_g + A_f}$$

where the $\Sigma(\psi_w \cdot l_w)$ describes the effects of installation. It is illustrated in Fig.2 for hypothetical window of excellent quality: Assumed thermal transmittance of glazing $0.60 \text{ W}/(\text{m}^2\text{K})$, frame U_f $0,60 \text{ W}/(\text{m}^2\text{K})$, thermal bridges of glazing edge expressed by linear thermal transmittance ψ_g $0,03 \text{ W}/(\text{mK})$, thermal bridge due to installation in the roof (ψ_w $0,05 \text{ W}/(\text{mK})$), considering the reference window size $1.14 \text{ m} \times 1.40 \text{ m}$. It can be seen that for improvements of roof windows all parts are of a high importance: glazing, frame and installation method and overall geometry.

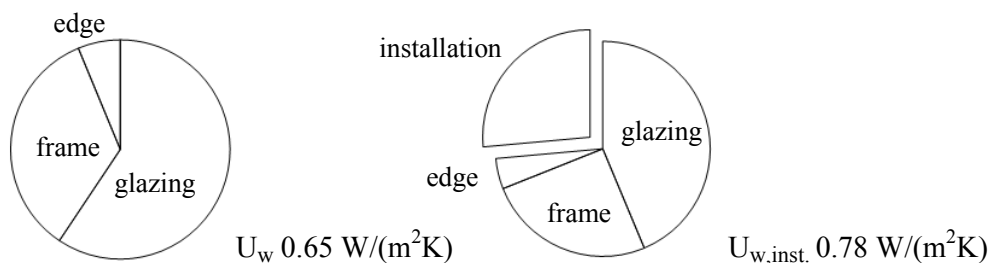


Figure 2. Result of a study for excellent roof window in typical position in pitched roof (see Fig.1). Heat transfer of window (left), heat transfer of window including installation in the pitched roof (right) based on 2D calculations for all relevant cross sections.

IMPORTANCE OF ROOF WINDOWS IN HEAT LOSS OF BUILDING ENVELOPE

Two studies were performed to show the influence of roof window in the overall transmission heat loss of a building envelope for simple single family house. Thermal transmittances used here are based on standard requirements (CSN 73 0540-2, 2011) as well as on recommendations for passive buildings published there. First study (Fig.3, Tab.1) deals with the whole building envelope. The second one (Tab.2) is focused to pitched roof only – with or without windows, considering different thermal qualities. At the pitched roof of 140 m² for a passive house is the opaque part responsible for 77 % and the roof windows (6 pcs a 1 m²) for 23 % of heat losses respectively. This corresponds to and ¼ increase of heat losses compared to the roof without windows.

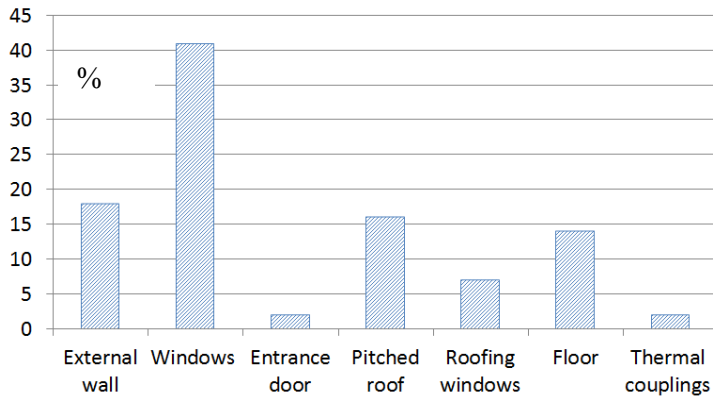


Figure 3. Distribution (%) of transmission heat loss for simple single family house with typical values needed for reaching passive house level.

Table 1. Data for case study – Effect of 6 roof windows in the building envelope.

	Thermal transmittance [W/(m ² K)]	Area [m ²]
External walls	0.15	120
Windows in walls	0.8	46
Doors	1.0	2
Pitched roof	0.10	134
Roof windows (6pcs a 1m ²)	0.8	6
Floor	0.25	100
Overall effect of thermal couplings between building components	+2 %	--

Table 2. Distribution of transmittance heat loss for a pitched roof of the family house with 6 roof windows. Alternative **A** corresponds to traditional solution around year 2000, alternative **B** for passive house quality roof with traditional roof windows, alternative **C** for passive house quality with high performing windows.

	Thermal transmittance	Heat transfer coefficient		Overall increase [%] (100 % = no windows)
		[W/K]	[%]	
A				
Roof	0.3 W/(m ² K)	40.2	69	69
Roof windows	1.8 W/(m ² K)	10.8	19	} 31
Thermal coupling by installation	0.3 W/(mK)	7.2	12	
Total		58.2	100	139
B				
Roof	0.1 W/(m ² K)	13.4	49	49
Roof windows	1.5 W/(m ² K)	9.0	33	} 51
Thermal coupling by installation	0.2 W/(mK)	4.8	18	
Total		27.2	100	194
C				
Roof	0.1 W/(m ² K)	13.4	77	77
Roof windows	0.6 W/(m ² K)	3.6	21	} 23
Thermal coupling by installation	0.02 W/(mK)	0.5	2	
Total		17.5	100	125

DETAILED STUDY

A roof window in typical geometry, usual opening system (horizontal pivot casement) and typical installation in the roof was the subject of thermal analysis during our real development process (UCEEB, 2017) (Figure 5). Frame combining wood (assumed thermal conductivity 0.12 W/(mK)) and hard polymer parts (0.04 W/(mK)) together with two types of glazing (U_g 0.30 and 0.50 W/(m²K)) units were used. Installation is assumed to be carried out using thermal insulating installation frame in the roof (demonstrated here by block of extruded polystyrene thickness 100 mm) or traditionally without such additional frame. Two geometries of interior side lining are assumed: perpendicular to the window or symmetrically slanted (opened) to the interior with an angle of 45°. All data are based on 2D calculations of heat conduction for 4 typical cross sections of windows and related to the reference size 1.14 m x 1.40 m. The thermal transmittance of respective frames and linear thermal transmittance of glazing edges were calculated according to EN ISO 10 077-2. Adiabatic boundary layer was set according to EN ISO 12 567-2. The ratio of glazed area to full projected area of the window is 0.63.

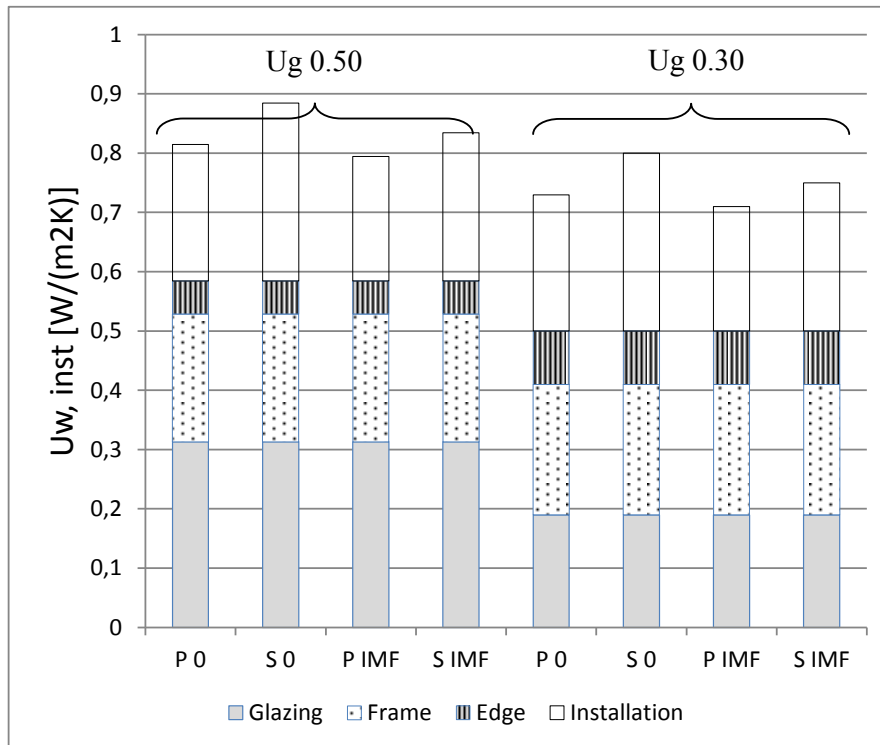


Figure 5. Thermal transmittance of roof windows with the newly developed frame (U_f 0.59 W/(m²K)) and two types of glazing (U_g 0.30 and U_g 0.50 W/(m²K) respectively). (P for perpendicular, S for slanted side lining, IMF for insulating mounted frame)

The results presented in Fig. 5 can be summarized as follows: Even with the (still un-usual) best glazing unit ($U_g = 0.30$ W/(m²K)) and optimized window frame ($U_f = 0.59$ W/(m²K)), the U -value of the window installed in typical configuration (P 0) is 0.72 W/(m²K). With a standard triple-glazed unit ($U_g = 0.50$ W/(m²K)) the overall U -value rises to 0.88 W/(m²K).

The thermal coupling due to installation, which can be hardly avoided, plays a significant role in both cases ($\psi_w \cdot l_w = 0.23$ W/(m²K)).

The additional thermal insulating frame (IMF) has effect only in combination with slanted interior lining (S), where it lowers the thermal transmittance of about 0.05 W/(m²K). The installation with slanted interior lining (S 0) has higher thermal transmittance of about 0.05 W/(m²K) compared to perpendicular case (P 0). However, this solution may still be preferable due to better distribution of daylight.

RESULTS

The relative high influence of roof window for overall thermal transmittance was identified. In order to reach the passive house criteria the increased thermal loss even by the best possible roof windows has to be compensated. It is advantageous to combine the best glazing with a frame having the thermal transmittance in the same range. Best option seems to be the use of a high performing insulation material directly in the frame. In order to reduce the negative impact of the installation in the roof additional installation components (mounting frames) can be used or (better) the window frame itself should contain corresponding continuing thermal insulation material on its perimeter.

The geometry of side lining (widening to interior) has no significant negative influence on heat loss due to limited amount of thermal insulation there (UCEEB, 2017).

CONCLUSION AND OUTLOOK

Consistent and complex application of building physics instruments can effectively accompany ongoing development works. All parts of future roof window should be optimized in order to achieve plausible results: Of critical importance is the frame in terms of material choice and shape. The form of installation has a big influence on the final result as well.

Based on these findings our research will continue in following directions:

- a) Developing and testing of a real solution together with industrial partner according to already performed theoretical and experimental studies (not published here). It is expected that the frames will be alternatively made of hard polymer with appropriate surface layer (high pressure laminate, veneer lumber etc.) or made of high quality wood profiles combined with hard polymer.
- b) Continuation in theoretical and experimental research concerning heat transfer at surfaces of windows in order to guarantee no condensation risk there, especially for situations without possible positive effects of heating bodies placed below.
- c) Continuation (UCEEB, 2017) in day-lighting experimental studies for optimum size and installation. The side lining widened to interior can support better distribution of daylight. In general, such measure can lead to sufficient daylight with smaller window areas which has an additional energy saving effect.
- d) Studies about optimum shading and estimation of overheating risks.

ACKNOWLEDGEMENT

This work has been supported by the Ministry of Education, Youth and Sports within National Sustainability Programme I, project No. LO1605 and by Technology Agency of the Czech Republic, project No. TH01021120.

References

- EN ISO 10 077-2. Thermal performance of windows, doors and shutters - Calculation of thermal transmittance - Part 2: Numerical method for frames
- EN ISO 12 567-2. Thermal performance of windows and doors - Determination of thermal transmittance by hot box method - Part 2: Roof windows and other projecting windows
- PHI, 2018a: https://database.passivehouse.com/de/components/list/roof_window. 25.2.2018
- PHI, 2018b: http://www.passiv.de/downloads/03_zertifizierungskriterien_transparente_bauteile.pdf
- UCEEB, 2017. Project TH01021120 Interim report, not public.
- CSN 73 0540-2, 2011 Thermal protection of buildings. Part 2 -Requirements, UNMZ 2011

Nomenclature

U thermal transmittance $W/(m^2K)$

A area m^2

l length m

ψ linear thermal transmittance $W/(m.K)$

indexes

g glazing, f frame, w window, inst installed

Sensitivity Analysis Using the SWMM LID Control for an Extensive Green Roof in Syracuse, NY

Lucie L. Worthen^{1,*} and Cliff I. Davidson^{1,2}

¹Department of Civil and Environmental Engineering, Syracuse University, 151 Link Hall, Syracuse, NY 13210

²Center of Excellence in Environmental and Energy Systems, Syracuse University, Syracuse, NY 13210

**Corresponding email: llworthe@syr.edu*

ABSTRACT

Green roofs are a popular form of sustainable drainage infrastructure. They provide many environmental benefits, such as reducing peak urban stormwater runoff by enabling retention and evapotranspiration similar to natural conditions. Each green roof has unique hydrologic behavior based on physical properties of its growth medium, types of vegetation, structural design, and climate. To improve the application of green roof technology at a site, there is a need to predict stormwater mitigation for several designs before commencing green roof construction. The Storm Water Management Model (SWMM) includes a low impact development control module which makes it possible to model the hydrologic performance of a green roof by directly defining the physical characteristics of its layers. In this study we compare the outputs of the SWMM model with hydrologic performance data from a large extensive green roof in Syracuse, NY from April 2017 to October 2017. Our objectives are to evaluate the performance of SWMM as a long-term modeling software appropriate for predicting the hydrologic performance of a green roof, and to explore changing parameters that might improve hydrologic performance when designing future green roofs. It is expected that this work will help designers of green roofs in climates similar to those of Central NY. In the future, more extensive hydrologic data will be obtained to enable better assessment of SWMM as a tool to help design green roofs.

KEYWORDS

Green roof, SWMM, Green roof modelling, Stormwater management, Green infrastructure

INTRODUCTION

Urbanization contributes to an increase in impervious surfaces and a decrease in land area covered by soil and vegetation. This reduces ecosystem services such as infiltration and evapotranspiration, leading to an increase in urban stormwater runoff. Green infrastructure (GI), which is an important component of low impact development (LID), is being used in urban settings to restore ecosystem services. Green roofs, a form of GI, can restore ecosystem services by retaining and detaining stormwater runoff (Carson et al. 2013; Li and Babcock, 2014) and increasing urban biodiversity (Baumann, 2006; Francis and Lormier, 2011).

Monitoring studies have been conducted to understand the hydrologic performance of green roofs (Peng and Stovin, 2017). Since green roofs vary in configuration, they can range in retention and detention rates (Carson et al. 2013). Though many studies have aided in understanding green roof performance (Heusinger et al. 2018), this indicates the need for engineers to accurately forecast green roof performance through the application of modelling whenever a new green roof is built. The Storm Water Management Model (SWMM) is the most

commonly used commercial hydrologic and hydraulic model and provides a quick assessment tool for quantifying the hydrologic performance of GI (Li and Babcock 2014).

The first objective of this study is to assess the SWMM model as a tool for predicting hydrologic performance of a green roof by comparing model outputs with monitoring data from a full-scale, extensive green roof located in Syracuse, NY. The second objective is to perform a sensitivity analysis which will lead to future adjustment of the model parameters and verification. This research is still in an early phase.

METHODS

Green Roof Test Site

The study site is a 5550 sq. meter green roof located on the roof of the Nicholas J. Pirro Convention Center (the OnCenter) in downtown Syracuse, New York (43.04368N, 76.14824W). See Squier-Babcock and Davidson (2018) for a detailed description of the site, drainage design, and monitoring equipment.

Precipitation, runoff, and temperature data have been collected between 4/1/17 and 10/31/17 at 5-minute intervals. Common retention and detention metrics are used to quantify performance. Retention is calculated cumulatively for the entire monitoring period. For the purposes of comparison, rainfall and runoff are expressed as equivalent depth in mm.

EPA SWMM Model

The EPA Storm Water Management Model (SWMM version 5.1.012) is a dynamic hydrology, hydraulic, and water quality simulation model that can be used for both single-event or continuous simulation (Rossman, 2015). The LID controls in SWMM are designed to specifically model GI, such as green roofs. The LID controls work by performing and tracking moisture balances between different vertical layers that are defined by parameters in the graphical user interface.

To model restoration of retention capacity, SWMM has five methods for calculating Potential ET (PET). In this study, following the methods of Peng and Stovin (2017), monthly PET values are calculated using the Hargreaves equation (Marasco et al. 2015) which is standard in SWMM. Note that SWMM models ET strictly as a constant proportion of PET and does not automatically account for the reduction in actual ET (AET) that occurs during moisture limited periods. The proportion can generally be used to account for crop variability or moisture limited months (Peng and Stovin, 2017). For this analysis, the proportion was initially set to 1.

The green roof is modelled in SWMM as a subcatchment that is 100% occupied by the green roof and has an outlet. The dimensions of the subcatchment are 111 m width by 50 m length since the water flow path is perpendicular to the width, which represents the actual flow path of the OnCenter roof. To test the accuracy of the ET component of the model for predicting long-term retention, SWMM is used to generate runoff for the period of 4/1/17 to 10/31/17 at an hourly temporal resolution, avoiding periods of freezing.

The long-term simulation used observed precipitation from the OnCenter green roof site. Monthly PET values were calculated with monthly temperature minimums, maximums, averages, and the geospatial location of the OnCenter. The initial green roof parameter values were estimated from field measurements by Squier and Davidson (2016), Yang and Davidson (2017), and CH2M who performed the initial modelling studies of the OnCenter green roof, and SWMM default values. The values and sources for each parameter utilized in the SWMM Bioretention Module are presented in Table 1.

Table 1. SWMM Parameters and Initial Values for Uncalibrated Simulations

Parameter	Initial Value	Data Source
<u>Subcatchment</u>		
ET coefficient	1	Default
Area	5600 m ²	Squier and Davidson (2016)
Width	110.8 m	Squier and Davidson (2016)
<u>Surface Layer</u>		
Berm Height	0	CH2M Estimate
Vegetation Volume	0	CH2M Estimate
Surface Roughness	0.4	CH2M Estimate
Surface slope	1%	Squier and Davidson (2016)
<u>Soil (substrate)</u>		
Thickness	7.6 cm	Squier and Davidson (2016)
Porosity	0.5	Yang and Davidson (2017)
Field capacity	0.2	CH2M Estimate
Wilting point	0.1	CH2M Estimate
Conductivity	32,400 mm/hr	Yang and Davidson (2017)
Conductivity slope	10	CH2M Estimate
Suction head	41.7 mm	CH2M Estimate
<u>Storage</u>		
Thickness	304.8 mm	CH2M Estimate
Void ratio	0.02	CH2M Estimate
Seepage Rate	0	CH2M Estimate
Clogging Factor	0	CH2M Estimate
<u>Drain</u>		
Flow coefficient	0.075	CH2M Estimate
Flow exponent	0.5	CH2M Estimate
Offset Height	0	CH2M Estimate

Sensitivity Analysis

To determine the parameters that would most effectively minimize the difference between observed and simulated results, a sensitivity analysis was performed using the long-term simulation results. The method suggested by Rosa et al. (2015) and Peng and Stovin (2017) was followed, where each single parameter is adjusted over a range of plus or minus 10 and 50 percent of its original value while holding the other parameter values constant. The difference in annual retention and annual runoff volume were determined for the long-term simulation. Sensitivity was calculated using Eq. (1) (Rosa et al. 2015; Peng and Stovin, 2017):

$$Sensitivity = \left(\frac{\delta R}{\delta P} \right) \left(\frac{P}{R} \right) \quad (1)$$

Where δR = the difference between the original and the new model output; δP = the difference between the original and the adjusted parameter value; R = the original model output; and P = the original value of the parameter.

Validation

The Nash-Sutcliffe model efficiency (NSME) coefficient in Eq. 2 (Nash and Sutcliffe, 1970) was used to reflect the accuracy of the model results as compared to the collected data. An NSME value equal to 1 indicates that the model predicted the performance of the green roof

perfectly, while an NSME value greater than 0.5 is still an indication of acceptable model performance (Rosa et al. 2015, Peng and Stovin, 2017). The long-term simulation hourly results were compared in this study to determine an NSME value.

$$NSME = 1 - \left[\frac{\sum_1^N (Q_m - Q_p)^2}{\sum_1^N (Q_m - Q_{Am})^2} \right] \quad (2)$$

where N = number of samples; Q_m = runoff observed; Q_p = modeled runoff; and Q_{Am} = mean observed runoff.

In the future continuation of this work, single events will be modelled and evaluated with NSME. The subsequent NSME values from this study and future studies will lead to evaluation of the model.

RESULTS

Uncalibrated Long-Term Simulations

Long-term simulations run with these initial parameter values show less than ideal agreement. The cumulative runoff predicted by SWMM totaled 345 mm while the cumulative runoff collected from the green roof totaled 451 mm, or about 100 mm difference. As Figure 1 shows, the model consistently underestimates the amount of runoff compared with the observations. The value of NSME is -0.07. One possible cause of the disagreement is that SWMM may be overestimating ET; work is underway to explore the reasons for the difference. These are the very first results using SWMM with this green roof, and we expect results will improve as we continue to measure roof characteristics rather than using default values and estimates.

Sensitivity Analysis

The results of the sensitivity analysis are presented in Table 2. The negative sensitivity values indicate a decrease in corresponding runoff volume or annual retention, while positive values indicate an increase. The total runoff volume and annual retention were found to be influenced by the ET coefficient, the soil field capacity, and the soil wilting point. The surface slope, soil porosity, soil conductivity, conductivity slope, suction head, storage void ratio, drain flow coefficient, and drain flow exponent were found to have less impact on the model results. For one run, the values were not valid because porosity cannot be smaller than field capacity. Both the annual retention and the total annual runoff were most sensitive to a change in the soil field capacity, followed by the wilting point, and then the ET coefficient. Field capacity influences the retention capacity; wilting point and ET influence retention recovery. Both retention capacity and recovery are essential contributors to annual retention performance. The importance of both ET and field capacity in green roof performance have been cited in many studies (Peng and Stovin, 2017; Cipolla et al. 2016; Stovin et al. 2013).

DISCUSSION

The SWMM bioretention module for a green roof with a drain has the potential to be an accurate model representation. However, the initial results of consistently underestimating runoff points to the way that a green roof's storage capacity is restored – ET. The sensitivity analysis identifies the importance of ET in green roof retention, which is well supported by many studies (Stovin et al. 2013; Peng and Stovin, 2017). The use of the Hargreaves equation, a temperature-based model for ET, and the standard option in SWMM, could contribute to overestimate ET during moisture limited conditions. Further examination of alternative options for ET modeling will be explored, specifically related to energy-based models and PET versus AET, in pursuit of model simulation and observed agreement with data.

Table 2. Sensitivity of Annual Retention and Annual Runoff Volume to SWMM Bioretention Parameters Adjusted $\pm 10\%$ and $\pm 50\%$

Parameter	-50%		-10%		10%		50%	
	Annual Retention	Runoff Volume	Annual Retention	Runoff Volume	Annual Retention	Runoff Volume	Annual Retention	Runoff Volume
ET coefficient	-0.343	0.369	-0.277	0.292	0.229	-0.247	0.187	-0.202
Surface slope	0	0	0	0	0	0	0	0
Soil porosity	-0.0004	0.0004	0	0	0	0	0	0
Soil field capacity	-	-	-1.045	1.127	0.936	-1.010	0.667	-0.720
Soil wilting point	0.414	-0.447	0.471	-0.508	-0.508	0.547	-0.583	0.629
Soil conductivity	0	0	0	0	0	0	0	0
Conductivity slope	0	0	0	0	0	0	0	0
Suction head	0	0	0	0	0	0	0	0
Storage void ratio	0.003	-0.004	0.005	-0.005	0	0	0	0
Drain flow coefficient	0.001	-0.002	0	0	0	0	0	0
Drain flow exponent	0.001	-0.002	0	0	0	0	0	0

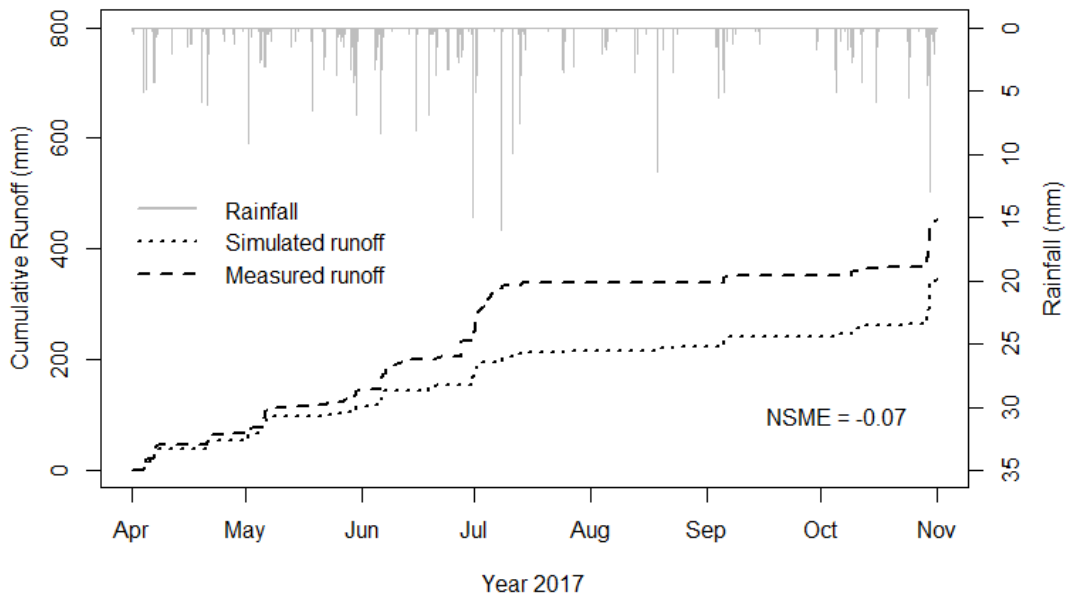


Figure 1. Uncalibrated long-term simulation. NSME calculated from hourly runoff. The rainfall is given in mm for each 1 hr timestep. The runoff is given as cumulative depth in mm.

CONCLUSIONS

The initial comparison of the results obtained from the OnCenter green roof and the SWMM bioretention module needs further investigation before concluding that the model can represent the hydrology of a green roof. The concepts of accurate PET versus AET and antecedent dry weather period are important for green roof model representation. This study is merely a first step in validating SWMM as an accurate model for a green roof in Syracuse, NY.

ACKNOWLEDGMENTS

This material is based upon work supported by the National Science Foundation under Grant No. DGE-1449617 and Grant No. SBE-1444755. Any opinions, findings, and conclusions or recommendations expressed in this paper are those of the authors and do not necessarily reflect the views of the National Science Foundation.

REFERENCES TO BE UPDATED

- Baumann, N. (2006). "Ground-nesting birds on green roofs in Switzerland: Preliminary observations." *Urban Habitats*, 4(1), 37–50.
- Carson, T. B., Marasco, D. E., Culligan, P. J., and McGillis, W. R. (2013). "Hydrological performance of extensive green roofs in New York City: observations and multi-year modeling of three full-scale systems." *Environmental Research Letters*, 8(2), 024036.
- Cipolla, S. S., Maglionico, M., & Stojkov, I. (2016). A long-term hydrological modelling of an extensive green roof by means of SWMM. *Ecological Engineering*, 95, 876–887.
- Francis, R.A. and Lorimer, J., 2011. "Urban reconciliation ecology: the potential of living roofs and walls." *Journal of Environmental Management*, 92, 1429–1437.
- Heusinger, J., Sailor, D. J., & Weber, S. (2018). "Modeling the reduction of urban excess heat by green roofs with respect to different irrigation scenarios." *Building and Environment*, 131, 174–183.
- Li, Y. and Babcock, R.W., 2014. "Green roof hydrologic performance and modeling: a review." *Water Science and Technology*, 69, 727–738.
- Marasco, D. E., Culligan, P. J., & McGillis, W. R. (2015). "Evaluation of common evapotranspiration models based on measurements from two extensive green roofs in New York City." *Ecological Engineering*, 84, 451–462.
- Nash, J. E., and Sutcliffe, J. V. (1970). "River flow forecasting through conceptual models. Part I: A discussion of principles." *J. Hydrol. (Amsterdam, Neth.)*, 10(3), 282–290.
- Peng, Z., & Stovin, V. (2017). Independent Validation of the SWMM Green Roof Module. *Journal of Hydrologic Engineering*, 22(9), 1–12.
- Rossman, L., 2015. Storm Water Management Model Reference Manual Volume I-Hydrology.
- Squier, M. and C. I. Davidson (2016), "Heat flux and seasonal thermal performance of an extensive green roof." *Building and Environment*, 107 235-44.
- Squier-Babcock, M and C. I. Davidson (2018), "Hydrologic performance of an extensive green roof system in Syracuse, NY." Manuscript in preparation.
- Stovin, V., Poë, S., & Berretta, C. (2013). "A modelling study of long term green roof retention performance." *Journal of Environmental Management*, 131, 206–215.
- Yang, Y. and C. I. Davidson (2017), "Green roof performance influenced by growth medium characteristics", Poster Presentation, 15th Annual New York State Green Building Conference, Syracuse, NY, March 30-31, 2017.

Simulation of Building Physics for Beginning Design Students

Alexander Timmer¹

¹University of Wisconsin – Milwaukee, Milwaukee

*Corresponding email: timmer@uwm.edu

ABSTRACT

Concepts such as heat transfer, stack effect, natural ventilation, and other problems related to building physics are taught to beginning design students through architectural examples, deterministic diagrams, and rules of thumb. Unlike the approach to teaching form, which involves exploration and iteration within a studio environment, often suspending disbelief to allow exploration, these exercises see architecture through the lenses of optimization, equilibrium, and objective outcomes. They are taught as steady state concepts. Instead of leaning on teaching techniques derived from an engineering standpoint, often technocratic and deterministic, it would serve beginning design students well to explore these concepts through experimentation and scaled built models that demonstrate the intended atmosphere effect. Can we ask the students to think compositionally about an architectural atmosphere in the way we ask them to think about form, proportion, sequence, and hierarchy? The goal then is to have students learn to think about atmosphere and energy from a design standpoint. As Kiel Moe notes, this point of view comes from an understanding of architecture and energy as one of magnificence and not of management. (Moe, 2017) With the help of students at the University of Wisconsin – Milwaukee, this research looks to explore reciprocal design techniques that allow students to iterate within an open system of their design. This ongoing investigation looks to grow the rigor and accessibility of scaled physical simulation of atmosphere and energy in buildings within a beginning design student studio.

KEYWORDS

Buoyancy Ventilation, Simulation, Physical Models, Early Design Education, Design Process

INTRODUCTION

This research is focused on the physical simulation of building physics. This ongoing research attempts to balance a desire for the visual representation of building physics for use in the architectural design studio with a repeatable and measurable outcome. While the primary purpose of the model is not measurement, the various inputs of heat and matter are scaled appropriately. Using the concept of similitude, this model is scaled to allow for the building of a representational section, which can then be heated to demonstrate the flow of fluid through the section. While focusing primarily on the simulation of buoyancy ventilation in two dimensions, this project develops a working methodology that encourages iteration. Students design parts within Rhino 3D, print them with a 3D printer, test them in the rheoscopic fluid bath, document them with a long exposure camera, evaluate the results and then repeat the process. This work was completed as part of an exhibition and workshop at the University of Wisconsin – Milwaukee.

METHODS

This design exercise asked students to work through a fixed loop. Students design a section within Rhino 3D, print them with a 3D printer, test them in a rheoscopic fluid bath, document them with a long exposure camera, evaluate the results and then repeat the process. The first

step is the design of an initial section in Rhino 3D, a NURBS modelling software. Students are asked to produce sectional models in which the wall thickness is fixed at .8mm. While the first section is a guess on the student's part, the next model made will be informed by the process to come. The second step is the printing of the student's design. Students print their sections 6mm thick out of PLA plastic. For the third step students place their prints into a heated bath. The parts are pinched between a piece of glass and the milled aluminium back which heats that fluid. The medium of the bath is a rheoscopic fluid that makes the flow visible. (Figure 3) A heating element is mounted to the back of the aluminium half of the tank. After this, students document the sections with a camera, make changes to their design and repeat the process. The models were scaled using similitude and the Galileo Number. (Etheridge, 2011)

RESULTS

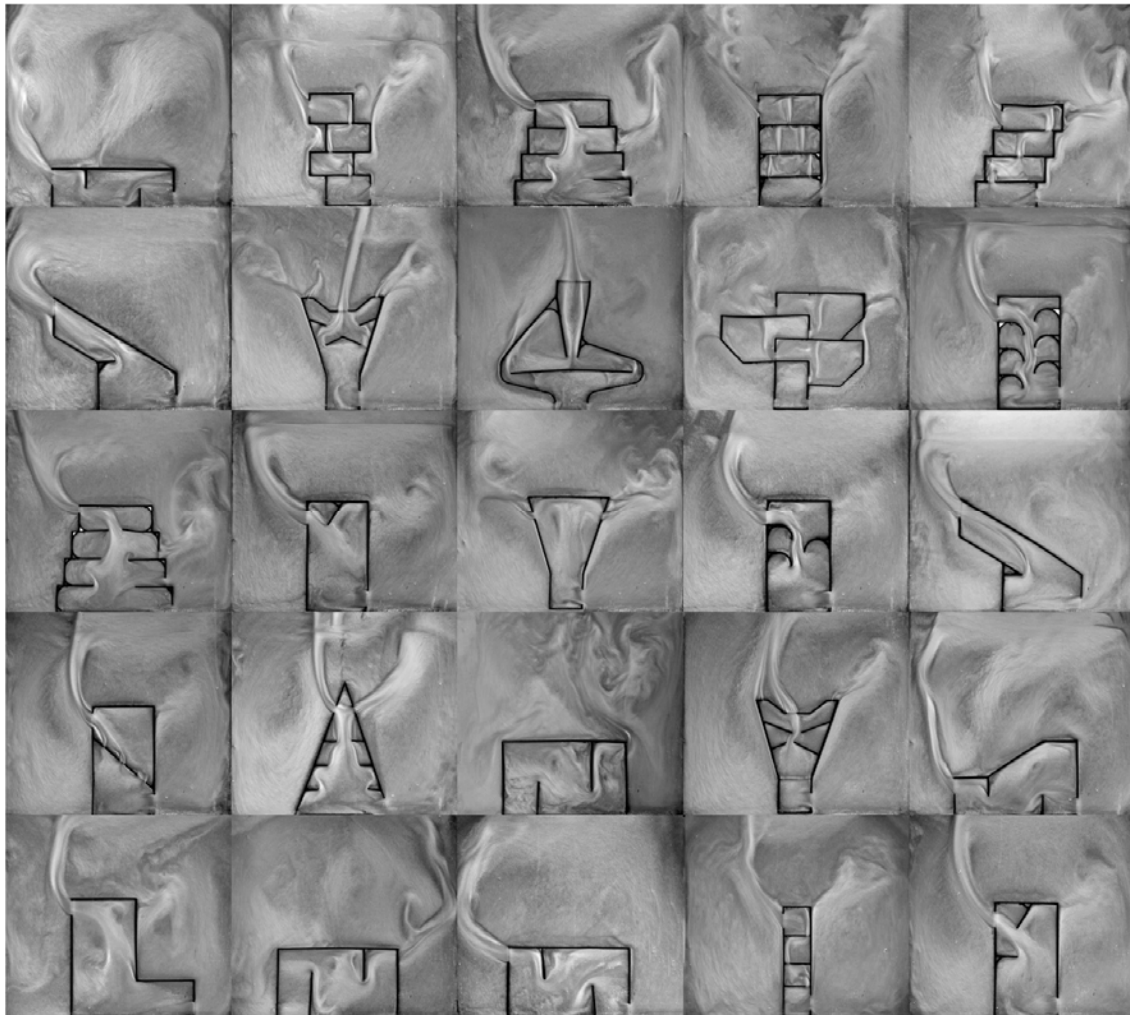


Figure 1. Iterations produced by the students.

The students produced a wide range of examples. (Figure 1,2) The studies often led to a series of variations in which each student explored the role of shape, form, and proportion in the flow of fluid by buoyancy ventilation. The more successful explorations used simple forms to better understand the effects of their design decisions. While the models are essentially two dimensional, they offer a way into the process of natural ventilation from the point of view of

a designer. The work was exhibited and functioned as a workshop to introduce the students to the concept of buoyancy ventilation. (Figure 4, 5, 6)



Figure 2. Long exposure documentation of rheoscopic fluid.



Figure 3. Rheoscopic fluid tank with section.



Figure 4. Exhibition and workshop.



Figure 5. Exhibition and workshop.

Equations

$$Ga_M \equiv \left[\frac{\Delta T_0}{T_0} \right]_P \left[\frac{\Delta T_0}{T_0} \right]_M Ga_P \quad (1)$$

Using dimensionless analysis similarity between the model and prototype can be achieved by increasing the ΔT_0 in the model. This equation assumes a simple single cell enclosure in which ventilation is achieved with buoyancy only. (Etheridge, 2011)

Names and units

Ga	Galileo Number
T	Temperature, C°

DISCUSSIONS

The most problematic aspect of these models is the lack of three dimensionality. While the two-dimensional model allows students to understand some of the basic concepts of buoyancy ventilation, it lacks the complex reality of a three-dimensional model. The appropriate application of this pedagogy to the design of a building, not merely proto architectural objects, requires more research. In general, though the next steps in this research will require a transition to three dimensions. Additionally, while this modeling technique allows for the visual approximation of heat driven flows, it does not at this time allow for the measurement of the rate of flow. Although, the appropriate scaling of the model and its heat input should allow for a measurable rate of flow through the openings by mathematical means. As mentioned before, the intended goal of this exercise is the development of a pedagogy that encourages design students to explore building physics as an opportunity for design and spatial innovation.

CONCLUSIONS

When we think of architectural models, we think of them as objects, representational at best, a stand-in for a larger construct. While this has not always been the case historically, new digital measures seek to reduce the physical model further to merely the output of a printer: a stereotomic afterthought. Renaissance model makers, for example, used the model as a stand-in for construction documents that were intended to assist the builders with complex geometry, calculating structural loads, and testing the quality of light. These models participated in the construction of buildings. At the Bauhaus, making was integral to the introductory design exercises, asking students to fold the paper and imagine the spatial and sculptural qualities. The paper though was not a stand-in for another material but the material of study itself. With the advent of the digital model, and more recently the BIM model, the physical artifact has been pushed out. In its transformation, it has lost its material intelligence and its active role in the design process. It has been reduced to a representational artifact and an imperfect imitation of its digital doppelganger. What then is the role of the contemporary physical model, what could its role be in contemporary design practice?

These new operative artifacts find themselves between a study model and a finished representational model. They hang ambiguously between these two states. They are far from pristine, but they are highly rigorous and intensely participatory. They are objects that both represent a complete thought and speak to a possible future. These objects develop out of an understanding of design as an open system, a series of inputs and outputs, in which the model is understood as an active participant in the design process rather than passive byproduct.

ACKNOWLEDGEMENT

I would like to acknowledge the students at University of Wisconsin – Milwaukee and specifically Max Rodencal who helped in the development and initial testing of this pedagogy. This ongoing research was supported through the UWM SURF Grant program.

REFERENCES

- Etheridge, D. (2011). Natural ventilation of buildings: theory, measurement and design. Retrieved from <https://ebookcentral.proquest.com>
- Moe, K. (2017). Magnificence: On the Appearance of the Baths of Caracalla, *Journal of Architectural Education*, 71:2, 241-246

Study on multivariate regression model of indoor and outdoor particulate pollution in severe cold area of China

Yang Lv^{1,*}, Haifeng Wang¹, Yuwei Zhou¹, Tongke Zhao¹, Bin Chen¹, Lei Zhang², Qi Zhao²

¹Dalian University of Technology, Dalian

²Northeast Petroleum University, Daqing

*Corresponding email: lyyang@dlut.edu.cn

ABSTRACT

At present, the widespread existence of haze phenomenon has a serious impact on indoor air quality. Indoor particulate pollution has been paid more and more attention by the society. However, the correlation and diffusion mechanism of indoor and outdoor particulate matter are still controversial. In order to explore the correlation between indoor and outdoor particulate matter of different building types in heating season and non-heating season, the indoor and outdoor particulate concentrations and meteorological parameters of 110 stations in severe cold area of China were monitored by experiments. The analysis shows that indoor and outdoor temperature, humidity, air velocity, wind direction and atmospheric pressure are the main factors affecting indoor and outdoor particulate concentration. And based on these factors, it can model the indoor predicted particulate concentrations by multivariate regression. It also shows a significant difference in the relationship between the concentration of particulate matter and factors of indoor and outdoor particulate matter. Therefore, this study provides a good premise for exploring the health risks and control measures of particulate matter.

KEYWORDS

Particulate Matter, Severe Cold Area, Correlation Analysis, Regression Model

INTRODUCTION

Human inhalable particulate matter (PM₁₀, PM_{2.5}) is the primary pollutant in most cities in China, especially for fine particulate matter (PM_{2.5}). More and more epidemiologists show that there is a positive correlation between human morbidity, mortality and mass concentration of particulate matter (Dockery et al. 1993; Zhao et al. 2015; Tseng et al. 2015; Cohen et al. 2017; Klemm R J et al. 1996). People spend 90% of their time indoors, so indoor air quality plays an important role in human health. The study showed that the outdoor pollution components can enter into the indoor air through natural ventilation, mechanical ventilation and infiltration ventilation. There is a significant correlation between the indoor and outdoor particles. The proportion of indoor PM_{2.5} from outdoor is 30~75% (Dockery and Spengler, 1981; Koutrakis et al., 1992; Ozkaynak et al. 1995; Xiong et al. 2004).

The situation of indoor and outdoor particulate matter in severe cold area of China is different from that in other regions because of geographical location, climatic condition and building type. This paper will via the long-term monitoring of indoor and outdoor particulate concentrations to analyze the correlation between indoor particles concentrations and indoor and outdoor influencing factors of different building types in Daqing, which will provide parameters and basis for indoor particulate matter exposure assessment.

METHODS

Selection of measured objects and sampling points

The sampling points were located in five districts of Daqing which were total of 110 sampling points, including 30 classrooms, 30 offices and 50 residences, among which were divided into urban and rural residences. To get the seasonal variations of particulate pollution, we collected data of summer and winter from November 2016 to April 2017 and June to August 2016, respectively. A sampling point was sited in and out of each room, measured simultaneously. Each point was collected seven days of valid data. To analyze more accurately, the hourly average value of each sampling point was calculated. The measuring instrument includes QT50 particulate online monitor ($\pm 1 \mu\text{g}/\text{m}^3$). The measurements contents include indoor and outdoor temperature, relative humidity and $\text{PM}_{2.5}$ mass concentration. The monitoring time was set to start every 15 minutes, and the data were collected for 5 minutes each time.

Data analysis and processing method

In this paper, the analysis data is mainly based on the hourly average of each parameter. With the SPSS software, the statistical analysis of sampling data was completed, and finished the multiple analysis such as bivariate correlation analysis and multiple linear regression.

Bivariate correlation analysis is an important method to evaluate the relationship between two of variables. Pearson coefficient (r) could measure the extent of correlations, which could be expressed as:

$$r = \frac{\sum(X - \bar{X})(Y - \bar{Y})}{\sqrt{(\sum(X - \bar{X})^2)(\sum(Y - \bar{Y})^2)}} \quad (1)$$

Where X and Y - variables, \bar{X} and \bar{Y} - the averages of variables. In this part, Pearson coefficient (r) is used to express the relationship between indoor particulate concentration and indoor and outdoor influencing factors (such as outdoor particulate concentration, temperature and humidity, etc.).

Multivariate linear regression is a regression with one dependent variable and two or more independent variables, each of which is a single term. It is one of the most commonly used statistical methods in the measurement of microenvironment or exposure of particulate matter. The mathematical model of multivariate linear regression can be expressed as follows:

$$y = a + b_1x_1 + b_2x_2 + \dots + b_nx_n \quad (2)$$

Where, y is a dependent variable; $x_1, x_2 \dots x_n$ are independent variables; $b_1, b_2 \dots b_n$ are coefficients of independence variables; a is a constant term. To ensure the accuracy of the regression model, the errors between the observed and predicted values of five performance

indexes are used in this paper: the normalized absolute error (NAE), the root mean square error (RMSE), the prediction accuracy (PA), the determinant coefficient (R^2) and the index of agreement (IA).

RESULTS AND DISCUSSIONS

Correlation Analysis between Indoor $PM_{2.5}$ concentration and factors

There are many factors affecting indoor particulate concentration, such as indoor particulate source strength, settling rate, air exchanges rate, penetration coefficient, building types and meteorological conditions. The results show that there is a certain relationship between indoor particulate concentration and them above, while little attention has been paid to this aspect in the present researches. By the method of bivariate analysis, Pearson correlation coefficient (r) was used to express the extent of the linear correlation between the indoor particulate concentration and these factors. The probability distribution value ($P < 0.05$) was considered to be statistically significant.

Table 1. The correlation analysis between indoor $PM_{2.5}$ concentration and affecting factors

Building type		T_{in}	RH_{in}	$PM_{2.5}(Out)$	T_{out}	RH_{out}	P	WD	WS	
Office	Summer	r	0.027	0.289	0.734	0.030	0.126	-0.048	-0.183	0.092
		P	0.392	0.000	0.000	0.341	0.000	0.126	0.000	0.003
		N	1041	1041	1041	1041	1041	1041	1041	1032
	Winter	r	0.001	0.007	0.903	0.206	-0.063	-0.296	-0.036	0.198
		P	0.978	0.846	0.000	0.000	0.075	0.000	0.305	0.000
		N	806	806	806	806	806	806	806	806
Classroom	Summer	r	0.199	0.245	0.745	0.143	0.118	-0.083	-0.176	0.052
		P	0.000	0.000	0.000	0.000	0.000	0.008	0.000	0.038
		N	1032	1032	1032	1032	1032	1032	1032	1032
	Winter	r	-0.006	0.349	0.809	0.227	0.071	-0.076	-0.101	0.000
		P	0.862	0.000	0.000	0.000	0.034	0.024	0.003	0.990
		N	886	886	886	886	886	886	886	886
Urban residence	Summer	r	0.071	0.497	0.837	0.21	0.067	-0.235	0.038	0.112
		P	0.006	0.000	0.000	0.000	0.009	0.000	0.146	0.000
		N	1485	1485	1485	1485	1485	1485	1485	1485
	Winter	r	0.008	0.045	0.604	-0.111	0.144	0.027	-0.04	0.033
		P	0.797	0.152	0.000	0.000	0.000	0.392	0.195	0.291
		N	1028	1028	1028	1028	1028	1028	1028	1028
Rural residence	Summer	r	0.159	0.336	0.848	0.205	0.02	-0.217	0.129	0.13
		P	0.010	0.000	0.000	0.001	0.750	0.000	0.037	0.035
		N	263	263	263	263	263	263	263	263
	Winter	r	0.284	0.123	0.862	0.105	-0.034	-0.02	-0.089	0.092
		P	0.000	0.123	0.000	0.190	0.669	0.802	0.267	0.248
		N	158	158	158	158	158	158	158	158

Note: r -Correlation, P - Significance, N - Sampling times, T - Temperature, RH - Relative humidity, P - Atmospheric pressure, WD - Wind direction, WS - Wind speed

Table 1 compares the correlation analysis between indoor PM_{2.5} concentration and indoor and outdoor factors of four building types in summer and winter, statistics of which have significant correlation has been bold. On the whole, it can be found that outdoor PM_{2.5} concentration has the strongest correlation with indoor PM_{2.5} whether it is summer or winter. Indoor PM_{2.5} concentration is positively correlated with indoor and outdoor temperature, humidity and outdoor wind speed, negatively correlated with outdoor atmospheric pressure, and both positively and negatively correlated with outdoor wind direction. However, all these factors are significantly related to indoor particulate concentration for summer. For winter, the main factor of indoor PM_{2.5} concentration is outdoor particulate concentration, the influence of other factors is relatively little. The primary explanation is that the main ventilation mode of the measured buildings is natural ventilation during summer, outdoor particulate matter can enter into the indoor environment which is vulnerable to wind pressure and hot pressure. Outdoor wind speed and atmospheric pressure will affect the indoor and outdoor air exchange rate and the concentration of indoor particulate matter. For the season of winter, the indoor temperature is constant due to the use of heating equipments, which has little effect on the diffusion and transfer of particulate matter. At the meanwhile, doors and windows are always closed and the impermeability of enclosure structure is well, the change of outdoor atmospheric pressure has little effect on the permeation process of indoor particulate matter.

Multivariate regression model fitting

According to the correlation analysis above, it found that all the factors mentioned could affect indoor particulate concentration. Based on these factors, a multivariate linear regression model of indoor PM_{2.5} concentration prediction was proposed. In order to ensure the reliability of the results, the data is divided into two groups, one composed of 70% of the original data for regression, and the other 30% is used to verify the regression model. Table 2 shows the regression model between indoor particulate concentration and factors of four building types in summer and winter. The simulation results are standardized to ensure the comparability among the model parameters, which can be found that the range of determining coefficient R² obtained by calculation of four building types in summer and winter is 0.57 ~ 0.85, indicating that the model has a strong fitting.

Table 2. The regression model between indoor particulate concentrations

	Season	R ²	model
Office	Summer	0.57	$y=0.15x_1+0.28x_2+0.62x_3+0.09x_4+0.04x_5-0.05x_6-0.10x_7-0.05x_8$
	Winter	0.85	$y=0.02x_1-0.03x_2+0.94x_3-0.01x_4+0.01x_5+0.06x_6+0.06x_7+0.04x_8$
Classroom	Summer	0.67	$y=0.09x_1+0.14x_2+0.77x_3+0.02x_4+0.04x_5+0.14x_6-0.03x_7+0.02x_8$
	Winter	0.69	$y=-0.03x_1+0.15x_2+0.80x_3-0.10x_4-0.05x_5+0.01x_6+0.02x_7-0.03x_8$
Urban residence	Summer	0.67	$y=0.09x_1+0.23x_2+0.76x_3-0.02x_4-0.02x_5+0.02x_6-0.03x_7-0.05x_8$
	Winter	0.69	$y=0.08x_1+0.07x_2+0.65x_3-0.04x_4+0.02x_5+0.01x_6+0.01x_7+0.02x_8$
Rural residence	Summer	0.67	$y=0.22x_1+0.14x_2+0.73x_3-0.06x_4-0.11x_5-0.05x_6+0.05x_7+0.03x_8$
	Winter	0.69	$y=0.20x_1+0.06x_2+0.83x_3-0.03x_4-0.09x_5+0.11x_6-0.05x_7-0.02x_8$

Note: x_1 - Indoor temperature; x_2 -Indoor humidity; x_3 -Outdoor PM_{2.5} concentration; x_4 -Outdoor temperature ; x_5 -Outdoor humidity; x_6 -Outdoor atmospheric pressure; x_7 -Outdoor Wind Direction; x_8 -Outdoor air velocity

Table 3. The results analysis of performance indicators

	Office		Classroom		Urban residence		Rural residence	
	Summer	Winter	Summer	Winter	Summer	Winter	Summer	Winter
NAE	0.290	0.344	0.341	0.306	0.271	0.385	0.269	0.527
RMSE	10.250	20.540	8.420	9.710	10.730	14.510	16.890	32.230
R ²	0.740	0.868	0.684	0.664	0.773	0.743	0.876	0.756
PA	0.537	0.834	0.820	0.630	0.122	0.661	0.405	0.628
AI	0.719	0.680	0.724	0.682	0.699	0.997	0.700	0.556

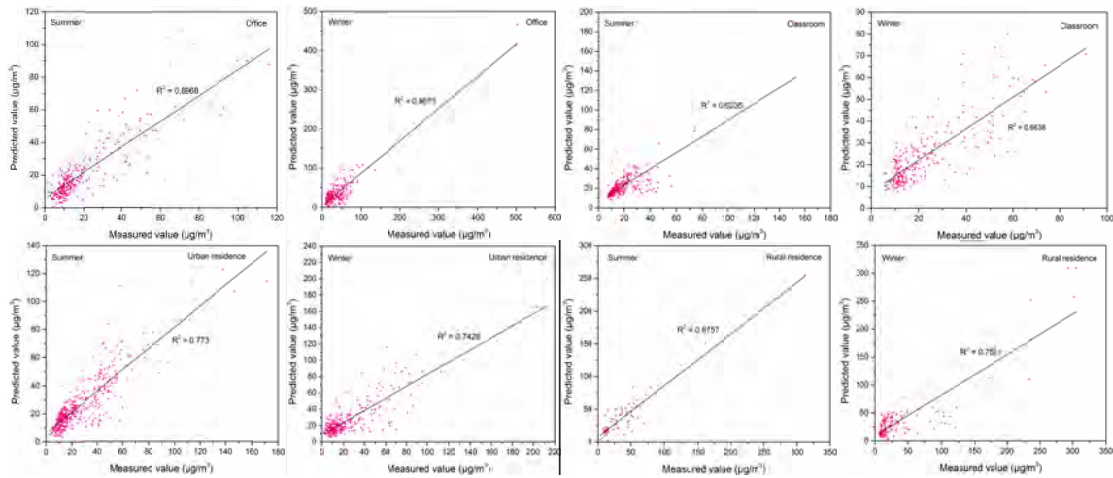


Figure 1. The comparison between predicted and measured values of regression model

According to the results of regression model in Table 2, the predicted value of the model is compared with the measured by 30% test data. Figure 1 is the result of comparison of each model. It can be found that there is a strong correlation between the measured and predicted values of indoor PM_{2.5} concentration. Table 3 shows the analysis results of the errors between the measured values and the predicted values of five performance indexes, the values of NAE, RMSE are relatively small and R², PA and IA are close to 1, which indicates that the prediction model and the method are practical to some extent.

Comparative analysis of model parameters

Table 2 shows the regression results of the model parameters standardization. According to the comparative analysis, it can be found that the outdoor PM_{2.5} concentration plays a leading role in the model, whether it is summer or winter, air velocity and wind direction are relatively weak, while the other parameters have their diversities respectively. For heating season, the influence of indoor temperature and humidity account for a large proportion of the model, while small in the non-heating season. Therefore, the correlation between indoor particulate concentration and all the parameters has significant seasonal differences, while no for different building types.

CONCLUSIONS

In this paper, the indoor and outdoor particulate concentrations of four building types were monitored to analyze the correlation and factors of indoor and outdoor particulate concentrations and establish the prediction model of indoor particulate concentration. Specific conclusions are as followed:

- (1) Outdoor temperature and humidity, air velocity, wind direction and atmospheric pressure are the main factors affecting indoor particulate concentration. According to the results, indoor $PM_{2.5}$ concentration is positively correlated with indoor and outdoor temperature and humidity as well as outdoor air velocity, negatively with outdoor atmospheric pressure and both positively and negatively with outdoor wind direction.
- (2) Based on these factors, the study uses multivariate linear regression to establish the indoor $PM_{2.5}$ concentration prediction model. No matter in summer and winter season, outdoor $PM_{2.5}$ concentration plays a leading role in the model, the outdoor air velocity and wind directions are relatively weak, while the other parameters have their diversities respectively.

ACKNOWLEDGEMENT

This research is supported by the China Environmental Protection Project (201509063), the National Nature Science Foundation of China (91743102, 51578103).

REFERENCES

- Dockery D W, Pope C A, Xu X P, et al. 1993. An association between air pollution and mortality in six United-States cities. *New England Journal of Medicine*, 329(24), 753-759.
- Zhao J, Bo L, Gong C, et al. 2015. Preliminary study to explore gene- $PM_{2.5}$ interactive effects on respiratory system in traffic policemen. *International journal of occupational medicine and environmental health*, 28(6), 971-983.
- Tseng E, Ho W C, Lin M H, et al. 2015. Chronic exposure to particulate matter and risk of cardiovascular mortality: cohort study from Taiwan. *BMC public health*, 15(1), 936.
- Cohen A J, Brauer M, Burnett R, et al. 2017. Estimates and 25-year trends of the global burden of disease attributable to ambient air pollution: an analysis of data from the Global Burden of Diseases Study 2015. *The Lancet*.
- Klemm R J, Mason R M, Heilig C M, et al. 1996. Is daily mortality associated specifically with fine particles? *Journal of the Air & Waste Management Association*, 46(10), 927-965.
- Dockery D W, Spengler J D. 1981. Indoor-outdoor relationships of respirable sulfates and particles. *Atmospheric Environment (1967)*, 15(3), 335-343.
- Koutrakis P, Briggs S L K, Leaderer B P. 1992. Source apportionment of indoor aerosols in Suffolk and Onondaga Counties, New York. *Environmental Science & Technology*, 26(3), 521-527.
- Ozkaynak H, Xue J, Spengler J, et al. 1995. Personal exposure to airborne particles and metals: results from the Particle TEAM study in Riverside, California. *Journal of Exposure Analysis and Environmental Epidemiology*, 6(1), 57-78.
- Xiong ZM, Zhang GQ, Peng JQ, et al. 2004. The research status of indoor inhalable particulate matter pollution. *HVAC*, 34 (4), 32-36.

The Design, Construction and Commissioning of a Small Scale Dynamic Calibrated Hot Box (CHB)

Timothy P. O’Leary^{1,*}, Aidan Duffy²

¹Dublin Institute of Technology, Ireland

²Dublin Institute of Technology, Ireland

**Timothy.oleary@dit.ie*

ABSTRACT

Sustainable construction and in particular the sustainability of materials is a global issue with legislation on material properties and product performance at the forefront. In traditional constructed buildings however, it can be extremely challenging to get accurate data on performance. The variability of building materials design, manufacture and construction from different eras is substantial, even within local areas due to the vernacular nature of construction from these periods. Material properties testing can be expensive and is not always readily available when required and is therefore often ignored, particularly in the retrofitting of historic buildings. This can have major adverse effects on the building fabric and for its inhabitant’s health if the appropriate material interventions are not chosen. An inexpensive environmental chamber for testing such materials has been designed and built at the Dublin Institute of Technology, (DIT) Ireland, adopting comparable standards from EN ISO 8990 and ASTM C1363. This paper describes the design requirements for the construction of an affordable and mobile calibrated hot box (CHB) for the testing of historic materials. A characterisation panel has been used to carry out early calibration testing and the results of this are discussed. Improvements and tweaking of the first test are also discussed.

KEYWORDS

Calibrated hot box, Historic materials, Characterisation panel, Data acquisition.

INTRODUCTION

Buildings’ energy consumption accounts for approximately 40% of total energy use in developed countries. The legislation on energy efficiency in buildings, such as the EU Directive 2010/31 has tried to raise minimum energy efficiency standards, for both the single components and the entire building. The building fabric plays a fundamental role in its energy balance, particularly the thermal properties when exposed to moisture and often generic values are used in ideal situations when modelling. In solid walled structures these values are, expensive and difficult to accurately ascertain due to the inconsistency of materials.

To establish accurate and reliable data on structures with different materials used in the one homogenous unit requires different approaches such as numerical simulation, but this is only as accurate as the accuracy of the inputs which often tend not to be validated. Hot boxes have been used to establish accurate properties with guarded hot boxes used mainly for commercial use and calibrated hot boxes used in laboratory work, where often it is necessary for greater levels of refinement and accuracy be achieved. The design of the hot box produced at the DIT was motivated by the need for such testing of small building elements from historic buildings primarily. These material dimensions influenced the design and construction of the whole apparatus and in particular the dimensions of the panel which hosts the sample.

Hot boxes require two closed rooms kept at constant, individual temperatures: a metering chamber, which is warm and the environmental chamber that is cold. A test wall typically containing the specimen under test, divides the two chambers. The overall thermal resistance

is evaluated from the heat flux between the two chambers including that of the internal and external air resistances. This research paper looks at the design, build and calibration of a calibrated hot box (CHB) constructed in the Dublin Institute of Technology, incorporating guidelines from EN ISO 8990 and ASTM C1363-05 with the primary aim of designing and constructing an affordable dynamic environmental test chamber. The construction of the facility was carried out in the Dublin Institute of Technology (DIT) workshops and Labs.

Objectives

a) Design and construct a dynamic environmental hot box to meet the input requirements for a later hygrothermal simulation, establishing thermodynamic properties b) Calibrate a small-scale, affordable apparatus for thermal testing of non-conventional materials using a characterisation panel of known thermal conductivity and c) Analyse and compare measured versus theoretical data to establish % error.

Literature review

Typical thermal testing of multilayer wall systems is conducted using a hot box apparatus according to standards comparable to ASTM C1363 [2] and EN ISO 8990 [4]. The properties of non-conventional materials can create challenges when conducting thermal tests using apparatus designed for conventional materials. For example, past tests conducted on historic brick varied in reliability due to poor fit inside conventional testing frames (Baker, 2011). EN ISO 6990 & ASTM Standard C1363-11 details the requirements for design and operation of a test apparatus for evaluating thermal performance of building materials and envelope assemblies by means of a hot box apparatus. The sensors measure the surface-to-surface heat transfer rather than the overall thermal resistance, and the initial performance is evaluated using heat transfer calculations.

Ulgen (2002) measured the time lag and decrement factor using wall compositions of opaque materials in a hot box simulation. Sala et al., (2008) conducted dynamic testing of insulated brick walls using a calibrated guarded hot box. The two types commonly used are the: Guarded hot box : In the guarded hot box, the metering box is surrounded by a guard box in which the environment is controlled to minimize lateral heat flow in the specimen. The total heat flow through the specimen will then be equal to the heat input to the metering box. In practice, there will be a limit in detecting imbalance in each test. (EN ISO 8990) [4]

Calibrated hot box : The calibrated hot box is surrounded by a temperature-controlled space not necessarily at the same air temperature as inside the metering box. The heat losses through the box walls are kept low by using a construction of high thermal resistance. The power input shall be corrected for the wall and flanking losses. The correction for chamber and flanking losses are determined by tests on specimens of known thermal resistance. For flanking loss calibration, the calibration specimens should cover the same thickness and conductivity range as the specimens to be measured and the temperature range of intended use. (EN ISO 8990) Schumacher, et., al.,(2013) constructed a hot box and concluded that the thermal performance of wall assemblies is complex and heavily influenced by factors such as insulation level, air leakage, thermal bridging, operating conditions, moisture content and installation defects and argue that simple R value calculation is not sufficient to address the above factors. They contend that more sophisticated testing is required before a new metric for testing is established. They used finite element programme analysis for the flanking losses.

International Standards lays down the principles for the design of the apparatus and minimum requirement that shall be met. It does not, however, specify a particular design since requirements vary, particularly in terms of size, and also to a lesser extent in terms of operating conditions. This International Standard describes also the apparatus, measurement technique and necessary data reporting.

The air exchange rate (AER) is not often measured in hot box construction and three methods using tracer gases exist for its determination. These are the concentration decay method, the constant injection method, and the constant concentration method (Laussman et al. 2011). The primary function being to establish additional heat losses at junction interfaces.

METHODOLOGY

All thermal bridge calculations were carried out according to EN ISO 10211. Numerical simulations were performed using the 2D and 3D finite element program Psi Therm. The U-value of the metering chamber was calculated according to EN ISO 6946:2007

Design for construction

Concept: It was determined that a calibrated hot box would be the most suitable for the testing requirements within the DIT. The limiting factors in design and dimensioning of the apparatus were the size of the door openings in different buildings as it was constructed in the Bolton street campus, 4-5 Km away. Transportation also determined the overall weight and mobility of the unit and had to be factored into the design and construction. The maximum specimen area achieved was 715mm (L) by 715 mm (H) by 200mm (T). 200mm was chosen as being capable of testing a panel of representative material to achieve accurate results. Bricks from a historic building have been prepared to a test standard size of 180 x 80 x 55mm for testing in the chamber. The following items were addressed: Identification of experiments to be carried out, Comply with standards, Capable of testing historic elements, Self-contained unit, Logging capabilities/ dynamic, Humidifier capacity and location, Highly insulated, Thermal bridge free or as low as practicably possible, Constructible in DIT and mobile, Good compactness ratio, Robust but adaptable specimen holder panel, Cost effective, Compliance and Practical implications re; budget, size, mobility.

Construction of CHB

The hot box, shown in Figure 1 was constructed using a 45 mm medium density fibreboard (mdf) outer structural layer, with one layer of 200mm EPS insulation glued to the inside surfaces with PVA glue. Air leakage was prevented by using a brush-on waterproof tanking layer, this also ensuring that the insulation and mdf thermal properties do not change due to moisture uptake from within. A 100mm wide mdf strip was glued on internally to provide fixings for the heaters/fans thus ensuring no fixings penetrated the eps. Heating is produced by a single 60W resistance heater located as far as is practicably possible away from the specimen. Cooling is provided by the environmental chamber on the other half of the apparatus, -a insulated box identical in size and construction to the metering box. The cooling is provided by a chiller unit placed on top of the unit with the evaporator connected internally. The identical dimensioning of the hot box ensures that air circulation and velocity across the sample face should be almost identical as they are placed in the same position in both boxes. Both boxes were designed to accommodate a 6mm mdf baffle painted matt black, installed 200mm from the face of the test specimen. Air circulation is provided by 2 computer fans per box placed behind the baffles in identical positions. Each specimen prepared for testing, is fitted with insulation plugs around its perimeter, identical to the layers insulating the hot box.

Four castors per box allow for easy opening and closing of the units. External threaded bars are used to tighten the two chambers together during testing, minimising air leakage. A humidifier has been fixed to the outside of the chamber and each chamber is equipped with a humidity probe and 8 thermocouples. All data is acquired and managed by the use of a single National Instruments cRio datalogger using Labview programming.

Calibration: The accuracy of each individual apparatus shall be estimated with reference to homogeneous specimens of thermal conductance extending over a range of temperatures, close to what the final testing conditions are likely to be. The metering chamber was set up to keep steady-state conditions: the set point was 30 °C, with an air flow rate of 3.8 m/s measured and RH that ranges in average between 30% - 47% with the environmental (cold) chamber value 'set point' changing at 5 °C intervals from 25, 20, 15, 10, and 0 °C, until steady state environment was reached at each.

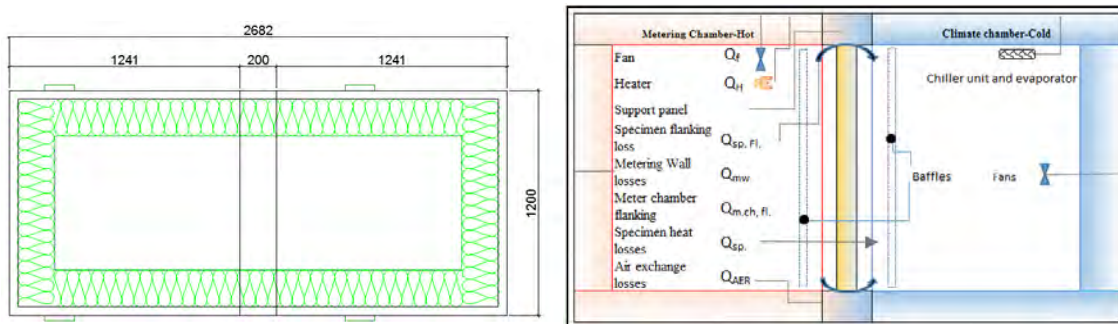


Figure 1. Horizontal section through apparatus. Figure 2. Components and Heat Pathways

Air Exchange Rate (AER)

The air change rate (ACR) through the box as a whole was determined through standard tracer gas measurement. After CO₂ was released into the chamber, its concentration decays exponentially, if no further CO₂ supply occurs and if the driving forces for air exchange remain constant. After introduction of the CO₂ into the sealed enclosure, the concentration of the gas decreased as air entered and exited. Plotting the natural logarithm of this exponential decay curve against time normally result in a straight line, the slope of which is the (AER) air changes per unit time. The mass balance equation is used to describe the relationship between the concentrations of gas in a space as a function of time. The general form of the equation for calculating air exchange per unit time is given as follows:

$$N = [\ln(C_{\text{int } t_0} - C_{\text{ext}}) - \ln(C_{\text{int } t_1} - C_{\text{ext}})] / (t_1 - t_0) \quad (1)$$

where N = number of air changes, $C_{\text{int } t_0}$ = internal concentration of tracer gas in enclosure at start, C_{ext} = external concentration of tracer gas in room, $C_{\text{int } t_1}$ = internal concentration of tracer gas in enclosure at end, t_0 = time at start (days), t_1 = time at end (days) and ln = natural logarithm.

CHARACTERISATION AND ESTIMATION OF LOSSES

A characterization panel of known thermal resistance (wood fibre board λ 0.04 W/mK) is used in a number of tests, over the expected operating temperature range. Each test determines the difference between the measured heat input to the metering chamber and the heat transfer through the characterization specimen, calculated from the measured temperature drop across it and its known resistance.

Calculations: A significant difference in temperature across the specimen is suggested. The air velocity on both sides was held constant and the heat flow across the sample was measured.

EN ISO 8990 and ASTM C1363-05 requires the following heat balance equation be verified. A schematic showing the heat transfer pathways is given in Figure 2.

$$Q_{Source} = Q_{Heater} + Q_{Fans}, \quad \text{Specimen} = U_{Specimen} \times A_{Specimen} \times \Delta T \quad \text{and}$$

$$Q_{metering\ chamber\ losses} = U_{Chamber} \times A_{Chamber} \times \Delta T + Vc_p\rho\Delta T + Q_{flanking}(W) \quad (2)$$

Where: $A_{Specimen}$ = Sample area (m^2), $Q_{Heaters}$ = Heat input from heaters (W), Q_{Fans} = Heat input from fans (W), $Q_{m\ ch}$ = Heat transfer rate through metering walls, floor and ceiling (W), $Q_{flanking}$ = Heat transfer rate at junction of specimen to frame (W), $U_{chamber}$ = Thermal conductivity of the chamber ($W/m^2.K$), $A_{chamber}$ = Area of chamber walls where losses occur (m^2), \dot{V} = Air exfiltration rate m^3/s , c_p = A Specific Heat Capacity of $1007\ J/kg.K$ at $30\ ^\circ C$ is used, ρ = Air density between $1.16 - 1.27\ kg/m^3$ used, ΔT_{air} = Inside to outside temperature difference ($^\circ C$), $\Delta T_{surfaces}$ = Temperature difference between hot and cold surfaces ($^\circ C$), $U_{Specimen}$ = Thermal conductivity of the sample ($W/m^2.K$)

RESULTS

The results of the CO₂ analysis are shown in Figure 3, where the air exchange rate equals the slope of the line at 0.087 ach and this is multiplied by the chamber volume to get a volume per second time of 1.313E-05 to be used in the heat balance equation. The test was conducted at ambient temperature only and accounted for less than 2% of the overall energy input, however further tests at different temperatures should further verify this figure.

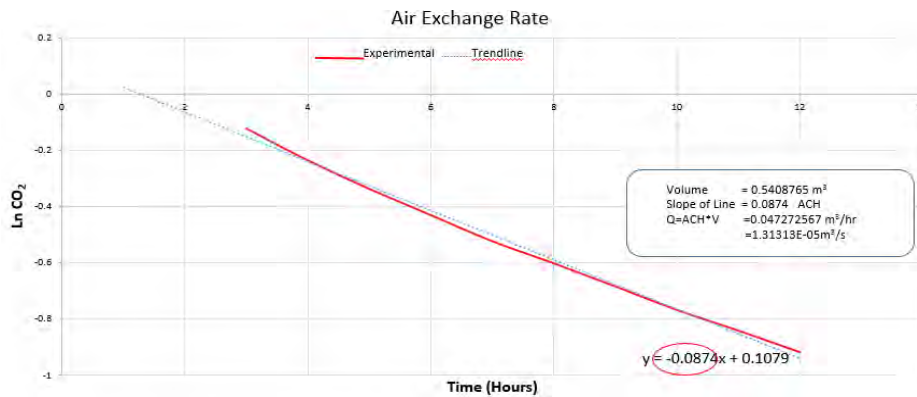


Figure 3. CO₂ results for air leakage of the chambers.

Table 1. Measured and calculated results over delta T of 5, 10, 15, 20 & 25 $^\circ C$

Delta T	30_25	30_20	30_15	30_10	30_05	30_00
Q_{fl}	1.28	1.21	1.22	0.93	0.86	1.14
$U_{ch} * A_{ch} * dT_{surf}$	3.85	3.70	3.71	3.23	3.01	3.45
$V * C_p * \rho * dT_{air}$	0.13	0.12	0.12	0.10	0.09	0.11
$Q_{fl\ sample}$	0.18	0.40	0.62	0.85	1.08	1.14
$U * A * dT_{specimen}$	0.99	2.21	3.47	4.73	6.06	6.35
Q_{H+F}	6.76	7.94	9.04	10.26	11.39	12.55
Balance equation	0.33	0.29	-0.10	0.42	0.29	0.37
$Q_{AER} + Q_{fl} + Q_{fl} + Q_{mw}$	6.43	7.64	9.14	9.83	11.10	12.18
% Error	4.83	3.69	-1.09	4.14	2.55	2.94

Characterisation results

Table 1 shows the inputs for the heat balance equation measured over five delta T's during the testing of an 80mm woodfibre board. The stated manufacturer's lambda value for this panel is $0.04\ W/mK$ and is used in the U value component (Table 1) of the $U * A * dT_{specimen}$. As the balance equation should read 0, the percentage error shown in the last row is just under 5%. The theoretical and experimental results are plotted in Figure 3 and can be seen to have good correlation with the distance between the lines representing the gap to be identified.

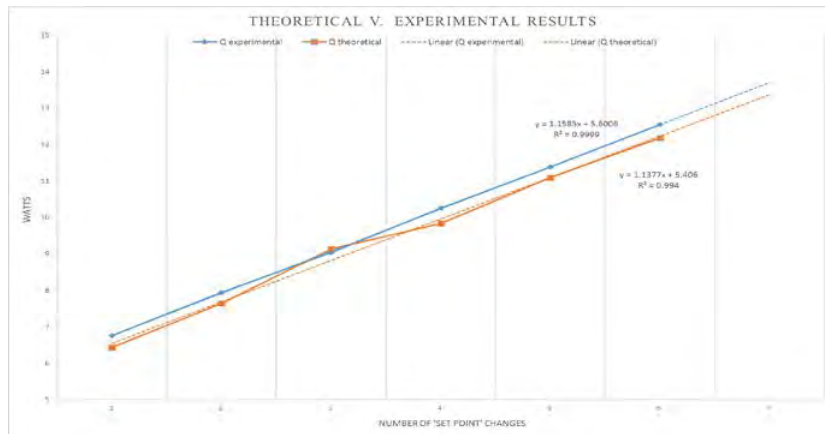


Figure 3. Theoretical versus Experimental losses of wood fibre board over 5 ΔT 's

ANALYSIS AND DISCUSSION

The limitations of this CHB are its relatively small size and also the fine levels of accuracy of some of the equipment but these have been counteracted by the extra care taken in the construction and calibration process. The maximum size of 715mm by 715mm sample area size requires that the thermal bridge calculation needs to be extremely accurately identified. The advantages of reduced dimensions over more traditional hot box systems however, provides a reduced mass and, thus, reduced thermal inertia of the overall system. First tests on a wood fibre board of an accepted conductivity (0.04 W/mK) shows very close relationship between theoretical and experimental data. The percentages of error varies by approximately 5%. The average temperatures in both chambers were steady throughout the testing period. Investigation is required to establish the cause of the slight non-linearity at delta T, of 15 °C. Finally the CHB built in the DIT set out to design and build an affordable testing chamber for establishing the material properties of historic building materials with the first step of calibrating a panel thickness of 80mm of known thermal conductivity. This was satisfactorily achieved and the percentages error of approximately 5% is acceptable for this apparatus. The next steps of testing historic building materials from a case study building is currently underway, with the results being inputted to a hygrothermal simulation.

REFERENCES

- Asdrubali, F., Baldinelli, G., 2011. Thermal Transmittance measurements with the hot box method; Energy Build.
- ASTM C1363-11. 2005. Standard Test Method for Thermal Performance of Building Materials and Envelope Assemblies by Means of a Hot Box Apparatus.
- Baker P. H., 2011; U-values and Traditional Buildings: Historic Scotland Technical Paper 10; Edinburgh: Historic Scotland;
- EN ISO 8990:1996. Thermal insulation –Determination of steady state thermal transmission properties –Calibrated and guarded hot box.
- Laussmann, D, & Helm, D, 2011. Air Change Measurements Using Tracer Gases: Methods and Results. Significance of air change for indoor air quality. DOI. 10.5772/18600
- Sala, J.M., Urresti, A., Martín, K, Flores, I., Apaolaza, 2008. A., Static and dynamic thermal characterisation of hollow brick wall: Tests and numerical analysis, Energy and Buildings.
- Schumacher, C.J. et al., 2013. Development of a New Hot Box Apparatus to Measure Building Enclosure Thermal Performance. Proceedings of Building XII.
- Ulgen K., 2002. Experimental and theoretical investigation of effects of wall's thermophysical properties on time lag and decrement factor, Energy Build.

The Effect of Human Walking on Distribution Characteristics of Indoor Particulate Matter

Yang Lv^{1,*}, Haifeng Wang¹, Hiroshi Yoshino², Hiroshi Yonekura², Rie Takaki³, and Genta Kurihara⁴

¹School of Civil Engineering, Dalian University of Technology, China

²Department of Architecture & Building Science, Tohoku University, Japan

³Tohoku Institute of Technology, Japan

⁴Kajima Construction, Japan

*Corresponding email: lvyang@dlut.edu.cn

ABSTRACT

In modern society, house dust particulate matters pollution had become serious. Ventilation is an important method for removing house dust particulate matters and it is very important to explore the removal efficiency of house dust particulate matters under different ventilation modes. This study analyses the removal effect of house dust particulate matters under the two typical ventilation modes called ceiling exhaust and slit exhaust strategy through experiments and data analysis. In the process of experiments, riboflavin particles were used as the house dust particulate matters, instantaneous microbial detection (IMD) was used to measure the house dust particulate matters. Walking test was carried on after the ventilation system running for some time, which aimed to explore the influence of human behaviour on the house dust particulate matters distribution under two different ventilation modes. It is concluded that larger size particles had larger sedimentation velocity and sedimentation velocity of particles would be faster significantly after the ventilation system working. After walking experiment, particles concentration returned to background concentrations due to the effect of the ventilation system. Particles concentration in slit exhaust strategy was lower than ceiling exhaust so that the effect of slit exhaust strategy is superior to the ceiling exhaust.

KEYWORDS

Ventilation strategy; House dust particulate matters; Experiment; Concentration distribution; Walking test

INTRODUCTION

In modern society, people spend 80% of the time in indoor environment (Peggy et al., 1992; Robinson and Nelson, 1995), thus indoor air quality is particularly important. With the worsening of atmosphere particle pollution, indoor particle pollution has become increasingly severe due to the infiltration by building exterior and other reasons. US Environmental Protection Agency had conducted an investigation for 5 years, which found that indoor pollution was serious in residential and public building (Zhu, 2002). Due to the limitations of various factors in China, indoor air environment can't build a more comprehensive monitoring network, resulting to indoor air quality is even more worrying.

Epidemiological studies showed that short or long-term exposure to dust particle would lead to widespread adverse effects on human multiple systems. "Global Environment Outlook" published UNEP pointed out that nearly 2 million premature deaths were related with particulate matter pollution. There was a positive correlation between the particle mass concentration with human mortality and morbidity, even the concentration lower than the

national limits standards (Yang, 2014). Dockery (1993) conducted a prospective study in six cities, and it found that particle pollution was related with cardiovascular diseases. With the increase of the annual average concentration of particulate matter, all-cause mortality, cardiovascular mortality and lung cancer mortality was significantly increased after controlling confounding factors (Pope et al., 2002). Under the same concentration, house dust particulate matters pollution was more harmful to the human body (Dockery et al., 1993; Pope et al., 2002; Guo et al., 2010; Tinker and Roberts, 1999). House dust particulate matters can enter the lungs to made greater harm to human body (Wang et al., 2013; Wang et al., 2007; Nikasinovic et al., 2006; Neas et al., 1994; Delfino et al., 2006; Zhu et al., 2015).

A growing number of epidemiological studies had shown that population incidence and mortality were associated with the particle mass concentration, especially significantly the indoor particulate matter concentrations (Yang, 2014; Dockery et al., 1993; Pope et al., 2002; Guo et al., 2010; Tinker and Roberts, 1999; Wang et al., 2013; Wang et al., 2007). Thus, the distribution characteristics of indoor particles and the health risks have been common concern in environmental science and engineering. Zhang and Chen (2006) studied particle transportation and distribution in ventilation chamber using experimental and numerical methods, who found that different ventilation forms had a great impact on indoor particle concentration distribution. Munat (2001) investigated and analysed the influence of different airflow forms on particle suspension, and the results showed that displacement ventilation system had small resuspension harm. Zhao B (2004) compared the diffusion characteristics of indoor particulate matter in displacement ventilation and mixing ventilation using numerical simulation method.

Many indoor air environment-related research study have been carried out, but it's not clear how indoor human behaviour affects indoor particle distribution under different ventilation. To solve this problem, the study made a research to figure out the effect of indoor human behaviours' influence to house dust particle distribution under different airflow. It will improve the prevention and control level of indoor air pollution and provide scientific basis of human health.

METHODS

Selection of particles

In the experimental study of house dust particulate matters, Japan used JIS-11 as experimental particles (Liu et al., 1996). JIS-11 test powder is non-biological particles produced by volcanic ash. The concentration of non-biological particles was high in the air, and its impact on the health is not clear, so in this study, riboflavin particles were used as the test particles because it is harmless for biological particles (Kurihara et al., 2010). Riboflavin is a special kind of biological particles which can emit fluoresce when it is exposed to light sources with certain specific wavelength. And it can be detected by particle detector (IMD) based on optical sensors and fluorescence detection techniques as biological particles. Studies have shown that value of riboflavin powder is low in the air, so it doesn't affect experimental results (Kurihara et al., 2010).

Ventilation systems and experiment process

Figure 1 shows experimental room ($L \times W \times H = 5.37\text{m} \times 2.74\text{m} \times 2.25\text{m}$) and ventilation systems. The window is sheltered by aluminum foil corrugated board to prevent solar radiation, and the walls are insulated by expanded polystyrene board. This study analyses the effect of the human walk activity on indoor particles distribution under two typical ventilation modes including ceiling exhaust and slit exhaust. Ceiling exhaust is the traditional ventilation way. For the slit exhaust strategy, delivery outlet was located in the center of the ceiling (In this study, delivery outlet of two ventilation system was same), the exhaust port is located at

the junction of walls and floors. Delivery outlet size of two ventilation systems were $0.05\text{m} \times 0.10\text{m}$. The exhaust port size in ceiling exhaust was $0.05\text{m} \times 0.10\text{m}$. As for the slit exhaust system, exhaust port size in the east was $4.2\text{m} \times 0.005\text{m}$, $4.53\text{m} \times 0.005\text{m}$ in the west. Figure 2 shows ceiling exhaust and slit exhaust system. Ventilation time was 0.75 times/h during the experiment

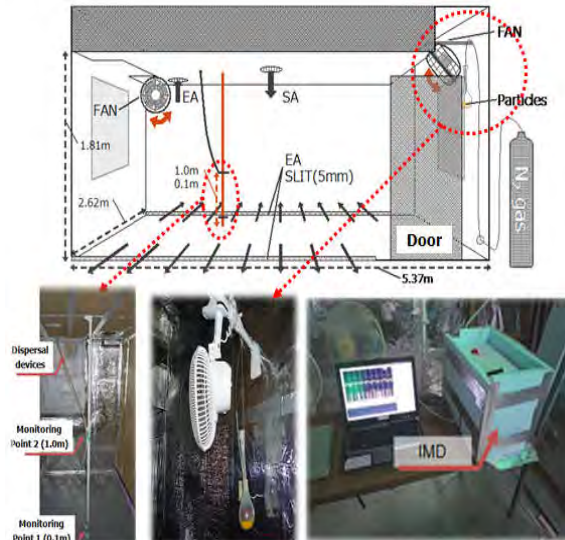


Figure 1. Experimental room and ventilation systems.

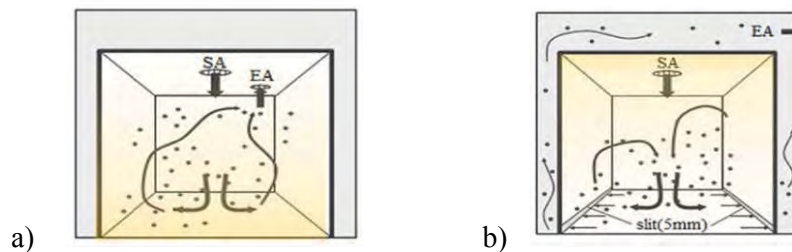


Figure 2. Two ventilation system. a) ceiling exhaust, b) slit exhaust

Indoor particles distribution was shown in Figure 1. The house dust particles were put in a measuring flask, which was fixed at the corner near the ceiling of the room. Nitrogen gas was blown into the measuring flask to disperse the house dust particles. Nitrogen gas flow rate was set as 10 L/min. To make the distribution of house dust particles as evenly as possible in the room, the house dust particles were mixed by an electric fan which was fixed close to the flask. Taking into the account of the height of the child, the position of the monitoring point was set at 0.1m and 1.0m. IMD (instantaneous microbial detection; IMD-A 200-1, BioVigilant Systems) was used to measure the particles, which is based on optical fluorescence sensor technology and is capable of detecting the size of biological or non-biological particles in the environmental air. Particle sizes were classified as the following six levels: $0.5\text{-}1.0\ \mu\text{m}$, $1.0\text{-}3.0\ \mu\text{m}$, $3.0\text{-}5.0\ \mu\text{m}$, $5.0\text{-}7.0\ \mu\text{m}$, $7.0\text{-}10.0\ \mu\text{m}$, and $10.0\text{-}15.0\ \mu\text{m}$. Experimental procedure (total 42 hours): the first hour - indoor particles spreading; 2 to 9 hours - indoor particles free settling; 10 to 42 hours - the ventilation system running. Indoor people started walking test from 27th hours. The purpose of the walking test was to explore the impact of walking behaviour to indoor particle concentration distribution under two different ventilation modes. Research was determined according to Liu Yu's experimental

methods from Japan's National Public Health Institute (Lu et al., 1982). In the study, male experimenter entered to room doing walk test, and walked in the room for 10min according to designated route (60 steps/ minute, 60 cm/step, a total of 600 steps). Figure 3 shows the walk test details.

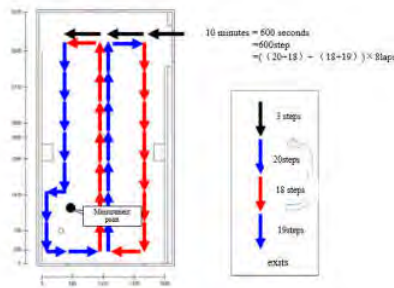
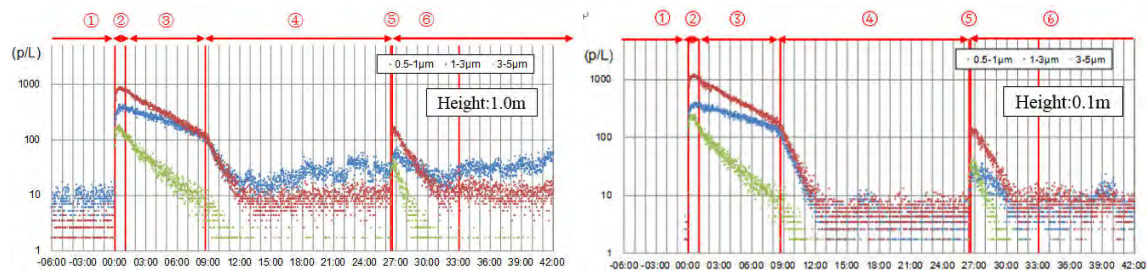


Figure 3. The walk test details

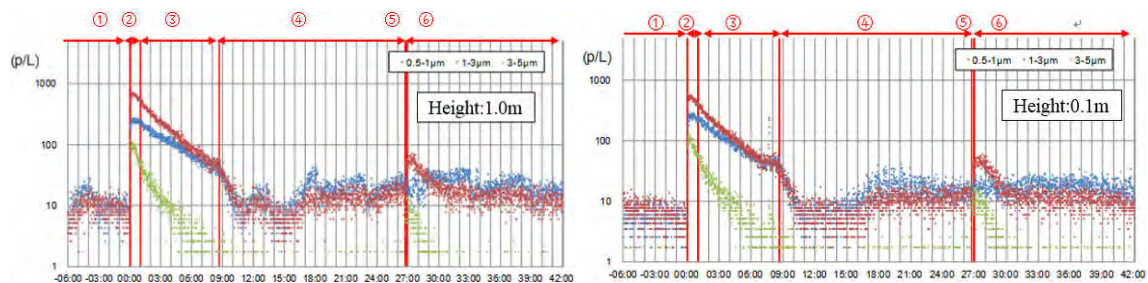
RESULTS AND DISCUSSIONS

The results in the ceiling exhaust strategy

Figure 4 shows the variation of particles concentration (0.5-1.0 μm , 1.0-3.0 μm , 3.0-5.0 μm) in two different measuring points (from the ground 0.1 meters and 1.0 meters) in the ceiling exhaust strategy. It shows that: ① Before spreading powder (-6-0h), all size particles' background concentration was low in air (about 10P/L). ② When powders walked for 1 hour (0-1h), indoor particles concentration increased rapidly; After 8 hours (1-9h), different size particles (0.5-1.0 μm , 1.0-3.0 μm , 3.0-5.0 μm) exhibited different settlement curve because of gravity; The larger particle size, the faster fall velocity. ③ After running the ventilation system (9h ~), all size particles accelerated subsidence (settlement curve sudden step in figure 6); When did walk test (27h-), particles concentration increased significantly, which may be due to suspended caused by disturbance of human walking; After the walk test, particles concentration returned to background concentration under the action of the ventilation system running continuously. Two measuring points showed above trend.



Remarks: ①background values; ②powder spreading; ③free settling; ④ventilation; ⑤walk test; ⑥ventilation
Figure 4. Variation of particle concentration in the ceiling exhaust strategy



Remarks: ①background values; ②powder spreading; ③free settling; ④ventilation; ⑤walk test; ⑥ventilation
Figure 5. Variation of particle concentration in the slit exhaust strategy

The results in the slit exhaust strategy

Figure 5 shows the particles concentration variation of two different measuring points (from the ground 0.1 m and 1.0 m) in the slit exhaust strategy. The variation trend of particles concentration in two measurement point was basically same with Figure 4, but there were some differences in concentration distribution.

Comparison of indoor particles concentration distribution in both ventilation systems

Figure 6 shows the different size particles concentration after ventilation system running (9h-) under two ventilation modes. Figure 6a shows the results in the height of 1.0m, and Figure 6b shows the results in the height of 0.1m. The results indicate that particles concentration in slit exhaust was lower than that of ceiling exhaust in the two measurement points. The lower the height, the more obvious of the effect for slit exhaust. The exhaust outlet was located at the junction of walls and floors for the slit exhaust, thus indoor particle gathered in the corner and excluded.

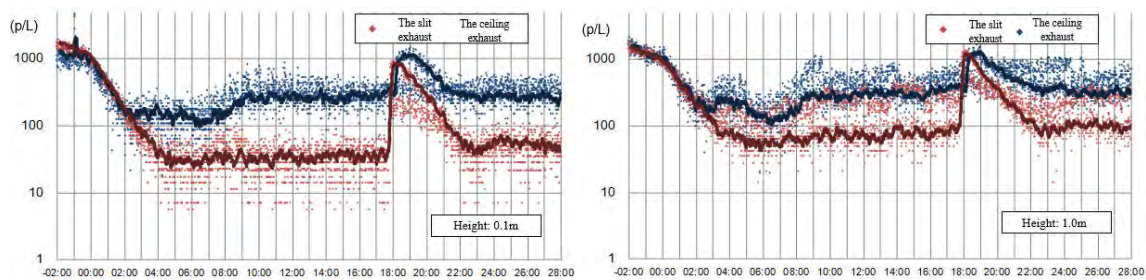


Figure 6. Particles concentration after ventilation system running in two ventilation systems.

CONCLUSIONS

This paper clarifies the effect of human walk behaviours on house dust particle distribution under different ventilation modes (including ceiling exhaust and slit exhaust). The following conclusions have been drawn:

- 1) Riboflavin was used to indoor house dust particles and IMD was used to measure the riboflavin particles concentration.
- 2) Larger size particles had larger sedimentation velocity and sedimentation velocity of particles accelerated significantly after the ventilation system working. Comparison of the number of particle in experimental monitoring point shows that the number of house dust particles in the ceiling exhaust was higher than that of the slit exhaust after house dust particles decreased as same level as background.
- 3) At the beginning of walking test, particles concentration increased significantly. After the walking test, particles concentration returned to background concentration under the action of the ventilation system running continuously.
- 4) Particles concentration in slit exhaust strategy was lower than that of the ceiling exhaust, thus the effect of slit exhaust is superior to the ceiling exhaust.

ACKNOWLEDGEMENT

This research is supported by the Ministry of Land, Infrastructure, Transport and Tourism of Japan and the Fundamental Research Funds for the Central Universities of China, Dalian Science and Technology Fund projects, the China Environmental Protection Project (201509063), and the National Nature Science Foundation of China (91743102, 51308088, and 51578103).

REFERENCES

- Peggy L. Jenkins, Phillips Thomas J., Mulberg Elliot J., et al. 1992. Activity patterns of Californians: use of and proximity to indoor pollutant sources. *Atmospheric Environment Part A General Topics*, 26(12), 2141-2148.
- Robinson J, Nelson W.C. 1995. National human activity pattern survey data base. *US EPA, Research Triangle Park*.
- Zhu LT. 2002. Indoor air pollution control .BeiJing: Chemical Industry Press.
- Yang L. 2014. Communication and control of indoor air pollution. *BeiJing: Machinery Industry Press*.
- Dockery D W, Pope C A, Xu X P, et al. 1993. An association between air pollution and mortality in six United-States cities. *New England Journal of Medicine*, 329(24), 753-759.
- Pope C A, Burnett R T, Thun M J, et al. 2002. Lung cancer, cardiopulmonary mortality, and long-term exposure to fine particulate air pollution. *Journal of the American Medical Association*, 287(9), 1132-1141.
- Guo Q B, Cheng X F, Hou h, et al. 2010. Pollution characteristics and morphology analysis of PM10 and PM2.5 in winter. *Environmental Monitoring in China*, 26(4), 55-58.
- Tinker J. A. , D. Roberts. 1999. Modeling air quality and bacteria levels in an operating theatre. *In Proceedings of Indoor Air' 99*, Edinburgh, 4, 731
- Wang WF, Yu J, Xu DD, et al. 2013. Pollution characteristics of particles and its main components in ningbo urban atmosphere. *Environmental Monitoring in China*, 29(5), 43-44.
- Wang YX, Niu JP, Ding GW, Noordim MM, Chen XY. 2007. Effects of air pollution on juvenile lung function in Lanzhou. *J Environ Health*, 24(6), 415-418.
- Nikasinovic L, Just J, Sahraoui F, et al. (2006). Nasal inflammation and personal exposure to fine particles PM2.5 in asthmatic children. *J Allergy Clin Immunol*, 117(6), 1382-1388.
- Neas LM, Dockery DW, Ware JH, et al. 1994. Concentration of indoor particulate matter as a determinant of respiratory health in Children. *Am J Epidemiol*, 139(11), 1088-1099.
- Delfino RJ, Staimer N, Gillen D, et al. 2006. Personal and ambient air pollution is associated with increased exhaled nitric oxide in children with asthma. *Environ Health Perspect*, 114(11), 1736-1743.
- Zhu SW, Wei Cai, Hiroshi Yoshino, et al. 2015. Primary pollutants in schoolchildren's homes in Wuhan, China. *Building and Environment*, 2015, 1-13.
- Zhang Z, Chen Q. 2006. Experimental measurements and numerical simulations of particle transport and distribution in ventilated rooms. *Atmospheric Environment*, 40(18), 3396-3408
- Mundt E. 2001. Non-buoyant pollutant sources and particles in displacement ventilation. *Building and Environment*, 36(7), 829-836.
- Zhao B, Zhang Y, et al. 2004. Comparison of Indoor Aerosol particle Concentration and Deposition in Different ventilated Rooms by Numerical Method. *Building and Environment*, 39(1), 1-8.
- Liu Yu, Ikeda Kouichi, Irie Tatehisa, Hiraoka Kenji. 1996. Characterization of re-dispersion of settled particulates into the space with raised floor and conventional ceiling HVAC system. *Journal of architecture, planning and environmental engineering*, (483), 49-54.
- Kurihara Genta, Yoshino Hiroshi, Yonekura Hiroshi, Takaki Rie, Lu Yang. 2010. Experimental method for determining removal efficiency of house dust by mechanical ventilation. *31st conference of the Air Infiltration and Ventilation Centre (AIVC2010)*, Korea, 78-92.
- Yang Lu, Jing Liu, Hiroshi Yoshino, et al. 2015. Study on Distribution and Deposition of House Dust by Different Ventilation Systems in a Full-scale Residential Room. *International Journal of Ventilation*, 13(4), 417-426.

Thermal performance analysis of traditional housing in Albania

Rudina Belba^{1,*} and Sokol Dervishi^{1,2}

¹ Epoka University, Faculty of Architecture, Tirana/Albania

² Vienna University of Technology, Institute of Architecture Science, Vienna/ Austria

**rbelba12@epoka.edu.al*

ABSTRACT

This paper introduces the results of a one-year research, to gather and analyse data on the traditional housing buildings in Kukes region, Albania. The energy performance and the thermal comfort conditions in five different buildings were examined. The Design Builder Energy simulation software was used to analyse the thermal performance of the selected typologies. Detailed construction activity and weather information was applied in modelling the houses. Simulation results showed that these buildings require only heating during the winter. As for the first villa, seven improvement scenarios were applied and examined. The same scenarios incorporate the use of thermal insulation of the walls and the roof as well as the use of double glazing. The results suggest that improvements and insulations in building fabrics could reduce the annual energy consumption up to 35 %.

KEYWORDS

Thermal performance, Traditional building, Parametric simulation, Design Builder

INTRODUCTION

Adaptive reuse contributes to the sustainability of the urban generation, as it extends the life cycle of the buildings, avoids demolition waste, encourages energy efficient solutions, and provides significant social and economic benefits to the society (Resuli and Dervishi, 2015). Due to the difficulty of finding maintained buildings, very few researches analyze the energy efficiency of traditional buildings in Albania (Rexhepi and Mahdavi, 2010). Previous studies have identified effective ways for the energy conservation in the existing buildings (Kaleci and Dervishi, 2014). The renovation of the existing buildings is one of them, consisting of interventions on improving the functionality and sustainability of traditional buildings. This study consists of five traditional buildings located in Lume village, in the Region of Kukes, Albania, on which, records on thermal conditions and the energy use were gathered over a period of one year.

This paper is specifically related to five case studies of traditional houses in the villages of Kukës and identifying their sustainable potentials. The selected houses have been historically exploited as a shelter for the locals, guests, and foreigners. Nowadays their conditions have deteriorated and a large amount of energy is used for heating. Increase of energy consumption is caused by the low temperatures of this area, and the absence of insulations in old buildings, specifically the wall insulation, roof insulation, and double glazing. In most case studies, the building design does not consider orientation, glazing ratio, shading devices, or thermal mass. The sustainable environment is achieved using natural resources (sun, wind, temperature variation) in sustainable approaches, which directly affect the quality of the inner space (comfort, energy efficiency, and lighting) (Rashani and Mahdavi, 2015), and hence, this study is concerned with the following objectives: i) analyzing the energy consumption and

how it affects thermal conditions; ii) evaluating the thermal performance; iii) analyzing the comfort of inner spaces; and iv) developing strategies towards improvement.

METHODS

The five selected buildings diverge in terms of construction period, location, orientation and occupancy. Table 1 summarizes general information regarding the concerned houses such as area, function, construction year, presence of Kulla, and the materials used.

Table 1. Overview of the selected houses (year of construction, area, interventions, material used).

	H 1	H 2	H 3	H 4	H 5
Approximate year of construction	1930	1920	1915	1965	1940
Occupancy	full	non	non	full	partial
Interventions	*				*
Two story house	*	*	*		*
Warehouse and livestock		*	*		
Both inner and outer stairs					*
Presence of wood in main façade	*	*	*		*
Materials: Clay, Stone, Wood	*			*	*
Presence of inner wall	*	*	*	*	*

Indoor thermal Condition and Energy Used

Indoor climate parameters (indoor air temperature and relative humidity) and the energy use were simulated for all houses (living room and in the entire building over a period of one year (Jan 1st- Dec 31th). In order to evaluate the existing indoor thermal conditions, the ratios of air temperature and relative humidity are diagrammed in psychometric charts. Based on the questionnaires' and gathered information, building performance simulation models were generated and secondarily used to test various improvement scenarios by means of parametric simulation software [Design Builder 2013], (see Table 2).

Table 2. Questionnaire output (thermal insulation, heating equipment, cooling equipment, lamps, thermal comfort)

Questions	H1-Results	H2-Results	H3-Results	H4-results	H5-Results
Thermo insulation	No	No	No	No	No
Heating Equipment	Mineral wood	-	-	Mineral wood	Mineral wood
Cooling Equipment	No	No	No	No	No
Lamps	Economical fluorescent lighting	-	-	Economical fluorescent lighting	Economical fluorescent lighting
Energy used for cooking	Mineral wood	-	-	Mineral wood	Electric
Thermal Comfort (Summer)	Hot-Ground floor	Neutral-Ground floor	Neutral-Ground floor	Hot	Neutral-Ground floor
	Hot-First floor	Neutral-First floor	Neutral-First floor		Hot-First floor
Thermal Comfort (Winter)	Neutral	Cold	Cold	Neutral	Neutral

Simulation study

Five buildings, respectively H1, H2, H3, H4, and H5 were simulated over a period of one year. The gathered geometry and the construction records were used to generate the base case simulation models. Assumptions were made based on in situ observations, historical documents, and questionnaires'. Simulation assumptions regarding actual construction data

are summarized in Table 3. To run the simulations, weather files were generated based Meteororm (2007) software platform.

Table 3. Base case construction materials and respective U values for all houses (H1-H5).

Code	Scenario	U-Values	Description
BC 1	Base case- H1	$U_{\text{Walls}} = 1.31 \text{ W.m}^{-2}.\text{K}^{-1}$ $U_{\text{roof}} = 1.95 \text{ W.m}^{-2}.\text{K}^{-1}$	Wall- 60 cm stone wall Roof- Uninsulated pitched roof, Heavy weight
	Base case- H2	$U_{\text{Window}} = 2.6 \text{ W.m}^{-2}.\text{K}^{-1}$	Window- Double glazing, Clear, Argon filled
BC 2	Base case- H3	$U_{\text{Walls}} = 1.46 \text{ W.m}^{-2}.\text{K}^{-1}$ $U_{\text{roof}} = 2.11 \text{ W.m}^{-2}.\text{K}^{-1}$	Wall- 60 cm stone wall Roof- Uninsulated pitched roof, Medium weight
		$U_{\text{Window}} = 5.5 \text{ W.m}^{-2}.\text{K}^{-1}$	Window- 4 mm Single glazing, Clear
BC 3	Base case- H4	$U_{\text{Walls}} = 1.61 \text{ W.m}^{-2}.\text{K}^{-1}$ $U_{\text{roof}} = 2.11 \text{ W.m}^{-2}.\text{K}^{-1}$	Wall- 50 cm stone wall Roof- Uninsulated pitched roof, Medium weight
		$U_{\text{Window}} = 5.5 \text{ W.m}^{-2}.\text{K}^{-1}$	Window- 4 mm Single glazing, Clear
BC 4	Base case- H5	$U_{\text{Walls}} = 1.22 \text{ W.m}^{-2}.\text{K}^{-1}$ $U_{\text{roof}} = 1.95 \text{ W.m}^{-2}.\text{K}^{-1}$	Wall- 60 cm stone wall Roof- Uninsulated pitched roof, Heavy weight
		$U_{\text{Window}} = 2.6 \text{ W.m}^{-2}.\text{K}^{-1}$	Window- Double glazing, Clear, Argon filled
BC 5		$U_{\text{Walls}} = 1.38 \text{ W.m}^{-2}.\text{K}^{-1}$ $U_{\text{roof}} = 1.95 \text{ W.m}^{-2}.\text{K}^{-1}$	Wall- 70 cm stone wall Roof- Uninsulated pitched roof, Medium
		$U_{\text{Window}} = 2.6 \text{ W.m}^{-2}.\text{K}^{-1}$	Window- 6 mm Single glazing, Clear

Improvement scenarios

To demonstrate thermal improvement possibilities a number of seven improvement scenarios (S1-S7) were introduced only for the first typology (H1) for parametric simulations in a 2 day interval (1st and 2nd of July). The first scenario (S1) explores the impact of the thermal insulation on the external walls. The second scenario (S2) involves the thermal insulation of the roof. The third scenario (S3) involves the use of double glazing as a replacement for of single glazing. The fourth, fifth, sixth, and seventh scenarios (S4-S7) comprise the combination of the aforementioned scenarios. The purpose is to achieve a more stable temperature in the indoor environment and to reduce energy consumption. Table 4 summarizes improvement scenarios for one selected representative house.

Table 4. Improved scenarios for H1 (WI, RI, DG, WI+RI, WI+DG, RI+DG, WI+RI+DG)

Code	Scenario	U-Values	Description
WI	Wall Insulation	$U_{\text{Walls}} = 0.26 \text{ W.m}^{-2}.\text{K}^{-1}$	Inner Insulation PVC= 12 cm
RI	Roof insulation	$U_{\text{roof}} = 0.151 \text{ W.m}^{-2}.\text{K}^{-1}$	Glass Wool 8 cm
DG	Double glazing	$U_{\text{Window}} = 1.07 \text{ W.m}^{-2}.\text{K}^{-1}$	Replacement of Single Glazing with Double Glazing
WI+RI			
WI+DG			
RI+DG			
WI+RI+DG			

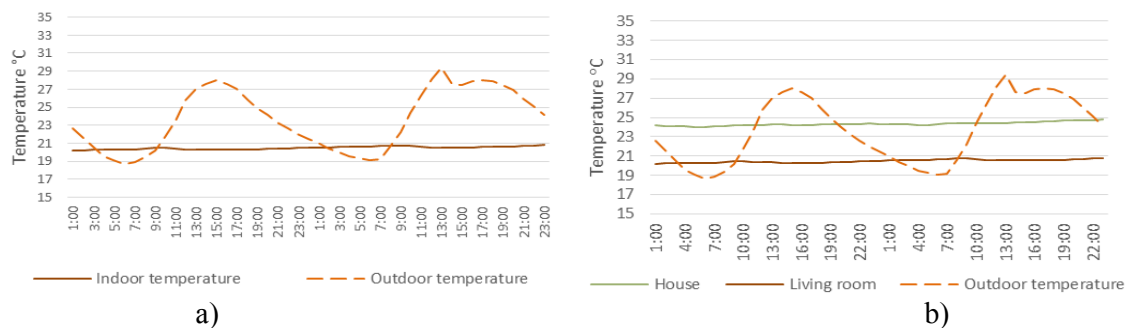
RESULTS AND DISCUSSION

Figure 1 shows an indication of the existing thermal performance only in the first house (H1) based on the simulation results in a course of a 2 day interval (1st and 2nd of July 2017). Taking into account the weather conditions in Kukes, no cooling took place during simulation, and ventilation was considered during day and night hours with altered recesses (see Table 5). Figure 2a shows the assessment of indoor temperatures of all selected houses, compared with the outdoor temperature for a 2 day interval measurements (1st and 2nd of July 2017). As indicated in the relevant figures, the indoor temperature is more constant during day and night, compared to the outdoor temperature. Owing to that stone is the material that

was used in outer walls its conductivity directly brings about a stable room temperature. A considerable difference is shown between indoor temperatures of occupied houses (H1, H4, and H5) and unoccupied houses (H2 and H3), as the absence of activity affects the sustainability of internal temperatures in H2 and H3. Figure 2b compares the humidity measurements of all houses in the 2 day interval (1st and 2nd of July 2017). Based on the results, the amount of humidity is lower in the occupied houses (H1, H4, and H5) because the unoccupied houses (H2 and H3) are unventilated. Additionally, Figure 3a shows the comparison of energy between five houses in one year interval, while Figure 3b,c shows the ratio of indoor temperatures and relative humidity for one month (July 2017) for H1 (occupied) and H2 (unoccupied) represented by psychometric charts. As it is shown in the charts, the houses are positioned differently related to the comfort zone. The first typology (H1) is the most comfortable one, since its construction belongs to more recent years whilst the second typology (H2) is out of the comfort zone, since it is unoccupied and the amount of humidity is bigger. Figure 4a,b and shows that energy and temperature are changed based on improvement scenarios for the first typology (H1). As shown in the figure 4b the lowest value consists the first typology (H1) due to its recent interventions and insulation system. The second lowest value consists of the fifth typology (H5) which has the same material as the fourth typology (H4) but its activity takes place only during the summer period. For the unoccupied houses (H2 and H3) the results show relatively low performance. The implementation of all scenarios together reduces the amount of energy consumption (yearly) and decreases the indoor temperature in the 2 day interval (1st and 2nd of July). As expected, interventions in the external wall, roof and windows affect directly the indoor temperature and energy consumption. The combinations of the all scenarios (WI + RI + DG) decrease the average of the indoor temperature from 25°C to 22°C during summer period and reduce the annual amount of energy consumption from 74 kWhY.m-2 to 45 kWhY.m-2.

Table 5. Ventilation schedule for all houses (H1-H5)

	H1		H2		H3		H4		H5	
	Day	Night	Day	Night	Day	Night	Day	Night	Day	Night
Ventilation hours	09:00-17:00	22:00-01:00	-	-	-	-	09:00-17:00	22:00-01:00	09:00-17:00	22:00-01:00
% of opening	80 %	20 %	-	-	-	-	80 %	20 %	80 %	20 %

Figure 1. a) Base case temperature (living room of H1), b) Symptoms. Base case temperature (living room and H1) in a 2 day interval (1st and 2nd of July 2017).

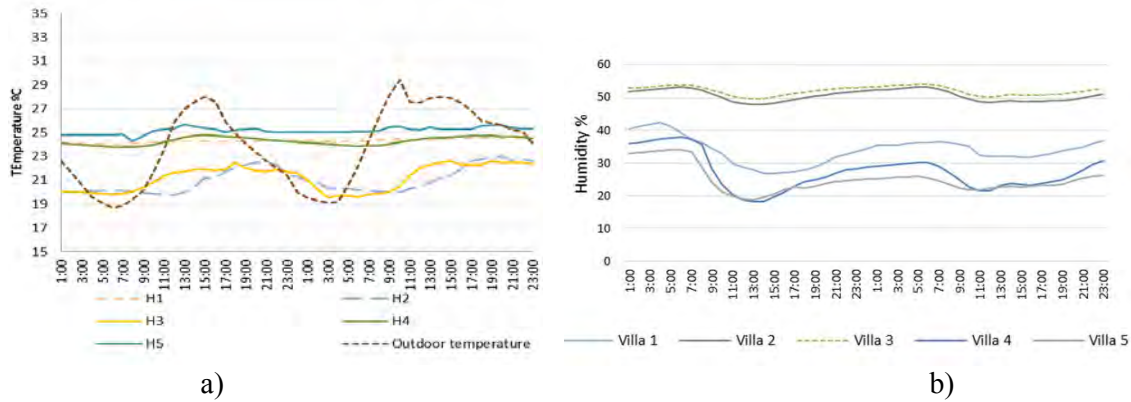


Figure 2. a) Comparisons of BC temperatures (H1-H5), b) Comparisons of BC humidity's (H1-H5).

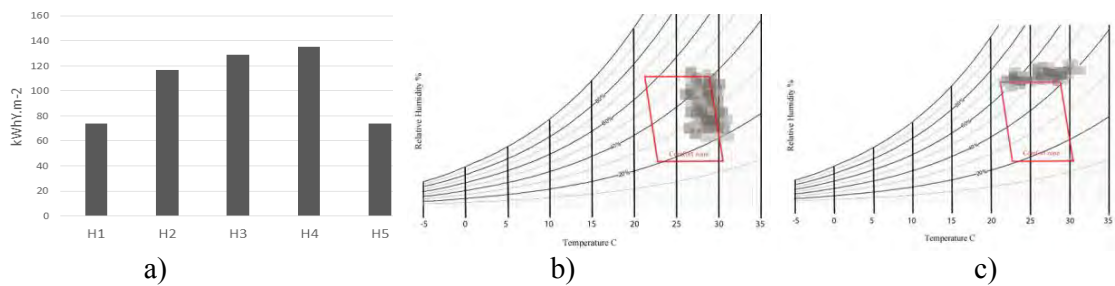


Figure 3. a) Simulated heating loads/yearly (H1-H5), b) Hourly temperature and relative humidity H1, c) Hourly temperature and relative humidity H2.

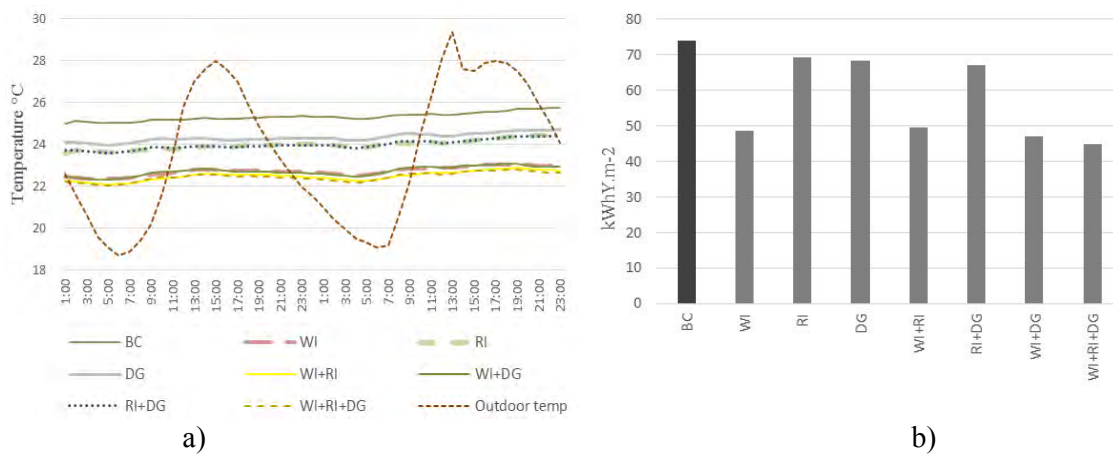


Figure 4. a) Comparison of BC and Scenario Temperatures (H1-H5), b) Scenarios heating loads (H1).

CONCLUSIONS

The paper is about a study conducted on the comfort and energy consumption of five traditional housing conditions in Northern Albania, using one year simulation measurements. Given the climatic conditions in Kukes, traditional houses require only heating during the winter and no cooling in summer. The simulation results establish that thermal comfort is

directly connected to the climate conditions, manufacture fabrics, dwelling shape, and occupants' activity. Altered involvements to the building's fabrics can bring about better performance. Certain combinations of improvement measures (such as insulations in walls, roof, and double glazing) have the ability to recover the thermal performance of the buildings in the climatic context of Kukes, Albania. Wall insulation and other related arrangements have significantly increased the temperatures and condensed the energy consumption, compared with the other scenarios (30 to 35%). Replacement of glazing and roof insulation affects less the thermal comfort (2 to 10%). Future studies may address the impact of the change of the structure and activity on the energy consumption of the building.

REFERENCES

- Rashani M. and Mahdavi A. 2015. Energy performance assessment of existing multi-family apartment buildings in Kosovo. In: *Proceedings of the 6th International Building Physics Conference the IBPC 2015*, Torino, pp. 782-787.
- Resuli P., Dervishi S. 2015. Thermal performance of cultural heritage Italian housing in Albania. In: *Proceedings of the 6th International Building Physics Conference, IBPC 2015*, Torino, pp. 753-758.
- Mahdavi A. and Orehousing K. et al. 2007, Analyzing Traditional Buildings Empirically Calibrated Building Performance Models. In: *Proceedings of the 10th International Building Performance Simulation Association Conference and Exhibition IBSA 2007*, Beijing, (China), pp. 75-78.
- Marino C. and Minichiello F. 2015. Existing buildings and HVAC systems: incidence of innovative surface finishes on the energy requirements. In: *Proceedings of the 70th Conference of the Engineering Association ATI 2015*, Roma, pp 499-505.
- Zhang H. and Lei S L. 2012. An Assessment Framework for the Renovation of Existing Residential Buildings regarding Environmental Efficiency. In: *Proceedings of the Pacific International Conference on Environment-Behaviour Studies AicE-Bs 2012*, Cairo, pp. 549-563.
- Kaleci E. and Dervishi S. 2014. Implementation Challenges to the Adaptive Reuse of a Heritage Building in Tirana, Albania. In: *Proceedings of the 2nd International Conference in Architecture and Urban Design Epoka University ICAUD 2014*, Tirana, Albania, pp. 1-10.
- Giombini M. and Pinchi E. M. 2015. Energy functional retrofitting of historic residential buildings: the case study of the historic center of Perugia. In: *Proceedings of the 70th Conference of the Engineering Association ATI 2015*, Roma, pp 1009-1016.
- Vieites E. and Vassileva I. et al. 2015. European initiatives towards improving the energy efficiency in existing and historic buildings. In: *Proceedings of the 3rd International Conference on Advanced Electromaterials ICAE 2015*, ICC Jeju, Korea, pp 1679-1685.
- Akande O. K. and Odeleye D. et al. 2016. Performance evaluation of operational energy use in refurbishment, reuse, and conservation of heritage buildings for optimum sustainability. In: *Proceedings of the Foundation for Auditing Research FAR 2016*, pp. 371-382.
- Rexhepi A. and Mahdavi A. 2010. Empirical and computational study of the Thermal Performance of a traditional housing type in Kosovo. In: *Proceedings of the 3rd German-Austrian IBPCA Conference, IBPCA 2010*, Vienna, Austria, pp. 1-6.

Uncertainty in Building Energy Performance Characterization: Impact of Gas Consumption Decomposition on Estimated Heat Loss Coefficient

Marieline Senave^{1,2,3,*}, Glenn Reynders^{1,3}, Behzad Sodagar⁴ and Dirk Saelens^{1,3}

¹KU Leuven, Department of Civil Engineering, Building Physics Section, Belgium

²VITO, Smart Energy and Built Environment Unit, Belgium

³EnergyVille, Cities in Transition Section, Belgium

⁴University of Lincoln, School of Architecture and the Built Environment, United Kingdom

*Corresponding email: marieline.senave@kuleuven.be

ABSTRACT

Characterization of building energy performance indicators such as the Heat Loss Coefficient (HLC) based on in-situ measurement data calls for thorough building physical insight, a well-designed measurement set-up to collect sufficient, qualitative data and adequate data analysis methods. On-board monitoring may be an alternative for dedicated experiments to perform the data collection task. This paper analyses the sensitivity of the end-result of the characterization, the HLC estimate, to flaws in the monitoring data set. More specifically, the impact of not installing submeters to disentangle the gas consumption for space heating and the production of domestic hot water is evaluated. Hereto, multiple gas decomposition methods are applied on a case study monitoring data set, after which the HLC is assessed. The results show deviations up to 33% for the mean estimate and non-overlapping 95% confidence intervals.

KEYWORDS

Characterization, Heat Loss Coefficient, On-board Monitoring, Gas Consumption Decomposition, Sensitivity Analysis.

INTRODUCTION

Building energy performance (BEP) characterization based on in-situ measurements has recently been gaining much attention in the framework of IEA EBC Annex projects 58 and 71. Furthermore, Bauwens (2015), Deconinck (2017) and Farmer et al. (2017) demonstrate how the thermal resistance of building elements and the HLC of building envelopes can be estimated through application of statistical modelling techniques on data collected in on-site steady-state and dynamical measurement experiments. The HLC hereby describes the amount of heating power needed to maintain a temperature difference of 1 degree Kelvin over the entire building envelope [W/K]. The case studies investigated to date, however, mainly focus on mock-ups or unoccupied dwellings. Not only because the measurement conditions can be better controlled, but also because the measurement set-up can be perceived as intrusive and costly.

On-board monitoring, using sensors to collect data of an occupied, in-use building, is put forward as a solution to the issues of cost and intrusiveness (Saelens and Reynders, 2016). However, much uncertainty still exists about the optimal sensor set-up, the way disturbances induced by occupants should be handled, etc.

The present paper aims to address a particular data related challenge that researchers, aspiring to estimate the HLC, might have to face; namely that the same type of fuel has been used for both space heating (SH) and the production of domestic hot water (DHW), and that no submeters can or have been installed to differentiate between both end uses.

The dynamic heat balance for a single zone (Eq.1), which forms the framework for both the

monitoring campaign and the data analysis model, stipulates that the HLC at each timestep t depends on the effective heat capacity C_i [J/K] of the zone, the difference between the interior and exterior temperature (T_i and T_e resp. in [K]), the heat flow rates due to mechanical ventilation with heat recovery, internal and solar gains ($\varphi_{vent,hr}$, φ_{int} and φ_{sol} resp.), and the net power supplied by the heating system φ_H [W]. This final term not only implies that the gross fuel consumption has to be converted in net energy use on the basis of the system efficiency, but also that the energy use for SH should be separated from that for DHW production and that the latter should be eliminated from the analysis for as far that it does not induce internal gains.

$$C_i \cdot \frac{dT_i}{dt} = HLC \cdot (T_{i,t} - T_{e,t}) + \varphi_{vent,hr;t} + \varphi_{int;t} + \varphi_{sol;t} + \varphi_{H;t} \quad (1)$$

Not decomposing the fuel consumption results in an overestimate of the HLC. However, disentangling it incorrectly might just as much lead to an erroneous estimate. This paper will therefore evaluate the sensitivity of the HLC estimate to the approach used to determine the not-monitored fuel (gas) consumption for space heating.

The first part of the methodology section describes the case study dwelling and on-board monitoring campaign used to this end. Next, three different ways to decompose the gas consumption and thus approach φ_H are discussed. In the final part of the methodology section, the data analysis procedure used to estimate the HLC is delineated. In the results section, differences between the decomposition outcomes are shown, and, more importantly, their impact on the characterization of HLC is demonstrated. Finally, conclusions are drawn on the present study and recommendations are given for future research.

METHODOLOGY

Case study dwelling and on-board monitoring campaign

The object of this study is a semi-detached, two-story house built in 2012 in Gainsborough, UK. A theoretical HLC of 47 W/K is calculated based on the target U-values and surface areas of the building envelope parts, the average result of three blowerdoor tests, and the assumption that the efficiency of the mechanical ventilation heat recovery unit equals 100 %. SH and DHW are provided by a gas fired combi boiler. Together with the other dwellings in its terrace, the house has been the subject of a monitoring campaign conducted from October 2012 until November 2015. During this period, the dwelling was inhabited by three persons. The interior temperature of the living room and bedroom (both from the studied and neighbouring dwelling), the exterior temperature, the gas, water and electricity consumption and the PV production were monitored with a 5 min sample frequency. Hourly averaged values of the global horizontal solar irradiance (GHR) were obtained from a RAF weather station located 30 km from the site. A detailed description of the dwelling and performed monitoring campaign can be found in (Sodagar and Starkey, 2016), in which the dwelling is referred to as ‘House 1’.

Gas consumption decomposition methods (DMs)

Classifying all gas consumption for the production of DHW as internal gains and thus assessing HLC based on the total gas consumption (‘No decomposition’) is incorrect since the hot tap water directly leaves the dwelling through the sewage system.

A first decomposition method to disentangle both end uses (‘DM1’) could therefore be the application of a default distribution. In this case study there will be opted for a 76/24 distribution for the end uses SH/DHW, as reported by Menkveld (2009). A major drawback of this method is that it does not take the actual consumption, SH demand or occupant behavior into account.

The second decomposition method (‘DM2’) is fully based on the assumptions that (1) in the case of the combi boiler, the production of DHW and SH do not occur at the same time and (2)

the gas consumption for DHW production perfectly coincides with the DHW consumption. It involves the implementation of two rules on the 5min-interval monitoring data. The first rule stipulates that the gas consumption for DHW production must be set to 0 when mains water consumption is 0, else gas consumption for the production of DHW must be set equal to the total monitored gas consumption. The second rule states that the gas consumption for SH must be set to 0 when mains water is consumed, else gas consumption for SH must be set equal to the total monitored gas consumption.

This DM is straightforward and easy to implement. However, a number of potential flaws can be identified. First, the assumptions imply that all cold water tapplings occurring while gas is used for SH are classified as DHW usage. The fact that grey water is used to flush the toilets though makes this assumption more reasonable. Secondly, the hot water tapplings could be significantly shorter than the 5 min sampling time. Yet, from the moment water consumption is observed, however small, the full gas consumption for that 5 min period is allocated to DHW production. Higher frequency logging could solve this issue. Thirdly, small time delays between starting and stopping of water and gas consumption will create some error.

The third approach, ‘DM3’, which was demonstrated by Bacher et al (2016), uses a robust, zero order, Gaussian kernel smoother to estimate the ‘gas consumption for SH’-profile underlying the noisy 5 min gas consumption data. Next, all spikes of the total gas consumption significantly above this kernel (smoother) estimate are classified as DHW heating spikes and their values are obtained by subtraction of the kernel estimate. Finally, subtraction of the estimated heat load for the production of DHW from the total heat load gives an estimate for the heat load for SH. The parameters of the kernel smoother procedure were tuned with an eye on limiting the gas consumption classified as ‘gas used for space heating’ during the summer months. The final model parameter values are as follows: kernel window: 1 h, bandwidth: 0.5 h, threshold for bisquare robust estimation γ : 7 MJ/h, separation threshold q_{tres} : 1.1.

Just like DM2, this decomposition method has not been verified on a case study where the total gas consumption and the consumption for the production of DHW and SH were measured separately. In contrast with the previously described approach, this method assumes that gas consumption for both end uses can occur simultaneously. It should furthermore be noted that all peaks are classified as DHW heating, although the start-up of the space heating might also result in a similar peak in the fuel consumption.

Determination of HLC

For the characterization exercise, four periods were selected from the entire data set: a relatively long model training period, extending from the 1st of October 2014 till the 31st of March 2015, and three different shorter model validation periods, in January, February and March 2014. With the heat balance equation (Eq.1) in mind, the following variables were selected from the monitoring data; the exterior temperature T_e , the interior temperature of the dwelling itself and the neighbouring dwelling (T_i and T_n , resp). Both T_i and T_n are approximately determined as the arithmetic mean of the sensor data collected in the living room and bedroom. In the absence of data on the incident radiation on the different facades, the GHR will be used to represent I_{sol} . After adaptation with the calorific values published by National Grid (2017) and decomposition through one of the above-mentioned decomposition methods, the gas consumption data will be used as φ_H . The system efficiency is thus assumed to be equal to 100 %. Although this value is uncertain and in reality not even constant, this will not pose an issue for this study, which focuses on the relative differences caused by DMs used for gas consumption. The same holds for the other assumptions made. Finally, the internal gains φ_{int} are neglected in a first run ($\varphi_{int} = 0$) and assumed to equal the total electricity consumption in a second run ($\varphi_{int} > 0$). The latter variable is hereby approximated as the mains electricity consumption plus half of the PV

production to account for the not-submetered electricity that is directly fed to the grid. Next, an Auto-regressive with eXogenous input (ARX) model is fitted on the selected time series data, utilizing the ‘lm’ function in R-Studio:

$$\varphi_i(B) \cdot T_{i,t} = \omega_e(B) \cdot T_{e,t} + \omega_n(B) \cdot T_{n,t} + \omega_{sol}(B) \cdot I_{sol,t} + \omega_H(B) \cdot (\varphi_{H,t} + \varphi_{int,t}) + Int + \varepsilon_t \quad (4)$$

with T_i , T_e , T_n , I_{sol} , φ_H and φ_{int} the previously determined variables, resampled to hourly values, and $\varphi_i(B)$ an input polynomial of order p_i in the backshift operator B . Likewise, the $\omega_x(B)$'s are output polynomials of order p_x . Int is a constant intercept term and ε_t the residual (error) (Madsen, 2016).

To decide on the model order, a backward elimination procedure is followed, starting from a model including 24 lags for each of the considered polynomials. After every run, the significance of the fitted model coefficients is verified using a t-test (threshold of $p < 0.05$), starting with the highest available order. When coefficients of a certain order prove insignificant, their variables are eliminated from the model description and the model is refitted. The iterative process ends when all model coefficients present are significant.

To validate the developed models, it is verified whether their residuals resemble white-noise in plots of the autocorrelation function (ACF) and cumulated periodogram (CP). By comparing the normalized RMSE (nRMSE) [%] between the measured interior temperature and its one-step-ahead prediction for both the training and a validation period, it is checked whether the model is not overfitted.

If the model is accepted, HLC is calculated as the quotient of steady-state gains $\omega_e(1)/\omega_H(1)$. Finally, the models are compared based on (1) their score for the Akaike Information Criterion (AIC) and (2) the nRMSE between the observed and simulated interior temperature for the cross-validation periods. For both criteria, a lower value indicates a better model.

RESULTS ANALYSIS AND DISCUSSION

Differences between the gas consumption for SH estimated by the DMs

Table 1 compares the decomposition of gas consumption for SH and DHW production obtained through the different approaches. The default method (DM1) almost always results in a higher gas consumption for SH than DM2 and DM3. The method with the robust kernel smoother (DM3) uses a certain threshold instead of selectively classifying the gas consumption as either gas consumption for SH or production of DHW as DM2 does. This way it appears to systematically obtain a lower gas consumption for SH.

Table 1: Total gas consumption [kWh] and the gas consumption for SH as estimated by the four approaches [expressed as a percentage of the total gas consumption], per month.

	Oct 2014	Nov 2014	Dec 2014	Jan 2015	Feb 2015	Mar 2015
Total gas consumption	188 kWh	286 kWh	486 kWh	526 kWh	428 kWh	267 kWh
No decomposition	100 %	100 %	100 %	100 %	100 %	100 %
DM 1	76 %	76 %	76 %	76 %	76 %	76 %
DM 2	58 %	69 %	74 %	77 %	74 %	59 %
DM 3	44 %	55 %	62 %	63 %	59 %	45 %

Validation of developed ARX models

Given the applied model selection procedure, all finally included parameters of the 8 models (4 variants for φ_H times 2 scenarios for φ_{int}) are significant. Except for the models with φ_H based on DM2 or DM3 and $\varphi_{int}=0$, the interior temperature of the neighboring dwelling appeared to be an insignificant model input, probably because of a nearly constant profile of T_n . For the

other validation tests, the results were positive for all models: the nRMSE did only increase with about 1 % for the one-step-ahead cross-validation test, and the ACF and CP plots indicated white noise residuals. All models thus appear to be statistically valid.

Comparison of resulting HLC

Figure 1 shows the impact of the applied gas decomposition method on the HLC estimate, and this for the two different φ_{int} scenarios. The models appear to yield fairly different results, with 95 % confidence intervals that do not all overlap. In the case of $\varphi_{int} = 0$ the mean estimates range from 47 to 71 W/K, which is a difference of 33 %. The assumption that the internal gains equal the (approximated) total electricity consumption not only slightly reduces the uncertainty on the outcomes, but also lowers the impact of the choice for a certain DM (maximal difference of 25 % between the means). Nonetheless, the mean outcomes for DM2 and DM3 still differ with 14 %. Notably, the observed deviances are dwelling and occupant specific. In the case of a less-insulated dwelling with a lower DHW consumption and higher setpoint temperature of the heating system, the sensitivity of the characterization result to the applied DM may be lower.

The majority of the estimates fall above the calculated reference value, suggesting that the actual HLC is higher. As neither DM2 nor DM3 has yet been validated and the information available on the boiler is limited, it is impossible to claim that one of the HLC outcomes

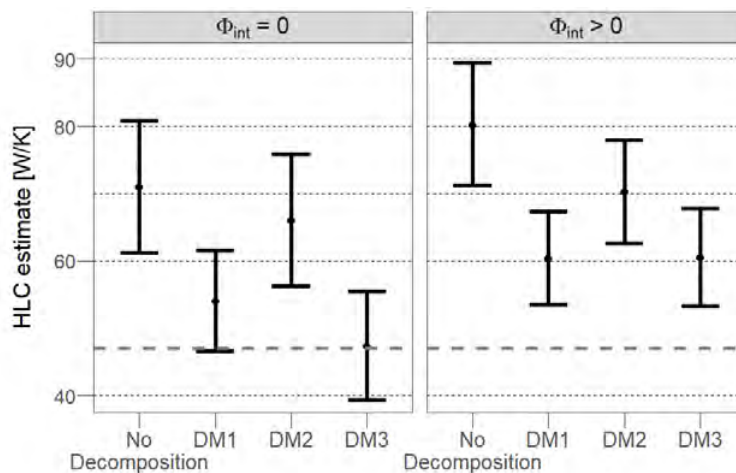


Figure 1: Overview of the HLC estimates and their related 95 % confidence intervals for the different models. The dashed line indicates the theoretically calculated reference value.

Table 2: Comparison of the different models based on the AIC and nRMSE between the measured (T_i) and simulated (\hat{T}_i) interior temperature.

	AIC	nRMSE(T_i, \hat{T}_i) [%] for validation periods in:		
	Training period	Jan '14	Jan-Feb '14	Feb-Mar '14
$\varphi_{int} = 0$				
No decomposition	-4319.60	24.52	18.59	33.62
DM 1	-4316.53	24.51	18.62	33.69
DM 2	-4585.14	14.07	10.13	14.72
DM 3	-4515.00	18.10	17.25	16.76
$\varphi_{int} > 0$				
No decomposition	-3415.77	35.74	28.44	43.49
DM 1	-3390.58	43.01	34.22	48.54
DM 2	-3558.96	22.05	16.04	23.96
DM 3	-3548.66	26.94	26.75	30.34

is correct. However, some conclusions can be drawn from a statistical point of view. When comparing the models' AIC and their nRMSEs for the simulation validation periods (Table 2), we see that the models with $\varphi_{int}=0$, and the models where DM2 (and DM3) are applied, are better capable of predicting the interior temperature. The more accurate predictions on cross-validation data may indicate more correct input data and a more accurate model structure, and are therefore argued to be a reason for favoring the outcome of those models.

CONCLUSION

The present paper explored how the HLC of a building envelope can be characterized based on on-board monitoring data. The focus was on the sensitivity of the characterization outcome to the preciseness of the knowledge on the supplied net heating power. This way the paper aimed to address the common problem that the two end-uses of gas (SH and DHW) are not submetered. By means of a case study, diverse approaches to approximate the unknown gas consumption for SH were illustrated. It was uncovered how, depending on the approach used, the HLC outcome can be 33 % apart. Uncertainty regarding other variables involved, e.g. the internal gains, furthermore influences this result. Since the applied gas decomposition methods have not yet been validated, the 'correct' characterization outcome could not be identified. However, based on statistical model comparison tests, suggestions on the trustworthiness of the outcomes were given. Submetering the gas consumption would, however, clear all doubts and increase the accuracy of the outcome. In next steps the applied decomposition techniques should be validated and the sensitivity of the HLC estimate towards assumptions on other variables (e.g. the system efficiency, interior temperature, incident solar radiation) should be explored.

ACKNOWLEDGEMENT

The authors gratefully acknowledge the Research Foundation Flanders (FWO) and the Flemish Institute for Technology (VITO) for funding this research.

REFERENCES

- Bacher P., de Saint-Aubain P.A., Christiansen L.E., and Madsen H. 2016. Non-parametric method for separating domestic hot water heating spikes and space heating. *Energy and Buildings*, 130, 107-112.
- Bauwens G. 2015. In situ testing of a building's overall heat loss coefficient. *Ph.D. Thesis*, KU Leuven (Belgium), 200 pages.
- Deconinck A.H. 2017. Reliable thermal resistance estimation of building components from on-site measurements. *Ph.D. Thesis*, KU Leuven (Belgium), 224 pages.
- Farmer D., Gorse C., Swan W., Fitton R., Brooke-Peat M., Miles-Shenton D., and Johnston D. 2017. Measuring thermal performance in steady-state conditions at each stage of a full fabric retrofit to a solid wall dwelling. *Energy and Buildings*, 156, 404-414.
- Madsen H., Bacher P., Bauwens G., Deconinck A., Reynders G., Roels S., ... Lethé G. 2016. IEA EBC Annex 58: Report of Subtask 3, part 2: Thermal performance characterisation using time series data - statistical guidelines. KU Leuven (Belgium), 83 pages.
- Menkveld M. 2009. Kentallen warmtevraag woningen. Final Report for RVO. ECN, 7 pages.
- National Grid UK. 2017. Calorific Value (CV): CV Data: Data Item Explorer. National Grid UK: <https://www.nationalgrid.com/uk/gas/market-operations-and-data/calorific-value-c>, consulted October 6, 2017.
- Saelens D., and Reynders G. 2016. IEA EBC Annex 58: Report of Subtask 4b: Towards a characterisation of buildings based on in situ testing and smart meter readings and potential for applications in smart grids. KU Leuven (Belgium), 25 pages.
- Sodagar B., and Starkey D. 2016. The monitored performance of four social houses certified to the Code for Sustainable Homes Level 5. *Energy and Buildings*, 110, 245-256.

Ventilation Potential Assessments for Residential Building Arrangements Based on Exceedance Probability Analysis

Wei You¹, Lian Tang¹ and Wowo Ding^{1,*}

¹ School of Architecture and Urban Planning, Nanjing University, Nanjing 210093, China

*Corresponding email: dww@nju.edu.cn

ABSTRACT

In this study, the building ventilation potentials were assessed at building group level. Exceedance probability analysis was applied to estimate the uncertainties associated with the influence of climate on wind environment. The criterion was proposed based on building facade pressures. Two typical residential building arrangements were investigated. Simulation results show that facade pressure based exceedance probability are efficient in assessing the natural ventilation potentials of building groups and building height variations are important for improving building natural ventilation potentials.

KEYWORDS

Residential buildings, Ventilation potential, Exceedance probability, Facade wind pressure.

INTRODUCTION

Natural ventilation is a common adopted passive building design strategy. It can improve indoor thermal comfort and air quality by removing excess heat and airborne contaminants. Optimizing building natural ventilation design is not only related to building façade opening size and location, but also refers to the arrangements of buildings. Thus, the assessments of natural ventilation potentials require an investigation at building group level.

For building natural ventilation, wind pressure distribution of building facade is an important boundary condition, as wind is the driving force. Many studies had investigated the indoor natural ventilation in terms of wind pressures for building groups. Tsutsumi et al. (1992) experimentally studied the wind pressure on a building surrounded by a group of buildings. The relations between average wind pressure coefficients and various layouts of buildings are discussed under different wind conditions. Similar studies were also carried out by Kim et al. (2012) and Shirzadi et al. (2018). In addition, Asfour (2010) investigated the effect of building layout patterns on ventilation potential of these buildings. Six hypothetical arrangements of buildings were assessed by calculating wind pressure difference. Bady et al. (2011) carried out wind tunnel experiments to study wind pressure characteristics on groups of buildings located within high density building arrays. The results all show that buildings configuration and wind direction are important factors in determining urban ventilation. However, most studies had investigated single building under typical wind directions.

For wind environment evaluation considering the uncertain upper wind parameters, some researches introduced the probability analysis into wind performance studies. This method estimates the probability of ventilation performance satisfying certain criteria. In past researches, probability analysis had most been applied in investigation of pedestrian-level wind environment, generally focusing on wind comfort/safety issues (Blocken and Persoon, 2009; Du et al. 2017). Recently, several researchers had introduced the probability concept into other wind performance area. Pietrzyk (2008) developed a probabilistic model and

studied the problem of air infiltration in low-rise buildings. Bu et al. (2009) analyzed the exceedance probability of local air change rate and local kinetic energy for investigating the ventilation performance and thermal comfort within urban street canyons.

This study attempted to introduce probability concept into wind-driven natural ventilation area for valuating natural ventilation potentials of building groups. Exceedance probability was calculated in terms of wind pressure on building facades. Two typical residential building arrangements, namely multi-story buildings and high-rise buildings, were adopted as the evaluation objects. The cases were located at a typical southeast monsoon wind city - Nanjing. And residential building units were investigated for natural ventilation potentials. To calculate building facade pressures, computational fluid dynamics (CFD) method with ANSYS-Fluent was adopted. The exceedance probabilities were post-processed by MATLAB and ArcGIS.

RESIDENTIAL BUILDING GROUP CONFIGURATION

A 3 x 3 building group were built for building arrangement analysis. The central group (CG) was the analysis unit, and surrounding units (SG) were arranged around the studied area as environmental conditions, as shown by Figure 1a. Road widths (Sr1, Sr2) were determined as 30m according to design code. Two residential building types were established for case comparison (Figure 1b-c). Case A was multi-storey building group (building height $H=18\text{m}$), and Case B was high-rise building group ($H=36\text{m}$). Building widths L and depth D were determined as 72 and 12m, respectively. Lateral spacing S were 12m, and north-south spacing was 24m and 48m for multi-storey and high-rise building group. Figure 1d shows the data extracted zones for probability calculation and comparison. W1-W6 numbered the south and north facade of living units. W0 and W7 numbered the east and west facade of living units. For vertical partition, multi-storey building was divide into three part, which represent the living unit at low, middle and high levels, and high-rise building was divide into six levels.

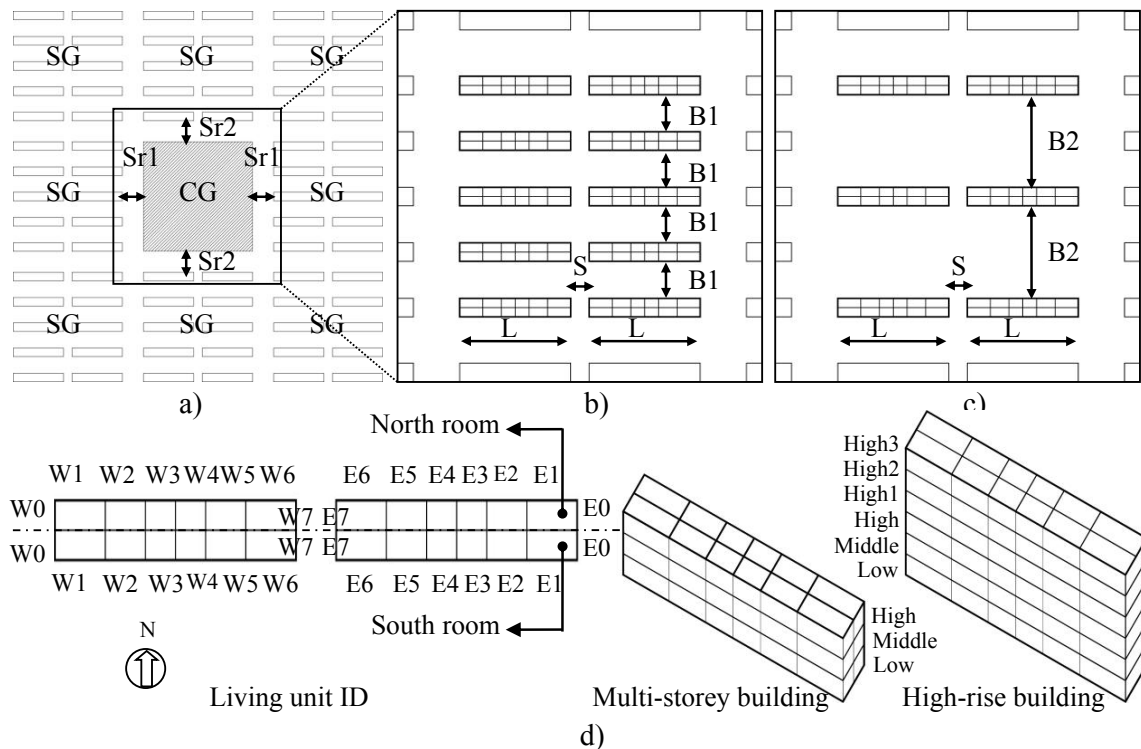


Figure 1. a) Building groups setting, b) Case A, c) Case B, d) Data extracted zones

EXCEEDANCE PROBABILITY CALCULATION FOR VENTILATION POTENTIALS

The exceedance probability based building ventilation assessment consisted of three parts, as shown in Figure 2. The first part was the base data collection, which include weather data, building geometry data and wind flow data. The second part was MATLAB based data processing. In this step, wind data and façade pressure data were extract from the weather file and simulation results. Exceedance probability for each building façade were calculated by processing façade pressure data. At last, building façade geometry and the corresponding probability data were linked and by ArcGIS's spatial join tool for further ventilation potential analysis. The probability distributions were also visualized for each studied surface.

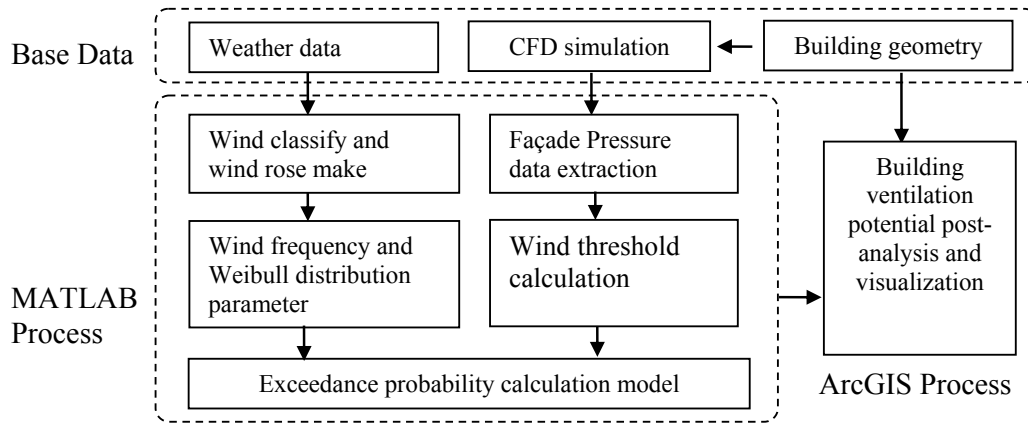


Figure 2. Flow chart of exceedance probability calculation

Base data obtaining

The wind climate of Nanjing was obtained from calibrating the hourly wind data of the solar and Wind Energy Resource Assessment (SWERA) weather file, which were download from EnergyPlus Weather Data (EPW) website. Building façade pressure data were obtained from CFD simulation results. The study referred to the AIJ (Architectural Institute of Japan) guidelines (Tominaga et al. 2008). For turbulence model selection, the Reynolds-Averaged Navier-Stokes (RANS) approach with standard $k-\varepsilon$ model was adopted in this study due to its less time consumption and less complexity in boundary condition setting.

Exceedance probability calculation

The pressure based exceedance probability (P_g -EP) at each point above building facade was assumed to follow a two-parameter Weibull distribution in this study. And the P_g -EP for 12 azimuths was calculated as follow:

$$P(P_g > P_g^*) = \sum_{i=1}^{12} A(i) \exp \left[- \left(\frac{\sqrt{P_g^*}}{R \cdot C(i)} \cdot \left(\frac{H_{met}}{\delta_{met}} \right)^{\alpha_{met}} \right)^{k(i)} \right] \quad (3)$$

$$R = \frac{\sqrt{\text{abs}(P_g)}}{V_{ref}} \cdot \left(\frac{H}{\delta} \right)^\alpha \quad (2)$$

Where $P(P_g > P_g^*)$ is the probability of exceeding the specified P_g^* . i is the wind direction number, and $A(i)$ is the occurrence frequency, and $K(i)$, $C(i)$ are two parameters of Weibull distribution. P_g is the façade pressure extracted from CFD simulation results. V_{ref} is the

reference up wind speed at the height H . α , α_{met} , δ and δ_{met} are the wind speed profile exponent and boundary layer thickness of the studied building located terrain and the weather station located terrain. H_{met} is the wind measured height at the the weather station.

RESULTS AND DISCUSSION

Figure 3 showed the distributions of exceedance probability percentage (P_g -EP) on building facade for multi-story and high-rise buildings. In subplot (a)-(b), the facade P_g -EP distribution were viewed from southeast and in subplot (c)-(d), the P_g -EP distribution were viewed from northeast. The natural ventilation potentials of the building groups were clearly revealed by the P_g -EP distribution on each building facades. High-rise buildings obviously improved the building natural ventilation potentials, comparing with that of multi-story buildings. The variation range of P_g -EP was between 30% and 70% for high-rise buildings, while between 20% and 60% for multi-story buildings. For high-rise building group, the more ventilation living units were located at the first (south) and third (north) row, which the P_g -EPs of first row building's south facade (Figure 3b) and the third row building's north facade (Figure 3d) were almost above 60%. It was because the surrounding buildings were multi-story buildings, which wind can directly reach the up part of the high-rise building facades. For the multi-story building group (Figure 3a) and the middle row high-rise buildings (Figure 3b), the more ventilation living units were located at the building's eastside. It was due to effect of southeast monsoon in summer. Due to the recirculation flow phenomenon, the middle level P_g -EPs of the multi-story buildings' north facade increase (Figure 3c). It revealed the ventilation potentials of north living units at the third and fourth storey building are improved.

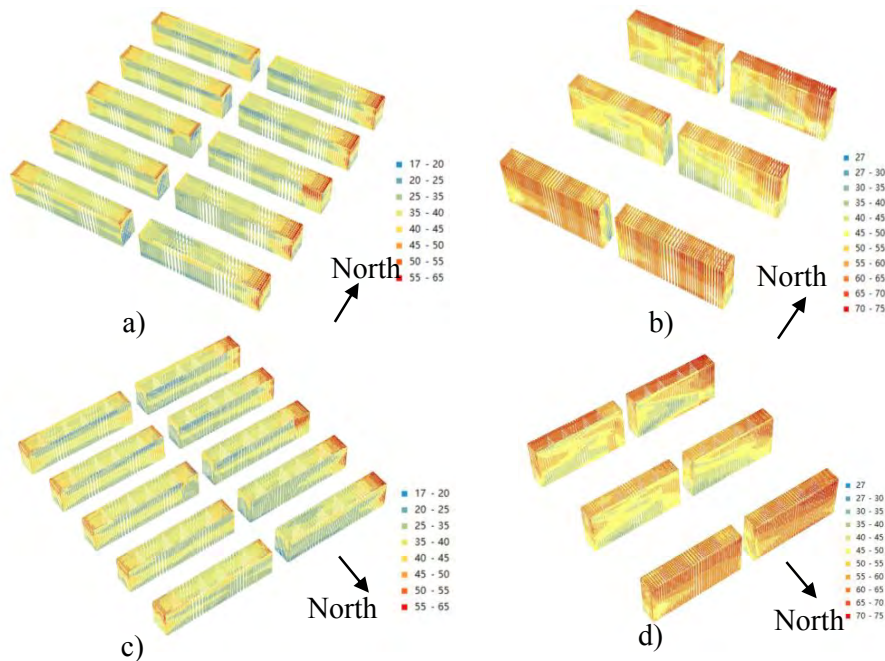


Figure 3. Distributions of the exceedance probability percentage on building facades.

More detailed quantitative analysis of natural ventilation potentials of the building groups was shown in Figure 4 and Figure 5. Figure 4 were the P_g -EP compassion of different height level residential units for multi-story and high-rise buildings. From the figure, it can be found that for the multi-story building group, the P_g -EPs were all below 50% (Figure 4a). And the natural ventilation potentials of low, middle and high levels of high-rise building units all increased, with P_g -EP around 50% (Figure 4b). It was due to the strengthen of air flow by the

upper facade of the high-rise building. The natural ventilation potentials of higher levels (high1 high2 and high3) of high-rise buildings were improved greatly due to the less effect of surrounding buildings. The P_g -EPs of these areas were all generally above 50% (Figure 4c). In terms of the positions of residential units at one storey, ventilation potentials of side units are better than that of middle units, and ventilation potentials of east side units are better than that of west side units. It is more obviously reflected within the multi-story building group. Figure 5 shows the P_g -EPs of south and north units for multi-story and high-rise buildings. The simulation results showed that P_g -EPs of north units were slightly better than that of south room for multi-story building. It was due to the turbulence flow, which acted on the north facade of the multi-story residential building, which discussed above.

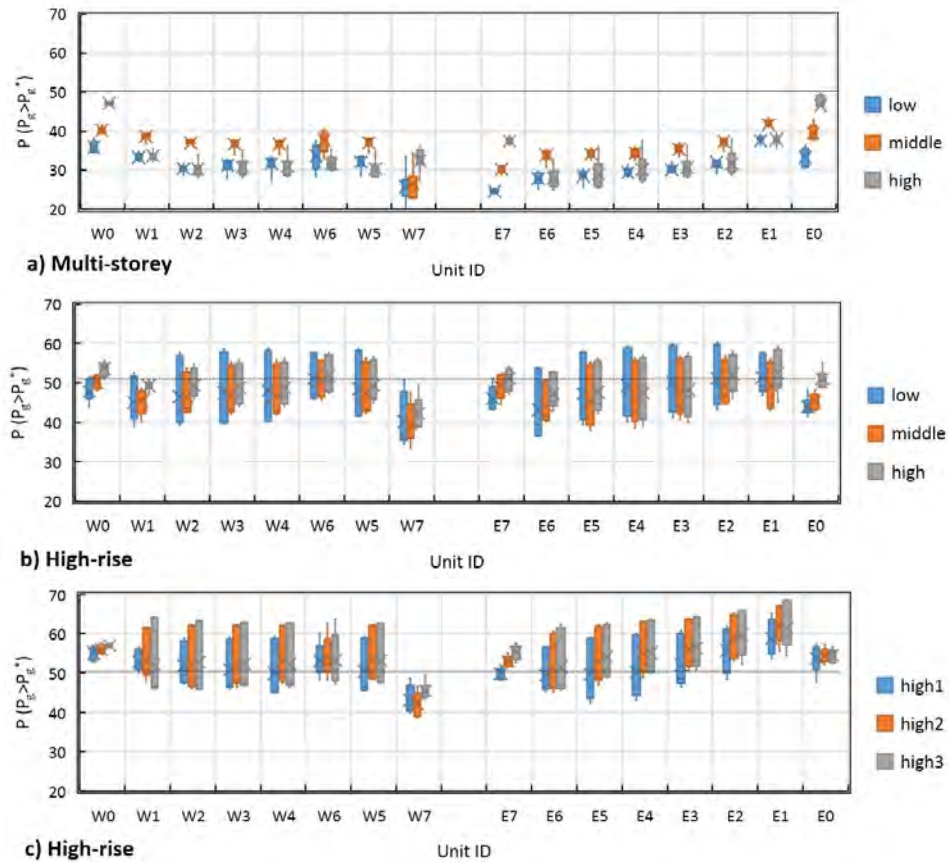


Figure 4. Comparison of different living-unit levels for multi-story and high-rise buildings.

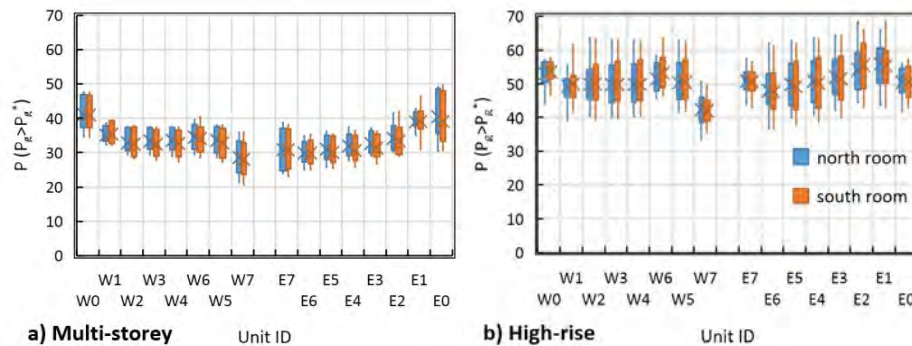


Figure 5. Comparison of living-unit facade directions for multi-story and high-rise buildings.

CONCLUSIONS

This paper provided a simple method to assess building group's natural ventilation potentials considering the effect of local wind climate. The cases studies show that, by calculation the exceedance probability of wind pressure on building facades, the natural ventilation potentials of building group can be revealed for each living units. Two typical residential building arrangements were investigated using the façade pressure based exceedance probability. Simulation results show that high-rise buildings could obviously improve the building's natural ventilation potentials by increasing P_g -Eps of around 20%, comparing to that of the same levels (1-6 storey) of multi-story buildings. In southeast monsoon regions, the ventilation potentials of eastside living units is indeed improved especially for multi-story buildings. The P_g -Eps could increase by about 10%. And the ventilation of north façade living units could also be beneficial by the turbulence flows.

This study is a preliminary test of using façade pressure based exceedance probability as an indicator for assessing of building natural ventilation potentials. Only two typical residential building groups were investigated. In the following study, more building arrangement cases will be evaluated to provide design strategies for architects.

ACKNOWLEDGEMENT

The project is supported by the National Natural Science Foundation of China (Nos.51508262 and 51538005).

REFERENCES

- Blocken B. and Persoon J. 2009. Pedestrian wind comfort around a large football stadium in an urban environment: CFD simulation, validation and application of the new Dutch wind nuisance standard. *Journal of Wind Engineering and Industrial Aerodynamics*, 97, 255-270
- Du Y.X, Mak C.M, Kwok K, Tse K-T, Lee T-C, Ai Z.T, Liu J.L, and Niu J.L. 2017. New criteria for assessing low wind environment at pedestrian level in Hong Kong. *Building and Environment*, 123, 23-36
- Bady M, Kato S, Takahashi T, and Huang H. 2011. Experimental investigations of the indoor natural ventilation for different building configurations and incidences. *Building and Environment*, 46, 65-74
- Shirzadi M, Naghashzadegan M, and Mirzaei P.A. 2018. Improving the CFD modelling of cross-ventilation in highly-packed urban areas. *Sustainable Cities and Society*, 37, 451-465
- Asfour, O.S. 2010. Prediction of wind environment in different grouping patterns of housing blocks. *Energy and Buildings*, 42, 2061-2069.
- Tsutsumi J, Katayama T, and Nishida M. 1992. Wind tunnel tests of wind pressure on regularly aligned buildings. *Journal of Wind Engineering and Industrial Aerodynamics*, 43, 1799-1810
- Kim Y.C, Yoshida A, and Tamur Y. 2012. Characteristics of surface wind pressures on low-rise building located among large group of surrounding buildings. *Engineering Structures*, 35,18-28.
- Pietrzyk K, Hagentoft C-E. 2008. Probabilistic analysis of air infiltration in low-rise buildings. *Building and Environment*, 43(4), 537-49.
- Bu Z, Kato S, Ishida Y, and Huang H. New criteria for assessing local wind environment at pedestrian level based on exceedance probability analysis. *Building and Environment*, 44, 1501-1508
- Tominaga, Y.; Mochida, A.; Yoshie, R.; Kataoka, H.; Nozue, H.; Yoshikawa, M.; Shirasawa, T. 2008. AIJ guidelines for practical applications of CFD to pedestrian wind environment around buildings. *Journal of Wind Engineering and Industrial Aerodynamics*, 96, 1749-1761

Author Index

First Name	Last Name	ID	Session Number
Marc	Abadie	308	MS-7
Masaru	Abuku	328	EC-1
Mark	Adams	232	MS-5
Michelle	Addington	500	Keynote
Deborah	Adkins	324	HF-3
Timothy	Aduralere	426	MS-1
Riham	Ahmed	137	IE-1
Abdulghafar	Al Tair	430	GB-1
Francisco	Albornoz	104	GB-2
Danai	Alifragki	7	IM-1
Noor	Alkhalili	60	HF-4
Jonas	Allegrini	338	GB-2
Jonas	Allegrini	386	EP-2
Mark	Allen	484	HF-1
Moonis	Ally	244	EP-2
Manuela	Almeida	269	IE-3
Manuela	Almeida	270	IE-3
Mohamed	Aly	255	BE-10
Armin	Amirazar	411	HF-4
Armin	Amirazar	452	IE-3
Vishal	Anand	42	IE-6
Brandon	Andow	255	BE-10
Karen	Angeles	291	MS-4
Marco	Arnesano	101	PS
Marco	Arnesano	102	IE-1
Rocio	Arriola-Cepeda	104	GB-2
Roshanak	Ashrafi	411	HF-4
Roshanak	Ashrafi	452	IE-3
Silje	Asphaug	331	BE-5
Andreas	Athienitis	107	PE-1
Andreas	Athienitis	134	PS
Dorit	Aviv	463	IE-6
Mona	Azarbayjani	411	HF-4
Mona	Azarbayjani	452	IE-3
Azizan	Aziz	318	MS-6
Marina	Bagaric	98	PS
Ali	Bahloul	363	IE-5
Christopher	Baldwin	181	EP-1
Ilaria	Ballarini	238	MS-8
Amir	Baniassadi	245	IE-2
Ivana	Banjad Pecur	98	PS

First Name	Last Name	ID	Session Number
Diane	Bastien	468	BE-9
Brent	Bauer	85	HF-4
Thomas	Bednar	161	MS-4
Thomas	Bednar	407	BE-9
Thomas	Bednar	419	BE-6
Mehmet	Bekar	105	IE-6
Rudina	Belba	94	PS
Nicolás	Benavente	438	MS-8
Ernesto	Benini	71	MS-3
Sally	Benson	259	EP-2
Umberto	Berardi	106	BE-3
Umberto	Berardi	13	BE-7
Umberto	Berardi	208	BE-6
Umberto	Berardi	444	BE-7
Daniela	Besser	24	MS-1
Daniel	Betts	244	EP-2
Lorenza	Bianco	235	BE-5
Melissa	Bilec	427	MS-1
Ayman	Bishara	387	IM-1
Nadja	Bishara	392	MS-8
Søren	Bjarløv	223	BE-5
Ivar	Björnsson	57	PE-1
Vincent	Blouin	384	MS-1
C.R.	Boardman	428	BE-4
Biayna	Bogosian	430	GB-1
Martha	Bohm	240	BE-5
Dario	Bottino Leone	239	PS
Elie	Bou-Zeid	283	GB-3
Elie	Bou-Zeid	400	GB-3
Elie	Bou-Zeid	402	GB-2
Elie	Bou-Zeid	424	MS-5
Elie	Bou-Zeid	430	GB-1
Michael	Bozlar	276	EC-1
Michael	Bozlar	454	IE-6
Wolf	Bracke	72	HF-3
Arianna	Brambilla	31	HF-3
Rudina	Brecani	150	PS
Sébastien	Brideau	474	BE-7
Johannes	Brozovsky	362	BE-1
Federica	Brunone	31	HF-3
Yanhui	Bu	46	HF-4

First Name	Last Name	ID	Session Number
Yanhui	Bu	88	IE-3
Aimee	Buccellato	291	MS-4
Scott	Bucking	86	MS-6
Adrian	Bucur	307	PS
Alexander	Buff	463	IE-6
Tanyel	Bulbul	383	MS-4
Michal	Bureš	405	BE-6
Esfand	Burman	162	IE-4
Esfand	Burman	165	IE-4
Waldo	Bustamante	436	BE-10
Waldo	Bustamante	438	MS-8
Waldo	Bustamante	448	MS-3
Luisa F	Cabeza	219	PS
Klaas	Calle	330	BE-2
Vitezslav	Calta	182	PS
José	Candanedo	134	PS
Francesca	Cappelletti	357	PE-1
Francesca	Cappelletti	396	IE-2
Stefan	Carl	373	BE-2
Jan	Carmeliet	216	BE-2
Jan	Carmeliet	338	GB-2
Jan	Carmeliet	369	BE-9
Jan	Carmeliet	373	BE-2
Jan	Carmeliet	376	GB-2
Jan	Carmeliet	386	EP-2
Jan	Carmeliet	395	BE-9
Jan	Carmeliet	398	MS-4
Jan	Carmeliet	399	EP-2
Jan	Carmeliet	496	Keynote
Mark	Carver	440	BE-3
Mark	Carver	474	BE-7
Veronica Lucia	Castaldo	230	PS
Veronica Lucia	Castaldo	231	GB-3
Sergio	Castano	225	IM-1
Miroslav	Cekon	300	BE-10
Miroslav	Cekon	406	PS
Robert	Cerny	32	MS-3
Marta	Chafer	219	PS
Bin	Chen	469	IE-1
Bin	Chen	479	IE-6
Mingyang	Chen	369	BE-9

First Name	Last Name	ID	Session Number
Mingyang	Chen	395	BE-9
Qingyan	Chen	28	HF-1
Qingyan	Chen	42	IE-6
Wanyu	Chen	361	MS-6
Siyu	Cheng	131	BE-6
Siyuan	Cheng	145	EC-1
Peter	Childs	324	HF-3
Wonjun	Choi	33	MS-5
Kingston	Chow	428	BE-4
Giovanni	Ciampi	270	IE-3
Steven	Claes	83	MS-7
Steven	Claes	84	BE-1
Johan	Claesson	27	MS-8
Livia	Claudi	101	PS
Nicholas	Clements	85	HF-4
Brock	Conley	440	BE-3
Brock	Conley	474	BE-7
Stefano Paolo	Corgnati	347	PE-1
Stefano Paolo	Corgnati	356	HF-2
Cristina	Cornaro	213	IE-1
Vincenzo	Corrado	211	PS
Vincenzo	Corrado	238	MS-8
Franco	Cotana	230	PS
Paul	Crovella	317	BE-9
Cynthia	Cruickshank	181	EP-1
Cynthia	Cruickshank	440	BE-3
Patricia	Culligan	499	Keynote
Jakub	Curpek	300	BE-10
Emmy	Dahlström	49	MS-6
Andrea	Dal Monte	71	MS-3
Alessandro	Dama	465	BE-5
Rui	Dang	118	MS-4
Rui	Dang	120	IE-1
Rui	Dang	131	BE-6
Rui	Dang	207	IE-2
Rui	Dang	46	HF-4
Rui	Dang	88	IE-3
Mohamed	Dardir	289	PS
Cliff	Davidson	149	PS
Cliff	Davidson	313	PS
Cliff	Davidson	417	PS

First Name	Last Name	ID	Session Number
Cliff	Davidson	423	GB-2
Cliff	Davidson	447	GB-2
Cliff	Davidson	453	PS
Julia	Day	81	HF-1
Alessandra	De Angelis	211	PS
Jacques	de Chalendar	259	EP-2
Richard	de Dear	497	Keynote
Giovanna	De Luca	238	MS-8
Thijs	Defraeye	338	GB-2
Marc	Delghust	72	HF-3
Marc	Delghust	74	HF-3
Zhipeng	Deng	28	HF-1
Dominique	Derome	216	BE-2
Dominique	Derome	338	GB-2
Dominique	Derome	369	BE-9
Dominique	Derome	373	BE-2
Dominique	Derome	376	GB-2
Dominique	Derome	395	BE-9
Sokol	Dervishi	150	PS
Sokol	Dervishi	94	PS
Guyline	Desmarais	216	BE-2
Yueqiang	Di	132	IE-4
Wowo	Ding	157	PS
Wowo	Ding	429	GB-3
Domenico	Dirutigliano	238	MS-8
Brandi	Dodge	372	BE-8
Timur	Dogan	358	MS-5
Magdalena	Dolezelova	37	BE-4
William	Dols	380	MS-4
Fredrik	Domhagen	195	IE-2
Matteo	Dopudi	465	BE-5
Thomas	Dougherty	34	IM-1
Joshua	Draper	316	HF-2
Aidan	Duffy	241	PS
Marco	Dutto	277	BE-7
Anna	Dyson	316	HF-2
Hagar	Elarga	7	IM-1
Hagar	Elarga	71	MS-3
Mohamed	El-Mankibi	289	PS
Idil	Erdemir Kocagil	287	GB-3
Valentina	Fabi	356	HF-2

First Name	Last Name	ID	Session Number
Claudia	Fabiani	230	PS
Claudia	Fabiani	283	GB-3
Xinying	Fan	469	IE-1
Jinzhong	Fang	260	MS-7
David	Fannon	304	HF-2
David	Fannon	426	MS-1
Stefano	Fantucci	235	BE-5
Stefano	Fantucci	277	BE-7
Fabio	Favoino	471	IE-3
Juliana	Felkner	433	BE-7
Chi	Feng	58	BE-4
Chi	Feng	59	BE-4
Hongxin	Feng	130	BE-10
Elisa	Fenoglio	277	BE-7
Endla	Feustel	417	PS
Scott	Fisher	430	GB-1
Kimberly	Fitzgerald	453	PS
Gilles	Flamant	448	MS-3
Carli	Flynn	447	GB-2
Sebastian	Forthuber	233	PE-1
Aurélie	Fouquier	248	MS-7
Gilles	Fraisse	248	MS-7
Francesca	Frasca	213	IE-1
Maria	Fredriksson	59	BE-4
Maira	Freitas	310	MS-2
Brian	Fricke	232	MS-5
Hagen	Fritzzy	34	IM-1
Jason	Frost	259	EP-2
Kazuma	Fukui	116	BE-4
Akira	Fukushima	328	EC-1
Anthony	Fuller	81	HF-1
Benjamin	Futrell	411	HF-4
Neşe	Ganiç Sağlam	347	PE-1
Lei	Gao	431	EP-2
Zhi	Gao	429	GB-3
Ziang	Gao	46	HF-4
Marina	Garcia	310	MS-2
Andrea	Gasparella	303	MS-6
Andrea	Gasparella	357	PE-1
Andrea	Gasparella	392	MS-8
Andrea	Gasparella	396	IE-2

First Name	Last Name	ID	Session Number
Vincenzo	Gentile	352	EC-1
Mehdi	Ghobadi	73	MS-3
Sara	Gilani	147	HF-1
Sara	Gilani	148	HF-1
Jeremy	Gilbert	257	PS
Luigi	Giovannini	471	IE-3
Samuel	Glass	428	BE-4
Jeanne	Goffart	192	EP-1
Francesco	Goia	179	IE-4
Francesco	Goia	215	BE-10
Francesco	Goia	71	MS-3
Gregory	Goldstein	445	IE-2
Juliana	Gonçalves	273	MS-2
Alice	Gorodetsky	285	GB-1
Klodian	Gradeci	208	BE-6
Klodian	Gradeci	95	BE-2
Anna	Gralka	102	IE-1
Matt	Gregg	243	IE-2
Giulia	Grosso	277	BE-7
John	Grunewald	239	PS
Steinar	Grynning	179	IE-4
Steinar	Grynning	215	BE-10
Steinar	Grynning	331	BE-5
Steinar	Grynning	95	BE-2
Lars	Gullbrekken	331	BE-5
Lars	Gullbrekken	95	BE-2
Charitha	Gunawardana	447	GB-2
H. Burak	Gunay	147	HF-1
H. Burak	Gunay	87	HF-4
Hongshan	Guo	198	EP-1
Hongshan	Guo	281	MS-5
Juanli	Guo	130	BE-10
Juanli	Guo	133	PS
Rajat	Gupta	243	IE-2
Matthias	Haase	362	BE-1
Carl-Eric	Hagentoft	195	IE-2
Carl-Eric	Hagentoft	205	MS-3
Fariborz	Haghighat	289	PS
Fariborz	Haghighat	363	IE-5
Maryam	Hamidpour	384	MS-1
Mengtao	Han	53	MS-5

First Name	Last Name	ID	Session Number
Morten	Hansen	223	BE-5
Thor	Hansen	199	BE-3
Michael	Hartner	233	PE-1
Vaclav	Hasik	427	MS-1
Chuan	He	229	MS-7
Guoqing	He	65	BE-8
Dariusz	Heim	36	IE-3
Dariusz	Heim	38	BE-10
Dariusz	Heim	92	BE-1
Farhad	Hemmati	458	PS
Eline	Himpe	72	HF-3
Shuichi	Hokoi	116	BE-4
Shuichi	Hokoi	166	EP-1
Shuichi	Hokoi	177	EC-1
Akinori	Hosoi	328	EC-1
Amir	Hosseinzadeh Zarrabi	411	HF-4
Amir	Hosseinzadeh Zarrabi	452	IE-3
Tianfeng	Hou	70	PS
Ming	Hu	11	MS-1
Ming	Hu	4	MS-2
Ming	Hu	445	IE-2
Tianwei	Hu	364	IE-5
Ge	Hua	107	PE-1
Ge	Hua	190	MS-3
Mélanie	Huard	363	IE-5
Stephanie	Huynh	85	HF-4
Yunho	Hwang	431	EP-2
Chiemi	Iba	116	BE-4
Chiemi	Iba	166	EP-1
Chiemi	Iba	177	EC-1
Hideo	Ichiboji	328	EC-1
Emishaw	Iffa	202	BE-2
Piljae	Im	232	MS-5
Marco	Imperadori	31	HF-3
Kana	Inamoto	177	EC-1
Robert	Irving	243	IE-2
Jacqueline	Isaacs	426	MS-1
Francesco	Isaia	235	BE-5
Islah	Islahuddin	83	MS-7
Giuseppina	Iuliano	269	IE-3
Lisa	Iulo	427	MS-1

First Name	Last Name	ID	Session Number
Anja	Jamrozik	85	HF-4
Hans	Janssen	197	BE-1
Hans	Janssen	58	BE-4
Hans	Janssen	59	BE-4
Hans	Janssen	70	PS
Hans	Janssen	80	BE-1
Hans	Janssen	83	MS-7
Hans	Janssen	84	BE-1
Hans	Janssen	91	MS-6
Arnold	Janssens	72	HF-3
Arnold	Janssens	74	HF-3
Arnaud	Jay	336	PS
Nickolaj	Jensen	223	BE-5
Milos	Jerman	37	BE-4
Lin	Jiang	260	MS-7
Sihang	Jiang	114	MS-2
Sihang	Jiang	115	BE-1
Maria	Jiménez	225	IM-1
Pär	Johansson	206	BE-3
Pär	Johansson	99	BE-7
Camille	John	134	PS
Alexander	Johnson	447	GB-2
Alexander	Johnson	453	PS
Christopher	Johnston	223	BE-5
Sarah	Juricic	248	MS-7
Burak	Kakillioglu	285	GB-1
Targo	Kalamees	220	PS
Jarl	Kampen	17	IE-6
Jérôme	Kämpf	56	MS-2
Achilles	Karagiozis	446	BE-5
Patrick	Kastner	358	MS-5
Theo	Keeley-LeClaire	276	EC-1
Ted	Kesik	60	HF-4
Basak	Keskin	492	PS
Kristina	Kiesel	303	MS-6
Tracy	Kijewski-Correa	291	MS-4
Hideki	Kikumoto	53	MS-5
Donghwan	Kim	433	BE-7
Nicholas	Kincaid	448	MS-3
Daisuke	Kitagawa	328	EC-1
Paul	Klößeiko	220	PS

First Name	Last Name	ID	Session Number
Dominika	Knera	36	IE-3
Dominika	Knera	92	BE-1
Jan	Koci	37	BE-4
Vaclav	Koci	32	MS-3
Vaclav	Koci	37	BE-4
Gul	Koclar Oral	287	GB-3
Meng	Kong	173	IE-4
Meng	Kong	364	IE-5
Pavel	Kopecký	405	BE-6
Naoyuki	Koshiishi	272	BE-8
Piotr	Kosiński	40	IE-1
Piotr	Kosiński	41	BE-8
Bryan	Kovisto	106	BE-3
Helge	Kramberger	387	IM-1
Lukas	Kranzl	233	PE-1
Aytaç	Kubilay	338	GB-2
Aytaç	Kubilay	376	GB-2
Liu	Kuixing	131	BE-6
Liu	Kuixing	132	IE-4
Villu	Kukk	410	BE-9
Sinem	Kültür	413	MS-8
Teja	Kuruganti	174	GB-1
Michael	Lacasse	253	BE-2
Dongfang	Lai	260	MS-7
Khee Poh	Lam	66	EC-1
Adrian	Lamano	361	MS-6
Evi	Lambie	377	IM-1
Evi	Lambie	464	IM-1
Jelle	Langmans	123	BE-6
Marco	Larcher	239	PS
Marijana	Larma	473	EP-1
Olena	Larsen	465	BE-5
Bertrand	Lasternas	318	MS-6
Leen	Lauriks	17	IE-6
Jelle	Laverge	72	HF-3
Jelle	Laverge	74	HF-3
Jérôme	Le Dréau	172	EP-1
Chang-Seo	Lee	363	IE-5
Jonathan	Lehmann	273	MS-2
Boyu	Li	445	IE-2
Chaoen	Li	175	BE-8

First Name	Last Name	ID	Session Number
Qi	Li	424	MS-5
Rongling	Li	186	HF-3
Rongling	Li	473	EP-1
Xianting	Li	114	MS-2
Xianting	Li	115	BE-1
Yuguo	Li	501	Keynote
Yunyi	Li	73	MS-3
Tang	Lian	157	PS
Amanda	Liberty	285	GB-1
Michele	Libralato	211	PS
Serena	Lim	153	GB-1
Gang	Liu	118	MS-4
Gang	Liu	120	IE-1
Gang	Liu	130	BE-10
Gang	Liu	131	BE-6
Gang	Liu	132	IE-4
Gang	Liu	207	IE-2
Gang	Liu	46	HF-4
Gang	Liu	88	IE-3
Rui	Liu	372	BE-8
Shichao	Liu	475	IE-5
Yu	Liu	65	BE-8
Zhenlei	Liu	308	MS-7
Valerio Roberto Maria	Lo Verso	326	MS-2
Valerio Roberto Maria	Lo Verso	471	IE-3
Vivian	Loftness	318	MS-6
Vivian	Loftness	498	Keynote
Mae-Ling	Lokko	155	PS
Nicola	Lolli	362	BE-1
Valeria	Longo	235	BE-5
Alessandra	Luna-Navarro	466	HF-2
Qihuang	Luo	65	BE-8
Yongqiang	Luo	463	IE-6
Weihua	Lv	115	BE-1
Yang	Lv	26	PS
Yang	Lv	67	PS
Carlo	Macciò	102	IE-1
Jiri	Madera	32	MS-3
Jiri	Madera	37	BE-4
Luigi	Maffei	269	IE-3
Luigi	Maffei	270	IE-3

First Name	Last Name	ID	Session Number
Ardeshir	Mahdavi	303	MS-6
Ina	Maia	233	PE-1
Lenka	Maierová	333	PS
Kanako	Makita	328	EC-1
Suzi Dilara	Mangan	287	GB-3
Lento	Manickathan	338	GB-2
Gulten	Manioglu	105	IE-6
Valentina	Marino	277	BE-7
Berardo	Matalucci	255	BE-10
Berardo	Matalucci	316	HF-2
Georgios	Mavromatidis	398	MS-4
Georgios	Mavromatidis	399	EP-2
Forrest	Megggers	276	EC-1
Forrest	Megggers	281	MS-5
Forrest	Megggers	454	IE-6
Forrest	Megggers	463	IE-6
Gillian	Menzies	241	PS
Yannis	Merlet	336	PS
Alberto	Messico	490	MS-1
Johann	Meulemans	172	EP-1
Michele	Mililli	102	IE-1
Simon	Miller	427	MS-1
William	Miller	446	BE-5
Bojan	Milovanovic	98	PS
Ioan	Moga	309	MS-8
Ligia	Moga	307	PS
Ligia	Moga	309	MS-8
Germán	Molina	448	MS-3
Eva	Møller	199	BE-3
Eva	Møller	93	BE-6
Miklós	Molnár	57	PE-1
Renata	Morbiducci	490	MS-1
Martin	Morelli	93	BE-6
Andrea	Morini	490	MS-1
Naomi	Morishita	419	BE-6
Christopher	Morse	255	BE-10
Andreas	Müller	233	PE-1
Dejan	Mumovic	137	IE-1
Maidier	Munitxa	430	GB-1
Giovanni	Murano	211	PS
Giovanni	Murano	238	MS-8

First Name	Last Name	ID	Session Number
Sayaka	Murata	328	EC-1
NaveenKumar	Muthumanickam	427	MS-1
Zoltan	Nagy	34	IM-1
Federica	Naspi	101	PS
Joshua	New	232	MS-5
Bing Feng	Ng	361	MS-6
Jennifer	Nguyen	85	HF-4
Andreas	Nicolai	308	MS-7
Vahid	Nik	146	EP-2
Alessandro	Nocente	179	IE-4
Alessandro	Nocente	362	BE-1
Gang	Nong	73	MS-3
Camila	Novais	415	HF-4
Nicholas	Novelli	255	BE-10
Atila	Novoselac	475	IE-5
Simon	Obelz	463	IE-6
Liam	O'Brien	147	HF-1
Liam	O'Brien	148	HF-1
Liam	O'Brien	60	HF-4
Liam	O'Brien	81	HF-1
Liam	O'Brien	86	MS-6
Liam	O'Brien	87	HF-4
Fabian	Ochs	274	PE-1
Daisuke	Ogura	116	BE-4
Daisuke	Ogura	177	EC-1
Daisuke	Ogura	342	BE-3
Timothy	O'Leary	241	PS
Cassandra	Olenick	245	IE-2
Lars	Olsson	205	MS-3
Hamidreza	Omidvar	400	GB-3
Ryozo	Ooka	33	MS-5
Ryozo	Ooka	53	MS-5
Kristina	Orehounig	398	MS-4
Kristina	Orehounig	399	EP-2
Mohamed	Ouf	87	HF-4
Scott	Overall	255	BE-10
Mauro	Overend	466	HF-2
Mauro	Overend	484	HF-1
Norbert	Palz	470	PS
Argun	Paragamyan	326	MS-2
Anil	Parekh	474	BE-7

First Name	Last Name	ID	Session Number
June Young	Park	34	IM-1
Galina	Paskaleva	161	MS-4
Dimitrios	Patsialis	291	MS-4
Jingjing	Pei	229	MS-7
Anna	Pellegrino	326	MS-2
Anna	Pellegrino	471	IE-3
Yunlong	Peng	429	GB-3
Andréa	Pereira	415	HF-4
Gabrie	Perez	219	PS
Marco	Perino	277	BE-7
Giovanni	Pernigotto	303	MS-6
Terri	Peters	60	HF-4
Ruut	Peuhkuri	223	BE-5
Krystyna	Pietrzyk	422	GB-1
Ilaria	Pigliautile	169	HF-2
Ilaria	Pigliautile	219	PS
Ilaria	Pigliautile	231	GB-3
Camilo	Pinto	448	MS-3
Cristina	Piselli	169	HF-2
Cristina	Piselli	219	PS
Anna Laura	Pisello	169	HF-2
Anna Laura	Pisello	219	PS
Anna Laura	Pisello	230	PS
Anna Laura	Pisello	231	GB-3
Anna Laura	Pisello	283	GB-3
Lorenza	Pistore	396	IE-2
Ilaria	Pittana	396	IE-2
Alyssa	Pizzi	313	PS
Casper	Pold	223	BE-5
Alessandro	Prada	357	PE-1
Elisa	Primo	238	MS-8
Menghao	Qin	145	EC-1
Menghao	Qin	167	BE-4
Menghao	Qin	308	MS-7
Jianzhen	Qiu	39	PS
David	Radcliff	430	GB-1
Reinhard	Radermacher	431	EP-2
Eva	Raggi	102	IE-1
Tarek	Rakha	285	GB-1
Christian	Ramos	85	HF-4
Torben	Rasmussen	5	IE-5

First Name	Last Name	ID	Session Number
Jamaica	Reese-Julien	304	HF-2
Georg	Reichard	383	MS-4
Alexandra	Rempel	153	GB-1
Alexandra	Rempel	155	PS
Iva	Rešetar	470	PS
Gian Marco	Revel	101	PS
Gian Marco	Revel	102	IE-1
Glenn	Reynders	273	MS-2
Glenn	Reynders	371	PS
Jan	Richter	405	BE-6
Carsten	Rode	186	HF-3
Carsten	Rode	473	EP-1
Carsten	Rode	7	IM-1
Staf	Roels	123	BE-6
Staf	Roels	197	BE-1
Staf	Roels	70	PS
Staf	Roels	91	MS-6
Piercarlo	Romagnoni	396	IE-2
Linus	Rönn	49	MS-6
Antonio	Rosato	269	IE-3
Antonio	Rosato	270	IE-3
Simon	Rouchier	225	IM-1
Simon	Rouchier	248	MS-7
Simon	Rouchier	336	PS
Adam	Rysanek	463	IE-6
Youngryel	Ryu	430	GB-1
Dirk	Saelens	273	MS-2
Dirk	Saelens	371	PS
Dirk	Saelens	377	IM-1
Dirk	Saelens	464	IM-1
David	Sailor	245	IE-2
Baris	Salman	492	PS
Mikael	Salonvaara	446	BE-5
Alberto	Sangiorgio	31	HF-3
Onorio	Saro	211	PS
Angela	Sasic Kalagasidis	49	MS-6
Jean-Louis	Scartezzini	56	MS-2
Roger	Schmidt	257	PS
Matthias	Schuss	303	MS-6
Marcel	Schweiker	356	HF-2
Marcel	Schweiker	81	HF-1

First Name	Last Name	ID	Session Number
Michelangelo	Scorpio	269	IE-3
Rizal	Sebastian	102	IE-1
Beata	Semen	41	BE-8
Marieline	Senave	371	PS
Marieline	Senave	464	IM-1
Federico	Seri	101	PS
Valentina	Serra	235	BE-5
Valentina	Serra	277	BE-7
Valentina	Serra	471	IE-3
Zahra	Shayegan	363	IE-5
Chong	Shen	114	MS-2
Chong	Shen	115	BE-1
Xing	Shi	90	PS
Zhu	Shi	42	IE-6
Zixiao	Shi	86	MS-6
Suin	Shim	276	EC-1
Masanori	Shukuya	33	MS-5
Binghui	Si	90	PS
Anna Maria	Siani	213	IE-1
Sergio	Siblio	269	IE-3
Sergio	Siblio	270	IE-3
Marco	Simonetti	352	EC-1
Nikolaos	Skandalos	333	PS
Behzad	Sodagar	371	PS
Jie	Song	364	IE-5
Shahrzad	Soudian	13	BE-7
Roberta	Souza	310	MS-2
Roberta	Souza	415	HF-4
Roberta	Souza	52	HF-1
Irem	Sozen	287	GB-3
Giorgia	Spigliantini	356	HF-2
Mallory	Squier	447	GB-2
Kamil	Stanek	182	PS
Kamil	Stanek	333	PS
Kamil	Staněk	405	BE-6
Michael	Starke	174	GB-1
Ursula	Steinfort	104	GB-2
Howard	Stone	276	EC-1
Meiling	Sun	469	IE-1
Paulo	Tabares-Velasco	448	MS-3
Alexandros	Taflanidis	291	MS-4

First Name	Last Name	ID	Session Number
Satoru	Takada	177	EC-1
Shun	Takano	166	EP-1
Huijiao	Tan	118	MS-4
Huijiao	Tan	120	IE-1
Mingfang	Tang	260	MS-7
Fitsum	Tariku	194	BE-8
Fitsum	Tariku	202	BE-2
Fitsum	Tariku	261	MS-7
Fitsum	Tariku	458	PS
Ellika	Taveres-Cachat	215	BE-10
Ellika	Taveres-Cachat	331	BE-5
Eric	Teitelbaum	276	EC-1
Eric	Teitelbaum	454	IE-6
Eric	Teitelbaum	463	IE-6
Asok	Thirunavukarasu	107	PE-1
Emmanouil	Thrampoulidis	398	MS-4
Astrid	Tijskens	91	MS-6
Berit	Time	331	BE-5
Alex	Timmer	442	PS
Achalu	Tirfe	249	IE-4
Jelena	Todorovic	84	BE-1
Alexandra	Troi	239	PS
Tsukasa	Tsukidate	328	EC-1
Jan	Tywniak	182	PS
Jan	Tywniak	333	PS
Jan	Tywniak	405	BE-6
Marcella	Ucci	137	IE-1
Lindsay	Underhill	380	MS-4
Tina	Unwalla	427	MS-1
Daniel	Uribe	436	BE-10
Daniel	Uribe	438	MS-8
Charalampos	Vallianos	134	PS
Joris	Van Acker	123	BE-6
Stijn	Van Craenendonck	17	IE-6
Wouter	Van De Walle	80	BE-1
Wouter	Van De Walle	83	MS-7
Nathan	Van Den Bossche	253	BE-2
Nathan	Van Den Bossche	330	BE-2
Jan	Van den Bulcke	123	BE-6
Stephanie	Van Linden	253	BE-2
Giuseppe Peter	Vanoli	269	IE-3

First Name	Last Name	ID	Session Number
Giuseppe Peter	Vanoli	270	IE-3
Michiel	Vanpachtenbeke	123	BE-6
Charles	Vardeman	291	MS-4
Ali	Vaseghi	194	BE-8
Senem	Velipasalar	285	GB-1
Ana Carolina	Veloso	310	MS-2
Ana Carolina	Veloso	52	HF-1
Sergio	Vera	104	GB-2
Sergio	Vera	436	BE-10
Sergio	Vera	438	MS-8
Sergio	Vera	448	MS-3
Silke	Verbruggen	72	HF-3
Silke	Verbruggen	74	HF-3
Evy	Vereecken	197	BE-1
Clara	Vite	490	MS-1
Frank	Vogdt	24	MS-1
Peter	Vontobel	216	BE-2
Peter	Vontobel	373	BE-2
Cedric	Vuye	17	IE-6
Paula	Wahlgren	195	IE-2
Paula	Wahlgren	99	BE-7
Petter	Wallenten	27	MS-8
Man Pun	Wan	361	MS-6
Andong	Wang	186	HF-3
Haifeng	Wang	26	PS
Haifeng	Wang	67	PS
Jiehui	Wang	130	BE-10
Jiehui	Wang	133	PS
Lihui	Wang	364	IE-5
Lin	Wang	190	MS-3
Nan	Wang	118	MS-4
Nan	Wang	120	IE-1
Qingchen	Wang	46	HF-4
Qingchen	Wang	88	IE-3
Zhi-Hua	Wang	424	MS-5
Gordon	Warn	427	MS-1
Andreas	Weder	387	IM-1
Paul	Wegerer	407	BE-9
Paul	Wegerer	419	BE-6
Lai	Wei	207	IE-2
Anna	Wieprzkowicz	38	BE-10

First Name	Last Name	ID	Session Number
Anna	Wieprzkowicz	92	BE-1
Martin	Winther-Gaasvig	468	BE-9
Robert	Wójcik	40	IE-1
Robert	Wójcik	41	BE-8
Sabine	Wolny	161	MS-4
Monika	Woloszyn	192	EP-1
Monika	Woloszyn	336	PS
Lucie	Worthen	149	PS
Lucie	Worthen	447	GB-2
Shuo-xian	Wu	39	PS
Yujie	Wu	56	MS-2
Yunjie	Xiong	383	MS-4
Yi	Xu	131	BE-6
Yujie	Xu	318	MS-6
Alula	Yadete	261	MS-7
Midori	Yamada	272	BE-8
Hideya	Yamamoto	342	BE-3
Shuai	Yan	115	BE-1
Jiachuan	Yang	283	GB-3
Jiachuan	Yang	402	GB-2
Jiachuan	Yang	424	MS-5
Shiyu	Yang	361	MS-6
Xinyue	Yang	133	PS
Yige	Yang	417	PS
Yige	Yang	423	GB-2
Yige	Yang	447	GB-2
Yuchen	Yang	146	EP-2
Borjen	Yeh	428	BE-4
Ayşe	Yılmaz	347	PE-1
Shi	You	186	HF-3
Wei	You	157	PS
Ye	Yuan	207	IE-2
Syed	Zaidi	106	BE-3
Lorenzo	Zampetti	102	IE-1
Helia	Zandi	174	GB-1
Luca	Zaniboni	303	MS-6
Bijan	Zarrabi	146	EP-2
Bijan	Zarrabi	187	BE-3
Bijan	Zarrabi	206	BE-3
Chenlu	Zhang	66	EC-1
Chi	Zhang	395	BE-9

First Name	Last Name	ID	Session Number
Fan	Zhang	497	Keynote
Jensen	Zhang	173	IE-4
Jensen	Zhang	229	MS-7
Jensen	Zhang	249	IE-4
Jensen	Zhang	257	PS
Jensen	Zhang	308	MS-7
Jensen	Zhang	364	IE-5
Jihua	Zhang	364	IE-5
Rui	Zhang	257	PS
Xueyan	Zhang	479	IE-6
Zhe	Zhang	361	MS-6
Zhiang	Zhang	66	EC-1
Jie	Zhao	85	HF-4
Tongke	Zhao	469	IE-1
Yi	Zheng	364	IE-5
Wu	Zhimin	167	BE-4
Liang	Zhou	73	MS-3
Xiaohai	Zhou	216	BE-2
Yuwei	Zhou	26	PS
Jiayi	Zhu	65	BE-8